2026 IEEE NSS MIC RTSD

IEEE NPSS
NUCLEAR & PLASMA SCIENCES SOCIETY

Nuclear Science Symposium,
Medical Imaging Conference and
Room Temperature Semiconductor
Detector Conference



7 Nov – 14 Nov 2026

GRANADA, SPAIN

ABSTRACT SUBMISSION
DEADLINE: 12 MAY 2026

General Chair:	Stefan Ritt
Deputy Chair:	Juan M Górriz
NSS Chair:	Audrey Corbeil Therrien
NSS Deputy Chair:	Giulia Hull
MIC Chair:	Vesna Sossi
MIC Deputy Chair:	Roger Fulton
RTSD Co-Chair:	Michael Fiederle
RTSD Co-Chair:	Gerard Ariño

HYBRID

Welcome

Dear Colleagues,

We are delighted to announce that the upcoming onsite and hybrid IEEE Nuclear Science Symposium, Medical Imaging Conference, and Room Temperature Semiconductor Detectors Symposium will be held in **Granada, Spain, in November 7 – 14, 2026.** Nestled at the foot of the Sierra Nevada mountains in southern Spain, Granada is a city rich in history, culture, and natural beauty — a truly unique setting for our conference.

Granada is world-renowned for the **Alhambra**, a breathtaking Moorish palace and fortress complex that stands as one of Europe's greatest architectural treasures.

Pro tip: tickets often sell out weeks in advance, so if you want to visit — and you should — book at least a month ahead… seriously!

The city's distinctive blend of **Arab, Jewish, and Christian heritage** gives rise to a dynamic cultural atmosphere, visible in everything from its historic neighborhoods to its vibrant local cuisine and flamenco traditions. The modern **Palacio de Congresos** will serve as our venue, offering excellent facilities within walking distance of the historic city center. You will also find a wealth of museums, gardens, and scenic viewpoints nearby.

The technical program will be enriched by a diverse selection of **short courses** designed to strengthen the skills of early-career researchers and students, while also serving as valuable refreshers for experienced professionals. Further opportunities for engagement and development will be offered through **workshops and special events**, including Women in Engineering (WIE), Young Professionals (YP), and plenary sessions featured in the main program. The conference offers a hybrid option for people who cannot attend in-person, but those will miss the onsite Spanish flavor. We are confident that you will enjoy the warm Andalusian hospitality, outstanding gastronomy and the inspiring surroundings that Granada provides.

Yes, tapas come for free if you have a drink in most bars!

A spacious exhibition area will be available to connect with industry partners and fellow researchers in this culturally rich and welcoming city.

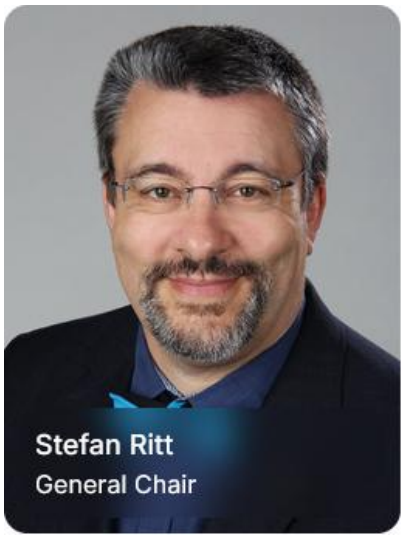



Contents

Welcome ... 2
Contents ... 3
Sponsors ... 7
Exhibitors ... 8
Weekly Agenda ... 9
Short Courses ... 190
7 November, 2026 ... 191
SC-01 | Front-End Electronics for Radiation Detectors ... 192
SC-02 | Analog and digital SPAD-based photodetectors ... 196
8 November, 2026 ... 199
SC-04 | State-of-the-art semiconductor detectors in basic science, applied science and in industry ... 200
SC-03 | Scientific Writing ... 204
9 November, 2026 ... 206
SC-05 | Fast-timing scintillation detectors for medical and other applications ... 207
SC-06 | Medical predictions from imaging with machine learning: The implementation gap ... 210
10 November, 2026 ... 213
SC-07 | Medical Image Reconstruction: from Foundations to AI ... 214
SC-08 | Fundamentals of Total-Body PET ... 216
Workshops ... 217
8 November, 2026 ... 218
WS-01 | AI in Nuclear Sciences and Nuclear Medical Imaging – Review and future expectations (onsite only) ... 219
WS-02 | Digital SiPM and SPAD-based sensors (onsite only) ... 227
14 November, 2026 ... 237
WS-03 | Total-Body Kinetic Modeling Workshop ... 238
WS-04 | Emerging Directions in Theranostic Imaging: From PET and SPECT to Novel Modalities (onsite only) ... 243
Joint Sessions ... 261
10 November, 2026 ... 262
JS-01 | Joint Session NSS-MIC-RTSD ... 263
JS-02 | Joint Session - NSS-MIC ... 269
JS-03 | Joint Session NSS-RTSD ... 278
NSS ... 284
9 November, 2026 ... 285
NP-01 | NSS Plenary Session ... 286
NP-02 | NSS Plenary Session ... 289
N-LT-01 | NSS Lightning Talks 1 ... 291
N-LT-02 | NSS Lightning Talks 2 ... 306
NSS-01 | NSS Poster Session ... 320

NSS-02 | Neutron and gamma-ray detectors and applications, including security, dosimetry and other related applications ····454
NSS-03 | NSS DAQ, front-end and electronics ····461
NSS-04 | Semiconductor detectors ····467
10 November, 2026 ····475
NSS-05 | Neutron and gamma-ray detectors and applications, including security, dosimetry and other related applications ····476
NSS-06 | Detector modeling and simulation ····484
NSS-07 | Scintillators ····492
NSS-08 | Synchrotron, FEL and XFEL detectors ····499
NSS-09 | Neutron and gamma-ray detectors and applications, including security, dosimetry and other related applications ····507
11 November, 2026 ····514
NSS-10 | Analog and Digital Circuits I ····515
NSS-11 | AI and ML for radiation detection ····522
NSS-12 | Novel detectors and associated technologies ····528
N-LT-03 | NSS Lightning Talks 3 ····537
N-LT-04 | NSS Lightning Talks 4 ····550
NSS-13 | NSS Poster Session ····563
NSS-14 | Analog and digital circuits II ····698
NSS-15 | Computational methods and data analysis ····706
NSS-16 | Scintillators ····713
NSS-17 | DAQ, front-end and electronics ····721
NSS-18 | Neutron and gamma-ray detectors and applications, including security, dosimetry and other related applications ····728
NSS-19 | Nuclear, HEP and astrophysics detectors ····734
12 November, 2026 ····740
NSS-20 | DAQ, front-end and electronics ····741
NSS-21 | Photodetectors ····749
NSS-22 | Neutron and gamma-ray detectors and applications, including security, dosimetry and other related applications ····758
NSS-23 | Analog and digital circuits III ····764
NSS-24 | Gas detectors ····771
NSS-25 | Nuclear, HEP and astrophysics detectors ····777
NSS-26 | AI and ML for radiation detection ····783
NSS-27 | Scintillators ····791
NSS-28 | Semiconductor detectors ····800
NSS-29 | NSS closing session and Student Paper Awards ····810
MIC ····814
11 November, 2026 ····815
MP-01 | MIC Plenary Session 1 ····816

MIC-01 | Advanced tomographic reconstruction techniques (1) ····822
MIC-02 | High resolution imaging systems (organ-dedicated, small animal systems (1) ····828
M-LT-01 | Advanced tomographic reconstruction techniques, X-ray imaging systems (CT, spectral CT, photo-counting CT) ····834
M-LT-02 | High resolution imaging systems (organ-dedicated, small animal systems, X-ray imaging systems (CT, spectral CT, photo-counting CT), Quantitative imaging, image assessment and standardization ····845
MIC-03 | X-ray imaging systems (CT, spectral CT, photo-counting CT)····855
MIC-04 | Quantitative imaging, image assessment and standardization ····863
MIC-05 | MIC Poster Session 1····872
12 November, 2026 ····1019
MP-02 | MIC Plenary Session 2 ····1020
MIC-06 | Simulation and modeling of medical imaging systems (1)····1026
MIC-07 | Multi-modality imaging systems including applications and High resolution imaging systems (organ-dedicated, small animal systems) (2) ····1032
M-LT-03 | New radiation detector technologies for medical imaging,Novel applications of AI in radiation-based medical imaging ····1037
M-LT-04 | New radiation detector technologies for medical imaging, Simulation and modeling of medical imaging system, Multi-modality imaging systems including applicationss ····1047
MIC-08 | Novel applications of AI in radiation-based medical imaging (1) ····1057
MIC-09 | New radiation detector technologies for medical imaging (1) ····1066
MIC-10 | MIC Poster Session 2····1076
13 November, 2026 ····1222
MIC-11 | Young Investigator Session (oral)····1223
MIC-12 | New Concepts and Emerging Applications ····1232
MIC-13 | New radiation detector technologies for medical imaging (2) ····1241
MIC-14 | Novel applications of AI in radiation-based medical imaging (2) ····1247
M-LT-05 | Kinetic modeling, molecular connectivity analysis and radiomics, Theranostics, Imaging and dosimetry in therapy (particle, radiopharmaceutical, surgery), Total body imaging systems including applications ····1253
M-LT-06 | Signal and Data Processing, New Concepts and Emerging Applications····1263
MIC-15 | MIC Poster Session 3····1274
MIC-16 | Simulation and modeling of medical imaging systems (2)····1419
MIC-17 | Theranostics, Imaging and dosimetry in therapy (particle, radiopharmaceutical, surgery) (1)····1427
14 November, 2026 ····1434
MIC-18 | Advanced tomographic reconstruction techniques (2) ····1435
MIC-19 | Signal and data processing····1444
MIC-20 | Total body imaging systems including applications and kinetic modeling, molecular connectivity and radiomics ····1452
MIC-21 | Theranostics, Imaging and dosimetry in therapy (particle, radiopharmaceutical, surgery) (2)····1458
MIC-22 | Closing····1465
RTSD ····1466
9 November, 2026 ····1467

RTSD-01 | RTSD Opening ····· 1468
RTSD-02 | RTSD Aviation Inspection & Security Applications ····· 1477
10 November, 2026 ····· 1483
RTSD-03 | RTSD Pixel Detectors ····· 1484
RTSD-04 | RTSD Poster Session ····· 1493
11 November, 2026 ····· 1538
RTSD-05 | RTSD Perovskite Detectors ····· 1539
RTSD-06 | RTSD Perovskite Detectors II ····· 1546
RTSD-07 | RTSD Pixel Detectors II ····· 1552
RTSD-08 | RTSD Medipix/Timepix Detectors ····· 1560
12 November, 2026 ····· 1566
RTSD-09 | RTSD CZT Detectors ····· 1567
RTSD-10 | RTSD Awards and Closing ····· 1576
Special Events ····· 1583
11 November, 2026 ····· 1584
TS-02 | Technical Sessions 2 ····· 1585
SimSET | SimSET User Meeting (onsite only) ····· 1590
TS-03 | Technical Sessions 3 ····· 1591
12 November, 2026 ····· 1594
WIE & YP | WIE & YP ····· 1595
STIR | STIR Users' & Developers' Meeting (onsite only) ····· 1596
Index ····· 1601
Author Index ····· 1602

Sponsors









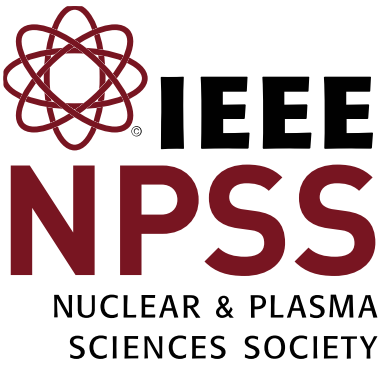

















* The organizers gratefully acknowledge the financial support provided by the PID2022-137451OB-I00 project, funded by the MICIU/AEI/10.13039/501100011033 and by FEDER, EU.

Exhibitors


5N+
ACRORAD
ADVAFAB
Alpha Spectra, Inc.
SCINTILLATION DETECTORS
AMETEK
Applied Diamond, Inc
BSI BALTIC SCIENTIFIC INSTRUMENTS
BRIGHTSPEC
BROADCOM
C&A Corporation
CAEN Tools for Discovery
CapeSym
CLEAR-PULSE
crytur
Epic-Crystal
ET Enterprises electron tubes
Field Viewers
GalaxRay Innovation in radiation safety
GOHI 国瀚瑞海
HED
HAMAMATSU PHOTON IS OUR BUSINESS
宇称电子 MICROPARITY Sensor and Science
Shalom EO
Hellma Materials When every photon counts
Hilger Crystals
Hyperion Hybrid Imaging Systems
ideas
Institute of High Energy Physics Chinese Academy of Sciences
JTC
Leading Crystal 领晶光电
LND, INC.
LUXIUM excelitas
MIRION TECHNOLOGIES
EBOCRYSTAL
NALU SCIENTIFIC
Nuclear Instruments
NUCLEAR SHIELDS
ORTEC AMETEK
OXIDE
PETsys Electronics
RAYQUANT
ROTUNDA
AMCRYS ScintiTech
scintacor THE CENTRE OF SCINTILLATION
SCIONIX
SINTEF
TechnoAP
XIA Instruments That Advance The Art
Kitec

Weekly Agenda


Saturday, 7 November, 2026
Sunday, 8 November, 2026
Monday, 9 November, 2026
Tuesday, 10 November, 2026
Wednesday, 11 November, 2026
Thursday, 12 November, 2026
Friday, 13 November, 2026
Saturday, 14 November, 2026
9:00
10:00
11:00
12:00
13:00
14:00
15:00
16:00
17:00
18:00
19:00
20:00
21:00
22:00
Short Course
Short Course
Workshop
Workshop
Welcome Reception
Short Courses
NSS Session
Break
NSS Session
NSS Session
Break
NSS Session
RTSD Session
Short Course
Break
NSS Session
RTSD Session
NSS Session
NSS Session
Joint Session
NSS Session
RTSD Session
NSS Session
MIC Session
RTSD Session
Special Event
Break
Special Event
Break
Joint Session
NSS Session
RTSD Session
NSS Session
MIC Session
RTSD Session
Special Event
Break
What is IEEE?
Joint Session
NSS Session
NSS Session
MIC Session
RTSD Session
Exhibitor Happy Hour
Conference Reception
NSS Dinner
NSS Session
NSS Session
MIC Session
RTSD Session
Special Event
Break
Special Event
Break
NSS Session
MIC Session
RTSD Session
RTSD Lunch
MIC Sess.
Break
Break
NSS Session
MIC Session
Special Event
MIC Session
MIC Session
Break
MIC Session
MIC Session
Break
Conference Closing Party
Break
Workshop
Workshop
Break
MIC Session
Break
MIC Session
MIC Dinner

7 November, 2026

9:00 – 18:00 Alhamar @Hotel Saray Granada
SC-01 Front-End Electronics for Radiation Detectors

9:00 **SC-01-01**
Part I: Fundamentals
Gianluigi De Geronimo

11:00 **SC-01-02**
Morning Coffee

11:30 **SC-01-03**
Part II: Fundamentals
Gianluigi De Geronimo

13:30 **SC-01-04**
Lunch

14:30 **SC-01-05**
Part III: Fundamentals
Gianluigi De Geronimo

16:00 **SC-01-06**
Afternoon Coffee

16:30 **SC-01-07**
Part IV: Radiation Tolerance
Lodovico Ratti

9:00 – 18:00 Partal @Hotel Saray Granada
SC-02 Analog and digital SPAD-based photodetectors

9:00 **SC-02-01**
Part I: SPAD physics
Fabrice Retiere

11:00 **SC-02-02**
Morning Coffee

11:30 **SC-02-03**
Part II: Analog SiPMs, timing and read-out (metrology)
Stefan Gundacker

13:30 **SC-02-04**
Lunch

14:30 **SC-02-05**
Part III: Digital SiPMs: Introduction (quenching circuits, metrology)
Serge Charlebois

16:00 **SC-02-06**
Afternoon Coffee

16:30 **SC-02-07**
Part IV: Digital SiPMs: Architectures and Applications
Claudio Bruschini

17:30 **SC-02-08**
Part V: Demos

8 November, 2026

9:00 – 18:00 **Alhamar @Hotel Saray Granada**
SC-04 **State-of-the-art semiconductor detectors in basic science, applied science and in industry**

9:00 **SC-04-01**
Semiconductor detector physics

10:30 **SC-04-02**
Electronics I

11:00 **SC-04-03**
Morning Coffee

11:30 **SC-04-04**
Electronics II

12:30 **SC-04-05**
Astrophysics

13:30 **SC-04-06**
Lunch

14:30 **SC-04-07**
Semiconductor detectors in material and life sciences

15:30 **SC-04-08**
Semiconductor detectors in high energy physics I

16:00 **SC-04-09**
Afternoon Coffee

16:30 **SC-04-10**
Semiconductor detectors in high energy physics II

17:30 **SC-04-11**
Concluding remarks

9:00 – 18:00 **Partal @Hotel Saray Granada**
SC-03 **Scientific Writing**

9:00 **SC-03-01**
Scientific Writing
Johan Knapen

9 November, 2026

9:00 – 19:00 **Alhamar @Hotel Saray Granada**
SC-05 **Fast-timing scintillation detectors for medical and other applications**

9:00 **SC-05-01**
Part 1

11:00 **SC-05-02**
Morning Coffee

11:30 **SC-05-03**
Part 2

13:30 **SC-05-04**
Lunch

14:30 **SC-05-05**
Part 3

16:00 **SC-05-06**
Afternoon Coffee

16:30 **SC-05-07**
Part 4

9:00 – 18:00 **Partal @Hotel Saray Granada**
SC-06 **Medical predictions from imaging with machine learning: The implementation gap**

9:00 **SC-06-01**
Part I - Statistical testing for medical imaging

11:00 **SC-06-02**
Morning Coffee

11:30 **SC-06-03**
Part II - An introduction to Statistical Learning Theory

13:30 **SC-06-04**
Lunch

14:30 **SC-06-05**
Part III - The implementation gap

16:00 **SC-06-06**
Afternoon Coffee

16:30 **SC-06-07**
Part IV

10 November, 2026

9:00 – 18:00 **Alhamar @Hotel Saray Granada**
SC-07 **Medical Image Reconstruction: from Foundations to AI**

9:00 **SC-07-01**
Part 1 - Image reconstruction foundations

11:00 **SC-07-02**
Morning Coffee

11:30 **SC-07-03**
Part 2 - AI for image reconstruction: introduction

13:30 **SC-07-04**
Lunch

14:30 **SC-07-05**
Part 3 - Kernel and deep image prior methods

16:00 **SC-07-06**
Afternoon Coffee

16:30 **SC-07-07**
Part 4 - Generative AI for image reconstruction

9:00 – 18:00 **Partal @Hotel Saray Granada**
SC-08 **Fundamentals of Total-Body PET**

9:00 **SC-08-01**
Welcome and Introduction to Short Course
Ben Spencer, Steven Meikle, Georgios Angelis

9:15 **SC-08-02**
History and Motivation for Development of TB-PET
Ben Spencer

10:15 **SC-08-03**
Clinical and Research Applications of TB-PET
Steven Meikle

11:00 **SC-08-04**
Morning Coffee

11:30 **SC-08-05**
Performance of LAFOV PET Systems
Steven Meikle

12:20 **SC-08-06**
QC/QA of TB-PET Systems
Ben Spencer

13:10 **SC-08-07**
Pulse check Q & A
Steven Meikle, Ben Spencer, Georgios Angelis

13:30 **SC-08-08**
Lunch

14:30 **SC-08-09**
Acquisition Protocols for TB-PET
Ben Spencer

15:15 **SC-08-10**
Data Corrections for TB-PET
Georgios Angelis

16:00 **SC-08-11**
Afternoon Coffee

16:30 **SC-08-12**
Reconstruction for TB-PET
Georgios Angelis

17:15 **SC-08-13**
Data Analysis Tools for TB-PET
Steven Meikle

17:45 **SC-08-14**
Q & A and Course Review
Georgios Angelis, Steven Meikle, Ben Spencer

8 November, 2026

11:30 – 17:00 ANDALUCÍA II & III
WS-01 AI in Nuclear Sciences and Nuclear Medical Imaging – Review and future expectations (onsite only)

Chairs:
Jean-Baptiste Michaud (Sherbrooke)
Francis Loignon-Houle (Valencia)

11:30 **WS-01-01**
Kolmogorov-Arnold Networks: A New Paradigm for Explainable Prediction

11:45 **WS-01-02**
AI at the Front End: Machine Learning for Raw-Signal Processing in Semiconductor Detectors

12:00 **WS-01-03**
Edge-AI with CMOS In-Memory Computing for Radiation Detector Acquisition Chains

12:15 **WS-01-04**
AI in PET: are we ready for more than better images?

12:30 **WS-01-05**
AI in nuclear imaging and neuroscience: a look at the initial impact

12:45 **WS-01-06**
Lunch Break

15:00 **WS-01-07**
Delegate, Verify, Understand : Agentic AI in the Medical Imaging Research Workflow

15:15 **WS-01-08**
Panel - AI in Nuclear Sciences and Nuclear Medical Imaging – Review and future expectations

14:30 – 19:40 ALBÉNIZ & MACHUCA
WS-02 Digital SiPM and SPAD-based sensors (onsite only)

14:30 **WS-02-01**
Opening words

14:39
14:40 - 16:00 - Topic 1 - Status of ongoing projects

14:40 **WS-02-02**
Status of project DIGILOG
Samuele Bisi

14:47 **WS-02-03**
Status of the PetVision project
Rok Dolenec

14:54 **WS-02-04**
Photon-to-Digital Converters: Update and Future development
Serge A. Charlebois

15:01 **WS-02-05**
Status of project at TRIUMF
Fabrice Retiere

15:08 **WS-02-06**
Status of the Picopix project
Rafael Ballabriga

15:15 **WS-02-07**
Recent progress in TSV, 2.5D and 3D integration of SiPMs at FBK
Alberto Gola

15:22 **WS-02-08**
Status of project PLATON
Kodai Kaneyasu

15:29 **WS-02-09**
Status of ASPIDES project
Tommaso M. Floris, On behalf of ASPIDES-Collaboration

15:43 **WS-02-10**
Status of project spadRICH
Prabhleen Singh

16:00
15:53 - 16:15 - Break

16:14
16:15 - 17:00 - Invited Talk - Digital SPAD detectors: a broader perspective on trends and markets

16:15 **WS-02-11**
Packing Functionality under SPADs with nanometer scale 3D Stacking Technologies
Robert K. Henderson

17:00
17:00 - 17:30 - Coffee break

17:29
17:30 - 18:30 - Topic 2 - Vision

17:30 **WS-02-12**
ASPIDES: a digital SiPM in 110nm CMOS - rationale, technology choice and open challenges
Lodovico Ratti, On behalf of the ASPIDES collaboration

17:45 **WS-02-13**
PLATON - lessons learned on strategy and funding
Davide Sgalaberna

18:00 **WS-02-14**
SPADs in DRDs
Fabrice Retiere

18:15 **WS-02-15**
Digital SiPM initiatives in the USA
Shiva Abbaszadeh

18:29
18:30 - 18:45 - Topic 3 - Foundry perspective

18:30 **WS-02-16**
End-to-End SPAD Technology at Fraunhofer IMS
Jennifer Ruskowski

18:44
18:45 - 19:30 - Topic 4 - How could one size fits all - A panel and group discussion

18:45 **WS-02-17**
Discussion/debate: on collaboration and funding strategies to bring these technologies to use

19:30 **WS-02-18**
Summary and conclusions

19:35 **WS-02-19**
Cocktail

14 November, 2026

14:30 – 19:30 FEDERICO GARCÍA LORCA
WS-03 Total-Body Kinetic Modeling Workshop

14:30 **WS-03-01**
Welcome and Introduction
Negar Omidvari, Steven Meikle

14:39
14:40–15:40 - Session 1: Cutting Edge Methods in Total-Body Kinetic Modeling and Analysis
Richard Carson, Jing Wu

14:40 **WS-03-02**
Total-Body PET Kinetic Modeling: Challenges and Opportunities
Guobao Wang

15:00 **WS-03-03**
A pragmatic approach to ultrashort time-frame total-body PET image reconstruction
Andrew Reader

15:20 **WS-03-04**
Exploring inter-organ connectivity using static and dynamic whole-body PET
Irène Buvat

15:39
15:40–16:40 - Session 2: Emerging Frontiers
Negar Omidvari, Yun Zhao

15:40 **WS-03-05**
New hopes or old illusions? Image-derived input functions in the era of next-generation (brain) PET imaging
Tommaso Volpi

16:00 **WS-03-06**
High-Temporal Resolution PET Kinetic Modeling
Kevin Chung

16:20 **WS-03-07**
Whole-Body Functional [18F]FDG PET
Sharna Jamadar

16:40 **WS-03-08**
Coffee break

16:59
17:00–18:00 - Session 3: Industrial Perspectives – Translating TB-PET Kinetic Modeling into Practice
Negar Omidvari, Yun Zhao

17:00 **WS-03-09**
Enabling dynamic/parametric imaging applications in the era of ultra high sensitivity PET with Omni128
Elise Emond

17:15 **WS-03-10**
Practical Total-Body PET Kinetic Modeling with the Quadra
Paul Schleyer

17:30 **WS-03-11**
Practical Barriers, Innovative Solutions: Total-Body PET Kinetic Modeling for Research and Clinical Use
Qing Ye

17:45 **WS-03-12**
Short break

18:00 **WS-03-13**
18:00–19:00 - Session 4: SlicerDynamicPET Tutorial
Daniele Dall'Olio

19:00 **WS-03-14**
Drinks, Canapés, and Networking

15:00 – 19:00 MANUEL DE FALLA
WS-04 Emerging Directions in Theranostic Imaging: From PET and SPECT to Novel Modalities (onsite only)

Chairs:
Shiva Abbaszadeh (Santa Cruz)
Javier Caravaca (Berkeley)

15:00 **WS-04-01**
Radiotheranostics Beyond Boundaries: Hardware, AI, and the Future of Quantitative Imaging
Youngho Seo

15:15 **WS-04-02**
A Long Axial-FOV PET System with Embedded Spectroscopic Gamma-Cameras for In Vivo Imaging of Radiopharmaceutical Therapy
Ling-Jian Meng

15:30 **WS-04-03**
A High-Resolution Mobile Gamma-Camera for optimizing dosimetry in Molecular Radiotherapy : first clinical feasibility study for treatment of thyroid diseases with Radioactive Iodine
Laurent Menard

15:37 **WS-04-04**
The Personalized Remote Radiation Tracking Portable Organ Dosimetry Device
Robert S. Miyaoka

15:44 **WS-04-05**
Incorporating X-Ray and gamma-Ray Coincidence Detection for Improved Detection Efficiency and Image Quality in ^{177}Lu Imaging
Qingyang Wei

15:51 **WS-04-06**
Physics-Corrected List-Mode MLEM Reconstruction for Quantitative ^{177}Lu Cascade Gamma Coincidence Imaging
Hanshen Ye

15:58 **WS-04-07**
Learning Support Priors from ^{177}Lu with Projection-Domain Constraint for Quantitative ^{225}Ac SPECT Reconstruction
Zhengkun Dong

16:05 **WS-04-08**
Rapid Extended-Distance ^{177}Lu Imaging with a Portable Telephoto-Lens Magic-Cube Gamma Camera for Intra-Procedural Theranostic Assessment
Yuxi Zhang

16:12
Open Discussion I

16:40
Coffee Break

17:10 **WS-04-09**
Implementation of Radiation Detection Technologies, Quality Assurance, and Harmonized Control Standards for Theragnostic Programs in Emerging Healthcare Systems.
Ian M. Rossi

17:25 **WS-04-10**
New Horizons in Ultra-High Resolution 3D CZT Detectors and its impact on preclinical SPECT/PET
Alexander Cherlin

17:39 **WS-04-11**
A multimodal C-arm enabling concurrent X-ray and nuclear imaging for cost-effective theragnostic interventions
Dennis R. Schaart

17:46 **WS-04-12**
Theranostic SPECT with High Energy Resolution CZT Detectors
Peter G. Hotvedt

17:53 **WS-04-13**
Fast Timing for High-Energy Gammas with GAGG and BGO for Improved Theranostic
Fiammetta Pagano

18:00 **WS-04-14**
Event-Based Alpha- and Beta- Particle Imaging with iQID: From Quantitative Digital Autoradiography to Isotope Identification
Brian W. Miller

18:07 **WS-04-15**
How the next generation digital autoradiography can provide insight into theranostic bioequivalence
Stephen Adler

18:14 **WS-04-16**
Gamma-Positron Imaging and Event-Correlated Simulation for Emerging Theranostics
Matthew A. Kupinski

18:21 **WS-04-17**
Multiplexed PET for Theranostic Imaging
Joaquín López Herraiz

18:28
Open Discussion II

10 November, 2026

11:30 – 13:00 FEDERICO GARCÍA LORCA
JS-01 Joint Session NSS-MIC-RTSD

Chairs:
John Valentine (Berkeley)

11:30 **JS-01-01**
Uniformity, Stability and High-Flux X-ray Detection Performance of $FAPbBr_3$, $CsPbBr_3$ and CZT
Isabel Braddock

11:45 **JS-01-02**
Estimating requirements for scintillator-based photon counting detectors in CT
Scott Hsieh

12:00 **JS-01-03**
A four side buttable system in package for medical and industrial Photon-Counting CT
Torsten Solf

12:15 **JS-01-04**
A Vibrational-Scanning Single-Photon Emission Microscope (SPEM) for In Vivo 3-D Autoradiography of Targeted Alpha Therapy
Weijian Zhang

12:30 **JS-01-05**
Multi-Agent Pipeline with Local Large Language Models for Automated MCNP Script Review
Byoungil Jeon

12:45 **JS-01-06**
A Compact Educational Platform for Demonstrating TDAQ Concepts in Particle Detector Systems
Raffaele Giordano

15:00 – 17:05 FEDERICO GARCÍA LORCA
JS-02 Joint Session - NSS-MIC

Chairs:
Cinzia DaVia (Manchester)
Roger Lecomte (Sherbrooke)

15:00 **JS-02-01**
2026 IEEE TNS Best Paper Award

15:05 **JS-02-02**
Systematic Defect and Crystal-Field Engineering of LYSO-U Scintillators for Photon-Counting CT
Dongzhou Ding

15:20 **JS-02-03**
Energy resolved imaging with a fine-pitch YAGG-SiPM based indirect photon counting detector
Kenji Shimazoe

15:35 **JS-02-04**
Latest update on the glass-less TSV FBK SiPM for 2.5D integrated ToF-PET modules
Michele Penna

15:50 **JS-02-05**
The DIGILOG Project: μSiPM Sensor and Sub-20 ps Readout Electronics for ToF-PET
Samuele Bisi

16:05 **JS-02-06**
Real-Time DOI Layer Prediction in TOF-PET Detectors via FPGA Neural Network
Shuiting Xin

16:20 **JS-02-07**
Physics-Informed Deep Learning on FPGA for Inter-Crystal Scattering Correction in ToF-CT
Lamyae Jdid

16:35 **JS-02-08**
Cherenkov Photon Counting, Labeling, and Multi-Photon Timing Estimation for sub-100 ps CTR BGO TOF-PET Detectors
Joshua W. Cates

16:50 **JS-02-09**
3D-cylindrical microdetector arrays for microdosimetryin proton therapy
Consuelo Guardiola

17:30 – 19:00 FEDERICO GARCÍA LORCA
JS-03 Joint Session NSS-RTSD

Chairs:
Shariar Motakef (Natick)
Chiara Guazzoni (Milano)

17:30 **JS-03-01**
Role of Al_2O_3passivation on high-resolution 4H-SiC radiation detectors
Krishna C. Mandal

17:45 **JS-03-02**
Vacuum-deposited metal halide perovskite film as a radiation scintillator
Muzzamer Zahid

18:00 **JS-03-03**
FAST NEUTRON DETECTION USING A SINGLE-CRYSTAL DIAMOND DETECTOR
Bohumír Zaťko, Bohumír Zaťko

18:15 **JS-03-04**
Improving the spectral resolution of photons in silicon Timepix3 by correcting for the cluster size and by lowering the Krummenacher current
Jindrich Jelinek

18:30 **JS-03-05**
Simulation-based inference for uncertainty-aware interaction reconstruction in 3D CZT drift strip detectors
Alejandro Valverde Mahou

18:45 **JS-03-06**
One-Year Performance Analysis of the cadmium zinc TElluride Radiation Imager (TERI) in Orbit
Nicholas Kirschner

9 November, 2026

9:00 – 11:00 FEDERICO GARCÍA LORCA
NP-01 NSS Plenary Session

Chairs:
Audrey Corbeil Therrien (Sherbrooke)
Giulia Hull (Orsay)

9:00 **NP-01-01**
Welcoming remarks
Stefan Ritt

9:30 **NP-01-02**
The Shape of Light
Sara Cazzoli

10:20 **NP-01-03**
2026 Radiation Instrumentation Early Career Award (NSS)

10:30 **NP-01-04**
2026 IEEE Emilio Gatti Radiation Instrumentation Technical Achievement Award (NSS)

10:40 **NP-01-05**
2026 IEEE Glenn F. Knoll Radiation Instrumentation Outstanding Achievement Award (NSS)

11:30 – 12:30 FEDERICO GARCÍA LORCA
NP-02 NSS Plenary Session

Chairs:
Audrey Corbeil Therrien (Sherbrooke)
Giulia Hull (Orsay)

11:30 **NP-02-01**
Environmental sustainability in research
Hannah Wakeling

12:20 **NP-02-02**
2026 Valentin T. Jordanov Radiation Instrumentation Travel Grants and 2026 Paul Phelps Continuing Education Grant

12:25 **NP-02-03**
Introduction to lighning talks

12:30 – 13:00 FEDERICO GARCÍA LORCA
N-LT-01 NSS Lightning Talks 1

Chairs:
Audrey Corbeil Therrien (Sherbrooke)
Giulia Hull (Orsay)

12:30 **N-LT-01-01**
Facile, scalable and high-yield synthesis of zero-dimensional copper halide $Cs_3Cu_2Cl_5$ scintillator with near-unity quantum yield for high-resolution X-ray imaging applications
Byungha Shin

12:32 **N-LT-01-02**
Hydrophobic Solvent-Based Polishing for Performance Enhancement of Water-Sensitive Perovskite Scintillator Crystals
Seungho Song

12:34 **N-LT-01-03**
Organic Scintillator Light Yield Models for Sub-MeV Neutrons in EJ301D and d-stilbene
Christian A. Irvine

12:36 **N-LT-01-04**
Application of neutron sensitising layers to plastic scintillator
Matt P. Taggart

12:38 **N-LT-01-05**
Scintillation light quenching for energetic charged particles in GAGG:Ce
Felix Liang

12:40 **N-LT-01-06**
Temperature Dependence of Pulse Shape Discrimination in SiPM-Based EJ-276D Detectors
John Leland

12:42 **N-LT-01-07**
Performance evaluation of GaGG(Ce) scintillators with different photosensors
Miriam Caballero Rodríguez

12:44 **N-LT-01-08**
Combining cross-luminescent scintillators and µSiPMs for better timing in ToF-PET
Katrin Herweg

12:46 **N-LT-01-09**
Fast or Adapt: Proportional Gas in γ-ray Fields
David O'Connor

12:48 **N-LT-01-10**
Characterisation of edge-on fully-depleted monolithic CMOS silicon sensors
Matteo Barbagiovanni, On behalf of 1MICRON Collaboration

12:50 **N-LT-01-11**
Gain suppression study on LGADs with different gain layer designs
Leo Cavazzini

12:52 **N-LT-01-12**
Pulse-Shape-Based Slow-Rising Pulse Rejection for Reliable Charge-Carrier Transport Characterization in a Semiconductor Radiation Detector
Jihwan Boo

12:56 **N-LT-01-13**
Diagnosing Mechanisms for Charged Particle Attenuation Enhancement in Nanostructured Materials
Niko P. Speck

12:58 **N-LT-01-14**
Monolithic integration of cooling microchannels in all-silicon ladders for vertex detectors
Javier Fernández-Tejero

12:30 – 13:00 ALBÉNIZ & MACHUCA
N-LT-02 NSS Lightning Talks 2

12:30 **N-LT-02-01**
Ultra High-Rate Neutron Detection with ^{3}He Tubes via CF_4 Prompt Scintillation Readout
Luis M. Margato

12:32 **N-LT-02-02**
Characterization of 3D ultra-thin silicon-based thermal neutron detectors
Felipe Zamorano

12:34 **N-LT-02-03**
Scintillator Size Effects in Fiber-Based Neutron Detectors With Pulse-Shape Discrimination for BNCT
Hong-Da Liu, Hong-Da Liu

12:36 **N-LT-02-04**
Time-Resolved Imaging of Radioactive Gas with the 4π Gamma-Ray Imager C3G
Yoshiharu Kitayama

12:38 **N-LT-02-05**
Method for determining lithium ore's grade based on photoneutrons' lifetime measurement
Minfeng Yu

12:40 **N-LT-02-06**
Template-Matching Position Solving on FPGAs for a Thermal Neutron Detector
Matthew Loyd

12:42 **N-LT-02-07**
Localization of uranium samples in large cemented nuclear waste using active photon interrogation and a Bayesian inversion
Malo Lebreton, Malo Lebreton

12:44 **N-LT-02-08**
Hybrid Temperature Compensation and Radiation Damage Recovery with Scintillation Detectors
Dae yang Oh

12:46 **N-LT-02-09**
Simulations of A Novel Time-of-Flight β/γ Transmission Tomography Scanner
Robert Carmichael, Robert Carmichael

12:48 **N-LT-02-10**
Revealing Disorder Faster: Detector Upgrades for SANDALS-II
Sarah E. Mann, Sarah E. Mann

12:50 **N-LT-02-11**
Characterization and Radiation Damage Mitigation of Silicon Photomultipliers for Low Earth Orbit Applications
Shideh Davarpanah, On behalf of NUSES Collaboration

12:52 **N-LT-02-12**
Graphene Photodetectors for Vacuum-UV Through Visible Wavelengths
Alec Lindman

12:54 **N-LT-02-13**
FPGA-Based Real-Time SiPM Emulator with Sub-Nanosecond Temporal Quantization
Stefano Carsi

12:56 **N-LT-02-14**
Self-Powered Wireless Communication via Ambient Gamma-Ray Harvesting at Fukushima Daiichi
Takeshi Fujiwara

12:58 **N-LT-02-15**
Basic Development of a Wide-Field EUV Polarimeter for High-Energy Transient Sources
Soken Kuwabara

15:00 – 17:00 Poster Area
NSS-01 NSS Poster Session

Chairs:
Matteo Porro (Schenefeld)

15:00 **NSS-01-001**
Fast or Adapt: Proportional Gas in γ-ray Fields
David O'Connor

15:00 **NSS-01-003**
Development of a Monte Carlo Simulation–Based Analysis Technique for High-Pressure Ionization Chambers (HPIC)
Kyeong Hyeon Sung

15:00 **NSS-01-005**
High Granularity Readout Time Projection Chamber R&D for Future Circular e+e- Colliders
Huirong Qi, On behalf of Linear Collider Time Projection Chamber International Collaboration

15:00 **NSS-01-007**
A Semi-Analytical Method for Sensitivity Estimation of Parallel-Plate Boron-Coated

Ionization Chambers
Peng Tang

15:00 **NSS-01-009**
A New Efficient n-γ Pulse Shape Discrimination Technique for Fast Scintillation Detectors
Stefano Riboldi

15:00 **NSS-01-011**
Near infrared scintillation properties of rare earth doped fluorapatite transparent ceramics
Takayuki Yanagida

15:00 **NSS-01-013**
Hydrophobic Solvent-Based Polishing for Performance Enhancement of Water-Sensitive Perovskite Scintillator Crystals
Seungho Song

15:00 **NSS-01-015**
Combining cross-luminescent scintillators and µSiPMs for better timing in ToF-PET
Katrin Herweg

15:00 **NSS-01-017**
Temperature Dependence of Pulse Shape Discrimination in SiPM-Based EJ-276D Detectors
John Leland

15:00 **NSS-01-019**
Scintillation light quenching for energetic charged particles in GAGG:Ce
Felix Liang

15:00 **NSS-01-021**
Facile, scalable and high-yield synthesis of zero-dimensional copper halide $Cs_3Cu_2Cl_5$ scintillator with near-unity quantum yield for high-resolution X-ray imaging applications
Byungha Shin

15:00 **NSS-01-023**
Spectral-feature-based radionuclide and radiation-type discrimination using a plastic scintillation fiber detector for in-situ pipe measurements
Tomohisa Abe

15:00 **NSS-01-025**
Investigation of Coincidence Time Resolution in BaF_2:Y Scintillators for TOF PET

Applications
Junfeng Chen

15:00 **NSS-01-027**
Experimental Study of DOI Effects on the Timing Response of a 1”×2” LaBr3 Detector
Sara Gaitán Dominguez

15:00 **NSS-01-029**
Development of Mo-Doped Cs_2HfCl_6 for Dosimetry in High Dose-Rate Environment
Shinichiro Kondo

15:00 **NSS-01-031**
From $LaBr_3$:Ce to $Cs_2LiLa(Br,Cl)_6$:Ce Mixed-Halide Elpasolites: Tailoring Scintillation Response for High-Precision Gamma-Ray and Neutron Detection
Zhuochen Cai

15:00 **NSS-01-033**
Application of neutron sensitising layers to plastic scintillator
Matt P. Taggart

15:00 **NSS-01-035**
Micropower Generation and Radiation Detection with Cr-doped Al_2O_3 Transparent Ceramics
Noriaki Kawaguchi

15:00 **NSS-01-037**
Single-ended Multiplexed Readout Scintillation Detector With Depth of Interaction Capability: Architecture and Optical Simulation
Gabriela Jazvac

15:00 **NSS-01-039**
Performance evaluation of GaGG(Ce) scintillators with different photosensors
Miriam Caballero Rodríguez

15:00 **NSS-01-041**
Cosmic-Ray Muon Position Reconstruction via Dual-End Readout of Triangular Plastic Scintillators
Yaofeng Zhang

15:00 **NSS-01-043**
Scintillation Properties of ^{6}Li-doped CsI:Tl Crystals for Thermal Neutron Detection
Anil K. Gourishetty

15:00 **NSS-01-045**
Development of Plastic Scintillator by Thermal Polymerization for Gamma Spectroscopy
Anil K. Gourishetty

15:00 **NSS-01-047**
Comparative Analysis of Scintillators for TOF-DXA Detectors in the Low-Energy X-ray Region
Jiwon Nam

15:00 **NSS-01-049**
Improved Low-Energy Threshold Performance of a Vacuum-Compatible Hybrid Pixel Detector for Soft X-ray Applications
Yasukazu Nakaye

15:00 **NSS-01-053**
Development and Testing of the Strip Pairing Algorithm for the COSI Data Pipeline
Julian Gerber

15:00 **NSS-01-055**
Temperature-Dependent Charge Transport in Diamond Radiation Detectors
Owen A. Johnson

15:00 **NSS-01-057**
Monitoring neutron exposure in hyper-pure germanium detectors with in-situ capture reactions
Thomas Round

15:00 **NSS-01-059**
Pixel Architecture Effects on Neutron-Induced White Spot Generation in CMOS Image Sensors
Jihun Jeong

15:00 **NSS-01-061**
Characterisation of edge-on fully-depleted monolithic CMOS silicon sensors
Matteo Barbagiovanni, On behalf of 1MICRON Collaboration

15:00 **NSS-01-063**
Gain suppression study on LGADs with different gain layer designs
Leo Cavazzini

15:00 **NSS-01-065**
Pulse-Shape-Based Slow-Rising Pulse Rejection for Reliable Charge-Carrier Transport

Characterization in a Semiconductor Radiation Detector
Jihwan Boo

15:00 **NSS-01-067**
The Sensor, Packaging and INtegration (SPIN) group at Fondazione Bruno Kessler (FBK): capabilities, facilities and expertise
Pietro Tosato

15:00 **NSS-01-069**
High-voltage stress test and thermal recovery of an amorphous-silicon-passivated planar HPGe detector
LiHui Han

15:00 **NSS-01-071**
Development of a SiC-Based Muon Beam Monitor for the COMET Experiment
Kenya Okabe

15:00 **NSS-01-073**
Argon Ion-Assisted Polycrystalline PbO Layers for Direct-Conversion X-ray Imaging Detectors
Mikhail Vostokov

15:00 **NSS-01-075**
Quantum Dots-Based Short-Wave Infrared Avalanche Photodetectors
Xingzhan Wei

15:00 **NSS-01-077**
Characterization and Radiation Damage Mitigation of Silicon Photomultipliers for Low Earth Orbit Applications
Shideh Davarpanah, On behalf of NUSES Collaboration

15:00 **NSS-01-079**
Toward SiPM Single-Photon Detection Matrix using Ultrafast, Low Power RF Readout
Dominique F. Yvon

15:00 **NSS-01-081**
FPGA-Based Real-Time SiPM Emulator with Sub-Nanosecond Temporal Quantization
Stefano Carsi

15:00 **NSS-01-083**
Design and Single-Cell Verification of an Integrated Temperature-Compensation Architecture for Digital SiPMs in Extreme Environments
Jin-Seok Oh

15:00 **NSS-01-085**
Graphene Photodetectors for Vacuum-UV Through Visible Wavelengths
Alec Lindman

15:00 **NSS-01-087**
Development of a PLL-less 6.25Gbps Serializer and CML Transmitter for the LCLS-II Upgrade
Aseem Gupta

15:00 **NSS-01-089**
Performance Evaluation of Differential Amplifiers for Fast Scintillating Fiber Readout in Proton Therapy
Bayram Deniz

15:00 **NSS-01-091**

15:00 **NSS-01-093**
Design of the new Matterhorn detector for the 4th generation synchrotrons
Davide Mezza

15:00 **NSS-01-095**
A Low-Latency 28-nm CMOS ASIC for Superconducting Quantum Readout
Yunzhuo Zhang

15:00 **NSS-01-097**
Radiation Effects on COTS On-Board Computer and Boot/Data-Storage Media Configurations for Super-Low-Earth-Orbit Optical Satellites
Jongdae Sohn

15:00 **NSS-01-099**
A Versatile High Linearity Front-End Preamplifier with Wide Dynamic Range for Multiple SiPM Sensors
Jara García-Barrena, On behalf of NEXT collaboration

15:00 **NSS-01-101**
SPAGHETTI : An original instrument for the continuous gamma-ray based monitoring of hydrothermal volcanoes
Hervé Chanal

15:00 **NSS-01-103**
Evaluating AMD's Versal Architecture for Tapped Delay Line Time-to-Digital Converters.
Julien Rossignol

15:00 **NSS-01-105**
Probing Sub-20 ps Intrinsic Timing Limits of MVT-SiPM Readout for TOF-PET
Hui Lao

15:00 **NSS-01-109**
Design and characterization of a 28 nm CMOS asynchronous front-end for the readout of hybrid pixel sensors in future colliders
Luigi Gaioni

15:00 **NSS-01-111**
A 5.12-GS/s Time-Interleaved VCO-Based ADC With Digital Calibration for High-Speed Detector Waveform Digitization
Chenxi Chen

15:00 **NSS-01-113**
Development of an FPGA-based Hardware Data Injector for High-Energy Experiments
Marcel M. Boonen

15:00 **NSS-01-115**

15:00 **NSS-01-117**
MU-STAR-mini: A 5-GS/s Prototype Sampling Array for High-Resolution Multi-Channel Streaming Readout
Luca Macchiarulo

15:00 **NSS-01-119**
Implementation of FPGA-Based Time-to-Digital Converters with Zero Measurement Dead Time
Xinren Qi

15:00 **NSS-01-121**
A Pre-Study of a General-Purpose Trigger Processing Unit for the CEPC TDAQ System
Dong Liu

15:00 **NSS-01-123**
Design of the Ultra-Low-Power Readout Electronics for the Large Area ^{3}He Tube Array Detector at China Spallation Neutron Source
Weigang Yin

15:00 **NSS-01-125**
A modular, self-triggered firmware for the FPGA-based readout of electromagnetic

calorimeters at the INSIGHT@ELSA experiment
Benedikt Otto, On behalf of the INSIGHT collaboration

15:00 **NSS-01-127**
A Self-Triggered, Event-Driven Readout ASIC for the eXTP PFA X-ray Polarimeter
Ke Wang

15:00 **NSS-01-129**
Pulse shape discrimination by digital pulse processing
Felix Liang

15:00 **NSS-01-131**
Intrinsic time jitter of alternate data acquisition systems for the HISTARS project
Víctor Martínez Nouvilas

15:00 **NSS-01-133**
Feasibility Study of Analog Pulse Processing ASIC for SDD Array in High Count Rate XRF
Yuji Okubo

15:00 **NSS-01-135**
High-performance upgrade for Track Lab: processing Timepix4 hits efficiently at scale
Petr Mánek

15:00 **NSS-01-137**
A Scalable High-Throughput DAQ Architecture for Real-Time Proton Beam Monitoring Applications
Bayram Deniz, On Behalf of NOVO Collaboration

15:00 **NSS-01-139**
A Modular High-Bandwidth DAQ System for the Medipix4 ASIC Based on FPGA Ethernet Readout
Nicolò Vladi Biesuz

15:00 **NSS-01-141**
Measurement of Energy-Dependent Neutron-Induced Single-Event-Upset Rates for Multiple FPGA Types
Shunya Ueda

15:00 **NSS-01-143**
Wireless Dosimetry System for Interventional Radiology
Pedro M.M. Correia

15:00 **NSS-01-145**
FPGA firmware for ^{3}He resistive wire tube readout with CAEN R5560 ADC.
Davide Raspino

15:00 **NSS-01-147**
LDMX Silicon Tracker Data Acquisition System
Benjamin Reese

15:00 **NSS-01-149**
Latest Upgrades and Operation of the Neutron Veto Data Acquisition System for the XENONnT Experiment
Stefano Mastroianni, on behalf of the XENON Collaboration

15:00 **NSS-01-151**
Design and Integration of a Modular $LiInP_2Se_6$ Neutron Detector Prototype for Single-Crystal Diffractometry Applications
Mohamed El Amine Benkechkache

15:00 **NSS-01-153**
Improvement of Ambient dose equivalent rate Estimation for Airborne Radiation Monitoring Using Artificial Neural Networks with Vegetation and Topographic Information
Ayumu Miyahara

15:00 **NSS-01-155**
Explainable Radionuclide Identification Using FWHM-Aware Adaptive Banding in Gamma-Ray Spectroscopy
Seoyun Jang

15:00 **NSS-01-157**
Source-Transferable Machine Learning-based Pulse Shape Discrimination in 3D-Printed Plastic Scintillators
Anil K. Gourishetty

15:00 **NSS-01-159**
Spectro-Temporal Gamma-Ray Anomaly Detection with Context-Adaptive Background Modeling
Hannah Parrilla

15:00 **NSS-01-161**

15:00 **NSS-01-163**
Generative Overlay Augmentation for Robust Structural Region Segmentation in Dual-

Energy X-Ray Cargo Container Imagery
Yeon-Wook Kim

15:00 **NSS-01-165**
Development of Realistic Gamma-ray Spectrum Database Using Geant4 and U-Net-based Sim-to-Real Translation
Geon Kim

15:00 **NSS-01-167**
Real-Time Nuclide Identification via Physics-Region Preprocessing
Dongseong Shin

15:00 **NSS-01-169**
Development of a vehicle-mounted Directional radiation monitoring system using multiple NaI(Tl) detectors and an ANN algorithm
Hee Kyun Baek

15:00 **NSS-01-171**
Wavelet optimisation for improved photopeak extraction in low-count gamma-ray spectra
James Biggs

15:00 **NSS-01-173**
Real-Time Particle Hit Detection Using a 1D Convolutional Neural Network on a CAEN FPGA-Based Digitizer
Carlo Tintori

15:00 **NSS-01-175**
Development of an ANN-based Gamma-ray Spectrum Correction Algorithm for PVT Detectors
Jiwon Ra

15:00 **NSS-01-177**
measurement-guided x-ray image restoration using fourier stochastic differential equations
Seokwon Oh

15:00 **NSS-01-179**
A General-Purpose Radionuclide Identification Model for HPGe Gamma-Ray Spectrometry
Jim Zickefoose

15:00 **NSS-01-181**

15:00 **NSS-01-183**

15:00 **NSS-01-185**
High-Fidelity 3D MCNP Modeling for Waste Classification in PWRs
Changyeon Yoon

15:00 **NSS-01-187**
Six-Degree-of-Freedom Pose Estimation for Safety Monitoring in a Nuclear Glovebox
Lewis Mead

15:00 **NSS-01-189**
Photonuclear Processes in a Tungsten Matrix Collimator for Spatially Fractionated Radiation Therapy
Igor E. Anokhin

15:00 **NSS-01-191**
A Low-Energy X-ray Transmission Imaging Method for Detecting Metallic Microparticles in Single-Layer $LiFePO_4$ Batteries
Dehao Wang

15:00 **NSS-01-193**

15:00 **NSS-01-195**
Improved Scattering Modeling in CIVA-RT using a Next-Event Estimator
Sheraz Blas

15:00 **NSS-01-197**
Development of a spectral unmixing method for gamma-ray spectra analysis : application to airborne measurements
Luc Patryl

15:00 **NSS-01-199**

15:00 **NSS-01-201**
Hybrid Semantic–Keyword Analysis for the Classification of Nuclear Fuel Cycle Activities Using Open-Source Information
Yeon Woo Lee

15:00 **NSS-01-203**
Selective Use of Directionally Informative Non-Photopeak Events for Low-Count

Industrial Gamma Imaging
Linxin Lei

15:00 **NSS-01-205**
An Optical Surrogate Framework for Three-Dimensional Fusion Source Reconstruction
Zhong Zhang

15:00 **NSS-01-207**
Adaptive Tetrahedral Mesh Reconstruction for Industrial Computed Tomography
Junho Lee

15:00 **NSS-01-209**
Forward Simulation of High-Energy XPCI Using XRM-Derived Semiconductor Package Phantoms
Uijin Lee

15:00 **NSS-01-211**
Investigating Identifiability in Joint Transmission–Backscatter X-ray Image Registration with Energy-Dependent Source Geometry
Youngchol Choi

15:00 **NSS-01-213**
Development of a UAV-Mounted Radiation Survey System Integrating LaBr3(Ce) Detectors and LiDAR
Young-Yong Ji

15:00 **NSS-01-215**
Development of a Handheld Uranium Enrichment Analyzer Based on LaBr3 Detector and Relative Detection Efficiency Self-Calibration Method
Guorong Liu

15:00 **NSS-01-217**
Neutron Response Evaluation of Miniature Spherical Li-glass scintillators for Optical-Fiber-Based Detectors
Yutaro Saito

15:00 **NSS-01-219**
Time-Resolved Imaging of Radioactive Gas with the 4π Gamma-Ray Imager C3G
Yoshiharu Kitayama

15:00 **NSS-01-221**
Performance Evaluation of a Fast Fission Neutron Coincidence Counting System
Yosuke Toh

15:00 **NSS-01-223**
Development and Validation of Neutron Diagnostics on ASP in Support of Future Facilities
Lucy A. Wilson

15:00 **NSS-01-225**
Development and test of a novel neutron and gamma imaging detector
Yancheng Yu

15:00 **NSS-01-227**
Multilayer Scintillator for Improved Gamma-ray Discrimination at Thermal Neutron Scattering Beamlines
Ahmed Moustafa

15:00 **NSS-01-229**
Feasibility of Organic Scintillator-Based Coincidence Counting for Photonuclear Nondestructive Assay of Nuclear Materials
Kosuke Tanabe

15:00 **NSS-01-231**
Localization of uranium samples in large cemented nuclear waste using active photon interrogation and a Bayesian inversion
Malo Lebreton, Malo Lebreton

15:00 **NSS-01-233**
Development and Performance Evaluation of a Four-Detector RMS in Compliance with IEC 60532
Dongam Yang

15:00 **NSS-01-235**
Template-Matching Position Solving on FPGAs for a Thermal Neutron Detector
Matthew Loyd

15:00 **NSS-01-237**
Method for determining lithium ore's grade based on photoneutrons' lifetime measurement
Minfeng Yu

15:00 **NSS-01-239**
EJ309-Based Neutron–Photon Detection for Photoneutron Characterisation and High-Altitude Radiation Assessment
Khalil Al Khouri

15:00 **NSS-01-241**
Multimodal extension of the Feynman model for thermal neutron multiplicity counters
Gabriel Chartier

15:00 **NSS-01-243**
Building a Two-Stage Compton Camera with $LaBr_3$:Ce Detector Assemblies
Sello Mashinini

15:00 **NSS-01-245**
Dosimetry and Beam-Condition Characterization of Mixed-Field Irradiation Positions at CERN CHARM
Salvatore Fiore

15:00 **NSS-01-247**
Hybrid Temperature Compensation and Radiation Damage Recovery with Scintillation Detectors
Dae yang Oh

15:00 **NSS-01-249**
Simulations of A Novel Time-of-Flight β/γ Transmission Tomography Scanner
Robert Carmichael, Robert Carmichael

15:00 **NSS-01-251**
A Large-Area Spectroscopic Alpha Imaging Detector for Dual-Isotope Imaging of ^{225}Ac and ^{213}Bi in Targeted Alpha Therapy
Jong-Guk Kim

15:00 **NSS-01-253**
Scintillator Size Effects in Fiber-Based Neutron Detectors With Pulse-Shape Discrimination for BNCT
Hong-Da Liu, Hong-Da Liu

15:00 **NSS-01-255**
Performance Evaluation of a DOI-Based Directional Radiation Monitoring System for Moving Radiation Source Tracking
Juwan Kang

15:00 **NSS-01-257**
Development of a Portable High-Gamma-Ray-resistant Alpha and Beta Dust Monitor
Misaki Hirato

15:00 **NSS-01-259**
Investigation of Structure-Dependent Neutron-Induced Displacement Damage in Silicon

MOSFETs
Jin-Seok Oh

15:00 **NSS-01-261**
Solid-State Large-Area Contamination Detector Using Lightlink™ technology for Contamination and clearance equipment
Philippe Talent

15:00 **NSS-01-263**
Performance Evaluation of the SNIPER-GN Portable Gamma–Neutron Detection System
Fabio Davolio

15:00 **NSS-01-265**
Development of A Cold Neutron Imaging Detector based on Structured $^{10}B_2O_3$-ZnS:Cu Screen
Deyuan Li

15:00 **NSS-01-267**
Revealing Disorder Faster: Detector Upgrades for SANDALS-II
Sarah E. Mann, Sarah E. Mann

15:00 **NSS-01-269**
PGNAA-Based Composition Analysis Using $LaBr_3$(Ce) and NaI(Tl) Detectors
Ki-Yoon Lee

15:00 **NSS-01-271**
Ultra High-Rate Neutron Detection with ^{3}He Tubes via CF_4 Prompt Scintillation Readout
Luis M. Margato

15:00 **NSS-01-273**
Imaging detection and spectral tracking of neutrons in wide range by Timepix detectors with Si, SiC, GaAs and CdTe sensors
Carlos Granja

15:00 **NSS-01-275**
Characterization of 3D ultra-thin silicon-based thermal neutron detectors
Felipe Zamorano

15:00 **NSS-01-277**
A Full Rank Pileup Deconvolution Scheme Suitable for Calorimeter Online Trigger Primitive Generation
Jinyuan Wu

15:00 **NSS-01-279**
In-orbit performance of the Tl_2LiYCl_6:Ce (TLYC) detector onboard the Neutron Radiation Detection Instrument-1A (NeRDI-1A)
Karla G. Oñate Melecio

15:00 **NSS-01-281**
Technical Design and Geometric Acceptance of the Assessing Lunar Ion-Generated Neutrons (ALIGN) Payload for Chang'E-8
Kullapha Chaiwongkhot

15:00 **NSS-01-283**
Cluster Size Simulation to Predict LHCb Upgrade I VELO Performance
Sean J. Williams, On behalf of the LHCb VELO group

15:00 **NSS-01-285**
Design of Readout Electronics for a CdZnTe Detector Prototype for Polar-orbiting Solar Hard X-ray Imaging Telescope
ZeKun Wang

15:00 **NSS-01-287**
Stability of the ATLAS Timepix3 Detector Network for Relative Luminosity Measurement in Run 3
Catalina Lesmes

15:00 **NSS-01-289**
Radiation Studies for the LHCb Upgrade II Detector: Impact of the Upgraded Electromagnetic Calorimeter and Muon System Shielding
Sacha E.R. Medaer

15:00 **NSS-01-291**
Timing properties of the FARCOS detection system
Chiara Guazzoni, on behalf of the fARCOS collaboration

15:00 **NSS-01-293**
Thermal and In Situ annealing tests for SiPM radiation damage mitigation
Suomi Bez Baruah

15:00 **NSS-01-295**
Axial Reactivity Profile Measurement of Polaris Using CR-39 Nuclear Track Detectors
Sara Alawabdeh

15:00 **NSS-01-297**
On-detector Electronics for the ATLAS Liquid Argon Calorimeter Phase-II Upgrade at the

High-Luminosity LHC
Emmanuel Josue Molina Gonzalez, On behalf of the ATLAS Collaboration

15:00 **NSS-01-299**
Airborne Measurement of Terrestrial Gamma-Ray Flashes with the High Elevation Radiation Array
Juan J. Manfredi

15:00 **NSS-01-301**
Systematic X-ray irradiations of a back illuminated, HPGe, microstrip sensor.
Daniel Thacker

15:00 **NSS-01-303**
Energy-resolved Laue Diffraction: a New Tool for Crystal Structure determination
David P. Siddons

15:00 **NSS-01-305**
Pile-Up Resilient X-Ray Spectroscopy via Direct Sampling and Waveform Fitting in SDDs
Andrea Abba

15:00 **NSS-01-307**
High-resolution Germanium Detector system for Fluorescence-Mode X-ray Absorption Spectroscopy
Abdul K. Rumaiz

15:00 **NSS-01-309**
Visualization of beta-emitting nuclides in water using a CCD camera and CaF_2 scintillator
Yuki Morishita

15:00 **NSS-01-311**
Diagnosing Mechanisms for Charged Particle Attenuation Enhancement in Nanostructured Materials
Niko P. Speck

15:00 **NSS-01-313**
Monolithic integration of cooling microchannels in all-silicon ladders for vertex detectors
Javier Fernández-Tejero

15:00 **NSS-01-315**
A spin-selective detector for quantum sensing with neutrons
Thomas Neulinger

15:00 **NSS-01-317**
Higher-Order Gain-Drift Correction in Magnetic Microcalorimeters for Decay Energy Spectrometry
Ryan Wood

15:00 **NSS-01-319**
Pixelated Array for Low-Energy Electron Beam Mapping
Marcos Turqueti

15:00 **NSS-01-321**
Self-Powered Wireless Communication via Ambient Gamma-Ray Harvesting at Fukushima Daiichi
Takeshi Fujiwara

15:00 **NSS-01-323**
Optimizing Tritium Uptake and Detection Sensitivity in a Metal-Hydride Gas Detector
Tzu-Hsiang Lin

15:00 **NSS-01-325**
Basic Development of a Wide-Field EUV Polarimeter for High-Energy Transient Sources
Soken Kuwabara

15:00 **NSS-01-327**
Cryogenic and Underground Performance of the Diffuse BGO Scintillator Array in the KAPAE Phase II Detector
Dongwoo Jeong

15:00 **NSS-13-329**
Organic Scintillator Light Yield Models for Sub-MeV Neutrons in EJ301D and d-stilbene
Christian A. Irvine

17:30 – 19:00 FEDERICO GARCÍA LORCA

NSS-02 Neutron and gamma-ray detectors and applications, including security, dosimetry and other related applications

Chairs:
Abdallah LYOUSSI (Saint Paul-lez-Durance)
Malcolm J. Joyce (Lancaster)

17:30 **NSS-02-01**
Dead time and self-absorption corrections at high uranium grade for total count rate gamma probes
Bertrand Pérot

17:45 **NSS-02-02**
Identification and Reconstruction of Pair-Production Events in an Electron-Tracking Compton Camera via 3D Track Analysis
Taiyo Sato, Taiyo Sato

18:00 **NSS-02-03**
Design of a 2D neutron and gamma imager based on CPRE64
Chaoyang Zhao

18:15 **NSS-02-04**
Evaluation of a High-Efficiency Portable Compton-Imaging System for Radioactive Waste Characterization and Nuclear Decommissioning
Victor Babiano-Suárez

18:30 **NSS-02-05**
Development of a high-sensitivity portable gamma-ray imaging system for identifying radioactive material carriers
Goeun Lee

18:45 **NSS-02-06**
Development of a new gamma-ray spectrometer for measurements inside reservoirs
Yuki Morishita, Yuki Morishita

17:30 – 19:00 ALBÉNIZ & MACHUCA
NSS-03 NSS DAQ, front-end and electronics

Chairs:
Eric J. Mannel (Upton)

17:30 **NSS-03-01**
Dual Time-Over-Threshold Energy and PSD Readout of SiPMs Using FPGA-Based TDCs
Aaron Nowack

17:45 **NSS-03-02**
Development of Readout Electronics for a SiPM-Based Compton Camera
Alessio Brunamonti

18:00 **NSS-03-03**
High Count-Rate Modular Readout System for SiPM-Based Gamma-Ray Detectors
Martina Piroddi

18:15 **NSS-03-04**
High-Rate FPGA-Based Fully Digital SiPM Readout for Photon-Number-Resolving

Measurements in Quantum Optics and Quantum Communications
Stefano Carsi

18:30 **NSS-03-05**
Towards Multi-channel Direct Positron Emission Imaging using Cherenkov-Radiator-Integrated MCP-PMTs, FastIC+, and Time-to-Digital Converters in FPGA.
Julien Rossignol

18:45 **NSS-03-06**
TEMPOROC3 : A 64-channel SiPM read-out chip for time-of-flight measurement on monolithic crystal
Vsevolod Yeroshenko

17:30 – 19:00 PICASSO
NSS-04 Semiconductor detectors

Chairs:
Chiara Guazzoni (Milano)
Davide Mezza (Villigen)

17:30 **NSS-04-01**
Very-High-Energy Electron FLASH Radiotherapy at the PEER Beamline - Dosimetry and Biological Benchmarking
Dean Cutajar

17:45 **NSS-04-02**
New approach in 2D microdosimetry using Alpide pixelated detector
Dean Cutajar

18:00 **NSS-04-03**
AlphaBeast : A CMOS-based detector for real-time neutron production monitoring
Lucia Victoria Garcia Garcia

18:15 **NSS-04-04**
Comparative Performance Evaluation of pnCCD Sensor Variants with 36 µm Pixel Size
Šejla Hadžić, Šejla Hadžić

18:30 **NSS-04-05**
fine-pitch HPGe strip detectors for high-rate gamma-ray spectroscopy and imaging
Joanna M. Szornel

18:45 **NSS-04-06**
Repairing Proton Radiation Damage on n-type, Cross-Strip Germanium Detectors
Sophia E. Haight

10 November, 2026

9:00 – 11:00 FEDERICO GARCÍA LORCA
NSS-05 Neutron and gamma-ray detectors and applications, including security, dosimetry and other related applications

Chairs:
Anne-Sophie Lalleman (GIF SUR YVETTE)
Malcolm J. Joyce (Lancaster)

9:00 **NSS-05-01**
Time-of-Flight Neutron Imaging With a Segmented Organic Imager Cell
William Heriot, This work was supported in part by the Consortium for Monitoring, Technology, and Verification under Department of Energy National Nuclear Security Administration, award number DE-NA0003920.

9:15 **NSS-05-02**
Development of an omnidirectional neutron imager with fractal geometry
Nishiki Matsubayashi

9:30 **NSS-05-03**
Neutron Spectroscopy Using a Spatially Resolved He-3 Slab Detector
Madeline L. Lockhart

9:45 **NSS-05-04**
Residual Interpulse 14-MeV Neutron Emission in Active Interrogation with Neutron Generators
Valentin Fondement

10:00 **NSS-05-05**
Neutron Flux Monitor (NFM): A Micromegas-Based Beam Monitor for the European Spallation Source
Ioannis Katsioulas

10:15 **NSS-05-06**
Development of a Handheld Fast Neutron Spectrometer Using Deuterated Scintillators and Spectrum Unfolding
Ariel A. Alcaide, Ariel A. Alcaide

10:30 **NSS-05-07**
Innovative neutron counting for high-rate double-differential cross-section in fragmentation events.
Iram B. Rivas Ortiz

10:45 **NSS-05-08**
First 3D-PDC Experimental Measurements of Fast Neutrons and PSD Performance
Amanda Steinhebel, Amanda Steinhebel

9:00 – 11:00 ALBÉNIZ & MACHUCA
NSS-06 Detector modeling and simulation

Chairs:
Shaun D. Clarke (Ann Arbor)
Angela Di Fulvio (Urbana)

9:00 **NSS-06-01**
ARES: A Web-Based Platform for Registration, Access, and Analysis of Radiation Simulation Results
Sacha E.R. Medaer

9:15 **NSS-06-02**
Monte Carlo simulation of a new Optical Neutron Detector geometry for generation-IV Sodium-cooled Fast Reactors
Valentin Gerenton, Valentin Gerenton

9:30 **NSS-06-03**
A Validated GEANT4 Model of a Dual-HPGe γ–γ Coincidence Spectrometer for Detection Sensitivity Evaluation
Thomas C. Stokes

9:45 **NSS-06-04**
Monte Carlo Quantum Imaging with Annihilation Photons
Ana Marija Kožuljević

10:00 **NSS-06-05**
Bringing Synchrotron X-ray Minibeam Radiotherapy into Clinical Relevance: Monte Carlo Validation of Clinically Relevant Treatment Fields at the Australian Synchrotron
Dean Cutajar

10:15 **NSS-06-06**
SimpleMC: A Simple and Flexible Monte Carlo Simulation Tool for Timepix Detectors
Chia-Wei Huang

10:30 **NSS-06-07**
Photodetector model for the ClearMind project: Toward ultra-high time resolution
Zoé Zobundzija

10:45 **NSS-06-08**
3-D simulation of carrier transport and signal formation in silicon detectors for charged particle identification
Andrea Castoldi

9:00 – 11:00 PICASSO
NSS-07 Scintillators

Chairs:
Etiennette Auffray (Geneva)
Shunsuke Kurosawa (Nagoya)

9:00 **NSS-07-01**
Crucible-Free Growth of High Melting Temperature Scintillators by the OCCC Method
Kei Kamada

9:15 **NSS-07-02**
$Cs_3Cu_2I_5$ Single Crystals Grown with Oleic- and Formic-Acid-Assisted Additives: Effects on Crystal Quality and Scintillation Properties
Bhavika Bansal

9:30 **NSS-07-03**
Novel $Cs_3Cu_2I_5$:Tl Scintillator Films for X-ray Imaging
Lakshmi Soundara Pandian

9:45 **NSS-07-04**
Growth and Pellet Fabrication of 2D Perovskite Scintillator Radiation Detectors
Amy J. Dickinson

10:00 **NSS-07-05**
Enhanced Light Outputs in Cs_2ZnCl_4 Single Crystals via Hydrothermal Purification and Cd Doping
Mingxue Deng

10:15 **NSS-07-06**
Scintillation Properties of Ce^{3+}-, Pr^{3+}-, and Eu^{2+}-Doped LiCl, LiBr, and LiI Single Crystals
Jarek Glodo

10:30 **NSS-07-07**
Characterising ZnSe(Al,O) for Real-Time Sr-90 Beta Spectroscopy
Arjana Kolnikaj

10:45 **NSS-07-08**
Exploring wavelength-shifting properties of nanocrystal layers and nanocomposites
Vojtech Zabloudil

15:00 – 17:00 ALBÉNIZ & MACHUCA
NSS-08 Synchrotron, FEL and XFEL detectors

Chairs:
Beatrice Pedretti (Milano)
Matteo Porro (Schenefeld)

15:00 **NSS-08-01**
Production Results of DEPFET-Based Modules for the DSSC Imager at the European XFEL
Stefano Maffessanti

15:15 **NSS-08-02**
Performance of the pFREYA16 ASIC for pixelated detectors in continuous-wave x-ray applications
Paolo Lazzaroni

15:30 **NSS-08-03**
DIANA: An LGAD-Based Architecture for Soft X-Ray Detection
Francesca Capocasa

15:45 **NSS-08-04**
Matterhorn: Initial Characterization of Single-Chip Assemblies
Viveka Gautam, On behalf of the detector group whose members include M. Anastasi, M. Bruckner, S. Ebner, S. Emiliani, K. Ferjaoui, D. Greiffenberg, S. Hasanaj, V. Hinger, V. Kedych, T. King, S. Li, C. Lopez-Cuenca, L. Lunin, A. Mazzoleni, S. Moses, A. Mozzanica, J. Mulvey, M. Muller, C. Ruder, B. Schmitt, S. Silletta, D. Thattil, X. Xie and J. Zhan

16:00 **NSS-08-05**
ORBIS: an X-ray SDD Array with Optimized Backscattering Detection Geometry
Pietro Barcella

16:15 **NSS-08-06**
Experimental Characterization of a Front-End Stage for Future XFEL Detectors
Adele Ciavarella-Ciavarella

16:30 **NSS-08-07**
Mapping of the charge collection function of hexagonal DEPFET pixels with the mesh experiment
Andrea Mason, Andrea Mason

16:45 **NSS-08-08**
Gated MCP High Resolution Detectors for UV, Soft X-ray photons, Ions, Neutrons and Electrons
Anton Tremsin

17:30 – 19:00 ALBÉNIZ & MACHUCA
NSS-09 Neutron and gamma-ray detectors and applications, including security, dosimetry and other related applications

Chairs:
Andrea Sagatova (Bratislava)
Lei R. Cao (Columbus)

17:30 **NSS-09-01**
Development and Experimental Validation of a Numerical Model for Fission Particles Multiplicity Counting using Polyvinyl Toluene Scintillators
Filip d'Almeida

17:45 **NSS-09-02**
Recent Advances in Developing Fluoride Eutectic Scintillators for Neutron Detection
Cai L. Wang

18:00 **NSS-09-03**
3D Boron-Coated Straw Detector Array for Tomographic Multiplicity Counting
Ming Fang

18:15 **NSS-09-04**
An Imaging and Spectroscopy Detector for High-Energy and High-Rate Gamma-Ray Measurements
Korbinian Urban

18:30 **NSS-09-05**
Ratiometric Alpha-Particle and Gamma-Ray Imaging with a Ligand-Stabilized $CsPbBr_3$Perovskite-Nanoparticle Coating on a 4.8-Megapixel Stacked CMOS Sensor
Viktor Gruev

18:45 **NSS-09-06**
Evolution of ZnS:Ag/^{6}LiF wavelength shifting fibre detectors from flat to tilted geometry
Giacomo Mauri

11 November, 2026

9:00 – 10:30 ALBÉNIZ & MACHUCA
NSS-10 Analog and Digital Circuits I

Chairs:
Giuseppe Bertuccio (Como)
Matteo Porro (Schenefeld)

9:00 **NSS-10-01**
NSX1: A 64-Channel Low-Power Front-End ASIC for Broadband Energy Silicon Drift Detectors Arrays
Gianluigi De Geronimo

9:15 **NSS-10-02**
Towards a 150 kHz Continuous Imager: The CoRDIA 0.5 Prototype 20 k Pixel Array
Ulrich Trunk

9:30 **NSS-10-03**
LID: A 10-GS/s Self-Triggered Readout IC for Tightly Coupled Strip and Pixel LGAD Arrays
Luca Macchiarulo

9:45 **NSS-10-04**
SparkPix-S: A Sparsified Readout Detector for 1 MHz Frame-Rate X-Ray Imaging - Design Progress and Early Characterization Results
Christos Bakalis

10:00 **NSS-10-05**
Global-ramp single-slope ADC with pixel-level comparison and built-in compression for large pixel arrays
Lodovico Ratti

10:15 **NSS-10-06**
Characterization of the Ignite64 ASIC in CMOS 28-nm technology for high time-resolution tracking
Luca Pacher, on behalf of IGNITE-Collaboration

9:00 – 10:30 MACHADO
NSS-11 AI and ML for radiation detection

Chairs:
Marco Carminati (Milano)

9:00 **NSS-11-01**
ML-based radiological clearance of activated metallic waste at CERN using synthetic data
Andrea Gomes

9:15 **NSS-11-02**
Inverse reconstruction of ^{137}Cs depth-dependent contamination in concrete from gamma spectrometry measurements
Antoine Hayek

9:30 **NSS-11-03**
Joint autoencoder-classifier network for particle-type identification in organic scintillator pulse pileup
Annamaria R. McHugh

9:45 **NSS-11-04**
Joint Neutron Source Localization and Identification using Machine-Learning-based Spectral Imaging
David Breitenmoser

10:00 **NSS-11-05**
Machine-Learning-Based Real-Time Gamma-Ray Direction Estimation Using Fractal Radiation Imaging Element
Miyuki Sasaki

10:15 **NSS-11-06**
Evaluating isotope identification methods for use with count-starved gamma spectra
James Biggs

9:00 – 11:00 **PICASSO**
NSS-12 **Novel detectors and associated technologies**

Chairs:
Christian Scharf (Berlin)
Miguel Ullan (Barcelona)

9:00 **NSS-12-01**
PLATON: a plenoptic single-photon camera with sub-nanosecond time resolution for particle detection through monolithic scintillating volumes
Davide Sgalaberna

9:15 **NSS-12-02**
A Capacitively Coupled GaAs SAM-APD with Cross-Delay Lines for Fully Digital 3D Hard X-ray Photon Imaging
Nicola Lusardi

9:30 **NSS-12-03**
Characterization of 4H-SiC implanted LGADs after 23 MeV Proton Irradiation
Arianna Morozzi

9:45 **NSS-12-04**
Status of GRAiNITA, a next generation calorimeter
Hervé Chanal

10:00 **NSS-12-05**
Small Dose Monitor based on Silicon Carbide diodes for FLASH radiotherapy
Celeste Fleta

10:15 **NSS-12-06**
Thin-Film and Single-Crystal Perovskite Detectors for Real-Time FLASH Radiotherapy
Mara Bruzzi

10:30 **NSS-12-07**
Particle-by-Particle Characterization of Clinical Carbon Ion Beams with a Silicon Strip Detector and High-Rate DAQ Systems
Felix Mas Milian

10:45 **NSS-12-08**
Diamond Quantum Sensor for High Fluence Neutron Detection
Raymond Cao

10:30 – 11:00 ALBÉNIZ & MACHUCA
N-LT-03 NSS Lightning Talks 3

Chairs:
Rejean Fontaine (Sherbrooke)

10:30 **N-LT-03-01**
Radiation-Hardened VCO in 28 nm FDSOI with Enhanced Frequency Stability Under Total Ionizing Dose
Muhammad Adeel Anwar, Muhammad Adeel Anwar

10:32 **N-LT-03-02**
Preamplifier Readout Electronics for Summing SiPMs Enhanced Circuit (PRESSEC) for Advanced SiPM Camera
Daniel David Marín

10:36 **N-LT-03-03**
Characterization of MAGIC: a SiPM Readout ASIC for Monolithic PET Detectors
Tommaso D'Incà, Tommaso D'Incà

10:38 **N-LT-03-04**
Photon Counting with FPGA Gigabit Transceivers: A Proof-of-Concept SiPM Readout for

TOF-PET
Marcos Turqueti

10:40 **N-LT-03-05**
Design and Implementation of an FPGA-Based Nuclear-Like Signal Generator
Yao Yang, Yao Yang

10:42 **N-LT-03-06**
High-performance preamplifier for spectroscopy systems based on High-Purity Germanium detectors
Fernando Ojeda, Fernando Ojeda

10:44 **N-LT-03-07**
Preliminary Test Results on Latest Version of FESA Readout ASIC for TOF-PET Detectors
Yuhao Yang

10:46 **N-LT-03-08**
Single-Shot Precision Decomposition of a 64-Channel FPGA TDC for TOF-PET
Giancarlo Sportelli

10:48 **N-LT-03-09**
SEU Evaluation of an Atom Switch-based FPGA for Slow-Control Systems
Kazuki Ueno

10:50 **N-LT-03-10**
MAPSSIC: Toward a Wireless Implantable Positron Probe for Molecular Neuroimaging of Awake and Freely Moving Rats
Mathieu Dupont

10:52 **N-LT-03-11**
Realistic Detector Response Model for COMET Phase-I Cylindrical Drift Chamber
Siyuan Sun

10:54 **N-LT-03-12**
Measurement and correction of high intensity effects on the pixel response of the DSSC DEPFET camera
Maurizio Ghisetti

10:56 **N-LT-03-13**
Towards a 64-Channel Monolithic SDD X-Ray Spectrometer for High-Throughput Synchrotron Applications
Beatrice Pedretti

10:58 **N-LT-03-14**
Education kit for radiation measurements
Masaharu Nomachi

10:30 – 11:00 MACHADO
N-LT-04 NSS Lightning Talks 4

Chairs:
Martin Grossmann (Villigen)
Trang Hoang (Ho Chi Minh)

10:30 **N-LT-04-01**
Recoil electron tracking in 3D CZT drift strip detectors: a feasibility study
Michał Kossakowski

10:32 **N-LT-04-02**
CVAE-Based Synthetic Thermoluminescence Silica Glass Jewellery Bead Glow Curve Generation
Lukasz Tomaszewski

10:34 **N-LT-04-03**
Characterizing Neutron Detection Efficiency in Timepix3: A Bayesian-Optimized FLUKA Approach
Sharmistha Mukhopadhyay

10:36 **N-LT-04-04**
Enhanced Spent Nuclear Fuel Characterization Using Sequential Detector Responses through Deep Learning
Beomkyu Kwon

10:38 **N-LT-04-05**
Robust Dual-Target Radioisotope Quantification Under Increasing Unseen Contaminant Complexity
Yeongjun Kim

10:40 **N-LT-04-06**
Automated Monte Carlo-Based Efficiency Transfer Integrated into HPGe Gamma Spectroscopy Workflows for High-Throughput Laboratories
Spencer Behling

10:42 **N-LT-04-07**
Neutron and secondary photon dose mapping of deuterium-deuterium (D-D) and deuterium-tritium (D-T) neutron generators via PHITS simulations
Andrea G. Alipio

10:44 **N-LT-04-08**
Bayesian Filtering Image Reconstruction for SourceLocalization and Tracking in Compton Imaging
John Leland

10:46 **N-LT-04-09**
Count-Level Effects on Radiomics Robustness and Harmonization in Total-Body PET Imaging
Mohamed Saber Azimi

10:48 **N-LT-04-10**
Development of a Single-Layer Dual-Ended Readout Compton Camera Prototype for Enhanced Spatial Imaging
Haoqi Wen

10:50 **N-LT-04-11**
Crystal Dual-Readout Calorimetry for Future e^+e^- Higgs Factories
Marcello Campajola

10:52 **N-LT-04-12**
Design of the ePIC Hadronic Barrel Calorimeter, Status of the Test stand and Prospects for Physics at the EIC.
Eric J. Mannel

10:54 **N-LT-04-13**
Off-detector Readout and Real-time Signal Processing for the ATLAS Liquid ArgonCalorimeter at the High-Luminosity LHC
Pablo Collado Soto, On behalf of the ATLAS Collaboration

10:56 **N-LT-04-14**
The LS3 Enhancement of the LHCb Electromagnetic Calorimeter
Eduardo Picatoste, on behalf of the LHCb ECAL Upgrade II RD Group

11:30 – 13:00 Poster Area
NSS-13 NSS Poster Session

Chairs:
Andrea Gonzalez Montoro (Valencia)

11:30 **NSS-13-002**
Gas Circulation and Pressure Protection System for the COMET Cylindrical Drift Chamber
Ryo Nagai

11:30 **NSS-13-004**
Performance of a 2D-THCOBRA Gaseous Detector with Ar/Xe Mixtures for X-Ray Imaging
Ana Luísa M. Silva

11:30 **NSS-13-006**
The effect of hole geometry on the ion-backflow of a single gas electron multiplier foil
Hussam Badran

11:30 **NSS-13-008**
Feasibility of a Compact Detector for LINAC Radioactivation Monitoring
Jeongho Kim

11:30 **NSS-13-010**
Temperature Dependence of Energy Resolution in a SiPM-Based Scintillation Detector for PET Applications
Solano Rigotti Caiano

11:30 **NSS-13-012**
Development of transparent ceramic Tl:NaI scintillators for gamma-ray detectors
Takayuki Yanagida

11:30 **NSS-13-014**
Simulation of Electron Escape within Thin Organic Scintillators
Ethan Schneider

11:30 **NSS-13-016**
Alignments of the Dual-Layer Flat-Panel Detectors and their Modulation Transfer Functions
Dong Sik Kim

11:30 **NSS-13-018**
Loading Surface-Modified $LiAlO_2$ Nanoparticles in Plastic Scintillators for Thermal Neutron Detection
Masanori Koshimizu

11:30 **NSS-13-020**
Development of Perovskite Quantum Dots with High Photoluminescence Quantum Yields and Their Loading in Plastic Scintillators
Masanori Koshimizu

11:30 **NSS-13-022**
Effect of geometry on the properties of 3D-printed scintillators
Anil K. Gourishetty

11:30 **NSS-13-024**
Development of a Gamma Camera for Real-Time Monitoring of High-Energy Gamma-Ray Environments
Youngjoo Park

11:30 **NSS-13-026**
Study on the Influence of Grain Size for the GAGG powder-PMMA composite scintillator Detector
Yantao Liu

11:30 **NSS-13-028**
Thermal Neutron Detection with Dy-doped LiF/CaF_2 Eutectic Composite
Noriaki Kawaguchi

11:30 **NSS-13-030**
Development of Afterglow and NIR Decay Curve Measurement Systems using a Field Emission-type Pulsed X-ray Source
Hiromi Kimura

11:30 **NSS-13-032**
One Dimensional TPE-4Br Supramolecular Scintillator for High-Speed X-ray Imaging
Xiaoqing Liu

11:30 **NSS-13-034**
Development of a Large-Area Diode-Multiplexed Scintillation Detector for Prompt Gamma Monitoring in Proton Therapy
Xiaodong Mo

11:30 **NSS-13-036**
Development of a Hand-Foot Monitor for Visualizing Alpha Contamination
Naoki Sagawa

11:30 **NSS-13-038**
Room-Temperature Synthesis of Na^+-Doped $Cs_3Cu_2I_5$ Single Crystals: Structural, Optical and Scintillation Properties
Anil K. Gourishetty

11:30 **NSS-13-040**
Thermal Cycling of Optical Coupling Material to Investigate Performance Degradation in Detectors
Zoe H. Sharpe

11:30 **NSS-13-042**

11:30 **NSS-13-044**
Performance of Improved CsI:Tl Coupled SiPM Detectors for Imaging Applications
Rastgo Hawrami, Rastgo Hawrami

11:30 **NSS-13-046**
Optical Control of Valence State in LuAG:Ce,Ca
Colleen Campbell

11:30 **NSS-13-048**
Study of elpasolite crystals for neutron/gamma spectroscopy : First measurements with CLYC:Ce
Isaac Zeghni

11:30 **NSS-13-050**
A feasibility study on CsPbBr3 perovskite crystals for time-of-flight PET
Chien-Min Kao

11:30 **NSS-13-052**
From Collision Cascades to Device Response: A Multiscale Study of Proton-Induced Defects in Silicon
Sarah Shoorian

11:30 **NSS-13-054**
DREAM : A miniaturized spectrometer for protons and electrons measurement in space
Arnaud Dufour

11:30 **NSS-13-056**
Bulk Stoichiometry and van der Waals Interface Engineering of CdTe for Room-Temperature X/γ-Ray Detectors
Qinghua Zhao

11:30 **NSS-13-058**
Alpha Particle Detection with sCMOS imager
Makoto Sasano

11:30 **NSS-13-060**
Development of Silicon Drift Detector Technology from Single-Element Devices to a 19-Pixel Module for X-ray Spectroscopy Applications
Ziyu Bao

11:30 **NSS-13-062**
Oxygen-Ion-Assisted Amorphous PbO Layers for Direct-Conversion X-ray Detectors
Galina Nagicheva

11:30 **NSS-13-064**
Custom Geometries for Broader Applications of the GAPS Si(Li) Detectors
Kelsey Yee

11:30 **NSS-13-066**
Neutron Measurements of ^{252}Cf in High-Gamma-Ray Environments Using Silicon Carbide (SiC) Semiconductor Detector
Kanta Nagai

11:30 **NSS-13-068**
Development of amorphous germanium blocking contact multi-electrode coaxial HPGe detectors for highcount-rate applications
Siyuan Yu

11:30 **NSS-13-070**
A Novel Compton-Polarimeter in Telescope Configuration for X-Ray Energies up to 1 MeV
Tobias Over-Winter

11:30 **NSS-13-072**
Benefits from the latest Clover and Custom Desgined HPGe Detector Technologies
Gabriela Ilie

11:30 **NSS-13-074**
An automated testing and characterization system for SiPM device arrays
Ciro Boiano

11:30 **NSS-13-076**
Construction and Testing of An In-Situ Magnetron Sputtering Plasma Monitoring Setup
Burak Bilki

11:30 **NSS-13-078**
Utilisation of the ISIS Digital Data Pipeline for Afterpulsing Analysis of PMT & SiPM Signals
Daniel E. Pooley

11:30 **NSS-13-080**
Dark Count Rate of LHCb Scintillating Fibre Tracker SiPMs as an In-Situ Radiation Monitor
Sacha E.R. Medaer

11:30 **NSS-13-082**
Radiation-Hardened CMOS-SPAD Design for Stable Geiger-Mode Operation
Doo-Hee Son

11:30 **NSS-13-084**
ClearMind: fast photo-detection for TOF-PET
Viatcheslav Sharyy

11:30 **NSS-13-086**
Characterization of High-Speed Photomultiplier Tubes with $LaBr_3$(Ce) scintillators
Miriam Caballero Rodríguez

11:30 **NSS-13-088**
TID irradiations of a Shunt-LDO designed in a 110 nm CMOS process for EPIC-SVT
Matthew Buckland

11:30 **NSS-13-090**
Characterization of Single-Event Upsets in a 90 nm Commercial Off-the-shelf SRAM caused by Low-Energy Protons
Shintaro Ishihara

11:30 **NSS-13-092**
Design and Implementation of an FPGA-Based Nuclear-Like Signal Generator
Yao Yang, Yao Yang

11:30 **NSS-13-094**
Radiation-Hardened VCO in 28 nm FDSOI with Enhanced Frequency Stability Under Total Ionizing Dose
Muhammad Adeel Anwar, Muhammad Adeel Anwar

11:30 **NSS-13-096**
A Radiation-Hardened R-2R Digital-to-Analog Converter with Branch-Local Diode-Replica Dummy Biasing
Duckhyun Kim

11:30 **NSS-13-098**
Preamplifier Readout Electronics for Summing SiPMs Enhanced Circuit (PRESSEC) for Advanced SiPM Camera
Daniel David Marín

11:30 **NSS-13-100**
Feasibility studies on readout topologies for a MHz-framerate continuous wave-mode X-

ray detector in 45nm SOI CMOS technology
Pradeep Kalavakuru

11:30 **NSS-13-102**
Characterization of MAGIC: a SiPM Readout ASIC for Monolithic PET Detectors
Tommaso D'Incà, Tommaso D'Incà

11:30 **NSS-13-104**
A Modular Warm Time-Division MultiplexedReadout Platform for SQUID Applications
Benjamin A. Reese

11:30 **NSS-13-106**
A Scalable Test Vehicle ASIC in 28-nm CMOS for Cryogenic Device Characterization
Panagiotis Zarkos

11:30 **NSS-13-108**
Intermediate-Dose Close-In Phase-Noise Instability in a 55-nm CMOS PLL Irradiated to 100 Mrad(Si)
Peng Zheng

11:30 **NSS-13-110**
A Low-Noise Multi-Channel Readout ASIC for High-Purity Germanium Detectors
Li He

11:30 **NSS-13-112**
A precision bandgap reference with improved noise performance for spectroscopy ASICs in 180 nm CMOS technology
Yinhe Zhu

11:30 **NSS-01-116**
Photon Counting with FPGA Gigabit Transceivers: A Proof-of-Concept SiPM Readout for TOF-PET
Marcos Turqueti

11:30 **NSS-13-118**
A 640 MHz Phase Locked Loop for High Energy Physics Environment in 28nm CMOS Bulk
Fabio D'Ottavi

11:30 **NSS-13-120**
Machine-Protection System for the PIP-II Linear Accelerator: Architecture and Data Processing Schemes
Jinyuan Wu

11:30 **NSS-13-122**
Comparison of discrete non-gated charge-to-time converters for SPECT application
Pauline Lafoux

11:30 **NSS-13-124**
150 Gbps data transfer Bay simulating Agata detector Readout
Nabil Karkour

11:30 **NSS-13-126**
Performance Testing and Characterization of CPRE12-64CZT: A Low-Noise 64-Channel Readout ASIC for 3-D Position-Sensitive CdZnTe Detectors
Long Wei

11:30 **NSS-13-128**
Fast timing performance of a front-end ASIC designed for high purity germanium strip detectors
Clio Sleator

11:30 **NSS-13-130**
A Fully FPGA-Based 3D (x–y–t) Imager with 24 µm Spatial Resolution for Cross Delay-Line Detectors
Nicola Lusardi

11:30 **NSS-13-132**
High-performance preamplifier for spectroscopy systems based on High-Purity Germanium detectors
Fernando Ojeda, Fernando Ojeda

11:30 **NSS-13-134**
MAPSSIC: Toward a Wireless Implantable Positron Probe for Molecular Neuroimaging of Awake and Freely Moving Rats
Mathieu Dupont

11:30 **NSS-13-136**
Single-Shot Precision Decomposition of a 64-Channel FPGA TDC for TOF-PET
Giancarlo Sportelli

11:30 **NSS-13-138**
Education kit for radiation measurements
Masaharu Nomachi

11:30 **NSS-13-140**
Preliminary Test Results on Latest Version of FESA Readout ASIC for TOF-PET Detectors
Yuhao Yang

11:30 **NSS-13-142**
SEU Evaluation of an Atom Switch-based FPGA for Slow-Control Systems
Kazuki Ueno

11:30 **NSS-13-144**
Validation and Integration of the COMET Phase-I Trigger System
Chihiro Yamada

11:30 **NSS-13-146**
Evaluation of a Charge Sharing Compensation with Synchrotron Radiation
Piotr G. Maj

11:30 **NSS-13-148**
A High-Precision and Wide-Dynamic Range Energy Acquisition Method based on MVT with Pulse-Shape for Elemental Logging
Huan Liu

11:30 **NSS-13-150**
Realistic Detector Response Model for COMET Phase-I Cylindrical Drift Chamber
Siyuan Sun

11:30 **NSS-13-152**
Improving UAV-Based Radiation Monitoring in Mountainous Forests Using ANN with Spectral Information
Kazuhiro Suzuki

11:30 **NSS-13-154**
Figure-Grounded Multimodal Retrieval-Augmented Generation for Radiation Equipment Manual Question-Answering
Minjong Kim

11:30 **NSS-13-156**
Physics Enhanced Machine Learning for Thermoluminescence Glow Curve Deconvolution
Lukasz Tomaszewski

11:30 **NSS-13-158**
A High-Fidelity Robotics Simulation Framework for Autonomous Radiation Source

Search
Lance M. Drouet

11:30 **NSS-13-160**
Robust Dual-Target Radioisotope Quantification Under Increasing Unseen Contaminant Complexity
Yeongjun Kim

11:30 **NSS-13-162**
Recoil electron tracking in 3D CZT drift strip detectors: a feasibility study
Michał Kossakowski

11:30 **NSS-13-164**
Enhanced Spent Nuclear Fuel Characterization Using Sequential Detector Responses through Deep Learning
Beomkyu Kwon

11:30 **NSS-13-166**
Development of a PINN-Based Defect Verification Algorithm for CANDU Spent Nuclear Fuel Bundles
Juwan Kang

11:30 **NSS-13-168**
Towards Spiking Neural Network-Inspired In-Pixel Processing for Radiation Detectors
Anna Kozioł

11:30 **NSS-13-170**
CVAE-Based Synthetic Thermoluminescence Silica Glass Jewellery Bead Glow Curve Generation
Lukasz Tomaszewski

11:30 **NSS-13-172**
Gamma-Ray Image Denoising and Source Enhancement Based on a Residual Convolutional Autoencoder
Jonghyun Park

11:30 **NSS-13-174**
Neural-Network Surrogate Modeling of TID-Induced Degradation in 180 nm Bulk NMOS Transistors
Minuk Seung

11:30 **NSS-13-176**
Deep Learning Positioning and Depth of Interaction Prediction with Automatic Gain

Mismatch Correction
Matthew Dilsizian

11:30 **NSS-13-178**
Deep learning for precise gamma-ray interaction in an hexagonal monolithic scintillation crystals for PET imaging
Lidia Jiménez Algarra

11:30 **NSS-13-180**
Characterizing Neutron Detection Efficiency in Timepix3: A Bayesian-Optimized FLUKA Approach
Sharmistha Mukhopadhyay

11:30 **NSS-13-182**
Background pattern recognition and its reconstruction during radiation shadowing by scanned vehicles in Radiation Portal Monitors.
Vladislav Kondrashov

11:30 **NSS-13-184**
Effect of Source Intensity Imbalance on Two-Point Angular Resolution in Coded-Aperture Imaging
Yuhang Qiu

11:30 **NSS-13-186**
X-Ray Measurement of Tubes Using Closed-Loop Residual-Driven Optimization Algorithm
Yuchang Sun

11:30 **NSS-13-188**
Verification of a Rapid Dose Assessment Program Against MCNP for Nuclear Power Plant Decommissioning
Changyeon Yoon

11:30 **NSS-13-190**
High-Reliability Tritium Monitoring Using Hardware Alpha Suppression and AI-Based Smoothing Filter
Sungho Lee

11:30 **NSS-13-192**
Automated Monte Carlo-Based Efficiency Transfer Integrated into HPGe Gamma Spectroscopy Workflows for High-Throughput Laboratories
Spencer Behling

11:30 **NSS-13-194**
Graph-Based Modeling of Organ and Lesion Radiomics Interactions in Theranostic SPECT/CT Imaging
Mohamed Saber Azimi

11:30 **NSS-13-196**
Quantitative Neutron Emission Tomography of Plutonium-Bearing Materials using a Boron-Coated Straw Detector Array
David Breitenmoser

11:30 **NSS-13-198**
Caesium 137 Radiation Transport Profile Modelling for Application to Physical and Simulation Environments
Emmanuel Leo

11:30 **NSS-13-200**
Bayesian Filtering Image Reconstruction for SourceLocalization and Tracking in Compton Imaging
John Leland

11:30 **NSS-13-202**
An Iterative Based Gain Calibration Method for Multi-Channel Readout Scintillation Detectors
Zijun Yan

11:30 **NSS-13-204**
A Python-based Tool for Automated Geant4 Simulations of Scintillation Detectors
Ayush Priyadarshi

11:30 **NSS-13-206**
Development and deployment of a compact beta/gamma spectrometry chain for autonomous ground vehicles in nuclear decommissioning
Pierre-Louis Antonsanti

11:30 **NSS-13-208**
Neutron and secondary photon dose mapping of deuterium-deuterium (D-D) and deuterium-tritium (D-T) neutron generators via PHITS simulations
Andrea G. Alipio

11:30 **NSS-13-210**
Count-Level Effects on Radiomics Robustness and Harmonization in Total-Body PET Imaging
Mohamed Saber Azimi

11:30 **NSS-13-212**
A Geant4 add-on package to emulate surface electron response in Monte-Carlo simulation
Georgios Konstantinou

11:30 **NSS-13-214**
Multi-energy Radiography Using a Three-energy Accelerator and Dual-layer Detectors
Zhusong Mei

11:30 **NSS-13-216**
Portable African Neutron-Gamma Laboratory for Innovative Nuclear Science
Pete Jones

11:30 **NSS-13-218**
Feasibility Study on Ghost Imaging-based Neutron Depth Profiling for 3D Lithium Distribution Mapping
Junhyeok Kim

11:30 **NSS-13-220**
Feasibility Study of Thermal-Neutron Localization Using a GAGG-Based Directional Probe
Yuhang Qiu

11:30 **NSS-13-222**
Empirical Test of Gamma Emission Tomography for Detecting Partial-defect within PWR-type Spent Nuclear Fuel
Hyung Joo Choi

11:30 **NSS-13-224**
Enrichment-Dependent Neutron Interrogation Spectrum Optimization for Delayed Neutron Temporal Measurement
Caryanne R. Wilson

11:30 **NSS-13-226**
Improving contraband thermal neutron capture gamma detection in low and medium-Z cargo with pulsed D-T active neutron interrogation
Ketaki Joshi

11:30 **NSS-13-228**
Detection of Water in Spent Nuclear Fuel by Prompt Gamma Activation Analysis
Brendan Green

11:30 **NSS-13-230**
Development of a Portable Alpha–Beta Detection Device for Decommissioning Sites
Yuki Morishita

11:30 **NSS-13-232**
Proof-of-Concept Pulsed Neutron Detection Using a Timestamping SOI Pixel Detector SOFIST3
Ayaki Takeda

11:30 **NSS-13-234**
Experimental and Simulation Studies of FFCC Measurements Using a D-D Neutron Generator
Makoto Maeda

11:30 **NSS-13-236**
Compact and modular ^{6}LiF:ZnS(Ag) neutron detectors
Felix Liang

11:30 **NSS-13-238**
Characterization of a Leak-Tight Radon Chamber for Exhalation Rate Measurements of NORM Products
Jin-Goo Kang

11:30 **NSS-13-240**
Compton Scattering Imaging for On-site Nondestructive Testing of Cultural Heritage
Xin Li

11:30 **NSS-13-242**
In Situ 300-m Depth Underwater Environmental Radiation Monitoring System with Cesium Preconcentration
Min Sun Lee

11:30 **NSS-13-244**
Vehicle Based Detection System for Gamma-Neutron Background Measurements
Luke G. Morris

11:30 **NSS-13-246**
Performance Evaluation of a Portable MMXRF for Safeguards Environmental Sample Analysis under Transport-induced Alignment Changes
Sung-Woo Kwak

11:30 **NSS-13-248**
Measurement of 3-dimentional Distribution of ^{60}Co in a Graphite Block by Three Pinhole

Gamma Cameras
Jun Kawarabayashi

11:30 **NSS-13-250**
Verification of the Outer Space Treaty with trapped Protons in the VanAllen Radiation belt
Areg Danagoulian

11:30 **NSS-13-252**
Optimization of Detector Configuration for Enhanced Neutron Imaging Reconstruction Accuracy in Tokamak Fusion Reactor
Gyeongjin Choi

11:30 **NSS-13-254**

11:30 **NSS-13-256**
Characterization of Floating Gate Dosimeter Structures through a Standardized FPGA-Based Radiation-Test Platform
Evgenia Leonida

11:30 **NSS-13-258**
Physics-Informed Response Matrix Optimization for Neutron Flux Unfolding
Kilyoung Ko

11:30 **NSS-13-260**
Comprehensive Modeling and Experimental Validation of a SiPM-Based Neutron–Gamma Pulse Shape Discrimination System
Orith Halfon

11:30 **NSS-13-262**
Blade Checker – Radioisotope-free Positron Generator coupled with HPGe-based Doppler Broadening Spectroscopy for aircraft components maintenance operation
Damian Ralet

11:30 **NSS-13-264**
Optimization of the neutron source size for compensated neutron well logging
Yu Xiang Liu

11:30 **NSS-13-266**
Three-Dimensional Radiation Source Reconstruction with a Compound-Eye Compton Camera Using a NeRF-Inspired Neural Field
Yongshun Xiao

11:30 **NSS-13-268**
Advancing Beam Diagnostics on ESS Neutron Beamlines: Simulation and Validation of Ionization Chamber Monitors
Evangelos Samouilidis

11:30 **NSS-13-270**
Indoor 3D Gamma Radiation Mapping Based on VSLAM and Its Application in NPPs
Hui Li

11:30 **NSS-13-272**
Photofission Prompt Neutron Measurements from Active Photon Interrogation of Depleted Uranium with a Superheated Droplet Detector
Johann Piekar

11:30 **NSS-13-274**
Characterization and Comparison of State-of-the-Art Handheld Gamma-Imaging Field Spectrometers
Ariel A. Alcaide

11:30 **NSS-13-276**

11:30 **NSS-13-278**
Prototyping ALPIDE-based Modules for the R^3B Target Recoil Tracker Detector
Matthew Buckland

11:30 **NSS-13-280**
Development of a Single-Layer Dual-Ended Readout Compton Camera Prototype for Enhanced Spatial Imaging
Haoqi Wen

11:30 **NSS-13-282**
A GRID CubeSat Phoswich Payload for Space-Based Neutron Lifetime Measurement
Qidong Wang, On behalf of GRID Collaboration

11:30 **NSS-13-284**
Crosstalk and Charge collection in the ATLASPix3.1
Sean Williams

11:30 **NSS-13-286**
Radiation-Tolerant Fast Analogue Pixel Test Structures in TPSCo 65 nm CMOS Technology for the ALICE ITS3 Upgrade
Umberto Savino

11:30 **NSS-13-288**
Off-detector Readout and Real-time Signal Processing for the ATLAS Liquid ArgonCalorimeter at the High-Luminosity LHC
Pablo Collado Soto, On behalf of the ATLAS Collaboration

11:30 **NSS-13-290**
Crystal Dual-Readout Calorimetry for Future e^+e^- Higgs Factories
Marcello Campajola

11:30 **NSS-13-292**
The LS3 Enhancement of the LHCb Electromagnetic Calorimeter
Eduardo Picatoste, on behalf of the LHCb ECAL Upgrade II RD Group

11:30 **NSS-13-294**
Design of the ePIC Hadronic Barrel Calorimeter, Status of the Test stand and Prospects for Physics at the EIC.
Eric J. Mannel

11:30 **NSS-13-296**

11:30 **NSS-13-298**
Operations and performance of a FD-MAPS Telescope based on the ARCADIA sensors
Piero Giubilato

11:30 **NSS-13-300**
Measurement and correction of high intensity effects on the pixel response of the DSSC DEPFET camera
Maurizio Ghisetti

11:30 **NSS-13-302**
XSTREAM Pathfinder: A Modular R&D Framework for Next-Generation High-Throughput X-ray Detectors at the European XFEL
Matteo Porro

11:30 **NSS-13-304**
Redesign of the DSSC IOB for Near- and Long-Term High-Rate Operation
Gabriele Fiumicelli

11:30 **NSS-13-306**
Towards a 64-Channel Monolithic SDD X-Ray Spectrometer for High-Throughput Synchrotron Applications
Beatrice Pedretti

11:30 **NSS-13-308**
Novel Alpha Spectrometer for Aqueous and Molten Salt Systems
Owen A. Johnson

11:30 **NSS-13-310**
The Beta Rhizotron: a Radioisotope Imaging System for Plant Biology Research
Andrew Weisenberger

11:30 **NSS-13-312**
True Random Number Generation for Post-Quantum Applications
Edward Cazalas

11:30 **NSS-13-314**

11:30 **NSS-13-316**
Optimization of working point for TES microcalorimetric gamma spectroscopy
Nolan I. Kowitt

11:30 **NSS-13-318**
Radiation Damage to Quantum Dots
Edward Cazalas

11:30 **NSS-13-320**
Simulation-based evaluation of a position-sensitive TES microcalorimeter for gamma-ray detection
Nao Hata

11:30 **NSS-13-322**
Architecture and Qualification of the GlowRIA radiation monitor: An Optical fibre based dosimeter compatible with Cubesat missions
Nourdine Kerboub

11:30 **NSS-13-324**
Scintillation imaging with Coded Aperture masks
Valentina Cicero

11:30 **NSS-13-326**
Application of a Compact Electrically Cooled HPGe Detector to Quality Control in Radiopharmaceutical Isotope Production
Gabriela Ilie

15:00 – 17:00 ALBÉNIZ & MACHUCA
NSS-14 Analog and digital circuits II

Chairs:
Gianluigi De Geronimo (Syosset)
Serge A. Charlebois

15:15 **NSS-14-01**
Graphene-Based Front-End Amplifier for Nuclear Instrumentation
Marcos Turqueti

15:00 **NSS-14-02**
ToRA : a 64-channel ASIC for the readout of gaseous detectors in a CMOS 65 nm technology
Giovanni Mazza

15:15 **NSS-14-03**
CHASER: A Charge Sensitive Amplifier and Sampling Circuit for CZT Detectors
Leonardo Bernardini

15:30 **NSS-14-04**
Design and Experimental Characterization of a 65 nm CMOS Readout Channel for the Si(Li) Tracker Upgrade of the GAPS Experiment
Luca Ghislotti

15:45 **NSS-14-05**
Measurements of HPSoCv3 - an integrated 9-channel 10 Gsps Waveform Digitizer for high density LGAD array
Luca Macchiarulo

16:00 **NSS-14-06**
Cryogenic MOSFET Modeling Applied to CSA Design for Germanium Detector Readout
Joel Georgeous

16:30 **NSS-14-07**
A Fully Charge-Pump-Based Powering Scheme for SDDs in 180 nm SOI Technology
Tobias Michel, Tobias Michel

16:45 **NSS-14-08**
Development and testing of the ASIX region: a low-noise 128-pixel building block with event-driven readout and on-chip A/D conversion
Massimo Minuti

15:00 – 17:00 MACHADO
NSS-15 Computational methods and data analysis

Chairs:
Martin Grossmann (Villigen)
Chulhee Min (Wonju)

15:00 **NSS-15-01**
Improving the Estimation Accuracy of the Inverse Estimation of the Radioactive Source Distribution at the Fukushima Daiichi Nuclear Power Station Using L2 Normalization
Dai Tateishi, Dai Tateishi

15:15 **NSS-15-02**
Template-Based Decomposition of Gamma Spectra for NORM Quantification
Fabio Davolio

15:30 **NSS-15-03**
Enhancing Low-Energy MVT Bi-exponential Convergence via Adaptive Initial Value Estimation
Guanning Su, Guanning Su

15:45 **NSS-15-04**
Dual-Modality Muon Imaging via Trigger Optimization and Image Fusion
Zhi Zhou

16:00 **NSS-15-05**
Effects of Inverse Compton Scattering Source Parameters on Output X-Ray Spectra for Medical Applications.
Henry Priestley

16:15 **NSS-15-06**
Latent-Space Modeling for Multi-Organ Radiomics Phenotyping in ^{177}Lu-Based SPECT/CT Imaging
Mohamed Saber Azimi, Mohamed Saber Azimi

15:00 – 17:00 PICASSO
NSS-16 Scintillators

Chairs:
Jarek Glodo

15:00 **NSS-16-01**
Asymmetry in time difference histograms for scintillators with different decay constants in coincidence
Akram Hamato

15:15 **NSS-16-02**
Ultrafast and Efficient 2D Perovskite Scintillators for Sub-50 ps TOF-PET and High-Resolution X-ray Imaging
Jiaqi Liu

15:30 **NSS-16-03**
Thick Optical-guiding Scintillator with Enhanced Crystal Quality for High-Resolution and High-Sensitivity X-ray Imaging
Yuhei Nakata

15:45 **NSS-16-04**
Development of 3D-Printable Plastic Scintillator Using Stereolithography for Radiation Detection Applications
Kunlanan Puprasit

16:00 **NSS-16-05**
Energy Spectroscopy Using Tin-Loaded Organic Glass Scintillators of Varying Sizes
Erin Neely

16:15 **NSS-16-06**
Position-Sensitive and Energy-Constrained Characterization of an Opaque Scintillation Detector
Sander Katz, On Behalf of the LiquidO Consortium

16:30 **NSS-16-07**
Large Scale Lu_2O_3:Yb Ceramics for High-Rate Calorimetry
Lakshmi Soundara Pandian

16:45 **NSS-16-08**
Calibration of the Light Detection System of the XEMIS2 Liquid Xenon Compton Camera
Yohann Ramsi

17:30 – 19:00 ALBÉNIZ & MACHUCA
NSS-17 DAQ, front-end and electronics

Chairs:
Eric J. Mannel (Upton)

17:30 **NSS-17-01**
A Configurable Dual-CDL Sigma-Delta Readout Circuit for Dual-Polarity and High-Precision Signal Detection in CsI: Tl SPECT
Xi Zhang

17:45 **NSS-17-02**
Design and Preliminary Characterization of a Waveform-Sampling ASIC-Based Readout System for the MASS-Cube CZT Detector
Chen Li

18:00 **NSS-17-03**
MALTA2 Sensor Characterization with a New Asynchronous Oversampling Readout
Fuat Kerem Işık

18:15 **NSS-17-04**
A fully-programmable mixed-signal RISC-V SoC for direct readout of radiation sensors
Valerio Pagliarino

18:30 **NSS-17-05**
The MIZAR ASIC: from mixed-signal design to the PBR mission
Andrea Di Salvo, On behalf of the JEM-EUSO Collaboration

18:45 **NSS-17-06**
A Timepix4-based High-Speed Imaging System for Energy-Resolved Neutron Imaging at CSNS
Yimie Yuan

17:30 – 19:00 MACHADO
NSS-18 Neutron and gamma-ray detectors and applications, including security, dosimetry and other related applications

Chairs:
Abdallah LYOUSSI (Saint Paul-lez-Durance)
Igor Jovanovic (Berkeley)

17:30 **NSS-18-01**
Fast Neutron Spectrometer for Fusion Diagnostics
Fabrice Retiere

17:45 **NSS-18-02**
Pixel Size-Induced Visibility Degradation and Its Mitigation for X-ray Dark-Field Baggage Scanners
Zhexin Wang

18:00 **NSS-18-03**
Three-Dimensional Isotopic Imaging via Portable Neutron Resonance Transmission Analysis
Kevin Sanchez

18:15 **NSS-18-04**
Neutron diffraction-contrast tomography demonstration using event-based Timepix camera
Anton Khaplanov

18:30 **NSS-18-05**
Associated-Particle Neutron Time-of-Flight Measurements of Curium-244 and Californium-252
Malcolm J. Joyce

18:45 **NSS-18-06**
Quantitative Contamination Mapping Using an Electron-Tracking Compton Camera for Nuclear Decommissioning
Shinya Sonoda

17:30 – 19:00 PICASSO
NSS-19 Nuclear, HEP and astrophysics detectors

Chairs:
Chiara Guazzoni (Milano)

17:30 **NSS-19-01**
Status of the Phase-2 Upgrade of the CMS Outer Tracker
Michael Tytgat, On behalf of the CMS Collaboration

17:45 **NSS-19-02**
Operation and Performance of the ATLAS Liquid Argon Calorimeter During LHC Run 3
Nick Fritzsche, On behalf of the ATLAS Collaboration

18:00 **NSS-19-03**
Building the TRISTAN Phase-1 Detector: Characterization of 1000 SDD Pixels
Marco Carminati, On behalf of KATRIN Collaboration

18:15 **NSS-19-04**
Detector Performance Results on the MOSAIX Stitched Sensor Structures for ALICE ITS3
Livia Terlizzi, On behalf of the ALICE Collaboration

18:30 **NSS-19-05**
The LHCb PicoCal: a New Radiation-hard ECAL with Picosecond Time Resolution
Eduardo Picatoste, on behalf of the LHCb ECAL Upgrade II R&D Group

18:45 **NSS-19-06**
digital SiPMs for future RICH detectors
Prabhleen Singh

12 November, 2026

9:00 – 11:00 ALBÉNIZ & MACHUCA
NSS-20 DAQ, front-end and electronics

Chairs:
David J. Abbott (Newport News)

9:00 **NSS-20-01**
Development and validation of the Forward Feature Extractor Prototype for high-speed data processing in the ATLAS L0Calo trigger systems
ATLAS Collaboration ATLAS Collaboration, On behalf of the ATLAS Collaboration

9:15 **NSS-20-02**
Lessons Learned from the sPHENIX Experiment
Martin L. Purschke

9:30 **NSS-20-03**
Architecture and Performance of a Versatile Trigger, Tracking and Readout System for Particle Detector Beam Tests
Liliana Congedo

9:45 **NSS-20-04**
TD-Link: A Daisy-Chain Optical Architecture for Integrated Data Readout and Deterministic Timing Distribution in Large-Scale Detector Systems
Andrea Abba

10:00 **NSS-20-05**
Design and test of a readout board for the ePIC dRICH detector
Davide Falchieri

10:15 **NSS-20-06**
Performance evaluation of SPIDER and ICECAL65 for the upgrade II of the LHCb calorimeter detector
Eduardo Picatoste, On behalf of the LHCb ECAL Upgrade II R&D Group

10:30 **NSS-20-07**
Design and Performance of the Fermilab Constant-Fraction Discriminator (FCFD) Readout ASIC for ePIC Barrel Time-of-Flight Detector
Datao Gong

10:45 **NSS-20-08**
LDMX Timing Distribution and Data AcquisitionSystem
Benjamin A. Reese

9:00 – 11:00 MACHADO
NSS-21 Photodetectors

Chairs:
Fabrice Retiere (Vancouver)
Stefan Gundacker (Vienna)

9:00 **NSS-21-01**
Development of a Cost-Effective PCCT Detector Based on Sub-Millimeter EQR SiPM and LYSO Array with High Count Rate and Adequate Energy Resolution
Yongqiang Yan

9:15 **NSS-21-02**
First Characterisation Results on Backside-Illuminated SiPM Prototypes from the IBIS Project
Roberto Preghenella, On behalf of the IBIS and IBIS_NEXT Collaborations

9:30 **NSS-21-03**
Photon-to-Digital Converters Enabling Event Classification Through Pulse Shape Discrimination
Serge A. Charlebois

9:45 **NSS-21-04**
Progress on Single-cell-access TSVs for 3D-integrated microSiPM readout in fast-timing SiPM detectors
Alberto Gola

10:00 **NSS-21-05**
PlatonSPAD: A Scalable Sensor for Elementary Particle Detection
Kodai Kaneyasu, Kodai Kaneyasu

10:15 **NSS-21-06**
Study of neutron irradiated CMOS SPADs for RICH detector applications
Rok Dolenec

10:30 **NSS-21-07**
Comparative Study of NIEL Effects on Dark Count Rate in 110 nm CMOS SPADs Under Neutron, Proton and Electron Irradiation
Marcello Campajola

10:45 **NSS-21-08**
First developments of NUV-DJ SiPM arrays forcryogenic operation for the LHCb SciFi tracker Upgrade II
Carina Antonia Trippl

9:00 – 11:00 PICASSO

NSS-22 Neutron and gamma-ray detectors and applications, including security, dosimetry and other related applications

Chairs:
Marek Flaska (University Park)
Bertrand Pérot (Saint-Paul-lez-Durance)

9:00 **NSS-22-01**
Learning Real-World Spectral Templates from a City-Scale Radiological Sensor Network
Hannah Parrilla

9:15 **NSS-22-02**
Spatially-derived Enhancement of Time-domain PSD and Spectroscopy Measurements
Patrick M. Collins-Price

9:30 **NSS-22-03**
Impact of Air Activation on Tritium Monitoring in Fusion Energy Systems
Shaun D. Clarke

9:45 **NSS-22-04**
Attention-Biased Additive Point Source Localization
Brian J. Quiter

10:00 **NSS-22-05**
VETTR: A Robotic Landmine Detection System via Associated Particle Imaging
Ryan Pavlovsky

10:15 **NSS-22-06**
Development of a Real-time Dose Rate Monitoring System Reading with Optical Fiber under the High-Dose Rate Condition
Shunsuke Kurosawa

11:30 – 13:00 ALBÉNIZ & MACHUCA

NSS-23 Analog and digital circuits III

Chairs:
Stefan Gundacker (Vienna)
Lodovico Ratti (Pavia)

11:45 **NSS-23-01**
A Timing ASIC for Large-area SiPM Readout with Channel Delay Compensation
Yi Fu

11:30 **NSS-23-02**
CMOS-Based QUBO Solver ASIC for Charged Particle Tracking
Hyunjoon Kim

12:00 **NSS-23-03**
Scalable FPGA-Based Dual-Threshold Time-Over-Threshold Readout Circuit for Fast-Component Discrimination in BaF_2
Min Hyeong Son

12:15 **NSS-23-04**
A Flexible Multi-Mode Digital Readout Architecture for High-Precision Low-Rate Time-of-Flight Detectors
Manuel Viqueira Rodriguez, On behalf of PetVision project

12:30 **NSS-23-05**
Analog Neural Network ASIC for In-Detector Processing: Experimental Validation of an Advanced Prototype
Michele Ronchi

12:45 **NSS-23-06**
ASIC Development of Rad-hard Embedded FPGA in 28nm for Machine Learning in Particle Detector
Aseem Gupta

11:30 – 13:00 MACHADO
NSS-24 Gas detectors

Chairs:
Michael Tytgat (Brussel)
Takeshi Fujiwara (Tskuba)

11:30 **NSS-24-01**
GEM detectors for the CMS muon system
Chiara Aimè, On behalf of CMS Collaboration

11:45 **NSS-24-02**
A new detector technology for the LHCb Muon system in the high luminosity era
Francesco Debernardis

12:00 **NSS-24-03**
A Straw Tube Chamber Prototype for the Inner Detector of a Future e^+e^- Collider Experiment
Julia Okfen

12:15 **NSS-24-04**
Characterisation of a Multitube detector for the CSPEC Cold Neutron Spectrometer
William Saenz-Arevalo

12:30 **NSS-24-05**
Characterization of a High-efficiency Multi Element Thick Gas Electron Multiplier Based Neutron Dosemeter
Haoshuai Wang

12:45 **NSS-24-06**
Xe-SF_6 mixtures for negative-ion detectors
Afonso P. Marques

11:30 – 13:00 PICASSO
NSS-25 Nuclear, HEP and astrophysics detectors

Chairs:
Hartmut Hillemans
Maurizio Ghisetti (Milano)

11:30 **NSS-25-01**
Early On-Orbit Characterization of the Neutron Radiation Detection Instrument-1B (NeRDI-1B)
Anthony L. Hutcheson

11:45 **NSS-25-02**
High-speed single-photoelectron detection for Cherenkov astronomy
Luca Giangrande

12:00 **NSS-25-03**
Experimental demonstration of thermal neutron effects and their suppression in a sampling-type veto detector
Toru Matsumura

12:15 **NSS-25-04**
A High-Performance Mid-Format SiC based Detection System for Radioactive Ion Beam Tagging and Diagnostics
Chiara Guazzoni

12:30 **NSS-25-05**
The General Antiparticle Spectrometer (GAPS) Instrument: Design, Performance, and First Antarctic Flight
Kelsey Yee, On behalf of the GAPS collaboration

12:45 **NSS-25-06**
The Future of In-Beam Gamma-ray Spectroscopy at RIBF: $CeBr_3$ Development for the HYPATIA Array
Luke Tetley, On behalf of the HYPATIA Collaboration

15:00 – 17:00 ALBÉNIZ & MACHUCA
NSS-26 AI and ML for radiation detection

Chairs:
Marco Carminati (Milano)

15:00 **NSS-26-01**
Emergent Physical Interpretability in Transformer Encoders for Radiation Anomaly Detection
Derian M. Mowen

15:15 **NSS-26-02**
Ground-Truth-Free Validation of Surface Radiation Mapping via Forward-Simulation Round-Trip
Byoung-Jik Kim

15:30 **NSS-26-03**
Backscattered Spectral Network Imaging Method Based on a Combined Long–ShortCrystal Detector
Junjun Li

15:45 **NSS-26-04**
A Machine Learning Approach to Inter-Crystal Scattering Kinematics for Multiple Emission Tomography
Luca Presotto

16:00 **NSS-26-05**
Real-Time Data Compression Using Machine Learning for the ARGO Dark Matter Detector
Sajedeh Esmaeilzadeh

16:15 **NSS-26-06**
Machine-Learning Based Rapid Characterization of HPGe Detectors Based on Full-Energy Peak Efficiency Responses
Kainan Zhang

16:30 **NSS-26-07**
Comprehensive Strategy for Track Signal Extraction in the COMET Phase-I Experiment using Deep Learning Algorithms
Joe Sato

16:45 **NSS-26-08**
Signal Electron Extraction and Energy Resolution the COMET Experiment
Yuya Kojima

15:00 – 17:00 MACHADO
NSS-27 Scintillators

Chairs:
Marco Pizzichemi (Geneva)
Lakshmi Soundara Pandian (Watertown)

15:00 **NSS-27-01**
Measurement of the Cross Section of $^{14}N(n, p)^{14}C$ Reaction Using Sample-Added Scintillator
Gengchen Li, Gengchen Li

15:15 **NSS-27-02**
Development of thermal neutron detector using co-doped Ce:$LaBr_3$/^{6}LiBr Eutectic Scintillators for High Gamma-Ray Backgrounds
Kei Kamada

15:30 **NSS-27-03**
Scintillators based on 2D perovskite single-crystals for the detection of rapid neutrons and gamma/neutron discrimination.
Fanny Thorimbert

15:45 **NSS-27-04**
Optimization of $Cs_2LiLa(Br,Cl)_6$:Ce Scintillation Crystals for Neutron Detection and n/γ Discrimination
Zhuochen Cai, Zhuochen Cai

16:00 **NSS-27-05**
Development of Tl and ^{6}Li Co-Doped $Cs_3Cu_2I_5$ for Remote Thermal Neutron Detection
Chihaya Fujiwara

16:15 **NSS-27-06**
Gamma-Neutron Detection with Intrinsic and Doped Ternary Halide Scintillators
Elsa Ariesanti

16:30 **NSS-27-07**
Neutron and Gamma Ray Pulse Shape Discrimination in Small, Fiber-Coupled Organic Glass Scintillators
Schuyler Tyler

16:45 **NSS-27-08**
Pulse Shape Discrimination in a 3D-Printable Perovskite–Polysiloxane Nanocomposite Scintillator
Matteo Polo

15:00 – 17:00 PICASSO
NSS-28 Semiconductor detectors

Chairs:
Shiva Abbaszadeh (Santa Cruz)
Lars R. Furenlid (Tucson)

15:00 **NSS-28-01**
Methylpiperazinium Perovskitoid for High-Performance X-Ray Detection
Hong Li

15:15 **NSS-28-02**
Design and Evaluation of Graphene Strip Arrays for Radiation Detection
Marcos Turqueti

15:30 **NSS-28-03**
Geometry-Defined Impact Ionization in Two-Stage Mesa-Type Silicon Electron Multipliers
Hironori Sonobe

15:45 **NSS-28-04**
Electrical and UHDR characterization of trench-isolated thin segmented silicon detectors
Diango M. Montalvan Olivares

16:00 **NSS-28-05**
Development and Electrical Performance Characterization of 3D Column-Trench Detector
Huimin Ji, Huimin Ji

16:15 **NSS-28-06**
Large-Area Silicon Pixel Sensor Processing on 8-Inch High-Resistivity Wafers
Juha Kalliopuska

16:30 **NSS-28-07**
Results from irradiated nLGAD sensors
Marco Ferrero

16:45 **NSS-28-08**
Insights into DC-coupled Resistive Silicon Detector (DC-RSD) results
Marco Ferrero

17:30 – 19:00 FEDERICO GARCÍA LORCA
NSS-29 NSS closing session and Student Paper Awards

Chairs:
Audrey Corbeil Therrien (Sherbrooke)
Giulia Hull (Orsay)

17:30 **NSS-29-01**
Summary of the conference

17:40 **NSS-29-02**
Student Paper Awards - Runner-Up Poster presentation

17:45 **NSS-29-03**
Runner-up Poster Presentation

17:50 **NSS-29-04**
Student Paper Awards - Winner Poster presentation

17:55 **NSS-29-05**
Winner Poster Presentation

18:00 **NSS-29-06**
Student Paper Awards - Runner-Up Oral Presentation

18:05 **NSS-29-07**
Runner-up Oral Presentation

18:20 **NSS-29-08**
Student Paper Awards - Winner Oral Presentation

18:25 **NSS-29-09**
Winner Oral Presentation

18:40 **NSS-29-10**
Closing and passing to NSS 2027

11 November, 2026

9:00 – 11:00 FEDERICO GARCÍA LORCA
MP-01 MIC Plenary Session 1

Chairs:
Vesna Sossi (Vancouver)
Roger Fulton (Sydney)

9:00 **MP-01-01**
Opening ceremony; General Chair and MIC welcome
Stefan Ritt, Vesna Sossi, Roger Fulton

9:15 **MP-01-02**
Marie Sklodowska-Curie Technical Field Award Introduction
Sara A. Pozzi

9:25 **MP-01-03**
Marie Sklodowska-Curie Technical Field Awardee Presentation | Decoding the Cancer Ecosystem Through Multiscale Imaging for Precision Medicine
Irene Buvat

10:10 **MP-01-04**
NPSS Richard F. Shea Distinguished Member Awardee Announcement
Steven R. Meikle

10:14 **MP-01-05**
NPSS Richard F. Shea Distinguished Member Presentation
Tba Tba

10:29 **MP-01-06**
Edward J. Hoffman Early Career Development Grant Introduction
Steven R. Meikle

10:31 **MP-01-07**
Edward J. Hoffman Early Career Development Grant Presentation
Tba Tba

10:41 **MP-01-08**
Ronald J. Jaszczak Graduate Award Introduction
Steven R. Meikle

10:42 **MP-01-09**
Ronald J. Jaszczak Graduate Award Presentation
Tba Tba

10:45 **MP-01-10**
Glenn F. Knoll Post Doctoral Educational Grant Introduction
Steven R. Meikle

10:46 **MP-01-11**
Glenn F. Knoll Post Doctoral Educational Grant Presentation
Tba Tba

10:49 **MP-01-12**
NPSS Glenn F. Knoll Graduate Educational Grant Introduction
Steven R. Meikle

10:50 **MP-01-13**
NPSS Glenn F. Knoll Graduate Educational Grant Presentation
Tba Tba

10:52 **MP-01-14**
NPSS Graduate Scholarship Award Introduction
Steven R. Meikle

10:53 **MP-01-15**
NPSS Graduate Scholarship Award Introduction Presentation
Steven R. Meikle

10:55 **MP-01-16**
Awardee Introductions: Jordanov Awards and Phelps Grants
Lorenzo Fabris

11:30 – 12:45 FEDERICO GARCÍA LORCA
MIC-01 Advanced tomographic reconstruction techniques (1)

Chairs:
Andrew J. Reader (London)

11:30 **MIC-01-01**
3D Diffusion Posterior Sampling with Patient-Specific PET Priors for Ultra-Low-Count SPECT in alpha therapy
Alejandro Lopez-Montes

11:45 **MIC-01-02**
Joint Reconstruction of Activity and Attenuation with Motion Estimation in PET using Diffusion Models
Clémentine Phung-Ngoc, Clémentine Phung-Ngoc

12:00 **MIC-01-03**
Flow Models for PET Image Reconstruction
George Webber

12:15 **MIC-01-04**
Flow Matching for PET Image Reconstruction
Fumio Hashimoto

12:30 **MIC-01-05**
Data-Driven Kernel EM Reconstruction Using Attention-Based Learning for Dynamic PET
Haoran Chang

11:30 – 12:45 MANUEL DE FALLA
MIC-02 High resolution imaging systems (organ-dedicated, small animal systems (1)

Chairs:
Tianyu Ma (Beijing)
Elena Maria Zannoni (Austin)

11:30 **MIC-02-01**
Development and Evaluation of Gym-PET for Functional Brain Imaging of Awake Running Mice
Xin Yu, Xin Yu

11:45 **MIC-02-02**
Preliminary Validation of Flexible On-Demand Customized Ultra-Resolution System for Targeted Performance Enhancement in Preclinical PET
Kexin Wang

12:00 **MIC-02-03**
Initial Performance Characterization of the SAVANT Ultra-High-Resolution Phoswich-Based DOI Brain PET Scanner
Roger Lecomte

12:15 **MIC-02-04**
A Physics-Guided Deep Learning Method for Fast System Matrix Modeling in Self-Collimating SPECT Using Sparse Point-Source Calibration
Qiqi Ye

12:30 **MIC-02-05**
BuckyPET: Performance Evaluation and NEMA Adaptation for Compact PET Geometries
David Perez-Benito

12:45 – 13:05 FEDERICO GARCÍA LORCA
M-LT-01 Advanced tomographic reconstruction techniques, X-ray imaging systems (CT, spectral CT, photo-counting CT)

Chairs:
Andrew J. Reader (London)

12:45 **M-LT-01-01**
SPECT Reconstruction via Diffusion Sampling from a PET Image Manifold for Theranostics
Huanzhe Wei

12:47 **M-LT-01-02**
Event-by-Event Energy-Dependent List-Mode Reconstruction for Quantitative ^{90}Y Bremsstrahlung SPECT
Chenyu Yan

12:49 **M-LT-01-03**
Introducing "T-Index"—A Metric for Quantifying Data Range and Sampling Sufficiency
Katsuyuki Taguchi

12:51 **M-LT-01-04**
Time-of-Flight X-ray Imaging with Scatter Rejection and Subtraction
Altea Lorenzon, Altea Lorenzon

12:53 **M-LT-01-05**
Robustness to Scatter in Dual Energy Bone Suppression for Chest Radiography
Wojciech Zbijewski

12:55 **M-LT-01-06**
Unrolled relaxed algorithm for 3D SPECT reconstruction
Corentin Constanza

12:57 **M-LT-01-07**
Three-Photon Bayesian Imaging of Ortho-Positronium
Wojciech Krzemien, On behalf of IMPET project

12:59 **M-LT-01-08**
Lutetium-176-Aided Joint Activity and Attenuation Reconstruction in TOF-PET Using Trust-Region Cubic Surrogate Optimization
Xin Zhao

13:01 **M-LT-01-09**
List-Mode Derived Synthetic Kernel-Based Image Reconstruction for Dynamic Total Body PET
Movindu Dassanayake

13:03 **M-LT-01-10**
Unsupervised micro-CT reconstruction from limited-angle and truncated data in cone-

beam geometry
Keisuke Izumitani

12:45 – 13:05 MANUEL DE FALLA
M-LT-02 High resolution imaging systems (organ-dedicated, small animal systems, X-ray imaging systems (CT, spectral CT, photo-counting CT), Quantitative imaging, image assessment and standardization

Chairs:
Tianyu Ma (Beijing)
Elena Maria Zannoni (Austin)

12:45 **M-LT-02-01**
Experimental Results from Novel Monolithic PET Detector and Application to Axillary Lymph Node Imaging
Timothy Cotroneo

12:47 **M-LT-02-02**
Spatial Characterization of PET Detectors Based on BGO Pseudo-slabs
Neus Cucarella

12:49 **M-LT-02-03**
SurfaceCam: A Close-Proximity Multi-Pinhole CZT Brain SPECT system with Enhanced Geometric Sensitivity and Spatial Resolution
Shubham Mandot

12:51 **M-LT-02-04**
In vivo Gold Nanoparticle Imaging in Mice for Tumor Detection Using SiPM-Based Photon-Counting CT
Shuma Midorikawa, Shuma Midorikawa

12:53 **M-LT-02-05**
Quantitative Evaluation of Liver Disease through Multi-modality Approach Combining SiPM-based PC-CT and MRI—Approach to the Visualization of Inflammation through Water Fraction Estimation —
Yu Furuta, On behalf of the joint research group of Kanazawa University, Waseda University, Ishikawa Prefectural University, and Proterial Ltd.

12:55 **M-LT-02-06**
Position-, direction- and contrast-dependent measurement of MLEM-reconstructed PET resolution using a 3D-printed cube
Santiago Alvarado Orozco

12:57 **M-LT-02-07**
A Clinically Viable, Scalable Implementation of Monte Carlo Scatter Correction for PET/CT
Michal Edelstein

12:59 **M-LT-02-08**
Evaluation of Motion Correction Methods on the NeuroEXPLORER Using Multi-Tracer Human Data
Jiazhen Zhang

13:01 **M-LT-02-09**
SSS Optimised for Monte Carlo Scatter Estimation for PET
Antonia Reeves

13:03 **M-LT-02-10**
Positron Range Confinement in Preclinical PET/MRI: A Multi-Isotope, Multi-Density Experimental Study
Andrea Gonzalez-Montoro, Andrea Gonzalez-Montoro

15:00 – 17:00 FEDERICO GARCÍA LORCA
MIC-03 X-ray imaging systems (CT, spectral CT, photo-counting CT)

Chairs:
Dimitra G. Darambara (London)
Katsuyuki Taguchi (Baltimore)

15:00 **MIC-03-01**
LUCID: Model-Free High-Rate Photon Counting
Paul Scoullar

15:15 **MIC-03-02**
Comparison of scintillator and semiconductor based photon counting detectors via a unique, modular, multi-level simulation framework (PC-SIM).
Oliver L.P. Pickford Scienti

15:30 **MIC-03-03**
Single Energy Material Decomposition via X-ray Grating Interferometry
Longchao Men

15:45 **MIC-03-04**
Performance Evaluation of Low-Dose 3D Small-Animal Imaging Using YSO/SiPM-Based Photon-Counting CT
Rui Zheng

16:00 **MIC-03-05**
Photon-Counting Spectral Dark-Field Micro-CT for Enhanced Tooth Microcrack Detection
Qianyue Ma

16:15 **MIC-03-06**
ePixUHR-100k: A 100 kfps Full-Frame Imager for the LCLS X-Ray FEL Upgrade
Aldo Pena-Perez

16:30 **MIC-03-07**
Inverse Analysis of Pulse Pile-Up and Charge Sharing in Photon-Counting Detectors
Rikuto Sawada

16:45 **MIC-03-08**
Towards the first ToF-CT X-ray image: acquisition and scatter correction
Gabriel Belanger

15:00 – 17:00 MANUEL DE FALLA
MIC-04 Quantitative imaging, image assessment and standardization

Chairs:
Christoph W. Lerche (Jülich)
Jorge Roser (Lübeck)

15:00 **MIC-04-01**
Single-Source Cross-Tracer Brain PET Attenuation Correction via Anchored Flow Matching with Attenuation Maps from Simultaneous Reconstruction
Min Jeong Cho

15:15 **MIC-04-02**
High-Energy Penetration Correction in Multi-Aperture SPECT Using Aperture–Plate Ray Decomposition
Yusheng Li

15:30 **MIC-04-03**
Improving Lutetium Background Radiation-based Attenuation Correction for CT-less PET Using Singles-derived Randoms
Bing Dai, Bing Dai

15:45 **MIC-04-04**
Estimation of random events in PET imaging using the time differences of uncorrelated singles
Maxime Toussaint

16:00 **MIC-04-05**
Quantitative Activities Evaluation of Ac-225 and Daughter Nuclides Using the Alpha-SPECT Mini System
Yong Du

16:15 **MIC-04-06**
Physics-Driven Methods for Standardizing Radiomics Features in CT Data
Joseph W. Stayman

16:30 **MIC-04-07**
Uncertainty estimation for ^{123}I-DaTSCAN
Kelley M. Ferreira

16:45 **MIC-04-08**
Towards Absolute Resolution Characterization in OSEM Reconstructed Images without Ground Truth: Using FBP Reconstructed Images as the Bridge
Yifan Hu

17:30 – 19:00 Poster Area
MIC-05 MIC Poster Session 1

Chairs:
Margaret E. Daube-Witherspoon (Philadelphia)
Fabian P. Schmidt (Tuebingen)

17:30 **MIC-05-001**
Variable Angle Slant-Hole Collimator for Molecular Breast Imaging System
Andrew Weisenberger

19:00 **MIC-05-004**
Characterization of the CHLOE readout for dual-ended BGO crystals for PET with the FastIC+
Claudio San Martín Valenzuela

20:30 **MIC-05-007**
A 0.32 mm Pitch GAGG Array-Based SPECT Detector
Junwei Du

22:00 **MIC-05-010**
Sub-millimeter PET detectors using multiplexed readout with ASIC
Zheng Liu

23:30 **MIC-05-013**
Performance Evaluation of a Position Sensitive SiPM for Decoding Ultra-Small Crystal

Arrays
Jianlang Hua

1:00 **MIC-05-016**
Joint Deconvolution Framework for Photon-Train Reconstruction from Dual-Channel SiPM Readouts
Minseok Yi

2:30 **MIC-05-019**
Pushing the CTR limits in thick dual-ended crystals readout with FastIC+
David Mazzanti

4:00 **MIC-05-022**
Deep Learning Depth-of-Interaction Estimation from Full-Waveform Single-Ended PET Readout: Spatial Resolution Limits
Luca Macchiarulo

5:30 **MIC-05-025**
Optical-Guiding Crystal Scintillator for Single-Cell Resolution Imaging
Fumihiko Nishikido

7:00 **MIC-05-028**
Crystal Topology and Channel Compression Optimization for a high-resolution Neuro PET/MRI TOF-DOI PET Detector
Thore Meyer

8:30 **MIC-05-031**
An ultralow-afterglow γ-camera prototype for hybrid interventional X-ray and scintigraphy imaging
Marc Snoeyink

10:00 **MIC-05-034**
CRYSP: towards an accessible TBPET
Laura Navarro-Cozcolluela, On behalf of the CRYSP group

11:30 **MIC-05-037**
Evaluation of a Low-Noise Ultra-Fast SiPM Time-of Flight Analog Readout Chip (LUSTAR)
Joshua W. Cates, Joshua W. Cates

13:00 **MIC-05-040**
A Dual-Ended Readout PET Detector Module With 0.75 mm Pitch LYSO Arrays for High-Resolution Small-Animal Imaging
Xianchao Huang

14:30 **MIC-05-043**
CNN-Based 2D Source Localization Using Collimator-Free Staggered Scintillator Arrays
Bryan Casanelli

16:00 **MIC-05-046**
Development and Experimental Characterization of a Fine-Pitch CZT SPECT Detector Head with Simulation-Guided Matched-Pixel Collimator Selection
Rui Wang

17:30 **MIC-05-049**
Monte Carlo simulations of positrons in uniform magnetic fields with PENELOPE
Héctor Alva-Sánchez

19:00 **MIC-05-052**
Impact of a Breast PET Insert on Lesion Detectability in Whole-Body PET/MRI
Hong Phuc Vo

20:30 **MIC-05-055**
Proposal of an L-shaped Dual-detector Multi-pinhole Myocardial SPECT System Using a CNN
Takumi Akatsuka

22:00 **MIC-05-058**
EduPETSIM: An Educational Web-Based Framework Integrating Simulation, Reconstruction, and Generative AI for Rapid Source Modeling
Trang Hoang, On behalf of EduPET Collaboration

23:30 **MIC-05-061**
Accelerating Monte Carlo Light Transport in Turbid Media with an Analytically Invertible Simplified Phase Function
Aristotelis-Nikolaos Rapsomanikis

1:00 **MIC-05-064**
Fast On-the-Fly System Matrix Computation for Broad-Energy Multi-Pinhole SPECT
Bo Gao

2:30 **MIC-05-067**
Monte Carlo Based Performance Evaluation of a Dual Panel PET&SPECT Trimodal Imager
Hang Yang

4:00 **MIC-05-070**
Experimental Validation and Calibration of a GATE Simulation Model for a Dedicated

Breast PET/MR Insert
Elnaz Olyaei

5:30 **MIC-05-073**
An Integrated Digital Twin Framework for Accurate Quantification of Preclinical Immuno-PET
Claudia Dominguez-Borrero

7:00 **MIC-05-076**
Tensor-Based Multi-Stage Evolution for Generative Design of Arbitrary Permanent Magnet Geometries for PET-compatible Low-Field MRI
Fumihiko Nishikido

8:30 **MIC-05-079**
Design of SSLE-PET with GATE Simulation Towards Sub-Second Dynamic Mouse Imaging
Han Gyu Kang

10:00 **MIC-05-082**
SPECT vs. Compton Camera for Prompt Gamma Monitoring in BNCT: a simulation study.
Tommaso Ferri

11:30 **MIC-05-085**
A Novel Inter-Crystal Scatter Positioning Method Using Variable-Bin Stochastic Conditional Probability Based on Energy and Depth-of-Interaction Ordering
Hyeongseok Shim

13:00 **MIC-05-088**
Validation of Compton camera simulations using GATE version 10 through experimental data
Zaina J. Hurani

14:30 **MIC-05-091**
Convertible Whole-Body Extension of a Brain-Dedicated Whole Gamma Imaging System:A Simulation Study
Go Akamatsu

16:00 **MIC-05-094**
Translating CLS Detector Technology from Brain to Whole-Body PET Imaging: A Simulation Study
Mizuki Furuta

17:30 **MIC-05-097**
Photon-Counting CT in the Context of Ultra-Low-Dose PET/CT
Samaneh Mostafapour

19:00 **MIC-05-100**
DMGR-Net: Dual-Modal Gated Residual Network for Lightweight PET/MRI Brain Parcellation
Minjie Wang

20:30 **MIC-05-103**
New Hyperion Detector Platform Electronics: Highly Integrated Mainboard, Tile Cable, and Sensor Tile
Bjoern Weissler

22:00 **MIC-05-106**
Development of a Shielded Digital PET Detector System for a Brain PET/MRI Insert
Oleksandr Bubon

23:30 **MIC-05-109**
Design and Performance Evaluation of a Full-Ring SPECT System Based on the Continuous LaBr3(Ce)
Kui Wang

1:00 **MIC-05-112**
Image quality assessment of a positron emission mammography prototype
Valeria Pérez-Martínez

2:30 **MIC-05-115**
Experimental Results from Novel Monolithic PET Detector and Application to Axillary Lymph Node Imaging
Timothy Cotroneo

4:00 **MIC-05-118**
Spatial Characterization of PET Detectors Based on BGO Pseudo-slabs
Neus Cucarella

5:30 **MIC-05-121**
Positron Range Confinement in Preclinical PET/MRI: A Multi-Isotope, Multi-Density Experimental Study
Andrea Gonzalez-Montoro, Andrea Gonzalez-Montoro

7:00 **MIC-05-124**
Resolution-Sensitivity Optimization with Expanded Position Maps in the CLS-7: A TOF-

DOI Brain PET System
Kurumi Narita

8:30 **MIC-05-127**
Performance evaluation of N-PET, a high-resolution TOF-DOI PET dedicated to brain imaging
Ming Niu

10:00 **MIC-05-130**
DOI-Dependent Energy Window for Reducing Lu Background in In-Beam SIRMIO PET
Munetaka Nitta

11:30 **MIC-05-133**
NEMA NU-2 performance tests of a prototype PET scanner using novel detectors capable of measuring the gamma interaction point in 3D
August Blomgren

13:00 **MIC-05-136**
SurfaceCam: A Close-Proximity Multi-Pinhole CZT Brain SPECT system with Enhanced Geometric Sensitivity and Spatial Resolution
Shubham Mandot

14:30 **MIC-05-139**
Local Activity and Uncertainty Quantification for Pre-clinical Compton Imaging of ^{213}Bi
Oscar H. Matousek

16:00 **MIC-05-142**
A Compact X-ray Dark-Field Imaging Setup and Corresponding Image Optimization
Xiaolei Yan

17:30 **MIC-05-145**
Digital phantoms that can reproduce diseases aiming for virtual radiation imaging experiments
Rina Nishigami, This is a collaborative study between Kanazawa University and Okayama University.

19:00 **MIC-05-148**
A novel computational scatter estimation method in CBCT with half ASG
Jiongtao Zhu

20:30 **MIC-05-151**
Quantitative Evaluation of Liver Disease through Multi-modality Approach Combining SiPM-based PC-CT and MRI—Approach to the Visualization of Inflammation through

Water Fraction Estimation —
Yu Furuta, On behalf of the joint research group of Kanazawa University, Waseda University, Ishikawa Prefectural University, and Proterial Ltd.

22:00 **MIC-05-154**
Introducing “T-Index”—A Metric for Quantifying Data Range and Sampling Sufficiency
Katsuyuki Taguchi

23:30 **MIC-05-157**
In vivo Gold Nanoparticle Imaging in Mice for Tumor Detection Using SiPM-Based Photon-Counting CT
Shuma Midorikawa, Shuma Midorikawa

1:00 **MIC-05-160**
End-to-End Simultaneous Combined Scatter Correction and Metal Projection Segmentation for CBCT Metal Artifact Reduction Network
Junjie Zhou

2:30 **MIC-05-163**
X-ray Scattering in Dual-Layer Flat-Panel Detectors
Dong Sik Kim

4:00 **MIC-05-166**
Development and Experimental Validation of a Low-Cost Benchtop Micro-CT System
Pedro M.M. Correia

5:30 **MIC-05-169**
Development of a Robot-Arm-Based Automated Transmission and Backscatter X-ray Image Acquisition System for AI Training Data Generation
JeongHee Lee

7:00 **MIC-05-172**
Robustness to Scatter in Dual Energy Bone Suppression for Chest Radiography
Wojciech Zbijewski

8:30 **MIC-05-175**
Time-of-Flight X-ray Imaging with Scatter Rejection and Subtraction
Altea Lorenzon, Altea Lorenzon

10:00 **MIC-05-178**
Iodine Sensitivity in Photon Counting CT Using Conventional and Diffusion-Based Material Decomposition Algorithms
Grace J. Gang

11:30 **MIC-05-181**
TCMnet: An Automatic Tube Current Modulation Policy Based on Neural Network
Haoyu Zhang

13:00 **MIC-05-184**
A Fully Quantitative Reconstruction Framework Tailored for Depth-of-Interaction PET Systems
Yihao Chen

14:30 **MIC-05-187**
Unsupervised micro-CT reconstruction from limited-angle and truncated data in cone-beam geometry
Keisuke Izumitani

16:00 **MIC-05-190**
A Self-Supervised Framework for Simultaneous Reconstruction of Activity and Attenuation in TOF-PET
Hao Jia

17:30 **MIC-05-193**
Extended Field-of-View Reconstruction for Full-Ring Multi-Pinhole SPECT
Qiao Liu

19:00 **MIC-05-196**
CT Image Reconstruction Using Deep Image Prior with VoxelMorph
Kensuke Hori

20:30 **MIC-05-199**
A Boosting Diffusion Model for Ultra-Sparse-View CT reconstruction
Yura Kimura

22:00 **MIC-05-202**
SPECT Reconstruction via Diffusion Sampling from a PET Image Manifold for Theranostics
Huanzhe Wei

23:30 **MIC-05-205**
Plug-and-Play PET Image Reconstruction Using Diffusion Models
Tomoya Minagawa

1:00 **MIC-05-208**
List-Mode Reconstruction for Gamma-Positron Imaging
Matthew A. Kupinski

2:30 **MIC-05-211**
Pilot Clinical Evaluation of CT-Less PET Attenuation Correction Using Back-Scatter Coincidences on the NeuroEXPLORER System
Zhongzhi Liu

4:00 **MIC-05-214**
Unrolled relaxed algorithm for 3D SPECT reconstruction
Corentin Constanza

5:30 **MIC-05-217**
Multiple Emission Tomography: GPU-Accelerated LM-OSEM Reconstruction for Compton Events
Matteo N. Colombo

7:00 **MIC-05-220**
List-Mode Derived Synthetic Kernel-Based Image Reconstruction for Dynamic Total Body PET
Movindu Dassanayake

8:30 **MIC-05-223**
Three-Photon Bayesian Imaging of Ortho-Positronium
Wojciech Krzemien, On behalf of IMPET project

10:00 **MIC-05-226**
Event-by-Event Energy-Dependent List-Mode Reconstruction for Quantitative ^{90}Y Bremsstrahlung SPECT
Chenyu Yan

11:30 **MIC-05-229**
Evaluation of Cash C as a Cost Function for xSPECT Conjugate Gradient
Francesc Massanes

13:00 **MIC-05-232**
Investigation of Ray Driven Collimator Detector Response Model for Multi-Photopeak SPECT Reconstruction
Thibaut Merlin

14:30 **MIC-05-235**
Deep Kernel Gaussian Process Prior for Robust, Anatomically Guided Radiation Image Reconstruction
Jaewon Lee

16:00 MIC-05-238
ChameleonIQ: Bridging NEMA NU-2 and NU-4 Standards through Automated Image Analysis
Edwing Y. Ulin-Briseño

17:30 MIC-05-241
Position-, direction- and contrast-dependent measurement of MLEM-reconstructed PET resolution using a 3D-printed cube
Santiago Alvarado Orozco

19:00 MIC-05-244
Evaluation of Motion Correction Methods on the NeuroEXPLORER Using Multi-Tracer Human Data
Jiazhen Zhang

20:30 MIC-05-247
A Clinically Viable, Scalable Implementation of Monte Carlo Scatter Correction for PET/CT
Michal Edelstein

22:00 MIC-05-250
Down-Scatter Correction for PET-induced contamination in simultaneous PET&SPECT imaging
Hengyi Li

23:30 MIC-05-253
A Quantitative Reconstruction Framework for Variable-Pitch Multi-Layer DOI Brain PET
Yihao Chen

1:00 MIC-05-256
Intra-frame motion correction for dynamic PET using mutual information-based registration
Simon Noë

2:30 MIC-05-259
Head Motion Correction Improves Machine Learning Classification of Alzheimer's Disease from PET
Eléonore V. Lieffrig

4:00 MIC-05-262
CT-less Data Corrections For Dedicated Cardiac PET Scanners
Florence M. Muller

5:30 **MIC-05-265**
AmyPET: A Comprehensive Automated Framework for Static and Dynamic NeuroPET Quantification
Pawel J. Markiewicz

7:00 **MIC-05-268**
SSS Optimised for Monte Carlo Scatter Estimation for PET
Antonia Reeves

8:30 **MIC-05-271**
Quantitative Activities Evaluation of Ac-225 and Daughter Nuclides Using the Alpha-SPECT Mini System
Yong Du

10:00 **MIC-05-274**
Exploring a Novel Timing Calibration Approach for a Brain-Dedicated Time-of-Flight PET Scanner
James D. Ho

11:30 **MIC-05-277**
Preliminary Study on Thick-Slab Image Generation of Digital Breast Tomosynthesis
Subong Hyun

13:00 **MIC-05-280**
Torch-Enabled STIR: Validation on CPU and GPU
Nikos Efthimiou

14:30 **MIC-05-283**
Post-Reconstruction Spill-In Correction Methods in Lung PET Under Heterogeneous Conditions
Claire J. Brooks

16:00 **MIC-05-286**
Data-Driven Motion Artifact Correction for Wearable PET
Qiyu Peng

17:30 **MIC-05-289**
Radiographic Scatter Correction via Pixelwise Alpha Blending of Dark and Bright Channel Priors
Sanghyun Cho

19:00 **MIC-05-292**
Adapting Timepix4 single-particle trackinginstrumentation for medical X-ray imaging
Petr Mánek

20:30 **MIC-05-295**
A phase shifting method to provode three dimensional position information of an incident gamma ray
Shuwei Zhao

22:00 **MIC-05-298**
Simultaneous Dose Reduction and Resolution Recovery in Preclinical SPECT via Deep Learning
Elise Taragola

23:30 **MIC-05-301**
Self-supervised PET Denoising Based on the Noise2Noise Principle
Sacha Bouchez-Delotte

1:00 **MIC-05-304**
Python Integration in CASToR: Application to the End-to-End DIP-Based PET Reconstruction
Nasrin Taheri

2:30 **MIC-05-307**
DOI Calibration and Resolution Estimation in PET Detector Panels Using Uncollimated Irradiations
Francisco E. Enriquez-Mier-y-Teran

4:00 **MIC-05-310**
Virtual Imaging Trial to Evaluate the Impact of Acquisition Protocols on Harmonized Radiomic features in multi-site PDAC CT
Debojyoti Pal

5:30 **MIC-05-313**
Allometric Scaling of PSMA Uptake as a Novel Biomarker for Predicting Biochemical Response in Prostate Cancer
Fereshteh Yousefirizi

7:00 **MIC-05-316**
A Cucker–Smale Flocking Model for Edge-Aware Medical Image Analysis
Amirreza Hashemi

8:30 **MIC-05-319**
ComBat-Driven Latent Representation Learning for Robust Multicenter Radiomics in Theranostic SPECT/CT Imaging
Mohamed Saber Azimi

10:00 **MIC-05-322**
Evaluation of Dose Rate Dependent Alanine/ESR Response under Carbon Ion FLASH Irradiation
Chul Hee Min

11:30 **MIC-05-325**
Preclinical Evaluation of an In-Room All-Digital PET System for Post-Irradiation Proton Range Verification
Qingguo Xie

13:00 **MIC-05-328**
Proton range verification via coaxial prompt gamma-ray monitoring: experimental proof-of-concept at clinical beam currents
Fernando Hueso-González

14:30 **MIC-05-331**
Sub-Millimeter Range Verification in Carbon-Ion Therapy Using In-Beam All-Digital PET
Qingguo Xie

16:00 **MIC-05-334**
Effect of Radionuclide Distribution on DNA Damage Yields: A Comparative Study between ^{134}Ce/^{134}La and other radionuclides
Sangho Lee

17:30 **MIC-05-337**
Range Monitoring and Tissue Identification in Particle Therapy with the TIARA Detector
Sara Marcatili

19:00 **MIC-05-340**
Secondary Electron Bremsstrahlung Imaging with a Knife-Edge Slit Camera for Range Verification in Carbon-Ion Therapy
Michiko Tsuda

20:30 **MIC-05-343**
A Deep Learning-Based 3D Dose Reconstruction Using a Dual-Panel PET in Proton Therapy
Xiaolong Jiang

22:00 **MIC-05-346**
Validation of Dose-to-PET Conversion for OpenPET Range Verification in Carbon-Ion Therapy
Hideaki Tashima

23:30 **MIC-05-349**
EasyPET.3D imaging of positron-emitter distributions in proton-irradiated PMMA phantoms
Ana Luísa M. Silva

1:00 **MIC-05-352**
Dosimetry-Oriented Structure-Weighted CT-Guided Registration for Multi-Time-Point SPECT/CT in Radionuclide Therapy
Yanzhen Du

2:30 **MIC-05-355**
Characterization and biological validation of a BNCT irradiation field using PADC detectors, RCF and microdosimetric modelling
Joan Flors Marti

4:00 **MIC-05-358**
MACACO III+ Compton camera imaging of ^{225}Ac in mice
Karol Brzeziński

5:30 **MIC-05-361**
Boron Imaging with a Compton Camera: Toward Real-Time Dosimetry in BNCT Treatments
Pablo Torres-Sánchez

7:00 **MIC-05-364**
Feasibility of In-vivo Dosimetry for Proton Therapy using a Mobile Point-of-Care (PoC) PET Imaging System
Samarth Aggarwal

8:30 **MIC-05-367**
Unfolding Temporal Behavior in Emerging ^{161}Tb-FAPI-2286 Dosimetry: Role of Partial Volume Correction in Lesion and Organ Quantification
Mohamed Saber Azimi

10:00 **MIC-05-370**
COXIRIS: A Novel Real-Time Platform for Integrated Cancer Detection, Medical Imagen and Targeted Treatment; Deep EDXRF Detection

Bryan Casanelli, National Research and Development Agency of Chile (ANID) and the Frontera Uninversity

11:30 **MIC-05-373**
Attenuation Correction Using 176Lu Background in Limited-Angle Flat-Panel Total-Body PET
Thibault D'Hulster

13:00 **MIC-05-376**
System Characterization of a DOI-Enabled High-Resolution Total-Body TOF PET Scanner
Qiyu Peng

14:30 **MIC-05-379**
Implementation and Evaluation of TOF and Scatter correction for the IMAS TB-PET
Antonio J. Gonzalez

16:00 **MIC-05-382**
Addressing Scatter Phantom Length Limitations: A Single-Scan Multi-Position Method for NEMA NU 2 Testing of Long Axial FOV PET Systems
Liuchun He

17:30 **MIC-05-385**
Characterizing Smoking Effects Across Lung Cancer Subtypes by Integrating Systemic Metabolic Networks and Tumor Habitat Imaging from Total-Body ^{18}F-FDG PET/CT
Haiyan Wang

19:00 **MIC-05-388**
Improving Generalization of PET Image-Enhancing Deep Learned Models Through Domain Randomization
Pablo Aguiar

20:30 **MIC-05-391**
Unsupervised Deep Learning for Prompt Gamma Emission Reconstruction in Time and Space
Julius Werner

22:00 **MIC-05-394**
Supervised Contrastive Pretraining Enables Few-Shot Alzheimer's Disease Classification on Multi-Site ECD SPECT
Yu-Ching Ni

23:30 **MIC-05-397**
Large Language Models for Generating Descriptions of 3D Medical Image Volumes
Joshua Schaefferkoetter

1:00 **MIC-05-400**
Preliminary Region-Aware MRI-to-sCT Synthesis for Radiotherapy-Oriented Imaging in Nasopharyngeal Carcinoma
Zhigang Sun

2:30 **MIC-05-403**
Deep Learning-Based Tau Positivity Estimation from Multimodal Amyloid and FDG PET
Yiyi Hu

4:00 **MIC-05-406**
Compton Camera Image Reconstruction Using Compton Physics-Prior Fusion and Set Transformers for Actinium-225 Targeted Alpha Therapy
Yazeed Balasmeh

5:30 **MIC-05-409**
CNN-Based Classification Performance Across Axial, Coronal, and Sagittal Imaging Orientations in ^{18}F-PSMA PET Images
Anting Li

7:00 **MIC-05-412**

8:30 **MIC-05-415**
Equilibrium Matching for PET Image Denoising: Signal vs. Velocity Parameterization Under Identical Conditions
Shaghayegh Afshari

10:00 **MIC-05-418**
CT-VDETR: Semi-supervised 3D Trauma Detection in Computed Tomography (CT) scans using Dense Vertex Relative Position Encoding
Shivam Chaudhary

11:30 **MIC-05-421**
An AI Model for Breast Density Estimation using Spectroscopic X-Ray Data
Megan A. Eaton

13:00 **MIC-05-424**
Positron Range Correction with Texture Preservation in ^{82}Rb PET
Nerea Encina-Baranda

14:30 **MIC-05-430**
Genetic algorithm-based PET sinogram denoising using a Poisson noise fitness criterion
Fernando Guedan

16:00 **MIC-05-433**
Comparative Analysis of Cross-Validation Strategies for Classification of Major Adverse Cardiac Events Using Stress-phase PET Polar Maps
Monire Vatandoust, Monire Vatandoust

17:30 **MIC-05-436**
High-Sensitivity Compton Imaging via a Virtual Multi-Stage Edge-On CZT Architecture
Greyson Shoop

19:00 **MIC-05-439**
3D reconstruction of radioluminescence microscopy data via MAP with optimized total variation regularization
Youngho Seo

20:30 **MIC-05-442**
Physics-Informed Jointly Constrained Spectral Signal Decomposition for High-Resolution X-Ray Fluorescence Computed Tomography
Liang Li

22:00 **MIC-05-445**
Evaluation of Dual Tracer [^{18}F]FDG:[^{11}C]choline PET: A Simulation Study
Avishan Elkayee Dehno

23:30 **MIC-05-448**
EduPET - Development of a portable benchtop ToF-PET system for educational applications
Ana Luísa M. Silva, On behalf of EduPET Collaboration

1:00 **MIC-05-451**
Telephoto-Lens Magic-Cube: A Hybrid-Encoded Portable Gamma Camera for Extended-Distance Intraoperative Radiotracer Imaging
Yuxi Zhang

2:30 **MIC-05-454**
Whole gamma imaging prototype V: a proof-of-concept system with thin HRGAGG toward simultaneous PET/SPECT imaging
Go Akamatsu

4:00 **MIC-05-457**
Methodology to determine the absolute values of 3γ/2γ annihilation rate ratio with J-PET
Neha Chug, On behalf of J-PET collaboration

5:30 **MIC-05-460**
Development of MACACOX2 dual-Compton camera system
Siddharth Parashari

7:00 **MIC-05-463**
MEDICAL THERMAL TOMOGRAPHY: EXPERIMENTAL DEMONSTRATION WITH HARDWARE PHANTOMS
Anna Frixou

8:30 **MIC-05-466**

10:00 **MIC-05-469**
A Computational Assessment of Quantum SimulationVersus Classical Simulation for Quantum-InspiredMedical Imaging
Hamid Sabet

12 November, 2026

9:00 – 11:00 FEDERICO GARCÍA LORCA
MP-02 MIC Plenary Session 2

Chairs:
Vesna Sossi (Vancouver)
Roger Fulton (Sydney)

9:00 **MP-02-01**
NPSS President
Sara A. Pozzi, Vesna Sossi, Roger Fulton

9:10 **MP-02-02**
Plenary Talk | Nuclear Fusion – Energy source for the future: An overview with emphasis on control and imaging
Axel Winter

10:00 **MP-02-03**
NPSS merit award Introduction
Steven R. Meikle

10:05 **MP-02-04**
NPSS merit award presentation
Tba Tba

10:15 **MP-02-05**
Edward J. Hoffman Medical Imaging Scientist Award Introduction
Youngho Seo

10:17 **MP-02-06**
Edward J. Hoffman Medical Imaging Scientist Awardee Introduction
Suleman Surti

10:19 **MP-02-07**
Edward J. Hoffman Medical Imaging Scientist Awardee Presentation
Dimitris Visvikis

10:29 **MP-02-08**
Freek J. Beekman Medical Imaging Technical Achievement Award Introduction
Youngho Seo

10:31 **MP-02-09**
Freek J. Beekman Medical Imaging Technical Achievement Awardee Introduction
Xiaochuan Pan

10:33 **MP-02-10**
Freek J. Beekman Medical Imaging Technical Achievement Awardee Presentation
Ken Taguchi

10:43 **MP-02-11**
Bruce H. Hasegawa Young Investigator Medical Imaging Award Introduction
Youngho Seo

10:45 **MP-02-12**
Bruce H. Hasegawa Young Investigator Medical Imaging Awardee Introduction
Ciprian Catana

10:47 **MP-02-13**
Bruce H. Hasegawa Young Investigator Medical Imaging Awardee Presentation
Kevin Jaeyoung Chung

10:52 **MP-02-14**
IEEE TRPMS Best Paper Award
Dimitris Visvikis

11:30 – 12:45 FEDERICO GARCÍA LORCA
MIC-06 Simulation and modeling of medical imaging systems (1)

Chairs:
Julien Bert (Brest)
Min Sun Lee (Daegu)

11:30 **MIC-06-01**
Minkhole Collimators for SPECT: Minkowski-Sum Aperture Geometry and Closed-Form Ray Tracing
Yusheng Li

11:45 **MIC-06-02**
Monte Carlo simulation model of the ring CZT based VERITON SPECT-CT system
David Sarrut

12:00 **MIC-06-03**
Intraoperative Position-Sensitive Positron Emission Counter (PEC): A Simulation Study
Ryotaro Ohashi

12:15 **MIC-06-04**
A metascintillator-based, ultra-ToF enabled, brain PET scanner simulation
Georgios Konstantinou

12:30 **MIC-06-05**
Towards the Ultimate Sub-0.4 mm Resolution: GATE Simulation of a Mouse Brain PET System
Han Gyu Kang

11:30 – 12:45 MANUEL DE FALLA
MIC-07 Multi-modality imaging systems including applications and High resolution imaging systems (organ-dedicated, small animal systems) (2)

Chairs:
Volkmar Schulz (Aachen)
Nikos Efthimiou (Groningen)

11:30 **MIC-07-01**
Experimental Feasibility of Dual-Mode C-arm CT/SPECT Imaging Using a Commercial X-ray Detector for Online Brachytherapy Delivery Verification
Saerom Sung

11:45 **MIC-07-02**
Development of Biological Microenvironment Imaging Technique Using ^{111}In Cascade

Gamma-Ray Correlation
Boyu Feng

12:00 **MIC-07-03**
SmartBrain-EEG: First-in-Human Wearable PET/EEG Imaging in Epilepsy
Han Liu, Han Liu

12:15 **MIC-07-04**
Human Subject and Phantom Imaging Performance of PETcoil Gen II Brain-Dedicated PET System
Grant H.-S. Park

12:30 **MIC-07-05**
Development of SIAT 9.4T MRI compatible animal PET scanner
Haonan Li

12:45 – 13:05 FEDERICO GARCÍA LORCA
M-LT-03 New radiation detector technologies for medical imaging,Novel applications of AI in radiation-based medical imaging

Chairs:
Min Sun Lee (Daegu)
Julien Bert (Brest)

12:45 **M-LT-03-01**
MRI-Informed SPECT-only Spatial Normalization for Reliable Brain Perfusion Quantification
Euijin You

12:47 **M-LT-03-02**
Developments in fabrication and design flexibility of amorphous silicon microchannel plates
Georgios Konstantinou

12:49 **M-LT-03-03**
Fabrication of diamond detectors with graphitic contacts for tissue equivalent dosimetry
Ivan Lopez Paz, Ivan Lopez Paz

12:51 **M-LT-03-04**
Scintillation Properties of $(Lu,Y)_2O_3$:La Ceramic Pixels for PET
Jarek Glodo

12:53 **M-LT-03-05**
Ultrahigh Spatial Resolution Perovskite-based Direct X-ray Imagers for Low-lag Medical

Applications
Amlan Datta

12:55 **M-LT-03-06**
PhysiCal-PET: Physics-based neural networks for the rapid position Calibration of PET Scanners
Mojahed Abushawish

12:57 **M-LT-03-07**
Adaptive Spatio-Temporal Denoising for Low-Dose Fluoroscopy via Motion-Gradient Weighting
Nerea León

12:59 **M-LT-03-08**
An Ensemble of Deep-Learning Classifiers for 3D Anatomical Change Reconstruction in Carbon-Ion Radiotherapy (CIRT)
Maria Martisikova

13:01 **M-LT-03-09**
Zero-Shot PET Image Super-Resolution via Cross-Modal Mutual Information Guidance
Yilin He

13:03 **M-LT-03-10**
3D Photon Position Estimation Using Neural Networks in Monolithic-Based PET Systems
Marta Freire

12:45 – 13:05 MANUEL DE FALLA

M-LT-04 New radiation detector technologies for medical imaging, Simulation and modeling of medical imaging system, Multi-modality imaging systems including applicationss

Chairs:
Volkmar Schulz (Aachen)
Nikos Efthimiou (Groningen)

12:45 **M-LT-04-01**
Development of a PET/MRI Compatible Fluorescence Microscope for Simultaneous Cell Tracking in a Small Animal PET/MRI Scanner
Philipp Renn

12:47 **M-LT-04-02**
Hybrid PGI-PET Imaging for Ion-Range Monitoring in Hadron Therapy
Javier Balibrea-Correa

12:49 **M-LT-04-03**
Intercrystal Compton Scattering Detection in Pixelated LYSO Detectors via Quantum Localization
Amirreza Hashemi

12:51 **M-LT-04-04**
PETRARCA: a Positron Emission Tomography Real-Time Analog Re-Configurable ANN Detector
Maurizio Pandocchi

12:53 **M-LT-04-05**
MIMOSA: Medical IMaging MOnte Carlo Simulation Algorithms for fast proton therapy range monitoring
Declan D. Garvey

12:55 **M-LT-04-06**
Analytical modeling and inclusion of object scatter in non-TOF 3D PET for low-count data
Jorge Roser

12:57 **M-LT-04-07**
Quantitative Impact of Inter-Crystal Scatter on Image Quality and Sensitivity across LabPET-II Scanner Architectures: A Comparative GATE Simulation Study
Alexandre Bernier

12:59 **M-LT-04-08**
Validated Optical Simulation for High-Energy Gamma Response in a 3-Layer LYSO DOI Detector
Shan Jiang

13:01 **M-LT-04-09**
Identification of ICS Pixels in a high-resolution 3-Layer DOI-PET Detector Using a CNN
Shan Jiang

13:03 **M-LT-04-10**
Study on the axial extension of the small-fish PET scanner MERMAID
Magdalena Kolodziej

15:00 – 17:00 FEDERICO GARCÍA LORCA
MIC-08 Novel applications of AI in radiation-based medical imaging (1)

Chairs:
Quanzheng Li (Boston)
Nicolas A. Karakatsanis (New York)

15:00 **MIC-08-01**
Sensitivity-Informed Network for Image Restoration in Sparse-Detector PET
Yucun Hou

15:15 **MIC-08-02**
Anatomy-Guided Null-Space Learning for Self-Supervised Blind PET Deblurring
Ziyuan Zhou

15:30 **MIC-08-03**
Brownian Bridge Diffusion Model for Ultra-Low-Dose Total-Body PET Denoising
Narges Aghakhanolia

15:45 **MIC-08-04**
Self-Supervised Low-Dose SPECT Denoising from a Single Standard-Dose Scan via Poisson Thinning
Haowen Zheng

16:00 **MIC-08-05**
VLM-Guided Conditional Flow Matching for CT-Free total-body PET Correction
Jianming Rong

16:15 **MIC-08-06**
Implicit Neural Representations for Joint Motion-Resolved PET Reconstruction and Respiratory Gating
Nicolas De Bie

16:30 **MIC-08-07**
Towards CT-Free Multi-Time-Point [^{18}F]PSMA-1007 LAFOV PET Protocols: Evaluation of Synthetic Attenuation Maps Versus Elastic Co-Registration for Longitudinal Imaging
Elnaz Olyaei, Elnaz Olyaei

16:45 **MIC-08-08**
3D Latent Implicit Diffusion for Scalable Volume Generation
Antoine De Paepe

15:00 – 17:00 MANUEL DE FALLA
MIC-09 New radiation detector technologies for medical imaging (1)

Chairs:
Joshua W. Cates (Berkeley)
Marta Freire (Valencia)

15:00 **MIC-09-01**
Deep learning-based estimation of individual scintillation photon arrival times for

enhanced TOF resolution
Yuya Onishi, Yuya Onishi

15:15 **MIC-09-02**
Inter-Crystal Scattering Recovery in Semi-Monolithic Crystals: an Experimental and Simulation Study
Fiammetta Pagano

15:30 **MIC-09-03**
A High Resolution Semi-Monolithic GAGG Detector Aiming for SPECT Imaging
Yangyang Zhao

15:45 **MIC-09-04**
Feasibility of Cherenkov-only Radiation Emitters Coupled to SiPMs for PET
Afonso Xavier Pinto

16:00 **MIC-09-05**
Scan Time and Effective Dose Reduction using an Ultra-Fast Molecular Breast Imaging System
Alexander Cherlin

16:15 **MIC-09-06**
Scalable Cherenkov-Enhanced Timing in BGO with FastIC+
Francis Loignon-Houle

16:30 **MIC-09-07**
An Optimized Two-Layer PET&SPECT Shared Detector based on a Scintillator-as-Collimator Design
Yangyang Zhao

16:45 **MIC-09-08**
Unlocking Next-Generation Time-of-Flight Imaging with the PoETIC ASIC
David Gascón

17:30 – 19:00 Poster Area
MIC-10 MIC Poster Session 2

Chairs:
Dennis R. Schaart (Delft)
Hideaki Tashima (Chiba)

17:30 **MIC-10-002**
Detection efficiency of a lead-loaded plastic scintillator for positron emission

tomography detectors : A Monte Carlo study
Makoto Yamazaki

17:30 **MIC-10-005**
Exploring CTR improvement through structural refinement of orthogonally stacked PET detector
Ryosuke Ota

17:30 **MIC-10-008**
A Cost-Effective Neural Network Approach for DOI Estimation in a State-of-the-Art PET Detector
Qi Liu

17:30 **MIC-10-011**
X-ray Imaging Performance of Mg Co-doped $Y_3(Al,Ga)_5O_{12}$:Ce for Photon-counting CT
Hisato Suezumi

17:30 **MIC-10-014**
Optimal Radiator Refractive Index for Cherenkov-Radiator-Integrated PET Detectors: A Simulation Study
Taiyo Ishikawa

17:30 **MIC-10-017**
Fabrication of diamond detectors with graphitic contacts for tissue equivalent dosimetry
Ivan Lopez Paz, Ivan Lopez Paz

17:30 **MIC-10-020**
Experimental Evaluation of Classification MLP for Position Estimation in Semi-Monolithic LYSO Cassettes for Ultra-High-Performance Brain PET
Nicolas A. Karakatsanis

17:30 **MIC-10-023**
AI-based DOI determination for hexagonal monolithic LYSO scintillators with hexagonal cells engraved with laser: A simulation/experiment study
Jose Udias

17:30 **MIC-10-026**
Exploring the Performance of Light-Sharing Based Single-ended BGO DOI-PET Detectors
Yong Hwan Sul

17:30 **MIC-10-029**
Experimental Evaluation of Coincidence Time Resolution in LYSO Scintillators with

Photonic Crystal Pattern
Suyeon Hyeon

17:30 **MIC-10-032**
X-ray fluorescence imaging for breast cancer characterization within the IMMPRINT project
Karol Brzeziński

17:30 **MIC-10-035**
Characterization of DOI-enabled Three-Layer Trapezoidal Pixelated LYSO Detector
Siddharth Parashari

17:30 **MIC-10-038**
PETRARCA: a Positron Emission Tomography Real-Time Analog Re-Configurable ANN Detector
Maurizio Pandocchi

17:30 **MIC-10-041**
Scintillation Properties of $(Lu,Y)_2O_3$:La Ceramic Pixels for PET
Jarek Glodo

17:30 **MIC-10-044**
Ultrahigh Spatial Resolution Perovskite-based Direct X-ray Imagers for Low-lag Medical Applications
Amlan Datta

17:30 **MIC-10-047**
Timing and Spatial Properties of HRPPD coupled to LGSO/LYSO for TOF-PET Applications
Chien-Min Kao

17:30 **MIC-10-050**
Analytical modeling and inclusion of object scatter in non-TOF 3D PET for low-count data
Jorge Roser

17:30 **MIC-10-053**
Noise Modeling of Three Material Dual Energy Computed Tomography with a Pathlength Constraint
Andrew E. Ferretti

17:30 **MIC-10-056**
Optimization of Pinhole Diameter in Fully Stationary Multi-Pinhole Brain SPECT:

Prioritizing Spatial Resolution via CNN-Based Correction
Takumi Akatsuka

17:30 **MIC-10-059**
Validated Optical Simulation for High-Energy Gamma Response in a 3-Layer LYSO DOI Detector
Shan Jiang

17:30 **MIC-10-062**
A Mesh-Type Reference Computational Phantom Platform for Multi-Modality Monte Carlo Simulation in OpenGATE
Jin Jegal

17:30 **MIC-10-065**
Inter-Crystal Scattering in LYSO-SiPM PET: Integrated Analysis via Geant4/GATE Simulation, CNN, and Multi-Pitch Experiments
Tianyi Deng

17:30 **MIC-10-068**
Design of a brain SPECT scanner based on high intrinsic resolution CZT detectors and multi-pinhole collimators
Kris Thielemans

17:30 **MIC-10-071**
Modeling analog SiPMs with temporal crosstalk integration for fast timing in medical imaging
Nicolaus Kratochwil

17:30 **MIC-10-074**
Study on the axial extension of the small-fish PET scanner MERMAID
Magdalena Kolodziej

17:30 **MIC-10-077**
Design and Modeling of BetaBox 2.0: a System for Quantitative Measurement of Beta Emitters in Single Cells
Kyle Klein

17:30 **MIC-10-080**
Hardware Ray-Tracing-Accelerated Optical Photon Transport in TOPAS on Apple Silicon
YoungMoon Goh

17:30 **MIC-10-083**
Identification of ICS Pixels in a high-resolution 3-Layer DOI-PET Detector Using a CNN
Shan Jiang

17:30 **MIC-10-086**
Impact of PET energy window extent on trues normalization and reconstructions
Simon Noë

17:30 **MIC-10-089**
MIMOSA: Medical IMaging MOnte Carlo Simulation Algorithms for fast proton therapy range monitoring
Declan D. Garvey

17:30 **MIC-10-092**
Quantitative Impact of Inter-Crystal Scatter on Image Quality and Sensitivity across LabPET-II Scanner Architectures: A Comparative GATE Simulation Study
Alexandre Bernier

17:30 **MIC-10-095**
Effects of Beam Filtration on Time-of-Flight-Based Scatter Rejection in Computed Tomography
Guen Bae Ko

17:30 **MIC-10-098**
Hybrid PGI-PET Imaging for Ion-Range Monitoring in Hadron Therapy
Javier Balibrea-Correa

17:30 **MIC-10-101**
Development of a PET/MRI Compatible Fluorescence Microscope for Simultaneous Cell Tracking in a Small Animal PET/MRI Scanner
Philipp Renn

17:30 **MIC-10-104**
Toward Simultaneous PET/SPECT/MR System for Theranostic Imaging
Yifei Jin

17:30 **MIC-10-107**
Development of a Preclinical Simultaneous Ultrasensitive SPECT and PET Imager
Ruiying Zhu

17:30 **MIC-10-110**
A Dual-Ring Super-Resolution PET System
Chien-Min Kao

17:30 **MIC-10-113**
Performance Evaluation of a DOI-Enabled Dedicated Brain PETCT System
Qiyu Peng

17:30 **MIC-10-116**
Design and Preliminary Validation of a Heart-Dedicated TOF-PET Scanner with Sub-250ps Timing Resolution
Qiyu Peng

17:30 **MIC-10-119**
Design and Quantitative Characterization of a High-Performance Brain-Dedicated PET System via Virtual Pinhole PET Technique
Yihao Chen

17:30 **MIC-10-122**
Design and Performance Characterization of a Sparsely Populated DOI capable Breast PET/MRI Insert
Janina Hohnholz

17:30 **MIC-10-125**
Enabling DOI capability in Low-Cost BGO PET System for Small-Animal Imaging
Haoyu Zou

17:30 **MIC-10-128**
Nested plastic scintillator PET detector geometries have distinct spatial resolution advantages
Martin Rädler, On behalf of the J-PET collaboration

17:30 **MIC-10-131**
Adapt-PET: A Hardware-Algorithm Co-evolution Framework for Versatile, Ultra-High-Resolution Targeted Imaging
Jianyong Jiang

17:30 **MIC-10-134**

17:30 **MIC-10-137**
Performance evaluation of the third generation of TOF-DOI Prism-PET detector modules
Soroush Shabani Sichani

17:30 **MIC-10-140**
Clinical Validation of MoDeCo: A Motion Detection and Correction Method for a

Dedicated Brain PET Scanner
Enrique Muñoz

17:30 **MIC-10-143**
Impact of beam hardening and detector response function corrections when using photon-counting imaging detectors
Hiroaki Hayashi

17:30 **MIC-10-146**
Evaluation of Lead-Free Composite for X-ray Shielding using LD-V1 Film
Seungwoo Park

17:30 **MIC-10-149**
Evaluation of image resolution for Novel Dual-energy X-ray Absorptiometry System
Hyuntae Leem

17:30 **MIC-10-152**
Physics-Guided Retinexformer for Beam Hardening Artifact Correction in Rock CBCT
Yuanjue Ma

17:30 **MIC-10-155**

17:30 **MIC-10-158**
Mitigating Scatter-Induced BMD Errors in Wide Fan-Beam DXA Using Anti-Scatter Grids
Myungwoo Oh

17:30 **MIC-10-161**
Empirical Decomposition for Quantification of Multi-Contrast-Agent
Zhe Wang

17:30 **MIC-10-164**
Empirical Correction of Detector Response for Quantitative X-Ray Transmission Modelling and its Application to Computed Tomography
Qingxiang Chen

17:30 **MIC-10-167**
Synthetic generation of the dental anatomy for cone-beam CT simulation from patient data
Idris Tatachak

17:30 **MIC-10-170**
Image Quality Evaluation of Cone Beam Computed Tomography (CBCT) in an O-arm

Fluoroscopy Machine Using the SedentexCT IQ Phantom
John Patrick Ryan S. De Guzman

17:30 **MIC-10-173**
Validation of conventional mammography material decomposition using VICTRE simulated breast data
Xiaochuan Pan

17:30 **MIC-10-176**

17:30 **MIC-10-179**
Development of a 64-Channel Energy and Timing Acquisition System for TOF-DXA
Sang-Hyun Chun

17:30 **MIC-10-182**
GARM: Geometry-Aware Reconstruction Method for Static CT Generalizable across Diverse Scanning Strategies
Peixuan Song

17:30 **MIC-10-185**
Impact of Small-Angle Event Selection in Compton Cone Imaging
Elisabetta Medina

17:30 **MIC-10-188**
Deep Learning-based 3D SPECT Reconstruction from Biplanar Projections and CT Scout Views
Jiarui Huang

17:30 **MIC-10-191**
The Inverse Problem of Spatiotemporal Emission Reconstruction from Prompt Gamma Timing Data
Julius Werner

17:30 **MIC-10-194**
Recent updates to STIR, a community effort of a quarter century
Nikos Efthimiou

17:30 **MIC-10-197**
Developments in fabrication and design flexibility of amorphous silicon microchannel plates
Georgios Konstantinou

17:30 **MIC-10-200**
A Universal Geometric Calibration Method for CBCT Systems with Arbitrary Trajectories
Tong Jia

17:30 **MIC-10-203**
CT-less Attenuation Maps as Priors for Robust Joint Activity–Attenuation Estimation in TOF and Non-TOF PET
Elise Emond

17:30 **MIC-10-206**
Convergence-Informed AI-Assisted Reconstruction for Dual-Panel PET Imaging
Abdollah Saberi Manesh

17:30 **MIC-10-209**
Anatomically Guided Adaptive Gaussian Representation for PET Image Reconstruction
Zhihao Li

17:30 **MIC-10-212**
MRI guided PET reconstruction in meningioma [^{68}Ga]DOTATOC patients, pituitary adenoma [^{18}F]FET, and neurodegenerative [^{18}F]FDG patients
Thomas L. Andersen

17:30 **MIC-10-215**
A Hybrid Neural Network Model for DaTscan Diagnosis of Neurodegenerative Disorders
Efstratios Roupas

17:30 **MIC-10-218**
A Global-Local Latent Diffusion Model for Limited-Angle CT Reconstruction
Tong Jia

17:30 **MIC-10-221**
Iterative proton CT reconstruction from list-mode data of a sandwich time-of-flight scanner
Aurélien Coussat

17:30 **MIC-10-224**
Direct normalization correction for a brain PET system with multi-resolution detector design
Chengzhi Yang

17:30 **MIC-10-227**
Effect of Cardiac Reorientation on Deep Learning-Based Denoising for Low-Dose Cardiac

SPECT
Jovan G. Brankov

17:30 **MIC-10-230**
Ghost Artifact Suppression in Multiplexed Self-Collimating SPECT via Total Variation Regularization
Rutao Yao

17:30 **MIC-10-233**
Integrating In-Patient Scattered Events in PET Reconstruction via a Monte Carlo Projector
Mathis Moulin

17:30 **MIC-10-236**
List-Mode Subspace-Based Dynamic PET: 1-Second Temporal Resolution on the NeuroEXPLORER
Thibault Marin

17:30 **MIC-10-239**
Hierarchical ROI-free Learning for GFR Category Stratification in Dynamic ^{99m}Tc-DTPA Renography
Zhuoyuan Xu

17:30 **MIC-10-242**
Design and Construction of Physical and Digital Phantoms for Image-Derived Input Function Validation Studies in Brain PET Imaging
Usman Khalid

17:30 **MIC-10-245**
TRACE: A New Phantom for Simultaneous Multi-Method Assessment of PET Spatial Resolution
Deepa Choudhary

17:30 **MIC-10-248**
A Reconstruction-Agnostic Paper Made Fan Phantom for Task-Relevant PET Spatial Resolution Assessment
Benjamin A. Spencer

17:30 **MIC-10-251**
Quantitative Image Quality Evaluation of ^{177}LuSPECT Using a NEMA NU 4-based SPECT IQPhantom
Yirong Zhang

17:30 **MIC-10-254**
Investigation of the stability of energy-based scatter estimation in PET
SeyedAmir ZamanPour

17:30 **MIC-10-257**
A Quantitative Comparison of PET Image Reconstruction Methods for Amyloid-Beta Plaque Identification in Alzheimer's Disease
Azeezat Azeez

17:30 **MIC-10-260**
Dose-Dependent Electron Density CT Images for PET Attenuation Correction
Debora Niekämper

17:30 **MIC-10-263**
TOF-Aware Single Scatter Simulation in STIR: Implementation and Validation Against Monte Carlo
Manil Sabeur

17:30 **MIC-10-266**
Event-by-Event Energy-Based Scatter Correction via Bayesian Likelihood Estimation
Mohammadreza Teimoorisichani

17:30 **MIC-10-269**
Synthetic CT Generation for Attenuation Correction in Respiratory-Gated Rb-82 Cardiac PET Using 3D Diffusion Models
Boxiao Yu

17:30 **MIC-10-272**
Beyond the Single-Tissue Voxel:A Spin-Echo–Based Multi-Tissue Decomposition Framework with Implications for Synthetic MRI and Machine Learning Diagnosis
Larry Zeng

17:30 **MIC-10-275**
Assessment of Cortical Defect Discriminability in Reduced-Dose Pediatric Tc-99m DMSA Renal SPECT
Michael A. King

17:30 **MIC-10-278**
Automated Coronary Artery Extraction up to Distal Vessels Based on Hessian Matrix and 3D Skeletonization to Compensate for Incomplete Labels
Ryutaro Ide

17:30 **MIC-10-281**
Differential Diagnosis of PD, PSP, and MSA: An XGBoost Approach to Retinal Layer Analysis
Francisco J. Martínez Murcia

17:30 **MIC-10-284**
Multi-step Nonlinear Iteration Method for ECT Energy Spectrum Decomposition
Junxu Mu

17:30 **MIC-10-287**

17:30 **MIC-10-290**
Low-Dimensional Embeddings of Structural MRI for Multi-Disease Brain Morphometry
Carmen Jiménez-Mesa

17:30 **MIC-10-293**
Detector design in the AIDER Compton Camera Using Neural Networks: A Hybrid CNN-DNN Approach
Deniel Rodriguez Almora

17:30 **MIC-10-296**
Impact of Spatial Normalization on the Performance of Deep Learning-Based Systems for Neurodegenerative Disease Classification
Fermin Segovia

17:30 **MIC-10-299**
Edge-Guided Deformation Field Fusion for Robust PET Motion Correction
Wenyuan Qi

17:30 **MIC-10-302**
Simulation Trained Convolutional Neural Network For Clinical Inter-Crystal Scattering Filtering
Oleksandr Bubon

17:30 **MIC-10-305**
Temporally and Spatially-Variant Penalty for Dynamic PET Reconstruction
Nasrin Taheri

17:30 **MIC-10-308**
SAR-Based Brain Aging Validation Using Functional Connectivity Correlation Matrices from UK Biobank
Alejandro Hernández

17:30 **MIC-10-311**
Interpreting Prognostic [^{18}F]FDG PET Radiomic Signatures Using Parametric Tumour Simulation
Lara M. Bonney

17:30 **MIC-10-314**
Parameter Estimation of Arterial Input Function Using Nonlinear Mixed-Effects Modeling With Reduced Sampling
Yong Du

17:30 **MIC-10-317**
Orbital MRI radiomics in thyroid eye disease: A multi-structure stability analysis using perturbation-based methods
Farbod Semnani

17:30 **MIC-10-320**
Feasibility of portal imaging in proton therapy: concept and phantom experiments
Christian Bäumer

17:30 **MIC-10-323**
A Feasibility Study of Patient-Specific Integral Dose Verification Using a 3D-Printed Tumor Model Scintillator for Radiosurgery
Hye Jeong Yang

17:30 **MIC-10-326**
Attenuation Correction for Targeted Alpha Therapy Monitoring with Compton Camera MACACO III+
Yuemeng Feng

17:30 **MIC-10-329**
Monte Carlo-Based PET Range Verification for Carbon-Ion Therapy
Qingguo Xie

17:30 **MIC-10-332**
Performance of a state-of-the-art ToF-PET detector in a proton therapy in-beam radiation environment
Thomas Fogg

17:30 **MIC-10-335**
In-Beam All-Digital PET for Dose-Guided Particle Therapy: Vision, Roadmap, and Progress
Ao Qiu

17:30 **MIC-10-338**
Feasibility Study of In-Beam Range Verification Using Pixelated CZT Detectors in Carbon Ion Therapy
Dian Guo

17:30 **MIC-10-341**
Experimental setup for radiobiological studies with laser-accelerated protons at high dose rates
Lucia Velasco Peñarrubia

17:30 **MIC-10-344**
Design and Development of a BGO-based PET Scanner for Dose Verification after Proton Therapy
Marta Freire

17:30 **MIC-10-347**
A Software Framework for Real-Time Prompt Gamma Range Verification
Korbinian Urban

17:30 **MIC-10-350**
Construction and positioning accuracy of a prototype Portable Organ Dosimetry Device (PODD) for RPT
William C.J. Hunter

17:30 **MIC-10-353**
^{224}Ra Experimental and simulation studies with the MACACO III+ Compton camera prototype
Luis Barrientos

17:30 **MIC-10-356**
AIDER Compton Camera for Targeted Radionuclide Therapy
Gabriela Llosá, On behalf of AIDER Collaboration

17:30 **MIC-10-359**
Gamma Detection for Source Localisation in Targeted Alpha Therapy
Sean Williams

17:30 **MIC-10-362**
Cellular-Scale Imaging of Theranostic Radiopharmaceutical Uptake with a Lensless Radiomicroscopy Sensor
Nicola Belcari

17:30 **MIC-10-365**
Intercrystal Compton Scattering Detection in Pixelated LYSO Detectors via Quantum Localization
Amirreza Hashemi

17:30 **MIC-10-368**
A Learned Unfolded Deconvolution Framework for Partial Volume Correction in Total-Body PET Imaging
Mohamed Saber Azimi

17:30 **MIC-10-371**
Direct Theranostic Dose Estimation using a Multi-Pinhole Model of the Sparse Portable Organ Dosimetry Device
Adam M. Alessio

17:30 **MIC-10-374**
FastPET for low-count reconstruction scenarios
Vanessa Nadig

17:30 **MIC-10-377**
Quantitative Reconstruction and Correction for Long-Axial FOV PET: Optimizing Component-Based Normalization and Scatter Estimation
Jianyong Jiang

17:30 **MIC-10-380**
Optimized Partial Field-of-View Reconstruction by Limited TOF Axial Rebinning in Long-Axial PET
Inki Hong

17:30 **MIC-10-383**
Generalizable CT-Free Low-Dose PET Restoration: Few-Shot Adaptation Across Multi-Scanners
Xiaoya Qiao

17:30 **MIC-10-386**
3D Photon Position Estimation Using Neural Networks in Monolithic-Based PET Systems
Marta Freire

17:30 **MIC-10-389**
Depth Attention and Volume Attention Module for 3D Medical Image Segmentation
Xiaoshuo Kan

17:30 **MIC-10-392**
Comparing the anatomical accuracy of a PET(O15) reconstructed algorithm (AGR) on Moyamoya Patients
Azeezat Azeez

17:30 **MIC-10-395**
MRI-Informed SPECT-only Spatial Normalization for Reliable Brain Perfusion Quantification
Euijin You

17:30 **MIC-10-398**
When Do TAC and ROI Features Help? Residual Multimodal Learning for GFR Estimation in Dynamic ^{99m}Tc-DTPA Renography
Yuanhao Zhu

17:30 **MIC-10-401**
Uncertainty-Guided Localized Diffusion Refinement for Lumbar Spine MRI Segmentation
Quang Vinh Pham

17:30 **MIC-10-404**
PhysiCal-PET: Physics-based neural networks for the rapid position Calibration of PET Scanners
Mojahed Abushawish

17:30 **MIC-10-407**
Nonsubsampled Contourlet Transform-based Generative Adversarial Networks for Anatomical Structure-Preserving Low Dose CT Denoising
Sanghyun Cho

17:30 **MIC-10-410**
Preliminary Results of Generative Model-Based Positron Range Correction in PET Imaging
Yucun Hou

17:30 **MIC-10-413**
Wavelet-Conditioned Rectified Flow for Efficient Whole-Body Low-Dose PET Denoising
Luxiang Xie

17:30 **MIC-10-416**
Adaptive Spatio-Temporal Denoising for Low-Dose Fluoroscopy via Motion-Gradient Weighting
Nerea León

17:30 **MIC-10-419**
An Ensemble of Deep-Learning Classifiers for 3D Anatomical Change Reconstruction in Carbon-Ion Radiotherapy (CIRT)
Maria Martisikova

17:30 **MIC-10-422**
Reduction of Breathing and Metallic Implant Artifacts in PET with Synthetic CT Attenuation
Zoe Wilson

17:30 **MIC-10-425**
Frozen Stable Diffusion VAE as a Slice-Wise Encoder for Scalable 3-D Medical Image Generation
Antoine De Paepe

17:30 **MIC-10-427**
Deep learning-based 3D SPECT generation model for 225Ac-DOTATATE quantification using CT and 2D Planar images
Jingyu Yang

17:30 **MIC-10-428**
No CT, No Problem: Synthetic PET Enables Attenuation Correction in Dedicated Brain Scanners
Alejandro Merino-Balaguer

17:30 **MIC-10-431**
Alpha-CenterNet: A Heatmap-Based Detector for Alpha-Particle Localization in Scintillator-Camera Imagery
Donghee Kang

17:30 **MIC-10-434**
AI-Assisted Circuitry Design for a Timing-Sensitive SiPM Front-End Readout
Boren Wang

17:30 **MIC-10-437**
Simultaneous Dual Tracer PET Separation in reconstruction: Validation on LAFOV Data
Zekai Li

17:30 **MIC-10-440**
High-Energy Proton Scattering Radiography of a Geant4 Hand Phantom under Constant-Energy Loss
Reshma S. Ughade

17:30 **MIC-10-443**
Multiple Emission Tomography: A High-Sensitivity Single-Layer Simultaneous PET Compton-Camera
Marco Pizzichemi

17:30 **MIC-10-446**
A Scalable NaI(Tl)-SiPM Photon-Counting Scintillator Detector for Gold and Gadolinium XRF Imaging
Bryan Casanelli

17:30 **MIC-10-449**
A Preclinical PET System for Simultaneous Acquisition and Separation of Multiple Tracers
Jackson W. Foster

17:30 **MIC-10-452**
On the Pseudo Dark-Field Signal in X-Ray Scattering Tensor Tomography
Ruifeng Liu

17:30 **MIC-10-455**
A Proof-of-Concept Tri-Mode PET and SPECT Imager with a Shared Scintillator-as-Collimator Detector
Xiangtao Zeng

17:30 **MIC-10-458**
Zero-Shot PET Image Super-Resolution via Cross-Modal Mutual Information Guidance
Yilin He

17:30 **MIC-10-461**
Extracting total and Compton attenuation coefficients via ghost imaging-like photon counting
Gregory R. Romanchek

17:30 **MIC-10-464**
Enhancement of Charged-Particle Shielding via Lightweight Nanocomposites
Gabrielle J. Grey

17:30 **MIC-10-467**
Detector Geometry Optimization of a Sensing Collimation Imager (SCI)
Ling Cai

17:30 **MIC-10-470**
Toward Whole-Body Whole Gamma Imaging: Monte Carlo Simulation of ^{89}Zr PET-

Compton Hybrid Imaging
Mizuki Miyahara

13 November, 2026

9:00 – 11:00 FEDERICO GARCÍA LORCA
MIC-11 Young Investigator Session (oral)

Chairs:
Emilie Roncali (Davis)
Ciprian Catana (Charlestown)

9:00 **MIC-11-01**
Toward Clinical Deployment of Complex PET Designs via Fast In-System Calibration
Julian Thull, Julian Thull

9:15 **MIC-11-02**
A Compact Preclinical PET Scanner Achieving NEMA-Standard Sub-0.5 mm Spatial Resolution via Analytic FBP Reconstruction
Chenxi Li

9:30 **MIC-11-03**
Development of a ring-type Quantum Entanglement PET Imaging System and Application of a Novel Image Reconstruction Algorithm to In-Vivo Imaging
Koki Nakamura

9:45 **MIC-11-04**
SIMPLE-DIP: Positronium Lifetime Image Reconstruction Using Deep Image Prior
Bangyan Huang

10:00 **MIC-11-05**
AI-Based Predictive Dosimetry from PET for 177Lu-PSMA Radiopharmaceutical Therapy for Prostate Cancer
Bowen Lei

10:15 **MIC-11-06**
Event-Resolved Parent-Progeny Discrimination Using CMOS Lensless Radiomicroscopy for ^{225}Ac Targeted Alpha Therapy
Hyeyeun Chu

10:30 **MIC-11-07**
Physics-Guided Implicit Neural Representation for 3D Ac-225 Compton Imaging
Gyohyeok Song

10:45 **MIC-11-08**
Attenuation Map Estimation from NAC Brain PET Images Using a 3D Patch-Based U-Net: A Multi-Tracer Study on the NeuroEXPLORER
Max Keppens

9:00 – 11:00 MANUEL DE FALLA
MIC-12 New Concepts and Emerging Applications

Chairs:
Magdalena Rafecas (Lübeck)

9:00 **MIC-12-01**
Direct clinical imaging of alpha therapy in a PET/CT scanner via cascade gamma-rays imaging
Javier Caravaca

9:15 **MIC-12-02**
From MeV Gamma to PET Signal: Experimental Demonstration of Pair Production Tomography for Theranostic Imaging
Biswajit Das

9:30 **MIC-12-03**
Quantitative evaluation of pair-produced positrons using a clinical linear accelerator for pair-production tomography
Ryosuke Ota

9:45 **MIC-12-04**
Terbium-149: a Laboratory for Three-Photon Events
Lorenzo Mercolli

10:00 **MIC-12-05**
The first in vivo quantum entanglement imaging of a human subject
Pawel Moskal

10:15 **MIC-12-06**
Constraining CP Invariance in Ortho-Positronium Decays at 7 T with NeuroSphere MR-Compatible PET Modules
Magdelena S. Allen

10:30 **MIC-12-07**
Novel Spatial Encoding Using Larmor Precession in Nuclear Medicine: A Study on Imaging Robustness
Hiroto Suzuki

10:45 **MIC-12-08**
Real-Time Task-Based Adaptive SPECT Imaging via Optimized System Sampling Strategies Using a Robotic Clinical SPECT Platform
Yifei Jin

11:30 – 12:45 FEDERICO GARCÍA LORCA
MIC-13 New radiation detector technologies for medical imaging (2)

Chairs:
Paul R. Lecoq (Geneva)
Han Gyu Kang (Chiba)

11:30 **MIC-13-01**
Cramér–Rao–Efficient Timing with Photon Counting: Theory and Proof-of-Concept Demonstration for Cherenkov TOF-PET
Nicolaus Kratochwil

11:45 **MIC-13-02**
Sparse-to-Dense SiPM Readout Upsampling for Position Estimation in PET Detectors
Francis Loignon-Houle

12:00 **MIC-13-03**
Crosshair Light-Sharing Detectors with Diode-based Multiplexing for High-Resolution TOF-DOI PET
Han Gyu Kang

12:15 **MIC-13-04**
High-performance 4×4-channel microchannel plate photomultiplier tubes with bismuth germanate window faceplate
Ryosuke Ota

12:30 **MIC-13-05**
Achieving Sub-100 ps CTR and Sub-2 mm DOI Resolution in TOF-PET Modules
Giulia Terragni

11:30 – 12:45 MANUEL DE FALLA
MIC-14 Novel applications of AI in radiation-based medical imaging (2)

Chairs:
Joyita Dutta (Amherst)

11:30 **MIC-14-01**
Deep Learning Limited Angle Artefact Correction for dual panel PET in Shearlet Domain
Jens Maebe

11:45 **MIC-14-02**
Multi-Objective Bayesian Optimization of Self-Collimating SPECT System Design Using Quantitative Imaging Metrics
Syed O. Shah

12:00 **MIC-14-03**
Sensitivity-Aware Gated Deep Reconstruction for Cascade γ Coincidence Imaging
Hao Jia

12:15 **MIC-14-04**
Two-Stage Retrieval-Augmented 3D Detection of Bone Metastatic Lesions via SPECT/CT
Yangshi Lin

12:30 **MIC-14-05**
Data Augmentation Strategy Analysis for Noninvasive Lung Cancer Subtype Classification
Xinyu Hu

12:45 – 13:05 FEDERICO GARCÍA LORCA
M-LT-05 Kinetic modeling, molecular connectivity analysis and radiomics, Theranostics, Imaging and dosimetry in therapy (particle, radiopharmaceutical, surgery), Total body imaging systems including applications

Chairs:
Paul R. Lecoq (Geneva)
Han Gyu Kang (Chiba)

12:45 **M-LT-05-01**
Pixelated Cherenkov Crystals for Prompt-Gamma Imaging in Proton Range Verification
Leonor Rebolo

12:47 **M-LT-05-02**
Coded-Mask PGI for Proton Range Verification With Pure Cherenkov Crystal Detectors
Salvador M. Gómez

12:49 **M-LT-05-03**
Deep Learning-based CT-Free Deformable Registration for PET-CT Misalignment Correction
Abolfazl Mehranian

12:51 **M-LT-05-04**
Evaluation of TOF-DOI Crystal Topologies for the HD-MetaPET MRI Insert
Thore Meyer

12:53 **M-LT-05-05**
Noise-Robust Bayesian Parameter Estimation of Two-Tissue Compartment Kinetic Model for dynamic SPECT imaging
Dandan Zhang

12:55 **M-LT-05-06**
Conditional Flow-Matching-based Kinetic Refinement for Low-Count SRTM-based Parametric Imaging in Dynamic PET
Yu Jin Seol, Yu Jin Seol

12:57 **M-LT-05-07**
Attenuation Images from Time-of-Flight PET for Metal Artifact Reduction: A Phantom Study
Ann-Kristin Lüvelsmeyer

12:59 **M-LT-05-08**
An FPGA-based data acquisition system for remote wireless radiation monitoring
Robert S. Miyaoka

13:01 **M-LT-05-09**
Energy-Shifting: an efficient approach for Monte Carlo Particle Therapy Dose Calculation
Julien Bert

13:03 **M-LT-05-10**
Treatment Monitoring System for Proton Therapy Based on Beam Range Measurement
SeHyun Jang

12:45 – 13:05 MANUEL DE FALLA
M-LT-06 Signal and Data Processing, New Concepts and Emerging Applications

Chairs:
Joyita Dutta (Amherst)

12:45 **M-LT-06-01**
Development of a Dual-Modality Imaging Capsule for Laparoscopic Radio-Guided Surgery
Krishan Patel

12:47 **M-LT-06-02**
Development of a High Sensitivity Cascade Gamma Photon Coincidence Imaging System
Qingyang Wei

12:49 **M-LT-06-03**
Quantum entanglement of annihilation photons as a function of the annihilation

mechanism
Deepak Kumar

12:51 **M-LT-06-04**
First In-Vivo Positronium Ratio Imaging (PRI) using F-18 FDG: A Preliminary Study with Phantom and a Mouse Model
Macoto Fujimoto

12:53 **M-LT-06-05**
Quantitative 4D PET Imaging of Photosynthate Transport and Rhizosphere Carbon Partitioning in Intact Plant–Soil Systems
Muhammad Nasir Ullah

12:55 **M-LT-06-06**
Comparative Evaluation of Respiratory Motion Correction Methods for Upright Walk-Through PET Using XCAT Simulations
Rabia Aziz

12:57 **M-LT-06-07**
Dementia Risk Estimation From a Positron Emission Tomography-Derived Latent Biomarker
Cristóbal Vázquez García

12:59 **M-LT-06-08**
Data-Driven Selection of Representative Motion Models for Simulation in Dynamic Cardiac PET
Nader Nemati, Nader Nemati

13:01 **M-LT-06-09**
A Quality Control Framework for Deep Learning-based Attenuation Map Synthesis in PET
Yihuan Lu

13:03 **M-LT-06-10**
Characterizing Noise in Clinical Nuclear Medicine Modalities via Quantum-Inspired Framework
Amirreza Hashemi

15:00 – 17:00 Poster Area
MIC-15 MIC Poster Session 3

Chairs:
Georg Schramm
Charalampos Tsoumpas (Groningen)

15:00 **MIC-15-003**
Dual-ended Redout PET Detectors based on 0.25 mm pitch LYSO/GAGG arrays
Junwei Du

15:00 **MIC-15-006**
Study of the response of comercial CMOS sensors to soft X-rays
Lucía Velasco

15:00 **MIC-15-009**
Asymmetric dual-ended readout using diode-based multiplexing circuits for TOF-DOI PET detectors
Ruipeng Dai

15:00 **MIC-15-012**
Development of a TOF-DOI PET Detector Using Dual-ended Interleaved Multiplexing Readout
Xiaolong Jiang

15:00 **MIC-15-015**
Design of a Single-Ended Readout DOI PET Detector with BGO and Deep Learning
Sungwook Hong

15:00 **MIC-15-018**
A pulse-train model for X-ray photon-counting scintillation detectors with pile-up
Lukas Schröder

15:00 **MIC-15-021**
Monte Carlo Simulations of a Penumbra-Based Collimator-less SPECT Detector for Targeted Radionuclide Therapy Monitoring
Iara Neves

15:00 **MIC-15-024**
A covariance-based framework for quantifying circuit and intrinsic CTR limits in TOF-PET detectors
Hyeongseok Shim

15:00 **MIC-15-027**
Identification and Mitigation of Inter-Crystal Scatter in Dual-Layer DOI Configurations Under Highly Multiplexed Readout
Lukas U. Rauscher

15:00 **MIC-15-030**
Characterization of a multiplexed SiPM readout with free-running ADC for BGO PET

detectors
Nicola Belcari

15:00 **MIC-15-033**

15:00 **MIC-15-036**
Evaluating a novel type of silicon photomultiplier for X-ray photon-counting CT applications
Lukas Schröder

15:00 **MIC-15-039**
Ultra-High-Definition, 8 µm pitch, Low-Dose X-ray Detector for Microfocus Clinical Applications: From Dental to Medical Imaging
Michele Sannino

15:00 **MIC-15-042**
Dual-Ended Readout PET Detector Based on Semi-Monolithic Laser-Engraved Scintillators
Victor Sánchez-Tembleque

15:00 **MIC-15-045**
PETVision: An Ultra-High TOF Resolution PET System with 2.5D Modular Flat-Panel Detectors
Yue Zhuo

15:00 **MIC-15-048**
Comparative Evaluation of NUV-MT and NUV-DJ SiPM Timing Performance for TOF-PET Detector Application
Suhan Choi

15:00 **MIC-15-051**
Decomposing Optical Photon Transport in PET Detectors: Geometric Priors and Generative Models of Residual Stochasticity
Stephan Naunheim

15:00 **MIC-15-054**
Scaling TOF-PET Timing Calibration via Structured Detector-Wise Learning
Julian Thull

15:00 **MIC-15-057**
GPU-Accelerated Monte Carlo Simulation for SPECT Imaging
Feng Zhou

15:00 **MIC-15-060**
Monte Carlo Validation of a Positron Emission Mammography Scanner Using GATE 9.4: Sensitivity Analysis with an Aluminum Sleeve Phantom
Sara H. El-Sallabi

15:00 **MIC-15-063**
Heuristic seeding for GA-based optimization of halbach magnets for PET-compatible low-field MRI
Fumihiko Nishikido

15:00 **MIC-15-066**
Experimentally Validated GATE Model of a Commercial PET System with Sub-200 ps TOF
Michel Atieh

15:00 **MIC-15-069**
Experimental and simulation-guided light-sharing characterization of hexagonal laser-engraved PET detectors.
Clara N. Golhen Mateo

15:00 **MIC-15-072**
Microstructure-Informed Single-Grid Dark-Field X-ray Imaging for Breast Microcalcification Typing
Sunghoon Choi

15:00 **MIC-15-075**
SimTBPET: A faster framework for Total Body Monte Carlo PET simulations
Arnau Farré-Melero

15:00 **MIC-15-078**
Performance Comparison of Low-Multiplexing and High-Multiplexing Multi-Pinhole Collimators for a Large-Animal Cardiac SPECT System
Jiali Yan

15:00 **MIC-15-081**
Is 20 mm Still Optimal? Revisiting Scintillator Length in Modern TOF-PET Systems
Mizuki Furuta

15:00 **MIC-15-084**
Comparison Between GATE and SimSET Monte Carlo Simulations on GE Omni Legend PET scanner geometry
SeyedAmir ZamanPour

15:00 **MIC-15-087**
Hybrid Least-Square and k-Nearest-Neighbour Event Positioning for a Compact Gamma Camera with Monolithic NaI(Tl) Scintillator
Zhongyi Wu

15:00 **MIC-15-090**
Ultra-fast Positron Range Simulator for Patient-Specific PET Imaging
Robert J. Paneque-Yunta

15:00 **MIC-15-093**
Analytic Determination of Minkhole Collimator Sensitivity With Penetration
Yusheng Li

15:00 **MIC-15-096**

15:00 **MIC-15-099**
Performance evaluation of Compton-PET with MACACO-PET system
Siddharth Parashari

15:00 **MIC-15-102**
Dosimetry Assessment and Noise Scaling Laws in Proton Computed Tomography
Mara Bruzzi

15:00 **MIC-15-105**
Feasibility of 511 keV photon detection in the presence of scattered x-rays for simultaneous PET and CT imaging
Paul E. Kinahan

15:00 **MIC-15-108**
Integrating X-ray Dark-Field and Fluorescence Modalities for Molecular Imaging in Personalized Medicine: Initial Specifications of Setup Design and Integration Parameters
Xiaolei Yan

15:00 **MIC-15-111**
A Dual-Head Positron Imaging System
Matthias Streun

15:00 **MIC-15-114**
Development of the CT extension of the MERMAID PET prototype
Rebecca Kantorek

15:00 **MIC-15-117**
Initial performance evaluation of a dual-panel, high-resolution TOF-DOI PET prototype
Ming Niu

15:00 **MIC-15-120**
Development of a Four-Layer DOI Detector Based Preclinical PET System
Hang Yang

15:00 **MIC-15-123**
Experimental Evaluation of 3D Imaging Point Spread Function for the Ultra-High Performance Brain PET (UHB-PET) Scanner
Nicolas A. Karakatsanis

15:00 **MIC-15-126**
System integration of a Breast PET/MR Insert in a Whole-Body PET/MRI System: Data Driven Temperature Drift Correction and Synchronization
Janina Hohnholz

15:00 **MIC-15-129**
Performance Evaluation of the Motion-Adaptive Molecular and Behavioral Observation (MAMBO)-PET System
Francisco E. Enriquez-Mier-y-Teran

15:00 **MIC-15-132**
First experimental and phantom results of the DC-SPECT scanner: a cardiac-dedicated SPECT with Laser-Processed CsI:Tl Detector Modules
Xi Zhang

15:00 **MIC-15-135**
Validation of an Image Based Method of Estimating Mechanical Offsets in a Rotating Flat-Panel PET Scanner with Phantom and Clinical Data
Anirudh Shahi

15:00 **MIC-15-138**
Detector Stability and Effects on Time and Energy Resolution in Novel Clinical Brain PET Scanners
Luis Batres

15:00 **MIC-15-141**
Counting loss correction of photon counting detector: the need to consider the effective atomic number of the target object in clinical applications
Natsumi Kimoto, This is a collaborative study between JOB CORPORATION and Junshin Gakuen University.

15:00 **MIC-15-144**
An algorithm to generate effective atomic number and mass density images from photon-counting CT: application for lung disease assessment
Takashi Asahara

15:00 **MIC-15-147**
Dual-Energy CT Metal Artifact Reduction Using VMI-Guided Iterative Reconstruction Refinement
Sungmin Park

15:00 **MIC-15-150**
Magnification Effect Evaluation for Novel Dual-Energy X-Ray Absorptiometry System
Chanwoo Kwon

15:00 **MIC-15-153**
Transient radiative transport equation solution for ToF-CT ballistic X-ray photons
Maëlle Fromont

15:00 **MIC-15-156**
Characterization of a Photon-Counting CT Modality for Preclinical PET/CT
João F.C.A. Veloso

15:00 **MIC-15-159**
Characterization of a LYSO:Ce/SiPM detector array for photon-counting CT
João Filipe C.D.A. Veloso

15:00 **MIC-15-162**
Linearizing the Transformation from CT Hounsfield Units to Linear Attenuation Coefficient for PET Attenuation Map Generation using Virtual Non-Contrast Images
Heba Alrakh

15:00 **MIC-15-165**

15:00 **MIC-15-168**
Image Improvement in X-ray Fluorescence Computed Tomography Using Deep Image Prior with X-ray Transmission Images
Tsutomu Zeniya

15:00 **MIC-15-171**
Experimental Characterization and Materials-Driven Optimization of Fine-Pitch CZT Detectors for Photon-Counting CT
Aziz Ikhlef

15:00 **MIC-15-174**
Longitudinal Cone-Beam CT and MRI Integration for High-Fidelity Synthetic CT Generation
Vincent Jaouen

15:00 **MIC-15-177**
Dynamic hepatocyte-specific liver imaging using a two-dimensional SiPM-based photon counting CT: Comparison between healthy and liver tumor mouse models
Fitri Lucyana

15:00 **MIC-15-180**
Improved Material Decomposition Method in DXA Using Scatter-Induced Arrival Time Difference
Sena Kwon

15:00 **MIC-15-183**
Limited-Angle and Few-View Image Reconstruction Using Point Spread Functions
Gengsheng Zeng

15:00 **MIC-15-186**
Accelerating CGCIS Iterative Reconstruction Based on Location Priors from the DBP Algorithm
Kui Wang

15:00 **MIC-15-189**
DeepDreaming SPECT: Gradient-Based Reconstruction via Differentiable Physics Simulation
Francesc Massanes

15:00 **MIC-15-192**
Plug-and-Play Learned Regularization in PET Reconstruction: Integration of DeepInverse and STIR through SIRF
Kathiresan Chandrasekaran

15:00 **MIC-15-195**
Optimization of CT Reconstruction for Improved Image Quality in Lithium-Ion Battery Modules for Electric Wheelchairs
Donghee Kim

15:00 **MIC-15-198**
Frequency Guided Network for Quantitative PET Reconstruction with Improved Scatter Correction
Yucun Hou

15:00 **MIC-15-201**
Image-guided depth-of-interaction recovery for parallax-mitigated PET image reconstruction
Carlos Galindo-Morata

15:00 **MIC-15-204**
Patient-Adaptable Smoothing with Deep Learning Denoising for Cardiac-gated SPECT Studies
Xirang Zhang

15:00 **MIC-15-207**
LAFOV scanner SAFOV imaging: Sensitivity Restoration by Local Tomography Approach
Vladimir Panin

15:00 **MIC-15-210**
Clinically Feasible Deep-Learning–Enabled Dual-Gating Reconstruction for Cardiac PET
Kuan-Hao Su

15:00 **MIC-15-213**
Regularized Tomographic Reconstruction for Fast Ultrasound-Modulated Optical Tomography
Lucas Duclos

15:00 **MIC-15-216**
Multiresolution Proximal Stochastic Denoising Regularization for Accelerated Sparse-View CT Reconstruction
Antoine De Paepe

15:00 **MIC-15-219**
MLEM Positron Range Corrector for PET/CT
Joaquín López Herraiz

15:00 **MIC-15-222**
Lutetium-176-Aided Joint Activity and Attenuation Reconstruction in TOF-PET Using Trust-Region Cubic Surrogate Optimization
Xin Zhao

15:00 **MIC-15-225**
Organ-based Motion Correction for PET Image Reconstruction using Artificial Intelligence to Segment Organs
Deepak Bharkhada

15:00 **MIC-15-228**
Multi-information Joint Iterative Reconstruction Algorithm for Cascaded Gamma Photon Coincidence
Shuyu Xu

15:00 **MIC-15-231**
Detector-Block-Level Geometric Calibration for Full-Ring Multi-Aperture SPECT Using Analytical Ray-Tracing Simulation
Qian Wang

15:00 **MIC-15-234**
A flexible convex optimization framework for list-mode PET reconstruction with explicit regularization using Primal-Dual Hybrid Gradient
Alejandro Lopez-Montes

15:00 **MIC-15-237**
Investigation of hybrid CT-free attenuation correction framework with TOF-MLAA and deep learning
Yuya Onishi

15:00 **MIC-15-240**
Crystal-Wise Dead-Time Correction: Application to VRAIN
Hideaki Tashima

15:00 **MIC-15-243**
Beyond NEMA Standards: Spatial Resolution Assessment of a Dual-Rotation Preclinical PET System
João F.C.A. Veloso

15:00 **MIC-15-246**
PET Spatial Resolution Repeatability and Reproducibility Following the NEMA NU 2 Standard
Benjamin A. Spencer

15:00 **MIC-15-249**
Characterization and Correction of Dynamic Changes in Sensitivity Patterns for the Jülich BrainPET-7T
Juergen J. Scheins

15:00 **MIC-15-252**
Evaluation of the Impact of Motion Correction on PET Quantification of Early Diagnosis of Alzheimer's Disease
Viet A. Dao

15:00 **MIC-15-255**
Investigation of PET-only Data-driven Motion Detection and Correction Methods
Natia Beriashvili

15:00 **MIC-15-258**
Rigorous and accurate estimation of spatial resolution of MLEM reconstructions in PET
Martin Rädler, On behalf of the J-PET collaboration

15:00 **MIC-15-261**
Randomand Scatter Correction for a Brain PET System Based on List-Mode Data
Zexing Wu

15:00 **MIC-15-264**
Attenuation Correction Strategies for Bain Scans in State-of-the-art TOF PET/MRI
Mohammadreza Teimoorisichani

15:00 **MIC-15-267**
Performance Evaluation of DSAC in LYSO and Plastic Scintillators: A Comparative Simulation Study for CT-less PET
Satyam Tiwari

15:00 **MIC-15-270**
Random Estimation for a PET Scanner Dedicated to Plant Rhizosphere Imaging Using LORs Outside the Reconstruction Volume
Muhammad Nasir Ullah

15:00 **MIC-15-273**
An Exponential Total Variation Functional to Replace the Total Variation Norm
Gengsheng L. Zeng

15:00 **MIC-15-276**
Comparative Evaluation of Respiratory Motion Correction Methods for Upright Walk-Through PET Using XCAT Simulations
Rabia Aziz

15:00 **MIC-15-279**
Multi-parametric calibration and correction procedures for clinical and preclinical PET scanners: improving timing and energy resolution
Iván Colmenarejo Allavena

15:00 **MIC-15-282**
Dementia Risk Estimation From a Positron Emission Tomography-Derived Latent

Biomarker
Cristóbal Vázquez García

15:00 **MIC-15-285**
Affine rotation and scaling transformations directly over the sinogram domain images for data augmentation
Alejandro Sanz-Sánchez

15:00 **MIC-15-288**
Multi-Hit Event Recovery in Multiplexed PET
Kurumi Narita

15:00 **MIC-15-291**
Hyperion DAQ: A Versatile Data Acquisition and Processing Platform
David Schug

15:00 **MIC-15-294**
Quantifying the Effect of Partial Volume Correction on Lesion Dosimetry in ^{161}Tb-FAPI-2286 and ^{177}Lu-FAPI SPECT/CT imaging
Mohamed Saber Azimi

15:00 **MIC-15-297**
A Quality Control Framework for Deep Learning-based Attenuation Map Synthesis in PET
Yihuan Lu

15:00 **MIC-15-300**
Generating synthetic PET/CT scans with latent diffusion models
Kevin H. Leung

15:00 **MIC-15-303**
Characterizing Noise in Clinical Nuclear Medicine Modalities via Quantum-Inspired Framework
Amirreza Hashemi

15:00 **MIC-15-306**
Data-Driven Selection of Representative Motion Models for Simulation in Dynamic Cardiac PET
Nader Nemati, Nader Nemati

15:00 **MIC-15-309**
Initial Validation of a High-Precision External Head-Motion Tracking System for γβ$^+$ Brain PET Imaging
Michael A. King

15:00 **MIC-15-312**
Noise-Robust Bayesian Parameter Estimation of Two-Tissue Compartment Kinetic Model for dynamic SPECT imaging
Dandan Zhang

15:00 **MIC-15-315**
Conditional Flow-Matching-based Kinetic Refinement for Low-Count SRTM-based Parametric Imaging in Dynamic PET
Yu Jin Seol, Yu Jin Seol

15:00 **MIC-15-318**
Treatment Monitoring System for Proton Therapy Based on Beam Range Measurement
SeHyun Jang

15:00 **MIC-15-321**
Pixelated Cherenkov Crystals for Prompt-Gamma Imaging in Proton Range Verification
Leonor Rebolo

15:00 **MIC-15-324**
Coded-Mask PGI for Proton Range Verification With Pure Cherenkov Crystal Detectors
Salvador M. Gómez

15:00 **MIC-15-327**
An FPGA-based data acquisition system for remote wireless radiation monitoring
Robert S. Miyaoka

15:00 **MIC-15-330**
Attenuation Images from Time-of-Flight PET for Metal Artifact Reduction: A Phantom Study
Ann-Kristin Lüvelsmeyer

15:00 **MIC-15-333**
Depth-Resolved Multi-Nuclide Decomposition of Carbon-Ion PET for Range Verification
Qingguo Xie

15:00 **MIC-15-336**
FARO: Feasibility of Adaptative Surface-Guided Radiation Oncology
Nataly Castellanos

15:00 **MIC-15-339**
A Cherenkov-Based Prompt Gamma Imaging for Proton Range and Dose Prediction Using a Multilayer Perceptron
Xiangtao Zeng

15:00 **MIC-15-342**

Compact Handheld Compton Camera versus Planar Gamma Camera for Post-Iodine-131 Therapy Imaging: A GATE/Geant4 Monte Carlo Study

Mina-Ermioni Tomazinaki

15:00 **MIC-15-345**

Comparison of CNN-Based Reduced-Time-Point and Conventional Single-Time-Point Voxel Dosimetry for ^{177}Lu-DOTATATE SPECT/CT

Stathis Varzakis, This work is supported by the EPSRC-funded UCL Centre for Doctoral Training in Intelligent, Integrated Imaging in Healthcare (i4health) (EP/S021930/1), the National Physical Laboratory (NPL) and the UK National Measurement System of the UK Government's Department for Science, Innovation and Technology (DSIT). SIRF and STIR software maintenance is part-funded via CCP SyneRBI (funded by the EPSRC grant EP/T026693/1) and by STFC through the UKRI Digital Research Infrastructure programme.

15:00 **MIC-15-348**

Design and characterization of detector modules and readout electronics for a dual head PET system for proton therapy verification

Pedro Rato-Mendes

15:00 **MIC-15-351**

Characterization of Prompt Gamma-Ray Emission for Helium-Ion Beam Range Verification: A Monte Carlo Study

Weigang Duan

15:00 **MIC-15-354**

GPU-Accelerated Voxel-Wise Mono/Bi-Exponential Fitting for Lu-177 SPECT Time-Integrated Activity Estimation

Haotian Tan

15:00 **MIC-15-357**

A Three-Stage Scintillator-Compton Camera for BNCT: From Point-Source Resolution to Phantom Reconstruction

Sergio López Martínez

15:00 **MIC-15-360**

Impact of PET Energy Window Selection on Y-90 Radioembolization Dosimetry

Matthew Strugari

15:00 **MIC-15-363**

A Compton Camera Using GAGG Scintillators Coupled with SiPM Array Readout for Online Monitoring in Particle Therapy

Yun Wang

15:00 **MIC-15-366**
***In Silico* Optimization of [^{177}Lu]Lu-PSMA-617 Therapy Regimens**
Marc Ryhiner

15:00 **MIC-15-369**
Energy-Shifting: an efficient approach for Monte Carlo Particle Therapy Dose Calculation
Julien Bert

15:00 **MIC-15-372**
Human Single Time Point Dosimetry Using Weight-Based Extrapolated Mouse Effective Half-Life
Jingyu Yang

15:00 **MIC-15-375**
Deep Learning-based CT-Free Deformable Registration for PET-CT Misalignment Correction
Abolfazl Mehranian

15:00 **MIC-15-378**
Investigation of Image Quality Gains Using Variable Time Windows in Long-Axial PET Systems
Jianyong Jiang

15:00 **MIC-15-381**
Evaluation of TOF-DOI Crystal Topologies for the HD-MetaPET MRI Insert
Thore Meyer

15:00 **MIC-15-384**
Towards Clinically Compatible Dynamic PET: Enabling Kinetic Analysis with 20-Minute Acquisitions
Irene Incicco

15:00 **MIC-15-387**
SADCA-ResDiff: A Structure-Aware Dual Cross-Attention Residual Diffusion Network for MR-Free Partial Volume Correction in Amyloid Brain PET
Runxiang Huang

15:00 **MIC-15-390**
A comparison of deep-learning-based attenuation correction methods in brain perfusion SPECT
Raúl Osorio Durán

15:00 **MIC-15-393**
Assisting Total-Body Multiplexed PET Separation Using Synthetic Paired Data
Denis Prokopenko

15:00 **MIC-15-396**
A Multi-Client Split Federated Diffusion Framework for Resource-Efficient Cardiac-Gated MP-SPECT Denoising
Zhigang Sun

15:00 **MIC-15-399**
Weakly Supervised Cyclic Disentanglement for Delayed PET Image Synthesis
Zhigang Sun

15:00 **MIC-15-402**
Neural Radiance Field-Based Reconstruction of Object Changes in Stationary Computed Tomography with Linearly Distributed Sources
Haoyuan Qian

15:00 **MIC-15-405**
Methods for Reconstruction Aware Completion of Partial PET Sinograms
Ziad Burbar

15:00 **MIC-15-408**
Symmetry-Enhanced YOLOv11 for Bone Metastatic Lesion Detection in Whole-Body Bone Scintigraphy
Fenghua Weng

15:00 **MIC-15-411**
HyperAβ: Brain Region Hypergraph Neural Network with Dynamic Margin Loss for Amyloid PET/CT Classification
Gan Zhan

15:00 **MIC-15-414**
A Wavelet-Enhanced Trajectory-Refined Flow Matching Model for MR-to-CT Synthesis in Nasopharyngeal Carcinoma
Yueyu Huang

15:00 **MIC-15-417**
Quantitative Unpaired Low-Dose PET Image Translation with a Poisson-Aware Identity Loss
Sihyun Lee

15:00 **MIC-15-420**
Deep Learning with Physics-Corrected Histo-Images for Robust Low-Dose Scatter Correction on uMI Panorama GS
Xu Zhang

15:00 **MIC-15-423**
Quantum-Geometric Radiomics Classification of Pancreatic Lesions
Hyeonmin Yang

15:00 **MIC-15-426**
Zero-Shot Vision-Language Refinement for PET-CT Multi-Organ Segmentation
Cindy Duan

15:00 **MIC-15-429**
Beyond AUC: Decision-Level Discordance and XAI Interpretation of a CBAM-CNN and a Vision Transformer on PET Polar Maps
Anting Li

15:00 **MIC-15-432**
Multitracer Conditional Diffusion Model for CT-Less Attenuation Correction in Preclinical PET Imaging
Mathieu Vachon, University of Sherbrooke, Department of Electrical and Computer Engineering

15:00 **MIC-15-435**
Joint Self-Collimation Compton SPECT for Wide-Energy and High-SNR Imaging
Peize Li

15:00 **MIC-15-438**
A Robot-Assisted SPECT Platform for Adaptive Functional Imaging using Non-Conventional Trajectories
Lorenzo Confalonieri

15:00 **MIC-15-441**
Estimating ejection fractions from standard of care F18-FDG PET/CT: a feasibility study
Zoe Wilson

15:00 **MIC-15-444**
Experimental validation of inter-crystal scatter recovery using forward Compton kinematics and polarization correlations in PET imaging
Mihael Makek

15:00 **MIC-15-447**
Development of a Dual-Modality Imaging Capsule for Laparoscopic Radio-Guided

Surgery
Krishan Patel

15:00 **MIC-15-450**
Development of a High Sensitivity Cascade Gamma Photon Coincidence Imaging System
Qingyang Wei

15:00 **MIC-15-453**
Development of High-Time Resolution Ring-Type GFAG Pixel Detector System for pH Sensing via Time-Differential Perturbed Angular Correlation
Mizuki Uenomachi

15:00 **MIC-15-456**
Quantum entanglement of annihilation photons as a function of the annihilation mechanism
Deepak Kumar

15:00 **MIC-15-459**
First In-Vivo Positronium Ratio Imaging (PRI) using F-18 FDG: A Preliminary Study with Phantom and a Mouse Model
Macoto Fujimoto

15:00 **MIC-15-462**
Ortho-Positronium Lifetime Measurements from Pile-up Single Events
José A. Avellaneda

15:00 **MIC-15-465**
Quantitative 4D PET Imaging of Photosynthate Transport and Rhizosphere Carbon Partitioning in Intact Plant–Soil Systems
Muhammad Nasir Ullah

15:00 **MIC-15-468**
Investigating an Optical Approach for Microliter-Scale Droplet Geometry Correction in Radioactivity Quantification
Shawn Shin

17:30 – 19:00 FEDERICO GARCÍA LORCA
MIC-16 Simulation and modeling of medical imaging systems (2)

Chairs:
Munetaka Nitta (Garching)
David Sarrut (Villeurbanne)

17:30 **MIC-16-01**
How well do we know non-collinearity in PET? A simulation and a new analysis of past and recent experiments
Jose M. Udias

17:45 **MIC-16-02**
PAL-G4: A Geant4-based code with PAL parametrisation
Ana Ros

18:00 **MIC-16-03**
Data-Driven System Response Modeling for SPECT via Maximum Likelihood Estimation (MLE) of Directional Penetration Maps from Experimental Sparse Scanning Data
Yifei Jin

18:15 **MIC-16-04**
Wasserstein Pullback Metric for Intrinsic Difficulty of Scintillation Detector Inverse Problems
Sangjin Bae

18:30 **MIC-16-05**
Zero-Knowledge Calibration: PET Geometry Recovery from Unlocalized Point Sources
Tim Freye

18:45 **MIC-16-06**
A Multi-Channel Positronium Decay Source Model in GATE
Wojciech Krzemien, For the IMPET project

17:30 – 19:00 MANUEL DE FALLA
MIC-17 Theranostics, Imaging and dosimetry in therapy (particle, radiopharmaceutical, surgery) (1)

Chairs:
Akram Hamato (Chiba)
Francesco Pennazio (Torino)

17:30 **MIC-17-01**
Detection of deep seated anatomical changes in patients undergoing ion beam radiotherapy
Maria Martisikova

17:45 **MIC-17-02**
Proton Range Verification in 3D Pencil Beam Scanning Lattice via a Dual-head Multi-slit 3D Prompt Gamma Imaging System
Hongyang Zhang

18:00 **MIC-17-03**
Design and Experimental Validation of the REALPATH Prompt Gamma Camera for Range Verification in Hadrontherapy
Martina Piroddi

18:15 **MIC-17-04**
First Tests of Hybrid n/gamma-ray Imaging for Proton Therapy Range Verification at a Clinical Proton Beam
Sara T. Mueller, On behalf of the NOVO collaboration

18:30 **MIC-17-05**
First Demonstration of Short-Interval Proton Range-Verification and FAZA PET on SIRMIO
Chie Toramatsu

18:45 **MIC-17-06**
Beyond short-lived positron emitters: feasibility of ^{18}F detection for range verification in carbon ion therapy
Akram Hamato

14 November, 2026

9:00 – 11:00 **FEDERICO GARCÍA LORCA**
MIC-18 **Advanced tomographic reconstruction techniques (2)**

Chairs:
Jinyi Qi (Davis)

9:00 **MIC-18-01**
Steerable Kernel Based Emission Tomography Reconstruction
Huanzhe Wei

9:15 **MIC-18-02**
Cross-Tracer PET Image Reconstruction Using an ^{18}F-FDG-Trained Deep Kernel Model
Siqi Li

9:30 **MIC-18-03**
List-mode PET Image Reconstruction with Neural Radiance Fields
Haoyu Lu, Haoyu Lu

9:45 **MIC-18-04**
Dynamic image reconstruction for high-resolution SAVANT scanner using non-negative low-rank constraint
Yassir Najmaoui

10:00 **MIC-18-05**
A Generalized Tuy-Type Completeness Analysis for X-Ray Scattering Tensor Tomography
Ruifeng Liu

10:15 **MIC-18-06**
Hamiltonian Monte Carlo Ensemble Features for DATSCAN SPECT Analysis in Parkinson's Disease
Theodoros Leontiou

10:30 **MIC-18-07**
Monte Carlo–based reconstruction in Ac-225 SPECT: impact on image quality, quantitative accuracy, and computational burden.
Chenguang Li

10:45 **MIC-18-08**
Sparse-View ^{177}Lu SPECT Reconstruction for Pre-Treatment Dosimetry using Gaussian Mixtures
Hyun Ji Lee

9:00 – 11:00 MANUEL DE FALLA
MIC-19 Signal and data processing

Chairs:
Jae Sung Lee (Seoul)
Fumio Hashimoto (Gainesville)

9:00 **MIC-19-01**
Noise-Aware Brownian Bridge Diffusion Model for Denoising of Low-Dose PET Images
Wolf De Mits

9:15 **MIC-19-02**
N2N-DiffPET: Self-supervised Diffusion for Low-dose PET Image Denoising
Quanzheng Li

9:30 **MIC-19-03**
Multi-Dose PET Image Denoising using Consistency Flow Matching
Joo Hyun Lee

9:45 **MIC-19-04**
High-Temporal-Resolution Data-Driven Respiratory Motion Estimation in Cardiac PET Imaging
Chen Sun

10:00 **MIC-19-05**
Spatial-variant fast non-linear energy calibration for a high resolution SSLE pixelated PET detector
Lidia Jiménez Algarra

10:15 **MIC-19-06**
Random Coincidence Correction for Inter-Crystal Scatter Events in PET
Hyeongseok Shim

10:30 **MIC-19-07**
A Software-Based Coincidence Sorters for Simultaneous PET Emission and Lu-176 Intrinsic Transmission Data Extraction
Xin Zhao, Xin Zhao

10:45 **MIC-19-08**
Characterisation of Positron Emission Particle Tracking (PEPT) Performance for In-vivo Blood Flow Estimation in Preclinical PET
Laurence Vass

11:30 – 12:45 FEDERICO GARCÍA LORCA
MIC-20 Total body imaging systems including applications and kinetic modeling, molecular connectivity and radiomics

Chairs:
Stefaan Vandenberghe (Ghent)
Kevin Chung (Boston)

11:30 **MIC-20-01**
Evaluation of Sparse-Geometry Designs for Long-Axial Field-of-View Preclinical SPECT
Elissa L. Avila

11:45 **MIC-20-02**
Feasibility study of ^{68}Ga/^{18}F multiplexed PET imaging on a total-body PET scanner
Wen He

12:00 **MIC-20-03**
Positronium Lifetime Imaging on LAFOV PET: Impact of Estimation Methods and Count Statistics
Lukas U. Rauscher

12:15 **MIC-20-04**
Intercept Graphical Plot with Normalization for Total-Body PET Parametric Imaging with Reduced Input Function Data and Enhanced Inter-Subject Quantification
Yiran Wang

12:30 **MIC-20-05**
Generative Consistency Model for Bayesian Kinetic Model Selection in Dynamic Total-Body PET
Yun Zhao

11:30 – 12:45 MANUEL DE FALLA
MIC-21 Theranostics, Imaging and dosimetry in therapy (particle, radiopharmaceutical, surgery) (2)

Chairs:
Youngho Seo (San Francisco)
Andrea Gonzalez Montoro (Valencia)

11:30 **MIC-21-01**
Experimental System Performance Characterization of Alpha-SPECT and Exploration of Angular Sampling Enhancement via Collimator Micro-Rotation
Shubham Mandot

11:45 **MIC-21-02**
First Validation of a BNCT-SPECT System Based on a Detector with Embedded AI in a Clinical-Like Facility
Tommaso Ferri

12:00 **MIC-21-03**
Imaging of TAT in Clinical Phantoms with a CZT Compton Camera
Biswajit Das

12:15 **MIC-21-04**
Design of a PET&SPECT shared Detector with Low- and Medium-Energy Scintillator-as-Collimator for Lu-177 Imaging
Xiangtao Zeng

12:30 **MIC-21-05**
Dosimetry Evaluation Studies in Non-Melanoma Skin Cancers Using a Novel Thin-Layer Scintillation Detector
Giulia Tosetti, This project has received financial support from the CNRS through the MITI interdisciplinary programs.

12:45 – 13:05 FEDERICO GARCÍA LORCA
MIC-22 Closing

Chairs:
Vesna Sossi (Vancouver)
Roger Fulton (Sydney)

9 November, 2026

15:00 – 17:00 ANDALUCÍA II & III
RTSD-01 RTSD Opening

Chairs:
Michael Fiederle (Freiburg)
Gerard Arino-Estrada (Barcelona)

15:00 **RTSD-01-01**
Exploring 4x4x3 cm^3 3D-CdZnTe Semiconductor Gamma-Ray Detectors
Zhong He

15:15 **RTSD-01-02**
Visualizing the Hidden Physics of CdTe Detectors: Direct Spatiotemporal Imaging of Charge Clouds
Adriano Cola

15:30 **RTSD-01-03**
Compton Imaging Capability of 1-cm-Thick Pixelated TlBr Detectors
Keitaro Hitomi

15:45 **RTSD-01-04**
Effect of the Anode Irradiation by X-ray on the Polarization of a CdTe Imaging Sensor
Petr Praus

16:00 **RTSD-01-05**
Identification and control of interfacial limits enabling high-performance photon-counting perovskite radiation detectors
Ganbaatar Tumen-Ulzii

16:15 **RTSD-01-06**
High-Z Sensor Characterisation and Readout Development for X-ray Detectors at PSI
Jonathan Mulvey, On behalf of the detector group whose members include:J. Mulvey, M. Anastasi, A. Bergamaschi, M. Brueckner, M. Carulla, R. Dinapoli, S. Ebner, S. Emiliani,K. Ferjaoui, E. Fr¨ojdh, V. Gautam, D. Greiffenberg, S. Hasanaj, V. Hinger, V. Kedych, T. King, S. Li,C. Lopez-Cuenca, L. Lunin, A. Mazzoleni, D. Mezza, S. Moses, K. Moustakas, A. Mozzanica, M. Mueller,C. Ruder, B. Schmitt, S. Silletta, D. Thattil, X. Xie and J. Zhang

16:30 **RTSD-01-07**
Response of a Timepix4 CdTe spectral imaging detector for radiographic applications
Laura A. Cerbone

16:45 **RTSD-01-08**

Exploring the X-ray imaging with single-crystalline integrated perovskite sensors

Vitalii Bartosh, Vitalii Bartosh

17:30 – 19:00 ANDALUCÍA II & III

RTSD-02 RTSD Aviation Inspection & Security Applications

Chairs:
Zhong He (Ann Arbor)
Jan S. Iwanczyk (Los Angeles)

17:30 **RTSD-02-01**

Next Generation Room Temperature Semiconductor Detectors, Sources, and Methods for Computed Tomography in Aviation Security

William C. Barber, William C. Barber

18:00 **RTSD-02-02**

A new compact prototype for 3D gamma coded-aperture spectro-imaging

Giulia Rosso

18:15 **RTSD-02-03**

Characterization of a miniature prototype photon counting detector system and evaluation of its imaging performance for potential use in threat and explosive detection CT scanners; A new paradigm for security screening.

Georgios Prekas

18:30 **RTSD-02-04**

Tileable Imager Architecture using HiSPECT Gamma Imaging Modules and Applications

Guillaume Montémont, Guillaume Montémont

18:45 **RTSD-02-05**

Activity Quantification Using Experimentally Imaged Source Distributions

Christopher G. Wahl, Christopher G. Wahl

10 November, 2026

9:00 – 11:00 ANDALUCÍA II & III

RTSD-03 RTSD Pixel Detectors

Chairs:
Dominic Greiffenberg (Villigen)
Filippo Mele (Milano)

9:00 **RTSD-03-01**

Flat-Panel Intensity Normalization for Fully Spectroscopic CT-Based Material

Identification with 1 mm CdTe Timepix3 Detectors
Michael K. Schütz

9:15 **RTSD-03-02**
A Pixelated CCl TlBr Detector for Time-Resolved Multi-MeV Gamma Detection
Leonor Rebolo

9:30 **RTSD-03-03**
Self-Consistent Simulation of Charge Sharing in CZT Pixel Detectors
Andrea Zappettini

9:45 **RTSD-03-04**
Waveform-Based Depth-of-Interaction Characterization in 5-mm Cross-Strip CdZnTe
Max Teicheira

10:00 **RTSD-03-05**
Ultra-High Resolution CZT Gamma Camera Using Machine-Learning Based 3D Interaction Localisation
Alexander Cherlin

10:15 **RTSD-03-06**
Optimized femtosecond laser ablation processing of hybrid semiconductor detectors for enhanced spectroscopic and imaging performance
Zuzana Melnikova

10:30 **RTSD-03-07**
Energy, Spatial and Timing Performance of CZT Drift Strip Detectors
Andrea Zappettini

10:45 **RTSD-03-08**
Circularity-Based Spectroscopic Correction for Small-Pixel CdTe/Timepix Detectors
Elena Maria Zannoni

15:00 – 17:00 Poster Area
RTSD-04 RTSD Poster Session

Chairs:
Michael Fiederle (Freiburg)
Gerard Arino-Estrada (Barcelona)

15:00 **RTSD-04-350**
Characterization of Bremsstrahlung Photon Contamination in Clinical Electron Beams via CdZnTe Detectors
Chansun Park

15:00 **RTSD-04-351**
Engineering Low-Reverse-Current $CsPbBr_3$ Sensor Structures through Surface Passivation and Deposition of Different Contacts
Volodymyr Gnatyuk

15:00 **RTSD-04-352**
Additive Engineering of $Cs_2AgBiBr_6$ Double Perovskite Single Crystals: Growth Optimization, Structural Characterization, and Radiation Detector Evaluation
Nazire S. Sahsuvar

15:00 **RTSD-04-353**
Solution Growth and Material Characterization of $Cs_2AgBiBr_6$ Double Perovskite Crystals for X-Ray Detection: Crystal Quality, Electrical Transport Properties, and Structural Defects
Zeynep Cihan

15:00 **RTSD-04-354**
A new approach for studying phase equilibria in the CdTe-MnTe system
Aleksey Bolotnikov

15:00 **RTSD-04-355**
First Clinical Evaluation of a Gallium Nitride Diode Array for Proton Pencil Beam Scanning
Luisa Parschat

15:00 **RTSD-04-356**
An Integrated Purification-Growth Strategy for High-Performance Perovskite $CsPbBr_3$ Crystals
Junfeng Chen

15:00 **RTSD-04-357**
Spectral Performance of GaAs:Cr Photon-Counting Detectors with Various Thicknesses
Boren Wang

15:00 **RTSD-04-358**
Optical manipulation of space charge in rectifying CdZnTe/CdTe radiation detectors
Samuel Kačenga

15:00 **RTSD-04-359**
High-Voltage Tolerant Ni/YSZ/4H-SiC MOS Detectors for Thick Active Layers
Marcel Talacko

15:00 **RTSD-04-360**
Polycrystalline Based Semiconductors (PBS) TlBr for High Energy X-ray Detection and Radiography
Jarek Glodo

15:00 **RTSD-04-361**
Lateral Expansion of the Active Region in Semi-Insulating GaAs Radiation Detectors with Different Schottky Contact Sizes
Nikola Kurucova

15:00 **RTSD-04-362**
Depth-Resolved Measurement of Charge-Cloud Formation and Transport in a 2.0 mm CdTe-Timepix3 Detector
Duarte S. Rodrigues

15:00 **RTSD-04-363**
When 0 V Is Not Really 0 V: Remnant Fields in $MAPbBr_3$ X-Ray Detectors
Jean-Marie Verilhac

15:00 **RTSD-04-364**
Vibration-suppressed solution growth of perovskite single crystals for high-resolution gamma-ray detection
Haodi Wu

15:00 **RTSD-04-365**
Investigation of the anisotropy of the electronic properties of $CsPbBr_3$
Aleksey Bolotnikov

15:00 **RTSD-04-366**
Controllable Fabrication of High-performance Perovskite Single Crystals in Solution toward Efficient X-ray Detection
Yu Chen

15:00 **RTSD-04-367**
Improved Stability of Perovskite Single Crystal Semiconductor X-ray Detector via 2D Layer Formation
Dakyoung Lee

15:00 **RTSD-04-368**
Highly Radiation-Hard Flexible Perovskite Imaging Arrays for Real-Time Proton Beam Monitoring
Yang Zhang

15:00 **RTSD-04-369**
FAPbBr3 Single Crystal Perovskite Radiation Detector with Embedded Electrode Array Architecture
Seán Cardiff

15:00 **RTSD-04-370**

15:00 **RTSD-04-371**
Evaluation of carrier transport properties of TlBr semiconductor detectors
Kenichi Watanabe

15:00 **RTSD-04-372**
Fabrication of Flexible Nanostructured Polymer for Nanomaterial-based Detectors
Ill-Hyuk Han

15:00 **RTSD-04-373**
Enhanced Imaging Uniformity of Perovskite X-ray Detectors via Combined Uniform Particle Dispersion and Solution-assisted Hot Pressing Treatment
Xulong Pang

15:00 **RTSD-04-374**
Investigation of Metal Oxides as Contact Materials for CdTe X-Ray, Gamma-Ray Detectors
Madan Niraula

15:00 **RTSD-04-375**
Transport Properties of CdTe Semiconductor after Laser Ablation
Jakub Dřevo

15:00 **RTSD-04-376**
Contact Characterization of High-Flux Stable GaAs:Cr Detector
Boren Wang

15:00 **RTSD-04-377**
Validation of FAPbBr3 Perovskite Radiation Stability: Monte Carlo Simulation and Proton-Irradiation Experiment
Zeqi Huang

15:00 **RTSD-04-378**
CZT Strip Detectors Characteristics After the Euro Material Ageing Mission
Andrea Zappettini

15:00 **RTSD-04-379**
Development of a Compact CdTe-Based Gamma Spectroscopy System with Dual-Side Readout for High-Resolution Gamma Imaging
Siyao Chang

15:00 **RTSD-04-380**
An Event Reconstruction ASIC for 3D CdZnTe Gamma-Ray Detectors
Farah Mohammed Rafee

15:00 **RTSD-04-381**
Spectroscopic Performance of SOI-CMOS Pixel Detector at Elevated Temperatures
Haruno Takamoto

15:00 **RTSD-04-382**
Development of Zero-Grid-Bias Operation in Coplanar Grid Type TlBr Detectors
Seishiro Tanaka

15:00 **RTSD-04-383**
A Monte-Carlo Simulation of Unipolar Charge-Sensing Amorphous Selenium X-ray Detector for Photon Counting Imaging
Arev Koc

15:00 **RTSD-04-384**
Study of the spectroscopic performance of Timepix4 with highly ionizing particles
Petr Smolyanskiy

15:00 **RTSD-04-385**
Investigation of Gain Instability of a 3-D CdZnTe Detector
Matthew Granados

15:00 **RTSD-04-386**
Bias Scan Analysis of Si-Timepix Detector with Various Sensor Thickness
Andrea Sagatova

15:00 **RTSD-04-387**
Multidimensional Parameter-Space Analysis of Fast Neutron-Induced Tracks in Timepix Detectors
Matej Balušík

15:00 **RTSD-04-388**
A 512 × 256 a-IGZO Dual-Gate TFT 2T-APS Array for Low-Dose Direct-Conversion X-Ray Flat-Panel Detector
Yihong Qi

15:00 **RTSD-04-389**
Development of a Self-Triggering Pixelated TlBr Detector with Cherenkov Light Detection
Tsubasa Komaki

15:00 **RTSD-04-390**
Readout Electronics of SPECTRE CZT detector
Damanio Cabiati, On behalf of SPECTRE Collaboration

15:00 **RTSD-04-391**
Spectral Response and Counting Characteristics of a Peak-finding ASIC for GaAs:Cr Detectors
Xiaochun Lai

15:00 **RTSD-04-392**
Thickness-dependent front-end noise in CdTe Timepix3 detectors
Juan S. Useche Parra

15:00 **RTSD-04-393**
SiC Timepix3 detector response to fast neutrons: effect of varying sensor bias
Katarina Foss

15:00 **RTSD-04-394**
A neural network determining the gamma interaction position in pixelated CZT detectors
Adeiza S. Anumah

15:00 **RTSD-04-395**
Robust and reliable radionuclide identification under realistic measurement conditions
Andrea Zappettini

15:00 **RTSD-04-396**
In-situ high-resolution gamma spectroscopy for characterization of radiological environmental sites.
Bertrand Rossé

15:00 **RTSD-04-397**
Gamma Spectroscopy Analysis and Benchmarking of Nuclear Fuel for Next Generation Reactor Designs
Daryl T. Giglio

15:00 **RTSD-04-398**
Comparison of the simulated response of the in-house DT hybrid pixel detector with synchrotron beam tests
Mélissa Leroy

15:00 **RTSD-04-399**
Characterization and Compensation of Radiation-Induced Leakage Current in CdTe/CZT Detectors Under High-flux X-ray Irradiation
Xinchi Ran

15:00 **RTSD-04-400**
Compton Polarimetric Potential of a Low Power CdTe Timepix3 Frame Mode Detector
Duarte Rodrigues

15:00 **RTSD-04-401**
Imaging Performance Comparison of a GaAs Photon-Counting Detector and an Energy-Integrating Detector under Various Photon-Flux Conditions
Boren Wang

11 November, 2026

9:00 – 11:00 ANDALUCÍA II & III
RTSD-05 RTSD Perovskite Detectors

Chairs:
Andrea Zappettini (Parma)
Paul Sellin (Guildford)

9:00 **RTSD-05-01**
Performance Improvements on Perovskite Gamma-Ray Detectors Using Depth-Dependent Shaping Optimizations
Max Robbins

9:15 **RTSD-05-02**
On Technological Aspects In The Development Of Perovskite Gamma Radiation Detectors
Normunds Grundmanis

9:30 **RTSD-05-03**
Metal-Halide Perovskites for Fast Hard-Radiation Detection
Anastasiia Sakhatska

9:45 **RTSD-05-04**
Growth of $MAPbBr_3$ Single Crystals for X-Ray, Gamma Ray Detection by Slow Solvent Evaporation at Room-Temperature
Madan Niraula, Madan Niraula

10:00 **RTSD-05-05**
Millimeter-Thick Perovskite Single-Crystal X-ray Detectors with Unity Charge Extraction

in Photovoltaic Mode
Kostiantyn Sakhatskyi

10:15 **RTSD-05-06**
Multipixel 2D Perovskite Thin-Film Array for High-Resolution Proton Beam Profiling
Ilaria Fratelli

10:30 **RTSD-05-07**
Phase-Pure Orthorhombic $CsPbBr_3$ Perovskite Materials for Low-Lag, Ultrahigh-Resolution Direct X-ray Detectors
Shariar Motakef

11:30 – 13:00 ANDALUCÍA II & III
RTSD-06 RTSD Perovskite Detectors II

Chairs:
Juan S. Useche Parra (Freiburg)
Ge Yang (Raleigh)

11:30 **RTSD-06-01**
Influence of the Active Layer Thickness on the Performance of Metal-Halide-Perovskite Thin Films for X-ray Detectors
Marco Girolami

11:45 **RTSD-06-02**
Optimization of $FAPbBr_3$ Single Crystals for Photon Counting Radiation Detection
Paul Sellin

12:00 **RTSD-06-03**
Transient Currents in 4H–SiC Radiation Sensors with Graphene Electrodes
Eduard Belas

12:15 **RTSD-06-04**
Perovskite $CsPbBr_3$ Cherenkov charge induction gamma-ray detector with sub-ns timing resolution
Lei Pan

12:30 **RTSD-06-05**
Unraveling Atmosphere-Dependent Trap-Mediated X-Ray Detection in Organic Field-Effect Transistors
Giulia Napolitano

12:45 **RTSD-06-06**
Li- and B-Doped $CsPbBr_3$ Composites for Fast Radiation Scintillation Detection
Mohamed Boukhicha

15:00 – 17:00 ANDALUCÍA II & III
RTSD-07 RTSD Pixel Detectors II

Chairs:
Krishna C. Mandal (Columbia)
Chris G. Wahl (Ann Arbor)

15:00 **RTSD-07-01**
Physics-Informed 3D Gaussian Splatting for Multi-View Compton Camera Imaging
Rui Ma

15:15 **RTSD-07-02**
Benchmark of the H3DD_UMv5 Waveform Sampling ASIC for Pixelated Room-Temperature Semiconductor Detectors
Yuefeng Zhu

15:30 **RTSD-07-03**
Optimizing Array Configurations of Position-Sensitive Virtual Frisch-grid Detectors for Coded Aperture Telescopes
Aleksey Bolotnikov

15:45 **RTSD-07-04**
Measurement of the energy response function of a photon counting prototype detector using the HEX-27 beamline at the Brookhaven National Laboratory; A method to derive an empirical model of the detector non-ideal behavior and to improve material discrimination by spectrum deconvolution.
Georgios Prekas

16:00 **RTSD-07-05**
3D Integration and Interconnects for the Readout of Hybrid Pixel Detectors
Francisco Piernas Diaz, On behalf of the Medipix Collaboration and the EP R&D Work Package 5.

16:15 **RTSD-07-06**
Carrier Dynamics and Polarization in GaAs:Cr Detectors Under High X-ray Flux
Boren Wang

16:30 **RTSD-07-07**
Evaluation of Cr-Compensated GaAs Sensors with Different Thicknesses by Photon-

Counting ReadoutElectronics
Juha Kalliopuska

17:30 – 19:00 ANDALUCÍA II & III
RTSD-08 RTSD Medipix/Timepix Detectors

Chairs:
Amlan Datta (Natick)
Christer Frojdh

17:30 **RTSD-08-01**
The Timepix ASIC Family: Past, Present, and Future
Rafael Ballabriga, On behalf of the Medipix2, Medipix3 and Medipix4 Collaborations

18:00 **RTSD-08-02**
Timepix4 based photon-counting detector for full-spectral X-ray micro computed tomography
Paolo Cardarelli

18:15 **RTSD-08-03**
Machine learning pipeline for spectral material identification with a CdTe-Timepix3 detector
Juan S. Useche Parra

18:30 **RTSD-08-04**
Full Scale Microstructural Imaging Based on Energy dispersive X-ray Diffraction using Timepix3/4 with CdTe Sensor
Jan Jakubek

18:45 **RTSD-08-05**
Energy-resolved Grating-based Phase-contrast Imaging with Timepix4
Markus Schneider

12 November, 2026

9:00 – 11:00 ANDALUCÍA II & III
RTSD-09 RTSD CZT Detectors

Chairs:
Aleksey E. Bolotnikov (Upton)

9:00 **RTSD-09-01**
4π Visualization of Extended, Low-Level GammaEmission Sources Using a Rotating 3-D PositionSensitive CdZnTe Imager
Amii O. Lamm

9:15 **RTSD-09-02**
High-Energy Gamma Transmission Imaging with a 3D-CZT Detector Using Ring Localization
Peter G. Hotvedt

9:30 **RTSD-09-03**
A 128-Channel Mixed-Signal Readout ASIC for 3D Position-Sensitive CZT Detectors with Integrated ADC and TDC
Zirui Yang

9:45 **RTSD-09-04**
X-ray direct detectors from solution-processed CdZnTe quantum dots
Marco Ruggieri

10:00 **RTSD-09-05**
High-Flux Performance of a Photon-Counting Detector for Spectral CT Based on the ColorCT ASIC
Andrea Brambilla

10:15 **RTSD-09-06**
A CZT Readout ASIC for Double-Layer Compton Imaging Applications
Will B. Wright

10:30 **RTSD-09-07**
Performance evaluation of CZTS grown with higher purity CdSe starting material
Utpal N. Roy

10:45 **RTSD-09-08**
Merit-Function-Guided Porosity Control in Directional Solidification of CZT
Aimen E. Gheribi

11:30 – 13:00 ANDALUCÍA II & III
RTSD-10 RTSD Awards and Closing

Chairs:
Michael Fiederle (Freiburg)
Gerard Arino-Estrada (Barcelona)

11:30 **RTSD-10-01**
Energy-Resolved Effective Focal-Spot Characterization of a CdTe-Timepix3 Nanofocus XCT System Using Orthogonal Slanted-Edge Measurements
Gerardo A. Roque

11:45 **RTSD-10-02**
Digital Signal Processing of Large-Volume, Pixelated $CsPbBr_3$ for Gamma-ray Spectroscopy
Michael Streicher

12:00 **RTSD-10-03**
A spectroscopic CdZnTe/CMOS hybrid linear array detection system based on wedge-bondable HDI interposer
Filippo Mele

12:15 **RTSD-10-04**
Stabilizing the Detector Response of $CsPbBr_3$ Gamma-Ray Detectors
Matthew Petryk

12:30 **RTSD-10-05**
Neutron Irradiation Effects in β-Ga_2O_3 Radiation Detector Materials Investigated by Raman and Positron Annihilation Spectroscopy
Shams Noor

12:45
Awards and closing remarks
Michael Fiederle

11 November, 2026

11:30 – 13:00 Seminar Room 3/4
TS-02 Technical Sessions 2

11:30 **TS-02-01**
ROIC/ASICs for Radiation Detection and Imaging
Dirk Meier

11:45 **TS-02-02**
Toward Information-Efficient Photon Detection: CMOS SiPMs and Multi-Threshold Readout ASICs
Hui Lao

12:00 **TS-02-03**
From Semiconductor Sensors to Hybrid Pixel Detectors: Advafab's Fabrication and Integration Capabilities
Ben Panesar

12:15 **TS-02-04**
Real-Time Pile-Up Recovery and High-Resolution Signal Processing for SDDs using PurSamurAI
Kazuki Otomo

12:30 **TS-02-05**
Sci-Compiler: Towards Cross-Platform FPGA Development and Automated CI/CD Workflows for Scientific Data Acquisition
Andrea Abba

12:45 **TS-02-06**
Broadcom's Silicon Photomultiplier: Technology, Performance, Status and Roadmap
Stefan Brunner, on behalf of the Broadcom SiPM team

13:15 – 14:30 ALBÉNIZ & MACHUCA
SimSET SimSET User Meeting (onsite only)

Chairs:
Paul E. Kinahan (Seattle)
Robert S. Miyaoka (Seattle)

15:00 – 17:00 Seminar Room 3/4
TS-03 Technical Sessions 3

15:00 **TS-03-01**
Recent Advances in Photosensors and Radiation Detectors for Nuclear Science and High Energy Physics
Mauro Bombonati

15:15 **TS-03-02**
Introduction to Representative Achievements of Jinan Laboratory of Applied Nuclear Sciences in the Field of Nuclear Technology Applications
Kunliang Liu, Ray Image Testing Technology；The Palace Museum；Shandong Nuclear Power Co., Ltd

15:30 **TS-03-03**
TBA

15:45 **TS-03-04**
TBA

16:00 **TS-03-05**
TBA

16:15 **TS-03-06**
TBA

16:30 **TS-03-07**
TBA

16:45 **TS-03-08**
TBA

12 November, 2026

13:00 – 15:00 **Z1**
WIE & YP **WIE & YP**

Chairs:
Audrey Corbeil Therrien (Sherbrooke)
Andrea Gonzalez Montoro (Valencia)

13:30 – 15:00 **ANDALUCÍA II & III**
OG-WS **OpenGATE Workshop (onsite only)**

19:00 – 21:30 **ANDALUCÍA II & III**
STIR **STIR Users' & Developers' Meeting (onsite only)**

19:00 **STIR-01**
Welcome and Introduction
Charalampos Tsoumpas

19:10 **STIR-02**
A STIR-based reconstruction pipeline for the Philips Vereos PET/CT scanner
Charalampos Tsoumpas

19:15 **STIR-03**
Scatter Correction for Long Axial Field-of-View PET Scanners in STIR Library
Charalampos Tsoumpas

19:20 **STIR-04**
Adding time-of-flight scatter estimation to STIR
Kris Thielemans

19:25 **STIR-05**
Fully Automated Motion Detection, Estimation and Correction For Rigid Motion
Charalampos Tsoumpas

19:30 **STIR-06**
Simultaneous Dual Tracer PET Separation in reconstruction: Validation on LAFOV Data
Charalampos Tsoumpas

19:35 **STIR-07**
Simulation-Based Evaluation of SPECT Image Reconstruction in STIR
Kris Thielemans

19:40 **STIR-08**
Exploring Starguide GX SPECT-CT system in STIR
Valentina Ferri

19:50 **STIR-09**
Introduction to the STIR new SPECT GPU projector
Daniel Deidda

19:55 **STIR-10**
Optimization of GPU memory management in STIR
Kris Thielemans

20:10 **STIR-11**
Dead-time correction for STIR and PETSIRD
Alan Osys

20:25 **STIR-12**
PETRIC2: overview and results
Kris Thielemans

20:35 **STIR-13**
Democratizing AI attenuation correction research with STIR: results and experiences from the BIC-MAC MICCAI challenge
Christian Hinge

20:50 **STIR-14**
Future of STIR and related projects
Kris Thielemans

8 November, 2026

18:00 – 19:00	**Conference Center**
WR	**Welcome Reception**

10 November, 2026

19:00 – 19:20 **FEDERICO GARCÍA LORCA**
WIS **What is IEEE?**

19:00 **WIS-01**
What is IEEE?
Vesna Sossi

19:30 – 21:00 **Conference Center - Exhibits**
EHH **Exhibitor - Happy Hour**

11 November, 2026

19:30 – 21:00 **Conference Center**
CR **Conference Reception**

14 November, 2026

13:15 – 14:15 **Conference Center**
CCP **Conference Closing Party**

9 November, 2026

19:45 – 22:00 **El Claustro de Santa Paola, Hotel**
NSS-D **NSS Dinner**

12 November, 2026

14:00 – 17:00 **Carmen de los Chapiteles**
RTSD-L **RTSD Lunch**

13 November, 2026

19:45 – 22:00 **Carmen de los Chapiteles**
MIC-D **MIC Dinner**

9 November, 2026

11:00 – 11:30 ALBÉNIZ & MACHUCA,ANDALUCÍA II & III,FEDERICO GARCÍA LORCA,PICASSO,Poster Area
Coffee Break

13:00 – 15:00 ALBÉNIZ & MACHUCA,ANDALUCÍA II & III,FEDERICO GARCÍA LORCA,PICASSO
Lunch Break

17:00 – 17:30 ALBÉNIZ & MACHUCA,ANDALUCÍA II & III,FEDERICO GARCÍA LORCA,PICASSO,Poster Area
Coffee Break

10 November, 2026

11:00 – 11:30 ALBÉNIZ & MACHUCA,ANDALUCÍA II & III,FEDERICO GARCÍA LORCA,PICASSO,Poster Area
Coffee Break

13:00 – 15:00 ALBÉNIZ & MACHUCA,ANDALUCÍA II & III,FEDERICO GARCÍA LORCA,Poster Area,PICASSO
Lunch Break

17:05 – 17:30 FEDERICO GARCÍA LORCA,PICASSO,Poster Area
Coffee Break

11 November, 2026

11:00 – 11:30 ALBÉNIZ & MACHUCA,ANDALUCÍA II & III,FEDERICO GARCÍA LORCA,MACHADO,MANUEL DE FALLA,PICASSO,Seminar Room 3/4,Poster Area
Coffee Break

13:00 – 15:00 ANDALUCÍA II & III,PICASSO,MACHADO,Seminar Room 3/4,Poster Area,FEDERICO GARCÍA LORCA,MANUEL DE FALLA
Lunch Break

17:00 – 17:30 ALBÉNIZ & MACHUCA,ANDALUCÍA II & III,FEDERICO GARCÍA LORCA,MACHADO,MANUEL DE FALLA,PICASSO,Seminar Room 3/4,Poster Area
Coffee Break

12 November, 2026

11:00 – 11:30 ALBÉNIZ & MACHUCA,ANDALUCÍA II & III,FEDERICO GARCÍA LORCA,MACHADO,MANUEL DE FALLA,PICASSO,Poster Area,Z1
Coffee Break

13:00 – 15:00 ALBÉNIZ & MACHUCA,FEDERICO GARCÍA LORCA,MACHADO,MANUEL DE FALLA,PICASSO,Poster Area
Lunch Break

17:00 – 17:30 ALBÉNIZ & MACHUCA,ANDALUCÍA II & III,FEDERICO GARCÍA LORCA,MACHADO,MANUEL DE FALLA,PICASSO,Poster Area,Z1
Coffee Break

13 November, 2026

11:00 – 11:30 FEDERICO GARCÍA LORCA,MANUEL DE FALLA
Coffee break

13:05 – 15:00 FEDERICO GARCÍA LORCA,Poster Area,MANUEL DE FALLA
Lunch Break

17:00 – 17:30 FEDERICO GARCÍA LORCA,Poster Area,MANUEL DE FALLA
Coffee Break

14 November, 2026

11:00 – 11:30 **FEDERICO GARCÍA LORCA,MANUEL DE FALLA**
Coffee Break

13:05 – 15:00 **MANUEL DE FALLA,FEDERICO GARCÍA LORCA**
Lunch break

Short Courses

7 November, 2026

Time:
7 November, 2026
9:00 – 18:00

Room:
Alhamar @Hotel Saray Granada

SC-01 | Front-End Electronics for Radiation Detectors

Material for preparation can be downloaded here

Schedule

08:00-09:00 Breakfast & Registration
09:00-11:00 Part 1
11:00-11:30 Morning Coffee
11:30-13:30 Part 2
13:30-14:30 Lunch
14:30-16:00 Part 3
16:00-16:30 Afternoon Coffee
16:30-18:00 Part 4

Location

Course and all breaks in Hotel Saray

Description

Successful front-end electronics developments emerge from tight collaboration between electronics engineers and specialists in detectors, data acquisition, and system integration. This one-day short course delivers the core concepts required to understand front-end design, enabling clearer communication and more effective interdisciplinary teamwork.

The course is ideal for both seasoned engineers and those new to the field—circuit designers, physicists, and detector specialists alike—providing a solid foundation in low-noise front-end circuit design. Participants will actively work alongside the instructor on practical examples of noise analysis, circuit design, and simulation. **Attendees must bring a laptop with the required software pre-installed** (see the instructions in the attached document - yellow button "Material for preparation can be downloaded here").

The final segment explores in depth a topic of broad interest to the NSS-MIC community: radiation tolerance.

Outline

Part I: Fundamentals – Gianluigi De Geronimo

- Noise sources and equivalent noise charge
- Noise analysis in frequency domain
- Interactive noise analysis, design and simulations

Part II: Fundamentals – Gianluigi De Geronimo

- Noise analysis in time domain
- Charge amplifier design
- Interactive noise analysis, design and simulations

Part III: Fundamentals – Gianluigi De Geronimo

- Filter design
- Mixed-signal circuits
- Waveform sampling and digitization
- Interactive noise analysis, design and simulations

Part IV: Radiation Tolerance – Lodovico Ratti

- Introduction: radiation environments and radiation sources
- Ionizing radiation effects on MOSFET transistors
- Ionizing radiation effects: from low to extreme doses
- Ionizing radiation effects: from bulk CMOS to finFETs

Instructor's Biographies

Gianluigi De Geronimo received his M.S. and Ph.D. in Electronics from Politecnico di Milano, Italy. He joined the Instrumentation Division at Brookhaven National Laboratory (BNL) shortly thereafter, where he specialized in the design of low-noise integrated circuits for ionizing radiation detectors. Over his career at BNL, he advanced from Assistant Scientist to Tenured Scientist and Head of the Microelectronics Group. Dr. De Geronimo has developed numerous high-performance front-end ASICs for applications in medical imaging, space, security, defense, and fundamental physics research. He is the founder of **DG Circuits**, where he continues his work as an independent ASIC designer and consultant. He also serves as Adjunct Professor at Stony Brook University and as an Editor for the IEEE Transactions on Nuclear Science. He has co-authored more than 150 scientific publications and two book chapters, and is the recipient of the 2008 BNL Science and Technology Award, three R&D 100 Awards (2009, 2011, 2014), the 2012 CSIRO Award, the 2012 Battelle Inventor of the Year Award, and the 2018 IEEE Long Island Section Charles Hirsch Award

Lodovico Ratti is Full Professor of Electronics at the University of Pavia, Department of Electrical, Computer and Biomedical Engineering, Italy. His main research expertise lies in front-end electronics for highly segmented radiation detectors, photodetectors (SPADs, SiPMs), and monolithic sensors, particularly those based on CMOS processes. His work also focuses on ionizing radiation effects, bulk damage, and noise characterization in microelectronic devices and circuits. The target applications of his research include high-energy physics, astrophysics, and photon science experiments. Lodovico Ratti serves as Secretary of the Radiation Instrumentation Steering Committee (RISC) of the Nuclear and Plasma Science Society (NPSS). He is also a Technology

Research Fellow with the National Institute for Nuclear Physics (INFN), Italy. He is the author or co-author of more than 360 publications, including peer-reviewed journal papers, conference proceedings, contributions to international conferences, and book chapters. He also serves as editor for IEEE Transactions on Nuclear Science, Frontiers in Physics, and MDPI Electronics.

-

Time:
7 November, 2026
9:00 – 18:00

Room:
Partal @Hotel Saray Granada

SC-02 | Analog and digital SPAD-based photodetectors

Schedule

08:00-09:00 Breakfast & Registration
09:00-11:00 Part 1
11:00-11:30 Morning Coffee
11:30-13:30 Part 2
13:30-14:30 Lunch
14:30-16:00 Part 3
16:00-16:30 Afternoon Coffee
16:30-18:00 Part 4

Location

Course and all breaks in Hotel Saray

Outline

Part I: SPAD physics [Fabrice Retière]
Single Photon Avalanche Diodes (SPADs) are the building blocks of Silicon Photomultiplier (implicitly analog) and digital SPAD array. SPADs operate following several steps: 1.1) transmission (as opposed to reflection or absorption) of photons into the silicon, 1.2) absorption of the photons within the silicon at wavelength-dependent depth, 1.3) production of electron-hole pairs considering quantum yield, 1.4) drift or diffusion of the carrier towards the high field region, 2.1) initiation and evolution of the avalanche, 2.2) quenching, 2.3) production of a detectable signal. SPADs carry a set of undesirable features: 3.) dark noise, 4.) carrier trapping and detrapping yielding to after-pulse, 5.) light production in avalanche yielding to internal and external optical crosstalk. Each item will be discussed in detail.

Part II: Analog SiPMs, timing and read-out (metrology) [Stefan Gundaker]
The silicon photomultiplier (SiPM) has become the standard device in many time-critical applications, ranging from

single-photon detection in quantum cryptography or light detection and ranging (LiDAR) to multi-photon detection in high-energy physics and time-of-flight positron emission tomography. The basic working principles of the SiPM will be introduced, and the most important parameters, such as photon detection efficiency, single-photon time resolution, and noise sources, will be discussed. The front-end electronics, an important aspect of the readout of analog-SiPMs, will be examined, and basic principles will be presented. Furthermore, the impact on SiPM parameters and electronic readout on timing will be explained when applied to scintillation, Cherenkov emission and single-photon detection. Prominent examples of applications will be reviewed, and the possible future of analog-SiPMs will be evaluated.

Part III: Digital SiPMs: Introduction (quenching circuits, metrology) [Serge Charlebois]
Review of various quenching circuit architectures, edge discriminators, and control of the quenching-recharge cycle. Methods to characterize performances adapted to digital SPADs.

Part IV: Digital SiPMs: Architectures and Applications [Claudio Bruschini]
We will provide a short overview of some of the main chip and system architectures which have been explored over the years for SPAD arrays and digital SiPMs, with an eye on the specificities of high-energy and nuclear physics applications. This will be complemented by a brief technology-oriented discussion.

Part V: Demos
We will provide examples of various data output obtained from digital SPAD detectors and demonstrate basic analysis performed on them (e.g., event rate, crosstalk, pulse shape analysis, single-photon timing resolution, coincidence timing resolution). We will also strive at bringing physical demonstrations of digital SPAD detectors.

Instructors

- Fabrice Retière, Université de Sherbrooke
- Serge Charlebois, Université de Sherbrooke
- Claudio Bruschini, Ecole Polytechnique Fédérale Lausanne
- Stefan Gundaker, Oesterreichische Akademie der Wissenschaften Vienna

8 November, 2026

Time:
8 November, 2026
9:00 – 18:00

Room:
Alhamar @Hotel Saray Granada

SC-04 | State-of-the-art semiconductor detectors in basic science, applied science and in industry

Schedule

08:00-09:00 Breakfast & Registration
09:00-11:00 Part 1
11:00-11:30 Morning Coffee
11:30-13:30 Part 2
13:30-14:30 Lunch
14:30-16:00 Part 3
16:00-16:30 Afternoon Coffee
16:30-18:00 Part 4

Location

Course and all breaks in Hotel Saray

Description

A solid understanding of the physics and technology underlying semiconductor detectors enables researchers to align experimental measurements more effectively with the scientific questions under investigation. It further facilitates the optimization of data analysis procedures, allowing experiments to approach the intrinsic resolution limits of the measurement setup. Moreover, such knowledge empowers users to formulate well-founded proposals for improving measurement processes in both hardware and software.

This one-day course begins with the fundamentals of semiconductor physics, followed by an overview of the interaction of ionizing radiation with semiconductor materials. Key concepts such as charge carrier generation and transport, basic device architectures, and an introduction to process and device simulation will be covered.

Depending on the application, semiconductor detectors require dedicated electronics characterized by low noise and high speed. Accordingly, noise sources and mitigation strategies will be discussed in detail. The course will

also introduce application-specific integrated circuit (ASIC) developments for signal amplification and data processing, concluding with an overview of state-of-the-art ASIC designs that enable complex detector systems.

Applications of semiconductor detectors across astrophysics, materials science, life sciences, and high-energy physics will be presented, each beginning with a clear motivation and a description of the relevant experimental constraints. In astrophysics, both space-based missions - such as XMM-Newton, Chandra, eROSITA, and BepiColombo - and future projects like ATHENA and LISA will be discussed, alongside ground-based systems employing e.g. adaptive optics.

In materials and life sciences, experiments conducted in institutional laboratories, synchrotrons, and X-ray free-electron lasers rely on electrons, protons, and X-rays to probe for example, crystal structures, molecular bonds, electric and magnetic fields, mechanical stress and many more. These applications impose diverse requirements on detectors, including high dynamic range, spectroscopic imaging capabilities, ultrafast response and count rate capability.

High-energy particle and nuclear physics have historically driven the development of advanced detector technologies. Examples include accelerator-based experiments at CERN, DESY and KEK, as well as underground experiments such as DUNE and GERDA. Recent technology developments lead to record performance (in spatial resolution, timing information resolution, radiation hardness, large area coverage) and to a broad variety of applications extending to astrophysics, beam and dose monitoring in hadron therapy, and more.

The basics of semiconductor physics and technology will be treated in detail. By providing a comprehensive overview of a broad range of applications, the course aims to stimulate new experimental ideas and support students and researchers in refining their experimental scientific research.

Outline

Part I: Semiconductor detector physics – 100 min

Part II: Electronics for semiconductor detectors – 90 min

Part III: Semiconductor detectors in astronomy and astrophysics – 60 min

Part IV: Semiconductor detectors in material and life sciences – 90 min

Part V: Semiconductor detectors in high energy physics – 90 min

Part VI: Summary and discussion – 30 min

Instructors

Lothar Strüder is professor at the University of Siegen. He earned his PhD in Physics at the Technical University Munich in 1988. His major scientific interests include position-, energy- and time resolving detectors for photons and particles. He is author and co-author of more than 500 technical and scientific publications with over 25.000 citations. He holds 15 worldwide patents in scientific instrumentation. Among other awards he received the Glenn F. Knoll Radiation Instrumentation Outstanding Achievement Award of the IEEE in 2019 and became Fellow of the MAS in 2020.

Giuseppe Bertuccio is professor of electronics and head of the Semiconductor Detector and Integrated Circuits Laboratory at Politecnico di Milano, where he began in 1987 in Prof. Emilio Gatti's research group. He has been visiting researcher at Brookhaven National Laboratory and at Canberra Industries, and has collaborated with numerous universities, research centers and companies worldwide on radiation detectors and low-noise electronics for scientific, industrial, and medical applications. He received the 2019 RTSD Scientist Award in recognition of his contributions to the field of room-temperature semiconductor detectors, electronics and systems.

Silvia Masciocchi is professor for experimental particle and nuclear physics at the University in Heidelberg, and head of the ALICE department at GSI, the Helmholtz Center for Heavy Ion Research in Darmstadt. Her research interests include heavy-ion physics and the development of particle detectors, with a particular focus on high precision tracking and vertexing, and on particle identification. After working with silicon strip detectors and with the large-volume Time Projection Chamber in ALICE, she recently moved to the development and integration of monolithic active pixel sensors (MAPS) produced in CMOS technology. Within the Helmholtz Matter program, she is the speaker of the Detector Technology and Systems topic.

Andrew Fram is Product Manager for detector systems at PNDetector GmbH. He has worked with X-ray and electron detector systems for more than eight years, holding product management and technical sales roles. His experience spans OEM instrument manufacturers, synchrotron facilities and research institutions worldwide. He has provided technical input on detector requirements, system configuration and application-specific integrations for energy-resolving X-ray and electron detection systems. His perspective is based on practical work with users, applications teams and engineering groups across the detector-system lifecycle. He holds a BEng (Hons) in Mechanical Engineering Design.

Time:
8 November, 2026
9:00 – 18:00

Room:
Partal @Hotel Saray Granada

SC-03 | Scientific Writing

Schedule

08:00-09:00 Breakfast & Registration
09:00-11:00 Part 1
11:00-11:30 Morning Coffee
11:30-13:30 Part 2
13:30-14:30 Lunch
14:30-16:00 Part 3
16:00-16:30 Afternoon Coffee
16:30-18:00 Part 4

Location

Course and all breaks in Hotel Saray

Description

This course is an introduction on how to get your message across in writing as a physical scientist. We concentrate on refereed papers and proposals/job applications but also touch upon other formats. The course is aimed at beginning scientific writers, PhD students and junior postdocs, but more experienced writers may find many aspects interesting, eye-opening, or simply useful in developing their own writing. The skills learned in this course will be more generally applicable as well, whether or not you not plan to build a further career as an academic.

During the course and the exercises, you will refer to your own writing when we discuss items like title, abstract, introduction, or paragraph and sentence structure, so bring with you your latest paper, whether in early draft form or already submitted to a journal.

Syllabus:

1. Writing in science

Refereed papers are an important vehicle in science, but not the only format where writing is needed. We will start the course by analysing what writing in science is about, and how you can optimise your written products. Among other aspects, we will study the optimum structure of a paper: where and how do you provide the information?

How to transform your scientific results in a story? And how to then write that story in a clear and precise way so you can produce a good paper? How do you put emphasis?

We will analyse how you catch a reader's attention in our current era of information overload, and highlight the importance of title and abstract.

2. How to write your papers?

You will learn to optimally structure your text, from the entire text down to the paragraphs and to individual sentences, thereby writing for the reader. How can topic sentences make paragraphs do their job?

We will highlight grammar rules you need to know so that you will write papers that are pleasant to read as well as correctly written. We will also revise the typesetting conventions that are used in our field, referring to publishers' Instructions for Authors and to LaTeX.

3. How to write a proposal or job application?

Whether you want to get experiment time on a large facility, access to supercomputers, apply for a post-doc position or a prestigious fellowship, get a tenured job, or get funding for your research, you will need to write proposals. And they need to stand out in order to be successful. In this session, you will learn the recipes to follow and the pitfalls to avoid.We will also highlight how you can make and maintain an effective CV, and discuss how you can enhance the effect of your reference letters.

4. How to make optimal use of AI tools?

AI tools, including large language models (LLMs) like ChatGPT or Claude, are revolutionising our lives as scientists. We will consider the advantages and possible pitfalls of the use of AI in preparing your written products, and analyse how you can optimise their use.

This course expands on what we wrote in the following Perspective papers in Nature Astronomy. They are widely applicable across the physical sciences, even though they were specifically written for astronomers. More general papers and books about scientific writing are referenced. We recommend participants to read these three papers before attending the Short Course.

- Chamba et al. 2022: https://rdcu.be/cVdtK How to plan your astronomy research paper in ten steps
- Knapen et al. 2022: https://rdcu.be/cVdtJ How to write and develop your astronomy research paper
- Knapen et al. 2025: https://rdcu.be/evDCt How to prepare competitive proposals and job applications

Instructor

Johan Knapen is a Research Professor at the Instituto de Astrofísica de Canarias in Tenerife, Spain. His research focusses on the structure and evolution of the central regions and the disks of galaxies, combining the exploitation of the sharpest and deepest possible imaging across a range of wavelengths with the use of AI tools. He has published almost 300 refereed papers. He is PI and coordinator of the EU Doctoral Network EDUCADO, and of the EU-funded Twinning network ExGal-Twin. Mentoring and coaching, in particular of young scientists from developing countries, is an increasingly important part of his activities, as is advanced training in scientific writing.

9 November, 2026

Time:
9 November, 2026
9:00 – 19:00

Room:
Alhamar @Hotel Saray Granada

SC-05 | Fast-timing scintillation detectors for medical and other applications

Schedule

08:00-09:00 Breakfast & Registration
09:00-11:00 Part 1
11:00-11:30 Morning Coffee
11:30-13:30 Part 2
13:30-14:30 Lunch
14:30-16:00 Part 3
16:00-16:30 Afternoon Coffee
16:30-19:00 Part 4

Location

Course and all breaks in Hotel Saray

Description

Remarkable progress is being made with regard to the timing performance of scintillation detectors. For example, the time resolution of clinical time-of-flight positron emission tomography (TOF-PET) systems has improved from 500 – 700 ps FWHM in the second half of the 2000s to less than 200 ps FWHM for the latest available systems. In the laboratory, coincident detection of annihilation photon pairs with a time resolution better than 50 ps FWHM has been demonstrated. These advancements are driven by innovations in scintillation materials, photosensors, readout electronics, detector design, and signal processing. In addition to medical imaging, the results of these developments are used in many other domains, such as materials science, nuclear physics, and high-energy physics.

The improvement of scintillation detector time resolution requires the optimization of the full detection chain. A sound understanding of the underlying physics and statistics greatly facilitates such efforts. Therefore, a substantial part of the course will be devoted to the theory of scintillation detector time resolution. It will be shown how the

physical limits of time resolution are governed by scintillation photon counting statistics and, as such, by fundamental properties of the scintillator (e.g. its light yield and pulse shape) and the photosensor (e.g. its photodetection efficiency and single-photon time resolution).

Based on the insights offered by this analysis, we will study the history, state-of-the-art, and ongoing developments in scintillation materials, photosensors, readout electronics, and signal processing. Special attention will be paid to detectors based on silicon photomultipliers (SiPMs), as the introduction of this new light sensing technology is a key driver of time resolution improvement in TOF-PET. Attention will also be paid to the increasing importance of detector design, which affects the kinetics of scintillation photon transport, as well as on the possibilities to mitigate the resulting loss of time information though the concept of time resolution recovery.

Instructors

- Dennis Schaart, TU Delft
- Joshua Cates, Lawrence Berkely National Laboratory

Time:
9 November, 2026
9:00 – 18:00

Room:
Partal @Hotel Saray Granada

SC-06 | Medical predictions from imaging with machine learning: The implementation gap

Schedule

08:00-09:00 Breakfast & Registration
09:00-11:00 Part 1
11:00-11:30 Morning Coffee
11:30-13:30 Part 2
13:30-14:30 Lunch
14:30-16:00 Part 3
16:00-16:30 Afternoon Coffee
16:30-18:00 Part 4

Location

Course and all breaks in Hotel Saray

Description

This course addresses the question of why so few machine learning (ML) systems for medical decision-making go beyond proof-of-concept to implementation. In doing so we take the scenic route, first discussing frequentist and Bayes statistical methods that are already successfully deployed with imaging in research and clinical contexts, and the estimates they make that are useful, and how this information is communicated in a way that improves the patient's experience. We then take an introductory tour of statistical learning theory (SLT), arguably the first and most comprehensive framework for ML developments including supervised, unsupervised, and reinforcement learning, and how SLT has been applied to imaging data. Validation and performance testing is an important component to these systems, and after describing the primary techniques, we also discuss contemporary alliances of ML with statistical inference. Finally, we explore the technical, ethical, and organisational reasons why ML systems are particularly absent from routine healthcare, even though they appear to offer an empirical advantage.

Outline

Part I: Statistical testing for medical imaging

- Images as an ordered dataset
- Frequentist and Bayes statistical approaches for imaging
- Including spatial information in test statistics
- The reproducibility crisis and response

Part II: An introduction to Statistical Learning Theory

- Preliminaries
- Components of a ML system
- Cross-validation
- Statistical Agnostic Learning

Part III: The implementation gap

- Technical – the right outputs for the right questions
- Ethical – bias, privacy, and explainability
- Organisational – agency and responsibility, interacting with electronic health records, integration into healthcare processes

Instructors

- John Suckling, niversity of Cambridge
- Subati Abulikemu, Univerysity of Cambridge)

10 November, 2026

Time:
10 November, 2026
9:00 – 18:00

Room:
Alhamar @Hotel Saray Granada

SC-07 | Medical Image Reconstruction: from Foundations to AI

Schedule

08:00-09:00 Breakfast & Registration
09:00-11:00 Part 1
11:00-11:30 Morning Coffee
11:30-13:30 Part 2
13:30-14:30 Lunch
14:30-16:00 Part 3
16:00-16:30 Afternoon Coffee
16:30-18:00 Part 4

Location

Course and all breaks in Hotel Saray

Description

Using the primary example of positron emission tomography (PET), core image reconstruction methods will be explained, from unregularised to regularised methods, through to kernel-based and generative AI-based image reconstruction. The coverage of reconstruction and deep learning principles will also touch on implementation aspects for core methods as well as state of the art methodology.

Image reconstruction foundations

- Reconstruction basics: object representation and forward models
- Maximum likelihood expectation maximisation (MLEM)
- Maximum *a posteriori* EM (MAPEM)
  - Priors

- Algorithms

AI for image reconstruction: introduction

- Basic principles of deep learning
- Direct methods (CNNs and CEDs)
- Unrolled iterative deep-learned methods (e.g. FBSEM-Net)
- Methods without training data

Kernel and deep image prior methods

- Conventional kernel EM (KEM)
- Deep image prior (DIP)
- Kernel methods with deep learning

Generative AI for image reconstruction

- Overview of generative models for inverse problems
- Diffusion models and integration with PET image reconstruction
- Unsupervised and supervised approaches

Test-time adaptation: steerable diffusion and deep diffusion image prior

Instructors

- Andrew Reader, King’s College London
- George Webber, King’s College London
- Siqi Li, UC Davis

Time:
10 November, 2026
9:00 – 18:00

Room:
Partal @Hotel Saray Granada

SC-08 | Fundamentals of Total-Body PET

Schedule

08:00-09:00 Breakfast & Registration
09:00-11:00 Part 1
11:00-11:30 Morning Coffee
11:30-13:30 Part 2
13:30-14:30 Lunch
14:30-16:00 Part 3
16:00-16:30 Afternoon Coffee
16:30-18:00 Part 4

Location

Course and all breaks in Hotel Saray

Description

This course focusses on the unique features of Total-Body and long axial field-of-view PET (TB-PET) systems that an imaging scientist needs to know to extract optimal performance from such systems, along with the clinical and research applications enabled by this technology. Participants will explore challenges and solutions for managing the QC, image reconstruction and data processing of TB-PET systems, and how to exploit their unique advantages in a range of applications.

Instructors

- Steve Meikle, University of Sydney
- Ben Spencer, UC Davis
- Georgios Angelis, University of Sydney

Workshops

8 November, 2026

Time:
8 November, 2026
11:30 – 17:00

Room:
ANDALUCÍA II & III

WS-01 | AI in Nuclear Sciences and Nuclear Medical Imaging – Review and future expectations (onsite only)

Chairs:

Jean-Baptiste Michaud (Sherbrooke)
Francis Loignon-Houle (Valencia)

Summary

In many nuclear sciences and medical imaging applications, AI has come a long way and in some instances it has (almost!) become the gold standard. The workshop will outline the major milestone in the last 10 years, the current hot topics and issues, and discuss where future breakthroughs could come from and what our collective priorities should be for the next 10 years.

Contacts

- jean-baptiste.michaud@usherbrooke.ca
- floignon@i3m.upv.es**Panelists** (in alphabetical order)

Irène Buvat

Irène Buvat, PhD, is a Senior researcher at CNRS, and Head of the IRIS lab at Institut Curie, Orsay, France. She obtained her PhD degree in “Nuclear and Particle Physics” from Paris Sud University, France, and focused her research on applications of physics to medical imaging. She is currently the head of the Imaging, innovative Radlation therapy and Systems medicine (IRIS) lab at Institut Curie in Orsay, France. Her research interests focus on the use of positron emission tomography (PET) to understand biological mechanisms involved in cancer and optimize patient management, using multi-scale and multimodal data analysis powered by artificial intelligence (AI). She is highly involved in radiomics and AI research to enhance the role of medical imaging in precision medicine. Her lab has developed the user-friendly LIFEx software to facilitate reproducible radiomic studies (>10,000 users

worldwide). In 2020, she introduced a novel PET biomarker for measuring the dissemination of cancer, that has now been validated in thousands of patients and is commercially available. She promotes open-access to state-of-the-art research material (GATE, LIFEx) and resource sharing to accelerate the development and validation of AI-based methods. She is a member of the SNMMI AI task force and an Associate Editor of the Journal of Nuclear Medicine.

Marco Carminati

Marco Carminati (B.Sc. 2003, M.Sc. 2005, Ph.D. 2010) is currently an Associate Professor of Electronics at Politecnico di Milano (Italy) and Associate with INFN where he coordinates the KATRIN_TRITAN experiment on neutrino physics. His research interests include sensors, low-noise electronics, radiation detectors and nuclear instrumentation for medical imaging, with increasing interest in analog implementations of machine learning for in-sensor processing. He has authored 400+ publications, 6400+ citations, holds 7 patents, and received 3 IEEE Best Paper Awards. He is Senior IEEE member, Chair of the IEEE NPSS Italy Chapter and a Member-at-Large of the NPSS RISC Technical Committee.

Audrey Corbeil Therrien

Audrey Corbeil Therrien is an Associate Professor in the Department of Electrical and Computer Engineering at the Université de Sherbrooke in Québec, Canada. She currently holds the Tier-2 Canada Research Chair in real-time embedded intelligence for ultra-high-rate detectors. Her research aims to improve real-time analyses at the edge with the integration of machine learning in high performance radiation instrumentation systems. These systems can generate hundreds of gigabytes per second and more. Reducing that data at the edge within the detector greatly improves the efficiency of instruments, including high precision medical scanners and dark matter detectors.

Luca Presotto

Luca Presotto is associate professor of applied physics at the University of Milano-Bicocca (Milano, Italy) department of physics. He has previously worked for more than 10 years in the nuclear medicine unit of Ospedale San Raffaele. He served a quick stint as senior PET scientist in IXICO, a contract research organization devoted to brain imaging. His current research interests include image reconstruction and AI-based image analysis. He is part of the scientific board of the Milan Centre for Neuroscience. Also his teaching duties focus on the application of AI in medical imaging. In neuroscience, he has mostly worked in studying neurodegenerative diseases (especially Alzheimer's and Parkinson's disease) using FDG-PET and other tracers targeting amyloid proteins. He has participated in more than 40 scientific publications for which he curated the automated image analysis, accumulating more than 1700 citations.

Ye Qing

Dr. Qing Ye has been leading PET kinetic modeling research and development at United Imaging Healthcare since 2020. She has played a key role in the development and release of multiple AI-based advanced imaging applications. Her research focuses on dynamic and parametric PET imaging, motion correction, and quantitative PET reconstruction, bridging cutting-edge imaging methodologies with clinical applications. Dr. Ye is also an active contributor to the scientific community, having authored or co-authored more than 30 scientific publications.**Panel Moderators**

Francis Loignon-Houle

Francis Loignon-Houle, PhD, is a postdoctoral researcher at the Institute for Instrumentation in Molecular Imaging (i3M) in Valencia, Spain, a joint center of the Spanish National Research Council (CSIC) and the Universitat Politècnica de València (UPV). He obtained his PhD degree in Radiation Sciences and Biomedical Imaging from the Université de Sherbrooke, Canada, and focused his research on instrumentation for positron emission tomography (PET), in particular on the fundamental limits of timing resolution in scintillation detectors. He has contributed to the development and characterization of several organ-dedicated and high-resolution PET scanners, to machine learning–based waveform analysis, and to time-of-flight (TOF) PET image reconstruction. He is

currently working on improving both timing and positioning in new TOF-PET detectors, exploiting Cherenkov emission in BGO with scalable ASIC-based readout electronics and developing machine learning methods for interaction positioning.

Jean-Baptiste Michaud

Jean-Baptiste Michaud is professor of Electrical and Computer Engineering at the Université de Sherbrooke (Quebec, Canada) and an interdisciplinary research leader in artificial intelligence (AI), with prior experience in cutting-edge industrial R&D. For more than twenty years, he has been developing electronic and software technologies, data analysis methods, and AI algorithms for health applications. His contributions center on three collaborations: bra-based breast cancer detection, predictive modeling in the intensive care unit, and medical imaging instrumentation. He provides the vision and technical expertise that drive the resulting biomedical advances. He holds or has filed patent applications in each of his projects, all of which involve a partner company for commercialization, and he also contributes to clinical and preclinical trials within them.

WS-01-01

Kolmogorov-Arnold Networks: A New Paradigm for Explainable Prediction

M. J. Neuer (1,2), I. Garmaev (1)
1 RWTH-Aachen University
2 innoRIID-Ametek, Düsseldorf

In 1957, the findings of Kolmogorov and Arnold showed that continuous multivariate functions can be represented by combinations of simpler, univariate functions. Based on this work, Liu et al. [1] presented in 2024 a novel architecture for formulating neural networks — the Kolmogorov-Arnold network (KAN).
The paper will first introduce shortly the basic foundations of KAN, including how to design, train and apply them. Their structure differs from common multilayer perceptrons (MLP) because KANs train univariate functions on the edges of the network graph. In these functions, typically B-splines, instead of training weights like a MLP, KANs train the control coefficients of the splines. Nodes of the network consequently act as pure transfer points of the internal data. An advantage of this new network type is intrinsic explainability. After training, the splines on the edges represent human-interpretable mathematical functions. They can be visually studied to understand the decision logic within the network. The paper will also show the conversion of a KAN into an symbolic expressions. Secondly, several emerging KAN applications will be reviewed and compared to existing classical machine learning solutions. KANs have already been successfully applied to industrial problems, including cancer screening [2], mechanical predictions [3], time-series prediction [4], bioinformatics [5], soft-sensor solutions [6] andhyperspectral image classification [7]. These recent works show the potential of the approach for application to radiation detection, nuclear security and safety, as well as nuclear medicine.
The present paper will provide a brief outlook on how to use KAN for gamma spectroscopy. One canonical scenario — the differentiation of special nuclear material like weapon-grade plutonium (WGPu) and enriched uranium (HEU) from masking nuclides like iodine (I-131) or gallium (Ga-67, Ga-68) — is used to illustrate thebenefits of the new approach.
[1] Liu, Z., et al. (2024). KAN: Kolmogorov-Arnold Networks. arXiv:2404.19756
[2] Wang, J., Zhang, L., & Liu, Y. (2025). Kan-AAE-driven synthetic SERS spectra generation method for cancer screening. Journal of Molecular Liquids, Volume 419, 126950
[3] Abueidda, Diab W.; Pantidis, Panos; Mobasher, Mostafa E. DeepOKAN: Deep Operator Network Based on Kolmogorov Arnold Networks for Mechanics Problems. Computer Methods in Applied Mechanics and Engineering, 2024/2025
[4] Xu, Kunpeng; Chen, Lifei; Wang, Shengrui. Kolmogorov-Arnold Networks for Time Series: Bridging Predictive Power and Interpretability. arXiv:2406.02496
[5] Dumontet, Louis; Han, So-Ra; Prouvost, Axel; Lee, Jun Hyuck; Oh, Tae-Jin; Kang, Mingon. Interpretable Kolmogorov-Arnold Networks for Enzyme Commission Number Prediction. npj Artificial Intelligence 2, Article 11, 2026

[6] Sun, Huanqi; Liu, Wentao; Zeng, Fengrong; Sui, Lin; Yao, Le; Xiong, Weili. A Temporal Convolutional-Based Kolmogorov-Arnold Network for Industrial Soft Sensor Modeling. IEEE Transactions on Instrumentation and Measurement 74, 1-13, 2025
[7] Arya, Rajat Kumar; Chattopadhyay, Pratik; Srivastava, Rajeev. Hyperspectral Image Classification Using Gated Adaptable Convolutional-Based Kolmogorov-Arnold Network. IEEE Geoscience and Remote Sensing Letters 22, Article 5507005, 2025

WS-01-02

AI at the Front End: Machine Learning for Raw-Signal Processing in Semiconductor Detectors

A. Cherlin, N. Atkins, M. Exley, T. Winterbottom
Kromek Ltd., County Durham, UK

Over the past decade, ML (machine learning) methods in nuclear detection and medical imaging have advanced most rapidly at the back end of the processing pipeline, i.e. enhancement, correction and interpretation of already reconstructed images and spectra. In medical imaging, deep learning is now widely used to suppress noise, automate lesion segmentation, reduce patient dose and scan time, and flag abnormalities to support diagnostic decisions.
However, ML application at the front end of low-level detector signal processing remains comparatively underexplored, even though the conversion of raw detector signals into event information significantly affects all subsequent steps. This review focuses on this stage, with particular attention to room-temperature semiconductor detectors, such as CdZnTe (CZT).
Detector performance has traditionally been improved through theoretical and phenomenological modelling, extensive calibrations and, often, costly hardware modifications such as reducing pixel size to improve position resolution. The review outlines how ML is changing this landscape: models trained on raw detector signals can estimate energy, position and timing significantly more accurately than current signal processing methods, reducing the need for major hardware upgrades.
The underlying ground truth of individual events cannot be measured directly, and characterising every detector in a real system in full detail is usually impractical. Such models therefore rely heavily on simulated training data, which can further be supplemented by experimental data. One of the central challenges is thus the gap between simulation and reality: real detectors exhibit material non-uniformities operating-condition drift, and other effects that simulations and calibrations usually do not fully capture. This review presents strategies reported to date for closing this gap: from generating more representative training data to adapting models to real measurements. These include the authors' recent results, which show that incorporating realistic calibration variations into simulated training data reduces the domain shift between simulated and real data and improves downstream

spectral and image reconstruction. The review concludes with practical considerations for deployment, including real-time implementation and its impact on system performance.

WS-01-03

Edge-AI with CMOS In-Memory Computing for Radiation Detector Acquisition Chains

M. Ronchi, M. Pandocchi, M. Amadori, M. Carminati, G. Borghi, C. E. Fiorini
Politecnico di Milano, Dipartimento di Elettronica, Informazione e Bioingegneria, Milan, Italy
Istituto Nazionale di Fisica Nucleare (INFN), Sezione di Milano, Milan, Italy

We propose a review of digital and analog edge-AI in-memory computing (IMC) solutions for nuclear and medical imaging acquisition chains, with a focus on CMOS based approaches. We start by covering the motivation and historical context for IMC, driven by the von Neumann bottleneck, and its growing relevance to nuclear physics applications as high-density pixel detectors and high-luminosity, high-rate experiments push data-bandwidth demands higher. We then present the two main hardware directions pursued in the field: emerging non-volatile memory devices (memristors, phase-change memory, etc.) versus CMOS/SRAM-based IMC, comparing their trade-offs in maturity, reliability, and PDK availability. We survey how research groups across the nuclear field are approaching edge-AI implementation. We will then present a case study, that is our analog neural network ASIC (ANNA), an in-memory CMOS accelerator designed to be embedded in the analog front-end of Anger-camera PET/SPECT detectors. We briefly detail the initial ANNA V1 proof of concept and the ongoing ANNA V2 validation and monolithic crystal demonstrator. We discuss the advantages and disadvantages we observed with capacitive-based analog computing and the main difficulties encountered. We discuss figures of merit to compare in-memory computing devices, with a focus on energy efficiency (GOPs/W). We close by highlighting the main opportunities and unresolved questions for IMC adoption in nuclear instrumentation going forward. Although studies on the application of these devices to medical imaging and nuclear physics remain limited, we consider this a promising direction for the future of radiation and particle detectors.

WS-01-04

AI in PET: are we ready for more than better images?

I. Buvat
Institut Curie, Paris

Artificial Intelligence is rapidly transforming Positron Emission Tomography imaging. From image enhancement and automated quantification to prognostic models and AI agents, this presentation will explore how AI is reshaping the field. Through selected examples, we will examine what is already clinically available, what still requires extensive validation, and what may come next.

WS-01-05

AI in nuclear imaging and neuroscience: a look at the initial impact

L. Presotto
University of Milano-Bicocca, Italy

In the last decade, the number of medical devices approved for clinical use involving AI has increased exponentially. Most of them are for imaging based applications, due initially to the effectiveness of convolutional neural networks in extracting image features. Translating models into practice opens a large set of challenges, due to "distribution shifts". Such shift are often quite hard to predict and detect before the application is deployed to the end-user setting.
In this review, I will focus mostly on imaging-based neuroscience, a field that developed robust automated analysis algorithms earlier than most others (SPM was released in 1996!). I will select a number of cases of interest to highlight which problems AI can effectively solve and where its inclusion in a full clinical or research pipeline is still suboptimal.

WS-01-06

Lunch Break

WS-01-07

Delegate, Verify, Understand : Agentic AI in the Medical Imaging Research Workflow

G. Bélanger, M. Fromont, J.B. Michaud
Electrical and Computer Engineering, Université de Sherbrooke

Large language models have moved from conversational assistants to agents that can act within a research environment. Operating within a software harness that provides tools and feedback, they read code and data, run analyses, generate figures and revise their work based on what they observe. As these tools evolve rapidly, research groups need to consider how to adopt them in a controlled and transparent manner. Starting from a defined research question, this presentation examines where an agent may contribute at each step of the methodology and how its contribution can be verified. Agents can substantially accelerate tasks that are well established, precisely specified and easily verified, such as implementing known algorithms, standard statistical analyses, data visualization and publication figures, which occupy much of researchers' time. Tasks involving complex reasoning, such as literature synthesis, method selection or new numerical methods, remain possible but require closer supervision and independent validation. Two projects from our group illustrate both regimes. For a deterministic X-ray transport solver, an agent contributed to implementation, optimization and GPU porting, with validation against analytical and Monte Carlo references. For scatter estimation in time-of-flight computed tomography, an agent-assisted literature search led to a well-documented closed-form solution, complemented by active-set methods to enforce non-negativity, replacing our original purely iterative algorithm. Combined with a GPU implementation, this improved accuracy and reduced processing time, for example from about 11 minutes to 0.1 s per projection. Finally, we discuss the risks that accompany these tools. Results obtained with AI assistance should be understood and validated by researchers and reviewed by human peers; how to guarantee this in practice remains an open question.

WS-01-08

Panel - AI in Nuclear Sciences and Nuclear Medical Imaging – Review and future expectations

Time:
8 November, 2026
14:30 – 19:40

Room:
ALBÉNIZ & MACHUCA

WS-02 | Digital SiPM and SPAD-based sensors (onsite only)

Summary

Digital SiPMs and SPAD-based devices see increased development activity with the potential of improving photon-counting systems. The main NSS program reports on technology performance and application use of available technologies.

The goal of the workshop is to provide a place where upcoming/future technologies can be described by their developers, development roadmaps can be disclosed, and application niches or markets are aimed for.

This is not the type of communication easily accepted in the main program.

To make sure everyone is included, we invite groups who develop digital SPAD systems or have proposals to use this type of photodetectors to contact us for a participation in the workshop.

Tentative topics for the workshop structure:

- Roadmap presented by technology developers (short talks)
- Discussion/debate on collaboration and funding strategies to bring these technologies to use

We will invite spin-offs that commercialize SPAD based detectors to attend the event and participate in the discussion/debate.

Contact

Serge Charlebois, Université de Sherbrooke, Canada (serge.charlebois@usherbrooke.ca)
Catherine Pepin, Université de Sherbrooke, Canada (catherine.pepin@usherbrooke.ca)
Stefan Gundacker, ÖAW, Austria (stefan.gundacker@oeaw.ac.at)
Claudio Bruschini, EPFL, Switzerland (claudio.bruschini@epfl.ch)
Fabrice Retière, TRIUMF, Canada (fretiere@triumf.ca)

WS-02-01

Opening words

14:40 - 16:00 - Topic 1 - Status of ongoing projects

WS-02-02

Status of project DIGILOG (#3409)

Samuele Bisi

École Polytechnique Fédérale de Lausanne, Neuchâtel, Switzerland

Abstract
Please complete

WS-02-03

Status of the PetVision project (#3410)

Rok Dolenec[1,2], David Gascón[3], Alberto Gola[4], Jose Maria Benlloch[5], David G. Sanchez[6], Rafael Ballabriga[7], Wolfgang Weber[8], Georges El Fakhri[9], Rok Pestotnik[2]

[1] University of Ljubljana, Faculty of Mathematics and Physics, Ljubljana, Slovenia; [2] Jožef Stefan Institute, Experimental Particle Physics Department, Ljubljana, Slovenia; [3] University of Barcelona, Dept. Física Quàntica i Astrofísica, Institut de Ciències Del Cosmos, Barcelona, Spain; [4] Fondazione Bruno Kessler, Trento, Italy; [5] The Institute of Instrumentation for Molecular Imaging, Valencia, Spain; [6] Oncovision, Valencia, Spain; [7] European Organisation for Nuclear Research - CERN, Geneva, Switzerland; [8] Technical University of Munich (TUM-MED), Munich, Germany; [9] University of California Davis, Dept. of Biomedical Engineering, Davis, USA

This project has received funding from the European Union's Horizon Europe research and innovation programme under grant agreement No 101099896

Abstract
With coincidence timing resolution (CTR) below 100 ps positron emission tomography (PET) with limited angular coverage and even small flat panels could reach state-of-the-art image quality. The PetVision project is developing a novel modular PET detector concept based on high-resolution time-of-flight (TOF) capabilities that approach the physical limits of current scintillator technology.

Achieving this performance requires dedicated development and optimized integration of key PET detector components. We are designing a low noise, high dynamic range frontend electronics, specifically a next generation ASIC with 20 ps intrinsic time resolution and on-chip time-to-digital conversion (TDC). Concurrently, we are advancing SiPM sensor technology to enhance photon detection efficiency and reduce jitter. We also explore 2.5D integration between the photodetector and electronics to minimise parasitic effects and timing dispersion.

This contribution present the project's vision and progress in technology development, focusing on the ASIC design, production of dedicated SiPMs and preliminary tests of 2.5D integration approaches.

WS-02-04

Photon-to-Digital Converters: Update and Future development (#3401)

Serge A. Charlebois

Université de Sherbrooke, Génie électrique et génie informatique, Institut interdisciplinaire d'innovation technologique (3IT, Sherbrooke, Canada

Abstract
We will present an update on the development of the Low-Power Photon-to-Digital converter (PDC) fabrication and performances for large area detector systems and on the design of the Timing-Optimized PDC for medical imaging and timing sensitive applications.
We will discuss the current migration of the PDC process to a 200 mm wafer production line and the timeline toward an MPW-type runs of the PDC technology.

WS-02-05

Status of project at TRIUMF (#3411)

Fabrice Retiere

TRIUMF, Science Technology Department, Vancouver, Canada

Abstract
Please complete

WS-02-06

Status of the Picopix project (#3412)

Rafael Ballabriga

Conseil européen pour la Recherche Nucléaire (CERN), Geneva, Switzerland

The presentation is on behalf of the design team: X. Llopart, O. C. Akgun, M. Andorno, R. Ballabriga, G. Bergamin, S. Biereigel, F. Brambilla, A. Caratelli, D. Ceresa, T. Daros, F. De Benedetti, B. Denkinger, A. Fiergolski, V. Gromov, J. Kaplon, S. Kulis, M. Lupi, A. Pulli, S. Scarfi, T. Silva, V. Sriskaran, L. Timmermans, O. Y. Wong

Abstract

PicoPix is a large-area hybrid pixel detector readout ASIC being developed in 28 nm CMOS by CERN and Nikhef. Its main target is the LHCb VELO Upgrade II. It is also aimed at beam loss monitoring and at applications within the Medipix collaboration framework. The design builds on almost two decades of hybrid pixel development in the CERN EP-ESE-ME group. From Timepix (2007, 10 ns time bin) through Timepix3 (2013, ~1.56 ns) and VeloPix (2016) to Timepix4 (2020, 200 ps). PicoPix pushes timing precision into the picosecond regime while keeping fine spatial granularity and very high rate capability.

The chip has a 256 × 384 matrix of 50 µm square pixels and can be tiled seamlessly on three sides, so it can create large detector areas with minimal dead space. It targets a time resolution below 50 ps rms per hybrid (ASIC plus sensor). To survive the extreme radiation environment of the upgraded LHCb VELO, the logic uses triple modular redundancy and is designed for total ionizing doses up to 1 Grad. The chip can handle up to 96 events per 25 ns bunch crossing, which is up to 3.84 × 10^9 events per chip per second. To keep this rate manageable, programmable on-chip data reduction performs event clustering, vetoing, filtering and sorting. Data leave the chip through a data-driven readout over up to four 25.6 Gbps serial links, for a total bandwidth of 102.4 Gbps.

WS-02-07

Recent progress in TSV, 2.5D and 3D integration of SiPMs at FBK (#3413)

Alberto Gola

Fondazione Bruno Kessler (FBK), Trento, Italy

Abstract

FBK is developing a set of integration technologies to overcome the limits of wire-bonded, front-side-contacted SiPMs in large-area, high-granularity detectors. We report on the latest progress of our through-silicon-via (TSV) platform. A first run of a glass-less TSV process has been carried out alongside the standard front-side production flow, and the transfer of the process to an external foundry has been assessed. TSVs allow 6x6 mm^2 SiPMs to be

segmented into independently read sub-pixels down to 1 mm^2 on the same die, and a single-cell-access TSV layout, giving back-side access to individual microcells, has been taped out. In parallel, we are pursuing 2.5D and 3D integration with front-end electronics, including 3D stacking of SiPMs on readout ASICs developed with an industrial partner. These approaches enable four-side tileable modules with minimal dead area, and aim at finer segmentation and improved timing for TOF-PET, high-energy physics and space applications.

WS-02-08

Status of project PLATON (#3414)

Kodai Kaneyasu[1], **Davide Sgalaberna**[2]

[1] École Polytechnique Fédérale de Lausanne, Neuchâtel, Switzerland; [2] ETH Zurich, Inst. f. Teilchen- und Astrophysik, Zürich, Switzerland

Abstract
The PLATON project is developing scintillator-based detectors for high-resolution particle tracking in applications such as neutrino experiments. This talk presents the development status of PlatonSPAD, a 9 mm × 9 mm sensor fabricated in a 110 nm CMOS image sensor process for single-photon readout in tiled detector modules.
The sensor contains 192 × 160 single-photon avalanche diodes (SPADs) organized into 48 × 40 macro-pixels. Each macro-pixel comprises a 4 × 4 array of SPADs and two event-driven time-to-digital converters (TDCs) with a nominal bin width of 200 ps. The first hit within a macro-pixel triggers timestamp capture and starts a programmable delay. When the delay expires, that macro-pixel latches the states of its 16 SPADs to form a hit map. Each macro-pixel can independently record up to two hit maps per measurement cycle, each paired with its corresponding first-hit timestamp.
Resistively coupled on-chip ring oscillators provide the TDC clocks, and an on-chip phase-locked loop locks them to a nominal frequency of 315 MHz. A selectable buffer chain delays the input reference clock in 70 ps steps, with a maximum delay of 1.12 ns, to compensate for board-level clock skew and align timestamps across tiled chips.

WS-02-09

Status of ASPIDES project (#3415)

Tommaso M. Floris[1,2,3], On behalf of ASPIDES-Collaboration

[1] Universita di Pavia, Pavia, Italy; [2] Istituto Nazionale di Fisica Nucleare, Pavia, Italy; [3] Fondazione Bruno Kessler, Trento, Italy

The activity leading to the results presented in this paper was carried out in the framework of the ASPIDES project, funded by the National Institute for Nuclear Physics (INFN), Italy.

Abstract
As part of the ASPIDES collaboration, a prototype of a fully digital SiPM in 110 nm CMOS technology, based on a fast parallel adder and featuring first-photon timing and time-over-threshold measurement capabilities, was submitted in December 2025. The development of a dedicated test board has been completed, and the measurement setup is currently being finalized. Pending the results of the initial experimental characterization, the design of a scalable demonstrator has been initiated. This new version is designed to interconnect multiple digital SiPMs, similar to those currently under evaluation, through a simplified serial input/output interface. This approach minimizes the physical interconnect overhead toward the control FPGA, thereby enabling a single FPGA to manage a considerably larger number of devices.
The digital interface electronics must support two main functions: the configuration of internal structures and the retrieval of data from all integrated modules. The communication process is based upon a 32-bits instruction-based protocol, which enables individual module addressing, thereby supporting SiPM programming and command execution. This protocol includes functions such as pixel reset, acquisition window control, configuration register menagement and control of the output data format. The demonstrator is targeted for completion in spring 2027.

WS-02-10

Status of project spadRICH (#3417)

Prabhleen Singh[1], **Rok Dolenec**[2]

[1] École polytechnique fédérale de Lausanne, AQUA Laboratory, Neuchâtel, Switzerland; [2] University of Ljubljana, Faculty of Mathematics and Physics, Ljubljana, Slovenia

Abstract
Please complete

15:53 - 16:15 - Break

16:15 - 17:00 - Invited Talk - Digital SPAD detectors: a broader perspective on trends and markets

WS-02-11

Packing Functionality under SPADs with nanometer scale 3D Stacking Technologies (#3418)

Robert K. Henderson

University of Edinburgh, School of Engineering, Edinburgh, UK

Abstract
This talk will look at recent 3D stacked SPAD sensors and consider the limits of what electronics can be packed under SPAD detectors. In latest 3D stacked nanometer-scale SPAD technologies. We will consider examples of high resolution arrays for HDR intensity imaging, LIDAR arrays and computational pixels for life-science applications. The prospects for the nuclear science community to harness these largely consumer/automotive driven technologies will be discussed.

17:00 - 17:30 - Coffee break

17:30 - 18:30 - Topic 2 - Vision

WS-02-12

ASPIDES: a digital SiPM in 110nm CMOS - rationale, technology choice and open challenges (#3419)

Lodovico Ratti, On behalf of the ASPIDES collaboration

Universita di Pavia, Dipartimento di Ingegneria Industriale e dell'Informazione, Pavia, Italy

Abstract
ASPIDES is an R&D project funded by INFN and involving several groups, targeting HEP applications such as dual-readout calorimetry and RICH detectors. It aims at a proof of principle of a fully digital SiPM in CMOS technology, where photon counting and timing are performed on chip by a parallel counter and a NAND-tree network feeding sub-100 ps TDCs. The talk presents the rationale behind the choice of the LFoundry 110 nm CIS process and the status of the first prototype, with SPAD characterization, including irradiation and cryogenic tests, as an integral part of the activity. The challenges of a planar implementation and the collaboration and funding strategy are also discussed.

WS-02-13

PLATON - lessons learned on strategy and funding (#3420)

Davide Sgalaberna

ETH Zürich, Inst. f. Teilchen- und Astrophysik, Zürich, Switzerland

Abstract
The PLATON project aims to develop a 9x9 mm^2 SPAD array sensor (PLATON SPAD) for high-resolution particle tracking in scintillator-based neutrino detectors. PLATON SPAD is being developed for counting photons produced and transported by very thin scintillating fibers (0.5 mm diameter or lower) or as imaging sensor of plenoptic cameras that view unsegmented scintillator. PLATON SPAD requires single-photon capability. Sub-nanosecond timestamping allows to exploit the very fast response of the scintillator to reject random noise. Finally, the required ton-scale scintillator mass implies covering a few m^2 surface with PLATON SPAD sensors. In this talk, I will review the requirements of the high-resolution neutrino detectors under development within the PLATON project, focusing on both the advantages brought by SPAD arrays and the challenges that lead to the design choises. After elaborating possible funding strategies and mass production towards the realisation of the PLATON detectors and discussing about the lessons learned thus far, I will report on potential applications of SPAD array sensors beyond neutrino experiments, such as a novel monolithic PET scanner under design within the PLATON project, and the related technical challenges to overcome.

WS-02-14

SPADs in DRDs (#3421)

Fabrice Retiere

TRIUMF, Science Technology Department, Vancouver, Canada

Abstract
Please complete

WS-02-15

Digital SiPM initiatives in the USA (#3422)

Shiva Abbaszadeh

UC Santa Cruz, Electrical and Computer Engineering, Santa Cruz, USA

Abstract
R&D Collaboration on photodetectors (RDC-2) brings together the U.S. detector-development community to advance next-generation photon detection technologies for particle physics experiments within the broader CPAD framework.
The collaboration coordinates R&D in innovative photosensors, photodetector instrumentation, and large-area photon-detection systems.
Its mission is to foster collaboration across institutions, identify common technology needs, and accelerate the development of photodetectors that enable future neutrino, dark matter, and other frontier physics experiments.
We will present the main R&D activities on SPADs and SPAD-based systems ongoing in the U.S.A.

18:30 - 18:45 - Topic 3 - Foundry perspective

WS-02-16

End-to-End SPAD Technology at Fraunhofer IMS (#3423)

Jennifer Ruskowski[1], Peter vom Stein[1], Martin Figge[1], Stephan Kolnsberg[1], Anton Grabmaier[1,2]

[1] Fraunhofer Institute for Microelectronic Circuits and Systems, Duisburg, Germany; [2] University Duisburg-Essen, Duisburg, Germany

Abstract
The development of the Fraunhofer IMS SPAD technology was originally driven by the requirements of large-scale SPAD arrays for LiDAR. Today, a 200 mm backside-illuminated SPAD process with wafer-to-wafer bonding is available, providing a versatile platform for highly integrated photon detection systems. The approach allows SPAD detectors and CMOS circuitry to be designed and optimized separately and subsequently combined, with the electronics positioned directly underneath the detector to maximize the photosensitive area and reach perfect timing symmetry.
Fraunhofer IMS covers the complete development chain, from SPAD and circuit design to semiconductor manufacturing and electro-optical waferlevel test, enabling sensor solutions tailored to specific detection challenges. The presentation will introduce this end-to-end approach, the rationale behind the technology, key

lessons learned during its development, and its potential for highly integrated digital SiPMs, including applications in particle physics.

18:45 - 19:30 - Topic 4 - How could one size fits all - A panel and group discussion

WS-02-17

Discussion/debate: on collaboration and funding strategies to bring these technologies to use

WS-02-18

Summary and conclusions

WS-02-19

Cocktail

14 November, 2026

Time:
14 November, 2026
14:30 – 19:30

Room:
FEDERICO GARCÍA LORCA

WS-03 | Total-Body Kinetic Modeling Workshop

Summary

This workshop is designed to serve as a forum for discussing the emerging field of total-body PET kinetic modeling and its future directions. There are currently about 100 total-body PET and long axial field-of-view PET scanners operating across four continents. This workshop is timely to discuss the growing need for effective handling of total-body data for dynamic imaging and kinetic modeling. Such advancements are essential for extracting physiologically significant information that traditional static imaging methods could not achieve. We have invited experts with various levels of experience, including both senior and junior researchers, to present an overview of the technical challenges, progress, and clinical applications in this field. The workshop will facilitate not only rich exchanges of ideas but also offer a kinetic modeling an open-source software demonstrattion. Importantly, this workshop is designed to complement the existing MIC program on kinetic modeling, providing invited talks and practical sessions without overlapping with current offerings.

Instructors

- Negar Omidvari (UC Davis)
- Steven Meikle (University of Sydney)
- Kevin Chung (Massachusetts General Hospital)
- Yun Zhao (University of Sydney)
- Qinlin (Alistair) Gu (University of Sydney)

Contact

Steven Meikle, University of Sydney, Australia (steven.meikle@sydney.edu.au)

WS-03-01

Welcome and Introduction

Steven Meikle, Negar Omidvari

University of Sydney, Sydney, Australia; University of California, Davis, USA

14:40–15:40 - Session 1: Cutting Edge Methods in Total-Body Kinetic Modeling and Analysis

Richard Carson, Jing Wu

Yale University, New Haven, USA; Beijing Normal University, Beijing, China

WS-03-02

Total-Body PET Kinetic Modeling: Challenges and Opportunities

Guobao Wang

University of California, Davis, USA

WS-03-03

A pragmatic approach to ultrashort time-frame total-body PET image reconstruction

Andrew Reader

King's College London, London, UK

WS-03-04

Exploring inter-organ connectivity using static and dynamic whole-body PET

Irène Buvat

Institut Curie, Paris, France

15:40–16:40 - Session 2: Emerging Frontiers

Negar Omidvari, Yun Zhao

UC Davis, Davis, USA; University of Sydney, Sydney, Australia

WS-03-05

New hopes or old illusions? Image-derived input functions in the era of next-generation (brain) PET imaging

Tommaso Volpi

Yale University, New Haven, USA

WS-03-06

High-Temporal Resolution PET Kinetic Modeling

Kevin Chung

Massachusetts General Hospital, Boston, USA

WS-03-07

Whole-Body Functional [18F]FDG PET

Sharna Jamadar

Monash University, Melbourne, Australia

WS-03-08

Coffee break

17:00–18:00 - Session 3: Industrial Perspectives – Translating TB-PET Kinetic Modeling into Practice

Negar Omidvari, Yun Zhao

UC Davis, Davis, USA; University of Sydney, Sydney, Australia

WS-03-09

Enabling dynamic/parametric imaging applications in the era of ultra high sensitivity PET with Omni128

Elise Emond

GE HealthCare, Zurich, Switzerland

WS-03-10

Practical Total-Body PET Kinetic Modeling with the Quadra

Paul Schleyer

Siemens Healthineers, Knoxville, USA

WS-03-11

Practical Barriers, Innovative Solutions: Total-Body PET Kinetic Modeling for Research and Clinical Use

Qing Ye

United Imaging Healthcare, Beijing, China

WS-03-12

Short break

WS-03-13

18:00–19:00 - Session 4: SlicerDynamicPET Tutorial

Daniele Dall'Olio

University of Bologna, Bologna, Italy

WS-03-14

Drinks, Canapés, and Networking

Time:
14 November, 2026
15:00 – 19:00

Room:
MANUEL DE FALLA

WS-04 | Emerging Directions in Theranostic Imaging: From PET and SPECT to Novel Modalities (onsite only)

Chairs:
Shiva Abbaszadeh (Santa Cruz)
Javier Caravaca (Berkeley)

sponsored by

Summary

Radiotheranostics, combining targeted molecular therapies with diagnostic imaging, holds great promise to transform healthcare decision-making by supporting individualized treatment planning, monitoring, and optimization. However, advanced imaging technologies for radiotheranostics are still emerging, and significant scientific, technical, and clinical challenges must be addressed to unlock their full potential in clinical environments. This workshop provides a dedicated forum for interested researchers to review past achievements, report recent progress and novel techniques, and discuss remaining challenges and future directions toward clinical translations. Key focus areas include optimizing the application of alpha and beta emitters enabled by novel imaging instrumentation, unconventional imaging techniques, advanced image reconstruction, dosimetry methods, simulation toolkits, and AI/ML methods for radiotheranostics.

We will invite interested presenters to submit separate abstracts to this workshop by August 31. We also invite industry partners and collaborators to attend and support this workshop.

We have created a special issue related to the content of this workshop in IEEE Transactions on Radiation and Plasma Medical Sciences (TRPMS). This Special Issue (https://ieee-trpms.org/current-special-issues/) will be a

collection of manuscripts associated with presentations and submitted abstracts in this workshop, after peer-review processes for the journal acceptance.

Contact

Youngho Seo, University of California, San Francisco (youngho.seo@ucsf.edu)
Shiva Abbaszadeh, University of California, Santa Cruz (sabbasza@ucsc.edu)
Javier Caravaca, Lawrence Berkeley National Laboratory (jcaravacarodriguez@lbl.gov)
Joshua Cates, Siemens Healthineers (joshuawcates@gmail.com)
Pedro Correia, University of Aveiro (pmcorreia@ua.pt)
Andrea Gonzalez-Montoro, i3M CSIC-UPV, Valencia (andrea.gm@i3m.upv.es)

WS-04-01

Radiotheranostics Beyond Boundaries: Hardware, AI, and the Future of Quantitative Imaging (#3328)

Pedro M.M. Correia[1], **Andrea Gonzalez-Montoro**[2], **Shiva Abbaszadeh**[3], **Javier Caravaca**[4,5], **Joshua W. Cates**[6], **Youngho Seo**[5,7,8]

[1] University of Aveiro, Institute for Nanostructures, Nanomodelling and Nanofabrication (i3N), Aveiro, Portugal; [2] CSIC-UPV, Institute for Instrumentation in Molecular Imaging (I3M), Valencia, Spain; [3] University of California, Santa Cruz, Department of Electrical and Computer Engineering, Santa Cruz, USA; [4] Lawrence Berkeley National Laboratory, Nuclear Science Division, Berkeley, USA; [5] University of California, San Francisco, Department of Radiology and Biomedical Imaging, San Francisco, USA; [6] Siemens Healthineers, Molecular Imaging, Knoxville, USA; [7] University of California, Berkeley, Department of Nuclear Engineering, Berkeley, USA; [8] Lawrence Berkeley National Laboratory, Molecular Biophysics & Integrated Bioimaging Division, Berkeley, USA

Abstract

Cancer treatment has shifted from empirical, toxicity-based dosing toward precision oncology guided by the specific genetic and molecular profiles of individual tumors. Within this framework, physicians, medical physicists, engineers, and scientists share the responsibility of developing tools to deliver high-precision treatments, predict therapeutic responses, and track disease progression. Radiotheranostics contributes to this approach by leveraging advanced radiochemistry to design highly selective molecules that deliver diagnostic or therapeutic radionuclides to target cells. Although routine at major medical centers for metastatic disease, broader adoption requires advances in imaging performance and targeted radiopharmaceuticals. Conventional PET and SPECT systems remain constrained by physical limits in spatial resolution, sensitivity, and quantitative accuracy, all of which are critical for clinical translation. Addressing these gaps requires higher sensitivity and spatial resolution, refined reconstruction algorithms for improved image clarity, precise image-based dose calculations, and system standardization. These needs drive hardware development toward total-body and organ-specific PET and SPECT systems, as well as new gamma, x-ray, and hybrid imaging methods. For high linear-energy transfer approaches like targeted alpha therapy, ex vivo micro-scale imaging is increasingly important to measure dose heterogeneity at the suborgan/cellular level. Concurrently, artificial intelligence is improving image reconstruction and dose prediction. Finally, key translational challenges must be addressed: ensuring trial reproducibility, integrating new methodologies into clinical workflows, and demonstrating cost-effectiveness alongside tangible patient benefit. This workshop brings together experts across these areas to collaborate and advance next-generation radiotheranostic technologies.

WS-04-02

A Long Axial-FOV PET System with Embedded Spectroscopic Gamma-Cameras for In Vivo Imaging of Radiopharmaceutical Therapy (#3322)

Yifei Jin[1], Junwei Du[2], Simon R. Cherry[2,3], **Ling-Jian Meng**[1,4,5]

[1] University of Illinois at Urbana and Champaign, Department of Nuclear, Plasma and Radiological Engineering, Urbana, USA; [2] University of California at Davis, Department of Biomedical Engineering, Davis, USA; [3] King's College London, School of Biomedical Engineering and Imaging Sciences, London, UK; [4] University of Illinois at Urbana-Champaign, Beckman Institute for Advanced Science and Technology, Urbana, USA; [5] University of Illinois at Urbana-Champaign, Department of Bioengineering, Urbana, USA

Abstract

The development of radiotheranostics would greatly benefit from quantitative imaging techniques that can simultaneously map the distributions of diagnostic and therapeutic radionuclides across spatial, temporal, and functional domains. To address this need, we will present the design of a proposed preclinical PET/SPECT platform consisting of a long-axial-FOV PET scanner with embedded CZT pinhole camera modules. The system is designed to simultaneously image both PET tracers and typical SPECT isotopes, as well as therapeutic radionuclides, such as Lu-177, Ac-225, Ra-223, and At-211.

The PET subsystem is based on dual-ended-readout BGO detectors with a diameter of 16 cm and an axial length of 16 cm. The BGO detectors in the central portion are purposefully positioned to leave small gaps to accommodate micro-gamma-camera elements (MGCE's) based on high-resolution CZT detectors with pinhole collimation for radionuclides. The MGCE's are designed to cover a wide dynamic range of 20 keV to 700 keV, so the combined PET and SPECT system will be capable of imaging virtually all commonly used SPECT isotopes and therapeutic radionuclides. In addition, data acquisition for the PET and SPECT subsystems is synchronized via a unified clock-and-trigger architecture. It enables coincidence detection of both PET and single-photon signals. Correlations among detected photons in the spectral and temporal domains are used to reject down-scattering noise in SPECT acquisition and to identify cascade emission of gamma rays from Lu-177 and Ac-225.

In this presentation, we will discuss a comprehensive design study of an integrated PET/SPECT imaging system and its potential to characterize the complex pharmacokinetics of radionuclide therapies.

WS-04-03

A High-Resolution Mobile Gamma-Camera for optimizing dosimetry in Molecular Radiotherapy : first clinical feasibility study for treatment of thyroid diseases with Radioactive Iodine (#3281)

Théo Bossis[1], Marc-Antoine Verdier[1,2], Lavinia Vija[4], Frédéric Courbon[5], Delphine Vallot[6], Camila Nascimento[4], Olivier Caselles[6], Tiffany Beaumont[3], Françoise Bouvet[1], Laurent Pinot[1], Laurent Menard[1,2]

[1] Université Paris-Saclay, CNRS/INP3, IJCLab, Orsay, France; [2] Université Paris Cité, IJCLab, Orsay, France; [3] ASNR, LEDI, Fontenay-aux-roses, France; [4] Nuclear Medicine Department, Oncopole Claudius Regaud, Toulouse, France; [5] Nuclear Medicine Department, Oncopole Claudius Regaud and Toulouse University, Toulouse, France; [6] Medical Physics Department, Oncopole Claudius Regaud, Toulouse, France

Abstract

Molecular radiotherapy requires personalized dosimetry for efficient treatment and reduced toxicity, but current clinical imaging systems and miniaturized gamma-cameras lack the required capabilities. We developed a mobile gamma-camera with a 10×10 cm^2 field of view tailored for quantitative assessment of ^{131}I biokinetics during therapy of thyroid diseases. The system combines interchangeable 3D-printed tungsten collimators, a monolithic scintillator read out by a SiPM array, and commercial electronics. It achieves an intrinsic spatial resolution of 1.15 mm FWHM and negligible deadtime up to 150 kcps. Images are reconstructed in real time using an experimental data-trained convolutional neural network. The collimators and shielding were adjusted with Monte-Carlo simulations in order to reduce septal penetration and scattering. Preclinical studies demonstrated high quantitative accuracy, with activity bias below 5%, even for small sources. These performances stem from the camera's compactness and mobile design, which enables shorter detector-to-target distances, optimized viewing angles, as well as from its high overall spatial resolution (4–6 mm at 365 keV). Its mobility also avoids transporting radioactive patients, reducing radiation exposure for staff and other patients. A first clinical feasibility study involving 20 patients with benign thyroid diseases was completed in March 2025, to assess patient acceptance and image quality during planning and post-treatment follow-up, compared with a standard gamma camera (Syngula). Results indicate unprecedented image quality around 400 keV with direct quantitative information, particularly for post-therapeutic imaging, enabling improved assessment of heterogeneous ^{131}I distribution, including for Graves' disease. This highlights the potential of the camera for personalizing administered activity and, more importantly, estimating the dose actually absorbed during treatment, directly linked to therapeutic success.

WS-04-04

The Personalized Remote Radiation Tracking Portable Organ Dosimetry Device (#3335)

Robert S. Miyaoka[1], William C.J. Hunter[1], Pavan S. Guntha[3], Gabriel Maliakal[2], Ethan Ingalls[3], Thomas M. Whalen[3], Mia T. Kim[3], Geoff Jones[3], Scott A. Hauck[3], Adam M. Alessio[2]

[1] University of Washington, Radiology / Nuclear Medicine, Seattle, USA; [2] Michigan State University, CMSE, BME, and Radiology, Lansing, USA; [3] University of Washington, Department of Electrical Engineering, Seattle, USA

This work was supported by NIH R01CA287205. We thank Robert Harrison for extensions to SimSET.

Abstract

We are developing a Personalized Remote Radiation Tracking Portable Organ Dosimetry Device (PRRT PODD) for at-home monitoring of patients receiving radiopharmaceutical therapy. The goal of this work is to provide a user and facility friendly device to enable organ at risk (OAR) dosimetry for patients undergoing Lu-177 DOTATATE treatment. The PRRT PODD consists of a portable frame with wings that encircle the patient's torso from the base of their kidneys to the top of their liver. In addition, there is a registration pad that enables precise positioning of the patient in the PODD for daily measurements. The patient lies down in a PODD template during their therapy qualifying PET/CT scan. This registers the PODD to their anatomy. Using software tools, a sensitivity matrix between the patient's OAR and tumors is determined for a two-dimensional (2D) array of potential detector locations along the surface of the PODD. Using this matrix, 16-32 detector locations are selected based upon the patient's specific anatomy to enable activity estimation for the patient's OAR. After a quantitative SPECT/CT scan acquired 24-hours after treatment, a PODD measurement will be made in clinic to normalize with the SPECT/CT scan. The PODD will then be sent home with the patient for fourteen 5-minute daily measurements. The PODD utilizes a carbon fiber base plate, a vacuumable Styrofoam registration pad, 3D printed wings, compact pinhole SiPM-based radiation detectors, battery-operated acquisition electronics, and a cell phone app that supports wireless transmission from the PODD's detector to a remote computer workstation. Our updated simulation software supports placement of a virtual 2D array of detectors on the polygonal surface defined by the PODD. An overview of the PODD development along with results from simulations based on human imaging examples will be provided at the workshop.

WS-04-05

Incorporating X-Ray and gamma-Ray Coincidence Detection for Improved Detection Efficiency and Image Quality in ^{177}Lu Imaging

(#3306)

Kui Wang[1], Tiantian Dai[2], Zhongbin Hang[3], Hui Liu[4], Jing Wu[5], Yaqiang Liu[4], Zuoxiang He[3], **Qingyang Wei**[1]

[1] University of Science and Technology Beijing, Beijing Engineering Research Center of Industrial Spectrum Imaging, School of Automation and Electrical Engineering, Beijing, China; [2] China–Japan Friendship Hospital, Department of Radiation Oncology, Beijing, China; [3] Tsinghua University, Beijing Tsinghua Changgung Hospital, Beijing, China; [4] Tsinghua University, Department of Engineering Physics, Beijing, China; [5] Beijing Normal University, Center for Advanced Quantum Studies, Beijing, China

This work was supported in part by the National Key Research and Development Program of China under Grant 2022YFC2402001; in part by the National Natural Science Foundation of China under Grant 12375337; and in part by the Beijing Natural Science Foundation under Grant L232126.

Abstract

In conventional ^{177}Lu imaging that relies solely on single photons or cascade gamma photons, the detection efficiency is fundamentally limited by the low photon emission probabilities. The decay of ^{177}Lu produces not only γ photons but also characteristic X-rays through the internal conversion process. In this work, we propose a multi-type time coincidence imaging strategy that exploits characteristic X-rays together with γ photons to improve the detection efficiency and image quality of ^{177}Lu imaging. The feasibility of X–X, X–γ, and γ–γ coincidence detection is analyzed based on the decay characteristics of ^{177}Lu, and a full-ring coincidence imaging system is subsequently employed for performance evaluation. Experimental results show that the integration of multiple coincidence-event types increases the system detection efficiency by 107.60\% and improves the contrast-to-noise ratio (CNR) by 8.39\% compared with conventional γ–γ coincidence imaging, while preserving nearly unchanged spatial resolution.

WS-04-06

Physics-Corrected List-Mode MLEM Reconstruction for Quantitative ^{177}Lu Cascade Gamma Coincidence Imaging (#3289)

Hanshen Ye[1,2,3], Hui Liu[4], Qingyang Wei[5], Hao Jia[6], Hai Hu[1,2,7], Zhongbin Hang[7], Tiantian Dai[8], Zuoxiang He[7], Yaqiang Liu[4], Jing Wu[1,2,3]

[1] Beijing Normal University, Center for Advanced Quantum Studies, School of Physics and Astronomy, Beijing, China; [2] Beijing Normal University, Key Laboratory of Multiscale Spin Physics, Ministry of Education, Beijing, China; [3] Beijing Normal University, Center for Health and Aging, Beijing, China; [4] Tsinghua University, Department of Engineering Physics, Beijing, China; [5] University of Science and Technology Beijing, School of Automation and Electrical Engineering, Beijing, China; [6] Tsinghua University, School of Biomedical Engineering, Beijing, China; [7] Tsinghua University Changgung Hospital, Changgung Hospital, Beijing, China; [8] China-Japan Friendship Hospital, Department of Radiation Oncology, Beijing, China

Supported by National Key Research and Development (R&D) Program of China (2022YFC2402003, 2022YFC2402002), National Natural Science Foundation of China (No. 12305379, No.12205166), Beijing Natural Science Foundation (Z220010), CIRP Open Fund of Radiation Protection Laboratories (TNMPP-2024-No.1).

Abstract

Cascade gamma coincidence imaging is an alternative to conventional single photon imaging for therapeutic radionuclides such as ^{177}Lu by exploiting time-correlated cascade photon pairs. However, high spatial resolution and reliable quantitative accuracy remain challenging because of photon attenuation, scatter, partial volume effects. We developed a cascade-coincidence list-mode maximum-likelihood expectation-maximization (CCLM-MLEM) framework for a full-ring ^{177}Lu cascade gamma coincidence imaging system. Attenuation correction (AC) and scatter correction (SC) were incorporated into reconstruction, followed by absolute quantification and post-reconstruction partial volume correction (PVC). The system response matrix was modeled according to the cascade-photon detection geometry. The framework was evaluated using seven-point-source and hot-rod phantoms for spatial-resolution assessment, the modified image-quality phantom for quantitative evaluation, and the Mouse Whole-Body (MOBY) digital phantom for small-animal imaging. Direct backprojection (DBP) was used for comparison. CCLM-MLEM reduced the mean point-source FWHM from 2.20±0.10 mm with DBP to 1.51±0.27 mm and resolved 1.0-mm rods, compared with 1.5-mm rods using DBP. In the modified image-quality phantom, AC and SC improved activity and contrast recovery at comparable noise levels. In the MOBY phantom, the relative bias for a 4-mm tumor decreased from -57.19% without correction to 1.83% after AC, SC, and PVC. These results support high-resolution quantitative ^{177}Lu cascade gamma coincidence imaging and its potential for preclinical radiopharmaceutical imaging and dosimetry.

WS-04-07

Learning Support Priors from ^{177}Lu with Projection-Domain Constraint for Quantitative ^{225}Ac SPECT Reconstruction (#3267)

Zhengkun Dong[1], Xiangxi Meng[2], Xiao Jin[2], Wei Liu[1], Xiangxiang Ding[2], Yi Sun[2], Ling Yuan[4], Nan Li[2], Zhi Yang[2], Ming Lu[3], Jie Li[3], Qiushi Ren[1], Jiangyuan Yu[2], Zhaoheng Xie[1,5]

[1] Peking University, National Biomedical Imaging Center, College of Future Technology, Beijing, China; [2] Peking University Cancer Hospital & Institute, Department of Nuclear Medicine, Beijing, China; [3] Peking University Cancer Hospital & Institute, Department of Gastrointestinal Oncology, Beijing, China; [4] Beijing Sinotau International Pharmaceutical Technology Co., Ltd., Beijing, China; [5] Peking University Health Science Center, Peking University, Institute of Medical Technology, Beijing, China

Supported by NSFC Grant 62394311, 62394310, 625B2004, and 12505390.

Abstract

Background: ^{225}Ac targeted alpha therapy requires quantitative post-therapy SPECT for verification and dosimetry. Multiple emissions, scatter, and inter-window crosstalk complicate reconstruction.

Methods: We developed a ^{177}Lu-informed deep support-driven kernel (DSDK). A support generator was pretrained on 63 clinical [^{177}Lu]Lu-DOTATATE SPECT scans using simulated projections at multiple count levels and a projection-consistency objective. For ^{225}Ac reconstruction, the learned support was used only to construct an image-domain kernel prior; activity remains governed by measured multi-energy projections and a Poisson model. Scatter and crosstalk are explicit projection-space physical models using MC-optimized DEW and self-consistent crosstalk correction for 218-keV, 440-keV, and joint-window reconstruction. Evaluation included MC calibration, single-sphere NEMA IQ scatter-window validation, dual-sphere IQ CNR-COV assessment at 15/30/60 s, and 10-patient [^{225}Ac]Ac-DOTATATE SPECT/CT evaluation. Baselines included OSEM, DDIP-TTA, and PET-guided methods; PET was not a DSDK input.

Results: MC selected a narrow 5% lower scatter window beside ±10% photopeak windows, with projection MSEs of 0.16/0.10 at 218/440 keV. Single-sphere joint-window CNR/SBR rose from 3.032/8.390 without scatter correction to 3.104/9.081. Dual-sphere DSDK with crosstalk improved the CNR-COV trade-off, especially at 15/30 s; at a representative joint window, CNR/COV was 22.2/0.87 versus 17.1/1.19 for DDIP-TTA. Clinically, joint-window DSDK achieved TBR 2.43 ± 1.27 and the highest lesion CNR among non-PET-prior methods. DSDK also achieved the highest joint-window lesion SSIM, 0.88 ± 0.05, without a PET-derived prior.

Conclusion: DSDK integrates support-level transfer, projection-consistent statistical reconstruction, and crosstalk physical modeling for quantitative multi-window ^{225}Ac SPECT and may support patient-specific dosimetry.

WS-04-08

Rapid Extended-Distance ^{177}Lu Imaging with a Portable Telephoto-Lens Magic-Cube Gamma Camera for Intra-Procedural Theranostic Assessment (#3290)

Yuxi Zhang[1], Zhenlei Lyu[1,2], Jiachang Xu[2], Yifan Hu[3], Yufang Zhang[1,2], Wangzhao Chi[2], Zeqing Zhao[2], Wendi Cheng[4,5], Kexin Chen[4,5], Huawei Cai[4,5], Tianyu Ma[1]

[1] Tsinghua university, Department of Engineering Physics, Beijing, China; [2] Greater Bay Area National Center of Technology Innovation, Guangzhou, China; [3] Yale University, Department of Radiology and Biomedical Imaging, New Haven, USA; [4] Sichuan University, Laboratory of Clinical Nuclear Medicine and Department of Nuclear Medicine, West China Hospital, Chengdu, China; [5] Sichuan University, Sichuan Provincial Engineering Research Center of Radiopharmaceutical Clinical Translation, Chengdu, China

Abstract

Immediate visualization of therapeutic radionuclide distributions could provide useful spatial feedback during or shortly after interventional radionuclide therapy, but this use case requires a portable camera to acquire images quickly without close contact with the target region. We evaluated a Telephoto-Lens Magic-Cube portable gamma camera for rapid ^{177}Lu imaging using hybrid front-end long-hole geometric encoding and detector-side self-collimation encoding. A measured ^{177}Lu system matrix covered an 80 × 80 mm² field of view and source-to-camera distances of 8–22 cm. Across 54 point-source positions from 10–20 cm, mean absolute localization errors were 0.26, 0.32, and 2.58 mm along the x, y, and z axes, respectively. Representative dual-source reconstructions showed visually distinguishable hotspots separated by 5–7 mm at distances of 10–18 cm. At approximately 16 cm, all principal hotspots remained visible in 1 s reconstructions of three phantoms and an in vivo rat liver, with NCC values of 0.942–0.992 and transverse hotspot displacements of 0.27–1.12 mm relative to 300 s references. An excised rat liver containing 72.2 μCi of residual ^{177}Lu also showed a localized activity region. These results demonstrate the feasibility of rapid ^{177}Lu distribution imaging at extended working distances for procedure-room theranostic assessment.

Open Discussion I

Coffee Break

WS-04-09

Implementation of Radiation Detection Technologies, Quality Assurance, and Harmonized Control Standards for Theragnostic Programs in Emerging Healthcare Systems. (#3321)

Ian M. Rossi[1,2], María C. Plazas[1], Paul N. Martinez[1]

[1] Universidad Nacional de Colombia, Physics Department, Bogotá D.C., Colombia; [2] IEEE, Colombian Section, New York, USA

We gratefully acknowledge the support of the Universidad Nacional de Colombia and Vicerrectoría de Investigación through research project HERMES 64204, funded under the 2024 Innovation and Artistic Creation Projects Call.

Abstract

Theragnostic imaging is an emerging approach in precision oncology that combines molecular imaging with targeted radionuclide therapy. Its safe and effective implementation requires not only advanced radiopharmaceuticals, but also reliable radiation detection systems, standardized quality control (QC), and comprehensive quality assurance (QA) throughout the imaging and treatment workflow. This work focuses on the role of radiation detection technologies in theragnostics, including detector performance, calibration and verification of QC equipment, and radiopharmaceutical quality assessment.

Particular attention is given to radionuclide and radiochemical purity, activity calibrator verification, measurement traceability, and harmonized QA protocols. The work also addresses challenges in conventional gamma spectrometry, particularly spectral overlap in composite and low-activity samples, highlighting maximum-likelihood estimation (MLE) approaches for improved activity quantification of theragnostic radionuclides using NaI(Tl) detectors. In addition, emerging detector materials such as graphene quantum dots are considered for their potential to enhance radiation detection technologies.

The study discusses the challenges of implementing theragnostic programs in emerging healthcare systems, emphasizing the need for international standards, specialized training, appropriate infrastructure, and adaptable regulatory frameworks. These elements are essential to achieving accurate personalized dosimetry, reliable treatment planning, and safe, standardized theragnostic practices.

WS-04-10

New Horizons in Ultra-High Resolution 3D CZT Detectors and its impact on preclinical SPECT/PET (#3309)

Alexander Cherlin[1], Freek Beekman[2,3,4]

[1] Kromek Ltd., Sedgefield, UK; [2] TU Delft, dept. Radiation Science & Technology, Delft, Netherlands; [3] Free Bee Int'l, Delft, Netherlands; [4] The Molecular Imaging Foundation, Delft, Netherlands

Abstract

Clinical and preclinical demand for higher-precision molecular imaging across an extended energy range is pushing gamma-ray detectors beyond the limits of conventional SPECT. CZT detectors offer excellent energy resolution and good sensitivity for high-energy isotopes, but position resolution and spectral distortions, including charge sharing and depth dependence, remain limited by pixel size, detector thickness, and cost of scaling readout electronics.

A novel approach is presented, using machine learning models trained on high-fidelity simulations to extract sub-pixel and depth-of-interaction (DOI) information from anode signals. Implemented in a prototype CZT gamma camera, the method achieves 10×10 sub-pixelisation of 2 mm pixels, DOI resolution of ~500-800 µm, and gamma-camera-level energy resolution with spatial precision approaching mid-range x-ray detectors, pointing toward a new class of high-resolution SPECT instrumentation.

A key challenge is the increased demand on readout speed and bandwidth. Accurate positioning requires acquisition of positive and negative signals across pixel clusters, increasing data volume and processing requirements while limiting real-time operation and scalability.

To address this, we explore neural network inference integrated directly into the detector front-end, enabling photon-by-photon signal processing. A dedicated ASIC will digitise and buffer electrode signals, which are then characterised by a neural-state machine that outputs high-level interaction data. A pulse-level simulation framework is being developed to train and validate front-end neural network models.We will present the first implementation of this framework on pixelated and drift-strip CZT detectors, with simulation results demonstrating improved multi-interaction event discrimination and reconstruction. This work provides a route to compact, high-resolution gamma detectors for next-generation theranostic imaging, from radionuclide therapy dosimetry to hybrid modalities. An example will be shown on what the impact of using high-end 3D CZT instead of traditional NaI Anger detectors could be on the architecture and performance of a new multi-isotope PET/PET PET/SPECT imaging module in Free Bee International's U-VET preclinical open PET/SPECT/CT/Optical/Ultrasound platform (World Molecular Imaging Society Innovation of the Year 2026)

WS-04-11

A multimodal C-arm enabling concurrent X-ray and nuclear imaging for cost-effective theragnostic interventions (#3316)

Dennis R. Schaart[1], Martijn M.A. Dietze[2], Camiel E. Kerckhaert[2], Lukas Schröder[1], Marc Snoeyink[1], Niek Wijnen[2], Hugo W. De Jong[2]

[1] Delft University of Technology, Medical Physics & Technology, Delft, Netherlands; [2] University Medical Center Utrecht, Radiology and Nuclear Medicine, Utrecht, Netherlands

This work was funded in part by EU Horizon grant 101257367.

Abstract

Theragnostic interventions commonly require both fluoroscopic and nuclear image guidance. In liver tumor radioembolization, for example, ^{90}Y microspheres are injected into the liver bloodstream under fluoroscopy. First, ^{99m}Tc microspheres are administered, and a SPECT scan is made. Therapeutic ^{90}Y microsphere delivery is typically performed two weeks later, based on the results of the pre-treatment procedure. If a SPECT scan of the ^{99m}Tc microsphere distribution can be made inside the intervention room, the pre-treatment and treatment procedures can be merged into a single session, enabling in-situ adaptation of the catheter position and near-real time, personalized dosimetric treatment planning. Moreover, the burden for the patient as well as the overall cost of treatment are reduced. To this end, a first prototype of an interventional X-ray and scintigraphy imaging (IXSI) system was built at UMC Utrecht. It consists of a C-arm equipped with an X-ray tube and a detector stack consisting of an adapted X-ray flat panel detector positioned in front of a gamma camera fitted with a cone-beam collimator. Here, we report on two recent developments. First, a clinical trial is ongoing in which the first patients with liver cancer are receiving single-session radioembolization using the IXSI prototype. Second, X-ray imaging is currently limited to 70 kVp and the X-ray tube is translated off-focus from the focal point of the cone-beam collimator by 5 cm, to avoid blinding of the gamma camera by X-rays penetrating through the flat-panel detector. To enable concurrent, intrinsically co-registered X-ray and nuclear imaging using X-ray spectra up to 120 kVp, a novel detector stack is under development, comprising a gamma camera based on a low-afterglow, pixelated NaI(Tl) scintillator read out by SiPMs. An update of these developments will be presented at the workshop.

WS-04-12

Theranostic SPECT with High Energy Resolution CZT Detectors (#3334)

John R. Kuchta[1], Peter G. Hotvedt[1,2], Zhonghua Ouyang[1], David Paylan[1]

[1] MH3D Inc., Ann Arbor, USA; [2] University of Michigan, Nuclear Engineering and Radiological Sciences, Ann Arbor, USA

Abstract

An increasing number of isotopes have seen use in theranostic applications but have generally been limited by poor image quality or low quantification accuracy. These limitations are caused by factors like low emission intensities, clustered photopeaks, or lower system sensitivity. These factors drive the use of easier to image surrogate isotopes for biodistribution studies. Theranostic SPECT with CZT semiconductors reduces the need for traditional cut-and-count measurements and can produce quality reconstructions for isotopes that are otherwise difficult to image. The Alpha-SPECT^{TM} Mini preclinical device utilizes CZT semiconductors as the detecting medium, providing the highest energy resolution with a full-body field-of-view for mice. This SPECT imager has a 2.5% single-pixel energy resolution at 140 keV, and it has been used in the imaging of popular isotopes such as ^{225}Ac, ^{213}Bi, ^{212}Pb, ^{211}At, ^{177}Lu, ^{111}In, and ^{99m}Tc.

The detectors' superior energy resolution allows for discrimination of the clustered photopeaks in the X-ray energy regions of ^{225}Ac and ^{212}Pb. Projection windows with sufficient separation from the tungsten characteristic X-ray at 60 keV allow for removal of excess scatter in reconstructed images, one of the major image degradation factors in low-emission isotope imaging. The system's high sensitivity enables the dynamic imaging of fast decaying isotopes over the whole body of a mouse, such as ^{213}Bi with its 45-minute half-life. The dynamic imaging function has been utilized for binning as small as 2 seconds for ^{99m}Tc, 1 minute for ^{211}At, 15 minutes for ^{213}Bi, and 30 minutes for ^{225}Ac. This functionality unveils important information on theranostic isotope distribution shortly post-injection.

WS-04-13

Fast Timing for High-Energy Gammas with GAGG and BGO for Improved Theranostic (#3313)

Fiammetta Pagano[1], Andrea Gonzalez-Montoro[1], Francis Loignon-Houle[1], Antonio Olmos Risen[1], Joshua W. Cates[2], Javier Caravaca[2], Antonio J. Gonzalez[1]

[1] Institute for Instrumentation in Molecular Imaging (I3M), CSIC-Universitat Politècnica de València, Valencia, Spain; [2] Lawrence Berkeley National Laboratory, Nuclear Science Division, Berkley, USA

This work was partially funded by the European Union (ERC, PHOENIX, 101164363). The authors express their gratitude to César Domingo-Pardo and his team for hosting the measurements in their laboratory.

Abstract
Time-of-flight (TOF) improves effective sensitivity and image signal-to-noise ratio in positron emission tomography (PET). Other medical applications that benefit from high time resolution include ion range verification in hadron therapy via prompt gamma imaging and dose verification in targeted alpha therapy via cascade gamma imaging. All these applications would benefit from intrinsically radiation-free scintillators, motivating the search for alternatives to LYSO. GAGG is a strong candidate due its high light yield, which enables good energy resolution, and to its fast decay time, which makes GAGG's time resolution very competitive. At high gamma energies — between 1–7 MeV, the range relevant to prompt gammas in hadron therapy and to characteristic gammas emitted in cascade by alpha-emitting isotopes — BGO also becomes particularly attractive, as its prompt Cherenkov photon yield increases significantly in this range.
Here, we present a proof-of-concept measurement of the time resolution of BGO and GAGG at ~1 MeV. Pairs of 3×3×15 mm³ BGO and GAGG crystals, coupled to FBK-NUV-MT SiPMs, were read out using state-of-the-art high-frequency electronics. Each crystal pair detected in coincidence the gamma cascade from a ^{60}Co source (1173 keV and 1333 keV gamma rays emitted with a sub-picosecond half-life). In our preliminary studies, we achieved a coincidence time resolution (CTR) FWHM of 120 ps for GAGG and 188 ps for BGO, while for 511 keV the CTRs are 179 ps and 245 ps, respectively. Additionally, simulations are used to investigate Cherenkov photon detection yield and time resolution as a function of gamma-ray energy. These results highlight the potential of GAGG and BGO both for TOF-PET and other emerging applications involving high-gamma energies.

WS-04-14

Event-Based Alpha- and Beta- Particle Imaging with iQID: From Quantitative Digital Autoradiography to Isotope Identification (#3326)

Brian W. Miller[1,2], Jared W. Moore[2]

[1] The University of Arizona, Radiation Oncology and Radiology & Imaging Sciences, Tucson, USA; [2] QScint Imaging Solutions, Tucson, USA

Research reported in this publication was supported by the NIBIB of the NIH under SBIR Award Number R44EB035459.

Abstract
The growth of radiopharmaceutical therapy (RPT) has created an increasing need to characterize RPT distributions at microscopic spatial scales, where heterogeneity can strongly influence absorbed dose and biological response. This is particularly important for alpha-particle therapies, where information of the activity distributions is needed at spatial scales comparable to alpha-particle ranges in tissue (40–100 μm). The ionizing-radiation Quantum Imaging Detector (iQID) is a high-resolution imaging system developed for quantitative digital autoradiography of alpha- and beta-particle emitters at these spatial scales. iQID combines scintillation-based detection with CMOS-camera

imaging and real-time processing to localize individual particle interactions and record their spatial, temporal, and intensity information. Unlike phosphor imaging plate autoradiography, which integrates the cumulative signal from all radioactive decay events over an exposure, iQID detects and localizes individual scintillation events in real time. Event size, intensity, position, and time are retained as list-mode data, enabling high-resolution quantitative imaging of radioactive sources and radiolabeled tissue sections. Event characteristics can also distinguish alpha- and beta-particle interactions, allowing both emission types to be imaged simultaneously. The spatial and temporal information retained by iQID provides additional capabilities for characterizing radioactive sources. Changes in activity and decay behavior can be followed over time, and measured decay signatures can help distinguish radionuclides within mixed sources. This presentation will describe the iQID imaging approach and highlight applications in quantitative alpha/beta autoradiography, source characterization, isotope identification, radiopharmaceutical biodistribution, and micro-scale dosimetry.

WS-04-15

How the next generation digital autoradiography can provide insight into theranostic bioequivalence (#3315)

Stephen Adler

Frederick National Laboratory For Cancer Research, Clinical Research Directorate, Bethesda, USA

Funded by the NCI Contract No. 75N91019D00024.

Abstract

Introduction: Theranostic cancer treatments rely on ligands which can be tagged with two different isotopes. One for imaging and one for treatment. The imaging ligand is used as a proxy for monitoring the ligand used to treat the target tissue. Key to using the imaging agent to measure the dosimetry of the treatment ligand is knowing the bio-equivalence of the ligand pair. Bio-equivalence is defined as equal biological interaction of two ligands within tissue. This can be achieved with the Quantitative Particle Identification Autoradiograph (QPID).

Materials and Methods: The next generation of spectral autoradiograph has been developed which mates a Timepix3 sensor developed by the CERN Medipix collaboration with a CeBr3 scintillation crystal. This allows one to use the gamma emission energy in forming autoradiograph images of tissue samples harvested in bio-distribution studies. The QPID time resolution is on the order of 1.6 ns allowing for the detection of single decays, thus achieving alpha and beta identification through ionization topology and energy deposition in the Timepix3 sensor, and spectral gamma emissions from the imaged sample.

Results: The QPID can segregate alpha and positron emissions, generating separate quantitative alpha and positron autoradiograph images from a sample which contains both an alpha and positron emitting ligand. This provides a mechanism to analyze co-injected theranostic imaging and treatment ligands. Using these separate images, one can measure the uptake and distribution in the same tissue sample. Furthermore, one can directly measure the pharmacokinetic properties of both ligands and measure their bio-equivalence.

Conclusion: Measuring any bio-equivalent deviation of the two ligands can be used to adjust the imaging agent activity and pharmacokinetic properties to more accurately be used as a proxy to measure the treatment effects and dosimetry results of the treatment ligand.

WS-04-16

Gamma-Positron Imaging and Event-Correlated Simulation for Emerging Theranostics (#3341)

Matthew A. Kupinski[1,2], Michael A. King[3], Shiva Abbaszadeh[4], Lars R. Furenlid[1,2]

[1] University of Arizona, College of Optical Sciences, Tucson, USA; [2] University of Arizona, Department of Medical Imaging, Tucson, USA; [3] University of Massachusetts Chan Medical School, Department of Radiology, Worchester, USA; [4] University of California, Santa Cruz, Baskin School of Engineering, Santa Cruz, USA

This work was supported by NIH UH3EB034686.

Abstract

PET and SPECT are often used even when radionuclides emit complementary radiations. Gamma-positron imaging exploits nuclides that emit a prompt gamma with a positron: annihilation photons define a PET line of response and prompt-gamma Compton interactions define a cone. Their intersection can estimate the radionuclide decay location more directly than PET alone.

We are developing a brain-dedicated gamma-positron imager using crossed-strip CZT detectors, event-correlated radiation transport, and GPU-accelerated list-mode reconstruction. The system records PET coincidences, prompt-gamma Compton events, and triple events in which both signatures arise from one decay. We evaluated event-class-specific LM-MLEM, conventional joint-Poisson reconstruction, and an event-type-conditioned method designed to preserve the localization value of triple events.

UAMonteCarlo preserves the lineage of prompt photons, positrons, annihilation photons, and secondaries from emission through detector interaction, allowing detector response, event classification, sensitivity, and reconstruction to be evaluated in one framework. In simulated 44Sc studies, all event classes localized point sources correctly. In a hot-rod phantom, rod-to-background contrast was 1.36 for PET-only, 1.14 for prompt-only, 4.93 for triple-only, 3.24 for conventional combined, and 3.86 for event-type-conditioned combined reconstruction, showing that triple events are uncommon but spatially informative.

The project also applies complete radiation-transport histories to emerging theranostic imaging. For 149Tb, gamma-positron events from the positron branch could image the same radiopharmaceutical responsible for alpha therapy. We are also applying the framework to 203Pb surrogate imaging for 212Pb-targeted alpha therapy. Together, these studies show how preserving decay and particle histories can inform detector design, reconstruction, quantitative imaging, and dosimetry.

WS-04-17

Multiplexed PET for Theranostic Imaging (#3342)

Nerea Encina-Baranda[1,2], Alejandro Lopez-Montes[3], Edwin C. Pratt[4], Trong-Nghia Nguyen[5], Axel Rominger[3], Lukas Carter[5], Jorge Cabello[6], Maurizio Conti[6], Hasan Sari[3,7], Kuangyu Shi[3], Elisa Körner[8], Fabian Schmidt[8], Jose M. Udias[1], Jan Grimm[5], **Joaquín López Herraiz**[1,2]

[1] Complutense University of Madrid, Dep. of Structure of the Matter. Nuclear Physics Group., Madrid, Spain; [2] Hospital Clinico San Carlos, Health Research Institute, Madrid, Spain; [3] Bern University Hospital, Dep. of Nuclear Medicine, Inselpital, Bern, Switzerland; [4] Stony Brook Cancer Center, Dep. of Radiology, Stony Brook, USA; [5] Memorial Sloan Kettering Cancer Center, Dep. of Radiology, New York, USA; [6] Siemens Medical Solutions USA, Inc., Tennessee, USA; [7] Siemens Healthineers International AG, Zurich, Switzerland; [8] University of Tübingen, Dep. of Nuclear Medicine and Clinical Molecular Imaging, Tübingen, Germany

Support from NIH R01-EB03300-02, Comunidad de Madrid TEC-2024/TEC-43, and Siemens Research Grant

Abstract

Multiplexed PET (mPET) enables simultaneous imaging of multiple radiotracers in a single acquisition by exploiting radionuclide-specific signatures beyond conventional 511-keV annihilation photons. Positron–prompt gamma emitters such as ^{124}I, ^{86}Y, or ^{44}Sc can generate triple coincidences that help distinguish them from pure positron emitters. This opens new opportunities for theranostic imaging, where complementary tracers could simultaneously characterize therapeutic targets and tumor biology, investigate intra- and inter-lesion heterogeneity, assess radiopharmaceutical biodistribution and dosimetry, or monitor early biological response to treatment.

We present a modular mPET framework applicable to different radionuclides and scanners. It incorporates all the corrections and reconstructions required for quantitative PET while adapting to different scanner capabilities. When available, we exploit energy and time-of-flight information, while coincidence multiplicity alone provides radionuclide-specific information in more limited systems. The method also includes radionuclide-specific positron-range correction for each separated image.

We quantitatively evaluated the approach with combinations such as ^{18}F+^{124}I, ^{18}F+^{52}Mn, ^{68}Ga+^{86}Y, and ^{89}Zr+^{86}Y across several preclinical and clinical PET scanners. Studies ranging from simultaneous tracer imaging in mice to multi-radionuclide phantom experiments demonstrated recovery of the individual radionuclide distributions across systems with different detector characteristics.

These results demonstrate the translation of mPET across PET scanners and radionuclide combinations. mPET could extend PET from a predominantly single-tracer technique toward a multidimensional molecular imaging platform in which complementary aspects of patient selection, treatment delivery, and response are interrogated within the same imaging session.

Open Discussion II

Joint Sessions

10 November, 2026

Time:
10 November, 2026
11:30 – 13:00

Room:
FEDERICO GARCÍA LORCA

JS-01 | Joint Session NSS-MIC-RTSD

Chairs:
John Valentine (Berkeley)

JS-01-01

Uniformity, Stability and High-Flux X-ray Detection Performance of $FAPbBr_3$, $CsPbBr_3$ and CZT (#2658)

Isabel Braddock[1], William Brown[1], Seán Cardiff[2], Vishal Dhamgaye[4], Oliver Fox[4], Jayana Jayarathne[3], Sarina Joshi[1], Daniel McAleer[1], Ganbaatar Tumen-Ulzii[2], Tim Nicholls[1], Kawal Sawhney[4], Paul Sellin[3], Samuel Stranks[2], Matthew Veale[1]

[1] Science and Technology Facilities Council, Rutherford Appleton Laboratory, Harwell, UK; [2] University of Cambridge, Department of Chemical Engineering and Biotechnology, Cambridge, UK; [3] University of Surrey, School of Mathematics and Physics, Guildford, UK; [4] Diamond Light Source, Harwell, UK

Work completed at STFC was funded by the Centre for Instrumentation programmes ”High-Z Sensor Materials for Advanced Radiation Technologies (SMART)” and ”Perovskites and other Radiation Imaging Sensor Materials (PRISM)”. We thank Diamond Light Source for time on beamline B16 (proposal number OM41265) that contributed to the results presented here, and for the assistance of the beamline staff.

Abstract

Pixel detectors for X-ray science typically require pixel pitches of less than 1 mm and operation at photon fluxes greater than 10^9 ph s^{-1} mm^2. For lead halide perovskite detectors to be viable in these applications, they must demonstrate good spatial uniformity, as well as operational stability over a period of hours or days. Here, we present results of synchrotron experiments in which the detection performance of melt-grown $CsPbBr_3$ devices, solution-grown $FAPbBr_3$ devices and CZT were each measured at 20 keV X-ray fluxes up to 10^9 ph/s/mm^2, demonstrating the linear response of the material to changing X-ray fluxes. Microbeam maps of device response to single-photon fluxes of 50 keV X-rays were used to quantify spatial variations in the charge collection efficiency and rise time of events.

JS-01-02

Estimating requirements for scintillator-based photon counting detectors in CT (#1502)

Scott Hsieh[1], Soohyun Lee[1], Benjamin Wilson[1], Parmita Mondal[1], Dennis Schaart[3]

[1] Mayo Clinic, Radiology, Rochester, USA; [2] Johns Hopkins, Radiology, Baltimore, USA; [3] TU Delft, Radiation Sciences & Technology, Delft, Netherlands

This work is funded by the National Institutes of Health under R01EB035553 and R01EB036984. The views expressed here are those of the authors only and are not the official views of the National Institutes of Health.

Abstract
Scintillator-based photon counting detectors (PCDs) couple a fast scintillator with a silicon photomultiplier (SiPM) and associated readout electronics. The characteristics of the scintillator and SiPM that are required for competitive performance are not yet clear, and it is sometimes felt that bright scintillators and high photodetection efficiency are needed. We use numerical modeling to study this question, using a cascaded system model with multiple stages to quantify the effects of light yield, SiPM sensitivity, and energy binning. Effects such as SiPM saturation, Swank noise, and K-escape are also included as optional stages. We find that using relatively dim components (5x dimmer than that assumed in previous modeling studies) introduces little harm into spectral imaging tasks, but the penalty of K-escape is large. Future prototype detectors should emphasize K-escape, stopping power, and speed rather than light yield or photodetection efficiency.

JS-01-03

A four side buttable system in package for medical and industrial Photon-Counting CT (#1574)

Torsten Solf[1], Thomas Froehlich[2], Enrique Hostalet[3], Riad Kanan[2]

[1] AMS Osram, Garching, Germany, Germany; [2] AMS Osram, Jona, Switzerland; [3] AMS Osram, Valencia, Spain

Abstract
We present the second generation of a four-side buttable module solution (AS592xM) for spectral CT detectors with a pixel matrix of 72x24 covering an area of 24.5 mm x 8.57 mm with a pitch of 365 µm x 340 µm. In combination with a suitable direct detection material like CdTe or CZT it detects individual X-ray photons with five programmable thresholds. Improvements have been made to reduce power consumption down to 0.35mW/pixel while maintaining low noise performance (380 e rms). Count rate stability is based on two different methods: a static leakage compensation (SLC) as well as a base line restorer circuit (BLR). The new SLC in combination with an auto-zero scheme in the frontend suppresses the effect of potential 1/f and Random Telegraph Noise (RTN) noise from the amplifiers. The adjustable BLR compensates for static and dynamic baseline shifts up to 700nA of leakage current per pixel. Measurements with and without CZT will be shown to quantify the energy resolution and count rate stability over input flux for different operation modes to quantify S/N for the different energy bins. Additionally, the MTF is characterized to project spatial resolution on system level.

JS-01-04

A Vibrational-Scanning Single-Photon Emission Microscope (SPEM) for In Vivo 3-D Autoradiography of Targeted Alpha Therapy (#3062)

Weijian Zhang[1], Yifei Jin[1], Shubham Mandot[1], Shangzhen Shu[1], Elena Zannoni[2], Ling-Jian Meng[1,3]

[1] University of Illinois Urbana-Champaign, Department of Nuclear, Plasma, and Radiological Engineering, Champaign, USA; [2] University of Texas at Austin, Walker Department of Mechanical Engineering, Austin, USA; [3] University of Illinois Urbana-Champaign, Department of Bioengineering, Champaign, USA

This work was supported by NIH under Grant No. 1R01CA297470.

Abstract

In this presentation, we will report the design and imaging performance of our third-generation Alpha-SPECT-mini system (the Alpha-SPECT-mini-ZM, where ZM stands for Zoom-in Microscope), which combines ultra-narrow micro-ring collimators and a vibrational aperture-scanning scheme to provide ultrahigh spatial resolution for *in vivo* 3-D autoradiography of α-RPT in small lab animals. The system uses a cylindrical ring of 10 detector panels, each comprising 2×6 HEXITEC/CZT detector modules. Each CZT module has a 2×2 cm^2 active area with 80×80 pixel array at 250 μm pitch and offers 1.5 keV FWHM energy resolution at 122 keV. The Alpha-SPECT-mini-ZM system uses a two-section collimator ring that combines pinhole apertures for whole-body imaging and ultra-narrow micro-ring apertures for zoomed-in ultrahigh-resolution imaging of a focal area with a 5-mm-diameter FOV, switched via a motorized stage. To offer an ultrahigh imaging resolution that overcomes the limited detector pixel size, the system employs a vibrational scanning strategy with MUCRB-guided acquisition optimization. Preliminary simulations with micro-hot-rod phantoms show the micro-ring collimator achieving better than 160 μm resolution at practical sensitivity. Further phantom studies will be carried out to characterize the performance of the system.

References

[1] G. Sgouros, *Semin. Nucl. Med.*, 2020

[2] C. Kratochwil *et al.*, *J. Nucl. Med.*, 2016

[3] E. Maria Zannoni *et al.*, *IEEE TRPMS*, 2025

[4] C. Yang *et al.*, *IEEE NSSMICRTSD*, 2025

[5] L. J. Meng *et al.*, *IEEE Trans. Med. Imaging*, 2004

[6] N. Li *et al.*, *IEEE Trans. Nucl. Sci.*, 2011

[7] L. Jones *et al.*, *Nucl Instrum Methods Phys Res A*, 2009

JS-01-05

Multi-Agent Pipeline with Local Large Language Models for Automated MCNP Script Review (#1447)

Byoungil Jeon[1], Soobin Lim[2]

[1] Korea Atomic Energy Research Institute, Artificial Intelligence Section, Daejeon, South Korea; [2] Quamtum Beam Solution, Daejeon, South Korea

This study was funded by the Commercialization Promotion Agency for R&D Outcomes (COMPA), supported by Korea's Ministry of Science and ICT (MSIT, grant No. 2710086067), and by the Advanced GPU Utilization Support Program (No. 02-26-01-0492) of MSIT. The MCNP 6.3.0 Theory & User Manual is openly available as a technical report cleared for public release.

Abstract
Although large language models (LLMs) perform well on general-purpose programming tasks, their accuracy drops sharply when applied to domain-specific simulation codes such as Monte Carlo N-Particle (MCNP). Within the nuclear sector, security policies and export-control rules typically forbid uploading inputs to cloud-hosted LLM services, so review tools must instead run on-premise atop openly released models. This study introduces a coordinated multi-agent framework that automatically inspects and repairs MCNP input decks. Three role-specific agents—a Supervisor, a Fixer, and a Validator—drive the workflow, supported by 16 auxiliary tools and an optional retrieval-augmented generation (RAG) module that consults the MCNP user manual. To measure performance, we assembled a 360-case benchmark covering six representative nuclear-engineering scenarios. Our pipeline reaches a 75.8% success rate, exceeding a single-agent reference by 15.5 percentage points and confirming that role-based orchestration is an effective strategy for trustworthy MCNP code repair in fully local deployments.

JS-01-06

A Compact Educational Platform for Demonstrating TDAQ Concepts in Particle Detector Systems (#1734)

Raffaele Giordano[1,2], Mihai Cuciuc[3,4]

[1] University of Naples "Federico II", Naples, Italy; [2] INFN, Naples, Italy, Naples, Italy; [3] Extreme Light Infrastructure - Nuclear Physics, IFIN-HH, Magurele, Romania; [4] Pomelo Instrumentation SRL, Bucarest, Romania

The authors are sincerely grateful to Dr. Fulvio Coppola[1] from CESMA for ensuring the safety of radioactive materials. Work funded by CSN5 of INFN (MEMPHYS experiment).

Abstract

Particle physics experiments rely on complex detectors, where trigger and data acquisition (TDAQ) systems play a key role. These systems are typically expensive, large-scale, and accessible only in specialized laboratories, limiting students' early exposure to the fundamentals of TDAQ. To address this gap, we developed a compact, low-cost educational platform that reproduces the main elements of a particle-detector readout chain in a form suitable for university laboratories. The platform is based on an Arduino UNO R4 Wi-Fi, a custom piggy-back board, and a detector module consisting of a CsI(Tl) scintillator coupled to a silicon photomultiplier. The system integrates bias-voltage generation and temperature monitoring, programmable pulse amplitude discrimination, peak detection, digitization, and USB or Wi-Fi data transfer to a personal computer.

The platform enables students to explore the main TDAQ concepts, including trigger formation, latency, dead time, buffering, and threshold setting. By progressively implementing different firmware strategies, from simple trigger polling to interrupt-driven and hardware-assisted acquisition, students gain direct insight into the relation between system design and detector performance. Educational activities on slow control, such as bias-voltage calibration, detector monitoring, and gain stabilization, are also possible. After firmware development, students can perform gamma-spectroscopy measurements using low-activity radioactive materials. Examples include potassium chloride salt substitutes, where the 1460.8 keV photopeak from ^{40}K can be observed, and thoriated tungsten welding electrodes, which exhibit several gamma lines from thorium decay products. In this contribution, we discuss the platform, the TDAQ topics addressed, and student experiments that demonstrate its educational potential.

Time:
10 November, 2026
15:00 – 17:05

Room:
FEDERICO GARCÍA LORCA

JS-02 | Joint Session - NSS-MIC

Chairs:
Cinzia DaVia (Manchester)
Roger Lecomte (Sherbrooke)

JS-02-01

2026 IEEE TNS Best Paper Award

The 2026 IEEE TNS Best Paper Award is relevant to papers published in the third year prior to the year of the award (2023).The winner is the paper judged most useful to the Nuclear Science community according to the rate of downloads and citations in the 3 calendar years including the year of publication.

JS-02-02

Systematic Defect and Crystal-Field Engineering of LYSO-U Scintillators for Photon-Counting CT (#2274)

Chengyi Li[1,2], Zhongjun Xue[1,2], Peng Qiu[1,2], Shuwen Zhao[1,2], Bozhen Zhao[3], Bicheng Liu[3], **Dongzhou Ding**[1,2]

[1] Chinese Academy of Sciences, State Key Laboratory of Functional Crystals and Devices, Shanghai Institute of Ceramics, Shanghai, China; [2] Center of Materials Science and Optoelectronics Engineering, University of Chinese Academy of Sciences, Beijing, China; [3] Nuctech Company Limited, Beijing, China

This work was supported by the National Science and Technology Major Project (Grant No. 2026ZD0623000), the National Natural Science Foundation of China (Grant No. 12305212) and the Shanghai Eastern Talent Plan (Grant No. BJKJ2025007).

Abstract

Photon-counting computed tomography (PCCT) requires scintillators with ultrafast decay times, ultralow afterglow, and high light yields (LY) to prevent pulse pile-up and image ghosting under continuous high-flux X-rays. While cerium-doped lutetium yttrium oxyorthosilicate (LYSO:Ce) is a benchmark material, its intrinsic ~40 ns decay time and deep-trap-induced afterglow constrain its PCCT applications. This work demonstrates systematic defect and crystal-field engineering to modify LYSO:Ce crystals, establishing a highly customizable material platform.Four distinct codoping strategies are evaluated to overcome the speed-efficiency-afterglow trade-offs. First, multi-site co-doping was employed to convert Ce^{3+} in ultrafast LYSO (LYSO-U) scintillation crystals into fast-emitting Ce^{4+}, introducing a non-radiative path within the crystal. This breaks the intrinsic lifetime barrier, achieving a 7.3 ns decay component and suppressing afterglow to 0.02% at 40 ms, while preserving an LY of 25,000 photons/MeV. Second, multivalent Al/Mn codoping utilizes bidirectional energy transfer to deliver a 9.6 ns decay, 446 ppm afterglow at 40 ms, and an LY of 31,300 photons/MeV. Third, isovalent Ge substitution (LYSGO:Ce) increases local crystal-field

splitting to thermodynamically deepen emitting states for enhanced carrier capture, elevating the LY to 38,700 photons/MeV and supporting a 25.6 lp/mm spatial resolution. Finally, trace Co^{2+} doping (~330 ppm) passivates oxygen-vacancy traps without severe lattice distortion, boosting the LY to 37,800 photons/MeV. By elucidating these physical mechanisms, these tailored, charge-sharing-free scintillator platforms address the diverse architectural demands of advanced PCCT detectors.

References
[1] Li, C et al. 2025, 'Enabling sub-150 picosecond TOF-PET imaging with ultrafast-efficient oxide scintillators by synergistic defect and energy transfer engineering', Laser Photonics Rev., vol. 19, no. 23, p. e00767, Weinheim: Wiley-VCH
[2] Qiu, P et al. 2026, 'Substantial enhancement of light yield in LYSO:Ce crystals via trace Co^{2+} co-doping', Chem. Eng. J., vol. 529, p. 172884, Amsterdam: Elsevier

JS-02-03

Energy resolved imaging with a fine-pitch YAGG-SiPM based indirect photon counting detector (#2087)

Kenji Shimazoe[1], Yosuke Kobayashi[1], Kei Kamada[2], Yasuhiro Shoji[2], Masao Yoshino[2], Kyohei Sakamoto[3], Fabio Acerbi[4], Alberto Gola[4]

[1] University of Tokyo, Department of Nuclear Engineering and Management, Bunkyo, Japan; [2] Tohoku University, Sendai, Japan; [3] Diatrend Corporation, Osaka, Japan; [4] FBK, Trento, Italy

Abstract

Scintillation based photon counting detectors (PCDs) attracts great interest because of its fast time response, crystal separation to suppress the charge sharing and wider choices of sophisticated scintillation crytals. We have designed and fabricated a custom fine-pitch (250 μ m) 10 × 10 Ce:YAGG- SiPM array whose size is comparable to the current commercial compound semiconductor based PCD. The performance was characterized in terms of energy resolution, spatial resolution, count rate capability and imaging capability. The measured results shows 28% @ 122 keV moderate energy resolution, 2.9 LP/mm spatial resolution comparable to the existing CT, 20 Mcps/mm2 at 20 % loss count rate capability. The comparison between YAGG and GFAG shows the significant supression of K-α escape cross-talk in the energy spectrum. The investigation with other scintillation crystals, such as LYSO will be shown. The different concentration of Optiray contrast agent (Iodine) with 10 m-50 mg/mL was clearly identified with 4 thresholds photon counting system.

References
[1] Shimazoe, Kenji, et al. Communications Engineering 3.1 (2024): 167.

JS-02-04

Latest update on the glass-less TSV FBK SiPM for 2.5D integrated ToF-PET modules (#2474)

Michele Penna[1], Carina Trippl[1], Fabio Acerbi[1], Ibrahim Hany[1], Fabiola Caso[1], Jacopo Dalmasson[1], Rok Dolenec[3], Dina O.E. Elgewaily[1], Andrea Ficorella[1], Priyanka Kachru[1], David Mazzanti[4], Laura Parellada-Monreal[1], Giovanni Paternoster[1], Maria Ruzzarin[1], Andreau Sanuy[4], Oscar A.M. Villarreal[1], Nicola Zorzi[1], Rafael Ballabriga[2], Jose Maria Benlloch[5], Georges El Fakhri[6], David Gascón[4], Stanislaw Majewski[7], Rok Pestotnik[3], Alberto Gola[1]

[1] Fondazione Bruno Kessler, Povo, Italy; [2] CERN, Meyrin, Switzerland; [3] Jozef Stefan Institute, Ljubljana, Slovenia; [4] ICCUB, University of Barcelona, Barcelona, Spain; [5] UPV, Instituto de Instrumentacion Para Imagen Molecular, Velencia, Spain; [6] Yale School of Medicine, New Haven, USA; [7] University of California Davis, Davis, USA

Abstract

In this work, the latest developments in glass-less Through-Silicon Via (TSV) integration of FBK NUV-HD-MT Silicon Photomultipliers (SiPMs), targeting next-generation Time-of-Flight Positron Emission Tomography (ToF-PET) detectors in the framework of the PetVision project, are presented. The NUV-HD-MT technology platform provides an outstanding baseline for TSV integration, featuring Photon Detection Efficiency (PDE) exceeding 65% at $420\ \text{nm}$, optical crosstalk below 5% at $15\ \text{V}$ excess bias, and a Single-Photon Time Resolution (SPTR) as low as $\simeq 18\ \text{ps}$ FWHM for a single SPAD. The glass-less TSV architecture eliminates any permanent intermediate layer at the scintillator interface by removing the temporary glass carrier after backside thinning to $150\ \mu\text{m}$, enabling optimal optical coupling and preserving the fast-timing performance of the underlying technology. The TSV development follows a structured, learning-cycle-based R\&D approach. Preliminary characterization of the Learning Cycle 1 (LC1) front-side production confirms that timing performance remains at state-of-the-art levels, with a Coincidence Time Resolution (CTR) of $\simeq 75\ \text{ps}$ FWHM achieved using a $3\times3\ \text{mm}^2$ SiPM coupled to a $2.8\times2.8\times3\ \text{mm}^3$ L(Y)SO:Ce:Ca scintillator, and an SPTR of $\simeq 25\ \text{ps}$ FWHM obtained for a single $50\ \mu\text{m}$ SPAD. Back-side processing of the LC1 wafers has been completed and full electrical and functional characterization is now underway. The Learning Cycle 2 (LC2) design, featuring an optimized 4×2 SiPM array with a $3\ \text{mm}$ channel pitch for direct crystal matrix coupling and a reduced TSV count of one per channel for improved yield, represents a significant step toward a robust, production-ready solution.

JS-02-05

The DIGILOG Project: μSiPM Sensor and Sub-20 ps Readout Electronics for ToF-PET (#2623)

Samuele Bisi[1], Katrin Herweg[2,3], Andrada Muntean[4], David Schug[5,2], Volkmar Schulz[3,5], Laura Parellada-Monreal[7], Michele Penna[7], Alberto Gola[7], Stefan Gundacker[8,2], Makoto Motoyoshi[9], Claudio Bruschini[1], Edoardo Charbon[1]

[1] École polytechnique fédérale de Lausanne (EPFL), Advanced Quantum Architecture Lab, Neuchatel, Switzerland; [2] RWTH Aachen University, University Hospital RWTH Aachen, Aachen, Germany; [3] RWTH Aachen University, Institute of Imaging and Computer Vision, Aachen, Germany; [4] NovoViz S.A., Neuchatel, Neuchâtel, Switzerland; [5] Hyperion Hybrid Imaging Systems GmbH, Aachen, Germany; [6] RWTH Aachen university, 6Physics Institute III B, Aachen, Germany; [7] Fondazione Bruno Kessler, Trento, Italy; [8] Marietta Blau Institute for Particle Physics, Austrian Academy of Sciences, Vienna, Austria; [9] Tohoku-MicroTec Co., Ltd., Sendai, Japan

German Research Foundation - 500540345
SNSF - 200021L_208073

Abstract

In time-of-flight PET, coincidence time resolution (CTR) is essential, with the ultimate aim of reaching 10 ps CTR [1]. Cherenkov radiation in BGO crystals, offers a path toward this target, but its low photon yield demands detectors combining high photon detection efficiency, low dark count rate, and fast single-photon time resolution (SPTR) [2].

In DIGILOG, we segment state-of-the-art analog SiPMs into smaller clusters called μSiPMs [3]. With fewer SPADs per cell, μSiPMs have lower capacitive loading, enabling simpler, faster electronic interfaces and higher-resolution timestamping via time-to-digital converters (TDCs) in proximity through 3D stacking. Optical and system-level simulations identify a granularity of 6×6 SPADs per μSiPM (100 μSiPMs in 3×3 mm²) as optimal for Cherenkov-based BGO timing [4].

The μSiPM top tier, fabricated by FBK in NUV-HD-MT technology [5], uses Single-Cell TSVs for independent microcell cathode access without fill-factor loss. We present two 110 nm CMOS readout architectures, both based on a current-mirror front-end, a Vernier ring-oscillator TDC [6], and a serial interface. Two ring oscillators run at slightly different frequencies setting the LSB; the sequences are compared as in a Vernier line until pulses align, and T is computed from the counts n1 and n2. The first implementation, an 8×8 TDC array with 20 ps target LSB, has been fabricated; a Vernier LSB of 19 ps and 4.4 ps RMS jitter have been measured [7]. The second upscales to a 9×9 array with three TDCs per μSiPM on independent threshold levels of a multi-level comparator, enabling MD-SiPM-like operation [8] and order-statistics-based timing [9]. It targets a 6 ps LSB at 2.0 mW per channel, with an on-chip PLL (<5 ps FWHM jitter) stabilizing the oscillators against PVT. Post-layout simulations yield SPTR <20 ps (FWHM) and INL ±1.1 LSB. Die-to-die 3D bonding of the two tiers is ongoing at T-Micro.

References
[1] P. Lecoq *et al., Roadmap toward the 10 ps time-of-flight PET challenge,* PMB 65 (2020). DOI: 10.1088/1361-6560/ab9500
[2] S. Gundacker *et al., On timing-optimized SiPMs for Cherenkov detection to boost low cost time-of-flight PET,* PMB, 68(16) (2023). DOI: 10.1088/1361-6560/ace8ee

[3] S. Gundacker *et al., DIGILOG: A digital-analog SiPM towards 10 ps prompt-photon tagging in TOF-PET*, IEEE NSS MIC RTSD (2023). DOI: 10.1109/NSSMICRTSD49126.2023.10338522
[4] K. Herweg et al., *Exploring μSiPMs with BGO for Cherenkov time-of-flight in PET*, IEEE TRPMS, 2026 (under review)
[5] Merzi S. et al., "NUV-HD SiPMs with metal-filled trenches". Journal of Instrumentation, 2023; 18, P05040. doi: 0.1088/1748-0221/18/05/P05040
[6] G. Théberge-Dupuis *et al., Cascaded Vernier Time-to-Digital Converter: Toward Integration in an Array*, ISSW, R10.2 (2024)
[7] *S. Bisi et al., Achieving Sub-20 ps Resolution in Large Arrays of μSiPMs for the DIGILOG Project, IEEE NSS MIC RTSD (2025). DOI: 10.1109/NSS/MIC/RTSD57106.2025.11287428*
[8] A. Carimatto *et al., A 67,392-SPAD PVTB-compensated multi-channel digital SiPM with 432 column-parallel 48ps 17b TDCs for endoscopic time-of-flight PET*, IEEE International Solid-State Circuits Conference (ISSCC), 202-203 (2015). DOI: 10.1109/ISSCC.2015.7062996
[9] M.W. Fishburn and E. Charbon, *System tradeoffs in gamma-ray detection utilizing SPAD arrays and scintillators*, IEEE Transactions on Nuclear Science 57(5), 2549-2557 (2010). DOI: 10.1109/TNS.2010.2064788

JS-02-06

Real-Time DOI Layer Prediction in TOF-PET Detectors via FPGA Neural Network (#2254)

Shuiting Xin, Zhenjie Han, Xiang Zhang, Xinyu Lv, Shaoping Chu

united imaging, MI, Shanghai, China

Abstract

Depth-of-interaction (DOI) information is critical for improving time-of-flight (TOF) precision in positron emission tomography (PET) detectors. Traditional DOI estimation methods, such as dual-ended readout and layered crystal arrays, require complex fabrication or additional photodetector channels, increasing system cost and degrading timing performance. This paper presents a machine learning framework for real-time DOI layer prediction in single-ended readout LYSO crystal arrays (5×6 structure coupled to a 2×2 SiPM array). A neural network takes normalized SiPM energy ratios and crystal position as inputs and outputs DOI classification into 2, 3, or 6 depth layers. A symmetry-based training strategy is introduced to enhance model generalization across crystal positions, effectively quadrupling the training data through rotational coordinate transformations. Experiments with a collimated ^{22}Na source demonstrate classification accuracy of 40–80% across six depth layers. Validation using top radiation data confirms the model's generalization from lateral irradiation (training) to normal incidence (clinical deployment). DOI-corrected coincidence time resolution (CTR) evaluated on 4320 crystals shows improvements of 2.25 ps (2-layer), 3.41 ps (3-layer), and 5.18 ps (6-layer). The two-layer neural network has been implemented on FPGA with fixed-point arithmetic, achieving a processing rate for real-time inference. Ongoing work focuses on system-level integration and image quality evaluation.

References
[1] Yoshida, E., Yamaya, T. PET detectors with depth-of-interaction and time-of-flight capabilities. Radiol Phys Technol 17, 596–609 (2024). https://doi.org/10.1007/s12194-024-00821-x
[2] S. Xin, "Machine Learning-Based Depth-of-Interaction Identification in Single-Ended Scintillation Detectors,"doi:10.1109/NSS/MIC/RTSD57106.2025.11286387

JS-02-07

Physics-Informed Deep Learning on FPGA for Inter-Crystal Scattering Correction in ToF-CT (#1776)

Lamyae Jdid, Réjean Fontaine, Audrey C. Therrien

Université de Sherbrooke, Interdisciplinary Institute for Technological Innovation, Sherbrooke, Canada

This research was funded in part by the STRATEGIA Initiative of the FRQNT, Project 355619. Audrey Corbeil Therrien holds the Canada Research Chair in Real-time embedded intelligence for ultra high rate detectors. This research was enabled in part by support provided by Calcul Québec and the Digital Research Alliance of Canada.

Abstract

Time-of-Flight Computed Tomography (ToF-CT) enhances contrast-to-noise ratio by suppressing patient-scattered photons. However, the fine pixel pitch required for sub-millimeter spatial resolution intensifies inter-crystal scattering (ICS), a confounder that conventional energy-based discrimination cannot resolve under polychromatic X-ray sources, ultimately compromising spatial resolution. To overcome this limitation, we introduce the first real-time, physics-informed ICS correction framework deployed at the FPGA-based detector readout of ToF-CT systems. Built on Physics-Informed Knowledge Distillation (PI-KD), the framework compresses a high-capacity teacher (AUPRC = 0.99) into a compact student architecture suitable for embedded deployment. Specifically, the distillation objective constrains the student to remain consistent with Klein–Nishina scattering kinematics and Monte Carlo-derived interaction priors, thereby preserving the physical structure of its spatiotemporal and energetic representations under aggressive compression. Quantization-Aware Training (QAT) further enables hardware-native INT8 inference, reducing the parameter footprint to ~2.3 kB with negligible performance loss. Post-synthesis on a Xilinx ZCU104 at a 200 MHz target clock confirms real-time operation beyond the 1 MHz acquisition target, sustaining 1.32 MHz per inference instance with 0.83 µs latency, while INT8 LUT-based arithmetic leaves all DSP blocks free (28% LUT, 38% BRAM, 0% DSP).

References

[1] Rossignol, J, Martinez Turtos, R, Gundacker, S, Gaudreault, D, Auffray, E, Lecoq, P, Bérubé-Lauzière, Y & Fontaine, R 2020, 'Time-of-flight computed tomography: proof of principle', *Physics in Medicine & Biology*, vol. 65, no. 8, 085013, Bristol: IOP Publishing.

[2] Jan, S, Benoit, D, Becheva, E, Carlier, T, Cassol, F, Descourt, P, Frisson, T, Grevillot, L, Guigues, L, Maigne, L, Morel, C, Perrot, Y, Rehfeld, N, Sarrut, D, Schaart, DR, Stute, S, Pietrzyk, U, Visvikis, D, Zahra, N & Buvat, I 2011, 'GATE V6: a major enhancement of the GATE simulation platform enabling modelling of CT and radiotherapy', *Physics in Medicine and Biology*, vol. 56, no. 4, pp. 881-901, Bristol: IOP Publishing.

[3] Jdid, Lamyae & Bélanger, Gabriel & Fontaine, R. & Corbeil Therrien, Audrey. (2025). Physics-Informed Deep Neural Network for Inter-Crystal Scattering Recovery in ToF-CT. 1-1. 10.1109/NSS/MIC/RTSD57106.2025.11287152.

JS-02-08

Cherenkov Photon Counting, Labeling, and Multi-Photon Timing Estimation for sub-100 ps CTR BGO TOF-PET Detectors (#2761)

Joshua W. Cates, Seungeun Lee, Ryan Heller, Woon-Seng Choong

Lawrence Berkeley National Laboratory, Applied Nuclear Physics, Berkeley, USA

Abstract

We have developed a bismuth germanate (BGO) Cherenkov and Scintillation photon counting time-of-flight positron emission tomography (TOF-PET) detector which can count and provide unique timestamps for detected optical photons. This allows 511 keV photon time of interaction estimators to be derived from the prompt Cherenkov light without influence from scintillation light, which has a much higher variance from time of detection. This detector concept is also capable of three-dimensional positioning of 511 keV photon interactions, allowing for position and depth-of-interaction dependent optical transit time skew corrections to be applied to the prompt estimators. Information from this detector concept can be used to classify each detected optical photon as Cherenkov or scintillation. In this work, we show how labeling each detected photon as Cherenkov/scintillation and only incorporating prompt information into a timing estimator that averages timestamps for events with more than one detected Cherenkov photon significantly improves both achievable coincidence time resolution with BGO and also the TOF kernel shape by significantly reducing the long tails from time pickoff on scintillation light. We constructed a 16x16x15 mm^3 BGO photon counting detector prototype and evaluated its performance in coincidence with a fast reference detector. Incorporating the information from multiple labeled Cherenkov photons improved CTR from 159 ps to 137 ps FWHM, and the long scintillation tail was reduced to a small fraction of the total coincidence distribution. When considering all events with at least one Cherenkov photon detected, CTR was 122 ps FWHM with a Gaussian kernel shape. CTR improved to ≤100 ps for events containing 2 or more detected Cherenkov photons. We present these methods, along with a new detector concept with high Cherenkov photon detection efficiency to enable ≤100 ps CTR in a BGO TOF-PET detectors that also have high 511 keV photon detection efficiency.

JS-02-09

3D-cylindrical microdetector arrays for microdosimetryin proton therapy (#2475)

Carla Riera-Llobet[1], Celeste Fleta[1], Paula Ibáñez[2], Iván López[1], **Consuelo Guardiola**[1]

[1] National Center of Microelectronics (IMB-CNM, CSIC), Radiation Detectors Group, Barcelona, Spain; [2] Univ. Complutense de Madrid (UCM), Nuclear Physics Group, Madrid, Spain

The project has received support from the Spanish government through the ‘María de Maeztu Unit of Excellence’ accreditation (CEX2023-001397-M / AEI/10.13039/501100011033)

Abstract

Proton therapy provides high dose conformity, improving protection of organs at risk, especially for radioresistant tumours, sensitive locations, and paediatric cases. However, reported toxicities may be linked to high linear energy transfer (LET) effects. To address this issue, IMB-CNM has developed a new radiation detector architecture [1]: 3D-cylindrical silicon microdetectors, with micrometre-scale sensitivity to quantify LET. Starting from this kernel, different configurations have been designed and fabricated to cover a wide range of resolutions and radiation sensitive areas from a 11 × 11 array (2 mm × 2 mm) [2] to a linear array of 200 of those microdetectors covering 0.4 mm × 12 cm [3, 4], among others. To the best of our knowledge, these are the largest radiation sensitive surfaces covered with microdosimeters so far. Each of these multi–arrays are integrated in customized electronics readouts by using multichannel ASICs to DAQ. The ASIC enables the beam trigger and an analogue output for 128 microdetectors. Additionally, special pitch–adapters have been manufactured for each configuration to connect the signal channels with the ASIC readouts properly.

In this work we present the first measurements in proton therapy centres under clinical fluence rates (10^8 p/cm2s) across different regions of the beam. Additionally, Geant4-based Monte Carlo simulations were performed to crosscheck the experimental results. Representative microdosimetry energy spectra were obtained for some clinical depths as well as the comparison with the patient simulated LET values obtained by a treatment planning software.

The results show the feasibility of quantifying distributions of microdosimetry lineal energy values under clinical conditions, which are compared with clinically simulated for the first time.

References

[1] Guardiola C. et al., Phys Med Biol. 2021; 66(11):10.1088/1361 6560/abf811

[2] Bachiller Perea, D., et al., (2022). Scientific Reports, 12(1), 12240.

[3] C. Riera-Llobet *et al.*, in *IEEE Transactions on Radiation and Plasma Medical Sciences*, vol. 10, no. 2, pp. 288-298, Feb. 2026, doi: 10.1109/TRPMS.2025.3581801.

[4] Yuwei Z. et al., in *IEEE Transactions on Radiation and Plasma Medical Sciences*, vol. 10, no. 5, pp. 799-814, May 2026, doi: 10.1109/TRPMS.2025.3620266

Time:
10 November, 2026
17:30 – 19:00

Room:
FEDERICO GARCÍA LORCA

JS-03 | Joint Session NSS-RTSD

Chairs:
Shariar Motakef (Natick)
Chiara Guazzoni (Milano)

JS-03-01

Role of Al_2O_3passivation on high-resolution 4H-SiC radiation detectors

(#1671)

Krishna C. Mandal[1], Sandeep K. Chaudhuri[1], Frank H. Ruddy[2]

[1] University of South Carolina, Electrical Engineering Department, Columbia, USA; [2] Ruddy Consulting, Nuclear Detection and Imaging, Mount Pleasant, USA

The authors acknowledge research funding from Center of Resilience Excellence South Carolina Innovation Grant No.10013350 and NSF (ECCS-DMR) Grant No. 2404862.

Abstract

Oxide passivation plays a critical role in stabilizing semiconductor radiation detectors by suppressing surface states and enabling low-leakage, high-resolution operation. In this work, Al_2O_3-passivated Ni/4H-SiC Schottky radiation detectors were fabricated on n-type epitaxial layers of varying thickness (20, 150, and 250 μm) using pulsed laser deposition without post-deposition annealing. All devices exhibit uniform rectification with Schottky barrier heights of ~1.3 eV, low interface trap density (~10^9 $cm^{-2}eV^{-1}$), and reverse leakage dominated by Poole-Frenkel transport. Capacitance-voltage measurements indicate a flat-band potential of ~2.3 V due to fixed oxide charge, while frequency dispersion confirms minimal contribution from slow interface states. Under 5.486 MeV α-particle irradiation, the detectors demonstrate efficient self-biased operation with energy resolution of 3.3% at 0 V, improving to ~0.5-0.6% at -40 V. A detailed comparison of two nominally identical 150 μm detectors reveals significant variation in charge collection efficiency (~0.99 vs ~0.6) and energy resolution despite similar electrical characteristics, indicating that bulk carrier trapping dominates performance variability. Deep-level transient spectroscopy identifies $Z_{1/2}$ centers as the primary recombination-active defects limiting resolution across all thicknesses. A broad high-energy feature is definitively resolved, for the first time in Al_2O_3-passivated 4H-SiC Schottky detectors, using isothermal transient spectroscopy into two distinct defect levels at E_C-1.05 eV and E_C-1.1 eV, attributed to oxide-related ON2a/b states. This work establishes a unified understanding of interface and bulk defect effects in SiC radiation detectors for optimizing high-resolution operation in harsh environments.

References

[1] Mandal, KC, Chaudhuri, SK, Ruddy, FH 2023, "High-Resolution Alpha Spectrometry Using 4H-SiC Detectors: A Review of the State-of-the-Art," *IEEE Trans. Nucl. Sci.*, vol. 70, no. 5, pp. 823-830, doi: 10.1109/TNS.2023.3267996.

[2] Mandal, KC, Oner, C., Chaudhuri, SK, Nag, R., 2026, "Metal-free (p^+) diamond/(n)4H-SiC epitaxial heterojunction diodes for radiovoltaic applications," *IEEE Electron Device Lett.*, vol. 47, no. 2, pp. 257–260, doi: 10.1109/LED.2025.3640092.

[3] Nag, R, Chaudhuri, SK, Ruddy, FH, Mandal, KC, 2025, "High-resolution Cr/4H-SiC Schottky barrier radiation detector," *IEEE Trans. Nucl. Sci.*, vol. 72, no. 4, pp. 1644–1651, doi: 10.1109/TNS.2025.3547998.

[4] Nag, R, Oner, C, Chaudhuri, SK, Mandal, KC, 2025, "Investigating 4H-SiC epilayer thickness variation in high-resolution Ni/Y_2O_3/4H-SiC MOS detectors," *J. Mater. Sci. Mater. Electron.*, vol. 36, no. 34, p. 2172, doi: 10.1007/s10854-025-16272-y.

[5] Chaudhuri, SK, Nag, R, Stefurak, J, Lee, D, Seesi, E, Ahmad, I, Mandal, KC, 2026, "Electrically active oxide defects in Ni/Al_2O_3/4H-SiC diodes mimicking CAV-related defect levels," *Appl. Phys. Lett.*, vol. 128, no. 16, p. 162102, doi: 10.1063/5.0329725.

[6] Mandal, KC, Oner, C, Chaudhuri, SK, Nag, R, 2026, "Metal-free (p+)diamond/(n)4H-SiC epitaxial Heterojunction Diodes for Radiovoltaic Applications," *IEEE Electron Device Lett.*, 47(2), 257-260, 10.1109/LED.2025.3640092.

JS-03-02

Vacuum-deposited metal halide perovskite film as a radiation scintillator (#2471)

Muzzamer Zahid[1], Amy J. Dickinson[1], Jayana Jayarathne[1], Carol Crean[2], Paul Sellin[1]

[1] University of Surrey, School of Mathematics and Physics, Guildford, UK; [2] University of Surrey, School of Mathematics and Physics, Guildford, UK

Abstract

Metal halide perovskite (MHP) has been widely investigated as a radiation scintillator. Current solution-processing methods used to fabricate the MHP film suffer from toxic solvent issues and are limited in their ability to scale up for a large area detector. Single-source vapour deposition offers a solvent-free alternative that uses a single precursor, making it a promising technique for scalable film fabrication. In this study, $(BA)_2PbBr_4$ films were fabricated using SSVD onto glass substrates under high vacuum. The films were subsequently characterised, and the X-ray scintillation performance was evaluated. The results revealed that SSVD produces a thick film with a mean thickness of 10.5 ± 4.0 um and has a polycrystalline grain distribution. Energy-dispersive X-ray spectroscopy confirmed that the SSVD method preserved the composition, as the Br/Pb ratio is consistent with the theoretical value 4 for $(BA)_2PbBr_4$. Photoluminescence spectroscopy revealed a narrow peak emission 423 nm with FWHM 13 nm in close agreement with reported values for solution-grown crystals, confirming that the optoelectronic structure is preserved after deposition. Under 50 kVp X-ray irradiation, the film exhibited a fast, stable, linear dose rate response yielding scintillation sensitivity of 2464 μC Gy^{-1} cm^{-2}. These results demonstrate that SSVD is a viable, solvent-free method for fabricating MHP scintillator films with direct implications for scalable fabrication for next-generation medical imaging detectors.

JS-03-03

FAST NEUTRON DETECTION USING A SINGLE-CRYSTAL DIAMOND DETECTOR (#2449)

Bohumír Zaťko[1], Marian Varga[1], Andrea Šagátová[2], Eva Kováčová[1], Tomáš Slavíček[3], Rudolf Sýkora[3]

[1] Slovak Academy of Sciences, Institute of Electrical Engineering, Bratislava, Slovakia; [2] Slovak University of Technology, Faculty of Electrical Engineering and Information Technology, Bratislava, Slovakia; [3] Czech Technical University in Prague, Institute of Experimental and Applied Physics, Prague, Czech Republic

This work was supported by the Slovak Research and Development Agency by grant No. APVV-22-0382 and the grant of the Scientific Grant Agency of the Ministry of Education of the Slovak Republic and the Slovak Academy of Sciences No. 2/0084/20, and Funded by the EU Next Generation EU through the Recovery and Resilience Plan for Slovakia under the project No. 09I05-03-V02-00073.

Abstract
Diamond is a highly promising semiconductor material for ionizing radiation detection. Diamond-based detectors are excellent candidates for neutron detection due to interactions on relatively light carbon nuclei. Moreover, these detectors exhibit low sensitivity to X-ray and gamma radiation that often accompany neutron flux. Neutrons with energies below approximately 6 MeV are detected solely via elastic scattering on carbon nuclei within the diamond crystal. At higher energies, nuclear reactions occur, producing alpha particles, protons, and ions that can be detected by the detector. In this experiment, we use a single-crystal CVD diamond detector to detect fast neutrons with energies ranging from 300 keV to 18.5 MeV. A diamond detector has square contact dimensions of 3.6 × 3.6 mm^2 and a thickness of 0.5 mm. Testing the detector with an alpha-particle source showed a high-energy resolution of about 0.4% at 5.5 MeV. The detector was used to detect monoenergetic neutrons ranging from 250 keV to 911 keV, 3.5 MeV to 4.5 MeV, and 14.6 MeV to 18.5 MeV, generated by p-T, D-D, and D-T nuclear reactions at Van de Graaff accelerator, respectively. The single-crystal diamond detector showed good linearity and excellent detection properties. In the detected spectra, all main neutron-detector interactions were identified.

JS-03-04

Improving the spectral resolution of photons in silicon Timepix3 by correcting for the cluster size and by lowering the Krummenacher current (#1416)

Jindrich Jelinek[1,2], Benedikt Bergmann[1]

[1] Czech Technical University, Institute of Experimental and Applied Physics, Prague, Czech Republic; [2] University of Geneva, Department of Particle and Nuclear Physics, Geneva, Switzerland

B. Bergmann acknowledges support from the Czech Science Foundation under Registration Number GM23-04869M.

The authors would like to thank Petr Smolyanskiy (IEAP CTU) for his help with the measurements, Jan Zemlicka (IEAP CTU) for lending a piece of gadolinium metal, and Tomas Slavicek (IEAP CTU) and Bartolomej Biskup (IEAP CTU) for their assistance with the radioactive sources.

Abstract
We investigated ways to improve the spectral resolution of a Timepix3 hybrid pixel detector with a 1 mm thick silicon sensor for X-ray and soft gamma photons. A standard procedure is to calibrate the time-over-threshold (ToT) to deposited energy for each pixel, but even then, there remains room for improvement. The first

improvement was lowering the Krummenacher current (Ikrum) to increase the ToT at even low-energy deposits to get a finer resolution. The second novel improvement was creating an additional calibration on cluster energies, taking into account the cluster size. It was observed that clusters of larger size feature a higher energy than smaller clusters created by the same photon source. The cluster energy could therefore be corrected based on its size, and we found that this correction is linear for each cluster size. Both the lowering of the Ikrum together with the cluster size correction decreased the full width at half maximum (FWHM) by 17-35 % compared to the initial settings in the energy range of 4-136 keV. The higher the photon energy, the larger the percentage decrease in FWHM. We intend to utilize the enhanced spectral resolution in Compton X-ray polarimetry. There, the coincident events of a Compton scattering followed by a photoabsorption are measured. The sum of the deposited energies in the two events gives the original energy of the photon. The FWHM of coincident pairs of clusters decreased by 22-44 % compared to the initial settings in the energy range of 43-136 keV.

References
[1] T. Poikela, et al., 2014, 'Timepix3: a 65K channel hybrid pixel readout chip with simultaneous ToA/ToT and sparse readout,' *JINST*, vol. 9, no. 05, pp. C05013
[2] J. Jelinek, B. Bergmann, and P. Smolyanskiy, 2025, 'Evaluation of Timepix3 with a 1 mm thick silicon sensor as a Compton imaging polarimeter in the hard X-ray band,' *JINST*, vol. 20, no. 02, pp. C02006
[3] J. Jakubek, A. Cejnarova, T. Holy, S. Pospisil, J. Uher, and Z. Vykydal, 2008, 'Pixel detectors for imaging with heavy charged particles,' *Nucl. Instrum. Methods Phys. Res. A*, vol. 591, no. 1, pp. 155--158
[4] D. Turecek, J. Jakubek, and P. Soukup, 2016, 'USB 3.0 readout and time-walk correction method for Timepix3 detector,' *JINST*, vol. 11, no. 12, pp. C12065
[5] P. Burian, P. Broulím, M. Jára, V. Georgiev, and B. Bergmann, 2017, 'Katherine: Ethernet Embedded Readout Interface for Timepix3,' *JINST*, vol. 12, no. 11, pp. C11001

JS-03-05

Simulation-based inference for uncertainty-aware interaction reconstruction in 3D CZT drift strip detectors (#2532)

Alejandro Valverde Mahou[1], Michał Kossakowski[2], Irfan Kuvvetli[2], Søren Hauberg[1], Georgios Arvanitidis[1], Christian A. Naesseth[3]

[1] Technical University of Denmark, DTU Compute, Kgs. Lyngby, Denmark; [2] Technical University of Denmark, DTU Space, Kgs. Lyngby, Denmark; [3] University of Amsterdam, Informatics Institute, Amsterdam, Netherlands

Abstract

Accurate interaction position reconstruction in radiation detectors is often limited by the lack of tractable likelihood functions and the stochastic nature of particle transport and charge induction processes. In this work, we present a simulation-based inference framework for 3D Cadmium Zinc Telluride drift strip detectors (3D CZT DSD) that learns a probabilistic inverse mapping from Charge Induction Efficiency signals to interaction positions using Monte Carlo generated training data. We formulate the reconstruction problem as Neural Posterior Estimation and train a neural network to predict a Gaussian approximation of the posterior distribution over interaction positions. The model is optimized using negative log-likelihood, enabling simultaneous estimation of interaction positions and associated uncertainties in a single amortized inference step. Preliminary results on synthetic datasets show that the proposed method produces meaningful uncertainty estimates that provide insights into detector response variability compared to deterministic regression approaches.

References
[1] I. Kuvvetli, S. R. H. Owe, and C. Budtz-Jørgensen, "Advancements in CdZnTe Detectors with the Drift Strip Method," in CdTe and CdZnTe Materials: Material Properties and Applications, K. Iniewski, Ed. Cham, Switzerland: Springer Nature Switzerland, 2024, pp. 51–70.
[2] K. Cranmer, J. Brehmer, and G. Louppe, "The frontier of simulation-based inference," Proceedings of the National Academy of Sciences, vol.117, no. 48, pp. 30055–30062, 2020.
[3] G. Papamakarios, D. Sterratt, and I. Murray, "Sequential neural likelihood: Fast likelihood-free inference with autoregressive flows," in Proc.22nd Int. Conf. Artificial Intelligence and Statistics (AISTATS), Naha, Okinawa, Japan, 2019, pp. 837–848.

JS-03-06

One-Year Performance Analysis of the cadmium zinc TElluride Radiation Imager (TERI) in Orbit (#1229)

Nicholas Kirschner[1], Daniel Shy[2], Michael Streicher[3], Douglas M. Groves[3], Zhong He[3], Jason Jaworski[3], Willy Kaye[3], James Mason[3], Ryan Parsons[3], Feng Zhang[3], Yuefeng Zhu[3], Alena Thompson[2], Chi C. Cheung[2], Anthony L. Hutcheson[2], Mary V. Johnson-Rambert[2], Wiley N. Johnson[4], Bernard F. Phlips[2]

[1] National Research Council Research Associate resident, U.S. Naval Research Laboratory, Washington, USA; [2] U.S. Naval Research Laboratory, Washington, USA; [3] H3D, Inc., Ann Arbor, USA; [4] Technology Service Corporation, Arlington, USA

The authors are grateful to the Department of Defense (DoD) Space Test Program (STP) for providing space launch services and mission operations support for TERI. Special thanks to Scott Budzien for providing the NRL Payload Operations Control Center. The CdZnTe crystals were provided by the Defense Threat Reduction Agency. This work is supported by the Office of Naval Research 6.1 funds.

Abstract

The cadmium zinc TElluride Radiation Imager (TERI) was successfully launched to the International Space Station (ISS) on April 21, 2025 as a part of the Department of Defense's Space Test Program (STP-H10) mission. The primary mission of TERI is to space-qualify large-volume 4×4×1.5 cm^3 pixelated CdZnTe (CZT) detectors. The system is composed of four of these advanced detectors, each of which is 3D position sensitive, allowing for Compton event imaging. Here, we report on the one-year in-orbit performance results of TERI, including measurements of the background rate, which align with expected orbital variations. We analyze the 511 keV line and observe no significant degradation over nine months in orbit. Additionally, we observe multiple spectral lines, several of which are consistent with known activation lines.

References
[1] Shy, D., Streicher, D., Groves, M., He, Z., Jaworski, J., Kaye, W., Mason, J., Parsons, R., Zhang, F., Zhu, Y., Thompson, A., Garner, A., Hutcheson, A., Johnson-Rambert, M., Johnson, W. N., Phlips, B., 2024, 'Development of the cadmium zinc telluride radiation imager', *Journal of Astronomical Telescopes, Instruments, and Systems*, vol. 10, no. 04
[2] Shy, D., Goodman, D., Parson, R., Streicher, M., Kaye, W., Mitchell, L., He, Z., Phlips, B., 2023, 'Radiation damage of 2 x 2 x 1cm^3 pixelated CdZnTe due to high-energy protons', *Nuclear Instruments and Methods in Physics Research A*, vol 1056, p. 168622

NSS

9 November, 2026

Time:
9 November, 2026
9:00 – 11:00

Room:
FEDERICO GARCÍA LORCA

NP-01 | NSS Plenary Session

Chairs:
Audrey Corbeil Therrien (Sherbrooke)
Giulia Hull (Orsay)

NP-01-01

Welcoming remarks (#3450)

Stefan Ritt

Paul Scherrer Institute (PSI), Villigen, Switzerland

NP-01-02

The Shape of Light (#3451)

Sara Cazzoli

Instituto de Astrofísica de Andalucía, Astrophysics, Granada, Spain

Abstract

The term Big Bang evokes a deafening sound. Yet in the Universe, it is not sound but light that serves, so far, as the most powerful messenger of information. Our eyes were the first instruments through which humanity began to understand the nature of our Universe. Today, telescopes are our eyes to the cosmos, and they are coupled with a wide variety of instruments capable of collecting, manipulating, and transforming the light that we can ultimately study in order to unravel the secrets of the Universe. Thanks to them, we obtain information as distant and ancient as the Cosmic Microwave Background and as close and young as the whims of our own star, the Sun. What stories do the different forms of light tell us? Whether through “simple” photon counts, spectra, or even the absence of light, its many forms reveal different information about our Universe. Light is also a fundamental element in the arts. In the performing arts, it is crucial for creating emotions—often becoming a narrative language—in photography, it builds atmospheres, from the depth of black and white to the intensity of the most vivid colors; and in architecture, it defines spaces and highlights textures. Light is an essential element both in the artistic experience and in our understanding of the Universe. The Shape of Light is, more than a talk, a journey through light across astronomy, physics, and art.

NP-01-03

2026 Radiation Instrumentation Early Career Award (NSS)

NP-01-04

2026 IEEE Emilio Gatti Radiation Instrumentation Technical Achievement Award (NSS)

NP-01-05

2026 IEEE Glenn F. Knoll Radiation Instrumentation Outstanding Achievement Award (NSS)

Time:
9 November, 2026
11:30 – 12:30

Room:
FEDERICO GARCÍA LORCA

NP-02 | NSS Plenary Session

Chairs:
Audrey Corbeil Therrien (Sherbrooke)
Giulia Hull (Orsay)

NP-02-01

Environmental sustainability in research

Hannah Wakeling

University of Oxford, UK

NP-02-02

2026 Valentin T. Jordanov Radiation Instrumentation Travel Grants and 2026 Paul Phelps Continuing Education Grant

NP-02-03

Introduction to lighning talks

Time:
9 November, 2026
12:30 – 13:00

Room:
FEDERICO GARCÍA LORCA

N-LT-01 | NSS Lightning Talks 1

Chairs:
Audrey Corbeil Therrien (Sherbrooke)
Giulia Hull (Orsay)

N-LT-01-01

Facile, scalable and high-yield synthesis of zero-dimensional copper halide $Cs_3Cu_2Cl_5$ scintillator with near-unity quantum yield for high-resolution X-ray imaging applications (#1659)

Young Seung Choi[1], Jaeyoung Im[2], Kang Heo[3], Sung Oh Cho[2], Bo Kyung Cha[4], **Byungha Shin**[1]

[1] KAIST, Materials Science and Engineering, Daejeon, South Korea; [2] KAIST, Nuclear and Quantum Engineering, Daejeon, South Korea; [3] Viewworks, Anyang, South Korea; [4] KERI, Ansan, South Korea

Abstract

Metal halide perovskites, particularly copper halide variants, have emerged as promising scintillators owing to their large Stokes shift, high photoluminescence quantum yield (PLQY), and efficient radioluminescence. Here, we demonstrate a dioxolane-mediated reaction synthesis as a simple, scalable, and high-yield strategy for producing $Cs_3Cu_2Cl_5$ powders with near-complete conversion. By employing low-polarity yet water-miscible dioxolane as the reaction medium together with an aqueous H_3PO_2 additive, the solubility imbalance between the precursors inherent to low-polarity solvents is effectively addressed. This approach enables stoichiometry-controlled dissolution–precipitation under a low-polarity reaction environment and the formation of phase-pure $Cs_3Cu_2Cl_5$ powders with near-unity PLQY. The powders show bright green emission at ~530 nm and retain over 80% of their initial efficiency after 300 days of ambient storage without encapsulation, demonstrating remarkable intrinsic stability. $Cs_3Cu_2Cl_5$-based composite films deliver an ultrahigh light yield of ~98,000 photons MeV^{-1}, greatly surpassing that of commercial scintillators such as Gd_2O_2S and CsI:Tl, and exhibiting excellent dose linearity and long-term irradiation stability. When integrated into commercial flat-panel detectors, the $Cs_3Cu_2Cl_5$-based composite films successfully enabled high-quality 2D radiographic and 3D computed tomography imaging, directly verifying their compatibility with existing X-ray detection systems. This facile and efficient synthesis, together with the demonstrated device-level imaging performance, highlights $Cs_3Cu_2Cl_5$ as a scalable and practical candidate for next-generation X-ray scintillators.

N-LT-01-02

Hydrophobic Solvent-Based Polishing for Performance Enhancement of Water-Sensitive Perovskite Scintillator Crystals (#1236)

Seungho Song[1,2], Jiwon Seo[3], Dakyoung Lee[1,2], Chansun Park[4], Beomjun Park[5], Jung-Yeol Yeom[2,6]

[1] Korea University, Department of Bioengineering, Seoul, South Korea; [2] Korea University, Interdisciplinary Program in Precision Public Health, Seoul, South Korea; [3] Korea Institute of Fusion Energy, Dajeon, South Korea; [4] Korea University, Global Health Technology Research Center, Seoul, South Korea; [5] Seoul National University, Research Institute for Future Technology and Policy, Seoul, South Korea; [6] Korea University, School of Bioengineering, Seoul, South Korea

This work was supported by the National Research Foundation of Korea (NRF), funded by the Ministry of Science and ICT (RS-2023-NR077190, RS-2022-00165164), and by the National Research Foundation of Korea and the Commercializations Promotion Agency for R&D Outcomes (RS-2023-00234651).

Abstract

Halide perovskites are promising scintillator materials for radiation detection and medical imaging because of their excellent optical and scintillation properties. Since the surface quality of single-crystal scintillators strongly affects light extraction and detector performance, polishing is an essential step in scintillator fabrication. However, conventional wet polishing processes are not suitable for water-sensitive crystals such as $Cs_3Cu_2I_5$ (CCI). In this work, hydrophobic solvents were investigated as polishing media for water-sensitive CCI single crystals. Three hydrophobic solvents—squalane, silicone oil, and mineral oil— were used as dispersion media for 1 μm alumina abrasives, followed by toluene rinsing after polishing. Among them, squalane showed the best polishing performance, yielding the lowest surface roughness (R_q=17.29 nm), the highest transmittance of 78.21%, and the narrowest rocking-curve FWHM of 0.025°. In addition, sequential polishing in squalane using P2000 sandpaper, P4000 sandpaper, and 1 μm alumina enhanced the light yield and improved the energy resolution from 6.53% to 5.83%. These results identify squalane as a promising polishing medium for water-sensitive halide perovskite scintillators.

N-LT-01-03

Organic Scintillator Light Yield Models for Sub-MeV Neutrons in EJ301D and d-stilbene (#1369)

Christian A. Irvine[1,2], Tyler C. Borgwardt[1], Robert A. Weldon Jr.[1], John Mattingly[2]

[1] Los Alamos National Laboratory, NEN-2, Los Alamos, USA; [2] North Carolina State University, Nuclear Engineering, Raleigh, USA

This work was supported by the US Department of Energy through the Los Alamos National Laboratory. Los Alamos National Laboratory is operated by Triad National Security, LLC, for the National Nuclear Security Administration of U.S. Department of Energy (Contract No. 89233218CNA000001).

Abstract

Six commonly used models for neutron induced light yield in organic scintillators were fit and analyzed using measurements of a 2.54 cm diameter by 2.54 cm long right circular cylinder of EJ301D and a (5.08 cm)3 custom made cube of deuterated trans-stilbene-d12 (d-stilbene). Measured neutron energies spanned 300 keV to 2200 keV for the EJ301D scintillator and 200 keV to 2500 keV in d-stilbene. The model fits and experimental analysis methods were verified by examining the agreement between the predicted light output spectrum and the measured light output spectrum for several simulated quasi-monoenergetic neutron sources. Birks model inaccurately predicted highly quenched light yield for sub-MeV neutrons in both scintillators. The addition of a second order quenching term to the Birks model by Chou significantly improved the models accuracy, however its behavior is non-physical if extrapolated beyond the measured neutron energies. The model derived by Voltz accurately fit the measurement of both scintillators for all measured neutron energies. Further investigation into the ability to extrapolate based on these semi-empiric models would be valuable given the non-physical behavior of well-fitting models.

References

[1] Thibault A Laplace et al. “Modeling ionization quenching in organic scintillators”. In: Materials Advances 3.14 (2022), pp. 5871–5881

[2] Mark A. Norsworthy et al. “Evaluation of neutron light output response functions in EJ-309 organic scintillators”. In: Nuclear Instruments and Methods in Physics Research Section A: Accelerators, Spectrometers, Detectors and Associated Equipment 842 (2017), pp. 20–27. ISSN: 0168-9002. DOI: https://doi.org/10.1016/j.nima.2016.10.035.

[3] John Betteley Birks. The theory and practice of scintillation counting: International series of monographs in electronics and instrumentation. Vol. 27. Elsevier, 2013.

[4] CN Chou. “The nature of the saturation effect of fluorescent scintillators”. In: Physical Review 87.5 (1952), p. 904.

[5] J Hong et al. “The scintillation efficiency of carbon and hydrogen recoils in an organic liquid scintillator for dark matter searches”. In: Astroparticle Physics 16.3 (2002), pp. 333–338. ISSN: 0927-6505. DOI: https://doi.org/10.1016/S09276505(01)00114-1

[6] S Yoshida et al. “Light output response of KamLAND liquid scintillator for protons and 12C nuclei”. In: Nuclear Instruments and Methods in Physics Research Section A: Accelerators, Spectrometers, Detectors and Associated Equipment 622.3 (2010), pp. 574–582.

[7] R. Voltz et al. “Influence of the Nature of Ionizing Particles on the Specific Luminescence of Organic Scintillators”. In: The Journal of Chemical Physics 45.9 (Nov. 1966), pp. 3306–3311. ISSN: 0021-9606. DOI: 10.1063/1.1728106. eprint: https://pubs.aip.org/aip/jcp/article-pdf/45/9/3306/18846420/3306 1 online.pd

[9] G. Dietze and H. Klein. “Gamma-calibration of NE213 scintillation counters”. In: Nucl. Instr. and Meth. 193.3 (1982), pp. 549–556. ISSN: 0167-5087. DOI: 10.1016/0029-554X(82)90249-X.

[11] C. A. Irvine et al. “Low energy neutron light output characterization of EJ301D and deuterated stilbene with a comparison of light output characterization methods”. In: Submitted for review (2026).

N-LT-01-04

Application of neutron sensitising layers to plastic scintillator (#2414)

Jack R. Hitchens, Chris Allwork, Shivani L. Chauhan, Tom Crane, Tom Heather, Matt P. Taggart

AWE Nuclear Security Technologies, Reading, UK

Abstract

Eljen plastic scintillator disks have been coated with layers of neutron sensitiser in a systematic study on the thickness of neutron detection layers. Here we discuss the impact of enhancing standard plastic scintillator (PVT) with coatings containing both lithium and boron isotopes. The application of these layers enhances the material to provide a mechanism for detecting neutron radiation. A systematic study was performed to assess the impact of sensitiser thickness on neutron detection efficiency and neutron-gamma pulse shape discrimination (PSD) performance. Samples were exposed to the mixed radiation fields of a ^{252}Cf source, and a sample of plutonium. The results demonstrate clear neutron-gamma discrimination in sensitised samples, with measured figures of merit in excess of 3 recorded for optimised lithium-rich coatings. This is comparable performance to established dual-mode detectors. These findings show that thin, externally applied neutron-sensitising layers provide an effective route to enhancing the performance of conventional plastic scintillators. This approach may offer a low-cost means of upgrading existing detector systems in nuclear security applications.

References

[1] J. Glodo, et al., “Selected Properties of Cs2LiYCl6:Ce3+ Scintillator,” IEEE Trans. Nucl. Sci., vol. 56, pp. 873–880, 2009.

[2] R. Song, et al., “The Neutron-Gamma Pulse Shape Discrimination of CLLB Detector,” EPJ Web of Conferences, vol. 295, Art. No. 09031, 2024

[3] N. Zaitseva, et al., “Plastic scintillators with efficient neutron-gamma pulse shape discrimination,” Nuclear Instruments and Methods in Physics Research A, vol. 668, pp. 88-93, 2012

[4] R. Breuckers, C. Bartle and A. Edgar, "Transparent lithium loaded plastic scintillators for thermal neutron detection," Nuclear Instruments and Methods in Physics Research A, vol. 701, pp. 58-61, 2013

[5] I. Pawelczak, et al., “Boron-loaded plastic scintillators with neutron-γ discrimination capability,” Nuclear Instruments and Methods in Physics Research A, vol. 751, pp. 62-69, 2014

[6] N. Cherepy, et al., “Bismuth- and lithium-loaded plastic scintillators for gamma and neutron detection,” Nuclear Instruments and Methods in Physics Research A, vol. 778, pp. 126-132, 2015

N-LT-01-05

Scintillation light quenching for energetic charged particles in GAGG:Ce (#1607)

Felix Liang[1], Nicholas Floyd[1], Heshani Jayatissa[1], Philip Adsley[2], Arthur Alvarez[2], Robert Bartsch[2], Shayden Fritz[2], Travis Hankins[2], Bryan Harvey[2], Khang Pham[2], Elizabeth Schnorrenberg[2], David Shelden[2], Sherry Yennello[2]

[1] Los Alamos National Laboratory, ISR Division, Los Alamos, USA; [2] Texas A&M University, Cyclotron Institute, College Station, USA

Los Alamos National Laboratory is managed by Triad National Security, LLC for the U.S. Department of Energy's NNSA.

Abstract

Cerium-doped gadolinium gallium aluminium garnet (GAGG:Ce) is a novel scintillator with excellent scintillation properties. It is suitable for use in various basic science research and applications. Because the scintillation light is quenched for charged particle detection, it is necessary to use beams from accelerators to calibrate the energy response. Measurements of energetic charged particles incident on three GAGG:Ce crystals were performed using accelerated protons, ^{4}He, and ^{12}C at 0°C and 20°C in consideration for detecting charged particles in the earth's radiation belts for space weather modeling and for deploying in dosimetry devices in ion therapy, respectively. The Birks factor which quantitatively describes the extent of quenching was deduced from the experimental data. For all three GAGG:Ce scintillators, the Birks factor decreases with the atomic number Z of the incident ions. Furthermore, less light quenching, a smaller Birks factor, was observed for GAGG:Ce at 0°C. The quenching for the Mg-codoped GAGG:Ce which has a shorter decay time constant, was found to be less temperature dependent compared to the other two GAGG:Ce crystals.

References

[1] Wang, YQ, Burward-Hoy, JM, Tesmer, JR 2014, 'Production of high energy and low flux protons using ^{2}D(^{3}He,p)^{4}He for space detector calibrations', *Nucl. Instrum. Methods*, vol. B332, pp. 432-438.

[2] Espinoza, TN, *et al.* 2024, 'Proton quenching in rare-earth inorganic scintillators: GAGG:Ce and YSO:Ce', *IEEE Trans. Nucl. Sci.*, vol. 71, pp. 2102-2108.

[3] Birks, JB 1964, 'The theory and practice of scintillation counting', Pergamon Press, Oxford.

[4] Treytak, VI 2010, 'Semi-empirical calculation of quenching factors for ions in scintillators', *Astro. Phys.*, vol. 33, pp. 40-53.

[5] Ziegler, JF, Biersack, JP, Littmark, U 1985, 'The stopping and range of ions in solids', vol. 1, Pergamon Press, New York.

[6] Berger, MJ, Coursey, JS, Zucker, MA, Chang, J 2017, 'Stopping-power & range tables for electrons, protons and helium ions', https://dx.doi.org/10.18434/T4NC7P.

N-LT-01-06

Temperature Dependence of Pulse Shape Discrimination in SiPM-Based EJ-276D Detectors (#1585)

Jacob W. Fritchie, Angela Di Fulvio, Gabriella Gariazzo, Grant Roche, John Leland

University of Illinois Urbana-Champaign, Nuclear, Plasma, and Radiological Engineering, Urbana, USA

This work is funded in-part by Sandia National Laboratories (SNL) LDRD Award 2308289. SNL is a multimission laboratory managed and operated by National Technology & Engineering Solutions of Sandia, LLC, a wholly owned subsidiary of Honeywell International Inc., for the U.S. Department of Energy's National Nuclear Security Administration (NNSA) under contract DE-NA0003525. This research was performed under appointment to the Nuclear Nonproliferation International Safeguards Fellowship Program sponsored by the U.S. NNSA's Office of International Nuclear Safeguards.

Abstract

The temperature dependence of pulse shape discrimination performance was investigated for three commercial silicon photomultiplier technologies coupled to an EJ-276D organic scintillator. Measurements were conducted at 22 °C, 30 °C, 40 °C, and 50 °C using PuBe sources. Pulse shape discrimination was quantified using the tail-to-total ratio and figure of merit. For all devices, the figure of merit increased at 30 °C. The Broadcom device exhibited the highest performance, increasing from 1.12 at 22 °C to a maximum of 1.17 at 30 °C before decreasing to 0.76 at 50 °C. The Onsemi and Hamamatsu devices showed smaller improvements, with figure of merit values increasing from 0.86 to 0.89 and 0.84 to 0.90, respectively, between 22 °C and 30 °C. At 50 °C, all devices exhibited reduced performance due to increased silicon photomultiplier thermal noise. Temperature-dependent changes in pulse shape were observed, with increasing temperature producing faster decay and modifying the balance of prompt and delayed scintillation light, improving neutron-gamma separation at intermediate temperatures. Despite degradation at higher temperature, all devices maintained effective discrimination up to 50 °C. These results demonstrate that silicon photomultiplier-based detectors are capable of robust neutron-gamma discrimination at elevated temperatures relevant to safeguards applications.

References

[1] Acerbi, Fabio, Gundacker, Stefan 2019, 'Understanding and Simulating SiPMs', *Nulcear Insturments and Methods in Physics Research Section A: Accelerators, Spectrometers, Detectors and Associated Equipment*, 926, 16-35

[2] Borgwardt, TC, Oukrop, L, Bartlett, KD, Smith, K, Williamson, E, Meierbachtol, KC, Febbraro, M 2025, 'Temperature dependence of the nspec fieldable neutron spectrometer', Nuclear Instruments and Methods in Physics Research Section A: Accelerators, Spectrometers, Detectors and Associated Equipment, vol. 1072, article 170161.

[3] Arrue, J, Chandler, C, Duce, M, Lim, A, Sellinger, A, Erickson, A 2023, 'Impact of temperature on light yield and pulse shape discrimination of polysiloxane-based organic scintillators formulated with commercial resins', Nuclear Instruments and Methods in Physics Research Section A: Accelerators, Spectrometers, Detectors and Associated Equipment, vol. 1056, article 168650.

N-LT-01-07

Performance evaluation of GaGG(Ce) scintillators with different photosensors (#2850)

Miriam Caballero Rodríguez[1], Nikita Bernier[1], Victor Martínez Nouvilas[1], Luis M. Fraile[2,1], Odette Alonso-Sañudo[1], José A. Briz[1], Sara Gaitán Dominguez[1], Gabriel G. de Lorenzo[1], Pablo Gonzalez-Tarrio[1], Andrés Illana[3], Jose Udias[1]

[1] Universidad Complutense de Madrid, Facultad de Ciencias Físicas / Departamento de Estructura de la Materia, Física Térmica y Electrónica, Madrid, Spain; [2] CERN, ISOLDE, EP Department, Geneva, Spain; [3] CSIC, Instituto de Estructura de la Materia, Madrid, Spain

This work has been supported by the Spanish Ministerio de Ciencia e Innovaci\'on under projects PID2019-104714GB-C21 and PID2022-140400NB-C21.

Abstract

The HIE-ISOLDE Timing Array for Reaction Studies (HISTARS) project at CERN is developing a specialized detector system designed to measure the lifetimes of excited nuclear states. For efficient particle detection, thin square GaGG(Ce) are utilized alongside YSO due to their high density and fast scintillation properties. This work evaluates the performance of GAGG(Ce) crystals coupled with two distinct photosensors: a Hamamatsu R9779 photomultiplier tube (PMT) and an array of four silicon photomultipliers (SiPM) using a custom-designed circuit. These configurations were tested in combination with a $LaBr_3$(Ce) detector to facilitate coincidence measurements. Data acquisition was performed using high-speed digitizer to extract timing and energy information. This article reports on the comparative performance of both readout methods, specifically characterizing pulse shape discrimination capabilities, energy resolution, and the coincidence time resolution for alpha-gamma events. Although the energy resolution is acceptable and it has a good pulse shape discrimination capability, the measured timing limitations show that the current configuration is not ideal for the HISTARS array. These results will guide the selection of better-suited materials for high-precision timing at HIE-ISOLDE.

References

[1] Wang, Z, Guo, H, Qian, S 2020, 'Pulse shape discrimination of GAGG:Ce crystals for charged particle detection', Journal of Instrumentation, Vol. 15, p. C06031, Bristol: IOP Publishing.

[2] Tsuchida, N, Ikeda, M, Kamae, T 1997, 'A study of the GAGG:Ce crystal for its application in nuclear physics', Nuclear Instruments and Methods in Physics Research Section A, Vol. 385, pp. 290–298, Amsterdam: Elsevier.

[3] Vedia, V, Carmona-Gallardo, M, Fraile, LM 2017, 'Characterization of specialized $LaBr_3$(Ce) detectors for fast-timing lifetime measurements', Nuclear Instruments and Methods in Physics Research Section A, Vol. 857, pp. 98–105, Amsterdam: Elsevier

N-LT-01-08

Combining cross-luminescent scintillators and µSiPMs for better timing in ToF-PET (#1249)

Katrin Herweg[1,2], Samuele Bisi[3], Claudio Bruschini[3], Edoardo Charbon[3], Alberto Gola[4], Laura Parellada-Monreal[4], Michele Penna[4], David Schug[1,2], Volkmar Schulz[2], Stefan Gundacker[5]

[1] RWTH Aachen University, University Hospital RWTH Aachen, Aachen, Germany; [2] RWTH Aachen University, Institute of Imaging and Computer Vision, Aachen, Germany; [3] Ecole polythechnique fédérale de Lausanne, Advanced Quantum Architecture Laboratory, Neuchatel, Switzerland; [4] Fondazione Bruno Kessler, Trento, Italy; [5] Austrian Academy of Sciences, Marietta Blau Institute for Particle Physics, Vienna, Austria

This research is funded by the Deutsche Forschungsgemeinschaft (DFG, German Research Foundation) - 500540345 and the Swiss National Science Foundation (SNSF) - #200021L_208073.

Abstract

Time-of-flight positron emission tomography (ToF-PET) has boosted PET image quality significantly in the last years. During its first inception it was built with cross-luminescent BaF_2 crystals, which have since been replaced by LYSO. Recently, cross-luminescence has regained popularity with new scintillators being developed. However, BaF_2 and the recently developed Cs_2ZnCl_4 could not improve on the LYSO state-of-the-art coincidence time resolution (CTR) (56 ps for 2x2x3 mm³ and 95 ps for 3x3x19 mm³). As Cs_2ZnCl_4 shows a significant Cherenkov production, we combined it with the DIGILOG approach to boost its timing performance. The DIGILOG approach segments the sensor into µSiPMs and has shown an improved timing performance for BGO due to its Cherenkov radiation and an improved SPTR. Here, we simulated a 3x3x3 mm³ and a 3x3x20 mm³ Cs_2ZnCl_4 crystal coupled to seven different µSiPM arrays. The simulation included noise factors like dark counts, cross-talk, SPAD dead time and analog noise. It was designed with a PDE of 60 % and an SPTR of 25 ps. This resulted in an improved CTR of 34+/-4 ps for an array of 20x20 µSiPMs coupled to a 3x3x3 mm³ Cs_2ZnCl_4 crystal compared to the non-segmented SiPM at 48+/-3 ps. Furthermore, for the 3x3x20 mm³ crystal, a CTR of 64+/-4 ps was reached with a 10x10 µSiPM array, while the non-segmented SiPM showed a CTR of 84+/-3 ps. The results of the segmented SiPMs improve on the LYSO state-of-the-art. Additionally, they demonstrate that the DIGILOG SiPM approach improves timing performance not just for BGO, but also for other scintillators with high Cherenkov yield, ultra-fast emission and low light yield. We also provide motivation to optimize sensors for Cs_2ZnCl_4, which could enable better timing performance than the LYSO state-of-the-art.

References

[1] Wong, W. H. et al. 1984, 'Characteristics of small barium fluoride (BaF2) scintillator for high intrinsic resolution time-of-flight positron emission tomography', IEEE TNS

[2] Herweg, K. et al. 2023, 'On the Prospects of BaF2 as a Fast Scintillator for Time-of-Flight Positron Emission Tomography Systems', IEEE TRPMS

[3] Rutstrom, D. et al. 2022, 'Improved light yield and growth of large-volume ultrafast single crystal scintillators Cs2ZnCl4 and Cs3ZnCl5', Optical Materials

[4] Herweg, K. et al. 2024, 'Timing limits of ultrafast cross-luminescence emission in CsZnCl-based crystals for TOF-CT and TOF-PET', EJNMMI Physics

[5] Nadig, V. et al. 2023, 'Timing advances of commercial divalent-ion co- doped LYSO:Ce and SiPMs in sub-100 ps time-of-flight positron emission tomography', PMB

[6] Gundacker, S. et al. 2023, 'DIGILOG: A digital-analog SiPM towards 10 ps prompt-photon tagging in TOF-PET', 2023 IEEE NSS MIC RTSD

[7] Herweg, K. et al. 2024, 'Investigating µSiPMs to overcome the limits of BGO in ToF-PET', 2024 IEEE NSS MIC RTSD
[8] Herweg, K. et al. 2026, 'Exploring µSiPMs with BGO for Cherenkov time-of-flight in PET', revision submitted to IEEE TRPMS
[9] Zuo, X. et al. 2025, 'Scintillation performance of 1-inch-diameter Cs2ZnCl4 crystals', CrystEngComm

N-LT-01-09

Fast or Adapt: Proportional Gas in γ-ray Fields (#1278)

Jakub Prchlik, Eric Yokie, Arlo Petitjean, David O'Connor

Reuter-Stokes, LLC, Twinsburg, USA

Abstract

Background γ-ray fields complicate neutron measurements for Nondestructive Assay (NDA) of Nuclear Materials and the next generation of advanced reactor designs, including non-light water (non-LWR) and Small Modular Reactors (SMRs). Neutron sensitive proportional counter design for high γ-ray fields often focus on optimizing ion collection time and integrating low-Z materials. In these counters, the metal cathode produces most of the Compton scattered electrons, which deposit unwanted energy and signal in the gas. The long path length for Compton electrons in the counter gas means the counter gas pressures may be optimized to increase the ratio of ion-to-electron energy deposition. Here we present gas mixture and pressure optimization for ion-to-electron energy deposition using SRIM simulations. The simulation output is then tested experimentally for its effect on neutron sensitivity in γ-ray fields between 1 R/Hr and 100 R/Hr. The ion-to-electron energy deposition ratio shows promise as an additional design consideration for neutron sensitive proportional counters in γ-ray fields, even though the experimentally measured optimum pressure of 0.5 atm for He/N_2 95/5 is lower than the simulated optimum pressure. Future experiments with a current sensitive preamplifier (CAEN A1427) will improve neutron counting for 1 to 100 R/Hr γ-ray fields.

References
[1] DH Beddingfield, NH Johnson, and HO Menlove. 3he neutron proportional counter performance in high gamma-ray dose environments. Nuclear Instruments and Methods in Physics Research Section A: Accelerators, Spectrometers, Detectors and Associated Equipment, 455(3):670–682, 2000.
[2] D. C. Henzlova, M. P. Baker, K. Bartlett, A. Favalli, M. Iliev, M. A. Root, S. Sarnoski, T. Shin, and M. T. Swinhoe. Neutron Detectors, pages 325–358. Springer Nature Switzerland, Cham, 2024.
[3] Kevin S McKinny, Thomas R Anderson, and Nathan H Johnson. Neutron detector sensitivity measurements and their variation. In 2011 IEEE Nuclear Science Symposium Conference Record, pages 533–537. IEEE, 2011.
[4] J. Va'Vra. Review of wire chamber aging. Nuclear Instruments and Methods in Physics Research Section A: Accelerators, Spectrometers, Detectors and Associated Equipment, 252(2):547–563, 1986.

N-LT-01-10

Characterisation of edge-on fully-depleted monolithic CMOS silicon sensors (#1882)

Matteo Barbagiovanni[1,2], Anders Bjorklid[3], Alberto Bortone[2], Rickard Brunskog[6], Manuel D. Da Rocha Rolo[2], Mats Danielsson[6], Andreas Elihar[3], Umberto Follo[2], Sara Garbolino[2], Johan Hartman[4], Julia Herzen[7], Dominik John[7], Franz L. Klaus[7], Carolin Mogler[7], Lucio Pancheri[5], Julia Parnell[7,6], Mats Persson[6], Edoardo Posteraro[1,2], Martin Sjolin[3], Moa Y. Tamm[6], Sami Wirtensohn[7], On behalf of 1MICRON Collaboration

[1] Politecnico di Torino, Electronics and Telecommunications, Turin, Italy; [2] INFN Sezione Torino, Turin, Italy; [3] Prismatic Sensor, Stockholm, Sweden; [4] Karolinska Institutet, Stockholm, Sweden; [5] Università di Trento, Trento, Italy; [6] KTH Royal Institute of Technology, Stockholm, Sweden; [7] TUM, Munich, Germany

This study was carried out with support from the INFN CSN5 Call ARCADIA. This work was supported by the European Union's Horizon Europe research and innovation programme under the 1MICRON project – "New Technology for 1 MICRON Resolution Biomedical Imaging" (grant agreement No. 101186826).

Abstract

Monolithic silicon CMOS Sensors represent a considerable step forward in charged particle and photon sensing, and emerge as a promising embodiment for the design of novel deep-silicon photon-counting X-ray Computed Tomography scanners . This work presents the first characterization of the ARCADIA MD3 Fully-Depleted CMOS sensors, which technology is currently the baseline for the development of innovative sensors under the framework of the EIC Pathfinder Open 1MICRON project. We report on the characterisation results using an edge-on geometry and a focused synchrotron X-ray beam at the DESY test facility. The x-rays impinge on the edge of the sensor, increasing the active sensor depth seen by the photons, which consequently improves the quantum efficiency with respect to a face-on configuration. A 37 keV focused beam incident parallel to the sensor surface allowed scans along the two directions of the sensor edge, enabling the extraction of the active sensor thickness and mechanical tilt via pixel intensity profiles. Lateral scans across pixel boundaries revealed a periodicity of the spatial modulation of mean cluster size compatible with the pixel pitch of the matrix. Taking the cluster size as the main figure of merit, the performance of the sensor was evaluated at different thresholds and multiple bias voltages in order to assess the variation in the Coulomb cone and collection dynamic. The measurements are supported by Allpix Squared Monte Carlo framework, demonstrating good consistency between the simulated and the real domain.

References
[1] Da Rocha Rolo, Manuel 2025 'Arcadia fully depleted cmos maps development with lfoundry 110 nm cis', Frontiers in Sensors, vol. Volume 6 - 2025
[2] Bergamaschi, A., 2005, 'Edge on silicon microstrip detectors for medical imaging', Nuclear Instruments and Methods in Physics Research Section A: Accelerators, Spectrometers, Detectors and Associated Equipment, vol. 549, no. 1, pp. 199–204, Sep. 2005

N-LT-01-11

Gain suppression study on LGADs with different gain layer designs

(#2025)

Leo Cavazzini[1,2], Ashish Bisht[1], Maurizio Boscardin[1], Matteo Centis Vignali[1], Marcos Fernandez Garcia[3], Francesco Ficorella[1], Omar Hammad Alì[1], Veronika Kraus[4], Michael Moll[5], Giovanni Paternoster[1], Moritz Wiehe[5]

[1] Fondazione Bruno Kessler, Trento, Italy; [2] University of Trento, Department of Physics, Trento, Italy; [3] Instituto de Fisica de Cantabria, IFCA, Santander, Spain; [4] TU Wien, Faculty of Physics, Vienna, Austria; [5] CERN, Geneva, Switzerland

Abstract

High-energy physics experiments currently use Low Gain Avalanche Diodes (LGADs) as part of their time-of-flight layers to track particles, thanks to their unique temporal resolution and radiation hardness. With increasing deposited charge, the gain was observed to decrease. This gain suppression effect originates from the electrostatic field screening produced by the avalanche multiplication charge. This work investigates the resilience of the LGADs to the gain suppression by characterizing a set of detectors with different gain layer designs and thicknesses, using Transient Current Techniques.

References

[1] G. Pellegrini et al. “Technology developments and first measurements of Low Gain Avalanche Detectors (LGAD) for high energy physics applications”. In: Nucl. Instrum. Meth. A.765 (2014), pp. 12–16. DOI: https://www.doi.org/10.1016/j.nima.2014.06.008.

[2] N. Cartiglia et al. “Beam test results of a 16 ps timing system based on ultra-fast silicon detectors”. In: Nucl. Instrum. Meth. A.850 (2017), pp. 83–88. DOI: https://www.doi.org/10.1016/j.nima.2017.01.021.

[3] E. Curras et al. “Gain reduction mechanism observed in Low Gain Avalanche Diodes”. In: Nuclear Instruments and Methods in Physics Research Section A: Accelerators, Spectrometers, Detectors and Associated Equipment, 1031 (May 2022), p. 166530. ISSN: 0168-9002. DOI: http://www.doi.org/10.1016/j.nima.2022.166530.

[4] Sebastian Pape et al. “TCAD Simulation of Two Photon Absorption–Transient Current Technique Measurements on Silicon Detectors and LGADs”. In: Sensors 24.24 (2024). ISSN: 1424-8220. DOI: https://doi.org/10.3390/s24248032.

N-LT-01-12

Pulse-Shape-Based Slow-Rising Pulse Rejection for Reliable Charge-Carrier Transport Characterization in a Semiconductor Radiation Detector (#2231)

Jihwan Boo[1], Beomjun Park[2], Geehyun Kim[1,3]

[1] Seoul National University, Department of Energy Systems Engineering, Seoul, South Korea; [2] Seoul National University, Nuclear Research Institute for Future Technology and Policy (NIFTEP), Seoul, South Korea; [3] Seoul National University, Nuclear Engineering Department, Seoul, South Korea

This work was supported by the National Research Foundation of Korea (NRF) grant funded by the Korea government (Ministry of Science and ICT) (No. 2022M2D2A1A02063826).

Abstract

Mobility (μ), lifetime (τ), and mobility–lifetime product (μτ) are key metrics for semiconductor radiation detectors. Highly concentrated trapping centers or defects can distort the internal electric-field distribution, producing reduced-amplitude slow-rising charge-sensitive preamplifier pulses that degrade carrier-transit and charge-collection analyses. Although slow-rising-pulse rejection is commonly used to sharpen pulse-amplitude peaks and suppress low-amplitude tails, this work extends its use to charge-carrier transport characterization. A CdZnTeSe detector [1, 2] was characterized at room temperature under electron- and hole-transit-dominant conditions using ^{241}Am alpha irradiation. Pulse-shape analysis rejected slow-rising pulses for key metrics extraction. In electron-transit-dominant measurements, the fast-rising pulse events preserved the bias-dependent peak-centroid trend and yielded $(\mu\tau)_e$ = 5.7 × 10^{-4} cm²/V, μ_e = 576 cm²/V·s, and τ_e = 1.0 μs, consistent with reported values [3,4]. For hole-transit-dominant measurements, all-pulse events obscured the pulse-amplitude peak and hindered Hecht fitting. After rejection, we obtained $(\mu\tau)_h$ = 2.1 × 10^{-4} cm²/V, τ_h = 0.7 μs, comparable to reported values [5], with μ_h = 318 cm²/V·s. Using the rise-time peak as the representative transit time, both all-pulse and fast-rising-pulse events yielded similar μh values. However, when the median rise time of all-pulse events was used instead, drift velocity did not show a clear linear dependence on electric field, whereas fast-rising-pulse events retained linearity. This reflects the need for careful consideration of slow-rising components and the transit-time definition. These results show that slow-rising-pulse rejection enables reliable transport characterization beyond spectral improvement.

References

[1] Park, B., et al. 2022, 'Bandgap engineering of $Cd_{1-x}Zn_xTe_{1-y}Se_y$ (0< x< 0.27, 0< y< 0.026)', Nucl. Instrum. Methods Phys. Res. A. 1036, 166836.

[2] Park, B., et al. 2024 'Fabrication and Evaluation of Spectroscopic Grade Quasi-hemispherical CdZnTe Detector', J. Radiat. Prot. Res. 49(2), 85-90.

[3] Kleppinger, J.W., et al. 2021, 'Growth of $Cd_{0.9}Zn_{0.1}Te_{1-y}Se_y$ single crystals for room-temperature gamma ray detection, IEEE Trans. Nucl. Sci. 68(9), 2429-2434.

[4] Chaudhuri, S.K., et al. 2021, 'Quaternary semiconductor $Cd_{1-x}Zn_xTe_{1-y}Se_y$ for high-resolution, room-temperature gamma-ray detection', Crystals 11(7), 827.

[5] Pipek, J., et al. 2021, 'Charge transport and space-charge formation in $Cd_{1-x}Zn_xTe_{1-y}Se_y$ radiation detectors', Phys. Rev. Appl. 15(5) 054058.

N-LT-01-13

Diagnosing Mechanisms for Charged Particle Attenuation Enhancement in Nanostructured Materials (#1508)

Niko P. Speck[1], Gabrielle J. Grey[2], Drew A. Vecchio[1], Kathleen A. Cotterill[1], Alan I. Taub[2], Mark Hammig[1]

[1] University of Michigan, Nuclear Engineering and Radiological Sciences Department, Ann Arbor, USA; [2] University of Michigan, Materials Science and Engineering Department, Ann Arbor, USA

The authors acknowledge the financial support of the University of Michigan College of Engineering and technical support from the Michigan Center for Materials Characterization and Michigan Medicine Microscopy Core. Thank you to Tao Ma for guidance on operating the TFS Spectra 300 TEM and Megan Bennett for support on ultramicrotome sample preparation.

Abstract

This paper presents a methodology for measuring the trajectories of high-energy electrons through materials utilizing a transmission electron microscope (TEM). This novel technique is implemented to diagnose and quantify the mechanism for enhanced radiation attenuation via nanostructures. Rather than an imaging technique, the TEM is applied to radiation shielding measurements as an adaptable electron source with functionality for various beam energies, amperage, alignments, and exposure times alongside an array of precise electron detectors. By utilizing energy filtering and direct electron detection capabilities, scattering profiles are measured with minimal background contributions. This TEM method is leveraged to describe particle transport in nanostructures. Palladium nanoparticles at various monodisperse sizes are synthesized via heat injection and deposited into an epoxy matrix. The palladium epoxy nanocomposites are sectioned with an ultramicrotome to thicknesses of 70 to 1000 nm containing nanoparticle sizes of 5 to 50 nm at 20% of the total weight fraction. Scattering profile measurements at various beam energies are conducted with a variety of sample thicknesses, nanoparticle sizes, and composite fractions. Scattering profile measurements also include bulk, homogeneous palladium samples in contrast to nanomaterials composed of identical atomic percentages. Simulation of the experimental scattering profiles demonstrate an understanding for the phenomena behind nanostructured attenuation enhancement, bolstering advanced nuclear technology via a foundational description for particle transport in nanostructures.

References

[1] S. A. Thibeault, J. H. Kang, G. Sauti, C. Park, C. C. Fay, and G. C. King, “Nanomaterials for radiation shielding,” *MRS Bulletin*, vol. 40, no. 10, pp. 836--841, Oct. 2015, doi: 10.1557/mrs.2015.225.

[2] A. Rosh-Gorsky *et al.*, “3D Printing of Composite Radiation Shielding for Broad Spectrum Protection of Electronic Systems,” *Advanced Materials*, vol. 36, no. 33, p. e2403822, 2024, doi: 10.1002/adma.202403822.

[3] M. Steffens *et al.*, “Characterization of Novel Lightweight Radiation Shielding Materials for Space Applications,” *IEEE Transactions on Nuclear Science*, vol. 64, no. 8, pp. 2325--2332, Aug. 2017, doi: 10.1109/TNS.2017.2703312.

[4] A. Hamisu *et al.*, “The use of nanomaterial polymeric materials as ionizing radiation shields,” *Radiation Physics and Chemistry*, vol. 216, p. 111448, Mar. 2024, doi: 10.1016/j.radphyschem.2023.111448.

[5] P. Hosemann, E. Stergar, A. T. Nelson *et al.*, “Nanostructured Engineering Alloys for Nuclear Application,” *MRS Online Proceedings Library*, vol. 1298, pp. 217--226, 2011.

[6] V.-D. Le *et al.*, “X-ray and gamma-ray Sensing from Aqueous-Based Lead Sulfide Telluride Nanocomposites,” *Small*, vol. 21, 2025.

[7] A. Curtis *et al.*, “Micro-scale fusion in dense relativistic nanowire array plasmas,” *Nature Communications*, vol. 9, p. 1077, 2018, doi: 10.1038/s41467-018-03466-7.

N-LT-01-14

Monolithic integration of cooling microchannels in all-silicon ladders for vertex detectors (#1940)

Javier Fernández-Tejero[1], André Dias[1], Marta Duch[1], Roser Mas[1], Carlos Orero[2], Marcel Vos[2], Miguel Ullán[1]

[1] Centro Nacional de Microelectrónica (IMB-CNM, CSIC), Cerdanyola del Vallés, Spain; [2] Instituto de Física Corpuscular (IFIC, CSIC), Paterna, Spain

This work has received funding from the postdoctoral fellowships programme Beatriu de Pinós (Marie Skłodowska-Curie grant No 801370), and Spanish R&D grant PID2024-156645NB-C22 funded by MICIU/AEI/ 10.13039/501100011033 and by ERDF/EU.

Abstract

New generation of vertex detectors must have excellent thermo-mechanical stability, and all-silicon ladders are considered as promising solutions for future detectors. However, power consumption asymmetries between the active area and periphery can induce large temperature gradients, and in some cases a combination of air and liquid cooling will be required to achieve homogeneous thermal profiles. Microchannel cooling offers a competitive alternative to traditional cooling systems. The short thermal path between the heat load and sink gives an increased thermal evacuation performance, combined with the reduced material needed for the integrated microchannels and the reduced Coefficient of Thermal Expansion mismatch between the cooling and sensor materials to obtain an optimized cooling for radiation detectors. The development of the technology needed for the integration of the sensor with the microchannels in a single piece is an ambitious challenge, as the conditions for the microchannel formation must be compatible with the sensor, requiring the optimization of the fabrication to ensure the compatibility with CMOS processes. As a demonstrator, all-silicon ladder prototypes with integrated cooling microchannels are presented. Power consumptions for the active area and periphery of the ladders are emulated using integrated aluminum heaters. The bulk in the active area is thinned from 600 to 50 microns, and the design of the microchannels cooling circuit, integrated in the periphery of the ladder, is optimized using finite-element simulation packages. Variations of prototype ladders with different sizes, microchannel dimensions, and integrated using different wafer bonding techniques are fabricated and evaluated in detail in this work.

References

[1] de Aguiar Francisco OA, Buytaert J, Collins P, et al., 'Evaporative CO_2 microchannel cooling for the LHCb VELO pixel upgrade', *Journal of Instrumentation*, 10 (2015) C05014

[2] Andricek L, Boronat M, Fuster F, et al., 'Integrated cooling channels in position-sensitive silicon detectors', *Journal of Instrumentation*, 11 (2016) P06018

[3] Vos M, 'Micro-channel cooling in high energy physics', *Proceedings of science*, 287 (2016) 037

[4] Flaschel N, Ariza D, Díez S, et al., 'Thermal and hydrodynamic studies for micro-channel cooling for large area silicon sensors in high energy physics experiments', *Nuclear Instruments and Methods A*, 863 (2017) 26-34

[5] Ullán M, Correa J, Dauderys V, et al., 'Development of silicon interposers with embedded microchannels and metal re-distribution layer for the integration of hybrid detector systems', *Nuclear Instruments and Methods A*, 1065 (2024) 169490

Time:
9 November, 2026
12:30 – 13:00

Room:
ALBÉNIZ & MACHUCA

N-LT-02 | NSS Lightning Talks 2

N-LT-02-01

Ultra High-Rate Neutron Detection with ^{3}He Tubes via CF_4 Prompt Scintillation Readout (#3034)

Luis M. Margato[1,2], Andrey Morozov[1,2], Vladimir Solovov[1], Bruno Guérard[3], Julien Marchal[3]

[1] LIP-Coimbra, Coimbra, Portugal; [2] University of Coimbra, Dep. of Physics, Coimbra, Portugal; [3] ILL-Institut Laue-Langevin, Grenoble, France

This work was supported by the Portuguese national funds OE and Foundation for Science and Technology within the project Ref. 2023.15652.PEX (https://doi.org/10.54499/2023.15652.PEX). L. Margato acknowledges FCT-Portugal support through contract CEECINST/00106/2018/CP1494/CT0001.

Abstract

This work presents a novel neutron detector concept aiming to provide detection efficiency and background levels equivalent to conventional ^{3}He-based detectors, whilst boosting the maximum counting rate by several orders of magnitude. The detector retains the form-factor of a standard ^{3}He tube and uses the same working gas mixture of ^{3}He with admixture of CF_4 as the stopping gas. The key innovation is a fast optical readout of CF_4 prompt scintillation light using silicon photomultiplier (SiPM) sensors. The target performance is a detection efficiency equivalent to that of a standard ^{3}He tube under identical gas filling conditions, gamma sensitivity below 10^{-6}, and a maximum counting rate of 2 MHz/pixel, orders of magnitude improvement over existing detectors. The fast emission of CF_4 scintillation light is the enabling factor for achieving ultra-high counting rates. CF_4 exhibits a considerable photon yield, with one scintillation band in the UV and another in the visible region of the spectrum, with several thousands of photons emitted per neutron event. The efficient collection of light by the SiPMs constitutes a critical design parameter, addressed in this study through Monte Carlo optimization. The gas mixture composition is optimised to maximise the scintillation yield, and a gas purification system can be integrated into the detector to ensure long-term stability. The first experimental results of a detector prototype characterisation on a neutron beamline at the Institut Laue-Langevin (ILL) will be presented.

References

[1] Morozov, A, et al., “Photon yield for ultraviolet and visible emission from CF4 excited with α-particles”, Nuclear Instruments and Methods in Physics Research Section B: Beam Interactions with Materials and Atoms, vol. 268, no. 9, pp. 1456–1459, May 2010

[2] Morozov, A, et al., “Effect of the electric field on the primary scintillation from CF4”, Nuclear Instruments and Methods in Physics Research A 628 (2011) 360

[3] Morozov, A, Margato, L, Canezin, G, and Gonzalez, J, “Ants3 toolkit: Front-end for Geant4 with interactive GUI and Python scripting”, Computer Physics Communications, vol. 318, p. 109869, Jan. 2026

[4] Margato, L, et al., “Effect of the gas contamination on CF4 primary and secondary scintillation”, Nuclear Instruments and Methods in Physics Research A 695 (2012) 425

N-LT-02-02

Characterization of 3D ultra-thin silicon-based thermal neutron detectors (#3088)

Felipe Zamorano, Iván Lopez, Martín Pérez, Javier Bravo, Celeste Fleta, Consuelo Guardiola

Institute of Microelectronics of Barcelona, Barcelona, Spain

This project has received funding from the Consejo de Seguridad Nuclear (CSN) under the project Subvenciones 2022 SUB-08.

Abstract

Neutron contamination in advanced radiotherapy and other mixed radiation environments has become an increasing concern due to the limitations of conventional neutron detectors under intense gamma background conditions. In this work, ultra-thin 3D silicon neutron detectors specifically designed for operation in mixed radiation fields were experimentally characterized under thermal and high-energy irradiation conditions. The detectors, consisting of 20 µm-thick silicon sensors paired with ^{6}LiF neutron conversion layers, were tested at the FANT thermal neutron facility and at the CERN High-Energy Reference Field (CERF). Measurements included reproducibility, angular dependence, bias voltage operation, and discrimination threshold effects using a low-voltage FPGA-based readout system. The results showed stable operation under mixed radiation fields, moderate angular dependence, and strong dependence of the response on detector bias and discrimination threshold. The ultra-thin detector architecture enabled high gamma rejection capability, enabling reliable neutron detection under intense photon background conditions. These results demonstrate the suitability of 3D ultra-thin silicon detectors for compact real-time neutron monitoring in radiation protection and medical applications.

References

[1] *Zorloni G. et al. "Joint EURADOS WG9-WG11 rem-counter intercomparison in a Mevion S250i proton therapy facility with Hyperscan pulsed synchrocyclotron" Phys. Med. Biol. (2022).*

[2] *Guardiola C. et al. "Neutron measurements with ultra-thin 3D silicon sensors in a radiotherapy treatment room using a Siemens PRIMUS linac" Phys. Med. Biol. (2013).*

[3] *Zamorano F. et al. "Out-of-field thermal neutron characterization with thin 3D-silicon detectors in Varian TrueBeam and Elekta Synergy LINACs" Phys. Med. Biol. (2025).*

[4] *Pozzi F. et al.* "The CERN-EU high-energy Reference Field (CERF) facility: New FLUKA reference values of spectral fluences, present and newly proposed operational quantities" *NIMA (2020).*

N-LT-02-03

Scintillator Size Effects in Fiber-Based Neutron Detectors With Pulse-Shape Discrimination for BNCT (#2328)

Hong-Da Liu[1,2], **Hong-Da Liu**[1,2], Chun-Yen Chang[1], Chun-Yen Chang[1], Yi-Hsiang You[1], Yi-Hsiang You[1], Ya-Chen Chang[1], Ya-Chen Chang[1], Zhen-Fan You[2], Zhen-Fan You[2], Tzu-Hsiang Lin[1], Tzu-Hsiang Lin[1], Ming-Wei Lin[1], Ming-Wei Lin[1]

[1] National Tsing Hua University, Institute of Nuclear Engineering and Science, Hsinchu, Taiwan; [2] Heron Neutron Medical Corporation, Nuclear Science Department, Zhubei, Taiwan

This work was primarily supported by Heron Neutron Medical Corporation and the Industry–Academia Cooperative Ph.D. Project of the Ministry of Education in Taiwan. Partial financial support was also provided by the Institute of Nuclear Engineering and Science at National Tsing Hua University.

Abstract

Scintillator-on-fiber (SOF) detectors utilizing Liglass scintillators show strong potential for neutron flux monitoring in intense radiation environments due to their high radiation hardness and fast response. Previous studies have typically employed fragmented scintillators in SOF detectors due to the difficulty of μm-scale machining. In this work, Li-glass scintillators with well-defined dimensions (1×1×0.5 to 0.25×0.25×0.5 mm^3) were precisely fabricated using laser cutting, enabling a systematic investigation of the effect of scintillator size on neutron response linearity in an acceleratordriven neutron beam. With pulse-shape discrimination (PSD), the results show that neutron signals measured with scintillator sizes larger than 0.5×0.5×0.5 mm^3 become blurred in the P_{SP}-channel scatter plot due to gamma-ray contributions and pulse pile-up at an accelerator current of 250 μA. In contrast, the smallest scintillator (0.25×0.25×0.5 mm^3) maintains clear separation between neutron and gamma-ray signals. Analysis of the maximum shift error σ_m of the neutron peak centroid further indicates that this smallest scintillator effectively suppresses pileup, achieving $\sigma_m = 0$. In terms of linearity, scintillators with sizes below 0.75×0.75×0.5 mm^3 yield coefficients of determination $R^2 > 0.99$ when processed using a two-dimensional fiducial cut, satisfying the requirements for neutron flux monitoring in boron neutron capture therapy (BNCT). These results demonstrate the feasibility of optimizing Li-glass scintillator size and volume in SOF detectors to achieve reliable neutron flux monitoring in BNCT applications.

N-LT-02-04

Time-Resolved Imaging of Radioactive Gas with the 4π Gamma-Ray Imager C3G (#1185)

Yoshiharu Kitayama[1], Hiromi Nakai[1], Kazuyuki Enomoto[3], Naoto Yamada[3], Keitaro Hitomi[2], Mitsuhiro Nogami[2], Naoki Kawachi[3,1]

[1] Fukushima Institute for Research, Education and Innovation, Plant Imaging research Unit, Fukushima, Japan; [2] Tohoku University, Sendai, Japan; [3] National Institutes for Quantum Science and Technology, Takasaki, Japan

This work was supported by JSPS KAKENHI Grant Number 26K03212. The authors thank the members of the Radiotracer Imaging Project, QST, for their valuable support during the experiment.

Abstract

The Coded Cube Camera for Gamma-ray (C3G) is a 4π gamma-ray imager designed to estimate gamma-ray source distributions from direction-dependent detector response patterns. In this study, we developed a 24-detector C3G consisting of 24 HR-GAGG scintillators and applied it to a plant radioisotope (RI) imaging experiment using $^{11}CO_2$ gas. In the plant RI imaging experiment, approximately 300 MBq of $^{11}CO_2$ gas was supplied to a plant placed in an experimental chamber to image the transport of ^{11}C-labeled photosynthates within the plant. During this experiment, the C3G was placed outside the chamber, and the dynamics of $^{11}CO_2$ gas were continuously measured with an acquisition time of 1 s per measurement. As a result, the inflow of the gas into the chamber was clearly visualized. In addition, the reconstructed image intensity decreased exponentially over time. The half-life estimated from this intensity change was 20.70 min, which was in good agreement with the known half-life of ^{11}C, 20.34 min. These results demonstrate that the 24-detector C3G can visualize dynamic gaseous radioactive sources and estimate temporal changes in radioactivity from reconstructed image intensity. This capability is expected to be useful for applications such as radioactive gas leakage monitoring, environmental monitoring, and nuclear security.

N-LT-02-05

Method for determining lithium ore's grade based on photoneutrons' lifetime measurement (#1637)

Minfeng Yu[1,2], Yigang Yang[1,2]

[1] Tsinghua University, Department of Engineering Physics, Beijing, China; [2] Tsinghua University, Key Laboratory of Particle & Radiation Imaging, Beijing, China

This research was supported by the Natural Science Foundation of Beijing, China (Grant No. L252023).

Abstract

Analysis of lithium ore grade is industrially significant for efficient lithium resource development and utilization, enabling improved production efficiency and reduced costs. Lithium has a large neutron absorption cross-section, and changes in lithium grade can affect the neutron lifetime, which is inversely proportional to the macroscopic absorption cross-section of ore. In this paper, a method for determining lithium grade through neutron lifetime measurements based on an e-LINAC driven photoneutron source is applied to the online analysis of lithium ore grade. Since lithium does not emit gamma rays upon neutron absorption, the neutron lifetime is measured from the time distribution of capture gamma rays induced by neutrons in the matrix elements of the medium. The feasibility of this approach has been demonstrated in experiments using various lithium nitrate solutions as simplified media. Meanwhile, the effect of neutron diffusion was investigated by simulations. The potential of neutron-induced prompt gamma analysis for reducing interference caused by variations in matrix composition is discussed. Further simulation studies and system design are in progress.

References

[1] X. Zeng et al., “Commercialization of Lithium Battery Technologies for Electric Vehicles,” Advanced Energy Materials, vol. 9, no. 27, p. 1900161, Jun. 2019, doi: https://doi.org/10.1002/aenm.201900161.

[2] N Eswara Prasad, Amol Gokhale, and R J H Wanhill, Aluminum-Lithium Alloys : Processing, Properties, and Applications. Amsterdam: Elsevier Science, 2014. pp. 503–535.

[3] Dou L R, Liu H Q, Chang D K, et al. Challenges and countermeasures for lithium resources in China and analysis of global distribution and industry status. Bulletin of Chinese Academy of Sciences, 2025, 40(3): 494-510, doi: 10.16418/j.issn.1000-3045.20240326001.

[4] M. G. Aylmore et al., “Assessment of a spodumene ore by advanced analytical and mass spectrometry techniques to determine its amenability to processing for the extraction of lithium,” Minerals Engineering, vol. 119, pp. 137–148, Apr. 2018, doi: https://doi.org/10.1016/j.mineng.2018.01.010.

[5] C. Korbel et al., “Quantification of lithium using handheld instruments: application of LIBS and XRF spectroscopy to assay the lithium content of mineral processing products,” Journal of Analytical Atomic Spectrometry, vol. 39, no. 7, pp. 1838–1853, 2024, doi: https://doi.org/10.1039/d3ja00423f.

[6] Y. Liu, Y.-G. Yang, Y. Tai, and Z. Zhang, “A capture-gated fast neutron detection method,” Chinese Physics C, vol. 40, no. 7, p. 076201, Jun. 2016, doi: https://doi.org/10.1088/1674-1137/40/7/076201.

[7] J. S. Wahl, W. B. Nelligan, A. H. Frentrop, C. W. Johnstone, and R. J. Schwartz, “The Thermal Neutron Decay Time Log,” Society of Petroleum Engineers Journal, vol. 10, no. 04, pp. 365–379, Dec. 1970, doi: https://doi.org/10.2118/2252-PA.

[8] M. Yu, Y. Yang, C. Zong, and S. Ming, “Analysis of gadolinium concentration in solutions based on photoneutrons’ lifetime measurement,” Nuclear Instruments and Methods in Physics Research Section A Accelerators Spectrometers Detectors and Associated Equipment, vol. 1079, pp. 170661–170661, May 2025, doi: https://doi.org/10.1016/j.nima.2025.170661

N-LT-02-06

Template-Matching Position Solving on FPGAs for a Thermal Neutron Detector (#1591)

Matthew Loyd

Oak Ridge National Lab, Oak Ridge, USA

Notice: This summary has been authored by UT-Battelle, LLC, under contract DE-AC05-00OR22725 with the US Department of Energy (DOE).The US government retains and the publisher, by accepting the article for publi cation, acknowledges that the US government retains a nonexclusive,paid-up, irrevocable, worldwide license to publish or reproduce the published form of this manuscript, or allow others to do so, for US government purposes.DOE will provide public access to these results of federally sponsored research in accordance with the DOE Public Access Plan. This work was sponsored by the U.S. Department of Energy (DOE) Office of Science Early Career Research Program Award (KC0406021) under Contract No. DE-AC05-00OR22725

Abstract

Silicon photomultiplier (SiPM) based thermal neutron detectors have been developed at Oak Ridge National Laboratory for single crystal diffraction instruments. They have potential as good replacements for current 3He detectors on neutron reflectometers due to their high spatial resolution and fast scintillator decay time. The current software-implemented position fitting on these detectors is limited due to the processing required for the recursive least-squares algorithm. In this work, we present a fast method for determining neutron position that can be run on the Field-Programmable Gate Array (FPGA) chip that is already installed on the detector. This method compares the collected event data with pre-determined shapes stored on FPGA memory in parallel, and determines the one with the least linear error. Using this method for neutron positioning takes less time than the hardware defined dead time. Count-rate and spatial resolution results collected at the High-Flux Isotope Reactor are presented, with output count rates > 500 kcps achieved, an order of magnitude greater than the software fitting method.

N-LT-02-07

Localization of uranium samples in large cemented nuclear waste using active photon interrogation and a Bayesian inversion (#1492)

Malo Lebreton[1], **Malo Lebreton**[1], Benoit Geslot[1], Benoit Geslot[1], Cédric Carasco[1], Cédric Carasco[1], Bertrand Pérot[1], Bertrand Pérot[1], Claire Michelet[2], Claire Michelet[2]

[1] Commissariat à l'énergie atomique et aux énergies alternatives, CEA/DES/IRESNE, St Paul Lez Durance, France; [2] Université de Bordeaux, CNRS-IN2P3/LP2IB, Bordeaux, France

Abstract

CEA Cadarache currently manages over 6,000 historical 870 L nuclear waste packages. To ensure long-term safety, French regulatory authorities require a precise characterization of each unit, specifically regarding structural integrity, fissile material mass and total activity of alpha emitters. However, the high density and volume of 870 L concrete waste packages result in significant signal attenuation, making standard passive gamma spectrometry or passive and active neutron measurements inefficient to assess the mass of nuclear materials. To maximize the signal-to-noise ratio, a specific Active Photon Interrogation (API) approach is developed inside the CINPHONIE irradiation bunker of CHICADE facility, at CEA IRESNE, Cadarache, France. This method makes use of inorganic BGO scintillators to measure high-energy delayed gamma rays from short-lived photofission products induced with a high-energy bremsstrahlung photon source, i.e., a 18 MeV LINAC. A Bayesian framework is applied to infer both the mass and the position of nuclear materials from angular acquisitions. This article is focused on testing API

framework in the case where the source of the signal is located in a homogeneous environment. Based on the promising results presented here, future developments will focus on the heterogenous case.

References
[1] M. Lebreton *et al.*, "Photon flux characterization of a new electron LINAC in the CINPHONIE irradiation facility through a Bayesian framework," *IEEE Trans. Nucl. Sci.*, pp. 1–1, 2026, doi: 10.1109/TNS.2026.3653194.
[2] M. Delarue *et al.*, "Localization of nuclear materials in large concrete radioactive waste packages using photofission delayed gamma rays," *EPJ Web Conf.*, vol. 253, p. 08003, 2021, doi: 10.1051/epjconf/202125308003.
[3] C. Carasco *et al.*, "Photofission delayed gamma-ray measurements in a large cemented radioactive waste drum during LINAC irradiation," *Nucl. Instrum. Methods Phys. Res. Sect. Accel. Spectrometers Detect. Assoc. Equip.*, vol. 1053, p. 168360, Aug. 2023, doi: 10.1016/j.nima.2023.168360.
[4] C. Carasco, "A Bayesian approach for measuring nuclear material in radioactive waste using photofission," *Nucl. Instrum. Methods Phys. Res. Sect. Accel. Spectrometers Detect. Assoc. Equip.*, vol. 1057, p. 168728, Dec. 2023, doi: 10.1016/j.nima.2023.168728.
[5] "Home," FASTER. Accessed: Jan. 22, 2026. [Online]. Available: https://faster.in2p3.fr/

N-LT-02-08

Hybrid Temperature Compensation and Radiation Damage Recovery with Scintillation Detectors (#2243)

Dae yang Oh[1,2], Junseong Hwang[1,2], Geon Kim[1,2], Chanho Kim[3], Jung-Yeol Yeom[1,4]

[1] Korea University, Department of Bioengineering, Seoul, South Korea; [2] Korea University, Interdisciplinary Program in Precision Public Health, Seoul, South Korea; [3] Korea Atomic Energy Research Institute, Daejeon, South Korea; [4] Korea University, School of Biomedical Engineering, Seoul, South Korea

Abstract

Gamma-ray spectroscopy is a fundamental technique for identifying radioisotopes in safety-critical applications. However, in scenarios such as nuclear accidents, high-temperature and high-radiation environments severely degrade photomultiplier tube performance. Conventional temperature compensation systems face physical voltage limits, and prior deep-learning algorithms fail because they require preserved spectral shapes. To overcome these limitations, this study presents a comprehensive strategy to enhance detector stability. First, an active high-voltage control system mitigates initial temperature-induced gain loss. Because this hardware compensation eventually reaches its physical safety limits, the system integrates a deep learning (DL) technique – bidirectional long short-term memory network – to interpret residual spectral distortions, successfully achieving accurate multi-isotope quantification up to 185 °C. Second, to address radiation-induced damage localized within the photomultiplier tube, a targeted active thermal annealing protocol was applied. Following a 1.55 kGy cumulative gamma irradiation, detector output dropped to 23.5% of its baseline. Subsequent thermal annealing of the photomultiplier tube body at 145 °C successfully restored the output to 89.4%. Ultimately, this integration of hardware, software, and active recovery lays a foundation for robust radionuclide identification under concurrent high-temperature and high-radiation constraints.

References
[1] Park, M., Kim, C., Hwang, J., Yeom, J.-Y. 2026, 'Deep learning-based radioisotope quantification for extreme environments', *Radiation Physics and Chemistry*, 239, 113345, Amsterdam: Elsevier Ltd.
[2] Kim, C., Kim, D., Lee, Y., Park, C., Ullah, M. N., Kim, D., Kwon, I., Hur, S., Yeom, J.-Y. 2021, 'Radiation resistance and temperature dependence of Ce:GPS scintillation crystal', *Radiation Physics and Chemistry*, 183, 109396, Amsterdam: Elsevier Ltd.

N-LT-02-09

Simulations of A Novel Time-of-Flight β/γ Transmission Tomography Scanner (#2255)

Robert Carmichael[1,2], **Robert Carmichael**[1,2], Arion Chatziioannou[1,2], Arion Chatziioannou[1,2]

[1] University of California Los Angeles, Department of Molecular and Medical Pharmacology, Los Angeles, USA; [2] University of California Los Angeles, Crump Institute for Molecular Imaging, Los Angeles, USA

Abstract

Large cargo scanning presents a unique challenge for national security. Container size limitations pose challenges to tomographic imaging. This work proposes a new stationary, limited angle tomographic transmission scanner geometry with a unique β/γ source utilizing a pair of fixed flat panel detectors, known as Gamma Tomography (GT). A Gate 10 simulation evaluates the imaging capabilities of the scanner and explores time-of-flight (TOF) and energy discrimination as electronic collimation methods to reduce scattered radiation and improve image quality. A 600 μm thin plastic scintillator sheet encasing 100mCi of ^{60}Co as a near detector locally captures nearly all emitted β particles without significant γ interactions, while a far detector panel of 2 cm thick LYSO crystals captures the ~1.25 MeV energy ^{60}Co γ photons. Both panels were simulated as 50x80 cm with a thin, 2 cm thick, multi-material test object consisting of water, aluminum, titanium, steel, and uranium in the center of the field of view. The same simulation dataset was reconstructed with/without two separate electronic collimation schemes: valid coincidences with a 100 keV energy window around the ^{60}Co photopeaks, and valid coincidences with a 100 ps time resolution. Despite the short acquisition time (18sec), reconstructed images are low noise, with all objects visible above background and distinguishable. The images show attenuation coefficient under-estimation, due to object scatter. TOF and energy discrimination underestimate μ values by 25.8% and 34.3% respectively, but a large dynamic range and very high SNR in μ value is achieved for all reconstructions (SNR-water: 46, SNR-Uranium: 1369). Using time information in lieu of energy allows events scattered in the detector to be used to improve image quality and SNR, but further investigation will include achievable time resolution, panel construction, and source geometry optimization.

N-LT-02-10

Revealing Disorder Faster: Detector Upgrades for SANDALS-II (#2826)

Sarah E. Mann, **Sarah E. Mann**, Nigel J. Rhodes, Nigel J. Rhodes, Erik M. Schooneveld, Erik M. Schooneveld, Giacomo Mauri, Giacomo Mauri, Jack Day, Jack Day, Oliver L.G. Alderman, Oliver L.G. Alderman, Terri-Louise Hughes, Terri-Louise Hughes, Daniel T. Bowron, Daniel T. Bowron, G. Jeff Sykora, G. Jeff Sykora

STFC, ISIS, Harwell Campus, UK

Abstract

SANDALS-II is an instrument being developed at the ISIS Neutron and Muon Source as a next generation diffractometer for the study of amorphous and liquid materials. This upgrade will deliver count rates up to 11 times higher than the existing SANDALS instrument and will significantly expand its scientific capabilities. This work focuses on developments of a large area scintillator detector that are essential for achieving enhanced performance. Scintillation detectors for SANDALS-II will cover a solid angle of 0.67Ω, 2.4 times greater detector coverage than the current instrument. These detectors are required to have high efficiency, particularly at higher neutron energies (short wavelengths), which is achieved using a unique design employing tiles made from alternating layers of glass and scintillator. Scintillator and glass options are explored to optimise detector and instrument performance. Different low Li and B content glasses were tested to determine the most suitable option for the instrument that provides good neutron transmission while maintaining affordability. The ratio of ZnS:Ag to ^{6}LiF in the scintillator will be altered from 4:1 to 2:1 to enhance neutron absorption and therefore detection efficiency. At 30eV (0.05Å) this offers a 60% improvement in detection efficiency. The applicability of low-afterglow scintillator, ZnO:Zn/^{6}LiF, for use in SANDALS-II is also explored. ZnO:Zn/^{6}LiF is shown to offer a 2x increase in count rate capability over ZnS:Ag/^{6}LiF, but a 6% lower neutron detection efficiency. As the reduction in efficiency using ZnO:Zn/^{6}LiF is modest, this alternative scintillator offers a viable solution for the high count rate regions of SANDALS-II. With optimised glass and scintillator selection, the performance required for the upgraded instrument can be delivered. This will enable faster measurements, smaller sample studies, and time resolved experiments, making SANDALS-II a world leading disordered material neutron diffractometer.

N-LT-02-11

Characterization and Radiation Damage Mitigation of Silicon Photomultipliers for Low Earth Orbit Applications (#1902)

Shideh Davarpanah, On behalf of NUSES Collaboration

Université de Genève, Département de physique nucléaire et corpusculaire, Genève, Switzerland

Abstract

Silicon photomultipliers (SiPMs) are attractive photosensors for space applications because of their compact size, low cost, low operating voltage, high photon detection efficiency (PDE), and single-photon sensitivity. Their use in space applications, however, is limited by radiation-induced increases in dark count rate (DCR). This work presents the characterization and radiation tolerance study of FBK NUV-HD-MT SiPMs for the focal plane of the Terzina Cherenkov telescope onboard the NUSES mission, which will operate in a Sun-synchronous low Earth orbit (LEO) at an altitude of approximately 550 km. Devices with micro-cell sizes ranging from 25 to 50 μm were evaluated through a comprehensive characterization campaign comprising static (current-voltage), dynamic (noise and pulse-shape), and optical (photon detection efficiency) measurements to identify the sensor configuration best suited for this application. The 30 μm bare sensors were selected as the optimal solution, achieving a PDE greater than 50% at 400 nm, optical cross-talk below 2%, and a DCR below 60 kHz/mm^2 at 10 V overvoltage. The radiation environment was modeled using SPENVIS, and dose deposition in the focal plane was evaluated with Geant4 simulations. In parallel, radiation effects were investigated experimentally through two irradiation campaigns: a 50 MeV proton beam test and electron exposure using a Sr-90 source. Proton-induced damage produced a significant increase in leakage current and DCR, while electron-induced degradation was substantially smaller. Temperature-dependent measurements were used to extrapolate in-orbit performance and to evaluate recovery through thermal annealing. The results indicate that performing periodic annealing cycles at temperatures above 50°C can reduce the radiation-induced current by up to 40% after approximately 84 hours, helping preserve detector performance over the three-year mission.

References
[1] NUSES Collaboration, “The NUSES space mission,” PoS TAUP2023, p. 121, 2024.
[2] NUSES collaboration, The NUSES space mission, J. Phys. Conf. Ser. 2429 (2023) 012007.
[3] L. Burmistrov, “Terzina on board NUSES: A pathfinder for EAS Cherenkov light detection from space,” EPJ Web Conf., vol. 283, p. 06006, 2023.
[4] L. Burmistrova, S. Davarpanah, M. Heller, T. Montaruli, C. Trimarelli, R. Aloisio, et al., “Performance and radiation damage mitigation strategy for silicon photomultipliers on LEO space missions,” J. Cosmol. Astropart. Phys., vol. 2025, no. 07, p. 073, Jul. 2025.
[5] T. Montaruli and A. Nagai, “Properties of large SiPM at room temperature,” Nucl. Instrum. Methods Phys. Res. A, vol. 985, p. 164609, 2021.
[6] A. Nagai, C. Alispach, D. Della Volpe, M. Heller, T. Montaruli, S. Njoh, et al., “SiPM behaviour under continuous light,” JINST, vol. 14, p. P12016, 2019.
[7] Spenvis: The space environment information system, 2022.
[8] Geant4: Toolkit for the simulation of the passage of particles through matter. its areas of application include high energy, nuclear and accelerator physics, as well as studies in medical and space science, 2019.
[9] J. Swakon, P. Olko, D. Adamczyk, T. Cywicka-Jakiel, J. Dabrowska, B. Dulny et al., Facility for proton radiotherapy of eye cancer at ifj pan in krakow, Radiation Measurements 45 (2010) 1469.

N-LT-02-12

Graphene Photodetectors for Vacuum-UV Through Visible Wavelengths (#3124)

Alec Lindman[1], Marcos Turqueti[1], Lisa Schlueter[1], Gabriela R. Araujo[2]

[1] Lawrence Berkeley National Laboratory, Berkeley, USA; [2] University of Zurich, Zurich, Switzerland

This work was supported by the U.S. Department of Energy through the Laboratory Directed Research and Development program.

Abstract
Many experiments rely on measuring vacuum-ultraviolet light, which is emitted in situations as diverse as scintillation in cryogenic liquid noble gases (126.8 nm in argon) and laser spectroscopy of atomic hydrogen isotopes (121.6 nm). Graphene-monolayer photodetectors offer several attractive traits: they are naturally thin, sensitive to a broad range of wavelengths, relatively simple to fabricate (including with integrated readout circuitry with the same process), and can be made on flexible substrates. We present measurements with visible and UV light down to 115 nm, including at low intensity and with fast pulses, of graphene field-effect transistors (GFETs) of various sizes up to 2 mm square fabricated on silicon. These detectors show promise for experiments from neutrinoless double beta decay searches to absolute neutrino mass measurements, as well as dark-matter searches or other VUV-detection applications.

N-LT-02-13

FPGA-Based Real-Time SiPM Emulator with Sub-Nanosecond Temporal Quantization (#1987)

Andrea Abba[1], Stefano Carsi[1], Francesco Caponio[1], Edoardo Proserpio[1,2], Valentina Arosio[1]

[1] Nuclear Instruments SRL, Lambrugo, Italy; [2] Università dell'Insubria, Como, Italy

Abstract
This work presents a real-time FPGA-based Silicon Photomultiplier (SiPM) detector emulator capable of reproducing physically accurate detector waveforms at 16-bit resolution and 2.5 GS/s analog output rate. The proposed architecture combines microscopic event simulation with a temporally quantized event-streaming model, enabling real-time waveform synthesis directly inside FPGA logic while drastically reducing bandwidth requirements compared to traditional waveform streaming approaches. The emulator separates event generation from signal shaping: software layers generate timestamped photon-hit sequences derived either from analytical distributions, Geant4 simulations, or SimSiPM microscopic detector models, while the FPGA reconstructs the analog waveform through parallel Infinite Impulse Response (IIR) filter banks implementing the SiPM transfer function; a look-ahead recursive transformation enables II = 1 operation across all banks at 156.25 MHz, consuming approximately 235 DSP48E2 slices. A multi-phase temporal quantization architecture provides 0.8 ns effective timing precision using a 156.25 MHz fabric clock and eight temporal sub-phases. Experimental validation demonstrates excellent agreement between hardware-generated waveforms and analytical as well as SimSiPM-generated references, including pile-up scenarios with overlapping scintillation events reproduced through linear superposition. The prototype operates with an end-to-end latency of approximately 83 ns.

N-LT-02-14

Self-Powered Wireless Communication via Ambient Gamma-Ray Harvesting at Fukushima Daiichi (#2629)

Takeshi Fujiwara[1], Yasushi Shoji[1], Hiromi Kimura[1], Shunichiro Mae[2], Hiroshi Yoshimochi[2], Kohei Kawasaki[2], Hiroshi Kawamura[2], Katsuki Miyako[2]

[1] National Institute of Advanced Industrial Science and Technology (AIST), Tskuba, Japan; [2] Chiyoda Technol Corporation, Tokyo, Japan

Abstract

Reliable long-term monitoring in nuclear decommissioning facilities is hampered by the absence of permanent power infrastructure and by the radiation fields that degrade conventional electronics. We present a scintillator-photovoltaic converter that captures ambient gamma radiation and transforms it into electrical energy sufficient for periodic wireless data transmission. The converter pairs a 750 cm³ CsI(Tl) crystal with a compact GaInP photovoltaic array mounted on a single end face, following a "large absorber, minimal semiconductor" strategy.) On-site evaluation inside a contaminated-material storage building at the Fukushima Daiichi Nuclear Power Plant (~35 mSv/h) produced 273 nW per module. Two parallel modules, combined with ultra-low-power energy management and a sub-GHz radio, achieved seven autonomous transmission bursts totaling 32 packets over a 30 m link during a three-hour observation window—without any external power supply or dedicated radioactive source.

References

[1] IAEA, *Monitoring and Surveillance of Radioactive Waste Disposal Facilities*, Safety Reports Series No. 84, 2014.

[2] Fujiwara, Takeshi, et al. "Demonstration of self-powered wireless transmission using a gamma-ray battery in a nuclear decommissioning environment." *Available at SSRN 6191942*.

N-LT-02-15

Basic Development of a Wide-Field EUV Polarimeter for High-Energy Transient Sources (#3164)

Soken Kuwabara[1], Shuichi Gunji[2], Komei Chiba[1], Akira Takahashi[1], Mamoru Kitaura[2], Eiken Nakamura[3]

[1] Yamagata University, Graduate School of Science and Engineering, Yamagata, Japan; [2] Yamagata University, Faculty of Science, Yamagata, Japan; [3] Institute for Molecular Science, UVSOR Synchrotron Facility / Beamline Technical Staff, Aichi, Japan

The authors would like to thank the UVSOR staff for their technical support during the synchrotron radiation experiments. Portions of the manuscript preparation were assisted by a cloud-based AI language model.

Abstract

Polarization observations in extreme ultraviolet (EUV) band have not yet been achieved because it remains technically difficult to develop wide-field EUV detectors with sufficient sensitivity. However, EUV polarization measurements are expected to provide important insights into the emission mechanisms of gamma-ray bursts (GRBs) and ultraviolet flashes associated with supernova explosions. In this study, we propose a novel EUV polarimeter based on Lobster-Eye Optics (LEO), which combines a wide field of view with polarization sensitivity. Optical simulations show that EUV reflectivity on metal surfaces strongly depends on polarization. For example, at 40 eV and an incident angle of 75° on a gold-coated mirror, the reflectivity is about 40% for p-polarization and 60% for s-polarization, respectively. This difference produces an asymmetric cross-shaped image on the focal plane detector depending on the polarization direction. To verify this principle, we developed a test chamber and conducted a synchrotron radiation experiment using a gold-coated mirror and a microchannel plate (MCP) detector. By rotating the mirror around the beam axis, we measured the modulation of the MCP count rate and evaluated the detector modulation factor. The experimental results are presented and discussed in this paper.

References
[1] Fan, YZ & Wei, DM 2004, 'UV/optical emission accompanying gamma-ray bursts', Monthly Notices of the Royal Astronomical Society, vol. 351, no. 1, pp. 292–296.
[2] Di Marco, A., Fabiani, S., La Monaca, F., Muleri, F., Rankin, J., Soffitta, P., Xie, F., *et al.* 2022, 'Calibration of the IXPE focal plane X-ray polarimeters to polarized radiation', *Astronomical Journal*, 164(3), 103, Bristol: IOP Publishing.

Time:
9 November, 2026
15:00 – 17:00

Room:
Poster Area

NSS-01 | NSS Poster Session

Chairs:
Matteo Porro (Schenefeld)

NSS-01-001

Fast or Adapt: Proportional Gas in γ-ray Fields (#1278)

Jakub Prchlik, Eric Yokie, Arlo Petitjean, David O'Connor

Reuter-Stokes, LLC, Twinsburg, USA

Abstract

Background γ-ray fields complicate neutron measurements for Nondestructive Assay (NDA) of Nuclear Materials and the next generation of advanced reactor designs, including non-light water (non-LWR) and Small Modular Reactors (SMRs). Neutron sensitive proportional counter design for high γ-ray fields often focus on optimizing ion collection time and integrating low-Z materials. In these counters, the metal cathode produces most of the Compton scattered electrons, which deposit unwanted energy and signal in the gas. The long path length for Compton electrons in the counter gas means the counter gas pressures may be optimized to increase the ratio of ion-to-electron energy deposition. Here we present gas mixture and pressure optimization for ion-to-electron energy deposition using SRIM simulations. The simulation output is then tested experimentally for its effect on neutron sensitivity in γ-ray fields between 1 R/Hr and 100 R/Hr. The ion-to-electron energy deposition ratio shows promise as an additional design consideration for neutron sensitive proportional counters in γ-ray fields, even though the experimentally measured optimum pressure of 0.5 atm for He/N_2 95/5 is lower than the simulated optimum pressure. Future experiments with a current sensitive preamplifier (CAEN A1427) will improve neutron counting for 1 to 100 R/Hr γ-ray fields.

References

[1] DH Beddingfield, NH Johnson, and HO Menlove. 3he neutron proportional counter performance in high gamma-ray dose environments. Nuclear Instruments and Methods in Physics Research Section A: Accelerators, Spectrometers, Detectors and Associated Equipment, 455(3):670–682, 2000.

[2] D. C. Henzlova, M. P. Baker, K. Bartlett, A. Favalli, M. Iliev, M. A. Root, S. Sarnoski, T. Shin, and M. T. Swinhoe. Neutron Detectors, pages 325–358. Springer Nature Switzerland, Cham, 2024.

[3] Kevin S McKinny, Thomas R Anderson, and Nathan H Johnson. Neutron detector sensitivity measurements and their variation. In 2011 IEEE Nuclear Science Symposium Conference Record, pages 533–537. IEEE, 2011.

[4] J. Va'Vra. Review of wire chamber aging. Nuclear Instruments and Methods in Physics Research Section A: Accelerators, Spectrometers, Detectors and Associated Equipment, 252(2):547–563, 1986.

NSS-01-003

Development of a Monte Carlo Simulation–Based Analysis Technique for High-Pressure Ionization Chambers (HPIC) (#1858)

Kyeong Hyeon Sung[1], Chul Hee Min[1], Jung-Ki Shin[2]

[1] Yonsei University, Department of Radiation Convergence Engineering, Wonju, South Korea; [2] NeosisKorea, Daejeon, South Korea

This work was supported by the Nuclear Energy International Joint Research Project through the National Research Foundation of Korea (NRF) funded by the Ministry of Science and ICT (MSIT) (No. RS-2025-25396349).

Abstract
High-pressure ionization chambers (HPICs) are widely used for radiation monitoring owing to their high sensitivity and mechanical robustness. However, under low-dose conditions, the inherently small signal results in a low signal-to-noise ratio, making accurate characterization of detector response challenging. Therefore, detailed analysis of radiation interaction and charge transport processes in the detector is required for accurate characterization and optimization of HPIC performance. In this study, a simulation framework was developed to investigate and optimize the signal response characteristics of HPICs. A coupled simulation framework integrating Geant4 and Garfield++ is used to model the full signal formation process, including radiation dose deposition and charge transport under applied electric fields. A Kyocera HPIC was used to measure the current response as a function of applied voltage under irradiation from a 95 μCi Cs-137 source. In the Geant4 simulation, the HPIC geometry was modeled to calculate the spatial distribution of dose deposition within the gas volume, which is subsequently converted into ion pair distributions using the W-value. The electric field is modeled in Garfield++ to simulate charge transport under applied voltages, enabling the calculation of the resulting current response. The collected charge in the anode shows a plateau behavior at approximately 64.2 pA, while the experimental results exhibit a saturation around 54.8 pA. It is predicted that the discrepancy is attributed to additional physical effects such as ion recombination, feedthrough effects, and leakage currents. These findings demonstrate that the proposed approach provides a reliable framework for accurate analysis and optimization of HPIC.

References
[1] G. F. Knoll, Radiation Detection and Measurement, 4th ed. Hoboken, NJ, USA: Wiley, 2010.
[2] D. Pfeiffer, M. J. R. Hoch, S. R. Johnson, and A. Sharma, “Interfacing Geant4, Garfield++ and Degrad for the simulation of gaseous detectors,” Nucl. Instrum. Methods Phys. Res. A, vol. 935, pp. 121–134, 2019.
[3] ICRU, “Mean energy required to produce an ion pair,” ICRU Report 31, Bethesda, MD, USA: International Commission on Radiation Units and Measurements, 1979.

NSS-01-005

High Granularity Readout Time Projection Chamber R&D for Future Circular e+e- Colliders (#2530)

Huirong Qi[1,2], Maksym Titov[2], On behalf of Linear Collider Time Projection Chamber International Collaboration

[1] Institute of High Energy Physics, CAS, Beijing, China; [2] Linear Collider Time Projection Chamber International Collaboration, Hamburg, Germany

Abstract
A worldwide Lepton Collider Time Projection Chamber community of the physicists was working to realize an exceptional physics program of the energy-frontier, electron-positron collision, especially for Future Circular Collider (FCC-ee), Circular Electron Positron Collider (CEPC) and the International Linear Collier (ILC). In all proposed detector concepts, the Time Projection Chamber (TPC) serves as the main tracking detector, complemented by the

silicon tracking detectors both inside and outside the TPC, all embedded within a 3 T solenoid field. Many extensive R&D program for the track detector has been developed within the collaboration of LCTPC.
TPC performance is satisfactory in Higgs mode, but the high luminosity Z pole running poses substantial technical challenges. Based on MDI background simulation data to study ion-induced space charge effects, we have conducted a detailed assessment of TPC technical challenges and potential solutions, particularly under the high luminosity Z pole running conditions. In this talk, the feasibility and update progress of high precision TPC as the main track detector for e+ e− collider will be presented. TPC detection aims the good separation power with the cluster counting to be considered and the simulation results of the pad/pixelated TPC technology will be given. Compared with the pad readout using the simulation, the high granularity readout TPC options will obtain the better spatial resolution of single electrons, the very high detection efficiency in excellent tracking and good PID performance (less than 3σ). A large prototype TPC in a 1.0T magnetic field, which allow to accommodate up to seven identical Micro Pattern Gaseous Detector (MPGD) readout modules of the TPC being studied using the 5GeV electron beam at DESY, we will present the track reconstruction performance results and summarize the next steps of the pad/pixelated TPC technology for the future lepton colliders.

NSS-01-007

A Semi-Analytical Method for Sensitivity Estimation of Parallel-Plate Boron-Coated Ionization Chambers (#3076)

Peng Tang

tsinghua university, Institute of Nuclear and New Energy Technology, beijing, China

Abstract
This paper presents a semi-analytical method for sensitivity estimation of multilayer parallel-plate boron-coated ionization chambers. The model combines: (1) an overlap-geometry calculation for the distribution of crossed boron layers under oblique incidence, and (2) a microscopic-simulation-based depth-response function for single-layer effective signal generation. By coupling geometric crossing statistics, boron attenuation, and depth response, detector sensitivity can be rapidly evaluated versus incidence angle, boron thickness, and plate spacing. Compared with Geant4, the method reproduces both trend and magnitude of angular sensitivity, with better agreement at large angles. The framework is suitable for fast parameter screening before high-fidelity simulation.

NSS-01-009

A New Efficient n-γ Pulse Shape Discrimination Technique for Fast Scintillation Detectors (#1149)

Stefano Riboldi[1,2], Agnese Giaz[2], Sergio Brambilla[2], Ciro Boiano[2]

[1] *Università degli Studi di Milano, Fisica, Milano, Italy;* [2] *INFN, Milano, Milano, Italy*

Abstract

Pulse shape discrimination (PSD) is an effective technique for identifying the interacting particle (e.g., gamma rays or neutrons) in scintillation detectors.

In the simplest cases (e.g., the Cs_2LiYCl_6 scintillator, showing a large difference between gamma and neutron signals), the PSD procedure can be performed using the "charge integration" (CI) method, based on rectangular weighting functions. However, for scintillators with smaller differences in signal shape (e.g., the $LaCl_3$:Ce scintillator), different methods must be used.

Moreover, when digital acquisition systems are used, sampling the photodetector's analog signal at a finite time step can significantly affect the PSD results. Indeed, apart from the effects of electronic and quantization noise, the main cause of overlapping of the PSD regions of interest (ROI) of fast scintillator signals processed in the time domain is the temporal variability (ΔT) of the sampling comb relative to the onset of the analog pulse. In the case of relatively high DAQ's acquisition frequency (e.g., 500 MHz), increasing it further to mitigate this issue is not practical, and alternative techniques must be used.

One solution is to proceed via the absolute value of the discrete Fourier transform (DFT) of the signal, which completely solves the temporal variability issue, though at the cost of significant computational burden.

This paper presents a new analysis technique that solves the problem with a negligible computational overhead, making it especially suitable for online applications, by just linking the information on the time shift ΔT to the detector signal, and linearly filtering the whole dataset.

The filter weighting function is determined with the DPLMS optimal filter synthesis algorithm, employed here for the first time for this purpose.

The PSD results obtained with this technique, suitable as well for energy and time estimations, are here shown for experimentally acquired $LaCl_3$:Ce scintillator signals.

References

[1] S. Riboldi, et al., 2025, 'Neutron-Gamma Pulse Shape Discrimination Techniques for Scintillation Detectors,' IEEE NSS, Yokohama, Japan, doi: 10.1109/NSS/MIC/RTSD57106.2025.11287487

[2] D. Rigamonti, et al., 2025, 'A chlorine based detector (LaCl3(Ce)) for 2.5 MeV neutron spectroscopy in deuterium nuclear fusion plasmas with enhanced particle discrimination algorithm', Meas. Sci. Technol. 36 (2025), doi: 10.1088/1361-6501/ad8f4e

NSS-01-011

Near infrared scintillation properties of rare earth doped fluorapatite transparent ceramics (#1184)

Takayuki Yanagida[1], Keita Miyajima[1], Kai Okazaki[1], Takayuki Nakanishi[2], Hiroaki Furuse[2], Takumi Kato[1], Daisuke Nakauchi[1], Noriaki Kawaguchi[1]

[1] Nara Institute of Science and Technology, Ikoma, Japan; [2] NIMS, Tsukuba, Japan

Abstract

Near infrared (NIR) emitting scintillators have attracted attentions recently for radiation monitoring at high dose fields. In this work, NIR scintillation properties of Yb3+ and Nd3+ doped fluorapatite (Ca10(PO4)6F2, FAP) transparent ceramics with different doping concentration were investigated. These materials have been originally developed for laser applications. The most famous laser material, Nd:YAG transparent ceramic, can show good scintillation performance both UV-VIS emission and NIR emission, and following such a study, good performance can be expected in FAP transparent ceramic. When X-rays were irradiated, they exhibited 1000 nm (Yb) and 1064 (band) emission bands, and their scintillation decay time resulted several micro hundreds s. The most important property for high dose field monitoring, the lower detection limit (LDL), was investigated by coupling with InGaAs photodiode. Yb and Nd-doped FAP showed 1.2 and 0.6 mGy/hr, respectively. In the conference, scintillation properties as well as photoluminescence properties will be presented, and compared with other NIR emitting scintillators.

NSS-01-013

Hydrophobic Solvent-Based Polishing for Performance Enhancement of Water-Sensitive Perovskite Scintillator Crystals (#1236)

Seungho Song[1,2], Jiwon Seo[3], Dakyoung Lee[1,2], Chansun Park[4], Beomjun Park[5], Jung-Yeol Yeom[2,6]

[1] Korea University, Department of Bioengineering, Seoul, South Korea; [2] Korea University, Interdisciplinary Program in Precision Public Health, Seoul, South Korea; [3] Korea Institute of Fusion Energy, Dajeon, South Korea; [4] Korea University, Global Health Technology Research Center, Seoul, South Korea; [5] Seoul National University, Research Institute for Future Technology and Policy, Seoul, South Korea; [6] Korea University, School of Bioengineering, Seoul, South Korea

This work was supported by the National Research Foundation of Korea (NRF), funded by the Ministry of Science and ICT (RS-2023-NR077190, RS-2022-00165164), and by the National Research Foundation of Korea and the Commercializations Promotion Agency for R&D Outcomes (RS-2023-00234651).

Abstract

Halide perovskites are promising scintillator materials for radiation detection and medical imaging because of their excellent optical and scintillation properties. Since the surface quality of single-crystal scintillators strongly affects light extraction and detector performance, polishing is an essential step in scintillator fabrication. However, conventional wet polishing processes are not suitable for water-sensitive crystals such as $Cs_3Cu_2I_5$ (CCI). In this work, hydrophobic solvents were investigated as polishing media for water-sensitive CCI single crystals. Three hydrophobic solvents—squalane, silicone oil, and mineral oil— were used as dispersion media for 1 μm alumina abrasives, followed by toluene rinsing after polishing. Among them, squalane showed the best polishing performance, yielding the lowest surface roughness (R_q=17.29 nm), the highest transmittance of 78.21%, and the narrowest rocking-curve FWHM of 0.025°. In addition, sequential polishing in squalane using P2000 sandpaper, P4000 sandpaper, and 1 μm alumina enhanced the light yield and improved the energy resolution from 6.53% to 5.83%. These results identify squalane as a promising polishing medium for water-sensitive halide perovskite scintillators.

NSS-01-015

Combining cross-luminescent scintillators and μSiPMs for better timing in ToF-PET (#1249)

Katrin Herweg[1,2], Samuele Bisi[3], Claudio Bruschini[3], Edoardo Charbon[3], Alberto Gola[4], Laura Parellada-Monreal[4], Michele Penna[4], David Schug[1,2], Volkmar Schulz[2], Stefan Gundacker[5]

[1] RWTH Aachen University, University Hospital RWTH Aachen, Aachen, Germany; [2] RWTH Aachen University, Institute of Imaging and Computer Vision, Aachen, Germany; [3] Ecole polythechnique fédérale de Lausanne, Advanced Quantum Architecture Laboratory, Neuchatel, Switzerland; [4] Fondazione Bruno Kessler, Trento, Italy; [5] Austrian Academy of Sciences, Marietta Blau Institute for Particle Physics, Vienna, Austria

This research is funded by the Deutsche Forschungsgemeinschaft (DFG, German Research Foundation) - 500540345 and the Swiss National Science Foundation (SNSF) - #200021L_208073.

Abstract

Time-of-flight positron emission tomography (ToF-PET) has boosted PET image quality significantly in the last years. During its first inception it was built with cross-luminescent BaF_2 crystals, which have since been replaced by LYSO. Recently, cross-luminescence has regained popularity with new scintillators being developed. However, BaF_2 and the recently developed Cs_2ZnCl_4 could not improve on the LYSO state-of-the-art coincidence time resolution (CTR) (56 ps for 2x2x3 mm³ and 95 ps for 3x3x19 mm³). As Cs_2ZnCl_4 shows a significant Cherenkov production, we combined it with the DIGILOG approach to boost its timing performance. The DIGILOG approach segments the sensor into μSiPMs and has shown an improved timing performance for BGO due to its Cherenkov

radiation and an improved SPTR. Here, we simulated a 3x3x3 mm³ and a 3x3x20 mm³ Cs_2ZnCl_4 crystal coupled to seven different µSiPM arrays. The simulation included noise factors like dark counts, cross-talk, SPAD dead time and analog noise. It was designed with a PDE of 60 % and an SPTR of 25 ps. This resulted in an improved CTR of 34+/-4 ps for an array of 20x20 µSiPMs coupled to a 3x3x3 mm³ Cs_2ZnCl_4 crystal compared to the non-segmented SiPM at 48+/-3 ps. Furthermore, for the 3x3x20 mm³ crystal, a CTR of 64+/-4 ps was reached with a 10x10 µSiPM array, while the non-segmented SiPM showed a CTR of 84+/-3 ps. The results of the segmented SiPMs improve on the LYSO state-of-the-art. Additionally, they demonstrate that the DIGILOG SiPM approach improves timing performance not just for BGO, but also for other scintillators with high Cherenkov yield, ultra-fast emission and low light yield. We also provide motivation to optimize sensors for Cs_2ZnCl_4, which could enable better timing performance than the LYSO state-of-the-art.

References
[1] Wong, W. H. et al. 1984, 'Characteristics of small barium fluoride (BaF2) scintillator for high intrinsic resolution time-of-flight positron emission tomography', IEEE TNS
[2] Herweg, K. et al. 2023, 'On the Prospects of BaF2 as a Fast Scintillator for Time-of-Flight Positron Emission Tomography Systems', IEEE TRPMS
[3] Rutstrom, D. et al. 2022, 'Improved light yield and growth of large-volume ultrafast single crystal scintillators Cs2ZnCl4 and Cs3ZnCl5', Optical Materials
[4] Herweg, K. et al. 2024, 'Timing limits of ultrafast cross-luminescence emission in CsZnCl-based crystals for TOF-CT and TOF-PET', EJNMMI Physics
[5] Nadig, V. et al. 2023, 'Timing advances of commercial divalent-ion co- doped LYSO:Ce and SiPMs in sub-100 ps time-of-flight positron emission tomography', PMB
[6] Gundacker, S. et al. 2023, 'DIGILOG: A digital-analog SiPM towards 10 ps prompt-photon tagging in TOF-PET', 2023 IEEE NSS MIC RTSD
[7] Herweg, K. et al. 2024, 'Investigating µSiPMs to overcome the limits of BGO in ToF-PET', 2024 IEEE NSS MIC RTSD
[8] Herweg, K. et al. 2026, 'Exploring µSiPMs with BGO for Cherenkov time-of-flight in PET', revision submitted to IEEE TRPMS
[9] Zuo, X. et al. 2025, 'Scintillation performance of 1-inch-diameter Cs2ZnCl4 crystals', CrystEngComm

NSS-01-017

Temperature Dependence of Pulse Shape Discrimination in SiPM-Based EJ-276D Detectors (#1585)

Jacob W. Fritchie, Angela Di Fulvio, Gabriella Gariazzo, Grant Roche, John Leland

University of Illinois Urbana-Champaign, Nuclear, Plasma, and Radiological Engineering, Urbana, USA

This work is funded in-part by Sandia National Laboratories (SNL) LDRD Award 2308289. SNL is a multimission laboratory managed and operated by National Technology & Engineering Solutions of Sandia, LLC, a wholly owned subsidiary of Honeywell International Inc., for the U.S. Department of Energy's National Nuclear Security Administration (NNSA) under contract DE-NA0003525. This research was performed under appointment to the Nuclear Nonproliferation International Safeguards Fellowship Program sponsored by the U.S. NNSA's Office of International Nuclear Safeguards.

Abstract

The temperature dependence of pulse shape discrimination performance was investigated for three commercial silicon photomultiplier technologies coupled to an EJ-276D organic scintillator. Measurements were conducted at 22 °C, 30 °C, 40 °C, and 50 °C using PuBe sources. Pulse shape discrimination was quantified using the tail-to-total ratio and figure of merit. For all devices, the figure of merit increased at 30 °C. The Broadcom device exhibited the highest performance, increasing from 1.12 at 22 °C to a maximum of 1.17 at 30 °C before decreasing to 0.76 at 50 °C. The Onsemi and Hamamatsu devices showed smaller improvements, with figure of merit values increasing from 0.86 to 0.89 and 0.84 to 0.90, respectively, between 22 °C and 30 °C. At 50 °C, all devices exhibited reduced performance due to increased silicon photomultiplier thermal noise. Temperature-dependent changes in pulse shape were observed, with increasing temperature producing faster decay and modifying the balance of prompt and delayed scintillation light, improving neutron-gamma separation at intermediate temperatures. Despite degradation at higher temperature, all devices maintained effective discrimination up to 50 °C. These results demonstrate that silicon photomultiplier-based detectors are capable of robust neutron-gamma discrimination at elevated temperatures relevant to safeguards applications.

References
[1] Acerbi, Fabio, Gundacker, Stefan 2019, 'Understanding and Simulating SiPMs', *Nulcear Insturments and Methods in Physics Research Section A: Accelerators, Spectrometers, Detectors and Associated Equipment*, 926, 16-35
[2] Borgwardt, TC, Oukrop, L, Bartlett, KD, Smith, K, Williamson, E, Meierbachtol, KC, Febbraro, M 2025, 'Temperature dependence of the nspec fieldable neutron spectrometer', Nuclear Instruments and Methods in Physics Research Section A: Accelerators, Spectrometers, Detectors and Associated Equipment, vol. 1072, article 170161.
[3] Arrue, J, Chandler, C, Duce, M, Lim, A, Sellinger, A, Erickson, A 2023, 'Impact of temperature on light yield and pulse shape discrimination of polysiloxane-based organic scintillators formulated with commercial resins', Nuclear Instruments and Methods in Physics Research Section A: Accelerators, Spectrometers, Detectors and Associated Equipment, vol. 1056, article 168650.

NSS-01-019

Scintillation light quenching for energetic charged particles in GAGG:Ce (#1607)

Felix Liang[1], Nicholas Floyd[1], Heshani Jayatissa[1], Philip Adsley[2], Arthur Alvarez[2], Robert Bartsch[2], Shayden Fritz[2], Travis Hankins[2], Bryan Harvey[2], Khang Pham[2], Elizabeth Schnorrenberg[2], David Shelden[2], Sherry Yennello[2]

[1] Los Alamos National Laboratory, ISR Division, Los Alamos, USA; [2] Texas A&M University, Cyclotron Institute, College Station, USA

Los Alamos National Laboratory is managed by Triad National Security, LLC for the U.S. Department of Energy's NNSA.

Abstract

Cerium-doped gadolinium gallium aluminium garnet (GAGG:Ce) is a novel scintillator with excellent scintillation properties. It is suitable for use in various basic science research and applications. Because the scintillation light is quenched for charged particle detection, it is necessary to use beams from accelerators to calibrate the energy response. Measurements of energetic charged particles incident on three GAGG:Ce crystals were performed using accelerated protons, ^{4}He, and ^{12}C at 0°C and 20°C in consideration for detecting charged particles in the earth's

radiation belts for space weather modeling and for deploying in dosimetry devices in ion therapy, respectively. The Birks factor which quantitatively describes the extent of quenching was deduced from the experimental data. For all three GAGG:Ce scintillators, the Birks factor decreases with the atomic number Z of the incident ions. Furthermore, less light quenching, a smaller Birks factor, was observed for GAGG:Ce at 0°C. The quenching for the Mg-codoped GAGG:Ce which has a shorter decay time constant, was found to be less temperature dependent compared to the other two GAGG:Ce crystals.

References
[1] Wang, YQ, Burward-Hoy, JM, Tesmer, JR 2014, 'Production of high energy and low flux protons using $^{2}D(^{3}He,p)^{4}He$ for space detector calibrations', *Nucl. Instrum. Methods*, vol. B332, pp. 432-438.
[2] Espinoza, TN, *et al.* 2024, 'Proton quenching in rare-earth inorganic scintillators: GAGG:Ce and YSO:Ce', *IEEE Trans. Nucl. Sci.*, vol. 71, pp. 2102-2108.
[3] Birks, JB 1964, 'The theory and practice of scintillation counting', Pergamon Press, Oxford.
[4] Treytak, VI 2010, 'Semi-empirical calculation of quenching factors for ions in scintillators', *Astro. Phys.*, vol. 33, pp. 40-53.
[5] Ziegler, JF, Biersack, JP, Littmark, U 1985, 'The stopping and range of ions in solids', vol. 1, Pergamon Press, New York.
[6] Berger, MJ, Coursey, JS, Zucker, MA, Chang, J 2017, 'Stopping-power & range tables for electrons, protons and helium ions', https://dx.doi.org/10.18434/T4NC7P.

NSS-01-021

Facile, scalable and high-yield synthesis of zero-dimensional copper halide $Cs_3Cu_2Cl_5$ scintillator with near-unity quantum yield for high-resolution X-ray imaging applications (#1659)

Young Seung Choi[1], Jaeyoung Im[2], Kang Heo[3], Sung Oh Cho[2], Bo Kyung Cha[4], **Byungha Shin**[1]

[1] KAIST, Materials Science and Engineering, Daejeon, South Korea; [2] KAIST, Nuclear and Quantum Engineering, Daejeon, South Korea; [3] Viewworks, Anyang, South Korea; [4] KERI, Ansan, South Korea

Abstract
Metal halide perovskites, particularly copper halide variants, have emerged as promising scintillators owing to their large Stokes shift, high photoluminescence quantum yield (PLQY), and efficient radioluminescence. Here, we demonstrate a dioxolane-mediated reaction synthesis as a simple, scalable, and high-yield strategy for producing $Cs_3Cu_2Cl_5$ powders with near-complete conversion. By employing low-polarity yet water-miscible dioxolane as the reaction medium together with an aqueous H_3PO_2 additive, the solubility imbalance between the precursors inherent to low-polarity solvents is effectively addressed. This approach enables stoichiometry-controlled dissolution–precipitation under a low-polarity reaction environment and the formation of phase-pure $Cs_3Cu_2Cl_5$ powders with near-unity PLQY. The powders show bright green emission at ~530 nm and retain over 80% of their initial efficiency after 300 days of ambient storage without encapsulation, demonstrating remarkable intrinsic stability. $Cs_3Cu_2Cl_5$-based composite films deliver an ultrahigh light yield of ~98,000 photons MeV^{-1}, greatly surpassing that of commercial scintillators such as Gd_2O_2S and CsI:Tl, and exhibiting excellent dose linearity and long-term irradiation stability. When integrated into commercial flat-panel detectors, the $Cs_3Cu_2Cl_5$-based composite films successfully enabled high-quality 2D radiographic and 3D computed tomography imaging, directly verifying their compatibility with existing X-ray detection systems. This facile and efficient synthesis, together with

the demonstrated device-level imaging performance, highlights $Cs_3Cu_2Cl_5$ as a scalable and practical candidate for next-generation X-ray scintillators.

NSS-01-023

Spectral-feature-based radionuclide and radiation-type discrimination using a plastic scintillation fiber detector for in-situ pipe measurements

(#1767)

Tomohisa Abe[1], Takamasa Nakasone[2], Tsutomu Yamada[2], Marina Kanno[3], Yuki Morishita[1]

[1] Japan Atomic Energy Agency, Collaborative Laboratories for Advanced Decommissioning Science, Minamisomashi, Japan; [2] Japan Radiation Engineering Co.,Ltd., Hitachishi, Japan; [3] PESCO Co., Ltd., Minatoku, Japan

Abstract

A capillary-type plastic scintillation fiber (PSF) detector combined with a multi-channel analyzer (MCA) was investigated for radionuclide and radiation-type discrimination in in-situ pipe measurements. Plastic scintillators generally exhibit poor energy resolution, resulting in broadened spectra that complicate conventional peak-based identification. In this study, spectral features including the Compton edge (CE), endpoint, and centroid were extracted from β- and γ-ray spectra obtained using Sr-90/Y-90 and Cs-137 sources. The positional dependence of these features along the fiber was evaluated, and significantly reduced variation compared with previous studies was achieved by introducing a reflective structure at the fiber end. In addition, radiation-type discrimination under mixed β/γ conditions was investigated using a stainless-steel (SUS) cover to suppress β-ray components. The results demonstrated that the extracted spectral features remained stable against source position and that condition switching using the SUS cover enabled practical discrimination of β and γ components. These findings indicate that the proposed method is applicable to contamination assessment in confined environments such as piping systems.

References
[1] S. Song, J. H. Park, J. Kim, S. Kim, S. Jegal, S. Lee, and B. Lee, “Acquiring gamma-ray energy spectrum using a plastic scintillation optical fiber detector,” Photonics, vol. 11, p. 493, 2024.
[2] J. W. Bae and H. R. Kim, “Plastic scintillator beta ray scanner for in-situ discrimination of beta ray and gamma ray radioactivity in soil,” Nucl. Eng. Technol., vol. 52, pp. 1259–1265, 2020.

NSS-01-025

Investigation of Coincidence Time Resolution in BaF_2:Y Scintillators for TOF PET Applications (#1798)

Heejong Kim[1], Junfeng Chen[3], Jing Zhang[3], Jiawei Xu[3], Subramanian Sundramoorthy[2], Yingjie Wang[1], Chin-Tu Chen[1], Chien-Min Kao[1]

[1] University of Chicago, Department of Radiology, Chicago, USA; [2] University of Chicago, Department of Radiation and Cellular Oncology, Chicago, USA; [3] Chinese Academy of Sciences, Shanghai Institute of Ceramics, Shanghai, China

Abstract

We are investigating BaF_2:Y scintillators for TOF-PET applications. BaF_2 exhibits an ultra-fast scintillation component with a 0.6 ns decay time produced through cross-luminescence, making it an attractive material for achieving coincidence time resolutions below 100 ps. Recent advances in Vacuum-Ultraviolet (VUV) SiPMs, which provide high photon-detection efficiency in the deep-UV range, have made it increasingly feasible to reliably detect this fast component. In addition to the fast emission, BaF_2 also contains a slow scintillation component with a decay time of approximately 600 ns. This slow component can be substantially suppressed through doping—for example, BaF_2:Y, produced via yttrium doping. Effective suppression of the slow component is essential for applications requiring high count-rate capability, excellent timing performance, and minimal pulse pile-up, such as TOF-PET. In this work, we investigated the coincidence time resolution (CTR) of BaF_2:Y scintillators. The BaF_2 and BaF_2:Y crystals used in this study were grown and polished by the Shanghai Institute of Ceramics (SIC), China. For the BaF_2:Y samples, the yttrium concentration was set to 2 at%, which suppressed the slow component by approximately a factor of four while leaving the fast-component light yield unaffected. Hamamatsu S13370 VUV-MPPCs were used to detect the fast scintillation component. Pairs of BaF_2 and BaF_2:Y crystals with dimensions 2 × 2 × 3 mm^3 were optically coupled to S13370 VUV-MPPCs and irradiated with a ^{22}Na source placed between them in a coincidence setup. We measured CTR values of 86 ps for BaF_2 and 96 ps for BaF_2:Y. These initial results are highly promising, and we anticipate further improvements in CTR with a more optimized experimental setup. Here, we report our preliminary findings.

NSS-01-027

Experimental Study of DOI Effects on the Timing Response of a 1”×2” LaBr3 Detector (#1996)

Sara Gaitán Dominguez[1], Víctor Martínez Nouvilas[1], Miriam Caballero Rodríguez[1], José A. Briz[1], Luis M. Fraile[2], Jose Udias[1]

[1] Complutense University of Madrid, Group of Nuclear Physics, EMFTEL and IPARCOS, Madrid, UK; [2] Cern, ISOLDE, EP Department, Geneva, UK

This work was supported by the Spanish Government under grant PR38/23-HISTARS(MRR)

Abstract

Depth of interaction (DOI) effects can affect the timing response of scintillation detectors due to variations in optical photon transport inside the crystal volume. In this work, DOI-dependent timing measurements were performed using a 1”×2” $LaBr_3$ scintillation detector coupled to a photomultiplier tube (PMT) within the framework of the HiSTARs project. A ^{22}Na source was positioned at different locations along the crystal axis in coincidence with a fast SiPM-based reference detector, and signals were acquired using a DRS digitizer operating at 5 GS/s. The present study focuses on the comparison between interactions occurring close to the PMT side of the crystal and interactions occurring close to the opposite side. Coincidence timing distributions show a systematic shift of approximately 300 ps in the centroid position between both irradiation configurations. Coincidence timing resolutions of 287 ps and 268 ps FWHM were obtained for the two positions, respectively. The observed behavior is consistent with differences in optical photon propagation paths and light collection timing inside the scintillator. Although DOI effects introduce measurable timing shifts, the overall degradation of the timing resolution remains moderate for the studied configurations. Additional irradiation geometries and analysis conditions are currently under study in order to obtain a more complete characterization of DOI effects in long $LaBr_3$ scintillation detectors.

References

[1] Luxium Solutions, “LaBr3 Scintillation Crystals.” [Online]. Available: https://www.luxiumsolutions.com

[2] Hamamatsu Photonics, “Photomultiplier Tubes: Basics and Applications,” Hamamatsu, Japan. [Online]. Available: https://www.hamamatsu.com

[3] EPIC Crystal Company, “Scintillation Crystals.” [Online]. Available: http://www.epic-crystal.com

[4] S. Ritt, “DRS4 Handbook,” Paul Scherrer Inst., Villigen, Switzerland, Rev. 0.9, 2008

NSS-01-029

Development of Mo-Doped Cs_2HfCl_6 for Dosimetry in High Dose-Rate Environment (#2267)

Shinichiro Kondo[1], Chihaya Fujiwara[2,3], Akihiro Yamaji[3], Shunsuke Kurosawa[3,4]

[1] Nagoya University, School of Engineering, Nagoya, Japan; [2] Tohoku University, Department of Materials Science, Graduate School of Engineering, Sendai, Japan; [3] Nagoya University, Graduate School of Engineering, Nagoya, Japan; [4] Osaka University, Institute of Laser Engineering, Osaka, Japan

Abstract

In order to accomplish rapid and safe decommissioning of Fukushima Daiichi nuclear power plant, the remote and real-time dosimeter was required. To address this issue, detector systems comprising a scintillator coupled to an optical fiber have been proposed. In this system, emission wavelength of the scintillator itself should be in the near-infrared (NIR) band, to spectrally discriminate the scintillation signal from the Cherenkov component generated within the optical fiber itself. Therefore, in this study, we focus on Mo doped Cs_2HfCl_6 as the scintillator with NIR emission wavelength and high atmospheric stability. The Mo doped Cs_2HfCl_6 scintillators were grown via melt solidification method. The result of powder X-ray diffraction pattern suggested that the single phase of Mo: Cs_2HfCl_6 were successfully obtained. Furthermore, the emission wavelength of Mo doped Cs_2HfCl_6 was shifted to 900nm from 420 nm of host emission of C_2HfCl_6. These results indicate Mo: CHC is the promising scintillator for the real time remote monitoring system with optical fiber.

NSS-01-031

From $LaBr_3$:Ce to $Cs_2LiLa(Br,Cl)_6$:Ce Mixed-Halide Elpasolites: Tailoring Scintillation Response for High-Precision Gamma-Ray and Neutron Detection (#2321)

Zhuochen Cai[1], Ziang Yin[1], Xianggang Zhang[1], Zhe Kang[2], Jinbo Liu[2], Qinghua Zhao[1], Tao Wang[1]

[1] Northwestern Polytechnical University, State Key Laboratory of Solidification Processing, Xi'an, China; [2] Crystalab Corporation Ltd, Xi'an, China

Abstract

Halide scintillators provide a flexible material platform for detectors requiring high gamma-ray energy resolution, fast response, and, in lithium-containing compounds, intrinsic neutron sensitivity. This work presents CrystaLab Co., Ltd.'s compositional-engineering route from $LaBr_3$:Ce gamma-ray scintillators to $Cs_2LiLa(Br,Cl)_6$:Ce (CLLBC) mixed-halide Elpasolites for combined gamma-ray and neutron detection. Packaged $LaBr_3$:Ce detector modules demonstrate high-resolution gamma-ray spectroscopy, with a representative energy resolution of 2.37% at 662 keV and product specifications below 3% at 662 keV. $CeBr_3$ detectors provide a low-background lanthanide-halide

option with energy resolution below 4.5% at 662 keV. By introducing Li and tuning the Br/Cl halide sublattice, $Cs_2LiLaBr_6$ (CLLB) and CLLBC extend the platform to neutron-sensitive dual-mode detection with neutron-gamma pulse-shape discrimination (PSD). CLLB products provide gamma-ray energy resolution below 4.5% at 662 keV and room-temperature neutron-gamma figure of merit (FOM) values >1.2, while optimized 1-inch CLLBC crystals achieved 3.09% energy resolution at 662 keV and FOM = 2.1. These results show how halide composition, crystal growth, and detector integration can tailor scintillation response from high-precision gamma-ray spectroscopy toward compact mixed-field radiation detectors.

NSS-01-033

Application of neutron sensitising layers to plastic scintillator (#2414)

Jack R. Hitchens, Chris Allwork, Shivani L. Chauhan, Tom Crane, Tom Heather, Matt P. Taggart

AWE Nuclear Security Technologies, Reading, UK

Abstract

Eljen plastic scintillator disks have been coated with layers of neutron sensitiser in a systematic study on the thickness of neutron detection layers. Here we discuss the impact of enhancing standard plastic scintillator (PVT) with coatings containing both lithium and boron isotopes. The application of these layers enhances the material to provide a mechanism for detecting neutron radiation. A systematic study was performed to assess the impact of sensitiser thickness on neutron detection efficiency and neutron-gamma pulse shape discrimination (PSD) performance. Samples were exposed to the mixed radiation fields of a ^{252}Cf source, and a sample of plutonium. The results demonstrate clear neutron-gamma discrimination in sensitised samples, with measured figures of merit in excess of 3 recorded for optimised lithium-rich coatings. This is comparable performance to established dual-mode detectors. These findings show that thin, externally applied neutron-sensitising layers provide an effective route to enhancing the performance of conventional plastic scintillators. This approach may offer a low-cost means of upgrading existing detector systems in nuclear security applications.

References
[1] J. Glodo, et al., “Selected Properties of Cs2LiYCl6:Ce3+ Scintillator,” IEEE Trans. Nucl. Sci., vol. 56, pp. 873–880, 2009.
[2] R. Song, et al., “The Neutron-Gamma Pulse Shape Discrimination of CLLB Detector,” EPJ Web of Conferences, vol. 295, Art. No. 09031, 2024
[3] N. Zaitseva, et al., “Plastic scintillators with efficient neutron-gamma pulse shape discrimination,” Nuclear Instruments and Methods in Physics Research A, vol. 668, pp. 88-93, 2012
[4] R. Breuckers, C. Bartle and A. Edgar, "Transparent lithium loaded plastic scintillators for thermal neutron detection," Nuclear Instruments and Methods in Physics Research A, vol. 701, pp. 58-61, 2013
[5] I. Pawelczak, et al., “Boron-loaded plastic scintillators with neutron-γ discrimination capability,” Nuclear Instruments and Methods in Physics Research A, vol. 751, pp. 62-69, 2014
[6] N. Cherepy, et al., “Bismuth- and lithium-loaded plastic scintillators for gamma and neutron detection,” Nuclear Instruments and Methods in Physics Research A, vol. 778, pp. 126-132, 2015

NSS-01-035

Micropower Generation and Radiation Detection with Cr-doped Al_2O_3 Transparent Ceramics (#2416)

Noriaki Kawaguchi, Keita Miyajima, Kai Okazaki, Takumi Kato, Daisuke Nakauchi, Takauyuki Yanagida

Nara Institute of Science and Technology, Ikoma, Japan

This work was supported by the Cooperative Research Project of Research Center for Biomedical Engineering, Kazuchika Okura Memorial Foundation, Yashima Environment Technology Foundation, Iketani Science and Technology Foundation, and JSPS KAKENHI (22H00309, 24K03197, and 26K03208).

Abstract

We prepared 0.05–1% Cr-doped Al_2O_3 transparent ceramics with a diameter of approximately 10 mm by spark plasma sintering. The samples showed sharp emission peaks at around 700 nm, which matched the sensitivity of typical Si-photodetectors. When the samples were combined with a Si-photodetector and irradiated with X-, α-, and β-rays, currents ranging from picoamperes to nanoamperes were detected. The generated power was maximized when the dopant concentration was around 0.2–0.4 %.

NSS-01-037

Single-ended Multiplexed Readout Scintillation Detector With Depth of Interaction Capability: Architecture and Optical Simulation (#2505)

Gabriela Jazvac[1], Ana Marija Kožuljević[1], Luka Lotina[1], Luka Pavelić[1,2]

[1] Institute for Medical Research and Occupational Health, Division of Radiation Protection, Zagreb, Croatia; [2] Nucleometrix d.o.o., Zagreb, Croatia

This work was funded by the European Union – Next Generation EU and is part of the project Voxel matrix detector for full solid angle radiological imaging (VMDScan) - NPOO.C3.2.R2-I1.06.0084.

Abstract

An accurate and precise determination of the depth of interaction (DOI) of incident photons in scintillation detectors is paramount to increasing the spatial resolution of positron annihilation tomography (PET) systems. The high number of readout channels is a major source of cost and complexity of such systems, while light sharing multiplexed readouts suffer from edge effects. We have developed a pixelized scintillator detector with DOI capability and 4-to-1 multiplexing utilizing only single-ended readout and light-sharing light guides which can

improve signal-to-noise ratio and mitigate edge effects present in other solutions. The scintillator matrix is coupled to a silicon photomultiplier (SiPM) array on one end and light guides on the other. Adjacent crystals are connected in pairs via light guides to enable light sharing. The scintillation light of these crystal pairs is shared between exactly two SiPM pixels. DOI is determined using the ratio of signals on the two SiPM pixels. Pairing distant crystals on matrix edges avoids edge effects. We present the detector architecture and the results of optical simulations evaluating its DOI capability. The interaction position was swept along the central axis of one crystal and the number of incident photons was recorded in the interaction crystal and in the optically connected crystal. The number of rays incident on the sensor coupled to the interaction crystal is always higher than that of the connected crystal. This enables unambiguous determination of the interaction crystal. The ratio of the number of rays incident on the sensors spans three orders of magnitude and approaches unity as the source gets closer to the light guide. These properties demonstrate a favorable DOI capability of the presented detector configuration.

References
[1] LaBella, A, Cao, X, Zeng, X, Zhao, W, Goldan AH 2021, 'Sub-2 mm depth of interaction localization in PET detectors with prismatoid light guide arrays and single-ended readout using convolutional neural networks', *Med. Phys.*, 48, 1019-1025, AAPM
[2] Yu, X, Han, S, Liang, C, Liu, H, Zhang, X, Tao, J, Zhao, H, Xu, J, Peng, Q 2025, 'An optimized DOI decoding method for a PET detector with nine-crystal-to-one-photodetector coupling', *Phys. Med. Biol.*, 70, 175016, IPEM

NSS-01-039

Performance evaluation of GaGG(Ce) scintillators with different photosensors (#2850)

Miriam Caballero Rodríguez[1], Nikita Bernier[1], Victor Martínez Nouvilas[1], Luis M. Fraile[2,1], Odette Alonso-Sañudo[1], José A. Briz[1], Sara Gaitán Dominguez[1], Gabriel G. de Lorenzo[1], Pablo Gonzalez-Tarrio[1], Andrés Illana[3], Jose Udias[1]

[1] Universidad Complutense de Madrid, Facultad de Ciencias Físicas / Departamento de Estructura de la Materia, Física Térmica y Electrónica, Madrid, Spain; [2] CERN, ISOLDE, EP Department, Geneva, Spain; [3] CSIC, Instituto de Estructura de la Materia, Madrid, Spain

This work has been supported by the Spanish Ministerio de Ciencia e Innovaci\'on under projects PID2019-104714GB-C21 and PID2022-140400NB-C21.

Abstract
The HIE-ISOLDE Timing Array for Reaction Studies (HISTARS) project at CERN is developing a specialized detector system designed to measure the lifetimes of excited nuclear states. For efficient particle detection, thin square GaGG(Ce) are utilized alongside YSO due to their high density and fast scintillation properties. This work evaluates the performance of GAGG(Ce) crystals coupled with two distinct photosensors: a Hamamatsu R9779 photomultiplier tube (PMT) and an array of four silicon photomultipliers (SiPM) using a custom-designed circuit. These configurations were tested in combination with a $LaBr_3$(Ce) detector to facilitate coincidence measurements. Data acquisition was performed using high-speed digitizer to extract timing and energy information. This article reports on the comparative performance of both readout methods, specifically characterizing pulse shape

discrimination capabilities, energy resolution, and the coincidence time resolution for alpha-gamma events. Although the energy resolution is acceptable and it has a good pulse shape discrimination capability, the measured timing limitations show that the current configuration is not ideal for the HISTARS array. These results will guide the selection of better-suited materials for high-precision timing at HIE-ISOLDE.

References

[1] Wang, Z, Guo, H, Qian, S 2020, 'Pulse shape discrimination of GAGG:Ce crystals for charged particle detection', Journal of Instrumentation, Vol. 15, p. C06031, Bristol: IOP Publishing.
[2] Tsuchida, N, Ikeda, M, Kamae, T 1997, 'A study of the GAGG:Ce crystal for its application in nuclear physics', Nuclear Instruments and Methods in Physics Research Section A, Vol. 385, pp. 290–298, Amsterdam: Elsevier.
[3] Vedia, V, Carmona-Gallardo, M, Fraile, LM 2017, 'Characterization of specialized $LaBr_3$(Ce) detectors for fast-timing lifetime measurements', Nuclear Instruments and Methods in Physics Research Section A, Vol. 857, pp. 98–105, Amsterdam: Elsevier

NSS-01-041

Cosmic-Ray Muon Position Reconstruction via Dual-End Readout of Triangular Plastic Scintillators (#2888)

Ziqi Yin[1,2], Yaofeng Zhang[1,4], Jianjie Zhang[5], Li Wang[1,2], Yannan Huang[1,2], Xin Zhao[1,2], Jianping Cheng[1,3], Yuanyuan Liu[1,3]

[1] Beijing Normal University, School of Physics and Astronomy, Beijing, China; [2] Beijing Normal University, Joint Laboratory of Jinping Ultra-low Radiation Background Measurement of Ministry of Ecology and Environment, Beijing, China; [3] Jinping Deep Underground Frontier Science and Dark Matter Key Laboratory of Sichuan Province, Liangshan, China; [4] Beijing Normal University, Key Laboratory of Beam Technology of Ministry of Education, Beijing, China; [5] Chengdu University of Technology, College of Nuclear Technology and Automation Engineering, Chengdu, China

This work was supported by the National Natural Science Foundation of China (No.12222502).

Abstract

By measuring the time difference and amplitude ratio of the signals at both longitudinal ends of a triangular prism plastic scintillator through dual-end readout, it is theoretically possible to reconstruct the longitudinal position of an incident muon. This paper presents a cosmic-ray muon collimation device that determines the incident region via triple coincidence and features an adjustable incident area. Using natural cosmic-ray muons obtained with this device, dual-end positioning experiments were carried out on a triangular prism plastic scintillator. The threshold-crossing time and amplitude information were extracted from the complete waveforms and fitted, yielding well-fitted relationship functions of the threshold-crossing time difference and the logarithm of the amplitude ratio with respect to the hit position. Experimental results show that the longitudinal position resolution achieved by this method is 3 cm, confirming the effectiveness of the dual-end readout positioning method in triangular prism plastic scintillator array muon detectors and laying a foundation for future research on lightweight and efficient plastic scintillator array detectors.

References

[1] Nagamine, K, Iwasaki, M, Shimomura, K et al. 1995, 'Method of probing inner-structure of geophysical substance with the horizontal cosmic-ray muons and possible application to volcanic eruption prediction', *Nucl. Instrum. Methods Phys. Res. A*, vol. 356, no. 2-3, pp. 585-595, Amsterdam: Elsevier.
[2] Park, C, Kim, K B, Baek, M K et al. 2023, 'Development of a muon detector based on a plastic scintillator and WLS fibers to be used for muon tomography system', *Nuclear Engineering and Technology*, vol. 55, no. 3, pp. 1009-1014, Amsterdam: Elsevier.
[3] Wang, Z, Li, Z, Fan, X et al. 2025, 'Composition, structure and position resolution optimization of plastic scintillator units and arrays for a muon tomography detector', *Radiat. Phys. Chem.*, vol. 236, Art. no. 112893, Amsterdam: Elsevier.
[4] Sweany, M, Galindo-Tellez, A, Brown, J et al. 2019, 'Interaction position, time, and energy resolution in organic scintillator bars with dual-ended readout', *Nucl. Instrum. Methods Phys. Res. A*, vol. 927, pp. 451-462, Amsterdam: Elsevier.

NSS-01-043

Scintillation Properties of ^{6}Li-doped CsI:Tl Crystals for Thermal Neutron Detection (#2928)

Deepika Sharma[1,2], Anil K. Gourishetty[1], Mohit Tyagi[2], Manda Sonawane[2]

[1] India Institute of Technology Roorkee, Department of Physics, Roorkee, India; [2] Bhabha Atomic Research Centre, Technical Physics Division, Mumbai, India

Abstract

Alkali halide scintillators have emerged as promising low-cost alternatives to conventional thermal neutron detectors such as ^{3}He counters, through the incorporation of neutron sensitive isotopes such as ^{6}Li or ^{10}B, owing to their ease of growth and scalability. In this work, single crystals of CsI:Tl incorporating 2% ^{6}Li and varying concentration of Sr as dopants were grown using the Bridgman melt growth method and evaluated for their scintillation and neutron-gamma discrimination characteristics. The radioluminescence spectra are dominated by yellow-green emission from Tl activator sites. Under ^{137}Cs excitation, the light output of the crystals was observed to decrease with Sr incorporation compared to the ^{6}Li-only doped crystal, while the crystal doped with 2% Sr exhibit the best energy resolution of 6.8% at 662keV. The pulse shape discrimination (PSD) studies of the grown crystals demonstrate effective neutron-gamma discrimination, highlighting the potential of these crystals for use in mixed radiation fields and compact radiation system.

References
[1] Yang, KN, Menge, PR & Ouspenski, V 2017, 'Li co-doped NaI:Tl (NaIL)—A large volume neutron-gamma scintillator with exceptional pulse shape discrimination', *IEEE Transactions on Nuclear Science*, vol. 64, p. 2406, New York: IEEE.
[2] Wang, J, Wang, C, Li, H, Shi, J, Wen, X, Shan, C & Wu, Y 2023, 'Improvement of energy resolution and neutron–gamma discrimination of NaI:Tl, ^{6}Li single crystal scintillators by Ca^{2+} and Sr^{2+} co-doping', *IEEE Transactions on Nuclear Science*, vol. 70, p. 840, New York: IEEE.

NSS-01-045

Development of Plastic Scintillator by Thermal Polymerization for Gamma Spectroscopy (#2945)

Tanuj Kumar, Vivek Anand, Anil K. Gourishetty

Indian Institute of Technology Roorkee, Department of Physics, Roorkee, India

The authors would like to acknowledge Prof. Akash Kaithal and Mr. Manish Tiwari from Department of Chemistry, IIT Roorkee for their help in Argon purging.
This work was supported by the Council of Scientific and Industrial Research (CSIR), Human Resource Development Group (CSIR-HRDG), Government of India, under the Extra Mural Research (EMR) Scheme (ID: 35112355 and File No. 09/0143(21791)/2025-EMR-I). G. Anil Kumar would also like to acknowledge the financial support provided by the Anusandhan National Research Foundation (ANRF) under the projects ANR-2415-PHY-TSAH/24-25 and ANR-2863-PHY-TSAH/25-26.

Abstract

A series of polyvinyl toluene (PVT)-based scintillators was prepared via thermal polymerization to investigate the effect of the thermal initiator 2,2-Azobisisobutyronitrile (AIBN) on light output. Samples were synthesized both with varying weight percentages (wt%) of AIBN and without AIBN. All samples contained 2% 2,2-diphenyloxazole (PPO) and 0.05% 1,4-bis(5-phenyl-2-oxazolyl) benzene (POPOP), while the concentrations of vinyl toluene and AIBN were varied. The light output of the developed plastic scintillators (PS) was compared to the commercially available PS EJ-267D using the gamma spectrum from a Cs-137 radiation source. The results indicated that samples containing 0.1% AIBN without argon purging, 1% AIBN without purging, and 0% AIBN with argon purging yielded 24.40%, 28.23%, and 40.88% of the light output of EJ-267D, respectively.

References
[1] Lee, C.H., Son, J., Kim, T.-H., Kim, Y.K. 2017, 'Characteristics of plastic scintillators fabricated by a polymerization reaction', Nuclear Engineering and Technology,Volume 49, Issue 3, April 2017, Pages 592-597, South Korea: Korean Nuclear Society
[2] Lastname, GN, Lastname, GN YYYY, 'Article', *Journal*, Edition, Page, Place of publication: publishers
Fitriana, R., Febrianti, Y., Rahmawati, R. & Saputro, A.H. 2025, 'A Review on Plastic Scintillator Development and Performance for Gamma-Ray Detection', *Nuclear Science and Engineering*, vol. 00, pp. 1–29, Taylor & Francis.

NSS-01-047

Comparative Analysis of Scintillators for TOF-DXA Detectors in the Low-Energy X-ray Region (#3149)

Jiwon Nam, Jiwoong Jung, Sang-hyun Chun, Sena Kwon, Jin Ho Jung, Yong Choi

Sogang University, Department of Electronic Engineering, Intelligent Signal Processing System (ISPS) Laboratory, Seoul, South Korea

This research was supported by the Industrial Technology Innovation Program funded by the Ministry of Trade, Industry and Energy (no. P0030253), by the National Research Foundation of Korea (NRF) grant funded by the Korea government (MSIT) (no. RS-2023-00280177), and by the Basic Science Research Program through the National Research Foundation of Korea (NRF) funded by the Ministry of Education (no. RS-2026-25565373) of the Republic of Korea.

Abstract

TOF-DXA requires simultaneous energy and timing measurement in the low-energy X-ray region (<60 keV). However, the low X-ray energies result in reduced scintillation light output and small detector signals, making timing measurement challenging. The purpose of this study was to evaluate the performance of different scintillators for energy and timing measurement in low-energy TOF-DXA detectors.

An analog front-end circuit was developed for energy and timing measurement in low-energy TOF-DXA detectors. Detector signals in the energy path were amplified transmitted differentially to reduce common-mode noise and signal degradation. For timing path, a high slew-rate amplifier and comparator were used to generate LVDS preserving the rising-edge integrity of detector pulses. Three 3 × 3 × 3 mm^3 scintillators (LYSO, GFAG, and YAP) coupled with a NUV-MT SiPM were evaluated for simultaneous energy and timing measurement. Output pulses were measured using an Am-241 point source to evaluate energy resolution and pulse characteristics. In addition, X-ray spectra were acquired using an X-ray generator operated at 83 kVp and 0.2 mA with a Ce filter to evaluate detector performance in the DXA.

The energy resolutions measured with LYSO, GFAG, and YAP were 25.7%, 24.4%, and 30.9%, respectively. In the timing path, LYSO exhibited the highest slew rate (364.8 MV/s), followed by GFAG (354.9 MV/s) and YAP (220.8 MV/s). LYSO showed the highest peak-to-valley ratios for both the low- and high-energy peaks (3.96 and 1.62, respectively). For the low-energy peak, GFAG and YAP showed PVRs of 3.32 and 2.45, respectively, whereas YAP showed a slightly higher high-energy PVR (1.13) than GFAG (1.02).This overall performance may be attributed to the balanced characteristics of LYSO, which exhibited higher light output than YAP and faster decay time than GFAG.

These results indicated that LYSO was superior to GFAG and YAP for TOF-DXA applications requiring both energy and timing measurement.

References

[1] Pietrobelli, A, Formica, C, Wang, Z, Heymsfield, SB 1996, 'Dual-energy X-ray absorptiometry body composition model: review of physical concepts', *Am. J. Physiol.*, vol. 271, pp. E941–E951.

[2] Park, C, et al. 2020, 'Feasibility study of SiPM based scintillation detector for dual-energy X-ray absorptiometry', *Nucl. Eng. Technol.*, vol. 52, pp. 2346–2352

NSS-01-049

Improved Low-Energy Threshold Performance of a Vacuum-Compatible Hybrid Pixel Detector for Soft X-ray Applications (#1007)

Yasukazu Nakaye, Tomonao Inoue, Masaya Oka, Takuto Sakumura, Yasutaka Sakuma, Satoshi Mikusu

Rigaku Corporation, Detector Development Grp., Akishima, Japan

Abstract

We report characterization results of a vacuum-compatible, pre-production hybrid pixel array X-ray detector incorporating a silicon sensor and a low-noise photon-counting readout ASIC, with emphasis on extending the practical low-energy discriminator threshold. Calibration pulse measurements combined with refined noise characterization enabled evaluation of discriminator threshold settings down to approximately 450 eV. Considering measured RMS noise levels on the order of 70-80 e^-RMS, such threshold operation implies practical detectability of soft X-ray photons with energies around 500 eV, although uniform full-field operation at this threshold is not yet expected.

Low-threshold operation was found to be temporally stable, showing negligible threshold drift and no observable degradation of pixel operability during continuous operation over extended periods. Soft X-ray beam validation experiments are planned at the SPring-8 BL17SU beamline. Additional measurements at higher X-ray energies will be conducted at BL32-B2 and BL29XU to support fundamental characterization of detector and ASIC behavior.

The present study focuses on system-level noise correction and threshold optimization using a conventional silicon sensor. Evaluation with alternative sensor technologies, including iLGAD, is foreseen in future work.

References

[1] Grybos, P, Kmon, P, Maj, P & Szczygiel, R 2016, '32k Channel Readout IC for Single Photon Counting Pixel Detectors with 75 µm Pitch, Dead Time of 85 ns, 9 e^- rms Offset Spread and 2% rms Gain Spread', *IEEE Transactions on Nuclear Science*, vol. 63, no. 2, pp. 1155–1161, Piscataway, NJ: IEEE.

NSS-01-053

Development and Testing of the Strip Pairing Algorithm for the COSI Data Pipeline (#1263)

Julian Gerber[1], Andreas Zoglauer[2], Steven E. Boggs[1], Felix Hagemann[2], Carolyn Kierans[3], Sean N. Pike[1], Jarred M. Roberts[1], Field R. Rogers[2], John A. Tomsick[2]

[1] University of California, San Diego, Astronomy & Astrophysics, San Diego, USA; [2] University of California, Berkeley, Space Sciences Laboratory, Berkeley, USA; [3] NASA Goddard Space Flight Center, Greenbelt, USA

This work was supported in part by the Compton Spectrometer and Imager, a NASA Explorer project led by the University of California, Berkeley with funding from NASA, United States under contract 80GSFC21C0059.

Abstract
The Compton Spectrometer and Imager (COSI) is a NASA Small Explorer satellite mission scheduled for launch in August 2027. COSI's imaging capabilities are achieved by reconstructing Compton scattering events within a 2 x 2 x 4 stack of germanium detectors (GeDs). Each GeD contains orthogonal electrode strips on opposite faces of the detector, forming an x-y grid. An incident gamma ray interacts with the GeD by depositing energy in one or more strips on each face that are then read out simultaneously. The "strip pairing" algorithm reconstructs the 2D position of each scatter by comparing the measured energies on pairs of orthogonal strips through a reduced chi square statistic. While simple for a single-site event, the matching becomes more complex when considering multiple scatters within a detector, multiple scatters on a single strip, or charge sharing between neighboring strips. Here, we describe the strip pairing algorithm and how it is implemented into the COSI pipeline. We then test the algorithm's efficacy and use it to demonstrate the imaging and spectral performance of a COSI GeD. Using a ^{137}Cs calibration source and a single test detector, we find that the pipeline reconstructs the source's position and yields an energy resolution of less than 1% full width at half maximum at 662 keV.

References
[1] A. C. Zoglauer, "First light for the next generation of Compton and pair telescopes," Ph.D. dissertation, Technical University of Munich, Germany, Jan. 2005.
[2] F. R. Rogers et al., "Depth calibration of double-sided strip germanium detectors for the Compton Spectrometer and Imager satellite," Nuclear Instruments and Methods in Physics Research A, vol. 1086, p. 171332, Jun. 2026.
[3] J. Tomsick et al., "The Compton Spectrometer and Imager," in 38th International Cosmic Ray Conference, Sep. 2024, p. 745.

NSS-01-055

Temperature-Dependent Charge Transport in Diamond Radiation Detectors (#1377)

Owen A. Johnson[1,2], Richard Fitzhugh[2], Eric Lukosi[1]

[1] University of Tennessee Knoxville, Nuclear Engineering, Knoxville, USA; [2] Y-12 National Security Complex, Oak Ridge, USA

The information, data or work presented herein was funded in part by the Advanced Research Project Agency-Energy (ARPA-E), U.S. Department of Energy, under award
Number DE-AR0001603. This work was also supported in part by Consolidated Nuclear Security, LLC (CNS) as accounts of work sponsored by an agency of the United
States Government under Contract DE-NA-0001942 and under subcontract number 4300189680, both related to the operation of Y-12 National Security Complex.
Neither the United States Government nor any agency thereof, nor CNS, nor any of their employees, makes any warranty, express or implied, or assumes any legal liability or
responsibility to any non-governmental recipient hereof for the accuracy or usefulness of any information. The views and opinions of authors expressed herein do not necessarily state or reflect those of the United States Government or any agency or contractor thereof.

Abstract
Semiconductor radiation detectors are often limited due to thermal degradation of their electrical properties: as temperature increases, thermally activated carrier generation and other effects lead to elevated leakage currents and reduced signal to noise ratios. For more extreme environments such as advanced reactors and molten salt environments, detectors which operate at high temperatures are needed. Diamond, with its wide 5.47 eV bandgap, high carrier mobility, and radiation hardness is a promising material. Previous work in literature reported charge collection efficiency degradation in diamond at 230 °C, followed by recovery and stability of operation to 450 °C. However, this result has not been widely validated. This study evaluates three diamond samples of varying thickness at elevated temperatures, reevaluating carrier mobility and charge collection efficiency. Alpha traces at each temperature are analyzed to study the current transients, gaining insight into how thermal variations impact detector performance and mechanisms driving charge transport variation.

NSS-01-057

Monitoring neutron exposure in hyper-pure germanium detectors with in-situ capture reactions (#1736)

Thomas Round[1], Brendan Green[1], Stephen Croft[1], Joshua Moore[2], Alex Metcalfe[1], Malcolm J. Joyce[1]

[1] Lancaster University, Engineering Department, Lancaster, UK; [2] NSG Environmental, Chorley, UK

We acknowledge the support of NSG Ltd (Chorley, UK) and the UK Nuclear Decommissioning Authority.

Abstract
The potential to monitor neutron exposure in hyper-pure germanium detectors via capture-g reactions in the germanium crystal is explored. The short-lived reactions on ^{70}Ge and ^{74}Ge resulting in g rays in the 130 to 200 keV energy region have been studied in terms of their response to thermalization of neutrons incident on portable, mechanically cooled, reverse-electrode hyper-pure germanium detectors (REGe^{TM}). The relative sensitivity in terms of y rays emitted per unit neutron flux is estimated and a comparison is made with the inelastic response observed at higher energies, the latter often considered as cause of damage in such detectors. We report the potential for

these short-lived reactions to serve as a built-in neutron-sensitive diagnostic for germanium detector use in hot cells and realistic, mixed-field environments.

References
[1] J-H. Chao, Appl. Rad. Isot. (1993) 44 (3) pp. 605-611, https://doi.org/10.1016/0969-8043(93)90177-C.
[2] N. Soppera, M. Bossant and E. Dupont, Nuclear Data Sheets, (2014) 120 pp. 294-296, https://doi.org/10.1016/j.nds.2014.07.071.
[3] S. He et al., Anal. Methods, (2014) 6 (12) pp. 4402–4407, https://doi.org/10.1039/c4ay00068d
[4] L. Szentmiklósi, J. Radioanal. Nucl. Chem. 315 (2018) pp. 663-670, https://doi.org/10.1007/s10967-017-5589-z

NSS-01-059

Pixel Architecture Effects on Neutron-Induced White Spot Generation in CMOS Image Sensors (#1811)

Jihun Jeong[1], Seil Kim[2], Jungman Lim[2], Seungbae Lee[2], Inyong Kwon[1]

[1] Yonsei University, Radiation Convergence Engineering, Wonju, South Korea; [2] Samsung Electronics, Whaseong, South Korea

Abstract

This paper quantifies how pixel structural parameters, specifically pitch, photodiode type, and transfer gate design, independently influence neutron-induced white spot generation in CMOS image sensors. Six sensor families with pixel pitches of 0.64, 0.70, 1.00, 1.12, and 1.20 μm, covering single and dual photodiode configurations and single and dual transfer gate designs, were irradiated with neutrons at the TRIUMF facility across seven cumulative fluence steps up to approximately 7×10^8 n/cm². Ten samples per family were used, with dark-frame measurements performed at each step using eight-frame averaged images. White spot fractions were extracted using a baseline-subtracted delta counting method with Arrhenius-based temperature correction applied to the radiation-induced component. All six families exhibit a clear power-law dependence of white spot fraction on fluence. Spatial analysis reveals a monotonic increase in the 3×3 cluster ratio, defined as the ratio of the summed dark signal increase in neighboring pixels to that of the center hot pixel, from 0.14 at 1.20 μm to 0.24 at 0.64 μm, and this metric remains independent of fluence. A two-stage meta-regression model shows that increasing pitch from 0.64 to 1.20 μm raises the power-law amplitude by 2.12 times, adopting dual photodiode sharing raises it by 2.35 times, and employing a dual transfer gate reduces it by 0.49 times. Furthermore, the model is extended to predict white spot fractions for unmeasured pixel configurations, with potential for radiation-tolerant CIS design.

References
[1] J. R. Srour, C. J. Marshall and P. W. Marshall, "Review of displacement damage effects in silicon devices," in *IEEE Transactions on Nuclear Science*, vol. 50, no. 3, pp. 653-670, June 2003, doi: 10.1109/TNS.2003.813197.
[2] J. R. Srour and J. W. Palko, "Displacement Damage Effects in Irradiated Semiconductor Devices," in *IEEE Transactions on Nuclear Science*, vol. 60, no. 3, pp. 1740-1766, June 2013, doi: 10.1109/TNS.2013.2261316.
[3] C. Virmontois *et al.*, "Displacement Damage Effects Due to Neutron and Proton Irradiations on CMOS Image Sensors Manufactured in Deep Submicron Technology," in *IEEE Transactions on Nuclear Science*, vol. 57, no. 6, pp. 3101-3108, Dec. 2010, doi: 10.1109/TNS.2010.2085448.
[4] J.-M. Belloir, V. Goiffon, C. Virmontois, M. Raine, P. Paillet, O. Duhamel, M. Gaillardin, R. Molina, P. Magnan, and O. Gilard, "Pixel pitch and particle energy influence on the dark current distribution of neutron irradiated CMOS image sensors," *Optics Express*, vol. 24, no. 4, pp. 4299–4315, Feb. 2016, doi: 10.1364/OE.24.004299.
[5] V. Goiffon, M. Estribeau, P. Cervantes, R. Molina, M. Gaillardin and P. Magnan, "Influence of Transfer Gate Design and Bias on the Radiation Hardness of Pinned Photodiode CMOS Image Sensors," in *IEEE Transactions on Nuclear Science*, vol. 61, no. 6, pp. 3290-3301, Dec. 2014, doi: 10.1109/TNS.2014.2360773.

[6] S. Place, J. -P. Carrere, S. Allegret, P. Magnan, V. Goiffon and F. Roy, "Radiation Effects on CMOS Image Sensors With Sub-2 µm Pinned Photodiodes," in *IEEE Transactions on Nuclear Science*, vol. 59, no. 4, pp. 909-917, Aug. 2012, doi: 10.1109/TNS.2012.2193671.

NSS-01-061

Characterisation of edge-on fully-depleted monolithic CMOS silicon sensors (#1882)

Matteo Barbagiovanni[1,2], Anders Bjorklid[3], Alberto Bortone[2], Rickard Brunskog[6], Manuel D. Da Rocha Rolo[2], Mats Danielsson[6], Andreas Elihar[3], Umberto Follo[2], Sara Garbolino[2], Johan Hartman[4], Julia Herzen[7], Dominik John[7], Franz L. Klaus[7], Carolin Mogler[7], Lucio Pancheri[5], Julia Parnell[7,6], Mats Persson[6], Edoardo Posteraro[1,2], Martin Sjolin[3], Moa Y. Tamm[6], Sami Wirtensohn[7], On behalf of 1MICRON Collaboration

[1] Politecnico di Torino, Electronics and Telecommunications, Turin, Italy; [2] INFN Sezione Torino, Turin, Italy; [3] Prismatic Sensor, Stockholm, Sweden; [4] Karolinska Institutet, Stockholm, Sweden; [5] Università di Trento, Trento, Italy; [6] KTH Royal Institute of Technology, Stockholm, Sweden; [7] TUM, Munich, Germany

This study was carried out with support from the INFN CSN5 Call ARCADIA. This work was supported by the European Union's Horizon Europe research and innovation programme under the 1MICRON project – "New Technology for 1 MICRON Resolution Biomedical Imaging" (grant agreement No. 101186826).

Abstract

Monolithic silicon CMOS Sensors represent a considerable step forward in charged particle and photon sensing, and emerge as a promising embodiment for the design of novel deep-silicon photon-counting X-ray Computed Tomography scanners . This work presents the first characterization of the ARCADIA MD3 Fully-Depleted CMOS sensors, which technology is currently the baseline for the development of innovative sensors under the framework of the EIC Pathfinder Open 1MICRON project. We report on the characterisation results using an edge-on geometry and a focused synchrotron X-ray beam at the DESY test facility. The x-rays impinge on the edge of the sensor, increasing the active sensor depth seen by the photons, which consequently improves the quantum efficiency with respect to a face-on configuration. A 37 keV focused beam incident parallel to the sensor surface allowed scans along the two directions of the sensor edge, enabling the extraction of the active sensor thickness and mechanical tilt via pixel intensity profiles. Lateral scans across pixel boundaries revealed a periodicity of the spatial modulation of mean cluster size compatible with the pixel pitch of the matrix. Taking the cluster size as the main figure of merit, the performance of the sensor was evaluated at different thresholds and multiple bias voltages in order to assess the variation in the Coulomb cone and collection dynamic. The measurements are supported by Allpix Squared Monte Carlo framework, demonstrating good consistency between the simulated and the real domain.

References

[1] Da Rocha Rolo, Manuel 2025 'Arcadia fully depleted cmos maps development with lfoundry 110 nm cis', Frontiers in Sensors, vol. Volume 6 - 2025

[2] Bergamaschi, A., 2005, 'Edge on silicon microstrip detectors for medical imaging', Nuclear Instruments and Methods in Physics Research Section A: Accelerators, Spectrometers, Detectors and Associated Equipment, vol. 549, no. 1, pp. 199–204, Sep. 2005

NSS-01-063

Gain suppression study on LGADs with different gain layer designs

(#2025)

Leo Cavazzini[1,2], Ashish Bisht[1], Maurizio Boscardin[1], Matteo Centis Vignali[1], Marcos Fernandez Garcia[3], Francesco Ficorella[1], Omar Hammad Alì[1], Veronika Kraus[4], Michael Moll[5], Giovanni Paternoster[1], Moritz Wiehe[5]

[1] Fondazione Bruno Kessler, Trento, Italy; [2] University of Trento, Department of Physics, Trento, Italy; [3] Instituto de Fisica de Cantabria, IFCA, Santander, Spain; [4] TU Wien, Faculty of Physics, Vienna, Austria; [5] CERN, Geneva, Switzerland

Abstract

High-energy physics experiments currently use Low Gain Avalanche Diodes (LGADs) as part of their time-of-flight layers to track particles, thanks to their unique temporal resolution and radiation hardness. With increasing deposited charge, the gain was observed to decrease. This gain suppression effect originates from the electrostatic field screening produced by the avalanche multiplication charge. This work investigates the resilience of the LGADs to the gain suppression by characterizing a set of detectors with different gain layer designs and thicknesses, using Transient Current Techniques.

References

[1] G. Pellegrini et al. “Technology developments and first measurements of Low Gain Avalanche Detectors (LGAD) for high energy physics applications”. In: Nucl. Instrum. Meth. A.765 (2014), pp. 12–16. DOI: https://www.doi.org/10.1016/j.nima.2014.06.008.

[2] N. Cartiglia et al. “Beam test results of a 16 ps timing system based on ultra-fast silicon detectors”. In: Nucl. Instrum. Meth. A.850 (2017), pp. 83–88. DOI: https://www.doi.org/10.1016/j.nima.2017.01.021.

[3] E. Curras et al. “Gain reduction mechanism observed in Low Gain Avalanche Diodes”. In: Nuclear Instruments and Methods in Physics Research Section A: Accelerators, Spectrometers, Detectors and Associated Equipment, 1031 (May 2022), p. 166530. ISSN: 0168-9002. DOI: http://www.doi.org/10.1016/j.nima.2022.166530.

[4] Sebastian Pape et al. “TCAD Simulation of Two Photon Absorption–Transient Current Technique Measurements on Silicon Detectors and LGADs”. In: Sensors 24.24 (2024). ISSN: 1424-8220. DOI: https://doi.org/10.3390/s24248032.

NSS-01-065

Pulse-Shape-Based Slow-Rising Pulse Rejection for Reliable Charge-Carrier Transport Characterization in a Semiconductor Radiation Detector (#2231)

Jihwan Boo[1], Beomjun Park[2], Geehyun Kim[1,3]

[1] Seoul National University, Department of Energy Systems Engineering, Seoul, South Korea; [2] Seoul National University, Nuclear Research Institute for Future Technology and Policy (NIFTEP), Seoul, South Korea; [3] Seoul National University, Nuclear Engineering Department, Seoul, South Korea

This work was supported by the National Research Foundation of Korea (NRF) grant funded by the Korea government (Ministry of Science and ICT) (No. 2022M2D2A1A02063826).

Abstract

Mobility (μ), lifetime (τ), and mobility–lifetime product (μτ) are key metrics for semiconductor radiation detectors. Highly concentrated trapping centers or defects can distort the internal electric-field distribution, producing reduced-amplitude slow-rising charge-sensitive preamplifier pulses that degrade carrier-transit and charge-collection analyses. Although slow-rising-pulse rejection is commonly used to sharpen pulse-amplitude peaks and suppress low-amplitude tails, this work extends its use to charge-carrier transport characterization. A CdZnTeSe detector [1, 2] was characterized at room temperature under electron- and hole-transit-dominant conditions using ^{241}Am alpha irradiation. Pulse-shape analysis rejected slow-rising pulses for key metrics extraction. In electron-transit-dominant measurements, the fast-rising pulse events preserved the bias-dependent peak-centroid trend and yielded $(\mu\tau)_e$ = 5.7×10^{-4} cm²/V, μ_e = 576 cm²/V·s, and τ_e = 1.0 μs, consistent with reported values [3,4]. For hole-transit-dominant measurements, all-pulse events obscured the pulse-amplitude peak and hindered Hecht fitting. After rejection, we obtained $(\mu\tau)_h$ = 2.1×10^{-4} cm²/V, τ_h = 0.7 μs, comparable to reported values [5], with μ_h = 318 cm²/V·s. Using the rise-time peak as the representative transit time, both all-pulse and fast-rising-pulse events yielded similar μh values. However, when the median rise time of all-pulse events was used instead, drift velocity did not show a clear linear dependence on electric field, whereas fast-rising-pulse events retained linearity. This reflects the need for careful consideration of slow-rising components and the transit-time definition. These results show that slow-rising-pulse rejection enables reliable transport characterization beyond spectral improvement.

References

[1] Park, B., et al. 2022, 'Bandgap engineering of $Cd_{1-x}Zn_xTe_{1-y}Se_y$ (0< x< 0.27, 0< y< 0.026)', Nucl. Instrum. Methods Phys. Res. A. 1036, 166836.

[2] Park, B., et al. 2024 'Fabrication and Evaluation of Spectroscopic Grade Quasi-hemispherical CdZnTe Detector', J. Radiat. Prot. Res. 49(2), 85-90.

[3] Kleppinger, J.W., et al. 2021, 'Growth of $Cd_{0.9}Zn_{0.1}Te_{1-y}Se_y$ single crystals for room-temperature gamma ray detection, IEEE Trans. Nucl. Sci. 68(9), 2429-2434.

[4] Chaudhuri, S.K., et al. 2021, 'Quaternary semiconductor $Cd_{1-x}Zn_xTe_{1-y}Se_y$ for high-resolution, room-temperature gamma-ray detection', Crystals 11(7), 827.

[5] Pipek, J., et al. 2021, 'Charge transport and space-charge formation in $Cd_{1-x}Zn_xTe_{1-y}Se_y$ radiation detectors', Phys. Rev. Appl. 15(5) 054058.

NSS-01-067

The Sensor, Packaging and INtegration (SPIN) group at Fondazione Bruno Kessler (FBK): capabilities, facilities and expertise (#2415)

David Novel, Tiziano Facchinelli, Evgeny Demenev, Alessandro Lega, Pietro Tosato, Sara Ferrari

Fondazione Bruno Kessler, Trento, Italy

Abstract

This contribution presents the capabilities, infrastructure, and technical expertise of the Sensor, Packaging and Integration (SPIN) group at Fondazione Bruno Kessler (FBK). The SPIN unit has established experience in the miniaturisation and integration of electronic systems for radiation detectors, with demonstrated results in space instrumentation (e.g. THESEUS for ESA), high-energy physics (e.g. R&D for ALICE3), and medical applications (e.g. the BOA project within INFN). These domains impose stringent constraints on material budget, geometrical footprint, and signal integrity, motivating the development of dedicated integration strategies. The group core expertise lies in the co-design of sensors and front-end electronics for operation in highly constrained volumes, where standard packaging solutions are not applicable. This includes the optimisation of interconnect technologies (wire bonding, TAB, flip-chip), layout strategies and the implementation of low-noise architectures. Emphasis is placed on preserving signal integrity in high-density environments typical of modern detector systems. SPIN offers end-to-end capabilities covering system design, prototyping, assembly, and characterisation, supported by dedicated infrastructure for precision packaging and electrical testing. A key enabling technology is the use of flexible and hybrid electronics, allowing the development of low-mass, conformable interconnects and non-planar integration schemes. In particular, the group has developed dedicated processes for the fabrication and integration of ultra-thin Kapton-aluminium flexible circuits, optimised for low material budget and high mechanical compliance. These structures enable the realisation of fine-pitch routing on lightweight substrates, with controlled thickness and reduced radiation length, making them especially suitable for tracking detectors.

NSS-01-069

High-voltage stress test and thermal recovery of an amorphous-silicon-passivated planar HPGe detector (#2646)

LiHui Han[1,2], Yulan Li[1,2], Li He[1,2], Siyuan Yu[1,2], Xiuxia Li[1,3], Mingxin Yang[1,2], Yuanjing Li[1,2], Yang Tian[1,2]

[1] Tsinghua University, Department of Engineering Physics, Beijing, China; [2] Ministry of Education, Key Laboratory of Particle & Radiation Imaging (Tsinghua University), Beijing, China; [3] Greater Bay Area National Center of Technology Innovation, Guangzhou, China

Abstract

High-purity germanium (HPGe) detectors are widely used in low-background and rare-event measurements because of their excellent energy resolution and relatively high detection efficiency. Compared with a-Ge, sputtered a-Si provides a higher electron-injection barrier, which is attractive for planar detectors under high electric fields. However, the high-voltage (HV) stability of a-Si contacts and the recovery from HV-induced large leakage-current and resolution degradation remain insufficiently understood. The detector was fabricated using a planar p-type HPGe crystal (φ24 mm × 10 mm). A Li-diffused n+ contact was used as the high-voltage electrode, while the opposite face was coated with an a-Si layer deposited by magnetron sputtering. A central Al pad was formed on the a-Si layer by thermal evaporation and used as the signal readout electrode. I–V curves were measured with a picoammeter up to 2500 V, and 57Co spectra were acquired at 500–2000 V using a DSPEC-50 digital spectrometer. The stress test consisted of repeated biasing up to 2000 V, followed by 9 hours of room-temperature storage and 9 hours of thermal treatment with the crystal holder maintained below 70 degrees. After the high-voltage stress test, the leakage current at 1000 V increased to approximately 1.1 nA, more than two orders of magnitude higher than the initial level. After thermal treatment below 70 degrees, the leakage current at 1000 V decreased to less than 2 pA, close to the as-fabricated level. At 1000 V, the resolution broadened to 1.53 keV FWHM, suggesting larger noise and contact-related instability under a higher electric field. After thermal treatment, the resolution at 500 V recovered to 0.67 keV FWHM, comparable to the initial value. In the future, we will repeat stress-recovery cycles, and investigate the dependence on treatment temperature and duration. The possible underlying recovery mechanism related to the a-Si fermi level will also be studied.

References
[1] Hull E L, Pehl R H, Lavietes A D, et al. Amorphous-semiconductor blocking contacts on Ge radiation detectors. Nuclear Instruments and Methods in Physics Research Section A, 2014, 762: 130-134.
[2] Looker Q, Amman M, Vetter K. Leakage current in high-purity germanium detectors with amorphous semiconductor contacts. Nuclear Instruments and Methods in Physics Research Section A, 2015, 777: 138-144.
[3] Yang M, Li Y, Zeng Z, et al. A prototype segmented planar high purity germanium detector using wraparound lithium diffusion electrode and amorphous germanium blocking contact. Radiation Detection Technology and Methods, 2022, 6(4): 433-438.

NSS-01-071

Development of a SiC-Based Muon Beam Monitor for the COMET Experiment (#2912)

Kenya Okabe[1], Yoshinori Fukao[2], Youichi Igarashi[2], Yowichi Fujita[2], Eitaro Hamada[2], Tetsuichi Kishishita[3], Kazutoshi Kojima[4], Ryoji Kosugi[4], Satoshi Mihara[2], Hajime Nishiguchi[2], Masayoshi Shoji[2], Yasunori Tanaka[4], Yoshiki Yamaguchi[5], Yoshiki Yamada[5]

[1] The Graduate University for Advanced Studies, Particle and Nuclear Physics Program, Tsukuba, Japan; [2] High Energy Accelerator Research Organization, Institute of Particle and Nuclear Studies, Tsukuba, Japan; [3] Universität Bonn, Physikalisches Institut, Bonn, Germany; [4] National Institute of Advanced Industrial Science and Technology, Advanced Power Electronics Research Center, Tsukuba, Japan; [5] University of Tsukuba, Faculty of Engineering, Information and Systems, Tsukuba, Japan

This work was supported by JSPS KAKENHI Grant Numbers JP21H01117, JP22H00139, JP25K07348, and JST SPRING, Japan Grant Number JP-MJSP2104.

Abstract

The COMET Experiment at J-PARC aims to search for the muon-to-electron conversion process with a sensitivity of 10−17. In COMET Phase-I, the muon beam monitor (MBM) will be installed downstream of the primary detector system for background suppression and precise beam control. Since the MBM directly measures the high-intensity muon beam, silicon carbide (SiC), one of the wide-bandgap semiconductors with higher radiation tolerance, is employed as the detector material. The SiC sensor was jointly developed by KEK and AIST, and a beam test performed at J-PARC MLF in 2024 showed successful muon detection and sufficient linearity for operation in the COMET Experiment. In addition, a radiation-tolerant ASIC currently under development at KEK is planned for the SiC detector readout. While the initial prototype MBM board utilised a two-layer polyimide PCB to minimise the material budget, it suffered from external noise and inter-channel crosstalk, obscuring low-amplitude beta-ray signals. To address this and optimise the final MBM board design, we developed a test board equipped with seven SiC detectors. This study showed that noise can be reduced by implementing appropriate noise mitigation techniques, such as a ground plane in a standard PCB structure, enabling stable waveform acquisition of low-amplitude beta-ray signals. In addition, inter-channel crosstalk was effectively suppressed to a negligible level by introducing low-pass filters on the bias supply lines close to each detector. Based on these findings, a prototype MBM board for the final system is currently being developed. This presentation also reports on its design and initial performance evaluation.

References

[1] R. Abramishvili *et al.*, “COMET Phase-I Technical Design Report,” *PTEP*, vol. 2020, no. 3, p. 033C01, 2020.

[2] T. Kishishita *et al.*, “SiC p+n Junction Diodes Toward Beam Monitor Applications,” *IEEE Trans. Nucl. Sci.*, vol. 68, no. 12, pp. 2787–2793, 2021.

[3] K. Okabe *et al.*, “Performance review of the prototype SiC muon beam monitor for COMET experiment,” *Nucl. Instrum. Meth. A*, vol. 1080, p. 170798, 2025

NSS-01-073

Argon Ion-Assisted Polycrystalline PbO Layers for Direct-Conversion X-ray Imaging Detectors (#3080)

Mikhail Vostokov, Janos Rado, Galina Nagicheva, Amy Stieh, Alexander Alexandrov, Alla Reznik

Lakehead University, Physics Department, Thunder Bay, Canada

This research was supported by Teledyne DALSA and Natural Sciences and Engineering Research Council of Canada Discovery and Alliance programs, MITACS. The authors gratefully acknowledge their support.

Abstract

Lead oxide (PbO) is a high-atomic-number photoconductor for direct-conversion X-ray imaging. This work compares PbO layers produced by three deposition regimes: conventional physical vapor deposition from molten PbO powder, oxygen ion-assisted PVD, and argon ion-assisted PVD. All layers were deposited on indium tin oxide

coated glass substrates with a polyimide blocking layer to reduce dark current and were characterized by scanning electron microscopy, Raman spectroscopy, profilometry, density measurements, and X-ray photoconductivity. Deposition without ion assistance produced low-density polycrystalline PbO with noticeable lag in the X-ray response after irradiation. Oxygen ion-assisted growth yielded dense amorphous PbO with essentially lag-free temporal response. In contrast, argon ion-assisted deposition preserved the polycrystalline structure while producing a more uniform layer with intermediate density and needle-like surface crystallites. X-ray photocurrent measurements showed that the argon-assisted films had an electron–hole pair creation energy, W±, of approximately 6 eV/ehp at 10 V/μm, close to the fundamental limit. Under 30 Hz modulated X-ray irradiation, these films showed stable photocurrent during exposure and rapid signal decay after irradiation stopped, indicating negligible lag.

References
[1] S. O. Kasap, J. B. Frey, G. Belev, O. Tousignant, H. Mani, J. Greenspan, L. Laperriere, O. Bubon, A. Reznik, G. DeCrescenzo, K. S. Karim, and J. A. Rowlands, "Amorphous and polycrystalline photoconductors for direct conversion flat panel X-ray image sensors," Sensors, vol. 11, no. 5, pp. 5112-5157, 2011, doi: 10.3390/s110505112.
[2] O. Grynko and A. Reznik, "Progress in lead oxide X-ray photoconductive layers," in Photoconductivity and Photoconductive Materials, S. O. Kasap, Ed. Hoboken, NJ, USA: Wiley, 2022, ch. 16, pp. 643-688, doi: 10.1002/9781119579182.ch16.
[3] O. Semeniuk, O. Grynko, G. DeCrescenzo, G. Juska, K. Wang, and A. Reznik, "Characterization of polycrystalline lead oxide for application in direct conversion X-ray detectors," Scientific Reports, vol. 7, Art. no. 8659, 2017, doi: 10.1038/s41598-017-09154-w.
[4] O. Semeniuk, O. Grynko, G. Juska, and A. Reznik, "Amorphous lead oxide (a-PbO): suppression of signal lag via engineering of the layer structure," Scientific Reports, vol. 7, Art. no. 13272, 2017, doi: 10.1038/s41598-017-13572-7.
[5] O. Grynko, T. Thibault, E. Pineau, and A. Reznik, "Engineering of a blocking layer structure for low-lag operation of the a-PbO-based X-ray detector," IEEE Trans. Electron Devices, vol. 68, no. 5, pp. 2335-2341, May 2021, doi: 10.1109/TED.2021.3067616.
[6] A. Reznik and O. Semeniuk, "Lead oxide as material of choice for direct conversion detectors," in Oxide Electronics, 2021, ch. 7, doi: 10.1002/9781119529538.ch7.

NSS-01-075

Quantum Dots-Based Short-Wave Infrared Avalanche Photodetectors

(#1295)

Shilong Fang[1,3], Xingzhan Wei[2,3]

[1] Chongqing University of Posts and Telecommunications, Chongqing, China; [2] Chongqing Institute of Green and Intelligent Technology, Chinese Academy of Sciences, Chongqing, China; [3] Chongqing School, University of Chinese Academy of Sciences, Chongqing, China

This work is supported by National Key Research and Development Program of China (2024YFE0211900) and the Natural Science Foundation of Chongqing of China (CSTB2023NSCQ-LZX0087) .

Abstract

Short-wave infrared photodetectors based on colloidal quantum dots (QDs) have attracted substantial attention owing to their solution processability, tunable bandgaps, and natural compatibility with silicon-based readout integrated circuits. However, the performance of QDs photodetectors is fundamentally limited by the low intrinsic carrier mobility of colloidal QDs, which significantly hinders charge transport. In addition, conventional detector

architectures typically provide insufficient internal gain, thereby restricting detection sensitivity, particularly under weak infrared illumination. To address these challenges, we propose a hybrid avalanche photodetector that integrates a halogen-passivated PbS QDs absorption layer with a silicon multiplication region. After absorbing incident infrared photons in the QDs layer, photoexcited electrons are efficiently injected into the silicon multiplication region. The accelerated carriers then induce impact ionization, which enables strong avalanche multiplication and yields high internal gain for efficient carrier collection. Technology Computer-Aided Design (TCAD) simulations indicate that the proposed device delivers a responsivity of 29.5 A/W at a wavelength of 1550 nm, accompanied by fast rise and fall times of 305 ps and 306 ps, respectively. By integrating the spectral tunability of PbS QDs with the robust avalanche gain offered by mature silicon platforms, this architecture provides a highly promising, CMOS-compatible route toward next-generation, high-sensitivity infrared photodetection.

References
[1] F. de Arquer, D. Talapin, V. Klimov, et al., 'Semiconductor quantum dots: Technological progress and future challenges,' *Science*, vol. 373, no. 6555, pp. eaaz8541, American Association for the Advancement of Science
[2] Y. Wang, C. Deng, J. Liu, et al., 'Interface Engineering Enables High-performance PbS Colloidal Quantum Dots Imager via Tungsten Oxide Hydrophilic Layer,' *Laser & Photonics Reviews*, vol. 19, no. 19, pp. 9, Wiley-VCH
[3] J. Liu, P. Liu, D. Chen, et al., 'A near-infrared colloidal quantum dot imager with monolithically integrated readout circuitry,' *Nature Electronics*, vol. 5, no. 7, pp. 443–451, Springer Nature
[4] C. Hartley, and J. Dempsey, 'Revealing the Molecular Identity of Defect Sites on PbS Quantum Dot Surfaces with Redox-Active Chemical Probes,' *Chemistry of Materials*, vol. 33, no. 7, pp. 2655–2665, American Chemical Society
[5] J. Fu, C. Leng, R. Ma, et al., 'Photo-driven fin field-effect transistors,' *Opto-Electronic Science*, vol. 3, no. 5, pp. 230046, Science Press
[6] X. Xiao, K. Xu, M. Yin, et al., 'High quality silicon: Colloidal quantum dot heterojunction based infrared photodetector,' Applied Physics Letters, vol. 116, no. 10, pp. 4, American Institute of Physics
[7] G. Whitworth, M. Dalmases, N. Taghipour, et al., 'Solution-processed PbS quantum dot infrared laser with room-temperature tunable emission in the optical telecommunications window,' *Nature Photonics*, vol. 15, no. 10, pp. 738–742,Springer Nature

NSS-01-077

Characterization and Radiation Damage Mitigation of Silicon Photomultipliers for Low Earth Orbit Applications (#1902)

Shideh Davarpanah, On behalf of NUSES Collaboration

Université de Genève, Département de physique nucléaire et corpusculaire, Genève, Switzerland

Abstract
Silicon photomultipliers (SiPMs) are attractive photosensors for space applications because of their compact size, low cost, low operating voltage, high photon detection efficiency (PDE), and single-photon sensitivity. Their use in space applications, however, is limited by radiation-induced increases in dark count rate (DCR). This work presents the characterization and radiation tolerance study of FBK NUV-HD-MT SiPMs for the focal plane of the Terzina Cherenkov telescope onboard the NUSES mission, which will operate in a Sun-synchronous low Earth orbit (LEO) at an altitude of approximately 550 km. Devices with micro-cell sizes ranging from 25 to 50 μm were evaluated through a comprehensive characterization campaign comprising static (current-voltage), dynamic (noise and pulse-shape), and optical (photon detection efficiency) measurements to identify the sensor configuration best suited for this application. The 30 μm bare sensors were selected as the optimal solution, achieving a PDE greater than 50% at 400 nm, optical cross-talk below 2%, and a DCR below 60 kHz/mm^2 at 10 V overvoltage. The radiation environment was modeled using SPENVIS, and dose deposition in the focal plane was evaluated with Geant4

simulations. In parallel, radiation effects were investigated experimentally through two irradiation campaigns: a 50 MeV proton beam test and electron exposure using a Sr-90 source. Proton-induced damage produced a significant increase in leakage current and DCR, while electron-induced degradation was substantially smaller. Temperature-dependent measurements were used to extrapolate in-orbit performance and to evaluate recovery through thermal annealing. The results indicate that performing periodic annealing cycles at temperatures above 50°C can reduce the radiation-induced current by up to 40% after approximately 84 hours, helping preserve detector performance over the three-year mission.

References
[1] NUSES Collaboration, “The NUSES space mission,” PoS TAUP2023, p. 121, 2024.
[2] NUSES collaboration, The NUSES space mission, J. Phys. Conf. Ser. 2429 (2023) 012007.
[3] L. Burmistrov, “Terzina on board NUSES: A pathfinder for EAS Cherenkov light detection from space,” EPJ Web Conf., vol. 283, p. 06006, 2023.
[4] L. Burmistrova, S. Davarpanah, M. Heller, T. Montaruli, C. Trimarelli, R. Aloisio, et al., “Performance and radiation damage mitigation strategy for silicon photomultipliers on LEO space missions,” J. Cosmol. Astropart. Phys., vol. 2025, no. 07, p. 073, Jul. 2025.
[5] T. Montaruli and A. Nagai, “Properties of large SiPM at room temperature,” Nucl. Instrum. Methods Phys. Res. A, vol. 985, p. 164609, 2021.
[6] A. Nagai, C. Alispach, D. Della Volpe, M. Heller, T. Montaruli, S. Njoh, et al., “SiPM behaviour under continuous light,” JINST, vol. 14, p. P12016, 2019.
[7] Spenvis: The space environment information system, 2022.
[8] Geant4: Toolkit for the simulation of the passage of particles through matter. its areas of application include high energy, nuclear and accelerator physics, as well as studies in medical and space science, 2019.
[9] J. Swakon, P. Olko, D. Adamczyk, T. Cywicka-Jakiel, J. Dabrowska, B. Dulny et al., Facility for proton radiotherapy of eye cancer at ifj pan in krakow, Radiation Measurements 45 (2010) 1469.

NSS-01-079

Toward SiPM Single-Photon Detection Matrix using Ultrafast, Low Power RF Readout (#1939)

Rafik Belkacem[1], Dominique F. Yvon[1,4], David Baudin[2], Dominique Breton[3]

[1] CEA Saclay / Univ. Paris-Saclay, IRFU/DPhP, Gif sur Yvette, France; [2] CEA Saclay / Univ. Paris-Saclay, IRFU/DEDIP, Gif sur Yvette, France; [3] CNRS-IN2P3/ Univ. Paris-Saclay, IJCLab, Orsay, France; [4] UMR BioMaps/ Univ. Paris-Saclay, Orsay, France

Abstract

To enable the readout of fast signals from SiPM arrays, we have developed a SiPM chip readout based on a compact, low-power radio-frequency preamplifier, thus avoiding the use of ASICs. On a 16 mm² SiPM operating in single photoelectron mode, we measure a rise time of 450 ps and a timing resolution (SPTR) of 84 ps (FWHM), while amplifying the fast component of the SiPM pulses. Furthermore, the active output impedance of the preamplifier is on the order of kΩ, allowing these chips to be mounted along a transmission line without significantly affecting signal propagation. This enables the implementation of dense SiPM lines or arrays, reducing the number of digitization channels required for readout. Finally, an optimized passive pole-zero compensation network, placed at the ends of the line, suppresses the slow component of the SiPM pulses and achieves critical damping of the fast pulse shapes. Thus, pulse pile-up, expected during multiplexing of SiPM photodetectors, can be controlled even at high counting rates. We are currently working on the assembly of such SiPM arrays. We measured a

Coincidence Time Resolution of 69 ps (FWHM) using a 9 mm^3 LYSO crystal + SiPM spectrometers with our readout electronics.

References

[1] J. Huizenga et al., *Nucl. Instrum. Meth. A* **695** (2012) 379
[2] H. Kim et al., *Nucl. Instrum. Meth. A* **784** (2015) 557–564
[3] J. W. Cates et al., *Phys. Med. Biol.* 63 (2018) 185022
[4] S. Gundacker et al., *Phys. Med. Biol.* 65 (2020) 025001

NSS-01-081

FPGA-Based Real-Time SiPM Emulator with Sub-Nanosecond Temporal Quantization (#1987)

Andrea Abba[1], Stefano Carsi[1], Francesco Caponio[1], Edoardo Proserpio[1,2], Valentina Arosio[1]

[1] Nuclear Instruments SRL, Lambrugo, Italy; [2] Università dell'Insubria, Como, Italy

Abstract

This work presents a real-time FPGA-based Silicon Photomultiplier (SiPM) detector emulator capable of reproducing physically accurate detector waveforms at 16-bit resolution and 2.5 GS/s analog output rate. The proposed architecture combines microscopic event simulation with a temporally quantized event-streaming model, enabling real-time waveform synthesis directly inside FPGA logic while drastically reducing bandwidth requirements compared to traditional waveform streaming approaches. The emulator separates event generation from signal shaping: software layers generate timestamped photon-hit sequences derived either from analytical distributions, Geant4 simulations, or SimSiPM microscopic detector models, while the FPGA reconstructs the analog waveform through parallel Infinite Impulse Response (IIR) filter banks implementing the SiPM transfer function; a look-ahead recursive transformation enables II = 1 operation across all banks at 156.25 MHz, consuming approximately 235 DSP48E2 slices. A multi-phase temporal quantization architecture provides 0.8 ns effective timing precision using a 156.25 MHz fabric clock and eight temporal sub-phases. Experimental validation demonstrates excellent agreement between hardware-generated waveforms and analytical as well as SimSiPM-generated references, including pile-up scenarios with overlapping scintillation events reproduced through linear superposition. The prototype operates with an end-to-end latency of approximately 83 ns.

NSS-01-083

Design and Single-Cell Verification of an Integrated Temperature-Compensation Architecture for Digital SiPMs in Extreme Environments

(#2580)

Jin-Seok Oh[1], Hur Seop[2], Koo Seo-Ryong[2], Kwon Inyong[3]

[1] Korea University of Science and Technology (UST), Daejeon, South Korea; [2] Korea Atomic Energy Research Institute (KAERI), Daejeon, South Korea; [3] Yonsei University, Wonju, South Korea

This work was supported in part by the National Research Foundation (NRF) funded by the Korean government (MSIT) (RS-2025-04162969, RS-2022-00144324, RS-2022-00144419, and RS-2022-00165164), the Regional Innovation System & Education (RISE) program through the Gangwon RISE Center, funded by the Ministry of Education (MOE) and the Gangwon State (G.S.), Republic of Korea. (2025-RISE-10-006), the National Research Council of Science & Technology (NST) grant by the Korea government (MSIT) (No. GTL25051-000), and the Basic Science Research Program through the National Research Foundation of Korea (NRF) funded by the Ministry of Science and ICT (RS-2026-00144324).

Abstract

This paper presents the single-cell design and verification of a digital SiPM building block with an integrated temperature-compensation architecture that eliminates external sensors by exploiting SPAD output-amplitude tracking as an intrinsic thermal indicator. A low-power SPAD with a P+/N-well junction and P-well guard ring was fabricated in a 180 nm CMOS process, exhibiting a 10.3 V breakdown voltage, while the digital-cell employs a high-speed comparator to suppress pulse-width variation and premature edge breakdown. The extracted amplitude trend drives an integrated PMIC in a closed loop to dynamically adjust the SPAD bias, maintaining a constant overvoltage and providing instantaneous compensation for thermal drifts.

References

[1] C. Veerappan and E. Charbon, "A Low Dark Count p-i-n Diode Based SPAD in CMOS Technology," IEEE Transactions on Electron Devices, vol. 63, no. 1, pp. 65–71, Jan. 2016, doi: 10.1109/TED.2015.2475355.

[2] F. Nolet et al., "A 2D Proof of Principle Towards a 3D Digital SiPM in HV CMOS With Low Output Capacitance," IEEE Transactions on Nuclear Science, vol. 63, no. 4, pp. 2293–2299, Aug. 2016, doi: 10.1109/TNS.2016.2582686.

[3] F. Licciulli and C. Marzocca, "An Active Compensation System for the Temperature Dependence of SiPM Gain," IEEE Transactions on Nuclear Science, vol. 62, no. 1, pp. 228–235, Feb. 2015, doi: 10.1109/TNS.2015.2388580.

NSS-01-085

Graphene Photodetectors for Vacuum-UV Through Visible Wavelengths (#3124)

Alec Lindman[1], Marcos Turqueti[1], Lisa Schlueter[1], Gabriela R. Araujo[2]

[1] Lawrence Berkeley National Laboratory, Berkeley, USA; [2] University of Zurich, Zurich, Switzerland

This work was supported by the U.S. Department of Energy through the Laboratory Directed Research and Development program.

Abstract

Many experiments rely on measuring vacuum-ultraviolet light, which is emitted in situations as diverse as scintillation in cryogenic liquid noble gases (126.8 nm in argon) and laser spectroscopy of atomic hydrogen isotopes (121.6 nm). Graphene-monolayer photodetectors offer several attractive traits: they are naturally thin, sensitive to a broad range of wavelengths, relatively simple to fabricate (including with integrated readout circuitry with the same process), and can be made on flexible substrates. We present measurements with visible and UV light down to 115 nm, including at low intensity and with fast pulses, of graphene field-effect transistors (GFETs) of various sizes up to 2 mm square fabricated on silicon. These detectors show promise for experiments from neutrinoless double beta decay searches to absolute neutrino mass measurements, as well as dark-matter searches or other VUV-detection applications.

NSS-01-087

Development of a PLL-less 6.25Gbps Serializer and CML Transmitter for the LCLS-II Upgrade (#1129)

Gang Liu, Hampus Sandberg, Aldo Pena-Perez, Bojan Markovic, Aseem Gupta, Hyunjoon Kim, Lorenzo Rota, Dionisio Doering, Larry Ruckman

Stanford University, SLAC National Accelerator Laboratory, Menlo Park, USA

Work supported by the U.S. Department of Energy, under contract number DE-AC02-76SF00515.

Abstract

Linac Coherent Light Source (LCLS) at SLAC National Laboratory has been going through a major upgrade, called LCLS-II, where the repetition rates are increasing from 120Hz to almost a MegaHertz. Custom ASICs that support x-ray data measurements at these rates are in development for both full frame and sparse data readout. For these

ASIC designs we are departing from conventional internal PLL architectures, and instead implementing a 6.25 Gbps serializer with high-speed current-mode logic (CML) receivers (for clock) and transmitters (for data). This approach simplifies the whole chip design, reduces the power consumption and minimizes the noise sensitivity between the high-speed data path and the low-noise front-end blocks. This paper presents detailed performance measurements in a prototype ASIC, followed by the description of their circuit design and implementation.

NSS-01-089

Performance Evaluation of Differential Amplifiers for Fast Scintillating Fiber Readout in Proton Therapy (#1449)

Bayram Deniz[1,2], Ali Eksim[1,2]

[1] TUBITAK BILGEM, KOCAELI, Turkey; [2] Gebze Technical University, KOCAELI, Turkey

The authors thank the TUBITAK BILGEM Embedded Systems and Digital Design Team and the NOVO Project Team for their technical support and collaboration throughout this work.

Abstract

Real time range verification in proton therapy requires analog front end electronics that can process fast, low amplitude signals from scintillating fibers with sub nanosecond precision. This work compares two COTS differential amplifiers (ADA4930 vs. ADA4938) for the NOVO project's detector. Using actual scintillator derived PWL pulses (0.3 V peak, 18 ns rise time) and a 5th order 250 MHz Butterworth filter, we show that small signal bandwidth governs transient performance. The ADA4930 achieved 660 V/µs pre filter and 350.56 V/µs post filter slew rate, versus 550 and 289.44 V/µs for the ADA4938. Noise analysis reveals the ADA4930 is "resistor noise limited" (61.4% passive resistors), while the ADA4938 is "IC noise limited" (71.6% internal noise). The ADA4930 yields SNR = 65 dB and ENOB = 10.6 bits, outperforming the ADA4938 (62 dB, 10.0 bits). The ADA4930 is therefore the optimal driver for maximizing slope to noise ratio and minimizing timing jitter.

NSS-01-091

NSS-01-093

Design of the new Matterhorn detector for the 4th generation synchrotrons (#1694)

Davide Mezza, Michele Anastasi, Anna Bergamaschi, Martin Brueckner, Roberto Dinapoli, Maria Carulla, Simon Ebner, Simone Emiliani, Khalil Ferjaoui, Viveka Gautam, Dominic Greiffenberg, Erik Froejdh, Shqipe Hasanaj, Viktoria Hinger, Markus Huerst, Vadym Kedych, Thomas King, Shuqi Li, Carlos Lopez-Cuenca, Leonid Lunin, Alice Mazzoleni, Scharon Moses, Kostantinos Moustakas, Aldo Mozzanica, Jonathan Mulvey, Martin Mueller, Christian Ruder, Bernd Schmitt, Saverio Silletta, Dhanya Thattil, Xiangyu Xie, Jiaguo Zhang

Paul Scherrer Institute (PSI), SLS Detector Group, Villigen, Switzerland

Abstract

The new fourth-generation storage rings (diffraction-limited storage rings), such as those at MAX IV Laboratory, ESRF EBS, and Swiss Light Source 2.0, will provide significantly higher brilliance than third-generation sources, resulting in a much larger photon flux at the pixel level. This increased flux will exceed the count-rate capabilities of many single-photon counting detectors currently in use, making them unsuitable for future experiments at these facilities. Matterhorn is a 2-D hybrid pixel detector developed by the PSD detector group at the Paul Scherrer Institute for operation at SLS 2.0. Its main objective is to extend the count rate capability to a target of 20 Mcounts/pixel/s using multi-threshold circuitry implemented in each pixel. The Matterhorn ASIC features a 256 × 256 pixel matrix with 75 µm pitch and is implemented in UMC 110 nm technology. Each pixel includes a charge-sensitive amplifier and a shaper connected to four comparators with independently adjustable thresholds. Setting thresholds above the photon energy enables an extension of the effective count-rate capability. Each comparator is connected to an independently gateable 16-bit counter. The target frame rate for reading out one 16-bit counter per pixel is 10 kHz. To support this rate, the ASIC periphery includes four serial links operating in double data rate mode at up to 3.125 GHz, driven by a 1.5625 GHz clock generated by an on-chip PLL. A fully synthesized digital periphery provides flexible ASIC configuration. Since January 2026, the final ASIC, which is fully functional, has been under test to evaluate its performance. This contribution focuses primarily on the ASIC design and detector architecture, and reports the main performance parameters measured so far, while a detailed discussion of the full characterization results will be presented in a separate contribution.

NSS-01-095

A Low-Latency 28-nm CMOS ASIC for Superconducting Quantum Readout (#1815)

Yunzhuo Zhang[1], Cheng Guo[2], Xinzhe Wang[2], Wenyi Peng[2], Futian Liang[2]

[1] University of Science and Technology of China, school of physical science, hefei, China; [2] University of Science and Technology of China, Hefei National Laboratory, hefei, China

Abstract

As the scale of the superconducting quantum control system continues to expand, traditional field-programmable gate array architectures face bottlenecks such as high energy consumption, low scalability, and severe signal attenuation. This paper proposes a highly integrated, low-latency digital front-end architecture fabricated in a 28-nm CMOS process to meet dynamic feedback requirements and optimize power, performance,and area. The front-end includes an arbitrary waveform generator and a data acquisition module, independently managed by a microcontroller. At the transmitter, a digital-to-analog converter
is used to output analog signals, with a measured spurious free dynamic range of 52 dB. At the receiver, a low-latency analog-to-digital converter captures analog signals, which the data acquisition module demodulates and ultimately uploads via a low-voltage differential signaling interface. The total hardware latency is restricted to approximately 100 ns. Under full-load testing conditions—including continuous waveform generation,concurrent demodulation of 16 qubits, and state feedback—the total digital power consumption is limited to 539 mW(33.7 mW/qubit). This design achieves extremely low latency and excellent energy efficiency, satisfying the real-time control demands of scalable fault-tolerant quantum computers.

References

[1] F. Arute et al., “Quantum supremacy using a programmable superconducting processor,” Nature, vol. 574, no. 7779, pp. 505–510, Oct. 2019.

[2] J. P. G. van Dijk et al., “Impact of Classical Control Electronics on Qubit Fidelity,” Physical Review Applied, vol. 12, no. 4, p. 044054, Oct. 2019.

[3] J. C. Bardin et al., “Design and Characterization of a 28-nm Cryo-CMOS Core for Control of Transmon Qubits,” IEEE Journal of Solid-State Circuits, vol. 54, no. 11, pp. 3043–3060, Nov. 2019.

[4] C. A. Ryan et al., “Hardware for dynamic quantum operations,” Physical Review A, vol. 95, no. 6, p. 062317, Jun. 2017.

NSS-01-097

Radiation Effects on COTS On-Board Computer and Boot/Data-Storage Media Configurations for Super-Low-Earth-Orbit Optical Satellites

(#1893)

Jongdae Sohn[1,2], Hojin Lee[1,2], Hyosang Yoon[3]

[1] Korea Astronomy and Space Science Institute, Division of Space Exploration, Daejeon, South Korea; [2] University of Science and Technology, Department of Astronomy and Space Science, Daejeon, South Korea; [3] Korea Advanced Institute of Science and Technology, Department of Aerospace Engineering, Daejeon, South Korea

Abstract

Super-low-Earth-orbit (SLEO) optical satellites require compact on-board computing and data-storage electronics, but commercial off-the-shelf (COTS) on-board computers (OBCs) and boot/data-storage media must retain boot, communication, and read/write functions under the mission radiation environment. This paper reports a configuration-level radiation screening of COTS OBC candidates for a 300 km-class, 2-year SLEO optical satellite. A SPENVIS/SHIELDOSE-2 dose assessment gave a total ionizing dose of 14.345 krad(Si) for the design case; therefore, a conservative 30 krad(Si) TID screening target was selected by applying a margin factor of approximately 2. The screening campaign included Arduino and Raspberry Pi family boards, and the detailed design interpretation focused on Raspberry Pi Compute Module 4 (CM4) with input/output board and nonvolatile boot/data-storage media, including Secure Digital (SD) cards, embedded MultiMediaCard (eMMC), solid-state drives (SSDs), and hard disk drives (HDDs). Devices were irradiated with cobalt-60 gamma rays, 10 MeV electrons, and 100 MeV protons, and were evaluated by boot status, communication, supply-current and voltage behavior, read/write operation, and recovery after irradiation. The results indicate that CM4-based configurations were more suitable than the other screened modules for the SLEO OBC candidate. Among storage options, eMMC showed the most favorable radiation and operational suitability, SSDs were identified as a practical secondary storage option after configuration-level verification, and HDDs were not recommended for spacecraft on-board use although some configurations survived to approximately 30 krad(Si), because rotating mechanical parts can affect spacecraft operation. These results support qualifying the exact OBC and boot/data-storage configuration, rather than only the processor board, for COTS-based SLEO on-board computing and storage electronics.

References

[1] Heynderickx, D, Quaghebeur, B, Wera, J, Daly, EJ, Evans, HDR 2004, 'New radiation environment and effects models in the European Space Agency's Space Environment Information System (SPENVIS)', Space Weather, vol. 2, no. 10, S10S03, doi:10.1029/2004SW000073.

[2] Seltzer, SM 1994, 'Updated calculations for routine space-shielding radiation dose estimates: SHIELDOSE-2', NIST Interagency/Internal Report 5477, Gaithersburg, MD: National Institute of Standards and Technology.

[3] Raspberry Pi Ltd. 2026, 'Raspberry Pi Compute Module 4 Datasheet', Product Datasheet, Cambridge, United Kingdom: Raspberry Pi Ltd.

[4] European Space Components Coordination 2016, 'Total Dose Steady-State Irradiation Test Method', ESCC Basic Specification No. 22900, Issue 5, Noordwijk, The Netherlands: European Space Agency.

[5] U.S. Department of Defense 2013, 'Method 1019.9: Ionizing Radiation (Total Dose) Test Procedure', MIL-STD-883J, Test Method Standard Microcircuits, Washington, DC: U.S. Department of Defense.

[6] NASA Tech Briefs 2010, 'Solid-State Recorders Enhance Scientific Data Collection', NASA Tech Briefs, December 2010, Washington, DC: National Aeronautics and Space Administration.

[7] Fleetwood, DM 2013, 'Total ionizing dose effects in MOS and low-dose-rate-sensitive linear-bipolar devices', IEEE Transactions on Nuclear Science, vol. 60, no. 3, pp. 1706–1730, doi:10.1109/TNS.2013.2259260.

NSS-01-099

A Versatile High Linearity Front-End Preamplifier with Wide Dynamic Range for Multiple SiPM Sensors (#1920)

Jara García-Barrena[1], Vicente Herrero[1], Cristo Mourani[2], Raúl Esteve[1], Jose F. Toledo[1], Francisco J. Mora[1], Francisco Ballester[1], Vicente Álvarez[1], Juan José Gómez-Cadenas[2], On behalf of NEXT collaboration

[1] Universitat Politècnica de València (UPV), Instituto de Instrumentación de Imagen Molecular (I3M), Valencia, Spain; [2] Donosti International Physics Center (DIPC), San Sebastián, Spain

This work was supported by the Agencia Española de Investigación (AEI) through project PID2024-161553NB-C53. The authors gratefully acknowledge this funding, which enabled the research presented in this study.

Abstract

The integration of Silicon Photomultipliers (SiPMs) into high-resolution radiation detection systems has become increasingly relevant in the search for novel methodologies in precision energy measurement. This fact implies the need of front-end electronics capable of properly working with these sensors, whose parasitics change among different parts. In the signal processing chain, the initial stage must offer maximal linearity to preserve signal integrity throughout the subsequent architectures. A low-noise goal is also important in order to optimize energy resolution since first stage is critical in noise budget. Consequently, a specialized preamplifier design is presented in this paper in order to address these requirements. The primary design challenge involves achieving a very good linearity through high internal loop gain without compromising system stability. To ensure a controlled frequency response, the circuit employs a Miller compensation scheme whose dominant pole is inside the circuit. Constructing a robust stability topology, the architecture can handle diverse parasitic components in its input due to the use of different SiPM devices. In a first amplification stage, a key innovative structure has been developed as a translinear wideband inner gain stage. Furthermore, to ensure an extended dynamic range which allows working in both photon counting and high amplitude signal conditions without design reconfiguration, a digitally controlled attenuator system is integrated at the output of the first stage. The attenuator uses a R-2R ladder architecture implemented with MOSFET technology, allowing for direct gain adjustments and accurate calibration through external control logic.

References

[1] T. Contreras, B. Palmeiro, H. Almazán et al., “Measurement of energy resolution with the next-white silicon photomultipliers,” Journal of High Energy Physics, vol. 2024, no. 9, p. 112, 2024.

[2] C. Adloff et al., “Hadronic energy resolution of a highly granular scintillator-steel hadron calorimeter using software compensation techniques,” Journal of Instrumentation, vol. 7, no. 09, p. P09017, 2012.

[3] F. Corsi et al., “Modelling a silicon photomultiplier (sipm) as a signal source for optimum front-end design,” Nuclear Instruments and Methods in Physics Research Section A, vol. 572, no. 1, pp. 416–418, 2007.

[4] F. Corsi, M. Foresta, C. Marzocca, G. Matarrese, and A. Del Guerra, “Basic: An 8-channel front-end asic for silicon photomultiplier detectors,” Nuclear Science Symposium Conference Record (NSS/MIC), 2009 IEEE, pp. 1082 – 1087, 24 2009-nov. 1 2009.

[5] W. Cheng, F. Cossio, M. D. R. Rolo, A. Rivetti, and Z. Wang, “A mixed-signal large dynamic range front-end asic for high capacitance detectors,” Journal of Instrumentation, vol. 14, no. 08, p. P08013, aug 2019. [Online]. Available: https://doi.org/10.1088/1748-0221/14/08/P08013

[6] R. J. Wiegerink, Analysis and Synthesis of MOS Translinear Circuits, ser. The Kluwer International Series in Engineering and Computer Science. Dordrecht, The Netherlands: Kluwer Academic Publishers, 1993, vol. 232.

[7] K. Bult and G. Geelen, “An inherently linear and compact most-only current-division technique,” Solid-State Circuits Conference, 1992. Digest of Technical Papers. 39th ISSCC, 1992 IEEE International, pp. 198–199, 281, Feb 1992.

NSS-01-101

SPAGHETTI : An original instrument for the continuous gamma-ray based monitoring of hydrothermal volcanoes (#2092)

Hervé Chanal, Cyrille Achard, Jonathan Bonnard, Vincent Breton, Emmanuel Busato, Christophe Insa, Jonathan Lao, Gilles Magaud, Hervé Croizet, Magali Magne, Valentin Niess, David Picard, Valentin Rabant, Luca Terray

Université Clermont Auvergne, CNRS/IN2P3, LPCA, Clermont-Ferrand, France

Abstract

Hydrothermal volcanic systems are associated with major hazards such as magmatic/phreatic eruptions and toxic gaz emissions.
Monitoring fluid circulation within these systems is a key scientific challenge.
The SPAGHETTI project (Spectral Panoptic Analyzers of Gamma rays in Hydrothermal Environments for Transport Time Inference) aims to develop
an original instrument dedicated to the continuous and high-frequency monitoring of radon using gamma-ray spectroscopy.
The instrument relies on NaI scintillation detectors coupled to a specific signal processing electronics.
The whole system is designed to withstand high temperatures, extreme humidity, and acidic corrosion.
This contribution focuses on the FPGA-based digital signal processing chain implemented on a low-cost ADC-SoC platform.
Real-time triggering, digital filtering, and amplitude extraction are performed directly in programmable logic.
First tests aiming to demonstrate the capability of the system to continuously
acquire and process scintillation signals in conditions representative of volcanic hydrothermal environments will be presented.

NSS-01-103

Evaluating AMD's Versal Architecture for Tapped Delay Line Time-to-Digital Converters. (#2179)

Julien Rossignol, Sun Il Kwon

University of California, Davis, Biomedical engineering, Davis, USA

This work was supported by the National Institutes of Health under grant R01 EB033536.

Abstract

Performances of tapped delay line (TDL) time-to-digital converters (TDCs) in FPGAs are strongly linked to the FPGA fabrication process, with newer fabrication processes usually yielding smaller propagation delays, thus improving the resolution and precision of the fine measurement. This study evaluates TDLs designed inside the Versal architecture, AMD's newest architecture that uses a 7 nm fabrication process. Since the Versal architecture's new configurable logic blocks (CLB) allow for multiple propagation paths through them, three different implementations of a TDL were evaluated. Code density and single-shot precision measurements were performed on five pairs of channels for each implementation. The lowest quantization error, 4.47 ps, was obtained using a mix of the outputs of the carry propagation circuit and the look-up tables (LUTs) of the CLB, while the best single-shot precision, 7.51 ps, was obtained by using only the output of the LUTs. Because of the change in the CLB design, TDL TDCs perform significantly worse than in AMD's previous architecture.

References

[1] H. Xia et al., A Review of Advancements and Trends in Time-to-Digital Converters Based on FPGA. IEEE T. Instrum. Meas. Vol. 73, June 2024.

[2] J. Rossignol et al., Simulating and Optimizing Tapped Delay Lines for Time-to-Digital Converters in FPGA using a Precision Model based on Circuit Characteristics. SSRN, Oct. 2025.

[3] J. Rossignol et al., Tapped Delay Lines Time-to-Digital Converter Design and Performance in Versal Architectur. IEEE Real-Time Conference, 2026.

[4] Q. Wingering et al., FPGA Based Time-To-Digital Converter for Time of Flight Computed Tomography, IEEE NSS MIC RTSD, 2024.

NSS-01-105

Probing Sub-20 ps Intrinsic Timing Limits of MVT-SiPM Readout for TOF-PET (#2205)

Hui Lao[1], Qingguo Xie[1], Guanning Su[3], Zereng Wang[4], Jingbin Chen[1], Jing Wang[4], Haoxuan Xu[1], Junhao Yu[2], Lu Li[2]

[1] University of Science and Technology of China, Department of Electronic Engineering and Information Science, hefei, China; [2] Huazhong University of Science and Technology, Biomedical Engineering Department, Wuhan, China; [3] University of Science and Technology of China, School of Gifted Young, hefei, China; [4] University of Science and Technology of China, School of Microelectronics, hefei, China

This work was supported in part by the National Key R\&D Program of China under Grant 2024YFE0113500, in part by the start-up fund of USTC "Research on total solid Angle PET-EPR multimodal intelligent imaging".
Hui Lao, Guanning Su, Jingbin Chen, Haoxuan Xu, Zereng Wang, Jing Wang (e-mail: jw2019@ustc.edu.cn) and Qingguo Xie (e-mail: qgxie@ustc.edu.cn) are with University of Science and Technology of China, Hefei, China. Junhao Yu and Lu Li are with Biomedical Engineering Department,Huazhong University of Science and Technology, Wuhan,China.

Abstract

The Multi-Voltage Threshold (MVT) method is widely employed in particle detection. However, limited by discrete hardware architectures, existing FPGA-based digitization systems struggle to fully exploit the fundamental timing potential of photodetectors. To investigate these performance limits, we systematically evaluate the ultimate timing performance of a detection chain comprising a CMOS SiPM and an in-house-developed MVT ASIC. This ASIC features picosecond time quantization and a wide dynamic range. Experimental results show that, under excitation from a synchronized picosecond laser source, the MVT ASIC achieves an intrinsic electronic time resolution of 16.94 ps (FWHM) and a coincidence time resolution (CTR) of 16.58 ps (FWHM). Benchmarking against a high-performance digital oscilloscope demonstrates that the timing precision of the MVT ASIC closely approaches that of laboratory-grade instrumentation (11.74 ps). This work validates the potential of the MVT ASIC for time-of-flight (TOF) measurement systems and establishes a promising technical foundation for ultra-high-resolution TOF detection.

References
[1] Xie, Q. , et al. "A New Approach for Pulse Processing in Positron Emission Tomography." IEEE Transactions on Nuclear Science 52.4(2005):988-995.
[2] Xi, Daoming , et al. "FPGA-Only MVT Digitizer for TOF PET." IEEE Transactions on Nuclear Science 60.5 Part1(2013):3253-3261.

NSS-01-109

Design and characterization of a 28 nm CMOS asynchronous front-end for the readout of hybrid pixel sensors in future colliders (#2384)

Luigi Gaioni[1,3], Lodovico Ratti[2,3], Valerio Re[1,3], Gianluca Traversi[1,3], Simone Gerardin[4], Davide Falchieri[5], Luca Frontini[6], Alberto Stabile[7]

[1] University of Bergamo, Dept. of Engineering and Applied Sciences, Bergamo, Italy; [2] University of Pavia, Dept. of Electrical, Computer and Biomedical Engineering, Pavia, Italy; [3] INFN - Istituto Nazionale di Fisica Nucleare, Sezione di Pavia, Pavia, Italy; [4] University of Padova, Dept. of Information Engineering, Padova, Italy; [5] INFN - Istituto Nazionale di Fisica Nucleare, Sezione di Bologna, Bologna, Italy; [6] INFN - Istituto Nazionale di Fisica Nucleare, Sezione di Milano, Milano, Italy; [7] University of Milano, Dept. of Physics, Milano, Italy

This work was carried out in the framework of the PiHex project, CUP F53D23001490006 - PRIN 2022, funded by NextGenerationEU - M4, C2, 1.1.

Abstract

A demonstrator chip integrating a matrix of 32 x 8 readout channels for hybrid pixel detectors has been designed and tested in the framework of the PiHEX project, funded by the Italian Ministry of University and Research. The front-end channels include a low-noise charge sensitive amplifier with detector leakage compensation, an asynchronous, differential comparator, and a 5-bit threshold tuning DAC. A Time-over-Threshold counter is integrated for signal digitization. The front-end channels have been developed in a 28 nm CMOS technology and feature an overall area of 25 um x 100 um with a current consumption close to 4.2 uA. Full details on the design and characterization of the prototype chip will be reported in the conference paper.

References

[1] I. Peric, “The FEI3 Readout Chip for the ATLAS Pixel Detector”, Nucl. Instrum. and Methods, A 565 (2006), 178-187.

[2] H. C. Kastli et al., “Design and performance of the CMS pixel detector readout chip”, Nucl. Instrum. and Methods, A 565 (2006), 188-194.

[3] O. Aberle et al., “High-Luminosity Large Hadron Collider (HL-LHC): Technical design report”, CERN-2020-010 (2020).

[4] G. Alimonti et al., “RD53 pixel readout integrated circuits for ATLAS and CMS HL-LHC upgrades”. J. Instrum., 20 P03024 (2025).

[5] F. Resta et al., “28nm Integrated Circuit for PIXel detector”, Nucl. Instrum. and Methods, A 904 (2018), 140-148.

[6] F. Bandi et al., “Analog IP blocks in 28nm CMOS for the high energy physics community: SLVS transmitter and receiver”, J. Instrum., 18 C01039 (2023).

[7] S. Bonaldo et al., “Ionizing-radiation response and low frequency noise of 28-nm MOSFETs at ultrahigh doses”, IEEE Trans. Nucl. Sci., 67(2020), 1302-1311.

NSS-01-111

A 5.12-GS/s Time-Interleaved VCO-Based ADC With Digital Calibration for High-Speed Detector Waveform Digitization (#2436)

Chenxi Chen, Yuchen Hu, Simeng Chen, Xueye Hu, Jinghong Wang

University of Science and Technology of China, Hefei, China

Abstract

This paper presents a 5.12-GS/s time-interleaved voltage-controlled-oscillator-based analog-to-digital converter (VCO-based ADC) for high-speed detector waveform digitization in nuclear science and high-energy physics experiments. The proposed ADC employs an 8-channel time-interleaved architecture, where each sub-channel operates at 640 MS/s, resulting in an aggregate sampling rate of 5.12 GS/s. VCO-based quantization is adopted to exploit time-domain signal processing and inherent first-order noise shaping. Each sub-channel integrates a high-linearity bootstrapped sampling switch, a 15-stage ring-VCO quantizer, multi-phase sampling flip-flops, and an asynchronous coarse counter to realize hybrid coarse-fine quantization. To address the major performance limitations of VCO-based and time-interleaved ADCs, a digital calibration scheme is introduced to compensate for the VCO voltage-to-frequency nonlinearity and inter-channel timing skew. The ADC is implemented in a 55-nm CMOS process. Post-layout simulation results show that, at an aggregate sampling rate of 5.12 GS/s with a 2.4-GHz input signal, the ADC achieves an SNDR of 37.5 dB and an effective number of bits of 5.94 bits after calibration. The simulated power consumption is 75 mW from a 1.2-V supply, corresponding to a Walden figure-of-merit of 239 fJ/conversion-step. Full-chip performance measurement is currently underway, and the measured results will be reported at the conference. These results demonstrate the potential of the proposed digitally calibrated TI VCO-based ADC for compact, high-speed detector readout systems.

References

[1] M. Wang et al., "Development of a High Counting Rate Waveform-Sampling Readout Electronics Based on DRS4 for TOF-PET Detector," in IEEE Transactions on Instrumentation and Measurement, vol. 74, pp. 1-9, 2025

[2] E. Delagnes et al., "The SAMPIC Waveform and Time to Digital Converter," 2014 IEEE Nuclear Science Symposium and Medical Imaging Conference (NSS/MIC), Seattle, WA, USA, 2014

[3] J. Kim et al., "Analysis and Design of Voltage-Controlled Oscillator Based Analog-to-Digital Converter," in IEEE Transactions on Circuits and Systems I: Regular Papers, vol. 57, no. 1, pp. 18-30, Jan. 2010,

NSS-01-113

Development of an FPGA-based Hardware Data Injector for High-Energy Experiments (#2845)

Marcel M. Boonen, Davide Cieri, Oliver Kortner, Sandra Kortner

Max Planck for Physics, Munich, Germany

Abstract

Most high-energy experiments at CERN are upgrading their trigger systems for the upcoming high-luminosity era of the LHC. At the same time, development started on the trigger systems of future collider experiments. To fully validate those new systems and developments, it is necessary to test both the algorithms and the underlying interfaces under consideration in a faithful manner. For the former, simulations are used, and for the latter small-scale hardware test stands are typically used. This project proposes the usage of an FPGA-based hardware data injector, which could replicate at the same time the expected fast trigger data rate and transmission protocols. By storing Monte-Carlo simulated data in a DDR4 memory and subsequently transmitting it continuously to a trigger board under test using Gigabit Transceivers, the emulator can mimic the expected low latency data flow.

References
[1] CERN Yellow Reports: Monographs. CERN Yellow Reports: Monographs, Vol. 10 (2020): High-Luminosity Large Hadron Collider (HL-LHC): Technical design report. 2020.
[2] Iacopo Longarini. “Status and testing of the MDT Trigger Processor for the ATLAS Level-0 Muon Trigger at HL-LHC”. In: PoS EPS-HEP2025 (2026), p. 563. DOI: 10.22323/1.485.0563.
[3] Eric Shearer Hazen et al. “The APOLLO ATCA Platform”. In: Proceedings of Topical Workshop on Electronics for Particle Physics — PoS(TWEPP2019). TWEPP2019. Sissa Medialab, Mar. 2020, p. 120. DOI : 10.22323/1.370.0120. URL: http://dx.doi.org/10.22323/1.370.0120.

NSS-01-115

NSS-01-117

MU-STAR-mini: A 5-GS/s Prototype Sampling Array for High-Resolution Multi-Channel Streaming Readout (#3057)

Luca Macchiarulo, Isar Mostafanezhad, Eyan Forsythe, Justine Horikawa, Kahiwa Hoe, Greg Uehara, Joseph Cardenas, Christopher Chock

Nalu Scientific, LLC, Honolulu, USA

This work was partially funded under U.S. DOE DE-SC0025827 award.

Abstract

In this article we describe the design and prototyping of the MUlti-channel Streaming Autonomous Readout chip (MU-STAR-mini) to explore the design limits of fast (5 Gsps) sampling array architectures for high voltage resolution, and probe the hypothesis that such architecture can be competitive in resolution and advantageous in terms of power, density and data reduction when compared with traditional ADC architectures for impulsive applications as they are often found in particle physics. We will describe the design and fabrication of the sampling array architecture, the design and fabrication of its test board, and its initial testing.

References
[1] S. Ritt, "Design and performance of the 6 GHz waveform digitizing chip DRS4," 2008 IEEE NSS 2008 Dresden, Germany, 2008,
[2] L. Macchiarulo, et al., "Design improvements and first results for the revision 3 of AARDVARC Waveform Sampling System On Chip," IEEE NSS-MIC 2021, Virtual Presentation, October 2021.
[3] L. Macchiarulo et al. "HPSoCv3 - an integrated 9-channel 10 Gsps Waveform Digitizer for high density LGAD array" 2025 IEEE NSS, Yokohama, Japan, 2025
[4] Luca Macchiarulo, et al, "Design and Measurement Results for the High Density Digitizer System on Chip (HDSoC): A 64 Channel 1 GSa/s Waveform Digitizer for High Density Detectors, " IEEE NSS conference, October 2021.

NSS-01-119

Implementation of FPGA-Based Time-to-Digital Converters with Zero Measurement Dead Time (#1024)

Xinren Qi, Yonggang Wang

University of Science and Technology of China, Department of Modern Physics, Hefei, China

Abstract

Field programmable gate array (FPGA)-based time-to-digital converter (TDC) has played a very important role in facilities of high-energy physics and scientific instrumentation. Some applications even require TDCs without measurement dead time. In this paper, normal tapped delay line (TDL) based TDC structure is modified towards the realization of zero dead time without losing any TDC original performance. The major challenge in this situation is that there will be more than one signal transition edge in the latched TDL status, therefore, a robust multi-signal transition edge detection circuit module and calibration module are crucial. On a Xilinx UltraScale FPGA, the latched TDL status is first decomposed into 32 divisions, which execute the transition edge picking up parallel before they are combined together to give out all the edges. Since there is only one calibration table in the system, all the edges have to be calibrated sequentially through a specially designed data queue. For performance evaluation, the TDC prototype is implemented on the FPGA with a system clock frequency of 700 MHz. The TDC resolutions for the rising and falling edges are measured as 2.44 ps and 2.31 ps respectively, meanwhile the root-mean-square (RMS) time-interval measurement precisions are measured in the range of 3.5 to 6.5 ps. Applying two trigger signals with 500 ps separation into the TDC repeatedly, all the edges are captured and correctly measured, which demonstrates the capability of zero measurement dead time of the design.

References
[1] Y. Wang, X. Zhou, Z. Song, J. Kuang, and Q. Cao, "A 3.0-ps rms precision 277-MSamples/s throughput time-to-digital converter using multi-edge encoding scheme in a Kintex-7 FPGA," *IEEE Trans. Nucl. Sci.*, vol. 66, no. 10, pp. 2275–2281, Oct. 2019, doi: 10.1109/TNS.2019.2938571.
[2] X. Qi, J. Zhang, and Y. Wang, "Realization of zero measurement dead time on FPGA-based time-to-digital converters," *IEEE Trans. Instrum. Meas.*, vol. 74, pp. 1-8, Dec. 2024, Art no. 2001008, doi: 10.1109/TIM.2024.3509597.

NSS-01-121

A Pre-Study of a General-Purpose Trigger Processing Unit for the CEPC TDAQ System (#1197)

Dong Liu[1,2], Jingzhou Zhao[1], Haoxin Wang[1,2], Sheng Dong[1], Boping Chen[1], Kejun Zhu[1,2], Wenxuan Gong[1], Canming Li[1,2], Fei Li[1], Xin Cao[1,2], Qianyuan Zhao[1,2], Zhenan Liu[1,2]

[1] Institute of High Energy Physics, Beijing, China; [2] University of Chinese Academy of Sciences, Beijing, China

Abstract

The Circular Electron Positron Collider (CEPC) is a large-scale international high-energy physics facility with the Higgs boson as its primary scientific goal. Three operation modes are foreseen: Higgs, Z, and W+W-. The CEPC Trigger and Data Acquisition (TDAQ) system faces a fundamental challenge: extracting rare physics events from an extremely high background rate. For example, in the Higgs mode, simulation results indicate that the target physics event rate is approximately 0.5 kHz, while the bunch crossing rate reaches 1.34 MHz. To cope with this challenge, the required Level-1 (L1) trigger rate for the Higgs mode is about 20 kHz.This extremely low signal-to-background ratio demands a trigger system capable of making efficient and real-time trigger decisions to achieve high-purity event selection while maintaining high efficiency for rare physics signals.To facilitate research and verification of the trigger system design, this talk presents a general-purpose Advanced Telecommunications Computing Architecture (ATCA) processing unit for the CEPC TDAQ system. The unit features an AMD Virtex UltraScale+ field-programmable gate array (FPGA) as its computing core, providing high-density parallel processing. High-speed data transmission is achieved via the FPGA's Gigabit Transceiver (GT) and optical transceivers, offering standardized interfaces for electronic subsystems. The design incorporates 11 Quad Small Form-factor Pluggable (QSFP) modules providing 44 high-speed lanes up to 25 Gbps each, 16 GB of Double Data Rate (DDR) memory for hundreds of milliseconds of buffering, and an Intelligent Platform Management Controller (IPMC) + K26 system-on-module (SOM) for intelligent management. Developed as a flexible testbed, this unit enables the implementation and evaluation of various trigger algorithms and architectures. The test results of related trigger functionalities and performance will be presented in the talk at the conference.

References

[1] S. P. Adhya et al. (CEPC Study Group), “CEPC Technical Design Report - Reference Detector,” arXiv:2510.05260 [hep-ex] (2025).

NSS-01-123

Design of the Ultra-Low-Power Readout Electronics for the Large Area ^{3}He Tube Array Detector at China Spallation Neutron Source (#1266)

Weigang Yin[1,2], Yanlin Lai[1,2], Hongbin Liu[1,2], Qinglei Xiu[1,2], Yubin Zhao[1,2]

[1] Institute of High Energy Physics, Chinese Academy of Sciences, Beijing, China; [2] Spallation Neutron Source Science Center, Dongguan, China

Abstract

The China Spallation Neutron Source (CSNS) is currently upgrading to CSNS-II, increasing the proton beam power to 500 kW and constructing several new neutron spectrometers. The CSNS-II upgrade poses significant challenges for detector and electronics systems, including higher counting rate, improved position resolution requirement, and vacuum operating environment. The large-area ^{3}He tube array detector has been adopted as the major neutron detector owing to the high detection efficiency, the excellent neutron/gamma discrimination, and the ability to construct the detector with large area coverage. In this paper, we present an ultra-low-power front-end readout electronics designed for ^{3}He tube detectors in CSNS-II spectrometers. The circuit design, FPGA algorithms, and laboratory test results of the electronics will be discussed. Experimental results demonstrate that the new electronics system can achieve a single-tube counting rate of 100K/s while maintaining a position resolution about 6 mm. Test also confirmed the system's capability to operate under vacuum conditions. These results meet the requirements for neutron signal readout in CSNS-II spectrometers.

NSS-01-125

A modular, self-triggered firmware for the FPGA-based readout of electromagnetic calorimeters at the INSIGHT@ELSA experiment (#1294)

Benedikt Otto, On behalf of the INSIGHT collaboration

Bonn University, Helmholtz-Institut für Strahlen- und Kernphysik, Bonn, Germany

Abstract

This paper presents a modular, per-channel self-triggered firmware architecture for the FPGA-based readout of electromagnetic calorimeters at the INSIGHT experiment. The firmware integrates a compact deconvolution stage to compensate preamplifier trailing-edge ringing, a configurable, pipelined feature extraction chain (baseline estimation, peak-based trigger with interpolation, pileup detection), and a lightweight network module. The implementation uses a decomposition of the deconvolution kernel to reduce resource usage. Despite the computational demands, the implementation of the deconvolution is resource-efficient and leaves headroom for further extensions. A Python-based simulation framework guided the selection and tuning of algorithms and numerical parameters. Test-beam measurements with a detector module showed an effective ringing suppression

without affecting the pulse amplitude and timing; cooling the detector to the nominal operating temperature in upcoming runs is expected to further reduce residual artifacts. The resulting firmware framework provides a base for both electromagnetic calorimeters, the Crystal Barrel and the PANDA forward endcap calorimeter, in the INSIGHT experiment and will reduce maintenance effort.

NSS-01-127

A Self-Triggered, Event-Driven Readout ASIC for the eXTP PFA X-ray Polarimeter (#1382)

Na Wang[1], Ke Wang[1], Yacong Zhang[2], Ke Wei[2], Yuan Shi[2], Minghang Li[3], Tian Luo[3], Zhongjian Chen[2], Wengao Lu[2], Yingying Cui[2], Wei Wei[1], Weichun Jiang[1], Xiaohua Liu[1], Hong Li[1], Hongwei Liu[1], Haolong Liao[1], Hua Feng[1]

[1] Institute of High Energy Physics,Chinese Academy of Sciences, Beijing, China; [2] School of Integrated Circuits, Peking University, Beijing 100871, Peoples R China, Beijing, China; [3] School of Software and Microelectronics, Peking University, Beijing 100871, Peoples R China, Beijing, China

Abstract

The Polarimetry Focusing Array (PFA) onboard the planned enhanced X-ray Timing and Polarimetry (eXTP) observatory comprises three identical X-ray imaging telescopes, providing X-ray polarimetry in the 2–8 keV energy range with high spatial, spectral, and temporal resolution. To meet these requirements, each detector unit integrates a radiation sensor with a dedicated Application-Specific Integrated Circuit (ASIC) for precise charge extraction and digitization of individual X-ray events.

This paper presents a readout ASIC designed for this application. The proposed ASIC features a self-triggering mechanism that enables event-driven readout with dynamically configurable windows. To satisfy stringent performance requirements, a two-stage analog readout architecture is adopted. Although the target system employs a 352 × 304 pixel array, a prototype ASIC with a 70 × 60 pixel matrix and a pitch of 50 μm was fabricated in a 180-nm CMOS process to validate the design.

Measurement results demonstrate an Equivalent Noise Charge (ENC) below 40 e^- rms. With a 12.5 MHz readout clock, the dead time for a typical event involving approximately 1000 pixels is maintained below 100 μs. These results verify the feasibility of the proposed ASIC architecture for the eXTP PFA instrument.

NSS-01-129

Pulse shape discrimination by digital pulse processing (#1608)

Felix Liang[1], Nicholas Floyd[1], Heshani Jayatissa[1], Philip Adsley[2], Arthur Alvarez[2], Robert Bartsch[2], Shayden Fritz[2], Travis Hankins[2], Bryan Harvey[2], Khang Pham[2], Elizabeth Schnorrenberg[2], David Shelden[2], Sherry Yennello[2]

[1] Los Alamos National Laboratory, ISR Division, Los Alamos, USA; [2] Texas A&M University, Cyclotron Institute, College Station, USA

Los Alamos National Laboratory is managed by Triad National Security, LLC for the U.S. Department of Energy's NNSA.

Abstract

Cerium doped gadolinium aluminium gallium garnet (GAGG:Ce) is capable of detecting both photons and charged particles. Particle identification capabilities present GAGG:Ce as a useful detector in nuclear physics research, and in medical, industry, security and space applications. This work explores the feasibility of using trapezoidal filtering for pulse shape discrimination (PSD) to perform particle identification so that the pulse height analysis (PHA) mode in commercially available waveform digitizers can be used without developing custom PSD firmware. Waveforms recorded from proton and alpha scattering measurements were analyzed offline to optimize the trapezoidal filter parameters. Satisfactory pulse shape discrimination was achieved with a figure of merit of 0.68. Future work will incorporate the optimized parameters in the waveform digitizers for heavy-ion reaction experiments to improve particle identification in real time.

References

[1] Wuenschel, S, *et al.* 2009, 'NIMROD-ISIS, a versatile tool for studying the isotopic degree of freedom in heavy ion collisions', Nucl. *Instrum. Methods*, vol. A604, pp. 578-583.

[2] Sarantites, D, *et al.* 1996, 'The microball', *Nucl. Instrum. Methods*, vol. A381, pp. 418-432.

[3] HV, Richardson, IG, von Rosenvinge, TT 2010, 'A study of solar energetic particle events of 1997-2006: Their composition and associations', *J. Geophys. Res.*, vol. 225, A014848.

[4] Rawat, S, *et al.* 2016, 'Pulse shape discrimination properties of $Gd_3Ga_3Al_2O_{12}$:Ce,B single crystal in comparison with CsI:Tl', *Nucl. Instrum. Methods*, vol. A840, pp. 186-191.

[5] Jordanov, VT, Knoll, GF, Huber, AC, Pantazis, JP 1994, 'Digital techniques for real-time pulse shaping in radiation measurements', *Nucl. Instrum. Methods*, vol. A533, pp. 261-264.

NSS-01-131

Intrinsic time jitter of alternate data acquisition systems for the HISTARS project (#1947)

Víctor Martínez Nouvilas[1], Sara Gaitán Dominguez[1], Luis M. Fraile[2,1], Miriam Caballero Rodríguez[1], Nikita Bernier[1], Andrés Illana[3,1], José A. Briz[1], José Manuel Udías[1]

[1] Universidad Complutense de Madrid, Grupo de Física Nuclear, Madrid, Spain; [2] CERN, ISOLDE, Meyrin, Switzerland; [3] CSIC, Instituto de Estructura de la Materia, Madrid, Spain

This work was funded by the Spanish Government under grant PR38/23-HISTARS (MRR), and by the Comunidad de Madrid CT85/23 under grant PIPF-2023/SAL-GL-30761.

Abstract

The HIE-ISOLDE Timing Array for Reaction Studies (HISTARS) is being developed for the measurement of lifetimes of excited nuclear states produced in reactions at HIE-ISOLDE (CERN). It is based on fast particle and gamma scintillator detectors that will require a fast data acquisition system capable of handling more than 60 channels with good time and energy resolution. Digitizing the fast scintillator signals will allow for a flexible signal processing, while preserving the pulse time structure, and potentially enabling high-precision timing.

In this work we measure the intrinsic time resolution of several digitizer systems for data acquisition and processing of data stemming from fast scintillators, such as LaBr$_3$(Ce). A very promising high-performance candidate is the CAEN 2751 digitizer, providing 14-bit, 1 GS/s, 16 channels, and embedded FPGA processing for advanced waveform acquisition and digital pulse processing.

The DRS4 Evaluation Board uses the DRS4 switched-capacitor array chip developed at Paul Scherrer Institute with 4 input channels, sampling rates of 0.7 to 5 GS/s with 1024 sampling cells at 14-bit resolution. The CAEN DT5742B is a 16-channel switched-capacitor digitizer based on the same DRS4 chip, providing 14-bit resolution and up to 5 GS/s sampling rate.

The CAEN DT5751 is a desktop digitizer 4 channels, 10-bit resolution, and sampling rate of 1 GS/s per channel.

An in-house custom microcontroller-based data acquisition system, capable of analog pulse integration and timestamp assignment based on a bespoke time to amplitude converter (TAC), is also included in the DAQ systems comparison. These results will guide the choice of the data acquisition system for the HISTARS project and determine its baseline contribution to the timing capabilities of the array.

NSS-01-133

Feasibility Study of Analog Pulse Processing ASIC for SDD Array in High Count Rate XRF (#2211)

Yuji Okubo[1], Daisuke Matsunaga[1], Carlo E. Fiorini[2,3], Giacomo Borghi[2,3]

[1] HORIBA, Ltd., Advanced R&D Center, Kyoto, Japan; [2] Politecnico di Milano, Dipartimento di Elettronica, Informazione e Bioingegneria, Milan, Italy; [3] INFN, Sezione di Milano, Milan, Italy

Abstract

Silicon Drift Detectors (SDDs) are the most widely used sensors for energy dispersive X-ray detection in the energy range from a few hundred eV to some tens of keV. When connected to a state-of-the-art CMOS preamplifier, they provide high energy resolution at short peaking times, allowing for high count rates. In high-count-rate X-ray fluorescence (XRF) measurements, SDD arrays are also considered; however, using conventional Digital Pulse Processors (DPPs) requires a large number of ADCs and FPGAs, leading to an increase in overall system size. To keep the total system compact, this study proposes an approach using the analog pulse processing ASIC "SCARLET" and investigates its feasibility. Using an actual XRF setup, a single SDD signal was input into the ASIC as an initial evaluation of its fundamental throughput performance and energy spectrum at an input count rate of up to 1.8 Mcps. The results show that with a 400 ns shaping pulse width, the ASIC could potentially achieve faster throughput compared to a conventional DPP with an equivalent filter length. However, with a 200 ns pulse width, the throughput decreased, and incorrect energy measurements were observed, such as the appearance of an unexpected peak on the lower energy side. This indicates that there are remaining issues in the peak detection logic within the ASIC. This study provides fundamental insights into the effectiveness of the analog ASIC for high-count-rate XRF measurements and highlights areas for future improvement.

References

[1] R. Quaglia, et al., “Silicon Drift Detectors and CUBE preamplifiers for high-resolution X-ray spectroscopy “, IEEE Trans. Nucl. Sci., Vol. 62, No. 1, pp. 221-227, 2015

[2] G. Bellotti, et al. "The detection module of ARDESIA: A new, versatile array of SDDs for X-ray spectroscopy synchrotron applications", Proc. IEEE NSS/MIC/RTSD, pp. 1-4, 2016

[3] I. Hafizh et al., “TERA: Throughput-Enhanced Readout ASIC for High-Rate Energy-Dispersive X-ray Detection,” IEEE Trans. Nucl. Sci., Vol. 67, No. 7, p. 1746, 2020

[4] G. Deda, et al., “SCARLET: Readout ASIC for Bump-bonded SDD Array for Large Event Throughput”, IEEE Trans. Nucl. Sci., Vol. 71, No. 10, pp. 2323-2333, 2024

NSS-01-135

High-performance upgrade for Track Lab: processing Timepix4 hits efficiently at scale (#2433)

Petr Mánek[1], Benedikt Bergmann[1], Petr Burian[1,2], Tomáš Čelko[1,3], Radu E. Mihai[1,4], Petr Smolyanskiy[1]

[1] Czech Technical University in Prague, Institute of Experimental and Applied Physics, Prague, Czech Republic; [2] University of West Bohemia in Pilsen, Faculty of Electrical Engineering, Pilsen, Czech Republic; [3] Charles University, Department of Computer Science Education, Prague, Czech Republic; [4] Horia Hulubei National Institute for R&D in Physics and Nuclear Engineering, Department of Nuclear Physics, Bucharest-Magurele, Romania

B.B. and P.M. and P.S. acknowledge funding from the Czech Science Foundation under Registration Number GM23-04869M. P.B. acknowledges funding from the Technology Agency of the Czech Republic under grant number TN02000012.

Abstract

Timepix4 represents a significant advancement in the Timepix family of hybrid active pixel detectors, particularly attractive due to its fine time resolution (195 ps) and high supported hit rates (up to 5 GHz/mm2). To address performance challenges presented by these new features, an upgrade has been implemented for the Track Lab software package, which has become a standard tool for data collection and analysis of many Timepix-based systems. Above all, the presented upgrade adds support for a 40 Gb/s PCI-express readout interface, capable of reaching hit rates of 300–400 MHz. To facilitate efficient analysis of such data volumes, the presented work implements a number of optimizations, including memory-level bit packing, deduplication and GPU offload for hit clustering, a required step for most event-based analysis algorithms. This work will present details of these improvements, characterize Track Lab's response under heavy load and present results of a performance benchmark. The upgraded software is expected to find plentiful applications in high-intensity X-ray imaging, γ-imaging and the forthcoming high-luminosity campaign at the Large Hadron Collider.

References

[1] P. Mánek, P. Burian, E. David-Bosne, P. Smolyanskiy, and B. Bergmann, "Track Lab: extensible data acquisition software for fast pixel detectors, online analysis and automation," *J. Instrum.*, vol. 19, Jan. 2024, Art. no. C01008, 10.1088/1748-0221/19/01/C01008.

[2] X. Llopart et al., "Timepix4, a large area pixel detector readout chip which can be tiled on 4 sides providing sub-200 ps timestamp bin-ning," *J. Instrum.*, vol. 17, Jan. 2022, Art. no. C01044, 10.1088/1748-0221/17/01/C01044.

[3] O.Růžička et al., "Timepix4 chipboard and readout concept," *J. Instrum.*, vol. 20, Jun. 2025, Art. no. C06074, 10.1088/1748-0221/20/06/C06074.

[4] T. Čelko, F. Mráz, B. Bergmann, and P. Mánek, "Parallel CPU- and GPU-based connected component algorithms for event building for hybrid pixel detectors," *J. Instrum.*, vol. 20, Jan. 2025, Art. no. C01041, 10.1088/1748-0221/20/01/C01041.

NSS-01-137

A Scalable High-Throughput DAQ Architecture for Real-Time Proton Beam Monitoring Applications (#2452)

Burcu Yerli[1], Ugur Demir[1], Hasan O. Caliskan[1], Bayram Deniz[1], Furkan Caliskan[1], Meyra Ayyildiz[1], Kıvanc Nurdan[1,2], Bora Akgun[2,3], On Behalf of NOVO Collaboration

[1] TÜBİTAK, Informatics and Information Security Research Center (BİLGEM), Kocaeli, Turkey; [2] Bogazici University, Department of Physics, İstanbul, Turkey; [3] Bogazici University, Center for Targeted Therapy Technologies, İstanbul, Turkey

The authors would like to acknowledge the support of The Scientific and Technological Research Council of Türkiye (TÜBİTAK). This work was carried out within the framework of the NOVO Collaboration, whose support and collaborative environment are gratefully appreciated.

Abstract

This paper presents a scalable and high-throughput data acquisition (DAQ) architecture developed for real-time proton beam monitoring applications in advanced proton therapy systems. The proposed system is designed to support detector-based tracking of proton energy deposition, enabling continuous monitoring of beam delivery and allowing treatment parameters to be adjusted dynamically during operation. By providing precise localization of proton energy release within the target region, the system contributes to improved dose accuracy while minimizing radiation exposure to surrounding healthy tissue. The DAQ architecture integrates high-speed digitization, synchronized timing distribution, and efficient event aggregation within a modular rack-based platform optimized for detector readout applications. The system consists of eight digitizer boards supporting 64 analog input channels corresponding to 32 detector elements. Differential signal readout is employed to improve signal integrity and reduce noise susceptibility during acquisition. A dedicated Data Collection Board equipped with 40 Gbps QSFP+ communication links aggregates and transfers acquired event data to a host DAQ server with high bandwidth and low latency. System-wide synchronization is maintained through a centralized Clock Distribution Board, while an OpenVPX-compliant Power Supply Board ensures reliable operation of all modules. The proposed architecture provides a compact, scalable, and synchronized solution for real-time proton therapy monitoring and high-performance medical imaging applications.

References

[1] Bortfeld, Thomas, and Wolfgang Schlegel. "An analytical approximation of depth-dose distributions for therapeutic proton beams." Physics in Medicine & Biology 41.8 (1996): 1331-1339.

[2] Medina, Elisabetta. "Solid-state detectors for beam monitoring in FLASH radiotherapy and for other harsh environment applications." (2025).

[3] Halfon, Orith, et al. "A position sensitive detector with real-time gamma/neutron discrimination capability." IEEE Transactions on Nuclear Science (2025).

[4] Halfon, O., et al. "First Experimental Measurement of Prompt Gamma Imaging with Real-Time Neutron Rejection via Pulse Shape Discrimination." IEEE Transactions on Radiation and Plasma Medical Sciences (2026).

[5] Matamoros, A., et al. "Analysis of the mixed secondary radiation field in proton therapy using a Timepix detector." Physics in Medicine & Biology 70.16 (2025): 165002.

[6] Liu, Zhengyao, et al. "Design of highly reliable and rugged PHYTIUM computing unit based on OpenVPX." International Conference on Internet of Things and Machine Learning (IoTML 2021). Vol. 12174. SPIE, 2022.

[7] Paganetti, Harald, et al. "Roadmap: proton therapy physics and biology." Physics in Medicine & Biology 66.5 (2021): 05RM01.

NSS-01-139

A Modular High-Bandwidth DAQ System for the Medipix4 ASIC Based on FPGA Ethernet Readout (#2665)

Nicolò Vladi Biesuz[1], Rafael Ballabriga[2], Jerome A. Alozy[2], Riccardo Bolzonella[2], Michael Campbell[2], Massimiliano Fiorini[3,1], Xavier Llopart Cudie[2]

[1] Istituto Nazionale di Fisica Nucleare (INFN), Ferrara Division, Ferrara, Italy; [2] CERN, EP Department, Geneva, Switzerland; [3] Università di Ferrara, Ferrara, Italy

Abstract

The Medipix4 ASIC is a hybrid pixel detector developed for high-rate spectroscopic X-ray imaging and photon-counting applications. Its synchronous frame-based architecture supports multiple acquisition modes and up to sixteen DDR output links, requiring scalable off-detector electronics. This work presents a modular FPGA-based Data Acquisition (DAQ) system developed for Medipix4 characterization and detector integration.

The system is composed of a Xilinx Kintex UltraScale FPGA DAQ board and a dedicated CERN-developed Medipix4 chipboard directly interfaced through FMC connectivity. The firmware reuses the IPbus-based control path developed for the Timepix4 ASIC while implementing a dedicated Medipix4 synchronous acquisition pipeline. Sixteen independent DDR interfaces operate at selectable clock frequencies of 20, 40, 80, 160 and 320 MHz. Each detector link is connected to a deserializer implementing frame detection, header decoding and 64-bit payload reconstruction. The decoded headers allow the firmware to determine the active acquisition configuration, including counter depth, active links and payload size.

The sixteen parallel data streams are packetized and transmitted through two independent 10~Gigabit Ethernet UDP links. The aggregate detector bandwidth of 10.24 Gb/s is compatible with the measured sustained transmission throughput of 2 X 8.85 Gb/s. The firmware uses reusable open-source HDL components where possible and is distributed within the Medipix collaboration as Open Hardware under the CERN Open Hardware Licence. Ongoing developments include migration toward lower-cost FPGA platforms and support for simultaneous acquisition from multiple Medipix4 ASICs.

References

[1] Sriskaran, V., Alozy, J., Ballabriga, R., Campbell, M., Christodoulou, P., Heijne, E., Koukab, A. Kugathasan, T., Llopart, X., Piller, M., Pulli, A., Sallese, J.-M., Tlustos, L. 2024, *'High-rate, high-resolution single photon X-ray imaging: Medipix4, a large 4-side buttable pixel readout chip with high granularity and spectroscopic capabilities'*, Journal of Instrumentation, **19** (02) P02024 , online: IOP Publishing

[2] Llopart, X., Alozy, J., Ballabriga, R., Campbell, M., Casanova, R., Gromov, V., Heijne, E.H.M., Poikela, T., Santin, E., Sriskaran, V., Tlustos, L., Vitkovskiy, A., 2022, *'Timepix4, a large area pixel detector readout chip which can be tiled on 4 sides providing sub-200 ps timestamp binning'*, Journal of Instrumentation, 17 (01), C01044, online: IOP Publishing

[3] *C. Ghabrous Larrea, K. Harder, D. Newbold, D. Sankey, A. Rose, A. Thea and T. Williams, 2015, "IPbus: a flexible Ethernet-based control system for xTCA hardware"*, Journal of Instrumentation ***10*** *(02), C02019*, online: IOP Publishing

[4] Biesuz, N.V., Caballero, R., Cieri, D., Giangiacomi, N., Gonnella, F., Loustau De Linares, G., Peck, A., 2023, *`Hog 2023.1: a collaborative management tool to handle Git-based HDL repository'*, Proceedings of the 3rd Workshop on Open-Source Design Automation (OSDA), arXiv:2304.02437

[5] Forencich, A., Han, S., 2025, *`verilog-ethernet: Ethernet MAC, PHY, and networking stack in Verilog'*, GitHub repository, [Online]: https://github.com/alexforencich/verilog-ethernet

[6] Bruendler, O., 2026, *`Open-Logic: reusable open-source FPGA building blocks'*, GitHub repository. [Online], https://github.com/open-logic/open-logic

NSS-01-141

Measurement of Energy-Dependent Neutron-Induced Single-Event-Upset Rates for Multiple FPGA Types (#2544)

Shunya Ueda[1], Hanwook Bae[2], Eitaro Hamada[3], Youichi Igarashi[3], Yu Nakazawa[3], Shin-ichiro Meigo[4,5], Haruki Miyai[1], Kou Oishi[3], Kazuki Ueno[1], Chihiro Yamada[1]

[1] The University of Osaka, Toyonaka, Japan; [2] Tohoku University, Sendai, Japan; [3] High Energy Accelerator Research Organization, Tukuba, Japan; [4] Japan Atomic Energy Agency, Naka, Japan; [5] J-PARC Center, Naka, Japan

The neutron experiment at the J-PARC MLF BL10 NOBORU was performed under a user program (Proposal No. 2025B0064). The
authors would like to express their sincere thanks to
Dr. K. Oikawa, Dr. M. Harada, and Dr. Y. Tsuchikawa at J-PARC for their support during this experiment.
This work was supported by the Japan Society for the Promotion of Science (JSPS) KAKENHI under Grant JP21H04971.

Abstract

We measured energy-dependent single-event-upset (SEU) rates for three field-programmable gate array (FPGA) types under neutron irradiation at the BL10 beamline of the Materials and Life Science Experimental Facility (MLF) at the Japan Proton Accelerator Research Complex (J-PARC). Two 28-nm complementary metal oxide semiconductor (CMOS) devices and one 65-nm CMOS device was irradiated with neutrons over a wide energy range from meV to MeV. Dedicated firmware detected SEUs with high timing precision, and the time-of-flight (TOF) method identified the neutron energies that caused the SEUs. We estimated the neutron fluence from a PHITS simulation of the beam spectrum and normalized the SEU counts to the fluence for each FPGA type.

The SEU rates clearly depended on neutron energy.
One 28-nm device had an SEU rate in the 10^{-8}-10^{-7} MeV region about one order of magnitude higher than that at 1 MeV, whereas the other devices showed no significant low-energy enhancement. Below 0.1 MeV, the SEU rate increased as neutron energy decreased, approximately following the $1/v$ dependence, where v is the neutron velocity.

The two 28-nm devices responded differently despite using the same process technology. In contrast, the 65-nm device had a low-to-high-energy change similar to that of one 28-nm device.
These results suggest that device structure or neutron-sensitive materials, rather than process technology alone, contribute to neutron-induced SEUs.

References

[1] Iwashita, H, Kiuchi, R, Hiroshima, Y, ,Okugawa, Y, Sebe, T, Takeda, M 2023, 'Energy-Resolved SEU Cross Section From 10-meV to 800-MeV Neutrons by Time-of-Flight Measurement,' in *IEEE Transactions on Nuclear Science*, vol. 70, no. 3, pp. 216-221
[2] Yamada, C, Bae, H, Hamada, E, Miyai, H, Nakazawa, Y, Oishi, K, Ueda, S, Ueno, K, 2026 "Thermal-neutron-induced single event upsets in an FPGA used in particle physics experiments," *Nucl. Instrument. Methods. Phys. Res. A*, Vol. 1083, p. 171149.
[3] Hasemi, H, Harada, M, Kai, T, Shinohara, T, Ooi, M, Sato, H, Kino, K, Segawa, M, Kamiyama, T, Kiyanagi, Y, 2015 "Evaluation of nuclide density by neutron resonance transmission at the NOBORU instrument in J-PARC/MLF," *Nucl. Instrum. Methods Phys. Res. A*, Vol. 773, pp. 1137–1149.
[4] Iwasem, H, Niita, K, Nakamura, T, 2002 "Development of general-purpose particle and heavy ion transport Monte Carlo code," *J. Nucl. Sci. Technol.*, Vol. 39, No. 11, pp. 1142–1151.

NSS-01-143

Wireless Dosimetry System for Interventional Radiology (#2676)

Marta Moniz, Pedro M.M. Correia, Ana Luísa M. Silva, João F.C.A. Veloso, Carlos D.R. Azevedo

University of Aveiro, i3N - Physics Department, Aveiro, Portugal

This work was supported in part by project CENTRO2030-FEDER-02363500 (easyPET.CT), funded by the FEDER program through CENTRO2030 and by national funds through FCT - Fundação para a Ciência e a Tecnologia, I.P., under the project UID/50025/2025 (doi.org/10.54499/UID/50025/2025), UID/PRR/50025/2025 (doi.org/10.54499/UID/PRR/50025/2025), UID/PRR2/50025/2025 (doi.org/10.54499/UID/PRR2/50025/2025) and the Associate Laboratory I3N -- LA/P/0037/2020 (doi.org/10.54499/LA/P/0037/2020).

Abstract

This work presents the design and characterisation of the front-end eletronics of a wireless active personal dosimeter for interventional radiology. The device is a low-cost, single-channel sensing unit that can be replicated across the thorax, neck, hands, and eyes, providing operators with continuous dose-rate feedback at these four anatomical regions. Each dosimeter consists of a tissue-equivalent plastic scintillator coupled to a silicon photomultiplier, read out by a charge-sensitive amplifier, a semi-Gaussian shaper with pole-zero cancellation, and a peak-and-hold circuit triggered by a comparator. Power management and wireless transmission are handled by a battery-operated microcontroller, keeping the assembly compact and unobtrusive to the operator. Dose-rate data are transmitted to a remote display with visual and sound alarms. The front-end has been characterised under dark-count conditions, with a dead time of 11.6 microseconds expected to extend to approximately 20 microseconds once analog-to-digital conversion is included in the readout loop. Energy and dose calibration of the coupled detector, together with the four-channel graphical interface, are the next development steps.

References
[1] National Council on Radiation Protection and Measurements, ``NCRP Report No. 168: Radiation dose management for fluoroscopically guided interventional medical procedures,'' Bethesda, MD, USA, Tech. Rep., Jul. 2010.
[2] L. Servoli, L. Bissi, S. Fabiani, D. Magalotti, P. Placidi, A. Scorzoni, A. Calandra, R. Cicioni, S. Chiocchini, A. C. Dipilato, N. Forini, M. Paolucci, R. D. Lorenzo, F. P. Cappotto, M. Scarpignato, A. Maselli, and A. Pentiricci, "Personnel real time dosimetry in interventional radiology," Physica Medica, vol. 32, pp. 1724–1730, 12 2016.
[3] R. Sanchez, E. Vano, J. M. Fernandez, and J. J. Gallego, "Staff radiation doses in a real-time display inside the angiography room," CardioVascular and Interventional Radiology, vol. 33, pp. 1210–1214, 12 2010.

[4] R. Baumgartner, K. Libuit, D. Ren, O. Bakr, N. Singh, U. Kandemir, M. T. Marmor, and S. Morshed, “Reduction of radiation exposure from c-arm fluoroscopy during orthopaedic trauma operations with introduction of real-time dosimetry,” Journal of Orthopaedic Trauma, vol. 30, pp. 53–58, Feb. 2016
[5] V. Koch, L. M. Conrades, L. D. Gruenewald, K. Eichler, S. S. Martin, C. Booz, T. D’Angelo, I. Yel, S. Bernatz, S. Mahmoudi, M. H. Albrecht, J. E. Scholtz, A. Thalhammer, S. Zangos, T. J. Vogl, and T. Gruber-Rouh, “Reduction of radiation dose using real-time visual feedback dosimetry during angiographic interventions,” Journal of Applied Clinical Medical Physics, vol. 24, 2 2023.
[6] J. Racadio, R. Nachabe, B. Carelsen, J. Racadio, N. Hilvert, N. Johnson, K. Kukreja, and M. Patel, “Effect of real-time radiation dose feedback on pediatric interventional radiology staff radiation exposure,” Journal of Vascular and Interventional Radiology, vol. 25, pp. 119–126, 2014.
[7] James, R. F., Wainwright, K. J., Kanaan, H. A., Hudson, S., Wainwright, M. E., Hightower, J. H., & Delaney, J. J. (2015). Analysis of occupational radiation exposure during cerebral angiography utilizing a new real time radiation dose monitoring system. Journal of neurointerventional surgery, 7(7), 503–508. https://doi.org/10.1136/neurintsurg-2014-011215
[8] U. O’Connor, E. Carinou, I. Clairand, O. Ciraj-Bjelac, F. De Monte, J. Domienik-Andrzejewska, P. Ferrari, M. Ginjaume, H. Hrˇsak, O. Hupe, Z. Kneˇzevi´c, M. Sans Merce, S. Sarmento, T. Siiskonen, and F. Van- ˇ havere, “Recommendations for the use of active personal dosemeters (apds) in interventional workplaces in hospitals,” Physica Medica, vol. 87, pp. 131–135, 2021.
[9] Radiological protection---X and gamma reference radiation for calibrating dosemeters and doserate meters and for determining their response as a function of photon energy---Part 1: Radiation characteristics and production methods}, ISO Standard 4037-1:2019, Jan. 2019.

NSS-01-145

FPGA firmware for ³He resistive wire tube readout with CAEN R5560 ADC. (#2794)

Davide Raspino[1], Andrea Abba[2], Erik Schooneveld[1], Stefano Carsi[2], Jeff Sykora[1]

[1] UKRI- STFC, ISIS, Chilton Didcot, UK; [2] Nuclear Instrument, Comom, Italy

Abstract

This work presents the development of a versatile FPGA firmware for the readout of ³He resistive wire tubes widely used in neutron scattering instruments. These detectors are deployed in large numbers across major neutron facilities, including ISIS, ILL, SNS, FRM2, ESS, MLF, and CNCS.

In typical configurations, detector signals are first conditioned by front-end preamplifiers located near the tubes, then digitized by ADC systems positioned up to 40 m away. The FPGA-based processing extracts pulse amplitudes to determine the neutron interaction position along the detector. The implemented system is based on the R5560 ADC, operating at a sampling rate of 125 MHz.

The firmware, developed using SCI-Compiler, is organized into two main blocks: signal processing and data transmission. The signal processing stage includes baseline correction and gain scaling to maximize ADC dynamic range, followed by configurable filtering. The latter consists of cascaded moving-average integrators and a differentiator, with user-defined parameters (number and length of filters) adjustable via control registers to accommodate different instrument requirements.

To ensure compatibility with both legacy and next-generation data acquisition systems, the firmware supports multiple communication interfaces. At ISIS, the ADC serial interface is currently used for integration with the existing Data Acquisition Electronics (DAE), as demonstrated on the OSIRIS instrument. In parallel, a high-throughput UDP-based optical fibre link has been developed for future deployment, including WISH and µRWELL-based detector systems. Additionally, a TCP/IP Ethernet interface provides a flexible solution for diagnostics and lower-rate data acquisition.

This architecture enables a scalable and adaptable readout solution for current and future neutron detector systems.

References
[1] ISIS Annual Report, https://www.isis.stfc.ac.uk/wp-content/uploads/2025/10/ISIS_Annual_Report_2025_final.pdf
[2] CAEN R5560 ADC Family, https://www.caen.it/products/r5560/
[3] Visual Programming Language for Open FPGA, https://www.sci-compiler.com/
[4] M. T. F. Telling and K. H. Andersen , *Phys. Chem. Chem. Phys.*, 2005, **7** , 1255 –1261, https://doi.org/10.1039/B413934H
[5] L. C. Chapon, P. Manuel, P. G. Radaelli, C. Benson, L. Perrott, S. Ansell, N. J. Rhodes, D. Raspino, D. Duxbury, E. Spill, J. Norris, Wish: The new powder and single crystal magnetic diffractometer on the second target station. *Neutron News* **22**, 22–25 (2011).
[6] R. Hafeji,et al, Gain measurements of µRWELLs in ^{3}He-CF_4 mixtures for thermal neutron detectors, Nuclear Instruments and Methods in Physics Research Section A, Volume 1048, 2023, https://doi.org/10.1016/j.nima.2022.167976.

NSS-01-147

LDMX Silicon Tracker Data Acquisition System (#2807)

Benjamin Reese, Timothy K. Nelson, Matthew Gignac, Christos Bakalis

SLAC National Accelerator Laboratory, Menlo Park, USA

Abstract

The Light Dark Matter eXperiment (LDMX) is a proposed fixed-target experiment that will search for sub-GeV dark matter using a missing-momentum signature in high-rate electron interactions. Its Silicon Tagging Tracker (STT) and Silicon Recoil Tracker (SRT) measure incoming and outgoing charged particles around the target, providing trajectory and momentum information needed to identify events with invisible final-state particles and reject backgrounds. The Tracker data acquisition (DAQ) system is built around APV25-based silicon strip modules, front-end boards (FEBs), and a Bittware PCI Express back end integrated with the common LDMX timing, fast-control, and event-building infrastructure. Each FEB distributes APV25 clock, trigger, reset, I2C control, low-voltage power, and sensor bias. It also digitizes APV25 analog streams, formats three-sample channel records, and transmits Tracker event records to the back end. The architecture is constrained by the APV25 pipeline latency and must preserve bunch timing while scaling to the final multi-FEB Tracker. During the 2025 LDMX test at SLAC End Station A, a Tracker DAQ vertical slice operated one FEB with four silicon Hybrid modules and the Bittware back end. The system acquired coherent data with other LDMX subsystems, demonstrated stable noise performance, was timed in to beam, and observed beam-induced hits with the expected timing behavior.

NSS-01-149

Latest Upgrades and Operation of the Neutron Veto Data Acquisition System for the XENONnT Experiment (#2929)

Stefano Mastroianni, on behalf of the XENON Collaboration

INFN, Sec. Naples, Naples, Italy

Abstract

The Neutron Veto (NV) of the XENONnT experiment is a gadolinium-doped water Cherenkov detector surrounding the central xenon time projection chamber (TPC). It is instrumented with 120 photomultiplier tubes (PMTs) to reduce the nuclear recoil background induced by radiogenic neutrons originating from detector materials, which can mimic WIMP-like signatures. During the third science run (SR2), conducted between October 2023 and March 2025, XENONnT achieved a significantly reduced background configuration. In particular, the neutron background was suppressed by loading the water tank with 500 ppm of gadolinium sulfate, resulting in an approximately twofold reduction compared to earlier runs performed with pure water. Following maintenance activities initiated in summer 2025, the detector is currently being recommissioned in preparation for the next science run. This work presents the latest upgrades and the operational performance of the NV data acquisition (DAQ) and online processing systems. The NV DAQ is based on a fully triggerless architecture in which PMT waveforms are continuously digitized, enabling software-based coincidence searches within time windows of several hundred nanoseconds.To enhance long-term reliability and stability, the DAQ system has been upgraded with new-generation CAEN PCIe readout cards. Concurrently, the front-end server has been upgraded to ensure compatibility with latest operating systems, while improving fault tolerance, system monitoring, and integration with the experiment-wide online processing system. A further improvement is the deployment of a dedicated FPGA-based monitoring board for the NV data readout. This board processes digitizer monitoring signals such as buffer occupancy, busy and flow-control flags, timing and synchronization signals, and error conditions during both science data taking and calibration runs, enabling continuous checks of DAQ performance and stability.

NSS-01-151

Design and Integration of a Modular $LiInP_2Se_6$ Neutron Detector Prototype for Single-Crystal Diffractometry Applications (#3158)

Mohamed El Amine Benkechkache[1,2], Erick Hoegberg[1,2], Alireza Kargar[3], James Christian[3], Charles Sosa[3], Huicong Hong[3], Mercouri G. Kanatzidis[4], Khasim Saheb[4], Safdar Imam[4], Eric Lukosi[1]

[1] University of Tennessee, Nuclear Engineering Department, Knoxville, USA; [2] UT Institute for Advanced Materials & Manufacturing, Knoxville, USA; [3] Radiation Monitoring Devices, Inc., Watertown, USA; [4] Northwestern University, Department of Chemistry, Evanston, USA

This material is based upon work supported by the U.S. Department of Energy under grant no. DE-SC0021554. Disclaimer: The views and conclusions contained in this document are those of the authors and should not be interpreted as necessarily representing the official policies, either expressed or implied, of the U.S. Department of Energy.

Abstract

Lithium Indium Phosphorus Selenide ($LiInP_2Se_6$) has emerged as a promising semiconductor material for neutron detection due to its high neutron capture cross-section, suitable bandgap, and favorable charge transport properties. This work reports on the development of a modular $LiInP_2Se_6$ detector prototype for single-crystal diffractometry (SCD) applications. The prototype consists of an 8 × 2 array of $LiInP_2Se_6$ strip sensors with a 300 µm pitch configuration integrated onto a custom sensor baseboard. Initial sensor characterization includes electrical IV measurements and preliminary radiation-response evaluation. The sensors are coupled to a dual-ASICs daughterboard based on VATAGP7 ASICs for signal readout and processing, while detector control and data acquisition are managed through the LISeDAQ acquisition system. This work demonstrates the integration of $LiInP_2Se_6$ sensors, front-end electronics, and acquisition hardware into a scalable detector module architecture toward future high-resolution SCD detector systems.

References

[1] C.C. Wilson, ” Single-crystal neutron diffraction from molecular materials”. Vol. 2. World Scientific Publishing Company, 2000.

[2] Y. Liu, et al. ”PIONEER, a high-resolution single-crystal polarized neutron diffractometer.” Review of Scientific Instruments 93.7 (2022).

[3] C.L. Wang, et al. ”Bright Eu2+-activated polycrystalline ceramic neutron scintillators.” Nuclear Instruments and Methods in Physics Research Section A: Accelerators, Spectrometers, Detectors and Associated Equipment 883 (2018): 1-8.

[4] D. Chica, et al., ”Direct thermal neutron detection by the 2D semiconductor 6LiInP2Se6”. Nature, 577(7790), (2020).

[5] M.A. Benkechkache, et al. ”Front-end Electronics of a LiInP2Se6 Neutron Detector for Single Crystal Diffractometer.” 2024 IEEE Nuclear Science Symposium (NSS), Medical Imaging Conference (MIC) and Room Temperature Semiconductor Detector Conference (RTSD). IEEE, 2024.

[6] IDEAS, Inc. (Norway), http://ideas.no/.

NSS-01-153

Improvement of Ambient dose equivalent rate Estimation for Airborne Radiation Monitoring Using Artificial Neural Networks with Vegetation and Topographic Information (#1454)

Ayumu Miyahara, Miyuki Sasaki, Kazuhiro Suzuki, Yuki Morishita, Hironori Funaki

Japan Atomic Energy Agency, 1. Collaborative Laboratories for Advanced Decommissioning Science, Minamisoma, Japan

Abstract

In airborne radiation monitoring using unmanned aerial vehicles conducted in Japan following the Fukushima Daiichi nuclear power plant accident, a flat-source model is used to estimate the ambient dose equivalent rate at ground level from count rates. However, its assumptions are not suitable for mountainous and forested areas. To improve reliability in these areas, an artificial neural network was constructed that incorporates topographic and

vegetation information as input variables in addition to count rate information, and its impact on estimation performance was evaluated.
The ambient dose equivalent rate map generated by the artificial neural network model reproduced spatial variation in more detail compared to the map created by the flat-source model. Vegetation information helped distinguish between forests and open land, contributing to improved estimation accuracy and precision. Topographic information reduced errors in mountainous areas where the relative position of the detector and the ground changes drastically. An artificial neural network incorporating this information can contribute to identifying hotspots and determining whether evacuation orders can be lifted for small areas.

References
[1] Sasaki, M., Sanada, Y., Katengeza, E.W., Yamamoto, A., 2021, 'New method for visualizing the dose rate distribution around the Fukushima Daiichi Nuclear Power Plant using artificial neural networks', Scientific Reports, vol. 11, article 1857
[2] Sasaki, M. & Sanada, Y. 2022, 'Improvement of training data for dose rate distribution using an artificial neural network', Journal of Advanced Simulation in Science and Engineering, vol. 9, no. 1, pp. 30–39
[3] Sasaki, M., Ochi, K., Sanada, Y., Joung, S., Choi, Y., Lee, E., Ji, W. & Ji, Y.-Y. 2025, 'Expanding the Applicability of Air Dose Rate Conversion Artificial Neural Networks Constructed from Fukushima Experience to Other Detectors', Journal of Radiation Protection and Research, vol. 50, suppl. 1, pp. S112–S123

NSS-01-155

Explainable Radionuclide Identification Using FWHM-Aware Adaptive Banding in Gamma-Ray Spectroscopy (#1543)

Seoyun Jang[1], Gyohyeok Song[1], Uijin Lee[1], Jeonghoon Lee[1], Daeseung Kim[2], Jisoo Kim[1], Gyuseong Cho[1]

[1] KAIST (Korea Advanced Institute of Science and Technology), Department of Nuclear and Quantum Engineering, Daejeon, South Korea; [2] Pusan National University, Nuclear Systems Major, School of Mechanical Engineering, Pusan, South Korea

Abstract
Machine learning has shown strong potential for radionuclide identification using gamma-ray spectroscopy. However, its black-box nature limits the physical interpretation of model predictions. In this study, a spectroscopy-tailored explainable artificial intelligence (XAI) framework for a 1D-CNN-based radionuclide identification model was investigated using gamma-ray spectra measured with a NaI(Tl) detector. The model was trained to classify four radionuclides: ^{22}Na, ^{60}Co, ^{137}Cs, and ^{54}Mn. To identify the spectral regions contributing to the CNN predictions, Grad-CAM, LIME, and Kernel SHAP were applied. In particular, because perturbation-based XAI methods are strongly affected by the definition of input features, two spectral banding strategies were compared: conventional uniform banding and FWHM-aware adaptive banding. The results showed that compared with uniform banding, the proposed adaptive banding provided more localized and physically interpretable attribution results in several cases. These findings suggest that detector-resolution-aware banding can improve the reliability and interpretability of XAI for gamma-ray spectroscopy.

References
[1] M. S. Bandstra, J. C. Curtis, J. M. Ghawaly Jr, A. C. Jones, and T. H. Joshi, "Explaining machine-learning models for gamma-ray detection and identification," Plos one, vol. 18, no. 6, p. e0286829, 2023.

[2] J. Contreras and T. Bocklitz, “Explainable artificial intelligence for spectroscopy data: a review,” Pflügers Archiv-European Journal of Physiology,
vol. 477, no. 4, pp. 603–615, 2025.
[3] Y. Wang, Q. Yao, Q. Zhang, H. Zhang, Y. Lu, Q. Fan, N. Jiang, and W. Yu, “Explainable radionuclide identification algorithm based on the convolutional neural network and class activation mapping,” Nuclear Engineering and Technology, vol. 54, no. 12, pp. 4684–4692, 2022.
[4] B. Jeon, J. Kim, and M. Moon, “Explanation of deep learning-based radioisotope identifier for plastic scintillation detector,” Nuclear Technology, vol. 209, no. 1, pp. 1–14, 2023.

NSS-01-157

Source-Transferable Machine Learning-based Pulse Shape Discrimination in 3D-Printed Plastic Scintillators (#1703)

Vivek Anand, Kuneh Shah, Anil K. Gourishetty

Indian Institute of Technology Roorkee, Roorkee, India

This work was supported by the Ministry of Higher Education (MHRD), Government of India.

Abstract

This work demonstrates source-transferable neutron-gamma pulse-shape discrimination in 3D-printed plastic scintillators using compact deep neural networks trained on experimental waveforms. Additively manufactured plastic scintillators are attractive for application-specific neutron detectors because printing can produce nonplanar and architected geometries. However, their pulse shapes can depend on resin chemistry, dopant loading, and curing conditions. Therefore, discrimination algorithms validated on conventional liquid or cast plastic scintillators cannot be assumed to transfer directly to printed scintillators. Pulses were collected from ^{252}Cf and AmBe sources using CAEN DT5751 and DT5730 digitizers, respectively, and analyzed using charge-comparison pulse-shape discrimination, unsupervised clustering, tree-based classifiers, one-dimensional convolutional neural networks, and fully connected deep neural networks. Charge-comparison methods were limited to 92-93% accuracy for the more overlapping ^{252}Cf dataset, whereas the optimized network used smoothed, peak-aligned, amplitude-normalized waveforms and achieved 99.55% test accuracy on ^{252}Cf. Without retraining, the same model achieved 99.91% inference accuracy on the independent AmBe dataset. Peak alignment was found to be essential as AmBe inference accuracy increased from 88.11% for unaligned raw waveforms to 99.91% for aligned waveforms. These results establish peak-aligned waveform learning as an effective route for robust neutron-gamma discrimination in 3D-printed plastic scintillators.

NSS-01-159

Spectro-Temporal Gamma-Ray Anomaly Detection with Context-Adaptive Background Modeling (#2215)

Hannah Parrilla, Mark Bandstra, Reynold Cooper

Lawrence Berkeley National Laboratory, Berkeley, USA

This work was performed under the auspices of the U.S. Department of Energy by Lawrence Berkeley National Laboratory (LBNL) under Contract DE-AC02-05CH11231. The project was funded by the U.S. Department of Energy, National Nuclear Security Administration, Office of Defense Nuclear Nonproliferation Research and Development.

Abstract

Gamma-ray anomaly detection and identification in complex environments requires background models that are accurate, robust to environmental variation, and interpretable enough to support adaptation given contextual information. We present Gaussian Process Prior NMF (GPP-NMF) spectro-temporal background modeling, combining the physically meaningful structure of Non-negative Matrix Factorization (NMF) in the spectral dimension with a Gaussian process prior (GPP) in the temporal dimension, parameterized by a smoothing hyperparameter λ_T. Evaluated on RADAI synthetic mobile search data, GPP-NMF outperforms standard spectral NMF in the low false alarm rate regime of operational interest, with a single fixed calibrated λ_T. We validate a principled approach for λ_T adaptation to contextual information by showing that the power spectrum of the logarithm of the total building solid angle seen by the detector — extractable from camera data in real time — closely matches the GPP prior power spectrum. Full contextual integration results, including on real-world data, will be presented.

NSS-01-161

NSS-01-163

Generative Overlay Augmentation for Robust Structural Region Segmentation in Dual-Energy X-Ray Cargo Container Imagery (#2263)

Yeon-Wook Kim, Kiyoung Kim, Trinh T.D. Pham

Infiniq, AI Lab, Seoul, South Korea

This work was supported by the National Research Foundation of Korea (NRF) grant funded by the Korea government (MSIT, KCS) (IRIS RS-2025-25459707).

Abstract

Non-intrusive inspection of cargo containers via dual-energy X-ray radiography increasingly faces threats concealed within the container's own structural void spaces, making segmentation of the structural region a necessary prerequisite for downstream anomaly detection. Two compounding factors hinder this task: inconsistent geometric distortion across operational scans, and path-integral structure–cargo overlay that prevents pixel-level human annotation in densely loaded regions. We formulate the task as binary segmentation and propose a regionwise generative overlay augmentation pipeline, in which Stable Diffusion is adapted via a three-stage scheme—LoRA, ControlNet, and inpainting—to synthesise structure–cargo overlay imagery. Polygon annotation is partitioned by visual confidence: structural polygons supply segmentation labels and ControlNet conditions, while cargo polygons serve as inpainting masks. The central hypothesis is that a model trained with the proposed structure–cargo overlay augmentation outperforms a baseline trained on real annotations alone, evaluated on two test partitions defined by the visual clarity of structure–cargo separation under overlay: Easy (clearly distinguishable) and Hard (separation challenging but feasible).

References

[1] T. W. Rogers et al., "Automated X-ray image analysis for cargo security," J. X-Ray Sci. Technol., vol. 25, no. 1, pp. 33–56, 2017.
[2] N. Jaccard et al., "Detection of concealed cars in complex cargo X-ray imagery using deep learning," J. X-Ray Sci. Technol., vol. 25, no. 3, pp. 323–339, 2017.
[3] World Customs Organization, Infiltration of Maritime Cargo Supply Chains: Organized Crime, Cocaine and the Internal Conspirator, Brussels, 2025.
[4] R. Rombach et al., "High-resolution image synthesis with latent diffusion models," Proc. CVPR, 2022, pp. 10684–10695.
[5] E. J. Hu et al., "LoRA: Low-rank adaptation of large language models," Proc. ICLR, 2022.
[6] L. Zhang, A. Rao, and M. Agrawala, "Adding conditional control to textto-image diffusion models," Proc. ICCV, 2023, pp. 3836–3847.
[7] R. Sapkota et al., "YOLO26: Key architectural enhancements and performance benchmarking for real-time object detection," arXiv:2509.25164, 2025.
[8] F. Li et al., "Mask DINO: Towards a unified transformer-based framework for object detection and segmentation," Proc. CVPR, 2023, pp. 3041– 3050.
[9] Y. Fang et al., "EVA-02: A visual representation for neon genesis," arXiv:2303.11331, 2023.

NSS-01-165

Development of Realistic Gamma-ray Spectrum Database Using Geant4 and U-Net-based Sim-to-Real Translation (#2356)

Geon Kim[1,2], Junseong Hwang[1,2], Dae yang Oh[1,2], Chanho Kim[3], Jung-Yeol Yeom[1,4]

[1] Korea University, Department of Bioengineering, Seoul, South Korea; [2] Korea University, Interdisciplinary Program in Precision Public Health, Seoul, South Korea; [3] Korea Atomic Energy Research Institute, Daejeon, South Korea; [4] Korea University, School of Biomedical Engineering, Seoul, South Korea

Abstract

Reliable gamma-ray spectrum databases are needed for data-driven radioisotope identification, but direct measurements of accident-related or short-lived radionuclides are often limited by safety regulations and isotope availability. Geant4 can generate synthetic spectra, but simulated spectra may differ from measured detector-domain spectra because of detector response, energy resolution, gain variation, and channel-domain distortion. In this study, we evaluated a U-Net-based sim-to-real translation framework to transform Geant4-simulated spectra toward measured detector spectra. Measured detector energy-resolution broadening and channel-domain augmentation were applied before translation, and a spatial-transformer-integrated U-Net was used to compensate for gain- and offset-related channel shifts. In validation, the model achieved a mixed-isotope training mean absolute error of 0.045214 and leave-one-out mean absolute error values of 0.068125 for unseen ^{22}Na and 0.047816 for ^{137}Cs. A photopeak-based fidelity analysis showed that 44% of ^{22}Na samples and 24% of ^{137}Cs samples satisfied the defined peak-position and peak-height criterion and a peak-height difference threshold of 0.05. These results indicate that U-Net-based translation can partially reduce the sim-to-real discrepancy in gamma-ray spectroscopy, while consistent reconstruction of detailed photopeak structures remains limited.

References

[1] Chanho Kim, Dongyoung Kim, Yeeun Lee, Chansun Park, Muhammad Nasir Ullah, Duckhyun Kim, Inyong Kwon, Seop Hur, Jung-Yeol Yeom, “Radiation resistance and temperature dependence of Ce:GPS

[2] S. Agostinelli et al., "Geant4-a simulation toolkit," Nuclear Instruments and Methods in Physics Research Section A: Accelerators, Spectrometers, Detectors and Associated Equipment, vol. 506, no. 3, pp. 250-303, 2003.

[3] O. Ronneberger, P. Fischer, and T. Brox, “U-Net: Convolutional networks for biomedical image segmentation,” in Proc. Medical Image Computing and Computer-Assisted Intervention (MICCAI), 2015, pp. 234–241.

NSS-01-167

Real-Time Nuclide Identification via Physics-Region Preprocessing (#2437)

Dongseong Shin[1], Inyong Kwon[2]

[1] Korea Atomic Energy Research Institute, Department of Advanced I&C Research, Daejeon, South Korea; [2] Yonsei University, Department of Radiological Science, Wonju, South Korea

This work was supported in part by the Basic Science Research Program through the National Research Foundation of Korea (NRF) funded by the Ministry of Science and ICT (RS-2022-00165164, RS-2022-00144419)

Abstract

This work addresses real-time identification of gamma-emitting nuclides released outside a damaged reactor using a network of low-cost Silicon photomultiplier (SiPM)–scintillator gamma detectors. Of all fission products, only a few reach the plant exterior in amounts sufficient to produce measurable photopeaks; using the NUREG-1465 source term for Pressurized Water Reactor (PWR) severe accidents, we reduce the monitored set to the dominant nuclides ^{85}Kr, ^{131}I, ^{132}Te, ^{137}Cs, ^{60}Co, and ^{140}Ba. For this set, we design a 2K+1 physics-region preprocessing front-end that places one region of interest on each target photopeak and Compton edge, producing compact features for small downstream classifiers, including the target on-chip deep-learning core. Because direct validation on a real off-site release is impractical, we evaluate the pipeline on a K=5 surrogate set of ^{133}Ba, ^{22}Na, ^{137}Cs, ^{54}Mn, and ^{60}Co spanning the same 80 keV-to-1.3 MeV band on a NaI(Tl)-SiPM detector. On this surrogate, the 2K+1 preprocessing achieves 83.9% accuracy at 25 photopeak counts per window and 97.8% at 100, compared with 75.4% and 94.3% for a raw pulse-vector baseline.

References

[1] IAEA, “The Fukushima Daiichi Accident: Technical Volume 1,” IAEA, Vienna, 2015.
[2] IAEA, “Method for Developing Arrangements for Response to a Nuclear or Radiological Emergency,” IAEA EPR-METHOD, Vienna, 2003.
[3] L. Soffer et al., “Accident Source Terms for Light-Water Nuclear Power Plants,” NUREG-1465, U.S. NRC, 1995.
[4] G. F. Knoll, Radiation Detection and Measurement, 4th ed., Wiley, 2010.
[5] C. G. Ryan et al., “SNIP, a statistics-sensitive background treatment,” Nucl. Instrum. Methods B, vol. 34, pp. 396–402, 1988.
[6] L. A. Currie, “Limits for qualitative detection and quantitative determination,” Anal. Chem., vol. 40, no. 3, pp. 586–593, 1968.
[7] M. Kamuda, J. Stinnett, and C. J. Sullivan, “Automated isotope identification algorithm using artificial neural networks,” IEEE Trans. Nucl. Sci., vol. 64, no. 7, pp. 1858–1864, 2017.
[8] ANSI N42.34, “Performance Criteria for Hand-Held Instruments for the Detection and Identification of Radionuclides,” American National Standards Institute, 2015.
[9] I. Kwon, D. Shin, J. Oh, C.-H. Kim and H. Kim, “Preprocessing Energy Intervals on Spectrum for Real-Time Radionuclide Identification,” IEEE Trans. Nucl. Sci., vol. 68, no. 8, pp. 2202–2209, Aug. 2021, doi: 10.1109/TNS.2021.3097389.

NSS-01-169

Development of a vehicle-mounted Directional radiation monitoring system using multiple NaI(Tl) detectors and an ANN algorithm (#2628)

Hee Kyun Baek[1], Jin Won Lee[1], Sung Min Park[1], Min Yong Park[1], Seong Jae Jeong[1], Seong Hun Choi[1], Jae seung Heo[1], Yong Hyun Chung[2], Sang Yong Kim[1], Jung Ki Shin[1]

[1] Neosiskorea Co., Ltd., Daejeon, South Korea; [2] Yonsei University, Department of Radiation Convergence Engineering, Wonju, South Korea

This work was supported by the Nuclear Energy International Joint Research Project through the National Research Foundation of Korea (NRF) funded by the Ministry of Science and ICT (MSIT) (No. RS-2025-25458886).

Abstract

Vehicle-based radiation monitoring systems are widely used for environmental radiation surveillance, nuclear emergency response, and radioactive contamination mapping. Conventional systems use large-area NaI(Tl) scintillation detectors with high sensitivity for low-count-rate radiation measurements. However, they have limitations such as poor energy resolution and the inability to provide directional information of radiation sources. To overcome these limitations, this study developed a vehicle-based radiation source direction detection system using nine NaI(Tl) detectors while maintaining high sensitivity and energy resolution. The system consists of nine Φ3” × 3” NaI(Tl) detectors. Four upper-layer detectors were arranged for rapid direction identification, one center detector was used for dose assessment, and four lower-layer detectors with lead collimators improved directional accuracy. Radiation source direction was estimated using detector count-rate ratios according to incident direction and distance. An ANN-based algorithm was applied for direction estimation. System performance was evaluated using a 137Cs (100 μCi). Energy resolution and sensitivity were evaluated at 23 cm, while angular resolution tests were conducted at 6 m with source angles varied from 0° to 90° at 10° intervals. The developed system showed approximately 6.8 times higher detection sensitivity than a conventional large-area NaI(Tl) detector system. The angular resolution was evaluated as 45° and 10° for the upper and lower detector layers, respectively, confirming the feasibility of radiation source direction detection in a vehicle-based system. Future work will focus on miniaturization through compact optical sensors, detector rearrangement, and signal-processing optimization.

NSS-01-171

Wavelet optimisation for improved photopeak extraction in low-count gamma-ray spectra (#2656)

James Biggs, Caroline Shenton-Taylor

University of Surrey, School of Maths and Physics, Guildford, UK

Abstract

Detector networks are a potential method of surveillance of radiological material moving through urban environments. Such a network would require ways of automatically assessing collected spectra for non-background isotopes, particularly in count-starved spectra collected in environments with complex backgrounds. In 2018, the London-based SIGMA trial gathered 1.5 billion one-second gamma spectra using both stationary and mobile scintillator detectors. This work presents a wavelet analysis method optimised for use with count-starved gamma spectra. A range of ^{137}Cs spectra were collected, both experimentally and simulated in Geant4, and combined with real-world SIGMA background data. A continuous wavelet transform was conducted on each spectrum, producing an associated scalogram with wavelet transform modulus maxima lines arising from spectral features. By using the ’straightness’ of these lines, it was shown to be possible to identify the presence of ^{137}Cs with 95% accuracy, with a number of false positive identifications. Constraining certain metrics within the method reduced the number of false positives at the expense of overall detection accuracy. UK Ministry of Defence © Crown Owned Copyright 2026/AWE

NSS-01-173

Real-Time Particle Hit Detection Using a 1D Convolutional Neural Network on a CAEN FPGA-Based Digitizer (#2722)

Carlo Tintori[1], Matteo Brini[1], Alberto Potenza[1], Ferdinando Giordano[1], Marco Zanetti[2,3], Andrea Triossi[2,3], **Michail Sapkas**[2,3]

[1] CAEN S.p.A., Viareggio, Italy; [2] University of Padova, Physics and Astronomy, Padova, Italy; [3] INFN Padova, Padova, Italy

Abstract

This study proposes a 1D Convolutional Neural Network (CNN) architecture designed for real-time particle hit detection, moving beyond traditional rigid triggering thresholds. By processing continuous data streams, including high-noise environments, our model demonstrates superior sensitivity in low Signal-to-Noise Ratio (SNR) regimes and pile-up events. We demonstrate that this approach successfully identifies particle signals and provides precise temporal metadata in real time, offering a robust alternative to conventional signal processing methods. Performance was evaluated on a scintillating detector.

References

[1] F. Fahim et al., "hls4ml: An Open-Source Codesign Workflow to Empower Scientific Low-Power Machine Learning Devices," arXiv:2103.05579, 2021

NSS-01-175

Development of an ANN-based Gamma-ray Spectrum Correction Algorithm for PVT Detectors (#2762)

Jiwon Ra, Juwan Kang, Yoon Soo Chung, Yong Hyun Chung

Yonsei University, Department of Radiation Convergence Engineering, Wonju, South Korea

This research was supported by the Regional Innovation System & Education(RISE) program through the Gangwon RISE Center, funded by the Ministry of Education(MOE) and the Gangwon State(G.S.), Republic of Korea.(2025-RISE-10-006)

Abstract

Environmental radiation monitoring systems require detectors that can measure radiation in real time and rapidly identify radionuclides. This study developed an artificial intelligence–based spectrum Correction algorithm that converts gamma-ray spectra acquired from polyvinyl toluene (PVT) detectors with limited energy resolution into

spectra comparable to those of NaI(Tl) detectors. The proposed model used an artificial neural network (ANN)-based multi-layer perceptron (MLP) regressor with two hidden layers, each containing 64 nodes. Rectified Linear Unit (ReLU) and Adaptive Moment Estimation (Adam) were employed as the activation function and optimizer, respectively. The model was trained using PVT spectra as input and NaI(Tl) spectra as target output data to learn the spectral relationship between the two detector systems. Training datasets were generated using Geant4 Application for Tomographic Emission (GATE) for four radionuclides: Co-57, Ba-133, Cs-137, and Co-60. The simulation results demonstrated that the proposed model successfully generated NaI(Tl) photopeak features from PVT spectra. Representative results for Cs-137 yielded a Pearson correlation coefficient of 0.9996 and a root mean square error (RMSE) of 0.0038. Additionally, the energy resolutions at the 662 keV photopeak were found to be 5.94% for the actual NaI(Tl) spectrum and 5.96% for the predicted spectrum, indicating that the two spectra have highly consistent energy resolution characteristics. These results imply that the proposed model can generate spectra with characteristics comparable to those of NaI(Tl) detectors while maintaining the practical benefits of PVT detectors for radiation monitoring applications.

References
[1] Lowdon M, Martin PG, Hubbard MWJ, Taggart MP, Connor DT, Verbelen Y, Sellin PJ, Scott TB. Evaluation of Scintillator Detection Materials for Application within Airborne Environmental Radiation Monitoring. Sensors (Basel). 2019 Sep 4;19(18):3828.
[2] Knoll, G. F. (2010). Radiation detection and measurement. John Wiley & Sons.
[3] Daniel, G., Ceraudo, F., Limousin, O., Maier, D., & Meuris, A. (2020). Automatic and real-time identification of radionuclides in gamma-ray spectra: a new method based on convolutional neural network trained with synthetic data set. IEEE Transactions on Nuclear Science, 67(4), 644-653.

NSS-01-177

measurement-guided x-ray image restoration using fourier stochastic differential equations (#2948)

Seokwon Oh, Junho Lee, Seungjun Yoo, Jeonghyeon Kim, Ho Kyung Kim

Pusan National University, school of mechanical engineering, Busan, South Korea

This work was supported by the National Research Foundation of Korea (NRF) grant funded by the Korea government (MSIT) under Grant RS-2024-00340520. S. Oh was supported by the Basic Science Research Program through the NRF funded by the Ministry of Education under Grant RS-2024-00408137.

Abstract
Industrial X-ray imaging for nondestructive inspection requires high spatial resolution and high sensitivity, but phosphor-based detectors face a trade-off because increased phosphor thickness improves X-ray absorption while degrading spatial resolution through optical spreading. This study investigates a measurement-guided Fourier stochastic differential equation for detector X-ray image restoration. The proposed method defines a degradation path in the Fourier domain using measured detector characteristics. The relative modulation transfer function (MTF) models deterministic resolution loss, and the measured noise power spectrum guides stochastic perturbation. A neural restoration network is trained to reconstruct high-resolution images from intermediate degraded states conditioned on low-resolution observations. Experiments on printed circuit board X-ray images compared the

proposed method with Wiener filtering, a regression baseline, and a conditional diffusion model (CDM). The proposed method improved low-resolution images and achieved image domain restoration quality comparable to the regression baseline and better than Wiener filtering, while CDM showed slightly lower structural fidelity in representative regions. Frequency domain analysis using MTF, contrast transfer function (CTF), and NNPS showed that both CDM and the proposed method closely followed the high-resolution MTF and that the proposed method showed higher CTF recovery in the mid-to-high frequency range. These results indicate that X-ray image restoration methods should be assessed using both image domain metrics and frequency domain characteristics.

References
[1] R. C. Gonzalez and R. E. Woods, Digital Image Processing, 4th ed. New York, NY, USA: Pearson, 2018.
[2] O. Ronneberger, P. Fischer, and T. Brox, "U-Net: Convolutional networks for biomedical image segmentation," in *Proc. Med. Image Comput. Comput.-Assist. Intervent. (MICCAI)*, 2015, pp. 234–241.
[3] C. Dong, C. C. Loy, K. He, and X. Tang, "Image super-resolution using deep convolutional networks," *IEEE Trans. Pattern Anal. Mach. Intell.*, vol. 38, no. 2, pp. 295–307, Feb. 2016.
[4] J. Ho, A. Jain, and P. Abbeel, "Denoising diffusion probabilistic models," in *Adv. Neural Inf. Process. Syst.*, vol. 33, 2020, pp. 6840–6851.
[5] C. Saharia, J. Ho, W. Chan, T. Salimans, D. J. Fleet, and M. Norouzi, "Image super-resolution via iterative refinement," *IEEE Trans. Pattern Anal. Mach. Intell.*, vol. 45, no. 4, pp. 4713–4726, Apr. 2023.
[6] Y. Song, J. Sohl-Dickstein, D. P. Kingma, A. Kumar, S. Ermon, and B. Poole, "Score-based generative modeling through stochastic differential equations," in *Proc. Int. Conf. Learn. Represent. (ICLR)*, 2021.
[7] D. P. Kingma and J. Ba, "Adam: A method for stochastic optimization," in *Proc. Int. Conf. Learn. Represent. (ICLR)*, 2015.

NSS-01-179

A General-Purpose Radionuclide Identification Model for HPGe Gamma-Ray Spectrometry (#3209)

Jim Zickefoose, **Henrik Persson**, Cameron Cianci

Mirion Technologies (Canberra) Inc, Physics, Meriden, USA

Abstract
Radionuclide identification in high-purity germanium (HPGe) gamma-ray spectra can be a challenging and time-consuming task, particularly when complex samples contain many radionuclides that produce overlapping spectral features. In addition to sample emissions, HPGe detectors measure contributions from naturally occurring and environmental radionuclides, referred to as background. The measured sample spectrum is therefore the sum of sample and background contributions, and in most applications it is desirable to identify only the radionuclides present in the sample itself. While background subtraction is commonly performed using a separate background measurement, accurate identification near critical detection limits remains difficult, especially for low-count or cluttered spectra.
We present a Siamese Neural Network (SNN)–based approach for radionuclide identification with background subtraction in HPGe gamma-ray spectra that is generalizable to many detector models and geometries. By directly learning a similarity metric between foreground and background spectra, the method enhances sensitivity to weak spectral features while maintaining low false-positive rates.
The network is trained on a large dataset containing spectra from over 500 radionuclides, generated using Monte Carlo simulations spanning more than 50 detector and geometry combinations and augmented with measured background data. We present the data generation methodology, training procedure, and performance results on

both simulated and measured spectra. The results demonstrate that the SNN approach achieves performance comparable to or exceeding that of traditional spectral analysis techniques. This work provides a foundation for robust, automated radionuclide identification across diverse measurement conditions.

NSS-01-181

NSS-01-183

NSS-01-185

High-Fidelity 3D MCNP Modeling for Waste Classification in PWRs

(#1189)

Changyeon Yoon

Korea Hydro & Nuclear CO., LTD, Central Research Institute, Daejeon, South Korea

Abstract

Accurate classification of radioactive waste is critical for determining disposal costs and ensuring safety during nuclear power plant decommissioning. However, generic models with simplified geometries and material compositions can lead to systematic misclassification. In this study, a high-fidelity 3D MCNP model of a pressurized water reactor (PWR) was developed to evaluate activation source terms and classify waste based on IAEA Safety Standards Series. The model includes the reactor pressure vessel (RPV), reactor vessel internals (RVI), and bioshield concrete, enabling realistic representation of complex structures. Activation analysis shows that Fe-55, Co-60, and Mn-54 are the dominant radionuclides in both the RPV and bioshield, qualitatively aligning with widely recognized reactor activation data and thereby validating the developed model. Based on specific activity, Fe-55

accounts for over 99% in both structures. However, applying radionuclide-specific activity limits results in a dramatic shift in the dominant contributor. In the bioshield concrete, the contribution of Fe-55 decreases from over 99% to approximately 16%, while C-14 becomes dominant at approximately 76%. This indicates that classification based solely on specific activity can lead to fundamental misclassification. The RPV is classified as low-level waste (LLW), whereas the bioshield meets the criteria for very low-level waste (VLLW). In contrast, generic models fail to accurately represent the reactor configuration, which can result in over-classifying the bioshield as LLW. The high-fidelity approach provides a quantitative basis for reclassification, directly contributing to the reduction of disposal volume. These results demonstrate that high-fidelity activation modeling is essential not only for improving classification reliability but also for avoiding systematic overestimation of waste classes and enabling more economically efficient decommissioning strategies.

NSS-01-187

Six-Degree-of-Freedom Pose Estimation for Safety Monitoring in a Nuclear Glovebox (#1287)

Lewis Mead, Charlie Kind, Tom Scott

University Of Bristol, Interface Analysis Centre, Bristol, UK

Thanks to my supervisors Charlie Kind and Tom Scott, and colleagues at the Interface Analysis Centre, for their guidance, technical support, and feedback throughout this work.

Abstract

Nuclear glovebox monitoring must recognise not only which objects are present, but whether their position and orientation indicate an operationally relevant state, such as an inverted container, a handled tool, or an object moving close to a glove during potentially hazardous work. This paper evaluates a two-camera six-degree-of-freedom vision pipeline for advisory operator support in a tabletop analogue of a nuclear glovebox containing a can, pliers, and screwdriver. Offline colour-and-depth pseudo-labels are generated and filtered to train a lightweight object detector and keypoint regressor. During live operation, the system performs object detection, keypoint-based pose recovery, masked depth refinement, temporal smoothing, and safety-state logging. On the validation split, the detector achieved 99.3% mean average precision at an intersection-over-union threshold of 0.5, and the live keypoint-and-depth-refinement pipeline ran at 8.5 frames per second on constrained hardware. These results show that pose-aware monitoring can support prototype glovebox alarms and auditable event records without running a high- capacity pose model online, suggesting a practical route toward advisory systems that improve situational awareness and post- task review while preserving operator judgement. Before such systems could be used operationally, further work is required to establish independent ground truth, model articulated tools, validate longer-term reliability, and build the necessary safety case.

References
[1] O. Tokatli, P. Das, R. Nath, L. Pangione, A. Altobelli, G. Burroughes, E. T. Jonasson, M. F. Turner, and R. Skilton, “Robot-Assisted Glovebox Teleoperation for Nuclear Industry,” Robotics, vol. 10, no. 3, p. 85, 2021.

[2] B. Wen, W. Yang, J. Kautz, and S. Birchfield, “FoundationPose: Unified 6D Pose Estimation and Tracking of Novel Objects,” in Proc. IEEE/CVF Conf. Comput. Vis. Pattern Recognit., 2024, pp. 17868–17879.
[3] C. Rother, V. Kolmogorov, and A. Blake, “GrabCut: Interactive Foreground Extraction Using Iterated Graph Cuts,” in ACM SIGGRAPH 2004 Papers, 2004, pp. 309–314.
[4] G. Jocher and J. Qiu, “Ultralytics YOLO11,” version 11.0.0, 2024. [Online]. Available: https://github.com/ultralytics/ultralytics
[5] V. Lepetit, F. Moreno-Noguer, and P. Fua, “EPnP: An Accurate O(n) Solution to the PnP Problem,” Int. J. Comput. Vis., vol. 81, no. 2, pp. 155–166, 2009.
[6] M. A. Fischler and R. C. Bolles, “Random Sample Consensus: A Paradigm for Model Fitting with Applications to Image Analysis and Automated Cartography,” Commun. ACM, vol. 24, no. 6, pp. 381–395, 1981.
[7] P. J. Besl and N. D. McKay, “A Method for Registration of 3-D Shapes,” IEEE Trans. Pattern Anal. Mach. Intell., vol. 14, no. 2, pp. 239–256, 1992.
[8] J. Park, Q.-Y. Zhou, and V. Koltun, “Colored Point Cloud Registration Revisited,” in Proc. IEEE Int. Conf. Comput. Vis., 2017, pp. 143–152.
[9] T. Hodaˇn, M. Sundermeyer, B. Drost, Y. Labbé, E. Brachmann, F. Michel, C. Rother, and J. Matas, “BOP Challenge 2023 on Detection, Segmentation and Pose Estimation of Seen and Unseen Rigid Objects,” in Proc. IEEE/CVF Conf. Comput. Vis. Pattern Recognit. Workshops, 2024.

NSS-01-189

Photonuclear Processes in a Tungsten Matrix Collimator for Spatially Fractionated Radiation Therapy (#1326)

Igor E. Anokhin, Dmytro Ramazanov

Institute for Nuclear Research, Kyiv, Ukraine

Abstract

Spatially fractionated radiation therapy using tungsten matrix collimators enables high peak-to-valley dose ratios and improved normal tissue sparing. At photon energies near 25 MeV, photonuclear interactions in tungsten induce activation and produce secondary neutrons, potentially affecting both dosimetric performance and radiation safety. In this work, these processes were investigated using FLUKA Monte Carlo simulations of a modular tungsten-matrix collimator irradiated by a 25-MeV photon beam. Secondary neutron fluence distributions, energy spectra, and absorbed-dose maps in a silicon detector plane were evaluated and normalized to a photon fluence of approximately 1×10^{9} cm^{-2}. The calculated absorbed-dose profile exhibits a pronounced mini-beam structure with a peak dose of 6.16×10^{-4} Gy, a valley dose of 2.53×10^{-5} Gy, and a peak-to-valley dose ratio of 24.4. Neutron production is highest at the entrance to the collimator and decreases significantly beyond approximately 5 cm along the beam path, indicating substantial attenuation within the 9 cm tungsten structure. Folding the neutron spectra with energy-dependent fluence-to-dose conversion coefficients yields an ambient dose equivalent of 102 μSv in the collimator region and 0.62 μSv in the phantom region for the same irradiation.

The results demonstrate that photoneutron generation is strongly influenced by the collimator configuration and exhibits distinct spatial and spectral characteristics. Photoneutrons contribute to the dose outside the primary irradiation field, thereby increasing the valley dose and affecting the achievable peak-to-valley dose ratio. These

findings underscore the importance of accounting for photonuclear effects during collimator optimization and shielding design for high-energy photon mini-beam therapy systems.

References
[1] Anokhin I. E., Pugatch V. M., Ramazanov D. M., and Storozhyk D. V., "Matrix metal collimators studies for the spatially fractionated radiation therapy," 2020 IEEE Nuclear Science Symposium and Medical Imaging Conference, NSS-11
[2] Anokhin I. E., Pugatch V. M., and Ramazanov D. M., "Matrix metal collimators studies for the spatially fractionated radiation therapy. Part II: Tungsten, Tantalum and Iron Collimators," 2021 IEEE Nuclear Science Symposium and Medical Imaging Conference, N-28-194
[3] Anokhin I. E., Pugatch V. M., and Ramazanov D. M., "Matrix metal collimators studies for the spatially fractionated radiation therapy. Part III: Particle spectrums," 2022 IEEE NSS/MIC/RTSD, NSS-03-243
[4] FLUKA Collaboration, FLUKA: a multi-particle transport code, https://fluka.cern
[5] ICRP, Conversion Coefficients for use in Radiological Protection against External Radiation, ICRP Publication 74, Ann. ICRP 26(3-4), 1996

NSS-01-191

A Low-Energy X-ray Transmission Imaging Method for Detecting Metallic Microparticles in Single-Layer $LiFePO_4$ Batteries (#1517)

Dehao Wang, Yigang Yang

Tsinghua University, Department of Engineering Physics, Beijing, China

The authors would like to thank the Department of Engineering Physics, Tsinghua University, for experimental support and helpful discussions.

Abstract

Metallic foreign particles are critical safety hazards in lithium-ion battery manufacturing. To address the difficulty of detecting metallic microparticles in single-layer $LiFePO_4$ cells, this work proposes a nondestructive detection method based on low-energy X-ray transmission imaging. Cu, Fe, and Ni particles are analyzed through attenuation modeling and simulation to evaluate the effects of photon energy, particle material, and particle thickness on transmission contrast. Preliminary imaging experiments are performed using 40keV X-rays, and weak abnormal signals are extracted by normal-sample normalization, filtering enhancement, threshold segmentation, and local SNR analysis. The results show that metallic microparticles can produce detectable local attenuation anomalies in low-energy X-ray images.

References
[1] J. Grabow, M. Osenberg, J. Hilger, I. Manke, and A. Latz, "Particle contamination in commercial lithium-ion cells---Risk assessment with focus on internal short circuits and replication by currently discussed trigger methods," Batteries, vol. 9, no. 1, 2023.
[2] P. R. Shearing, J. Gelb, N. P. Brandon, and S. J. Harris, "X-ray tomography for lithium ion battery research", Annual Review of Materials Research, vol. 48, pp. 1--27, 2018.

NSS-01-193

NSS-01-195

Improved Scattering Modeling in CIVA-RT using a Next-Event Estimator

(#1959)

Sheraz Blas[1], Anthony Touron[1], Henri Hutinet[2], Odile Petit[3], Jean Michel Létang[4], Cindy Le Loirec[2]

[1] Université Paris-Saclay, CEA, List, Palaiseau, France; [2] CEA, DES, IRESNE, DER, Service de Physique des Reacteurs et du Cycle, Cadarache, France; [3] Université Paris-Saclay, CEA, Service d'Etudes des Réacteurs et de Mathématiques Appliquées, Gif-sur-Yvette, France; [4] INSA-Lyon, Université Claude Bernard Lyon 1, CNRS, Inserm, CREATIS UMR 5220 U1294, Villeurbanne, France

We acknowledge the financial support of the Cross-Disciplinary Program on Numerical simulation of CEA, the French Alternative Energies and Atomic Energy Commission.

Abstract

In non-destructive testing (NDT), simulation is used to study radiation–matter interactions for various cases. CIVA software includes a radiographic testing (RT) module, which combines analytical and Monte Carlo (MC) approaches. The analytical component models primary photons, while the MC component handles scattered photons — a process that can become computationally intensive in complex configurations. Building on this, we introduce an estimator based on a split exponential track length method (seTLE) in the MC component of CIVA-RT, designed to reduce statistical variance and computational cost. This next-event estimator increases the probability of photon contributions to the detector by creating multiple pseudo-photons during the simulation. Its performance is evaluated using a convergence index and a Figure of Merit. Three configurations are studied: a simple configuration, a step wedge configuration with a distant detector, and an industrial weld case. Results show that the estimator provides significant efficiency gains. A detailed analysis of seTLE simulation shows that rare high-weight photons can cause sudden signal variations. These results demonstrate that the approach provides efficiency gains, making high fidelity simulations more tractable in industrial contexts.

References

[1] H. Hutinet, "Développement d'un estimateur déterministe appliqué au transport de particules neutres en méthode Monte-Carlo" Thèse de doctorat, Aix Marseille Université, 2024. [Online]. Available: https://theses.fr/s376078

[2] F.-X. Hugot *et al.*, "Overview of the TRIPOLI-4 Monte Carlo code, version 12," *EPJ Nucl. Sci. Technol.*, vol. 10, p. 17, 2024, doi: 10.1051/epjn/2024018.

[3] N. Freud, J.-M. Letang, and D. Babot, "A hybrid approach to simulate X-ray imaging techniques, combining Monte Carlo and deterministic algorithms," in *IEEE Symposium Conference Record Nuclear Science 2004.*, Rome, Italy: IEEE, 2004, pp. 3075–3079. doi: 10.1109/NSSMIC.2004.1466331.
[4] H. Hutinet, P.-L. Antonsanti, C. Le Loirec, and D. Mancusi, "Accelerating split-exponential track length estimator on GPU for Monte Carlo simulations," *EPJ Nucl. Sci. Technol.*, vol. 11, p. 62, 2025, doi: 10.1051/epjn/2025053.

NSS-01-197

Development of a spectral unmixing method for gamma-ray spectra analysis : application to airborne measurements (#2081)

Killian Castillo[1], Luc Patryl[1], Charles-Philippe Mano[1], Hugues Paradis[1], Frédérick Carrel[2], Jérôme Bobin[3]

[1] CEA, DAM-DIF, ARPAJON, France; [2] CEA, LIST, SACLAY, France; [3] CEA, IRFU, SACLAY, France

Abstract

The CEA develops and uses airborne detectors to carry out gamma mapping missions for various private and public entities, and various national and international authorities. The main objectives of these missions are : site monitoring (natural and anthropic contributions to environmental radioactivity), mapping contaminated areas, detecting and identifying radionuclides and radioactive sources.

Methods for analyzing the spectra acquired during these missions are being studied, with a view to improve decision thresholds and detection limits for various radionuclides of interest. A spectral analysis method called "spectral unmixing" has been developed, using a full spectrum analysis instead of the reference method based on regions of interest. This algorithm takes into account the response of the detector under study to an individual radionuclide, and estimates the proportions of the different radionuclides using a likelihood estimator. This method was shown to be accurate for reconstructing radionuclide activities, with improved sensitivity compared to the reference method.

The application of this algorithm to airborne detectors raises a number of challenging problems, such as taking into account the variability of spectral signatures linked to the environment and source shielding. An algorithm has been developed to address this problem. The algorithm was validated on simulated and experimental data, and improved the results of an airborne measurements campaign. This method can be implemented on the measurement system for real-time radionuclide identification.

NSS-01-199

NSS-01-201

Hybrid Semantic–Keyword Analysis for the Classification of Nuclear Fuel Cycle Activities Using Open-Source Information (#2241)

Yeon Woo Lee[1], **Seung A Choi**[1], Seul Ah Kim[1], Chul Hee Min[2], Yong Hyun Chung[2], Jae Joon Ahn[1]

[1] Yonsei University, Division of Data Science, Wonju, South Korea; [2] Yonsei University, Department of Radiation Convergence Engineering, Wonju, South Korea

This work was supported by the Nuclear Safety Research Program through the Korea Foundation Of Nuclear Safety using the financial resource granted by the Nuclear Safety and Security Commission of the Republic of Korea (No. RS-2026-25538205)

Abstract

This study proposes a hybrid semantic–keyword analysis framework for automatically identifying and classifying nuclear fuel cycle-related activities using open-source text data. In the safeguards system of the International Atomic Energy Agency, continuous monitoring and analysis of nuclear fuel cycle activities are required; however, existing approaches rely heavily on expert-driven manual review, limiting efficient processing of large volumes of unstructured text data. To address this issue, nuclear fuel cycle-related news articles collected from Google News were used to construct profiles for seven nuclear fuel cycle activities. Each activity was represented by combining semantic information derived from Sentence-BERT embeddings with keyword importance obtained using class-based TF-IDF. Subsequently, key sentences were extracted from IAEA news articles, and activity classification was performed by integrating semantic and keyword similarity for each activity category. Performance evaluation results showed that the proposed method achieved a Top-1 accuracy of 57.14%, a Top-3 accuracy of 85.71%, and a mean reciprocal rank of 0.738. In addition, the actual activity category was generally included within the top candidate groups, showing that the proposed framework reflects the semantic relationships and complex characteristics among nuclear fuel cycle activities. This study demonstrates the feasibility of automating open-source-based nuclear fuel cycle activity analysis and suggests the potential for future extension to an Additional Protocol-based automatic declaration target identification system. The results also highlight the applicability of data-driven analytical approaches for safeguards and regulatory support.

References

[1] N. Reimers and I. Gurevych, “Sentence-BERT: Sentence embeddings using siamese BERT-networks,” in Proc. 2019 Conf. Empirical Methods Natural Language Processing and 9th Int. Joint Conf. Natural Language Processing (EMNLP-IJCNLP), Hong Kong, China, 2019, pp. 3982–3992.
[2] M. Grootendorst, “BERTopic: Neural topic modeling with a class-based TF-IDF procedure,” 2022, arXiv:2203.05794.
[3] International Atomic Energy Agency, “Information collection and evaluation.” Accessed: May 11, 2026, [Online]. Available: https://www.iaea.org/topics/information-collection-and-evaluation

NSS-01-203

Selective Use of Directionally Informative Non-Photopeak Events for Low-Count Industrial Gamma Imaging (#2392)

Linxin Lei, Debin Zhang, Yuxi Zhang, Zhenlei Lyu, Tianyu Ma

Tsinghua University, Beijing, China

Abstract

High-performance industrial gamma imaging under count-limited conditions is challenging, particularly for medium- and high-energy radionuclides where photopeak statistics are limited. However, some non-photopeak Compton-related events still retain directional information. We propose a directionally informed multi-energy-window reconstruction method that selectively incorporates such events. Monte Carlo spectral decomposition was used to define energy windows and estimate useful-event fractions. Window-specific projection data were paired with matched system matrices and jointly reconstructed using weighted MLEM.

The method was evaluated with a self-collimating industrial gamma camera for ^{137}Cs imaging. In point-source experiments, 30 s multi-window reconstruction achieved localization accuracy comparable to 90 s photopeak-window-only MLEM. In structured-source and short-frame dynamic imaging, it reduced background artifacts and improved localization stability. These results show that selective use of directionally informative non-photopeak events can improve event utilization and reconstruction robustness under low-count industrial gamma imaging conditions.

NSS-01-205

An Optical Surrogate Framework for Three-Dimensional Fusion Source Reconstruction (#2548)

Zhong Zhang[1,2], Yigang Yang[1,2]

[1] Tsinghua University, Department of Engineering Physics, Beijing, China; [2] Tsinghua University, Key Laboratory of Particle and Radiation Imaging, Ministry of Education, Beijing, China

Abstract

Three-dimensional reconstruction of fusion neutron sources is critical for diagnosing burn-region morphology and implosion asymmetry in inertial confinement fusion, yet the recoverable morphology is severely limited by sparse and geometrically constrained diagnostic views. This work proposes an optical surrogate framework to study information-driven sparse-channel layout design for fusion neutron source reconstruction, offering controllable source morphology, low cost, and ease of iteration compared to direct neutron diagnostics. The core motivation is to treat limited-view reconstruction not only as an inverse-algorithm problem, but also as a constrained layout-design problem. A conceptual design employing Latin hypercube sampling generates candidate layouts within admissible geometries, followed by greedy selection. The optical surrogate tests the shared inverse-problem structure using movable point-like optical sources, directional fiber channels, rather than reproducing neutron transport physics. Preliminary fiber-response measurements reveal finite-acceptance soft-channel behavior with a transverse full width at half maximum of approximately 2.7 mm. Theoretical reconstruction using a discrete multi-point-source design yields a detector-domain residual of 0.038, a source-correlation coefficient of 0.998, and a maximum relative strength-ratio error of approximately 7.2%. These results establish a forward-model basis for subsequent layout optimization and future migration to neutron-response matrices.

References
[1] D. N. Fittinghoff, N. Birge, and V. Geppert-Kleinrath, “Neutron imaging of inertial confinement fusion implosions,” Rev. Sci. Instrum., vol. 94, no. 2, Art. no. 021101, Feb. 2023, doi: 10.1063/5.0124074.
[2] P. L. Volegov, C. R. Danly, F. E. Merrill, R. Simpson, and C. H. Wilde, “On three-dimensional reconstruction of a neutron/x-ray source from very few two-dimensional projections,” J. Appl. Phys., vol. 118, no. 20, Art. no. 205903, Nov. 2015, doi: 10.1063/1.4936319.
[3] P. L. Volegov et al., “Three-dimensional reconstruction of neutron, gamma-ray, and x-ray sources using spherical harmonic decomposition,” J. Appl. Phys., vol. 122, no. 17, Art. no. 175901, Nov. 2017, doi: 10.1063/1.4986652.
[4] P. L. Volegov et al., “Three-dimensional reconstruction of neutron, gamma-ray, and x-ray sources using a cylindrical-harmonics expansion,” Rev. Sci. Instrum., vol. 92, no. 3, Art. no. 033508, Mar. 2021, doi: 10.1063/5.0042860.
[5] F. E. Merrill et al., “The neutron imaging diagnostic at NIF (invited),” Rev. Sci. Instrum., vol. 83, no. 10, Art. no. 10D317, Aug. 2012, doi: 10.1063/1.4739242.
[6] M. D. McKay, R. J. Beckman, and W. J. Conover, “A comparison of three methods for selecting values of input variables in the analysis of output from a computer code,” Technometrics, vol. 21, no. 2, pp. 239–245, May 1979, doi: 10.1080/00401706.1979.10489755.

NSS-01-207

Adaptive Tetrahedral Mesh Reconstruction for Industrial Computed Tomography (#2942)

Junho Lee, Yoonsang Hong, Seungjun Yoo, Seokwon Oh, Ho Kyung Kim

Pusan National University, Computational X-ray Imaging Laboratory, School of Mechanical Engineering, Busan, South Korea

This work was supported by the National Research Foundation of Korea (NRF) grant funded by the Korea government (MSIT) under Grant RS-2024-00340520. J. Lee and Y. Hong were supported by the Korea Institute of Energy Technology Evaluation and Planning (KETEP) and the Ministry of Climate, Energy and Environment (MCEE) of the Republic of Korea under Grant RS-2024-00398425.

Abstract

Industrial X-ray computed tomography (CT) is widely used for non-destructive inspection and generation of geometric models. However, conventional voxel-based CT reconstruction on a fixed Cartesian grid causes partial-volume blurring and possible geometric errors when converted into surface or CAD models. This work presents an interface-adaptive tetrahedral mesh-based iterative reconstruction framework for industrial CT. The method estimates nodal attenuation coefficients directly on an unstructured mesh. X-ray projection and backprojection are performed by an NVIDIA OptiX-accelerated projector, which computes ray-mesh intersections, segment lengths, and barycentric weights, and backprojects residuals using the SIRT algorithm. To improve boundary representation, the reconstructed field is used to detect interface-related edges, locally refine the mesh, and displace vertices. For each candidate vertex, a local attenuation-gradient direction is estimated from neighboring nodes. The neighbors are divided across the estimated normal, and the vertex is shifted toward the attenuation mid-level between regions while enforcing element quality constraints. Simulated projection studies showed the proposed adaptive mesh reconstruction preserved overall structure while producing sharper material boundaries than voxel-based SIRT. Global structural similarity improved, particularly in regions containing material interfaces. These results indicate the framework reduces boundary blurring, supporting more accurate defect sizing and dimensional measurement in industrial testing.

References
[1] Merckx, J., den Dekker, A. J., Sijbers, J., De Beenhouwer, J. 2025, 'DAMMER: Direct Adaptive Multi-Resolution MEsh Reconstruction From X-Ray Measurements', IEEE Trans. Comput. Imag., vol. 11, pp. 926–941
[2] Nagai, Y., Ohtake, Y., Suzuki, H. 2016, 'CT reconstruction on unstructured mesh for multi-material object', Proc. 19th World Conf. Non-Destructive Testing, Munich, Germany
[3] Buyens, F., Quinto, M. A., Houzet, D. 2013, 'Adaptive mesh reconstruction in X-ray tomography', Proc. MICCAI Workshop Mesh Processing Med. Image Anal., Nagoya, Japan
[4] Boutchko, R., Sitek, A., Gullberg, G. T. 2013, 'Practical implementation of tetrahedral mesh reconstruction in emission tomography', Phys. Med. Biol., vol. 58, no. 9, pp. 3001–3022

NSS-01-209

Forward Simulation of High-Energy XPCI Using XRM-Derived Semiconductor Package Phantoms (#2980)

Uijin Lee[1], Seoyun Jang[1], Daeseung Kim[1,2], Sangho Lee[1], Yeaeun Kim[1], Gyohyeok Song[1], Jeonghoon Lee[1], Gyuseong Cho[1], Jisoo Kim[1]

[1] Korea Advanced Institute of Science and Technology, Department of Nuclear and Quantum Engineering, Daejeon, South Korea; [2] Pusan National University, Nuclear Systems Major, School of Mechanical Engineering, Busan, South Korea

Abstract

This study presents a forward simulation of high-energy X-ray phase-contrast imaging (XPCI) for semiconductor package inspection using an X-ray microscopy (XRM)-derived structural phantom. A projected phantom from an experimental laboratory XRM reconstruction stack was used as a geometry prior rather than quantitative material ground truth. The projected grayscale phantom was percentile-normalized and mapped to simplified Cu/Si refractive-index distributions. Under the proposed long-beamline high-energy synchrotron XPCI conditions, the simulated XPCI intensity and retrieved phase images reproduced characteristic package structures, including stacked layers and metal interconnect regions. The finite-source-induced blur was on the order of the detector pixel size, while the selected intra-bump feature showed higher local visibility in the retrieved phase image than in the simulated intensity image. This work extends idealized-phantom simulations to a laboratory-XRM-reconstructed semiconductor package structure under long-beamline high-energy synchrotron XPCI conditions.

References

[1] A. Snigirev, I. Snigireva, V. Kohn, S. Kuznetsov, and I. Schelokov, "On the possibilities of x-ray phase contrast microimaging by coherent high-energy synchrotron radiation," *Rev. Sci. Instrum.*, vol. 66, no. 12, pp. 5486–5492, Dec. 1995

[2] J. Kim and J.-H. Lim, "Exploring high-energy X-ray phase-contrast microscopy at a diffraction-limited storage ring," *NDT&E Int.*, vol. 155, Art. no. 103395, 2025.

[3] S. Huhn, L. M. Lohse, J. Lucht, and T. Salditt, "Fast algorithms for nonlinear and constrained phase retrieval in near-field X-ray holography based on Tikhonov regularization," *Opt. Express*, vol. 30, no. 18, pp. 32871–32898, 2022.

NSS-01-211

Investigating Identifiability in Joint Transmission–Backscatter X-ray Image Registration with Energy-Dependent Source Geometry (#1740)

Hosung Joo[1], Youngchol Choi[2], Jongwon Park[2], Chang Hwy Lim[3], JeongHee Lee[2], Hyun Jong Yang[4,5]

[1] Pohang University of Science and Technology (POSTECH), Department of Electrical Engineering, Pohang, South Korea; [2] Korea Research Institute of Ships and Ocean Engineering (KRISO), Daejeon, South Korea; [3] M1 International Inc., Daejeon, South Korea; [4] Seoul National University, Department of Electrical and Computer Engineering, Seoul, South Korea; [5] Seoul National University, Institute of New Media and Communications, Seoul, South Korea

Abstract

X-ray scannings are widely adopted by customs to control containers. Transmission and backscatter X-ray imaging are often jointly employed to enhance material discrimination and detection robustness in cargo inspection systems. However, the two modalities typically operate at substantially different photon energy levels, leading to energy-dependent interaction volumes and effective source geometries that cannot be simultaneously aligned. As a result, image registration becomes a prerequisite for joint analysis and decision-making based on transmitted and backscattered measurements, yet it is fundamentally ill-posed because consistent spatial correspondence between the two imaging processes is not directly observable. In this work, we investigate this identifiability issue in joint transmission--backscatter X-ray image registration by explicitly modeling energy-dependent source geometry and imaging physics. We show that mismatched photon energies can induce structural ambiguity, such that multiple spatial alignments may remain similarly plausible under joint interpretation.

References

[1] A. M. Wajid, M. R. Abdelnour, A. Naz, G. Liu, Y. Wang, Z. Li, X. Li, L. Zhang, Z. Liu, and J. Liu, 'X-ray backscattering: design, applications, and prospects in non-destructive evaluation', J. Radioanal. Nucl. Chem., vol. 334, no. 5, pp. 3033–3054, May 2025.
[2] B. Tracey, M. Schiefele, C. Alvino, E. Miller, and O. Al-Kofani, "Combined use of backscattered and transmitted images in x-ray personnel screening systems," in Signal Processing, Sensor Fusion, and Target Recognition XXI. SPIE, May 2012.
[3] G. An, J. Park, and H. Seo, "Dual-energy backscatter X-ray imaging for material discrimination," in 2024 IEEE Nuclear Science Symposium (NSS), Medical Imaging Conference (MIC) and Room Temperature Semiconductor Detector Conference (RTSD). IEEE, Oct. 2024, pp. 1–1.
[4] S. Huang, X. Wang, Y. Chen, J. Xu, T. Tang, and B. Mu, "Modeling and quantitative analysis of X-ray transmission and backscatter imaging aimed at security inspection," Opt. Express, vol. 27, no. 2, pp. 337–349, Jan. 2019.

NSS-01-213

Development of a UAV-Mounted Radiation Survey System Integrating LaBr3(Ce) Detectors and LiDAR (#1003)

Young-Yong Ji, Wanook Ji, Kyungmin Kim, Myoung Jung Kim

Korea Atomic Energy Research Institute, Environmental Safety Technology Research Division, Daejeon, South Korea

This work was supported by the Ministry of Science and ICT (MSIT) of the Republic of Korea (Project No. RS-2022-00144210).

Abstract

To facilitate the highly efficient and accurate surveying of radioactively contaminated areas, this study presents the development of an advanced UAV-mounted integrated survey system capable of the simultaneous, real-time measurement of 3D geospatial information and environmental radiation data. The hardware architecture is robustly constructed, integrating two sets of two-inch LaBr3(Ce) detectors for high-resolution gamma spectrometry. This is combined with a LiDAR sensor for acquiring precise 3D terrain topography, a GPS, and a laser altimeter to ensure accurate spatial referencing. To guarantee operational stability during flight, the payload design incorporates specialized vibration-damping mounts and a lightweight 1.5-millimeter aluminum housing. Furthermore, a high-speed LTE router network was introduced to reliably handle the transmission of large-capacity data streams to the ground station.

The practical efficacy of the system was rigorously validated through extensive flight tests conducted over radioactively contaminated regions in Fukushima. When aerial measurements were mathematically converted to dose rates at one meter above ground level, the results demonstrated highly satisfactory performance, showing a strong statistical correlation with baseline data obtained using conventional backpack-type ground survey equipment. Crucially, by mapping real-time energy spectra directly onto the acquired 3D geospatial models, the system successfully enabled the comprehensive, multi-dimensional identification of specific high-level contamination hotspots. Moving forward, by integrating AI to further refine advanced topographical correction algorithms, this autonomous system is expected to significantly enhance the rapid and precise generation of contamination maps, providing critical support for emergency response.

References
[1] Y. Sanada and T. Torii, “Aerial radiation monitoring around the Fukushima Adi-ichi nuclear power plant using an unmanned helicopter,” J. Enviorn. Radioact. vol. 139, pp. 294-299, 2015.
[2] Y. Sanada, T. Orita, and T. Torii, “Temporal variation of dose rate distribution around the Fukushima Daiichi nuclear power station using unmanned helicopter,” Appl. Radiat. Isot. vol. 118, pp. 208-216, 2016.
[3] Y.-Y. Ji, S. Joung, W. Ji, K. Ochi, M. Sasaki, and Y. Sanada, “Performance of UAV-based airborne gamma-ray spectrometry for wide-area radiation monitoring of contaminated sites,” J. Radiol. Prot. vol. 45, 042501, 2025.
[4] Y.-Y. Ji, W. Ji, K. Kim, M.J. Kim, K. Ochi, Y. Morishita, and Y. Sanada, “Practical approach of airborne gamma-ray spectrometry using UAVs for evaluating ground-level dose rates,” Radiat. Phys. Chem. vol. 244, 113781, 2026.

NSS-01-215

Development of a Handheld Uranium Enrichment Analyzer Based on LaBr3 Detector and Relative Detection Efficiency Self-Calibration Method (#1069)

Guorong Liu, Hao Zhou, Jinghuai Li

China institute of atomic energy, Department of Radiochemistry, Beijing, China

Abstract

To meet the on-site inspection requirements for uranium materials, a handheld uranium enrichment analyzer based on a LaBr3 detector and the relative detection efficiency self-calibration method was developed. The adopted LaBr3:Ce crystal has a size of 38.1mm in diameter and 25.4mm in thickness, with an energy resolution of 2.9% at 662keV. The handheld uranium enrichment analyzer is equipped with a 4.5-inch touchscreen. It features overall dimensions of 145×75×58mm and a weight of 800g, supporting continuous operation for more than 8 hours. Test results from six NBS standard samples show that for uranium samples with a mass≥200g, a ^{235}U enrichment≥0.711%, and a measurement time≥1800s, the relative deviation of the measured ^{235}U enrichment is less than 8.0%. This device can be applied to the verification and measurement of ^{235}U enrichment in uranium materials.

References
[1] T.E. Sampson, T.A. Kelley, and D.T. Vo. Application Guide to Gamma-Ray Isotopic Analysis Using the FRAM Software. Los Alamos National Laboratory report LA-14018 (2003)
[2] Vo Duc Ta, McMath, Garrett Ear. Testing the HM-5s and NaIGEM code. Los Alamos National Laboratory report LA-UR-20-23051(2020)
[3] P. Mortreau, R.Berndt. Measurement of ^{235}U enrichment with a $LaBr_3$ scintillation detector. Nuclear Instruments and Methods in Physics Research A 620 (2010) 324–331.
[4] William H. Geist, Peter A. Santi, Martyn T. Swinhoe. Nondestructive Assay of Nuclear Materials for Safeguards and Security(Second Edition).ISBN 978-3-031-58277-6.2024

NSS-01-217

Neutron Response Evaluation of Miniature Spherical Li-glass scintillators for Optical-Fiber-Based Detectors (#1115)

Yutaro Saito, Yuya Oshima, Wakako Kitsuki, Kenichi Watanabe

Kyushu University, Applied Quantum Physics and Nuclear Engineering, Fukuoka, Japan

This work was supported by a research grant from Murata Science and Education Foundation.

Abstract

Boron Neutron Capture Therapy (BNCT) and high-flux pulsed neutron sources such as J-PARC require reliable real-time neutron monitoring with minimal perturbation of the irradiation field. We have been developing miniature optical-fiber-based neutron detectors using small Li-glass scintillators mounted at the fiber tip. Conventionally, the scintillator pieces were prepared by crushing bulk Li-glass, producing irregularly shaped fragments that introduce geometric uncertainties and complicate quantitative response evaluation by Monte Carlo simulation. To overcome this, an aerodynamic polishing technique was established to shape Li-glass fragments into well-defined spherical particles with diameters of 100 to 500 μm without significant degradation in light yield. The spherical geometry enabled quantitative prediction of the wall effect through PHITS Monte Carlo simulations with a quenching model based on Birks' law, and the simulated pulse-height spectra showed excellent agreement with experimental data obtained from spheres of various diameters (220–450 μm). This approach provides a robust framework for the precise design and manufacturing of miniature neutron detectors for high-intensity fields.

References

[1] H. Tanaka, Y. Sakurai, T. Takata et al., Note: Development of real-time epithermal neutron detector for boron neutron capture therapy, *Rev. Sci. Instrum.*, 88, 023303 (2017).

[2] A. Ishikawa, K. Watanabe, A. Yamazaki et al., Evaluation of the thermal neutron sensitivity, output linearity, and gamma-ray response of optical fiber-based neutron detectors using Li-glass scintillator, *Nucl. Instrum. Methods Phys. Res. A*, 1025, 166074 (2022).

[3] T. Sato, Y. Iwamoto, S. Hashimoto et al., Recent improvements of the particle and heavy ion transport code system – PHITS version 3.33, *J. Nucl. Sci. Technol.*, 61, 127–135 (2024).

[4] K. Watanabe, Y. Oshima, N. Shigyo, Y. Hirata, Evaluation of quenching characteristics of Li-containing scintillators, *Jpn. J. Appl. Phys.*, 63, 042001 (2024).

NSS-01-219

Time-Resolved Imaging of Radioactive Gas with the 4π Gamma-Ray Imager C3G (#1185)

Yoshiharu Kitayama[1], Hiromi Nakai[1], Kazuyuki Enomoto[3], Naoto Yamada[3], Keitaro Hitomi[2], Mitsuhiro Nogami[2], Naoki Kawachi[3,1]

[1] Fukushima Institute for Research, Education and Innovation, Plant Imaging research Unit, Fukushima, Japan; [2] Tohoku University, Sendai, Japan; [3] National Institutes for Quantum Science and Technology, Takasaki, Japan

This work was supported by JSPS KAKENHI Grant Number 26K03212. The authors thank the members of the Radiotracer Imaging Project, QST, for their valuable support during the experiment.

Abstract

The Coded Cube Camera for Gamma-ray (C3G) is a 4π gamma-ray imager designed to estimate gamma-ray source distributions from direction-dependent detector response patterns. In this study, we developed a 24-detector C3G consisting of 24 HR-GAGG scintillators and applied it to a plant radioisotope (RI) imaging experiment using $^{11}CO_2$ gas. In the plant RI imaging experiment, approximately 300 MBq of $^{11}CO_2$ gas was supplied to a plant placed in an experimental chamber to image the transport of ^{11}C-labeled photosynthates within the plant. During this experiment, the C3G was placed outside the chamber, and the dynamics of $^{11}CO_2$ gas were continuously measured with an acquisition time of 1 s per measurement. As a result, the inflow of the gas into the chamber was clearly visualized. In addition, the reconstructed image intensity decreased exponentially over time. The half-life estimated from this intensity change was 20.70 min, which was in good agreement with the known half-life of ^{11}C, 20.34 min. These results demonstrate that the 24-detector C3G can visualize dynamic gaseous radioactive sources and estimate temporal changes in radioactivity from reconstructed image intensity. This capability is expected to be useful for applications such as radioactive gas leakage monitoring, environmental monitoring, and nuclear security.

NSS-01-221

Performance Evaluation of a Fast Fission Neutron Coincidence Counting System (#1196)

Yosuke Toh, Makoto Maeda, Masao Komeda

Japan Atomic Energy Agency, Nuclear Science and Engineering Center, Ibaraki, Japan

This work supported by the Decommissioning, Contaminated Water and Treated Water Management Project funded by the Ministry of Economy, Trade and Industry (METI), Japan.

Abstract
Characterization of nuclear fuel in fuel debris is essential for the decommissioning of the Fukushima Daiichi Nuclear Power Station. The fast fission neutron coincidence counting (FFCC) method, which is less sensitive to neutron absorbers than conventional thermal-neutron-based techniques, was investigated using Monte Carlo simulations with PHITS. A cylindrical unit can containing fuel debris was modeled, and four detector configurations with 24–72 liquid scintillator detectors were compared. Fast neutron coincidence counting efficiency decreased as the number of detectors decreased, whereas the quantification limit did not vary monotonically; the 56-detector configuration provided the best performance. This indicates that an optimal number of detectors exists, as gains in coincidence events are offset by reduced efficiency in distant detectors and increased background counts. Evaluation of the effective dose showed that shielding with lead and boron-loaded polyethylene reduced the dose around the system below the access limit for personnel, without significantly affecting measurement performance. These findings provide useful guidelines for the design of practical FFCC systems.

NSS-01-223

Development and Validation of Neutron Diagnostics on ASP in Support of Future Facilities (#1227)

Lucy A. Wilson, Colin Horsfield, Alex Leatherland, Gareth Davies, Thomas Harrington, Sam Morley, Simon Rice, Sebastian Tanner, Aaron Stott, Andrew Simons, William Tominey, Verity Woolhead, David Wright

AWE - Nuclear Security Technologies, Reading, UK

Abstract
The ASP neutron facility at AWE – Nuclear Security Technologies (AWE-NST) Aldermaston, is undergoing upgrades to both the accelerator beamline and the supporting diagnostics. This is driven by evolving customer requirements, particularly its increasing use as a platform for fundamental nuclear data measurements. Neutron flux monitoring on ASP is provided by fission chambers and is supported by external activation foil calibrations and internal cross-calibration measurements. A recommissioned associated-particle technique provides improved accuracy for lower-fluence measurements, while ongoing work is improving neutron spectral characterisation using a range of techniques including activation, Single crystal chemical vapour deposited diamond detectors, proton recoil and Helium - 3 spectrometers. These activities reduce uncertainties in current measurements, and establish the diagnostic techniques required for a future facility (VENTURE) capable of delivering higher fluxes and a wider range of quasi-monoenergetic neutron energies. The calibration and diagnostics strategy for the VENTURE facility is outlined, with an emphasis on delivering the well characterised source required for nuclear data experiments.
UK Ministry of Defence © Crown owned copyright 2026/AWE

NSS-01-225

Development and test of a novel neutron and gamma imaging detector (#1280)

Yancheng Yu[1], Yujie Liu[3], Xin Liu[1], Zhihong Qiao[1], Nianming Jiang[1], Qingyang Wei[3], Yaqiang Liu[2]

[1] Chengdu Novel Medical Equipment Ltd., Chengdu, China; [2] Tsinghua University, Beijing, China; [3] University of Science and Technology Beijing, Beijing, China

Abstract

As the demand for the detection of special nuclear materials increases, the use of imaging instruments that can sensitively image both gamma-ray and neutron signatures has become necessary. The radioactive waste streams can contain neutron-emitting radioactive materials, hence localisation of neutron sources plays an important part in nuclear decommissioning. Neutron detector design based on the MURA revealed promising results when tested in security applications. Due to the requirement of ensuring high detection efficiency for both neutrons and gamma rays, the plastic scintillator used is typically thick. As demonstrated in our previous study, the dual-layer design exhibits better imaging performance and produces fewer artifacts. In this paper, we propose a dual-layer DOI (depth of interaction) detector design and have successfully developed a prototype module. The first and second layer of the crystals are clearly resolved from the flood histograms, demonstrating its capability to provide two-layer depth encoding. The energy resolution of each layer is improved by 50% compared with that of a single-layer detector with the same thickness, and the neutron/gamma discrimination figure of merit (FOM) is also significantly enhanced. Validation and testing of the imaging performance are currently underway.

NSS-01-227

Multilayer Scintillator for Improved Gamma-ray Discrimination at Thermal Neutron Scattering Beamlines (#1365)

Ahmed Moustafa, Matthew Loyd

Oak Ridge National Laboratory, Oak Ridge, USA

This work was sponsored by the U.S. Department of Energy (DOE) Office of Science Early Career Research Program Award (KC0406021) under Contract No. DE-AC05- 00OR22725.

Abstract

Scintillator-based thermal neutron detectors are utilized at scattering beamline facilities around the world. The Anger camera is one example that was designed and deployed at Oak Ridge National Laboratory. The camera uses enriched ^{6}Li-glass (GS20) that offers advantages over the widely used ^{3}He gas proportional counters,

including sub-millimeter spatial resolution, higher count rate capability, and high neutron absorption efficiency. However, GS20 has higher γ-ray sensitivity due to its solid state, potentially reducing the neutron signal to background ratio. Gamma rejection using pulse height discrimination is feasible, but it suffers when there is greater overlapping between the neutron and gamma spectral features in intense background fields, like with certain beamline configurations. Additionally, pulse shape discrimination is unfeasible with GS20. Previous work demonstrated a new approach to discrimination by optimizing the scintillator shape and reducing its size. In this work, we demonstrate improved gamma discrimination by segmenting the GS20 scintillator layer of the Anger camera. The layer is divided into several thinner layers with the same overall thickness, and coupled together using non-scintillating quartz layers. The neutron absorption products fully deposit their energy in the GS20 layers due to their significantly shorter range compared to the Compton-scattered electrons from γ-rays that only partially deposit their energy. This allows for better separation between the respective features on the pulse height spectrum, and therefore improved discrimination, while maintaining the same high neutron absorption efficiency.

NSS-01-229

Feasibility of Organic Scintillator-Based Coincidence Counting for Photonuclear Nondestructive Assay of Nuclear Materials (#1414)

Kosuke Tanabe[1], Hiroshi Sagara[2], Tatsuya Katabuchi[2], Kazushi Terada[3], Yoshiyuki Takahashi[3], Jun-ichi Hori[3], Krittanai Kiatkongkaew[2], Risa Kunitomo[2]

[1] National Research Institute of Police Science, Physics Section, Chiba, Japan; [2] Institute of Science Tokyo, Laboratory for Zero-Carbon Energy, Tokyo, Japan; [3] Kyoto University, Institute for Integrated Radiation and Nuclear Science, Osaka, Japan

This work was supported by JSPS KAKENHI Grant Number JP25K01706.

Abstract

This study demonstrates organic scintillator-based neutron coincidence counting as a promising approach for photonuclear nondestructive assay (NDA) of nuclear materials. Four organic scintillators—organic glass scintillator (OGS), EJ-276D, stilbene, and BC-501A—were systematically evaluated in terms of fast-neutron detection efficiency, pulse shape discrimination (PSD) capability, and timing response. In addition, three-detector coincidence counting systems based on OGS and stilbene detectors were constructed and tested using a ^{252}Cf source. Stilbene and BC-501A exhibited excellent PSD performance, EJ-276D showed high fast-neutron detection efficiency, and OGS provided superior timing response. The OGS-based system successfully measured neutron double- and triple-coincidence events with and without lead shielding, whereas the stilbene-based system showed a marked reduction in coincidence events under unshielded conditions. These results indicate that combining PSD, neutron coincidence counting, and gamma-ray shielding enhances the extraction of correlated neutron signals in photonuclear NDA. The proposed OGS-based approach is a promising for active interrogation systems in nuclear security and safeguards.

References

[1] K. W. Chin, H. Sagara, C. Y. Han, "Application of photofission reaction to identify high-enriched uranium by bremsstrahlung photons", *Annals Nuclear Energy*, **158**, 108295, (2021).
[2] K. Tanabe, H. Sagara, "A novel method of neptunium-237 detection in its separated form and advanced fuel based on photonuclear reactions", *Annals of Nuclear Energy*, **170**, 108990, (2022).
[3] K. Tanabe, H. Sagara, "Feasibility of americium detection and verification based on photonuclear reactions", *Annals of Nuclear Energy*, **227**, 112005, (2026).
[4] A.J. Jinia, T.E. Maurer, C.A. Meert, O.V. Pakari, S.D. Clarke, H.S. Kim, D.D. Wentzloff, and S.A. Pozzi, "Prompt Photofission Neutron Detection in Depleted Uranium", *Phys. Rev. Applied*, **19**, 054073, (2023).
[5] O. Searfus, C. Meert, S. Clarke, S. Pozzi, and I. Jovanovic, "Detection of uranium-photofission neutrons with a ^{4}He scintillation detector", *Phys. Rev. Applied*, **22**, 064080, (2024).
[6] K. W. Chin, H. Sagara, J. Hori, Y. Takahashi, "Measurement System Requirements for Photofission Signal Detection with Coincidence Neutron Counting Method", *Progress Nuclear Science Technology*, **7**, 91-96, (2025).

NSS-01-231

Localization of uranium samples in large cemented nuclear waste using active photon interrogation and a Bayesian inversion (#1492)

Malo Lebreton[1], **Malo Lebreton**[1], Benoit Geslot[1], Benoit Geslot[1], Cédric Carasco[1], Cédric Carasco[1], Bertrand Pérot[1], Bertrand Pérot[1], Claire Michelet[2], Claire Michelet[2]

[1] Commissariat à l'énergie atomique et aux énergies alternatives, CEA/DES/IRESNE, St Paul Lez Durance, France; [2] Université de Bordeaux, CNRS-IN2P3/LP2IB, Bordeaux, France

Abstract

CEA Cadarache currently manages over 6,000 historical 870 L nuclear waste packages. To ensure long-term safety, French regulatory authorities require a precise characterization of each unit, specifically regarding structural integrity, fissile material mass and total activity of alpha emitters. However, the high density and volume of 870 L concrete waste packages result in significant signal attenuation, making standard passive gamma spectrometry or passive and active neutron measurements inefficient to assess the mass of nuclear materials. To maximize the signal-to-noise ratio, a specific Active Photon Interrogation (API) approach is developed inside the CINPHONIE irradiation bunker of CHICADE facility, at CEA IRESNE, Cadarache, France. This method makes use of inorganic BGO scintillators to measure high-energy delayed gamma rays from short-lived photofission products induced with a high-energy bremsstrahlung photon source, i.e., a 18 MeV LINAC. A Bayesian framework is applied to infer both the mass and the position of nuclear materials from angular acquisitions. This article is focused on testing API framework in the case where the source of the signal is located in a homogeneous environment. Based on the promising results presented here, future developments will focus on the heterogenous case.

References
[1] M. Lebreton *et al.*, "Photon flux characterization of a new electron LINAC in the CINPHONIE irradiation facility through a Bayesian framework," *IEEE Trans. Nucl. Sci.*, pp. 1–1, 2026, doi: 10.1109/TNS.2026.3653194.
[2] M. Delarue *et al.*, "Localization of nuclear materials in large concrete radioactive waste packages using photofission delayed gamma rays," *EPJ Web Conf.*, vol. 253, p. 08003, 2021, doi: 10.1051/epjconf/202125308003.
[3] C. Carasco *et al.*, "Photofission delayed gamma-ray measurements in a large cemented radioactive waste drum during LINAC irradiation," *Nucl. Instrum. Methods Phys. Res. Sect. Accel. Spectrometers Detect. Assoc. Equip.*, vol. 1053, p. 168360, Aug. 2023, doi: 10.1016/j.nima.2023.168360.
[4] C. Carasco, "A Bayesian approach for measuring nuclear material in radioactive waste using photofission," *Nucl. Instrum. Methods Phys. Res. Sect. Accel. Spectrometers Detect. Assoc. Equip.*, vol. 1057, p. 168728, Dec. 2023, doi: 10.1016/j.nima.2023.168728.
[5] "Home," FASTER. Accessed: Jan. 22, 2026. [Online]. Available: https://faster.in2p3.fr/

NSS-01-233

Development and Performance Evaluation of a Four-Detector RMS in Compliance with IEC 60532 (#1540)

Dongam Yang, Sungho Lee

Korea Atomic Energy Research Institute (KAERI), Radiation Safety Management Division, Daejeon, South Korea

This work was supported by Korea Atomic Energy Research Institute (KAERI) R&D Program (No. 522430-26)

Abstract

Radiation monitoring systems (RMS) are essential for continuous radiation surveillance and rapid alarm generation in nuclear facilities. This paper presents the development and performance evaluation of a miniaturized Local Processing and Display Unit (LPDU)-based RMS designed to reduce installation space and radioactive waste generation while maintaining reliable monitoring performance. The developed RMS adopts a 1:4 architecture that enables a single LPDU to process and display signals from four independent detectors. The system was implemented using a Texas Instruments TMS2800137-based edge device and a Canberra G64IC detector. Firmware was developed to support pulse counting, EEPROM operation, RS-232/RS-485 communication, and real-time data processing. A dedicated communication protocol with Cyclic Redundancy Check (CRC) verification was also implemented to enhance data integrity. In addition, a Centered Significant Test (CST)-based adaptive filtering algorithm was embedded in the edge device to improve noise suppression and detector signal monitoring under field conditions. Performance verification tests were conducted in accordance with IEC 60532:2010 using a calibrated Cs-137 gamma radiation source. The developed RMS satisfied the acceptance criteria for linearity, statistical fluctuations, response time, and alarm response time and stability. The maximum linearity deviation was 2.1%, the coefficient of variation was 0.0203%, and all response times were below 6 s. These results demonstrate that the proposed RMS provides reliable radiation monitoring performance in a compact multi-detector configuration.

References

[1] S. H. Lee and D. A. Yang, “Development of a Low-cost Radiation Monitor with Quadruple Detectors,” in *Proc. Korean Nuclear Society Autumn Meeting*, 2025.

NSS-01-235

Template-Matching Position Solving on FPGAs for a Thermal Neutron Detector (#1591)

Matthew Loyd

Oak Ridge National Lab, Oak Ridge, USA

Notice: This summary has been authored by UT-Battelle, LLC, under contract DE-AC05-00OR22725 with the US Department of Energy (DOE).The US government retains and the publisher, by accepting the article for publi cation, acknowledges that the US government retains a nonexclusive,paid-up, irrevocable, worldwide license to publish or reproduce the published form of this manuscript, or allow others to do so, for US government purposes.DOE will provide public access to these results of federally sponsored research in accordance with the DOE Public Access Plan. This work was sponsored by the U.S. Department of Energy (DOE) Office of Science Early Career Research Program Award (KC0406021) under Contract No. DE-AC05-00OR22725

Abstract

Silicon photomultiplier (SiPM) based thermal neutron detectors have been developed at Oak Ridge National Laboratory for single crystal diffraction instruments. They have potential as good replacements for current 3He detectors on neutron reflectometers due to their high spatial resolution and fast scintillator decay time. The current software-implemented position fitting on these detectors is limited due to the processing required for the recursive least-squares algorithm. In this work, we present a fast method for determining neutron position that can be run on the Field-Programmable Gate Array (FPGA) chip that is already installed on the detector. This method compares the collected event data with pre-determined shapes stored on FPGA memory in parallel, and determines the one with the least linear error. Using this method for neutron positioning takes less time than the hardware defined dead time. Count-rate and spatial resolution results collected at the High-Flux Isotope Reactor are presented, with output count rates > 500 kcps achieved, an order of magnitude greater than the software fitting method.

NSS-01-237

Method for determining lithium ore's grade based on photoneutrons' lifetime measurement (#1637)

Minfeng Yu[1,2], Yigang Yang[1,2]

[1] Tsinghua University, Department of Engineering Physics, Beijing, China; [2] Tsinghua University, Key Laboratory of Particle & Radiation Imaging, Beijing, China

This research was supported by the Natural Science Foundation of Beijing, China (Grant No. L252023).

Abstract

Analysis of lithium ore grade is industrially significant for efficient lithium resource development and utilization, enabling improved production efficiency and reduced costs. Lithium has a large neutron absorption cross-section, and changes in lithium grade can affect the neutron lifetime, which is inversely proportional to the macroscopic absorption cross-section of ore. In this paper, a method for determining lithium grade through neutron lifetime measurements based on an e-LINAC driven photoneutron source is applied to the online analysis of lithium ore grade. Since lithium does not emit gamma rays upon neutron absorption, the neutron lifetime is measured from the time distribution of capture gamma rays induced by neutrons in the matrix elements of the medium. The feasibility of this approach has been demonstrated in experiments using various lithium nitrate solutions as simplified media. Meanwhile, the effect of neutron diffusion was investigated by simulations. The potential of neutron-induced prompt gamma analysis for reducing interference caused by variations in matrix composition is discussed. Further simulation studies and system design are in progress.

References

[1] X. Zeng et al., “Commercialization of Lithium Battery Technologies for Electric Vehicles,” Advanced Energy Materials, vol. 9, no. 27, p. 1900161, Jun. 2019, doi: https://doi.org/10.1002/aenm.201900161.

[2] N Eswara Prasad, Amol Gokhale, and R J H Wanhill, Aluminum-Lithium Alloys : Processing, Properties, and Applications. Amsterdam: Elsevier Science, 2014. pp. 503–535.

[3] Dou L R, Liu H Q, Chang D K, et al. Challenges and countermeasures for lithium resources in China and analysis of global distribution and industry status. Bulletin of Chinese Academy of Sciences, 2025, 40(3): 494-510, doi: 10.16418/j.issn.1000-3045.20240326001.

[4] M. G. Aylmore et al., “Assessment of a spodumene ore by advanced analytical and mass spectrometry techniques to determine its amenability to processing for the extraction of lithium,” Minerals Engineering, vol. 119, pp. 137–148, Apr. 2018, doi: https://doi.org/10.1016/j.mineng.2018.01.010.

[5] C. Korbel et al., “Quantification of lithium using handheld instruments: application of LIBS and XRF spectroscopy to assay the lithium content of mineral processing products,” Journal of Analytical Atomic Spectrometry, vol. 39, no. 7, pp. 1838–1853, 2024, doi: https://doi.org/10.1039/d3ja00423f.

[6] Y. Liu, Y.-G. Yang, Y. Tai, and Z. Zhang, “A capture-gated fast neutron detection method,” Chinese Physics C, vol. 40, no. 7, p. 076201, Jun. 2016, doi: https://doi.org/10.1088/1674-1137/40/7/076201.

[7] J. S. Wahl, W. B. Nelligan, A. H. Frentrop, C. W. Johnstone, and R. J. Schwartz, “The Thermal Neutron Decay Time Log,” Society of Petroleum Engineers Journal, vol. 10, no. 04, pp. 365–379, Dec. 1970, doi: https://doi.org/10.2118/2252-PA.

[8] M. Yu, Y. Yang, C. Zong, and S. Ming, “Analysis of gadolinium concentration in solutions based on photoneutrons’ lifetime measurement,” Nuclear Instruments and Methods in Physics Research Section A Accelerators Spectrometers Detectors and Associated Equipment, vol. 1079, pp. 170661–170661, May 2025, doi: https://doi.org/10.1016/j.nima.2025.170661

NSS-01-239

EJ309-Based Neutron–Photon Detection for Photoneutron Characterisation and High-Altitude Radiation Assessment (#1848)

Khalil Al Khouri[1], Mathis Bony[1], Valentin Blideanu[1], Benjamin Rapp[2]

[1] Université Paris-Saclay, Laboratoire National Henri Becquerel at CEA, Paris, France; [2] Université Paris-Saclay, IRFU at CEA, Paris, France

Abstract

This work presents an EJ309 organic liquid scintillator system for neutron–photon detection in mixed radiation fields. The performances achieved are illustrated through two complementary use cases. The first concern photoneutron production in pulsed high-energy photon fields generated by a TrueBeam medical electron LINAC and it has been used to characterise neutron–photon pulse-shape discrimination, integrated-charge observables, pile-up and saturation signatures, and the response of the acquisition chain under short intense irradiation pulses. This configuration simulates closely enough the energies involved in high-altitude cosmic-ray neutron production allowing the use of the previously qualified detection system to be used for neutron monitoring at the Jungfraujoch research station (Switzerland, at 3600 m), where the neutron field is mainly produced by atmospheric secondary cascades, including proton- and alphainduced spallation reactions. The detection set-up and analysis framework will be used to measure time-resolved neutron-like and photon-like event populations, pulse-shape discrimination distributions, and spectral observables over long acquisition periods. The work demonstrates the use of EJ309 scintillators for fast-neutron detection in controlled photoneutron fields and supports their application to natural high-altitude cosmic-ray environments, atmospheric radiation monitoring, and photoneutron studies relevant to intense high-energy photon fields.

References
[1] A. Tomanin, J. Paepen, P. Schillebeeckx, R. Wynants, R. Nolte, A. Lavietes, “Characterization of a cubic EJ-309 liquid scintillator detector” in Nuclear Instruments and Methods in Physics Research Section A: Accelerators, Spectrometers, Detectors and Associated Equipment, vol. 756, 2014, ISSN 0168-9002, https://doi.org/10.1016/j.nima.2014.03.028.
[2] C. Besnard-Vauterin, B. Rapp, V. Blideanu, “New Measurements of Photoneutron Spectra investigating specific signatures of Carbon, Nitrogen, and Oxygen” in Radiation Physics and Chemistry, vol. 229, 2025, ISSN 0969-806X, https://doi.org/10.1016/j.radphyschem.2025.112566
[3] C. Besnard-Vauterin, B. Rapp, V. Blideanu, “Neutron detection in mixed short-pulsed fields with intense photon flashes for LINAC-based active interrogation applications” in Nuclear Instruments and Methods in Physics Research Section A: Accelerators, Spectrometers, Detectors and Associated Equipment, vol. 1064, 2024, ISSN 0168-9002, https://doi.org/10.1016/j.nima.2024.169403.

NSS-01-241

Multimodal extension of the Feynman model for thermal neutron multiplicity counters (#1916)

Gabriel Chartier[1], Jonathan Dumazert[1], Benoit Laurent[1], Louis Cavallini[1], Marc Labalme[2]

[1] Commissariat à l'Énergie Atomique, DAM, DIF, Arpajon, France; [2] LPC Caen, Normandie Univ, ENSICAEN, UNICAEN, CNRS/IN2P3, Caen, France

Abstract
The point kinetics model can be extended to multiple regions or energy groups to account for system heterogeneities. This paper presents an extension of the Feynman-α technique in diverse measurement configurations relevant to nuclear safeguards. This extension is achieved by incorporating phase-type distributions into the heuristic derivation of the Feynman model. Phase-type distributions effectively capture the absorption times of finite-state Markov processes. The resulting expressions are specifically tailored to each experimental configuration. In a bare source configuration using an array of ^{3}He-filled proportional counters, the neutron decay exhibits bimodal behavior. When a supplementary reflector is added to the setup, a third term emerges in the expression, as expected. However, the shape of this additional term depends on the type of reflector, due to

assumptions in the system's transition matrix. When fitted to simulated datasets, these new models show the fundamental decay mode of the detector (approximately 70 μs) and are validated with a 95% confidence χ2 test.

References
[1] Chartier, G., Denis-Petit, D., Aubert, D., Lavallou, F., Dufour N., Laurent, B., Lelaizant, G., Dumazert, J. 2026, 'Bayesian calibration of the Feynman-Y technique for correlated neutron source characterization', *Annals of Nuclear Energy*, Vol. 231, 112211.
[2] Feynman, R. P., de Hoffmann, F., Serber, R. 1956, 'Dispersion of the neutron emission in U-235 fission', *Journal of Nuclear Energy*, Vol. 3, pp. 64–69.
[3] Chernikova, D., Ziguan, W., Pázsit, I., Pál, L., 2014, 'A general analytical solution for the variance-to-mean Feynman-alpha formulas for a two-group two-point, a two-group one-point and a one-group two-point cases', *European Physics Journal Plus*, Vol. 129, 259.
[4] Hua, M., Hutchinson, J., McKenzie, G., Clarke, S., Pozzi, S., 2021, 'On the Feynman-α method for reflected fissile assemblies', *Annals of Nuclear Energy*, Vol. 155, 108082.
[5] Mogens, B., 2005, 'A Review on Phase-type Distributions and their Use in Risk Theory', *ASTIN Bulletin*, Vol. 35, pp.145–161.
[6] Furuhashi, A., Izumi, A., 1968, 'Third moment of the number of neutrons detected in short time intervals', *Journal of Nuclear Science and Technology*, Vol. 5, pp. 48–59, 1968.

NSS-01-243

Building a Two-Stage Compton Camera with $LaBr_3$:Ce Detector Assemblies (#1962)

Shanyn Hart[1], Pete Jones[1], Sello Mashinini[4], Luna Pellegri[3], Christo van Tubbergh[2]

[1] iThemba LABS, Separated Sector Cyclotron Laboratory, Cape Town, South Africa; [2] iThemba LABS, Research and Development Technical Support, Cape Town, South Africa; [3] University of the Witwatersrand, School of Physics, Johannesburg, South Africa; [4] Stellenbosch University, Cape Town, South Africa

This work is based on the research supported wholly by National Research Foundation of South Africa (90741, 99037, 127116) and iThemba LABS.
Supported 2023-24 by the Technology Innovation Agency under Grant number 14606/01

Abstract
A two-stage Compton camera prototype was developed for compact gamma-ray imaging applications in medicine [1]. Each camera layer consists of four monolithic 14 × 14 × 25.4 mm^3 $LaBr_3$:Ce scintillation detector assemblies manufactured by CapeScint, each coupled to a single-channel silicon photomultiplier (SiPM) readout. This configuration does not provide intrinsic position sensitivity within individual crystals.
Detector performance was experimentally characterised and modelled using the TOPAS Monte Carlo toolkit, with validation performed against standard gamma-ray calibration sources [2]. Data acquisition was performed using a XIA PIXIE-16 fully digital signal processing system operating in list-mode, enabling event-by-event energy and timing extraction with digital pulse processing [3]. The detectors achieved an energy resolution of approximately 3.4% at 662 keV and a coincidence timing resolution of 988(17) ps.
Imaging performance was evaluated using a GBq ^{137}Cs source at multiple source-to-detector distances. Reconstructed experimental images were compared with validated simulations, with simulations yielding a full width at half maximum (FWHM) of 3.36(1) mm and an angular resolution measure (ARM) of 1.47(13)°.

Results demonstrate agreement between experiment and simulation, validating the modelling framework and supporting the feasibility of compact $LaBr_3$:Ce-based Compton camera systems for medical gamma-ray imaging applications.

References
[1] Hart, S, Jones, P, Pellegri, L, Peterson, S 2025, 'Building a Hybrid Compton Camera System for Improving Medical Imaging Applications', *IEEE NSS MIC RTSD*, DOI: 10.1109/NSS/MIC/RTSD57106.2025.11287197, USA: IEEE.
[2] TOPAS MC Inc, 2022, 'TOPAS: A Tool for Particle Simulation', TOPAS Monte Carlo, Available: http://www.topasmc.org/, USA: TOPAS MC Inc.
[3] XIA LLC 2019, 'Pixie-16 User Manual', XIA LLC, Available: https://docs.frib.msu.edu/daq/newsite/pixie16/Pixie16_UserManual.pdf, Accessed: 12-03-2024, USA: XIA LLC.

NSS-01-245

Dosimetry and Beam-Condition Characterization of Mixed-Field Irradiation Positions at CERN CHARM (#2131)

Salvatore Fiore, Federico Ravotti, Salvatore Danzeca

CERN, Geneva, Switzerland

Abstract

Mixed-field irradiation facilities require accurate and traceable dosimetry to support the qualification of electronic components and systems for accelerator environments. This work presents an updated dosimetry and beam-condition characterization of the CERN High-energy AcceleRator Mixed-field facility (CHARM), focusing on the comparison of different irradiation positions and on the extension of the available test conditions to new high dose-rate and high fluence locations close to the target. The study combines active and passive dosimetry methods, including CERN RadMon radiation monitors, radiophotoluminescent glass dosimeters and alanine dosimeters, to evaluate Total Ionizing Dose and fluence-related quantities under representative operating conditions. Measurements acquired during commissioning are compared with data collected during user operation to assess the stability and reproducibility of the delivered radiation fields. In addition, the effect of upstream IRRAD samples on the residual beam reaching the CHARM target is investigated using the IRRAD beam position monitors and the multi-wire proportional chamber installed at the end of the T8 beam line. Variations in the upstream material configuration are shown to affect the transported beam properties, including divergence, with a measurable impact on the resulting mixed field. The combined dosimetry and beam instrumentation data are used to validate the new irradiation positions, compare independent dosimetry techniques and define operational reference conditions for CHARM tests. These results improve the traceability of dose and fluence delivery in mixed-field accelerator irradiation campaigns and support more robust interpretation of radiation effects tests performed at CHARM.

NSS-01-247

Hybrid Temperature Compensation and Radiation Damage Recovery with Scintillation Detectors (#2243)

Dae yang Oh[1,2], Junseong Hwang[1,2], Geon Kim[1,2], Chanho Kim[3], Jung-Yeol Yeom[1,4]

[1] Korea University, Department of Bioengineering, Seoul, South Korea; [2] Korea University, Interdisciplinary Program in Precision Public Health, Seoul, South Korea; [3] Korea Atomic Energy Research Institute, Daejeon, South Korea; [4] Korea University, School of Biomedical Engineering, Seoul, South Korea

Abstract

Gamma-ray spectroscopy is a fundamental technique for identifying radioisotopes in safety-critical applications. However, in scenarios such as nuclear accidents, high-temperature and high-radiation environments severely degrade photomultiplier tube performance. Conventional temperature compensation systems face physical voltage limits, and prior deep-learning algorithms fail because they require preserved spectral shapes. To overcome these limitations, this study presents a comprehensive strategy to enhance detector stability. First, an active high-voltage control system mitigates initial temperature-induced gain loss. Because this hardware compensation eventually reaches its physical safety limits, the system integrates a deep learning (DL) technique – bidirectional long short-term memory network – to interpret residual spectral distortions, successfully achieving accurate multi-isotope quantification up to 185 °C. Second, to address radiation-induced damage localized within the photomultiplier tube, a targeted active thermal annealing protocol was applied. Following a 1.55 kGy cumulative gamma irradiation, detector output dropped to 23.5% of its baseline. Subsequent thermal annealing of the photomultiplier tube body at 145 °C successfully restored the output to 89.4%. Ultimately, this integration of hardware, software, and active recovery lays a foundation for robust radionuclide identification under concurrent high-temperature and high-radiation constraints.

References

[1] Park, M., Kim, C., Hwang, J., Yeom, J.-Y. 2026, 'Deep learning-based radioisotope quantification for extreme environments', *Radiation Physics and Chemistry*, 239, 113345, Amsterdam: Elsevier Ltd.

[2] Kim, C., Kim, D., Lee, Y., Park, C., Ullah, M. N., Kim, D., Kwon, I., Hur, S., Yeom, J.-Y. 2021, 'Radiation resistance and temperature dependence of Ce:GPS scintillation crystal', *Radiation Physics and Chemistry*, 183, 109396, Amsterdam: Elsevier Ltd.

NSS-01-249

Simulations of A Novel Time-of-Flight β/γ Transmission Tomography Scanner (#2255)

Robert Carmichael[1,2], **Robert Carmichael**[1,2], Arion Chatziioannou[1,2], Arion Chatziioannou[1,2]

[1] University of California Los Angeles, Department of Molecular and Medical Pharmacology, Los Angeles, USA; [2] University of California Los Angeles, Crump Institute for Molecular Imaging, Los Angeles, USA

Abstract

Large cargo scanning presents a unique challenge for national security. Container size limitations pose challenges to tomographic imaging. This work proposes a new stationary, limited angle tomographic transmission scanner geometry with a unique β/γ source utilizing a pair of fixed flat panel detectors, known as Gamma Tomography (GT). A Gate 10 simulation evaluates the imaging capabilities of the scanner and explores time-of-flight (TOF) and energy discrimination as electronic collimation methods to reduce scattered radiation and improve image quality. A 600 μm thin plastic scintillator sheet encasing 100mCi of ^{60}Co as a near detector locally captures nearly all emitted β particles without significant γ interactions, while a far detector panel of 2 cm thick LYSO crystals captures the ~1.25 MeV energy ^{60}Co γ photons. Both panels were simulated as 50x80 cm with a thin, 2 cm thick, multi-material test object consisting of water, aluminum, titanium, steel, and uranium in the center of the field of view. The same simulation dataset was reconstructed with/without two separate electronic collimation schemes: valid coincidences with a 100 keV energy window around the ^{60}Co photopeaks, and valid coincidences with a 100 ps time resolution. Despite the short acquisition time (18sec), reconstructed images are low noise, with all objects visible above background and distinguishable. The images show attenuation coefficient under-estimation, due to object scatter. TOF and energy discrimination underestimate μ values by 25.8% and 34.3% respectively, but a large dynamic range and very high SNR in μ value is achieved for all reconstructions (SNR-water: 46, SNR-Uranium: 1369). Using time information in lieu of energy allows events scattered in the detector to be used to improve image quality and SNR, but further investigation will include achievable time resolution, panel construction, and source geometry optimization.

NSS-01-251

A Large-Area Spectroscopic Alpha Imaging Detector for Dual-Isotope Imaging of ^{225}Ac and ^{213}Bi in Targeted Alpha Therapy (#2275)

Jong-Guk Kim, Byoung Soo Kim, Ilhan Lim, Kyo Chul Lee

Korea Institute of Radiological and Medical Sciences, Seoul, South Korea

Abstract

Alpha particle autoradiography is an emerging modality for mapping the biodistribution of alpha-emitting radionuclides in preclinical studies, supporting the development of radiopharmaceuticals for targeted alpha therapy (TAT). Considerable effort has been directed toward achieving high spatial resolution, with recent advances emphasizing single-event processing and energy-resolved detection to identify the nuclide of origin of individual alpha particles. Our previous work validated a spectrum decomposition method for dual-isotope imaging of ^{225}Ac and ^{213}Bi using a spectroscopic alpha imaging detector, confirming its feasibility with therapeutic amounts of ^{225}Ac. However, the active area of that system was constrained to 2.5 cm × 2.5 cm, limiting its applicability to small fields of view. To overcome this constraint and accommodate simultaneous imaging of multiple tissue sections or organs from larger animals, we developed a large-area spectroscopic alpha imaging detector with an active area of 5 cm × 5 cm, representing a fourfold increase over the prior system. The detector achieved an energy resolution of 4.3% FWHM at 5 MeV and a spatial resolution of approximately 600 μm, representing a substantial improvement over the prior system. Future work will include demonstration of dual-isotope spectral imaging of ^{225}Ac and ^{213}Bi to support preclinical TAT evaluations.

NSS-01-253

Scintillator Size Effects in Fiber-Based Neutron Detectors With Pulse-Shape Discrimination for BNCT (#2328)

Hong-Da Liu[1,2], **Hong-Da Liu**[1,2], Chun-Yen Chang[1], Chun-Yen Chang[1], Yi-Hsiang You[1], Yi-Hsiang You[1], Ya-Chen Chang[1], Ya-Chen Chang[1], Zhen-Fan You[2], Zhen-Fan You[2], Tzu-Hsiang Lin[1], Tzu-Hsiang Lin[1], Ming-Wei Lin[1], Ming-Wei Lin[1]

[1] National Tsing Hua University, Institute of Nuclear Engineering and Science, Hsinchu, Taiwan; [2] Heron Neutron Medical Corporation, Nuclear Science Department, Zhubei, Taiwan

This work was primarily supported by Heron Neutron Medical Corporation and the Industry–Academia Cooperative Ph.D. Project of the Ministry of Education in Taiwan. Partial financial support was also provided by the Institute of Nuclear Engineering and Science at National Tsing Hua University.

Abstract

Scintillator-on-fiber (SOF) detectors utilizing Liglass scintillators show strong potential for neutron flux monitoring in intense radiation environments due to their high radiation hardness and fast response. Previous studies have typically employed fragmented scintillators in SOF detectors due to the difficulty of μm-scale machining. In this work, Li-glass scintillators with well-defined dimensions (1×1×0.5 to 0.25×0.25×0.5 mm^3) were precisely fabricated using laser cutting, enabling a systematic investigation of the effect of scintillator size on neutron response linearity in an acceleratordriven neutron beam. With pulse-shape discrimination (PSD), the results show that neutron signals measured with scintillator sizes larger than 0.5×0.5×0.5 mm^3 become blurred in the P_{SP}-channel scatter plot due to gamma-ray contributions and pulse pile-up at an accelerator current of 250 μA. In contrast, the smallest scintillator (0.25×0.25×0.5 mm^3) maintains clear separation between neutron and gamma-ray signals. Analysis of the maximum shift error σ_m of the neutron peak centroid further indicates that this smallest scintillator effectively suppresses pileup, achieving σ_m = 0. In terms of linearity, scintillators with sizes below 0.75×0.75×0.5 mm^3 yield

coefficients of determination $R^2 > 0.99$ when processed using a two-dimensional fiducial cut, satisfying the requirements for neutron flux monitoring in boron neutron capture therapy (BNCT). These results demonstrate the feasibility of optimizing Li-glass scintillator size and volume in SOF detectors to achieve reliable neutron flux monitoring in BNCT applications.

NSS-01-255

Performance Evaluation of a DOI-Based Directional Radiation Monitoring System for Moving Radiation Source Tracking (#2334)

Yoon Soo Chung, Juwan Kang, Jiwon Ra, Yong Hyun Chung

Yonsei University, Radiation Convergence Engineering, Wonju, South Korea

Abstract

Radiation accident response requires real-time source-direction and radionuclide information. However, conventional systems are limited in simultaneously achieving radionuclide identification, direction estimation, 360° monitoring, real-time processing, and multiple-source detection. To address this, a directional radiation monitoring system (DRMS) using the depth-of-interaction (DOI) method was developed previously, and its feasibility for 360° monitoring and multiple-source detection was verified. This study evaluated the real-time direction detection performance of the developed DRMS under moving-source conditions. The DRMS consisted of a CsI(Tl) scintillator (1" diameter, 4" height), two photomultiplier tubes coupled to both ends, a cylindrical collimator with eight slots arranged in different directions, and an FPGA-based DAQ. The system calculated gamma-ray energy and DOI using the sum and ratio of the two PMT signals, respectively, and generated radiation distribution maps in real time based on the slot direction corresponding to the estimated DOI layer. Evaluation was conducted assuming an accident scenario in which a 5 TBq radiation source mounted on a vehicle moved at 40 km/h, 100 m from the system. To reproduce this in a laboratory, measurements used a 3.17 MBq ^{137}Cs source moved at 4.23 cm/min, 1 m from the system, under the same count-rate condition. Energy windows were applied to the data, and the nuclide was identified when counts within its window satisfied the criterion. A nuclide distribution map updated at fixed count intervals to reflect the real-time source position and an accumulated distribution map reflecting the total response were generated. The results confirmed that the system could visually reflect the position change and movement trajectory of a moving source. These results demonstrate the potential of the DOI-based DRMS for real-time source-direction monitoring in radiation accident response and mobile radiation detection.

References
[1] International Atomic Energy Agency, Preparedness and Response for a Nuclear or Radiological Emergency: General Safety Requirements. in IAEA Safety Standards Series No. GSR Part 7, no. v. GSR Part 7. Vienna: IAEA, 2015.
[2] International Atomic Energy Agency, Generic Procedures for Assessment and Response During a Radiological Emergency, IAEA-TECDOC-1162. Vienna, Austria: IAEA, Aug. 2000 (emended version, Mar. 2013).
[3] Y. S. Chung, M. K. Baek, S. Lee, J. Kang, and Y. H. Chung, “A novel directional radiation monitoring system for real-time nuclide identification and source localization using DOI method,” Nuclear Engineering and Technology, vol. 57, no. 10, p. 103710, Oct. 2025, doi: 10.1016/j.net.2025.103710.
[4] Y. S. Chung, S. Lee, J. Kang, J. Ra, J. Lee, and Y. H. Chung, “Design optimization and validation of a DOI-based directional radiation monitoring system for real-time nuclide identification and source localization,” Nuclear Engineering and Technology, vol. 58, no. 7, p. 104265, Jul. 2026, doi: 10.1016/j.net.2026.104265.

NSS-01-257

Development of a Portable High-Gamma-Ray-resistant Alpha and Beta Dust Monitor (#2423)

Misaki Hirato

Japan Atomic Energy Agency, Plutonium Radiation Control Section Radiation Protection Department, Muramatsu, Tokai-Mura, Naka-gun, Japan

This work was supported by JAEA Nuclear Energy S&T and Human Resource Development Project Grant Number JPJA25P 25135771.

Abstract

Measuring the radioactivity concentrations of airborne dust is crucial for selecting appropriate protective equipment for radiation workers and assessing internal exposure of them. In this study, we aim to develop a portable dust monitor that can measure alpha and beta rays simultaneously without being affected by ambient gamma rays. For the development, we utilize the clothing contamination monitor, which has been successfully put into practical use in previous research.

We investigated whether it was possible to distinguish between alpha and beta rays based on their respective energy spectra by irradiation tests. The results showed that by setting appropriate regions of interest (ROIs), we were able to minimize the influence of gamma rays and successfully distinguish and measure alpha and beta rays.

NSS-01-259

Investigation of Structure-Dependent Neutron-Induced Displacement Damage in Silicon MOSFETs (#2564)

Jin-Seok Oh[1,2], Hur Seop[2], Koo Seo-Ryong[2], Kwon Inyong[3]

[1] Korea University of Science and Technology (UST), Daejeon, South Korea; [2] Korea Atomic Energy Research Institute (KAERI), Daejeon, South Korea; [3] Yonsei University, Wonju, South Korea

This work was supported in part by the National Research Foundation (NRF) funded by the Korean government (MSIT) (RS-2025-04162969, RS-2022-00144324, RS-2022-00144419, and RS-2022-00165164), the Regional Innovation System & Education (RISE) program through the Gangwon RISE Center, funded by the Ministry of Education (MOE) and the Gangwon State (G.S.), Republic of Korea. (2025-RISE-10-006), the National Research Council of Science & Technology (NST) grant by the Korea government (MSIT) (No. GTL25051-000), and the Basic Science Research Program through the National Research Foundation of Korea (NRF) funded by the Ministry of Science and ICT (RS-2026-00144324).

Abstract

This work systematically characterizes how transistor geometry governs neutron displacement damage (DD)-induced degradation in silicon MOSFETs. A monolithic single-chip array integrating 1.8 V and 3.3 V NMOS/PMOS devices with seven channel widths and 1-, 5-, and 10-finger layouts was fabricated as the device under test, and a hierarchical 1 GHz multiplexing readout was developed to track 84 transistors in real time during irradiation at TRIUMF (10^6–10^{10} n/cm², five incremental steps, annealing monitored up to 40 days). For 1.8 V NMOS devices, the post-irradiation output-voltage shift scaled with channel width, while the threshold-voltage shift after 40-day annealing varied strongly with finger configuration at the same total channel width. These results indicate a strong dependence of DD-induced degradation on finger topology, beyond what channel-width scaling alone can explain, with 10-finger layouts exhibiting anomalous nonlinearity attributable to parasitic coupling and non-uniform damage.

References
[1] J. R. Srour and J. W. Palko, “Displacement Damage Effects in Irradiated Semiconductor Devices,” in IEEE Transactions on Nuclear Science, vol. 60, no. 3, pp. 1740-1766, June 2013, doi: 10.1109/TNS.2013.2261316.
[2] H. J. Barnaby, “Total-Ionizing-Dose Effects in Modern CMOS Technologies,” in IEEE Transactions on Nuclear Science, vol. 53, no. 6, pp. 3103-3121, Dec. 2006, doi: 10.1109/TNS.2006.885952.
[3] F. Faccio and G. Cervelli, “Radiation-induced edge effects in deep submicron CMOS transistors,” in IEEE Transactions on Nuclear Science, vol. 52, no. 6, pp. 2413-2420, Dec. 2005, doi: 10.1109/TNS.2005.860698.
[4] E. Simoen et al., “Radiation Effects in Advanced Multiple Gate and Silicon-on-Insulator Transistors,” in IEEE Transactions on Nuclear Science, vol. 60, no. 3, pp. 1970-1991, June 2013, doi: 10.1109/TNS.2013.2255313.

NSS-01-261

Solid-State Large-Area Contamination Detector Using Lightlink™ technology for Contamination and clearance equipment (#2688)

Philippe Talent

Mirion Technologies, R&D, Lamanon, France

Abstract

This paper presents a solid-state detection technology designed to improve large-area surface contamination measurements and enable integration into contamination and clearance equipment or robotics.
The primary objective is to replace photomultiplier-based detectors with compact architecture using solid-state photosensors and embedded digital processing, while maintaining or improving detection performance.
The proposed detector consists of a 579cm² sensitive surface divided into two independent channels, each coupled to integrated electronics performing biasing, signal processing, self-test, and communication. A daisy-chain configuration was implemented to evaluate system scalability, allowing up to fifty detectors to operate

synchronously within a single network. Measurements demonstrate detection homogeneity better than plus or minus fifteen percent over the active area and typical hemispherical efficiencies up to forty-six percent for high-energy beta emitters. The acquisition architecture enables rapid readout compatible with moving platforms, with sampling rates reaching one hundred measurements per second for moderate network sizes.
Compared with legacy systems, the proposed solution significantly reduces mass while improving robustness and insensitivity to magnetic fields and eliminates the need for complex external electronics. These results confirm that solid-state based large-area detectors can achieve high-performance contamination monitoring while enabling modular, scalable, and easily deployable systems. The approach opens new perspectives for robotic applications and large-area inspection in nuclear environments.

NSS-01-263

Performance Evaluation of the SNIPER-GN Portable Gamma–Neutron Detection System (#2692)

Paola Garosi, **Fabio Davolio**, Cristiana Del Bene, Giacomo Mangiagalli, Massimo Morichi, Carlo Uguccioni

CAEN S.p.A., Viareggio, Italy

Abstract
This work presents the experimental validation of SNIPER-GN, a portable gamma–neutron detection and identification system whose core innovation is a patented neutron identification algorithm (U.S. Patent No. 11835477). The algorithm enables robust and reliable neutron identification under challenging operational conditions, including shielding, moderation effects, and intense masking gamma radiation fields, representing a significant advancement over conventional detection approaches. The system integrates a high-efficiency gamma–neutron counter with a mid–high-resolution scintillation detector for rapid localization and characterization of radioactive threats, including Special Nuclear Material. The patented algorithm constitutes the enabling technology of the system and was the primary focus of the experimental verification campaign. Extensive performance testing was conducted in several international laboratories using calibrated sources under both static and dynamic measurement conditions. The system successfully identified neutron-emitting sources down to approximately 1 count per second with background levels below 0.1 counts per second, while gamma identification remained stable above 60 net counts per second over background. Tests employing polyethylene and lead shielding demonstrated identification success rates up to 100% depending on source geometry and activity, confirming robustness in realistic scenarios. Dynamic tests compliant with ANSI N42.53 confirmed reliable alarm performance for moving sources. Additional validation for field applications, such as rapid analysis of air-sampler filters and iodine cartridges for post-fallout monitoring, showed astonishing minimum detectable activities within measurement times shorter than five minutes.
Overall, these results validate the patented technology and demonstrate the suitability of SNIPER-GN for homeland security, emergency response, and radiological field deployment scenarios.

NSS-01-265

Development of A Cold Neutron Imaging Detector based on Structured $^{10}B_2O_3$-ZnS:Cu Screen (#2717)

Deyuan Li, Pengpeng Zhang, Xuewen Yan, Hui Li, Bo Yuan

China Institute for Radiation Protection, Taiyuan, China

This work was supported by the National Natural Science Foundation of China (No.12175202).

Abstract

Neutron imaging plays an irreplaceable role in the restoration of cultural relics and the study of lithium battery charging and discharging behaviors. The performance of neutron imaging detector directly determines the imaging quality. A cold neutron imaging detector based on a structured $^{10}B_2O_3$-ZnS:Cu scintillation screen was developed and tested at China Mianyang Research Reactor (CMRR) Cold Neutron Radiography Facility. The structured screen was made of glass microchannel plate (MCP), B_2O_3, ZnS:Cu and UV-curable binders. The refractive index contrast between the MCP (1.5) and the UV curable adhesive(1.62) leads to total internal reflection, thereby forming a light confinement structure. The spatial resolution was measured to be about 33μm with a Siemens Star Chart, and the cold neutron absorption efficiency was measured to be 24.4%

References

[1] Li, Deyuan, et al. "Design Optimization and Characterization of Cold Neutron Imaging Detector Based on Novel Gadolinium Scintillation Glass Fiber Arrays and Infinity Corrected Optics." IEEE Transactions on Nuclear Science 69.10 (2022): 2162-2167.

[2] Li, De-Yuan, et al. "High spatial resolution cold neutron imaging with new Tb^{3+}/Ce^{3+} co-doped Gd_2O_3 scintillation glass fiber arrays." Nuclear Instruments and Methods in Physics Research Section A: Accelerators, Spectrometers, Detectors and Associated Equipment 949 (2020): 162829.

NSS-01-267

Revealing Disorder Faster: Detector Upgrades for SANDALS-II (#2826)

Sarah E. Mann, **Sarah E. Mann**, Nigel J. Rhodes, Nigel J. Rhodes, Erik M. Schooneveld, Erik M. Schooneveld, Giacomo Mauri, Giacomo Mauri, Jack Day, Jack Day, Oliver L.G. Alderman, Oliver L.G. Alderman, Terri-Louise Hughes, Terri-Louise Hughes, Daniel T. Bowron, Daniel T. Bowron, G. Jeff Sykora, G. Jeff Sykora

STFC, ISIS, Harwell Campus, UK

Abstract

SANDALS-II is an instrument being developed at the ISIS Neutron and Muon Source as a next generation diffractometer for the study of amorphous and liquid materials. This upgrade will deliver count rates up to 11 times

higher than the existing SANDALS instrument and will significantly expand its scientific capabilities. This work focuses on developments of a large area scintillator detector that are essential for achieving enhanced performance. Scintillation detectors for SANDALS-II will cover a solid angle of 0.67Ω, 2.4 times greater detector coverage than the current instrument. These detectors are required to have high efficiency, particularly at higher neutron energies (short wavelengths), which is achieved using a unique design employing tiles made from alternating layers of glass and scintillator. Scintillator and glass options are explored to optimise detector and instrument performance. Different low Li and B content glasses were tested to determine the most suitable option for the instrument that provides good neutron transmission while maintaining affordability. The ratio of ZnS:Ag to ^{6}LiF in the scintillator will be altered from 4:1 to 2:1 to enhance neutron absorption and therefore detection efficiency. At 30eV (0.05Å) this offers a 60% improvement in detection efficiency. The applicability of low-afterglow scintillator, ZnO:Zn/^{6}LiF, for use in SANDALS-II is also explored. ZnO:Zn/^{6}LiF is shown to offer a 2x increase in count rate capability over ZnS:Ag/^{6}LiF, but a 6% lower neutron detection efficiency. As the reduction in efficiency using ZnO:Zn/^{6}LiF is modest, this alternative scintillator offers a viable solution for the high count rate regions of SANDALS-II. With optimised glass and scintillator selection, the performance required for the upgraded instrument can be delivered. This will enable faster measurements, smaller sample studies, and time resolved experiments, making SANDALS-II a world leading disordered material neutron diffractometer.

NSS-01-269

PGNAA-Based Composition Analysis Using $LaBr_3$(Ce) and NaI(Tl) Detectors (#2849)

Ki-Yoon Lee[1,2], Hyund-Dong Kim[1], Hyun-Soo Ha[1], Kyung-Hwan Jung[1], Jung-Hyeon Eo[2], JunYoung Shin[2], Jong-Yul Kim[3], Jae-Hyeon Kim[4], Kyung-Min Oh[4], Jin-Hyung Park[4], Cheol-Ha Baek[1,5]

[1] Kangwon National University, Medical Health Science, Samcheok, South Korea; [2] 3I Solution, Suwon, South Korea; [3] Korea Atomic Energy Research Institute, Neutron Science Center, Daejeon, North Korea; [4] Korea Atomic Energy Research Institute, Advanced Radiation Technology Institute, Jeongeup, South Korea; [5] Kangwon National University, Radiological Science, Samcheok, Germany

This work was supported by the Technology development Program(RS-2024-00469068) funded by the Ministry of SMEs and Startups(MSS, Korea)

Abstract

This study evaluated the performance of a $LaBr_3$(Ce) scintillation detector for elemental identification and mass-fraction estimation in a thermal-neutron-based prompt gamma-ray neutron activation analysis (PGNAA) system, in comparison with a conventional NaI(Tl) detector. PGNAA spectra were acquired at the Four-Circle Diffractometer (FCD) beamline of the HANARO research reactor at the Korea Atomic Energy Research Institute. The measured samples included pure Mn, Fe, Co, and Ni samples; binary Fe–Mn, Fe–Co, and Fe–Ni mixtures; and ternary NCM622 and NCM811 samples simulating spent lithium-ion battery cathode materials. Elemental identification was performed using Gaussian-derivative-convolution-based peak detection, SNIP baseline correction, and Currie-criterion-based significance testing. Mass fractions were estimated using region-of-interest-based weighted non-

negative least squares (WNNLS) with attenuation-integration correction. $LaBr_3(Ce)$ produced higher Z-scores, smaller energy-matching errors, and more stable characteristic peak combinations in mixed samples than NaI(Tl). For NCM622 and NCM811, $LaBr_3(Ce)$ achieved mean absolute errors of 4.3 and 1.9 percentage points, respectively, while also providing higher R^2 values for spectral-shape reproduction. These results indicate that $LaBr_3(Ce)$ offers improved peak separation and compositional estimation capability for nondestructive analysis of complex industrial samples, including spent lithium-ion battery cathode materials.

References
[1] T. Gozani, M. Elsalim, D. Strellis, and D. Brown, 2003, "Fusion of time-dependent gamma production spectra from thermal neutron capture and fast neutron inelastic scattering to improve material detection", Nucl. Instrum. Methods Phys. Res. A, vol. 505, no. 1–2, pp. 438–441, Elsevier.
[2] G. Molnár, 2004, "Handbook of Prompt Gamma Activation Analysis with Neutron Beams", 1st ed., Dordrecht, Netherlands: Springer, pp. 244-291, Springer

NSS-01-271

Ultra High-Rate Neutron Detection with ^{3}He Tubes via CF_4 Prompt Scintillation Readout (#3034)

Luis M. Margato[1,2], Andrey Morozov[1,2], Vladimir Solovov[1], Bruno Guérard[3], Julien Marchal[3]

[1] LIP-Coimbra, Coimbra, Portugal; [2] University of Coimbra, Dep. of Physics, Coimbra, Portugal; [3] ILL-Institut Laue-Langevin, Grenoble, France

This work was supported by the Portuguese national funds OE and Foundation for Science and Technology within the project Ref. 2023.15652.PEX (https://doi.org/10.54499/2023.15652.PEX). L. Margato acknowledges FCT-Portugal support through contract CEECINST/00106/2018/CP1494/CT0001.

Abstract
This work presents a novel neutron detector concept aiming to provide detection efficiency and background levels equivalent to conventional ^{3}He-based detectors, whilst boosting the maximum counting rate by several orders of magnitude. The detector retains the form-factor of a standard ^{3}He tube and uses the same working gas mixture of ^{3}He with admixture of CF_4 as the stopping gas. The key innovation is a fast optical readout of CF_4 prompt scintillation light using silicon photomultiplier (SiPM) sensors. The target performance is a detection efficiency equivalent to that of a standard ^{3}He tube under identical gas filling conditions, gamma sensitivity below 10^{-6}, and a maximum counting rate of 2 MHz/pixel, orders of magnitude improvement over existing detectors. The fast emission of CF_4 scintillation light is the enabling factor for achieving ultra-high counting rates. CF_4 exhibits a considerable photon yield, with one scintillation band in the UV and another in the visible region of the spectrum, with several thousands of photons emitted per neutron event. The efficient collection of light by the SiPMs constitutes a critical design parameter, addressed in this study through Monte Carlo optimization. The gas mixture composition is optimised to maximise the scintillation yield, and a gas purification system can be integrated into the detector to ensure long-term stability. The first experimental results of a detector prototype characterisation on a neutron beamline at the Institut Laue-Langevin (ILL) will be presented.

References

[1] Morozov, A, et al., “Photon yield for ultraviolet and visible emission from CF4 excited with α-particles”, Nuclear Instruments and Methods in Physics Research Section B: Beam Interactions with Materials and Atoms, vol. 268, no. 9, pp. 1456–1459, May 2010
[2] Morozov, A, et al., “Effect of the electric field on the primary scintillation from CF4”, Nuclear Instruments and Methods in Physics Research A 628 (2011) 360
[3] Morozov, A, Margato, L, Canezin, G, and Gonzalez, J, “Ants3 toolkit: Front-end for Geant4 with interactive GUI and Python scripting”, Computer Physics Communications, vol. 318, p. 109869, Jan. 2026
[4] Margato, L, et al., “Effect of the gas contamination on CF4 primary and secondary scintillation”, Nuclear Instruments and Methods in Physics Research A 695 (2012) 425

NSS-01-273

Imaging detection and spectral tracking of neutrons in wide range by Timepix detectors with Si, SiC, GaAs and CdTe sensors (#3044)

Carlos Granja[1], Andrea Sagatova[1], Tomas Slavicek[2], Stanislav Pospisil[2], Cristina Oancea[3], Petr Alexa[4], Zdenek Vykydal[5]

[1] Slovak University of Technology, Faculty of Electrical Engineering and Computer Science, Bratislava, Slovakia; [2] Czech Technical University, Institute of Experimental and Applied Physics, Prague, Czech Republic; [3] Advacam, Prague, Czech Republic; [4] VSB-Tech. Univ. Ostrava, Faculty of Electrical Engineering and Computer Science, Ostrava, Czech Republic; [5] Czech Metrology Institute, Prague, Czech Republic; [6] Czech Metrology Institute, Prague, Czech Republic

Work at the STU Bratislava was partially supported by grants APVV-22-0382 and DS-FR-24-0020 of the Slovak Research and Development Agency and funded by the EU NextGenerationEU through the Recovery and Resilience Plan for Slovakia under the project No. 09I05-03-V02-00073.

Abstract

The response of Timepix detectors with different sensors (Si, SiC, GaAs, CdTe) to thermal, slow, and fast neutrons is studied. Measurements at tunable mono-energetic neutron fields are compared and analyzed with nuclear-reaction models and numerical calculations. Specific radiation-type and sensor-material interaction neutron detection channels are derived for each detector-sensor configuration. These results serve to better and more completely process radiation data acquired with these detectors. Combining multi-detector measurements expands and enhances the resolving power of field decomposition.

References
[1] C. Zeitlin, “Physical Interactions of Charged Particles for Radiotherapy and Space Applications”, Health Physics, vol. 103, pp. 540-546, 2012.
[2] E. H. Lehmann, et al., “Neutron imaging – Detector options in progress”, J. of Instrum. vol. 6, 2011, Art no. C01050.
[3] C. Granja, et al., “Detection of fast neutrons with the pixel detector Timepix3”, J. of Instrum., vol. 18, 2023, Art no. P01003.
[4] R. Ballabriga, et. al., “ASIC developments for radiation imaging applications: The medipix and timepix family”, Nucl. Instrum. Meth. A, vol. 878, pp. 10-23, 2018R. Ballabriga, et. al., “ASIC developments for radiation imaging applications: The medipix and timepix family”, Nucl. Instrum. Meth. A, vol. 878, pp. 10-23, 2018.
[5] C. Granja, et al, "Detection resolving power of SiC Timepix3 detector to electrons, neutrons, ions and protons", J. of Instrum. vol. 19, 2024, Art no. C11007.
[6] J. Jakubek, S. Pospisil, et al., "Neutron detector based on TimePix pixel device with micrometer spatial resolution", Proc. SPIE 7449, Hard X-Ray, Gamma-Ray, and Neutron Detector Physics XI, 2009, Art no. 744910.

[7] C. Granja, et al., "Composition and Spectral Characterization of Mixed-Radiation Fields with Enhanced Resolving Power by Quantum Imaging Detection and Spectral-Sensitive Particle Tracking", IEEE Trans. Nucl. Sci., vol. 71, 2024, Art no. 921-931.
[8] B. Bergmann, S. Pospisil, et al., "Ionizing Energy Depositions After Fast Neutron Interactions in Silicon", IEEE Trans. Nucl. Sci. vol. 63, 2016, Art no. 2372-2378.
[9] C. Granja, et al., "Resolving power of pixel detector Timepix for wide-range electron, proton and ion detection", Nuclear Instr. Methods A, vol. 908, 2018, Art no. 60-71.

NSS-01-275

Characterization of 3D ultra-thin silicon-based thermal neutron detectors (#3088)

Felipe Zamorano, Iván Lopez, Martín Pérez, Javier Bravo, Celeste Fleta, Consuelo Guardiola

Institute of Microelectronics of Barcelona, Barcelona, Spain

This project has received funding from the Consejo de Seguridad Nuclear (CSN) under the project Subvenciones 2022 SUB-08.

Abstract

Neutron contamination in advanced radiotherapy and other mixed radiation environments has become an increasing concern due to the limitations of conventional neutron detectors under intense gamma background conditions. In this work, ultra-thin 3D silicon neutron detectors specifically designed for operation in mixed radiation fields were experimentally characterized under thermal and high-energy irradiation conditions. The detectors, consisting of 20 µm-thick silicon sensors paired with ^{6}LiF neutron conversion layers, were tested at the FANT thermal neutron facility and at the CERN High-Energy Reference Field (CERF). Measurements included reproducibility, angular dependence, bias voltage operation, and discrimination threshold effects using a low-voltage FPGA-based readout system. The results showed stable operation under mixed radiation fields, moderate angular dependence, and strong dependence of the response on detector bias and discrimination threshold. The ultra-thin detector architecture enabled high gamma rejection capability, enabling reliable neutron detection under intense photon background conditions. These results demonstrate the suitability of 3D ultra-thin silicon detectors for compact real-time neutron monitoring in radiation protection and medical applications.

References
[1] *Zorloni G. et al. "Joint EURADOS WG9-WG11 rem-counter intercomparison in a Mevion S250i proton therapy facility with Hyperscan pulsed synchrocyclotron" Phys. Med. Biol. (2022).*
[2] *Guardiola C. et al. "Neutron measurements with ultra-thin 3D silicon sensors in a radiotherapy treatment room using a Siemens PRIMUS linac" Phys. Med. Biol. (2013).*
[3] *Zamorano F. et al. "Out-of-field thermal neutron characterization with thin 3D-silicon detectors in Varian TrueBeam and Elekta Synergy LINACs" Phys. Med. Biol. (2025).*
[4] *Pozzi F. et al. "The CERN-EU high-energy Reference Field (CERF) facility: New FLUKA reference values of spectral fluences, present and newly proposed operational quantities" NIMA (2020).*

NSS-01-277

A Full Rank Pileup Deconvolution Scheme Suitable for Calorimeter Online Trigger Primitive Generation (#1091)

Jinyuan Wu

Fermi National Accelerator Laboratory, Batavia, USA

This manuscript has been authored by Fermi Forward Discovery Group, LLC under Contract No. 89243024CSC000002 with the U.S. Department of Energy, Office of Science, Office of High Energy Physics.

Abstract

In this document, a pileup deconvolution scheme not relying on any mathematics guessing is presented. In high energy physics experiment, as the luminosity increases, pile-up issues on detectors such as calorimeters become non-negligible. Deconvolution approaches developed for data taken from DAQ systems are usually rank-deficient or underdetermined, having less equations than unknowns, even with the ADC values from multiple beam crossings are collected. These deconvolution approaches need mathematic pre-assumptions such as Sparse Representation. For online computation tasks such as for trigger primitive creation, signal availability is significantly different as in offline data analysis stage, and therefore, it is possible to use different (yet simpler) algorithms. In this situation, number of ADC values of the calorimeter outputs is the same as the number of beam crossings (or 4 times number of beam crossings, depending on the ADC sampling rate), and therefore, the number of equations can be arranged to be the same as number of unknowns. This way, a determined deconvolution scheme with a full-rank squared convolution (and deconvolution) matrix becomes possible. The robustness of deconvolution over long time windows is also studied in this paper.

NSS-01-279

In-orbit performance of the Tl_2LiYCl_6:Ce (TLYC) detector onboard the Neutron Radiation Detection Instrument-1A (NeRDI-1A) (#1372)

Karla G. Oñate Melecio[1], Anthony L. Hutcheson[2], Bernard F. Phlips[2], Joseph M. Davis[2], Theodore T. Finne[2], Wiley N. Johnson[3], Lee J. Mitchell[2], Mary V. Johnson-Rambert[2], Joshua M. Wolf[2], Richard S. Woolf[2], Rose S. Perea[4]

[1] Research Associate with the National Research Council, Resident at the United States Naval Research Lab, Washington D.C., USA; [2] United States Naval Research Lab, Washington D.C., USA; [3] Technology Service Corporation, Arlington, USA; [4] Former NRC Research Associate at the U.S. NRL, Washington D.C., USA

This work was sponsored by the Office of Naval Research (ONR) as part of 6.1 funding.

Abstract
The Neutron Radiation Detection Instrument-1A (NeRDI-1A) is a technology demonstration payload on the International Space Station (ISS) as part of the Department of Defense Space Test Program (STP) mission STP-H9. The primary objective of NeRDI-1A is to space-qualify two detector technologies: a dual-mode gamma-neutron scintillator (Thallium-doped Cesium Lithium Yttrium Chloride, Tl_2LiYCl_6:Ce, or TLYC) and Domino microstructured semiconductor neutron detectors (MSNDs). The full NeRDI-1A suite includes a TLYC detector, three Domino MSNDs with varying moderation, and an EJ-270 plastic scintillator. This work focuses on the TLYC detector within NeRDI-1A. Here we present an analysis of the TLYC detector's response within distinct orbital regions--including the auroral regions and the South Atlantic Anomaly--during a period of minimal solar variability. We also present the evolution of the TLYC detector's performance over its operational lifetime.

References
[1] Hutcheson, A. L., et al. 2023, "Neutron radiation detection instrument-1A (NeRDI-1A)," Proc. SPIE 12696, Hard X-Ray, Gamma-Ray, and Neutron Detector Physics XXV, 1269603, https://doi.org/10.1117/12.2682621
[2] Hawrami, R., et al. 2017, "TL_2LiYCl_6: Large Diameter, High Performing Dual Mode Scintillator," Cryst. Growth Des., vol. 17, no. 7, pp. 3960-3964, American Chemical Society.
[3] Clark, S. 2023, "U.S. Military Experiments Hitching Ride to Space Station on SpaceX Cargo Ship," SpaceFlightNow.com, Spaceflight Now Inc.

NSS-01-281

Technical Design and Geometric Acceptance of the Assessing Lunar Ion-Generated Neutrons (ALIGN) Payload for Chang'E-8 (#1701)

Kullapha Chaiwongkhot[1], Koth Amratisha[1], Kanatip Anuchit[2], Sunruthai Burom[1], Sarawit Chindaratchakul[1], Hou Donghui[3], Paparin Jamlongkul[2], Pakorn Khonsri[2], Jidapa Lakronwat[1], Shariff Manuthasna[2], Tanawish Marsri[2], Warit Mitthumsiri[1], Pradiphat Muangha[2], Thanayuth Panyalert[2], Yaowarat Pittayang[2], Kunlanan Puprasit[4], David Ruffolo[1], Zhang Shenyi[3], Jetawee Wannasorn[2], Natthapong Treesakul[2], Ratchanonth Plumanut[2], Wutthiphat Hantrakul[2], Peerapong Torteeka[2]

[1] Mahidol University, Bangkok, Thailand; [2] National Astronomical Research Institute of Thailand, National Astronomical Research Institute of Thaila, Thailand; [3] National Space Science Center, Chinese Academy of Sciences, Beijing, China; [4] Chulabhorn Royal Academy, Bangkok, Thailand

This research was supported from the NSRF via the Research and Innovation Acceleration Agency for Competitiveness and Area Development (RCAD) (Program Management Unit for Technology and Innovation for Future Industries (PMU-B): Brainpower for Future Industries) [grant number B39G690003]

Abstract
The Assessing Lunar Ion-Generated Neutrons (ALIGN) payload is an advanced spectrometer developed to characterize the lunar radiation environment during the Chang'E-8 mission. Designed to operate within a stringent mass allocation of 4.8 kg and optimized for low electrical consumption, the payload features a highly integrated coincidence telescope statically oriented at -30 degrees from the horizontal. This presentation details the

instrumental architecture and multi-particle detection methodologies of the payload. The detector array comprises Double-Sided Silicon Strip Detectors (DSSDs), an EJ-254 boron-loaded plastic scintillator, and a primary CLYC calorimeter, all enveloped by an active BC-408 plastic scintillator veto. The system employs the Δ[if gte msEquation 12]><m:oMath><span style='font-size:12.0pt;mso-bidi-font-size:15.0pt;line-height:115%;font-family: "Cambria Math",serif;mso-fareast-font-family:DengXian;mso-fareast-theme-font: minor-fareast;mso-bidi-font-family:"Cordia New";mso-bidi-theme-font:minor-bidi; mso-ansi-language:EN-US;mso-fareast-language:ZH-CN;mso-bidi-language:TH'><m:r><m:rPr><m:scr m:val="roman"/><m:sty m:val="p"/></m:rPr>Δ</m:r></m:oMath><![endif][if gte vml 1]><v:shape id="_x0000_i1025" type="#_x0000_t75" style='width:7.2pt;height:16.2pt'> <v:imagedata src="file:///C:/Users/Admin/AppData/Local/Packages/oice_16_974fa576_32c1d314_c6d/AC/Temp/msohtmlclip1/01/clip_image003.png" o:title="" chromakey="white"/></v:shape><![endif]E-E technique—correlating initial energy loss in the DSSD transmission trackers with total energy deposited in the scintillators—to separate upward-moving albedo protons (20–140 MeV) from background electrons. Concurrently, intrinsic Pulse Shape Discrimination (PSD) within the CLYC crystal is utilized to accurately separate epithermal neutrons from gamma-ray interactions. To achieve definitive particle identification within these strict size, weight, and power constraints, a dedicated onboard FPGA executes priority-based signal processing. Geant4 simulations evaluated the instrument's overall geometric acceptance as a function of incident kinetic energy. By combining these advanced onboard logic techniques with a streamlined composite radiation shield, structural design is expected to successfully isolate lunar albedo signals from localized lander interference while fully satisfying the mission's strict engineering constraints.

References
[1] S. Zhang et al., “First measurements of the radiation dose on the lunar surface,” *Science Advances*, vol. 6, eaaz1334, 2020.
[2] T.B. McCord et al., “Sources and physical processes responsible for OH/H2O in the lunar soil as revealed by the Moon Mineralogy Mapper,”*JGR (Planets)*, vol. 116, E00G05, 2011.
[3] Z. Xu et al., “Primary and albedo protons detected by the lunar lander neutron and dosimetry experiment on the lunar farside,” Front. Astron.*Space Sci.*, vol. 9, 2022.

NSS-01-283

Cluster Size Simulation to Predict LHCb Upgrade I VELO Performance

(#1945)

Sean J. Williams[1], Emma Buchanan[2], David Friday[3], Jaap Velthuis[1], On behalf of the LHCb VELO group

[1] University of Bristol, H.H. Wills Physics Laboratory, Bristol, UK; [2] University of Edinburgh, School of Physics and Astronomy, Edinburgh, UK; [3] University of Manchester, Department of Physics and Astronomy, Manchester, UK

Abstract

The LHCb experiment recently underwent an extensive upgrade program to allow operation at higher luminosities. The VErtex LOcator (VELO) was redesigned to a hybrid pixel layout with 130nm CMOS technology. As a result of the upgrade, the VELO will be exposed to an extreme radiation environment – over an order of magnitude greater than before. At the end of its lifetime, the innermost regions are expected to be exposed to $8x10^{15}$MeV n_{eq} cm^{-2} [1]. Previous analysis of bias voltage scans (presented at IEEE Yokohama, 2025) has shown the VELO is at risk of exceeding the maximum 1000V bias voltage limit to remain at operational performance. Here, we present a data-

driven simulation of clusters in the VELO, to predict the performance at the end of its lifetime. Extensive validation of the simulation to testbeam data is performed, with angle and bias voltage scans showing very good agreement. Furthermore, charge sharing via diffusion in the simulation is authenticated with the charge collection vs intra-pixel hit position for size 2 clusters. Excellent agreement is seen. Comparison to Run III data is presented, showing good correspondence with the installed sensor. Extrapolations of the sensor performance at $8x10^{15}$MeV n_{eq} cm^{-2} are performed. Preliminary results estimate the hit efficiency to be 89.41±0.14\% and the spatial resolution to be 19.98±0.37μm (a 19.8% increase from non-irradiated). These results highlight the need to make use of beneficial annealing for the rest of the sensor lifetime, to ensure performance remains as good as possible.

References
[1] I. Bediaga. *LHCb VELO Upgrade Technical Design Report*. 11 2013.

NSS-01-285

Design of Readout Electronics for a CdZnTe Detector Prototype for Polar-orbiting Solar Hard X-ray Imaging Telescope (#2200)

ZeKun Wang[1,2], Shen Wang[1], Zhe Zhang[1]

[1] Purple Mountain Observatory, Chinese Academy of Sciences, Nanjing, China; [2] University of Science and Technology of China, School of Astronomy and Space Science, Nanjing, China

Abstract

To support the X-ray Imaging Telescope (XIT) onboard China's Solar Polar Orbiting Observatory, which aims to perform the first-ever imaging of the Sun polar regions and study high-energy processes in solar eruptions, we have developed a prototype readout electronics system for a CdZnTe hard X-ray detector. The system consists of a 2 mm thick CdZnTe detector with an effective area of 15 × 15 mm² segmented into four strip electrodes with switchable area ratios, a front-end electronics board employing the IDE4281 charge-sensitive preamplifier ASIC, and a FPGA-based data acquisition unit with integrated calibration and high-voltage supply. The IDE4281 chip provides 12 channels with programmable shaping times, self-triggering, and peak-hold outputs. In the readout prototype, the equivalent noise charge after common-mode noise subtraction ranges from 149 to 189 e^- across all channels. Using a ^{241}Am radioactive source, the detector demonstrates a full-width at half-maximum energy resolution of 4.92 keV at 59.5 keV, fulfilling the scientific requirement of better than 5 keV at that energy. These results validate the prototype design and establish the basis for the forthcoming X-ray imaging telescope instrument.

NSS-01-287

Stability of the ATLAS Timepix3 Detector Network for Relative Luminosity Measurement in Run 3 (#2499)

Catalina Lesmes[1,2], Benedikt Bergmann[1], Milan Beneš[1], Pavel Broulím[1], Petr Burian[1,3], Martin Farkaš[3], Tomáš Kulhánek[3], Petr Mánek[1], Stanislav Pospíšil[1], Ondrej Růžička[3], Petr Smolyanskiy[1], Ondrej Urban[3], Jan Zich[3]

[1] Czech Technical University in Prague, Institute of Experimental and Applied Physics, Prague, Czech Republic; [2] Czech Technical University in Prague, Faculty of Nuclear Sciences and Physical Engineering, Prague, Czech Republic; [3] University of West Bohemia, Faculty of Electrical Engineering, Pilsen, Czech Republic

Abstract

Since its installation, the Timepix3 detector network has demonstrated utility within the ATLAS cavern by providing radiation field measurements and relative luminosity monitoring. This work evaluates the performance and internal stability of the network during the entire LHC Run 3. To ensure robust monitoring and assess systematic uncertainties, three distinct algorithms were evaluated and compared: cluster counting, thermal neutron counting, and heavy and straight track counting.

Clean signal was achieved by identifying and masking noisy pixels and by modeling and subtracting background activation by a recursive growth and decay model. Internal consistency was verified through both short-term (intra-fill) and long-term (yearly) stability analyses across detectors situated at different distances from the interaction point. The presented results demonstrate that the distributed Timepix3 network provides a stable and robust relative luminosity measurement, complementing primary ATLAS luminometers during Run 3.

References

[1] P. Burian, et al., "Timepix3 detector network at ATLAS experiment,'' J. Instrum., vol. 13, p. C11024, Nov. 2018.

[2] B. Bergmann, et al., "Relative luminosity measurement with Timepix3 in ATLAS,'' J. Instrum., vol. 15, p. C01039, Jan. 2020.

[3] B. Bergmann, P. Burian, E. David-Bosne, et al., "Evaluation of Timepix3 as a luminosity detector at LHC during 2018 pp collisions at $\sqrt{s} = 13$ TeV,'' Eur. Phys. J. C, vol. 85, no. 904, 2025.

[4] T. Holy, et al., "Pattern recognition of tracks induced by individual quanta of ionizing radiation in Medipix2 silicon detector,'' Nucl. Instrum. Meth. A, vol. 591, no. 1, pp. 287--290, June 2008.

[5] M. Campbell, et al., "Induced radioactivity in ATLAS cavern measured by MPX detector network,'' J. Instrum., vol. 14, p. P03010, Mar. 2019.

NSS-01-289

Radiation Studies for the LHCb Upgrade II Detector: Impact of the Upgraded Electromagnetic Calorimeter and Muon System Shielding

(#2517)

Sacha E.R. Medaer, Gloria Corti

CERN, LHCb Collaboration, Geneva, Switzerland

The authors would like to thank M. Karacson and M. Pycior for their contributions to the FLUKA model, L. Granado Cardosos and F. Sborzacchi for their support with the computing infrastructure, as well as P. Roloff, S. Kholodenko, A. Saputi, and A. Satta for their assistance with the detector geometry descriptions.

Abstract

The LHCb Upgrade II, planned for Run5, will operate at a substantially higher luminosity than previous runs, motivating dedicated FLUKA simulations of the resulting mixed-field radiation environment. This work addresses the impact of two major changes: the upgraded Electromagnetic Calorimeter, referred to as PicoCal, and the shielding of the Muon System. The increased fraction of high-density material in the PicoCal central modules modifies shower development and neutron production, while additional shielding is required to preserve Muon System performance. All comparisons are made with respect to the same Run4 reference configuration without additional Muon System shielding. Two Muon System shielding solutions are evaluated: i) replacement of the Hadronic Calorimeter by an iron-and-concrete shield with borated-polyethylene plates upstream and downstream, and ii) retention of the present Hadronic Calorimeter followed by a ductile cast iron, borated-polyethylene and steel wall. The simulations show increased local neutron production around the PicoCal central modules, while the existing polyethylene-and-boron shield upstream of the calorimeter limits the impact on upstream sub-detectors. For the Muon System, both shielding strategies reduce the charged-particle fluence relevant for detector performance, with different spatial and particle-composition trade-offs. These results support the optimization of the LHCb Upgrade II layout and illustrate the role of detector radiation studies for shielding design in mixed-field high-energy physics environments.

References

[1] LHCb-Collaboration, “Framework tdr for the lhcb upgrade ii-opportunities in flavour physics, and beyond, in the hl-lhc era,” Technical Reports CERN-LHCC-2021-012 and LHCB-TDR-023, 2021

[2] R. Aaij, A. S. W. Abdelmotteleb, C. Abellan Beteta, F. Abudin´en, C. Achard, T. Ackernley, B. Adeva, M. Adinolfi, P. Adlarson, H. Af- sharnia et al., “The lhcb upgrade i,” Journal of Instrumentation, vol. 19, no. 05, p. P05065, 2024.

[3] G. Battistoni, T. Boehlen, F. Cerutti, P. W. Chin, L. S. Esposito, A. Fasso, A. Ferrari, A. Lechner, A. Empl, A. Mairani et al., “Overview of the fluka code,” Annals of Nuclear Energy, vol. 82, pp. 10–18, 2015.

[4] C. Ahdida, D. Bozzato, D. Calzolari, F. Cerutti, N. Charitonidis, A. Cim- mino, A. Coronetti, G. D’alessandro, A. Donadon Servelle, L. Esposito et al., “New capabilities of the fluka multi-purpose code,” Frontiers in Physics, vol. 9, p. 788253, 2022.

NSS-01-291

Timing properties of the FARCOS detection system (#2838)

Andrea Castoldi[1,2], **Chiara Guazzoni**[1,2], Andrea Mason[1,2], Mattia Pozzi[1,2], Riccardo Zambolo[1,2], on behalf of the fARCOS collaboration

[1] Politecnico di Milano and INFN, Dipartimento di Elettronica, Informazione e Bioingegneria, Milano, Italy; [2] INFN, Sezione di Milano, Milano, Italy

Abstract

FARCOS is a Femtoscope Array for Correlation and Spectroscopy designed to perform studies of two- and multi-particle and Intermediate Mass Fragments (IMFs) correlations in heavy-ion collisions at Fermi energies with stable and radioactive beams. The FARCOS system is a modular assembly of up to 20 telescopes to be used in combination with 4π detectors like the CHIMERA multidetector. Each telescope features two Silicon detection layers (32 + 32 channels Double Side Silicon Strip Detectors 300μm and 1500μm thick and a third calorimetric stage, made of four truncated pyramidal CsI(Tl) crystals arranged in a 2 x 2 matrix). Particular care has been posed in the design of the frontend electronics for the different stages. For the first time we performed a detailed qualification of the timing properties of the FARCOS frontend electronics and of the different detection stages. The achievable resolution was optimized thanks to an accurate analysis of the waveform shape. The remarkable time resolution measured at zero pf capacitive input load, with the FARCOS frontend electronics, below 100 ps rms at 1.1 MeV injected charge on the 100 MeV full-scale energy range, thanks to the excellent energy resolution below 15 keV FWHM paves the way to widen the range of experiments in which the FARCOS system will be applied. The measured time resolution improves to 25 ps rms at 5 MeV injected charge. The selectable gain factor allows the extension of the full-scale energy range up to a gain factor of 0.5mV/MeV over the full-scale range of 1.1V, with a small compromise on the time resolution, translating in a dynamic range of more than 15bits. The INL keeps below 0.5% over the full dynamic range. The timing performance of the Silicon layers of the FARCOS telescopes was then qualified with a near-infrared pulsed laser system and with alpha particles. This contribution presents the results of this qualification together with some highlights of the recent applications of the FARCOS telescopes.

References

[1] FARCOS Technical Design Report, available online at https://drive.google.com/file/d/0B5CgGWz8LpOOc3pGTWdOcDBoWFE/view.

[2] L. Acosta et al., *"Present status of the FARCOS detection system"*, 2017 IEEE Nuclear Science Symposium and Medical Imaging Conference Records, 2017 IEEE, Atlanta, Georgia, Oct. 21-Oct. 28, 2017, pp. 1– 4.

[3] L. Acosta et al., *"The FARCOS detection system: the first application in a real experiment"*, 2019 IEEE Nuclear Science Symposium and Medical Imaging Conference Records, 2019 IEEE, Manchester, United Kingdom, Oct. 26-Nov. 2, 2019, pp. 1– 4.

[4] A. Pagano, "Studies of Nuclear Reactions and Time Scale with the 4pi Detector CHIMERA", Nuclear Physics News International, 22, No.1, 28–33 (2012).

[5] A. Castoldi, C. Guazzoni, T. Parsani, V. L. Sicari, *"Implementation and Qualification of the FARCOS Frontend Electronics"*, 2018 IEEE Nuclear Science Symposium and Medical Imaging Conference Records, November 10-17, 2018, Sydney (Australia).

[6] A. Castoldi, C. Guazzoni and V. L. Sicari on behalf of the FARCOS collaboration, *"Widening the application range of the FARCOS frontend electronics"*, 2020 IEEE Nuclear Science Symposium and Medical Imaging Conference Records, pp. 1-4.

NSS-01-293

Thermal and In Situ annealing tests for SiPM radiation damage mitigation (#2917)

Suomi Bez Baruah[1,2], Maria S. Ruzzarin[1], Fabio Acerbi[1], Alberto Gola[1]

[1] *Fondazione Bruno Kessler, CRS, Trento, Italy;* [2] *University of Trento, Physics, Trento, Italy*

National PhD Program in Space Science and Technology (University of Trento)

Abstract

Silicon Photomultipliers (SiPMs) are solid-state photodetectors increasingly employed in astrophysics and space missions due to their high photon detection efficiency (PDE), compactness, insensitivity to magnetic fields, and operation at relatively low bias voltages. However, exposure to radiation, through both Ionizing Energy Loss (IEL) and Non-Ionizing Energy Loss (NIEL) effects, can degrade their key performance parameters.

To mitigate radiation-induced damage, annealing strategies have been explored. This work presents the results of two annealing tests performed on FBK SiPMs, after x-ray irradiation and proton irradiation, highlighting their respective advantages and limitations: (1) thermal annealing, involves storing the devices in a climatic chamber without active heating, while periodically performing electrical measurements to track recovery over time. (2) In-situ current annealing progressively increases the SiPM bias current to induce self-heating via resistive effects. Electrical measurements have been done after each step, and a thermocamera have been used to monitor device temperature.

References

[1] R. Preghenella et al., Nucl. Instrum. Methods Phys. Res. A, Vol. 1056, pp. 168578, 2023

[2] S. Merzi, S.E. Brunner, A. Gola, A. Inglese, A. Mazzi, G. Paternoster, M. Penna, C. Piemonte and M. Ruzzarin, J. Instrum., vol. 18, P05040, May 2023

[3] F. Acerbi, A.R. Altamura, B. Di Ruzza, S. Merzi, P. Spinnato and A. Gola, Nucl. Instrum. Methods Phys Res. A., vol. 1045, 167502, 2023

[4] A.R. altamura, F. Acerbi, B. Di Ruzza, E. Verroi, S. Merzi, A. Mazzi, and A. Gola, Nucl. Instrum. Methods Phys. Res. A., vol. 1045, 167488, 2023

NSS-01-295

Axial Reactivity Profile Measurement of Polaris Using CR-39 Nuclear Track Detectors (#2958)

Sara Alawabdeh, Perry Young, Nate Kaneshige, Wolfgang Hennig, Daniel Cech, John Peterson, Ron Grazioso, Michael Y. Hua

Helion Energy, Nuclear Diagnostics, Everett, USA

Abstract

This work presents the measurement of the axial neutron emission profile of the Polaris field-reversed configuration (FRC) fusion machine using CR-39 solid-state nuclear track detectors (SSNTDs). Passive detectors were deployed at multiple axial positions along the Polaris compression section, accumulating neutron-induced proton recoil tracks over several pulses of moderate yield, sufficiently low to resolve tracks. Chemical etching in 6M NaOH at 85°C for 2.5 hours revealed latent damage tracks, which were analyzed using a custom Python-based image processing pipeline incorporating a trained Random Forest classifier achieving 94.1% ± 2.2% cross-validation accuracy in neutron track identification. The resulting axial track density profile is symmetric and centrally peaked, in agreement with MCNP-simulated neutron dose distributions for a thermonuclear DT fusion source confined within the FRC plasmoid. The absence of asymmetric structure - characteristic of beam-target dominated reactions - provides compelling experimental evidence of spatially confined thermonuclear fusion on Polaris. This represents the first deployment of CR-39 diagnostics for reactivity profiling on a pulsed FRC machine and establishes passive track detectors as an effective tool for fusion burn characterization.

References

[1] Frenje, JA, Li, CK, Seguin, FH, Hicks, DG, Kurebayashi, S, Petrasso, RD 2002, 'Absolute measurements of neutron yields from DD and DT implosions at the OMEGA laser facility using CR-39 track detectors', *Review of Scientific Instruments*, vol. 73, no. 7, pp. 2597–2605, New York: AIP Publishing.

[2] Seguin, FH, Frenje, JA, Li, CK, Hicks, DG, Kurebayashi, S, Petrasso, RD 2003, 'Spectrometry of charged particles from inertial confinement-fusion plasmas', *Review of Scientific Instruments*, vol. 74, no. 2, pp. 975–995, New York: AIP Publishing.

[3] Casey, DT, Frenje, JA, Seguin, FH, Li, CK, Rosenberg, MJ, Petrasso, RD 2011, 'The coincidence counting technique for orders of magnitude background reduction in data obtained with the Magnetic Recoil Spectrometer at OMEGA and the NIF', MIT Plasma Science and Fusion Center, Rep. PSFC/JA-11-11, Cambridge: MIT.

[4] Helion Energy 2026, 'Helion Energy' [Online], Everett: Helion Energy. Available: https://www.helionenergy.com [Accessed: 7 May 2026].

[5] Lahmann, B, Gatu Johnson, M, Frenje, JA, Glebov, VY, Séguin, FH, Petrasso, RD 2020, 'CR-39 nuclear track detector response to ions from 10 keV to 1.1 MeV/u', *Review of Scientific Instruments*, vol. 91, no. 5, p. 053502, New York: AIP Publishing.

[6] Lengar, I, Skvarc, J, Ilic, R 2003, 'Calibration of a CR-39 detector for neutron measurements by the track-diameter method', *Radiation Measurements*, vol. 36, pp. 245–248, Oxford: Elsevier.

NSS-01-297

On-detector Electronics for the ATLAS Liquid Argon Calorimeter Phase-II Upgrade at the High-Luminosity LHC (#2989)

Emmanuel Josue Molina Gonzalez[2], **Nikiforos Nikiforou**[1], On behalf of the ATLAS Collaboration

[1] CERN, Geneve, Switzerland; [2] Université Paris-Saclay, IRFU, CEA, PAris, France

Abstract

The ATLAS Liquid Argon (LAr) calorimeter readout electronics are being upgraded for operation at the High-Luminosity Large Hadron Collider (HL-LHC), where up to 200 proton-proton interactions per bunch crossing will significantly increase detector occupancy, trigger rates, and radiation levels. While the calorimeter detectors themselves remain unchanged, the complete readout electronics chain is being replaced. The upgraded on-detector electronics readout system continuously amplifies, shapes, digitizes, and transmits calorimeter signals from approximately 182000 channels at the 40 MHz bunch-crossing rate. The new Front-End Boards (FEB2) integrate custom radiation-hard ASICs including the ALFE2 preamplifier/shaper, the COLUTA analog-to-digital converter, and lpGBT optical communication devices. Prototype boards and ASICs have been developed and extensively tested in laboratory and integration environments. This contribution presents the architecture, development status, and recent performance results of the Phase-II front-end electronics for the ATLAS LAr calorimeter.

References
[1] ATLAS Collaboration, “The ATLAS Experiment at the CERN Large Hadron Collider,” JINST, no. 3, S08003, 2008.
[2] ATLAS Collaboration, “Technical Design Report for the Phase-II Upgrade of the ATLAS LAr Calorimeter,” CERN-LHCC-2017-018, ATLAS-TDR-027, 2017.
[3] G. Aad et al., “The Phase-I trigger readout electronics upgrade of the ATLAS Liquid Argon calorimeters,” JINST 17, P05024, 2022.

NSS-01-299

Airborne Measurement of Terrestrial Gamma-Ray Flashes with the High Elevation Radiation Array (#2287)

Juan J. Manfredi[1], Jeffrey M. Chaffin[2,1], Vaun Clagett[1], Michael Rynders[1], Jacob Weinberg[1], William Erwin[3]

[1] Air Force Institute of Technology, Department of Engineering Physics, Wright-Patterson AFB, USA; [2] California Polytechnic State University, San Luis Obispo, Physics Department, San Luis Obispo, USA; [3] Air Force Research Laboratory, 711th Human Performance Wing, Wright-Patterson AFB, USA

Abstract

This study investigates the unique high-energy radiation environment of thunderstorms, focusing on terrestrial gamma-ray flashes (TGFs). Led by the Air Force Institute of Technology, the United States Air Force School of Aerospace Medicine, and the Air Force Research Laboratory, this effort deploys custom-built High Elevation Radiation Array (HERA) instruments aboard ten WC-130J “Hurricane Hunter” aircraft. These planes fly into hurricanes and tropical storms for the purpose of measuring weather data, potentially bringing them into proximity of TGF radiation. Each HERA unit contains a sodium iodide scintillator, a plastic scintillator, and associated data acquisition hardware. HERA represents the largest airborne campaign to date for near-source TGF observations and aims to improve understanding of TGF mechanisms, occurrence rates, and associated radiation risks to aircrew and equipment. All HERA detectors have been installed on aircraft and will collect data during the full 2026 Atlantic hurricane season.

NSS-01-301

Systematic X-ray irradiations of a back illuminated, HPGe, microstrip sensor. (#1420)

Daniel Thacker, Marcello Borri, Matthew Buckland, William Helsby, Andrew Hill, Konrad Sutowski

UKRI - Science & Technology Facilities Council, Technology Department, Warrington, UK

The authors would like to acknowledge the UKRI-STFC for funding the X-ray irradiations facility (ST X004837-1), and the UKRI-STFC Centre for Instrumentation for funding R&D on HPGe sensors.

Abstract

Back illuminated, HPGe, microstrip sensors are operated in the cryogenic detector system called XH. XH enables the collection of energy dispersive X-ray absorption spectra to investigate near-instantaneous structural variations in experimental samples. XH detects the transmitted radiation of a bright, single flash of X-rays that is delayed with respect to a laser pulse, which also hits the sample and creates an excited state of matter. Each strip in the HPGe sensor detects the intensity of a spectral component ($\Delta E \sim 1.5$ eV) of the transmitted, dispersed polychromatic beam, which has a typical bandwidth of ~1 keV. The HPGe sensor can be exposed to beam intensities as high as 1×10^{13} ph/mm^2/s from polychromatic beams with a central energy in the range ~5 keV to ~25keV. The operation in this radiation harsh condition benefits from a systematic irradiation campaign to investigate ageing effects created by Total Ionising Dose (TID). The TID effects on the HPGe sensor are mitigated by design by adopting a back illumination approach in order to shield the strip contacts, and by the selection of a proprietary, commercial lithographic process. XH was irradiated at the X-ray Irradiation Facility at Daresbury Laboratory (UK). The 1024 strip sensor was repeatedly exposed to X-rays in finite time steps. Total leakage and strip currents were monitored regularly with X-rays on and off. The X-ray peak energy was limited to 20 keV, which was fully absorbed in the 1.5 mm thick HPGe sensor. This protected the strip contacts from radiation. Beam collimation within the active area of the HPGe sensor showed a steady performance, which was immune from TID. Evidence of deterioration in surface leakage current was measured when the beam was hitting the sensor edge and its supporting PCB.

References

[1] M.Borri et al, 'Prototyping experience with Ge micro-strip sensors for EDXAS experiments', Nuclear Instruments and Methods in Physics Research A 1017 (2021) 165800
[2] M.Borri et al, 'Characterisation of Ge micro-strip sensors with a microfocused X-ray beam', Nuclear Instruments and Methods in Physics Research A 988 (2021) 164932
[3] N.Sevelin-Radiguet et al, 'Towards a dynamic compression facility at the ´ ESRF', Journal of Synchrotron Radiation 29 167-179
[4] Hernandez, J. A. et al, 'The high power laser facility at beamline ID24- ED at the ESRF', High Pressure Research, 44(3), 372–399
[5] Rosa, A. D. at al, 'New Opportunities for Earth Science at the Extremely Brilliant Source of the European Synchrotron Radiation Facility', Synchrotron Radiation News, 35(6), 8–16
[6] M.Borri et al, Commissioning of an X-ray irradiation facility to test HPGe sensors and to irradiate CMOS electronics, 2024 IEEE NSS MIC RTSD, https://doi.org/10.1109/NSS/MIC/RTSD57108.2024.10655927

NSS-01-303

Energy-resolved Laue Diffraction: a New Tool for Crystal Structure determination (#1715)

David P. Siddons[1], Abdul K. Rumaiz[1], Michael Drakopoulos Drakopoulos[1], Nghia Vo[1], Zhong Zhong[1], Anthony J. Kuczewski[1], Anthony J. Kuczewski[2], Ji Li[1], Wei Chen[2]

[1] Brookhaven National Laboratory, NSLS-II, Upton, USA; [2] Brookhaven National Laboratory, Instrumentation, Upton, USA

This research used resources of the National Synchrotron Light Source II, a U.S. Department of Energy (DOE) Office of Science User Facility operated for the DOE Office of Science by Brookhaven National Laboratory under Contract No. DE-SC0012704.

Abstract

White beam Laue diffraction is well-known as a means to orient single-crystal samples, but its use as a structure-determining tool is less exploited. One of the difficulties with the method is its incomplete measurement of the diffraction vector. Only its direction can be determined, but not its length, since conventional instrumentation does not provide the diffracted beam energy. In this paper we propose to use a high-resolution energy resolving detector to provide that information, together with NSLS-II's HEX beamline, which has a spectral range up to 200keV. We have developed a series of microstrip germanium detectors, and present here some measurements using one of them together with a horizontal aperture to emulate a 192 x 1 pixel detector with 250 micrometer pixels. By scanning this device in one dimension we could simulate a 2-dimensional detector with good energy resolution,. We have further designed and built a custom detector for this purpose, which has 192x2 pixels, each 250 x 250 micrometers, and so does not need the aperture, and which requires half the number of measurements. Data collected with these detectors will be presented.

NSS-01-305

Pile-Up Resilient X-Ray Spectroscopy via Direct Sampling and Waveform Fitting in SDDs (#1993)

Andrea Abba[1], Valentina Arosio[1], Pietro Barcella[2], Francesco Caponio[1], Marco Carminati[2], Edoardo Carlotti[1], Stefano Carsi[1], Alberto Cusimano[1], Carlo E. Fiorini[2], Monica Lazari[1], Beatrice Pedretti[2], Edoardo Proserpio[1], Carlo Tintori[3], Yuri Venturini[3]

[1] Nuclear Instruments SRL, Lambrugo, Italy; [2] Politecnico di Milano, DEIB, Milano, Italy; [3] CAEN SPA, Viareggio, Italy

Abstract

A fully digital readout architecture is described for high-throughput X-ray spectroscopy with silicon drift detectors (SDDs). The core challenge is the large-amplitude voltage ramp produced by transistor reset preamplifiers, which conventionally prevents direct digitization at spectroscopic resolution. In this work, sampling the preamplifier output with a 20-bit SAR ADC achieves a dynamic range exceeding 10^6, eliminating any analog conditioning stage upstream of the digitizer.

Throughput is sustained by combining four converters in a time-interleaved scheme, yielding an aggregate sampling rate of 160 Msps. A Zynq SoC provides the processing backbone, performing inter-channel timing alignment, gain equalization, and concurrent execution of the signal processing pipelines.

Two energy estimation algorithms run in parallel on the digitised data: a ramp-corrected trapezoidal filter and a model-based least-squares fitter that uses linear regression over the full inter-event sample record, remaining accurate even when pulse separation shrinks to sub-microsecond intervals. Experimental characterisation with ARDESIA multi-pixel SDD arrays and KETEK single-pixel detectors yields an energy resolution of 120.7 eV FWHM at low rate, 150 eV at 1 Mcps, and 180 eV at 2 Mcps, with live time exceeding 90% throughout.

NSS-01-307

High-resolution Germanium Detector system for Fluorescence-Mode X-ray Absorption Spectroscopy (#2626)

Abdul K. Rumaiz[1], Francesca Capocasa[2], Anthony J. Kuczewski[1], Giovanni Pinaroli[2], Thomas Krings[3], Bruce Ravel[4], David P. Siddons[1]

[1] Brookhaven National Laboratory, NSLS II, Upton, USA; [2] Brookhaven National Laboratory, Instrumentation Department, Upton, USA; [3] Forschungszentrum, Jülich, Germany; [4] National Institute of Standards and Technology, Gaithersburg, USA

Abstract

Fluorescence-mode X-ray Absorption Spectroscopy (XAS) at high photon energies require detectors with both high stopping power and excellent energy resolution to measure weak element-specific fluorescence signals. Conventional silicon-based detectors suffer from poor absorption efficiency above ~20 keV, while most high-Z semiconductor materials such as cadmium telluride (CdTe), cadmium zinc telluride (CZT), and gallium arsenide (GaAs) have largely been developed for imaging applications with comparatively limited spectroscopic performance. In contrast, Germanium combines excellent stopping power with superior intrinsic energy resolution owing to its low Fano factor and favorable charge transport properties, making it particularly attractive for spectroscopy in the 15-100 keV range. Here we report the development, fabrication, and characterization of Gepta-EX, a compact multi-channel high-purity germanium (HPGe) detector system designed for fluorescence-mode XAS. Gepta-EX incorporates a monolithic seven-channel HPGe pixel array integrated with low-noise CUBE charge-sensitive preamplifiers inside a thermally isolated compact cryostat operating near 90K. The detector achieves energy resolutions of 218 eV at 5.9 keV using an ^{55}Fe source and 373 eV at 59.5 keV using an ^{241}Am source, with uniform response across all channels. By avoiding the escape-peak interference commonly associated with silicon detectors while maintaining stable high-resolution performance at elevated X-ray energies, Gepta-EX provides a powerful platform for high-energy X-ray spectroscopy and fluorescence-mode XAS applications.

NSS-01-309

Visualization of beta-emitting nuclides in water using a CCD camera and CaF_2 scintillator (#1462)

Yuki Morishita[1], Marina Kanno[2]

[1] Japan Atomic Energy Agency, Collaborative Laboratories for Advanced Decommissioning Science (CLADS), Futaba County, Japan; [2] PESCO Co., Ltd., Tokyo, Japan

Abstract

At nuclear facilities such as decommissioning sites and reprocessing plants, continuous monitoring of radioactive liquid waste is essential to prevent the spread of contamination. While gamma-emitting radionuclides can be detected relatively easily using gamma-ray detectors, radionuclides emitting only alpha or beta radiation are difficult to measure remotely because these particles are strongly absorbed in water. Conventional liquid scintillation counting requires sample collection and pretreatment, making real-time monitoring difficult. In this study, a real-time visualization method for beta-emitting nuclides in water was developed using a calcium fluoride (CaF_2) scintillator and an Electron Multiplying CCD (EM-CCD) camera. The scintillator was designed with a water-permeable structure to allow contaminated water to flow through it, enabling direct detection of beta radiation in water. Radiation source measurements were performed in a dark room using a 90Sr–90Y beta source. Scintillation light generated in the CaF_2 scintillator was captured by the EM-CCD camera. The results demonstrated that the position of the beta source could be successfully visualized with acquisition times as short as 1 s, and the detected intensity increased with measurement time. Measurements conducted while moving the source confirmed that changes in source position could also be visualized, indicating the capability to monitor moving contamination in water. In addition, water infiltration tests confirmed that water could successfully pass through the scintillator structure. These results demonstrate that the proposed system is promising for real-time monitoring and visualization of beta-emitting radionuclides in radioactive liquid waste and aquatic environments.

References
[1] Montaña, M., et al. "The presence of radionuclides in wastewater treatment plants in Spain and their effect on human health." Journal of cleaner production 60 (2013): 77-82.
[2] Yeung, K. H., H. Y. Mok, and H. K. Lam. "An on-line water contamination monitoring system." Nuclear Instruments and Methods in Physics Research Section A: Accelerators, Spectrometers, Detectors and Associated Equipment 353.1-3 (1994): 550-552.
[3] Choi, Woo Nyun, et al. "Continuous beta monitoring technology for uncontrolled radiological release in underwater using integrated beta and gamma detection system." Nuclear Engineering and Technology 57.3 (2025): 103248.
[4] [4] Tarancón, A., et al. "Development of an equipment for real-time continuous monitoring of alpha and beta radioactivity in river water." Applied Radiation and Isotopes 187 (2022): 110322.

NSS-01-311

Diagnosing Mechanisms for Charged Particle Attenuation Enhancement in Nanostructured Materials (#1508)

Niko P. Speck[1], Gabrielle J. Grey[2], Drew A. Vecchio[1], Kathleen A. Cotterill[1], Alan I. Taub[2], Mark Hammig[1]

[1] University of Michigan, Nuclear Engineering and Radiological Sciences Department, Ann Arbor, USA; [2] University of Michigan, Materials Science and Engineering Department, Ann Arbor, USA

The authors acknowledge the financial support of the University of Michigan College of Engineering and technical support from the Michigan Center for Materials Characterization and Michigan Medicine Microscopy Core. Thank you to Tao Ma for guidance on operating the TFS Spectra 300 TEM and Megan Bennett for support on ultramicrotome sample preparation.

Abstract

This paper presents a methodology for measuring the trajectories of high-energy electrons through materials utilizing a transmission electron microscope (TEM). This novel technique is implemented to diagnose and quantify the mechanism for enhanced radiation attenuation via nanostructures. Rather than an imaging technique, the TEM is applied to radiation shielding measurements as an adaptable electron source with functionality for various beam energies, amperage, alignments, and exposure times alongside an array of precise electron detectors. By utilizing energy filtering and direct electron detection capabilities, scattering profiles are measured with minimal background contributions. This TEM method is leveraged to describe particle transport in nanostructures. Palladium nanoparticles at various monodisperse sizes are synthesized via heat injection and deposited into an epoxy matrix. The palladium epoxy nanocomposites are sectioned with an ultramicrotome to thicknesses of 70 to 1000 nm containing nanoparticle sizes of 5 to 50 nm at 20% of the total weight fraction. Scattering profile measurements at various beam energies are conducted with a variety of sample thicknesses, nanoparticle sizes, and composite fractions. Scattering profile measurements also include bulk, homogeneous palladium samples in contrast to nanomaterials composed of identical atomic percentages. Simulation of the experimental scattering profiles demonstrate an understanding for the phenomena behind nanostructured attenuation enhancement, bolstering advanced nuclear technology via a foundational description for particle transport in nanostructures.

References

[1] S. A. Thibeault, J. H. Kang, G. Sauti, C. Park, C. C. Fay, and G. C. King, "Nanomaterials for radiation shielding," *MRS Bulletin*, vol. 40, no. 10, pp. 836--841, Oct. 2015, doi: 10.1557/mrs.2015.225.
[2] A. Rosh-Gorsky *et al.*, "3D Printing of Composite Radiation Shielding for Broad Spectrum Protection of Electronic Systems," *Advanced Materials*, vol. 36, no. 33, p. e2403822, 2024, doi: 10.1002/adma.202403822.
[3] M. Steffens *et al.*, "Characterization of Novel Lightweight Radiation Shielding Materials for Space Applications," *IEEE Transactions on Nuclear Science*, vol. 64, no. 8, pp. 2325--2332, Aug. 2017, doi: 10.1109/TNS.2017.2703312.
[4] A. Hamisu *et al.*, "The use of nanomaterial polymeric materials as ionizing radiation shields," *Radiation Physics and Chemistry*, vol. 216, p. 111448, Mar. 2024, doi: 10.1016/j.radphyschem.2023.111448.
[5] P. Hosemann, E. Stergar, A. T. Nelson *et al.*, "Nanostructured Engineering Alloys for Nuclear Application," *MRS Online Proceedings Library*, vol. 1298, pp. 217--226, 2011.
[6] V.-D. Le *et al.*, "X-ray and gamma-ray Sensing from Aqueous-Based Lead Sulfide Telluride Nanocomposites," *Small*, vol. 21, 2025.
[7] A. Curtis *et al.*, "Micro-scale fusion in dense relativistic nanowire array plasmas," *Nature Communications*, vol. 9, p. 1077, 2018, doi: 10.1038/s41467-018-03466-7.

NSS-01-313

Monolithic integration of cooling microchannels in all-silicon ladders for vertex detectors (#1940)

Javier Fernández-Tejero[1], André Dias[1], Marta Duch[1], Roser Mas[1], Carlos Orero[2], Marcel Vos[2], Miguel Ullán[1]

[1] Centro Nacional de Microelectrónica (IMB-CNM, CSIC), Cerdanyola del Vallés, Spain; [2] Instituto de Física Corpuscular (IFIC, CSIC), Paterna, Spain

This work has received funding from the postdoctoral fellowships programme Beatriu de Pinós (Marie Skłodowska-Curie grant No 801370), and Spanish R&D grant PID2024-156645NB-C22 funded by MICIU/AEI/ 10.13039/501100011033 and by ERDF/EU.

Abstract

New generation of vertex detectors must have excellent thermo-mechanical stability, and all-silicon ladders are considered as promising solutions for future detectors. However, power consumption asymmetries between the active area and periphery can induce large temperature gradients, and in some cases a combination of air and liquid cooling will be required to achieve homogeneous thermal profiles. Microchannel cooling offers a competitive alternative to traditional cooling systems. The short thermal path between the heat load and sink gives an increased thermal evacuation performance, combined with the reduced material needed for the integrated microchannels and the reduced Coefficient of Thermal Expansion mismatch between the cooling and sensor materials to obtain an optimized cooling for radiation detectors. The development of the technology needed for the integration of the sensor with the microchannels in a single piece is an ambitious challenge, as the conditions for the microchannel formation must be compatible with the sensor, requiring the optimization of the fabrication to ensure the compatibility with CMOS processes. As a demonstrator, all-silicon ladder prototypes with integrated cooling microchannels are presented. Power consumptions for the active area and periphery of the ladders are emulated using integrated aluminum heaters. The bulk in the active area is thinned from 600 to 50 microns, and the design of the microchannels cooling circuit, integrated in the periphery of the ladder, is optimized using finite-

element simulation packages. Variations of prototype ladders with different sizes, microchannel dimensions, and integrated using different wafer bonding techniques are fabricated and evaluated in detail in this work.

References
[1] de Aguiar Francisco OA, Buytaert J, Collins P, et al., 'Evaporative CO_2 microchannel cooling for the LHCb VELO pixel upgrade', *Journal of Instrumentation*, 10 (2015) C05014
[2] Andricek L, Boronat M, Fuster F, et al., 'Integrated cooling channels in position-sensitive silicon detectors', *Journal of Instrumentation*, 11 (2016) P06018
[3] Vos M, 'Micro-channel cooling in high energy physics', *Proceedings of science*, 287 (2016) 037
[4] Flaschel N, Ariza D, Díez S, et al., 'Thermal and hydrodynamic studies for micro-channel cooling for large area silicon sensors in high energy physics experiments', *Nuclear Instruments and Methods A*, 863 (2017) 26-34
[5] Ullán M, Correa J, Dauderys V, et al., 'Development of silicon interposers with embedded microchannels and metal re-distribution layer for the integration of hybrid detector systems', *Nuclear Instruments and Methods A*, 1065 (2024) 169490

NSS-01-315

A spin-selective detector for quantum sensing with neutrons (#1977)

Thomas Neulinger[1], Skyler Degenkolb[2], Roman Gernhäuser[3], Robert Georgii[1], Christoph Grüner[1], Harald Haese[4], Sebastian Kempf[5,6], Tim Sandmann[2], Josef Tremmel[2], Mathias Wegner[6,5]

[1] Technische Universität München, Forschungs-Neutronenquelle Heinz Maier-Leibnitz, Garching, Germany; [2] Universität Heidelberg, Physikalisches Institut, Heidelberg, Germany; [3] Technische Universität München, E12 Dense and Strange Hadronic Matter, Garching, Germany; [4] S-DH GmbH, Heidelberg, Germany; [5] Institute of Micro- and Nanoelectronics Systems, Karlsruhe Institute of Technology, Karlsruhe, Germany; [6] Institute for Data Processing and Electronics, Karlsruhe Institute of Technology, Karlsruhe, Germany

Abstract
We present performance calculations for a proof-of-concept, spin-selective neutron detector in which the magnetic field of a microfabricated planar superconducting coil controls the quantum mechanical absorption resonance in a multilayer structure. For first tests with cold neutrons, depolarization calculations favor a parallel over a meander geometry, the latter of which should nevertheless offer enhanced detector sensitivity in the ultracold neutron regime. Simulations predict that spin contrasts can be efficiently demonstrated using polarized cold neutron reflectometry at existing facilities.

References
[1] S. Degenkolb, P. Fierlinger, and O. Zimmer "Approaches to high-density storage experiments with *in-situ* production and detection of ultracold neutrons," *J. Neutron Res.*, vol. 24, pp. 123-143, Sep. 2022, 10.3233/JNR-220044.
[2] S. Kempf, A. Fleischmann, L. Gastaldo, and C. Enss, "Physics and Applications of Metallic Magnetic Calorimeters," *J. Low Temp. Phys.*, vol. 193, no. 3, pp. 365--379, Nov. 2018, 10.1007/s10909-018-1891-6.
[3] A. Vorobiev *et al.*, "Recent upgrade of the polarized neutron reflectometer Super ADAM," *Neutron News*, vol. 26, no. 3, pp. 25--26, Aug. 2015, 10.1080/10448632.2015.1057054
[4] J. F. Ziegler, M. D. Ziegler, and J. P. Biersack, "SRIM – The stopping and range of ions in matter (2010)," *Nucl. Instrum. Methods Phys. Res. B*, vol. 268, no. 11--12, pp. 1818--1823, 2010, 10.1016/j.nimb.2010.02.091.

NSS-01-317

Higher-Order Gain-Drift Correction in Magnetic Microcalorimeters for Decay Energy Spectrometry (#2186)

Ryan Wood[1,2], Igor Jovanovic[1], Geon-bo Kim[2]

[1] University of California, Berkeley, Nuclear Engineering, Berkeley, USA; [2] Lawrence Livermore National Laboratory, Livermore, USA

This work was performed under the auspices of the U.S. Department of Energy by Lawrence Livermore National Laboratory under Contract DE-AC52-07NA27344. This material is based upon work supported by the Consortium for Nuclear Forensics under Department of Energy, National Nuclear Security Administration award number DE-NA0004142. This work was supported by the Laboratory Directed Research and Development program of Lawrence Livermore National Laboratory under Project No. 23-LW-043.

Abstract

Metallic magnetic calorimeters can provide excellent energy resolution for decay-energy spectrometry of alpha- and beta-emitting radionuclides, but temperature-dependent gain drift can broaden peaks during long acquisitions. This work compares two post-acquisition correction models for data acquired with a gold-erbium paramagnetic sensor in the MAGNETO-v neutrino experiment. The pre-trigger baseline is used as an event-by-event proxy for detector temperature. The lower-order model includes linear baseline dependence, whereas the higher-order model adds baseline-energy cross terms and second-order baseline dependence to capture nonlinear drift. Model parameters are estimated with a likelihood-based fit to known plutonium and americium reference peaks, and each event is calibrated by solving the fitted response model for deposited energy. Performance is evaluated from isotope-resolved peak widths in the corrected alpha-decay region of the spectrum. Across the reference groups considered here, the higher-order model produces consistently narrower fitted peaks, with the clearest improvements in the higher-statistical-weight isotope groups. These results indicate that higher-order baseline terms can improve spectral resolution when baseline-correlated drift is present.

References

[1] S. Kempf, A. Fleischmann, L. Gastaldo, and C. Enss, “Physics and applications of metallic magnetic calorimeters,” J. Low Temp. Phys., vol. 193, pp. 365-379, 2018, doi: 10.1007/s10909-018-1891-6.

[2] R. Wood, G.-B. Kim, I. Jovanovic, C. Lee, N. Hines, and T. Parsons-Davis, “Radioisotope dating of nuclear materials using cryogenic decay energy spectrometry,” J. Radioanal. Nucl. Chem., vol. 335, pp. 2371-2379, 2026, doi: 10.1007/s10967-026-10742-1.

[3] J. W. Fowler et al., “The practice of pulse processing,” J. Low Temp. Phys., vol. 184, no. 1-2, pp. 374-381, 2016, doi: 10.1007/s10909-015-1380-0.

[4] M. O. Herdrich et al., “Application of a metallic-magnetic calorimeter for high-resolution x-ray spectroscopy of Fe at an EBIT,” J. Phys. B At. Mol. Opt. Phys., vol. 57, Art. no. 085001, 2024, doi: 10.1088/1361-6455/ad34a2.

[5] M. L. Zahir, M. Rodrigues, M. Loidl, and A. Kaur, “Energy non-linearity study of a high-resolution metallic magnetic calorimeter,” Radiat. Phys. Chem., vol. 220, Art. no. 111730, 2024, doi: 10.1016/j.radphyschem.2024.111730.

[6] C. Lee et al., “Search for a heavy neutral lepton with the MAGNETO-v experiment using 241Pu β− decays,” Phys. Rev. C, vol. 113, Art. no. 024620, 2026, doi: 10.1103/4xt7-mdyv.

NSS-01-319

Pixelated Array for Low-Energy Electron Beam Mapping (#2374)

Marcos Turqueti, Om Aggarwal

Lawrence Berkeley National Laboratory, Engineering Division, Berkeley, USA

Abstract

We present a low-energy electron beam position detector based on a segmented capacitive sensing architecture designed for precision monitoring of electron beams in the 500 eV to 2000 eV energy range. The detector employs a 3 mm × 3 mm capacitive sensor structure optimized for non-invasive beam position measurements with micrometer scale spatial resolution. Low-energy electron beams present unique diagnostic challenges due to their sensitivity to electromagnetic perturbations, beam spreading, and reduced signal levels. Conventional beam diagnostics often suffer from limited sensitivity or introduce disturbances that alter the beam trajectory.

The proposed detector addresses these limitations through a pixelated capacitive pickup array combined with low-noise front-end electronics and differential signal processing techniques. Variations in induced charge distribution along the sensing electrodes are used to reconstruct the transverse beam position with high precision while maintaining minimal interaction with the electron beam. The array enables accurate position tracking over extended beam paths and improves sensitivity to small beam displacements.

Analytical modeling and preliminary experimental characterization demonstrate that the sensor can resolve beam motion at the micrometer level across the targeted energy range. The detector response was evaluated as a function of beam energy, beam current, and electrode geometry, showing stable operation and high linearity under low-energy conditions. Noise mitigation strategies, including shielding and optimized capacitance matching, were implemented to preserve signal integrity and reduce environmental interference.

This detector architecture is well suited for applications requiring compact, high-resolution diagnostics of low-energy electron beams, including micro cathode ray magnetic probes, electron optics experiments, and vacuum electronic devices.

References

[1] Takahiro Nishi, Tamaki Watanabe, Taihei Adachi, Ryo Koyama, Naruhiko Sakamoto, Kazunari Yamada, and Osamu Kamigaito," Nondestructive beam envelope measurements using beam position monitors for low-beta heavy ion beams in a superconducting linear accelerator",Phys. Rev. Accel. Beams **28**, 092803 – **2025**,DOI: https://doi.org/10.1103/8ct7-x1xf

[2] Jun He, Yanfeng Sui, Yong Li, Huizhou Ma, Yaoyao Du, Ying Zhao, Wan Zhang, Shujun Wei, Taoguang Xu, Junhui Yue,"Beam position monitor design for the High Energy Photon Source ",Measurement Science and Technology, Volume 33, Number 11,2022,**DOI** 10.1088/1361-6501/ac8277

[3] Yong Zhang (张雍), Jun-Xia Wu (武军霞), Guang-Yu Zhu (朱光宇), Huan Jia (贾欢), Zong-Heng Xue (薛纵横), Hai Zheng (郑海), Hong-Ming Xie (谢宏明), Xin-Cai Kang (康新才), Yuan He (何源), Lin Li (李林), " Chinese Physics C Paper Capacitive beam position monitors for the low-β beam of the Chinese ADS proton linac*",Chinese Physics C, Volume 40, Number 2,2016, **DOI** 10.1088/1674-1137/40/2/027003

[4] S. Bheesette and M. Turqueti, "Simulation Studies For The Electron Gun Based Magnetic Probe," *2021 IEEE Nuclear Science Symposium and Medical Imaging Conference (NSS/MIC)*, Piscataway, NJ, USA, 2021, pp. 1-2, doi: 10.1109/NSS/MIC44867.2021.9875587.

[5] P. Li, B. G. Sun, Q. Luo, X. H. Wang, H. L. Xu and P. Lu, "New methods of measuring emittance using beam position monitors," *2007 IEEE Nuclear Science Symposium Conference Record*, Honolulu, HI, USA, 2007, pp. 1675-1678, doi: 10.1109/NSSMIC.2007.4437322.

NSS-01-321

Self-Powered Wireless Communication via Ambient Gamma-Ray Harvesting at Fukushima Daiichi (#2629)

Takeshi Fujiwara[1], Yasushi Shoji[1], Hiromi Kimura[1], Shunichiro Mae[2], Hiroshi Yoshimochi[2], Kohei Kawasaki[2], Hiroshi Kawamura[2], Katsuki Miyako[2]

[1] National Institute of Advanced Industrial Science and Technology (AIST), Tskuba, Japan; [2] Chiyoda Technol Corporation, Tokyo, Japan

Abstract

Reliable long-term monitoring in nuclear decommissioning facilities is hampered by the absence of permanent power infrastructure and by the radiation fields that degrade conventional electronics. We present a scintillator-photovoltaic converter that captures ambient gamma radiation and transforms it into electrical energy sufficient for periodic wireless data transmission. The converter pairs a 750 cm³ CsI(Tl) crystal with a compact GaInP photovoltaic array mounted on a single end face, following a "large absorber, minimal semiconductor" strategy.) On-site evaluation inside a contaminated-material storage building at the Fukushima Daiichi Nuclear Power Plant (~35 mSv/h) produced 273 nW per module. Two parallel modules, combined with ultra-low-power energy management and a sub-GHz radio, achieved seven autonomous transmission bursts totaling 32 packets over a 30 m link during a three-hour observation window—without any external power supply or dedicated radioactive source.

References

[1] IAEA, *Monitoring and Surveillance of Radioactive Waste Disposal Facilities*, Safety Reports Series No. 84, 2014.

[2] Fujiwara, Takeshi, et al. "Demonstration of self-powered wireless transmission using a gamma-ray battery in a nuclear decommissioning environment." *Available at SSRN 6191942*.

NSS-01-323

Optimizing Tritium Uptake and Detection Sensitivity in a Metal-Hydride Gas Detector (#2734)

Praneeth Kandlakunta, Lei R. Cao, Tzu-Hsiang Lin, Rhys Young, Ashton Hoffman

The Ohio State University, Department of Mechanical and Aerospace Engineering, Columbus, USA

This research is supported by the U. S. Department of Energy / National Nuclear Security Administration under Award Number DE-NA0004196.

Abstract

The Metal-Hydride and Gas (MEGA) detector is a recently proposed approach for high-selectivity tritium (T_2) monitoring that combines hydrogen (H_2) storage metals with gas proportional counting. Previous work demonstrated the feasibility of T_2 absorption in palladium (Pd), formation of metal-tritide, and subsequent T_2 release into a proportional counter for measurement. In this work, we investigate pathways toward improving the overall detection efficiency of the MEGA detector through optimization of T_2 absorption, retention, desorption, and counting characteristics. A simplified efficiency framework is introduced to identify the dominant efficiency-limiting processes. The pressure–composition behavior of the Pd–H system is examined to evaluate approaches for enhancing isotope uptake at low T_2 partial pressures through reduced operating temperature and increased local pressure. Preliminary Monte Carlo simulations of tritium β-particle transport in Pd indicate strong self-absorption effects, with the simulated maximum penetration depth of 18.6-keV β-particles in Pd limited to a few hundred nanometers. These results support the need for optimized Pd geometry and efficient thermal desorption approaches to maximize gas-phase T_2 release and proportional counting efficiency. The present work establishes a quantitative framework for future optimization of MEGA detector sensitivity for environmental and nuclear safeguards applications.

NSS-01-325

Basic Development of a Wide-Field EUV Polarimeter for High-Energy Transient Sources (#3164)

Soken Kuwabara[1], Shuichi Gunji[2], Komei Chiba[1], Akira Takahashi[1], Mamoru Kitaura[2], Eiken Nakamura[3]

[1] Yamagata University, Graduate School of Science and Engineering, Yamagata, Japan; [2] Yamagata University, Faculty of Science, Yamagata, Japan; [3] Institute for Molecular Science, UVSOR Synchrotron Facility / Beamline Technical Staff, Aichi, Japan

The authors would like to thank the UVSOR staff for their technical support during the synchrotron radiation experiments. Portions of the manuscript preparation were assisted by a cloud-based AI language model.

Abstract

Polarization observations in extreme ultraviolet (EUV) band have not yet been achieved because it remains technically difficult to develop wide-field EUV detectors with sufficient sensitivity. However, EUV polarization measurements are expected to provide important insights into the emission mechanisms of gamma-ray bursts (GRBs) and ultraviolet flashes associated with supernova explosions. In this study, we propose a novel EUV polarimeter based on Lobster-Eye Optics (LEO), which combines a wide field of view with polarization sensitivity. Optical simulations show that EUV reflectivity on metal surfaces strongly depends on polarization. For example, at 40 eV and an incident angle of 75° on a gold-coated mirror, the reflectivity is about 40% for p-polarization and 60% for s-polarization, respectively. This difference produces an asymmetric cross-shaped image on the focal plane detector depending on the polarization direction. To verify this principle, we developed a test chamber and conducted a synchrotron radiation experiment using a gold-coated mirror and a microchannel plate (MCP) detector. By rotating the mirror around the beam axis, we measured the modulation of the MCP count rate and evaluated the detector modulation factor. The experimental results are presented and discussed in this paper.

References
[1] Fan, YZ & Wei, DM 2004, 'UV/optical emission accompanying gamma-ray bursts', Monthly Notices of the Royal Astronomical Society, vol. 351, no. 1, pp. 292–296.
[2] Di Marco, A., Fabiani, S., La Monaca, F., Muleri, F., Rankin, J., Soffitta, P., Xie, F., *et al.* 2022, 'Calibration of the IXPE focal plane X-ray polarimeters to polarized radiation', *Astronomical Journal*, 164(3), 103, Bristol: IOP Publishing.

NSS-01-327

Cryogenic and Underground Performance of the Diffuse BGO Scintillator Array in the KAPAE Phase II Detector (#3216)

Dongwoo Jeong[1], Hong Joo Kim[2,1], Jaeyoung Cho[1], HyeoungWoo Park[3]

[1] Kyungpook National University, Center for High Energy Physics, Daegu, South Korea; [2] Kyungpook National University, Department of Physics, Daegu, South Korea; [3] 2Central Research Institute, Korea Hydro & Nuclear Power Co., Ltd., DaeJeon, South Korea

These investigations were supported by the National Research Foundation of Korea (NRF), funded by the Ministry of Science and Technology, Korea (MEST) (RS-2024-00348317).

Abstract

The KNU Advanced Positronium Annihilation Experiment (KAPAE) Phase II searches for invisible positronium decays using a compact 4π BGO scintillation calorimeter. Stable operation, efficient photon collection, and low-background performance are essential for this rare-event measurement. We report the cryogenic and underground performance of a chemically diffused BGO scintillator array developed for KAPAE Phase II.

The BGO crystal surfaces were chemically diffused to enhance photon collection and coupled to SiPM-based readout for low-temperature operation. At approximately −37 °C, reduced SiPM thermal noise and improved light collection yielded an energy resolution of 9% at 662 keV. The scintillation decay time was approximately 960 ns. This performance improves upon earlier BGO-based positronium calorimeters, including the ETH Zurich experiment, which reported an energy resolution of approximately 15% [1].

The detector was installed and operated at Yemilab underground. A continuous 120-day run demonstrated stable detector response, trigger operation, and long-term data-taking capability under cryogenic conditions. Calibration data were used to tune and validate a Geant4 detector simulation, which was applied to evaluate energy containment, gamma-ray leakage, and the expected sensitivity for invisible para-positronium decay searches. Based on measured performance and validated simulations, KAPAE Phase II achieves the expected sensitivity of 10−8 for invisible para-positronium branching-ratio measurements.

This study demonstrates that chemically diffused BGO scintillator arrays can provide stable, high-resolution calorimetric performance under cryogenic underground conditions.

References
[1] A. Badertscher et al., "Improved limit on invisible decays of positronium," Phys. Rev. D 75, 032004 (2007).

NSS-13-329

Organic Scintillator Light Yield Models for Sub-MeV Neutrons in EJ301D and d-stilbene (#1369)

Christian A. Irvine[1,2], Tyler C. Borgwardt[1], Robert A. Weldon Jr.[1], John Mattingly[2]

[1] Los Alamos National Laboratory, NEN-2, Los Alamos, USA; [2] North Carolina State University, Nuclear Engineering, Raleigh, USA

This work was supported by the US Department of Energy through the Los Alamos National Laboratory. Los Alamos National Laboratory is operated by Triad National Security, LLC, for the National Nuclear Security Administration of U.S. Department of Energy (Contract No. 89233218CNA000001).

Abstract

Six commonly used models for neutron induced light yield in organic scintillators were fit and analyzed using measurements of a 2.54 cm diameter by 2.54 cm long right circular cylinder of EJ301D and a (5.08 cm)3 custom made cube of deuterated trans-stilbene-d12 (d-stilbene). Measured neutron energies spanned 300 keV to 2200 keV for the EJ301D scintillator and 200 keV to 2500 keV in d-stilbene. The model fits and experimental analysis methods were verified by examining the agreement between the predicted light output spectrum and the measured light output spectrum for several simulated quasi-monoenergetic neutron sources. Birks model inaccurately predicted highly quenched light yield for sub-MeV neutrons in both scintillators. The addition of a second order quenching term to the Birks model by Chou significantly improved the models accuracy, however its behavior is non-physical if extrapolated beyond the measured neutron energies. The model derived by Voltz accurately fit the measurement of both scintillators for all measured neutron energies. Further investigation into the ability to extrapolate based on these semi-empiric models would be valuable given the non-physical behavior of well-fitting models.

References

[1] Thibault A Laplace et al. “Modeling ionization quenching in organic scintillators”. In: Materials Advances 3.14 (2022), pp. 5871–5881

[2] Mark A. Norsworthy et al. “Evaluation of neutron light output response functions in EJ-309 organic scintillators”. In: Nuclear Instruments and Methods in Physics Research Section A: Accelerators, Spectrometers, Detectors and Associated Equipment 842 (2017), pp. 20–27. ISSN: 0168-9002. DOI: https://doi.org/10.1016/j.nima.2016.10.035.

[3] John Betteley Birks. The theory and practice of scintillation counting: International series of monographs in electronics and instrumentation. Vol. 27. Elsevier, 2013.

[4] CN Chou. “The nature of the saturation effect of fluorescent scintillators”. In: Physical Review 87.5 (1952), p. 904.

[5] J Hong et al. “The scintillation efficiency of carbon and hydrogen recoils in an organic liquid scintillator for dark matter searches”. In: Astroparticle Physics 16.3 (2002), pp. 333–338. ISSN: 0927-6505. DOI: https://doi.org/10.1016/S09276505(01)00114-1

[6] S Yoshida et al. “Light output response of KamLAND liquid scintillator for protons and 12C nuclei”. In: Nuclear Instruments and Methods in Physics Research Section A: Accelerators, Spectrometers, Detectors and Associated Equipment 622.3 (2010), pp. 574–582.

[7] R. Voltz et al. “Influence of the Nature of Ionizing Particles on the Specific Luminescence of Organic Scintillators”. In: The Journal of Chemical Physics 45.9 (Nov. 1966), pp. 3306–3311. ISSN: 0021-9606. DOI: 10.1063/1.1728106. eprint: https://pubs.aip.org/aip/jcp/article-pdf/45/9/3306/18846420/3306 1 online.pd

[9] G. Dietze and H. Klein. “Gamma-calibration of NE213 scintillation counters”. In: Nucl. Instr. and Meth. 193.3 (1982), pp. 549–556. ISSN: 0167-5087. DOI: 10.1016/0029-554X(82)90249-X.

[11] C. A. Irvine et al. “Low energy neutron light output characterization of EJ301D and deuterated stilbene with a comparison of light output characterization methods”. In: Submitted for review (2026).

Time:
9 November, 2026
17:30 – 19:00

Room:
FEDERICO GARCÍA LORCA

NSS-02 | Neutron and gamma-ray detectors and applications, including security, dosimetry and other related applications

Chairs:
Abdallah LYOUSSI (Saint Paul-lez-Durance)
Malcolm J. Joyce (Lancaster)

NSS-02-01

Dead time and self-absorption corrections at high uranium grade for total count rate gamma probes (#1014)

Bertrand Pérot[1], Thomas Marchais[1], Abdelwahab Miloudi[2], Hervé Toubon[2], Trevor Allen[4], Romain Mieszkalski[2], Youcef Bensedik[2], Sébastien Hocquet[2], Adrien Gruel[1], Clément Besnard-Vauterin[3]

[1] CEA, DES, IRESNE, Nuclear Measurement Laboratory, Saint-Paul-lez-Durance, France; [2] Orano Mining, Châtillon, France; [3] Orano Mining, CIME, Bessines-sur-Gartempe, France; [4] Orano Canada Inc., Saskatoon, Canada

Abstract

In high-grade uranium mines such as the Orano Canada Inc. (OCI) operated McClean Lake Mine, gamma logging probes deal with a non-linear behavior due to both gamma self-absorption in uranium and electronics dead-time, which may lead to a significant underestimation of the resources. Up to now, quantitative uranium grade measurements were conducted through coring and subsequent laboratory analysis. However, the SABRE mining method involves larger diameter drilling, making systematic coring impractical due to the additional costs. Therefore, Orano Mining and CEA have developed and qualified a combined correction for electronics dead-time and gamma self- absorption. These phenomena are significant above a uranium grade of about 1% w/w U, leading to huge resource underestimations at high grade, for instance nearly a factor 3 at 50% w/w U, just for self-absorption. In this work, we detail the tests conducted at Orano La Hague irradiator to estimate the dead-time of different NaI(Tl) and Geiger Muller probes, the MCNP Monte Carlo calculations to assess uranium self- absorption on a large uranium grade range, a new method developed to jointly correct for these two phenomena, and its experimental qualification through the comparison of gamma logging with core sample analyses from high-grade boreholes.

References

[1] T. Marchais et al., “Characterization of Uranium Ore Samples by HPGe Gamma-Ray Spectroscopy,” IEEE Trans. Nucl. Sci., vol. 67, no. 4, pp. 654–661, Apr. 2020, doi: 10.1109/TNS.2020.2966824

[2] T. Marchais, B. Pérot, C. Carasco, P-G. Allinei, H. Toubon, R. Goupillou, Y. Bensedik, “Low-resolution gamma spectroscopy of uranium ores to determine U concentration and U/Rn imbalance,” in IEEE Trans. on Nucl. Sci., DOI 10.1109/TNS.2021.3129343

[3] B. Pérot, T. Marchais, P-G. Allinei, H. Toubon, Y. Bensedik, R. Goupillou, A. Berland, Development of Gamma Spectroscopic Tools for Uranium Ore Samples and Borehole Exploration, 2022 IEEE Nuclear Science Symposium, 5 – 12 November 2022, Milano, Italy, DOI: 10.1109/NSS/MIC44845.2022.10398898

[4] T Marchais, B. Pérot, Hervé Toubon, Youcef Bensedik, Romain Mieszkalski, Sebastien Hocquet, Dragomir Savov, Matthew Schubert, Bruno Legros, Patrick Van Eyll, Michaël Pernette, CeBr3 gamma-ray logging probe qualification for uranium mining applications, ANIMMA 2025 international conference, Valencia, 9-13 June 2025, EPJ Web Conf., 338 (2025) 05002, https://doi.org/10.1051/epjconf/202533805002

[5] C. Carasco, B. Pérot, J.L. Ma, H. Toubon, L. Pauthier, A. Dubille-Auchère, Improving gross count gamma-ray logging in uranium mining with the NGRS probe, IEEE Transactions on Nuclear Science, Vol. 65, No. 3, March 2018

NSS-02-02

Identification and Reconstruction of Pair-Production Events in an Electron-Tracking Compton Camera via 3D Track Analysis (#1466)

Taiyo Sato[1], **Taiyo Sato**[1], Atsushi Takada[1], Atsushi Takada[1], Hiroki Yoneda[1], Hiroki Yoneda[1], Soma Deguchi[1], Soma Deguchi[1], Sana Okumura[1], Sana Okumura[1], Mitsuru Abe[1], Mitsuru Abe[1], Kai Matsunaga[1], Kai Matsunaga[1], Takeshi Nakamori[2], Takeshi Nakamori[2], Haruki Iiyama[2], Haruki Iiyama[2], Shun Suzuki[2], Shun Suzuki[2], Tatsuya Sawano[3], Tatsuya Sawano[3], Yusuke Munakata[3], Yusuke Munakata[3], Kanaho Okamoto[3], Kanaho Okamoto[3], Masaki Mori[4], Masaki Mori[4], Tomohiko Oka[5], Tomohiko Oka[5], Yoshitaka Mizumura[6], Yoshitaka Mizumura[6], Kenji Hamaguchi[7], Kenji Hamaguchi[7], Junko Kushida[8], Junko Kushida[8], Shunsuke Kurosawa[9], Shunsuke Kurosawa[9], Kentaro Miuchi[10], Kentaro Miuchi[10], Toru Tanimori[11], Toru Tanimori[11]

[1] Kyoto University, Department of Physics II, Graduate School of Science, Kyoto, Japan; [2] Yamagata University, Department of Science, Faculty of Science, Yamagata, Japan; [3] Kanazawa University, Division of Mathematical and Physical Sciences, Graduate School of Natural Science and Technology, Kanazawa, Japan; [4] Osaka Metropolitan University, Graduate School of Science, Osaka, Japan; [5] Julius-Maximilians-Universität Würzburg, Astronomy / AG Siegert, Würzburg, Germany; [6] ISAS/JAXA, Institute of Space and Astronautical Science, Department of Interdisciplinary Space Science, Sagamihara, Japan; [7] UMBC, Center for Space Sciences and Technology, Catonsville, USA; [8] Tokai University, Department of Physics, School of Science, Hiratsuka, Japan; [9] Nagoya University, Department of Energy Engineering and Science, Graduate School of Engineering, Nagoya, Japan; [10] Kobe University, Graduate School of Science, Kobe, Japan; [11] Kitasato University, School of Frontier Engineering, Sagamihara, Japan

Abstract

The 1–30 MeV gamma ray observation holds key astrophysical signatures—nucleosynthesis, cosmic-ray interactions, and possible dark-matter signatures—yet remains the least explored window in high-energy astronomy. The electron-tracking Compton camera (ETCC) tracks the recoil electron to constrain the photon direction to a single point on the sky, enabling bijective imaging. We are developing the ETCC for SMILE-3, planned for 2028, extending the observation band to 5 MeV via a double-hit analysis. Beyond this, reconstructing pair-production events inside the time projection chamber (TPC) offers a further extension above ∼ 10 MeV and enables cross-calibration between Compton and pair-production channels in the same detector—an important advantage for MeV observations, where background control is critical. Additionally, identifying pair events removes a source of misreconstruction in the double-hit analysis, where atmospheric gamma rays above 10 MeV undergoing pair production are misidentified as Compton events and leak through the zenith-angle cut. We developed a geometry-based algorithm to identify pair-production events from the 3D point-cloud of TPC tracks. Voxelization and DBSCAN separate track clusters from noise; local PCA estimates direction vectors, and intersecting pairs define vertex candidates evaluated by a log-likelihood ratio (LLR) test. Accepted events are reconstructed from the vector sum of the two track directions. We validated the algorithm using inverse-Compton-scattered gamma rays at 3.3, 4.8, and 6.6 MeV from the UVSOR BL1U beamline. At 6.6 MeV, the 68% containment angle was 16.2◦ for beam-synchronous events and 12.0◦ for asynchronous events, consistent with the nuclear-recoil kinematic limit. Monte Carlo simulations with the SMILE-3 geometry are underway to quantify identification efficiency and leakage improvement.

References
[1] Tsuji, N., et al. 2023, 'MeV Gamma-Ray source contribution to the inner galactic diffuse emission', ApJ, 943(1), 48.
[2] Boddy, K. K., et al. 2015, 'Indirect detection of dark matter using MeV-range gamma-ray telescopes', Phys. Rev. D, 92(2), 023533.
[3] Carr, B. J., et al. 2010, 'New cosmological constraints on primordial black holes', Phys. Rev. D, 81(10), 104019.
[4] Tanimori, T., et al. 2015, 'An electron-tracking Compton telescope for a survey of the deep universe by MeV Gamma-Rays', ApJ, 810(1), 28.
[5] Oka, T., et al. 2024, 'High-energy extension of the gamma-ray band observable with an electron-tracking Compton camera', Nucl. Instrum. Methods Phys. Res. A, 1063, 169242.
[6] Takada, A., et al. 2022, 'First Observation of the MeV Gamma-Ray Universe with Bijective Imaging Spectroscopy Using the Electron-tracking Compton Telescope on Board SMILE-2+', ApJ, 930, 6.
[7] Gros, P., et al. 2018, 'Performance measurement of HARPO: A time projection chamber as a gamma-ray telescope and polarimeter', Astropart. Phys., 97, 10–18.

NSS-02-03

Design of a 2D neutron and gamma imager based on CPRE64 (#1589)

Chaoyang Zhao[1], Jifeng Han[1], Jing Ren[2], Ke Wang[3]

[1] Sichuan University, Institute of Nuclear Science and Technology, Chengdu, China; [2] Harbin Engineering University, College of Physics and Optoelectronic Engineering, Harbin, China; [3] Chinese Academy of Sciences, Institute of High Energy Physics, Beijing, China

This work is supported by the National Key R&D program of China (2023YFF0721700).

Abstract

Dual gamma and neutron imaging is promising owing to their complementary characteristics, and has been widely applied in nuclear material monitoring, defect analysis of aerospace materials, and cultural heritage authentication. A gamma and neutron imager with an active area of about 20 cm × 20 cm is currently under development. The imager employs a home-developed Ce^{3+}-doped lithium glass scintillator coupled to 4096 silicon photomultipliers (SiPMs), each with a size of 3 mm × 3 mm. To achieve optimal imaging performance, each SiPM is individually read out using a newly custom-designed 64-channel application-specific integrated circuit (ASIC), designated CPRE64. A total of 64 CPRE64 chips are integrated into the system to read out the 4096 SiPM channels. This paper introduces the overall design of the two-dimensional (2D) neutron and gamma imager. A 2D neutron and gamma imager prototype, using a 25 mm × 25 mm × 5 mm scintillator coupled to an 8 × 8 SiPM array (3 mm × 3 mm pixel size), has been fabricated and characterized. The scintillator exhibits a light yield of approximately 4700 photon/MeV and an energy resolution of 14.5% for 662 keV gamma rays. Meanwhile, it provides a high light yield of roughly 7058 photon/neutron, which is approximately 1.18 times that of the reference GS20 glass. The baseline variation across CPRE64 channels was measured to be ± 10%, spanning from 1.3V to 1.7V, whereas the channel uniformity of the CPRE64 channels exceeded 90%. The prototype has been successfully used for gamma and neutron imaging, achieving an experimental neutron spatial resolution better than 1mm.

References
[1] R. Song, et al., "A high light-yield neutron scintillator based on Ce^{3+}-doped lithium glass," Chin. Phys. B, vol. 34, Feb. 2025, Art. no. 050703.

[2] C. Yi, et al., "Development of SiPM batch aging and performance measurement system," Nucl. Tech., vol. 48, Apr. 2025, Art. no. 030402.
[3] H. Liao, et al., "CPRE64: a low-noise 64-channel front-end readout ASIC for 3-D position-sensitive CdZnTe detectors," in Proc. IEEE Nucl. Sci. Symp. Med. Imaging Conf. Room Temp. Semicond. Detector Conf. (NSS/MIC/RTSD), Dec. 2025.
[4] Y. Long, et al., "The calibration and performance of a 2D planar neutron and gamma imaging detector," Nucl. Instrum. Methods Phys. Res. A, vol. 1082, Feb. 2026, Art. no. 171068.

NSS-02-04

Evaluation of a High-Efficiency Portable Compton-Imaging System for Radioactive Waste Characterization and Nuclear Decommissioning

(#1393)

Victor Babiano-Suárez[1], Javier Balibrea-Correa[1], Jorge Lerendegui-Marco[1], Ion Ladarescu[1], Pablo Torres-Sánchez[1], Ariel Tarifeño-Saldivia[1], Guillem Cortés[2], José Luis Leganés-Nieto[3], César Domingo-Pardo[1]

[1] Instituto de Física Corpuscular (CSIC - Universitat de Valencia), Experimental Nuclear Physics, Valencia, Spain; [2] Universitat Politècnica de Catalunya, Escola Tècnica Superior d'Enginyeria Industrial de Barcelona (ETSEIB), Barcelona, Spain; [3] ENRESA, Empresa Nacional de Residuos radiactivos, Madrid, Spain

Authors acknowledge funding from the Margarita Salas grant (European Union, NextGenerationUE), and from Convenio CSIC-ENRESA (2014-2018). This work was also supported by the Spanish Ministerio de Ciencia e Innovaci\'on (PID2022-138297NB-C21, PID2019-104714GB-C21, FPA2017-83946-C2-1-P), CSIC (PIE-201750I26), and HYMNS ERC-CoG Grant (Agreement Nr.681740).

Abstract

Nuclear energy remains a pivotal low-carbon alternative for mitigating climate change, yet the management of radioactive waste presents significant technical and economic challenges. Optimizing waste characterization is essential to minimize disposal volumes and ensure safe decommissioning. This work evaluates a high-efficiency, portable Compton camera designed for the visualization and quantification of low- and intermediate-level waste (LILW).

The system was validated through three extensive field campaigns at the El Cabril disposal facility and the Santa María de Garoña nuclear power plant in Spain. These evaluations encompassed diverse waste containers and isotopic inventories to assess characterization performance in real industrial environments. Our findings demonstrate the robustness of Compton imaging, particularly regarding detection efficiency and reduced acquisition times. The system's performance was enhanced by integrating computer-vision techniques with GPU-accelerated Maximum-Likelihood Expectation Maximization (MLEM) algorithms, enabling real-time radiological-visual fusion.

Furthermore, we demonstrate the feasibility of 3D tomographic reconstructions derived from multi-pose measurements. A significant highlight is the first field deployment of GNVision, a novel dual-particle imager for simultaneous neutron and gamma-ray mapping, aimed at identifying actinide-bearing residues. These results

underscore the potential of advanced imaging to streamline waste classification and enhance safety in decommissioning workflows.

References
[1] World Nuclear Association, ``World Nuclear Performance Report 2022'', England (2025).
[2] V. Babiano-Suárez et al., "A computer-vision aided Compton-imaging system for radioactive waste characterization and decommissioning of nuclear power plants", NIM A, 1076 (2025).
[3] J. Lerendegui-Marco et al., "Simultaneous Gamma-Neutron Vision device: a portable and versatile tool for nuclear inspections", EPJ Techn Instrum 11, 2 (2024).
[4] C. Domingo-Pardo, "i-TED: A novel concept for high-sensitivity (n,γ) cross-section measurements, Nucl. Instrum. Methods Phys. Res. A 825 (2016).
[5] C. Domingo-Pardo, "High-sensitivitY Measurements of key stellar Nucleo-Synthesis reactions (HYMNS)", ERC-consolidator grant agreement no. 681740.
[6] V. Babiano et al., "γ-Ray position reconstruction in large monolithic LaCl3(Ce) crystals with SiPM readout", Nucl. Instrum. Methods Phys. Res. A 931 (2019).
[7] V. Babiano et al., "First i-TED demonstrator: A Compton imager with Dynamic Electronic Collimation", Nucl. Instrum. Methods Phys. Res. A 953 (2020).
[8] J. Balibrea-Correa et al., "Machine learning aided 3D-position reconstruction in large LaCl3 crystals, Nucl. Instrum. Methods Phys. Res. Sect. A 1001 (2021).
[9] J. Lerendegui-Marco et al., "Device for the simultaneous Detection, Identification, Quantification and/or location of gamma radiation and neutron sources" International Patent WO2021229132A1 (2021).

NSS-02-05

Development of a high-sensitivity portable gamma-ray imaging system for identifying radioactive material carriers (#1453)

Goeun Lee, Junyoung Lee, Taehyeon Eom, Jaeho Cho, Sehyun Jang, Chan Hyeong Kim

Hanyang University, Nuclear engineering, Seoul, South Korea

Abstract

Gamma-ray imaging is an emerging technology to identify individuals smuggling radioactive materials at international points of entry. However, imaging moving subjects requires high efficiency due to the limited data acquisition time as sources pass the imaging system. We developed a high-sensitivity gamma camera named the portable fast gamma imager (pFGI). The pFGI integrates an imaging module, an RGB-D camera, and other components into an enclosure. The imaging module combines Compton and coded aperture modalities using two position-sensitive detectors and a MURA coded aperture mask. Each detector comprises a monolithic NaI(Tl) scintillator (14.6×14.6×2.5 cm^3) coupled to a 3×3 square-type photomultiplier tube array. The detectors are placed 16 cm apart, with the mask 6 cm in front of the front detector. To achieve superior imaging performance across a broad energy range, a hybrid imaging method was employed, which acquires coded aperture and Compton images, respectively, and then fuses them via pixel-wisemultiplication. Furthermore, an AI-based motion-compensated method was used to integrate data along the moving subject's trajectory. The YOLOv11 and BoT-SORT algorithms were applied to the RGB images acquired from the RGB-D camera to extract displacement vectors for each subject; then, the radiation image for each subject was translated and fused according to the trajectories. The pFGI achieved a 7° angular resolution and high sensitivity, imaging the location of a 137Cs source, producing an incremental dose rate of 0.1 μSv/h within 1 s. Additionally, in a dynamic multi-person scenario, the imager successfully and continuously imaged the moving source and identified the source carrier among multiple people. These results highlight the pFGI as a robust solution for national security.

NSS-02-06

Development of a new gamma-ray spectrometer for measurements inside reservoirs (#1461)

Yuki Morishita[1], **Yuki Morishita**[1], Tsutomu Yamada[2], Tsutomu Yamada[2], Kengo Kajiyama[3], Kengo Kajiyama[3]

[1] Japan Atomic Energy Agency, Collaborative Laboratories for Advanced Decommissioning Science (CLADS), Futaba County, Japan; [2] Japan Radiation Engineering Co. Ltd, Hitachi, Japan; [3] NUCLEAR ENGINEERING Co.,Ltd., Tokai-mura, Japan

Abstract

Radioactive materials released during the accident at the Fukushima Daiichi Nuclear Power Station were deposited not only on land surfaces but also in aquatic environments such as irrigation ponds. Monitoring radiation levels in these environments is important for environmental assessment and decontamination activities. In this study, a waterproof gamma-ray spectrometer based on a Ce-doped $Gd_2Si_2O_7$ (Ce:GPS) scintillator coupled with a photomultiplier tube was developed for underwater radiation measurements. The detector employed a 10 mm × 10 mm Ce:GPS scintillator and an FPGA-based data acquisition system for event-by-event signal processing and energy spectrum acquisition. To enable pond-bottom measurements, the detector was integrated into a pipe structure approximately 4 m in length. Field measurements were conducted in an irrigation pond in Fukushima Prefecture, where the detector was submerged and placed on the pond bottom. A clear 662 keV photopeak originating from cesium-137 was observed, and the measured energy resolution was 9.8% FWHM. Energy spectra were also measured at different heights above the pond bottom. The cesium-137 photopeak was clearly detected at the bottom and at 50 cm above the bottom, whereas scattered gamma-ray components became dominant at greater heights because of attenuation and scattering in water. The results demonstrate that the developed waterproof Ce:GPS spectrometer is effective for in-situ underwater gamma-ray measurements and radionuclide identification in aquatic environments contaminated by radioactive cesium.

References

[1] Poltabtim, Worawat, et al. "Estimation of ambient dose equivalent rate distribution map using walking survey technique in Hirosaki City, Aomori, Japan." International Journal of Environmental Research and Public Health 20.3 (2023): 2657.

[2] Vlachos, D. S., and C. Tsabaris. "Response function calculation of an underwater gamma ray NaI (Tl) spectrometer." Nuclear Instruments and Methods in Physics Research Section A: Accelerators, Spectrometers, Detectors and Associated Equipment 539.1-2 (2005): 414-420.

[3] Kim, Chanho, et al. "Radiation resistance and temperature dependence of Ce: GPS scintillation crystal." Radiation Physics and Chemistry 183 (2021): 109396.

Time:
9 November, 2026
17:30 – 19:00

Room:
ALBÉNIZ & MACHUCA

NSS-03 | NSS DAQ, front-end and electronics

Chairs:
Eric J. Mannel (Upton)

NSS-03-01

Dual Time-Over-Threshold Energy and PSD Readout of SiPMs Using FPGA-Based TDCs (#1724)

Aaron Nowack[1], John Leland[2,1], Erik Brubaker[1], John Steele[1], Melinda Sweany[1]

[1] Sandia National Laboratories, Dept 08647 - Radiation and Nuclear Detection Systems, Livermore, USA; [2] University of Illinois, Urbana-Champaign, Department of Nuclear, Plasma, and Radiological Engineering, Urbana, USA

Abstract

Independent readout of highly pixelated organic scintillator detectors is needed for next-generation associated particle imaging, neutron radiography, and single-volume scatter cameras. Field-programmable gate arrays (FPGAs) are an attractive solution as they have hundreds to thousands of IO pins and can be programmed for a variety of applications while minimizing cost as compared to ASICs. We detail a dual time-over-threshold (ToT) method for measuring the deposited energy and pulse width of gamma and neutron interactions in scintillator using a Time-to-Digital Converter (TDC) realized with an FPGA and minimal external components. We compare a simple DC threshold and an active feedback rising edge signal for PSD and energy estimation. Simulated ToT results using digitized data are presented, with hardware details for an upcoming data campaign. For each circuit, the performance of energy resolution and PSD capability is weighed against the complexity and power requirements of the external analog components. In this work we present each of these approaches for SiPM readout, detail current progress, and experimental results.

NSS-03-02

Development of Readout Electronics for a SiPM-Based Compton Camera (#2016)

Alessio Brunamonti[1,2], Beatrice Morellato[1], Filippo Ghisio[1,2], Giacomo Borghi[1,2], Marco Carminati[1,2], Gabriela Llosá[3], Alain Iltis[4], Carlo E. Fiorini[1,2]

[1] Politecnico di Milano, Dipartimento di Elettronica, Informazione and Bioingegneria, Milano, Italy; [2] Istituto Nazionale di Fisica Nucleare, Sezione di Milano, Milano, Italy; [3] Instituto de Fisica Corpuscolar (IFIC, CSIC-UV), Paterma, Spain; [4] Damavan Imaging, Troyes, France

Abstract

This work, conducted within the framework of the AIDER project, presents the design and preliminary characterization of an electronics readout architecture for SiPM-based Compton cameras (CCs) in nuclear applications. The system includes two front-end units, serving the absorber and the scatterer layers. Each module integrates four GAMMA ASICs to interface with up to 64 SiPMs per layer, performing individual charge integration

while providing an aggregated sum-current output. To mitigate amplitude-walk effects over the broad energy spectra typical of Compton imaging, time stamps are extracted by a custom designed Constant Fraction Discriminator (CFD) circuit. A central FPGA with embedded Time-to-Digital Converters (TDCs) synchronizes energy and timing data across both layers. A pre-trained Artificial Neural Network (ANN) is embedded directly into the FPGA logic to provide real-time estimation of the interaction position, reducing data throughput. SiPM are biased by a custom module that dynamically compensates for temperature fluctuations. The electronics, coupled with a 25 mm x 25 mm x 5 mm LaBr3 scintillator and a 16 SiPMs tile, yielded an energy resolution of 3.6% FWHM at 662 keV. Preliminary characterization of the CFD circuit with current pulses injected into the ASICs yielded a 140 ps resolution at 511 keV maintaining a sub nanosecond resolution down to 45 keV. The amplitude walk on such dynamic range was limited to 2.15 ns.

References
[1] Llosá, G, 2019 'SiPM-based Compton cameras', *Nuclear Instruments and Methods in Physics Research Section A: Accelerators, Spectrometers, Detectors and Associated Equipment*, 924, 148-152, https://doi.org/10.1016/j.nima.2018.09.053.
[2] Flux, GD 2017, 'Imaging and dosimetry for radium-223: the potential for personalized treatment', *Br J Radiol.*, 90, 20160748, doi: 10.1259/bjr.20160748.
[3] Buonanno, L, Di Vita, D, Carminati, M, Fiorini, C 2021, 'GAMMA: A 16-Channel Spectroscopic ASIC for SiPMs Readout With 84-dB Dynamic Range', *IEEE Transactions on Nuclear Science*, 68, 2559-2572, doi: 10.1109/TNS.2021.3107333
[4] Caracciolo, A, Buonanno, L, Di Vita, D, D'Adda, I, Chacon, A, Kielly, M, Carminati, M, Safavi-Naeini, M, Fiorini, C 2022, 'BeNEdiCTE (Boron Neutron Capture): A Versatile Gamma-Ray Detection Module for Boron Neutron Capture Therapy', *IEEE Transactions on Radiation and Plasma Medical Sciences*, 6, 886-892, doi: 10.1109/TRPMS.2022.3154232

NSS-03-03

High Count-Rate Modular Readout System for SiPM-Based Gamma-Ray Detectors (#2622)

Andrea Forgione[1,2], Martina Piroddi[1,2], Christian Riboldi[1,2], Enrico Ronconi[1], Korbinian Urban[1,2], Fabio Garzetti[1], Giacomo Borghi[1,2], Marco Carminati[1,2], Angelo Geraci[1], Carlo E. Fiorini[1,2]

[1] Politecnico di Milano, DEIB, Milano, Italy; [2] National Institute for Nuclear Physics (INFN), Milan Section, Milano, Italy

This work was supported by the REALPATH project (Italian MUR), grant n. FISA-2022-00779

Abstract
In this work, we present a scalable high-performance readout system for LYSO-coupled SiPMs. The project aims to enable real-time beam range monitoring in proton therapy through Prompt Gamma Imaging (PGI), detecting prompt gamma rays emitted during proton–tissue interactions [1]. This application requires operation over a wide energy range, from 3 MeV to 10 MeV, together with high count-rate capability up to 1 Mcps/channel.
The resulting platform is suitable for a broad range of gamma-ray detection applications. A compact DAQ board has been developed integrating all the electronics required for gamma event acquisition, processing, and data transmission without the need for external units [2]. The system is able to detect gamma rays with energies above 10 MeV using 12-bit energy digitization and 300 ps (FWHM) timing resolution.

The module is connected to LYSO-coupled SiPMs (Hamamatsu S14160-6015PS) featuring a 6 × 6 mm² photosensitive area and 15 µm pixel pitch. Tests with calibration sources show a 10.2% FWHM resolution at 511 keV and 6.2% at 1275 keV.
A custom ASIC specifically developed for high-energy gamma-ray detection is used for the readout of SiPM currents. With a minimum integration and readout time of 350 ns, the ASIC supports output count rates above 1 Mcps/channel.
While each module supports 32 SiPM channels, multiple identical modules can be connected in a daisy-chain configuration to support larger detector arrays. The PCB mechanical design allows multiple boards to be stacked without inactive regions between modules, with the only limitation being the available 10 Gbps transmission bandwidth.

References
[1] G. Pausch et al., 2020, Nuclear Instruments and Methods in Physics Research Section A: Accelerators, Spectrometers, Detectors and Associated Equipment.
[2] C. Riboldi et al, 2025, Journal of Instrumentation.
[3] I. D'Adda et al., 2024, IEEE Transactions on Nuclear Science
[4] N. Lusardi et al, 2021 IEEE Nuclear Science Symposium and Medical Imaging Conference (NSS/MIC)

NSS-03-04

High-Rate FPGA-Based Fully Digital SiPM Readout for Photon-Number-Resolving Measurements in Quantum Optics and Quantum Communications (#2050)

Stefano Carsi[1,2], Andrea Abba[1], Alessia Allevi[2], Alex Pozzoli[2], Marco Lamperti[2]

[1] Nuclear Instruments SRL, Lambrugo, Italy; [2] Università degli Studi dell'Insubria, Dipartimento di Scienza e Alta Tecnologia, Como, Italy

Abstract
Photon-number-resolving (PNR) detection based on Silicon Photomultipliers (SiPMs) is emerging as a promising approach for high-rate quantum optics and quantum communication experiments, particularly for the possible implementation of hybrid schemes. We present a fully digital SiPM readout platform combining a 14-bit, 1 GS/s waveform digitizer with a real-time FPGA-based signal-processing chain optimized for fast charge extraction and photon-number reconstruction. The system is implemented on an open-FPGA architecture programmable through the Sci-Compiler framework, enabling custom firmware development without dedicated HDL design.
The firmware performs real-time baseline restoration, digital pole-zero compensation, synchronous triggering, and charge integration entirely inside the FPGA pipeline at full sampling rate. The system supports synchronous operation with externally or internally triggered laser sources and enables deterministic acquisition windows with nanosecond-scale integration gates.
Different Hamamatsu SiPM models were characterized using coherent and twin-beam optical states to evaluate the impact of detector gain, pixel pitch, pile-up, and photon detection efficiency on photon-number reconstruction. Measurements demonstrate reliable operation from mean photon numbers well below 1 up to more than 50

detected photons per pulse at repetition rates up to 1 MHz, with operation extendable toward 10–20 MHz depending on the analog front-end configuration. The digital processing chain significantly improves peak separation, dynamic range, and noise performance compared with conventional boxcar-based acquisition systems. The presented architecture demonstrates how modern FPGA-based real-time digital processing can transform SiPM detectors into scalable, high-speed PNR systems suitable for next-generation quantum optics instrumentation and quantum communication protocols.

NSS-03-05

Towards Multi-channel Direct Positron Emission Imaging using Cherenkov-Radiator-Integrated MCP-PMTs, FastIC+, and Time-to-Digital Converters in FPGA. (#2177)

Julien Rossignol[1], Ryosuke Ota[1,2], José María Fernández-Tenllado[3], Joan Mauricio[5], Jerome A. Alozy[4], Sergio Gomez[5], Rafael Ballabriga[4], David Gascón[3], Sun Il Kwon[1]

[1] University of California, Davis, Biomedical engineering, Davis, USA; [2] Hamamatsu Photonics K.K., Central Research Laboratory, Hamamatsu, Japan; [3] University of Barcelona, ICCUB, Barcelona, Spain; [4] CERN, Meyrin, Switzerland; [5] Universitat Politècnica de Catalunya, Barcelona, Spain

This work was supported by the National Institutes of Health under grant R01 EB033536.

Abstract

Direct positron emission imaging (dPEI) enables imaging of positron-emitting radionuclide distributions without tomographic reconstruction by directly localizing annihilation events using ultrafast time-of-flight measurements. This modality was first demonstrated experimentally in 2021 using two Cherenkov-radiator-integrated microchannel plate photomultiplier tubes (CR-IMPs) read out by an oscilloscope. However, to scale to a larger number of channels for clinical applications, the oscilloscope must be replaced with an embedded front-end and digitizer. In this study, a dPEI acquisition chain for multi-channel readout was designed using two CR-IMPs, a FastIC+ front-end, and a tapped delay line time-to-digital converter implemented inside an UltraScale+ FPGA. A single-shot RMS precision of 4.0 ps was achieved by the front-end and the TDC when measuring pulses from a function generator. This timing precision is sufficient to digitize CR-IMP signals while preserving the timing performance required to approach the best coincidence timing resolution (CTR) currently measured using an oscilloscope. After evaluating the combined FastIC+ and TDC system, a complete readout chain from two CR-IMPs through the FastIC+ to the TDC was successfully configured, and coincidence events from a Na-22 source were successfully acquired during preliminary operation. We are currently optimizing the front-end parameters to achieve the best CTR between the two CR-IMPs. This study highlights the capability of the FastIC+ to read out CR-IMP signals and the ability of the combined FastIC+ and FPGA-based TDC system to digitize events with sufficient precision for dPEI.

References
[1] S. I. Kwon et al., Ultrafast Timing Enables Reconstruction-free Positron Emission Imaging. Nat. Photon. 15, 914–918 (2021).
[2] R. Ota et al., High-performance 4×4-channel microchannel plate photomultiplier tubes with bismuth germanate window faceplate. Submitted to IEEE NSS MIC RTSD 2026

[3] D. Mazzanti et al., Below 100 ps CTR using FastIC+, an ASIC Including On-chip Digitization for ToF-PET and Beyond. IEEE Trans. Radiat. Plasma Med. Sci., 2026
[4] J. Rossignol et al., Simulating and Optimizing Tapped Delay Lines for Time-to-Digital Converters in FPGA using a Precision Model Based on Circuit Characteristics. SSRN, Oct. 2025
[5] R. Ota et al., Coincidence time resolution of 30 ps FWHM using a pair of Cherenkov-radiator-integrated MCP-PMTs. Phys. Med. & Biol. 64, (2019)

NSS-03-06

TEMPOROC3 : A 64-channel SiPM read-out chip for time-of-flight measurement on monolithic crystal (#3068)

Salleh Ahmad, Jean-Baptiste Cizel, Cyrille Derrien, Julien Fleury, Amar Haddar, Maxime Morenas, Florent Perrez, **Vsevolod Yeroshenko**

Weeroc, Villebon-sur-Yvette, France

Abstract

TEMPOROC3 is a 64-channel mixed-signal SiPM read-out application-specific integrated circuit (ASIC) designed in TSMC130 technology. The ASIC aims at measuring the energy with a 10-bit analogue-to-digital converter (ADC), time-of-arrival (TOA) and time-over-threshold (TOT) with a 40-ps bin time-to-digital converter (TDC). The analogue front-end offers a dynamic range up to 500 pC. The dual discriminator allows for measuring either two TOA at different threshold levels or the time between a rising and falling edge, giving a TOT. The dual-gain charge measurement integrates the input signal over a tuneable range from 20 to 300 ns. The 64 channels are divided into 4 clusters, each outputting data at 320 Mbps. The clusters can be synchronised to stream all channel data whenever a channel from the matrix has triggered. The number of triggered channels (per cluster) required to launch the data serialisation is programmable, as well as the window duration for accepting new triggers. At 450 kEvents/s per cluster (with 1 TDC + 1 ADC per channel), the power consumption is about 8 mW per channel. The trigger scheme for the monolithic matrix readout was successfully validated by acquiring a gamma spectrum of an ^{11}Na source with a large LYSO(Ce) crystal coupled to a 61-channel SiPM. Event filtering using a charge discriminator was validated, allowing for data rate reduction in the ASIC. Temporal characteristics were evaluated using external trigger, charge injection, laser pulses with SiPM, and coincident gamma from an ^{11}Na source. Measurements in coincidence between 2 channels from 2 ASICs have shown TDC coincidence time resolution (CTR) as low as 60 ps FWHM. Coincident annihilation gamma measurement using LYSO(Ce) crystals with SiPM demonstrated spatial sensitivity to the source displacement, providing CTR as low as 139 ps FWHM. TEMPOROC3 has been shown to be a versatile read-out ASIC with numerous configuration parameters that can be applied in ToF-PET, Compton cameras, LIDAR.

References
[1] RETIMAGER : www.retimager.eu
[2] Iltis, A., Snoussi, H., De Magalhaes, L. Rodrigues, et al. Temporal imaging CeBr3 Compton camera: A new concept for nuclear decommissioning and nuclear waste management. In : EPJ Web of Conferences. EDP Sciences, 2018. p. 06003.
[3] W. Zhang et al., "A Low-Power Time-to-Digital Converter for the CMS Endcap Timing Layer (ETL) Upgrade," in IEEE Transactions on Nuclear Science, vol. 68, no. 8, pp. 1984-1992, Aug. 2021, doi: 10.1109/TNS.2021.3085564

Time:
9 November, 2026
17:30 – 19:00

Room:
PICASSO

NSS-04 | Semiconductor detectors

Chairs:
Chiara Guazzoni (Milano)
Davide Mezza (Villigen)

Radiation measurement, spectroscopy, neutron monitoring, electron imaging, microdosimetry, medical physics, and detector system performance.

NSS-04-01

Very-High-Energy Electron FLASH Radiotherapy at the PEER Beamline - Dosimetry and Biological Benchmarking (#2494)

James Cayley[1], Dean Cutajar[1], Elette Engels[2,1], Chelsey Skee[1], Anatoly Rosenfeld[1], Yaw-Ren E. Tan[3], Michael Lerch[1]

[1] University of Wollongong, Centre for Medical Radiation Physics, Wollongong, Australia; [2] Peter MacCallum Cancer Centre and University of Melbourne Sir Peter MacCallum Department of Oncology, Melbourne, Australia; [3] ANSTO, Australian Synchrotron, Melbourne, Australia

Abstract

Very-high-energy electrons delivered at ultra-high dose rates, are being investigated for their promise within radiotherapy to treat deep-seated tumours. VHEE FLASH radiotherapy research requires two major components; a real-time dosimeter that remains linear at the required dose-per-pulse, and an accelerator that is stable, biologically benchmarked, and suitable for in vivo studies. Investigations have been conducted at the Pulsed Energetic Electrons for Research (PEER) beamline of the ANSTO Australian Synchrotron to realise this reality. Utilising a 100 MeV electron linac, PEER provides irradiation fields comprised of 100 ps bunches with a 2 ns spacing, forming bunchtrains with average and instantaneous dose-rates as high as 10^8 Gy/s and 10^9 Gy/s, respectively. The MOSkin detector was tested for linearity with a dose-per-pulse as high as 23 Gy within 200 ns. During this work, EBT-XD radiochromic film was employed as a reference dosimeter, however, a dose-rate dependence of the film was discovered. This was confirmed with another experiment which allowed calculation of a correction factor, enabling use of the film as an independent measurement of dose. Three cell lines (A549, T98G, and MDCK) were irradiated utilising real-time dosimetry, and mouse cadavers were irradiated to assess the feasibility of small animal experiments. These results support PEER as being suitable for future in vivo VHEE FLASH research.

References

[1] J. Cayley et al., “Establishing linearity of the MOSkin detector for ultra-high dose-per-pulse, very-high-energy electron radiotherapy using dose- rate-corrected EBT-XD film,” Appl. Sci., vol. 15, no. 14, Art. no. 8101, Jul. 2025, doi: 10.3390/app15148101.

[2] J. Cayley et al., “PEERing into the future: benchmarking the ANSTO Australian Synchrotron’s very-high-energy electron linac for ultra-high dose-rate, in vivo FLASH radiotherapy research,” Cancers, vol. 18, no. 4, Art. no. 640, Feb. 2026, doi: 10.3390/cancers18040640.

NSS-04-02

New approach in 2D microdosimetry using Alpide pixelated detector

(#3171)

Linh Tran[1], Qiuyu Lu[1], James Vohradsky[1], Alexander Schilling[2], Vladimir Panin[1], Marco Petasecca[1], Michael Lerch[1], Susanna Guatelli[1], Odd Harald Oddland[4], Matthias Richter[3], Dieter Röhrich[3], Anatoly Rosenfeld[1], Dean Cutajar[1]

[1] University of Wollongong, Centre for Medical Radiation Physics, Wollongong, Australia; [2] Tech Univ Kaiserslautern, Chair Sci Comp, Kaiserslautern, Germany; [3] University of Bergen, Bergen, Norway; [4] Haukeland Hospital, Dept Oncol & Med Phys, Bergen, Norway

This work was supported by the NHMRC Development grant GNT2039887 from the National Health and Medical Research Council, Australia and Career Development Fellowship 2021/CDF1112 from the Cancer Institute of NSW

Abstract

This work investigates the feasibility of using the ALPIDE pixelated detector for two-dimensional microdosimetry applications in proton therapy. The detector offers several advantages for microdosimetry, including low noise, fast readout capability, flexible spatial sampling, and very high spatial resolution. Detailed Geant4 simulations were developed to model an experimental setup using an 80 MeV proton beam passing through different aluminium thicknesses. A strong agreement was observed between the responses of the ALPIDE detector and the SOI microdosimeter, demonstrating the capability of ALPIDE to accurately characterise LET distributions in proton radiation fields. In addition, the proposed calibration approach showed that the cluster size measured by the ALPIDE detector can be reliably converted to LET in silicon. Thanks to its pixelated architecture, arbitrary groups of pixels can be selected and analysed, enabling high-resolution two-dimensional LET mapping of complex radiation fields. These results demonstrate the strong potential of the ALPIDE detector as a versatile and cost-effective tool for advanced microdosimetry and proton beam LET_d characterisation.

References

[1] Lühr, Cläre von Neubeck, Jörg Pawelke, Annekatrin Seidlitz, Claudia Peitzsch, Søren M Bentzen, Thomas Bortfeld, Jürgen Debus, Eric Deutsch, Johannes A Langendijk, Jay S Loeffler, Radhe Mohan, Michael Scholz, Brita S Sørensen, Damien C Weber, Michael Baumann, Mechthild Krause (2018), "Radiobiology of Proton Therapy": Results of an international expert workshop", Radiother Oncol. 128(1):56-67.

[2] Linh T. Tran, Lachlan Chartier, David Bolst, Alex Pogossov, Susanna Guatelli, Dale A. Prokopovich, Marco Petasecca, Michael L. F. Lerch, Mark I. Reinhard, Benjamin Clasie, Nicolas Depauw, Hanne Kooy, Jay Flanz, Aimee McNamara, Harald Paganetti, Chris Beltran, Keith Furutani, Vladimir L. Perevertaylo, Michael Jackson and Anatoly B. Rosenfeld (2017), "Characterization of proton pencil beam scanning and passive beam using a high spatial resolution solid-state microdosimeter", Med. Phys. 44 (11): 6085-6095.

[3] ald Paganetti (2014), "Relative biological effectiveness (RBE) values for proton beam therapy. Variations as a function of biological endpoint, dose, and linear energy transfer", Phys Med Biol. 59(22): 419-72.

[4] VA Pan, LT Tran, T Madden, B Clasie, H Kooy, AB Rosenfeld, N Depauw (2024) "LETd Optimization Verification With an SOI Microdosimeter", Int J Radiation Oncol. Biol. Phys., 119(3):946-956, 2024

[5] Gianluca Aglieri Rinella, "The ALPIDE pixel sensor chip for the upgrade of the ALICE Inner Tracking System", Nuclear Instruments and Methods in Physics Research Section A: Accelerators, Spectrometers, Detectors and Associated Equipment, Volume 845, 2017, Pages 583-587,

[6] S. Senyukov, J. Baudot, A. Besson, G. Claus, L. Cousin, A. Dorokhov, W. Dulinski, M. Goffe, C. Hu-Guo, M. Winter, "Charged particle detection performances of CMOS pixel sensors produced in a process with a high resistivity epitaxial layer", Nucl. Instrum. Methods Phys. Res. Sect. A: Accel. Spectromet. Detect. Assoc. Equip.730(2013)115–118, proceedings of the 9th International Conference on Radiation Effects on Semiconductor Materials Detectors and Devices, October 9-122012, Dipartimento di Fisica e Astronomia, Firenze, http://dx.doi.org/10.1016/j.nima.2013.03.017.

[7] ALICE Collaboration, Journal of Physics G 41 (2014) 087002.

NSS-04-03

AlphaBeast : A CMOS-based detector for real-time neutron production monitoring (#1169)

Lucia Victoria Garcia Garcia[1], Nicolas Arbor[1], Djokhar Betelgueriev[1], Stéphane Higueret[1], The-Duc Le[1], Jean-Michel Horodynski[2]

[1] Université de Strasbourg, CNRS, IPHC UMR 7178, Strasbourg, France; [2] Ingénierie Radioprotection Sûreté Démantèlement (iRSD) - CNRS, Paris, France

Abstract

Neutrons produced around particle accelerators are a major concern for radiation protection in research, medical, and industrial facilities due to their contribution to occupational exposure, patient dose, and material activation. Accurate characterisation of neutron fields is therefore essential, but conventional techniques such as activation foils, Bonner sphere systems, and solid-state nuclear track detectors are limited by their lack of real-time capability. In this work, we present the AlphaBeast, a CMOS-based detector designed for real-time monitoring of thermal and fast neutrons. This sensor has been designed as an electronic alternative to solid-state track detectors, using polyethene and 10B converters for fast and thermal neutron detection with on-chip discrimination thresholds. The system was calibrated using the irradiation facilities available at the Institut Pluridisciplinaire Hubert Curien in Strasbourg, France. A GATE/Geant4 Monte Carlo model was developed to simulate the detector response and optimise its performance. The AlphaBeast sensor was then tested in various mixed radiation fields, including radiotherapy rooms and accelerator casemates. Experimental results show good agreement with simulations and demonstrate its potential for real-time neutron monitoring in particle accelerator facilities.

References

[1] N. Arbor, S. Higueret, and D. Husson, “Micro-scale characterization of a CMOS-based neutron detector for in-phantom measurements in radiation therapy,” Nuclear Instruments and Methods in Physics Research Section A: Accelerators, Spectrometers, Detectors and Associated Equipment, vol. 888, pp. 103–109, Apr. 2018. [Online]. Available: https://linkinghub.elsevier.com/retrieve/pii/S0168900218300755

[2] N. Arbor, S. Higueret, H. Elazhar, R. Combe, P. Meyer, N. Dehaynin, F. Taupin, and D. Husson, “Real-time detection of fast and thermal neutrons in radiotherapy with CMOS sensors,” Physics in Medicine and Biology, vol. 62, no. 5, pp. 1920–1934, Mar. 2017. [Online]. Available: https://iopscience.iop.org/article/10.1088/1361-6560/aa5bc9

NSS-04-04

Comparative Performance Evaluation of pnCCD Sensor Variants with 36 µm Pixel Size (#2493)

Šejla Hadžić, **Šejla Hadžić**, Johannes Treis, Johannes Treis, Alexander Bähr, Alexander Bähr, Rainer H. Richter, Rainer H. Richter, Jelena Ninković, Jelena Ninković, Florian Schopper, Florian Schopper, Mikhail Polovykh, Mikhail Polovykh, Martin Hensel, Martin Hensel, Christian Koffmane, Christian Koffmane, Chanyoung So, Chanyoung So, Basanth Kondasani, Basanth Kondasani, Hua Ye, Hua Ye, Danilo Mießner, Danilo Mießner, Irina Riazanova, Irina Riazanova

Semiconductor Laboratory of the Max Planck Society, Garching, Germany

Abstract

Fully depleted silicon pnCCD sensors are used for X-ray spectroscopy in applications ranging from X-ray astronomy to synchrotron radiation sources and free-electron lasers, due to their outstanding capabilities, such as high energy resolution, low electronic noise and excellent quantum efficiency. At HLL, a new series of pnCCD sensors with a 36 µm pixel size has been fabricated to investigate the performance of small-pixel pnCCD devices. Applications requiring high spatial resolution can benefit from smaller pixel sizes, utilizing position reconstruction based on charge sharing. This contribution focuses on the systematic comparison of different designs within this pnCCD production run. The investigated sensors include devices based on our standard JFET amplifier, as well as variants with modified readout anodes, different options for the biasing of the MOS structures between the p-registers, and an option for a sensor design with self-aligned channel guide implants. Since the devices share the same basic geometry and sensor thickness, their comparison allows design-dependent effects on the detector performance to be directly assessed, while also exploring possible simplifications of the fabrication process and the overall detector system. For this purpose, the sensor variants are tested under comparable operating conditions using a newly developed experimental setup at HLL. The sensors are read out in a column-parallel architecture using the VERITAS 2.1 ASIC. Their spectral performance is evaluated in terms of noise behavior, gain uniformity, charge transfer inefficiency, and energy resolution. The observed performance differences between the variants will be discussed as a basis for identifying optimization paths for future pnCCD sensor designs.

NSS-04-05

fine-pitch HPGe strip detectors for high-rate gamma-ray spectroscopy and imaging (#3145)

Joanna M. Szornel[1]

[1] Lawrence Berkeley National Laboratory, Nuclear Science Division, Berkeley, USA; [2] Lawrence Berkeley National Laboratory, Nuclear Science Division, Berkeley, USA; [3] Lawrence Berkeley National Laboratory, Berkeley, USA; [4] Lawrence Berkeley National Laboratory, Berkeley, USA

This work was supported by the Laboratory Directed Research and Development (LDRD) program of Lawrence Berkeley National Laboratory under Contract No. DE-AC02-05CH11231 with the U.S. Department of Energy.

Abstract

A prototype high-purity germanium (HPGe) double-sided strip detector has been developed to maintain high energy resolution and high throughput at count rates relevant to MHz-rate gamma-ray spectroscopy and imaging. Conventional HPGe detectors provide excellent energy resolution but suffer from throughput loss and resolution degradation at elevated count rates, limiting their use in applications such as beam diagnostics, nuclear decommissioning, medical imaging, and prompt spectroscopy of superheavy elements.

This work presents the design, fabrication, and characterization of fine-pitch HPGe double-sided strip detectors developed for high-rate spectroscopy and imaging. A 0.5 mm strip pitch detector geometry was selected using analytical calculations and numerical simulations of efficiency, charge collection, throughput, timing, energy resolution, and position resolution. This prototype demonstrated an energy resolution of 1.8 keV FWHM at 662 keV under low-rate conditions, consistent with predicted performance, and has now undergone additional characterization at higher rates. Extensive characterization has also been performed on 1.16 mm-pitch HPGe strip detectors, providing a broader experimental basis for evaluating fabrication yield, leakage current, strip-to-strip uniformity, charge sharing, charge loss, and spectroscopic performance.

Results from both the 1.16 mm-pitch and 0.5 mm-pitch detectors will be presented. Energy resolution and throughput are evaluated as functions of shaping time, strip geometry, and incident count rate. These results demonstrate progress toward fine-pitch HPGe detector systems capable of high-resolution spectroscopy, three-dimensional position sensitivity, and sustained performance in high-rate environments.

NSS-04-06

Repairing Proton Radiation Damage on n-type, Cross-Strip Germanium Detectors (#1121)

Sophia E. Haight[1], Jarred Roberts[1], Steven E. Boggs[1], Sean N. Pike[1], Julian Gerber[1], Emily Broadbent[1], John Tomsick[2], Joanna Szornel[4], Albert Shih[3], Aravind Valluvan[1], Andreas Zoglauer[2]

[1] University of California San Diego, Department of Astronomy and Astrophysics, La Jolla, USA; [2] University of California Berkeley, Space Sciences Laboratory, Berkeley, USA; [3] NASA, Goddard Space Flight Center, Greenbelt, USA; [4] Lawrence Berkeley National Laboratory, Berkeley, USA

This work was supported by the NASA Astrophysics Research and Analysis (APRA) program, grant 80NSSC22K1881. The Compton Spectrometer and Imager is a NASA Explorer project led by the University of California, Berkeley with funding from NASA, United States under contract 80GSFC21C0059.

Abstract

We performed a high-energy proton irradiation on a cross-strip germanium detector with the goals of measuring the subsequent loss to detector spectral resolution and characterizing the effectiveness of high-temperature annealing in repairing radiation damage. This work aims to address the expected radiation damage to the Compton Spectrometer and Imager (COSI) during two-year primary mission in low-Earth orbit and evaluate methods for maintenance of spectral resolution. COSI's cross-strip germanium detectors are susceptible to damage induced by the space radiation environment. Negatively charged dislocations induced by high-energy protons trap charge carriers as they drift in the applied bias voltage. The result is a degraded hole-collection signal characterized by widened spectral lines and loss to detector spectral resolution. We irradiated a non-flight detector with a fluence of $1.1 \cdot 10^7$ p^+/cm^2 — COSI's expected exposure over prime mission (95% confidence level). After irradiation, we executed a series of high-temperature anneals aimed at physically repairing the damaged germanium. We track spectral resolution by measuring the full width half maximum (FWHM) of the 662 keV spectral line emitted by the isotope Cesium-137. We repaired widened FWHMs through high-temperature annealing to within 12% of its preradiation value, repairing to 2.97 keV compared to the original 2.67 keV. We track spectral resolution across annealing processes and characterize a timescale for repair. We find the anneal time needed to repair damage from COSI's primary mission within 1% of the spectral broadening from residual damage. We project the repair time required at 90°C to be 54 +/- 10 hours.

References

[1] J. Tomsick, S. Boggs, A. Zoglauer, D. Hartmann, M. Ajello, E. Burns, *et al.*, The Compton Spectrometer and Imager, Proc. ICRC2023, vol. 444, 2023, p. 745.

[2] L. S. Darken, R. C. Trammell, T. W. Raudorf, R. H. Pehl, and J. H. Elliott, "Mechanism for fast neutron damage of Ge(HP) detectors," NuclearInstruments and Methods, vol. 171, no. 1, pp. 49–59, 1980.

[3] J. Beechert, H. Lazar, S. E. Boggs, T. J. Brandt, Y.-C. Chang, C.-Y. Chu, H. Gulick, C. Kierans, A. Lowell, N. Pellegrini, J. M. Roberts, T. Siegert, C. Sleator, J. A. Tomsick, and A. Zoglauer, "Calibrations of the Compton Spectrometer and Imager," Nuclear Instruments and Methods in Physics Research A, vol. 1031, p. 166510, May 2022.

[4] S. E. Haight, S. E. Boggs, G. Brewster, S. N. Pike, J. M. Roberts, A. Y.Shih, J. M. Szornel, J. A. Tomsick, A. B. Valluvan, and A. Zoglauer, "Proton radiation damage and annealing of COSI p-type cross-strip hpge detectors," Nuclear Instruments and Methods in Physics Research Section A: Accelerators, Spectrometers, Detectors and Associated Equipment, vol.1077, p. 170538, 2025.

[5] J. Ripa, G. Dilillo, R. Campana, and G. Galgoczi, "A comparison of trapped particle models in low earth orbit," in Space Telescopes and Instrumentation 2020: Ultraviolet to Gamma Ray, Eds. SPIE, Dec. 2020.

[6] M. Koenen, J. Bruckner, M. Korfer, I. Taylor, and H. Wankel, "Radiation damage in large-volume n- and p-type high-purity germanium detectors irradiated by 1.5 GeV protons," in Proceedings of 1994 IEEE Nuclear Science Symposium - NSS'94 vol. 1, 1994, pp. 201–205 vol.1.

10 November, 2026

Time:
10 November, 2026
9:00 – 11:00

Room:
FEDERICO GARCÍA LORCA

NSS-05 | Neutron and gamma-ray detectors and applications, including security, dosimetry and other related applications

Chairs:
Anne-Sophie Lalleman (GIF SUR YVETTE)
Malcolm J. Joyce (Lancaster)

NSS-05-01

Time-of-Flight Neutron Imaging With a Segmented Organic Imager Cell

(#2120)

William Heriot[1], David Breitenmoser[1], Peter Marleu[2], Keith Vaigneur[3], Shaun D. Clarke[1], Sara A. Pozzi[1],
This work was supported in part by the Consortium for Monitoring, Technology, and Verification under Department of Energy National Nuclear Security Administration, award number DE-NA0003920.

[1] University of Michigan, Nuclear Engineering and Radiological Sciences, Ann Arbor, USA; [2] Sandia National Laboratories, Livermore, USA; [3] Oakridge National Laboratories, Oakridge, USA

The authors would like to acknowledge Keith Vaigneur and Paul Hausladen at Oakridge National Laboratory for supplying our team with our detector volume and Erik Brubaker at Sandia National Laboratories for their input throughout the design process. This work was funded in-part by the Consortium for Monitoring, Technology, and Verification under Department of Energy National Nuclear Security Administration, United States of America award number DE-NA0003920. Sandia National Laboratories is a multimission laboratory managed and operated by National Technology & Engineering Solutions of Sandia, LLC, a wholly owned subsidiary of Honeywell International Inc., for the U.S. Department of Energy's National Nuclear Security Administration under contract DE-NA0003525. SAND2026- 20469A

Abstract

Neutron imaging arrays are critical tools in nuclear non-proliferation, with applications in neutron source localization in wide-area source searches and cargo inspections. However, they commonly have large form factors due to needing large data acquisition systems, complicating deployment. A solution with simplified data acquisition is needed to make portable and field-deployable neutron imaging arrays. Organic scintillator-based neutron imaging arrays typically require pulse shape discrimination (PSD) to differentiate between neutron and gamma-ray events. This method requires full waveform data acquisition, which results in a high data throughput, and utilizes expensive analog-to-digital converters. In order to alleviate the need for full waveform acquisition, this work seeks to develop a system that instead leverages time-of-flight particle discrimination. To discriminate neutrons from gamma events using time-of-flight particle discrimination, a Segmented Organic Neutron Imager Cell, SONIC, has been constructed of 64 5x0.6x0.6 cm3 bars of EJ200. 14 of the 16 tested bars show typical pulse-integral spectra for Cs-137. This work details the introductory characterization of this imager array and evaluates its validity for future work in achieving a field-deployable, handheld neutron scatter imager.

NSS-05-02

Development of an omnidirectional neutron imager with fractal geometry (#1531)

Nishiki Matsubayashi[1], Tatsuo Torii[2], Miyuki Sasaki[3], Shunsuke Kurosawa[4]

[1] Tokyo University of Agriculture and Technology, Tokyo, Japan; [2] Fukushima University, Fukushima, Japan; [3] Japan Atomic Energy Agency, Minamisoma, Japan; [4] Nagoya University, Nagoya, Japan

In making the detector, we got help from N. Miyazaki and Y. Furuta at Clear Pulse Co., Ltd., and T. Sugita at SSL Inc. for response analysis. In addition, this research was conducted using funds from the JAEA/CLADS project (problem-solving program for decommissioning research, FY2024).

Abstract

In areas where radiation sources are diffused three-dimensionally, it is important to develop a compact imaging sensor that can detect radiation distributions in the 4π direction. A radiation imager that detects the distribution of radiation sources with a fractal Sierpinski tetrahedron shape was developed before. The imager has 16 sensors arranged in a Sierpinski tetrahedron shape, with the space between the sensors filled with a shielding material. We have been developing a neutron imager to measure radiation distribution within the site of the Fukushima Daiichi Nuclear Power Plant (FDNPP) and in the environment contaminated by the FDNPP accident. The reactor buildings contain large amounts of radiation sources. Since the nuclear fuel and debris contained in the reactor pressure vessel (RPV) will be removed in the future, it is extremely important to identify neutron sources originating from nuclear fuel in high dose rate areas for criticality management and radiation protection of workers. Therefore, we developed a compact omnidirectional neutron imager to locate neutron sources in the reactor building. This sensor consists of thin triangular scintillators (^{6}LiF/ZnS:Ag) for neutron detection attached to a tetrahedral acrylic surface and arranged in a Sierpinski tetrahedron shape, with B_4C mixed with resin for neutron shielding filled between the sensors. In this presentation, we report the results of performance evaluations of the imager using a neutron source and research reactor.

References

[1] T. Torii, M. Sasaki, and Y. Sanada, “Development of an omnidirectional detector for beta and gamma-ray imaging with fractal geometry,” in Proc. IEEE NSS/MIC/RTSD, 2023

[2] M. Sasaki, Y. Abe, Y. Sanada, and T. Torii, “Evaluation of the distribution accuracy of radioactivity from a gamma-ray source using an omnidirectional detector for radiation imaging with fractal geometry,” Nucl. Instrum. Methods Phys. Res., Sect. A, vol. 1072, p. 170207, Mar. 2025.

[3] T. Torii, M. Sasaki, Y. Sanada, N. Matsubayashi and S. Kurosawa, “Development of an omnidirectional detector for neutron imaging with fractal geometry” 2025 IEEE NSS MIC RTSD, N-16-150, November, 2025.

[4] T. Sato et al. Features of Particle and Heavy Ion Transport code System, J. Nucle. Sci. and Tech., 55:6 (2018), 684.

NSS-05-03

Neutron Spectroscopy Using a Spatially Resolved He-3 Slab Detector

(#2047)

Madeline L. Lockhart[1], Jason P. Hayward[1], Amanda Youmans[2], Phil Kerr[2]

[1] University of Tennessee, Department of Nuclear Engineering, Knoxville, USA; [2] Lawrence Livermore National Laboraatory, Livermore, USA

This work was performed under the auspices of the U.S. Department of Energy by Lawrence Livermore National Laboratory under Contract DE-AC52-07NA27344.
This material is based upon work supported by the Department of Energy National Nuclear Security Administration through Defense Nuclear Nonproliferation's Enabling Capabilities in Technology Consortium under Award Number DE-NA0004197.

Abstract

This work presents a He-3 based slab detector for neutron spectroscopy that leverages spatially resolved detector response to infer incident neutron energy. In moderated detector systems, neutron energy information is typically degraded prior to detection, complicating spectrum unfolding. The proposed detector addresses this limitation through channel-by-channel list-mode acquisition, enabling analysis of spatial response variations correlated with neutron energy. Additional moderating and absorbing configurations are investigated to improve spectral sensitivity. A model of the detector is developed using Monte Carlo simulation and benchmarked against experimental measurements with monoenergetic neutron sources. This model will be used to generate energy-dependent response functions for use in spectral unfolding. Results indicate that combining spatial response information with multiple detector configurations will improve the conditioning of the neutron spectrum unfolding problem and enhance reconstruction accuracy. This approach provides a pathway toward information-optimized neutron spectrometry for nuclear security and safeguards applications.

NSS-05-04

Residual Interpulse 14-MeV Neutron Emission in Active Interrogation with Neutron Generators (#2076)

Valentin Fondement[1], Igor Jovanovic[2]

[1] University Of Michigan, Nuclear Engineering & Radiological Sciences, Ann Arbor, USA; [2] University of California, Berkeley, Nuclear Engineering, Berkeley, USA

This work has been supported in part by the US Department of Homeland Security, Countering Weapons of Mass Destruction (CWMD) Office, Academic Research Initiative
cooperative agreement number 21CWDARI00040-01-0.

Abstract
We report residual 14 MeV neutron emission between pulses of a Thermo Fisher Scientific P 211 DT neutron generator operated at 100 Hz with a 0.1% duty cycle. Using a liquid organic scintillator with pulse-shape discrimination, we detect a significant population of neutron events with light output consistent with DT neutrons. The interpulse time structure follows a two-component exponential decay with time constants of 0.8 ms and 4.7 ms, inconsistent with ^{17}N β-delayed neutron emission. The interpulse yield represents 0.1% of the total emission (~10^{-6} of instantaneous pulse intensity). These results demonstrate that the assumption of zero interpulse emission can be violated even when both the ion source and the high voltage are nominally pulsed, with direct implications for low-SNR delayed-signature measurements.

References
[1] Thermo Scientific P 211 Neutron Generator: Product Specifications. URL: https://www.thermofisher.com/order/catalog/product/1512521C
[2] T. A. Laplace *et al.*, "Comparative scintillation performance of EJ-309, EJ-276, and a novel organic glass," J. Inst., vol. 15, no. 11, pp. P11020–P11020, Nov. 2020, doi: 10.1088/1748-0221/15/11/P11020.
[3] CAEN, DT5730S User Manual Rev. 8, CAEN (2023) URL: https://www.caen.it/products/dt5730
[4] C. Graham, *et al.*, "Improved contraband detection using an experimentally optimized neutron active interrogation pulse structure," NIM A, vol. 1083, p. 171157, Mar. 2026, doi: 10.1016/j.nima.2025.171157.
[5] V. Fondement *et al.*, "Electronics and ^{3}He Counter Acquisition Tests During the Pulses of a D-T Neutron Generator," 2022 IEEE NSS/MIC, Italy, 2022, pp. 1-6, doi: 10.1109/NSS/MIC44845.2022.10399200.
[6] V. Fondement *et al.*, "Development of a neutron probe to perform a combined measurement of uranium concentration and hydrogen porosity for mining applications," NIM A, vol. 1059, p. 168888, Feb. 2024, doi: 10.1016/j.nima.2023.168888.

NSS-05-05

Neutron Flux Monitor (NFM): A Micromegas-Based Beam Monitor for the European Spallation Source (#2999)

Ioannis Katsioulas[1], Ali Altingün[1], Alexandros Gardikiotis[3], Mariam Kebbiri[2], Christos Lampoudis[3], Brahim A. Moreno[2], Thomas Papaevangelou[2], Evangelos Samouilidis[3,1], Ourania Sidiropoulou[1]

[1] European Spallation Source, Detector Group, Lund, Sweden; [2] Université Paris-Saclay, IRFU, CEA, Gif-sur-Yvette, France; [3] Aristotle University of Thessaloniki, Physics Department, Thessaloniki, Greece

We would like to thank Dr Jochen Stahn (PSI) and Dr Davide Raspino for providing beam time and their support during the measurements at the AMOR and MORPHEUS instruments at the Paul Scherrer Institute (CH) and the EMMA beamline in the ISIS facility at the Rutherford Appleton Laboratory (UK).

Abstract
The European Spallation Source (ESS) requires advanced neutron-beam monitors capable of stable operation under high-rate conditions while maintaining low beam attenuation. To address these requirements, a Micromegas-based Neutron Flux Monitor (NFM) has been developed by the ESS Detector Group in collaboration with DEDIP

(IRFU) and CEA Saclay. The detector employs a novel bulk Micromegas implementation directly on AlMg3 alloy substrates, minimizing the use of hydrogen-rich materials and therefore reducing neutron attenuation and moderation effects along the beamline. Initial detector characterization using X-ray sources demonstrated good gain uniformity, stable high-gain operation, and good energy resolution. Subsequent neutron measurements performed with different gas mixtures and front-end electronics confirmed stable operation under representative ESS-like conditions. Measurements performed at the EMMA beamline at ISIS investigated detector performance at high neutron rates and provided important input for the optimisation of the final NFM readout architecture for future ESS deployment.

References
[1] Andersen, KH, Argyriou, DN, Jackson, AJ, Houston, J, Henry, PF, Deen, PP, et al. 2020, 'The instrument suite of the European Spallation Source', *Nuclear Instruments and Methods in Physics Research Section A*, vol. 957, Art. no. 163402, Amsterdam: Elsevier.
[2] Garoby, R, et al. 2018, 'The European Spallation Source Design', *Physica Scripta*, vol. 93, Art. no. 014001, Bristol: IOP Publishing.
[3] Giomataris, I, Rebourgeard, Ph, Robert, JP, Charpak, G 1996, 'MICROMEGAS: A high-granularity position-sensitive gaseous detector for high particle-flux environments', *Nuclear Instruments and Methods in Physics Research Section A*, vol. 376, pp. 29–35, Amsterdam: Elsevier.
[4] Giomataris, I, et al. 2006, 'Micromegas in a bulk', *Nuclear Instruments and Methods in Physics Research Section A*, vol. 560, pp. 405–408, Amsterdam: Elsevier.
[5] Segui, L, et al. 2023, 'Detector design and performance tests of the ESS-neutron Beam Loss Monitor detectors', *Journal of Instrumentation*, vol. 18, P01013, Bristol: IOP Publishing.

NSS-05-06

Development of a Handheld Fast Neutron Spectrometer Using Deuterated Scintillators and Spectrum Unfolding (#3014)

Ariel A. Alcaide[1], **Ariel A. Alcaide**[1], Tyler C. Borgwardt[2], Tyler C. Borgwardt[2], Carl Brune[3], Carl Brune[3], Lorenzo Fabris[4], Lorenzo Fabris[4], Michael Febbraro[1], Michael Febbraro[1], Juan J. Manfredi[1], Juan J. Manfredi[1], Thomas Massey[3], Thomas Massey[3], James Matta[4], James Matta[4], David Matthews[4], David Matthews[4], Cody Parker[3], Cody Parker[3], Daniel Rutstrom[1], Daniel Rutstrom[1], Natalia Zaitseva[5], Natalia Zaitseva[5]

[1] Air Force Institute of Technology, Engineering Physics, Dayton, USA; [2] Los Alamos National Laboratory, Los Alamos, USA; [3] Ohio University, Athens, USA; [4] Oak Ridge National Laboratory, Oak Ridge, USA; [5] Lawrence Livermore National Laboratory, Livermore, USA

Abstract
Fast neutron spectroscopy has the potential to offer critical information for safeguards, nonproliferation, and field radiation detection applications where neutron energy distributions provide source characteristics inaccessible through conventional moderated neutron counters. Traditional portable neutron detection systems primarily rely on moderation and thermal neutron counting, which remove incident neutron energy information and limit spectroscopic capability. In this work, the nSpec system is developed as a handheld fast neutron spectrometer utilizing four novel deuterated polystyrene (dPS) scintillator detectors coupled to photomultiplier tubes in a compact, field-deployable architecture. By leveraging neutron--deuteron elastic scattering interactions, the system preserves energy-dependent neutron response while maintaining portability suitable for operational environments. Pulse shape discrimination is employed to separate neutron and gamma interactions, while detector response

matrices (DRMs) derived from high-flux neutron characterization are used to reconstruct incident neutron spectra through maximum likelihood expectation maximization (MLEM) unfolding. Prototype evaluations using representative neutron sources, including AmBe and Cf-252, demonstrate successful spectral unfolding and source discrimination capability. Ongoing development focuses on onboard electronics integration, firmware implementation, shielding optimization, and validation against simulated and experimental DRMs. These results establish nSpec as a promising pathway toward practical handheld fast neutron spectroscopy for safeguards and field applications.

NSS-05-07

Innovative neutron counting for high-rate double-differential cross-section in fragmentation events. (#2947)

Iram B. Rivas Ortiz[1], Emanuele M. Data[2], Veronica Ferrero[2], Elisa Fiorina[1], Simona Giordanengo[1], Felix Mas Milian[1,3], Alessio Mereghetti[4], Diango M. Montalvan Olivares[1,2], Francesco Pennazio[1], Marco Pullia[4], Sahar Ranjbar[2], Roberto Sacchi[1,2], Anna Vignati[1,2], Piergiorgio Cerello[1]

[1] Instituto Nazionale di Fisica Nucleare, Sezione di Torino, Torino, Italy; [2] Universita degli Studi di Torino, Torino, Italy; [3] Universidade Estadual de Santa Cruz, Bahia, Brazil; [4] Fondazione Centro Nazionale di Adronterapia Oncologica, Pavia, Italy

Abstract

Neutron production cross-sections are critical for dose assessment in particle therapy and space radiation protection, yet double-differential data remain scarce. We present a consistent framework for Time-Of-Flight (TOF)-based measurement built around the use of Low Gain Avalanche Detectors (LGADs) segmented into strips on the primary beam, enabling large statistical samples and precise time measurement, and a secondary neutron detector split into layers to accurately reconstruct neutron production as a function of kinetic energy and angular direction. A preliminary beam test was conducted to validate the methodology. The setup comprises an 8-strip beam monitor for primary particle tagging, a $LaBr_3$(Ce) scintillator with Silicon Photomultiplier (SiPM) readout as secondary radiation detector, and a plastic veto for charged-particle rejection. Neutron kinetic energy is reconstructed via relativistic TOF analysis from approximately 16 MeV to several hundred MeV. A novel Beer-Lambert fitting approach enables efficiency-independent neutron flux estimation from the attenuation pattern along the detection depth, overcoming systematic uncertainties of conventional scaling methods. Monte Carlo (MC) simulations validate both TOF distributions and flux reconstruction at the few-percent level, with computed cross-sections in good agreement with MC truth values. Combined with a rotary-translation stage enabling systematic angular scanning for full double-differential cross-section mapping, the proposed approach provides a robust and scalable framework for neutron production measurements in fragmentation events, with direct application to out-of-field dose characterization in particle therapy and astronaut radiation exposure assessment.

NSS-05-08

First 3D-PDC Experimental Measurements of Fast Neutrons and PSD Performance (#1598)

Amanda Steinhebel[1], **Amanda Steinhebel**[1], Serge A. Charlebois[2], Serge A. Charlebois[2], Lorenzo Fabris[1], Lorenzo Fabris[1], Paul Hausladen[1], Paul Hausladen[1], Gabriel Lessard[2], Gabriel Lessard[2], Catherine M. Pepin[2], Catherine M. Pepin[2], Jean-François Pratte[2], Jean-François Pratte[2], Tommy Rossignol[2], Tommy Rossignol[2], Nicolas Roy[2], Nicolas Roy[2], Frederic Vachon[2], Frederic Vachon[2]

[1] Oak Ridge National Laboratory, Bldg 3500, MS 6010, Oak Ridge, USA; [2] Universite de Sherbrooke, Interdisciplinary Institute for Technological Innovation and Department of Electrical and Computer Engineering, Sherbrooke, Canada

The present work was supported in part by the United States Department of Energy, Office of Defense Nuclear Nonproliferation Research and Development in the National Nuclear Security Administration and by the United States Department of Energy, Office of High Energy Physics.

Abstract

Novel Photon-to-Digital Converters (3D-PDCs) are arrays of Single Photon Avalanche Diodes (SPADs) vertically-integrated with low power CMOS digital readouts, offering high timing precision (<200 ps FWHM) and individual-pixel control. As single-photon counters, 3D-PDCs can be coupled to scintillators for radiation detection. This talk will discuss the first 3D-PDC measurements of fast neutrons. The 3D-PDCs are used to read out an organic plastic scintillator with Pulse Shape Discrimination (PSD) capabilities, making incident neutrons and gamma rays discernible by the pulse shape of the induced scintillator signal. First PSD results will be shown and compared to standard commercial silicon photomultipliers.

References

[1] A. Pietropaolo, et al., “Neutron detection techniques from μeV to GeV,” Phys. Reports, vol. 875, pp. 1-65, Sept, 2020, 10.1016/j.physrep.2020.06.003.

[2] M. L. Roush, M. A. Wilson, and W. F. Hornyak, “Pulse shape discrimination,” Nucl. Instrum. Methods, vol. 31, pp. 112-124, June, 1964.

[3] J.-F. Pratte, et al., “3D Photon-To-Digital Converter for radiation instrumentation: Motivation and future works,” Sensors, vol. 21, no. 2, pp. 598, Jan, 2021, 10.3390/s21020598.

[4] T. Rossignol, et al., “A 3D photon-to-digital converter readout for low-power and large-area applications,” JINST, vol. 19, Sept, 2024, 10.1088/1748-0221/19/09/P09017.

[5] C.M. Pepin, et al.. (2025, Nov.). Performance of 3D Photon-to-Digital Converters. Presented at 2025 IEEE NSS MIC RTSD. [In-person]. Available: https://inspirehep.net/literature/3102109. Accessed on: May 06, 2026.

Time:
10 November, 2026
9:00 – 11:00

Room:
ALBÉNIZ & MACHUCA

NSS-06 | Detector modeling and simulation

Chairs:
Shaun D. Clarke (Ann Arbor)
Angela Di Fulvio (Urbana)

NSS-06-01

ARES: A Web-Based Platform for Registration, Access, and Analysis of Radiation Simulation Results (#3019)

Sacha E.R. Medaer[1], Carlos H. Ferreira Brito Filho[2], Pedro Glaser De Senna[2], Andre Freitas Pacifico[2], Joel Closier[1], Gloria Corti[1]

[1] CERN, LHCb Collaboration, Geneva, Switzerland; [2] Universidade Federal do Rio de Janeiro, COPPE/EE/IF, Rio De Janeiro, Brazil

Abstract

Radiation simulations are essential for the design, operation, upgrade, and radiation protection assessment of high-energy physics experiments and other complex accelerator or irradiation facilities. However, their outputs are often difficult to organise, document, retrieve, compare, and share consistently, particularly when many studies, configurations, and users are involved. We present the Analysis platform for Radiation Environment Simulations (ARES), a web-based system developed within the LHCb experiment to support the workflow from registration to analysis of radiation simulation results obtained with the FLUKA particle transport code. ARES provides a database-backed interface for registering radiation estimators together with metadata describing the simulation context, scoring configuration, estimator location, and other relevant information. This structured registration makes results traceable, searchable, reproducible, and easier to reuse. Users can browse and query available estimators through a dedicated search interface and open selected data in a standalone visualisation and analysis service. The platform has been deployed for LHCb radiation studies covering prompt radiation and induced activity use cases, supporting quantities such as fluence, dose, and activation-related estimators. By centralising validated results and providing common tools for access and analysis, ARES improves collaboration between stakeholders involved in simulation production, detector studies, operations, upgrades, and radiation protection. This work demonstrates that a dedicated data-management and analysis layer can make radiation simulations more accessible and more effectively exploitable within a large experimental environment. Future developments include support for additional Monte-Carlo based codes and broader applicability beyond current LHCb use cases.

References

[1] L. Collaboration, A. A. Alves Jr, L. Andrade Filho, A. Barbosa, I. Bediaga, G. Cernicchiaro, G. Guerrer, H. Lima Jr, A. Machado, J. Magnin et al., “The lhcb detector at the lhc,” Journal of instrumentation, vol. 3, no. 08, pp. S08 005–S08 005, 2008.

[2] G. Battistoni, T. Boehlen, F. Cerutti, P. W. Chin, L. S. Esposito, A. Fasso, A. Ferrari, A. Lechner, A. Empl, A. Mairani et al., “Overview of the fluka code,” Annals of Nuclear Energy, vol. 82, pp. 10–18, 2015.

[3] C. Ahdida, D. Bozzato, D. Calzolari, F. Cerutti, N. Charitonidis, A. Cimmino, A. Coronetti, G. D’alessandro, A. Donadon Servelle, L. Esposito et al., “New capabilities of the fluka multi-purpose code,” Frontiers in Physics, vol. 9, p. 788253, 2022.

[4] G. J. Souza e Silva, C. H. Ferreira Brito Filho, G. Corti, and J. Closier, “Glance search library,” in EPJ Web of Conferences, vol. 295. EDP Sciences, 2024, p. 05006.

[5] A. J. Peters, E. A. Sindrilaru, and G. Adde, “Eos as the present and future solution for data storage at cern,” in Journal of Physics: Conference Series, vol. 664, no. 4. IOP Publishing, 2015, p. 042042.

NSS-06-02

Monte Carlo simulation of a new Optical Neutron Detector geometry for generation-IV Sodium-cooled Fast Reactors (#1285)

Valentin Gerenton, **Valentin Gerenton**, Philippe Filliatre, Philippe Filliatre, Grégoire De Izarra, Grégoire De Izarra

CEA, DEN / DER / Instrumentation, Sensors and Dosimetry Laboratory, Saint-Paul-lez-Durance, France

This work was supported by the CEA, DEN, Reactor Research Department, Saint-Paul-lez-Durance, France.

Abstract

Generation-IV sodium-cooled fast reactors impose severe constraints on neutron flux measurement instruments, particularly due to sustained temperatures that can exceed 550 °C [1]. In this context, optical neutron detectors (ONDs) represent a promising alternative to conventional fission chambers. These devices convert the kinetic energy of fission fragments into optical photons via gas-plasma luminescence and transmit the signal via an optical fiber, allowing electronic components to be placed out of pile, away from radiation. However, the photon collection efficiency of current prototypes is only $\eta \approx 1.78 \times 10^{-7}$, limiting detector sensitivity [2]. This work presents a dedicated Monte Carlo simulation code, written in C, that estimates the impact of a new OND geometry—combining a hemispherical fissile deposit and a parabolic mirror—on photon collection efficiency, while accounting for the thermal radiation generated at high temperatures. The code comprises three coupled Monte Carlo loops: heavy-ion transport in gas (using polynomial moderation laws from COSICAF), plasma-photon propagation by ray tracing, and thermal wall-radiation modeling at 600 °C. A parametric study identified the negligible impact of the focal length of the parabolic mirror around the geometrically calculated value and quantified the impact of the reflective surfaces, and gas density. The proposed geometry achieves $\eta = 5.4 \times 10^{-6}$, a factor of 30 improvement over to current prototypes. These results call for progressive experimental validation, from out-of-reactor thermal characterization to in-reactor testing.

References

[1] Guidez, J, Bonin, B, 2014, ‘Réacteurs nucléaires à caloporteur sodium’, CEA Saclay, Groupe Moniteur

[2] Pouradier-Duteil, M, 2024, ‘Study and optimization of the signal-to-noise ratio of optical neutron detectors applied to reactor environments’, Ph.D. thesis, Fluid mechanics, energy and processes, Grenoble Alpes Univ., Grenoble, France

NSS-06-03

A Validated GEANT4 Model of a Dual-HPGe γ–γ Coincidence Spectrometer for Detection Sensitivity Evaluation (#1900)

Thomas C. Stokes[1,2], Matthew Goodwin[1], Mark Jackson[1], Andrew Boston[2]

[1] AWE Nuclear Security Technologies, Aldermaston, UK; [2] The Oliver Lodge Laboratory, The University of Liverpool, Liverpool, UK

Abstract

Gamma-gamma (γ-γ) coincidence is an advanced radiometric detection technique that has been widely demonstrated to reduce detection limits for many radionuclides in a variety of sample types and applications. The superior selectivity of γ-γ coincidence spectrometry in comparison to traditional single detector analysis, reduces the sensitivity of detection limits to changes in the activity of impurity radionuclides. This is particularly true in the case of impurities that do not emit coincident gamma photons (e.g. ^{137}Cs). In this work, a GEANT4 model of a dual high-purity germanium γ-γ coincidence system has been developed and validated against experimental measurements. Additionally, a method to generate modelled time-stamped list mode (T-List) data is presented and demonstrated using long and short-lived radionuclides. By processing the modelled T-List data, the effect on the detection limit for an analyte of interest in the presence of an impurity radionuclide can be studied. These preliminary results demonstrate how the detection limit of ^{134}Cs shows no measurable dependence on the activity of ^{137}Cs over the simulated range of 0.2-100 kBq. Future work will seek to investigate the influencing factors on detection limits for coincidence spectrometry as well as demonstrate the use of γ-γ coincidence alongside radiochemical separations to accelerate analytical timelines.

NSS-06-04

Monte Carlo Quantum Imaging with Annihilation Photons (#2481)

Ana Marija Kožuljević[1], Gabriela Jazvac[1], Luka Lotina[1], Mihael Makek[2], Siddharth Parashari[3], Petar Žugec[2], Luka Pavelić[1,4]

[1] Institute for Medical Research and Occupational Health, Divison of Radiation Protection, Zagreb, Croatia; [2] University of Zagreb Faculty of Science, Department of Physics, Zagreb, Croatia; [3] Instituto de Fisica Corpuscular, Valencia, Spain; [4] Nucleometrix d.o.o., Zagreb, Croatia

This work was funded by the European Union – Next Generation EU and is part of the project Voxel matrix detector for full solid angle radiological imaging (VMDScan) - NPOO.C3.2.R2-I1.06.0084.

Abstract

Quantum imaging with annihilation photons has recently emerged as a promising imaging modality [1, 2]. Positron annihilation photons are correlated particles, carrying the same energy of 511 keV and opposite momenta. The technique relies on coincidence measurements of the annihilation photons' energies and positions, with an object placed in front of one of the detectors. As a result, a ghost image of the object forms in the other detector, and the real image is enhanced by background noise reduction, since the noise lacks the photons' correlations. In this work, we explore the limits of the modality for background noise reduction via Geant4 simulations. The coincidence measurements are simulated for an experimental setup encompassing two segmented scintillating detectors, comprised of 64 Gadolinium Aluminum Gallium Garnet (GAGG) crystals and assembled into an 8x8 square matrix with 3.2 mm pitch [3]. We have found that quantum imaging outperforms classical gamma transmission imaging by retaining the contrast-to-noise ratio (CNR) of noiseless conditions regardless of the background noise intensity. We have also tested the penetrative aspect of annihilation gamma rays, exploring the possibility of detecting attenuation variations in optically dense, high-Z materials.

References
[1] Schneider, A, Mahon, R, Goodrich, J, Hanrahan, J, Stoll, S, Da Via, C 2026, 'Quantum imaging with positronium-decay-emitted gamma rays', *Phys. Rev, A*, 113, 013715, APS
[2] Romanchek, G, Yu, Z, Abbaszadeh, S 2026 'Monte Carlo validation of signal-to-noise improvements in transmission imaging using correlated annihilation photon pairs', *Sci Rep*, Nature
[3] Makek M, Bosnar D, Kožuljević AM, Pavelić L 2020 'Investigation of GaGG:Ce with TOFPET2 ASIC Readout for Applications in Gamma Imaging Systems', *Crystals*, 10, 1073, MDPI

NSS-06-05

Bringing Synchrotron X-ray Minibeam Radiotherapy into Clinical Relevance: Monte Carlo Validation of Clinically Relevant Treatment Fields at the Australian Synchrotron (#1459)

Vincent T. de Rover[1], Kiarn Roughley[1], John Paul Bustillo[1,2], Samuel Au[1], Matthew Cameron[3], Moeava Tehei[1], Elette Engels[1,5], Michael Grams[4], Sean Park[4], Anatoly Rosenfeld[1], Claire Phillips[5], Marco Petasecca[1], Dean Cutajar[1], Stephanie Corde[1,6], Susanna Guatelli[1], Michael Lerch[1]

[1] University of Wollongong, Centre for Medical Radiation Physics, Wollongong, Australia; [2] University of the Philippines Manila, Department of Physical Sciences and Mathematics, College of Arts and Sciences, Manila, Philippines; [3] Australian Synchrotron, Imaging and Medical Beamline, Melbourne, Australia; [4] Mayo Clinic, Department of Radiation Oncology, Rochester, USA; [5] Peter MacCallum Cancer Centre, Parkville, Australia; [6] Prince of Wales Hospital, Department of Radiation Oncology, Randwick, Australia

V.d.R. is a recipient of the Australian Government Research Training Program Award and of the Australian Institute of Nuclear Science and Engineering (AINSE) Postgraduate Research Award. The authors would like to acknowledge the facilities and assistance of the Imaging and Medical Beamline (IMBL), at the Australian Synchrotron, where the experimentals were performed under proposal ID 23802. This research was undertaken with the assistance of resources from the Australian National Computer Infrastructure (NCI) supercomputer cluster.

Abstract

To progress synchrotron-based, spatially fractionated X-ray radiotherapy towards clinical trials, the efficacy of clinically relevant treatment fields must be assessed. In this paper, we present the development and validation of a Geant4 model for human-relevant broad beam (BB) and minibeam radiotherapy (MBRT) treatment fields (up to 7 x 7 cm^2) in an experimental hutch located 140m from the synchrotron source at the Imaging and Medical Beamline at the ANSTO Australian Synchrotron. Both broad beam and MBRT treatment fields were modelled for different beam energies and field sizes, with two minibeam fields of different peak spacing investigated. BB and MBRT (peak and valley) depth doses were investigated up to 7cm in a solid water phantom. There was excellent agreement in broad beam percentage depth dose curves (within 4%) as well as the minibeam peak depth dose curves (within 6%), with the model and experimental results agreeing within combined uncertainty for all depths and configurations investigated. There was good agreement in valley dose when comparing EBT-XD Gafchromic film to the model with most results within 10% and within uncertainty. However, there was disagreement between the valley dose measured by the microdiamond detector and the Geant4 model up to 15%. This model will be useful for further MBRT experiments performed at IMBL, with future work validating this model for 3D printed patient volumes.

References
[1] Slatkin, D.N., Spanne, P., Dilmanian, F.A., et. al. 1995, “Subacute neuropathological effects of microplanar beams of x-rays from a synchrotron wiggler”, Proc. Natl. Acad. Sci. U.S.A. 92 (19) 8783-8787.
[2] Dilmanian, F.A., Zhong, Z., Bacarian, T., et. al. 2006, “Interlaced x-ray microplanar beams: A radiosurgery approach with clinical potential”, Proc. Natl. Acad. Sci. U.S.A. 103 (25) 9709-9714.
[3] Grams, M.P., Mateus, C., Mashayekhi, M., et. al. 2024, “Minibeam radiation therapy treatment (mbrt): Commissioning and first clinical implementation”, International Journal of Radiation Oncology*Biology*Physics, 120(5):1423-1434.
[4] Schneider, T., Fernandez-Palomo, C., Bertho, A., et. al. 2022, “Combining FLASH and spatially fractionated radiation therapy: The best of both worlds”, Radiotherapy and Oncology 175, 169-177.
[5] Treibel, F., Nguyen, M., Ahmed, M., et. al. 2021, “Establishment of microbeam radiation therapy at a small-animal irradiator”, International Journal of Radiation Oncology*Biology*Physics, 109(2):626–636.
[6] Agostinelli, S., Allison, J., Amako K., et. al. 2003, “Geant4—a simulation toolkit”, Nuclear Instru ments and Methods in Physics Research Section A: Accelerators, Spectrometers, Detectors and Associated Equipment, 506(3):250–303.
[7] Davis, J.A., Petasecca, M., Cullen A., et. al. 2019, “X-Tream dosimetry of synchrotron radiation with the PTW microdiamond” J. Instrum. 14 P10037.
[8] Dipuglia, A., Cameron, M., Davis J.A., et. al. 2019, “Validation of a monte carlo simulation for microbeam radiation therapy on the imaging and medical beamline at the australian synchrotron”, Scientific Reports, 9(17696).

NSS-06-06

SimpleMC: A Simple and Flexible Monte Carlo Simulation Tool for Timepix Detectors (#2518)

Chia-Wei Huang[1], Jaroslav Čeřovský[1], Štěpán Malec[1], Vladimír Linhart[1], Kamilla Sabirzyanova[2], Karolína Melovská[2], Eliška Soharová[2]

[1] Czech Technical University in Prague, Faculty of Nuclear Sciences and Physical Engineering, Prague, Czech Republic; [2] ADVACAM, Prague, Czech Republic

This project is co-financed by the Technology Agency of the Czech Republic (TACR) within the SIGMA Program, project no. TQ15000215.

Abstract

Timepix type pixel detectors enable event-by-event radiation measurements [1], but classification of mixed fields remains challenging due to scarce labeled data and detector dependent effects. We present SimpleMC, an Allpix^2 [2, 3] based framework for generating realistic synthetic Timepix datasets by combining Monte Carlo transport simulation with detector response modeling and data driven refinement. Photon and electron benchmarks are improved using two complementary approaches: a tuned digitizer and a simplified Gaussian smearing model. These approaches enhance agreement with calibration and spectral measurements. For proton and alpha particles, generative models are used to bridge the sim-to-real gap, including Contrastive Unpaired Translation (CUT) and Conditional Diffusion Denoising Probabilistic Models (CDDPM). The models are trained to map simulated cluster representations to experimental-like responses. CDDPM outperorms CUT in capturing experimental variability and improving generalization to unseen geometries and irradiation conditions. The framework is evaluated across photons, electrons, and heavy charged particles, showing good agreement in both energy related observables and cluster morphology. Additional experimental datasets from complex radiation environments, including fusion relevant tokamak conditions, are collected for future validation. SimpleMC provides a flexible framework for realistic synthetic data generation, supporting detector characterization and the development of advanced simulation based analysis tools. It will be further developed into a user-friendly toolkit with documentation for the broader radiation detection community.

References
[1] R. Al Darwish, L. Marcu, and E. Bezak, “Overview of current applications of the Timepix detector in spectroscopy, radiation and medical physics,” Appl. Spectrosc. Rev., vol. 55, no. 3, pp. 243–261, Mar. 2020.
[2] S. Spannagel et al., “Allpix^2: A modular simulation framework for silicon detectors,” Nucl. Instrum. Methods Phys. Res. Sect. Accel. Spectrometers Detect. Assoc. Equip., vol. 901, pp. 164–172, Sep. 2018.
[3] R. Ballabriga Sune et al., “A simulator for Timepix-like pixel front-ends,” J. Instrum., vol. 19, no. 3, p. C03022, Mar. 2024.

NSS-06-07

Photodetector model for the ClearMind project: Toward ultra-high time resolution (#1979)

Zoé Zobundzija[1], Viatcheslav Sharyy[1,2], Dominique Yvon[1,2], Geoffrey Daniel[3], Theo Kaprelian[3], Christian Morel[4], Mathieu Dupont[4]

[1] Université Paris-Saclay, CEA, IRFU/Département de Physique des Particules, Gif-sur-Yvette, France; [2] Université Paris-Saclay, CEA, CNRS, INSERN, Laboratoire BIOMAPS, Orsay, France; [3] Université Paris-Saclay, CEA, Service de Génie Logiciel pour la simulation, Gif-sur-Yvette, France; [4] Aix-Marseille Université, CNRS/IN2P3, CPPM, Marseille, France

Abstract
The ClearMind collaboration is developing a next-generation Time-of-Flight PET detector aiming at sub-100 ps coincidence resolving time, high detection efficiency and precise spatial resolution. This presentation discusses the modeling of the ClearMind gamma detector, made of crystal with direct photocathode deposition and microchannel plate (MCP) electron multiplication. The simulation model uses Geant4 software to simulate gamma interactions within the crystal and the propagation of optical photons. Photoelectron generation, multiplication and signal processing are described through a parametrized simulation. This model is crutial for both understanding and optimizing the ClearMind prototype and for development of machine learning-based reconstruction algorithms. To

validate the model, we compare simulation results with experimental measurments PbF_2, $PbWO_4$, BaF_2 and LYSO crystals assembled with the Incom HRPPD MCP-PMT in a conventional configuration. We also explore various factors contributing to the detector's time resolution, including photon collection efficiency, photocathode efficiency, single-photon time resolution and signal pile-up effects. Additionally, we investigated new estimators using deep learning models trained on simulation for time reconstruction and event-by-event associated uncertainty estimation enabling us to select the most precise events. The preliminary results show a time resolution below 100 ps.

References
[1] A. Galindo et et al, First ClearMind gamma detector prototype for TOF-PET imaging, 2024, JINST, 19 P07037, doi: 10.1088/1748-0221/19/07/P07037 arXiv:2312.13169 [physics.ins-det]
[2] M. Follin et al, High resolution MCP-PMT readout using transmission lines, Engineering Applications of Artificial Intelligence, vol. 131, p. 107876, 2024. doi: 10.1016/j.engappai.2024.107876
[3] C.-H. Sung et al, Detailed simulation for the ClearMind prototype detection module and event reconstruction using artificial intelligence,*Nucl. Instrum. Meth. A*, vol. 1053, p. 168357, 2023. doi: 10.1016/j.nima.2023.168357.
[4] G. Daniel et al, Deep learning reconstruction with uncertainty estimation for gamma photon interaction in fast scintillator detectors, *Nucl. Instrum. Meth. A*, vol. 1053, p. 168357, 2023. doi: 10.1016/j.nima.2023.168357.
[5] D. Breton et al, Measurements of timing resolution of ultra-fast silicon detectors with the SAMPIC waveform digitizer,*Nucl. Instrum. Meth. A*, vol. 835, suppl. C, pp. 51--60, 2016. doi: 10.1016/j.nima.2016.08.019.

NSS-06-08

3-D simulation of carrier transport and signal formation in silicon detectors for charged particle identification (#2910)

Andrea Castoldi[1,2], Chiara Guazzoni[1,2], Filippo Buda[1]

[1] Politecnico di Milano, DEIB, Milano, Italy; [2] INFN, Sezione di Milano, Milano, Italy

Abstract

Fast simulation of carrier generation, transport and signal formation is a powerful tool for the optimization of segmented detector arrays targeted to charged particle identification in nuclear physics experiments. A custom numerical tool for the self-consistent computation of the electron-hole dynamics has been used to study ion tracks in silicon and non-silicon detectors. The code includes the effect of thermal diffusion and Coulomb interaction among the mobile carriers in a microscopic fashion, essential for the correct simulation of high-density ionization tracks in which plasma-like effects (field screening, transient distortions, collection slowdown, and marked nonlinearities) become significant, like in the case of heavy ion interactions. We addressed the challenging case of intermediate mass fragments stopping in the typically few hundred microns of the first detection layer of a telescope configuration, where particle identification critically relies on pulse-shape analysis. Simulations were carried out for several ions - from Li6 to Na22 - impinging on a silicon detector with energies up to the punch-through condition. We studied the impact of the relevant properties of detector and preamplifier response and of the effectiveness of different pulse-shape algorithms to assess the minimum energy threshold and the achievable resolution in charged particle separation in mass (A) and atomic number (Z).

Time:
10 November, 2026
9:00 – 11:00

Room:
PICASSO

NSS-07 | Scintillators

Chairs:
Etiennette Auffray (Geneva)
Shunsuke Kurosawa (Nagoya)

NSS-07-01

Crucible-Free Growth of High Melting Temperature Scintillators by the OCCC Method (#2280)

Kei Kamada[1,2], Taketoshi Tomida[1], Masao Yoshino[1,2], Masanori Kitahara[1,2], Vladimir Kochurikhin[2], Rikito Murakami[1,2], Yasuhiro Shoji[2], Koichi Kakimoto[1], Akira Yoshikawa[1,2]

[1] Tohoku Univ., Sendai, Japan; [2] C&A corp., Sendai, Japan

Abstract

High-melting-point oxide scintillators are key materials for radiation imaging and harsh-environment radiation detection, but their scaling is limited by iridium crucibles, melt contamination, and composition fluctuation. We report crucible-free growth and scaling of Ce:LYSO and Y_2O_3 scintillators using the oxide crystal growth from cold crucible (OCCC) method. In OCCC growth, the oxide melt is directly heated by high-frequency induction and retained by a self-formed solidified raw-material layer in a water-cooled copper basket. Ce:LYSO was grown in air, and EPMA showed host-cation segregation coefficients close to unity for Lu, Y, and Si. The straight-body region exhibited light-output variation within ±20%, with a maximum light output of approximately 16,000 photons/MeV under ^{137}Cs 662-keV excitation. Most importantly, an ultrahigh-melting-point Y_2O_3 scintillator was successfully grown to a 3-inch diameter by OCCC, and polished Y_2O_3 samples exhibited transparent appearance and a clear scintillation response under ^{137}Cs excitation. The OCCC method is a promising platform for scaling high-melting-point oxide scintillators without precious-metal crucibles.

NSS-07-02

$Cs_3Cu_2I_5$ Single Crystals Grown with Oleic- and Formic-Acid-Assisted Additives: Effects on Crystal Quality and Scintillation Properties (#2527)

Bhavika Bansal, Vivek Anand, Anil K. Gourishetty

Indian Institute of Technology Roorkee, Department of Physics, Roorkee, India

Abstract

$Cs_3Cu_2I_5$ single crystals were grown at room temperature via a solvent evaporation method using two organic acid additives: oleic acid (OA) and formic acid (FA), and their effects on crystal quality and scintillation performance were systematically investigated. X-ray photoelectron spectroscopy confirmed the absence of Cu^{2+} features in both samples, demonstrating that organic acid additives effectively suppress Cu^{+} oxidation during growth. Single-crystal X-ray diffraction and rocking curve analysis revealed that formic-acid-assisted crystals exhibit superior crystalline quality, with a narrower rocking-curve FWHM of 0.009° compared to 0.016° for OA-assisted crystals. Scintillation measurements using a ^{137}Cs γ-ray source (662 keV) coupled to a SiPM photosensor showed an improved energy resolution of 5.4% for formic-acid-grown crystals versus 5.8% for OA-grown crystals. The enhanced performance of

FA-assisted crystals is attributed to formic acid's ability to regulate iodide ion availability through slow reaction with I^{3-} species, reducing the crystallization rate and extending the metastable growth regime, thereby suppressing defect formation. In contrast, the long-chain nature of oleic acid promotes residual ligand incorporation and non-uniform solvent evaporation, slightly degrading optical transparency and crystallinity

NSS-07-03

Novel $Cs_3Cu_2I_5$:Tl Scintillator Films for X-ray Imaging (#2891)

Lakshmi Soundara Pandian, Jun Wang, Govinda Adhikari, Edgar van Loef, Jarek Glodo, Vivek Nagarkar

Radiation Monitoring Devices, Inc., Imaging Sensors and Applications, Watertown, USA

Abstract

Tl-doped cesium copper iodide ($Cs_3Cu_2I_5$:Tl, CCI:Tl) has emerged as a promising scintillator for medical imaging, offering higher light yield than the long-established CsI:Tl while remaining non-hygroscopic and lead free. Its emission (445–500 nm) matches the quantum efficiency of CCD, CMOS, and flat panel readouts, making it an excellent choice as a converter for advanced X-ray detectors. Detectors based on CCI:Tl have potential for providing dose efficiency in medical applications including digital mammography, radiography, and cone-beam CT. The high brightness of CCI:Tl will enable their use in high framerate or otherwise light starved applications in both medical and industrial fields.

We report on the development of polycrystalline CCI:Tl scintillating films grown by hot wall evaporation (HWE), a technique previously used to produce columnar, low stress CsI:Tl films and extended here to the ternary CCI system. CCI crystals were first grown and then used as the source for evaporation. Material quality was characterized by SEM and EDX. EDX confirms stoichiometric Cs:Cu:I ratio of 3:2:5. Scintillation properties were measured under gamma and X-ray excitation, including pulse-height spectra, emission, light yield relative to CsI:Tl, scintillation decay time, and afterglow. X-ray imaging performance was evaluated through quantification of contrast transfer function (CTF(f)) and measurements of modulation transfer function (MTF(f)) using a slit method. with films demonstrating resolution 5 lp/mm at 70 kVp for thickness in excess of 150µm. The results indicate structured growth and demonstrate that HWE grown CCI:Tl films offer a viable, potentially higher luminosity alternative to CsI:Tl for indirect medical-imaging detection while also revealing the deposition parameters that govern film morphology and scintillation response. Results from both crystals and films and applications of CCI:Tl films will be presented.

NSS-07-04

Growth and Pellet Fabrication of 2D Perovskite Scintillator Radiation Detectors (#2585)

Amy J. Dickinson[1], Carol Crean[1], Joydip Ghosh[2], Phasit Petisiwaveth[1,3], Paul Sellin[1]

[1] University of Surrey, School of Mathematics and Physics, Guildford, UK; [2] University of Oxford, Department of Chemistry, Oxford, UK; [3] University of Wollongong, School of Physics, Wollongong, Australia

Abstract

Two-dimensional (2D) metal halide perovskites have emerged as promising scintillator materials for radiation detection due to their high x-ray and gamma-ray absorption coefficients, high light yields, and fast scintillation decay times. Their structural flexibility enables precise tuning of optical and scintillation properties through variation of the organic spacer, halide composition, and dopant incorporation [1]. This work presents the synthesis, optical characterisation, and pellet fabrication of several 2D perovskite scintillators, including the Ruddlesden-Popper (RP) phase materials $(BA)_2PbBr_4$ and $(PEA)_2PbBr_4$, and the Dion-Jacobson (DJ) phase material $(TMPDA)PbBr_4$. Crystals were synthesised using a slow-cooling solution growth method and subsequently processed into pellets using a cold-pressing technique to increase thickness while improving uniformity and reproducibility. The effects of manganese and rubidium doping in $(BA)_2PbBr_4$ were also investigated, demonstrating enhanced light yield and tuneable emission behaviour. Under x-ray excitation, $(PEA)_2PbBr_4$ exhibited a light yield exceeding that of LYSO, while all investigated materials demonstrated promising gamma-ray scintillation responses with resolvable peaks. These results highlight the strong potential of 2D perovskite scintillators for next-generation radiation detection technologies.

NSS-07-05

Enhanced Light Outputs in Cs_2ZnCl_4 Single Crystals via Hydrothermal Purification and Cd Doping (#2781)

Yuzhe Wu, Mingxue Deng, Shaohan Wang, Jie Ma, Tong Wu, Junfeng Chen

Shanghai Institute of Ceramics, Chinese Academy of Sciences, State Key Laboratory of Functional Crystals and Devices, Shanghai, China

This work was supported by the National Key Research and Development Program of China (2023YFA1606300), the National Natural Science Foundation of China (12405227).

Abstract

Cs_2ZnCl_4 single crystals exhibit ultrafast cross-luminescence and show great potential for high-repetition-rate and fast timing radiation detection areas. However, their light output is severely limited by synthesis-induced impurities and intrinsic defects. To address this bottleneck, this work systematically investigates two parallel strategies: hydrothermal purification and Cd doping. High optical-quality single crystals were grown via the vertical Bridgman method using hydrothermally purified method, followed by systematic optical transmittance, luminescence, and absolute light output characterizations. The results demonstrate that hydrothermal purification effectively eliminates heavy metal impurities in the precursors, significantly enhancing the light output (LO) from 680 ph/MeV to 1078 ph/MeV (a 58.5% increase) while fully preserving the crystal's ultrafast decay constant of 1.76 ns. Furthermore, Cd doping increases the light output to 3689 ph/MeV, representing an enhancement of 126.6%. This study provides two effective strategies for enhancing the light output of ultrafast halide light-emitting materials.

References
[1] P. Lecoq, "On the way to the 10 ps time-of-flight PET challenge," The European Physical Journal Plus, vol. 137, no. 8, 2022.
[2] P. Lecoq, "Pushing the Limits in Time-of-Flight PET Imaging," IEEE Transactions on Radiation and Plasma Medical Sciences, vol. 1, no. 6, pp. 473-485, 2017.
[3] K. Herweg et al., "Timing limits of ultrafast cross-luminescence emission in CsZnCl-based crystals for TOF-CT and TOF-PET," EJNMMI Phys, vol. 11, no. 1, p. 59, Jul 9 2024.
[4] X. Zuo et al., "Scintillation performance of 1-inch-diameter Cs_2ZnCl_4 crystals," CrystEngComm, vol. 27, no. 22, pp. 3682-3689, 2025.

NSS-07-06

Scintillation Properties of Ce^{3+}-, Pr^{3+}-, and Eu^{2+}-Doped LiCl, LiBr, and LiI Single Crystals (#2238)

Jarek Glodo, Edgar van Loef, Lakshmi Soundara Pandian

Radiation Monitoring Devices, Inc., Watertown, USA

Abstract

Lithium-rich scintillators are widely used to detect thermal neutrons, with Eu-doped lithium iodide (LiI:Eu) serving as the long-standing benchmark. LiI:Eu, however, has high gamma sensitivity, slow scintillation decay, and limited ability to distinguish neutrons from gamma rays. As a result, we have shifted our focus towards the lighter binary lithium halides, such as lithium chloride (LiCl) and lithium bromide (LiBr), which offer intrinsically lower gamma sensitivity. We also investigated Ce^{3+} and Pr^{3+} with the goal of evaluating their ability for fast *d-f* type emission and neutron-gamma discrimination.

Single crystals were grown by the vertical Bridgman method and characterized by X-ray luminescence, light yield, decay time, and neutron response using a moderated Am/Be source. Initial results show that LiBr:Ce delivers a clear thermal-neutron peak at 3.1 MeVee with a light yield of 7,300 ph/n (comparable to GS20) and pulse-shape discrimination capability. Full data and comparison across all dopant-host combinations will be presented.

NSS-07-07

Characterising ZnSe(Al,O) for Real-Time Sr-90 Beta Spectroscopy

(#2965)

Arjana Kolnikaj, Kelum A.A. Gamage, Olaoluwa R. Popoola

University of Glasgow, James Watt School of Engineering, Glasgow, UK

The author acknowledges the School of Physics and Astronomy at the University of Glasgow for access to laboratory facilities. Special thanks are given to Mx Thomas Queen for access to the nuclear laboratory, and to Dr Graham Gibson for access to the laser system and guidance on the Brewster-angle refractive-index measurement.

Abstract

ZnSe(Al,O) is a promising scintillator for compact beta spectroscopy, but its detector-relevant properties are poorly documented and strongly dependent on dopant composition, growth quality, and optical transport. This work experimentally characterises a commercially supplied ZnSe(Al,O) crystal intended for use in a silicon photomultiplier-coupled beta detector for strontium-90 monitoring. The crystal measured 42 mm in diameter and 2.1 mm in thickness. Scanning electron microscopy with energy-dispersive X-ray spectroscopy confirmed a zinc selenide composition with aluminium and oxygen impurities, giving measured atomic abundances of 49.2% zinc, 46.1% selenium, 3.50% oxygen, and 1.2% aluminium. The measured density was 5.31 g cm^−3, and the refractive index determined using a Brewster-angle method was 2.475. Scintillation waveforms were recorded under strontium-90/yttrium-90 beta irradiation using silicon photomultiplier readout and analysed to extract charge spectra and decay behaviour. The light yield was estimated to be approximately 7.8 × 10^4 photons MeV^−1, while the decay constant was measured as 9.41 us, with a waveform-to-waveform standard deviation of 1.1 us. These values are broadly consistent with the range reported for zinc-selenide-based scintillators, while providing a single experimentally derived parameter set for this specific ZnSe(Al,O) sample. The results support the suitability of ZnSe(Al,O) for silicon photomultiplier-based beta spectroscopy and provide material inputs required for improved detector modelling, optical design, and future development of compact detectors for environmental strontium-90 monitoring.

NSS-07-08

Exploring wavelength-shifting properties of nanocrystal layers and nanocomposites (#3052)

Vojtech Zabloudil[1,2], Jan Kral[2,3], Vladimir Masek[2], Julie Delenne[1,4], Jean-Louis Faure[5], Solangel Rojas[2], Etiennette Auffray[1]

[1] CERN, Geneva, Switzerland; [2] Czech Technical University in Prague, Prague, Czech Republic; [3] Institute of Physics of the Czech Academy of Sciences, Prague, Czech Republic; [4] Université de Strasbourg, UMR7178, CNRS, IPHC, Strasbourg, France; [5] CEA Saclay, Paris, France

This work is performed in the framework of the Crystal Clear Collaboration (CCC) and the European Pathfinder Open project UNICORN (GA 101098649). Additional support was provided by the Grant Agency of the Czech Technical University in Prague, Grant Number SGS24/145/OHK4/3T/14.

Abstract

Efficient detection of fast ultraviolet scintillation is essential for the next generation of high-speed radiation detectors. We investigate $CsPbX_3$ nanocrystals as a versatile wavelength-shifting platform, leveraging their sub-nanosecond response times and tunable bandgaps to match the peak sensitivity of standard photodetectors. As a proof-of-concept, using radioluminescence measurements, we characterize the conversion of scintillation light from a LYSO:Ce reference crystal by $CsPbBr_3$ nanocrystal layers and polymer-based nanocomposites. It has been observed that concentrated drop-cast layers perform better than nanocomposites and achieve total extinction of the broad scintillation peak of LYSO:Ce at 430 nm, shifting it to 535 nm, corresponding to the nanocrystal emission. Rigorous validation tests confirm that the observed green emission is a product of wavelength-shifting rather than a result of direct nanocrystal excitation or spectral attenuation of the primary light. This performance establishes a foundation for modular wavelength-shifting interfaces that can be tailored to various scintillators and radiators, including BaF_2 (cross-luminescence), CeF_3, and PbF_2 (Cherenkov light).

References

[1] Doser, M, Auffray, E, Brunbauer, FM, Frank, I, Hillemanns, H, Orlandini, G, Kornakov, G 2022, 'Quantum Systems for Enhanced High Energy Particle Physics Detectors', *Front. Phys.*, 10, 887738, Lausanne: Frontiers Media SA

[2] Král, J, Děcká, K, Zabloudil, V, Liška, P, Hájek, F, Horák, M, Čuba, V, Mihóková, E, Auffray, E 2021, 'On the Cs4PbBr6 Phase in the Luminescence Performance of Bright CsPbBr3 Nanocrystals', *Nanomaterials*, 11(8), 1935, Basel: MDPI

[3] Haddad, Y, Arora, D, Auffray, E, Doser, M, Salomoni, M, Weber, M 2025, 'Quantum dot based chromatic calorimetry: a proposal', *Journal of Instrumentation*, 20(08), P08029, Bristol: IOP Publishing

Time:
10 November, 2026
15:00 – 17:00

Room:
ALBÉNIZ & MACHUCA

NSS-08 | Synchrotron, FEL and XFEL detectors

Chairs:
Beatrice Pedretti (Milano)
Matteo Porro (Schenefeld)

NSS-08-01

Production Results of DEPFET-Based Modules for the DSSC Imager at the European XFEL (#1421)

Stefano Maffessanti[1], Karsten Hansen[1], Pradeep Kalavakuru[1], Christian Reckleben[1], Stefan Aschauer[2], Andrea Castoldi[3,4], Carlo E. Fiorini[3,4], Elisa Riceputi[5,6], Lothar Strüder[2,7], Matteo Porro[8,9]

[1] Deutsches Elektronen-Synchrotron DESY, Hamburg, Germany; [2] PNSensor GmbH, Munich, Germany; [3] Politecnico di Milano, Dipartimento di Elettronica, Informazione e Bioingegneria, Milano, Italy; [4] Istituto Nazionale di Fisica Nucleare, Sezione di Milano, Milano, Italy; [5] Università di Bergamo, Dalmine, Italy; [6] Istituto Nazionale di Fisica Nucleare, Sezione di Pavia, Pavia, Italy; [7] University of Siegen, Siegen, Germany; [8] European XFEL, Schenefeld, Germany; [9] Ca' Foscari University of Venice, with Department of Molecular Sciences and Nanosystems, Venezia, Italy

This work was supported by the European XFEL GmbH in the DSSC project framework.

Abstract

The DEPFET Sensor with Signal Compression (DSSC) is a 1-megapixel, 2D X-ray detector designed for the European XFEL, capable of operating at MHz frame rates. This work presents the characterization results of the second-generation DSSC focal-plane modules (FPMs), which incorporate active DEPFET sensors to improve dynamic range and performance compared to the first-generation mini-SDD-based camera. Each FPM—the smallest independent unit of the camera—comprises two sensors read by eight ASICs and underwent rigorous geometric characterization, with sensor-to-sensor systematic deviation of 32.9 ± 68.9 µm and −48.6 ± 66.9 µm in the x- and y-direction, respectively. Functional tests were run under vacuum at 18°C. Key metrics demonstrated excellent reproducibility of prototype characterization, with tight distributions in sensitivity (199.4 ± 5.4 eV/ADU), equivalent-noise charge (23.2 ± 1.2 e- rms), first gain-compression energy (74.9 ± 4.3 keV) and in-pixel leakage current (1.3 ± 0.3 pA/pixel). The results validate the reliability of the DEPFET FPMs for integration into the 1-megapixel camera, ensuring uniform performance.

References

[1] M. Porro et al., "The MiniSDD-Based 1-Mpixel Camera of the DSSC Project for the European XFEL," IEEE Trans. Nucl. Sci., vol. 68, no. 6, pp. 1334–1350, 2021, doi: 10.1109/TNS.2021.3076602.

[2] S. Maffessanti et al., "A 64k pixel CMOS-DEPFET module for the soft X-rays DSSC imager operating at MHz-frame rates," Sci. Rep., vol. 13, no. 1, p. 11799, Jul. 2023, doi: 10.1038/s41598-023-38508-9.

[3] K. Hansen et al., "Qualification and Integration Aspects of the DSSC Mega-Pixel X-Ray Imager," IEEE Trans. Nucl. Sci., vol. 66, no. 8, pp. 1966–1975, Aug. 2019, doi: 10.1109/TNS.2019.2927421.

NSS-08-02

Performance of the pFREYA16 ASIC for pixelated detectors in continuous-wave x-ray applications (#2037)

Paolo Lazzaroni[1,2], Mike Hammer[3], Massimo Manghisoni[1,2], Antonino Miceli[3], Lodovico Ratti[4,2], Valerio Re[1,2]

[1] Università degli Studi di Bergamo, Dipartimento di Ingegneria e Scienze Applicate, Dalmine (BG), Italy; [2] INFN, Sezione di Pavia, Pavia, Italy; [3] Argonne National Laboratory, X-ray Science Division, Lemont, USA; [4] Università di Pavia, Dipartimento di Ingegneria Industriale e dell'Informazione, Pavia, Italy

Abstract

The fourth generation of synchrotron light sources brings unprecedented brightness to the experimental stations of the x-ray science community. As light sources improve their performance, detector instrumentation requirements become more demanding. Among these, readout electronics should be capable of achieving zero dead-time, handling an inter-bunch spacing of just a few nanoseconds, and including a digital backend able to deal with the expected data stream. In this context, a prototype readout channel has been developed in a commercial 65 nm CMOS technology and assembled in a 16-pixel matrix, named pFREYA16. Each pixel features a low-noise Charge-Sensitive Amplifier, a semi-Gaussian unipolar RC-CR shaper with four selectable peaking times, a pseudo-differential discrimination chain to enable zero-suppression, and an A/D chain with a differential S/H and a differential 10-bit SAR ADC, along with a basic digital backend to shift data out and configure the matrix. The prototype has been fully characterised at each stage of the signal processing chain. It exhibits a linear input-output transfer characteristic over a full-well capacity of 256 photons at 5, 9, 15, and 25 keV, single-photon resolution with a measured ENC of 380 e- rms at 9 keV at a frame rate of 1 MHz, and a power consumption of approximately 220 uW per pixel.

References

[1] R. Hettel, "Status of the APS-U Project," *Proc. IPAC2021*, vol. IPAC2021, pp. 1–6, 2021, doi: 10.18429/JACOW-IPAC2021-MOXA02.

[2] S. Strempfer *et al.*, "A lightweight, user-configurable detector ASIC digital architecture with on-chip data compression for MHz X-ray coherent diffraction imaging," *J. Instrum.*, vol. 17, no. 10, p. P10042, Oct. 2022, doi: 10.1088/1748-0221/17/10/P10042.

[3] C. Jacobsen, J. Deng, and Y. Nashed, "Strategies for high-throughput focused-beam ptychography," *J. Synchrotron Rad.*, vol. 24, no. 5, pp. 1078–1081, Sep. 2017, doi: 10.1107/S1600577517009869.

[4] P. Lazzaroni, "Design of a pixel readout processor for nano-meter resolution x-ray ptychography," Doctoral Thesis, Università degli studi di Bergamo, 2024. doi: 10.13122/lazzaroni-paolo_phd2024-04-18.

[5] P. Lazzaroni *et al.*, "Analog Readout Channel for Continuous-wave X-ray Science Applications," *IEEE Trans. Nucl. Sci.*, pp. 1–1, 2025, doi: 10.1109/TNS.2025.3565911.

NSS-08-03

DIANA: An LGAD-Based Architecture for Soft X-Ray Detection (#2095)

Francesca Capocasa[1], Abdul Rumaiz[2], Giovanni Pinaroli[1], Gabriele Giacomini[1], Anthony J. Kuczewski[2], David P. Siddons[2], Gabriella Carini[3]

[1] Brookhaven National Laboratory, Instrumentation, Upton, USA; [2] Brookhaven National Laboratory, NSLS II, Upton, USA; [3] Brookhaven National Laboratory, Discovery Technology Directorate, Upton, USA

Abstract

Soft X-ray detection is essential for synchrotron and free-electron laser science, but existing detector technologies remain limited in quantum efficiency, signal-to-noise ratio, and readout performance at low photon energies. In this work, we present DIANA, a Low-Gain Avalanche Diode (LGAD)-based detector architecture optimized for soft X-ray applications. The device employs a p-type entrance window for high transparency and places the gain layer on the readout side, allowing charge carriers generated near the entrance surface to drift through the full silicon thickness before undergoing controlled internal amplification. An additional n-type buffer layer is introduced between the gain layer and segmented readout electrodes to mitigate electric field non-uniformities and improve stability. TCAD simulations and first prototype fabrication at Brookhaven National Laboratory demonstrate stable operation above full depletion and confirm the effectiveness of the buffer layer in shaping the electric field. Electrical characterization shows clear charge multiplication with gains up to approximately 3, while spectroscopic measurements demonstrate stable and nearly energy-independent amplification across the investigated photon-energy range. These results validate the DIANA concept as a promising candidate for next-generation soft X-ray detectors.

NSS-08-04

Matterhorn: Initial Characterization of Single-Chip Assemblies (#2805)

Viveka Gautam, Anna Bergamaschi, Roberto Dinapoli, Erik Frojdh, Davide Mezza, Konstantinos Moustakas, On behalf of the detector group whose members include M. Anastasi, M. Bruckner, S. Ebner, S. Emiliani, K. Ferjaoui, D. Greiffenberg, S. Hasanaj, V. Hinger, V. Kedych, T. King, S. Li, C. Lopez-Cuenca, L. Lunin, A. Mazzoleni, S. Moses, A. Mozzanica, J. Mulvey, M. Muller, C. Ruder, B. Schmitt, S. Silletta, D. Thattil, X. Xie and J. Zhan

PSI, Center for photon science, Villigen, Switzerland

Abstract

The upgrade of synchrotron facilities, such as Swiss Light Source 2.0 (SLS 2.0), will provide significantly higher brilliance and photon flux than current-generation sources. These operating conditions will exceed the count-rate capability of many existing single-photon-counting detectors. Although higher photon flux improves acquisition capability, synchrotron experiments still often rely on detecting weak features where only a few photons contain

important information. Preserving sensitivity while operating at very high photon flux therefore becomes a major challenge. To address these limitations, Matterhorn, a single photon counting hybrid pixel detector, is developed at the Paul Scherrer Institute for future high-flux synchrotron experiments. The detector implements a multi-threshold photon-counting architecture with four independently adjustable thresholds in each pixel to improve count-rate performance under high-flux condi- tions. The detector targets count rate up to 20 Mcounts/pixel/s through the implementation of multi-threshold circuitry in each pixel. The ASIC consists of a 256 × 256 pixel matrix with a pixel pitch of 75 × 75 µm 2 and is implemented in UMC 110 nm technology. Single-chip assemblies (i.e. a single chip bump- bonded to a single-chip sensor) are characterized using both a laboratory X-ray source and measurements at the SLS beamline. Preliminary measurements demonstrate stable operation of the full-size ASIC and reproduce the performance from the prototype studies. This contribution presents the current characterization status and summarizes the main performance results obtained so far, while a more detailed discussion of the detector architecture will be presented in a separate contribution.

NSS-08-05

ORBIS: an X-ray SDD Array with Optimized Backscattering Detection Geometry (#2839)

Pietro Barcella[1,2], Beatrice Pedretti[1,2], Giacomo Borghi[1,2], Marco Carminati[1,2], Matteo Centis Vignali[4], Francesco Ficorella[4], Gerald Falkenberg[3], Axel Rosenhahn[5], Carlo E. Fiorini[1,2]

[1] Politecnico di Milano, Dipartimento di Elettronica,Informazione e Bioingegneria, Milano, Italy; [2] Istituto Nazionale di Fisica Nucleare, Sezione di Milano, Milano, Italy; [3] Deutsches Elektronen-Syncrotron, Hamburg, Germany; [4] Fondazione Bruno Kessler, Trento, Italy; [5] Ruhr-University Bochum, Bochum, Germany

Abstract

In X-Ray Fluorescence Microscopy, where the analyses can take up to several hours, optimizing the solid angle of the spectrometer is critical. Moreover, the use of multichannel spectrometers is now a necessity due to the high throughput required from the incread brilliance achieved by modern, 4th generation synchrotrons.

ORBIS is a 16-channel monolithic SDD array optimized for backscattering configurations, with a geometry that can guarantee an uncollimated total solid angle coverage of 2.35 sr while ensuring uniform irradiation of all the pixels. The project, supported by Ruhr University Bochum (RUB) and Deutsches Elektronen-Synchrotron (DESY) aims to develop a novel, vacuum compatible spectrometer to be used for biological experiments.

A preliminary characterization of the SDD array shows promising results, with FWHM resolutions as low as 131 eV measured at the Mn-kα line at 800 ns peaking time, and 171 eV FWHM at 32 ns peaking time.

The first tests in P06 beamline are planned in June 2026, during which the instrument performance will be evaluated. The results of this campaign will be reported at the conference.

References

[1] Utica, G., Fabbrica, E., Carminati, M., Borghi, G., Zorzi, N., Ficorella, F., ... & Fiorini, C. (2021). ARDESIA-16: a 16-channel SDD-based spectrometer for energy dispersive X-ray fluorescence spectroscopy. *Journal of Instrumentation*, *16*(07), P07057.

[2] Ryan, C. G., Siddons, D. P., Kirkham, R., Li, Z. Y., De Jonge, M. D., Paterson, D. J., ... & Borg, S. (2014, April). Maia X-ray fluorescence imaging: Capturing detail in complex natural samples. In *Journal of Physics: Conference Series* (Vol. 499, No. 1, p. 012002).

[3] Rumancev, C., Gräfenstein, A., Vöpel, T., Stuhr, S., Von Gundlach, A. R., Senkbeil, T., ... & Rosenhahn, A. (2020). X-ray fluorescence analysis of metal distributions in cryogenic biological samples using large-acceptance-angle SDD detection and continuous scanning at the Hard X-ray Micro/Nano-Probe beamline P06 at PETRA III. *Synchrotron Radiation*, *27*(1), 60-66.
[4] Ticchi, G., Venturelli, M., Utica, G., Carminati, M., Borghi, G., Zorzi, N., ... & Fiorini, C. (2022, December). Optimization of solid angle and count rate capability of an X-ray detector with backscattering geometry. In *Journal of Physics: Conference Series* (Vol. 2380, No. 1, p. 012099). IOP Publishing.
[5] Iguaz, F. J., Bombelli, L., Meo, S., Orsini, F., Schöder, S., Tocchio, A., ... & Vantelon, D. (2023). DANTE Digital Pulse Processor for XRF and XAS experiments. *Journal of Instrumentation*, *18*(06), T06011.

NSS-08-06

Experimental Characterization of a Front-End Stage for Future XFEL Detectors (#2843)

Adele Ciavarella-Ciavarella[1,2], Pietro Barcella[1,2], Giacomo Borghi[1,2], Marco Carminati[1,2], Matteo Porro[3,4], Carlo E. Fiorini[1,2]

[1] Politecnico di Milano, Dipartimento di Elettronica, Informazione e Bioingegneria, Milan, Italy; [2] Istituto Nazionale di Fisica Nucleare, Sezione di Milano, Milan, Italy; [3] European XFEL, Schenefeld, Germany; [4] Università di Venezia Ca' Foscari, Dipartimento di Scienze Molecolari e Nanosistemi, Venice, Italy

Abstract

The evolving requirements of X-ray Free Electron Laser (XFEL) applications in terms of speed, dynamic range, and noise motivate the development of new X-ray pixel detectors. The next generation of detectors must provide a high dynamic range while maintaining low-noise performance to ensure single-photon detection at low energies. In this work, we present a front-end architecture employing a Charge Sensitive Amplifier (CSA) with predictive gain switching and a Flip-Capacitor filter. The CSA is designed to achieve both a high dynamic range up to 10^4 photons and single-photon resolution by means of active gain control. The novel predictive gain switching circuit sets the optimal gain by measuring the time required for the CSA output signal to exceed a fixed threshold. The trapezoidal filter, by reducing the electronic noise, enables single-photon resolution at low energies when the CSA operates in its highest gain configuration. A dedicated voltage-to-current converter has been designed to couple the CSA and the filter. The proposed front-end is implemented in 65 nm CMOS technology, and preliminary characterization has been performed to evaluate gain switching and noise performance. The ASIC has been coupled to a Silicon Drift Detector (SDD), and an Equivalent Noise Charge of 35 e^- has been measured. Further measurements, including tests with a mini-SDD, are planned. This front-end architecture will be proposed for the XSTREAM (Xray detector System with high-Throughput REadout Architecture and Modularity) Pathfinder.

References
[1] Ciavarella-Ciavarella , et al. Design of a front-end stage for future european xfel detectors. IEEE Transactions on Nuclear Science, 73(1):34–40, 2026.
[2] Buonanno, et al. Gamma: A 16-channel spectroscopic asic for sipms readout with 84-db dynamic range. IEEE Transactions on Nuclear Science, 68(10):2559–2572, 2021.
[3] Facchinetti, et al. Characterization of the flip capacitor filter for the xfel dssc project. IEEE Transactions on Nuclear Science, 58(4):2032–2038, 2011.

NSS-08-07

Mapping of the charge collection function of hexagonal DEPFET pixels with the mesh experiment (#2892)

Andrea Castoldi[1,2], Andrea Castoldi[1,2], Maurizio Ghisetti[1,2], Maurizio Ghisetti[1,2], Chiara Guazzoni[1,2], Chiara Guazzoni[1,2], **Andrea Mason**[1,2], **Andrea Mason**[1,2], Stefano Maffessanti[3], Stefano Maffessanti[3], Cyril Danilevski[4], Cyril Danilevski[4], Loïc Le Guyader[4], Loïc Le Guyader[4], David Lomidze[4], David Lomidze[4], Matteo Porro[4,5], Matteo Porro[4,5], Monica Turcato[4], Monica Turcato[4], Sergey Usenko[4], Sergey Usenko[4]

[1] Politecnico di Milano, DEIB, Milano, Italy; [2] INFN, Sezione di Milano, Milano, Italy; [3] DESY, Hamburg, Germany; [4] European XFEL, Schenefeld, Germany; [5] Università Ca' Foscari, Venezia, Italy

Abstract

We performed the mesh experiment to map the charge collection function of hexagonal DEPFET pixels of the DSSC camera, a 1024x1024 hybrid pixel detector targeted at soft X-ray imaging experiments at the European XFEL with stringent requirements on noise, speed and dynamic range. With a read noise of few electrons rms, the measurement of the pixel charge collection function and its correlation to pixel layout and operating conditions are essential to assess the spectroscopic performance of the camera and detect possible optimizations. The obtained virtual scan of the hexagonal pixel of one DSSC sensor (256x128 pixels) highlights a non-uniform charge collection that can affect the camera spectroscopic performance, proving the effectiveness of this technique to optimize the performance of large, low-noise detectors.

NSS-08-08

Gated MCP High Resolution Detectors for UV, Soft X-ray photons, Ions, Neutrons and Electrons (#3099)

Anton Tremsin[1], Travis Curtis[1], Dennis Tercero[1], John Vallerga[1], Richard Raffanti[2], Niko Pontius[3], Christian Schüßler-Langeheinee[3]

[1] University of California, Berkeley, Space Sciences Laboratory, Berkeley, USA; [2] Techne Instruments, Oakland, USA; [3] Helmholtz-Zentrum Berlin für Materialien und Energie, Berlin, Germany

Development of MCP/Timepix detectors was partially supported by NASA Grant #80NSSC20K0496, DOE Contract No. DE-AC02-05CH11231 and several other sources.

Abstract

High-resolution particle detectors based on microchannel plates (MCPs) provide unique capabilities for applications requiring detection of photons, electrons, ions, and neutrons with high spatial and temporal resolution. Recent advances in readout technologies have substantially increased the counting-rate capabilities of these detectors, with rates exceeding 10^8 particles/s/cm². However, experiments with even higher incident fluxes remain limited by the number of particles that MCP detectors can process.

In some high-flux applications, only a small fraction of the incident particles needs to be recorded, while the total flux can be extremely high. In such cases, fast gating of the detector can prevent unnecessary charge extraction and allow MCP-based detectors to operate under otherwise unsustainable flux conditions. For soft X-ray, gamma photons, electron, neutron and ion detection, the primary particle conversion occurs at the front surface of the MCP itself. In this case, the MCP itself must be gated directly, which is challenging because of the MCP's large capacitance and high operating bias.

In this paper, we present results from gated MCP detectors that can be switched on and off on a time scale of approximately 5 ns. We demonstrate this capability using an MCP detector with a Timepix readout, selectively detecting chosen synchrotron pulses while suppressing detection of the remaining bunches. Without gating, the detector is oversaturated and cannot operate under the same incident flux. This gating approach is applicable to a broad range of MCP readout configurations, not only Timepix-based systems, and enables high-resolution MCP detectors to be used in applications where the total input flux would otherwise exceed their sustainable operating range.

Time:
10 November, 2026
17:30 – 19:00

Room:
ALBÉNIZ & MACHUCA

NSS-09 | Neutron and gamma-ray detectors and applications, including security, dosimetry and other related applications

Chairs:
Andrea Sagatova (Bratislava)
Lei R. Cao (Columbus)

NSS-09-01

Development and Experimental Validation of a Numerical Model for Fission Particles Multiplicity Counting using Polyvinyl Toluene Scintillators (#1470)

Filip d'Almeida[1], Vincent Bottau[1], Cyrille Eleon[1], Bertrand Pérot[1], Cédric Carasco[1], Mohamed Abdelli[1], Jacob Lamblin[3], Olivier Litaize[2], Achment Chalil[1]

[1] CEA IRESNE, DTN/SMTA/LMN, Saint-Paul-Lez-Durance, France; [2] CEA IRESNE, DER/SPRC/LEPh, Saint-Paul-Lez-Durance, France; [3] Grenoble Alpes University, CNRS / Grenoble INP / LPSC-IN2P3, Grenoble, France

Abstract

A system comprising sixteen polyvinyl toluene (PVT) scintillators is under development at the Nuclear Measurements Laboratory (CEA IRESNE) for the passive nondestructive assay of alpha-contaminated waste drums. Although PVT scintillators offer a low-cost alternative to ^{3}He counters, their sensitivity to gamma rays and scattering cross-talk restricts the use of traditional multiplicity equations for determining spontaneous fission rates. Machine learning methods provide a viable solution to this inverse problem but require extensive training datasets, necessitating a reliable, experimentally validated numerical model. Therefore, a novel calculation scheme utilizing the FIFRELIN and PHITS Monte Carlo codes is introduced. This framework generates and transports prompt fission particles, extracting raw time-of-flight and energy deposition data. The resulting files are subsequently processed using ROOT scripts to model the detectors' response. Specifically, the energy resolution function implemented in the simulation is derived from a ^{60}Co source measurement, utilizing parameters adjusted to align the simulated and experimental spectra. The full framework demonstrates good agreement with the measurement of ^{252}Cf doubles and triples counts, enabling the generation of training data for regression models capable of accurately predicting spontaneous fission rates across various measured mock drum configurations.

References

[1] B. Simony *et al.*, "Passive neutron coincidence counting with plastic scintillators for the characterization of radioactive waste drums," IEEE Trans. Nucl. Sci., vol. 64, no. 10, pp. 2719–2724, Oct. 2017.

[2] V. Bottau *et al.*, "Detection of Fission Coincidences with Plastic Scintillators for the Characterization of Radioactive Waste Drums," IEEE Transactions on Nuclear Science, vol. 69, no. 4, pp. 818-824, April 2022, doi: 10.1109/TNS.2022.3144346.

[3] I. Pázsit, A. Enqvist, S. Avdic, "Combined use of neutron and gamma multiplicities for determining sample parameters," Proceedings of the 2009 International Conference on Mathematics, Computational Methods & Reactor Physics (M&C 2009).

[4] R. Sarwar *et al.*, "An event-triggered coincidence algorithm for fast-neutron multiplicity assay corrected for cross-talk and photon breakthrough," Nucl. Instr. Methods Phys. Res. A: Accel., Spectrom., Detect. Assoc. Equip., vol. 903, pp. 152-161, 2018, doi: 10.1016/j.nima.2018.06.056.

[5] https://faster.in2p3.fr

[6] O. Litaize, O. Serot, & L. Berge, "Fission modelling with FIFRELIN". Eur. Phys. J. A 51, 177 (2015). https://doi.org/10.1140/epja/i2015-15177-9

[7] T. Ogawa *et al.*, "Overview of PHITS Ver. 3.34 with particular focus on track-structure calculation", EPJ Nuclear Sci. Technol. 10, 13 (2024), https://doi.org/10.1051/epjn/2024012

[8] R. Brun, F. Rademakers, "ROOT – An object-oriented data analysis framework", Nucl. Instr and Meth. In Phys. Res. A, Vol. 389, 1997, https://doi.org/10.1016/S0168-9002(97)00048-X

[9] N. Ensslin, "Principles of neutron coincidence counting," in Passive Nondestructive Assay of Nuclear Materials. Los Alamos, NM, USA: Los Alamos Nat. Lab., 1991, ch. 16, pp. 457–491.

NSS-09-02

Recent Advances in Developing Fluoride Eutectic Scintillators for Neutron Detection (#1651)

Cai L. Wang[1,2], Xunsheng Zhou[1,2]

[1] Songshan Lake Materials Laboratory, Neutron Science-Imaging Science and Technology, Dongguan, China; [2] Dongguan Institute of Materials Science and Technology, Division of Advanced Scientific Instruments and Equipment, Donguan, China; [3] Quantum Science Center of Guangdong-Hongkong-Macao Greater Bay Area, Division of Instruments, Shenzhen, China

This research was supported by National Natural Science Foundation of China Major Instrument Project (52127817), and Guangdong Provincial Quantum Science Strategic Initiative (GDZX23032006).

Abstract

The ^{6}Li-glass (GS20) Scintillator-based Anger cameras have been used for single-crystal neutron diffractometry. To expand their applications for more neutron-scattering instruments and Boron Neutron Capture Therapy (BNCT) with a neutron flux~10^{9} n/s/cm^{2}, there are urgent needs to improve the neutron detection efficiency, light yield, and neutron-gamma discrimination ratio (NGD ratio, or efficiency ratio), and to reduce the light decay lifetime of the neutron scintillator. We have developed Eu^{2+}:CaF_2/^{6}LiF eutectic scintillators to potentially replace the GS20 in neutron Anger cameras. In this work, we show our further endeavors in i). enhancing light yield of the eutectics in casting method; ii). improving transparency and uniformity of the eutectics in oriented growth; iii). reducing the light decay lifetime to about 4 ns via Pr^{3+} doping; iv). the enhancement in the NGD ratio using an optimized multi-layer graph filter under a self-supervised learning framework. Therefore, future Eu:CaF_2/^{6}LiF eutectic neutron scintillators are expected to find wider applications not only in neutron scattering and BNCT, but also in nuclear power plants and homeland security.

References

[1] C. L. Wang and R. A. Riedel, “Improved neutron-gamma discrimination for a ^{6}Li-glass neutron detector using digital signal analysis methods”, *Rev. Sci. Instrum.*, vol.87, 013301, 2016.

[2] C. L. Wang, M. P. Paranthaman, R. A. Riedel, J. P. Hodges, J. J. Karlic, R. A. Veatch, L. Li, and C. A. Bridges, “Bright Eu^{2+}-activated polycrystalline ceramic neutron scintillators”, *Nucl. Instrum. Methods A*, vol. 883, pp.1-8, 2018.

[3] X. Zhou, B. Zhao, L. Yao, W. Gui, L. Chen, C. Li, S. Zhang, and C. L. Wang, “Al^{3+} co-doped LiF-CaF_2:Eu^{2+}bright eutectic scintillators for large-area thermal neutron detectors”, *ACS Appl. Opt. Mater.*, vol. 2, pp.1495-1504, 2024.

[4] C. L. Wang, “Optimizing event graphs in particle discrimination for neutron detectors”, *IEEE Nuclear Science Symposium and Medical Imaging Conference*, Nov. 2024, p.1.

[5] C. L. Wang, “Gd-containing scintillators for thermal neutron detection via graph-based particle discrimination”, *Rev. Sci. Instrum.*, vol. 92, 103304, 2021.

NSS-09-03

3D Boron-Coated Straw Detector Array for Tomographic Multiplicity Counting (#1768)

Ming Fang[1], David Breitenmoser[2], Shaun D. Clarke[2], Sara A. Pozzi[2], Scott Thompson[3], David L. Chichester[3], Angela Di Fulvio[1]

[1] University of Illinois Urbana-Champaign, Department of Nuclear, Plasma, and Radiological Engineering, Urbana, USA; [2] University of Michigan, Department of Nuclear Engineering & Radiological Sciences, Ann Arbor, USA; [3] Idaho National Laboratory, Radiochemistry and Nuclear Measurements Department, Idaho Falls, USA

This material is based upon work supported by the Department of Energy Office of Nuclear Energy's Nuclear Energy University Program under Award Number DE-NE0009507.

Abstract

Accurate assessment of plutonium content during pyroprocessing is needed to enhance the proliferation resistance. Matrix isotopic heterogeneity, source non-uniformity, and high gamma-ray emission rate prevent the application of traditional non-destructive assay (NDA) systems and methods. We aim to develop a novel NDA system that can withstand pyroprocessing harsh environments and have consistent sensitivity and accuracy despite different fuel form factors. The proposed NDA system encompasses two system modules, a boron-coated-straw (BCS) multiplicity module and a 3D boron-coated-straw detector array (3D-BCSDA) tomography module. The multiplicity module performs multiplicity counting and provides assay observables, whereas the tomographic module reduces systematic biases by enabling geometry-aware corrections. In this work, we report the development of the multiplicity module and the 3D-BCSDA tomography module. The multiplicity module consists of six 64-straw BCS panels, with a measured neutron detection efficiency of 12.4% and die-away time of 42 μs. The tomography module is a moderated array incorporating thirty one-meter-long boron-coated straws with double-sided readout. Time delay lines and charge sharing have been implemented to enable 3D localization of the neutron interaction event. We will begin experimental testing with laboratory sources at UIUC and plutonium sources at INL to assess the system’s accuracy in real-world conditions, supporting the integration of tomographic imaging with neutron multiplicity counting for bulk plutonium assay.

NSS-09-04

An Imaging and Spectroscopy Detector for High-Energy and High-Rate Gamma-Ray Measurements (#2645)

Korbinian Urban[1,2], Martina Piroddi[1,2], Christian Riboldi[1,2], Andrea Forgione[1,2], Letizia Santini[1,2], Fabio Garzetti[1], Giacomo Borghi[1,2], Marco Carminati[1,2], Emma S. Bellotti[3], Davide Bortot[3], Davide Mazzucconi[3], Carlo E. Fiorini[1,2]

[1] Politecnico di Milano, Department of Electronics, Information and Bioengineering (DEIB), Milan, Italy; [2] National Institute for Nuclear Physics (INFN), Milan Section, Milan, Italy; [3] Politecnico di Milano, Department of Energy (DENG), Milan, Italy

This work was supported by the REALPATH project (Italian MUR), grant n. FISA-2022-00779

Abstract

The REALPATH detector and readout platform is a pixilated scintillation detector developed for prompt gamma imaging in proton therapy. Prompt gamma imaging aims to provide online verification of proton range via the position-sensitive detection of prompt gamma rays emitted during proton treatment. Due to the high fluence of modern medical proton accelerators, the detector is designed to cope with rates of up to 1 Mcps per pixel across 512 pixels. At the same time, good spectroscopic performance at high energies in the range of 3 MeV to 6 MeV is beneficial for neutron background rejection and prompt-gamma emission analysis. To address these requirements, each LYSO pixel features an independent SiPM readout, implemented with the custom SITH (spectroscopy imaging timing hadrontherapy) ASIC. In this work, we present the experimental characterization of the first 64-channel detector module. Using a ^{137}Cs source, we measured an average resolution of 8.5% at 662 keV for all pixels at low rates. The high source activity allowed us to characterize the detector up to 1.9 Mcps input count rate per channel. The high-energy performance was tested with a ^{241}Am-Be source that provides gamma rays of 4.44 MeV. By applying a light-sharing correction and combining data from coincident events across multiple pixels, we achieved an energy resolution of 4.8% at the 4.44 MeV full-energy peak. With these characteristics, the detector may also be suited for applications beyond prompt gamma imaging that require position-resolved high-rate gamma spectroscopy.

References

[1] Pinto, Marco, 2024, Prompt-gamma imaging in particle therapy, Eur. Phys. J. Plus , Vol. 139, No. 10

[2] Jolly et. al., 2020, Technical challenges for FLASH proton therapy, Phys. Medica , Vol. 78, p. 71-82

[3] D'Adda et. al., 2024, SITH: An SiPM Readout ASIC for Prompt Gamma-Ray Detection in Hadrontherapy Applications, IEEE Trans. Nucl. Sci. , Vol. 71, No. 9, p. 2140-2150

[4] Riboldi et. al., 2025, Design of a 64-channel modular platform for high-speed readout of scintillator-based detectors for range monitoring in hadrontherapy, J. Instrum. , Vol. 20, No. 09, p. P09037

NSS-09-05

Ratiometric Alpha-Particle and Gamma-Ray Imaging with a Ligand-Stabilized $CsPbBr_3$Perovskite-Nanoparticle Coating on a 4.8-Megapixel Stacked CMOS Sensor (#2798)

Haoxiang Chang[1], Shubham Mandot[2], Shangzhen Zhu[2], Ming Fang[2], Angela Di Fulvio[2], Shuming Nie[3,4], Ling-Jian Meng[2,4], Viktor Gruev[1,4]

[1] University of Illinois at Urbana-Champaign, Department of Electrical and Computer Engineering, Champaign, USA; [2] University of Illinois at Urbana-Champaign, Department of Nuclear, Plasma, and Radiological Engineering, Champaign, USA; [3] University of Illinois at Urbana-Champaign, Department of Bioengineering, Champaign, USA; [4] University of Illinois at Urbana-Champaign, Beckman Institute for Advance Science and Technology, Champaign, USA

Abstract

Conventional alpha/gamma instruments often use bulk scintillators coupled to photomultiplier or silicon-photomultiplier pulse processing, or hybrid pixel detectors optimized for timing or deposited-energy readout; compact megapixel imaging with ratiometric particle-type contrast remains less developed. A monolithic alternative is demonstrated by spin-coating a 10-μm film of ligand-stabilized $CsPbBr_3$ perovskite nanoparticles (PNCs) onto a vertically stacked 4.8-megapixel complementary metal-oxide-semiconductor (CMOS) image sensor containing three photodiodes per pixel. Gamma-ray interactions in the PNC layer generate green scintillation photons that are registered differentially by the top, middle, and bottom photodiodes, whereas alpha particles deposit energy primarily in the top photodiode layer. Comparing these spatially registered photodiode responses with cluster amplitude and event footprint yields ratiometric single-frame alpha/gamma signatures without an external scintillator/photomultiplier timing chain. Radiation-induced events were extracted from full-frame readout as temporally nonpersistent, 8-connected pixel clusters. Relative to the uncoated sensor, the coated detector increased gamma-candidate event yield by 10^3-10^4 in Am-241, Co-57, and Ac-225 measurements. Gamma-candidate clusters exhibited median signal-to-noise ratios of 10.9-11.0 and a median footprint of one pixel. In unfiltered Ac-225 free-path measurements, the coated sensor preserved the direct alpha-particle response while adding gamma sensitivity. These results establish a spin-coated PNC/three-photodiode stacked CMOS architecture for compact, spatially resolved, ratiometric alpha/gamma imaging.

References

[1] G. F. Knoll, Radiation Detection and Measurement, 4th ed. Hoboken, NJ, USA: Wiley, 2010.

[2] X. Llopart, R. Ballabriga, M. Campbell, L. Tlustos, and W. Wong, "Timepix, a 65k programmable pixel readout chip for arrival time, energy and/or photon counting measurements," *Nucl. Instrum. Methods Phys. Res. A*, vol. 581, no. 1-2, pp. 485-494, 2007.

[3] F. Cova et al., "Scintillation Properties of CsPbBr3 Nanocrystals Prepared by Ligand-Assisted Reprecipitation and Dual Effect of Polyacrylate Encapsulation toward Scalable Ultrafast Radiation Detectors," *Nano Lett.*, vol. 24, no. 3, pp. 905-913, 2024.

NSS-09-06

Evolution of ZnS:Ag/^{6}LiF wavelength shifting fibre detectors from flat to tilted geometry (#2905)

Giacomo Mauri[1], Jeff G. Sykora[1], Sarah E. Mann[1], Erik M. Schooneveld[1], Nigel J. Rhodes[1]

[1] STFC, ISIS, Harwell Campus, UK; [2] STFC/ISIS, Didcot, UK

Abstract

Scintillator-based neutron detectors have been developed at ISIS for over three decades, with ongoing research and development focused on enhancing performance and meeting increasingly demanding instrument requirements. The Endeavour programme places new demands on detector technology, particularly in achieving large-area coverage, high spatial resolution, and high counting-rate capability.

Conventional WLSF detectors are built from stacked flat scintillator screens interleaved with fibre planes. Achieving high neutron efficiency (~80% at 1.8 Å) requires four scintillator layers and two fibre planes. This work presents a novel approach to the design and manufacture of ZnS:Ag/^{6}LiF wavelength-shifting fibre (WLSF) detectors, with the potential to significantly improve both performance and cost-efficiency for next-generation systems.

This concept instead exploits the increase in neutron path length by tilting the scintillator relative to the incident beam. A V-shaped strip geometry is introduced, where the angle can be tuned to control detection efficiency and fibre spacing. This design also provides optical isolation between strips, enabling parallel signal processing for neutron event identification, which significantly reduces the detector dead time.A first linear position-sensitive detector prototype was developed featuring four regions with varying fibre pitches and tilt angles. This was followed by a 2D position-sensitive detector based on the same principle. The designs and performance results from tests on ISIS instruments are presented, along with a discussion of simplified manufacturing and reduced costs.

Overall, these advancements enhance detector capability and support the continued evolution of the ISIS science programme, enabling future instrument upgrades.

11 November, 2026

Time:
11 November, 2026
9:00 – 10:30

Room:
ALBÉNIZ & MACHUCA

NSS-10 | Analog and Digital Circuits I

Chairs:
Giuseppe Bertuccio (Como)
Matteo Porro (Schenefeld)

NSS-10-01

NSX1: A 64-Channel Low-Power Front-End ASIC for Broadband Energy Silicon Drift Detectors Arrays (#1411)

Gianluigi De Geronimo[1,2], Wayne H. Baumgartner[3], Sukanya Chakrabarti[4], Wesley Hodge[4], Nabin Poudyal[4], Paul S. Ray[3], Jarred Roberts[5], Colleen A. Wilson-Hodge[6], Eric A. Wulf[3]

[1] DG Circuits, Syosset, USA; [2] Stony Brook University, Stony Brook, USA; [3] U.S. Naval Research Laboratory, Washington, USA; [4] University of Alabama in Huntsville, Huntsville, USA; [5] University of California San Diego, San Diego, USA; [6] NASA Marshall Space Flight Center, Huntsville, USA

This work was supported by NASA (Proposal No. 22-APRA22-0026)

Abstract

We present NSX1, a very-low-power 64-channel front-end ASIC developed for large-area broadband-energy X-ray Silicon Drift Detectors (SDD) for space applications. Fabricated in 180 nm CMOS, it integrates dual-gain charge amplification, shaping, discrimination, peak detection, analog multiplexing, and 12-bit analog-to-digital conversion. The ASIC offers extensive programmability, including high-resolution mode, various discrimination modes, neighbor-channel/chip processing, peak processing modes, and power-down options. At less than 600 µW per channel and ~110 fF input capacitance (SDD anode + wirebond), it achieves an Equivalent Noise Charge (ENC) below 7 e^- (< 6 e^- in high-resolution mode), meeting or exceeding STROBE-X requirements.

NSS-10-02

Towards a 150 kHz Continuous Imager: The CoRDIA 0.5 Prototype 20 k Pixel Array (#2886)

Ulrich Trunk[1,2], Alexander Klujev[1,2], Sabine Lange[1,2], Alessandro Marras[1,2], David Pennicard[1,2], Cornelia B. Wunderer[1,2], Hans Krueger[3], Simon Spannagel[1], Tomas Vanat[1], Heinz Graafsma[1,4]

[1] DESY - Deutsches Elektronensynchrotron, Photon Science – Detector Systems Group, Hamburg, Germany; [2] DESY - Deutsches Elektronensynchrotron, CFEL, Hamburg, Germany; [3] Universität Bonn, Physikalisches Institut, Bonn, Germany; [4] Mid-Sweden University, Sundsvall, Sweden

NIKHEF (particularly V. Gromov and A. Vitkovskiy), for allowing the authors to include a version of the PCS-GWT circuit in the CoRDIA design, for fast data readout;
CERN, for allowing the reuse of CMOS IO pads and SOFIC ESD structures in the MPW design;
Europractice, IMEC and CERN for their MPW and design tool support.

Abstract
The Continuous Readout Digitizing Imager Array (CoRDIA) is an X-ray hybrid pixel detector currently being developed for scientific experiments exploiting the performance of 4th generation light sources, in particular that of PETRA IV, but also CW free electron lasers (FELs). Operating on the charge-integrating principle, it adopts the dynamic gain switching architecture and circuit topology of the AGIPD detector at the European XFEL to combine single photon sensitivity with a large dynamic range. Implementing the readout ASIC in a 65 nm CMOS technology enables a small pixel size of 110 × 110 μm^2.
To ensure up to 150 kframes/s dead time free operation, images are stored by a sample and hold (S&H) circuit, before digitisation by an 11 bit SAR ADC serving blocks of 16 pixels each. Data from 128 ADCs (2 kpixels) is driven off-chip by a 5.12 Gbit/s wire transmitter (GWT).
In spring of 2026 we completed the design of the ’20 k’ prototype CoRDIA 0.5, which combines the full signal chain consisting of 1232 4 × 4 pixel blocks (tested on CoRDIA 0.2) with 14 GWTs (tested on Timepix4 and CoRDIA 0.3). This chip also contains a programmable sequencer, controlling the ADC and readout operation. This sequencer is based on an SRAM memory and thus much more flexible than counter-based solutions as implemented e.g. on the AGIPD chip.
In addition to wirebond pads through silicon via (TSV) landing pads are evenly distributed across the whole chip area enabling ’local powering’ for future gapless detectors.
We will present the design of CoRDIA 0.5 with emphasis on the implementation of the readout sequencer, and new characterisation results.

References
[1] C. G. Schroer, et al., "PETRA IV: upgrade of PETRA III to the Ultimate 3D X-ray microscope. Conceptual Design Report," Deutsches Elektronen-Synchrotron DESY, 2019
[2] A. Marras, et al., "Development of the Continuous Readout Digitising Imager Array detector," JINST, 19 C03006, Mar. 2024.
[3] A. Allahgholi, et al., "The Adaptive Gain Integrating Pixel Detector at the European XFEL," J. Synchrotron Rad., vol. 26, no. 1, pp. 74–82, Jan. 2019.
[4] Y. Otarid, et al., "Caribou – A versatile data acquisition system for silicon pixel detector prototyping," JINST 20 C07043, Jul. 2025

NSS-10-03

LID: A 10-GS/s Self-Triggered Readout IC for Tightly Coupled Strip and Pixel LGAD Arrays (#2955)

Luca Macchiarulo[1], Isar Mostafanezhad[1], Eyan Forsythe[1], Gregory Uehara[1], Simone Mazza[2], Jennifer Ott[2], Christopher Chock[1]

[1] Nalu Scientific, LLC, HONOLULU, USA; [2] University of California, Santa Cruz, Santa Cruz Institute for Particle Physics (SCIPP), Santa Cruz, USA; [3] University of Hawaii at Manoa, Electical and Computer Engineering Department, Honolulu, USA

This work was partially funded under U.S. DOE DE-SC0025826 award.

Abstract

In this article we describe the design of the LGAD Integrated Digitizer (LID) - a readout Integrated circuit that is meant for tight coupling with dense LGAD arrays. The circuit is a multi-channel device that performs internal pre-amplification and self-triggered high rate digitization (10 Gsps) and digital processing. The RoIC is an evolution of previous HPSoC chips[1][2][3], and it features variants of the front end Transimpedance amplifier (TIA) that are capable of handling the higher capacitance of strip detectors. The paper will detail the design and performance of the TIAs, the planned integration with sensors, and the definition and hardware implementation of algorithms using waveforms from multiple channels to extract accurate position and timing information. Simulation results in the presence of noise show that the system is capable of fine location to within 10 percent of the sensor pitch and up to 9 ps of timing resolution in the best case.

References

[1] L. Macchiarulo, et al. "Design of HPSoC – a 10GSa/s Waveform Digitizer for Readout of Dense Sensor Arrays," 2022 IEEE (NSS), Italy

[2] L. Macchiarulo, et al., "HPSoCv2 - design and testing of an improved prototype for high density sensor array 10GSa/s Waveform Digitizer," 2024 IEEE (NSS), Tampa, FL, USA

[3] L. Macchiarulo et al. “HPSoCv3 - an integrated 9-channel 10 Gsps Waveform Digitizer for high density LGAD array” 2025 IEEE NSS, Yokohama, Japan, 2025.

[4] H. F. W. Sadrozinski et al., Ultra-fast silicon detectors, NIM-A 730 (2013) 226-231

NSS-10-04

SparkPix-S: A Sparsified Readout Detector for 1 MHz Frame-Rate X-Ray Imaging - Design Progress and Early Characterization Results (#1438)

Hyunjoon Kim[1], Lorenzo Rota[1], Aldo Pena-Perez[1], Christos Bakalis[1], Llorenç Fanals-i-Batllori[1], Dawood Alnajjar[1], Gang Liu[1], Xavier Defay[1], Dionisio Doering[1], Aseem Gupta[1], Alexandre Habib[3], Mike Hammer[2], Ping-Chen Huang[1], Chris Kenny[1], Hugo Hernandez[1], Bojan Markovic[1], Filippo Mele[5], Henry Shi[2], Ryan Herbst[1], Pietro King[4], Angelo Dragone[1]

[1] SLAC National Accelerator Laboratory, TID/ID/IC, Menlo Park, USA; [2] Argonne National Laboratory, Lemont, USA; [3] CentraleSupélec, Université Paris-Saclay, Gif-sur-Yvette, France; [4] European Organization for Nuclear Research (CERN), Geneva, Switzerland; [5] Politecnico di Milano, Milan, Italy

Use of the Linac Coherent Light Source (LCLS), SLAC National Accelerator Laboratory, is supported by the U.S. Department of Energy, Office of Science, Office of Basic Energy Sciences under Contract No. DE-AC02-76SF00515.

Abstract

We present the design progress and early test results of SparkPix-S, a charge-integrating readout application specific integrated circuit (ASIC) developed for next-generation X-ray cameras operating at the 1 MHz frame rate of LCLS-II. The SparkPix-S detector is being developed for X-ray Photon Correlation Spectroscopy (XPCS) and Speckle Visibility Spectroscopy (XSVS) experiments, where the inherent sparsity of the data — with average frame occupancies well below 1 % — enables a fundamentally different readout approach compared to conventional full-frame readout ASIC architectures. The pixel front-end architecture combines a charge-integrating front-end, coupled to an in-pixel discriminator to control the sparse readout architecture. 1 MHz operation is achieved through the combination of per-pixel asynchronous sparse readout logic, high-speed CML serial links, and a novel frame-work for sparse readouts named Pix2PGP. The first full-reticle (312 × 384 pixels) prototype has been fabricated in 130 nm CMOS technology. Electrical characterization of the front-end confirms noise performance below 60 electrons r.m.s., enabling single-photon sensitivity for tender X-ray energies. We report on the chip architecture, preliminary measurement results with a silicon sensor bump-bonded to the ASIC, and first results from the sample X-ray source testing with Cd-109 and Am-241, demonstrating the viability of the sparsified readout concept for MHz-rate photon science at free-electron laser facilities.

References

[1] Gr¨ubel, Gerhard, Madsen, Anders, and Robert, Aymeric 2008, “X-Ray Photon Correlation Spectroscopy (XPCS)”. In: Soft Matter Characterization. Ed. by Redouane Borsali and Robert Pecora. Dordrecht: Springer Netherlands,2008, pp. 953–995. ISBN: 978-1-4020-4465-6. DOI: 10.1007/978-1- 4020- 4465- 6 18. URL: https://doi.org/10.1007/978-1-4020-4465-6 18.

[2] Pena-Perez, Aldo et al. 2026, “A Low-Power Single-Ended SAR ADC With Energy-Efficient Differential Switching for Ultrafast X-Ray Imagers”. In: IEEE Open Journal of Circuits and Systems 7, pp. 255–268. DOI: 10.1109/OJCAS.2025.3628857.

[3] Rota, Lorenzo et al. 2024, “The SparkPix-S ASIC for the sparsified readout of 1 MHz frame-rate X-ray cameras at LCLS-II: pixel design and simulation results”. In: Journal of Instrumentation 19.01, p. C01010. DOI: 10.1088/1748- 0221/19/01/C01010. URL: https://doi.org/10.1088/1748-0221/19/01/C01010.

[4] Sandberg, Hampus et al. 2025, “GT Readout – A Development Platform for 1 MHz Frame-Rate Detectors at LCLS-II”. In: Journal of Instrumentation 20.08,P 08019. DOI: {10.1088/1748-0221 / 20 / 08 / P08019}. URL: %7Bhttps : / / doi . org / 10 . 1088 / 1748 -0221/20/08/P08019%7D.
[5] Inoue, Ichiro, Shinohara, Yuya, Watanabe, Akira, and Amemiya, Yoshiyuki 2012, “Effect of shot noise on X-ray speckle visibility spectroscopy,” Optics Express, vol. 20, no. 24, pp. 26 878–26 887. DOI: 10 . 1364 / OE . 20 . 026878.

NSS-10-05

Global-ramp single-slope ADC with pixel-level comparison and built-in compression for large pixel arrays (#1705)

Lodovico Ratti[1,2], Sergio Bottinelli[3], Tommaso M. Floris[1,2], Tomasz Hemperek[3], Paolo Lazzaroni[4,2], Massimo Manghisoni[4,2], Valerio Re[4,2], Carla Vacchi[1,2]

[1] University of Pavia, Pavia, Italy; [2] University of Bergamo, Dalmine, Italy; [3] DECTRIS AG Ltd., Baden- Daettwil, Switzerland; [4] INFN - Istituto Nazionale di Fisica Nucleare, Sezione di Pavia, Dalmine, Italy

Abstract

A 10-bit single-slope analog-to-digital converter has been developed in a 110 nm CMOS technology for amplitude measurements in large-area pixel detectors for X-ray imaging. The converter generates the linear ramp and the timestamp in the chip periphery and distributes them to the 256x256 pixels in the chip core for comparison with the local amplitude sample. This approach reduces power dissipation in the chip core and achieves an optimal trade-off between IR-drop effects and front-end noise performance, while preserving the integrity of the analog sample at the pixel level. Although the current detector design targets frame rates in the tens-of-kHz range, the possibility of scaling to higher rates is explored through the implementation of a compression feature that accounts for Poisson noise in the photon signal.

References
[1] P. Aller, A.M. Orville, "Dynamic Structural Biology Experiments at XFEL or Synchrotron Sources," Methods Mol. Biol., vol. 2305, pp.~203-228, 2021.
[2] L. Schaper, S. Ackermann, E. Allaria, P. Amstutz, K. Baev, M. Beye et al., "Flexible and Coherent Soft X-ray Pulses at High Repetition Rate: Current Research and Perspectives," Appl. Sci., vol. 11, no. 20, article no. 9729, 2021.
[3] M. Chergui, M. Beye, S. Mukamel, C. Svetina e C. Masciovecchio, "Progress and prospects in nonlinear extreme-ultraviolet and X-ray optics and spectroscopy," Nat. Rev. Phys., vol. 5, pp.~578-596, 2023.
[4] M. Porro, "Ultra-Low Noise Imaging of Soft X-Rays at Rates of Up To 4.5 Mega-Frames per Second Using the DSSC Camera at the European XFEL," 2025 IEEE NSS MIC RTSD Conference, Yokohama, Japan, Nov. 1-8, 2025.
[5] A. Gupta, D. Doering, M. P. Hammer, H. Shi, J. Weizeorick, S. Strempfer et al., "SparkPix-RT2: The design of a 192x168 pixel detector ASIC with on-chip data processing for ultra-fast photon science," 2024 IEEE NSS MIC RTSD Conference, Tampa, USA, Oct. 26-Nov. 2, 2024.
[6] D. Magalhães, P. Fajardo, P. Grybos, R. Kleczek, P. Kmon, P. Otfinowski et al., "Very High Rate X-ray Photon Counting 2D Detectors with Small Pixels: the SPHIRD Project", 2022 IEEE NSS MIC Conference, Milan, Italy, Nov. 5-12, 2022.
[7] M. F. Snoeij, A. J. P. Theuwissen, K. A. A. Makinwa, and J. H. Huijsing, "Column-parallel single-slope ADCs for CMOS image sensors," Proc. Eurosensors XX, vol. 2, pp.~284-287, 2006.
[8] R. Hogervorst, J. P. Tero, R. G. H. Eschauzier, J. H. Huijsing, "A Compact, Power-Efficient 3 V CMOS rail-to-rail Input/Output Operational Amplifier for VLSI Cell Libraries," J. Solid-State Circuits, vol. 29, no. 12, pp.~1505-1513.

NSS-10-06

Characterization of the Ignite64 ASIC in CMOS 28-nm technology for high time-resolution tracking (#1913)

Luca Pacher[2], **Adriano Lai**[1], on behalf of IGNITE-Collaboration

[1] Istituto Nazionale Fisica Nucleare, Cagliari, Cagliari, Italy; [2] University of Turin and INFN Torino, Torino, Italy

Abstract

The IGNITE project is developing advanced technical solutions in 28-nm CMOS technology for next-generation collider tracking systems, targeting time resolutions below 40 ps RMS while preserving the key constraints of current inner trackers, namely small pixel dimensions (~50 µm pitch) and low power density (1–2 W/cm.).

This contribution presents characterization results for the Ignite64 prototype ASIC, featuring a 64x64-pixel matrix with 55 µm pitch and one TDC per pixel. The chip has been conceived as a test platform for advanced silicon sensor technologies, including 3D sensors, TI-LGADs, and i-LGADs. The Ignite64 adopts a modular architecture that is directly scalable to the final IgnitER ASIC, currently close to submission.

The prototype implements and validates dedicated solutions for accurate power delivery and low-jitter clock distribution, both essential for achieving uniform timing performance across large pixel matrices. Several alternative Analog Front-End architectures have also been integrated and experimentally evaluated to optimize the trade-off among timing performance, power consumption, and Total Ionizing Dose tolerance.

At an input charge of 1 fC and a power consumption of 10 µW per pixel, the measured timing resolution is approximately 20 ps RMS at zero input capacitance, remaining around 35 ps RMS at a typical pixel capacitance of 100 fF. Performance uniformity across the full matrix is well controlled, with an RMS spread of about 5 ps in the distribution of pixel time resolutions, demonstrating the effectiveness of the adopted architectural and powering strategies.

Comprehensive laboratory characterization results are presented for operation both with and without connected sensors. Measurements include tests performed using the integrated pulsing system, radioactive sources, and a dedicated infrared laser setup capable of accurately reproducing the charge deposition profile generated by charged particles in silicon sensors.

References

[1] TimeSPOT collaboration, Characterisation of highly irradiated 3D trench silicon pixel sensors for 4D tracking with 10 ps timing accuracy, Frontiers in Phys. 12 (2024).

[2] TimeSPOT collaboration, Characterisation of 3D trench silicon pixel sensors irradiated at 1·1017 1 MeV neq cm-2, Frontiers in Phys. 12 (2024).

[3] Brundu D. et al, Accurate modelling of 3D-trench silicon sensor with enhanced timing performance and comparison with test beam measurements. J Instrumentation (2021) 16: P09028. 10.1088/1748-0221/16/09/p09028.

Time:
11 November, 2026
9:00 – 10:30

Room:
MACHADO

NSS-11 | AI and ML for radiation detection

Chairs:
Marco Carminati (Milano)

NSS-11-01

ML-based radiological clearance of activated metallic waste at CERN using synthetic data (#1357)

Andrea Gomes[2,1], Markus Helej[1], Matteo Magistris[1], Francisco Ogallar Ruiz[1], Maria Elisso Stamati[1], Christian Theis[1], Helmut Vincke[1]

[1] CERN, HSE-RP, Geneva, Switzerland; [2] University of Geneva, Physics Department, Geneva, Switzerland

Abstract

The maintenance and dismantling of high-energy accelerators at CERN generate activated waste with significant variability in irradiation history, cooling time, and material composition. If activity levels are negligible, waste can be cleared from regulatory control in Switzerland and reused as conventional material. We present a method for radiological classification which is conservative, without being as penalizing as more traditional approaches based on a worst-case scenario. More specifically, we classify accelerator components as conventional or radioactive based on a radiation measurement (e.g. with a bismuth germanate detector), and on the application of a predictive model. The models here presented were trained over ~60,000 synthetic waste items and their radiological properties. Each synthetic item represents a specific activation scenario, generated through probabilistic sampling of operational parameters. The associated radiological properties were computed with ActiWiz, a CERN-developed activation code based on FLUKA Monte Carlo simulations and evaluated neutron data libraries. Focusing on the classification of metallic accelerator components, we compare the performance of logistic regression based on a bismuth germanate detector response, with that of a neural network model incorporating both the detector response and the item mass. Results show that the neural network improves classification performance and robustness relative to logistic regression, reducing misclassification of borderline cases while maintaining compliance with Swiss regulatory criteria. The proposed framework establishes a robust and scalable clearance workflow, adaptable to the evolving requirements of large-scale research facilities.

NSS-11-02

Inverse reconstruction of ^{137}Cs depth-dependent contamination in concrete from gamma spectrometry measurements (#1469)

Antoine Hayek[1], Julien Venara[1], Geoffrey Daniel[2], Clément Lynde[3], Pierre-Louis Antonsanti[1], Marie Cuozzo[1], Charly Mahé[1], Ziad El Bitar[4]

[1] CEA, Univ. Montpellier, Marcoule, DES, ISEC, DPME, SEIP, LNPA, F-30207 Bagnols-sur-Cèze Cedex, France; [2] Université Paris-Saclay, CEA, Service de Génie Logiciel pour la Simulation, 91191 Gif-sur-Yvette, France; [3] Université Paris-Saclay, CEA, Service de Physico-Chimie, 91191 Gif-sur-Yvette, France; [4] Université de Strasbourg, CNRS, IPHC UMR 7178, 67000 Strasbourg, France

Abstract

Radiological characterization is a key step in nuclear decommissioning, particularly during final operations where contaminated concrete structures must be assessed prior to decontamination. Conventional approaches combine surface measurements with radiochemical analyses of samples at different depths, and use geostatistical methods to estimate 3D contamination distributions. Despite their efficacy, these methods remain intrusive, time-consuming, and costly. In this work, we investigate a complementary non-destructive methodology based on in situ gamma spectrometry conducted at the surface using a HPGe detector. The primary objective of this methodology is to reduce the need for destructive sampling and improving the understanding of contamination phenomena in concrete. This study focuses on the analysis of ^{137}Cs, a predominant gamma-emitting radionuclide frequently encountered in nuclear facilities. The proposed approach relies on inverse reconstruction of depth contamination profiles, where the volume of concrete is discretized into layers. The feasibility of the approach was confirmed through simulations. The detector response is modeled using Monte Carlo simulations with MCNP and is combined with the ML-EM algorithm to solve the inverse problem. However, investigations also revealed limitations, especially ambiguities and non-unique solutions in complex configurations. We propose to integrate prior knowledge on the contamination profile (Fickian diffusion) and demonstrate its benefits in addressing the aforementioned limitations. In controlled laboratory conditions, the experimental validation was executed with a calibrated ^{137}Cs point source shielded with a concrete barrier. With this configuration, the ability to estimate source position by using relevant energy ranges were demonstrated. These results highlight both the potential and inherent limitations of ML-EM, thus motivating hybrid approaches combining physics-based modeling and learning methods.

NSS-11-03

Joint autoencoder-classifier network for particle-type identification in organic scintillator pulse pileup (#1374)

Annamaria R. McHugh, Kurt Beyer, Shaun D. Clarke, Sara A. Pozzi, Majdi I. Radaideh

University of Michigan, Department of Nuclear Engineering and Radiological Sciences, Ann Arbor, USA

This work was supported in part by the Consortium for Monitoring, Technology, and Verification under Department of Energy National Nuclear Security Administration, award number DE-NA0003920. The authors would like to thank Dr. Abbas Jinia from the University of Michigan Detection for Nuclear Non-proliferation Group (DNNG) for supplying the waveform dataset used in this study.

Abstract

Charge-comparison pulse-shape discrimination in organic scintillators fails at high irradiation rates due to the effects of pulse pileup. While pileup rejection reduces particle misclassification, this severely degrades detector efficiency. We present a new machine-learning pipeline to extract particle-type information from piled-up trans-stilbene waveforms using a novel joint autoencoder–classifier design. Events are classified as single or pileup, then routed to separate multi-task convolutional autoencoders, which extract the important features of the input waveform and perform n/γ classification. Trained on 519,910 labeled

Time-of-Flight waveforms and synthetically generated pileup data, the system achieves 97.66% accuracy for single/pileup detection, 99.42% n/γ classification accuracy on single pulses, and 90.15% classification accuracy of both constituents in pileup waveforms. This approach is shown to substantially outperform charge-comparison-based analytical pulse-shape discrimination by improving pileup detection and preserving neutron and gamma-ray counts.

NSS-11-04

Joint Neutron Source Localization and Identification using Machine-Learning-based Spectral Imaging (#2042)

David Breitenmoser, Shaun D. Clarke, Sara A. Pozzi

University of Michigan, Department of Nuclear Engineering and Radiological Sciences, Ann Arbor, USA

This work was supported in part by the Consortium for Monitoring, Technology, and Verification under Department of Energy National Nuclear Security Administration, award number DE-NA0003920.

Abstract

Neutron source localization and identification are critical for nuclear safeguards and security, yet current scatter-based imaging pipelines typically decouple spatial reconstruction from spectral analysis, treating both as separate post-processing steps. This work introduces a unified machine-learning framework for joint spectral-directional neutron source inference using energy-resolved simple back-projection (SBP) images. The proposed framework combines unsupervised Gaussian mixture model localization with a lightweight k-nearest neighbors classifier. Despite its simplicity, the approach achieves strong performance on controlled laboratory data involving Cf-252 and PuBe sources in single- and mixed-source configurations, with a mean angular localization error <5º and a source classification accuracy >98%. These results demonstrate that low-complexity statistical learning applied to energy-resolved SBP data enables fully automated, end-to-end inference of both source direction and source identity without manual region selection or separate spectral analysis, offering a practical pathway toward more scalable and deployable neutron imaging systems for real-world safeguards and security operations.

NSS-11-05

Machine-Learning-Based Real-Time Gamma-Ray Direction Estimation Using Fractal Radiation Imaging Element (#1755)

Miyuki Sasaki[1], Tatsuo Torii[2], Yuki Morishita[1], Shunsuke Kurosawa[3], Nishiki Matsubayashi[4]

[1] Japan Atomic Energy Agency, Minamisoma, Japan; [2] Fukushima University, Fukushima, Japan; [3] Nagoya University, Nagya, Japan; [4] Tokyo University of Agriculture and Technology, Tokyo, Japan

The authors would like to express their sincere gratitude to Tsutomu Yamada, Takamasa Nakasone and Marina Kanno of the Japan Atomic Energy Agency Environmental Monitoring Group for their valuable support and cooperation during the experiments. The authors also acknowledge the cooperation of Clear Pulse Co., Ltd. and C&A Corporation.
This manuscript was partially prepared with the assistance of ChatGPT by OpenAI. The tool was used to help draft and revise portions of the text under the direct supervision of the authors.

Abstract

In this study, a real-time gamma-ray contribution direction imaging system using a Fractal Radiation Imaging Element (FRIE) detector and a Multi-Layer Perceptron (MLP) was developed and evaluated. The system consists of an FRIE detector composed of sixteen GFAG scintillators, a 360-degree camera, and a PC for real-time analysis and visualization. Radiation contribution directions were estimated from count-rate data of the sixteen detectors using an MLP trained with Cs-137 point-source irradiation data including statistical fluctuations. Evaluation results showed that the average angular estimation error was approximately five degrees, and the estimation accuracy improved as the count rate increased. Experiments using measured data demonstrated that the estimated source direction gradually converged through temporal accumulation of measurement data, even under low count-rate conditions. Compared with the conventional similarity-based method, the proposed method reduced the direction estimation error while enabling real-time gamma-ray contribution direction estimation. These results demonstrate the effectiveness of the proposed system for real-time localization of gamma-ray sources in nuclear decommissioning environments.

References
[1] T. Torii, M. Sasaki, and Y. Sanada, “Development of an omnidirectional detector for beta and gamma-ray imaging with fractal geometry,” in Proc. IEEE NSS/MIC/RTSD, 2023. doi: 10.1109/NSSMICRTSD49126.2023.10337827.
[2] M. Sasaki, Y. Abe, Y. Sanada, and T. Torii, “Evaluation of the distribution accuracy of radioactivity from a gamma-ray source using an omnidirectional detector for radiation imaging with fractal geometry,” Nucl. Instrum. Methods Phys. Res., Sect. A, vol. 1072, p. 170207, Mar. 2025. doi: 10.1016/j.nima.2025.170207.
[3] M. Sasaki, Y. Sanada, and T. Torii, “Development of real-time imaging technology using an omnidirectional detector,” IEEE Trans. Nucl. Sci., p. 1-1, March 2026. doi: 10.1109/TNS.2026.3675230
[4] T. Akiba, S. Sano, T. Yanase, T. Ohta, and M. Koyama, “Optuna: A next-generation hyperparameter optimization framework,” Proc. ACM SIGKDD Int. Conf. Knowl. Discov. Data Min., 2019. doi: 10.1145/3292500.3330701

NSS-11-06

Evaluating isotope identification methods for use with count-starved gamma spectra (#2536)

James Biggs, Caroline Shenton-Taylor

University of Surrey, School of Mathematics and Physics, Guildford, UK

Abstract

Radiation detector networks provide a potential means of monitoring the movement of radiological material within urban environments. Such systems require automated methods capable of identifying non-background isotopes within collected spectra, particularly for count-starved measurements acquired in complex backgrounds. In 2018, the London-based SIGMA trial collected approximately 1.5 billion one-second gamma spectra using a combination of stationary and mobile scintillation detectors. This work presents a comparison between three viable isotope identification tools, to ascertain which is best placed to be used in environments with count-starved gamma spectra, such as those typically seen in large datasets like SIGMA. Representative spectra were created by combining laboratory collected spectra and Geant4 simulated spectra with real-world SIGMA background. Tranches of spectra were tested in each of the chosen methods: InterSpec, wavelets, and a convolutional neural network. Although all three methods showed promise when identifying a range of ^{137}Cs spectra, the CNN outperformed the others when presented with spectra with the smallest photopeaks, making it the preferred approach for isotope detection in urban landscapes.

UK Ministry of Defence © Crown Owned Copyright 2026/AWE

Time:
11 November, 2026
9:00 – 11:00

Room:
PICASSO

NSS-12 | Novel detectors and associated technologies

Chairs:
Christian Scharf (Berlin)
Miguel Ullan (Barcelona)

This session focuses on innovative detector concepts, materials, architectures, and enabling technologies. It aims to provide a forum for researchers and engineers to present the latest developments and discuss future directions in detector technologies and their associated systems.

NSS-12-01

PLATON: a plenoptic single-photon camera with sub-nanosecond time resolution for particle detection through monolithic scintillating volumes (#1339)

Till C. Dieminger[1], Saul Alonso-Monsalve[1], Kodai Kaneyasu[2], Marco Barbieri[4], Vincenzo Berardi[3], Claudio Bruschini[2], Edoardo Charbon[2], **Davide Sgalaberna**[1]

[1] ETH Zurich, Zurich, Switzerland; [2] EPFL, Lausanne, Switzerland; [3] Politecnico di Bari, Bari, Italy; [4] Università degli Studi Roma Tre, Rome, Italy

This work was supported by Swiss National Science Foundation under grants PCEFP2_203261 and 20QT21_187716 Qu3D ``Quantum 3D Imaging at high speed and high resolution"), the National Energy Research Scientific Computing Center (NERSC), a U.S. Department of Energy User Facility, under the AI4Sci@NERSC award DDR-ERCAP0034642, Swiss AI Initiative grant from the Swiss National Supercomputing Centre (CSCS), project ID a149, on the Alps system.

Abstract

High-resolution scintillator detectors achieve precise particle tracking through fine segmentation down to a few hundred micrometres, making complexity and costs prohibitive when scaling up to large volumes. We propose a change of paradigm: 3D imaging of particle interactions in an unsegmented monolithic volume of scintillator obtained by combining plenoptic imaging with a Single-Photon Avalanche Diode (SPAD) array sensor. We report the performance of the first SPAD-based plenoptic camera for particle detection, built around the SwissSPAD2 sensor. Results obtained from ^{90}Sr radioactive source, a point light source and a controlled two-photon-absorption setup as well as novel analytical and artificial-intelligence-driven 3D imaging techniques will be described. A simulation case study on neutrino detection demonstrates the unique potential of this approach and its scalability to medium (1 x 1 x 1 m^3) and large (10 x 10 x 10 m^3) scale scintillator volumes, with sub-millimeter 3D spatial resolution. A new custom SPAD array required to enhance the resolution currently under development is also presented. This work sets the path forward for a new system for high-precision particle tracking in dense volumes. Applications of the PLATON concept can also extend to medical imaging.

References
[1] A. Blondel et al., JINST, vol. 13, no. 02, pp. P02 006–P02 006, feb 2018
[2] S. Abe et al., arXiv:2603.14921 [physics.ins-det]
[3] A. Agarwal et al., Phys. Lett. B, vol. 840, p. 137843, 2023
[4] C. Joram et al., Tech. Rep., 2015
[5] T. Dieminger et al., Nature Communications, vol. 17, no. 1, p. 4204, 2026
[6] Ulku et al., IEEE Journal of Selected Topics in Quantum Electronics, vol. 25, pp. 1–12, 1 2019
[7] K. Kaneyasu et al., Platon SPAD: A scalable sensor for elementary particle detection NSS-MIC 2026 - abstract ID #1496

NSS-12-02

A Capacitively Coupled GaAs SAM-APD with Cross-Delay Lines for Fully Digital 3D Hard X-ray Photon Imaging (#1810)

Nicola Lusardi[1,7], Fulvia Arfelli[3,2], Giorgio Biasiol[4], Francesco Driussi[8], Matias Antonelli[2], Marco Cautero[3,5], Matija Colja[5], Fabio Garzetti[1], Giuseppe Cautero[5,2], Ralf H. Menk[5,2], Andrea Costa[1], Gabriele Fiumicelli[1], Enrico Ronconi[1], Gabriele Bonanno[1], Gabriele Brajnik[5], Sergio Carrato[6], Davide Curcio[4], Simone Dal Zilio[4], Daniele Ercolani[4], Angelo Geraci[1,7], Alessandro Pilotto[8], Luca Sbuelz[4], Rudi Sergo[5], Luigi Stebel[5]

[1] Politecnico di Milano, Dipartimento di Elettronica, Informazione e Bioingegneria, Milano, Italy; [2] INFN, Trieste, Trieste, Italy; [3] University of Trieste, Department of Physics, Trieste, Italy; [4] CNR, ISTITUTO OFFICINA DEI MATERIALI, Trieste, Italy; [5] Elettra Sincrotrone, Trieste, Italy; [6] University of Trieste, DIA, Trieste, Italy; [7] INFN, Milano, Milano, Italy; [8] Università degli Studi di Udine, DPIA, Udine, Italy

The work is supported by PRIN 2022 - Code 20227N9LW7

Abstract

Time-resolved ultrafast phenomena with hard X-rays are central to applications such as pump–probe spectroscopy, driving advances in detector and multichannel acquisition technologies. This work proposes a fully digital 3D (x–y–time) imager for hard X-rays. Key challenges include improving time and spatial resolution—often limited by pixelated approaches—and overcoming the low quantum efficiency of silicon detectors at high photon energies. To address these issues, we adopt a Separate Absorption and Multiplication Avalanche Photodiode (SAM-APD) based on III–V semiconductors. GaAs alloys, with higher atomic number and carrier mobility than silicon, enable significantly improved absorption efficiency and faster response. On the readout side, the shift toward multichannel systems and stringent constraints on power and area per channel motivate a transition from voltage-mode pixel electronics to time-based acquisition, where spatial (x, y) and temporal information are encoded in the detection time. The proposed architecture couples a large-area GaAs SAM-APD (mm-scale diameter) with two Cross Delay Lines (CDLs) and a 4-channel Field-Programmable Gate Array (FPGA)-based Time-to-Digital Converter (TDC) with 15 ps precision. The main challenges are preserving spatial coherence between the interaction point on the detector and the corresponding charge readout location on the CDL, and ensuring capacitive coupling with high signal integrity. Preliminary tests were performed using a 10 × 5 mm² p–i–n diode and laser pulses achieving a spatial precision of <100 µm r.m.s. and a temporal jitter of 68.3 ps r.m.s. Additional measurements show intensity discrimination capability with resolvable signal changes of ~1.2–1.6×. The approach offers a compact and scalable alternative to pixelated detectors, eliminating the need for advanced lithography and per-pixel readout, while relying on only four acquisition channels.

References

[1] F. Capasso et al., “Enhancement of electron impact ionization in a superlattice: A new avalanche photodiode with a large ionization rate ratio,” Applied Physics Letters, vol. 40, no. 1, pp. 38–40, 01 1982. [Online]. Available: https://doi.org/10.1063/1.92910

[2] J. Lauter et al., “Algaas/gaas sam-avalanche photodiode: An x-ray detector for low energy photons,” Nuclear Instruments and Methods in Physics Research Section A: Accelerators, Spectrometers, Detectors and Associated Equipment, vol. 356, no. 2, pp. 324–329, 1995. [Online]. Available: https://www.sciencedirect.com/science/article/pii/0168900294012377

[3] N. Lusardi et al., “Advanced system in fpga for 3d (x, y, t) imaging with cross delay-lines,” in 2019 IEEE Nuclear Science Symposium and Medical Imaging Conference (NSS/MIC), 2019, pp. 1–4.

NSS-12-03

Characterization of 4H-SiC implanted LGADs after 23 MeV Proton Irradiation (#1845)

Francesco Moscatelli[1,2], Arianna Morozzi[2], Valentina Sola[3], Daniele Passeri[4], Peter Svihra[5,6], Radek Novotny[5], Vojtech Kracmar[5], Jiri Kroll[6], Brendan Regnery[7], Robert White[8], Marco Ferrero[8], Marta Tornago[3,8], Anna Rita Altamura[3,8], Mara Bruzzi[9], Sebastian A. Onder[10], Alexander Dierlamm[7], Thomas Bergauer[10]

[1] CNR-Istituto Officina dei Materiali (IOM), Perugia, Italy; [2] INFN of Perugia, Perugia, Italy; [3] University of Torino, Department of Physics, Torino, Italy; [4] University of Perugia, Department of Engineering, Perugia, Italy; [5] FNSPE CTU in Prague, Department of Physics, Prague, Czech Republic; [6] FZU CAS, Department of Detector Development and Data Processing, Prague, Czech Republic; [7] Karlsruhe Institute of Technology, Karlsruhe, Germany; [8] INFN Torino, Torino, Italy; [9] University of Florence, Department of Physics and Astronomy, Firenze, Italy; [10] MBI for Particle Physics, Wien, Austria

This work was supported by INFN CSN5 with the SiC4GAIN research project

Abstract

The demand for radiation-hard 4D detectors capable of simultaneous high-precision timing and spatial resolution is driving the investigation of 4H-Silicon Carbide (4H-SiC) as a robust alternative to silicon. While 4H-SiC offers superior thermal stability and radiation tolerance, its wide bandgap and current epitaxial thickness limits necessitate the use of internal charge multiplication. This work presents an extensive performance evaluation of 4H-SiC LGADs and PN junction diodes fabricated by Onsemi on 6-inch wafers 50 μm epitaxial layer, n=5 $\cdot 10^{13}$ cm^{-3}. The devices were subjected to 23 MeV proton irradiation, covering five fluences from 1.3 $\cdot 10^{14}$ to 2 $\cdot 10^{15}$ p/cm^2. They have been characterized in terms of current–voltage I-V and capacitance–voltage C-V measurements. The study is complemented by ongoing Transient Current Technique (TCT) and Charge Collection Efficiency (CCE) measurements using a beta source. Furthermore, the impact of temperature (up to 200°C for I-V/C-V and 100°C for beta tests) is investigated to evaluate defect dynamics and the operational stability of 4H-SiC LGADs in extreme environments.

NSS-12-04

Status of GRAiNITA, a next generation calorimeter (#1928)

Hervé Chanal[1], Duccio Abbaneo[5], Sergey Barsuk[2], Oleg Bezshyyko[4], Ianina Boyarintseva[2,3], Andrey Boyarintsev[3], Dominique Breton[2], Matteo DeFranchis[5], Alexender M. Dubovik[3], Larysa Golina-Bezshyyko[4], David d'Enterria[5], Brieuc François[5], Yingrui Hou[1], Fangyi Guo[5], Giulia Hull[2], Patrick Janot[5], Denys Klekots[4,2], Andrii Kotenko[4], Jacques Lefrançois[2], Jihane Maalmi[2], Magali Magne[1], Andre David Tinoco Mendes[5], Stéphane Monteil[1], Emmanuel Perez[5], David Picard[1], Marie-Hélène Schune[2], Michele Selvaggi[5], Nazard Semkiv[4], Irina Tupitsyna[3], Mykhailo Yeresko[2]

[1] Université Clermont Auvergne, LPCA, CNRS/IN2P3, Clermont-Ferrand, France; [2] Université Paris-Saclay, IJCLab, CNRS/IN2P3, Saclay, France; [3] Institute for Scintillation Materials of the National Academy of Sciences of Ukraine, Kharkiv, Ukraine; [4] Kyiv National Taras Shevchenko University, Kyiv, Ukraine; [5] CERN, European Organization for Nuclear Research, Geneva, Switzerland

Abstract

The GRAiNITA project aims to develop a novel design for a next-generation calorimeter. It is an innovative approach which uses a mixture of millimeter-sized inorganic scintillating crystals (approximately 1-2 mm) dispersed within a high-density, transparent liquid. Compared to other sampling calorimeter with sensitive material of plastic scintillator, liquid argon, or silicon detector the sampling fluctuation impact on the resolution is predicted by simulation to be much smaller (<2%/sqrt{E}) due to the high density of the scintillator grains compared to the liquid and the smallness of the grains. A test beam operated in June 2024 at CERN allowed to study the performance of a small-scale GRAiNITA prototype. The light light yield was confirmed to be approximately 10 kPE/GeV and we demonstrated the feasibility of achieving sub-2% stochastic and constant terms. Since, the project has advanced significantly. This article presents the latest developments, including the design of a full-scale demonstrator module, advanced Geant4 simulations which are used to evaluate its expected performance, and detailed characterization studies scintillation properties of ZnWO$_4$ using proton beams. These efforts pave the way for the comprehensive validation of a full-scale detector.

NSS-12-05

Small Dose Monitor based on Silicon Carbide diodes for FLASH radiotherapy (#2594)

Celeste Fleta[1], Iván López[1], Ángela Henao[1], Sophie Heinrich[2], **Consuelo Guardiola**[1]

[1] National Center of Microelectronics (IMB-CNM, CSIC), Barcelona, Spain; [2] University Paris-Saclay, Orsay, France, Institut Curie, Inserm U1021-CNRS UMR 3347, Orsay, France

The project has received support from the Spanish government through the ‘María de Maeztu Unit of Excellence’ accreditation (CEX2023-001397-M / AEI/10.13039/501100011033).

Abstract

FLASH radiotherapy (FLASH RT), delivered at ultra-high dose rates (>40 Gy/s), has shown potential to reduce toxicity in healthy tissues while preserving tumor control. However, accurate, real-time dosimetry at such conditions remains challenging due to limitations of conventional detectors, including saturation effects and insufficient temporal resolution. In this work, silicon carbide (SiC) diodes are investigated as a promising solution for ultra-high dose rate (UHDR) dosimetry due to their high radiation hardness, fast response, and low sensitivity to saturation [1].

A 4 × 4 array of SiC diodes (1 mm diameter, 2.2 mm pitch) and a single 2.2 mm diode were tested using pulsed 7 MeV electron beams under FLASH conditions. The detectors were evaluated in terms of linearity, time response, and spatial dose measurement capabilities using a clinical reference dosimeter and radiochromic films for comparison. The single diode demonstrated excellent linearity better than 3.5% up to 10 Gy per pulse, with no evidence of saturation or radiation damage. Time-resolved measurements confirmed the capability to resolve sub-microsecond pulse structures, consistent with accelerator signals.

The SiC array prototype enabled spatially resolved dose measurements over areas up to 70 × 50 mm², producing 2D dose maps with millimeter-scale resolution under UHDR conditions. Good agreement with independent film measurements demonstrates its accuracy for beam profiling. These results highlight the feasibility of SiC-based detectors as scalable, position-sensitive dose monitors for FLASH RT [2].

Overall, this work demonstrates the potential of SiC technology for real-time, high-resolution dosimetry in FLASH radiotherapy, paving the way for future large-area detector systems and improved quality assurance in UHDR treatments.

References

[1] Fleta C, Pellegrini G, Godignon P, et al. State-of -the-art silicon carbide diode dosimeters for ultra-high dose-per-pulse radiation at FLASH radiotherapy. *Phys Med Biol*. 2024;69(9):095013. doi:10.1088/1361-6560/ad37eb

[2] Lopez Paz I, Fleta C, Henao Á, Heinrich S, Guardiola C. Small dose monitor based on silicon-carbide diodes for FLASH radiotherapy. Med Phys. 2026 Mar;53(3):e70354. doi: 10.1002/mp.70354. PMID: 41757409; PMCID: PMC12947054.

NSS-12-06

Thin-Film and Single-Crystal Perovskite Detectors for Real-Time FLASH Radiotherapy (#2664)

Mara Bruzzi[1,2], Lucia Baldesi[1,2], Laura Basiricò[7,10], Maria Giuseppina Bisogni[3,4], Giovanni Casini[1], Andrea Cavalieri[8,9], Carlo Civinini[1], Leonardo Forcieri[2,1], Beatrice Fraboni[7,10], Fabio Di Martino[6,8], Anna Vinattieri[1], Enrico Verroi[5]

[1] INFN - Istituto Nazionale di Fisica Nucleare, Sezione di Firenze, Firenze, Italy; [2] Università di Firenze, Firenze, Italy; [3] Università di Pisa, Pisa, Italy; [4] INFN - Istituto di Fisica Nucleare, Sezione di Pisa, Pisa, Italy; [5] INFN - Istituto di Fisica Nucleare, TIFPA - Sezione di Trento, Trento, Italy; [6] Unit of Medical Physics, Pisa University Hospital, Azienda Ospedaliero-Universitaria Pisana, Pisa, Italy; [7] Università di Bologna, Bologna, Italy; [8] Centro Pisano ricerca e implementazione clinica Flash Radiotherapy (CPFR@CISUP), Pisa, Italy; [9] Center for Instrument Sharing of the University of Pisa (CISUP), University of Pisa, Pisa, Italy; [10] INFN- Istituto di Fisica Nucleare, Sezione di Bologna, Bologna, Italy

Work performed under the framework of the PROVIDE CSN5 project. We thank Fondazione Pisa for funding CPFR with the grant prog. n.134/2021

Abstract

Ultra-high dose rate (UHDR) radiotherapy, commonly known as FLASH radio-therapy, is a revolutionary oncological approach that spares healthy tissue while preserving tumor control. Clinical translation of this method needs radiation detectors that provide real-time dosimetry under extreme dose rates, exceeding 40-100 Gy/s. Standard dosimeters, such as ionization chambers and traditional semiconductors, may face limitations like charge recombination and signal saturation in these environments. This study investigates full-inorganic metal-halide perovskites ($CsPbBr_3$) as viable detector material due to its high stopping power and moderately wide bandgap. We evaluated two distinct device architectures: thin-film (TF) and single-crystal (SC) detectors. The 1 µm-thick TF detectors were fabricated using radio-frequency magnetron sputtering (MS) on flexible Kapton substrates with interdigitated electrodes. SC detectors featured Schottky-Ohmic electrodes (Ti/Au and Au) deposited by DC-MS on pure commercial crystals. Characterization indicated a dominant CsPbBr3 phase, a forbidden gap of 2.32 eV, and a dark resistivity of approximately 10^7 Ωcm. Experimental validation was performed using a 9 MeV electron beam at Centro Pisano FLASH Radiotherapy (CPFR) and a 228 MeV proton beam at APSS (Azienda Provinciali Servizi Sanitari) Trento proton-therapy center. The tests with 9MeV electron beams covered a dose-per-pulse (DPP) range of 0.1 to 5.0 Gy delivered in 4us-long pulses, while proton testing reached dose-rates of 300 Gy/s with pulse durations of 10-25ms. Both detector types demonstrated good signal linearity and showed no evidence of saturation at the highest tested intensities. Ultimately, these results confirm that CsPbBr3 perovskite detectors are suitable for real-time monitoring in both electron and proton FLASH radiotherapy.

References

[1] V. Favaudon, L. Caplier, V. Monceau, F. Pouzoulet, M. Sayarath, C. Fouillade et al, "Ultrahigh dose-rate FLASH irradiation increases the differential response between normal and tumor tissue in mice" Sci translational Med., Vol. 6, 2014.

[2] Pablo P. Yepes, Solid-State Detector for FLASH Radiotherapy: Dosimetric Applications and Emerging Concepts, Condens. Matter 11, 2026, 3.

[3] H. Wei, J. Huang, Halide lead perovskites for ionizing radiation detection. Nat Commun Vol. 10, 2019, p. 1066.
[4] M. Bruzzi, L. Forcieri, C. Civinini, A. Vinattieri, L. Basiricò, B. Fraboni Development of thin-film inorganic perovskite UV photodetectors, in press on JINST.
[5] F. Di Martino et al. "Architecture, flexibility and performance of a special electron linac dedicated to Flash radiotherapy research: electronFlash with a triode gun of the centro pisano flash radiotherapy (CPFR)", Front. Phys.. Sec. Medical Physics and Imaging Vol. 11 Nov. 2023.

NSS-12-07

Particle-by-Particle Characterization of Clinical Carbon Ion Beams with a Silicon Strip Detector and High-Rate DAQ Systems (#3038)

Felix Mas Milian[1], Mohammad Fadavi Mazinani[1], Piergiorgio Cerello[1], Stefano De Astis[1,2], Miguel D. Fernandez Moreira[1], Veronica Ferrero[1,2], Elisa Fiorina[1], Diango M. Montalvan Olivares[1,2], Francesco Pennazio[1], Marco Pullia[3], Sahar Ranjbar[1,2], Iram B. Rivas Ortiz[1], Roberto Sacchi[1,2], Anna Vignati[1,2], **Simona Giordanengo**[1]

[1] Istituto Nazionale di Fisica Nucleare, Section Torino, Torino, Italy; [2] Università di Torino, Department of Physics, Torino, Italy; [3] Centro Nazionale di Adroterapia Oncologica, Pavia, Italy

This research was supported by the INFN CSN5 project SIG and SIG PNR funding.

Abstract

At CNAO, carbon-ion beams are delivered by the standard scheme which uses betatron-core extraction of a debunched beam, while RF Knock-Out (RFKO) extraction keeps the beam bunched and drives particles transversely toward extraction. To resolve the fine temporal structure of these modes beyond the 100 ms limit of standard ESA-ABACUS readout, a High-Rate DAQ system with 10 ns time bins was developed. The system used the LVDS outputs of 48 central channels from two ABACUS ASICs connected to a Xilinx Kintex-7 FPGA implementing custom VHDL firmware. Counts were aggregated in 10 ns windows, stored in DDR3 memory, and analyzed offline to reconstruct beam-rate waveforms and frequency components.

Tests were performed at CNAO with clinical carbon-ion beams using Betatron and RFKO extraction at four energies (115, 209, 304, and 398 MeV/u) and three intensity levels (20%, 50%, 100%).

A CAEN DT5203 picoTDC was also used as an independent acquisition system to record leading- and trailing-edge timing information from 32 ESA-ABACUS outputs in Streaming mode. The High-Rate DAQ resolved clear differences between the two extraction modes: RFKO showed a more compact and regular bunched time structure, while Betatron extraction showed the broader temporal distribution expected from a debunched coasting beam.

Fast Fourier Transform analysis of the High-Rate DAQ waveforms allowed the main accelerator RF components to be estimated with deviations below 0.25% for all tested conditions.

The DT5203 provided complementary hit-by-hit timing and enabled bunch-spacing estimation with <1.5% deviations, but suffered rate saturation at high intensities.

Overall, the High-Rate DAQ proved suitable for fine beam-structure measurements under clinical carbon-ion conditions, supporting accelerator tuning, particularly for RFKO operation.

References

[1] E. Bressi, L. Falbo, C. Priano, S. Foglio, *Betatron Core Slow Extraction at CNAO*, IPAC2018.
[2] S. Savazzi et al., *Implementation of RF-KO Extraction at CNAO*, IPAC2019.
[3] E. M. Data et al, "Characterization of a 144-channel front-end board for ion beam counting in particle therapy," Nuclear Instruments and Methods in Physics Research A 1080 (2025) 170712
[4] E. Data et al. "A novel detector for 4D tracking in particle therapy" Nuclear Instruments and Methods A,1068 (2024) 169690

NSS-12-08

Diamond Quantum Sensor for High Fluence Neutron Detection (#3048)

Luke Shoen[1], Yuhan Tong[2], Jack Lanza[1], Jennifer Choy[2], **Raymond Cao**[1]

[1] The Ohio State University, Nuclear Engineering, Mechanical and Aerospace Engineering, Columbus, USA; [2] University of Wisconsin at Madison, Electrical and Computer Engineering, Madison, USA

This research is supported by the U. S. Department of Energy/National Nuclear Security Administration under Award Number DE-NA0004196 for the ETI consortia and is also partially supported by Helion Energy.

Abstract

This work investigates diamond nitrogen-vacancy (NV) centers as a new class of neutron dosimetry that uses neutron-induced defect formation as the sensing mechanism rather than treating radiation damage as a failure mode. There is no device fabrication, wire connection, or charge collection as the diamond works purely as a passive dosimeter. Fast neutrons generate carbon vacancies in nitrogen-enriched diamond, followed by high-temperature annealing to form stable NV centers exhibiting characteristic photoluminescence and optically detected magnetic resonance responses. Eight nitrogen-rich diamond samples were irradiated at The Ohio State University Research Reactor, with fluence ranging from 10^{15} n/cm^2 to 10^{17} n/cm^2, and then annealed at 800 °C for a few hours. The results demonstrated a strong linear correlation between fluorescence intensity and neutron fluence, with up to 403× fluorescence increase observed after annealing compared to control samples. The results support the feasibility of applying diamond as compact, passive, and radiation-hardened sensors for high-fluence neutron detection in nuclear fission and fusion systems. The ongoing work is also exploring the real-time sensing using a diamond quantum sensor.

Time:
11 November, 2026
10:30 – 11:00

Room:
ALBÉNIZ & MACHUCA

N-LT-03 | NSS Lightning Talks 3

Chairs:
Rejean Fontaine (Sherbrooke)

N-LT-03-01

Radiation-Hardened VCO in 28 nm FDSOI with Enhanced Frequency Stability Under Total Ionizing Dose (#1750)

Muhammad Adeel Anwar[1,4], **Muhammad Adeel Anwar**[1,4], Dong Seok Kim[3,5], Dong Seok Kim[3,5], Seo Ryong Koo[1,4], Seo Ryong Koo[1,4], Inyong Kwon[2], Inyong Kwon[2]

[1] Korea University of Science and Technology (UST), Nuclear Science and Technology, Daejeon, South Korea; [2] Yonsei University Mirae Campus, Department of Radiological Science, Wonju, South Korea; [3] Korea University of Science and Technology (UST), Radiation Science, Daejeon, South Korea; [4] Korea Atomic Energy Research Institute (KAERI), Daejeon, South Korea; [5] Korea Atomic Energy Research Institute (KAERI), Gyeongju, South Korea

This work was supported in part by the National Research Foundation of Korea (NRF) funded by MSIT under Grants RS-2022-00144419, RS-2022-00144324, and RS-2022-00165164; by MSS under Grant RS-2023-00322102; by NST (MSIT) under Grant GTL25051-000; and by the RISE program (MOE and Gangwon State) under Grant 2025-RISE-10-006.

Abstract

Ensuring reliable RF operation in radiation-prone is critical for wireless monitoring systems in nuclear and space applications. This work presents a radiation-hardened-by-design (RHBD) voltage-controlled oscillator (VCO) implemented in a 28 nm Fully-Depleted Silicon-On-Insulator (FDSOI) process and experimentally evaluated under total ionizing dose (TID) conditions. The proposed RHBD VCO is compared with a conventional design up to 370 kGy(Si) using a Cobalt-60 gamma irradiation source at KAERI. Measurement results demonstrate that the RHBD VCO significantly improves frequency stability, achieving up to 57% reduction in frequency drift compared to the conventional counterpart. In addition, enhanced output power stability and reduced supply current variation are observed under irradiation. The results highlight the combined benefits of FDSOI technology and circuit-level hardening techniques, demonstrating a robust solution for radiation-tolerant RF circuit design.

References

[1] H. Jeon, I. Kwon and M. Je, "Radiation-Hardened Sensor Interface Circuit for Monitoring Severe Accidents in Nuclear Power Plants," in IEEE Transactions on Nuclear Science, vol. 67, no. 7, pp. 1738-1745, July 2020, doi: 10.1109/TNS.2020.3002421.

[2] J. D. Seo, L. D. Trang, J. -W. Han, J. Kim, S. Lee and I. -J. Chang, "Total Ionizing Dose Effect on Ring Oscillator Frequency in 28-nm FD-SOI Technology," in IEEE Electron Device Letters, vol. 39, no. 11, pp. 1728-1731, Nov. 2018, doi: 10.1109/LED.2018.2872345.

[3] A. Urena-Acuna and J. M. Armani, "Circuit-level Simulation of TID and Thermal Regeneration Effects on 28nm FDSOI Technology," 2024 24th European Conference on Radiation and Its Effects on Components and Systems (RADECS), Maspalomas, Spain, 2024, pp. 1-8, doi: 10.1109/RADECS61970.2024.11298612.

[4] J. R. Schwank et al., "Radiation Effects in MOS Oxides," in IEEE Transactions on Nuclear Science, vol. 55, no. 4, pp. 1833-1853, Aug. 2008, doi: 10.1109/TNS.2008.2001040.

N-LT-03-02

Preamplifier Readout Electronics for Summing SiPMs Enhanced Circuit (PRESSEC) for Advanced SiPM Camera (#1992)

Daniel David Marín[1], Alberto López[1], Diego Mateo[2], Josep Altet[2], Enrique Barajas[2], Xavier Aragones[2], Joan Serrano[1], Joan Mauricio[1], Rafel Manera[1], Eduardo Picatoste[1], Sergio Gómez[2]

[1] Universitat de Barcelona, Institut de Ciències del Cosmos, Barcelona, Spain; [2] Universitat Politécnica de Barcelona, Electronics Department, Barcelona, Spain

Thanks to the grants “Gamma-Ray Astronomy with CTA-North and MAGIC, Project 1” (PID2022-138172NB-C43)

Abstract

The next generation of imaging atmospheric Cherenkov telescope (IACT) cameras is transitioning to silicon photomultipliers (SiPMs) due to their stability, robustness, and superior sensitivity compared to PMTs. Specifically, we are developing an ASIC for the advanced SiPM camera (AdvCam). This ASIC, designated as PRESSEC (Preamplifier Readout Electronics for Summing SiPMs Enhanced Circuit), is implemented in 65 nm CMOS technology. The PRESSEC utilizes a 32-input scheme for large-area sensor readout. Its primary function is to generate analog outputs by summing signals from four sensors into a single channel, effectively reducing the total output count to eight channels. The main functionality of this ASIC is housed in the energy path, which integrates a single-ended-to-differential converter and a pole-zero cancellation circuit. This structure is instrumental in reducing the pulse’s Full Width at Half Maximum (FWHM) to 3 to 5 ns, thereby mitigating pileup effects in high activity environments. Simultaneously, these signals feed a trigger system for rapid event identification via a fast comparator. Additionally, a dedicated Night-Sky Background (NSB) monitoring circuit is included to measure ambient noise from sources like moonlight, employing a slow integrator with adjustable high-value pseudo-resistors to achieve integration time constants in the order of the milliseconds. Rigorous performance benchmarks, validated using Hamamatsu and FBK SiPMs, show a signal-to-noise ratio of at least 5, a dynamic range of 300 photons, and a linearity error below 3% for both energy and NSB paths, while presenting a power consumption of approximately 10 mW per input channel.

References

[1] “Cherenkov Telescope Array website.” [Online]. Available: https://www.cta-observatory.org/

[2] M. Heller and et. al., “The next generation cameras for the largesized telescopes of the cherenkov telescope array observatory,” in 38th International Cosmic Ray Conference, 2023.

[3] S. Gomez, J. Alozy, M. Campbell, J. Fernandez-Tenllado, R. Manera, J. Mauricio, C. Pujol, D. Sanchez, A. Sanmukh, A. Sanuy, R. Ballabriga, and D. Gascon, “Fastic: a fast integrated circuit for the readout of high performance detectors,” Journal of Instrumentation, vol. 17, no. 05, p. C05027, may 2022. [Online]. Available: https://doi.org/10.1088/1748-0221/17/05/C05027

[4] A. Rivetti, CMOS: Front-End Electronics for Radiation Sensors, 06 2015.

[5] “KM3NeT website.” [Online]. Available: https://www.km3net.org/

[6] A. Tajalli, Y. Leblebici, and E. Brauer, “Implementing ultra-high-value floating tunable cmos resistors,” Electronics Letters, vol. 44, 02 2008.

[7] A. Lopez, “Design of a rail-to-rail ota in 65 nm cmos technology for a particle detector sensor,” 2023. [Online]. Available: https://upcommons.upc.edu/handle/2117/403133

N-LT-03-03

Characterization of MAGIC: a SiPM Readout ASIC for Monolithic PET Detectors (#2162)

Leonardo Nassi[1,2], **Leonardo Nassi**[1,2], Tommaso D'Incà[2], Tommaso D'Incà[2], Ilenia D'Adda[2], Ilenia D'Adda[2], Giacomo Borghi[1,2], Giacomo Borghi[1,2], Carlo E. Fiorini[1,2], Carlo E. Fiorini[1,2], Marco Carminati[1,2], Marco Carminati[1,2]

[1] INFN - Istituto Nazionale di Fisica Nucleare, Sezione di Milano, Milano, Italy; [2] Politecnico di Milano, Dipartimento di Elettronica, Informazione e Bioingegneria, Milano, Italy

Support by Politecnico di Milano, INFN and EU under project CLARITY is acknowledged.

Abstract

The experimental characterization of MAGIC (Multichannel Analog Gamma- ray detection Integrated Circuit) is here presented. This ASIC is designed in CMOS 110 nm technology and it is intended to readout the current signals coming from SiPMs coupled with monolithic scintillators that are used in medical imaging applications. The circuit is divided into three main sections: an energy path that provides a differential voltage proportional to the energy of the gamma photon, a timing path that gives information about the time of arrival of the photon, and a validation path for event discrimination. For the experimental characterization two PCBs, a mainboard and a carrier, have been designed. In this testing phase all the functionalities have been validated and the key performance of the ASIC have been characterized, in particular the power dissipation (5 mW/channel), the linearity of the energy chain to demonstrate the direct proportionality between the measured charge and the one generated by photon interaction, and the time jitter which affects the propagation delay through the timing path. The results are within the specifications and confirmed by simulations: the linearity error is below 1% and the time jitter is below 20 ps. Such a low value enables its use also in TOF-PET applications.

References

[1] Nassi, L, et al. 2025 “MAGIC: A SiPM Readout ASIC for Monolithic PET Detectors”. *Proc. 2025 IEEE NSS/MIC/RTSD*.

[2] Temes, GC, et al. 1987, “Fast CMOS current amplifier and buffer stage”. *Electronics letters*, 23.13, pp. 696–697.

[3] Buonanno, L, et al. 2021, “GAMMA: A 16-channel spectroscopic ASIC for SiPMs readout with 84-dB dynamic range”, *IEEE Transactions on Nuclear Science*, 68.10, pp. 2559–2572.

N-LT-03-04

Photon Counting with FPGA Gigabit Transceivers: A Proof-of-Concept SiPM Readout for TOF-PET (#2884)

Tarun Prakash, Joshua W. Cates, Woon-Seng Choong, Marcos Turqueti

Lawrence Berkeley National Laboratory, Berkeley, USA

This work was supported in part by NIH Research under Grant R01EB033402

Abstract

Achieving 100ps FWHM coincidence time resolution (CTR) in time-of-flight positron emission tomography (TOF-PET) is benefited by electronics that can resolve individual scintillation photons with high temporal precision. We report a proof-of-concept readout in which silicon photomultiplier (SiPM) single-photon pulses are discriminated by a high-speed comparator and digitized directly by GTY transceivers of a Xilinx Virtex UltraScale XCVU095 FPGA (VCU1287 board) at 16Gbps, encoding photon arrival times as bit positions with 62.5ps resolution. Signal integrity analysis showed that an initial LVDS comparator produced common-mode voltage and differential swing below GTY receiver specifications; switching to a CML comparator substantially reduced bit errors. Room-temperature SiPM dark count bitstreams were captured with a random FPGA clock trigger and post-processed to produce a finger plot showing 1-, 2-, and 3-photoelectron peaks, providing a preliminary validation of the bitstream-based photon-counting concept. These results support the feasibility of FPGA gigabit transceivers as scalable digitizers for single-photon pulse streams in next-generation TOF-PET detector modules.

References

[1] S. Surti and J. S. Karp, “Update on latest advances in time-of-flight PET,” Physica Medica, vol. 80, pp. 251–258, 2020, doi: 10.1016/j.ejmp.2020.10.031.

[2] S. Pourashraf, A. Gonzalez-Montoro, J. Y. Won, M. S. Lee, J. W. Cates, Z. Zhao, J. S. Lee, and C. S. Levin, “Scalable electronic readout design for a 100 ps coincidence time resolution TOF-PET system,” Phys. Med. Biol., vol. 66, no. 8, Apr. 2021, doi: 10.1088/1361-6560/abf1bc.

[3] S. Pourashraf, A. Gonzalez-Montoro, M. S. Lee, J. W. Cates, J. Y. Won, J. S. Lee, and C. S. Levin, “Investigation of electronic signal processing chains for a prototype TOF-PET system with 100-ps coincidence time resolution,” IEEE Trans. Radiat. Plasma Med. Sci., vol. 6, no. 6, pp. 690–696, Jul. 2022, doi: 10.1109/TRPMS.2021.3124756.

[4] S. Pourashraf, J. W. Cates, and C. S. Levin, “A scalable dynamic TOT circuit for a 100 ps TOF-PET detector design to improve energy linearity and dynamic range,” IEEE Trans. Radiat. Plasma Med. Sci., vol. 8, no. 3, pp. 237–247, Mar. 2024, doi: 10.1109/TRPMS.2023.3344399.

[5] Analog Devices, “Rail-to-Rail, Very Fast, 2.5 V to 5.5 V, Single-Supply CML Comparators,” ADCMP606/ADCMP607 datasheet, Rev. C, 2016. [Online]. Available: https://www.analog.com/media/en/technical-documentation/data-sheets/ADCMP606_607.pdf

N-LT-03-05

Design and Implementation of an FPGA-Based Nuclear-Like Signal Generator (#1615)

Yao Yang[1,2], Yao Yang[1,2], Xiaohui Li[1,2], Xiaohui Li[1,2], Teng Tong[1,2], Teng Tong[1,2], Fanhui Meng[1,2], Fanhui Meng[1,2], Shuangquan Liu[1,2], Shuangquan Liu[1,2], Zhiming Zhang[1,2], Zhiming Zhang[1,2], Cunfeng Wei[1,2], Cunfeng Wei[1,2], Long Wei[1,2], Long Wei[1,2]

[1] Chinese Academy of Sciences, Institute of High Energy Physics, Beijing, China; [2] Jinan Laboratory of Applied Nuclear Science, Jinan Laboratory of Applied Nuclear Science, Jinan, China

This work was supported by the National Natural Science Foundation of China (Grant No. 12505356)

Abstract

Traditional radioactive source testing involves health risks, regulatory limitations, and operational inconvenience. To address these issues, this paper presents a nuclear-like signal generator capable of reproducing the waveform, amplitude, and timing characteristics of real nuclear radiation signals. The proposed system is implemented on a Xilinx K7 FPGA and supports parameter configuration through a touch screen, USB, Ethernet, or host computer software. In the waveform-generation module, photon emission timing is modeled according to scintillator light yield and decay time, while photoelectric conversion jitter and Gaussian pulse responses are introduced to synthesize realistic macroscopic waveforms. In the amplitude-generation module, a cumulative distribution function threshold table derived from measured energy spectra is used to reproduce statistical energy distributions. In the timing module, event occurrence is modeled as a Poisson process with exponentially distributed intervals. The system supports multiple radioactive sources and scintillator materials, including Na, Cs, LYSO, NaI, CsI, and BGO, with independent dual-channel output capability.

N-LT-03-06

High-performance preamplifier for spectroscopy systems based on High-Purity Germanium detectors (#1999)

Fernando Ojeda, Fernando Ojeda, Brian Nelson, Brian Nelson

AMETEK ORTEC, Oak Ridge, USA

The authors wish to acknowledge the valuable contributions to this work from the Engineering, Production, and Detector Test teams.

Abstract
Preamplifiers play a primary role in the resolution, linearity, and sensitivity of ionizing radiation spectrometers, converting the small charges collected by photo detectors into usable voltage signals that are further amplified, digitized, and processed to obtain the intended spectra. Additionally, the accuracy and thermal stability of such charge-to-voltage conversion must be assured to keep a constant performance over time and across different detectors, wiring configurations, and radiation scenarios. This article presents electronic simulations and the first laboratory results showing recent improvements in a new preamplifier designed for High-Purity Germanium spectroscopy systems, in terms of dynamic response, noise, linearity, thermal stability, symmetry, tolerance to reactive loads, piling-up, saturation recovery, and power consumption. The impact of these improvements is also discussed.

References
[1] H. Spieler, Semiconductor Detector Systems, Oxford, UK: Oxford University Press, 2005.
[2] T.R. Twomey, R.M. Keyser, M.L. Simpson, and S.E. Wagner, H. Spieler, "High-Count-Rate Spectroscopy with Ge Detectors: Quantitative Evaluation of the Performance of High-Rate Systems," 2002, ORTEC [online]. Available https://www.ortec-online.com/. Accessed on: May 12th, 2026
[3] Ronald M. Keyser and Timothy R. Twomey, "Optimization of pulse processing parameters for HPGe gamma-ray spectroscopy systems used in extreme count rate conditions and wide count rate ranges," Journal of Radioanalytical and Nuclear Chemistry, vol. 296, pp. 503-508, 2013.

N-LT-03-07

Preliminary Test Results on Latest Version of FESA Readout ASIC for TOF-PET Detectors (#2565)

Yuhao Yang, Yonggang Wang, Xinchi Xu, Xiang Zhang, Huandong Huang

University of Science and Technology of China, Department of Modern Physics, Hefei, China

Abstract
The latest version of the low-power 64-channel Front-End readout chip for SiPM Array (FESA4.0) with the preliminary test results is presented in this paper. Using a row-column summing readout method, FESA compresses the 64 input signals into 16 output digital pulses, which then is digitized by the followed field programmable gate array (FPGA). In the pathway of each summing output, there are two threshold current comparators used for signal pickup, one with a low threshold for signal timing and the other with a high threshold for signal validation. Since the signal amplitude is converted into the pulse time-width via the linear discharge method, both the signals timing and amplitude can be measured by the time-to-digital converter (TDC) in the FPGA. The new version of FESA incorporates a time-over-threshold (TOT) measurement capability, which allows to identify the signals originating from different scintillators. The chip offers prominent advantages of simple architecture, low power consumption, and high performance. Through electronics tests, FESA4.0 has a measurement linearity of 99. 1% with a dynamic range of 140. The intrinsic time measurement precision is measured better than 30 ps. Combined with a TOF-PET detector with an 8×8 LYSO crystal coupled to an 8x8 SiPM, the energy resolution and time coincidence resolution are measured as 279 ps and 12.4% respectively.

These test results show that FESA4.0 is very promising for the construction of highly integrated TOF-PET scanners.

References
[1] A. D. Francesco et al., “TOFPET2: A high-performance ASIC for time and amplitude measurements of SiPM signals in time-of-flight applications,” J. Instrum., vol. 11, no. 3, Mar. 2016, Art. no. C03042, doi: 10.1088/1748-0221/11/03/c03042.
[2] X. Xu, Y. Wang, X. Zhang, H. Huang, Y. Zhou and Z. Song, "A Low-Power 8×8 SiPM Readout ASIC With Row-Column Summing Structure for Compact TOF-PET Detectors," in IEEE Transactions on Circuits and Systems I: Regular Papers, vol. 73, no. 2, pp. 961-971, Feb. 2026, doi: 10.1109/TCSI.2025.3617034.
[3] X. Zhang, Y. Wang, M. Wang and X. Kong, "An FPGA-Based 64-Channel Readout Electronics for High-Resolution TOF-PET Detectors," in IEEE Transactions on Radiation and Plasma Medical Sciences, vol. 9, no. 1, pp. 11-19, Jan. 2025, doi: 10.1109/TRPMS.2024.3443831.

N-LT-03-08

Single-Shot Precision Decomposition of a 64-Channel FPGA TDC for TOF-PET (#2381)

Giancarlo Sportelli[1,2], Matteo Morrocchi[1,2], Nicola Belcari[1,2]

[1] University of Pisa, Department of Physics "E. Fermi", Pisa, Italy; [2] INFN, Sezione di Pisa, Pisa, Italy

The authors would like to thank TEDIEL s.r.l. for the technical support on FPGA TDC architecture implementation and validation.

Abstract

We report a channel-level characterization of a calibrated 64-channel FPGA Time-to-Digital Converter (TDC) for fast-timing TOF-PET, with explicit decomposition of the single-shot precision (SSP) into quantization and jitter contributions. The TDC is implemented on an Altera Cyclone 10 GX device and operates with a 256-tap, 64-bin tapped-delay-line (TDL) at ~400 MHz, calibrated offline via code-density histograms. Two implementation strategies are compared: the default arithmetic carry-chain inference, and a placement-aware variant in which the TDLs are constrained to regular structures. Across all 64 channels, controlled placement reduces the ultra-bin width from 160 ± 76 ps to 101 ± 12 ps, the equivalent LSB (LSBeq) from 83 ± 32 ps to 63 ± 4 ps, and the quantization noise σ_Q from 24.5 ± 7.3 ps rms to 18.1 ± 0.8 ps rms. The placement-constrained implementation also substantially improves channel-to-channel uniformity. The constrained routing increases σ_{jitter} which makes jitter the dominant SSP contribution once σ_Q is reduced. A system-level projection onto previously characterized UTOFPET monolithic modules indicates that the TDC accounts for 59% of the measured CRT² in a 12 mm LYSO/256-channel module (CRT ≈ 150 ps FWHM), but only ~8% in 16–20 mm BGO/64-channel modules (CRT ≈ 400 ps FWHM). This identifies σ_{jitter} as the dominant architectural ceiling and motivates wave-union/multi-TDC averaging or finer-node FPGAs for full LYSO exploitation.

N-LT-03-09

SEU Evaluation of an Atom Switch-based FPGA for Slow-Control Systems (#2501)

Kazuki Ueno[1], Nanae Taniguchi[2], Toshitsugu Sakamoto[3], Makoto Miyamura[3]

[1] The University of Osaka, Department of Physics, Osaka, Japan; [2] KEK, Institute of Particle and Nuclear Studies, Tsukuba, Japan; [3] NanoBridge Semiconductor, Inc., Tsukuba, Japan

Abstract

Atom Switch-based FPGAs (AS-FPGAs) are being developed as next-generation FPGAs with expected high radiation tolerance. Their application to various radiation environments is anticipated, and we are also investigating their potential use in detector electronics for future high-energy physics experiments. In this study, neutron irradiation tests were performed to evaluate the Single Event Upset (SEU) tolerance of digital resources implemented in a 65 nm AS-FPGA. A prototype slow-control board equipped with the AS-FPGA was developed and used for the irradiation test. Two independent block RAM (BRAM) blocks and D-type flip-flop (DFF) blocks were implemented in the FPGA for SEU evaluation, and data mismatches detected during irradiation were counted as SEU events. Neutron irradiation tests were carried out using the tandem accelerator at Kobe University. The neutron fluence reached 1.2×10^{11} n/cm^2. No SEUs were observed in the DFF blocks, while approximately 10 SEUs were detected in the BRAM blocks. The preliminary SEU cross section for the BRAMs was estimated to be on the order of 10^{-9} cm^2/Mbit. In parallel with the irradiation studies, stable acquisition of temperature and pressure data from a commercial environmental sensor connected to the prototype slow-control board was successfully demonstrated during neutron irradiation, indicating the applicability of the AS-FPGA to detector slow-control systems in radiation environments.

N-LT-03-10

MAPSSIC: Toward a Wireless Implantable Positron Probe for Molecular Neuroimaging of Awake and Freely Moving Rats (#2143)

Mathieu Dupont[1], Samir El katera[3,2], Franck Agnese[5], Luis Ammour[6], Jérome Baudot[5], Sandrine Bouvard[7], Fabrice Gensolen[1], Maciej Kachel[5], Jérome Laurence[1], Patrick Pangaud[1], Teo Weicherding[1], Luc Zimmer[7], Phillipe Lanièce[3,4], Marc Antoine Verdier[3,4], Christian Morel[1]

[1] Aix-Marseille Univ, CNRS/IN2P3, CPPM, Marseille, France; [2] Centre de Radiothérapie St. Louis, Toulon, France; [3] Université Paris Cité, CNRS/IN2P3, IJCLab, Orsay, France; [4] Université Paris Saclay, CNRS/IN2P3, IJCLab, Orsay, France; [5] Université de Strasbourg, CNRS, IPHC UMR 7178, Strasbourg, France; [6] Nantes Université, CHU Nantes, Nantes, France; [7] Universitée Lyon 1, CERMEP, CNRS, INSERM, HCL, Lyon, France

Abstract

Correlating molecular neuroimaging with behavior in preclinical models requires acquisitions in awake and freely moving animals, whereas most current positron emission tomography procedures are still performed under anesthesia.
The MAPSSIC project addresses this limitation with an implantable intracerebral probe based on monolithic active pixel sensors (MAPS) for direct positron detection in targeted brain structures of awake, freely moving rats, thereby avoiding the pharmacological bias of anesthesia. Following sensor characterization and simulation studies previously reported, this contribution presents the transition to a fully wireless system. The acquisition chain combines four IMIC2 sensor chips, a STM32L4 microcontroller, 1 Gbit on-board flash memory, and a bidirectional 2.4 GHz radio link to a Raspberry Pi ground station. The complete software stack is implemented in Rust with the Embassy asynchronous framework, providing memory safety and concurrent peripheral management without dynamic allocation. Planned validation with ^{18}F, ^{11}C phantoms, and anesthetized implanted rats will mark the shift from sensor feasibility to system-level wireless validation.

N-LT-03-11

Realistic Detector Response Model for COMET Phase-I Cylindrical Drift Chamber (#2941)

Siyuan Sun[1], Masaharu Aoki[1], Andreas Jansen[2], Masaki Miyataki[1], Yohei Nakatsugawa[3], Yoshi Uchida[4], Kazuki Ueno[1], Chen Wu[5], Tianyu Xing[6], Chihiro Yamada[1], Ye Yuan[5], Yao Zhang[5]

[1] The University of Osaka, Department of Physics, Toyonaka, Japan; [2] Dresden University of Technology, Department of Physics, Dresden, Germany; [3] Wakayama Medical University, School of Medicine, Wakayama, Japan; [4] Imperial College London, Department of Physics, London, UK; [5] Institute of High Energy Physics, Chinese Academy of Sciences, Beijing, China; [6] Istituto Nazionale di Fisica Nucleare, Milan, Italy

This work was supported by QLEAR fellowship grant No. Q21-017, and the National Natural Science Foundation of China (NSFC) under grant No. 12575207.

Abstract
The COMET (COherent Muon to Electron Transition) Phase-I experiment at J-PARC searches for coherent muon-to-electron conversion in aluminum with a single-event sensitivity of 3 x 10^-15. A key detector challenge is the high instantaneous beam rate, which produces background hits in the Cylindrical Drift Chamber (CDC). In particular, low-energy protons can generate large ionization signals that drive the readout electronics into nonlinear regions, producing waveform saturation and pileups. These effects may reduce hit efficiency by masking later signal or background hits and therefore must be modeled realistically in performance studies. We developed a detector response model for the CDC that combines Geant4-based ionization with the Photon Absorption Ionization (PAI) model, Garfield++-based drift time calculation, and an electronics response emulation based on measured response functions. The model explicitly includes nonlinear saturation effects in the circuit and was validated using cosmic-ray test data. The measured-response model reproduces the main features of the data more accurately than a simple linear-response model. The remaining discrepancy corresponds to a limited uncertainty in the pileup-effect evaluation, providing a realistic basis for COMET Phase-I reconstruction and performance studies.

References
[1] Abramishvili, R et al. 2020, ‘COMET Phase-I technical design report’, Progress of Theoretical and Experimental Physics, vol. 2020, no. 3, Art. no. 033C01.
[2] Allison, J et al. 2016, ‘Recent developments in Geant4’, Nuclear Instruments and Methods in Physics Research Section A, vol. 835, pp. 186–225.
[3] Veenhof, R 1993, ‘Garfield, a drift chamber simulation program’, presented at the International Conference on Programming and Mathematical Methods for Solving Physical Problems, Dubna, Russia.
[4] Shimazaki, S et al. 2014, ‘Front-end electronics of the Belle II drift chamber’, Nuclear Instruments and Methods in Physics Research Section A, vol. 735, pp. 193–197.
[5] Pagano, D, Bonomi, G, Donzella, A, Zenoni, A, Zumerle, G & Zurlo, N 2021, ‘EcoMug: An efficient cosmic muon generator for cosmic-ray muon applications’, Nuclear Instruments and Methods in Physics Research Section A, vol. 1014, Art. no. 165732.

N-LT-03-12

Measurement and correction of high intensity effects on the pixel response of the DSSC DEPFET camera (#1557)

Andrea Castoldi[1,2], **Maurizio Ghisetti**[1,2], Chiara Guazzoni[1,2], Stefano Maffessanti[3], Cyril Danilevski[4], Loïc Le Guyader[4], David Lomidze[4], Yevheniy Ovcharenko[4], Matteo Porro[4,5]

[1] Politecnico di Milano, DEIB, Milano, Italy; [2] INFN, Sezione di Milano, Milano, Italy; [3] DESY, Hamburg, Germany; [4] European XFEL, Schenefeld, Germany; [5] Università Ca' Foscari, Venezia, Italy

Abstract

This work reports on the experimental characterization, modeling and correction of high intensity effects on the pixel response of the DEPFET Sensor with Signal Compression (DSSC) camera, an active pixel detector targeted at soft X-ray imaging experiments at the European XFEL. Experimental tests with up to 5 MeV/pixel deposited energy have been performed at the European XFEL, showing evidence of a shift of the pedestal value growing with X-ray intensity. Moreover, the signal compression provided by the DEPFET (DEpleted P-type Field Effect Transistor), integrated in each pixel, enhances the impact of this systematic effect on the measurement accuracy. The observed shift is assumed to be proportional to the signal dependent drop of the power supply lines along each ASIC column and can be modeled by two parameters. We devised a procedure to efficiently measure the two model parameters by means of a custom mask that shields a fraction of each ASIC column, irradiated with a flat field. The main results of the characterization of the signal dependent pedestal shift parameters and the application of the resulting correction to X-ray images of different patterned masks (dots, stripes, 2D shapes etc.) acquired at increasing intensities will be presented and discussed.

N-LT-03-13

Towards a 64-Channel Monolithic SDD X-Ray Spectrometer for High-Throughput Synchrotron Applications (#2776)

Beatrice Pedretti[1,2], Pietro Barcella[1,2], Andrea Abba[3], Giacomo Borghi[1,2], Marco Carminati[1,2], Carlo E. Fiorini[1,2]

[1] Politecnico di Milano, DEIB, Milano, Italy; [2] INFN, Milano, Milano, Italy; [3] Nuclear Instruments srl, Lambrugo, Italy

Abstract

The increasing brilliance of fourth-generation synchrotron sources drives a growing demand for energy-dispersive X-ray fluorescence (XRF) spectrometers capable of handling extreme photon fluxes.

We present the design and characterization of the ARDESIA-64 instrument, a complete X-ray fluorescence (XRF) spectrometer for high-throughput synchrotron applications.

The instrument integrates a highly scaled 64-channel monolithic Silicon Drift Detector (SDD) array, featuring a pixel pitch of 2.5 mm, within a compact, vacuum-compatible mechanical housing tailored for beamline integration.

At the conference, we will present the instrument design and comprehensive spectroscopic characterization results.

The collimated 450 µm-thick sensor variant demonstrates an excellent average energy resolution of 125.9 eV FWHM at 5.9 keV. Preliminary high-rate tests confirm exceptional throughput capabilities, sustaining Input Count Rates (ICR) exceeding 800 kcps per channel while preserving an energy resolution of ~150 eV. The readout is performed by a 64-channel Digital Pulse Processor (DPP) based on the CAEN DT5560SE digitizer with firmware specifically adapted for high-throughput X-ray spectroscopy in synchrotrons.

References

[1] Pedretti, B., Ticchi, G., Barcella, P., Borghi, G., Carminati, M., & Fiorini, C. (2025). High-throughput X-ray spectroscopy: characterization of the ARDESIA detector with high-end digital pulse processors. *Synchrotron Radiation*, *32*(6).

[2] Utica, G., Fabbrica, E., Carminati, M., Borghi, G., Zorzi, N., Ficorella, F., ... & Fiorini, C. (2021). ARDESIA-16: a 16-channel SDD-based spectrometer for energy dispersive X-ray fluorescence spectroscopy. *Journal of Instrumentation*, *16*(07), P07057.

N-LT-03-14

Education kit for radiation measurements (#2477)

Masaharu Nomachi

The University of Osaka, RCNP, Ibaraki/Osaka, Japan

This work is supported by IEEE/NPSS Initiative.

Abstract

We have been organizing schools on radiation measurements for students from ASEAN countries. Hands-on experience with radiation measurements is very important, and we prepare radiation measurement systems for practical exercises.

To host as many students as possible, we considered organizing the schools in ASEAN countries. However, the shipping cost of the equipment was extremely high. As a result, we could not conduct hands-on exercises on radiation measurement.

Driven by recent large-scale experiments, electronics for radiation measurements have become compact, highly integrated, and low-cost. This development now makes it possible to carry equipment to schools.

Today, compact detector systems are available at affordable prices, making it much easier to conduct practical radiation measurement exercises in schools.

However, modern compact electronics have introduced a new problem: they are too small to probe easily with an oscilloscope. In modern electronics, waveform processing is increasingly performed digitally. Nevertheless, we believe that analogue processing remains important and highly educational for students. This motivated us to develop electronics specifically for educational purposes.

We have developed an “education kit” for radiation measurement education. By plugging in a SiPM and a small scintillator crystal module, the board functions as a complete radiation measurement system. An on-board FPGA interfaces with a PC through a USB connection. The board is the size of a Raspberry Pi board. Optionally, it can be plugged onto a Raspberry Pi.

Although the board is compact, it provides sufficient space for probing signals. The design of the board will be released as open-source hardware. Students can modify the design and develop their own versions of the board. The “education kit” will serve as an entry point to radiation measurement electronics.

Time:
11 November, 2026
10:30 – 11:00

Room:
MACHADO

N-LT-04 | NSS Lightning Talks 4

Chairs:
Martin Grossmann (Villigen)
Trang Hoang (Ho Chi Minh)

N-LT-04-01

Recoil electron tracking in 3D CZT drift strip detectors: a feasibility study (#2296)

Michał Kossakowski[1], Alejandro Valverde Mahou[2], Søren Hauberg[2], Irfan Kuvvetli[1]

[1] Technical University of Denmark, Space Research and Technology, Lyngby, Denmark; [2] Technical University of Denmark, Applied Mathematics and Computer Science, Lyngby, Denmark

This work was supported by the Danish Data Science Academy, funded by the Novo Nordisk Foundation (NNF21SA0069429) and the VILLUM FONDEN (40516). The first author also acknowledges the i-RASE (Intelligent Radiation Sensor Readout System) project team for their support and collaboration.

Abstract

Bridging the *MeV gap* remains difficult due to the interplay of competing photon interaction processes, leaving a persistent sensitivity gap in gamma-ray astronomy. Compton telescopes based on 3D CZT Drift Strip Detectors (DSD) are promising candidates for bridging this gap, offering room-temperature operation, high stopping power, excellent energy and position resolution. A key open question is whether recoil electron tracking, which significantly improves angular resolution and detector sensitivity is achievable from raw detector signals. We investigate this using a machine learning approach trained on forward simulations of the 3D CZT DSD response. Principal Component Analysis of simulated electron tracks confirms that track structure is encodable in a low-dimensional representation, and neural network training to regress the recoil direction directly from detector waveforms is ongoing.

References

[1] S. R. Owe, I. Kuvvetli, A. Zoglauer, and C. Budtz-Jørgensen, “Feasibility of using 3d czt drift strip detectors for small compton camera space missions,” Journal of Instrumentation, vol. 19, no. 01, p. C01005, 2024

[2] A. C. Zoglauer, “First light for the next generation of compton and pair telescopes,” Ph.D. dissertation, Technische Universitat Munchen, 2005

N-LT-04-02

CVAE-Based Synthetic Thermoluminescence Silica Glass Jewellery Bead Glow Curve Generation (#2606)

Lukasz Tomaszewski, Caroline Shenton-Taylor

University of Surrey, Department of Physics, Guildford, UK

This work was funded and supported by the Nuclear Threat Reduction Network (NTR-Net), UK Ministry of Defence
© Crown Owned Copyright 2026/AWE.

Abstract
Micro silica glass jewellery beads have emerged as a viable material for thermoluminescence dosimetry (TLD), offering a low-cost and widely accessible option for personal dose assessment. Their linear glow curve responses, governed by irradiation, thermal conditions, and sample characteristics, exhibit unique spectral elements and structure variability. While machine learning (ML) methods have been successfully applied to dose estimation and irradiation analysis, can ML be used to elevate silica glass beads beyond just decorative jewellery? In this work, a Conditional Variational Autoencoder (CVAE) is implemented to model and generate thermoluminescent glow curves from silica glass beads conditioned on experimental parameters. The model is trained on a dataset of experimentally acquired responses, augmented with Poisson noise to increase the dataset size and robustness. Conditioning variables include temperature profiles, irradiation and sample characteristics, enabling the model to learn relationships between physical conditions and the glow curve. Results show that the CVAE model can generate realistic glow curves that reflect the underlying conditioning variables. Generated predications maintain peak structure and overall shape, while also reproducing the expected linear relationship between total counts and absorbed dose. Model performance remains consistent when evaluated on previously unseen testing data with a mean figure of merit of 7.5%, although accuracy declines at low dose levels due to diminished signal intensity. The proposed approach demonstrates the potential of generative ML techniques for supporting dosimetry simulation, calibration, and data augmentation workflows for future research.
UK Ministry of Defence © Crown Owned Copyright 2026/AWE.

N-LT-04-03

Characterizing Neutron Detection Efficiency in Timepix3: A Bayesian-Optimized FLUKA Approach (#3239)

Angel Mercado, Sharmistha Mukhopadhyay, Malachi West, Patrick Connolly, Shaheen Dewji

Georgia Institute of Technology, Atlanta, USA

Abstract
Characterization of converter layer geometry is critical for determining the absolute detection efficiency of pixelated thermal neutron detectors. However, uncertainties in film deposition and source strength often lead to significant discrepancies between simulated models and actual experimental performance. This work addresses these challenges by implementing a Bayesian optimized FLUKA framework to determine the effective enriched Lithium-6 Fluoride converter thickness for an ADVACAM Timepix3 detector with a 1000 µm Silicon sensor. The FLUKA Monte Carlo model was benchmarked against experimental measurements using an Americium-Beryllium source with a nominal activity of 40 mCi and a documented tolerance of fifteen percent. The Bayesian optimizer successfully converged to an effective thickness of 5 µm after forty evaluations by minimizing the residuals between the nominal source activity and the simulation-implied activities. This methodology demonstrates a robust approach to resolving geometric uncertainties in hybrid semiconductor detectors where direct physical measurement of internal components is not feasible post-assembly. The resulting validated geometry provides a

high-fidelity foundation for modeling future detection efficiency benchmarks across diverse neutron spectra. This work demonstrates a practical approach for integrating machine-learning optimization with Monte Carlo transport modeling to address geometric uncertainties in neutron detectors.

N-LT-04-04

Enhanced Spent Nuclear Fuel Characterization Using Sequential Detector Responses through Deep Learning (#2393)

Beomkyu Kwon[1], Wooseong Hong[1,2], Jaehyo Kim[1,2], Geehyun Kim[1,2]

[1] Seoul National University, Nuclear Engineering, seoul, South Korea; [2] Seoul National University, Energy Systems Engineering, seoul, South Korea

This work was supported by the Nuclear Safety Research Program through the Korea Foundation of Nuclear Safety (KoFONS) using the financial resource granted by the Nuclear Safety and Security Commission (NSSC) of the Republic of Korea. (RS-2022-KN073410)

Abstract

Accurate characterization of spent nuclear fuel (SNF) is essential for verifying operator-declared information in nuclear safeguards. Conventional nondestructive assay (NDA) approaches for such characterization based on gamma-ray spectroscopy typically rely on extracting specific photopeak information (ex. 662 keV peak of ^{137}Cs), which compresses high-dimensional detector responses into a limited number of variables and may lead to information loss. To address this limitation, we propose a deep learning–based SNF characterization approach that directly utilizes sequential detector-response data for advanced characterization performance. The training dataset was generated through integrated ORIGEN and MCNP simulations for 5000 realistic SNF conditions, covering variations in initial enrichment, burnup, and cooling time. The proposed C2C-GRU-v2 architecture was designed to process long sequential detector-response data by combining Coordinate-to-Context embedding and GRU-based recurrent sequence modeling, enabling both event-level contextual learning and sequence-level generalization. For comparison, a conventional spectrum-based regression method using ^{137}Cs peak counts was also implemented under identical conditions. The proposed approach demonstrated improved characterization performance compared with the conventional method, particularly for cooling time estimation, achieving Relative Root Mean Square Errors (RRMSE) of 0.157 for burnup and 0.0456 for cooling time prediction. These results demonstrate the feasibility of deep learning–based sequential detector-response analysis for advanced SNF characterization in nuclear safeguards applications.

References
[1] Willman, Christofer, et al. "Nondestructive assay of spent nuclear fuel with gamma-ray spectroscopy." Annals of Nuclear Energy 33.5 (2006): 427-438.
[2] Hong, Wooseong, Beomkyu Kwon, and Geehyun Kim. "Characterization of Spent Fuel Parameters using Non-destructive Assay and Machine Learning."
[3] Bell, M. J. ORIGEN: the ORNL isotope generation and depletion code. No. ORNL--4628. Oak Ridge National Lab., Tenn.(USA), 1973.
[4] Kulesza, Joel A., et al. MCNP® code version 6.3. 1 theory & user manual. No. LA-UR--24-24602. Los Alamos National Laboratory (LANL), Los Alamos, NM (United States), 2024.

[5] Favalli, Andrea, et al. "Determining initial enrichment, burnup, and cooling time of pressurized-water-reactor spent fuel assemblies by analyzing passive gamma spectra measured at the Clab interim-fuel storage facility in Sweden." Nuclear Instruments and Methods in Physics Research Section A: Accelerators, Spectrometers, Detectors and Associated Equipment 820 (2016): 102-111.

N-LT-04-05

Robust Dual-Target Radioisotope Quantification Under Increasing Unseen Contaminant Complexity (#2217)

Chanho Kim[1], Yeongjun Kim[1], Geon Kim[2], Dae yang Oh[2]

[1] Korea Atomic Energy Research Institute, Daejeon, South Korea; [2] Korea University, Department of Bioengineering, Seoul, South Korea

This work was supported by the National Research Foundation of Korea (NRF) grant funded by the Korea government (Ministry of Science and ICT) (No. RS-2022-00165164).

Abstract

Gamma-ray spectroscopy is a fundamental technique for radioisotope identification and quantification across safety-critical applications, where deep learning models have recently emerged as a data-driven alternative to traditional library-dependent methods. However, most existing deep learning approaches operate under a closed-set assumption that all isotopes during deployment are present in the training set; field deployments frequently violate this assumption, and the introduction of unknown isotopes leads to silent degradation. Recent OOD-detection studies have been reported, but they treat OOD spectra as anomalies to be flagged rather than quantified, and systematic evaluation under increasing unseen contaminant complexity remains lacking. This study proposes a denoising autoencoder (DAE) framework that reconstructs the clean target spectrum (^{137}Cs, ^{133}Ba) from contaminated measurements while simultaneously estimating target fractions through a dual-head architecture. Using Ce:GPS scintillator pulse data under a leave-one-out unknown noise (LOO-UN) protocol, the DAE achieved a mean absolute error (MAE) of 0.024 at 20% out-of-distribution (OOD) contamination in the two-unseen configuration, outperforming NNLS-known (0.038) and MLP (0.031), with near-constant accuracy as the unseen contaminant count increased from one to two (0.025 → 0.024).

References

[1] M. Park, C. Kim, J. Hwang, and J. Y. Yeom, "Deep learning-based radioisotope quantification for extreme environments," Radiat. Phys. Chem., vol. 239, p. 113345, 2025.

[2] B. Van Omen et al., "Multilabel deep learning approach for radioisotope proportion estimation and out-of-distribution detection," Ann. Nucl. Energy, vol. 208, p. 110777, 2024.

[3] C. Kim et al., "Radiation resistance and temperature dependence of Ce:GPS scintillation crystal," Radiat. Phys. Chem., vol. 183, p. 109396, 2021.

[4] D. Hendrycks and K. Gimpel, "A baseline for detecting misclassified and out-of-distribution examples in neural networks," in Proc. Int. Conf. Learn. Representations (ICLR), 2017.

[5] P. Vincent, H. Larochelle, I. Lajoie, Y. Bengio, and P.-A. Manzagol, "Stacked denoising autoencoders: Learning useful representations in a deep network with a local denoising criterion," J. Mach. Learn. Res., vol. 11, pp. 3371–3408, 2010.

N-LT-04-06

Automated Monte Carlo-Based Efficiency Transfer Integrated into HPGe Gamma Spectroscopy Workflows for High-Throughput Laboratories (#1579)

Spencer Behling[1], Felix Diel[3], Marc Breidenbach[2]

[1] Ametek, Ortec, Oak Ridge, USA; [2] AMETEK GmbH, Meerbusch, Duesseldorf, Germany; [3] AMETEK GmbH, InnoRIID, Duesseldorf, Germany

Abstract

High-purity germanium (HPGe) detector systems are widely used for gamma spectroscopy; however, increasing throughput demands, expanding measurement configurations, and a declining base of expert users have made traditional efficiency calibration and transfer workflows increasingly impractical. Efficiency transfer between counting geometries has historically required manual configuration, custom made sources, and/or execution of Monte Carlo simulations by trained computational physicists, limiting scalability in routine laboratory environments. We present an approach that embeds Monte Carlo-based efficiency transfer directly within a commercial spectral analysis software stack, enabling automated operation without additional user intervention. At runtime, sample geometries—already specified by laboratory personnel using standard container templates such as Marinelli beakers—are used to drive a ray-tracing-based gamma transport simulation coupled to detector interaction and pulse-processing models. The approach operates over an energy range of 20 keV to 2.5 MeV and produces both full spectra and efficiency curves.

Validation is performed through comparison of simulated spectra and efficiency curves against measured data and results from the Geant4 Monte Carlo toolkit. While not intended to match the full generality of Geant4, the proposed approach demonstrates comparable practical accuracy for routine laboratory configurations while significantly reducing user complexity. Additionally, seamless integration into existing workflows is demonstrated, enabling non-expert users to apply physics-based efficiency transfer without specialized training.

This work provides a scalable solution for automated, high-throughput gamma spectroscopy, bridging the gap between rigorous Monte Carlo modeling and practical laboratory usability.

N-LT-04-07

Neutron and secondary photon dose mapping of deuterium-deuterium (D-D) and deuterium-tritium (D-T) neutron generators via PHITS simulations (#2970)

Andrea G. Alipio[1], Christine L. Dulohan[1], Bernhard Egwolf[2], Alvie Asuncion-Astronomo[3]

[1] University of Santo Tomas, The Graduate School, Manila, Philippines; [2] University of Santo Tomas, Department of Mathematics and Physics, Manila, Philippines; [3] Department of Science and Technology, Philippine Nuclear Research Institute, Quezon City, Philippines

This work is supported by the DOST-PCIEERD-funded project NURAD Component 2: "Accelerator Driven Subcritical Nuclear Reactor" with Project Number 1211979.

Abstract

The Monte Carlo-based Particle Heavy Ion Transport Code System (PHITS) was used to model deuterium-deuterium (D-D) and deuterium-tritium (D-T) neutron generators for preliminary radiation safety assessment of the ongoing establishment of the Neutron Irradiation Facility (NIF) of the Philippine Nuclear Research Institute (PNRI). Neutron and secondary photon dose distributions were obtained for fully shielded, partially shielded, and unshielded configurations. In both D-D and D-T cases, the counting room dose rates were acceptable with respect to occupational dose limits for a 500-hour annual operating time. However, additional shielding should be explored for the D-T setup to further reduce dose rates in the work area. The dose maps presented the significance of the configuration of moderating and shielding materials in minimizing radiological doses during operation. The findings of this work will serve as a reference for the safe and reliable installation of the country's first neutron generator laboratory.

N-LT-04-08

Bayesian Filtering Image Reconstruction for SourceLocalization and Tracking in Compton Imaging (#2167)

John Leland[1], Cecilia Tarpau[2], Ming Fang[1], Yoann Altmann[3], Angela Di Fulvio[1]

[1] University of Illinois Urbana-Champaign, Nuclear, Plasma, and Radiological Engineering, Urbana, USA; [2] University of Edinburgh, Maxwell Institute for Mathematical Sciences, Bayes Center, Edinburgh, UK; [3] Heriot-Watt University, School of Engineering and Physical Sciences, Edinburgh, UK

This material is based upon work supported in part by the Department of Energy National Nuclear Security Administration through the Nuclear Science and Security Consortium under Award Number DE-NA0003996.

Abstract

Stand-off detection of special nuclear materials (SNM) in safeguards and non-proliferation applications demands imaging systems capable of tracking sources across dynamic environments. In this work, we introduce a Bayesian-Filtering (BF) algorithm for simultaneous source localization and tracking where existing reconstruction methods, such as simple back-projection (SBP) and maximum likelihood expectation maximization (MLEM), are insufficient. We evaluate the BF algorithm using synthetic data generated with MCNPX-PoliMi for a simulated Compton imager consisting of a 4 x 7 array of LYSO scintillator crystals. Two independent sources are simulated, one sweeping in azimuth and one in elevation, each traveling from -90° to +90° at 1 m/s. The BF algorithm successfully tracked both sources across the full angular sweep, achieving mean angular errors of 6.4° and 6.03° for the azimuth and elevation cases, respectively. Additionally, preliminary results for multi-source tracking are successful with the algorithm tracking both sources up until their paths intersect which is a known challenge we are currently investigating.

References

[1] E. Padovani, S. Pozzi, S. Clarke, and E. Miller, MCNPX-Polimi Users Manual.

[2] C. Tarpau, M. Fang, K. C. Zygalakis, M. Pereyra, A. Di Fulvio, and Y. Altmann. Statistical modelling and bayesian inversion for a compton imaging system: application to radioactive source localization. Inverse Problems, 40:125028, 2024. doi:10.1088/1361-6420/ad96de

N-LT-04-09

Count-Level Effects on Radiomics Robustness and Harmonization in Total-Body PET Imaging (#3090)

Mohamed Saber Azimi[5], Maryam Cheraghi[7], Habib Zaidi[1]

[1] Geneva University Hospital, Division of Nuclear Medicine & Molecular Imaging, Geneva, Switzerland; [2] Geneva University Hospital, Division of Nuclear Medicine & Molecular Imaging, Geneva, Switzerland; [3] Odense University Hospital, Deptartment of Nuclear Medicine, Odense, Denmark; [4] Odense University Hospital, Deptartment of Nuclear Medicine, Odense, Denmark; [5] Obuda University, University Research and Innovation Cente, Budapest, Hungary; [6] Obuda University, University Research and Innovation Cente, Budapest, Hungary; [7] Shahid Beheshti University, Department of Nuclear Medicin, Tehran, Iran; [8] Shahid Beheshti University, Department of Nuclear Medicin, Tehran, Iran

This study was financially supported by the Swiss National Science Foundation (SNSF, grant No. 30030–231742) and the Geneva League Against Cancer (grant No. LGC 2402).

Abstract

Radiomics analysis in total-body PET imaging is highly sensitive to acquisition variability, particularly count reduction, which directly affects noise characteristics and feature reliability. In this study, we investigate the impact of count reduction and multi-parametric harmonization on the robustness of multi-organ radiomics. A retrospective

dataset of 550 patients from two centers was analyzed. Multiple count levels were generated from list-mode data, including standard and reduced counts (reduction factors up to 100). Multi-organ segmentation was performed automatically, and 107 IBSI-compliant radiomics features were extracted from SUV-normalized images. Feature harmonization was applied using ComBat under different configurations, including scanner, voxel size, radiopharmaceutical, and scatter correction. Reproducibility was evaluated using intraclass correlation coefficients across count levels and anatomical regions. Results show that radiomics stability is strongly dependent on both count level and feature type. Approximately 31% of features achieved good reproducibility (ICC ≥ 0.75) in at least one organ. Shape and first-order features remained relatively stable under moderate count reduction (CRF ≤ 20), while higher-order texture features exhibited substantial degradation at extreme count levels (CRF ≥ 50). Harmonization improved feature consistency, particularly for scanner- and resolution-related variations, but had limited impact under severe noise conditions. Taken together, the results indicate that preserving quantitative reliability in low-count PET requires careful consideration of both feature selection and acquisition variability. Rather than relying solely on harmonization, robust radiomics analysis should incorporate count-aware strategies, especially when extending to multi-center or ultra-low-count imaging scenarios.

N-LT-04-10

Development of a Single-Layer Dual-Ended Readout Compton Camera Prototype for Enhanced Spatial Imaging (#1799)

Haoqi Wen, Chenxi Li, Yucun Hou, Kexin Wang, Jianyong Jiang

Beijing Normal University, Key Laboratory of Beam Technology of Ministry of Education, School of Physics and Astronomy, Bejing, China

This work was supported by the NSFC (No. 12475336).

Abstract

The Compton camera has emerged as a pivotal gamma-ray imaging technique, with critical applications in astrophysical observation, nuclear safety monitoring, and environmental radiation detection. In nuclear astrophysics, the detection and localization of gamma rays in the MeV range are indispensable for probing high-energy cosmic phenomena. Despite its importance, the advancement of MeV gamma-ray imaging instrumentation remains constrained by low interaction probabilities and high imaging complexity. This study presents a single-layer Compton camera prototype designed for enhanced spatial imaging, building upon the mission heritage of the BNU-120—a space-borne detector successfully deployed for monitoring gamma-ray bursts (GRBs). To transcend the original system's lack of spatial imaging capability, we propose a high-performance architecture that leverages the established BNU-120 framework while integrating a dual-ended readout to achieve a 4π detection solid angle. The prototype uses a 8×8 Ce:GAGG array coupled to Hamamatsu Multi-Pixel Photon Counters (MPPC, S14161-3050HS-08) at both ends. Each crystal measures 3×3×25 mm^3 and is optically isolated by 0.2-mm-thick $BaSO_4$ reflective layers. System characterization demonstrated an energy resolution of approximately 5% (FWHM) at 511 keV. Depth-of-interaction (DOI) information, extracted via the energy ratio method, yielded a DOI resolution of roughly 2 mm (FWHM) along the crystal axis. Computational validation using GATE simulations of a U-shaped 511

keV planar source showed that the source geometry was clearly distinguishable through a back-projection (BP) algorithm. Subsequent point-source experiments verified the detector's capability to localize discrete sources. Future work will focus on realistic physical imaging experiments and the exploration of more advanced reconstruction algorithms to fully evaluate the module's Compton imaging performance.

References
[1] W. Jiang, et al., “Calibrations of the BNU-120 gamma-ray detector based on GAGG Scintillators,” J. Beijing Normal Univ. (Nat. Sci.), vol. 58, pp. 1-6, 2022.
[2] J. Jiang et al., “A prototype of aerial radiation monitoring system using an unmanned helicopter mounting a GAGG scintillator Compton camera,” Journal of Nuclear Science and Technology, vol. 53, no. 7, pp. 1067–1075, Jul. 2016, doi: 10.1080/00223131.2015.1089796.
[3] C. Li et al., “Performance characterization of a Compton camera prototype based on a novel epitaxial-quenching-resistor SiPM,” J. Inst., vol. 20, no. 05, p. P05048, May 2025, doi: 10.1088/1748-0221/20/05/P05048.
[4] B. Das, B. Mehrdel, D. Goodman, M. Streicher, Y. Seo and J. Caravaca, "Compton Imaging of Ac-225 in Preclinical Phantoms With a 3D-positioning CZT Camera," in *IEEE Transactions on Radiation and Plasma Medical Sciences*, vol. 10, no. 1, pp. 112-125, Jan. 2026, doi: 10.1109/TRPMS.2025.3577212.
[5] Z. Kuang et al., “Dual-ended readout small animal PET detector by using 0.5 mm pixelated LYSO crystal arrays and SiPMs,” Nuclear Instruments and Methods in Physics Research Section A: Accelerators, Spectrometers, Detectors and Associated Equipment, vol. 917, pp. 1–8, Feb. 2019, doi: 10.1016/j.nima.2018.11.011.

N-LT-04-11

Crystal Dual-Readout Calorimetry for Future e^+e^- Higgs Factories (#2842)

Marcello Campajola[1], Mariagrazia Alviggi[2,1], Benedetta Argiento[3,1], Etiennette Auffray[4], Andrea Benaglia[5], Maurizio Biasini[7,8], Valeria Bisignani[2,1], Daniele Boccanfuso[6,1], Lucrezia Borriello[3,1], Claudia Cecchi[7,8], Francesco Cirotto[2,1], Francesco Conventi[3,1], Antonio D'Avanzo[2,1], Julie Delenne[9,4], Guglielmo De Nardo[2,1], Carlo Di Fraia[2,1], Adelina D'Onofrio[1], Leonardo Favilla[6,1], Marco Francesconi[1], Giovanni Gaudino[1], Orso Alberto Maria Iorio[2,1], Vincenzo Izzo[1], Marco Toliman Lucchini[10,5], Elisa Manoni[8], Marco Mirra[1], Stefano Moneta[8], Pierluigi Paolucci[1], Simone Perna[3,1], Biaggio Rossi[1], Elvira Rossi[2,1], Julia Scamardella[2,1], Givi Sekhniaidze[1]

[1] INFN, Sezione di Napoli, Napoli, Italy; [2] Università degli Studi di Napoli Federico II, Napoli, Italy; [3] Università degli Studi di Napoli Parthenope, Napoli, Italy; [4] CERN, Ginevra, Switzerland; [5] INFN, Sezione di Milano-Bicocca, Milano, Italy; [6] Scuola Superiore Meridionale, Napoli, Italy; [7] Università degli Studi di Napoli Perugia, Perugia, Italy; [8] INFN, Sezione di Perugia, Perugia, Italy; [9] Université de Strasbour, Strasbour, France; [10] Università degli Studi di Milano-Bicocca, Milano, Italy

This work was performed in the framework of DRDcalo. It received funding from the European Union – Next Generation EU programme, Mission 4, Component 1 (CUP H53D23001120006), and from the Horizon Europe ERA Widening Project no. 101078960 TWISMA.

Abstract
Precision physics at future e+e− Higgs factories set stringent requirements on calorimetric performance, with 3%/√E for electromagnetic particles and ∼ 30%/√E for neutral hadrons identified as key benchmarks. A hybrid dual-readout approach, combining a homogeneous crystal electromagnetic section with a fiber-based hadronic section, offers a cost-effective path toward simultaneously achieving both targets. Reaching such performance requires enhancing the longitudinal and transverse granularity of the crystal section beyond what is available in conventional

homogeneous calorimeters and equipping each crystal cell with two independent readout channels to simultaneously collect Cherenkov and scintillation light. These features enable advanced particle-flow dual-readout reconstruction algorithms to exploit the maximum available information from each event. This work will present extensive laboratory characterizations together with beam-test measurements carried out at CERN on single-crystal PWO, BGO, and BSO cells instrumented with optical filters and SiPMs. These studies demonstrate event-by-event separation of Cherenkov and scintillation light, with both scintillation and Cherenkov yields exceeding the thresholds required for optimal electromagnetic and hadronic energy resolution. The results have guided the technological choices for the ongoing construction of full-containment calorimeter prototypes

References
[1] Abada et al., “FCC-ee: The Lepton Collider: Future Circular Collider Conceptual Design Report Volume 2,” Eur. Phys. J. Special Topics, vol. 228, no. 2, pp. 261–623, 2019. doi:10.1140/epjst/e2019-900045-4
[2] T. C. S. Group, “CEPC Conceptual Design Report: Volume 2 – Physics & Detector,” 2018. arXiv:1811.10545.
[3] M. T. Lucchini et al.,“Particle flow with a hybrid segmented crystal and fiber dual-readout calorimeter,” JINST, vol. 17, no. 06, P06008, 2022. arXiv:2202.01474
[4] R. Ferrari et al., “Dual-readout calorimetry,” Int. J. Mod. Phys. A, vol. 34, no. 13n14, p. 1940019, 2019. doi:10.1142/S0217751X19400190.
[5] N. Akchurin et al., “Separation of crystal signals into scintillation and Cherenkov components,” Nucl. Instrum. Methods Phys. Res. A, vol. 595, no. 2, pp. 359–374, 2008. doi: 10.1016/j.nima.2008.07.136.
[6] M. Abbrescia et al. [IDEA Study Group], “The IDEA detector concept for FCC-ee,”. arXiv:2502.21223.
[7] R. Hirosky et al., “Dual-readout calorimetry with homogeneous crystals,” EPJ Web Conf., vol. 320, p. 00021, 2025. arXiv:2408.11973
[8] A. Benaglia et al., “Characterization of thin optical filters for high purity Cherenkov light readout from scintillating crystals”, JINST 21 (2026) P03025, arXiv:2512.04965
[9] M. Alviggi et al., “Cherenkov and scintillation light separation in BGO and BSO crystals coupled to SiPMs for dual-readout electromagnetic calorimetry at future colliders. arXiv:2604.09918v1

N-LT-04-12

Design of the ePIC Hadronic Barrel Calorimeter, Status of the Test stand and Prospects for Physics at the EIC. (#2964)

Eric J. Mannel

Brookhaven National Laboratory, Physics Dept, Upton, USA

This work is supported by the United States Department of Energy.

Abstract
ePIC is the general purpose detector for the Electron-Ion Collider (EIC) that is being built at Brookhaven National Laboratory and will be ready for first physics when the Electron-Ion Collider turns on. ePIC is based on a new 1.7T superconducting solenoid magnet. The detector consists of precision tracking, particle identification and calorimeter (electromagnetic and hadronic) to measure the properties of electron-Ion collisions that will occur at the EIC. In this paper we will present the over all design of the ePIC detector, with a focus on the Barrel Hadronic Calorimeter (BHCal) which is the repurposed sPHENIX Outer Hadronic Calorimeter (HCal). We will also present the current status of the BHCal design, test stand and preliminary results of the new electronics readout system based on the CaloROC chip designed for ePIC

N-LT-04-13

Off-detector Readout and Real-time Signal Processing for the ATLAS Liquid ArgonCalorimeter at the High-Luminosity LHC (#2635)

Pablo Collado Soto[2], **Nikiforos Nikiforou**[1], On behalf of the ATLAS Collaboration

[1] CERN, Geneve, Switzerland; [2] Universidad Autonoma de Madrid, Physics Department, Madrid, Spain

Abstract

The ATLAS Liquid Argon (LAr) calorimeter readout electronics are being upgraded for operation at the High-Luminosity Large Hadron Collider (HL-LHC), where up to approximately 200 proton-proton interactions per bunch crossing will significantly increase detector occupancy, data throughput, and trigger rates. While the calorimeter detectors themselves remain unchanged, the full readout electronics chain is being replaced. The upgraded off-detector processing system continuously receives digitized calorimeter signals from approximately 182000 channels at the 40 MHz bunch-crossing rate through high-speed optical links. The processing architecture is implemented in Advanced Telecommunications Computing Architecture (ATCA) systems hosting large FPGAs performing real-time reconstruction of energy and timing while satisfying stringent trigger latency requirements. Prototype hardware and firmware have been developed and validated in integration setups combining front-end electronics, timing distribution, and data acquisition systems. In parallel, advanced reconstruction methods including machine-learning approaches optimized for FPGA implementation are being investigated to improve robustness against pileup and overlapping pulses.

N-LT-04-14

The LS3 Enhancement of the LHCb Electromagnetic Calorimeter (#2898)

Eduardo Picatoste[1], Sergio Gómez[2], on behalf of the LHCb ECAL Upgrade II RD Group

[1] Universitat de Barcelona, Institute of Cosmos Sciences of the University of Barcelona, Barcelona, Spain; [2] Universitat Politècnica de Catalunya, Barcelona, Spain

Abstract

An upgrade of the LHCb electromagnetic calorimeter (ECAL) is planned for Long Shutdown 3 (LS3) to address significant aging effects in the central region caused by radiation damage and high particle flux. The innermost ECAL modules will be replaced with a new design based on Spaghetti Calorimeter (SpaCal) technology, optimized for radiation tolerance and improved performance under high occupancy conditions. A total of 176 SpaCal modules will be installed. These are based on scintillating plastic fibers embedded in dense absorbers. The innermost 32 modules will use 3D-printed tungsten absorbers to withstand the highest radiation levels, while the remaining 144 modules will employ lead absorbers produced through an innovative casting technique. Both configurations have

been prototyped and extensively validated in test beam campaigns at DESY-II and CERN SPS. The measured energy resolution for electron beams is consistent with performance requirements and shows good agreement with detailed Monte Carlo simulations. The scintillating fibers will be read out using radiation-hard hollow light guides coupled to fast photon detectors. In total, 3072 new readout channels will be implemented with dedicated front-end electronics. In parallel with the installation of the new SpaCal modules, the current Shashlik calorimeter modules will be rearranged to better match the spatial distribution of particle occupancy. Simulation studies demonstrate a significant reduction in per-cell occupancy after the LS3 upgrade, improving detector performance in Run 4 conditions. Benchmark analyses of key physics channels confirm that this enhancement leads to a substantial gain in reconstruction efficiency and measurement precision. Overall, the LS3 ECAL upgrade represents a crucial step toward coping with higher luminosity conditions and anticipates key design features of the future PicoCal system foreseen for implementation during LS4.

References
[1] The LHCb Collaboration, 2023, ‘LHCb Particle Identification Enhancement Technical Design Report,’ CERN-LHCC-2023-005
[2] The LHCb Collaboration, 2022, ‘LHCb Framework TDR for the LHCb Upgrade II Opportunities in flavour physics, and beyond, in the HL-LHC era’, CERN-LHCC-2021-012
[3] The LHCb Collaboration, 2024, ‘LHCb Upgrade II Scoping Document’, CERN-LHCC-2024-010

Time:
11 November, 2026
11:30 – 13:00

Room:
Poster Area

NSS-13 | NSS Poster Session

Chairs:
Andrea Gonzalez Montoro (Valencia)

NSS-13-002

Gas Circulation and Pressure Protection System for the COMET Cylindrical Drift Chamber (#1762)

Ryo Nagai[1], Shukei Kawano[1], Shunya Ueda[1], Yuuki Nakano[2], Akira Sato[1], Kazuki Ueno[1]

[1] The University of Osaka, Department of Physics, Osaka, Japan; [2] University of Toyama, Faculty of Science, Toyama, Japan

This work was supported by JSPS KAKENHI Grant Number 21H04971.

Abstract

The COMET Cylindrical Drift Chamber is a large, low-mass gaseous detector. Gas exchange through the detector volume affects gas quality, gain stability, and wire aging, which are important for stable detector operation. Increasing the gas-flow rate in a once-through operation would increase fresh-gas consumption and cost, and would also impose constraints on exhaust handling from the experimental area. For this reason, a gas circulation system is adopted. At the same time, safe operation of the chamber requires the differential pressure between the chamber volume and the surrounding atmosphere to be maintained within a narrow range, because the large-radius, low-mass inner wall adopted to suppress backgrounds imposes a strict mechanical limit on the allowable differential pressure. Pressure excursions caused by pump operation, environmental variations, or abnormal exhaust conditions must be suppressed. While the system consists of standard gas-system components, their configuration and operating parameters were quantitatively evaluated against the mechanical constraints and gas-flow requirements of the chamber. A simplified analysis based on a resistance-compliance model was introduced to interpret pressure propagation in the gas system. Preliminary gas-system commissioning tests, including pump-start and exhaust-transient measurements, were performed to characterize the pressure response and to evaluate the roles of buffer tanks and restricted flow paths. The results are being used to define the buffer-tank configuration, emergency-exhaust conductance, pump operating conditions, and a staged gas-commissioning procedure, enabling safe commissioning and stable long-term operation of the detector.

References

[1] The COMET Collaboration, “COMET Phase-I technical design report”, Prog. Theor. Exp. Phys. 2020, 033C01.

[2] A. Sato, et al., “Design and construction of the cylindrical drift chamber for the COMET Phase-I experiment”, Nucl.Instrum.Meth.A 1069 (2024) 169926.

NSS-13-004

Performance of a 2D-THCOBRA Gaseous Detector with Ar/Xe Mixtures for X-Ray Imaging (#2168)

Flávia Daniela Leite[1], Sofia Pessanha[2], João Veloso[1], Ana Luísa M. Silva[1]

[1] Universidade Aveiro, Physics Department, Aveiro, Portugal; [2] Universidade NOVA de Lisboa, Physics Department, Caparica, Portugal

This work is financed by national funds through FCT - Fundação para a Ciência e a Tecnologia, I.P. and the Ministry of Science, Technology and Higher Education under the project UID/50025/2025 (doi.org/10.54499/UID/50025/2025), UID/PRR/50025/2025 (doi.org/10.54499/UID/PRR/50025/2025), UID/PRR2/50025/2025 (doi.org/10.54499/UID/PRR2/50025/2025) and the Associate Laboratory I3N – LA/P/0037/2020 (doi.org/10.54499/LA/P/0037/2020) and under the project COMPETE2030-FEDER-00785100. F. D. Leite is grateful to FCT (Portugal) for the PhD grant 2022.10237.BD.

This project was funded by Agenda ILLIANCE" [C644919832-00000035 | Project nº 46] – WP4 OLI Health, financed by PRR – "Plano de Recuperação e Resiliência" under the Next Generation EU from the European Union.

Abstract

In this work, we present a systematic characterization of a 2D-THCOBRA detector operated in pure argon (Ar) and Ar/Xe mixtures (Ar/Xe 98/2, 95/5 and 90/10), exploiting the Penning effect to enhance detector performance. The detector is characterized in terms of gain, energy resolution, linearity, and intrinsic spatial resolution. The addition of Xe to Ar significantly reduces the required operating voltage, with equivalent gains achieved at voltages approximately 300 V lower than those required for pure Ar. The energy resolution improved from 24.4% (pure Ar) to 18.3% FWHM at 5.9 keV (Ar/Xe 95/5 mixture), and the intrinsic spatial resolution improves from 1.8 mm (pure Ar) to 1.5 mm FWHM Ar/Xe 95/5. These initial results demonstrate the strong potential of the 2D-THCOBRA operating in Ar/Xe mixtures for X-ray fluorescence imaging and spectral X-ray imaging applications.

References

[1] F. Sauli, *Micro-Pattern Gaseous Detectors: Principles of Operation and Applications*. World Scientific Publishing, 2020.

[2] S. Bressler, L. Moleri, A. Jash, A. Tesi, and D. Zavazieva, "The Thick Gas Electron Multiplier and its derivatives: Physics, technologies and applications," *Prog. Part. Nucl. Phys.*, vol. 130, p. 104029, 2023, doi: 10.1016/j.ppnp.2023.104029.

[3] F. Sauli, "The gas electron multiplier (GEM): Operating principles and applications," *Nucl. Instruments Methods Phys. Res. Sect. A Accel. Spectrometers, Detect. Assoc. Equip.*, vol. 805, pp. 2–24, Jan. 2016, doi: 10.1016/J.NIMA.2015.07.060.

[4] R. Alon *et al.*, "Operation of a Thick Gas Electron Multiplier (THGEM) in Ar, Xe and Ar-Xe," *J. Instrum.*, vol. 3, no. 01, Jan. 2008, doi: 10.1088/1748-0221/3/01/P01005

[5] A. L. M. Silva *et al.*, "X-ray imaging detector based on a position sensitive THCOBRA with resistive line," *J. Instrum.*, vol. 8, no. 05, pp. P05016–P05016, May 2013, doi: 10.1088/1748-0221/8/05/P05016.

[6] L. F. N. D. Carramate *et al.*, "THCOBRA X-ray imaging detector operating in pure Kr," *J. Instrum.*, 2017, doi: 10.1088/1748-0221/12/05/T05003.

[7] "Line Pair Patterns." https://quart.de/en/products/test-phantoms/resolution-patterns/line-pair-patterns (accessed May 12, 2026)

[8] A. L. M. Silva, C. D. R. Azevedo, C. A. B. Oliveira, J. M. F. Dos Santos, M. L. Carvalho, and J. F. C. A. Veloso, "Characterization of an energy dispersive X-ray fluorescence imaging system based on a Micropattern Gaseous Detector," *Spectrochim. Acta Part B At. Spectrosc.*, vol. 66, no. 5, pp. 308–313, May 2011, doi: 10.1016/J.SAB.2011.03.002.

[9] F. D. Leite *et al.*, "Analysis of Zebrafish contamination with heavy metals using a FF-XRF imaging system based on a MPGD," *Spectrochim. Acta Part B At. Spectrosc.*, vol. 198, p. 106545, 2022, doi: 10.1016/j.sab.2022.106545

NSS-13-006

The effect of hole geometry on the ion-backflow of a single gas electron multiplier foil (#2631)

Hussam Badran[1], **Erik Brücken**[1,2], Jouni Heino[1], Timo Hildén[1]

[1] Helsinki Institute of Physics, Helsinki, Finland; [2] University of Helsinki, Department of Physics, Helsinki, Finland

Abstract

A systematic study of the ion-backflow (IBF) contribution of single GEM foils with respect to the hole sizes and geometries is presented. The effective gain and the IBF of single GEM foils in a standard gas enclosure with a 2D strip readout plane were measured, using Ar-CO2 (70-30) gas mixture. The X-ray exposure using ^{55}Fe source was performed separately for each foil segment to compare the performance differences of the different hole geometries. A clear dependency of the IBF to the size and shape of the GEM holes was found. The results were compared to simulations using the Garfield++ toolkit. We present that choosing the right foils for a TPC readout chamber can effectively limit the IBF.

References

[1] F. Sauli, GEM: A new concept for electron amplification in gas detectors, Nucl. Instr. Meth. A 386, (1997) 531.

[2] J. Adolfsson et al. [ALICE TPC collaboration], The upgrade of the ALICE TPC with GEMs and continuous readout, JINST 16 (2021) no.03, P03022.

[3] T. Hildén et al., Optical quality assurance of GEM foils, Nucl. Instrum. Meth. A 770 (2015) 113.

[4] E. Brücken et al., Hole Misalignment and Gain Performance of Gaseous Electron Multipliers, Nucl. Instrum. Meth. A 1002 (2021), 165271.

[5] A. Utrobicic et al., A floating multi-channel picoammeter for micropattern gaseous detector current monitoring, Nucl. Instr. Meth. A 801 (2015) 21.

NSS-13-008

Feasibility of a Compact Detector for LINAC Radioactivation Monitoring (#1053)

Jeongho Kim[1], Byungdo Park[2], Jihoon Choi[2]

[1] Samsung changwon hospital, Research and Suport, Changwon, South Korea; [2] Samsung changwon hospital, Radition Oncology, Changwon, South Korea

This research was supported by the Challengeable Future Defense Technology Research and Development Program through the Agency for Defense Development (ADD) funded by the Defense Acquisition Program Administration (DAPA) in 2024 (No. UI247016TE).

Abstract

A compact SiPM–GAGG(Ce) radiation detector without conventional front-end electronics was evaluated for LINAC radioactivation monitoring. The proposed detector employed a simplified signal-processing architecture without a preamplifier, shaping amplifier, or comparator. Spectroscopic performance was evaluated at SiPM operating voltages from 58 V to 61 V. The best energy resolution for the 662 keV photopeak of Cs-137 was 8.31% at 61 V, corresponding to an overvoltage of approximately 7 V from the measured breakdown voltage of 53.88 V. Mixed-source measurements using Ba-133, Cs-137, and Co-60 demonstrated distinguishable radionuclide peaks and channel-energy linearity greater than 0.99. The detector was subsequently applied to LINAC radioactivation measurements, where characteristic gamma-ray peaks of W-187 were successfully detected near the LINAC head after high-energy photon beam irradiation. The results demonstrate the feasibility of compact and simplified LINAC radioactivation monitoring using the proposed detector system.

References

[1] J. Kim, J. Park, B. Park, Y. Kim, B. Park, and S. H. Park, “Compact and real-time radiation dosimeter using silicon photomultipliers for in vivo dosimetry in radiation therapy,” Sensors, vol. 25, no. 3, 2025, Art. no. 857.

[2] G. F. Knoll, Radiation Detection and Measurement, 4th ed. Hoboken, NJ, USA: Wiley, 2010.

[3] B. Sanaei, M. T. Baei, and S. Z. Sayyed-Alangi, “Characterization of a new silicon photomultiplier in comparison with a conventional photomultiplier tube,” J. Mod. Phys., vol. 6, pp. 425–433, 2015.

[4] J. H. Kim et al., “Development of a wireless radiation detection backpack based on an array silicon-photomultiplier,” Nucl. Eng. Technol., vol. 52, no. 11, pp. 2568–2577, 2020.

[5] E. Roncali and S. R. Cherry, “Application of silicon photomultipliers to positron emission tomography,” Ann. Biomed. Eng., vol. 39, no. 4, pp. 1358–1377, 2011.

[6] J. Kim, B. Park, B. Park, H. Park, J. Park, and J. Choi, “Compact radiation detector based on SiPM-GAGG(Ce) without front-end electronics,” J. Instrum., vol. 21, no. 03, Mar. 2026, Art. no. P03040

NSS-13-010

Temperature Dependence of Energy Resolution in a SiPM-Based Scintillation Detector for PET Applications (#1177)

Solano Rigotti Caiano[1], Daniel Alexandre Baptista Bonifacio[1], Helio Massaharu Murata[1], Marcio Bottaro[2], Mauricio Moralles[1]

[1] University of São Paulo (USP), Institute of Energy and Nuclear Research (IPEN), São Paulo, Brazil; [2] University of São Paulo (USP), Institute of Energy and Environment (IEE), São Paulo, Brazil

Abstract

Silicon photomultipliers (SiPMs) are widely used in PET detectors due to their compact size and compatibility with magnetic fields. However, their performance is strongly dependent on temperature. In this work, the temperature dependence of energy resolution in a SiPM-based scintillation detector coupled to a LYSO crystal is experimentally investigated. Measurements were carried out over a temperature range from 10 to 50 degrees Celsius using a controlled climatic chamber. Preliminary results show a systematic degradation in energy resolution with increasing temperature. A simplified physical interpretation based on the temperature dependence of breakdown voltage,

gain, photon detection efficiency (PDE), and noise contributions is proposed. Ongoing work focuses on developing a quantitative model and compensation strategies for detector stabilization.

References
[1] Acerbi, F; Gundacker, S 2019, 'Understanding and simulating SiPMs', Nuclear Instruments and Methods in Physics Research Section A, vol. 926, pp. 16–35, Amsterdam: Elsevier.
[2] Murata, HM; Moralles, M; Bonifácio, DAB 2018, 'Evaluation of digital methods for energy calculation and timing pick-off in positron emission tomography', Journal of Instrumentation, vol. 13, no. 09, p. P09024, Bristol: IOP Publishing.
[3] Wang, Q et al. 2022, 'Temperature dependence of SiPM array coupled Cs2LiYCl6:Ce3+ detector performance', Nuclear Instruments and Methods in Physics Research Section A, vol. 1025, p. 166112, Amsterdam: Elsevier.
[4] Thompson, W 2022, 'Red Pitaya multichannel analyser', GitHub repository, viewed 2026, <https://github.com/sefffal/redpitaya-multichannelanalyser>.
[5] Swiderski, L et al. 2019, 'Scintillation response to gamma-rays measured at wide temperature range for Tl-doped CsI with SiPM readout', Nuclear Instruments and Methods in Physics Research Section A, vol. 916, pp. 32–36, Amsterdam: Elsevier.

NSS-13-012

Development of transparent ceramic Tl:NaI scintillators for gamma-ray detectors (#1187)

Takayuki Yanagida, Takumi Kato, Daisuke Nakauchi, Noriaki Kawaguchi

Nara Institute of Science and Technology, Ikoma, Japan

This work was supported by the Cooperative Research Project of Research Center for Biomedical Engineering, Kazuchika Okura Memorial Foundation, Yashima Environment Technology Foundation, Iketani Science and Technology Foundation, and JSPS KAKENHI (22H00309, 24K03197, and 26K03208).

Abstract

Tl-doped NaI (Tl:NaI) single crystal has been a one of the standard scintillators from mid 20th century, and in this time, we will report a development of transparent ceramic Tl:NaI. Tl 0.05, 0.1, 0.3, and 0.5% doped NaI transparent ceramics were fabricated by the spark plasma sintering (SPS) method. Under X-ray irradiation, these ceramics showed a typical emission wavelength at 420 nm with a typical decay time (~200 ms) due to $^3P_1 \rightarrow {}^1S_0$ electronic transitions of Tl^+. When 662 keV gamma-rays from 137Cs were irradiated, all the samples exhibited a clear photoabsorption peak, and among all the samples, 0.1% doped one had the highest scintillation light yield, reaching to 36000 ph/MeV, which was equivalent to common commercial Tl:NaI single crystal.

NSS-13-014

Simulation of Electron Escape within Thin Organic Scintillators (#1248)

Ethan Schneider, Colton Graham, Erin Neely, David Breitenmoser, Shaun D. Clarke, Sara A. Pozzi

University of Michigan, Ann Arbor, USA

This work was supported in part by the Consortium for Monitoring, Technology, and Verification under Department of Energy National Nuclear Security Administration, award number DE-NA0003920.

Abstract

Organic scintillators are fast detectors that are sensitive to both neutrons and gamma rays. Measurements of neutron timing in an intense gamma-ray field can be studied with thin organics, as recoil electrons produced by Compton scatters have a path length significantly longer than those of recoil protons. Past work in characterization of such samples has been hindered by the lack of clear energy calibration with samples with thicknesses less than 2 mm, as the spectral features used for an energy calibration are significantly broadened from electron escapes. To address this issue, the gamma spectrum was observed for three gamma check sources, Cs-137, Na-22, and Co-60, within four organic glass scintillators, from 6 mm to 1 mm, and compared with Monte Carlo models MCNPX-PoliMi. A genetic algorithm was used to broaden the simulated spectra to match the measured spectra. Thinner samples displayed greater broadening of Compton edges, which suggests an increase in electron escape. Simulations show an increase in electron escape probability between the 6 mm sample and the 1 mm sample of 12% ± 1% to 26.1% ± 0.3%.

NSS-13-016

Alignments of the Dual-Layer Flat-Panel Detectors and their Modulation Transfer Functions (#1465)

Dong Sik Kim

Hankuk University of Foreign Studies, Division of Semiconductor and Electronics Engineering, Sungnam, South Korea

This work was supported by the National Research Foundation of Korea (NRF) grants funded by the Korean government (MSIP) (No. RS-2024-00459219).

Abstract

In radiographic imaging, dual-layer flat-panel detectors (DFDs) can be used for two purposes: acquiring high-quality x-ray images and performing material decomposition.

A convex combination of the x-ray images acquired from DFD can yield significantly improved detective quantum efficient. The DFD structure consists of stacked upper and lower flat-panel detectors, and can provide different modulation transfer function (MTF) characteristics depending on the orientation of the stacked detectors with respect to the incident x-ray. In this paper, we consider three different stacked structures for DFD and find the optimal DFD structure by experimentally observing the MTF curves using fabricated DFD prototypes. Because the inverted layers have a back-irradiation geometry, the MTF performance is better than that of the normal case. Therefore, we can select a DFD structure having an inverted lower layer to acquire high-DQE x-ray images.

References
[1] Lu, M et al. 2019, “Dual energy imaging with a dual-layer flat panel detector,” in Med. Imag.: Phys. Med. Imag., vol. 10948. SPIE, pp. 269–278.
[2] Jhala, R et al. 2026, “Measurement of scatter and evaluation of grid performance for dual-layer flat-panel detector prototype,” in Med. Imag.: Phys. Med. Imag., vol. 13924. SPIE, p. 139240V.
[3] Kim, D. S. and Lee, D 2025, “Performance of dual-layer flat-panel detectors,” Diagnostics, vol. 15, no. 15.
[4] Kim, D. S. and Lee, D 2024, “Two-step image registration for dual-layer flat-panel detectors,” Diagnostics, vol. 14, no. 23.
[5] Howansky, A et al. 2019, “Comparison of CsI:Tl and Gd2O2S:Tb indirect flat panel detector x-ray imaging performance in front- and back-irradiation geometries,” Med. Phys., vol. 46, no. 11, pp. 4857–4868.
[6] A. R. Lubinsky et al., “Back-irradiated and dual-screen sandwich detector configurations for radiography,” Jour. Med. Imag., vol. 6, no. 3, pp.033 501–1–10, 2019.
[7] Kim, D. S. 2023, “Convex combination of images from dual-layer detectors for high detective quantum efficiencies,” IEEE Trans. Biomed. Eng., vol. 70, no. 6, pp. 1804–1814.
[8] Lee, D and Kim, D. S. 2024, “Subpixel registration for dual-layer detectors based on the amplitude response,” IEEE Access, vol. 12, pp. 153 019–153 029.

NSS-13-018

Loading Surface-Modified $LiAlO_2$ Nanoparticles in Plastic Scintillators for Thermal Neutron Detection (#1484)

Haruhisa Tsukahara[1], Kenichi Watanabe[2], **Masanori Koshimizu**[1,3]

[1] Shizuoka University, Graduate School of Integrated Science and Technology, Hamamatsu, Japan; [2] Kyushu University, Department of Applied Quantum Physics and Nuclear Engineering, Fukuoka, Japan; [3] Shizuoka University, Research Institute of Electronics, Hamamatsu, Japan

Abstract
We report the development of plastic scintillators for thermal neutron detection by incorporating surface-modified $LiAlO_2$ nanoparticles. Conventionally, thermal neutrons have been detected using ^{3}He gas counters, but the scarcity of ^{3}He has driven the search for alternative technologies. Plastic scintillators are attractive due to their low cost and ease of fabrication; however, loading neutron-reactive isotopes such as ^{6}Li into plastics is challenging because conventional organometallic compounds suffer from poor solubility and strong quenching effects.
To overcome these limitations, $LiAlO_2$ nanoparticles enriched with ^{6}Li were synthesized via a sol–gel method and their surfaces were modified with trimethoxyphenylsilane to improve compatibility with a polystyrene matrix. Structural and spectroscopic analyses confirmed that the nanoparticles retained the γ-$LiAlO_2$ phase and were successfully functionalized with phenyl groups, without significant changes in particle size. The surface modification greatly enhanced nanoparticle dispersion within the plastic scintillator, as evidenced by uniform elemental mapping.Scintillation measurements demonstrated that the emission originated from the organic fluor and that the modified nanoparticles did not introduce additional emission bands. The scintillation light yields of 2400–3000

photons per neutron were achieved, depending on nanoparticle loading, which is substantially higher than those of boron-loaded commercial plastic scintillators and plastics containing unmodified $LiAlO_2$ nanoparticles. These results highlight surface modification as an effective strategy for improving the performance of nanoparticle-loaded plastic scintillators for thermal neutron detection.

NSS-13-020

Development of Perovskite Quantum Dots with High Photoluminescence Quantum Yields and Their Loading in Plastic Scintillators (#1618)

Itsutoshi Ishihara[1], Kazuki Asou[1], **Masanori Koshimizu**[1,2]

[1] Shizuoka University, Faculty of Engineering, Hamamatsu, Japan; [2] Shizuoka University, Research Institute of Electronics, Hamamatsu, Japan

Abstract

Fast plastic scintillators are attractive for radiation detection owing to their nanosecond decay times, low cost, and scalability; however, their practical application is limited by low scintillation light yield and poor detection efficiency for X- and γ-rays. In this study, we report the development of plastic scintillators loaded with perovskite quantum dots (QDs) exhibiting high photoluminescence quantum yields (PL QYs). Cesium lead halide perovskite QDs with various halogen compositions were synthesized via a facile solution process under ambient conditions. Surface modification using oleyl amine was employed to passivate surface defects and enhance radiative recombination. Transmission electron microscopy revealed spherical QDs with diameters of approximately 10 nm and a narrow size distribution. The oleyl amine modification markedly improved PL QYs, achieving values exceeding 80% for $CsPbBr_3$ QDs. By tuning the halogen composition, the emission wavelength was controllably varied from ~420 to 540 nm. These high-PL-QY QDs were uniformly loaded into polystyrene-based plastic scintillators. Scintillation spectra demonstrated dominant QD emission without defect-related luminescence, indicating fast emission owing to the interband transition within the QDs. Although clear full-energy peaks were not observed in pulse-height spectra, enhanced scintillation responses were evident for samples containing surface-modified QDs. These results demonstrate that surface-engineered perovskite QDs are promising additives for improving the performance of fast plastic scintillators.

NSS-13-022

Effect of geometry on the properties of 3D-printed scintillators (#1708)

Vivek Anand, Anjali Sharma, Utkarsh Bajpai, Bhavika Bansal, Anil K. Gourishetty

Indian Institute of Technology Roorkee, Roorkee, India

This work was supported by the Ministry of Higher Education (MHRD), Government of India.

Abstract

This work investigates how scintillator geometry influences light collection in 3D-printed plastic scintillators, motivated by the ability of additive manufacturing to fabricate detector shapes that are difficult to realize by conventional casting or machining. Four geometries, including a cylinder, truncated cone, cone, and paraboloid, were fabricated using a digital light processing based 3D printing method and evaluated experimentally. Complementary Geant4 optical-photon simulations were performed to study photon transport and collection trends for the same geometry family. Both experiment and simulation indicate that geometry modifies photon escape, internal reflection, and collection at the readout face. Taking the cylinder as the reference at 100%, the truncated cone, paraboloid-like geometry, and cone show increased relative light outputs of 151%, 156%, and 180%, respectively, suggesting that non-cylindrical 3D-printed scintillator shapes can improve photon collection at the readout face, most likely by reducing unfavorable optical paths and repeated reflections. The simulations reproduce the qualitative trend observed experimentally, although the absolute values do not agree number by number because the present model does not fully include fabrication-specific effects such as print-layer scattering, surface roughness, optical coupling variations, reflector response, and sensor nonuniformity. These results demonstrate that geometry is an important design parameter for additively manufactured scintillators and should be optimized together with material composition and photosensor coupling.

NSS-13-024

Development of a Gamma Camera for Real-Time Monitoring of High-Energy Gamma-Ray Environments (#1777)

Youngjoo Park[1,2], Taewoong Lee[3], Seongmin Jo[3], Jungyeol Yeom[1], Hakjae Lee[4], Kisung Lee[1]

[1] Korea University, Department of Bioengineering, Seoul, South Korea; [2] Korea University, Interdisciplinary program in precision public health, Seoul, South Korea; [3] KEPCO KPS Global Institute of Technology, Naju-si, South Korea; [4] ARALE Laboratory, Seoul, South Korea

This work was supported by the National Research Foundation of Korea and Commercialization Promotion Agency for R&D Outcomes (RS-2023-00234651).

Abstract

In June 2025, Kori Unit 1, the first commercial nuclear power plant in the Republic of Korea, obtained final approval for decommissioning. This milestone highlights the growing need for radiation-imaging technologies that can support radiation surveillance during nuclear decommissioning and in other high-radiation environments. In this study, we developed a portable gamma camera for real-time monitoring of high-energy gamma-ray fields and evaluated its basic detector characteristics and imaging performance. The spatial response of the GAGG-SiPM detector array was investigated using flood-map measurements and line-profile analysis. The obtained flood maps showed that all scintillator pixels were distinctly resolved, with minimal signal overlap between adjacent pixels. The average full width at half maximum (FWHM) was measured to be approximately 0.58 mm, corresponding to about 41% of the 1.41 mm pixel pitch, indicating stable intrinsic spatial resolution across the detector array. The intrinsic energy resolution was assessed using a Co-60 point source. The measured energy resolutions were 7.42% and 6.68% FWHM at the 1.17 MeV and 1.33 MeV photopeaks, respectively. In addition, the detectable imaging distance was examined by acquiring Co-60 point-source images at source-to-detector distances from 10 cm to 300 cm. The source location was successfully identified throughout the tested range, and clear gamma-ray imaging was achieved even at a distance of 3 m. These results demonstrate that the proposed portable gamma camera provides stable detector response, high-energy gamma-ray imaging capability, and practical source-localization performance for radiation monitoring in nuclear decommissioning environments.

References

[1] Han, D.-H., et al., *Development and evaluation of a compact gamma camera for radiation monitoring.* Nuclear Engineering and Technology, 2023. **55**(8): p. 2873–2878.

[2] Sueoka, K., et al., *Development of a new pinhole camera for imaging in high dose-rate environments.* Nuclear Instruments and Methods in Physics Research Section A: Accelerators, Spectrometers, Detectors and Associated Equipment, 2018. **912**: p. 115–118.

[3] Yamamoto, S., et al., *Development of a GAGG gamma camera for the imaging of prompt gammas during proton beam irradiation.* Physica Medica, 2024. **127**: p. 104847.

NSS-13-026

Study on the Influence of Grain Size for the GAGG powder-PMMA composite scintillator Detector (#1895)

Zexin Zhang[1,2], Yuzhong Feng[1,2], Wei Zhou[1,2], Xiaoming Wang[1], Xin Li[1,2], Aoyang Wei[1,2], **Yantao Liu**[1,2]

[1] Beijing Engineering Research Center of Radiographic Techniques and Equipment, Institute of High Energy Physics, Chinese Academy of Sciences, Beijing, China; [2] School of Nuclear Science and Technology, University of Chinese Academy of Sciences, Beijing, China

This research is supported by the National Natural Science Foundation of China (Grant No. 11975248) and the Youth Innovation Promotion Association of the Chinese Academy of Sciences (CAS YIPA) (Grant No. 2021014).

Abstract

A SiPM-based detector using GAGG powder-PMMA composite scintillators was developed and evaluated. There were 8 scintillator samples with the identical GAGG mass fraction but different powder grain sizes. Each scintillator has an active area of 40 mm × 40 mm and a total thickness of 3.6 ± 0.1 mm. The detector system consisted of the scintillator module, front-end analog electronics for filtering, shaping, and amplification, and an 8-channel back-end digital acquisition system. Under identical measurement conditions, the count rate measured with a 50 μCi 22Na source increased from approximately 1.7 × 10^3 cps for Sample #1 to 1.6×10^4 cps for Sample #8. Waveform measurements also showed higher output amplitude for the larger-powder sample. The results indicate that the grain size of GAGG powder strongly affects photon transport and effective detector response in the composite scintillators.

References
[1] K. Kamada, T. Yanagida, T. Endo, K. Tsutumi, Y. Usuki, M. Nikl, Y. Fujimoto, A. Fukabori, and A. Yoshikawa, “2 inch diameter single crystal growth and scintillation properties of Ce:Gd3Al2Ga3O12,” Journal of Crystal Growth, vol. 352, no. 1, pp. 88–90, 2012.
[2] O. Sakthong, W. Chewpraditkul, C. Wanarak, K. Kamada, A. Yoshikawa, P. Prusa, and M. Nikl, “Scintillation properties of Gd3Al2Ga3O12:Ce3+ single crystal scintillators,” Nuclear Instruments and Methods in Physics Research Section A, vol. 751, pp. 1–5, 2014.
[3] F. Acerbi and S. Gundacker, “Understanding and simulating SiPMs,” Nuclear Instruments and Methods in Physics Research Section A, vol. 926, pp. 16–35, 2019.

NSS-13-028

Thermal Neutron Detection with Dy-doped LiF/CaF_2 Eutectic Composite

(#2150)

Noriaki Kawaguchi[1], Hiromi Kimura[2], Akihiro Nishikawa[1], Takumi Kato[1], Daisuke Nakauchi[1], Takauyuki Yanagida[1]

[1] Nara Institute of Science and Technology, Ikoma, Japan; [2] National Institute of Advanced Industrial Science and Technology, Tsukuba, Japan

This work was supported by the Cooperative Research Project of Research Center for Biomedical Engineering, Kazuchika Okura Memorial Foundation, Yashima Environment Technology Foundation, Iketani Science and Technology Foundation, and JSPS KAKENHI (22H00309, 24K03197, and 26K03208).

Abstract

We studied thermal neutron detection using a LiF/CaF_2:Dy eutectic composite which can be used for thermoluminescence dosimetry. Emissions of the sample due to the self-trapped exciton of CaF_2 and 4f-4f transitions of Dy^{3+} ions were confirmed in the X-ray excited spectrum and decay curve measurements. The thermoluminescence spectrum at 230 ℃ showed only the emission peaks due to Dy^{3+}. This result indicates that Dy-doping in LiF/CaF_2 is efficient for thermoluminescence dosimetry applications. Thermal neutron detection was performed using the LiF/CaF_2:Dy eutectic composite, and its light yield was 3000 photons/neutron. This measurement was achieved due to the fast emission of the self-trapped exciton. The LiF/CaF_2:Dy eutectic composite can act as a dual functional material for radiation dosimetry and detection.

NSS-13-030

Development of Afterglow and NIR Decay Curve Measurement Systems using a Field Emission-type Pulsed X-ray Source (#2269)

Hiromi Kimura[1], Hidetoshi Kato[1], Koji Michishio[1], Ryoichi Suzuki[1], Daisuke Nakauchi[2], Takayuki Yanagida[2], Kenichi Watanabe[3], Takeshi Fujiwara[1]

[1] National Institute of Advanced Industrial Science and Technology, Tsukuba, Japan; [2] Nara Institute of Science and Technology, Ikoma, Japan; [3] Kyushu University, Nishi, Japan

This work was supported by Grants-in-Aid for Early Career Scientists (25K21506) from the Japan Society for the Promotion of Science.

Abstract

Scintillation detectors are widely used in various fields. Since the performance of scintillators directly affects detector properties, the evaluation of scintillation properties is essential. Scintillators are required to exhibit specific properties, including a high light yield, a short decay time, and a low afterglow. So far, afterglow measurements have not yet been standardized, and each manufacturer employs its own measurement setup and evaluation criteria. In conventional systems, their temporal resolution is limited to several milliseconds, which is insufficient for accurate characterization of afterglow in the short-time region. Separately, although near infrared (NIR)-emitting scintillators have recently attracted considerable attention and their emission spectra have been investigated, their NIR decay curves have not been sufficiently evaluated. In this study, we developed the afterglow and NIR decay curve measurement systems by combining a field-emission pulse X-ray source with the two types of detection units: an afterglow detection unit and an NIR detection unit. The performance of the developed system was evaluated by measuring the afterglow of CWO, BGO, and CsI:Tl, as well as the NIR decay curve of the NIR-emitting Yb:Lu_2O_3 transparent ceramics. The afterglow levels of CWO, BGO, and CsI:Tl were approximately 2.5, 0.5, and 450 ppm, respectively. The X-ray-induced NIR decay time constants of 0.1%–3.0% Yb:Lu_2O_3 transparent ceramics were 0.66–1.05 ms. Since these values were comparable to previously reported afterglow levels and PL decay time constants, the present results are considered to be valid.

NSS-13-032

One Dimensional TPE-4Br Supramolecular Scintillator for High-Speed X-ray Imaging (#2373)

Xiaoqing Liu[1,2]

[1] Wuhan University of Technology, State key Laboratory of Advanced Glass Materials, Wuhan, China; [2] Wuhan University of Technology, School of Materials Science and Engineering, Wuhan, China

This work was supported in part by the National Natural Science Foundation of China (U2330115, 62134003, 62275206) and National Key Research and Development Program of China (2024YFE0217100)

Abstract

Next-generation radiation detection, such as TOF-PET and high-flux X-ray imaging, requires scintillators that combine high light yield with ultrafast response. However, organic scintillators are often limited by inefficient exciton utilization and non-radiative quenching of high-energy states. In this work, we report a 1D supramolecular organic architecture based on the luminophore TPE-4Br. By shifting the molecular packing from a discrete 0D form into an ordered 1D configuration, we achieve a structural "locking" effect that rigidifies the lattice and suppresses vibrational quenching. This configuration results in an increase in Young's modulus (6.44 GPa) and hardness (0.24 GPa) compared to 0D crystals. Under X-ray excitation, the 1D framework exhibits an enhanced light yield that is 1.5 times higher. Furthermore, real-time dynamic X-ray imaging at 67 fps is demonstrated, showing minimal afterglow and the ability to track moving objects with high signal fidelity. This combination of luminosity, timing, and mechanical robustness positions the TPE-4Br-based 1D framework as a candidate for high-speed nuclear instrumentation and medical CT systems

References

[1] J. X. Wang *et al.*, "Heavy-atom engineering of thermally activated delayed fluorophores for high-performance X-ray imaging scintillators," *Nature Photonics*, vol. 16, no. 12, pp. 869-875, 2022.

[2] W. Ma *et al.*, "Thermally activated delayed fluorescence (TADF) organic molecules for efficient X-ray scintillation and imaging," *Nature materials*, vol. 21, no. 2, pp. 210-216, 2022.

[3] H. Uoyama, K. Goushi, K. Shizu, H. Nomura, and C. Adachi, "Highly efficient organic light-emitting diodes from delayed fluorescence," Nature, vol. 492, no. 7428, pp. 234-238, 2012.

[4] F. Brooks, "Development of organic scintillators," Nuclear Instruments and Methods, vol. 162, no. 1-3, pp. 477-505, 1979.

[5] X. Du et al., "Efficient and ultrafast organic scintillators by hot exciton manipulation," Nature Photonics, vol. 18, no. 2, pp. 162-169, 2024.

[6] Z. Deng et al., "Revealing the excited-state mechanisms of the polymorphs of a hot exciton material," Nature Communications, vol. 16, no. 1, p. 258, 2025.

[7] L. Yao et al., "Highly efficient near-infrared organic light-emitting diode based on a butterfly-shaped donor-acceptor chromophore with strong solid-state fluorescence and a large proportion of radiative excitons," Angewandte Chemie, vol. 126, no. 8, pp. 2151-2155, 2014.

NSS-13-034

Development of a Large-Area Diode-Multiplexed Scintillation Detector for Prompt Gamma Monitoring in Proton Therapy (#2409)

Xiaodong Mo, Chunhui Zhang, Xiangdong Cai, Yongzhi Yin

Lanzhou University, School of Nuclear Science and Technology, Lanzhou, China

Abstract

This work presents the development of a large-area flat-panel scintillation detector designed for prompt gamma monitoring in proton therapy. The detector comprises a 2x2 of ArrayJ-60035-64P silicon photomultiplier arrays, coupled with a 14x14 Lutetium-yttrium oxyorthosilicate crystal array. To address the challenge of high channel density, a diode-based row-column multiplexing circuit was implemented, reducing the total number of readout channels from 256 to 64. The system interfaces with the PETsys TOFPET2 ASIC via a custom adapter board utilizing LSHM-140 connectors. Preliminary laboratory tests using a 22Na point source demonstrate the feasibility of the multiplexing scheme and its potential for high-resolution gamma-ray imaging in clinical environments.

NSS-13-036

Development of a Hand-Foot Monitor for Visualizing Alpha Contamination (#2451)

Naoki Sagawa

Japan Atomic Energy Agency, Plutonium Radiation Control Section Radiation Protection Department, Muramatsu, Tokai-Mura, Naka-Gun, Japan

This work was supported by JAEA Nuclear Energy S&T and Human Resource Development Project Grant Number JPJA25P 25135771.

Abstract

When exiting controlled areas such as nuclear facilities, contamination control is of the utmost importance to prevent the removal of contaminants outside the area. Currently used hand and foot monitors and personnel contamination monitors are equipped with multiple detectors near the clothing and limbs, enabling the simultaneous measurement of radioactive contamination on the body surface.
However, conventional detectors make it difficult to pinpoint contaminated areas in detail. Accurately visualizing contamination distribution is crucial for preventing internal exposure and conducting efficient decontamination operations.

This study aimed to develop a personnel contamination monitor capable of visualizing contaminated areas. Contamination visualization is achieved by combining an electron-multiplying charge-coupled device (EMCCD) camera or a quantitative complementary metal-oxide-semiconductor (qCMOS) camera with multiple scintillators, such as ZnS(Ag) scintillators and rare-earth complex high-luminescence scintillators.
This device utilizes a CCD camera (ImagEMX2, Hamamatsu Photonics K.K.) or a CMOS camera (ORCA-Quest, Hamamatsu Photonics K.K.) in combination with a 3.25 mg/cm² ZnS(Ag) scintillator (EJ-440, Eljen Technology), a rare-earth complex high-luminescence scintillator (manufactured by Hokkaido University), and a large-area plastic scintillator containing dispersed europium complexes (manufactured by Hokkaido University). The system was irradiated with alpha rays, and the resulting images were analyzed using ImageJ.As a result, the luminous intensities of the various scintillators were confirmed, and we were able to select the optimal combination of scintillators and device configuration conditions for visualizing contaminated areas.

References
[1] Morishita, Yuki, et al. "Development of a large-area alpha imaging detector for hand and foot monitors." Nuclear Instruments and Methods in Physics Research Section A: Accelerators, Spectrometers, Detectors and Associated Equipment 1057 (2023): 168-702.
[2] Adadurov, A, et al. "Plastic scintillator with phosphorescent dopants for a-particles registration." Nuclear Instruments and Methods in Physics Research Section A: Accelerators, Spectrometers, Detectors and Associated Equipment 621 (2010): 354-357.

NSS-13-038

Room-Temperature Synthesis of Na^+-Doped $Cs_3Cu_2I_5$ Single Crystals: Structural, Optical and Scintillation Properties (#2545)

Bhavika Bansal[1], Anil K. Gourishetty[1]

[1] Indian Institute of Technology Roorkee, Department of Physics, Roorkee, India; [2] Indian Institute of Technology Roorkee, Department of Physics, Roorkee, India

Abstract
Copper-based halide perovskite $Cs_3Cu_2I_5$ has emerged as a promising lead-free scintillator for ionizing radiation detection. In this work, Na^+-doped and undoped $Cs_3Cu_2I_5$ single crystals were grown at room temperature via a formic-acid-assisted solvent evaporation method. Both crystals exhibit ordered diffraction planes and excellent crystallinity, confirmed by rocking-curve full width at half maximum (FWHM) values of 0.009° (undoped) and 0.008° (Na^+-doped). X-ray photoelectron spectroscopy confirms that Cu^+ remains in its monovalent state in both samples. Optical analyses show that Na^+ incorporation enhances the photoluminescence (PL) intensity by 11% and increases the self-trapped exciton (STE) decay time from 1090 ns to 1146 ns, attributed to shallow defect passivation and suppressed non-radiative recombination. The Na^+-doped crystal demonstrates superior scintillation performance with a light output of 42,000 ph/MeV and an energy resolution of 4.9% at 662 keV, compared to 39,000 ph/MeV and 5.4% for the undoped crystal, corresponding to improvements of ~7.6% and ~9%, respectively. These results establish Na^+ doping as an effective strategy for defect suppression and scintillation enhancement in lead-free halide perovskite single crystals.

NSS-13-040

Thermal Cycling of Optical Coupling Material to Investigate Performance Degradation in Detectors (#2575)

Zoe H. Sharpe[1,2], **Kerri L. Loughney**[1,2], Chris Allwork[1,2], Paul J. Sellin[2]

[1] AWE NST, Reading, UK; [2] University of Surrey, Physics, Guildford, UK

Abstract

Thermal cycling is used to accelerate the ageing process through an exaggerated version of diurnal temperature variations a detector/material may experience during use/storage over the lifetime of a detector. For this investigation, samples of optical grease were thermally cycled between +5 and +75°C in an environmental chamber. Four sets of samples were created with different preparation methods, volumes and substrates used, consisting of: 0.02g between microscope slides, 2ml petri dish, and 1” & 2” diameter discs in petri slides. A total of 15 samples per set were created that were divided into three subsets: Cyclical (C), Duration (D) and Room (R) samples. The percentage transmission (%T) for all samples was measured using a spectrophotometer for a wavelength range of 300-700nm for comparison with the emission range of common scintillators, such as EJ200. Identical “blank” samples with air were used for baseline/zero corrections performed for the spectrophotometer, meaning all %T values are relative to air. C samples were recharacterised at the end of each year equivalent cycle, while D and R were only recharacterised after the final cycle as controls for the removal from the chamber and the passage of real time respectively. Samples were cycled to equivalent of a maximum 20 years, with an additional set of “no bubble” (NB) samples introduced at the start of the 11th year equivalent cycle to determine the impact of air bubbles on %T. The 1” petri slide samples displayed the greatest average variation in %T across the range 400-500nm, with a drop of 20% %T value between pre and post-20 year characterisation (28% percentage difference), while 2” petri slide samples showed an average 10% decrease in %T value (15% percentage difference). Microscope slides and petri dish samples displayed a 2.6% average %T decrease (3% percentage difference) and 3.9% average %T increase (4.7% percentage difference) respectively.

UK Ministry of Defence © Crown owned copyright 2026/AWE

References

[1] Sato, K., Yamada, R., Takahashi, Y., Nagano, T., Yamamoto, K., 2013, "The reliability and reproducibility of MPPC," 2013 IEEE Nuclear Science Symposium and Medical Imaging Conference (2013 NSS/MIC), Seoul, Korea (South), pp. 1-3, doi: 10.1109/NSSMIC.2013.6829584.

[2] Loughney, K. L., 2023, “Investigating the Stability in Optical Properties of Portable Radiation Detector Components Through Accelerated Ageing”, Diss. University of Surrey

[3] Met Office, “A review of the UK’s Climate in 2024”, Met Office: A review of the UK’s climate in 2024 - Carbon Brief

NSS-13-042

NSS-13-044

Performance of Improved CsI:Tl Coupled SiPM Detectors for Imaging Applications (#2931)

Rastgo Hawrami[1], **Rastgo Hawrami**[1], Hamid Sabet[2], Hamid Sabet[2]

[1] Xtallized Intelligence, Inc. (XI, Inc.), Chapmansboro, USA; [2] Massachusetts General Hospital – Harvard Medical School, Charlestown, USA

This work was supported in part by the U.S. National Institute of Health Award 1R01EB034785-01.

Abstract

Scintillators play an important role in radiation detection and imaging. Thallium-doped cesium iodide (CsI:Tl) is one of the major scintillators that have been used for many applications for many decades. Coupling CsI:Tl crystals to silicon photomultipliers (SiPMs) makes them into compact and portable detectors, enabling them to be incorporated in many modular detector designs. This paper presents a performance study of improved CsI:Tl crystals coupled to silicon photomultipliers (SiPMs). Iterations of electronic designs as well as CsI:Tl crystal growth, processing, and characterization with both photomultiplier tubes (PMTs) and SiPMs will be presented.

References

[1] R. Hawrami, E. Ariesanti, A. Farsoni, D. Szydel, H. Sabet, "Growth and Evaluation of Improved CsI:Tl and NaI:Tl Scintillators," Crystals, vol. 12, no. 11, p. 1517, 2022.

NSS-13-046

Optical Control of Valence State in LuAG:Ce,Ca (#2991)

Colleen Campbell[1], Stephen Rand[2], Jarek Glodo[3], Matthias Muller[3], Arthur Kim[3], David Wehe[1]

[1] University of Michigan, NERS, Ann Arbor, USA; [2] University of Michigan, EECS, Physics, Ann Arbor, USA; [3] Radiation Monitoring Devices, Inc., Watertown, USA

This material is based upon work supported by the Defense Threat Reduction Agency under Contract No. HDTRA1-20-2-0002. Any opinions, findings and conclusions or recommendations expressed in this material are those of the authors and do not necessarily reflect the views of the Defense Threat Reduction Agency.

Abstract

Scintillator energy resolution is ultimately limited by light yield. One theoretical pathway for increasing this light yield in inorganic scintillators is optical re-excitation of activator ions. $Lu_3Al_5O_{12}$ (LuAG) with Ce^{3+} activator ions is investigated as a candidate for verifying the mechanism. Ca co-doping is used to convert the Ce^{3+} to Ce^{4+} during manufacturing, so Ce^{3+} is only present in the material after a radiation interaction occurs, allowing for multiplication of the radiation-induced signal. Optical spectroscopy is used to evaluate the impact of co-doping ratios on the concentration of Ce^{4+} in several samples. The impact of
stimulation wavelength on the intensity of previously observed optically-induced valence change indicates the valence change originates from charge-transfer absorption of the Ce^{4+}. A dual-beam optical and x-ray excitation experiment with a chopperwheel and lock-in amplifier is used to compare the scintillation response of LuAG:Ce and LuAG:Ce,Ca samples to single- and dual-beam excitation. The difference between these responses is evaluated with a lock-in amplifier and using a program which superimposes the single-beam signals and minimizes the variance of this superposition with respect to the dual-beam signal. After optical characterization, the responses of LuAG samples with different Ce concentrations and co-doping ratios will be tested in this dual-beam experiment to identify optimal doping concentrations for re-excitation.

References

[1] Blahuta, S, Bessiere, A, Viana, B, Dorenbos, P, Ouspenski, V 2013, "Evidence and consequences of Ce^{4+} in LYSO:Ce,Ca and LYSO:Ce,Mg single crystals for medical imaging applications," *IEEE Transactions on Nuclear Science*, vol. 60, no. 4, pp. 3134–3141.

[2] Dorenbos, P 2000, "The 5d level positions of the trivalent lanthanides in inorganic compounds," *Journal of Luminescence*, vol. 91, no. 3, pp. 155–176.

[3] Hu, C, Liu, S, Fasoli, M, Vedda, A, Nikl, M, Feng, X, Pan, Y 2015, "ESR and TSL study of hole and electron traps in LuAG:Ce,Mg ceramic scintillator," *Optical Materials*, vol. 45, pp. 252–257.

NSS-13-048

Study of elpasolite crystals for neutron/gamma spectroscopy : First measurements with CLYC:Ce (#3212)

Isaac Zeghni, Clément Delafosse

CNRS, IJCLab, Orsay, France

This project has received funding from the French Agence Nationale de la Recherche under grant agreement No. ANR-24-CE31-7626-01 (ANR SENSE).

Abstract

The spectroscopy of decay products is one of the three pillars of low-energy beam exploitation techniques produced by the ISOL method. Decay stations can be found in all facilities using the ISOL technique to produce radioactive beams, such as ALTO (France), ISOLDE (CERN), and IGISOL (Finland), as well as in future facilities like SPES (Italy) and DESIR (France), to name a few in Europe.

In the context of β decay, it is important to note that the total energy released during this process, denoted as Q_β, can exceed 10 MeV as we venture further from nuclear stability. At the same time, the energy required to remove a neutron (S_n) decreases, resulting in the emission of unbound neutron(s) alongside the expected γ-rays.

Elpasolite crystals containing ^{35}Cl such as CLYC:Ce represent a promising way to detect and discriminate both neutrons and γ-rays coming from such decay while measuring their energies. The ANR project SENSE (Scintillating Elpasolite for Neutron Spectroscopy Enhancement) aims to study such crystals using detailed Geant4 simulations in association with experimental measurements.

We started this project using a 3"x4" CLYC:Ce crystal in order to measure several physical quantities such as its resolution, efficiency and homogeneity. Those measurements were first performed for gamma only and are combined with simulations performed via Geant4 for comparaison. So far, the study of neutron interaction with the crystal is being studied and experiments using ALTO facilities are planned. Also, Geant4 does not implement well the cross-section of neutron interacting with chlorine and this part of the work is still in progress. Our presentation will share the results we have obtained for this CLYC crystal and the on-going work that is performed at IJCLab.

NSS-13-050

A feasibility study on CsPbBr3 perovskite crystals for time-of-flight PET (#1120)

Heejong Kim[1], Yingjie Wang[1], Subramanian Sundramoorthy[2], Mythra V. Nemallapudi[1], Chin-Tu Chen[1], Chien-Min Kao[1]

[1] University of Chicago, Department of Radiology, Chicago, USA; [2] University of Chicago, Department of Radiation and Cellular Oncology, Chicago, USA

Abstract

We are evaluating the potential of $CsPbBr_3$ crystals as Cherenkov light generating materials for TOF PET applications. $CsPbBr_3$, a lead halide perovskite semiconductor, has recently emerged as a highly efficient and cost-effective alternative to traditional radiation detection materials such as CZT and CdTe for X-ray and gamma-ray imaging. Its high carrier mobility and excellent energy resolution characteristics make it attractive for next generation radiation detector technologies. Furthermore, its high refractive index (~2.4) enables efficient generation of Cherenkov light, positioning this material as a promising candidate for fast timing applications, including TOF PET. To assess its timing performance, we investigated the coincidence time resolution (CTR) of $CsPbBr_3$ samples. Two crystal sizes—5 × 5 × 10 mm^3 and 3 × 3 × 3 mm^3—were used to study how crystal length affects CTR. Each crystal was optically coupled to a Broadcom NUV-MT SiPM (S4N44P014M or S4N66P014M) and irradiated with a ^{22}Na positron source in a coincidence timing measurement setup. A CTR of ~339 ps was achieved using a pair of 3 × 3 × 3 mm^3 $CsPbBr_3$ detectors. This preliminary result is highly encouraging and demonstrates the strong potential of $CsPbBr_3$ crystals for fast-timing radiation detection applications. In this work, we present our initial findings and discuss the associated challenges, along with potential strategies for further improving the CTR.

NSS-13-052

From Collision Cascades to Device Response: A Multiscale Study of Proton-Induced Defects in Silicon (#1178)

Sarah Shoorian, Hamid Jafari

Shahid Beheshti University, Nuclear Engineering, Tehran, Iran

In memory of Dr. Seyed Amirhossein Feghhi

Abstract

This study presents a comprehensive multi-scale computational and experimental investigation into displacement damage effects induced by high-energy proton irradiation in silicon-based photodiodes. The developed methodology systematically integrates SRIM-based analysis of primary knock-on atom (PKA) energy spectra, molecular dynamics (MD) simulations using LAMMPS to model atomic-level defect formation, and TCAD-based device-level electrical modeling in SILVACO. MD simulations revealed a nonlinear increase in stable Frenkel pair formation, ranging from minimal defects at low PKA energies (≤200 eV) to substantial defect clustering at higher energies (≥500 eV), with approximately 40 stable defects per 2 keV event. These atomistic results were used to inform TCAD models, which demonstrated that increasing mid-gap trap densities significantly amplify reverse-bias leakage currents via trap-assisted recombination mechanisms, consistent with the Shockley–Read–Hall (SRH) recombination theory. Experimental validation using BPX65 photodiodes irradiated with 3 MeV protons, corroborated simulation predictions. Leakage current increased dramatically with proton fluence, exhibiting linear trends at lower fluences. Forward current measurements showed only modest degradation, confirming trap-assisted recombination as the primary mechanism behind device deterioration. The combined results underscore the dominant role of trap-assisted recombination in leakage current enhancement and validate the SRH framework in describing carrier lifetime degradation due to mid-gap traps. Deviations at high fluence were attributed to interface effects and charge compensation mechanisms. These findings demonstrate the effectiveness of integrating atomic-scale simulations with device-level modeling to predict and interpret radiation effects in semiconductor detectors, providing a foundation for future radiation-hardened electronics design.

References
[1] Moll M. Radiation Damage in Silicon Particle Detectors: Microscopic Defects and Macroscopic Properties. PhD thesis. University of Hamburg; 1999. DESY-THESIS-1999-040.
[2] Srour JR, Marshall CJ, Marshall PW. Review of displacement damage effects in silicon devices. IEEE Trans Nucl Sci. 2003;50(3):653–670.
[3] Nordlund K, et al. Improving atomic displacement and replacement calculations. Nat Commun. 2018;9:1084. doi:10.1038/s41467-018-03415-5
[4] Norgett MJ, Robinson MT, Torrens IM. A proposed method of calculating displacement dose rates. Nucl Eng Des. 1975;33:50–54. doi:10.1016/0029-5493(75)90035-7
[5] Iwamoto Y, et al. Estimation of reliable displacements-per-atom based on athermal-recombination-corrected model. J Nucl Sci Technol. 2020;57:1164–1177.

NSS-13-054

DREAM : A miniaturized spectrometer for protons and electrons measurement in space (#1273)

Arnaud Dufour[1], Robert Ecoffet[1], Julien Mekki[1], Alix Pierre-Louis[2], Jérôme Sadowy[2]

[1] CNES, Toulouse, France; [2] STEEL Electronique, Martres-Tolosane, France

This instrument has been funded by CNES.
CNES thanks STEEL and N7 Consulting for their technical contributions to this instrument.

Abstract

This paper describes a compact charged particles spectrometer called DREAM (French abbreviation of « Détecteur Radiation Energétique Adaptable et Miniaturisé »). It is a cubesat compatible radiation monitor, designed to measure protons (13 MeV – 200 MeV) and electrons (350 keV – 3 MeV) in space, essentially in the Earth's magnetic field. Built around silicon diode detectors co designed with STEEL Electronique and N7 Consulting, DREAM weighs around 400 g, fits within a 0.6 U volume (55 × 100 × 100 mm), and consumes less than 3W at 5 V.

The main goal of this instrument is to measure the dynamic behaviour of trapped charged particles flux in the magnetosphere, mainly disturbed by solar flares. It will then help to predict anormal fluxes that may damage satellites or humans in space. Experimental results show a good agreement between simulated and experimental spectra obtained at the UCL (62 MeV beam) and Partrec (184MeV beam) proton accelerators.

Qualification activities (radiation latch up tests, vibration, thermal cycling in vacuum, …) have been performed in 2025 and a detailed summary will be available in the paper. This instrument is already identified in several missions (mainly for the spaceweather), like the ESA S2P (Space Safety Programme) mission.

References

[1] S. Bourdarie and D. Boscher, "The space radiation environment," in Space Radiation Environment and Its Effects on Spacecraft Components and Systems. Toulouse, France: Cepadus, 2004, pp. 57–82.
[2] D. Baker, "The occurrence of operational anomalies in spacecraft and their relationship to space weather," IEEE Trans. Plasma Sci., vol. 28, no. 6, pp. 2007–2016, Dec. 2000.
[3] D. Boscher et al., "In-flight measurements of radiation environment on board the argentinean satellite SAC-D," IEEE Trans. Nucl. Sci., vol. 61, no. 6, pp. 3395–3400, Dec. 2014.
[4] D. Boscher et al., "In flight measurements of radiation environment on board the french satellite JASON-2," IEEE Trans. Nucl. Sci., vol. 58, no. 3, pp. 916–922, Jun. 2011.
[5] D. Falguere et al., "In-flight observations of the radiation environment and its effects on devices in the SAC-C polar orbit," IEEE Trans. Nucl. Sci., vol. 49, no. 6, pp. 2782–2787, Dec. 2002.
[6] M. Ruffenach et al., "A Proton Sensor for Energies From 2 to 20 MeV," IEEE Trans. Nucl. Sci., vol. 67, no. 7, pp. 1351-1359, Jul. 2020.
[7] K. Yando, R. M. Millan, J. C. Green, and D. S. Evans, "A Monte Carlo simulation of the NOAA POES medium energy proton and electron detector instrument: Technique," J. Geophys. Res., vol. 116, no. A10, Oct. 2011
[8] J. B. Blake et al., "The magnetic electron ion spectrometer (MagEIS) instruments aboard the radiation belt storm probes (RBSP) spacecraft," in The Van Allen Probes Mission, N. Fox and J. L. Burch, Eds. Boston, MA, USA: Springer, 2014, pp. 383–421.
[9] Y. Sasaki, H. Matsumoto, T. Goka, T. Nakamura, K. Terasawa, and H. Kitamura, "Technical data acquisition equipment for GOSAT," in Proc. 30th Int. Cosmic Ray Conf. (ICRC), 2007, pp. 643–646.

NSS-13-056

Bulk Stoichiometry and van der Waals Interface Engineering of CdTe for Room-Temperature X/γ-Ray Detectors (#1617)

Qinghua Zhao[1], Zhengyi Sun[1], Tao Wang[1], Volodymyr Gnatyuk[2]

[1] Northwestern Polytechnical University, School of Material Science and Engineering, Xi'an, China; [2] Advafab Oy, Helsinki, Finland

This work was supported in part by the National Key Research and Development Program of China under Grant 2023YFE0108500 and Grant 2023YFF0719500; in part by the National Natural Science Foundation of China under Grant 52072300, Grant 52302199, and Grant 52472014; in part by the Guangdong Basic and Applied Basic Research Foundation under Grant 2022A1515110538; in part by the Key Research and Development Program of Shaanxi under Grant 2023-GHZD-48.

Abstract

Cadmium telluride (CdTe) is a leading room-temperature semiconductor for direct X- and γ-ray detection, but its performance is limited by bulk stoichiometric defects and interface-induced leakage current. Here, we report an integrated strategy combining vapor-pressure-controlled CdTe(Cl) crystal growth with noninvasive van der Waals (vdW) Au contacts to enhance bulk charge transport and interfacial charge control. Detector-grade CdTe(Cl) single crystals were grown by vertical gradient freeze using a Cd reservoir to stabilize Cd partial pressure and Cl doping to regulate compensation. This approach suppressed large Te inclusions below 5 μm, achieved ~60% infrared transmittance, and yielded high resistivity of 1.5×10^{10} Ω·cm, electron mobility of 1055 ± 88 $cm^2 V^{-1} s^{-1}$, and electron mobility–lifetime product of ~1.1×10^{-4} $cm^2 V^{-1}$. Planar Au/CdTe(Cl)/Au detectors showed clear ^{241}Am α-particle response. Mechanically transferred Au electrodes further formed vdW contacts that avoided atomic intermixing, preserved surface chemistry, reduced defect-related photoluminescence, and increased the Schottky barrier height from 0.78 to 0.83 eV. Consequently, vdW-contact CdTe detectors suppressed dark current and improved 59.5 keV γ ray energy resolution from 14.4% to 11.8%.

References

[1] Sun, Z, Liu, Y, Zheng, D, Liu, H, Li, J, Yin, Z, Zhang, B, Chen, S, Han, N, Zhao, Q, Gnatyuk, V & Wang, T 2025, 'Enhanced Au/Semi-Insulating Single-Crystal CdTe Schottky-Type Radiation Detectors Based on van der Waals Contacts', IEEE Transactions on Nuclear Science, vol. 72, no. 12, pp. 3792–3800.

[2] Yin, Z-A, Zhang, Y-R, Kang, Z, Zhang, X-G, Liu, J-B, Liu, K-J, Sun, Z-Y, Jie, W-Q, Zhao, Q-H & Wang, T 2025, 'Achieving detector-grade CdTe(Cl) single crystals through vapor-pressure-controlled vertical gradient freeze growth', Nuclear Science and Techniques, vol. 36, article 130.

NSS-13-058

Alpha Particle Detection with sCMOS imager (#1770)

Makoto Sasano[1,3], Masateru Hayashi[1], Nobukazu Teranishi[2]

[1] Mitsubishi Electric Corporation, Advanced R&D center, Amagasaki, Japan; [2] Shizuoka University, Research Institute of Electronics, Hamamatsu, Japan; [3] Hirosaki University, Institute of Radiation Emergency Medicine, Hirosaki, Japan

Abstract

We investigated the alpha-particle response of a back-illuminated CMOS imager for radionuclide measurements in nuclear decommissioning. A GSENSE2020-BSI sensor with an approximately 10 μm-thick sensitive layer was used. To prevent alpha particles from reaching the circuit layer, measurements were performed with an 11 μm-thick aluminum foil and aluminized polymer sheets. The alpha-particle energy was varied by changing the number of sheets, and the resulting event images and deposited energy were analyzed. The expected deposited energy was calculated using Geant4, and single events were extracted using OpenCV-based image processing. The image intensity was calibrated to deposited energy using a ^{241}Am gamma-ray source.

Alpha-particle events appeared as spatially spread images. Under unsaturated conditions, the measured energy spectra agreed well with simulation, whereas ADC saturation caused underestimation at higher energies. Reliable energy information was obtained when the deposited energy was approximately 1.5 MeV or lower. The event area increased with deposited energy, following area is proportional to $E_{dep}^{1/3}$. These results demonstrate the potential of a back-illuminated CMOS imager for alpha-particle detection and nuclide identification.

References
[1] M. Sasano, M. Hayashi, and N. Teranishi, "Evaluation of beta ray maximum energy using sCMOS Imager." [Online]. Available: https://ssrn.com/abstract=6447307
[2] "GSENSE2020BSI." Accessed: Feb. 25, 2026. [Online]. Available: https://gpixel.com/en/pro_details_1194.html
[3] J. Allison *et al.*, "Recent developments in GEANT4," *Nucl. Instrum. Methods Phys. Res. A*, vol. 835, pp. 186–225, 2016, doi: 10.1016/j.nima.2016.06.125.
[4] J. Jakubek, A. Cejnarova, T. Holy, S. Pospisil, J. Uher, and Z. Vykydal, "Pixel detectors for imaging with heavy charged particles," *Nucl. Instrum. Methods Phys. Res. A*, vol. 591, no. 1, pp. 155–158, Jun. 2008, doi: 10.1016/j.nima.2008.03.091.

NSS-13-060

Development of Silicon Drift Detector Technology from Single-Element Devices to a 19-Pixel Module for X-ray Spectroscopy Applications

(#1826)

Ziyu Bao[1,2], Zhenjie Li[1,2], Yaoguang Liu[1], Wei Li[3], Yusa Wang[3]

[1] Institute of High Energy Physics, Chinese Academy of Sciences, Beijing Synchrotron Radiation Facility and High Energy Photon Source, Beijing, China; [2] University of Chinese Academy of Sciences, Beijing, China; [3] Institute of High Energy Physics, Chinese Academy of Sciences, the State Key Laboratory of Particle Astrophysics, Beijing, China

This work is supported by China's Space Origins Exploration Program, Chinese Academy of Sciences (XDA15020500).

Abstract

Silicon drift detectors (SDDs) are promising sensors for high-resolution X-ray spectroscopy because of their low anode capacitance, good timing capability, and scalability to large-area and multi-pixel detector systems. This work presents recent progress on single-pixel and array SDD technologies developed for space astronomy and synchrotron radiation applications. Single-pixel SDDs with sensitive areas from 15 to 85 mm² were designed and fabricated through optimization of the drift field, anode structure, leakage-current suppression, and dedicated semiconductor process. Low-noise front-end electronics, semiconductor packaging, and digital pulse-processing readout electronics were developed to support detector characterization and module integration. A 30 mm² single-pixel detector achieved an energy resolution of 135 eV at 5.9 keV at −40 °C, demonstrating the effectiveness of the device and readout design. Based on these developments, a first 19-pixel SDD module with a hexagonal 1+6+12 layout was fabricated, packaged, and tested for the Spectroscopy Focusing Array of the enhanced X-ray Timing and Polarimetry mission. The module integrates the SDD sensor, ceramic substrate package, low-noise front-end electronics, and high-density flexible readout interface. Low-temperature X-ray measurements showed that most

pixels satisfied the energy-resolution requirement, whereas the remaining pixels were mainly limited by increased dark current. The measured spectral response indicates the capability of the module to cover the required 0.5–10 keV energy range. These results validate the feasibility of the developed SDD technology for compact, low-noise, multi-pixel X-ray spectroscopy modules. The next stage will focus on the second-generation 19-pixel prototype and a 7-pixel SDD detector system for synchrotron radiation applications.

References
[1] Gatti, E & Rehak, P 1984, 'Semiconductor drift chamber – An application of a novel charge transport scheme', Nuclear Instruments and Methods in Physics Research, vol. 225, no. 3, pp. 608–614.
[2] Gatti, E, Manfredi, P F, Sampietro, M et al. 1990, 'Suboptimal filtering of 1/f-noise in detector charge measurements', Nuclear Instruments and Methods in Physics Research Section A: Accelerators, Spectrometers, Detectors and Associated Equipment, vol. 297, no. 3, pp. 467–478.
[3] Zhang, S-N, Santangelo, A, Xu, Y, Feng, H, Lu, F, Chen, Y, Ge, M, Nandra, K, Wu, X, Feroci, M et al. 2025, 'The enhanced X-ray Timing and Polarimetry mission eXTP for launch in 2030', Science China Physics, Mechanics & Astronomy, vol. 68, no. 11, 119502.
[4] Bao, Z, Li, Z, Liu, Y, Wang, Y, Jiang, X, Hu, J, Liu, M, Li, H, Li, H, Li, Q & Liu, P 2024, 'Development of silicon drift detectors for synchrotron radiation sources', Nuclear Instruments and Methods in Physics Research Section A: Accelerators, Spectrometers, Detectors and Associated Equipment, vol. 1069, 169927.

NSS-13-062

Oxygen-Ion-Assisted Amorphous PbO Layers for Direct-Conversion X-ray Detectors (#2091)

Galina Nagicheva, Janos Rado, Mikhail Vostokov, Amy Stieh, Alexander Alexandrov, Alla Reznik

Lakehead University, The Department of Physics, Thunder Bay, Canada

This research was supported by Teledyne DALSA and Natural Sciences and Engineering Research Council of Canada Discovery and Alliance programs, MITACS. The authors gratefully acknowledge their support.

Abstract
Lead oxide (PbO) is a promising high-atomic-number photoconductor for direct-conversion x-ray detectors because of its high x-ray stopping power and low intrinsic electron–hole pair creation energy. A key challenge is depositing detector-grade thick PbO layers directly onto flat-panel imaging electronics while keeping the substrate temperature compatible with thin-film transistor and CMOS readout arrays. In conventional physical vapor deposition, limited adatom mobility at substrate temperatures below approximately 200 °C can promote porous, platelet-like polycrystalline PbO with reduced charge collection, temporal lag, and structural instability. In this work, oxygen-ion-assisted thermal evaporation was investigated as a low-temperature route for producing amorphous PbO photoconductors. Low-energy oxygen-ion bombardment supplied additional energy to the growing film surface without increasing the substrate temperature. The deposition conditions were optimized with respect to x-ray-to-charge conversion, evaluated using the average electron–hole pair creation energy, W±. Amorphous PbO layers with W± as low as approximately 7.5 eV/ehp and effective hole mobility on the order of 10^{-1} cm²/V·s at 10 V/μm were achieved. These results indicate that oxygen-ion-assisted deposition can produce amorphous PbO layers with detector-relevant charge generation and transport properties for direct-conversion flat-panel X-ray detectors.

References

[1] Kasap, SO, Frey, JB, Belev, G, Tousignant, O, Mani, H, Greenspan, J, Laperriere, L, Bubon, O, Reznik, A, DeCrescenzo, G, Karim, KS & Rowlands, JA 2011, 'Amorphous and polycrystalline photoconductors for direct conversion flat panel X-ray image sensors', *Sensors*, vol. 11, no. 5, pp. 5112–5157, doi: 10.3390/s110505112.
[2] Semeniuk, O, Csík, A, Kökényesi, S & Reznik, A 2017, 'Ion-assisted deposition of amorphous PbO layers', *Journal of Materials Science*, vol. 52, no. 13, pp. 7937–7946, doi: 10.1007/s10853-017-0998-5.
[3] Grynko, O, Thibault, T, Pineau, E & Reznik, A 2021, 'Engineering of a blocking layer structure for low-lag operation of the a-PbO-based X-ray detector', *IEEE Transactions on Electron Devices*, vol. 68, no. 5, pp. 2335–2341, doi: 10.1109/TED.2021.3067616
[4] Pineau, E, Grynko, O, Thibault, T, Alexandrov, A, Csík, A, Kökényesi, S & Reznik, A 2022, 'Comparative analysis of multilayer lead oxide-based X-ray detector prototypes', *Sensors*, vol. 22, no. 16, article no. 5998, doi: 10.3390/s22165998
[5] Juška, G, Arlauskas, K, Viliūnas, M & Kočka, J 2000, 'Extraction current transients: New method of study of charge transport in microcrystalline silicon', *Physical Review Letters*, vol. 84, no. 21, pp. 4946–4949, doi: 10.1103/PhysRevLett.84.4946
[6] Semeniuk, O, Juška, G, Oelerich, J-O, Wiemer, M, Baranovskii, SD & Reznik, A 2016, 'Charge transport mechanism in lead oxide revealed by CELIV technique', *Scientific Reports*, vol. 6, article no. 33359, doi: 10.1038/srep33359
[7] Baranovskii, SD 2014, 'Theoretical description of charge transport in disordered organic semiconductors', *Physica Status Solidi B*, vol. 251, no. 3, pp. 487–525, doi: 10.1002/pssb.201350339

NSS-13-064

Custom Geometries for Broader Applications of the GAPS Si(Li) Detectors (#2180)

Kelsey Yee[1], Hideyuki Fuke[2], Tanmay Gupta[3], Masayoshi Kozai[4], William Ostling[3], Kaliroë Pappas[3], Kerstin Perez[3], Yuki Shimizu[5], Sarah Vickers[3], Mengjiao Xiao[6]

[1] Massachusetts Institute of Technology, Cambridge, USA; [2] Institute of Space and Astronautical Science, Japan Aerospace Exploration Agency (ISAS/JAXA), Sagamihara, Japan; [3] Columbia University, New York, USA; [4] Research Organization of Information and Systems, Tokyo, Japan; [5] Kanagawa University, Yokohama, Japan; [6] School of Physics and Astronomy, Shanghai Jiao Tong University, Shanghai, China

K. Yee is supported through the NSF Graduate Research Fellowship under grant 2141064. The Columbia University GAPS group is supported by the Heising-Simons Foundation award 2025-6055. H. Fuke, M. Kozai, and Y. Shimizu are supported by JSPS KAKENHI grants; H. Fuke (JP17H01136, JP19H05198, JP22KK0042, JP22H00147), M. Kozai (JP20K14505), and Y. Shimizu (JP20K04002, JP22KK0042, JP23K03436). M. Xiao receives support from the Yangyang Development Fund.

Abstract

The General Antiparticle Spectrometer (GAPS) is an Antarctic long-duration balloon experiment designed to measure low-energy (< 0.25 GeV/n) cosmic antinuclei as signatures of dark matter. The distinctive GAPS particle identification technique relies on a tracker composed of > 1000 lithium-drifted silicon (Si(Li)) detectors – over 10 m^2 of silicon sensors – that both captures an incoming antinucleus into an exotic atom and measures the de-excitation X-ray and nuclear annihilation products. The GAPS program established the techniques necessary to produce large-area Si(Li) detectors, operable 150 ^oC above the liquid nitrogen temperatures typically required to achieve fine X-ray resolution, for an order of magnitude lower cost than previous commercially-available detectors. The distinctive detector geometry, together with custom polyimide passivation coatings that protect against humidity and organic contamination, has enabled remarkably robust operation: stable performance has now been

demonstrated after more than five years without requiring HV bias or low-temperature storage to prevent lithium redistribution. Detector segmentation, previously achieved through ultrasonic impact grinding, has now been demonstrated using a DISCO dicing saw, a less expensive alternative suitable for mass-production that opens new flexibility in detector and readout geometries. In this contribution, we review the features of such Si(Li) detector design and performance, and discuss the broader applications enabled by custom detector geometries.

NSS-13-066

Neutron Measurements of ^{252}Cf in High-Gamma-Ray Environments Using Silicon Carbide (SiC) Semiconductor Detector (#2326)

Kanta Nagai[1], Kei Aoyama[2], Takahito Suzuki[2], Takashi Nakamura[2,3], Tetsuro Matsumoto[4], Akihiko Masuda[4], Seiya Manabe[4], Junya Ishii[4], Kenji Shimazoe[1]

[1] University of Tokyo, the Nuclear Enginnering and Management, the Graduate School of Engineering, Tokyo, Japan; [2] Fuji Electric Co., Hino, Japan; [3] Tohoku University, Sendai, Japan; [4] National Institute of Advanced Industrial Science and Technology, Tsukuba, Japan

Abstract

Neutron measurement technology is essential for the decommissioning of the Fukushima Daiichi Nuclear Power Plant and for monitoring special nuclear materials. In the former case in particular, high-dose gamma radiation is present, and there are significant constraints on size and weight. As a neutron detector suited to these environments, we focused on a neutron detector using silicon carbide (SiC) semiconductors, which offer higher radiation resistance than silicon semiconductors. In this study, we verified whether it is possible to distinguish and detect neutrons emitted from a ^{252}Cf neutron source from gamma rays in a high-dose gamma-ray background environment. The results showed that it is possible to distinguish between neutrons and gamma rays in a gamma-ray environment of up to 132 Gy/h.

References

[1] Linyue Liu, Xiao Ouyang, Runlong Gao, Pengying Wan, and Xiaoping Ouyang ; “Latest developments in room-temperature semiconductor neutron detectors: Prospects and challenges” ; SCIENCE CHINA Physics, Mechanics & Astronomy ; March 2023 Vol. 66 No. 3: 232001

[2] T. Natsume, H. Doi, F. Ruddy, J. Seidel, and A. Dulloo, “Spent fuel monitoring with silicon carbide semiconductor neutron/gamma detectors,” J. ASTM Int., vol. 3, no. 3, p. 13430, 2006.

[3] K Nagai, K Aoyama, T Suzuki, T Nakamura, H Tanaka, J Ishii, K Shimazoe, “Performance evaluation of a silicon carbide semiconductor-based neutron detector for neutron-gamma discrimination”, Nuclear Instruments and Methods in Physics Research Section A: Accelerators, Spectrometers, Detectors and Associated Equipment ; April 2026 Vol 1084 171265

[4] Yuichi Hashizume, Takashi Uchida, Naoyuki Ose: Fuji Electric Technical Review 2020 vol.93 no.4 p262~264 2nd Generation SiC-SBD

[5] Yohei Abe, Development of a real-time neutron personal radiation dosimeter using inverted thin silicon diodes (2022), p. 22.

[6] T. Sato, Y. Iwamoto, S. Hashimoto, *et.al*. Features of Particle and Heavy Ion Transport code System (PHITS) version 3.02, J. Nucl. Sci. Technol. 55, 684-690 (2018).

NSS-13-068

Development of amorphous germanium blocking contact multi-electrode coaxial HPGe detectors for highcount-rate applications (#2621)

Siyuan Yu[1,2], Yang Tian[1,2], Li He[1,2], XiuXia Li[1,3], LiHui Han[1,2], MingXin Yang[1,2], Yuanjing Li[1,2], Yulan Li[1,2]

[1] Tsinghua University, Department of Engineering Physics, Beijing, China; [2] Key Laboratory of Particle & Radiation Imaging (Tsinghua University), Ministry of Education, Beijing, China; [3] Greater Bay Area National Center of Technology Innovation, Beijing, China

Abstract

High-purity germanium (HPGe) detectors are widely used in high-resolution gamma-ray spectroscopy and high-count-rate radiation measurements because of their excellent energy resolution and detection efficiency. Multi-electrode HPGe detectors can improve count-rate capability and provide local response information, but the calibration and summation of segmented-electrode signals remain challenging due to charge sharing, inter-electrode coupling, crosstalk and transient induced signals. In this work, a coaxial four-electrode HPGe prototype based on amorphous germanium blocking contacts was developed and tested. The detector consists of a small boron-implanted central P^+ electrode and three outer n-type segmented electrodes defined by amorphous germanium coating and aluminum metallization. The leakage current was below 10 pA at 200 V. Measurements with a ^{137}Cs source showed energy resolutions of 1.43–1.45 keV for the outer electrodes and 1.78 keV for the central electrode at 662 keV. Experimental and simulated four-channel waveforms were compared to evaluate induced responses in neighboring electrodes. Non-zero residual baselines observed in the experimental neighboring channels indicate coupling effects in the present frontend design. Simulated ^{137}Cs segment spectra and Ch1+Ch2 sum reconstruction further show that the central-electrode energy can serve as a reference for segment-energy calibration. These results demonstrate the feasibility of the amorphous-germanium-contact multi-electrode HPGe design and provide a basis for central-electrode-referenced correction and reliable segment-sum reconstruction in high-count-rate measurements.

References

[1] Akkoyun S, Algora A, Alikhani B, et al. Agata–advanced gamma tracking array[J]. Nuclear Instruments and Methods in Physics Research Section A: Accelerators, Spectrometers, Detectors and Associated Equipment, 2012, 668: 26-58.

[2] Amman M. High purity germanium based radiation detectors with segmented amorphous semiconductor electrical contacts: Fabrication procedures[J]. arXiv preprint arXiv:2006.05471, 2020.

NSS-13-070

A Novel Compton-Polarimeter in Telescope Configuration for X-Ray Energies up to 1 MeV (#2758)

Tobias Over-Winter[1,2], Anton Kononov[1], Thomas Krings[3], Wilko Middents[1,2], Uwe Spillmann[1], Günter Weber[1,4], Thomas Stöhlker[1,2]

[1] GSI Helmholtzzentrum für Schwerionenforschung GmbH, Darmstadt, Germany; [2] Friedrich-Schiller-Universität Jena, Institute of Optics and Quantum Electronics, Jena, Germany; [3] Forschungszentrum Jülich, Nuclear Physics Institute, Jülich, Germany; [4] Helmholtz-Institut Jena, Jena, Germany

Abstract

Compton polarimeters enable the detailed study of polarization sensitivity of fundamental radiative processes in the hard x-ray regime, i.e. for photon energies between 60 keV and 1 MeV. These detectors are based on double-sided segmented planar semiconductor crystals in which the recoil electron and the scattered photon of the Compton process are measured simultaneously. Within the SPARC collaboration (Stored Particles Atomic Physics Research Collaboration), a new Compton polarimeter in telescope configuration consisting of a Si(Li)- and a HPGe-detector has been developed, aiming for polarization experiments at particle accelerators and synchrotron facilities to analyze atomic or nuclear processes. A polarimeter consisting of only the first crystal, the Si(Li), was already operated in stand-alone mode in the energy range starting at 60 keV up to 250 keV. In a study of polarizazion-dependence of elastic scattering at the PETRAIII synchrotron facility of DESY, it proofed to be working well. Now the second crystal, the HPGe, was added to extend the accessible energy range up to the 1 MeV regime to widen the investigation of radiative processes. The main construction of the new detector system was performed at the detector laboratory of the Forschungszentrum Jülich, which is now relocating to the university of Cologne. We will report on the design of the novel Compton-polarimeter and first experimental applications.

NSS-13-072

Benefits from the latest Clover and Custom Desgined HPGe Detector Technologies (#3051)

Gabriela Ilie

Mirion Technologies, Product Management, Meriden, USA

Abstract

Mirion has been supplying sophisticated HPGe detectors and instrumentation which are used in cutting-edge materials analysis, fundamental nuclear physics research, and space studies to world's leading research institutes. The Clover [1] detector is one of Mirion unique product, recognized as an advanced gamma-ray detection system widely used in a variaty of different nuclear physics experiments. Clover detectors consist of four high-purity

germanium (HPGe) crystals, arranged in a compact cloverleaf-like configuration within a single cryostat. This unique geometry enhances its efficiency, enabling precise gamma-ray detection and energy resolution. The detectors design minimizes dead space, improving sensitivity to weak signals and increasing the likelihood of coincident gamma-ray detection for advanced spectroscopic studies. The Clover detectors versatility is augmented by its segmented configuration, which allows for effective background suppression and Doppler shift correction, making it invaluable for nuclear physics experiments and high-energy gamma-rays. Recent advancements in signal processing and digital electronics have further enhanced the performance of Clover detectors which continue to be a cornerstone in gamma-ray spectroscopy due to its high efficiency, excellent energy resolution, and timing. This presentation will provide an overview of various technologies for Mirion Clover detectors, highlighting the benefits of recent advancements like electrical cooling, an expanded energy dynamic range, and more.

References
[1] https://www.mirion.com/products/technologies/spectroscopy-scientific-analysis/research-education-and-industrial-solutions/special-hpge-sili-detectors/clover-detectors-four-coaxial-germanium-detectors

NSS-13-074

An automated testing and characterization system for SiPM device arrays (#1148)

Stefano Riboldi[1,2], Agnese Giaz[2], Ciro Boiano[2], Sergio Brambilla[2], Franco Camera[1,2]

[1] *Universita degli Studi di Milano, Dipartimento di Fisica, Milano, Italy;* [2] *INFN, Milano, Milano, Italy*

Abstract
Large-area photodetectors in the form of silicon photomultiplier (SiPM) array detectors are becoming increasingly widespread in basic physics, medical, industrial, and security applications.
Various suitable devices are commercially available from companies such as Broadcom, Hamamatsu, and OnSemi. Alternatively, they can be constructed from individual SiPM devices.
After repeated use and initial testing of self-constructed devices, it is useful to characterize the electrical properties of each SiPM photodetector to determine the operating conditions of the array.
If the operational readout of the photodetector is based on a combination of theoretically available anode signals — for example, by short-circuiting all anode signals into a single readout channel — this verification procedure must be conducted using an independent test system.
This paper discusses the possible general structure of a fully automated test system, its implementation details, and its practical application by the user.
Through the implemented test procedures, the following can be determined:
Short circuits and open circuits on the printed circuit board housing the array under test
The individual I-V characteristic curves of the SiPM devices and the homogeneity of their operating parameters (e.g., breakdown voltage)
The operability, electro-optical conversion gain, response time, and saturation level of the signal of the individual SiPM devices through the injection of optical photons from a light-emitting diode (LED)
Depending on the tests performed, this test system can fully automatically determine the operational status of the SiPM device array within a time interval ranging from a few seconds to about ten minutes.

References
[1] J. Delgado et al., 2024, 'Comparative Study of SiPM Arrays Performances for Neutron Detectors', IEEE TNS, doi: 10.1109/TNS.2024.3387075
[2] M. Bonesini, et al., 2022, 'Large area LaBr3:Ce crystals read by SiPM arrays with improved timing and temperature gain drift control', NIM A, Elsevier, doi:10.1016/j.nima.2022.167677

NSS-13-076

Construction and Testing of An In-Situ Magnetron Sputtering Plasma Monitoring Setup (#1340)

Burak Bilki[1], Mehmet Tosun[1,2], Sena Acikgoz[1,3]

[1] Turkish Accelerator and Radiation Laboratory, Ankara, Turkey; [2] Istinye University, Istanbul, Turkey; [3] Ankara University, Ankara, Turkey

This work is supported under TÜBİTAK Grant No: 124F091.

Abstract

Magnetron sputtering is a widely used technique for depositing both metallic and insulating thin films on diverse substrates. Its strength lies in the precise control it enables over film thickness and morphology, achievable through a detailed understanding of key physical processes such as gas ionization, plasma behavior, target sputtering, and film deposition. This level of control is particularly critical for high-energy physics detector technologies, where thin, uniform, and functional coatings such as those implemented in hybrid Resistive Plate Chambers are essential for optimizing detector performance, stability, and signal fidelity.

A promising pathway toward improving this control is the investigation of plasma-emitted light, which encodes valuable information about the composition, density, and dynamics of both working gas species and sputtered material. However, existing studies have largely relied on external optical observations or diagnostic techniques that perturb the plasma, limiting their effectiveness.

To address these challenges, we developed a high-precision, multi-parameter optical monitoring system capable of probing plasma emission directly within the sputtering chamber. The system samples light at key locations along the target-to-substrate trajectory with a timing resolution of up to 320 ps. Quartz optical fibers are integrated into the vacuum environment and coupled through a dedicated feedthrough to an external detection system. Signal acquisition is performed using Silicon Photomultipliers mounted on a custom-designed readout board.

This approach provides detailed insight into the temporal and spatial evolution of magnetron plasmas, enabling improved understanding of thin-film growth mechanisms. These results will contribute to the optimization of coating processes for next-generation detector systems in high-energy physics, enhancing their performance, robustness, and scalability.

NSS-13-078

Utilisation of the ISIS Digital Data Pipeline for Afterpulsing Analysis of PMT & SiPM Signals (#1732)

James S Lord[1], Andrea Abba[2], Peter J Baker[1], Francesco Caponio[2], Piers Coode[1], Stephen P. Cottrell[1], Day Jack[1], Kirk Daniel[1], Anthony Lim[1], Lisa Malliolio[3], Nixon Daniel[1], Daniel E. Pooley[1], Dave Templeman[1]

[1] STFC Rutherford Appleton Laboratory, Didcot, UK; [2] Nuclear Instruments SRL, Lambrugo, Italy; [3] The University of Pavia, Pavia, Italy

This work is partially supported by the Erasmus+ programme.

Abstract

This paper reports on the recently deployed ISIS Digital Data Pipeline, which has facilitated an in-depth examination at the detector signals coming from the suite of Muon Spectrometers. Signal processing and event-mode analysis has been used to understand the afterpulsing characteristics of three types of photosensor; the HAMAMATSU R5505 1-inch PMT, the EMI-9954 2-inch PMT and S13360-1325PE HAMAMATSU SiPM. The R5505 was found to produce significant afterpulsing that can be identified via pulse shape discrimination due to their characteristically shorter fall time. This indicates impurity ionization, as the signals are not convolved with the scintillation response. The data pipeline has been tuned to suppress the afterpulses, producing data sets without this background contribution.

NSS-13-080

Dark Count Rate of LHCb Scintillating Fibre Tracker SiPMs as an In-Situ Radiation Monitor (#2507)

Sacha E.R. Medaer[1], Federico Ronchetti[2], Elisabeth M. Niel[2,3], Gloria Corti[1], Guido Haefeli[2]

[1] CERN, LHCb Collaboration, Geneva, Switzerland; [2] École Polytechnique Fédérale de Lausanne, Institute of Physics, Lausanne, Switzerland; [3] Leprince-Ringuet Laboratory, Institut Polytechnique de Paris, École Polytechnique, CNRS/IN2P3, Palaiseau, France

The authors would like to thank B. Leverington for his assistance with the SciFi geometry description as well as the SciFi team for the construction and operation of the SciFi detector.

Abstract

In high-energy physics detectors, Silicon photomultipliers (SiPMs) operated in mixed radiation fields show a dramatic increase in dark count rate (DCR), which affects detector performance. This work investigates whether the DCR of the SiPMs in the LHCb Scintillating Fibre Tracker can be used as an in-situ monitor of accumulated radiation exposure. The DCR at three delivered luminosities was recorded at the end of three consecutive yearly shutdowns and converted to area-normalized DCR. The results obtained were compared with radiation estimators obtained from particle-transport simulations using the latest detector geometry. The study focuses on total ionizing dose and 1 MeV neutron-equivalent fluence, which represent ionizing energy deposition and displacement-damage effects, respectively. The measured DCR was fitted as a linear function of each radiation estimator. Both estimators show a monotonic correlation with the measured DCR. The fitted slopes are approximately Gaussian after normalization, with relative dispersions of about 17 percent when all tracking stations are combined and about 13 percent when the stations are treated separately. This reduction indicates that part of the response spread is associated with station-dependent effects rather than with channel-to-channel variations only. The two radiation estimators cannot be uniquely separated with the present dataset. The results therefore support an empirical parameterization of DCR as a proxy for the considered radiation estimators, rather than a unique identification of the underlying damage mechanism. With appropriate station-wise calibration, this approach could provide a way to estimate the accumulated total ionizing dose or 1 MeV neutron equivalent fluence from post-shutdown DCR measurements.

References
[1] J.-L. Agram, W. Barter, M. Baselga, M. Battaglia, J. Beyer, H. M. Borecka-Bielska, D. Brzhechko, A. de Cosa, I. Dawson, F. Djama et al., “Measurements of radiation damage on silicon sensors,” CERN Yellow Reports: Monographs, vol. 2021, pp. 59–85, 2021.
[2] O. Girard, G. Haefeli, A. Kuonen, L. Pescatore, O. Schneider, and M. E. Stramaglia, “Characterisation of silicon photomultipliers based on statistical analysis of pulse-shape and time distributions,” arXiv preprint arXiv:1808.05775, 2018.
[3] G. Battistoni, T. Boehlen, F. Cerutti, P. W. Chin, L. S. Esposito, A. Fasso, A. Ferrari, A. Lechner, A. Empl, A. Mairani et al., “Overview of the fluka code,” Annals of Nuclear Energy, vol. 82, pp. 10–18, 2015.
[4] C. Ahdida, D. Bozzato, D. Calzolari, F. Cerutti, N. Charitonidis, A. Cim- mino, A. Coronetti, G. D’alessandro, A. Donadon Servelle, L. Esposito et al., “New capabilities of the fluka multi-purpose code,” Frontiers in Physics, vol. 9, p. 788253, 2022.
[5] L. Collaboration et al., “Lhcb tracker upgrade technical design report,” CERN, Tech. Rep., 2014.

NSS-13-082

Radiation-Hardened CMOS-SPAD Design for Stable Geiger-Mode Operation (#2314)

Doo-Hee Son, Doyoon Eom, Myung-Jae Lee

Yonsei University, Department of Electrical and Electronic Engineering, Seoul, South Korea

Manuscript received May 12, 2025. This work was supported by the Yonsei University Research Fund of 2025 (2025-22-0433), the Institute of Information & Communications Technology Planning & Evaluation (IITP) grant funded by the Ministry of Science and ICT (MSIT) (RS-2025-02218723), and the National Research Council of Science & Technology (NST) grant by the Korea government (MSIT) (GTL25011-000).

Abstract

Single-photon avalanche diodes (SPADs) are advanced semiconductor photodetectors that operate in Geiger mode, offering single-photon sensitivity and sub-nanosecond timing resolution for biomedical and space applications where robust radiation hardness is essential. In these environments, prolonged gamma-ray irradiation causes total ionizing dose effects, in which holes generated in silicon dioxide become trapped near the silicon/silicon dioxide interface, forming positive oxide-trapped charges and promoting interface trap formation. The progressive accumulation of these charges distorts the local electric field distribution near the guard ring periphery, causing field crowding that can promote premature edge breakdown and compromise stable Geiger-mode operation. This work employs technology computer-aided design (TCAD) simulations using the Sentaurus tool to compare a conventional virtual guard ring structure with a proposed physical guard ring realized by a deep p-well, available in complementary metal-oxide-semiconductor (CMOS) processes. Simulation results demonstrate that the virtual guard ring exhibits persistent edge field crowding exceeding the device junction field across all irradiation conditions, whereas the physical guard ring maintains its edge field below the junction level over a wide irradiation range. These results confirm that the deep p-well-based physical guard ring effectively reduces the risk of premature edge breakdown, offering a promising radiation-tolerant design strategy for CMOS SPADs.

References
[1] Choi, H-S et al. 2026, 'Optimization of backside-illuminated single-photon avalanche diodes in 90 nm CIS technology for scintillator-based biomedical applications', *APL Photonics*, vol. 11, no. 4, pp. 046106-1–046106-10.
[2] Oldham, TR & McLean, FB 2003, 'Total ionizing dose effects in MOS oxides and devices', *IEEE Transactions on Nuclear Science*, vol. 50, no. 3, pp. 483–499.
[3] Shojaee, F, Zarei, M, Ratti, L & Karami, MA 2022, 'A new guard ring for ionizing radiation tolerance enhancement in single-photon avalanche diodes', *Microelectronics Reliability*, vol. 135, art. no. 114573.
[4] Marcelot, O, Goiffon, V & Magnan, P 2019, 'Exploration of pinned photodiode radiation hardening solutions through TCAD simulations', *IEEE Transactions on Electron Devices*, vol. 66, no. 8, pp. 3411–3416.

NSS-13-084

ClearMind: fast photo-detection for TOF-PET (#2741)

Viatcheslav Sharyy[1,2], Zoe Zobundzija[1], Dominique Yvon[1,2], Eric Delagnes[1], Dominique Breton[5], Jihane Maalmi[5], Mathieu Dupont[4], Christian Morel[4], Geoffrey Daniel[4], Theo Kaprelian[4], Michael Minot[6], Mark Popecki[6], Alexey Lyashenko[6]

[1] CEA, IRFU, Gif sur Yvette, France; [2] CEA, CNRS, INSERM, BIOMAPS, Orsay, France; [3] CEA, Service de Génie Logiciel pour la Simulation, Gif-sur-Yvette, France; [4] CNRS, CPPM, Marseille, France; [5] CNRS, IJCLab, Orsay, France; [6] Incom Inc., Charltom, USA

This project has received funding from the French National Research Agency under grant No. **ANR-19-CE19-0009-01** and **ANR-24-CE45-7518**.

Abstract
The ClearMind project aims to improve Time-of-Flight Positron Emission Tomography by developing detection modules with a Coincidence Time Resolution of 100 ps FWHM or better. This performance is achieved through the simultaneous detection of Cherenkov and scintillation photons within the PWO crystal window of a Micro-Channel-Plate PhotoMultiplicator Tube read out by transmission lines. The first prototype, assembled by Photek (UK), demonstrated the feasibility of such technology but has a suboptimal time resolution of 370 ps

(FWHM) when detecting 511 keV gamma photons. To address these challenges, we are improving the photocathode design, with the next prototype to be assembled by Incom (USA). As a first step, we evaluated the performance of standard Incom's High-Resolution Photon Detector (HRPPD) MCP-PMT with a capacitive readout. Tests were conducted using both a pulsed laser in single-photon mode and a ^{22}Na radioactive source. The HRPPD's capacitive readout system, which is compatible with the ClearMind's transmission line design, has achieved a single-photon Transit Time Spread as low as 50 ps (FWHM) for high-gain events and a spatial resolution of about 1 mm (FWHM). Photocathode deposition on PWO trials at Incom remains stable over time and confirms its feasibility. Through realistic simulations combined with machine learning-based reconstruction, we investigate the factors limiting the time resolution in ClearMind technology and demonstrate that a time resolution below 100 ps is achievable for large-size PWO modules under certain conditions.

NSS-13-086

Characterization of High-Speed Photomultiplier Tubes with $LaBr_3(Ce)$ scintillators (#2829)

Miriam Caballero Rodríguez[1], Luis M. Fraile[1], Sara Gaitán Dominguez[2], Víctor Martínez Nouvilas[1], Víctor Sánchez-Tembleque[1], Jose Udias[1]

[1] Universidad Complutense de Madrid, Facultad de Ciencias Físicas, EMFTEL and IPARCOS, Madrid, Spain; [2] CERN, ISOLDE, EP Department, Geneva, Switzerland

This work has been supported by the Spanish Ministerio de Ciencia e Innovaci\'on under projects PID2019-104714GB-C21 and PID2022-140400NB-C21.

Abstract

Fast-timing γ-ray spectroscopy based on $LaBr_3(Ce)$ scintillators coupled to photomultiplier tubes (PMT) is a well-established technique for measuring lifetimes of excited nuclear states in the picosecond-to-nanosecond range. In this work, we present a comparative characterization of different $LaBr_3(Ce)$ crystals of various sizes and geometries coupled to several Hamamatsu PMT models: R9779 (H10570), R13089 (H13719-Y006 and H13719-Y007), and R13408-Y006. The study focuses on timing performance, linearity, and energy resolution using digital signal processing. While the discontinued R9779 remains a benchmark for timing performance, the newer PMT models exhibit good linearity, comparable energy resolution for a given crystal, and competitive coincidence time resolution.

References
[1] Vedia, V, et al. 2015, 'Enhanced time response of 1-in. $LaBr_3(Ce)$ crystals by leading edge and constant fraction techniques', Nucl. Instrum. Methods Phys. Res. A, vol. 795, pp. 144–150, Amsterdam: Elsevier
[2] Vedia, V, et al. 2015, 'Performance evaluation of $LaBr_3(Ce)$ crystal geometries designed for fast timing applications', 2015 IEEE Nuclear Science Symposium and Medical Imaging Conference (NSS/MIC), vol. 1, pp. 1–2, Piscataway, NJ: IEEE
[3] Sánchez-Tembleque, V, et al. 2019, 'Optimizing time-pickup algorithms in radiation detectors with a genetic algorithm', Nucl. Instrum. Methods Phys. Res. A, vol. 927, pp. 54–62, Amsterdam: Elsevier

NSS-13-088

TID irradiations of a Shunt-LDO designed in a 110 nm CMOS process for EPIC-SVT (#1430)

Marcello Borri[1], Matthew Buckland[1], James J. Glover[2], Liam Godfrey[1], Andrew Hill[1], Amanda Krieger[3], Lochana Ranatunge[5], Iain Sedgwick[1], Liliana Teodorescu[5], Che S. Tse[2], Roy Wastie[4]

[1] UKRI Science and Technology Facilities Council, Technology Department, Warrington, UK; [2] University of Birmingham, Department of Physics, Birmingham, UK; [3] Lawrence Berkeley National Laboratory, Engineering Division, Berkeley, USA; [4] University of Oxford, Department of Physics, Oxford, UK; [5] Brunel University of London, College of Engineering, Design and Physical Sciences, London, UK

The authors would like to acknowledge the UKRI-STFC for funding this work via the following grants: ST-X004837-1 and ST-W00450X-1.

Abstract

The Silicon Vertex Tracker (SVT) of the EPIC detector adopts a serial powering scheme to distribute electrical power to Monolithic Active Pixel Sensors (MAPS) that are mounted on outer barrels, and electron and hadron end caps. Serial powering is an advantageous powering scheme because it reduces the mass required by electrical services. This is important in order to achieve the target material budget in staves and disks, which can be as low as 0.25% X/X_0.

The Shunt Low Drop Out (SLDO) voltage regulator is key to the serial powering scheme. Four SLDOs are connected to each MAPS to supply its 4 different power domains. This forms a coherent electrical unit that is repeated in a serial chain. A constant current is distributed through the SLDOs in this serial chain.

The SLDO is a bespoke circuit design. It supplies up to ~1.0 A of output current with an output voltage in range 1.1 V to 1.4 V. The chip was designed in a 110 nm process.

A series of SLDO chips were irradiated at the X-ray Irradiation Facility at Daresbury Laboratory (UK). X-rays were produced via Bremsstrahlung from electrons hitting a Tungsten target. The irradiation campaign studied the circuit response against the Total Ionising Dose (TID) requirements of the EPIC detector. The target TID for EPIC-SVT is estimated to be of the order of 200 krad(SiO_2), integrated over a period of 10 years of operations. This estimate is based on a worst case scenario where a beam of 100 GeV electrons collides with a beam of 275 GeV protons for a period of 6 months per year.

TID irradiations characterised the performance of the SLDO chip for different settings of input voltage, output loads, and different temperatures. Irradiations were carried out at different dose rates, as high as ~100 krad(SiO_2)/min. Annealing was monitored after irradiation.

References

[1] J.J.Glover et al, EIC vertex and tracking detector, PoS VERTEX2025 (2025) 001, https://doi.org/10.22323/1.513.0001

[2] L.Gonella et al, Development of a Silicon Vertex and Tracking Detector for the Electron-Ion Collider, PoS VERTEX2023 (2024) 038, https://doi.org/10.22323/1.448.0038
[3] I.Sedgwick et al, A Shunt-LDO for the Electron Ion Collider in a 110nm CMOS process, 2026 JINST 21 C03031, https://doi.org/10.1088/1748-0221/21/03/C03031
[4] L.Gonella et al, The shunt-LDO regulator to power the upgraded ATLAS pixel detector, 2012 JINST 7 C01034, https://doi.org/10.1088/1748-0221/7/01/C01034
[5] M.Borri et al, Commissioning of an X-ray irradiation facility to test HPGe sensors and to irradiate CMOS electronics, 2024 IEEE NSS MIC RTSD, https://doi.org/10.1109/NSS/MIC/RTSD57108.2024.10655927
[6] M. Borri et al, TID Irradiations of a 65 nm CTLE Prototype for ePIC SVT, 2025 IEEE NSS MIC RTSD, https://doi.org/10.1109/NSS/MIC/RTSD57106.2025.11286260

NSS-13-090

Characterization of Single-Event Upsets in a 90 nm Commercial Off-the-shelf SRAM caused by Low-Energy Protons (#1482)

Shintaro Ishihara, Yukimune Uchida, Sho Toyama, Wataru Kada, Shigeo Matsuyama

Tohoku University, Department of Quantum science and Energy Engineering, Graduate school of Engineering, Sendai, Japan

The authors gratefully acknowledge N. Shibanuma for constructing the single-event effect irradiation field used in this study.

Abstract

In contradistinction to conventionally manufactured radiation-hardened devices, which demonstrate radiation tolerance and reliability, commercial off-the-shelf (COTS) devices may exhibit vulnerability to single-event effects (SEEs) resulting from direct ionization in environments dominated by protons, such as in low earth orbit (LEO). The issue of limited cross-section data availability for such protons with low energies has been addressed by a dedicated SEE, particularly single-event upset (SEU), evaluation field based on a 1MV tandem accelerator. In the present study, low-energy proton beams with an energy range of between 0.40 and 1.65 MeV have been irradiated to 90-nm COTS SRAM. The proton-induced SEU cross-sections were found to be several orders of magnitude lower than the predicted values through the Weibull plot derived from conventional data. Moreover, an approximate tenfold enhancement in SEU cross-section was observed at the energy of 0.447 MeV, coinciding with a roughly twofold increase in accumulated fluence. The findings present novel experimental insights into the energy- and ion-species- dependent mechanisms underpinning SEU occurrence in COTS.

References
[1] Leyva-Mayorga, I., Soret, B., Röper, M., Wübben, D., Matthiesen, B., Dekorsy, A. and Popovski, P. 2020, 'LEO Small-Satellite Constellations for 5G and Beyond-5G Communications', *IEEE Access*, vol. 8, pp. 184955–184964, Piscataway, NJ: IEEE.
[2] Glorieux, M., Bonnoit, T., Lange, T., Gaillard, R., Nofal, I., Artola, L., Poivey, C., Levacq, D., Rey, R., Kettunen, H. and Polo, C.B. 2024, 'Methods for Proton Direct Ionization SEU Characterization and Orbital Error-Rate Estimation', *IEEE Transactions on Nuclear Science*, vol. 71, no. 8, pp. 1707–1714, Piscataway, NJ: IEEE.
[3] Kobayashi, D. 2021, 'Scaling Trends of Digital Single-Event Effects: A Survey of SEU and SET Parameters and Comparison with Transistor Performance', *IEEE Transactions on Nuclear Science*, vol. 68, no. 2, pp. 124–148, Piscataway, NJ: IEEE.
[4] Toyama, S., Shibanuma, N., Matsumoto, T., Otsuka, Y., Nakatsuma, A., Maruta, K., Miwa, M., Kada, W. and Matsuyama, S. 2026, 'Calibration of an Electrostatic Accelerator for Single-Event-Effects Tests', *Nuclear Instruments and Methods in Physics Research Section B: Beam Interactions with Materials and Atoms*, vol. 572, article no. 166006, Amsterdam: Elsevier.

[5] Shibanuma, N., Kada, W., Toyama, S., Miwa, M. and Matsuyama, S. 2025, 'Establishment of a Single Event Effect Evaluation Field Based on a Compact Ion Accelerator for Commercial Off-the-Shelf Devices Utilized in Low Earth Orbit', *2025 IEEE Nuclear Science Symposium, Medical Imaging Conference and Room-Temperature Semiconductor Detector Conference (NSS/MIC/RTSD)*, pp. 1, Piscataway, NJ: IEEE.

NSS-13-092

Design and Implementation of an FPGA-Based Nuclear-Like Signal Generator (#1615)

Yao Yang[1,2], **Yao Yang**[1,2], Xiaohui Li[1,2], Xiaohui Li[1,2], Teng Tong[1,2], Teng Tong[1,2], Fanhui Meng[1,2], Fanhui Meng[1,2], Shuangquan Liu[1,2], Shuangquan Liu[1,2], Zhiming Zhang[1,2], Zhiming Zhang[1,2], Cunfeng Wei[1,2], Cunfeng Wei[1,2], Long Wei[1,2], Long Wei[1,2]

[1] Chinese Academy of Sciences, Institute of High Energy Physics, Beijing, China; [2] Jinan Laboratory of Applied Nuclear Science, Jinan Laboratory of Applied Nuclear Science, Jinan, China

This work was supported by the National Natural Science Foundation of China (Grant No. 12505356)

Abstract

Traditional radioactive source testing involves health risks, regulatory limitations, and operational inconvenience. To address these issues, this paper presents a nuclear-like signal generator capable of reproducing the waveform, amplitude, and timing characteristics of real nuclear radiation signals. The proposed system is implemented on a Xilinx K7 FPGA and supports parameter configuration through a touch screen, USB, Ethernet, or host computer software. In the waveform-generation module, photon emission timing is modeled according to scintillator light yield and decay time, while photoelectric conversion jitter and Gaussian pulse responses are introduced to synthesize realistic macroscopic waveforms. In the amplitude-generation module, a cumulative distribution function threshold table derived from measured energy spectra is used to reproduce statistical energy distributions. In the timing module, event occurrence is modeled as a Poisson process with exponentially distributed intervals. The system supports multiple radioactive sources and scintillator materials, including Na, Cs, LYSO, NaI, CsI, and BGO, with independent dual-channel output capability.

NSS-13-094

Radiation-Hardened VCO in 28 nm FDSOI with Enhanced Frequency Stability Under Total Ionizing Dose (#1750)

Muhammad Adeel Anwar[1,4], **Muhammad Adeel Anwar**[1,4], Dong Seok Kim[3,5], Dong Seok Kim[3,5], Seo Ryong Koo[1,4], Seo Ryong Koo[1,4], Inyong Kwon[2], Inyong Kwon[2]

[1] Korea University of Science and Technology (UST), Nuclear Science and Technology, Daejeon, South Korea; [2] Yonsei University Mirae Campus, Department of Radiological Science, Wonju, South Korea; [3] Korea University of Science and Technology (UST), Radiation Science, Daejeon, South Korea; [4] Korea Atomic Energy Research Institute (KAERI), Daejeon, South Korea; [5] Korea Atomic Energy Research Institute (KAERI), Gyeongju, South Korea

This work was supported in part by the National Research Foundation of Korea (NRF) funded by MSIT under Grants RS-2022-00144419, RS-2022-00144324, and RS-2022-00165164; by MSS under Grant RS-2023-00322102; by NST (MSIT) under Grant GTL25051-000; and by the RISE program (MOE and Gangwon State) under Grant 2025-RISE-10-006.

Abstract

Ensuring reliable RF operation in radiation-prone is critical for wireless monitoring systems in nuclear and space applications. This work presents a radiation-hardened-by-design (RHBD) voltage-controlled oscillator (VCO) implemented in a 28 nm Fully-Depleted Silicon-On-Insulator (FDSOI) process and experimentally evaluated under total ionizing dose (TID) conditions. The proposed RHBD VCO is compared with a conventional design up to 370 kGy(Si) using a Cobalt-60 gamma irradiation source at KAERI. Measurement results demonstrate that the RHBD VCO significantly improves frequency stability, achieving up to 57% reduction in frequency drift compared to the conventional counterpart. In addition, enhanced output power stability and reduced supply current variation are observed under irradiation. The results highlight the combined benefits of FDSOI technology and circuit-level hardening techniques, demonstrating a robust solution for radiation-tolerant RF circuit design.

References

[1] H. Jeon, I. Kwon and M. Je, "Radiation-Hardened Sensor Interface Circuit for Monitoring Severe Accidents in Nuclear Power Plants," in IEEE Transactions on Nuclear Science, vol. 67, no. 7, pp. 1738-1745, July 2020, doi: 10.1109/TNS.2020.3002421.

[2] J. D. Seo, L. D. Trang, J. -W. Han, J. Kim, S. Lee and I. -J. Chang, "Total Ionizing Dose Effect on Ring Oscillator Frequency in 28-nm FD-SOI Technology," in IEEE Electron Device Letters, vol. 39, no. 11, pp. 1728-1731, Nov. 2018, doi: 10.1109/LED.2018.2872345.

[3] A. Urena-Acuna and J. M. Armani, "Circuit-level Simulation of TID and Thermal Regeneration Effects on 28nm FDSOI Technology," 2024 24th European Conference on Radiation and Its Effects on Components and Systems (RADECS), Maspalomas, Spain, 2024, pp. 1-8, doi: 10.1109/RADECS61970.2024.11298612.

[4] J. R. Schwank et al., "Radiation Effects in MOS Oxides," in IEEE Transactions on Nuclear Science, vol. 55, no. 4, pp. 1833-1853, Aug. 2008, doi: 10.1109/TNS.2008.2001040.

NSS-13-096

A Radiation-Hardened R-2R Digital-to-Analog Converter with Branch-Local Diode-Replica Dummy Biasing (#1844)

Duckhyun Kim[1,2], Gyuseong Cho[1], Inyong Kwon[3]

[1] Korea Advanced Institute of Science and Technology (KAIST), Department of Nuclear and Quantum Engineering, Daejeon, South Korea; [2] Korea Atomic Energy Research Institute (KAERI), Advanced Instrumentation and Control Research Division, Daejeon, South Korea; [3] Yonsei University, Department of Radiological Science, Wonju, South Korea

This work was supported in part by the National Research Foundation of Korea (NRF, RS-2022-00144324), the National Research Council of Science and Technology (NST, GTL25051-201), the Korea Technology and Information Promotion Agency for SMEs (TIPA, RS-2023-00322102), and the Gangwon RISE Center (2025-RISE-10-006), all funded by the Korean government.

Abstract

R-2R ladder converters in nuclear instrumentation are vulnerable to total ionizing dose (TID) because threshold-voltage shifts in NMOS switching transistors perturb on-resistance ratios that govern ladder accuracy. Preliminary irradiation measurements motivate a circuit-level solution: a modest on-resistance increase already drives worst DNL beyond 1 LSB. The proposed converter in 0.18 μm BCD employs a two-layer hardening strategy. The first layer uses a switch-compensated R-2R topology where all resistors share the same R+Ron unit, canceling Ron[if gte msEquation 12]><m:oMath><m:sSub><m:sSubPr><m:ctrlPr></m:ctrlPr></m:sSubPr><m:e><span lang=EN-US style='font-size:10.0pt; font-family:"Cambria Math",serif;mso-fareast-font-family:"맑은 고딕";mso-fareast-theme-font: minor-fareast;mso-bidi-font-family:"Times New Roman";mso-ansi-language:EN-US; mso-fareast-language:EN-US;mso-bidi-language:AR-SA'><m:r><m:rPr><m:scr m:val="roman"/><m:sty m:val="b"/></m:rPr>R</m:r></m:e><m:sub><span lang=EN-US style='font-size:10.0pt;font-family:"Cambria Math",serif; mso-fareast-font-family:"맑은 고딕";mso-fareast-theme-font:minor-fareast; mso-bidi-font-family:"Times New Roman";mso-ansi-language:EN-US;mso-fareast-language: EN-US;mso-bidi-language:AR-SA'><m:r><m:rPr><m:scr m:val="roman"/><m:sty m:val="b"/></m:rPr>on</m:r></m:sub></m:sSub></m:oMath><![endif] in the transfer function. The second layer preserves this cancellation through branch-local diode-replica biasing: a per-branch source-tracking loop and a scaled NMOS replica enforce uniform VGS,Ref on every dummy switch, with a constant-transconductance reference anchoring gm,rep to a poly-silicon ratio. Simulations across multiplicities 5–50 at 27 ℃ and 200 ℃ show the proposed converter achieves the 1 LSB target at multiplicity 15 vs. 40 for the conventional reference (2.7× area reduction). At multiplicity 20, worst DNL is 0.564 LSB at 200 ℃ vs. 2.471 LSB, with ~4.4× major-carry DNL improvement.

References

[1] Barnaby, H. J. 2006, 'Total-ionizing-dose effects in modern CMOS technologies', IEEE Trans. Nucl. Sci., vol. 53, no. 6, 3103–3121.
[2] Schwank, J. R. et al. 2008, 'Radiation effects in MOS oxides', IEEE Trans. Nucl. Sci., vol. 55, no. 4, 1833–1853.
[3] Fan, H. et al. 2018, 'A 4-channel 12-bit high-voltage radiation-hardened DAC for low orbit satellite applications', IEEE Trans. Circuits Syst. I, vol. 65, no. 11, 3698–3706.
[4] Yao, Y., Dai, F., Jaeger, R. C., Cressler, J. D. 2008, 'A 12-bit cryogenic and radiation-tolerant DAC for aerospace extreme environment applications', IEEE Trans. Ind. Electron., vol. 55, no. 7, 2810–2819.
[5] Marche, D., Savaria, Y., Gagnon, Y. 2009, 'An improved switch compensation technique for inverted R-2R ladder DACs', IEEE Trans. Circuits Syst. I, vol. 56, no. 6, 1115–1124.
[6] Asazawa, H. 1992, 'D/A Converter for Minimizing Nonlinear Error', U.S. Patent 5,119,095.
[7] Tahar, C. et al. 2025, '12-bit high-voltage current-steering-assisted R-2R DAC with RCM and parallel switch for satellite applications', IEEE Trans. Nucl. Sci., vol. 72, no. 4, 1425–1432.

NSS-13-098

Preamplifier Readout Electronics for Summing SiPMs Enhanced Circuit (PRESSEC) for Advanced SiPM Camera (#1992)

Daniel David Marín[1], Alberto López[1], Diego Mateo[2], Josep Altet[2], Enrique Barajas[2], Xavier Aragones[2], Joan Serrano[1], Joan Mauricio[1], Rafel Manera[1], Eduardo Picatoste[1], Sergio Gómez[2]

[1] Universitat de Barcelona, Institut de Ciències del Cosmos, Barcelona, Spain; [2] Universitat Politécnica de Barcelona, Electronics Department, Barcelona, Spain

Thanks to the grants "Gamma-Ray Astronomy with CTA-North and MAGIC, Project 1" (PID2022-138172NB-C43)

Abstract

The next generation of imaging atmospheric Cherenkov telescope (IACT) cameras is transitioning to silicon photomultipliers (SiPMs) due to their stability, robustness, and superior sensitivity compared to PMTs. Specifically, we are developing an ASIC for the advanced SiPM camera (AdvCam). This ASIC, designated as PRESSEC (Preamplifier Readout Electronics for Summing SiPMs Enhanced Circuit), is implemented in 65 nm CMOS technology. The PRESSEC utilizes a 32-input scheme for large-area sensor readout. Its primary function is to generate analog outputs by summing signals from four sensors into a single channel, effectively reducing the total output count to eight channels. The main functionality of this ASIC is housed in the energy path, which integrates a single-ended-to-differential converter and a pole-zero cancellation circuit. This structure is instrumental in reducing the pulse's Full Width at Half Maximum (FWHM) to 3 to 5 ns, thereby mitigating pileup effects in high activity environments. Simultaneously, these signals feed a trigger system for rapid event identification via a fast comparator. Additionally, a dedicated Night-Sky Background (NSB) monitoring circuit is included to measure ambient noise from sources like moonlight, employing a slow integrator with adjustable high-value pseudo-resistors to achieve integration time constants in the order of the milliseconds. Rigorous performance benchmarks, validated using Hamamatsu and FBK SiPMs, show a signal-to-noise ratio of at least 5, a dynamic range of 300 photons, and a linearity error below 3% for both energy and NSB paths, while presenting a power consumption of approximately 10 mW per input channel.

References
[1] "Cherenkov Telescope Array website." [Online]. Available: https://www.cta-observatory.org/

[2] M. Heller and et. al., “The next generation cameras for the largesized telescopes of the cherenkov telescope array observatory,” in 38th International Cosmic Ray Conference, 2023.
[3] S. Gomez, J. Alozy, M. Campbell, J. Fernandez-Tenllado, R. Manera, J. Mauricio, C. Pujol, D. Sanchez, A. Sanmukh, A. Sanuy, R. Ballabriga, and D. Gascon, “Fastic: a fast integrated circuit for the readout of high performance detectors,” Journal of Instrumentation, vol. 17, no. 05, p. C05027, may 2022. [Online]. Available: https://doi.org/10.1088/1748-0221/17/05/C05027
[4] A. Rivetti, CMOS: Front-End Electronics for Radiation Sensors, 06 2015.
[5] “KM3NeT website.” [Online]. Available: https://www.km3net.org/
[6] A. Tajalli, Y. Leblebici, and E. Brauer, “Implementing ultra-high-value floating tunable cmos resistors,” Electronics Letters, vol. 44, 02 2008.
[7] A. Lopez, “Design of a rail-to-rail ota in 65 nm cmos technology for a particle detector sensor,” 2023. [Online]. Available: https://upcommons.upc.edu/handle/2117/403133

NSS-13-100

Feasibility studies on readout topologies for a MHz-framerate continuous wave-mode X-ray detector in 45nm SOI CMOS technology

(#2069)

Pradeep Kalavakuru, Karsten Hansen, Stefano Maffessanti, Christian Reckleben, Inge Diehl, Uttal Ghosh

DESY - Deutsches Elektronensynchrotron, FE, Hamburg, Germany

The authors would like to thank Eric Wüstenhagen for technical discussions.

Abstract

This work presents a concept and feasibility study of a data readout circuit topology for a pixel matrix with in-pixel digitization, enabling continuous wave-mode X-ray detectors operating at MHz frame rates. The key components comprise dedicated high-speed column and row serializers based on custom-designed flip-flops with an optimized timing scheme. The readout topology is tailored to interface with silicon photonics electronic-photonic integrated circuits, enabling high-bandwidth and scalable data transmission. For a 64×64-pixel configuration, simulations confirm achievable frame rates of up to 4.5 MHz with the proposed architecture. At 1.125 MHz, the total readout circuitry consumes 100 µW per pixel at a supply voltage of 1 V. Design trade-offs in area, speed, mechanical integration and power consumption are analyzed, demonstrating the modularity of the architecture for high-frame-rate detector systems.

References
[1] M. Porro *et al.*, "The MiniSDD-Based 1-Mpixel Camera of the DSSC Project for the European XFEL," in *IEEE Transactions on Nuclear Science*, vol. 68, no. 6, pp. 1334-1350, June 2021.
[2] P. Kalavakuru et al., "A 50-Gbps 4-Channel DWDM Transceiver in monolithic 45-nm CMOS Si-Photonics SOI Technology - Concept and Design," *2024 IEEE (NSS/MIC/RTSD)*, Tampa, FL, USA, 2024, pp. 1-1.
[3] S. Maffessanti et al., “A 64k pixel CMOS-DEPFET module for the soft X-rays DSSC imager operating at MHz-frame rates,” Sci. Rep., vol. 13, no. 1, p. 11799, Jul. 2023, doi: 10.1038/s41598-023-38508-9.

NSS-13-102

Characterization of MAGIC: a SiPM Readout ASIC for Monolithic PET Detectors (#2162)

Leonardo Nassi[1,2], **Leonardo Nassi**[1,2], Tommaso D'Incà[2], Tommaso D'Incà[2], Ilenia D'Adda[2], Ilenia D'Adda[2], Giacomo Borghi[1,2], Giacomo Borghi[1,2], Carlo E. Fiorini[1,2], Carlo E. Fiorini[1,2], Marco Carminati[1,2], Marco Carminati[1,2]

[1] INFN - Istituto Nazionale di Fisica Nucleare, Sezione di Milano, Milano, Italy; [2] Politecnico di Milano, Dipartimento di Elettronica, Informazione e Bioingegneria, Milano, Italy

Support by Politecnico di Milano, INFN and EU under project CLARITY is acknowledged.

Abstract

The experimental characterization of MAGIC (Multichannel Analog Gamma- ray detection Integrated Circuit) is here presented. This ASIC is designed in CMOS 110 nm technology and it is intended to readout the current signals coming from SiPMs coupled with monolithic scintillators that are used in medical imaging applications. The circuit is divided into three main sections: an energy path that provides a differential voltage proportional to the energy of the gamma photon, a timing path that gives information about the time of arrival of the photon, and a validation path for event discrimination. For the experimental characterization two PCBs, a mainboard and a carrier, have been designed. In this testing phase all the functionalities have been validated and the key performance of the ASIC have been characterized, in particular the power dissipation (5 mW/channel), the linearity of the energy chain to demonstrate the direct proportionality between the measured charge and the one generated by photon interaction, and the time jitter which affects the propagation delay through the timing path. The results are within the specifications and confirmed by simulations: the linearity error is below 1% and the time jitter is below 20 ps. Such a low value enables its use also in TOF-PET applications.

References

[1] Nassi, L, et al. 2025 “MAGIC: A SiPM Readout ASIC for Monolithic PET Detectors”. *Proc. 2025 IEEE NSS/MIC/RTSD*.

[2] Temes, GC, et al. 1987, “Fast CMOS current amplifier and buffer stage”. *Electronics letters*, 23.13, pp. 696–697.

[3] Buonanno, L, et al. 2021, “GAMMA: A 16-channel spectroscopic ASIC for SiPMs readout with 84-dB dynamic range”, *IEEE Transactions on Nuclear Science*, 68.10, pp. 2559–2572.

NSS-13-104

A Modular Warm Time-Division MultiplexedReadout Platform for SQUID Applications (#2181)

Benjamin A. Reese, Gunther Haller, Shawn W. Henderson, Leonid Sapozhnikov, Zeeshan Ahmed

SLAC National Accelerator Laboratory, Menlo Park, USA

Abstract

Many low-temperature detector experiments require a maintainable replacement for the warm Multi-Channel Electronics used for time-division multiplexed (TDM) readout of superconducting quantum interference device (SQUID) amplifiers. This work presents a modular warm TDM readout platform whose architecture replaces the MCE backplane model with a common FPGA carrier, pluggable analog front ends, simple 12 V board power, and commodity network interfaces. The carrier hosts 16 two-channel fast DACs for 32 waveform outputs and an eight-channel 125 MSPS ADC. In a column-readout configuration, the fast DACs provide SQUID Series Array (SSA) feedback, Stage 1 SQUID (SQ1) bias, and SQ1 feedback for eight columns, while the column front end provides SSA bias, transition-edge sensor (TES) bias, and amplification of SSA return signals. In a row-select configuration, the same carrier drives 32 fully differential analog outputs that support two-level row and chip selection. Shared firmware provides timing distribution, configuration, data streaming, and communications, while role-specific firmware implements row-select sequencing or column ADC processing with SQUID flux-locked-loop feedback. Multiple carriers with attached front ends form scalable readout groups. One carrier in each group is configured as the coordinator and provides the SFP+ 10 Gb/s Ethernet interface to the back-end DAQ and configuration system. The platform has demonstrated 1 MHz row rates with 80 active rows.

NSS-13-106

A Scalable Test Vehicle ASIC in 28-nm CMOS for Cryogenic Device Characterization (#2278)

Panagiotis Zarkos[1], Aldo Pena-Perez[2], Meriam Gay Bautista[1], Maurice Garcia-Sciveres[1], Carl Grace[1], Timon Heim[1], Shawn W. Henderson[2], Brian Lenardo[2], Aikaterini Papadopoulou[1], Lorenzo Rota[2], William Henry[1]

[1] Lawrence Berkeley National Laboratory, Berkeley, USA; [2] Stanford Linear Accelerator National Laboratory, Menlo Park, USA

This work was supported in part by the U.S. Department of Energy under Contract No. DE-AC02-05CH11231

Abstract

This work presents the design and preliminary experimental validation of an ASIC developed as a test vehicle toward a comprehensive cryo-CMOS process development kit (PDK) for a commercially available 28\,nm bulk CMOS process. A CMOS device array utilizing a row-column addressing architecture for rapid characterization of nearly 2000 NMOS and PMOS devices with different geometries and threshold-voltage flavors, has been fabricated and experimentally validated. The complete transistor array can be evaluated using only 16 external wires, making the platform easily adaptable in a dilution fridge for deep-cryo testing. Separate gate-bias control of unselected devices is implemented to minimize leakage current, while a 4-wire sensing scheme improves measurement accuracy. The large-scale cryogenic characterization enabled by this approach represents an important step toward the development of accurate cryo-CMOS PDKs and reliable IC design methodologies for high-energy physics (HEP), quantum computing, and other cryogenic applications in deeply scaled CMOS technologies.

The fabricated die comprises 13 subarrays covering 10 device flavors, including NMOS and PMOS transistors with high-, regular-, low-, and ultra-low-threshold voltage options, native as well as deep N-well NMOS devices. In addition, duplicated regular-Vt arrays are included to evaluate intra-chip process variations. An integrated scan chain selects one transistor at a time, with all remaining device gates independently biased to suppress leakage during measurement. Preliminary results confirm correct scan-chain operation and successful device selection, with measured I_d - V_{gs} characteristics showing expected current scaling across different device geometries. Comprehensive cryogenic characterization from 77K down to mK temperatures is planned as the next step toward completing the cryo-CMOS PDK.

References
[1] X. Xue et al., “CMOS-based cryogenic control of silicon quantum circuits,” Nature, vol. 593, no. 7858, pp. 205–210, May 2021.
[2] D. A. Dwyer et al., “Larpix: Demonstration of low-power 3d pixelated charge readout for liquid argon time projection chambers,” Journal of Instrumentation, vol. 13, no. 10, P10007, 2018.
[3] A. Beckers et al., “Cryogenic characterization of 28 nm bulk cmos technology for quantum computing,” in 2017 47th European Solid-State Device Research Conference (ESSDERC), IEEE, 2017, pp. 62–65
[4] A. Papadopoulou, “Characterization of variability in deeply-scaled fully depleted SOI devices,” 2012.

NSS-13-108

Intermediate-Dose Close-In Phase-Noise Instability in a 55-nm CMOS PLL Irradiated to 100 Mrad(Si) (#2358)

Peng Zheng, Yiming Wu, Chao Lv, Wanchang Wang, Xueye Hu, Jinhong Wang

University of Science and Technology of China, Department of Physics, Hefei, China

Abstract

This work presents an in-situ total ionizing dose (TID) characterization of a 2.56 GHz charge-pump phase-locked loop (PLL) implemented in a commercial 55 nm CMOS process for high-energy physics front-end clocking applications. The chip was irradiated with X-rays up to 100 Mrad(Si), while phase noise, integrated jitter, supply current, and lock status were monitored throughout dose accumulation. Although the endpoint degradation is limited, with the RMS jitter integrated from 1 kHz to 10 MHz increasing from approximately 550 fs to 700 fs after 100 Mrad(Si), the in-situ measurements reveal a more critical intermediate-dose effect. Around 10 Mrad(Si), the

PLL exhibits strong close-in phase-noise instability, mainly from 1 kHz to 100 kHz offset frequency. Standalone VCO measurements show no similar fluctuation, indicating that the observed behavior is unlikely to originate from the LC-VCO and is more consistent with radiation-enhanced low-frequency noise in the loop-control path. These results show that final-dose measurements alone may underestimate the worst-case phase-noise degradation of PLLs under TID exposure.

References
[1] B. Razavi, "Phase-Locking in High-Performance Systems: From Devices to Architectures," IEEE Solid-State Circuits Magazine, vol. 11, no. 3, pp. 8–18, Summer 2019.
[2] D. M. Fleetwood, "1/f Noise and Defects in Microelectronic Materials and Devices," IEEE Trans. Nucl. Sci., vol. 62, no. 4, pp. 1462–1486, Aug. 2015.
[3] T. Komawaki, M. Yabuuchi, R. Kishida, J. Furuta, T. Matsumoto and K. Kobayashi, "Circuit-level simulation methodology for Random Telegraph Noise by using Verilog-AMS," 2017 IEEE International Conference on IC Design and Technology (ICICDT), Austin, TX, USA, 2017, pp. 1-4, doi: 10.1109/ICICDT.2017.7993526.
[4] R. Wang et al., "Too Noisy at the Bottom? —Random Telegraph Noise (RTN) in Advanced Logic Devices and Circuits," 2018 IEEE International Electron Devices Meeting (IEDM), San Francisco, CA, USA, 2018, pp. 17.2.1-17.2.4, doi: 10.1109/IEDM.2018.8614594.

NSS-13-110

A Low-Noise Multi-Channel Readout ASIC for High-Purity Germanium Detectors (#2413)

Li He[1,2], Yulan Li[1,2], Yang Tian[1,2], Yuanjing Li[1,2]

[1] Tsinghua University, Department of Engineering Physics, Beijing, China; [2] Ministry of Education, Key Laboratory of Particle & Radiation Imaging (Tsinghua University), Beijing, China

Abstract

Multi-electrode High-Purity Germanium (HPGe) detectors are promising for high-count-rate gamma spectroscopy, but traditional JFET readouts suffer from excessive power (~200 mW per channel, >3.2 W for 16 channels), bulky volume, and severe outgassing. This paper presents a low-noise, high-integration readout ASIC implemented in TSMC 0.18μm CMOS, featuring 18 P+ and 18 N+ channels. Each channel consists of a continuous-feedback charge-sensitive amplifier (CSA), a CR-RC shaper employing ICON cells (1 GΩ equivalent resistance) for large time constants, and a class-AB buffer. A PMOS-input folded-cascode topology is utilized for optimal noise performance. Room-temperature measurements demonstrate a total power consumption of 594 mW (180 mA @ 3.3 V) for all 36 channels, presenting a significant advantage over JFET solutions. The ASIC achieves a gain of 11.3 mV/fC, an integral non-linearity (INL) < 1% over 40 keV to 1.5 MeV, and a rise time of ~65 ns. With a 10 μs shaping time, the equivalent noise charge (ENC) is approximately 58 e^- at zero input capacitance. Future work will focus on cryogenic evaluation with HPGe detectors and noise slope characterization.

References
[1] B. VanDevender, M. Dion, J. Fast, et al., High purity germanium spectroscopy at rates in excess of 106 events/s, IEEE Transactions on Nuclear Science 2014, 61(5): 2619-2627.
[2] M. Amman, High purity germanium based radiation detectors with segmented amorphous semiconductor electrical contacts: fabrication procedures, arXiv:2006.05471,2020. 07.
[3] Gianluigi De Geronimo, Paul O'Connor,A CMOS detector leakage current self-adaptable continuous reset system: Theoretical analysis,Nuclear Instruments and Methods in Physics Research Section A: Accelerators, Spectrometers, Detectors and Associated Equipment,Volume 421, Issues 1–2,1999,Pages 322-333

[4] G. De Geronimo, P. O'Connor and J. Grosholz, "A generation of CMOS readout ASICs for CZT detectors," *1999 IEEE Nuclear Science Symposium. Conference Record. 1999 Nuclear Science Symposium and Medical Imaging Conference (Cat. No.99CH37019)*, Seattle, WA, USA, 1999, pp. 518-528 vol.1
[5] G. De Geronimo *et al.*, "Front-end ASIC for a GEM based time projection chamber," in *IEEE Transactions on Nuclear Science*, vol. 51, no. 4, pp. 1312-1317, Aug. 2004
[6] C. Fiorini, M. Porro and T. Frizzi, "An 8-Channel DRAGO Readout Circuit for Silicon Detectors With Integrated Front-End JFET," in *IEEE Transactions on Nuclear Science*, vol. 53, no. 5, pp. 2998-3003, Oct. 2006
[7] C. Fiorini and M. Porro, "Integrated RC cell for time-invariant shaping amplifiers," in *IEEE Transactions on Nuclear Science*, vol. 51, no. 5, pp. 1953-1960, Oct. 2004
[8] W. M. C. Sansen, *Analog Design Essentials*. Dordrecht, The Netherlands: Springer, 2006.

NSS-13-112

A precision bandgap reference with improved noise performance for spectroscopy ASICs in 180 nm CMOS technology (#2577)

Yinhe Zhu[1], Filippo Mele[1,2], Giuseppe Bertuccio[1,3]

[1] Politecnico di Milano, Department of Electronics, Information and Bioengineering, Milano, Italy; [2] Istituto Nazionale di Astrofisica (INAF), Istituto di Astrofisica e Planetologia Spaziali (IAPS), Roma, Italy; [3] Istituto Nazionale di Fisica Nucleare (INFN), Sezione di Milano, MIlano, Italy

Abstract

We present the design of a low-noise and low-offset bandgap reference (BGR) circuit intended for front-end readout ASICs for semiconductor radiation detectors (SRDs). To suppress low-frequency noise and reduce process-induced dispersion of the reference voltage and proportional-to-absolute-temperature (PTAT) current, a voltage-domain BGR architecture employing local positive feedback is designed [1]. The circuit technique suppresses the dominant noise and offset contributions originating from the error amplifier. Compared to a conventional topology operating at the same power consumption of 50 µW, the proposed circuit achieves a tenfold reduction in low-frequency noise. The circuit is implemented in a 180 nm deep N-well CMOS process from amsOSRAM and operates from a 1.8 V supply voltage, occupying a total area of 0.024 mm^2. Post-layout simulation results show a tenfold reduction in the 1/f noise, a voltage power spectral density of 200 nV/√Hz from 100 Hz up to 1 MHz and a DC accuracy of 0.06 %. In addition, the proposed BGR achieves a temperature coefficient of 30 ppm/°C over the temperature range from -40 °C to 125 °C.

References

[1] Liu, L. et al., 2019, “A 3.6-µvrms noise, 3 ppm/◦c tc bandgap reference with offset/noise suppression and five-piece linear compensation,” *IEEE Transactions on Circuits and Systems I: Regular Papers*, vol. 66, no. 10, pp. 3786–3796.

NSS-01-116

Photon Counting with FPGA Gigabit Transceivers: A Proof-of-Concept SiPM Readout for TOF-PET (#2884)

Tarun Prakash, Joshua W. Cates, Woon-Seng Choong, Marcos Turqueti

Lawrence Berkeley National Laboratory, Berkeley, USA

This work was supported in part by NIH Research under Grant R01EB033402

Abstract

Achieving 100ps FWHM coincidence time resolution (CTR) in time-of-flight positron emission tomography (TOF-PET) is benefited by electronics that can resolve individual scintillation photons with high temporal precision. We report a proof-of-concept readout in which silicon photomultiplier (SiPM) single-photon pulses are discriminated by a high-speed comparator and digitized directly by GTY transceivers of a Xilinx Virtex UltraScale XCVU095 FPGA (VCU1287 board) at 16Gbps, encoding photon arrival times as bit positions with 62.5ps resolution. Signal integrity analysis showed that an initial LVDS comparator produced common-mode voltage and differential swing below GTY receiver specifications; switching to a CML comparator substantially reduced bit errors. Room-temperature SiPM dark count bitstreams were captured with a random FPGA clock trigger and post-processed to produce a finger plot showing 1-, 2-, and 3-photoelectron peaks, providing a preliminary validation of the bitstream-based photon-counting concept. These results support the feasibility of FPGA gigabit transceivers as scalable digitizers for single-photon pulse streams in next-generation TOF-PET detector modules.

References

[1] S. Surti and J. S. Karp, “Update on latest advances in time-of-flight PET,” Physica Medica, vol. 80, pp. 251–258, 2020, doi: 10.1016/j.ejmp.2020.10.031.

[2] S. Pourashraf, A. Gonzalez-Montoro, J. Y. Won, M. S. Lee, J. W. Cates, Z. Zhao, J. S. Lee, and C. S. Levin, “Scalable electronic readout design for a 100 ps coincidence time resolution TOF-PET system,” Phys. Med. Biol., vol. 66, no. 8, Apr. 2021, doi: 10.1088/1361-6560/abf1bc.

[3] S. Pourashraf, A. Gonzalez-Montoro, M. S. Lee, J. W. Cates, J. Y. Won, J. S. Lee, and C. S. Levin, “Investigation of electronic signal processing chains for a prototype TOF-PET system with 100-ps coincidence time resolution,” IEEE Trans. Radiat. Plasma Med. Sci., vol. 6, no. 6, pp. 690–696, Jul. 2022, doi: 10.1109/TRPMS.2021.3124756.

[4] S. Pourashraf, J. W. Cates, and C. S. Levin, “A scalable dynamic TOT circuit for a 100 ps TOF-PET detector design to improve energy linearity and dynamic range,” IEEE Trans. Radiat. Plasma Med. Sci., vol. 8, no. 3, pp. 237–247, Mar. 2024, doi: 10.1109/TRPMS.2023.3344399.

[5] Analog Devices, “Rail-to-Rail, Very Fast, 2.5 V to 5.5 V, Single-Supply CML Comparators,” ADCMP606/ADCMP607 datasheet, Rev. C, 2016. [Online]. Available: https://www.analog.com/media/en/technical-documentation/data-sheets/ADCMP606_607.pdf

NSS-13-118

A 640 MHz Phase Locked Loop for High Energy Physics Environment in 28nm CMOS Bulk (#3108)

Matteo Chiariello[1], Fabio D'Ottavi[2], Luca Palini[2], Mirco Malanchini[1], Marco Privitera[3], Ciro Esposito[1], Luca Gelmi[2], Valeria Vadalà[1], Alberto Stabile[4], Marcello De Matteis[1]

[1] University of Milano-Bicocca, Milano, Italy; [2] University of Pavia, Pavia, Italy; [3] University of Catania, Catania, Italy; [4] University of Milano, Milano, Italy

This work is supported by the IGNITE project (INFN Ground-up INITiative-on micro- Electronics developments) of the Italian National Institute for Nuclear Physics (INFN), and PNRR(National Recovery and Resilience Plan) Etic (Einstein Telescope Infrastructure Consortium) project.

Abstract

This work presents a Phase-Locked Loop (PLL) integrated in 28 nm Bulk CMOS HPC+ technology, developed within the INFN Ground-up iNITiative for Electronics developments (IGNITE) project. It is designed to generate low-jitter clock signals at 40 MHz for high-time-resolution charge measurement, and at 640 MHz for high-speed data serialization.

In High Energy Physics, mixed-signal circuits must withstand severe radiation damage, both cumulative, in the form of Total Ionizing Dose (TID) up to 1 GRad, and event-driven, in the form of Single Event Effects (SEEs) induced by particles with Linear Energy Transfer (LET) values up to 60 MeV·cm²/mg. To address these effects, the PLL was implemented using radiation- hardened-by-design-oriented techniques. Experimental validation in time and frequency domains confirmed cycle-to-cycle jitter values of 11.437 ps RMS and 1.95 ps RMS for the 40 MHz and 640 MHz outputs, respectively. Power consumption is 8.4 mA from a 900 mV supply. The total active area is 0.0174 mm².

References

[1] S. Cadeddu et al., “Recent developments in the IGNITE project on front-end design in CMOS 28-nm technology,” JINST, Jan. 2024

[2] F. Resta et al., ”1GigaRad TID impact on 28nm HEP analog circuits,” 2017 13th Conference on Ph.D. Research in Microelectronics and Electronics (PRIME)

[3] L. Gelmi et al., ”28 nm MOS Transistor SPICE BSIM Model based on Equivalent Gate Oxide Capacitance supporting Electrical Effects of 1-Grad Total Ionizing Dose,” 2024 IEEE Nuclear Science Symposium (NSS)

[4] M. Chiariello et al., ”A 900-MHz Hardening-by-Design Voltage Controlled Oscillator in 28nm CMOS,” 2024 31st IEEE International Conference on Electronics, Circuits and Systems (ICECS)

[5] G. C. Messenger, ”Collection of Charge on Junction Nodes from Ion Tracks,” in IEEE Transactions on Nuclear Science

[6] G. Borghello, ”Radiation effects on 28nm CMOS technology”, 2023 CERN 28nm Mixed-Signal Design Workshop

NSS-13-120

Machine-Protection System for the PIP-II Linear Accelerator: Architecture and Data Processing Schemes (#1193)

Jinyuan Wu, Arden Waner, Jonathan Eisch, Mark Austin

Fermi National Accelerator Laboratory, Batavia, USA

This manuscript has been authored by Fermi Forward Discovery Group, LLC under Contract No. 89243024CSC000002 with the U.S. Department of Energy, Office of Science, Office of High Energy Physics.

Abstract

PIP-II at Fermilab features a brand-new, 800 MeV leading-edge Linear Accelerator (Linac) that will enable the Fermilab complex to deliver more than a megawatt of beam power to the Long Base-line Neutrino Facility (LBNF), requiring a robust Machine Protection System (MPS) to prevent beam-induced damage to delicate cryomodules and vacuum components. Signals in various accelerator components, in both analog and digital format, are collected and processed to assest the operating conditions of the accelerator. In the situation a potential damage is foreseen, the beam permit signal will be drop. A critical element of this system is the fast Analog Machine Protection System, a high-bandwidth platform designed for real-time beam loss monitoring. The system utilizes a modular, FPGA-based architecture to digitize signals from beam-sensing devices, such as AC Current Transformers (ACCTs), non-invasive Ring Pickups (RPUs) and beam scrapers. To eliminate both high frequency as well as 60 Hz noise that might be picked up in the industrial environment, data processing schemes beyond regular digital filtering are planned and implemented.

NSS-13-122

Comparison of discrete non-gated charge-to-time converters for SPECT application (#1264)

Pauline Lafoux, Nicolas Chevillon, Christian Fuchs, Tom Robert, Virgile Bekaert, Frederic Boisson

Université de Strasbourg, CNRS, Institut Pluridisciplinaire Hubert Curien UMR7178, Strasbourg, France

Abstract

In the context of tomographic imaging, a simple and modular readout combines non-gated charge-to-time converters (QTC), composed of few discrete analog components, and time-to-digital converters implemented in FPGA. The choice of discrete QTC's architecture depends on a compromise between number of components per channel, charge RMS resolution and dead time. Because temperature drift can lead to high measurement error and temperature compensation circuit costs lot of surface per channel, another key parameter to consider is the QTC's

response stability to variation of temperature. This study compares three continuous-reset QTC topologies, named after their feedback circuit (RC, diode, and MOSFET). Each circuit is implemented with discrete components and tested in a dynamic range from 2 pC to 35 pC, for a Single-Photon Emission Computed Tomography (SPECT) application. Unlike previous work, we compare them on conventional figures of merit and also evaluate their TOT-Q characteristics stability for temperature variation over 20 °C. Experimental results show that the RC QTC reduces dead time by a factor of 2 compared to linear designs, while the diode-QTC and MOSFET QTC achieve sub-0.1pC charge RMS resolution. However, the MOSFET QTC exhibits a 1.2 %/°C relative error due to temperature-dependent drain current. And diode-QTC requires a temperature compensation circuit to remain stable as RC-QTC (<0.2 %/°C).

References

[1] C. Parl et al., IEEE TNS, 59(5), 1809–1814, 2012.
[2] S. Liu et al., NIM-A, 621(1), 513-518, 2010.

NSS-13-124

150 Gbps data transfer Bay simulating Agata detector Readout (#1274)

Nabil Karkour, Xavier LAfay

Université Paris–Saclay, CNRS/IN2P3, IJCLab 91405 Orsay, France, Electronic, Orsay, France

The authors acknowledge the support of the AGATA collaboration in the work described in this publication and who helped us financially to achieve our goals. The 150 Gbps Bay development have been financed by CNRS, IN2P3, France. Special thanks to Gustav Vinther-Jørgensen and to Andrea Triossi who supported the STARE Proof Of Concept. . Many thanks would like to thank the IJCLAB Orsay AGATA team to make this project successful.

Abstract
The Advanced Gamma Tracking Array (AGATA) spectrometer consists of 180 high-purity germanium detectors, each segmented into 38 segments. The trigger rate of each detector can go up to 50 kHz. The data transfer rate per detector ranges from 5 to 8 Gbps. Moreover, continuous monitoring data is sent over the network using another link, resulting in a total outgoing data rate of approximately 18 Gbps using User Datagram Protocol (UDP). The total transfer rate of 180 detectors can go up to 3.2 Tbps during a period of 1 to 3 weeks of continuous operation. The bay is designed in parallel with the Phase 2 front-end electronics development and production so that the complex readout system from these electronics to the computer farm is validated. The 10 Gbps UDP transfer is not totally secure; at such a data readout speed, the computer receiver uses most of its processing and memory capacities. The bay simulates the Phase 2 electronics data readout of more than 12 AGATA detectors using the Serial Transfer and Readout over Ethernet (STARE) modules. The bay is designed to validate the complex readout system from the Phase 2 electronics to the computer farm and to test the overall data acquisition system reliability. Data quality is mandatory for the scientific results, and any data loss could degrade the physics case and the system efficiency. This article will show how the bay simulates the multiple-source data readout to the computer farm at over 100 Gbps.

References

[1] S. Akkoyun, et al., Nuclear Instruments and Methods in Physics Research Section A: Accelerators, Spectrometers, Detectors and Associated Equipment 668, 26 (2012). DOI 10.1016/j.nima.2011.11.081
[2] N. Karkour et al., "A Development of a 40-Gb/s Readout Interface STARE for the AGATA Project," in IEEE Transactions on Nuclear Science, vol. 68, no. 8, pp. 2005-2011, Aug. 2021, doi: 10.1109/TNS.2021.3086684.
[3] J. Collado *et al.*, "A new preprocessing and control board for the phase 2 electronics of AGATA experiment," *2016 IEEE-NPSS Real Time Conference (RT)*, Padua, 2016, pp. 1-4, doi: 10.1109/RTC.2016.7543161.
[4]
Collado, J., Capra, S., Pullia, A. *et al.* AGATA phase 2 advancements in front-end electronics. *Eur. Phys. J. A* **59**, 133 (2023). https://doi.org/10.1140/epja/s10050-023-01045-0

NSS-13-126

Performance Testing and Characterization of CPRE12-64CZT: A Low-Noise 64-Channel Readout ASIC for 3-D Position-Sensitive CdZnTe Detectors (#1303)

Haolong Liao[1,2], Ke Wang[1], Na Wng[1], Jiale Cai[1,3], Xiaoxuan Li[1,2], Xiaopan Jiang[1], Cunfeng Wei[1,2], Zhiming Zhang[1,2], Lei Shuai[1,3], Yao Yang[1], Yi Liu[1,2], Long Wei[1,2], Xiaohui Li[1,3]

[1] Institute of High Energy Physics, Chinese Academy of Sciences, Beijing, China; [2] School of Nuclear Science and Technology, University of Chinese Academy of Sciences, Beijing, China; [3] Jinan Laboratory of Applied Nuclear Science, Jinan, China; [4] CAEA Center of Excellence on Nuclear Technology Applications for Nuclear Detection and Imaging, Beijing, China

This work was supported in part by the National Key Research and Development Program of China under Grant 2023YFF0721700.

Abstract

CPRE64 is a 64ch readout ASIC specifically optimized for three-dimensional position-sensitive Cadmium–Zinc–Telluride (CZT) detectors, developed from the CPRE32 . The chip is capable of reading both cathode and anode signals, allowing it to match pixelated, virtual Frisch-grid CZT or silicon detectors. Each channel integrates a low-noise charge-sensitive amplifier (CSA), high-order shaper, peak detect-and-hold (PDH) circuit for energy measurement, and sample-and-hold circuit for timing measurement. Power consumption is below 5 mW per channel. The ASIC incorporates a layout designed for SEE hardening, resulting in a die area of 7.10 mm × 12.44 mm^2. The chip layout features pins on three sides for permitting expansion to 128 channels . Experimental results show: when a CZT sensor connected and biased, the electronic resolution better than 150 e^-(rms) for anode channel, better than 250 e^-(rms) for cathode channel. The readout channel exhibits linearity with ≤1.5% integral nonlinearity, with a maximum dynamic range reaching 350 fC. Spectral measurements applying a simple depth correction demonstrated a single-pixel resolution of 0.78%(FWHM) at 662 keV.

References
[1] Y. Eisen and A. Shor, “CdTe and CdZnTe materials for room-temperature X-ray and gamma ray detectors,” Journal of Crystal Growth, vol. 184–185, pp. 1302–1312, Feb. 1998, doi: 10.1016/S0022-0248(98)80270-4.
[2] V. Ivanov, L. Alekseeva, P. Dorogov, and A. Loutchanski, “Correlation between quality of CZT crystals and spectrometric performance of hemispherical radiation detectors,” in IEEE Symposium Conference Record Nuclear Science 2004., Oct. 2004, pp. 4415–4419. doi: 10.1109/NSSMIC.2004.1466864.
[9] P. N. Luke, “Unipolar charge sensing with coplanar electrodes-application to semiconductor detectors,” IEEE Transactions on Nuclear Science, vol. 42, no. 4, pp. 207–213, Aug. 1995, doi: 10.1109/23.467848.

[4] Y. Cui, A. Bolotnikov, G. Camarda, A. Hossain, G. Yang, and R. B. James, "CZT virtual Frisch-grid detector: Principles and applications," in 2009 IEEE Long Island Systems, Applications and Technology Conference, May 2009, pp. 1–5. doi: 10.1109/LISAT.2009.5031559.
[8] F. P. Doty et al., "Pixellated CdZnTe detector arrays," Nuclear Instruments and Methods in Physics Research Section A: Accelerators, Spectrometers, Detectors and Associated Equipment, vol. 353, no. 1, pp. 356–360, Dec. 1994, doi: 10.1016/0168-9002(94)91675-6.
[6] F. Zhang, C. Herman, Z. He, G. De Geronimo, E. Vernon, and J. Fried, "Characterization of the H3D ASIC Readout System and 6.0 cm3 3-D Position Sensitive CdZnTe Detectors," IEEE Transactions on Nuclear Science, vol. 59, no. 1, pp. 236–242, Feb. 2012, doi: 10.1109/TNS.2011.2175948.
[9] Y. Zhu and Z. He, "Performance of Larger-Volume 40 × 40 × 10- and 40 × 40 × 15-mm³ CdZnTe Detectors," IEEE Transactions on Nuclear Science, vol. 68, no. 2, pp. 250–255, Feb. 2021, doi: 10.1109/TNS.2021.3052133.
[9] L. A. Ocampo Giraldo et al., "Arrays of Position-Sensitive Virtual Frisch-Grid CdZnTe Detectors: Results From a 4 $\times$ 4 Array Prototype," IEEE Transactions on Nuclear Science, vol. 64, no. 10, pp. 2698–2705, Oct. 2017, doi: 10.1109/TNS.2017.2743160.
[7] Y. Kim, K. Shin, A. Bolotnikov, and W. Lee, "Positional correction of a 3D position-sensitive virtual Frisch-grid CZT detector for gamma spectroscopy and imaging based on a theoretical assumption," Nuclear Engineering and Technology, vol. 55, no. 5, pp. 1718–1733, May 2023, doi: 10.1016/j.net.2023.01.014.

NSS-13-128

Fast timing performance of a front-end ASIC designed for high purity germanium strip detectors (#1504)

Clio Sleator[1], Eric A. Wulf[1], Gianluigi De Geronimo[2,3], Alex Lowell[4], Brent Mochizuki[4], Jarred M. Roberts[5], Field R. Rogers[4], John A. Tomsick[4]

[1] U.S. Naval Research Laboratory, Space Science Division, Washington, USA; [2] DG Circuits, Syosset, USA; [3] Stony Brook University, Stony Brook, USA; [4] University of California Berkeley, Space Science Division, Berkeley, USA; [5] University of California San Diego, Department of Astronomy and Astrophysics, La Jolla, USA

This work was supported by NASA under Contract 80GSFC21C0059.

Abstract

We have developed an application-specific integrated circuit (ASIC) to read out high-purity germanium (HPGe) strip detectors, which will be used as the front-end readout for the HPGe double-sided strip detectors flown aboard the Compton Spectrometer and Imager NASA Small Explorer mission. Here we present an overview of the ASIC, focusing on its fast timing capabilities. The ASIC has 32 channels, each of which contains two shaping circuits to allow for high-resolution measurements of both the charge collected, which is proportional to the energy deposited, and the time of collection. By taking the difference between the charge carrier arrival times on each side of the detector, we can determine the interaction depth in the detector. We evaluated the performance of the ASICs using engineering models of the COSI flight boards. To assess the timing performance in particular, we used a dual-channel function generator to pulse two ASICs, with one channel delayed from the other by various amounts. We also present preliminary measurements of the ASIC timing performance on a COSI-like detector using a fan beam collimator placed to illuminate discrete depths.

NSS-13-130

A Fully FPGA-Based 3D (x–y–t) Imager with 24 µm Spatial Resolution for Cross Delay-Line Detectors (#1821)

Fabio Garzetti[1], Nicola Lusardi[1,2], Andrea Costa[1], Enrico Ronconi[1], Gabriele Fiumicelli[1], Angelo Geraci[1,2], Marco Cautero[3,4], Matija Colja[4], Sergio Carrato[5], Luigi Stebel[4], Rudi Sergo[4], Giuseppe Cautero[4,6]

[1] Politecnico di Milano, Dipartimento di Elettronica, Informazione e Bioingegneria, Milano, Italy; [2] INFN, Milano, Milano, Italy; [3] University of Trieste, Department of Physics, Trieste, Italy; [4] Elettra Sincrotrone, Trieste, Trieste, Italy; [5] University of Trieste, DIA, Trieste, Italy; [6] INFN, Trieste, Trieste, Italy

Abstract

Advanced X-ray sources such as synchrotrons and Free Electron Lasers (FELs) enable ultrafast time-resolved experiments, requiring acquisition systems with event-by-event timing and spatial resolution. Cross Delay-Line (CDL) detectors are well suited for simultaneous time–space encoding via time-to-space conversion. Standard high-performance architectures rely on Application-Specific Integrated Circuit (ASIC)-based Time-to-Digital Converters (TDCs) or Time-to-Amplitude Converters (TACs), followed by Field-Programmable Gate Array (FPGA) processing, but lack reconfigurability. We present a high-performance, fully FPGA-based reconfigurable acquisition system implementing both the TDC and real-time 3D (x, y, t) reconstruction in programmable logic, eliminating ASIC dependence while maintaining state-of-the-art performance and enabling full adaptability to experimental conditions. The system employs a two-FPGA architecture, with a 8-channel TDC and a dedicated reconstruction unit. The TDC achieves 12 ps rms timing precision, 9.6 ns dead time, and 4 ps integral non-linearity, corresponding to 24 and 27 µm spatial resolution on the CDL for the x and the y coordinates, respectively. This approach enables scalable, high-throughput, fully digital, and reconfigurable time-resolved imaging with spatial and temporal resolution comparable to state-of-the-art ASIC-based solutions.

References

[1] O. Siegmund et al., “Cross delay line detectors for high time resolution astronomical polarimetry and biological fluorescence imaging,” in IEEE Nuclear Science Symposium Conference Record, 2005, vol. 1, Oct. 2005, pp. 448–452, iSSN: 1082-3654

[2] O. Seigmund et al., “Delay Line Detectors for the UVCS and Sumer Instruments on the SOHO Satellite,” Proceedings of SPIE - The International Society for Optical Engineering, vol. 2280, Jun. 1994.

[3] O. Jagutzki et al., “A position and time-sensitive photon-counting detector with delay-line read-out,” in Optical Sensing Technology and Applications, vol. 6585. SPIE, May 2007, pp. 391–401.

[4] G. Cautero et al., “A two-dimensional detector for pump-and-probe and time resolved experiments,” Nuclear Instruments and Methods in Physics Research Section A: Accelerators, Spectrometers, Detectors and Associated Equipment, vol. 595, no. 2, pp. 447–459, Oct. 2008. [Online]. Available: https://linkinghub.elsevier.com/retrieve/pii/S0168900208009121

NSS-13-132

High-performance preamplifier for spectroscopy systems based on High-Purity Germanium detectors (#1999)

Fernando Ojeda, **Fernando Ojeda**, Brian Nelson, Brian Nelson

AMETEK ORTEC, Oak Ridge, USA

The authors wish to acknowledge the valuable contributions to this work from the Engineering, Production, and Detector Test teams.

Abstract

Preamplifiers play a primary role in the resolution, linearity, and sensitivity of ionizing radiation spectrometers, converting the small charges collected by photo detectors into usable voltage signals that are further amplified, digitized, and processed to obtain the intended spectra. Additionally, the accuracy and thermal stability of such charge-to-voltage conversion must be assured to keep a constant performance over time and across different detectors, wiring configurations, and radiation scenarios. This article presents electronic simulations and the first laboratory results showing recent improvements in a new preamplifier designed for High-Purity Germanium spectroscopy systems, in terms of dynamic response, noise, linearity, thermal stability, symmetry, tolerance to reactive loads, piling-up, saturation recovery, and power consumption. The impact of these improvements is also discussed.

References

[1] H. Spieler, Semiconductor Detector Systems, Oxford, UK: Oxford University Press, 2005.

[2] T.R. Twomey, R.M. Keyser, M.L. Simpson, and S.E. Wagner, H. Spieler, “High-Count-Rate Spectroscopy with Ge Detectors: Quantitative Evaluation of the Performance of High-Rate Systems,” 2002, ORTEC [online]. Available https://www.ortec-online.com/. Accessed on: May 12th, 2026

[3] Ronald M. Keyser and Timothy R. Twomey, “Optimization of pulse processing parameters for HPGe gamma-ray spectroscopy systems used in extreme count rate conditions and wide count rate ranges,” Journal of Radioanalytical and Nuclear Chemistry, vol. 296, pp. 503-508, 2013.

NSS-13-134

MAPSSIC: Toward a Wireless Implantable Positron Probe for Molecular Neuroimaging of Awake and Freely Moving Rats (#2143)

Mathieu Dupont[1], Samir El katera[3,2], Franck Agnese[5], Luis Ammour[6], Jérome Baudot[5], Sandrine Bouvard[7], Fabrice Gensolen[1], Maciej Kachel[5], Jérome Laurence[1], Patrick Pangaud[1], Teo Weicherding[1], Luc Zimmer[7], Phillipe Lanièce[3,4], Marc Antoine Verdier[3,4], Christian Morel[1]

[1] Aix-Marseille Univ, CNRS/IN2P3, CPPM, Marseille, France; [2] Centre de Radiothérapie St. Louis, Toulon, France; [3] Université Paris Cité, CNRS/IN2P3, IJCLab, Orsay, France; [4] Université Paris Saclay, CNRS/IN2P3, IJCLab, Orsay, France; [5] Université de Strasbourg, CNRS, IPHC UMR 7178, Strasbourg, France; [6] Nantes Université, CHU Nantes, Nantes, France; [7] Universitée Lyon 1, CERMEP, CNRS, INSERM, HCL, Lyon, France

Abstract

Correlating molecular neuroimaging with behavior in preclinical models requires acquisitions in awake and freely moving animals, whereas most current positron emission tomography procedures are still performed under anesthesia.

The MAPSSIC project addresses this limitation with an implantable intracerebral probe based on monolithic active pixel sensors (MAPS) for direct positron detection in targeted brain structures of awake, freely moving rats, thereby avoiding the pharmacological bias of anesthesia. Following sensor characterization and simulation studies previously reported, this contribution presents the transition to a fully wireless system. The acquisition chain combines four IMIC2 sensor chips, a STM32L4 microcontroller, 1 Gbit on-board flash memory, and a bidirectional 2.4 GHz radio link to a Raspberry Pi ground station. The complete software stack is implemented in Rust with the Embassy asynchronous framework, providing memory safety and concurrent peripheral management without dynamic allocation. Planned validation with ^{18}F, ^{11}C phantoms, and anesthetized implanted rats will mark the shift from sensor feasibility to system-level wireless validation.

NSS-13-136

Single-Shot Precision Decomposition of a 64-Channel FPGA TDC for TOF-PET (#2381)

Giancarlo Sportelli[1,2], Matteo Morrocchi[1,2], Nicola Belcari[1,2]

[1] University of Pisa, Department of Physics "E. Fermi", Pisa, Italy; [2] INFN, Sezione di Pisa, Pisa, Italy

The authors would like to thank TEDIEL s.r.l. for the technical support on FPGA TDC architecture implementation and validation.

Abstract
We report a channel-level characterization of a calibrated 64-channel FPGA Time-to-Digital Converter (TDC) for fast-timing TOF-PET, with explicit decomposition of the single-shot precision (SSP) into quantization and jitter contributions. The TDC is implemented on an Altera Cyclone 10 GX device and operates with a 256-tap, 64-bin tapped-delay-line (TDL) at ~400 MHz, calibrated offline via code-density histograms. Two implementation strategies are compared: the default arithmetic carry-chain inference, and a placement-aware variant in which the TDLs are constrained to regular structures. Across all 64 channels, controlled placement reduces the ultra-bin width from 160 ± 76 ps to 101 ± 12 ps, the equivalent LSB (LSBeq) from 83 ± 32 ps to 63 ± 4 ps, and the quantization noise σ_Q from 24.5 ± 7.3 ps rms to 18.1 ± 0.8 ps rms. The placement-constrained implementation also substantially improves channel-to-channel uniformity. The constrained routing increases σ_{jitter} which makes jitter the dominant SSP contribution once σ_Q is reduced. A system-level projection onto previously characterized UTOFPET monolithic modules indicates that the TDC accounts for 59% of the measured CRT² in a 12 mm LYSO/256-channel module (CRT ≈ 150 ps FWHM), but only ~8% in 16–20 mm BGO/64-channel modules (CRT ≈ 400 ps FWHM). This identifies σ_{jitter} as the dominant architectural ceiling and motivates wave-union/multi-TDC averaging or finer-node FPGAs for full LYSO exploitation.

NSS-13-138

Education kit for radiation measurements (#2477)

Masaharu Nomachi

The University of Osaka, RCNP, Ibaraki/Osaka, Japan

This work is supported by IEEE/NPSS Initiative.

Abstract
We have been organizing schools on radiation measurements for students from ASEAN countries. Hands-on experience with radiation measurements is very important, and we prepare radiation measurement systems for practical exercises.
To host as many students as possible, we considered organizing the schools in ASEAN countries. However, the shipping cost of the equipment was extremely high. As a result, we could not conduct hands-on exercises on radiation measurement.
Driven by recent large-scale experiments, electronics for radiation measurements have become compact, highly integrated, and low-cost. This development now makes it possible to carry equipment to schools.
Today, compact detector systems are available at affordable prices, making it much easier to conduct practical radiation measurement exercises in schools.
However, modern compact electronics have introduced a new problem: they are too small to probe easily with an oscilloscope. In modern electronics, waveform processing is increasingly performed digitally. Nevertheless, we

believe that analogue processing remains important and highly educational for students. This motivated us to develop electronics specifically for educational purposes.
We have developed an “education kit” for radiation measurement education. By plugging in a SiPM and a small scintillator crystal module, the board functions as a complete radiation measurement system. An on-board FPGA interfaces with a PC through a USB connection. The board is the size of a Raspberry Pi board. Optionally, it can be plugged onto a Raspberry Pi.
Although the board is compact, it provides sufficient space for probing signals. The design of the board will be released as open-source hardware. Students can modify the design and develop their own versions of the board. The “education kit” will serve as an entry point to radiation measurement electronics.

NSS-13-140

Preliminary Test Results on Latest Version of FESA Readout ASIC for TOF-PET Detectors (#2565)

Yuhao Yang, Yonggang Wang, Xinchi Xu, Xiang Zhang, Huandong Huang

University of Science and Technology of China, Department of Modern Physics, Hefei, China

Abstract
The latest version of the low-power 64-channel Front-End readout chip for SiPM Array (FESA4.0) with the preliminary test results is presented in this paper. Using a row-column summing readout method, FESA compresses the 64 input signals into 16 output digital pulses, which then is digitized by the followed field programmable gate array (FPGA). In the pathway of each summing output, there are two threshold current comparators used for signal pickup, one with a low threshold for signal timing and the other with a high threshold for signal validation. Since the signal amplitude is converted into the pulse time-width via the linear discharge method, both the signals timing and amplitude can be measured by the time-to-digital converter (TDC) in the FPGA. The new version of FESA incorporates a time-over-threshold (TOT) measurement capability, which allows to identify the signals originating from different scintillators. The chip offers prominent advantages of simple architecture, low power consumption, and high performance. Through electronics tests, FESA4.0 has a measurement linearity of 99. 1% with a dynamic range of 140. The intrinsic time measurement precision is measured better than 30 ps. Combined with a TOF-PET detector with an 8×8 LYSO crystal coupled to an 8x8 SiPM, the energy resolution and time coincidence resolution are measured as 279 ps and 12.4% respectively. These test results show that FESA4.0 is very promising for the construction of highly integrated TOF-PET scanners.

References
[1] A. D. Francesco et al., “TOFPET2: A high-performance ASIC for time and amplitude measurements of SiPM signals in time-of-flight applications,” J. Instrum., vol. 11, no. 3, Mar. 2016, Art. no. C03042, doi: 10.1088/1748-0221/11/03/c03042.
[2] X. Xu, Y. Wang, X. Zhang, H. Huang, Y. Zhou and Z. Song, "A Low-Power 8×8 SiPM Readout ASIC With Row-Column Summing Structure for Compact TOF-PET Detectors," in IEEE Transactions on Circuits and Systems I: Regular Papers, vol. 73, no. 2, pp. 961-971, Feb. 2026, doi: 10.1109/TCSI.2025.3617034.
[3] X. Zhang, Y. Wang, M. Wang and X. Kong, "An FPGA-Based 64-Channel Readout Electronics for High-Resolution TOF-PET Detectors," in IEEE Transactions on Radiation and Plasma Medical Sciences, vol. 9, no. 1, pp. 11-19, Jan. 2025, doi: 10.1109/TRPMS.2024.3443831.

NSS-13-142

SEU Evaluation of an Atom Switch-based FPGA for Slow-Control Systems (#2501)

Kazuki Ueno[1], Nanae Taniguchi[2], Toshitsugu Sakamoto[3], Makoto Miyamura[3]

[1] The University of Osaka, Department of Physics, Osaka, Japan; [2] KEK, Institute of Particle and Nuclear Studies, Tsukuba, Japan; [3] NanoBridge Semiconductor, Inc., Tsukuba, Japan

Abstract

Atom Switch-based FPGAs (AS-FPGAs) are being developed as next-generation FPGAs with expected high radiation tolerance. Their application to various radiation environments is anticipated, and we are also investigating their potential use in detector electronics for future high-energy physics experiments. In this study, neutron irradiation tests were performed to evaluate the Single Event Upset (SEU) tolerance of digital resources implemented in a 65 nm AS-FPGA. A prototype slow-control board equipped with the AS-FPGA was developed and used for the irradiation test. Two independent block RAM (BRAM) blocks and D-type flip-flop (DFF) blocks were implemented in the FPGA for SEU evaluation, and data mismatches detected during irradiation were counted as SEU events. Neutron irradiation tests were carried out using the tandem accelerator at Kobe University. The neutron fluence reached 1.2×10^{11} n/cm^2. No SEUs were observed in the DFF blocks, while approximately 10 SEUs were detected in the BRAM blocks. The preliminary SEU cross section for the BRAMs was estimated to be on the order of 10^{-9} cm^2/Mbit. In parallel with the irradiation studies, stable acquisition of temperature and pressure data from a commercial environmental sensor connected to the prototype slow-control board was successfully demonstrated during neutron irradiation, indicating the applicability of the AS-FPGA to detector slow-control systems in radiation environments.

NSS-13-144

Validation and Integration of the COMET Phase-I Trigger System (#2756)

Chihiro Yamada[1], Yuki Fujii[2], Youichi Igarashi[3], MyeongJae Lee[4], Haruki Miyai[1], Masaki Miyataki[1], Yu Nakazawa[3], Kou Oishi[3], Shunya Ueda[1], Kazuki Ueno[1]

[1] The University of Osaka, physics, Osaka, Japan; [2] Imperial College London, physics, London, UK; [3] High Energy Accelerator Research Organization (KEK), Tsukuba, Japan; [4] Sungkyunkwan University, physics, Suwon, South Korea

This work was supported by JSPS KAKENHI Grant Numbers 25KJ1715 and 21H04971.

Abstract
The COMET Phase-I experiment at J-PARC searches for muon-to-electron conversion in muonic atoms, which is a charged-lepton-flavor-violating process. The signal electron is monoenergetic, and its momentum is reconstructed using hit information from the Cylindrical Drift Chamber (CDC) and timing information from the Cylindrical Trigger Hodoscope (CTH). The trigger system must provide high event-selection efficiency, be robust against radiation, return trigger decisions within 8.5 μs, and operate stably. To achieve high event-selection efficiency, a multi-stage hardware trigger system was previously developed in which the CDC and CTH trigger candidates are processed in parallel and required to be in coincidence. However, FPGA reconfiguration in the CDC trigger path could change the communication latency, shifting 10 MHz CDC hit frames and degrading the time consistency required for online track finding. This work reports the development and validation of fixed-latency CDC trigger firmware using a setup with one board of each type. Repeated communication-link reset tests show that the latency is fixed with path-to-path variations less than 1 ns. The total latency is 3.5–3.6 μs, satisfying the requirement with sufficient margin, and input-pulse tests demonstrate 100% trigger response efficiency. These results establish a basis for ongoing full-board CDC validation and CDC–CTH trigger-system integration toward Phase-I data-taking.

References
[1] Abramishvili, R et al.2020, ‘COMET Phase-I technical design report’, *Prog. Theor. Exp. Phys.*, vol. 2020, no. 3, Art. no. 033C01.
[2] Nakazawa, Y et al.2021, ‘An FPGA-based trigger system with online track recognition in COMET Phase-I’, *IEEE Trans. Nucl. Sci.*, vol. 68, no. 8, pp. 2028–2034.
[3] Miyataki, M et al. 2024, ‘Neural network based event selection on FPGA for COMET Phase-I’, in *Proc. 2024 IEEE Nucl. Sci. Symp., Med. Imag. Conf. and Room Temperature Semiconductor Detector Conf.*, pp. 1–1, Tampa, FL, USA.
[4] Pesaresi, M et al. 2015, ‘The FC7 AMC for generic DAQ & control applications in CMS’, *J. Instrum.*, vol. 10, Mar. 2015, Art. no. C03036.
[5] *LogiCORE IP Aurora 8B/10B v5.3 User Guide (UG353), AMD Inc., 2012.*
[6] Giordano, R and Aloisio, A 2011, ‘Fixed-latency, multi-gigabit serial links with Xilinx FPGAs’, *IEEE Trans. Nucl. Sci.*, vol. 58, no. 1, pp. 194–201, Piscataway, NJ, USA: IEEE.

NSS-13-146

Evaluation of a Charge Sharing Compensation with Synchrotron Radiation (#2795)

Piotr G. Maj[1], Dominik S. Gorni[1], Grzegorz W. Deptuch[1], David P. Siddons[2], Abdul Rumaiz[2]

[1] Brookhaven National Laboratory, Instrumentation Department, Upton, USA; [2] Brookhaven National Laboratory, NSLSII, Upton, USA

The work wouldn’t be accomplished without dedication of the high-density interconnection group led by Donald Pinelli at Instrumentation Department at BNL as well as the continuous support Anthony Kuczewski from NSLSII.

Abstract
Charge-sharing compensation results obtained with the 3FI ASIC bump-bonded to a pixelated silicon sensor and tested on an NSLS-II synchrotron beamline are presented. The 3FI is a 32×32-pixel readout ASIC fabricated in 65

nm CMOS for Full-Field Fluorescence spectral X-ray Imaging, with 100 µm pixel pitch and event-driven analog output. Building on previously reported functionality and noise performance, this work focuses on the charge-sharing regime. A micrometer-diameter pinhole beam was stepped across pixel boundaries, and event-by-event charge data were recorded at each position. When the beam is directed precisely between two pixels, raw individual-pixel spectra exhibit split-charge events with degraded energy resolution. Offline charge summation of coincident neighboring pixels restores the full photon energy, recovering spectral integrity at the cost of a √2 noise increase. Furthermore, since the shared event is independently sampled by both neighbors, averaging the two reconstructed values cancels the noise penalty entirely, making the detector effectively insensitive to charge sharing across the inter-pixel region. The correction is validated against single-pixel hits recorded away from pixel boundaries, demonstrating full spectral restoration.

References
[1] Gorni, D. S., Deptuch, G. W., & Miryala, S. (2022). *Event driven readout architecture with non-priority arbitration for radiation detectors*. Journal of Instrumentation, 17(04), C04027.
[2] Siddons, D. P., Kuczewski, A. J., Rumaiz, A. K., Tappero, R., Idir, M., Nakhoda, K., Khanfri, J., Singh, V., Farquhar, E. R., Sullivan, M., Abel, D., Brady, D. J., & Yuan, X. (2020). *A coded aperture microscope for X-ray fluorescence full-field imaging*. Journal of Synchrotron Radiation, 27(6), 1703–1706.

NSS-13-148

A High-Precision and Wide-Dynamic Range Energy Acquisition Method based on MVT with Pulse-Shape for Elemental Logging (#2841)

Huan Liu[1], Junhao Yu[2], Qingguo Xie[1,2]

[1] University of Science and Technology of China, Department of Electronic Engineering and Information Science, Hefei, China; [2] Huazhong University of Science and Technology, Department of Biomedical Engineering, Wuhan, China

This work was supported in part by the National Natural Science Foundation of China under Grant 62201194, in part by the Sino-German Mobility Programme under Grant M-0387, and in part by the start-up fund of USTC ”Research on total solid Angle PET-EPR multimodal intelligent imaging”.

Abstract
As unconventional oil and gas exploration extends toward deep and ultra-deep wells, downhole nuclear logging systems are required to operate under high-temperature, high count-rate, and high energy-precision conditions over a wide dynamic range, which are difficult to simultaneously achieve using conventional pulse sampling methods. The multi-voltage threshold (MVT) technique provides inherent advantages under these constraints; however, conventional power-exponential pulse models exhibit limited robustness to waveform variations among detectors of different types and sizes, resulting in degraded pulse reconstruction accuracy and energy linearity. To address this issue, an energy-linearity optimization method is proposed for MVT-based neutron elemental logging instruments. A dedicated front-end signal conditioning and pulse-shaping circuit was developed to regulate the detector pulse shape for improved matching with the power-exponential model, thereby enhancing fitting accuracy. This approach effectively reduces reconstruction error and improves spectral performance across a wide energy

range. Experimental results demonstrate that the coefficient of determination (R^2) was significantly improved from 0.1380 to 0.9851. The energy resolution was enhanced from 10.5% to 6.2%, closely approaching the oscilloscope-based result of 6.0% with a deviation of only 0.2%. In addition, the proposed method demonstrated good compatibility with detectors of different types and sizes, indicating strong potential for applications in ultra-deep (~10,000 m) and extreme downhole environments.

References
[1] Q. Xie, C. M. Kao, Z. Hsiau, *et al.*, "A new approach for pulse processing in positron emission tomography," *IEEE Trans. Nucl. Sci.*, vol. 52, no. 4, pp. 988–995, 2005.
[2] D. Xi, C. M. Kao, W. Liu, *et al.*, "FPGA-only MVT digitizer for TOF PET," IEEE Trans. *Nucl. Sci.*, vol. 60, no. 5, pp. 3253–3261, 2013.
[3] S. Li, X. Lyu, F. Wang, *et al.*, "An accurate semi-empirical model for PMT pulse signal analysis," *PLoS One*, vol. 19, no. 11, p. e0313999, 2024.

NSS-13-150

Realistic Detector Response Model for COMET Phase-I Cylindrical Drift Chamber (#2941)

Siyuan Sun[1], Masaharu Aoki[1], Andreas Jansen[2], Masaki Miyataki[1], Yohei Nakatsugawa[3], Yoshi Uchida[4], Kazuki Ueno[1], Chen Wu[5], Tianyu Xing[6], Chihiro Yamada[1], Ye Yuan[5], Yao Zhang[5]

[1] The University of Osaka, Department of Physics, Toyonaka, Japan; [2] Dresden University of Technology, Department of Physics, Dresden, Germany; [3] Wakayama Medical University, School of Medicine, Wakayama, Japan; [4] Imperial College London, Department of Physics, London, UK; [5] Institute of High Energy Physics, Chinese Academy of Sciences, Beijing, China; [6] Istituto Nazionale di Fisica Nucleare, Milan, Italy

This work was supported by QLEAR fellowship grant No. Q21-017, and the National Natural Science Foundation of China (NSFC) under grant No. 12575207.

Abstract
The COMET (COherent Muon to Electron Transition) Phase-I experiment at J-PARC searches for coherent muon-to-electron conversion in aluminum with a single-event sensitivity of 3 x 10^-15. A key detector challenge is the high instantaneous beam rate, which produces background hits in the Cylindrical Drift Chamber (CDC). In particular, low-energy protons can generate large ionization signals that drive the readout electronics into nonlinear regions, producing waveform saturation and pileups. These effects may reduce hit efficiency by masking later signal or background hits and therefore must be modeled realistically in performance studies. We developed a detector response model for the CDC that combines Geant4-based ionization with the Photon Absorption Ionization (PAI) model, Garfield++-based drift time calculation, and an electronics response emulation based on measured response functions. The model explicitly includes nonlinear saturation effects in the circuit and was validated using cosmic-ray test data. The measured-response model reproduces the main features of the data more accurately than a simple linear-response model. The remaining discrepancy corresponds to a limited uncertainty in the pileup-effect evaluation, providing a realistic basis for COMET Phase-I reconstruction and performance studies.

References

[1] Abramishvili, R et al. 2020, 'COMET Phase-I technical design report', Progress of Theoretical and Experimental Physics, vol. 2020, no. 3, Art. no. 033C01.
[2] Allison, J et al. 2016, 'Recent developments in Geant4', Nuclear Instruments and Methods in Physics Research Section A, vol. 835, pp. 186–225.
[3] Veenhof, R 1993, 'Garfield, a drift chamber simulation program', presented at the International Conference on Programming and Mathematical Methods for Solving Physical Problems, Dubna, Russia.
[4] Shimazaki, S et al. 2014, 'Front-end electronics of the Belle II drift chamber', Nuclear Instruments and Methods in Physics Research Section A, vol. 735, pp. 193–197.
[5] Pagano, D, Bonomi, G, Donzella, A, Zenoni, A, Zumerle, G & Zurlo, N 2021, 'EcoMug: An efficient cosmic muon generator for cosmic-ray muon applications', Nuclear Instruments and Methods in Physics Research Section A, vol. 1014, Art. no. 165732.

NSS-13-152

Improving UAV-Based Radiation Monitoring in Mountainous Forests Using ANN with Spectral Information (#1212)

Kazuhiro Suzuki[1,2], Miyuki Sasaki[1], Ayumu Miyahara[1], Yuki Morishita[1], Hironori Funaki[1]

[1] Japan Atomic Energy Agency, Collaborative Laboratories for Advanced Decommissioning Science, Fukushima, Japan; [2] Hirosaki University, Graduate School of Health Sciences, Aomori, Japan

Abstract

Unmanned aerial vehicles (UAVs) are widely used to estimate ambient dose equivalent rates in mountainous forests. However, improving estimation accuracy remains challenging due to complex terrain and forest structure. In this study, an artificial neural network (ANN) model was constructed using UAV measurement data, and its applicability to estimating ambient dose equivalent rates at 1 m above ground level in mountainous forests was evaluated. In addition, the effect of explicitly incorporating direct and scattered radiation components on estimation accuracy was examined. These results show that the proposed ANN-based approach incorporating physically informed spectral information reduces root mean square error by 23% relative to the conventional Flat Source Model in mountainous forests, with explicit separation of radiation components further improving both estimation accuracy and physical interpretability.

References
[1] International Atomic Energy Agency (IAEA) 2003, 'Guidelines for radioelement mapping using gamma ray spectrometry data', IAEA-TECDOC-1363
[2] Sasaki, M., Sanada, Y., Katengeza, E. W., Yamamoto, A. 2021, 'New method for visualizing the dose rate distribution around the Fukushima Daiichi Nuclear Plant using artificial neural networks', *Scientific Reports*, 11, 1857.
[3] Cresswell, A. J., Sanderson, D. C. W., Yamaguchi, K. 2018, 'Assessment of the calibration of gamma spectrometry systems in forest environments', *J. Environ. Radioact.*, 181, 70–77.

NSS-13-154

Figure-Grounded Multimodal Retrieval-Augmented Generation for Radiation Equipment Manual Question-Answering (#1505)

Minjong Kim[1], Jinhyung Kwon[2], Jonghoon Park[2], Sangmin Lee[2], Byeonghyeon Park[2]

[1] Korea Atomic Energy Research Institute, Applied Artificial Intelligence Section, Daejeon, South Korea; [2] Korea Institute of Nuclear Safety, Radiation Regulation Division, Daejeon, South Korea

This research was supported by a grant from the Korea Atomic Energy Research Institute (KAERI) R&D Program (No. KAERI-526140-26). This work was also supported by a grant from the Korea Institute of Nuclear Safety (KINS), funded by the Nuclear Safety and Security Commission (NSSC) of the Republic of Korea in 2026 (No. 26-24-FD) for the project titled "Development of User-Customized AI-Based Radiation Equipment Management System."

Abstract

Radiation equipment manuals are multimodal documents in which textual content and safety-related visual materials jointly carry critical information. Existing retrieval-augmented generation (RAG) methods are predominantly text-centric and either fail to reflect visual information or include figures unrelated to the answer. This paper proposes a figure-grounded multimodal RAG pipeline that delivers an answer together with its supporting figures. The proposed method comprises figure-to-section alignment via a document map, hybrid sparse–dense retrieval, and answer generation accompanied by relevant figures. To evaluate multimodal performance, we construct an answer-grounded ground-truth figure set and define Figure Precision@k and Figure Recall@k as evaluation metrics. On a benchmark of ten radiation-equipment manuals (800 questions), the proposed method improves Figure Precision@5 from 0.06 to 0.30 and Figure Recall@5 from 0.15 to 0.61 over an image-embedding baseline, with textual answer quality comparable to a long-context text-RAG baseline in BERTScore-F1 and slightly lower in ROUGE-L.

References

[1] P. Lewis et al., "Retrieval augmented generation for knowledge-intensive NLP tasks," in Adv. Neural Inf. Process. Syst. (NeurIPS), vol. 33, 2020, pp. 9459–9474.

[2] S. Robertson and H. Zaragoza, "The probabilistic relevance framework: BM25 and beyond," Found. Trends Inf. Retr., vol. 3, no. 4, pp. 333–389, 2009.

[3] V. Karpukhin et al., "Dense passage retrieval for open-domain question answering," in Proc. EMNLP, 2020, pp. 6769–6781.

[4] G. V. Cormack, C. L. A. Clarke, and S. Büttcher, "Reciprocal rank fusion outperforms Condorcet and individual rank learning methods," in Proc. SIGIR, 2009, pp. 758–759.

[5] A. Yang et al. (Qwen Team), "Qwen3 technical report," arXiv preprint arXiv:2505.09388, 2025.

[6] L. Zheng et al., "Judging LLM-as-a-judge with MT-Bench and Chatbot Arena," in Adv. Neural Inf. Process. Syst. (NeurIPS), vol. 36, 2023.

[7] A. Radford et al., "Learning transferable visual models from natural language supervision," in Proc. ICML, PMLR 139, 2021, pp. 8748–8763.

[8] C.-Y. Lin, "ROUGE: A package for automatic evaluation of summaries," in Proc. Workshop Text Summarization Branches Out, ACL, 2004, pp. 74–81.

[9] T. Zhang, V. Kishore, F. Wu, K. Q. Weinberger, and Y. Artzi, "BERTScore: Evaluating text generation with BERT," in Proc. Int. Conf. Learn. Represent. (ICLR), 2020.

NSS-13-156

Physics Enhanced Machine Learning for Thermoluminescence Glow Curve Deconvolution (#1623)

Lukasz Tomaszewski, Caroline Shenton-Taylor

University of Surrey, Department of Physics, Guildford, UK

This work was funded and supported by the Nuclear Threat Reduction Network (NTR-Net), UK Ministry of Defence
© Crown Owned Copyright 2026/AWE.

Abstract

Thermoluminescence dosimetry (TLD) relies on accurate glow curve deconvolution to characterise trapping parameters, yet conventional methods are computationally intensive and rely on expert-defined initial parameters. This study explores a machine learning (ML) framework to automate glow curve analysis while preserving interpretability and decreasing user input. A hybrid CNN–GRU model was developed and trained on 658 experimental glow curves from silica glass beads and 10,000 synthetic mathematical glow curves derived from kinetic order equations. The model demonstrates the ability to reconstruct glow curves and infer peak structures without explicit user-defined initialisation, achieving an average figure of merit (FOM) of 8.3% on unseen experimental data. Notably, the ML approach consistently identifies the primary glow peak at the same temperature positions as conventional deconvolution methods, indicating that prominent physical features are reliably captured. Although traditional deconvolution techniques yield lower FOM values (~1%), they require optimisation and expert guidance. However, the ML model provides rapid, repeatable predictions and scales efficiently to large datasets. The results suggest that ML is not a replacement for conventional approaches but a complementary tool, in which ML predicts the initial parameters rather than a user. This work highlights the potential for hybrid ML-physics strategies to advance TL analysis.
UK Ministry of Defence © Crown Owned Copyright 2026/AWE

NSS-13-158

A High-Fidelity Robotics Simulation Framework for Autonomous Radiation Source Search (#2144)

Lance M. Drouet[1,2], Kalie Knecht[2], John Sparger[2], Michael Willis[2], Peter Sobel[2], Nicholas Prins[2], Jason Karcz[2]

[1] University of Tennessee, Department of Nuclear Engineering, Knoxville, USA; [2] Oak Ridge National Laboratory, Oak Ridge, USA

This research was supported by the U.S. National Nuclear Security Administration (NNSA) Office of Defense Nuclear Nonproliferation Research and Development within the U.S. Department of Energy under Contract AC05-00OR2272.

Abstract

Radiological source search requires timely threat assessment to ensure the security of the public. Existing methods rely on personnel to conduct radiation surveys with mobile detector systems, potentially exposing them to hazardous environments. Recent advancements in physical AI have presented the opportunity to improve radiological source search with robotics, machine learning, and artificial intelligence. Prior work at Oak Ridge National Laboratory (ORNL) has developed a radiation search platform that equips the Boston Dynamics Spot quadruped with a radiation imager, LiDAR, IMU, camera, and onboard computer for real-time 3D radiation imaging during autonomous navigation of complex environments. However, the development and field testing of autonomous robotic platforms are resource intensive and operationally constrained, motivating a simulation framework to refine autonomy algorithms and evaluate search performance across complex environments that would otherwise be infeasible to access. Building on the physical system, this work presents a high-fidelity simulation framework for developing and testing autonomous radiation search workflows in NVIDIA Isaac Sim. The framework centers on a model of the Spot quadruped equipped with simulated contextual sensors, including 3D LiDAR, RGB, and depth cameras, and exposes velocity-command control through a ROS 2 bridge. The current implementation provides end-to-end integration of sensor streaming, command interfaces, and a Python-based autonomy pipeline. Preliminary mapping outputs are presented as qualitative system-integration results and sandbox visualizations to support future autonomy and radiation-modeling studies.

References
[1] K. Knecht, J. Sparger, P. Sobel, J. Karcz, N. Prins, and M. Willis, “Coordinated autonomous navigable instruments for nuclear emergency search (canines),” in Proceedings of the INMM Annual Meeting, Washington, D.C., USA, 2025.
[2] K. Knecht et al., “Integrating agentic ai and real-time radiation mapping for autonomous source search,” 2026, work in progress.
[3] Boston Dynamics, “Spot®,” https://bostondynamics.com/products/spot/.
[4] NVIDIA, “Isaac Sim.” [Online]. Available: https://github.com/isaac-sim/IsaacSim
[5] Ouster, “Os0 ultra-wide view high-resolution imaging lidar,” https://data.ouster.io/downloads/datasheets/datasheet-rev7-v3p0-os0.pdf, 2026, accessed: 2026-03-27.
[6] H3D Inc., “M400 Custom Integrable Detector Module,” https://h3dgamma.com/m400.php.
[7] J. M. Ghawaly et al., “Radai: A large-scale realistic dataset for radiation detection algorithm development,” IEEE Transactions on Nuclear Science, 2026.

NSS-13-160

Robust Dual-Target Radioisotope Quantification Under Increasing Unseen Contaminant Complexity (#2217)

Chanho Kim[1], Yeongjun Kim[1], Geon Kim[2], Dae yang Oh[2]

[1] Korea Atomic Energy Research Institute, Daejeon, South Korea; [2] Korea University, Department of Bioengineering, Seoul, South Korea

This work was supported by the National Research Foundation of Korea (NRF) grant funded by the Korea government (Ministry of Science and ICT) (No. RS-2022-00165164).

Abstract

Gamma-ray spectroscopy is a fundamental technique for radioisotope identification and quantification across safety-critical applications, where deep learning models have recently emerged as a data-driven alternative to traditional library-dependent methods. However, most existing deep learning approaches operate under a closed-set assumption that all isotopes during deployment are present in the training set; field deployments frequently violate this assumption, and the introduction of unknown isotopes leads to silent degradation. Recent OOD-detection studies have been reported, but they treat OOD spectra as anomalies to be flagged rather than quantified, and systematic evaluation under increasing unseen contaminant complexity remains lacking. This study proposes a denoising autoencoder (DAE) framework that reconstructs the clean target spectrum (^{137}Cs, ^{133}Ba) from contaminated measurements while simultaneously estimating target fractions through a dual-head architecture. Using Ce:GPS scintillator pulse data under a leave-one-out unknown noise (LOO-UN) protocol, the DAE achieved a mean absolute error (MAE) of 0.024 at 20% out-of-distribution (OOD) contamination in the two-unseen configuration, outperforming NNLS-known (0.038) and MLP (0.031), with near-constant accuracy as the unseen contaminant count increased from one to two (0.025 → 0.024).

References

[1] M. Park, C. Kim, J. Hwang, and J. Y. Yeom, "Deep learning-based radioisotope quantification for extreme environments," Radiat. Phys. Chem., vol. 239, p. 113345, 2025.

[2] B. Van Omen et al., "Multilabel deep learning approach for radioisotope proportion estimation and out-of-distribution detection," Ann. Nucl. Energy, vol. 208, p. 110777, 2024.

[3] C. Kim et al., "Radiation resistance and temperature dependence of Ce:GPS scintillation crystal," Radiat. Phys. Chem., vol. 183, p. 109396, 2021.

[4] D. Hendrycks and K. Gimpel, "A baseline for detecting misclassified and out-of-distribution examples in neural networks," in Proc. Int. Conf. Learn. Representations (ICLR), 2017.

[5] P. Vincent, H. Larochelle, I. Lajoie, Y. Bengio, and P.-A. Manzagol, "Stacked denoising autoencoders: Learning useful representations in a deep network with a local denoising criterion," J. Mach. Learn. Res., vol. 11, pp. 3371–3408, 2010.

NSS-13-162

Recoil electron tracking in 3D CZT drift strip detectors: a feasibility study (#2296)

Michał Kossakowski[1], Alejandro Valverde Mahou[2], Søren Hauberg[2], Irfan Kuvvetli[1]

[1] Technical University of Denmark, Space Research and Technology, Lyngby, Denmark; [2] Technical University of Denmark, Applied Mathematics and Computer Science, Lyngby, Denmark

This work was supported by the Danish Data Science Academy, funded by the Novo Nordisk Foundation (NNF21SA0069429) and the VILLUM FONDEN (40516). The first author also acknowledges the i-RASE (Intelligent Radiation Sensor Readout System) project team for their support and collaboration.

Abstract

Bridging the *MeV gap* remains difficult due to the interplay of competing photon interaction processes, leaving a persistent sensitivity gap in gamma-ray astronomy. Compton telescopes based on 3D CZT Drift Strip Detectors (DSD) are promising candidates for bridging this gap, offering room-temperature operation, high stopping power, excellent energy and position resolution. A key open question is whether recoil electron tracking, which significantly improves angular resolution and detector sensitivity is achievable from raw detector signals. We investigate this using a machine learning approach trained on forward simulations of the 3D CZT DSD response. Principal Component Analysis of simulated electron tracks confirms that track structure is encodable in a low-dimensional representation, and neural network training to regress the recoil direction directly from detector waveforms is ongoing.

References
[1] S. R. Owe, I. Kuvvetli, A. Zoglauer, and C. Budtz-Jørgensen, “Feasibility of using 3d czt drift strip detectors for small compton camera space missions,” Journal of Instrumentation, vol. 19, no. 01, p. C01005, 2024
[2] A. C. Zoglauer, “First light for the next generation of compton and pair telescopes,” Ph.D. dissertation, Technische Universitat Munchen, 2005

NSS-13-164

Enhanced Spent Nuclear Fuel Characterization Using Sequential Detector Responses through Deep Learning (#2393)

Beomkyu Kwon[1], Wooseong Hong[1,2], Jaehyo Kim[1,2], Geehyun Kim[1,2]

[1] Seoul National University, Nuclear Engineering, seoul, South Korea; [2] Seoul National University, Energy Systems Engineering, seoul, South Korea

This work was supported by the Nuclear Safety Research Program through the Korea Foundation of Nuclear Safety (KoFONS) using the financial resource granted by the Nuclear Safety and Security Commission (NSSC) of the Republic of Korea. (RS-2022-KN073410)

Abstract

Accurate characterization of spent nuclear fuel (SNF) is essential for verifying operator-declared information in nuclear safeguards. Conventional nondestructive assay (NDA) approaches for such characterization based on gamma-ray spectroscopy typically rely on extracting specific photopeak information (ex. 662 keV peak of ^{137}Cs), which compresses high-dimensional detector responses into a limited number of variables and may lead to information loss. To address this limitation, we propose a deep learning–based SNF characterization approach that directly utilizes sequential detector-response data for advanced characterization performance. The training dataset was generated through integrated ORIGEN and MCNP simulations for 5000 realistic SNF conditions, covering variations in initial enrichment, burnup, and cooling time. The proposed C2C-GRU-v2 architecture was designed to process long sequential detector-response data by combining Coordinate-to-Context embedding and GRU-based recurrent sequence modeling, enabling both event-level contextual learning and sequence-level generalization. For comparison, a conventional spectrum-based regression method using ^{137}Cs peak counts was also implemented under identical conditions. The proposed approach demonstrated improved characterization performance compared with the conventional method, particularly for cooling time estimation, achieving Relative Root Mean

Square Errors (RRMSE) of 0.157 for burnup and 0.0456 for cooling time prediction. These results demonstrate the feasibility of deep learning–based sequential detector-response analysis for advanced SNF characterization in nuclear safeguards applications.

References
[1] Willman, Christofer, et al. "Nondestructive assay of spent nuclear fuel with gamma-ray spectroscopy." Annals of Nuclear Energy 33.5 (2006): 427-438.
[2] Hong, Wooseong, Beomkyu Kwon, and Geehyun Kim. "Characterization of Spent Fuel Parameters using Non-destructive Assay and Machine Learning."
[3] Bell, M. J. ORIGEN: the ORNL isotope generation and depletion code. No. ORNL--4628. Oak Ridge National Lab., Tenn.(USA), 1973.
[4] Kulesza, Joel A., et al. MCNP® code version 6.3. 1 theory & user manual. No. LA-UR--24-24602. Los Alamos National Laboratory (LANL), Los Alamos, NM (United States), 2024.
[5] Favalli, Andrea, et al. "Determining initial enrichment, burnup, and cooling time of pressurized-water-reactor spent fuel assemblies by analyzing passive gamma spectra measured at the Clab interim-fuel storage facility in Sweden." Nuclear Instruments and Methods in Physics Research Section A: Accelerators, Spectrometers, Detectors and Associated Equipment 820 (2016): 102-111.

NSS-13-166

Development of a PINN-Based Defect Verification Algorithm for CANDU Spent Nuclear Fuel Bundles (#2403)

Juwan Kang[1], Yoon Soo Chung[1], Jiwon Ra[1], Jae Joon Ahn[2], Yong Hyun Chung[1]

[1] Yonsei University, Department of Radiation Convergence Engineering, Wonju-si, South Korea; [2] Yonsei University, Division of Data Science, Wonju-si, South Korea

This work was supported by the Nuclear Safety Research Program through the Korea Foundation Of Nuclear Safety (KoFONS) using the financial resource granted by the Nuclear Safety and Security Commission (NSSC) of the Republic of Korea (No. RS-2024-00405144)

Abstract

The 37-element CANDU (CANadian Deuterium Uranium) spent fuel bundles at the Wolsong heavy water reactor are stored vertically in 19 layers within a wet storage facility. The Improved Optical fiber-based VErification System (IOVES), comprising a scintillator, optical fiber, and photomultiplier tube, traverses vertically between bundles to measure radiation profiles. Operators manually count profile peaks to verify bundle integrity, but reliability degrades when peaks are indistinct.

This study presents a Physics-Informed Neural Network (PINN)-based algorithm for automated defect verification of spent fuel bundles. The model learns physical characteristics of radiation profiles to generate predicted profiles, which are compared against measured profiles to localize defective bundles.

A three-head output structure independently predicts the defect status per layer, the number of defective bundles per layer, and the left/right defect probability. The total loss, comprising the three head-specific losses and a mean squared error profile of prediction loss, was optimized using the Adam optimizer.

The dataset comprised three scenarios (0, 1, and 2 defective bundles), with 200,000 samples each, totaling 600,000 samples, split 70%, 15%, and 15% for training, validation, and testing.

Defect classification accuracy per layer reached 99.7%. 19-layer exact match accuracy was 97.2%, with 100% accuracy on defect-free arrays.
This work demonstrates the feasibility of an automated verification system that overcomes operator-dependent inspection limitations. Future work will target improved left/right defect localization accuracy.

References
[1] PARK, Seunghoon; KIM, Yewon; JOUNG, Sungyeop. Radiological characteristics of CANDU spent fuel stacks using optical fiber probe. In: 2019 IEEE Nuclear Science Symposium and Medical Imaging Conference (NSS/MIC). IEEE, 2019. p. 1-3.
[2] Kwak, S. W., Kim, H., Kim, J., Kim, Y., & Lim, K. T. (2024). Field tests for performance evaluation of a new spent-fuel verification system in heavy water reactor. *Journal of Instrumentation*, *19*(03), C03057.
[3] Raissi, M., Perdikaris, P., & Karniadakis, G. E. (2019). Physics-informed neural networks: A deep learning framework for solving forward and inverse problems involving nonlinear partial differential equations. Journal of Computational physics, 378, 686-707.

NSS-13-168

Towards Spiking Neural Network-Inspired In-Pixel Processing for Radiation Detectors (#2446)

Anna Kozioł

AGH University of Krakow, Department of Measurement and Electronics, Cracow, Poland

The research leading to these results has received the Dean's financial support from the Faculty of Electrical Engineering, Automation, Computer Science and Biomedical Engineering at the AGH University of Krakow.

Abstract
This work introduces a neuromorphic in-pixel processing concept for next-generation high-flux radiation detectors. By leveraging event-driven principles inspired by Spiking Neural Networks, the proposed approach aims to move part of the signal interpretation directly into the pixel matrix, rather than relying solely on external readout and post-processing. This enables local extraction of photon timing, energy-related features, and mitigation of pile-up effects under extreme photon flux conditions. The concept builds on recent developments in hybrid pixel detectors and emerging intelligent in-pixel architectures, and extends them towards fully event driven detector operation. The proposed paradigm may open new directions for adaptive, low-latency radiation imaging at future synchrotron and XFEL facilities.

References
[1] Y. Lin and E. Charbon, "Spiking Neural Networks for Active Time-Resolved SPAD Imaging," *Proc. - 2024 IEEE Winter Conf. Appl. Comput. Vision, WACV 2024*, pp. 8132–8141, 2024, doi: 10.1109/WACV57701.2024.00796.
[2] V. Sriskaran *et al.*, "High-rate, high-resolution single photon X-ray imaging: Medipix4, a large 4-side buttable pixel readout chip with high granularity and spectroscopic capabilities," *J. Instrum.*, vol. 19, no. 2, 2024, doi: 10.1088/1748-0221/19/02/P02024.
[3] K. Heijhoff *et al.*, "Timing performance of the Timepix4 front-end," *J. Instrum.*, vol. 17, no. 7, 2022, doi: 10.1088/1748-0221/17/07/P07006.
[4] M. Ronchi, S. Di Giacomo, M. Amadori, G. Borghi, M. Carminati, and C. Fiorini, "Design, Implementation, and Analysis of an Integrated Switched Capacitor Analog Neuron for Edge Computing AI Accelerators," *IEEE Trans. Circuits Syst. I Regul. Pap.*, vol. PP, pp. 1–14, 2025, doi: 10.1109/TCSI.2025.3546521.
[5] A. Muntean *et al.*, "On-Chip Fully Reconfigurable Artificial Neural Network in 16 nm FinFET for Positron Emission Tomography," *IEEE J. Sel. Top. Quantum Electron.*, vol. 30, no. 1, pp. 1–13, 2024, doi: 10.1109/JSTQE.2023.3346957.

[6] A. Koziol *et al.*, "Artificial neural network on-chip and in-pixel implementation towards pulse amplitude measurement," *J. Instrum.*, vol. 18, no. 2, 2023, doi: 10.1088/1748-0221/18/02/C02048.
[7] A. Koziol *et al.*, "Measurements of IntelPixel – a readout IC with in-pixel artificial neural network for X-ray photon energy estimation in pixel sensors," *IEEE Nucl. Sci. Symp. Med. Imaging Conf. 2025*, pp. 1–2, doi: 10.1109/JSTQE.2023.3346957.S.

NSS-13-170

CVAE-Based Synthetic Thermoluminescence Silica Glass Jewellery Bead Glow Curve Generation (#2606)

Lukasz Tomaszewski, Caroline Shenton-Taylor

University of Surrey, Department of Physics, Guildford, UK

This work was funded and supported by the Nuclear Threat Reduction Network (NTR-Net), UK Ministry of Defence
© Crown Owned Copyright 2026/AWE.

Abstract
Micro silica glass jewellery beads have emerged as a viable material for thermoluminescence dosimetry (TLD), offering a low-cost and widely accessible option for personal dose assessment. Their linear glow curve responses, governed by irradiation, thermal conditions, and sample characteristics, exhibit unique spectral elements and structure variability. While machine learning (ML) methods have been successfully applied to dose estimation and irradiation analysis, can ML be used to elevate silica glass beads beyond just decorative jewellery? In this work, a Conditional Variational Autoencoder (CVAE) is implemented to model and generate thermoluminescent glow curves from silica glass beads conditioned on experimental parameters. The model is trained on a dataset of experimentally acquired responses, augmented with Poisson noise to increase the dataset size and robustness. Conditioning variables include temperature profiles, irradiation and sample characteristics, enabling the model to learn relationships between physical conditions and the glow curve. Results show that the CVAE model can generate realistic glow curves that reflect the underlying conditioning variables. Generated predications maintain peak structure and overall shape, while also reproducing the expected linear relationship between total counts and absorbed dose. Model performance remains consistent when evaluated on previously unseen testing data with a mean figure of merit of 7.5%, although accuracy declines at low dose levels due to diminished signal intensity. The proposed approach demonstrates the potential of generative ML techniques for supporting dosimetry simulation, calibration, and data augmentation workflows for future research.
UK Ministry of Defence © Crown Owned Copyright 2026/AWE.

NSS-13-172

Gamma-Ray Image Denoising and Source Enhancement Based on a Residual Convolutional Autoencoder (#2662)

Jonghyun Park[1,2], Youngjoo Park[1,2], Ilwoong Choi[1], Hakjae Lee[3], Kisung Lee[1]

[1] Korea University, Department of Bioengineering, Seoul, South Korea; [2] Korea University, Interdisciplinary program in precision public health, Seoul, South Korea; [3] ARALE Laboratory, Co., Ltd, Seoul, South Korea

This work was supported by the National Research Foundation of Korea and Commercialization Promotion Agency for R&D Outcomes (RS-2023-00234651).

Abstract

In radiation-guided cancer surgery, the amount of radioactive isotopes administered is limited, resulting in the acquisition of low-count, low-resolution gamma images that are further degraded by scattered radiation. In this study, a Residual Convolutional Autoencoder (Residual CAE) was developed to suppress background noise and enhance source-related signals in low-count [if gte msEquation 12]><m:oMath><span lang=EN-US style='font-size:8.0pt; mso-bidi-font-size:10.0pt;font-family:"Cambria Math",serif;mso-fareast-font-family: "맑은 고딕";mso-fareast-theme-font:minor-fareast;mso-bidi-font-family:"Times New Roman"; mso-ansi-language:EN-US;mso-fareast-language:EN-US;mso-bidi-language:AR-SA'><m:r><m:rPr><m:scr m:val="roman"/><m:sty m:val="b"/></m:rPr>13</m:r><m:r><m:rPr><m:scr m:val="roman"/><m:sty m:val="b"/></m:rPr>×</m:r><m:r><m:rPr><m:scr m:val="roman"/><m:sty m:val="b"/></m:rPr>13</m:r></m:oMath><![endif] gamma-ray images. The input images were zero-padded to [if gte msEquation 12]><m:oMath><span lang=EN-US style='font-size:8.0pt;mso-bidi-font-size:10.0pt; font-family:"Cambria Math",serif;mso-fareast-font-family:"맑은 고딕";mso-fareast-theme-font: minor-fareast;mso-bidi-font-family:"Times New Roman";color:black;mso-ansi-language: EN-US;mso-fareast-language:EN-US;mso-bidi-language:AR-SA'><m:r><m:rPr><m:scr m:val="roman"/><m:sty m:val="b"/></m:rPr>16</m:r><m:r><m:rPr><m:scr m:val="roman"/><m:sty m:val="b"/></m:rPr>×</m:r><m:r><m:rPr><m:scr m:val="roman"/><m:sty m:val="b"/></m:rPr>16</m:r></m:oMath><![endif] and normalized by the image-wise maximum value. The Residual CAE was configured as an encoder-decoder network with a residual connection that adds the first shallow feature map to the final decoder feature map, thereby preserving source location and spatial details. In test results, the Residual CAE achieved an MSE of 0.0007, SSIM of 0.9682, peak bias of 0.2416 pixels, and [if gte msEquation 12]><m:oMath><span lang=EN-US style='font-size:10.0pt; font-family:"Cambria Math",serif;mso-fareast-font-family:"맑은 고딕";mso-fareast-theme-font: minor-fareast;mso-bidi-font-family:"Times New Roman";mso-ansi-language:EN-US; mso-fareast-language:EN-US;mso-bidi-language:AR-SA'><m:r><m:rPr><m:scr m:val="roman"/><m:sty m:val="b"/></m:rPr>Δ</m:r></m:oMath><![endif] FWHM of 0.0441 pixels. To enable direct deployment of the trained model on the gamma camera and the monitoring software the model was converted to the Open Neural Network Exchange (ONNX) format, allowing its inference performance to be evaluated in an

embedded environment. The entire deployment pipeline, including preprocessing, inference, and postprocessing, was implemented. The converted ONNX model produced outputs that were highly consistent with the trained model and demonstrated low-latency inference suitable for real-time gamma-ray image processing. After conversion to ONNX, the model maintained reliable inference performance, achieving a mean peak bias of 1.35 pixels, a minimum Δ FWHM of −0.711 pixels, and 95.73% overall classification accuracy. These results demonstrate that the Residual CAE is effective for gamma-ray image denoising and source enhancement while preserving source localization and spatial resolution, supporting its feasibility for real-time deployment.

References
[1] A. L. Farnworth and S. L. Bugby, “Intraoperative gamma cameras: A review of development in the last decade and future outlook,” J. Imaging, vol. 9, no. 5, p. 102, May 2023.
[2] R. A. Gregory, I. Murray, J. Gear, M. D. Aldridge, D. Levine, L. Fowkes, W. A. Waddington, S. Chua, and G. Flux, “Objective comparison of lesion detectability in low and medium-energy collimator iodine-123 mIBG images using a channelized Hotelling observer,” Phys. Med. Biol., vol. 62, no. 1, pp. 17–30, Jan. 2017.
[3] X.-J. Mao, C. Shen, and Y.-B. Yang, “Image Restoration Using Very Deep Convolutional Encoder-Decoder Networks with Symmetric Skip Connections,” in *Advances in Neural Information Processing Systems 29 (NIPS)*, pp. 2802–2810, 2016.
[4] L. Gondara, “Medical Image Denoising Using Convolutional Denoising Autoencoders,” in *Proc. 2016 IEEE 16th International Conference on Data Mining Workshops (ICDMW)*, pp. 241–246, Dec. 2016.
[5] F. Chollet et al., “Keras,” 2015. [Online]. Available: https://keras.io.
[6] K. He, X. Zhang, S. Ren, and J. Sun, “Deep Residual Learning for Image Recognition,” in Proc. IEEE Conf. Comput. Vis. Pattern Recogn. (CVPR), pp. 770–778, Jun. 2016.
[7] ONNX, “Open Neural Network Exchange,” 2017. [Online]. Available: https://github.com/onnx/onnx.

NSS-13-174

Neural-Network Surrogate Modeling of TID-Induced Degradation in 180 nm Bulk NMOS Transistors (#2739)

Minuk Seung, Seop Hur, Chanho Kim

Korea Atomic Energy Research Institute, Daejeon, South Korea

This work was supported in part by the Basic Science Research Program through the National Research Foundation of Korea (NRF) funded by the Ministry of Science and ICT (RS-2022-00144324, RS-2022-00165164 and RS-2023-00258052).

Abstract
This paper presents a neural-network surrogate model for predicting Total Ionizing Dose (TID) induced degradation in a 180 nm bulk CMOS NMOS transistor. The proposed model uses only the gate length L, gate width W, W/L, total dose, and log(1+dose) as input features, where the layout parameters are extractable from a PDK netlist. The model predicts the dose-dependent changes in V_{th}, I_{on}, I_{off}, g_m, and SS. Using 180 nm NMOS data generated by a 3D drift-diffusion TCAD framework, the model is evaluated under three holdout conditions: 15 kGy(SiO_2) interpolation, 50 kGy(SiO_2) extrapolation, and a held-out geometry (L, W)=(240nm, 750nm). With 3-fold cross-validation along the dose axis and five random-seed repetitions, the worst-case absolute relative errors of V_{th}, I_{on}, g_m, and SS are below 0.30% in the INTERP/EXTRAP conditions, while those of I_{off} are 0.99–1.45% and 2.16–

2.52%, respectively. In the held-out geometry condition, the worst-case errors of all five metrics remain within 2%, indicating that TCAD-level TID degradation trends can be approximated using layout and total dose variables.

References
[1] T. R. Oldham and F. B. McLean, "Total ionizing dose effects in MOS oxides and devices," IEEE Trans. Nucl. Sci., vol. 50, no. 3, pp. 483–499, Jun. 2003.
[2] P. S. Winokur et al., "Charge build-up in MOS system under ionizing radiation," Microelectron. Reliab., vol. 21, no. 5, 1981.
[3] M. Manghisoni, L. Ratti, V. Re, V. Speziali, G. Traversi, and A. Candelori, "Comparison of Ionizing Radiation Effects in 0.18 and 0.25 µm CMOS Technologies for Analog Applications," IEEE Trans. Nucl. Sci., vol. 50, no. 6, pp. 1827–1833, Dec. 2003.
[4] Y.-C. Wu and Y.-R. Jhan, "2D MOSFET Simulation," in 3D TCAD Simulation for CMOS Nanoelectronic Devices, Singapore: Springer, 2017.

NSS-13-176

Deep Learning Positioning and Depth of Interaction Prediction with Automatic Gain Mismatch Correction (#2882)

Matthew Dilsizian, Hongdi Li, Yusheng Li

United Imaging, Molecular Imaging, Houston, USA

Abstract

This paper describes a deep learning algorithm for the estimation of axial, transverse, and depth of interaction (DOI) positions of detected events in SPECT. The algorithm includes a method for automatic calibration of the gain factor mismatches between detectors. The training data is obtained by simulation. The model consists of three feed-forward networks, one for each parameter to estimate. The axial is a continuous estimate, while transverse and DOI and discrete. The axial estimate is passed as an additional parameter to the DOI estimate, which improves estimates near the detector edge. A single base model is trained with data from a reference detector that is taken to have perfect gains, then calibration learns factors relative to this detector. Log-gains are learned to smoothly enforce strict positivity, from which the gains can be easily recovered. The algorithm achieves an axial FWHM of 1.40 mm, transverse FWHM of 0.83 mm, and a DOI FWHM of 1.24 mm. The gain factor estimates, based on histogram data, are within 0.001%.

References
[1] Kelkar, Sneha S., and Theresa M. Reineke. "Theranostics: combining imaging and therapy." *Bioconjugate chemistry* 22.10 (2011): 1879-1903
[2] A. B. Hwang, K. Iwata and B. H. Hasegawa, "Simulation of depth of interaction effects for pinhole SPECT," 2001 IEEE Nuclear Science Symposium Conference Record

NSS-13-178

Deep learning for precise gamma-ray interaction in an hexagonal monolithic scintillation crystals for PET imaging (#2968)

Lidia Jiménez Algarra[1], David Pérez-Benito[1], David Izquierdo-Garcia[1], Juan J. Vaquero López[1,2]

[1] Universidad Carlos III, Departamento de Bioingeniería, Leganés, Spain; [2] Instituto de Investigación Sanitaria Gregorio Marañón, Madrid, Spain

Abstract

The estimation of scintillation positioning with a high degree of precision in PET detectors is a crucial factor in determining the spatial resolution of the final image. Nevertheless, intra-crystal Compton scatter, optical diffusion, edge effects, and DOI ambiguity collectively limit the accuracy of first-interaction localization. Consequently, reducing this uncertainty will have a significant impact on the LOR definition and, in turn, will enhance the quality of the final PET image. Machine learning and deep learning methodologies have been shown to be particularly effective in this domain, resolving non-linear relationships between data and often outperforming other traditional approaches. In this study, we investigate various pipelines and deep learning techniques for enhancing gamma-positioning precision through the utilization of validated Monte Carlo simulations in a monolithic PET crystal with a specific hexagonal-shaped scintillation crystal. The validation of the selected models was done using experimental data specifically acquired for this study. The findings suggest that the most effective approach involves the utilization of a net trained with photoelectric and scatter events. The final FWHM mean in the corner and center are 1.2 mm and 1.7 mm for the simulated data respectively, while 1.74 and 2.63 mm, respectively for the validation. The bias achieved was 0.25 mm in the Z direction for the simulation.

References

[1] A Iborra et al. “Ensemble of neural networks for 3D position estimation in monolithic PET detectors”. In: Physics in Medicine amp; Biology 64.19 (Oct. 2019), p. 195010. ISSN: 1361-6560. DOI: 10.1088/1361-6560/ ab3b86.

[2] ON Semiconductor. Linearity of the Silicon Photomultiplier. Tech. rep. AND9776/D. Rev. 2. ON Semiconductor, Sept. 2018

NSS-13-180

Characterizing Neutron Detection Efficiency in Timepix3: A Bayesian-Optimized FLUKA Approach (#3239)

Angel Mercado, Sharmistha Mukhopadhyay, Malachi West, Patrick Connolly, Shaheen Dewji

Georgia Institute of Technology, Atlanta, USA

Abstract

Characterization of converter layer geometry is critical for determining the absolute detection efficiency of pixelated thermal neutron detectors. However, uncertainties in film deposition and source strength often lead to significant

discrepancies between simulated models and actual experimental performance. This work addresses these challenges by implementing a Bayesian optimized FLUKA framework to determine the effective enriched Lithium-6 Fluoride converter thickness for an ADVACAM Timepix3 detector with a 1000 µm Silicon sensor. The FLUKA Monte Carlo model was benchmarked against experimental measurements using an Americium-Beryllium source with a nominal activity of 40 mCi and a documented tolerance of fifteen percent. The Bayesian optimizer successfully converged to an effective thickness of 5 µm after forty evaluations by minimizing the residuals between the nominal source activity and the simulation-implied activities. This methodology demonstrates a robust approach to resolving geometric uncertainties in hybrid semiconductor detectors where direct physical measurement of internal components is not feasible post-assembly. The resulting validated geometry provides a high-fidelity foundation for modeling future detection efficiency benchmarks across diverse neutron spectra. This work demonstrates a practical approach for integrating machine-learning optimization with Monte Carlo transport modeling to address geometric uncertainties in neutron detectors.

NSS-13-182

Background pattern recognition and its reconstruction during radiation shadowing by scanned vehicles in Radiation Portal Monitors. (#1109)

Vladislav Kondrashov

GalaxRay LLC, radiation detectors, Mississauga, Canada

We are grateful to Dr. Eva Rimbauer, ALARA expert for her review and invaluable advices.

Abstract
The author has presented the approach to ambient radiation background pattern recognition and reconstruction for plastic scintillator-based Radiation Portal Monitors during vehicle scanning in situations when the ambient background is depressed (shadowed) by a vehicle. The principle is based on a correlation-significance test derived from the paired Student's t-tests and Pearson correlation coefficients. The author establishes criteria to recognize background depression and radiation source presence in the occupancy spectrum.
After determining the scale of depression for defined energy windows, the given approach presents the formalism to reconstruct the depressed background during the scan which is based on Aluminum variable thickness sheet as a vehicle equivalent model and the method for evaluating the signal-to-noise ratio to detect the radiation source under such scan conditions.

References
[1] L Kagan, A Stavrov "Radioactive source detection by vehicle radiation portal monitors considering background suppression", P02.160 v2, IPRA13, 2012
[2] JungHyun Bae et al, Radiation portal monitor data file format for comprehensive background radiation monitoring, Nuclear Instruments and Methods in Physics Research, A 1076 (2025) 170516

NSS-13-184

Effect of Source Intensity Imbalance on Two-Point Angular Resolution in Coded-Aperture Imaging (#1160)

Yuhang Qiu[1], Tiantian Dai[2], Qingyang Wei[1]

[1] University of Science and Technology Beijing, School of Automation and Electrical Engineering, Beijing, China; [2] China-Japan Friendship Hospital, Department of Radiation Oncology, Beijing, China

This work was supported by Project “Vice President of Science and Technology” of Changping District, Beijing (Grant No. 202503003030).

Abstract

Far-field angular resolution of coded-aperture gamma-ray imagers is often assessed by the smallest angular separation at which two point sources can still be distinguished, but the effect of unequal source activities on such measurements remains unclear. In this work, Monte Carlo simulations were performed to quantify how source-count imbalance influences two-point-source resolution tests in coded-aperture imaging. Images were reconstructed using the maximum-likelihood expectation-maximization algorithm, and reconstruction quality was evaluated using the valley-to-weak-peak ratio and localization bias. An appropriate stopping point was determined by jointly examining both metrics. Under ideal noise-free conditions, increasing source-count imbalance progressively degraded two-source discrimination. When the valid-count mismatch did not exceed 20%, acceptable discrimination was maintained near the nominal angular resolution limit, whereas larger mismatches caused a marked increase in localization bias. These results indicate that source-count imbalance can bias two-point-source resolution measurements and should be controlled in practical evaluations of coded-aperture systems.

References

[1] S. Park, J. Boo, M. Hammig, and M. Jeong, “Impact of aperture thickness on the real-time imaging characteristics of coded-aperture gamma cameras,” *Nucl. Eng. Technol.*, vol. 53, no. 4, pp. 1266–1276, 2021.

[2] A. Laminack, K.-P. Ziock, J. Daughhetee, P. Gibbs, K. Schmitt, and V. Nwadeyi, “3d source reconstruction using coded aperture gamma ray imaging,” Oak Ridge National Laboratory (ORNL), Oak Ridge, TN (United States), Tech. Rep., 2023.

[3] K. Lange and R. Carson, “EM reconstruction algorithms for emission and transmission tomography,” *J. Comput. Assist. Tomogr.*, vol. 8, no. 2, pp. 306–316, 1984.

NSS-13-186

X-Ray Measurement of Tubes Using Closed-Loop Residual-Driven Optimization Algorithm (#1269)

Yuchang Sun, Tianchen Zeng, Liqiang Wang

Tsinghua university, Bejing, China

Abstract

The geometric cross-sectional parameters of circular tubes, such as cables and rubber hoses, including inner and outer diameters, wall thickness, and eccentricity, are key indicators of manufacturing quality. However, existing X-ray digital imaging-based inspection methods generally rely on locating edge transition points (ETPs) in attenuation profiles, which degrades the accuracy and reliability of parameter reconstruction. To address these limitations, this paper develops a closed-loop residual-driven optimization (CRO) algorithm. The residual at ETPs between the measured projection and the analytical projection of the parameterized contour model is used as the feedback signal, and the contour parameters are corrected through a sign-driven update rule. Monte Carlo (MC) simulation data as the measured data demonstrates that, for a detector pixel size of 0.04mm, introducing CRO reduces the MAE of contour parameters by 69.44%, with a maximum error of 0.03mm.

References

[1] L. Wang, C. S. Wang, et al., ``Mathematical model establishment for cable eccentricity online detection system based on X-ray,'' in Proc. 29th Chinese Control and Decision Conference, 2017, pp. 5957--5960.

[2] Y. H. Feng, X. J. Xu, et al., ``X-ray tube wall thickness eccentricity measurement platform,'' Science and Technology and Innovation, no. 19, pp. 14--15, 2015.

[3] Y. H. Tang, X. Q. Xia, et al., ``Pipe wall thickness measurement method based on mobile X-ray detection system,'' Pipeline Technique and Equipment, no. 2, pp. 35--41, 2022.

[4] W. Sun, F. Shi, et al., ``X-ray-based cable eccentricity detection method used in online monitoring of cable eccentricity, involving calculating eccentricity of the cable under test based on geometric center coordinates of outer and inner candidate ellipses in screened candidate pairs,'' China Patent CN 121074027 A, Dec. 5, 2025.

[5] G. Sansoni, P. Bellandi, et al., ``3D system for the measurement of tube eccentricity: An improved, rugged, easy-to-calibrate layout,'' Measurement Science and Technology, vol. 24, no. 12, 2011.

[6] Y. C. Liu, Q. Lin, et al., ``A novel method of eccentricity detection for cross-linking cable,'' Nuclear Electronics and Detection Technology, no. 10, pp. 1216--1220, 2012.

[7] E. Y. Sidky, C.-M. Kao, et al., ``Accurate image reconstruction from few-views and limited-angle data in divergent-beam CT,'' Journal of X-ray Science and Technology, vol. 14, pp. 119--139, 2006.

[8] J. Willemink and B. No{\"e}l, ``The evolution of image reconstruction for CT---from filtered back projection to artificial intelligence,'' European Radiology, vol. 29, pp. 2185--2195, 2019.

[9] M. Beister, D. Kolditz, et al., ``Iterative reconstruction methods in X-ray CT,'' Physica Medica, vol. 28, no. 2, pp. 94--108, 2012.

NSS-13-188

Verification of a Rapid Dose Assessment Program Against MCNP for Nuclear Power Plant Decommissioning (#1310)

Changyeon Yoon

Korea Hydro & Nuclear CO., LTD, Central Research Institute, Daejeon, South Korea

Abstract

Accurate prediction of radiation exposure for workers during nuclear facility decommissioning is important for radiation protection and work planning. To support this, a previously developed dose assessment program based on the Electric Power Research Institute (EPRI) algorithm was verified in this study. The program inversely estimates source activity from known source positions and measured dose rates at selected locations, and then calculates worker exposure based on the estimated activity. To verify the performance of the program, its results were compared with those from MCNP, a widely used Monte Carlo radiation transport code. Three representative scenarios were considered: (1) multiple workers and multiple sources, (2) presence of thick shielding, and (3) changes in shielding and source location. For each scenario, dose rates were first calculated using MCNP and used as reference values, and the developed program predicted doses under the same conditions. In addition, the Average Fractional Error (AFE) was evaluated by comparing the measured dose rates with the dose rates recalculated at the same points using the estimated source activity. The results show that the prediction error is within 10% for most cases, while the shielding scenario shows a higher deviation, with a maximum error of 18.2%. The AFE results also support this trend, with a maximum value of 34% for the shielding case and less than 6% for the other scenarios, which are within the acceptable range based on the EPRI algorithm criterion. These results indicate that the program provides reliable results overall, while some deviation appears under strong shielding conditions. Since decommissioning environments change frequently, repeated MCNP simulations can be time-consuming. The developed program provides results within a few seconds, allowing quick estimation of worker dose under changing conditions and supporting practical work planning.

NSS-13-190

High-Reliability Tritium Monitoring Using Hardware Alpha Suppression and AI-Based Smoothing Filter (#1370)

Sungho Lee

Korea Atomic Energy Research Institute, Department of Radiation Safety Control, Daejeon, South Korea

This work was supported by KAERI R&D Program (No. KAERI-522430-26)

Abstract

Tritium monitoring in research reactors is essential for radiation safety because tritium is released as a low-energy beta emitter and is therefore difficult to measure accurately in real time. In particular, the reliability of tritium measurements can be degraded by two major factors: unavoidable statistical fluctuations in the ion chamber output and transient interference caused by radon and its alpha-emitting progeny. Radon-induced alpha events generate large ionization signals in the ion chamber, producing spike-like transients that can distort the measured current, while statistical fluctuations reduce the stability and precision of the monitoring data. To address these limitations, this study proposes a tritium monitoring system that combines a hardware-based alpha suppression function with an AI-based smoothing filter. The proposed monitor consists of two ion chambers, a pump, and a membrane separator, enabling gamma compensation and the exclusion of beta-emitting noble gases. The alpha suppression circuit detects and removes alpha-induced transients before they affect the measurement output. In addition, a piecewise learning-based smoothing filter is applied to reduce statistical fluctuations while preserving the response to actual changes in tritium concentration. The filter employs a two-stage framework consisting of change point detection and local regression, and is implemented using ONNX Runtime in a C#-based real-time monitoring system. Experimental results show that the proposed approach improves both measurement stability and responsiveness, demonstrating its applicability to reliable tritium monitoring in research reactor stack environments.

NSS-13-192

Automated Monte Carlo-Based Efficiency Transfer Integrated into HPGe Gamma Spectroscopy Workflows for High-Throughput Laboratories (#1579)

Spencer Behling[1], Felix Diel[3], Marc Breidenbach[2]

[1] Ametek, Ortec, Oak Ridge, USA; [2] AMETEK GmbH, Meerbusch, Duesseldorf, Germany; [3] AMETEK GmbH, InnoRIID, Duesseldorf, Germany

Abstract

High-purity germanium (HPGe) detector systems are widely used for gamma spectroscopy; however, increasing throughput demands, expanding measurement configurations, and a declining base of expert users have made traditional efficiency calibration and transfer workflows increasingly impractical. Efficiency transfer between counting geometries has historically required manual configuration, custom made sources, and/or execution of Monte Carlo simulations by trained computational physicists, limiting scalability in routine laboratory environments. We present an approach that embeds Monte Carlo-based efficiency transfer directly within a commercial spectral analysis software stack, enabling automated operation without additional user intervention. At runtime, sample geometries—already specified by laboratory personnel using standard container templates such as Marinelli beakers—are used to drive a ray-tracing-based gamma transport simulation coupled to detector interaction and pulse-processing models. The approach operates over an energy range of 20 keV to 2.5 MeV and produces both full spectra and efficiency curves.

Validation is performed through comparison of simulated spectra and efficiency curves against measured data and results from the Geant4 Monte Carlo toolkit. While not intended to match the full generality of Geant4, the proposed approach demonstrates comparable practical accuracy for routine laboratory configurations while significantly reducing user complexity. Additionally, seamless integration into existing workflows is demonstrated, enabling non-expert users to apply physics-based efficiency transfer without specialized training.
This work provides a scalable solution for automated, high-throughput gamma spectroscopy, bridging the gap between rigorous Monte Carlo modeling and practical laboratory usability.

NSS-13-194

Graph-Based Modeling of Organ and Lesion Radiomics Interactions in Theranostic SPECT/CT Imaging (#3206)

Mohamed Saber Azimi[3], Maryam Cheraghi[4], Mohammad A. Ghodsi-Rad[4], Ghasemali Divband[5], Habib Zaidi[1,2]

[1] Geneva University Hospital, Division of Nuclear Medicine & Molecular Imaging, Geneva, Switzerland; [2] Odense University Hospital, Deptartment of Nuclear Medicine, Odense, Denmark; [3] Obuda University, University Research and Innovation Center, Budapest, Hungary; [4] Shahid Beheshti University, Department of Nuclear Medicine, Tehran, Iran; [5] Jam Hospital, Department of Nuclear Medicine, Tehran, Iran

Abstract
Current radiomics approaches primarily focus on individual organs or lesions, which limits the ability to describe interactions within the body holistically. To address this limitation, we introduce a graph-based framework for modeling radiomics relationships between organs and lesions in theranostic SPECT/CT imaging. A cohort of 57 patients treated with ^{177}Lu-based radiopharmaceuticals was analyzed using post-therapy SPECT/CT. Organs were segmented using a deep learning–based approach, and lesions were delineated semi-automatically on SPECT images. From each region, 107 standardized radiomic features were extracted. Interactions between organs and lesions were quantified using a combination of linear similarity measures (Pearson, Spearman, cosine) and a nonlinear dependency metric based on normalized mutual information. These relationships were then represented as patient-specific graphs to capture system-level radiomics organization. The results reveal a non-uniform interaction pattern, where only a subset of organs exhibits strong associations with lesion characteristics. The highest coupling was observed in physiologically active regions such as the kidneys, liver, and spleen, with normalized mutual information values reaching approximately 0.66. Across all regions, nonlinear dependencies consistently showed higher values than linear metrics, indicating that complex relationships dominate radiomics interactions. Network representations further demonstrated a densely connected structure without prominent hubs, suggesting a distributed interaction model. Stability analysis confirmed reproducible patterns across patients, with near-perfect rank consistency and high agreement among top-ranked regions. These findings demonstrate that radiomics interactions between organs and lesions are structured, nonlinear, and reproducible. The proposed framework enables system-level interpretation of imaging data and may support the development of more informative biomarkers.

NSS-13-196

Quantitative Neutron Emission Tomography of Plutonium-Bearing Materials using a Boron-Coated Straw Detector Array (#2009)

David Breitenmoser[1], Ming Fang[2], David L. Chichester[3], Scott Thompson[3], Shaun D. Clarke[1], Angela Di Fulvio[2], Sara A. Pozzi[1]

[1] University of Michigan, Department of Nuclear Engineering and Radiological Sciences, Ann Arbor, USA; [2] University of Illinois, Department of Nuclear, Plasma, and Radiological Engineering, Urbana-Champaign, USA; [3] Idaho National Laboratory, Radiochemistry and Nuclear Measurements Department, Idaho Falls, USA

This work was funded in part by the Department of Energy through award number DE-NE0009507 “Non-Destructive Plutonium Assay in Pyroprocessing Bulk Materials with a 3D Boron-Coated-Straw Detector Array”.

Abstract

Neutron-based non-destructive assay (NDA) is a cornerstone of nuclear safeguards. Yet conventional techniques relying on integral counting suffer from significant biases if the spatial distribution and emission strength of neutron sources are unknown. This work presents a new, quantitative neutron emission tomography framework using a custom boron-coated straw detector array, enabling simultaneous localization and emission rate estimation of plutonium-bearing materials. Using high-fidelity Monte Carlo simulations and a custom iterative support-refined non-negative least squares algorithm, we demonstrate that centimeter-scale spatial resolution and percent-level accuracy in emission rate reconstruction can be achieved for realistic counting statistics. These results highlight the potential of neutron emission tomography as a next-generation NDA technique for advanced nuclear fuel cycles and reprocessing technologies.

NSS-13-198

Caesium 137 Radiation Transport Profile Modelling for Application to Physical and Simulation Environments (#2147)

Emmanuel Leo, Kelum A.A. Gamage, Olaoluwa R. Popoola

University of Glasgow, James Watts School of Engineering, Glasgow, UK

Supervisors: Prof. Kelum A. A. Gamage, Dr. Olaoluwa R. Popoola

Abstract

Towards the assembly of a virtual component of a radiological monitoring digital twin, an analysis of Caesium 137's mixed field radiation transport is presented. Caesium 137 decays by both beta and gamma radiation which can allow for long range detection of radioactive leakage events. First, a preliminary screening of the source-to-sensor distances of electrons in air was undertaken using the NIST ESTAR dataset. Following this, a Geant4 study was developed to investigate the profile of Caesium 137 activity with respect to distance from a source and threshold variation. This study confirmed that detection efficiency diminished with increased sensor thresholds and confirmed that the change in activity with respect to distance closely follows Poisson statistics. This sets the ground for creating engineering surrogate models that could be employed for application to the radiation field models and the creation of a physical simulation for radiation. The work carried out enables the application of digital twin methodologies to facilitate semi-autonomous radiological monitoring in Nuclear Power Plant environments.

References
[1] Madni, A. M., Madni, C. C., Lucero, S. D. 2019 “Leveraging Digital Twin Technology in Model-Based Systems Engineering”. en. In: Systems 7.1 , p. 7. ISSN: 2079-8954. DOI: 10.3390/systems7010007. URL: https://www.mdpi.com/2079-8954/7/1/7
[2] Fitzgerald, J., Larsen, P. G., Pierce, K. 2019 “Multi-modelling and Co-simulation in the Engineering of Cyber-Physical Systems: Towards the Digital Twin”. en. In: From Software Engineering to Formal Methods and Tools, and Back. Ed. by Maurice H. Ter Beek, Alessandro Fantechi, and Laura Semini. Vol. 11865. Series Title: Lecture Notes in Computer Science. Cham: Springer International Publishing, pp. 40–55. ISBN: 978-3-030-30984-8 978-3-030-30985-5. DOI: 10 . 1007 / 978-3-030-30985-5 4. URL: http://link.springer.com/10.1007/978-3-030-30985-5 4 (visited on 03/18/2026).
[3] Knoll, G. F. 2010 "Radiation Detection and Measurement." 4th ed. Wiley
[4] Leblond, S. 2024 “DDEP re-evaluation of the radioactive decay scheme of 137Cs”. In: Applied Radiation and Isotopes 206 (Apr. 2024), p. 111191. ISSN: 09698043. DOI: 10 . 1016 / j . apradiso. 111191. URL: https : / / www . sciencedirect . com / science / article / pii / S0969804324000198 (visited on 03/30/2026).
[5] Polo, M., et al. 2023 “Assessment of a NaIL detector performance for radiation monitoring applications”. English. In: European Physical Journal-Special Topics 232.10 (Aug. 2023). Num Pages: 10 Web of Science ID: WOS:001000195900001, pp. 1477–1486. ISSN: 19516355, 1951-6401. DOI: 10.1140/epjs/s11734-023-00896-4.
[6] Ghalehasadi, A., et al. 2026 “Enhanced radioisotope identification via dual-spectrum analysis using scintillation detectors”. In: Nuclear Engineering and Technology 58.4 (2026), p. 104107. URL: https : / / www . sciencedirect . com/science/article/pii/S1738573325006758 (visited on 03/30/2026).
[7] Goodwin, M., et al. 2026 “A – coincidence spectrometry detector system in the Boulby Deep Underground Laboratory”. In: Nuclear Instruments and Methods in Physics Research Section A: Accelerators, Spectrometers, Detectors and Associated Equipment 1087 (2026), p. 171419. URL: https://www.sciencedirect.com/science/article/pii/S0168900226001452 (visited on 03/30/2026).

NSS-13-200

Bayesian Filtering Image Reconstruction for SourceLocalization and Tracking in Compton Imaging (#2167)

John Leland[1], Cecilia Tarpau[2], Ming Fang[1], Yoann Altmann[3], Angela Di Fulvio[1]

[1] University of Illinois Urbana-Champaign, Nuclear, Plasma, and Radiological Engineering, Urbana, USA; [2] University of Edinburgh, Maxwell Institute for Mathematical Sciences, Bayes Center, Edinburgh, UK; [3] Heriot-Watt University, School of Engineering and Physical Sciences, Edinburgh, UK

This material is based upon work supported in part by the Department of Energy National Nuclear Security Administration through the Nuclear Science and Security Consortium under Award Number DE-NA0003996.

Abstract

Stand-off detection of special nuclear materials (SNM) in safeguards and non-proliferation applications demands imaging systems capable of tracking sources across dynamic environments. In this work, we introduce a Bayesian-Filtering (BF) algorithm for simultaneous source localization and tracking where existing reconstruction methods, such as simple back-projection (SBP) and maximum likelihood expectation maximization (MLEM), are insufficient. We evaluate the BF algorithm using synthetic data generated with MCNPX-PoliMi for a simulated Compton imager consisting of a 4 x 7 array of LYSO scintillator crystals. Two independent sources are simulated, one sweeping in azimuth and one in elevation, each traveling from -90° to +90° at 1 m/s. The BF algorithm successfully tracked both sources across the full angular sweep, achieving mean angular errors of 6.4° and 6.03° for the azimuth and elevation cases, respectively. Additionally, preliminary results for multi-source tracking are successful with the algorithm tracking both sources up until their paths intersect which is a known challenge we are currently investigating.

References

[1] E. Padovani, S. Pozzi, S. Clarke, and E. Miller, MCNPX-Polimi Users Manual.

[2] C. Tarpau, M. Fang, K. C. Zygalakis, M. Pereyra, A. Di Fulvio, and Y. Altmann. Statistical modelling and bayesian inversion for a compton imaging system: application to radioactive source localization. Inverse Problems, 40:125028, 2024. doi:10.1088/1361-6420/ad96de

NSS-13-202

An Iterative Based Gain Calibration Method for Multi-Channel Readout Scintillation Detectors (#2248)

Zijun Yan, Yangyang Zhao, Qingyang Wei

University of Science and Technology Beijing, Beijing Engineering Research Center of Industrial Spectrum Imaging and School of Automation and Electrical Engineering, Beijing, China

This work was supported in part by the National Key Research and Development Program of China under Grant 2022YFC2402001;and in part by Beijing Natural Science Foundation (Grant Number: L232126); and in part by National Natural Science Foundation of China (Grant Number:12375337)

Abstract

To address the common issue of channel gain non-uniformity in multi-channel readout scintillation detectors, this paper proposes an iterative correction method based on raw event data.The proposed method requires no additional hardware support and directly calibrates the gain coefficients of each channel directly using event data acquired by the detector. Channel energy data are extracted for each event, and the total energy is computed to locate the photopeak position.An energy selection window is then applied to retain valid events, thereby suppressing the influence of scattered and noise events. On this basis, an iterative optimization process is employed to refine the gain coefficients of each channel, gradually converging the event energy distribution toward

the photopeak. The correction effect is assessed by the energy resolution derived from the resulting energy spectrum. Experimental results show that the proposed method effectively compensates for channel response inconsistencies, significantly improves detector performance including energy resolution, and consequently enhances imaging quality and accuracy. The method is simple to implement and highly practical, and can be directly integrated into the data processing pipeline of existing detection systems.

References
[1] Dali Zhang et al ,Gain stabilization and consistency correction approach for multiple SiPM-based gamma-ray detectors on GECAM,Nuclear Instruments and Methods in Physics Research 2022,166222,ISSN0168-9002
[2] E.V. D.van Loef,et al, High-energy-resolution scintillator: Ce3+ activated LaBr3 .Appl. Phys. Lett. 3 September 2001; 79 (10): 1573–1575.

NSS-13-204

A Python-based Tool for Automated Geant4 Simulations of Scintillation Detectors (#2509)

Ayush Priyadarshi[1], Anil K. Gourishetty[1,2], Kavish Madhan[1], Virendra Ranga[2,1]

[1] Indian Institute of Technology, Roorkee, Department of Physics, Roorkee, India; [2] Tata Institute of Fundamental Research, Mumbai, Dept of Nuclear and Atomic Physics, Mumbai, India

I am grateful to G. Anil Gourishetty for this opportunity. I would also like to thank my parents, Capt. Arvind K. Prasad and Kumari Priyadarshini, along with my sister Ashika.

Abstract

This paper presents the development of a compact Geant4-Python simulation-analysis tool for a reproducible gamma response scintillation detector. The tool couples a configurable Geant4 C++ backend with Python automation for macro generation, simulation execution, ROOT-file validation, deposited-energy spectrum generation, count extraction and summarisation in a table. Unlike a general-purpose detector framework, the present implementation is focused on the end-to-end workflow required for scintillation detector response studies using solid cylindrical, hollow cylindrical, and near-4π soccerball-style geometries. Simulations with Cs-137 for 10^8 events demonstrate the complete workflow, while higher-statistics validation runs on PARAMGanga (Super-Computer at IITR) indicate that the same structure can be extended to larger detector-response campaigns. The resulting tool reduces manual intervention, improves traceability, and provides a reusable starting point for systematic Geant4-based gamma-spectroscopy simulations.

References
[1] Agostinelli, S et al. 2003, ‘GEANT4—a simulation toolkit’, Nuclear Instruments and Methods in Physics Research Section A, vol. 506, no. 3, pp. 250–303, Amsterdam: Elsevier.
[2] Priyadarshi, A 2026, ‘geant4-detector-simulation-pipeline: A reproducible Geant4–Python repository for automated scintillation detector simulations’, GitHub repository, Available: https://github.com/ayushpriyadarshi-18/geant4-detector-simulation-pipeline.
[3] Kumar, GA, Mazumdar, I & Gothe, DA 2009, ‘Efficiency calibration and simulation of a $LaBr_3$(Ce) detector in close-geometry’, Nuclear Instruments and Methods in Physics Research Section A, vol. 609, pp. 183–186, Amsterdam: Elsevier.

[4] Dhibar, M, Mankad, D, Mazumdar, I & Kumar, GA 2016, 'Efficiency calibration and coincidence summing correction for a large volume (946 cm^3) $LaBr_3$(Ce) detector: GEANT4 simulations and experimental measurements', Applied Radiation and Isotopes, vol. 118, pp. 32–37, Amsterdam: Elsevier.
[5] Kittelmann, T, Stefanescu, I, Kanaki, K, Boin, M, Hall-Wilton, R & Zeitelhack, K 2014, 'Geant4 based simulations for novel neutron detector development', Journal of Physics: Conference Series, vol. 513, p. 022017, Bristol: IOP Publishing.

NSS-13-206

Development and deployment of a compact beta/gamma spectrometry chain for autonomous ground vehicles in nuclear decommissioning

(#2624)

Pierre-Louis Antonsanti[1], Julien Venara[1], Marie Cuozzo[1], Thibaud Durand[1], Jérémy Seyssaud[1], Matteo Pacini[3], Eric Cantrel[2]

[1] Université de Montpellier / CEA, DES/ISEC/DPME/SEIP/LNPA, Bagnols-sur-Cèze, France; [2] Université de Montpellier / CEA, DES/ISEC/DPME, Bagnols-sur-Cèze, France; [3] Sigma Ingegneria, Lucca, Italy

This work was supported in part by the European project XS ABILITY under Grant BS123456.

Abstract

The XS ABILITY project aims to deploy a swarm of autonomous unmanned ground/aerial vehicles equipped with advanced radiation detection technologies for Dismantling & Decommissioning operations. As part of this effort, we developed a compact beta/gamma spectrometry chain to monitor concrete surfaces potentially contaminated with ^{137}Cs or ^{90}Sr, the main fission products encountered in nuclear facilities. The detection system comprises a 4-mm-thick plastic scintillator coupled to a photomultiplier tube, optimized for ^{90}Sr/^{90}Y full beta energy deposition. Analog signal processing is performed using a wireless, portable multichannel analyzer (CAEN Gammastream), adapted to both payload constraints and real-time measurements. It is currently being integrated into the Sigma Rover for automated floor/wall measurements. Energy calibration and resolution were estimated in laboratory using standard sources (^{137}Cs, ^{207}Bi, ^{241}Am), complemented by an uncertainty analysis addressing calibration parameters, measurement geometry, and background noise. A Monte Carlo model of the spectrometer was developed and validated against experimental data, facilitating simulations of configurations infeasible in laboratory settings. One of the target test cases of XS Ability being the CEA Marcoule G2 reactor currently undergoing dismantlement, a campaign of automated background noise measurements in the building is scheduled. The analysis of the spatial variability of the signal and the accessibility of the facility are key steps in the development of robust and automated scans. The measures will complement the uncertainty analysis, thus improving the contamination detection and reducing the false alarm and false negative rates. Ongoing work focuses on developing machine-learning-based algorithms for source identification (^{137}Cs, ^{90}Sr) and localization, targeting both surface and subsurface contamination.

NSS-13-208

Neutron and secondary photon dose mapping of deuterium-deuterium (D-D) and deuterium-tritium (D-T) neutron generators via PHITS simulations (#2970)

Andrea G. Alipio[1], Christine L. Dulohan[1], Bernhard Egwolf[2], Alvie Asuncion-Astronomo[3]

[1] University of Santo Tomas, The Graduate School, Manila, Philippines; [2] University of Santo Tomas, Department of Mathematics and Physics, Manila, Philippines; [3] Department of Science and Technology, Philippine Nuclear Research Institute, Quezon City, Philippines

This work is supported by the DOST-PCIEERD-funded project NURAD Component 2: "Accelerator Driven Subcritical Nuclear Reactor" with Project Number 1211979.

Abstract

The Monte Carlo-based Particle Heavy Ion Transport Code System (PHITS) was used to model deuterium-deuterium (D-D) and deuterium-tritium (D-T) neutron generators for preliminary radiation safety assessment of the ongoing establishment of the Neutron Irradiation Facility (NIF) of the Philippine Nuclear Research Institute (PNRI). Neutron and secondary photon dose distributions were obtained for fully shielded, partially shielded, and unshielded configurations. In both D-D and D-T cases, the counting room dose rates were acceptable with respect to occupational dose limits for a 500-hour annual operating time. However, additional shielding should be explored for the D-T setup to further reduce dose rates in the work area. The dose maps presented the significance of the configuration of moderating and shielding materials in minimizing radiological doses during operation. The findings of this work will serve as a reference for the safe and reliable installation of the country's first neutron generator laboratory.

NSS-13-210

Count-Level Effects on Radiomics Robustness and Harmonization in Total-Body PET Imaging (#3090)

Mohamed Saber Azimi[5], Maryam Cheraghi[7], Habib Zaidi[1]

[1] Geneva University Hospital, Division of Nuclear Medicine & Molecular Imaging, Geneva, Switzerland; [2] Geneva University Hospital, Division of Nuclear Medicine & Molecular Imaging, Geneva, Switzerland; [3] Odense University Hospital, Deptartment of Nuclear Medicine, Odense, Denmark; [4] Odense University Hospital, Deptartment of Nuclear Medicine, Odense, Denmark; [5] Obuda University, University Research and Innovation Cente, Budapest, Hungary; [6] Obuda University, University Research and Innovation Cente, Budapest, Hungary; [7] Shahid Beheshti University, Department of Nuclear Medicin, Tehran, Iran; [8] Shahid Beheshti University, Department of Nuclear Medicin, Tehran, Iran

This study was financially supported by the Swiss National Science Foundation (SNSF, grant No. 30030–231742) and the Geneva League Against Cancer (grant No. LGC 2402).

Abstract

Radiomics analysis in total-body PET imaging is highly sensitive to acquisition variability, particularly count reduction, which directly affects noise characteristics and feature reliability. In this study, we investigate the impact of count reduction and multi-parametric harmonization on the robustness of multi-organ radiomics. A retrospective dataset of 550 patients from two centers was analyzed. Multiple count levels were generated from list-mode data, including standard and reduced counts (reduction factors up to 100). Multi-organ segmentation was performed automatically, and 107 IBSI-compliant radiomics features were extracted from SUV-normalized images. Feature harmonization was applied using ComBat under different configurations, including scanner, voxel size, radiopharmaceutical, and scatter correction. Reproducibility was evaluated using intraclass correlation coefficients across count levels and anatomical regions. Results show that radiomics stability is strongly dependent on both count level and feature type. Approximately 31% of features achieved good reproducibility (ICC ≥ 0.75) in at least one organ. Shape and first-order features remained relatively stable under moderate count reduction (CRF ≤ 20), while higher-order texture features exhibited substantial degradation at extreme count levels (CRF ≥ 50). Harmonization improved feature consistency, particularly for scanner- and resolution-related variations, but had limited impact under severe noise conditions. Taken together, the results indicate that preserving quantitative reliability in low-count PET requires careful consideration of both feature selection and acquisition variability. Rather than relying solely on harmonization, robust radiomics analysis should incorporate count-aware strategies, especially when extending to multi-center or ultra-low-count imaging scenarios.

NSS-13-212

A Geant4 add-on package to emulate surface electron response in Monte-Carlo simulation (#3237)

Georgios Konstantinou, Sara El Akel, Christophe Baillif, Nicolas Wyrsch

EPFL, PV Lab, Neuchatel, Switzerland

Abstract

One of the most complex aspects of understanding and simulating accurately micro-channel plate structures is the accurate estimation of surface response of electron impacts, an integral part of the avalanche driven multiplication process that dictates gain and temporal charge profiles. Electron behavior is heavily affected by the surface quality, roughness, material thickness, deposition process and other details that are difficult to model. For this reason, a lot of groups rely on measurements, which are then introduced in different simulators, such as COMSOL Multiphysics, SimIon or others. Geant4 is the state-of-the-art community-based Monte-Carlo simulation software. Several new physics packages have been introduced over the years to simulate low-energy electron interactions; however, it is very difficult to emulate the entirety of optimizations that can lead to accurate simulation. For this reason we develop an package that allows accurate electron response on surfaces by allowing import of experimental data and is calibrated through an emulation run. The purpose is not to substitute the scatter/back-scatter mechanism that is native to Geant4, but allow light-weight and accurate surface responses to be integrated in full MCP simulations, including multichannel and broad range primary kinetic energies. The model is benchmarked against a fully developed COMSOL model and experimental gain results and tried in various primary scenarios, including direct alpha, beta, beta+ and gamma absorption.

NSS-13-214

Multi-energy Radiography Using a Three-energy Accelerator and Dual-layer Detectors (#1028)

Zhusong Mei[1], Yongle Dang[1], Chunguang Zong[1,2], Yanwei Xu[1,2], Lei Liu[1,2], Bicheng Liu[1]

[1] Nuctech Company Limited, Beijing, China; [2] Tsinghua University, Department of Engineering Physics, Beijing, China

Abstract

Traditional dual-energy X-ray cargo inspection systems are limited in thin-material discrimination and detail visibility because low- and high-energy information is mixed within broad bremsstrahlung spectra. This work presents a multi-energy imaging system based on a 6/3/0.3 MeV three-energy accelerator and dual-layer detectors, enabling acquisition of six effective energy channels in a single scan. Experimental results show that the 0.3 MeV channel significantly improves detail resolution, achieving a wire resolution of 0.9 mm. A random forest classifier achieves

92% overall accuracy for four representative materials over a mass-thickness range of 1–120 g/cm2, outperforming a conventional dual-energy configuration by approximately 28%. These results demonstrate that the proposed architecture is a promising solution for high-precision cargo and vehicle inspection.

References
[1] Y. Liu, B. D. Sowerby, and J. R. Tickner, ”Comparison of neutronand high-energy X-ray dual-beam radiography for air cargo inspection”,Appl Radiat Isotopes, vol. 66, no. 4, pp. 463-473, 2008
[2] Z.-Q. Chen, T. Zhao, and L. Li, ”A curve-based material recognitionmethod in MeV dual-energy X-ray imaging system”, Nuclear Science and Techniques, vol. 27, no. 01, pp. 173-180, 2016.

NSS-13-216

Portable African Neutron-Gamma Laboratory for Innovative Nuclear Science (#1078)

Pete Jones[1], Shanyn Hart[1], Mark Johnson[2], Omer Mahgoub[2], Steyn Meyer[2], Luna Pellegri[3,1], Maahir Rahman[2], Nieldane Stodart[1], Glen Taylor[2], Ferdinand van Niekerk[4], Christo van Tubbergh[1], Ahmed Vanker[2], Stephan Woodborne[5], Donovan Wyngaard[1]

[1] iThemba LABS, Cape Town, South Africa; [2] South African Radio Astronomy Observatory, Cape Town, South Africa; [3] University of the Witwatersrand, Cape Town, South Africa; [4] Tshwane Technical University, Cape Town, South Africa; [5] iThemba LABS, Johannesburg, South Africa

This work is based on the research supported wholly by National Research Foundation of South Africa (90741, 99037, 127116) and iThemba LABS.
Supported 2023-24 by the Technology Innovation Agency under Grant number 14606/01

Abstract
iThemba LABS has pioneered a mobile gamma-ray detection unit [1] which allows a user to operate in the field and chart the location, strength and energy of gamma radiation. The system incorporates a sensitive scintillation detector [2] typically used for accelerator-based spectroscopy at the SSC laboratory and was integrated into a backpack incorporating a fast 125 MHz digitiser for readout and a GPS enabled Raspberry Pi microprocessor system, allowing in situ measurements of radiation around the Cape Town site, with collected data streamed to the cloud and analysed offline. The Portable African Neutron-Gamma Laboratory for Innovative Nuclear Science (PANGoLINS) project [3] aims to investigate measurements of both gamma rays and neutrons which forms an important component part on site or in transit and the detection of both fissile material for the use in decarbonised energy sources or disposal thereof. A core component of the project is be to miniaturize the weight of the gamma-ray detection device and associated infrastructure so that it can be loaded on an uncrewed aerial vehicle to enable access to, and enhance performance of radiation monitoring measurements at remote sites leading to autonomous operations. PANGoLINS incorporates commercial detector assemblies of $LaBr_3$(Ce), SrI_2(Eu) and/or CLYC(Ce) for spectroscopy. In addition, the project encompasses the instrumentation of other scintillation detectors with silicon photomultiplier technologies. The coupling of these to readout devices such as high-density ADC readout are planned for applications for nuclear science, medical imaging or astronomy.

References
[1] Jones, P. *et al.*, IEEE Nuclear Science Symposium (2023) DOI: 10.1109/NSSMICRTSD49126.2023.10338129
[2] Msebi, L. *et al.*, NIM-A. **1026** (2022) 166195, DOI: 10.1016/j.nima.2021.166195
[3] Jones, P. *et al.*, IEEE Nuclear Science Symposium (2025) DOI: 10.1109/NSS/MIC/RTSD57106.2025.11286641

NSS-13-218

Feasibility Study on Ghost Imaging-based Neutron Depth Profiling for 3D Lithium Distribution Mapping (#1125)

Junhyeok Kim, Jinhwan Kim

Korea Atomic Energy Research Institute, DAEJEON, South Korea

This research was supported by the Korea government (MSIT) (1711078081) and by the National Research Council of Science & Technology (NST) grant by the Korea government (MSIT) (No. CAP25031-000).

Abstract

This paper investigates the feasibility of three-dimensional lithium distribution mapping in solid-state electrolytes by integrating ghost imaging with neutron depth profiling. In the proposed system, a cold neutron beam is spatially modulated by a sequence of 32×32 Hadamard-patterned cadmium masks, and a single-pixel charged-particle detector records the energy spectrum for each pattern. Since each energy bin corresponds to a specific depth layer via the stopping power, reconstructing a lateral image independently for every energy bin and stacking them along the depth axis produces a complete three-dimensional lithium map without mechanical scanning. Monte Carlo simulations were performed with 1024 mask patterns and 5×10^8 neutron histories per pattern. Images were reconstructed using an untrained neural network-based algorithm at sampling ratios of 25%, 50%, 75%, and 100%. At 100% sampling, the peak signal-to-noise ratio and structural similarity index reached 7.5 dB and 0.577, respectively. Although these quantitative scores remain modest due to limited source statistics, the reconstructed images qualitatively resolve the target lithium-rich structures across all depth layers. Compared to conventional pinhole-scanning approaches that require exhaustive spatial sampling, the proposed method would achieve comparable image quality at 50% sampling, directly halving beam time and making three-dimensional characterization practically feasible.

References
[1] H. Jeong, J. Kim, B. G. Park, and K. T. Lim, “ANN-based pulse shape discrimination for background reduction in neutron depth profiling,” Nuclear Engineering and Technology, vol. 57, no. 12, Dec. 2025, doi:10.1016/j.net.2025.103816.
[2] T. Yi, E. Zhao, Y. He, T. Liang, and H. Wang, “Quantification and visualization of spatial distribution of dendrites in solid polymer electrolytes,” eScience, vol. 4, no. 1, Feb. 2024, doi:10.1016/j.esci.2023.100182.
[3] S. Liu, X. Meng, Y. Yin, H. Wu, and W. Jiang, “Computational ghost imaging based on an untrained neural network,” Opt. Lasers Eng., vol. 147, no. June, p. 106744, 2021, doi: 10.1016/j.optlaseng.2021.106744.
[4] D. Sarrut et al., “GATE 10 Monte Carlo particle transport simulation: I. Development and new features,” Phys. Med. Biol., vol. 71, no. 1, Jan. 2026, doi: 10.1088/1361-6560/ae237b.

NSS-13-220

Feasibility Study of Thermal-Neutron Localization Using a GAGG-Based Directional Probe (#1183)

Yuhang Qiu[1], Tiantian Dai[2], Qingyang Wei[1]

[1] University of Science and Technology Beijing, School of Automation and Electrical Engineering, Beijing, China; [2] China-Japan Friendship Hospital, Department of Radiation Oncology, Beijing, China

This work was supported by Project “Vice President of Science and Technology” of Changping District, Beijing (Grant No. 202503003030).

Abstract

This work evaluated the feasibility of thermal-neutron localization using a directional probe originally developed for gamma-ray source localization. The probe consisted of 30 GAGG scintillator bars surrounding a tungsten cylinder and was modeled by Monte Carlo simulation. Thermal neutrons were generated from a ^{252}Cf point source placed at the center of a spherical high-density polyethylene moderator. Localization was performed using a centroid vector method based on events recorded within the energy window around the characteristic 80 keV capture-related peak. Ten source directions at a source-to-detector distance of 0.5 m were evaluated under ideal noise-free conditions. Representative results showed the localization accuracy improved as the number of valid counts in the selected energy window increased. The mean angular bias decreased from 4.12° at 100 valid counts to 0.78° at 2700 valid counts, demonstrating sub-degree average localization accuracy at higher count levels. These results support the feasibility of thermal-neutron localization with a compact GAGG-based directional probe and suggest potential future use in simultaneous neutron and gamma-ray localization for nuclear security applications.

References

[1] J. Dumazert, R. Coulon, Q. Lecomte, G. H. Bertrand, and M. Hamel, “Gadolinium for neutron detection in current nuclear instrumentation research: A review,” *Nucl. Instrum. MethodsPhys. Res. A*, vol. 882, pp. 53–68, 2018.

[2] M. Taggart, M. Nakhostin, and P. Sellin, “Investigation into the potential of gagg:ce as a neutron detector,” *Nucl. Instrum. MethodsPhys. Res. A*, vol. 931, pp. 121–126, 2019.

[3] Q. Wei, Z. Yang, and T. Dai, “A novel radiation source location detector based on attenuation,” in *Proc. 2018IEEENucl. Sci. Symp. Med. ImagingConf. (NSS/MIC)*. IEEE, 2018, pp. 1–3.

[4] Y. Qiu, G. Wang, and Q. Wei, “Rapid low-energy gamma-ray source localization via centroid vector method,” in *Proc. 2025IEEENucl. Sci. Symp., Med. ImagingConf., andRoom-TemperatureSemicond. DetectorConf. (NSS/MIC/RTSD)*. IEEE, 2025, pp. 1–1.

[5] S. Jan, G. Santin, D. Strul, S. Staelens, K. Assié, D. Autret, S.Avner, R. Barbier, M. Bardiès, P. Bloomfield *et al.*, “Gate: a simulation toolkit for pet and spect,” *Phys. Med. Biol.*, vol. 49, no. 19, pp. 4543–4561, 2004.

NSS-13-222

Empirical Test of Gamma Emission Tomography for Detecting Partial-defect within PWR-type Spent Nuclear Fuel (#1220)

Hyung Joo Choi[1], Hee Kyun Baek[2], Jung-ki Shin[2], Sung-Woo Kwak[3], Chul Hee Min[1]

[1] Yonsei University, Radiation Convergence Engineering, Wonju, South Korea; [2] NeosisKorea Co. Ltd., Daejeon, South Korea; [3] Korea Institute of Nuclear Nonproliferation and Control, Safeguards team, Daejeon, South Korea

This work was supported by the Nuclear Safety Research Program through the Korea Foundation Of Nuclear Safety (KoFONS) using financial resources granted by the Nuclear Safety and Security Commission (NSSC) of the RoK (RS-2021-KN050310), and the Basic Science Research Program through the National Research Foundation of Korea (NRF) funded by the Ministry of Education (RS-2024-00412203).

Abstract

Spent Nuclear Fuel (SNF) contains various radionuclides and emits significant levels of radiation; therefore, accurate and effective inspection methods for identifying partial defects within SNF are essential. In our previous study, we proposed and fabricated a scintillator-based Gamma Emission Tomography (GET) system named the Yonsei Single-photon Emission Computed Tomography (YSECT). The purpose of this study is to experimentally evaluate the its performance and applicability under conditions mimicking actual inspection conditions. The YSECT system consists of four detection modules, a data acquisition module, a Peltier-based cooling system, and a rotation module. For employing the YSECT instrument to partial-defect inspection, a waterproof test was conducted at a depth of 1.58 m for 120 minutes. In addition, the performance and applicability of the YSECT instrument were evaluated by acquiring projection and tomographic images. The waterproof test confirmed that water intrusion was not assessed into the instrument. While a comparison of projection images obtained in air and water revealed some degradation in image quality—specifically regarding noise levels and spatial resolution—and an exponential decrease in pixel intensities in the inner layers due to water attenuation and lead dummy pins, the source distribution remained clearly distinguishable across the entire SNF region. These results demonstrate that the YSECT instrument is highly effective for detecting partial defects in SNF. Future studies will focus on validating the system under actual SNF inspection conditions.

References

[1] M. Mayorov, “Gamma emission tomography for the inspection of spent nuclear fuel,” in 2017 IEEE Nuclear Science Symposium and Medical Imaging Conference (NSS/MIC), p. 1-2.

[2] Virta, R., “Improved passive gamma emission tomography image quality in the central region of spent fuel,” in Scientific Reports, Vol 12(1), 12473.

[3] H. J. Choi, “Optimization of Yonsei single-photon emission computed tomography (YSECT) detector for fast inspection of spent nuclear fuel in water storage,” in Journal or Radiation Protection and Research, Vol 49(1), 29-39.

NSS-13-224

Enrichment-Dependent Neutron Interrogation Spectrum Optimization for Delayed Neutron Temporal Measurement (#1250)

Caryanne R. Wilson[1], Kristofer Ogren[2], Shaun D. Clarke[3], Sara A. Pozzi[3], Igor Jovanovic[1], Oskar Searfus[4]

[1] University of California, Berkeley, Department of Nuclear Engineering, Berkeley, USA; [2] Los Alamos National Laboratory, Los Alamos, USA; [3] University of Michigan, Department of Nuclear Engineering and Radiological Sciences, Ann Arbor, USA; [4] Sandia National Labratories, Livermore, USA

This research was performed under appointment to the Nuclear Nonproliferation International Safeguards Fellowship Program sponsored by the National Nuclear Security Administration's Office of International Nuclear Safeguards (NA-241). This work has been supported in part by the US Department of Homeland Security, Countering Weapons of Mass Destruction (CWMD) Office, Academic Research Initiative cooperative agreement number 21CWDARI00040-01-00. Sandia National Laboratories is a multimission laboratory managed and operated by National Technology & Engineering Solutions of Sandia, LLC, for the U.S. Department of Energy's National Nuclear Security Administration under contract DE-NA0003525.

Abstract

The time-emission profile of delayed neutrons (DNs) emitted by decaying fission fragments and induced by an external, time-modulated interrogating source can be used to identify the isotopic composition of uranium samples. In low- and high-enriched samples, a single isotope dominates the DN temporal profile, complicating measurements of isotopic composition. By suitably moderating the neutron spectrum of an interrogating neutron source, the large thermal fission cross-section of ^{235}U can be leveraged to amplify its signal, thereby improving the ability to measure lower enrichments. This work evaluates the use of neutron moderation in DN-based enrichment measurements using a Monte Carlo simulation. The ^{235}U-to-^{238}U fission ratio serves as the optimization metric, since DN production is proportional to the number of fissions. Optimal moderating configurations that yield a near-unity ^{235}U to ^{238}U DN emission ratio for low-enriched and high-assay low-enriched uranium were determined. Based on this analysis, an experimental design has been developed for future validation. DN temporal analysis offers the prospect of nondestructive uranium assay across the entire ^{235}U enrichment range, from depleted (0.3% ^{235}U) to highly enriched (93.0% ^{235}U) uranium.

References
[1] International Atomic Energy Agency, ed., Safeguards techniques and equipment. No. no.1 (Rev. 2) in International nuclear verification series, Vienna: International Atomic Energy Agency, 2011 edition ed., 2011.
[2] J. Nattress et al., "Discriminating Uranium Isotopes Using the Time- Emission Profiles of Long-Lived Delayed Neutrons," Phys. Rev. Appl., vol. 10, p. 024049, Aug. 2018.
[3] K. Ogren et al., "Discriminating Uranium Isotopes Based on Fission Signatures Induced by Delayed Neutrons," Phys. Rev. Appl., vol. 14, p. 014033, July 2020.
[4] O. Searfus et al., "Passive and active neutron signatures of 233U for nondestructive assay," Phys. Rev. Appl., vol. 20, p. 064038, Dec. 2023.
[5] P. Dimitriou et al., "Development of a Reference Database for Beta- Delayed Neutron Emission," Nucl. Data Sheets, vol. 173, pp. 144–238, Mar. 2021.
[6] IAEA, "ITV tables and method descriptions (narratives) library." https://nucleus.iaea.org/sites/connect/ITVPublic/SitePages/Home.aspx. Accessed: April 28, 2026.

NSS-13-226

Improving contraband thermal neutron capture gamma detection in low and medium-Z cargo with pulsed D-T active neutron interrogation

(#1300)

Ketaki Joshi, Xianfei Wen, Jason P. Hayward

University of Tennessee, Department of Nuclear Engineering, Knoxville, USA

This material is based upon the work supported by the Department of Homeland Security and the Department of Energy National Nuclear Security Administration through Defense Nuclear Nonproliferation's Enabling Capabilities in Technology Consortium under the award numbers 21CWDARI00041-01-00 and DE-NA0004197.

Abstract

Identification of shielded contraband like chemical weapons, explosives, and drugs being illegally transported in cargo containers can be achieved by detecting gamma rays produced using active pulsed D-T neutron interrogation. The time-dependent active gamma background produced by various low to medium-Z benign cargo-filling materials can interfere with contraband gammas and can make rapid and reliable detection of such contraband challenging. Using optimized timing gates depending on cargo-type for gamma spectra analysis can improve the signal-background ratio of contraband gammas. In this work we use a 6x6 array of 3"x8" NaI(Tl) detectors with coincidence-summing addback for full energy peak reconstruction and a pulsed D-T neutron generator to understand the gamma background produced by empty cargo, and paper and steel cargo filled to 0.6 g/cc density in our cargo inspection setup. We identify optimized timing windows for each cargo and validate the optimization with d_a signal sensitivity calculations.

NSS-13-228

Detection of Water in Spent Nuclear Fuel by Prompt Gamma Activation Analysis (#1400)

Brendan Green[1], Kartikey Mathur[1], Andrew Kennedy[1], Damilola Folley[1], Stephen Croft[1], David Hambley[2], Robert Mills[2], Malcolm J. Joyce[1]

[1] Lancaster University, Engineering Department, Lancaster, UK; [2] United Kingdom National Nuclear Laboratory, Central Laboratory, Seascale, UK

This summary is part of work funded by the Nuclear Decommissioning Authority via a PhD studentship (B. J. Green) and the United Kingdom's ESPRC grant EP/X038327/1. B. J. Green, K. Mathur, A. Kennedy, D. Folley, S. Croft, and M. J. Joyce are with Department of Engineering, Lancaster University, Bailrigg, Lancashire, United Kingdom, LA1 4YR (e-mail: b.j.green@lancaster.ac.uk).
R. Mills and D. Hambley are with the United Kingdom National Nuclear Laboratory, Central Laboratory, Sellafield, Seascale, Cumbria, CA20 1PG, United Kingdom (e-mail: robert.w.mills@uknnl.com)

Abstract
The detection of water in a mock advanced gas reactor slotted can has been carried out using non-radioactive surrogate materials. The method of detecting water is via prompt gamma activation analysis of hydrogen. This results in a prompt 2.223 MeV γ-ray. Due to the absence of hydrogenous materials in the fuel matrix, the 2.223 MeV γ-ray is indicative of the presence of water. GEANT4 simulations of the mock slotted can have demonstrated the variation in 2.223 MeV γ-ray intensity dependent on the location of water. High density polyethylene blocks equivalent to and above water mass detection limits set out in literature were exposed to ^{252}Cf sources. The γ spectra obtained were examined.

References
[1] B. Green *et al.* "Prompt γ-ray techniques based on neutron capture in hydrogen for the detection of water in nuclear legacy environments: a review" *Progress in Nuclear Energy*, vol.189, p. 105905, 2025, doi: 10.1016/j.pnucene.2025.105905.
[2] C. Binnersley et al., "Quantifying water in spent fuel assemblies with neutrons: A simulation-based approach," Progress in Nuclear Energy, vol. 145, p. 104110, 2022, doi: 10.1016/j.pnucene.2021.104110.

NSS-13-230

Development of a Portable Alpha–Beta Detection Device for Decommissioning Sites (#1464)

Yuki Morishita[1], Naoki Sagawa[2], Misaki Hirato[2], Mitsugu Sohma[3], Jun Akedo[3], Naoya Yamaishi[4], Junichi H. Kaneko[4], Mikio Higuchi[4], Yuichi Kitagawa[4]

[1] Japan Atomic Energy Agency, Collaborative Laboratories for Advanced Decommissioning Science (CLADS), Futaba County, Japan; [2] Japan Atomic Energy Agency, Nuclear Fuel Cycle Engineering Laboratories, Tokai-mura, Japan; [3] National Institute of Advanced Industrial Science and Technology (AIST）, Tsukuba, Japan; [4] Hokkaido University, Graduate School and School of Engineering, Sapporo, Japan

This work was supported by JAEA Nuclear Energy S&T and Human Resource Development Project Grant Number JPJA25P 25135771.

Abstract
A compact handheld alpha–beta radiation detector was developed for field applications in nuclear decommissioning environments. At decommissioning sites such as the Fukushima Daiichi Nuclear Power Plant, mixed contamination from alpha- and beta-emitting radionuclides requires rapid and reliable on-site radiation measurements. To address these challenges, the developed detector enables real-time alpha–beta discrimination

while maintaining compact size, lightweight design, and battery-powered operation. The detector employs a Ce-doped Gd 2Si2O7 (GPS) scintillator coupled with a Multi-Pixel Photon Counter (MPPC). Signal processing and radiation discrimination were performed using an FPGA, and the measured count rates and energy spectra were displayed in real time on an LCD via a Raspberry Pi Pico microcontroller. The device weighs approximately 1.3 kg and can operate continuously for up to 8 hours on battery power. Pulse height spectra showed a speak for alpha particles, while beta particles exhibited continuous spectra. The detector achieved a detection efficiency of 90.7% under the measurement conditions. By applying a low-energy threshold (LLD) at channel 190, more than 80% of the alpha counts were retained, whereas the beta counts were reduced to 6.4%, demonstrating effective alpha–beta discrimination. Real-time measurement results, including count rates and spectra, were successfully displayed on the LCD screen. These results demonstrate that the developed handheld detector provides effective alpha–beta discrimination and is suitable for rapid, on-site radiation measurements in mixed contamination environments encountered during nuclear decommissioning activities.

References
[1] Morishita, Yuki, et al. "Performance comparison of scintillators for alpha particle detectors." Nuclear Instruments and Methods in Physics Research Section A: Accelerators, Spectrometers, Detectors and Associated Equipment 764 (2014): 383-386.
[2] Morishita, Yuki, et al. "A phoswich alpha/beta detector for monitoring in the site of Fukushima Daiichi Nuclear Power Station." Radiation Measurements 160 (2023): 106896.

NSS-13-232

Proof-of-Concept Pulsed Neutron Detection Using a Timestamping SOI Pixel Detector SOFIST3 (#1510)

Ayaki Takeda[1], Rikuto Kawashima[1], Asahi Shiokawa[1], Soshi Kudo[1], Kenji Shimazoe[2], Mizuki Uenomachi[3], Kanta Nagai[2], Miho Yamada[4]

[1] University of Miyazaki, Engineering, Miyazaki, Japan; [2] The University of Tokyo, Engineering, Tokyo, Japan; [3] Institute of Science Tokyo, Institute of Integrated Research, Tokyo, Japan; [4] Tokyo Metropolitan College of Industrial Technology, Information and Telecommunication Engineering Program, Tokyo, Japan

Abstract

We report a proof-of-concept pulsed neutron de- tection experiment using SOFIST3, a silicon-on-insulator (SOI) pixel detector with per-pixel energy and timestamp recording. SOFIST3 was tested at the NOBORU beamline (BL-10) of J-PARC/MLF using a ^{10}B conversion layer. Two-dimensional spatial distributions of charge signal and timestamp were recorded, confirming simultaneous per-pixel energy and timing measurement under neutron irradiation. The pixel occupancy increased proportionally with beam intensity—from approximately 1.7×10^4 to 5.1×10^4 hits/cm^2/s over a factor of ~3 in intensity—demonstrating count rate performance free from the system-wide dead time that limits conventional SOI pixel detectors. These results provide a foundation for developing dedicated high count rate neutron imaging detectors based on SOI pixel technology.

References
[1] M. Zubair and Y. Adel, “Advances in neutron imaging for non-destructive testing: Developing techniques, challenges, and future directions,” Kuwait J. Sci., vol. 53, p. 100546, 2026.
[2] Y. Kamiya, T. Miyoshi, H. Iwase et al., “Development of a neutron imaging sensor using INTPIX4-SOI pixelated silicon devices,” Nucl. Instrum. Methods Phys. Res. A, vol. 979, p. 164400, 2020.

[3] A. Takeda, Y. Arai, S. G. Ryu et al., "Design and evaluation of an SOI pixel sensor for trigger-driven X-ray readout," IEEE Trans. Nucl. Sci., vol. 60, pp. 586–591, 2013.
[4] A.Takeda,K.Mori,Y.Nishiokaetal.,"Developmentofon-chippattern processing in event-driven SOI pixel detector for X-ray astronomy with background rejection purpose," J. Instrum., vol. 15, p. P12025, 2020.
[5] S. Ono, M. Yamada, M. Togawa et al., "Development of a monolithic pixel sensor based on SOI technology for the ILC vertex detector," Nucl. Instrum. Methods Phys. Res. A, vol. 924, pp. 431–435, 2019.

NSS-13-234

Experimental and Simulation Studies of FFCC Measurements Using a D-D Neutron Generator (#1563)

Makoto Maeda, Masao Komeda, Yosuke Toh

Japan Atomic Energy Agency, Nuclear Science and Engineering Center, Tokai-mura, Japan

This work supported by the Decommissioning, Contaminated Water and Treated Water Management Project funded by the Ministry of Economy, Trade and Industry (METI), Japan.

Abstract

Quantification of nuclear material in fuel debris at the Fukushima Daiichi Nuclear Power Station is expected to contribute to the streamlining of processing and management. The Fast Fission neutron Coincidence Counting (FFCC) method has been proposed as a non-destructive assay technique that utilizes fast neutrons, which are less affected by neutron absorbers contained in the debris. In FFCC measurements, an external neutron source is used to induce fission. Compared with conventional D-T systems, D-D neutron generators are more suitable for on-site deployment due to the absence of tritium and the lower neutron energy, which reduces shielding requirements. However, their lower neutron yield and smaller fission cross-sections pose challenges for measurement. In this study, the feasibility of FFCC measurements using a D-D neutron generator was experimentally demonstrated with EJ-301 liquid scintillation detectors. Time-difference spectra were obtained from uranium samples with and without B_4C neutron absorbers. Clear coincidence peaks were observed in both cases, indicating that fission neutrons can be successfully detected even in the presence of neutron absorbers, with less than a 10% reduction in counts. In addition, Monte Carlo simulations were performed using a designed measurement system to evaluate the feasibility of measurements within a practical measurement time. The results indicate that sufficient counting statistics can be obtained. These results demonstrate the feasibility of the FFCC method using a D-D neutron generator and its potential applicability to the non-destructive assay of fuel debris.

NSS-13-236

Compact and modular ^{6}LiF:ZnS(Ag) neutron detectors (#1609)

Felix Liang, Adam Esquibel, Nicholas Floyd, Heshani Jayatissa

Los Alamos National Laboratory, ISR Division, Los Alamos, USA

Los Alamos National Laboratory is managed by Triad National Security, LLC for the U.S. Department of Energy's NNSA.

Abstract

Neutron detection plays an important role in nuclear security, industrial applications, space exploration, and basic science research. Some compact neutron detectors made with ^{6}LiF:ZnS(Ag) and wavelength shifters have been deployed in portable instruments for nuclear security. In such detectors where photosensors are attached to one end of the wavelength shifter, high photon propagation efficiency for the wavelength shifter is required so that the signal-to-noise ratio of the photosensor is adequate for signal processing. Monte Carlo simulations using Geant4 were performed to study photon propagation efficiency for wavelength shifter panels and bars. Compact neutron detector modules were constructed according to the results of the Geant4 simulations. An initial test using a ^{252}Cf source shows the 10x10x45 mm^3 bar detects more neutrons than the 10x10x30 mm^3 bar and a majority of events have a small pulse height resulting from neutrons detected further away from the photodiodes. Although the count rate of the 45 mm bar for HDPE moderated neutrons was 67% lower than a 10 atm ^{3}He tube, its length is 3 times shorter than the ^{3}He tube.

References

[1] van Eijk, CWE 2004, 'Inorganic scintillators for thermal neutron detection', *Radiat. Measur.*, vol. 38, pp. 337-342.

[2] Barton, JC, *et al.*, 'A novel neutron multiplicity detector using lithium fluoride and zinc sulphide scintillator', *J. Phys. G: Nucl. Part. Phys.*, vol. 17, pp. 1885-1899.

[3] Ramsden, D, Foster, MA 2017, 'Neutron detector and method for detecting neutrons', US Patent No. 9720111 B2.

NSS-13-238

Characterization of a Leak-Tight Radon Chamber for Exhalation Rate Measurements of NORM Products (#1748)

Jin-Goo Kang[1], Ill-hyuk Han[2], Juhyun Lee[1], Jeongsoo Kang[1], Jung-Seok Chae[1], Geehyun Kim[2]

[1] Korea Institute of Nuclear Safety (KINS), Dept. of NORM Radiation Safety Assessment, Daejeon, South Korea; [2] Seoul National University, Dept. of Energy System Eng., Dept. of Nuclear Eng. and Institute of Eng. Research, Seoul, South Korea

This work was supported by a grant from "Establishment of Technical Basis for Implementation on Safety Management of Radiation in the Natural Environment" carried out by Korea Institute of Nuclear Safety (KINS).

Abstract

Accurate quantification of radon (^{222}Rn) exhalation rate from consumer products containing naturally occurring radioactive materials (NORM) is essential for source-term-based safety evaluation. This requires a sealed measurement chamber whose tightness and internal radon concentration homogeneity are characterized to ensure data integrity. We characterize a 0.343 m³ stainless-steel radon chamber housing two Durridge RAD7 alpha spectrometers for low-emanation NORM measurements. Chamber tightness, evaluated via the radon decay curve method over ~24 days, yielded a fitted leak rate constant statistically consistent with zero (1σ uncertainty 1.7×10^{-5} h^{-1}), more than an order of magnitude below the 5 % × λ_{Rn} acceptance criterion. To support spatial homogeneity evaluation, a MATLAB advection–diffusion solver with a real Navier–Stokes velocity field (Chorin projection method) was developed as a transferable computational framework, deliberately trading full turbulence-model fidelity for accessibility. Preliminary simulations indicate that fan-driven advection (2.0 m/s) reduces the spatial coefficient of variation (CV) below the 5 % target within ~10^1 arbitrary time units, approximately three orders of magnitude faster than under natural diffusion alone (~10^4 a.u.). Experimental cross-validation using a calibrated Pylon ^{226}Ra source and two RAD7 units in a crossover configuration is in progress and will be presented at the conference. This integrated experimental and computational protocol qualifies the chamber for high-precision radon exhalation measurements of NORM products, enabling consistent and conservative safety regulation.

References

[1] KINS, “Establishment of Technical Basis for Implementation on Safety Management of Radiation in the Natural Environment,” KINS/ER-337 Vol. 11 (2025).

[2] F. Leonardi et al. "A study on natural radioactivity and radon exhalation rate in building materials containing NORM residues: preliminary results." Construction and Building Materials 173 (2018).

[3] J.-G. Kang, “Effects of geometric factors on radon exhalation rates evaluation using closed chamber method,” M.S. thesis, Dept. of Energy Syst. Eng., Seoul National Univ., Seoul, Republic of Korea, 2022.

[4] ISO 11665, “Measurement of radioactivity in the environment – Air: radon-222 – Part 7: Accumulation method for estimating surface exhalation rate (2012) and Part 9: Test methods for exhalation rate of building materials (2019).”

[5] M. Abo-Elmagd, "Radon exhalation rates corrected for leakage and back diffusion–evaluation of radon chambers and radon sources with application to ceramic tile." *Journal of Radiation Research and Applied Sciences* 7.4 (2014).

[6] X. Zhang, Y. Zhang, Y. Liu, and B. Tang, "Evaluation of the uniformity of concentration of radon in a radon chamber." *Applied Radiation and Isotopes* 110 (2016).

NSS-13-240

Compton Scattering Imaging for On-site Nondestructive Testing of Cultural Heritage (#1857)

Xin Li[1,2], **Yantao Liu**[1,2], Wei Zhou[1,2], Yuzhong Feng[1,2], Aoyang Wei[1,2], Zhiming Zhang[1,2], Long Wei[1,2]

[1] Institute of High Energy Physics, Chinese Academy of Sciences, Beijing Engineering Research Center of Radiographic Techniques and Equipment, Beijing, China; [2] University of Chinese Academy of Sciences, School of Nuclear Science and Technology, Beijing, China

This research is supported by the National Natural Science Foundation of China (Grant No. 11975248) and the Youth Innovation Promotion Association of the Chinese Academy of Sciences (CAS YIPA) (Grant No. 2021014).

Abstract

Cultural heritage preservation requires non-invasive in-situ detection techniques to avoid irreversible damage to fragile relics. Compton scattering imaging (CSI), based on single-sided backscattering detection, offers a promising alternative to X-ray transmission imaging for nondestructive testing (NDT) at archaeological sites. This paper presents two push-broom CSI systems for on-site in-situ NDT of cultural heritage. A modified 2D CSI system was deployed at an auxiliary pit in Xi'an, effectively revealing shallow subsurface burial features and locating unexcavated relics. A 3D Compton scattering tomography system was further developed to address depth limitations, featuring a soil penetration depth of over 10 cm and a spatial resolution of 1cm with preliminary experiments verifying its technical feasibility for 3D structural characterization of buried artifacts.

References

[1] A. M. Wajid et al., "X-ray backscattering: design, applications, and prospects in non-destructive evaluation," J. Radioanal. Nucl. Chem., vol. 334, no. 5, pp. 3033–3054, May 2025, doi: 10.1007/s10967-025-10103-4.

[2] C. Shi et al., "Rapid and high-resolution handheld X-ray backscatter subsurface imaging for field archaeology prediction," Archaeometry, vol.67, no. 3, pp. 738–747, Jun. 2025, doi: 10.1111/arcm.13039.

[3] G. Harding and E. Harding, "Compton scatter imaging: A tool for historical exploration," Appl. Radiat. Isot., vol. 68, no. 6, pp. 993–1005, Jun. 2010, doi: 10.1016/j.apradiso.2010.01.035

[4] X. Xiong et al., "A compact, high signal-to-noise ratio line-detector array Compton scatter imaging system based on silicon photomultipliers," Appl. Radiat. Isot., vol. 154, p. 108845, Dec. 2019, doi: 10.1016/j.apradiso.2019.108845.

NSS-13-242

In Situ 300-m Depth Underwater Environmental Radiation Monitoring System with Cesium Preconcentration (#1925)

Min Sun Lee[1], Jiyoung Park[2], Jungmin Seo[3], Mee Jang[2], Hyemi Cha[2], Soo Mee Kim[3]

[1] Daegu Gyeongbuk Institute of Science and Technology (DGIST), Electrical Engineering and Computer Science, Daegu, South Korea; [2] Korea Atomic Energy Research Institute, Environmental Radioactivity Assessment Team, Daejeon, South Korea; [3] Korea Institute of Ocean Science and Technology, Maritime ICT & Mobility Research Department, Busan, South Korea

This work was supported by a research grant from Korea Institute of Ocean Science and Technology (PEA0402), a research grant from Korea Atomic Energy Research Institute Institutional Program (Project No. 522610-26), and a research grant from National Research Foundation of Korea (RS-2025-02316993).

Abstract

The prompt detection of marine environmental radioactivity is essential in the wake of accidents such as the Fukushima event, yet conventional methods relying on bulk seawater sampling and offline analysis cannot provide timely information. We developed an in-situ underwater gamma-ray monitoring system, operable down to 300 m depth, that integrates real-time cesium preconcentration with a low-background gamma-ray spectrometer for deployment on unmanned surface vehicles, underwater gliders, and mooring platforms. The 18.54 kg system

houses a seawater circulator, a pressure regulator, a dual-head gamma-ray detector, and a battery within a 58 cm × 21.4 cm watertight enclosure. Each detector head consists of a 2×2 tiled array of 48×48×20 mm³ monolithic GAGG:Ce crystals (96×96 mm² active area) coupled to a 16×16 SiPM array, with a KNiFC resin column placed between the opposing heads for selective ^{137}Cs adsorption. KNiFC-based preconcentration yielded over 92% ^{137}Cs recovery from spiked seawater. In a 30-bar pressure chamber, the system operated stably for 1 hour, and underwater background counts in the 662 keV region were reduced by a factor of 17 owing to water shielding. Under this low-background condition, two ^{137}Cs-preloaded adsorbent columns containing as low as 11.4 mBq and 73.2 mBq were observable within the 662 keV photopeak window, with net counts scaling consistently with the loaded activities. With a photopeak detection efficiency of 0.13, the system achieved a minimum detectable activity of 5.8 mBq/L for a 60 L sample within a 1-hour measurement, demonstrating sub-10 mBq/L sensitivity for in-situ ^{137}Cs detection in deep-sea environments.

NSS-13-244

Vehicle Based Detection System for Gamma-Neutron Background Measurements (#2083)

Luke G. Morris, Tom Crane, Maxim B. Joseph, Matt P. Taggart

AWE Nuclear Security Technologies, Reading, UK

Abstract

The variability of background radiation, primarily gamma rays and neutrons, can have a significant impact on the performance of detector systems. In nuclear security, background-limited minimal detectable activity constrains which sources can be detected with acceptable confidence. Furthermore, the radiation background can have direct impact on the false alarm rate; higher background levels can lead to increased false alarm rates, normally mitigated by increasing thresholds, which decreases the system sensitivity. The local environment is one of the main factors in background rate variation. Therefore, a vehicle-based system is a well-suited detector platform to investigate dynamically changing environments. This work summarises the design and creation of a custom vehicle-based system assembled at AWE-NST as a platform for experimental gamma and neutron background measurements. This platform can also be used to benchmark novel anomaly detection algorithms. This work details the results from the first measurement campaign taken in July 2025 with the system driven over 247 miles around the counties of Hampshire and Berkshire in the UK.

References
[1] OpenStreetMap contributors, “Copyright and license,” OpenStreetMap. [Online]. Available: https://www.openstreetmap.org/copyright. Accessed on: July. 23, 2025.
[2] G. Pausch et al., “Fast- and thermal-neutron detection with common NaI (Tl) detectors,” arXiv:2208.06696 [physics.ins-det], Aug. 2022. [Online]. Available: https://doi.org/10.48550/arXiv.2208.06696. Accessed on: Apr. 23, 2026.

NSS-13-246

Performance Evaluation of a Portable MMXRF for Safeguards Environmental Sample Analysis under Transport-induced Alignment Changes (#2222)

Sung-Woo Kwak[1], Woojin Kim[1], Jinho Ryu[1], Juwan Kang[2], Yong Hyun Chung[2]

[1] Korea Institute of Nuclear Nonproliferation and Control, Safeguard Division, Daejeon, South Korea; [2] Yonsei University, Department of Radiation Convergence Engineering, Wonju, South Korea

This work was supported by the Nuclear Safety Research Program through the Korea Foundation Of Nuclear Safety(KoFONS) using financial resources granted by the Nuclear Safety and Security Commission (NSSC) of the Republic of Korea (RS-2021-KN063810).

Abstract

The Korea Institute of Nuclear Nonproliferation and Control (KINAC) has developed a portable Monochromatic Micro X-Ray Fluorescence (MMXRF) analyzer. This device is designed for the on-site measurement and evaluation of safeguards environmental samples to rapidly identify and respond to undeclared nuclear activities. Due to its portable nature for field inspections, the equipment is frequently subject to transportation. This movement can lead to misalignments between critical components which must remain precisely fixed for optimal performance. In this study, we conducted experiments to evaluate how transportation-induced alignment errors and environmental background noise affect the device's performance. The MMXRF system was transported from KINAC to two places. We measured the shift in the X-ray focal spot and background noise before and after each transit. Experimental results indicated a focal spot displacement of approximately 1.7 mm following transportation. While background noise levels remained relatively stable, significant performance degradation was observed during measurements of uranium-deposited swipe standard samples. These findings suggest that the shift in the X-ray focal spot is a primary driver of performance loss. In conclusion, this study confirms that the alignment stability of the X-ray generator is a critical factor in maintaining the reliability of portable safeguards equipment. We will discuss detailed methodologies and technical solutions to mitigate these alignment issues at the conference to ensure the high-fidelity performance of portable MMXRF systems in the field.

NSS-13-248

Measurement of 3-dimentional Distribution of ^{60}Co in a Graphite Block by Three Pinhole Gamma Cameras (#2268)

Jun Kawarabayashi, Yusuke Takabayashi, Naoto Hagura

Tokyo City University, Department of Nuclear Safty Engineering, Setagaya-ku, Japan

Abstract

Cobalt-60 isotopes are sometimes detected in graphite blocks used in research reactors with small cores. One possible cause of this cobalt-60 is the activation of impurities within the graphite blocks by neutrons. Another possible cause is the activation of rust adhering to the surface of the graphite blocks. When disposing of these graphite blocks, the distribution of radioactive materials measured by non-destructive methods would greatly contribute to improving the accuracy of radioactive material quantification. Therefore, we prototyped simple gamma camera combining a pinhole collimator and a phosphor plate. Using this camera, we imaged the block from three directions and attempted to measure the three-dimensional distribution of radioactive materials based on the acquired data. We prepared the detector response function in advance through Monte Carlo simulation. Images were captured by the gamma camera experimentally with a PLA resin block embedded with a cobalt-60 source and estimated the position of the source using ML-EM algorithm. From these results, when the source was placed at the corner of the block, the location of the source was estimated in the correct position. On the other hand, when the source was placed at the center, it was estimated to be at an adjacent position. Improving the accuracy of the response function is the next step of this study.

NSS-13-250

Verification of the Outer Space Treaty with trapped Protons in the VanAllen Radiation belt (#2270)

Areg Danagoulian

Massachusetts Institute of Technology, Nuclear Science and Engineering, CAMBRIDGE, USA

See https://arxiv.org/abs/2512.20016 for full a list of acknowledgements.

Abstract

The Outer Space Treaty (OST), opened for signature in 1967 and ratified by 117 countries including the U.S., Russia, and China, prohibits the placement of nuclear weapons in outer space. The OST, however, lacks any verification mechanism, and no peer-reviewed methodology for verification has been proposed in the open literature. Recent concerns over Russia's Kosmos2553, suspected of testing nuclear-armed anti-satellite (ASAT)

components, and a U.S. executive order calling for the detection of nuclear weapons in space, have made the need for a credible verification capability urgent. A nuclear detonation in Low Earth Orbit (LEO) could destroy most LEO satellites, as the 1962 Starfish Prime test demonstrated. This study presents a concept and feasibility analysis for verifying a satellite's compliance with the OST by detecting neutrons induced by proton spallation on the thermonuclear device's high-Z (uranium) radiation case. The interrogating GeV-energy protons are naturally provided by the inner Van Allen belt, requiring no active source. The proposed inspector is a 9U-CubeSat-sized directional neutron detector consisting of two 30x30 pixel planes, with each pixel formed by an EJ-276 PSD plastic scintillator wrapped in CVD-diamond active vetoes. Geant4 simulations characterize anti-coincidence rejection of the harsh proton/electron environment, directional discrimination of spallation neutrons from atmospheric albedo neutrons via neutron-scatter-camera kinematic reconstruction, and dead-time effects due to the high charged-particle flux. Combined with IRENE AP9/AE9 belt models and Carpenter's spallation yield, the analysis shows that the 9U inspector can confirm the presence of a thermonuclear weapon from a stand-off of 4 km in approximately one week, with a false-positive rate <1.1%. A constellation of ten inspectors at 1 km reduces this to a single-flyby inspection.

NSS-13-252

Optimization of Detector Configuration for Enhanced Neutron Imaging Reconstruction Accuracy in Tokamak Fusion Reactor (#2283)

Gyeongjin Choi, Beomkyu Kwon, Ill-Hyuk Han, Kyoung-Jae Chung

Department of Energy System Engineering, Seoul National University, Seoul, South Korea

This work was supported by the National Research Foundation of Korea (NRF) funded by the Ministry of Science and ICT (RS-2023-00281276) of the Republic of Korea.

Abstract

This study investigated the quantitative effects of neutron camera configuration with various parameter—the number of channels, colimator window diameter, and channel allocation for each port—on imaging performance in Deuterium-Tritium (DT) fusion reactor environments. Plasma neutron emission profiles were generated using the TRIASSIC code, which generating plasma shape, and detector signals were calculated in both 2-D and MCNP-based 3-D environments. Neutron image reconstruction was performed using the calculated detector signals, and reconstruction accuracy was evaluated using the Normalized Mean Square Error (NMSE). First, neutron image reconstruction was performed using the reference neutron camera configuration proposed for ITER and EURO-DEMO, resulting in an NMSE of 3.12%. To improve reconstruction accuracy, an expanded neutron camera configuration consisting of 10 and 16 channels for each vertical and radial neutron camera(VNC and RNC) port, respectively, was applied. The reconstructed results yielded NMSE values of 1.59% in the 2-D and 1.85% in the 3-D environment, both lower than the reference value. Reconstruction accuracy was strongly affected not only by the total number of detector channels but also by the channel distribution and Line-of-Sight (LoS) coverage. In particular, asymmetric detector distributions in the VNC ports generally produced lower NMSE values than symmetric configurations, while increasing the detector channel number in the RNC port improved reconstruction

accuracy overall. These results indicate that appropriate neutron camera configuration can enhance neutron imaging performance in DT fusion reactor environments and may provide fundamental data for future neutron camera design and optimization for DEMO-class fusion reactors.

References
[1] Lee, C. Y., et al. "Development of integrated suite of codes and its validation on KSTAR." Nuclear Fusion 61.9 (2021): 096020.
[2] Bertalot, Luciano, et al. "Concept design and integration aspects of ITER vertical neutron camera." *First EPs Conf. on Plasma Diagnostics (1st ECPD). Villa Mondragone, Frascati (Rome), Italy*. 2015.
[3] Cecconello, Marco, et al. "Pre-conceptual study of the European DEMO neutron diagnostics." *Journal of Instrumentation* 14.09 (2019): C09001.
[4] Bruyant, P. P., Analytic and Iterative Reconstruction Algorithms in SPECT, Nuclear Spectroscopy and Image Processing Research Group, Biophysics Laboratory, Claude Bernard University, Lyon, France, PhD Thesis, 2002.

NSS-13-254

NSS-13-256

Characterization of Floating Gate Dosimeter Structures through a Standardized FPGA-Based Radiation-Test Platform (#2338)

Evgenia Leonida[1,2], Salvatore Fiore[2], Antonio Scialdone[2], Salvatore Danzeca[2], Frederic Wrobel[1], Jerome Boch[1]

[1] University of Montpellier, IES - Institute of Electronics and Systems, Montpellier, France; [2] CERN, BE-CEM-EPR, Geneva, Switzerland

Abstract
Floating-gate dosimeters (FGDOS) are being investigated at CERN as candidates for the next generation of Total Ionizing Dose monitoring devices in the accelerator complex. This work presents the characterization of floating-gate dosimeter structures through a standardized CERN BE-CEM-EPR radiation-test platform using a common carrier board, dedicated sensor daughterboards with standardized pinout, and a Pynq FPGA readout implementing reusable gateware libraries and continuous-integration firmware validation. The platform allows the same device under test to transition from laboratory bring-up to irradiation facilities without setup modifications. The sensor is fabricated in a 0.6 µm CMOS process and exploits a digital control component — handling structure selection, bias control, charge injection, and frequency readout — combined with analog floating-gate NMOS structures, each paired with a matched dummy reference transistor for differential read-out. Two structures with different floating-

gate area to NMOS readout transistor ratios were characterized: a reduced-area variant at one quarter of the baseline retaining the same NMOS (TC994), and a variant with larger sensor area and optimized NMOS for lower noise (TC994). Four recharge modes were compared: disabled, comparator-based, counter-based, and bit-based. Temperature dependence of the sensor frequency was observed and used to validate the acquisition chain; sensor-to- reference frequency ratios were evaluated as a first-order thermal compensation method. The platform is being extended to a new generation of structures integrating normal NMOS, high-voltage NMOS, and parasitic NMOS readout implementations (TC994), whose laboratory and irradiation results will be presented with emphasis on suitability for future RadMon and BatMon Total Ionizing Dose monitoring at CERN.

References
[1] S. Fiore et al., “RadMon: a versatile, integrated radiation monitoring system for accelerators and experiments electronics at CERN” JINST20, 06 (2025) pp.C06015.
[2] A. Zimmaro et al., “Testing and Validation Methodology for a Radiation Monitoring System for Electronics in Particle Accelerators” IEEE Trans. Nucl. Sci., vol. 69, no. 7, pp. 1642-1650, July 2022.
[3] A. Zimmaro, R. Ferraro, S. Fiore, G. Lerner, A. Masi and S. Danzeca, “Advancing Radiation Hardness Assurance at CERN: Improved HEH Sensor for Enhanced Radiation Monitoring and Reliability System Study” IEEE Trans. Nucl. Sci., vol. 73, no. 4, pp. 1054-1062, April 2026.
[4] M. Brucoli et al., “Floating gate dosimeter suitability for accelerator-like environments,” IEEE Trans. Nucl. Sci., vol. 64, no. 8, pp. 2054–2060, Aug. 2017.
[5] M. Rizzo et al., “An enhanced sensitivity operation mode for floating gate dosimeters,” IEEE Trans. Nucl. Sci., vol. 69, no. 8, pp. 1876–1883, Aug. 2022
[6] S. Danzeca et al., “Characterization and modeling of a floating gate dosimeter with gamma and protons at various energies,” IEEE Trans. Nucl. Sci., vol. 61, no. 6, pp. 3451–3457, Dec. 2014

NSS-13-258

Physics-Informed Response Matrix Optimization for Neutron Flux Unfolding (#2476)

Kilyoung Ko, Wonku Kim, Jongbum Kim, Kibeak Shin, Jinjoo Kim, Sunjin Kim, Jin Kim, Gujin Kang, Jintae Hong

Korea Atomic Eneregy Research Institute, Radioisotope Research Division, Daejeon, South Korea

This work was supported by Korea Research Institute for defense Technology planning and advancement (KRIT) grant funded by the Korea 310 government (DAPA, Defense Acquisition Program Administration) (22-107-C00-007) (JRIT-CT-23-055)

Abstract
Accurate characterization of neutron fields is crucial in applications involving neutron-emitting radioisotopes, as surrounding materials can alter these energy distributions. This necessitates a detailed reconstruction of neutron flux distributions beyond just dose-rate measurements. Reliable neutron flux reconstruction using compact organic scintillation detectors remains challenging under spectrally modified neutron fields owing to nonlinear light yield and detector resolution effects. In this study, we investigated the robustness of neutron flux unfolding using a stilbene scintillation detector with response matrices optimized using a physics-informed genetic algorithm (GA) framework. Although local differences in the unfolded flux distributions were observed under source-or neutron field–

mismatched conditions, the overall spectral shapes remained stable. The approach aids neutron flux reconstruction for various safety and evaluation applications. It enhances assessments in mixed radiation fields and nuclear environments.

References
[1] R. M. Ambrosi et al., “European radioisotope thermoelectric generators (RTGs) and radioisotope heater units (RHUs) for space science and exploration,” Space Science Reviews, vol. 215, no. 55, 2019.
[2] C. Haodong, Y. Zhang, C. Zhang, H. Chen, Q. Xiang, J. Zeng, G. Hu, and Y. Liu, “Characterization of 238PuO2 neutron and gamma radiation based on the latest nuclear databases,” Radiation Physics and Chemistry, vol. 232, no. 112659, 2025.
[3] A. J. Zillmer et al., “Light Weight Radioisotope Heater Unit (LWRHU) User’s Guide,” Idaho National Laboratory, Idaho Falls, ID, USA, Tech. Rep. INL/LTD-21-64869, 2022.
[4] N. J. Roberts et al., “Radionuclide neutron source characterization techniques,” Metrologia, vol. 48, no. 6, pp. S239–S253, 2011.
[5] G. F. Knoll, Radiation Detection and Measurement, 4th ed. Hoboken, NJ, USA: John Wiley & Sons, 2010.
[6] J. B. Birks, The Theory and Practice of Scintillation Counting. Oxford, U.K.: Pergamon Press, 1964.
[7] V. Suman and P. K. Sarkar, “Neutron spectrum unfolding using genetic algorithm in a Monte Carlo simulation,” Nuclear Instruments and Methods in Physics Research Section A, vol. 737, pp. 76–86, 2014.
[8] H. Shahabinejad, S.A. Hosseini, M. Sohrabpour, “A new neutron energy spectrum unfolding code using a two-step genetic algorithm,” Nuclear Instruments and Methods in Physics Research Section A, vol. 811, pp. 82–93, 2016.
[9] S. A. Hosseini, “Neutron spectrum unfolding using artificial neural network and modified least square method,” Radiation Physics and Chemistry, vol. 126, pp. 75–84, 2016.

NSS-13-260

Comprehensive Modeling and Experimental Validation of a SiPM-Based Neutron–Gamma Pulse Shape Discrimination System (#2568)

Orith Halfon[1,3], Christian Riboldi[1,3], Korbinian Urban[1,3], Giacomo Borghi[1,3], Marco Carminati[1,3], Franco Camera[2,3], Olga Maiatska[4], Juergen Stein[4], Guntram Pausch[4], Carlo E. Fiorini[1,3]

[1] Politecnico di Milano, Dipartimento di Elettronica, Informazione e Bioingegneria, Milan, Italy; [2] Università degli studi di Milano, Dipartimento di Fisica, Milan, Italy; [3] Istituto Nazionale di Fisica Nucleare, Sezione di Milano, Milan, Italy; [4] Rapiscan Systems GmbH, Wuppertal, Germany

This work is partially supported by the REALPATH project.

Abstract
In recent years, increasing attention in nuclear and medical applications has focused on detectors capable of neutron–gamma discrimination, with Pulse Shape Discrimination (PSD) being one of the most widely used and versatile techniques. A compact real-time detector has been previously developed, providing an event-by-event digital PSD parameter and a flexible platform for both organic and inorganic scintillators, as demonstrated using the CLYC crystal and, more recently, the M-700 scintillator. The system is based on a scintillator coupled to NUV-HD SiPM arrays and compact front-end electronics enabling real-time acquisition and processing. The detector achieves moderate Figures of Merit (FOM) while ensuring reliable neutron–gamma separation. To investigate the factors limiting its performance, an analytical model of the full detection chain was developed, including scintillator–SiPM coupling, readout electronics, and the main noise contributions (electronic noise, statistical fluctuations, time jitter, amplitude walk, and finite bandwidth-induced shaping in the analog chain). This framework allows the decoupling and quantitative evaluation of the effects limiting discrimination accuracy. Preliminary results show good

agreement with experimental data and identify the dominant limiting factors, providing guidance for targeted improvements and further performance enhancement.

References
[1] L. Buonanno , et al. GAMMA: A 16-Channel Spectroscopic ASIC for SiPMs Readout With 84-dB Dynamic Range. IEEE Trans. Nucl. Sci., 2021.
[2] O. Halfon , et al. A position sensitive detector with real-time gamma/neutron discrimination capability. IEEE Transactions on Nuclear Science, 72(7):2215–2221, 2025.
[3] O. Maiatska , et al. Polyurethane-based scintillators for neutron and gamma radiation detection in medical and industrial applications. Radi ation Measurements, 193:107647, 2026
[4] A. Gola , et al. Nuv-sensitive silicon photomultiplier technologies developed at fondazione bruno kessler. Sensors, 19:308, 01 2019

NSS-13-262

Blade Checker – Radioisotope-free Positron Generator coupled with HPGe-based Doppler Broadening Spectroscopy for aircraft components maintenance operation (#2689)

Michael Ginsz[1], **Damian Ralet**[1], Jean-Michel Rey[2]

[1] MIRION Technologies, Lingolsheim, France; [2] POSITHOT, Villebon sur Yvette, France

Abstract
Accessing an early stage of damage evolution is a key factor for the aircraft industry. Positron annihilation allows very accurate and nondestructive measurement of defect density, and its future evolution, as probed by Doppler Broadening Spectroscopy. Once the limited availability of positrons is addressed using a nonradioactive positron generator, application of positron annihilation can be foreseen for maintenance activity addressing the aircraft industry.
The Blade Checker project is a proof of concept to demonstrate this capability. Although Blade Checker is focusing on the aircraft industry, this technique could be extended to other fields. It consists of a novel accelerator-based, radioisotope-free positron generator, custom HPGe detectors and an experimental setup allowing the defect density measurement on mechanical parts up to 3 dm^3.
The AM Gen is an accelerator-based positron generator, developed by POSITHOT, with a compact design and including the Xray shielding. Complemented by a beam stretching device, it provides a continuous positron flux of approximately 5.10^6 positrons per second. The generator has been commissioned by the French nuclear safety authority.
The signals coming from the positron annihilation require the resolving power of a High Purity Germanium (HPGe) detector focusing on the 511 keV peak shape analysis. MIRION Technologies developed a custom, 7-element, electrically cooled HPGe detector placed inside a vacuum chamber as close as possible to the sample to be measured. Several small elements are preferred over one large crystal to avoid pile-up effects. A time-listed multi-channel data-acquisition is used to have in-beam time correlation and coincidence.
A description of the systems, positron generator, HPGe system and readout, together with some results from material characterization and projected probing speed will be presented.

NSS-13-264

Optimization of the neutron source size for compensated neutron well logging (#2703)

Yu Xiang Liu, Yigang Yang

Tsinghua University, Department of Engineering Physics, Beijing, China

Abstract

Compensated neutron logging commonly employs isotopic neutron sources based on (α,n) reactions, such as Am–Be sources, which are typically approximated as point sources due to their small physical dimensions. However, alternative neutron sources based on (γ,n) reactions may require significantly larger target volumes to achieve sufficient neutron yield, making the point-source approximation no longer applicable. In this work, Monte Carlo simulations based on MCNP are performed to investigate the effect of neutron source length on compensated neutron logging response. A limestone–water formation model and a dual-detector configuration with near and far He-3 detectors are employed. The results show that the porosity sensitivity initially increases with source length, reaches a maximum at approximately 20 cm, and then gradually decreases. A figure-of-merit (FOM) combining sensitivity and statistical stability is further introduced, which increases monotonically with source length while gradually approaching saturation. The results provide a quantitative basis for neutron source optimization in compensated neutron logging.

NSS-13-266

Three-Dimensional Radiation Source Reconstruction with a Compound-Eye Compton Camera Using a NeRF-Inspired Neural Field (#2721)

Wenjie Yu, Minghao Dong, Yongshun Xiao

tsinghua university, beijing, China

Abstract

Compton cameras (CCs) have a large field of view and a wide energy detection range, and are useful in nuclear security monitoring, environmental radiation measurement, nuclear accident response, and radiation source localization. However, their depth accuracy is still limited in practical three-dimensional source localization. A single detector view provides weak spatial constraints, so traditional Compton reconstruction methods can produce depth errors, especially with few events, strong noise, or distant sources. Artifacts may also appear in the reconstructed images. To address this problem, we propose a three-dimensional radiation source reconstruction method for a compound-eye Compton camera based on a NeRF neural network structure. The aim is to improve localization accuracy by combining the compound-eye geometry with neural field learning. We simulated a compound-eye

detector system with 25 scatterers arranged on a spherical surface and absorbers arranged in a plane. For each detector view, list-mode Compton event data were used to perform independent MLEM reconstruction, and a source distribution image was obtained. These reconstructed images and the corresponding detector pose information were then used as training data for the neural field network. Preliminary results show that, after training with multi-detector data, the reconstructed three-dimensional radiation intensity distribution becomes more concentrated. The peak intensity position is closer to the true source position, and the depth shift is reduced. These results show that multi-detector geometric constraints can provide useful information for three-dimensional radiation source reconstruction, and that combining a compound-eye Compton camera with neural field reconstruction is feasible.

References
[1] Dong, M., Ouyang, X., Luo, X., & Xiao, Y. (2026). Compound-eye-vision-based 3-D position estimation of radioactive sources using a GAGG Compton camera. Measurement, 264, 120321.
[2] D. Dietz, et al., "3D Gamma-Ray Source Localization Using Deep Learning," IEEE Transactions on Nuclear Science, vol. 71, no. 7, pp. 1658-1666, July 2024.
[3] S. Sato, K. S. Tanaka, J. Kataoka; ComptonNet: A direct reconstruction model for Compton camera. Appl. Phys. Lett. 17 June 2024; 124 (25): 253702.
[4] Z. Shen, H. Wang, K. Yi, and S. K. Zhou, "NeRP: Implicit Neural Representation Learning with Prior Embedding for Sparse View CT Reconstruction," IEEE Transactions on Neural Networks and Learning Systems, vol. 35, no. 2, pp. 1923-1936, Feb. 2024.

NSS-13-268

Advancing Beam Diagnostics on ESS Neutron Beamlines: Simulation and Validation of Ionization Chamber Monitors (#2765)

Ali Altingün[2], Alexandros Gardikiotis[1], Ioannis Katsioulas[2], Martin Klein[4], Christos Lampoudis[1], **Evangelos Samouilidis**[1], Christian J. Schmidt[3]

[1] Aristotle University of Thessaloniki, Physics Department, Thessaloniki, Greece; [2] European Spallation Source, Lund, Sweden; [3] GSI Detector Laboratory, Darmstadt, Germany; [4] CDT CASCADE Detector Technologies GmbH, Heidelberg, Germany

We would like to thank Dr Jochen Stahn (PSI) and Dr Davide Raspino for the beam time and support during the measurements at the AMOR and MORPHEUS instruments at the Paul Scherrer (CH) Institute and the EMMA beam line in the ISIS facility at the Rutherford Appleton Laboratory (UK).

Abstract
The European Spallation Source (ESS), expected to start its scientific program in 2027, will be the world's most powerful neutron source. This facility requires advanced systems for accurate beam monitoring and diagnostics. To meet these requirements, dedicated detectors have been designed to operate at ESS, one of them being the Ionization chamber Beam Monitor (I-BM). This work presents detailed simulation studies, using Geant4, Garfield++ and LTspice, to investigate energy deposition, charge transport, induced current formation, and front-end electronics response. Experimental data from neutron beam test campaigns are also included to support the evaluation of the I-BM performance.

References
[1] K. H. Andersen, D. N. Argyriou, A. J. Jackson, J. Houston, P. F. Henry, P. P. Deen, et al., ”The instrument suite of the European Spallation Source,” Nucl. Instrum. Methods Phys. Res. A, vol. 957, Art. no. 163402, 2020, doi: 10.1016/j.nima.2020.163402.
[2] R. Garoby et al., ”The European Spallation Source Design,” Physica Scripta, vol. 93, no. 1, Art. no. 014001, Dec. 2017, doi: 10.1088/1402-4896/aa9bff.
[3] Ionization Chamber Neutron Beam Monitor (I-BM) Operating Manual, CDT CASCADE Detector Technologies GmbH, Heidelberg, Germany, Jul. 11, 2024.
[4] C. Cazzaniga, D. Raspino, G. J. Sykora, and C. D. Frost, ”Dosimetry of thermal neutron beamlines at a pulsed spallation source for application to the irradiation of microelectronics,” IEEE Trans. Nucl. Sci., vol. 68, no. 5, pp. 921–927, May 2021, doi: 10.1109/TNS.2021.3064681.

NSS-13-270

Indoor 3D Gamma Radiation Mapping Based on VSLAM and Its Application in NPPs (#2909)

Hui Li[1,2], Hua Li[1], Liye Liu[1], Qing Fan[1], Mingmin Wang[1], Faguo Chen[1]

[1] China Institute for Radiation Protection, TaiYuan, China; [2] University of Science and Technology of China, Hefei, China

This work was supported by the Youth Science Research Project of the Shanxi Provincial Basic Research Program (No. 202403021212024) and the Young Talent Program of China National Nuclear Corporation (Nos. JY24070301 and JY25070303).

The authors thank the participating nuclear power plant staff and project team members for their support during laboratory tests, field measurements and digital-system integration.

Abstract

Fast, spatially complete and digitally usable radiation information is essential for radiation protection in nuclear power plants (NPPs), particularly during maintenance, decommissioning and emergency response. Conventional surveys usually separate geometric measurement from dose-rate measurement, which makes data acquisition slow, labor-intensive and difficult to integrate with digital radiation-protection platforms. This paper presents an indoor three-dimensional (3D) gamma radiation mapping method based on visual simultaneous localization and mapping (VSLAM). The developed DoseMap system combines an RGB-D VSLAM module with a hot-pluggable Geiger--Muller gamma dose-rate detector. Environmental point clouds, measurement trajectories and gamma dose-rate data are fused through timestamp synchronization and an integral path midpoint method, enabling real-time 3D visualization, radiation-field interpolation and hotspot localization. Tests in laboratories and NPP environments show that more than 80\% of the reconstructed scene point cloud is within 0.2 m of the reference cloud, the trajectory localization error is approximately 4 cm, the single-source hotspot localization error is less than 0.2 m, and measurement efficiency is improved by a factor of 26.8 compared with traditional survey workflows. The method has also been linked with the smart radiation-protection support system(SMARP), demonstrating its potential for digital twins, ALARA planning and remote or robotic radiation surveys.

References
[1] Young, K. L., Phillips, C. K., Reyes, M. D., et al. (2025). Mission results: Creating a 3D map of a very high radiation confined space using the LiDAR-equipped Elios 3 drone. *Nuclear Science and Engineering*, 199(8), 1351–1363.
[2] Vavrek, J. R., Pavlovsky, R., Negut, V., & others. (2025). Demonstration of a new CLLBC-based gamma- and neutron-sensitive free-moving omnidirectional imaging detector. *arXiv preprint*, arXiv:2503.09862.Knoll, G. F. (2010). *Radiation Detection and Measurement* (4th ed.). Wiley.
[3] Hautot F, Dubart P, Bacri C O, et al. (2017). Visual simultaneous localization and mapping (VSLAM) methods applied to indoor 3D topographical and radiological mapping in real time. *EPJ Web of Conferences*, **153**, 01005.
[4] Hautot F, Dubart P, Bacri C O, et al. (2017). Visual simultaneous localization and mapping (VSLAM) methods applied to indoor 3D topographical and radiological mapping in real time. *EPJ Web of Conferences*, **153**, 01005.
[5] Vetter, K. (2016). Multi-sensor radiation detection, imaging, and fusion. *Nuclear Instruments and Methods in Physics Research Section A: Accelerators, Spectrometers, Detectors and Associated Equipment*, 805, 127–134.
[6] H. Li, Q. Fan, H. Li, et al. (2024). Research on automatic measurement method of three-dimensional gamma dose rate radiation field based on VSLAM, Atomic Energy Science and Technology, vol. 58, no. S, pp. 157--166

NSS-13-272

Photofission Prompt Neutron Measurements from Active Photon Interrogation of Depleted Uranium with a Superheated Droplet Detector

(#2913)

Johann Piekar, Jeanne Vinoy, Vesna Simic, Adrien Sari

Université Paris - Saclay, CEA, LIST, F - 91120, Palaiseau, France

Abstract

Illicit transport of uranium-bearing materials remains a concern for nuclear security when passive radiation signatures are weak, shielded, or ambiguous. Active photon interrogation can induce photofission in uranium using a Bremsstrahlung field generated by 9 MeV electrons and provide neutron signatures from this reaction. Established photofission approaches commonly exploit delayed neutrons or delayed gamma rays measured after irradiation or in beam-off windows, which helps reject prompt radiation fields but imposes constraints on timing, sufficient decay statistics, and acquisition duration. Here, we propose a proof-of-concept measurement of prompt photofission neutrons using a depleted uranium bar and a commercial superheated droplet detector. Such passive neutron sensors rely on nuclear recoils that form bubbles when local energy deposition exceeds a thermodynamic threshold, while photon-induced low-LET interactions are strongly suppressed. Although superheated droplet detectors are established for neutron dosimetry and photon rejection, their use for measuring prompt neutrons from photofission during active photon interrogation has not, to our knowledge, been demonstrated experimentally. Measurements will be acquired with and without uranium under identical beam, geometry, shielding, and temperature conditions. The integrated response will be normalized to irradiation time under fixed beam settings, with beam-current or dose-monitor information used to check the stability of the photon output. A 20°C temperature-controlled bath stabilizes detector response. Polyethylene shielding is placed within the direct solid angle of the converter as seen by the detector, in order to reduce the linac-induced photoneutron component reaching the measurement region. The experiment will test whether uranium produces a reproducible excess above this background and will define requirements for prompt photofission neutron measurements at sub-10 MeV electron energy.

NSS-13-274

Characterization and Comparison of State-of-the-Art Handheld Gamma-Imaging Field Spectrometers (#3056)

Ariel A. Alcaide[1], Juan J. Manfredi[1], Michael Ford[1], Bal Parajuli[2]

[1] Air Force Institute of Technology, Engineering Physics, Dayton, USA; [2] U.S. Air Force School of Aerospace Medicine, Dayton, USA

Abstract

Portable gamma-ray spectrometers with integrated imaging capability represent a significant advancement in field radiation detection by combining radionuclide identification with real-time source localization. These systems have the potential to reduce operator dose through stand-off detection while improving situational awareness in safeguards, emergency response, and radiological assessment missions. This work characterizes and compares two novel handheld gamma-imaging spectrometers: the PHDS GeGI, a mechanically cooled high-purity germanium (HPGe) system, and the H3D H420, a cadmium zinc telluride (CZT)-based detector employing room-temperature semiconductor technology. Baseline performance testing evaluated energy resolution, intrinsic photopeak efficiency, imaging capability, and operational factors including power consumption. Laboratory measurements confirmed that both detectors achieved manufacturer-stated energy resolution at 662 keV, with the GeGI demonstrating superior spectroscopic resolution while the H420 exhibited greater intrinsic photopeak efficiency across much of the tested energy range due to detector geometry and material characteristics. High-gamma-flux testing revealed that the H420 maintained functional spectroscopy and reliable gamma-imaging performance at significantly closer source distances, whereas the GeGI experienced degradation in spectral quality, imaging accuracy, and mission suitability under elevated exposure conditions. The results demonstrate complementary advantages between the two systems: the GeGI provides superior high-resolution isotope identification, while the H420 offers improved operational robustness, imaging stability, and field deployability. These findings support the development of expanded field-performance evaluation frameworks for next-generation gamma-imaging spectrometers and provide guidance for mission-specific detector selection.

NSS-13-276

NSS-13-278

Prototyping ALPIDE-based Modules for the R^{3}B Target Recoil Tracker Detector (#1352)

Beatriz Amorim[4], Paul Booker[2], Marcello Borri[2], **Matthew Buckland**[2], Liam Godfrey[2], William Helsby[2], Andrew Hill[2], Oleg Kiselev[1], Marc Labiche[2], John Lipp[2], Paul Morrall[2], Stefanos Paschalis[4], Marina Petri[4], Luke Rose[4], Dave Seddon[3], Konrad Sutowski[2]

[1] GSI Helmholtzzentrum für Schwerionenforschung GmbH, Darmstadt, Germany; [2] UKRI Science and Technology Facilities Council, Technology Department, Warrington, UK; [3] University of Liverpool, Department of Physics, Liverpool, UK; [4] University of York, Department of Physics, York, UK

The authors would like to acknowledge the UKRI Science and Technology Facilities Council (STFC) for funding this project (ST/X006573/1).

Abstract

R3B is a fixed target experiment at the Facility for Antiproton and Ion Research (FAIR) (DE). The setup comprises different sub-detectors that perform kinematically complete measurements of reactions with high-energy radioactive beams. One such sub-detector is the Target Recoil Tracker (TRT), placed in vacuum around a target. The TRT aims to detect light charged particles with an efficiency of ≥ 65 % and provide precise tracking (≤ 10 μm), angular resolution (≲ 2 mrad), and reaction vertex reconstruction, over a large acceptance (≈10° to 90°). It consists of two concentric barrels with radii 5 cm and 6.5 cm, and a total active length of ~ 27 cm. It utilizes silicon Monolithic Active Pixel Sensors (MAPS) thinned down to 50 μm. The ALPIDE sensor, developed by ALICE/CERN, was chosen as its technology is mature and fulfills the R3B detector requirements.

A module consists of 9 chips glued to an aluminum-based Flexible Printed Circuit (FPC) and wire-bonded, with a total material budget of ~ 0.16% X/X_0. The assembly has undergone extensive prototyping through low-, mid-, and high-readiness modules, during which assembly procedures, quality assurance, databases, manuals, and electrical tests were developed in preparation for launching pre-production. The last batch of high-readiness prototypes has been assembled with all final materials and tested. The prototypes show a functional response from all chips, demonstrating the ability to construct fully working production-level modules. Validation tests include a scan of the module with a ^{90}Sr source coupled to an external trigger, and vacuum tests down to 1×10^{-4} mbar. This paper will present the latest developments from the last prototyping stage. UKRI-STFC Laboratories and the University of York aim to deliver 60 production-level modules to FAIR by October 2027.

References

[1] H. Gutbrod et al., “FAIR Baseline Technical Report”, vol. 4, ISBN3-9811298-0-6P, pp.41-82, March 2006.

[2] R3B Collaboration, “Technical Report for the Design, Construction and Commissioning of the Pixel-based Target Recoil Tracker (TRT) for R3B,” July 2024. [Online] Available: https://edms.cern.ch/document/3129317/1. Accessed on: April 29, 2026.

[3] M. Borri et al., “FAIR R3B-TRT: a MAPS-based Si-tracker,” 2024 IEEE NSS MIC RTSD, Tampa, FL, USA, Sept 2024, pp. 1-1.

[4] A. Di Mauro, “The new inner tracking system for the ALICE upgrade at the LHC,” Nucl. Instr. Meth. A936, Aug 2019.

[5] M. Buckland. (2020). Series Production and Test of Hybrid Modules for the ALICE ITS Upgrade. 063. https://doi.org/10.22323/1.373.0063.

NSS-13-280

Development of a Single-Layer Dual-Ended Readout Compton Camera Prototype for Enhanced Spatial Imaging (#1799)

Haoqi Wen, Chenxi Li, Yucun Hou, Kexin Wang, Jianyong Jiang

Beijing Normal University, Key Laboratory of Beam Technology of Ministry of Education, School of Physics and Astronomy, Bejing, China

This work was supported by the NSFC (No. 12475336).

Abstract

The Compton camera has emerged as a pivotal gamma-ray imaging technique, with critical applications in astrophysical observation, nuclear safety monitoring, and environmental radiation detection. In nuclear astrophysics, the detection and localization of gamma rays in the MeV range are indispensable for probing high-energy cosmic phenomena. Despite its importance, the advancement of MeV gamma-ray imaging instrumentation remains constrained by low interaction probabilities and high imaging complexity. This study presents a single-layer Compton camera prototype designed for enhanced spatial imaging, building upon the mission heritage of the BNU-120—a space-borne detector successfully deployed for monitoring gamma-ray bursts (GRBs). To transcend the original system's lack of spatial imaging capability, we propose a high-performance architecture that leverages the established BNU-120 framework while integrating a dual-ended readout to achieve a 4π detection solid angle. The prototype uses a 8×8 Ce:GAGG array coupled to Hamamatsu Multi-Pixel Photon Counters (MPPC, S14161-3050HS-08) at both ends. Each crystal measures 3×3×25 mm^3 and is optically isolated by 0.2-mm-thick $BaSO_4$ reflective layers. System characterization demonstrated an energy resolution of approximately 5% (FWHM) at 511 keV. Depth-of-interaction (DOI) information, extracted via the energy ratio method, yielded a DOI resolution of roughly 2 mm (FWHM) along the crystal axis. Computational validation using GATE simulations of a U-shaped 511 keV planar source showed that the source geometry was clearly distinguishable through a back-projection (BP) algorithm. Subsequent point-source experiments verified the detector's capability to localize discrete sources. Future work will focus on realistic physical imaging experiments and the exploration of more advanced reconstruction algorithms to fully evaluate the module's Compton imaging performance.

References
[1] W. Jiang, et al., “Calibrations of the BNU-120 gamma-ray detector based on GAGG Scintillators,” J. Beijing Normal Univ. (Nat. Sci.), vol. 58, pp. 1-6, 2022.
[2] J. Jiang et al., “A prototype of aerial radiation monitoring system using an unmanned helicopter mounting a GAGG scintillator Compton camera,” Journal of Nuclear Science and Technology, vol. 53, no. 7, pp. 1067–1075, Jul. 2016, doi: 10.1080/00223131.2015.1089796.
[3] C. Li et al., “Performance characterization of a Compton camera prototype based on a novel epitaxial-quenching-resistor SiPM,” J. Inst., vol. 20, no. 05, p. P05048, May 2025, doi: 10.1088/1748-0221/20/05/P05048.
[4] B. Das, B. Mehrdel, D. Goodman, M. Streicher, Y. Seo and J. Caravaca, "Compton Imaging of Ac-225 in Preclinical Phantoms With a 3D-positioning CZT Camera," in *IEEE Transactions on Radiation and Plasma Medical Sciences*, vol. 10, no. 1, pp. 112-125, Jan. 2026, doi: 10.1109/TRPMS.2025.3577212.
[5] Z. Kuang et al., “Dual-ended readout small animal PET detector by using 0.5 mm pixelated LYSO crystal arrays and SiPMs,” Nuclear Instruments and Methods in Physics Research Section A: Accelerators, Spectrometers, Detectors and Associated Equipment, vol. 917, pp. 1–8, Feb. 2019, doi: 10.1016/j.nima.2018.11.011.

NSS-13-282

A GRID CubeSat Phoswich Payload for Space-Based Neutron Lifetime Measurement (#1825)

Qidong Wang[1], Haotian Qi[2], Fei Sha[1], Longhao Li[1], Xiaopeng Zhou[2], Baohua Sun[2], Xutao Zheng[1], Ming Zeng[1], On behalf of GRID Collaboration

[1] Tsinghua University, Department of Engineering Physics, Beijing, China; [2] Beihang University, School of Physics, Beijing, China

This work is supported by the Tsinghua University Initiative Scientific Research Program, and the Tsinghua-Kunshan Student Innovation and Entrepreneurship Talent Cultivation Agreement.

Abstract

A 1U-CubeSat payload for the Gamma-Ray Integrated Detectors (GRID) mission has been developed, expanding its scientific scope from transient gamma-ray burst (GRB) monitoring to include space-based neutron lifetime measurements in Low Earth Orbit (LEO). Constrained by a strict form factor (1U, 1.3 kg, 8 W), the payload retains two legacy GAGG scintillators for GRB detection while introducing two novel CLYC-plastic phoswich probes for thermal neutron measurement. To discriminate thermal neutrons within complex orbital backgrounds, the phoswich architecture enables robust pulse shape discrimination (PSD). To mitigate spacecraft-induced secondary neutrons, Gadolinium (Gd) shielding is applied to the sides and backs of both phoswich probes. Furthermore, a differential front-shielding design is employed to extract the thermal neutron flux. An in-orbit Charge Comparison Method (CCM) algorithm is implemented, which optimizes telemetry by processing the PSD signals in real-time, adding only two bytes per event. Ground calibrations demonstrate a neutron-gamma Figure of Merit (FoM) of 1.25, and preliminary cold neutron beam tests validate the differential shielding concept. The payload successfully balances multi-messenger astronomy and fundamental physics goals, verifying its readiness for flight.

References

[1] J. T. Wilson, D. J. Lawrence, P. N. Peplowski, V. R. Eke, and J. A. Kegerreis, "Measurement of the free neutron lifetime using the neutron spectrometer on NASA's Lunar Prospector mission," *Phys. Rev. C*, vol. 104, no. 4, p. 045501, Oct. 2021, doi: 10.1103/PhysRevC.104.045501.

[2] J.-X. Wen *et al.*, "Compact CubeSat Gamma-ray detector for GRID mission," *NUCL SCI TECH*, vol. 32, no. 9, p. 99, Sep. 2021, doi: 10.1007/s41365-021-00937-4.

[3] A. Giaz *et al.*, "The CLYC-6 and CLYC-7 response to γ-rays, fast and thermal neutrons," *Nuclear Instruments and Methods in Physics Research Section A: Accelerators, Spectrometers, Detectors and Associated Equipment*, vol. 810, pp. 132–139, Feb. 2016, doi: 10.1016/j.nima.2015.11.119.

NSS-13-284

Crosstalk and Charge collection in the ATLASPix3.1 (#2166)

Sean Williams[1], Attilio Andreazza[2], Richard Ballard[1], Henry Bichard[1], Roushi Dong[3,4], Jens Dopke[5], Harald Fox[6], Yanyan Gao[7], Elizabeth Hutchinson[6], Tim Jones[8], Yiming Li[4], Lingxin Meng[6], Daniel Muenstermann[9], Ivan Peric[3], Fabrizio Sabatini[2], Fuat Ustuner[7], **Jaap J. Velthuis**[1], Fergus Wilson[5], Riccardo Zanzottera[2], Shenghui Zeng[1]

[1] University of Bristol, School of Physics, Bristol, UK; [2] Università degli Studi di Milano and INFN Sezione di Milano, Milano, Italy; [3] Karlsruhe Institute of Technology, ASIC and Detector Lab / IPE, Karlsruhe, Germany; [4] Institute of High Energy Physics, Chinese Academy of Sciences, Beijing, China; [5] STFC Rutherford Appleton Laboratory, Particle Physics, Didcot, UK; [6] Lancaster University, Department of Physics, Lancaster, UK; [7] University of Edinburgh, School of Physics and Astronomy, Edinburgh, UK; [8] University of Liverpool, Department of Physics, Liverpool, UK; [9] RheinMain University of Applied Sciences, Faculty of Engineering, Wiesbaden, Germany

Abstract

The ATLASPix3.1 is a full reticle HV-CMOS sensor [1]. It is under study for future lepton colliders [2] and is part of the family of sensors leading to the MightyPix for LHCb and the MuPix for Mu3e. This makes detailed studies of the sensor performance important. We previously reported signal to noise, cluster size and position resolution [3]. Here a detailed study of cross talk and charge collection is presented. Between ATLASPix3.0 and ATLASPix3.1 masks were changed to improve the chip properties at the cost of introducing cross talk. Two types of cross talk were found. Type I yields small signal at fixed positions determined by the hit location. These typically have a signal less than 15% of the original signal. Around 99% of these clusters can be suppressed using a simple minimal signal cut. There is a second type of cross talk hits that yield high signals. An attempt was made to identify these cross talk hits using a gradient-boosted decision tree analysis with variables reflecting cluster shape & signal and signal spread over the pixels. We show that it is not possible to efficiently remove these hits based on cluster properties. This can result in a track candidates with similar χ^2. This can be addressed in an updated design of the sensor and/or by further optimising settings. Using a grazing angle scan the charge collection was studied. In the depletion zone, the charge will be collected quickly. Charge generated in the non-depleted zone will yield a lower and later signal. The depth of the depletion zone was derived as a function of bias voltage. The results show that the depletion depth is proportional to the square root of the bias volrage as would be expected for a planar silicon detector. The experiments have shown that the sensor has very good performance, serving as a promising candidate for future lepton colliders.

References
[1] M. Prathapan et al., PoS(TWEPP2019)010
[2] The IDEA Study Group, arXiv:2502.21223v4 (2025)
[3] L. Meng, Proceedings VERTEX2022

NSS-13-286

Radiation-Tolerant Fast Analogue Pixel Test Structures in TPSCo 65 nm CMOS Technology for the ALICE ITS3 Upgrade (#2439)

Umberto Savino[1,2]

[1] University of Torino, Department of Physics, Torino, Italy; [2] INFN, Section of Torino, Torino, Italy

Abstract

The ALICE ITS3 upgrade represents a major advancement in silicon tracking, exploiting the commercial 65 nm CMOS imaging technology to develop ultra-thin monolithic active pixel sensors (MAPS) for high-energy physics applications. The target detector performance includes an extremely low material budget below 0.09% X0 per layer, with a spatial resolution below 5 μm, and radiation tolerance up to 4×10^{12} 1 MeV n_{eq} cm^{-2}.

Several pixel test structures have been designed and fabricated to investigate both sensor geometries and front-end architectures. In particular, analogue pixel test structures (APTS) featuring a fast operational amplifier (APTS-OA) as output buffer have been developed to study charge collection dynamics and the intrinsic timing performance of the sensor. Measurements performed in charged-

particle beam tests demonstrated a best time resolution of 63 ps, combined with a charge collection efficiency above 99% and a spatial resolution better than 3 μm, while maintaining stable performance up to 1×10^{14} 1 MeV n_{eq} cm^{-2}.

Building on these results, a second engineering run (ER2) introduced three novel chip variants targeting enhanced detector performance and improved radiation robustness. In particular, the optimization of the low-dose n-implant located below the n-well collection electrode aims at reducing the sensor capacitance while enhancing the lateral electric field, thereby improving sensor

depletion and restoring charge collection performance after radiation damage.

This contribution presents the characterization of the new APTS-OA variants and discusses their impact on timing performance, charge collection efficiency, and radiation tolerance through measurements performed on both irradiated and non-irradiated devices.

Laboratory characterization results will be presented providing insight into the effectiveness of the ER2 design optimizations for radiation-tolerant fast MAPS detectors.

NSS-13-288

Off-detector Readout and Real-time Signal Processing for the ATLAS Liquid ArgonCalorimeter at the High-Luminosity LHC (#2635)

Pablo Collado Soto[2], **Nikiforos Nikiforou**[1], On behalf of the ATLAS Collaboration

[1] CERN, Geneve, Switzerland; [2] Universidad Autonoma de Madrid, Physics Department, Madrid, Spain

Abstract
The ATLAS Liquid Argon (LAr) calorimeter readout electronics are being upgraded for operation at the High-Luminosity Large Hadron Collider (HL-LHC), where up to approximately 200 proton-proton interactions per bunch crossing will significantly increase detector occupancy, data throughput, and trigger rates. While the calorimeter detectors themselves remain unchanged, the full readout electronics chain is being replaced. The upgraded off-detector processing system continuously receives digitized calorimeter signals from approximately 182000 channels at the 40 MHz bunch-crossing rate through high-speed optical links. The processing architecture is implemented in Advanced Telecommunications Computing Architecture (ATCA) systems hosting large FPGAs performing real-time reconstruction of energy and timing while satisfying stringent trigger latency requirements. Prototype hardware and firmware have been developed and validated in integration setups combining front-end electronics, timing distribution, and data acquisition systems. In parallel, advanced reconstruction methods including machine-learning approaches optimized for FPGA implementation are being investigated to improve robustness against pileup and overlapping pulses.

NSS-13-290

Crystal Dual-Readout Calorimetry for Future e^+e^- Higgs Factories (#2842)

Marcello Campajola[1], Mariagrazia Alviggi[2,1], Benedetta Argiento[3,1], Etiennette Auffray[4], Andrea Benaglia[5], Maurizio Biasini[7,8], Valeria Bisignani[2,1], Daniele Boccanfuso[6,1], Lucrezia Borriello[3,1], Claudia Cecchi[7,8], Francesco Cirotto[2,1], Francesco Conventi[3,1], Antonio D'Avanzo[2,1], Julie Delenne[9,4], Guglielmo De Nardo[2,1], Carlo Di Fraia[2,1], Adelina D'Onofrio[1], Leonardo Favilla[6,1], Marco Francesconi[1], Giovanni Gaudino[1], Orso Alberto Maria Iorio[2,1], Vincenzo Izzo[1], Marco Toliman Lucchini[10,5], Elisa Manoni[8], Marco Mirra[1], Stefano Moneta[8], Pierluigi Paolucci[1], Simone Perna[3,1], Biaggio Rossi[1], Elvira Rossi[2,1], Julia Scamardella[2,1], Givi Sekhniaidze[1]

[1] INFN, Sezione di Napoli, Napoli, Italy; [2] Università degli Studi di Napoli Federico II, Napoli, Italy; [3] Università degli Studi di Napoli Parthenope, Napoli, Italy; [4] CERN, Ginevra, Switzerland; [5] INFN, Sezione di Milano-Bicocca, Milano, Italy; [6] Scuola Superiore Meridionale, Napoli, Italy; [7] Università degli Studi di Napoli Perugia, Perugia, Italy; [8] INFN, Sezione di Perugia, Perugia, Italy; [9] Université de Strasbour, Strasbour, France; [10] Università degli Studi di Milano-Bicocca, Milano, Italy

This work was performed in the framework of DRDcalo. It received funding from the European Union – Next Generation EU programme, Mission 4, Component 1 (CUP H53D23001120006), and from the Horizon Europe ERA Widening Project no. 101078960 TWISMA.

Abstract
Precision physics at future e+e− Higgs factories set stringent requirements on calorimetric performance, with 3%/√E for electromagnetic particles and ∼ 30%/√E for neutral hadrons identified as key benchmarks. A hybrid dual-readout approach, combining a homogeneous crystal electromagnetic section with a fiber-based hadronic section, offers a cost-effective path toward simultaneously achieving both targets. Reaching such performance requires enhancing the longitudinal and transverse granularity of the crystal section beyond what is available in conventional

homogeneous calorimeters and equipping each crystal cell with two independent readout channels to simultaneously collect Cherenkov and scintillation light. These features enable advanced particle-flow dual-readout reconstruction algorithms to exploit the maximum available information from each event. This work will present extensive laboratory characterizations together with beam-test measurements carried out at CERN on single-crystal PWO, BGO, and BSO cells instrumented with optical filters and SiPMs. These studies demonstrate event-by-event separation of Cherenkov and scintillation light, with both scintillation and Cherenkov yields exceeding the thresholds required for optimal electromagnetic and hadronic energy resolution. The results have guided the technological choices for the ongoing construction of full-containment calorimeter prototypes

References
[1] Abada et al., “FCC-ee: The Lepton Collider: Future Circular Collider Conceptual Design Report Volume 2,” Eur. Phys. J. Special Topics, vol. 228, no. 2, pp. 261–623, 2019. doi:10.1140/epjst/e2019-900045-4
[2] T. C. S. Group, “CEPC Conceptual Design Report: Volume 2 – Physics & Detector,” 2018. arXiv:1811.10545.
[3] M. T. Lucchini et al.,“Particle flow with a hybrid segmented crystal and fiber dual-readout calorimeter,” JINST, vol. 17, no. 06, P06008, 2022. arXiv:2202.01474
[4] R. Ferrari et al., “Dual-readout calorimetry,” Int. J. Mod. Phys. A, vol. 34, no. 13n14, p. 1940019, 2019. doi:10.1142/S0217751X19400190.
[5] N. Akchurin et al., “Separation of crystal signals into scintillation and Cherenkov components,” Nucl. Instrum. Methods Phys. Res. A, vol. 595, no. 2, pp. 359–374, 2008. doi: 10.1016/j.nima.2008.07.136.
[6] M. Abbrescia et al. [IDEA Study Group], “The IDEA detector concept for FCC-ee,”. arXiv:2502.21223.
[7] R. Hirosky et al., “Dual-readout calorimetry with homogeneous crystals,” EPJ Web Conf., vol. 320, p. 00021, 2025. arXiv:2408.11973
[8] A. Benaglia et al., “Characterization of thin optical filters for high purity Cherenkov light readout from scintillating crystals”, JINST 21 (2026) P03025, arXiv:2512.04965
[9] M. Alviggi et al., “Cherenkov and scintillation light separation in BGO and BSO crystals coupled to SiPMs for dual-readout electromagnetic calorimetry at future colliders. arXiv:2604.09918v1

NSS-13-292

The LS3 Enhancement of the LHCb Electromagnetic Calorimeter (#2898)

Eduardo Picatoste[1], Sergio Gómez[2], on behalf of the LHCb ECAL Upgrade II RD Group

[1] Universitat de Barcelona, Institute of Cosmos Sciences of the University of Barcelona, Barcelona, Spain; [2] Universitat Politècnica de Catalunya, Barcelona, Spain

Abstract
An upgrade of the LHCb electromagnetic calorimeter (ECAL) is planned for Long Shutdown 3 (LS3) to address significant aging effects in the central region caused by radiation damage and high particle flux. The innermost ECAL modules will be replaced with a new design based on Spaghetti Calorimeter (SpaCal) technology, optimized for radiation tolerance and improved performance under high occupancy conditions. A total of 176 SpaCal modules will be installed. These are based on scintillating plastic fibers embedded in dense absorbers. The innermost 32 modules will use 3D-printed tungsten absorbers to withstand the highest radiation levels, while the remaining 144 modules will employ lead absorbers produced through an innovative casting technique. Both configurations have been prototyped and extensively validated in test beam campaigns at DESY-II and CERN SPS. The measured energy resolution for electron beams is consistent with performance requirements and shows good agreement with detailed Monte Carlo simulations. The scintillating fibers will be read out using radiation-hard hollow light guides coupled to fast photon detectors. In total, 3072 new readout channels will be implemented with dedicated front-end electronics. In parallel with the installation of the new SpaCal modules, the current Shashlik calorimeter modules

will be rearranged to better match the spatial distribution of particle occupancy. Simulation studies demonstrate a significant reduction in per-cell occupancy after the LS3 upgrade, improving detector performance in Run 4 conditions. Benchmark analyses of key physics channels confirm that this enhancement leads to a substantial gain in reconstruction efficiency and measurement precision. Overall, the LS3 ECAL upgrade represents a crucial step toward coping with higher luminosity conditions and anticipates key design features of the future PicoCal system foreseen for implementation during LS4.

References
[1] The LHCb Collaboration, 2023, 'LHCb Particle Identification Enhancement Technical Design Report,' CERN-LHCC-2023-005
[2] The LHCb Collaboration, 2022, 'LHCb Framework TDR for the LHCb Upgrade II Opportunities in flavour physics, and beyond, in the HL-LHC era', CERN-LHCC-2021-012
[3] The LHCb Collaboration, 2024, 'LHCb Upgrade II Scoping Document', CERN-LHCC-2024-010

NSS-13-294

Design of the ePIC Hadronic Barrel Calorimeter, Status of the Test stand and Prospects for Physics at the EIC. (#2964)

Eric J. Mannel

Brookhaven National Laboratory, Physics Dept, Upton, USA

This work is supported by the United States Department of Energy.

Abstract
ePIC is the general purpose detector for the Electron-Ion Collider (EIC) that is being built at Brookhaven National Laboratory and will be ready for first physics when the Electron-Ion Collider turns on. ePIC is based on a new 1.7T superconducting solenoid magnet. The detector consists of precision tracking, particle identification and calorimeter (electromagnetic and hadronic) to measure the properties of electron-Ion collisions that will occur at the EIC. In this paper we will present the over all design of the ePIC detector, with a focus on the Barrel Hadronic Calorimeter (BHCal) which is the repurposed sPHENIX Outer Hadronic Calorimeter (HCal). We will also present the current status of the BHCal design, test stand and preliminary results of the new electronics readout system based on the CaloROC chip designed for ePIC

NSS-13-296

NSS-13-298

Operations and performance of a FD-MAPS Telescope based on the ARCADIA sensors (#3113)

Piero Giubilato[1,2], Serena Mattiazzo[1,2], Devis Pantano[1,2], Chiara Bonini[6,2], Caterina Pantouvakis[1,2], Michele Rignanese[1,2], Sabrina Ciarlantini[6,2], Alessandra Zingaretti[1,2], Manuel Rolo[3], Davide Falchieri[4], Romualdo Santoro[5]

[1] University of Padova, Physics and Astronomy, Padova, Italy; [2] INFN, Padova, Padova, Italy; [3] INFN, Torino, Torino, Italy; [4] INFN, Bologna, Bologna, Italy; [5] University of Insubria, Science and Advanced Technology, Como, Italy; [6] University of Padova, Space Studies Center Giuseppe Colombo, Padova, Italy

Abstract

In the framework of the ARCADIA collaboration several INFN groups developed a Monolithic Active Pixel Sensor realized in 110 nm CMOS technology capable to operate with fully depleted substrate. Several prototypes embedding different substrate thickness have been produced and tested. In this contribution we detail the design and operation of the first multilayer particle tracking telescope realized with such technology, and successfully tested at the DESY II Test Beam Facility.

The telescope uses 6 tracking planes, each realized with an ARCADIA sensor, and is paired to a 7th layer, the device under test, which was also an ARCADIA sensor, only with a different substrate thickness. The tracking apparatus includes a scintillator based triggering system, a complete synchronization electronics, and a parallel DAQ system for control and data readout.

Together with a brief description of the sensor, the whole telescope system is depicted, detailing the relevant design choices and the expected performances. Maximum rates, resolution and other key metrics are derived from the telescope technical characteristics, and bench-marked against test-beam results. Measured performance are also compared with respect to the gold-standard MIMOSA telescope available at the same test-beam facility, which was used to characterize the same Device Under Test for reference.

A discussion about the strength and weaknesses of the technology, as well as the foreseen improvements and potential applications will close the discussion. Also, potential area of application, both in physics research and in applied fields will be highlighted.

NSS-13-300

Measurement and correction of high intensity effects on the pixel response of the DSSC DEPFET camera (#1557)

Andrea Castoldi[1,2], **Maurizio Ghisetti**[1,2], Chiara Guazzoni[1,2], Stefano Maffessanti[3], Cyril Danilevski[4], Loïc Le Guyader[4], David Lomidze[4], Yevheniy Ovcharenko[4], Matteo Porro[4,5]

[1] Politecnico di Milano, DEIB, Milano, Italy; [2] INFN, Sezione di Milano, Milano, Italy; [3] DESY, Hamburg, Germany; [4] European XFEL, Schenefeld, Germany; [5] Università Ca' Foscari, Venezia, Italy

Abstract

This work reports on the experimental characterization, modeling and correction of high intensity effects on the pixel response of the DEPFET Sensor with Signal Compression (DSSC) camera, an active pixel detector targeted at soft X-ray imaging experiments at the European XFEL. Experimental tests with up to 5 MeV/pixel deposited energy have been performed at the European XFEL, showing evidence of a shift of the pedestal value growing with X-ray intensity. Moreover, the signal compression provided by the DEPFET (DEpleted P-type Field Effect Transistor), integrated in each pixel, enhances the impact of this systematic effect on the measurement accuracy. The observed shift is assumed to be proportional to the signal dependent drop of the power supply lines along each ASIC column and can be modeled by two parameters. We devised a procedure to efficiently measure the two model parameters by means of a custom mask that shields a fraction of each ASIC column, irradiated with a flat field. The main results of the characterization of the signal dependent pedestal shift parameters and the application of the resulting correction to X-ray images of different patterned masks (dots, stripes, 2D shapes etc.) acquired at increasing intensities will be presented and discussed.

NSS-13-302

XSTREAM Pathfinder: A Modular R&D Framework for Next-Generation High-Throughput X-ray Detectors at the European XFEL (#1690)

Matteo Porro[1,2], Monica Turcato[1]

[1] European XFEL, Schenefeld, Germany; [2] Ca' Foscari University of Venice, Department of Molecular Sciences and Nanosystems, Venezia, Italy

Abstract

We present the XSTREAM Pathfinder, an exploratory R&D effort at the European XFEL aimed at defining detector technologies for a potential facility upgrade. The activity addresses a broad photon-energy range, from soft X-rays starting at about 250 eV to hard X-rays up to 50 keV, and is structured around three main building blocks: sensor and interconnection technologies, prototype readout ASICs, and a first-stage DAQ system at camera level. The goal is to investigate detector concepts combining pixel sizes of about 100 µm, MHz-rate capability, and flexibility

with respect to possible future XFEL timing structures. Baseline sensor options include silicon diodes and MiniSDDs for soft X-rays, and (thick) silicon diodes for hard X-rays in the 9–12 keV range, with high-Z materials (e.g. CdTe, CZT) considered for extending the operation toward higher photon energies. More advanced options for soft X-rays, including DEPFETs and LGADs, are also under investigation. On the ASIC side, prototype developments will be implemented in scaled CMOS technologies (28 nm or 22 nm), aiming at maximizing the reuse of both analog and digital building blocks across different sensor implementations. While sensor-specific front-end adaptations are required, a common architecture is pursued for key elements such as analog filtering, predictive gain switching, in-pixel digitization, and high-speed data serialization. A central challenge is the development of a high-throughput readout enabling continuous operation at up to 1 MHz, opening the path toward CW or high-duty-cycle modes, while maintaining backward compatibility with burst-mode operation. The Pathfinder will progressively validate the readout chain from sensor to digital output, including early studies of DAQ-level real-time data reduction.

References
[1] A. Allahgholi et al., J. Synchrotron Rad. (2019). 26, 74-82, https://doi.org/10.1107/S1600577518016077
[2] M. Porro et al., “The AGIPD detector for the European XFEL,” IEEE Trans. Nucl. Sci., vol. 59, no. 6, pp. 3339–3351, Dec. 2012.
[3] M.C. Veale et al., 2017 JINST 12 P12003
[4] S.Aschauer, et al., J. Instrum. 12, P11013. https://doi.org/10.1088/1748-0221/12/11/p11013
[5] S. Maffessanti, et al., “A 64k pixel CMOS-DEPFET module for the soft X-rays DSSC imager operating at MHz-frame rates”, Sci Rep 13, 11799 (2023)
[6] J. Zhang et al., "Development of LGAD sensors with a thin entrance window for soft X-ray detection”, 2022 JINST 17 C11011
[7] A. Ciavarella-Ciavarella, et al., "Design of a Front-End Stage for Future European XFEL Detectors," in IEEE Transactions on Nuclear Science, vol. 73, no. 1, pp. 34-40, Jan. 2026, doi: 10.1109/TNS.2025.3637403

NSS-13-304

Redesign of the DSSC IOB for Near- and Long-Term High-Rate Operation (#1870)

Gabriele Fiumicelli[1], Luca Colzani[1], Andrea Costa[1], Fabio Garzetti[1], Nicola Lusardi[1,2], Enrico Ronconi[1], Gabriele Bonanno[1], Angelo Geraci[1,2], Stefano Maffessanti[3], Karsten Hansen[3], Cyril Danilevski[4], Konstantin Sukharnikov[4], Andrea Bannwart Perina[4], David Lomidze[4], Monica Turcato[4], Matteo Porro[4,5]

[1] Politecnico di Milano, Dipartimento di Elettronica, Informazione e Bioingegneria, Milano, Italy; [2] INFN, Milano, MIlano, Italy; [3] Deutsches Elektronen-Synchrotron DESY, Hamburg, Germany; [4] European XFEL, Schenefeld, Germany; [5] Ca’ Foscari University of Venice, DMSN, Venezia, Italy

This work is financed by the European XFEL.

Abstract
The Data Acquisition (DAQ) system of the DEPFET Sensor with Signal Compression (DSSC) megapixel (Mpx) camera at the European X-ray Free-Electron Laser (EuXFEL) is being revisited to support higher-performance detectors. The current digital front-end consists of two Field-Prgrammable Gate Array (FPGA)-based stages: the Input Output Board (IOB), responsible for initial data acquisition from Application Specific Integrated Circuits

(ASICs), and the Patch Panel Transceiver (PPT), which manages data reordering and remote control. In the present 1-Mpx configuration with 9-bit pixel resolution, each IOB serves 16 ASICs (0.29 Gbps), four IOBs form a quadrant (18.88 Gbps), and four PPTs handle the full camera (75.49 Gbps). Since the AISCs and IOBs operate inside a vacuum enclosure at about −20 °C, any upgrade must comply with strict constraints on size, power delivery, and thermal management. In this context, EuXFEL is exploring both near- and long-term upgrade paths driven by the evolution of DSSC toward a 4-Mpx detector with 10-bit pixel resolution and higher throughput. The current system stores about 8,000 frames per second out of the 27,000 pulses per second produced by EuXFEL; near-term targets are 10,000 fps and 27,000 fps, while the long-term goal is continuous operation up to 1 Mfps. These modes would increase the required data transfer rate by factors ranging from about 5.55 to 15 in the near-term, and up to 555 in the long-term scenario, highlighting the main limitation of the current IOB. The IOB must be redesigned with a more powerful FPGA to meet near-term targets while enabling advanced data processing for long-term scenarios (e.g., lossless compression). The current capacitor bank—a simple power approach for DEPFETs—is therefore reconsidered; its removal frees up to about 50% of the IOB area, allowing the integration of additional memory and paving the way toward significantly higher data rates.

NSS-13-306

Towards a 64-Channel Monolithic SDD X-Ray Spectrometer for High-Throughput Synchrotron Applications (#2776)

Beatrice Pedretti[1,2], Pietro Barcella[1,2], Andrea Abba[3], Giacomo Borghi[1,2], Marco Carminati[1,2], Carlo E. Fiorini[1,2]

[1] Politecnico di Milano, DEIB, Milano, Italy; [2] INFN, Milano, Milano, Italy; [3] Nuclear Instruments srl, Lambrugo, Italy

Abstract

The increasing brilliance of fourth-generation synchrotron sources drives a growing demand for energy-dispersive X-ray fluorescence (XRF) spectrometers capable of handling extreme photon fluxes.

We present the design and characterization of the ARDESIA-64 instrument, a complete X-ray fluorescence (XRF) spectrometer for high-throughput synchrotron applications.

The instrument integrates a highly scaled 64-channel monolithic Silicon Drift Detector (SDD) array, featuring a pixel pitch of 2.5 mm, within a compact, vacuum-compatible mechanical housing tailored for beamline integration.

At the conference, we will present the instrument design and comprehensive spectroscopic characterization results.

The collimated 450 µm-thick sensor variant demonstrates an excellent average energy resolution of 125.9 eV FWHM at 5.9 keV. Preliminary high-rate tests confirm exceptional throughput capabilities, sustaining Input Count Rates (ICR) exceeding 800 kcps per channel while preserving an energy resolution of ~150 eV. The readout is performed by a 64-channel Digital Pulse Processor (DPP) based on the CAEN DT5560SE digitizer with firmware specifically adapted for high-throughput X-ray spectroscopy in synchrotrons.

References

[1] Pedretti, B., Ticchi, G., Barcella, P., Borghi, G., Carminati, M., & Fiorini, C. (2025). High-throughput X-ray spectroscopy: characterization of the ARDESIA detector with high-end digital pulse processors. *Synchrotron Radiation*, *32*(6).

[2] Utica, G., Fabbrica, E., Carminati, M., Borghi, G., Zorzi, N., Ficorella, F., ... & Fiorini, C. (2021). ARDESIA-16: a 16-channel SDD-based spectrometer for energy dispersive X-ray fluorescence spectroscopy. *Journal of Instrumentation*, *16*(07), P07057.

NSS-13-308

Novel Alpha Spectrometer for Aqueous and Molten Salt Systems (#1378)

Owen A. Johnson[1], Colin Patricelli[1], Courtnee Staine[1], Sam Bonick[1], Brian Canfield[2], Will Doniger[3], Val Konvalov[4], Eric Lukosi[1]

[1] University of Tennessee, Nuclear Engineering, Knoxville, USA; [2] University of Tennessee Space Institute, Center for Laser Applications, Tullahoma, USA; [3] Argonne National Laboratory, Process Simulation and Safeguards, Lemont, USA; [4] Applied Diamond, Wilmington, USA

The information, data, or work presented herein was funded in part by the Advanced Research Projects Agency-Energy (ARPA-E), U.S. Department of Energy, under Award Number DE-AR0001603. The views and opinions of authors expressed herein do not necessarily state or reflect those of the United States Government or any agency thereof.

Abstract

Conducting isotopic level material control and accountancy of radioactive materials in fluids is challenging for multiple reasons: optical and electronic methods only provide elemental information, gamma-based methods face difficulties quantifying total concentrations, and destructive mass spectroscopy is costly and time consuming. Alpha-based techniques are typically not feasible due to the particles short (10-20 μm) range in dense matter and often require radiochemical separations in conjunction with electroplating. In this presentation we will present a novel sensor design that utilizes microfluidic structures which constrain the sample to a thin volume, limiting the energy loss of alpha particles, enabling spectroscopic measurements. If the alpha-particle energy is properly conserved it will allow for identification of the isotopes present, while the known sample volume will provide a means of calculating the isotope mass and subsequent concentration.

NSS-13-310

The Beta Rhizotron: a Radioisotope Imaging System for Plant Biology Research (#1603)

Seung J. Lee[1], Eric Christy[1], Kondo Gnanvo[1], **Andrew Weisenberger**[1], Shiva Abbaszadeh[2], Weixin Cheng[2], Gregory Bonito[3], Katharina Domnanich[3], Gregory Severin[3]

[1] Thomas Jefferson National Accelerator Facility, Detector Development Group, Newport News, USA; [2] University of California Santa Cruz, Santa Cruz, USA; [3] Michigan State University, East Lansing, USA

Work supported by the U.S. Department of Energy, Office of Science, Office of Nuclear Physics under contract DE-AC05-06OR23177.

Abstract

The rhizosphere is the zone surrounding plant roots where there is mutual influence exerted between soil microbes and the roots. In this zone biological and chemical activity is driven by compounds exuded by or present in the root and consumed by specialized types of fungi and bacteria that inhabit or surround the roots. Understanding the dynamics occurring in the rhizosphere regarding plant-microbe, plant-plant and microbe-microbe interaction is the focus of much plant ecophysiology research. Plant biologists often use radioisotopes of carbon, iron, phosphorous and calcium to study this plant-microbe interaction but their radioisotope imaging methods are static and destructive. The Beta Rhizotron is a beta (b)particle imaging detector designed for dynamic, non-invasive, *in-vivo/in-situ* imaging of plant roots being studied using b-particle emitting radioisotope tracers. Potential tracers include ^{14}C, ^{32}P, ^{45}Ca and ^{64}Cu via detection of their emitted b-particles from roots grown in a special container called a rhizotron/rhizobox. The detector is a gas based charged particle detector known as a micro-pattern gaseous detector (MPGD). Large area MPGDs are used in particle physics research. The use of a MPGD coupled to a rhizobox for low energy b-particle detection requires an MPGD able to operate in a varying temperature and humidity environment of standard growth chambers to obtain dynamic images of the bio-distribution of b-particle emitting radioisotopes. A key optimization of MPGD construction we are reporting here is the choice of window material.To estimate the expected 2-D intensity histograms simulations were performed using GEANT4 for ^{64}Cu with the b+ endpoint energy of ~0.65 MeV.Simulated was an 8 μm Kapton window, a 6 μm aluminized Mylar MPGD cathode/window, a 3 mm thick MPGD drift gas volume and a 1 x 1 x 70 mm^3 water column with a uniform spatial distribution of the β-particle emitter to approximate a root. Results indicated adequate imaging results.

NSS-13-312

True Random Number Generation for Post-Quantum Applications

(#1622)

Edward Cazalas, Cara Blick

University of Utah, Nuclear Engineering Program, Salt Lake City, USA

None

Abstract

This project advances a self-contained, portable True Random Number Generator (TRNG) grounded in the quantum-physical randomness of radioactive decay, integrated with an AI-driven monitoring and adaptive control system, for post-quantum cryptography (PQC) in mission-critical environments where remote connectivity is unavailable or constitutes an unacceptable security risk. Conventional cryptographic methods are projected to be vulnerable to quantum computing attacks by 2030, and NIST has mandated migration to PQC standards (FIPS 203–205) by 2030–2035. A fundamental requirement of PQC is a hardware TRNG capable of producing certified entropy without software-based pseudo-randomness. Existing solutions, e.g., cloud-connected beacons, large optical facilities, are incompatible with the remote, radiation-exposed, and network-denied settings of nuclear power plants, satellites, submarines, and forward military installations. Silicon SoC (system on a chip)-based TRNGs further fail in these environments, as ionizing radiation effects (total ionizing dose, single event upsets, direct damage) can bias, degrade, or manipulate their entropy output. Radioactive decay is a quantum-physical process that is intrinsically random, radiation-environment-tolerant, and scalable to NRC-exempt activity levels, making it ideally suited to this application.

NSS-13-314

NSS-13-316

Optimization of working point for TES microcalorimetric gamma spectroscopy (#2121)

Nolan I. Kowitt, Areg Danagoulian

Massachusetts Institute of Technology, Nuclear Science and Engineering, Cambridge, USA

This work was partially supported by the NSSC4 Consortium under grant number DE-NA0004277.

Abstract

Cryogenic microcalorimeters are low-noise thermal detectors that have demonstrated gamma-ray resolution better than 100 eV at 100 keV, resolving lines unresolvable by conventional spectrometers. Achieving this resolution with an array of transition-edge sensors (TESs), however, requires that all TESs, each with a slightly different transition temperature, be simultaneously biased near their individual operating points. Because the TESs on a given readout line share a common bias, ensemble performance is determined by global parameters: the mixing-chamber temperature, the TES bias current, and the readout electronics configuration. A parametric study was performed to identify the operating point that maximizes the number of usefully contributing pixels and the combined energy resolution. Results of this study will be discussed, along with the methodology for combining and analyzing spectra across the array.

References

[1] K. A. Schreiber, K. E. Koehler, M. P. Croce, E. N. Stark, D. G. McNeel, M. H. Carpenter, D. J. Mercer, E. P. Abel, B. Archambault, L. Arrigo *et al.*, "Applications of ultra-high resolution microcalorimeter gamma- ray spectrometry," *Frontiers in Nuclear Engineering*, vol. 4, p. 1654123, 2025

[2] K. D. Irwin and G. C. Hilton, "Transition-edge sensors," in *Cryogenic particle detection*. Springer, 2005, pp. 63–150.

[3] S.Moseley, J.C.Mather, and D.McCammon,"Thermaldetectorsasx-ray spectrometers," *Journal of Applied Physics*, vol. 56, no. 5, pp. 1257–1262, 1984.

[4] D. Chow, M. Lindeman, M. Cunningham, M. Frank, T. Barbee Jr, and S. Labov, "Gamma-ray spectrometers using a bulk sn absorber coupled to a mo/cu multilayer superconducting transition edge sensor," *Nuclear Instruments and Methods in Physics Research Section A: Accelerators, Spectrometers, Detectors and Associated Equipment*, vol. 444, no. 1-2, pp. 196–200, 2000.

[5] D. A. Bennett, R. D. Horansky, D. R. Schmidt, A. Hoover, R. Winkler, B. K. Alpert, J. A. Beall, W. B. Doriese, J. W. Fowler, C. Fitzgerald *et al.*, "A high resolution gamma-ray spectrometer based on superconducting microcalorimeters," *Review of Scientific Instruments*, vol. 83, no. 9, 2012.

[6] R. Smith, T. Kikuchi, Y. Sato, F. Hirayama, A. Sato, S. Kohjiro, and H. Takahashi, "Development of transition edge sensor array for wide energy range gamma-ray spectroscopy," *IEEE Transactions on Applied Superconductivity*, vol. 35, no. 5, pp. 1–4, 2024.

[7] M. Bacrania, A. Hoover, P. Karpius, M. Rabin, C. Rudy, D. Vo, J. Beall, D. A. Bennett, W. Doriese, G. Hilton *et al.*, "Large-area microcalorimeter detectors for ultra-high-resolution x-ray and gamma-ray spectroscopy," *IEEE Transactions on Nuclear Science*, vol. 56, no. 4, pp. 2299–2302, 2009.

[8] O. Noroozian, J. A. Mates, D. A. Bennett, J. A. Brevik, J. W. Fowler, J. Gao, G. C. Hilton, R. D. Horansky, K. D. Irwin, Z. Kang *et al.*, "High-resolution gamma-ray spectroscopy with a microwave-multiplexed transition-edge sensor array," *Applied Physics Letters*, vol. 103, no. 20, 2013.

NSS-13-318

Radiation Damage to Quantum Dots (#2264)

Jesse Snow, Edward Cazalas

university of Utah, Nuclear Engineering Program, Salt Lake City, USA

We would like to thank faculty and staff at the University of Utah NanoFab and Materials Characterization Lab for their assistance in measurement systems use and training. This material is based upon work supported by the Consortium for Nuclear Forensics (CNF) under the U.S. Department of Energy (DOE) National Nuclear Security Administration (NNSA) award number DE-NA0004142.

Abstract

QD nanostructures have emerged as highly versatile materials for sensing ionizing radiation. However, comparatively little is known about how QDs respond to non-ionizing radiation such as fast and thermal neutrons, where neutron capture, rather than ionization, is the dominant interaction mechanism. This study examines the viability of graphene QDs as neutron dosimeters or neutron–gamma discriminators. Additionally, research into QDs can aid in nuclear non-proliferation and dosimetry. The goal of this research is to investigate the effects of neutron irradiation on the optical properties of graphene QDs for non-proliferation applications. The results of this work provide insight into the mechanisms through which neutrons alter QD electronic structure and optical response. This study will contribute to the broader effort to develop hybrid or stand-alone QD-based radiation sensors and markers capable of operating across diverse radiation environments and even being incorporated into fuel.

NSS-13-320

Simulation-based evaluation of a position-sensitive TES microcalorimeter for gamma-ray detection (#2462)

Nao Hata[1], Rintaro Moriyama[1], Ryusei Arai[1], Amane Kawamoto[1], Naoko Iyomoto[1], Takehiro Ueno[1], Noriko Yamasaki[2], Tasuku Hayashi[3], Kazuhisa Mitsuda[4]

[1] Kyushu University, the Department of Applied Quantum Physics and Nuclear Engineering, Fukuoka, Japan; [2] Japan Aerospace Exploration Agency, Insutitute of Space and Astronautical Science, Sagamihara, Japan; [3] RIKEN, Nishina Center for Accelerator-Based Science, Wako, Japan; [4] National Astronomical Observatory of Japan, Advanced Technology Center, Mitaka, Japan

This work was partially supported by a travel grant from the Dentsu Scholarship Foundation. The authors gratefully acknowledge their financial support for participation in this international conference.

Abstract

Transition-edge Edge Sensor (TES) microcalorimeters (TES) are attractive promising detectors for gamma-ray spectroscopy because of their excellent energy resolution[1]. However, TES detectors microcalorimeters generally have small sensitive effective areas, and large-scale arrays are required to achieve high detection efficiency. Since TESs operate at cryogenic temperatures, increasing the number of TESs increases Joule heating and readout complexity.

To address this issue, a Position-Sensitive TES (PoST) structure microcalorimeters haves been proposed to realize a large effective detection area with a small number of TESs. The Our gamma-ray PoST consists of a long lead absorber with TESs attached to both ends, and the incident position of gamma rays is estimated from differences in pulse shapes.

In this study, we evaluated the energy resolution and position resolution of the PoST detector by simulations considering thermal intrinsic noise and gamma-ray multiple scatteringinteractions. The simulations were performed using a finite element model coupling thermal conduction and TES electrical circuits. Sub-millimeter position resolution was achieved for 1333 keV1.33 MeV gamma rays.

References

[1] E. Figueroa-Feliciano, Nucl. Instr. And Meth. A, 520, 496(2024)

NSS-13-322

Architecture and Qualification of the GlowRIA radiation monitor: An Optical fibre based dosimeter compatible with Cubesat missions (#2601)

Nourdine Kerboub[1], Nicolas Balcon[1], Steven Fosset[1], Mathieu Bergont[2], Pierrick Cheiney[2], Sylvain Girard[3,4], Julien Mekki[1]

[1] CNES, Toulouse, France; [2] Exail, Lannion, France; [3] Université Jean Monnet, Saint-Etienne, France; [4] IUF, Paris, France

This instrument development has been funded by CNES and supported by EXAIL & Laboratory Hubert Curien, through their joint laboratory LABH6.

Abstract

Optical-fiber dosimetry, based on Radiation-Induced Attenuation (RIA) or Radiation-Induced Luminescence (RIL), has progressed from particle-accelerator research to space applications. The first space-borne implementation, the LUMINA experiment, flew on the International Space Station during the ALPHA mission. LUMINA used several kilometres of specially selected silica fiber to provide dose-rate-independent, temperature-independent, and particle-type-independent measurements, successfully monitoring the ISS radiation environment, including each passage through the South Atlantic Anomaly.

To meet the more demanding radiation levels, mass, volume, and power constraints of CubeSat missions, we have miniaturized the LUMINA architecture into GlowRIA. In this new design, the fiber length was reduced to a few hundred metres and can be adjusted according to the expected mission dose. The optoelectronics, including the laser and photodiodes, were selected for lower power consumption and a more compact form factor. In addition, the read-out electronics were replaced by a radiation-tolerant microcontroller, eliminating the Raspberry-Pi board used on LUMINA and ensuring resilience to both cumulative dose effects and single-event effects.
GlowRIA has been subjected to a comprehensive qualification campaign reproducing harsh orbital conditions such as vacuum, large temperature excursions, electromagnetic interference, and total ionizing dose. The tests confirm that the dosimeter retains its performance while meeting CubeSat power and mass budgets.
We are also conducting Total Ionizing Dose calibration of the instrument using a Co-60 source, while Single Event Effects testing is planned at a later stage. The results of the environmental, radiation, and performance qualification campaigns will be presented in the full article.

References
[1] M. Roche *et al.*, « Solar Particle Event Detection With the LUMINA Optical Fiber Dosimeter Aboard the International Space Station », *IEEE Trans. Nucl. Sci.*, vol. 71, n° 8, p. 1580-1588, août 2024, doi: 10.1109/TNS.2024.3368137.
[2] A. Dufour *et al.*, « DREAM: A Miniaturized Spectrometer for Measurement of Protons and Electrons on Orbit », *IEEE Trans. Nucl. Sci.*, vol. 70, n° 8, p. 1541-1547, août 2023, doi: 10.1109/TNS.2023.3264461.
[3] S. Girard *et al.*, « Recent advances in radiation-hardened fiber-based technologies for space applications », *J. Opt.*, vol. 20, n° 9, p. 093001, sept. 2018, doi: 10.1088/2040-8986/aad271.
[4] S. Girard *et al.*, « Radiation Effects on Silica-Based Optical Fibers: Recent Advances and Future Challenges », *IEEE Trans. Nucl. Sci.*, vol. 60, n° 3, Art. n° 3, juin 2013, doi: 10.1109/TNS.2012.2235464.

NSS-13-324

Scintillation imaging with Coded Aperture masks (#2853)

Valentina Cicero[1], Nicolò Tosi[1], Alessandro Montanari[1], Valerio Pia[1], Filippo Mei[3,1], Luigi Martina[2], Giovanni De Matteis[2]

[1] Istituto Nazionale di Fisica Nucleare, Bologna, Bologna, Italy; [2] Università del Salento, Mathematics and Physics, Lecce, Italy; [3] Università di Bologna, Physics and Astronomy, Bologna, Italy

This work is part of the project “Imaging calorimetry in scintillating media for high energy physics and tomography” (PRIN 2022KJZSYB), funded by the European Union Next Generation EU, Mission 4, Component 1, CUP I53D23001230006.

Abstract
Large volumes of liquid argon or xenon serve as highly effective media for detecting neutrino interactions and searching for dark matter. Conventional noble-liquid detectors typically use scintillation light for timing or calorimetric measurements only, while relying on charge drift in a time projection chamber for spatial reconstruction.
Direct optical reconstruction of events by imaging scintillation light could provide an alternative to the slow charge collection, also eliminating the necessity for an electric drift field. The increased rate capability enables new applications, including detectors at high-intensity neutrino beams and medical imaging (whole-body PET).

Thanks to finely segmented Silicon PhotoMultiplier arrays and appropriate optical systems, it is feasible to create cameras capable of ``photographing" the primary scintillation light. A significant challenge is presented by the fact that both argon and xenon emit scintillation light in the vacuum-ultraviolet spectrum. To overcome this, coded aperture masks are employed instead of conventional lenses, enabling the construction of thin cameras with wide and deep fields of view. A reconstruction algorithm based on Maximum Likelihood Expectation Maximization has been developed to generate a 3D map of energy deposition. The most recent results from simulations and reconstructions of particles tracks in a liquid argon detector equipped with these cameras will be discussed.

NSS-13-326

Application of a Compact Electrically Cooled HPGe Detector to Quality Control in Radiopharmaceutical Isotope Production (#2856)

Gabriela Ilie

Mirion Technologies, Radiometric Physics, Meriden, USA

Abstract

Since their invention in the 1970s, high purity germanium (HPGe) detectors have been the gold standard for the detection and spectroscopy of gamma rays. Developments in the fabrication, packaging, and operation of HPGe detectors, as well as in readout electronics and signal processing, have led to their application in fields as diverse as fundamental nuclear and particle physics, nuclear security and safety, and nuclear medicine. Based on decades of experience in electrical cooling technology, in recent years Mirion Technologies has developed rugged germanium detectors that can be used in difficult conditions traditionally considered too challenging for HPGe detectors. An example of such a detector is our newest product: the MicroGe detector. Due to it is small form factor and rapid deployment capability, the MicroGe detector can be used in medical radioisotope production facilities where high resolution is critical to identify impurities in samples. The MicroGe detector is capable of going from storage to measurement in less than 30 minutes which is a revolutionary achievement for HPGes. This paper presents results of the evaluation of a novel ultra-compact electrically cooled germanium detector as a quality-control instrument for quantification of for radionuclide impurity of samples.

References

[1] https://www.mirion.com/products/search-measurement-analysis-instrumentation

Time:
11 November, 2026
15:00 – 17:00

Room:
ALBÉNIZ & MACHUCA

NSS-14 | Analog and digital circuits II

Chairs:
Gianluigi De Geronimo (Syosset)
Serge A. Charlebois

NSS-14-01

Graphene-Based Front-End Amplifier for Nuclear Instrumentation (#2349)

Marcos Turqueti[1], Alec Lindman[2], Om Aggarwal[1], Alan Poon[2]

[1] Lawrence Berkeley National Laboratory, Engineering Division, Berkeley, USA; [2] Lawrence Berkeley National Laboratory, Nuclear Science Division, Berkeley, USA

Abstract

Front-end electronics for nuclear instrumentation require ultra-low noise, high bandwidth, radiation tolerance, and low power consumption to accurately process weak signals generated by radiation detectors. Conventional silicon-based amplifiers face increasing limitations in applications demanding extreme sensitivity, cryogenic operation, and compact integration. This work investigates the use of graphene-based electronic devices as a novel platform for next-generation front-end amplifiers for nuclear science applications. Owing to its exceptional carrier mobility, high thermal conductivity, mechanical flexibility, and potential for low-noise operation, graphene presents a promising alternative material for advanced detector readout electronics.

We present the conceptual design and preliminary evaluation of a graphene-based front-end amplifier architecture intended for integration with nuclear radiation detectors including silicon photomultipliers (SiPMs), cadmium zinc telluride (CZT) detectors, and other low-signal sensing systems. The proposed approach focuses on achieving improved signal amplification while minimizing electronic noise and power dissipation. Device-level considerations including transconductance behavior, impedance matching, frequency response, and low-temperature performance are analyzed to assess suitability for nuclear instrumentation environments.

Theoretical analyses indicate that graphene-enabled amplifier structures can provide enhanced sensitivity and bandwidth compared to conventional semiconductor implementations, particularly in low-temperature and low-signal regimes relevant to modern nuclear physics experiments and radiation detection systems. The results demonstrate the potential of graphene-based front-end electronics as an enabling technology for next-generation nuclear instrumentation, with applications spanning particle physics, medical imaging, homeland security, and advanced scientific sensing platforms.

References

[1] Butseraen, G., Ranadive, A., Aparicio, N. *et al.* A gate-tunable graphene Josephson parametric amplifier. *Nat. Nanotechnol.* **17**, 1153–1158 (2022). https://doi.org/10.1038/s41565-022-01235-9

[2] Yuya Takatsuka; Kazuhiro Takahagi; Eiichi Sano; Victor Ryzhii; Taiichi Otsuji, "Gain enhancement in graphene terahertz amplifiers with resonant structures ",*J. Appl. Phys.* 112, 033103 (2012),https://doi.org/10.1063/1.4742998

[3] T. Hanna, N. Deltimple, M.S. Khenissa, E. Pallecchi, H. Happy, S. Frégonèse,"2.5GHz integrated graphene RF power amplifier on SiC substrate",Solid-State Electronics,Volume 127,2017,Pages 26-31,ISSN 0038-1101,https://doi.org/10.1016/j.sse.2016.10.002.

NSS-14-02

ToRA : a 64-channel ASIC for the readout of gaseous detectors in a CMOS 65 nm technology (#1949)

Giovanni Mazza[1], Maxim Alexeev[1,2], Oleg Denisov[1], Lorenzo Marcellino[2], Chiara Alice[2], Marco Mignone[1], Richard J. Wheadon[1]

[1] INFN - Istituto Nazionale di Fisica Nucleare, Sezione di Torino, Torino, Italy; [2] Università di Torino, Dipartimento di Fisica, Torino, Italy

Abstract

ToRA is a 64 channel ASIC for the readout of gaseous detectors used in high energy physics experiments. Its driving application is the readout of the MicroMega detectors for the AMBER experiment upgrade. However, it is designed to be highly flexible in order to be used also for other types of gaseous detectors, e.g. straw detectors. Each ToRA channel provides programmable signal amplification and shaping. The ASIC provides the time measurement of the time of arrival, the time over threshold and the peak position of the shaper signal. Moreover, the peak value is hold and converted with a single ramp ADC.

A fully digital interface, based on differential serial links and including a data and a control interface, has been implemented. The events are packed into 32-bit words and transmitted over two 200 Mb/s links.

References

[1] C. Alice et al., “Development and test of the Micromegas detector prototype and its readout electronics for the AMBER experiment at CERN,” J. Instrum, vol. 18, July 2023, Art. no. C07004

[2] G. De Geronimo, “Low-Noise Electronics for Radiation Sensors,” in Medical Imaging: Principles, Detectors and Electronics, K. Iniewski Editor, Wiley, 2009.

[3] G. De Geronimo and S. Li, “Shaper design in CMOS for high dynamic range,” IEEE Trans. Nucl. Sci., vol. 58, no. 5, pp. 2382-2390, 2011.

NSS-14-03

CHASER: A Charge Sensitive Amplifier and Sampling Circuit for CZT Detectors (#1963)

Leonardo Bernardini[1,2], Samuele Formenti[1], Adele Ciavarella-Ciavarella[1,2], Giacomo Borghi[1,2], Carlo E. Fiorini[1,2], Marco Carminati[1,2]

[1] Politecnico di Milano, Dipartimento di Elettronica, Informazione e Bioingegneria, Milan, Italy; [2] Istituto Nazionale di Fisica Nucleare, Sezione di Milano, Milan, Italy

This work is supported by Horizon Europe under Grant 101130550 (i-RASE).

Abstract

This work presents an 8-channel ASIC designed in 180 nm CMOS technology for γ-ray spectroscopy as part of the EU-funded project i-RASE. i-RASE aims at developing a novel generation of radiation detectors capable of performing real-time processing by adopting artificial neural networks (ANN) to reconstruct energy, position, and timing of incoming photons. The ASIC is specifically tailored for room temperature detectors, featuring large detector capacitance (up to 50 pF), like CdZnTe. It includes dual-polarity charge sensitive amplifiers (CSA) with pulsed-reset and leakage current compensation (LCC), sample-and-hold circuitry controlled by a digital logic shared among the channels, and both single-ended and differential output architectures. Two readout modes are supported: a continuous mode, compatible with conventional analog and digital readout and shaping chains, and a high-speed sampling mode, in which a switched capacitor array (SCA) continuously samples the analog output of the CSA at frequencies up to 100 MHz. The samples are stored in 256 capacitors and subsequently buffered to an external differential ADC, triggered by the ASIC event thresholds, and controlled by the FPGA running the ANN. The preliminary results of the ASIC characterization (rise time of 100 ns, linearity of 0.5%), performed by injecting test signals, are presented and match simulations.

References

[1] S. H. Owe, I. Kuvvetli, and C. Budtz-Jørgensen, “Carrier Lifetime and Mobility Characterization Using the DTU 3-D CZT Drift Strip Detector”, IEEE Trans. Nucl. Sci., vol. 68, no. 9, pp. 2440–2446, 2021.

[2] G. Song, B. Das, Y. Seo, G. Cho, and J. Caravaca, “Performance evaluation of single-and double-layer czt compton cameras for 225 ac imaging”, IEEE Transactions on Nuclear Science, 2026.

[3] B. N. Hauptmann and et al., “Performance evaluation of new large area 3D CdZnTe drift strip detectors”, vol. 13093. SPIE, 2024, p. 130931D.

NSS-14-04

Design and Experimental Characterization of a 65 nm CMOS Readout Channel for the Si(Li) Tracker Upgrade of the GAPS Experiment (#2371)

Luca Ghislotti[1,2], Paolo Lazzaroni[2,1], Massimo Manghisoni[2,1], Lodovico Ratti[3,1], Valerio Re[2,1], Elisa Riceputi[2,1]

[1] INFN, Sezione di Pavia, Pavia, Italy; [2] Università degli Studi di Bergamo, Dipartimento di Ingegneria e Scienze Applicate, Dalmine, Italy; [3] Università di Pavia, Dipartimento di Ingegneria Industriale e dell’Informazione, Pavia, Italy

Abstract

This work presents the design and experimental characterization of a prototype channel developed in a 65 nm CMOS process for the readout of the large-area lithium-drifted silicon detectors of the General Antiparticle Spectrometer tracker. To simultaneously achieve high-resolution X-ray spectroscopy below 100 keV and a wide dynamic range up to 100 MeV, the charge-sensitive amplifier employs a dynamic-threshold MOS feedback capacitor exploiting dynamic signal compression. An enhanced Krummenacher network provides continuous feedback discharge, compensating detector leakage currents up to 200 nA. Experimental results demonstrate an energy resolution of 3.2 keV full width at half maximum (379 e^- rms equivalent noise charge) and an integral

nonlinearity below 1.5%. A compensation technique to mitigate temperature-induced variations in the charge-sensitive amplifier response is also presented.

References
[1] The GAPS Collaboration et al. 2026, 'The general antiparticle spectrometer (GAPS) antarctic balloon payload', Apr. 2026.
[2] Manghisoni, M et al. 2024, 'A 32-channel readout ASIC for X-ray spectrometry and tracking in the GAPS experiment', *IEEE Trans. Nucl. Sci.*, vol. 71, no. 1, pp. 96-105.
[3] Ghislotti, L et al. 2025, 'Design of the ANTARES4 readout ASIC for the second flight of the GAPS experiment: Motivations and requirements', *Particles*, vol. 8, no. 4, p. 89.
[4] Ghislotti, L et al. 2024, 'Low-noise wide dynamic range charge sensitive amplifier in 65 nm CMOS technology for the second flight of the GAPS experiment', *Proc. 19th Conf. Ph.D. Res. Microelectron. Electron. (PRIME)*, pp. 1-4.
[5] Assaderaghi, F 2000, 'DTMOS: Its derivatives and variations, and their potential applications', *Proc. 12th Int. Conf. Microelectron. (ICM)*, pp. 9-10.

NSS-14-05

Measurements of HPSoCv3 - an integrated 9-channel 10 Gsps Waveform Digitizer for high density LGAD array (#3007)

Luca Macchiarulo[1], Isar Mostafanezhad[1], Eyan Forsythe[1], Gregory Uehara[1], Simone Mazza[2], Jennifer Ott[3], Kahiwa Hoe[1], Christopher Chock[1]

[1] Nalu Scientific, LLC, HONOLULU, USA; [2] University of California, Santa Cruz, Santa Cruz Institute for Particle Physics (SCIPP), Santa Cruz, USA; [3] University of Hawaii at Manoa, Electrical and Computer Engineering Department, Honolulu, USA

This work was partially funded under U.S. DOE DE-SC0025826 grant and Jlab PO 24-D0681.

Abstract

We present the first measurements for the third revision of the High Pitch digitizer System-on-Chip (HPSoC), a 9 channel Readout Integrated Circuit (ROIC) prototype. The HPSoC concept is that of a high channel density and scalable waveform digitization ROIC with an embedded interface to advanced high-speed sensor arrays such as e.g. AC-LGADs. The chip was fabricated in 65nm technology and targets picosecond-level timing resolution via high speed waveform sampling (in excess of 10 Gsps), autonomous chip triggering and feature extraction. In this paper, we present the results of testing of the chip's timing generation and digitization.

References
[1] H. F. W. Sadrozinski et al., Ultra-fast silicon detectors, NIM-A 730 (2013) 226-231
[2] L. Macchiarulo, et al. "Design of HPSoC – a 10GSa/s WaveformDigitizer for Readout of Dense Sensor Arrays," 2022 IEEE Nuclear Science Symposium and Medical Imaging Conference (NSS/MIC), Italy, 2022, pp. 1-2, doi: 10.1109/NSS/MIC44845.2022.10399322.
[3] L. Macchiarulo, et al., "HPSoCv2 - design and testing of an improved prototype for high density sensor array 10GSa/s Waveform Digitizer," 2024 IEEE Nuclear Science Symposium (NSS), Medical Imaging Conference (MIC) and Room Temperature Semiconductor
Detector Conference (RTSD), Tampa, FL, USA, 2024, pp. 1-1, doi: 10.1109/NSS/MIC/RTSD57108.2024.10657998
[4] L. Macchiarulo et al. "HPSoCv3 - an integrated 9-channel 10 GspsWaveform Digitizer for high density LGAD array" 2025 IEEE Nuclear
Science Symposium (NSS), Medical Imaging Conference (MIC) andRoom Temperature Semiconductor Detector Conference (RTSD),
Yokohama, Japan, 2025

NSS-14-06

Cryogenic MOSFET Modeling Applied to CSA Design for Germanium Detector Readout (#2571)

Joel Georgeous[1], Carlo E. Fiorini[1], Federico Chiesa[1], Adele Ciavarella-Ciavarella[1], Marco Carminati[1], Giacomo Borghi[1], Michael Willers[2], Susanne Mertens[3]

[1] Politecnico di Milano, Department of Information Technology, Milano, Italy; [2] Technical University of Munich, Munich, Germany; [3] Max Planck Institute for Nuclear Physics, Heidelberg, Germany

Abstract

The LEGEND (Large Enriched Germanium Exper iment for Neutrinoless double beta Decay) experiment aims to detect neutrinoless double beta decay (0νββ) in 76Ge using large scale cryogenic germanium detectors. A 0.35µm LUIGI ASIC was designed as a detector readout, ensuring low noise and high radiopurity conditions. Such front-end ASIC, when assembled to the Ge detector, must operate at cryogenic temperatures, typically 87 K using liquid argon (LAr). At cryogenic temperatures, semiconductor characteristics shift significantly, while standard transistor models, typically validated only to −55◦C (218.15 K), become inaccurate. therefore, this work presents a workflow for cryogenic MOSFET modeling based on BSIM4, using experimen tal data measured at 77 K. The model is extracted from mea surements at both room and cryogenic temperatures, validated with corresponding Cadence models at room temperature, and is then used to assess the impact of cryogenic effects on analog circuit performance. Further experimental characterization on a new set of transistors will be made is required to refine and improve the accuracy of the model.

References

[1] F Edzards, M Willers, A Alborini, L Bombelli, D Fink, Matthew P Green, M Laubenstein, S Mertens, G Othman, David C Radford, et al. Investigation of asic-based signal readout electronics for legend-1000. Journal of Instrumentation, 15(09):P09022, 2020.

[2] LEGEND Collaboration et al., “LEGEND-1000 Preconceptual Design Report,” arXiv.org, Jul. 23, 2021. https://arxiv.org/abs/2107.11462 arXiv preprint arXiv:2107.11462, 2021.

[3] G. Gilmore, Practical Gamma-Ray Spectroscopy, 2nd ed. Chichester, U.K.: Wiley, 2008.

[4] C Fiorini and Matteo Porro. Integrated re cell for time-invariant shaping amplifiers. IEEE TNS, 51(5):1953-1960, 2004. IEEE TNS, 71(9):2171–2179, 2024.

[5] D. Butta, G. Borghi, M. Carminati, G. Ferrari, A. Gieb, F. Henkes, M. Willers, S. Mertens, S. Riboldi, and C. Fiorini. Design and characteri zation of a low-noise and low-background charge sensitive amplifier for the readout of germanium detectors. 421(1-2):322–333, 1999.

[6] A. Kabao˘glu, N. S¸. Solmaz, S. ˙ Ilik, Y. Uzun and M. B. Yelten, ”Sta tistical MOSFET Modeling Methodology for Cryogenic Conditions,” in IEEE Transactions on Electron Devices, vol. 66, no. 1, pp. 66-72, Jan. 2019, doi: 10.1109/TED.2018.2877942

NSS-14-07

A Fully Charge-Pump-Based Powering Scheme for SDDs in 180 nm SOI Technology (#1836)

Tobias Michel[1], **Tobias Michel**[1], Peter Iskra[2], Peter Iskra[2], Florian Wiest[3], Florian Wiest[3], Werner Buttler[4], Werner Buttler[4], Linus Maurer[5], Linus Maurer[5]

[1] University of the Bundeswehr Munich, Institute for Integrated Systems, Neubiberg, Germany; [2] KETEK GmbH, Munich, Germany; [3] KETEK GmbH, Munich, Germany; [4] Ingenieurbüro Werner Buttler, Essen, Germany; [5] University of the Bundeswehr Munich, Institute for Integrated Systems, Neubiberg, Germany

The authors would like to acknowledge the support by the ”Bayerisches Verbundforschungsprogramm” of the Free State of Bavaria and VDI/VDE Innovation + Technik GmbH.

Abstract

X-ray fluorescence analysis is a fast, non-destructive technique for material characterization and recycling, where silicon drift detector-based systems provide high energy resolution. Portable applications require a high integration density, while conventional state of the art solutions depend on external highvoltage electronics occupying more than 250 mm^2. To address this challenge, this work presents an application-specific integrated circuit fabricated in 180 nm silicon-on-insulator technology that generates all negative high voltages required for silicon drift detector operation in the range from -20 V to -130 V. Each voltage supply is implemented using a CMOS DC/DC converter based on a Pelliconi charge pump. The employed topology utilizes low-voltage transistors and a simple two-phase clock scheme driven by a ring oscillator at 10 MHz, enabling high efficiency while reducing chip area. The stability, noise, and spectral performance of a silicon drift detector operated with the proposed charge-pump-based supply is compared to those obtained with a conventional power supply. The results show that operation of a silicon drift detector module using an external ASIC-based charge pump is possible with high energy resolution for peaking times exceeding 1 µs, provided that the generated voltages are sufficiently smoothed using external capacitors. These results facilitate the development of more compact and cost-effective silicon drift detector power supply solutions.

References

[1] Lutz, G. 2007, *Semiconductor Radiation Detectors*, Berlin, Heidelberg: Springer Berlin Heidelberg, p. 35.

[2] Suman, S., Sharma, K. G., Ghosh, P. K. 2016, ‘Analysis and design of current starved ring VCO’, *2016 International Conference on Electrical, Electronics, and Optimization Techniques (ICEEOT)*, pp. 3222–3227, Chennai, India: IEEE.

[3] Pelliconi, R., Iezzi, D., Baroni, A., Pasotti, M., Rolandi, P. 2003, ‘Power efficient charge pump in deep submicron standard CMOS technology’, *IEEE Journal of Solid-State Circuits*, vol. 38, no. 6, pp. 1068–1071

[4] Adeel, S., Tolkiehn, M. 2022, ‘Digital signal processing algorithms for energy dispersive x-rays detectors’, *Journal of Physics: Conference Series*, vol. 2380, no. 1, p. 012098.

NSS-14-08

Development and testing of the ASIX region: a low-noise 128-pixel building block with event-driven readout and on-chip A/D conversion

(#2954)

Massimo Minuti[1], Luigi Gaioni[5], Massimo Manghisoni[5], Gianluca Traversi[5], Lodovico Ratti[7], Luca Frontini[4], Valentino Liberali[6], Luca Palini[4], Alberto Stabile[6], Paolo Bruschi[8], Francesco Gagliardi[8], Massimo Piotto[8], Luca Baldini[9], Roberto Beccherle[1], Ronaldo Bellazzini[1], Alessandro Brez[1], Marco Ceccanti[1], Pasquale Delogu[9], Luca Latronico[2], Guido Magazzu[1], Andrea Ria[8], Alberto Manfreda[3], Fabio Morsani[1], Leonardo Orsini[1], Melissa Pesce-Rollins[1], Michele Pinchera[1], Alessandro Profeti[1], Paolo Prosperi[1], Carmelo Sgrò[1], Stefano Silvestri[1], Gloria Spandre[1]

[1] Istituto Nazionale di Fisca Nucleare, Pisa, Pisa, Italy; [2] Istituto Nazionale di Fisca Nucleare, Torino, Torino, Italy; [3] Istituto Nazionale di Fisca Nucleare, Napoli, Napoli, Italy; [4] Istituto Nazionale di Fisca Nucleare, Milano, Milano, Italy; [5] University of Bergamo, Dept. of Engineering and Applied Sciences, Bergamo, Italy; [6] University of Milano, Dept. of Physics, Milano, Italy; [7] University of Pavia, Dept. of Electrical, Computer and Biomedical Engineering, Pavia, Italy; [8] University of Pisa, University of Pisa, Dept. of Information Engineering, Pisa, Italy; [9] University of Pisa, Dept. of Physics, Pisa, Italy

This work is funded by INFN CSN5

Abstract

The Analog Spectral Imager for X-rays (ASIX) is a technology demonstrator for a Hybrid Pixel Detector (HPD) aimed at delivering high-resolution measurements in both spatial and energy domains, thus enabling advanced X-ray spectral imaging. ASIX features 50~μm pixels arranged into a hexagonal array. An in-pixel ultra-low noise front-end (<30 ENC at Cd=100 fF), together with a self-triggering logic, and a highly segmented readout, enables precise identification of the charge clusters on a photon-by-photon basis.

The readout architecture is based on regions. Each region comprises a 16 X 8 pixel matrix and dedicated readout electronics including a compact 10-bit SAR ADC, a data-out FIFO and the readout-controller sequencing logic. The full demonstrator chip will be composed of a 6 X 12 array of regions, corresponding to a 96 X 96 pixel matrix, together with a digital output logic responsible for collecting, formatting and serializing data.

We developed a 2 X 2 mm^2 prototype readout chip in a commercial 65 nm CMOS process featuring a fully functional region.

Given its 4-side abuttable layout and its almost exclusively digital interfaces, this can be regarded as the main building block for readout matrices in larger-scale ASICs such as the future full-scale demonstrator.

Time:
11 November, 2026
15:00 – 17:00

Room:
MACHADO

NSS-15 | Computational methods and data analysis

Chairs:
Martin Grossmann (Villigen)
Chulhee Min (Wonju)

NSS-15-01

Improving the Estimation Accuracy of the Inverse Estimation of the Radioactive Source Distribution at the Fukushima Daiichi Nuclear Power Station Using L2 Normalization (#1751)

Dai Tateishi[1,2], **Dai Tateishi**[1,2], Masahiko Machida[2], Masahiko Machida[2], Susumu Yamada[3], Susumu Yamada[3], Yuta Terasaka[1,2], Yuta Terasaka[1,2], Yuki Sato[1,2], Yuki Sato[1,2], Yuta Ichiba[4], Yuta Ichiba[4]

[1] Japan Atomic Energy Agency, Fukushima Research and Engineering Institute, Collaborative Laboratories for Advanced Decommissioning Science, Radiation Sensing and Digitization Group, Naraha-machi, Futaba-gun, Fukushima, Japan; [2] Japan Atomic Energy Agency, Fukushima Research and Engineering Institute, Naraha Center for Remote Control Technology Development, Facility Use Promotion and Technology Section, Naraha-machi, Futaba-gun, Fukushima, Japan; [3] Japan Atomic Energy Agency, Center for Computational Science and e-Systems, Wakashiba, Kashiwa, Chiba, Japan; [4] Tokyo Electric Power Company Holdings, Fukushima Daiichi Decontamination and Decommissioning Engineering Company, Ohkuma, Fukushima, Japan

Two of the authors (M.M. and S.Y.) are indebted to T.Yoshida and H.Hasegawa in RIST for L2 normalization implementation in 3D-AI.

Abstract

To ensure the safe decommissioning of the reactor buildings at the Fukushima Daiichi Nuclear Power Station, it is essential to reduce the external exposure of workers. In order to achieve this objective, it is necessary to accurately estimate the distribution of [if gte msEquation 12]><m:oMath><m:sPre><m:sPrePr><span style='font-family:"Cambria Math",serif;mso-ascii-font-family:"Cambria Math"; mso-hansi-font-family:"Cambria Math";color:black;mso-themecolor:text1; mso-fareast-language:JA;font-style:italic;mso-bidi-font-style:normal'><m:ctrlPr></m:ctrlPr></m:sPrePr><m:sub></m:sub><m:sup><span lang=EN-US style='font-size:10.0pt; font-family:"Cambria Math",serif;mso-fareast-font-family:游明朝;mso-fareast-theme-font: minor-fareast;mso-bidi-font-family:"Times New Roman";color:black;mso-themecolor: text1;mso-ansi-language:EN-US;mso-fareast-language:JA;mso-bidi-language: AR-SA'><m:r>137</m:r></m:sup><m:e><span lang=EN-US style='font-size:10.0pt;font-family:"Cambria Math",serif;mso-fareast-font-family: 游明朝;mso-fareast-theme-font:minor-fareast;mso-bidi-font-family:"Times New Roman"; color:black;mso-themecolor:text1;mso-ansi-language:EN-US;mso-fareast-language: JA;mso-bidi-language:AR-SA'><m:r><m:rPr><m:scr m:val="roman"/><m:sty m:val="p"/></m:rPr>Cs</m:r></m:e></m:sPre></m:oMath><![endif] contamination density — the primary source of external exposure — and to evaluate dose rates in each working space within R/Bs with high precision. 3D Air Dose Rate Evaluation System -Indoor (3D-AI) estimates distributions of contamination density and dose rate in the working space using dose-rate data and point clouds via LASSO regression. In this work, we introduce an L2-normalization method that balances each source's contribution to measurement points to improve sensitivity to remote contaminations. To test the ability of this method, we analyzed data measured near the startup transformer of the Fukushima Daiichi Nuclear Power Station Unit 3 and compared them with maps estimated by the Compton camera. Results show that both conventional and new systems estimated contamination distributions and dose rates with high accuracy near the measurement points. In contrast, in areas distant from measurement points, the

new method better matches the Compton images and improves surface dose-rate estimates, reducing the ~1/50 underestimation to within a few factors.

References
[1] Machida, M., et al. 2022, 'R&D of digital technology on inverse estimation of radioactive source distributions and related source countermeasures; R&D status of digital platform including 3D-ADRES-indoor', *RIST News*, vol. 68, pp. 3–19, Japan
[2] Machida, M., et al. 2024, 'R&D Status of Digital Technology on Inverse Estimation of Radioactive Source Distributions and Related Source Countermeasures – Fast Digital Twin Tech. in Decommissioning Field: 3D-ADRES-Indoor FrontEnd –', RIST News, vol. 70, pp. 3–22, Japan
[3] Shi, W., Machida, M., Yamada, S., Okamoto, K. 2026, 'Development of LASSO based optimized scheme for reconstructing radioactive source distributions using monitoring air dose rates', Measurement, vol. 258, Art. no. 119444.
[4] Sato, Y., Terasaka, Y., Ichiba, Y. 2025, 'Visualization of radioactive contamination around the startup transformer of the Fukushima Daiichi Nuclear Power Station Unit 3 using an integrated Radiation Imaging System based on a Compton camera', Journal of Nuclear Science and Technology, vol. 62, no. 4, pp. 389–400.

NSS-15-02

Template-Based Decomposition of Gamma Spectra for NORM Quantification (#2804)

Massimo Morichi, Bruno Angelucci, **Fabio Davolio**, Cristiana Del Bene, Erica Fanchini, Paola Garosi, Carlo Uguccioni

CAEN S.p.A., Viareggio, Italy

Abstract
This paper describes a template-based gamma spectral decomposition algorithm developed for quantitative analysis of Naturally Occurring Radioactive Material (NORM). The method uses a Monte Carlo-simulated template to decompose measured spectra into contributions from the 40K, and the 238U and 232Th decay chains, and to estimate the corresponding absorbed dose rates. The algorithm is integrated into the CAEN Gamon-Drone platform and supports both $CeBr_3$ and NaI(Tl) scintillation detectors. The proposed approach addresses two operational scenarios. In airborne surveys, dynamic integration and spectral reweighting are applied to continuously acquired spectra to reduce statistical fluctuations. This processing improves detection sensitivity and allows for high-resolution radiological mapping. In ground-based measurements, the same analytical framework provides rapid in situ characterization of soils, rocks, and construction materials through direct estimation of radionuclide concentrations. Validation tests showed strong consistency between reconstructed activities and reference values for multiple detector configurations and environmental conditions. The results demonstrate that Monte Carlo template decomposition can provide accurate and robust NORM quantification using compact scintillation-based gamma spectroscopy systems.

NSS-15-03

Enhancing Low-Energy MVT Bi-exponential Convergence via Adaptive Initial Value Estimation (#2818)

Bowen Xu, **Bowen Xu**, Hao Lan, Hao Lan, Guanning Su, Guanning Su, Qingguo Xie, Qingguo Xie

University of Science and Technology of China, Department of Electronic Engineering and Information Science, Hefei, China

Abstract

Multi-Voltage Threshold (MVT) technology, serving as an advanced method for scintillation pulse digitization, achieves pulse waveform reconstruction and energy calculation in PET systems through a bi-exponential model. However, with the gradual application of crystal miniaturization and 1:1:1 readout technologies, the fitting of low-energy pulses faces severe convergence challenges. This leads to a large number of pulses being discarded, which severely restricts system sensitivity. To address this issue, this paper proposes an effective initial value estimation method. Experiments were conducted using four-threshold MVT sampling and bi-exponential fitting, utilizing the Root Mean Square Error (RMSE) of the fitted waveforms, the proportion of severe deviations, the absolute mean of the pulse area relative error, and the standard deviation as evaluation metrics. Results on low-energy band pulses (40-150 keV) indicate that after utilizing the proposed initial value estimation method, the waveform RMSE was effectively restricted, and the three relative area error metrics were improved by 61.5%, 105.8, and 341.0, respectively, thereby significantly reducing fitting convergence failures.

References

[1] Q. Xie, C. M. Kao, Z. Hsiau, *et al.*, "A new approach for pulse processing in positron emission tomography," *IEEE Trans. Nucl. Sci.*, vol. 52, no. 4, pp. 988–995, 2005.

[2] H. T. Van Dam, S. Seifert, R. Vinke, *et al.*, "A comprehensive model of the response of silicon photomultipliers," *IEEE Trans. Nucl. Sci.*, vol. 57, no. 4, pp. 2254–2266, 2010.

[3] S. Yamamoto, J. Kataoka, K. Kamada, *et al.*, "An ultrahigh spatial resolution radiation-imaging detector using 0.1 mm×0.1 mm pixelated GAGG plate combined with 1 mm channel size Si-PM array," *Nucl. Instrum. Methods Phys. Res. A*, vol. 919, pp. 125–133, 2019.

[4] L. Bläckberg, S. Sajedi, G. El Fakhri, *et al.*, "A layered single-side readout depth of interaction time-of-flight-PET detector," *Phys. Med. Biol.*, vol. 66, no. 4, Art. no. 045025, 2021

NSS-15-04

Dual-Modality Muon Imaging via Trigger Optimization and Image Fusion (#2927)

Zhi Zhou[1,2], Jianjie Zhang[5,2], Yaofen Zhang[1,4], Yini Wu[5,2], Xin Zhao[1,2], Li Wang[1,2], Wenwan Ding[1,2], Ni Su[1,2], Ziqi Yin[1,2], Yannan Huang[1,2], Jianping Cheng[1,3], Yuanyuan Liu[1,3]

[1] Beijing Normal University, School of Physics and Astronomy, Beijing, China; [2] Beijing Normal University, Joint Laboratory of Jinping Ultra-low Radiation Background Measurement of Ministry of Ecology and Environment, Beijing, China; [3] Jinping Deep Underground Frontier Science and Dark Matter Key Laboratory of Sichuan Province, Jinping, China; [4] Beijing Normal University, Key Laboratory of Beam Technology of Ministry of Education, Beijing, China; [5] Chengdu University of Technology, College of Nuclear Technology and Automation Engineering, Chengdu, China

Abstract

Muon scattering imaging (MSI) is sensitive to high-Z materials; however, the inherently low cosmic muon flux usually requires long acquisition times to achieve acceptable image quality. To address this limitation, we propose a statistically enhanced dual-modality muon imaging framework based on trigger redesign in a muon scattering tomography system consisting of 8 detector layers. By relaxing the conventional strict coincidence requirement and redesigning the event selection logic, previously discarded non-penetrating muon events can be effectively incorporated into muon absorption imaging (MAI), while penetrating events are retained for MSI reconstruction. This event reutilization significantly increases the effective statistics without additional hardware, thereby improving imaging efficiency and reducing the required measurement time.

To further exploit the complementary information from MAI and MSI, multiple image fusion methods were investigated, including linear weighted fusion, Fourier decomposition filtering fusion, and Principal Component Analysis-based fusion. Experimental results show that the maximum a posteriori (MAP)-based fusion method achieves the best reconstruction performance. Imaging experiments were conducted using an eight-layer 50 cm × 50 cm plastic scintillator detector system. The target consisted of fifteen 5 cm × 5 cm × 5 cm lead blocks arranged in a U-shaped structure. A total of 4.3 × 10^4 muon events were collected. Compared with conventional MSI reconstruction, the proposed framework produces clearer structural boundaries, higher contrast, and significantly suppressed background noise. Quantitative evaluation using the structural similarity index (SSIM) shows an improvement from 0.212 to 0.389, corresponding to an increase of approximately 83%.

The proposed trigger optimization and image fusion strategy enable faster, higher-quality, and more practical muon scattering imaging for security and high-Z material identification.

References

[1] Tanaka, H. K. M., et al. 2023, ‘Muography’, Nature Reviews Methods Primers, vol. 3, no. 1, p. 88.

[2] Borozdin, K. N., et al. 2003, ‘Radiographic imaging with cosmic-ray muons’, Nature, vol. 422, no. 6929, pp. 277.

[3] Wu, Y.-N., et al. 2026, ‘Reinforcement learning for muon scattering tomography enhancement’, Nuclear Science and Techniques, vol. 37, no. 5, p. 81.

[4] Bae, J., Montgomery, R., and Chatzidakis, S. 2024, ‘Image reconstruction algorithm for momentum dependent muon scattering tomography’, Nuclear Engineering and Technology, vol. 56, no. 5, pp. 1553–1561.

NSS-15-05

Effects of Inverse Compton Scattering Source Parameters on Output X-Ray Spectra for Medical Applications. (#3102)

Henry Priestley[1], Gianfranco Paterno[2], Marie Jacquet[3], Kevin Dupraz[3], Adrian Wilson[4], Jon Duffy[4], Alberto Bravin[5], Sarah Bugby[1], Jenny Spiga[1]

[1] Loughborough University, Department of Physics, Loughborough, UK; [2] University of Ferrara, Department of Physics and Earth Science, Ferrara, Italy; [3] Universite Paris-Saclay, IJCLab, Paris, France; [4] University of Warwick, Department of Physics, Warwick, UK; [5] Università degli Studi di Milano-Bicocca and INFN, Dipartimento di Fisica, Milan, Italy

We are grateful to support provided by the ThomX facility.

Abstract

This work investigates Inverse Compton Scattering (ICS) sources and their potential for synchrotron-based medical applications, particularly Microbeam Radiation Therapy (MRT). As compact alternatives to large synchrotron facilities, ICS sources are rapidly approaching the flux and energy requirements necessary for MRT, but require detailed characterisation before clinical implementation can be considered. Geant4 Monte Carlo simulations inspired by the ThomX ICS source were performed to evaluate the influence of key source parameters on the emitted x-ray spectrum. Parameters studied included electron beam energy, energy spread, emittance, and laser wavelength. The simulations show that variations in these parameters produce measurable shifts in spectral peak energy, directly relevant to MRT beam optimisation, as well as asymmetric spectral broadening across the spectrum. These results are the first ICS simulations of these parameters at MRT relevant energies and aid the evaluation of ICS sources as compact alternatives to synchrotron radiation sources.

References

[1] S. Bartzsch *et al.*, "Technical advances in x-ray microbeam radiation therapy," Jan. 16, 2020, *Institute of Physics Publishing*. doi: 10.1088/1361-6560/ab5507.

[2] [2] K. Dupraz *et al.*, "The ThomX ICS source," *Physics Open*, vol. 5, Dec. 2020, doi: 10.1016/j.physo.2020.100051.

[3] E. Eggl *et al.*, "The Munich Compact Light Source: initial performance measures," *J. Synchrotron Rad*, vol. 23, pp. 1137–1142, 2016, doi: 10.1107/S160057751600967X.

[4] G. Paternò *et al.*, "Generation of primary photons through inverse Compton scattering using a Monte Carlo simulation code," *Physical Review Accelerators and Beams*, vol. 25, no. 8, Aug. 2022, doi: 10.1103/PhysRevAccelBeams.25.084601.

[5] J. Livingstone, A. W. Stevenson, D. Häusermann, and J.-F. Adam, "Experimental optimisation of the X-ray energy in microbeam radiation therapy," *Physica Medica European Journal of Medical Physics*, vol. 45, pp. 156–161, 2018, doi: 10.1016/j.ejmp.2017.12.017i.

[6] M. Jacquet, "High intensity compact Compton X-ray sources: Challenges and potential of applications," *Nucl. Instrum. Methods Phys. Res. B*, vol. 331, pp. 1–5, Jul. 2014, doi: 10.1016/j.nimb.2013.10.078.

[7] G. A. Krafft *et al.*, "Laser pulsing in linear Compton scattering," *Physical Review Accelerators and Beams*, vol. 19, no. 12, p. 121302, Dec. 2016, doi: 10.1103/PhysRevAccelBeams.19.121302.

NSS-15-06

Latent-Space Modeling for Multi-Organ Radiomics Phenotyping in ^{177}Lu-Based SPECT/CT Imaging (#3205)

Mohamed Saber Azimi[3], **Mohamed Saber Azimi**[3], Maryam Cheraghi[4], Maryam Cheraghi[4], Mohammad A. Ghodsi-Rad[4], Mohammad A. Ghodsi-Rad[4], Ghasemali Divband[5], Ghasemali Divband[5], Habib Zaidi[1,2], Habib Zaidi[1,2]

[1] Geneva University Hospital, Division of Nuclear Medicine & Molecular Imaging, Geneva, Switzerland; [2] Odense University Hospital, Deptartment of Nuclear Medicine, Odense, Denmark; [3] Obuda University, Research and Innovation Center, Budapest, Hungary; [4] Shahid Beheshti University, Department of Nuclear Medicine, Tehran, Iran; [5] Jam Hospital, Department of Nuclear Medicine, Tehran, Iran

This study was financially supported by the Swiss National Science Foundation (SNSF, grant No. 30030–231742) and the Geneva League Against Cancer (grant No. LGC 2402).

Abstract

Radiomics analysis in nuclear medicine is commonly performed on predefined features extracted from individual regions, which limits its ability to describe global imaging patterns across the whole body. In this work, we propose a latent-space digital twin framework to characterize multi-organ radiomics behavior in theranostic SPECT/CT imaging. Post-therapy SPECT/CT data from 57 patients treated with ^{177}Lu-based radiopharmaceuticals were analyzed. Multi-organ and lesion segmentations were obtained, and 107 standardized radiomics features were extracted for each region. These features were aggregated into patient-level representations and projected into a low-dimensional latent space using principal component analysis. Unsupervised clustering and distance-based analysis were then applied to identify underlying radiomics phenotypes and quantify inter-patient variability. The learned latent space revealed structured organization of radiomics patterns, with the first two principal components capturing more than half of the total variance (PC1: 34%, PC2: 19%). Distinct patient groups emerged with clear separation, characterized by lower intra-group distances (≈6) and substantially higher inter-group distances (≈12). Analysis of latent components indicated that structural regions predominantly contributed to the first component, while soft-tissue and vascular regions influenced the second component. In addition, the latent representation enabled identification of outlier patients, reflecting substantial heterogeneity in multi-organ radiomics profiles. These findings demonstrate that latent-space modeling provides a compact and interpretable representation of complex radiomics data. The proposed digital twin framework enables system-level phenotyping and may support improved patient stratification in theranostic SPECT/CT imaging.

Time:
11 November, 2026
15:00 – 17:00

Room:
PICASSO

NSS-16 | Scintillators

Chairs:
Jarek Glodo

NSS-16-01

Asymmetry in time difference histograms for scintillators with different decay constants in coincidence (#2202)

Akram Hamato[1,2], Nicolaus Kratochwil[2], Ryosuke Ota[2,4], Jarek Glodo[3], Taiga Yamaya[1], Simon R. Cherry[2], Sun Il Kwon[2]

[1] National Institutes for Quantum Science and Technology (QST), Advanced Nuclear Medicine Sciences, Chiba, Japan; [2] University of California Davis, Biomedical Engineering, Davis, USA; [3] Radiation Monitoring Devices Inc., Watertown, USA; [4] Hamamatsu Photonics K.K, Central Research Laboratory, Hamamatsu, Japan

This work was supported by the National Institutes of Health under grant R01 EB030538.

Abstract

Coincidence timing resolution is a critical performance parameter in time-of-flight PET and other timing sensitive applications. The timing performance of scintillation detectors is governed by intrinsic scintillator properties such as light yield, rise time, and decay constant. When detectors with different scintillation characteristics are in coincidence, these differences can distort the coincidence timing spectrum, leading to deviations from an ideal symmetric Gaussian distribution. Differences in scintillator decay constants can introduce measurable asymmetry in coincidence timing histograms. In this work, the influence of scintillator decay constant on coincidence timing histogram was investigated using several scintillators with different decay constants. The scintillators (Lu_2O_3:Yb, EPS-100 plastic scintillator, $LaBr_3$:Ce, LYSO:Ce, GAGG, NaI:Tl, and BGO) with dimensions of 3×3×5 mm^3 mounted on identical silicon photomultipliers were placed in coincidence with a reference LYSO detector. Time difference histograms were acquired for each detector pair and quantitatively analyzed using the mean, median, and skewness of the measured distributions. The results showed nearly symmetric timing histograms for EPS-100, $LaBr_3$, and LYSO scintillators, whereas other scintillators exhibited increasing asymmetry. The longest tail was observed for BGO on one side of the histogram. Time difference histograms were also analytically calculated based on the arrival time distribution of the 10th detected photon. The analytical results reproduced the main trends observed experimentally. These findings demonstrate that scintillator decay constants significantly influence the shape and asymmetry of coincidence timing histograms for non-identical detector pairs with substantially different decay constants, providing insight relevant to the design and optimization of mixed scintillator timing systems.

References
[1] T. V. D Herman et al., Phys. Med. Biol., 58, 3243, 2013.
[2] S. Gundacker et al., J. Inst., 8, P07014, 2013.
[3] F. Acerbi et al., J. Inst., 10, P07014, 2015.
[4] M. Piller et al., Phys. Med. Biol., 69, 115014, 2024.
[5] R. Ota et al., arxiv:2510.03488, 2025.

NSS-16-02

Ultrafast and Efficient 2D Perovskite Scintillators for Sub-50 ps TOF-PET and High-Resolution X-ray Imaging (#2541)

Jiaqi Liu

Wuhan University of Technology, School of Materials Science and Engineering, Wuhan, China

Abstract

Ultrafast radiation detection has been persistently limited by the formidable challenge of achieving scintillators that combine sub-nanosecond response times with high scintillation efficiency. Here, we identify atomic-level exciton confinement, achieved through the synergistic regulation of A-site organic cations in 2D perovskites, as a critical factor for breaking this performance bottleneck. The resulting (1,4-CMA)$PbBr_4$ crystals exhibit a rare combination of a 0.62 ns radioluminescence decay time and a high light yield of 19,730 photons/MeV, surpassing leading commercial benchmarks such as BaF_2 and LYSO:Ce. Detectors based on this material achieved a record-breaking coincidence timing resolution (CTR) of 43.3 ps for reconstruction-free Time-of-Flight Positron Emission Tomography (TOF-PET) and a high spatial resolution of 32.3 lp mm^{-1} for X-ray imaging. These results establish rational lattice distortion engineering as a key principle for the development of high-performance, scalable perovskite scintillators for next-generation medical and industrial imaging.

NSS-16-03

Thick Optical-guiding Scintillator with Enhanced Crystal Quality for High-Resolution and High-Sensitivity X-ray Imaging (#2557)

Yuhei Nakata[1,2], Kei Kamada[3,2], Masao Yoshino[2,3], Tetsuo Kudo[4], Rikito Murakami[2], Satoshi Ishizawa[2], Yuui Yokota[2,3], Akira Yoshikawa[2,3]

[1] Tohoku University, Department of Materials Science / Graduate School of Engineering, Sendai, Japan; [2] Tohoku University, Institute for Materials Research, Sendai, Japan; [3] Tohoku University, New Industry Creation Hatchery Center, Sendai, Japan; [4] C&A Corporation, Sendai, Japan

Abstract

This study presents the fabrication and evaluation of an Optical-guiding Crystal Scintillator (OCS), a structured scintillator that achieves both high spatial resolution and high detection sensitivity in X-ray imaging. Conventional scintillators face a trade-off between these two properties, and structured scintillators have been developed to overcome this trade-off. However, simultaneously achieving fine waveguiding channels with sufficient thickness at bulk scale remains a challenge. The OCS has been proposed to address this issue [1–2]. It has regularly arrayed single-crystal scintillator cores embedded in a low-refractive-index glass cladding. Each core confines scintillation light by total internal reflection. In this work, we grew Tl-doped $Cs_3Cu_2I_5$ (CCI:Tl, n = 1.92) single-crystal cores

through directional solidification from a melt within the 5 μm-diameter channels of a borosilicate glass plate (n = 1.47). Electron backscatter diffraction analysis of the cross-section sample confirmed that each core is a single crystal, and X-ray-excited radioluminescence showed an emission peak at 517 nm, consistent with previously reported values for CCI:Tl single crystals [3]. We evaluated spatial resolution by imaging test charts with a microfocus X-ray tube and calculating the contrast transfer function (CTF). A 500 μm-thick OCS achieved CTF = 35% at 10 lp/mm, compared with 10% for a commercial CsI:Tl columnar scintillator of the same thickness. The OCS maintained spatial resolution over a thickness range of 200 to 700 μm, whereas the commercial scintillator exhibited a sharp decline. Light yield was higher than that of the commercial CsI:Tl columnar scintillator. These results demonstrate that the OCS overcomes the conventional trade-off between spatial resolution and detection sensitivity, opening new possibilities for high-energy X-ray imaging, industrial nondestructive testing, and medical diagnostics.

References
[1] Ryuga, Yajima, Akira, Yoshikawa, *et al.*, 2023, 'Prototype fabrication of optical-guiding Tl:CsI crystal scintillators and investigation of the crystallization process', *Jpn. J. Appl. Phys.*, vol. 62, p. SC1064.
[2] Kei, kamada, *et al.*, 2026, 'Development of Optical-Guiding Scintillators with Ultrafine (~12 μm) Uniform Scintillator Cores for High-Resolution X-Ray Imaging', *Materials*, vol. 19, no. 9, p. 1834.
[3] Yuan, Dongsheng, 2020, 'Air-stable bulk halide single-crystal scintillator $Cs_3Cu_2I_5$ by melt growth: Intrinsic and Tl doped with high light yield', *ACS Appl. Mater. Interfaces*, vol. 12, no. 34, pp. 38333–38340.

NSS-16-04

Development of 3D-Printable Plastic Scintillator Using Stereolithography for Radiation Detection Applications (#1653)

Kunlanan Puprasit[1,2], Nattasit Mattayom[1], Kullapha Chaiwongkhot[3], Koth Amratisha[3], Akapong Phunpueok[4], Nantawat Udee[5]

[1] Chulabhorn Royal Academy/Princess Srisavangavadhana Faculty of Medicine/Medical Physics Program, Bangkok, Thailand; [2] Chulabhorn Royal Academy/Personalized Radiotherapy and Imaging in Medicine (PRIME) Excellent Research Group, Bangkok, Thailand; [3] Mahidol University/Faculty of Science/Department of Physics, Bangkok, Thailand; [4] Rajamangala University of Technology Thanyaburi/Faculty of Science and Technology/Division of Physics, Pathum Thani, Thailand; [5] Naresuan University/Faculty of Allied Health Sciences/Department of Radiological Technology, Phitsanulok, Thailand

This research was supported by the NSRF via the Research and Innovation Acceleration Agency for Competitiveness and Area Development (RCAD), Program Management Unit for Technology and Innovation for Future Industries (PMU-B): Brainpower for Future Industries (grant number B39G690003). The authors also acknowledge the support of the Personalized Radiotherapy and Imaging in Medicine (PRIME) Excellent Research Group, Chulabhorn Royal Academy, Bangkok, Thailand.

Abstract
Plastic scintillators are widely used in radiation detection; however, conventional fabrication constrains detector geometry to simple shapes, limiting applicability in complex dosimetry configurations. We report the development of a geometrically flexible plastic scintillator fabricated via stereolithography (SLA) 3D printing, enabling arbitrary-

geometry detector production. The formulation incorporated vinyltoluene (VT, 0–20 wt%) as an aromatic co-monomer, 2,5-diphenyloxazole (PPO, 1–2 wt%) as the primary fluorophore, 1,4-bis(2-methylstyryl)benzene (Bis-MSB, 0–0.01 wt%) as a wavelength shifter, and TPO as the photoinitiator in a commercial acrylate photopolymer host matrix. A post-print resin-dipping technique using the identical formulation improved optical transmittance from 11% to 72%. Main-effect analysis across nine formulations showed that VT at 10 wt% yields optimal optical clarity (~72% at 800 nm), while PPO at 2.0 wt% produces the highest emission intensity at 367–368 nm without concentration quenching. Self-absorption arising from PPO emission–absorption spectral overlap and a host-resin transmission cut-off at 410 nm was identified as the primary optical challenge, establishing Bis-MSB wavelength shifting as essential for light collection beyond the cut-off. Active scintillation was confirmed under Sr-90 via silicon photomultiplier (SiPM) readout, with pulse amplitude 20 times lower than EJ-200. Dosimetric characterization under Cs-137 and Co-60 with EJ-200 benchmarking will be presented.

References
[1] J. B. Birks, The Theory and Practice of Scintillation Counting. Oxford: Pergamon, 1964.
[2] M. Nikl et al., "Synthesis and development of a vinyltoluene-based plastic scintillator," J. Lumin., vol. 193, pp. 1–6, 2018.
[3] R. R. Raylman et al., "Evaluation of advanced methods and materials for construction of scintillation detector light guides," Front. Phys., vol. 9, 2021.
[4] K. Yoon et al., "Fast-, light-cured scintillating plastic for 3D-printing applications," J. Nucl. Eng., vol. 4, no. 1, pp. 241–257, 2023.
[5] M. Hamel et al., "Preparation and characterization of cross-linked plastic scintillators," Polymer, vol. 207, p. 122906, 2020.
[6] T. Kaptanoglu et al., "Fluorescence quantum yield of bis-MSB," arXiv:1506.00240, 2015.
[7] Eljen Technology, "EJ-200 Data Sheet." [Online]. Available: https://eljentechnology.com
[8] A. Sharma et al., "Novel epoxy-bPBD-BisMSB composite plastic scintillator," Sci. Rep., vol. 14, p. 6640, 2024.

NSS-16-05

Energy Spectroscopy Using Tin-Loaded Organic Glass Scintillators of Varying Sizes (#2113)

Erin Neely[1,2], Ethan Schneider[2], Charles Sosa[3], Shaun D. Clarke[2], Sara A. Pozzi[2]

[1] University of Michigan, Department of Applied Physics, Ann Arbor, USA; [2] University of Michigan, Department of Nuclear Engineering and Radiological Sciences, Ann Arbor, USA; [3] Radiation Monitoring Devices, Boston, USA

This work was supported in part by the Consortium for Monitoring, Technology, and Verification under Department of Energy National Nuclear Security Administration, award number DE-NA0003920.

Abstract
Organic scintillators doped with heavy metals are promising for nonproliferation work as they combine the low-Z sensitivity to neutrons with the high-Z sensitivity to photoelectric absorption of gammas. Organic glass scintillators (OGS), in particular, are easy to shape and perform almost as well as trans-stilbene in light yield, energy resolution, and pulse shape discrimination. The Detection for Nuclear Nonproliferation Group (DNNG) at the University of Michigan has already completed work on 6-mm and 12-mm cubes of the tin-loaded OGS (or Sn-OGS), finding good agreement between experimental results and MCNP simulations of reasonable fidelity. The measured energy

resolution of the photopeak from the 12-mm Sn-OGS is on the order of 10% and the intrinsic efficiency is visible on a log scale, both with uniform energy-dependent trends. DNNG and RMD have just entered into an agreement to further investigate this material in the form of a 1” x 1” cylinder. We anticipate that similar basic gamma spectroscopy will reveal increased photopeak efficiency and a diminished X-ray escape peak as multiple scatters are more likely in a larger volume; however, the effect of detector volume on energy resolution is unknown. In addition, we hope to present data from Compton coincidence experiments, and begin work with gamma/neutron sources for pulse shape discrimination. This work will also be compared to MCNP simulations.

NSS-16-06

Position-Sensitive and Energy-Constrained Characterization of an Opaque Scintillation Detector (#1047)

Sander Katz[1], Garrett Wendel[2], Jacob Moffatt[2], Andrew Wilhelm[3], Minfang Yeh[4], Douglas F. Cowen[2], Igor Jovanovic[1], On Behalf of the LiquidO Consortium

[1] University of California, Berkeley, Department of Nuclear Engineering, Berkeley, USA; [2] Pennsylvania State University, Department of Physics, University Park, USA; [3] United States Military Academy West Point, Department of Physics & Nuclear Engineering, West Point, USA; [4] Brookhaven National Laboratory, Chemistry Division, Upton, USA

This research is partly sponsored by the Defense Threat Reduction Agency (DTRA) as part of the Interaction of Ionizing Radiation with Matter University Research Alliance (IIRM-URA) under contract number HDTRA1-20-2-0002.

Abstract

LiquidO detectors stochastically confine scintillation and Cherenkov light around energy depositions by using media with a short optical scattering length. Wavelength-shifting fibers latticed throughout the volume capture the confined light, re-emit it, and transport it to photosensors, creating an optically segmented detector without physical optical barriers. Optical segmentation offers the prospect of effective particle identification and directional reconstruction by using the time of flight, energy deposition, and topology of events that deposit energy at multiple locations in the detector volume. A critical first step toward this capability is a position-sensitive calibration to evaluate detector homogeneity and single-scatter spatial and energy resolution. To achieve this, a four-liter LiquidO prototype detector was constructed and exposed to a collimated Cs-137 source in a tagged Compton scattering configuration. A sodium-iodide detector views the scattering region, providing spatially and energetically constrained event tagging. A Monte Carlo simulation of the experimental geometry models optical photon propagation, light collection, and photosensor noise. Initial measurements indicate a light collection of ~100 photoelectrons per MeV can be achieved in the detector center, and ongoing analysis compares measured and simulated detector responses to quantify the spatial and energy resolution.

NSS-16-07

Large Scale Lu_2O_3:Yb Ceramics for High-Rate Calorimetry (#2903)

Lakshmi Soundara Pandian[1], Matthias Muller[1], Govinda Adhikari[1], Arthur Kim[1], Suyoung Kim[1], Liyuan Zhang[2], Harvey Newman[2], Patrick Albert[3], Justin Reiss[3], Yimin Wang[1], Jarek Glodo[1]

[1] Radiation Monitoring Devices, Inc., Watertown, USA; [2] California Institute of Technology, Physics, Mathematics and Astronomy Division, Pasadena, USA; [3] Pennsylvania State University, Applied Research Laboratory, State College, USA

This work was supported by the United States Department of Energy through competitively awarded contract number DE-SC0021686. This support does not constitute an express or implied endorsement on the part of the Government.

Abstract

Future high-luminosity collider experiments require scintillators that combine high density, ultrafast response, and strong radiation tolerance. Yb-doped lutetium oxide (Lu_2O_3:Yb) is a promising candidate due to its 9.4 g/cm³ density, sub-2 ns charge transfer luminescence, and light yield near 500 photons/MeV. Due to its very high melting point, Lu_2O_3 is more effectively fabricated through ceramic processing, which enables scalable production of transparent, large volume components for calorimetry and fast timing systems.

Our current effort advances two complementary ceramic routes for producing Lu_2O_3 at detector relevant sizes. In collaboration with PSU/ARL, Field-Assisted Sintering Technology (FAST) approach is being developed to achieve monolithic parts with target dimensions of 2 × 2 × 15 cm³. In parallel, RMD is fabricating 2.5 cm-scale cubes and thin plates using a sinter-plus-HIP process. Optical and scintillation measurements show that thin plates, including 1-inch squares and 14 × 14 × 3 mm³ samples, reach light yields near 500 ph/MeV, while larger cubes currently exhibit reduced output due to limited transparency. All samples emit near 350 nm under X-ray excitation and maintain decay times of approximately 2 ns.

In collaboration with Caltech we also produce Lu_2O_3 plates for the RaDiCAL experiment as potential replacement for LYSO, leveraging the material's high density and ultrafast timing. The combination of fast response, radiation hardness, and scalable fabrication positions Lu_2O_3 ceramics as a strong candidate for next-generation HEP calorimeters and timing detectors. Our results from the latest FAST-processed Lu_2O_3 samples will also be presented at the conference.

NSS-16-08

Calibration of the Light Detection System of the XEMIS2 Liquid Xenon Compton Camera (#3185)

Yohann Ramsi[1], Nicolas Beaupere[1], Jean-Luc Beney[1], Halim Benhabiles[7], Théo Bossis[1], Pierre Crespi[2], Sara Diglio[1], Debora Giovagnoli[6], Amaury Hervo[1], Jérôme Idier[3], Vincent Jaouen[5], Frédéric Lefevre[1], Olivier Lemaire[1], Patrick Le Ray[1], Julien Masbou[1], Eric Morteau[1], Patrice Pichot[1], Christophe Renard[1], Martin Staempflin[2], Simon Stute[4], Jean-Sébastien Stutzmann[1], Dominique Thers[1]

[1] Subatech, IMT Atlantique, CNRS/IN2P3, Nantes Université., Nantes, France; [2] Air Liquide Advanced Technologies, Sassenage, France; [3] Nantes Université, École Centrale Nantes, CNRS, LS2N., Nantes, France; [4] CRCI2 NA, INSERM UMR 1307, Nantes University, Nantes, France, Nantes, France; [5] IMT Atlantique, Data Science Department and LaTIM, Inserm, Brest, France., Brest, France; [6] IMT Atlantique, Data Science Department, Brest, France, Brest, France; [7] IMT Nord Europe, Lille, France., Lille, France

This project has received financial support from the CNRS through the MITI interdisciplinary programs

Abstract

XEMIS2 is a liquid xenon Compton camera developed at the Subatech laboratory in Nantes, France, designed to demonstrate 3 gamma nuclear imaging on small animals for the first time. This technique exploits the three gamma rays simultaneously emitted by Scandium-44, whose combined detection constrains the emitter position in 3D, enabling a reduction of the injected activity by a factor of 100 compared to conventional Positron Emission Tomography while maintaining equivalent image quality. The detector simultaneously measures two complementary signals: scintillation light, detected by 64 photomultiplier tubes surrounding the liquid xenon active volume, and ionisation electrons, drifted by a 2 kV/cm electric field toward a pixelised anode. Accurate image reconstruction relies critically on the precise calibration of the light acquisition system. The full light calibration chain developed for XEMIS2 is presented, covering the determination of detection thresholds, the photomultiplier tubes gain calibration procedure, and the inter-channel time delay correction validated on both simulation and experimental data.

References

[1] L. Gallego Manzano. Optimization of a single-phase liquid xenon Compton camera for 3 gamma medical imaging. Nuclear Experiment [nucl-ex]. Ecole des Mines de Nantes, 2016.

[2] Y. Xing. Studies and optimization of ionization signal measurement for the 3-gamma imaging XEMIS2 liquid xenon Compton camera. Nuclear Experiment [nucl-ex]. Ecole nationale supérieure Mines-Télécom Atlantique, 2021.

[3] D. Cai. Contributions to instrumental developments for the XEMIS2 camera, on-board ionization and scintillation measurements. Nuclear Experiment [nucl-ex]. Ecole nationale supérieure Mines-Télécom Atlantique, 2024.

Time:
11 November, 2026
17:30 – 19:00

Room:
ALBÉNIZ & MACHUCA

NSS-17 | DAQ, front-end and electronics

Chairs:
Eric J. Mannel (Upton)

NSS-17-01

A Configurable Dual-CDL Sigma-Delta Readout Circuit for Dual-Polarity and High-Precision Signal Detection in CsI: Tl SPECT (#2067)

Xi Zhang, Hamid Sabet

Harvard Medical School, Massachusetts General Hospital, Malden, USA

This work was supported in part by NIH Grant No. R01HL145160 and R01EB034785.

Abstract

Conventional readout electronics for silicon photomultiplier-coupled cesium iodide scintillation detectors are bulky, costly, and difficult to integrate into compact single-photon emission computed tomography systems. Prior sigma-delta modulation charge-to-digital converter implementations are limited to single-polarity operation or require firmware modification for polarity switching. We propose a configurable dual controlled discharging line sigma-delta readout circuit that simultaneously supports dual-polarity readout and high-precision single-polarity charge integration without firmware or hardware modification. The circuit employs a sigma-delta modulator directly integrating silicon photomultiplier charge, with two controlled discharging lines supporting dual-polarity mode for concurrent handling of both signal polarities, and single-polarity mode for fast baseline recovery and precise charge zeroing. Three CsI :Tl crystal configurations were evaluated against a commercial digitizer using Hamamatsu silicon photomultiplier arrays: a small unprocessed crystal with ^{22}Na and ^{137}Cs sources, a monolithic 50×50×8 mm³ crystal with ^{57}Co, and a laser-processed 25×25 pixel array under collimated and flood irradiation. On the small crystal, energy resolutions of 8.49% and 7.47% at 511 keV and 662 keV. On the monolithic crystal, the proposed circuit achieves 7.88% energy resolution at 122 keV versus 13.86% for the CAEN digitizer, a 1.76-fold improvement. On the laser-processed array, a 9% higher peak-to-valley ratio and superior energy resolution are obtained under collimated irradiation, with cleaner pixel separation under flood irradiation. The proposed dual-CDLs sigma-delta readout circuit outperforms commercial digitizers in energy resolution, event rate, and pixel separability across all configurations, offering a scalable, low-cost solution for next-generation SPECT systems.

References

[1] Z. Zhao *et al.*, “A Novel Read-Out Electronics Design Based on 1-Bit Sigma-Delta Modulation,” *IEEE Trans. Nucl. Sci.*, vol. 64, no. 2, pp. 820–828, 2017.1e’, *Journal*, Edition, Page, Place of publication: publishers

[2] X. Cheng, K. Hu, and Y. Shao, “Dual-Polarity SiPM Readout Electronics Based on 1-bit Sigma-Delta Modulation Circuit for PET Detector Applications,” *IEEE Trans. Nucl. Sci.*, vol. 66, no. 9, pp. 2107–2113, 2019.‘Article’, *Journal*, Edition, Page, Place of publication: publishers

[3] M. Ruiz-Gonzalez and L. R. Furenlid, “Design of a 2-Bit Sigma-Delta Modulator for Scintillation Waveform Capture,” in *2017 IEEE Nuclear Science Symposium and Medical Imaging Conference (NSS/MIC)*, 2017, pp. 1–2.

[4] H. Sabet, L. Blackberg, D. Uzun-Ozsahin, and G. El Fakhri, “Novel laser-processed CsI:Tl detector for SPECT,” *Med. Phys.*, vol. 43, no. 5, pp. 2630–2638, 2016.

NSS-17-02

Design and Preliminary Characterization of a Waveform-Sampling ASIC-Based Readout System for the MASS-Cube CZT Detector (#2596)

Chen Li[1,2], Fei Sha[1,2], Xutao Zheng[1,2], Ming Zeng[1,2]

[1] Tsinghua University, Department of Engineering Physics, Beijing, China; [2] Tsinghua University, Key Laboratory of Particle and Radiation Imaging, Ministry of Education, Beijing, China

This work is supported by the Tsinghua University Initiative Scientific Research Program, and the Tsinghua-Kunshan Student Innovation and Entrepreneurship Talent Cultivation Agreement.

Abstract

MeV gamma-ray astronomy provides an important observational window for studying cosmic nucleosynthesis, compact objects and high-energy transients. The MeV Astrophysical Spectroscopic Surveyor (MASS) is a 3-D position-sensitive CdZnTe (CZT) detector concept proposed for MeV gamma-ray detection. Its pathfinder payload, MASS-Cube, has been launched on September 5, 2025. To further improve the event reconstruction capability of CZT detectors, this work presents a readout system based on a waveform-sampling ASIC for the future upgrades of MASS-Cube. Preliminary test results show that the readout system can reliably acquire signal waveforms from the CZT detector. With a ^{137}Cs source, FWHM energy resolutions of 1.33% for single-interaction events and 0.69% for single-pixel spectrum were achieved at 662 keV. These results demonstrate the feasibility of the proposed readout chain and provide a foundation for future waveform-based 3-D position reconstruction and imaging optimization.

References

[1] J. Zhu *et al.*, "MeV astrophysical spectroscopic surveyor (MASS): a compton telescope mission concept," *Experimental Astronomy*, 2024.

[2] Y. Zhu, S. E. Anderson, and Z. He, "Sub-Pixel Position Sensing for Pixelated, 3-D Position Sensitive, Wide Band-Gap, Semiconductor, Gamma-Ray Detectors," *IEEE Trans. Nucl. Sci.*, vol. 58, no. 3, pp. 1400–1409, Jun. 2011, doi: 10.1109/TNS.2011.2132738.

[3] GDS-10-Datasheet V2R0, www.ideas.no.

NSS-17-03

MALTA2 Sensor Characterization with a New Asynchronous Oversampling Readout (#2808)

Fuat Kerem Işık[1], Carlos A. Solans Sanchez[2], İlkay Türk Çakır[1], Milou van Rijnbach[2], Prafulla Behera[3], D. Vlad Berlea[4], Daniela Bortoletto[5], Craig Buttar[6], Theertha Chembakan[3], Valerio Dao[7], Ganapati Dash[3], Yuji Enari[8], Lucian Fasselt[4], Sebastian Haberl[2,9], Tomohiro Inada[2], Cigdem Issever[4], Long Li[10], Xuan Li[11], Yuta Okazaki[8], Heinz Pernegger[2], Petra Riedler[2], Walter Snoeys[2], Anna Swoboda[2], Anusree Vijay[3], Steven Worm[4]

[1] Ankara University, Institute Of Accelerator Technologies, Ankara, Turkey; [2] CERN, Meyrin, Switzerland; [3] Indian Institute of Technology Madras, Chennai, India; [4] Deutsches Elektronen-Synchrotron DESY, Zeuthen, Germany; [5] University of Oxford, Oxford, UK; [6] University of Glasgow, Glasgow, UK; [7] Stony Brook University, Stony Brook, USA; [8] High Energy Accelerator Research Organization (KEK), Tsukuba, Japan; [9] University of Innsbruck, Innsbruck, Austria; [10] University of Birmingham, Birmingham, UK; [11] Los Alamos National Laboratory, Los Alamos, USA

Abstract

The MALTA2 depleted monolithic active pixel sensor, implemented in 180 nm complementary metal-oxide-semiconductor imaging technology, has demonstrated hit detection efficiencies of up to 98% after neutron irradiation to 3 × 10^{15} 1 MeV n_eq/cm². Measurements at higher fluence motivate further sensor-characterization and test-beam studies, including planned investigations of UHD-modified samples. This contribution presents a new asynchronous oversampling readout developed to support these measurements through more stable sampling of MALTA2 hit signals. The system provides the readout basis for ongoing studies at the CERN Super Proton Synchrotron H6 beam line and future beam-test campaigns at KEK.

References

[1] Garcia-Sciveres, M., Wermes, N. 2018, 'A review of advances in pixel detectors for experiments with high rate and radiation', Reports on Progress in Physics, 81, 066101.

[2] Snoeys, W. et al. 2017, 'A process modification for CMOS monolithic active pixel sensors for enhanced depletion, timing performance and radiation tolerance', Nuclear Instruments and Methods in Physics Research Section A, 871, 90–96.

[3] Cardella, R. et al. 2019, 'MALTA: An asynchronous readout CMOS monolithic pixel detector for the ATLAS High-Luminosity upgrade', Journal of Instrumentation, 14, C06019.

[4] Berlea, D. V. et al. 2023, 'Radiation hardness of MALTA2, a monolithic active pixel sensor for tracking applications', IEEE Transactions on Nuclear Science, 70, 2303–2309.

[5] van Rijnbach, M. et al. 2023, 'Performance of the MALTA telescope', Journal of Instrumentation, 18, C03009.

[6] van Rijnbach, M. et al. 2024, 'Radiation hardness of MALTA2 monolithic CMOS imaging sensors on Czochralski substrates', European Physical Journal C, 84, 251.

NSS-17-04

A fully-programmable mixed-signal RISC-V SoC for direct readout of radiation sensors (#3010)

Valerio Pagliarino[1,2], Luigi Borge[1,2], Alessandra Dolmeta[1], Stefano Durando[2], Luigi Giuffrida[1], Enrico Manfredi[1], Maurizio Martina[1], Guido Masera[1], Marco Mignone[2], Valeria Piscopo[1], Angelo Rivetti[2], Manuel D. Da Rocha Rolo[2,3]

[1] Politecnico di Torino, Dipartimento di Elettronica (DET), Torino, Italy; [2] INFN, Sezione di Torino, Torino, Italy; [3] Università degli Studi di Torino, Dipartimento di Fisica, Torino, Italy

Abstract

A 6U CubeSat scheduled for launch in March 2027 will be equipped with a payload for in-orbit charged-particle spectroscopy, requiring on-board signal processing and feature extraction to comply with the narrow-band downlink. To satisfy these requirements, while testing and validating in a space environment a novel technology, an FPGA has been installed implementing the digital logic of the MAIA SoC. The solution is currently entering the testing phase.

MAIA is a fully-programmable mixed-signal System-on-Chip for readout of particle detectors, targeting a 28 nm CMOS node. Each channel integrates selectable analog front-ends a 320 MSps 10-bit waveform sampling ADC, a programmable DSP for continuous-time signal conditioning, a feature extraction engine and four 1.28 Gbps data links. A global trigger unit with real-time pattern analysis capability is integrated as well. The system control is provided by a multi-core cv32e40p RISC-V CPU with radiation-tolerant lock-step operation support and DMA engine, implementing closed-loop real-time control of the signal processing parameters. A chiplet-compatible architecture enables cost-effective channel scaling and connection to external chips. The encapsulation of the UART and JTAG slow-control interfaces on a full-duplex 320 Mbps 8b10b-encoded data link allow remote control of the SoC when integrated in medium or large-scale experiments.

This approach based on high-level of programmability of the signal processing chain can reduce the cost with the respect to producing dedicated front-end ASICs in 110/65 nm for different experiments. All the features of the digital logic of MAIA SoC will be implemented on the satellite FPGA, while the analog front-end and the ADCs will be replaced by the "MIZAR" chip. The payload will be characterized using a particle beam in the next months and the results will be presented at the conference, while the submission of the complete MAIA SoC to the foundry is planned for 2027.

NSS-17-05

The MIZAR ASIC: from mixed-signal design to the PBR mission (#3041)

Andrea Di Salvo[1], Emanuele Trossarello[3,1], Matteo Bussi[2], Federico Reynaud[1], Matteo Abrate[1], Sofia Durandetto[2], Richard Wheadon[1], Marco Mignone[1], Angelo Rivetti[1], Sara Garbolino[1], Mario E. Bertaina[2,1], On behalf of the JEM-EUSO Collaboration

[1] National Institute for Nuclear Physics, Section of Torino, Torino, Italy; [2] University of Torino, Department of Physics, Torino, Italy; [3] Politecnico di Torino, Department of Electronics, Torino, Italy

The authors would also like to thank Paolo De Remigis for his support during the setup of the LASER, Marco Ferrero for his fundamental contribution during the bonding stage and Giorgio Cotto for the mechanical support of the SiPMs.

Abstract

The POEMMA Balloon with Radio (PBR) is a NASA's mission to achieve the dual purpose of detecting Ultra-High Energy Cosmic Rays (UHECRs) and performing neutrino astronomy. Planned to operate at stratospheric altitudes, this mission is equipped with two payloads, fluorescence light and Cherenkov light detectors respectively. To detect the latter, a new ASIC was designed in a commercial 65 nm CMOS technology. The Multi-channel Integrated Zone-sampling Analogue-memory based Readout (MIZAR) chip is a 64-channel ASIC developed to read out the signals generated in a tile of Silicon Photo-Multipliers (SiPMs). A single channel is made of 256 cells based on analog memories and working at the sampling frequency of 100 MHz. Each cell allows the local digitization of the events using a configurable Wilkinson Analog-to-Digital Converter (ADC) in the range 8-12 bits. When an event of interest is detected, MIZAR sends out to an FPGA a 64-bit hitmap. This raw information in used as first-level trigger and if it is validated the event is digitized, then the data is serialized through a dedicated Low Voltage Differential Signaling (LVDS) line at 200 MHz in Double Data Rate (DDR). This work describes the scientific context of the PBR mission and the design stages of the MIZAR ASIC. The general results of the test campaign in laboratory are shown, then a focus on the performances in terms of single photo-electron sensitivity and linearity are presented.

References

[1] James H. Adams Jr.; others, The EUSO-SPB2 fluorescence telescope for the detection of Ultra-High Energy Cosmic Rays. Astroparticle Physics; Volume 165, February 2025, 103046.

[2] M. Battisti and others for the JEM-EUSO collaboration, POEMMA-Balloon with Radio: A balloon-born multi-messenger multi-detector observatory, Nuclear Instruments and Methods in Physics Research Section A: Accelerators, Spectrometers, Detectors and Associated Equipment, Volume 1069, 2024.

[3] Hamamatsu Company; MPPC (SiPM) array (https://www.hamamatsu.com/eu/en/product/optical-sensors/mppc/mppc mppc-array/S13361-3050NE-08.html).

[4] Di Salvo, A.; others, The MIZAR ASIC: 64-channel zone-sampling based ASIC for Cherenkov light detection from sub-orbital and orbital altitudes. Nuclear Instruments and Methods in Physics Research Section A: Accelerators, Spectrometers, Detectors and Associated Equipment, Volume 1069, December 2024, 169856.

[5] Di Salvo, A.; others, Preliminary characterization of the 64-channel MIZAR ASIC for Cherenkov light detection. Journal of Instrumentation, Volume 21, April 2026.

NSS-17-06

A Timepix4-based High-Speed Imaging System for Energy-Resolved Neutron Imaging at CSNS (#3077)

Hongbin Liu[1,2], Qicai Li[1,3], Yujie Zhou[5,6], Chengshuo Zhang[4,2], Haoran Guo[4,2], Weile Gong[1,3], Yimie Yuan[1,3]

[1] Chinese Academy of Sciences, Institute of High Energy Physics, Beijing, China; [2] Spallation Neutron Source Science Center, Dongguan, China; [3] University of Chinese Academy of Sciences, Beijing, China; [4] University of Electronic Science and Technology of China, Chengdu, China; [5] Chinese Academy of Sciences, Purple Mountain Observatory, Nanjing, China; [6] University of Science and Technology of China, Hefei, China

Abstract

The China Spallation Neutron Source (CSNS) is undergoing a beam power upgrade to 500 kW. This upgrade requires new detector readout systems for the Energy-Resolved Neutron Imaging (ERNI) instrument. We present CTPX1, a data-driven camera system based on the Timepix4 ASIC, designed to overcome the 80 Mhits/s bandwidth limit of legacy Timepix3 systems. The CTPX1 integrates a custom high-voltage bias supply with a noise floor below 1 mV, a thermoelectric cooling unit that maintains the sensor temperature within 0.1°C, and a Zynq UltraScale+ FPGA-based readout system. The FPGA aggregates sixteen 5.12 Gbps serial links from the ASIC. The system provides a buffered mode for short data bursts up to 81.92 Gbps and a continuous streaming mode up to 64 Gbps via a QSFP+ interface. In high-flux X-ray tests, the system achieved a peak event rate of 1.17 Ghits/s without data loss. During neutron imaging tests at the CSNS BL-20 beamline, using a ^{6}LiF/ZnS:Ag scintillator coupled with an image intensifier, the system obtained a spatial resolution of 55 μm. Furthermore, time-of-flight measurements on austenitic stainless steel successfully identified the Bragg edges corresponding to the expected fcc lattice planes. Quantitative energy calibration using X-ray fluorescence (XRF) also showed a highly linear ToT-to-energy relationship. These results indicate that the CTPX1 meets the high-throughput requirements for energy-resolved neutron imaging, making it a suitable candidate for the ERNI upgrade at CSNS-II. Future work will explore its application at high-flux synchrotron light sources, such as HEPS.

Time:
11 November, 2026
17:30 – 19:00

Room:
MACHADO

NSS-18 | Neutron and gamma-ray detectors and applications, including security, dosimetry and other related applications

Chairs:
Abdallah LYOUSSI (Saint Paul-lez-Durance)
Igor Jovanovic (Berkeley)

NSS-18-01

Fast Neutron Spectrometer for Fusion Diagnostics (#3079)

Kartikeya Sharma, Fabrice Retiere

a. TRIUMF, 4004 Wesbrook Mall, Vancouver, British Columbia V6T 2A3, Canada, Vancouver, Canada

This work was supported in part by the Natural Sciences and Engineering Research Council of Canada (NSERC).

Abstract

Advancements in Silicon Photomultiplier (SiPM) performance in recent years have demonstrated success across a broad range of fields, including particle and nuclear physics, Positron Emission Tomography, Light Detection and Ranging technology, Fusion diagnostics, among others. This work develops a time-of-flight (ToF)–based neutron spectrometer using SiPMs coupled to plastic scintillators as a plasma fusion diagnostic tool. A Deuterium-fueled plasma fusion emits 2.45MeV neutrons with an energy spectrum broadened by ion kinematics. The achievable neutron energy resolution of the spectrometer is correlated to the relative uncertainty on the inferred plasma ion temperature, a critical parameter for evaluating plasma performance and viability of the fusion approach. The target relative uncertainty on temperature is below 20%, therefore constraining the neutron interaction time and position resolution within the spectrometer. A two-layer (L1–L2) detector array is in development at TRIUMF. The detector coupled with fast data acquisition is expected to successfully detect neutrons at GHz rate. Timing-Position resolution of the chosen scintillators (Eljen L1: EJ232Q 0.5% Benzophenone doped; L2: EJ230) paired with Broadcom series AFBR-S4N SiPMs is presented as proof of concept in the neutron energy range of interest. A 511keV-gamma source is used to characterize the timing and position response of a single scintillator–SiPM assembly, incorporating the light yield differences between gamma and neutron interactions accounted for via Birks' law. Techniques and results demonstrating time resolution ranging 60 to 120ps with energy in Layer 1 and preliminary work on Layer 2 will be presented.

NSS-18-02

Pixel Size-Induced Visibility Degradation and Its Mitigation for X-ray Dark-Field Baggage Scanners (#2055)

Zhexin Wang[1], Peiyuan Guo[1], Jie Tian[2], Longchao Men[1], Xinbin Li[3], Chengpeng Wu[4,1], Xinchi Ran[1], Zhi Deng[1], Li Zhang[1], Zhentian Wang[1]

[1] Tsinghua University, Department of Engineering Physics, Beijing, China; [2] Science and Technology Research Center of China Customs, Beijing, China; [3] Nuctech Company Limited, Beijing, China; [4] Technical University of Denmark, Department of Physics, Kongens Lyngby, Denmark

This work was supported in part by National Key Research and Development Program of China (No. 2023YFC2605802) and National Natural Science Foundation of China (No. 62227804).

Abstract

X-ray dark-field (DF) imaging enables detection of low-Z scattering materials such as powdered explosives and narcotics, which are indistinguishable in conventional absorption imaging, making it a transformative technology for security screening. However, industrial baggage scanners face an inherent trade-off: high-throughput operation requires large-pixel detectors to capture sufficient photon flux at 160 kV operating voltages, but this causes severe Moiré fringe blurring that fundamentally limits DF sensitivity. In our previous work, we developed a 160 kV dark-field baggage scanner prototype, but found that the 2.7 mm × 3.0 mm large-pixel detectors we used only achieved a fringe visibility of ~7.3% under practical operating conditions, severely limiting DF sensitivity. To address this bottleneck, this study quantitatively investigates pixel size-induced visibility degradation through physics-informed simulations and experimental validation on a benchtop grating interferometry platform. Results confirm the visibility decay trend predicted by the sinc model, and show that a 0.5 mm small-pixel detector achieves ~30% improvement in DF sensitivity for high-energy X-ray dark-field baggage scanners. This work provides critical quantitative guidance for optimizing these systems to improve hazardous material detection.

References

[1] F. Pfeiffer, M. Bech, O. Bunk, et al., "Hard-X-ray dark-field imaging using a grating interferometer," Nature Materials, vol. 7, pp. 134–137, 2008.

[2] J. H. Hubbell, W. J. Veigele, E. A. Briggs, et al., "Atomic form factors, incoherent scattering functions, and photon scattering cross sections," J. Phys. Chem. Ref. Data, vol. 4, pp. 471–538, 1975.

[3] A. P. Sauter, J. Andrejewski, M. Frank, et al., "Correlation of image quality parameters with tube voltage in X-ray dark-field chest radiography: a phantom study," Scientific Reports, vol. 11, Art. no. 14130, 2021.

[4] X. Ran, Z. Deng, Y. Song, and H. Gao, “Development of a Simultaneous Photon Counting and Energy Integrating Detector for X-Ray Imaging Applications,” IEEE Trans. Nucl. Sci., vol. 73, no. 1, pp. 147–156, Jan. 2026.

[5] C. Wu, “Research on information retrieval theory and performance optimization methods for grating-based X-ray multi-contrast imaging,” Ph.D. dissertation, Dept. Eng. Phys., Tsinghua Univ., Beijing, China, 2022.

NSS-18-03

Three-Dimensional Isotopic Imaging via Portable Neutron Resonance Transmission Analysis (#2122)

Kevin Sanchez, Areg Danagoulian, Nolan I. Kowitt

MIT, NSE, Cambridge, USA

Abstract

Nuclear material safeguards demand portable, isotope specific verification methods capable of operating across diverse deployment contexts. Neutron Resonance Transmission Analysis (NRTA) exploits isotope-specific resonances in neutron cross sections to provide definitive material identification, but portable implementations have been constrained to one-dimensional areal density measurements. Here we present a compact pixelated NRTA system that achieves three-dimensional isotopic imaging through a deuterium-tritium neutron generator, a multi-element GS20 ^{6}Li scintillator array, and Algebraic Reconstruction Technique (ART) algorithms. Systematic benchmarking establishes operational limits: maximum target dimensions of 17.5 × 17.5 × 17.5 cm, stand-off distances up to 17.5 cm, spatial resolution of 2.5 cm, and complete three-dimensional reconstruction within four

hours using eight measurement angles at 30 minutes per angle. Three-dimensional reconstruction of both homogeneous and non-homogeneous tungsten and silver targets is demonstrated experimentally. This system extends portable NRTA beyond one-dimensional assay, enabling field-deployable isotopic imaging previously available only at large centralized neutron facilities.

References
[1] Prasad, S. et al. Nonproliferation improvements and challenges presented by small modular reactors. Prog. Nucl. Energy 80, 102–109 (2015).
[2] Anderson, I. S. et al. Research opportunities with compact accelerator driven neutron sources. Phys. Rep. 654, 1–58 (2016).
[3] Postma, H. & Schillebeeckx, P. Neutron resonance capture and transmission analysis. In Encyclopedia of Analytical Chemistry (Wiley, 2009).
[4] Gozani, T. Active Nondestructive Assay of Nuclear Materials: Principles and Applications. NUREG/CR-0602 (US NRC, 1981).
[5] Klein, E. A. et al. Neutron-resonance transmission analysis with a compact deuterium-tritium neutron generator. Phys. Rev. Appl. 15,054026 (2021).
[6] Rahon, J. M. Compact Capabilities: Developing and Evaluating a Field-Portable Neutron Resonance Capture Analysis System. Thesis, Massachusetts Institute of Technology (2024).
[7] Brown, D. et al. ENDF/B-VIII.0: the 8th major release of the nuclear reaction data library with CIELO-project cross sections, new standards and thermal scattering data. Nucl. Data Sheets 148, 1–142 (2018).
[8] Gordon, R., Bender, R. & Herman, G. T. Algebraic reconstruction techniques (ART) for three-dimensional electron microscopy and X-ray photography. J. Theor. Biol. 29, 471–481 (1970).

NSS-18-04

Neutron diffraction-contrast tomography demonstration using event-based Timepix camera (#2157)

Anton Khaplanov, Ke An, Saurabh Kabra, Shuo Qian, Gergeley Nagy, Chen Zhang

Oak Ridge National Laboratory, NScD, Oak Ridge, USA

This research used resources of the Spallation Neutron Source, High-Flux Isotope Reactor at ORNL. ORNL is managed by UT-Battelle LLC for DOE's Office of Science, the single largest supporter of basic research in the physical sciences in the US.

Abstract
Diffraction contrast tomography is used extensively on x-ray scattering instruments, however, its neutron counterpart has up till now been elusive, in part due to detector limitations. Scintillator-coupled Timepix detectors offer high spatial resolution, event-mode readout, and improved rate capability, making them attractive for neutron scattering and imaging applications. Here we evaluate a LumaCam detector equipped with a TPX3Cam and a ZnO:Zn:6LiF scintillator in a near-field diffraction setup. Scintillation light was focused in a lens onto a 25mm-diameter MCP-based image intensifier. Intensified light was refocused onto a 0.3mm-thick Si sensor with a thin window bonded to a Timepix3 ASIC. Hits were collected in and clusterie to increase position resolution beyond the native pixelation of the ASIC. The detector was placed 10 cm from the sample at 90 degrees to the beam and calibrated using a silicon powder sample. A refractory alloy sample with grains up to 1mm was measured over 180 degrees of rotation. Diffraction spots were assigned to reflections from several crystallographic orientations. By correlating angular separations and relative intensities, 75 grains were identified. Results demonstrate the

feasibility of compact grain-resolved neutron diffraction using Timepix camera technology. Irregular spot shapes indicate sensitivity to grain morphology, however, resolution is smeared by beam divergence. Thus, to fully exploit available detector resolution, shorter sample-to-detector distances are currently being explored. Ongoing work combines near-field diffraction with simultaneous transmission imaging to achieve neutron diffraction contrast tomography by relating diffraction spots to grain locations.

NSS-18-05

Associated-Particle Neutron Time-of-Flight Measurements of Curium-244 and Californium-252 (#2360)

Andrew Parker[1], Michael D. Aspinall[3], Frank Cave[2], Stephen Croft[1], Alex Grievson[5], Bryan Swinson[4], Malcolm J. Joyce[1,2]

[1] Lancaster University (Lancaster), School of Engineering, Lancaster, UK; [2] Hybrid Instruments Ltd, Gillow Avenue, Lancaster, UK; [3] Aspinall Instruments, Lancaster, UK; [4] Alpha Safety PSC, Sante Fe, USA; [5] Mirion Technologies UK Ltd, Warrington, UK

This work was fund by the UKs Science and Technolgies Funding Council, via the DSI: Late-stage commercialisation for time-of-flight neutron spectrometer grant.

Abstract

γ-triggered neutron time-of-flight technique was used to measure fast-neutron spectra from spontaneous fission sources using two EJ-309 liquid scintillator detectors operated in coincidence. Prompt γ-ray detection provided the timing reference for neutron energy reconstruction. Measurements were performed using bare ^{244}Cm and ^{252}Cf sources, together with a moderated ^{252}Cf configuration to investigate scattering effects. Time-of-flight spectra were reconstructed into neutron energy distributions with corrections for detector efficiency and the non-linear time–energy relationship, supported by GEANT4 detector-response simulations. The reconstructed spectra were fitted using Maxwellian and Watt functions. Extracted Maxwellian temperatures were 1.89 MeV for bare ^{252}Cf, 1.41–1.51 MeV for moderated ^{252}Cf, and 1.48 MeV for ^{244}Cm, demonstrating the expected spectral softening caused by moderation. Although systematic deviations from literature values were observed due to detector threshold and efficiency limitations, the method successfully resolved relative differences between source configurations. The results demonstrate the suitability of γ-triggered nToF spectrometry for comparative neutron spectral characterisation.

NSS-18-06

Quantitative Contamination Mapping Using an Electron-Tracking Compton Camera for Nuclear Decommissioning (#1819)

Daiki Satoh[1], Atsushi Takada[2], Yuya Koda[1], Shinya Sonoda[3,2], Toru Tanimori[4,3]

[1] Japan Atomic Energy Agency, Ibaraki, Japan; [2] Kyoto University, Kyoto, Japan; [3] ERRAI Corporation, Kyoto, Japan; [4] Kitasato University, Kanagawa, Japan

The authors would like to thank the staff of the FUGEN Decommissioning Engineering Center for their dedicated support during the experiments. This work was supported by JSPS KAKENHI Grant Number JP23K26591.

Abstract

Quantitative evaluation of radioactive contamination is essential for nuclear decommissioning; however, conventional survey methods provide limited spatial information, and conventional Compton cameras lack quantitative imaging capability due to their non-unique source reconstruction, in which the source position spreads into a cone. In this work, we investigate the applicability of an Electron-Tracking Compton Camera (ETCC) [1] to quantitative gamma-ray imaging in a decommissioning environment. The ETCC consists of a gaseous Time Projection Chamber (TPC) as the scatterer and a pixel scintillator array as the absorber. By reconstructing recoil electron tracks in the TPC, the ETCC uniquely solves the Compton kinematics, enabling a one-to-one correspondence between the source direction and the reconstructed image, in contrast to conventional Compton cameras. Measurements were conducted at the Prototype Advanced Thermal Reactor "FUGEN," currently under decommissioning. A ^{60}Co hot spot with a dose rate of approximately 1 μSv/h was successfully identified and imaged, and the dose rate estimated from the ETCC data was consistent with that obtained from a survey meter. In addition, weak ^{60}Co contamination at approximately 0.08 μSv/h, close to the background level and below the sensitivity limit of conventional survey meters, was visualized through direction-resolved analysis. These results demonstrate that the ETCC enables quantitative and sensitive imaging of radioactive contamination and can complement conventional survey methods, with potential to improve the efficiency of contamination assessment and clearance verification in nuclear decommissioning.

References

[1] Takada, A, Takemura, T, Yoshikawa, K, Mizumura, Y, Ikeda, T, Nakamura, Y, Onozaka, K, Abe, M, Hamaguchi, K, Kubo, H, Kurosawa, S, Miuchi, K, Saito, K, Sawano, T & Tanimori, T 2022, 'First Observation of the MeV Gamma-Ray Universe with Bijective Imaging Spectroscopy Using the Electron-tracking Compton Telescope on Board SMILE-2+', *The Astrophysical Journal*, vol. 930, no. 1, Art. no. 6, Bristol: IOP Publishing.

Time:
11 November, 2026
17:30 – 19:00

Room:
PICASSO

NSS-19 | Nuclear, HEP and astrophysics detectors

Chairs:
Chiara Guazzoni (Milano)

NSS-19-01

Status of the Phase-2 Upgrade of the CMS Outer Tracker (#1573)

Michael Tytgat, On behalf of the CMS Collaboration

Vrije Universiteit Brussel, Inter-University Institute for High Energies, Brussels, Belgium

This work was supported in part by the FWO (grant I001123N) and WEWIS in Flanders/Belgium.

Abstract

The Silicon Tracker of the Compact Muon Solenoid (CMS) is the innermost sub-detector, measuring charged particles produced in high-energy collisions at the Large Hadron Collider (LHC), and is the world's largest silicon tracking system operational today. The High-Luminosity LHC (HL LHC) will increase luminosity by up to an order of magnitude, delivering 3000–4000 fb^{-1} of data with up to 200 simultaneous interactions per bunch crossing. To cope with these extreme conditions, CMS will replace its entire tracking system during the Phase-2 Upgrade. The new tracker will feature enhanced radiation tolerance, finer granularity, and extended coverage, significantly improving tracking efficiency, vertex resolution, and momentum measurement. A key innovation is the inclusion of tracking information at the Level-1 trigger. This is enabled by p_t-modules in the Outer Tracker, each consisting of two closely spaced sensors that correlate hits to identify high-p_t track candidates in real time. The Outer Tracker will comprise over 13,000 such modules, produced worldwide, with a large-scale production underway since 2025. This contribution will detail the Outer Tracker design and the ongoing module production and integration efforts leading up to the installation and commissioning of the new tracker during the upcoming LHC Long Shutdown 3.

References
[1] CMS Collaboration, The Phase-2 Upgrade of the CMS Tracker, CERNLHCC-2017-009, CMS-TDR-014 (2017).
[2] I. Zoi, Design and construction of the CMS Outer Tracker for the Phase-2 Upgrade, Nucl. Instrum. Meth. A 1078 (2025) 170599.
[3] I. Sohail, Beam test characterization of an irradiated pixel-strip module for the HL-LHC CMS tracker upgrade, Nucl. Instrum. Meth. A 1080 (2025) 170683.

NSS-19-02

Operation and Performance of the ATLAS Liquid Argon Calorimeter During LHC Run 3 (#2118)

Nick Fritzsche, On behalf of the ATLAS Collaboration

CERN, Experimental Physics, Geneve, Switzerland

Abstract

The ATLAS Liquid Argon (LAr) calorimeter provides electromagnetic calorimetry for |η|<3.2 and hadronic and forward calorimetry up to |η|=4.9, playing a central role in the reconstruction and triggering of electrons, photons,

jets, and missing transverse momentum at the Large Hadron Collider. During LHC Run 3, the detector operated under increased instantaneous luminosity and pileup conditions reaching up to approximately 65 interactions per bunch crossing. A major evolution during this period was the commissioning and operation of the Phase-I Digital Trigger readout system based on longitudinally segmented supercells and real-time FPGA processing. The upgraded trigger path provides finer granularity and improved trigger performance compared to the legacy trigger architecture. In addition, the Digital Trigger enables advanced online detector monitoring and demonstrates strong potential for luminosity measurements using statistical properties of digitized supercell signals. Run 3 data show stable detector operation, excellent trigger-readout agreement, and enhanced trigger efficiency for physics objects.

References
[1] ATLAS Collaboration, "The ATLAS Experiment at the CERN Large Hadron Collider," JINST, no. 3, S08003, 2008.
[2] ATLAS Collaboration, "The ATLAS experiment at the CERN Large Hadron Collider: a description of the detector configuration for Run 3," JINST 19, no. 05, P05063 (2024).
[3] G. Aad, et al. "The Phase-I trigger readout electronics upgrade of the ATLAS Liquid Argon calorimeters," JINST 17, no. 05, P05024, 2022.

NSS-19-03

Building the TRISTAN Phase-1 Detector: Characterization of 1000 SDD Pixels (#2158)

Marco Carminati[1,2], On behalf of KATRIN Collaboration

[1] INFN - Istituto Nazionale di Fisica Nucleare, Sezione di Milano, Milano, Italy; [2] Politecnico di Milano, Dipartimento di Elettronica, Informazione e Bioingegneria, Milano, Italy

The author acknowledges support from Politecnico di Milano, INFN (CSN2 KATRIN_TRISTAN Experiment), MPP, KATRIN and KIT.

Abstract
The TRISTAN detector, an array of 9 modules based on monolithic arrays of 166 Silicon Drift Detectors (SDD) pixels is being realized for high accuracy (1 ppm) beta spectroscopy. It will be installed in the KATRIN focal plane by the end of 2026 in order to extend the use of the KATRIN Tritium facility for searching the sterile neutrino in the keV mass range. Each detection module is 4-side buttable and has an area of 4 by 4 cm^2. Here, the progress in detectors assembly is reported. Currently, more than 25 modules have been realized and tested, allowing to select the best 7 modules, out of the final set of 9. They are being characterized in a chamber replicating the operating conditions in terms of vacuum, electric and magnetic fields. Out of the final target value of 1494 pixels, currently a total of 981 pixels are operational, making this system the largest array of spectroscopic SDD detectors ever commissioned. The challenges of this phase are mostly related to production yield and reliability of the complex assembly phase. All pixels show an average FWHM energy resolution below 300 eV for electrons of 20 keV.

References
[1] KATRIN Collaboration, 2025, "Direct neutrino-mass measurement based on 259 days of katrin data," *Science*, vol. 388, no. 6743, pp. 180–185.
[2] KATRIN Collaboration, 2025, "Sterile-neutrino search based on 259 days of katrin data," *Nature*, vol. 648, no. 8092, pp. 70–75.

[3] Mertens, S, et al., 2020, "Characterization of silicon drift detectors with electrons for the tristan project," *Journal of Physics G: Nuclear and Particle Physics*, vol. 48, no. 1, p. 015008.
[4] Siegmann, D et al., 2024, "Development of a silicon drift detector array to search for kev-scale sterile neutrinos with the katrin experiment," *Journal of Physics G: Nuclear and Particle Physics*, vol. 51, no. 8, p. 085202.
[5] Spreng, D, et al.,2024, "Investigation of electron backscattering on silicon drift detectors for the sterile neutrino search with tristan," *Journal of Instrumentation*, vol. 19, no. 12, p. P12009.
[6] Carminati, M, et al., 2023, "The tristan 166-pixel detector: Preliminary results with a planar setup," *Nuclear Instruments and Methods in Physics Research Section A: Accelerators, Spectrometers, Detectors and Associated Equipment*, p. 168046.
[7] Urban, K, et al., 2024, "A thermionic electron gun to characterize silicon drift detectors with electrons," *Journal of Instrumentation*, vol. 19, no. 06, p. P06004.
[8] Acharya, H, et al., 2026 "KATRIN sensitivity to kev sterile neutrinos with the TRISTAN detector upgrade," *arXiv preprint* arXiv:2603.23256.

NSS-19-04

Detector Performance Results on the MOSAIX Stitched Sensor Structures for ALICE ITS3 (#2617)

Hartmut Hillemanns, Livia Terlizzi, On behalf of the ALICE Collaboration

CERN, Geneva, Switzerland

Abstract

The ALICE collaboration is currently developing a new vertex detector ("ITS3"), scheduled for installation in 2028 - 2029 during LHC long shutdown 3 to replace the three innermost layers (Inner Barrel) of the existing Inner Tracking System as from Run 4 onwards. ITS3 comprises the use of ultra-thin (down to 50 micrometers) silicon wafers and stitching technologies in 65nm CMOS imaging process , enabling the production of large area (9.8cm x 26.7cm) Monolithic Active Pixels Sensors sensors which will be bent to half-cylindrical shapes of 19, 25.2 and 31.5 mm bending radii for layer 0, 1 and 2 respectively, and supported by carbon foam structures. The very low power consumption of about 40mV/cm^2 allows for air cooling, and the bent shape allows for a minimum of mechanical support using carbon foam only. The very low material budget of less than 0.09% of a radiation length per layer ensures extremely good tracking and vertexing performance. Following an extensive R\&D program for the ITS3, large area stitched prototype structures (MOSAIX) with a final pixel pitch of 20.8µm x 22.8µm, matrix sizes and all other features have been produced and will be tested throughout this year before and after irradiation with TID and NIEL in order to validate the final design for production. In this contribution we present and discuss an overview of detection performance measurements in various test beams.

NSS-19-05

The LHCb PicoCal: a New Radiation-hard ECAL with Picosecond Time Resolution (#2732)

Eduardo Picatoste, on behalf of the LHCb ECAL Upgrade II R&D Group

Universitat de Barcelona, Institute of Cosmos Science of the University of Barcelona, Barcelona, Spain

Abstract

The LHCb Upgrade II program aims to operate at an instantaneous luminosity of up to 1.0×10^{34} cm^{-2} s^{-1}, during the High-Luminosity LHC Run 5, targeting an integrated dataset of 300 fb^{-1}. This ambitious goal requires a complete redesign of the electromagnetic calorimeter (ECAL), leading to the development of the PicoCal detector. The upgrade addresses the challenges of extreme pile-up, high particle densities, and severe radiation levels—reaching up to 1 MGy in the innermost regions—by introducing enhanced transverse granularity and precision timing capabilities at the level of O(10) picoseconds. The PicoCal design combines different technologies optimized for distinct detector regions. The central, high-radiation zones will employ Spaghetti Calorimeter (SpaCal) modules, based on dense absorbers coupled with fast scintillating materials. The
outer regions will be instrumented with upgraded Shashlik calorimeters with fast wavelength-shifting fibers to improve timing performance. Extensive R&D efforts have focused on scintillators, photodetectors, and front-end electronics, with several photomultiplier tube (PMT) candidates evaluated for their timing precision and radiation tolerance. Prototype modules of both SpaCal and Shashlik technologies have been successfully designed, constructed, and tested. Test beam campaigns demonstrate that the calorimeter achieves an energy resolution with a stochastic term of about 10% sampling contribution and 1% constant term, while timing resolutions better than 20 ps are achieved at high energies across different scintillator options. In parallel, the SPIDER ASIC prototype has been validated in beam tests, achieving timing performance comparable to standard digitizer-based readout systems. These results collectively demonstrate that the PicoCal concept meets the stringent performance requirements of LHCb Upgrade II, ensuring precise energy and time measurements
under extreme HL-LHC conditions.

References

[1] The LHCb collaboration, 2008 JINST 3, 08, S08005

[2] L. An, et al., 2023, 'Performance of a spaghetti calorimeter prototype with tungsten absorber and garnet crystal fibres', *Nuclear Instruments and Methods in Physics Research Section A: Accelerators, Spectrometers, Detectors and Associated Equipment*, vol. 1045, p. 167629

[3] LHCb collaboration, 2023, 'LHCb Particle Identification Enhancement Technical Design Report', CERN-LHCC-2023-005

[4] L. Martinazzoli, et al., 2022, 'Compositional engineering of multicomponent garnet scintillators: Towards an ultra-accelerated scintillation response', *Materials Advances*, 3, 6842-6852

[5] D. Breton, C. Cheikali, E. Delagnes, J. Maalmi, P. Rusquart, P. Vallerand 2019, 'Fast electronics for particle Time-Of-Flight measurement, with focus on the SAMPIC ASIC', *Nuovo Cim.C*, vol. 43, no. 1, Italy

NSS-19-06

digital SiPMs for future RICH detectors (#2857)

Prabhleen Singh[1], Rok Dolenec[2], Claudio Bruschini[1], Edoardo Charbon[1]

[1] EPFL, STI IEM AQUA, Neuchatel, Switzerland; [2] Jozef Stefan Institute, Experimental Particle Physics Department, Ljubljana, Slovenia

Abstract

Planned upgrades to Ring Imaging Cherenkov (RICH) detectors in the LHCb, Belle II, and ALICE 3 high energy physics experiments require photodetectors capable of single-photon detection at high event rates and neutron fluences up to a few 10^{13} 1-MeV equivalent/cm². The spadRICH project develops a CMOS-based single-photon avalanche diode (SPAD) array optimized for radiation hardness and cryogenic operation to meet these requirements.

This paper presents a decision-maker (DM) circuit architecture for use in digital silicon photomultiplier (dSiPM) readout. The DM identifies the first-firing SPAD along with its address among competing channels and disables both the winning and losing SPADs immediately after the decision, thus suppressing subsequent avalanches. Combined with fast quenching, this reduces afterpulsing and lowers power consumption in multi-channel readout — critical for operation in high-radiation cryogenic environments. The DM can be cascaded into a binary tree topology to implement full dSiPM functionality. dSiPMs with varying aspect ratios and SPAD sizes are fabricated in the GlobalFoundries 55 nm BCDLite® process. In addition to dSiPMs, we have also implemented analog SiPMs (aSiPMs) to compare the advantage of its high fill factor with selective deactivation of SPADs and time-gating features of dSiPMs in high radiation environments.

References

[1] A. Ronchini Ximenes, P. Padmanabhan, M.-J. Lee, Y. Yamashita, D.-N. Yaung, and E. Charbon, “A Modular, Direct Time-of-Flight Depth Sensor in 45/65-nm 3-D-Stacked CMOS Technology,” IEEE Journal of Solid-State Circuits, vol. 54, pp. 3203–3214, Nov. 2019.

12 November, 2026

Time:
12 November, 2026
9:00 – 11:00

Room:
ALBÉNIZ & MACHUCA

NSS-20 | DAQ, front-end and electronics

Chairs:
David J. Abbott (Newport News)

NSS-20-01

Development and validation of the Forward Feature Extractor Prototype for high-speed data processing in the ATLAS L0Calo trigger systems

(#2816)

ATLAS Collaboration ATLAS Collaboration, On behalf of the ATLAS Collaboration

ATLAS Collaboration, CERN, Geneva, Switzerland

Abstract

We present the development and validation of the Forward Feature Extractor (fFEX) prototype module, a key component of the ATLAS Experiment's Phase-II Level-0 Calorimeter (L0Calo) trigger system for real-time event filtering and feature extraction. The prototype module has been produced and validated through an extensive test campaign. Hardware validation demonstrates stable power delivery, full main-board core functionality, reliable FPGA operation including high-speed transceivers and bit-error-rate tests at 25.8 Gbps per link, robust clock distribution including jitter cleaners and fanout stages, and complete control and monitoring functionality. In addition, integration tests with other ATLAS Phase-II subsystems have been carried out and the results are reported, confirming interoperability and being suitable for operation within the experiment's complex trigger and data-acquisition architecture. The system achieves a total throughput of 2.5 Tbps per main FPGA, including real-time processing and data-handling operations. On the firmware side, a modular design has been implemented, comprising the infrastructure layer, including an implementation of the Interlaken protocol (Core1990) and a simple-packet based protocol called IPBus, the readout firmware, and the algorithmic firmware. In this article, particular emphasis is placed on the readout path and the handling of multiple data types and trigger objects, including the formatting, error-correction and flow-control aspects. The algorithmic firmware supports the identification of jets, electromagnetic clusters, and hadronic tau candidates, and the calculation of global quantities such as missing transverse energy (MET). These results demonstrate the technical readiness of the fFEX prototype for further system-level integration, timing and performance studies.

NSS-20-02

Lessons Learned from the sPHENIX Experiment (#1595)

Martin L. Purschke

Brookhaven National Laboratory, Physics, Upton, USA

for the sPHENIX collaboration

Abstract

The sPHENIX experiment at the Relativistic Heavy Ion Collider (RHIC), and RHIC itself, concluded their beam operations on Feb. 6, 2026. RHIC and the experiments are now being decommissioned to begin construction of the Electron-Ion Collider. This marks the end of 25 years of Heavy-Ion and polarized proton-proton Physics at the facility.

sPHENIX was designed as a high-rate detector optimized for precision measurements of jets, heavy flavor, and quarkonia in Relativistic Heavy-Ion collisions. Following a successful commissioning phase, the experiment collected high-quality data in p-p , Au-Au, and O-O collision systems.
To summarize our key performance numbers:

- The sPHENIX DAQ system has exceeded the design event rate of 15 kHz
- We were able to sustain a DAQ data rate of more than 70 GB/s
- We accumulated just under 300 PB of data on tape with beam, and crossed the 300 PB threshold with the post-shutdown calibration data.We present key lessons learned from the design, commissioning, and operation of the sPHENIX data acquisition system. We also briefly discuss ongoing analysis efforts and the anticipated physics legacy of the sPHENIX program.

NSS-20-03

Architecture and Performance of a Versatile Trigger, Tracking and Readout System for Particle Detector Beam Tests (#1917)

Liliana Congedo[1], Roberta Pillera[1], Davide Cerasole[1,2], Giuseppe De Robertis[1], Leonardo Di Venere[1], Fabio Gargano[1], Mario Giliberti[1,2], Francesco Licciulli[1], Antonio Liguori[1,2], Rocco Liotino[1,2], Pierpaolo Loizzo[1,3], Francesco Loparco[1,2], Leonarda Lorusso[1], Mario Nicola Mazziotta[1], Nicola Nicassio[1,2], Giuliana Panzarini[1]

[1] Istituto Nazionale di Fisica Nucleare, Sezione di Bari, Bari, Italy; [2] Dipartimento di Fisica "M. Merlin", Università e Politecnico di Bari, Bari, Italy; [3] Dipartimento di Fisica, Università di Trento, Trento, Italy

Abstract
This work presents the development and validation of a Trigger, Tracking, and Readout System for the beam test characterization of novel particle detectors, designed to address the challenges of providing precise reference tracking for event reconstruction while integrating heterogeneous front-end electronics. The system combines a scalable tracking apparatus based on scintillating fibers coupled to Silicon Photomultipliers, a Centralized Control Unit for trigger generation and system synchronization and a modular readout architecture based on Field Programmable Gate Arrays. A dedicated software platform provides unified control of data acquisition, configuration and monitoring, ensuring efficient system operation. The overall design approach relies on hardware modularity and the use of commercial components, complemented by adaptable firmware and software to interface multiple detector technologies with minimal customization effort. The system has been validated during beam test campaigns of a Ring Imaging Cherenkov detector prototype for the future ALICE3 experiment, foreseen at the High-Luminosity Large Hadron Collider. The results demonstrate accurate event reconstruction capability, with a data matching efficiency among independent readout boards exceeding 99%, ensuring reliable synchronization

across different subsystems. In addition, a time resolution at the level of a few tens of picoseconds have been measured, highlighting the remarkable timing performance of the system and its suitability for the characterization of high-precision timing detectors. The results confirm the effectiveness of the proposed system as a cost-effective, flexible, scalable, and portable solution that can be readily employed for the development and beam test validation of future particle detectors based on a wide range of technologies.

References
[1] D. Cerasole et al., Development of a light tracker based on thin scintillating fibers and Silicon Photomultipliers for space application. Nucl.Instrum. Meth. A 1082 (2026).
[2] S. Ahmad et al., Petiroc2A: Characterization and Experimental Results, NSS/MIC (2018).
[3] G. De Robertis et al., A MOdular System for Acquisition, Interface and Control (MOSAIC) of detectors and their related electronics for high energy physics experiment. EPJ Web Conf. 174 (2018).
[4] A. R. Altamura et al., Beam test studies for a SiPM-based RICH detector prototype for the future ALICE 3 experiment". Eur. Phys. J. C 85.5 (2025).
[5] ALICE Collaboration, Letter of intent for ALICE 3: A next generation heavy-ion experiment at the LHC, CERN-LHCC-2022-009 (2022).
[6] T. Saleem et al., Study experimental time resolution limits of recent ASICs at Weeroc with different SiPMs and scintillators, JINST 18.10 P10005 (2023).
[7] S. Altruda et al., PicoTDC: a flexible 64 channel TDC with picosecond resolution, JINST 18.07 P07012 (2023).

NSS-20-04

TD-Link: A Daisy-Chain Optical Architecture for Integrated Data Readout and Deterministic Timing Distribution in Large-Scale Detector Systems (#1971)

Andrea Abba[1], Valentina Arosio[1], Gianluca Becuzzi[2], Matteo Bianchini[2], Francesco Caponio[1], Stefano Carsi[1], Alberto Cusimano[1], Camilla Maggio[2], Annalisa Mati[2], Daniele Ninci[2], Andrea Picchi[2], Carlo Tintori[2], Yuri Venturini[2]

[1] Nuclear Instruments SRL, Lambrugo, Italy; [2] CAEN SPA, Viareggio, Italy

Abstract
TD-Link is a versatile optical communication architecture combining high-throughput data readout and sub-nanosecond timing synchronization over a single optical fiber for large-scale detector systems. The protocol adopts a multidrop daisy-chain ring topology connecting one Data Concentrator to up to sixteen FERS front-end boards per link, with multiple independent links per concentrator, enabling scalable instrumentation with reduced optical infrastructure. Operating at 3.25 Gb/s, TD-Link transports data, synchronization, and control traffic within the same serial stream through a token-based protocol minimizing per-hop latency and supporting packet fragmentation. The synchronization system distributes a global time reference (T0) with deterministic latency. On the concentrator, transmitter lane alignment exploits the half-full condition of the transceiver elastic buffer as a 1-bit phase detector. A firmware state machine iteratively adjusts the TX phase interpolator until the write-to-read pointer difference reaches half the buffer depth, locking the lane to a deterministic phase condition. A Digital Dual Mixer Time Difference (DDMTD) circuit is used only for inter-concentrator synchronization, compensating the phase offset between the recovered transceiver clock and the FPGA fabric reference clock.
On FERS boards, recovered clocks are cleaned through an external zero-delay PLL and retransmitted

downstream, preserving phase coherence along the daisy chain. Deterministic T0 latency is ensured by disabling elastic buffers and routing timing signals through calibrated delay paths.
Experimental validation with CERN PicoTDC-equipped FERS boards demonstrates a synchronization sigma of 6 ps for boards sharing the same coaxial clock reference and below 25 ps for boards connected to different concentrators. The performance remains stable across repeated power cycles, confirming the robustness of the phase alignment strategy.

NSS-20-05

Design and test of a readout board for the ePIC dRICH detector (#2620)

Davide Falchieri[1], Pietro Antonioli[1], Luca Barion[2], Marco Contalbrigo[2], Fabio Cossio[3], Giulio Della Casa[3], Sandro Geminiani[4], Roberto Malaguti[2], Matilda Panza[4], Roberto Preghenella[1], Luigi P. Rignanese[1], Giovanni Torromeo[1]

[1] INFN Sezione di Bologna, Section of Bologna, BOLOGNA, Italy; [2] INFN Sezione di Ferrara, Section of Ferrara, Ferrara, Italy; [3] INFN Sezione di Torino, Section of Torino, Torino, Italy; [4] INFN Bologna and UNIBO, Section of Bologna and UNIBO, Bologna, Italy

The authors wish to thanks INFN Bologna, Ferrara and Torino for funding the project.

Abstract
This paper presents the design of a board named RDO (ReaDOut module) which is the main building block of the readout system for the dual-radiator RICH (dRICH) of the ePIC experiment at the future Electron-Ion Collider (EIC). The main purpose of the board is to provide an interface towards the front-end ASICs (the ALCOR chips) and towards the main data acquisition system (the FELIX boards) through a high-speed optical link based on the CERN VTRx+ optical transceiver. Among the many requirements, the board needs to fit a very limited size and must withstand a moderately hostile radiation environment. The board has already been used in a test-beam at CERN and it has also undergone irradiation tests of its main components: the most significant results will be presented and discussed.

References
[1] S. Dalla Torre, “The Electron-Ion Collider and the ePIC experiment”, *Il nuovo Cimento C*, year 2024, issue 4, July-August.
[2] F. Cossio et al, “ALCOR: a mixed-signal ASIC for the dRICH detector of the ePIC experiment at the EIC”, *Frontier Detectors for Frontier Physics*, La Biodola, 2024.
[3] M. Rentsch Ersdal et al, “External scrubber implementation for the ALICE ITS Readout Unit”, Processdings of Science (TWEPP2019)136, DOI: 10.22323/1.370.0136.
[4] J. Troska, A. Brandon-Bravo, S. Detraz, A. Kraxner, L. Olantera, C. Scarcella, C. Sigaud, C. Soos, F. Vasey, “The VTRx+, an optical module for data transmission at HL-LHC”, *TWEPP 2017*, DOI: 10.22323/1.313.0048.
[5] IBIS Version 8.0, https://ibis.org/ver8.0, IBIS Open Forum.
[6] C. Ghabrous Larrea, K. Harder. D. Nwebold, D. Sankey, A. Rose, A. Thea, T. Williams, “Ipbus: a flexible Ethernet-based control system for xTCA hardware”, *JINST 10 (2015) n. 02*, C02019, DOI: 10.1088/1748-0221/10/02/C02019.

NSS-20-06

Performance evaluation of SPIDER and ICECAL65 for the upgrade II of the LHCb calorimeter detector (#2654)

Alberto López[1], Josep Altet[2], Ludovic Alvado[6], Xavier Aragonés[2], Nicolas Arveuf[5], Enrique Barajas[2], Edouard Bechetoille[7], Dominique Breton[4], Guillaume Blanchard[5], Sergio Gómez[2,1], Baptiste Joly[5], Laurent Leterrier[6], Jihane Maalmi[4], Samuel Manen[5], Daniel David Marín[1], Diego Mateo[2], Hervé Mathez[7], Joan Mauricio[1], José Mazorra[3], Eduardo Picatoste[1], Joan Serrano[1], Christophe Sylvia[4], Philippe Vallerand[4], Richard Vandaele[5], On behalf of the LHCb ECAL Upgrade II R&D Group

[1] Universitat de Barcelona, ICCUB, Barcelona, Spain; [2] Universitat Politècnica de Catalunya, Departament d'Enginyeria Electrònica, Barcelona, Spain; [3] Universitat de Valencia, IFIC, Valencia, Spain; [4] Université de Paris-Saclay, CNRS / IN2P3 / IJCLab, Orsay, France; [5] Université Clermont-Auvergne, CNRS / IN2P3 / LPCA, Clermont-Ferrand, France; [6] Université de Caen Normandie, CNRS / IN2P3 / LPC, Caen, France; [7] Université de Lyon, CNRS / IN2P3 / IP2I, Lyon, France

Abstract

The LHCb Phase-II electromagnetic calorimeter upgrade, known as PicoCal, requires new radiation-tolerant front-end electronics capable of providing precise energy and timing measurements under the demanding conditions expected after the High-Luminosity LHC upgrade. Two dedicated ASICs are being developed for this purpose in TSMC65 technology: ICECAL65 for energy measurement, and SPIDER for picosecond timing reconstruction. ICECAL65 follows the scheme in the ASIC currently used in the LHCb calorimeter. Nonetheless, it adopts a dual-gain architecture with time-interleaved subchannels to achieve 12-bit precision over a wide dynamic range while eliminating dead time between input samples. The analog chain integrates configurable shaping, tunable integration, and high-speed track-and-hold stages synchronized through an integrated PLL. Post-layout simulations indicate a power consumption of 40 mW per channel, output noise compatible with 12-bit precision, linearity errors below 1%, and spillover below 2.5%. SPIDER is a waveform digitizer ASIC dedicated to ultra-fast timing measurements. Based on the Waveform Time-to-Digital Converter concept, it samples detector signals inside programmable windows synchronized with the 40 MHz LHC clock. The architecture combines analog memory banks, embedded discriminators, DLL-based timing control, and massively parallel Wilkinson ADC conversion. Configurable sampling frequencies from 1.6 to 20 GS/s enable timing resolutions well below 10 ps rms. While post-layout simulations of ICECAL65 are still pending verification, first measurements of SPIDER_V0 demonstrate a Time Difference Resolution of 7.13 ps rms between two asynchronous pulses, corresponding to a single-channel precision close to 5 ps. Together, ICECAL65 and SPIDER provide a complete front-end solution for the PicoCal upgrade and represent a promising platform for future fast-timing detectors in high-energy physics.

References

[1] E. Picatoste, D. Gascón, C. Abellán, J. Lefrancois, F. Machefert, O. Duarte, E. Grauges, L. Garrido, and X. Vilasis, “Low noise front-end ICECAL ASIC for the upgrade of the LHCb calorimeter.”

[2] A. López, “Design of a rail-to-rail ota in 65 nm cmos technology for a particle detector sensor,” Master’s thesis, UPC, 2023, master’s thesis.

[3] Lastname, GN, Lastname, GN YYYY, ‘Article’, *Journal*, Edition, Page, Place of publication: publishersD. Breton, C. Cheikali, E. Delagnes, J. Maalmi, P. Rusquart, and P. Vallerand, “Fast electronics for particle time-of-flight measurement, with focus on the SAMPIC ASIC.”

NSS-20-07

Design and Performance of the Fermilab Constant-Fraction Discriminator (FCFD) Readout ASIC for ePIC Barrel Time-of-Flight Detector (#2797)

Artur Apresyan[1], Cristinel V. Gingu[1], Datao Gong[1], Neha S. Kharwadkar[1], Sergey Los[1], Cristian Pena[1], Chinar Syal[1], Shuoxing Wu[1], Si Xie[1,2], Todd Zenger[1], Thomas Zimmerman[1]

[1] Fermi National Accelerator Laboratory, Batavia, USA; [2] California Institute of Technology, Pasadena, USA

Abstract

We present the design and performance of the FCFD1.1 constant-fraction discriminator ASIC for precision timing detectors based on AC-LGAD sensors. The chip, implemented in 65 nm CMOS, achieves ~ 40 ps time resolution and 15-20 μm spatial resolution in beam tests, with full detection efficiency over the sensor surface. The design integrates on-chip time-walk correction, reducing reliance on offline calibration. Building on this result, we introduce FCFD1.2, a six-channel full-chain prototype for AC-LGAD readout. Each channel includes a constant-fraction discriminator, an ADC block, and a self-calibrated TDC, while the six channels share a common readout block that packs the data into frames and outputs them through a serializer. The chip was submitted in April 2026, and preliminary test results are expected to be presented at the conference. Its architecture targets ~ 45 ps overall timing resolution, with less than 10 ps contribution from the internal electronics, enabling scalable, low-power timing readout for future detector systems.

References

[1] W.~Zhang, H.~Sun, C.~Edwards, D.~Gong, X.~Huang, C.~Liu, T.~Liu, T.~Liu, J.~Olsen, Q.~Sun, X.~Sun, J.~Wu, J.~Ye, and L.~Zhang, ``A low-power time-to-digital converter for the CMS Endcap Timing Layer (ETL) upgrade,'' \emph{IEEE Transactions on Nuclear Science}, vol.~68, no.~8, pp.~1984--1992, Aug. 2021, doi: 10.1109/TNS.2021.3085564.

NSS-20-08

LDMX Timing Distribution and Data AcquisitionSystem (#2940)

Benjamin A. Reese[1], Christos Bakalis[1], Ryan Herbst[1], Timothy K. Nelson[1], Lauren Tompkins[2], Elizabeth Berzin[2], Matt Weaver[1]

[1] SLAC National Accelerator Laboratory, Menlo Park, USA; [2] Stanford University, Stanford, USA

Abstract

The Light Dark Matter eXperiment (LDMX) will search for sub-GeV dark matter with a fixed-target missing-momentum technique requiring time-aligned detector data from several independent subsystems, including the Trigger Scintillator, Silicon Tracker, Electromagnetic Calorimeter, and Hadronic Calorimeter. This work presents the LDMX trigger and data acquisition (TDAQ) system for timing distribution, fast control, and event tagging. The

central timing node is implemented on an APx ATCA board originally developed for CMS. It receives the LCLS-II accelerator timing stream and recovers the 185.714 MHz timing clock and timing frames. Firmware combines accelerator pulse identifiers, run state, and Global Trigger decisions into fixed-latency 3.714 Gbps PGP Fast Control (PGPFC) messages for endpoints. Timing Messages carry a 56-bit pulse ID, 4-bit run state, and state-changed flag. Readout Request (RoR) messages, analogous to Level-1 Accept triggers, carry pulse ID and a 6-bit bunch count. Endpoints recover the fast-control clock, derive a 37.14 MHz bunch clock, align RoRs to bunch boundaries, and write the common timestamp into DAQ event headers. Common firmware blocks provide fast-control reception and event formatting for subsystem designs, enabling offline alignment and future real-time event building. Run states support trigger-data alignment and RoR-latency calibration before physics. In a 2025 beamline test at End Station A at SLAC, this architecture acquired coherent data at 10 Hz for up to 12 hours with aligned contributions from participating reduced-scale detector-subsystem slices.

Time:
12 November, 2026
9:00 – 11:00

Room:
MACHADO

NSS-21 | Photodetectors

Chairs:
Fabrice Retiere (Vancouver)
Stefan Gundacker (Vienna)

NSS-21-01

Development of a Cost-Effective PCCT Detector Based on Sub-Millimeter EQR SiPM and LYSO Array with High Count Rate and Adequate Energy Resolution (#6)

Yongqiang Yan[1], Mingyue Huang[1], Xu Zhang[1], Kun Liang[1], Ru Yang[1], Dejun Han[1,2]

[1] Beijing Normal University, school of Physics and Astronomy, Beijing, China; [2] Beijing Normal University, Applied Optics Beijing Area Major Laboratory, Beijing, China

Abstract

Among the detector candidates for clinical photon-counting CT (PCCT), SiPM-based fast-scintillation photon-counting detectors (PCD) represent a cost-effective solution. However, their practical implementation is constrained by the incompatible trade-off between count-rate capability and energy resolution. To address this limitation, we developed a scintillation PCD designed to achieve both high counting rate and improved energy resolution. The detector consists of a 26-channel pixelated LYSO scintillator array coupled to an epitaxial-quenching-resistor (EQR) SiPM array with a 0.5-mm pixel pitch and 15-μm microcells. Benefiting from the EQR architecture, the SiPM pixels exhibit a fast recovery time of 3.2 ns, a 64% fill factor, and a photon detection efficiency exceeding 40% at 420 nm. A multi-channel FPGA-based photon-counting readout circuit with per-channel pole-zero cancellation was developed to suppress signal tailing and mitigate pulse pile-up. This PCD achieved a maximum count rate of 46.3 Mcps/mm² while maintaining an energy resolution of 33.7% at 59.5 keV. The spatial resolution of 1.86 lp/mm (537 μm) was achieved under 120-keV X-rays, which agreed closely with the 0.5-mm physical pixel pitch of the detector. A more sophisticated PCD based on a 64-channel EQR SiPM array with 0.25-mm pixel pitch and 10-μm microcells, coupled to a corresponding pixelated LYSO scintillator array, will also be presented. Those results indicate that the proposed scintillation PCD is a promising cost-effective candidate for clinical PCCT applications.

References

[1] Willemink, MJ, Persson, M, Pourmorteza, A, Pelc, NJ & Fleischmann. 2018, 'Photon-counting CT: Technical Principles and Clinical Prospects', *Radiology*, vol. 289, no. 2, pp. 293–312, Easton: Radiological Society of North America.

[2] Yan, Y, et al. 2026, 'Epitaxial Quenching Resistor SiPM With Counting Rate Enhanced Technique Aiming at Photon-Counting CT Applications', *IEEE Transactions on Radiation and Plasma Medical Sciences*, pp. 1-1, Piscataway: IEEE.

[3] Yan, Y, et al. 2026, 'A high-count-rate X-ray photon-counting detector based on EQR SiPM array aiming at PCCT', *Nucl. Instrum. Methods Phys. Res. A*, vol. 1087, p. 171393, Amsterdam: Elsevier.

[4] Zhang G. *et al.* 2010,'Demonstration of a silicon photomultiplier with bulk integrated quenching resistors on epitaxial silicon,'*Nucl. Instrum. Methods Phys. Res. A*, vol. 621, no. 1–3, pp. 116–120., Amsterdam: Elsevier.

NSS-21-02

First Characterisation Results on Backside-Illuminated SiPM Prototypes from the IBIS Project (#2930)

Roberto Preghenella[1], Fabio Acerbi[2], Pietro Antonioli[1], Eleonora Bertolin[2,4], Francesca Carnesecchi[1], Fabiola Caso[2], Dina O.E. Elgewaily[2], Giulia Fadini[1,3], Andrea Ficorella[2], Camilla Forza[2], Alberto Gola[2], Priyanka Kachru[2], Elisabetta Montagna[1], Alessandro Montanari[1], Rosario Nania[1], Laura Parellada-Monreal[2], Giovanni Paternoster[2], Riccardo Ricci[1], Luigi Rignanese[1], Edoardo Rovati[1,3], Bianca Sabiu[1,3], Gabriele Sirri[1], Nicolò Tosi[1], Carina Trippl[2], Oscar A.M. Villarreal[2], On behalf of the IBIS and IBIS_NEXT Collaborations

[1] Istituto Nazionale di Fisica Nucleare, Sezione di Bologna, Bologna, Italy; [2] Fondazione Bruno Kessler, Trento, Italy; [3] Università di Bologna, Bologna, Italy; [4] Università di Milano Bicocca e INFN Sezione Milano Bicocca, Milano, Italy

The authors acknowledge INFN and FBK for support and sensor production, and the CERN PS facility for beam test operations.

Abstract

We report on the development and characterisation of innovative Backside-Illuminated Silicon Photomultipliers (BSI-SiPMs) within the INFN IBIS and IBIS_NEXT projects. The BSI architecture relocates the photon entrance window to the back side of the device, enabling high fill factor and improved photon detection efficiency while preserving compatibility with advanced front-end electronics integration, and offering the potential for enhanced sensitivity in the VUV region.

A preliminary experimental campaign has been performed on partially processed BSI prototype devices, including electrical characterisation over a wide temperature range, dark count rate measurements, irradiation studies, annealing tests, and timing performance evaluation using both pulsed laser excitation and minimum ionising particles (MIPs) at CERN.

Irradiation up to 10^9 n_{eq}/cm^2 results in an increase in dark count rate. Preliminary annealing studies show recovery of dark current by nearly one order of magnitude. Timing measurements yield resolutions of order ~100 ps, demonstrating the potential of BSI-SiPMs for fast timing applications in high-energy physics.

NSS-21-03

Photon-to-Digital Converters Enabling Event Classification Through Pulse Shape Discrimination (#1301)

Gabriel Lessard[1], Catherine M. Pepin[1], Tommy Rossignol[1], Nicolas Roy[1], Frédéric Vachon[1], Romain Espagnet[1], Gaétan Lemaire[1], Amanda L. Steinhebel[2], Paul Hausladen[2], Lorenzo Fabris[2], Roger Lecomte[3], Réjean Fontaine[1], Jean-François Pratte[1], Serge A. Charlebois[1]

[1] Université de Sherbrooke, Interdisciplinary Institute for Technological Innovation and Department of Electrical and Computer Engineering, Sherbrooke, Canada; [2] Oak Ridge National Laboratory, Oak Ridge, USA; [3] Université de Sherbrooke, Sherbrooke Molecular Imaging Center and Department of Medical Imaging and Radiation Sciences, Sherbrooke, Canada

The present work was supported in part by the United States Department of Energy, Office of Defense Nuclear Nonproliferation Research and Development in the National Nuclear Security Administration.

Abstract

Digital silicon photomultipliers (SiPMs) are being developed to circumvent many of the shortfalls inherent to analog SiPMs and their associated readout electronics. We design 3D-integrated digital SiPMs, called Photon-to-Digital Converters (PDCs), to simultaneously optimize the photosensitive area, remove analog noise contributions, and embed signal processing. With a low-power-optimized readout architecture providing high timing resolution, we demonstrate fully digital measurement approaches and their benefits across multiple fields, including time-of-flight medical imaging and neutron imaging. Leveraging the high-timing precision of the PDC through pulse shape discrimination, the components of an LGSO (Fast/Slow) phoswich scintillator assembly are precisely classified, while maintaining the expected energy resolution for the scintillators irradiated with calibration isotopes such as a 68Ge source. Coincidence timing resolution is also assessed for this configuration. These results position PDCs as great candidates for depth-of-interaction reconstruction in PET imaging, ToF measurement in CT imaging, and particle identification in neutron imaging.

References

[1] J.-F. Pratte et al., “3D Photon-To-Digital Converter for Radiation Instrumentation: Motivation and Future Works,” Sensors, vol. 21, no. 2, p.598, Jan. 2021, number: 2 Publisher: Multidisciplinary Digital Publishing Institute. URL: https://www.mdpi.com/1424-8220/21/2/598

[2] S. Parent et al., “Wafer-Level Characterization and Monitoring Platform for Single-Photon Avalanche Diodes,” IEEE Journal of the Electron Devices Society, vol. 12, pp. 127–137, 2024. URL: https://doi.org/10.1109/JEDS.2024.3359088

[3] T. Rossignol et al., “A 3D photon-to-digital converter readout for low-power and large-area applications,” Journal of Instrumentation, vol. 19, no. 09, p. P09017, Sep. 2024. URL: https://dx.doi.org/10.1088/1748-0221/19/09/P09017

NSS-21-04

Progress on Single-cell-access TSVs for 3D-integrated microSiPM readout in fast-timing SiPM detectors (#2683)

Alberto Gola[1], Samuele Bisi[2], Claudio Bruschini[2], Edoardo Charbon[2], Stefan Gundacker[4,3], Katrin Herweg[3,5], Priyanka Kachru[1], Laura Parellada-Monreal[1], Giovanni Paternoster[1], Michele Penna[1], Maria Ruzzarin[1], David Schug[3,5], Volkmar Schulz[5,6], Nicola Zorzi[1]

[1] Fondazione Bruno Kessler (FBK), Trento, Italy; [2] Ecole Polythechnique federale de Lausanne (EPFL), AQUA Lab, Neuchatel, Switzerland; [3] University Hospital RWTH Aachen, Aachen, Germany; [4] Austrian Academy of Sciences, Institute of High Energy Physics, Vienna, Austria; [5] RWTH Aachen University, Institute of Imaging and Computer Vision, Aachen, Germany; [6] Hyperion Hybrid Imaging Systems GmbH, Aachen, Germany; [7] RWTH Aachen University, Physics Institute III B, Aachen, Germany

Abstract

Segmentation of the SiPM active area into smaller, independently read out elements is one of the most promising routes to improve the single-photon time resolution (SPTR) required by next-generation time-of-flight PET systems. We report on Single-Cell Access through-silicon vias (SCA-TSVs), a custom TSV technology under development at Fondazione Bruno Kessler (FBK), Trento, and applied to the NUV-HD-MT SiPM platform. SCA-TSVs exploit the deep-trench isolation (DTI) already present in this technology to physically separate and independently access each SiPM microcell from the backside, with essentially no loss of fill factor. A backside redistribution layer (RDL) can then regroup microcells with an arbitrary segmentation level, according to application requirements. The first implementation targets the DIGILOG project, where a 3 × 3 mm² SiPM with 50 µm cells is segmented into 3 × 3- or 6 × 6-cell clusters, referred to as microSiPMs. These units are designed to be read out independently by a matched ASIC developed at EPFL and connected through chip-to-chip 3D integration. This approach preserves the SPTR of a single SPAD, approximately 25 ps FWHM, while avoiding the complexity of full single-cell readout. The first SCA-TSV learning cycle (LC1) required modifications to the original NUV-HD-MT technology, mainly an increase of the DTI depth beyond 20 µm. Front-side characterization showed that the timing performance was preserved. The first backside integration runs also revealed a reduced TSV yield. The analysis identified both layout-related and backside-process-related limitations, which are being addressed through optimized LC1 backend process splits and in the second technology learning cycle (LC2). The presentation will discuss the SCA-TSV concept, LC1 fabrication and characterization results, and the latest LC2 developments toward 3D-integrated microSiPM/ASIC chips for fast-timing applications.

References

[1] A. Gola, " FBK roadmap towards the next-generation of 3D-integrated SiPM and SPAD technologies.", PD 2024 Conference, Vancouver, Canada.

[2] S. Merzi et al., "NUV-HD SiPMs with metal-filled trenches," J. Instrum., vol. 18, no. 05, P05040, 2023.

[3] S. Gundacker et al., "DIGILOG: A digital-analog SiPM towards 10 ps prompt-photon tagging in TOF-PET," in 2023 IEEE NSS/MIC/RTSD, 2023.

[4] F. Acerbi et al., "Characterization of single-photon time resolution: from single SPAD to silicon photomultiplier," IEEE Trans. Nucl. Sci., vol. 61, no. 5, pp. 2678-2686, 2014.

NSS-21-05

PlatonSPAD: A Scalable Sensor for Elementary Particle Detection

(#1496)

Kodai Kaneyasu[1], **Kodai Kaneyasu**[1], Till C. Dieminger[2], Till C. Dieminger[2], Jan Soerensen[2], Jan Soerensen[2], Davide Sgalaberna[2], Davide Sgalaberna[2], Claudio Bruschini[1], Claudio Bruschini[1], Edoardo Charbon[1], Edoardo Charbon[1]

[1] *Ecole polytechnique fédérale de Lausanne (EPFL), Advanced Quantum Architecture lab, Neuchatel, Switzerland;*
[2] *ETH Zurich, Institute for Particle Physics and Astrophysics, Zurich, Switzerland*

This work was supported by the SNSF grant PCEFP2 203261, Switzerland.

Abstract

Precise detection of elementary particles such as neutrinos, gammas, or electrons in an unsegmented scintillating volume requires three-dimensional tracking with sub-nanosecond timing resolution [1], [2]. However, conventional detectors based on analog silicon photomultipliers are inherently constrained by trade-offs between spatial resolution and scalability, making them less suitable for large-scale implementations [3]. To overcome these limitations, CMOS single-photon avalanche diode (SPAD)-based detectors have emerged as a promising alternative for high-resolution particle detection [4], [5]. Here, we propose a dedicated large-format SPAD array sensor fabricated in 110 nm CMOS image sensor (CIS) technology, targeting both high timing precision and scalability. The sensor incorporates a high photon-detection-efficiency SPAD pixel architecture that triggers time-to-digital converters (TDCs) in an event-driven manner with a resolution of 200 ps to detect sparse photons generated by probabilistic events such as particle interactions. All TDCs are synchronized with a global reference clock distributed through an on-chip phase-locked loop, ensuring precise timing alignment across the entire sensor array. Furthermore, a tunable clock shifting feature is implemented to compensate for clock skew in multiple-chip operation. As a result, this chip serves as a fundamental building block for a scalable, multi-chip tiled detector system in which all timing information is globally synchronized, enabling future large-scale, high-resolution particle tracking applications.

References

[1] D. Sgalaberna, The Super Fine-Grained Detector (SuperFGD) for the T2K neutrino oscillation experiment, Detector Seminar at CERN, December 13 (2024). https://indico.cern.ch/event/1484063.

[2] T. Dieminger et al., An ultrafast plenoptic-camera system for high-resolution 3D particle tracking in unsegmented scintillators, Nature Comm. (2026). DOI: 10.1038/s41467-026-70918-x

[3] D. Douqa et al., The SuperFGD for the T2K near detector upgrade, J. Phys. Conf. Ser. 1690, 012070 (2020). DOI: 10.1088/1742-6596/1690/1/012070

[4] M. Franks et al., Demonstration of particle tracking with scintillating fibres read out by a SPAD array sensor and application as a neutrino active target, Eur. Phys. J. C 84, 202 (2024). DOI: 10.1140/epjc/s10052-024-12509-y

[5] K. Kaneyasu et al., PlatonSPAD: a novel SPAD sensor for large-scale high-resolution particle detectors. In Proc. International Image Sensor Workshop (IISW), 1–4 (2025). DOI: 10.60928/486s-zwmd

NSS-21-06

Study of neutron irradiated CMOS SPADs for RICH detector applications (#2502)

Rok Dolenec[1,2], Halil Kerim Yildirim[3], Gia Van Tran[3], Alexandre Germain Philippe Domenech[3], Baris Can Efe[3], Won Yong Ha[3], Utku Karaca[3], Prabhleen Singh[3], Gregor G. Taylor[3], Samo Korpar[4,1], Peter Križan[1,2], Rok Pestotnik[1], Andrej Seljak[1], Edoardo Charbon[3], Claudio Bruschini[3]

[1] Jožef Stefan Institute, Ljubljana, Slovenia; [2] University of Ljubljana, Faculty of Mathematics and Physics, Ljubljana, Slovenia; [3] École polytechnique fédérale de Lausanne, AQUA Laboratory, Neuchâtel, Switzerland; [4] University of Maribor, Faculty of Chemistry and Chemical Engineering, Maribor, Slovenia

This project has received funding from the Slovenian Research and Innovation Agency (project J1-50009) and the Swiss National Science Foundation (project No 200021E 218853).

Abstract

Single-photon avalanche diodes (SPAD) produced in CMOS technologies are increasingly being considered as photodetector candidates for future Ring imaging Cherenkov (RICH) detectors. CMOS SPAD based sensors with integrated electronics can be designed and optimized specifically for RICH detector applications, making it easier to achieve the high photon detection efficiency, excellent single photon timing resolution and hardness to neutron radiation as required in the planned high energy physics experiments. To help guide the design of first digital SiPM targeting RICH detector applications being developed in the spadRICH project, existing single SPADs as well as a 144x32 SPAD array were studied in terms of their operation after neutron irradiation. Dark count rates were measured for neutron irradiation as high as 10^{12} 1-MeV neutron equivalent/cm^2. Thermal annealing and operation at temperatures down to liquid nitrogen were explored. In terms of cryogenic operation, afterpulsing probability and behavior of the photon detection efficiency were also studied. Simulations were used to assess the possible performance of microlenses specifically for the highly collimated Cherenkov photon light as expected in the upgraded LHCb RICH detector.

References

[1] D. Consuegra Rodríguez et al., Characterization of neutron-irradiated SiPMs down to liquid nitrogen temperature, Eur. Phys. J. C (2024) 84:970.

[2] A. Muntean et al., Blumino: The First Fully Integrated Analog SiPM With On-Chip Time Conversion, IEEE Trans. Radiat. Plasma Med. Sci, 5(5) 671-678 (2020).

[3] F. Gramuglia et al., Engineering Breakdown Probability Profile for PDP and DCR Optimization in a SPAD Fabricated in a Standard 55 nm BCD Process, IEEE J. Sel. Top. Quantum Electron. 28(2) (2022) 3802410.

[4] G.G. Taylor et al., Developing photodetectors for future RICH particle detector applications, Proc. SPIE (2025) 13373.

[5] R. Dolenec et al., SiPM and CMOS SPAD characterization at liquid nitrogen temperatures, JINST 20 (2025) P06052.

[6] C. Bruschini et al., Challenges and prospects for multi-chip microlens imprints on front-side illuminated SPAD imagers, Opt. Express 31, 21935-21953 (2023).

[7] H.K. Yildirim et al., Room-temperature, 96×96 pixel 3D-stacked InGaAs/InP SPAD sensor with complementary gating for flash LiDAR, Opt. Express. 34(3) (2026) 5064:5078.

[8] M.-Lo. Wu et al., Radiation Hardness Study of Single-Photon Avalanche Diode for Space and High Energy Physics Applications, Sensors. 22(8) (2022) 2919.

[9] F. Liu et al., Doping Engineering for PDP Optimization in SPADs Implemented in 55-nm BCD Process, IEEE J. Sel. Top. Quantum Electron. 30(1) (2024) 3801407.

NSS-21-07

Comparative Study of NIEL Effects on Dark Count Rate in 110 nm CMOS SPADs Under Neutron, Proton and Electron Irradiation (#1251)

Marcello Campajola[1], Alexander Burdyko[2], Gianmaria Collazuol[3], Manuel D. Da Rocha Rolo[4], Guglielmo De Nardo[5,1], Francesco Di Capua[5], Davide Falchieri[6], Francesco Fienga[5], Giuliana Fiorillo[5,1], Tommaso M. Floris[7], Francesco Licciulli[8], Luca Maresca[5,1], Mario Nicola Mazziotta[8], Lucio Pancheri[9], Roberto Preghenella[6], Lodovico Ratti[7], Luigi Rignanese[6], Romualdo Santoro[2], Fatemeh Shojaei[7], Carla Vacchi[7]

[1] INFN, Sezione di Napoli, Napoli, Italy; [2] Università degli Studi dell'Insubria and INFN Sezione di Milano, Como, Italy; [3] Università degli Studi di Padova and INFN Sezione di Padova, Padova, Italy; [4] INFN, Sezione di Torino, Torino, Italy; [5] Università degli Sudi di Napoli 'Federico II', Napoli, Italy; [6] INFN, Sezione di Bologna, Bologna, Italy; [7] Università degli Sudi di Pavia and INFN Sezione di Pavia, Pavia, Italy; [8] INFN, Sezione di Bari, Bari, Italy; [9] Università di Trento and INFN TIFPA, Trento, Italy

Abstract

Single-photon avalanche diodes (SPADs) fabricated in a 110 nm CMOS technology were irradiated with neutrons, protons, and electrons over a range of fluences up to 10^{11} 1 MeV neutron-equivalent cm^{-2}. The dark count rate (DCR) evolution was systematically characterized as a function of displacement damage dose; online monitoring during neutron and proton irradiation allowed individual scattering events and short-term annealing dynamics to be resolved at the single-pixel level, providing direct insight into defect formation and recovery. Statistical characterization of the DCR distributions reveals that the average DCR alone is insufficient to describe radiation-induced degradation in SPAD arrays: the particle type critically determines both the magnitude and spatial uniformity of damage. These differences reflect distinct defect morphologies - clustered damage for hadrons, isolated point defects for electrons - a key aspect not captured by NIEL scaling alone.

References
[1] E. Charbon, "Single-photon imaging in complementary metal oxide semiconductor processes," Philos. Trans. Roy. Soc. London A, vol. 372, article no. 20130100, Feb. 2014.
[2] S. Gundacker et al., "The silicon photomultiplier: fundamentals and applications of a modern solid-state photon detector," Phys. Med. Biol. vol. 65, no. 17, 2020.
[3] C. Virmontois et al., "Similarities Between Proton and Neutron Induced Dark Current Distribution in CMOS Image Sensors," IEEE Trans. Nucl. Sci., vol. 59, pp. 927–936, 2012.
[4] G. Torilla, A test platform for CMOS SPADs and digital SiPMs in a 110 nm technology, Ph.D. dissertation, Dept. Elect., Comput. Biomed. Eng., Univ. Pavia, Pavia, Italy, 2024.
[5] L. Ratti et al., "Total Ionizing Dose Effects on the Dark Count Rate in 110 nm CMOS SPADs," to be presented at IEEE NSREC, 2026.
[6] A. Jouni et al., "Proton-Induced Displacement Damages in 2-D and Stacked CMOS SPADs: Study of Dark Count Rate Degradation," IEEE Trans. Nucl. Sci., vol. 70, no. 4, pp. 515–522, Apr. 2023.
[7] M. Campajola et al., "Proton induced dark count rate degradation in 150-nm CMOS single-photon avalanche diodes," Nucl. Instrum. Meth. A, vol. 947, 2019.

NSS-21-08

First developments of NUV-DJ SiPM arrays forcryogenic operation for the LHCb SciFi tracker Upgrade II (#2830)

Carina Antonia Trippl[1], Fabio Acerbi[1], Esteban Curras Rivera[2], Guido Haefeli[2], Oscar A.M. Villarreal[1], Shuqi Sheng[2], Alberto Gola[1]

[1] Fondazione Bruno Kessler, CRS, Trento, Italy; [2] École Polytechnique Fédérale de Lausanne, LPHE, Lausanne, Switzerland

Abstract

This work presents the first cryogenic performance evaluation of the novel Near-Ultraviolet Deep-Junction (NUV-DJ) SiPM technology developed by Fondazione Bruno Kessler (FBK). By relocating the high-electric field region deeper within the substrate, the NUV-DJ architecture achieves a state-of-the-art photo-detection efficiency of approximately 70% at 420 nm and a timing resolution of 60 ps FWHM at room temperature with a 4 x 4 mm^2 SiPM. We report on a comprehensive dark characterisation of these sensors from 300 K down to 77 K, extracting the activation energy (Ea) to identify dominant carrier generation mechanisms, and evaluating the stability of correlated noise and gain. These studies serve as a foundation for a new dedicated production run for the LHCb Scintillating Fibre (SciFi) Tracker Upgrade II, in collaboration with EPFL, featuring custom 0.4 mm2 geometries and advanced afterpulsing suppression. The main goal is to assess whether the enhanced blue-green sensitivity of NUV-DJ, which is advantageous for the readout of irradiated blue-emitting scintillating fibres, can be combined with radiation tolerance and stable cryogenic operation at liquid-nitrogen temperature.

References

[1] **Marti Villarreal, OA, Acerbi, F, Paternoster, G, Penna, M, Zorzi, N and Gola, A 2026**, 'Novel NUV-sensitive Deep-Junction Silicon Photomultiplier', *manuscript in preparation*.

[2] **Merzi, S et al. 2023**, 'NUV-HD SiPMs with metal-filled trenches', *Journal of Instrumentation*, vol. 18, p. P05040.

[3] **LHCb Collaboration 2021**, 'Technical Design Report for the LHCb Upgrade II: Framework TDR', *CERN*, LHCB-TDR-023, Geneva: CERN.

[4] **Witola, L and LHCb Collaboration 2025**, 'Performance of the LHCb Scintillating Fibre Tracker in Run 3', *Nuclear Instruments and Methods in Physics Research Section A*, vol. 1079, p. 170606.

[5] **Trippl, C 2024**, 'Development of high-resolution and radiation-tolerant Scintillating Fibre trackers for the LHCb experiment', *PhD Thesis*, Lausanne: EPFL.

[6] **Haefeli, G et al. 2025**, 'Microlens-enhanced SiPMs for the LHCb SciFi tracker Upgrade II: update and recent results', *Nuclear Instruments and Methods in Physics Research Section A*, vol. 1080, p. 170607.

[7] **Acerbi, F et al. 2017**, 'Cryogenic Characterization of FBK HD Near-UV Sensitive SiPMs', *IEEE Transactions on Electron Devices*, vol. 64, no. 2, pp. 521-526.

Time:
12 November, 2026
9:00 – 11:00

Room:
PICASSO

NSS-22 | Neutron and gamma-ray detectors and applications, including security, dosimetry and other related applications

Chairs:
Marek Flaska (University Park)
Bertrand Pérot (Saint-Paul-lez-Durance)

NSS-22-01

Learning Real-World Spectral Templates from a City-Scale Radiological Sensor Network (#1381)

Hannah Parrilla[1], Nicolas Abgrall[1], Mark Bandstra[1], Reynold Cooper[1], Yongho Kim[2], Marco Salathe[1], Rajesh Sankaran[2], Sean Shahkarami[2]

[1] Lawrence Berkeley National Laboratory, Berkeley, USA; [2] Argonne National Laboratory, Lemont, USA

This work was performed under the auspices of the U.S. Department of Energy by Lawrence Berkeley National Laboratory (LBNL) under Contract DE-AC02-05CH11231. The project was funded by the U.S. Department of Energy, National Nuclear Security Administration, Office of Defense Nuclear Nonproliferation Research and Development.

Abstract

Spectral templates used for radiological anomaly detection and isotope identification are most commonly derived from simulation, yet real-world source encounters are subject to a diversity of shielding configurations, scattering geometries, and encounter dynamics that simulation does not fully capture. The PANDAWN sensor network — fourteen statically deployed, multi-modal radiological detection nodes distributed across Chicago, IL — provides a unique opportunity to learn spectral templates directly from real-world data. In this talk, we present the application of regularized Non-Negative Matrix Factorization clustering to anomalous gamma-ray spectra, which recovers multiple spectrally distinct templates for nuisance isotope encounters observed across the network, each corresponding to physically interpretable differences in source attenuation and encounter geometry. Examining how these cluster components trigger isotope identification during known source encounters reveals distinct temporal patterns, further demonstrating that the learned templates capture meaningful structure in the real-world encounter environment. We will discuss what these results reveal about source encounters across the network, present an assessment of template transferability across nodes, and examine how developing a taxonomy of data-driven source templates of this kind can improve detection and isotope identification performance.

NSS-22-02

Spatially-derived Enhancement of Time-domain PSD and Spectroscopy Measurements (#1991)

Patrick M. Collins-Price, Ioannis Tsitsimpelis, Michael D. Aspinall, Malcolm J. Joyce

Lancaster University, Engineering, Lancaster, UK

Abstract

Geometrical event removal (GER) via a position-sensitive multianode photomultiplier tube (MAPMT) is used to enhance mixed-field pulse-shape discrimination (PSD) in an organic EJ-276 scintillator and gamma spectroscopy peak-to-continuum ratio in a CeBr3 crystal scintillator. Significant (~21.3%) improvements in PSD figure-of-merit (FoM) are shown without the need for an energy cut-off, allowing for real-time spectrum-agnostic enhancement of time-domeain PSD methods. This allows greater separation of the neutron and gamma plumes at low energies without the need for a low-energy cutoff, thereby preserving the ability to measure across the full range of neutron spectra. The position sensitivity of the detector has also been exploited to create 2D flux map images of gamma fields attenuated through various lightweight 3D-printed collimators, and to identify the isotope and relative direction of individual point gamma sources in a multi-isotope combined field.

NSS-22-03

Impact of Air Activation on Tritium Monitoring in Fusion Energy Systems (#2627)

Shaun D. Clarke[1], David Breitenmoser[1], Michael Y. Hua[2], Sara A. Pozzi[1]

[1] University of Michigan, Department of Nuclear Engineering & Radiological Sciences, Ann Arbor, USA; [2] Helion Energy, Inc., Everett, USA; [3] Helion Energy, Inc., Everett, USA

This work was supported in-part by the Consortium for Monitoring, Technology, and Verification under Department of Energy National Nuclear Security Administration award number DE-NA0003920.

Abstract

Robust tritium monitoring is essential for fusion energy systems, where rapid detection of low-level airborne releases is needed to support safe operation and accident response. However, intense neutron fields in fusion environments activate surrounding air and produce radioactive products that can contribute beta, gamma-ray, and X-ray backgrounds, complicating tritium detection. In this work, we investigate the impact of air-activation products on a proposed tritium detection concept that combines a thin plastic scintillator beta cell with a surrounding NaI(Tl) anti-coincidence shield. The plastic scintillator provides sensitivity to the low-energy beta particles from tritium decay, while the NaI(Tl) detector enables rejection of coincident photon backgrounds. Monte Carlo simulations were performed using MCNP6 to estimate the detector response to tritium and relevant air-activation radionuclides, including beta emitters such as 13N, 14C, 39Ar, 39Cl, and 41Ar, as well as associated gamma-ray, X-ray, and bremsstrahlung contributions. A 1.3-mm-thick plastic scintillator cell was modeled to match commercially available thin-walled beta cells used in radioxenon detection. Preliminary results show that several air-activation products produce signals in the same low-energy region as tritium and may represent important background contributions, particularly when gamma rays are not detected in coincidence. Subsequent simulations will be performed using the MCNPX-PoliMi code to accurately treat the correlated detection of electrons and photons in the plastic and NaI(Tl) cells.

NSS-22-04

Attention-Biased Additive Point Source Localization (#2925)

Emil Rofors, Brian J. Quiter, Victor Negut

Lawrence Berkeley National Laboratory, Berkeley, USA

This work was performed under the auspices of the U.S. Department of Energy by Lawrence Berkeley National Laboratory (LBNL) under Contract DE-AC02-05CH11231. The project was funded by the U.S. Department of Energy, National Nuclear Security Administration, Office of Defense Nuclear Nonproliferation Research and Development.

Abstract

We present Attention-Biased Additive Point Source Localization (ABAPSL), a fast reconstruction method for localizing multiple radioactive point sources from mobile gamma-ray measurements. The method extends our prior gridded multi-source localization work, which found sources one at a time and added confirmed sources into a growing background model. ABAPSL instead re-fits all active sources at each reconstruction while using an attention metric to place fine test points only where the data support high sensitivity or high source likelihood. This provides local 10cm-scale refinement without requiring a uniformly fine grid over the full survey area. We also introduce multi-resolution spatial measurement binning, replacing fixed time bins with trajectory-aligned spatial bins that remain fine near candidate sources yet are coarser in background-dominated regions. The resulting system matrix is small enough for online reconstruction on mobile computers such as the onboard compute used in a Localization and Mapping Platform (LAMP) system. We demonstrate the approach with simulations around multiple radioactive point sources, with LAMP measurement validation to follow.

NSS-22-05

VETTR: A Robotic Landmine Detection System via Associated Particle Imaging (#2957)

Ryan Pavlovsky, Patrick Freeman, Victor Goicoecheaca, Seth DuBridge, Justin Ellin, Justin Oshiro, Brooke Bilyeu, Erika Suzuki, Andrew Haefner, Kai Vetter

Gamma Reality Inc, Berkeley, USA

Abstract

Gamma Reality Inc has developed and demonstrated, to our knowledge, the first robotic deployment of Associated Particle Imaging (API) for the application of rapid-assessment, detection and 3D imaging of buried landmines. We utilize a deuterium-tritium (DT) reaction to generate momentum-tagged neutrons, at rates up to 5E8 n/s, that

stimulate characteristic gamma-ray emissions. The result is 3D voxel-spectral information that we combine with contextual sensed scenes, via 3D LiDAR, providing a centimeter resolution map of isotopic compositions within a specific scene. There are many non-destructive assay applications for such a system, however we identify landmine detection as our first application space. Modern landmine detectors are sensitive to secondary characteristics of mines, such as low mass-metal content within the mines, and struggle with false-positive probabilities. Our method targets the primary characteristics of mines, which has the potential for a very large reduction in false positive rate compared to current methods, which can be 30 to 1 or often worse. In this paper we present results of our field demonstrations and domestic tests, where we identify surrogate mine materials constructed of ammonium nitrate and carbon against common background and nuisance objects (organic materials, metal objects, & etc). We present results for 20 min, 5min and 1min detections over mine surrogates in soil. We will also present the results of field-testing over TNT and other explosive fills in replica casings.

References
[1] G. Vourvopoulos, R. A. Sullivan, and D. T. Holslin, “Evaluation of PELAN as a confirmation sensor for landmines and explosives,” Science Applications International Corporation (SAIC), San Diego, CA, USA, Jun. 20, 2008. [Online]. Available: https://www-pub.iaea.org/MTCD/publications/PDF/P1441_CD/Papers2007/vourvopoulos.pdf
[2] E. A. Rhodes, C. E. Dickerman, and M. Frey, “Advances in associated-particle neutron probe diagnostics for substance detection,” in Law Enforcement Technologies, Proc. SPIE, vol. 2511, pp. 2–13, Sep. 1995, doi: 10.1117/12.219583.
[3] R. Keeley, Understanding Landmines and Mine Action. Mines Action Canada, Sep. 2003. [Online]. Available: https://web.mit.edu/demining/assignments/understanding-landmines.pdf

NSS-22-06

Development of a Real-time Dose Rate Monitoring System Reading with Optical Fiber under the High-Dose Rate Condition (#3167)

Shunsuke Kurosawa[1], Akihiro Yamaji[1], Chihaya Fujiwara[1], Yusuke Urano[2]

[1] Nagoya University, Graduate School of Engineering, Nagoya, Japan; [2] Kyoto University, Institute for Integrated Radiation and Nuclear Science, Kumatori, Japan; [3] Kyoto University, Institute for Integrated Radiation and Nuclear Science, Kumatori, Japan

This work was supported by Eichi jigyo and JSPS KAKENHI Grant Number 24H00788.

Abstract
Dosimetry under the high dose-rate conditions is required such as internal survey of the Fukushima Daiichi Nuclear Power Plant for the decommissioning. We have developed a dose-rate monitor consisting of optical fiber and scintillators. Since the optical fiber has lower collection efficiency of the scintillation photons compared to that of direct contacting between a scintillator and photomultiplier tube, higher light output was required. Moreover, long emission wavelength of over 650 nm is required to obtain sufficient sensitivity. Cr-doped oxides are expected to have emission wavelength in the red or infra-red region, and garnet crystals can be optimized the emission wavelength by changing crystal fields. Thus, we focused on Cr-doped $(Y, Gd)_3(Al, Ga)_5O_{12}$ materials as red oxide scintillators, and $Gd_3(Ga_{0.995}\ Cr_{0.005})_5O_{12}$ (Cr:GGG) single crystals grown by the micro-pulling-down method had an emission wavelength of Cr:GGG was 731 nm, which achieved the emission goal. Using this Cr:GGG sample we

have developed the real-time dose monitor, and such system was found to operate the survey even under the high dose rate of around 1 kSv/h. Moreover, we evaluated the absorption dose with different gamma-ray energies with geant4 (gamma-ray energy response), and the result was consistent with gamma-ray irradiation test with ^{137}Cs and ^{60}Co sources.

Time:
12 November, 2026
11:30 – 13:00

Room:
ALBÉNIZ & MACHUCA

NSS-23 | Analog and digital circuits III

Chairs:
Stefan Gundacker (Vienna)
Lodovico Ratti (Pavia)

NSS-23-01

A Timing ASIC for Large-area SiPM Readout with Channel Delay Compensation (#2660)

Yi Fu, Weihao Wu, Mingxin Wang

Shanghai Jiao Tong University, Institute of Nuclear and Particle Physics, School of Physics and Astronomy, Shanghai, China

This work was supported by National Key R&D Program of China (Grant No. 2023YFA1606203) , National Natural Science Foundation of China (Grant No. 12575197), Shanghai Pilot Program for Basic Research — Shanghai Jiao Tong University (Grant No. 21TQ1400218).

Abstract

The detector of TRopIcal DEep-sea Neutrino Telescope (TRIDENT) will use large-area silicon photomultiplier (SiPM) arrays combined with photomultiplier tubes to boost photon detection efficiency and pointing capability. An application-specific integrated circuit (ASIC) is being developed to aim at high-resolution time measurement of large-area SiPM arrays. 16 front-end channels are embedded in the ASIC, with output logical-ORed on LVDS output to interface external TDC. Each channel includes a front-end buffer and a discriminator, both in current mode for higher bandwidth while reducing power. To compensate for inconsistency of propagation delay due to detector array layout and process variation, a programmable delay line is introduced for each channel. The delay line consists of coarse and fine delay cells with 165 ps and 33 ps resolution respectively and a dynamic range of 3000 ps. When connected to 16 2s2p SiPM (Hamamatsu S13360-3050PE) arrays with a total area of 5.76 cm², the system achieved a timing jitter of <500 ps FWHM.

References

[1] Z.P. Ye et al., A multi-cubic-kilometre neutrino telescope in the western Pacific Ocean, Nature Astron. 7 (2023) 1497 [arXiv:2207.04519].

[2] F. Hu, Z. Li and D. Xu, Exploring a PMT+SiPM hybrid optical module for next generation neutrino telescopes, PoS ICRC2021 (2021) 1043 [arXiv:2108.05515].

[3] S. Ahmad et al., Petiroc2A: Characterization and Experimental Results, in the proceedings of the IEEE Nuclear Science Symposium and Medical Imaging Conference Proceedings, Sydney, NSW, Australia, November 10–17 (2018) [DOI:10.1109/nssmic.2018.8824464].

[4] R. Bugalho et al., Experimental characterization of the TOFPET2 ASIC, 2019 JINST 14 P03029.

[5] M.X. Wang et al., Exploration of optimized front-end readout circuit for time measurement of large-area SiPM arrays, 2025 JINST 20 T08002.

NSS-23-02

CMOS-Based QUBO Solver ASIC for Charged Particle Tracking (#1611)

Hyunjoon Kim[1], Jooyoung Bae[2], Chanwho Park[3], Chaeyun Shim[5], Bongjin Kim[4], Lorenzo Rota[1], Aldo Pena-Perez[1], Bojan Markovic[1], Llorenç Fanals-i-Batllori[1], Aseem Gupta[1], Hugo Hernandez[1], Ping-Chen Huang[1], Gang Liu[1], Victor Turbiner[6], Ariel G. Schwartzman[1], Rainer Bartoldus[1], Ryan Herbst[1], Angelo Dragone[1]

[1] SLAC National Accelerator Laboratory, Menlo Park, USA; [2] Kwangwoon University, Seoul, South Korea; [3] Georgia Institute of Technology, Atlanta, USA; [4] Korea Advanced Institute of Science & Technology, Daejeon, South Korea; [5] University of California - Santa Barbara, Santa Barbara, USA; [6] Stanford University, Menlo Park, USA

Abstract

We present a CMOS-based QUBO solver ASIC architecture and its application to charged particle track reconstruction for high-energy physics. The solver implements a fully parallel spin-update engine operating on the Ising Hamiltonian Y = −(SUMij si Jij sj − Hi si) with 8-bit fixed-point coupling interaction coefficients, which gets mapped to Quadratic Unconstrained Binary Optimization(QUBO) problems via the standard spin-to-binary substitution xi = (si + 1)/2. The QUBO encodes track-finding physics through diagonal terms (geometric edge quality) and off-diagonal terms (triplet collinearity rewards and bifurcation penalties) derived from the Denby-Peterson formulation. The solver is evaluated as a front-end edge discriminator in a two-stage track reconstruction pipeline on TrackML simulated data. Unlike prior quantum annealing-inspired approaches that rely on a Gaussian KDE trained on ground-truth edge features, our method requires no supervised training or labeled-edge fitting — edge quality is determined entirely by the solver's combinatorial optimization over local neighborhoods. The pipeline achieves F1 = 84.1% (precision 89.3%, recall 79.6%), within 4% of the KDE-dependent baseline while exceeding it in precision.

References

[1] Golling, Tobias, et al 2019, 'TrackML : a tracking Machine Learning challenge'. PoS ICHEP2018, p. 159. DOI: 10.22323/1.340.0159.

[2] Zlokapa, Alexander, et al 2021, 'Charged particle tracking with quantum annealing optimization'. Quantum Machine Intelligence 3.2 (2021), p. 27. ISSN: 2524-4914. DOI: 10 . 1007 / s42484 - 021 - 00054 - w. URL: https://doi.org/10.1007/s42484-021-00054-w.

NSS-23-03

Scalable FPGA-Based Dual-Threshold Time-Over-Threshold Readout Circuit for Fast-Component Discrimination in BaF_2 (#3182)

Min Hyeong Son, Jiwoong Jung, Jin Ho Jung, Yong Choi

Sogang University, Department of Electronic Engineering, Intelligent Signal Processing System (ISPS) Laboratory, Seoul, South Korea

This research was supported by the Korea Medical Device Development Foundation Grant funded by the Ministry of Science and ICT, the Ministry of Trade, Industry and Resources, the Ministry of Health & Welfare, the Ministry of Food and Drug Safety (no. 2410019162, no. RS-2026-25540876), by the Technology Innovation Development Program funded by the Ministry of SMEs and Startups (no. RS-2024-00487344), and by the National Research Foundation of Korea (NRF) grant funded by the Korea government (MSIT) (no. RS-2025-21682968) of the Republic of Korea.

Abstract

BaF_2 emits a prompt fast component with a sub-nanosecond decay time (~0.6 ns), ideal for ultrafast timing applications. Previous studies proved discriminated fast-component-dominant events based on pulse amplitude and slew rate characteristics could improve coincidence time resolution (CTR) in BaF_2. In this work, the fast-component discrimination method was implemented using FPGA-based dual-threshold time-over-threshold (DTOT) readout circuit, providing scalable architecture for multi-channel systems.

To reproduce the pulse amplitude and slew-rate characteristics used in previous full-waveform analysis using oscilloscope, the proposed DTOT method extracted amplitude-related, slew-rate-related parameters using two voltage thresholds applied to the pulse. Low-threshold TOT width provided amplitude-correlated parameter, while the timing difference between low- and high-threshold crossings provided pulse slew rate. Because fast-component-dominant events exhibited steeper rising edges, these parameters enabled fast-component discrimination without full waveform sampling.

The FPGA-based DTOT readout circuit consisted of BaF_2 coupled to VUV-MPPC SiPM, two-stage high frequency amplifier designed to provide sufficient gain with preserving rising-edge profile of fast component, low-latency comparators for accurate slew-rate extraction, and FPGA-based TDC for timestamping threshold crossings.In previous full-waveform analysis, CTR improved from 115 ps to 98 ps (14.8%) using the fast-component-dominant events. With the FPGA-based DTOT readout circuit, CTR improved from 126 ps to 109 ps (13.2%) using the fast-component-dominant events. These results demonstrated that FPGA-based DTOT readout circuit could identify the fast-component events and achieved considerable CTR improvement without full waveform sampling, providing a scalable and practically implementable method for ultrafast timing applications.

References

[1] Peng, C., Zhang, K., Yang, L., Zheng, J., Lu, Y., Hou, Y., ... & Yang, F. (2022). Investigation on the fast component light yield of BaF 2: Y crystal. *IEEE Transactions on Nuclear Science*, *69*(9), 2083-2088.

[2] Gundacker, S., Pots, R. H., Nepomnyashchikh, A., Radzhabov, E., Shendrik, R., Omelkov, S., ... & Auffray, E. (2021). Vacuum ultraviolet silicon photomultipliers applied to BaF2 cross-luminescence detection for high-rate ultrafast timing applications. *Physics in Medicine & Biology*, *66*(11), 114002.

[3] Han, J., Jung, J., Jung, J. H., Lee, I., Hwang, D., Kwon, S., ... & Choi, Y. (2025, November). Development of a Fast Component Discrimination Method to Obtain Fast Coincidence Time Resolution Using BaF 2. In *2025 IEEE Nuclear Science Symposium (NSS), Medical Imaging Conference (MIC) and Room Temperature Semiconductor Detector Conference (RTSD)* (pp. 1-1). IEEE.
[4] Grant, A. M., & Levin, C. S. (2014). A new dual threshold time-over-threshold circuit for fast timing in PET. *Physics in medicine and biology*, *59*(13), 3421-3430.

NSS-23-04

A Flexible Multi-Mode Digital Readout Architecture for High-Precision Low-Rate Time-of-Flight Detectors (#2425)

Manuel Viqueira Rodriguez[1], Joan Mauricio Ferré[2], Albert Espinya Rojas[2], José María Fernández-Tenllado[2], Miquel Ribalda Galvez[2], Rafel Manera Escalero[2], Juan José Silva García[2], Sara Portero Castillo[2], Gianmario Bergamin[1], Rafael Ballabriga[1], David Gascón[2], On behalf of PetVision project

[1] CERN, EP-ESE-ME, Meyrin, Switzerland; [2] Universitat de Barcelona, Institut de Ciències del Cosmos de la Universitat de Barcelona (ICCUB), Barcelona, Spain

Abstract

As chip design costs and complexity rises, the industry is increasingly shifting toward application versatility. The digital readout of the PoETIC chip, designed for custom Silicon Photomultiplier (SiPM) detectors within the PetVision project, embodies this philosophy, supporting Positron Emission Tomography (PET), mass spectrometry, and other high- precision low-rate (≤1 MHz) Time-of-Flight (ToF) applications. The architecture has 16 channels, with three thresholds each: (1) ≤1 photon Low Threshold (ThL), (2) a few-photons High Threshold (ThH), and (3) above ten photons Trigger Threshold (ThT). ThL and ThH are connected to dedicated Time-to-Digital Converters (TDCs), while the ThT signals are ORed into two groups of eight channels, connected to a separate TDC channel. Each TDC channel provides a ToF of 24.4ps time-bin and a Time-over-Threshold (ToT) of 390ps. Each channel integrates a track-and-hold circuit connected to an ADC for linear energy measurements. To optimize data transmission across diverse applications, the readout supports multiple operational modes and configurations. In low-bandwidth setups, several PoETIC chips can be daisy-chained to share a single communication link, reducing the required system resources. For data compression, a trigger operation mode reduces the data volume by transmitting a full bit-width reference ToF timestamp grouped with delta- encoded timestamps of other hits. For systems requiring external validation, the TDC digitizes the trigger validation signal generated by an external coincidence system so that only validated trigger events are transmitted. A data-driven operation mode allows the transmission of all hits in independent packets. The chip also offers control over ToF, non-linear energy measurement (ToT), and linear energy measurement data, allowing users to configure which information is sent, bit widths, and filtering to balance precision and bandwidth according to the specific requirements of the target application.

NSS-23-05

Analog Neural Network ASIC for In-Detector Processing: Experimental Validation of an Advanced Prototype (#2723)

Michele Ronchi[1,2], Mattia Amadori[1,2], Marco Carminati[1,2], Giacomo Borghi[1,2], Carlo E. Fiorini[1,2]

[1] Politecnico di Milano, Department of Electronics, Information and Bioengineering (DEIB), Milano, Italy; [2] Istituto Nazionale di Fisica Nucleare (INFN), Sezione Milano, Milano, Italy

This work is supported by Politecnico di Milano and by the Italian National Institute for Nuclear Physics (INFN), under project Analog Neural Network ASIC (ANNA) under Grant CSN5.

Abstract

Analog neural networks (ANN) are promising solutions for achieving fast and efficient data processing, usually trading-off accuracy for ultra-low power operation. For instance, in scintillator-based PET and SPECT gamma cameras, analog processing embedded in the analog acquisition chain can simplify the system design, reducing throughput, power consumption and scanner cost. After a first proof-of-concept, last year we proposed the design of a more advanced version of an Analog Neural Network ASIC (ANNA). We now present the preliminary experimental results of this ANNAv2 chip, fabricated in 110 nm CMOS technology. It features a fully analog charge-domain processing architecture enabling the implementation of configurable feedforward fully connected ANN. Each neuron consists of an efficient inverter-based charge integrator. Thanks to this programmability, its employment is not limited to emission tomography, but can be tailored to other scenarios in processing signals of "intelligent" detectors. The maximum supported complexity is 70 analog inputs with 5 weighted layers, up to 32 neurons per layer, and 32 analog outputs. Weights are quantized over 63 analog levels, with programmable non-linear activation functions. Preliminary measurements performed on the ASIC validate the correct operation of the proposed architecture and demonstrate the feasibility of fully analog end-to-end inference (with an energy cost of 2nJ/inference) for sensor front-end applications.

References

[1] S. Di Giacomo, M. Ronchi, M. Amadori, G. Borghi, M. Carminati and C. Fiorini, "Experimental Validation of ANNA: Analog Neural Network ASIC for Event Positioning in Monolithic Scintillation Detectors," in *IEEE Transactions on Radiation and Plasma Medical Sciences*, vol. 9, no. 5, pp. 542-552, May 2025, doi: 10.1109/TRPMS.2025.3530774.

[2] M. Ronchi, S. D. Giacomo, M. Amadori, G. Borghi, M. Carminati and C. Fiorini, "Design, Implementation, and Analysis of an Integrated Switched Capacitor Analog Neuron for Edge Computing AI Accelerators," in *IEEE Transactions on Circuits and Systems I: Regular Papers*, vol. 72, no. 8, pp. 3947-3960, Aug. 2025, doi: 10.1109/TCSI.2025.3546521

NSS-23-06

ASIC Development of Rad-hard Embedded FPGA in 28nm for Machine Learning in Particle Detector (#2082)

Aseem Gupta[1], Larry Ruckman[1], Qibin Liu[1], Liangyu Wu[1,2], Julia Gonski[1], Lorenzo Rota[1]

[1] SLAC National Laboratory, Technology Innovation Directorate, Menlo Park, USA; [2] Stanford University, Physics, Palo Alto, USA

Work supported by the U.S. Department of Energy, under contract number DE-AC02-76SF00515.

Abstract

Embedded FPGAs (eFPGAs) combine the performance and efficiency of custom silicon with the flexibility of programmable logic as reconfigurable digital logic can directly be integrated into ASICs. When designed with radiation tolerance techniques such as Triple Modular Redundancy (TMR), eFPGAs can support fault-tolerant and intelligent front-end processing. This enables systems to adapt to evolving data handling needs and environmental conditions, while also supporting local data reduction to lower cabling, power and backend processing demands. Building on previous prototype developments in 130nm and 28nm at SLAC, this paper details the ASIC development of a radiation-hardened eFPGA in 28nm CMOS using radiation-mitigation techniques to realize a reconfigurable logic fabric capable of reliable operation under fault-inducing conditions.

Time:
12 November, 2026
11:30 – 13:00

Room:
MACHADO

NSS-24 | Gas detectors

Chairs:
Michael Tytgat (Brussel)
Takeshi Fujiwara (Tskuba)

NSS-24-01

GEM detectors for the CMS muon system (#1040)

Chiara Aimè, On behalf of CMS Collaboration

Istituto Nazionale di Fisica Nucleare, Sezione di Pavia, Pavia, Italy

Abstract

The High-Luminosity upgrade of the Large Hadron Collider (HL-LHC) will subject the Compact Muon Solenoid (CMS) experiment to unprecedented particle rates and radiation levels. To maintain high-efficiency muon triggering and reconstruction in this challenging environment, CMS is upgrading its forward muon system, including Gas Electron Multiplier (GEM) technology. This program introduces two key stations: GE1/1 and ME0.

The GE1/1 station, composed of triple-GEM detectors, was installed during Long Shutdown 2 to complement the existing Cathode Strip Chamber stations in the $1.6 < |\eta| < 2.15$ region. Operational since the start of Run 3, GE1/1 has significantly enhanced redundancy and Level-1 trigger performance. This presentation reviews the operational experience gained during Run 3, focusing on detector performance, electronics optimizations, and the continuous improvements implemented to ensure seamless system integration.

Looking further ahead, the ME0 station is designed for installation during Long Shutdown 3 to extend the muon system's coverage up to $|\eta| = 2.8$. To withstand the high-rate environment of the HL-LHC, ME0 incorporates advanced design optimizations and robust background rejection capabilities. We present the current status of the ME0 project, including results from the latest prototype studies, time resolution performance, and the progress of the ongoing mass production.

Together, these GEM upgrades are pivotal for extending the physics reach of CMS, ensuring high-quality muon identification and tracking in the most demanding regions of the detector.

NSS-24-02

A new detector technology for the LHCb Muon system in the high luminosity era (#2159)

Francesco Debernardis

INFN-Bari, Fisica, Bari, Italy

Abstract

A novel Micro-Pattern Gaseous Detector (MPGD) technology based on μ-RWELL is under development as a potential replacement for the most irradiated regions of the LHCb muon system at CERN, in view of the Upgrade II

program. The μRWELL is a resistive MPGD featuring a compact single-stage amplification structure with typical gains up to 10^4, making it well suited for operation in harsh radiation environments. An improved detector layout, the G-RWELL, is currently under study. This configuration enhances the standard μ-RWELL design by introducing a single GEM pre-amplification stage, allowing gains up to 10^5 under stable operating conditions. These features make the technology suitable for the extreme rate capability required at the future LHC high-luminosity conditions, where peak luminosity of L = 1.5×10^{34} $cm^{-2}sec^{-1}$ is planned. The presentation will focus on the ongoing research activities on these detector technologies in the context of the LHCb muon Upgrade II. Particular emphasis will be given to recent testbeam campaigns at the CERN PS beam line, involving the use of the FATIC front-end electronics, currently under development, and a dedicated data analysis framework optimized for this readout.

NSS-24-03

A Straw Tube Chamber Prototype for the Inner Detector of a Future e^+e^- Collider Experiment (#2774)

Oliver Kortner, Sandra Kortner, Hubert Kroha, Nick Meier, **Julia Okfen**, Robert Richter, Jörg Zimmermann

Max Planck Institute for Physics, ATLAS Research Group, Munich, Germany

Abstract

The Future Circular electron-positron Collider, proposed as future flagship at CERN, offers a unique opportunity for precision measurements of the Higgs boson and electroweak properties. To meet the stringent requirements of a future Inner Tracker in terms of momentum resolution, particle identification, and minimal material budget, a scalable, ultra-light gaseous detector concept based on straw tubes is under development.

This contribution presents the design and construction of a 1.5 m-long straw tube chamber prototype.

As part of the mechanical feasibility study, the importance of the tube wall pre-tensioning during assembly was identified to prevent a drift radius asymmetry.

Via a CERN test beam validation a comprehensive study of the prototype has been performed. The applied grounding scheme was successful, since the noise rates are below 100 Hz.

Through a muon detection efficiency of 100% except for a narrow region close to the tube wall and a spatial resolution of 118 μm, the suitability of the straw tube tracker for an inner detector of a future e^+e^- collider experiment is demonstrated.

Combining the test beam data with Garfield++ simulations allows for a prediction of the expected the particle identification capabilities, yielding a π/K separation mostly better than 3σ up to momenta of 10 GeV.

Owing to their reduced material budget, straw tubes exhibit a low gamma conversion probability, although the resulting Compton electrons are not stopped within the thin tube wall.

Subsequently, crucial input for the optimization of future prototypes is provided, which is directly addressed in the next generation 4 m-long straw tube chamber prototype.

This contribution will additionally present the latest performance results from the up-scaled 4m prototype, obtained during the upcoming CERN test beam campaign in July.

References

[1] H. Beauchemin *et al.*, ``A Straw Tracker for an FCC-ee experiment'', Expression of Interest (EOI) for the ALLEGRO Concept, Feb. 2025.
[2] ATLAS Collaboration, ``Technical Design Report for the Phase-II Upgrade of the ATLAS Muon Spectrometer'', CERN, Geneva, 2017. [Online]. Available: *https://cds.cern.ch/record/2285580*.

NSS-24-04

Characterisation of a Multitube detector for the CSPEC Cold Neutron Spectrometer (#2800)

Jean-Claude Buffet[1], Sylvain Cuccaro[1], Nathaly De La Rosa[2], Kevin Fissum[2], Bruno Guerard[1], Antoine Lepine[2], Julien Marchal[1], Bernhard Meirose[2], Thomas Neulinger[3], Daria Noferini[2], Jerome Pentenero[1], Dorothea Pfeiffer[2], Davide Raspino[4], **William Saenz-Arevalo**[1], Nicolas Sartor[1], Ourania Sidiropoulou[2]

[1] Institut Laue Langevin, Grenoble, France; [2] European Spallation Source, Lund, Sweden; [3] Forschungs-Neutronenquelle Heinz Maier-Leibnitz, Garching, Germany; [4] ISIS Neutron and Muon Source, Didcot, UK

Abstract

This work presents performance measurements of the first neutron detector module developed for the Cold Neutron Spectrometer (CSPEC) hosted at the European Spallation Source (ESS). Designed and built at the Laue-Langevin Institute (ILL), the detector employs a two-dimensional Multitube architecture to meet the CSPEC requirements in terms of spatial resolution count rate capability and amplification gain stability and uniformity. Experimental tests completed at the CT2 detector test beamline of ILL, confirm compliance to these detection features while validating the production process for the next modules.

References
[1] Neutron News, 21, 2 (2010)
[2] EPJ Web of Conferences 272, 02001 (2022)
[3] Rev. Sci. Instrum. 92, 105104 (2021)

NSS-24-05

Characterization of a High-efficiency Multi Element Thick Gas Electron Multiplier Based Neutron Dosemeter (#1312)

Haoshuai Wang[1,2], Soo Hyun Byun[1,2]

[1] McMaster University, Department of Physics and Astronomy, Hamilton, Canada; [2] McMaster University, Radiation Sciences Graduate Program, Hamilton, Canada

The authors would like to thank the CANDU Owners Group (COG), Canada, and the Natural Sciences and Engineering Research Council (NSERC), Canada for financially supporting this work.

Abstract

We report characterization of a high-efficiency multi-element neutron dosemeter built by the Thick Gas Electron Multiplier (THGEM) technology. The multi-element configuration is an excellent way to increase neutron detection efficiency and is well suited for the development of tissue-equivalent proportional counters (TEPCs) for microdosimetric measurements in low-intensity neutron fields. Compared to conventional TEPCs, the THGEM-based design eliminates the need for anode wire structures, thereby simplifying fabrication and assembly processes. Moreover, the capability of cascading multiple THGEM layers to achieve higher gain, combined with its low cost, mechanical robustness, and large-area scalability, are advantageous features of the THGEM for building multi-element detectors. Following the successful development of an initial prototype consisting of twenty-one gaseous sensitive volumes, an upgraded detector with ninety-five sensitive volumes has been developed to increase neutron efficiency even higher. Experimental characterization of the new detector is currently underway using ^{238}PuBe and ^{7}Li(p,n) neutron sources at the McMaster Accelerator Laboratory. The signal performance and dosimetric response of the detector will be presented and compared with Monte Carlo simulation results.

NSS-24-06

Xe-SF_6 mixtures for negative-ion detectors (#3195)

Afonso P. Marques[1,2], José F. Sousa[1,2], Alexandre M.F. Trindade[1,2], Duarte S. Rodrigues[1,2], Filipa I.G.M. Borges[1,2], Filomena P. Santos[1,2]

[1] University of Coimbra, Department of Physics, Coimbra, Portugal; [2] Laboratory of Instrumentation and Experimental Particle Physics, Coimbra, Portugal

Abstract

Conventional gaseous detectors rely on electron drift, but this transport is intrinsically limited by diffusion, particularly in noble-gas mixtures and over long drift distances. Electronegative additives offer an attractive alternative because they rapidly capture electrons and form negative ions, which drift with much smaller diffusion, enabling improved spatial resolution. In this work, Xe-SF_6 mixtures were investigated using a dedicated experimental setup to study electron attachment, ion mobility, electron detachment, charge multiplication, and electroluminescence. Near-total electron attachment was observed in all cases, confirming the efficient formation of negative ions in Xe-SF_6 mixtures. In the low-field regime, two negative-ion species, SF_6^- and clustered $SF_6^-(SF_6)$, were identified, with reduced mobilities remaining independent of the electric field. High electric fields inside GEM holes enabled electron detachment and subsequent amplification, with EL and multiplication thresholds shifting to lower fields and gas gains increasing as the SF_6 concentration decreased. Xenon electroluminescence was also observed in these mixtures, both inside the GEM and after, although strongly quenched by the electronegative additive. The increase in the thresholds for both scintillation and charge multiplication with increasing SF_6 fraction, highlight the central role of the detachment processes in the amplification mechanisms. These results demonstrate that even a very small addition of SF_6 can substantially modify xenon transport properties. However, the usual amplification stages are not immune to these changes.

References
[1] Phan, N, Lafler, R, Lauer, R, et al. 2017, 'The novel properties of SF_6 for directional dark matter experiments', *Journal of Instrumentation*, vol. 12, no. 2, Art. no. P02012, Bristol: IOP Publishing.
[2] Marques, AP, Sousa, JF, Trindade, AMF, Escada, J, Borges, FIGM & Santos, FP 2026, 'Negative ions as charge carriers in gaseous detectors: results in Xe, SF_6 and Xe-SF_6 mixtures', *Nuclear Instruments and Methods in Physics Research Section A*, vol. 1077, Art. no. 170178, Amsterdam: Elsevier.

Time:
12 November, 2026
11:30 – 13:00

Room:
PICASSO

NSS-25 | Nuclear, HEP and astrophysics detectors

Chairs:
Hartmut Hillemans
Maurizio Ghisetti (Milano)

NSS-25-01

Early On-Orbit Characterization of the Neutron Radiation Detection Instrument-1B (NeRDI-1B) (#1373)

Anthony L. Hutcheson[1], Bernard F. Phlips[1], Wiley N. Johnson[2], Mary V. Johnson-Rambert[1], Alena M. Thompson[1]

[1] U.S. Naval Research Laboratory, Washington, DC, USA; [2] Technology Service Corporation, Arlington, USA

This work was sponsored by the Office of Naval Research (ONR) as part of 6.1 funding.

Abstract

The objective of the Neutron Radiation Detection Instrument (NeRDI) series of experiments is to space qualify and characterize the long-term performance of these new detector technologies in on-orbit radiation environments. The second of this series of experiments, NeRDI-1B, launched on 21 April 2025 to the International Space Station as part of the Department of Defense Space Test Program-Houston 10 (STP-H10) mission. The NeRDI-1B instrument comprises two arrays of Domino microstructured semiconductor neutron detectors (MSNDs), a single separate MSND sensor, and an EJ-270 plastic scintillator read out by a custom array of silicon photomultipliers. Here we describe the NeRDI-1B instrument and present an analysis of its first year of on-orbit operations, with particular focus on the characterization of the MSNDs.

NSS-25-02

High-speed single-photoelectron detection for Cherenkov astronomy (#1412)

Luca Giangrande[1], Matthieu Heller[2], Teresa Montaruli[2]

[1] University of Geneva, Particle and nuclear physics, Geneva, Switzerland; [2] University of Geneva, Département de physique nucléaire et corpusculaire - DPNC, Geneva, Switzerland

Abstract

Silicon photomultipliers are increasingly replacing photomultiplier tubes in Cherenkov telescope cameras, but achieving single-photoelectron resolution with nanosecond timing in a low-noise, scalable detector system emains challenging. We present a co-designed SiPM sensor and front-end application specific integrated circuit (ASIC) that meets these requirements. The custom hexagonal sensor, developed with Hamamatsu Photonics, incorporates an integrated optical filter and fourfold pixel segmentation. The readout is performed by a second prototype of the FANSIC ASIC, optimized for this application and fabricated in 65 nm standard CMOS technology, provides eight channels with on-chip analog summing of sub-channels on a 3.5×3.5 mm2 die, while consuming only 24 mW per

channel. We demonstrate clear single-photoelectron peak separation
with a gain of 2.7 × 10−12 V · s , and an impulse response below 4 ns full width at half maximum with a 1.7 ns rise time, preserving the nanosecond-scale structure of Cherenkov pulses. The system esponds linearly from 1 to 130 photoelectrons, and 55 distinct photoelectron peaks are resolved by varying the source intensity.These results demonstrate that the integrated sensorelectronics architecture delivers the speed, resolution, and dynamic range required for imaging atmospheric Cherenkov telescopes, and provides a scalable path toward large-area camera modules.

References
[1] Biland, A., et al., 2014, "Calibration and performance of the photon sensor response of FACT—the first G-APD Cherenkov telescope." Journal of Instrumentation 9.10, P10012.
[2] Fleury, J., et al., 2014, 'Petiroc and Citiroc: front-end ASICs for SiPM read-out and ToF applications.' *Journal of Instrumentation* 9.01, C01049-C01049.
[3] Bugalho, R., et al., 2019, "Experimental characterization of the TOFPET2 ASIC." Journal of Instrumentation, 14.03, P03029-P03029.
[4] Albert, A., et al.,2017, "TARGET 5: A new multi-channel digitizer with triggering capabilities for gamma-ray atmospheric Cherenkov telescopes.", Astroparticle Physics 92, 49-61.
[5] Giangrande, L., et al., 2025, "FANSIC: A Fast ANalog SiPM Interface Circuit for the readout of large silicon photomultipliers." Nuclear Instruments and Methods in Physics Research Section A, 1077, 170523.
[6] Sanuy, A., et al., 2012, "Wideband (500 MHz) 16 bit dynamic range current mode PreAmplifier for the CTA cameras (PACTA)." *Journal of Instrumentation* 7.01, C01100-C01100.
[7] Cta Consortium, 2018, "*Science with the Cherenkov Telescope Array*.", World Scientific.

NSS-25-03

Experimental demonstration of thermal neutron effects and their suppression in a sampling-type veto detector (#1440)

Toru Matsumura[1], Gei Y. Lim[2], Katsushige Kotera[3], Koji Shiomi[2], Hajime Nanjo[3], Hiroaki Watanabe[2], Tadashi Nomura[2], Mifuyu Ukai[2], Takeshi O. Yamamoto[4]

[1] National Defense Academy of Japan, Department of Applied Physics, Yokosuka, Japan; [2] High Energy Accelerator Research Organization (KEK), Institute of Particle and Nuclear Studies, Tsukuba, Japan; [3] Osaka University, Department of Physics, Toyonaka, Japan; [4] Japan Atomic Energy Agency, Advanced Science Research Center, Tokai, Japan

Abstract
This paper reports on the effects of thermal neutrons in a plastic-scintillator-based sampling calorimeter for a rare kaon decay experiment and the results of experimental studies demonstrating their suppression. We prepared a prototype detector consisting of a lead/scintillator sampling calorimeter with a transverse size of 25 × 25 cm² and 25 alternate layers of 1-mm-lead and 5-mm-scintillator. The prototype can accommodate 50 boron carbide sheets (0.1 mm thick), detachably mounted between the lead and scintillator layers to absorb thermal neutrons. We irradiated the prototype detector with a 0.9 GeV/c π^- beam at J-PARC and demonstrated the existence of late signals which are thought to be γ-rays from capture of thermal neutrons induced by the interaction of charged pions. Furthermore, we separately confirmed, by utilizing a radioactive neutron source, that the insertion of boron carbide sheets reduces the detection of thermal neutrons. These results demonstrate that boron loading is effective in suppressing accidental signals originating from pion-induced thermal neutrons.

NSS-25-04

A High-Performance Mid-Format SiC based Detection System for Radioactive Ion Beam Tagging and Diagnostics (#2221)

Luis Acosta[1,4], Carmen Altana[2], Alice Barbon[3,4], Giuseppe Cardella[4], Andrea Castoldi[5,6], Giuseppe D'Agata[3,4], Enrico De Filippo[4], Saverio de Luca[2], Francesco De Pretto[5,6], Elena Geraci[3,4], **Chiara Guazzoni**[5,6], Cettina Maiolino[2], Andrea Mason[5,6], Emanuele V. Pagano[2], Sara Pirrone[4], Guseppe Politi[3,4], Lucia Quattrocchi[7,4], Mattia Pozzi[5,6], Fabio Risitano[7,4], Francesca Rizzo[3,4], Paolo Russotto[2], Marina Trimarchi[7,4], Salvo Tudisco[2], Cristina Zagami[3,4], Riccardo Zambolo[5,6]

[1] CSIC, Madrid, Spain; [2] INFN, LNS, Catania, Italy; [3] Universita' degli Studi di Catania, Dipartimento di Fisica e Astronomia, Catania, Italy; [4] INFN, Sezione di Catania, Catania, Italy; [5] Politecnico di Milano and INFN, Dipartimento di Elettronica, Informazione e Bioingegneria, Milano, Italy; [6] INFN, Sezione di Milano, Milano, Italy; [7] Universita' di Messina, Dip. di Scienze MIFT, Messina, Italy

The authors greatly acknowledge Sergio Masci, Politecnico di Milano for the careful bonding of the detector prototypes.

Abstract

Radioactive Ion Beams (RIBs) are the frontier in Nuclear Physics, allowing investigations of low cross-section reactions and of nuclei far from the stability valley. Silicon carbide (SiC) material can overperform Silicon as a charged-particle detector, offering nearly zero leakage current and visible-light blindness thanks to the high bandgap. The high displacement energy of SiC is synonymous of radiation hardness and the saturation velocity higher than Si makes SiC an excellent material for fast, high-rate radiation detectors in nuclear and medical physics. In order to provide effectively RIBs tagging, even in the case of high intensity beams, like the ones foreseen at the Laboratori Nazionali del Sud of INFN in Catania (Italy), produced by the novel high intensity Radioactive Ion Beams (RIBs) facility named FRAISE, novel detection systems for the diagnostics and the tagging of RIBs along the transport line and in the measurement chamber are requested. To this aim and for the need of other particle accelerators around the world, we are developing a novel high performance, mid-format detection system, based on an array of Silicon Carbide (SiC) diodes, readout by an optimized fast frontend electronics. This contribution deals with the design, the study and the experimental qualification of the performance of the proposed mid-format detection system with particular care in the characterization of the timing properties and in the analysis of the limiting factors affecting the time resolution. For deposited energies above 2 MeV the time resolution keeps below 100 ps rms at zero added input capacitance. At 22pF added capacitance, the measured time resolution is below 100 ps rms above 5 MeV injected energy.

NSS-25-05

The General Antiparticle Spectrometer (GAPS) Instrument: Design, Performance, and First Antarctic Flight (#2247)

Kelsey Yee, On behalf of the GAPS collaboration

Massachusetts Institute of Technology, Cambridge, USA

GAPS is a collaboration of over 60 scientists and engineers. The work presented here is possible thanks to all of their contributions. The GAPS Experiment is funded in the U.S. by the NASA APRA program grants NNX17AB44G, NNX17AB46G, NNX17AB47G, and 80NSSC21K187, in Japan by the JAXA/ISAS Small Science Program FY2017, and in Italy by Istituto Nazionale di Fisica Nucleare (INFN) and the Italian Space Agency (ASI) through the ASI INFN agreement No. 2018-22-HH.0. The Columbia University GAPS group is supported by the Heising-Simons Foundation award 2025-6055. K. Yee is supported through the NSF Graduate Research Fellowship under grant 2141064.

Abstract

The General Antiparticle Spectrometer (GAPS) is an Antarctic balloon experiment designed to search for low-energy cosmic antiparticles as signatures of dark matter. The GAPS instrument flew on an Antarctic long-duration balloon platform for 25 days in the 2025 austral summer, proving several novel technologies for the first time in flight. The detection method employed by GAPS involves a low-energy antiparticle slowing to a stop within the tracker, forming an exotic atom; the subsequent decay releases characteristic X-rays and nuclear annihilation products that are detectable by the instrument. GAPS utilizes a plastic scintillator time-of-flight (TOF) system that measures energy depositions and velocities and provides a system trigger, together with a tracker consisting of over 1000 lithium-drifted silicon (Si(Li)) strip detectors that provides energy and position measurements, as well as X-ray detections. The tracker operating temperature of < -35 °C is achieved with a novel multi-loop capillary heat pipe (MCHP) thermal system that passively transfers heat generated in the tracker to a large-area radiator. This contribution details the instrument design, performance from ground commissioning, and first Antarctic flight of the GAPS instrument.

NSS-25-06

The Future of In-Beam Gamma-ray Spectroscopy at RIBF: $CeBr_3$ Development for the HYPATIA Array (#2810)

Luke Tetley[1], Ting Gao[1], Joshua Sharpe[1], William Marshall[1], Sidong Chen[1], Timothy Ayers[1], Jason Flatt[1], David Hesp[1], Bob Hide[1], Pankaj Joshi[1], Marc Labiche[2], David O'Donnell[3], Dave Seddon[4], Robert Shearman[5], Francis Thomson[3], Carl Unsworth[2], Pieter Doornenbal[6], Stefanos Paschalis[1], Marina Petri[1], On behalf of the HYPATIA Collaboration

[1] University of York, School of Physics, Engineering and Technology, York, UK; [2] STFC, Daresbury Laboratory, Warrington, UK; [3] University of the West of Scotland, School of Computing, Engineering & Physical Sciences, Paisley, UK; [4] University of Liverpool, School of Physical Sciences, Liverpool, UK; [5] National Physical Laboratory, Nuclear Metrology Group, Teddington, UK; [6] RIKEN, Radioactive Isotope Physics Group, Wako, UK

This work was supported by the UK Science and Technology Facilities Council (STFC) under Grant ST/Y00308X/1.

Abstract

HYPATIA is a next-generation scintillator detector array under development for in-beam gamma-ray spectroscopy of exotic nuclei at the Rare Isotope Beam Factory (RIBF), at the RIKEN Nishina Center for Accelerator-Based Science. When completed, the array will consist of 1008 advanced scintillator detector crystals (384 HR-GAGG and 624 $CeBr_3$), in a hybrid configuration to deliver improved energy resolution, fast timing, enhanced background suppression and peak-to-total. This work presents the development and characterisation of $CeBr_3$ detector modules produced at the University of York for integration into the HYPATIA array. Each module consists of four $CeBr_3$ crystals coupled to silicon photomultiplier arrays within a compact, hermetically sealed housing, designed to ensure the long-term performance stability of the hygroscopic scintillators, whilst optimising the detection efficiency. Experimental characterisation demonstrates an energy resolution of 4.1% – 4.3% at 662 keV and a timing resolution of approximately 0.6 ns (FWHM) for the coincident ^{60}Co gamma rays. These results validate the module design and confirm its suitability for the high-precision spectroscopic measurements required to explore the limits of nuclear stability.

Time:
12 November, 2026
15:00 – 17:00

Room:
ALBÉNIZ & MACHUCA

NSS-26 | AI and ML for radiation detection

Chairs:
Marco Carminati (Milano)

NSS-26-01

Emergent Physical Interpretability in Transformer Encoders for Radiation Anomaly Detection (#1513)

Derian M. Mowen, Miltiadis Alamaniotis

University of Texas at San Antonio, Electrical Engineering, San Antonio, USA

This material is based upon work supported by the Department of Energy National Nuclear Security Administration through Defense Nuclear Nonproliferation's Enabling Capabilities in Technology Consortium under Award Number DE-NA0004197.

Abstract

Constraining a Transformer decoder to a known physical generative structure induces emergent interpretability in the encoder's self-attention without labels or supervision. We demonstrate this in gamma-ray spectroscopy, where measurements are Poisson-sparse at one-second mobile survey dwell times, environments are nonstationary, and labeled decompositions are unavailable. Observed spectra arise as nonnegative additive superpositions of source contributions, which we encode using a Nonnegative Matrix Factorization (NMF)-constrained decoder paired with a Transformer encoder. The learned representations organize into physically meaningful components, separating environmental substructures and recovering known photopeak features at correct energies. In contrast, an identical Transformer with an unconstrained decoder produces unstructured latent representations, with 48.6% of weights taking negative values that are inconsistent with photon-counting physics, isolating the decoder constraint as the causal mechanism. The proposed architecture achieves state-of-the-art anomaly detection on 6,221 field-collected spectra, outperforming linear baselines and unconstrained autoencoders while exhibiting reduced run-to-run variance, demonstrating that embedding known generative structure into decoder design can induce interpretable representations across domains governed by additive physical processes.

NSS-26-02

Ground-Truth-Free Validation of Surface Radiation Mapping via Forward-Simulation Round-Trip (#1723)

Byoung-Jik Kim[1,2]

[1] Changwon National University, Nuclear Engineering, Changwon, South Korea; [2] Reversible Inc., Changwon, South Korea

This research was supported by Changwon National University in 2025 ~ 2026.
This research was funded by the 'New Faculty Research Support Grant' at Changwon National University in 2025.

Abstract

Reconstruction of surface radiation contamination from sparse airborne measurements has matured rapidly with deep learning, but a validation gap persists: the surface activity is rarely measurable in operational deployments, leaving no oracle for evaluating predictions. We address this by reframing airborne mapping as an inverse deconvolution problem in which a known forward operator maps surface activity to aerial fluence via altitude blur and detector response. The framing yields a ground-truth-free validation protocol: each candidate surface reconstruction is forward-simulated through the operator and compared to held-out aerial measurements. We characterize the protocol on a synthetic benchmark with a 64-by-64 ground-truth surface of Gaussian hotspots, a fixed Gaussian forward kernel, 150 sparse aerial samples per scene, and 200 held-out validation points. Four reconstructions are compared: inverse distance weighting (IDW), ordinary kriging, IDW followed by Wiener deconvolution, and a small encoder-decoder convolutional network. Across 40 scenes per method, the round-trip aerial-space root-mean-square error correlated with the oracle surface-space root-mean-square error, with a pooled Pearson correlation of 0.871 across methods and within-method correlations from 0.71 to 0.82. The protocol identified the encoder-decoder network as the most accurate reconstruction in agreement with the oracle ranking, without access to ground truth. These findings suggest that round-trip forward-simulation residuals can serve as a practical proxy for surface reconstruction quality, supporting evaluation and benchmarking of radiation mapping methods when direct surface ground truth is limited or unavailable.

References

[1] Kim, B-J, Sasaki, M, Sanada, Y 2019, 'Comparison of the Fukushima radioactive mapping by two different aerial radiation monitoring systems', Progress in Nuclear Science and Technology, vol. 6, pp. 130-133, doi: 10.15669/pnst.6.130

[2] Sasaki, M, Sanada, Y, Katengeza, EW, Yamamoto, A 2021, 'New method for visualizing the dose rate distribution around the Fukushima Daiichi Nuclear Power Plant using artificial neural networks', Scientific Reports, vol. 11, art. 1857, doi: 10.1038/s41598-021-81546-4

[3] Sasaki, M, Sanada, Y 2022, 'Improvement of training data for dose rate distribution using an artificial neural network', Journal of Advanced Simulation in Science and Engineering, vol. 9, no. 1, pp. 30-39, doi: 10.15748/jasse.9.30

[4] Murphy, B, Yurchak, R, Müller, S 2025, 'GeoStat-Framework/PyKrige: v1.7.3', Zenodo, doi: 10.5281/zenodo.17372225

[5] Ronneberger, O, Fischer, P, Brox, T 2015, 'U-Net: convolutional networks for biomedical image segmentation', Medical Image Computing and Computer-Assisted Intervention, pp. 234-241

NSS-26-03

Backscattered Spectral Network Imaging Method Based on a Combined Long–ShortCrystal Detector (#2600)

Junjun Li[1,3], Yongshun Xiao[1,3]

[1] Tsinghua University, Department of Engineering Physics, Beijing, China; [2] Tsinghua University, Department of Engineering Physics, Beijing, China; [3] Key Laboratory of Particle & Radiation Imaging (Tsinghua University), Ministry of Education, Beijing, Beijing, China; [4] Key Laboratory of Particle & Radiation Imaging (Tsinghua University), Ministry of Education, Beijing, Beijing, China

Abstract

Compton backscatter imaging (CBST) is a promising non-contact technique for nondestructive testing of complex structures, but its performance is limited by the trade-off between detection efficiency and spatial resolution. In this work, we propose a backscattered spectral network imaging framework based on a combined long–short crystal (CLSC) detector and a spectral fusion neural network. The CLSC detector integrates alternating long and short scintillation crystals to improve photon detection efficiency while retaining geometric selectivity, and segmented metal collimation is introduced to provide depth-dependent scattering information. The acquired multi-crystal spectra are processed by a dual-branch fusion network that jointly exploits spectral and spatial features for defect reconstruction. Geant4 simulations with varying defect sizes and depths under realistic noise conditions demonstrate that the proposed method outperforms conventional count-based and collimator-free approaches under low-count conditions, enabling more reliable detection of deep and small defects.

References

[1] C. Shi, Y. Xiao, M. Dong, X. Ouyang, M. Shen, D. Lan, and P. Ma, “Multiple scattering correction with Monte Carlo simulations for Compton backscatter tomography,” Nucl. Instrum. Methods Phys. Res., Sect. A, vol. 1075, p. 170411, 2025, doi: 10.1016/j.nima.2025.170411.

[2] C. Shi, X. Ouyang, M. Dong, M. Shen, D. Lan, P. Ma, and Y. Xiao, “Deep learning based Compton backscatter imaging with scattered X-ray spectrum data: A Monte Carlo study,” Radiat. Phys. Chem., vol. 225, p. 112148, 2024, doi: 10.1016/j.radphyschem.2024.112148.

[3] J. Li and Y. Xiao, "Backscatter Resolution Recovery Imaging System Based on Position-Sensitive Detectors," 2025 IEEE Nuclear Science Symposium (NSS), Medical Imaging Conference (MIC) and Room Temperature Semiconductor Detector Conference (RTSD), Yokohama, Japan, 2025, pp.1-1,doi:10.1109/NSS/MIC/RTSD57106.2025.11287602.

NSS-26-04

A Machine Learning Approach to Inter-Crystal Scattering Kinematics for Multiple Emission Tomography (#2796)

Lisa Arnone[1], Matteo N. Colombo[1], Giulia Terragni[2], Francesco Pennazio[3], Marco Paganoni[1], Luca Presotto[1], Etiennette Auffray[2], Marco Pizzichemi[1,2]

[1] University of Milano-Bicocca, Milan, Italy; [2] CERN, Geneva, Switzerland; [3] INFN Torino, Turin, Italy

This work is supported by the European Union-Next Generation EU, Mission 4 Component 1 CUP H53D23007430001 “Multiple Emission Tomography”, and carried out in association with the CERN Crystal Clear Collaboration.

Abstract

High spatial resolution and sensitivity in Positron Emission Tomography (PET) are essential for early diagnosis and treatment monitoring. However, in modern pixelated detectors, a large fraction of coincidence events involves Inter-Crystal Scatter (ICS), where a gamma ray deposits its energy across multiple scintillators through a Compton interaction followed by photoelectric absorption.These events are difficult to exploit because the sequence of interactions cannot be directly determined, degrading the reconstruction of the Line of Response and, consequently, the spatial resolution. For this reason, ICS events are often discarded, leading to a significant loss in sensitivity. The Multiple Emission Tomography (MET) project aims to recover these events and use them to enable

a hybrid imaging approach combining PET and Compton camera capabilities. In conventional approaches, ICS reconstruction relies on analytical methods based on chi-squared minimization and manually tuned selection cuts. Although effective, these methods are computationally intensive and strongly dependent on user-defined criteria, limiting both efficiency and scalability. In this work, we introduce a Machine Learning (ML) pipeline integrated into the MET prototype to automatically identify ICS events and determine their interaction sequence. By replacing the analytical reconstruction with XGBoost classifiers and a Convolutional Neural Network, the proposed approach provides a more flexible and efficient solution, improving the identification of the first interaction point and enabling a more effective use of multi-crystal events.

NSS-26-05

Real-Time Data Compression Using Machine Learning for the ARGO Dark Matter Detector (#1376)

Sajedeh Esmaeilzadeh[1], Charles-Etienne Granger[1], Hamza Ezzaoui Rahali[1], Kevin Gracequist[2], Simon Viel[2], Audrey C. Therrien[1]

[1] Sherbrooke universuity, Interdisciplinary Institute for Technological Innovation(3IT), Sherbrooke, Canada; [2] Carleton University, Department of Physics, Ottawa, Canada

This research was undertaken, in part, thanks to funding from Canada Foundation for Innovation, CMC Microsystems, NSERC discovery grant program and Canada Research Chairs Program. Audrey C. Therrien holds the Canada Research Chair in Real-Time Intelligence Embedded for High-Speed Sensors.

Abstract

Abstract—The search for dark matter requires increasingly advanced detectors and data processing systems. The ARGO detector, under development, uses liquid argon as the detection medium and will deploy Single Photon Avalanche Diodes (SPAD) over approximately 200 m2. These SPAD matrices, arranged in mm2 units, will generate millions of data channels, with potential drawbacks such as high power consumption, complex cabling, and costly high-speed data storage. To address these challenges, we investigate a unified real-time machine learning (ML) approach capable of simultaneously performing particle identification and event position reconstruction. The proposed Convolutional Neural Network (CNN) architecture classifies events as nuclear recoils (NR), electron recoils (ER), or alpha decays, while concurrently reconstructing the interaction position inside the detector. This multi-task approach reduces computational resources, making it well suited for resource- constrained edge environments near the detector. Future work will focus on optimizing the models and implementing them on edge hardware.

References
[1] Aalseth, CE, *et al.* 2018, 'DarkSide-20k: A 20 tonne two-phase LAr TPC for direct dark matter detection at LNGS', *The European Physical Journal Plus*, vol. 133, pp. 1–129, Berlin: Springer.
[2] Therrien, AC, Gouin-Ferland, B, Rahimifar, MM 2022, 'Potential of edge machine learning for instrumentation', *Applied Optics*, vol. 61, no. 8, pp. 1930–1937, Washington, DC: Optical Society of America.
[3] Ajaj, R, *et al.* 2019, 'Search for dark matter with a 231-day exposure of liquid argon using DEAP-3600 at SNOLAB', *Physical Review D*, vol. 100, no. 2, pp. 022004, College Park, MD: American Physical Society.

[4] Adhikari, P, *et al*. 2021, 'Pulse-shape discrimination against low-energy Ar-39 beta decays in liquid argon with 4.5 tonne-years of DEAP-3600 data', *The European Physical Journal C*, vol. 81, pp. 1–13, Berlin: Springer.
[5] Adhikari, P, *et al*. 2023, 'Machine learning approach for event position reconstruction in the DEAP-3600 dark matter search experiment', *Physics*, vol. 2023, no. 5(2), pp. 483–491, Basel: MDPI.
[6] Rahimifar, M.M. Thesis, Universite de Sherbrooke, 2025
[7] T. Bolton, D. Gastler, J. Klein, H. Lippincott, A. Mastbaum, J. Nikkel, G. Orebi Gann, M. Akashi-Ronquest, S. Seibert, S. Sekula et al., "Rat (is an analysis tool) user's guide (2018)," URL https://rat. readthedocs. io, 2023.
[8] S. Esmaeilzadeh, A. Moharana, H. E. Rahali, Student, IEEE, C.-E. Granger, Student, IEEE, K. Gracequist, S. Viel, A. C. Therrien, Member, IEEE, "Event Classification using Machine Learning for the ARGO Dark Matter Detector", 2025 IEEE Nuclear Science Symposium and Medical Imaging Conference (NSS-MIC), Japan

NSS-26-06

Machine-Learning Based Rapid Characterization of HPGe Detectors Based on Full-Energy Peak Efficiency Responses (#1052)

Kainan Zhang[1,2], Pengwen Su[1,2], Zhen Wu[1,3], Ankang Hu[1,2], Hui Zhang[1,2], Junli Li[1,2], Rui Qiu[1,2]

[1] Tsinghua University, Department of Engineering Physics, Beijing, China; [2] Key Laboratory of Particle & Radiation Imaging, Tsinghua University, Ministry of Education, Beijing, China; [3] Nuctech Company Limited, Beijing, China

Abstract

Full-energy peak efficiency (FEPE) is a critical quantity for quantitative gamma-ray spectrometry using HPGe detectors. However, the FEPE response may vary during long-term operation because of operational history and environmental conditions. Conventional detector characterization usually requires repeated Monte Carlo simulations, in which selected geometrical parameters are manually adjusted until the simulated FEPE curve agrees with experimental measurements. This iterative procedure is computationally expensive and strongly dependent on operator expertise.

To address this limitation, this work proposes a machine-learning-based rapid characterization framework using a sparsely connected multilayer perceptron (MLP) with multiple attention heads. By taking experimentally determined FEPE values and fixed detector parameters as inputs, the network directly determines key characterization parameters, including the crystal radius, crystal length, and dead layer thickness.On a test set comprising 13 detector instances with different specifications, the proposed framework performed detector characterization, and the simulated FEPEs of the characterized detectors agreed closely with the corresponding experimental FEPEs, demonstrating the broad applicability of the approach. Owing to the feed-forward nature of the MLP architecture, the characterization procedure can be completed rapidly through a single forward pass, providing an efficient alternative to the conventional manual Monte Carlo adjustment workflow.

References
[1] W. Khan, Q. Zhang, C. He, and M. Saleh, "Monte Carlo simulation of the full energy peak efficiency of an HPGe detector," Appl. Radiat. Isot., vol. 131, pp. 67–70, Jan. 2018.
[2] E. Uyar and M. H. Bölükdemir, "Characterisation of two p-type HPGe detectors by measurements and Monte Carlo simulations," Measurement, vol. 204, Art. no. 112092, Nov. 2022.
[3] S. Devi, K. Tiwari, S. S. Kaintura, and P. P. Singh, "Performance analysis and dead layer profiling of a carbon-fiber encapsulated p-type HPGe detector," Sci. Rep., vol. 16, Art. no. 2581, 2026.

NSS-26-07

Comprehensive Strategy for Track Signal Extraction in the COMET Phase-I Experiment using Deep Learning Algorithms (#2397)

Joe Sato

Yokohama National University, Deapartment of Physics, Yokohama, Japan

This work was supported by the Japan Society for the Promotion of Science (JSPS) KAKENHI Grant Numbers JP18H05231, JP18H05543, and 25H01524.

Abstract

The COMET Phase-I experiment searches for the neutrinoless muon-to-electron conversion with a target sensitivity of 7×10^{-15}. A critical challenge is identifying signal hits amid a high background occupancy of approximately 40\% in the Cylindrical Drift Chamber (CDC). Traditional methods struggle under such dense environments. We present a deep-learning-based hit filtering strategy using a U-Net architecture with an EfficientNet backbone. By optimizing image formats and multi-hit handling, we achieved a purity of 98\% and a retention of 90\%, significantly surpassing design goals. This framework establishes a robust foundation for track reconstruction in high-occupancy environments.

References
[1] R. Abramishvili et al. (COMET Collaboration), ``COMET Phase-I Technical Design Report,'' \textit{PTEP}, vol. 2020, no. 3, 033C01, 2020.
[2] F. Kaneko, J. Sato, et al., ``Extracting Signal Electron Trajectories in COMET using Deep Learning,'' \textit{PTEP} 2025 (2025) 5, 053C01.
[3] O. Ronneberger et al., ``U-Net: Convolutional Networks for Biomedical Image Segmentation,'' \textit{MICCAI}, 2015.

NSS-26-08

Signal Electron Extraction and Energy Resolution the COMET Experiment (#1795)

Yuya Kojima

Yokohama National University, Graduate School of Engineering Science, yokohama, Japan

Abstract

Charged lepton flavor violation (CLFV) is a promising probe of physics beyond the Standard Model. The COMET Phase-I experiment searches for coherent muon-to-electron conversion ($\mu^- \text{–} e^-$ conversion), which produces a mono-energetic electron with an energy close to 105 MeV. However, Decay-In-Orbit (DIO) electrons form a major background near the signal region, requiring precise track reconstruction and energy estimation.

In this study, a U-Net–based deep-learning method was applied to Cylindrical Drift Chamber (CDC) hit information represented as two-dimensional images. Hit wires with deep-learning scores above a threshold were treated as signal hits and passed to GenFit for track reconstruction. Quality cuts based on the p-value, the number of degrees of freedom (NDF), and reduced χ^2 were also applied to improve the reconstruction quality.
The ROC curve evaluation demonstrated effective discrimination between signal-electron hits and background hits. Furthermore, applying the selected hits to GenFit improved the momentum residual distributions compared with the conventional reconstruction method. In particular, the combination of hit selection and quality cuts suppressed events with large momentum residuals contributing to the DIO background and reduced the overlap between the DIO background and the signal region. Smearing evaluations using the obtained momentum residual distributions and the theoretical DIO spectrum indicated improved energy reconstruction performance under the condition corresponding to a conversion rate of CR = 3.0×10^{-15}. These results suggest that deep-learning-based hit selection can improve track reconstruction and energy estimation performance in the COMET experiment.

References
[1] COMETCollaborationCOMETPhase-I Technical Design Report
[2] Fumihiro Kaneko, Yoshitaka Kuno, Joe Sato, Ikuya Sato, Dorian Pieters, and Chen Wu. Extracting signal electron trajectories in the comet phase- I cylindrical drift chamber using deep learning. hep-ex, 2024.
[3] Olaf Ronneberger, Philipp Fischer, and Thomas BroxU-Net: Convolutional Networks for Biomedical Image Segmentation

Time:
12 November, 2026
15:00 – 17:00

Room:
MACHADO

NSS-27 | Scintillators

Chairs:
Marco Pizzichemi (Geneva)
Lakshmi Soundara Pandian (Watertown)

NSS-27-01

Measurement of the Cross Section of $^{14}N(n, p)^{14}C$ Reaction Using Sample-Added Scintillator (#2201)

Gengchen Li[1], **Gengchen Li**[1], Tatsuya Katabuchi[1], Tatsuya Katabuchi[1], Ziyue Zhu[1], Ziyue Zhu[1], Maxwell C. Maloney[1], Maxwell C. Maloney[1], Risa Kunitomo[1], Risa Kunitomo[1], Zefeng Shao[1], Zefeng Shao[1], Atsushi Kimura[2], Atsushi Kimura[2], Shunsuke Endo[2], Shunsuke Endo[2], Rovira L. Gerard[2], Rovira L. Gerard[2]

[1] Institute of Science Tokyo, Department of Transdisciplinary Science and Engineering, Tokyo, Japan; [2] Japan Atomic Energy Agency, Ibaraki, Japan

The work was supported by JST SPRING, Japan under Grant Number JPMJSP2180， the InfoSyEnergy Consortium and ANSET-CP at the Institute of Science Tokyo. The authors acknowledge the staff at J-PARC for their support.

Abstract

Conventional measurements of neutron-induced charged-particle emission cross sections with semiconductor detectors are limited by particle energy loss in samples and stringent experimental constraints.The $^{14}N(n, p)$ reaction is critical for dose evaluation in boron neutron capture therapy, as it dominates radiation dose to healthy tissue under thermal and epi-thermal neutron irradiation. High-precision cross-section data with uncertainties below 5% are indispensable for safe treatment planning, while existing datasets are currently under re-evaluation. This work aims to accurately measure the $^{14}N(n, p)$ reaction cross section from 2.6×10^{-3} to 1.8 eV using a homemade sample-added scintillator detector. The scintillator consists of a base matrix, ^{14}N-containing luminescent agent, wavelength shifter and photoinitiator. Pure scintillators and sample-added scintillator with lithium fluoride and gold powder are fabricated as active targets, attached directly on the surface of a photomultiplier tube, and aligned on the neutron beam. Experiments are carried out at the ANNRI beamline of the MLF of the JPARC with a flight length of 28.41 m. Waveform signals were recorded by a digitizer, with long-gate pulse height area, short-gate pulse shape discrimination area and time-of-flight data acquired for each event. The $^{14}N(n, p)$ cross section was determined relative to the $^{6}Li(n, \alpha)$ reaction. Results indicates that the cross sections obtained in the present work show an overall energy dependence consistent with the expected low-energy 1/v behavior, and the measured values are consistent within uncertainty with the past experimental values and evaluated cross section data. This study demonstrates the feasibility of using self-made sample-added scintillators for measurements.

References

[1] Torres-Sánchez, P, et al. 2023, 'Measurement of the 14N(n,p)14C cross section at the CERN n_TOF facility from subthermal energy to 800 keV', *Physical Review C*, vol. 107, no. 6, Art. no. 064617, College Park: American Physical Society.

[2] Koehler, PE & O'Brien, HA 1989, '14N(n,p)14C cross section from 61 meV to 34.6 keV and its astrophysical implications', *Physical Review C*, vol. 39, p. 1655, College Park: American Physical Society.

[3] Gledenov, YM & Salatski, VI 1993, 'The 14N(n,p)14C reaction cross section for thermal neutrons', *Zeitschrift für Physik A*, vol. 346, p. 307, Berlin: Springer.

[4] Wagemans, J & Wagemans, C 2000, 'Experimental determination of the 14N(n,p)14C reaction cross section for thermal neutrons', *Physical Review C*, vol. 61, Art. no. 064601, College Park: American Physical Society.

[5] Kitahara, R & Hirota, K 2019, 'Improved accuracy in the determination of the thermal cross section for neutron lifetime measurement', *Progress of Theoretical and Experimental Physics*, vol. 2019, no. 9, Oxford: Oxford University Press.

[6] deBoer, RJ & Junghans, AR 2025, 'Total cross section of 14N + n from 0.1 to 12 MeV', *Physical Review C*, vol. 112, Art. no. 025805, College Park: American Physical Society.
[7] Shinjo, Y & Kin, T 2020, 'Advancement of plastic scintillator made with 3D printer', *Ionizing Radiation*, vol. 46, pp. 39–48, Tokyo: Japan Radioisotope Association.
[8] Katabuchi, T & Sato, Y 2024, 'Measurement of the neutron capture cross section of 185Re in the keV energy region', *Journal of Nuclear Science and Technology*, vol. 61, no. 2, pp. 224–229, London: Taylor & Francis.
[9] Rovira, G & Kimura, A 2024, 'Neutron capture cross section measurement of 129I and 127I using the NaI(Tl) spectrometer of the ANNRI beamline at J-PARC', *European Physical Journal A*, vol. 60, Art. no. 120, Heidelberg: Springer.

NSS-27-02

Development of thermal neutron detector using co-doped Ce:$LaBr_3$/^{6}LiBr Eutectic Scintillators for High Gamma-Ray Backgrounds

(#2226)

Kei Kamada[1,2], Kyoung Jin Kim[1,2], Masao Yoshino[1,2], Masaaki Kaburagi[4], Junya Ishii[4], Tetsuro Matsumoto[4], Seiya Manabe[4], Akihiko Masuda[4], Hideki Harano[4], Masahiro Kato[4], Kenji Shimazoe[5], Akira Yoshikawa[1,2]

[1] Tohoku Univ., Sendai, Japan; [2] C&A corp., Sendai, Japan; [3] Japan Atomic Energy Agency, Tokai, Japan; [4] National Institute of Advanced Industrial Science and Technology, Tsukuba, Japan; [5] The University of Tokyo, Tokyo, Japan

Abstract

Thermal-neutron detection in intense gamma-ray fields is required for fuel-debris monitoring and criticality safety during nuclear decommissioning. We developed co-doped Ce:$LaBr_3$/^{6}LiBr eutectic scintillators in which the ^{6}LiBr phase converts thermal neutrons through the ^{6}Li(n,α)^{3}H reaction and the Ce:$LaBr_3$ phase produces fast scintillation light. Building on eutectic-scintillator design concepts that enable higher Li content than stoichiometric single crystals, Sr^{2+} and Ba^{2+} co-doping were investigated to improve pulse-shape discrimination (PSD). Sr co-doping produced only limited improvement in the eutectic because Sr-rich secondary regions were formed, whereas Ba co-doping gave clearer α/γ PSD mapping. A Ce:$LaBr_3$/^{6}LiBr detector was then evaluated in the same ^{252}Cf-neutron/^{137}Cs-gamma mixed-field configuration and digital processing scheme as the optimized LiCAF:Ce detector benchmark. Neutron-source detection was demonstrated up to 5.4 Gy/h with an effective thermal-neutron sensitivity of approximately 0.3 cps/nv, indicating the potential of Ba,Ce:$LaBr_3$/^{6}LiBr eutectics for compact neutron monitoring in decommissioning environments.

NSS-27-03

Scintillators based on 2D perovskite single-crystals for the detection of rapid neutrons and gamma/neutron discrimination. (#1344)

Fanny Thorimbert[1], Eric Gros-Daillon[2], David Tisseur[3], Olivier Llido[3], Victor Buridon[5], Dominique Tromson[5], Jean-Marie Verilhac[1]

[1] Université Grenoble Alpes, CEA/LITEN, Grenoble, France; [2] Université Grenoble Alpes, CEA/LETI, Grenoble, France; [3] CEA, IRESNE, Saint-Paul les Durance, France; [4] CEA, IRESNE, Saint-Paul les Durance, France; [5] Université Paris-Saclay, CEA/LIST, Palaiseau, France; [6] Université Paris-Saclay, CEA/LIST, Palaiseau, France; [7] Université Grenoble Alpes, CEA/LITEN, Grenoble, France

Abstract

Fast neutron detectors are essential for quantifying neutron flux in nuclear reactors, imaging the internal structure of large equipment, and detecting contraband or radioactive nuclear materials. However, no ideal technology currently enables efficient, accurate, and real-time detection of fast neutrons, which are high-energy, highly penetrating particles. There is a growing interest in hybrid organic–inorganic halide perovskites, which exhibit scintillation under X-rays, gamma rays, and fast neutrons within a single material platform. In particular, two-dimensional (2D) perovskites contain both light elements, such as hydrogen in long organic cations, which are suitable for neutron detection, and heavy elements, such as lead, which enhance X- and gamma-ray absorption [1,2].

In this presentation, I will present our approach to grow from solution by solvent evaporation, centimeter-sized single crystals of 2D perovskites, namely PEA_2PbBr_4. The optical characterizations of this single-phase, perfectly ordered crystal present two photoluminescence (PL) peaks, at 411 and 426 nm, attributed respectively to the emission from the surface and the bulk, a PLQY (Photoluminescence Quantum Yield) of 26 %, and a time decay of ≈ 3 ns. The radioluminescent measurements show a result of 20000 to 30000 Ph/MeV vs LYSO, which is better than organic scintillators, like EJ200~10000 Ph/MeV. In a second step, we will dope the reference material with cations such as Zn^{2+} or Mn^{2+} to enhance the light yield and increase the Stokes shift in order to reduce the self-absorption. We will also investigate the effects of dimensionality and halide composition to achieve a PL redshift. All synthesized materials will be evaluated under realistic neutron flux conditions, with particular attention to their stability. In parallel, their ability to discriminate between neutron and gamma radiation will also be investigated on a laboratory bench, using a ^{252}Cf source.

References

[1] M. Xia *et al.*, 2022 « Organic–inorganic hybrid perovskite scintillators for mixed field radiation detection », *InfoMat*, vol. 4, n° 9, p. e12325

[2] B. Yang *et al.*, 2024 « Inch-sized 2D perovskite single-crystal scintillators for high-resolution neutron and X-ray imaging », *InfoMat*, vol. 7, n° 4, p. e12648

NSS-27-04

Optimization of $Cs_2LiLa(Br,Cl)_6$:Ce Scintillation Crystals for Neutron Detection and n/γ Discrimination (#1789)

Zhuochen Cai[1], **Zhuochen Cai**[1], Xianggang Zhang[1], Xianggang Zhang[1], Ziang Yin[1], Ziang Yin[1], Jinbo Liu[2], Jinbo Liu[2], Zhe Kang[2], Zhe Kang[2], Qinghua Zhao[1], Qinghua Zhao[1], Tao Wang[1], Tao Wang[1]

[1] Northwestern Polytechnical University, State Key Laboratory of Solidification, Xi'an, China; [2] Crystalab Corporation Ltd, Xi'an, China

Abstract

$Cs_2LiLa(Br,Cl)_6$:Ce (CLLBC) is a promising Elpasolite scintillator for compact gamma-ray spectroscopy and thermal-neutron detection, but the effect of Ce concentration on neutron-gamma pulse-shape discrimination (PSD) remains insufficiently quantified. In this work, CLLBC crystals with 20% Cl substitution and nominal Ce concentrations of 2%, 3%, and 4% were grown by the vertical Bridgman method. When Ce concentration increasing from 2.05% to 5.46%, the 662 keV energy resolution improved from about 3.5% to 3.2%, the relative light output increased by 9.4%, and the neutron-gamma figure of merit (FOM) increased from 1.6 to 2.0. Scintillation-decay measurements and coupled rate-transport calculations indicate that higher Ce concentration enhances energy transfer and excitation-density-dependent quenching, making neutron-like pulses more distinct from gamma-ray pulses. Continued growth optimization further enabled a 1 inch SiPM-coupled CLLBC detector that achieved 3.19% energy resolution at 662 keV and FOM = 2.37. These results demonstrate a practical route for improving CLLBC scintillators for compact mixed-field radiation detectors.

References

[1] J. Glodo, E. van Loef, R. Hawrami, W. M. Higgins, A. Churilov, U. Shirwadkar *et al.*, "Selected Properties of Cs_2LiYCl_6, $Cs_2LiLaCl_6$, and $Cs_2LiLaBr_6$ Scintillators," IEEE Trans. Nucl. Sci., vol. 58, no. 1, pp. 333-338, 2011.

[2] R. Hawrami, L. S. Pandian, J. G. E. Ariesanti, J. Finkelstein, and K. S. J. Tower, "$Cs_2LiLa(Br, Cl)_6$ Crystals for Nuclear Security Applications," IEEE Trans. Nucl. Sci.,vol. 63, no. 2, pp. 509-512, 2016.

[3] J. Cang, X. Fang, Z. Zeng, M. Zeng, Y. Liu, Z. Sun, *et al.*, "Ionization-density-dependent scintillation pulse shape and mechanism of luminescence quenching in $LaBr_3$: Ce," Phys. Rev. Appl., vol. 14, no. 6, p. 064075, 2020.

NSS-27-05

Development of Tl and ^{6}Li Co-Doped $Cs_3Cu_2I_5$ for Remote Thermal Neutron Detection (#1524)

Chihaya Fujiwara[1,2], Yusuke Urano[3], Akihiro Yamaji[2], Nishiki Matsubayashi[3], Takushi Takata[3], Hiroki Tanaka[3], Mátyás Hunyadi[4], Lóránt Csige[4], Shunsuke Kurosawa[2,5]

[1] Tohoku University, Department of Materials Science, Graduate School of Engineering, Sendai, Japan; [2] Nagoya University, Graduate School of Engineering, Nagoya, Japan; [3] Kyoto University, Institute for Integrated Radiation and Nuclear Science, Osaka, Japan; [4] HUN-REN Institute for Nuclear Research, Debrecen, Hungary; [5] Osaka University, Institute of Laser Engineering, Osaka, Japan

Abstract

Tl- and ^{6}Li-co-doped $Cs_3Cu_2I_5$ crystals were grown by the Bridgman method and evaluated as thermal neutron scintillators for application in fiber-optic-coupled neutron flux monitoring systems. The grown crystals (5 × 5 × 3 mm) exhibited a light yield of approximately 140,000 ph./n_{th}excited thermal neutron, which is approximately 24 times higher than that of the conventional and widely used GS20 neutron scintillator. A detector was constructed by optically coupling a small crystal piece (1 × 1 × 0.2 mm) to the tip of a 20 m optical fiber. Neutron irradiation experiments were conducted at the Kyoto University Research Reactor. The neutron excited radioluminescence spectra of Tl,^{6}Li doped $Cs_3Cu_2I_5$ were confirmed. In addition, the scintillation intensity varied linearly with neutron flux, with a coefficient of determination of R^2 = 0.996. These results indicate that ^{6}Li- and Tl-co-doped $Cs_3Cu_2I_5$ is a highly promising scintillator material for real-time neutron dosimetry in high-flux environments such as boron neutron capture therapy.

NSS-27-06

Gamma-Neutron Detection with Intrinsic and Doped Ternary Halide Scintillators (#2873)

Elsa Ariesanti[1], Rastgo Hawrami[1], Raphael Hermann[2], Matthew Loyd[2]

[1] Fisk University, Life and Physical Sciences (Physics), Nashville, USA; [2] Oak Ridge National Laboratory, Oak Ridge, USA

This work was supported in part by the U.S. Department of Energy under Grant DE-SC0025877.

Abstract

Traditionally dual-mode radiation detection requires a combination of two or more radiation detectors that work synchronously. In recent years more novel and advanced scintillation detector materials for dual-mode detection

have been discovered and developed. Recent elpasolite scintillators, such as cerium doped CLYC, CLLB, and TLYC, which contain neutron sensitive materials, have been investigated as dual mode detectors. Because of the complexity of their phase diagrams, crystal growth yield, including bulk uniformity and detection performance, is lower than ideal, which eventually leads to a high final product cost. As a result, there is not a widespread interest in using these scintillators due to their high costs and scarcity although they have good detection and gamma-neutron performance. Simpler compounds like binary and ternary halides have less complicated phase diagrams due to fewer reacting compounds in the growth systems. This paper describes the efforts to grow scintillators that are capable of simultaneous neutron and gamma ray detection with lithium-doped or containing ternary halide compounds. The presence of lithium, whether it be natural or enriched ^{6}Li, improves the neutron sensitivity of the compounds and allows for simultaneous detection of gamma-ray and thermal neutrons. Fast or scattered neutron detection is also possible with ternary chloride compounds. This paper presents the growth and characterization of lithium based ternary halide scintillation crystals for dual-mode neutron-gamma detection and imaging. Early results show an energy resolution about 4% (FWHM) for 662 keV gamma-rays and a primary decay constant about 800 ns. Other properties, such as melting points, transmittance and absorbance spectra, x-ray excitation optical emission spectra, as well as preliminary neutron gamma discrimination and crystal structure measurements will be presented.

References
[1] R Hawrami, E Ariesanti, A Burger, P Sellin, "Latest growth of large diameter Tl-based elpasolite scintillation crystals," Opt. Mater., vol. 128, pp. 112324, June 2022.
[2] R. Hawrami, E. Ariesanti, A. Burger, E. Neely, J. Glodo, L. Pandian, C. Ji, S. Stepanoff, D.E. Wolfe, F. Liang, "Characterization of large diameter dual-mode cerium-doped Tl_2LiYCl_6 advanced scintillator," Nucl. Instrum. Meth. Phys. Res. A, vol. 1056, pp. 168626, Nov. 2023.
[3] L. Soundara-Pandian, R. Hawrami, J. Glodo, E. Ariesanti, E. V. van Loef, K. Shah, "Lithium Alkaline Halides—Next Generation of Dual Mode Scintillators," IEEE Trans. Nucl. Sci., vol. 63, no. 2, pp. 490-496, April 2016.

NSS-27-07

Neutron and Gamma Ray Pulse Shape Discrimination in Small, Fiber-Coupled Organic Glass Scintillators (#1730)

Schuyler Tyler, Oscar Stennes, Shaun D. Clarke, Sara A. Pozzi

The University of Michigan, Department of Nuclear Engineering and Radiological Sciences, Ann Arbor, USA

This work was supported in-part by the Consortium for Monitoring, Technology, and Verification under Department of Energy National Nuclear Security Administration award number DE-NA0003920. The authors thank collaborators at École Polytechnique Fédérale de Lausanne (EPFL) for their technical discussions, continued support, and contribution of detector materials used in this work.

Abstract
Miniature fiber-coupled organic scintillators are promising candidates for distributed neutron measurements in confined or high-radiation environments where remote placement of photodetectors and electronics is desirable. In this work, organic glass scintillator (OGS) droplets coupled to polymethyl methacrylate (PMMA) optical fibers were

characterized to investigate how optical transport distance affects pulse-shape discrimination (PSD) behavior and neutron-sensitive response. Measurements were performed using direct coupling and fiber lengths up to 12 m with ^{252}Cf and ^{137}Cs sources. Tail-to-total PSD was used to compare neutron and gamma-ray event populations under fixed photomultiplier operating conditions. Increasing fiber length produced substantial attenuation and broadening of both pulse populations, with the gamma-ray band degrading more rapidly than the neutron band. Low-light transport effects, coupling conditions, and threshold migration also significantly altered the PSD morphology as fiber length increased. Although low-energy calibration features were difficult to interpret due to the small scintillator geometry and probable electron escape effects, measurable neutron-sensitive PSD structure remained observable across all tested fiber lengths. These results suggest that long PMMA optical transport may preferentially suppress gamma-ray response while preserving neutron-sensitive discrimination capability relevant to neutron-signature analysis and remote neutron monitoring applications.

References
[1] F. Vitullo, V. Lamirand, J.-B. Mosset, P. Frajtag, O. Pakari, P. Gregory, and A. Pautz, “Developing and testing a miniature fiber-coupled scintillator for in-core neutron counting in CROCUS,” EPJ Web of Conferences, vol. 225, p. 04018, 2020.
[2] F. Vitullo, “Miniature and Minimalistic Neutron Detectors for Online High-Resolution Experiments in the Zero-Power Reactor CROCUS,” Ph.D. dissertation, École Polytechnique Fédérale de Lausanne (EPFL), Lausanne, Switzerland, 2022.
[3] S. A. Pozzi, E. Schneider, E. Neely, R. Lopez, P. Feng, and S. D. Clarke, “Organic glass scintillators: Material properties, performance characterization, and applications,” Radiation Measurements, vol. 193, p. 107627, 2026, doi: 10.1016/j.radmeas.2026.107627.
[4] Industrial Fiber Optics, Inc., “ESKA® SH8001 jacketed PMMA optical fiber cable,” Accessed: May 9, 2026. [Online]. Available: https://i-fiberoptics.com/eska-jacketed-cable-detail.php?id=21&sum=80
[5] J. K. Polack, M. Flaska, A. Enqvist, C. S. Sosa, C. C. Lawrence, and S. A. Pozzi, “An algorithm for charge-integration, pulse-shape discrimination and estimation of neutron/photon misclassification in organic scintillators,” Nucl. Instrum. Methods Phys. Res. A, vol. 795, pp. 253–267, 2015.

NSS-27-08

Pulse Shape Discrimination in a 3D-Printable Perovskite–Polysiloxane Nanocomposite Scintillator (#2064)

Matteo Polo[1,2], Sara M. Carturan[3,4], Marco Cinausero[4], Sandra Moretto[3,5], Gian-Franco Dalla Betta[1,2], Anna Paola Caricato[6,7], Alberto Quaranta[1,2]

[1] University of Trento, Department of Industrial Engineering, Trento, Italy; [2] INFN-TIFPA, Trento, Italy; [3] University of Padova, Department of Physics and Astronomy, Padova, Italy; [4] INFN-LNL, Legnaro, Italy; [5] INFN-Padova, Padova, Italy; [6] University of Salento, Department of Physics and Mathematics, Lecce, Italy; [7] INFN-Lecce, Lecce, Italy; [8] CEDAD, Brindisi, Italy

This work was supported by the National Institute of Nuclear Physics (INFN) of Italy, through the CSN5 SHINE project.

Abstract
Scintillators, which convert ionizing radiation into visible photons, are essential in applications ranging from high-energy physics to medical imaging. Plastic scintillators are especially attractive due to their low cost, fast response, and simple fabrication. However, their limited radiation hardness and poor geometrical adaptability restrict their use

in demanding environments such as hadron therapy and real-time dosimetry. In this work, a novel nanocomposite scintillator designed for 3D printing is investigated. The material consists of a photocurable polysiloxane matrix embedding metal-halide perovskite (CsPbBr3) nanocrystals, enabling the fabrication of complex detector geometries. Beyond its manufacturability, the composite exhibits an unusual scintillation response: under alpha-particle excitation, the emitted signal shows a significantly longer decay time compared with the fast emission typical of pure perovskites. These temporal features allow effective pulse shape discrimination between gamma photons and alpha particles, representing, to the best of the authors' knowledge, the first demonstration of this capability in hybrid perovskite-based scintillators. Preliminary optical characterization was carried out through spectrofluorimetric analysis to study the interaction between the polymer matrix and the perovskite phase, while UV--visible transmittance measurements confirmed adequate transparency for efficient light transport. Scintillation performance was then evaluated using an alpha source. Comparison with a commercial plastic scintillator benchmark highlights the potential of the proposed nanocomposite for advanced and customizable dosimetry applications, especially where flexible detector geometries and particle discrimination are required.

References
[1] G. F. Knoll, Radiation detection and measurement. John Wiley & Sons, 2010.
[2] A. Quaranta, S. Carturan, M. Cinausero, T. Marchi, F. Gramegna, M. Degerlier, A. Cemmi, and S. Baccaro, "Characterization of polysiloxane organic scintillators produced with different phenyl containing blends," Materials Chemistry and Physics, vol. 137, no. 3, pp. 951–958, 2013.
[3] J. Ghosh, J. O'Neill, M. G. Masteghin, I. Braddock, C. Crean, R. Dorey, H. Salway, M. Anaya, J. Reiss, D. Wolfe, et al., "Surfactant-dependent bulk scale mechanochemical synthesis of cspbbr3 nanocrystals for plastic scintillator-based x-ray imaging," ACS applied nano materials, vol. 6, no. 16, pp. 14980–14990, 2023.
[4] S. Mourdikoudis and L. M. Liz-Marz´an, "Oleylamine in nanoparticle synthesis," Chemistry of Materials, vol. 25, no. 9, pp. 1465–1476, 2013.
[5] A. Giuri, A. C. Chekkallur, et al., "3d printed ultra-fast plastic scintillators based on perovskite-photocurable polymer composite," Advanced Functional Materials, vol. 35, no. 12, p. 2417653, 2025

Time:
12 November, 2026
15:00 – 17:00

Room:
PICASSO

NSS-28 | Semiconductor detectors

Chairs:
Shiva Abbaszadeh (Santa Cruz)
Lars R. Furenlid (Tucson)

Detector materials, silicon device technologies, avalanche multiplication, radiation hardness, and electrical characterization.

NSS-28-01

Methylpiperazinium Perovskitoid for High-Performance X-Ray Detection (#2343)

Hong Li

wuhan university of technology, HuBei, China

This work was financially supported by the Guangdong Major Project of Basic and Applied Basic Research (grant no.2021B0301030001), National Natural Science Foundation of China (U2330115.62275206).

Abstract

Abstract — Metal halide perovskites are promising for direct X-ray detection, but phase impurity in conventional quasi-2D systems limit device performance. Here we report a methylpiperazinium (MPZ) based quasi-2D perovskitoid, $(mpz)_5Pb_8Br_{26}\cdot 2H_2O$. The crystal features a unique segmented architecture: four corner-sharing $PbBr_6$ octahedra form 3D-like conduction blocks, separated by 2D spacer regions where MPZ^{2+}. This design simultaneously achieves a high mobility-lifetime ($\mu\tau$) product of 6.1×10^{-3} cm^2 V^{-1}. A direct X-ray detector fabricated in the out-of-plane configuration exhibits a sensitivity of 33.18 μC Gy^{-1} cm^{-2} and a detection limit of 6.2 nGy s^{-1}, representing a record among lead-based quasi-2D perovskites. The successful construction of quasi-2D single crystals provides a versatile platform for high-performance optoelectronics, proving its efficacy for applications spanning photodetection, solar energy conversion, and light-emitting devices even under the most rigorous material requirements

References

[1] J. S. Kim, H.-D. Lee, J. H. Jung, T. Kim, S.-J. Woo, H. J. Yoon, J. Moon, C.-m. Kang, S.-E. Chang, D.-H. Kim, Nature Communications 2025, 16, 9590.

[2] K. Leng, I. Abdelwahab, I. Verzhbitskiy, M. Telychko, L. Chu, W. Fu, X. Chi, N. Guo, Z. Chen, Z. Chen, Nature materials 2018, 17, 908-914.

[3] B. Hailegnaw, S. Demchyshyn, C. Putz, L. E. Lehner, F. Mayr, D. Schiller, R. Pruckner, M. Cobet, D. Ziss, T. M. Krieger, Nature Energy 2024, 9, 677-690.

[4] X. Wang, L. Jin, A. Sergeev, W. Liu, S. Gu, N. Li, K. Fan, S.-c. Chen, K. S. Wong, X. Sun, Science Advances 2023, 9, eadj3476.

[5] R. Quintero-Bermudez, A. Gold-Parker, A. H. Proppe, R. Munir, Z. Yang, S. O. Kelley, A. Amassian, M. F. Toney, E. H. Sargent, Nature materials 2018, 17, 900-907.

NSS-28-02

Design and Evaluation of Graphene Strip Arrays for Radiation Detection (#2400)

Marcos Turqueti[1], Alec Lindman[2], Alan Poon[2]

[1] Lawrence Berkeley National Laboratory, Engineering Division, Berkeley, USA; [2] Lawrence Berkeley National Laboratory, Nuclear Science, Berkeley, USA

Abstract

Graphene has emerged as a promising material for next-generation sensing systems due to its exceptional carrier mobility, low electronic noise, mechanical flexibility, and high electrical conductivity. In this work, we present the design and evaluation of graphene strip arrays for radiation detection applications. The detector architecture employs segmented graphene sensing strips integrated connected to low-noise front-end electronics to investigate radiation-induced signal generation, spatial sensitivity, and charge transport characteristics. Conventional semiconductor radiation detectors often face challenges associated with fabrication complexity, radiation damage, and limitations in scaling toward lightweight and flexible detection systems. Graphene-based detectors provide an alternative approach with potential advantages in fast signal response, compact integration, and scalable fabrication.

The proposed detector consists of patterned graphene strip arrays fabricated on an silicon substrate with optimized strip geometry and differential signal readout. Radiation-induced charge variations are detected through low-noise charge amplification and signal conditioning electronics. Preliminary experimental characterization demonstrates measurable detector response under controlled irradiation conditions and stable electrical operation across multiple bias configurations. The segmented strip geometry enables position-sensitive radiation detection and supports scalability toward larger-area detector systems. The presented work demonstrates the feasibility of graphene strip arrays as compact, low-noise radiation detectors for advanced nuclear science and charged-particle instrumentation.

References

[1] A. Patil *et al.*, "Graphene field effect transistors for detection of ionizing radiation," *IEEE Nuclear Science Symposium & Medical Imaging Conference*, Knoxville, TN, USA, 2010, pp. 674-676, doi: 10.1109/NSSMIC.2010.5873845.

[2] Tawfik MW, Sharaf A, Serry M. Monolayer Graphene Radiation Sensor with Backend RF Ring Oscillator Transducer. Nanomaterials (Basel). 2022 Jan 18;12(3):305. doi: 10.3390/nano12030305. PMID: 35159652; PMCID: PMC8838122.

[3] M. Foxe *et al.*, "Detection of ionizing radiation using graphene field effect transistors," *2009 IEEE Nuclear Science Symposium Conference Record (NSS/MIC)*, Orlando, FL, USA, 2009, pp. 90-95, doi: 10.1109/NSSMIC.2009.5401864.

[4] M. Foxe *et al.*, "Numerical model of graphene-based radiation detector response," *IEEE Nuclear Science Symposium & Medical Imaging Conference*, Knoxville, TN, USA, 2010, pp. 667-670, doi: 10.1109/NSSMIC.2010.5873843.

[5] Merve Eren Yakişiklier, Hidayet Çetin, Seyhan Karaçavuş,"Ionizing radiation responses in graphene field effect transistor",Radiation Physics and Chemistry,Volume 244,2026,113745,ISSN 0969-806X,https://doi.org/10.1016/j.radphyschem.2026.113745.

[6] A. Patil *et al.*, "Graphene field effect transistor as radiation sensor," *2011 IEEE Nuclear Science Symposium Conference Record*, Valencia, Spain, 2011, pp. 455-459, doi: 10.1109/NSSMIC.2011.6154538.

[7] M. Foxe *et al.*, "Graphene-based neutron detectors," *2011 IEEE Nuclear Science Symposium Conference Record*, Valencia, Spain, 2011, pp. 352-355, doi: 10.1109/NSSMIC.2011.6154517.

NSS-28-03

Geometry-Defined Impact Ionization in Two-Stage Mesa-Type Silicon Electron Multipliers (#1064)

Hironori Sonobe, Naoki Kamiya, Tatsuya Kobayashi, Ryozo Shiozaki, Yusuke Matsunaga

Hamamatsu Photonics K.K., Solid State Division, Hamamatsu, Japan

Abstract

A silicon electron multiplier (SiEM) that achieves internal multiplication without a dedicated doped gain layer is demonstrated. The device employs a two-stage mesa-type architecture in which impact ionization occurs in a localized high-field region formed by geometric field crowding within a cylindrical mesa. A buried gate electrode independently controls carrier injection into the multiplication region. Devices were fabricated in a sub-micron CMOS process line. The structure consists of an injection stage and a multiplication stage. The injection stage uses a buried polysilicon gate to electrostatically steer carriers toward the center of the pixel, while the multiplication stage confines the high electric field within a constricted cylindrical mesa. Three-terminal operation enables independent control of multiplication through the gate bias. Electro-optical measurements were performed using 905 nm illumination with an absorption depth of approximately 30–35 μm in silicon. The devices exhibit a multiplication factor exceeding 100 for |Vgate| < 50 V. Scaling of the cylindrical mesa geometry shows that smaller diameters and reduced mesa height lower the bias required for multiplication. For example, reducing the mesa diameter from 3.0 μm to 1.6 μm increases the multiplication factor from approximately 1.5 to greater than 3 at |Vgate| = 40 V, and gains exceeding 400 are obtained at |Vgate| ≈ 50 V. Temperature measurements from −40 °C to 40 °C show a multiplication sensitivity of dVgate/dT = 24–30 mV/°C at constant gain (M = 10). This value is significantly smaller than those typically reported for gain-layer detectors. These results demonstrate geometry-defined impact ionization with electrostatically controlled carrier injection. The proposed SiEM provides a design framework for radiation-tolerant silicon detectors with internal multiplication.

References

[1] ScriptorStartFragmentGianotti, F et al 2005, ‘Physics potential and experimental challenges of the LHC luminosity upgrade’, The European Physical Journal C, Vol. 39, No. 3, pp. 293–333, Berlin & Heidelberg: Springer.ScriptorEndFragment

[2] ScriptorStartFragmentCartiglia, N et al 2015, ‘Design optimization of ultra-fast silicon detectors’, Nuclear Instruments and Methods in Physics Research Section A, Vol. 796, pp. 141–148, Amsterdam: Elsevier.ScriptorEndFragment

[3] ScriptorStartFragmentFerrero, M et al 2019, ‘Radiation resistant LGAD design’, Nuclear Instruments and Methods in Physics Research Section A, Vol. 919, pp. 16–26, Amsterdam: Elsevier.ScriptorEndFragment

[4] ScriptorStartFragmentHalvorsen, MM et al 2022, ‘The Silicon Electron Multiplier sensor’, Nuclear Instruments and Methods in Physics Research Section A, Vol. 1041, Article 167325, Amsterdam: Elsevier.ScriptorEndFragment

[5] ScriptorStartFragmentHalvorsen, MM et al 2024, ‘Fabrication of a Silicon Electron Multiplier sensor using metal assisted chemical etching and its characterisation’, Nuclear Instruments and Methods in Physics Research Section A, Vol. 1060, Article 169046, Amsterdam: Elsevier.ScriptorEndFragment

NSS-28-04

Electrical and UHDR characterization of trench-isolated thin segmented silicon detectors (#2529)

Diango M. Montalvan Olivares[1,2], Umberto Deut[1,2], Maria Giuseppina Bisogni[3,4], Maurizio Boscardin[5], Matteo Centis Vignali[5], Stefano De Astis[1,2], Marco Ferrero[2], Simona Giordanengo[2], Franco Mostardi[1,2], Roberto Sacchi[1,2], Anna Vignati[1,2]

[1] Università degli Studi di Torino, Deparment of Physics, Turin, Italy; [2] Istituto Nazionale di Fisica Nucleare, Turin, Italy; [3] Università di Pisa, Pisa, Italy; [4] Istituto Nazionale di Fisica Nucleare, Pisa, Italy; [5] Fondazione Bruno Kessler, Trento, Italy

Abstract

Thin segmented silicon sensors have attracted increasing interest for beam monitoring and microdosimetry in emerging radiotherapy modalities such as FLASH and spatially fractionated radiotherapy, owing to their excellent temporal response, high spatial precision, and robustness. In this study, thin planar silicon sensor manufactured by Fondazione Bruno Kessler and implementing different electrode-isolation strategies were investigated through electrical characterization and irradiation tests under ultra-high dose rate electron beams. The investigated devices included sensors with two different trench technologies, which were compared with segmented silicon detectors based on p-stop and Junction Termination Extension isolation techniques. Electric characterization was performed through current-voltage and capacitance-voltage measurements to extract relevant operational parameters. In addition, the detectors were exposed to electron beams delivered by a LINAC at dose-per-pulse values of 2.2 Gy in a 4μs pulse. Preliminary results showed comparable electrical performance for all detector technologies, with leakage currents in the nanoampere range and stable operation up to 200 V bias voltage. Nevertheless, segmented sensor without trench isolation exhibited deviations between collected charge and pad areas ratios, suggesting geometry-dependent contributions to charge collection, likely related to perimeter effects. Ongoing studies aim to evaluate whether trench isolation mitigates these effects and improves sensitive volume definition, as well as to assess the radiation hardness of the proposed detector technologies.

NSS-28-05

Development and Electrical Performance Characterization of 3D Column-Trench Detector (#2488)

Huimin Ji[1,2], **Huimin Ji**[1,2], Manwen Liu[1,2], Manwen Liu[1,2], Zhihua Li[1,2], Zhihua Li[1,2], Xiaohui Li[4], Xiaohui Li[4], Jun Luo[1,2], Jun Luo[1,2]

[1] the Key Laboratory of Fabrication Technologies for Integrated Circuits, Chinese Academy of Sciences, Beijing, China; [2] the Institute of Microelectronics, Chinese Academy of Sciences, Beijing, China; [3] University of Chinese Academy of Sciences, the School of Integrated Circuits, Beijing, China; [4] Institute of High Energy Physics, Chinese Academy of Sciences, Beijing, China

This work was supported in part by the National Natural Science Foundation of China under Grant 12375188 and in part by the National Key Research and Development Program of China under Grant 2023YFF0719600.

Abstract

In this work, a novel 3D column-trench detector based on a 30 $\mu $m thick high-resistivity P-type epitaxial silicon is proposed and experimentally validated. The detector is fabricated on the standard CMOS process platform of the Institute of Microelectronics, Chinese Academy of Sciences (IMECAS), featuring a hybrid 3D configuration that combines N-type column electrodes and P-type strip trench electrodes. Electrical characterizations performed on single-pixel device with central N-type electrode demonstrate that the proposed detector achieves a low leakage current of 0.3 nA and a small capacitance of 0.3 pF under a reverse bias voltage of 30 V. According to the analysis of current-voltage (IV) and capacitance-voltage (CV) characteristics, the device exhibits a full depletion voltage of approximately 3 V and a high breakdown voltage up to 130 V. In addition, the device design, layout, and electrical performance of the 3DCTS are systematically elaborated in this paper. The electrical test results indicate that the proposed device possesses promising application prospects in high-energy physics experiments, medical imaging, and space radiation detection.

References

[1] S. Parker, C. Kenney, and J. Segal, “3D — A proposed new architecture for solid-state radiation detectors,” *Nuclear Instruments and Methods in Physics Research Section A: Accelerators, Spectrometers, Detectors and Associated Equipment*, vol. 395, no. 3, pp. 328–343, 1997, proceedings of the Third International Workshop on Semiconductor Pixel Detectors for Particles and X-rays.

[2] C. Kenney, S. Parker, J. Segal, and C. Storment, “Silicon detectors with 3D electrode arrays: fabrication and initial test results,” *IEEE Transactions on Nuclear Science*, vol. 46, no. 4, pp. 1224–1236, 1999.

[3] M. Liu, T. Zhou, and Z. Li, “Electrical properties of ultra-fast 3d-trench electrode silicon detector,” *Micromachines*, vol. 11, no. 7, 2020.

[4] A. Montalbano, D. Bassignana, Z. Li, S. Liu, D. Lynn, G. Pellegrini, and D. Tsybychev, “A systematic study of bnl’s 3d-trench electrode detectors,” *Nuclear Instruments and Methods in Physics Research Section A: Accelerators, Spectrometers, Detectors and Associated Equipment*, vol. 765, pp. 23–28, 2014, hSTD-9 2013 - Proceedings of the 9th International ”Hiroshima” Symposium on Development and Application of Semiconductor Tracking Detectors.

NSS-28-06

Large-Area Silicon Pixel Sensor Processing on 8-Inch High-Resistivity Wafers (#2906)

Juha Kalliopuska, Jussi Marles, Sampson Andoh, Mikko Ilosalo, Naresh Giri, Olena Shtepura, Magdalena Järvenpää, Sami Vähänen

ADVAFAB, Helsinki, Finland

Abstract

The transition from 6-inch to 8-inch high-resistivity silicon wafer processing has been implemented for the fabrication of large-area pixel sensors for photon-counting applications. The upgraded production line enables a doubling of usable wafer area compared to conventional 6-inch wafers, allowing either larger sensor formats or increased number of sensors per wafer. Prototype 8- inch wafers were processed using stepper lithography with stitching to realize multiple sensor layouts compatible with Medipix3, Timepix3 and Timepix4 readout ASICs. Electrical characterization was performed prior to under-bump metallization (UBM) and flip-chip assembly. Leakage currents at a reverse bias of -300 V were compared with reference data from 6-inch production batches of 500 µm thick sensors. An approximately 60% increase in leakage current for sensors fabricated on 8-inch wafers is attributed to a non-uniform radial resistivity distribution observed in the prototype 8-inch material.

8-inch wafer processing has been successfully demonstrated for silicon pixel sensor fabrication. The process is compatible with existing 6-inch technology and supports large-area sensor production. Although an increased leakage current was observed due to resistivity non-uniformity, the results confirm the feasibility of the approach. Future 8-inch production wafers are expected to have an improved resistivity profile, which is anticipated to reduce the leakage current and improve sensor uniformity.

References

[1] R. Ballabriga, M. Campbell, and X. Llopart, “Asic developments for radiation imaging applications: The medipix and timepix family,” Nucl. Instrum. Methods Phys. Res. A, vol. 878, pp. 10–23, Jan. 2018, 10.1016/j.nima.2017.07.029.

[2] R. Ballabriga, M. Campbell, and X. Llopart, “An introduction to the Medipix family ASICs,” Radiat. Meas., vol. 136, pp. 1–3, Aug. 2020, Art no. 106271, 10.1016/j.radmeas.2020.106271.

[3] T. Poikela, J. Plosila, T. Westerlund, M. Campbell, M. De Gaspari, X. Llopart, et al., Timepix3: a 65K channel hybrid pixel readout chip with simultaneous ToA/ToT and sparse readout, J. Instrum., vol. 9, no 5, pp. 1–8, May 2014, Art. no. C05013, 10.1088/1748-0221/9/05/C05013.

[4] T. Poikela, J. Plosila, T. Westerlund, M. Campbell, M. De Gaspari, X. Llopart, et al.,“ Timepix4, a large area pixel detector readout chip which can be tiled on 4 sides providing sub-200 ps timestamp binning,” J. Instrum, vol. 17, no.1, pp. 1–13, Jan. 2022, Art. no. C01044, 10.1088/1748-0221/17/01/C01044.

NSS-28-07

Results from irradiated nLGAD sensors (#1742)

Marco Ferrero[1], Valentina Sola[2,1], Giovanni Paternoster[3], Arianna Morozzi[4], Anna Rita Altamura[2,1], Roberta Arcidiacono[5,1], Ashish Bisht[3], Maurizio Boscardin[3], Nicolò Cartiglia[1], Matteo Centis Vignali[3], Marco Costa[2,1], Tommaso Croci[4], Alessandro Fondacci[4], Simone Galletto[2], Omar Hammad Ali[3], Leonardo Lanteri[2,1], Ludovico Massaccesi[2,1], Francesco Moscatelli[6,4], Maria Margherita Obertino[2], Daniele Passeri[7,4], Nadia Pastrone[1], Federico Siviero[1], Marta Tornago[2,1], Robert White[1]

[1] Istituto Nazionale di Fisica Nucleare (INFN), INFN Torino, Torino, Italy; [2] Università degli Studi di Torino, Department of Physics, Torino, Italy; [3] Fondazione Bruno Kessler, Trento, Italy; [4] Istituto Nazionale di Fisica Nucleare (INFN), INFN Perugia, Perugia, Italy; [5] Università degli Studi del Piemonte Orientale, Novara, Italy; [6] 6CNR-IOM, Sede secondaria di Perugia, Perugia, Italy; [7] Università degli Studi di Perugia, Perugia, Italy

This project has received funding from the European Union's Horizon 2020 research and innovation programme under Grant Agreements Nos 101004761 (AIDAinnova) and 101057511 (EURO-LABS), the European Union – Next Generation EU, Mission 4 Component 1 CUP D53D23002870001 (Comon-Sens), the European Union (ERC, CompleX, 101124288), and the INFN CSN5 through the "eXFlu" research project. Views and opinions expressed are however those of the authors only and do not necessarily reflect those of the European Union or the European Research Council. Neither the European Union nor the granting authority can be held responsible for them.

Abstract

This contribution will present the first results on the radiation resistance of p-in-n Low-Gain Avalanche Diodes (nLGAD) produced at Fondazione Bruno Kessler (FBK), where signal multiplication is achieved through a high-concentration n-type dopant implant. The sensors are fabricated on thin epitaxial n-type substrates with an active thickness of 55 µm and incorporate a redesigned p^{++} ohmic contact and n^{+} gain layer, optimized to account for dopant activation and diffusion effects. Fourteen wafers were produced, exploring different implant depths, diffusion profiles, and employing two n-type dopants, Phosphorus and Arsenic. These devices provide a unique platform to study the donor removal mechanism at concentrations of ~10^{16} atoms/cm³, offering key input for the development of radiation-hard p^{+}–n^{+} compensated LGADs for operation at extreme fluences. We will present the first results on nLGAD sensors irradiated with neutrons in the fluence range 10^{14}–10^{15} n_{eq}/cm². The characterization pre- and post-irradiation focuses on the evolution of gain and charge collection, providing a first direct assessment of the radiation hardness of nLGAD in this fluence regime. The study of the radiation resistance of the gain layer will be further supported by the characterization of the n^{+} implant, through the characterization of irradiated Van der Pauw structures.

References

[1] G. Pellegrini *et al.*, "Technology developments and first measurements of Low Gain Avalanche Detectors (LGAD) for high energy physics applications", Nucl. Instrum. Methods A, vol. 765, pp. 12-16, Nov. 2014, DOI: 10.1016/j.nima.2014.06.008 [Online].

[2] M. Ferrero *et al.*, "An introduction to ultra-fast silicon detectors", CRC Press (2001) p. 184, DOI: 10.1201/9781003131946 [Online].

[3] V. Sola *et al.*, "A compensated design of the LGAD gain layer", Nucl. Instrum. Methods A, vol. 1040, no. 167232, Oct. 2022, DOI: 10.1016/j.nima.2022.167232

[4] V. Sola *et al.*, "The first batch of compensated LGAD sensors", Nucl. Instrum. Methods A, vol. 1064, no. 169453, Jul. 2024, DOI: 10.1016/j.nima.2024.169453

[5] A. Fondacci *et al.*, "TCAD investigation of Compensated LGAD Sensors for extreme fluence", Nucl. Inst. Methods A, vol. 1068, no. 169811, Nov. 2024, DOI: 10.1016/j.nima.2024.169811
[6] T. Croci *et al.*, "Enhancing guard-ring protection structures for the next generation of radiation-hard thin silicon particle detectors", Nucl. Instrum. Methods A, vol. 1080, no. 170753, Nov. 2025, DOI: 10.1016/j.nima.2025.170753
[7] V. Sola *et al.*, "Preliminary results from the first NLGAD batch of FBK", 17th Topical Seminar on Innovative Particle and Radiation Detectors – IPRD25, Siena (Italy).
[8] L. Massaccesi *et al.*, "Characterisation of the first 55 µm thick nLGAD sensors from FBK", 21st "Trento" Workshop on Advanced Silicon Radiation Detectors – TREDI 2026, Perugia (Italy).
[9] A. Fondacci *et al.*, "Compensated LGAD optimisation through van der Pauw test structures", Nucl. Inst. Methods A, vol. 1080, no., 170800, Nov. 2025, DOI: 10.1016/j.nima.2025.170800

NSS-28-08

Insights into DC-coupled Resistive Silicon Detector (DC-RSD) results

(#2041)

Marco Ferrero[1], Roberta Arcidiacono[2,1], Nicolò Cartiglia[1], Giulio Bardelli[3], Maurizio Boscardin[4,5], Matteo Centis Vignali[4,5], Antonio Cassese[3], Tommaso Croci[6], Alessandro Fondacci[9,6], Omar Hammad Ali[4,5], Matteo Durando[2,1], Arianna Morozzi[6], Luca Menzio[7], Francesco Moscatelli[8,6], Daniele Passeri[9,6], Giacomo Sguazzoni[3], Federico Siviero[1], Valentina Sola[10,1], Lorenzo Viliani[3], Giovanni Paternoster[4,5]

[1] Istituto nazionale di Fisica Nucleare (INFN), INFN Torino, Torino, Italy; [2] Università del Piemonte Orientale, Novara, Italy; [3] Istituto nazionale di Fisica Nucleare (INFN), INFN Firenze, Firenze, Italy; [4] Fondazione Bruno Kessler, Povo, Italy; [5] TIFPA-INFN, Trento, Italy; [6] Istituto nazionale di Fisica Nucleare (INFN), INFN Perugia, Perugia, Italy; [7] CERN, Meyrin, Switzerland; [8] CNR-IOM, CNR Perugia, Perugia, Italy; [9] Università degli Studi di Perugia, Perugia, Italy; [10] Università degli Studi di Torino, Torino, Italy

This work has received funding from: INFN CSN5 through the 4DSHARE research project; European Union-Next Generation EU, Mission 4 component 2, CUP C53D23001510006 (project 2022KLK4LB); European Union's Horizon Europe Research and Innovation program Grant Agreement No 101057511 (EURO- LABS).

Abstract

Recent progress in sensor technology has paved the way for high-resolution 4D-tracking silicon detectors capable of simultaneously measuring position and time of passage of charged particles. This is achieved through the innovative concepts of Low Gain Avalanche Diodes (LGAD) and Resistive Silicon Detectors (RSD). While standard LGADs aim at excellent temporal resolution, the RSD design also achieves high spatial resolution through signal sharing. This contribution presents the latest advancements in the DC-coupled RSD (DC-RSD) design, which utilizes trenches for cell isolation and signal sharing control. A major milestone of the 2026 campaign is the integration of the FAST3 ASIC, a custom-designed chip specifically optimized for high-precision timing measurements with LGAD-based sensors. For the first time, this readout electronics is employed to characterize the performance of DC-RSD sensors in a test beam environment before and after radiation exposure. We will present the results of an experimental campaign conducted on DC-RSD sensors irradiated at fluences 2×10^{14} and 4×10^{14} neq/cm². These measurements will represent the first test beam characterization performed on irradiated DC-RSD sensors. The analysis focuses on the evolution of timing and spatial resolution as a function of fluence,

comparing the performance of the FAST3 chip with previous readout solutions. The results, obtained at the DESY and CERN test beam facilities, offer insights into the radiation hardness and robustness of the DC-RSD principle.

References
[1] ECFA Detector R&D Roadmap Process Group, “The 2021 ECFA detector research and development roadmap”, ISBN: 978-92-9083-614-8, doi: 10.17181/CERN.XDPL.W2EX
[2] R. Arcidiacono et al, “High-accuracy 4D particle trackers with resistive silicon detectors (AC-LGAD)”, JINST, vol. 1040, No. C03013, Mar. 2022, DOI: 10.1088/1748-0221/17/03/C03013
[3] M. Tornago *et al.*, "Resistive AC-Coupled Silicon Detector principles of operation and first results from beam test and laser combined analysis", Nucl. Instrum. Methods A, vol. 1003, no. 165319, Jul. 2021, DOI: 10.1016/j.nima.2021.165319
[4] R. Arcidiacono *et al.*, "High precision 4D tracking with large pixels using thin resistive silicon detectors", Nucl. Instrum. Methods A, vol. 1057, no. 168671, Dec. 2023, DOI: 10.1016/j.nima.2023.168671
[5] F. Moscatelli *et al.*, "Measurements and TCAD simulations of innovative RSD and DC-RSD LGAD devices for future 4D tracking", Nucl. Instrum. Methods A, vol. 1064, no. 169380, Jul. 2024, DOI: 10.1016/j.nima.2024.169380
[6] R. Diener *et al.*, " The DESY II Test Beam Facility", Nucl. Instrum. Methods A, vol. 922, pp. 265-286, Apr. 2019, DOI: 10.1016/j.nima.2018.11.133
[7] M. Ferrero *et al.*, "FAST3 ASIC: an analog front-end with 30 ps resolution, designed to readout thin Low Gain Avalanche Diodes", JNST, vol. 20, no. C03007, Mar. 2025, DOI: 0.1088/1748-0221/20/03/C03007

Time:
12 November, 2026
17:30 – 19:00

Room:
FEDERICO GARCÍA LORCA

NSS-29 | NSS closing session and Student Paper Awards

Chairs:
Audrey Corbeil Therrien (Sherbrooke)
Giulia Hull (Orsay)

NSS-29-01

Summary of the conference

NSS-29-02

Student Paper Awards - Runner-Up Poster presentation

NSS-29-03

Runner-up Poster Presentation

NSS-29-04

Student Paper Awards - Winner Poster presentation

NSS-29-05

Winner Poster Presentation

NSS-29-06

Student Paper Awards - Runner-Up Oral Presentation

NSS-29-07

Runner-up Oral Presentation

NSS-29-08

Student Paper Awards - Winner Oral Presentation

NSS-29-09

Winner Oral Presentation

NSS-29-10

Closing and passing to NSS 2027

MIC

11 November, 2026

Time:
11 November, 2026
9:00 – 11:00

Room:
FEDERICO GARCÍA LORCA

MP-01 | MIC Plenary Session 1

Chairs:
Vesna Sossi (Vancouver)
Roger Fulton (Sydney)

MP-01-01

Opening ceremony; General Chair and MIC welcome (#3353)

Stefan Ritt[1], **Vesna Sossi**[2], **Roger Fulton**[3]

[1] Paul Scherrer Institute (PSI), Villigen, Switzerland; [2] University of British Columbia, Vancouver, Canada; [3] University of Sydney, Sydney, Australia

MP-01-02

Marie Sklodowska-Curie Technical Field Award Introduction (#3354)

Sara A. Pozzi

University of Michigan, Ann Arbor, USA

MP-01-03

Marie Sklodowska-Curie Technical Field Awardee Presentation | Decoding the Cancer Ecosystem Through Multiscale Imaging for Precision Medicine (#3355)

Irene Buvat

Institut Curie, PSL University, Inserm, Orsay, France

MP-01-04

NPSS Richard F. Shea Distinguished Member Awardee Announcement (#3356)

Steven R. Meikle

The University of Sydney, Sydney, Australia

MP-01-05

NPSS Richard F. Shea Distinguished Member Presentation (#3357)

Tba Tba

TBA, TBA, Germany

MP-01-06

Edward J. Hoffman Early Career Development Grant Introduction (#3358)

Steven R. Meikle

The University of Sydney, Sydney, Australia

MP-01-07

Edward J. Hoffman Early Career Development Grant Presentation (#3359)

Tba Tba

Tba, Tba, Germany

MP-01-08

Ronald J. Jaszczak Graduate Award Introduction (#3360)

Steven R. Meikle

The University of Sydney, Sydney, Australia

MP-01-09

Ronald J. Jaszczak Graduate Award Presentation (#3361)

Tba Tba

Tba, Tba, Germany

MP-01-10

Glenn F. Knoll Post Doctoral Educational Grant Introduction (#3362)

Steven R. Meikle

The University of Sydney, Sydney, Australia

MP-01-11

Glenn F. Knoll Post Doctoral Educational Grant Presentation (#3363)

Tba Tba

Tba, Tba, Germany

MP-01-12

NPSS Glenn F. Knoll Graduate Educational Grant Introduction (#3364)

Steven R. Meikle

The University of Sydney, Sydney, Australia

MP-01-13

NPSS Glenn F. Knoll Graduate Educational Grant Presentation (#3365)

Tba Tba

Tba, Tba, Germany

MP-01-14

NPSS Graduate Scholarship Award Introduction (#3434)

Steven R. Meikle

The University of Sydney, Sydney, Australia

MP-01-15

NPSS Graduate Scholarship Award Introduction Presentation (#3435)

Steven R. Meikle

The University of Sydney, Sydney, Australia

MP-01-16

Awardee Introductions: Jordanov Awards and Phelps Grants (#3366)

Lorenzo Fabris

Oak Ridge National Laboratory, Oak Ridge, USA

Time:
11 November, 2026
11:30 – 12:45

Room:
FEDERICO GARCÍA LORCA

MIC-01 | Advanced tomographic reconstruction techniques (1)

Chairs:
Andrew J. Reader (London)

MIC-01-01

3D Diffusion Posterior Sampling with Patient-Specific PET Priors for Ultra-Low-Count SPECT in alpha therapy (#2448)

Alejandro Lopez-Montes[1,2], Astrid Delker[3], Kamo Ramonaheng[4,5], Dennis Groschupf[3], Robert Seifert[1], Sandra Resch[3], Axel Rominger[1], Guido Boening[3], Mike Sathekge[4,5], Ali Afshar-Oromieh[1], Kuangyu Shi[1,2]

[1] University of Bern, Department of Nuclear Medicine, Bern, Switzerland; [2] University of Bern, Department of Digital Medicine, Bern, Switzerland; [3] Ludwig Maximillian University, Department of Nuclear Medicine, Munich, Germany; [4] University of Pretoria, Department of Nuclear Medicine, Pretoria, South Africa; [5] Steve Biko Hospital, Nuclear Medicine Research Infrastructure (NuMeRI), Pretoria, South Africa

Abstract

Ultra-low-count SPECT imaging in alpha-particle radiopharmaceutical therapy (α-RPT) remains challenged by low administered activities and severe noise amplification associated with conventional reconstruction. We propose a fully three-dimensional diffusion posterior sampling (3D-DPS) framework for physics-informed SPECT reconstruction integrating learned generative priors with a Poisson-consistent likelihood formulation for emission tomography. A 3D unconditional diffusion model was trained on PSMA PET volumes to learn tracer uptake distributions. To further constrain the inverse problem, patient-specific prior adaptation was introduced through synthetic subject-specific uptake realizations designed to model physiologically plausible tracer variability during training. During reconstruction, the learned priors are coupled with a physics-based SPECT forward model through a Poisson log-likelihood formulation consistent with MLEM reconstruction. Validation was performed using realistic ultra-low-count ^{225}Ac-PSMA simulations, as well as two clinical ^{177}Lu-PSMA SPECT acquisitions retrospectively degraded to mimic ^{225}Ac imaging conditions using Poisson thinning (~10^5 detected photons) and angular downsampling (120 to 30 projections). Compared with MLEM and regularized MLEM, the proposed framework reduced reconstruction error (NMAE = 0.34 ± 0.04 versus 0.53 ± 0.02 and 0.41 ± 0.05, respectively) and improved structural similarity (SSIM = 0.90 ± 0.05 versus 0.77 ± 0.13 and 0.85 ± 0.08, respectively) while preserving anatomical detail and projection-domain consistency. Reconstructions from degraded clinical acquisitions demonstrated substantially improved noise suppression and lesion preservation compared with conventional reconstruction. These results demonstrate the potential of diffusion-based reconstruction for quantitative ultra-low-count SPECT imaging and α-RPT dosimetry.

References

[1] Gosewisch A, Schleske & M, Gildehaus FJ, et al. Image-based dosimetry for 225 Ac-PSMA-I&T therapy using quantitative SPECT. *Eur J Nucl Med Mol Imaging*. 2021;48:1260-1261. doi:10.1007/s00259-020-05024-1

[2] Sathekge MM, Lawal IO, Bal C, et al. Actinium-225-PSMA radioligand therapy of metastatic castration-resistant prostate cancer (WARMTH Act): a multicentre, retrospective study. *Lancet Oncol*. 2024;25(2):175-183. doi:10.1016/S1470-2045(23)00638-1

[3] Liubchenko G, Böning G, Zacherl M, et al. Image-based dosimetry for [225Ac]Ac-PSMA-I&T therapy and the effect of daughter-specific pharmacokinetics. *Eur J Nucl Med Mol Imaging*. 2024;51(8):2504-2514. doi:10.1007/s00259-024-06681-2

[4] Lopez-Montes A, Yousefirizi F, Chen Y, Salimi Y, Seifert R, Afshar-Oromieh A, Uribe C, Rominger A, Zaidi H, Rahmim A, Shi K. Artificial Intelligence for Simplified Patient-centered Dosimetry in Radiopharmaceutical Therapies. PET Clin. 2026 Jan;21(1):73-88. doi: 10.1016/j.cpet.2025.09.010. PMID: 41271260.

[5] Rahmim A, Zaidi H. PET versus SPECT: strengths, limitations and challenges. *Nucl Med Commun*. 2008;29(3):193-207. doi:10.1097/MNM.0b013e3282f3a515

[6] Marquis H, Willowson KP, Schmidtlein CR and Bailey DL (2023) Investigation and optimization of PET-guided SPECT reconstructions for improved radionuclide therapy dosimetry estimates. Front. Nucl. Med. 3:1124283. doi: 10.3389/fnume.2023.1124283

[7] Chung H, Kim J, Mccann MT, Klasky ML, Ye JC. Diffusion Posterior Sampling for General Noisy Inverse Problems. In: *International Conference on Learning Representations*. 2023 https://doi.org/10.48550/arXiv.2209.14687
[8] Song YS, Sohl-Dickstein J, Brain G, et al. Score-Based Generative Modeling through Stochastic Differential Equations. In: *International Conference on Learning Representations*. 2021. https://doi.org/10.48550/arXiv.2011.13456
[9] Lopez-Montes A, Seifert R, Delker A, et al. Patient-specific AI for generation of 3D dosimetry imaging from two 2D-planar measurements. In: *IEEE NSS/MIC* ; 2025. https://doi.org/10.48550/arXiv.2510.21362

MIC-01-02

Joint Reconstruction of Activity and Attenuation with Motion Estimation in PET using Diffusion Models (#1403)

Clémentine Phung-Ngoc[1,2], **Clémentine Phung-Ngoc**[1,2], Antoine De Paepe[1], Antoine De Paepe[1], Hong-Phuong Dang[3], Hong-Phuong Dang[3], Olivier Saut[2,4], Olivier Saut[2,4], Dimitris Visvikis[1], Dimitris Visvikis[1], Alexandre Bousse[1], Alexandre Bousse[1]

[1] Univ. Brest, LaTIM, Inserm UMR 1101, Brest, France; [2] Inria Center, Univ. Bordeaux, MONC Project-Team, Talence, France; [3] CentraleSupélec, IETR, CNRS UMR 6164, Cesson-Sévigné, France; [4] Mathematics Institute of Bordeaux, UMR 5251, Univ. Bordeaux, CNRS, Bordeaux INP, Talence, France

This work was supported by the French National Institute of Health and Medical Research (Inserm) and by the French Institute for Research in Computer Science and Automation (Inria).

Abstract

Respiratory motion and attenuation mismatch degrade positron emission tomography (PET) reconstruction. Furthermore, the additional scan required for attenuation correction (AC) may complexify the imaging workflow and increase radiation exposure. Joint reconstruction of activity and attenuation with motion estimation (JRAAM) methods address these issues by jointly estimating activity, attenuation, and motion solely from emission data. We propose JRAAM-DPS, a diffusion model (DM)-based framework that leverages a diffusion prior on activity–attenuation image pairs to recover motion-compensated and attenuation-corrected PET images directly from respiratory-gated PET data. We evaluated the proposed method on simulated data, and demonstrated improved image quality compared to maximum likelihood activity and attenuation (MLAA) and the non-motion-corrected JRAA-DPS

References
[1] Bousse, A., Bertolli, O., Atkinson, D., Arridge, S., Ourselin, S., Hutton, B. F., & Thielemans, K. (2015). Maximum-likelihood joint image reconstruction/motion estimation in attenuation-corrected respiratory gated PET/CT using a single attenuation map. *IEEE transactions on medical imaging*, *35*(1), 217-228.
[2] Rezaei, A., Defrise, M., Bal, G., Michel, C., Conti, M., Watson, C., & Nuyts, J. (2012). Simultaneous reconstruction of activity and attenuation in time-of-flight PET. *IEEE transactions on medical imaging*, *31*(12), 2224-2233.
[3] Phung-Ngoc, C., Bousse, A., De Paepe, A., Merlin, T., Laurent, B., Dang, H. P., ... & Visvikis, D. (2025). Joint reconstruction of activity and attenuation in PET by diffusion posterior sampling in wavelet coefficient space. *arXiv preprint arXiv:2505.18782*.
[4] Elhamiasl, M., Jolivet, F., Rezaei, A., Fieseler, M., Schäfers, K., Nuyts, J., ... & Boada, F. (2025). Joint estimation of activity, attenuation and motion in respiratory-self-gated time-of-flight PET. *Physics in Medicine & Biology*, *70*(7), 075003.
[5] Chung, H., Kim, J., Mccann, M. T., Klasky, M. L., & Ye, J. C. (2022). Diffusion posterior sampling for general noisy inverse problems. *arXiv preprint arXiv:2209.14687*.

[6] De Paepe, A., Bousse, A., Phung-Ngoc, C., & Visvikis, D. (2025). Solving blind inverse problems: Adaptive diffusion models for motion-corrected sparse-view 4DCT. *arXiv preprint arXiv:2501.12249*.
[7] Cao, Y. H., Bourbonne, V., Lucia, F., Schick, U., Bert, J., Jaouen, V., & Visvikis, D. (2024). CT respiratory motion synthesis using joint supervised and adversarial learning. *Physics in Medicine & Biology*, *69*(9), 095001.
[8] Schramm, G., & Thielemans, K. (2024). PARALLELPROJ—an open-source framework for fast calculation of projections in tomography. *Frontiers in Nuclear Medicine*, *3*, 1324562.

MIC-01-03

Flow Models for PET Image Reconstruction (#1883)

George Webber[1], Alexander Hammers[2,1], Andrew P. King[1], Andrew J. Reader[1]

[1] King's College London, School of Biomedical Engineering and Imaging Sciences, London, UK; [2] Guy's and St Thomas' PET Centre, London, UK

G. Webber was funded by the EPSRC CDT in Smart Medical Imaging [EP/S022104/1] and by a GSK Studentship.
G. Webber (george.webber@kcl.ac.uk), A. P. King and A. J. Reader are with the School of Biomedical Engineering and Imaging Sciences, King's College London, UK.
A. Hammers is with the King's College London & Guy's and St Thomas' PET Centre.

Abstract

Flow-based generative models can be used as pre-trained priors for inverse problems; however, their use in PET image reconstruction remains largely unexplored. We present a proof-of-principle study using flow priors for 2D PET reconstruction. A U-Net was trained by flow matching on simple brain phantoms and used as an unconditional image prior. We used the MPC-Flow (Model Predictive Control) framework to condition the pre-trained flow via direct control of the generative dynamics, and adapted it to the PET setting by incorporating a Poisson likelihood and an explicit intensity scaling to address the dynamic range mismatch between the generative model and PET data. This method was used to reconstruct images from simulated low-count PET sinogram data. On held-out phantoms, MPC-Flow achieved lower error than diffusion-based reconstruction and conventional iterative baselines, likely due to the explicit control objective, which balances likelihood maximization with a penalty on deviations from the learned flow trajectory. These results demonstrate that flow priors can be coupled with PET likelihoods in a principled framework. Evaluation on more realistic anatomical phantoms and clinical data, where the learned manifold may be less accurate, will be a necessary next step.

References
[1] Singh, IRD, Denker, A, Barbano, R, Kereta, Ž, Jin, B, Thielemans, K, Maass, P & Arridge, S 2024, 'Score-based generative models for PET image reconstruction', *Machine Learning for Biomedical Imaging*, vol. 2, pp. 547–585.
[2] Webber, G, Mizuno, Y, Howes, OD, Hammers, A, King, AP & Reader, AJ 2025, 'Likelihood-scheduled score-based generative modeling for fully 3D PET image reconstruction', *IEEE Transactions on Medical Imaging*, vol. 44, no. 11, pp. 4445–4456.
[3] Lipman, Y, Chen, RTQ, Ben-Hamu, H, Nickel, M & Le, M 2023, 'Flow Matching for Generative Modeling', in *The Eleventh International Conference on Learning Representations (ICLR 2023)*, Kigali, Rwanda.
[4] Liu, X, Gong, C & Liu, Q 2023, 'Flow Straight and Fast: Learning to Generate and Transfer Data with Rectified Flow', in *The Eleventh International Conference on Learning Representations (ICLR 2023)*, Kigali, Rwanda.
[5] Webber, G, Denker, A, Barbano, R & Reader, AJ 2026, 'Solving Inverse Problems with Flow-based Models via Model Predictive Control', *arXiv*, arXiv:2601.23231.
[6] Schramm, G & Thielemans, K 2024, 'PARALLELPROJ—an open-source framework for fast calculation of projections in tomography', *Frontiers in Nuclear Medicine*, vol. 3, art. 1324562.

[7] Wang, G & Qi, J 2012, 'Penalized likelihood PET image reconstruction using patch-based edge-preserving regularization', *IEEE Transactions on Medical Imaging*, vol. 31, no. 12, pp. 2194–2204.

MIC-01-04

Flow Matching for PET Image Reconstruction (#1731)

Fumio Hashimoto, Ziqian Huang, Kuang Gong

University of Florida, Gainesville, USA

Abstract

Generative models, especially diffusion models, have recently demonstrated strong potential for positron emission tomography (PET) image reconstruction. However, diffusion models often require many sampling steps and incur a high computational cost, which may limit their practical use in PET image reconstruction. Flow matching is an attractive alternative, enabling continuous generative modeling with a simpler sampling procedure and a stable, efficient training framework. In this study, we present flow matching-based PET image reconstruction methods. We first establish PET-FlowDPS as a baseline by incorporating Poisson likelihood guidance into the FlowDPS framework. We then propose a model-based PET image reconstruction method that uses a pretrained flow matching model as a prior. The proposed reconstruction method iteratively performs three steps: (1) flow-based destination estimation to obtain a clean image estimate, (2) penalized PET image reconstruction refinement to enforce data consistency, and (3) flow-based propagation to update the image to the next time step. The proposed reconstruction method was evaluated using 10 low-dose clinical brain [^{18}F]FDG datasets. Experimental results showed that the flow matching-based methods reduced image noise while preserving cortical structures compared with the maximum *a posteriori* expectation-maximization (MAPEM) algorithm. The proposed method further improved image quality compared with PET-FlowDPS in terms of PSNR. In addition, the computation time of the proposed method was less than 2 minutes. These results demonstrate that flow matching is a promising generative prior for PET image reconstruction.

References

[1] I. R. Singh et al., "Score-Based Generative Models for PET Image Reconstruction," Mach. Learn. for Biomed. Imaging, vol. 2, pp. 547–585, 2024.

[2] F. Hashimoto and K. Gong, "PET Image Reconstruction Using Deep Diffusion Image Prior," IEEE Trans. Med. Imaging, pp. 1–1, 2026.

[3] X. Liu, C. Gong, and Q. Liu, "Learning to Generate and Transfer Data with Rectified Flow," in Proc. ICLR, 2023.

[4] J. Kim, B. S. Kim, and J. C. Ye, "FlowDPS: Flow-Driven Posterior Sampling for Inverse Problems," in Proc. ICCV, 2025, pp. 12 328–12 337

[5] M. Pourya, B. E. Rawas, and M. Unser, "Flower: A Flow-Matching Solver for Inverse Problems," in Proc. ICLR, 2026.

[6] S. D. Jamadar et al., "Monash DaCRA fPET-fMRI: A dataset for comparison of radiotracer administration for high temporal resolution functional FDG-PET," GigaScience, vol. 11, p. giac031, 01 2022.

[7] G. Schramm and K. Thielemans, "PARALLELPROJ—an open-source framework for fast calculation of projections in tomography," Front. Nucl. Med., vol. Volume 3 - 2023, 2024.

MIC-01-05

Data-Driven Kernel EM Reconstruction Using Attention-Based Learning for Dynamic PET (#3168)

Haoran Chang[1], Wenyuan Qi[2], Jeff Kolthammer[2], Jinyi Qi[1]

[1] University of California, Davis, Biomedical Engineering, Davis, USA; [2] Canon Medical Research USA, Vernon Hills, USA

Abstract

Dynamic positron emission tomography (PET) reconstruction remains challenging due to low count statistics in individual frames and the ill-posed nature of the inverse problem. Kernelized expectation maximization (KEM) methods have been developed to incorporate prior information through a kernel matrix; however, their performance strongly depends on the design of the kernel and the prior information, as well as the associated hyperparameters. In this work, we propose a data-driven framework for kernel construction based on attention-guided learning from dynamic PET images.

A neural network is used to learn spatial-temporal relationships from dynamic image frames, producing attention maps that encode pairwise similarities. These features are further analyzed via dimensionality reduction and clustering to identify regions of interest (ROIs) with similar spatial-temporal characteristics. The resulting ROI masks are used to define adaptive neighborhoods and compute kernel weights, producing a data-driven kernel that is subsequently integrated into the KEM reconstruction framework.

Experiments on simulated data demonstrate that the proposed method not only improves image quality but also enables accurate estimation of time-activity curves (TACs) across different ROIs. In real PET data, the method achieves enhanced reconstruction quality, while exhibiting reduced sensitivity to the choice of clustering parameters compared with the baseline approach that performs clustering directly on the dynamic PET images without attention-guided learning. In particular, stable reconstruction performance is maintained across a wide range of cluster numbers, whereas baseline approaches show strong parameter dependence and introduce noticeable noise at larger cluster sizes.

These results demonstrate that attention-based kernel learning provides a robust and effective strategy for improving dynamic PET reconstruction quality and quantitative accuracy.

References

[1] G. Wang and J. Qi, "PET Image Reconstruction Using Kernel Method," in *IEEE Transactions on Medical Imaging*, vol. 34, no. 1, pp. 61-71, Jan. 2015, doi: 10.1109/TMI.2014.2343916

[2] S. Li and G. Wang, "Deep Kernel Representation for Image Reconstruction in PET," in *IEEE Transactions on Medical Imaging*, vol. 41, no. 11, pp. 3029-3038, Nov. 2022, doi: 10.1109/TMI.2022.3176002

[3] S. Li, K. Gong, R. D. Badawi, E. J. Kim, J. Qi and G. Wang, "Neural KEM: A Kernel Method With Deep Coefficient Prior for PET Image Reconstruction," in *IEEE Transactions on Medical Imaging*, vol. 42, no. 3, pp. 785-796, March 2023, doi: 10.1109/TMI.2022.3217543

[4] S. Wang, S. Kim, K. P. Cosgrove, E. D. Morris, “A framework for designing dynamic lp-ntPET studies to maximize the sensitivity to transient neurotransmitter responses to drugs: Application to dopamine and smoking,” NeuroImage, Vol. 146, pp. 701–714, 2017

Time:
11 November, 2026
11:30 – 12:45

Room:
MANUEL DE FALLA

MIC-02 | High resolution imaging systems (organ-dedicated, small animal systems (1)

Chairs:
Tianyu Ma (Beijing)
Elena Maria Zannoni (Austin)

MIC-02-01

Development and Evaluation of Gym-PET for Functional Brain Imaging of Awake Running Mice (#2398)

Xin Yu[1], **Xin Yu**[1], Han Liu[1], Han Liu[1], Da Liang[1], Da Liang[1], Wenjing Zhu[1], Wenjing Zhu[1], Wangquan Ma[1], Wangquan Ma[1], Yibin Zhang[1], Yibin Zhang[1], Jinyong Tao[1], Jinyong Tao[1], Huiping Zhao[1], Huiping Zhao[1], Qiyu Peng[1], Qiyu Peng[1]

[1] Shenzhen Bay Laboratory, Shenzhen, China; [2] Shenzhen Bay Laboratory, Shenzhen, China

This work was supported by the National Natural Science Foundation of China (Grant no. 82327809), the National Key Research and Development Program of China (Grant No. 2024YFF0507700), National High-Level Hospital Clinical Research Funding (2025-PUMCH-D-003), Beijing Natural Science Foundation(L252047).

Abstract

Awake functional brain imaging is crucial for behavioral neuroscience, but conventional preclinical PET scanners typically require anesthesia, which suppresses brain glucose metabolism and limits natural behavioral studies. To address these limitations, we developed Gym-PET, a 75 g head-mounted wearable PET system optimized for awake running mice.

The wearable module features a compact detector ring (20.0 mm inner diameter) composed of 1 x 1 x 5 mm³ LYSO crystal arrays coupled to SiPMs, a short crystal design chosen to minimize parallax degradation under close-range conditions. To enable stable imaging during locomotion, the scanner is integrated with a customized treadmill platform using a lightweight suspension mechanism. Based on the NEMA NU-4 2008 standard, the system achieved 12.5% energy resolution, 0.8% peak sensitivity, and a high spatial resolution of 0.66 mm. Compared to conventional preclinical PET systems, Gym-PET demonstrated visibly improved delineation of small subcortical structures.

To validate the system's in vivo capabilities, dynamic 18F-FDG PET imaging was performed. The results successfully captured exercise-induced metabolic activation in the brainstem and thalamus of awake running mice. Furthermore, a three-day sleep deprivation study revealed the system's sensitivity to global metabolic suppression without anesthesia interference. Ultimately, the Gym-PET platform significantly reduces anesthesia-related metabolic interference, establishing a highly effective tool for high-resolution molecular neuroimaging in awake behavioral models.

References

[1] A. Miranda, D. Glorie, D. Bertoglio et al., “Awake 18f-fdg pet imaging of memantine-induced brain activation and test–retest in freely running mice,” Journal of Nuclear Medicine, vol. 60, no. 6, pp. 844–850, 2019.

[2] A. Miranda, S. Staelens, S. Stroobants et al., “Fast and accurate rat head motion tracking with point sources for awake brain pet,” IEEE transactions on medical imaging, vol. 36, no. 7, pp. 1573–1582, 2017.

[3] X. Yu, Z. Zhao, H. Liu, D. Liang, W. Zhu, Y. Lin, J. Zeng, C. Liu, J. Xu, S. Xie, W. Wang, and Q. Peng, “Development and performance evaluation of a benchtop small-animal pet/mri scanner,” IEEE Transactions on Radiation and Plasma Medical Sciences, vol. 9, no. 8, pp. 1118–1126, 2025.

MIC-02-02

Preliminary Validation of Flexible On-Demand Customized Ultra-Resolution System for Targeted Performance Enhancement in Preclinical PET (#3184)

Kexin Wang[1], Runze Liao[1], Ziquan Yuan[1], Yue Chen[1], Yihao Chen[1], Haoqi Wen[1], Chenxi Li[1], Yucun Hou[1], Shenghuan Gong[1], Yuanchuan Tai[2], Jianyong Jiang[1]

[1] Beijing Normal University, Beijing, China; [2] Washington University in St. Louis, Mallinckrodt Institute of Radiology, St. Louis, USA

This work was supported in part by the National Natural Science Foundation of China (No. 12475336), and the Fundamental Research Funds for the Central Universities (No. 310400209521).

Abstract

This study introduces Flexible On-demand Customized Ultra-resolution System for PET (FOCUS-PET), a novel technique designed to maximize spatial resolution and counting statistics within a predefined region of interest. The efficacy of FOCUS-PET was rigorously evaluated via Monte Carlo simulations and physical experiments using high-resolution add-on detector configurations. The simulated system employed an arc-shaped add-on detector comprised of a 4×2 module array, with each module housing 32×48 LYSO crystals (0.42×0.42×5.0 mm³). Sensitivity profiles were mapped using an axially stepped ^{22}Na point source, and a three-bed whole-body protocol was simulated utilizing a micro-Derenzo phantom. Simulation results demonstrated a 5.1% to 19.8% enhancement in absolute sensitivity. The system resolved 0.9-mm micro-rods, effectively surpassing native resolution limits, and improved the peak-to-valley ratio (PVR) and contrast recovery (CR) for 1.0-mm rods from 1.50 to 2.13 and 33.30% to 52.95%, respectively. Experimental validation was performed by integrating a flat-panel add-on detector—comprising two modules with 44×44 LYSO arrays (0.52×0.52×5.0 mm³)—into an ACTIVE 7 MAX preclinical scanner. Imaging of a physical Derenzo phantom was conducted to assess ultimate resolution and multi-bed stitching fidelity. Physical experiments corroborated the theoretical gains, with the flat-panel FOCUS-PET device consistently improving PVR (1.57 to 1.90) and CR (27.93% to 33.19%) for 1.25-mm hot rods compared to the baseline. In conclusion, FOCUS-PET significantly elevates system sensitivity and spatial resolution, providing a cost-effective pathway for ultra-high-resolution preclinical imaging and potential translation to clinical whole-body PET applications.

References
[1] S. Surti, Journal of Nuclear Medicine, vol. 56, pp. 98-105, Jan 2015.
[2] M. Janecek, *et al.*, IEEE Transactions on Nuclear Science, vol. 53, pp. 1143-1149, 2006.
[3] M. Janecek, *et al.*, IEEE Transactions on Nuclear Science, vol. 53, pp. 1143-1149, 2006.
[4] Z. Yuan, *et al.*, Medical Physics, vol. 53, no. 1, pp. e70216, 2026.

MIC-02-03

Initial Performance Characterization of the SAVANT Ultra-High-Resolution Phoswich-Based DOI Brain PET Scanner (#2935)

Roger Lecomte[1,5], Yassir Najmaoui[4,2], Maxime Gaudreault[1], Otman Sarrhini[3], Jean-François Beaudoin[3], Tommy Galarneau[3], Étienne Croteau[3], Éric Lavallée[3], Christian Thibaudeau[5], Romain Espagnet[4], Nicolas Viscogliosi[4], Jonathan Bouchard[4], Arnaud Samson[4], Maxime Toussaint[6], Thibault Marin[2], Yanis Chemli[2], Jean-Baptiste Michaud[4], Marc-André Tétrault[4], Réjean Fontaine[4], Georges El Fakhri[2]

[1] Université de Sherbrooke, Sherbrooke Molecular Imaging Center and Department of Medical Imaging and Radiation Sciences, Sherbrooke, Canada; [2] Yale University School of Medicine, Yale Biomedical Imaging Institute, New Haven, USA; [3] CRCHUS, Sherbrooke Molecular Imaging Center, Sherbrooke, Canada; [4] Université de Sherbrooke, Interdisciplinary Institute for Technological Innovation – 3IT, Sherbrooke, Canada; [5] Imaging Research and Technology (IR&T) Inc., Magog, Canada; [6] Nantes Université, Laboratoire CRCI2NA, INSERM, CNRS, Nantes, France

Abstract

High spatial resolution is essential to resolve small structures in the brain and to enable imaging of neurological pathways at the onset of diseases. A key challenge with ultra-high-resolution (UHR) PET scanners is the significant degradation of resolution that occurs beyond the central area of the field-of-view (FOV). The UHR Brain PET scanner was designed with short (12 mm) LYSO crystals to mitigate the parallax error off the FOV center, but at the expense of reduced sensitivity. To address these limitations, the LabPET II technology platform was upgraded to implement depth-of-interaction (DOI) measurement using longer (15 mm) dual LGSO phoswich detectors in the SAVANT. Simulation results indicate an estimated 40% gain in sensitivity, while maintaining the resolution below 2 mm FWHM at the edge of the brain. For DOI determination, the crystal identification between *slow* (43-48 ns decay time) and *fast* (30-35 ns decay time) LGSO scintillators uses a model-based dual-threshold time-over-threshold (ToT) discrimination technique, currently achieving better than 70% accuracy. The 6.5/8.5 mm length ratio of the top *slow* and bottom *fast* LGSO scintillators resulted from trade-offs between off-center spatial resolution and balanced coincidence detection efficiency of the two crystal layers. We report the initial experimental characterization of the partially assembled scanner (182 mm axial extent), which demonstrate the improvement in sensitivity and resolution uniformity across the radial FOV achieved using this simple DOI discrimination scheme. Point source and phantom measurements taken at various radial positions demonstrate the gain in spatial resolution compared to non-DOI measurements, though not reaching the resolution predicted by simulation. Further refinement of the crystal identification process using AI-based classification is expected to yield the forecasted benefits from simulation. Preliminary results for imaging the human brain will be presented.

References

[1] Gaudin, É., Toussaint, M., Thibaudeau, C., Paille,M., Fontaine, R., Lecomte, R., "Performance Simulation of an Ultrahigh Resolution Brain PET Scanner Using 1.2-mm Pixel Detectors," *IEEE Trans. Radiat. Plasma Med. Sci.*, vol. 3, no. 3, pp. 334–342, May 2019, doi: 10.1109/TRPMS.2018.2877511.

[2] Émilie Gaudin, Maxime Toussaint, Christian Thibaudeau, Réjean Fontaine, Marc D. Normandin, Yoann Petibon, Jinsong Ouyang, Georges N. El Fakhri, Roger Lecomte."Simulation studies of the SAVANT high resolution dedicated brain PET scanner using indi vidually coupled APD detectors and DOI encoding". *Society of Nuclear Medicine and Molecular Imaging (SNMMI) 2019 Annual Meeting*, Anaheim, CA, 22-25 June 2019. (*Journal of Nuclear Medicine*, vol. 60, suppl. 1, p. 531, 1st May 2019)

[3] Émilie Gaudin, Maxime Toussaint, Christian Thibaudeau, Étienne Croteau, Réjean Fontaine, Marc D. Normandin, Yoann Petibon, Jinsong Ouyang, Georges El Fakhri, Roger Lecomte. "SAVANT: a high resolution APD-based dedicated brain PET scanner with DOI encoding". *2019 IEEE Nuclear Science Symposium & Medical Imaging Conference*, Paper ID #2392, M-06-086, Manchester, UK, 26 October - 2 November 2019.
[4] Haithem Bouziri, Catherine M. Pepin, Konin Koua, Maher Benhouria, Caroline Paulin, Jinsong Ouyang, Marc Normandin, Jean-François Pratte, Georges El Fakhri, Roger Lecomte, Réjean Fontaine. "Investigation of a model-based time-over-threshold technique for phoswich crystal discrimination". Haithem Bouziri, Catherine M. Pepin, Konin Koua, Maher Benhouria, Caroline Paulin, Jinsong Ouyang, Marc Normandin, Jean-François Pratte, Georges El Fakhri, Roger Lecomte, Réjean Fontaine. *IEEE Transactions on Radiation and Plasma Medical Sciences*, vol. 6, no. 4, pp. 393-403, 1st April 2022. (DOI: 10.1109/TRPMS.2021.3077412)

MIC-02-04

A Physics-Guided Deep Learning Method for Fast System Matrix Modeling in Self-Collimating SPECT Using Sparse Point-Source Calibration (#2412)

Qiqi Ye[1], Debin Zhang[1], Huidong Xie[2], Zhenlei Lyu[1], Tianyu Ma[1]

[1] *Tsinghua University, Beijing, China;* [2] *Fudan University, Shanghai, China*

Abstract

Self-collimating SPECT (SC-SPECT) enables simultaneous high-resolution and high-sensitivity imaging using sparse-scintillator detector layers. Accurate system matrix (SM) estimation is essential but remains challenging in SC-SPECT, because dense point-source calibration is time-consuming and conventional modeling is limited by complex system physics, while geometry-dependent detector responses further complicate AI-based sparse-to-dense recovery. In this work, we propose a physics-guided sparse-to-dense SM modeling framework to recover the full SM from 10k point-source measurements. The framework uses a customized 3D encoder–decoder with anisotropic convolutions and modified down/up-sampling to preserve fine structures under limited sampling. Sparse response intensity, sampling positions, and detector angular information are encoded as four input channels, while LOR-directional profile and curvature-continuity losses enforce physically consistent recovery. The model is trained on simulated PPDFs, with ablation studies evaluating the input-channel, architecture, and loss designs. It is further validated using experimental SM-level metrics and MLEM reconstructions of hot-rod phantom and small-animal data. Results demonstrate improved PPDF recovery and reconstruction quality over interpolation-based SM estimation and a standard U-Net, while reducing the calibration time by over 97.5%.

References
[1] T. Ma, et al. Self-Collimating SPECT With Multi-Layer Interspaced Mosaic Detectors. IEEE TMI, 2021.
[2] D. Zhang, et al. A High-Performance Self-Collimation SPECT for Small Animal Imaging. IEEE TMI, 2026.
[3] D. Zhang, et al. Characterization and Assessment of Projection Probability Density Function and Enhanced Sampling in Self-Collimation SPECT. IEEE TMI, 2023.

MIC-02-05

BuckyPET: Performance Evaluation and NEMA Adaptation for Compact PET Geometries (#3115)

David Perez-Benito[1], Luis Batres[1], Lidia Jimenez Algarra[1], Marcos Vidal[1], Juan J. Vaquero[1,2]

[1] Universidad Carlos III de Madrid, Departamento de Bioingeniería, Madrid, Spain; [2] Instituto de Investigación Sanitaria Gregorio Marañón, Madrid, Spain

Abstract

Dedicated brain PET systems are attracting renewed interest due to their potential to overcome key limitations of conventional whole-body PET, particularly limited sensitivity and spatial resolution for neurological imaging. In this work, we present BuckyPET, an innovative dedicated brain PET scanner inspired by fullerene-like geometry. The system is based on 234 regular hexagonal LYSO detector modules arranged to closely approximate a spherical configuration, arguably the most efficient geometry for brain PET imaging. Each detector is laser-engraved to create customizable optical barriers defining hexagonal scintillation pixels and is coupled to a hexagonal Hamamatsu MPPC with 61 individually read channels.

Current clinical and preclinical NEMA standards rely on concepts such as sinograms, single-slice rebinning, axial axes, and transaxial planes, which are not directly applicable to spherical or highly enclosed geometries. We also discuss the need for a modified NEMA NU 2-2018-like protocol for non-cylindrical PET systems. We propose preserving the core performance metrics of the standard while reformulating the analysis in a geometry-independent framework.

Preliminary results demonstrate the high-sensitivity capabilities of BuckyPET, alongside a high noise-to-count ratio and spatial resolution in the range of 1.5-2 mm. Ongoing work focuses on fine-tuning the electronics and acquisition system and assessing robustness under different operating conditions. Thus, the final figures of merit are expected to further improve, while ongoing advances in the reconstruction framework are anticipated to push the spatial resolution beyond the 1 mm frontier. First studies for the clinical validation are scheduled for summer 2026.

References

[1] L. Moliner, M. J. Rodríguez-Alvarez, J. V. Catret, A. González, V. Ilisie, and J. M. Benlloch, “NEMA performance evaluation of CareMiBrain dedicated brain PET and comparison with the whole-body and dedicated brain PET systems,” Scientific Reports, vol. 9, pp. 1–10, 2019.

[2] H. Tashima, E. Yoshida, F. Nishikido, H. Wakizaka, M. Nitta, A. M. Ahmed, A. Mohammadi, S. Tazawa, Y. Kimura, T. Suhara, Y. Fujibayashi, and T. Yamaya, “Development of the helmet-chin PET prototype,” 2015 IEEE Nuclear Science Symposium and Medical Imaging Conference, pp. 1–3, 2015.

Time:
11 November, 2026
12:45 – 13:05

Room:
FEDERICO GARCÍA LORCA

M-LT-01 | Advanced tomographic reconstruction techniques, X-ray imaging systems (CT, spectral CT, photo-counting CT)

Chairs:
Andrew J. Reader (London)

M-LT-01-01

SPECT Reconstruction via Diffusion Sampling from a PET Image Manifold for Theranostics (#1954)

Huanzhe Wei[1], Lefteris Livieratos[1,2], George Webber[1], Andrew J. Reader[1]

[1] Kings College London, School of Biomedical Engineering and Imaging Sciences, London, UK; [2] Kings College London, Guy's and St Thomas' NHS Foundation Trust, London, UK

Abstract

Single photon emission computed tomography (SPECT) remains the standard modality for uptake verification and patient-specific dosimetry in molecular radiotherapy (MRT), however it has limited spatial resolution and noise characteristics compared to pre-therapy positron emission tomography (PET). Existing approaches that incorporate PET priors into SPECT reconstruction are often constrained by hand-crafted feature representations and suffer from inter-modality mismatch and registration-induced artifacts. In this work, we employ a conditional generative framework to enhance SPECT reconstruction toward PET-level image quality. A denoising diffusion probabilistic model (DDPM) is trained to learn the distribution of high-quality PET images. During inference, the reverse diffusion process is conditioned on measured SPECT data and CT images, enabling anatomically consistent, high-fidelity image synthesis. The method is initially assessed using 2D Zubal phantom simulations. Performance is compared with conventional maximum likelihood expectation maximization (MLEM) and kernel based methods. Both quantitative metrics and qualitative analysis demonstrate that the diffusion-based approach achieves enhanced edge preservation and superior noise suppression. The reconstructed images show closer agreement with reference data compared to MLEM and kernel based reconstructions. By avoiding explicit PET–SPECT registration, the framework mitigates spatial misalignment and associated artifacts. These results indicate that conditional diffusion sampling provides a principled and flexible approach to improve resolution and noise limitations in SPECT, with potential to improve quantitative accuracy in MRT applications.

References

[1] H. Marquis, D. Deidda, A. Gillman et al., “Theranostic SPECT reconstruction for improved resolution: application to radionuclide therapy dosimetry,” EJNMMI Phys., vol. 8, no. 1, p. 16, Feb. 2021.

[2] F. Liu, H. Zhu, J. Yu et al., “68Ga/177Lu-labeled DOTA-TATE shows similar imaging and biodistribution in neuroendocrine tumor model,”Tumour Biol., vol. 39, no. 6, p. 1010428317705519, Jun. 2017.

[3] H.Wei, L. Livieratos, and A. J. Reader, “PET Guided Kernel EM Methods for SPECT Reconstruction in Molecular Radiotherapy,” in Proc. IEEE Nucl. Sci. Symp. Med. Imaging Conf. (NSS/MIC), Nov. 2025, pp. 1–1.

[4] G. Webber and A. J. Reader, “Diffusion models for medical image reconstruction,” BJR—Artif. Intell., vol. 1, no. 1, p. ubae013, Mar. 2024.

[5] I. R. Singh, A. Denker, R. Barbano et al., “Score-Based Generative Models for PET Image Reconstruction,” Mach. Learn. Biomed. Imaging, vol. 2, no. Generative Models, pp. 547–585, Jan. 2024.

[6] K. Thielemans, C. Tsoumpas, S. Mustafovic et al., “STIR: software for tomographic image reconstruction release 2,” Phys. Med. Biol., vol. 57, no. 4, pp. 867–883, Feb. 2012.

M-LT-01-02

Event-by-Event Energy-Dependent List-Mode Reconstruction for Quantitative ^{90}Y Bremsstrahlung SPECT (#2953)

Chenyu Yan[1], Hai Hu[1], Jingjing Qin[1], Hanshen Ye[1], Chengzhi Yang[1], Faguo Chen[2,3], Ri Zhao[2,3], Hua Li[2,3], Zuoxiang He[4], Yaqiang Liu[5], Hui Liu[5], Jing Wu[1]

[1] Beijing Normal University, Center for Advanced Quantum Studies, School of Physics and Astronomy, Beijing, China; [2] China Institute for Radiation Protection, Shanxi, China; [3] Shanxi Provincial Key Laboratory for Translational Nuclear Medicine and Precision Protection, Shanxi, China; [4] Beijing Tsinghua Changgung Hospital, Department of Nuclear Medicine, Beijing, China; [5] Tsinghua University, Department of Engineering Physics, Beijing, China

This study was supported by National Natural Science Foundation of China (No. 12305379, No.12205166), Beijing Natural Science Foundation (Z220010), CIRP Open Fund of Radiation Protection Laboratories (TNMPP-2024-No.1).

Abstract

^{90}Y bremsstrahlung SPECT imaging remains challenging due to its broad continuous energy spectrum. In this study, we proposed and evaluated a novel event-by-event energy-dependent list-mode reconstruction algorithm for quantitative ^{90}Y bremsstrahlung SPECT. To enable real-time and reasonably accurate energy-dependent collimator-detector response modeling, we proposed and incorporated a True Half-Width method into the list-mode reconstruction framework. Monte Carlo simulations were performed using three energy windows: 90-160 keV, 105-285 keV, and 90-400 keV. Quantitative evaluation was performed using contrast recovery coefficient and background variability. Compared with projection-based reconstruction, list-mode reconstruction achieved the best quantitative performance using the 90-400 keV energy window, owing to accurate event-level energy-dependent system matrix modeling over the broad continuous energy spectrum. These results demonstrate that event-by-event energy-dependent list-mode reconstruction is essential for improving the quantitative accuracy of ^{90}Y bremsstrahlung SPECT.

References

[1] Se Y, Minh P, Thanh Q, et al. Algorithms and Analyses for Joint Spectral Image Reconstruction in Y-90 Bremsstrahlung SPECT. IEEE Trans. Med. Imaging, 2020,39:1369-1379.

[2] Nathan C, Muthana S, De Nadine A, et al. AAPM Medical Physics Practice Guideline 14.a: Yttrium-90 microsphere radioembolization. Med. Phys, 2023,25:1-28.

[3] Se Y, Jeffrey A, Yuni K. Correction for Collimator-Detector Response in SPECT Using Point Spread Function Template. IEEE Trans. Med. Imaging, 2013,32:295-305.

M-LT-01-03

Introducing “T-Index”—A Metric for Quantifying Data Range and Sampling Sufficiency (#2039)

Katsuyuki Taguchi, Jingyan Xu

Johns Hopkins University, Baltimore, USA

The work has been supported by NIH grants R01 NS126256, U01 EB037558, R01 EB036984, R21 EB034337, R21 EB033426, R21 EB037806.

Abstract

Many image reconstruction methods for x-ray computed tomography (CT) use optimization approaches with cost functions that consist of a data fidelity term and a prior term. Extensive efforts have been devoted to construct better priors, some using machine learning, for high resolution, low dose, and spectral imaging. There seems to be a belief that a good prior can overcome any problems in data acquisition, downplaying the data fidelity term. It would be desirable if we could quantify the sufficiency of the problem setting (or adequacy of the data acquisition) toward a set of desired imaging properties. We propose “Truth index” or “T-index” to quantify data range and data sampling issues in this work. When fully developed, the T-index will show, independent of specific image reconstruction methods used, how much the solution can be trusted or has a risk of hallucination.

References

[1] Lastname, GN, Lastname, GN YYYY, ‘Article’, *Journal*, Edition, Page, Place of publication: publishers Jørgensen, J. S., Sidky, E. Y., and Pan, X, 2012, "Quantifying admissible undersampling for sparsity-exploiting iterative image reconstruction in X-ray CT," *IEEE Trans Med Imaging,* vol. 32, no. 2, pp. 460-73, Feb 2013, doi: 10.1109/tmi.2012.2230185.

M-LT-01-04

Time-of-Flight X-ray Imaging with Scatter Rejection and Subtraction (#3042)

Altea Lorenzon, **Altea Lorenzon**, Zimo Liu, Zimo Liu, Xiao Jiang, Xiao Jiang, Wojciech Zbijewski, Wojciech Zbijewski, J Webster Stayman, J Webster Stayman

Johns Hopkins University, Biomedical Engineering, Baltimore, USA

This work is supported, in part, by grant #0030253 from the Korea Institute for Advancement of Technology.

Abstract

X-ray time of flight information can be used in computed tomography to characterize photon interactions and discriminate scattered from unscattered events. Specifically, photons undergoing Compton and Rayleigh scattering are subject to trajectory deviations that increase their path length relative to primary photons. Therefore, with adequate temporal resolution, scattered photons are detected with larger time delay with respect to primary photons, providing a physically grounded mechanism to reject scatter. Recent technological developments in ultra-fast X-ray sources (e.g: 50ps) and high-temporal-resolution photon-counting detectors may allow for this imaging modality.
In this work, Monte Carlo (MC) simulations of a water cylinder were performed assuming Gaussian source pulse shape and detector timing jitter, with combined full-width-half-maximum as low as 50ps. A threshold-based scatter rejection method was applied, sweeping multiple thresholds to find the optimal balance between scatter rejection efficiency (η) and primary retention (ε). Filtered-backprojection reconstructions were performed and evaluated in terms of root mean square error and bias. Rejection performances were compared with an ideal, MC-based scatter subtraction technique, that leverages template fitting to estimate the average scatter contribution from time-delay histograms. A combined rejection-subtraction approach was also evaluated.For rejection only, the optimal reconstruction accuracy is obtained with a threshold T'=30 ps, corresponding to η=59% and ε=80%. Residual scatter leads to bias in the reconstructed attenuation, preventing the method from achieving the same reconstruction accuracy as the ideal subtraction. However, rejection yields lower noise levels compared to subtraction. Combining rejection and subtraction may provide a better compromise between bias and noise.

M-LT-01-05

Robustness to Scatter in Dual Energy Bone Suppression for Chest Radiography (#3063)

Gengxin Shi[1], Jamin Schaefer[3], Sebastian Vogt[3], Amirreza Heshmat[3], Ludwig Ritschl[3], Steffen Kappler[3], Cheng T. Lin[2], Dilek Oncel[2], Selin Ocal[2], Wojciech Zbijewski[1]

[1] Johns Hopkins University, Department of Biomedical Engineering, Baltimore, USA; [2] Johns Hopkins University, Russel H. Morgan Dept. of Radiology and Radiological Science, Baltimore, USA; [3] Siemens Healthineers, Forchheim, Germany

This work was supported in part by Siemens Healthineers. The product/feature and/or service offerings mentioned herein are not commercially available in all countries and/or for all modalities. Their future availability cannot be guaranteed.

Abstract
We quantify the impact of scatter on the performance of bone suppression in virtual non-calcium chest radiographs (VNCa-CXR) generated with (i) a multi-layer flat-panel detector (ML-FPD, three 200-um thick CsI layers) and (ii) with a kV-switching protocol (60/140 kVp). We show that in the setting of log-subtraction, the decomposition weight (DW) can be adjusted for scatter-to-primary ratio (SPR) such that the scatter-induced bias in VNCa is locally corrected (scatter-compensating weight, DW-scat). However, DW-scat is spatially varying. If a constant DW is used in log-subtraction, the magnitude of bone residual in VNCa radiographs will depend on the degree of spatial

inhomogeneity in DW-scat. We investigate this effect is simulation studies in anthropomorphic chest phantoms (20 – 24 cm thickness) with and without an anti-scatter grid (ASG). Without a scatter-compensating DW, scatter-induced bone residual increased by >100% is most configurations except for ML-FPD with a grid. Applying DW-scat averaged over central lung region reduced the residual by up to 50% for ML-FPD without an ASG and by ~40% for kV-switching with an ASG. Overall, our results reveal that DE VNCa imaging is relatively robust to scatter in scenarios with a grid, where kV-switching appears to benefit from spatially-averaged scatter-compensating DW more than ML-FPD, likely due to differences in scatter content of the two energy channels. Without a grid, both configurations may require a spatially-dependent scatter compensation for optimal bone suppression.

M-LT-01-06

Unrolled relaxed algorithm for 3D SPECT reconstruction (#2388)

Corentin Constanza[1], David Sarrut[1], Ane Etxebeste[1,2]

[1] CREATIS, CNRS UMR 5220; INSERM U 1044, Université de Lyon; INSA-Lyon; Université Lyon 1, Villeurbanne, France; [2] Centre de lutte contre le cancer Léon-Bérard, Lyon, France

All authors declare that they have no known conflicts of interest.

Abstract

In this work, we propose an unrolled Block Sequential Regularized Expectation Maximization (BSREM) reconstruction framework in which the gradient of the regularization term is learned using a convolutional neural network. Building on our previous work, we adopt Jacobian-Free Unrolling (JFU) to enable memory-efficient training on 3D synthetic data. This training strategy backpropagates only through the final iteration of the unrolled optimization, significantly reducing memory consumption while improving training stability. We investigate the influence of relaxation strategies within the unrolled BSREM scheme and analyze their impact on convergence behavior, stability, and reconstruction quality. Experiments conducted on realistic simulated SPECT datasets and clinical ^{177}Lu-DOTATATE patient data show that JFU-based unrolling consistently outperforms classical unrolled training for an equivalent number of parameters and memory usage. Unlike classical unrolling, which requires strong relaxation to ensure stable training, JFU achieves optimal performance with weak or no relaxation. Excessive relaxation is shown to be suboptimal, leading to reduced quantitative accuracy. Quantitative evaluations demonstrate improvements in both global image quality and organ-level activity accuracy compared to OSEM and conventional BSREM with a Relative Difference Penalty prior. As observed in our previous study using Green's one-step-late algorithm, the proposed approach may introduce over-separation artifacts between regions of low and high activity. This behavior appears intrinsic to learning the regularization gradient rather than to the unrolling strategy itself. Overall, this work highlights the advantages of Jacobian-Free Unrolling for scalable and stable learning-based SPECT reconstruction and provides insights into the role of relaxation in unrolled optimization schemes.

References
[1] H. M. Hudson and R. S. Larkin, "Accelerated image reconstruction using ordered subsets of projection data," IEEE Transactions on Medical Imaging, 1994.

[2] S. Ahn, S. G. Ross, E. Asma, J. Miao, X. Jin, L. Cheng, S. D. Wollenweber, and R. M. Manjeshwar,, "Quantitative comparison of OSEM and penalized likelihood image reconstruction using relative difference penalties for clinical PET," Physics in Medicine & Biology, 2015.
[3] P. J. Green, "Bayesian reconstructions from emission tomography data using a modified EM algorithm," IEEE Transactions on Medical Imaging, 1990.
[4] S. Ahn and J. A. Fessler, "Globally convergent image reconstruction for emission tomography using relaxed ordered subsets algorithms," IEEE Transactions on Medical Imaging, 2003.
[5] V. Monga, Y. Li, and Y. C. Eldar, "Algorithm unrolling: Interpretable, efficient deep learning for signal and image processing," IEEE Signal Processing Magazine, 2021.
[6] S. W. Fung, H. Heaton, Q. Li, D. McKenzie, S. Osher, and W. Yin, "Jfb: Jacobian-free backpropagation for implicit networks," in AAAI Conference Proceedings, 2022.
[7] L. Davy, L. M. Briceno-Arias, and N. Pustelnik, "Restarted contractive operators to learn at equilibrium," arXiv preprint arXiv:2506.13239, 2025.
[8] T. Kaprélian, A. Etxebeste, and D. Sarrut, "Partial volume correction of SPECT images with deep learning trained on synthetic data," IEEE Transactions on Radiation and Plasma Medical Sciences, 2025
[9] J. Leube, J. Gustafsson, M. Lassmann, M. Salas-Ramirez, and J. Tran-Gia, "A deep-learning-based partial-volume correction method for quantitative 177Lu SPECT/CT imaging," Journal of Nuclear Medicine, 2024.

M-LT-01-07

Three-Photon Bayesian Imaging of Ortho-Positronium (#2897)

Wojciech Krzemien[1], Lech Raczyński[2], Aurélien Coussat[3], On behalf of IMPET project

[1] National Centre for Nuclear Research, Department of High Energy Physics, Otwock Swierk, Poland; [2] National Centre for Nuclear Research, Department of Complex Systems, Otwock Swierk, Poland; [3] INSA-Lyon, niversité Claude Bernard Lyon 1, CNRS, Inserm, CREATIS UMR 5220, U1294, F-69373, Lyon, France

The work was supported by the Foundation for Polish Science through the FIRST TEAM FENG.02.02-IP.05-0152/23 programme co-financed by the European Union under the European Funds for Smart Economy 2021-2027 (FENG). by the "PHC POLONIUM" program (project number: 55194PB), funded by the French Ministry for Europe and Foreign Affairs, the French Ministry for Higher Education, Research, and Space, and the Polish NAWA (BPN/BFR/2025/1/00036/ and BPN/BAT/2025/1/00009), and co-supported by the Austrian Ministry for Women, Science and Research (project WTZ PL 11/2026).

Abstract
Positron emission tomography provides functional images from two-photon coincidences. In human tissue, approximately 40% of annihilations are preceded by positronium formation, of which the ortho-positronium component partially decays into three photons [1]. This three-photon channel carries additional information about the local micro-environment [1], including the three-to-two-photon yield ratio as a potential diagnostic marker [3,2], and its exploitation does not require a prompt photon, making it compatible with standard radionuclides such as FDG. We propose the Three-Photon Bayesian Imaging of Ortho-Positronium algorithm, a novel event-by-event reconstruction method formulated as a Bayesian maximum a posteriori inference problem, which unifies time-based trilateration [4], energy-based reconstruction [3], and a physics-informed prior derived from the quantum electrodynamics description of ortho-positronium decay [5-6] within a single probabilistic framework. Monte Carlo simulations modelled after the Siemens Biograph Quadra scanner [7] demonstrate an improvement of a factor of two over time-based trilateration and by an order of magnitude over energy-based reconstruction. The proposed

approach is compatible with existing scanners capable of registering three-photon coincidences, broadening its applicability beyond positronium lifetime imaging to standard clinical radionuclides.

References
[1] Hourlier, A, Boisson, F & Brasse, D 2024, 'Experimental uses of positronium and potential for biological applications', *IEEE Transactions on Radiation and Plasma Medical Sciences*, vol. 8, no. 6, pp. 581–594
[2] Fujimoto, M et al. 2025, 'Advancing PET through direct imaging of three-photon decay using pure positron emitters', unpublished.
[3] Kacperski, K, Spyrou, NM & Smith, FA 2004, 'Three-gamma annihilation imaging in positron emission tomography', *IEEE Transactions on Medical Imaging*, vol. 23, no. 4, pp. 525–529.
[4] Gajos, A et al. 2016, 'Trilateration-based reconstruction of ortho-positronium decays into three photons with the J-PET detector', *Nuclear Instruments and Methods in Physics Research Section A*, vol. 819, pp. 54–59.
[5] Ore, A & Powell, JL 1949, 'Three-photon annihilation of an electron–positron pair', *Physical Review*, vol. 75, no. 11, pp. 1696–1699.
[6] Berestetskii, VB, Lifshitz, EM & Pitaevskii, LP 2008, *Quantum Electrodynamics*, 2nd edn, Butterworth-Heinemann, Oxford.
[7] Prenosil, GA et al. 2022, 'Performance characteristics of the Biograph Vision Quadra PET/CT system with a long axial field of view using the NEMA NU 2-2018 standard', *Journal of Nuclear Medicine*, vol. 63, no. 3, pp. 476–484.

M-LT-01-08

Lutetium-176-Aided Joint Activity and Attenuation Reconstruction in TOF-PET Using Trust-Region Cubic Surrogate Optimization (#2772)

Xin Zhao, Zhijun Zhao, Zhao Wang, Zhaoheng Xie

Peking University, Beijing, China

This work was supported by National Natural Science Foundation of China (62394311) and National Biomedical Imaging Facility Grant.

Abstract
Joint Maximum Likelihood Activity and Attenuation (MLAA) provides a promising CT-less attenuation correction framework but suffers from global scaling ambiguity. Intrinsic Lu-176 background radiation provides patient-specific transmission information to reduce this issue, while introducing a highly nonlinear and ill-conditioned joint likelihood. We propose the Separable Cubic Surrogate with Trust Region (SCS-TR) algorithm, utilizing an analytical Lipschitz constant and a vectorized solver to ensure strictly monotonic convergence and avoid local optima. The reconstruction is initialized with Maximum Likelihood Transmission Reconstruction (MLTR) results. GATE simulations studies demonstrate that SCS-TR effectively recovers clear bone structures and smooth uniform regions without explicit regularization. The proposed method recovered clear bony structures and uniform soft-tissue regions without explicit regularization, and maintained structural fidelity under 20% count statistics.

References
[1] Omidvari N, Cheng L, Leung E K, et al. Lutetium background radiation in total-body PET–A simulation study on opportunities and challenges in PET attenuation correction[J]. Frontiers in Nuclear Medicine, 2022, 2: 963067.
[2] Cartis C, Gould N I M, Toint P L. Adaptive cubic regularisation methods for unconstrained optimization. Part I: motivation, convergence and numerical results[J]. Mathematical Programming, 2011, 127(2): 245-295.
[3] Li T, He L, Liu Z, et al. CT-Less Attenuation Correction for PET using Backward Inter-Crystal Scattered Events[C]//2024 IEEE Nuclear Science Symposium (NSS), Medical Imaging Conference (MIC) and Room Temperature Semiconductor Detector Conference (RTSD). IEEE, 2024: 1-1

[4] Nesterov Y, Polyak B T. Cubic regularization of Newton method and its global performance[J]. Mathematical programming, 2006, 108(1): 177-205.

M-LT-01-09

List-Mode Derived Synthetic Kernel-Based Image Reconstruction for Dynamic Total Body PET (#2844)

Movindu Dassanayake[1], Laurence Vass[1], Paul K. Marsden[1], Julia A. Schnabel[1,2], Andrew J. Reader[1]

[1] King's College London, Department of Imaging Physics and Engineering at the School of Biomedical Engineering and Imaging Sciences, London, UK; [2] Technical University Munich, School of Computation, Information and Technology, Munich, Germany

MD would like to acknowledge funding from the EPSRC Centre for Doctoral Training in Smart Medical Imaging [EP/S022104/1] and via a Siemens Healthineers Studentship.

Abstract

Total-body positron emission tomography (TB-PET) provides significantly improved sensitivity, enabling ultra-short time framing for dynamic imaging. However, the resulting low count statistics lead to increased noise and unstable time activity curves (TACs), limiting quantitative accuracy. We investigate a kernel-based reconstruction approach within a list-mode (LM)-derived synthetic framework, where a vendor reconstruction is forward projected through an event-specific LM system matrix to generate synthetic data, implicitly includes attenuation, normalisation, scatter, and randoms effects while enabling flexible algorithm design.

Spatial, temporal, and spatio-temporal kernels are evaluated for short-frame FDG data acquired on a Biograph Vision Quadra system, with features constructed from multiple dynamic intervals. Reconstructions are compared with a 10x higher count vendor reference images using spatial and temporal PRMSE. Spatially, the spatio-temporal kernel achieves the lowest error. In addition, we demonstrated that kernel methods benefit from larger neighbourhoods resulting in improved visual quality compared to synthetic PET. This was computationally feasible on consumer hardware by using region-of-interest specific reconstructions.

These results demonstrate that LM-derived synthetic kernel reconstruction provides a flexible framework for incorporating spatial and temporal priors in TB-PET. While performance is currently limited by kernel parameter selection, the observed improvements in spatial and temporal behaviour indicate strong potential for optimisation through tuning the kernel strength and feature vector design.

References

[1] Wang, G, Qi, J, 2015, 'PET Image Reconstruction Using Kernel Method', IEEE Transactions on Medical Imaging, vol. 34, no. 1, pp. 61–71, 2015

[2] Hutchcroft, W et al., 2016, 'Anatomically-aided PET reconstruction using the kernel method', Physics in Medicine and Biology, vol. 61, no. 18, pp. 6668–6683,

[3] Bland, J, et al., 2018, 'MR-Guided Kernel EM Reconstruction for Reduced Dose PET Imaging', IEEE Transactions on Radiation and Plasma Medical Sciences, vol. 2, no. 3, pp. 235–243, 2018.

[4] Vass, L and Reader, AJ, 2023, 'Synthesized Image Reconstruction for Post-Reconstruction Resolution Recovery', IEEE Transactions on Radiation and Plasma Medical Sciences, vol. 7, no. 5, pp. 473–482, 2023

[5] Lastname, GN, Lastname, GN YYYY, 'Article', *Journal*, Edition, Page, Place of publication: publishers
Schramm, G and Thielemans, K, 2024, 'PARALLELPROJ—an open-source framework for fast calculation of projections in tomography', Frontiers in Nuclear Medicine

M-LT-01-10

Unsupervised micro-CT reconstruction from limited-angle and truncated data in cone-beam geometry (#1238)

Keisuke Izumitani[1,2], Tatsunori Shibuya[2,3], Hidetoshi Kato[2,3], Hideaki Haneishi[4], Takayuki Okamoto[4]

[1] Chiba University, Graduate School of Science and Engineering, Chiba, Japan; [2] National Institute of Advanced Industrial Science and Technology (AIST), Research Institute for Measurement and Analytical Instrumentation, National Metrology Institute of Japan, Tsukuba, Japan; [3] National Institute of Advanced Industrial Science and Technology (AIST), Non-Destructive Imaging Research Team, Integrated Research Center for Resilient Infrastructure, Tsukuba, Japan; [4] Chiba university, Center for Frontier Medical Engineering, Chiba, Japan

This study was supported by JSPS KAKENHI, Grant Number JP25K21580; JST, ACT-X, Grant Number JPMJAX23K5; and JSPS Program for Forming Japan's Peak Research Universities (J-PEAKS), Grant Number JPJS00420230002.

Abstract

Micro X-ray computed tomography (micro-CT) enables non-destructive visualization of fine internal structures. Resolving finer details requires higher geometric magnification, typically achieved by reducing the source-to-rotation-center distance (SRD). However, short-SRD acquisition can suffer from a limited angular range due to physical interference with the X-ray source and from projection truncation when the object extends beyond the field-of-view (FOV), causing streak artifacts and structural distortions. Supervised learning-based reconstruction methods have been investigated to mitigate such artifacts but applying them to non-destructive high-magnification micro-CT is difficult because fully sampled, non-truncated reference data cannot be readily acquired without destructive sample preparation. Moreover, many existing methods are designed for 2D fan-beam geometry rather than 3D cone-beam geometry commonly used in micro-CT. We propose an unsupervised reconstruction method that simultaneously reduces limited-angle and projection-truncation artifacts by incorporating long-SRD measurements. Long-SRD acquisition provides full-view, non-truncated projections, albeit at lower spatial resolution, complementing the high-resolution but incomplete short-SRD acquisition. By jointly using these complementary measurements, the proposed method preserves fine structural details while recovering the global object structure without requiring ground-truth images. Numerical experiments demonstrated that the proposed method reduced streak artifacts and recovered structural information outside the short-SRD FOV. To the best of our knowledge, this is the first unsupervised 3D cone-beam reconstruction method to simultaneously address both artifacts in high-magnification micro-CT.

References
[1] Y. Huang et al., "Data consistent CT reconstruction from insufficient data with learned prior images", arXiv preprint, 2005.10034, 2020.

[2] K. Izumitani, H. Haneishi, and T. Okamoto, “Weakly supervised limited-angle CT reconstruction using multiple projection geometries”, 2025 IEEE NSS MIC RTSD, Yokohama, Japan.
[3] H. Kim and K. Champley, “Differentiable forward projector for x-ray computed tomography,” arXiv preprint, 2307.05801, 2023.

Time:
11 November, 2026
12:45 – 13:05

Room:
MANUEL DE FALLA

M-LT-02 | High resolution imaging systems (organ-dedicated, small animal systems, X-ray imaging systems (CT, spectral CT, photo-counting CT), Quantitative imaging, image assessment and standardization

Chairs:
Tianyu Ma (Beijing)
Elena Maria Zannoni (Austin)

M-LT-02-01

Experimental Results from Novel Monolithic PET Detector and Application to Axillary Lymph Node Imaging (#1769)

Timothy Cotroneo[1], David Pare[1], Lemise Saleh[1], Paul Vaska[1,2]

[1] Stony Brook University, Biomedical Engineering, Stony Brook, USA; [2] Renaissance School of Medicine at Stony Brook University, Radiology, Stony Brook, USA

We thank the Carol M. Baldwin Foundation for Breast Cancer Research, Stony Brook University Graduate School, and the SBU OVPR seed funding program for their support.

Abstract

Monolithic scintillators are a promising alternative to standard pixelated crystals in positron emission tomography, as they can be more cost-effective, reduce dead space, and capture an unobstructed light distribution, which can be used for depth of interaction estimation. We focus on the improvements seen by using an array of integrated corner reflectors (ICR) machined directly into the entrance face of the monolith, which we previously showed via simulation to improve light collection and narrow the light distribution. In this study, we built a physical prototype of the device using a CNC machining process. We compared this prototype with other monolithic block designs. We show that the ICR monolith with the CNN positioning algorithm has potential for high-resolution imaging with ~1 mm resolution at 12 mm thickness. Using GATE simulations, we constructed a full scanner with the performance of the monolithic blocks and tested the capabilities compared to existing systems. We show the improved spatial resolution and feasibility for a non-cylindrical design for axillary lymph node scanning.

References

[1] A. Gonzalez-Montoro et al., "Evolution of PET Detectors and Event Positioning Algorithms Using Monolithic Scintillation Crystals," IEEE T Radiat Plasma, vol. 5, no. 3, pp. 282-305, 2021, doi: 10.1109/TRPMS.2021.3059181.

[2] Y. Wang, W. Zhu, X. Cheng, and D. Li, "3D position estimation using an artificial neural network for a continuous scintillator PET detector," Phys Med Biol, vol. 58, no. 5, pp. 1375-90, Mar 7 2013, doi: 10.1088/0031-9155/58/5/1375.

[3] R. A. Valdés, M. Pereira, Daphne, and van, “Breast Cancer,” Springer eBooks, pp. 1–37, Jan. 2022, doi: https://doi.org/10.1007/978-3-031-05497-6_1.

M-LT-02-02

Spatial Characterization of PET Detectors Based on BGO Pseudo-slabs

(#1981)

Neus Cucarella[1], Laura Gil-Bosch[1], Fiammetta Pagano[1], Francis Loignon-Houle[1], Marc Gil[1], Marta Freire[1], David Sanchez[2], Andrea Gonzalez-Montoro[1], Antonio J. Gonzalez[1]

[1] Instituto de Instrumentación para Imagen Molecular (I3M), Centro Mixto CSIC-Universitat Politècnica de València, DMIL, Valencia, Spain; [2] Oncovision SA, Valencia, Spain

This work was partially funded by the AEI (Grant PID2023-151999OB-I00), co-funded by the ERC (Grant No. 101164363). Views and opinions expressed are, however, those of the author(s) only and do not necessarily reflect those of the European Union or the ERC. Neither the European Union nor the granting authorities can be held responsible for them.
N.C. is supported by PTA2022-022459-I. M.F. and F.L.-H. are supported by CIAPOS/2023/141 and CIAPOS/2023/133, respectively.

Abstract

Pixelated crystal arrays are the standard in commercial PET scanners. However, these detectors usually lack DOI information, essential to achieve a homogenous spatial resolution along the entire FOV. Yet, studies have been already performed with pixelated detectors with DOI capabilities but at the cost of using extra hardware material and/or crystal assembling. Inspired by semi-monolithic crystal geometries, pseudo-slabs were proposed as an alternative. This geometry consists of an $N \times N$ pixel array optically isolated only in one direction, allowing light crosstalk in the orthogonal one. The N pixels sharing light in this direction form a pseudo-slab. The light sharing within a pseudo-slab is enough to enable DOI retrieval, while the physical separation between pixels confines the light more than in a pure slab geometry, yielding better time resolution.

In this work we evaluated the DOI resolution of a BGO block formed by 8×8 pixels, each measuring around 3×3×15 mm^3. Two different readout configurations were employed and compared. First, all the 64 channels corresponding to the TOFPET2 ASIC channels were digitized. Then, a multiplexing circuit was utilized, reducing the signals to 8+8 by summing rows and columns. The DOI was obtained using neural networks trained on experimental data.The results show a good DOI resolution for both readout configurations, achieving 3.8 ± 1.3 mm with the multiplexing circuit. These results show that pseudo-slabs are suitable for clinical PET scanners with DOI capabilities.

References

[1] M. Ito et al., *Biom. Eng. Let.*, 2011. DOI: 10.1007/s13534-011-0019-6.
[2] N. Cucarella et al., *TRPMS*, 2025. DOI: 10.1109/TRPMS.2025.3546998.
[3] R. Bugalho et al., *JINST*, 2019. DOI: 10.1088/1748-0221/14/03/P03029.
[4] A.J. Gonzalez et al., arXiv, 2926. DOI: 10.48550/arXiv.2603.09898.

M-LT-02-03

SurfaceCam: A Close-Proximity Multi-Pinhole CZT Brain SPECT system with Enhanced Geometric Sensitivity and Spatial Resolution (#3121)

Shubham Mandot[1], Scott D. Metzler[2], Ling-Jian Meng[1,3]

[1] University of Illinois at Urbana-Champaign, Department of Nuclear, Plasma and Radiological Engineering, Champaign, USA; [2] University of Pennsylvania at Philadelphia, Department of Radiology, Philadelphia, USA; [3] University of Illinois at Urbana-Champaign, Beckman Institute for Advance Science and Technology, Champaign, USA

We would like to thank NIH/NIBIB (BRAIN Initiative) for supporting this work under the grant UG3 EB034715.

Abstract

High-sensitivity, high-resolution brain-dedicated SPECT systems are critically important for advancing diagnosis and surgical planning in complex neurological disorders such as epilepsy, Parkinson's disease, and Alzheimer's disease. In this paper, we present *SurfaceCam*, a close-proximity multi-pinhole SPECT architecture with a radially adaptable rotating gantry, designed specifically for clinical brain imaging. The system comprises 15 detector-collimator panels distributed across three detector heads in a cylindrical arrangement, operating at a 1:8 minification geometry with a 28 cm bore. Each panel integrates 16 high-performance CZT sensors in a compact 2×8 configuration. The three detector heads translate radially to accommodate varying patient head sizes while maintaining close-proximity geometry, and the rotating gantry enables micro-rotation between acquisitions to facilitate angular super-sampling strategies. Pinholes are organized into groups of four with a twisted geometry, each subtending partial coverage of the 20 cm spherical FOV, while eliminating inter-pinhole projection multiplexing on the detector surface. Analytical comparison against a conventional 1:11 minification compound-eye reference design demonstrates approximately 1.4-fold higher geometric sensitivity and approximately 27% improvement in effective pinhole spatial resolution. The front-end electronics and data acquisition systems have been fully developed and validated, with Monte Carlo simulation studies and experimental phantom validation currently underway.

M-LT-02-04

In vivo Gold Nanoparticle Imaging in Mice for Tumor Detection Using SiPM-Based Photon-Counting CT (#1749)

Shuma Midorikawa[1], **Shuma Midorikawa**[1], Makoto Arimoto[1], Makoto Arimoto[1], Fitri Lucyana[1], Fitri Lucyana[1], Yu Furuta[1], Yu Furuta[1], Satoshi Kobayashi[1], Satoshi Kobayashi[1], Hiroki Kawashima[1], Hiroki Kawashima[1], Kenichiro Okumura[1], Kenichiro Okumura[1], Asuka Mizutani[1], Asuka Mizutani[1], Naoki Ohno[1], Naoki Ohno[1], Minori Oshima[1], Minori Oshima[1], Jun Kataoka[2], Jun Kataoka[2], Ro Takahiro[2], Ro Takahiro[2], Ryotaro MInagawa[2], Ryotaro MInagawa[2], Kazuhiro Murakami[3], Kazuhiro Murakami[3], Yuta Maeno[4], Yuta Maeno[4], Shinsuke Terazawa[4], Shinsuke Terazawa[4]

[1] Kanazawa University, Ishikawa, Japan; [2] Waseda University, Tokyo, Japan; [3] Ishikawa Prefectural University, Ishikawa, Japan; [4] Proterial Ltd, Tokyo, Japan

We gratefully acknowledge financial support from JSPS KAKENHI Grant Numbers JP19H04483 and JP19K22924, JST ERATO Grant Number JPMJER2102, Japan, the Naito Foundation, Japan, the Uehara Memorial Foundation, Japan, the Casio Science Promotion Foundation, Japan, the Murata Science Foundation, Japan, and the JSPS Leading Initiative for Excellent Young Researchers program, Japan .

Abstract

Photon-counting CT (PC-CT) is a powerful spectral imaging technique that identifies materials by counting individual X-ray photons. While direct-conversion systems are entering clinical practice, we are developing a cost-effective, large-area scintillator-based PC-CT system using YGAG:Ce coupled with silicon photomultipliers (SiPMs). PC-CT excels at identifying high-atomic-number elements like gold (Au) by utilizing its K-edge (80.7 keV). Gold nanoparticles (AuNPs) are promising for drug delivery, as their biodistribution can be controlled by particle size, enabling selective tumor accumulation via the enhanced permeability and retention (EPR) effect.

In this study, we evaluated the in vivo biodistribution of AuNPs in tumor-bearing mice using our SiPM-based PC-CT. Two sizes of AuNPs (1.9 nm and 15 nm) were intravenously administered, and their accumulation was quantitatively assessed using multi-energy CT concentration estimation. Results showed distinct size-dependent patterns: 1.9 nm AuNPs exhibited rapid renal clearance and bladder accumulation, while 15 nm AuNPs showed prolonged circulation and significant hepatic accumulation. Tumor accumulation was confirmed for both sizes, demonstrating the potential of our SiPM-based PC-CT for quantitative in vivo nanoparticle imaging.This presentation reports on the
experimental setup, the analysis methods, and the results obtained.

References
[1] H. Kiji, et al., “64-channel photon-counting computed tomography using a new MPPC-CT system,” Nucl. Instrum. Methods Phys. Res. A, vol. 984, p. 164610, 2020, doi: 10.1016/j.nima.2020.164610.
[2] M. Arimoto, et al., “Development of 64-channel LSI with ultrafast analog and digital signal processing dedicated for photon-counting computed tomography with multi-pixel photon counter,” Nucl. Instrum. Methods Phys. Res. A, vol. 1047, p. 167721, 2023, doi: 10.1016/j.nima.2022.167721.

[3] Y. Furuta, et al., "X-ray imaging of anticancer drugs and a Platinum-Iodine mixture encapsulated in liposomes using SiPM-based photon-counting CT," IEEE Trans. Nucl. Sci., vol. 73, no. 1, pp. 1–1, 2026, doi: 10.1109/TNS.2026.3662738

M-LT-02-05

Quantitative Evaluation of Liver Disease through Multi-modality Approach Combining SiPM-based PC-CT and MRI—Approach to the Visualization of Inflammation through Water Fraction Estimation —

(#1548)

Yu Furuta[1], Makoto Arimoto[1], Fitiri Lucyana[1], Shuma Midorikawa[1], Satoshi Kobayashi[1], Hiroki Kawashima[1], Kenichiro Okumura[1], Naoki Ohno[1], Takahiro Tomoda[1], Minori Oshima[1], Kazuhiro Murakami[2], Jun Kataoka[3], Ryotaro Minagawa[3], Takahiro Ro[3], Shinsuke Terazawa[4], Yuta Maeno[4], On behalf of the joint research group of Kanazawa University, Waseda University, Ishikawa Prefectural University, and Proterial Ltd.

[1] Kanazawa University, Kanazawa, Japan; [2] Ishikawa Prefectural University, Nonoichi, Japan; [3] Waseda University, Shinzyuku, Japan; [4] Proterial Ltd., Mishima, Japan

We gratefully acknowledge financial support from JSPS KAKENHI Grant Numbers JP19H04483 and JP19K22924, JST ERATO Grant Number JPMJER2102, Japan, the Naito Foundation, Japan, the Uehara Memorial Foundation, Japan, the Casio Science Promotion Foundation, Japan, the Murata Science Foundation, Japan, and the JSPS Leading Initiative for Excellent Young Researchers program, Japan.

Abstract

X-ray computed tomography (CT) is essential nondestructive internal imaging. Photon-counting computed tomography (PC-CT) acquires X-ray energy information to enable material identification and quantitative density evaluation. Combining PC-CT energy information with magnetic resonance imaging (MRI) data is expected to provide a novel diagnostic approach to visualize inflammation through tissue water fraction estimation. We developed a PC-CT system combining high-speed scintillators (YGAG:Ce) and silicon photomultipliers (SiPMs), specifically utilizing multi-pixel photon counters, MPPCs, which are optical semiconductor devices. This study evaluated healthy and fatty liver rat models (fed a high-fat diet for two or four weeks). Liver fat fractions, estimated from energy-dependent linear attenuation coefficients, showed good agreement with MRI and pathological results. Furthermore, we performed a detailed pathological evaluation focusing on inflammation induced changes in tissue water content. By integrating high reliability MRI fat fraction data with PC-CT data, we improved the estimation accuracy of water content and quantitatively visualized tissue "water-richness" (edema). Increased water proportions in fatty liver groups suggested inflammation progression. These findings demonstrate that PC-CT is highly valuable for quantitative evaluation of liver disease within a multi-modality imaging approach.

References
[1] H. Kiji et al. Nucl. Instr. Meth. A, 984:164610, 2020, DOI. 10.1016/j.nima.2020.164610.
[2] M. Arimoto et al. Nucl. Instr. Meth. A, 1047:167721, 2023, DOI. 10.1016/j.nima.2022.167721.

M-LT-02-06

Position-, direction- and contrast-dependent measurement of MLEM-reconstructed PET resolution using a 3D-printed cube (#1967)

Santiago Alvarado Orozco[1], Matthijs Sevenois[2], Georg Schramm[1]

[1] KU Leuven, Department of Imaging and Pathology, Leuven, Belgium; [2] UZ Leuven, Division of Nuclear Medicine, Leuven, Belgium

Abstract

The reconstructed spatial resolution of a PET image is determined by both intrinsic scanner properties and the chosen reconstruction algorithm. Standard NEMA measurements use point sources reconstructed with FBP and therefore mainly characterize the scanner. They are thus suboptimal for predicting the resolution of images reconstructed with MLEM and point-spread-function modeling, as is common in clinical practice.

We propose a 3D-printed resolution cube with an off-center inner compartment which, combined with a mid-acquisition phantom flip and a single reconstruction, produces sharp edges at finite (2:1) contrast along three orthogonal directions. Position-, direction- and contrast-dependent edge and line spread functions (ESFs, LSFs) are then extracted using smoothing-spline fits. As a proof of concept, the method is applied to the NeuroExplorer brain PET system at the isocenter and 10 cm off-center, with and without depth-of-interaction (DOI) modeling.

The LSFs are non-Gaussian with pronounced negative side lobes. With DOI, the resolution is approximately 2.5 mm FWHM in all directions at both positions; without DOI it degrades radially to about 4 mm at 10 cm off-center. Notably, differences between finite and infinite contrast are small in most configurations.

The method provides a position-, direction- and contrast-dependent characterization of PET resolution from clinically reconstructed images and complements NEMA point-source values for image quality comparison, harmonization and partial volume correction.

M-LT-02-07

A Clinically Viable, Scalable Implementation of Monte Carlo Scatter Correction for PET/CT (#2119)

Danielle Zeltser[1], Ester Hait-Fraenkel[1], Xuezhu Zhang[2], Michal Edelstein[1], Gali Elkin-Basudo[1], Yaniv Mizrachi[1], Yariv Grobshtein[1]

[1] GE HealthCare, Molecular Imaging, Haifa, Israel; [2] GE HealthCare, Molecular Imaging, Waukesha, USA

Abstract

Monte Carlo scatter correction is well established as a highly accurate approach for scatter estimation in PET/CT imaging. It demonstrates superior robustness compared with model based scatter estimation methods, particularly under extreme variations in activity distribution and in the presence of patient motion, conditions under which model based approaches often produce artifacts. Despite these advantages, Monte Carlo scatter correction is computationally intensive, and does not inherently account for out-of-field scatter. In this work, we address both limitations and propose an implementation suitable for integration into routine clinical workflows. A multi-GPU implementation, as well as parallel processing with efficient data streaming significantly reduce the processing time. To handle out-of-field scatter, we separately handle regions where information about out-of-field distribution is known, and can be used for a highly precise estimation. In regions where out-of-field information is inaccessible, the effect on scatter is approximated by the measured data, while ensuring a smooth transition in which the high-accuracy region governs the final estimate. Our approach is scalable and robust across system designs ranging from a standard axial field-of-view to a long axial field-of-view, each presenting distinct considerations for scatter estimation. We demonstrate the effectiveness of our method using phantom and clinical data.

M-LT-02-08

Evaluation of Motion Correction Methods on the NeuroEXPLORER Using Multi-Tracer Human Data (#2130)

Jiazhen Zhang, Tianyi Zeng, Yifan Hu, Kathryn Fontaine, Tommaso Volpi, Takuya Toyonaga, Richard E. Carson

Yale University, New Haven, USA

Research funding support: U01EB029811.

Abstract

Accurate motion correction is critical for dynamic brain PET, particularly on the high-resolution NeuroEXPLORER (NX), where residual head motion can blur focal targets and bias time-activity curves (TACs). We evaluated multiple motion correction (MC) strategies using 17 multi-tracer human NX PET scans, including no motion correction (NMC), post-reconstruction registration (PRR), registration before attenuation correction (RBA), UMT-based frame-averaged correction (AVG), and UMT-based event-by-event correction (EBE). Performance was assessed using qualitative image comparison and ROI-based residual TAC variability (%SD_{res}) from 20-70 min. All MC methods reduced %SD_{res} compared with NMC. Across all tracers, subjects, and ROIs, EBE achieved the lowest residual variability (1.40 ± 1.27%), followed by PRR (1.79 ± 1.49%), RBA (1.94 ± 1.64%), AVG (2.01 ± 1.63%), and NMC (4.68 ± 4.26%). Poisson noise-floor analysis further showed that residual motion effects were tracer- and count-statistics-dependent. Overall, UMT-based EBE provided the most effective reduction of residual motion effects in dynamic NX brain PET.

References
[1] T. Volpi, et al., "Exceptional brain PET images from the NeuroEXPLORER: scans with targeted radiopharmaceuticals and comparison to HRRT," *EJNMMI*, 2026.
[2] E. M. Revilla, et al., "Adaptive data-driven motion detection and optimized correction for brain PET," *Neuroimage*, 2022.

[3] Z. Cai, et al., "PET Head Motion Estimation Using Supervised Deep Learning with Attention," *IEEE TMI*, 2025.
[4] T. Zeng, et al., "Validation and application of markerless head motion tracking for a next-generation brain PET scanner," *IEEE MIC*, 2023.
[5] T. Zeng, et al., "Optimization of Brain PET Markerless Head Motion Correction in a Large Human Cohort," *EJNMMI Physics*, 2026.
[6] K. Fontaine, et al., "MOLAR-NX: building a PET reconstruction framework for exploring the novel features provided by the NeuroEXPLORER," *IEEE MIC*, 2024.
[7] J. Zhang, et al., "Cranberry: Combined Rigid and Nonrigid Event-by-Event Motion Correction at Yale," *IEEE MIC*, 2025.
[8] C. Sun, et al., "An objective evaluation method for head motion estimation in PET—motion corrected centroid-of-distribution," *Neuroimage*, 2022.
[9] J. Zhang, et al., "Evaluation of motion correction quality in brain, face, and neck for NeuroEXPLORER," *SNMMI*, 2024.

M-LT-02-09

SSS Optimised for Monte Carlo Scatter Estimation for PET (#3060)

Antonia Reeves[3,2], SeyedAmir ZamanPour[1], Simon Noe[1], Simon Arridge[4], Kris Thielemans[2,3]

[1] KU Leuven, Department of Imaging and Pathology, Leuven, Belgium; [2] University College London, Institute of Nuclear Medicine and the Hawkes Institute, London, UK; [3] University College London, Department of Medical Physics and Biomedical Engineering, London, UK; [4] University College London, Department of computer science, London, UK

This work was supported by the i4Health Centre for Doctoral Training, UCL and GE Healthcare. Software used in this project is maintained by CCP SyneRBI (UKRI support: EPSRC grant EP/T026693/1 and STFC through the DRI programme).

Abstract

Recent increases in computational power as well as new tools being more readily available have led to increased interest in Monte Carlo scatter estimation. However, Monte Carlo scatter simulation is still computationally expensive. This is exacerbated by the fact that model-based scatter estimation requires multiple iterations of scatter simulation and image reconstruction. We propose to combine the current clinical standard (analytic single scatter simulation and tail-fitting) with Monte Carlo scatter simulation.

M-LT-02-10

Positron Range Confinement in Preclinical PET/MRI: A Multi-Isotope, Multi-Density Experimental Study (#1930)

Fernando Lopez-Berenguer[1], **Fernando Lopez-Berenguer**[1], Andrea Gonzalez-Montoro[1], Andrea Gonzalez-Montoro[1], Stuart Berr[2], Stuart Berr[2], Mark Williams[2], Mark Williams[2], Antonio J. Gonzalez[1], Antonio J. Gonzalez[1]

[1] Instituto de Instrumentación para Imagen Molecular (i3M), Centro Mixto CSIC-Universitat Politècnica de València, Valencia, Spain; [2] University of Virginia, Department of Radiology and Medical Imaging, Charlottesville, USA

This work was supported by the Generalitat Valenciana under Grant No. CIPROM/2021/003 and funds from the Univ, VA FUS Cancer Immunotherapy Center.F.Lopez Berenguer is supported by the European Research Council (ERC) under the European Union's Horizon Europe research and innovation programme (Grant agreement No. 101164363).

Abstract

The spatial resolution of PET imaging is fundamentally limited by the positron range, whose extent depends on both the emission energy of the radionuclide and the electron density of the surrounding medium. In integrated PET/MRI systems, the static magnetic field exerts a Lorentz force on the positrons, confining their trajectories in the transverse plane to the main magnetic field, potentially improving image resolution. Two complementary experiments were performed using a dedicated monolithic-crystal based PET insert operated at 0T and inside a 9.4T MRI: capillary line sources embedded in three tissue-equivalent phantoms of increasing density (EPF, PLA, and Rigid10k resin), and a microDerenzo phantom. Both tests were carried out with three positron emitters (^{18}F, ^{89}Zr, and ^{68}Ga) eventually use in pre-clinical imaging. The results demonstrate that the magnetic field significantly enhances transverse spatial resolution for high-energy positron emitters in medium- and high-density materials, with FWTM reductions of ~60% for ^{68}Ga and ~18% for ^{89}Zr, while the axial direction remains largely unaffected. Rod resolvability improved at 9.4T from 1.5 mm to ~1.0 mm and from 1.2 mm to 0.9 mm for ^{68}Ga and ^{89}Zr, respectively. . These findings highlight the relevance of both positron energy and tissue-equivalent density in determining the magnitude of magnetic-field-induced resolution improvements in preclinical PET/MRI.

References

[1] Moses, WW 2011, 'Fundamental limits of spatial resolution in PET', *Nuclear Instruments and Methods in Physics Research A*, vol. 648, pp. S236–S240.

[2] Ku-Toval, D et al. 2024, 'Quantitative analysis of the effect of the magnetic field generated by a PET/MR scanner on positron range', *Physics in Medicine and Biology*, vol. 69, no. 18, p. 185006.

[3] Lopez-Berenguer, F et al. 2025, 'Positron Range Confinement in High-Field MRI, Enhancing PET Image Quality', *IEEE NSS/MIC*.

[4] Lopez-Berenguer, F et al. 2025, 'Evaluation of a PET insert for trimodal imaging: a step towards PET/MRI-guided focused ultrasound', *IEEE Transactions on Radiation and Plasma Medical Sciences*, in press.

Time:
11 November, 2026
15:00 – 17:00

Room:
FEDERICO GARCÍA LORCA

MIC-03 | X-ray imaging systems (CT, spectral CT, photo-counting CT)

Chairs:
Dimitra G. Darambara (London)
Katsuyuki Taguchi (Baltimore)

MIC-03-01

LUCID: Model-Free High-Rate Photon Counting (#1041)

Paul Scoullar, Chris Mc Lean

Southern Innovation, Melbourne, Australia

Abstract

Conventional photon-counting systems rely on dead-time models [1], [2] that saturate at high flux, introduce systematic bias, and require per-channel calibration that scales poorly to large pixel arrays [3]. We present LUCID (Linear Unbiased Count-rate from Interval Detection), which estimates photon flux by measuring the silence between pulses rather than counting individual arrivals, eliminating dead-time modelling entirely. The method assumes only that photon arrivals follow a Poisson process — a condition satisfied by all common detector types at constant source output — and requires no detector-specific dead-time model.

For a Poisson arrival process, the memoryless property of the exponential distribution ensures that gaps exceeding a configurable minimum duration θ_{gap} retain the full statistical information about the true rate λ, regardless of pile-up below that threshold. The unbiased estimator $\hat{\lambda} = (N-1)/T_{excess}$ requires only two hardware-accumulated quantities — valid gap count N and cumulative excess gap duration T_{excess} — and a single division. No knowledge of pulse shape, dead-time, or detector material is required. The estimator variance $\mathrm{Var}(\hat{\lambda}) \approx \lambda^2/(N_{total} \cdot \exp(-\lambda\theta_{gap}))$ provides closed-form uncertainty quantification with graceful degradation at extreme rates rather than a hard saturation limit.

LUCID has been validated from Monte Carlo simulation to commercial deployment, with no per-channel calibration. Simulation demonstrates sub-0.3% RMSE per pixel to 100 Mcps and continued accuracy to 300 Mcps. Eliminating count-rate non-linearity directly improves CT number accuracy, beam-hardening correction, and material decomposition fidelity in photon-counting CT. The architecture requires no high-speed ADC and is suited to FPGA, ASIC, or analogue comparator-integrator realisation [4]. We discuss current work extending the framework toward spectral recovery.

References

[1] G. F. Knoll, *Radiation Detection and Measurement*, 4th ed. New York, NY, USA: John Wiley & Sons, 2010.

[2] J. W. Müller, "Dead-time problems," *Nucl. Instrum. Methods*, vol. 112, no. 1–2, pp. 47–57, 1973.

[3] F. Y. Daniel and J. A. Fessler, "Mean and variance of single photon counting with deadtime," *Phys. Med. Biol.*, vol. 45, no. 7, pp. 2043–2058, 2000.

[4] P. A. Scoullar and R. J. Evans, "Maximum likelihood estimation techniques for high rate, high throughput digital pulse processing," in *Proc. IEEE Nucl. Sci. Symp. Conf. Rec.*, Dresden, Germany, Oct. 2008, pp. 1668–1672.

MIC-03-02

Comparison of scintillator and semiconductor based photon counting detectors via a unique, modular, multi-level simulation framework (PC-SIM). (#2811)

Oliver L.P. Pickford Scienti, Dimitra Darambara

Institute of Cancer Research and The Royal Marsden Hospital, Joint Department of Physics, London, UK

This work was funded by the EPSRC in the UK

Abstract

Spectral photon counting is widely seen as a revolution in medical imaging, however applications will be limited by the spectral performance of the x-ray sensor. Primarily these sensors are made of semiconductors such as CdTe, however in recent years there has been growing interest in whether scintillators could be used as an alternative. These materials lack the high energy resolution of the semiconductors, however they are not affected by the extensive low energy tailing seen in small pixelated semiconductor devices. As spectral photon counting is performed with coarse energy bins rather than fine spectral resolution, this raises the question of which factor is more important for spectral fidelity in energy binned tasks: a narrow intrinsic energy resolution (semiconductors) or the absence of charge sharing induced low energy tailing (scintillators)? This work sets out to compare the two sensor types to answer this question. To do this we use a new simulation tool called PC-SIM (Photon Counting Spectral Imaging Model), which is a modular framework, designed for flexible modelling of a range of spectral photon counting scanner designs. We combine this tool with Monte Carlo simulations performed in GATE to quantify the spectral fidelity of scintillator- and semiconductor-based detectors under a range of conditions, including various numbers of energy bins, pixel sizes, and differing beam spectra (polychromatic and monochromatic sources). This presentation will introduce PC-SIM, outlining its design philosophy, module options and how it was used to compare the scintillator and semiconductor systems as fairly as possible. Results will show under what conditions scintillators might provide comparable photon-counting performance compared with the current gold standard of semiconductor based detectors, but at a cheaper price-point. Limitations and assumptions of this work will be discussed, along with implications of the results.

References

[1] van der Sar, S. J., Leibold, D., & Schaart, D. R. 2026, 'Experimental investigation of the potential of LaBr3: Ce, LYSO: Ce, and YAP: Ce for scintillator-based x-ray photon-counting detectors', *Physics in Medicine & Biology*, *71*(2), 025003.

[2] Taguchi, K., Schaart, D. R., Goorden, M. C., & Hsieh, S. S. 2025, 'Imaging performance of a LaBr3: Ce scintillation detector for photon counting x-ray computed tomography: simulation study', *Medical physics*, *52*(1), 158-170

[3] Scienti, O. P., Bamber, J. C., & Darambara, D. G. 202, 'Inclusion of a charge sharing correction algorithm into an X-ray photon counting spectral detector simulation framework', *IEEE Transactions on Radiation and Plasma Medical Sciences*, *5*(4), 485-492.

MIC-03-03

Single Energy Material Decomposition via X-ray Grating Interferometry (#1679)

Longchao Men, Peiyuan Guo, Jincheng Lu, Li Zhang, Zhentian Wang

Tsinghua, Beijing, China

Abstract

We propose single-energy material decomposition (SEMD), a method that achieves quantitative basis material imaging from a single X-ray grating interferometry (XGI) acquisition without dual-energy scans. XGI inherently provides two independent spectra from a single acquisition, yielding the spectral separation required for material decomposition. SEMD is particularly valuable for dark-field CT, enabling material decomposition directly from the existing acquisition without requiring dual-energy hardware, greatly enhancing the clinical utility of these systems. Experimental results demonstrate that SEMD achieves decomposition accuracy comparable to conventional dual-energy material decomposition (DEMD), providing absorption, dark-field, and basis material images simultaneously from a single scan.

References
[1] \bibitem{pfeiffer2008} F. Pfeiffer \textit{et al.}, \textit{Nat. Mater.}, vol.~7, no.~2, pp.~134--137, 2008.
[2] \bibitem{viermetz2022} M. Viermetz \textit{et al.}, \textit{Proc. Natl. Acad. Sci.}, vol.~119, no.~8, e2118799119, 2022.
[3] \bibitem{alvarez1976} R. Alvarez \textit{et al.}, \textit{Phys. Med. Biol.}, vol.~21, no.~5, pp.~733--744, 1976.
[4] \bibitem{sidky2005} E. Sidky \textit{et al.}, \textit{J. Appl. Phys.}, vol.~97, no.~12, 124701, 2005.
[5] \bibitem{yashiro2015} W. Yashiro \textit{et al.}, \textit{Opt. Express}, vol.~23, no.~18, p.~23462, 2015.
[6] \bibitem{tang2023} R. Tang \textit{et al.}, \textit{Opt. Express}, vol.~31, no.~24, p.~40450, 2023.

MIC-03-04

Performance Evaluation of Low-Dose 3D Small-Animal Imaging Using YSO/SiPM-Based Photon-Counting CT (#2872)

Li Pan[1], Rui Zheng[1], Daoming Xi[2], Qiliang Hong[1], Peng Xiao[1,2], Qingguo Xie[1,2]

[1] University of Science and Technology of China, Department of Electronic Engineering and Information Science, Hefei, China; [2] Hefei Comprehensive National Science Center, Institute of Artificial Intelligence, Hefei, China

This work was supported in part by the National Key R&D Program of China under Grant 2024YFE0113500, and in part by the start-up fund of USTC "Research on total solid Angle PET-EPR multimodal intelligent imaging".

Abstract

Photon-counting computed tomography (PC-CT) shows remarkable potential in low-dose spectral imaging by binning X-ray photons into discrete energy windows. This study presents a novel PC-CT system integrating scintillation detectors and multi-voltage threshold (MVT) digitizers, extends its application to 3D *in vivo* spectral imaging, and specifically evaluates the low-dose imaging performance. Validation results show that the system achieves a detection efficiency of 94.78%, a dark count rate of 0.08 cps/pixel, and a peak count rate of 0.85 Mcps/pixel. Dosimetric evaluations at 120 kVp reveal a central $CTDI_{100}$ of 0.15–0.375 mGy, yielding a dose-normalized figure of merit (FOM) nearly tenfold higher than that of conventional micro-CT. Furthermore, *in vivo* experiments validate the system's capability for high-fidelity 3D material decomposition, even under photon-starved conditions. These results substantiate the potential of the YSO/SiPM-based PC-CT system for precise *in vivo* material decomposition at low radiation doses.

References
[1] S. J. Van der Sar and D. R. Schaart, "Performance of x-ray photon-counting scintillation detectors under pile-up conditions at 60 keV," *IEEE Trans. Radiat. Plasma Med. Sci.*, vol. 9, no. 6, pp. 708-720, 2025.
[2] D. Sato, *et al.*, "Multi-energy *in-vivo* imaging of multiple contrast agents in a mouse using MPPC-based photon-counting CT," *Nucl. Instrum. Methods Phys. Res. Sect. A*, vol. 1064, p. 169337, 2024.
[3] R. Chen, C. Cai, W. Liu, *et al.*, "Multi-voltage threshold digitizer using a time-varied threshold for photon-counting X-ray security inspection imaging," *Nucl. Instrum. Methods Phys. Res. A*, vol. 1048, p. 167886, 2023.
[4] D. Zhang, *et al.*, "Feasibility study of photon-counting CT for material identification based on YSO/SiPM detector: A proof of concept," *Med. Phys.*, vol. 51, no. 11, pp. 8151-8167, 2024.
[5] X. Liang, *et al.*, "NEMA-2008 and *in-vivo* animal and plant imaging performance of the large FOV preclinical digital PET/CT system discoverist 180," *IEEE Trans. Radiat. Plasma Med. Sci.*, vol. 4, no. 5, pp. 622-629, 2020.

MIC-03-05

Photon-Counting Spectral Dark-Field Micro-CT for Enhanced Tooth Microcrack Detection (#3183)

Qianyue Ma[1,2], Jincheng Lu[1,2], Sheng Peng[1], Yizhou Bai[2], Longchao Men[1], Li Zhang[1], Zhentian Wang[1]

[1] Tsinghua University, Department of Engineering Physics, Beijing, China; [2] Tsinghua University, School of Clinical Medicine, Beijing Tsinghua Changgung Hospital, Beijing, China

Abstract

Conventional absorption-based dental CT often fails to detect early tooth microcracks due to limited resolution and attenuation contrast. While X-ray dark-field imaging is highly sensitive to sub-pixel structures, traditional systems lack spectral capabilities. To address this, our study utilized a photon-counting grating-interferometry micro-CT system to perform energy-resolved CT imaging of an ex vivo human tooth. Using a 4.8 μm Talbot-Lau interferometer and dual-threshold detection (15 and 30 keV), absorption and dark-field signals were acquired across total-energy (TE), low-energy (LE), and high-energy (HE) channels. Results confirm the complementary nature of the two modalities: absorption imaging better differentiates enamel and dentin, whereas dark-field imaging reveals microcracks with significantly higher conspicuity. Regarding spectral performance, although increasing energy leads to higher overall image noise and decreased clarity (LE > TE > HE), microcrack contrast exhibits the exact opposite trend (HE > LE > TE), peaking in the HE channel with the maximum crack contrast. These findings highlight the advantages of photon-counting spectral dark-field micro-CT for highly sensitive dental crack detection.

References
[1] F. Pfeiffer, M. Bech, O. Bunk, P. Kraft, E. F. Eikenberry, C. Bronnimann, C. Grunzweig, and C. David, "Hard-x-ray dark-field imaging using a grating interferometer," Nat. Mater., vol. 7, no. 2, pp. 134-137, 2008.
[2] C. Gusenbauer, T. Krenkel, F. Beckmann, F. Pfeiffer, and D. M. Herzenberg, "Characterization of medical and biological samples with a Talbot-Lau grating interferometer µXCT in comparison to reference methods," Case Stud. Nondestruct. Test. Eval., vol. 6, pp. 1-9, 2016.
[3] C. Jud, Y. Sharma, B. Günther, J. Weitz, F. Pfeiffer, and D. Pfeiffer, "X-ray dark-field tomography reveals tooth cracks," Sci. Rep., vol. 11, no. 1, Art. no. 14017, 2021.

MIC-03-06

ePixUHR-100k: A 100 kfps Full-Frame Imager for the LCLS X-Ray FEL Upgrade (#1812)

Lorenzo Rota[1], Aldo Pena-Perez[1], Bojan Markovic[1], Aseem Gupta[1], Hugo Hernandez[1], Gang Liu[1], Pietro King[1], Hyunjoon Kim[1], Mike Hammer[2], Henry Shi[2], Antonino Miceli[2], Angelo Dragone[1]

[1] SLAC National Lab - Stanford University, TID-Instrumentation Division, Menlo Park, USA; [2] Argonne National Laboratory, X-ray Science Division of the Advanced Photon Source, Lemont, USA

Use of the Linac Coherent Light Source (LCLS), SLAC National Accelerator Laboratory, is supported by the U.S. Department of Energy, Office of Science, Office of Basic Energy Sciences under Contract No. DE-AC02-76SF00515.

Abstract

Next-generation X-ray sources, including 4th-generation synchrotrons and Free-Electron Lasers (FELs) such as LCLS-II, deliver photon rates that saturate conventional photon-counting detectors. ePixUHR-100k addresses this gap with a hybrid X-ray imager providing continuous 100 kfps readout with 104 dB dynamic range and single-photon sensitivity down to 2 keV, capturing single photon and > 1000-photon events with low cross-talk. Power-and area-efficient SAR A/D converters distributed across the pixel matrix enable massively parallel digitization, while a charge-integrating front-end with auto-gain switching sustains fluxes beyond 109 photons/s/pixel. Fabricated in a 130 nm CMOS process, the full-reticle 19.4 × 18.0 mm^2 ASIC is bump-bonded to a 144 × 192 pixel Si sensor and achieves 123 e- RMS noise. Validation of a prototype camera system with a 109Cd radioactive source and at the LCLS X-ray FEL confirms state-of-the-art continuous frame-rate and power-efficiency performance among reported X-ray detectors, including SPAD-based designs. Full ASIC architecture, A/D converter characterization, dynamic range evaluation, gain-switching performance, and comparison with state-of-the-art detectors will be presented at the conference. Scalability toward large-area X-ray cameras will also be discussed through tiled 2 × 2 and 2 × 3 ASIC configurations bump-bonded to large-format Si sensors, enabling systems from 0.5 to 16 Mpixels.

References
[1] P. Abbamonte et al., “New science opportunities enabled by LCLS-II X-ray lasers,” SLAC National Accelerator Laboratory, Tech. Rep. SLAC-R-1053, 2015.
[2] B. Park, H.-S. Choi, J. Jeong, J. Cheon, M.-J. Lee, and Y. Chae, “A 7.2 inch 5.5 mpixel 600mw spad x-ray detector with 116.7 db dynamic range,” IEEE VLSI Technology and Circuits, pp. 1–2, 2024.
[3] S. Lee, J. Jeong, T. Kim, C. Park, T. Kim, and Y. Chae, “28.3 a 5.2mpixel 88.4db-dr 12in cmos x-ray detector with 16b column-parallel continuous-time ΔΣ adcs,” IEEE ISSCC, pp. 434–436, 2020.
[4] H. Shike et al., “A global shutter wide dynamic range soft x-ray cmos image sensor with bsi pinned photodiode, two-stage lofic and voltage domain memory bank,” IEEE IEDM, pp. 16.4.1–16.4.4, 2020.

[5] A. Pena-Perez et al., "A low-power single-ended sar adc with energy-efficient differential switching for ultrafast x-ray imagers," IEEE OJCAS, pp. 1–1, 2025.
[6] P. Harpe, "A compact 10-b sar adc with unit-length capacitors and a passive fir filter," IEEE JSSC, vol. 54, no. 3, pp. 636–645, Mar. 2019.

MIC-03-07

Inverse Analysis of Pulse Pile-Up and Charge Sharing in Photon-Counting Detectors (#1582)

Rikuto Sawada[1], Katsuyuki Taguchi[2], Kenji Amaya[1]

[1] Institute of Science Tokyo, Department of Systems and Control Engineering, Otaku, Japan; [2] Johns Hopkins University, Department of Radiology and Radiological Science, Baltimore, USA

Abstract

Photon-counting detectors offer high spatial resolution and energy discrimination for advanced X-ray imaging. However, their performance is limited due to pulse pile-up and charge sharing, which distort the observed current waveforms.

In this study, we propose a Bayesian inverse analysis framework to estimate photon events directly from observed current waveforms. The detector response is modeled by the drift-diffusion equation. Photon events are parameterized by their energy, arrival time, and interaction position. The event parameters are estimated using Bayesian inference. Prior probability distributions of the number of events and interaction depths are incorporated to obtain physically plausible solutions.

Numerical simulation results demonstrated that the proposed method accurately estimated photon events under pulse pile-up and charge sharing conditions. Furthermore, the reconstructed energy spectra showed reduced distortion compared with the conventional method.

MIC-03-08

Towards the first ToF-CT X-ray image: acquisition and scatter correction (#1314)

Gabriel Belanger[1,2], Gaétan Lemaire[1,2], Julien Rossignol[1,2], Yves Bérubé-Lauzière[1,2], Audrey Corbeil Therrien[1,2], Marc-André Tétrault[1,2], Réjean Fontaine[1,2]

[1] Universite de Sherbrooke, Electrical and computer engineering, Sherbooke, Canada; [2] Universite de Sherbrooke, Institut Interdisciplinaire d'Innovation Technologique (3IT), Sherbrooke, Canada

Thank you to CRSNG and Chaire de recherche du Canada for funding this research.

Abstract

All components of a first Time-of-flight CT scanner prototype are now assembled at Université de Sherbrooke where both timing and energy measurements enabled to create first line profiles. Previous simulation studies have shown that, by using these measurements, the contribution of scattered photons to an image can be estimated and removed without an using anti-scatter grid. The scanner prototype can now explore and confirm the measurement and scatter correction methods used in simulation studies. The experimental setup is composed of a scintillator coupled to an SiPM readout and a Weerock front end board. This board includes a Radioroc ASIC along with a picoTDC. An FPGA harvest data and send them to a PC for signal processing. From these data, primary and scatter counts in each pixel can be recovered through the use of an iterative deconvolution algorithm. The experiment successfully produced a small photon counting projection image of an ACR phantom and produced time-of-flight distribution measurements for each pixel with around 550~ps FWHM resolution for the full energy spectrum (30 to 120 keV). Scatter correction lead to a contrast resolution improvement of 195\% in the irradiated bone-water region of the phantom. Its accuracy was partially validated with an analytical calculation of the X-ray's penetration through a part of the phantom with a 5.2\% penetration calculated, and a 10.8\% and 5.7\% penetration before and after scatter correction respectively.

References

[1] Rossignol, J., Turtos, R.M., Gundacker, S., Gaudreault, D., Auffray, E., Lecoq, P., Bérubé-Lauzière, Y. and Fontaine, R. 2020. “Time-of-flight computed tomography - proof of principle:” *Physics in Medicine & Biology*,IOP Publishing Vol. 65, No. 8, p. 085013.

[2] Lemaire, G., Espagnet, R., Haddar, A., Perez, F., Ahmad, S., Cizel, J.-B., Corbeil Therrien, A., Trétault, M.A., Bérubé-Lauzière, Y. and Fontaine, R. 2025. "Exploration of the Radioroc ASIC for Multipixel X-Ray Time-of-Flight Measurements for Medical Imaging". *2025 IEEE Nuclear Science Symposium (NSS), Medical Imaging Conference (MIC) and Room Temperature Semiconductor Detector Conference (RTSD).*

[3] Rossignol, J., Bélanger, G., Fromont, M., Therrien, A.C., Fontaine, R. and Bérubé-Lauzière, Y. 2024. “Scatter estimation and correction using time-of-flight and deconvolution in x-ray medical imaging:” *Physics in Medicine & Biology*,IOP Publishing Vol. 69, No. 17, p. 175017.

[4] Bélanger, G., Rossignol, J., Bérubé-Lauzière, Y., Therrien, A.C. and Fontaine, R. (2025). "Reduced Time-Of-Flight Measurements for Accurate Scatter Estimation and Correction X-Ray Ct". *2025 IEEE Nuclear Science Symposium (NSS), Medical Imaging Conference (MIC) and Room Temperature Semiconductor Detector Conference (RTSD).*

[5] Berger, M.J.,Hubbell, J.H., Seltzer, S.M., Chang, J., Coursey, J.S., Sukumar, R., Zucker, D.S., and Olsen, K., 2010, XCOM: Photon Cross Sections Database. *NIST Standard Reference Database 8 (XGAM). NIST, PML, Radiation Physics Division.*

Time:
11 November, 2026
15:00 – 17:00

Room:
MANUEL DE FALLA

MIC-04 | Quantitative imaging, image assessment and standardization

Chairs:
Christoph W. Lerche (Jülich)
Jorge Roser (Lübeck)

MIC-04-01

Single-Source Cross-Tracer Brain PET Attenuation Correction via Anchored Flow Matching with Attenuation Maps from Simultaneous Reconstruction (#1516)

Min Jeong Cho[1,2], Seung Kwan Kang[3], Jae Sung Lee[4,5]

[1] Seoul National University, Interdisciplinary Program of Bioengineering, Seoul, South Korea; [2] Seoul National University, Integrated Major in Innovative Medical Science, Seoul, South Korea; [3] Samsung Ventures, Seoul, South Korea; [4] Seoul National University, Department of Nuclear Medicine, Seoul, South Korea; [5] Brightonix Imaging Inc., Seoul, South Korea

This research was supported by the AI Computing Infrastructure Enhancement (GPU Rental Support) User Support Program funded by the Ministry of Science and ICT (MSIT), Republic of Korea. (No. RQT-25-090157)

Abstract

Accurate attenuation correction (AC) is essential for quantitative PET imaging, but CT-free AC across diverse radiotracers remains challenging. MLAA-derived μ-maps are useful inputs for deep learning-based AC. However, tracer-dependent biodistribution introduces domain shifts that limit the generalizability of models trained only on ^{18}F-FDG. We propose a single-source cross-tracer CT-free AC framework that combines tracer-robust U-Net regression with anchored flow matching. Local Gamma Field augmentation is used during U-Net training to mimic anatomy-preserving regional intensity and contrast variations in MLAA μ-maps, encouraging tracer-independent MLAA-to-CT mapping. The U-Net output is then used as an anchor for an unconditional flow-matching model trained on CT μ-maps, enabling generative refinement from a reliable deterministic estimate. The proposed method achieved the highest PSNR across all evaluated tracers and reduced MLAA noise, tracer-specific artifacts, and U-Net over-smoothing. AC PET analysis showed strong agreement with CT-based AC PET, with regional uptake correlations closest to the identity line. These results demonstrate that the proposed framework enables accurate and structurally faithful μ-map estimation across multiple tracers using only FDG training data.

References

[1] Hwang, D., Kang, S. K., Kim, K. Y., Seo, S., Paeng, J. C., Lee, D. S., & Lee, J. S. (2019). Generation of PET attenuation map for whole-body time-of-flight 18F-FDG PET/MRI using a deep neural network trained with simultaneously reconstructed activity and attenuation maps. *Journal of Nuclear Medicine*, *60*(8), 1183-1189.

[2] Lipman, Y., Chen, R. T., Ben-Hamu, H., Nickel, M., & Le, M. Flow Matching for Generative Modeling. In *The Eleventh International Conference on Learning Representations*.

MIC-04-02

High-Energy Penetration Correction in Multi-Aperture SPECT Using Aperture–Plate Ray Decomposition (#1606)

Yusheng Li[1], Qian Wang[2], Liuchun He[1], Hongdi Li[1]

[1] United Imaging Healthcare North America, MI, Houston, USA; [2] United Imaging Healthcare, MI, Shanghai, China

Abstract

Multi-aperture single-photon emission computed tomography (SPECT) at ¹³¹I (364 keV) exhibits a detector-wide plate-penetration halo: a 1.8 cm tungsten plate transmits ~4 × 10^{−4} at μ_W = 4.4 cm^{−1}. Prior corrections perform the aperture/plate split at the photon level via effective-radius point-spread function enlargement, or at the system-matrix level via per-ray full-physics tracing; both merge the two components at storage time, inflating memory by one to two orders of magnitude. We propose a storage-agnostic per-ray partition: a topological rule on the source-to-detector intersection list separates the response into a sparse, peaked aperture component A and a slowly varying plate halo B, upstream of any representation choice. The rule is mutually exclusive and jointly exhaustive, so A_{ij} + B_{ij} = C_{ij} holds bit-exactly against the unsplit baseline for any per-ray contribution functional; the plate path length is a closed-form slab chord minus an analytic aperture chord at O(N_{ap}) per ray. On a 34-module multi-aperture SPECT ring (small-aperture configuration), the identity holds bit-exactly across three projection modes (collimator-path, sensitivity, counts) for a centered single-photon source and across every pixel of 34 Jaszczak hot-rod ¹³¹I views, with per-pixel plate intensity ~10^{−4}–10^{−3} of the aperture peak. OSEM correction with a lagged plate estimate will be presented at the conference.

References

[1] K. van Audenhaege, R. Van Holen, S. Vandenberghe, C. Vanhove, S. D. Metzler, and S. C. Moore, “Review of SPECT collimator selection, optimization, and fabrication for clinical and preclinical imaging,” Med. Phys., vol. 42, no. 8, pp. 4796–4813, 2015. [Online]. Available: https://doi.org/10.1118/1.4927061

[2] M. F. Smith and R. J. Jaszczak, “An analytic model of pinhole aperture penetration for 3D pinhole SPECT image reconstruction,” Phys. Med. Biol., vol. 43, no. 4, pp. 761–775, 1998. [Online]. Available: https://doi.org/10.1088/0031-9155/43/4/006

[3] S. D. Metzler and S. C. Moore, “Analytic determination of rectangular-pinhole sensitivity with penetration,” IEEE Trans. Med. Imag., vol. 39, no. 4, pp. 833–843, Apr. 2020. [Online]. Available: https://doi.org/10.1109/TMI.2019.2936187

[4] K. Vunckx, J. Nuyts, H. Vanbilloen, M. De Saint-Hubert, D. Vanderghinste, D. Rattat, F. M. Mottaghy, and M. Defrise, “Optimized multipinhole design for mouse imaging,” IEEE Trans. Nucl. Sci., vol. 56, no. 5, pp. 2696–2705, 2009. [Online]. Available: https://doi.org/10.1109/TNS.2009.2030194

[5] H. M. Hudson and R. S. Larkin, “Accelerated image reconstruction using ordered subsets of projection data,” IEEE Trans. Med. Imag., vol. 13, no. 4, pp. 601–609, 1994. [Online]. Available: https://doi.org/10.1109/42.363108

[6] Y. Li and H. Li, “Minkhole collimators for SPECT: Minkowski-sum aperture geometry and closed-form ray tracing,” in Proc. IEEE Nucl. Sci. Symp. Med. Imag. Conf. (NSS/MIC) RTSD, 2026, submitted.

MIC-04-03

Improving Lutetium Background Radiation-based Attenuation Correction for CT-less PET Using Singles-derived Randoms (#2103)

Bing Dai[1], **Bing Dai**[1], Stephen C. Moore[1], Stephen C. Moore[1], Margaret E. Daube-Witherspoon[1], Margaret E. Daube-Witherspoon[1], Florence M. Muller[1,2], Florence M. Muller[1,2], Joel S. Karp[1], Joel S. Karp[1]

[1] University of Pennsylvania, Department of Radiology, Philadelphia, USA; [2] Ghent University, Faculty of Engineering and Architecture, Ghent, Belgium

This work was supported by NIH CA-113941. FMM acknowledges support from the Research Foundation Flanders (11P0E24N0). Authors thank S McDonald for phantom experiments.

Abstract

Lutetium background radiation in modern PET scanners enables activity- and tracer-independent transmission measurement for attenuation correction (AC) without CT scans. However, quantitative accuracy of attenuation maps (μ-maps) derived from lutetium transmission (Lu-Tx) is limited by low transmission statistics and noisy randoms estimation from delayed coincidences (DE). In this work, we investigate the use of singles-derived randoms (RS) to improve Lu-Tx-based AC for CT-less PET. Emission and Lu-Tx data were acquired simultaneously on the PennPET Explorer, a 142-cm long axial field-of-view (LAFOV) scanner. μ-maps were reconstructed using maximum-likelihood transmission reconstruction with randoms estimated from either delayed coincidences or singles data, then used for attenuation and scatter correction during PET image reconstruction. The methods were evaluated using physical phantoms, including uniform cylinders, a 190-cm pipe phantom, cylinders with non-uniform axial activity distributions, and an image quality (IQ) phantom. Data were subsampled to simulate low-count short clinical scans. RS produced substantially smoother sinograms while maintaining agreement with DE in total randoms counts. Incorporation of RS improved axial uniformity, reduced noise, and mitigated emission contamination-induced bias in μ-maps, particularly under low-count conditions and non-uniform activity distributions. In IQ phantom studies, AC PET images reconstructed using RS demonstrated contrast comparable to CT-AC PET, whereas DE led to reduced contrast and increased bias, especially for short scans. These results demonstrate that RS improves the quantitative accuracy of Lu-Tx-based AC and support the proposed method as a practical pathway towards CT-less PET for both long dynamic imaging and short clinical scans.

References

[1] Sari H, Teimoorisichani M, Viscione M, et al. Feasibility of an Ultra-Low-Dose PET Scan Protocol with CT-Based and LSO-TX–Based Attenuation Correction Using a Long–Axial-Field-of-View PET/CT Scanner. *Journal of Nuclear Medicine*. 2025. doi:10.2967/jnumed.124.268380

[2] Daube-Witherspoon ME, Moore SC, Karp JS. Randoms Estimation for Long Axial Field-of-View PET. *IEEE Transactions on Radiation and Plasma Medical Sciences*. 2025:1-1. doi:10.1109/TRPMS.2025.3591035

[3] Dai B, Daube-Witherspoon ME, McDonald S, et al. Performance evaluation of the PennPET explorer with expanded axial coverage. *Physics in Medicine & Biology*. 2023;68(9):095007. doi:10.1088/1361-6560/acc722

[4] Li Y, Matej S, Karp JS. Practical joint reconstruction of activity and attenuation with autonomous scaling for time-of-flight PET. *Phys Med Biol*. 2020;65(23):235037. doi:10.1088/1361-6560/ab8d75

MIC-04-04

Estimation of random events in PET imaging using the time differences of uncorrelated singles (#2578)

Maxime Toussaint[1], Thomas Carlier[1,2], Simon Stute[1,2]

[1] Nantes Université, Laboratoire CRCI2NA, INSERM, CNRS, Nantes, France; [2] Nantes University Hospital, Nuclear Medicine Department, Nantes, France

This work has been funded by the French INCA-DGOS-INSERM/ITMO Cancer 18011 (SIRIC ILIAD).

Abstract

Correction of random coincidences is required in clinical PET imaging. Several methods have been proposed to estimate their distributions in a PET acquisition and they mostly use singles detection and/or a delayed coincidence window (DCW). We propose a new approach to achieve this task, which uses the differences in arrival times between consecutive single events that are greater than the coincidence window. This approach is thus less susceptible to bias induced by true coincidences and has more statistics than a DCW. As a proof of concept, a first implementation of this approach was compared to the classic methods using simulations from a small-sized PET scanner. The acquisition of four phantoms, each with different challenges in terms of randoms estimation, were simulated over a range of activities. Overall, the proposed method was less biased than the classical methods while also being more precise than DCW.

References

[1] T. Carlier et al., “Assessment of acquisition protocols for routine imaging of Y-90 using PET/CT,” EJNMMI research, vol. 3, no. 1, p. 11, 2013

[2] S. R. Cherry et al., Physics in nuclear medicine. Saunders, 2003, vol. 3.

[3] M. Conti, “Effect of randoms on signal-to-noise-ratio in tof pet,” in IEEENuclear Science Symposium Conference Record, 2005, vol. 3.IEEE, 2005,pp. 6–pp.

[4] J. F. Oliver et al., “Improving the singles rate method for modeling accidentalcoincidences in high-resolution pet,” Physics in Medicine & Biology, vol. 55,no. 22, pp. 6951–6971, 2010.

[5] J. F. Oliver et al., “Modelling random coincidences in positron emission tomography byusing singles and prompts: a comparison study,” PloS one, vol. 11, no. 9, p.e0162096, 201

[6] D. Sarrut et al., “The opengate ecosystem for monte carlo simulation inmedical physics,” PMB, vol. 67, no. 18, p. 184001, sep 2022.

[7] C. C. Watson, “A hybrid algorithm for randoms variance reduction,” in 2009IEEE Nuclear Science Symposium Conference Record (NSS/MIC). IEEE,2009, pp. 3882–3885.

MIC-04-05

Quantitative Activities Evaluation of Ac-225 and Daughter Nuclides Using the Alpha-SPECT Mini System (#3094)

Wenbo Zhao[1], Xuhan Luo[1], Ling-Jian Meng[2], Yong Du[1]

[1] Johns Hopkins University School of Medicine, Baltimore, USA; [2] University of Illinois at Urbana and Champaign, Champaign Il, Champaign, USA

This research was funded by National Institutes of Health, grant number S10OD038221. The content is solely the responsibility of the authors and does not necessarily represent the official views of the National Institutes of Health.

Abstract

The Alpha-SPECT Mini system integrates SPECT imaging with CT-based attenuation correction, providing a platform for quantifying in vivo distributions of alpha-emitting radiopharmaceuticals and daughter radionuclides. In this study, three Ac-225 filled syringes with different volumes, 0.5, 4.2, and 18.0 mL, respectively, were scanned with Alpha-SPECT Mini. The ground truth activities were[YD1] 26.12 μCi, 21.62 μCi, and 18.80 μCi from the smallest to the largest syringe, respectively. SPECT listmode acquisition was performed for 20 minutes for each syringe, together with an 80 kV CT scan for attenuation correction. SPECT images were reconstructed for the following photopeaks: 100 keV for Ac-225, 218 keV for Fr-221, 440 keV for Bi-213, and 117 keV for Tl-209. Activities of Ac-225 and these daughter radionuclides, were then estimated from SPECT images using CT defined ROIs and compared with ground truth.

The results showed that quantification accuracy varied with the radionuclides and syringe sizes. Fr-221 and Bi-213 showed relatively lower errors (<5%), while Ac-225 and Tl-209 exhibited larger deviations. The higher errors likely due to the low abundance of low energy (100 keV for Ac-225 and 117 keV for Tl-209) photopeaks and interference from downscatter and collimator penetration from high energy photons. Tl-209 also exhibited larger deviations with a size-dependent trend, suggesting sensitivity to source geometry and scatter correction. Overall, the Alpha-SPECT Mini system showed potential for quantitative imaging of Ac-225 and daughter radionuclides. Future work includes further calibration and implementation of scatter correction.

MIC-04-06

Physics-Driven Methods for Standardizing Radiomics Features in CT Data (#2771)

Huay Din[1], Yijie Yuan[2], Grace H. Kim[3], Michael F. McNitt-Gray[3], Joseph W. Stayman[2], Grace J. Gang[1]

[1] University of Pennsylvania, Radiology, Philadelphia, USA; [2] Johns Hopkins University, Biomedical Engineering, Baltimore, USA; [3] University of California, Los Angeles, Radiology, Los Angeles, USA

This work was supported, in part, by the NIH Grant R01EB031592.

Abstract

Radiomics have demonstrated potential in numerous clinical applications. However, feature variability resulting from different scanner hardware and image processing degrades predictive ability and reduces model generalizability. We present a novel physics-driven framework for radiomics standardization. Assuming a linear, shift-invariant image formation model, we developed an analytical method to remove the dependency of radiomics features classes on known spatial resolution and noise properties. The method consists of two deconvolution operations: deconvolving the system blur from the reconstructed image, then deconvolving the noise probability density function from radiomics feature distributions. This approach is applicable to multiple feature classes. We further developed a workflow to implement this framework on a clinical CT scanner. The method was evaluated on an anthropomorphic lung phantom imaged at five dose levels and reconstructed using eight kernels. Results demonstrate that the standardization method effectively improves the consistency of radiomics features value with those at reference imaging conditions. As expected, standardizing from smoother kernels to sharp kernels is more challenging than the reverse. The proposed standardization method is a promising tool for improving the robustness and generalizability of radiomics models.

References

[1] D. Mackin, X. Fave, L. Zhang, J. Yang, A. K. Jones, C. S. Ng and L. Court, "Harmonizing the pixel size in retrospective computed tomography radiomics studies," PLoS One, vol. 13, no. 1, 2017.

[2] Mackin D, Ger R, Gay S, Dodge C, Zhang L, Yang J and Jones AK 2019. Matching and homogenizing convolution kernels for quantitative studies in computed tomography Investigative Radiol. 54 288–95

[3] H. Um, F. Tixier, D. Bermudez, J. O. Deasy, R. J. Young and H. Veeraraghavan, "Impact of image preprocessing on the scanner dependence of multi-parametric MRI radiomic features and covariate shift in multi-institutional glioblastoma datasets," Phys. med. Biol., vol. 64, 2019.

[4] W. E. Johnson, C. Li and A. Rabinovic, "Adjusting batch effects in microarray expression data using empirical Bayes," Biostatistics, vol. 8, no. 1, pp. 118-127, 2007.

[5] G. J. Gang, R. Deshpande and J. W. Stayman, "Standardization of histogram- and gray-level co-occurrence matrices-based radiomics in the presence of blur and noise," Phys Med Biol., 2021.

[6] G. J. Gang, W. Zbijewski, J. W. Stayman and J. H. Siewerdsen, "Cascaded systems analysis of noise and detectability in dual-energy cone-beam CT," Med. Phys, vol. 39, no. 8, pp. 5145-5156, 2012.

MIC-04-07

Uncertainty estimation for ^{123}I-DaTSCAN (#2802)

Kelley M. Ferreira[1,3], Andrew P. Robinson[3], Kevin M. Bradley[1,4], Daniel R. McGowan[1,2]

[1] Oxford University Hospitals NHS Foundation Trust, Department of Medical Physics and Clinical Engineering, Oxford, UK; [2] National Physical Laboratory (NPL), Teddington, UK; [3] University of Oxford, Department of Oncology, Oxford, UK; [4] University Hospital of Wales, Wales Research and Diagnostic Positron Emission Tomography Imaging Centre (PETIC), Wales, UK

The National Physical Laboratory is operated by NPL Management Ltd, a wholly owned company of the UK Department for Science, Innovation and Technology (DSIT).

Abstract

^{123}I-DaTSCAN is used to aid diagnosis of Parkinsonism. Visual analysis of ^{123}I-DaTSCAN is used in conjunction with patient clinical history and semi-quantification. Specific Binding Ratios (SBR) are commonly estimated for the right and left putamen and caudate using commercially available software. The estimation of uncertainties is not common for this clinical study; however, the benefits of estimating uncertainties have been recognised for other clinical applications. In this work, a method to evaluate the uncertainty associated with SBR is developed using phantom data and then applied to estimate uncertainties for imaging data from a cohort of patients. List mode data was acquired and bootstrapped to create equivalent sinograms. The sinograms were reconstructed and processed using BRASS software to obtain the distribution of SBR and respective standard deviations were estimated. The impact of estimating uncertainties in patient classification is also considered.

For the patient data, the estimated standard uncertainties varied between 2.8 % and 19 %. The correlation of SBR uncertainty with patient classification within the cohort is presented. Initial analysis suggests the patient classification does not change when considering uncertainty, but does provide confidence in the results.

This is the first time that uncertainties on SBR values are used to evaluate impact on patient classification. Future work will include analysing additional patient data to further investigate the impact of uncertainties in patient classification. Analysis to understand if the uncertainties can be reduced is also planned.

References

[1] JCGM, “Evaluation of measurement data-guide to the expression of uncertainty in measurement évaluation des données de mesure-guide pour l’expression de l’incertitude de mesure,” Tech. Rep., 2008. [Online]. Available: www.bipm.org.

[2] A. Possolo, “Simple guide for evaluating and expressing the uncertainty of NIST measurement results NIST technical note 1900,” National Institute of Standards and Technology, vol. 1297, pp. 1–20, 2015. [Online]. Available: http://dx.doi.org/10.6028/NIST.TN.1900.

[3] L. Mari *et* al. “Measurement fundamentals: A pragmatic view,” IEEE Transactions on Instrumentation and Measurement, vol. 61, pp. 2107–2115,
2012.

[4] S. Morbelli *et* al. “EANM practice guideline/SNMMI procedure standard for dopaminergic imaging in parkinsonian syndromes 1.0,” European Journal of Nuclear Medicine and Molecular Imaging, vol. 47, pp. 1885–1912, 2020.

[5] I. Buvat, “A non-parametric bootstrap approach for analysing the statistical properties of SPECT and PET images,” Physics in Medicine and Biology, vol. 47, pp. 1761–1775, 2002.

MIC-04-08

Towards Absolute Resolution Characterization in OSEM Reconstructed Images without Ground Truth: Using FBP Reconstructed Images as the Bridge (#2809)

Yifan Hu[1], Liang Guo[2], Tim Mulnix[1], Thibault Marin[1], Richard E. Carson[1,2]

[1] Yale University, Department of Radiology and Biomedical Imaging, New Haven, USA; [2] Yale University, Department of Biomedical Engineering, New Haven, USA

Abstract

Absolute resolution characterization of OSEM-reconstructed images is challenging because the OSEM algorithm is nonlinear and its resolution strongly depends on the activity distribution and the number of iterations. In contrast, the linear FBP algorithm provides a more consistent resolution, albeit with higher noise. In this work, we propose using FBP-reconstructed images as a bridge to estimate the absolute resolution of OSEM images without requiring ground truth. Two FBP-bridge approaches are investigated: an image-domain Gaussian fitting method and a frequency-domain modulation transfer function (MTF) ratio method. Hoffman phantom experimental results show that the Gaussian fitting approach has better agreement with the reference FWHM obtained using the known phantom ground truth. Both methods are further applied to human brain PET scans. This method also allows pixel-wise visualization of spatially variant image resolution. Future work will investigate the effects of noise and FBP filter selection.

Time:
11 November, 2026
17:30 – 19:00

Room:
Poster Area

MIC-05 | MIC Poster Session 1

Chairs:
Margaret E. Daube-Witherspoon (Philadelphia)
Fabian P. Schmidt (Tuebingen)

MIC-05-001

Variable Angle Slant-Hole Collimator for Molecular Breast Imaging System (#1035)

Seungjoon Lee[1], Andrew Weisenberger[1], Bradley Patt[2], James Hugg[2]

[1] Thomas Jefferson National Accelerator Facility, Nuclear Physics, Newport News, USA; [2] Smartbreast Corporation, Sherman Oaks, USA

Abstract

A Variable Angle Slant-Hole (VASH) collimator has been developed for integration with the SmartBreast's Eve ClearScan e750 Molecular Breast Imaging (MBI) system, formerly known as the GE Discovery NM750b. This effort builds upon prior success implementing VASH technology in the Dilon 6800 camera platform, where slanted collimator geometries demonstrated improved resolution and lesion detectability in breast imaging applications. The SmartBreast MBI system incor-porates high-resolution cadmium zinc telluride (CZT) detectors, replacing earlier NaI(Tl)-based designs, and thus necessitates a redesigned collimator geometry to fully leverage the intrinsic resolution and detector compactness. The new VASH design incorporates a reduced hole pitch of 1.84 mm, fixed septal thickness of 0.4 mm, and a shortened collimator depth of 13 mm, in contrast to the original lead-based parallel-hole collimator (2.46 mm pitch, 0.4 mm septa, 21 mm depth). These parameters were selected to balance sensitivity and spatial resolution. Ana-lytical calculations indicate that the redesigned VASH achieves comparable or improved resolution and sensitivity performance at clinically relevant object-to-collimator distances up to 60 mm. The first prototype is under construction, with mechanical inte-gration, phantom imaging, and angular performance evaluation scheduled for upcoming testing. The VASH system offers imaging flexibility in clinical MBI and has potential implications for improving detection of lesions at variable depths in dense breast tissue.

MIC-05-004

Characterization of the CHLOE readout for dual-ended BGO crystals for PET with the FastIC+ (#1221)

Claudio San Martín Valenzuela[1], Marino Maiorino[1], Afonso Xavier Pinto[3], Nicolaus Kratochwil[2], Elisabetta Medina[1], Carles Puigdengoles[1], Mokhtar Chmeissani[1], Gerard Ariño-Estrada[1,2]

[1] Institut de Física d'Altes Energies - Barcelona Institute of Science and Technology (IFAE - BIST), Bellaterra, Spain; [2] University of California at Davis (UC DAVIS), Department of Biomedical Engineering, Davis, USA; [3] University of Aveirno, Aveiro, Portugal

This work was supported by the European Research Council Starting Grant #101041972 and by the ATRAE grant #ATR2023-143812 from the Spanish Research Agency.
The authors would like to acknowledge the advice from the FastIC+ team at ICCUB.

Abstract
The performance of gamma detectors for time-of-flight positron emission tomography (TOF-PET) has improved significantly over the last decade. With commercial systems surpassing the 200~ps coincidence time resolution (CTR) barrier, the avenues for improving TOF-PET detector performance become progressively more limited. We report on CHLOE (Cherenkov Light Module), a PET detector readout with high channel density composed of dual ended readout bismuth germanate (BGO) crystals coupled one-to-one to silicon photomultipliers (SiPMs) with the goal of providing a trade-off between 3D detector segmentation, energy resolution, and scalability in an intrinsic radiation-free crystal. The electronics were based on the FastIC+ chip and the complete readout chain, from the front-end to the back-end was customized for this concept.

This work presents the first electronic and detector characterization of the CHLOE readout approach. The noise and dark counts contributions of the system are presented, including measurements of channel dependencies in the response. Energy spectra were obtained for ^{22}Na and ^{133}Ba sources. The work presented in this contribution represents the very first steps towards a full functional characterization of the CHLOE readout.

References
[1] Mariscal-Castilla, A. *et al.*, 2024, 'Toward Sub-100 ps TOF-PET Systems Employing the FastIC ASIC With Analog SiPMs,', *IEEE Transactions on Radiation and Plasma Medical Sciences*, vol. 8, no. 7, pp. 718-733, doi: 10.1109/TRPMS.2024.3414578.
[2] Mauricio, J. *et al.*, 2024, 'FastIC+: An Analog Front-End including on-chip TDCs for fast timing detectors,' *2024 IEEE Nuclear Science Symposium (NSS), Medical Imaging Conference (MIC) and Room Temperature Semiconductor Detector Conference (RTSD)*, Tampa, FL, USA, 2024, pp. 1-1, doi: 10.1109/NSS/MIC/RTSD57108.2024.10657159.

MIC-05-007

A 0.32 mm Pitch GAGG Array-Based SPECT Detector (#1596)

Jiahao Xie, Haibo Wang, Jinyi Qi, Simon R. Cherry, Junwei Du

University of California at Davis, Biomedical Engineering, Davis, USA

This work was supported by the NIH R01 EB031961.

Abstract
Multi-tracer preclinical single-photon emission computed tomography (SPECT) enables simultaneous tracking of multiple physiological processes inside organs, requiring detectors with high spatial and energy resolution over a broad energy range. In this study, we developed and evaluated a high-resolution detector comprising a 28 × 28 gadolinium aluminum gallium garnet (GAGG) array (0.32 mm pitch, 2 mm thickness) coupled to a linearly graded silicon photomultiplier (LG-SiPM) using radiation sources with different energies: 55, 122, 202, 307, 511 keV. Flood histograms demonstrated clear separation of crystal elements over a wide energy range from 55 keV to 511 keV.

Furthermore, the detector achieved energy resolutions of 18% at 122 keV and 12% at 511 keV, along with excellent energy linearity across 55–511 keV (R^2 = 0.996). These results demonstrate that the developed detector is a promising candidate for high-resolution small-animal SPECT systems.

References
[1] Y. Bouchareb *et al.*, "Technological Advances in SPECT and SPECT/CT Imaging," *Diagnostics*, vol. 14, no. 13, Jul. 2024, doi: 10.3390/diagnostics14131431.
[2] G. Soultanidis, J. L. Herraiz, Z. A. Fayad, J. Grimm, and A. J. P. Teunissen, "Multiplexed imaging of radionuclides," *Nat. Biomed. Eng*, vol. 9, no. 7, pp. 993–1006, Jul. 2025, doi: 10.1038/s41551-025-01406-8.
[3] F. Acerbi, S. Merzi, and A. Gola, "Large area tiles of position-sensitive silicon photomultipliers," *Nuclear Instruments and Methods in Physics Research Section A: Accelerators, Spectrometers, Detectors and Associated Equipment*, vol. 1067, p. 169650, Oct. 2024, doi: 10.1016/j.nima.2024.169650.
[4] J. Xie *et al.*, "High spatial resolution PET detectors based on 10 mm × 10 mm linearly-graded SiPMs and 0.5 mm pitch LYSO arrays," *Phys. Med. Biol.*, vol. 70, no. 2, p. 025016, Jan. 2025, doi: 10.1088/1361-6560/ada084.
[5] J. Xie, H. Wang, and J. Du, "High-resolution dual-ended readout PET detectors based on 0.5 mm pitch LYSO arrays with various reflectors," *Medical Physics*, vol. 52, no. 9, p. e18103, 2025, doi: 10.1002/mp.18103.
[6] J. Du *et al.*, "Characterization of Large-Area SiPM Array for PET Applications," *IEEE Transactions on Nuclear Science*, vol. 63, no. 1, pp. 8–16, Feb. 2016, doi: 10.1109/TNS.2015.2499726.

MIC-05-010

Sub-millimeter PET detectors using multiplexed readout with ASIC

(#1718)

Zhiqiang Zhu, Linjun Zhang, Hui Huang, Haonan Li, Yongfeng Yang, **Zheng Liu**

Shenzhen Institute of Advanced Technology, Chinese Academy of Sciences, Shenzhen, China

This work is supported by the National Natural Science Foundation of China (Grant No. 12375358), the National Key Research and Development Program of China (2023YFF0716000), the Shenzhen Science and Technology Program (JCYJ20220531100000001, JCYJ20220818101804009).

Abstract

This study presents a sub-millimeter resolution small-animal PET detector based on a dual-ended readout configuration with highly multiplexed signal processing, targeting applications in compact and MRI-compatible PET insert systems. The detector employs a LYSO crystal array coupled to silicon photomultiplier (SiPM) arrays on both ends. A row-column summation multiplexing scheme is adopted to compress multi-channel SiPM signals into a limited number of position-encoding outputs, while a dedicated multi-channel ASIC (MPT2321) is utilized for signal amplification, timing extraction, and digitization. The multiplexed signals are directly processed by the ASIC without requiring individual channel readout, significantly reducing the number of electronic channels and system complexity, which is particularly beneficial for integration in high-field MRI environments. Experimental results demonstrate that all crystal elements in the 26 × 26 LYSO array can be clearly resolved in the flood histogram. The detector achieves an average energy resolution of 15.3 ± 0.7%, a DOI resolution of 2.56 ± 0.46 mm, and a detector timing resolution (DTR) of 2.40 ± 0.20 ns. The proposed detector design demonstrates that highly multiplexed readout combined with ASIC-based signal processing can effectively reduce system complexity and cost while maintaining good spatial, energy, and DOI performance, making it suitable for high-resolution small-animal PET imaging and compact PET/MRI insert applications.

References
[1] Cherry, S.R. and S.S. Gambhir, Use of positron emission tomography in animal research. ILAR journal, 2001. 42(3): p. 219-232.

[2] Xi, W., M. Tian, and H. Zhang, Molecular imaging in neuroscience research with small-animal PET in rodents. Neuroscience research, 2011. 70(2): p. 133-143.
[3] Virdee, K., et al., Applications of positron emission tomography in animal models of neurological and neuropsychiatric disorders. Neuroscience & Biobehavioral Reviews, 2012. 36(4): p. 1188-1216.
[4] Miyaoka, R.S. and A.L. Lehnert, Small animal PET: a review of what we have done and where we are going. Physics in Medicine and Biology, 2020. 65(24).

MIC-05-013

Performance Evaluation of a Position Sensitive SiPM for Decoding Ultra-Small Crystal Arrays (#1901)

Jianlang Hua, Xiaoqin Zhang, Ming Niu, Hang Yang, RuiPeng Dai, Zheng Gu

Shenzhen Bay Laboratory, Institute of Biomedical Engineering, Shenzhen, China

This work is supported by the National Natural Science Foundation of China (Nos. 12275182 and 62371314), the National Key R&D Program of China (No. 2023YFC2414800), Guangdong Basic and Applied Basic Research Foundation (Nos. 2024A1515012154), the Guangdong Provincial Project (Grant No. 2023TQ07A233), the Major Program of Shenzhen Bay Laboratory (No. C1012530005) and the Shenzhen Bay Laboratory Proof-of Concept Grants (No. C1022430005).

Abstract

We evaluate the spatial decoding capability and energy resolution of a position sensitive SiPM (PS-SiPM, model PSS 11-6060-S, Capital Photonics Technology, China) with an active area of 6.24 mm × 6.24 mm. The PS-SiPM is optically coupled to a checkerboard-pattern scintillator array, which is composed of alternating LYSO and BGO crystals with a 0.38 mm crystal size and a 0.46 mm pitch, arranged in a 28 × 28 array. To compensate for the lower scintillation light yield of BGO, a custom amplifier board with a nominal gain of 16 was incorporated into the readout chain.

Delayed charge integration (DCI) technique was applied for distinguishing LYSO and BGO events based on pulse shape. The average rise and decay time constants were measured 31 ns and 313 ns for BGO, and 22 ns and 60 ns for LYSO, respectively. Using an Anger-logic positioning algorithm, the resulting flood image successfully resolved a 13 × 13 sub-region of the crystal array, with minimal edge decoding difficulty. It highlights the advantage of the PS-SiPM in identifying edge crystals.

Energy resolution was evaluated within a central 9 × 10 crystal pixels to mitigate intrinsic geometric constraints. The 45 LYSO crystals in this region achieved an average energy resolution of 18.52% ± 2.39%, and the 45 interleaved BGO crystals achieved 25.54% ± 2.48%. These results confirm the feasibility of using a PS-SiPM for decoding sub-millimeter crystal array, and provide a performance reference for the implementation of PS-SiPMs in ultra-high-resolution nuclear imaging detectors.

References

[1] Peng Y, Lv W, Dai L, et al. A square-bordered position-sensitive silicon photomultiplier toward distortion-free performance with high spatial resolution. IEEE Electron Device Letters, 2020, 41(12): 1802-1805.
[2] Gu Z, Yang H, Zhao Y, et al. An LYSO and BGO checkerboard pattern detector with inter-crystal scatter identification capability. 2023 IEEE NSS MIC RTSD. IEEE, 2023: 1-1.

MIC-05-016

Joint Deconvolution Framework for Photon-Train Reconstruction from Dual-Channel SiPM Readouts (#2012)

Minseok Yi[1,2], Guen Bae Ko[3], Jae Sung Lee[1,4]

[1] Seoul National University, Interdisciplinary Program in Bioengineering, Seoul, South Korea; [2] Seoul National University, Integrated Major in Innovative Medical Science, Seoul, South Korea; [3] Korea Advanced Institute of Science and Technology, Nuclear and Quantum Engineering, Seoul, South Korea; [4] Brightonix Imaging Inc., Seoul, South Korea

This work was supported by the National Research Foundation of Korea (NRF) grant funded by the Korea government (MSIT) (Grant No. RS-2024-00354123).

Abstract

We present a physics-constrained joint deconvolution framework for reconstructing photon arrival dynamics. In scintillator-based detectors, measured waveforms arise from the convolutional superposition of stochastic photon detection events, while finite analog signal shaping limits the observable temporal resolution. Mathematical deconvolution approaches implicitly assume continuous photon arrival recovery; however, such formulations are fundamentally ill-posed under band-limited measurements. In this work, we instead represent the latent photon arrival process on a discretized temporal grid as a sampled intensity. Dual-channel timing and energy waveforms are modeled as complementary observations of a shared latent process and jointly inverted using sparsity-constrained optimization. The proposed framework stabilized reconstruction in the presence of bipolar timing responses and temporal smearing, yielding physically consistent photon-train estimates. Joint modeling mitigates ambiguities inherent to single-channel reconstruction and improves robustness in timing extraction under degraded signal conditions. These results establish photon-train reconstruction as a physically grounded representation of detector response and a principled framework for interpreting temporally overlapping signals.

References
[1] Berg, E., Roncali, E., Hutchcroft, W., Qi, J., & Cherry, S. R. (2016). Improving depth, energy and timing estimation in PET detectors with deconvolution and maximum likelihood pulse shape discrimination. *IEEE transactions on medical imaging*, *35*(11), 2436-2446.
[2] Ota, R., & Ote, K. (2024). Emphasizing Cherenkov photons from bismuth germanate by single photon response deconvolution. *IEEE Transactions on Radiation and Plasma Medical Sciences*, *8*(6), 595-606.

MIC-05-019

Pushing the CTR limits in thick dual-ended crystals readout with FastIC+ (#2084)

David Mazzanti[1], Daniel Guberman[1], Joan Mauricio[1], Jerome A. Alozy[3], Franco Nahuel[3], MIchael Campdell[3], Rok Dolenec[5], Georges El Fakhri[6], José María Fernández-Tenllado[1], Alberto Gola[4], Sergio Gómez[2,1], Stanislaw Majewski[7], Rafel Manera[1], MIchele Penna[4], Rok Pestotnik[5], Andrea Paterno[3], Sara Portero[1], Miquel Ribalda[1], Andreu Sanuy[1], Juan J. Silva[1], Rafael Ballabriga[3], David Gascón[1]

[1] Universitat de Barcelona, Institut de Ciències del Cosmos, Barcelona, Spain; [2] Universitat Politècnica de Barcelona, Barcelona, Spain; [3] CERN, Microelectronics Section, Meyrin, Switzerland; [4] Fondazione Bruno Kessler, Trento, Italy; [5] Jožef Stefan Institute, Ljubljana, Slovenia; [6] Yale University School of Medicine, New Haven, USA; [7] University of California, Davis, Davis, USA

Abstract

Over the past years, significant advances have been achieved in Time-of-Flight Positron Emission Tomography (ToF-PET) systems, reaching coincidence time resolution (CTR) values below 100 ps. However, this performance has been demonstrated in small-scale detectors using short scintillation crystals, which favor timing performance at the expense of detection efficiency, and high-power electronics. In contrast, realistic system designs require scintillator crystals with thicknesses of >=10 mm to ensure high detection efficiency. Pushing the CTR limits in large crystals remains challenging due to optical photon transport effects and depth-of-interaction (DOI) uncertainties.

For this purpose, we investigate a dual-ended read out detector based on a 3x3x20 mm^3 LYSO:Ce,Ca crystal against a 2x2x3 mm^3 Fast-LGSO crystal used as a timing reference. The read out was performed with the FastIC+, a custom application-specific integrated circuit (ASIC) multi-channel front-end with on-chip digitization. This ASIC is specifically design for fast-timing applications and optimized for the read out of high-gain photodetectors such as silicon photomultipliers (SiPMs).

In this work, we apply an energy-based DOI correction method to improve the CTR performance of thick-crystal detectors. Using a dual-ended detector based on a 3x3x20 mm^3 LYSO:Ce,Ca crystal coupled to 4x4 mm^2 SiPMs and measured against a 2x2x3 mm^3 Fast-LGSO reference detector coupled to a 3x3 mm^2 SiPM, we achieve a CTR of (135 +/- 1) ps without DOI correction. After applying the correction, the CTR improves down to (110 +/- 1) ps. These results obtained for thick crystals opens a clear path toward sub-100 ps performance in realistic scanner configurations.

References

[1] Schaart, DR, Schramm, G, Nuyts, J and Surti, S 2021, 'Time of Flight in Perspective: Instrumental and Computational Aspects of Time Resolution in Positron Emission Tomography', *IEEE Transactions on Radiation and Plasma Medical Sciences*, vol. 5, no. 5, pp. 598–618, Piscataway: IEEE.

[2] Kratochwil, N, Roncali, E, Cates, JW and Ariño-Estrada, G 2025, 'High-Performance Dual-Ended SiPM Readout for TOF-PET With BGO and LYSO:Ce', *IEEE Transactions on Radiation and Plasma Medical Sciences*, vol. 9, no. 6, pp. 721–735, Piscataway: IEEE.

[3] Gundacker, S, Martinez Turtos, R, Kratochwil, N, Pots, RH, Paganoni, M, Lecoq, P and Auffray, E 2020, 'Experimental time resolution limits of modern SiPMs and TOF-PET detectors exploring different scintillators and Cherenkov emission', *Physics in Medicine & Biology*, vol. 65, no. 2, p. 025001, Bristol: IOP Publishing.

[4] Mazzanti, D *et al.* 2026, 'Below 100 ps CTR using FastIC+, an ASIC including on-chip digitization for ToF-PET and beyond', *IEEE Transactions on Radiation and Plasma Medical Sciences*, Piscataway: IEEE.

[5] Lee, S, Choong, W-S and Cates, JW 2024, 'Characterization of external optical crosstalk reduction for SiPM-based scintillation detectors with an optical bandpass filter', *Nuclear Instruments and Methods in Physics Research Section A: Accelerators, Spectrometers, Detectors and Associated Equipment*, vol. 1061, p. 169101, Amsterdam: Elsevier.

MIC-05-022

Deep Learning Depth-of-Interaction Estimation from Full-Waveform Single-Ended PET Readout: Spatial Resolution Limits (#2163)

Marcus Luck[1], Luca Macchiarulo[1], Christopher Chock[1], Isar Mostafanezhad[1], Hamid Sabet[2]

[1] Nalu Scientific, LLC, honolulu, USA; [2] Massachusetts General Hospital & Harvard Medical School, Radiology, Boston, USA

Abstract

Depth-of-interaction (DOI) estimation is a bottleneck in next-generation PET, contributing to parallax error and degraded timing resolution. Existing solutions using double-sided readout, phoswich, monolithic, or layered crystals require substantial modifications to the readout or detector stack. As part of the development of the SymPET waveform-digitizing readout ASIC, we investigate whether photon arrival-time waveforms alone carry sufficient information to recover DOI without auxiliary sensing. Using DETECT2000 Monte Carlo simulations of 2×2 mm LYSO rods coupled one-to-one to SiPMs, we compare polished and unpolished surface treatments at 12 and 20 mm lengths and train a hybrid 1D CNN-Transformer regressor on 50 ps-binned photon arrival-time histograms. Unpolished surfaces yield lower per-Z MAE and residual std than polished. Bundled high-SNR events reach 0.18 mm worst-per-Z MAE, while single-event MAE is 2.53 mm. Showing the information is present in the waveform, closing this SNR gap is the open problem. (Preliminary results.)

MIC-05-025

Optical-Guiding Crystal Scintillator for Single-Cell Resolution Imaging (#2253)

Fumihiko Nishikido[1], Kei Kamada[2,3], Yuhei Nakata[2], Tetsuo Kudo[3], Hidekatsu Wakizaka[1], Akira Yoshikawa[2,3], Taiga Yamaya[1]

[1] National Institutes for Quantum Science and Technology (QST), Chiba, Japan; [2] Tohoku University, Sendai, Japan; [3] C&A Corporation, Sendai, Japan

Abstract

This study is aimed at the development of a dynamic micro imaging technique based on nuclear medicine methods. Single-cell resolution imaging is strongly required to study the properties and mechanisms of cells for

improved efficiency of drug development. Conventional nuclear medicine imaging techniques are not suitable for this purpose due to their limited spatial resolution. Autoradiography works in terms of spatial resolution, but it cannot obtain dynamic images. Therefore, we are developing a micro radioisotope (RI) imaging system to realize dynamic cell observation. This system consists of a CCD camera and a scintillator plate. Instead of the eutectic scintillator that we introduced in the last IEEE MIC conference, which had non-uniformity and insensitive region issues for this purpose, in this study we use an optical-guiding crystal scintillator (OCS) which has a 10 μm fiber structure.We developed a prototype of the system using the OCS plate, an objective lens (x4) and an CCD camera (C9100-23B). The length, width and thickness of the OCS plate were approximately 2 mm × 5 mm and ~160 μm, respectively. The diameters of the cores in the OCS plate were ~10 μm. In evaluations, a slide chamber was filled with FDG solution, covered with an 8 μm thick polyimide film and then directly put on the OCS plate. The scintillation lights generated by irradiation of positrons from a FDG were detected with the CCD camera through an objective lens. As a result, optical and scintillation images were obtained with the developed system using the OCS. In addition, using half-life measurements, we confirmed the obtained scintillation images were exactly derived from the interactions between the positrons of the F-18 and the OCS. In the next step, we will evaluate performance of the prototype micro RI cell imaging system in measurements with actual cell samples.

MIC-05-028

Crystal Topology and Channel Compression Optimization for a high-resolution Neuro PET/MRI TOF-DOI PET Detector (#2364)

Thore Meyer[1], David Schug[1,2], Bjoern Weissler[1,2], Eike Gegenmantel[2], Oliver Muelhens[2], Giulia Terragni[3], Yannick Kuhl[1], Harald Radermacher[1], Christoph W. Lerche[4], Marco Pizzichemi[3,5], Etiennette Auffray[3], Volkmar Schulz[1,2]

[1] RWTH Aachen University, Chair of Imaging and Computer Vision, Aachen, Germany; [2] Hyperion Hybrid Imaging Systems GmbH, Aachen, Germany; [3] CERN, Geneva, Switzerland; [4] Forschungszentrum Jülich, Institute of Neuroscience and Medicine 4, Jülich, Germany; [5] University of Milano-Bicocca, Milan, Italy

This work is sponsored by BMFTR, contract numbers 13GW0609A, 13GW0609B, 13GW0621A and 13GW0621B. Part of this work was performed in the framework of Crystal Clear Collaboration.

Abstract
The S-PET project is developing a high-resolution positron emission tomography detector module intended for simultaneous brain positron emission tomography / magnetic resonance imaging. The detector needs to feature good position resolution including depth-of-interaction capabilities as well as good timing resolution. A core challenge is the limited space for electronics. The detector integrates 12×12 or even 16×12 SiPMs with one 64-channel TOFPET2 ASIC, necessitating efficient channel compression schemes without additional elements that leverage light-sharing for event positioning. Crucial optimization parameters for detector performance include the crystal topology and a matching compression scheme. This work evaluates Time-of-Flight and Depth-of-Interaction performance across multiple compression schemes and crystal topologies: continuous slabs, pseudoslabs, and pixelated arrays with a light guide coupled to the face opposite the photosensitive detector. This study utilizes

modular development boards, that allow for quick swapping of the compression scheme without reattaching the crystal array, and the first full-scale sensor tile with one of these compression schemes, the Hyperion Visor HD. Preliminary results with a 48×48 mm^2 BrainPET 7T crystal array on the latter show planar resolutions with Mean Absolute Error below 1.5 mm. First tests without compression schemes on a development board with 16×16 mm^2 crystal arrays (2 mm and 4 mm pixel size) with light guide on top show good timing (Coincidence Time Resolution of 235 ps) and Depth-of-Interaction resolution (Mean Absolute Error <1.5 mm). While these preliminary results are promising, the comprehensive evaluations utilizing several crystal topologies combined with the different compression schemes will be presented at the conference.

References
[1] Mueller, Florian, 2022, 'A Semi-Monolithic Detector providing intrinsic DOI-encoding and sub-200 ps CRT TOF-Capabilities for Clinical PET Applications', *Medical Physics*, Vol. 49, No. 12, 7469-7488
[2] Terragni, Giulia, 2025, 'Exploring the performance of a DOI-capable TOF-PET module using different SiPMs, customized and commercial readout electronics', *Physics in Medicine & Biology*, Vol. 70, No. 2, 025015
[3] Lerche, Christoph, 2025, 'Fast maximum likelihood positioning for a staggered layer scintillation PET detector', *Physics and Engineering in Medicine*, Vol. 70, No. 17, 175018
[4] Cucurella, Neus, 2025, 'Single-Ended Readout PET Detector Based on Pixelated Crystals With TOF and DOI Capabilities', *IEEE Transactions on Radiation and Plasma Medical Sciences*, Vol. 9, No. 7, 866-871

MIC-05-031

An ultralow-afterglow γ-camera prototype for hybrid interventional X-ray and scintigraphy imaging (#2497)

Marc Snoeyink[1], Lukas Schröder[1], Peter Menge[2], Dennis R. Schaart[1]

[1] *TU Delft, TNW/RST, Delft, Netherlands;* [2] *Luxium Solutions, Hiram, USA*

Abstract
Radioembolization is widely used for treating cancer, e.g. in the liver. The procedure currently consists of two sessions, one for imaging and one for treatment, typically several weeks apart. Cost-effectiveness, accuracy of treatment, and patient experience could all be improved if both steps could be combined into a single interventional session. A multimodal detector that integrates an X-ray flat panel with a γ-camera would make this possible, by capturing anatomical information and dose distribution at the same time. During X-ray imaging, however, a portion of the radiation passes through the flat panel and blinds the γ-camera. In principle, γ-photons could be detected in between X-ray pulses, but the high afterglow of the currently used NaI(Tl) scintillator interferes with the γ-photon signals. To overcome this, we explore the use of a low-afterglow scintillator in a pixelated γ-camera design. Reducing afterglow facilitates γ-detection shortly after X-ray exposure. Pixelation further increases the γ-photon signal intensity relative to the afterglow background. The pixels are coupled one-to-one to silicon photomultipliers (SiPM). Here, we characterize a prototype module based on NaI(Tl,Sr,Y), which we previously showed to have a low afterglow of 500ppm at 100ms. The module is hermetically sealed to protect the hygroscopic scintillator and comprises 6 x 6 crystals of 3.75 x 3.75mm x 9mm, separated by 0.25mm thick Teflon reflectors. The central 4 x 4 pixels are coupled to a 4 x 4 SiPM array. The 20 inactive outer pixels ensure equal inter-crystal scatter conditions for all active pixels. Event positioning is based on a winner-takes-all algorithm. The performance of the prototype detector is evaluated by measuring Am-241, Ce-141 and Co-57 pulse-height spectra of all active pixels, with and without simultaneous exposure to a pulsed X-ray source.

MIC-05-034

CRYSP: towards an accessible TBPET (#2598)

Laura Navarro-Cozcolluela[1,2], Stefano Roberto Soleti[1,3], Juan José Gómez-Cadenas[1,3], On behalf of the CRYSP group

[1] Donostia International Physics Center, Donostia, Spain; [2] Universidad del Pais Vasco (UPV/EHU), Department of Physics, Bilbao, Spain; [3] Ikerbasque (Basque Foundation for Science), Bilbao, Spain

LN-C acknowledges support of the Department of Education of the Basque Government of Spain under the predoctoral training program non-doctoral research personnel. SRS acknowledges support of a grant from the Basque Country Government with code PUE24-10.

Abstract

The dominant cost driver in total-body positron emission tomography (TBPET) systems is the scintillator material. Current commercial scanners rely on LYSO crystals, which are costly and depend on geographically concentrated rare-earth supply chains. CRYSP proposes an alternative TBPET design based on large monolithic pure cesium iodide (CsI) crystals operated at cryogenic temperatures (~100 K). At these temperatures, CsI achieves a light yield of ~10^5 photons/MeV, yielding an energy resolution below 7% at 511 keV. The monolithic geometry provides inherent depth-of-interaction (DOI) capability, enabling millimeter-scale spatial resolution in all three dimensions and minimizing parallax error. These properties compensate for the lower sensitivity and absence of time-of-flight information, allowing image quality competitive with state-of-the-art TBPET scanners at substantially reduced cost. The slow decay time of cryogenic CsI (~800 ns) renders conventional readout electronics unsuitable; a front-end based on the CAEN CITIROC ASIC, providing pulse-height analysis well suited for slow scintillators, was adopted instead for the prototype. Event position reconstruction employs both analytic methods and a deep-learning algorithm trained on Geant4 simulations, achieving millimeter-scale resolution including DOI in Monte Carlo studies. As a first proof-of-concept, a small-scale PET scanner comprising 18 monolithic CsI(Tl) crystals operating at room temperature is under development, providing hands-on experience with the full acquisition and reconstruction chain before advancing to a cryogenic prototype.

References

[1] Vandenberghe, S., Moskal, P., & Karp, J. S. (2020). State of the art in total body PET. *EJNMMI physics*, *7*(1), 35.

[2] Soleti, S. R., Dietz, P., Esteve, R., García-Barrena, J., Herrero, V., Lopez, F., ... & Gómez-Cadenas, J. J. (2026). CRYSP: a total-body PET based on cryogenic cesium iodide crystals. *Physics in Medicine & Biology*, *71*(2), 025001.

[3] Mikhailik, V. B., Kapustyanyk, V., Tsybulskyi, V., Rudyk, V., & Kraus, H. (2015). Luminescence and scintillation properties of CsI: A potential cryogenic scintillator. *physica status solidi (b)*, *252*(4), 804-810.

[4] Lewis, C. M., & Collar, J. I. (2021). Response of undoped cryogenic CsI to low-energy nuclear recoils. *Physical Review C*, *104*(1), 014612.

[5] Ding, K., Liu, J., Yang, Y., Scholberg, K., & Markoff, D. M. (2024). Performance of a liquid nitrogen cryostat setup for the study of nuclear recoils in undoped CsI crystals. *Nuclear Instruments and Methods in Physics Research Section A: Accelerators, Spectrometers, Detectors and Associated Equipment*, *1063*, 169283.

[6] Soleti, S. R., Castillo, A., del Barrio-Torregrosa, M., Echeverria, C., Seemann, M., Zerzion, D., ... & Collar, J. I. (2025). Cryogenic cesium iodide as a potential PET material. *Journal of Instrumentation*, *20*(06), P06038.

MIC-05-037

Evaluation of a Low-Noise Ultra-Fast SiPM Time-of Flight Analog Readout Chip (LUSTAR) (#2690)

Joshua W. Cates[1], **Joshua W. Cates**[1], Jyothisraj Johnson[2], Jyothisraj Johnson[2], Woon-Seng Choong[1], Woon-Seng Choong[1], Carl Grace[2], Carl Grace[2]

[1] Lawrence Berkeley National Laboratory, Applied Nuclear Physics, Berkeley, USA; [2] Lawrence Berkeley National Laboratory, Engineering, Berkeley, USA

The presented research was supported by National Institute of Biomedical Imaging and Bioengineering of the National Institutes of Health under award number R21EB034885.

Abstract

The precision to which the arrival time of 511 keV photons are able to be known directly affects the signal-to-noise-ratio (SNR) for reconstructed images in time-of-flight positron emission tomography (TOF-PET). Currently, significant research is ongoing to push the full-width-half-maximum (FWHM) coincidence time resolution (CTR) for TOF-PET systems well below 100 ps towards the few-10's-of-ps regime. In this work, we designed an application specific integrated circuit (ASIC) in a commercial 65nm CMOS process to translate ultra-fast timing performance currently demonstrated in state-of-the-art bench-top measurements into a fully integrated scalable topology for large scale time-of-flight positron emission tomography (TOF- PET) systems. We targeted a scalable, low-noise, ultra-fast silicon photomultiplier (SiPM) analog front-end that maintains excellent SNR for single photon response while achieving ≤35 ps FWHM electronic noise jitter for single photon detection with 4x4 mm^2 Broadcom AFBR-S4N44P014M Near-ultraviolet metal-trench SiPMs. This "analog" chip uses low-voltage differential signaling (LVDS) transmitters to drive discriminator data to an external time-to-digital converter (TDC). We present evaluation of achievable single photon time resolution and CTR with the first prototype test chip.

MIC-05-040

A Dual-Ended Readout PET Detector Module With 0.75 mm Pitch LYSO Arrays for High-Resolution Small-Animal Imaging (#2714)

Shihan Yang, Xianchao Huang, Xiaorou Han, Hang Yuan, Hanri Liao, Long Wei, Zhiming Zhang

Chinese Academy of Sciences, Institute of High Energy Physics, Beijing, China

This work was supported by the National Key R&D Program of China (Grant No. 2023YFF0716000).

Abstract

We present a high-resolution PET detector module with fine-pitch crystals and dual-ended readout for small-animal imaging. The detector employs a 28 × 28 LYSO crystal array with a pixel size of 0.75 mm × 0.75 mm × 15 mm, separated by 0.08 mm $BaSO_4$ reflector layers and read out at both ends by SiPM arrays. Experimental results demonstrated clear crystal separation with a corrected depth-of-interaction (DOI) resolution of 1.59 mm (FWHM) and an energy resolution of 14.9% in the selected 1/4 detector region. These results indicate that dual-ended readout can effectively improve DOI resolution in fine-pitch crystal arrays while preserving crystal separation, demonstrating the feasibility of fine-pitch dual-ended PET detectors for high-resolution small-animal PET imaging.

References

[1] Miyaoka, RS, Lehnert, AL 2020, 'Small animal PET: a review of what we have done and where we are going', *Physics in Medicine & Biology*, vol. 65, no. 24, Art. no. 24TR01, pp. 1-14, Bristol: IOP Publishing.

[2] Wang, H, Xie, J, Qi, J et al. 2025, 'Dual-ended readout TOF-DOI PET detectors based on 3.2 mm and 1.6 mm pitch LYSO arrays', *EJNMMI Physics*, vol. 12, Art. no. 51, pp. 1-12, Heidelberg: Springer Nature

[3] Selfridge, AR, Cherry, SR, Judenhofer, MS 2018, 'Optimization of a depth of interaction encoding PET block detector for a PET/MRI insert', *Physics in Medicine & Biology*, vol. 63, no. 23, Art. no. 235031, pp. 1-13, Bristol: IOP Publishing

[4] Gonzalez-Montoro, A et al. 2017, 'A method to measure the intrinsic detector resolution on monolithic crystals', in *Proceedings of the IEEE Nuclear Science Symposium and Medical Imaging Conference*, pp. 1-3, Atlanta, GA: IEEE

[5] Poladyan, H, Bubon, O, Teymurazyan, A, Senchurov, S, Reznik, A 2020, 'Gaussian position-weighted center of gravity algorithm for multiplexed readout', *Physics in Medicine & Biology*, vol. 65, no. 16, Art. no. 165003, pp. 1-11, Bristol: IOP Publishing

[6] Pizzichemi, M et al. 2016, 'A new method for depth of interaction determination in PET detectors', *Physics in Medicine & Biology*, vol. 61, no. 12, pp. 4679-4698, Bristol: IOP Publishing

MIC-05-043

CNN-Based 2D Source Localization Using Collimator-Free Staggered Scintillator Arrays (#2914)

Bryan Casanelli, Iara Neves, Ana Luísa M. Silva, Pedro M.M. Correia

University of Aveiro, Institute for Nanostructures, Nanomodelling and Nanofabrication (i3N), Department of Physics (DFis), Aveiro, Portugal

This work was supported by the "la Caixa" Foundation ID CI25-10265 under the CaixaImpulse program, and by project HadronPET COMPETE2030-FEDER-00755500, funded by FEDER program and by national funds through the FCT, Portugal. Is also funded by national funds through FCT - Fundação para a Ciência e a Tecnologia, I.P., under the project UID/50025/2025 (doi.org/10.54499/UID/50025/2025), UID/PRR/50025/2025 (doi.org/10.54499/UID/PRR/50025/2025), UID/PRR2/50025/2025 (doi.org/10.54499/UID/PRR2/50025/2025) and the Associate Laboratory I3N - LA/P/0037/2020 (doi.org/10.54499/LA/P/0037/2020).

Abstract

Mechanical collimators in SPECT introduce a fundamental sensitivity-resolution trade-off that becomes critical in targeted radionuclide therapy (TRT) imaging, where administered activities are low. We explore a collimator-free detector concept based on an 18x18 pixelated GAGG scintillator array in which collimation is achieved through staggering, that is, height offsets between neighboring pixels that produce characteristic shadow patterns in the resulting flood map. Three configurations are evaluated: a flat array (stagger-0), a single-pixel checkerboard (stagger-1), and a 3x3-block checkerboard (stagger-3). For each geometry, OpenGATE 10 Monte Carlo simulations of a 140 keV point source were performed at 400 positions on a fixed-height plane. The resulting flood maps were used to train a 2D convolutional neural network that regresses the source coordinates. Evaluated on 40 test positions, the 3D root-mean-square error of the neural network decreases with increasing staggering degree, from 0.44 mm (stagger-0) to 0.40 mm (stagger-1) and 0.34 mm (stagger-3), a 23% reduction that supports staggering as a promising strategy for collimator-free source localization.

References

[1] K. Van Audenhaege, R. Van Holen, S. Vandenberghe, C. Vanhove, S. D. Metzler, and S. C. Moore, “Review of SPECT collimator selection, optimization, and fabrication for clinical and preclinical imaging,” Medical Physics, vol. 42, no. 8, pp. 4796–4813, Aug. 2015, 10.1118/1.4927061.

[2] N. Lepareur, B. Ramée, M. Mougin-Degraef, and M. Bourgeois, “Clinical advances and perspectives in targeted radionuclide therapy,” Pharmaceutics, vol. 15, no. 6, p. 1733, Jun. 2023, 10.3390/pharmaceutics15061733.

[3] Y. Zhu, Z. Yu, Z. Lyu, Y. Liu, R. Yao, and T. Ma, “A collimator-less crisscrossed planar gamma scanner with a single-slim-scintillator detector,” Journal of Nuclear Medicine, vol. 64, no. supplement 1, p. P788, Jun. 2023. [Online]. Available: http://jnm.snmjournals.org/content/64/supplement_1/P788.abstract.

[4] R. Wang, D. Zhang, Y. Hu, Z. Lyu, and T. Ma, “High-sensitivity cardiac SPECT system design with collimator-less interspaced mosaic-patterned scintillators,” Frontiers in Medicine, vol. 10, p. 1145351, Jun. 2023, 10.3389/fmed.2023.1145351.

[5] A. Jo, D. Hong, and W. Lee, “Feasibility verification of deep-learning-based collimator-less imaging system using a voxelated GAGG(Ce) single-volume detector: A Monte Carlo simulation,” Applied Radiation and Isotopes, vol. 217, p. 111605, Mar. 2025, 10.1016/j.apradiso.2024.111605.

MIC-05-046

Development and Experimental Characterization of a Fine-Pitch CZT SPECT Detector Head with Simulation-Guided Matched-Pixel Collimator Selection (#3083)

Zhiyong Song[2], Rui Wang[1], Pengyu Ke[2], Xu Chen[2], Zifan Hao[2], Jingzhe Gong[3], Xinyu Lv[2], Shaohui An[2]

[1] Shanghai United Imaging Healthcare Advanced Technology Research Institute Co., Ltd, Shanghai, China; [2] United Imaging Healthcare Co., Ltd., Molecular Imaging, Shanghai, China; [3] ShanghaiTech University, School of Biomedical Engineering, Shanghai, China

Abstract

A fine-pitch CZT detector-head prototype was assembled and experimentally characterized for SPECT imaging. The head consists of a 5 × 10 tiled array of CZT modules, each containing 16 × 16 anodes with 1.45 mm pixels and a 1.6 mm pitch. The prototype achieved a global energy resolution of 4.8% at 140 keV. The intrinsic integral and differential uniformities were 0.56% and 0.44%, respectively. To exploit the fine intrinsic spatial sampling of the CZT detector, a fast ray-tracing Monte Carlo framework was used to explore dual-layer 1H/4HMPD matched-pixel collimator candidates and to compare them with the 1HL30.5 reference design, defined as a one-hole-per-pixel collimator with a 30.5 mm hole length, under prototype-constrained geometric and mechanical conditions. A representative dual-layer candidate showed an alternative main-lobe sensitivity–resolution trade-off, but GATE point-source simulations revealed more pronounced non-Gaussian tails than the 1HMPD reference. Therefore, the 1HL30.5 configuration was retained as the near-term practical collimator design. GATE-simulated Derenzo phantom reconstruction of this configuration showed that 5 mm hot rods were visually distinguishable at 10M and 5M total projection counts. These results support the feasibility of the fine-pitch CZT detector-head prototype and justify retaining 1HL30.5 for subsequent experimental phantom validation.

References

[1] F. Weng, S. Bagchi, Q. Huang, and Y. Seo, “Design Studies of a CZT-based Detector Combined with a Pixel-Geometry-Matching Collimator for SPECT Imaging.,” IEEE Nucl. Sci. Symp. Conf. Rec. (1997)., vol. 2013, pp. 1–4, Oct. 2013, doi: 10.1109/NSSMIC.2013.6829458.

[2] N. Boutaghane, M. Hesse, B. Bouzid, H. Zaidi, F. Jamar, and S. Walrand, “Dual-layer collimator for improved spatial resolution in SPECT with CZT camera: an analytical and Monte Carlo study,” Phys. Med. Biol., vol. 67, no. 6, p. 65006, 2022.

[3] N. Boutaghane, B. Bouzid, and H. Zaidi, “Conceptual design of a large pixelated CZT detector with four-hole collimator matched pixel detector for SPECT imaging: a Monte Carlo simulation study,” J. Instrum., vol. 14, no. 02, pp. P02026–P02026, 2019.

MIC-05-049

Monte Carlo simulations of positrons in uniform magnetic fields with PENELOPE (#1298)

Mario A. González-Ramírez, Mercedes Rodríguez-Villafuerte, Arnulfo Martínez-Dávalos, Héctor Alva-Sánchez

Universidad Nacional Autónoma de México, Instituto de Física, Mexico City, Mexico

We thank the support from PAEP-UNAM, PAPIIT-UNAM IN103726. This work has been partially supported by the ENEN2plus project (HORIZON-EURATOM-2021-NRT-01-13 101061677) founded by the European Union.

Abstract

This study investigates the influence of magnetic fields on F-18 and Ga-68 positrons and how they affect image quality metrics in tissue-equivalent phantoms relevant to PET/MR imaging. To this end, we performed Monte Carlo simulations using the PENELOPE code. Since the main PENELOPE routine penmain.f does not account for the influence of electromagnetic fields on radiation transport in matter, a modified version of the penfield.f module was used instead. Simulations were carried out in four representative media (lung, soft tissue, water, and cortical bone) and in NEMA-like image quality phantoms to assess the effect of uniform magnetic fields of 0, 3, and 9 T. We simulated positron point sources at the center of a 10 cm-radius spherical phantom of homogeneous materials and in a set of three image-quality phantoms to evaluate specific image-quality parameters: spill-over ratio, recovery coefficient, and lesion detectability, as in a previous experimental study. The results indicate that positron range significantly affects recovery coefficients and spill-over ratios, particularly for high-energy positron emitters in low-density tissues. In the recovery-coefficient phantom, when the cylinder separation distance is smaller than the positron range, a slight overestimation of the recovery coefficients is observed due to contributions from adjacent cylinders. The magnetic field reduces these effects in the direction perpendicular to the magnetic field lines, leading to improved spatial resolution and quantitative accuracy. These findings represent the maximum image quality that can be achieved under ideal conditions in a PET system in the presence of uniform magnetic fields and provide a physical basis for the development of positron-range correction methods in PET/MR imaging.

References

[1] Nuclear Energy Agency, PENELOPE 2018: A code system for Monte Carlo simulation of electron and photon transport: Workshop Proceedings, Barcelona, Spain, 2019.

[2] D. Ku-Toval, M. Rodríguez-Villafuerte, M. A. Ávila-Rodríguez et al, “Quantitative analysis of the effect of the magnetic field generated by a PET/MR scanner on positron range”, Phys. Med. Biol. 69 2024, 185006.

MIC-05-052

Impact of a Breast PET Insert on Lesion Detectability in Whole-Body PET/MRI (#1405)

Hong Phuc Vo[1], Jorge Roser[1], Elnaz Olyaei[2,3], Janina Hohnholz[2], Lukas Rauscher[2], Fabian P. Schmidt[2,3], Magdalena Rafecas[1]

[1] University of Luebeck, Institute of Medical Engineering, Luebeck, Germany; [2] Eberhard Karls University Tuebingen, Werner Siemens Imaging Center, Department of Preclinical Imaging and Radiopharmacy, Tuebingen, Germany; [3] University Hospital Tuebingen, Department of Nuclear Medicine and Clinical Molecular Imaging, Tuebingen, Germany

The project is supported by the German Research Foundation (DFG) under grant agreement no. 508064995. The authors gratefully acknowledge the computing time made available to them on the high-performance computer "Lise" at the NHR center NHR@ZIB, project no. shb00004. This center is jointly supported by the Federal Ministry of Research, Technology, and Space and the state governments participating in the NHR (www.nhr-verein.de).

Abstract

To improve the detectability of small lesions and early metastases, we are developing a breast PET insert that operates in conjunction with a whole-body (WB) PET/MRI scanner. We implemented a joint reconstruction framework with attenuation correction that explicitly accounts for the different coincidence types from the insert and the WB-PET, aiming to improve spatial resolution inside the insert field of view (iFOV), as well as outside. Performance was evaluated using Monte Carlo simulations of an anthropomorphic phantom with lesions of 4, 8, and 12 mm diameter and contrast ratios of 4:1 and 8:1 relative to the breast background. Lesions were placed at clinically relevant locations, including within the breast, as well as in axillary and parasternal lymph nodes. Compared to WB-PET alone, the inclusion of all coincidence types improved lesion conspicuity, particularly for small (4–8 mm) and low-contrast lesions. Within the iFOV, breast lesions show increases in contrast recovery coefficent (CRC) of up to 16.4% (4 mm, 8:1) and 16.9% (8 mm, 4:1), with 4-mm lesions becoming resolvable. Similar trends were observed for axillary lymph nodes, with CRC increases of up to 11.9% (8 mm, 4:1). Future work will extend this study beyond the idealized 511 keV case to more realistic energy windows with finite energy resolution and higher scatter contribution, as well as incorporate spatially variant point spread function modeling and scatter correction into the reconstruction framework.

References

[1] Zhang-Yin, J., 2023, "State of the Art in 2022 PET/CT in Breast Cancer: A Review", *Journal of Clinical Medicine*, 12, no. 3: 968, https://doi.org/10.3390/jcm12030968

[2] Pommranz, C.M., Schmidt, F.P., Mannheim, J.G., Diebold, S.J., Tenzer, C., Santangelo, A. and Pichler, B.J., 2023, "Design and performance simulation studies of a breast PET insert integrable into a clinical whole-body PET/MRI scanner", *Physics in Medicine & Biology*, *68*(5), p.055019.

[3] Vo, H.P., Pommranz, C., Schmidt, F.P. and Rafecas, M., 2024, "Towards Enhancing Auxiliary Lymph Node Detection Using a Breast Insert with a Whole-Body PET/MRI Scanner", In *2024 IEEE Nuclear Science Symposium (NSS), Medical Imaging Conference (MIC) and Room Temperature Semiconductor Detector Conference (RTSD)*, pp. 1-2, IEEE.

[4] Segars, W.P., Sturgeon, G., Mendonca, S., Grimes, J. and Tsui, B.M., 2010, "4D XCAT phantom for multimodality imaging research", *Medical physics*, *37*(9), pp.4902-4915.

[5] Vo, H.P., Williams, T., Doroud, K., Williams, C. and Rafecas, M., 2025, "Dedicated prostate DOI-TOF-PET based on the ProVision detection concept", *Physics in Medicine & Biology*, *70*(18), p.185001.

MIC-05-055

Proposal of an L-shaped Dual-detector Multi-pinhole Myocardial SPECT System Using a CNN (#1523)

Takumi Akatsuka[1], Koichi Ogawa[2]

[1] Hosei University, Applied Informatics, Graduate School of Science and Engineering, Koganei, Japan; [2] Hosei University, Applied Informatics, Faculty of Science and Engineering, Koganei, Japan

Abstract

Dedicated cardiac semiconductor SPECT systems enable short acquisition times owing to their high sensitivity; however, artifacts may occur depending on patient body habitus, and quantitative reconstruction images cannot be obtained because attenuation correction using X-ray CT images (μ-maps) is not available. In this study, we propose a novel SPECT system in which two gamma cameras equipped with NaI scintillators are arranged in an L-shaped configuration, allowing data acquisition while keeping the detectors stationary, and achieving attenuation, scatter, statistical noise and collimator aperture correction using a convolutional neural network (CNN). To improve sensitivity, 44 multi-pinhole collimators were employed, and projection images were acquired in an overlapped manner and accurately separated using the CNN. A U-Net++ architecture was adopted to construct a unified framework for overlap separation of projection data, statistical noise reduction, aperture correction and attenuation/scatter correction without requiring μ-maps. Image reconstruction was performed using the ML-EM algorithm, and image quality was evaluated using the normalized mean squared error (NMSE) of the polar map. As a result, approximately uniform image reconstruction was achieved without using μ-maps, and the NMSE was 0.0402, demonstrating the effectiveness of the proposed method.

References

[1] Garcia, E. V, Faber, T.L, Esteves, F.P 2011, 'Cardiac Dedicated Ultrafast SPECT Cameras: New Designs and Clinical Implications', *J. Nucl. Med.*, vol. 52, pp. 210–217.

[2] Sharir, T, Ben-Haim, S, Merzon, K, et al., 2008, 'High-Speed Myocardial Perfusion Imaging: Initial Clinical Comparison With Conventional Dual Detector Anger Camera Imaging', *JACC Cardiovasc. Imag.*, vol. 1, pp. 156–163.

[3] Herzog, B, Buechel, R, Katz, R, et al., 2010, 'Nuclear Myocardial Perfusion Imaging with a Cadmium-Zinc-Telluride Detector Technique: Optimized Protocol for Scan Time Reduction', *J. Nucl. Med.*, vol. 51, pp. 46–51.

[4] Inaba, S, Nawano, Y, Ogawa, K, 2026, 'Accurate CT-free correction of attenuation, scatter, and aperture effects using deep learning in dedicated cardiac pinhole SPECT', Ann. of Nucl. Med., https://doi.org/10.1007/s12149-026-02187-z.

[5] Mok, GSP, Benjamin MW, Beekman FJ,et al., 2011 'The effects of object activity distribution on multiplexing multi-pinhole SPECT', *Phys. Med. Biol.*, vol. 56, pp. 2635–2650.

[6] Akatsuka, T, Ogawa, K, ' Removal of Projection Data Overlaps Using Deep Learning in SPECT with a Large Number of Pinholes', IEEE NSS/MIC, https://doi.org/10.1109/NSS/MIC/ RTSD 57106.2025.11286491.

[7] Yagi, S, Usui, K, Ogawa, K, 2025, 'Scatter and beam hardening effect corrections in pelvic region cone-beam CT images using a convolutional neural network', *Radiol. Phys. Technol.*, vol. 18, pp. 457–468.

[8] Kinahan, P, Muzi, M, Bialecki, B, Herman, B, et al., 2019, 'Data from the ACRIN 6668 Trial NSCLC-FDG-PET', The Cancer Imaging Archive.

MIC-05-058

EduPETSIM: An Educational Web-Based Framework Integrating Simulation, Reconstruction, and Generative AI for Rapid Source Modeling (#1644)

Trang Hoang[1,2], Martin Grossmann[3], Andrea Gonzalez-Montoro[4], Pedro M.M. Correia[5], Ana Luísa M. Silva[5], João F. Veloso[5], Youngho Seo[6], On behalf of EduPET Collaboration

[1] University of Science, VNU-HCM, Physics, Ho Chi Minh, Vietnam; [2] Vietnam National University, Ho Chi Minh, Vietnam; [3] Paul Scherrer Institut PSI, Villigen, Switzerland; [4] Instituto de Instrumentación para Imagen Molecular (I3M), Centro Mixto CSIC-Universitat Politècnica de València, Detectors for Molecular Imaging Lab (DMIL), València, Spain; [5] University of Aveiro, the I3N Physics Department, Aveiro, Portugal; [6] University of California, San Francisco and Berkeley, USA

This work was supported by IEEE Nuclear and Plasma Sciences Society (NPSS).

Abstract

Accurate physics-based simulations are essential for assessing and validating scanner geometries and reconstruction algorithms. EduPET is an NPSS-supported educational PET technology demonstrator. This work introduces the Educational PET SIMulation system (EduPETSIM), an integrated web-based framework designed for educational purposes to streamline the entire PET workflow. The platform unites an OpenGATE-based simulation engine, a custom coincidence sorter, and an image reconstruction module within a unified environment. A primary novel contribution of this framework is the integration of a Conditional Wasserstein Generative Adversarial Network (cWGAN) to facilitate rapid source modeling, which significantly reduces the computational overhead associated with traditional particle transport simulation. Current developments focus on fine-tuning the cWGAN model for a ^{22}Na source within the two-detector EduPET system, with the completed model available for the upcoming IEEE NPSS schools on medical imaging.

References

[1] S. Agostinelli *et al.*, "Geant4—a simulation toolkit," *Nucl. Instrum. Methods Phys. Res. A, Accel. Spectrom. Detect. Assoc. Equip.*, vol. 506, no. 3, pp. 250–303, 2003.

[2] S. Jan *et al.*, "GATE: a simulation toolkit for PET and SPECT," *Phys. Med. Biol.*, vol. 49, no. 19, pp. 4543–4561, 2004.

[3] J. Salvadori *et al.*, "Monte Carlo simulation of digital photon counting PET," *EJNMMI Phys.*, vol. 7, no. 1, p. 23, 2020.

[4] J. Salvadori *et al.*, "PET digitization chain for Monte Carlo simulation in GATE," *Phys. Med. Biol.*, vol. 69, no. 16, Art. no. 165013, 2024.

[5] P. M. M. Correia *et al.*, "An EDUGATE simulation toolkit based on the educational easyPET," *Biomed. Phys. Eng. Express*, vol. 5, no. 2, Art. no. 025009, 2019.

[6] V. Arosio *et al.*, "The EasyPET: A novel concept for an educational cost-effective positron emission 2D scanner," in *Proc. IEEE NSS/MIC/RTSD*, 2016, pp. 1–3, doi: 10.1109/NSSMIC.2016.8069360.

MIC-05-061

Accelerating Monte Carlo Light Transport in Turbid Media with an Analytically Invertible Simplified Phase Function (#1704)

Aristotelis-Nikolaos Rapsomanikis[1,2], Mina-Ermioni Tomazinaki[1], Efstathios Stiliaris[1,3]

[1] National and Kapodistrian University of Athens, Department of Physics, Athens, Greece; [2] University of West Attica, Athens, Greece; [3] Institute of Accelerating Systems & Applications (IASA), Athens, Greece

Abstract

Modeling light scattering in biological media requires balancing the accuracy of Mie theory with the speed of simplified phase functions. We propose a new phase function that replaces the standard *cos(θ)* term with a quadratic θ^2 relationship, significantly improving large-angle fidelity compared to the Henyey-Greenstein (HG) model. A key advantage is the function's analytical invertibility, enabling direct Inverse Transform Sampling that accelerates Monte Carlo simulations by bypassing transcendental computations. Mathematical consistency is validated against the stochastic Rejection Method for various tissues. Transport simulations using the PhoSim package demonstrate enhanced spatial accuracy and closer alignment with the Mie ground truth, offering a high-speed framework for real-time IR tomography and Time-Resolved Optical Tomography.

References

[1] Binzoni, T. et al. 2006, 'The use of the Henyey–Greenstein phase function in Monte Carlo simulations in biomedical optics', Phys. Med. Biol. 51, N313-N322

[2] Yang, Y., Zhao, Z., Yang J. 2026, 'Research on analytical phase function model of chlorophyll water', Physics Letters A 580, 131537

[3] Rapsomanikis A.-N., Eleftheriou A., Mikeli M., Pafilis Ch., Zioga M. and Stiliaris E. 2016, 'PhoSim: A Software Simulation Package Designed for Macroscopic and Microscopic Studies in the Time-Resolved Optical Tomography', IEEE NSS & MIC Record

[4] Rapsomanikis A.-N., Stiliaris E. 2020, 'Stochastic Light Transport through Tissues in Optical Imaging with Inverted Functions', IEEE NSS & MIC Record

MIC-05-064

Fast On-the-Fly System Matrix Computation for Broad-Energy Multi-Pinhole SPECT (#1808)

Bo Gao, Beien Wang, Feng Zhou, Liuchun He, Yun Dong

United Imaging Healthcare, Molecular Imaging Business Unit, Shanghai, China

Abstract

We present a GPU-accelerated system matrix computation method for multi-pinhole SPECT based on spatial modeling of position-dependent point spread functions (PSFs). Sparse Monte Carlo-generated PSFs are fitted with an anisotropic Gaussian model, and the resulting parameters are expressed as geometry-dependent functions to enable estimation of voxel-dependent responses at unmeasured locations. Implemented in CUDA for forward and

backprojection, the method supports on-the-fly iterative reconstruction without storage of a fully precomputed system matrix. This approach was evaluated using Derenzo phantoms and NEMA image quality phantoms filled with isotopes whose emitted photon energies range from 140 to 440 keV, demonstrating its potential for efficient multi-isotope and theranostic SPECT imaging.

References
[1] K. Van Audenhaege, R. Van Holen, S. Vandenberghe, C. Vanhove, S. D. Metzler, and S. C. Moore, "Review of spect collimator selection, optimization, and fabrication for clinical and preclinical imaging," Medical Physics, vol. 42, no. 8, pp. 4796–4813.
[2] F. Van Der Have, B. Vastenhouw, M. Rentmeester, and F. Beekman, "System calibration and statistical image reconstruction for Ultra-High Resolution Stationary Pinhole SPECT," IEEE Transactions on Medical Imaging, vol. 27, no. 7, pp. 960–971, 6 2008.
[3] L. He, J. Li, C. Sun, Y. Lu, and Y. Dong, "GPU-Accelerated Monte Carlo Simulation for PET Imaging (Part I): Validation of Imaging Physics Simulation," in 2023 IEEE NSS MIC RTSD, 11 2023, p. 1.

MIC-05-067

Monte Carlo Based Performance Evaluation of a Dual Panel PET&SPECT Trimodal Imager (#1888)

Hang Yang[1,2], Xiangtao Zeng[1], Yangyang Zhao[1], Zexin Wu[1], Hengyi Li[1], Ming Niu[1], Zheng Gu[1]

[1] Shenzhen Bay Laboratory, Institute of Biomedical Engineering, Shenzhen, China; [2] Harbin Institute of Technology, School of Astronautics, Harbin, China

This work is supported by the National Key R&D Program of China (No. 2023YFC2414800), the Major Program of Shenzhen Bay Laboratory (No. C1012530005), the National Natural Science Foundation of China (Nos. 12275182 and 62371314), Guangdong Basic and Applied Basic Research Foundation (Nos. 2024A1515012154), the Guangdong Provincial Project (Grant No. 2023TQ07A233) and the Shenzhen Bay Laboratory Proof-of Concept Grants (No. C1022430005).

Abstract
This work presents a Monte Carlo based performance evaluation of a dual-panel PET&SPECT trimodal imaging system, in terms of spatial resolution, system sensitivity, and count rate performance following the NEMA NU 2-2018 standard. Spatial resolution measurements yield an average value of 1.01 mm for PET and 11.1 mm for SPECT. The SPECT sensitivity with a 700 mm length line source is 101.5 cps/MBq at the center of the field of view (axial offset z = 0 cm) and 103.0 cps/MBq at z = 10 cm. When using a 350 mm line source, SPECT sensitivity increases to 152.1 cps/MBq at z = 0 cm and 129.1 cps/MBq at z = 10 cm. The PET sensitivity measured with a 700 mm length line source achieves 43.4 cps/kBq at z = 0 cm and 43.5 cps/kBq at z = 10 cm. The PET peak noise equivalent count rate reaches 131.5 kcps at 193 MBq in standalone acquisition mode, and decreases under simultaneous PET&SPECT acquisition due to elevated dead time induced by SPECT detections. These results validate the overall system design, quantify the interference between PET and SPECT detections, and provide a foundation for further optimization toward clinical trimodal imaging applications.

References
[1] Zeng X, Yang H, Niu M, et al. 'Tri-mode PET, SPECT, and PET&SPECT imager using a novel scintillator-as-collimator detector', 2025 IEEE NSS MIC and RTSD, Yokohoma Japan.

[2] Zhao Y, Huang C, Zeng, X et al. 'Validation of an Optimized DOI-Capable Shared PET&SPECT Detector based on a Scintillator-as-Collimator Structure', 2026 IEEE NSS MIC and RTSD, submitted.
[3] Ryu HJ, Meikle SR, Willowson KP, et al. 'Performance evaluation of quantitative SPECT/CT using NEMA NU 2 PET methodology', Physics in Medicine & Biology, 2019, 64(14): 145017.

MIC-05-070

Experimental Validation and Calibration of a GATE Simulation Model for a Dedicated Breast PET/MR Insert (#2013)

Elnaz Olyaei[1,2], Janina Hohnholz[1], Hong P. Vo[3], Lukas U. Rauscher[1], Magda Rafecas[3], Bernd Pichler[1], Fabian P. Schmidt[1,2]

[1] University of Tuebingen, Werner Siemens Imaging Center, Department of Preclinical Imaging and Radiopharmacy, Tuebingen, Germany; [2] University Hospital of Tuebingen, Department of Nuclear Medicine and Clinical Molecular Imaging, Tuebingen, Germany; [3] University of Luebeck, Institute of Medical Engineering, Luebeck, Germany

Supported by bwHPC/DFG (455622343) (bwForCluster NEMO 2) and DFG grant agreement no. 508064995

Abstract

Advanced detector designs employing multi-layer crystal configurations and multiplexed readouts introduce complex light transport and inter-crystal scatter effects. These result in position-dependent differences in energy response and crystal identification that are difficult to reproduce using idealized simulations. We present an experimentally calibrated GATE simulation framework for a dual-layer depth-of-interaction capable detector developed for a dedicated breast PET/MRI insert. The detector block consists of a 10×10 bottom LSO crystal array (1.5×1.5×9.81 mm³) and a 9×9 top array (1.5×1.5×5.19 mm³). Simulations were performed using GATE v9.4.1 for two geometries and compared against experimental measurements. A reference configuration of 18 detector modules in a 100 mm ring was used to derive crystal-specific correction factors, then applied to the same 18 modules in a 178 mm ring representing the breast insert geometry. Measurements were acquired using a centered Na-22 point source for three energy windows (250–760 keV, 511±50 keV, and 430–610 keV) with experimentally informed coincidence timing resolutions. The uncorrected simulations systematically overestimated experimental coincidence count rates, with the largest deviations at edge and corner crystals of the bottom layer. Prior to calibration, mean absolute deviations for the 178 mm geometry were 37.1%, 38.0%, and 43.0%; following calibration, deviations were reduced to 9.3%, 8.4%, and 8.8%. Experimental detector blocks additionally showed substantially larger crystal-to-crystal variations in energy resolution (top: 12.5±1.1%, bottom: 11.0±1.2%) compared with the fixed simulated values, indicating complex optical transport and detector-specific effects are not yet fully reproduced in the current model.

References
[1] Pommranz, C.M., Schmidt, F.P., Mannheim, J.G., Diebold, S.J., Tenzer, C., Santangelo, A. and Pichler, B.J., 2023, "Design and performance simulation studies of a breast PET insert integrable into a clinical whole-body PET/MRI scanner", *Physics in Medicine & Biology*, *68*(5), p.055019.
[2] Vo, H.P., Pommranz, C., Schmidt, F.P. and Rafecas, M., 2024, "Towards Enhancing Auxiliary Lymph Node Detection Using a Breast Insert with a Whole-Body PET/MRI Scanner", In *2024 IEEE Nuclear Science Symposium (NSS), Medical Imaging Conference (MIC) and Room Temperature Semiconductor Detector Conference (RTSD)*, pp. 1-2, IEEE.

[3] Olyaei, E., Rauscher, L., Vo, HP., Pommranz, C., Lan, W. & Hohnholz, J. 2025, 'Towards Improved Simulation Models via Experimental Validation for a Dedicated Breast PET Insert Integrated with a PET/MR Scanner', in 2025 IEEE Nuclear Science Symposium (NSS), Medical Imaging Conference (MIC) and Room Temperature Semiconductor Detector Conference (RTSD), pp. 1–2, IEEE

MIC-05-073

An Integrated Digital Twin Framework for Accurate Quantification of Preclinical Immuno-PET (#2128)

Claudia Dominguez-Borrero[1,2], Xurxo García-Otero[1,2], Emma Ramos-Docampo[1], Jesús Rodríguez-Silva[3], Noemí Gómez-Lado[1,2], Soraya Groba de Antas[1], María Gómez-Muñoz[1,4], Jessica Codesido[2], Lara García-Varela[1,2], Pablo Aguiar[1,2]

[1] Molecular Imaging Biomarkers Group, Center for Research in Molecular Medicine and Chronic Diseases (CIMUS), Universidad de Santiago de Compostela, Santiago de Compostela, Spain; [2] Nuclear Medicine Department and Molecular Imaging Group, Health Research Institute of Santiago de Compostela (IDIS), Santiago de Compostela, Spain; [3] Reina Sofia Alzheimer Center, CIEN Foundation, Madrid, Spain; [4] Centro de Investigación Biomédica en Red en Enfermedades Neurodegenerativas (CIBERNED), Instituto de Salud Carlos III, Madrid, Spain

I would like to thank my supervisor and research group for their support and guidance throughout this project.

Abstract

Accurate quantification in preclinical PET remains a fundamental challenge due to the spatial resolution constraints inherent to small-animal imaging, where partial volume effects compromise biodistribution and dosimetry estimations in monoclonal antibody-based radiopharmaceuticals. Here, we present the first integrated digital-twin framework for immuno-PET quantification in preclinical imaging developed around a validated Monte Carlo model of the Bruker (BioSpec 3T) PET/MRI scanner implemented using the SimPET platform — which integrates the SimSET Monte Carlo engine and STIR reconstruction software — and validated following the NEMA NU 4-2008 standard. This validated model was then combined with physical and digital rodent phantoms to assess a highly accurate immuno-PET quantification pipeline. Scanner validation showed a good agreement between simulated and experimental data, with underestimation below 5%. On the other hand, quantification of a representative immuno-PET biodistribution using the Bio-Rat phantom revealed underestimations below 20% across most organs, consistent with partial volume effects at this spatial resolution.

This framework establishes a reproducible strategy to characterize and correct quantification biases in preclinical PET, with direct impact on the translational development of radiopharmaceuticals.

MIC-05-076

Tensor-Based Multi-Stage Evolution for Generative Design of Arbitrary Permanent Magnet Geometries for PET-compatible Low-Field MRI

(#2266)

Md Shahadat Hossain Akram[1], Fumihiko Nishikido[1], Takayuki Obata[2], Taiga Yamaya[1]

[1] National Institutes for Quantum Science and Technology (QST), Dept. of Advanced Nuclear Medicine Sciences, Chiba, Japan; [2] National Institutes for Quantum Science and Technology (QST), Applied MRI Research, Chiba, Japan

This work was supported by the JSPS Kakenhi grant number: 24K15805.

Abstract

The development of portable, low-field MRI systems is currently limited by the computational complexity of optimizing high-density permanent magnet arrays. While traditional Halbach cylinders offer a baseline for transverse fields, achieving medical-grade homogeneity in non-standard, compact geometries remains prohibitive using conventional loop-based physics. This work introduces an ultra-vectorized "Gen-Tensor" engine that revolutionizes the magnet design process by replacing iterative loops with 4D broadcasting and tensor evolution. By parameterizing 300 discrete magnets into a multiple of 2,100-variable generative DNA block (encompassing 3D position, 3-axis rotation, and activation masks), the framework enables the autonomous synthesis of inherently shimmed, multi-layered topologies.

A significant breakthrough of this study is the discovery of a non-standard Cassinian oval architecture that achieves a field magnitude nearly double that of traditional circular cylindrical benchmarks while maintaining high directional purity of the field. This 100% increase in field strength is achieved without an increase in the magnet budget, utilizing the algorithm's ability to exploit non-linear flux-path efficiencies and dynamic compaction. The optimization employs a dual-stage differential evolution protocol, transitioning from a high-entropy exploration phase to a low-mutation precision shimming phase.The resulting parallel flux streamlines, and high directional purity demonstrate a robust pathway for the realization of high-signal, portable MRI systems. This technology is specifically designed for side-by-side operation with existing PET systems in radiologically controlled environments, offering a computationally efficient solution for next-generation point-of-care molecular imaging without the need for intensive post-fabrication shimming.

MIC-05-079

Design of SSLE-PET with GATE Simulation Towards Sub-Second Dynamic Mouse Imaging (#2309)

Han Gyu Kang[1], Hideaki Tashima[1], Toshiaki Sakai[2], Taiga Yamaya[1]

[1] National Institutes for Quantum Science and Technology (QST), Advanced Nuclear Medicine Science, Chiba, Japan; [2] Hamamatsu Photonics, Hamamatsu, Japan

Abstract

Last year, we developed an ultrasensitive preclinical positron emission tomography (PET) scanner with 4-layer depth-of-interaction (DOI) detectors, thereby allowing sub-second dynamic imaging of a rat. However, the crystal pitch and DOI bins were 2.8 mm and 7.5 mm, which hampered mouse imaging. On the other hand, assembling smaller crystals remains technically challenging. In this study, we designed a novel preclinical PET scanner that uses a sub-surface laser engraving (SSLE) technique to fabricate the finely pixelized crystal elements, and we call it the SSLE-PET. The SSLE-PET consists of 12 DOI detectors, each of which has tapered LYSO crystals with a thickness of 20 mm. The LYSO crystals were pixelized by SSLE, providing fine crystal pitches (top=1.0 mm, bottom=1.6 mm) and 2.5 mm DOI bins. We used GATE simulation to investigate the effects of inner diameter (i.e. detector gap) and axial coverage on the performance of the SSLE-PET. To evaluate spatial resolution and sensitivity, a NEMA ^{22}Na source was used. For imaging performance evaluation, a resolution phantom was used. The GATE output was reconstructed by using a filtered back projection algorithm without any gap filling method. An energy window of 400-600 keV was used. The spatial resolution (1.27 mm) and resolvable rod diameter (1.0 mm) were not affected by the inner diameter. However, gap artifacts appeared for an inner diameter of 70 mm. Hence, an inner diameter of 65 mm would be the best choice to avoid any mechanical collision between detectors, while maintaining the image quality. With an axial coverage of 88 mm, sub-second PET imaging was demonstrated. As a next step, we plan to develop a prototype SSLE-PET scanner.

References

[1] H.G. Kang et al., “Development of an ultrasensitive small animal PET with 4-layer DOI detectors for sub-second dynamic rodent imaging”, *Phy. Med. Biol.*, vol. 70, No. 12, pp. 125014, 2025.

[2] Y. Yang, et al., “A Prototype High-Resolution Small-Animal PET Scanner Dedicated to Mouse Brain Imaging” Journal of Nuclear Medicine, vol. 57, no. 7, pp. 1130-1135, July 2016.

[3] T. Moriya et al., “Development of PET Detectors Using Monolithic Scintillation Crystals Processed With Sub-Surface Laser Engraving Technique”, *IEEE Trans. Nuc. Sci.*, vol. 57, No. 5, pp. 2455-2459, 2010.

[4] H.G. Kang et al., “Design optimization using GATE Monte Carlo simulations for a sub-0.5 mm resolution PET scanner with 3-layer DOI detectors”, *Phy. Med. Biol.*, vol. 71, No. 3, pp. 035001, 2026.

MIC-05-082

SPECT vs. Compton Camera for Prompt Gamma Monitoring in BNCT: a simulation study. (#2424)

Tommaso Ferri[1,2], Filippo Ghisio[1,2], Marco Carminati[1,2], Carlo E. Fiorini[1,2], Davide Mazzuzzoni[3,2], Gianluca Mocerino[3,2], Stefano Agosteo[3,2], Giacomo Borghi[1,2]

[1] Politecnico di Milano, Dipartimento di Elettronica, Informazione and Bioingegneria, Milano, Italy; [2] Istituto Nazionale di Fisica Nucleare (INFN), Sezione di Milano, Milano, Italy; [3] Politecnico di Milano, Dipartimento di Energia, Milano, Italy

Part of this work has been financed by INFN (CSN5), Italy (SPOC project), and by PRIN PNRR 2022 funding program of Ministero Dell'università e della Ricerca (MUR), Italy (BNCT-SPECT project).

Abstract

Real-time monitoring in Boron Neutron Capture Therapy (BNCT) exploiting the 478 keV gamma rays emitted by the neutron capture reaction, remains a major challenge due to the intense background present in the irradiation room during treatment. To date, no clinically established system is available, and the choice between SPECT and Compton camera approaches remains an open and highly relevant question.

Here, we present a Monte Carlo (MC) comparison study between a previously developed BNCT-SPECT detector and a LaBr3-based Compton camera for 478 keV prompt-gamma detection.

The goal is to assess the capability of Compton cameras to exploit electronic collimation and directionality for background rejection, thereby improving the signal-to-background ratio (SBR) with respect to SPECT. The results confirm that, in the absence of shielding, SPECT detection is severely dominated by room-induced background. For a vial containing 1000 ppm of ^{10}B irradiated with a thermal neutron flux of 3×10^6 n cm^{-2} s^{-1}, the SPECT configuration yielded an SBR of only 0.009, while the Compton camera achieved an SBR of 3.2. These findings suggest that a Compton camera-based system may represent a promising strategy to address one of the main limitations of BNCT-SPECT systems towards clinical applicability. However, the choice between the two approaches remains challenging, since properly shielded SPECT configurations can still provide high SBR values, while clinically relevant neutron fluences may increase the single-interaction rate in Compton cameras, making true-coincidence identification more demanding and possibly requiring dedicated shielding as well.

References

[1] Parajuli, R. at al. (2022), Development and Applications of Compton Camera—A Review. Sensors, 22(19), 7374.

[2] Ferri, T. at al., \textit{Development of an optimized SPECT module for BNCT applications with novel pinhole collimator and DOI estimation with ANN}. Submitted to IEEE Transactions on Radiation and Plasma Medical Sciences.

[3] Ferri, T. at al. Design and Validation of a SPECT Prototype for Treatment Monitoring in BNCT and First Experimental Tomographic Results. IEEE Transactions on Radiation and Plasma Medical Sciences, 10(1), 126–136.

[4] A. Caracciolo at al., “Prompt gamma-ray imaging in realistic background conditions of a boron neutron capture therapy facility,” Scientific Reports, vol. 15, no. 1, p. 18626, 2025.

MIC-05-085

A Novel Inter-Crystal Scatter Positioning Method Using Variable-Bin Stochastic Conditional Probability Based on Energy and Depth-of-Interaction Ordering (#2695)

Hyeongseok Shim[1,2], Guen Bae Ko[2]

[1] Korea Advanced Institute of Science and Technology, Department of Nuclear and Quantum Engineering, Daejeon, South Korea; [2] Korea Advanced Institute of Science and Technology, Mechanical Engineering Research Institute, Daejeon, South Korea

This work was supported by the National Research Foundation of Korea(NRF) grant funded by the Korea government(MSIT) (RS-2026-25490510).

Abstract

Inter-crystal scatter (ICS) in PET detectors causes multiple interactions within a detector block, and misidentification of the first interaction crystal can lead to incorrect LOR assignment and image degradation. Rejecting all ICS events avoids this error but reduces system sensitivity. This study proposes a stochastic conditional-probability-based ICS positioning method using ordering information from deposited energy and DOI. The method estimates first-interaction events by applying conditional probabilities defined over binned observables, where the conditioning variable is either the energy or DOI difference between two crystals involved in an ICS event. These probabilities were obtained statistically from GATE simulations of an 8×8 LYSO crystal array with 3.2 mm pitch. Point sources were placed at 5, 10, 20, and 25 cm, and two-crystal ICS events were selected for validation. The effects of bin count, binning strategy, and detector resolution were evaluated using 2, 4, and 8 bins with equiquantile and equal-width binning. Accuracy exceeded 85% using only 3% of the validation data, corresponding to approximately 20,000 ICS counts per detector block. DOI-based conditioning achieved slightly higher accuracy than energy-based method, suggesting that DOI ordering provides useful geometric information for first-crystal identification. However, the performance difference was small, indicating that either DOI or energy ordering can be used depending on detector readout capability. Accuracy was insensitive to bin count, binning strategy, and detector resolution. These results demonstrate that reliable ICS positioning can be achieved using predetermined conditional probabilities matched to detector characteristics, supporting practical recovery of ICS events without requiring high detector resolution or excessive readout complexity.

References

[1] Surti, S. and Karp, J. S. 2018, 'Impact of event positioning algorithm on performance of a whole-body PET scanner using one-to-one coupled detectors', *Physics in Medicine & Biology*, 63(5), 055008

[2] Abbaszadeh, S., Chinn, G. and Levin, C. S. 2018, 'Positioning true coincidences that undergo inter- and intra-crystal scatter for a sub-mm resolution cadmium zinc telluride-based PET system', *Physics in Medicine & Biology*, 63(2), 025012

[3] Rafecas, M., Böning, G., Pichler, B. J., Lorenz, E., Schwaiger, M. and Ziegler, S. I. 2003, 'Inter-crystal scatter in a dual layer, high resolution LSO-APD positron emission tomograph', Physics in Medicine & Biology, 48(7), 821–848

[4] Shim, H. S., Desai, F., Ullah, M. N., Levin, C. S., Lee, M. S. and Lee, J. S. 2025, 'A Novel Inter-Crystal Scattering Positioning Method Based on Energy Ordering and First-Interaction Crystal Correlation', *IEEE Conference Proceedings*, 2025(NSS/MIC/RTSD)

MIC-05-088

Validation of Compton camera simulations using GATE version 10 through experimental data (#2793)

Zaina J. Hurani[1], Luis Barrientos[2], Karol Brzeziński[2], Gabriela Llosá[2], David Sarrut[1], Ane Etxebeste[1]

[1] CREATIS, CNRS UMR 5220, INSERM U1044, Université de Lyon, INSA-Lyon, Université Lyon 1, Lyon, France; [2] Instituto de Física Corpuscular (IFIC), CSIC, Universitat de València, Valencia, Spain

This work has received funding from the European Union's EURATOM research and innovation program (AIDER project, G.A. 101061037).

Abstract

Compton cameras are electronically collimated imaging devices that reconstruct the origin of gamma rays using Compton kinematics, making them particularly suited for targeted radionuclide therapy (TRT), where conventional gamma cameras struggle with high-energy and low-activity emitters. The European project AIDER is developing a high-performance scintillator-based Compton camera to improve imaging and enable dosimetry in TRT, including targeted alpha therapy. Accurate Monte Carlo modeling is essential in this context for detector design and image reconstruction optimization. We present the validation of Compton camera simulations using GATE version 10, a major evolution of the Geant4-based Monte Carlo toolkit for medical physics with a Python based user interface. To this end, data acquired with MACACO1, a two-layer Compton camera prototype based on monolithic $LaBr_3$ scintillation crystals, developed at IFIC-Valencia, was employed. A Monte Carlo model of this system was previously validated using a dedicated Compton camera module in an older version of GATE based on legacy static macro-based files. In this work, the model was developed using GATE 10. The detector response was modeled by a digitizer chain that includes the measured energy and spatial resolution of the prototype. Time coincidences were obtained offline using a time coincidence window of 50 ns.

Simulated and experimental coincidence energy spectra showed good agreement despite small discrepancies at low energies. The angular resolution measure at 1275~keV was in good agreement between both simulated and experimental data with a relative difference of 0.7%. The validated framework for Compton camera simulations with the new GATE 10 modular version, provides a flexible platform for detector design and image reconstruction optimization.

References

[1] Sarrut, DN, et al. 2026, 'GATE 10 Monte Carlo particle transport simulation: I. Development and new features', *Physics in Medicine and Biology*, vol. 71, no. 1, p. 015042, Bristol: IOP Publishing.

[2] Todd, RW, Nightingale, JM, Everett, DB 1974, 'A proposed γ camera', *Nature*, vol. 251, pp. 132–134, London: Nature Publishing Group.

[3] Muñoz, E, et al. 2017, 'Performance evaluation of MACACO: a multilayer Compton camera', *Physics in Medicine and Biology*, vol. 62, no. 18, pp. 7321–7341, Bristol: IOP Publishing.

[4] Etxebeste, A, et al. 2020, 'CCMod: a GATE module for Compton camera imaging simulation', *Physics in Medicine and Biology*, vol. 65, no. 5, p. 055004, Bristol: IOP Publishing.

MIC-05-091

Convertible Whole-Body Extension of a Brain-Dedicated Whole Gamma Imaging System:A Simulation Study (#3053)

Ryogo Abe[1,2], Go Akamatsu[1], Hideaki Tashima[1], Taiga Yamaya[1]

[1] National Institutes for Quantum Science and Technology, Imaging physics groupe, Chiba, Japan; [2] Chiba University, Medical Engineering Course, Department of Fundamental Engineering, Graduate School of Science and Engineering, Chiba, Japan

Abstract

Whole gamma imaging (WGI) is a hybrid nuclear medicine technique under development at QST that integrates PET and Compton imaging by placing a scatterer detector ring inside a PET detector ring. This configuration is expected to enable simultaneous PET and SPECT tracer imaging and to allow high-sensitivity PET acquisition using radionuclides such as ^{89}Zr, which emit both positrons and prompt gamma rays. In this study, we investigated the feasibility of extending a previously optimized brain-dedicated WGI design to a whole-body configuration by scaling the scatterer-detector ring diameter. Our proposed system expands the scatterer detector ring diameter in the whole-body mode, and fills the missing data due to the detector gaps by a mechanical rotation. Monte Carlo simulations using Geant4 were performed to evaluate the detection performance of the proposed system for ^{89}Zr imaging in the whole-body mode, with particular emphasis on the effects of inter-detector gaps introduced by geometric scaling and the necessity of mechanical rotation in the scatterer-detector system. Point-source simulations were conducted to assess Compton sensitivity and angular resolution measure (ARM), and sparse detector configurations were reproduced by masking half of the scatterer detectors. The results showed that Compton sensitivity was approximately doubled when all scatterer modules were installed, indicating that sensitivity is primarily determined by the number of available detectors rather than the presence of gaps. In contrast, ARM exhibited minimal variation across configurations, suggesting that mechanical rotation has little influence on angular-resolution performance. These findings provide essential design guidelines for whole-body WGI systems and will be further validated through imaging simulations to quantify the impact of detector gaps and rotation on reconstructed image quality.

References

[1] E. Yoshida, *et al.*, "Whole gamma imaging: a new concept of PET combined with Compton imaging," Phys. Med. Biol., 65, 125013, 2020.

[2] G. Akamatsu et al., "Development of the 4th Whole Gamma Imaging Prototype for ^{89}Zr Mouse Imaging Demonstration", 2023 IEEE NSS, MIC-M-10-431

[3] G.Akamatsu et al., "Zr-89 mouse Compton imaging with the developed next-generation whole gamma imaging system", JNM. 65, suppl. 2, 241604, 2024

MIC-05-094

Translating CLS Detector Technology from Brain to Whole-Body PET Imaging: A Simulation Study (#3161)

Mizuki Furuta[1,2], Hideaki Tashima[1], Go Akamatsu[1], Taiga Yamaya[1]

[1] National Institutes for Quantum Science and Technology (QST), Department of Advanced Nuclear Medicine Sciences, Chiba, Japan; [2] Chiba University, Faculty of Engineering, Chiba, Japan

Abstract

We have achieved 1 mm rod separation performance in a brain-dedicated PET system, CLS-7, which employs our original crosshair light-sharing (CLS) detector with both time-of-flight (TOF) and depth-of-interaction (DOI) capabilities. From that work, our next question to explore is how CLS technology can improve whole-body PET imaging. PET is widely used in cancer diagnosis, and improving spatial resolution with low image noise is important for detecting small lesions at earlier stages. In this study using Monte Carlo simulation, we investigated the imaging performance of a whole-body PET system using CLS detectors. A whole-body CLS-PET system was modeled using the Geant4 with a ring diameter of 750 mm and an axial field-of-view of 228 mm. The detector was modeled as a 14 × 14 LGSO crystal array with 1.45 × 1.45 × 15 mm³ crystals divided into three depth segments for DOI modeling. The system had 92 detector blocks per ring and seven rings. Spatial resolution and image quality were evaluated by simulating point-source and image quality phantom measurements based on the NEMA NU 2 standard and compared to cases with and without DOI and TOF information. As a result, we found the use of DOI information improved spatial resolution by 40% compared with the no-DOI information condition, while TOF information substantially reduced image noise in the image-quality evaluation. These results suggest that whole-body PET using CLS detectors can suppress peripheral spatial-resolution degradation and improve contrast recovery for small lesions.

References

[1] E. Yoshida et al., “Air-CLS Detector: A Modified Crosshair Light Sharing PET Detector With Air Gaps in the U-Shape Light Path,” IEEE Transactions on Radiation and Medical Science, vol. 9, no. 7, pp. 872–878, Sep. 2025.

[2] K. Narita et al., “CLS-7: The 7-ring TOF-DOI Brain PET System with Crosshair Light-Sharing Detectors”, 2025 IEEE Nuclear Science Symposium (NSS), Medical Imaging Conference (MIC) and Room Temperature Semiconductor Detector Conference (RTSD), Yokohama, Japan, 2025

[3] National Electrical Manufacturers Association (NEMA), NEMA NU 2-2024: Performance Measurements of Positron Emission Tomographs (PET), NEMA, 2024

MIC-05-097

Photon-Counting CT in the Context of Ultra-Low-Dose PET/CT (#2394)

Samaneh Mostafapour[1], Joost F. Hop[2], Jan Braaksma[2], Marcel J.W. Greuter[2], Joyce van Sluis[1], Adriaan A. Lammertsma[1], Charalampos Tsoumpas[1]

[1] University Medical Center Groningen, University of Groningen, Nuclear medicine and molecular imaging department, Groningen, Netherlands; [2] University Medical Center Groningen, University of Groningen, Department of Radiology, Groningen, Netherlands

C. Tsoumpas, and S. Mostafapour are supported by the NWO AES Vici Talent program (doi: 10.61686/REEAR02777).

Abstract

Reducing radiation dose in positron emission tomography / computed tomography (PET/CT) is possible, but ultra-low-dose (ULD)-CT increases image noise which may affect quantitative reliability and accuracy due to attenuation correction. Photon-counting CT (PCCT) offers improved noise characteristics compared with conventional energy-integrating detector CT (EID-CT), particularly at low dose levels. This study compares PCCT and EID-CT under low-dose (LD) and ULD-CT conditions using a cadaver, an anthropomorphic phantom (PBU-60), and a tissue characterization phantom (Gammex 467). Quantitative evaluation is performed using CT values in HU and corresponding linear attenuation coefficients (μ). Results show that ULD increases noise in both systems, with stronger degradation and reconstruction dependency in EID-CT. Compared with EID-CT, PCCT shows less changes in mean HU values between LD and ULD acquisitions, particularly in dense materials, although noise remains present. After HU-to-μ conversion, variability is substantially reduced for both systems, though not uniformly across all conditions. These findings indicate that attenuation coefficients are less sensitive to dose reduction than CT values and suggest that PCCT may provide more robust quantitative performance than EID-CT under ULD conditions. However, given non-matched acquisition and reconstruction settings results should be interpreted with caution, and require validation in further standardized and PET-based studies.

References

[1] J. Hamill *et al*, "Can photon-counting CT improve PET/CT's quantitative accuracy?," Med. Phys., vol. 51, no. 10, pp. 7206–7213, 2024.

[2] J.P.J. Carney *et al*, "Method for transforming CT images for attenuation correction in PET/CT imaging," Med. Phys., 2006.

MIC-05-100

DMGR-Net: Dual-Modal Gated Residual Network for Lightweight PET/MRI Brain Parcellation (#2634)

Minjie Wang[1], **Gan Zhan**[2], Ye Tong[3], Jie Yang[4], Xianchen Liu[5], Yazhi Li[4], Shaojie Feng[4], Jing Zou[4], Siwei Xie[4]

[1] Sun Yat-sen University, School of Medicine, Shenzhen, China; [2] Shenzhen Bay Laboratory, Institute of Biomedical Engineering, Shenzhen, China; [3] Sun Yat-sen University, Zhongshan School of Medicine, Guangzhou, China; [4] Sun Yat-Sen University, School of Biomedical Engineering, Shenzhen, China; [5] Florida State University, Tallahassee, USA

This work was supported by grants from Shenzhen Medical Research Fund(A2403021), National Key Research and Development Program of China (2024YFF0727400) and the National Natural Science Foundation of China (82327809).

Abstract

Automated parcellation of the brain into correct regions using dual-modal PET and MRI is essential for quantitative neuroimaging. Existing high-performing fusion networks often rely on large model sizes, which limits their deployment in resource-constrained settings. This paper presents the DualModal Gated Residual Network (DMGR-Net), a lightweight architecture that integrates Bidirectional Cross-Modal Feature Gating (Bi-CMFG) and Residual Soft Deep Supervision (RSDS). Bi-CMFG performs spatial attention across modality-specific encoder branches to preserve fine structural details, while RSDS applies a boundary-weighted loss at multiple decoder scales to sharpen parcellation boundaries by explicitly penalizing errors along anatomical interfaces. Built upon a depthwise-separable 3D U-Net with only 0.121M parameters, DMGR-Net contains 0.206M parameters and 5.30 GFLOPs, yet achieves the lowest HD95 and ASSD among compared methods, surpassing substantially larger models on surface-distance metrics. Ablation studies confirm the complementary roles of each module, and qualitative comparisons illustrate progressively refined boundaries across configurations, demonstrating that a lightweight design can deliver precise surface delineation.

References

[1] Z. Shi, C. Zhang, D. Ye, P. Qin, R. Zhou, and L. Lei, “MMI-Fuse:Multimodal brain image fusion with multiattention module,” *IEEE Access*, vol. 10, pp. 37200–37214, 2022.

[2] H. Tang et al., “Automatic brain segmentation for PET/MR dual-modalimages through a cross-fusion mechanism,” *IEEE J. Biomed. Health Inform.*, vol. 29, no. 3, pp. 1982–1994, Mar. 2025.

[3] S. U. Khan, M. A. Khan, M. Azhar, F. Khan, Y. Lee, and M. Javed,“Multimodal medical image fusion towards future research: A review,” *J. King Saud Univ. – Comput. Inf. Sci.*, vol. 35, no. 8, Art. no. 101733, 2023.

[4] H. Kervadec, J. Bouchtiba, C. Desrosiers, E. Granger, J. Dolz, andI. B. Ayed, “Boundary loss for highly unbalanced segmentation,” *Med.Image Anal.*, vol. 67, Art. no. 101851, 2021.

[5] C. R. Jack Jr., M. A. Bernstein, N. C. Fox, P. Thompson, G. Alexander,D. Harvey, et al., “The Alzheimer’s disease neuroimaging initiative(ADNI): MRI methods,” *J. Magn. Reson. Imaging*, vol. 27, no. 4,pp. 685–691, 2008.

MIC-05-103

New Hyperion Detector Platform Electronics: Highly Integrated Mainboard, Tile Cable, and Sensor Tile (#2834)

Bjoern Weissler[1,2], David Schug[1,2], Eike Gegenmantel[2], Oliver Muelhens[2], Thore Meyer[1], Harald Radermacher[1], Julian Thull[1], Max Breuer[1], Christoph W. Lerche[3], Volkmar Schulz[1,2]

[1] RWTH Aachen University, Institute of Imaging & Computer Vision / Institute for Experimental Molecular Imaging, Aachen, Germany; [2] Hyperion Hybrid Imaging Systems GmbH, Aachen, Germany; [3] Forschungszentrum Juelich, Institute of Neuroscience and Medicine 4, Juelich, Germany

This work is sponsored by the German Federal Ministry of Education and Research, funding program “KMU-innovativ: Medizintechnik”, contract number 13GW0609(A/B) and 13GW0621(A/B/C).

Abstract

Combined PET/MRI is a powerful tool for studying neurological diseases, but resolving cortical structures requires a spatial resolution of about one millimeter. Dedicated brain inserts can achieve this by bringing high-resolution detectors close to the head, provided that the detector electronics meet stringent constraints on integration, thinness, width, length, and MRI compatibility.

The S-PET project develops such a scalable PET detector platform for neuro PET/MRI. The detector module concept is built around a single mounting and cooling structure that spans the full module length and carries sensor tiles, mainboard, and power supply.

The Visor HD sensor tile (49 × 49 mm²) combines a 12 × 12 Broadcom 4 mm NUV-MT SiPMs with a PETsys TOFPET2 ASIC. A dedicated compression scheme maps the 144 SiPM outputs to its maximum 64 ASIC channels: 36 SiPMs are read out directly, while the remaining channels each combine four spatially separated SiPMs that can be disambiguated through their direct neighbors.

The SuperVisor mainboard (134 × 49 mm²) hosts six sensor-tile connectors, an AMD/Xilinx Kintex-7 FPGA, individual voltage and current regulation per tile, and fiber-optic transceivers on a second PCB layer to keep the board short. A separate, exchangeable power-supply board feeds the module.

Thin flex-PCB tile cables, produced in precise lengths up to 454 mm, connect the sensor tiles to the mainboard on the opposite side of the cooling structure.

A first measurement with a BrainPET 7T crystal array (three DOI layers of LSO at 2 mm pitch), scanned across a fan-beam-collimated ^{22}Na source, yields a mean absolute error below 1.4 mm in both planar directions, confirming that the Visor HD compression scheme works as intended. SuperVisor PCBs are in production and expected in time for the conference.

References

[1] https://hyperion-his.com/pet-detector-platform/

[2] T. Meyer, et al., “Crystal Topology and Channel Compression Optimization for a high-resolution Neuro PET/MRI TOF-DOI PET Detector”, submitted to 2026 NSS-MIC-RTSD conference

[3] https://www.broadcom.com/products/optical-sensors/silicon-photomultiplier-sipm/high-performance-sipm-nuv-mt

[4] https://www.petsyselectronics.com/web/public/products/1

[5] D. Schug et al., “Hyperion DAQ: A Versatile Data Acquisition and Processing Platform”, submitted to 2026 NSS-MIC-RTSD conference

[6] C. Lerche et al., “Fast maximum likelihood positioning for a staggered layer scintillation PET detector”, Phys. Med. Biol. 70 (2025) 175018, https://doi.org/10.1088/1361-6560/adf8ab

MIC-05-106

Development of a Shielded Digital PET Detector System for a Brain PET/MRI Insert (#3066)

Bohdan Krauze[1], Yurii Shepelytskyi[3], Viktoriia Batarchuk[3], Brandon Baldassi[2], Mitchell Albert[3], Alla Reznik[1,3], Oleksandr Bubon[1,2]

[1] Lakehead University, Physics, Thunder Bay, Canada; [2] Radialis Inc., Thunder Bay, Canada; [3] Thunder Bay Regional Health Research Institute, Thunder Bay, Canada

We acknowledge the support from NSERC

Abstract

Simultaneous positron emission tomography/magnetic resonance imaging (PET/MRI) can combine PET functional information with MRI soft-tissue contrast in a single imaging session, offering potential benefits for neurological applications such as neurodegenerative disease assessment and brain tumor localization. However, fully integrated PET/MRI systems remain limited, motivating the development of compact PET inserts that can operate inside or around existing MRI scanners. In this work, radiofrequency shielding was developed and evaluated as an enabling step toward an MRI-compatible Radialis brain PET insert using digital detector electronics. Shielding was implemented for the digital front-end modules, data-acquisition electronics, high-speed data-transmission cable, and auxiliary power cable of a Radialis PET detector array. Each detector module consisted of a 24 × 24 cerium-doped lutetium yttrium orthosilicate scintillator array coupled through a borosilicate light guide to an 8 × 8 silicon photomultiplier array. The shielded detector configuration was evaluated during simultaneous acquisition on a 3.0 T MRI system using a ^{22}Na point source in a water phantom positioned within the MRI brain-coil geometry. The redesigned shielding enabled stable PET data acquisition, coincidence processing, and point-source image reconstruction during MRI operation. PET energy resolution was maintained at approximately 22.5–22.6% during simultaneous acquisition, although reconstructed image signal-to-noise ratio decreased from 76.64 outside the MRI environment to 37.83 during PET/MRI acquisition, likely reflecting residual MRI-related effects, head-coil attenuation, and source-positioning differences. These results demonstrate that targeted shielding of Radialis digital PET electronics enables reliable simultaneous PET/MRI operation and supports further development of a high-sensitivity brain PET/MRI insert.

References

[1] A. Kaushik *et al.*, "Estimation of radiation dose to patients from 18FDG whole body PET/CT investigations using dynamic PET scan protocol," *Indian J. Med. Res.*, vol. 142, no. 6, pp. 721–731, Dec. 2015, doi: 10.4103/0971-5916.174563.

[2] *Canadian Medical Imaging Inventory 2022–2023: Provincial and Territorial Overview: CMII Report*. in CADTH Health Technology Review. Ottawa (ON): Canadian Agency for Drugs and Technologies in Health, 2024. Accessed: May 11, 2026. [Online]. Available: http://www.ncbi.nlm.nih.gov/books/NBK607341/

[3] M. Rapley *et al.*, "A Shielding Free PET Insert for High Sensitivity PET/MRI of the Brain," in *2024 IEEE Nuclear Science Symposium (NSS), Medical Imaging Conference (MIC) and Room Temperature Semiconductor Detector Conference (RTSD)*, Oct. 2024, pp. 1–2. doi: 10.1109/NSS/MIC/RTSD57108.2024.10656764.

[4] B. J. Lee, R. D. Watkins, C.-M. Chang, I. Kwon, and C. S. Levin, "Detector shielding design of a PET inserts in a 3T MRI system," in *2016 IEEE Nuclear Science Symposium, Medical Imaging Conference and Room-Temperature Semiconductor Detector Workshop (NSS/MIC/RTSD)*, Oct. 2016, pp. 1–3. doi: 10.1109/NSSMIC.2016.8069610.

MIC-05-109

Design and Performance Evaluation of a Full-Ring SPECT System Based on the Continuous LaBr3(Ce) (#1199)

Kui Wang[1], Tiantian Dai[2], Qingyang Wei[1]

[1] University of Science and Technology Beijing, Beijing Engineering Research Center of Industrial Spectrum Imaging and School of Automation and Electrical Engineering, Beijing, China; [2] China–Japan Friendship Hospital, Department of Radiation Oncology, Beijing, China

Abstract

Small-animal single-photon emission computed tomography (SPECT) serves as a cornerstone of functional nuclear imaging, with extensive applications in preclinical research, drug discovery, and life sciences. Building upon our previously developed full-ring cascade gamma coincidence imaging system with continuous LaBr3 crystals, this work redesigns a multi-pinhole collimator to enable full-ring SPECT imaging for ^{99m}Tc. To optimize computational efficiency, the system transfer matrix is implemented using a sparse storage strategy. Furthermore, GPU acceleration is employed for key processes, including system matrix calculation, forward and backward projections, and image updates, significantly enhancing the performance of the iterative reconstruction algorithm. Experimental results demonstrate that the storage requirement for the system transfer matrix is reduced from 10.06 GB to 77.7 MB. Concurrently, the computational efficiency is significantly enhanced, achieving a single iteration time of 0.94 ms in binning mode. Moreover, the full-ring SPECT system achieves a 1.0×10^{-3} detection efficiency and successfully resolves 1.2 mm diameter hot rods. In conclusion, the proposed full-ring SPECT system achieves a high-performance balance between detection sensitivity and spatial resolution.

References
[1] K. P. Willowson and D. L. Bailey, “Evolving SPECT-CT technology,” *Br. J. Radiol.*, Oct. 2024.

MIC-05-112

Image quality assessment of a positron emission mammography prototype (#1431)

Valeria Pérez-Martínez, Karol F. Goyes-Acosta, Héctor Alva-Sánchez, Tirso Murrieta-Rodríguez, Arnulfo Martínez-Dávalos, Fernando G. Moncada-Gutiérrez, Mercedes Rodríguez-Villafuerte

Universidad Nacional Autónoma de México, Instituto de Física, CDMX, Mexico

We acknowledge the support from PAEP-UNAM and PAPIIT-UNAM IN103726.

Abstract
At the Biomedical Imaging Laboratory of the Institute of Physics, UNAM, a dual-panel positron emission mammography (PEM) prototype is under development. This work evaluated its spatial resolution through the line spread function, and image quality via recovery coefficients. A custom variable-geometry phantom was developed using 3D-printed supports for four ^{18}F line sources with a 0.69 mm internal diameter. Data acquisitions were performed at 11 in-plane positions and at different cross-planes heights to map the 17.4 cm × 17.4 cm × 6.0 cm effective field-of-view. Experimental setup included a panel separation distance of 6.0 cm, 8 ns coincidence window and a 360 – 757 keV energy window. The interaction position of each event is estimated using a raise-to-a-power center-of-gravity algorithm. Images are reconstructed using a list-mode ordered subsets expectation-maximization algorithm (3 iterations, 4 subsets) using a 1 mm isotropic voxel. Image quality was evaluated with a NEMA-like phantom containing 4 spherical lesions (diameters of 4, 6, 8 and 10 mm) filled with ^{18}F, placed at different field-of-view positions and phantom orientation. The effect of restricting oblique lines of response was also studied. In addition, the sensitivity was analyzed using a point-like ^{22}Na source in different field-of-view positions. The best spatial resolution was 2.1 ± 0.2 mm at the center of the PEM field-of-view and decreasing to 4.5 ± 0.3 mm at the PEM edges. FWHM values closest to the real sphere diameters were obtained at the detector center. Limiting oblique lines-of-response to reduce depth-of-interaction effects resulted in lower spatial resolution. Overall, the prototype showed good performance, with adequate image quality regardless of spherical-lesion position or orientation.

References
[1] L. T. Torres-Urzúa, H. Alva-Sánchez, A. Martínez-Dávalos *et al*, "A dedicated phantom design for positron emission mammography performance evaluation", *Phys. Med. Biol.* 65 (2020) 245003.
[2] F. G. Moncada-Gutiérrez, M. Rodríguez-Villafuerte, H. Alva-Sánchez *et al*, "Incorporation of Deep Learning Regularization in the Image Reconstruction Algorithm for a Dual-Panel PEM Scanner," 2025 IEEE NSS MIC RTSD, 2025.

MIC-05-115

Experimental Results from Novel Monolithic PET Detector and Application to Axillary Lymph Node Imaging (#1769)

Timothy Cotroneo[1], David Pare[1], Lemise Saleh[1], Paul Vaska[1,2]

[1] Stony Brook University, Biomedical Engineering, Stony Brook, USA; [2] Renaissance School of Medicine at Stony Brook University, Radiology, Stony Brook, USA

We thank the Carol M. Baldwin Foundation for Breast Cancer Research, Stony Brook University Graduate School, and the SBU OVPR seed funding program for their support.

Abstract
Monolithic scintillators are a promising alternative to standard pixelated crystals in positron emission tomography, as they can be more cost-effective, reduce dead space, and capture an unobstructed light distribution, which can be used for depth of interaction estimation. We focus on the improvements seen by using an array of integrated

corner reflectors (ICR) machined directly into the entrance face of the monolith, which we previously showed via simulation to improve light collection and narrow the light distribution. In this study, we built a physical prototype of the device using a CNC machining process. We compared this prototype with other monolithic block designs. We show that the ICR monolith with the CNN positioning algorithm has potential for high-resolution imaging with ~1 mm resolution at 12 mm thickness. Using GATE simulations, we constructed a full scanner with the performance of the monolithic blocks and tested the capabilities compared to existing systems. We show the improved spatial resolution and feasibility for a non-cylindrical design for axillary lymph node scanning.

References
[1] A. Gonzalez-Montoro et al., "Evolution of PET Detectors and Event Positioning Algorithms Using Monolithic Scintillation Crystals," IEEE T Radiat Plasma, vol. 5, no. 3, pp. 282-305, 2021, doi: 10.1109/TRPMS.2021.3059181.
[2] Y. Wang, W. Zhu, X. Cheng, and D. Li, "3D position estimation using an artificial neural network for a continuous scintillator PET detector," Phys Med Biol, vol. 58, no. 5, pp. 1375-90, Mar 7 2013, doi: 10.1088/0031-9155/58/5/1375.
[3] R. A. Valdés, M. Pereira, Daphne, and van, “Breast Cancer,” Springer eBooks, pp. 1–37, Jan. 2022, doi: https://doi.org/10.1007/978-3-031-05497-6_1.

MIC-05-118

Spatial Characterization of PET Detectors Based on BGO Pseudo-slabs

(#1981)

Neus Cucarella[1], Laura Gil-Bosch[1], Fiammetta Pagano[1], Francis Loignon-Houle[1], Marc Gil[1], Marta Freire[1], David Sanchez[2], Andrea Gonzalez-Montoro[1], Antonio J. Gonzalez[1]

[1] Instituto de Instrumentación para Imagen Molecular (I3M), Centro Mixto CSIC-Universitat Politècnica de València, DMIL, Valencia, Spain; [2] Oncovision SA, Valencia, Spain

This work was partially funded by the AEI (Grant PID2023-151999OB-I00), co-funded by the ERC (Grant No. 101164363). Views and opinions expressed are, however, those of the author(s) only and do not necessarily reflect those of the European Union or the ERC. Neither the European Union nor the granting authorities can be held responsible for them.
N.C. is supported by PTA2022-022459-I. M.F. and F.L.-H. are supported by CIAPOS/2023/141 and CIAPOS/2023/133, respectively.

Abstract
Pixelated crystal arrays are the standard in commercial PET scanners. However, these detectors usually lack DOI information, essential to achieve a homogenous spatial resolution along the entire FOV. Yet, studies have been already performed with pixelated detectors with DOI capabilities but at the cost of using extra hardware material and/or crystal assembling. Inspired by semi-monolithic crystal geometries, pseudo-slabs were proposed as an alternative. This geometry consists of an *N*×*N* pixel array optically isolated only in one direction, allowing light crosstalk in the orthogonal one. The *N* pixels sharing light in this direction form a pseudo-slab. The light sharing within a pseudo-slab is enough to enable DOI retrieval, while the physical separation between pixels confines the light more than in a pure slab geometry, yielding better time resolution.

In this work we evaluated the DOI resolution of a BGO block formed by 8×8 pixels, each measuring around 3×3×15 mm^3. Two different readout configurations were employed and compared. First, all the 64 channels corresponding to the TOFPET2 ASIC channels were digitized. Then, a multiplexing circuit was utilized, reducing the signals to 8+8 by summing rows and columns. The DOI was obtained using neural networks trained on experimental data.The results show a good DOI resolution for both readout configurations, achieving 3.8 ± 1.3 mm with the multiplexing circuit. These results show that pseudo-slabs are suitable for clinical PET scanners with DOI capabilities.

References
[1] M. Ito et al., *Biom. Eng. Let.*, 2011. DOI: 10.1007/s13534-011-0019-6.
[2] N. Cucarella et al., *TRPMS*, 2025. DOI: 10.1109/TRPMS.2025.3546998.
[3] R. Bugalho et al., *JINST*, 2019. DOI: 10.1088/1748-0221/14/03/P03029.
[4] A.J. Gonzalez et al., arXiv, 2926. DOI: 10.48550/arXiv.2603.09898.

MIC-05-121

Positron Range Confinement in Preclinical PET/MRI: A Multi-Isotope, Multi-Density Experimental Study (#1930)

Fernando Lopez-Berenguer[1], **Fernando Lopez-Berenguer**[1], Andrea Gonzalez-Montoro[1], Andrea Gonzalez-Montoro[1], Stuart Berr[2], Stuart Berr[2], Mark Williams[2], Mark Williams[2], Antonio J. Gonzalez[1], Antonio J. Gonzalez[1]

[1] Instituto de Instrumentación para Imagen Molecular (i3M), Centro Mixto CSIC-Universitat Politècnica de València, Valencia, Spain; [2] University of Virginia, Department of Radiology and Medical Imaging, Charlottesville, USA

This work was supported by the Generalitat Valenciana under Grant No. CIPROM/2021/003 and funds from the Univ, VA FUS Cancer Immunotherapy Center.F.Lopez Berenguer is supported by the European Research Council (ERC) under the European Union's Horizon Europe research and innovation programme (Grant agreement No. 101164363).

Abstract

The spatial resolution of PET imaging is fundamentally limited by the positron range, whose extent depends on both the emission energy of the radionuclide and the electron density of the surrounding medium. In integrated PET/MRI systems, the static magnetic field exerts a Lorentz force on the positrons, confining their trajectories in the transverse plane to the main magnetic field, potentially improving image resolution. Two complementary experiments were performed using a dedicated monolithic-crystal based PET insert operated at 0T and inside a 9.4T MRI: capillary line sources embedded in three tissue-equivalent phantoms of increasing density (EPF, PLA, and Rigid10k resin), and a microDerenzo phantom. Both tests were carried out with three positron emitters (^{18}F, ^{89}Zr, and ^{68}Ga) eventually use in pre-clinical imaging. The results demonstrate that the magnetic field significantly enhances transverse spatial resolution for high-energy positron emitters in medium- and high-density materials, with FWTM reductions of ~60% for ^{68}Ga and ~18% for ^{89}Zr, while the axial direction remains largely unaffected. Rod resolvability improved at 9.4T from 1.5 mm to ~1.0 mm and from 1.2 mm to 0.9 mm for ^{68}Ga and ^{89}Zr, respectively. . These findings highlight the relevance of both positron energy and tissue-equivalent density in determining the magnitude of magnetic-field-induced resolution improvements in preclinical PET/MRI.

References
[1] Moses, WW 2011, 'Fundamental limits of spatial resolution in PET', *Nuclear Instruments and Methods in Physics Research A*, vol. 648, pp. S236–S240.
[2] Ku-Toval, D et al. 2024, 'Quantitative analysis of the effect of the magnetic field generated by a PET/MR scanner on positron range', *Physics in Medicine and Biology*, vol. 69, no. 18, p. 185006.
[3] Lopez-Berenguer, F et al. 2025, 'Positron Range Confinement in High-Field MRI, Enhancing PET Image Quality', *IEEE NSS/MIC*.
[4] Lopez-Berenguer, F et al. 2025, 'Evaluation of a PET insert for trimodal imaging: a step towards PET/MRI-guided focused ultrasound', *IEEE Transactions on Radiation and Plasma Medical Sciences*, in press.

MIC-05-124

Resolution-Sensitivity Optimization with Expanded Position Maps in the CLS-7: A TOF-DOI Brain PET System (#2329)

Kurumi Narita[1,2], Go Akamatsu[1], Yuma Iwao[1], Eiji Yoshida[1], Hideaki Tashima[1], Miwako Takahashi[1], Taiga Yamaya[1]

[1] National Institutes for Quantum Science and Technology (QST), Institute for Quantum Medical Sciences, Chiba, Japan; [2] Chiba University, Graduate School of Science and Engineering, Chiba, Japan

This research was supported by AMED under Grant Number 23he2302010h0101, as well as by JST SPRING, Grant Number JPMJSP2109.

Abstract

The aim of this study was to optimize detector parameters of crosshair light-sharing (CLS) detectors to achieve a better resolution-sensitivity balance in the CLS-7, a brain-dedicated PET prototype we developed in 2025. In particular, we focused on position lookup tables (LUTs), which are generated from flood histograms calculated using Anger logic. In the 2025 model, restricted position LUTs fitted to crystal clusters were used to reduce inter-crystal scattering (ICS), thereby improving spatial and time-of-flight (TOF) resolution at the cost of decreased system sensitivity. In this study, we employed expanded position LUTs and compared the performance of restricted and expanded LUTs in the CLS-7. The detectors consisted of 15-mm-long fast-LGSO scintillators arranged with a crystal pitch of 1.6 mm. Sensitivity, noise-equivalent count rate (NECR), and TOF resolution at the peak NECR were evaluated for both settings. In addition, image quality was evaluated using a rod phantom, an IQ phantom, and a Hoffman phantom. Compared with the restricted LUTs, the expanded LUTs significantly improved sensitivity and the peak NECR by factors of 1.7 and 1.9, respectively. The loss in TOF resolution was only 12%, and no significant difference was observed in the rod phantom results. In both the IQ phantom and the Hoffman phantom, images obtained using the expanded LUTs had lower noise levels than those obtained using the restricted LUTs. These results demonstrate that expanded position LUTs can improve overall image quality despite some degradation in TOF resolution in the CLS-7 system.

References
[1] E. Yoshida, F. Obata, K. Kamada, A. Yoshikawa, and T. Yamaya, “Development of crosshair light sharing PET detector with TOF and DOI capabilities using fast LGSO scintillator,” *Physics in Medicine & Biology*, vol. 66, no. 22, p. 225003, Nov. 2021.
[2] National Electrical Manufacturers Association, “NEMA Standards Publication NU 2-2024: Performance Measurements of Positron Emission Tomographs,” Rosslyn, VA, USA, NEMA, 2024.

[3] E. Yoshida, F. Obata, and T. Yamaya, "Calibration method of crosshair light sharing PET detector with TOF and DOI capabilities," *Biomedical Physics & Engineering Express*, vol. 9, no. 5, p. 055031, Aug. 2023.

MIC-05-127

Performance evaluation of N-PET, a high-resolution TOF-DOI PET dedicated to brain imaging (#2442)

Ming Niu[1], Xiangtao Zeng[1], Hang Yang[1], Xiaolong Jiang[1], Wenjie Huang[1], Xin Zhao[1], Chen Huang[1], Zexing Wu[1], Hengyi Li[1], Xiaoqin Zhang[1], Yangyang Zhao[1,2], Jianlang Hua[1], Jing Wu[3], Qingyang Wei[2], Ji Dai[4], Ying Liang[5], Zheng Gu[1]

[1] Shenzhen Bay Laboratory, Institute of Biomedical Engineering, Shenzhen, China; [2] University of Science and Technology Beijing, School of Automation and Electrical Engineering, Beijing, China; [3] Beijing Normal University, School of Physics and Astronomy, Beijing, China; [4] Shenzhen Institute of Advanced Technology, Chinese Academy of Sciences, Shenzhen-Hong Kong Institute of Brain Science, Shenzhen, China; [5] National Cancer Center, Cancer Hospital & Shenzhen Hospital, Department of Nuclear Medicine, Shenzhen, China

The National Key R&D Program of China (No. 2023YFC2414800), the National Natural Science Foundation of China (Nos. 12275182 and 62371314), Guangdong Basic and Applied Basic Research Foundation (No. 2024A1515012154), the Major Program of Shenzhen Bay Laboratory (No. C1012530005) and the Shenzhen Bay Laboratory Proof-of Concept Grants (No. C1022430005).

Abstract

This study presents a performance evaluation of N-PET, a high-resolution TOF-DOI PET system designed for human brain imaging. The system has a compact ring geometry comprising 18 detector modules, with a ring diameter of 302 mm, a transaxial FOV of 210 mm, and an axial FOV of 52 mm. Each module employs dual-layer, multi-resolution LYSO detectors that enable both high spatial resolution and DOI measurement.System performance was first evaluated through count-rate measurements and phantom studies. Using a monkey-sized phantom, the scanner achieved a peak NECR of 44.0 kcps at 66.8 MBq, with a scatter fraction of 36.0%. After component-based normalization, the images of an image quality phantom showed a uniform background and high contrast hot spheres. Hot rod phantom imaging further demonstrated the high resolution of the system. With the phantom placed at the center of the FOV, rods of 1.2 mm diameter were resolved. When the phantom was placed at a 5-cm radial offset, reconstructed images using four DOI bins yields improved rod separation compared to that with one or two DOI bins, highlighting the benefit of DOI information in reducing resolution degradation near the edge of the FOV. In the Hoffman brain phantom images, gray matter structures are clearly delineated, and the PET images correlated well with anatomical structures derived from the CT image.

The imaging performance of N-PET was further evaluated in animal studies. In small animal scans, a rat ^{18}F-FDG imaging visualized the rat heart, while ^{18}F-NaF imaging clearly depicted rib structures. In a rhesus macaque brain study, PET and fused PET/CT images revealed major brain anatomy, with elevated FDG uptake in the cerebral cortex and subcortical nuclei. These results demonstrate that N-PET can provide high-resolution PET images in phantoms, small animal, and non-human-primate studies, supporting its feasibility for human brain imaging studies.

References
[1] Huang S, Jiang X, Chen Z, Zeng X, Huang W, Yang H, He W, Niu M, Wu J, Wei Q and Gu Z, "Optimization of TOF and DOI Performance in a Multi-Resolution Detector for Brain-dedicated PET", IEEE Transactions on Radiation and Plasma Medical Sciences. 2025.

MIC-05-130

DOI-Dependent Energy Window for Reducing Lu Background in In-Beam SIRMIO PET (#2637)

Munetaka Nitta[1], Giulio Lovatti[1], Francesco Evangelisat[1], Jonathan Bortfeldt[1], Ze Huang[1], Niels Bassler[2], Per Poulsen[2], Han Gyu Kang[3], Chiara Gianoli[1], Taiga Yamaya[3], Peter Thirolf[1], Katia Parodi[1]

[1] Ludwig Maximillian University Munich, Medical Physics, Garching, Germany; [2] Aarhus University Hospital, Danish Centre for Particle Therapy, Aarhus, Denmark; [3] National Institutes for Quantum Science and Technology, Chiba, Japan

This work was partly funded by the ERC under the European Union's Horizon 2020 research and innovation programme through the grant agreement number 725539.

Abstract

We have developed a high resolution small-animal in-beam PET scanner as part of the SIRMIO project for accurate image-guided proton irradiation at clinical facilities. The scanner consists of 56 three-layer depth-of-interaction (DOI) LYSO detectors with 1.0 mm-pitch scintillator pixels arranged in a compact spherical geometry with a with an entrance radius of 72 mm. Using different irradiation platform, we successfully demonstrated small-animal in-beam PET imaging. Since the number of positron emitters generated during irradiation is limited by the prescribed dose, intrinsic Lu background can contribute to background noise. In this study, we investigated the optimal energy window settings for different activity levels using Monte Carlo simulations based on coincidence count statistics in the SIRMIO PET scanner. The three-layer DOI detector structure enables independent energy window settings for each DOI layer. Since 511 keV gamma rays are more likely to interact near the shallow side of the detector, wider energy windows were selectively applied to shallow DOI layers, while narrower windows were used for deeper DOI layers to suppress Lu-176 background contributions. Geant4 simulations were performed for source activities ranging from 0.05 to 50 kBq. Net significance was evaluated for combinations of lower energy thresholds of 250 - 450 keV with a fixed upper threshold of 600 keV. For low-activity cases such as 0.05 kBq, the optimal lower energy thresholds were 400, 450, and 450 keV for the first, second, and third DOI layers, respectively. In contrast, wider energy windows became more advantageous at higher activity levels. These results indicate that layer-dependent energy window optimization is an effective method for improving low-count in-beam PET imaging performance.

References
[1] K. Parodi, et al., *Acta Oncologica, 58*(10), 1470-1475
[2] M. Nitta et al., IEEE NSS/MIC conference, M-15-01, 2023; 10.11.23
[3] G. Lovatti, et. al., PMB, 68(23), 235005, 2023.
[4] A. Goertzen et al., Journalof Nuclear Medicine, 48 (10), 1692-1698, 2007

MIC-05-133

NEMA NU-2 performance tests of a prototype PET scanner using novel detectors capable of measuring the gamma interaction point in 3D

(#2832)

August Blomgren[1], Benjamin Brunt[2], Marcus Palm[2], Christina Vallgren[2], Konstantinous Ziempekis[3], Marco Viscione[3], Axel Rominger[3], Kuangyu Shi[1]

[1] University of Bern, Department of Nuclear Medicine, Bern, Switzerland; [2] Terapet SA, Geneva, Switzerland; [3] Inselspital - University hospital of Bern, Bern, Switzerland

Abstract

Background: Depth-of-interaction (DOI) is one of the remaining challenges for high resolution PET. The resolution degradation stems from incorrect LOR endpoint estimation when photons impinge on the detector at oblique angles. This problem increases with distance from the symmetry axis and poses a challenge for LAFOV PET, where more LORs are acquired at oblique angles. Terapet SA manufactures radiation detectors capable of localising gamma ray interactions in 3D within the detector volume, potentially mitigating this effect. The aim of this project was to characterise the performance of a prototype PET scanner using Terapet's proprietary detectors, particularly the potential of DOI artefacts reduction.

Method: The NEMA NU-2 performance tests were conducted at the Department of Nuclear Medicine at Inselspital, Bern. Additionally, so far, two patient scans have been performed.

Results: The prototype achieved a FWHM of 2.56, 2.60 and 2.96 mm, averaged over all axes, at 10, 100 and 200 mm radial offset, respectively. The loss of resolution with increasing radial offset was lower in the prototype than in other clinical scanners, particularly along the radial axis.

The prototype had a low detection sensitivity of 0.99 cps/kBq. This is explained by the restrictive selection requirements on single- and coincidence events, optimised for high-quality data rather than high sensitivity.

The image-quality phantom and two patient images have been acquired. Results will be presented at the conference. The expectation is improved contrast recovery due to the improved spatial resolution, particularly for the smallest sphere.

Conclusion: The prototype demonstrated improved spatial resolution with the proprietary detectors. In particular, the spatial resolution is maintained with increasing radial offset. Future work will be aimed at improving the image reconstruction algorithms and correction methods. Construction of a LAFOV scanner using the same proprietary detectors is ongoing.

MIC-05-136

SurfaceCam: A Close-Proximity Multi-Pinhole CZT Brain SPECT system with Enhanced Geometric Sensitivity and Spatial Resolution (#3121)

Shubham Mandot[1], Scott D. Metzler[2], Ling-Jian Meng[1,3]

[1] University of Illinois at Urbana-Champaign, Department of Nuclear, Plasma and Radiological Engineering, Champaign, USA; [2] University of Pennsylvania at Philadelphia, Department of Radiology, Philadelphia, USA; [3] University of Illinois at Urbana-Champaign, Beckman Institute for Advance Science and Technology, Champaign, USA

We would like to thank NIH/NIBIB (BRAIN Initiative) for supporting this work under the grant UG3 EB034715.

Abstract

High-sensitivity, high-resolution brain-dedicated SPECT systems are critically important for advancing diagnosis and surgical planning in complex neurological disorders such as epilepsy, Parkinson's disease, and Alzheimer's disease. In this paper, we present *SurfaceCam*, a close-proximity multi-pinhole SPECT architecture with a radially adaptable rotating gantry, designed specifically for clinical brain imaging. The system comprises 15 detector-collimator panels distributed across three detector heads in a cylindrical arrangement, operating at a 1:8 minification geometry with a 28 cm bore. Each panel integrates 16 high-performance CZT sensors in a compact 2×8 configuration. The three detector heads translate radially to accommodate varying patient head sizes while maintaining close-proximity geometry, and the rotating gantry enables micro-rotation between acquisitions to facilitate angular super-sampling strategies. Pinholes are organized into groups of four with a twisted geometry, each subtending partial coverage of the 20 cm spherical FOV, while eliminating inter-pinhole projection multiplexing on the detector surface. Analytical comparison against a conventional 1:11 minification compound-eye reference design demonstrates approximately 1.4-fold higher geometric sensitivity and approximately 27% improvement in effective pinhole spatial resolution. The front-end electronics and data acquisition systems have been fully developed and validated, with Monte Carlo simulation studies and experimental phantom validation currently underway.

MIC-05-139

Local Activity and Uncertainty Quantification for Pre-clinical Compton Imaging of ^{213}Bi (#3138)

Oscar H. Matousek[1,2], Jaewon Lee[2], Biswajit Das[3,2], Javier Caravaca[2], Kai Vetter[1]

[1] University of California, Berkeley, Nuclear Engineering, Berkeley, USA; [2] Lawrence Berkeley National Laboratory, Nuclear Science Division, Berkeley, USA; [3] University of California, San Francisco, Department of Radiology, San Francisco, USA

Abstract

α-emitting radiopharmaceutical therapies (αRPT) show great potential to treat solid and diffuse tumors. However, following α-decay, the recoil energy and chemistry of daughter isotopes separate them from the targeting vector, exposing healthy tissue to an elevated radioactive dose. These effects must be studied in small animal experiments before new αRPTs make it to clinical trials. However, since extremely low activities are used, current single-photon emission computed tomography is insufficient due to its low sensitivity, especially for the 440 keV gamma ray emitted by ^{213}Bi (a daughter of one of the most promising radionuclides for αRPT, ^{225}Ac). In previous work, we used a high-purity Ge Compton camera as a high-sensitivity solution for pre-clinical imaging of αRPT. We demonstrated quantitative Compton imaging of ^{213}Bi using total-variation maximum-*a posteriori* expectation-maximization and a post-reconstruction global activity calibration. In this work, we improve upon this by implementing non-region-of-interest (nROI) reconstruction and a Gaussian Process Prior (GPP). We image a mouse phantom at relevant activity concentrations and measurement times to demonstrate that nROI reconstruction mitigates artifacts by redistributing events outside of the field-of-view across the image. We also show that, by using a GPP that correlates the activity in proximate voxels, we improve activity concentration quantification in all the volumes of the mouse phantom with respect to ML-EM. We modify both methods from previous iterations for local activity and uncertainty quantification, which is not straightforward in conventional ML-EM, and compare uncertainties obtained with the Laplace Approximation and preconditioned Crank-Nicholson Markov-Chain Monte Carlo to explain discrepancies from the ground truth. Finally, we experimentally measure a spatial resolution of ~3mm FWHM with a mini-Derenzo phantom.

MIC-05-142

A Compact X-ray Dark-Field Imaging Setup and Corresponding Image Optimization (#1107)

Xiaolei Yan, Christoph Hoeschen

Otto-von-Guericke- Universität Magdeburg, Institute of Medical Technology, Chair of Medical Systems Technology, Magdeburg, Germany

The author would like to express sincere appreciation to the supervisor and colleagues of the team for their support.

Abstract

Grating-based X-ray interferometry dark-field (DF) imaging provides exceptional sensitivity for detecting microstructures below the spatial resolution of standard detectors. Traditionally, this technique requires either large-scale synchrotron facilities or the integration of a source grating into a conventional X-ray tube setup. This study investigates a compact, simplified Talbot interferometer configuration utilizing a microfocus X-ray tube paired with a pixelated, energy-resolved photon-counting detector. In this setup, the microfocus source ensures the necessary spatial coherence, while the detector's energy-resolving capability enables the selection of specific energy bins—directly correlated to wavelength—to optimize reconstruction at the pixel level. Validation was conducted by imaging a metallic screw (0.5 mm pitch) using the phase-stepping method. Results demonstrate that while the sharp thread lines were heavily blurred in attenuation and phase-contrast modalities, they were clearly resolved in the dark-field images. Two optimization methods were evaluated for the full-energy dataset. Method 1, based on fitting effect correction through pixel filtering and interpolation, increased the Contrast-to-Noise Ratio (CNR). Method 2, based on the probability distribution approach, further improved the dark-field image quality compared to Method 1. This method resulted in a brighter signal along the threadline and significantly fewer rejected pixels, ensuring a more complete and better-defined representation of the object. These results demonstrate that high-resolution dark-field imaging is achievable through a compact laboratory setup combined with targeted data-processing optimizations.

References

[1] B. K. Blykers, C. Organista, M. N. Boone, M. Kagias, F. Marone, M. Stampanoni, T. Bultreys, V. Cnudde, and J. Aelterman, "Tunable x-ray dark-field imaging for sub-resolution feature size quantification in porous media," *Scientific reports*,vol. 11, no. 1, p. 18446, 2021.

[2] K. Scherer, E. Braig, S. Ehn, J. Schock, J. Wolf, L. Birnbacher, M. Chabior, J. Herzen, D. Mayr, S. Grandl et al., "Improved diagnostics by assessing the micromorphology of breast calcifications via x-ray dark-field radiography," Scientific reports, vol. 6, no. 1, p. 36991, 2016.

[3] R. Gradl, K. Morgan, M. Dierolf, C. Jud, L. Hehn, B. Günther, W. Möller, D. Kutschke, L. Yang, T. Stoeger et al., "Dynamic in vivo chest x-ray dark-field imaging in mice," IEEE transactions on medical imaging, vol. 38, no. 2, pp. 649–656, 2018.

[4] K. Willer, A. A. Fingerle, W. Noichl, F. De Marco, M. Frank, T. Urban, R. Schick, A. Gustschin, B. Gleich, J. Herzen et al., "X-ray dark-field chest imaging for detection and quantification of emphysema in patients with chronic obstructive pulmonary disease: a diagnostic accuracy study," The Lancet Digital Health, vol. 3, no. 11, pp. e733–e744, 2021.

[5] K. Willer, A. Fingerle, W. Noichl, F. De Marco, M. Frank, T. Urban, R. Schick, A. Gustschin, B. Gleich, J. Herzen et al., "X-ray dark-field chest imaging can detect and quantify emphysema in copd patients," medRxiv, pp. 2021–01, 2021.

[6] M. Ando, K. Yamasaki, F. Toyofuku, H. Sugiyama, C. Ohbayashi, G. Li, L. Pan, X. Jiang, W. Pattanasiriwisawa, D. Shimao et al., "Attempt at visualizing breast cancer with x-ray dark field imaging," Japanese journal of applied physics, vol. 44, no. 4L, p. L528, 2005.

[7] P. Guo, L. Zhang, J. Lu, H. Zhang, X. Zhu, C. Wu, X. Zhan, H. Yin, Z. Wang, Y. Xu et al., "Grating-based x-ray dark-field ct for lung cancer diagnosis in mice," European Radiology Experimental, vol. 8, no. 1, p. 12, 2024.R.

[8] T. Weitkamp, A. Diaz, C. David, F. Pfeiffer, M. Stampanoni, P. Cloetens, and E. Ziegler, "X-ray phase imaging with a grating interferometer," Opt. Express 13, 6296-6304 (2005).

MIC-05-145

Digital phantoms that can reproduce diseases aiming for virtual radiation imaging experiments (#1256)

Rina Nishigami[1], Takashi Asahara[2], Natsumi Kimoto[3], Mana Mitani[4], Daiki Kobayashi[1], Takuya Kasue[1], Noriaki Akagi[4], Toshihiro Iguchi[2], Takao Hiraki[5], Hiroaki Hayashi[6], This is a collaborative study between Kanazawa University and Okayama University.

[1] Kanazawa University, Graduate School of Medical Sciences, Kanazawa, Japan; [2] Okayama University, Department of Radiological Technology, Faculty of Health Sciences, Okayama, Japan; [3] Junshin Gakuen University, Department of Radiological Science, Faculty of Health Sciences, Fukuoka, Japan; [4] Okayama University Hospital, Division of Radiological Technology, Medical Support Department, Okayama, Japan; [5] Okayama University, Department of Radiology, Faculty of Medicine, Dentistry and Pharmaceutical Sciences, Okayama, Japan; [6] Kanazawa University, College of Transdisciplinary Sciences for Innovation, Kanazawa, Japan

This study was supported by JST SPRING (No. JPMJSP2135) and JSPS KAKENHI (Nos. JP24K03306, 25K21586, 25K21600, and 25KJ1355).

Abstract

Virtual X-ray imaging experiments are a crucial research technique in the development of X-ray technology. In recent years, advanced imaging detectors, such as photon-counting detectors, have been developed and are increasingly being used in clinical applications. It further increases the importance of virtual X-ray imaging experiments. To improve the reproducibility of patients in virtual experiments, the development of digital phantoms having diseases is desired. The purpose of this study is to develop a procedure for creating digital phantoms that can reproduce diseases. Virtual monoenergetic images (VMIs) at 40 keV and 130 keV were generated using a clinical photon-counting CT (PC-CT) system, and effective atomic number (Z_{eff}) and effective physical density (ρ_{eff}) were calculated using a newly developed algorithm. Z_{eff} was calculated by using the correlation between the ratio of measured linear attenuation coefficient (μ) values and atomic number (Z). ρ_{eff} was calculated from the fitting coefficient obtained by fitting the reaction cross-section (σ) of each Z material to the measured μ values. Then, 10 patient data examined using PC-CT were analyzed, and digital phantoms were created. We investigated the reproducibility of Z_{eff} and ρ_{eff} values of the disease tissues. Our procedure could reproduce the disease tissues by continuous Z_{eff} and ρ_{eff} distribution. In conclusion, we developed a methodology for constructing digital phantoms of patients having diseases from VMIs acquired with PC-CT.

References

[1] Segars WP, Sturgeon G, Mendonca S, Grimes J, Tsui BM, 2010, '4D XCAT phantom for multimodality imaging research', *Med Phys*, 37(9):4902–15

[2] Asahara T, Okada S, Hayashi H, Maeda T, Nishigami R, Kobayashi D, Kurose C, Kimoto N, Goto S, Hisatomi M, Yanagi Y, and Iguchi T, 2025, 'Helpfulness of effective atomic number image in forensic dental identification: Photon-counting computed tomography is suitable', *Comput Biol Med*, 184:109333

[3] Nishigami R, Kobayashi D, Kimoto N, Asahara T, Maeda T, Haba T, Kanazawa Y, Yamamoto S, and Hayashi H, 2025, 'Optimization of energy windows to calculate quantitative X-ray images using an energy-resolving photon-counting detector: A simulation study', *Rad Phys Chem*, 229:112460

[4] Hubbell JH, 1982, 'Photon Mass Attenuation and Energy-absorption Coefficients from 1 keV to 20 MeV', *Int J Appl Radiat Isot*, 33(11):1269–1290

[5] Kimoto N, Nishigami R, Asahara T, Kanazawa Y, Katsumata A, Yamamoto S, Hayashi H, 2026, 'Counting loss correction algorithm for an energy-resolving photon-counting detector for X-ray imaging of biological objects with effective atomic numbers between 3 and 20', *Rad Phys Chem*, 243, 113723

[6] Nishigami R, Kimoto N, Asahara T, Maeda T, Kobayashi D, Goto S, Haba T, Kanazawa Y, Yamamoto S, Hayashi H, 2026, 'Bone-enhanced high contrast X-ray images derived from attenuation estimation related to ultra-low energy X-rays – An application of an energy-resolving photon-counting detector (ERPCD)', *Rad Phys Chem*, 238, 113243
[7] Kimoto N, Hayashi H, Asakawa T, Lee C, Asahara T, Maeda T, Goto S, Kanazawa Y, Katsumata A, Yamamoto S, and Okada M, 2021, 'Effective atomic number image determination with an energy-resolving photon-counting detector using polychromatic X-ray attenuation by correcting for the beam hardening effect and detector response', *Appl Radiat Isot*, 170:109617
[8] Kimoto N, Hayashi H, Lee C, Maeda T, Ando M, Kanazawa Y, Katsumata A, Yamamoto S, and Okada M, 2021, 'A novel algorithm for extracting soft-tissue and bone images measured using a photon-counting type X-ray imaging detector with the help of effective atomic number analysis', *Appl Radiat Isot*. 176:109822

MIC-05-148

A novel computational scatter estimation method in CBCT with half ASG (#1343)

Jiongtao Zhu, Yuhang Tan, Zeqi Huang, Haodi Wu, **Yongshuai Ge**

Shenzhen Institutes of Advanced Technology, Chinese Academy of Sciences, Shenzhen, China

Abstract

CBCT image quality is strongly degraded by scattered radiation. Conventional anti-scatter grids (ASGs) are commonly used to mitigate this effect; however, they can only remove a portion of the scattered photons. In this study, we propose a novel computational scatter estimation method based on a half anti-scatter grid (h-ASG), which covers only half of the flat-panel detector. The full scatter distribution is estimated by combining two reconstructed CBCT images: one containing the full scatter component and the other containing a reduced scatter component. Experimental results using CatPhan and anthropomorphic head phantoms demonstrate that the proposed method effectively suppresses scatter-induced artifacts and significantly improves CBCT image quality.

References
[1] Cui, Han, Ting Su, Xin Zhang, Jiongtao Zhu, Yuhang Tan, Hairong Zheng, Dong Liang, and Yongshuai Ge. "Correction of scatter in CBCT with a new grid design." *Physics in Medicine & Biology* 69, no. 16 (2024): 165010.
[2] Zhang, Xin, Jixiong Xie, Yuhang Tan, Ting Su, Jiongtao Zhu, Han Cui, Dongmei Xia, Hairong Zheng, Dong Liang, and Yongshuai Ge. "Model-based CBCT scatter correction with dual-layer flat-panel detector." *Medical Physics* 52, no. 3 (2025): 1500-1514.
[3] Niu, Tianye, and Lei Zhu. "Scatter correction for full-fan volumetric CT using a stationary beam blocker in a single full scan." *Medical physics* 38, no. 11 (2011): 6027-6038.
[4] Zhu, Lei, Yaoqin Xie, Jing Wang, and Lei Xing. "Scatter correction for cone-beam CT in radiation therapy." *Medical physics* 36, no. 6Part1 (2009): 2258-2268.
[5] Schafer, S., J. W. Stayman, Wojciech Zbijewski, C. Schmidgunst, G. Kleinszig, and J. H. Siewerdsen. "Antiscatter grids in mobile C-arm cone-beam CT: effect on image quality and dose." *Medical physics* 39, no. 1 (2012): 153-159.

MIC-05-151

Quantitative Evaluation of Liver Disease through Multi-modality Approach Combining SiPM-based PC-CT and MRI—Approach to the Visualization of Inflammation through Water Fraction Estimation —

(#1548)

Yu Furuta[1], Makoto Arimoto[1], Fitiri Lucyana[1], Shuma Midorikawa[1], Satoshi Kobayashi[1], Hiroki Kawashima[1], Kenichiro Okumura[1], Naoki Ohno[1], Takahiro Tomoda[1], Minori Oshima[1], Kazuhiro Murakami[2], Jun Kataoka[3], Ryotaro Minagawa[3], Takahiro Ro[3], Shinsuke Terazawa[4], Yuta Maeno[4], On behalf of the joint research group of Kanazawa University, Waseda University, Ishikawa Prefectural University, and Proterial Ltd.

[1] Kanazawa University, Kanazawa, Japan; [2] Ishikawa Prefectural University, Nonoichi, Japan; [3] Waseda University, Shinzyuku, Japan; [4] Proterial Ltd., Mishima, Japan

We gratefully acknowledge financial support from JSPS KAKENHI Grant Numbers JP19H04483 and JP19K22924, JST ERATO Grant Number JPMJER2102, Japan, the Naito Foundation, Japan, the Uehara Memorial Foundation, Japan, the Casio Science Promotion Foundation, Japan, the Murata Science Foundation, Japan, and the JSPS Leading Initiative for Excellent Young Researchers program, Japan.

Abstract

X-ray computed tomography (CT) is essential nondestructive internal imaging. Photon-counting computed tomography (PC-CT) acquires X-ray energy information to enable material identification and quantitative density evaluation. Combining PC-CT energy information with magnetic resonance imaging (MRI) data is expected to provide a novel diagnostic approach to visualize inflammation through tissue water fraction estimation. We developed a PC-CT system combining high-speed scintillators (YGAG:Ce) and silicon photomultipliers (SiPMs), specifically utilizing multi-pixel photon counters, MPPCs, which are optical semiconductor devices. This study evaluated healthy and fatty liver rat models (fed a high-fat diet for two or four weeks). Liver fat fractions, estimated from energy-dependent linear attenuation coefficients, showed good agreement with MRI and pathological results. Furthermore, we performed a detailed pathological evaluation focusing on inflammation induced changes in tissue water content. By integrating high reliability MRI fat fraction data with PC-CT data, we improved the estimation accuracy of water content and quantitatively visualized tissue ”water-richness” (edema). Increased water proportions in fatty liver groups suggested inflammation progression. These findings demonstrate that PC-CT is highly valuable for quantitative evaluation of liver disease within a multi-modality imaging approach.

References

[1] H. Kiji et al. Nucl. Instr. Meth. A, 984:164610, 2020, DOI. 10.1016/j.nima.2020.164610.

[2] M. Arimoto et al. Nucl. Instr. Meth. A, 1047:167721, 2023, DOI. 10.1016/j.nima.2022.167721.

MIC-05-154

Introducing “T-Index”—A Metric for Quantifying Data Range and Sampling Sufficiency (#2039)

Katsuyuki Taguchi, Jingyan Xu

Johns Hopkins University, Baltimore, USA

The work has been supported by NIH grants R01 NS126256, U01 EB037558, R01 EB036984, R21 EB034337, R21 EB033426, R21 EB037806.

Abstract

Many image reconstruction methods for x-ray computed tomography (CT) use optimization approaches with cost functions that consist of a data fidelity term and a prior term. Extensive efforts have been devoted to construct better priors, some using machine learning, for high resolution, low dose, and spectral imaging. There seems to be a belief that a good prior can overcome any problems in data acquisition, downplaying the data fidelity term. It would be desirable if we could quantify the sufficiency of the problem setting (or adequacy of the data acquisition) toward a set of desired imaging properties. We propose “Truth index” or “T-index” to quantify data range and data sampling issues in this work. When fully developed, the T-index will show, independent of specific image reconstruction methods used, how much the solution can be trusted or has a risk of hallucination.

References

[1] Lastname, GN, Lastname, GN YYYY, ‘Article’, *Journal*, Edition, Page, Place of publication: publishers Jørgensen, J. S., Sidky, E. Y., and Pan, X, 2012, "Quantifying admissible undersampling for sparsity-exploiting iterative image reconstruction in X-ray CT," *IEEE Trans Med Imaging,* vol. 32, no. 2, pp. 460-73, Feb 2013, doi: 10.1109/tmi.2012.2230185.

MIC-05-157

In vivo Gold Nanoparticle Imaging in Mice for Tumor Detection Using SiPM-Based Photon-Counting CT (#1749)

Shuma Midorikawa[1], **Shuma Midorikawa**[1], Makoto Arimoto[1], Makoto Arimoto[1], Fitri Lucyana[1], Fitri Lucyana[1], Yu Furuta[1], Yu Furuta[1], Satoshi Kobayashi[1], Satoshi Kobayashi[1], Hiroki Kawashima[1], Hiroki Kawashima[1], Kenichiro Okumura[1], Kenichiro Okumura[1], Asuka Mizutani[1], Asuka Mizutani[1], Naoki Ohno[1], Naoki Ohno[1], Minori Oshima[1], Minori Oshima[1], Jun Kataoka[2], Jun Kataoka[2], Ro Takahiro[2], Ro Takahiro[2], Ryotaro MInagawa[2], Ryotaro MInagawa[2], Kazuhiro Murakami[3], Kazuhiro Murakami[3], Yuta Maeno[4], Yuta Maeno[4], Shinsuke Terazawa[4], Shinsuke Terazawa[4]

[1] Kanazawa University, Ishikawa, Japan; [2] Waseda University, Tokyo, Japan; [3] Ishikawa Prefectural University, Ishikawa, Japan; [4] Proterial Ltd, Tokyo, Japan

We gratefully acknowledge financial support from JSPS KAKENHI Grant Numbers JP19H04483 and JP19K22924, JST ERATO Grant Number JPMJER2102, Japan, the Naito Foundation, Japan, the Uehara Memorial Foundation, Japan, the Casio Science Promotion Foundation, Japan, the Murata Science Foundation, Japan, and the JSPS Leading Initiative for Excellent Young Researchers program, Japan .

Abstract

Photon-counting CT (PC-CT) is a powerful spectral imaging technique that identifies materials by counting individual X-ray photons. While direct-conversion systems are entering clinical practice, we are developing a cost-effective, large-area scintillator-based PC-CT system using YGAG:Ce coupled with silicon photomultipliers (SiPMs). PC-CT excels at identifying high-atomic-number elements like gold (Au) by utilizing its K-edge (80.7 keV). Gold nanoparticles (AuNPs) are promising for drug delivery, as their biodistribution can be controlled by particle size, enabling selective tumor accumulation via the enhanced permeability and retention (EPR) effect.

In this study, we evaluated the in vivo biodistribution of AuNPs in tumor-bearing mice using our SiPM-based PC-CT. Two sizes of AuNPs (1.9 nm and 15 nm) were intravenously administered, and their accumulation was quantitatively assessed using multi-energy CT concentration estimation. Results showed distinct size-dependent patterns: 1.9 nm AuNPs exhibited rapid renal clearance and bladder accumulation, while 15 nm AuNPs showed prolonged circulation and significant hepatic accumulation. Tumor accumulation was confirmed for both sizes, demonstrating the potential of our SiPM-based PC-CT for quantitative in vivo nanoparticle imaging.This presentation reports on the
experimental setup, the analysis methods, and the results obtained.

References
[1] H. Kiji, et al., “64-channel photon-counting computed tomography using a new MPPC-CT system,” Nucl. Instrum. Methods Phys. Res. A, vol. 984, p. 164610, 2020, doi: 10.1016/j.nima.2020.164610.
[2] M. Arimoto, et al., “Development of 64-channel LSI with ultrafast analog and digital signal processing dedicated for photon-counting computed tomography with multi-pixel photon counter,” Nucl. Instrum. Methods Phys. Res. A, vol. 1047, p. 167721, 2023, doi: 10.1016/j.nima.2022.167721.

[3] Y. Furuta, et al., "X-ray imaging of anticancer drugs and a Platinum-Iodine mixture encapsulated in liposomes using SiPM-based photon-counting CT," IEEE Trans. Nucl. Sci., vol. 73, no. 1, pp. 1–1, 2026, doi: 10.1109/TNS.2026.3662738

MIC-05-160

End-to-End Simultaneous Combined Scatter Correction and Metal Projection Segmentation for CBCT Metal Artifact Reduction Network

(#2385)

Junjie Zhou[1], Hongyang Qiao[2], Kai Chen[1], Ziqi Wang[3], Shipeng Xie[1], Hui Tang[3], Zhan Wu[3], Yang Chen[1,3]

[1] Nanjing University of Posts and Telecommunications, School of Communications and Information Engineering, Nanjing, China; [2] Qilu University of Technology, School of Computer Science and Technology, Jinan, China; [3] Southeast University, School of Computer Science and Engineering, Nanjing, China

This work was supported in part by the National Key Research and Development Program of China under Grant 2024YFC2417803, in part by the State Key Project of Research and Development Plan under Grant 2022YFC2401600, in part by the National Natural Science Foundation of China under Grant T2225025, in part by the Key Research and Development Programs in Jiangsu Province of China under Grant BE2021703 and BE2022768, in part by Natural Science Research Start-up Foundation of Recruiting Talents of Nanjing University of Posts and Telecommunications (No.XK0020925049), in part by the National Natural Science Foundation of China under Grant 62401141, the Jiangsu Province Science Foundation for Youths under Grant BK20241305. Junjie Zhou and Hongyang Qiao contributed equally to this work. Corresponding authors: Kai Chen, Hui Tang, and Shipeng Xie.

Abstract

Cone-beam computed tomography (CBCT) is a vital imaging modality rooted in nuclear science. It uses ionizing radiation and information processing to provide patients' internal anatomical details. When patients with metal implants undergo CT scans, projection data is contaminated. Consequently, reconstructions produce severe metal artifacts, compromising diagnostic accuracy. Thus, developing high-performance metal artifact reduction (MAR) methods for CBCT is essential for accurate clinical diagnosis. Some existing MAR methods ignore physical phenomena, like X-ray scattering, during imaging. Others use scatter correction as a preprocessing step; however, this non-end-to-end approach increases complexity. Here, we propose an end-to-end MAR method incorporating scatter correction and metal segmentation within the projection domain into a single network, followed by morphological post-processing and artifact suppression. Qualitative and quantitative analyses on simulated and real datasets demonstrate the superiority of this end-to-end method.

MIC-05-163

X-ray Scattering in Dual-Layer Flat-Panel Detectors (#2510)

Eunae Lee[1], Dong Sik Kim[2]

[1] Seoul National University, College of Medicine, Seoul, South Korea; [2] Hankuk University of Foreign Studies, Semiconductor and Electronics Engineering, Yonin, South Korea

This work was supported by the National Research Foundation of Korea (NRF) grants funded by the Korean government (MSIP) (No. RS-2024-00459219).

Abstract

In radiography imaging, dual-layer flat-panel detectors (DFDs) can be used for two purposes: acquiring high-quality x-ray images and performing material decomposition.

When using cone beam projection in DFD, the x-ray beam is scattered inside the object, increasing and distorting the intensity. In this paper, we experimentally observe x-ray scattering in acquiring images from DFD. The image acquired from the lower detector layer shows more scatter to prime ratios (SPRs) than the upper layer case due to the scattering inside the upper and intermediate layers. We perform parameter modeling for experimental SPR curves and simulations regarding the measurement of bone mineral density (BMD) estimates, including scattering intensity. We can observe that using the 2nd-order polynomial BMD function or fully connected neural network can successfully estimate BMD functions without scatter correction.

MIC-05-166

Development and Experimental Validation of a Low-Cost Benchtop Micro-CT System (#2591)

Pedro M.M. Correia, João M. Reis, Ana Luísa M. Silva

Universidade de Aveiro - i3N, Department of Physics, Aveiro, Portugal

This work was supported by project easyPET.CT - CENTRO2030-FEDER-02363500, funded by FEDER program through CENTRO2030; by project HadronPET - COMPETE2030-FEDER-00755500, funded by FEDER program and by national funds through the FCT, Portugal, by project UID/50025/2025, UID/PRR/50025/2025 and UID/PRR2/50025/2025 and the Associate Laboratory I3N - LA/P/0037/2020 (doi.org/10.54499/LA/P/0037/2020);

This project was funded by Agenda ILLIANCE" [C644919832-00000035 | Project nº 46] – WP4 OLI Health, financed by PRR – "Plano de Recuperação e Resiliência" under the Next Generation EU from the European Union.

Abstract

The growing demand for accessible, high-resolution imaging in pre-clinical and materials research has driven interest in low-cost micro-computed tomography (micro-CT) platforms. In this work, a bench-top micro-CT system was designed, assembled, and experimentally characterized, built around a microfocus X-ray tube, a CMOS flat-panel detector, low-cost open-source electronics based on an STM32 microcontroller, and the open-source TIGRE toolbox for volumetric reconstruction. A step-and-shoot acquisition strategy --- in which the sample rotates incrementally, and the detector captures frames only during active X-ray exposure via a hot duration trigger mode --- was employed for synchronized image acquisition. Three reconstruction approaches were implemented and comparatively evaluated: filtered back projection (FBP), Feldkamp-Davis-Kress (FDK) algorithm as the primary volumetric reconstruction method, and iterative techniques for noise suppression. System performance was assessed through established phantom protocols evaluating image uniformity, noise, signal-to-noise ratio (SNR), contrast-to-noise ratio (CNR), and a QRM micro-CT Bar-pattern phantom for spatial resolution characterization. While a persistent precession artefact attributed to rotation stage mechanical instability was identified as the primary performance limitation, the system demonstrated tomographic imaging capability and sub-millimeter spatial resolution, establishing a promising foundation for the development of accessible and cost-effective micro-CT platforms for laboratory research.

References
[1] Ritman, EL 2011, 'Current status of developments and applications of micro-CT', Annual Review of Biomedical Engineering, vol. 13, pp. 531-552.
[2] A. du Plessis, A et al. 2017, 'Laboratory x-ray micro-CT: a user guideline for biological samples', GigaScience, vol. 6, no. 6, Oxford: Oxford University Press.
[3] Zwanenburg, EA et al. 2023, 'Effective X-ray micro-CT imaging of carbon fibre composites', Composites Part B: Engineering, vol. 258.
[4] Cobos, SF et al. 2022, 'Cost-effective micro-CT for non-destructive testing of titanium 3D printed medical components', PLoS ONE, vol. 17, no. 10.
[5] Allphin, AJ et al. 2024, 'Turn-table micro-CT scanner for dynamic perfusion imaging in mice: design, implementation, and evaluation', Physics in Medicine and Biology, vol. 69, no. 17.
[6] Oxford Instruments n.d., 'Apogee 5500 Series Radiation Shielded X-ray Tube', datasheet, Oxford: Oxford Instruments.
[7] Spectrum Logic n.d., '1412HR CMOS X-ray Detector', datasheet: Spectrum Logic.
[8] Biguri, A et al. 2024, 'TIGRE v3: efficient and easy to use iterative computed tomographic reconstruction toolbox for real datasets', arXiv:2412.10129.

MIC-05-169

Development of a Robot-Arm-Based Automated Transmission and Backscatter X-ray Image Acquisition System for AI Training Data Generation (#2733)

JeongHee Lee[1], Chang Hwy Lim[2], Jongwon Park[1], Youngchol Choi[1]

[1] Korea Research Institute of Ship & Ocean Engineering, Dejeon, South Korea; [2] XsCan Inc, Dejeon, South Korea

This work was conducted as a part of the research projects of “Development of automatic screening and hybrid detection system for hazardous material detecting in port container” financially (RS-2020-KS201398) supported by the Ministry of Oceans and Fisheries, Korea.

Abstract

A large-scale X-ray image dataset acquired under diverse specimen and imaging conditions is essential for developing robust AI-based container-structure inspection models. However, single-view transmission imaging often fails to resolve structural ambiguities in complex container environments, where X-ray attenuation and scattering characteristics vary significantly with specimen geometry, material composition, and overlap conditions. In this study, a robot-arm-based automated transmission and backscatter X-ray image acquisition system was developed to enhance the diversity, reproducibility, and traceability of AI training data. The system employs a 225 kV, 13 mA X-ray source to sequentially acquire vertical and horizontal transmission images and horizontal backscatter images. The transmission unit consists of 1,408 detection channels based on eleven 1×128-pixel line-detector modules, whereas the backscatter unit incorporates four 600×500 mm plastic scintillation detectors. By precisely controlling specimen orientation using a robot arm, the system stores acquired images together with preprocessing results, quality-assessment data, and imaging-condition metadata for subsequent AI model training, validation, and evaluation.

References

[1] K. Moshkbar-Bakhshayesh, H. Afarideh, and R. Azimirad, “Inspection of cargo using dual-energy X-ray radiography: A review,” Radiation Physics and Chemistry, vol. 212, Art. no. 111180, 2023

[2] S. Akcay and T. P. Breckon, “Towards automatic threat detection: A survey of advances of deep learning within X-ray security imaging,” Pattern Recognition, vol. 122, Art. no. 108245, 2022

[3] X. Meng, H. Feng, Y. Ren, H. Zhang, W. Zou, and X. Ouyang, “Transformer-based dual-view X-ray security inspection image analysis,” Engineering Applications of Artificial Intelligence, vol. 136, Art. no. 109382, 2024.

[4] H. Cho, H. Park, I.-J. Kim, and J. Cho, “Data augmentation of backscatter X-ray images for deep learning-based automatic cargo inspection,” Sensors, vol. 21, no. 21, Art. no. 7294, 2021.

MIC-05-172

Robustness to Scatter in Dual Energy Bone Suppression for Chest Radiography (#3063)

Gengxin Shi[1], Jamin Schaefer[3], Sebastian Vogt[3], Amirreza Heshmat[3], Ludwig Ritschl[3], Steffen Kappler[3], Cheng T. Lin[2], Dilek Oncel[2], Selin Ocal[2], Wojciech Zbijewski[1]

[1] Johns Hopkins University, Department of Biomedical Engineering, Baltimore, USA; [2] Johns Hopkins University, Russel H. Morgan Dept. of Radiology and Radiological Science, Baltimore, USA; [3] Siemens Healthineers, Forchheim, Germany

This work was supported in part by Siemens Healthineers. The product/feature and/or service offerings mentioned herein are not commercially available in all countries and/or for all modalities. Their future availability cannot be guaranteed.

Abstract

We quantify the impact of scatter on the performance of bone suppression in virtual non-calcium chest radiographs (VNCa-CXR) generated with (i) a multi-layer flat-panel detector (ML-FPD, three 200-um thick CsI layers) and (ii) with a kV-switching protocol (60/140 kVp). We show that in the setting of log-subtraction, the decomposition weight (DW) can be adjusted for scatter-to-primary ratio (SPR) such that the scatter-induced bias in VNCa is locally corrected (scatter-compensating weight, DW-scat). However, DW-scat is spatially varying. If a constant DW is used in log-subtraction, the magnitude of bone residual in VNCa radiographs will depend on the degree of spatial inhomogeneity in DW-scat. We investigate this effect is simulation studies in anthropomorphic chest phantoms (20 – 24 cm thickness) with and without an anti-scatter grid (ASG). Without a scatter-compensating DW, scatter-induced bone residual increased by >100% is most configurations except for ML-FPD with a grid. Applying DW-scat averaged over central lung region reduced the residual by up to 50% for ML-FPD without an ASG and by ~40% for kV-switching with an ASG. Overall, our results reveal that DE VNCa imaging is relatively robust to scatter in scenarios with a grid, where kV-switching appears to benefit from spatially-averaged scatter-compensating DW more than ML-FPD, likely due to differences in scatter content of the two energy channels. Without a grid, both configurations may require a spatially-dependent scatter compensation for optimal bone suppression.

MIC-05-175

Time-of-Flight X-ray Imaging with Scatter Rejection and Subtraction

(#3042)

Altea Lorenzon, **Altea Lorenzon**, Zimo Liu, Zimo Liu, Xiao Jiang, Xiao Jiang, Wojciech Zbijewski, Wojciech Zbijewski, J Webster Stayman, J Webster Stayman

Johns Hopkins University, Biomedical Engineering, Baltimore, USA

This work is supported, in part, by grant #0030253 from the Korea Institute for Advancement of Technology.

Abstract

X-ray time of flight information can be used in computed tomography to characterize photon interactions and discriminate scattered from unscattered events. Specifically, photons undergoing Compton and Rayleigh scattering are subject to trajectory deviations that increase their path length relative to primary photons. Therefore, with adequate temporal resolution, scattered photons are detected with larger time delay with respect to primary photons, providing a physically grounded mechanism to reject scatter. Recent technological developments in ultra-fast X-ray sources (e.g: 50ps) and high-temporal-resolution photon-counting detectors may allow for this imaging modality.

In this work, Monte Carlo (MC) simulations of a water cylinder were performed assuming Gaussian source pulse shape and detector timing jitter, with combined full-width-half-maximum as low as 50ps. A threshold-based scatter rejection method was applied, sweeping multiple thresholds to find the optimal balance between scatter rejection efficiency (η) and primary retention (ε). Filtered-backprojection reconstructions were performed and evaluated in terms of root mean square error and bias. Rejection performances were compared with an ideal, MC-based scatter subtraction technique, that leverages template fitting to estimate the average scatter contribution from time-delay histograms. A combined rejection-subtraction approach was also evaluated.For rejection only, the optimal reconstruction accuracy is obtained with a threshold T'=30 ps, corresponding to η=59% and ε=80%. Residual scatter leads to bias in the reconstructed attenuation, preventing the method from achieving the same reconstruction accuracy as the ideal subtraction. However, rejection yields lower noise levels compared to subtraction. Combining rejection and subtraction may provide a better compromise between bias and noise.

MIC-05-178

Iodine Sensitivity in Photon Counting CT Using Conventional and Diffusion-Based Material Decomposition Algorithms (#3123)

Suyu Liao[1], Grace J. Gang[1]

[1] University of Pennsylvania, Radiology, Philadelphia, USA; [2] University of Pennsylvania, Radiology, Philadelphia, USA; [3] University of Pennsylvania, Radiology, Philadelphia, USA

This work is supported, in part, by ARPA-H grant AY1AX000089.

Abstract

Spectral CT enables material-specific imaging but suffers from noise amplification in low-concentration iodine decomposition. This work investigates advanced material decomposition algorithms for improving iodine detectability in a simulated four-channel photon-counting CT system. Diffusion Posterior Sampling (DPS) with hybrid priors was compared with conventional image-domain and projection-domain decomposition methods. Results demonstrate improved noise suppression and low-concentration vessel detectability while highlighting the noise-bias tradeoff in diffusion-based material decomposition.

References
[1] C. Vazia et al., IEEE Transactions on Radiation and Plasma Medical Sciences, pp. 1–1, 2026
[2] X. Jiang et al., IEEE Transactions on Biomedical Engineering, vol. 72, no. 8, pp. 2447–2461, 2025.
[3] J. Schlomka et al., Physics in Medicine & Biology, vol. 53, no. 15, p. 4031, 2008.

MIC-05-181

TCMnet: An Automatic Tube Current Modulation Policy Based on Neural Network (#3217)

Haoyu Zhang[1], Zhi Zeng[1], Yuxiang Xing[1]

[1] Tsinghua University, the Department of Engineering Physics, Beijing, China; [2] Tsinghua University, the Department of Engineering Physics, Beijing, China

This work is supported by Natural Science Foundation of Beijing (No. L242001).

Abstract

Low-dose computed tomography (LDCT) is essential for mitigating radiation risks to patients, and its effectiveness is significantly enhanced by automatic tube current modulation (TCM) that optimizes photon allocation across different projection angles to maintain image quality at reduced doses. However, most traditional methods offer

fixed modulation strategies based on typical human phantoms, thereby ignoring individual anatomical variations and failing to achieve personalized dose allocation. This paper proposes a personalized TCM method driven by an end-to-end neural network (TCMnet). Specifically, we construct a differentiable optimization chain that integrates the modulation strategy, forward projection, and image reconstruction into a unified framework, allowing the system to learn optimal, patient-specific current profiles by directly minimizing reconstruction errors under specific dose constraints. Experimental results demonstrate that, under identical photon count (radiation dose) constraints, the proposed method yields significantly higher reconstruction quality compared to conventional approaches. By analyzing the performance of these optimized profiles across varying dose levels, this study reveals an important physical phenomenon: under extreme low-photon-count conditions where photon resources are severely limited, the optimal modulation strategy shifts from seeking a globally balanced noise distribution to concentrating photons on fewer key projection angles in high-attenuation regions. This finding not only validates the optimization capabilities of the end-to-end framework under complex constraints but also provides new insights and design concepts for TCM mechanisms for ultra-low-dose CT.

References
[1] Callahan M J .CT dose reduction in practice[J].Pediatric Radiology, 2011, 41 Suppl 2(s2):488.DOI:10.1007/s00247-011-2099-y.
[2] Newman B , Callahan M J .ALARA (as low as reasonably achievable) CT 2011--executive summary..Pediatric radiology, 2011, 41(Suppla2).
[3] Slovis, Thomas L.The ALARA concept in pediatric CT: myth or reality?.Radiology, 2002, 223(1):5-6.DOI:10.1148/radiol.2231012100.
[4] Tack D .ALARA Concept for MDCT Optimization: What is Reasonable, What is Achievable?.Springer Berlin Heidelberg, 2011.DOI:10.1007/174_2011_458.
[5] Wang, T., Pelt, D. M., Lucka, F., van Leeuwen, T., & Batenburg, K. J. (2026). Deep Reinforcement Learning for Optimizing Angle Selection and Dose Allocation in CT Reconstruction. arXiv:2604.20939.
[6] Wu D , Yang X , Shen Z ,et al.Learning to scan: A deep reinforcement learning approach for personalized scanning in CT imaging[J].Inverse Problems and Imaging, 2022, 16(1):179-195.DOI:10.3934/ipi.2021045.

MIC-05-184

A Fully Quantitative Reconstruction Framework Tailored for Depth-of-Interaction PET Systems (#1140)

Yihao Chen, Ziquan Yuan, Yue Chen, Chenxi Li, Kexin Wang, Yucun Hou, Jianyong Jiang

Beijing Normal University, School of Physics and Astronomy, Beijing, China

This work was supported in part by the National Natural Science Foundation of China (No. 12475336), the Fundamental Research Funds for the Central Universities (No. 310400209521) and Beijing Natural Science Foundation (QY25290).

Abstract
Depth-of-interaction (DOI) encoding in positron emission tomography (PET) systems effectively mitigates parallax errors and improves spatial resolution, however, it introduces substantial complexities for accurate and efficient image reconstruction. Specifically, the dramatic increase in valid lines-of-response (LORs) and the inherent limitations of conventional correction methods—such as component-based normalization (CBN) and single scatter simulation (SSS)—often compromise quantitative accuracy in DOI enabled systems. To address these challenges,

we propose a fully GPU-accelerated reconstruction framework specifically designed for DOI-PET with complete correction techniques. The proposed framework extends standard CBN and SSS methods through sub-layer-based geometric modeling, enabling layer-specific normalization and scatter correction. A maximum-likelihood-based strategy is introduced to estimate DOI-dependent scatter scaling factors, incorporating inter-layer attenuation effects and axial response variations. The framework was evaluated using Monte Carlo simulations of the NeuroEXPLORER scanner. Our results demonstrate that the reconstructed uniform cylinder phantom exhibits high spatial homogeneity. Furthermore, the spatial resolution quantified via the Derenzo phantom and the quantitative accuracy achieved in a digital brain phantom are consistent with previously established benchmarks. These findings suggest that the proposed framework provides a robust and computationally efficient solution for high-resolution, quantitative reconstruction in DOI-PET systems.

References
[1] Panin, V 2008, 'Iterative algorithms for variance reduction on compressed sinogram random coincidences in PET', IEEE Nuclear Science Symposium Conference Record, 3719-3725, New York: IEEE
[2] Qi, J, Leahy, RM, Cherry, SR, Chatziioannou, A, Farquhar, TH 1998, 'High-resolution 3D Bayesian image reconstruction using the microPET small-animal scanner', Phys Med Biol, 43(4), 1001-1013, Bristol: IOP Publishing
[3] Hogg, D, Thielemans, K, Spinks, T, Spyrou, N 2001, 'Maximum-likelihood estimation of normalisation factors for PET', IEEE Nuclear Science Symposium Conference Record, vol. 4, 2065-2069, San Diego, CA: IEEE

MIC-05-187

Unsupervised micro-CT reconstruction from limited-angle and truncated data in cone-beam geometry (#1238)

Keisuke Izumitani[1,2], Tatsunori Shibuya[2,3], Hidetoshi Kato[2,3], Hideaki Haneishi[4], Takayuki Okamoto[4]

[1] Chiba University, Graduate School of Science and Engineering, Chiba, Japan; [2] National Institute of Advanced Industrial Science and Technology (AIST), Research Institute for Measurement and Analytical Instrumentation, National Metrology Institute of Japan, Tsukuba, Japan; [3] National Institute of Advanced Industrial Science and Technology (AIST), Non-Destructive Imaging Research Team, Integrated Research Center for Resilient Infrastructure, Tsukuba, Japan; [4] Chiba university, Center for Frontier Medical Engineering, Chiba, Japan

This study was supported by JSPS KAKENHI, Grant Number JP25K21580; JST, ACT-X, Grant Number JPMJAX23K5; and JSPS Program for Forming Japan's Peak Research Universities (J-PEAKS), Grant Number JPJS00420230002.

Abstract
Micro X-ray computed tomography (micro-CT) enables non-destructive visualization of fine internal structures. Resolving finer details requires higher geometric magnification, typically achieved by reducing the source-to-rotation-center distance (SRD). However, short-SRD acquisition can suffer from a limited angular range due to physical interference with the X-ray source and from projection truncation when the object extends beyond the field-of-view (FOV), causing streak artifacts and structural distortions. Supervised learning-based reconstruction methods have been investigated to mitigate such artifacts but applying them to non-destructive high-magnification micro-CT is difficult because fully sampled, non-truncated reference data cannot be readily acquired without destructive sample preparation. Moreover, many existing methods are designed for 2D fan-beam geometry rather

than 3D cone-beam geometry commonly used in micro-CT. We propose an unsupervised reconstruction method that simultaneously reduces limited-angle and projection-truncation artifacts by incorporating long-SRD measurements. Long-SRD acquisition provides full-view, non-truncated projections, albeit at lower spatial resolution, complementing the high-resolution but incomplete short-SRD acquisition. By jointly using these complementary measurements, the proposed method preserves fine structural details while recovering the global object structure without requiring ground-truth images. Numerical experiments demonstrated that the proposed method reduced streak artifacts and recovered structural information outside the short-SRD FOV. To the best of our knowledge, this is the first unsupervised 3D cone-beam reconstruction method to simultaneously address both artifacts in high-magnification micro-CT.

References
[1] Y. Huang et al., "Data consistent CT reconstruction from insufficient data with learned prior images", arXiv preprint, 2005.10034, 2020.
[2] K. Izumitani, H. Haneishi, and T. Okamoto, "Weakly supervised limited-angle CT reconstruction using multiple projection geometries", 2025 IEEE NSS MIC RTSD, Yokohama, Japan.
[3] H. Kim and K. Champley, "Differentiable forward projector for x-ray computed tomography," arXiv preprint, 2307.05801, 2023.

MIC-05-190

A Self-Supervised Framework for Simultaneous Reconstruction of Activity and Attenuation in TOF-PET (#1404)

Tan Gong[1], Hui Liu[2], Wenbo Huang[3], Hao Jia[1], Yaqiang Liu[2], Zuoxiang He[3]

[1] Tsinghua University, School of Biomedical Engineering, Beijing, China; [2] Tsinghua University, Department of Engineering Physics, Beijing, China; [3] Tsinghua University Changgung Hospital, Department of Nuclear Medicine, Beijing, China

This work was supported by the National Key Research and Development Program of China (No. 2022YFC2402000, No. 2022YFC2403802), and National Natural Science Foundation of China (No. 12205166)

Abstract

Time-of-flight PET (TOF-PET) enables CT-free attenuation correction (AC) through simultaneous activity and attenuation (SAA) reconstruction from emission alone. In this study, we propose a self-supervised SAA framework based on implicit neural representation. The proposed framework employs parallel hash encoders and multilayer perceptrons to learn the mapping from spatial coordinate to image space, thereby jointly reconstructing activity and attenuation maps. To further accelerate reconstruction and reduce GPU memory consumption, an ordered-subset training strategy is introduced, in which projection angles used for supervision are progressively increased during optimization. The proposed method was evaluated using analytical simulations based on a BrainWeb brain phantom with ^{18}F-FDG uptake. Compared with non-attenuation-corrected MLEM, maximum likelihood reconstruction of attenuation correction factors (MLACF) and maximum-likelihood activity and attenuation (MLAA), OSIR demonstrated improved visual consistency and quantitative accuracy. For activity reconstruction, OSIR achieved the highest PSNR of 24.62 dB and the lowest NRMSE of 5.87%, with SSIM comparable to MLAA. For

attenuation reconstruction, OSIR outperformed MLAA across all evaluation metrics. In addition, OSIR reduced the reconstruction time from 60 min to approximately 40 min. These results demonstrate that OSIR provides an efficient and robust solution for CT-free attenuation-corrected TOF-PET reconstruction, enabling accurate joint estimation of activity and attenuation maps without requiring CT images or large-scale training datasets.

References
[1] Rezaei, M. Defrise, G. Bal, et al., "Simultaneous reconstruction of activity and attenuation in time-of-flight PET," IEEE transactions on medical imaging, vol. 31, no. 12, pp. 2224-2233, 2012
[2] B. Mildenhall, P. P. Srinivasan, M. Tancik, J. T. Barron, R. Ramamoorthi, and R. Ng, "Nerf: Representing scenes as neural radiance fields for view synthesis," Communications of the ACM, vol. 65, no. 1, pp. 99-106, 2021.
[3] B. Aubert-Broche, M. Griffin, G. B. Pike, A. C. Evans, and D. L. Collins, "Twenty new digital brain phantoms for creation of validation image data bases," IEEE transactions on medical imaging, vol. 25, no. 11, pp. 1410-1416, 2006.
[4] G. Schramm and K. Thielemans, "PARALLELPROJ—an open-source framework for fast calculation of projections in tomography," Frontiers in Nuclear Medicine, vol. 3, p. 1324562, 2024

MIC-05-193

Extended Field-of-View Reconstruction for Full-Ring Multi-Pinhole SPECT (#1639)

Qiao Liu, Yang Lv, Fatih N. Gür

Shanghai Jiao Tong University, Global Institute of Future Technology, Shanghai, China

Abstract

Full-ring multi-pinhole SPECT offers high sensitivity and compact detector coverage, but eFOV reconstruction remains challenging due to projection truncation, incomplete angular sampling, and reduced peripheral sensitivity, especially for large-body or off-center activity distributions.

We propose a staged deep-learning-assisted OSEM framework for eFOV recovery. The framework combines a physics-based forward model, two-stage sinogram completion, and image-domain refinement. Truncated projections are first reconstructed by OSEM as the baseline. Two residual U-Nets then sequentially restore missing detector-width information and angular views in the sinogram domain. Finally, an image-domain network suppresses residual artifacts and improves structural continuity in the eFOV region.

Simulation studies used FDG activity distributions with randomized body scaling, translation, sparse sampling, and peripheral lesion insertion. Evaluation metrics included recovery coefficient, MAE, RMSE, SSIM, and lesion-level recovery. Compared with truncated-data OSEM, the proposed method improved peripheral lesion recovery and reduced reconstruction errors. In representative cases, recovery coefficient increased from 25.9% to 96.6% at 550 mm and from 10.1% to 82.5% at 650 mm. Preliminary 3D validation also showed lower errors and higher structural similarity in axial and sagittal views. These results suggest that combining physics-based modeling with dual-domain deep learning is feasible for eFOV reconstruction in full-ring multi-pinhole SPECT. Future work will validate the framework using physical phantom and clinical data.

MIC-05-196

CT Image Reconstruction Using Deep Image Prior with VoxelMorph

(#1782)

Kensuke Hori[1], Fumio Hashimoto[2], Takeyuki Hashimoto[3]

[1] Juntendo University, Department of Radiological Technology, Bunkyo-ku, Japan; [2] University of Florida, J. Crayton Pruitt Family Department of Biomedical Engineering, Gainesville, USA; [3] Kyorin University, Department of Radiological Technology, Mitaka-shi, Japan

Abstract

Motion during scanning results in motion artifacts that distort anatomical structures in computed tomography (CT) images. In radiation therapy, planning CT scan duration are high-speed, whereas linear accelerator gantry mounted CT takes more than 15 seconds, making them more susceptible to motion artifacts. Recently, CT image reconstruction methods using supervised learning have been shown to suppress motion artifacts. However, obtaining sufficient training data is difficult because actual organ motion cannot be directly visualized. In this study, we propose an unsupervised CT image reconstruction method incorporating deep image prior and VoxelMorph (DIP-VM). The proposed method iteratively alternates between DIP-based image reconstruction and VM-based estimation of the motion vector field, in which planning CT images are leveraged as reference images. The main advantage of the proposed DIP-VM is its ability to correct patient motion using only patient-specific data, without requiring large training datasets. The proposed DIP-VM was evaluated on an XCAT phantom with cardiac and respiratory motion. Experimental results demonstrate that, using only patient-specific projection data, the proposed DIP-VM method reduces motion artifacts more effectively than the comparison methods. This study provides an effective solution for suppressing motion artifacts using only patient-specific projection data, without requiring large training datasets.

References

[1] Chen Z, Li Q, Wu D. 'Estimate and compensate head motion in non-contrast head CT scans using partial angle reconstruction and deep learning', Med. Phys. vol. 51, pp. 3309-21, 2024.

[2] Ulyanov D, Vedaldi A, Lempitsky V, 'Deep image prior', International Journal of Computer Vision, vol. 128, pp. 1867-88, 2020.

[3] Balakrishnan G, Zhao A, Sabuncu MR, Guttag J, Dalca AV. 'VoxelMorph: a learning framework for deformable medical image registration', IEEE Trans. Med. Imag., vol. 38, pp. 1788-1800, 2019.

[4] Baguer DO, Leuschner J, Schmidt M. 'Computed tomography reconstruction using deep image prior and learned reconstruction methods', Inverse Problems. vol. 36, 094004, 2020.

[5] Segars WP, Mahesh M, Beck TJ, Frey EC, Tsui BM. 'Realistic CT simulation using the 4D XCAT phantom', Med. Phys., vol. 35, pp. 3800-8, 2008.

MIC-05-199

A Boosting Diffusion Model for Ultra-Sparse-View CT reconstruction

(#1840)

Yura Kimura[1], Sho Ozaki[1], Hideki Obara[2], Masahiko Aoki[3]

[1] Hirosaki University, Graduate School of Science and Technology, Aomori, Japan; [2] Hirosaki University School of Medicine and Hospital, Department of Radiology, Division of Medical Technology, Aomori, Japan; [3] Hirosaki University, Department of Radiation Oncology, Aomori, Japan

Sho Ozaki was partially supported by the JSPS Grant-in-Aid for Scientific Research (C), 25K15317.

Abstract

Recent advances in diffusion models for natural image processing [1] have led to the development of several diffusion prior-based methods for medical image reconstruction [2,3,4,5,6]. For these diffusion model-based methods, balancing fidelity to the observed data (e.g., projection data) and the diffusion prior is essential. In diffusion models, low noise levels correspond to fine-grained details and therefore better preserve consistency with the observed data, whereas high noise levels correspond to coarse-grained information and rely more heavily on the diffusion prior. In our previous study, we proposed an ensemble method using multiple diffusion priors [7]. This method successfully optimized the balance between observed-data fidelity and diffusion priors in moderately sparse-view settings. However, we found that the advantage of the ensemble method decreases in extremely sparse cases with fewer than 25 views. Under such extremely sparse conditions, a diffusion prior with a large time step alone performed better than the ensemble method.

In this study, we propose a boosting diffusion model for sparse-view CT reconstruction, particularly targeting cases with severe information loss in the observed data. In the proposed method, image reconstruction is first performed using a large time step, resulting in a coarse-grained reconstruction. Subsequently, reconstruction is refined using smaller time steps, leading to fine-grained image reconstruction. We compared the proposed method with existing methods, including iterative reconstruction (IR), DPS, and SDPS, in terms of SSIM and PSNR. The results demonstrated that the proposed method outperforms the existing methods in extremely sparse-view cases with fewer than 25 views.

References

[1] Ho J., Jain A., and Abbeel P., 2020, 'Denoising diffusion probabilistic models', in Advances in Neural Information Processing Systems, vol. 33, pp. 6840–6851.

[2] Song Y., Shen L., Xing L., and Ermon S., 2022, 'Solving Inverse Problems in Medical Imaging With Score-Based Generative Models', in The 10th International Conference on Learning Representations.

[3] Chung H., Sim B., Ryu D., and Ye J. C., 2022, 'Improving Diffusion Models for Inverse Problems using Manifold Constraints', in Advances in Neural Information Processing Systems, vol. 35, pp. 25683–25696.

[4] Xie J., Shao H.-C., Li Y., and Zhang Y. , 2024, 'Prior frequency guided diffusion model for limited angle (LA)-CBCT reconstruction', Phys. Med. Biol., vol. 69, no. 13, p. 135008.

[5] Chung H., Kim J., McCann M. T., Klasky M. L., and Ye J. C., 2023, 'Diffusion Posterior Sampling for General Noisy Inverse Problems', 11th Int. Conf. Learn. Represent. ICLR 2023, pp. 1–30.

[6] Jiang X., Li S., Teng P., Gang G., and Webster Stayman J., 2024, 'Strategies for CT Reconstruction using Diffusion Posterior Sampling with a Nonlinear Model', arXiv preprint arXiv: 2407.12956.

[7] Ozaki S., Kaji S., Imae T., Nawa K., Yamashita H., and Nakagawa K., 2025, 'Ensemble of Different Diffusion Priors for Sparse-View CT Reconstruction', in 2025 IEEE Nuclear Science Symposium (NSS), Medical Imaging Conference (MIC) and Room Temperature Semiconductor Detector Con-ference (RTSD).

MIC-05-202

SPECT Reconstruction via Diffusion Sampling from a PET Image Manifold for Theranostics (#1954)

Huanzhe Wei[1], Lefteris Livieratos[1,2], George Webber[1], Andrew J. Reader[1]

[1] Kings College London, School of Biomedical Engineering and Imaging Sciences, London, UK; [2] Kings College London, Guy's and St Thomas' NHS Foundation Trust, London, UK

Abstract

Single photon emission computed tomography (SPECT) remains the standard modality for uptake verification and patient-specific dosimetry in molecular radiotherapy (MRT), however it has limited spatial resolution and noise characteristics compared to pre-therapy positron emission tomography (PET). Existing approaches that incorporate PET priors into SPECT reconstruction are often constrained by hand-crafted feature representations and suffer from inter-modality mismatch and registration-induced artifacts. In this work, we employ a conditional generative framework to enhance SPECT reconstruction toward PET-level image quality. A denoising diffusion probabilistic model (DDPM) is trained to learn the distribution of high-quality PET images. During inference, the reverse diffusion process is conditioned on measured SPECT data and CT images, enabling anatomically consistent, high-fidelity image synthesis. The method is initially assessed using 2D Zubal phantom simulations. Performance is compared with conventional maximum likelihood expectation maximization (MLEM) and kernel based methods. Both quantitative metrics and qualitative analysis demonstrate that the diffusion-based approach achieves enhanced edge preservation and superior noise suppression. The reconstructed images show closer agreement with reference data compared to MLEM and kernel based reconstructions. By avoiding explicit PET–SPECT registration, the framework mitigates spatial misalignment and associated artifacts. These results indicate that conditional diffusion sampling provides a principled and flexible approach to improve resolution and noise limitations in SPECT, with potential to improve quantitative accuracy in MRT applications.

References

[1] H. Marquis, D. Deidda, A. Gillman et al., “Theranostic SPECT reconstruction for improved resolution: application to radionuclide therapy dosimetry,” EJNMMI Phys., vol. 8, no. 1, p. 16, Feb. 2021.

[2] F. Liu, H. Zhu, J. Yu et al., “68Ga/177Lu-labeled DOTA-TATE shows similar imaging and biodistribution in neuroendocrine tumor model,”Tumour Biol., vol. 39, no. 6, p. 1010428317705519, Jun. 2017.

[3] H.Wei, L. Livieratos, and A. J. Reader, “PET Guided Kernel EM Methods for SPECT Reconstruction in Molecular Radiotherapy,” in Proc. IEEE Nucl. Sci. Symp. Med. Imaging Conf. (NSS/MIC), Nov. 2025, pp. 1–1.

[4] G. Webber and A. J. Reader, “Diffusion models for medical image reconstruction,” BJR—Artif. Intell., vol. 1, no. 1, p. ubae013, Mar. 2024.

[5] I. R. Singh, A. Denker, R. Barbano et al., “Score-Based Generative Models for PET Image Reconstruction,” Mach. Learn. Biomed. Imaging, vol. 2, no. Generative Models, pp. 547–585, Jan. 2024.

[6] K. Thielemans, C. Tsoumpas, S. Mustafovic et al., “STIR: software for tomographic image reconstruction release 2,” Phys. Med. Biol., vol. 57, no. 4, pp. 867–883, Feb. 2012.

MIC-05-205

Plug-and-Play PET Image Reconstruction Using Diffusion Models

(#2071)

Tomoya Minagawa[1], Fumio Hashimoto[2], Kensuke Hori[3], Takeyuki Hashimoto[4]

[1] Toho University Ohashi Medical Center, Radiology, Tokyo, Japan; [2] University of Florida, J. Crayton Pruitt Family Department of Biomedical Engineering, Florida, USA; [3] Juntendo University, Radiological Technology, Tokyo, Japan; [4] Kyorin University, Medical Radiological Technology, Tokyo, Japan

We thank the members of the Department of Radiology at Toho University Ohashi Medical Center for their cooperation.

Abstract

Diffusion models (DMs) have recently demonstrated remarkable performance in positron emission tomography (PET) image reconstruction. However, in diffusion posterior sampling, data fidelity and diffusion prior are coupled within each sampling step, which can make the balance between them sensitive to parameter selection. In this study, we propose a plug-and-play diffusion-based PET image reconstruction method (PnP-DM) that enables explicit incorporation of a DM as a prior within a penalized reconstruction. The proposed method is formulated based on Bayes' theorem and employs a half-quadratic splitting algorithm to decouple the likelihood and prior terms into penalized reconstruction and diffusion sampling. The proposed method alternates between the likelihood and prior steps, where the likelihood step penalizes deviation from the diffusion result, while the prior step is guided by the reconstructed image from the likelihood step, thereby maintaining data consistency throughout the optimization process. We evaluated the proposed method using simulated [^{18}F]FDG BrainWeb phantom datasets. The proposed method suppressed noise while preserving structural details and achieved higher contrast-to-noise ratio and contrast recovery coefficient than maximum likelihood-expectation maximization (EM) and maximum a posteriori-EM. These results suggest that the proposed PnP method provides diffusion-based reconstruction that enables more stable optimization and flexible balancing between data fidelity and diffusion prior.

References

[1] F. Hashimoto and K. Gong, "PET image reconstruction using deep diffusion image prior," *IEEE Trans. Med Imaging*, 2026.

[2] K. Gong, et al., "PET image denoising based on denoising diffusion probabilistic model," *Eur. J. Nucl. Med. Mol. Imaging*, vol.51, pp. 358-368, 2024.

[3] I.R.D. Singh, et al., "Score-based generative models for PET image reconstruction," *J. Mach. Learn. Biomed. Imaging.*, vol. 2, pp. 547-585, 2023.

[4] Z. Wu, et al., "Principled probabilistic imaging using diffusion models as plug-and-play priors," *Advances in Neural information Processing Systems*, vol.37, pp. 118389-118427, 2024.

[5] D. Geman and C. Yang, "Nonlinear image recovery with half-quadratic regularization," *IEEE Trans. Image Process.*, vol. 4, pp. 932-946, 1995.

[6] J. Ho, et al., "Denoising diffusion probabilistic models," *Advances in Neural Information processing Systems*, vol. 33, pp. 6840-6851, 2020.

[7] B. Aubert-Broche, et al., "Twenty new digital brain phantoms for creation of validation image databases," *IEEE Trans. Med. Imaging.*, vol. 25, no. 11, pp. 1410-1416, 2006.

MIC-05-208

List-Mode Reconstruction for Gamma-Positron Imaging (#2124)

Matthew A. Kupinski[1,2], Michael A. King[3], Shiva Abbaszadeh[4], Lars R. Furenlid[1,2]

[1] University of Arizona, College of Optical Sciences, Tucson, USA; [2] University of Arizona, Department of Medical Imaging, Tucson, USA; [3] University of Massachusetts Chan Medical School, Department of Radiology, Worcester, USA; [4] University of California, Department of Electrical and Computer Engineering, Santa Cruz, USA

This research was supported by NIH Grants: UG3EB034686 and UH3EB034686.

Abstract

We present a GPU-accelerated list-mode reconstruction framework for gamma-positron brain imaging that models PET coincidences, prompt-gamma Compton events, and triple events, in which one decay produces both detected event classes. The goal is to reconstruct the radionuclide decay distribution, rather than only the positron annihilation location, by combining the sensitivity of 511-keV coincidences with the geometric constraint from a coincident prompt gamma. The framework uses UAMonteCarlo emission and detector simulations to generate sorted list-mode events and voxelized sensitivity maps for an edge-on crossed-strip CZT geometry. The test configuration contains 690 detectors on a 30-cm-diameter ring surrounding a 24-cm water sphere and models 44Sc, including emission and transport of a 1474 keV-max positron and a 1157 keV prompt gamma. Event likelihoods are evaluated for PET-only events, two-interaction prompt-gamma events, and triple events. PET likelihoods include annihilation-photon attenuation and positron range effects; prompt-gamma likelihoods include Compton kinematics, energy deposition, detector interaction type, and attenuation; triple-event likelihoods combine PET line-of-response and prompt Compton-cone constraints. The reconstruction code computes event probabilities on the GPU and applies a list-mode maximum-likelihood expectation-maximization update. Initial consistency studies with simulated 44Sc point-source data show that PET-only and prompt-only reconstructions recover point-source locations after three iterations using 2000 events per mode, while sensitivity maps and likelihood images show the tradeoff between high-sensitivity PET/prompt events and lower-sensitivity, higher-weight triple events. These results establish machinery for combined gamma-positron reconstructions and motivate tests with triple events, mixed event-type reconstructions, and further phantom studies.

MIC-05-211

Pilot Clinical Evaluation of CT-Less PET Attenuation Correction Using Back-Scatter Coincidences on the NeuroEXPLORER System (#2352)

Zhongzhi Liu[2,1], Tiantian Li[3], Liuchun He[1], Songsong Tang[1], Yun Dong[1]

[1] Shanghai United Imaging Healthcare Co., Ltd., Shanghai, China; [2] Wuhan United Imaging Life Science Instrument Co., Ltd., Wuhan, China; [3] United Imaging Healthcare North America, Inc., Houston, USA

Abstract

Attenuation correction (AC) is essential for quantitative PET imaging and is conventionally performed using CT-derived attenuation maps. In this work, we present an initial clinical evaluation of a CT-less AC approach based on detector backward inter-crystal scattered (BKS) coincidences on the NeuroEXPLORER (NX) PET/CT system. Two patient datasets were acquired with a full-energy-window protocol that preserved standard emission coincidences, BKS events, and (^{176})Lu background events within the same list-mode dataset. For each patient, three reconstruction pipelines were compared: CT-AC+OSEM, Lu-AC+OSEM, and BKS-AC+OSEM. Results showed that, in the higher-activity case, Lu-background data were more strongly affected by random events, leading to a noisier attenuation map, whereas the BKS-derived attenuation map showed improved quality, particularly in the skull region, and yielded PET images in closer agreement with the CT-AC reference. In the lower-activity case, BKS- and Lu-derived attenuation maps were generally comparable. A short-acquisition study further showed that BKS-derived attenuation maps remained reasonably consistent for acquisition times of 5 min or longer. These results indicate that BKS-based AC is a promising direction for CT-less PET attenuation correction and warrants further evaluation in larger studies.

References

[1] Li, T., et al. "CT-Less Attenuation Correction for PET using Backward Inter-Crystal Scattered Events." 2024 IEEE NSS-MIC.

[2] Liu, Z., et al. “Joint Activity and Attenuation Map Estimation for PET with TOF, Lu-176 background and back scatter “ 2025 IEEE NSS-MIC.

[3] Li, H., Badawi, R. D., et al. (2024). Performance characteristics of the NeuroEXPLORER, a next-generation human brain PET/CT imager. J. Nucl. Med., 65(8), 1320-1326.

MIC-05-214

Unrolled relaxed algorithm for 3D SPECT reconstruction (#2388)

Corentin Constanza[1], David Sarrut[1], Ane Etxebeste[1,2]

[1] CREATIS, CNRS UMR 5220; INSERM U 1044, Université de Lyon; INSA-Lyon; Université Lyon 1, Villeurbanne, France; [2] Centre de lutte contre le cancer Léon-Bérard, Lyon, France

All authors declare that they have no known conflicts of interest.

Abstract

In this work, we propose an unrolled Block Sequential Regularized Expectation Maximization (BSREM) reconstruction framework in which the gradient of the regularization term is learned using a convolutional neural network. Building on our previous work, we adopt Jacobian-Free Unrolling (JFU) to enable memory-efficient training on 3D synthetic data. This training strategy backpropagates only through the final iteration of the unrolled optimization, significantly reducing memory consumption while improving training stability. We investigate the influence of relaxation strategies within the unrolled BSREM scheme and analyze their impact on convergence behavior, stability, and reconstruction quality. Experiments conducted on realistic simulated SPECT datasets and clinical ^{177}Lu-DOTATATE patient data show that JFU-based unrolling consistently outperforms classical unrolled training for an equivalent number of parameters and memory usage. Unlike classical unrolling, which requires strong relaxation to ensure stable training, JFU achieves optimal performance with weak or no relaxation. Excessive relaxation is shown to be suboptimal, leading to reduced quantitative accuracy. Quantitative evaluations demonstrate improvements in both global image quality and organ-level activity accuracy compared to OSEM and conventional BSREM with a Relative Difference Penalty prior. As observed in our previous study using Green's one-step-late algorithm, the proposed approach may introduce over-separation artifacts between regions of low and high activity. This behavior appears intrinsic to learning the regularization gradient rather than to the unrolling strategy itself. Overall, this work highlights the advantages of Jacobian-Free Unrolling for scalable and stable learning-based SPECT reconstruction and provides insights into the role of relaxation in unrolled optimization schemes.

References

[1] H. M. Hudson and R. S. Larkin, "Accelerated image reconstruction using ordered subsets of projection data," IEEE Transactions on Medical Imaging, 1994.

[2] S. Ahn, S. G. Ross, E. Asma, J. Miao, X. Jin, L. Cheng, S. D. Wollenweber, and R. M. Manjeshwar,, "Quantitative comparison of OSEM and penalized likelihood image reconstruction using relative difference penalties for clinical PET," Physics in Medicine & Biology, 2015.

[3] P. J. Green, "Bayesian reconstructions from emission tomography data using a modified EM algorithm," IEEE Transactions on Medical Imaging, 1990.

[4] S. Ahn and J. A. Fessler, "Globally convergent image reconstruction for emission tomography using relaxed ordered subsets algorithms," IEEE Transactions on Medical Imaging, 2003.

[5] V. Monga, Y. Li, and Y. C. Eldar, "Algorithm unrolling: Interpretable, efficient deep learning for signal and image processing," IEEE Signal Processing Magazine, 2021.

[6] S. W. Fung, H. Heaton, Q. Li, D. McKenzie, S. Osher, and W. Yin, "Jfb: Jacobian-free backpropagation for implicit networks," in AAAI Conference Proceedings, 2022.

[7] L. Davy, L. M. Briceno-Arias, and N. Pustelnik, "Restarted contractive operators to learn at equilibrium," arXiv preprint arXiv:2506.13239, 2025.

[8] T. Kaprélian, A. Etxebeste, and D. Sarrut, "Partial volume correction of SPECT images with deep learning trained on synthetic data," IEEE Transactions on Radiation and Plasma Medical Sciences, 2025

[9] J. Leube, J. Gustafsson, M. Lassmann, M. Salas-Ramirez, and J. Tran-Gia, "A deep-learning-based partial-volume correction method for quantitative 177Lu SPECT/CT imaging," Journal of Nuclear Medicine, 2024.

MIC-05-217

Multiple Emission Tomography: GPU-Accelerated LM-OSEM Reconstruction for Compton Events (#2640)

Matteo N. Colombo[1], Marco Pizzichemi[1,2], Giulia Terragni[2], Francesco Pennazio[3], Marco Paganoni[1], Luca Presotto[1]

[1] University of Milano-Bicocca, Milan, Italy; [2] CERN, Meyrin, Switzerland; [3] INFN Torino, Turin, Italy

This work is supported by the European Union-Next Generation EU, Mission 4 Component 1 CUP H53D23007430001, and the Crystal Clear Collaboration at CERN.

Abstract

The Multiple Emission Tomography (MET) detector, a single-layer ring of LYSO:Ce scintillators, offers a versatile imaging platform combining Positron Emission Tomography (PET) with collimator-free Compton-mode Single-Photon Emission Computed Tomography (SPECT). However, Compton reconstruction for single-layer cylindrical geometries remains a major challenge due to high data dimensionality and a dense system matrix. In this work, we present a GPU-accelerated reconstruction framework based on List-Mode Ordered Subset Expectation Maximization (LM-OSEM). Building on the open-source CoReSi library, our framework introduces several contributions. i) High-Performance Architecture: we implement a vectorized PyTorch pipeline with fused broadcasting and event batching. This approach achieves O(batch size · voxels) peak GPU memory occupancy, enabling the processing of massive datasets. ii) Advanced Physics Modeling: we introduce a system matrix that incorporates a per-event Angular Resolution Measure (ARM). This model integrates Doppler broadening, energy resolution, and detector spatial resolution, allowing for optimal event weighting and noise suppression. iii) Geometry-Specific Sensitivity: we propose a novel sensitivity model tuned for the MET cylindrical geometry, accounting for solid-angle coverage and LYSO self-absorption.The framework is validated through Monte Carlo simulations of the MET prototype. We evaluate spatial resolution and noise on reconstructed images from 511 keV to 1 MeV. Spatial resolutions between 5 mm and 10 mm are achievable, confirming MET's potential for imaging high-energy exotic nuclei inaccessible to conventional gamma cameras. This work provides a scalable, fast, and physically accurate foundation for next-generation multi-modal molecular imaging.

MIC-05-220

List-Mode Derived Synthetic Kernel-Based Image Reconstruction for Dynamic Total Body PET (#2844)

Movindu Dassanayake[1], Laurence Vass[1], Paul K. Marsden[1], Julia A. Schnabel[1,2], Andrew J. Reader[1]

[1] King's College London, Department of Imaging Physics and Engineering at the School of Biomedical Engineering and Imaging Sciences, London, UK; [2] Technical University Munich, School of Computation, Information and Technology, Munich, Germany

MD would like to acknowledge funding from the EPSRC Centre for Doctoral Training in Smart Medical Imaging [EP/S022104/1] and via a Siemens Healthineers Studentship.

Abstract

Total-body positron emission tomography (TB-PET) provides significantly improved sensitivity, enabling ultra-short time framing for dynamic imaging. However, the resulting low count statistics lead to increased noise and unstable time activity curves (TACs), limiting quantitative accuracy. We investigate a kernel-based reconstruction approach within a list-mode (LM)-derived synthetic framework, where a vendor reconstruction is forward projected through an event-specific LM system matrix to generate synthetic data, implicitly includes attenuation, normalisation, scatter, and randoms effects while enabling flexible algorithm design.

Spatial, temporal, and spatio-temporal kernels are evaluated for short-frame FDG data acquired on a Biograph Vision Quadra system, with features constructed from multiple dynamic intervals. Reconstructions are compared with a 10x higher count vendor reference images using spatial and temporal PRMSE. Spatially, the spatio-temporal kernel achieves the lowest error. In addition, we demonstrated that kernel methods benefit from larger neighbourhoods resulting in improved visual quality compared to synthetic PET. This was computationally feasible on consumer hardware by using region-of-interest specific reconstructions.

These results demonstrate that LM-derived synthetic kernel reconstruction provides a flexible framework for incorporating spatial and temporal priors in TB-PET. While performance is currently limited by kernel parameter selection, the observed improvements in spatial and temporal behaviour indicate strong potential for optimisation through tuning the kernel strength and feature vector design.

References

[1] Wang, G, Qi, J, 2015, 'PET Image Reconstruction Using Kernel Method', IEEE Transactions on Medical Imaging, vol. 34, no. 1, pp. 61–71, 2015

[2] Hutchcroft, W et al., 2016, 'Anatomically-aided PET reconstruction using the kernel method', Physics in Medicine and Biology, vol. 61, no. 18, pp. 6668–6683,

[3] Bland, J, et al., 2018, 'MR-Guided Kernel EM Reconstruction for Reduced Dose PET Imaging', IEEE Transactions on Radiation and Plasma Medical Sciences, vol. 2, no. 3, pp. 235–243, 2018.

[4] Vass, L and Reader, AJ, 2023, 'Synthesized Image Reconstruction for Post-Reconstruction Resolution Recovery', IEEE Transactions on Radiation and Plasma Medical Sciences, vol. 7, no. 5, pp. 473–482, 2023

[5] Lastname, GN, Lastname, GN YYYY, 'Article', *Journal*, Edition, Page, Place of publication: publishers Schramm, G and Thielemans, K, 2024, 'PARALLELPROJ—an open-source framework for fast calculation of projections in tomography', Frontiers in Nuclear Medicine

MIC-05-223

Three-Photon Bayesian Imaging of Ortho-Positronium (#2897)

Wojciech Krzemien[1], Lech Raczyński[2], Aurélien Coussat[3], On behalf of IMPET project

[1] National Centre for Nuclear Research, Department of High Energy Physics, Otwock Swierk, Poland; [2] National Centre for Nuclear Research, Department of Complex Systems, Otwock Swierk, Poland; [3] INSA-Lyon, niversité Claude Bernard Lyon 1, CNRS, Inserm, CREATIS UMR 5220, U1294, F-69373, Lyon, France

The work was supported by the Foundation for Polish Science through the FIRST TEAM FENG.02.02-IP.05-0152/23 programme co-financed by the European Union under the European Funds for Smart Economy 2021-2027 (FENG). by the “PHC POLONIUM” program (project number: 55194PB), funded by the French Ministry for Europe and Foreign Affairs, the French Ministry for Higher Education, Research, and Space, and the Polish NAWA (BPN/BFR/2025/1/00036/ and BPN/BAT/2025/1/00009), and co-supported by the Austrian Ministry for Women, Science and Research (project WTZ PL 11/2026).

Abstract

Positron emission tomography provides functional images from two-photon coincidences. In human tissue, approximately 40% of annihilations are preceded by positronium formation, of which the ortho-positronium component partially decays into three photons [1]. This three-photon channel carries additional information about the local micro-environment [1], including the three-to-two-photon yield ratio as a potential diagnostic marker [3,2], and its exploitation does not require a prompt photon, making it compatible with standard radionuclides such as FDG. We propose the Three-Photon Bayesian Imaging of Ortho-Positronium algorithm, a novel event-by-event reconstruction method formulated as a Bayesian maximum a posteriori inference problem, which unifies time-based trilateration [4], energy-based reconstruction [3], and a physics-informed prior derived from the quantum electrodynamics description of ortho-positronium decay [5-6] within a single probabilistic framework. Monte Carlo simulations modelled after the Siemens Biograph Quadra scanner [7] demonstrate an improvement of a factor of two over time-based trilateration and by an order of magnitude over energy-based reconstruction. The proposed approach is compatible with existing scanners capable of registering three-photon coincidences, broadening its applicability beyond positronium lifetime imaging to standard clinical radionuclides.

References

[1] Hourlier, A, Boisson, F & Brasse, D 2024, 'Experimental uses of positronium and potential for biological applications', *IEEE Transactions on Radiation and Plasma Medical Sciences*, vol. 8, no. 6, pp. 581–594

[2] Fujimoto, M et al. 2025, 'Advancing PET through direct imaging of three-photon decay using pure positron emitters', unpublished.

[3] Kacperski, K, Spyrou, NM & Smith, FA 2004, 'Three-gamma annihilation imaging in positron emission tomography', *IEEE Transactions on Medical Imaging*, vol. 23, no. 4, pp. 525–529.

[4] Gajos, A et al. 2016, 'Trilateration-based reconstruction of ortho-positronium decays into three photons with the J-PET detector', *Nuclear Instruments and Methods in Physics Research Section A*, vol. 819, pp. 54–59.

[5] Ore, A & Powell, JL 1949, 'Three-photon annihilation of an electron–positron pair', *Physical Review*, vol. 75, no. 11, pp. 1696–1699.

[6] Berestetskii, VB, Lifshitz, EM & Pitaevskii, LP 2008, *Quantum Electrodynamics*, 2nd edn, Butterworth-Heinemann, Oxford.

[7] Prenosil, GA et al. 2022, 'Performance characteristics of the Biograph Vision Quadra PET/CT system with a long axial field of view using the NEMA NU 2-2018 standard', *Journal of Nuclear Medicine*, vol. 63, no. 3, pp. 476–484.

MIC-05-226

Event-by-Event Energy-Dependent List-Mode Reconstruction for Quantitative ^{90}Y Bremsstrahlung SPECT (#2953)

Chenyu Yan[1], Hai Hu[1], Jingjing Qin[1], Hanshen Ye[1], Chengzhi Yang[1], Faguo Chen[2,3], Ri Zhao[2,3], Hua Li[2,3], Zuoxiang He[4], Yaqiang Liu[5], Hui Liu[5], Jing Wu[1]

[1] Beijing Normal University, Center for Advanced Quantum Studies, School of Physics and Astronomy, Beijing, China; [2] China Institute for Radiation Protection, Shanxi, China; [3] Shanxi Provincial Key Laboratory for Translational Nuclear Medicine and Precision Protection, Shanxi, China; [4] Beijing Tsinghua Changgung Hospital, Department of Nuclear Medicine, Beijing, China; [5] Tsinghua University, Department of Engineering Physics, Beijing, China

This study was supported by National Natural Science Foundation of China (No. 12305379, No.12205166), Beijing Natural Science Foundation (Z220010), CIRP Open Fund of Radiation Protection Laboratories (TNMPP-2024-No.1).

Abstract

^{90}Y bremsstrahlung SPECT imaging remains challenging due to its broad continuous energy spectrum. In this study, we proposed and evaluated a novel event-by-event energy-dependent list-mode reconstruction algorithm for quantitative ^{90}Y bremsstrahlung SPECT. To enable real-time and reasonably accurate energy-dependent collimator-detector response modeling, we proposed and incorporated a True Half-Width method into the list-mode reconstruction framework. Monte Carlo simulations were performed using three energy windows: 90-160 keV, 105-285 keV, and 90-400 keV. Quantitative evaluation was performed using contrast recovery coefficient and background variability. Compared with projection-based reconstruction, list-mode reconstruction achieved the best quantitative performance using the 90-400 keV energy window, owing to accurate event-level energy-dependent system matrix modeling over the broad continuous energy spectrum. These results demonstrate that event-by-event energy-dependent list-mode reconstruction is essential for improving the quantitative accuracy of ^{90}Y bremsstrahlung SPECT.

References

[1] Se Y, Minh P, Thanh Q, et al. Algorithms and Analyses for Joint Spectral Image Reconstruction in Y-90 Bremsstrahlung SPECT. IEEE Trans. Med. Imaging, 2020,39:1369-1379.

[2] Nathan C, Muthana S, De Nadine A, et al. AAPM Medical Physics Practice Guideline 14.a: Yttrium-90 microsphere radioembolization. Med. Phys, 2023,25:1-28.

[3] Se Y, Jeffrey A, Yuni K. Correction for Collimator-Detector Response in SPECT Using Point Spread Function Template. IEEE Trans. Med. Imaging, 2013,32:295-305.

MIC-05-229

Evaluation of Cash C as a Cost Function for xSPECT Conjugate Gradient (#2962)

Francesc Massanes, Alexander H. Vija

Siemens Medical Solutions, MI SPECT Research, Hoffman Estates, USA

Abstract

xSPECT CG (Conjugate Gradient) SPECT reconstruction uses the Mighell Chi-Square (χ^2) statistic as its optimization cost function [3]. While effective under standard count conditions, the Mighell statistic is known to be suboptimal when Poisson statistics are poorly approximated at low counts. The Cash C statistic offers an alternative formulation derived from a modified chi-square for Poisson data, better suited to low-count regimes[2]. This work evaluates Cash C as a direct replacement for Mighell χ^2 in xSPECT CG, assessing resolution-noise trade-offs across count levels using a standard phantom. Resolution was quantified using a metric based on the approach described in [1], further developed here to handle arbitrary source-to-background contrasts. Cash C consistently achieved better noise properties at equivalent resolution compared to Mighell χ^2, with both algorithms converging to similar minimum resolution values 16.4 mm FWHM) at high update steps for the 8 mL sphere, confirming no loss of performance at high-count conditions. These characteristics are particularly relevant for clinical applications with limited count statistics, including cardiac SPECT [4] and emerging theranostic radiopharmaceuticals.

References

[1] A. H. Vija, “Characteristics of the xSPECT reconstruction method,” Siemens Healthineers, Molecular Imaging, White Paper, 2017.

[2] W. Cash, “Parameter estimation in astronomy through application of the likelihood ratio,” Astrophys. J., vol. 228, pp. 939–947, Mar. 1979, doi: 10.1086/156922.

[3] K. J. Mighell, “Parameter estimation in astronomy with Poisson-distributed data. I. The χ2 γ statistic,” Astrophys. J., vol. 518, pp. 380–393, Jun. 1999, doi: 10.1086/307253

[4] K. Nakajima, T. Shibutani, F. Massanes, T. Shimizu, S. Yoshida, M. Onoguchi, S. Kinuya, and A. H. Vija, “Myocardial perfusion imaging with retrospective gating and integrated correction of attenuation, scatter, respiration, motion, and arrhythmia,” J. Nucl. Cardiol., Sep. 2023, doi: 10.1007/s12350-023-03374-5.

MIC-05-232

Investigation of Ray Driven Collimator Detector Response Model for Multi-Photopeak SPECT Reconstruction (#3098)

Thibaut Merlin[1,3], Baptiste Laurent[1,3], Dimitris Visvikis[3]

[1] CHRU de Brest, Brest, France; [2] INSERM UMR1101 LaTIM, Brest, Germany; [3] LaTIM INSERM UMR 1101, Bâtiment 1, premier étage CHRU Morvan, Brest, France

Abstract

In SPECT imaging, accurate modeling of the collimator–detector response (CDR) function is essential for improving image resolution and quantitative accuracy. The CDR profile depends on several physical factors whose modeling can be complex and computationally demanding, particularly for multi-photopeak datasets, since the CDR, photon attenuation, and Compton scattering are energy dependent. In this work, we investigate the modeling of the CDR function using profiles generated through Monte Carlo simulations and its incorporation into the reconstruction process using a multi-line projector approach.
Monte-Carlo simulations were processed in order to generate CDRs of a SPECT intevo system with MELP collimator using 177Lu point sources located at different distances of the imaging system. These data were combined to generate CDR reponses for both 208kev and 113kev photopeaks. A multi-lines projector was implemented to integrate these profiles and processes the corrections specific to each photopeak. Simulations of NEMA IQP phantom was conducted to assess the proposed implementation, as well as phantom data acquired with the same system and variable source to collimator distance for each projections.
The proposed model improves the CRC-versus-noise trade-off as well as the overall image quality. Although increasing the number of projection lines enhances the signal-to-noise ratio, the evaluated metrics show limited improvement beyond a certain number of lines. These results suggest that for the studied acquisition and reconstruction setup, a reduced number of lines per detector channel may be sufficient to accurately model the CDR while limiting the computational cost of the reconstruction process.
Ongoing work includes the evaluation of the proposed implementation with different collimator geometries exhibiting various septal penetration and scattering characteristics. Future investigations will focus on simulations involving high-energy photon-emitting radionuclides.

MIC-05-235

Deep Kernel Gaussian Process Prior for Robust, Anatomically Guided Radiation Image Reconstruction (#3129)

Jaewon Lee, Javier Caravaca

Lawrence Berkeley National Laboratory, Applied Nuclear Physics (ANP), Berkeley, USA

Abstract
Newly emerging radiation imaging modalities—such as Compton camera imaging of alpha-emitting radiopharmaceuticals, positronium lifetime imaging, and dynamic PET imaging—frequently operate under count-starved, low signal-to-noise ratio (SNR) conditions, where the conventional maximum likelihood expectation maximization (ML-EM) algorithm is prone to severe overfitting. While recent neural network-based reconstruction methods have achieved impressive results, they require large amounts of task-specific training data, often neglect physics constraints, and largely lack principled uncertainty quantification frameworks.
In this work, we propose a Bayesian image reconstruction algorithm incorporating a Gaussian process (GP) prior with a neural network-based kernel, combining the robustness and principled uncertainty quantification of the GP framework with the representational flexibility of neural networks. The proposed method is highly robust against measurement noise, naturally incorporates physics constraints through the forward model, supports anatomically guided reconstruction through co-registered structural imaging data, and provides a full posterior covariance

characterization via variational inference. We demonstrate significant improvement in reconstruction quality over the conventional ML-EM algorithm alongside meaningful uncertainty estimates.

References
[1] Deep Kernel Learning, Wilson, AG, Hu, Z, Salakhutdinov, R & Xing, EP 2015, arXiv:1511.02222
[2] Radiation image reconstruction and uncertainty quantification using a Gaussian process prior, Lee, J, Joshi, TH, Bandstra, MS, Gunter, DL, Quiter, BJ, Cooper, RJ & Vetter, K 2024, Scientific Reports, vol. 14, p. 22958

MIC-05-238

ChameleonIQ: Bridging NEMA NU-2 and NU-4 Standards through Automated Image Analysis (#1243)

Edwing Y. Ulin-Briseño, Santiago Jiménez-Serrano, Antonio J. Gonzalez

CSIC-Universitat Politècnica de València, The Institute for Instrumentation in Molecular Imaging (I3M), Valencia, Spain

Abstract

Quantitative positron emission tomography (PET) requires standardized and reproducible image quality assessment to ensure comparability across scanners, protocols, and institutions. However, current workflows for NEMA-based evaluation often rely on manual region-of-interest (ROI) definition and fragmented analysis tools, limiting reproducibility and scalability. In this work, we present ChameleonIQ, an open-source, configuration-driven framework for automated PET image quality assessment. The platform supports both NEMA NU-2 2018 and NEMA NU-4 2008 protocols within a unified pipeline, providing automated ROI definition, deterministic metric computation, and structured reporting. Validation was performed using standardized IEC Body and NU-4 IQ phantoms. For the NEMA NU-2 protocol, contrast recovery ranged from 29.5% (10 mm sphere) to 55.1% (37 mm sphere), with background variability maintained between 6.1% and 7.0%. For the NEMA NU-4 phantom, recovery coefficients exceeded 0.8 for rods larger than 3 mm. The framework demonstrated high quantitative fidelity, achieving an average error in hot rod recovery of only 3.9% compared to reference manual evaluations. By providing a semi-automated pipeline that maintains this high precision while removing operator bias, ChameleonIQ facilitates efficient protocol optimization and multi-center benchmarking.

References
[1] Teoh, EJ, McGowan, DR, Macpherson, RE, Bradley, KM & Gleeson, FV 2016, 'Reproducibility of quantitative PET/CT imaging in multicenter trials', *European Journal of Nuclear Medicine and Molecular Imaging*, vol. 43, no. 7, pp. 1309-1318, Berlin, Heidelberg: Springer Berlin Heidelberg.
[2] National Electrical Manufacturers Association (NEMA) 2018, 'Performance Measurements of Positron Emission Tomographs', *NEMA Standard Publication*, NU 2-2018, Page 1-118, Rosslyn, Virginia: NEMA.
[3] National Electrical Manufacturers Association (NEMA) 2008, 'Performance Measurements of Small Animal Positron Emission Tomographs', *NEMA Standard Publication*, NU 4-2008, Page 1-56, Rosslyn, Virginia: NEMA.

[4] Cabrera-Martín, MN, Sánchez, D, Orcajo, MT, García-Cañamaque, L, Cussó, L, Desco, M & Vaquero, JJ 2021, 'Validation technique and improvements introduced in a new dedicated brain PET', *Revista Española de Medicina Nuclear e Imagen Molecular*, vol. 40, no. 4, pp. 239-248, Amsterdam: Elsevier.

[5] Sanchez, D, Lopez-Berenguer, F, Moliner, L, Ilisie, V, Gonzalez, AJ & Benlloch, JM 2024, 'Performance Evaluation of a High-Resolution PET Dedicated to Brain and Breast Imaging', *2024 IEEE Nuclear Science Symposium, Medical Imaging Conference and International Symposium on Room-Temperature Semiconductor Detectors (NSS MIC RTSD)*, pp. 1-3, Tampa, Florida: IEEE.

[6] Lopez-Berenguer, F, Sanchez, D, Moliner, L, Ilisie, V, Gonzalez, AJ & Benlloch, JM 2025, 'Evaluation of a PET Insert for Trimodal Imaging: A Step Towards PET/MRI-guided Focused Ultrasound', *IEEE Transactions on Radiation and Plasma Medical Sciences*, vol. 9, no. 1, pp. 1-1, Piscataway, New Jersey: IEEE.

MIC-05-241

Position-, direction- and contrast-dependent measurement of MLEM-reconstructed PET resolution using a 3D-printed cube (#1967)

Santiago Alvarado Orozco[1], Matthijs Sevenois[2], Georg Schramm[1]

[1] KU Leuven, Department of Imaging and Pathology, Leuven, Belgium; [2] UZ Leuven, Division of Nuclear Medicine, Leuven, Belgium

Abstract

The reconstructed spatial resolution of a PET image is determined by both intrinsic scanner properties and the chosen reconstruction algorithm. Standard NEMA measurements use point sources reconstructed with FBP and therefore mainly characterize the scanner. They are thus suboptimal for predicting the resolution of images reconstructed with MLEM and point-spread-function modeling, as is common in clinical practice.

We propose a 3D-printed resolution cube with an off-center inner compartment which, combined with a mid-acquisition phantom flip and a single reconstruction, produces sharp edges at finite (2:1) contrast along three orthogonal directions. Position-, direction- and contrast-dependent edge and line spread functions (ESFs, LSFs) are then extracted using smoothing-spline fits. As a proof of concept, the method is applied to the NeuroExplorer brain PET system at the isocenter and 10 cm off-center, with and without depth-of-interaction (DOI) modeling.

The LSFs are non-Gaussian with pronounced negative side lobes. With DOI, the resolution is approximately 2.5 mm FWHM in all directions at both positions; without DOI it degrades radially to about 4 mm at 10 cm off-center. Notably, differences between finite and infinite contrast are small in most configurations.

The method provides a position-, direction- and contrast-dependent characterization of PET resolution from clinically reconstructed images and complements NEMA point-source values for image quality comparison, harmonization and partial volume correction.

MIC-05-244

Evaluation of Motion Correction Methods on the NeuroEXPLORER Using Multi-Tracer Human Data (#2130)

Jiazhen Zhang, Tianyi Zeng, Yifan Hu, Kathryn Fontaine, Tommaso Volpi, Takuya Toyonaga, Richard E. Carson

Yale University, New Haven, USA

Research funding support: U01EB029811.

Abstract

Accurate motion correction is critical for dynamic brain PET, particularly on the high-resolution NeuroEXPLORER (NX), where residual head motion can blur focal targets and bias time-activity curves (TACs). We evaluated multiple motion correction (MC) strategies using 17 multi-tracer human NX PET scans, including no motion correction (NMC), post-reconstruction registration (PRR), registration before attenuation correction (RBA), UMT-based frame-averaged correction (AVG), and UMT-based event-by-event correction (EBE). Performance was assessed using qualitative image comparison and ROI-based residual TAC variability ($\%SD_{res}$) from 20-70 min. All MC methods reduced $\%SD_{res}$ compared with NMC. Across all tracers, subjects, and ROIs, EBE achieved the lowest residual variability (1.40 ± 1.27%), followed by PRR (1.79 ± 1.49%), RBA (1.94 ± 1.64%), AVG (2.01 ± 1.63%), and NMC (4.68 ± 4.26%). Poisson noise-floor analysis further showed that residual motion effects were tracer- and count-statistics-dependent. Overall, UMT-based EBE provided the most effective reduction of residual motion effects in dynamic NX brain PET.

References

[1] T. Volpi, et al., "Exceptional brain PET images from the NeuroEXPLORER: scans with targeted radiopharmaceuticals and comparison to HRRT," *EJNMMI*, 2026.

[2] E. M. Revilla, et al., "Adaptive data-driven motion detection and optimized correction for brain PET," *Neuroimage*, 2022.

[3] Z. Cai, et al., "PET Head Motion Estimation Using Supervised Deep Learning with Attention," *IEEE TMI*, 2025.

[4] T. Zeng, et al., "Validation and application of markerless head motion tracking for a next-generation brain PET scanner," *IEEE MIC*, 2023.

[5] T. Zeng, et al., "Optimization of Brain PET Markerless Head Motion Correction in a Large Human Cohort," *EJNMMI Physics*, 2026.

[6] K. Fontaine, et al., "MOLAR-NX: building a PET reconstruction framework for exploring the novel features provided by the NeuroEXPLORER," *IEEE MIC*, 2024.

[7] J. Zhang, et al., "Cranberry: Combined Rigid and Nonrigid Event-by-Event Motion Correction at Yale," *IEEE MIC*, 2025.

[8] C. Sun, et al., "An objective evaluation method for head motion estimation in PET—motion corrected centroid-of-distribution," *Neuroimage*, 2022.

[9] J. Zhang, et al., "Evaluation of motion correction quality in brain, face, and neck for NeuroEXPLORER," *SNMMI*, 2024.

MIC-05-247

A Clinically Viable, Scalable Implementation of Monte Carlo Scatter Correction for PET/CT (#2119)

Danielle Zeltser[1], Ester Hait-Fraenkel[1], Xuezhu Zhang[2], Michal Edelstein[1], Gali Elkin-Basudo[1], Yaniv Mizrachi[1], Yariv Grobshtein[1]

[1] GE HealthCare, Molecular Imaging, Haifa, Israel; [2] GE HealthCare, Molecular Imaging, Waukesha, USA

Abstract

Monte Carlo scatter correction is well established as a highly accurate approach for scatter estimation in PET/CT imaging. It demonstrates superior robustness compared with model based scatter estimation methods, particularly under extreme variations in activity distribution and in the presence of patient motion, conditions under which model based approaches often produce artifacts. Despite these advantages, Monte Carlo scatter correction is computationally intensive, and does not inherently account for out-of-field scatter. In this work, we address both limitations and propose an implementation suitable for integration into routine clinical workflows. A multi-GPU implementation, as well as parallel processing with efficient data streaming significantly reduce the processing time. To handle out-of-field scatter, we separately handle regions where information about out-of-field distribution is known, and can be used for a highly precise estimation. In regions where out-of-field information is inaccessible, the effect on scatter is approximated by the measured data, while ensuring a smooth transition in which the high-accuracy region governs the final estimate. Our approach is scalable and robust across system designs ranging from a standard axial field-of-view to a long axial field-of-view, each presenting distinct considerations for scatter estimation. We demonstrate the effectiveness of our method using phantom and clinical data.

MIC-05-250

Down-Scatter Correction for PET-induced contamination in simultaneous PET&SPECT imaging (#2341)

Hengyi Li[1,2], Hang Yang[1], Xiangtao Zeng[1], Ming Niu[1], Jing Wu[3], Zheng Gu[1]

[1] Shenzhen Bay Laboratory, Institute of Biomedical Engineering, Shenzhen, China; [2] Harbin Institute of Technology (Shenzhen), International Research Institute for Artificial Intelligence, Shenzhen, China; [3] Beijing Normal University, School of Physics and Astronomy, Beijing, China

This work is supported by the National Key R&D Program of China (No. 2023YFC2414800), the Major Program of Shenzhen Bay Laboratory (No. C1012530005), the National Natural Science Foundation of China (Nos. 12275182 and 62371314), Guangdong Basic and Applied Basic Research Foundation (Nos. 2024A1515012154), the Guangdong Provincial Project (Grant No. 2023TQ07A233) and the Shenzhen Bay Laboratory Proof-of Concept Grants (No. C1022430005).

Abstract

In simultaneous PET&SPECT imaging, PET-induced down-scatter contaminates SPECT data, degrading image quality and quantitative accuracy. This study presents a correction method that estimates PET down-scatter based on PET source modeling and corrects contaminated SPECT data to suppress PET interference.

A PET&SPECT simultaneous imaging system is modeled using GATE Monte Carlo simulation. The system adopts a dual-head detector rotating around the field of view. An image quality phantom consisting of background region, cold region, and multiple PET and SPECT hot regions is simulated to evaluate cross-modality interference. PET and SPECT activities are modeled using 511 keV annihilation photons and 140 keV gamma photons. A uniform PET activity distribution is simulated to establish a voxel-wise PET down-scatter contribution model. The actual PET activity distribution is obtained from reconstructed PET images, and the corresponding down-scatter components are estimated from the model and subtracted from the SPECT projections.

Experimental results demonstrate that PET-induced down-scatter significantly degrades SPECT projections and reconstructed image quality. The auxiliary energy window (AEW) method partially mitigates this degradation, while the proposed method achieves more effective suppression, yielding images closer to a pure SPECT reference. Quantitative evaluation shows that the proposed method outperforms AEW in terms of spillover ratio and contrast, confirming its effectiveness in simultaneous PET&SPECT imaging.

References
[1] X. Zeng, H. Yang, M. Niu, et al., “Tri-Mode PET, SPECT, and PET&SPECT Imager Using a Novel Scintillator-as-Collimator Detector,” 2025 IEEE NSS MIC and RTSD, Yokohama, Japan, 2025.
[2] R. Yao, T. Ma, Y. Shao, et al., “PET and SPECT dual-tracer imaging: correction of 511 keV photon’s down-scatter effect on SPECT,” presentation in 2007 IEEE Nuclear Science Symposium Conference Record.
[3] Y. Zhao, C. Huang, X. Zeng, et al. “Validation of an Optimized DOI-Capable Shared PET&SPECT Detector based on a Scintillator-as-Collimator Structure” 2026 IEEE NSS MIC and RTSD, submitted.

MIC-05-253

A Quantitative Reconstruction Framework for Variable-Pitch Multi-Layer DOI Brain PET (#2420)

Yihao Chen[1], Yue Chen[1], Xiangtao Zeng[2], Ming Niu[2], Zheng Gu[2], Jianyong Jiang[1]

[1] Beijing Normal University, School of Physics and Astronomy, Beijing, China; [2] Shenzhen Bay Laboratory, Institute of Biomedical Engineering, Shenzhen, China

This work was supported in part by the NSFC (No. 12475336), the FRFCU (No. 310400209521), the BNSF (QY25290), and the NKRDP (No. 2023YFC2414800).

Abstract

A dedicated brain positron emission tomography (PET) system utilizing multi-resolution depth-of-interaction (DOI) detectors is under development at Shenzhen Bay Laboratory. These detectors employ variable-pitch, multi-layer scintillators to optimize intrinsic spatial resolution and coincidence timing resolution while minimize parallax errors. However, the multi-resolution architecture introduces structural and detection heterogeneities that complicate quantitative image reconstruction. This study proposes an extended quantitative correction framework to address these challenges. We adapted standard component-based normalization (CBN) and single scatter simulation (SSS) via sub-layer-based geometric modeling to achieve layer-specific normalization and scatter correction. Specifically, a 3D fan-sum method was implemented to calculate crystal efficiencies by treating lines of response (LORs) within shared DOI layers as independent subsystems. Furthermore, a likelihood-based optimization framework was formulated to derive layer-specific scatter multipliers, compensating for detection biases caused by inter-layer shielding and axial sensitivity fluctuations. The framework was validated using GATE simulations. Ablation studies on uniform cylinder data confirmed the necessity of the integrated correction suite for spatial uniformity. Quantitative evaluation of a custom IQ phantom yielded contrast recovery coefficients (CRC) of 84.53%–65.13% and background variability (BV) of 1.69%–3.07% for spheres ranging from 37.0 to 13.0 mm. Reconstructed Derenzo phantom images resolved 1.0 mm rods at both central and off-center positions, validating its high spatial resolution. Finally, digital brain phantom studies indicate that the system's imaging performance is visually comparable to the NeuroEXPLORER benchmark.

References
[1] Huang, S et al. 2026, "Optimization of TOF and DOI Performance in a Multi-Resolution Detector for Brain-Dedicated PET", IEEE Transactions on Radiation and Plasma Medical Sciences, 10(3), 380-390, New York: IEEE
[2] Yuan, Z et al. 2026, "GPU-based list-mode TOF PET image reconstruction with complete correction techniques", Medical Physics, 53, e70216, Hoboken, NJ: John Wiley & Sons
[3] Li, H et al. 2024, "Performance Characteristics of the NeuroEXPLORER, a Next-Generation Human Brain PET/CT Imager", Journal of Nuclear Medicine, 65(8), 1320-1326, Reston, VA: Society of Nuclear Medicine and Molecular Imaging

MIC-05-256

Intra-frame motion correction for dynamic PET using mutual information-based registration (#2653)

Simon Noë[1], Matthew Spangler-Bickell[2], Ahmadreza Rezaei[1], Johan Nuyts[1], Georg Schramm[1]

[1] KU Leuven, Department of Imaging and Pathology, Nuclear Medicine & Molecular imaging, Leuven, Belgium; [2] GE HealthCare, Waukesha, USA

This work was supported by a KU Leuven C2 grant (3M220301): "Motion compensation for PET in TOF-PET/CT and TOF-PET/MR brain imaging".

Abstract

Patient motion remains a challenge for dynamic positron emission tomography (PET) imaging of the brain, due to long acquisition times. Data-driven registration-based motion estimation for static PET using sum of squared differences or normalized cross correlation as alignment metric (while popular for their simplicity and generalization potential) are not suitable for dynamic PET, as they cannot handle the changing tracer distribution throughout the scan. Alternative methods for dynamic PET motion estimation rely on the availability of a good kinetic model or suitable training data for deep learning, reducing their generalization potential. We therefore propose a registration method based on mutual information that makes it suitable for dynamic PET, and included the motion estimates in a listmode reconstruction using event-by-event motion correction. We tested this approach for 3 tracers on 2 patient scans each.

References
[1] Kyme, AZ, Fulton, RR 2021, 'Motion estimation and correction in SPECT, PET and CT', *Phys. Med. Biol.*, vol. 66, no. 18, p. 18TR02
[2] Spangler-Bickell, MG et al. 2022, 'Evaluation of Data-Driven Rigid Motion Correction in Clinical Brain PET Imaging', *J. Nucl. Med.*, vol. 63, no. 10, pp. 1604–1610
[3] Jiao, J et al. 2017, 'Direct Parametric Reconstruction With Joint Motion Estimation/Correction for Dynamic Brain PET Data', *IEEE Trans. Med. Imaging*, vol. 36, no. 1, pp. 203–213
[4] Sun, T, Wu, Y, Bai, Y, Wang, Z, Shen, C, Wang, W, Li, C, Hu, Z, Liang, D, Liu, X, Zheng, H, Yang, Y, Wang, M 2022, 'An iterative image-based inter-frame motion compensation method for dynamic brain PET imaging', *Phys. Med. Biol.*, vol. 67, no. 3, p. 035012
[5] Sundar, LKS et al. 2021, 'Conditional Generative Adversarial Networks Aided Motion Correction of Dynamic 18F-FDG PET Brain Studies', *J. Nucl. Med.*, vol. 62, no. 6, pp. 871–87

MIC-05-259

Head Motion Correction Improves Machine Learning Classification of Alzheimer's Disease from PET (#2752)

Eléonore V. Lieffrig[1], Takuya Toyonaga[2], Jiazhen Zhang[1], John Onofrey[1,2]

[1] Yale University, Department of Biomedical Engineering, New Haven, USA; [2] Yale University, Department of Radiology and Biomedical Imaging, New Haven, USA; [3] Yale University, Department of Urology, New Haven, USA

No funding was received to conduct this study. The authors have no relevant financial or non-financial interests to disclose.

Abstract

Head motion during PET data acquisition is a common source of artifact that degrades image quality and biases tracer uptake quantification. We hypothesize that motion correction improves the performance of a machine learning (ML) classifier for Alzheimer's disease versus cognitively normal subjects using brain PET images alone. A ResNet10 feature extractor combined with a Support Vector Machine classifier was applied to two cohorts encompassing a total of 301 ^{11}C-UCB-J and ^{18}F-FDG PET. On motion-corrected images, the classifier achieved AUROC of 0.96 (^{11}C-UCB-J) and 0.94 (^{18}F-FDG), with accuracy increases of 5% and 10%, respectively, when motion correction was applied. Our results highlight the critical need for efficient motion correction solutions to enable effective ML analysis of PET AD imaging.

References

[1] E. Passeri et al., “Alzheimer’s disease: Treatment strategies and their limitations,” Int. J. Mol. Sci., vol. 23, no. 22, p. 13954, 2022
[2] A. P. Mecca et al., “Synaptic density and cognitive performance in Alzheimer’s disease: A PET imaging study with [11C]UCB-J,” Alzheimer’s Dement., vol. 18, no. 12, pp. 2527–2536, 2022
[3] M. H. Azmi et al., “18F-FDG PET brain images as features for Alzheimer classification,” Proc. 13th Int. Symp. Rad. Phys., 2017
[4] B.-H. Yang et al., “Classification of Alzheimer’s disease from 18F-FDG and 11C-PiB PET imaging biomarkers using support vector machine,” J. Med. Biol. Eng., vol. 40, no. 4, pp. 545–554, 2020
[5] S. W. Park et al., “Deep learning application for the classification of alzheimer’s disease using 18fflortaucipir (av-1451) tau positron emission tomography” Sci. Rep., vol. 13, no. 1, 2023
[6] X. Jin et al., “Evaluation of motion correction methods in human brain PET imaging - a simulation study based on human motion data,” Med. Phys., vol. 40, no. 10, 2013
[7] R. E. Carson et al., “Design of a motion-compensation OSEM list-mode algorithm for resolution-recovery for the hrrt,” in 2003 IEEE NSS Conf. Rec., pp. 3281–3285
[8] K. He et al., “Deep residual learning for image recognition,” in 2016 IEEE CVPR, 2016
[9] S. Chen et al., “Med3D: Transfer learning for 3D medical image analysis,” arXiv:1904.00625, 2019

MIC-05-262

CT-less Data Corrections For Dedicated Cardiac PET Scanners (#2950)

Florence M. Muller[1,2], Shweta Majumder[1,3], Elizabeth J. Li[1], Margaret E. Daube-Witherspoon[1], Paco Bravo[1], Michael J. Parma[1], Joel S. Karp[1], Suleman Surti[1]

[1] University of Pennsylvania, Department of Radiology, Philadelphia, USA; [2] Ghent University, Faculty of Engineering and Architecture, Ghent, Belgium; [3] University of Pennsylvania, Department of Bioengineering, Philadelphia, USA

This work was supported by the Research Foundation Flanders (F Muller: 11P0E24N0) and the National Institutes of Health, R01-CA113941 (J Karp, PI), R01-EB035103 (S Surti, PI), and R01-HL137984 (P Bravo, PI). We are grateful to C. Tschabrunn for support of animal imaging. Data Courtesy (from UPenn): J. Dubroff, C. Wiers, E. McDonald, N. Taunk.

Abstract

This work develops and evaluates CT-less data correction methods for quantitative cardiac PET by combining deep learning-based attenuation correction (DLAC) with energy-based scatter (EBS) estimation. Robustness was assessed in three human FDG studies spanning a wide BMI range (24-50 kg/m²). DLAC showed stable performance across BMI groups, with mean myocardial SUV biases below 5% relative to CT-based AC (with single scatter simulation). For a low BMI case, the DLAC+EBS method resulted in low myocardial SUV bias (mean: 1.7%, P_5-P_{95}: [–2.1%, 10.8%]) relative to standard CT-based reconstruction. To assess generalization, the DLAC model (originally trained on supine non-cardiac human data) was extended to cardiac ^{82}Rb studies in pigs using transfer learning. These pig studies served as a surrogate for evaluating whether the network could be adapted to other imaging conditions (cross-tracer, cross-species, and other patient positionings, e.g., seated cardiac imaging) with limited re-training. With limited additional pig data (n=8), relative biases in mean myocardial SUV decreased to within 2%. Overall, these findings support CT-less data correction for cardiac PET systems.

References
[1] McMillan AB, Bradshaw TJ. (2021) AI-based data corrections for attenuation and scatterin PET and SPECT. *PET Clin.*

[2] Efthimiou N, Karp JS, and Surti S. (2022) Data-driven, energy-based method for estimation of scattered events in positron emission tomography. *PMB*.
[3] Muller FM, *et al.*, (2025)Deep Learning-based Attenuation Correction in TOF-PET using Histo-Image Data Partitioning and Dual-View Scouts. *Presented at IEEE MIC*.
[4] Majumder S, *et al.*, (2026) Evaluation of Data-Driven Energy-based Scatter Estimation and Correction in Positron Emission Tomography. *Presented atSNMMI*.

MIC-05-265

AmyPET: A Comprehensive Automated Framework for Static and Dynamic NeuroPET Quantification (#3013)

Pawel J. Markiewicz[1,2], Ariane Bollack[3,4], Kjell Erlandsson[5], Alle Meije Wink[6], Maqsood Yaqub[6], Lyduine E. Collij[6], Nienke Dijk[6], Robin Wolz[7], Richard Manber[7], David Vállez García[8,9], Beverley Holman[2], Teresa Szyszko[2], Alexander Hammers[10,11], Juan Domingo Gispert López[8], Frederik Barkhof[4,6]

[1] London South Bank University, School of Computer Science and Digital Technology, London, UK; [2] Royal Free Hospital, London, Nuclear Medicine, London, UK; [3] GE HealthCare, Chalfont St Giles, UK; [4] University College London, Medical Physics and Biomedical Engineering, Hawkes Institute, London, UK; [5] University College London, Institute of Nuclear Medicine, London, UK; [6] Vrije Universiteit, Amsterdam UMC, Department of Radiology & Nuclear Medicine, Amsterdam, Netherlands; [7] IXICO, London, Tanzania; [8] Barcelonaβeta Brain Research Center (BBRC), Pasqual Maragall Foundation, Barcelona, Spain; [9] Hospital del Mar Medical Research Institute (IMIM), Barcelona, Spain; [10] King's College London, School of Biomedical Engineering and Imaging Sciences, London, UK; [11] King's College London, King's College London & Guy's and St Thomas' PET Centre, London, UK

This work was supported by the Innovative Medicines Initiative 2 Joint Undertaking under grant agreement No 115952 (European Union's Horizon 2020), the UK MRC partnership grant (MR/N025792/1) and London South Bank University.

Abstract
Existing software solutions for PET quantification in neurological disorders remain fragmented and lack comprehensive end-to-end pipelines suitable for multi-site studies involving heterogeneous tracers, and scanners, including Total-Body PET systems. We present AmyPET, an open-source toolkit for automated end-to-end preprocessing and quantification of static and dynamic PET data directly from raw DICOM images. The framework supports processing in both native and MNI image spaces and integrates multiple brain atlases, motion correction, partial volume correction, and harmonised analysis within a single modular environment.
AmyPET comprises four integrated processing engines for static and dynamic PET analysis: (1) an alignment engine for moderate motion correction based on a novel displacement metric, (2) spatial normalisation and tissue segmentation, (3) regional sampling and image extraction, and (4) a post-processing engine enabling kinetic modelling, Centiloid quantification, and additional quantitative analyses, including dual-time-window acquisitions. Automated quality-control outputs are generated for all processing stages. The framework has been calibrated against the GAAIN reference datasets for amyloid PET and is extensible to tau and TSPO tracers.
Validation was performed using multiple amyloid PET cohorts, including test–retest studies, an amnestic mild cognitive impairment cohort, and the AMYPAD Prognostic and Natural History Study comprising more than 1500

scans. AmyPET demonstrated high repeatability (within-subject coefficient of variation, wCV=3.5%; ICC>0.98) and strong agreement with established clinical and research pipelines (R^2>0.96), supporting its use as a robust and scalable framework for quantitative neuroPET imaging.

References
[1] Markiewicz, PJ, Thompson, G, Wardlaw, JM et al. 2026, The Dementias Platform UK PET/MR harmonisation and test-retest study: assessment of PET repeatability and reproducibility across the national network. *Eur J Nucl Med Mol Imaging*. https://doi.org/10.1007/s00259-026-07885-4
[2] Bollack A, Schwarz AJ, et al., 2026, Comparability of Centiloid values from [^{18}F]flutemetamol scans using seven commercial and research software, *NeuroImage: Reports*. https://doi.org/10.1016/j.ynirp.2026.100343

[4] Markiewicz, Pawel J., Julian C. Matthews, John Ashburner, et al. 2021, Uncertainty Analysis of MR-PET Image Registration for Precision Neuro-PET Imaging.*NeuroImage*. https://doi.org/10.1016/j.neuroimage.2021.117821.
[3] Bollack, Ariane, Mahnaz Shekari, Lyduine E. Collij, et al. 2025, Implementing Robust Amyloid PET Quantification in Multi-Center Studies: AMYPAD Approach to Address Data Acquisition, Processing, Interpretation and Data Sharing Challenges. *Alzheimer's & Dementia: Translational Research & Clinical Interventions*. https://doi.org/10.1002/trc2.70190.

MIC-05-268

SSS Optimised for Monte Carlo Scatter Estimation for PET (#3060)

Antonia Reeves[3,2], SeyedAmir ZamanPour[1], Simon Noe[1], Simon Arridge[4], Kris Thielemans[2,3]

[1] KU Leuven, Department of Imaging and Pathology, Leuven, Belgium; [2] University College London, Institute of Nuclear Medicine and the Hawkes Institute, London, UK; [3] University College London, Department of Medical Physics and Biomedical Engineering, London, UK; [4] University College London, Department of computer science, London, UK

This work was supported by the i4Health Centre for Doctoral Training, UCL and GE Healthcare. Software used in this project is maintained by CCP SyneRBI (UKRI support: EPSRC grant EP/T026693/1 and STFC through the DRI programme).

Abstract
Recent increases in computational power as well as new tools being more readily available have led to increased interest in Monte Carlo scatter estimation. However, Monte Carlo scatter simulation is still computationally expensive. This is exacerbated by the fact that model-based scatter estimation requires multiple iterations of scatter simulation and image reconstruction. We propose to combine the current clinical standard (analytic single scatter simulation and tail-fitting) with Monte Carlo scatter simulation.

MIC-05-271

Quantitative Activities Evaluation of Ac-225 and Daughter Nuclides Using the Alpha-SPECT Mini System (#3094)

Wenbo Zhao[1], Xuhan Luo[1], Ling-Jian Meng[2], Yong Du[1]

[1] Johns Hopkins University School of Medicine, Baltimore, USA; [2] University of Illinois at Urbana and Champaign, Champaign Il, Champaign, USA

This research was funded by National Institutes of Health, grant number S10OD038221. The content is solely the responsibility of the authors and does not necessarily represent the official views of the National Institutes of Health.

Abstract

The Alpha-SPECT Mini system integrates SPECT imaging with CT-based attenuation correction, providing a platform for quantifying in vivo distributions of alpha-emitting radiopharmaceuticals and daughter radionuclides. In this study, three Ac-225 filled syringes with different volumes, 0.5, 4.2, and 18.0 mL, respectively, were scanned with Alpha-SPECT Mini. The ground truth activities were[YD1] 26.12 μCi, 21.62 μCi, and 18.80 μCi from the smallest to the largest syringe, respectively. SPECT listmode acquisition was performed for 20 minutes for each syringe, together with an 80 kV CT scan for attenuation correction. SPECT images were reconstructed for the following photopeaks: 100 keV for Ac-225, 218 keV for Fr-221, 440 keV for Bi-213, and 117 keV for Tl-209. Activities of Ac-225 and these daughter radionuclides, were then estimated from SPECT images using CT defined ROIs and compared with ground truth.

The results showed that quantification accuracy varied with the radionuclides and syringe sizes. Fr-221 and Bi-213 showed relatively lower errors (<5%), while Ac-225 and Tl-209 exhibited larger deviations. The higher errors likely due to the low abundance of low energy (100 keV for Ac-225 and 117 keV for Tl-209) photopeaks and interference from downscatter and collimator penetration from high energy photons. Tl-209 also exhibited larger deviations with a size-dependent trend, suggesting sensitivity to source geometry and scatter correction. Overall, the Alpha-SPECT Mini system showed potential for quantitative imaging of Ac-225 and daughter radionuclides. Future work includes further calibration and implementation of scatter correction.

MIC-05-274

Exploring a Novel Timing Calibration Approach for a Brain-Dedicated Time-of-Flight PET Scanner (#1341)

James D. Ho[1], Muhammad N. Ullah[2,3], Garry Chinn[2,3], Grant H.-S. Park[5], Eegan Ram[1], Wonu Park[5], Craig S. Levin[2,3]

[1] Stanford University, Physics, Stanford, USA; [2] Stanford University, Radiology, Stanford, USA; [3] Stanford University, Molecular imaging, Stanford, USA; [4] Stanford University, Bioengineering, Stanford, USA; [5] Stanford University, Electrical Engineering, Stanford, USA; [6] Stanford University, Engineering Physics, Stanford, USA

Some of the computing for this project was performed on the Sherlock cluster. We would like to thank Stanford University and the Stanford Research Computing Center for providing computational resources and support that contributed to these research results.
This work was supported in part by NIH-NIBIB Grant 5R01EB03103804

Abstract
PETcoil Gen II is a novel MRI-compatible time-of-flight (TOF) PET system for simultaneous PET-MRI brain imaging. Current calibration uses an annulus phantom to correct time skew on a per line-of-response (LOR) basis, leading to a large number of correction factors (order n^2). We propose a convex-optimization calibration method to calculate and store per-channel (order n) time skew offsets using rod phantoms. We evaluate the method using simulated annulus and rod phantoms with known applied skew offsets and point-source validation. The proposed per-channel approach achieves a mean absolute timing error of 19.9 ps (annulus-based) and 18.8 ps (rod-based) compared to 142 ps for the per-LOR method. When applied to point-source correction, the proposed approaches improve coincidence time resolution (CTR) performance by +18.7\% and 13.4\% using annulus and rod phantoms respectively, whereas the per-LOR approach resulted in a -70.0\% degradation relative to uncorrected data. Results demonstrate improved calibration accuracy and robustness in using rod-based phantoms. Future work will validate these methods experimentally and assess the quality of reconstructed images.

References
[1] Dong, Q. (2023). "PETcoil: A second-generation RF-penetrable TOF-PET insert for simultaneous brain PET/MRI". Order No. 31017900. PhD thesis. Stanford University.
[2] Park, S.-J. et al. (2006). "Digital Coincidence Processing for the RatCAP Conscious Rat Brain PET Scanner". In: 2006 *IEEE Nuclear Science Symposium Conference Record*. Vol. 5, pp. 3045–3048. DOI: 10 . 1109 / NSSMIC . 2006 . 356516.
[3] Reynolds, P. D. et al. (2011). "Convex optimization of coincidence time resolution for a high-resolution PET system". In: *IEEE Transactions on Medical Imaging* 30.2, pp. 391–400. DOI: 10.1109/TMI.2010.2080282.
[4] Ullah, M.N. et al. (2024). "Data Correction and Imaging Studies for PETCoil: A Second-Generation RF-Penetrable Brain TOF-PET Insert for Simultaneous PET/MRI". In: 2024 *IEEE Nuclear Science Symposium (NSS), Medical Imaging Conference (MIC) and Room Temperature Semiconductor Detector Conference (RTSD)*, pp. 1–2. DOI: 10.1109/NSS/MIC/RTSD57108.2024.10655515

MIC-05-277

Preliminary Study on Thick-Slab Image Generation of Digital Breast Tomosynthesis (#1451)

Subong Hyun[1], Donghyun Kim[1], Seoyoung Lee[1,2], Dohyun Lim[1], Seungryong Cho[1]

[1] KAIST, Nuclear and quantum engineering, Daejeon, South Korea; [2] Mayo clinic, Radiology, Rochester, USA

This work was supported in part by the Korean National Research Foundation (Grant Nos. RS-2026-25492331 and RS-2023-00285089)

Abstract

Digital breast tomosynthesis (DBT) improves lesion detection compared with 2D digital mammography (DM), but its large number of reconstructed slices leads to increased reading time and workload for radiologists. As a potential solution, thick-slab image generation can be used to combine adjacent reconstructed slices into fewer representative slab images. However, conventional slab generation methods typically rely on simple slice-combination strategies, such as maximum intensity projection (MIP) or average intensity projection (AIP) of adjacent slices, which may reduce image sharpness and obscure diagnostically relevant details. To overcome these limitations, we propose a new thick-slab image generation method. For each slab, the proposed method adaptively blends a representative slice with the corresponding MIP image. The representative slice is selected from the DBT slices within the slab based on linear structure information obtained using the oriented bins method. The blending map is generated by applying a 1D high-pass filter to the MIP image along the X-ray source travel direction. Using a numerical phantom, the proposed method was compared with conventional MIP- and AIP-based slab generation methods and showed improved image sharpness and structural preservation. These preliminary results suggest that the proposed thick-slab image generation method has the potential to reduce DBT review time by decreasing the number of images to be reviewed without substantial loss of diagnostically relevant information.

References

[1] Pujara, A. C., Joe, A. I., Patterson, S. K., Neal, C. H., Noroozian, M., Ma, T., Chan, H.-P., Helvie, M. A., and Maturen, K. E. 2020, 'Digital Breast Tomosynthesis Slab Thickness: Impact on Reader Performance and Interpretation Time', *Radiology*, 297(3), 534–542.

[2] Dustler, M., Andersson, M., Förnvik, D., Timberg, P., and Tingberg, A. 2013, 'A study of the feasibility of using slabbing to reduce tomosynthesis review time', *Medical Imaging 2013: Image Perception, Observer Performance, and Technology Assessment*, Proc. SPIE 8673, 86731L, Bellingham, WA: SPIE.

[3] Kim, H., Hong, J., Lee, T., Choi, Y. W., Kim, H. H., Chae, E. Y., Choi, W. J., and Cho, S. 2020, 'A synthesizing method for signal-enhanced and artifact-reduced mammogram from digital breast tomosynthesis', *Physics in Medicine and Biology*, 65(21), 215026.

MIC-05-280

Torch-Enabled STIR: Validation on CPU and GPU (#1661)

Nikos Efthimiou[1], Zekai Li[1], Valerio Cosmi[1], Kris Thielemans[2], Charalampos Tsoumpas[1]

[1] UMCG, Department of Nuclear Medicine, Groningen, Netherlands; [2] UCL, Institute of Nuclear Medicine, London, UK

Charalampos Tsoumpas, Nikos Efthimiou and Zekail Li are supported by the NWO AES Vici Talent program (doi: 10.61686/REEAR02777). Zekai Li was also supported by a Joint Scholarship from the China Scholarship Council and the University of Groningen (202210100011) and his placement at UCL by EPSRC CCP in Synergistic Reconstruction for Biomedical Imaging (EP/T026693/1). This work used the Dutch national e-infrastructure with the support of the SURF Cooperative using grant no. EINF-18121. STIR is partially maintained by CCP SyneRBI which is funded by the EPSRC grant EP/T026693/1 and by STFC through the UKRI Digital Research Infrastructure programme

Abstract

STIR is a widely used open-source framework for PET and SPECT image reconstruction; here we explored PyTorch as an alternative array backend for STIR. We replaced the STIR arrays with a tensor-based variant while preserving the existing reconstruction framework and backwards compatibility. Correctness was assessed using existing and newly developed unit tests. Performance was evaluated with dense arithmetic benchmarks, stir_timings, and stir_math. For image-based operations, the tensor backend accelerated in-memory processing, with the largest gains observed for larger volumes. In projection-data workflows, initial performance was limited by layout-conversion and storage overhead, but targeted optimization substantially reduced these costs. In projection-data stir_math tests, the Torch-backed implementation was faster than the native STIR Array backend in end-to-end execution, with gains of roughly 7% to 23% depending on the operation. Initial GPU benchmarking further showed that the tensor backend can exploit consumer GPU hardware for dense arithmetic, achieving an approximate 3.7x speedup over CPU in the tested workload. However, projector-style kernels based on sparse, irregular scalar access did not yet benefit consistently from direct backend substitution, indicating that these critical paths require further redesign.

References

[1] Thielemans, K, Tsoumpas, C, Mustafovic, S, Beisel, T, Aguiar, P, Dikaios, N & Jacobson, MW 2012, 'STIR: software for tomographic image reconstruction release 2', *Physics in Medicine and Biology*, vol. 57, no. 4, pp. 867–883.

MIC-05-283

Post-Reconstruction Spill-In Correction Methods in Lung PET Under Heterogeneous Conditions (#1891)

Claire J. Brooks[1], David Perez-Benito[1], María Felipe-Maestre[1], Céline Mayet[2], Candie Joly[2], Julien Lemaitre[2], Thibaut Nanink[2], Roger Le Grand[2], Juan José Vaquero[1,3]

[1] Universidad Carlos III de Madrid, Departamento de Bioingeniería, Leganés, Spain; [2] Immune Diseases, Microbiology and Innovative Therapies, Université Paris-Saclay, INSERM, CEA U1184 IMVA-HB/IDMIT, Fontenay-aux-Roses, France; [3] Instituto de Investigación Sanitaria Gregorio Marañón, Madrid, Spain

This work has received support from the Innovative Medicines Initiatives 2 Joint Undertaking (grant No 853989 ERA4TB). This work reflects only the author's views, and the JU is not responsible for any use that may be made of the information it contains.

Abstract

Accurate quantification of pulmonary PET activity is often limited by spill-in contamination from adjacent tissues. Although reconstruction-based partial volume correction techniques effectively reduce resolution-related blurring, residual spill-in can remain significant in pulmonary analysis due to respiratory motion and proximity to high-uptake extrapulmonary structures. Post-reconstruction correction methods often assume homogeneous activity within clearly defined anatomical compartments, assumptions not satisfied in inflammatory whole-lung volumes. As a result, manual refinement of the lung boundary is often necessary but is also time-intensive. Here, we compare three automatic post-reconstruction spill-in correction strategies in 18F-FDG PET scans of tuberculosis-infected macaques, using manually refined lung masks as a reference. Two methods directly adjust PET values within the lung: the first estimates spill-in from local background activity, while the second applies a more conservative correction using extrapulmonary hotspots. The third method automates conventional morphological mask refinement by adjusting the lung boundary. The value-based spill-in correction methods achieved higher agreement with manual refinement (mean log ratio 0.032 and 0.116) but showed greater sensitivity to boundary perturbation, whereas morphological correction showed lower boundary sensitivity but systematically underestimated uptake (mean log ratio -0.408). These findings suggest that localized spill-in correction methods may provide a practical alternative to manual mask refinement in 18F-FDG PET pulmonary imaging by reducing extrapulmonary contamination while preserving anatomical boundaries.

MIC-05-286

Data-Driven Motion Artifact Correction for Wearable PET (#2279)

Kaiming Hu[1,2], Ruiqing Meng[1,2], Han Liu[1,2], Wenkang Qu[1], Yuejie Lin[1], Xin Yu[1], Da Liang[1], Ying Lin[1], Xiaoying Zhang[1], Jingyong Tao[1], Dawei Shi[1], Wenbin Li[1], Huiping Zhao[1], Yibin Zhang[1], Gongning Luo[2], Qiyu Peng[1]

[1] Shenzhen Bay Laboratory, Institute of Biomedical Engineering, Shenzhen, China; [2] Harbin Institute of Technology, College of Artificial Intelligence, Harbin, China

This work was supported by the National Natural Science Foundation of China (Grant no. 82327809), the National Key Research and Development Program of China (Grant No. 2024YFF0507700), National High-Level Hospital Clinical Research Funding (2025-PUMCH-D-003), Beijing Natural Science Foundation(L252047).

Abstract

Wearable brain PET enables neuroimaging during free movement, but head motion causes severe degradation. Compact scanners are particularly sensitive because their small detector rings (~100 mm) amplify angular displacements at the event level. We compare five data-driven motion correction approaches on a wearable scanner using programmed Derenzo phantom motion, with all-data 3-DOF control groups isolating event retention from algorithmic accuracy. The hybrid phase-correlation with mutual-information 6-DOF method achieves the best resolution–noise trade-off—FWHM 4.68 mm vs. 5.42 mm for all-data 3-DOF and 15.15 mm for uncorrected—with SNR of 4,586. Results confirm that 6-DOF event-level correction is essential for compact-geometry wearable PET.

References

[1] S. Li *et al.*, "Performance Evaluation of SmartBrain: A Wearable PET System for Human Brain Imaging," *J. Nucl. Med.*, 2026.

[2] K. Gong *et al.*, "A Wearable Brain PET System: Design and Performance Evaluation," *Phys. Med. Biol.*, vol. 61, p. 3109, 2016.

[3] A. Rahmim *et al.*, "Motion Correction in PET/CT and PET/MRI: A Review of Methods, Mechanisms and Artifacts," *IEEE TRPMS*, 2013.

[4] A. Rahmim *et al.*, "Direct 6-Degree-of-Freedom Motion-Compensated List-Mode Reconstruction," *Phys. Med. Biol.*, vol. 49, p. 4589, 2004.

[5] P. J. Schleyer *et al.*, "Data-Driven Motion Detection and Event-by-Event Correction for Brain PET: Comparison with Vicra," *J. Nucl. Med.*,vol. 61, p. 1178, 2020.

[6] Y. Lu *et al.*, "Adaptive Data-Driven Motion Detection and Optimized Correction for Brain PET," *Phys. Med. Biol.*, vol. 67, p. 115009, 2022.

[7] Y. Najmaoui *et al.*, "YRT-PET: An Open-Source GPU-Accelerated Image Reconstruction Engine for PET," *IEEE TRPMS*, 2025.

[8] B. C. Lowekamp *et al.*, "The Design of SimpleITK," *Front. Neuroinform.*, vol. 7, p. 45, 2013.

[9] D. Mattes *et al.*, "PET-CT Image Registration with Joint Histogram Fitting and Information Theoretic Costs," *IEEE Trans. Med. Imaging*,vol. 22, p. 1207, 2003.

MIC-05-289

Radiographic Scatter Correction via Pixelwise Alpha Blending of Dark and Bright Channel Priors (#2340)

Jiwon Park[1], Sanghyun Cho[1], Yang Hyesun[1], Dae Yup Han[1], Duhee Jeon[2], Hyosung Cho[1]

[1] Yonsei University, Department of Radiation Convergence Engineering, Wonju, South Korea; [2] Yale School of Medicine, Department of Therapeutic Radiology, New Haven, USA

This work was supported by the National Research Foundation of Korea(NRF) grant funded by the Korea government(MSIT)(RS-2024-00347270).

Abstract

Radiographic image quality is degraded by X-ray scatter, which reduces contrast and obscures fine anatomical structures, especially in thick body regions. This study proposes a calibration-free software scatter correction method for radiographic imaging based on pixelwise alpha blending of dark channel prior and bright channel prior. The observed radiograph was modeled as attenuated primary radiation plus additive scatter. Scatter intensity was estimated using self-guided filtering, and transmission maps were generated from dark and bright channel priors. Because dark channel prior can fail in bright anatomical regions such as bone, an attenuation-based alpha weight was used to adaptively combine the two transmission maps. The restored radiograph was obtained using the estimated scatter intensity and refined transmission map. The method was evaluated using in vivo animal radiographs acquired with a mobile radiographic imaging system at 100 kVp and 40 mA. Rabbit, beagle dog, and mixed-breed dog images were used to assess performance across different body sizes and scatter conditions. Image quality was compared among the observed image, dark-channel-prior-only correction, and the proposed alpha-blended correction. The proposed method improved anatomical visibility and reduced overcompensation artifacts in bright bone regions. The contrast-to-noise ratio increased from 0.85 in the observed image and 1.78 with dark-channel-prior-only correction to 2.18 with the proposed method. These results demonstrate that pixelwise blending of dark and bright channel priors can improve radiographic contrast and fine-structure visibility without additional hardware or calibration.

References

[1] E. Rührnschopf and K. Klingenbeck, “A general framework and review of scatter correction methods in x-ray cone-beam computerized tomography. Part 1: Scatter compensation approaches,” Med. Phys., vol. 38, no. 7, pp. 4296–4311, 2011.

[2] K. He, J. Sun, and X. Tang, “Guided image filtering,” IEEE Trans. Pattern Anal. Mach. Intell., vol. 35, no. 6, pp. 1397–1409, 2013.

MIC-05-292

Adapting Timepix4 single-particle trackinginstrumentation for medical X-ray imaging (#2440)

Petr Mánek[1], Benedikt Bergmann[1], Petr Burian[1,2], Laura A. Cerbone[3,4], Radu E. Mihai[1,6], Stanislav Pospíšil[1], Martin P. Pichotka[5], Paolo Russo[3,4], Noah R. Schäfer[1], Jan Žemlička[1]

[1] Czech Technical University in Prague, Institute of Experimental and Applied Physics, Prague, Czech Republic; [2] University of West Bohemia in Pilsen, Faculty of Electrical Engineering, Pilsen, Czech Republic; [3] Universita di Napoli Federico II, Dipartimento di Fisica "Ettore Pancini", Napoli, Italy; [4] Istituto Nazionale di Fisica Nucleare, Sezione di Napoli, Napoli, Italy; [5] University of Freiburg, Department of Diagnostic and Interventional Radiology, University Medical Center Freiburg, Freiburg, Germany; [6] Horia Hulubei National Institute for R&D in Physics and Nuclear Engineering, Department of Nuclear Physics, Bucharest-Magurele, Romania

The authors wish to express their gratitude to Stanislav Pospíšil for valuable guidance, which enabled this effort. B.B. and P.M. acknowledge funding from the Czech Science Foundation under Registration Number M23-04869M. P.B. acknowledges funding from the Technology Agency of the Czech Republic under grant number TN02000012.

Abstract

Timepix4 hybrid pixel detectors, originally optimized for single-particle tracking applications, are increasingly attractive for medical X-ray imaging owing to their large area (~7 cm2), 4-side buttability and appreciable data-driven throughput (3.6 × 106 hits/mm2). Adapting them to imaging workflows, however, demands a substantial shift in data handling. A notable challenge is presented by coping with intensity-dependent data rates, and efficiently aggregating hits and clusters into fixed-size structures under heavy loads. This contribution describes a collection of stackable software tools that adapt an established event-driven tracking framework for Timepix-based systems to X-ray imaging, organized over a modular processing pipeline. The presented platform includes energy-band splitting of hit and cluster streams and corrections for commonly seen effects: internal fluorescence of CdTe sensors, per-pixel high-energy correction, cluster-volume energy loss, non-uniform flat field response and beam hardening. The composition order of these operations is treated as a user-driven parameter, permitting construction of dedicated processing workflows depending on the imaging task at hand. Fluorescence recovery, high-energy correction, and cluster volume correction are already operational and have been tested experimentally; the remaining features are under active development. The full platform is expected to be applied to representative medical imaging tasks over the summer of 2026, with quantitative results to be presented at the conference.

References

[1] X. Llopart, J. Alozy, R. Ballabriga, M. Campbell, R. Casanova, V. Gromov, E. H. M. Heijne, T. Poikela, E. Santin, V. Sriskaran, L. Tlustos, and A. Vitkovskiy, "Timepix4, a large area pixel detector readout chip which can be tiled on 4 sides providing sub-200 ps timestamp binning," J. Instrum., vol. 17, Jan. 2022, Art. no. C01044, 10.1088/1748-0221/17/01/C01044.

[2] O. Růžička, P. Burian, P. Broul´ım, B. Bergmann, T. Kulh´anek, M. Farka˘s, and P. Smolyanskiy, "Timepix4 chipboard and readout concept," J. Instrum., vol. 20, Jun. 2025, Art. no. C06074, 10.1088/1748-0221/20/06/C06074.

[3] P. M´anek, P. Burian, E. David-Bosne, P. Smolyanskiy, and B. Bergmann, "Track Lab: extensible data acquisition software for fast pixel detectors, online analysis and automation," J. Instrum., vol. 19, Jan. 2024, Art. no. C01008, 10.1088/1748-0221/19/01/C01008.

[4] S. P. George, M. Kroupa, S. Wheeler, S. Kodaira, H. Kitamura, L. Tlustos, T. Campbell-Ricketts, N. N. Stoffle, E. Semones, and L. Pinsky, "Very high energy calibration of silicon Timepix detectors," J. Instrum., vol. 13, Nov. 2018, Art. no. P11014, 10.1088/1748-0221/13/11/P11014.
[5] R. E. Mihai, B. Bergmann, and P. Smolyanskiy, "Extending the time-over-threshold calibration of Timepix3 for spatial-resolved ion spectroscopy," J. Instrum., vol. 20, May 2025, Art. no. P05040, 10.1088/1748-0221/20/05/P05040.

MIC-05-295

A phase shifting method to provode three dimensional position information of an incident gamma ray (#2533)

Shuwei Zhao, Hiroyuki Takahashi

The university of Tokyo, Graduate school of Engineering, Bunkyo City, Japan

Abstract

Phase-shifting sub-pixel sampling can improve the spatial granularity of compact gamma-ray detector modules without using analog charge sharing or Anger-logic interpolation.In this work, the phase-shifting concept is extended toward depth of-interaction (DOI) estimation by combining controlled detectordisplacement with double-sided MPPC readout. A monolithic scintillator is coupled to two readout sides, denoted as A and B, and the DOI-sensitive observable is defined by the signal ratio $A/(A + B)$. The detector is translated laterally by 1 mm steps relative to a narrow slit so that the effective irradiation position changes within the scintillator thickness. Coincidence signals are then analyzed using A-B correlation plots. The measured slopes vary systematically from the B-side region to the A-side region,
indicating that interaction depth information is preserved in the double-sided signals. These results demonstrate the feasibility of integrating phase-shifting sampling with DOI estimation for compact SPECT or Compton camera detector modules.

References
[1] Choghadi, M.A., Huang, S.C., Shimazoe, K. and Takahashi, H. (2021), Evaluation of dual-ended readout GAGG-based DOI-PET detectors with different surface treatments. Med. Phys., 48: 3470-3478.
[2] Xia Y, Ma T, Liu Y, et al. A modified spatial resolution formula for DOI-PET. IEEE Nucl Sci Conf. 2011; 2632.
[3] Kuang Z, Wang X, Li C, et al. Performance of a high-resolution depth encoding PET detector using barium sulfate reflector. *Phys Med Biol*. 2017; 62: 5945–5958.

MIC-05-298

Simultaneous Dose Reduction and Resolution Recovery in Preclinical SPECT via Deep Learning (#2608)

Elise Taragola[1], Sara Neyt[1], Wout Van de Velde[1], Stefaan Vandenberghe[1], Christian Vanhove[1], Florence M. Muller[1,2]

[1] Ghent University, Department of Electronics and Information Systems, Faculty of Engineering and Architecture, Ghent, Belgium; [2] University of Pennsylvania, Department of Radiology, Perelman School of Medicine, Philadelphia, USA

All animal experiments were approved by the Ghent University Ethical Committee (ECD 22-42). FM acknowledges support from the Research Foundation Flanders (FWO, 11P0E24N0).

Abstract

Micro-single photon emission computed tomography (µSPECT) is constrained by an inherent sensitivity-resolution trade-off imposed by the collimator. High-sensitivity collimators mitigate statistical noise but blur spatial details, whereas high-resolution collimators limit count sensitivity, thereby amplifying noise. To bridge this trade-off and overcome both low sensitivity and poor resolution, we propose and compare three frameworks for joint µSPECT denoising and super-resolution: a single Joint U-Net, a sequential Cascade U-Net, and a Dual-Encoder U-Net utilizing task-specific encoders and a shared decoder. Models were trained on paired mouse datasets to map noisy low-resolution acquisitions (10-50% of standard counts) to high-resolution targets, acquired with two different collimators. The Dual-Encoder architecture most effectively balanced the competing objectives of noise suppression and edge preservation by extracting distinct representations before merging. Compared to the input, the model achieved a 32% reduction in overall RMSE and an 8% improvement in SSIM. Furthermore, it demonstrated superior resolution recovery relative to the Joint and Cascade approaches, reducing edge map and spectral errors by 27% and 21% compared to the input, respectively. Visually, it was the only model capable of resolving rod peaks in a Derenzo phantom. This approach enables significant reductions in acquisition time or dose while maximizing precision for preclinical quantification.

References

[1] Balaji, V, *et al.* 2024, 'Artificial Intelligence for PET and SPECT Image Enhancement', *Journal of Nuclear Medicine*

[2] Taragola, E, *et al.* 2026, 'Cross-Modality Deep Learning Denoising for Low-Dose µSPECT: Transfer of PET-Trained U-Net and Diffusion Models', *Chemical and Biomedical Imaging*

[3] Cheng, Z, *et al.* 2025, 'A Review of State-of-the-Art Resolution Improvement Techniques in SPECT Imaging', *EJNMMI Physics*

MIC-05-301

Self-supervised PET Denoising Based on the Noise2Noise Principle (#2820)

Sacha Bouchez-Delotte[1], Jérôme Idier[1], Simon Stute[2], Clément Huneau[1]

[1] Nantes Université, École Centrale de Nantes, CNRS, LS2N, Nantes, France; [2] CHU Nantes, Serive de médecine nucléaire, CRCI2NA, INSERM UMR 1307, Nantes, France

Abstract

PET reconstruction aims to transform raw sinograms data into images using analytical, iterative or deep learning approaches. In addition to the ill-posedness of the problem, inherent Poisson noise in sinograms makes the problem more difficult, especially in low-dose contexts.

Using deep learning for image denoising and reconstruction has shown promising performances. However, supervised training requires large sets of paired data with corrupted images and their associated ground truth, which is hard or even impossible to acquire in the medical field, especially in emission tomography.

In this work, we adapted Noise2Noise, a self-supervised framework, to PET imaging in order to learn how to denoise images from noisy measurements only.

References

[1] Nuyts et al., IEEE Trans. Nuclear Sciences, vol. 49, no. 1, pp. 56–60,2002.
[2] Hashimoto et al., Radiol. Phys. Technol., vol. 17, no. 1, pp. 24–46, 2024.
[3] Gong et al., IEEE Trans. Med. Imaging, vol. 38, no. 7, pp. 1655–1665,2019.
[4] Lehtinen et al., in Proc. 35th Int. Conf. Machine Learning, 2018, vol. 80,pp. 2965–2974.
[5] Kang et al., Electronics, vol. 10, no. 13, pp. 1529, 2021.
[6] Monroy et al., Nucl. Med. Mol. Imaging, vol. 54, no. 6, pp. 299–304,2020.
[7] Monroy et al., Arxiv preprint 2412.04648, 2024.
[8] Schramm et al., Front. Nucl. Med., vol. 3, 2024.

MIC-05-304

Python Integration in CASToR: Application to the End-to-End DIP-Based PET Reconstruction (#2865)

Nasrin Taheri[1], Maxime Toussaint[1], Alexandre Merasli[3], Simon Stute[1,2]

[1] CRCI2NA, INSERM UMR 1307, Nantes University, Nantes, France; [2] Nuclear Medicine Department, Nantes University Hospital, Nantes, France; [3] Hematology Biology, Nantes University Hospital, Nantes, France

Abstract

Modern PET reconstruction methods increasingly rely on advanced optimization strategies and deep learning-based priors. However, integrating such approaches into established reconstruction toolkits remains challenging due to limited interoperability with high-level programming environments. In this work, we present a framework that enables Python integration within the CASToR reconstruction platform, allowing direct interaction between C++

reconstruction routines and Python-based modules. As a proof of concept, we implemented an end-to-end PET reconstruction approach incorporating the Deep Image Prior (DIP) and a forward projection model. This example illustrates how the proposed integration facilitates the use of modern Python libraries for deep learning within a physics-based reconstruction framework. This work opens the door to rapid prototyping and deployment of advanced reconstruction algorithms within CASToR using the Python ecosystem.

References
[1] F. Hashimoto et al., IEEE TRPMS, vol. 6, pp. 841–846, 2022.
[2] H. Hashimoto et al., IEEE TRPMS, vol. 5, pp. 322–332, 2021.
[3] T. Merlin et al., Phys. Med. Biol., vol. 63, p. 185005, 2018.
[4] S. Stute et al., IEEE NSS/MIC Conf. Rec., pp. 1–3, 2015.
[5] M. Savanier et al., Phys. Med. Biol., vol. 70, p. 195012, 2025.

MIC-05-307

DOI Calibration and Resolution Estimation in PET Detector Panels Using Uncollimated Irradiations (#3133)

Francisco E. Enriquez-Mier-y-Teran[1,2], Andre Z. Kyme[2,3], Steven R. Meikle[1]

[1] The University of Sydney, Faculty of Medicine and Health, Sydney, Australia; [2] The University of Sydney, Brain and Mind Centre, Sydney, Australia; [3] The University of Sydney, School of Biomedical Engineering, Sydney, Australia

NA

Abstract

High-resolution PET systems require accurate DOI calibration to reduce parallax errors. Conventional DOI calibration methods rely on lateral detector access and collimated irradiations, resulting in complex and time-consuming experimental setups. In this work, we investigated the use of an analytical DOI model and a multilayer perceptron (MLP) network for DOI calibration and DOI resolution estimation using only detector front-face irradiations. The methods were evaluated on a dual-ended-readout 4 × 4 detector panel. Crystal-wise DOI calibration estimates obtained using the analytical model and the MLP showed good agreement with ground-truth measurements, with median calibration RMSE values below 0.6 mm and 0.7 mm, respectively. However, the MLP yielded superior DOI resolution prediction, with consistent mean DOI resolution estimates of approximately 2.0 mm.

References
[1] M. Ito *et al.*, *Biomed. Eng. Lett.*, vol. 1, pp. 70-81, 2011.
[2] Y. Shao *et al.*, *Med. Phys.*, vol. 35, pp. 5829-40, 2008.
[3] Y. Yang *et al.*, *Phys. Med. Biol.*, vol. 54, p. 433, 2008.
[4] Lerche *et al.*, *IEEE Trans. Nucl. Sci.*, vol. 55, pp. 1344-51, 2008.
[5] Y. Kuhl *et al.*, *IEEE Trans. Radiat. Plasma Med. Sci.*, vol. 7, pp. 673-83, 2023.
[6] F.E. Enriquez-Mier-y-Teran *et al.*, *IEEE Trans. Radiat. Plasma Med. Sci.*, vol. 9, pp. 395-405, 2025.

MIC-05-310

Virtual Imaging Trial to Evaluate the Impact of Acquisition Protocols on Harmonized Radiomic features in multi-site PDAC CT (#2788)

Debojyoti Pal[1,2], Isabel Montero[4], Jingqin Luo[3], Allan Thomas[1], Ehsan Abadi[4], Kooresh I. Shoghi[1,2]

[1] Washington University School of Medicine, Department of Radiology, Saint Louis, USA; [2] Washington University in St. Louis, Imaging Science Program, Saint Louis, USA; [3] Washington University School of Medicine, Department of Surgery, Saint Louis, USA; [4] Duke University School of Medicine, Department of Radiology, Durham, USA

The authors thank Juan Carlos Ramirez Giraldo of Siemens for providing access to recon software.This study was supported by a research grant: U24CA209837, U24CA253531

Abstract

Radiomics is used to extract high-dimensional features from medical images such as computed tomography. However, radiomic features are susceptible to acquisition protocols in a multi-center setting. This results in domain shift in data distribution even when the patient anatomy is the same. This can increase intraclass variability and lead to algorithms learning protocol-specific artifacts rather than clinically relevant imaging information. In this work, we developed a virtual imaging trial (VIT) of pancreatic ductal adenocarcinoma (PDAC) patients scanned across multiple scanners and protocols to quantify protocol-induced radiomic variability post harmonization. A virtual patient cohort of 50 patients was generated using the XCAT. PDAC tumors extracted from clinical cases were implanted in individual virtual patients. DukeSim was used to simulate Siemens clinical scanners. For each scanner, two clinically representative acquisition protocols were designed by varying tube current, pitch, and reconstruction kernel. Radiomic features were extracted from tumor regions and harmonized using scanners and protocols as batch effect. Scanner and protocol dependency of each feature was assessed using Wilcoxon and Kruskal–Wallis tests, respectively. Feature robustness was quantified using intraclass correlation coefficient. Protocol-related batch effects were prominent in the non-harmonized data, with 85.98% of radiomic features dependent on protocols. Protocol-based CovBat achieved the best overall performance, reducing protocol-dependent features to 19.63% and increasing reproducible features by 3.8% post harmonization. Therefore, the proposed VIT-based framework can be used to evaluate harmonization methods and assess radiomic feature robustness before developing clinical decision-support models.

References

[1] A. E. Latenstein *et al.*, "Nationwide trends in incidence, treatment and survival of pancreatic ductal adenocarcinoma," *European Journal of Cancer*, vol. 125, pp. 83-93, 2020

[2] W. P. Segars, G. Sturgeon, S. Mendonca, J. Grimes, and B. M. Tsui, "4D XCAT phantom for multimodality imaging research," *Medical physics*, vol. 37, no. 9, pp. 4902-4915, 2010.

[3] D. R. White, Griffith, R. V., & Wilson, I. J., "ICRU reports. Reports of the International Commission on Radiation Units and Measurements," vol. (1), 203-205, 1992.

[4] E. Abadi, B. Harrawood, S. Sharma, A. Kapadia, W. P. Segars, and E. Samei, "DukeSim: a realistic, rapid, and scanner-specific simulation framework in computed tomography," *IEEE transactions on medical imaging*, vol. 38, no. 6, pp. 1457-1465, 2018

MIC-05-313

Allometric Scaling of PSMA Uptake as a Novel Biomarker for Predicting Biochemical Response in Prostate Cancer (#2104)

Fereshteh Yousefirizi[1,2], Taylor J. McColl[1,2], Rezvan Samimi[4], Elinaz Hosseinzadeh[4], Ghasemali Divband[5], Babak Nickkholgh[6], Zohreh Adinehpour[7], Shaghayegh Dastgerdi[8], Carlos Uribe[3,1], Arman Rahmim[2,1]

[1] University of British Columbia, Department of Radiology, Vancouver, Canada; [2] BC Cancer Research Institute, Department of Basic and Translational Research, Vancouver, Canada; [3] BC Cancer, Vancouver, Canada; [4] Shahid Beheshti University, Tehran, Iran; [5] Jam Hospital, Tehran, Iran; [6] PET/CT Centre, Tehran, Iran; [7] The Ottawa Hospital and University of Ottawa, Ottawa, Canada; [8] University of Isfahan, Isfahan, Iran

This research was funded by the BC Cancer Foundation.

Abstract

Prostate-specific membrane antigen (PSMA) PET/CT enables standardized quantitative tumor burden assessment, yet routine SPARC-aligned metrics, molecular tumor volume (MTV), total lesion activity (TLA), and total lesion fraction (TLF), show limited predictive value for early biochemical response. Allometric scaling laws (TLA ∝ MTV^β) govern metabolic activity superlinearly (β > 1) across multiple cancers, but their application to PSMA PET outcome prediction remains unexplored. We hypothesized that each patient's deviation from the cohort-level scaling line, the Distance from the Scaling Law (DSL), encodes biologically distinct information beyond raw burden metrics and predicts PSA50 biochemical response (PCWG3: ≥50% PSA decline). In 103 prostate cancer patients with PSMA PET/CT and paired PSA measurements from a real-world clinical cohort, we fitted the allometric law (TLA = α × MTV^β) and computed per-patient DSL residuals. The cohort exhibited a superlinear scaling law: TLA = 0.574 × MTV^1.157 (R^2 = 0.782, $p < 0.0001$) consistent with literature values (β ≈ 1.22–1.28). DSL ranked 4th among 12 candidate features in univariate discrimination (AUC = 0.668), outperforming standard SPARC burden metrics including TLF (0.589), TLA (0.588), and MTV (0.523). Non-responders showed lower DSL than responders (mean −0.243 vs +0.018; rank-biserial r = 0.336), indicating hypoactive PSMA uptake relative to tumor volume as a failure signature. Nine cost-sensitive classification strategies under 5-fold stratified cross-validation reached balanced accuracy of 0.57–0.64, constrained by extreme class imbalance (93.2% responders). These findings establish DSL as a physics-grounded, automatically computable biomarker that outperforms conventional burden metrics and is deployable within SPARC workflows.

MIC-05-316

A Cucker–Smale Flocking Model for Edge-Aware Medical Image Analysis (#3017)

Amirreza Hashemi, Hamid Sabet

Harvard Medical School/Massachusetts General Hospital, Radiology Department, Boston, USA

This work was supported in part by NIH grant R01EB034785.

Abstract

We propose a flocking-based framework for image structure analysis inspired by the Cucker–Smale model, interpreting pixels as interacting agents whose alignment patterns reveal self-organized regions. Here, we model each pixel as coupling with its neighbors through distance-weighted interactions, and identify structural boundaries via a normalized measure of local misalignment. This yields an edge-aware representation that suppresses intra-region variation while emphasizing transitions between self-organized flocks. We evaluate the method on diverse medical imaging data, including brain MRI, retinal fundus images, and microaneurysm patches. Across modalities, the approach robustly captures both large-scale anatomical boundaries and fine pathological details, adapting to different contrast regimes without requiring reference images. Quantitatively, strong-edge masks achieve edge/non-edge contrast ratios of ~66 in MRI, ~11 in fundus images, and ~4.4 in microaneurysm patches, with edge fractions ranging from 0.06 to 0.15—demonstrating high structural selectivity and reduced sensitivity to noise.

References

[1] A. Hashemi, S. Dutta, B. Georgeot, D. Kouamé, and H. Sabet, “A novel perspective on denoising using quantum localization with application to medical imaging,” *AIP Advances*, vol. 15, no. 8, p. 085012, Aug. 2025, doi: 10.1063/5.0267924.

[2] A. Hashemi, S. Dutta, B. Georgeot, D. KouamÉ, and H. Sabet, “Quantum-Inspired Denoising via Adaptive Planck Constant and Image Patching,” in *2024 IEEE Nuclear Science Symposium (NSS), Medical Imaging Conference (MIC) and Room Temperature Semiconductor Detector Conference (RTSD)*, Oct. 2024, pp. 1–1. doi: 10.1109/NSS/MIC/RTSD57108.2024.10657709.

[3] C. W. Reynolds, “Flocks, herds, and schools: a distributed behavioral model,” in *Seminal Graphics: Pioneering Efforts That Shaped the Field, Volume 1*, New York, NY, USA: Association for Computing Machinery, 1998, pp. 273–282. [Online]. Available: https://doi.org/10.1145/280811.281008

[4] Y.-P. Choi, S.-Y. Ha, and Z. Li, “Emergent Dynamics of the Cucker–Smale Flocking Model and Its Variants,” in *Active Particles, Volume 1 : Advances in Theory, Models, and Applications*, N. Bellomo, P. Degond, and E. Tadmor, Eds., Cham: Springer International Publishing, 2017, pp. 299–331. doi: 10.1007/978-3-319-49996-3_8.

[5] F. Cucker and S. Smale, “Emergent Behavior in Flocks,” *IEEE Transactions on Automatic Control*, vol. 52, no. 5, pp. 852–862, May 2007, doi: 10.1109/TAC.2007.895842.

MIC-05-319

ComBat-Driven Latent Representation Learning for Robust Multicenter Radiomics in Theranostic SPECT/CT Imaging (#3106)

Mohamed Saber Azimi[1,2], Maryam Cheraghi[3], Mohammad A. Ghodsi-Rad[4], Ghasemali Divband[5], Maryam Alhashim[6,7], Mahmoud Alabedi[7], Nahid Ibrahim[7], Enas Alwuhaib[7], Zahra Mansouri[8], Yazdan Salimi[8], Hossein Arabi[8], Jean Mathieu Beauregard[9], Arman Rahmim[10], Habib Zaidi[8,2]

[1] Obuda University, Doctoral School of Applied Informatics and Applied Mathematics, Budapest, Hungary; [2] Obuda University, University Research and Innovation Center, Budapest, Hungary; [3] Shahid Beheshti University of Medical Sciences, PET-CT Unit, Department of Nuclear Medicine, Tehran, Iran; [4] Shohada-e Tajrish Medical Center, Department of Nuclear Medicine, Tehran, Iran; [5] Jam Hospital, Department of Nuclear Medicine, Tehran, Iran; [6] Imam Abdulrahman Bin Faisal University, Department of Radiology, College of Medicine, Dammam, Saudi Arabia; [7] King Fahad Specialist Hospital Dammam, Medical Imaging Services Center, Dammam, Saudi Arabia; [8] Geneva University Hospital, Division of Nuclear Medicine & Molecular Imaging, Geneva, Switzerland; [9] Université Laval, Cancer Research Centre and Department of Radiology and Nuclear Medicine, Quebec, Canada; [10] University of British Columbia, Departments of Radiology and Physics, Vancouver, Canada

Abstract

Multicenter SPECT/CT radiomics is highly sensitive to variations in imaging protocols, reconstruction settings, and scanner configurations, limiting reproducibility and masking biological patterns. To address this challenge, we propose a harmonized latent radiomics framework for robust patient-level modeling in theranostic imaging. A retrospective multicenter dataset of ^{177}Lu-DOTATATE SPECT/CT scans from three institutions was analyzed. A total of 93 IBSI-compliant lesion-based radiomic features were extracted and harmonized using ComBat to reduce inter-center variability. Principal component analysis was then applied to generate a compact latent representation, followed by unsupervised clustering for lesion phenotype discovery. Patient-level representations were constructed by aggregating lesion embeddings. In addition, a perturbation strategy was implemented to assess latent-space stability and responsiveness. ComBat substantially reduced center-related variability, with η^2 values decreasing from 0.75 to near-zero levels (0.000–0.006). The latent representation demonstrated improved biological interpretability, with stronger association to intensity-related characteristics (0.351 to 0.956) and reduced dependence on texture-related confounding (0.967 to 0.528). Clustering results showed that lesion grouping was primarily driven by intrinsic phenotypic patterns rather than acquisition center. Perturbation analysis further revealed low phenotype transition rates (<10%) with gradual centroid shifts, indicating stable yet responsive latent behavior. The proposed framework combines harmonization and latent representation learning to improve robustness in multicenter radiomics and provides a promising foundation for digital twin modeling in theranostic imaging.

References

[1] A. Kopf and M. Claassen, "Latent representation learning in biology and translational medicine," *Patterns*, vol. 2, no. 3, 2021.

[2] J. Pan *et al.*, "Disentanglement of Biological and Technical Factors via Latent Space Rotation in Clinical Imaging Improves Disease Pattern Discovery," in *International Workshop on Applications of Medical AI*, 2025: Springer, pp. 309–319.

MIC-05-322

Evaluation of Dose Rate Dependent Alanine/ESR Response under Carbon Ion FLASH Irradiation (#1286)

Soo Min Lee[1], Ki-Taek Han[2], Mutsumi Tashiro[3], Shunsuke Inagaki[4], Chul Hee Min[1]

[1] Yonsei university, Department of Radiation Convergence Engineering, Wonju-si, Germany; [2] Korean Association for Radiation Application, Radiation Technology and Research Center, Jeongeup, Germany; [3] Gunma University, Gunma University Heavy Ion Medical Center, Gunma, Germany; [4] Gunma University, Department of Medical Physics for Heavy Ion Therapy, Graduate School of Medicine, Gunma, Germany

This work was supported by the Korea Hydro & Nuclear Power Co., LTD (No. 2023-Tech-11) and conducted as part of a research project on heavy ions at GHMC.

Abstract

Accurate dosimetry for ultra-high dose rate (FLASH) carbon ion irradiation is challenging because ionization chambers can exhibit dose rate dependent recombination and charge-collection inefficiency. Alanine/ESR dosimetry is a passive technique for high dose verification, but its response under FLASH conditions remains unclear. This study evaluated dose rate dependent alanine/ESR response by comparing calibration curves under conventional and FLASH irradiation. Alanine pellets were irradiated with a 290 MeV/u carbon ion beam at 10–100 Gy. Measurements were performed at SOBP centers under conventional irradiation at 0.09 Gy/s and FLASH irradiation at 174–265 Gy/s. An Advanced Markus chamber provided the reference absorbed dose to water. Monte Carlo simulations examined possible geometry-related dose perturbations and beam-quality effects. Under conventional irradiation, the ESR response was highly linear, and reconstructed doses agreed with the reference dose within 2%. However, applying this calibration to FLASH-irradiated alanine produced dose dependent deviations, with errors up to 28.6% in the low dose region and approximately 3–4% at higher doses. Simulations showed that chamber related scatter and positional dose differences at the alanine locations were below 1%, indicating that the discrepancy was not mainly caused by the irradiation geometry. A FLASH-specific calibration restored agreement within 1.31%, with an approximately 7.4% lower slope than the conventional calibration. These results indicate that alanine/ESR response is modified under FLASH irradiation, likely due to combined FLASH delivery and high-LET beam-quality effects. Therefore, conventional carbon ion calibration shows limited direct transferability to FLASH conditions, requiring FLASH-specific calibration for accurate dose verification.

References

[1] F. Romano, C. Bailat, P. G. Jorge, M. L. F. Lerch, and A. Darafsheh, “Ultra-high dose rate dosimetry: Challenges and opportunities for FLASH radiation therapy,” *Medical Physics*, vol. 49, no. 7, pp. 4912–4932, 2022, doi: 10.1002/mp.15649.

[2] D. F. Regulla and U. Deffner, “Dosimetry by ESR spectroscopy of alanine,” *The International Journal of Applied Radiation and Isotopes*, vol. 33, no. 11, pp. 1101–1114, Nov. 1982, doi: 10.1016/0020-708X(82)90238-1.

MIC-05-325

Preclinical Evaluation of an In-Room All-Digital PET System for Post-Irradiation Proton Range Verification (#1463)

Wentao Hu[1], Shiyu Ou[1], Dengyun Mu[1], Jingmin Zhu[1], Ao Qiu[1], Mengxin Chen[2], Yuhang Lai[2], Xingzhe Rao[2], Lin Wan[2], Qiuhui Ma[3,4], Qi Liu[3,4], Pengyuan Qi[3,4], Zhiyong Yang[3,4], Qingguo Xie[1,5]

[1] Huazhong University of Science and Technology, Department of Biomedical Engineering, Wuhan, China; [2] Huazhong University of Science and Technology, School of Software Engineering, Wuhan, China; [3] Huazhong University of Science and Technology, Tongji Medical College, Union Hospital, Hubei Key Laboratory of Precision Radiation Oncology, Institute of Radiation Oncology, Cancer Center, Wuhan, China; [4] Huazhong University of Science and Technology, Tongji Medical College, Union Hospital, Key Laboratory of Biological Targeted Therapy, Wuhan, China; [5] University of Science and Technology of China, Department of Electronic Engineering and Information Science, Hefei, China

This work was supported by the National Natural Science Foundation of China (Grant No. 625B2079).

Abstract

Accurate dose delivery in proton therapy requires reliable control of the proton range to ensure that the beam deposits its energy at the planned treatment position. However, the proton range is highly sensitive to tissue heterogeneities, anatomical changes, and patient positioning errors, making in vivo range verification an important component of proton therapy quality assurance. Positron emission tomography (PET) provides a non-invasive approach for range assessment by detecting proton-induced positron-emitting nuclei generated in the irradiated material. In this work, we demonstrate preclinical proton range verification using a dedicated in-room All-Digital PET system installed in a clinical proton treatment room. The system was evaluated using polymethyl methacrylate (PMMA) phantoms irradiated with a 130 MeV proton pencil beam. Controlled range perturbations were introduced using intact, 1 mm air-gap, and 4 mm air-gap phantom configurations. PET data were acquired for 300 s following irradiation, and one-dimensional activity profiles were extracted. At 130 MeV, the PET-derived activity profiles exhibited distinct distal fall-off shifts that correlated with the introduced air gaps. These results demonstrate the capability of the system to resolve millimeter-scale range perturbations under the tested phantom conditions and provide experimental support for future preclinical animal studies and clinical in-room proton therapy verification.

References

[1] H. Paganetti, “Range uncertainties in proton therapy and the role of Monte Carlo simulations,” Phys. Med. Biol., vol. 57, no. 11, pp. R99–R117, 2012.

[2] A.-C. Knopf and A. Lomax, “In vivo proton range verification: a review,”Phys. Med. Biol., vol. 58, no. 15, pp. R131–R160, 2013.

[3] K. Parodi and J. C. Polf, “In vivo range verification in particle therapy,” Med. Phys., vol. 45, no. 11, pp. e1036–e1056, 2018.

[4] W. Enghardt et al., “Charged hadron tumour therapy monitoring by means of PET,” Nucl. Instrum. Methods Phys. Res. A, vol. 525, no. 1–2, pp. 284–288, 2004.

[5] T. Hu et al., “Development and performance evaluation of an open-ring PET prototype for intraoperative metabolic monitoring,” IEEE Trans. Radiat. Plasma Med. Sci., early access, 2026,

MIC-05-328

Proton range verification via coaxial prompt gamma-ray monitoring: experimental proof-of-concept at clinical beam currents (#1433)

Iris García Rivas[1,2], Antonio Fernández Prieto[1], Pablo Vázquez Regueiro[1], Daniel García Fernández[2], Toni Kögler[3,4], Katja Römer[5], Fernando Hueso-González[6]

[1] University of Santiago de Compostela (USC), Instituto Galego de Física de Altas Enerxías (IGFAE), Santiago de Compostela, Spain; [2] TripleAlpha Innovation, Santiago de Compostela, Spain; [3] OncoRay – National Center for Radiation Research in Oncology, Medical Faculty and University Hospital Carl Gustav Carus, TUD Dresden University of Technology, Helmholtz-Zentrum Dresden - Rossendorf, Dresden, Germany; [4] Helmholtz-Zentrum Dresden - Rossendorf, Institute of Radiooncology – OncoRay, Dresden, Germany; [5] Helmholtz-Zentrum Dresden - Rossendorf, Institute of Nuclear Physics, Dresden, Germany; [6] Instituto de Física Corpuscular (IFIC), CSIC-UV, Paterna, Spain

Work supported by the Industrial Doctorates Program of the Xunta de Galicia (Galician Innovation Agency) and by the Generalitat Valenciana under grant number CDEIGENT/2019/011, the PTCOG Project Funding (Physics) 2024 as well as the European Union's 2020 research and innovation program under grant agreement No 101008126, corresponding to the RADNEXT project. IGFAE is supported by the CONSOLIDACIÓN 2022 GRC grant GI-1490 - Grupo de Altas Enerxías - GAES – ED431C/30 and funds from GENERACIÓN DE CONOCIMIENTO 2022 - (IGFAE-LHCb++). IFIC is supported by the Severo Ochoa Center of Excellence grant CEX2023-001292-S funded by MCIU/AEI.

Abstract

Proton therapy is recommended as the "new standard-of-care option for patients with head and neck oropharyngeal cancer". Still, the absence of a monitoring tool equivalent to electronic portal imaging hinders its upmost potential, and forces the application of safety margins and field-patching, thereby increasing the dose to normal tissue. Prompt gamma-rays produced along the proton track can cover this shortfall, since their production cross section is strongly correlated with the proton dose depth profile. We present the first experimental proof of principle of proton range verification with a single-channel prompt gamma-ray detector located behind the treated area, in coaxial geometry. Simple heterogeneous targets were irradiated with 1e8 protons at clinically realistic energies at beam currents of 1.6 nA. The mean statistical precision was 1 mm (sigma). The absolute experimental error with respect to the ground truth predicted by a Monte Carlo simulation was 2 mm on average. These findings encourage further investigations with anthropomorphic phantoms and realistic treatment plans, and could open up the door for proton range verification with a single scintillation detector, that may have better prospects of integration into rotating gantries and compact treatment rooms than collimated multi-channel systems.

MIC-05-331

Sub-Millimeter Range Verification in Carbon-Ion Therapy Using In-Beam All-Digital PET (#1474)

Jingmin Zhu[1], Ruolan Liu[1], Dengyun Mu[1], Wentao Hu[1], Ao Qiu[1], Tianjiao Hu[2], Weiwei Li[3,4], Yuki Nitta[3,4], Jiping Liu[3,4], Lin Wan[5], Ji Zhu[3,4], Qingguo Xie[1,2]

[1] Huazhong University of Science and Technology, Biomedical Engineering, Wuhan, China; [2] University of Science and Technology of China, Electronic Engineering and Information Science, Hefei, China; [3] Zhejiang Cancer Hospital, Radiation Oncology, Hangzhou, China; [4] Chinese Academy of Sciences, Hangzhou Institute of Medicine, Hangzhou, China; [5] Huazhong University of Science and Technology, Software Engineering, Wuhan, China

This work was supported by the National Natural Science Foundation of China under Grant 625B2079.

Abstract

Positron emission tomography (PET) has been widely investigated for range verification in carbon-ion radiotherapy (CIRT). All-Digital PET, based on multi-voltage threshold (MVT) direct digital signal acquisition with high count-rate capability, represents a promising new approach for in-beam monitoring. However, its application in CIRT remains largely unexplored, and experimental validation under realistic irradiation conditions is still lacking. In this study, we report the preliminary experimental validation of an in-beam All-Digital PET system for range verification in CIRT. A discrete 7x7 raster-scanned carbon-ion field (261.03 MeV/u) with a spot spacing of 5 mm and a delivery of 2000 MU per spot was delivered to a polymethyl methacrylate (PMMA) phantom (6x6x15 cm³). To simulate localized anatomical heterogeneity, a cylindrical air cavity with a diameter of 1 cm was embedded at a depth of 5 cm from the beam entrance, introducing an approximate local range shift of 10 mm. Two-dimensional distal range maps successfully revealed the irradiation field and clearly identified the cavity boundary. Within the region of interest, the measured localized range shift was 9.14 mm, with a residual error of only 0.86 mm compared with the ground truth. These results demonstrate the feasibility of All-Digital PET for accurate in-beam range verification under clinically relevant raster-scanned carbon-ion delivery conditions and support its potential for future CIRT applications.

References

[1] D. Schardt, T. Elsässer, and D. Schulz-Ertner, "Heavy-ion tumor therapy: Physical and radiobiological benefits," Rev. Mod. Phys., vol. 82, no. 1, pp. 383-425, 2010.

[2] T. Hofmann et al., "Dose reconstruction from PET images in carbon ion therapy: a deconvolution approach," Phys. Med. Biol., vol. 64, no. 2, p. 025011, 2019.

[3] L. Fang et al., "Development and evaluation of a new high-TOF-resolution all-digital brain PET system," Phys. Med. Biol., vol. 69, no. 2, p. 025019, 2024.

[4] B. Zhang et al., "Performance Evaluation of New PET/CT DigitMI 930," IEEE Trans. Radiat. Plasma Med. Sci., vol. 9, no. 5, pp. 578-585, 2025.

[5] F. Pennazio et al., "Carbon ions beam therapy monitoring with the INSIDE in-beam PET," Phys. Med. Biol., vol. 63, no. 14, p. 145018, 2018.

[6] Q. Zhang et al., "Feasibility study of LYSO-SiPM in-beam TOF-PET for dose monitoring in carbon-ion radiotherapy," Phys. Med. Biol., vol. 70, no. 17, p. 175017, 2025.

[7] T. Hu et al., "Development and Performance Evaluation of an Open-Ring PET Prototype for Intraoperative Metabolic Monitoring," IEEE Trans. Radiat. Plasma Med. Sci., early access, 2026.

MIC-05-334

Effect of Radionuclide Distribution on DNA Damage Yields: A Comparative Study between ^{134}Ce/^{134}La and other radionuclides (#1512)

Sangho Lee[1,2], Jungwook Shin[3], Yoonsuk Huh[4,5], Kondapa N. Bobba[6], Robert R. Flavell[2,7], Gyuseong Cho[1], Youngho Seo[2,8]

[1] Korea Advanced Institute of Science and Technology, Department of Nuclear and Quantum Engineering, Daejeon, South Korea; [2] University of California, San Francisco, Department of Radiology and Biomedical Imaging, San Francisco, USA; [3] National Institutes of Health, Division of Cancer Epidemiology and Genetics, National Cancer Institute, Rockville, USA; [4] Seoul National University Hospital, Department of Radiation Oncology, Seoul, South Korea; [5] Seoul National University Medical Research Center, Institute of Radiation Medicine, Seoul, South Korea; [6] University of Tennessee, Knoxville, Department of Nuclear Engineering, Knoxville, USA; [7] University of California, San Francisco, Department of Pharmaceutical Chemistry, San Francisco, USA; [8] University of California, Berkeley, Department of Nuclear Engineering, San Francisco, USA

This work was supported by the National Research Foundation of Korea (NRF) grant funded by the Korea government (MSIT) (RS- 2024-00345521), the Nuclear Safety Pre-practice Education Enhancement Program through the Korea Foundation Of Nuclear Safety(KoFONS) using the financial resource granted by the Nuclear Safety and Security Commission(NSSC) of the Republic of Korea, and the National Cancer Institute under grant R01CA279203.

Abstract

Targeted radionuclide therapy employs therapeutic radiation-producing radionuclides bound to targeting agents to selectively damage cancer cells. Recent interest has expanded beyond conventional beta emitters to include alpha emitters and Auger electron emitters. We investigated the therapeutic potential of the ^{134}Ce/^{134}La pair by comparing its DNA damage induction with commonly used radionuclides. A simplified human fibroblast cell model was implemented using Monte Carlo track-structure simulations to evaluate single-strand and double-strand DNA break yields. Particular attention was paid to the various spatial distributions of the radiation source. In this simulation, radionuclides were distributed at the cell surface, cytoplasm, and nucleus surface; both physical and chemical stages of radiation interaction were modeled, including indirect damage mediated by hydroxyl radicals. The results show that double-strand break yields increase as radionuclide localization approaches the nucleus, while single-strand break yields remain relatively stable. Indirect effects dominate DNA damage formation across all radionuclides and spatial distributions. The ^{134}Ce/^{134}La pair demonstrates DNA damage yields comparable to established beta and Auger electron emitters under all tested conditions. Although these findings do not directly translate to therapeutic efficacy, they indicate that this radionuclide pair has competitive radiobiological effectiveness and warrants further investigation for potential application in targeted radionuclide therapy.

References

[1] Bobba, KN. et al., 2023, 'Evaluation of ^{134}Ce/^{134}La as a PET Imaging Theranostic Pair for ^{225}Ac α-Radiotherapeutics', *Journal of Nuclear Medicine*, 67, 1076–1082.

[2] Bobba, KN. et al., 2025, 'Evaluation of ^{134}Ce/^{134}La-PSMA-617 for PET Imaging and Auger Electron Therapy of Prostate Cancer', *Journal of Nuclear Medicine*, 66, 1252–1257.

[3] Chatzipapas, KP. et al., 2023, 'Simulation of DNA damage using Geant4-DNA: an overview of the "molecularDNA" example application', *Precision Radiation Oncology*, 7, 4–14.

[4] Incerti, S. et al., 2010, 'The Geant4-DNA project', *International Journal of Modeling, Simulation, and Scientific Computing*, 1, 157–178.
[5] Incerti, S. et al., 2010, 'Comparison of Geant4 very low energy cross section models with experimental data in water', *Medical Physics*, 37, 4692–4708.
[6] Bernal, MA. et al., 2015, 'Track structure modeling in liquid water: A review of the Geant4-DNA very low energy extension of the Geant4 Monte Carlo simulation toolkit', *Physica Medica*, 31, 861–874.
[7] Incerti, S. et al., 2018, 'Geant4-DNA example applications for track structure simulations in liquid water: A report from the Geant4-DNA Project', *Medical Physics*, 45, e722–e739.
[8] Tran, HN. et al., 2024, 'Review of chemical models and applications in Geant4-DNA: Report from the ESA BioRad III Project', *Medical Physics*, 51, 5873–5889.
[9] Chatzipapas, KP. et al., 2025, 'In silico assessment of cellular damage from Lu-177, Ac-225, and Pb-212 therapeutic radionuclides', *Medical Physics*, 52, e70089.

MIC-05-337

Range Monitoring and Tissue Identification in Particle Therapy with the TIARA Detector (#1641)

Sara Marcatili[1], Adélie André[1], Maxime Pinson[1], Pavel Kavrigin[1], Chayma Abid[2], Mathieu Dupont[2], Giuseppe Fanciulli[1], Marie-Laure Gallin Martel[1], Alicia Garnier[2], Christophe Hoarau[1], Christian Morel[2], Jean-François Muraz[1], Dimitrios Psarras[3], Marco Pullia[4], Simone Savazzi[4], Nicola Toschi[3], Yannick Boursier[2], Daniel Maneval[5]

[1] Univ. Grenoble Alpes, CNRS, Grenoble INP, LPSC-IN2P3, Grenoble, France; [2] Aix-Marseille Univ, CNRS/IN2P3, CPPM, Marseille, France; [3] Università Roma Tor Vergata, Roma, Italy; [4] Centro Nazionale di Adroterapia Oncologica (CNAO), Pavia, Italy; [5] Centre Antoine Lacassagne, Nice, France

Abstract

Particle therapy with protons and carbon ions offers conformal dose delivery, but its clinical benefit strongly depends on accurate verification of the beam range inside the patient. The TIARA (Time-of-Flight Imaging ARray) detector has been developed to address this challenge through the exclusive measurement of Prompt-Gamma (PG) Time-of-Flight (TOF). The system combines a fast plastic beam monitor with arrays of Cherenkov gamma detectors based on PbF_2 crystals coupled to SiPMs, enabling sub-nanosecond timing performance and real-time treatment verification.

An 8-channel prototype has been tested with proton and carbon-ion beams delivered by cyclotrons, synchro-cyclotrons and synchrotrons. Measurements with 63 MeV protons at the MEDICYC cyclotron demonstrated a range accuracy of 3.3 ± 0.1 mm (2σ) for irradiation spots of about 2×10^7 protons, corresponding to roughly 3200 detected PG events. Experiments with carbon ions at the CNAO synchrotron achieved a range accuracy of 4.74 ± 0.36 mm (2σ) at clinical intensity by grouping four spots of 2.4×10^6 ions each, with approximately 5600 detected PGs. These results confirm the high sensitivity of the TOF approach for proton and carbon-ion therapy.

Beyond range monitoring, TIARA implements the Prompt Gamma Time Imaging (PGTI) method to identify anatomical changes occurring between treatment planning and dose delivery. An iterative reconstruction algorithm was developed to merge the TOF information from multiple detector modules and reconstruct both the PG emission profile and the proton beam average velocity evolution inside the patient. The method was validated using a RANDO head phantom irradiated at the Proteus One accelerator under two anatomical configurations simulating an empty and filled sinus cavity. The reconstructed PG distributions enabled localisation of the induced anatomical change, demonstrating the potential of TIARA for adaptive particle therapy and in vivo tissue identification.

MIC-05-340

Secondary Electron Bremsstrahlung Imaging with a Knife-Edge Slit Camera for Range Verification in Carbon-Ion Therapy (#1876)

Michiko Tsuda[1,2], Mitsutaka Yamaguchi[1], Yuto Nagao[1], Han Gyu Kang[3], Takuya Yabe[1], Eiji Yoshida[3], Taiga Yamaya[3], Makoto Sakama[4], Hideyuki Mizuno[4], Naoki Kawachi[1,5], Hiroshi Watabe[6]

[1] National Institutes for Quantum Science and Technology (QST), Takasaki Institute for Advanced Quantum Science, Gunma, Japan; [2] Postdoctoral Research Fellow of the Japan Society for the Promotion of Science (JSPS), Tokyo, Japan; [3] National Institutes for Quantum Science and Technology (QST), Institute for Quantum Medical Science, Chiba, Japan; [4] National Institutes for Quantum Science and Technology (QST), QST hospital, Chiba, Japan; [5] Fukushima Institute for Research, Education and Innovation (F-REI), Radiation Science, Medicine and Drug Development, & Industrial Applications for Radiation, Fukushima, Japan; [6] Tohoku University, Research Center for Accelerator and Radioisotope Science (RARiS), Miyagi, Japan

The irradiation experiments were conducted as part of the Research Project with the Heavy Ion Medical Accelerator in Chiba (HIMAC). This work was supported in part by JSPS KAKENHI under Grant Numbers JP23KJ0221 and JP23K28462.

Abstract

Accurate in-vivo range verification is essential for realizing the full dosimetric advantage of carbon-ion therapy [1]. Secondary electron bremsstrahlung (SEB), a low-energy photon emission produced along the beam trajectory inside the patient, has attracted attention as a prompt signal for non-invasive range monitoring [2]. While our prior work demonstrated the principle using a pinhole collimator, the limited collection efficiency of a pinhole aperture imposes a fundamental constraint on range estimation precision [3]. A knife-edge slit geometry offers a one-dimensional focusing advantage that substantially raises the collected photon flux compared to the pinhole-based approach. In this study, a knife-edge slit camera equipped with a Ce:GAGG scintillator array was constructed and evaluated through irradiation experiments with a 290 MeV/u carbon-ion beam at the Heavy Ion Medical Accelerator in Chiba (HIMAC). The camera employed a tungsten knife-edge slit collimator with a slit width of 1 mm and a thickness of 48 mm, positioned 490 mm from the beam axis with a collimator-to-detector distance of 49 mm. The Ce:GAGG scintillator array consisted of 1.5 × 1.5 × 1 mm³ crystals arranged in a 16 × 16 matrix with a pitch of 1.6 mm. One-dimensional SEB profiles were measured over a range of beam range conditions by varying the range-shifter thickness, and representative results are presented. The acquired distributions exhibited a systematic dependence on beam range, with a 5 mm increment reliably distinguished by visual inspection. Quantitative range estimation yielded an uncertainty of 2.89 mm for 10^8 ions; further details will be presented at the conference.

References

[1] K. Parodi and J. C. Polf, “In vivo range verification in particle therapy,” *Med. Phys.*, vol. 45, no. 11, pp. e1036–e1050, Nov. 2018.

[2] M. Yamaguchi *et al.*, “Beam range estimation by measuring bremsstrahlung,” *Phys. Med. Biol.*, vol. 57, no. 10, p. 2843, Apr. 2012.

[3] M. Tsuda *et al.*, “Uncertainty evaluation in simulation study on range-shift estimation due to statistical noise in secondary electron bremsstrahlung from a small number of carbon ions” *Jpn. J. Appl. Phys.*, vol. 64, no. 4, p. 047001, Apr. 2025.

MIC-05-343

A Deep Learning-Based 3D Dose Reconstruction Using a Dual-Panel PET in Proton Therapy (#1929)

Xiaolong Jiang[1,2], Chen Huang[1,3], Hang Yang[1], Xiangtao Zeng[1], Yangyang Zhao[1], Junqin Lei[4], Enzhuo Quan[4], Ming Niu[1], Zheng Gu[1]

[1] Shenzhen Bay Laboratory, Institute of Biomedical Engineering, Shenzhen, China; [2] Harbin Institute of Technology, School of Electronics and Information Engineering, Harbin, China; [3] Southern University of Science and Technology, Department of Electronic and Electrical Engineering, Shenzhen, China; [4] Chinese Academy of Medical Sciences and Peking Union Medical College, National Cancer Center/National Clinical Research Center for Cancer/Cancer Hospital & Shenzhen Hospital, Shenzhen, China

This work is supported by the National Key R&D Program of China (No. 2023YFC2414800), the National Natural Science Foundation of China (Nos. 12275182 and 62371314), Guangdong Basic and Applied Basic Research Foundation (Nos. 2024A1515012154), the Guangdong Provincial Project (Grant No. 2023TQ07A233), the Major Program of Shenzhen Bay Laboratory (No. C1012530005) and the Shenzhen Bay Laboratory Proof-of Concept Grants (No. C1022430005).

Abstract

Proton therapy requires accurate in *vivo* dose verification because proton range uncertainties may compromise treatment precision. This study aimed to develop and evaluate a deep learning-based method for three-dimensional (3D) dose reconstruction using positron emission tomography (PET) in proton therapy.

A dual-panel PET system with time-of-flight and depth-of-interaction (TOF-DOI) capability was modeled using GATE Monte Carlo simulations. PET activity images and corresponding ground-truth dose maps were generated for single pencil beams with energies across 60–120 MeV. A U-Net-based neural network was developed to reconstruct the 3D dose distributions from reconstructed PET activity images. Quantitative evaluation was performed using 3D gamma passing rates (GPRs) and distal range metrics (R_{50} and R_{90}).

The proposed method accurately reconstructed 3D dose distributions while reduced the impact of limited-angle artifacts inherent to the dual-panel PET geometry. GPRs exceeded 99% under the 3%/3 mm criterion and 98% under the 2%/2 mm criterion for all validation datasets. Submillimeter accuracy was achieved for distal range verification, with maximum deviations of 0.15 mm for R_{50} and 0.11 mm for R_{90}.

The results demonstrate the feasibility of using a dual-panel PET system with a deep learning method for accurate 3D dose reconstruction and proton range verification, supporting its potential in proton therapy quality assurance.

References

[1] M. Niu, *et al*, "Development of a dual-panel high-resolution TOF-DOI PET prototype dedicated to organ imaging," SNMMI 2026 Annual Meeting (accepted), 2026.

[2] S. Huang, *et al*, "Optimization of TOF and DOI performance in a multi-resolution detector for brain-dedicated PET," IEEE Transactions on Radiation and Plasma Medical Sciences, vol. 10, no. 3, pp. 380–390, 2026.

MIC-05-346

Validation of Dose-to-PET Conversion for OpenPET Range Verification in Carbon-Ion Therapy (#2077)

Hideaki Tashima[1], Tianxue Du[2], Chie Toramatsu[1], Takamitsu Masuda[1], Giulia Vallari[2], Marco Pinto[2], Akram Hamato[1], Yuma Iwao[1], Han Gyu Kang[1], Minoru Tajiri[1], Hideyuki Mizuno[1], Taku Inaniwa[1], Masashi Koto[1], Hiroaki Ikawa[1], Makoto Shinoto[1], Katia Parodi[2], Taiga Yamaya[1]

[1] National Institutes for Quantum Science and Technology, Department of Advanced Nuclear Medicine Sciences, Chiba, Japan; [2] Ludwig-Maximilians-Universität München, Department of Medical Physics, Munich, Germany

The authors acknowledge financial support from the DGMP Wolfgang Schlegel Stipendium, which supported Tianxue Du's research stay at QST.

Abstract

In-beam PET is a promising technique for range verification in particle therapy because positron emitters are produced along the beam path through nuclear fragmentation reactions. Over the past years, QST has developed a human-scale OpenPET system that enables three-dimensional PET imaging during and/or immediately after carbon-ion therapy. In parallel, LMU has developed an analytical approach based on a pencil beam algorithm for irradiation-plan-based PET image prediction. In the present study, we combine these two developments toward the clinical implementation of OpenPET for range verification in carbon ion therapy. The approach involves comparing measured OpenPET images with predicted PET images.

Phantom experiments were performed at HIMAC. OpenPET data were acquired during and after irradiation. To simplify PET image prediction, the present analysis was limited to the post-irradiation period, and list-mode data acquired from 0 to 600 s after the end of irradiation were extracted and reconstructed as the measured OpenPET image. A predicted PET image corresponding to the same 0-600 s post-irradiation period was generated from the irradiation plan and PET measurement conditions by modeling positron-emitter production and physical decay.

The predicted PET images showed an activity distribution corresponding to the planned irradiation fields, and the comparison indicated reasonable agreement between the predicted and measured images. These results demonstrate the feasibility of combining OpenPET with the irradiation-plan-based PET prediction, and they support the potential of the clinical use of OpenPET for range verification in carbon-ion therapy.

References

[1] K. Parodi and J. C. Polf, "*In vivo* range verification in particle therapy," *Medical Physics*, vol. 45, pp. e1036-e1050, Nov. 2018.

[2] T. Yamaya, et al., "A proposal of an open PET geometry," *Phys. Med. Biol.*, vol. 53, pp.757-73, Feb. 2008.

[3] H. Tashima, et al., "A single-ring OpenPET enabling PET imaging during radiotherapy," *Phys. Med. Biol.*, vol. 57, pp. 4705-18, July 2012.

[4] H. Tashima, et al., "Development of a multiuse human-scale single-ring OpenPET system," *IEEE TRPMS*, vol. 5, pp. 807-816, Nov. 2021.

[5] Y. Hirano et al., "Performance evaluation of a depth-of-interaction detector by use of position-sensitive PMT with a super-bialkali photocathode," *Radiol. Phys. Technol.*, vol. 7, pp. 57–66, Jan. 2014.

[6] H. Tashima, et al., "First Patient Study of In-Beam OpenPET for Range Verification in Carbon-Ion Therapy," *2024 IEEE NSS MIC RTSD*, Tampa, FL, USA, 2024. DOI:10.1109/NSS/MIC/RTSD57108.2024.10655431

[7] H. Tashima, et al., "Clinical OpenPET for Range Verification in Carbon-Ion Therapy: Gamma-Index Analysis for Inter-Fractional Comparison," *2025 IEEE NSS MIC RTSD*, Yokohama, Japan, 2025. DOI: 10.1109/NSS/MIC/RTSD57106.2025.11287913

[8] T. Du, J. Bauer, et al., "Validation of an analytical approach for in vivo PET verification in carbon ion therapy: comparison with Monte Carlo simulations and PET monitoring measurements," *Phys. Med. Biol.*, vol. 71, 095010, 2026.

MIC-05-349

EasyPET.3D imaging of positron-emitter distributions in proton-irradiated PMMA phantoms (#2152)

Ana C. Magalhães[1], Pedro M.M. Correia[1], Martin Grossmann[2], David Meer[2], João Veloso[1], Ana Luísa M. Silva[1]

[1] I3N -University of Aveiro, Physics Dpt., Aveiro, Portugal; [2] Paul Scherrer Institut, PSI, Villigen, Switzerland

- Project UID/50025/2025, UID/PRR/50025/2025 UID/PRR2/50025/2025 and the Associate Laboratory I3N – LA/P/0037/2020, financed by FCT/MEC;
- HadronPET - COMPETE2030-FEDER-00755500, funded by FEDER program and by FCT, Portugal;
- Grant to A. C. M. Magalhães (PRT/BD/153499/2021) through FCT, Portugal.

Abstract

Accurate quality assurance (QA) is essential in proton therapy, where the steep dose gradient of the Bragg peak requires precise knowledge of beam position to spare healthy tissue while ensuring full tumor coverage. This work presents the experimental evaluation of easyPET.3D, a compact and cost-effective preclinical PET scanner, as a potential tool for pretreatment QA in proton therapy using phantoms.Homogeneous PMMA phantoms were irradiated at the Paul Scherrer Institute (PSI) Gantry 1 facility with proton energies ranging from 138 to 195 MeV, delivering up to 6.4 × 10^{11} protons per irradiation. The resulting 3D β+ activity distributions were reconstructed and analyzed to characterize both longitudinal range and transverse beam profiles. A temporal convergence study determined the minimum acquisition time required for stable range estimation. In addition, a controlled displacement experiment, with longitudinal offsets of 1, 2, 3, and 5 mm, was performed to assess the system's ability to detect range variations.Transverse analysis revealed energy-dependent beam broadening, with mean FWHM values decreasing from 12.3 mm at 138 MeV to 9.6 mm at 195 MeV, and a characteristic widening near the distal end consistent with proton stopping at the Bragg peak. Range estimation converged within 10–12 cumulative frames (~30–35 min). Sensitivity tests showed that the system could detect longitudinal phantom displacements as small as 1 mm, with a linear response and a systematic overestimation of 13%, attributed to manual positioning uncertainties.These results demonstrate that easyPET.3D is a promising and accessible solution for pretreatment QA in proton therapy workflows.

References

[1] *A.-C. Knopf et al., PMB, vol. 58, no. 15, pp. R131–R160, 2013.*
[2] *A. Topi et al., Physica Medica, vol. 70, pp. 164–175, 2020.*
[3] *V. Ferrero et al., Scientific Reports, vol. 8, no. 1, p. 4100, 2018.*
[4] *K. Parodi et al., PMB, vol. 45, no. 11, pp. N151–N156, 2000.*
[5] *F. M. Ribeiro et al., IEEE TRPMS, vol. 9, no. 7, pp. 959–969, 2025.*
[6] *A. C. M. Magalh˜aes et al., BPEX, vol. 11, no. 6, p. 065037, 2025.*

MIC-05-352

Dosimetry-Oriented Structure-Weighted CT-Guided Registration for Multi-Time-Point SPECT/CT in Radionuclide Therapy (#2369)

Yanzhen Du[1], Zhaoxia Wu[1], Shi Wang[1], Yue Chen[2], Chi Qi[2], Hui Liu[1], Yaqiang Liu[1]

[1] Tsinghua University, Department of Engineering Physics, Beijing, China; [2] The Affiliated Hospital of Southwest Medical University, Department of Nuclear Medicine, Luzhou, China

This work was supported in part by the National Key Research and Development Program of China (No. 2022YFC2402002, No. 2022YFC2403802), and National Natural Science Foundation of China (No. 12205166)

Abstract

Multi-time-point SPECT/CT is used for patient-specific dosimetry after Lu-177-PSMA therapy. However, inter-scan motion, anatomical deformation, and time-dependent uptake variations can compromise volume-of-interest (VOI) activity extraction and time-integrated activity (TIA) estimation, thereby requiring accurate inter-time-point SPECT registration. This study proposes a structure-weighted CT-guided registration method for longitudinal SPECT/CT. Organ-specific dosimetric priorities and an uptake-derived activity-concentration term were integrated into a spatial weight map, which was incorporated into the CT registration similarity metric to emphasize structures with greater dosimetric relevance. The resulting CT-derived transformation was applied to SPECT images using physical-coordinate inverse mapping. Compared with Elastix and an unweighted baseline, the proposed method improved SPECT VOI Dice similarity coefficient (DSC) from 0.82 with Elastix and 0.87 with the unweighted baseline to 0.90. It also reduced fitting-residual-based TIA normalized root-mean-square error (nRMSE) across all evaluated structures, with additional reductions relative to the unweighted baseline of 15.8% in kidneys, 23.2% in prostate, and 49.2% in tumors. These results indicate that incorporating dosimetric structure weighting into CT-guided registration can improve dosimetry-relevant spatial consistency and temporal fitting stability in multi-time-point SPECT/CT workflows for radionuclide therapy.

References

[1] J. Luo et al., “Multi-timepoint SPECT image registration for PSMA-targeted radiopharmaceutical therapy dosimetry,” Journal of Nuclear Medicine, vol. 64, suppl. 1, p. P1275, Jun. 2023, abstr.

[2] K. M. Kim et al., “Enhancing voxel-based dosimetry accuracy with an unsupervised deep learning approach for hybrid medical image registration,” Medical Physics, vol. 51, no. 9, pp. 6432–6444, Sep. 2024.

[3] X. Tang et al., “Segmentation-guided multi-modal registration of liver images for dose estimation in SIRT,” EJNMMI Physics, vol. 9, no. 1, Art. no. 3, Jan. 2022.

MIC-05-355

Characterization and biological validation of a BNCT irradiation field using PADC detectors, RCF and microdosimetric modelling (#2456)

Joan Flors Marti[1], Michael Seimetz[1], Pablo Botella Asunción[2], Eva Rivero-Buceta[2], Marcin Balcerzyk[3], Christopher Geppert[4], Jörg Krämer[4], Sebastian Zahnreich[5], Jose Maria Benlloch[1]

[1] Instituto de Instrumentación para Imagen Molecular (i3M), CSIC-Universitat Politècnica de València, Valencia, Spain; [2] Instituto de Tecnologías Químicas (ITQ), CSIC-Universitat Politècnica de València, Valencia, Spain; [3] Bioaraba Health Research Institute & Basque Foundation for Science, Vitoria-Gasteiz, Spain; [4] Johannes Gutenberg-Universität Mainz, Mainz, Germany; [5] Universitätsmedizin der Johannes Gutenberg-Universität Mainz, Mainz, Germany

Abstract

Boron Neutron Capture Therapy (BNCT) is a binary radiation treatment relying on the selective uptake of B-10 in tumors, requiring a high thermal neutron flux with minimal fast neutron and gamma ray contamination. The reaction between the thermal neutron and the B-10 releases an alpha and lithium nucleus, two high-LET particles that deposit their energy inside the cell causing lethal damage. This work characterizes a BNCT-optimized irradiation field at a TRIGA Mark II reactor and compares the effects on various cell samples to standard radiation fields. The irradiation setup was localized within the graphite thermal column of the TRIGA reactor (Mainz). Gamma contamination was mitigated using lead shielding, while additional graphite bars further thermalized the neutrons. Dosimetric profiling was conducted using radiochromic films paired with specific radiation converters. Additionally, PADC plates were employed to quantify the alpha particle tracks emitted by the BNCT reaction, as well as proton tracks generated by the elastic scattering of fast neutrons. For biological validation, FaDu tumor cells and isolated lymphocytes were exposed to nominal doses (1–6 Gy) to evaluate clonogenic survival and DNA double-strand breaks (DSB) via the γH2AX foci assay. Experimental data were cross-referenced with Monte Carlo (GATE/Geant4) cellular microdosimetric models. Dose contributions from primary beam components were assessed across different shielding configurations to optimize the thermal neutron field, and microdosimetric models were applied to estimate biological sample doses. Results demonstrated linear dose-response relationships for lymphocyte DNA damage, while tumor cell survival was reduced compared to photon reference data, due to relative biological effectiveness of thermal neutrons.

Ultimately, this integrated experimental and computational methodology validates the reactor facility for advanced BNCT research.

References

[1] Jin, WH, et al., 2022, 'A review of Boron Neutron Capture Therapy: Its History and Current Challenges', *Int J. Part. Therm*,1,71-82

[2] Ziegner, M,et al., 2014, 'Confirmation of a realistic reactor model for BNCT dosimetry at the TRIGA Mainz', *Med Phy*, 11, 6-7

[3] Malouff, TD, et al., 2021, 'Boron Neutron Capture Therapy: A Review of Clinical Applications', *Front. Oncol*, 11, 1-5

[4] Pedrosa-Rivera, M, et al., 2020, 'Neutron Radiobiology studies with a pure cold neutron beam', *Nucl. Instr Meth. B*, 6, 24-31

MIC-05-358

MACACO III+ Compton camera imaging of ^{225}Ac in mice (#2614)

Karol Brzeziński[1], Luis Barrientos[1], Jorge Rodríguez[2], Unai Cossío[2], Jordi Llop[2], Gabriela Llosá[1]

[1] Instituto de Física Corpuscular (IFIC), CSIC-UV, Valencia, Spain; [2] CIC biomaGUNE, Basque Research and Technology Alliance (BRTA), San Sebastián, Spain

This work has received funding from the Spanish MICIN/AEI (project MIDAS, PID2022-143246OB-I00).

Abstract

Compton cameras are a potential tool for assessing translational targeted alpha therapy (TAT) treatments using ^{225}Ac in murine models. For this application, gamma cameras perform sub-optimally due to the extremely low activities used. The IRIS group at IFIC-Valencia is developing Compton cameras based on lanthanum bromide ($LaBr_3$) crystals, capable of visualizing ^{225}Ac distributions through the detection of the 440 keV gammas emitted during the decay of its short-lived daughter nuclide ^{213}Bi. Following successful imaging tests with ^{131}I in live mice at CIC biomaGUNE in San Sebastián, Spain, this work presents measurements performed using the current Compton camera prototype, MACACO III+, and a mouse phantom filled with ^{225}Ac. The system was shown to be capable of visualizing ^{225}Ac distributions in the phantom with two combinations of organ compartments filled with activity. Images obtained using the Compton camera are of comparable quality to those obtained using commercial pre-clinical SPECT systems at 440 keV. Monte Carlo simulations of a mouse phantom filled with ^{225}Ac have also demonstrated the improved image quality that can be achieved with an augmented Compton camera, MACACO IV, featuring a larger first plane detector and currently under development. Measurements using MACACO III+ for imaging live mice grafted with AR42J tumor cells and injected with [^{225}Ac]Ac-DOTATATE are planned for the near future.

References

[1] Morgenstern, A *et al* 2018, *Curr Radiopharm* 11, 200-208
[2] Scheinberg, DA *et al* 2011, *Curr Radiopharm* 4(4), 306–320
[3] Seo, Y 2019 *Nucl. Med. Mol. Imaging* 53, 182–188
[4] Kim, J-G *et al* 2024 *Applied Radiation and Isotopes* 206, 111236
[5] Robertson, AKH. *et al* 2017 *Phys. Med. Biol.* 62(11), pp. 4406-4420
[6] Roser, J *et al* 2025 *Physica Medica* vol. 132. 104928
[7] Brzezinski, K *et al*; *IEEE NSS MIC RTSD* Tampa, USA (2024)
[8] Barrientos, L *et al* 2026 *IEEE TRPMS* (provisionally accepted).
[9] Jan S *et al* 2004 *Phys. Med. Biol.*, 49(19), 4543-61

MIC-05-361

Boron Imaging with a Compton Camera: Toward Real-Time Dosimetry in BNCT Treatments (#2726)

Pablo Torres-Sánchez[1], Sebastián Valladares-Sánchez[1], Víctor Babiano-Suárez[1], Javier Balibrea-Correa[1], Bernardo Gameiro[1], Ion Ladarescu[1], Jorge Lerendegui-Marco[1], Silva Bortolussi[2,3], Setareh Fatemi[3], Ian Postuma[3], César Domingo-Pardo[1]

[1] Instituto de Física Corpuscular (CSIC-UV), Grupo de Espectroscopía Gamma, Valencia, Spain; [2] Università di Pavia, Dipartimento di Fisica, Pavia, Italy; [3] Istituto Nazionale di Fisica Nucleare, Sezione di Pavia, Pavia, Italy

Abstract

Boron Neutron Capture Therapy is a binary cancer treatment modality in which a tumour-selective boron-carrying drug is administered to the patient prior to irradiation with a neutron beam. The highly localised nuclear reaction between thermal neutrons and ^{10}B deposits a lethal radiation dose selectively within tumor cells. After recent advances driven by accelerator-based neutron sources and improved boron compounds, a critical gap remains: there is currently no method to image boron distribution in vivo during treatment, preventing real-time dose verification.

We present the development of a Compton camera system designed to detect the 478 keV prompt gamma rays emitted following ^{10}B neutron capture, thereby enabling direct spatial mapping of boron dose deposition. The detector is based on $LaCl_3$ and $CeBr_3$ scintillators arranged in a pyramidal geometry, inherited from nuclear physics instrumentation developed at CERN-n_TOF, which provides intrinsically low neutron sensitivity and high gamma-ray detection efficiency.

Experimental validation was carried out at Institut Laue-Langevin (ILL, Grenoble). A boron sample in water at 65 ppm, within the clinically relevant concentration range, was successfully imaged, yielding a signal-to-background ratio of 12. This constitutes, to our knowledge, the first experimental demonstration of Compton imaging of boron at clinical concentration levels.

At treatment-level neutron fluxes, however, the original detector suffered from count rate saturation. To address this, we redesigned the detector incorporating pixelated crystal arrays. The pixelated prototype was subsequently validated at the LENA reactor (U. Pavia) achieving a reduction in per-crystal count rate by a factor of approximately 250.

These results represent a substantive step toward a clinically deployable real-time boron imaging system, with implications both for treatment monitoring of patients and preclinical pharmacokinetic studies with animal models.

MIC-05-364

Feasibility of In-vivo Dosimetry for Proton Therapy using a Mobile Point-of-Care (PoC) PET Imaging System (#2876)

Samarth Aggarwal[1], Yao Hao[2], Xiandong Zhao[2], Ling Cai[1], Jaume R. Otaegui[3], Daniel Thorek[3], Richard Laforest[3], Stephanie Perkins[2], Yongjian Liu[3], Joseph O'Sullivan[1,4], Yuan-Chuan Tai[1,3]

[1] Washington University in St. Louis, Imaging Science Doctoral Program, St. Louis, USA; [2] Washington University in St. Louis, Radiation Oncology, St. Louis, USA; [3] Washington University in St. Louis, Radiology, St. Louis, USA; [4] Washington University in St. Louis, Electrical and Systems Engineering, St. Louis, USA

This work is funded in part by the National Institute of Biomedical Imaging and Bioengineering (NIBIB) of the National Institute of Health (NIH) (R01EB035144), Mallinckrodt Institute of Radiology internal allotment, the Siteman Cancer Center OIP Catalyst Award.
S.Aggarwal is partly funded by the Imaging Science Pathway Fellowship (NIH 5T32EB01485505).

Abstract

Proton therapy enables conformal tumor irradiation while reducing dose to surrounding healthy tissues. But anatomy, motion, and delivery uncertainty can cause differences between planned and delivered dose. PET can detect proton-induced positron-emitting radionuclides such as ^{15}O, ^{13}N, & ^{11}C, providing a method for post-irradiation in-vivo dosimetry verification. We evaluated a mobile PoC-PET system for imaging validation & MLEM-based radionuclide decomposition.

PoC-PET used 8 TOF detector modules. Imaging performance was evaluated with a Derenzo-style tumor phantom 3.3-11.4mm lesions at a 20:1 tumor:background ratio and with a FDG-injected mouse. To evaluate radionuclide decomposition, three vials with known ^{15}O, ^{13}N, & ^{11}C activities were imaged for 60 minutes. Counts were binned in 30s windows and reconstructed into PET image series. ROIs generated decay curves modeled as mixtures of exponential decay components using an MLEM-based fitting approach.

PoC-PET resolved all tumor clusters by the VPR < 0.735 criterion. Mouse imaging clearly showed regional FDG uptake with spatial agreement to MicroPET. In the multi-isotope experiment, the MLEM fit matched the large-ROI decay curve with a ~1% nRMSE. The fitted isotope allocation captured expected isotope behavior: ^{15}O dominating early, ^{13}N showing intermediate decay, and ^{11}C persisting throughout the scan. The injected mixture was 29% ^{11}C, 16% ^{13}N, and 55% ^{15}O, the MLEM estimated 27.7%, 15.7% and 56.6% respectively.

These results demonstrate the feasibility of using a mobile PoC-PET system and radionuclide decomposition for post-irradiation radionuclide characterization.

MIC-05-367

Unfolding Temporal Behavior in Emerging ^{161}Tb-FAPI-2286 Dosimetry: Role of Partial Volume Correction in Lesion and Organ Quantification

(#3025)

Mohamed Saber Azimi[1], Milad Peer-Firozjaei[2], Maryam Cheraghi[3], Ghasemali Divband[4], Swagat Dash[5], Vindhya Malasani[5], Kamal Yadav[5], Rakhee Vatsa[6], Parul Thakral[7], Priya Ashok[8], Naveen Sanchety[9], Vishnu Hari[10], Habibollah Dadgar[11], Majid Assadi[12], Hossein Arabi[13]

[1] Óbuda University, Doctoral School of Applied Informatics and Applied Mathematics, Budapest, Hungary; [2] Babol University of Medical Science, Student Research Committee, Babol, Iran; [3] Shahid Beheshti University of Medical Sciences, PET-CT Unit, Department of Nuclear Medicine, Masih Daneshvari Hospital, Tehran, Iran; [4] Jam Hospital, Department of Nuclear Medicine, Tehran, Iran; [5] Sarvodaya Hospital, Deptartment of Nuclear Medicine & Molecular Theranostics, Faridabad, India; [6] ABX-CRO, Advanced Pharmaceutical Services, New Delhi, India; [7] Fortis Memorial Research Institute, Department of Nuclear Medicine, Gurugram, India; [8] GE HealthCare, Molecular Imaging Application Specialist, Bengaluru, India; [9] Sarvodaya Hospital, Department of Surgical Oncology, Faridabad, India; [10] Sarvodaya Hospital, Department of Medical Oncology & Bone Marrow Transplant, Faridabad, India; [11] Imam Reza International University, Cancer Research Center, Mashhad, Iran; [12] The Persian Gulf Nuclear Medicine Research Center, Department of Molecular Imaging, and Theranostics, Bushehr, Iran; [13] Geneva University Hospital, Division of Nuclear Medicine and Molecular Imaging, Geneva, Switzerland

Abstract

Multi-time-point SPECT/CT imaging enables improved characterization of radiotracer kinetics for quantitative dosimetry, particularly in emerging radiopharmaceutical therapies. However, activity quantification is affected by partial volume effects (PVE), which introduce time-dependent bias in both lesion and organ dose estimation. This issue is especially relevant for novel radionuclides such as ^{161}Tb, where complex emission characteristics may lead to varying sensitivity to image correction across time. In this study, we analyze the temporal behavior of lesion and organ dosimetry for ^{161}Tb-FAPI-2286 and evaluate the influence of partial volume correction at multiple imaging time points (2 h, 24 h, and 96 h post-injection). Patient-specific SPECT/CT data were used, with lesions and organs segmented using semi-automatic and deep learning-based approaches. Two iterative correction methods, Richardson–Lucy and reblurred Van Cittert (RVC), were applied prior to dosimetric analysis. Absorbed dose values were estimated using Monte Carlo simulations, and relative differences were computed between corrected and non-corrected images. Results indicate minimal impact of correction at early imaging, with relative differences generally below ±3%. In contrast, substantial and heterogeneous variations were observed at later time points, with lesion-level dose changes ranging from approximately −30% to +38%. Bone lesions exhibited the largest positive deviations, whereas lung lesions showed consistent reductions at delayed imaging. Both correction methods demonstrated similar temporal patterns, with slightly lower variability for the RVC approach. These findings highlight the time-dependent nature of PVE in ^{161}Tb-based dosimetry and emphasize the importance of incorporating correction methods in delayed imaging. Temporal-aware quantitative strategies are therefore essential for improving the reliability of lesion-level dose estimation in emerging theranostic applications.

References

[1] H. Dadgar et al., "Exploring the efficacy of FAPI PET/CT in the diagnosis and treatment management of colorectal cancer: a comprehensive literature review and initial experience," Clinical and Translational Imaging, vol. 12, no. 3, pp. 235-252, 2024.

[2] H. Dadgar et al., "Targeted radioligand therapy: physics and biology, internal dosimetry and other practical aspects during 177Lu/225Ac treatment in neuroendocrine tumors and metastatic prostate cancer," Theranostics, vol. 15, no. 10, p. 4368, 2025.
[3] M. S. Azimi et al., "Critical review of partial volume correction methods in PET and SPECT imaging: benefits, pitfalls, challenges, and future outlook," European Journal of Nuclear Medicine and Molecular Imaging, pp. 1-32, 2025.
[4] M. S. Azimi et al., "Impact of partial volume correction on radiomics reproducibility in theranostic SPECT/CT imaging," Medical Physics, vol. 53, no. 4, p. e70427, 2026/04/03 2026, doi: 10.1002/mp.70427.

MIC-05-370

COXIRIS: A Novel Real-Time Platform for Integrated Cancer Detection, Medical Imagen and Targeted Treatment; Deep EDXRF Detection (#3141)

Rodolfo G. Figueroa Saavedra[1], Bryan Casanelli[2], Joan Sagardia[1], Mauro A. Valente[1], Natalia S. Villar[1], Manuel Cerna[1], Ana Luísa M. Silva[2], National Research and Development Agency of Chile (ANID) and the Frontera Uninversity

[1] Universidad de la Frontera, Center for Physics and Engineering in Health Please and Department of Physical Sciences, TEMUCO, Chile; [2] Aveiro University, Department of Physics, AVEIRO, Portugal

For the financial support of the Advanced Technologies Program of FONDEF TA 24I 10046 of the National Research and Development Agency of Chile

Abstract

The development of integrated strategies for simultaneous cancer detection and treatment is driving advanced theranostic platforms. In this context, the COXIRIS system (Confocal Orthovoltage X-Ray Induced Radiation Integral System) introduces a large-scale X-ray fluorescence (XRF) imaging architecture designed to combine real-time functional imaging with precision-guided therapy.This work evaluates the feasibility of COXIRIS for imaging and guiding treatment of tumors labeled with high-Z biomarkers or nanoparticles (e.g., Au, Gd). The system uses XRF detection with a collimated X-ray source directed toward a focal inspection region, while a synchronized high-sensitivity detection system performs three-dimensional scanning and tumor localization. The partially confocal detection geometry improves spatial selectivity at macroscopic scale and enables guidance of therapeutic modalities including radiotherapy, ablation, drug delivery, and surgical assistance.Experimental results demonstrated tumor localization at depths up to 15 cm in tissue-equivalent media using low radiation dose levels. Gadolinium-based targets were detected in less than 2 seconds at this depth. Although acquisition times are currently comparable to some nuclear medicine procedures, scalability through larger detector areas and optimized geometry indicates potential for sub-second detection.COXIRIS represents a novel large-scale XRF imaging and theranostic guidance platform that addresses limitations of existing micro-scale XRF techniques. Its compatibility with conventional radiotherapy systems, including linear accelerators and orthovoltage units, supports its translational potential for real-time and personalized cancer treatment.

References

[1] R. G. Figueroa, E. Lozano, F. Belmar and J. Veloso, *Radiation Physics and Chemistry*, vol. 95, pp. 288–291, 2014. doi: 10.1016/j.radphyschem.2013.10.005.
[2] B. L. Jones and S. H. Cho, "The feasibility of polychromatic cone-beam x-ray fluorescence computed tomography (XFCT) imaging of gold nanoparticle-loaded objects: a Monte Carlo study," *Physics in Medicine and Biology*, vol. 56, no. 12, pp. 3719–3730, 2011. doi: 10.1088/0031-9155/56/12/017.pp. N309–N315, 2004. doi: 10.1088/0031-9155/49/18/N03
[3] J. F. Hainfeld, D. N. Slatkin and H. M. Smilowitz, "The use of gold nanoparticles to enhance radiotherapy in mice," *Physics in Medicine and Biology*, vol. 49, no. 18, pp. N309–N315, 2004. doi: 10.1088/0031-9155/49/18/N03.
[4] L. Vincze, K. Janssens and F. Adams, "*Spectrochimica Acta Part B*, vol. 59, no. 10–11, pp. 1723–1730, 2004. doi: 10.1016/j.sab.2004.08.004.
[5] [D. Verellen, M. De Ridder, N. Linthout *et al.*, *Nature Reviews Cancer*, vol. 7, pp. 949–960, 2007. doi: 10.1038/nrc2288.
[6] R. G. Figueroa, M. Valente, J. Guarda, J. Leiva, E. Quilaguilque, B. Casanelli and F. Leyton, "OXIRIS project: Development of a new XRF device for the simultaneous detection and treatment of cancer," X-Ray Spectrometry, vol. 51, no. 3, pp. 251–259, 2022. doi: 10.1002/xrs.3272.
[7] J. Sagardia, M. Valente, F. Mattea, N. Villar, C. Toro, F. Jerez, M. Flores and R. Figueroa, "EDXRF analysis of Gdbased tumoral biomarker using a collimated 241Am source in a bioequivalent phantom," Radiation Physics and Chemistry, vol. 237, 113017, 2025.

MIC-05-373

Attenuation Correction Using 176Lu Background in Limited-Angle Flat-Panel Total-Body PET (#1490)

Thibault D'Hulster, Jens Maebe, Stefaan Vandenberghe

Ghent University, MEDISIP, Ghent, Belgium

Abstract

A novel flat-panel total-body walk-through PET system under development at Ghent University aims to improve patient throughput and cost-effectiveness compared to conventional total-body scanners. Its high sensitivity enables low-dose imaging protocols, where CT may be omitted to minimize radiation exposure. In this setting, an alternative CT-less attenuation correction method is required. The high sensitivity and large number of LYSO detector elements in the walk-through geometry also result in a substantial and potentially exploitable intrinsic background signal from ^{176}Lu.

This GATE simulation study investigates the feasibility of leveraging this intrinsic ^{176}Lu background activity in the LYSO detectors for transmission-based attenuation estimation. The limited angular coverage inherent to the flat-panel design introduces additional challenges for implementation of this method. To address this, a maximum likelihood transmission reconstruction (MLTR) algorithm was implemented. MLTR is particularly interesting for low-dose applications because it is independent of emission data and computationally efficient, making it suitable for clinical integration.

The effect of limited-angle artifacts on attenuation map convergence was evaluated, along with their impact on attenuation correction in PET image reconstruction, using a full angular coverage flat-panel geometry with side panels as reference. Simulations with a NEMA image quality phantom and the XCAT phantom demonstrated that limited angular coverage has minimal impact on attenuation correction in emission image reconstruction. These transmission-based attenuation maps may further serve as initial estimates for more advanced approaches, such as maximum likelihood reconstruction of attenuation and activity (MLAA) or physics-informed deep learning methods.

References
[1] Vandenberghe, S, Moskal, P, Karp, JS 2020, 'State of the art in total body PET', *EJNMMI Physics*, 7(1)
[2] Vandenberghe, S *et al*. 2023, 'Walk-through flat panel total-body PET: a patient-centered design for high throughput imaging at lower cost using DOI-capable high-resolution monolithic detectors', *EJNMMI*, 50(12), 3558-3571
[3] Sari, H *et al*. 2025, 'Feasibility of an Ultra-Low-Dose PET Scan Protocol with CT-based and LSO-TX-Based Attenuation Correction Using a Long-Axial-Field-of-View PET/CT Scanner', *Journal of Nuclear Medicine*, 66(6), 967-972

MIC-05-376

System Characterization of a DOI-Enabled High-Resolution Total-Body TOF PET Scanner (#1642)

Da Liang, Yuejie Lin, Han Liu, Xin Yu, Haoyu Zou, Ying Xu, Huiping Zhao, Jinyong Tao, Wenjing Zhu, Ying Lin, Wangquan Ma, Wenbin Li, Yibin Zhang, Dawei Shi, Jiayang Zeng, Qiushi Ren, Zhaoheng Xie, Wei Liu, Qiyu Peng

Shenzhen Bay Laboratory, Institute of Biomedical Engineering, Shenzhen, China

This work was supported by the National Natural Science Foundation of China (Grant no. 82327809), National High-Level Hospital Clinical Research Funding (2025-PUMCH-D-003), Beijing Natural Science Foundation(L252047), the National Key Research and Development Program of China (Grant No. 2024YFF0507700).

Abstract

A DOI-enabled total-body TOF PET system with a 200-cm axial field of view was developed using 2-mm-pitch LYSO crystal arrays and light-sharing-window-based DOI encoding. The system consists of seven detector rings with a transaxial diameter of 70 cm. Phantom experiments, including SZBL logo, Derenzo, and dynamic line-source phantoms, were performed to evaluate imaging performance. The reconstructed logo phantom demonstrated clear visualization of 2-mm structures, while rods down to 2.0 mm could be distinguished in the Derenzo phantom, indicating high spatial resolution consistent with the detector crystal pitch. Dynamic imaging results demonstrated continuous tracer propagation across consecutive 5-s frames, indicating high sensitivity and short-frame dynamic imaging capability. In addition, TOF resolution measurements based on the NEMA NU 2-2018 method achieved approximately 330 ps for both single-ring and dual-ring configurations. These results demonstrate the feasibility of integrating DOI capability, high spatial resolution, dynamic imaging capability, and stable TOF performance within a long axial field-of-view total-body PET system.

MIC-05-379

Implementation and Evaluation of TOF and Scatter correction for the IMAS TB-PET (#1989)

Álvaro Anreus-Valero[1], Marta Freire[1], David Sanchez[2], Santiago Jimenez-Serrano[1], Neus Cucarella[1], Andrea Gonzalez-Montoro[1], Alfonso Rios[3], Irene Torres-Espallardo[4], Luis F. Vidal[1], Marc Gil[1], Antonio J. Gonzalez[1]

[1] the Instituto de Instrumentación para Imagen Molecular (I3M), Centro Mixto CSIC–Universitat Politècnica de València, Valencia, Spain; [2] Oncovision S.A., Valencia, Spain; [3] Full Body Insight, Valencia, Spain; [4] Hospital La Fe, Clínical Area of Medical Imaging, Valencia, Spain

This work was partly supported by the Imagen Molecular de Alta Sensibilidad (IMAS) project launched by the Consellería de Sanitat Universal I Salut Publica of the Government of Valencia Region, announced in BOE 328, December 28, 2020, co-funded at 50% by the European Regional Development Fund (ERDF).
M. Freire was supported by the CIAPOS Program for Researchers in Postdoctoral Phase of the Generalitat Valenciana under Grant No. CIAPOS/2023/141

Abstract

Total-Body Positron Emission Tomography systems offer substantially increased sensitivity due to their extended axial FOV, enabling reduced dose, shorter acquisitions, or improved image quality. Incorporating TOF information further enhances image reconstruction by improving Signal-to-Noise Ratio. We have recently developed and installed a novel TB-PET scanner (IMAS) at Hospital La Fe in Valencia (Spain). The system is based on semi-monolithic LYSO crystals and provides TOF and Depth of Interaction (DOI) capabilities. In this work, we present the implementation and evaluation of TOF and scatter correction for the IMAS system, and we also present ongoing developments related to random, dead time, and quantification corrections are presented.

For the TOF information, an iterative skew correction was used. Scatter correction was applied using a TOF-based scaling method. For the random, dead-time and quantification correction study, the acquisition mode was modified allowing the acquisition of coincidences and singles at the same time.

A system CTR of 690 ps was measured at the NECR peak. The combined use of TOF and DOI information and the inclusion of scatter correction demonstrated a reduction in positional errors for off-center lesions and an improvement of the SNR, contributing to improving the image quality of the IMAS system.

References

[1] Surti, S., Pantel, A. R., & Karp, J. S. (2020). Total body PET: why, how, what for?. *IEEE transactions on radiation and plasma medical sciences*, *4*(3), 283-292.

[2] Vandenberghe, S., Moskal, P., & Karp, J. S. (2020). State of the art in total body PET. *EJNMMI physics*, *7*(1), 35.

[3] Gonzalez, A. J., Anreus-Valero, A., Sanchez, D., Jiménez-Serrano, S., Freire, M., Gonzalez-Montoro, A., ... & Torres-Espallardo, I. (2026). Initial Performance of a Long Axial FOV PET with TOF and DOI capabilities: IMAS system. *arXiv preprint arXiv:2603.09898*.

[4] Perkins, A. E., Werner, M., Kuhn, A., Surti, S., Muehllehner, G., & Karp, J. S. (2005, October). Time of flight coincidence timing calibration techniques using radioactive sources. In *IEEE Nuclear Science Symposium Conference Record, 2005* (Vol. 5, pp. 2488-2491). IEEE.

[5] Conti, M., Bendriem, B., Casey, M., Chen, M., Kehren, F., Michel, C., & Panin, V. (2005). First experimental results of time-of-flight reconstruction on an LSO PET scanner. *Physics in Medicine & Biology*, *50*(19), 4507-4526.

MIC-05-382

Addressing Scatter Phantom Length Limitations: A Single-Scan Multi-Position Method for NEMA NU 2 Testing of Long Axial FOV PET Systems (#2290)

Hancong Xu, Yifan Wu, Yilin Liu, Liuchun He, Yun Dong

United-imaging Healthcare Co., Ltd., MI-RECON, Shanghai, China

Abstract

The NEMA NU 2 scatter phantom (70 cm, ~20 kg) was designed for conventional PET scanners with axial fields-of-view (AFOV) under 30 cm. For long axial field-of-view (LAFOV) systems exceeding 70 cm, this phantom provides only a localized assessment that fails to capture out-of-FOV scatter and randoms from the full body. Scaling the phantom to 1.2–1.75 m would increase its weight to 34–50 kg, rendering routine use impractical. We propose a single-scan multi-position protocol that exploits the idle intervals between static acquisitions in a standard decay experiment to reposition the phantom axially within each time slot. A center-plus-off-center demonstration was performed on a uMI Panorama GS (1.5 m AFOV). The 70-cm phantom was measured at both the AFOV center and 10 cm beyond the AFOV edge, with the off-center position sampled twice per slot to enable interpolation to a common activity level. The two off-center acquisitions showed close agreement across all count rate metrics and scatter fraction (SF), confirming reproducibility. The SF at the off-center position was elevated due to out-of-FOV scatter contributions, consistent with total-body imaging conditions. This approach enables evaluation of LAFOV systems at multiple axial positions without additional phantom preparation, offering a practical basis for NEMA NU 2 evalution metrics related to the scatter phantom experiment.

References

[1] Spencer, B., et al. (2025). Assessing Scatter Phantom Suitability and Recommending an Appropriate Length for LAFOV and Total-Body PET Based on Human Data. 2025 MIC/NSS/RTSD.

[2] Spencer, B. A., et al. (2021). "Performance Evaluation of the uEXPLORER Total-Body PET/CT Scanner Based on NEMA NU 2-2018 with Additional Tests to Characterize PET Scanners with a Long Axial Field of View." J Nucl Med 62(6): 861-870.

[3] Zhang, H., et al. (2024). "Performance Characteristics of a New Generation 148-cm Axial Field-of-View uMI Panorama GS PET/CT System with Extended NEMA NU 2-2018 and EARL Standards." J Nucl Med 65(12): 1974-1982.

MIC-05-385

Characterizing Smoking Effects Across Lung Cancer Subtypes by Integrating Systemic Metabolic Networks and Tumor Habitat Imaging from Total-Body ^{18}F-FDG PET/CT (#2779)

Haiyan Wang[1,2], Yaping Wu[3], Yanhua Duan[4], Lianghua Li[5], Lubing Sun[3], Xuetong Tao[1,2], Na Zhang[1,2], Xiaowen Zhao[4], Jianjun Liu[5], Zilong Guan[1,2], Hairong Zheng[1,2], Dong Liang[1,2], Ruohua Chen[5], Zhaoping Cheng[4], Meiyun Wang[3], Greta S.P. Mok[6,7], Zhanli Hu[1,2]

[1] Shenzhen Institute of Advanced Technology, Chinese Academy of Sciences, Shenzhen, China; [2] Key Laboratory of Biomedical Imaging Science and System, Chinese Academy of Sciences, Shenzhen, China; [3] Henan Provincial People's Hospital, Henan, China; [4] The First Affiliated Hospital of Shandong First Medical University, Jinan, China; [5] Ren Ji Hospital, School of Medicine, Shanghai Jiao Tong University, Shanghai, China; [6] University of Macau, Faculty of Science and Technology, Macau, Macau; [7] University of Macau, Faculty of Health Science, Macau, Macau

Abstract

Lung cancer (LC) is increasingly recognized as a systemic disease, with metabolic alterations that may vary across histological subtypes. Smoking is a major LC risk factor, but its effects on systemic metabolism and tumor phenotypes across LC subtypes remain insufficiently characterized. We integrated systemic metabolic networks and tumor habitat imaging from static and dynamic total-body ^{18}F-FDG PET/CT to characterize smoking effects across LC subtypes. This multicenter study included 125 LC patients and 200 healthy controls from three centers. Thirty-seven regions spanning the central nervous system and peripheral organs were analyzed. Regional SUL_{mean} values and time–activity curves were harmonized using ComBat and adjusted for demographic covariates. Population-level metabolic networks were constructed from bootstrapped Pearson correlations of regional uptake, while individual-level networks were derived from residual time-activity curve correlations after third-order polynomial fitting to calculate organ-specific abnormality strength. Tumor habitats were defined using PET/CT intensity and entropy features, and their associations with smoking and organ abnormalities were assessed by multivariable regression and mediation analyses. Both network analyses showed that smoking disrupted systemic metabolic coordination in a subtype-dependent manner, with the liver emerging as a central hub. Tumor habitat imaging revealed a smoking-associated shift toward hypometabolic tumor microenvironments. Mediation analysis suggested that habitat composition modulated the association between smoking and hepatic metabolism, linking local tumor heterogeneity to systemic metabolic responses. These findings demonstrate that integrated metabolic network and tumor habitat imaging from total-body ^{18}F-FDG PET/CT provides quantitative insight into smoking-related systemic metabolic reprogramming in LC and may support imaging-based characterization across histological subtypes.

References

[1] Wang H, Guan Z, Qu J, Tao X, Wu Y, Liu Z, et al. Metabolic network analysis of lung adenocarcinoma and squamous cell carcinoma via static and dynamic total-body PET/CT imaging. Medical Physics. 2025;52:e70147.

[2] Sujit SJ, Aminu M, Karpinets TV, Chen P, Saad MB, Salehjahromi M, et al. Enhancing NSCLC recurrence prediction with PET/CT habitat imaging, ctDNA, and integrative radiogenomics-blood insights. Nature communications. 2024;15:3152.

MIC-05-388

Improving Generalization of PET Image-Enhancing Deep Learned Models Through Domain Randomization (#1058)

Jeremiah Poveda-Martínez[1,2], Juan Pablo Gómez-González[2], Francisco J. López-González[3], Claudia Dominguez-Borrero[1], Martín A. Belzunce[5,6], George Webber[4], Andrew J. Reader[4], Pablo Aguiar[1], Jesús Silva-Rodríguez[3]

[1] Universidad de Santiago de Compostela, Molecular Imaging Biomarkers and Theragnosis Lab, Center for Research in Molecular Medicine and Chronic Diseases (CIMUS), Santiago de Compostela, Spain; [2] Qubiotech Health Intelligence, Research & Development, La Coruña, Spain; [3] Reina Sofia Alzheimer Centre, CIEN Foundation, Madrid, Spain; [4] King's College London, School of Biomedical Engineering and Imaging Sciences, London, UK; [5] Instituto de Ciencias Físicas, Universidad Nacional de San Martínez, Buenos Aires, Argentina; [6] Centro Universitario de Imágenes Médicas, Universidad Nacional de San Martínez, Buenos Aires, Argentina

This research was supported by the Axencia Galega de Innovación (GAIN) under Grant[IN606D]. Jesús Silva-Rodríguez and was supported by the Instituto de Salud Carlos III – Fondo Europeo de Desarrollo Regional (ISCIII-FEDER) under Grant [PI24/00089] and “Fundación Reina Sofía” under Grant [E.6.4 FRS-CUERPOS DE LEWY].

Abstract

Deep learning models for PET image enhancement often struggle to generalize across unseen scanner configurations due to limited training data diversity. We introduce a Domain Randomization (DR) framework that utilizes Monte Carlo simulations via the SimPET platform to randomize scanner geometries and reconstruction protocols within clinically operational ranges. To mimic biological variability, this approach is supplemented by a tailored activity augmentation pipeline, resulting in a training dataset of 232 activity maps. To validate this methodology, we trained a 2.5D Attention U-Net to map simulations to high-quality activity maps. Performance was assessed across incremental data regimes ranging from 20 to 236 training instances. On unseen scanner domains, the DR strategy consistently outperformed the no-DR baseline in SSIM and relative contrast. Conversely, on the in-distribution source domain, the DR model achieved perceptual equivalence to the baseline, despite a minor trade-off in absolute pixel precision. Real-world validation with a Hoffman Phantom acquisition on a Philips Vereos scanner suggested a remaining sim-to-real gap on real data distributions. By demonstrating improved generalization without compromising structural fidelity on synthetic domains, this work presents a promising pathway for future research and democratizes access to high-quality, annotated training data through scalable and cost-effective deep learning tools.

References

[1] J. Tobin et al., “Domain Randomization for Transferring Deep Neural Networks from Simulation to the Real World.” arXiv, 20-Mar-2017.

[2] B. Marti-Fuster et al., “Including Anatomical and Functional Information in MC Simulation of PET and SPECT Brain Studies. Brain-VISET: A Voxel-Based Iterative Method,” *IEEE Transactions on Medical Imaging*, vol. 33, no. 10, pp. 1931–1938, Oct. 2014.

[3] F. J. López-González et al., “Intensity normalization methods in brain FDG-PET quantification,” *NeuroImage*, vol. 222, p. 117229, Nov. 2020.

[4] O. Oktay et al., “Attention U-Net: Learning Where to Look for the Pancreas.” arXiv, 20-May-2018.

MIC-05-391

Unsupervised Deep Learning for Prompt Gamma Emission Reconstruction in Time and Space (#1173)

Laura Hellwege[1,2], Julius Werner[1], Jona Kasprzak[1], Veronica Ferrero[3], Francesco Pennazio[4], Thorsten M. Buzug[1,2], Magdalena Rafecas[1], Maik Stille[2]

[1] University of Luebeck, Institute of Medical Engineering, Luebeck, Germany; [2] Fraunhofer Research Instution for Individualized Medical Technology and Engineering IMTE, Luebeck, Germany; [3] Universitá degli Studi di Torino, Department of Physics, Torino, Italy; [4] Istituto Nazionale di Fisica Nucleare, Sezione di Torino, Torino, Italy

This work was partially funded by the state of Schleswig-Holstein through the project ”Individualisierte Medizintechnik für bildgestützte, robotische Interventionen (IMTE 2)”, project number: 125 24 009 and the German Research Foundation (DFG) by Grant No. 51 658 7313 (PROSIT)

Abstract

Spatiotemporal Emission Reconstruction from Prompt Gamma Timing data (SER-PGT) has the potential to verify the stopping power through passive measurements during proton therapy. The underlying inverse problem is ill-posed and offers some unusual challenges compared to conventional emission or transmission reconstruction scenarios.In this work, we introduce an unsupervised deep learning framework for reconstructing prompt gamma emission distributions from simulated data, without requiring ground-truth images during training. Our method combines a physics-informed Poisson likelihood loss in the data domain with a UNet++ architecture with ResNeXt101 encoder. It operates on pseudo-inverse reconstructions from a system matrix modeling 110 detectors, 160 depth bins, and 100 time bins. Evaluation on 200 test samples yields comparable performance to MLEM in terms of Mean Absolute Error and Peak-Signal-to-Noise-Ratio in both image and data domains, demonstrating that accurate reconstruction is achievable through self-supervised learning. The approach showcases fast execution speed and a flexible framework. This makes it a promising candidate to move SER-PGT closer towards stopping power estimation in clinical scenarios.

References

[1] Ferrero, V., et al., "Estimating the stopping power distribution during proton therapy: A proof of concept,'' in *Front. Phys.*, vol 10-2022, 10:971767, 2022

[2] Pennazio, F., et al. "Proton therapy monitoring: spatiotemporal emission reconstruction with prompt gamma timing and implementation with PET detectors,'' *Phys. Med. Biol.*, vol. 67, no. 065005,, vol 10-2022, 10:971767

[3] Werner, J., et al. "Analytical model of prompt gamma timing for spatiotemporal emission reconstruction in particle therapy,'' in *Phys. Med. Biol.*, vol. 71, no. 075005, 2026

[4] Werner, J., et al. "Stopping power and range estimations in proton therapy based on prompt gamma timing: motion models and automated parameter optimization,'' *Phys. Med. Biol.*, vol. 69, no. 14NT02, 2024

[5] Hellwege, L. et al. "Unsupervised deep learning for inverse problems in computed tomography,'', arXiv, DOI: 10.48550/arXiv.2508.05321, 2025

[6] Zhou, Z. et al. "UNet++: A nested U-Net architecture for medical image segmentation,'' in *DLMIA/ML-CDS*, 2018

MIC-05-394

Supervised Contrastive Pretraining Enables Few-Shot Alzheimer's Disease Classification on Multi-Site ECD SPECT (#1384)

Hui-Chieh Yang[1], Fan-Pin Tseng[1], Yu-Ching Ni[1], Yen-Wen Wu[2,3], Guang-Uei Hung[4], Chia-Yu Lin[1], Yi-Chien Liu[5], Yu-Ming Fan[6,7], Shan-Ying Wang[2,8]

[1] National Atomic Research Institute, Department of Radiation Protection, Taoyuan, Taiwan; [2] Far Eastern Memorial Hospital, Department of Nuclear Medicine, New Taipei City, Taiwan; [3] National Yang Ming Chiao Tung University, School of Medicine, Taipei, Taiwan; [4] Chang Bing Show Chwan Memorial Hospital, Changhua, Taiwan; [5] Cardinal Tien Hospital, Department of Neurology, New Taipei City, Taiwan; [6] Cardinal Tien Hospital, Department of Nuclear Medicine, New Taipei City, Taiwan; [7] Fu Jen Catholic University, School of Medicine, New Taipei City, Taiwan; [8] Yuan Ze University, Electrical and Communication Engineering College, Taoyuan, Taiwan

Abstract

This study investigates the cross-site generalization of deep learning for Tc-99m ethyl cysteinate dimer (ECD) brain perfusion single-photon emission computed tomography (SPECT), where site-specific imaging variability often limits cross-site generalization of deep learning models. To address this, a multi-site supervised contrastive learning (SupCon) pretraining framework was developed using a 3D ResNet-18 encoder, which was trained on 2,242 images collected from five sites across eight diagnostic categories. The pretrained representation achieved a latent-space silhouette score of 0.815, while t-SNE visualization showed that samples from different sites were well mixed within diagnostic clusters, indicating that the learned features were more disease-discriminative than site-specific. To simulate deployment at a new hospital, a sixth site that had been entirely excluded from pretraining was reserved for downstream evaluation. In this hospital-held-out setting, where only 46 balanced samples were available for adaptation, few-shot fine-tuning achieved 80.4% accuracy for Alzheimer's disease-versus-Normal classification, with a macro F1-score of 0.801 and an area under the receiver operating characteristic curve (AUC) of 0.819. This performance substantially exceeded that of a randomly initialized baseline, which achieved 60.9% accuracy, a macro F1-score of 0.568, and an AUC of 0.639. These results suggest that multi-site SupCon pretraining may provide a practical route toward scalable cross-site deployment of brain SPECT classifiers with minimal site-specific annotation, potentially enabling rapid clinical adoption at new hospitals.

References

[1] Yang, F., Lei, B., Zhou, Z., Song, T. A., Balaji, V., & Dutta, J. 2025, 'AI in SPECT imaging: opportunities and challenges.', *Seminars in Nuclear Medicine*, Vol. 55, No. 3, pp. 294-312. WB Saunders.

[2] Khosla, P., Teterwak, P., Wang, C., Sarna, A., Tian, Y., Isola, P., ... & Krishnan, D. 2020, 'Supervised contrastive learning.', *Advances in neural information processing systems*, *33*, 18661-18673.

[3] Gryshchuk, V., Singh, D., Teipel, S., Dyrba, M., & ADNI, AIBL, FTLDNI study groups. 2025, 'Contrastive self-supervised learning for neurodegenerative disorder classification.', *Frontiers in Neuroinformatics*, *19*, 1527582.

[4] Kwak, M. G., Su, Y., Chen, K., Weidman, D., Wu, T., Lure, F., ... & Alzheimer's Disease Neuroimaging Initiative. 2023, 'Self-supervised contrastive learning to predict the progression of Alzheimer's disease with 3D amyloid-PET.', *Bioengineering*, *10*(10), 1141.

[5] He, K., Zhang, X., Ren, S., & Sun, J. 2016, 'Deep residual learning for image recognition.', *Proceedings of the IEEE conference on computer vision and pattern recognition*, pp. 770-778.

MIC-05-397

Large Language Models for Generating Descriptions of 3D Medical Image Volumes (#1604)

Joshua Schaefferkoetter, Paul Schleyer

Siemens Medical Solutions USA, Inc., Knoxville, USA

Abstract

This paper presents an approach for using large language models to automatically generate descriptions for 3d medical images. It describes a novel method for encoding volumetric data into a discrete set of tokens, which are then used to condition the text generated by a pre-trained foundational language model. Design considerations and model architecture are outlined, and the feasibility of the technique is demonstrated for generating descriptive captions of image volumes with information related to imaging modality, administered radiopharmaceutical and anatomical scan range.

References

[1] Ye, Yanfang, Zheyuan Zhang, Tianyi Ma, Zehong Wang, Yiyang Li, Shifu Hou, Weixiang Sun et al. "Llms4all: A review of large language models across academic disciplines." *arXiv preprint arXiv:2509.19580* (2025).

[2] Xiang, Lu, Yang Zhao, Yaping Zhang, and Chengqing Zong. "A survey of large language models in discipline-specific research: Challenges, methods and opportunities." *arXiv preprint arXiv:2507.08425* (2025).

[3] Sajjadi Mohammadabadi, Seyed Mahmoud, Burak Cem Kara, Can Eyupoglu, Can Uzay, Mehmet Serkan Tosun, and Oktay Karakuş. "A survey of large language models: evolution, architectures, adaptation, benchmarking, applications, challenges, and societal implications." *Electronics* 14, no. 18 (2025).

[4] Wang, Dandan, and Shiqing Zhang. "Large language models in medical and healthcare fields: applications, advances, and challenges." *Artificial intelligence review* 57, no. 11 (2024): 299.

[5] Carchiolo, Vincenza, and Michele Malgeri. "Trends, challenges, and applications of large language models in healthcare: a bibliometric and scoping review." *Future Internet* 17, no. 2 (2025): 76.

[6] Radford, Alec, Jong Wook Kim, Chris Hallacy, Aditya Ramesh, Gabriel Goh, Sandhini Agarwal, Girish Sastry et al. "Learning transferable visual models from natural language supervision." In *International conference on machine learning*, pp. 8748-8763. PmLR, 2021.

[7] Li, Junnan, Dongxu Li, Silvio Savarese, and Steven Hoi. "Blip-2: Bootstrapping language-image pre-training with frozen image encoders and large language models." In *International conference on machine learning*, pp. 19730-19742. PMLR, 2023.

[8] Alayrac, Jean-Baptiste, Jeff Donahue, Pauline Luc, Antoine Miech, Iain Barr, Yana Hasson, Karel Lenc et al. "Flamingo: a visual language model for few-shot learning." *Advances in neural information processing systems* 35 (2022): 23716-23736.

[9] Schaefferkoetter, J. et al. “Deep Learning Approach for Semantic, Multi-Organ Segmentation of PET Images.” PSMR (2024).

MIC-05-400

Preliminary Region-Aware MRI-to-sCT Synthesis for Radiotherapy-Oriented Imaging in Nasopharyngeal Carcinoma (#1752)

Qian Wang[1], Junnv Xu[2], Chunhao Li[1], Zhigang Sun[1], Huan Xiao[3], Wenbo Huang[4], Yuecan Zeng[2], Jingzhang Sun[1]

[1] Hainan University, Department of Data Science and Big Data, Haikou, China; [2] The Second Affiliated Hospital of Hainan Medical University, Department of Radiation Oncology, Cancer Treatment Center, Haikou, China; [3] The First Affiliated Hospital of Hainan Medical University, Department of Nuclear Medicine, Haikou, China; [4] Beijing Tsinghua Changgung Hospital, School of Clinical Medicine, Tsinghua University, Department of Nuclear Medicine, Haikou, China

This work was supported in part by the National Natural Science Foundation of China (12505396) and the Science and Technology Talents Innovation Project of Hainan Province (KJRC2023D30). Corresponding authors: Jingzhang Sun and Yuecan Zeng.

Abstract

Synthetic computed tomography (sCT) generation from magnetic resonance imaging (MRI) is an important component of MRI-only radiotherapy planning because MRI provides excellent soft-tissue contrast but lacks quantitative Hounsfield unit (HU) information for electron-density assignment. However, MRI-to-sCT synthesis remains challenging due to the indirect MRI representation of bone, the ambiguity between intra-body air and external background, and the heterogeneous HU distributions across anatomical regions. This study proposes a region-aware 3D supervised MRI-to-sCT synthesis framework using paired CT-referenced MRI and CT volumes. The network combines 3D convolutional feature extraction with a Project-and-Excite (PE) attention module to enhance volumetric anatomical representation. To improve HU fidelity in clinically relevant regions, MRI masks were used for input background suppression, CT body masks were used to define valid supervision and evaluation regions, and HU-derived masks were used to impose region-weighted constraints on body, background, intra-body air, and bone regions. The method was evaluated on 24 paired MRI/CT cases, including 16 training, 5 validation, and 3 independent testing cases. In ablation analysis, the full body–background–air–bone loss achieved the highest PSNR of 19.65 dB, while SSIM decreased to 0.53, suggesting improved control of large HU deviations rather than simple maximization of structural similarity. These preliminary results support the feasibility of region-aware HU optimization for MRI-to-sCT synthesis, while larger-scale validation, region-wise HU analysis, and dosimetric assessment remain necessary before clinical application.

References

[1] C. Hu, X. Hang, X. Li, D. Cao, H. Zhou, and N. Cao, "PelvicDiff: A novel diffusion model for high-fidelity synthetic CT generation from MRI in pelvic cancer radiotherapy," *Expert Systems with Applications*, p. 130236, 2025.

[2] M. A. Schmidt and G. S. Payne, "Radiotherapy planning using MRI," *Physics in Medicine & Biology*, vol. 60, no. 22, pp. R323-R361, 2015.

MIC-05-403

Deep Learning-Based Tau Positivity Estimation from Multimodal Amyloid and FDG PET (#1965)

Yiyi Hu[1], Cecilia Boccalini[1,2], Ghasem Hajianfar[1], Valentina Garibotto[1,2], Habib Zaidi[1,4], Amirhossein Sanaat[1]

[1] Geneva university hospital, Division of Nuclear Medicine and Molecular Imaging, Geneva, Switzerland; [2] University of Geneva, Geneva University Neurocenter and Faculty of Medicine, Geneva, Switzerland; [3] CIBM Center for Biomedical Imaging, Geneva, Switzerland; [4] University of Groningen, Department of Nuclear Medicine and Molecular Imaging, Groningen, Denmark

This work was supported by the Swiss National Science Foundation under Grant No. 320030_231742.
Data used in this study were obtained from the Alzheimer's Disease Neuroimaging Initiative (ADNI) database. As such, the investigators within ADNI contributed to the design and implementation of ADNI and/or provided data, but did not participate in the analysis or writing of this work. A complete listing of ADNI investigators can be found at: http://adni.loni.usc.edu/wp-content/uploads/how_to_apply/ADNI_Acknowledgement_List.pdf

Abstract

Tau positron emission tomography (PET) is strongly linked to cognitive impairment and disease progression in Alzheimer's disease, but direct tau imaging is not always available in routine clinical or research workflows. This study evaluated a multimodal deep learning framework that uses amyloid PET and fluorodeoxyglucose (FDG) PET to estimate binary ^{18}F-flortaucipir (FTP) positive/negative status. A total of 340 participants from Alzheimer's Disease Neuroimaging Initiative (ADNI) and the Geneva University Hospital cohort with available amyloid, FDG, and FTP PET were included. Images were registered to Montreal Neurological Institute space and used as two-channel volumetric input to a SwinUnetR-based classifier. The multimodal model setting was evaluated using stratified five-fold cross-validation on the combined cohort. The model achieved an accuracy of 0.853, sensitivity of 0.823, specificity of 0.871, and area under the receiver operating characteristic curve of 0.904. These findings suggest that combined amyloid and FDG PET contains complementary information relevant to tau status and may provide practical decision-support evidence when direct tau PET is unavailable or when the indication for tau imaging remains uncertain.

References
[1] J. Lagarde et al., "Tau-PET imaging predicts cognitive decline and brain atrophy progression in early Alzheimer's disease," *J. Neurol. Neurosurg. Psychiatry*, vol. 93, no. 5, pp. 459–467, 2022.
[2] C. Groot et al., "Tau positron emission tomography for predicting dementia in individuals with mild cognitive impairment," *JAMA Neurol.*, vol. 81, no. 8, pp. 845–856, 2024.
[3] G. D. Rabinovici et al., "Updated appropriate use criteria for amyloid and tau PET," *Alzheimers Dement.*, vol. 21, no. 1, p. e14338, 2025.
[4] S. C. Burnham et al., "A review of the flortaucipir literature for PET imaging of tau neurofibrillary tangles," *Brain Commun.*, vol. 6, no. 1, p. fcad305, 2024.
[5] G. Chételat et al., "Amyloid-PET and 18F-FDG-PET in the diagnostic investigation of Alzheimer's disease and other dementias," *Lancet Neurol.*, vol. 19, no. 11, pp. 951–962, 2020.
[6] C. R. Jack Jr. et al., "NIA-AA Research Framework: Toward a biological definition of Alzheimer's disease," *Alzheimers Dement.*, vol. 14, no. 4, pp. 535–562, 2018.
[7] V. Doré et al., "Relationship between amyloid and tau levels and its impact on tau spreading," *Eur. J. Nucl. Med. Mol. Imaging*, vol. 48, no. 7, pp. 2225–2232, 2021.
[8] R. Ossenkoppele et al., "Tau PET patterns mirror clinical and neuroanatomical variability in Alzheimer's disease," *Brain*, vol. 139, no. 5, pp. 1551–1567, 2016.

[9] A. Hatamizadeh, V. Nath, Y. Tang, D. Yang, H. R. Roth, and D. Xu, "Swin UNETR: Swin transformers for semantic segmentation of brain tumors in MRI images," in *Brainlesion: Glioma, Multiple Sclerosis, Stroke and Traumatic Brain Injuries*, Cham, Switzerland: Springer, 2022, pp. 272–284, doi: 10.1007/978-3-031-08999-2_22.

MIC-05-406

Compton Camera Image Reconstruction Using Compton Physics-Prior Fusion and Set Transformers for Actinium-225 Targeted Alpha Therapy

(#2148)

Yazeed Balasmeh[1], Ivor Fleck[1], Roman Obermaisser[2]

[1] University of Siegen, Department of Physics, Siegen, Germany; [2] University of Siegen, Embedded Systems, Department of Electrical Engineering and Computer Science, Siegen, Germany

Work supported by German Research Foundation.

Abstract

In this work, a physics-aware neural network architecture is proposed for Compton camera image reconstruction. The model incorporates physics-based features from coincidence events and uses backprojection as a prior. It is applied both to mono energetic sources as well as to targeted alpha therapy using Actinium-225 where the presence of multiple gamma-ray lines makes image reconstruction more challenging for existing medical imaging devices, such as single-photon emission computed tomography. The input data are preprocessed and categorized into scattering-only, absorption-only, and coincidence events. These data are used to generate feature maps through neural network layers and a transformer-based model, followed by an image reconstruction decoder. Training and testing data were generated using the Geant4 simulation toolkit. The model was first evaluated using controlled single-source simulations with different source sizes, energies, positions, and event statistics. It was then tested under more realistic conditions using a mouse phantom with Actinium-225 activity distributed in tumor and background regions. CPPF-Net achieved a mean peak-localization error of 1.0 ± 0.7 mm and a structural similarity index of 0.99 ± 0.01. These results indicate that CPPF-Net can provide accurate Compton camera image reconstruction for Actinium-225 targeted alpha therapy. Experimental validation with measured data is foreseen for the near future.

References

[1] Kim, SM & Lee, JS 2024, 'A comprehensive review on Compton camera image reconstruction: from principles to AI innovations', *Biomedical Engineering Letters*, vol. 14, no. 6, pp. 1175–1193.

[2] Parajuli, RK et al. 2022, 'Development and applications of Compton camera—a review', *Sensors*, vol. 22, no. 19, p. 7374.

[3] Agostinelli, S et al. 2003, 'Geant4—a simulation toolkit', *Nuclear Instruments and Methods in Physics Research Section A*, vol. 506, no. 3, pp. 250–303.

[4] Lee, T, Kim, M, Lee, W, Kim, B, Lim, I, Song, K & Kim, J 2019, 'Performance evaluation of a Compton SPECT imager for determining the position and distribution of 225Ac in targeted alpha therapy: A Monte Carlo simulation based phantom study', *Applied Radiation and Isotopes*, vol. 154, p. 108893.

[5] Caravaca, J et al. 2022, 'Compton and proximity imaging of 225Ac in vivo with a CZT gamma camera: a proof of principle with simulations', *IEEE Transactions on Radiation and Plasma Medical Sciences*, vol. 6, no. 8, pp. 904–915.

[6] Robertson, AKH, Ramogida, CF, Rodríguez-Rodríguez, C, Blinder, S, Kunz, P, Sossi, V & Schaffer, P 2017, 'Multi-isotope SPECT imaging of the 225Ac decay chain: feasibility studies', *Physics in Medicine & Biology*, vol. 62, no. 11, pp. 4406–4420.

[7] Lee, J, Lee, Y, Kim, J, Kosiorek, AR, Choi, S & Teh, YW 2019, 'Set Transformer: A Framework for Attention-Based Permutation-Invariant Neural Networks', *Proceedings of the 36th International Conference on Machine Learning*, pp. 3744–3753, PMLR.
[8] Sato, S, Tanaka, T & Kataoka, J 2024, 'ComptonNet: a direct reconstruction model for Compton camera', *Applied Physics Letters*, vol. 124, no. 25, p. 253702.
[9] Haefner, A, Gunter, D, Barnowski, R & Vetter, K 2015, 'A filtered back-projection algorithm for 4π Compton camera data', *IEEE Transactions on Nuclear Science*, vol. 62, no. 5, pp. 1911–1917.

MIC-05-409

CNN-Based Classification Performance Across Axial, Coronal, and Sagittal Imaging Orientations in ^{18}F-PSMA PET Images (#2302)

Anting Li[1,2], Oona Rainio[1], Maria K. Jaakkola[1], Ahti Vehmanen[1,2], Jukka Kemppainen[1,3], Riku Klén[1]

[1] University of Turku and Turku University Hospital, Turku PET Centre, Turku, Finland; [2] University of Turku, Faculty of Medicine, Turku, Finland; [3] Turku University Hospital, Department of Clinical Physiology and Nuclear Medicine, Turku, Finland

The authors would like to thank Jarmo Teuho for his feedback, comments and support during the research.

Abstract

Prostate cancer is one of the most commonly diagnosed cancers in men worldwide. Accurate detection using ^{18}F-prostate-specific membrane antigen (PSMA) positron emission tomography/computed tomography (PET/CT) enables reliable identification of the disease and supports clinical staging. In this study, we propose a deep learning framework for the slice-level classification of ^{18}F-PSMA PET/CT images using convolutional neural networks trained on axial, coronal, and sagittal views. The models achieved high discrimination performance, with an area under the receiver operating characteristic curve of 0.98 and a specificity of 0.98, while showing orientation-dependent differences in sensitivity and classification balance. However, lower performance in the hold-out dataset indicates limited generalization capability, highlighting the importance of imaging plane selection in prostate tumor classification. The classification model serves as a preliminary step for downstream segmentation by enabling slice-level localization of the region of interest.

References
[1] Rainio, O., Huhtanen, H., Vierula, J. P., Nurminen, J., Heikkinen, J., Nyman, M., ... & Hirvonen, J. (2025). Deep learning detects retropharyngeal edema on MRI in patients with acute neck infections. *European Radiology Experimental*, *9*(1), 60.
[2] Rainio, O., Lahti, J., Anttinen, M., Ettala, O., Seppänen, M., Boström, P., ... & Klén, R. (2023). New method of using a convolutional neural network for 2D intraprostatic tumor segmentation from PET images. *Research on biomedical engineering*, *39*(4), 905-913.
[3] *V. S. Viertonen, A. SirÅLen, M. Nyman, H. Huhtanen, R. KlÅLen, J. Hirvonen,and O. Rainio, "Acute deep neck infection mri: deep learning segmentationand clinical relevance of retropharyngeal edema volume," EuropeanRadiology Experimental, vol. 10, no. 1, p. 15, 2026.*
[4] Hellström, H., Liedes, J., Rainio, O., Malaspina, S., Kemppainen, J., & Klén, R. (2023). Classification of head and neck cancer from PET images using convolutional neural networks. *Scientific Reports*, *13*(1), 10528.

MIC-05-412

MIC-05-415

Equilibrium Matching for PET Image Denoising: Signal vs. Velocity Parameterization Under Identical Conditions (#2453)

Shaghayegh Afshari, Cheng-Ying Chou

National Taiwan University, Department of Biomechatronics Engineering, Taipei, Taiwan

The authors declare no external funding for this work.

Abstract

Low-count Positron Emission Tomography (PET) suffers from severe Poisson photon-counting noise, yet existing deep learning denoisers either rely on supervised regression networks that tend to oversmooth anatomical detail or on diffusion-based generative models designed for Gaussian corruption that require iterative, noise-level-dependent sampling at inference time. Equilibrium Matching (EqM) was recently proposed as a generative modeling framework that learns a time-invariant equilibrium gradient field toward the data manifold, but has not yet been explored for medical image restoration. We present a novel adaptation of EqM to PET denoising, reformulating its interpolation scheme for Poisson-corrupted acquisitions and introducing noise-level conditioning via Adaptive Group Normalization, and conduct a controlled comparison of its two parameterizations under identical training conditions: the signal form, which predicts the clean image directly with hyperparameter-free inference, and the velocity form, which predicts the noise residual via iterative Euler updates. Signal EqM achieves up to +5.26 dB PSNR gain at severe noise (N_peak = 50) with no step-size tuning. Velocity EqM consistently outperforms signal EqM on both PSNR and FID at all seven noise levels, with the PSNR gap growing from 0.13 dB at N_peak = 50 to 1.23 dB at N_peak = 5000, mirroring the x- vs. velocity-prediction trade-off in flow-based generative models.

References
[1] Xu, J, Gong, E, Pauly, J, Zaharchuk, G 2017, '200× low-dose PET reconstruction using deep learning', arXiv preprint arXiv:1712.04119
[2] Wang, Y, Yu, B, Wang, L, Zu, C, Lalush, DS, Lin, W, Wu, X, Zhou, J, Shen, D, Zhou, L 2018, '3D conditional generative adversarial networks for high-quality PET image estimation at low dose', NeuroImage, vol. 174, pp. 550–562
[3] Gao, Q, Li, Z, Zhang, J, Zhang, Y, Shan, H 2023, 'CoreDiff: Contextual error-modulated generalized diffusion model for low-dose CT denoising and generalization', IEEE Transactions on Medical Imaging, vol. 43, no. 2, pp. 745–759

[4] Wang, R, Du, Y 2025, 'Equilibrium matching: Generative modeling with implicit energy-based models', arXiv preprint arXiv:2510.02300
[5] Collins, DL, Zijdenbos, AP, Kollokian, V, Sled, JG, Kabani, NJ, Holmes, CJ, Evans, AC 1998, 'Design and construction of a realistic digital brain phantom', IEEE Transactions on Medical Imaging, vol. 17, no. 3, pp. 463–468
[6] Singh, I, Denker, A, Barbano, R 2024, 'Score-based generative models for PET image reconstruction', Zenodo, dataset, ver. 3, doi: 10.5281/zenodo.10509379

MIC-05-418

CT-VDETR: Semi-supervised 3D Trauma Detection in Computed Tomography (CT) scans using Dense Vertex Relative Position Encoding (#2592)

Shivam Chaudhary, Sheethal Bhat, Andreas Maier

Friedrich-Alexander-Universität Erlangen-Nürnberg, Pattern Recognition Lab, Erlangen, Germany

We sincerely acknowledge the Erlangen National High Performance Computing Center (NHR@FAU) of the Friedrich-Alexander-Universität Erlangen-Nürnberg (FAU) for providing the necessary computing resources that enabled this research.

Abstract

Accurate detection and localization of traumatic injuries in abdominal CT remain challenging because voxel-level annotations are limited and expensive to obtain. We present a label-efficient framework for 3D abdominal trauma detection that combines self-supervised pretraining with semi-supervised transformer-based detection. First, we use Masked Image Modeling (MIM) on 1098 CT volumes to pretrain a 3D U-Net encoder for anatomical representation learning. Next, we adapt V-DETR to dense volumetric CT through a feature adapter that converts the encoder feature grid into a compact token sequence for transformer decoding. The pretrained encoder is then integrated with V-DETR and 3D Vertex Relative Position Encoding (3D V-RPE) to improve the localization of irregularly shaped injuries. Finally, semi-supervised teacher–student consistency regularization leverages 2,000 additional unlabeled volumes during detector training. To the best of our knowledge, this is the first application of a 3D DETR-style detector to the RSNA abdominal trauma detection task. On this benchmark, the proposed method achieves 31.33% test mAP@0.50 using only 78 labeled training volumes, corresponding to a 1.53× improvement over supervised-only training. These results show that combining medical-domain pretraining with semi-supervised learning is an effective strategy for label-scarce 3D medical detection.

References
[1] S. Ren, K. He, R. Girshick, and J. Sun, “Faster R-CNN: Towards real-time object detection with region proposal networks,” in Advances in Neural Information Processing Systems, vol. 28, 2015.
[2] K. He, X. Chen, S. Xie, Y. Li, P. Doll´ar, and R. Girshick, “Masked autoencoders are scalable vision learners,” in Proceedings of the IEEE/CVF Conference on Computer Vision and Pattern Recognition (CVPR), 2022, pp. 16 000–16 009.
[3] K. Eckstein, C. Ulrich, M. Baumgartner, J. K¨achele, D. Bounias, T. Wald, R. Floca, and K. H. Maier-Hein, “The missing piece: A case for pre-training in 3D medical object detection,” arXiv preprint arXiv:2509.15947, 2024, medical Faculty Heidelberg, Heidelberg University.
[4] A. Tarvainen and H. Valpola, “Mean teachers are better role models: Weight-averaged consistency targets improve semi-supervised deep learning results,” in Advances in Neural Information Processing Systems, vol. 30, 2017.

[5] Y.-C. Liu, C.-Y. Ma, Z. He, C.-W. Kuo, K. Chen, P. Zhang, B. Wu, Z. Kira, and P. Vajda, "Unbiased teacher for semi-supervised object detection," in International Conference on Learning Representations (ICLR), 2021.
[6] N. Carion, F. Massa, G. Synnaert, N. Usunier, A. Kirillov, and S. Zagoruyko, "End-to-end object detection with transformers," in European Conference on Computer Vision (ECCV), 2020, pp. 213–229.
[7] I. Misra, R. Girdhar, and A. Joulin, "An end-to-end transformer model for 3D object detection," in Proceedings of the IEEE/CVF International Conference on Computer Vision (ICCV), 2021, pp. 2906–2917.
[8] Y. Shen, Z. Geng, Y. Yuan, Y. Lin, Z. Liu, C. Wang, H. Hu, N. Zheng, and B. Guo, "V-DETR: DETR with vertex relative position encoding for 3D object detection," in Proceedings of the IEEE/CVF International Conference on Computer Vision (ICCV), 2023, pp. 6857–6867.
[9] A. Dai, A. X. Chang, M. Savva, M. Halber, T. Funkhouser, and M. Nießner, "ScanNet: Richly-annotated 3D reconstructions of indoor scenes," in Proceedings of the IEEE Conference on Computer Vision and Pattern Recognition (CVPR), 2017.

MIC-05-421

An AI Model for Breast Density Estimation using Spectroscopic X-Ray Data (#2672)

Megan A. Eaton[1], Emma Lewis[2], Matt Wilson[3], Silvia Pani[1]

[1] University of Surrey, Department of Physics, Guildford, UK; [2] Royal Surrey County Hospital, Department of Medical Physics, Guildford, UK; [3] STFC Rutherford Appleton Laboratory, Detector Development, Didcot, UK

Thank you to the Engineering and Physical Sciences Research Council for funding this research.

Abstract

High breast density is a known risk factor for breast cancer. Current gold standard methods of density measurement are highly variable, and as such, reporting of density is not standard practice worldwide. The use of artificial intelligence has shown promise, but a lack of a definitive ground truth leads to less reliable predictions. This work combines artificial intelligence with spectroscopic X-ray imaging, which preserves compositional tissue information, as a novel density estimation method. A proof-of-concept study was performed by simulating the breast imaging process for breast tissue-equivalent phantoms to build a training set for a custom machine learning tool. This gave good results, having a mean squared error in the model's output of 0.013 +/- 0.002 %. Based on these results, further work focused on increasing the realism of the simulation and training data by modelling the charge transport in the detector as well as including anthropomorphic breast phantoms. This work will provide the foundations towards building a reliable and accurate way to measure breast density, allowing early cancer detection by tailoring patient pathways, and improving health outcomes.

References
[1] J. Chalfant and A. Hoyt, "Breast density: current knowledge, assessment methods, and clinical implications," *Journal of Breast Imaging*, vol. 4, no. 4, pp. 357–370, 2022.
[2] S. Pani, S. Saifuddin, F. Ferreira, N. Henthorn, P. Seller, P. Sellin, P. Stratmann, M. Veale, M. Wilson, and R. Cernik, "High energy resolution hyperspectral x-ray imaging for low-dose contrast-enhanced digital mammography," *IEEE Transactions on Medical Imaging*, vol. 36, no. 9, pp. 1784–1795, 2017.
[3] J. Pearl, J. Shin, J. Schumann, and H. Paganetti, "Topas: an innovative proton monte carlo platform for research and clinical applications," *Medical Physics*, vol. 39, no. 11, pp. 6818–6837, 2012.
[4] M. C. Veale, P. Seller, M. Wilson, and E. Liotti, "Hexitec: A high-energy x-ray spectroscopic imaging detector for synchrotron applications," *Synchrotron Radiation News*, vol. 31, no. 6, pp. 28–32, 2018.
[5] G. Poludniowski, A. Omar, R. Bujila, and P. Andreo, "Technical Note: SpekPy v2.0—a software toolkit for modeling x-ray tube spectra," *Medical Physics*, vol. 48, pp. 3630–3637, July 2021.

[6] O. Clark, M. Wilson, P. Evans, E. Harris, and S. Pani, "Corrections for fluorescence and charge-sharing effects to bremsstrahlung spectra for a hyperspectral pixelated czt x-ray detector," *IEEE Transactions on Nuclear Science*, vol. 70, no. 6, pp. 1202–1209, 2023.
[7] A. Badano, C. Graff, and A. Badal, "Evaluation of digital breast tomosynthesis as replacement of full-field digital mammography using an in silico imaging trial," *JAMA Network Open*, vol. 1, no. 7, 2018.
[8] M. Jeffreys, R. Warren, R. Highnam, and G. Davey Smith, "Initial experiences of using an automated volumetric measure of breast density: the standard mammogram form," *British Journal of Radiology*, vol. 79, no. 941, pp. 378–382, 2006.
[9] K. Feder and J.-H. Grunert, "Is individualizing breast compression during mammography useful? - investigations of pain indications during mammography relating to compression force and surface area of the compressed breast," *RoFo : Fortschritte auf dem Gebiete der Rontgenstrahlen und der Nuklearmedizin*, vol. 189, no. 1, p. 39–48, 2017.

MIC-05-424

Positron Range Correction with Texture Preservation in ^{82}Rb PET (#2819)

Nerea Encina-Baranda[1], Yifan Zheng[3], Jorge Cabello[3], Robert J. Paneque-Yunta[1], Alejandro Lopez-Montes[2], Maurizio Conti[3], Joaquín López Herraiz[1]

[1] Complutense University of Madrid, Grupo de Física Nuclear, EMFTEL & IPARCOS, Madrid, Spain; [2] Bern University Hospital, Department of Nuclear Medicine, Bern, Switzerland; [3] Siemens Medical Solutions USA, Inc., Knoxville, USA; [4] Universidad Complutense de Madrid, Facultad de Ciencias Físicas, Madrid, Spain

We acknowledge support from the following grants: PID2021-126998OB-I00, TED2021-349130592B-I00, and PDC2022-133057-I00, funded by the Spanish Ministry of Science, Innovation and Universities (MCIU) through AEI/10.13039/501100011033 and the European Union's NextGenerationEU/PRT program. Additional support was provided by the National Institutes of Health (NIH), USA, under grant R01 EB033000. Siemens Healthineers also supported this work with a research grant provided to UCM.

Abstract

The positron range (PR) is a fundamental resolution-limiting factor in positron emission tomography (PET), particularly for high-energy radionuclides such as ^{82}Rb. In cardiac PET, the long PR of ^{82}Rb causes spatial blurring, activity spill-out, and reduced myocardial contrast, especially across heterogeneous tissue interfaces. Deep learning-based PR correction (PRC) provides a practical post-reconstruction strategy, but supervised regression networks often produce over-smoothed outputs by attenuating high-frequency stochastic fluctuations. We propose a model-consistent framework that decouples structural PR correction from texture preservation by combining PRC, matched smoothing estimation, and deterministic texture reinjection. In simulated ^{82}Rb PET studies, the proposed framework improved the recovery coefficient by 13.8% relative to the uncorrected ^{82}Rb input, while restoring noise levels closer to the reference (9.74 ± 1.85% vs. 10.62 ± 0.82%), supporting structure–texture decoupling as a promising strategy for PET imaging.

References
[1] J. Cal-González et al., IEEE TMI, 2015. doi: 10.1109/TMI.2015.2436711
[2] J. L. Herraiz et al., Applied Sciences, 2021. doi: 10.3390/app11010266
[3] N. Encina-Baranda et al., arXiv preprint, 2025. doi:10.48550/arXiv.2504.19175
[4] H. H. Barrett et al., Foundations of Image Science. John Wiley \& Sons, 2004.
[5] S. Jan et al., PMB, 2004. doi: 10.1088/0031-9155/49/19/007
[6] H.-Y. Zhou et al., arXiv preprint, 2021. doi: 10.48550/arXiv.2109.03201

MIC-05-430

Genetic algorithm-based PET sinogram denoising using a Poisson noise fitness criterion (#2975)

Fernando Guedan[1], Juan Enrique Ortuño[3,2], George Kontaxakis[4]

[1] Universidad Politécnica de Madrid, ETSI Telecomunicación, Madrid, Spain; [2] Universidad Politécnica de Madrid, Biomedical Image Technologies Group, ETSI Telecomunicación, Madrid, Spain; [3] Instituto de Salud Carlos III, CIBER de Bioingeniería, Biomateriales y Nanomedicina, Madrid, Spain; [4] Universidad Politécnica de Madrid, Information Processing and Telecommunications Center, ETSI Telecomunicación, Madrid, Spain

This work has been partially funded by the project S2022/BMD-7236 MINA-CM of the Autonomous Community of Madrid, Spain.

Abstract

This paper presents a genetic-algorithm-inspired methodology for denoising positron emission tomography (PET) sinograms from a single noisy acquisition. The method assumes that a noise-free sinogram (NFS) is embedded within the noisy sinogram (NS) and formulates denoising as the search for chromosome-encoded parameters capable of recovering it. Each chromosome generates a candidate NFS by fitting continuous exponential curves to the measured sinogram data, with the exponential order and other generation parameters encoded in a reduced-size chromosome. For each candidate, the residual noise is computed as the difference between the NS and the generated NFS. The selection criterion is based exclusively on the statistic al properties of this residual noise, without requiring a ground-truth image or supervised training data. Since PET measurements are governed by photon-counting statistics, the residual noise is expected to exhibit Poisson-like behavior. Accordingly, the fitness function evaluates the mean-to-variance ratio over homogeneous count regions obtained by percentile-based stratification of the residual noise map. A ratio close to 1.0 indicates consistency with Poisson statistics. Experiments on simulated brain phantoms show a strong correlation between this noise-statistical criterion and the inverse of PSNR and SSIM after filtered back-projection reconstruction. These results indicate that chromosomes whose residual noise better satisfies Poisson statistics tend to produce higher-quality reconstructed images. The proposed method therefore provides a reference-free and interpretable framework for PET sinogram denoising, reducing dependence on annotated datasets and offering a mathematically evaluable alternative to supervised deep-learning approaches.

References

[1] A.M. Ali, B. Benjdira, A. Koubaa,W. El-Shafai, Z. Khan, and W. Boulila, “Vision Transformers in Image Restoration: A Survey”, Sensors, vol. 23, p. 2385, 2023. doi.org/10.3390/s23052385.A.M.

[2] C.H. Garcia-Capulin, F.J. Cuevas, G. Trejo-Caballero, H. Rostro-Gonzalez, “Hierarchical Genetic Algorithm for B-Spline Surface Approximation of Smooth Explicit Data”, *Mathematical Problems in Engineering*, 2014. doi.org/10.1155/2014/706247

[3] S. Guo, Y. Sheng, L. Chai, J. Zhang, “Kernel graph filtering–A new method for dynamic sinogram denoising”, PLoS ONE, vol. 16, nº 12, e0260374, 2021. doi.org/10.1371/journal.pone.0260374.

[4] X. Liu, Y. Hong, Q. Yin, and S. Zhang, “DnT: Learning Unsupervised Denoising Transformer from Single Noisy Image”. In *Proc. 4th Intl Conf. Imag. Proc & Machine Vision*, Hong Kong, China, 2022; pp. 50–56.

MIC-05-433

Comparative Analysis of Cross-Validation Strategies for Classification of Major Adverse Cardiac Events Using Stress-phase PET Polar Maps

(#3097)

Monire Vatandoust[1], **Monire Vatandoust**[1], Jarmo Teuho[1], Jarmo Teuho[1], Riku Klén[1], Riku Klén[1], Seyed Mohammadreza Hosseini[1], Seyed Mohammadreza Hosseini[1], Luis J. Orozco[2,3], Luis J. Orozco[2,3], Juhani Knuuti[1], Juhani Knuuti[1], Eero Lehtonen[1], Eero Lehtonen[1], Remco J. Knol[3], Remco J. Knol[3], Friso V.D. Zant[3], Friso V.D. Zant[3]

[1] University of Turku, Turku PET Centre, Turku, Finland; [2] UMC Utrecht, Utrecht, Netherlands; [3] Cardiac Imaging Division, Department of Nuclear Medicine, NWZ, Alkmaar, Netherlands

The authors wish to acknowledge CSC -- IT Centre for Science, Finland, for computational resources. This work was carried out with the support of the Turku PET Centre (University of Turku, Åbo Akademi University, and the Turku University Hospital, Turku, Finland). AI tools (e.g., GitHub Copilot) were used for the manuscript drafting and point extraction from experimental results; all content was reviewed and approved by the authors.

Abstract

The choice of cross-validation (CV) strategy can significantly affect reported performance in deep learning studies, but systematic comparisons of CV methods for medical image classification remain limited. This study systematically benchmarks seven common cross-validation strategies across nine mainstream deep learning models and a logistic regression baseline to classify major adverse cardiac events (MACE) utilising stress-phase PET MPI polar map data. For each model and CV combination, evaluated on identical data splits, we report average precision (AP) and area under the receiver operating characteristic curve (AUC) as primary metrics, with confidence intervals estimated by bootstrapping. Quantitative analysis shows that Stratified Shuffle consistently yields the highest and most stable AP and AUC scores, exemplified by SqueezeNet achieving an AP of 0.52, AUC of 0.85, and delivering reduced variability across models compared to the bootstrap approach. These results highlight the critical impact of CV strategy on reliable and reproducible model evaluation for imbalanced and limited-size biomedical datasets.

References

[1] [1] Betancur, J, et al. 2018, 'Deep learning for prediction of obstructive disease from fast myocardial perfusion SPECT: A multicenter study', *JACC: Cardiovascular Imaging*, vol. 11, no. 11, pp. 1654–1663.

[2] [2] Yeung, MW, et al. 2022, 'Multi-task deep learning of myocardial blood flow and cardiovascular risk traits from PET myocardial perfusion imaging', *Journal of Nuclear Cardiology*, vol. 29, no. 6, pp. 3300–3310.

[3] [3] Varoquaux, G, Colliot, O 2023, 'Evaluating machine learning models and their diagnostic value', *Machine Learning for Brain Disorders*, 1st ed., pp. 601–630, New York: Springer.

[4] [4] Le, J-O, van der Zant, FM, et al. 2017, 'Type 2 diabetes mellitus correlates with systolic function during myocardial stress perfusion scanning with nitrogen-13 ammonia pet', *Journal of Nuclear Cardiology*, vol. 24, no. 4, pp. 1305–1311.

[5] [5] Hutchins, GD, Schwaiger, M, Rosenspire, KC, Krivokapich, J, Schelbert, H, Kuhl, DE 1990, 'Noninvasive quantification of regional blood flow in the human heart using n-13 ammonia and dynamic positron emission tomographic imaging', *Journal of the American College of Cardiology*, vol. 15, no. 5, pp. 1032–1042.

MIC-05-436

High-Sensitivity Compton Imaging via a Virtual Multi-Stage Edge-On CZT Architecture (#1139)

Greyson Shoop[1], Gregory Romancheck[2], Matthew A. Kupinski[3], Lars R. Furenlid[4,3], Michael A. King[5], Shiva Abbaszadeh[1]

[1] University of California, Santa Cruz, Department of Electrical and Computer Engineering, Santa Cruz, USA; [2] University of Illinois at Urbana–Champaign, Department of Nuclear Plasma and Radiological Engineering, Champaign, USA; [3] The University of Arizona, James C. Wyant College of Optical Sciences, Tucson, USA; [4] The University of Arizona, Department of Medical Imaging, Tucson, USA; [5] University of Massachusetts Chan Medical School, Department of Radiology, Worcester, USA

All authors declare no conflicts of interest regarding competing financial interests or personal relationships that may influence the work reported in this paper. The authors acknowledge the support from the National Institute of Biomedical Imaging and Bioengineering of the National Institutes of Health under Award Numbers R01EB028091 and UH3EB034686.

Abstract

Optimizing detection efficiency and angular resolution in Compton cameras (CC) remains a challenge for its use in nuclear medical imaging of targeted alpha therapy (TAT) and prompt-gamma (γ) Positron Emission Tomography (PET) isotopes. A trade-off between detection efficiency and angular resolution must be considered when designing scattering layer material, thickness, and distance to the absorbing layer. We propose a novel approach by repurposing a cross-strip edgeon Cadmium Zinc Telluride (CZT) PET detector system as a high-sensitivity, single-layer CC. By leveraging 40 mm of CZT thickness and binning coincidences based on scattering distance, the system functions as a virtual multi-stage CC within a single volume. GATE simulations of γ's from 137Cs (662 keV) and 133Ba (356 keV) yield event sensitivities up to 4,508±7 and 1,239±4 cps/MBq and angular resolutions of 10.8° and 16.3° respectively. This work demonstrates the advantages of high energy resolution edge-on CZT, operating as a dual-mode PET/CC, providing a high-sensitivity where angular resolution can be further enhanced without sacrificing sensitivity. Future work aims to improve the existing design with advanced reconstruction algorithms, depth-of-interaction (DOI) correction, and detector optimization.

References

[1] H. Tashima and T. Yamaya, "Compton imaging for medical applications," Radiol Phys Technol, vol. 15, pp. 187–205, Sept. 2022.

[2] B. Das, B. Mehrdel, D. Goodman, M. Streicher, Y. Seo, and J. Caravaca, "Compton Imaging of Ac-225 in Preclinical Phantoms With a 3D-positioning CZT Camera," IEEE Transactions on Radiation and Plasma Medical Sciences, vol. 10, pp. 112–125, Jan. 2026.

[3] A. Omata, J. Kataoka, K. Fujieda, S. Sato, E. Kuriyama, H. Kato, A. Toyoshima, T. Teramoto, K. Ooe, Y. Liu, K. Matsunaga, T. Kamiya, T. Watabe, E. Shimosegawa, and J. Hatazawa, "Performance demonstration of a hybrid Compton camera with an active pinhole for wide-band X-ray and gamma-ray imaging," Scientific Reports, vol. 10, p. 14064, Aug. 2020.

[4] S. H. Owe, I. Kuvvetli, C. Budtz-JØrgensen, and A. Zoglauer, "Evaluation of a Compton camera concept using the 3D CdZnTe drift strip detectors," J. Inst., vol. 14, p. C01020, Jan. 2019.

[5] Y. F. Du, Z. He, G. F. Knoll, D. K. Wehe, and W. Li, "Evaluation of a Compton scattering camera using 3-D position sensitive CdZnTe detectors," Nuclear Instruments and Methods in Physics Research Section A: Accelerators, Spectrometers, Detectors and Associated Equipment, vol. 457, pp. 203–211, Jan. 2001.

[6] S. Abbaszadeh, G. Chinn, and C. S. Levin, "Positioning true coincidences that undergo inter-and intra-crystal scatter for a sub-mm resolution cadmium zinc telluride-based PET system," Physics in Medicine & Biology, vol. 63, p. 025012, Jan. 2018.
[7] D. Sarrut, M. Bała, M. Bardi`es, J. Bert, M. Chauvin, K. Chatzipapas, M. Dupont, A. Etxebeste, L. M Fanchon, S. Jan, G. Kayal, A. S Kirov, P. Kowalski, W. Krzemien, J. Labour, M. Lenz, G. Loudos, B. Mehadji, L. M´enard, C. Morel, P. Papadimitroulas, M. Rafecas, J. Salvadori, D. Seiter, M. Stockhoff, E. Testa, C. Trigila, U. Pietrzyk, S. Vandenberghe, M.-A. Verdier, D. Visvikis, K. Ziemons, M. Zvolsk´y, and E. Roncali, "Advanced Monte Carlo simulations of emission tomography imaging systems with GATE," Phys. Med. Biol., vol. 66, p. 10TR03, May 2021.
[8] K. Eckerman and A. Endo, "ICRP Publication 107. Nuclear decay data for dosimetric calculations," Ann ICRP, vol. 38, no. 3, pp. 7–96, 2008.

MIC-05-439

3D reconstruction of radioluminescence microscopy data via MAP with optimized total variation regularization (#1231)

Grant T. Gullberg[1], Qihui Lyu[2], Guillem Pratx[3], Youngho Seo[1], Yongjin Sung[4]

[1] University of California San Francisco, Radiology and Biomedical Imaging, San Francisco, USA; [2] University of California San Francisco, Radiation Oncology, San Francisco, USA; [3] Stanford University, Radiation Oncology, Stanford, USA; [4] University of Wisconsin-Milwaukee, Biomedical and Mechanical Engineering, Milwaukee, USA

Support from the NIH under Grant NIH 1 R21 EB035205-01.

Abstract

A new microscopic nuclear imaging instrument using radioluminescence microscopy (RLM) has been developed to image living cells at high resolution with radiotracers tagged with positron emitters. These are used in biological samples to mimic clinical applications in order to evaluate their effectiveness to target receptors, antigens, and proteins that are overexpressed during growth of cancerous cells. The methodology has demonstrated impressive results for planar applications using optical reconstruction of β-ionization tracks (ORBIT); however, 3D imaging presents a challenging problem of reconstructing the 3D distribution of the source requiring backtracking of the ionization track of the positron in the scintillator in order to determine its position and 3D orientation at the detector surface. Four microlens arrays are used to record projections, limiting the angle of projection measurements to 360° sampling in the azimuthal angle φ and 40° sampling in the polar angle θ. The angle information acts as a collimator but the limited angle acquisition presents a challenging reconstruction problem which increases in difficulty for sources further from the scintillator. We consider reconstruction of the image x as a hierarchical maximum a posteriori (MAP) estimation problem under a Poisson data model with a total variation (TV) prior. In our algorithm we treat the prior weight β as a variable and jointly estimate x and β by minimizing the sum of the negative Poisson log-likelihood and a TV penalty. An alternating optimization scheme is used in which x is updated by MAP-TV reconstruction and β is updated from the current image total variation using a deviance-based adaptive update method. Good results are demonstrated using Geant4 simulations of point sources as far as 98 μs from the face of the detector. The novelty is the microscopy application to image individual cells three-dimensionally with radiopharmaceuticals.

References
[1] Panin, VY, Zeng, GL, Gullberg, GT 1999, 'Total variation regulated EM algorithm', *IEEE Trans on Nucl Sci* 46:2202-2210.

[2] Sung, Y 2021, 'Snapshot three-dimensional absorption imaging of microscopic specimens,' *Physic Review Applied* 15(6):064065.
[3] Huesman, RH, Gullberg, GT, Greenberg, WL, Budinger, TF 1977 'Users Manual - -Donner Algorithms for Reconstruction Tomography,' PUB-214, Lawrence Berkeley Laboratory Publication.
[4] Siddon, RL 1985, 'Fast calculation of the exact radiological path for a three-dimensional CT array,' *Med Phys* 12:252-255.
[5] Abdalah, M, Mitra, D, Chen, S, Boutchko, R, Gullberg, GT 2013 'Optimization of regularization parameter in a reconstruction algorithm,' In: 2013 IEEE NSS/MIC Record, Oct. 27 – Nov. 2, 2013, Seoul, Korea.

MIC-05-442

Physics-Informed Jointly Constrained Spectral Signal Decomposition for High-Resolution X-Ray Fluorescence Computed Tomography (#1630)

Huahai Sun[1,2], Liang Li[1,2]

[1] *TsingHua University, Beijing, China;* [2] *Key Laboratory of Particle Radiation Imaging, Beijing, China*

This paper is supported by the grants from NNSFC 12575327.

Abstract

X-ray fluorescence computed tomography provides element-specific imaging, but weak fluorescence peaks are often obscured by a broad Compton-scatter continuum in photon-counting spectra. The objective of this study was to improve fluorescence projection extraction before reconstruction by replacing local empirical background fitting with a physics-informed hierarchical full-spectrum unmixing method. Each measured spectrum was modeled under Poisson counting statistics as the sum of a Klein--Nishina-constrained scatter template and a calibrated fluorescence-line template. The estimator was built hierarchically, progressing from pixel-wise spectral fitting to detector-plane joint unmixing and cross-angle projection-stack refinement. The method was evaluated on a simulated polymethyl methacrylate phantom with known fluorescence projections and on an experimental spectral data set. Under the default simulated Poisson-noise setting, the proposed method reduced projection root-mean-square error from 7.98 to 3.54 and background standard deviation from 3.92 to 1.39 relative to polynomial background extraction. On experimental data, it achieved the lowest contrast-to-noise-ratio-based detection limit, 0.305 mg/ml, compared with 0.370 mg/ml for polynomial extraction. These results indicate that structured full-spectrum unmixing can improve weak fluorescence extraction and downstream detectability while remaining compatible with existing reconstruction pipelines.

References

[1] [1] Cheong, SK, et al. 2010, 'X-ray fluorescence computed tomography imaging of gold nanoparticle-loaded objects using 110 kVp x-rays', *Phys. Med. Biol.*, vol. 55, no. 3, pp. 647–662.

[2] Li, L, et al. 2023, 'Full-field in vivo imaging of nanoparticles using benchtop cone-beam x-ray fluorescence computed tomography system with pixelated photon counting detector', *J. Biomed. Opt.*, vol. 28, no. 1.

[3] Gao, B, et al. 2020, 'An analytical simulation method for X-ray fluorescence computed tomography', *Radiat. Phys. Chem.*, vol. 168.

MIC-05-445

Evaluation of Dual Tracer [^{18}F]FDG:[^{11}C]choline PET: A Simulation Study (#2094)

Avishan Elkayee Dehno, Zekai Li, Joyce van Sluis, Walter Noordzij, Adriaan A. Lammertsma, Adrienne H. Brouwers, Charalampos Tsoumpas

University of Groningen, University Medical Center Groningen, Department of Nuclear Medicine and Molecular Imaging, Groningen, Netherlands

A.E. is supported by PUSH project funding from Siemens Healthineers and the University of Groningen (e-mail: a.elkayee.dehno@umcg.nl).
Z.L. is supported by a Joint Scholarship from the China Scholarship Council and the University of Groningen (e-mail: z.l.li@umcg.nl).

Abstract

[^{18}F]FDG and [^{11}C]choline ([^{11}C]CH) are used in hepatocellular carcinoma (HCC) lesions for more accurate characterization across various differentiation stages. In this study, we investigate a simultaneous dual tracer protocol, in which [^{11}C]CH is administered immediately following [^{18}F]FDG scanning, and assess whether dual tracer images can provide diagnostic information comparable with single tracer [^{18}F]FDG and [^{11}C]CH. We simulated single and dual tracer datasets to evaluate the impact of residual [^{18}F]FDG activity on [^{11}C]CH quantification. Realistic activity distributions were used, and lesions of varying sizes (1–4 cm) were inserted in the liver and spleen with different tumor-to-background ratio (TBR) uptake patterns. Analytic simulations were performed using STIR library for a long axial field-of-view PET scanner. Results indicated that all lesions remained detectable in dual tracer images, and TBR preserved differentiation dependent patterns. Averaged relative differences and standard deviation for SUV_{mean}, SUV_{max} and SUV_{peak} between the dual tracer and [^{11}C]CH images were -21.1±10.5%, -22.5±10.6% and -18.0±8.2%, respectively. To improve quantification, voxel-wise [^{18}F]FDG subtraction was applied as a separation step, reducing the mean absolute relative difference to 1.2±1.1% for SUV_{mean}, 4.4±4.1% for SUV_{max} and 1.2±1.08% for SUV_{peak}. These results demonstrate the clinical feasibility of a dual tracer [^{18}F]FDG:[^{11}C]CH imaging protocol and motivate further optimization of separation methods for simultaneous dual tracre clinical implementation.

References
[1] Veenstra, E.B., Ruiter, S.J., de Haas, R.J., de Jong, K.P., Erba, P.A., Dierckx, R.A. and Noordzij, W., 2023. A dual-tracer approach using [11C] CH and [18F] FDG in HCC clinical decision making. *EJNMMI research*, *13*(1), p.77.
[2] Li, Z., Mohr, P., Dao, V., Luurtsema, G., Brouwers, A.H., Lammertsma, A.A. and Tsoumpas, C., 2025. Simultaneous 15oh2o and 89zrmab scanning with long axial field-of-view PET: A simulation study using digital twins. *IEEE Transactions on Radiation and Plasma Medical Sciences*.
[3] Yamamoto, Y., Nishiyama, Y., Kameyama, R., Okano, K., Kashiwagi, H., Deguchi, A., Kaji, M. and Ohkawa, M., 2008. Detection of hepatocellular carcinoma using 11C-choline PET: comparison with 18F-FDG PET. *Journal of Nuclear Medicine*, *49*(8), pp.1245-1248.
[4] Thielemans, K., Tsoumpas, C., Mustafovic, S., Beisel, T., Aguiar, P., Dikaios, N. and Jacobson, M.W., 2012. STIR: software for tomographic image reconstruction release 2. *Physics in medicine and biology*, *57*(4), pp.867-883.

MIC-05-448

EduPET - Development of a portable benchtop ToF-PET system for educational applications (#2154)

Ana Luísa M. Silva[1], Tomás Gomes[1], Chiara Cuccui[1], Andrea Gonzalez-Montoro[2], Martin Grossmann[5], Stefan Ritt[5], Hoang T.K. Trang[3,4], Youngho Seo[6], João Veloso[1], Pedro M.M. Correia[1], On behalf of EduPET Collaboration

[1] University of Aveiro, I3N - Physics Dpt., Aveiro, Portugal; [2] Universitat Politécnica de Valência, Instituto de Instrumentacion para Imagen Molecular (I3M), Centro Mixto CSIC, Valencia, Spain; [3] University of Science - Ho Chi Minh City, Department of Nuclear Physics, Ho Chi Minh City, Vietnam; [4] Vietnam National University - Ho Chi Minh City, Ho Chi Minh City, Vietnam; [5] Paul Scherrer Institut PSI, Villigen, Switzerland; [6] University of California, San Francisco and Berkeley, USA

This work was supported by IEEE Nuclear and Plasma Sciences Society (NPSS); by project UID/50025/2025, UID/PRR/50025/2025 , UID/PRR2/50025/2025 and the Associate Laboratory I3N – LA/P/0037/2020 financed by Portuguese national funds through the FCT/MEC.

Abstract

The Nuclear Plasma Science Society (NPSS) Educational Committee (EduCom) oversees educational initiatives and manages the NPSS Schools as its main vehicle for sustainable education. One such initiative is the EduPET project, which aims to develop an educational system to be used in EduCom's instrumentation schools. The EduPET system was designed to demonstrate the fundamental principles of Time-of-Flight Positron Emission Tomography (ToF-PET) using modern detector instrumentation. The current prototype consists of two opposing detector modules, each comprising a 2×2×30 mm^3 LYSO:Ce crystal coupled to a Hamamatsu S13360-2050 silicon photomultiplier (SiPM), with signal digitization performed by a DRS4-based WaveDREAM board. Initial measurements included energy spectroscopy, coincidence timing, and ToF-based source localization using a ^{22}Na point source positioned at multiple locations along the detector axis. Coincidence time resolution (CTR) values ranging from 463 to 591 ps FWHM were obtained across the different positions. The timing resolution achieved was sufficient to resolve source displacements and demonstrate the probabilistic nature of ToF-based position estimation, confirming the suitability of EduPET system as an effective educational platform for illustrating key ToF-PET concepts and advanced instrumentation techniques. Future developments will focus on expanding the detector geometry toward a complete tomographic system.

References

[1] V. Arosio et al., 2016, doi: 10.1109/NSSMIC.2016.8069360.
[2] EasyPET, CAEN, https://www.caen.it/products/sp5700/.
[3] R. Pedro et al., 2013, doi: 10.1088/1748-0221/8/03/C03005.
[4] Ritt, Stefan et al., 2010, doi: 10.1016/j.nima.2010.03.045.

MIC-05-451

Telephoto-Lens Magic-Cube: A Hybrid-Encoded Portable Gamma Camera for Extended-Distance Intraoperative Radiotracer Imaging

(#2251)

Yuxi Zhang[1], Yifan Hu[3], Zhenlei Lyu[1,2], Zeqing Zhao[2], Yufang Zhang[1,2], Wangzhao Chi[2], Rutao Yao[6], Huawei Cai[4,5], Tianyu Ma[1]

[1] Tsinghua University, Beijing, China; [2] Greater Bay Area National Center of Technology Innovation, Guangzhou, China; [3] Yale University, Department of Radiology and Biomedical Imaging, New Haven, USA; [4] Sichuan University, West China Hospital, Chengdu, China; [5] Sichuan University, Sichuan Provincial Engineering Research Center of Radiopharmaceutical Clinical Translation, Chengdu, China; [6] University at Buffalo SUNY, Department of Radiology, Jacobs School of Medicine & Biomedical Sciences, Buffalo, USA

This work was supported in part by the National Natural Science Foundation of China (No. 92359204)

Abstract

Intraoperative radiotracer imaging requires gamma cameras to maintain adequate imaging performance at relatively large source-to-camera distances, because surgical targets are often separated from the detector by tissue, instruments, surgical access constraints, or sterile operating space.

In this work, we propose a Telephoto-Lens Magic-Cube gamma camera based on a hybrid encoding mechanism. The proposed system integrates front-end long-hole geometric encoding with detector-side self-collimation encoding, allowing distant radioactive sources to generate distinguishable detector responses.

The proposed system was evaluated using numerical simulations and radioactive-source prototype experiments. In simulations, the Telephoto-Lens Magic-Cube maintained better spatial resolution at large source-to-camera distances than the Magic-Cube system without the Telephoto-Lens and two conventional parallel-hole collimator systems. It also successfully detected low-activity hot spots under background activity at large distances, whereas the reference systems failed to provide reliable detection. Prototype experiments demonstrated a mean sensitivity of 118 cps/MBq over 50–200 mm, dual-source resolution of 3 mm at 100 mm and 5 mm at 150 mm, and accurate lateral localization of 10 μCi point sources. In an anthropomorphic prostate lymph-node phantom, the system visualized five low-activity deep lymph-node-like sources under background activity and organ-uptake interference. These results suggest that the hybrid-encoded Telephoto-Lens Magic-Cube gamma camera is promising for intraoperative localization of deep low-activity lesions or lymph nodes.

References

[1] Ma T, Wei Q, Lyu Z, et al. Self-Collimating SPECT With Multi-Layer Interspaced Mosaic Detectors[J]. IEEE Transactions on Medical Imaging, 2021, 40(8): 2152-2169.

[2] Hu, Y., Z. Lyu, et al. Preliminary Performance Evaluation of a Hand-Held Magic-Cube Spectral Intraoperative Gamma Camera. IEEE NSS/MIC 2023.

[3] Knoll P M S, Schwenkenbecher K, Barthel T. Performance Evaluation of a Solid-State Detector Based Handheld Gamma Camera System. [J]. Frontiers Biomed Technol, 2014.

MIC-05-454

Whole gamma imaging prototype V: a proof-of-concept system with thin HRGAGG toward simultaneous PET/SPECT imaging (#2353)

Go Akamatsu[1], Yuma Iwao[1], Hideaki Tashima[1], Ryogo Abe[1], Eiji Yoshida[1], Han Gyu Kang[1], Fumihiko Nishikido[1], Fujino Obata[1], Hidekatsu Wakizaka[1], Shigeki Ito[2], Kyoung Jin Kim[3], Kei Kamada[3], Akira Yoshikawa[3], Mariko Ishibashi[4], Yoichi Imai[5], Miwako Takahashi[1], Taiga Yamaya[1]

[1] National Institutes for Quantum Science and Technology (QST), Chiba, Japan; [2] Mirai Imaging Inc., Fukushima, Japan; [3] Tohoku University, Miyagi, Japan; [4] Nippon Medical School, Tokyo, Japan; [5] Dokkyo Medical University, Tochigi, Japan

This work is supported by Nakatani Foundation and JSPS KAKENHI 25K10901.

Abstract

Whole gamma imaging (WGI) is a novel imaging concept combining both PET and Compton camera using a dual-ring detector arrangement. We previously developed a series of WGI prototypes for proof-of-concept. In WGI Prototype IV (WGI-IV), reported in 2025, we targeted imaging of 909 keV γ-rays from ^{89}Zr, achieving a 3.0-mm rod resolution by Compton imaging. In this study, we aimed at further improving Compton imaging performance by using thin scatterer detectors, considering a potential extension to typical SPECT tracer imaging, and we developed WGI Prototype V (WGI-V). Compton imaging performance is determined mainly by the spatial resolution and energy resolution of scatterer detectors. Therefore, we used fine and thin 0.9×0.9×2.0 mm^3 HRGAGG scintillators to obtain high spatial resolution and high energy resolution. The outer absorber ring (304 mm diameter), which was composed of 216 fast-LGSO crystal blocks, was the same as that in WGI-IV. The inner scatterer ring (109.4 mm diameter) was remodeled with 10 HRGAGG crystal blocks (22×22 array). We evaluated energy resolution for scatterer detectors using ^{133}Ba, ^{241}Am, ^{99m}Tc and ^{176}Lu (background). Then, we evaluated small rod resolution using a ^{89}Zr-filled rod phantom (rod diameters: 1.0-4.8 mm). Energy resolutions for scatterer detectors were 37.6% at 31 keV, 27.3% at 59.5 keV, 21.5% at 81 keV, 15.0% at 141 keV, and 7.5% at 307 keV. These were superior to those for the previous scatterer detector (HRGAGG, 1.45×1.45×15 mm^3, 14×14 array). In the ^{89}Zr-filled rod phantom measurement, the 2.2-mm rods were resolved by WGI-V, whereas they could not be resolved by WGI-IV. High-resolution Compton imaging (2.2-mm rod resolution) was achieved by WGI-V with 0.9×0.9×2.0 mm^3 HRGAGG scatterer detectors. An application of the WGI-V to SPECT tracers will be presented at the conference.

References

[1] E. Yoshida, *et al.*, *Phys Med Biol*, vol. 65, p. 125013, 2020.
[2] G. Akamatsu, *et al.*, *IEEE NSS/MIC/RTSD* 2025, M-01-06.
[3] KJ. Kim, *et al.*, *JCrystGrowth*, vol. 652, p. 128014, 2025.
[4] S. Takyu, *et al.*, *IEEE TRPMS*, vol. 7, p. 570-579, 2023.
[5] H. Tashima, *et al.*, *Phys Med Biol*, vol. 65, p. 225038, 2020.

MIC-05-457

Methodology to determine the absolute values of 3γ/2γ annihilation rate ratio with J-PET (#2566)

Neha Chug[1,2], Paweł Moskal[1,2], On behalf of J-PET collaboration

[1] Jagiellonian University, Faculty of Physics, Astronomy and Applied Computer Science, Krakow, Poland; [2] Jagiellonian University, Center of Theranostics, Krakow, Poland

We acknowledge the support from National Science Center through grants: 2021/42/A/ST2/00423, 2021/43/B/ST2/0215; the European Research Council (ERC Advanced Grant POSITRONIUM no. 101199807); SciMat and qLife under Excellence Initiative at Jagiellonian Univetsity; and PLGrid infrastructure under grant no. PLG/2024/017688 and PLG/2025/018762.

Abstract

The measurement of the three-photon to two-photon annihilation rate ratio ($R_{3\gamma/2\gamma}$) in positronium decays emerges as a promising diagnostic indicator for accessing tissue hypoxia [1, 2, 3]. The triplet state of positronium (ortho-positronium) is highly sensitive to local molecular oxygen concentrations [4, 5]; thus, the $R_{3\gamma/2\gamma}$ ratio could reflect on the oxygenated level of tissues [6, 7]. This study presents methodology for determining the absolute values of this annihilation ratio using the Jagiellonian Positron Emission Tomograph (J-PET), the first PET scanner based on plastic scintillators [8]. We performed measurements with sodium-22 source enclosed in metal to characterize the detector response and geometrical acceptance for the $R_{3\gamma/2\gamma}$ ratio. Since the positronium formation is suppressed in metals the resulting annihilation ratio serves as a detector-dependent reference value. After calibrating with sodium-22 in metal, we have performed the studies with porous polymer material where the positronium formation is enhanced. The two-photon and three-photon annihilation events selection are described, and their respective lifetime distributions are presented. The results presented validate the event selection methodology and establish the detector calibration baseline for future quantitative $R_{3\gamma/2\gamma}$ studies in biological sample with J-PET.

References

[1] B. Jasińska, P. Moskal, "A New PET Diagnostic Indicator Based on the Ratio of 3γ/2γ Positron Annihilation", Acta Phys. Pol. B, vol. 48, no. 10, p. 1577, 2017.

[2] P. Moskal and E. Ł. Stępień, "Positronium as a biomarker of hypoxia," Bio-Algorithms Med. Syst., vol. 17, no. 4, pp. 311–319, Dec. 2021.

[3] P. Moskal *et al.*, "Positronium Imaging: History, Current Status, and Future Perspectives", IEEE Transactions on Radiation and Plasma Medical Sciences, vol. 9, no. 8, p. 981, Nov 2025.

[4] S. D. Bass, S. Mariazzi, P. Moskal, and E. Stępień, "Positronium physics and biomedical applications," Rev. Mod. Phys., vol. 95, no. 2, Art. no. 21002, May 2023.

[5] K. Shibuya *et al.*, "Oxygen sensing ability of positronium atom for tumor hypoxia imaging," Commun. Phys., vol. 3, Art. no. 173, Oct. 2020

[6] P. Moskal, "Quantum Entanglement Degree, Mean Positronium Lifetime, and the 3γ/2γ Annihilation-Rate Ratio as Novel PET Biomarkers for Hypoxia -- Concept, Challenges, and Predictions", *Bio-Algorithms Med. Syst.*, vol. 22, no. 1, p. 56, 2026 (arXiv: 2605.00021).

[7] K. Shimazoe and M. Uenomachi "Quantum sensing and imaging in the MeV regime of nuclear medicine", Appl. Phys. Express, vol. 19, no. 4, p. 040104, April 2026.

[8] P. Moskal *et al.*, "Positronium image of human brain in vivo," Sci. Adv., vol. 10, no. 37, p. eadp2840, Sep. 2024.

MIC-05-460

Development of MACACOX2 dual-Compton camera system (#2840)

Siddharth Parashari[1], Karol Brzeziński[1], John Barrio[2], Luis Barrientos[1], Gabriela Llosa[1]

[1] Instituto de Fisica Corpuscular (IFIC) CSIC-UV, Valencia, Spain; [2] Universitat Politècnica de València, Electronic Engineering Department, Valencia, Spain

This work has received funding from the Spanish MICIN/AEI (project MIDAS, PID2022-143246OB-I00). SP acknowledges the funding from Severo Ochoa Center of Excellence under the CEX2023-001292-S grant, funded by MCIN/AEI/10.13039/501100011033.

Abstract

Compton cameras (CCs) can be designed as compact and portable systems that can be employed in combination with other imaging modalities. These imaging systems provide 3D images with just one device. However, the resolution in the axis perpendicular to the first detector is degraded with respect to the parallel plane, especially at positions far from the detectors. Placing two CCs orthogonally can improve the uniformity of the 3D spatial resolution and also increase the usable size of the field of view (FOV). Following an initial study based on simulations carried out by the IRIS group, the current work aims at an experimental verification of operating two CCs positioned orthogonal to each other in the dual-CC MACACOX2 system. In this work, simulations are performed using a geometry that replicates the laboratory setup. Coincidence data are simulated with sources located at the center of the geometry, such that the scatterers of both CCs are positioned 30 mm from the center of the FOV. The image reconstruction algorithm has been developed and optimized by the group specifically for this imaging modality and is being applied in this work. Images of a ^{22}Na point source array obtained using the simulated two head CC system and reconstructed at 511 keV are obtained. Point sources separated by 8 mm can be clearly resolved at two, three, and four cm from the detector surface. Such successful findings provide foundation for the ongoing laboratory experiments with the MACACOX2 system.

References

[1] Y. Feng and H. Sabet, J. Nuclear Medicine, vol. 66 (2025) 251907.
[2] Y. Feng, et al., IEEE TRPMS (2026) 10.1109/TRPMS.2026.3664740.
[3] J. Roser, et. al., Physica Medica 132 (2025) 104928.
[4] K. Brzezinski et al; IEEE NSS MIC RTSD, Yokohama, Japan (2025).
[5] L. Barrientos et. al., Rad. Phys. Chem. vol. 208, (2023) 110922.
[6] J. Roser et al; Phys. Med Biol, vol. 67, (2022) 155009.
[7] S. Jan et al., Phys. Med. Biol., vol. 49 (19), (2004) 4543.
[8] S. Agostinelli et al., NIMA, vol. 506 (3), (2004) p. 250-303.

MIC-05-463

MEDICAL THERMAL TOMOGRAPHY: EXPERIMENTAL DEMONSTRATION WITH HARDWARE PHANTOMS (#2959)

Anna Frixou[1], Efstathios Stiliaris[2,1], Costas N. Papanicolas[1,3]

[1] The Cyprus Institute, Nicosia, Cyprus; [2] National and Kapodistrian University of Athens, Department of Physics, Athens, Greece; [3] The Cyprus Academy of Sciences, Letters and Arts, Cypru, Nicosia, Cyprus

The research activities and the engagement of C.N. Papanicolas were partly supported by the Cyprus Academy of Sciences, Letters and Arts. The authors also thank Prof. Kirsi Lauentz and Dr Anis Fatima for facilitating access to the BIOMERA platform, and providing the μCT images. This work was also supported by the Cyprus Research and Innovation Foundation (PERSPECT No. EXCELLENCE/0524/0410), “THALIA 2021-2027”, co-funded by the EU.

Abstract

Medical thermal imaging has long been explored as a non-invasive diagnostic modality for detecting localized sub-surface abnormalities associated with pathological processes. However, despite decades of investigation, conventional thermography has not achieved widespread clinical acceptance due to inconsistent and unreliable results. In this work, we experimentally validated a framework for medical thermal tomography combining high-precision thermal measurements in a controlled and monitored environment with physics-informed tomographic reconstruction. Following software-phantom studies, the methodology was validated using a dedicated automated experimental setup together with a suite of calibrations and temporal and spatial corrections, reducing the uncertainty in panoramic thermal projections to approximately 25 $^{\circ}$C. Reconstruction was performed using physics-informed forward thermal diffusion models within the AMIAS/RISE framework. Using this methodology, localized hot-spots with temperature differences as low as ΔT = 1.5 $^{\circ}$C were successfully detected and reconstructed at depths up to 3.3 cm in hardware phantoms. The reconstructed positions and temperatures were in good agreement with independent thermocouple and µCT measurements. These results provide strong evidence that thermal tomography is feasible when combined with precision thermal measurements and physics-informed reconstruction methods.

MIC-05-466

MIC-05-469

A Computational Assessment of Quantum SimulationVersus Classical Simulation for Quantum-InspiredMedical Imaging (#3117)

Amirreza Hashemi, Hamid Sabet

Massachusetts General Hospital, Harvard Medical School, Radiology, Boston, USA

This work was supported in part by NIH grant R01EB034785

Abstract

Quantum-inspired formulations have emerged as a promising approach for medical image denoising and segmentation by recasting image processing tasks as eigenvalue problems. While computationally demanding on classical hardware, these methods align naturally with quantum computing paradigms, particularly the Variational Quantum Eigensolver (VQE). In this work, we assess whether quantum simulation on classical hardware is justified in the absence of real quantum devices by comparing classical computing (CPU-based diagonalization), quantum simulation on CPU, and GPU-accelerated quantum simulation using Qiskit. Experiments on synthetic data and a clinical PET/CT case show consistent reconstruction and segmentation quality across implementations. Quantitatively, classical methods are faster for small problems (e.g., 0.0063 s vs 0.0229 s), while GPU-based quantum simulation reduces this gap (~0.003 s) and becomes slightly faster at larger scales (660.78 s vs 669.1 s). These results indicate that quantum simulation is not advantageous for small cases, but can become competitive or beneficial for larger problems within a quantum-inspired framework.

12 November, 2026

Time:
12 November, 2026
9:00 – 11:00

Room:
FEDERICO GARCÍA LORCA

MP-02 | MIC Plenary Session 2

Chairs:
Vesna Sossi (Vancouver)
Roger Fulton (Sydney)

MP-02-01

NPSS President (#3367)

Sara A. Pozzi[1], Vesna Sossi[2], Roger Fulton[3]

[1] University of Michigan, Ann Arbor, USA; [2] University of British Columbia, Vancouver, Canada; [3] University of Sydney, Sydney, Australia

MP-02-02

Plenary Talk | Nuclear Fusion – Energy source for the future: An overview with emphasis on control and imaging (#3368)

Axel Winter

Max Planck Institute for Plasma Physics, Greifswald, Germany

MP-02-03

NPSS merit award Introduction (#3369)

Steven R. Meikle

The University of Sydney, Sydney, Australia

MP-02-04

NPSS merit award presentation (#3370)

Tba Tba

Tba, Tba, Germany

MP-02-05

Edward J. Hoffman Medical Imaging Scientist Award Introduction

(#3371)

Youngho Seo

University of California, San Francisco, USA

MP-02-06

Edward J. Hoffman Medical Imaging Scientist Awardee Introduction

(#3372)

Suleman Surti

University of Pennsylvania, Department of Radiology, Philadelphia, USA

MP-02-07

Edward J. Hoffman Medical Imaging Scientist Awardee Presentation

(#3373)

Dimitris Visvikis

Univ. Brest, LaTIM, Inserm UMR 1101, Brest, France

MP-02-08

Freek J. Beekman Medical Imaging Technical Achievement Award Introduction (#3374)

Youngho Seo

University of California, San Francisco, USA

MP-02-09

Freek J. Beekman Medical Imaging Technical Achievement Awardee Introduction (#3375)

Xiaochuan Pan

University of Chicago, Department of Radiology, Chicago, USA

MP-02-10

Freek J. Beekman Medical Imaging Technical Achievement Awardee Presentation (#3376)

Ken Taguchi

Johns Hopkins University, Baltimore, USA

MP-02-11

Bruce H. Hasegawa Young Investigator Medical Imaging Award Introduction (#3377)

Youngho Seo

University of California, San Francisco, USA

MP-02-12

Bruce H. Hasegawa Young Investigator Medical Imaging Awardee Introduction (#3378)

Ciprian Catana

MGH and Harvard University, A. A. Martinos Center and Harvard Medical School, Cambridge, USA

MP-02-13

Bruce H. Hasegawa Young Investigator Medical Imaging Awardee Presentation (#3379)

Kevin Jaeyoung Chung

MGH and Harvard University, Cambridge, USA

MP-02-14

IEEE TRPMS Best Paper Award (#3380)

Dimitris Visvikis

Université de Bretagne Occidantal (UBO), Brest, France

Time:
12 November, 2026
11:30 – 12:45

Room:
FEDERICO GARCÍA LORCA

MIC-06 | Simulation and modeling of medical imaging systems (1)

Chairs:
Julien Bert (Brest)
Min Sun Lee (Daegu)

MIC-06-01

Minkhole Collimators for SPECT: Minkowski-Sum Aperture Geometry and Closed-Form Ray Tracing (#1605)

Yusheng Li[1], Hongdi Li[1]

[1] United Imaging Healthcare North America, MI, Houston, USA; [2] United Imaging Healthcare North America, MI, Houston, USA

Abstract

Single-photon emission computed tomography (SPECT) pinhole collimators trade isotropic resolution against detector coverage: circular apertures cover only 78.5% of a square detector. Rectangular pinholes (rectholes) fill the detector but introduce anisotropic resolution. Lofthole collimators linearly interpolate between a circular aperture and a rectangular exit; their non-developable lateral surfaces complicate fabrication and geometric calibration. We present the minkhole collimator, a knife-edge geometry whose half-frustum equals the Minkowski sum of a circular waist and a rectangular exit. The half-frustum boundary decomposes exactly into ten analytic patches: two caps, four ruled side planes, and four corner quadrics. Convexity of each half-frustum bounds a ray to at most two boundary intersections, giving a closed-form ray tracer of six linear and four quadratic solves with no iteration. We implement the 10-patch intersection and compare the minkhole to pinhole, recthole, and lofthole collimators on a common geometry. At matched sensitivity and field of view, minkhole projections are more symmetric than the recthole's and show less diagonal elongation than the lofthole's, while fully covering the detector. Its piecewise-developable surface (planar and sheared-conical patches) admits a compact analytic form that simplifies calibration, making the minkhole a practical building block for multi-aperture SPECT.

References

[1] S. D. Metzler, J. E. Bowsher, M. F. Smith, and R. J. Jaszczak, “Analytic determination of pinhole collimator sensitivity with penetration,” IEEE Trans. Med. Imag., vol. 20, no. 8, pp. 730–741, Aug. 2001, doi: 10.1109/42.938241.

[2] S. D. Metzler and S. C. Moore, “Analytic determination of rectangular-pinhole sensitivity with penetration,” IEEE Trans. Med. Imag., vol. 39, no. 4, pp. 833–843, Apr. 2019, doi: 10.1109/TMI.2019.2936187.

[3] K. Deprez, L. R. Pato, S. Vandenberghe, and R. Van Holen, “Characterization of a SPECT pinhole collimator for optimal detector usage (the lofthole),” Phys. Med. Biol., vol. 58, no. 4, Jan. 2013, doi: 10.1088/0031-9155/58/4/859.

[4] R. Schneider, Convex bodies: the Brunn–Minkowski theory. New York, NY: Cambridge University Press, 2nd edition, 2013, doi: 10.1017/CBO9781139003858.

MIC-06-02

Monte Carlo simulation model of the ring CZT based VERITON SPECT-CT system (#2273)

Ane Etxebeste[1,2], My Hoang Hoa Bui[1], Mary Erojo[4], Thomas Baudier[1], Jean Nöel Badel[1,2], Mikko Hakulinen[3,4], David Sarrut[1,2]

[1] CREATIS, INSA-Lyon, CNRS UMR 5220, Lyon, France; [2] Centre de lutte contre le cancer Léon Bérard, Lyon, France; [3] Diagnostic Imaging Center, Kuopio University Hospital, Kuopio, Finland; [4] University of Eastern Finland, Department of Technical Physics, Kuopio, Finland

The authors want to warmly thank all the team at Spectrum Dynamics, Justine McQuillan and Raphael Blum for very thorough discussions. M. Erojo would like to acknowledge that her work is supported by the Finnish Ministry of Education and Culture's Pilot for Doctoral Programmes (Pilot project Mathematics of Sensing, Imaging and Modelling).This work was performed within the framework of the SIRIC LYriCAN Grant INCa-DGOS-INSERM-ITMO cancer_18003, the LABEX PRIMES (ANR-11-LABX-0063) of Université de Lyon, within the program 'Investissements d'Avenir' (ANR-11-IDEX-0007) operated by the ANR.

Abstract

The aim of this study was to develop and evaluate a GATE Monte Carlo model of the ring CZT based VERITON SPECT-CT system against experimental data. System spatial resolution was evaluated using planar images with ^{99m}Tc point-like sources. Good agreement was obtained between both experimental and simulated data with consistent values within one sigma, except for the studied distances closest to the collimator surface (5 and 7 cm) where relative discrepancies of 25% and 7% were observed along X-axis. A tomographic acquisition, corresponding to 4 gantry rotations and 60 swivel positions per detector head, using the NEMA IEC body phantom was simulated within GATE 10. A qualitative comparison of profiles showed good agreement between both reconstructions.

We plan to further evaluate this model regarding quantitative imaging and extend it to additional radionuclides. Such a model could have a significant impact on the optimisation of acquisition protocols, image reconstruction and system design.

References

[1] L. Vergnaud et al., "Performance study of a 360◦ CZT camera for monitoring 177Lu-PSMA treatment," EJNMMI Physics, vol. 10, no. 1,p. 58, 2023.

[2] C. Desmonts et al., "Evaluation of a new multipurpose whole-body CZT- based camera: comparison with a dual-head anger camera and first clinical images," EJNMMI physics, vol. 7, no. 1, p. 18, 2020.

[3] S. Rit et al., "The Reconstruction Toolkit (RTK), an open-source cone-beam CT reconstruction toolkit based on the Insight Toolkit (ITK)," J. Phys: Conf. Ser., vol. 489, 02 2014.

[4] D. Sarrut et al., "GATE 10 Monte Carlo particle transport simulation: I. development and new features," Phys. Med. & Biol., vol. 71, no. 1, p. 015042, 2026.

[5] D. Sarrut et al., "Free flight angular acceptance variance reduction technique for SPECT Monte Carlo simulations," Phys. Med. & Biol., 2026.

MIC-06-03

Intraoperative Position-Sensitive Positron Emission Counter (PEC): A Simulation Study (#2337)

Ryotaro Ohashi[1,2], Shigeki Ito[3], Miwako Takahashi[1], Taiga Yamaya[1]

[1] National Institutes for Quantum Science and Technology, Chiba, Japan; [2] Chiba University, Graduate School of Science and Engineering, Chiba, Japan; [3] Mirai-Imaging Corporation, Fukushima, Japan

Abstract

For metastatic lymph-node localization in esophageal cancer surgery with ^{18}F-FDG injection, we have been developing an intraoperative positron emission counter (PEC). This device employs two BGO scintillators (~10×5×15 mm^3) on the tip of a forceps and it provides coincidence detection. The current design of the PEC is not position sensitive; however, quantitative radioactivity measurement requires recovery of the source distribution within the compact field of view (FOV) of the PEC, because position-dependent detection efficiency renders the integral count rate ambiguous. In this paper, we investigate the feasibility of source distribution visualization on a position-sensitive PEC variant featuring 2×2 segmentation of each scintillator (yielding 16 lines of response, LORs) together with a machine-learning (ML) decoder mapping these 16 LORs to a source distribution. Specifically, we designed a multi-layer perceptron (MLP) with a spatial-softmax head defined over the FOV. The MLP was trained with Kullback-Leibler (KL)-divergence supervision on random-walk phantoms (each yielding a 16-LOR expected count vector via Geant4 simulation, Poisson-sampled at a 100-count budget), with mixed single- and synthetic 2-source training samples. The pitch of the FOV reconstruction grid was 0.5 mm. On held-out single-source test phantoms, the predicted distribution provides the source center-of-gravity (CoG) with a median 3D Euclidean mean-absolute-error (MAE) of 0.73 mm and the per-axis source extent within ≤16% (sigma MAE 0.13–0.24 mm vs. ground-truth 1.2–1.5 mm). On disjoint 2-source pairs, 90.1% of the detected peaks lie within 2.5 mm of a true source (per-detected-peak median 1.40 mm; per-true-source median 1.58 mm). These results indicate that a position-sensitive PEC with an MLP-based decoder achieves not only the source localization but also the source distribution visualization from only 16 LOR counts.

References

[1] S. Yoshimura, et al., “One-by-one comparison of lymph nodes between ^{18}F-FDG uptake and pathological diagnosis in esophageal cancer,” Clin. Nucl. Med., vol. 45, no. 10, pp. 741–746, 2020.

[2] M. Takahashi, et al., “A design of forceps-type coincidence radiation detector for intraoperative LN diagnosis: Clinical impact estimated from LNs data of 20 esophageal cancer patients,” Ann. Nucl. Med., vol. 36, no. 3, pp. 285–292, 2022.

[3] R. Ohashi, et al., “Adding position-sensitive functionality to a forceps-type mini-PET prototype,” in 2023 IEEE NSS MIC RTSD, 2023.

MIC-06-04

A metascintillator-based, ultra-ToF enabled, brain PET scanner simulation (#2563)

Georgios Konstantinou[1,2], Paul Lecoq[2,3]

[1] EPFL, PV lab, Neuchatel, Switzerland; [2] Metacrystal SA, Geneve, Switzerland; [3] CERN, Geneve, Switzerland

Abstract
Metascintillator systems composed of LYSO:Ce and 2D organic lead halide perovskites were recently measured in the laboratory with high end electronics. The timing behavior of this metascintillator rendered two dominant subsets: 44% of fast, perovskite-led and shared events at 46 ps and 56% of slow, LYSO:Ce events at 110 ps. As this design reaches ultrafast ToF regimes, an opportunity to better understand the effect of such CTR on final image quality arises. The possibility of adapting this configuration to a photonic-driven semi-monolithic metascintillator also offers very good depth-of-interaction discrimination, at 4 mm. To benchmark this detector architecture, a brain PET scanner was designed in GATE, with a Hoffman brain and Derenzo phantoms for benchmarking. A series of reconstruction approaches, for instance using the fast subset as priors or weighing in on the different subsets been performed, but the drive for this exercise is to invite the reconstruction community to experiment with and demonstrate the potential of new generation high end ToF detectors for medical imaging.

MIC-06-05

Towards the Ultimate Sub-0.4 mm Resolution: GATE Simulation of a Mouse Brain PET System (#1832)

Han Gyu Kang, Hideaki Tashima, Taiga Yamaya

National Institutes for Quantum Science and Technology (QST), Advanced Nuclear Medicine Sciences, Chiba, Japan

This work was partly supported by 2023 IEEE Edward J. Hoffman Early Career Development Grant.

Abstract
Last year, we developed a sub-0.5 mm resolution positron emission tomography (PET) system using staggered 3-layer depth-of-interaction (DOI) detectors for mouse brain imaging. However, the crystal pitch of 0.8 mm limited the spatial resolution to 0.45 mm, which sparked our pursuit of the ultimate resolution. In this study, we investigate the spatial resolution of a newly proposed mouse brain PET system that uses a reduced crystal pitch as we move towards sub-0.4 mm resolution. The proposed system provides 48 mm inner diameter and 22.6 mm axial coverage. It consists of 32 DOI detectors with 2-ring geometry. Each DOI detector has staggered 3-layer LYSO crystals

(crystal pitch=0.6 mm) with a crystal layer thickness of 3+3+5 mm, thereby providing a 11 mm total thickness. We used GATE simulation to investigate the performance of the proposed PET design. For spatial resolution evaluation, an NEMA ^{22}Na source (D=0.25 mm) was scanned from the field-of-view center to the 15 mm radial offset position and it was reconstructed by using an FBP algorithm. For imaging performance evaluation, a resolution phantom having six different rod diameters was used. The PET images were reconstructed by using the OSEM algorithm. Compared to results of our previous work, the spatial resolution was improved from 0.75±0.02 mm to 0.55±0.07 mm. Unlike the previous work, the 0.4 mm rods of the resolution phantom were resolved with a valley-to-peak ratio of 0.763. In conclusion, the simulation showed that our proposed mouse brain PET system provided 0.4 mm resolution in resolution phantom imaging. As a next step, we plan to develop a prototype mouse brain PET scanner to achieve 0.4 mm resolution experimentally.

References

[1] R. S. Miyaoka et al., “Small animal PET - a review of what we have done and where we are going”, *Phys. Med. Biol.*, vol. 65, no. 24, pp. 24TR04, 2020.
[2] H.G. Kang et al., “Submillimeer-Resolution PET for High-Sensitivity Mouse Brain Imaging”, *J. Nucl. Med.*, vol. 64, No. 6, pp. 978-985, 2023.
[3] H.G. Kang et al., “Sub-0.5 mm Resolution PET Scanner With 3-Layer DOI Detectors for Rodent Neuroimaging”, *IEEE Trans. Med. Imaging.*, vol. 45, No. 4, pp. 1423-1431, 2026.
[4] H.G. Kang et al., “Design optimization using GATE Monte Carlo simulations for a sub-0.5 mm resolution PET scanner with 3-layer DOI detectors”, *Phy. Med. Biol.*, vol. 71, No. 3, pp. 035001, 2026.

Time:
12 November, 2026
11:30 – 12:45

Room:
MANUEL DE FALLA

MIC-07 | Multi-modality imaging systems including applications and High resolution imaging systems (organ-dedicated, small animal systems) (2)

Chairs:
Volkmar Schulz (Aachen)
Nikos Efthimiou (Groningen)

MIC-07-01

Experimental Feasibility of Dual-Mode C-arm CT/SPECT Imaging Using a Commercial X-ray Detector for Online Brachytherapy Delivery Verification (#1805)

Saerom Sung[1], Hyun Joon Choi[2], Sangwoon Jeong[2], Sei Hwan You[2], Chul Hee Min[1]

[1] Yonsei University, Department of Radiation Convergence Engineering, Wonju, South Korea; [2] Yonsei University Wonju College of Medicine, Wonju Severance Christian Hospital, Department of Radiation Oncology, Wonju, South Korea

This work was supported by NRF/MSIT, Republic of Korea (RS-2025-25438965), and the Gangwon RISE program (2025-RISE-10-006).

Abstract

Online brachytherapy delivery verification requires two complementary capabilities: anatomical verification of the applicator prior to irradiation and dynamic tracking of the radioactive source during dose delivery. This study experimentally evaluated the feasibility of a dual-mode C-arm CT/SPECT imaging concept using a single commercially available X-ray flat-panel detector. The core paradigm repurposes a standard X-ray detector into a shared hardware platform: an uncollimated mode for structural visualization, and a collimator-attached mode for radioactive source tracking. The experimental setup utilized a DRTECH EXT1616R digital detector. In the uncollimated X-ray mode, projection images of a PMMA–agar phantom containing a two-ovoid applicator were acquired at 90 kV and 10 mAs during rotational acquisition. The acquired projections successfully distinguished the applicator, air cavities, and phantom tissue surrogate layers. For the SPECT mode, a parallel-hole tungsten collimator was attached to the identical detector. Projection frames of a 58.12 GBq Co-60 source were acquired continuously at 1 frame/s during rotation. Following image intensity enhancement, the Co-60 source profile yielded full width at half maximum values of 3.80 mm and 2.91 mm in the x and y directions, respectively. Furthermore, to demonstrate the ultimate clinical utility of this dual-mode concept, a high-quality reference CT image of a patient-specific 3D-printed pelvic phantom was overlaid with the reconstructed SPECT source distribution, successfully illustrating CT/SPECT fusion feasibility. These findings robustly support the experimental viability of utilizing a commercial X-ray detector for both anatomical assessment and frame-based source delivery verification.

References

[1] P. Georg et al., “Dose-volume histogram parameters and late side effects in magnetic resonance image-guided adaptive cervical cancer brachytherapy,” Int. J. Radiat. Oncol. Biol. Phys., vol. 79, no. 2, pp. 356–362, 2011, 10.1016/j.ijrobp.2009.11.002

[2] S. Sung et al., “Feasibility of internal-source tracking with C-arm CT/SPECT imaging with limited-angle projection data for online in vivo dose verification in brachytherapy: A Monte Carlo simulation study,” Brachytherapy, vol. 22, no. 5, pp. 673–685, 2023, 10.1016/j.brachy.2023.05.003

MIC-07-02

Development of Biological Microenvironment Imaging Technique Using ^{111}In Cascade Gamma-Ray Correlation (#3120)

Boyu Feng[1], Moh Hamdan[2], Toshifumi Tatsumi[3], Sotaro Miyao[3], Akira Sugiyama[5], Mizuki Uenomachi[4], Hayato L. Mizuno[4], Yasutaka Anraku[4], Nobuyoshi Akimitsu[3], Kenji Shimazoe[1]

[1] The University of Tokyo, Graduate School of Engineering, Tokyo, Japan; [2] Fukushima Institute for Research, Education and Innovation (F-REI), Fukushima, Japan; [3] The University of Tokyo, Isotope Science Center, Tokyo, Japan; [4] Institute of Science Tokyo, Tokyo, Japan; [5] Hoshi University, Tokyo, Japan

Abstract

This study explores nuclear medicine imaging toward visualization of both radiotracer distribution and microscopic chemical environment using ^{111}In cascade gamma-ray correlation. PAC coefficients of ^{111}In-labeled agents were quantitatively evaluated under different pH conditions to assess local chemical-environment sensitivity. Cell experiments using ^{111}In-labeled molecular probes were performed to examine applicability to biological samples. In vivo DPECI visualized ^{111}In-labeled agent biodistribution in mice, showing liver and tumor signals consistent with ex vivo organ biodistribution. These results provide a basis for future multimodal imaging that integrates PAC-derived microscopic chemical information with DPECI-based spatial visualization.

MIC-07-03

SmartBrain-EEG: First-in-Human Wearable PET/EEG Imaging in Epilepsy (#2207)

Han Liu[1,2], **Han Liu**[1,2], Wenkang Qu[1], Wenkang Qu[1], Yuejie Lin[1], Yuejie Lin[1], Kaiming Hu[1,2], Kaiming Hu[1,2], Xin Yu[1], Xin Yu[1], Da Liang[1], Da Liang[1], Ying Lin[1], Ying Lin[1], Xiaoyin Zhang[1], Xiaoyin Zhang[1], Jinyong Tao[1], Jinyong Tao[1], Dawei Shi[1], Dawei Shi[1], Wenbin Li[1], Wenbin Li[1], Huiping Zhao[1], Huiping Zhao[1], Yibin Zhang[1], Yibin Zhang[1], Qiyu Peng[1], Qiyu Peng[1]

[1] Shenzhen Bay Laboratory, Institute of Biomedical Engineering, Shenzhen, China; [2] Harbin Institute of Technology, College of Artificial Intelligence, harbin, China

This work was supported by the National Natural Science Foundation of China (Grant no. 82327809), the National Key Research and Development Program of China (Grant No. 2024YFF0507700), National High-Level Hospital Clinical Research Funding (2025-PUMCH-D-003), Beijing Natural Science Foundation(L252047).

Abstract

In presurgical epilepsy evaluation, noninvasive localization remains challenging in patients with negative or suspicious magnetic resonance imaging findings or inconsistent multimodal results. Positron emission tomography provides metabolic information, while electroencephalography records abnormal electrical activity. However, conventional fixed PET systems usually require supine and constrained positioning, limiting simultaneous monitoring during seizure-related states, task conditions, or near-natural behaviors. To address this limitation, we integrated scalp electroencephalography with an ultra-light wearable motion-following brain PET system to evaluate the feasibility of simultaneous metabolic-electrophysiological imaging in epilepsy subjects. Compatibility was first assessed using an electroencephalography-equipped brain phantom. Phantom images acquired with and without electroencephalography electrodes showed comparable structures, and electroencephalography waveforms remained interpretable with and without PET operation. Initial human evaluation was then performed in an epilepsy patient. Wearable brain PET imaging and simultaneous wearable PET/EEG acquisition were successfully completed. During prolonged acquisition, the subject fell asleep, causing detector displacement and motion artifacts in reconstructed PET images. These results demonstrate the technical feasibility of simultaneous wearable metabolic-electrophysiological brain imaging and highlight the need for improved fixation, motion tracking, and motion correction in future natural-state neuroimaging studies.

References
[1] Traub-Weidinger, T, Arbizu, J, Barthel, H et al. 2024, 'EANM practice guidelines for an appropriate use of PET and SPECT for patients with epilepsy', *European Journal of Nuclear Medicine and Molecular Imaging*, vol. 51, pp. 1891–1908.
[2] Grouiller, F, Thornton, K, Groening, A et al. 2015, 'All-in-one interictal presurgical imaging in patients with epilepsy: single-session EEG/PET/(f)MRI', *European Journal of Nuclear Medicine and Molecular Imaging*, vol. 42, pp. 1133–1143.
[3] Liu, H, Qu, W, Liang, D et al. 2026, 'Performance Evaluation of SmartBrain: A Wearable PET System for Human Brain Imaging', *Journal of Nuclear Medicine*.
[4] Rajkumar, R, Rota Kops, E, Mauler, J et al. 2017, 'Simultaneous trimodal PET-MR-EEG imaging: Do EEG caps generate artefacts in PET images?', *PLOS ONE*, vol. 12, no. 9, e0184743.

MIC-07-04

Human Subject and Phantom Imaging Performance of PETcoil Gen II Brain-Dedicated PET System (#2894)

Grant H.-S. Park, Muhammad N. Ullah, Garry Chinn, Craig S. Levin

Stanford University, Radiology, Stanford, USA

This work was supported in part by NIH-NIBIB grant #5R01EB03103804. The authors thank Dr. Qian Dong for foundational contributions to the PETcoil Gen II system, Martin Schneider, our clinical coordinator for this study, and the patient who participated in this first clinical scan.

Abstract
PETcoil Gen II is a second-generation RF-penetrable time-of-flight (TOF) positron emission tomography (PET) brain insert designed for simultaneous PET/MRI. We evaluated initial imaging performance using a 3D Hoffman brain phantom and present the first clinical ^{18}F-FDG brain PET images acquired with the system. Randoms correction was performed using delayed-window (DW) estimates. A computed tomography (CT)-based attenuation

(μ) map was generated and extrapolated to 511 keV using piecewise linear interpolation, while scatter fractions were estimated via OpenSSS. In the Hoffman phantom and research subject scan, full corrections improved signal-to-background ratio from 3.48 to 4.50 and from 2.69 to 3.20, respectively, with improved visualization of cortical and subcortical structures. These results indicate that the correction methods are functioning and demonstrate the ability of the PETcoil Gen II to produce high-quality images.

References
[1] Q. Dong et al. 2024, 'Article', Physics in Medicine & Biology, 69, 185007, Bristol: IOP Publishing
[2] Ullah, MN 2024, 'Data Correction and Imaging Studies for PETCoil: A Second-Generation RF-Penetrable Brain TOF-PET Insert for Simultaneous PET/MRI', IEEE NSS/MIC/RTSD, Piscataway: IEEE
[3] Williams, CW et al. 1979, 'Article', Journal of Nuclear Medicine, 20, 695–696, Reston: Society of Nuclear Medicine
[4] Hudson, HM et al. 1994, 'Article', IEEE Transactions on Medical Imaging, 13, 601–609, Piscataway: IEEE

MIC-07-05

Development of SIAT 9.4T MRI compatible animal PET scanner (#1791)

Haonan Li, Hui Huang, Sen Yang, Zhonghua Kuang, Ning Ren, Zhanli Hu, Yongfeng Yang, Zheng Liu

Chinese Academy of Sciences, Paul C. Lauterbur Research Center for Biomedical Imaging, Shenzhen Institute of Advanced Technology, Shenzhen, China

This work is supported by the National Key Research and Development Program of China (2023YFF0716000), the National Natural Science Foundation of China (Grant No. 12375358), the Shenzhen Science and Technology Program (JCYJ20220531100000001, JCYJ20220818101804009).

Abstract

This study aims to develop a 9.4 T MRI-compatible small-animal PET insert with sub-millimeter spatial resolution and system-level magnetic compatibility. The PET insert consists of 84 dual-ended readout detector arrays arranged in 7 axial rings, with 12 detector modules per ring. Each detector array contains a 28 × 28 LYSO crystal matrix with a crystal size of 0.75 × 0.75 × 20 mm³. Compact front-end amplification electronics, row-column multiplexed readout, non-magnetic mechanical support, and inner/outer carbon-fiber tubes were integrated to meet the spatial and electromagnetic compatibility requirements of a 9.4 T MRI scanner. Point-source imaging was performed to evaluate spatial resolution. A prototype PET insert was developed and integrated. ^{22}Na point-source images reconstructed using OSEM with 5 iterations demonstrated sub-millimeter spatial resolution, indicating high-resolution imaging capability for 9.4 T small-animal PET/MRI applications.

References
[1] R. S. Miyaoka and A. L. Lehnert, "Small animal PET: a review of what we have done and where we are going," *Physics in Medicine & Biology,* vol. 65, no. 24, p. 24TR04, 2020.
[2] G. Stortz *et al.*, "Performance of a PET insert for high-resolution small-animal PET/MRI at 7 tesla," *Journal of Nuclear Medicine,* vol. 59, no. 3, pp. 536-542, 2018.
[3] Z. Kuang *et al.*, "Design and performance of SIAT aPET: a uniform high-resolution small animal PET scanner using dual-ended readout detectors," *Physics in Medicine & Biology,* vol. 65, no. 23, p. 235013, 2020.
[4] Z. Kuang *et al.*, "Development and performance of SIAT bPET: a high-resolution and high-sensitivity MR-compatible brain PET scanner using dual-ended readout detectors," *European Journal of Nuclear Medicine and Molecular Imaging,* vol. 51, no. 2, pp. 346-357, 2024.

Time:
12 November, 2026
12:45 – 13:05

Room:
FEDERICO GARCÍA LORCA

M-LT-03 | New radiation detector technologies for medical imaging,Novel applications of AI in radiation-based medical imaging

Chairs:
Min Sun Lee (Daegu)
Julien Bert (Brest)

M-LT-03-01

MRI-Informed SPECT-only Spatial Normalization for Reliable Brain Perfusion Quantification (#1410)

Euijin You[1,2], Yu Jin Seol[1,2], Hyun Gee Ryoo[3], Seung Kwan Kang[4], Jae Sung Lee[1,2]

[1] Seoul National University, Interdisciplinary Program in Bioengineering, Seoul, South Korea; [2] Seoul National University, Integrated Major in Innovative Medical Science, Seoul, South Korea; [3] Seoul National University, Department of Nuclear Medicine, Seoul, South Korea; [4] Samsung Ventures, Seoul, South Korea; [5] Brightonix Imaging Inc., Seoul, South Korea

Abstract

Spatial normalization enables standardized volume-of-interest quantification in brain perfusion single-photon emission computed tomography, but accurate alignment is difficult because of low resolution, noise, partial volume effects, and uptake-dependent variation. We propose a MRI-informed, SPECT-only framework that distills anatomical deformation fields and feature guidance from a magnetic resonance imaging registration teacher. The student disentangles anatomical and uptake-related representations to suppress functional-uptake interference while requiring only single-photon emission computed tomography at inference. In 173 paired imaging datasets, the method improved standardized uptake value ratio consistency between subject and template spaces, especially for fine-grained volumes of interest, supporting MRI-free, single-pass template-based quantification.

References

[1] Li, R., Figueredo, G., Auer, D., Wagner, C. and Chen, X. 2024, 'MrRegNet: Multi-resolution Mask Guided Convolutional Neural Network for Medical Image Registration with Large Deformations', 2024 IEEE International Symposium on Biomedical Imaging (ISBI), pp. 2349–2353, Piscataway, NJ: IEEE.

[2] Woo, S., Park, J., Lee, J.-Y. and Kweon, I.S. 2018, 'CBAM: Convolutional Block Attention Module', Proceedings of the European Conference on Computer Vision (ECCV), pp. 3–19, Cham: Springer.

[3] Kang, S.K., Kim, D., Shin, S.A., Kim, Y.K., Choi, H. and Lee, J.S. 2023, 'Fast and Accurate Amyloid Brain PET Quantification Without MRI Using Deep Neural Networks', Journal of Nuclear Medicine, vol. 64, no. 4, pp. 659–666, Reston, VA: Society of Nuclear Medicine and Molecular Imaging.

M-LT-03-02

Developments in fabrication and design flexibility of amorphous silicon microchannel plates (#2584)

Georgios Konstantinou, Loris Barraud, Christophe Baillif, Nicolas Wyrsch

EPFL, Neuchatel, Switzerland

The project is funded by the SNF SPARK grant no CRSK-2_237272

Abstract

The technology of amorphous silicon-based micro-channel plates (AMCPs) uses a versatile approach to stack hydrogenated amorphous silicon in thicknesses up to 100 µm, using plasma-enhanced chemical vapor deposition (PECVD) and etch microchannels of diameter below 2 µm every 5 µm, on a hexagonal pattern, by deep reactive ion etching. With gains up to 1000 for reverse bias less than 300 V, the design is possible to build on arrays of sensitive transimpedance amplifiers, integrated in read-out circuits with high channel density, such as for instance 15 by 15 µm. This ensures single photon detection with quantum efficiency up to 30% and noise rates below 50 Hz/cm², if combined with state of the art photocathodes such as the hi-QE from Photonis. Current fabrication runs focus on direct integration of the stack on ASICs, to be integrated with the photocathode over the next months. Measurements show timing response with jitter below 10 ps, making this high-precision photodetector ideal for radiation detectors combining ultra-fast photon emission and low light yield, such as Cherenkov.

M-LT-03-03

Fabrication of diamond detectors with graphitic contacts for tissue equivalent dosimetry (#2040)

Ivan Lopez Paz, **Ivan Lopez Paz**, Consuelo Guardiola, Consuelo Guardiola, Gemma Rius, Gemma Rius

Institut de Microelectronica de Barcelona (IMB-CNM, CSIC), Bellaterra, Spain

This work has been funded by the IMB-CNM (CSIC) TRIGGER projects PIACeD and CarDos4FLASH, supported by the ‘María de Maeztu Unit of Excellence’ accreditation (CEX2023-001397-M / AEI/10.13039/501100011033). This study was also funded RYC2024-050777-I project, financed by the MICIU / AEI / 10.13039/501100011033 and FSE+.

Abstract

Diamond-based dosimeters are popular for medical dosimetry in view of their fast response, radiation hardness and tissue equivalence. However, some design improvements to achieve better accuracy in signal readout and approach tissue equivalence are possible by the removal of the metallic contacts, sometimes covering the active area of said devices.

In this contribution, we explore the use of a simple processing and scalable solution to obtain non-metal, low Z electrical contact. Thus, the fabrication of diamond detectors with graphitic contacts at the Microelectronics Institute of Barcelona are shown. Several approaches are explored, some of which never utilised before for radiation detector fabrication, namely pyrolytic photoresist film, nickel catalysis and ion surface graphitisation.

A prototype of such device using the pyrolytic photoresist film process for the first time has been produced and was tested under a 60 kV X-ray tube. We report the fabrication and preliminary performance results of such device. Although the substrate material quality is not ideal for radiation detection, it was possible to observe radiation response using the PPF as an interface material. The prototype features a linearity better than 3% as tested in a laboratory X-ray chamber, proving it a promising technology for detector operation. Finally, the technology

challenges are finally discussed to assess the feasibility of PPF-diamond technology for dosimeter batch production.

M-LT-03-04

Scintillation Properties of $(Lu,Y)_2O_3$:La Ceramic Pixels for PET (#2881)

Jarek Glodo[1], Suyoung Kim[1], Arthur Kim[1], Matthias Muller[1], Charles Sosa[1], Jiahao Xie[2], Simon R. Cherry[2], Junwei Du[2]

[1] Radiation Monitoring Devices, Inc., Watertown, USA; [2] University of California, Davis, Department of Biomedical Engineering, Davis, USA

This work was supported by the US NIH NIBIB through competitively awarded contracts number 4R44MH135525-02.

Abstract

Lutetium oxide–based scintillators are of growing interest for positron emission tomography (PET) because of their high density and high effective atomic number, which provide efficient stopping of 511 keV annihilation photons. Lanthanum-doped $(Lu,Y)_2O_3$ (LYO:La) is a transparent ceramic variant that retains the favorable stopping power of Lu_2O_3 while being easier to fabricate, making it an attractive candidate for next-generation PET detector arrays. In this work we report a scintillation characterization of LYO:La pixels in two geometries relevant to PET, 1×1×10 mm^3 for high-resolution preclinical and dedicated-organ imaging, and 3×3×10 mm^3 for whole-body clinical systems. Pixels were cut from LYO:La ceramic disks, polished on all faces, and evaluated with a range of side reflectors (Teflon, Tyvek, ESR film, and Spectralon) in both flat and upright coupling orientations. We measured X-ray-excited radioluminescence emission spectra, ^{22}Na (511 keV) pulse height spectra, relative light yield, energy resolution, scintillation decay time profiles, and timing resolution. The results illustrate the influence of pixel geometry, coupling face, and reflector choice on light collection and energy resolution, and show that LYO:La pixels offer a promising combination of stopping power, light yield, and timing performance for PET detector modules.

M-LT-03-05

Ultrahigh Spatial Resolution Perovskite-based Direct X-ray Imagers for Low-lag Medical Applications (#3045)

Brandon Dunham[1], Shariar Motakef[1], **Amlan Datta**[1]

[1] CapeSym, Inc., Research and Developement, Natick, USA; [2] Massachusetts General Hospital, Department of Radiology, Boston, USA

This research was supported by the U.S. National Institutes of Health under award R44EB038123.

Abstract

Dynamic medical X-ray imaging requires detectors that combine high quantum efficiency, low residual lag, and high spatial resolution without the optical spread and afterglow of scintillator-based flat panels. We report a fully inorganic perovskite-based direct-conversion perovskite X-ray imager fabricated from phase-pure orthorhombic Cesium Lead Bromide (CPB) sensor material and integrated with active-pixel readout arrays. Phase-pure CPB was obtained by controlled crystal growth and converted into dense blade-coated films; non-phase-pure starting materials containing secondary phases produced nonuniform films and degraded images, confirming the importance of phase control for reproducible detector performance. The optimized CPB detector demonstrated high linear X-ray response, sensitivity of 55,400 μC $Gyair^{-1}$ cm^{-2} at 30 keV and 0.5 V/μm, a limit of detection of 417 pGyair s^{-1}, a mobility-lifetime product of 8.0×10^{-4} cm^2 V^{-1}, and a calculated detective quantum efficiency near 85% at practical dose levels. In flat-panel imaging, CPB imagers reached 6.9 lp/mm at 20% modulation transfer function on a 100 μm-pitch amorphous-silicon array and resolved 20 lp/mm after integration with a CMOS readout. Most importantly for low-lag medical applications, improvements in phase purity and charge-transport stability reduced residual detector lag from 8.9% to 1.1%. These results show that all-inorganic perovskite direct conversion can provide a path to low-dose, low-lag, high-resolution imaging for fluoroscopy, tomosynthesis, dental cone-beam computed tomography, and other image-guided procedures.

M-LT-03-06

PhysiCal-PET: Physics-based neural networks for the rapid position Calibration of PET Scanners (#2036)

Mojahed Abushawish[1], Pablo Galve[3,1], Iván Colmenarejo Allavena[1], Sara Gaitán Dominguez[1], Carlos Galindo-Morata[1], Victor Martínez Nouvilas[1], Jose Manuel Udias[1,2]

[1] Universidad Complutense de Madrid, Grupo de Física Nuclear, EMFTEL & IPARCOS, Madrid, Spain; [2] Health Research Institute of the Hospital Cínico San Carlos (IdISSC), Madrid, Spain; [3] Spanish National Research Council (CSIC), Institute for Physical and Information Technologies "Leonardo Torres Quevedo", ITEFI, Madrid, Spain

P. Galve acknowledges grant JDC2023-051754-I, funded by MCIU/AEI/10.13039/501100011033 and ESF+.

Abstract

Total-body positron emission tomography (PET) increases system sensitivity and enables whole-body dynamic imaging, but its extended axial field of view makes accurate depth-of-interaction (DOI) calibration essential for maintaining uniform spatial resolution and reducing parallax error. Conventional DOI calibration requires mechanically scanned collimated sources or detector-specific reference measurements, which become impractical as the number of detector modules increases. PhysiCal-PET introduces a physics-based neural-network framework for autonomous in-system DOI calibration of PET scanners. The method trains a network to map raw detector signals to DOI using coincidence data acquired with an uncollimated positron source at known positions. For each event, the loss function enforces annihilation geometry by requiring the predicted line of response to be consistent with the source position, thereby providing supervision without measured DOI labels. The framework was tested on realistic PET simulations and applied to data from a real preclinical PET scanner. Using this procedure, the DOI response of all 144 detector modules was calibrated in less than 2 hours of point-source measurement time. These results demonstrate that the annihilation physics can replace labor-intensive DOI calibration hardware and enable rapid, routine calibration of high-resolution PET systems. PhysiCal-PET therefore provides a scalable path toward autonomous calibration for total-body PET and other systems that rely on accurate DOI positioning. notionvc: 49ace5df-389b-489a-b611-1abe67c4c114

M-LT-03-07

Adaptive Spatio-Temporal Denoising for Low-Dose Fluoroscopy via Motion-Gradient Weighting (#2582)

Nerea León[1,2], Xiaolin Ye[1], Jesús L. Longas[1], Juan Manuel Arco[1], Jose María Ortega[1], Mailyn Pérez-Liva[2], Joaquín López Herraiz[2], Alejandro Sisniega[1]

[1] Sedecal Molecular Imaging, Madrid, Spain; [2] Universidad Complutense de Madrid, Nuclear Physics Group and IPARCOS, Universidad Complutense de Madrid, Madrid, Spain

The authors would like to express their sincere gratitude to the Image Processing and AI Group at Sedecal Molecular Imaging for their invaluable technical support and expertise. We also thank the Nuclear Physics Group and IPARCOS at the Universidad Complutense de Madrid for their collaboration and the resources provided for this research.
We acknowledge support from the Comunidad de Madrid regional government through the LUNABRAIN project (TEC-2024/TEC-43) and the Industrial PhD program IND2023/BMD-28275.

Abstract

A spatio-temporal denoising training strategy for low-dose fluoroscopy is proposed, based on a spatially-adaptive temporal consistency metric. This approach acts on a small set of consecutive frames coupling a conventional denoising operator with an adaptive motion-gradient attention gate to selectively modulate the temporal consistency terms within the loss function, ensuring effective noise suppression and flickering reduction while maintaining high anatomical fidelity in dynamic regions.
The proposed method was used to train a denoising operator in which a three-frame temporal window is used as input. The model was trained across multiple dose reduction factors (qF), and demonstrated superior structural recovery and enhanced temporal stability in the processed image sequences, compared to single-frame models. Quantitative and qualitative evaluation of image quality, along with stability maps—defined as the Normalized Cross-Correlation (NCC) of temporal Coefficient of Variation (CV) maps—confirms high fidelity relative to high-dose reference acquisitions, effectively mitigating stochastic fluctuations without introducing motion artifacts.

References

[1] Dierckx, P. *et al.* 2007, "Spatio-temporal adaptive filter for low-dose fluoroscopy", *IEEE Nuclear Science Symposium Conference Record*, pp. 3450–3453.

[2] Wang, X. *et al.* 2019, "EDVR: Video restoration with enhanced deformable convolutional networks", *IEEE/CVF Conference on Computer Vision and Pattern Recognition Workshops (CVPRW)*.

[3] Chen, H. *et al.* 2017, "Low-dose CT with a residual encoder-decoder convolutional neural network", *IEEE Transactions on Medical Imaging*, vol. 36, no. 12, pp. 2524–2535.

[4] Lehtinen, J. *et al.* 2018, "Noise2Noise: Learning image restoration without clean data", *Proceedings of the International Conference on Machine Learning (ICML)*.

[5] Zhao, W., Rowlands, J. A. 1995, "X-ray imaging using amorphous selenium: Feasibility of a flat panel self-scanned detector for digital radiology", *Medical Physics*, vol. 22, no. 10, pp. 1595–1604.

[6] Cunningham, I. A. 2000, "Applied linear-systems theory", in *Handbook of Medical Imaging*, vol. 1, Sonka, M., Fitzpatrick, J. M. (eds.), pp. 79–160, Bellingham, WA: SPIE.

M-LT-03-08

An Ensemble of Deep-Learning Classifiers for 3D Anatomical Change Reconstruction in Carbon-Ion Radiotherapy (CIRT) (#2644)

Patrice Schlegel[1,3], Rebekka Kirchgässner[1,2], Pamela Ochoa-Parra[1,2], Erik Bartelme[1,2], Ralf Mikut[4], Oliver Jäkel[1,2], Maria Martisikova[1,2]

[1] DKFZ, Division of Medical Physics in Radiation Oncology, E040, Heidelberg, Germany; [2] Heidelberg Institute for Radiation Oncology (HIRO), National Center for Research in Radiation Oncology (NCRO), Heidelberg, Germany; [3] University, Heidelberg, Medical Faculty, Heidelberg, Germany; [4] Karlsruhe Institute of Technology (KIT), Institute for Automation and Applied Informatics (IAI), Karlsruhe, Germany

Abstract

Carbon-ion radiotherapy (CIRT) combines high biological effectiveness with outstanding treatment precision. Since treatment plans are based on the most recent Computed Tomography (CT), anatomical changes during multi-week treatments may compromise dose delivery accuracy. To address the increasing uncertainty about the patient's anatomical state with time elapsed since the planning CT, our group developed an in vivo monitoring method using secondary charged particles emitted during therapy. This non-invasive approach requires no additional dose and reduces uncertainty about patient anatomy and thus, loss of treatment accuracy. It uses a custom detection system to detect nuclear fragments emmited from the patient and allows approximating their origin. To reconstruct these changes in 3D, we utilize our recently published method for detecting the depth (z) of changes along the beam axis and apply it to a sliding window (x,y) along the transverse plane. However, splitting reconstructed nuclear fragment origins into smaller subsets reduces the statistical stability of each subset distribution. In this study, we present an approach to robustly distinguish whether a windowed subset belongs to a region with or without an anatomical change based on correlation matrices generated by our depth detection method. These images contain location-wise correlations of joined frequency band variations between projections of nuclear fragment measurements from different treatment days. To classify regions of change and approximate change depth, we train an ensemble of deep learning-based image classifiers with different architectures *(i.e. ResNet, RegNet and ConvNeXt)* and combine their outputs into an ensemble decision. The approach was validated using dedicated irradiation measurements with coin-sized cavities inserted into PMMA head phantoms. Despite limited training data, we achieved robust improvements in change localization using an ensemble of different deep learning architectures.

References

[1] Schlegel, P., Kirchgässner, R., Ochoa-Parra, P., Kelleter, L., Gertz, M., Mikut, R., Jäkel, O. and Martišíková, M. 2025, 'A data analysis framework for in vivo monitoring in carbon-ion radiotherapy (CIRT): towards 3D reconstruction of interfractional anatomical changes', *Physics in Medicine & Biology*, 70, 245009, Bristol: IOP Publishing.

[2] Kirchgässner, R., Martišíková, M., Schlegel, P., Ochoa-Parra, P., Harrabi, S., Jäkel, O., Debus, J. and Kelleter, L. 2026, 'Out-of-beam artifact suppression in charged nuclear fragment-based carbon-ion radiotherapy monitoring', *Medical Physics*, 53, e70351, Hoboken: Wiley.

[3] Ghesquière-Diérickx, L., Félix-Bautista, R., Schlechter, A., Kelleter, L., Reimold, M., Echner, G., Soukup, P., Jäkel, O., Gehrke, T. and Martišíková, M. 2022, 'Detecting perturbations of a radiation field inside a head-sized phantom exposed to therapeutic carbon-ion beams through charged-fragment tracking', *Medical Physics*, 49, Hoboken: Wiley.

[4] Kelleter, L., Schmidt, S., Subramanian, M., Marek, L., Granja, C., Jakubek, J., Jäkel, O., Debus, J. and Martišíková, M. 2024, 'Characterisation of a customised 4-chip Timepix3 module for charged-particle tracking', *Radiation Measurements*, 173, Amsterdam: Elsevier.

M-LT-03-09

Zero-Shot PET Image Super-Resolution via Cross-Modal Mutual Information Guidance (#2526)

Yilin He, Yang Lv

Shanghai United Imaging Medical Technology Co., Ltd, Molecular Imaging Business Unit, Shanghai, China

This work was supported in part by Shanghai United Imaging Medical Technology Co., Ltd., through its internal research program. The authors gratefully acknowledge the Molecular Imaging team for their technical support and helpful discussions.

Abstract

Diffusion models have shown strong potential for improving PET image quality. However, existing methods based on unconditional pretrained diffusion priors often struggle to balance realism and fidelity, particularly in preserving high-resolution details. To address this issue, we propose MI-ResShift, a zero-shot mutual information-guided diffusion model with residual shifting for PET image super-resolution. MI-ResShift introduces a differentiable local-wise mutual information layer to guide the denoising process using structural information from CT or MRI, enabling robust cross-modal feature alignment in the statistical domain. By combining mutual information guidance with residual shifting, the proposed method enhances PET detail fidelity and robustness while reducing diffusion-based inference to only four steps. Experiments on PET/MR brain datasets demonstrate that MI-ResShift improves image quality over classical interpolation methods and provides an efficient solution for cross-modal PET super-resolution.

References
[1] Z. Wang et al., "Mutual Information Guided Diffusion for Zero-Shot Cross-Modality Medical Image Translation," in IEEE Transactions on Medical Imaging, vol. 43, no. 8, pp. 2825-2838, Aug. 2024, doi: 10.1109/TMI.2024.3382043.
[2] Z. Yue, J. Wang and C. C. Loy, "Efficient Diffusion Model for Image Restoration by Residual Shifting," in IEEE Transactions on Pattern Analysis and Machine Intelligence, vol. 47, no. 1, pp. 116-130, Jan. 2025, doi: 10.1109/TPAMI.2024.3461721.

M-LT-03-10

3D Photon Position Estimation Using Neural Networks in Monolithic-Based PET Systems (#2663)

Pau Piera-Sapiña, **Marta Freire**, Fernando Lopez-Berenguer, Andrea Gonzalez-Montoro, Antonio J. Gonzalez

Instituto de Instrumentación para Imagen Molecular (I3M), Centro Mixto CSIC—Universitat Politècnica de València, Valencia, Spain

This work was supported by the Generalitat Valenciana under Grant No. CIPROM/2021/003 and funding from the University of Virginia Focused Ultrasound Cancer Immunotherapy Center and the FUS Foundation. M. Freire was supported by the CIAPOS Program for Researchers in Postdoctoral Phase of the Generalitat Valenciana under Grant No. CIAPOS/2023/141.

Abstract

Neural Network (NN) models have emerged as a promising tool for determining 3D photon impact positions in Positron Emission Tomography (PET) detectors based on monolithic scintillators. Nevertheless, NNs typically require long acquisitions of reference data training, becoming a time-consuming process that requires extensive experimental data for each individual detector module. To reduce calibration time, we propose a new methodology based on NNs trained entirely using simulated data to predict the 3D impact position of gamma rays. The feasibility of the proposed approach was verified using a real preclinical PET system composed of two rings of 8 LYSO:Ce monolithic scintillators each.

The simulation of a single detector was implemented in GATE and reference data moving a pencil beam in 1 mm steps was simulated to train two Multilayer Perceptrons (MLPs), MLP_X and MLP_Y, to predict the *x*- and *y*- impact positions, respectively. To validate the introduced methodology at reconstructed image level, experimental data was acquired using a ^{22}Na point source at the center of the preclinical system and processed using both the presented framework and the system's standard calibration methodology.

Results have demonstrated that similar spatial resolution was obtained with both approaches, thus demonstrating that NNs trained exclusively with Monte Carlo simulations can generate coherent reconstructed images and thus eliminate the need for calibration measurements for each individual detector module.

References

[1] Gonzalez-Montoro A, et al. 2021, IEEE Trans. on Rad. and Plasma Med. Sci., 5, 282-305
[2] Iborra A, et. al. 2019, Phys. Med. Biol., 64, 195010
[3] Lopez-Berenguer F, et al. 2025, IEEE Trans. on Rad. and Plasma Med. Sci., 10, 789-798
[4] Gonzalez-Montoro A, et al. 2017, IEEE Trans. on Rad. and Plasma Med. Sci., 1, 229-237
[5] Freire M, et al. 2020, IEEE Trans. on Rad. and Plasma Med. Sci., 4, 350-360
[6] Jan S, et al. 2004, Phys. Med. Biol., 49, 4543-4543
[7] Freire M, et al. 2022, Phys. Med. Biol., 67, 245011

Time:
12 November, 2026
12:45 – 13:05

Room:
MANUEL DE FALLA

M-LT-04 | New radiation detector technologies for medical imaging, Simulation and modeling of medical imaging system, Multi-modality imaging systems including applicationss

Chairs:
Volkmar Schulz (Aachen)
Nikos Efthimiou (Groningen)

M-LT-04-01

Development of a PET/MRI Compatible Fluorescence Microscope for Simultaneous Cell Tracking in a Small Animal PET/MRI Scanner (#2535)

Philipp Renn[1], Jakob Schäfers[1], Noah Jurisa[1], Christian Pilger[2], Thomas Huser[2], Klaus Schäfers[1]

[1] University of Münster, European Institute for Molecular Imaging, 48149, Germany; [2] Bielefeld University, Biomolecular Photonics Research Group, Department of Physics, 33615, Germany

This work was funded by the Deutsche Forschungsgemeinschaft (DFG) – CRC 1450 – 431460824.

Abstract

Cell tracking in vivo is a key challenge in translational medicine. Positron emission tomography (PET) and magnetic resonance imaging (MRI) offer complementary strengths for this task, yet the validation of tracking algorithms against a reliable ground truth remains unresolved. Fluorescence microscopy can fulfill this role, but its integration into the highly constrained PET/MRI environment poses significant technical challenges. Here, we present a fluorescence microscope (FM) designed for simultaneous operation inside a small-animal PET/MRI scanner, with all custom structural and housing components 3D printed in polylactic acid (PLA). The assembled instrument has a total length of 95 cm and fits within the 35 mm PET insert bore, accommodating sample diameters of up to 21 mm. The imaging probe is rotated via a non-ferromagnetic, friction-driven mechanism, enabling multi-angle acquisition without repositioning the sample, and reliable rotation over the full 360° range was demonstrated under manual control. The system follows an epi-fluorescence configuration with 10× magnification, an excitation wavelength of 488 nm, and a 500 nm longpass filter in the detection path. Characterization with a calibration slide and a Convallaria majalis test specimen yielded a pixel pitch of 0.144 µm/pixel (6.96 pixels/µm), a spatial resolution of 2.32 µm (FWHM), a signal-to-noise ratio (SNR) of 7.21, and a field of view (FoV) of 0.55 × 0.31 mm2 (3816 × 2160 pixels), sufficient to resolve individual cells. These results establish the feasibility of integrating fluorescence microscopy into a PET/MRI scanner and provide the basis for future multimodal cell tracking studies with a reliable optical ground truth.

References

[1] Wapler, MC, Testud, F, Hucker, P, Leupold, J, v. Elverfeldt, D, Zaitsev, M & Wallrabe, U 2021, 'MR-compatible optical microscope for in-situ dual-mode MR-optical microscopy', *PLOS ONE*, vol. 16, no. 5, p. e0250903: PLOS.

[2] Cui, M, Zhou, Y, Wei, B, Zhu, X-H, Zhu, W, Sanders, MA, Ugurbil, K & Chen, W 2017, 'A proof-of-concept study for developing integrated two-photon microscopic and magnetic resonance imaging modality at ultra-high field of 16.4 tesla', *Scientific Reports*, vol. 7, no. 1, p. 2733: Nature Publishing Group.

[3] Zhu, X, Li, R, Li, H, Gu, L, Chen, L, Xu, J, Chen, J, Li, Y, Rudin, M, Thompson, G, Zhou, N & Ren, W 2026, 'MR-Scope: a multi-scale and simultaneous MRI-miniaturized microscopy system for elucidating neurovascular coupling': bioRxiv.

[4] Li, C, Yang, Y, Mitchell, GS & Cherry, SR 2011, 'Simultaneous PET and multispectral 3-dimensional fluorescence optical tomography imaging system', *Journal of Nuclear Medicine: Official Publication, Society of Nuclear Medicine*, vol. 52, no. 8, pp. 1268–1275: Society of Nuclear Medicine.

M-LT-04-02

Hybrid PGI-PET Imaging for Ion-Range Monitoring in Hadron Therapy

(#2044)

Javier Balibrea-Correa[1], Victor Babiano-Suárez[1], Jorge Lerendegui-Marco[1], Pablo Torres-Sánchez[1], Ion Ladarescu[1], César Domingo-Pardo[1], Ariel Tarifeño-Saldivia[1], Max Pallás[2], Benedetta Brusasco[2], Joerg Wulff[3], Christian Bäumer[3], Severine Rossomme[4], Alexis Warnier[4]

[1] Instituto de Física Corpuscular (CSIC-University of Valencia), Física Nuclear Experimental, Valencia, Spain; [2] Universitat Politècnica de Catalunya, Física Nuclear, Barcelona, Spain; [3] West German Proton Therapy Centre, Essen, Germany; [4] Ion Beam Applications, Louvain, Belgium

Abstract

Hadron therapy is a highly conformal cancer treatment technique that enables superior dose delivery to the tumor while sparing surrounding healthy tissues. However, its full clinical benefit is still limited by uncertainties in proton range within tissue, mainly due to the indirect estimation of ion stopping power from X-ray CT images. These uncertainties lead to safety margins that reduce treatment precision. Real-time, high-accuracy ion-range verification is essential to improve dose delivery and further enhance the therapeutic potential of proton therapy. Among the available approaches, PGI and PET are regarded as the most promising, as they provide complementary information. PGI offers direct correlation with the Bragg peak during irradiation, whereas PET yields high-resolution activity distributions from beta+ emitters produced along the proton path.

In this work, we report recent developments and experimental results obtained with a hybrid PGI-PET system for in situ proton range verification. The system is based on four high-efficiency two-plane Compton imagers arranged in a cross configuration, specifically optimized to enhance PGI sensitivity at the expense of a reduced PET field of view. Experimental campaigns were carried out at commercial IBA Proteus Plus and Proteus One proton therapy facilities using 100 and 125 MeV pencil beams delivered at minimum clinical currents. Polyethylene phantoms were irradiated at controlled positions and data were acquired during both in-spill and off-spill periods.

The first reconstructed 2D images demonstrate that PGI can directly identify the Bragg peak position through the maximum of the PGI distribution over a broad field of view, while PET provides a narrower and higher-resolution distribution associated with the induced beta+ activity. These results confirm the feasibility and complementarity of the hybrid PGI-PET approach and support its potential for accurate, clinically relevant proton range verification.

M-LT-04-03

Intercrystal Compton Scattering Detection in Pixelated LYSO Detectors via Quantum Localization (#2993)

Amirreza Hashemi, Xi Zhang, Hamid Sabet

Harvard Medical School/Massachusetts General Hospital, Radiology Department, Boston, USA

This work was supported in part by NIH grant R01EB034785.

Abstract

We introduce a novel quantum-inspired method for identifying intercrystal Compton scattering in pixelated scintillation detectors. The approach treats each SiPM readout as a spatial signal and converts it into a discrete eigenfunction representation using a Hamiltonian built from the measured intensity distribution. Event structure is then assessed through quantum localization, quantified by the participation ratio. Single-site events produce highly localized dominant modes, whereas Compton-scattered events produce multiple localized modes associated with distinct interaction sites. A dual criterion based on quantum localization and eigenvalue proximity is used to classify multi-site events without calibration-intensive response modeling or supervised training. The method was evaluated with Geant4 optical photon simulations and measurements from LYSO:Ce detector arrays with thicknesses from 2 to 25 mm. Experimental classification agreed closely with simulation, with differences below 1% for most thicknesses and below 5% in all cases. These results indicate that the proposed representation captures the topology of gamma-ray interactions directly from detector signals.

References

[1] M. S. Lee, H. S. Shim, and J. S. Lee, “Strategies for mitigating inter-crystal scattering effects in positron emission tomography: a comprehensive review,” *Biomedical Engineering Letters*, vol. 14, no. 6, pp. 1243–1258, Nov. 2024, doi: 10.1007/s13534-024-00427-7.

[2] S. Lee, K. Y. Kim, M. S. Lee, and J. S. Lee, “Recovery of inter-detector and inter-crystal scattering in brain PET based on LSO and GAGG crystals,” *Phys. Med. Biol.*, vol. 65, no. 19, p. 195005, Oct. 2020, doi: 10.1088/1361-6560/ab9f5c.

[3] M. N. Ullah and C. S. Levin, “Application of Artificial Intelligence in PET Instrumentation,” *PET Clinics*, vol. 17, no. 1, pp. 175–182, Jan. 2022, doi: 10.1016/j.cpet.2021.09.011.

[4] A. Hashemi, S. Dutta, B. Georgeot, D. Kouamé, and H. Sabet, “A novel perspective on denoising using quantum localization with application to medical imaging,” *AIP Advances*, vol. 15, no. 8, p. 085012, Aug. 2025, doi: 10.1063/5.0267924.

[5] A. Hashemi, S. Dutta, B. Georgeot, D. KouamÉ, and H. Sabet, “Quantum-Inspired Denoising via Adaptive Planck Constant and Image Patching,” in *2024 IEEE Nuclear Science Symposium (NSS), Medical Imaging Conference (MIC) and Room Temperature Semiconductor Detector Conference (RTSD)*, Oct. 2024, pp. 1–1. doi: 10.1109/NSS/MIC/RTSD57108.2024.10657709.

[6] A. Hashemi, H. Babaei, and S. Lee, “Effects of medium range order on propagon thermal conductivity in amorphous silicon,” *Journal of Applied Physics*, vol. 127, no. 4, p. 045109, Jan. 2020, doi: 10.1063/1.5124821.

M-LT-04-04

PETRARCA: a Positron Emission Tomography Real-Time Analog Re-Configurable ANN Detector (#2827)

Maurizio Pandocchi[1,2], Mattia Amadori[1,2], Michele Ronchi[1,2], Giacomo Borghi[1,2], Marco Carminati[1,2], Carlo E. Fiorini[1,2]

[1] Politecnico di Milano, Dipartimento di Elettronica Informazione e Bioingegneria, Milano, Italy; [2] Istituto Nazionale di Fisica Nucleare, Sezione di Milano, Milano, Italy; [3] Ministero dell'Università e della Ricerca, Milano, Italy

Abstract

Positron emission tomography systems are becoming increasingly complex due to the growing number of detector channels and the large amount of data generated, especially in total-body imaging configurations. In this work, we present PETRARCA, a positron emission tomography detector system integrating an analog neural network ASIC (ANNA) for real-time edge computing of gamma-ray interaction coordinates within a monolithic scintillation crystal. The system consists of a 32 mm × 32 mm × 10 mm monolithic LYSO crystal coupled to an 8 × 8 SiPM matrix read out by dedicated front-end electronics. The detector architecture includes both a conventional digital acquisition path and a parallel analog inference path based on the ANNA ASIC, enabling simultaneous acquisition of sensor data and hardware neural-network predictions. A first evaluation of the system has been carried out using simulated data and the real ASIC response to emulate a reduced-scale configuration using a 4 × 4 SiPM array coupled to a 26 mm × 26 mm × 10 mm monolithic crystal. The performances of the ASIC in predicting the interaction coordinates were tested, and proved to have a mean absolute error (MAE) of around 1 mm on both the x and y axes. The preliminary results demonstrate the feasibility of analog neural-network edge computing for spatial localization in PET detectors and support further developments toward fully integrated real-time detector systems.

References

[1] Nanni et al., “Total body positron emission tomography/computed tomography: Current status in oncology,” Semin. Nucl. Med., vol. 55, no. 1, pp. 31–40, 2025

[2] S. Di Giacomo et al., “Implementing an Integrated Neural Network for Real-Time Position Reconstruction in Emission Tomography With Monolithic Scintillators,” IEEE Trans. Radiat. Plasma Med. Sci., vol. 8, no. 5, pp. 501-510, May 2024.

[3] A. Gonzalez-Montoro et al., “Evolution of PET detectors and event positioning algorithms using monolithic scintillation crystals,” IEEE Trans. Radiat. Plasma Med. Sci., vol. 5, pp. 282–305, 2021.

[4] I. D’Adda et al., “SITH: An SiPM Readout ASIC for Prompt Gamma-Ray Detection in Hadrontherapy Applications,” IEEE Trans. Nucl. Sci., vol. 71, no. 9, pp. 2140–2150, 2024.

M-LT-04-05

MIMOSA: Medical IMaging MOnte Carlo Simulation Algorithms for fast proton therapy range monitoring (#2751)

Declan D. Garvey, Gabriela Llosá, Fernando Hueso-González

IFIC, CSIC-UV, Valencia, Spain

This work has been funded by the Conselleria de Educación, Investigación, Cultura y Deporte (Generalitat Valenciana), Spain, under grant number CDEIGENT/2019/011, by CSIC's JAEPRE23-19 grant, and by the MIDAS project PID2022-143246OB-I00 (MICIU/AEI). IFIC is supported by the Severo Ochoa Center of Excellence grant CEX2023-001292-S funded by MCIU/AEI

Abstract

Monte Carlo simulations play a vital role in many aspects of proton therapy treatment, including proton depth of penetration monitoring. A key limiting factor of full simulation engines is computation time: simulations can take several days, far longer than the time between treatment fractions. This project aims to develop a Monte Carlo simulation software, MIMOSA, for prompt gamma-ray based proton range verification, that is fast enough to be deployed before the next treatment fraction. Clinically acceptable gamma pass rates above 99% for 2%/2 mm and 97% for 1%/1 mm with respect to TOPAS were achieved on both homogenous and heterogenous phantoms. To benchmark computational speed, state-of-the-art GPU codes MOQUI and FRED were tested on the same computer. Comparatively, MIMOSA achieved a notable speed increase, able to simulate 1e9 primary protons with a 200 MeV energy in approximately 3 minutes. Along with maintaining accuracy and increasing computational speed, the project uses the hardware agnostic SYCL standard, and will be available with an open-source license and extensive documentation. Ongoing work is devoted to simulating realistic radiotherapy treatment plans, and including prompt gamma-ray transport and detector response.

References

[1] F. Hueso-Gonzalez and T. Bortfeld, “Compact method for proton range verification based on coaxial prompt gamma-ray monitoring: A theoretical study,” IEEE Transactions on Radiation and Plasma Medical Sciences, vol. 4, no. 2, p. 170–183, Mar. 2020. [Online]. Available: http://dx.doi.org/10.1109/TRPMS.2019.2930362

[2] J. Perl, J. Shin, J. Schumann, B. Faddegon, and H. Paganetti, “TOPAS: An innovative proton Monte Carlo platform for research and clinical applications,” Medical Physics, vol. 39, no. 11, pp. 6818–6837, November 2012

[3] H. Lee, J. Shin, J. M. Verburg et al., “MOQUI: an open-source GPU-based Monte Carlo code for proton dose calculation with efficient data structure,” Physics in Medicine & Biology, vol. 67, no. 17, p. 175001, 2022, published August 30, 2022. [Online]. Available: https://doi.org/10.1088/1361-6560/ac8716

[4] M. D. Simoni, M. Fischetti, E. Gioscio, M. Marafini, R. Mirabelli, V. Patera, A. Sarti, A. Schiavi, A. Sciubba, and G. Traini, “FRED: A fast Monte Carlo code on GPU for quality control in particle therapy,” Journal of Physics: Conference Series, vol. 1548, no. 1, p. 012020, may 2020. [Online]. Available: https://doi.org/10.1088/1742-6596/1548/1/012020

[5] A. Alpay and V. Heuveline, “Adaptivity in AdaptiveCpp: Optimizing performance by leveraging runtime information during JIT-compilation,” in Proceedings of the 13th International Workshop on OpenCL and SYCL, ser. IWOCL ’25. New York, NY, USA: Association for Computing Machinery, 2025. [Online]. Available: https://doi.org/10.1145/3731125.3731127

M-LT-04-06

Analytical modeling and inclusion of object scatter in non-TOF 3D PET for low-count data (#1275)

Jorge Roser, Hong P. Vo, Magdalena Rafecas

Universität zu Lübeck, Institute of Medical Engineering, Lübeck, Germany

This work was supported by the European Union's Horizon 2024 research and innovation programme under the Marie Skłodowska-Curie grant agreement no. 101207067, and partly by the German Research Foundation (DFG) under grant agreement no. 508064995.

Abstract

Compton scattering in Positron Emission Tomography (PET) is commonly seen as an important degrading factor for the image quality. In particular, object scattering is known to reduce image contrast and distort quantification. Conventional scatter correction techniques do not model scatter directly in the system matrix, despite its potential to better handle low-count data scenarios. In this work, we propose an analytical model for single Compton scattering events and subsequently derive expressions of the system matrix and sensitivity. We validate the obtained expressions with Monte Carlo simulations. Ongoing work includes studying the impact of such approach by using low-count simulated data, and a comparison of the proposed method with conventional scatter correction techniques.

References

[1] Zaidi, H, Koral, KF 2004, 'Scatter modelling and compensation in emission tomography', *Eur J Nucl Med Mol Imaging* **31**, 761–782. DOI: 10.1007/s00259-004-1495-z

[2] Watson, CC, et al. 1996, 'A Single Scatter Simulation Technique for Scatter Correction in 3D PET', In: Grangeat, P., Amans, JL. (eds) Three-Dimensional Image Reconstruction in Radiology and Nuclear Medicine. Computational Imaging and Vision, vol 4. Springer, Dordrecht. DOI: 10.1007/978-94-015-8749-5

[3] Tamal, M, et al. 2006, 'Noise Properties of Four Strategies for Incorporation of Scatter and Attenuation Information in PET Reconstruction Using the EM-ML Algorithm', *IEEE Transactions on Nuclear Science*, vol. 53, no. 5, pp. 2778-2786. DOI: 10.1109/TNS.2006.880973

[4] Markiewicz, PJ, et al. 2007, 'High accuracy multiple scatter modelling for 3D whole body PET', *Phys. Med. Biol.* **52** 829. DOI: 10.1088/0031-9155/52/3/021

[5] Schaar, M, Rafecas, M 2019, 'Modelling of Scatter in the System Matrix for 3D PET Image Reconstruction: a Comparative Study', *2019 IEEE Nuclear Science Symposium and Medical Imaging Conference (NSS/MIC)*, Manchester, UK. DOI: 10.1109/NSS/MIC42101.2019.9059797

[6] Roser, J, et al. 2026, 'Inclusion of Inter-crystal Scattering in PET: Analytical Models and Dedicated Reconstruction', preprint. DOI: 10.48550/arXiv.2601.05717

M-LT-04-07

Quantitative Impact of Inter-Crystal Scatter on Image Quality and Sensitivity across LabPET-II Scanner Architectures: A Comparative GATE Simulation Study (#2983)

Alexandre Bernier[1,2], Maxime Gaudreault[5], Jean-François Beaudoin[3], Roger Lecomte[4,5], Jean-Baptiste Michaud[1,2]

[1] University of Sherbrooke, Department of Electrical and Computer Engineering, Sherbrooke, Canada; [2] University of Sherbrooke, Interdisciplinary Institute for Technological Innovation, Sherbrooke, Canada; [3] CRCHUS, Sherbrooke Molecular Imaging Center, Sherbrooke, Sherbrooke, Canada; [4] Imaging Research & Technology, Sherbrooke, Canada; [5] University of Sherbrooke, Department of Medical Imaging and Radiation Sciences, Sherbrooke, Canada

This work was supported in part by the Arbour foundation, the Faculty of Engineering and the Dept of electrical and computer engineering.

M-LT-04-08

Validated Optical Simulation for High-Energy Gamma Response in a 3-Layer LYSO DOI Detector (#1668)

Shan Jiang, Giulio Lovatti, Francesco Evangelista, Peter Thirolf, Katia Parodi, Munetaka Nitta

Ludwig-Maximilians-Universität München, München, Germany

Abstract

We have developed a 3-layer staggered LYSO de tector with DOI capability within the project SIRMIO (Small animal proton irradiator for research in molecular image-guided radiation-oncology) for proton range verification via PET imag ing. To evaluate the feasibility of detecting prompt gamma rays for quasi-instantaneous monitoring of proton beams, we propose a workflow that includes the validation of optical simulation settings and the implementation of the saturation effect of the SiPM photonsensor in the Geant4 simulation. Measurement data with ^{152}Eu, ^{22}Na and ^{137}Cs radioactive sources are utilized for modeling the saturation effect of SiPM, and also for validating optical boundary settings in Geant4. The measured spectra of ^{22}Na and ^{137}Cs point sources are well reproduced with the proposed simulation workflow. The responses to prompt gamma rays are then simu lated. According to the floodmaps and profiles, LYSO pixel can be identified at 2.2, 4.4 and 6.2 MeV, but the contrast decreases strongly when energy reaches 6.2 MeV. The peak-to-valley ratios drop by up to 53% at 4.4 MeV and 62% at 6.2 MeV (relative to 2.2 MeV), primarily due to the energy deposition occurring more frequently in multiple LYSO pixels. These predictions suggest the detector’s potential for detecting prompt gamma rays, while accurately

recovering or rejecting inter-crystal scatter events is essential to maintain detector performance at higher gamma energy.

References
[1] K. Parodi et al., Acta Oncol., vol. 58, no. 10, p. 1470, 2019.
[2] T. M. Fitzpatrick, Ph.D. dissertation, lmu, 2022.
[3] J. Allison et al., Nucl. Instrum. Meth. A, vol. 835, p. 186, 2016.
[4] K. Kotera et al., arXiv:1510.01102, 2015.
[5] M. Janecek et al., IEEE Trans. Nucl. Sci., vol. 57, no. 3, p. 964, 2010.

M-LT-04-09

Identification of ICS Pixels in a high-resolution 3-Layer DOI-PET Detector Using a CNN (#2619)

Shan Jiang, Giulio Lovatti, Francesco Evangelist, Peter Thirolf, Katia Parodi, Munetaka Nitta

Ludwig-Maximilians-Universität München, München, Germany

Abstract

We have developed a 3-layer staggered LYSO DOI detector for the SIRMIO (Small animal proton irradiator for research in molecular image-guided radiation-oncology) project, with a crystal pitch of 1.0 mm. Due to the small crystal size, inter-crystal scatter (ICS) events degrade spatial resolution, while discarding them causes significant sensitivity loss. In our detector, ICS events account for approximately 50% of all interactions at 511 keV and result in a median lateral positioning error of approximately 2 mm. To solve this problem, we propose a dual-head convolutional neural network (CNN) for separating the 8×8 MPPC total response of two-pixel ICS events into two individual response matrices, from which the pixel positions and energy fractions can be obtained—a precondition for recovering the ICS events. The CNN correctly identifies both scattering pixels in 69.3% of test events, and in 26.4% of cases one pixel is correctly identified. Among the events with one pixel mismatched, the lateral error of the misidentified pixel falls within 1.0 mm in 91.0% of cases. Meanwhile, the median energy fractions prediction error is 0.016 per pixel. The results demonstrate that CNN-based MPPC response decomposition can serve as the enabling foundation for complete ICS recovery in 3-layer staggered DOI detectors, addressing a limitation explicitly acknowledged in recent physics-based ICS studies.

References
[1] F. Evangelista et al., in 2024 IEEE NSS MIC RTSD, 2024.
[2] K. Parodi et al., Acta Oncol., vol. 58, no. 10, p. 1470, 2019.
[3] M. S. Lee et al., Biomedical Engineering Letters, vol. 14, no. 6, 2024.
[4] Q. Liu et al., Physics in Medicine and Biology, 2026.
[5] S. Jiang et al., submitted to IEEE NSS MIC RTSD 2026 (#1668).

M-LT-04-10

Study on the axial extension of the small-fish PET scanner MERMAID

(#2065)

Magdalena Kolodziej[1], Jorge Roser[1], Steven Seeger[1,2], Hong P. Vo[1], Rebecca Kantorek[1,2], Magdalena Rafecas[1]

[1] University of Luebeck, Institute of Medical Engineering, Luebeck, Germany; [2] University of Luebeck, Isotope Laboratory of the Natural Science Section, Luebeck, Germany

The project is partially supported by the German Research Foundation (DFG) under grant agreement no. 496099829 and the DFG Cluster of Excellence PMI under grant agreement no. 390884018.

Abstract

MERMAID is the first PET scanner prototype dedicated to study small aquatic animals. Particularly, it aims to support the use of adult zebrafish as a model of human diseases. The current prototype, which consists of four detection modules composed of LYSO:Ce crystals, has demonstrated the capability of providing images with submillimeter resolution. An extension of MERMAID by another four modules is planned, aimed to increase the system sensitivity and allow for shorter scan times, making it more suitable for in-vivo imaging. In the presented work, various configurations for the extended MERMAID system are characterized by means of simulations and tailored reconstruction framework; modifications of imaging protocol for the system are investigated.

References

[1] S. Seeger et al., 2023 IEEE NSS MIC RTSD, 2023. doi: 10.1109/NSSMICRTSD49126.2023.10338697.

[2] J. Roser et al., IEEE TRPMS, 2026. doi: 10.1109/TRPMS.2026.3691192.

Time:
12 November, 2026
15:00 – 17:00

Room:
FEDERICO GARCÍA LORCA

MIC-08 | Novel applications of AI in radiation-based medical imaging (1)

Chairs:
Quanzheng Li (Boston)
Nicolas A. Karakatsanis (New York)

MIC-08-01

Sensitivity-Informed Network for Image Restoration in Sparse-Detector PET (#1881)

Yucun Hou[1], Yihao Chen[1], Fenglin Zhan[2,3], Jianyong Jiang[1]

[1] Beijing Normal University, School of Physics and Astronomy, beijing, China; [2] The First Affiliated Hospital of USTC, Department of Nuclear Medicine, Hefei, China; [3] Jiangnan University, Wuxi School of Medicine, Wuxi, China

This work was supported in part by the National Natural Science Foundation of China (No. 12475336), and the Fundamental Research Funds for the Central Universities (No. 310400209521).

Abstract

Positron emission tomography (PET) requires dense detector crystals and associated electronics, resulting in high manufacturing costs. Sparse detector configurations can reduce hardware complexity but may degrade image quality due to reduced coincidence events, incomplete line-of-response coverage, and geometry-dependent artifacts. In this study, different sparse detector configurations were investigated for clinical PET imaging, and a sensitivity-informed network, termed SIU-Net, was proposed to recover image quality from sparse ring reconstructions. The residual sensitivity image was used as structural guidance to improve the restoration of degradation caused by detector sparsity. Experiments on 303 clinical brain datasets showed that the 1/2-TS-AR configuration achieved the best image quality among the evaluated sparse designs. SIU-Net consistently outperformed the baseline models across seven degraded image settings. These results demonstrate the potential of combining optimized sparse detector geometry with sensitivity-guided deep learning restoration for cost-effective PET imaging.

References

[1] Berg, E & Cherry, SR 2018, 'Innovations in Instrumentation for Positron Emission Tomography', *Seminars in Nuclear Medicine*, vol. 48, no. 4, pp. 311–331, Elsevier.

[2] Gao, M, Daube-Witherspoon, ME, Karp, JS & Surti, S 2025, 'Total-body PET system designs with axial and transverse gaps: a study of lesion quantification and detectability', *Journal of Nuclear Medicine*, vol. 66, no. 2, pp. 323–329, Society of Nuclear Medicine and Molecular Imaging.

[3] Yuan, Z, Zhan, F, Lu, H, Hou, Y, Liao, R, Li, C, et al. 2026, 'GPU-based list-mode TOF PET image reconstruction with complete correction techniques', *Medical Physics*, vol. 53, no. 1, e70216, Wiley.

[4] Hou, Y, Zhan, F, Liu, J, Cheng, X, Li, C, Yuan, Z, et al. 2026, 'Cycle-constrained adversarial denoising convolutional network for PET image denoising: Multi-dimensional validation on large datasets with reader study and real low-dose data', *Medical Image Analysis*, vol. 107, 103826, Elsevier.

MIC-08-02

Anatomy-Guided Null-Space Learning for Self-Supervised Blind PET Deblurring (#2189)

Ziyuan Zhou, Ziwei Liu, Tzu-An Song, Fan Yang, Joyita Dutta

University of Massachusetts Amherst, Biomedical Engineering, Amherst, USA

Abstract

The intrinsically limited spatial resolution of positron emission tomography (PET) confounds image quantitation. Post-reconstruction deblurring is an ill-posed inverse problem in which the blur kernel is often unknown, and noise renders direct inversion infeasible. We present a principled framework for self-supervised blind PET image deblurring that incorporates high-resolution MRI anatomical guidance in a data-consistent way. The central contribution is an observation-dependent spectral decomposition of the PET image into a practical range space, i.e., the set of spatial frequencies recoverable from the blurry PET observation at a specified signal-to-noise ratio (SNR) threshold, and a complementary practical null space whose content cannot be estimated from the PET data alone, regardless of the estimator. A self-supervised deep learning framework, Anatomy-Guided Null-Space Learning (AGNS), instantiates this decomposition with three jointly optimized components: a blind 3D kernel estimation network, a range-space Wiener deconvolution, and an MRI-guided null-space imputation network. Joint optimization proceeds via the alternating direction method of multipliers (ADMM). Methodological evaluation is performed through clinical paired-resolution validation using images from the HRRT and NeuroEXPLORER (NX) scanners, where the NX images are only used as the validation ground-truth. AGNS produces strong qualitative and quantitative benchmarks relative to competing unsupervised and non-AI approaches.

References

[1] Tohka, J, Reilhac, A 2008, 'Deconvolution-based partial volume correction in Raclopride-PET and Monte Carlo comparison to MR-based method', *NeuroImage*, vol. 39, no. 4, pp. 1570–1584.

[2] Sample, C, Rahmim, A, Uribe, C, Bénard, F, Wu, J, Fedrigo, R, Clark, H 2024, 'Neural blind deconvolution for deblurring and supersampling PSMA PET', *Physics in Medicine & Biology*, vol. 69, no. 8.

[3] Ren, D, Zhang, K, Wang, Q, Hu, Q, Zuo, W 2020, 'Neural Blind Deconvolution Using Deep Priors', *arXiv*, arXiv:1908.02197.

[4] Volpi, T, Toyonaga, T, Khattar, N, Gallezot, JD, Naganawa, M, Vanderlinden, G, Honhar, P, Zeng, T, Fontaine, K, Mulnix, T, Hu, L, Sun, X, Henry, S, Matuskey, D, Radhakrishnan, R, Guo, L, Hu, Y, Zhang, J, Zheng, X, Nabulsi, N, Huang, Y, Badawi, RD, Cherry, SR, Hillmer, AT, Jones, T, Liu, C, Morris, E, Qi, J, Li, H, Carson, RE 2026, 'Exceptional brain PET images from the NeuroEXPLORER: scans with targeted radiopharmaceuticals and comparison to HRRT', *European Journal of Nuclear Medicine and Molecular Imaging*, vol. 53, no. 3, pp. 2110–2121.

[5] Zhou, Z, Song, T-A, Lei, B, Yang, F, Gomez, CL, Johnson, K, Dutta, J 2024, 'Unsupervised Tau PET Image Super-Resolution Using Cross-Domain Diffusion Posterior Sampling', *2024 IEEE Nuclear Science Symposium (NSS), Medical Imaging Conference (MIC) and Room Temperature Semiconductor Detector Conference (RTSD)*, pp. 1–1: IEEE.

[6] Liu, Z, Song, T, Yang, F, Banerjee, A, Zhou, Z, Lei, B, Saranathan, M, Dutta, J 2025, 'Segmentation Guided Neural Blind Deconvolution for Unsupervised 3D Brain PET Image Partial Volume Correction', *2025 IEEE Nuclear Science Symposium (NSS), Medical Imaging Conference (MIC) and Room Temperature Semiconductor Detector Conference (RTSD)*, [edition missing], pp. 1–1: IEEE.

[7] Song, T-A, Yang, F, Chowdhury, SR, Kim, K, Johnson, KA, El Fakhri, G, Li, Q, Dutta, J 2019, 'PET Image Deblurring and Super-Resolution With an MR-Based Joint Entropy Prior', *IEEE Transactions on Computational Imaging*, vol. 5, no. 4, pp. 530–539: IEEE.

MIC-08-03

Brownian Bridge Diffusion Model for Ultra-Low-Dose Total-Body PET Denoising (#1889)

Narges Aghakhanolia[1], Alireza Rafiei Sardouei[2], James Fowler[3], Alejandro Lopez-Montes[4], Kuangyu Shi[4], Pedro Esquinas[5], Arman Rahmim[6]

[1] University of British Columbia, School of Biomedical Engineering, Vancouver, Canada; [2] University of British Columbia, Department of Electrical and Computer Engineering, Vancouver, Canada; [3] University of British Columbia, Department of Physics & Astronomy, Vancouver, Canada; [4] Bern University Hospital, Department of Nuclear Medicine, Bern, Switzerland; [5] University of British Columbia, Department of Radiology, Vancouver, Canada; [6] BC Cancer Research Institute, Department of Basic and Translational Research, Vancouver, Canada

Abstract

PET imaging enables quantitative assessment of disease burden and treatment response, but performance is constrained by a trade-off between radiation dose and image quality. Reducing injected adiotracer activity decreases patient exposure, yet increases image noise, degrading lesion detectability and quantitative accuracy. Total-body PET systems, with substantially increased sensitivity, enable significant dose reduction. However, ultra-low-dose acquisitions remain highly noisy, limiting their clinical utility. In this work, we investigate Brownian Bridge Diffusion Models (BBDM) as a novel framework for ultra-low-dose PET denoising. BBDM formulates dose-level image translation as a stochastic bridge between paired standard- and low-dose PET images, with the diffusion process constrained at both endpoints. This formulation is well-suited for dose translation. The proposed method was evaluated on a multi-center, multi-scanner total-body 18F-FDG PET/CT dataset of 80 patients. Paired full-dose and simulated 1/10-dose datasets were generated through statistical count reduction in the list-mode data. The model was trained with T = 1000 diffusion steps, and inference was accelerated using S = 200 sampling steps. On the held-out test cohort, BBDM achieved substantial gains across both global image-quality and lesion-level quantitative metrics. Compared with low-dose inputs, BBDM increased PSNR by approximately 26.6% and SSIM by 8.9%, while reducing RMSE by 60.0%. Across evaluated lesions, SUVmean and SUVmax biases decreased by 54.5% and 70.9%, respectively. Lesion noise was also reduced by 45.8%. The approach effectively preserves both image quality and lesion quantification at substantially reduced dose levels, highlighting its potential for ultra-low-dose total-body PET imaging.

References

[1] S. J. McQuaid et al., “Cumulative radiation doses from recurrent PET-CT examinations,” British Journal of Radiology, vol. 94, no. 1124, 2021.

[2] S. R. Cherry, T. Jones, J. S. Karp, M. Sibomana, and R. D. Badawi, “Total-body PET: maximizing sensitivity to create new opportunities for clinical research and patient care,” Journal of Nuclear Medicine, vol. 59, no. 1, pp. 3–12, 2018.

[3] K. Gong, J. Guan, C.-C. Liu, and J. Qi, “PET image denoising using a deep neural network through fine structure preservation,” IEEE Transactions on Radiation and Plasma Medical Sciences, vol. 3, no. 1, pp. 26–34, 2018.

[4] B. Yu and K. Gong, “Robust whole-body PET image denoising using 3D diffusion models: evaluation across various scanners, tracers, and dose levels,” Physics in Medicine & Biology, vol. 70, no. 4, p. 045005, 2025.

[5] B. Li, K. Xue, B. Liu, and Y.-K. Lai, “BBDM: Image-to-image translation with Brownian Bridge Diffusion Models,” in Proceedings of the IEEE/CVF Conference on Computer Vision and Pattern Recognition (CVPR), pp. 1952–1961, 2023.

MIC-08-04

Self-Supervised Low-Dose SPECT Denoising from a Single Standard-Dose Scan via Poisson Thinning (#2519)

Haowen Zheng[1], Li Cheng[2], Lilei Gao[2], Shi Wang[1], Zhaoxia Wu[1], Hui Liu[1], Yaqiang Liu[1]

[1] Tsinghua University, Beijing, China; [2] Chengdu NOVEL MEDICAL Equipment Co., Ltd., Chengdu, China

This work was supported in part by the National Key Research and Development Program of China (No. 2022YFC2402002, No. 2022YFC2403802), and National Natural Science Foundation of China (No. 12205166)

Abstract

Low-dose or fast-scan single-photon emission computed tomography/computed tomography (SPECT/CT) suffers from Poisson noise, but clinical archives usually provide only one noisy standard-dose projection per patient and no noise-free target. A common single-scan workaround synthesizes a low-dose input from the standard-dose scan and uses the original projection as the supervised target. This creates a nested pair because the target contains the input photons, so the objective can learn a noisy full-dose image with input-noise leakage. We propose a self-supervised projection-domain framework based on mutually exclusive Poisson thinning. Each standard-dose projection is partitioned online into $K \in \{2,3,4,5\}$ disjoint equal-dose subsets by multinomial assignment, and two subsets are randomly paired for Noise2Noise training. These paired subsets contain disjoint photons and are conditionally independent given the underlying count rate while preserving the same dose; mean-square or Poisson-likelihood training therefore targets the clean same-dose conditional mean rather than a noisy full-dose target. A three-dimensional residual U-Net is trained only from thinned noisy pairs and applied before OSEM reconstruction. Training used 225 clinical bone SPECT/CT cases. On 31 held-out cases evaluated by patient-specific controlled Poisson resampling over 1×--5× fast-scan factors, the method achieved 45.72 dB PSNR and 0.9862 SSIM in the projection domain, outperforming an architecture-matched low-to-standard-dose supervised baseline by 2.68 dB; the paired gain increased from 1.82 dB at 1× to 3.34 dB at 5×. The framework enables low-dose bone SPECT/CT denoising from routinely stored projections without clean ground truth or repeated acquisitions.

References

[1] Lehtinen, J, Munkberg, J, Hasselgren, J, Laine, S, Karras, T, Aittala, M and Aila, T 2018, 'Noise2Noise: Learning Image Restoration without Clean Data', Proceedings of the 35th International Conference on Machine Learning, Proceedings of Machine Learning Research, vol. 80, pp. 2965–2974, PMLR.

[2] Pan, B et al. 2022, 'Ultra high speed SPECT bone imaging enabled by a deep learning enhancement method: a proof of concept', EJNMMI Physics, vol. 9, article 43.

[3] Aghakhan Olia, N et al. 2022, 'Deep learning–based denoising of low-dose SPECT myocardial perfusion images: quantitative assessment and clinical performance', European Journal of Nuclear Medicine and Molecular Imaging, vol. 49, pp. 1508–1522.

[4] Sun, J et al. 2023, 'Deep learning-based denoising in projection-domain and reconstruction-domain for low-dose myocardial perfusion SPECT', Journal of Nuclear Cardiology, vol. 30, no. 3, pp. 970–985.

[5] Liu, J, Yang, Y, Wernick, MN, Pretorius, PH and King, MA 2021, 'Deep learning with noise-to-noise training for denoising in SPECT myocardial perfusion imaging', Medical Physics, vol. 48, no. 1, pp. 156–168.

[6] Yie, SY et al. 2024, 'Enhancing bone scan image quality: an improved self-supervised denoising approach', Physics in Medicine & Biology, vol. 69, no. 21, article 215020.

MIC-08-05

VLM-Guided Conditional Flow Matching for CT-Free total-body PET Correction (#2298)

Jianming Rong[1], Sichun Li[2], Chunyan Yang[1], Lianghua Li[2], Jianjun Liu[2], Ruohua Chen[2], **Zhenxing Huang**[1]

[1] Shenzhen Institutes of Advanced Technology, Chinese Academy of Sciences, Research Center for Medical AI, Shenzhen, China; [2] Ren Ji Hospital, School of Medicine, Shanghai Jiao Tong University, Department of Nuclear Medicine, Shanghai, China

This work was supported by National Natural Science Foundation of China (62471461), Guangdong Basic and Applied Basic Research Foundation (2025A1515010783), Shenzhen Science and Technology Program (JCYJ20250604182905007, JCYJ20240813155913017).

Abstract

Accurate attenuation and scatter correction is important for positron emission tomography (PET) to improve diagnosis. Conventional PET correction pipelines rely heavily on CT-derived attenuation information, which inevitably increases radiation exposure during clinical examinations, especially in total-body PET/CT imaging. In this study, we introduce a vision-language-model-guided conditional flow framework for CT-free PET attenuation and scatter correction. Specifically, non-corrected PET slices are analyzed to generate organ-aware textual prompts, which are subsequently encoded as semantic representations and integrated into a latent-space flow generation process. Then, a cross-modal attention mechanism is further designed to establish interactions between semantic prompts and PET image features under multiple scales during conditional flow matching. Experiments were performed on 264 clinical subjects under total-body PET/CT scans. Comparison methods consist of several representative deep learning approaches, including UNet, Uformer, CycleGAN, latent diffusion models, and VM-UNet. Quantitative evaluation demonstrated that the proposed framework achieved the highest metric index, reaching 38.66 dB PSNR and 0.9754 SSIM on the testing dataset. Visual assessment and Correlation Analysis additionally confirmed improved anatomical continuity and more accurate tracer uptake recovery. The study suggests that semantic-aware flow modeling offers an effective strategy for CT-free PET correction.

References

[1] S. Surti, A. R. Pantel, and J. S. Karp, “Total body pet: why, how, what for?” IEEE transactions on radiation and plasma medical sciences, vol. 4, no. 3, pp. 283–292, 2020.

[2] R. Guo, S. Xue, J. Hu, H. Sari, C. Mingels, K. Zeimpekis, G. Prenosil, Y. Wang, Y. Zhang, M. Viscione et al., “Using domain knowledge for robust and generalizable deep learning-based ct-free pet attenuation and scatter correction,” Nature Communications, vol. 13, no. 1, p. 5882, 2022.

[3] C. Li, C. Wong, S. Zhang, N. Usuyama, H. Liu, J. Yang, T. Naumann, H. Poon, and J. Gao, “Llava-med: Training a large language-and-vision assistant for biomedicine in one day,” Advances in Neural Information Processing Systems, vol. 36, pp. 28 541–28 564, 2023.

[4] M. Yazdani, Y. Medghalchi, P. Ashrafian, I. Hacihaliloglu, and D. Shahriari, “Flow matching for medical image synthesis: Bridging the gap between speed and quality,” in International Conference on Medical Image Computing and Computer-Assisted Intervention. Springer, 2025, pp. 216–226.

MIC-08-06

Implicit Neural Representations for Joint Motion-Resolved PET Reconstruction and Respiratory Gating (#3089)

Nicolas De Bie, Massimiliano Colarieti Tosti

KTH Royal Institute of Technology, Department of Biomedical Engineering and Health Systems, Stockholm, Sweden

Abstract

Respiratory motion during acquisition degrades image quality in positron emission tomography (PET). Data-driven gating (DDG) extracts a respiratory signal directly from the measurement data, but classical methods such as axial center-of-mass and principal component analysis (PCA) degrade under irregular breathing and at low count rates. We propose a self-supervised framework based on implicit neural representations (INRs) that jointly estimates a respiratory gating signal and a motion-corrected reconstruction. Two coordinate-based networks parametrize a motion-free canonical activity image and a deformation field conditioned on learnable per-frame latent codes that encode the respiratory state. We evaluate the framework on XCAT thoracic phantom simulations of an 18F-FDG acquisition at clinically realistic count levels under regular and irregular breathing. The recovered gating signal achieves Spearman correlations of 0.87 (regular) and 0.85 (irregular) with the ground-truth respiratory signal, exceeding center-of-mass (0.62; 0.30) and PCA-based (0.74; 0.34) DDG baselines, and the framework simultaneously produces a motion-resolved reconstruction with PSNR comparable to maximum likelihood expectation maximization (MLEM) reconstruction.

References

[1] Y. Moussaoui, et al., “Implicit Neural Representations for End-to-End PET Reconstruction,” in 2025 IEEE 22nd International Symposium on Biomedical Imaging (ISBI), Apr. 2025

[2] R. J. Santo, et al., “From Ultra-Short Timeframes to Ultra-Fast Motion: Maximum-Likelihood Motion and Activity (MLMA) Reconstruction for Cardiac Gateless TOF-PET,” in 2025 IEEE NSS MIC RTSD conference, Nov. 2025

[3] V. Sitzmann et al., “Implicit Neural Representations with Periodic Activation Functions,” Jun. 2020.

[4] K. Thielemans et al, “Device-less gating for PET/CT using PCA,” in 2011 IEEE Nuclear Science Symposium Conference Record, Oct. 2011

MIC-08-07

Towards CT-Free Multi-Time-Point [^{18}F]PSMA-1007 LAFOV PET Protocols: Evaluation of Synthetic Attenuation Maps Versus Elastic Co-Registration for Longitudinal Imaging (#1865)

Elnaz Olyaei[1,2], **Elnaz Olyaei**[1,2], Joshua Schaefferkoetter[3], Joshua Schaefferkoetter[3], Eduardo Calderón Ochoa[1], Eduardo Calderón Ochoa[1], Christian P. Reinert[1,5], Christian P. Reinert[1,5], Lena S. Kiefer[1], Lena S. Kiefer[1], Christian la Fougère[1,4], Christian la Fougère[1,4], Fabian P. Schmidt[1,2], Fabian P. Schmidt[1,2]

[1] University Hospital Tuebingen, Department of Nuclear Medicine and Clinical Molecular Imaging, Tuebingen, Germany; [2] Eberhard-Karls University Tuebingen, Werner Siemens Imaging Center, Department of Preclinical Imaging and Radiopharmacy, Tuebingen, Germany; [3] Siemens Medical Solutions USA, Inc, Knoxville, USA; [4] University Hospital Tuebingen, Cluster of Excellence iFIT (EXC 2180) "Image Guided and Functionally Instructed Tumor Therapies", Tuebingen, Germany; [5] University Hospital Tuebingen, Diagnostic and Interventional Radiology, Tuebingen, Germany

Abstract

Long axial field-of-view (LAFOV) PET enables imaging at very late timepoints but requires repeated CT acquisitions for attenuation correction (AC) in multi-time-point protocols, increasing radiation exposure. This study evaluates two CT-free AC strategies for [^{18}F]PSMA-1007 LAFOV PET at delayed imaging timepoints: synthetic μ-maps derived from non-attenuation-corrected PET imaging using a ResNet-based model (Synth-AC) and elastic co-registration of CT-based μ-maps from the initial scan (CoReg-AC). Ten patients were scanned on a Siemens Biograph Vision Quadra LAFOV system at 90 min, 3 h, and 5 h p.i. Quantitative evaluation was performed based on relative differences in SUV_{mean} across seven major organs. Lesion quantification was assessed for SUV_{mean} (28 lesions at 3 h p.i., 20 lesions at 5 h p.i.) using Bland–Altman analysis and linear regression. Visually, synthetic μ-maps appeared smoother, while co-registration preserved more anatomical detail but showed localized inconsistencies. In PET images, Synth-AC exhibited smaller and more homogeneous deviations (±5%), whereas CoReg-AC showed more pronounced peripheral differences. At organ level, reduced variability was observed at 5 h for both methods. CoReg-AC showed a positive bias in high-uptake organs (liver +1.7% to +4.3%, spleen +2.7% to +4.3%), while Synth-AC shifted from near agreement at 3 h to moderate negative bias at 5 h (liver −2.1%, heart −13.5%). Both methods demonstrated a pronounced positive bias in lung regions. Linear regression demonstrated strong agreement with CT-based AC (R^2 = 0.993–0.998), and Bland–Altman analysis at 3 h p.i. showed a mean bias of −0.97% with limits of agreement [−12.11%; +10.17%] for Synth-AC and +1.40% [−8.71%; +11.52%] for CoReg-AC. Both CT-free approaches enable robust quantitative imaging in delayed LAFOV PET. Observed differences are primarily driven by organ-level bias patterns, while lesion quantification remains stable.

References

[1] Schaefferkoetter, J, 2021, 'Deep learning for whole-body medical image generation', *European Journal of Nuclear Medicine and Molecular Imaging*, vol. 48, no. 12, pp. 3817–3826, vol. 48, no. 12, pp. 3817–3826, Springer Nature.

[2] Schaefferkoetter, J , 2023, 'Deep learning for improving PET/CT attenuation correction by elastic registration of anatomical data', *European Journal of Nuclear Medicine and Molecular Imaging*, vol. 50, no. 8, pp. 2292–2304, Springer Nature

MIC-08-08

3D Latent Implicit Diffusion for Scalable Volume Generation (#2875)

Youness Mellak, Alexandre Bousse, Antoine De Paepe, Dimitris Visvikis

Université de Bretagne Occidentale, LaTIM, INSERM, UMR 1101, Brest, France

Abstract

Full-volume 3-D medical image generation at clinical resolutions remains a significant challenge due to GPU memory constraints. Direct voxel-space generative modeling becomes increasingly difficult once spatial resolution exceeds 256^3, especially on single-GPU hardware. Latent diffusion approaches reduce this burden by performing generation in a compact representation [1], but decoding onto a dense fixed grid remains costly at high resolution. Implicit neural representations offer an attractive alternative, as they reconstruct images by querying continuous spatial coordinates rather than materializing a full voxel grid [2], making them naturally suited to memory-efficient volumetric generation.

We propose a memory-efficient 3-D latent implicit diffusion framework that combines a lightweight 3-D encoder with a coordinate-conditioned local implicit decoder, inspired by [3]. The encoder compresses the input volume into a compact latent grid, while the implicit decoder reconstructs the volume by querying continuous spatial coordinates from learned latent features, avoiding the need to materialize the full voxel grid during training. A full-volume 3-D diffusion model is then trained directly in this compact latent space. At inference, new volumes are generated by sampling from the diffusion model and rendering the full grid through the implicit decoder.

We validate our framework on CT and MRI volumes at resolutions up to 512^3 on a single consumer-grade GPU, demonstrating coherent full-volume generation across axial, coronal, and sagittal planes without materializing the full voxel grid at any stage of training.

References

[1] Rombach, R., Blattmann, A., Lorenz, D., Esser, P. and Ommer, B., 2022. High-resolution image synthesis with latent diffusion models. In *Proceedings of the IEEE/CVF conference on computer vision and pattern recognition* (pp. 10684-10695).

[2] Chen, Y., Liu, S. and Wang, X., 2021. Learning continuous image representation with local implicit image function. In *Proceedings of the IEEE/CVF conference on computer vision and pattern recognition* (pp. 8628-8638).

[3] Kim, J. and Kim, T.K., 2024. Arbitrary-scale image generation and upsampling using latent diffusion model and implicit neural decoder. In *Proceedings of the IEEE/CVF Conference on Computer Vision and Pattern Recognition* (pp. 9202-9211).

Time:
12 November, 2026
15:00 – 17:00

Room:
MANUEL DE FALLA

MIC-09 | New radiation detector technologies for medical imaging (1)

Chairs:
Joshua W. Cates (Berkeley)
Marta Freire (Valencia)

MIC-09-01

Deep learning-based estimation of individual scintillation photon arrival times for enhanced TOF resolution (#1210)

Yuya Onishi[1,2], **Yuya Onishi**[1,2], Ryosuke Ota[1], Ryosuke Ota[1], Fumio Hashimoto[4], Fumio Hashimoto[4], Kibo Ote[1], Kibo Ote[1], Go Akamatsu[3], Go Akamatsu[3], Hideaki Tashima[3], Hideaki Tashima[3], Taiga Yamaya[3,2], Taiga Yamaya[3,2]

[1] Hamamatsu Photonics K.K., Central Research Laboratory, Hamamatsu, Japan; [2] Chiba University, Graduate School of Science and Engineering, Chiba, Japan; [3] National Institutes for Quantum Science and Technology, Department of Advanced Nuclear Medicine Sciences, Chiba, Japan; [4] University of Florida, J. Crayton Pruitt Family Department of Biomedical Engineering, Gainesville, USA

Abstract

The coincidence time resolution of scintillation detectors plays a critical role in time-of-flight positron emission tomography (TOF-PET) and it is fundamentally limited by the emission, transport, and detection processes of scintillation photons. Although previous analytical and Monte Carlo simulation studies have suggested that exploiting multiple timing information of scintillation photons could approach the theoretical timing limits, direct experimental access to all detected photon timestamps remains unavailable with standard PET detectors using analog silicon photomultipliers (SiPMs). To address this challenge, we previously proposed a deep learning-based approach to recover photon timestamps on an event-by-event basis by removing the SiPM degradation factor from detector waveforms within an unsupervised learning framework. Our experimental evaluations demonstrated that the recovered photon behavior is consistent with previous findings, although the absence of ground-truth timestamps inevitably limited a rigorous and quantitative assessment of its validity and reliability. In this study, we evaluate the proposed method using Monte Carlo simulation data with fully known photon-level information. The recovered photon timestamps were quantitatively compared with the true timestamps in terms of timing bias, timing uncertainty, and total photon count fidelity. The results showed that the proposed method achieves timing biases within approximately 10 ps and maintains acceptable timing precision across photons while accurately preserving the number of detected photons per event. With the optimized parameter settings, we will further improve temporal precision in timestamp recovery using experimental data.

References

[1] D. Schaart. Physics and technology of time-of-flight PET detectors. *Phys. Med. Biol.*, 66, 09TR01, 2021.
[2] S. Gundacker *et al*. On the comparison of analog and digital SiPM readout in terms of expected timing performance. *Nucl. Instrum. Methods Phys. Res. A.* 787, 6-11, 2015.
[3] J. Cate *et al*. Analytical calculation of the lower bound on timing resolution for pet scintillation detectors comprising high-aspect-ratio crystal elements. *Phys. Med. Biol.*, 60, 5141, 2015.
[4] N. Kratochwil *et al*. Analytic timing calculations and timing limits with prompt photons, high-aspect-ratio crystals, and complex TOF-kernels in TOF-PET. *IEEE Trans. Radiat. Plasma. Med. Sci.*, 2026.
[5] Y. Onishi *et al*. Single Photon Response Deconvolution for Boosting an Understanding of BGO Emission. *2024 IEEE NSS/MIC/RTSD*, 2024.
[6] Y. Onishi *et al*. Single Photon Response-Informed Neural Network for Photon Timestamp Recovery and Improved CTR. *2025 IEEE NSS/MIC/RTSD*, 2025.

MIC-09-02

Inter-Crystal Scattering Recovery in Semi-Monolithic Crystals: an Experimental and Simulation Study (#1581)

Fiammetta Pagano[1], Francis Loignon-Houle[1], David Sanchez[2], Ezzat Elmoujarkach[3], Nicolas A. Karakatsanis[3], Juan Cateret[2], Sadek A. Nehmeh[3], Antonio J. Gonzalez[1]

[1] CSIC-Universitat Politècnica de València, Institute for Instrumentation in Molecular Imaging (I3M), Valencia, Spain; [2] Oncovision, Valencia, Spain; [3] Weill Cornell Medical College, Department of Radiology, New York, USA

This work was partially supported by the National Institutes of Health (NIH) under award number 1R01CA275942-01A1

Abstract

In positron emission tomography (PET), inter-crystal scattering (ICS) is a major source of uncertainty contributing to spatial resolution. While rejecting ICS events can improve the resolution, it comes at the cost of sensitivity. Accurately recovering the first interaction position is therefore crucial for maintaining both high sensitivity and spatial resolution.

In this work, we apply ICS recovery to experimental data from semi-monolithic detectors, with a 2:1 slab-to-SiPM ratio using both analytical and deep-learning (DL) approaches. We developed a GATE Monte Carlo simulation framework tuned to reproduce experimental signals for data augmentation. A multilayer perceptron (MLP) achieved ~78% exact layer prediction, with an additional ~15% misassigned by only one slab, leaving just ~7% exceeding 1.5 mm (one slab thickness). This outperforms analytical methods, particularly for ICS-only events, where the MLP is 16 percentage points more accurate, and the analytical method fails entirely at edge slabs. We show simulated signals closely match experimental data; additional tuning will enable their use in training networks for experimental application.

This study takes a first step toward combining simulated and experimental data for DL-based ICS recovery, which could bypass individual detector array calibration.

References

[1] Lee, Min Sun, Hyeong Seok Shim, and Jae Sung Lee. "Strategies for mitigating inter-crystal scattering effects in positron emission tomography: a comprehensive review." *Biomedical Engineering Letters* 14.6 (2024): 1243-1258.

[2] Kuang, Zhonghua, et al. "Effects of inter-crystal scattering events on the performance of SIAT aPET." *Physics in Medicine & Biology* 70.17 (2025): 17NT01.

[3] Chung, Yong Hyun, et al. "New design of a quasi-monolithic detector module with DOI capability for small animal pet." *Nuclear Instruments and Methods in Physics Research Section A: Accelerators, Spectrometers, Detectors and Associated Equipment* 593.3 (2008): 588-591.

[4] Pagano, Fiammetta, et al. "Semi-monolithic detectors for TOF-DOI brain PET: Optimization of time, energy, and positioning resolutions with varying surface treatments." *IEEE Transactions on Radiation and Plasma Medical Sciences* (2025).

[5] Loignon-Houle, Francis, et al. "Reflectivity quenching of ESR multilayer polymer film reflector in optically bonded scintillator arrays." *Nuclear Instruments and Methods in Physics Research Section A: Accelerators, Spectrometers, Detectors and Associated Equipment* 851 (2017): 62-67.

MIC-09-03

A High Resolution Semi-Monolithic GAGG Detector Aiming for SPECT Imaging (#2693)

Yangyang Zhao[1,2], Kui Wang[1], Jiaxin Dang[1], Wenjie Huang[2], Zijun Yan[1], Zheng Gu[2], Qingyang Wei[1]

[1] University of Science and Technology Beijing, School of Automation and Electrical Engineering, Beijing, China; [2] Shenzhen Bay Laboratory, Institute of Biomedical Engineering, Shenzhen, China

This work was supported in part by National Natural Science Foundation of China (Grant Number:12375337) and Beijing Natural Science Foundation (Grant Number: L232126).

Abstract

High-resolution SPECT imaging requires detectors with high intrinsic spatial resolution, good energy resolution, and high detection efficiency. Pixelated scintillator arrays are commonly used to improve the intrinsic spatial resolution, but sub-millimeter pixels increase fabrication complexity and cost, and inter-crystal gaps may reduce detection efficiency.

In this work, we developed and evaluated a semi-monolithic GAGG SPECT detector composed of 29 stacked continuous crystal slabs. Each slab measured 25.8 × 0.8 × 6 mm³, and adjacent slabs were separated by 0.08 mm-thick $BaSO_4$ reflectors. The detector was coupled to a silicon photomultiplier (SiPM) array (Hamamatsu MPPC S14161-3050HS) and read out using a PETsys TOFPET2 ASIC. A tungsten parallel-slit collimator with 13 slits, a 2 mm pitch, and a 0.8 mm slit width was placed directly in front of the detector entrance surface for flood image, energy resolution (ER), and intrinsic spatial resolution (ISR) measurements.

Most pseudo-pixels (defined as discrete areas on the flood image based on the crystal look-up table) were clearly resolved in the flood image, except for several edge crystal pixels, with average peak-to-valley ratios of 5.4 ± 2.1 and 7.4 ± 3.9 in the X and Y directions, respectively. Within a 110–170 keV energy window, DOI-based energy correction improved the average ER from 15.37% ± 1.75% to 11.07% ± 0.77% at 140 keV. The average ISR were 1.02 ± 0.36 mm and 0.42 ± 0.29 mm in the X and Y directions, respectively.

In conclusion, these results demonstrate that the proposed semi-monolithic GAGG detector can achieve good energy resolution and sub-millimeter-level intrinsic spatial resolution, showing potential for high-resolution SPECT imaging.

References

[1] Yu Z, Lyu Z, Fan P, Wu J, Liu Y, Ma T.Submillimeter Pixelated SPECT Detector Using GAGG:Ce and Light Guide With Optical Barrier Slits. IEEE Trans. Radiat. Plasma Med. Sci.,2025, 9 (8): 1015-1024.

[2] Wei Q, Ma T, Jiang N, Xu T, Lyu Z, Hu Y, Liu Y.A side-by-side LYSO/GAGG phoswich detector aiming for SPECT imaging. Nucl. Instrum. Methods Phys. Res. A,2020, 953.

MIC-09-04

Feasibility of Cherenkov-only Radiation Emitters Coupled to SiPMs for PET (#1180)

Afonso Xavier Pinto[1], Nicolaus Kratochwil[2], Leonor Rebolo[2,1], Alexander H. LeBeau[4], Ryan Hernandez[4], João Veloso[1], Brahim Mehadji[2], Pedro M.M. Correia[1], Ana Luísa M. Silva[1], Gerard Ariño-Estrada[2,3]

[1] University of Aveiro, I3N Physics Department, Aveiro, Portugal; [2] University of California Davis, Department of Biomedical Engineering, Davis, USA; [3] Institut de Física d'Altes Energies - Barcelona Institute of Science and Technology (IFAE-BIST), Barcelona, Spain; [4] University of California, Department of Radiation Oncology, School of Medicine, Davis, USA

This work was supported by the Prototera grant PRT/BD/154558/2023; by national funds through Fundação para a Ciência e a Tecnologia (FCT), I.P., and the Ministry of Science, Technology and Higher Education under projects UID/50025/2025 (10.54499/UID/50025/2025), UID/PRR/50025/2025 (10.54499/UID/PRR/50025/2025), and UID/PRR2/50025/2025 (10.54499/UID/PRR2/50025/2025); and by the Associate Laboratory Institute of Nanostructures, Nanomodelling and Nanofabrication under project LA/P/0037/2020 (10.54499/LA/P/037/2020).

Abstract

Recent applications of Positron Emission Tomography (PET) in dosimetry such as Pair Production Tomography (P2T) or Proton Range Verification (PRV) require a detector count rate capacity far beyond the conventional range for diagnostic-oriented PET. Most commonly used PET detectors use scintillation crystal coupled to silicon photomultipliers (SiPMs). For high count rate situations the scintillation decay time in the range of tens of nanoseconds can lead to undesired pile-up effects.

In this work, we explore the feasibility of using Cherenkov-only emitter based on PbF_2 coupled to SiPMs to overcome the limitation posed by the long scintillation tails. While Cherenkov-only emitters have been proposed and tested for ultra-fast timing in time-of-flight PET (TOF-PET), the goal of this work is to evaluate the feasibility of using them in readily scalable setup.

We used 3×3×3-20 mm^3 PbF_2 crystals coupled to Broadcom NUV-MT SiPMs (4×4 mm^2) and custom low-noise high-frequency (LN-HF) readout electronics. SiPM over-voltages from +2 to +8 V and different trigger levels were evaluated to determine the optimal performance for this type of application, focusing on the true coincidence fraction (TCF), coincidence ratio and coincidence timing resolution (CTR), in order to assess if the Cherenkov signals are discernible from background noise. Additionally, we tested the same setup read out by an ASIC (FastIC evaluation board) to understand the impact of an integrated system-applicable readout. Using LN-HF-readout electronics and an excess bias voltage of +4 V we measure a TCF of 81% and a CTR of 240±2 ps. Using the FastIC ASIC, the best results were a TCF of 81% and a CTR of 506±6 ps. Our results demonstrate the potential of Cherenkov-only radiators for high count rate PET applications.

References

[1] Lyu, Q, Neph, R, Sheng, K 2023, 'Tomographic detection of photon pairs produced from high-energy X-rays for the monitoring of radiotherapy dosing', *Nature Biomedical Engineering*, vol. 7, no. 3, pp. 323–334, New York: Springer Nature

[2] Consuegra, D, Korpar, S, Križan, P, Pestotnik, R, Razdevšek, G, Dolenec, R 2020, 'Simulation study to improve the performance of a whole-body PbF_2 Cherenkov TOF-PET scanner', *Physics in Medicine & Biology*, vol. 65, no. 5, article 055013, Bristol: IOP Publishing.Consuegra, D, Korpar, S, Križan, P, Pestotnik, R, Razdevšek, G, Dolenec, R 2020, 'Simulation study to improve the performance of a whole-body PbF_2 Cherenkov TOF-PET scanner', *Physics in Medicine & Biology*, vol. 65, no. 5, article 055013, Bristol: IOP Publishing.
[3] Kratochwil, N, Gundacker, S, Auffray, E 2021, 'Roadmap toward Cherenkov-based PET', *Physics in Medicine & Biology*, Bristol: IOP Publishing. DOI: 10.1088/1361-6560/ac212a.
[4] Cates, JW, Gundacker, S, Auffray, E, Lecoq, P, Levin, CS 2018, 'Improved single photon time resolution for analog SiPMs', *Physics in Medicine & Biology*, Bristol: IOP Publishing. DOI: 10.1088/1361-6560/aadbcd.
[5] Gómez, S, Alozy, J, Campbell, M, Fernandez-Tenllado, JM, Manera, R, Mauricio, J, Pujol, C, Sanchez, D, Sanmukh, A, Sanuy, A, Ballabriga, R, Gascon, D 2022, 'FastIC: a fast integrated circuit for timing applications', *Journal of Instrumentation*, vol. 17, no. 5, article C05027, Bristol: IOP Publishing. DOI: 10.1088/1748-0221/17/05/C05027.
[6] Pinto, AX, Kratochwil, N, Gómez, S, Gascón, D, Correia, P, Veloso, J, Roncali, E, Silva, AL, Ariño-Estrada, G 2025, 'Improving Cherenkov PET detector performance using FastIC readout electronics', *IEEE Transactions on Radiation and Plasma Medical Sciences*, New York: IEEE. DOI: 10.1109/TRPMS.2025.3532794.

MIC-09-05

Scan Time and Effective Dose Reduction using an Ultra-Fast Molecular Breast Imaging System (#2691)

Alexander Cherlin[1], Matthew Exley[1], Nathan Atkins[1], Kjell Erlandsson[2], Ian Baistow[1], Brian F. Hutton[2], Michael O'Connor[3], Carrie Hruska[3], Kris Thielemans[2]

[1] Kromek Ltd., Sedgefield, UK; [2] University College London, Institute of Nuclear Medicine, London, UK; [3] Mayo Clinic, Department of Radiology, Rochester, USA

Abstract

A prototype stationary tomographic ultra-fast Molecular Breast Imaging system (UFMBI) has been developed and characterised using phantom studies. The system combines ultra-high resolution CZT detectors with depth-of-interaction (DOI) sensitivity and wide-angle sampling from densely packed multi-pinhole (MPH) collimators, together with novel de-multiplexing reconstruction to mitigate multiplexing artefacts. This approach enables substantial reductions in scan time (~40 min) and radiation dose (~2.4 mSv) compared with conventional MBI, supporting wider adoption as a supplemental screening tool for women with dense breast tissue.

A dual-head prototype with a field-of-view of 132mm x 88mm has been designed and built. Each head consists of a 6x4 array of 5 mm thick CZT detectors with 11x11 grid of 2 mm pixels. Raw detector data are processed using a machine learning model providing 10x10 sub-pixelisation and DOI sensitivity. Image reconstruction uses OSEM algorithm incorporating attenuation, collimator blurring, septal penetration and multiplexing effects.

Performance was evaluated using uniform and spherical lesion phantoms (5–9 mm) at tumour-to-background ratios of 10–20:1, with comparison to a clinical planar MBI system by imaging ^{99m}Tc-infused gel phantoms. Dose/time reduction factors (DRF) were evaluated by resampling measured data relative to the reference equivalent to current clinical practice. Lesion detectability was assessed using contrast-to-noise ratio (CNR) and the Rose criterion (CNR>3). Sphere studies demonstrated detectability of 5–7 mm lesions at DRF = 8. Gel phantom experiments showed that UFMBI achieved ~2.9× higher CNR than the clinical system at reference conditions and ~2× higher at DRF = 6.

These results demonstrate the feasibility of UFMBI as a high-throughput tomographic extension of conventional MBI, with potential application as a supplemental screening tool for women with dense breasts.

References
[1] Rhodes, D et al. 2015 “JOURNAL CLUB: Molecular Breast Imaging at Reduced Radiation Dose for Supplemental Screening in Mammographically Dense Breasts”, AJR Am J Roentgenol. vol. 204, pp. 241-251.
[2] Erlandsson, K, Wirth, A, Thielemans, K, Baistow, I, Cherlin, A, Hutton, BF et al. 2023 “Design of a Low-Dose, Stationary, Tomographic Molecular Breast Imaging System Using 3-D Position Sensitive CZT Detectors”, IEEE Transactions on Radiation and Plasma Medical Sciences, vol. 7(3), pp. 225-232.
[3] Cherlin, A, Atkins, N, Baistow, I, Erlandsson, K, Thielemans, K, Hutton, BF “Performance of the prototype of an ultra-low-dose stationary tomographic Molecular Breast Imaging (ULDMBI) camera”, in 2024 IEEE RTSD, Tampa, FL, USA.
[4] Long, Z, Conners, A, Hunt, KN, Hruska, CB, O'Connor, M 2016 “Performance characteristics of dedicated molecular breast imaging systems at low doses”, Med. Phys. 43 (6) p. 3062.

MIC-09-06

Scalable Cherenkov-Enhanced Timing in BGO with FastIC+ (#1562)

Francis Loignon-Houle[1], Fiammetta Pagano[1], David Mazzanti[2], Antonio Olmos-Risen[1], Neus Cucarella[1], Daniel Guberman[2], Oscar de la Torre[2], Sergio Gomez[3], David Gascón[2], Antonio J. Gonzalez[1], Andrea Gonzalez-Montoro[1]

[1] Institute for Instrumentation in Molecular Imaging (i3M), CSIC-UPV, Valencia, Spain; [2] Institute of Cosmos Science, University of Barcelona, Barcelona, Spain; [3] Universitat Politècnica de Cataluña, Barcelona, Spain

This work was funded by the European Union (ERC, PHOENIX, 101164363). Views and opinions expressed are however those of the author(s) only and do not necessarily reflect those of the European Union or the European Research Council. Neither the European Union nor the granting authority can be held responsible for them.

Abstract

The ultrafast nature of Cherenkov photon emission offers an avenue to improve the coincidence time resolution (CTR) of time-of-flight positron emission tomography (TOF-PET) detectors. Bismuth germanate (BGO) provides a higher Cherenkov photon yield than conventional lutetium-based crystals, but its slow scintillation component induces large variations in signal shape. Measuring the rise time of the signals, obtained from the time difference between two threshold crossings, enables classification of events by Cherenkov yield and time-offset correction to improve the CTR. While this principle has been demonstrated with dedicated fast electronics, scalable implementation remains a challenge. Here, we exploit the dual-threshold capability of the new FastIC+ ASIC to extract rise-time information in BGO-based detectors and study the influence of bias voltage, settings of thresholds, and rise-time correction methods on CTR performance. We obtained a 32% CTR improvement, from 577 to 395 ps FWHM, with 3×3×15 mm^3 polished BGO coupled to 3×3 mm^2 FBK NUV-MT SiPMs biased at 49 V, and we show trade-offs between noise rejection and rise-time correction efficiency as a function of the two selected thresholds. This work marks a concrete step toward a scalable approach to exploiting BGO's mixed Cherenkov–scintillation emission in TOF-PET imaging.

References
[1] G Ariño-Estrada et al, "Current Status of Cherenkov-Based Gamma Detectors for TOF-PET and Proton Range Verification", IEEE Trans. Radiat. Plasma Med. Sci., 10(1), pp. 1–15, 2026
[2] S Gundacker et al, "Experimental time resolution limits of modern SiPMs and TOF-PET detectors exploring different scintillators and Cherenkov emission", Phys. Med. Biol, 65(2), pp. 025001, 2020
[3] N Kratochwil et al, "Exploring Cherenkov Emission of BGO for TOF-PET", IEEE Trans. Radiat. Plasma Med. Sci., 5(5), pp. 619–629, 2021

[4] A Gonzalez-Montoro et al, "Cherenkov Radiation-Based Coincidence Time Resolution Measurements in BGO Scintillators", Front Phys, 10, 2022
[5] F Loignon-Houle et al, "Improving timing resolution of BGO for TOF-PET: a comparative analysis with and without deep learning", EJNMMI Phys, 12(1), 2025
[6] D Mazzanti et al, "Below 100 ps CTR using FastIC+, an ASIC including on-chip digitization for ToF-PET and beyond", IEEE Trans. Radiat. Plasma Med. Sci., 2026
[7] S Xie et al, "Methods to Compensate the Time Walk Errors in Timing Measurements for PET Detectors", IEEE Trans. Radiat. Plasma Med. Sci., 4(5), pp. 555-562, 2020
[8] J Nuyts et al, "The SNR of Positron Emission Data With Gaussian and Non-Gaussian Time-of-Flight Kernels, With Application to Prompt Photon Coincidence", IEEE TMI, 42(5), pp. 1254-1264, 20

MIC-09-07

An Optimized Two-Layer PET&SPECT Shared Detector based on a Scintillator-as-Collimator Design (#1674)

Yangyang Zhao[1,2], Chen Huang[1], Xiangtao Zeng[1], Hang Yang[1], Wenjie Huang[1], Xiaolong Jiang[1,2], Xiaoqing Zhang[1], Ming Niu[1], Ying Liang[3], Qingyang Wei[2], Zheng Gu[1]

[1] Shenzhen Bay Laboratory, Institute of Biomedical Engineering, Shenzhen, China; [2] University of Science and Technology Beijing, University of Science and Technology Beijing, Beijing, China; [3] Cancer Hospital Chinese Academy of Medical Sciences, Department of Nuclear Medicine, Shenzhen, China

This work is supported by the National Key R&D Program of China (No. 2023YFC2414800), the Major Program of Shenzhen Bay Laboratory (No. C1012530005), the National Natural Science Foundation of China (Nos. 12275182 and 62371314), Guangdong Basic and Applied Basic Research Foundation (Nos. 2024A1515012154), the Guangdong Provincial Project (Grant No. 2023TQ07A233) and the Shenzhen Bay Laboratory Proof-of Concept Grants (No. C1022430005).

Abstract

Simultaneous PET and SPECT imaging enables concurrent characterization of multiple biological processes, but conventional multi-modality systems typically require separate detector subsystems. We previously proposed a scintillator-as-collimator design for a PET&SPECT shared detector, and demonstrated PET, SPECT, and simultaneous PET&SPECT imaging capabilities. Nevertheless, the scintillator-as-collimator volume (SCV) lacked depth-of-interaction (DOI) discrimination in PET mode, and the thickness of the SPECT Detector volume (SD) was not optimized, compromising its time-of-flight (TOF) PET performance. To address these limitations, we developed an optimized two-layer PET&SPECT detector with a top 16×16 LYSO array (1.53×1.53×10 mm³) and a bottom 8×8 LYSO array (3×3×10 mm³), separated by two 2-mm light guides. The block was coupled to an MPPC array and read out by a PETsys TOFPET2 ASIC. To evaluate the effect of hole drilling on performance, two prototype detectors were fabricated: a drilled detector with holes in the top LYSO array and light guides, and a non-drilled reference. Both detectors used unpolished crystal sides with $BaSO_4$ reflectors. Flood images, energy resolution (ER), DOI resolution, and coincidence time resolution (CTR) were evaluated.

The drilled detector achieved effective DOI discrimination in both SCV and SD. After excluding ICS events, DOI resolutions of 3.60 ± 0.43 mm and 2.18 ± 0.15 mm were obtained in the top and bottom layers, with a bottom-to-bottom CTR of 259 ps. The DOI and CTR are comparable to those of the non-drilled reference detector.

In conclusion, these results validate the optimized two-layer scintillator-as-collimator design and demonstrate its potential for a PET&SPECT shared detector with high DOI and TOF performance. Future work will evaluate the capability of the SD region in detecting 140 keV gamma photons and develop a prototype system for imaging validation.

References
[1] X Zeng, H Yang, M Niu, W Huang, X Jiang, S Huang, C Huang, Z Chen, X Zhang, Y Liang and Z Gu, Tri-mode PET, SPECT, and PET&SPECT imager using a novel scintillator-as-collimator, IEEE Nuclear Science Symposium and Medical Imaging Conference, 2025.
[2] He, W, Zhao, Y, Huang, W, Zhao, X, Niu, M, Yang, H, Zhang, L, Ren, Q, & Gu, Z. A multi-resolution TOF-DOI detector for human brain dedicated PET scanner. Physics in Medicine and Biology, 69(2), 2024.

MIC-09-08

Unlocking Next-Generation Time-of-Flight Imaging with the PoETIC ASIC (#1270)

José María Fernández-Tenllado[1], Miquel Ribalda[1], Joan Mauricio[1], Albert Espinya Rojas[1], Manuel Viqueira Rodriguez[2], Juan J. Silva[1], Sara Portero[1], Gianmario Bergamin[2], David Mazzanti[1], Lucas J. Imas[1], Daniel Guberman[1], Andreu Sanuy[1], Jerome A. Alozy[2], Oscar de la Torre[1], Michele Penna[4], Rok Dolenec[3], Carina Trippl[4], Jose Maria Benlloch[5], David Sanchez[6], Stanislaw Majewski[8], Alberto Gola[4], Georges El Fakhri[7], Rok Pestotnik[3], Rafael Ballabriga[2], **David Gascón**[1]

[1] Universitat de Barcelona (UB), Institut de Ciències del Cosmos (ICCUB), Barcelona, Spain; [2] Conseil Européen pour la recherche nucléaire (CERN), Microelectronics Section, Meyrin, Switzerland; [3] Jožef Stefan Institute (JSI), Experimental Particle Physics, Ljubljana, Slovenia; [4] Fondazione Bruno Kessler (FBK), Custom Radiation Sensors, Trento, Italy; [5] Consejo Superior de Investigaciones Cientificas (CSIC), Institute for Instrumentation in Molecular Imaging (I3M), Valencia, Spain; [6] Oncovision, Valencia, Spain; [7] Yale University, PET Center at Yale School of Medicine, New Haven, USA; [8] Univeristy of California, Biomedical Engineering, Davis, USA

The authors acknowledge financial support from Grant/Award Number: 101099896 (EIC-Patfinder Petvision).

Abstract
Time-of-Flight Positron Emission Tomography requires readout electronics capable of extracting precise timing information. The Positron Emission Tomography Integrated Circuit (PoETIC) has been developed to bridge the performance gap between the intrinsic timing resolution of the detector and that achievable with integrated readout solutions, while remaining scalable in channel count and power consumption. PoETIC introduces a novel channel architecture based on two fully independent analog front-ends per channel, separately optimized for timing and energy measurements, and thereby relaxing conflicting design requirements at the input stage. Fabricated in 65 nm CMOS technology, the PoETIC die integrates fast low-noise front ends, dual-threshold discriminators and a TDC with 24.4 ps time binning. Four 16-channel dies are combined into a 64-channel 2.5D Integrated Circuit. A custom high-speed serial interface supports daisy-chained data and trigger distribution, significantly reducing interconnect complexity. The power consumption is 10 mW per channel. Measurements of a first prototype show a single-photon time resolution of 57 ± 1 ps FWHM and 85 ± 1 ps FWHM using FBK NUV-HD-MT SiPMs of 1×1 mm² and 3×3 mm², respectively. Preliminary measurements yield a coincidence time resolution of 74 ± 1 ps FWHM with the

3×3 mm² SiPMs and LGSO crystals of 2×2×3 mm³. To the best of our knowledge, these results represent state-of-the-art timing performance for an ASIC and suggest that PoETIC approaches the intrinsic timing performance of scintillator crystals while offering a flexible and scalable readout solution for next-generation PET systems and other fast-timing applications.

References
[1] Nadig, V, Gundacker, S, Herweg, K, Naunheim, SN, Schug, D, Weissler, B, Schulz, VA 2025, 'ASICs in PET: what we have and what we need', *EJNMMI Physics*, 12(1), 16, Heidelberg: Springer Nature. DOI: 10.1186/s40658-025-00717-8
[2] Gundacker, S, Martinez Turtos, R, Auffray, E, Paganoni, M, Lecoq, P 2019, 'High-frequency SiPM readout advances measured coincidence time resolution limits in TOF-PET', *Physics in Medicine & Biology*, 64(5), 055012, Bristol: IOP Publishing. DOI: 10.1088/1361-6560/aafd52
[3] Kratochwil, N, Gundacker, S, Lecoq, P, Auffray, E 2020, 'Pushing Cherenkov PET with BGO via coincidence time resolution classification and correction', *Physics in Medicine & Biology*, 65(11), 115004, Bristol: IOP Publishing. DOI: 10.1088/1361-6560/ab87f9
[4] Orehar, M, Dolenec, R, El Fakhri, G, Korpar, S, Križan, P, Razdevšek, G, Marin, T, Žontar, D, Pestotnik, R 2024, 'Design optimisation of a flat-panel, limited-angle TOF-PET scanner: a simulation study', *Diagnostics*, 14(17), 1976, Basel: MDPI. DOI: 10.3390/diagnostics14171976
[5] Mazzanti, D, Gómez, S, Mauricio, J, Alozy, J, Bandi, FN, Campbell, M, Dolenec, R, El Fakhri, G, Fernández-Tenllado, JM, Gola, A, Guberman, D, Majewski, S, Manera, R, Mariscal-Castilla, A, Penna, M, Pestotnik, R, Portero, S, Paternò, A, Sanuy, A, Silva, JJ, Ballabriga, R, Gascón, D 2026, '100 ps CTR using FastIC+, an ASIC including on-chip digitization for TOF-PET and beyond', *IEEE Transactions on Radiation and Plasma Medical Sciences*, Early Access, 1–1, Piscataway, NJ: IEEE. DOI: 10.1109/TRPMS.2026.XXXX

Time:
12 November, 2026
17:30 – 19:00

Room:
Poster Area

MIC-10 | MIC Poster Session 2

Chairs:
Dennis R. Schaart (Delft)
Hideaki Tashima (Chiba)

MIC-10-002

Detection efficiency of a lead-loaded plastic scintillator for positron emission tomography detectors : A Monte Carlo study (#1086)

Makoto Yamazaki[1], Masahiro Sato[2]

[1] Gunma Prefectural College of Health Sciences, Department of Radiological Technology, School of Radiological Technology, Gunma, Japan; [2] Shinshu University, Graduate School of Medicine, Science and Technology, Nagano, Japan

This study was supported by the individual research fund and overseas travel grant of Gunma Prefectural College of Health Sciences.

Abstract

Lead-loaded plastic scintillators are promising candidates for next-generation positron emission tomography (PET) detectors, combining the fast timing response and low cost of organic scintillators with enhanced gamma-ray stopping power due to heavy-element doping. This study evaluates the 511-keV photon detection performance of EJ-256, a commercially available plastic scintillator containing 5 wt% lead, relative to a conventional polyvinyltoluene (PVT) scintillator using Monte Carlo simulations. All simulations were performed in Geant4 (v11.1.1). Monoenergetic 511-keV gamma rays were incident on scintillator blocks with a fixed cross-section of 4 × 4 mm² and thicknesses ranging from 20 to 200 mm in 5-mm increments. For each configuration, 100,000 primary events were simulated, and the resulting energy-deposition spectra were analyzed in ROOT. Detection efficiency was defined as the fraction of incident photons depositing 505–515 keV within the scintillator volume. EJ-256 exhibited a distinct fullenergy peak at 511 keV, whereas the reference PVT scintillator showed only a broad Compton continuum. Detection efficiency for EJ-256 increased from 0.9% at 20-mm thickness to 2.9% at 200 mm, consistent with enhanced photon absorption at greater thicknesses. However, efficiency gains became marginal beyond approximately 135 mm, indicating practical saturation. The energy resolution remained approximately constant at ~10% full width at half maximum across the investigated thickness range. These results indicate that moderate lead loading enhances 511-keV photon detection in plastic scintillators without compromising spectral stability, supporting the potential of EJ-256 as a cost-effective candidate for PET detector modules.

References

[1] S. Agostinelli et al.,“Geant4—a simulation toolkit,”*Nuclear Instruments and Methods in Physics Research A*, vol. 506, pp. 250–303, 2003.
[2] J. Allison et al.,“Recent developments in Geant4,”*Nuclear Instruments and Methods in Physics Research A*, vol. 835, pp. 186–225, 2016.
[3] W. Moskal et al.,“Time-of-flight PET detector based on plastic scintillators,”*Physics in Medicine & Biology*, vol. 61, pp. 2025–2047, 2016.
[4] W. Moskal et al.,“Feasibility study of the J-PET detector for whole-body PET imaging,”*Physics in Medicine & Biology*, vol. 59, pp. 5395–5410, 2014.
[5] S. Surti and J. S. Karp,“Advances in time-of-flight PET,”*Physics in Medicine & Biology*, vol. 60, pp. R112–R137, 2015.
[6] P. Lecoq,“Pushing the limits in time-of-flight PET imaging,”*IEEE Transactions on Radiation and Plasma Medical Sciences*, vol. 1, pp. 473–485, 2017.
[7] Eljen Technology,“EJ-256 Lead-Loaded Plastic Scintillator Data Sheet,”Eljen Technology, 2023.
[8] H. Zaidi and K. S. Koral,“Scatter modelling and correction strategies in fully 3-D PET,”*Nuclear Medicine Communications*, vol. 26, pp. 1181–1184, 2005.
[9] S. Jan et al.,“GATE: a simulation toolkit for PET and SPECT,”*Physics in Medicine & Biology*, vol. 49, pp. 4543–4561, 2004.

MIC-10-005

Exploring CTR improvement through structural refinement of orthogonally stacked PET detector (#1253)

Arisa Sanzen, Yuya Onishi, Ryosuke Ota

Hamamatsu Photonics K.K., Central Research Laboratory, Hamamatsu, Japan

Abstract

Time of flight positron emission tomography (TOF-PET) plays an important role in the diagnosis of Alzheimer's disease and cancer because it enables localized estimation of lesion positions. Improving coincidence time resolution (CTR) is essential for enhancing the precision of lesion position estimation. Currently, commercially available PET systems achieve a CTR of approximately 200 ps full width at half maximum(FWHM), while the next goal is to reach 100 ps FWHM at the system level. However, commercial PET systems employ thick scintillators for high detection efficiency, resulting in a trade-off between CTR and detection efficiency due to photon transport time spread. To overcome this trade-off, we proposed xDetector, a readout scheme in which detector groups are orthogonally stacked. xDetector employs shorter scintillators than conventional detectors to improve CTR, while maintaining detection efficiency through multiple layers stacked. In addition, by orthogonally stacking detector groups via air coupling, it is possible to estimate the interaction position within the scintillator, which contributes to further CTR improvement. In previous study scintillator crystals and multi pixel photon counters (MPPC)s with 4.2 mm pitch were optimized for CTR measurements together with a high-frequency readout circuit. However, it was demonstrated that the CTR of xDetector with 3.2 mm pitch was 10% faster than that with 4.2 mm pitch, which can be attributed to faster time response of 3 mm MPPC than 4 mm. Thus, in this study, we aimed to further improve CTR by leveraging geometric flexibility and adopting small crystals with the same cross-sectional pitch of MPPCs compared to previous configurations. Through this investigation, we explore the potential of xDetector towards realizing 100 ps CTR.

References

[1] Y. Onishi, A. Sanzen, and R. Ota, "Optimizing configuration of orthogonally stacked PET detectors towards 100 ps CTR with DOI-based timing correction", *IEEE NSS/MIC* Yokohama, Japan 2025

[2] Y. Onishi and R. Ota, "Alleviating the trade-off between coincidence time resolution and sensitivity using scalable TOF-DOI detectors", *Phys. Med. Biol.*, vol 70 2025 06500

MIC-10-008

A Cost-Effective Neural Network Approach for DOI Estimation in a State-of-the-Art PET Detector (#1688)

Qi Liu[1,2], David Arutinov[3], Keith G. Ciantar[1], Gudrun Wagenknecht[3], N. Jon Shah[1,4], Christoph W. Lerche[1]

[1] Forschungszentrum Jülich GmbH, Institute of Neuroscience and Medicine 4, Jülich, Germany; [2] Chengdu University of Technology, College of Nuclear Technology and Automation Engineering, Chengdu, China; [3] Forschungszentrum Jülich GmbH, Peter Grünberg Institute 4, Jülich, Germany; [4] RWTH Aachen University, Department of Physics, Aachen, Germany

Abstract

Depth-of-interaction (DOI) estimation can reduce parallax error in PET imaging, but conventional pixelated detectors usually require additional DOI-encoding hardware or modified detector geometries. This study investigates a cost-effective neural network approach to recover DOI information from a state-of-the-art air-coupled pixelated PET detector using only compact engineered features, which could be extracted directly by front-end ASICs without digitizing all silicon photomultiplier (SiPM) channels. A Geant4 optical simulation was performed, and neural networks were trained for both 3D position regression and DOI-bin classification. The feature-only model achieved DOI performance comparable to models using the full raw SiPM counts, with an MAE_z of 1.107±0.001 mm, and an F1 score of 0.790 for DOI-bin classification, with most classification errors occurring between neighboring bins. These results demonstrate a practical and cost-effective pathway to enable DOI capability without changing the detector geometry, while reducing readout complexity, system cost and power consumption.

References

[1] Zaidi, H, Salimi, Y, Amini, M, Mathoux, G, Mainta, I, Garibotto, V 2025, 'Performance Evaluation of the Biograph Vision.X: A High Time-of-Flight Coincidence Time Resolution PET/CT Scanner', Journal of Nuclear Medicine, 66, 251754.

[2] Teimoorisichani, M, Cho, S, Sharghi, VK, Judenhofer, M, Cabello, J, Panin, V, Aykac, M, Conti, M 2023, 'A Depth-encoding Technique for the Biograph Vision PET/CT Scanner', 2023 IEEE Nuclear Science Symposium, Medical Imaging Conference and International Symposium on Room-Temperature Semiconductor Detectors (NSS MIC RTSD), 1–1, Vancouver, BC, Canada: IEEE.

[3] Yoshida, E, Yamaya, T 2024, 'PET Detectors with Depth-of-Interaction and Time-of-Flight Capabilities', Radiological Physics and Technology, 17(3), 596–609.

[4] Lerche, CW, Herrero-Bosch, V, Ferrando-Jodar, N, Gadea-Girones, R, Sanchez-Martinez, F, Mora-Más, FJ 2010, 'Efficient Readout Electronics for Multi-Anode Photomultiplier', SPIE Optical Engineering + Applications, 78050V, San Diego, California, United States.

MIC-10-011

X-ray Imaging Performance of Mg Co-doped $Y_3(Al,Ga)_5O_{12}$:Ce for Photon-counting CT (#1759)

Hisato Suezumi[1,2], Kei Kamada[3,4], Masao Yoshino[2,3], Liudmila Gushchina[3], Kohei Nakanishi[5], Rikito Murakami[2,3], Satoshi Ishizawa[2,3], Yuui Yokota[2,4], Akira Yoshikawa[2,4]

[1] Tohoku University, Graduate School of Engineering, Sendai, Japan; [2] Tohoku University, Institute for Materials Research, Sendai, Japan; [3] C&A corporation, Sendai, Japan; [4] Tohoku University, New Industry Creation Hatchery Center, Sendai, Japan; [5] Nagoya University, Department of Integrated Health Science, Graduate School of Medicine, Nagoya, Japan

Abstract

Photon-counting computed tomography (PCCT) has attracted attention because of its potential for high spatial resolution, low-dose imaging. Although semiconductor detectors are widely studied for PCCT, indirect-conversion detectors with fast and bright scintillators combined with silicon-photomultipliers arrays (SiPMs) have recently emerged as promising alternatives owing to their potential for the scalability and cost effectiveness. Though $Gd_3(Al,Ga)_5O_{12}$ or $(Lu,Y)_2SiO_5$ shows an excellent scintillation properties, Kα escape peak of Gd (43 keV), and Lu (55 keV) degrade the accurate photon counting. Instead, Mg co-doped $Y_3(Al,Ga)_5O_{12}$:Ce (YAGG) garnet scintillators with lower Kα escape peak (<15 keV) is developed for X-ray imaging applications. The effect of Mg co-doping on scintillation properties results in representing 5-7 folds increase in the light yield of 35,000 photons/MeV@662 keV and the decay time of <50 ns. In addition, synchrotron X-ray imaging performance demonstrates that the spatial resolution of Mg co-doped $Y_3Al_3Ga_2O_{12}$:Ce is comparable to that of LuAG:Ce with the 1 mm sample thickness. Although the density of YAGG:Ce,Mg (5.08–5.33 g/cm) is lower than that of LuAG:Ce (6.67 g/cm), there is a concern regarding X-ray stopping power and deterioration of spatial resolution, the linear attenuation coefficients at 12.4 keV are sufficiently high (273–350 cm^{-1} for YAGG:Ce,Mg and 943 cm^{-1} for LuAG:Ce), resulting in X-ray absorption efficiencies exceeding 99.99% for 1 mm thickness samples, indicating negligible influence on imaging performance in the lower energy range. Moreover, we also demonstrate the feasibility of YAGG:Ce,Mg to medical field from the success in clear imaging of small, dried fish. These results show that YAGG:Ce,Mg scintillators are promising candidates for next-generation X-ray imaging detectors and can be applied for indirect-conversion PCCT applications.

References

[1] M. Nikl and A. Yoshikawa, "Recent R&D Trends in Inorganic Single-Crystal Scintillator Materials for Radiation Detection," Advanced Optical Materials 3, no. 4 (2015): 463–481.

[2] M. J. Willemink, M. Persson, A. Pourmorteza, N. J. Pelc, and D. Fleischmann, "Photon-Counting CT: Technical Principles and Clinical Prospects," Radiology 289, no. 2 (2018): 293–312.

[3] K. Kamada, T. Endo, K. Tsutumi, T. Yanagida, Y. Fujimoto, A. Fukabori, *et al.*, "Composition Engineering in Cerium-Doped (Lu, Gd)3(Ga, Al)5O12 Single-Crystal Scintillators," Crystal Growth & Design 11, no. 10 (2011): 4484–4490.

[4] K. Shimazoe, D. Kim, M. Hamdan, Y. Kobayashi, K. Kamada, M. Yoshino, *et al.*, "An energy-resolving photon-counting X-ray detector for computed tomography combining silicon-photomultiplier arrays and scintillation crystals." Communications Engineering 3.1 (2024): 167.

[5] H. Suezumi, K. Kamada, L. Gushchina, M. Yoshino, K. J. Kim, S. Ishizawa, *et al.*, "Bulk Single Crystal Growth and Scintillation Properties of Ce and Mg Co-Doped Y3Ga3Al2O12 for Advanced X-ray Imaging," Scientific Reports (2026).

[6] M. Yoshino, S. Yamamoto, K. Nakanishi, K. Yogo, K. Kamada, N. Koshikawa, *et al.*, "Development and Performance Evaluation of a Thin GAGG: Ce Scintillator Plate for High Resolution Synchrotron Radiation X-ray Imaging," Journal of Instrumentation 19, no. 10 (2024): P10030.

MIC-10-014

Optimal Radiator Refractive Index for Cherenkov-Radiator-Integrated PET Detectors: A Simulation Study (#1942)

Taiyo Ishikawa[1,2], Ryosuke Ota[3,4], Hideaki Haneishi[5], Taiga Yamaya[2,5]

[1] Chiba University, Graduate School of Science and Engineering, Chiba, Japan; [2] National Institutes for Quantum Science and Technology, Institute for Quantum Medical Science, Chiba, Japan; [3] Hamamatsu Photonics K.K., Central Research Laboratory, Hamamatsu, Japan; [4] University of California, Davis, Department of Biomedical Engineering, Davis, USA; [5] Chiba University, Center for Frontier Medical Engineering, Chiba, Japan

Abstract

In positron emission tomography, time-of-flight information can localize source positions along lines of response. Cherenkov-radiator-integrated microchannel-plate photomultiplier tubes (CRI-MCP-PMTs) with a 3.2-mm-thick lead glass window (n~1.5) have achieved 30-ps coincidence time resolution (CTR). However, improving coincidence detection efficiency remains a challenge, as increasing the radiator thickness degrades the CTR. In this study, we focused on the radiator refractive index. Based on the Frank-Tamm formula, we hypothesized that ultraviolet-transparent materials with a high refractive index would increase Cherenkov photon production, reducing event loss. Furthermore, increased Cherenkov photon detection would improve effective single-photon time resolution, thus enhancing CTR. We tested this hypothesis using Geant4 simulations of point-source measurements with paired CRI-MCP-PMTs incorporating optical and detector characteristics. Assuming wavelength-independent refractive indices from 1.7 to 3.0, we found coincidence detection efficiency increased from 1.1% to 3.0% whereas CTR deteriorated from 41.5 to 49.6 ps. Contrary to our expectations, the reduced speed of light in the medium increased timing jitter, overriding the CTR benefits from detecting more Cherenkov photons. A similar simulation for lead fluoride radiators (n~1.7–2.1)—expected to improve efficiency while maintaining the CTR—showed a worse CTR (46.4 ps) was obtained than for the wavelength-independent cases (~42.0 ps). Wavelength-resolved analysis showed a CTR of 53.3 ps for 240–340 nm photons, which was unexpectedly worse than that of 39.9 ps for 540–640 nm photons, despite the higher theoretical photon production in the shorter band. One possible cause is the steep refractive index dispersion in the shorter band. In summary, while higher refractive indices improve coincidence detection efficiency, they can degrade CTR. Minimizing refractive index dispersion is critical for fast timing.

References

[1] R. Ota *et al.*, "Coincidence time resolution of 30 ps FWHM using a pair of Cherenkov-radiator-integrated MCP-PMTs," *Phys. Med. Biol.*, vol. 64, no. 7, p. 07LT01, Mar. 2019.

[2] R. Ota *et al.*, "Lead-free MCP to improve coincidence time resolution and reduce MCP direct interactions," *Phys. Med. Biol.*, vol. 66, no. 6, p. 064006, Mar. 2021.

[3] T. Ishikawa *et al.*, "Imaging Simulation of a Dual-Panel PET Geometry With Ultrafast TOF Detectors," *IEEE Trans. Radiat. Plasma Med. Sci.*, vol. 10, no. 3, pp. 418–426, Mar. 2026.

[4] T. Ishikawa *et al.*, "Monte Carlo Simulation of Cherenkov-Radiator-Integrated MCP-PMT with Full Modeling of Optics and Waveform," in *2025 IEEE NSS-MIC-RTSD*, Nov. 2025.

[5] R. Ota *et al.*, "Timing-performance evaluation of Cherenkov-based radiation detectors," *Nucl. Instrum. Methods Phys. Res. A*, vol. 923, pp. 1–4, Apr. 2019.

[6] N. Kratochwil *et al.*, "A roadmap for sole Cherenkov radiators with SiPMs in TOF-PET," *Phys. Med. Biol.*, vol. 66, no. 19, p. 195001, Sep. 2021.

[7] R. D. Shannon *et al.*, "Refractive Index and Dispersion of Fluorides and Oxides," *J. Phys. Chem. Ref. Data*, vol. 31, no. 4, pp. 931–970, Oct. 2002.

MIC-10-017

Fabrication of diamond detectors with graphitic contacts for tissue equivalent dosimetry (#2040)

Ivan Lopez Paz, **Ivan Lopez Paz**, Consuelo Guardiola, Consuelo Guardiola, Gemma Rius, Gemma Rius

Institut de Microelectronica de Barcelona (IMB-CNM, CSIC), Bellaterra, Spain

This work has been funded by the IMB-CNM (CSIC) TRIGGER projects PIACeD and CarDos4FLASH, supported by the 'María de Maeztu Unit of Excellence' accreditation (CEX2023-001397-M / AEI/10.13039/501100011033). This study was also funded RYC2024-050777-I project, financed by the MICIU / AEI / 10.13039/501100011033 and FSE+.

Abstract

Diamond-based dosimeters are popular for medical dosimetry in view of their fast response, radiation hardness and tissue equivalence. However, some design improvements to achieve better accuracy in signal readout and approach tissue equivalence are possible by the removal of the metallic contacts, sometimes covering the active area of said devices.

In this contribution, we explore the use of a simple processing and scalable solution to obtain non-metal, low Z electrical contact. Thus, the fabrication of diamond detectors with graphitic contacts at the Microelectronics Institute of Barcelona are shown. Several approaches are explored, some of which never utilised before for radiation detector fabrication, namely pyrolytic photoresist film, nickel catalysis and ion surface graphitisation.

A prototype of such device using the pyrolytic photoresist film process for the first time has been produced and was tested under a 60 kV X-ray tube. We report the fabrication and preliminary performance results of such device. Although the substrate material quality is not ideal for radiation detection, it was possible to observe radiation response using the PPF as an interface material. The prototype features a linearity better than 3% as tested in a laboratory X-ray chamber, proving it a promising technology for detector operation. Finally, the technology challenges are finally discussed to assess the feasibility of PPF-diamond technology for dosimeter batch production.

MIC-10-020

Experimental Evaluation of Classification MLP for Position Estimation in Semi-Monolithic LYSO Cassettes for Ultra-High-Performance Brain PET (#2111)

Ezzat Elmoujarkach[1], Fiammetta Pagano[2], Francis Loignon-Houle[2], Antonio J. Gonzalez[2], David Sanchez[3], Juan Vicente Catret[3], Mert Sabuncu[1,4], Nicolas A. Karakatsanis[1], Sadek A. Nehmeh[1]

[1] Weill Cornell Medical College, Department of Radiology, New York, USA; [2] CSIC-Universitat Politècnica de València, Institute for Instrumentation in Molecular Imaging (I3M), Valencia, Spain; [3] Oncovision, Valencia, Spain; [4] Cornell University, School of Electrical and Computer Engineering, Ithaca, USA

This work was supported by the National Institutes of Health (NIH) under award number 1R01CA275942-01A1.

Abstract

Accurate localization of annihilation γ-ray interaction positions within detector block is essential for achieving high spatial resolution in positron emission tomography (PET). Conventional high-resolution PET detectors often use finely pixelated scintillator arrays resulting in increased system cost due to the larger number of crystal elements and number of readout-channels. Semi-monolithic scintillator detectors offer an alternative solution by enabling signal-based position estimation with reduced readout. In this work, we experimentally evaluated a classification-based multilayer perceptron (class-MLP) for estimating the γ-photons interaction position direction within each semi-monolithic LYSO detector slab across a cassette of 40 mini-modules (mM), each comprised of 16 LYSO slabs coupled to 8x8 SiPMs and read by 16 readout channels, developed for the Ultra-High-Performance Brain PET (UHB-PET) system. Calibration data were acquired from each of the 40 mM, and operated on a benchtop setup using a 0.5mm slit-collimated source translated in 0.5mm steps. The class-MLP used 24 multiplexed readout and classified events into 49 position bins spanning 0-24mm along the monolithic. Independent MLPs were trained for the individual mM. After correction for the finite collimator resolution, the mean positioning-error FWHM was 1.29±0.13mm (range: 0.85 to 1.41mm). The corresponding FWTM was 3.91±0.29mm (range: 3.29 to 4.73mm). Our results demonstrate that class-MLP can achieve near-millimeter detector mean spatial resolution along the monolithic dimension in 20mm-thick semi-monolithic LYSO detectors with minimal variability across all mM of a UHB-PET cassette. Future work will focus on acquiring calibration data from all cassettes in the fully assembled UHB-PET scanner to characterize its system-wide detector spatial resolution using the current calibration strategy per mM.

References

[1] Du, J., and Du, S., 'Performance Comparison of DOI-Encoding PET Detectors Based on 1.1-mm Pitch BGO Arrays With Different Reflectors', IEEE Trans. Radiat. Plasma Med. Sci., vol. 8, no. 3, pp. 257-262, 2024

[2] LaBella, A. et al., 'High-Resolution Depth-Encoding PET Detector Module with Prismatoid Light-Guide Array', J. Nucl. Med 61 (10) 1528-1533, 2020

[3] Karakatsanis, NA, et al, 'Monte Carlo Evaluation of the Ultra-High Physical Performance Brain PET (UHB-PET) scanner with semi-monolithic detectors', IEEE NSS/MIC/RTSD, 2024

[4] Pagano, F., et al., 'Semi-Monolithic Detectors for TOF-DOI Brain PET: Optimization of Time, Energy, and Positioning Resolutions With Varying Surface Treatments', IEEE Trans. Radiat. Plasma Med. Sci., vol. 10, no. 2, pp. 276-287, 2026

[5] Elmoujarkach, E, et al., 'Sub-Millimeter 2D Intrinsic Resolution Recovery in Semi-Monolithic PET Detector using Neural Networks - a Monte Carlo Simulation', IEEE NSS/MIC, 2025

[6] Pagano, F, et al., 'Performance evaluation of a multiplexing circuit combined with ASIC readout for cost-effective brain PET imaging', Phys. Med. Biol. 70 205001, 2025
[7] Freire, M., et al., 'Position estimation using neural networks in semi-monolithic PET detectors', Phys. Med. Biol. 67 245011, 2022
[8] Loignon-Houle, F., et al,'Multi-Input Interaction Positioning and Signal Demultiplexing With Deep Learning in Semi-Monolithic Detectors', IEEE NSS/MIC/RTSD, 2024

MIC-10-023

AI-based DOI determination for hexagonal monolithic LYSO scintillators with hexagonal cells engraved with laser: A simulation/experiment study (#2234)

Mojahed Abushawish[1], **Jose Udias**[1,2], Clara N. Golhen Mateo[1], Carlos Galindo-Morata[1], Pablo Galve[3,1], Victor Sánchez-Tembleque[4], Lidia Jiménez Algarra[4], David Perez-Benito[4], Luis Batres[4], Juan José Vaquero[4]

[1] Universidad Complutense de Madrid, Grupo de Física Nuclear, EMFTEL & IPARCOS, Madrid, Spain; [2] Hospital Clínico San Carlos, Health Research Institute of the Hospital Cínico San Carlos (IdISSC), Madrid, Spain, Madrid, Spain; [3] Spanish National Research Council (CSIC), Institute for Physical and Information Technologies "Leonardo Torres Quevedo", ITEFI, Madrid, Spain; [4] Universidad Carlos III de Madrid, Departamento de Bioingeniería, Universidad Carlos III de Madrid, Madrid, Spain

We acknowledge support from Spanish Government and Next GenerationEU Recovery and Resilience Facility (RRF) CPP 2021-008751 NEWMBI; European Union, the European Innovation Council's Pathfinder Open Programme: RETIMAGER, 101099096; Spanish Government and Next Generation EU/PRTR: DI2M: Smart detectors for molecular imaging (2021/C005/00147498); P. Galve acknowledges grant JDC2023-051754-I, funded by MCIU/AEI/10.13039/501100011033 and ESF+.

Abstract
Laser engraving of monolithic scintillators to create pixel boundaries has been around already for some time, with the promise of good pixel identification as in conventional pixelated detectors, but at a much lower cost. However, their use is hindered by the fact that the pixel boundaries are semi-transparent, making it difficult to identify the pixel of interaction with the algorithms applied to fully pixelated detectors. The RETIMAGER project proposes laser-engraved (LE) pixelated LYSO blocks, with optimized transparency of pixel boundaries that might be exploited to obtain depth-of-interaction (DOI) based on the light spread in the SiPM array, while keeping crystal pixel identification. Hexagonal SiPM arrays, scintillators and pixel cells are introduced, improving packing fraction and reducing gaps in between detectors, but adding difficulty when applying ordinary vertex identification strategies. We present the experimental DOI performance for several RETIMAGER detectors, engraved with different optical densities (and thus trasparencies) por hexagons of 1.25 mm side. Data is acquired in a testbench with a collimated source, and employed to train an NN algorithm, to predict DOI. For a 13 mm thick crystal, DOI assignation uncertainty ranges from 2.4 to 3.2 mm FWHM, depending on the trasparency of the boundaries, with the highest trasparency detectors exhibiting the best results. Experimental results follow the trend of the simulations, which can be used to further optimize the DOI performance and to reduce bias.

MIC-10-026

Exploring the Performance of Light-Sharing Based Single-ended BGO DOI-PET Detectors (#2339)

Yong Hwan Sul[1], Minseok Yi[2,3], Guen Bae Ko[4], Jae Sung Lee[1,5]

[1] Seoul National University, Department of Nuclear Medicine, Seoul, South Korea; [2] Seoul National University, Interdisciplinary Program in Bioengineering, Seoul, South Korea; [3] Seoul National University, Integrated Major in Innovative Medical Science, Seoul, South Korea; [4] Korea Advanced Institute of Science and Technology, Department of Nuclear and Quantum Engineering, Daejeon, South Korea; [5] Brightonix Imaging Inc., Seoul, South Korea

This work was supported by the National Research Foundation of Korea(NRF) grant funded by the Korea government(MSIT) (Grant No. RS-2024-00354123).

Abstract

Bismuth germanate (BGO) is a high-density and cost-effective scintillator for PET detectors, but depth-of-interaction (DOI) encoding with single-ended readout remains challenging due to its relatively low light yield. This study investigated a light-sharing based BGO detector using paired crystals for DOI encoding. The effects of reflector geometry and lateral surface treatment were evaluated to optimize detector performance. Among the unpolished configurations, the trapezoidal reflector provided the best DOI encoding capability, achieving an average DOI resolution of 5.29 mm FWHM and an energy resolution of 20.4%. Partial surface polishing improved energy and timing performance but degraded DOI encoding capability. After applying timing correction based on DOI and rise-time correction, the timing resolution of the unpolished trapezoidal configuration improved from 427 ps to 353 ps FWHM. These results suggest the feasibility of a single-ended DOI approach for BGO PET detectors with potential time-of-flight (TOF) applications.

References

[1] M. Ito, S. J. Hong, and J. S. Lee, "PET detectors with depth-of-interaction capability," *Biomed. Eng. Lett.*, vol. 1, no. 2, pp. 70–81, 2011.

[2] J. Du, "Performance of dual-ended readout PET detectors based on BGO arrays and $BaSO_4$ reflector," *IEEE TRPMS*, vol. 6, no. 5, pp. 522–528, 2021.

[3] R. S. Miyaoka, T. K. Lewellen, H. Yu, and D. L. McDaniel, "Design of a DOI PET detector module," *IEEE TNS*, vol. 45, no. 3, pp. 1069–1073, 1998.

[4] J. W. Cates, S. Gundacker, E. Auffray, P. Lecoq, and C. S. Levin, "Improved SPTR for analog SiPMs with front-end readout that reduces influence of electronic noise," *PMB*, vol. 63, no. 18, Art. no. 185022, 2018.

[5] M. Yi, G. B. Ko, and J. S. Lee, "Pushing the limit of BGO-based dual-ended Cherenkov PET detectors through photon transit time correction," *PMB*, vol. 69, no. 2, Art. no. 025005, 2024.

[6] N. Kratochwil, S. Gundacker, P. Lecoq, and E. Auffray, "Pushing Cherenkov PET with BGO via CTR classification and correction," *PMB*, vol. 65, no. 11, Art. no. 115004, 2020.

MIC-10-029

Experimental Evaluation of Coincidence Time Resolution in LYSO Scintillators with Photonic Crystal Pattern (#2465)

Suyeon Hyeon[1], Suhan Choi[2], Guen Bae Ko[2], Min Sun Lee[1]

[1] Daegu Gyeongbuk Institute of Science and Technology (DGIST), Electrical Engineering and Computer Science, Daegu, South Korea; [2] Korea Advanced Institute of Science and Technology (KAIST), Nuclear and Quantum Engineering, Daejeon, South Korea

This work was supported by National Research Foundation of Korea (Grant No. RS-2025-02316993).

Abstract

Time-of-flight (TOF) positron emission tomography (PET) performance is governed by the coincidence time resolution (CTR), which is fundamentally constrained by the number and arrival-time distribution of scintillation photons reaching the photosensor. To enhance both quantities, we fabricated nano-scale line- and hole-type photonic crystal (PhC) patterns with a 1.2 μm period on the polished 3×3×20 mm³ surfaces of lutetium-yttrium oxyorthosilicate (LYSO) scintillators via flex-mold soft lithography using a UV-curable optical resin (n = 1.5). Six SiPM coupling conditions were evaluated: bare LYSO with and without grease, and line- and hole-type PhC patterns each with and without grease.

The intrinsic scintillation photon arrival-time distribution was reconstructed by deconvolving each measured waveform with the single-photoelectron (SPE) response of a photomultiplier tube (PMT), and the absolute light gain of each PhC geometry was independently assessed in an airgap PMT configuration by comparing the photopeak before and after patterning. PhC-patterned crystals achieved a 42.8% reduction in deconvolved rise time and light gains of 1.20 (line) and 1.18 (hole). To quantify the redistribution of photon arrivals, fractional yields were computed within three time windows — early (0–1 ns), mid (1–10 ns), and late (10–50 ns) — normalized to the total yield over 0–50 ns. The early-window yield increased from 0.7% to 0.9% (a 33.5% relative gain), the mid-window yield rose from 19.8% to 21.2%, and the late-window yield decreased from 79.5% to 77.9%, confirming a redistribution of photon arrivals toward the earlier windows.

In SiPM CTR measurements, the line-type PhC combined with grease achieved the best CTR of 180.6 ps, a 29.5% improvement over the bare crystal. These findings demonstrate that nano-scale PhC patterning improves CTR in LYSO-based TOF-PET by enhancing both the absolute light yield and the prompt photon density.

References

[1] Hyeon, S, et al., 2025, 'Experimental Evaluation of Flex-Molded Nanopatterns and Coupling Interfaces for Light Extraction Improvement for Scintillator-based PET detectors', 2025 IEEE NSS/MIC Conf. Record

MIC-10-032

X-ray fluorescence imaging for breast cancer characterization within the IMMPRINT project (#2531)

Karol Brzeziński[1], Siddharth Parashari[1], Oihan Elesgaray[1], Kunal Kumar[2], Christoph Hoeschen[2], Carlos Lacasta[1], Marko Mikuz[3], Andrej Studen[3], Johannes Treis[4], Jelena Ninković[4], Gabriela Llosá[1]

[1] Instituto de Física Corpuscular (IFIC), CSIC-UV, Valencia, Spain; [2] Otto von Guericke University, Magdeburg, Germany; [3] Jozef Stefan Institut, Ljubljana, Slovenia; [4] MPG Halbleiterlabor, Garching, Germany

This work has received funding from the European Union's EURATOM research and innovation program, IMMPRINT Project (G.A. 101061037). S.P. acknowledges the Severo Ochoa fellowship (CEX2023-001292-S grant), funded by MCIN/AEI/10.13039/501100011033.

Abstract

X-ray fluorescence imaging (XFI) is an emerging molecular imaging technique that combines high sensitivity with high spatial resolution, offering significant penetration depth in tissues while minimizing ionizing radiation exposure compared to other existing methods. This makes XFI a promising tool for tumor characterization and personalized treatment. The IMMPRINT project aims to develop a proof-of-principle demonstrator that leverages X-ray fluorescence computed tomography as a novel hybrid modality for tumor profiling, with a focus on breast cancer. The pnCCD silicon sensors produced by MPG HLL, Munich, have been chosen for the proof-of-principle studies. Fluorescence photons are generated when gold nanoparticles are excited by incident X-rays and are detected by the pnCCD. A specific system has been designed to operate up to four pnCCDs, including a cooling system to stabilize sensors' temperature between 0ºC and 20ºC, and it is under construction. Simulations are also performed which support the system design.

References

[1] Staufer, T and Grüner, F. 2023 *Int. J. Mol. Sci.* 24(13), 10990.
[2] Kumar, K. et al. 2024 *Int. J. Mol. Sci.* 25(9), 4733.
[3] Kumar, K. et al. 2024 Proc. SPIE 13924, 661-667
[4] Meidinger N. et al. 2006 Nuc. Instr. Meth. A. vol 568, 141-148

MIC-10-035

Characterization of DOI-enabled Three-Layer Trapezoidal Pixelated LYSO Detector (#2616)

Siddharth Parashari[1], Kristiyan M. Popov[2], Fernando Hueso-González[1], Munetaka Nitta[2], Peter G. Thirolf[2], Katia Parodi[2], Gabriela Llosa[1]

[1] Instituto de Fisica Corpuscular (IFIC), CSIC-UV, Valencia, Spain; [2] Ludwig-Maximilians-Universität, Department of Physics, Munich, Germany

This work was supported by the Spanish MICIN/AEI (MIDAS, PID2022-143246OB-I00). SP acknowledges support from the Severo Ochoa grant CEX2023-001292-S (MCIN/AEI/10.13039/501100011033). KMP acknowledges funding from the European Union's Erasmus+ programme. LMU members acknowledge support from ERC grant 725539 and from T. Yamaya and H.G. Kang (NIRS/QST) for the LMU detector development.

Abstract

In the context of the "Small Animal Proton Irradiator for Research in Molecular Image-guided Radiation Oncology" (SIRMIO) project, a high-resolution depth-of-interaction (DOI) LYSO-based detector has been developed for a small-animal in-beam PET scanner. In addition to PET applications, the DOI detector may also be suitable for the detection of high-energy prompt gamma rays originating from excited nuclei such as 12C and 16O, enabling potential applications in Compton camera imaging for ion-beam therapy monitoring. However, the interaction mechanisms of high-energy gamma rays differ from those of 511 keV annihilation gamma rays, particularly in terms of the relative contributions of photoabsorption and Compton scattering processes. In this study, we experimentally investigated the performance of the DOI detector for high-energy gamma-ray detection to gain a better understanding of its applicability to prompt gamma imaging. The detector consists of a three-layer pixelated scintillation block coupled to a 64-channel silicon photomultiplier array. The use of the PETsys TOFPET2 ASIC, employed in the Compton camera MACACOp developed by the IRIS group, is a potential alternative to the current electronics employed in the SIRMIO project, which enables individual channel readout. The study demonstrates the feasibility of operating the detector with PETsys electronics, and characterizes its response with 60Co and 22Na sources.

References
[1] G. Lovatti, et. al., PMB, 68 (23), (2023) 235005.
[2] T. Binder, et. al., Front. Phys. 10 (2022) 954204.
[3] R.Viegas, et. al., Rad. Phys. Chem. 202 (2023) 110507.

MIC-10-038

PETRARCA: a Positron Emission Tomography Real-Time Analog Re-Configurable ANN Detector (#2827)

Maurizio Pandocchi[1,2], Mattia Amadori[1,2], Michele Ronchi[1,2], Giacomo Borghi[1,2], Marco Carminati[1,2], Carlo E. Fiorini[1,2]

[1] Politecnico di Milano, Dipartimento di Elettronica Informazione e Bioingegneria, Milano, Italy; [2] Istituto Nazionale di Fisica Nucleare, Sezione di Milano, Milano, Italy; [3] Ministero dell'Università e della Ricerca, Milano, Italy

Abstract

Positron emission tomography systems are becoming increasingly complex due to the growing number of detector channels and the large amount of data generated, especially in total-body imaging configurations. In this work, we present PETRARCA, a positron emission tomography detector system integrating an analog neural network ASIC (ANNA) for real-time edge computing of gamma-ray interaction coordinates within a monolithic scintillation crystal. The system consists of a 32 mm × 32 mm × 10 mm monolithic LYSO crystal coupled to an 8 × 8 SiPM matrix read out by dedicated front-end electronics. The detector architecture includes both a conventional digital acquisition path and a parallel analog inference path based on the ANNA ASIC, enabling simultaneous acquisition of sensor data and hardware neural-network predictions. A first evaluation of the system has been carried out using simulated data and the real ASIC response to emulate a reduced-scale configuration using a 4 × 4 SiPM array coupled to a 26 mm × 26 mm × 10 mm monolithic crystal. The performances of the ASIC in predicting the interaction coordinates were tested, and proved to have a mean absolute error (MAE) of around 1 mm on both the x and y axes. The preliminary results demonstrate the feasibility of analog neural-network edge computing for spatial localization in PET detectors and support further developments toward fully integrated real-time detector systems.

References

[1] Nanni et al., “Total body positron emission tomography/computed tomography: Current status in oncology,” Semin. Nucl. Med., vol. 55, no. 1, pp. 31–40, 2025

[2] S. Di Giacomo et al., “Implementing an Integrated Neural Network for Real-Time Position Reconstruction in Emission Tomography With Monolithic Scintillators,” IEEE Trans. Radiat. Plasma Med. Sci., vol. 8, no. 5, pp. 501-510, May 2024.

[3] A. Gonzalez-Montoro et al., “Evolution of PET detectors and event positioning algorithms using monolithic scintillation crystals,” IEEE Trans. Radiat. Plasma Med. Sci., vol. 5, pp. 282–305, 2021.

[4] I. D’Adda et al., “SITH: An SiPM Readout ASIC for Prompt Gamma-Ray Detection in Hadrontherapy Applications,” IEEE Trans. Nucl. Sci., vol. 71, no. 9, pp. 2140–2150, 2024.

MIC-10-041

Scintillation Properties of $(Lu,Y)_2O_3$:La Ceramic Pixels for PET (#2881)

Jarek Glodo[1], Suyoung Kim[1], Arthur Kim[1], Matthias Muller[1], Charles Sosa[1], Jiahao Xie[2], Simon R. Cherry[2], Junwei Du[2]

[1] Radiation Monitoring Devices, Inc., Watertown, USA; [2] University of California, Davis, Department of Biomedical Engineering, Davis, USA

This work was supported by the US NIH NIBIB through competitively awarded contracts number 4R44MH135525-02.

Abstract

Lutetium oxide–based scintillators are of growing interest for positron emission tomography (PET) because of their high density and high effective atomic number, which provide efficient stopping of 511 keV annihilation photons. Lanthanum-doped $(Lu,Y)_2O_3$ (LYO:La) is a transparent ceramic variant that retains the favorable stopping power of Lu_2O_3 while being easier to fabricate, making it an attractive candidate for next-generation PET detector arrays. In this work we report a scintillation characterization of LYO:La pixels in two geometries relevant to PET, 1×1×10 mm^3 for high-resolution preclinical and dedicated-organ imaging, and 3×3×10 mm^3 for whole-body clinical systems. Pixels were cut from LYO:La ceramic disks, polished on all faces, and evaluated with a range of side reflectors (Teflon, Tyvek, ESR film, and Spectralon) in both flat and upright coupling orientations. We measured X-ray-excited radioluminescence emission spectra, ^{22}Na (511 keV) pulse height spectra, relative light yield, energy resolution, scintillation decay time profiles, and timing resolution. The results illustrate the influence of pixel geometry, coupling face, and reflector choice on light collection and energy resolution, and show that LYO:La pixels offer a promising combination of stopping power, light yield, and timing performance for PET detector modules.

MIC-10-044

Ultrahigh Spatial Resolution Perovskite-based Direct X-ray Imagers for Low-lag Medical Applications (#3045)

Brandon Dunham[1], Shariar Motakef[1], **Amlan Datta**[1]

[1] CapeSym, Inc., Research and Developement, Natick, USA; [2] Massachusetts General Hospital, Department of Radiology, Boston, USA

This research was supported by the U.S. National Institutes of Health under award R44EB038123.

Abstract

Dynamic medical X-ray imaging requires detectors that combine high quantum efficiency, low residual lag, and high spatial resolution without the optical spread and afterglow of scintillator-based flat panels. We report a fully inorganic perovskite-based direct-conversion perovskite X-ray imager fabricated from phase-pure orthorhombic Cesium Lead Bromide (CPB) sensor material and integrated with active-pixel readout arrays. Phase-pure CPB was obtained by controlled crystal growth and converted into dense blade-coated films; non-phase-pure starting materials containing secondary phases produced nonuniform films and degraded images, confirming the importance of phase control for reproducible detector performance. The optimized CPB detector demonstrated high linear X-ray response, sensitivity of 55,400 μC $Gyair^{-1}$ cm^{-2} at 30 keV and 0.5 V/μm, a limit of detection of 417 pGyair s^{-1}, a mobility-lifetime product of 8.0 × 10^{-4} cm^2 V^{-1}, and a calculated detective quantum efficiency near 85% at practical dose levels. In flat-panel imaging, CPB imagers reached 6.9 lp/mm at 20% modulation transfer function on a 100 μm-pitch amorphous-silicon array and resolved 20 lp/mm after integration with a CMOS readout. Most importantly for low-lag medical applications, improvements in phase purity and charge-transport stability reduced residual detector lag from 8.9% to 1.1%. These results show that all-inorganic perovskite direct conversion can provide a path to low-dose, low-lag, high-resolution imaging for fluoroscopy, tomosynthesis, dental cone-beam computed tomography, and other image-guided procedures.

MIC-10-047

Timing and Spatial Properties of HRPPD coupled to LGSO/LYSO for TOF-PET Applications (#3103)

Yingjie Wang[1], Mark Popecki[2], Heejong Kim[1], Alexey Lyashenko[2], Mythra V. Nemallapudi[1], Michael Minot[2], Chien-Min Kao[1], Chin-Tu Chen[1]

[1] University of Chicago, Radiology, Chicago, USA; [2] Incom Inc., Research and Development, Charlton, USA

Abstract

Large-area microchannel plate photomultipliers (MCP-PMT) such as the Large-Area Picosecond Photon Detector (LAPPD) and High-Rate Picosecond Photon Detector (HRPPD), are attractive for time-of-flight positron emission tomography (TOF-PET) due to their superior single-photon time resolution (SPTR) and low-cost potential. However, when coupling them with popular TOF-PET scintillators, it was previously reported worse-than 250 ps coincidence time resolutions (CTR) for annihilation photons. In this work, by applying a custom high-frequency (HF) amplifier to the outputs of an HRPPD (10×10cm^2 window) coupled to a 3×3×3 mm^3 LGSO crystal and an SiPM-based reference detector, we measured a 144 ps CTR. In addition, we showed that individual crystals of a 4×4 array of 3×3×10 mm^3 LYSOs can be resolved using this HRPPD whose output was 4×4 pads having a 25 mm pitch. We also constructed a detector model for investigating key factors affecting CTR. These factors include scintillation yield, light transport in the crystal and HRPPD window, photon detection efficiency and charge collection of the HRPPD, and electronics contributions, with parameters derived from analytical calculations, Geant4 simulations, or experimental measurements. This model predicted a CTR that was consistent with the measured value. Based on this model, a development roadmap with quantitative performance targets and near-term milestones is presented.

References

[1] Lecoq, P 2017, 'Pushing the Limits in Time-of-Flight PET Imaging', IEEE Transactions on Radiation and Plasma Medical Sciences, 1(6), pp. 473–485.
[2] Lyashenko, AV et al. 2026, 'HRPPD photosensors for RICH detectors with a high resolution timing capability', Nuclear Instruments and Methods in Physics Research A, 1082, 170964.
[3] Korpar, S et al. 2024, 'Timing Resolution of a LAPPD Prototype Measured with CERN PS Test Beams', Nuclear Instruments and Methods in Physics Research A, 1069, 169838.
[4] Minot, MJ et al. 2025, 'Advancing HRPPD Technologies for Next-Generation High-Performance TOF-PET Systems', IEEE NSS/MIC.
[5] Zobundzija, Z et al. 2025, 'Pixel and Transmission Line Readouts in Capacitive-Coupled HRPPD MCP-PMTs for High-Precision Timing', IEEE NSS/MIC.

MIC-10-050

Analytical modeling and inclusion of object scatter in non-TOF 3D PET for low-count data (#1275)

Jorge Roser, Hong P. Vo, Magdalena Rafecas

Universität zu Lübeck, Institute of Medical Engineering, Lübeck, Germany

This work was supported by the European Union's Horizon 2024 research and innovation programme under the Marie Skłodowska-Curie grant agreement no. 101207067, and partly by the German Research Foundation (DFG) under grant agreement no. 508064995.

Abstract

Compton scattering in Positron Emission Tomography (PET) is commonly seen as an important degrading factor for the image quality. In particular, object scattering is known to reduce image contrast and distort quantification. Conventional scatter correction techniques do not model scatter directly in the system matrix, despite its potential to better handle low-count data scenarios. In this work, we propose an analytical model for single Compton scattering events and subsequently derive expressions of the system matrix and sensitivity. We validate the obtained expressions with Monte Carlo simulations. Ongoing work includes studying the impact of such approach by using low-count simulated data, and a comparison of the proposed method with conventional scatter correction techniques.

References
[1] Zaidi, H, Koral, KF 2004, 'Scatter modelling and compensation in emission tomography', *Eur J Nucl Med Mol Imaging* **31**, 761–782. DOI: 10.1007/s00259-004-1495-z
[2] Watson, CC, et al. 1996, 'A Single Scatter Simulation Technique for Scatter Correction in 3D PET', In: Grangeat, P., Amans, JL. (eds) Three-Dimensional Image Reconstruction in Radiology and Nuclear Medicine. Computational Imaging and Vision, vol 4. Springer, Dordrecht. DOI: 10.1007/978-94-015-8749-5
[3] Tamal, M, et al. 2006, 'Noise Properties of Four Strategies for Incorporation of Scatter and Attenuation Information in PET Reconstruction Using the EM-ML Algorithm', *IEEE Transactions on Nuclear Science*, vol. 53, no. 5, pp. 2778-2786. DOI: 10.1109/TNS.2006.880973
[4] Markiewicz, PJ, et al. 2007, 'High accuracy multiple scatter modelling for 3D whole body PET', *Phys. Med. Biol.* **52** 829. DOI: 10.1088/0031-9155/52/3/021
[5] Schaar, M, Rafecas, M 2019, 'Modelling of Scatter in the System Matrix for 3D PET Image Reconstruction: a Comparative Study', *2019 IEEE Nuclear Science Symposium and Medical Imaging Conference (NSS/MIC)*, Manchester, UK. DOI: 10.1109/NSS/MIC42101.2019.9059797
[6] Roser, J, et al. 2026, 'Inclusion of Inter-crystal Scattering in PET: Analytical Models and Dedicated Reconstruction', preprint. DOI: 10.48550/arXiv.2601.05717

MIC-10-053

Noise Modeling of Three Material Dual Energy Computed Tomography with a Pathlength Constraint (#1443)

Andrew E. Ferretti, Emil Sidky, John Paul Phillips, Xiaochuan Pan

University of Chicago, Department of Radiology, Chicago, USA

This work is supported in part by NIH grant No. R01-CA287302. The contents of this article are solely the responsibility of the authors and do not necessarily represent the official views of the National Institutes of Health.

Abstract

Dual energy computed tomography (DECT) utilizes transmission measurements through a sample with two distinct X-ray spectra to produce a two material decomposition. By introducing a path-length constraint to DECT measurements, it is possible to obtain a three material decomposition. In both cases, the stability of the resulting decompositions and noise properties of the virtual monochromatic images (VMIs) are sensitive to acquisition choices like beam energy. We aim to extend a theoretical noise-propagation framework for choosing optimal beam energies and VMI energy for two material decompositions to the three material case. We then demonstrate the utility of this framework for a proposed use-case of contrast enhanced breast tomography. In particular, by assuming linear propagation of noise through material sinogram estimation and filtered backprojection, a compound Poisson noise process in X-ray measurements, and Gaussian-distributed distance constraints, we obtain analytic expressions for the Jacobian of the material sinogram-to-data transformation, the variance of VMI pixels, and the VMI contrast to noise ratio (CNR). We then use the VICTRE software to generate a realistic computational breast phantom, modeled as consisting of glandular tissue, adipose, and iodine contrast agent. For this phantom, we find that tube potential pairings of 30-40 kVp and 55-80 kVp give a high value of the material sinogram-to-data transformation Jacobian determinant, indicating good stability and minimal noise propagation. For this phantom and spectra, we compare analytically predicted and empirically realized VMI CNR versus monoenergy, and find good agreement between them with a maximum CNR of 9.6 for a VMI monoenergy of 65.5 keV in both cases.

References

[1] Kis, B.J., Sarnyai Z., Kákonyi, R., Erdélyi, M., Szabó, G., 2012, 'Single-energy material decomposition using X-ray path length estimation', *Journal of Computer Assisted Tomography*, vol. 36, no. 6, pp. 768–777

[2] Terzioglu, F., Sidky, E., Phillips, J.P., Reiser, I., Bal, G., Xiaochuan, P., 2024, 'Optimizing dual-energy CT technique for iodine-based contrast-to-noise ratio, a theoretical study', *Medical Physics*, vol. 51, no. 4, pp. 2871–2881

[3] Bal, G., Gong, R., Terzioglu, F., 2022, 'An inversion algorithm for *P*-functions with applications to multi-energy CT', *Inverse Problems*, vol. 38, no. 3, p. 035011

[4] Whiting, B. R., 'Signal statistics in x-ray computed tomography', 2002, *Medical Imaging 2002: Physics of Medical Imaging*, vol. 4682, pp. 53-60, International Society for Optics and Photonics

[5] U.S. Food and Drug Administration, 'VICTRE: In Silico Breast Imaging Pipeline' (RST24MX01.01). https://cdrh-rst.fda.gov/victre-silico-breast-imaging-pipeline

[6] Hubbell, J.H., Seltzer, S.M., 1995 'Tables of X-ray mass attenuation coefficients and mass energy-absorption coefficients 1 keV to 20 MeV for elements Z = 1 to 92 and 48 additional substances of dosimetric interest', Technical report, *National Inst. of Standards and Technology*

[7] Salvat, F., Fernandez-Varea, J. M., Sempauand, J., 2008, 'PENELOPE2006, A Code System for Monte-Carlo Simulation of Electron and Photon Transport', *Organisation for Economic Co-Operation and Development, Nuclear Energy Agency - OECD/NEA*, Le Seine Saint-Germain, 12 boulevard des Iles, F-92130 Issy-les-Moulineaux (France),
[8] Kim, B., et al., 2021, 'Adaptive image rescaling for weakly contrast-enhanced lesions in dedicated breast CT: A phantom study', *Journal of the Korean Society of Radiology*, vol. 82, no. 6, p. 1477-1492
[9] Poludniowski, G., Omar, A. , Bujila, R., Andreo, P., 2021, 'Technical note: Spekpy v2.0—a software toolkit for modeling x-ray Tube Spectra', *Medical Physics*, vol. 48, no. 7, pp. 3630–3637

MIC-10-056

Optimization of Pinhole Diameter in Fully Stationary Multi-Pinhole Brain SPECT: Prioritizing Spatial Resolution via CNN-Based Correction

(#1530)

Takumi Akatsuka[1], Koichi Ogawa[2]

[1] Hosei University, Applied Informatics, Graduate School of Science and Engineering, Koganei, Japan; [2] Hosei University, Applied Informatics, Faculty of Science and Engineering, Koganei, Japan

Abstract

Multi-pinhole SPECT enables static data acquisition without rotating the detectors, reducing patient burden. In brain SPECT, particularly for diagnosing neurodegenerative diseases like Alzheimer's, high spatial resolution is critical for visualizing minute regional functions. However, increasing the number of pinholes to secure sufficient sensitivity causes projection overlaps on the detector. Furthermore, physical factors such as gamma-ray attenuation and scattering within the object degrade the quantitative accuracy of reconstructed images. In addition to these issues, a significant trade-off exists regarding the pinhole aperture size. While a larger diameter (e.g., 5 mm) increases photon counts and reduces statistical noise, it exacerbates projection blur and degrades spatial resolution. Conversely, a smaller diameter (e.g., 2 mm) preserves resolution but suffers from increased noise. Previously, we proposed a convolutional neural network (CNN) approach using U-Net++ for a three-detector multi-pinhole SPECT that simultaneously performs overlap separation and various physical corrections. In this study, we applied this framework to brain SPECT to determine the optimal aperture size by comparing 2-mm and 5-mm pinhole diameters. Our results demonstrated that the 2-mm aperture, which maintains spatial resolution, outperformed the 5-mm aperture across quantitative image quality metrics, including NMSE, PSNR, and SSIM, confirming its superiority for detailed brain imaging.

References
[1] Ogawa, K, Ichimura, Y, 2014, 'Simulation study on a stationary data acquisition SPECT system with multi-pinhole collimators attached to a triple head gamma camera system', *Ann. Nucl. Med.*, vol. 28, pp. 716–724.
[2] Mok, GSP, Tsui, BMW, Beekman, FJ, 'The effects of object activity distribution on multiplexing multi- pinhole SPECT', 2011, *Phys. Med. Biol.*, vol. 56, pp. 2635–2650.
[3] N. Zeraatkar, Kalluri, KS, Auer, B, et al., 2021, 'Investigation of Axial and Angular Sampling in Multi-Detector Pinhole-SPECT Brain Imaging' *Phys. Med. Biol.*, vol. 66, p. 065004.
[4] Moore, SC, Cervo, M, Metzler, S.D, et al., 2015, 'An Iterative Method for Eliminating Artifacts from Multiplexed Data in Pinhole SPECT', in *Proc. 13th Fully 3D*, pp. 515–517S.
[5] Akatsuka, T, Ogawa, K, 2025, 'Removal of Projection Data Overlaps Using Deep Learning in SPECT with a Large Number of Pinholes', IEEE NSS/MIC, https://doi.org/10.1109/NSS/MIC/ RTSD 57106.2025.11286491.
[6] Motomura, N, Ogawa, K, Shidahara, M, et al., 2007, 'Development of Digital Phantoms for Evaluation of Fundamental Performance on SPECT', IEEE NSS MIC, CD-ROM.
[7] Allen Inst. Brain Sci., 'Allen Human Brain Atlas', https://human.brain-map.org/mri_viewers/data.
[8] Caron, M, 2022, 'MRI brain dataset', Kaggle, https://www.kaggle.com/datasets/medericcar/mribrain.

[9] Yagi, S, Usui, K, Ogawa, K, 2025, 'Scatter and beam hardening effect corrections in pelvic region cone beam CT images using a convolutional neural network', 2025, *Radiol. Phys. Technol.*, vol. 18, pp. 457–468.

MIC-10-059

Validated Optical Simulation for High-Energy Gamma Response in a 3-Layer LYSO DOI Detector (#1668)

Shan Jiang, Giulio Lovatti, Francesco Evangelista, Peter Thirolf, Katia Parodi, Munetaka Nitta

Ludwig-Maximilians-Universität München, München, Germany

Abstract

We have developed a 3-layer staggered LYSO de tector with DOI capability within the project SIRMIO (Small animal proton irradiator for research in molecular image-guided radiation-oncology) for proton range verification via PET imag ing. To evaluate the feasibility of detecting prompt gamma rays for quasi-instantaneous monitoring of proton beams, we propose a workflow that includes the validation of optical simulation settings and the implementation of the saturation effect of the SiPM photonsensor in the Geant4 simulation. Measurement data with ^{152}Eu, ^{22}Na and ^{137}Cs radioactive sources are utilized for modeling the saturation effect of SiPM, and also for validating optical boundary settings in Geant4. The measured spectra of ^{22}Na and ^{137}Cs point sources are well reproduced with the proposed simulation workflow. The responses to prompt gamma rays are then simu lated. According to the floodmaps and profiles, LYSO pixel can be identified at 2.2, 4.4 and 6.2 MeV, but the contrast decreases strongly when energy reaches 6.2 MeV. The peak-to-valley ratios drop by up to 53% at 4.4 MeV and 62% at 6.2 MeV (relative to 2.2 MeV), primarily due to the energy deposition occurring more frequently in multiple LYSO pixels. These predictions suggest the detector’s potential for detecting prompt gamma rays, while accurately recovering or rejecting inter-crystal scatter events is essential to maintain detector performance at higher gamma energy.

References

[1] K. Parodi et al., Acta Oncol., vol. 58, no. 10, p. 1470, 2019.
[2] T. M. Fitzpatrick, Ph.D. dissertation, lmu, 2022.
[3] J. Allison et al., Nucl. Instrum. Meth. A, vol. 835, p. 186, 2016.
[4] K. Kotera et al., arXiv:1510.01102, 2015.
[5] M. Janecek et al., IEEE Trans. Nucl. Sci., vol. 57, no. 3, p. 964, 2010.

MIC-10-062

A Mesh-Type Reference Computational Phantom Platform for Multi-Modality Monte Carlo Simulation in OpenGATE (#1743)

Jin Jegal[1], Kum Bae Kim[1], Yeon soo Yeom[3], Jaewon Yang[4], Chang Heon Choi[2], Jung-in Kim[2], Youngho Seo[5], **Yoonsuk Huh**[2,5]

[1] Korea Institute of Radiological and Medical Sciences, Department of Radiation Ocology, Seoul, South Korea; [2] Seoul National University Hospital, Department of Radiation Ocology, Seoul, South Korea; [3] Yonsei University, Departement of Radiation Convergence Engineering, Wonju, South Korea; [4] UT Southwestern medical Center, Department of Radiology, Texas, USA; [5] University of California, Department of Biomedical Imaging and Radiology, San Francisco, USA

None.

Abstract

Mesh-type Reference Computational (MRCP) Phantoms provide anatomically realistic tetrahedral organ structures, but their practical use in OpenGATE-based imaging and dosimetry simulations remains limited. In our previous work, a simplified tetrahedral phantom was imported using a tessellated-solid-based workflow and evaluated with heart and body geometries. In this study, we extended the approach to a whole-body tetrahedral phantom framework using parameterised tetrahedral geometry construction and region-aware dose scoring. The updated workflow reads mesh, material, organ-region, and visualization information, constructs the complete phantom in OpenGATE, and enables selected-organ three-dimensional dose scoring while preserving full-phantom particle transport. A copy-number-based filtering method was introduced to associate tetrahedral elements with anatomical regions, avoiding material-name-based selection. The complete phantom, including all anatomical organs, was successfully loaded with a memory usage of 23.84 GB. Three-dimensional deposited energy and dose distributions were generated for selected organs. Multi-threaded performance was evaluated using 8 million x-ray beam particles, reducing computation time from 2453.13 s with 1 CPU thread to 429.43 s with 8 CPU threads, corresponding to a 5.7-fold speed improvement. In the 8-thread simulation, dose scoring for four selected organs, including blood, heart wall, and both lungs, was completed in approximately 5 minutes. These results demonstrate the feasibility of multi-threaded, organ-specific MRCP dosimetry and provide a basis for extending mesh-type phantom simulation to CT, PET, SPECT, and linac workflows in OpenGATE.

MIC-10-065

Inter-Crystal Scattering in LYSO-SiPM PET: Integrated Analysis via Geant4/GATE Simulation, CNN, and Multi-Pitch Experiments (#1859)

Tianyi Deng, Qinghua Zhang, Hongqiang Zhang, Xiangdong Cai, Chunhui Zhang, Yongzhi Yin

Lanzhou University, School of Nuclear Science and Technology, Lanzhou, China

Abstract

This study integrates GEANT4/GATE Monte Carlo simulations with hardware experiments to investigate and correct inter-crystal scattering (ICS) in Lutetium Yttrium Oxyorthosilicate (LYSO) Positron Emission Tomography (PET) detectors. In the simulation phase, 10^7 valid events from a 511 keV gamma-ray point source were tracked across a 16 x 16 LYSO array (2.1 mm pitch) to analyze 3D energy spread and depth of interaction (DOI) characteristics. To correct ICS-induced parallax errors, we designed a physics-guided Convolutional Neural Network (CNN) with an energy masking constraint to recover the initial interaction coordinates. Furthermore, we established a physical experimental platform using arrays of various pitches (2.1 mm, 3.2 mm, and 4.1 mm). Deploying the pretrained CNN on physical hardware and conducting preliminary iterative training with empirical data demonstrated the predictive potential of machine learning for measured signals. During system image reconstruction, perfect CNN prediction of ICS events could theoretically improve spatial resolution from 1.45 mm to 1.21 mm. By synergistically applying algorithmic ICS correction and DOI information, the full width at half maximum (FWHM) can be further compressed to 0.99 mm. This study provides a conceptual solution and initial attempt for mitigating inter-crystal scattering in future high-resolution PET detectors.

MIC-10-068

Design of a brain SPECT scanner based on high intrinsic resolution CZT detectors and multi-pinhole collimators (#1985)

Kjell Erlandsson[1], Francesco Fraioli[1], Alexander Cherlin[2], Brian F. Hutton[1], Kris Thielemans[1]

[1] University College London, Institute of Nuclear Medicine, London, UK; [2] Kromek Ltd, Department of imaging, Sedgefield, UK

This work was supported by funding from the UKRI EPSRC Impact Acceleration award to UCL (EP/X525649/1). INM staff are partly funded by the NIHR University College London Hospitals Biomedical Research Centre.

Abstract

SPECT is useful for investigating a range of neurological and psychiatric conditions, such as Parkinson's disease, epilepsy and schizophrenia. Most clinical brain SPECT studies are performed with rotating gamma-cameras with

parallel-hole collimators, which results in sub-optimal image quality. Multi-pinhole (MPH) collimators can provide an improved sensitivity vs. resolution trade-off, while Cadmium-Zinc-Telluride (CZT) detectors offer better intrinsic spatial resolution as well as superior energy resolution compared to scintillation detectors. In collaboration with Kromek Ltd, we have developed a molecular breast imaging system based on CZT detectors and MPH collimators. Here we report initial results on designing a dedicated brain SPECT scanner using similar technology. The system will consist of a polygon of planar detectors and will be completely stationary, allowing for dynamic imaging. We performed computer simulations for various design configurations, based on a 20-cm diameter spherical field-of-view (FOV), assuming an intrinsic detector resolution of 0.4x0.4 mm and a depth-of-interaction (DOI) resolution of 1 mm. The simulations were based on an analytical system model, and images were reconstructed using an ML-EM algorithm. Our initial evaluations involved two different digital phantoms: A grid of 7x7 point-sources with a non-zero background; and the Hoffman brain phantom. With the target resolution set to 9 mm at the center and a degree of multiplexing of ~30%, the sensitivity was ~6×10^{-4}. An average reconstructed resolution of ~5 mm FWHM was obtained, going from 9 mm at the center down to 2-3 mm towards the edge of the FOV. In conclusion, our initial results show that high image quality can be obtained with this type of SPECT system.

References
[1] K. Erlandsson et al. 2023, IEEE Trans. Radiat. Plas. Med. Sci., 7(3):225-232.

MIC-10-071

Modeling analog SiPMs with temporal crosstalk integration for fast timing in medical imaging (#2021)

Nicolaus Kratochwil[1], Emilie Roncali[1], Gerard Ariño-Estrada[1,2]

[1] University of California, Davis, Department of Biomedical Engineering, Davis, USA; [2] Barcelona Institute of Science and Technology in Barcelona, Institut de Fisica d'Altes Energies, Barcelona, Spain

This work was supported by NIH grant R01EB034062.

Abstract

Silicon photomultipliers (SiPMs) coupled to scintillators are widely used in medical imaging, particularly in fast-timing applications such as time-of-flight positron emission tomography (TOF-PET) . While significant progress has been made in modeling detector response and correlated noise, recent advances in SiPM technology and fast readout electronics require a reassessment of the full analog signal formation process. In particular, the transition from idealized digital timestamps to realistic analog signals introduces information loss due to bandwidth limitations, electronic noise, and correlated effects such as optical crosstalk.

We present a comprehensive simulation framework that bridges this gap by modeling both analog waveform formation and generation-dependent optical crosstalk with explicit temporal structure. The framework enables systematic separation of different degradation mechanisms affecting timing performance. We investigate the impact of bandwidth limitation, electronic noise, and correlated noise on coincidence time resolution, as well as the information loss transitioning form digital to analog signals.

Our results show a clear degradation of timing resolution when moving from ideal timestamps to realistic analog

readout conditions, in agreement with experimental measurements. Furthermore, we observe that optical crosstalk can, in certain scintillator configurations, improve timing performance by effectively enhancing early signal amplitude, while simultaneously degrading higher-level temporal information relevant for event characterization. The presented framework provides a flexible tool for disentangling these effects and guiding SiPM and readout optimization for future fast-timing detector systems.

References
[1] Kratochwil et al 2026, https://doi.org/10.1109/TRPMS.2026.3665464.
[2] Vinogradov 2012, https://doi.org/10.1016/j.nima.2011.11.086.
[3] Herweg et al 2025, https://doi.org/10.3389/fphy.2025.1603556.
[4] Kratochwil et al 2020, https://doi.org/10.1088/1361-6560/ab87f9.
[5] Gundacker et al 2015, https://doi.org/10.1016/j.nima.2014.10.020.
[6] Gundacker et al 2020, https://doi.org/10.1088/1361-6560/ab63b4.
[7] Kratochwil et al 2025, https://doi.org/10.1016/j.sna.2025.116782.

MIC-10-074

Study on the axial extension of the small-fish PET scanner MERMAID

(#2065)

Magdalena Kolodziej[1], Jorge Roser[1], Steven Seeger[1,2], Hong P. Vo[1], Rebecca Kantorek[1,2], Magdalena Rafecas[1]

[1] University of Luebeck, Institute of Medical Engineering, Luebeck, Germany; [2] University of Luebeck, Isotope Laboratory of the Natural Science Section, Luebeck, Germany

The project is partially supported by the German Research Foundation (DFG) under grant agreement no. 496099829 and the DFG Cluster of Excellence PMI under grant agreement no. 390884018.

Abstract

MERMAID is the first PET scanner prototype dedicated to study small aquatic animals. Particularly, it aims to support the use of adult zebrafish as a model of human diseases. The current prototype, which consists of four detection modules composed of LYSO:Ce crystals, has demonstrated the capability of providing images with submillimeter resolution. An extension of MERMAID by another four modules is planned, aimed to increase the system sensitivity and allow for shorter scan times, making it more suitable for in-vivo imaging. In the presented work, various configurations for the extended MERMAID system are characterized by means of simulations and tailored reconstruction framework; modifications of imaging protocol for the system are investigated.

References
[1] S. Seeger et al., 2023 IEEE NSS MIC RTSD, 2023. doi: 10.1109/NSSMICRTSD49126.2023.10338697.
[2] J. Roser et al., IEEE TRPMS, 2026. doi: 10.1109/TRPMS.2026.3691192.

MIC-10-077

Design and Modeling of BetaBox 2.0: a System for Quantitative Measurement of Beta Emitters in Single Cells (#2271)

Kyle Klein, Juan Alex Leal Doblado, David Prout, Peter Clark, Mike van Dam, Arion Chatziioannou

University of California Los Angeles (UCLA), Pharmacology, Los Angeles, USA

This work is supported in part by the National Institute of Health under Grants R01CA289908, and T32EB002101.

Abstract

Single cell radiation measurements are an integral part of interrogating the biological heterogeneity of cancerous tumors. Identifying cell types present in bulk tumors via FDG uptake can elucidate cell types resistant to treatments, that would potentially be obscured via macroscopic FDG PET imaging. The BetaBox 1.0 was previously constructed to perform these single cell radiation measurements, but suffers from a lack of scale and inability to isolate cells after radiation measurement for further study. To address these challenges, we are constructing the BetaBox 2.0, which will be a high-sensitivity, low-noise device capable of performing many simultaneous single cell radiation measurements via the detection of beta particles in a pixelated array of organic scintillators coupled to SiPMs. The design of BetaBox 2.0 is considered and modeled in GATE simulations, which are used to determine an optimal organic scintillator thickness for the device. These simulations are then expanded on via experimental measurements taken with a SiPM pixel read out by PETsys readout electronics. These datasets jointly suggest the BetaBox 2.0 will be capable of isolating the signal from single cells, and quantitatively assessing their radiation uptake.

MIC-10-080

Hardware Ray-Tracing-Accelerated Optical Photon Transport in TOPAS on Apple Silicon (#2319)

YoungMoon Goh, Keum M. Back, Ui-Seob Lee, Sung-Woo Kim, Si Y. Song

Asan Medical Center, Department of Radiation Oncology, Seoul, South Korea

This work was supported by the National Research Foundation of Korea (NRF), funded by the Ministry of Science and Information and Communication Technology of Korea (grant number 2026OK9045).

Abstract

Optical photon transport in scintillator-based imaging detectors dominates TOPAS Monte Carlo wall time because each primary spawns tens of thousands of secondary photons, and TOPAS itself has no released GPU backend. We present MetalOpticalPhoton, a TOPAS extension that ports the optical physics chain to Apple Metal hardware ray tracing while reusing existing TOPAS material/surface/geometry tables. On an Apple M3 Ultra (80 GPU cores), execution wall time on a 100K-event scintillator-plus-lens benchmark is 25–28× shorter than a 30-thread M3 CPU baseline and about 10× shorter than a 90-thread AMD 7995WX baseline, sustaining roughly 33×10^6 photons/s GPU throughput. Two corrections to vanilla OpenTOPAS—a parallel-world envelope coincident-boundary loop suppressing 75–80% of the sensor-integrated CPU optical fluence, and a primary polarization initialization typo—were required for a self-consistent CPU reference and are relevant to TOPAS optical Monte Carlo independently of GPU acceleration. After patching, CPU–GPU agreement reaches the sub-1% level reported for production GPU optical Monte Carlo (sensor-integrated fluence sum ratio 0.993 ± 0.002 over five seeds).

References
[1] Allison, J et al. 2016, 'Recent developments in Geant4', Nucl. Instrum. Methods Phys. Res. A, vol. 835, pp. 186–225, Amsterdam: Elsevier.
[2] Perl, J, Shin, J, Schümann, J, Faddegon, B, Paganetti, H 2012, 'TOPAS: an innovative proton Monte Carlo platform for research and clinical applications', Med. Phys., vol. 39, no. 11, pp. 6818–6837, Hoboken: Wiley.
[3] Blyth, SC 2019, 'Opticks: GPU optical photon simulation via NVIDIA OptiX', EPJ Web Conf., vol. 214, art. no. 02027, Les Ulis: EDP Sciences.
[4] Apple Inc. 2026, 'Metal Shading Language Specification: Ray Tracing', Cupertino, CA: Apple Inc.

MIC-10-083

Identification of ICS Pixels in a high-resolution 3-Layer DOI-PET Detector Using a CNN (#2619)

Shan Jiang, Giulio Lovatti, Francesco Evangelist, Peter Thirolf, Katia Parodi, Munetaka Nitta

Ludwig-Maximilians-Universität München, München, Germany

Abstract

We have developed a 3-layer staggered LYSO DOI detector for the SIRMIO (Small animal proton irradiator for research in molecular image-guided radiation-oncology) project, with a crystal pitch of 1.0 mm. Due to the small crystal size, inter-crystal scatter (ICS) events degrade spatial resolution, while discarding them causes significant sensitivity loss. In our detector, ICS events account for approximately 50% of all interactions at 511 keV and result in a median lateral positioning error of approximately 2 mm. To solve this problem, we propose a dual-head convolutional neural network (CNN) for separating the 8×8 MPPC total response of two-pixel ICS events into two individual response matrices, from which the pixel positions and energy fractions can be obtained—a precondition for recovering the ICS events. The CNN correctly identifies both scattering pixels in 69.3% of test events, and in 26.4% of cases one pixel is correctly identified. Among the events with one pixel mismatched, the lateral error of the misidentified pixel falls within 1.0 mm in 91.0% of cases. Meanwhile, the median energy fractions prediction error is 0.016 per pixel. The results demonstrate that CNN-based MPPC response decomposition can serve as the enabling foundation for complete ICS recovery in 3-layer staggered DOI detectors, addressing a limitation explicitly acknowledged in recent physics-based ICS studies.

References
[1] F. Evangelista et al., in 2024 IEEE NSS MIC RTSD, 2024.

[2] K. Parodi et al., Acta Oncol., vol. 58, no. 10, p. 1470, 2019.
[3] M. S. Lee et al., Biomedical Engineering Letters, vol. 14, no. 6, 2024.
[4] Q. Liu et al., Physics in Medicine and Biology, 2026.
[5] S. Jiang et al., submitted to IEEE NSS MIC RTSD 2026 (#1668).

MIC-10-086

Impact of PET energy window extent on trues normalization and reconstructions (#2712)

Simon Noë[1], Seyed Amir Zaman Pour[1], Antonia Reeves[2], Ahmadreza Rezaei[1], Johan Nuyts[1], Georg Schramm[1], Kris Thielemans[2]

[1] KU Leuven, Department of Imaging and Pathology, Nuclear Medicine & Molecular imaging, Leuven, Belgium; [2] University College London, Institute of Nuclear Medicine and the Hawkes Institute, London, UK

This work was supported by the i4Health Centre for Doctoral Training, UCL, CCP SyneRBI funded by STFC through the DRI programme.

Abstract

PET systems require (among others) normalization corrections for the geometric sensitivity of the scanner, the result of the spatial arrangement of the detector crystals and energy readout area. It is estimated for a given extent of the photon energy acceptance window, and must be re-estimated if the lower energy threshold (LET) is changed, e.g. when optimizing the number of noise-equivalent counts for a given object, or to improve joint estimation of activity and attenuation. To investigate the effect of changing the LET on the geometric sensitivity, we performed a simulation study in SimSET and compared sensitivity sinograms, reconstructions and properties of accepted photons. We found that the effects are dependent on detector location and photon incidence angle, and likely due to the finite extent of the energy readout area.

References
[1] Theodorakis, L, Loudos, G, Prassopoulos, V, Kappas, C, Tsougos, I, Georgoulias, P 2013, 'A review of PET normalization: Striving for count rate uniformity', *Nucl. Med. Commun.*, vol. 34, no. 11, pp. 1033–1045
[2] Badawi, RD, Marsden, PK, Cronin, F, Sutcliffe, JL 1996, 'Optimization of noise-equivalent count rates in 3D PET', *Phys. Med. Biol.*, vol. 41, pp. 1755–1776
[3] Reeves, A, Arridge, S, Thielemans, K 2025, 'Spatial Optimisation of Lower Energy Discriminator for PET Data Using Noise Equivalent Counts', in *Proc. IEEE NSS/MIC/RTSD*, IEEE, pp. 1–1
[4] Brusaferri, L, Emond, EC, Bousse, A, Twyman, R, Whitehead, AC, Atkinson, D, Ourselin, S, Hutton, BF, Arridge, S, Thielemans, K 2022, 'Detection Efficiency Modeling and Joint Activity and Attenuation Reconstruction in Non-TOF 3-D PET from Multiple-Energy Window Data', *IEEE Trans. Radiat. Plasma Med. Sci.*, vol. 6, no. 1, pp. 87–97
[5] Wagadarikar, AA, Ivan, A, Dolinsky, S, McDaniel, DL 2014, 'Sensitivity improvement of time-of-flight (ToF) PET detector through recovery of Compton scattered annihilation photons', *IEEE Trans. Nucl. Sci.*, vol. 61, no. 1, pp. 121–125

MIC-10-089

MIMOSA: Medical IMaging MOnte Carlo Simulation Algorithms for fast proton therapy range monitoring (#2751)

Declan D. Garvey, Gabriela Llosá, Fernando Hueso-González

IFIC, CSIC-UV, Valencia, Spain

This work has been funded by the Conselleria de Educación, Investigación, Cultura y Deporte (Generalitat Valenciana), Spain, under grant number CDEIGENT/2019/011, by CSIC's JAEPRE23-19 grant, and by the MIDAS project PID2022-143246OB-I00 (MICIU/AEI). IFIC is supported by the Severo Ochoa Center of Excellence grant CEX2023-001292-S funded by MCIU/AEI

Abstract

Monte Carlo simulations play a vital role in many aspects of proton therapy treatment, including proton depth of penetration monitoring. A key limiting factor of full simulation engines is computation time: simulations can take several days, far longer than the time between treatment fractions. This project aims to develop a Monte Carlo simulation software, MIMOSA, for prompt gamma-ray based proton range verification, that is fast enough to be deployed before the next treatment fraction. Clinically acceptable gamma pass rates above 99% for 2%/2 mm and 97% for 1%/1 mm with respect to TOPAS were achieved on both homogenous and heterogenous phantoms. To benchmark computational speed, state-of-the-art GPU codes MOQUI and FRED were tested on the same computer. Comparatively, MIMOSA achieved a notable speed increase, able to simulate 1e9 primary protons with a 200 MeV energy in approximately 3 minutes. Along with maintaining accuracy and increasing computational speed, the project uses the hardware agnostic SYCL standard, and will be available with an open-source license and extensive documentation. Ongoing work is devoted to simulating realistic radiotherapy treatment plans, and including prompt gamma-ray transport and detector response.

References

[1] F. Hueso-Gonzalez and T. Bortfeld, “Compact method for proton range verification based on coaxial prompt gamma-ray monitoring: A theoretical study,” IEEE Transactions on Radiation and Plasma Medical Sciences, vol. 4, no. 2, p. 170–183, Mar. 2020. [Online]. Available: http://dx.doi.org/10.1109/TRPMS.2019.2930362

[2] J. Perl, J. Shin, J. Schumann, B. Faddegon, and H. Paganetti, “TOPAS: An innovative proton Monte Carlo platform for research and clinical applications,” Medical Physics, vol. 39, no. 11, pp. 6818–6837, November 2012

[3] H. Lee, J. Shin, J. M. Verburg et al., “MOQUI: an open-source GPU-based Monte Carlo code for proton dose calculation with efficient data structure,” Physics in Medicine & Biology, vol. 67, no. 17, p. 175001, 2022, published August 30, 2022. [Online]. Available: https://doi.org/10.1088/1361-6560/ac8716

[4] M. D. Simoni, M. Fischetti, E. Gioscio, M. Marafini, R. Mirabelli, V. Patera, A. Sarti, A. Schiavi, A. Sciubba, and G. Traini, “FRED: A fast Monte Carlo code on GPU for quality control in particle therapy,” Journal of Physics: Conference Series, vol. 1548, no. 1, p. 012020, may 2020. [Online]. Available: https://doi.org/10.1088/1742-6596/1548/1/012020

[5] A. Alpay and V. Heuveline, “Adaptivity in AdaptiveCpp: Optimizing performance by leveraging runtime information during JIT-compilation,” in Proceedings of the 13th International Workshop on OpenCL and SYCL, ser. IWOCL ’25. New York, NY, USA: Association for Computing Machinery, 2025. [Online]. Available: https://doi.org/10.1145/3731125.3731127

MIC-10-092

Quantitative Impact of Inter-Crystal Scatter on Image Quality and Sensitivity across LabPET-II Scanner Architectures: A Comparative GATE Simulation Study (#2983)

Alexandre Bernier[1,2], Maxime Gaudreault[5], Jean-François Beaudoin[3], Roger Lecomte[4,5], Jean-Baptiste Michaud[1,2]

[1] University of Sherbrooke, Department of Electrical and Computer Engineering, Sherbrooke, Canada; [2] University of Sherbrooke, Interdisciplinary Institute for Technological Innovation, Sherbrooke, Canada; [3] CRCHUS, Sherbrooke Molecular Imaging Center, Sherbrooke, Sherbrooke, Canada; [4] Imaging Research & Technology, Sherbrooke, Canada; [5] University of Sherbrooke, Department of Medical Imaging and Radiation Sciences, Sherbrooke, Canada

This work was supported in part by the Arbour foundation, the Faculty of Engineering and the Dept of electrical and computer engineering.

MIC-10-095

Effects of Beam Filtration on Time-of-Flight-Based Scatter Rejection in Computed Tomography (#3162)

Jisoo Lee[1,2], Seohan Kim[1,2], Guen Bae Ko[4], Wonmo Sung[1,3]

[1] The Catholic University of Korea, Department of Biomedical Engineering, College of Medicine, Seoul, South Korea; [2] The Graduate School of The Catholic University of Korea, Department of Medical Sciences, Seoul, South Korea; [3] The Catholic Medical Center of The Catholic University of Korea, CMC Institute for Basic Medical Science, Seoul, South Korea; [4] The Korea Advanced Institute of Science and Technology (KAIST), Department of Nuclear and Quantum Engineering, Daejeon, South Korea

This work was supported by KOREA HYDRO & NUCLEAR POWER CO., LTD (No. 2025-Tech-17).
This work was supported by the National Research Foundation of Korea(NRF) grant funded by the Korea government(MSIT)(RS-2026-25471484).
This research was supported by Basic Medical Science Facilitation Program through the Catholic Medical Center of the Catholic University of Korea funded by the Catholic Education Foundation.

Abstract

Computed tomography image quality is degraded by scattered photons, which reduce image contrast and quantitative accuracy. Time-of-flight-based scatter rejection has been proposed as a method to distinguish primary and scattered photons using their arrival-time differences, but the influence of beam filtration under polychromatic x-ray spectrum has not been fully evaluated. This study investigated the effects of tube voltage and beam filtration on time-of-flight-based scatter rejection using Monte Carlo simulation. X-ray spectrum were generated at 40 and 120 kVp, and four filtration conditions were compared: no filter, 1.06mm aluminum, 0.15mm copper, and 0.6mm tin. Polymethyl methacrylate phantoms with thicknesses of 50 and 200 mm were simulated. Scatter rejection performance was evaluated using the scatter rejection rate as a function of timing jitter from 0 to 1000 ps, and the area under the curve was used as a summary metric. At 120 kVp, tin filtration increased the area under the curve by 11.1% in the 200mm phantom and by 30.6% in the 50mm phantom compared with the no-filter condition. In contrast, at 40 kVp, the filtration effect was small, with a maximum area under the curve difference of 0.010 in the 50mm phantom. These results indicate that tin filtration improves timeof-flight scatter rejection at 120 kVp, whereas filter optimization has a limited effect at 40 kVp.

References
[1] G. Lemaire, R. Espagnet, J. Rossignol, L.-D. Gaulin, E. Villemure, A. Corbeil Therrien, Y. Bérubé-Lauzière, M.-A. Tétrault, and R. Fontaine, “Time-of-flight x-ray measurements for computed tomography,” arXiv preprint arXiv:2311.18087, Nov. 2023.
[2] J. Rossignol, R. Martinez Turtos, S. Gundacker, D. Gaudreault, E. Auffray, P. Lecoq, Y. Bérubé-Lauzière, and R. Fontaine, “Time-of-flight computed tomography—proof of principle,” Phys. Med. Biol., vol. 65, no. 8, Art. no. 085013, Apr. 2020, doi: 10.1088/1361-6560/ab78bf.
[3] G. Bélanger, J. Rossignol, Y. Bérubé-Lauzière, and R. Fontaine, “Study of dose reduction in computed tomography using a time-of-flight scatter rejection mechanism in a 3D voxelized phantom,” Phys. Med. Biol., vol. 70, Art. no. 235030, Dec. 2025, doi: 10.1088/1361-6560/ae222f.

MIC-10-098

Hybrid PGI-PET Imaging for Ion-Range Monitoring in Hadron Therapy

(#2044)

Javier Balibrea-Correa[1], Victor Babiano-Suárez[1], Jorge Lerendegui-Marco[1], Pablo Torres-Sánchez[1], Ion Ladarescu[1], César Domingo-Pardo[1], Ariel Tarifeño-Saldivia[1], Max Pallás[2], Benedetta Brusasco[2], Joerg Wulff[3], Christian Bäumer[3], Severine Rossomme[4], Alexis Warnier[4]

[1] Instituto de Física Corpuscular (CSIC-University of Valencia), Física Nuclear Experimental, Valencia, Spain; [2] Universitat Politècnica de Catalunya, Física Nuclear, Barcelona, Spain; [3] West German Proton Therapy Centre, Essen, Germany; [4] Ion Beam Applications, Louvain, Belgium

Abstract

Hadron therapy is a highly conformal cancer treatment technique that enables superior dose delivery to the tumor while sparing surrounding healthy tissues. However, its full clinical benefit is still limited by uncertainties in proton range within tissue, mainly due to the indirect estimation of ion stopping power from X-ray CT images. These uncertainties lead to safety margins that reduce treatment precision. Real-time, high-accuracy ion-range verification is essential to improve dose delivery and further enhance the therapeutic potential of proton therapy. Among the available approaches, PGI and PET are regarded as the most promising, as they provide complementary information. PGI offers direct correlation with the Bragg peak during irradiation, whereas PET yields high-resolution activity distributions from beta+ emitters produced along the proton path.

In this work, we report recent developments and experimental results obtained with a hybrid PGI-PET system for in situ proton range verification. The system is based on four high-efficiency two-plane Compton imagers arranged in a cross configuration, specifically optimized to enhance PGI sensitivity at the expense of a reduced PET field of view. Experimental campaigns were carried out at commercial IBA Proteus Plus and Proteus One proton therapy facilities using 100 and 125 MeV pencil beams delivered at minimum clinical currents. Polyethylene phantoms were irradiated at controlled positions and data were acquired during both in-spill and off-spill periods.
The first reconstructed 2D images demonstrate that PGI can directly identify the Bragg peak position through the maximum of the PGI distribution over a broad field of view, while PET provides a narrower and higher-resolution distribution associated with the induced beta+ activity. These results confirm the feasibility and complementarity of the hybrid PGI-PET approach and support its potential for accurate, clinically relevant proton range verification.

MIC-10-101

Development of a PET/MRI Compatible Fluorescence Microscope for Simultaneous Cell Tracking in a Small Animal PET/MRI Scanner (#2535)

Philipp Renn[1], Jakob Schäfers[1], Noah Jurisa[1], Christian Pilger[2], Thomas Huser[2], Klaus Schäfers[1]

[1] University of Münster, European Institute for Molecular Imaging, 48149, Germany; [2] Bielefeld University, Biomolecular Photonics Research Group, Department of Physics, 33615, Germany

This work was funded by the Deutsche Forschungsgemeinschaft (DFG) – CRC 1450 – 431460824.

Abstract
Cell tracking in vivo is a key challenge in translational medicine. Positron emission tomography (PET) and magnetic resonance imaging (MRI) offer complementary strengths for this task, yet the validation of tracking algorithms against a reliable ground truth remains unresolved. Fluorescence microscopy can fulfill this role, but its integration into the highly constrained PET/MRI environment poses significant technical challenges. Here, we present a fluorescence microscope (FM) designed for simultaneous operation inside a small-animal PET/MRI scanner, with all custom structural and housing components 3D printed in polylactic acid (PLA). The assembled instrument has a total length of 95 cm and fits within the 35 mm PET insert bore, accommodating sample diameters of up to 21 mm. The imaging probe is rotated via a non-ferromagnetic, friction-driven mechanism, enabling multi-angle acquisition without repositioning the sample, and reliable rotation over the full 360° range was demonstrated under manual control. The system follows an epi-fluorescence configuration with 10× magnification, an excitation wavelength of 488 nm, and a 500 nm longpass filter in the detection path. Characterization with a calibration slide and a Convallaria majalis test specimen yielded a pixel pitch of 0.144 µm/pixel (6.96 pixels/µm), a spatial resolution of 2.32 µm (FWHM), a signal-to-noise ratio (SNR) of 7.21, and a field of view (FoV) of 0.55 × 0.31 mm2 (3816 × 2160 pixels), sufficient to resolve individual cells. These results establish the feasibility of integrating fluorescence microscopy into a PET/MRI scanner and provide the basis for future multimodal cell tracking studies with a reliable optical ground truth.

References

[1] Wapler, MC, Testud, F, Hucker, P, Leupold, J, v. Elverfeldt, D, Zaitsev, M & Wallrabe, U 2021, 'MR-compatible optical microscope for in-situ dual-mode MR-optical microscopy', *PLOS ONE*, vol. 16, no. 5, p. e0250903: PLOS.
[2] Cui, M, Zhou, Y, Wei, B, Zhu, X-H, Zhu, W, Sanders, MA, Ugurbil, K & Chen, W 2017, 'A proof-of-concept study for developing integrated two-photon microscopic and magnetic resonance imaging modality at ultra-high field of 16.4 tesla', *Scientific Reports*, vol. 7, no. 1, p. 2733: Nature Publishing Group.
[3] Zhu, X, Li, R, Li, H, Gu, L, Chen, L, Xu, J, Chen, J, Li, Y, Rudin, M, Thompson, G, Zhou, N & Ren, W 2026, 'MR-Scope: a multi-scale and simultaneous MRI-miniaturized microscopy system for elucidating neurovascular coupling': bioRxiv.
[4] Li, C, Yang, Y, Mitchell, GS & Cherry, SR 2011, 'Simultaneous PET and multispectral 3-dimensional fluorescence optical tomography imaging system', *Journal of Nuclear Medicine: Official Publication, Society of Nuclear Medicine*, vol. 52, no. 8, pp. 1268–1275: Society of Nuclear Medicine.

MIC-10-104

Toward Simultaneous PET/SPECT/MR System for Theranostic Imaging

(#2904)

Yifei Jin[1], Junwei Du[2], Simon R. Cherry[2], Ling-Jian Meng[1,3]

[1] University of Illinois at Urbana and Champaign, Department of Nuclear, Plasma, and Radiological Engineering, Urbana, USA; [2] University of California at Davis, Department of Biomedical Engineering, Davis, USA; [3] University of Illinois at Urbana and Champaign, Beckman Institute for Advanced Science and Technology, Urbana, USA; [4] University of Illinois at Urbana and Champaign, Department of Bioengineering, Urbana, USA

This work was supported by the National Institutes of Health under grant numbers R01HL145786 (National Heart, Lung, and Blood Institute) and U01EB031798 (National Institute of Biomedical Imaging and Bioengineering).

Abstract

We report a design study for a combined preclinical scanner that integrates PET, SPECT, and MRI for simultaneous acquisition of PET, SPECT, and MR images for broad-band multi-isotope imaging capability critical for theranostics applications. The PET subsystem provides a very high-sensitivity and benefits from a wide variety of existing tracers. The SPECT subsystem allows for broad-band multi-isotope imaging capability critical for imaging therapeutic radioisotopes and their daughters. MRI offers unmatched soft-tissue contrast and high-resolution anatomical reference. The PET/SPECT insert consists of 12 detector rings. The central four PET rings are integrated with four rings of micro camera elements (MCEs) that are "looking at" the object through the small gaps between the PET detector blocks. This compact design provides approximately 16% PET sensitivity at the center and 1-mm PET imaging resolution across the 8-cm transverse by 28-cm axial FOV. The 64 CZT SPECT cameras provide approximately 1-mm spatial resolution over a 6-cm transverse and 9-cm axial FOV. To support simultaneous PET/SPECT operation, the design incorporates our previously developed anti-coincidence rejection strategy to suppress PET-induced contamination in SPECT data. Prior F-18/Tc-99m PET/SPECT simulations demonstrated up to 83.7% rejection of scatter contamination in projection-domain analysis, supporting the feasibility of acquisition-level cross-modality rejection. These design elements resulted in a compact and high performance tri-modality imaging platform for simultaneous PET/SPECT/MR imaging for preclinical theragnostic applications.

References

[1] M. L. James and S. S. Gambhir, "A molecular imaging primer: modalities, imaging agents, and applications," *Physiol. Rev.*, vol. 92, no. 2, pp. 897–965, Apr. 2012, doi: 10.1152/physrev.00049.2010.
[2] S. R. Cherry, "Multimodality in vivo imaging systems: twice the power or double the trouble?," *Annu. Rev. Biomed. Eng.*, vol. 8, pp. 35–62, 2006, doi: 10.1146/annurev.bioeng.8.061505.095728.
[3] A. Delker *et al.*, "Biodistribution and dosimetry for combined [177Lu]Lu-PSMA-I&T/[225Ac]Ac-PSMA-I&T therapy using multi-isotope quantitative SPECT imaging," *Eur. J. Nucl. Med. Mol. Imaging*, vol. 50, no. 5, pp. 1280–1290, Apr. 2023, doi: 10.1007/s00259-022-06092-1.
[4] M. S. Judenhofer *et al.*, "Simultaneous PET-MRI: a new approach for functional and morphological imaging," *Nat. Med.*, vol. 14, no. 4, pp. 459–465, Apr. 2008, doi: 10.1038/nm1700.
[5] G. Delso *et al.*, "Performance measurements of the Siemens mMR integrated whole-body PET/MR scanner," *J. Nucl. Med. Off. Publ. Soc. Nucl. Med.*, vol. 52, no. 12, pp. 1914–1922, Dec. 2011, doi: 10.2967/jnumed.111.092726.
[6] S. Vandenberghe and P. K. Marsden, "PET-MRI: a review of challenges and solutions in the development of integrated multimodality imaging," *Phys. Med. Biol.*, vol. 60, no. 4, pp. R115-154, Feb. 2015, doi: 10.1088/0031-9155/60/4/R115.
[7] E. M. Zannoni, "Development of the MRC-SPECT-II system: a MR-compatible small-animal SPECT system based on semiconductor imaging spectrometers and a Synthetic Compound-Eye gamma camera design," Thesis, University of Illinois at Urbana-Champaign, 2021. Accessed: May 06, 2026. [Online]. Available: https://hdl.handle.net/2142/113249
[8] Y. Jin, J. Du, S. R. Cherry, and L.-J. Meng, "Exploring Anti-Coincidence Technique for Scattering Contamination Rejection in a Simultaneous PET/SPECT Imaging System," *IEEE Trans. Radiat. Plasma Med. Sci.*, pp. 1–1, 2025, doi: 10.1109/TRPMS.2025.3649623.
[9] L. Cai, X. Lai, Z. Shen, C.-T. Chen, and L.-J. Meng, "MRC-SPECT: A sub-500 μm resolution MR-compatible SPECT system for simultaneous dual-modality study of small animals," *Nucl. Instrum. Methods Phys. Res. Sect. Accel. Spectrometers Detect. Assoc. Equip.*, vol. 734, no. B, pp. 147–151, Jan. 2014, doi: 10.1016/j.nima.2013.08.080.

MIC-10-107

Development of a Preclinical Simultaneous Ultrasensitive SPECT and PET Imager (#3109)

Ruiying Zhu[1], Cai Ling[1], Fardeen Ahmed[3], Abhinav K. Jha[3,1], Joseph A. O'Sullivan[1], Yuan-Chuan Tai[1,2]

[1] Washington University in St. Louis, Imaging Science, saint louis, USA; [2] Washington University in St. Louis, Mallinckrodt Institute of Radiology, saint louis, USA; [3] Washington University in St. Louis, Biomedical Engineering, saint louis, USA

This work was supported in part by the Mallinckrodt Institute of Radiology at Washington University at St. Louis through an internal fund allotment. We also acknowledge the support from NIH (R01-EB031962, R01-CA240711) and NSF CAREER Award (2239707).

Abstract

We previously proposed a Broadband Ultrasensitive Gamma Imager (BUGI) that uses a sensing collimator imager to encode and detect gamma rays without a metal collimator. When combined with fast scintillators, this approach enables simultaneous high-sensitivity SPECT and time-of-flight-capable PET imaging, with potential applications in monitoring alpha-particle radiopharmaceutical therapy (RPT). Unlike conventional simultaneous PET/SPECT systems, which use high-energy collimators that reduce PET sensitivity to SPECT levels, BUGI raises SPECT sensitivity toward that of PET.In this study, we evaluated two preclinical BUGI detector designs using GATE Monte Carlo simulations: a pinhole-inspired geometry and a parallel-hole-inspired geometry. The scanner consists of an octagonal arrangement of 8 detector blocks, each containing 1 × 4 arrays of self-collimating mini-modules built from 3×3×3 mm³ GAGG crystals. A dual-isotope cylindrical phantom was simulated with a ^{99m}Tc background, a ^{99m}Tc spherical tumor, and an ^{18}F spherical tumor, with a tumor-to-background ratio of 4:1. SPECT events and PET

coincidence events were reconstructed independently using a GPU-based MLEM framework.Both detector geometries produced usable simultaneous SPECT and PET images with comparable tumor contrast . The parallel-hole design showed better background uniformity, improved preservation of the cylindrical phantom shape, and sharper tumor edges.The pinhole design showed an octagonal artifact pattern that may be reduced with increased angular sampling. PET images were sharp and visually similar between the two designs. Future work will focus on developing and validating multi-energy-window SPECT and PET reconstruction methods for the BUGI system.

MIC-10-110

A Dual-Ring Super-Resolution PET System (#1259)

Youdong Lang[1,2], Qingguo Xie[1,3], Chien-Min Kao[4]

[1] Huazhong University of Science and Technology, Biomedical Engineering Department, Wuhan, China; [2] Huazhong University of Science and Technology, Institute of Artificial Intelligence, Wuhan, China; [3] University of Science and Technology of China, Department of Electronic Engineering and Information Science, Hefei, China; [4] University of Chicago, Department of Radiology, Chicago, USA

This work was supported in part by the Key Program of National Natural Science of China under Grant 62131009.

Abstract

Building upon previous works that explored the feasibility of super-resolution (SR) positron emission tomography (PET) by applying the principle of structured illumination microscopy (SIM), in this work we propose the concept of a dual-ring SR PET system design. Such a PET system contains a rotatable inner detector ring that serves the dual purpose of creating the needed measurement modulation for performing SIM-based SR as well as increasing event detection to eliminate a major drawback of the previous approach in which the modulator could considerably diminish the imaging sensitivity. We simulated a 2d PET system comprising 576 4.2 mm (transaxial) x 4.2 mm (axial) x 20 mm (radial) LYSO crystals on a 770 mm diameter ring. On the other hand, the inner ring consisted of repeating 2.8 mm-width attenuating material or detector and 5.6 mm-width air. The attenuating material was either 5 mm thick tungsten (W) or 10 mm thick LYSO. The outer detector was 20 mm thick LYSO. Axially, the inner ring was uniform and had the same 4.2 mm length as the outer detector ring. An SR dataset was made of three measurements acquired at three rotational positions of the inner ring. We also considered point-spread function (PSF) reconstruction when not using the inner ring, and also the situation when detector wobble motion was introduced to increase sampling. Our simulation results show that the dual-ring image can resolve 1.2 mm sources in the case of noise-free data and the image quality is visually superior to the PSF and Wobble+PSF images. For a noisy data set, it yields an overall better image quality than the other two SIM-based SR images using W or LYSO modulators for it has higher coincidence detection sensitivity. Quantitative performance evaluation based on the contrast-recovery-coefficient versus the background noise also shows superior results with the dual-ring system.

References
[1] Y. Lang et al., IEEE NSS/MIC, pp. 1-1, 2023.
[2] Y. Lang et al., https://doi.org/10.48550/arXiv:2409.16085.
[3] R. A. Brooks et al., IEEE Transactions on Nuclear Science26:2760–2763, 1979.

MIC-10-113

Performance Evaluation of a DOI-Enabled Dedicated Brain PETCT System (#1479)

Da Liang, Yuejie Lin, Han Liu, Xin Yu, Haoyu Zou, Ying Xu, Huiping Zhao, Jinyong Tao, Wenjing Zhu, Ying Lin, Wangquan Ma, Wenbin Li, Yibin Zhang, Dawei Shi, Jiayang Zeng, Qiushi Ren, Zhaoheng Xie, Wei Liu, Qiyu Peng

Shenzhen Bay Laboratory, Institute of Biomedical Engineering, Shenzhen, China

This work was supported by the National Natural Science Foundation of China (Grant no. 82327809), the National Key Research and Development Program of China (Grant No. 2024YFF0507700), National High-Level Hospital Clinical Research Funding (2025-PUMCH-D-003), Beijing Natural Science Foundation(L252047).

Abstract

Dedicated brain positron emission tomography (PET) systems can achieve higher sensitivity and spatial resolution than whole-body PET scanners due to their compact detector geometry. However, the reduced detector aperture introduces parallax error, making depth-of-interaction (DOI) capability important for maintaining spatial resolution uniformity across the field of view. In this work, we present a comprehensive performance evaluation of a DOI-enabled dedicated brain PET system based on light-sharing window (LSW) detector technology. The system consists of ten detector panels with an axial field of view of 280.6 mm and employs 2.0 × 2.0 × 20.0 mm^3 LYSO crystal arrays with DOI encoding capability.Performance measurements were conducted following the NEMA NU 2-2018 standard, including spatial resolution, sensitivity, count rate performance, scatter fraction, and time-of-flight (TOF) resolution. The measured sensitivity reached 14.31 cps/kBq at the center of the field of view and 15.08 cps/kBq at a radial offset of 10 cm. The peak noise-equivalent count rate (NECR) was 39.54 kcps at 5.11 kBq/mL. The TOF resolution was 298 ps at peak NECR and improved to 281 ps at low activity concentrations. Spatial resolution measurements demonstrated that DOI encoding significantly mitigated parallax error at large radial offsets. Preliminary clinical imaging studies further demonstrated the capability of the proposed system for high-resolution brain PET imaging

MIC-10-116

Design and Preliminary Validation of a Heart-Dedicated TOF-PET Scanner with Sub-250ps Timing Resolution (#1614)

Yuejie Lin, Haoyu Zou, Da Liang, Zhijun Zhao, Han Liu, Xin Yu, Jinyong Tao, Huiping Zhao, Xiaoyin Zhang, Wenjing Zhu, Wenbin Li, Dawei Shi, Yibin Zhang, Qiyu Peng

Shenzhen Bay Laboratory, Institute of Biomedical Engineering, Shenzhen, China

This work was supported by the National Key Research and Development Program of China (Grant No. 2024YFF0507700), the National Natural Science Foundation of China (Grant no. 82327809), National High-Level Hospital Clinical Research Funding (2025-PUMCH-D-003), Beijing Natural Science Foundation(L252047).

Abstract

General-purpose positron emission tomography scanners often face challenges with the high-frequency motion and small target volumes inherent in cardiac imaging. This study introduces a heart-dedicated positron emission tomography prototype featuring twenty detector panels in a cylindrical geometry with a 493.28 millimeter aperture and a 236.4 millimeter axial field of view. The detectors utilize lutetium-yttrium oxyorthosilicate crystals coupled to multi-pixel photon counters with depth-of-interaction capability. Performance was validated through Geant4 Application for Tomographic Emission simulations, detector bench tests, and in vivo experiments. Results demonstrate a coincidence resolving time of 234 picoseconds full width at half maximum and a spatial resolution of 1.0 millimeter under idealized conditions. Furthermore, electrocardiogram-gated imaging in rat and rabbit models successfully captured eight cardiac phases from end-systole to end-diastole, providing distinct myocardial structures without significant motion blur. These results validate the system's high sensitivity and timing precision, establishing a foundation for extracting functional parameters such as ejection fraction. Future work will implement depth-of-interaction correction across the full field of view to maintain high peripheral resolution for precise cardiovascular research and clinical diagnostics.

MIC-10-119

Design and Quantitative Characterization of a High-Performance Brain-Dedicated PET System via Virtual Pinhole PET Technique (#1919)

Yihao Chen[1], Ziquan Yuan[1], Yue Chen[1], Chenxi Li[1], Kexin Wang[1], Yucun Hou[1], Yuan-Chuan Tai[2], Jianyong Jiang[1]

[1] Beijing Normal University, School of Physics and Astronomy, Beijing, China; [2] Washington University in St. Louis, Mallinckrodt Institute of Radiology, St. Louis, USA

This work was supported in part by NSFC (12475336), FRFCU (310400209521) and BNSF (QY25290).

Abstract

Positron emission tomography (PET) is an indispensable tool in neuroscience, yet its efficacy in early lesion detection and advanced brain research is often constrained by the fundamental trade-offs between spatial resolution and sensitivity. To surpass these limitations, this study introduces the NeuroEXPLORER with Insert (NXI), a high-performance dedicated brain PET system that integrates Virtual Pinhole (VP-PET) technology into the NeuroEXPLORER (NX) platform. We developed a comprehensive quantitative reconstruction framework incorporating a full suite of physical correction techniques tailored for the NXI's asymmetric geometry. The system's performance was rigorously validated through Monte Carlo simulations using GATE. Point-source evaluations demonstrated a enhancement in overall sensitivity, driven by an increased proportion of high-resolution insert-scanner (IS) coincidence events in the vicinity of the insert. An ablation study performed on uniform cylinder data, demonstrated the effectiveness of the integrated correction suite, including normalization, attenuation, random, and scatter corrections. In Derenzo phantom experiments, the NXI system successfully resolved 0.6 mm hot rods, a benchmark that remained unresolvable by the standard NX configuration. Furthermore, high-resolution digital brain phantom studies confirmed the system's clinical potential, showing a 5.74% increase in data acquisition volume and a 19.31% improvement in the contrast-to-noise ratio (CNR) of gray and white matter compared to the NX system. By synergizing optimized hardware design with specialized reconstruction algorithms, this work verifies that the NXI architecture substantially elevates both sensitivity and spatial resolution, providing a robust technical pathway for the development of next-generation dedicated brain PET instrumentation.

References

[1] Li, H et al. 2024, 'Performance Characteristics of the NeuroEXPLORER, a Next-Generation Human Brain PET/CT Imager', Journal of Nuclear Medicine, 65(8), 1320-1326, Reston, VA: Society of Nuclear Medicine and Molecular Imaging

[2] Jiang, J et al. 2023, 'A virtual-pinhole PET device for improving contrast recovery and enhancing lesion detectability of a one-meter-long PET scanner: a simulation study', Phys Med Biol, 68(14), Bristol: IOP Publishing

[3] Jan, S et al. 2004, 'GATE: a simulation toolkit for PET and SPECT', Phys Med Biol, 49(19), 4543-4561, Bristol: IOP Publishing

[4] Yuan, Z et al. 2026, 'GPU-based list-mode TOF PET image reconstruction with complete correction techniques', Med Phys, 53, e70216, Hoboken, NJ: John Wiley & Sons

MIC-10-122

Design and Performance Characterization of a Sparsely Populated DOI capable Breast PET/MRI Insert (#2070)

Janina Hohnholz[1], Lukas U. Rauscher[1], Martin Judenhofer[2], Elnaz Olyaei[1,3], Hong P. Vo[4], Magdalena Rafecas[4], Bernd Pichler[1,5], Fabian Schmidt[1,3]

[1] Werner Siemens Imaging Center, Department of Preclinical Imaging and Radiopharmacy, University of Tuebingen, Tuebingen, Germany; [2] Siemens Medical Solutions USA, Inc., Knoxville, USA; [3] University Hospital Tuebingen, Nuclear Medicine and Clinical Molecular Imaging, Tuebingen, Germany; [4] Institute of Medical Engineering, University of Luebeck, Luebeck, Germany; [5] Cluster of Excellence iFIT (EXC2180) "Image Guided and Functionally Instructed Tumor Therapies", Tuebingen, Germany

Funding DFG 508064995

Abstract
To improve diagnostic accuracy in hybrid breast imaging, we develop a dedicated PET/MR breast insert for integration into a clinical whole-body PET/MR system. The final insert consists of two cylindrical detector rings (⌀ = 178 mm, height = 95 mm), each comprising five rings with 32 detector blocks per ring. A sparsely populated (18/32 blocks) single-ring prototype was realized, using dual-layer, depth-of-interaction capable 10×10/9×9 LSO scintillator arrays (1.6×1.6×9.8 / 5.2 mm³) and SiPM readout connected via 30 cm flexible cables to MRI-compatible front-end electronics. Detector calibration and bias voltage optimization demonstrated changes in CRT of up to 100 ps between 42-47V. A bias voltage of 45 V was selected as a stable operating point, maintaining consistent energy resolution and coincidence count rates. Reliable crystal identification was achieved for both layers, with a peak-to-valley ratio of 3.7. At this operation point, the prototype achieved energy resolutions of 13.1 ± 1.8% FWHM (top layer) and 11.8 ± 2.4% (bottom layer). CRT depended on the applied energy window, yielding 383 ± 34 ps FWHM for 430–610 keV and improving to 349 ± 32 ps for a 511±50 keV window, while degrading to 483 ± 175 ps for 250–760 keV. Compared to previous system configurations (>500 ps), the updated readout enabled a substantial improvement in timing performance. These results demonstrate robust energy and timing performance of a sparsely populated, DOI-capable PET/MR insert under realistic integration constraints, including extended signal routing and MRI-compatible system design. The findings support the scalability towards a fully populated double-ring system currently under construction, enabling systematic evaluation of PET/MR performance under stress-test sequences and realistic breast imaging conditions within a clinical PET/MR scanner.

References
[1] *L. U. Rauscher et al., 2025 IEEE NSS MIC RTSD Conference, Nov 2025.*

MIC-10-125

Enabling DOI capability in Low-Cost BGO PET System for Small-Animal Imaging (#2378)

Haoyu Zou[1], Siyuan Han[2], Xin Yu[2], Weidun Wang[1], Liyan Zhao[1], Lei Zhao[1], Da Liang[1], Huiping Zhao[1], Jinyong Tao[1], Han Liu[1], Yibin Zhang[1], Qiyu Peng[1]

[1] Shenzhen Bay Laboratory, Institute of Biomedical Engineering, Shenzhen, China; [2] Huazhong University of Science and Technology, School of Mechanical Science and Engineering, Wuhan, China

This work was supported by the National Natural Science Foundation of China (Grant no. 82327809), the National Key Research and Development Program of China (Grant No. 2024YFF0507700 and 2024YFF0727400), National High-Level Hospital Clinical Research Funding (2025-PUMCH-D-003), Beijing Natural Science Foundation(L252047).

Abstract
This work presents a low-cost small-animal PET system based on BGO crystals with depth-of-interaction (DOI) capability. A 10×8 BGO array (1.5×1.5×20 mm³) is coupled to an MPPC array in a 2×2 configuration, and a 6-mm

light-sharing window (LSW) encodes DOI-dependent light sharing. Using a rapid calibration method (vertical line source + histogram matching), the detector achieves an average DOI resolution of 4.9 mm FWHM and an energy resolution of 17.4% at 511 keV. System-level evaluation shows a spatial resolution of 1.43 mm FWHM at the center and resolves 1.5-mm hot rods. The design eliminates labor-intensive mechanical collimation, offering an affordable, maintainable solution for high-sensitivity preclinical imaging.

References
[1] Gong, K., Cherry, S. R. & Qi, J. On the assessment of spatial resolution of PET systems with iterative image reconstruction. Phys. Med. Biol. 61, N193–N202 (2016)

MIC-10-128

Nested plastic scintillator PET detector geometries have distinct spatial resolution advantages (#2558)

Martin Rädler[1,2], Paweł Moskal[1,2], On behalf of the J-PET collaboration

[1] Jagiellonian University, Centre for Theranostics, Kraków, Poland; [2] Jagiellonian University, Faculty of Physics, Astronomy and Applied Computer Science, Kraków, Poland

National Science Centre of Poland (2021/42/A/ST2/ 00423, 2021/43/B/ST2/02150, 2022/47/I/NZ7/03112), SciMat and qLife under the Excellence Initiative at Jagiellonian University, and PLGrid (ACK Cyfronet AGH, PLG/2024/017688).

Abstract
The J-PET (Jagiellonian Positron Emission Tomography) collaboration is developing a large Field-Of-View (FOV) Total-Body J-PET (TB-J-PET) scanner [1,2,3,4] enabling, among others, low dose imaging, short scan times, and dynamic imaging. The key distinctive feature, i.e., the utilization of cost-effective plastic scintillators, could facilitate a wider adoption of large FOV scanners. In this work, we study the benefit of combining the TB-J-PET with a Brain PET Insert (BI) via Monte Carlo simulations. We show that the proposed detector configuration has unique advantages enhancing the spatial resolution. For this purpose, we first developed a rigorous and accurate scheme to estimate spatial resolution from Maximum Likelihood Expectation Maximization (MLEM) reconstructions. We thereby address known challenges of MLEM-based spatial resolution assessment [5], which is discouraged by NEMA standards that continue to rely on the suboptimal Filtered Back-Projection (FBP). We then investigate the impact of the detector geometry on the resolution. The BI uses narrower scintillators than the TB-J-PET (4 vs. 6 mm). We show that this is a resource-efficient approach to achieve high resolution inside the BI, since the coincidences between TB-J-PET and BI (~50% of sensitivity) have particularly low uncertainty. We also show that this detector configuration is geometrically optimal and suppresses the non-collinearity effect. We back up our findings with theoretical analyses. We also investigate other factors influencing spatial resolution, including event selection, detector scattering, phantom scattering, and positron range. We provide intuitive insights, offering compelling arguments for the experimental realization of the detector geometry under investigation.

References

[1] Moskal, P. et al. 2020, 'Prospects and clinical perspectives of total-body PET imaging using plastic scintillators', *PET clinics*, 15.4, 439-452
[2] Moskal, P. et al. 2020, 'Simulating NEMA characteristics of the modular total-body J-PET scanner - an economic total-body PET from plastic scintillators', *Physics in Medicine & Biology*, 66.17, 175015
[3] Baran, J. et al. 2025, 'Realistic total-body J-PET geometry optimization: Monte Carlo study', *Medical Physics*, 52.4, 2961-2975
[4] Tayefi Ardebili, K et al. 2025, 'Development of a Cost-Effective Total Body J-PET From Plastic Scintillators: Definitive Design', *IEEE NSS MIC RTSD conference*, 1-2
[5] Gong, K. et al. 2016, 'On the assessment of spatial resolution of PET systems with iterative image reconstruction', *Physics in Medicine & Biology*, 61.5, N193–N202

MIC-10-131

Adapt-PET: A Hardware-Algorithm Co-evolution Framework for Versatile, Ultra-High-Resolution Targeted Imaging (#2661)

Runze Liao[1], Ziquan Yuan[1], Kexin Wang[1], Yue Chen[1], Yihao Chen[1], Yuanchuan Tai[2], Jianyong Jiang[1]

[1] Beijing Normal University, School of Physics and Astronomy, Beijing, China; [2] Washington University in St. Louis, Mallinckrodt Institute of Radiology, St. Louis, China

NSFC (No.12475336)

Abstract

PET remains a cornerstone of molecular imaging,yet the trade-off between spatial resolution,sensitivity,and system versatility persists.While integrating high-resolution inserts into existing systems can enhance performance within a targeted field-of-view,conventional designs lack geometric symmetry in insert-scanner(IS)and insert-insert(II)LORs.This asymmetry necessitates exhaustive,configuration-specific normalization data,severely limiting the mobility and clinical adaptability of the insert.To overcome these limitations,we propose the Adapt-PET(Adaptive-geometry PET)design strategy,which utilizes a "Hardware-Algorithm Co-evolution" approach featuring a movable,DOI-capable insert.The insert geometry is derived by proportionally downscaling the base scanner's transaxial dimensions while maintaining axial consistency,followed by systematic crystal subdivision.This configuration enables a unified geometric mapping strategy that projects IS and II LORs onto a standard scanner-scanner(SS)space.By exploiting intrinsic symmetries,our approach achieves geometric compression ratios comparable to baseline systems,effectively decoupling system normalization from hardware geometry and eliminating the need for re-normalization upon insert relocation.The proposed strategy was validated through GATE simulations of two prototypes integrated with a Siemens Biograph Vision scanner.Positioned at an inner radius of 200-mm,each insert comprised 24 modules of 30×40 subdivided crystal arrays(1.047×0.749×15 mm^3)with a 6-bin,2.5-mm DOI resolution.Evaluations using a uniform cylinder show that the system achieves near-quantitative reconstruction accuracy.Derenzo phantom imaging results reveal that the peak-to-valley ratio can be improved by up to 20%,while torso phantom results demonstrate a substantial enhancement in the detectability of 4-mm lesions.This study establishes a practical framework for flexible,organ-targeted PET imaging through hardware-algorithm synergy.

References

[1] Tai, Yuan-Chuan, et al. 2008, 'Virtual-pinhole PET', Journal of Nuclear Medicine, 49.3, 471-479, Reston, VA: Society of Nuclear Medicine and Molecular Imaging
[2] Zhou, Jian, Qi, Jinyi 2009, 'Theoretical analysis and simulation study of a high-resolution zoom-in PET system', Physics in Medicine & Biology, 54.17, 5193-5208, Bristol, UK: IOP Publishing
[3] Yuan, Ziquan, et al. 2026, 'GPU-based list-mode TOF PET image reconstruction with complete correction techniques', Medical Physics, 53.1, e70216, Hoboken, NJ: John Wiley & Sons
[4] Qi, Jinyi, et al. 1998, 'High-resolution 3D Bayesian image reconstruction using the microPET small-animal scanner', Physics in medicine & biology, 43.4, 1001-1013, Bristol, UK: IOP Publishing

MIC-10-134

MIC-10-137

Performance evaluation of the third generation of TOF-DOI Prism-PET detector modules (#3032)

Soroush Shabani Sichani[1,2], Zipai Wang[1], Wanbin Tan[1], David A. Muller[3], Jinyi Qi[4], Gloria C.-Y. Chiang[1], Amir H. Goldan[1]

[1] Weill Cornell Medicine, Radiology, New York, USA; [2] Cornell University, Physics, Ithaca, USA; [3] Cornell University, Applied Physics, Ithaca, USA; [4] University of California, Davis, Biomedical Engineering, Davis, USA

Abstract

Poor spatial resolution and partial volume effect (PVE) limit PET's ability to accurately quantify radiotracer uptake in small brainstem nuclei such as the locus coeruleus, one of the earliest sites to undergo neuropathological changes in the early stages of tau accumulation associated with Alzheimer's disease. Prism-PET is designed to improve spatial resolution and mitigate the PVE by combining ultrahigh-resolution detector modules with high scanner sensitivity in a practical and cost-effective system.

Latest generation of Prism-PET detector module was evaluated using both qualitative and quantitative performance assessments. The module's flood map was examined to assess crystal separation, pattern stability, and the reliability of crystal identification across the detector module. The tested module produced a clear and stable flood map with well-separated crystal patterns, indicating robust event localization. Quantitatively, we measured the detector's energy resolution, depth-of-interaction (DOI) resolution, and coincidence timing resolution. The tested module achieved 10.34% energy resolution, 3.23 mm FWHM DOI resolution, and 337 ps coincidence timing resolution. In the future work, we will report on the performance of the third generation Prism-PET scanner.

References

[1] Tan, W., Wang, Z., Zeng, X., Boccia, A., Wang, X., Li, Y., Li, Y., Fung, E.K., Qi, J., Zeng, T., Gupta, A. and Goldan, A.H. 2025, 'High-resolution motion compensation for brain PET imaging using real-time electromagnetic motion tracking', Medical Physics, vol. 52, no. 1, pp. 201–218, United States: Wiley/AAPM.
[2] Zeng, X., Wang, Z., Tan, W., Petersen, E., Cao, X., LaBella, A., Boccia, A., Franceschi, D., de Leon, M., Chiang, G.C.-Y., Qi, J., Biegon, A., Zhao, W. and Goldan, A.H. 2023, 'A conformal TOF–DOI Prism-PET prototype scanner for high-resolution quantitative neuroimaging', Medical Physics, vol. 50, no. 6, pp. 3401–3417, United States: Wiley/AAPM.
[3] Li, Y., LaBella, A., Zeng, X., Wang, Z., Petersen, E., Cao, X., Zhao, W. and Goldan, A.H. 2023, 'Interleaved signal multiplexing readout in depth encoding Prism-PET detectors', Medical Physics, vol. 50, no. 7, pp. 4234–4243, United States: Wiley/AAPM.
[4] Wang, Z., Cao, X., LaBella, A., Zeng, X., Biegon, A., Franceschi, D., Petersen, E., Clayton, N., Ulaner, G.A., Zhao, W. and Goldan, A.H. 2022, 'High-resolution and high-sensitivity PET for quantitative molecular imaging of the monoaminergic nuclei: A GATE simulation study', Medical Physics, vol. 49, no. 7, pp. 4430–4444, United States: Wiley/AAPM.
[5] Merlin, T., Stute, S., Benoit, D., Bert, J., Carlier, T., Comtat, C., Filipovic, M., Lamare, F. and Visvikis, D. 2018, 'CASToR: A generic data organization and processing code framework for multi-modal and multi-dimensional tomographic reconstruction', Physics in Medicine & Biology, vol. 63, no. 18, Art. no. 185005, Bristol, UK: IOP Publishing.

MIC-10-140

Clinical Validation of MoDeCo: A Motion Detection and Correction Method for a Dedicated Brain PET Scanner (#3187)

Enrique Muñoz[1], David Sánchez[1], Pablo Bascuñana[3], María Nieves Cabrera-Martín[3], Juan Vicente Catret[2]

[1] Oncovision, Image Department, Valencia, Spain; [2] Oncovision, CTO, Valencia, Spain; [3] Hospital Clínico San Carlos, Nuclear Medicine, Madrid, Spain

The authors thank the Nuclear Medicine Department of Hospital Clínico San Carlos (Madrid) for support in patient recruitment, image acquisition, and clinical evaluation.

Abstract

Patient motion during PET acquisition is a well-known source of image degradation. In dedicated brain PET systems such as CareMiBrain (Oncovision), patients occasionally slide downward during acquisition despite head immobilization, compromising diagnostic quality in a clinically relevant subset of studies. We present MoDeCo (Motion Detection and Correction), a modified iterative reconstruction algorithm that detects and compensates for intra-acquisition rigid head motion without requiring external tracking hardware. The listmode data are split into temporal fragments; fast preliminary reconstructions are co-registered to the first fragment to estimate rigid transformations, and a modified MLEM/OSEM algorithm applies them within each subiteration to combine the partial back-projections. Head motion was quantified on 256 [18F]FDG patient studies acquired at Hospital Clínico San Carlos (Madrid), and a qualitative clinical comparison was performed on 15 selected studies. Maximum head displacement during acquisition exceeded 5 mm in 14% of patients. In the high-motion subset (n = 10), MoDeCo was rated significantly superior to standard OSEM in 60% of cases and moderately superior in 20%; mild-motion studies (n = 5) were rated as equivalent. No case showed standard reconstruction outperforming MoDeCo. MoDeCo improves image quality in patients with significant motion while preserving equivalence in those without appreciable motion.

References
[1] P. M. Bloomfield et al., "A motion correction scheme for neurological PET," Phys. Med. Biol., vol. 48, no. 8, pp. 959-978, 2003.
[2] Y. Iwao, H. Tashima, E. Yoshida, F. Nishikido, T. Ida, and T. Yamaya, "Seated versus supine: consideration of the optimum measurement posture for brain-dedicated PET," Phys. Med. Biol., vol. 64, no. 12, p. 125003, Jun. 2019, doi: 10.1088/1361-6560/ab221d.
[3] Oncovision, "CareMiBrain dedicated brain PET scanner," Technical documentation, Valencia, Spain, 2023.
[4] R. R. Fulton et al., "Correction for head movements in PET using an optical motion-tracking system," IEEE Trans. Nucl. Sci., vol. 49, no. 1, pp. 116-123, Feb. 2002.

MIC-10-143

Impact of beam hardening and detector response function corrections when using photon-counting imaging detectors (#1206)

Hiroaki Hayashi[1], Rina Nishigami[2], Daiki Kobayashi[2], Takuya Kasue[2], Natsumi Kimoto[3], Takashi Asahara[4]

[1] Kanazawa University, College of Transdisciplinary Sciences for Innovation, Kanazawa, Japan; [2] Kanazawa University, Graduate School of Medical Sciences, Kanazawa, Japan; [3] Junshin Gakuen University, Department of Radiological Science, Faculty of Health Sciences, Fukuoka, Japan; [4] Okayama University, Faculty of Health Sciences, Okayama, Japan; [5] Kanazawa University, Ishikawa, Japan

The authors declare the following financial interests/personal relationships which may be considered as potential competing interests: This work was supported by JSPS KAKENHI Grant Number [KAKENHI: 24K03306 (Hayashi), 25K21586 (Asahara), 25K21600 (Kimoto), 25KJ1355 (Kobayashi)], and the Sasakawa Scientific Research Grant.

Abstract

Photon-counting detectors (PCDs) can perform quantitative imaging by utilizing the differences in the individual energies of X-ray photons, but this analysis requires various corrections, such as charge sharing, to determine the correct attenuation amount. The purpose of this study is to quantitatively clarify the importance of beam hardening and detector response corrections, which can be applied by software processing, when performing imaging with polychromatic X-rays using a line-sensor-type PCD having an anti-coincidence mode. Our PCD was a CdTe detector manufactured by Varex Imaging (pixel size 0.1 mm, thickness 0.75 mm). The response characteristics were calculated using the Monte Carlo simulation code EGS5, and the charge summing effect related to the "anti-coincidence mode" in the four clustered pixels was reproduced in a simple way. The evaluation method involved examining the reproducibility of quantitative values in the effective atomic number (Z_{eff}) images. Simulations using various virtual phantoms and experiments using a non-destructive testing system with the PCD-type line sensor were conducted. As a result, we demonstrated that by including our proposed correction procedure with the anti-coincidence mode, it is possible to generate highly quantitative Z_{eff} images. In conclusion, this study verified that when using PCDs, it is important to implement software-based beam hardening and detector response function corrections in addition to using the anti-coincidence modes.

References
[1] Hou B., Chen Q., Yi L., Sellin P., Sun H.T., Wong L. J., Liu X., 2024, 'Materials innovation and electrical engineering in X-ray detection', *Nature Reviews Electrical Engineering* 1, 639-655.

[2] Kimoto N., Hayashi H., Asakawa T., Lee C., Asahara T., Maeda T., Goto S., Kanazawa Y., Katsumata A., Yamamoto S., Okada M., 2021, 'Effective atomic number image determination with an energy-resolving photon-counting detector using polychromatic X-ray attenuation by correcting for the beam hardening effect and detector response', *Applied Radiation and Isotopes* 170, 109617.
[3] Kimoto N., Hayashi H., Lee C., Maeda T., Ando M., Kanazawa Y., Katsumata A., Yamamoto S., Okada M., 2021, 'A novel algorithm for extracting soft-tissue and bone images measured using a photon-counting type X-ray imaging detector with the help of effective atomic number analysis', *Applied Radiation and Isotopes* 176, 109822.
[4] Asahara T., Okada S., Hayashi H., Maeda T., Nishigami R., Kobayashi D., Kurose C., Kimoto N., Goto S., Hisatomi M., Yanagi Y., Iguchi T., 2025, 'Helpfulness of effective atomic number image in forensic dental identification: photon-counting computed tomography is suitable', *Computers in Biology and Medicine* 184, 109333.
[5] Asahara T., Mitani M., Kimoto N., Nishigami R., Takegami K., Morimitsu Y., Akagi N., Miyoshi T., Kanazawa Y., Iguchi T., Hayashi H., 2025, 'Applicability of effective atomic number (Z_{eff}) image analysis of coronary plaques measured with photon counting computed tomography', *Investigative Radiology*, in press.
[6] Nishigami R., Kobayashi D., Kimoto N., Asahara T., Maeda T., Haba T., Kanazawa Y., Yamamoto S., Hayashi H., 2025, 'Optimization of energy windows to calculate quantitative X-ray images using an energy-resolving photon-counting detector: A simulation study', *Radiation Physics and Chemistry* 229, 112460.
[7] Nishigami R., Kimoto N., Asahara T., Maeda T., Kobayashi D., Goto S., Haba T., Kanazawa Y., Yamamoto S., Hayashi H., 2026, 'Bone-enhanced high contrast X-ray images derived from attenuation estimation related to ultra-low energy X-rays – An application of an energy-resolving photon-counting detector (ERPCD) –', *Radiation Physics and Chemistry* 238, 113243.
[8] Kimoto N., Nishigami R., Asahara T., Kanazawa Y., Katsumata A., Yamamoto S., Hayashi H., 2026, 'Counting loss correction algorithm for an energy-resolving photon-counting detector for X-ray imaging of biological objects with effective atomic numbers between 3 and 20', *Radiation Physics and Chemistry* 243, 113723.

MIC-10-146

Evaluation of Lead-Free Composite for X-ray Shielding using LD-V1 Film (#1319)

Dung T. Tran[1,2], Minho Kim[1], Seungwoo Park[1,2]

[1] Korea Institute of Radiological and Medical Sciences, Seoul, South Korea; [2] University of Science and Technology, Radiological and Medico-Oncological Sciences, Seoul, South Korea

This work was supported by the Commercialization Promotion Agency for R&D Outcomes(COMPA) grant funded by the Korea government(Ministry of Science and ICT) (RS-2025-02309416).

Abstract

This study evaluated a lead-free $BaSO_4$–silicone composite for diagnostic X-ray shielding (60–100 kVp) using LD-V1 film, combining MCNP6 simulation with experimental validation. Evaluation of a 2 mm thick composite demonstrated shielding efficiencies ranging from 68.79% to 83.50%. Simulated results showed good agreement with experimental measurements, with a maximum deviation of 10.28%. Furthermore, the two-dimensional dose distribution map revealed an average radiation reduction of approximately 60.34% across the material. This result confirms effective attenuation of X-ray radiation across the irradiated field. The dose reduction was also spatially uniform over the entire protected area. In addition, the consistent dose reduction pattern indicates a homogeneous dispersion of $BaSO_4$ particles within the silicone matrix. These findings establish the $BaSO_4$–Si composite as an effective lead-free alternative and demonstrate the utility of LD-V1 film for both quantitative dosimetry and spatial validation in clinical X-ray systems.

MIC-10-149

Evaluation of image resolution for Novel Dual-energy X-ray Absorptiometry System (#1441)

Hyuntae Leem, Youngbok Ahn, Sunghyun Min, Myungwoo Oh, Chanwoo Kwon

Osteosys Corp., RnD center, Seoul, South Korea

This research was financially supported by the Ministry of Trade, Industry and Resources (**MOTIR**), Korea, under the “Global Industrial Technology Cooperation Center(GITCC) program” supervised by the Korea Institute for Advancement of Technology (**KIAT**).(Task No. P0030253)

Abstract

DXA has evolved beyond standard BMD measurement to include sarcopenia diagnosis and bone quality assessment via the TBS. As TBS is now a recognized modifier in the WHO FRAX Tool , image resolution has become the paramount technical factor determining the performance of DXA systems. This study evaluates the image resolution of iNSiGHT C510 (Osteosys, Korea), the novel DXA model designed for high-resolution whole-body imaging within 3 minutes.

The image resolution of iNSiGHT C510 was quantitatively assessed using a line phantom. The system achieved a vertical resolution of 0.63 lp/mm and a horizontal resolution of 0.9 lp/mm, demonstrating superior resolution capabilities compared to the industry-leading GE Prodigy. Anatomical discriminability was further verified using the spine phantom with increasing BMD levels. Analysis of peak-to-valley ratios, which represent the contrast clarity between bone and intervertebral discs, confirmed that iNSiGHT C510 maintains excellent discriminability despite its longitudinal scan architecture. These quantitative results suggest that the system minimizes ROI setting errors, ensuring high clinical reproducibility for TBS calculations that are highly sensitive to subtle signal variations.This study confirms that iNSiGHT C510 provides image resolution equivalent to global standards. Hardware architecture establishes a technical foundation for reducing identification errors in spinal measurements and improving ROI precision. Consequently, iNSiGHT C510 satisfies the performance requirements demanded by the high-precision sarcopenia diagnostic market. Future work will involve integrating ToF technology to suppress scatter noise inherent in wide fan-beam architectures.

References

[1] Osterhoff, G, McCloskey, EV 2016, 'Bone mechanical properties and changes with osteoporosis', *Injury*, vol. 47, Suppl. 2, pp. S11–S20.

[2] McCloskey, EV et al. 2016, 'A meta-analysis of trabecular bone score in fracture risk prediction and its relationship to FRAX', *Journal of Bone and Mineral Research*, vol. 31, no. 5, pp. 940–948.

[3] Martineau, P, Leslie, WD 2015, 'Spine trabecular bone score precision, a comparison between GE Lunar standard and high-resolution densitometers', *Journal of Clinical Densitometry*, vol. 18, no. 1, pp. 92–97.

[4] Binkley, N et al. 2015, 'Dual-energy X-ray absorptiometry image resolution and TBS precision', *Journal of Clinical Densitometry*, vol. 18, no. 4, pp. 434–435.

[5] Ha, YC, Kim, S, Yoo, JI 2025, 'Correlation of Lean Mass Measurements Between a Novel Whole-body X-ray Bone Densitometer (iNSiGHT C510) and Magnetic Resonance Imaging: A Single-center Comparative study', *Journal of Clinical Densitometry*, vol. 28, p. 101585.

[6] Takata, W et al. 2016, 'Simulated increased soft tissue thickness artefactually decreases trabecular bone score: a phantom study', *BMC Musculoskeletal Disorders*, vol. 17, no. 1, p. 13.

[7] Boudousq, V et al. 2005, 'Image resolution and magnification using a cone beam densitometer: optimizing data acquisition for hip morphometric analysis', *Osteoporosis International*, vol. 16, pp. 813–822.

[8] Hind, K, Cooper, W, Oldroyd, B, Davies, A, Rhodes, L 2015, 'A cross-calibration study of the GE-Lunar iDXA and Prodigy for the assessment of lumbar spine and total hip bone parameters via three statistical methods', *Journal of Clinical Densitometry*, vol. 18, no. 1, pp. 86–92.
[9] Rossignol, J, Martinez Turtos, R, Gundacker, S, Gaudreault, D, Auffray, E, Lecoq, P, Bérubé-Lauzière, Y, Fontaine, R 2020, 'Time-of-flight computed tomography - proof of principle', *Physics in Medicine and Biology*, vol. 65, no. 8, p. 085013.

MIC-10-152

Physics-Guided Retinexformer for Beam Hardening Artifact Correction in Rock CBCT (#1537)

Yuanjue Ma, Liang Li

Tsinghua University, Department of Engineering Physics, Beijing, China

The authors would like to acknowledge Yuanhao Cai and the co-authors of Retinexformer for making their source code publicly available, which significantly facilitated the implementation and development of our proposed architecture.

Abstract

Beam hardening in cone-beam computed tomography (CBCT) of high-density rock causes cupping artifacts and nonlinear CT value deviations, hindering quantitative mineral analysis. Conventional deep learning methods often over-smooth microstructures due to a lack of physical constraints. We propose a physics-informed Retinexformer framework that reformulates the polychromatic X-ray degradation as a multiplicative Retinex model. Under this paradigm, the non-uniform hardening field is treated as a degraded illumination map, while the pristine rock structure represents the ideal reflectance. A pre-trained Denoising Diffusion Implicit Model (DDIM), combined with mask-guided moment matching, is utilized to explicitly generate a statistically aligned physical hardening field prior. Furthermore, a multi-scale feature encoder extracts high-frequency structural details from the residuals between the input and the prior to guide the denoising process. Experiments on a 10-cm diameter underground rock dataset show that our method significantly corrects CT value deviations while preserving the fine structure. Quantitatively, it achieves a PSNR of 37.13 dB and an SSIM of 0.940, reducing RMSE to 0.0149—significantly outperforming SOTA baselines (NAFNet, Retinexformer, MambaIRv2). Notably, our model achieves this with only 2.00M parameters and 19.42G FLOPs, offering a highly efficient and interpretable solution for CT artifacts correction in dense media.

References
[1] L. Chen et al., “Simple baselines for image restoration,” European Conference on Computer Vision (ECCV), Springer, pp. 17-33, 2022, doi: https://doi.org/10.1007/978-3-031-20071-7_2.
[2] H. Guo et al., “Mambairv2: Attentive state space restoration,” Proceedings of the Computer Vision and Pattern Recognition Conference, 2025.
[3] Y. Cai et al., “Retinexformer: One-stage Retinex-based Transformer for Low-light Image Enhancement,” Proceedings of the IEEE/CVF International Conference on Computer Vision (ICCV), pp. 12504-12513, 2023.
[4] J. Song, C. Meng, and S. Ermon, “Denoising diffusion implicit models,” in International Conference on Learning Representations (ICLR), 2021, doi: https://doi.org/10.48550/arXiv.2010.02502.

MIC-10-155

MIC-10-158

Mitigating Scatter-Induced BMD Errors in Wide Fan-Beam DXA Using Anti-Scatter Grids (#2260)

Myungwoo Oh, Youngbok Ahn, Sunghyun Min, Hyuntae Leem, Chanwoo Kwon

Osteosys Corp., R&D Center, seoul, South Korea

This research was financially supported by the Ministry of Trade, Industry and Resource (MOTIR), Korea, under the “Global Industrial Technology Cooperation Center (GITCC) program” supervised by the Korea Institute for Advancement of Technology (KIAT) (Task No. P0030253).

Abstract

Dual-energy X-ray absorptiometry (DXA) is the clinical standard for bone mineral density (BMD) assessment. Modern wide fan-beam DXA architectures (fan angle ≥ 20°) shorten whole-body acquisition to under three minutes but enlarge the irradiated volume, raising the scatter-to-primary ratio with field size. Conventional DXA omits anti-scatter grids, relying on the long object-to-image-detector distance (OID > 580 mm) for scatter rejection via the air-gap effect. Whether this assumption holds for wide fan-beam DXA has not been directly tested. We investigated residual scatter in an experimental wide fan-beam DXA system using three complementary experiments on step-wedge and anthropomorphic phantoms. First, we implemented an outer-channel scatter probe and detected measurable scatter at outer channels even at OID > 580 mm. Second, with an 8:1 anti-scatter grid we quantified the dual-energy mass attenuation difference Δ(μ/ρ); at the maximum phantom configuration (25 cm polycarbonate + 4.9 cm aluminum), scatter caused an inversion of Δ(μ/ρ) in the no-grid configuration (−0.018 cm²/g); the 8:1 grid restored Δ(μ/ρ) to 0.076 cm²/g — a partial recovery only. Third, a 14:1 grid successfully suppressed the spurious BMD elevation. Compared to the no-grid baseline which showed a severe thickness-dependent BMD bias (coefficient of variation of approximately 19%), the 14:1 grid reduced the variability to 3% across 0–140 mm of added polycarbonate layers. These findings establish that explicit scatter compensation — whether through anti-scatter grids or software-based correction — is essential for thick-patient measurements at wide fan-beam DXA.

References
[1] Blake, GM, Fogelman, I 2007, ‘Role of dual-energy X-ray absorptiometry in the diagnosis and treatment of osteoporosis’, J. Clin. Densitom., vol. 10, no. 1, pp. 102–110.

[2] Messina, C et al. 2020, 'Body composition with dual-energy X-ray absorptiometry: from basics to new tools', Quant. Imag. Med. Surg., vol. 10, no. 8, pp. 1687–1698
[3] Blake, GM, Fogelman, I 2010, 'An update on dual-energy X-ray absorptiometry', Semin. Nucl. Med., vol. 40, no. 1, pp. 62–73.
[4] Sorenson, JA, Floch, J 1985, 'Scatter rejection by air gaps: an empirical model', Med. Phys., vol. 12, no. 3, pp. 308–316.
[5] Persliden, J, Carlsson, GA 1997, 'Scatter rejection by air gaps in diagnostic radiology: calculations using a Monte Carlo collision density method', Phys. Med. Biol., vol. 42, no. 1, pp. 155–175.
[6] Neitzel, U 1992, 'Grids or air gaps for scatter reduction in digital radiography: a model calculation', Med. Phys., vol. 19, no. 2, pp. 475–481.
[7] Libouban, H et al. 2002, 'Comparison of pencil-, fan-, and cone-beam dual X-ray absorptiometers for evaluation of bone mineral content in excised rat bone', J. Clin. Densitom., vol. 5, no. 4, pp. 355–361.
[8] Boone, JM, Cooper III, VN 2000, 'Scatter/primary in mammography: Monte Carlo validation', Med. Phys., vol. 27, no. 8, pp. 1818–1831.
[9] Njeh, CF et al. 1999, 'Radiation exposure in bone mineral density assessment', Appl. Radiat. Isot., vol. 50, no. 1, pp. 215–236.

MIC-10-161

Empirical Decomposition for Quantification of Multi-Contrast-Agent

(#2472)

Pengfei Chen[1,2], Zhe Wang[1], Chengmin Wang[1,2], Tong Jia[1], Shili Xie[1,2], Cunfeng Wei[1]

[1] Institute of High Energy Physics, Beijing Engineering Research Center of Radiographic Techniques and Equipment, Beijing, China; [2] University of Chinese Academy of Sciences, School of Nuclear Science and Technology, Beijing, China

Abstract

Contrast agents play an important role in spectral CT because they enhance the visibility of vessels, organs, tumors, and lesions, thereby improving image interpretation and lesion identification. However, accurately quantitative contrast-agent decomposition remains challenging. Conventional material decomposition algorithms still suffer from limited quantitative accuracy even in contrast-agent imaging. This problem becomes more severe when multiple contrast agents coexist. To address this limitation, we propose an empirical multi-agent decomposition method. The proposed method first applies conventional empirical decomposition to obtain initial decomposition results and estimate the corresponding decomposition errors. Then, bivariate error surfaces are constructed to model the relationship between iodine and gadolinium concentrations and their decomposition errors. These fitted error surfaces are subsequently used to compensate for the errors produced by conventional empirical decomposition. Simulated experiments demonstrate that the proposed method can simultaneously decompose iodine and gadolinium with improved quantitative accuracy, and the global MAPE and NRMSE are effectively reduced compared with the image-domain decomposition method for the test phantoms.

References
[1] S. Hamid, M. U. Nasir, A. So, G. Andrews, S. Nicolaou, and S. R. Qamar,"Clinical applications of dual-energy ct," *Korean Journal of Radiology*, vol. 22, no. 6, pp. 970–982, jun 2021 .
[2] C. Wang, Z. Wang, M. Li, Y. Liu, X. Zhang, C. Wei, and L. Wei,"Empirical correction decomposition method (ECDM): enhancing accuracy of quantitative measurement in spectral CT," *Physics in Medicine & Biology*, vol. 70, no. 1, p. 015021, Jan. 2025.
[3] M. Weiss and T. Meisen,"Reviewing material-sensitive computed tomography: From handcrafted algorithms to modern deep learning," *NDT*, vol. 2, no. 3, pp. 286–310, jul 2024 .

MIC-10-164

Empirical Correction of Detector Response for Quantitative X-Ray Transmission Modelling and its Application to Computed Tomography

(#2574)

Qingxiang Chen, Ben James, Yi Liu

The Commonwealth Scientific and Industrial Research Organisation, Mineral Resources, Lucas Heights, Australia

Abstract

X-ray computed tomography (CT) relies fundamentally on accurate transmission measurements to reconstruct meaningful attenuation maps. However, detector response non-linearity systematically biases transmission measurements away from the values predicted by the polychromatic forward model, propagating these errors into reconstructed data. To address this, a combined spectral modelling and empirical calibration framework was developed for a high-resolution flat-panel detector, enabling prediction of measured transmission values across a broad range of sample thicknesses and compositions. A polychromatic spectral model was constructed by combining tube-spectrum estimates with Beer–Lambert attenuation using NIST/XCOM coefficients, convolved with an effective CsI scintillator response function. Predicted transmission values were compared against experimental measurements obtained using high purity elemental foils spanning a wide range of thicknesses. Consistent and reproducible discrepancies between modelled and measured values revealed a structured detector response non-linearity not captured by the forward model. A first-order empirical correction was derived from the model–experiment residuals, yielding a fitted detector-response exponent of $\alpha = 1.47$ applied to model predictions to reproduce experimental detector behaviour. The calibrated model can therefore generate realistic transmission values consistent with measured detector output across a range of sample configurations. These findings highlight the broader potential of this framework, particularly for dual-energy CT, where material decomposition relies critically on the relative contrast between acquisitions at different tube voltages. A calibrated forward model of this kind offers a pathway toward improved relative CT threshold accuracy, supporting more reliable separation of materials with overlapping attenuation properties and more robust quantitative interpretation of reconstructed data.

References

[1] Mesina, M. B., de Jong, T. P. R. and Dalmijn, W. L. 2007, “Automatic sorting of scrap metals with a combined electromagnetic and dual energy X-ray transmission sensor,” International Journal of Mineral Processing, vol. 82, no. 4, pp. 222–232.

[2] Zhang, Y., Yoon, N. and Holuszko, M. E. 2021, “Assessment of sortability using a dual-energy X-ray transmission system for studied sulphide ore,” Minerals, vol. 11, no. 5, Art. no. 490.

[3] Moshkbar-Bakhshayesh, K., Afarideh, H. and Azimirad, R. 2023, “Inspection of cargo using dual-energy X-ray radiography: A review,” Radiation Physics and Chemistry, vol. 212, Art. no. 111180.

[4] Taguchi, K. and Iwanczyk, J. S. 2013, “Vision 20/20: Single photon counting X-ray detectors in medical imaging,” Medical Physics, vol. 40, no. 10, Art. no. 100901.

[5] Huang, S.-Y., Yang, K., Abbey, C. K. and Boone, J. M. 2012, “A semiempirical linear model of indirect, flat-panel X-ray detectors,” Medical Physics, vol. 39, no. 4, pp. 2108–2118.

[6] Berger, M. J., Hubbell, J. H., Seltzer, S. M., Chang, J., Coursey, J. S., Sukumar, R., Zucker, D. S. and Olsen, K. 2010, “XCOM: Photon Cross Sections Database,” NIST Standard Reference Database 8 (XGAM), National Institute of Standards and Technology.

MIC-10-167

Synthetic generation of the dental anatomy for cone-beam CT simulation from patient data (#2593)

Idris Tatachak[1,3], Luis Kabongo[3], Nicolas Papadakis[2], Xavier Ripoche[3], Simon Rit[1]

[1] Creatis, INSA-Lyon, Universite Claude Bernard Lyon 1, CNRS, Inserm, CREATIS UMR 5220, U1294, F-69373, Lyon, France; [2] Univ. Bordeaux, CNRS, Inria, Bordeaux INP, IMB, UMR 5251, Bordeaux, France; [3] ACTEON Group, Mérignac, France

This work was supported by the French National Association for Technical Research (ANRT) and the France 2030 BPI project Cone Beam AI and was performed within the framework of the SIRIC LYriCAN+ (INCa-DGOS-INSERM-ITMO cancer 18003) and the LABEX PRIMES (ANR-11-LABX-0063) of Université de Lyon, within the program 'Investissements d'Avenir' (ANR- 11-IDEX-0007) operated by the ANR.

Abstract

This paper develops a pipeline for generating synthetic cone-beam computed tomography (CBCT) projections from real dental CBCT acquisitions, providing a reference for supervised learning. To this end, we segment and synthesize fine structures from real CBCT acquisitions to obtain a material map of the head volume. Using the characteristics of the CBCT scanner, notably the effective spectrum, we simulate the acquisitions by modeling a polychromatic X-ray source and adding compound Poisson noise. The results demonstrate the realism of the generated synthetic CBCT acquisitions, as well as the plausibility of the simulated artifacts.

References

[1] W. P. Segars, G. Sturgeon, S. Mendonca, J. Grimes, and B. M. W. Tsui, "4D XCAT phantom for multimodality imaging research," Medical Physics, vol. 37, no. 9, pp. 4902–4915, 2010.

[2] M. ZANKL, "Adult male and female reference computational phantoms (icrp publication 110)," Japanese Journal of Health Physics, vol. 45, no. 4, pp. 357–369, 2010.

[3] K. Merken, J. Monnens, N. Marshall, N. Johan, D. M. Brasil, G. M. Santaella, C. Politis, R. Jacobs, and H. Bosmans, "Development and validation of a 3d anthropomorphic phantom for dental cbct imaging research," Medical Physics, vol. 50, no. 11, pp. 6714–6736, 2023.

[4] A. Takeya, K. Watanabe, and A. Haga, "Fine structural human phantom in dentistry and instance tooth segmentation," Sci Rep, vol. 14, no. 1, p. 12630, 2024.

[5] N. van Nistelrooij, L. Kr¨amer, S. Kempers, M. Beyer, F. Bolelli, T. Xi, S. Berg´e, M. Heiland, K. H. Maier-Hein, S. Vinayahalingam, and F. Isensee, "Toothseg: Robust tooth instance segmentation and numbering in cbct using deep learning and self-correction," IEEE Journal of Biomedical and Health Informatics, 2025.

[6] F. Isensee, P. F. Jaeger, S. A. A. Kohl, J. Petersen, and K. H. Maier-Hein, "nnU-Net: a self-configuring method for deep learning-based biomedical image segmentation," Nature Methods, vol. 18, no. 2, pp. 203–211, 2021.

[7] L. A. Feldkamp, L. C. Davis, and J. W. Kress, "Practical cone-beam algorithm," J. Opt. Soc. Am. A, vol. 1, no. 6, pp. 612–619, 1984.

[8] S. Rit, S. Brousmiche, J. Finet, G. C. Sharp, and P. Steininger, "Reconstruction Toolkit (RTK) v2, an Insight Toolkit (ITK) module for tomographic reconstruction," in International Conference on the use of Computers in Radiation therapy (ICCR), Lyon, France, 2024.

[9] M. Genisa, S. Shuib, Z. Rajion, E. Arief, and M. Hermana, "Density estimation based on the hounsfield unit value of cone beam computed tomography imaging of the jawbone system," proceedings of the Institution of Mechanical Engineers. Part H, Journal of engineering in medicine, vol. 232, p. 954411918806333, 10 2018.

MIC-10-170

Image Quality Evaluation of Cone Beam Computed Tomography (CBCT) in an O-arm Fluoroscopy Machine Using the SedentexCT IQ Phantom (#2974)

John Patrick Ryan S. De Guzman[1,2], Agnette Peralta[2]

[1] Philippine General Hospital, Department of Radiology, Manila, Philippines; [2] University of Santo Tomas, The Graduate School, Manila, Philippines

The accomplishment of this research was attained because of the wonderful people who have contributed, showed support, and served as inspiration to this research and the researcher. I would like to express my sincere gratitude to my advisers, Ms. Agnette P. Peralta and Ms. Melanie Marquez. Ma'am Agnette's admirable dedication to medical physics was an inspiration to contribute and make advancements in knowledge for the medical physics community in the Philippines. I am thankful for the endless support of Ma'am Melanie; she gave me the opportunity to progress with this research. Her uplifting and joyful personality always gave me hope and perseverance in finishing this research.

Abstract

The O-arm fluoroscopy machine, an application of cone beam computed tomography (CBCT) for interventional procedures, lacks a dedicated image quality (IQ) phantom for system image performance evaluation. This study aimed to investigate the viability and limitations of using the SedentexCT IQ phantom, a phantom originally designed for dental CBCT, to assess the image quality of resultant CBCT images of an interventional O-arm unit. Six CBCT image quality tests were performed (i.e. Uniformity, Image Noise, Geometric Accuracy, Voxel Intensity Values, Contrast Resolution, and Spatial Resolution), and corresponding parameters were assessed as baseline data in the low dose, standard dose, high dose, and enhanced cranial modes of the O-arm machine. The procedures were structured to the EFOMP-ESTRO-IAEA CBCT quality control protocol. An observed limitation of the phantom was the evaluation of the spatial resolution (lp/mm), since the lowest resolution of the SedentexCT IQ phantom is 1.0 lp/mm. Overall, since the phantom was applicable for the required CBCT image quality tests, the SedentexCT IQ phantom can be considered as a viable tool for image quality testing of the O-arm machine.

MIC-10-173

Validation of conventional mammography material decomposition using VICTRE simulated breast data (#3018)

John Paul Phillips, Emil Sidky, Ingrid Reiser, Zheng Zhang, Kirti Kulkarni, Xiaochuan Pan

The University of Chicago, Department of Radiology, Chicago, USA

This research was supported in part by the National Institut of Biomedical Imaging and Bioengineering of the National Institutes of Health under award numbers R01CA287302.

Abstract

The purpose of this work is to validate basis material decomposition in breast cancer screening mammography using a conventional single-kV scan. We employ mammography system physics modeling and a pathlength constraint to enable estimation of the basis material images. Using 3D breast phantoms and low noise Monte Carlo projection data generated with the FDA VICTRE software, we decompose transmission data into pathlength basis images of adipose and glandular tissue. The decomposition recovered adipose and glandular maps with mean absolute errors of 3.47 mm and 1.83 mm respectively. Accuracy along the skinline and nipple is degraded due to material mismatch. The results indicate material decomposition in mammography using a single energy acquisition is feasible to enable the quantitative recovery of adipose and glandular material maps.

References

[1] D'Orsi, CJ 1991, 'Early detection of breast cancer: mammography', Breast Cancer Research and Treatment, vol. 18, suppl. 1, pp. S107--S109, Dordrecht: Springer.

[2] Duncan, KA, Needham, G, Gilbert, FJ, Deans, HE 1998, 'Incident round cancers: what lessons can we learn?', Clinical Radiology, vol. 53, no. 1, pp. 29--32, Amsterdam: Elsevier.

[3] Smith, BJ, Dey, J, Medlock, L, Solis, D, Kirby, K 2025, 'Maximum-likelihood estimation of glandular fraction for mammography and its effect on microcalcification detection', Physical and Engineering Sciences in Medicine, vol. 48, no. 2, pp. 743--758, Cham: Springer Nature.

[4] Nissan, N, Comstock, CE, Sevilimedu, V, Gluskin, J, Mango, VL, Hughes, M, Ochoa-Albiztegui, RE, Sung, JS, Jochelson, MS 2024, 'Diagnostic accuracy of screening contrast-enhanced mammography for women with extremely dense breasts at increased risk of breast cancer', Radiology, vol. 313, no. 1, p. e232580, Oak Brook, IL: Radiological Society of North America.

[5] Leong, LT, Malkov, S, Drukker, K, Niell, BL, Sadowski, P, Wolfgruber, T, Greenwood, HI, Joe, BN, Kerlikowske, K, Giger, ML, Shepherd, JA 2021, 'Dual-energy three-compartment breast imaging for compositional biomarkers to improve detection of malignant lesions', Communications Medicine, vol. 1, no. 1, p. 29, London: Nature Publishing Group.

[6] Kis, BJ, Sarnyai, Z, K\'akonyi, R, Erd\'elyi, M, Szab\'o, G 2012, 'Single-energy material decomposition using x-ray path length estimation', Journal of Computer Assisted Tomography, vol. 36, no. 6, pp. 768--777, Philadelphia, PA: Lippincott Williams \& Wilkins.

[7] Poludniowski, G, Omar, A, Bujila, R, Andreo, P 2021, 'Technical Note: SpekPy v2.0---a software toolkit for modeling x-ray tube spectra', Medical Physics, vol. 48, no. 7, pp. 3630--3637, Hoboken, NJ: Wiley.

[8] Badano, A, Graff, CG, Badal, A, Sharma, D, Zeng, R, Samuelson, FW, Glick, SJ, Myers, KJ 2018, 'Evaluation of digital breast tomosynthesis as replacement of full-field digital mammography using an in silico imaging trial', JAMA Network Open, vol. 1, no. 7, p. e185474, Chicago, IL: American Medical Association.

[9] Huber, PJ 1964, 'Robust estimation of a location parameter', Annals of Mathematical Statistics, vol. 35, no. 1, pp. 73--101, Hayward, CA: Institute of Mathematical Statistics.

MIC-10-176

MIC-10-179

Development of a 64-Channel Energy and Timing Acquisition System for TOF-DXA (#3146)

Sang-Hyun Chun, Jiwoong Jung, Jiwon Nam, Sena Kwon, Jin Ho Jung, Yong Choi

Sogang University, Department of Electronic Engineering, Intelligent Signal Processing System (ISPS) Laboratory, Seoul, South Korea

This research was supported by the Industrial Technology Innovation Program funded by the Ministry of Trade, Industry and Energy (no. P0030253), by the Korea Medical Device Development Foundation Grant funded by the Ministry of Science and ICT, the Ministry of Trade, Industry and Resources, the Ministry of Health & Welfare, the Ministry of Food and Drug Safety (no. 2410019162, no. RS-2026-25540876), and by the Basic Science Research Program through the National Research Foundation of Korea (NRF) funded by the Ministry of Education (no. RS-2026-25565373) of the Republic of Korea.

Abstract

Time-of-flight dual-energy X-ray absorptiometry (TOF-DXA) is proposed as a method for enhancing material decomposition by incorporating timing information into conventional dual-energy attenuation measurements. In this study, a 64-channel energy and timing acquisition system was developed for TOF-DXA.

The detector consisted of a 64-channel LYSO array with a pixel size of 3 × 3 × 3 mm³, coupled to four 16-channel Broadcom NUV-MT SiPM arrays. Detector signals were split into independent energy and timing paths. For the energy path, signals were processed through differential amplifiers and digitized using 10-bit multichannel analog-to-digital converters. Timing signals were processed using front-end comparators and a Kintex-7 FPGA-based tapped delay line (TDL) time-to-digital converter. The TDL was implemented using a single-chain architecture based on CARRY4 primitives.

This dual-path configuration enabled synchronized acquisition of energy and timing information on an event-by-event basis. The FPGA logic measured energy values through peak detection and synchronized them with timing data stored in a timing FIFO to ensure event-by-event alignment. The energy resolution was evaluated using a Co-57 source at 122 keV, while the timing resolution was evaluated in coincidence with a reference detector using a

Na-22 source. X-ray spectra were acquired using an X-ray generator operated at 83 kVp and 0.2 mA with a Ce filter (K-edge: 40.4 keV) to evaluate system performance in the DEXA energy range.
The energy resolution was 16.3% at 122 keV, and the coincidence timing resolution was 104 ps at 511 keV. The low- and high-energy peaks were clearly resolved in the acquired X-ray spectrum.
These results demonstrated that the developed 64-channel acquisition system could simultaneously measure energy and timing information for TOF-DXA. Optimization of the acquisition board is currently in progress, and comprehensive system performance results will be presented at the conference.

References
[1] S. B. Heymsfield, et al., "Dual-energy X-ray absorptiometry: review of physical concepts," American Journal of Physiology-Endocrinology and Metabolism, vol. 271, no. 6, pp. E941–E951, 1996.
[2] G. M. Blake and I. Fogelman, "An Update on Dual-Energy X-Ray Absorptiometry," Seminars in Nuclear Medicine, vol. 40, no. 1, pp. 62–73, 2010.
[3] J. Jung, et al., "Development of SiPM-based DEXA detector for large detection area," Nuclear Instruments and Methods in Physics Research Section A, vol. 1084, p. 171218, 2026.
[4] D. Portaluppi, et al., "Multi-Channel FPGA Time-to-Digital Converter With 10 ps Bin and 40 ps FWHM," IEEE Transactions on Instrumentation and Measurement, vol. 71, p. 2002109, 2022.

MIC-10-182

GARM: Geometry-Aware Reconstruction Method for Static CT Generalizable across Diverse Scanning Strategies (#1076)

Peixuan Song[1,2], Changyu Chen[1,2], Zhiqiang Chen[1,2], Yuxiang Xing[1,2]

[1] Tsinghua University, Department of Engineering Physics, Beijing, China; [2] Tsinghua University, Key Laboratory of Particle & Radiation Imaging, Ministry of Education, Beijing, China

This work was supported in part by the Natural Science Foundation of Beijing (No.L242001), the National Natural Science Foundation of China (No. 12327809) and China Postdoctoral Science Foundation (No. 2025M780861)

Abstract
Static computed tomography (SCT) enables fast, task-specific imaging through ultrafast and flexible firing among distributed focal spots. However, it introduces irregular and incomplete data acquisition, which poses great challenges to reconstruction. In this work, we propose Geometry-Aware Reconstruction Method (GARM) for SCT across diverse scanning strategies. The Geometry-Guided Dimension Reduction (G2DR) Network first transforms irregular 3D projections into slice-wise 2D fan-beam projections using geometric information derived from ray positions. A 2D dual-domain network then suppresses sparse-view artifacts guided by geometric and Radon-space information. Simulated experiments demonstrate that GARM achieves high-quality reconstruction from irregular and incomplete projections with strong generalization capability across diverse scan strategies.

References
[1] Zheng, A, Gao, H, Zhang, L, et al. 2020, 'A dual-domain deep learning-based reconstruction method for fully 3D sparse data helical CT', Physics in Medicine & Biology, vol. 65, no. 24, p. 245030, Bristol: IOP Publishing.
[2] Zhang, T, et al. 2020, 'Stationary computed tomography with source and detector in linear symmetric geometry: Direct filtered backprojection reconstruction', Medical Physics, vol. 47, no. 5, pp. 2222–2236, Hoboken: Wiley.

[3] Chen, C, et al. 2025, 'Static CT With Sources and Detectors Distributed in a Multi-Segment Manner: System Analysis and Analytical Reconstruction', IEEE Transactions on Computational Imaging, vol. 11, pp. 251–264, Piscataway: IEEE.

MIC-10-185

Impact of Small-Angle Event Selection in Compton Cone Imaging (#1168)

Elisabetta Medina[1], Machiel Kolstein[1], Javier Caravaca[2], Mokthar Chmeissani[1], Brahim Mehadji[4], Gerard Ariño-Estrada[1,3]

[1] Institut de Física d'Altes Energies - Barcelona Institute of Science and Technology (IFAE-BIST), Medical Physics Group, Bellaterra, Barcelona, Spain; [2] Lawrence Berkeley National Laboratory, Berkeley, CA, USA; [3] University of California Davis, Department of Biomedical Engineering, Davis, CA, USA; [4] University of California Davis, Department of Radiology in the School of Medicine, Davis, CA, USA

This work was supported by the European Research Council Starting Grant #101041972 and by the ATRAE grant #ATR2023-143812 from the Spanish Research Agency.

Abstract

Compton cameras are imaging systems that detect Compton-scattered gamma rays using two position-sensitive detectors, typically called the scatterer and the absorber.

Each interaction pair defines a Compton cone enabling three-dimensional image reconstruction.

In this work, we investigate how the selection of low scattering angle events influences image quality.

A GATE-based simulation of a Si/CdTe Compton camera system was developed to generate Compton cone data.

A 511 keV rod phantom with source cylinders of radii from 1.5 mm to 0.75 mm was implemented, and 100 M primary photons were simulated.

Images were reconstructed from subsets obtained by applying a maximum threshold on Compton electron energy in the scatterer.

Energy selections of 5, 10, and 15 keV (corresponding to scattering angles of 8°, 11.4°, and 14°) were used, along with a reference dataset without any energy cut for standard CC reconstruction comparison.

We show that for two rods of 1.5 mm and 1.25 mm radius, the peak-to-valley ratio (PVR) without any energy selection is approximately 3.5. By selecting energy deposits below 15 keV (14°) the PVR nearly triples, with further improvements observed for lower energy thresholds, reaching a value of 13.8 for a 5 keV energy cut

For smaller rod radii, the PVR remains below 3, although low-energy event selection still yields enhancements of approximately 60%, 30%, and 17% for radii of 1 mm, 0.75 mm, and 0.51 mm, respectively.

These findings support event-selection strategies for CC systems capable of triggering at low energies in the scatterer.

Restricting to the most informative events can reduce computational load and improve reconstruction performance, with the strongest benefits observed for rods with radii above 1 mm.

References

[1] Kim, SM, Lee, JS 2024, 'A comprehensive review on Compton camera image reconstruction: from principles to AI innovations', Biomedical Engineering Letters, 14.6, 1175–1193, Seoul: Springer Nature.

[2] Delogu, P, et al. 2024, 'Validation of Timepix4 energy calibration procedures with synchrotron X-ray beams', Nuclear Instruments and Methods in Physics Research Section A: Accelerators, Spectrometers, Detectors and Associated Equipment, 1068, 169716, Amsterdam: Elsevier.
[3] Kolstein, M, De Lorenzo, G, Chmeissani, M 2014, 'Evaluation of list-mode ordered subset expectation maximization image reconstruction for pixelated solid-state Compton gamma camera with large number of channels', Journal of Instrumentation, 9.04, C04034–C04034, London: IOP Publishing.

MIC-10-188

Deep Learning-based 3D SPECT Reconstruction from Biplanar Projections and CT Scout Views (#1262)

Jiarui Huang[1,2], Qiulei Yao[1,2], Haonan Han[2], Huifang Xie[2], Guohua Cao[1], Yang Lv[2]

[1] ShanghaiTech University, School of Biomedical Engineering, Shanghai, China; [2] Shanghai United Imaging Healthcare, Shanghai, China

Abstract

Dual-view SPECT planar imaging is a widely used method in clinical bone scan screening due to its efficiency and low radiation dose compared to whole-body SPECT/CT imaging. However, its diagnostic efficacy is often limited by anatomical overlap and the absence of depth information. Achieving high-quality 3D image from only two projections remains a challenge for traditional methods. Furthermore, existing deep learning-based approaches for ultra-sparse-view SPECT reconstruction are mainly designed for cardiac imaging and cannot be directly adapted to bone scintigraphy. To address these limitations, we propose a deep learning framework for 3D SPECT reconstruction from orthogonal biplanar projections and CT Scout views. The framework comprises a 3D condition map generation module and a structure-guided 2D conditional diffusion module, facilitating a two-stage reconstruction process including an initial coarse reconstruction followed by iterative refinement via a diffusion model. Quantitative results demonstrate that the proposed method achieves better recovery coefficients for bone tissues and metastatic lesions, as well as improved LPIPS scores for perceptual quality. Qualitative assessments further reveal that the reconstructed images exhibit highly realistic textures and shows strong agreement with standard full-view scans. This method provides a fast, low-radiation 3D reconstruction strategy with considerable potential to optimize clinical bone scan workflows, enhance diagnostic accuracy and improve patient comfort.

MIC-10-191

The Inverse Problem of Spatiotemporal Emission Reconstruction from Prompt Gamma Timing Data (#1478)

Julius Werner[1], Malte Schmidt[1], Jorge Roser[1], Jona Kasprzak[1], Yuemeng Feng[1], Veronica Ferrero[2], Francesco Pennazio[3], Magdalena Rafecas[1]

[1] University of Luebeck, Institute of Medical Engineering, Lübeck, Germany; [2] Universitá degli Studi di Torino, Department of Physics, Torino, Italy; [3] Istituto Nazionale di Fisica Nucleare, Sezione di Torino, Torino, Italy

This work was supported in part by the German Research Foundation (DFG) by Grant No. 51 658 7313 (PROSIT).

Abstract

Reconstructing the emission distribution of prompt gamma radiation in time and space offers a unique advantage: it reveals the primary particle motion inside the irradiation target during particle therapy. Similar to typical tomographic emission reconstruction scenarios, the measurement process based on Prompt Gamma Timing can be described by a linear system model and Poisson-distributed measurement data. However, the structure of the emission domain (emission time and position of the prompt gammas) and the detection domain (detector index and event time difference relative to a primary particle signal) are unique. In this work, we inspect some features of this inverse problem and analyze related fundamental limitations based on reconstructions with ideal data and the singular value decomposition of the system matrix. The results show a need for regularization and help identify possible improvements to the approach. Additionally, understanding this inverse problem in-depth also supports the development of other Prompt-Gamma-Timing-based techniques.

References

[1] Pennazio, F et al. 2022, 'Proton therapy monitoring: spatiotemporal emission reconstruction with prompt gamma timing and implementation with PET detectors', *Phys. Med. Biol.*, 67, 065005

[2] Werner, J et al. 2024, 'Stopping power and range estimations in proton therapy based on prompt gamma timing: motion models and automated parameter optimization', *Phys. Med. Biol.*,69, 14NT02

[3] Werner, J et al. 2025, 'Stopping power monitoring during proton therapy by means of prompt gamma timing: first experimental results with a homogeneous phantom', *arXiv*, 2511.21344

[4] Ferrero, V et al. 2022, 'Estimating the stopping power distribution during proton therapy: A proof of concept', *Front. Phys.*, 10:971767

[5] Werner, J et al. 2026, 'Analytical model of prompt gamma timing for spatiotemporal emission reconstruction in particle therapy', *Phys. Med. Biol.*, 71, 075005

[6] Tong, S et al. 2011, 'Properties and Mitigation of Edge Artifacts in PSF-Based PET Reconstruction', *IEEE Transactions on Nuclear Science*, 85-5, 2264-2275

MIC-10-194

Recent updates to STIR, a community effort of a quarter century (#1658)

Nikos Efthimiou[1], Daniel Deidda[2], Viet A. Dao[1], Zekai Li[1], Charalampos Tsoumpas[1], Kris Thielemans[3]

[1] UMCG, Department of Nuclear Medicine, Groningen, Netherlands; [2] National Physical Laboratory, Teddington, UK; [3] UCL, Institute of Nuclear Medicine, London, UK

C. Tsoumpas, N. Efthimiou and Z. Li are supported by the NWO AES Vici Talent program (doi: 10.61686/REEAR02777). Z. Li was also supported by a Joint Scholarship from the China Scholarship Council and the University of Groningen (202210100011) and his placement at UCL by EPSRC CCP in Synergistic Reconstruction for Biomedical Imaging (EP/T026693/1). Viet Dao was supported by an E0SRC CASE PhD scholarship in partnership with Positrigo. This work used the Dutch national e-infrastructure with the support of the SURF Cooperative using grant no. EINF-18121.
STIR is partially maintained by CCP SyneRBI which is funded by the EPSRC grant EP/T026693/1 and by STFC through the UKRI Digital Research Infrastructure programme

Abstract

The Software for Tomographic Image Reconstruction (STIR) is a long-standing open-source platform for PET and SPECT reconstruction that has supported tomographic imaging research for more than two decades. Public STIR documentation dates to the early 2000s, and the project remains actively developed, with a current public release in November 2025 and a GitHub repository reporting 9,409 commits, 146 stars, and 108 forks. Recently there have been major contributions, that have expanded substantially the framework in scanner support, motion correction, and raw-data interoperability. Advances include support for the Siemens Biograph Vision Quadra long axial field-of-view PET/CT system, a data-driven rigid head motion-correction workflow for brain PET, and PETSIRD as a vendor-independent raw-data interface. Here, we demonstrate the impact of motion on clinically relevant quantitative measures. Together, these developments reinforce STIR's position as a mature, community-driven platform for modern PET reconstruction research.

References

[1] Thielemans, K, Tsoumpas, C, Mustafovic, S, Beisel, T, Aguiar, P, Dikaios, N & Jacobson, MW 2012, 'STIR: software for tomographic image reconstruction release 2', *Physics in Medicine and Biology*, vol. 57, no. 4, pp. 867–883.

[2] Brusaferri, L et al. 2020, 'Joint Activity and Attenuation Reconstruction From Multiple Energy Window Data With Photopeak Scatter Re-Estimation in Non-TOF 3-D PET', *IEEE Transactions on Radiation and Plasma Medical Sciences*, vol. 4, no. 4, pp. 410–421.

[3] Biguri, A et al. 2021, 'Recent Progress in STIR 5.0', *2021 IEEE Nuclear Science Symposium and Medical Imaging Conference (NSS/MIC)*, pp. 1–3

[4] Dao, V, Mikhaylova, E, Ahnen, ML, Fischer, J, Thielemans, K & Tsoumpas, C 2022, 'Evaluation of STIR Library Adapted for PET Scanners with Non-Cylindrical Geometry', *Journal of Imaging*, vol. 8, no. 6, article 172.

[5] Efthimiou, N, Emond, E, Wadhwa, P, Cawthorne, C, Tsoumpas, C & Thielemans, K 2019, 'Implementation and validation of time-of-flight PET image reconstruction module for listmode and sinogram projection data in the STIR library', *Physics in Medicine and Biology*, vol. 64, no. 3, article 035004.

[6] Prenosil, GA, Sari, H, Fürstner, M, Afshar-Oromieh, A, Shi, K, Rominger, A & Hentschel, M 2022, 'Performance Characteristics of the Biograph Vision Quadra PET/CT System with a Long Axial Field of View Using the NEMA NU 2-2018 Standard', *Journal of Nuclear Medicine*, vol. 63, no. 3, pp. 476–484.

[7] Efthimiou, N, Whitehead, AC, Stockhoff, M, Thyssen, C, Archibald, SJ & Vandenberghe, S 2019, 'Preliminary investigation of the impact of Axial Ring Splitting on Image Quality for the Cost Reduction of Total-Body PET', *2019 IEEE Nuclear Science Symposium and Medical Imaging Conference (NSS/MIC)*, Manchester, UK: IEEE. https://doi.org/10.1109/NSS/MIC42101.2019.9059650

[8] Dao, VA, Mikhaylova, E, Lesnic, E, Aykroyd, RG, Tsoumpas,C, 'Data Driven Motion Detection, Estimation and Correction for Brain Pet Scanners' pp. 1–1, Dec. 2025, doi: 10.1109/NSS/MIC/RTSD57106.2025.11286795.
[9] Efthimiou, N 2020, 'New Challenges for PET Image Reconstruction for Total-Body Imaging', *PET Clinics*, vol. 15, no. 4, pp. 453–461.
[10] Thielemans, K., E. Asma, M. Cook, et al. 2025. 'Final Draft of PETSIRD v1.0: A Proposed Standard for PET Raw Data'. 2025 IEEE Nuclear Science Symposium (NSS), Medical Imaging Conference (MIC) and Room Temperature Semiconductor Detector Conference (RTSD), November, 1–2. https://doi.org/10.1109/NSS/MIC/RTSD57106.2025.11287540

MIC-10-197

Developments in fabrication and design flexibility of amorphous silicon microchannel plates (#2584)

Georgios Konstantinou, Loris Barraud, Christophe Baillif, Nicolas Wyrsch

EPFL, Neuchatel, Switzerland

The project is funded by the SNF SPARK grant no CRSK-2_237272

Abstract

The technology of amorphous silicon-based micro-channel plates (AMCPs) uses a versatile approach to stack hydrogenated amorphous silicon in thicknesses up to 100 µm, using plasma-enhanced chemical vapor deposition (PECVD) and etch microchannels of diameter below 2 µm every 5 µm, on a hexagonal pattern, by deep reactive ion etching. With gains up to 1000 for reverse bias less than 300 V, the design is possible to build on arrays of sensitive transimpedance amplifiers, integrated in read-out circuits with high channel density, such as for instance 15 by 15 µm. This ensures single photon detection with quantum efficiency up to 30% and noise rates below 50 Hz/cm², if combined with state of the art photocathodes such as the hi-QE from Photonis. Current fabrication runs focus on direct integration of the stack on ASICs, to be integrated with the photocathode over the next months. Measurements show timing response with jitter below 10 ps, making this high-precision photodetector ideal for radiation detectors combining ultra-fast photon emission and low light yield, such as Cherenkov.

MIC-10-200

A Universal Geometric Calibration Method for CBCT Systems with Arbitrary Trajectories (#1877)

Tong Jia[1], Chengmin Wang[1,3], Baodong Liu[1,3], Yanfang Wang[1,3], Long Wei[1,3], Zhe Wang[1,3], Cunfeng Wei[1,3]

[1] Institute of High Energy Physics, Chinese Academy of Sciences, Beijing Engineering Research Center of Radiographic Techniques and Equipment, Beijing, China; [2] University of Chinese Academy of Sciences, Nuclear Science and Technology, Beijing, China; [3] University of Chinese Academy of Sciences, Nuclear Science and Technology, Beijing, China; [4] University of Chinese Academy of Sciences, Nuclear Science and Technology, Beijing, China

Abstract

This paper presents a universal calibration method based on spatial vector decomposition to address the challenge of dynamically changing and difficult-to-calibrate geometric parameters in cone-beam computed tomography (CT) systems with complex scanning trajectories. The proposed method enables high-precision and robust calibration for a broad range of CT imaging systems. First, the projection matrix at each scanning angle is computed using a calibration phantom. This matrix is then decomposed into spatial vectors representing the system's geometric state, including the position of the X-ray source, the detector reference point, and orientation vectors. These vectors can be directly used for image reconstruction or converted into device-specific parameters. A vector-based detector mapping algorithm is also introduced to facilitate efficient projection data correction. Experiments on Micro-CT, CL and robotic-arm CT systems confirm that the method significantly improves image clarity, suppresses artifacts and distortions, and accurately reconstructs the actual motion trajectories of the X-ray source and detector. The method demonstrates high accuracy and versatility, providing a reliable calibration solution for high-degree-of-freedom CT systems.

References

[1] N. S. O'Brien, R. P. Boardman, I. Sinclair and T. Blumensath. Recent advances in X-ray cone-beam computed laminography[J]. Journal of X-ray Science and Technology, 2016, 24: 691-707.

[2] Grunz J P, Kunz A S, Gietzen C H, et al. 3D cone-beam CT of the ankle using a novel twin robotic X-ray system: assessment of image quality and radiation dose[J]. European Journal of Radiology, 2019, 119: 108659.

[3] F. Noo, R. Clackdoyle, C. Mennessier, T. A. White and T. J. Roney. Analytic method based on identification of ellipse parameters for scanner calibration in cone-beam tomography[J]. Physics in Medicine & Biology, 2000, 45: 3489.

[4] Y. Sun, Y. Hou, F. Zhao and J. Hu. A calibration method for misaligned scanner geometry in cone-beam computed tomography[J]. Ndt & E International, 2006, 39: 499-513.

MIC-10-203

CT-less Attenuation Maps as Priors for Robust Joint Activity–Attenuation Estimation in TOF and Non-TOF PET (#2048)

Elise Emond[1], Zacharias Chalampalakis[2], Abolfazl Mehranian[3], Kuan-Hao Su[5], Sangtae Ahn[6], Fotis Kotasidis[4]

[1] GE HealthCare GmbH, Düsseldorf, Germany; [2] GE HealthCare, Buc, France; [3] GE HealthCare, Oxford, UK; [4] GE HealthCare, Zurich, Switzerland; [5] GE HealthCare, Waukesha, USA; [6] GE HealthCare Technology and Innovation Center, Niskayuna, USA

The authors acknowledge the Cincinnati Children's Hospital Medical Center, USA, for providing the data and Sangtae Ahn and Kuan-Hao Su (GE HealthCare) for their contributions to the methodological and code development of MAP-AA within the GE HealthCare PET reconstruction MATLAB package.

Abstract

CT-less attenuation correction in PET has gained increasing interest as a means to reduce patient radiation exposure, with recent AI-based methods providing anatomically plausible attenuation estimates from emission data and complementary inputs. However, residual inaccuracies in such attenuation maps can still impact PET quantification.

Joint estimation of activity and attenuation provides a physics-based framework to mitigate these effects, but remains less well constrained in the absence of time-of-flight (TOF) information.

This work evaluates the use of AI-generated CT-less attenuation maps as spatial priors for joint estimation of activity and attenuation in TOF and non-TOF PET. Using a maximum-a-posteriori formulation, the CT-less attenuation map is employed both as an initial estimate and as a regularising prior.

Experiments on paediatric PET datasets show that this approach stabilises joint reconstruction and recovers anatomically plausible attenuation maps, including in the non-TOF case. These results support the use of CT-less attenuation maps as effective priors for robust PET reconstruction.

MIC-10-206

Convergence-Informed AI-Assisted Reconstruction for Dual-Panel PET Imaging (#2078)

Abdollah Saberi Manesh[1], Mehdi Amini[1], Yazdan Salimi[1], Ghasem Hajianfar[1], Katayoun Doroud[2], Hossein Arabi[1], Habib Zaidi[1]

[1] University of Geneva, Department of Medical Imaging, Geneva University Hospital, Geneva, Switzerland; [2] Picotech, St Genis Pouilly, France

This work was supported by the Eurostars programme of the European Commission under grant E! 114021 ProVision and the Private Foundation of Geneva University Hospitals under Grant RC-06-01.

Abstract

Dual-panel positron emission tomography (PET) scanners offer compact, cost-effective, and organ-dedicated imaging geometries, but their limited angular coverage introduces anisotropic resolution loss and elongation artifacts. This work presents a convergence-informed artificial intelligence (AI)-guided iterative reconstruction framework for the ProVision dual-panel PET system. The proposed approach exploits voxel-wise convergence information (VCI) extracted from the first 15 iterations of list-mode multi-ray maximum likelihood expectation maximization (MLEM) reconstruction. VCI was incorporated into five reconstruction strategies: analytic VCI-guided MLEM, multilayer perceptron-based VCI-guided MLEM, standalone 3D Swin-UNet reconstruction, AI-guided maximum a posteriori reconstruction (AI-MAP), and AI-initialized MLEM (AI-MLEM). Training and evaluation were performed using Monte Carlo simulations, a scaled NEMA image quality phantom, an external simulated patient test set, and an experimental anthropomorphic pelvis phantom. Compared with conventional MLEM, the proposed hybrid methods substantially improved contrast recovery, background uniformity, and geometric fidelity. AI-MLEM increased the contrast recovery coefficient from 53.16% to 82.35%, reduced background variability from 12.38% to 8.25%, and reduced the elongation ratio from 1.48 to 1.15. On the external simulated patient test set, AI-MLEM improved structural similarity from 0.446 to 0.816 and reduced normalized mean absolute error from 0.405 to 0.215. Experimental phantom results further confirmed improved lesion conspicuity and reduced vertical spreading. These results demonstrate that early-iteration convergence behavior provides useful voxel-wise guidance for mitigating limited-angle artifacts while preserving data consistency in dual-panel PET reconstruction.

References

[1] A. Sanaat, M. Amini, H. Arabi, and H. Zaidi, "The quest for multifunctional and dedicated PET instrumentation with irregular geometries," *Annals of Nuclear Medicine*, vol. 38, no. 1, pp. 31–70, 2024/01/01 2024, doi: 10.1007/s12149-023-01881-6.

[2] H. Arabi, A. S. Manesh, and H. Zaidi, "Innovations in dedicated PET instrumentation: from the operating room to specimen imaging," *Physics in Medicine & Biology*, vol. 69, no. 11, p. 11TR03, 2024.

[3] M. Xia *et al.*, "On Hallucinations in Artificial Intelligence-Generated Content for Nuclear Medicine Imaging (the DREAM Report)," (in eng), *J Nucl Med*, vol. 67, no. 2, pp. 166–174, Feb 2 2026, doi: 10.2967/jnumed.125.270653.

[4] A. S. Manesh *et al.*, "Dedicated Image Reconstruction with Elongation Correction for a Dual-Panel Prostate PET Scanner," in *2024 IEEE Nuclear Science Symposium (NSS), Medical Imaging Conference (MIC) and Room Temperature Semiconductor Detector Conference (RTSD)*, 2024: IEEE, pp. 1–1.

[5] M. Amini *et al.*, "Acquisition Protocol Optimization of a Dual-Panel PET Scanner Dedicated to Prostate Cancer Imaging," in *2025 IEEE Nuclear Science Symposium (NSS), Medical Imaging Conference (MIC) and Room Temperature Semiconductor Detector Conference (RTSD)*, 2025: IEEE, pp. 1–2.

[6] M. A. A. Saberi Manesh, H. Arabi, K. Doroud, C. Williams, H. Zaidi, "Conceptual design of a Dual-Panel Dedicated Prostate PET Scanner: A Monte Carlo Simulation Study," *IEEE Nuclear Science Symposium and Medical Imaging Conference (NSS/MIC)*, 2022.

MIC-10-209

Anatomically Guided Adaptive Gaussian Representation for PET Image Reconstruction (#2133)

Zhihao Li[1], Zhao Wang[2], Xin Zhao[1], Yikuang Yuluo[1], Yixing Huang[1], Zhaoheng Xie[1,2]

[1] Peking University, The Institute of Medical Technology, Beijing, China; [2] Peking University, National Biomedical Imaging Center, Beijing, China

This work was supported by National Natural Science Foundation of China (62394311).

Abstract

We propose a continuous Gaussian representation for PET reconstruction, modeling the activity distribution with normalized Gaussian basis functions. This reformulates PET reconstruction as a compact differentiable optimization problem by coupling an analytical Gaussian forward model with Poisson likelihood. The key component is an anatomically guided adaptive density control strategy, which dynamically prunes, splits, and clones Gaussian primitives according to contribution, gradient, and MRI-derived mask constraints, thereby allocating representation capacity to informative regions while suppressing redundant components. Image-domain Huber-TV regularization is incorporated to stabilize reconstruction. Experiments on 2D simulations demonstrate competitive performance across count levels and clear advantages under low-count conditions, suggesting the potential of adaptive continuous representations for PET reconstruction.

References

[1] Shepp, L.A. and Y. Vardi, *Maximum Likelihood Reconstruction for Emission Tomography*. IEEE Transactions on Medical Imaging, 1982. **1**(2): p. 113-122.

[2] Kerbl, B., et al., *3d gaussian splatting for real-time radiance field rendering*. ACM Trans. Graph., 2023. **42**(4): p. 139:1-139:14.

[3] Zha, R., et al., *R $^ 2$-Gaussian: Rectifying Radiative Gaussian Splatting for Tomographic Reconstruction*. arXiv preprint arXiv:2405.20693, 2024.

[4] Kingma, D.P. and J. Ba, *Adam: A Method for Stochastic Optimization*. CoRR, 2014. **abs/1412.6980**.

MIC-10-212

MRI guided PET reconstruction in meningioma [^{68}Ga]DOTATOC patients, pituitary adenoma [^{18}F]FET, and neurodegenerative [^{18}F]FDG patients (#2361)

Emil S. Christensen[1,2], Andreas Clemmensen[1,2], Patrick Lehmann[3], Jorge Cabello[4], Otto M. Henriksen[1], Ian Law[1,5], Andreas Kjaer[1,2], Thomas L. Andersen[1,5]

[1] Copenhagen University Hospital, Department of Clinical Physiology and Nuclear Medicine, Copenhagen, Denmark; [2] University of Copenhagen, Department of Biomedical Sciences, Cluster for Molecular Imaging, Copenhagen, Denmark; [3] Siemens Healthcare A/S, Ballerup, Denmark; [4] Siemens Medical Solutions USA, Knoxville, USA; [5] University of Copenhagen, Department of Clinical Medicine, Copenhagen, Denmark

Abstract

The latest generation of simultaneous positron emission tomography and magnetic resonance imaging (PET/MRI) scanners is now at the forefront of hybrid imaging. As of now, the reconstruction of both modalities is independent, but research is ongoing in MRI-guided (MRIg) PET reconstruction, where information from the MRI is used as prior information in the iterative PET reconstruction.

We present three different clinical cohorts: meningioma patients (n=8) scanned with [^{68}Ga]DOTATOC, a single pituitary adenoma scanned dynamically with [^{18}F]FET and a neurodegenerative cohort (n=10) scanned with [^{18}F]FDG. The cohorts have been analyzed with standard OSEM reconstruction (b=0) versus MRIg reconstruction. The meningioma cohort showed an increased volume with standardized uptake values (SUV) above 2.5 when using MRIg reconstruction, and an increased SUV_{max} in the tumor. The pituitary adenoma showed increase time-activity curve both for β=1 and β=2. The neurodegenerative cohort showed stable SUV ratios of the cerebral-to-cerebellar cortex down to 3 minutes.

This preliminary work shows the clinical value in utilizing the information from the MRI in PET reconstruction with applications both to increase image quality and resolution, but also to facilitate faster imaging.

References

[1] Henriksen OM, Korsholm K, Loft A, et al. First Clinical Experiences with the Ultra-Fast Time-of-Flight BIOGRAPH One Next-Generation Hybrid PET/MRI System. *Diagnostics*. 2026;16:398.

[2] Afshar-Oromieh A, Wolf MB, Kratochwil C, et al. Comparison of 68Ga-DOTATOC-PET/CT and PET/MRI hybrid systems in patients with cranial meningioma: Initial results. *Neuro-Oncology*. 2015;17:312-319.

[3] Pruis IJ, Verburg FA, Balvers RK, et al. [18F] FET PET/MRI: an accurate technique for detection of small functional pituitary tumors. *Journal of Nuclear Medicine*. 2024;65:688-692.

[4] Acquah IK. *Comparison of Methods of μ-Map Generation: MR-Based Method in PET/MR Imaging Versus Pseudo-CT Method in Radiotherapy Dose Planning*, University of Ghana; 2019.

[5] Kazantsev D, Bousse A, Pedemonte S, Arridge SR, Hutton BF, Ourselin S. Edge preserving bowsher prior with nonlocal weighting for 3D spect reconstruction. Paper presented at: 2011 IEEE International Symposium on Biomedical Imaging: From Nano to Macro, 2011.

[6] Bowsher JE, Yuan H, Hedlund LW, et al. Utilizing MRI information to estimate F18-FDG distributions in rat flank tumors. Paper presented at: IEEE Symposium Conference Record Nuclear Science 2004., 2004.

[7] Na S, Kang DW, Kim GH, et al. The usefulness of 18F-FDG PET to differentiate subtypes of dementia: The systematic review and meta-analysis. *Dementia and Neurocognitive Disorders*. 2024;23:54.

MIC-10-215

A Hybrid Neural Network Model for DaTscan Diagnosis of Neurodegenerative Disorders (#2498)

Efstratios Roupas[1], Aikaterini Koukopoulou[1], Eleni Mitsou[1], Efstathios Stiliaris[2]

[1] National and Kapodistrian University of Athens, Medical School, Athens, Greece; [2] National and Kapodistrian University of Athens, Department of Physics, Athens, Greece

Abstract

This study presents the development of a hybrid Neural Network designed to simultaneously reconstruct medical images from their sinograms and to predict diagnostic parameters for neurodegenerative disorders, specifically Parkinson's disease. The training pipeline utilizes simulated Dopamine Transporter Scan (DaTscan) brain images and their corresponding sinograms, generated via a custom Monte Carlo based framework that employs analytically driven functions to model realistic hotspot and background noise characteristics. The architecture integrates image reconstruction and disease-specific parameter estimation into a unified framework. Key diagnostic features include the bilateral asymmetry of radiotracer uptake within the caudate nuclei; deviations in spatial distribution or intensity within predefined Regions of Interest (RoIs) serve as primary indicators of neuropathology. This dual-function approach advances automated, AI-assisted functional neuroimaging, offering a robust pathway for early, non-invasive diagnosis of neurodegenerative conditions.

References

[1] Duan T, Chen W, Ruan M, Zhang X, Shen S and Gu W, 2025, 'Unsupervised deep learning-based medical image registration: a survey', Physics in Medicine & Biology 70, 02TR01

[2] Paschalis P, Giokaris ND, Karabarbounis A, Loudos GK, Maintas D, Papanicolas CN, Spanoudaki V, Tsoumpas Ch and Stiliaris E, 2004, 'Tomographic image reconstruction using Artificial Neural Networks', Nuclear Instruments & Methods A 527, 151-156

[3] Argyrou M, Maintas D, Tsoumpas Ch and Stiliaris E, 2012, 'Tomographic Image Reconstruction based on Artificial Neural Network (ANN) Techniques', IEEE MIC Record M17-12, 3324-3327

[4] Hwang D and Zeng GL, 2006, 'Convergence study of an accelerated ML-EM algorithm using bigger step size', Physics in Medicine & Biology 51, 237

[5] Wang Z, Bovik AC, Sheikh HR, Simoncelli EP, 2004, 'Image quality assessment: from error visibility to structural similarity', IEEE Transactions on Image Processing 13, 600–612

MIC-10-218

A Global-Local Latent Diffusion Model for Limited-Angle CT Reconstruction (#2642)

Yifan Wang[1,2], Cunfeng Wei[1,2], Tong Jia[1], Qiong Xu[1,3]

[1] Institute of High Energy Physics, Chinese Academy of Sciences, Beijing, China; [2] University of Chinese Academy of Sciences, School of Nuclear Science and Technology, Beijing, China; [3] Jinan Laboratory of Applied Nuclear Science, Jinan, China

National Natural Science Foundation of China (NSFC) (No.12475313) and Excellent Youth Fund of Shandong Natural Science Foundation (ZR2024YQ066)

Abstract

Limited-angle computed tomography (LACT) reconstruction is highly ill-posed because missing projection views lead to severe artifacts and incomplete boundaries. This work proposes a global-local latent diffusion framework for limited-angle CT reconstruction. The proposed method performs diffusion reconstruction in the latent space of a variational autoencoder and jointly incorporates U-Net-based local modeling and transformer-based global modeling into the denoising process. The U-Net component captures multiscale spatial details and boundary continuity, whereas the transformer component models long-range dependencies and global structural relationships associated with missing-angle information. These complementary priors are adaptively integrated to guide latent-space denoising. During sampling, a physics-guided data-consistency constraint is further introduced. Specifically, the intermediate latent prediction produced by the model is decoded back to the image domain, processed with a projection-consistency operation, and then re-encoded into the latent diffusion trajectory. Preliminary experiments on a simulated data set show favorable reconstruction quality, indicating that the proposed global-local diffusion framework can improve structural fidelity and projection consistency for limited-angle CT reconstruction.

References

[1] R. Rombach, A. Blattmann, D. Lorenz, P. Esser, and B. Ommer, "High-Resolution Image Synthesis with Latent Diffusion Models," *Proceedings of the IEEE Computer Society Conference on Computer Vision and Pattern Recognition*, vol. 2022-June, pp. 10674–10685, Dec. 2021.

[2] W. Peebles and S. Xie, "Scalable Diffusion Models with Transformers," *Proceedings of the IEEE International Conference on Computer Vision*, pp. 4172–4182, Dec. 2022.

MIC-10-221

Iterative proton CT reconstruction from list-mode data of a sandwich time-of-flight scanner (#2821)

Aurélien Coussat, Jean Michel Létang, Simon Rit

INSA-Lyon, Université Claude Bernard Lyon 1, CNRS, Inserm, CREATIS, UMR 5220, U1294, F-69373, Lyon, France

With financial support from IT Cancer of Inserm within the framework of the 2021-2030 Cancer Control Strategy, on funds administered by Inserm, within the framework of the SIRIC LYriCAN+ (INCa-DGOS-INSERM-ITMO cancer 18003) and the LABEX PRIMES (ANR-11-LABX-0063) of Université de Lyon, within the program ”Investissements d’Avenir” (ANR-11-IDEX-0007) operated by the ANR.

Abstract

Proton CT is a promising alternative to X-ray CT for proton therapy treatment planning, allowing direct estimation of the relative stopping power map within the patient body without relying on conversion from Hounsfield units. Conventional list-mode proton CT scanners measure the energy loss of each individual proton to estimate the integral of the relative stopping power along its path, the water-equivalent path length, but do not meet the requirements for clinical use due to their low acquisition rates. An alternative proton CT scanner design was recently proposed where the time-of-flight of each proton is measured between two detectors located before and after the patient along the proton beam. The main advantages of this sandwich time-of-flight design are its compactness and high acquisition rates. However, conversion from sandwich time-of-flight data to water-equivalent path length is not possible. In this work, we propose an iterative reconstruction of the sought relative stopping power map based on the non-linear forward problem. The method is assessed using Monte Carlo simulations of the acquisition of four simple phantoms. Although computationally expensive, this method accurately recovers the relative stopping power map.

References

[1] A. Coussat, N. Krah, J. M. Létang, and S. Rit. “Proton computed tomography reconstruction from sandwich time-of-flight using a lookup table approach”. In: Fully3D. Shanghai, China, May 2025, pp. 646–649.

[2] R. P. Johnson. “Meeting the detector challenges for pre-clinical proton and ion computed tomography”. In: Phys Med Biol 69.11 (May 2024), 11TR02.

[3] F. Ulrich-Pur, T. Bergauer, A. Hirtl, C. Irmler, et al. “Novel ion imaging concept based on time-of-flight measurements with low gain avalanche detectors”. In: Journal of Instrumentation 18.02 (2023), p. C02062.

MIC-10-224

Direct normalization correction for a brain PET system with multi-resolution detector design (#2848)

Chengzhi Yang[1], Hanshen Ye[1], Chen Huang[2], Zexin Wu[2], Hui Liu[3], Qingyang Wei[4], Zheng Gu[2], Jing Wu[1]

[1] Beijing Normal University, Center for Advanced Quantum Studies, School of Physics and Astronomy, Beijing, China; [2] Shenzhen Bay Laboratory, Institute of Biomedical Engineering, Shenzhen, China; [3] Tsinghua University, Department of Engineering Physics, Beijing, China; [4] University of Science and Technology Beijing, School of Automation and Electrical Engineering, Beijing, Germany

This study was supported by National Key Research and Development (R&D) Program of China (No.2023YFC2414800), National Natural Science Foundation of China (No. 12305379, No.12205166), and CIRP Open Fund of Radiation Protection Laboratories (TNMPP-2024-No.1).

Abstract

A high-sensitivity, high-resolution brain PET system with a multi-resolution detector design has been developed. However, image reconstruction without normalization correction produces pronounced image artifacts. In this study, we implemented list-mode reconstruction with direct normalization correction using normalization factors derived from simulation data for this multi-resolution PET system. The effect of normalization correction on reconstructed image quality was evaluated using Monte Carlo simulations and real scan data from a modified image-quality phantom. The results showed that normalization-corrected reconstruction substantially reduced image artifacts and improved image uniformity in simulated data, while residual nonuniformity remained in real scan data due to the lack of experimentally measured crystal efficiencies. Overall, this work demonstrates the feasibility of normalization correction for the dual-layer brain PET system and provides a basis for further experimental normalization using measured crystal efficiencies

References

[1] Z. Chen et al., "Initial System Performance Evaluation of N-PET, a High-Sensitivity and High-Resolution TOF-DOI PET Prototype Dedicated for Human Brain Imaging," *2025 IEEE Nuclear Science Symposium (NSS), Medical Imaging Conference (MIC) and Room Temperature Semiconductor Detector Conference (RTSD)*, Yokohama, Japan, 2025, pp. 1-2

MIC-10-227

Effect of Cardiac Reorientation on Deep Learning-Based Denoising for Low-Dose Cardiac SPECT (#2932)

Mehdi Toumi[1], Yongyi Yang[1], Michael A. King[2], **Jovan G. Brankov**[1]

[1] Illinois Institute of Technology, Electrical and Computer Engineering, Chicago, USA; [2] University of Massachusetts Chan Medical School, Department of Radiology, Worcester, USA

Research reported in this publication was supported by the National Institute of Biomedical Imaging and Bioengineering(NIBIB) and the National Heart, Lung, and Blood Institute (NHLBI) of the National Institutes of Health under Award Numbers **R01EB036082** and **R01HL154687**. The content is solely the responsibility of the authors and does not necessarily represent the official views of the National Institutes of Health.

Abstract

In low-dose (LD) myocardial perfusion imaging (MPI) with single-photon emission computed tomography (SPECT), radiation exposure is reduced at the expense of image quality, potentially impairing perfusion defect detection. Deep learning methods have shown promise in reducing noise in LD MPI images. However, clinical data exhibit varying cardiac orientations, increasing the complexity of the learning task for denoising models. We hypothesize that standardizing cardiac orientation with respect to a common reference prior to training can reduce this complexity and improve denoising performance. We evaluated this approach with a previously proposed edge-aware convolutional autoencoder (EdgeCAE) across four levels of trade-off between edge preservation and mean-squared error (MSE) fidelity. The model was trained on 738 clinical subjects and tested on 300 noise realizations derived from two independent patient anatomies, with and without pre-reorientation. Our results demonstrated that cardiac reorientation consistently reduced the MSE compared to the full-dose reference images. This was also supported by visual assessment on an independent patient cohort.

References

[1] M. D. Cerqueira et al., “Standardized myocardial segmentation and nomenclature for tomographic imaging of the heart,” Circulation, vol. 105, pp. 539–542, 2002.

[2] P. J. Slomka et al., “Cardiac imaging with myocardial perfusion SPECT,” J. Nucl. Med., vol. 60, pp. 1100–1108, 2019.

[3] I. Shiri et al., “Standard SPECT myocardial perfusion estimation from half-time acquisitions using deep convolutional residual neural networks,” J. Nucl. Cardiol., vol. 28, pp. 2761–2779, 202

[4] A. J. Ramon et al., “Initial investigation of low-dose SPECT-MPI via deep learning,” IEEE Trans. Radiat. Plasma Med. Sci., vol. 4, pp. 65–72, 2020.

[5] M. Toumi et al., “Edge-aware convolutional autoencoder for low-dose SPECT myocardial perfusion image enhancement,” IEEE NSS-MIC Conf. Rec., 2024.

[6] E. V. Garcia et al., “Quantification of rotational thallium-201 myocardial tomography,” J. Nucl. Med., vol. 26, pp. 17–26, 1985.

[7] H. H. Barrett and K. J. Myers, Foundations of Image Science. Hoboken, NJ: Wiley, 2004.

[8] T. Marin, J. G. Brankov, “Deformable left-ventricle mesh model for motion-compensated filtering in cardiac gated SPECT,” Med Phys. vol. 37, no. 10, pp. 5471-81, 2010/ doi: 10.1118/3483098. PMID: 21089783; PMCID: PMC2962663.

[9] B. Feng, “Modeling of the left ventricle (LV) by using mechanical models and image data,” Ph.D. thesis, The University of Utah, 2002.

MIC-10-230

Ghost Artifact Suppression in Multiplexed Self-Collimating SPECT via Total Variation Regularization (#2996)

Siddharth Mehta[1], Harsh Tripathi[1], Tridev Methuku[1], Tessa Skirsky[2], Leslie Ying[4], Tianyu Ma[3], Rutao Yao[2]

[1] The State University of New York at Buffalo, Department of Computer Science and Engineering, Buffalo, USA; [2] The State University of New York at Buffalo, Department of Radiology, Buffalo, USA; [3] Tsinghua University, Department of Engineering Physics, Beijing, China; [4] The State University of New York at Buffalo, Biomedical Department, Buffalo, USA

This work is supported by the National Institute of Biomedical Imaging and Bioengineering of the National Institutes of Health, USA, under Grant R21EB032993. Computation work has been carried out on the high-performance computing platform supported by the Center for Computational Research at the University at Buffalo.

Abstract

Multiplexing in SPECT renders the measurement operator underdetermined. In symmetric multi-source configurations, iterative ambiguity reinforcement sustains persistent ghost artifacts. Established mitigation strategies require supplemental single-beam nonmultiplexed projections, constraining collimator design and sacrificing sensitivity. Sparsity in gradients for common tracer distributions motivate total-variation (TV) regularization as a natural demultiplexing strategy: ghost artifacts produce extra gradient support that TV prior penalizes, breaking the ambiguity cycle. We demonstrate that MAP-TV (maximum a posteriori total variation) acts as an active reconstruction-stage demultiplexer, a supplemental approach to modifying the projection set in the data acquisition stage.

References

[1] Chambolle, A, Pock, T 2011, 'A first-order primal-dual algorithm for convex problems with applications to imaging', *Journal of Mathematical Imaging and Vision*, vol. 40, no. 1, pp. 120–145, Springer: New York

[2] Panin, VY, Zeng, GL, Gullberg, GT 1999, 'Total variation regulated EM algorithm [SPECT reconstruction]', *IEEE Transactions on Nuclear Science*, vol. 46, no. 6, pp. 2202–2210, IEEE: Piscataway.

[3] Mok, GSP, Tsui, BMW, Beekman, FJ 2011, 'The effects of object activity distribution on multiplexing multi-pinhole SPECT', *PhysicsinMedicineand Biology*, vol. 56, no. 8, pp. 2635–2650, IOP Publishing: Bristol.

[4] Pells, S, Shestakova, I, Khalil, M, Hugg, J, Majewski, S, Bhatt, P, Bhatt, D 2024, 'Correction of multiplexing artefacts in multi-pinhole SPECT through temporal shuttering, de-multiplexing of projections, and alternating reconstruction', *PhysicsinMedicineandBiology*, vol. 69, no. 12, art. no. 125004, IOP Publishing: Bristol

MIC-10-233

Integrating In-Patient Scattered Events in PET Reconstruction via a Monte Carlo Projector (#3119)

Mathis Moulin[1,3], Guillaume Montémont[1], Hugo de las Heras Gala[1], Jean Michel Létang[3]

[1] CEA-LETI, Université Grenoble-Alpes, Grenoble, France; [2] CEA-LETI, Université Grenoble-Alpes, Grenoble, France; [3] INSA-Lyon, Université Claude Bernard Lyon 1, UJM- Saint Etienne, CNRS, Inserm, Lyon, France; [4] INSA-Lyon, Université Claude Bernard Lyon 1, UJM- Saint Etienne, CNRS, Inserm, Lyon, France

Abstract

In this paper, we propose a new projection method for PET, called Monte Carlo Point Projectors (MCPP), which back-projects measured gamma interactions in the detector by sampling potential positions of the event source within the field of view (FoV). We apply this method to scattered events using a projector for scattered lines of response (ScLoR), as well as a combination of scattered lines of response and Compton cones of response (CoR). The simulated system is a cylinder with a radius of 15~cm and a length of 16~cm, composed of 12 Cadmium Zinc Telluride panels, with a 7~cm radius water sphere at the center to simulate in-patient scatter. We show that for this system, the point spread function (PSF) resolutions were 8.3~cm for CoR and 5.3--4.7~cm for the proposed ScLoR projector and the combination with the CoR, demonstrating the advantage of using scattered events with the MCPP method. We also studied how the missing energy of scattered events influences the PSFs obtained with MCPP, noting that lower missing energy yields better resolution. Its combination with a scatter classification method on experimental data is being evaluated. In conclusion, the MCPP approach facilitates the integration of different projectors to process a maximum of detected events.

References

[1] Efthimiou, N., Karp, J.S., Surti, S. 2022, 'Data-driven,energy-based method for estimation of scattered events in positron emission tomography', *Physics in Medicine & Biology*, vol 67, p. 095010

[2] Moulin, M, Montémont, G, Létang, J 2025, 'Efficiency of an Event Neural Network Classifier for Positron Emission Tomography', *2025 IEEE Nuclear Science Symposium (NSS), Medical Imaging Conference (MIC) and Room Temperature Semiconductor Detector Conference (RTSD)*,(Yokohama Japan),p. 1

[3] Chinn, G, Foudray, MK, Levin, CS, 2006, 'Accurately Positioning and Incorporating Tissue-Scattered Photons into PET Image Reconstruction', *2006 IEEE Nuclear Science Symposium Conference Record*, vol 3, pp. 1746-1751

MIC-10-236

List-Mode Subspace-Based Dynamic PET: 1-Second Temporal Resolution on the NeuroEXPLORER (#3210)

Yanis Djebra, Yassir Najmaoui, Dimitri Szezurek, Yanis Chemli, Kathryn Fontaine, Jean-Dominique Gallezot, Takuya Toyonaga, Marc Normandin, Georges El Fakhri, Chao Ma, Thibault Marin

Yale University, Yale Biomedical Imaging, New Haven, USA

This work was supported in part by the National Institutes of Health under the grants R01EB035093, R01AG076153, and P41EB022544.

Abstract

Dynamic PET imaging is becoming increasingly valuable in neuroimaging and cardiac imaging, thanks to its ability to track functional changes over time.

Conventional approaches to dynamic PET imaging need to find a balance between frame duration and noise: shorter temporal frames can provide important information on rapid physiological processes, but at the expense of increased noise. Traditional filtering strategies aim at reducing noise, but inherently cause loss of spatial and/or temporal resolution.

In this work, we represent dynamic PET images using a subspace model during image reconstruction to substantially reduce noise while preserving spatial and temporal information, thereby exploiting the spatiotemporal correlations in dynamic images. We demonstrate the power of the proposed approach on an in-vivo scan of a nonhuman primate performed on the high-sensitivity, high-resolution NeuroEXPLORER scanner. Dynamic images reconstructed at 1-second frames exhibit high resolution and dramatically reduced noise compared to conventional reconstructions, enabling the visualization of early tracer perfusion, respiratory motion and contrast changes in the whole body, without any gating. The proposed method shows promise for short-frame imaging of the brain and body.

References

[1] H. Li et al., “Performance Characteristics of the NeuroEXPLORER, a Next-Generation Human Brain PET/CT Imager,” Journal of Nuclear Medicine, 2024.

[2] Y. Djebra et al., “LR-PET: A Subspace-Based Dynamic PET Imaging via Explicit Non-Negative Low-Rank Factorization,” in 2025 IEEE NSS/MIC/RTSD, 2025.

[3] J. Qi et al., “Iterative reconstruction techniques in emission computed tomography,” Physics in Medicine and Biology, 2006.

[4] K. Lange et al., “EM reconstruction algorithms for emission and transmission tomography,” Journal of Computer Assisted Tomography, 1984.

[5] H. M. Hudson et al., “Accelerated image reconstruction using ordered subsets of projection data,” IEEE Transactions on Medical Imaging, 1994.

MIC-10-239

Hierarchical ROI-free Learning for GFR Category Stratification in Dynamic ^{99m}Tc-DTPA Renography (#1527)

Zhuoyuan Xu[1], Jinlin Li[2], Chunhao Li[1], Jiaqi Zhong[2], Wen Sun[2], Jingxian Chen[3], Jiahui Dong[1], Zhigang Sun[1], Yuecan Zeng[4], Huan Xiao[2], Jingzhang Sun[1]

[1] Hainan University, Department of Data Science and Big Data, Haikou, China; [2] The First Affiliated Hospital of Hainan Medical University, Department of Nuclear Medicine, Haikou, China; [3] Hainan General Hospital, Haikou, China; [4] The Second Affiliated Hospital of Hainan Medical University, Department of Radiation Oncology, Cancer Treatment Center, Haikou, China

This work was supported in part by the National Natural Science Foundation of China (12505396) and the Science and Technology Talents Innovation Project of Hainan Province (KJRC2023D30). Corresponding authors: Jingzhang Sun and Huan Xiao.

Abstract

Dynamic ^{99m}Tc-diethylenetriaminepentaacetic acid (DTPA) planar renography is widely used for quantitative renal function assessment, but Gates-based glomerular filtration rate (GFR) estimation depends on manually defined kidney and background regions of interest (ROIs), which is time-consuming and operator-dependent. We developed RFVGG, an ROI-free hierarchical deep learning framework that learns directly from dynamic renography image sequences using routinely available Gates-derived labels. This retrospective study included 728 consecutive patients who underwent dynamic ^{99m}Tc-DTPA planar renography. RFVGG was built on a shared 3D VGG-style backbone with hierarchical task-specific heads for three-, five-, and six-category GFR stratification. Model development followed five-fold cross-validation, and RFVGG was compared with CNN, ResNet-18, and DenseNet under identical evaluation settings. Classification performance was evaluated using accuracy, precision, recall, and specificity. RFVGG achieved accuracies of 0.842±0.020, 0.705±0.043, and 0.606±0.042 for the three-, five-, and six-category tasks, respectively. The corresponding precisions were 0.846±0.017, 0.668±0.037, and 0.614±0.034; recalls were 0.843±0.024, 0.689±0.045, and 0.642±0.039; and specificities were 0.915±0.012, 0.920±0.012, and 0.920±0.008, respectively. These results indicate that RFVGG can perform automated ROI-free GFR category stratification from dynamic ^{99m}Tc-DTPA planar renography without contour-based kidney or background ROI tracing

References
[1] A. Levin *et al.*, "Kidney Disease: Improving Global Outcomes (KDIGO) CKD Work Group. KDIGO 2012 clinical practice guideline for the evaluation and management of chronic kidney disease," *Kidney international supplements*, vol. 3, no. 1, pp. 1-150, 2013.
[2] Y. Pi *et al.*, "Deep regression using 99mTc-DTPA dynamic renal imaging for automatic calculation of the glomerular filtration rate," *European Radiology*, vol. 33, no. 1, pp. 34-42, 2023.

MIC-10-242

Design and Construction of Physical and Digital Phantoms for Image-Derived Input Function Validation Studies in Brain PET Imaging (#1866)

Usman Khalid[1,2], Ceren Memis[1], Lutz Tellmann[1], Manfred Lennartz[3], Tobias Meurer[3], Philipp Lohmann[1,4], Hidehiro Iida[5], Martin Wiesmann[6], Hans Herzog[1], Jürgen Scheins[1], Nadim J. Shah[1,7], Christoph W. Lerche[1], Cláudia R. Brambilla[1]

[1] Forschungszentrum Jülich GmbH, Institute of Neuroscience and Medicine, INM-4, Jülich, Germany; [2] RWTH Aachen University, Faculty of Medicine, Aachen, Germany; [3] Forschungszentrum Jülich GmbH, Institute of Energy Technologies (IET), Jülich, Germany; [4] RWTH Aachen, Department of Nuclear Medicine, Aachen, Germany; [5] University of Turku, Turku PET center, Institute of Biomedicine, Faculty of Medicine, Turku, Finland; [6] Uniklinik Aachen, Clinic for Diagnostic and Interventional Neuroradiology, Aachen, Germany; [7] RWTH Aachen, Department of Neurology, Aachen, Germany

The authors would like to acknowledge their gratitude to Claire Rick for English proofreading. This work was supported by the Horizon EIC 2022 Pathfinder Open– RETIMAGER, Project ID:101099096.

Abstract
Quantitative brain PET studies often require arterial input functions (AIF), which can be derived from radiotracer concentrations through the internal carotid arteries (ICAs) in dynamic PET images. Image-derived input function (IDIF) methods avoid invasiveness; however, challenges in precise quantification of dynamic flow conditions and correction of partial volume effects (PVE) persist. Recently developed dedicated PET systems for brain imaging, such as the RETIMAGER System, offer excellent spatial and temporal resolution, which is of high relevance for IDIF determination. In addition, hybrid systems offer complementary information for improved IDIF validation. This study shows the design and development of digital and physical phantoms for future validation of IDIF methods in Brain PET systems. A two-phase approach employs the design and construction of a cylindrical phantom with an ICA insert matching real structural geometries. Phase 1 uses a digitalized phantom with Monte Carlo (MC) simulations to validate and optimize acquisition and reconstruction parameters. Phase 2 is in progress for experimental versus simulation validations using a physical phantom with an ICA insert to simulate flow dynamics using an injector. Additionally, a 3D head phantom incorporating gray matter (GM), white matter (WM), scalp, and ICA structures has been designed and is in fabrication for future comprehensive validation.

References
[1] Y. F. Tai et al, J. Neurol. Neurosurg. Psych, vol. 75, no. 5, pp. 669–76, 2004.
[2] H. Zaidi et al., Med. Phys., vol. 38, no. 10, pp. 5667–89, 2011.
[3] P. Ziegler-Fregonara et al., J. Cereb. Blood Flow Metab., vol. 31, no. 10, pp. 1986–98, 2011.
[4] P. Ziegler-Fregonara et al., J. Cereb. Blood Flow Metab., vol. 29, no. 11, pp. 1825–35, 2009.
[5] C. R. Brambilla et al., Front. Neurosci., vol. 19, p. 1725728, 2025.
[6] M. L. Thorne et al., Ultrasound Med. Biol., vol. 35, no. 1, pp. 120–28, 2009.
[7] H. Iida et al., Ann. Nucl. Med., vol. 27, no. 1, pp. 25–36, 2013.
[8] A. Haddar et al., “RETIMAGER”, in Proc. IEEE, pp. 1–1, 2025.

MIC-10-245

TRACE: A New Phantom for Simultaneous Multi-Method Assessment of PET Spatial Resolution (#2135)

Deepa Choudhary[1,2], Brahim Mehadji[1], Ramsey D. Badawi[1], Negar Omidvari[1], Benjamin A. Spencer[1]

[1] UC Davis Health, Radiology, Sacramento, USA; [2] UC Davis, Biomedical Engineering, Davis, USA

Abstract
Spatial resolution assessment in positron emission tomography (PET) typically relies on the full-width at half-maximum (FWHM) of point-like line sources reconstructed with filtered back-projection (FBP), yet modern clinical imaging predominantly uses iterative reconstruction methods, motivating the need for phantoms that evaluate resolution under clinically relevant protocols. To address this, we present TRACE (Tapered Rod Array for Continuous-resolution Evaluation), a 3D-printed phantom enabling simultaneous spatial resolution assessment via four complementary methods – FBP FWHM, modulation transfer function (MTF), Rayleigh criterion, and visual assessment – in a single acquisition. TRACE consists of a tapered cone with continuously decreasing fillable conical rod diameters (4.8–1.2 mm over 10 cm) and three integrated capillary slots for NEMA-compatible line

source measurements. The phantom was scanned on the uEXPLORER total-body PET scanner in transverse (XY) and axial (XZ) orientations. FBP FWHM yielded mean transverse resolutions of 3.0 ± 0.2 mm (radial) and 3.4 ± 0.2 mm (tangential), and 2.9 ± 0.5 mm axially. Under OSEM reconstruction, the Rayleigh criterion and visual assessment resolved rods down to 1.8 mm (XY) and 2.0 mm (XZ), while the 50% and 10% MTF were achieved at 2.8 mm and 1.6 mm (XY), and 2.6 mm and 1.7 mm (XZ), respectively. TRACE bridges standardized and clinically relevant resolution assessment, delivering all four metrics in a single acquisition and offering a comprehensive framework for PET spatial resolution characterization

References
[1] NU 2-2018. National Electrical Manufacturers Association; 2018
[2] S. E. Derenzo, T. F. Budinger, J. L. Cahoon, R. H. Huesman and H. G. Jackson, "High Resolution Computed Tomography of Positron Emitters," in *IEEE Transactions on Nuclear Science*, vol. 24, no. 1, pp. 544-558, Feb. 1977, doi: 10.1109/TNS.1977.4328738.
[3] Spencer, Benjamin A., et al. "Performance evaluation of the uEXPLORER total-body PET/CT scanner based on NEMA NU 2-2018 with additional tests to characterize PET scanners with a long axial field of view." *Journal of nuclear medicine* 62.6 (2021): 861-870.
[4] Toussaint M, Lecomte R, Dussault JP. Improvement of Spatial Resolution with Iterative PET Reconstruction using UltraFast TOF. IEEE Trans Radiat Plasma Med Sci. 2021 Sep;5(5):729-737. doi: 10.1109/trpms.2020.3033561. Epub 2020 Oct 26. PMID: 35059544; PMCID: PMC8765719.

MIC-10-248

A Reconstruction-Agnostic Paper Made Fan Phantom for Task-Relevant PET Spatial Resolution Assessment (#2307)

Brahim Mehadji[1], Ramsey D. Badawi[1,2], Lorenzo Nardo[1], Benjamin A. Spencer[1]

[1] UC Davis, Radiology, Sacramento, USA; [2] UC Davis, Biomedical Engineering, Davis, USA

This work was supported by the NIH NIBIB grant No. R03EB036611.

Abstract
Conventional methods for assessing PET spatial resolution, such as the NEMA NU-2 protocol and ACR guidelines, provide limited insight into the effective resolution achieved with modern clinical reconstruction techniques. In this work, we propose a simple and low-cost fan-pattern paper phantom enabling modulation transfer function (MTF)-based analysis for continuous spatial resolution characterization. The phantom consists of laser-cut paper in a fan geometry with gap sizes decreasing from 5 mm to 1 mm which is briefly immersed in an F-18 solution. Reproducibility and repeatability were evaluated on a uEXPLORER PET/CT system. Images were reconstructed using filtered back projection (FBP) and multiple clinical reconstruction algorithms, including OSEM and artificial intelligence (AI)-based methods. Spatial resolution full width at half maximum (FWHM) was derived from the MTF using the 50% frequency criterion. Results demonstrate an average radial resolution of 3.23 ± 0.034 mm for reproducibility and 3.22 ± 0.054 mm for repeatability, consistent with NEMA NU-2 measurements but with lower uncertainties, which can be attributed to the robustness of the MTF evaluation method. The proposed approach enables rapid (<5 min), robust, and continuous assessment of spatial resolution, including under clinical and AI-based reconstruction conditions. The proposed phantom provides a practical tool for PET system characterization and reconstruction optimization and will be made available to facilitate wider adoption.

References
[1] NU 2-2018. National Electrical Manufacturers Association; 2018.
[2] Measurements-of-Positron-Emission-Tomographs, ACR; 2025
[3] G. Li et al., 2024, DOI: 10.2967/jnumed.123.265929

MIC-10-251

Quantitative Image Quality Evaluation of ^{177}LuSPECT Using a NEMA NU 4-based SPECT IQPhantom (#2365)

Yirong Zhang[1], Daan Boreel[2], Milou Boswinkel[2], Ruud M. Ramakers[3], Konstantinos Chatzipapas[1], Marlies C. Goorden[1]

[1] TUDelft, Radiation Science & Technology Department, Delft, Netherlands; [2] Radboud University Medical Center, Department of medical Imaging, Nijmegen, Netherlands; [3] MILabs B.V, Utrecht, Netherlands

This work was supported by the research Grant UNRANU - Understanding the radiobiology of therapeutic medical radionuclides (project no.15311), which is funded by the Dutch Research Council (NWO).

Abstract

Lutetium-177, a combined gamma and beta emitter, is gaining significant attention as a theranostic isotope with clinical applications in metastatic prostate cancer and neuroendocrine tumors. Quantitative imaging of ^{177}Lu in a preclinical setting is important for therapy optimization. This study evaluates the image quality performance of a small-animal SPECT scanner equipped with an ultra-high-sensitivity collimator for ^{177}Lu using a SPECT IQ phantom adapted from the NEMA NU 4 PET phantom. Whole-body acquisitions were performed using a multi-bed protocol, and projection data were reconstructed with an iterative algorithm under different post-filtering conditions. Image quality was assessed using recovery coefficients (RCs) for rods of varying diameters, and image noise was quantified as the percentage standard deviation (%STDunif) within a uniform region. The results show that RC varies with rod size, iteration number, and post-reconstruction filtering. Effective recovery was observed for 1.35 mm rods (RC ~0.77), while RC values decreased to approximately 0.38 and 0.23 for 1.15 mm and 0.95 mm rods, respectively, indicating that reliable recovery is achieved for rod sizes of about 1.5 mm. Image noise increases with iteration number and decreases with stronger smoothing, reflecting the expected resolution–noise trade-off. These initialfindings demonstrate the capability of the SPECT IQ phantom for quantitative performance evaluation and protocol optimization in high-resolution SPECT imaging.

MIC-10-254

Investigation of the stability of energy-based scatter estimation in PET (#2546)

SeyedAmir ZamanPour, Ahmadreza Rezaei, Johan Nuyts, Georg Schramm

KU Leuven, Department of Imaging and Pathology, Leuven, Belgium

Abstract

Energy-based scatter estimation in PET estimates scatter from the energy information of detected photon pairs, without relying on an attenuation map. Recent work demonstrated promising results using a model that decomposes the 2D energy histogram into true and scattered coincidences via three basis functions. This model rests on two fundamental assumptions. First, that the **shape** of the scattered energy spectrum is sufficiently stable across varying activity distributions and time-of-flight (TOF) bins to be represented by fixed weights on two basis functions ($c_1 p_1 + c_2 p_2$). Second, that the scattered and true energy distributions remain **statistically distinguishable** given the finite energy resolution of the scanner: when low-angle Compton scatter dominates (as in LORs through high-contrast hot regions at central TOF bins) the scatter spectrum shifts towards 511 keV and the two distributions may become so spectrally similar that reliable decomposition is mathematically infeasible, regardless of counting statistics. In this work, we investigate the validity of both assumptions using long MCGPU-PET Monte Carlo simulations of an elliptical phantom with hot-sphere inserts of radii 1, 3, and 5 cm and contrast ratios of 1:10 and 1:100. Scattered energy spectra are extracted and inspected across TOF bins, hot-region sizes, and contrast ratios; challenging cases are identified for each assumption; and the feasibility of the nine-component 2D energy histogram decomposition from S.A. Zaman Pour et al. is evaluated.

MIC-10-257

A Quantitative Comparison of PET Image Reconstruction Methods for Amyloid-Beta Plaque Identification in Alzheimer's Disease (#2744)

Azeezat Azeez[1], Mehdi Khalighi[1], Andrzej Sokolowski[2], Elizabeth Mormino[2], Christina Young[3], Fernando Boada[1]

[1] Stanford School of Medicine, Radiological Sciences Laboratory, Palo Alto, USA; [2] Stanford School of Medicine, Department of Neurology and Neurological Sciences, Palo Alto, USA; [3] University of California Davis, Department of Radiology, Davis, Davis, USA

This work was supported in part by PHS Grant EB029306.

Abstract
The accurate quantification of amyloid-beta (Aβ) plaques with Positron Emission Tomography (PET) is critical for the early diagnosis and management of Alzheimer's Disease (AD). However, the diagnostic accuracy of PET imaging is heavily dependent on the image reconstruction algorithm employed. This study provides a quantitative comparison of three distinct PET image reconstruction methods to determine their efficacy for Aβ plaque identification. Using a clinical AD dataset, each of the three algorithms was applied to generate enhanced PET images. The resulting Aβ burden was quantified using the standardized Centiloid scale(CL), and a rigorous statistical analysis was performed to evaluate the performance differences between the methods. Identifying the optimal reconstruction technique is paramount, as its implementation can lead to more sensitive early detection of AD, improved monitoring of disease progression, and ultimately, the enhancement of therapeutic outcomes.

MIC-10-260

Dose-Dependent Electron Density CT Images for PET Attenuation Correction (#2877)

Debora Niekämper[1,2], Samaneh Mostafapour[2], Lutz Tellmann[1], Sebastian Faby[4], Heba Alrakh[1], Jürgen Scheins[1], Jan Braaksma[3], Daniel Overbeek[2], Marcel J.W. Greuter[3], N. Jon Shah[1,5], Charalampos Tsoumpas[2], Christoph W. Lerche[1]

[1] Forschungszentrum Jülich GmbH, Institute of Neuroscience and Medicine 4, Jülich, Germany; [2] University of Groningen, University Medical Center Groningen, Nuclear Medicine and Molecular Imaging, Groningen, Netherlands; [3] University of Groningen, University Medical Center Groningen, Department of Radiology, Groningen, Netherlands; [4] Siemens Healthineers AG, Department of Computed Tomography, Forchheim, Germany; [5] RWTH Aachen University, Department of Neurology, Aachen, Germany

DN and CT were partially supported by the NWO AES Vici Talent program (doi: 10.61686/REEAR02777).

Abstract
Generating accurate attenuation maps from CT images is essential for quantitative PET/CT imaging, while minimising radiation exposure is also important. In conventional CT, the attenuation contributions from Compton effect and photoelectric absorption are combined into a single attenuation value and transformed together from the CT energy spectrum to the PET imaging energy, despite their different energy dependencies. In contrast, spectral CT enables separate electron density and effective atomic number images to be reconstructed. This allows to transform the relevant Compton attenuation contribution independently by applying a scaling factor to the electron density image. In this study, we compare attenuation maps obtained using this approach with those obtained via a bilinear transformation. Measurements of phantoms containing various tissue-equivalent inserts are performed using a PET/CT with twin-beam dual-energy capability and a photon-counting CT. In additional measurements, selected inserts are replaced by compartments containing activity in order to evaluate the effect of

the different attenuation maps on reconstructed PET images. The measurements are performed across a wide dose range to investigate how far the radiation dose can be reduced while still obtaining accurate attenuation maps. Preliminary results show good agreement between attenuation values obtained at different dose levels, with the highest discrepancies between both transformation methods observed for bone-equivalent inserts.
Using electron density and effective atomic number reconstructions from spectral scanners to generate attenuation correction values may improve quantitative PET imaging.

References
[1] Carney, JPJ et al. 2006, 'Method for transforming CT images for attenuation correction in PET/CT imaging', *Medical Physics*, 33 4

[2] Guy, MJ et al. 1998, 'DETECT - Dual Energy Transmission Estimation CT - for improved attenuation correction in SPECT and PET', *IEEE Trans. Nucl. Sci*, 45 3

[3] Mostafapour, S et al. 2024, 'Ultra-low dose CT scanning for PET/CT', *Medical Physics*, 51 1

MIC-10-263

TOF-Aware Single Scatter Simulation in STIR: Implementation and Validation Against Monte Carlo (#2967)

Manil Sabeur[1,2], SeyedAmir ZamanPour[4], Simon Stute[2], Younes Moussaoui[1,2], Saïd Moussaoui[1], Kris Thielemans[3]

[1] Nantes Université, Ecole Centrale de Nantes, LS2N, Department of Medical Imaging, Nantes, France; [2] CHU Nantes, Section of Nuclear Medicine, Nantes, France; [3] University College London, Institute of Nuclear Medicine, London, UK; [4] KU Leuven, Department of Imaging and Pathology, Leuven, Belgium

The authors thank the STIR open-source community.
This work was supported by LS2N, Ecole Centrale de Nantes, and by CCP SyneRBI which is funded by the EPSRC grant EP/T026693/1 and by STFC through the UKRI Digital Research Infrastructure programme.

Abstract
Single scatter simulation (SSS) combined with tail-fitting is the standard analytical method for scatter correction in PET. Extending SSS to time-of-flight (TOF) data requires non-trivial adaptations to the scatter kernel. The open-source Software for Tomographic Image Reconstruction (STIR) library has a widely used implementation of SSS for non-TOF data. Here, we present a fully TOF-aware SSS implementation in STIR with two contributions: (i) the TOF kernel ε_t in the scatter-arm emission integral is computed via erf (error function) as opposed to central point approximation in Watson, avoiding the need for an extra normalisation step. (ii) re-use of cached integrals from the non-TOF implementation. The implementation is validated against MCGPU Monte Carlo on a 9-ring compact PET scanner (27 TOF bins, 169 ps, uniform phantom), confirming strong agreement with MC single scatter (r=0.985 full 4-D sinogram; r=0.994 TOF-summed spatial). This contribution opens the door to fully quantitative PET reconstructions for TOF-PET in STIR.

References
[1] C. Watson, “Extension of single scatter simulation to scatter correction of time-of-flight PET,” IEEE Trans. Nucl. Sci., vol. 54, no. 5, pp. 1679–1686, 2007. doi: 10.1109/TNS.2007.901227.
[2] K. Thielemans, C. Tsoumpas, S. Mustafovic et al., “STIR: software for tomographic image reconstruction release 2,” Phys. Med. Biol., vol. 57, no. 4, pp. 867–883, 2012. doi: 10.1088/0031-9155/57/4/867.
[3] Polycarpou, K. Thielemans, R. Manjeshwar, P. Aguiar, P. Marsden, and C. Tsoumpas, “Comparative evaluation of scatter correction in 3D PET using different scatter-level approximations”, Annals of Nuclear Medicine, vol. 25, no. 9, pp. 643–649, Nov. 2011, doi: 10.1007/s12149-011-0514-y.
[4] J. L. Herraiz, A. Lopez-Montes, and A. Badal, “MCGPU-PET: an open-source real-time Monte Carlo PET simulator,” Comput. Phys. Commun., vol. 296, p. 109008, Mar. 2024. doi: 10.1016/j.cpc.2023.109008.
[5] R. José Santo, A. Salomon, H. W. A. M. de Jong et al., “openSSS: an open-source implementation of scatter estimation for 3D TOF-PET,” EJNMMI Phys., vol. 12, p. 17, 2025. doi: 10.1186/s40658-025-00730-x.

MIC-10-266

Event-by-Event Energy-Based Scatter Correction via Bayesian Likelihood Estimation (#3026)

Mohammadreza Teimoorisichani

Siemens Medical Solutions USA Inc., Knoxville, USA

Abstract

Energy-based scatter (EBS) correction is increasingly utilized in PET image reconstruction. This work introduces a novel EBS framework that assigns scatter probabilities to individual listmode events via analytical Bayesian calculations. The method utilizes pre-defined energy distributions of scatter kernels as basis functions. By analyzing the global energy spectrum, the algorithm estimates the fractional probability for each event type and subsequently calculates the likelihood of Compton scattering for individual coincidences. The approach was validated using two phantom datasets acquired on a Biograph Vision PET/CT scanner (Siemens Healthineers). Reconstructed images were compared against standard vendor-implemented single-scatter simulation (SSS) with tail-fitting. Results demonstrate high consistency, with scatter fraction estimates differing by less than 3% from SSS. Furthermore, uniform and NEMA image quality phantom analyses showed less than 1% divergence in contrast recovery and background variability. These findings suggest that the proposed EBS method provides a robust, computationally efficient alternative for scatter estimation in clinical PET reconstruction.

References
[1] Watson, C., *Extension of Single Scatter Simulation to Scatter Correction of Time-of-Flight PET*. IEEE Transactions on Nuclear Science, 2007. 54(5): p. 1679-1686.
[2] Herraiz, J.L., A. Lopez-Montes, and A. Badal, *MCGPU-PET: An open-source real-time Monte Carlo PET simulator*. Computer Physics Communications, 2024. 296.
[3] Efthimiou, N., J.S. Karp, and S. Surti, *Data-driven, energy-based method for estimation of scattered events in positron emission tomography*. Phys Med Biol, 2022. 67(9).
[4] Hamill, J.J., et al., *Energy-based scatter estimation in clinical PET*. Med Phys, 2024. 51(1): p. 54-69.

MIC-10-269

Synthetic CT Generation for Attenuation Correction in Respiratory-Gated Rb-82 Cardiac PET Using 3D Diffusion Models (#3061)

Boxiao Yu[1], Wenyuan Qi[2], Jeff Kolthammer[2], Kuang Gong[1]

[1] University of Florida, J. Crayton Pruitt Family Department of Biomedical Engineering, Gainesville, USA; [2] Canon Medical Research USA, Inc., Vernon Hills, USA

Abstract

Accurate attenuation correction (AC) using computed tomography (CT) is critical for quantitative PET imaging. However, in respiratory-gated cardiac PET, respiratory phase mismatch between gated PET and CT can compromise the accuracy of CT-based AC, while acquiring additional phase-matched CT scans is impractical due to radiation dose concerns. To address these limitations, we employed a 3D Denoising Diffusion Probabilistic Model (DDPM) to generate synthetic CT images directly from non-attenuation corrected (NAC) PET data for gated PET AC. The model was trained using paired non-gated Rb-82 myocardial perfusion PET scans and CT-derived attenuation maps, and directly applied to respiratory-gated PET without retraining. Visual evaluation showed that 3D DDPM generated synthetic CT images with superior anatomical fidelity and improved respiratory phase alignment with gated PET compared with 3D GAN, 3D UNet, and 2D DDPM. Regional quantitative analysis near the diaphragm further demonstrated that 3D DDPM achieved improved attenuation correction in regions most affected by respiratory mismatch.

References

[1] Yu, B., Ozdemir, S., Dong, Y., Shao, W., Pan, T., Shi, K., & Gong, K. (2025). Robust whole-body PET image denoising using 3D diffusion models: evaluation across various scanners, tracers, and dose levels. *European Journal of Nuclear Medicine and Molecular Imaging*, *52*(7), 2549-2562.

[2] Pan, T., Thomas, M. A., & Luo, D. (2022). Data-driven gated CT: an automated respiratory gating method to enable data-driven gated PET/CT. *Medical physics*, *49*(6), 3597-3611.

MIC-10-272

Beyond the Single-Tissue Voxel:A Spin-Echo–Based Multi-Tissue Decomposition Framework with Implications for Synthetic MRI and Machine Learning Diagnosis (#1194)

Haiyi Li[1], Qingfei Luo[2], Marc J. Pomeroy[3], Haifang Li[4], Youngwook Kee[4], Xiaohong J. Zhou[2], Zhengrong J. Liang[4,1], Larry Zeng[5]

[1] Stony Brook University, Electrical and Computer Engineering, Stony Brook, USA; [2] University of Illinois College of Medicine at Chicago, Radiology, Chicago, USA; [3] Stony Brook University, Biomedical Engineering, Stony Brook, USA; [4] Stony Brook University, Radiology, Stony Brook, USA; [5] Utah Valley University, Computer Sience, Orem, USA

Abstract

Conventional synthetic MRI generates contrast images from a single effective set of voxel-wise quantitative parameters: proton density (PD), T1, and T2, which may be insufficient when any two or all three of gray matter (GM), white matter (WM), and cerebrospinal fluid (CSF) coexist within the same image voxel. This work presents an exploratory framework using the standard spin-echo signal generation model with a purity-weighted Expectation-Maximization algorithm for tissue prototype estimation that systematically quantifies the prevalence of such multi-tissue voxels. From three co-registered spin-echo MR brain images at distinct Time to Echo (TE), Time to Repetition (TR) settings, per-voxel PD, T1, and T2 relaxation maps are recovered via a robust nonlinear inversion pipeline and validated by re-synthesizing the original images. Each voxel is then decomposed into fractional contributions of GM, WM, and CSF using three methodologically independent models: a Signal-Domain Mixture Model, Parameter-Domain Mixture Model and Mean Parameter-Domain Mixture Model. All three consistently show that 52% – 62% of brain image voxels contain contributions from multiple tissue types, demonstrating model-independently that the single-effective-parameter representation is insufficient in most brain voxels and that conventional synMRI parameter maps can be systematically biased. A tissue-aware synthesis framework is proposed that generates physically grounded MRI contrasts across the full spin-echo (TE, TR) measurement space, providing a quantitative basis for more reliable synthetic MRI. Future work will extend this framework to multi-subject validation and evaluate the synthesized contrast library for machine learning-based lesion diagnosis.

References

[1] D. W. McRobbie, E. A. Moore, et al. “MRI from Picture to Proton,” in Cambridge Univ. Press Cambridge, 2nd ed.U.K.2006.

[2] JBM. Warntjes, et al. “Rapid magnetic resonance quantification on the brain: Optimization for clinical usage,” *Magnetic Resonance in Medicine*, vol. 60, no. 2, pp. 320–329, 2008.

[3] I. Blystad, et al. “Synthetic MRI of the brain in a clinical setting,” *Acta Radiol.*, vol. 53, no. 10, pp. 1158–1163, 2012.

[4] M. A. González Ballester, A. Zisserman, and M. Brady, “Estimation of the partial volume effect in MRI,” *Med Image Anal.*, vol. 6, no. 4, pp. 389–405, 2002.

[5] Y. Zhang, M. Brady, and S. Smith, “Segmentation of brain MR images through a hidden Markov random field model and the expectation-maximization algorithm,” *IEEE Trans Med Imaging*, vol. 20, no. 1, pp. 45–57, 2001.

[6] Z. Liang and S. Wang, “An EM approach to MAP solution of segmenting tissue mixtures: a numerical analysis,” *IEEE Trans Med Imaging*, vol. 28, no. 2, pp. 297–310, 2009.

[7] P. Tofts, Ed., “Quantitative MRI of the Brain: Measuring Changes Caused by Disease.” Chichester, U.K.: Wiley, 2003.

[8] Z. Liang, S. Chang, Y. Gao, et al. "Leveraging prior knowledge in machine intelligence to improve lesion diagnosis for early cancer detection,” *Medical Physics*, vol. 52, no. 7, pp.1–14, 2025.

[9] H. Li, Pomeroy, M. J, et al. "Enhancing classification of indeterminate pulmonary nodules at multiple scans in NLST dataset through integrated spectral CT radiomics." Medical Imaging 2026: Imaging Informatics. Vol. 13930. SPIE, 2026.

MIC-10-275

Assessment of Cortical Defect Discriminability in Reduced-Dose Pediatric Tc-99m DMSA Renal SPECT (#1422)

Weibin Fu[1], Yongyi Yang[1], Neha Kwatra[2,3], S. Ted Treves[2,3], Frederic Fahey[2], Michael A. King[4]

[1] Illinois Institute of Technology, Electrical and Computer Engineering, Chicago, USA; [2] Harvard Medical School, Radiology, Boston, USA; [3] Boston Children's Hospital, Radiology, Boston, USA; [4] University of Massachusetts Medical Center, Radiology, Worcester, USA

This work was supported under NIH Grant R01-EB029315.

Abstract

In prior work, deep-learning (DL) based denoising was demonstrated to be capable of yielding images comparable to standard-dose studies when the imaging dose is reduced several-fold in pediatric Tc-99m DMSA renal SPECT, based on both quantitative image quality metrics and visual assessment by clinical experts. In this study, we further evaluate the diagnostic utility of DL-denoised images by employing a DL-based classifier to perform a task-based assessment of cortical defects, where a 3D convolutional neural network (CNN) was used to differentiate kidneys with cortical defects from those with normal uptake. We demonstrated this approach with a set of clinical data acquired from 956 subjects, with performance quantified using receiver-operating characteristic (ROC) analysis. The results showed that, without DL denoising, the quarter-dose data achieved a lower classification performance than the full-dose in terms of the area under the ROC curve (p-value < 0.001); however, with DL denoising, the quarter-dose data achieved a statistically comparable performance to that of the full-dose data (p-value = 0.452).

MIC-10-278

Automated Coronary Artery Extraction up to Distal Vessels Based on Hessian Matrix and 3D Skeletonization to Compensate for Incomplete Labels (#1528)

Ryutaro Ide[1], Koichi Ogawa[2]

[1] Hosei University, Applied Informatics, Graduate School of Science and Engineering, Tokyo, Japan; [2] Hosei University, Applied Informatics, Faculty of Science and Engineering, Tokyo, Japan

Abstract

While deep learning has become the mainstream approach for coronary artery extraction from coronary computed tomography angiography (CCTA) images, its reliance on training data makes it difficult to accurately extract fine distal vessels using existing datasets with insufficient annotations. Therefore, this study proposes a hybrid extraction method utilizing image feature analysis. This method consists of three stages. First, an initial extraction is performed based on anatomical features and CT values. Second, a chained connection algorithm combining tubular structure enhancement via the Hessian matrix and three-dimensional (3D) skeletonization is employed to connect vessel fragments through local search, thereby recovering continuity. Third, volume expansion is performed using an adaptive threshold corresponding to local intensity to restore the accurate vessel diameter. Application of this method to an open dataset demonstrated extreme robustness against CT value degradation caused by insufficient contrast agent perfusion. We successfully extracted and reconstructed fine distal vessels that were missing in the existing labels while maintaining their continuity. Future work involves collaborating with clinical specialists to reconstruct high-quality ground truth labels and conduct rigorous quantitative evaluations.

References

[1] Zeng, A, Wu, C, Lin, G, et al. 2023, 'ImageCAS: A large-scale dataset and benchmark for coronary artery segmentation based on computed tomography angiography images,' Computerized Medical Imaging and Graphics, Vol.109, https://doi.org/10.1016/j.compmedimag.2023.102287

[2] Xu, X 2023, 'ImageCAS: A Large-Scale Dataset and Benchmark for Coronary Artery Segmentation based on CT,' Kaggle

[3] Zhao, B, Peng, J, Zhang, K, et al. 2025, 'TMN-Net: A Hybrid 2.5D Multi-Branch Transformer Network for Coronary Artery Segmentation in Cardiac Diagnosis,' IEEE Access, pp. 115581-115603

[4] Tayebi, RM, Wirza, R, Sulaiman, PSB, et al., 2014, 'Cardiac Components Categorization and Coronary Artery Enhancement in CT Angiography,' International Conference on Computer Assisted System in Health, https://doi.org/10.1109/CASH.2014.19

MIC-10-281

Differential Diagnosis of PD, PSP, and MSA: An XGBoost Approach to Retinal Layer Analysis (#1850)

Marina Rodriguez-Rubio[1], **Francisco J. Martínez Murcia**[1,2], Juan E. Arco[3], Ignacio Álvarez Illán[1,2], Fermin Segovia[1,2], Carmen Jiménez-Mesa[2], Cristóbal Vazquez-Garcia[1,2], Juan Manuel Gorriz[1,2], Javier Ramirez[1,2], Sonja Schönecker[4], Sebastian Kamp[4], Lukas Klatte[4], Sabrina Katzdobler[4,6], Lena Marth[4,6], Olivia Wagemann[4,6], Carla Palleis[4,6], Urban Fietzek[4], Endy Weidinger[4,6], Adrian Danek[4], Gunter Hölinger[4,6], Joachim Havla[7], Alexander Bernhardt[4], Alexander Jäck[4], Johannes Levin[4,6]

[1] University of Granada, Department of Signal Theory, Networking and Communications, Granada, Spain; [2] Andalusian Research Institute in Data Science and Computational Intelligence, Granada, Spain; [3] Mind, Brain and Behavior Research Center (CIMCYC), Granada, Spain; [4] Ludwig-Maximilians-Universität München, Department of Neurology, LMU University Hospital, Munich, Germany; [5] SyNergy, Munich Cluster for Systems Neurology, Munich, Germany; [6] German Center for Neurodegenerative Diseases (DZNE), Munich, Germany; [7] Ludwig-Maximilians-Universität München, Institute of Clinical Neuroimmunology, Biomedical Center and University Hospital, Munich, Germany

This research is part of the projects PID2022-137629OA-I00, {CNS2024-154296} and PID2022-137451OB-I00, funded by MICIU/AEI/10.13039/501100011033 and by ERDF/ EU, and TIC251-G-FEDER project, funded by ERDF/EU. The Friedrich-Baur-Stiftung and the “FöFoLe” Program of the Faculty of Medicine of the Ludwig-Maximilians-Universität München have supported the work of S.S.

Abstract

Optical coherence tomography (OCT) provides non-invasive retinal biomarkers that may reflect the distinct neurodegenerative patterns of underlying proteinopathies. This study evaluates a machine learning framework to classify synucleinopathies (Parkinson’s disease [PD] and multiple system atrophy [MSA]) and tauopathies (progressive supranuclear palsy [PSP]) using retinal layer morphometry. Several classification tasks were assessed, ranging from healthy control (HC) discrimination to the differential classification of proteinopathic groups. XGBoost was employed as the primary classifier and evaluated using nested cross-validation. To minimize intra-subject variability, only the most recent visit per patient was included, with features aggregated as the average of both eyes to represent bilateral neurodegenerative involvement. The model demonstrated notable efficacy in distinguishing synucleinopathies (PD+MSA) from tauopathies (PSP), achieving an accuracy of 0.704 ± 0.057. This performance was comparable to the binary classification of HCs vs. all pathological cases (0.724 ± 0.079). In contrast, multi-class settings proved more challenging. These findings suggest that while fine-grained clinical subtype differentiation remains a challenge, OCT-derived biomarkers are highly effective at capturing the broad divergent impacts of alpha-synuclein and tau pathology on the retina.

References

[1] C. Palleis et al., “Biomarker-based classification of corticobasal syndrome,” Brain, 2026.

[1] Luo, X, et al. 2023, ‘Retinal Structure Abnormalities in Parkinson's Disease and Atypical Parkinsonism’, Biomolecules, 13, 218, Basel: MDPI.

[2] Mammadova, N, et al. 2026, ‘Retinal Thickness Profiles in Parkinsonian Syndromes: Discerning Parkinson's Disease, Multiple System Atrophy, and Progressive Supranuclear Palsy via Optical Coherence Tomography’, Biomedicines, 14, 249, Basel: MDPI.

[3] Visser, F, et al. 2024, 'Optical Coherence Tomography as a Biomarker in the Differential Diagnosis between Parkinson's Disease and Atypical Parkinsonian Syndromes: A Narrative Review', Applied Sciences, 14, 2491, Basel: MDPI.
[4] Zhang, Y, et al. 2023, 'Applications of Machine Learning to Diagnosis of Parkinson's Disease', Brain Sciences, 13, 1546, Basel: MDPI.

MIC-10-284

Multi-step Nonlinear Iteration Method for ECT Energy Spectrum Decomposition (#1885)

Junxu Mu, Zhenrui Lu, Jiangpeng Peng, Zerui Yu, Dongdong Bi, Shaohui An

United Imaging Healthcare Co., Ltd, MI BU Detector R&D Center, Shanghai, China

Abstract

Theranostic radionuclide molecular imaging represents a core technology in precision nuclear medicine. However, its clinical application is hindered by scatter interference and complex background signals in spectral analysis. To address this bottleneck, this paper proposes a multi-step nonlinear iterative method for energy spectrum background subtraction and full-energy peak analysis, suitable for emission computed tomography detectors. The method realizes high-precision background subtraction and peak stripping via a systematic workflow consisting of peak localization, Log-Log-Square root transformation, interval iterative calculation, and Gaussian fitting. Experimental validation is conducted under both single-nuclide and multi-nuclide conditions. The results demonstrate that the proposed method can effectively separate full-energy peaks submerged by scatter in single-nuclide spectra. For the CsI detector, the energy resolution is improved from 12.9% to10.97%. For multi-nuclide and multi-peak spectra, it successfully separates overlapping peaks, suppresses Compton continuum interference, and optimizes energy resolution to around 10.6%. This method improves detector energy resolution, provides solid technical support for the clinical translation of theranostic radionuclide molecular imaging, and exhibits favorable adaptability and correction accuracy. Future work will focus on optimizing iterative efficiency and extending the method's applicability to more complex clinical scenarios.

References
[1] N. Pandit-Taskar, S. M. Larson, and J. A. Carrasquillo, "Theranostics in nuclear medicine: current status and future directions," J. Nucl. Med., vol. 59, no. 1, pp. 15-22, Jan. 2018, doi:10.2967/jnumed.117.198945.
[2] M. Morhac and V. Matousek, "Peak clipping algorithms for background estimation in spectroscopic data," Appl. Spectrosc., vol. 62, no. 1, pp. 91–106, Jan. 2008, 10.1366/000370208783412762.
[3] W. Zhang, Y. Li, H. Wang, Y. Zhang, and Z. Li, "System performance characterization of United Imaging Healthcare's Micro-SPECT/CT platform for preclinical imaging," in Proc. IEEE Nucl. Sci. Symp. Med. Imaging Conf. (NSS/MIC), Beijing, China, 2024, pp. 1-4, doi:10.1109/NSS/MIC48546.2024.10765432.

MIC-10-287

MIC-10-290

Low-Dimensional Embeddings of Structural MRI for Multi-Disease Brain Morphometry (#2362)

Carmen Jiménez-Mesa[1,2], Michail Mamalakis[3,4], Cristobal Vazquez-Garcia[2,5], Francisco J. Martínez Murcia[2,5], Juan E. Arco[2,6], Fermin Segovia[2,5], Javier Ramirez[2,5], Andres Ortiz[1,2], John Suckling[3], Juan Manuel Gorriz[2,3]

[1] University of Malaga, Department of Communications Engineering, Malaga, Spain; [2] University of Granada, DaSCI Andalusian Institute of Data Science and Computational Intelligence, Granada, Spain; [3] University of Cambridge, Department of Psychiatry, Cambridge, UK; [4] University of Cambridge, Cancer Research United Kingdom Cambridge Institute, Cambridge, UK; [5] University of Granada, Department of Signal Theory, Telematics and Communications, Granada, Spain; [6] University of Granada, Mind, Brain, and Behavior Research Center, Granada, Spain

This research is part of the PID2022-137451OB-I00 and PID2022-137629OA-I00 projects, funded by the MICIU/AEI /10.13039/501100011033 and by "ERDF/EU". C.J.M is supported by grant JDC2023-051807-I funded by MICIU/AEI/10.13039/501100011033 and by ESF+.

Abstract

The differential diagnosis of neurological disorders such as Alzheimer's disease (AD), frontotemporal dementia (FTD), Parkinson's disease (PD), and multiple sclerosis (MS) remains a clinical challenge due to overlapping neuroanatomical atrophy patterns in structural Magnetic Resonance Imaging (MRI). This work investigates whether low-dimensional embeddings derived from T1-weighted MRI can reveal a consistent neuroanatomical organisation across these conditions. Using a dataset of 528 subjects, we compared two feature extraction strategies: (i) high-dimensional voxel-wise representations and (ii) regional embeddings based on the Automated Anatomical Labeling (AAL) atlas (116 regions). Dimensionality reduction was performed using Principal Component Analysis (PCA) followed by Uniform Manifold Approximation and Projection (UMAP) to project subjects into a two-dimensional manifold embedding. Our results demonstrate that the neuroanatomical manifold is remarkably scale-invariant as both voxel-wise and regional embeddings yielded consistent topological distributions. Centroid distance analysis in the embedding space revealed a progressive deviation from the HC baseline across disorders. Interestingly, while the model was built on the HC-AD axis, MS and FTD cohorts exhibited the largest structural displacements

(d_{MS}=7.24, d_{FTD}=5.59) compared to AD (dAD=3.57) and PD (d_{PD}=4.27). These findings suggest that low-dimensional manifold representations derived from structural MRI are robust to spatial aggregation and may provide an interpretable framework for studying shared and disease-specific brain alterations across heterogeneous neurological disorders.

References
[1] Jimenez-Mesa, C., Ramirez, J., Suckling, J., Vöglein, J., Levin, J., Gorriz, J. M., & Alzheimer's Disease Neuroimaging Initiative. (2023). A non-parametric statistical inference framework for deep learning in current neuroimaging. *Information Fusion*, *91*, 598-611.
[2] Vázquez-García, C., Martínez-Murcia, F. J., Segovia, F., Forte, A., Ramírez, J., Illán, I., Hernández-Segura, A., Jiménez-Mesa, C., & Górriz, J. M. (2026). An explainable framework for the relationship between dementia and metabolism patterns. *NeuroImage*, 330, 121855.
[3] Prado, P., Medel, V., Gonzalez-Gomez, R., Sainz-Ballesteros, A., Vidal, V., Santamaría-García, H., ... & Ibañez, A. (2023). The BrainLat project, a multimodal neuroimaging dataset of neurodegeneration from underrepresented backgrounds. *Scientific Data*, *10*(1), 889.
[4] Tzourio-Mazoyer, N., Landeau, B., Papathanassiou, D., Crivello, F., Etard, O., Delcroix, N., ... & Joliot, M. (2002). Automated anatomical labeling of activations in SPM using a macroscopic anatomical parcellation of the MNI MRI single-subject brain. *Neuroimage*, *15*(1), 273-289.

MIC-10-293

Detector design in the AIDER Compton Camera Using Neural Networks: A Hybrid CNN-DNN Approach (#2484)

Deniel Rodriguez Almora[1], Jose Altube[1], Luis Barrientos[1], Alessio Brunamonti[2], Karol Brzezinski[1], Carlo E. Fiorini[2], Filippo Ghisio[2], Andrea Hanna[3], Alain Iltis[3], Siddharth Parashari[1], Javier Pérez Curbelo[1], Gabriela Llosá[1]

[1] Instituto de Física Corpuscular (IFIC-CSIC/UVEG), Valencia, Spain; [2] Politecnico di Milano, Dipartimento di Elettronica, Informazione and Bioingegneria, Milano, Italy; [3] DAMAVAN Imaging, Troyes, France

This work has received funding from the Spanish MICIU / AEI (project MIDAS, PID2022-143246OB-I00) and from the European Union's EURATOM research and innovation program (AIDER project, G.A. 101061037). S.P. acknowledges the Severo Ochoa CEX2023-001292-S grant, funded by MCIN/AEI/10.13039/501100011033

Abstract
This paper presents the development of a high-performance Compton camera for targeted radionuclide therapy within the framework of the European project AIDER. The camera is composed of two detector planes, each made of four $LaBr_3$ or $CeBr_3$ monolithic crystals of 50 mm x 50 mm size coupled to Silicon Photomultiplier (SiPM) arrays. In order to determine the optimum pixel size, a hybrid analysis approach based on convolutional neural networks (CNN) and dense networks (DNN) has been developed to estimate the interaction position of the photons. Starting from Monte Carlo simulation data (GATE v7.0) and using a reference based on an analytical model, the proposed alternative incorporates the systematic error of this model as an additional input for the NNs. This achieves active correction of the edge effect and improves the overall spatial resolution (FWHM) from a range of 1.80–2.25 mm down to 0.63–0.70 mm. Results show the benefits of the combined NN approach and indicate the possibility of employing SiPM arrays with large pixel sizes, effectively restricting the amount of readout channels. Experimental tests are ongoing.

References
[1] https://aider.ific.uv.es/aider/
[2] L. Barrientos et al., *Radiat. Phys. Chem.*, vol. 208, p. 110922, 2023.
[3] J. Roser et al., *Phys. Med.*, vol. 104956, 2025. doi: 10.1016/j.ejmp.2025.104928.
[4] Li, Z., et al. (2010). IEEE Transactions on Nuclear Science. Vol. 57, No. 5, pp. 2450-2456. 2010. 10.1109/TNS.2010.2051457
[5] G. Jaliparthi, P. F. Martone, A. V. Stolin, and R. R. Raylman, *Phys. Med. Biol.*, vol. 66, no. 14, p. 145008, 2021.
[6] J. Jo and J. S. Lee, *Nucl. Instrum. Methods Phys. Res. A, 2024.DOI: 10.1016/j.nima.2023.168925*
[7] S. Cho and J. S. Lee, *J. Korean Phys. Soc., 2024.DOI: 10.1007/s40042-023-00971-w*
[8] R. Liu et al., *arXiv*:1807.03247, 2018.
[9] A. Nibali et al., *arXiv*:1801.07372, 2018.

MIC-10-296

Impact of Spatial Normalization on the Performance of Deep Learning-Based Systems for Neurodegenerative Disease Classification (#2537)

Fermin Segovia[1,3], Rafael López[1], Cristóbal Vázquez-García[1,3], Alejandro Hernández[1], Álvaro Zorrilla[1], Carmen Jiménez-Mesa[2,3], Francisco J. Martínez Murcia[1,3], Ignacio Álvarez Illán[1,3], Javier Ramírez[1,3], Teodoro Martín-Noguerol[4], Juan M. Górriz[1,3]

[1] Univiersity of Granada, Department of Signal Theory, Networking and Communications, Granada, Spain; [2] University of Malaga, Department of Communications Engineering, Málaga, Spain; [3] Andalusian Institute of Data Science and Computational Intelligence (DaSCI), Granada, Spain; [4] HT Medica, Radiology department, Granada, Spain

This work is part of the projects PID2022-137629OA-I00 and PID2022-137451OB-I00 funded by MICIU/AEI/10.13039/501100011033 and by ERDF/EU, and the C-ING-183-UGR23 project, cofunded by the Consejería de Universidad, Investigación e Innovación and by European Union, funded by Programa FEDER Andalucía 2021-2027

Abstract

This study evaluates the suitability of spatial registration in deep learning for neuroimaging, focusing on the balance between reducing inter-subject anatomical variability and preserving data fidelity. We hypothesize that processing images in their native anatomical space avoids morphological distortions introduced by registration, enabling neural networks to detect subtle structural biomarkers that may be altered in normalized spaces. To test this, a standard densely connected neural network was used to classify two balanced cohorts: one focused on the diagnosis of Parkinson's disease (PD) and the other on the diagnosis of Alzheimer's disease (AD). The experimental design compared four input modalities: whole-brain volumes and gray matter maps, each in native space and registered to a standard reference space. For PD classification, native and registered spaces achieved similar accuracy, although registration produced a marked imbalance between sensitivity and specificity. For AD, the best performance was obtained using gray matter in native space, confirming that preserving topological integrity is critical in pathologies with pronounced atrophy. These findings suggest that spatial registration should not be considered an indispensable preprocessing step in deep learning-based neuroimaging, but rather a methodological choice that must be evaluated based on the task and dataset. Processing in native space is an effective alternative

that simplifies preprocessing while preserving diagnostically relevant information, opening future research directions on model robustness to anatomical variability without prior transformation.

References
[1] M. Klingenberg et al., “MRI Image Registration Considerably Improves CNN-Based Disease Classification”, in Machine Learning in Clinical Neuroimaging: 4th International Workshop, MLCN 2021, Held in Conjunction with MICCAI 2021, Strasbourg, France, September 27, 2021, Proceedings. Berlin, Heidelberg: Springer-Verlag, Sep. 2021, pp. 44–52.
[2] D. Fujibayashi et al., “Nonlinear registration as an effective preprocessing technique for Deep learning based classification of disease,” IEEE Engineering in Medicine and Biology Society. Annual International Conference, vol. 2021, pp. 3245–3250, Nov. 2021.
[3] H. He et al., “Landmark-guided region-based spatial normalization for functional magnetic resonance imaging,” Human Brain Mapping, vol. 43, no. 11, pp. 3524–3544, Apr. 2022.
[4] J. Kim et al., “An interactive cascaded deep learning framework with expert refinement for accurate striatal subregion segmentation,” Scientific Reports, vol. 16, no. 1, p. 6550, Jan. 2026.
[5] V. Ramineni et al., “STN-MRI: A Spatial Transformer Network-Based Pipeline for ROI-Aware Brain MRI Preprocessing and Alignment,” in 2025 29th International Computer Science and Engineering Conference (ICSEC), Nov. 2025, pp. 406–409.

MIC-10-299

Edge-Guided Deformation Field Fusion for Robust PET Motion Correction (#2650)

Qiong Liu, Wenyuan Qi, Jeff Kolthammer

Canon Medical Research USA, Vernon Hills, USA

The authors have no disclosures to report.

Abstract
Non-rigid motion correction for gated PET is challenging due to low contrast and high noise in homogeneous regions, where deformation estimates may drift, while strong smoothness regularization can oversmooth boundaries and suppress localized motion near lesions. We propose an edge-guided flow fusion method that combines two deformation fields predicted by identical registration architectures trained with different smoothness weights. For each moving--fixed PET pair, we compute an edge probability map from the gradient magnitude of the Gaussian-smoothed absolute intensity difference, followed by percentile normalization and logistic mapping. After thresholding and morphological dilation, the resulting mask defines an edge-dominant region. We fuse the two predicted flows by selecting the low-regularization flow near edges and the high-regularization flow in homogeneous background regions, then warp the moving PET volume using a spatial transformer. This approach preserves deformation flexibility at boundaries while maintaining smooth motion in low-contrast regions, without changing network architecture.

MIC-10-302

Simulation Trained Convolutional Neural Network For Clinical Inter-Crystal Scattering Filtering (#2835)

Henry Maa-Hacquoil[1], Elliott De Benetti[1], Alla Reznik[1,2], Oleksandr Bubon[1,2]

[1] Lakehead University, Department of Physics, Thunder Bay, Canada; [2] Radialis Inc., Thunder Bay, Canada; [3] Thunder Bay Regional Health Research Institute, Thunder Bay, Canada; [4] Ontario Institute for Cancer Research, Toronto, Canada

We acknowledge the support from the Natural Sciences and Engineering Research of Canada (NSERC). We thank Lakehead
University, the Thunder Bay Regional Health Research Institute, and Radialis Inc.

Abstract

PET detectors often use a Center of Gravity (CoG) algorithm applied to the output signal of sensor modules to perform coordinate reconstruction. CoG assumes that the spread of optical photons emitted by a pixelated scintillator crystal is symmetric about the point of interaction. A photoelectric (PE) event, where energy is deposited within a single scintillator pixel, produces such a distribution. Inter-crystal scatter (ICS) events, however, occur when a gamma photon deposits energy into multiple scintillator pixels, producing multiple photon distributions that degrade CoG accuracy and spatial resolution. Convolutional neural networks (CNNs) have proven effective for identifying and recovering ICS events in simulated data and in real systems when trained on experimentally acquired datasets, typically obtained using collimated measurements to isolate scintillator pixels. However, acquiring collimated datasets is time-consuming and requires high precision, motivating the use of simulated data as a primary training source. In this work, PET data was generated using GATE and used to train a small CNN to identify and remove ICS events based on softmax confidence values for a detector consisting of a 24×24 LYSO array coupled to an 8×8 SiPM array. A NU-4 image quality phantom and Na-22 point source acquired on a clinical system demonstrated improvements in recovery coefficient (RC) and peak-to-valley ratio for all RC five rod sizes, along with modest improvements in spatial resolution and spill-over ratio. The results demonstrate the feasibility of using imulated data as a primary training source for ICS filtering and recovery. Thus, a hybrid approach incorporating limited real data may further improve performance without requiring a large number of collimated acquisitions.

References

[1] Maa-Hacquoil, H., Poladyan, H., Baldassi, B., Komarov, B., Rado, J., Bubon, O. and Reznik, A., 2025. Improved Edge Pixel Resolution in Modular PET Detectors with Partly Segmented Light Guides. *Sensors*, *25*(22), p.7062.

[2] Zhang, C., Sang, Z., Wang, X., Zhang, X. and Yang, Y., 2019. The effects of inter-crystal scattering events on the performance of PET detectors. *Physics in Medicine & Biology*, *64*(20), p.205004.

[3] Lee, S. and Lee, J.S., 2021. Inter-crystal scattering recovery of light-sharing PET detectors using convolutional neural networks. *Physics in Medicine & Biology*, *66*(18), p.185004.

[4] Park, H. and Lee, J.S., 2020. SiPM signal readout for inter-crystal scatter event identification in PET detectors. *Physics in Medicine & Biology*, *65*(20), p.205010.

[5] Lee, S. and Lee, J.S., 2023. Experimental evaluation of convolutional neural network-based inter-crystal scattering recovery for high-resolution PET detectors. *Physics in Medicine & Biology*, *68*(9), p.095017.

[6] Stiles, J., Baldassi, B., Bubon, O., Poladyan, H., Freitas, V., Scaranelo, A., Mulligan, A.M., Waterston, M. and Reznik, A., 2022. Evaluation of a high-sensitivity organ-targeted PET camera. *Sensors*, *22*(13), p.4678.

[7] Jan, S., Santin, G., Strul, D., Staelens, S., Assié, K., Autret, D., Avner, S., Barbier, R., Bardiès, M., Bloomfield, P.M. and Brasse, D., 2004. GATE: a simulation toolkit for PET and SPECT. *Physics in Medicine & Biology*, *49*(19), pp.4543-4561.

MIC-10-305

Temporally and Spatially-Variant Penalty for Dynamic PET Reconstruction (#2858)

Nasrin Taheri[1], Thomas Carlier[2], Simon Stute[2]

[1] CRCI2NA, INSERM UMR 1307, Nantes University, Nantes, France; [2] Nuclear Medicine Department, Nantes University Hospital, Nantes, France

Abstract

Dynamic PET reconstruction is challenging due to strong temporal variations in count statistics, leading to non-uniform noise and spatial resolution across frames. In this work, we simply extend previous works to propose a temporally and spatially-variant regularization strategy for dynamic penalized maximum-likelihood (PML) reconstruction based on a time-and-space-dependent modulation factor derived from the Fisher information matrix. A modified estimation of the modulation factor is used to improve robustness in low-count conditions by removing dependence on noisy measurements. The method was evaluated using dynamic FDG simulations based on the 2D Zubal brain phantom and compared with OSEM and PML reconstruction without modulation.

Results showed improved preservation of anatomical structures and lower RMSE values in the cortex, putamen, and caudate regions while avoiding the excessive smoothing observed with conventional PML reconstruction. These results suggest that automatic temporally and spatially adaptive regularization can improve image quality and quantitative accuracy in dynamic PET imaging.

References

[1] J. N. et al., IEEE TNS, vol. 49, no. 1, pp. 56–60, 2002.
[2] S. A. et al., PMB, vol. 60, pp. 5733–51, 2015.
[3] Y. T. et al., IEEE TMI, vol. 39, no. 1, pp. 11–22, 2020.
[4] J. A. Fessler, IEEE TMI, vol. 13, no. 2, pp. 290–300, 1994.
[5] S. Stute et al., IEEE NSS/MIC Conf. Rec., pp. 1–3, 2015.

MIC-10-308

SAR-Based Brain Aging Validation Using Functional Connectivity Correlation Matrices from UK Biobank (#3186)

Alejandro Hernández[1,3], Ignacio Álvarez Illán[1,3], Javier Ramírez[1,3], Fermín Segovia[1,3], Diego Salas-González[1,3], Carmen Jiménez-Mesa[2,3], Cristóbal Vázquez-García[1,3], Francisco J. Martínez Murcia[1,3], Johannes Levin[4], Juan M. Górriz[1,3]

[1] University of Granada, Department of Signal Theory, Networking and Communications, Granada, Spain; [2] University of Malaga, Department of Communications Engineering, Málaga, Spain; [3] Andalusian Institute of Data Science and Computational Intelligence (DaSCI), Granada, Spain; [4] Ludwig-Maximilians-University, Department of Neurology, Munich, Germany

This work is part of the projects PID2022-137451OB-I00 and PID2022-137629OA-I00 funded by MICIU/AEI/10.13039/501100011033 and by ERDF/EU, and the C-ING-183-UGR23 project, cofunded by the Consejería de Universidad, Investigación e Innovación and by European Union, funded by Programa FEDER Andalucía 2021-2027.

Abstract

This study applies the Statistical Agnostic Regression (SAR) methodology to validate predictive model for brain aging using gray matter functional connectivity derived from fMRI data from the UK Biobank database. The method evaluates significant linear relationships between age and functional connectivity correlation matrices, by resampling and estimating an upper bound on the expected risk through a Bayesian threshold under the worst-case scenario. The SAR power quantifies the probability of detecting a true linear relationship using the expected risk statistic, via Monte Carlo simulations under the null distribution. Predictive performance is assessed through Principal Component Analysis (PCA) applied to the global correlation matrices, which are constructed from subjects whose ages fall within the extreme percentiles (below the 15th and above the 85th percentile). This framework enables the identification of connectivity signatures associated with aging within a unified representation of functional brain connectivity dynamics. Functional connectivity matrices of gray matter were computed from preprocessed fMRI data by extracting region-wise time series and estimating pairwise statistical dependencies using Pearson correlation coefficients. The results support the development of a statistically significant model for predicting age from functional connectivity correlation matrices and demonstrate that combining rigorously validated predictive models with SAR and PCA methodologies can characterize age-related variability in functional connectivity and improve understanding of brain aging using large-scale population neuroimaging data.

References

[1] Varoquaux, G., 2018, 'Cross- Validation failure: Small sample sizes lead to large error bars', *NeuroImage*, 180, 68-77.

[2] LeCun, Y., 2015, 'Deep learning', *Nature*, 521, 436–444.

[3] Leming, M., Górriz, J. M., Suckling, J., 2020, 'Ensemble Deep Learning on Large, Mixed-Site fMRI Datasets in Autism and Other Tasks', *International Journal of Neural Systems*, 30(7), 2050012.

[4] Górriz, J. M., *et al.*, 2026, 'Statistical Agnostic Regression: A machine learning method to validate regression models', *Journal of Advanced Research*, 80, 503-533.

[5] Pan, Y., *et al.*, 2024, 'Brain-wide functional connectome analysis of 40,000 individuals reveals brain networks that show aging effects in older adults', *Imaging Neuroscience*, 2, imag–2–00394.

MIC-10-311

Interpreting Prognostic [^{18}F]FDG PET Radiomic Signatures Using Parametric Tumour Simulation (#1849)

Lara M. Bonney[1,2], Kevin M. Bradley[3], Andrew B. Hassan[1], Daniel R. McGowan[2,4]

[1] University of Oxford, Sir William Dunn School of Pathology, Oxford, UK; [2] Oxford University Hospitals NHS Foundation Trust, Department of Medical Physics and Clinical Engineering, Oxford, UK; [3] Cardiff University, Wales Research and Diagnostic Positron Emission Tomography Imaging Centre (PETIC), Cardiff, UK; [4] University of Oxford, Department of Oncology, Oxford, UK

Abstract

Radiomic features derived from [^{18}F]FDG PET/CT imaging can quantify intratumoural spatial heterogeneity and have demonstrated prognostic utility across multiple oncological indications, including sarcoma. However, the biological interpretation of radiomic risk scores remains poorly understood, partly due to confounding in clinical datasets and the absence of ground-truth tumour parameters. A simulation-based approach offers a controlled framework for mapping image-derived features to biologically and physically meaningful tumour properties.

In this study, a parametric tumour model incorporating eight biologically motivated parameters—including uptake intensity, radial signal gradients, compartmental structure, multifocal uptake, and morphological deformation—was used to generate 1,024 synthetic tumour volumes across physiologically plausible parameter ranges. In parallel, a prognostic radiomic risk score was derived from [^{18}F]FDG PET/CT images of 115 sarcoma patients enrolled in the Oxford Precision Oncology for Sarcoma (OxPOS) study. This trained model was subsequently applied to each simulated volume to infer a radiomic risk score, and correlation analysis identified simulation parameters most strongly associated with predicted risk.

Three parameters; baseline uptake intensity, radial signal gradient, and fractional high-uptake volume, exhibited moderate but statistically significant correlations with the model-derived risk score ($|r|$= 0.41, 0.38, and 0.52, respectively). These findings provide mechanistic insight consistent with known tumour biology; for example, elevated radial signal gradients are characteristic of tumours with necrotic cores.

This work demonstrates the utility of simulation for enhancing biological interpretability and communicability of radiomic prognostic models. Ongoing work aims to expand the simulation framework and integrate genomic data to further elucidate the biological underpinnings of radiomic signatures in sarcoma.

References

[1] P. Lambin et al., Radiomics: extracting more information from medical images using advanced feature analysis, Eur. J. Cancer, vol. 48, no. 4, pp. 441--446, 2012.

[2] A. Zwanenburg et al., The Image Biomarker Standardization Initiative: standardized quantitative radiomics for high-throughput image-based phenotyping, Radiology, vol. 295, no. 2, pp. 328--338, 2020.

[3] J. J. M. van Griethuysen et al., Computational radiomics system to decode the radiographic phenotype, Cancer Research, vol. 77, no. 21, pp. e104--e107, 2017.

[4] R. Boellaard et al., 18F-FDG PET/CT: EANM procedure guidelines for tumour imaging: version 3.0, The EANM Journal, vol. 1, 2025.

MIC-10-314

Parameter Estimation of Arterial Input Function Using Nonlinear Mixed-Effects Modeling With Reduced Sampling (#2685)

Junan Jiang[2], Zirui Jiang[1], Junyu Chen[1], Yong Du[1]

[1] Johns Hopkins University School of Medicine, Department of Radiology, Baltimore, USA; [2] Johns Hopkins University Whiting School of Engineering, Department of Applied Mathematics and Statistics, Baltimore, USA

Abstract

Dynamic positron emission tomography (PET) requires dense arterial blood sampling to estimate arterial input functions (AIFs), creating substantial clinical burden and limiting practical implementation. To reduce number of samples, we developed a data-driven method for AIF estimation under sparse sampling conditions using nonlinear mixed-effects modeling. The study dataset included 90-min dynamic brain PET AIF data from 26 healthy subjects acquired with the 11C-DPA-713. A three-exponential nonlinear mixed-effects model was used to characterize the AIF, with fixed effects representing population-level kinetics and random effects capturing inter-individual variability. The AIF was modeled using a deterministic five-point subsampling strategy that selected representative early, intermediate, and late decay-phase observations. Model parameters were estimated using the stochastic approximation expectation maximization algorithm, and reduced-sampling predictions were compared with reference ground truth generated from the full dataset. The reduced five-point strategy produced AIF estimates that closely matched the full-data reference, yielding a root mean squared error of 0.37 and a mean relative error of ranging from 19% to 27.8%. Visual comparisons further demonstrated strong agreement between predicted and reference AIFs across subjects, indicating that plasma activity characteristics were preserved despite reduction in sampling density. These findings suggest that sparse sampling combined with nonlinear mixed-effects modeling can provide reliable AIF estimation while reducing the burden of arterial blood collection in dynamic PET studies.

References

[1] Zanotti-Fregonara P, Chen K, Liow JS, Fujita M, Innis RB, “Image-derived input function for brain PET studies: many challenges and few opportunities,” J. Cereb. Blood Flow Metab., vol. 31, no. 10, pp. 1986–1998, 2011, doi: 10.1038/jcbfm.2011.107.

[2] Xiu Z, Muzi M, Huang J, Wolsztynski E, “Patient-adaptive population-based modeling of arterial input functions,” IEEE Trans. Med. Imaging, vol. 42, no. 6, pp. 1698–1709, 2023, doi:10.1109/TMI.2023.3248454.

[3] Comets E, Lavenu A, Lavielle M, “Parameter estimation in nonlinear mixed effect models using saemix, an R implementation of the SAEM algorithm,” J. Stat. Softw., vol. 80, no. 3, pp. 1–41, 2017, doi: 10.18637/jss.v080.i03.

MIC-10-317

Orbital MRI radiomics in thyroid eye disease: A multi-structure stability analysis using perturbation-based methods (#3226)

Farbod Semnani[1], Seyed Sahab Aarabi[1], Ali Jafarizadeh[2], Maysam Abbasi[3], Armin Doostparast[4], Mirsaeed Abdollahi[2], Roohallah Alizadehsani[5], Juan M. Gorriz[6,7]

[1] School of Medicine, Tehran University of Medical Sciences (TUMS), Tehran, Iran; [2] Nikookari Eye Center, Tabriz University of Medical School, Tabriz, Iran; [3] School of Medicine, Hormozgan University of Medical Sciences (HUMS), Bandar Abbas, Iran; [4] Eye Research Center, Mashhad University of Medical Sciences, Mashhad, Iran; [5] School of medicine, Queensland University of Technology, Brisbane, Australia; [6] Data Science and Computational Intelligence Institute, Universidad de Granada, Granada, Spain; [7] Department of Psychiatry, University of Cambridge, Cambridge, UK

As a declaration of interests, J.M.G serves as Deputy General Chair of the 2026 IEEE NSS MIC RTSD.

Abstract

Thyroid eye disease (TED), the most common autoimmune orbital disorder and a major cause of orbital morbidity, is still assessed largely through subjective clinical measures. Although orbital MRI radiomics offers potential quantitative biomarkers for disease activity and treatment response, the reproducibility of these features under real-world imaging variability has not been systematically evaluated, limiting clinical translation. We performed a perturbation-based stability analysis using 150 patients from the public TOM500 dataset, extracting 293 radiomic features from seven Image Biomarker Standardization Initiative (IBSI)-compliant families across nine bilateral orbital structures using original and Laplacian-of-Gaussian filtered MRI images. We used ten perturbations per patient with combined rigid transformations, Gaussian noise, and 1-voxel mask modifications, and assessed stability using ICC(A,1). Across 2,637 structure-feature combinations, mean ICC was 0.72, and 53% of features achieved Good or Excellent stability (ICC ≥ 0.75). The medial rectus (ICC 0.84), followed by superior rectus and optic nerve (both 0.81) were the most robust structures, whereas the eyeball (0.55) and lateral rectus (0.61) were least stable. Laplacian-of-Gaussian filtering improved texture feature reproducibility, increasing median texture ICC from 0.73 to 0.80 and enhancing stability in medial rectus, lacrimal gland, and orbital fat features. Stability rankings were nearly identical between active and inactive disease groups (Pearson r = 0.92), indicating that disease severity did not influence feature reliability. These findings provide the first large-scale reproducibility assessment of orbital MRI radiomics in TED and establish a foundation for future biomarker and predictive modeling studies.

References

[1] Bartalena, L, et al., 2021, 'The 2021 European Group on Graves' orbitopathy (EUGOGO) clinical practice guidelines for the medical management of Graves' orbitopathy'. European journal of endocrinology, 185(4), G43–G67. https://doi.org/10.1530/EJE-21-0479

[2] Mourits, MP, Prummel, MF, Wiersinga, WM, and Koornneef, L, 1997, 'Clinical activity score as a guide in the management of patients with Graves' ophthalmopathy'. Clinical endocrinology, 47(1), 9–14. https://doi.org/10.1046/j.1365-2265.1997.2331047.x

[3] Hu, H, et al., 2022, 'T2 -Weighted MR Imaging-Derived Radiomics for Pretreatment Determination of Therapeutic Response to Glucocorticoid in Patients With Thyroid-Associated Ophthalmopathy: Comparison With Semiquantitative Evaluation'. Journal of magnetic resonance imaging : JMRI, 56(3), 862–872. https://doi.org/10.1002/jmri.28088

[4] Zhang, H., et al., 2025, 'TOM500: A Multi-Organ Annotated Orbital MRI Dataset for Thyroid Eye Disease'. Scientific data, 12(1), 60. https://doi.org/10.1038/s41597-025-04427-9

[5] van Griethuysen, JJM, et al., 2017, 'Computational Radiomics System to Decode the Radiographic Phenotype'. Cancer research, 77(21), e104–e107. https://doi.org/10.1158/0008-5472.CAN-17-0339
[6] Zwanenburg, A., et al., 2020, 'The Image Biomarker Standardization Initiative: Standardized Quantitative Radiomics for High-Throughput Image-based Phenotyping'. Radiology, 295(2), 328–338. https://doi.org/10.1148/radiol.2020191145
[7] Koo, TK, and Li, MY, 2016, 'A Guideline of Selecting and Reporting Intraclass Correlation Coefficients for Reliability Research'. Journal of chiropractic medicine, 15(2), 155–163. https://doi.org/10.1016/j.jcm.2016.02.012
[8] Zhang, H, et al., 2024, 'Whole-orbit radiomics: machine learning-based multi- and fused- region radiomics signatures for intravenous glucocorticoid response prediction in thyroid eye disease'. Journal of translational medicine, 22(1), 56. https://doi.org/10.1186/s12967-023-04792-2

MIC-10-320

Feasibility of portal imaging in proton therapy: concept and phantom experiments (#1070)

Johannes N. Esser[1,4], Claus M. Bäcker[1], Abdelkhalek Hammi[2], Beate Timmermann[1,3], Jens Weingarten[2], Jörg Wulff[2], Christian Bäumer[1,2]

[1] West German Proton Therapy Centre Essen, Medical Physics, Essen, Germany; [2] TU Dortmund University, Department of Physics, Dortmund, Germany; [3] University Medicine of Essen, Department of Particle Therapy, Essen, Germany; [4] University of Duisburg Essen, Faculty of Medicine, Essen, Germany

This work was supported by the MERCUR graduate school “Präzisionsprotonentherapie — Praxisbezogene Physik und Chemie an der Schnittstelle zur Medizin” (grant-number St-2019-0007).

Abstract

The aim of the study was to investigate whether proton therapy fields can be verified in vivo during treatment using film-based transit portal dosimetry. Potential clinical treatment plans were checked for downstream dose contributions. The complete proton portal imaging workflow was verified in experiments with an anthropomorphic phantom. Head-and-neck, mediastinal, thoracic, abdominal and cranio-spinal axis irradiations (CSIs) yielded downstream dose areas, which enable portal imaging. The cranial fields of CSI plans were deemed as most suitable and tested with the phantom in a simplified setup. Radiochromic films, mounted on top of the patient couch, served as portal imaging detectors. Phantom tests indicate that the patient setup can be verified within an accuracy of ≈1 mm per direction. In conclusion, a novel, straight-forward procedure has been developed for in-vivo dosimetry in proton therapy for some patients with specific indications.

References
[1] Dogan, B. J. Mijnheer, K. Padgett, A. Nalichowski, C. Wu, M. J. Nyflot, A. J. Olch, N. Papanikolaou, J. Shi, S. M. Holmes, et al., Use of electronic portal imaging devices for pre-treatment and in vivo dosimetry patient-specific IMRT and VMAT: Report of AAPM task group 307, Medical physics 50 (8) (2023) e865 (2023).

MIC-10-323

A Feasibility Study of Patient-Specific Integral Dose Verification Using a 3D-Printed Tumor Model Scintillator for Radiosurgery (#1239)

Hye Jeong Yang[1], Tae Hoon Kim[2], Yong Kyun Kim[3], Haksoo Kim[1], Hyun-Thai Chung[4]

[1] National Cancer Center Korea, Proton Therapy Center, Goyang, South Korea; [2] Radexel Inc., Research and Development Team, Seoul, South Korea; [3] Hanyang University, Department of Nuclear Engineering, Seoul, South Korea; [4] Seoul National University College of Medicine, Department of Neurosurgery, Seoul, South Korea

This research was supported by the National Cancer Center Korea (NCC-2410960).

Abstract

We developed a patient-specific volumetric dosimetry system using a tumor-shaped plastic scintillator derived from patient MR images for integral dose verification in Gamma Knife radiosurgery. Three tumor model scintillators (TMSs) representing a vestibular schwannoma (0.39 cm³) were irradiated using a nine-shot plan prescribing 8 Gy to the 60% isodose line. The integral dose, defined as the energy absorbed over the entire tumor volume, was measured and compared with the value calculated by the Leksell GammaPlan® treatment planning system. Two independent calibration methods were employed: calibration at a secondary standard dosimetry laboratory and Monte Carlo simulation-based calibration using Geant4. The integral dose measured by the simulation-based calibration was (2.00[if gte msEquation 12]><m:oMath><span lang=EN-US style='font-size:10.0pt;font-family:"Cambria Math",serif; mso-fareast-font-family:"맑은 고딕";mso-fareast-theme-font:minor-fareast; mso-bidi-font-family:"Times New Roman";mso-ansi-language:EN-US;mso-fareast-language: EN-US;mso-bidi-language:AR-SA'><m:r><m:rPr><m:scr m:val="roman"/><m:sty m:val="bi"/></m:rPr>±</m:r></m:oMath><![endif] 0.76)% higher than the planned value of 5.01 mJ, falling within the acceptable 3% tolerance for Gamma Knife absolute dosimetry. The laboratory-based calibration yielded an integral dose (5.84[if gte msEquation 12]><m:oMath><span lang=EN-US style='font-size:10.0pt;font-family:"Cambria Math",serif; mso-fareast-font-family:"맑은 고딕";mso-fareast-theme-font:minor-fareast; mso-bidi-font-family:"Times New Roman";mso-ansi-language:EN-US;mso-fareast-language: EN-US;mso-bidi-language:AR-SA'><m:r><m:rPr><m:scr m:val="roman"/><m:sty m:val="bi"/></m:rPr>±</m:r></m:oMath><![endif] 3.56)% lower than the reference value of 4.30 mJ; the larger deviation is attributed to probe reassembly uncertainty and the angular dependence of the calibration coefficient. These results demonstrate that the TMS system can serve as a practical tool for verifying the three-dimensional integral dose calculated by a treatment planning system.

MIC-10-326

Attenuation Correction for Targeted Alpha Therapy Monitoring with Compton Camera MACACO III+ (#1402)

Yuemeng Feng[1], Jorge Roser[1], Julius Werner[1], Jona Kasprzak[1], Luis Barrientos[2], Siddharth Parashari[2], Karol Brzeziński[2], Gabriela Llosá[2], Magdalena Rafecas[1]

[1] University of Luebeck, Institute of Medical Engineering, Luebeck, Germany; [2] University of Valencia, Institute for Corpuscular Physics, Valencia, Spain

The authors acknowledge the Advanced Imaging DEtector for targeted Radionuclide therapy (AIDER) programme (Grant agreement ID: 101165088), funded under the Euratom Research and Training Programme (EURATOM).

Abstract

Compton cameras are being explored as a promising technique for treatment monitoring of targeted alpha therapy, by imaging the gamma emissions produced during the decay of the alpha-emitting radionuclides. To improve image accuracy, attenuation correction is essential. Here we analyze the effects achieved by incorporating attenuation correction into the list-mode MLEM reconstruction of MACACO III+ synthetic data using ideal simulation. The results demonstrate that, without attenuation correction, contrast recovery coefficients of 97.2%, 84.7%, 73.5%, 47.8% are achieved for rods with diameters of 6, 5, 4 and 3 mm, respectively, using a total activity of 0.135 MBq of 440 keV gammas, a major gamma peak in the decay of ^{225}Ac and a hot to background ratio 10:1, simulated over 2 hours. Combined energy reconstruction at 218 and 440 keV yields improved image contrast when attenuation correction is applied. This work was carried out within the frame of the Advanced Imaging DEtector for targeted Radionuclide therapy (AIDER) project.

References

[1] JANG, Albert, et al. Targeted alpha-particle therapy: a review of current trials. *International journal of molecular sciences*, 2023, 24. Jg., Nr. 14, S. 11626.

[2] BENABDALLAH, Nadia, et al. Practical considerations for quantitative clinical SPECT/CT imaging of alpha particle emitting radioisotopes. *Theranostics*, 2021, 11. Jg., Nr. 20, S. 9721.

[3] FENG, Yuemeng, et al. Evaluation of a Compton Camera System for Whole-body Imaging of Ac-225: A Simulation Study. *IEEE Transactions on Radiation and Plasma Medical Sciences*, 2026.

[4] ROSER, Jorge, et al. Radiopharmaceutical imaging of phantoms and patients with MACACO III Compton camera. *Physica Medica*, 2025, 132. Jg., S. 104928.

[5] BARRIENTOS, L., et al. 131 I imaging with MACACO Compton camera. In: *2024 IEEE Nuclear Science Symposium (NSS), Medical Imaging Conference (MIC) and Room Temperature Semiconductor Detector Conference (RTSD)*. IEEE, 2024. S. 1-1.

[6] REN, Yuan, et al. Compton-camera-based radiopharmaceutical imaging with an attenuation-corrected LM-MLEM reconstruction strategy. *Radiation Measurements*, 2025, 181. Jg., S. 107379.

[7] MUNOZ, Enrique, et al. Study and comparison of different sensitivity models for a two-plane Compton camera. *Physics in Medicine & Biology*, 2018, 63. Jg., Nr. 13, S. 135004.

[8] MUNOZ, Enrique, et al. Imaging of polychromatic sources through Compton spectral reconstruction. *Physics in Medicine & Biology*, 2022, 67. Jg., Nr. 19, S. 195017.

MIC-10-329

Monte Carlo-Based PET Range Verification for Carbon-Ion Therapy

(#1456)

Ruolan Liu[1], Dengyun Mu[1], Jingmin Zhu[1], Ao Qiu[1], Tianjiao Hu[3], Weiwei Li[4], Yuki Nitta[4], Jiping Liu[4], Lin Wan[2], Peng Xiao[1], Ji Zhu[4], Qingguo Xie[1,3]

[1] Huazhong University of Science and Technology, Department of Biomedical Engineering, Wuhan, China; [2] Huazhong University of Science and Technology, School of Software Engineering, Wuhan, China; [3] University of Science and Technology of China, Department of Electronic Engineering and Information Science, Hefei, China; [4] Zhejiang Cancer Hospital, Hangzhou Institute of Medicine (HIM), Chinese Academy of Sciences, Department of Radiation Oncology, Hangzhou, China

This work was supported by the National Natural Science Foundation of China (Grant No. 625B2079).

Abstract

Positron emission tomography (PET) is an effective non-invasive modality for in vivo range verification in carbon-ion therapy. This study evaluates an all-digital PET system for in-beam monitoring of carbon-ion treatment plans. Clinical DICOM RT plans were converted into a GATE/Geant4 model of single-field pencil beam scanning (PBS) carbon-ion irradiation in a polymethylmethacrylate (PMMA) phantom. Simulated dose and positron-emitter distributions were compared with treatment planning system (TPS) dose and measured PET data. TPS and GATE showed good dosimetric agreement, with nearly identical planning target volume (PTV) D50% and a 3D gamma passing rate of 97.66% (2%/2 mm). PET validation yielded R50,sim = 124.33 mm and R50,exp = 125.00 mm, corresponding to ΔR50 = 0.67 mm. These results support millimeter-level PET-based range verification for carbon-ion therapy.

References

[1] W. Enghardt, P. Crespo, F. Fiedler, R. Hinz, K. Parodi, J. Pawelke, and F. Pönisch, "Charged hadron tumour therapy monitoring by means of PET," Nucl. Instrum. Methods Phys. Res. A, vol. 525, no. 1, pp. 284–288, Jun. 2004. DOI: 10.1016/j.nima.2004.03.128

[2] T. Hu, J. Hu, X. Zhang, S. Zheng, T. Zhou, Q. Liu, W. Hu, A. Qiu, Y. Xia, B. Li, P. Xiao, and Q. Xie, "Development and Performance Evaluation of an Open-Ring PET Prototype for Intraoperative Metabolic Monitoring," IEEE Trans. Radiat. Plasma Med. Sci., vol. PP, pp. 1–1, Jan. 2026. DOI: 10.1109/TRPMS.2026.3676872

[3] L. Grevillot, D. J. Boersma, H. Fuchs, A. Aitkenhead, A. Elia, M. Bolsa, C. Winterhalter, M. Vidal, S. Jan, U. Pietrzyk, L. Maigne, and D. Sarrut, "Technical Note: GATE-RTion: a GATE/Geant4 release for clinical applications in scanned ion beam therapy," Med. Phys., vol. 47, no. 8, pp. 3675–3681, 2020. DOI: 10.1002/mp.14242

MIC-10-332

Performance of a state-of-the-art ToF-PET detector in a proton therapy in-beam radiation environment (#1485)

Thomas Fogg, Peter Dendooven

University Medical Center Groningen, Particle Therapy Research Center & Department of Radiation Oncology, Groningen, Netherlands

Abstract

In-vivo positron emission tomography (PET) imaging of positron emitters produced by the therapeutic proton beam in the patient is a well-studied irradiation verification tool. Adaptive treatment planning benefits from fast feedback, down to the sub-second time scale, requiring an in-beam PET scanner operating during beam delivery for N-12 imaging. Use in clinical routine requires that the performance of such detectors is not significantly affected by radiation exposure over time. We have studied the performance of four state-of-the-art time-of-flight Hamamatsu C13500-4075YC-12 (ToF)-PET detectors in a proton therapy radiation environment. A 150 MeV proton beam (pulsed with intensities of 0.3, 1 and 3 nA at 10% and 1.5% duty cycles) was stopped in PMMA phantoms whilst PET data was acquired. The coincidence energy spectra obtained in-beam (both with the beam on and between beam pulses) show the N-12 511 keV peak. As the experiment progressed, the data output shows cumulative faults from an increasing percentage of corrupt events. Whilst the accumulation of these faults was partially mitigated by system resets during the experiment, comparison of data acquisitions with a combined Na-22 & Ga-68 source before and after the experiment show that the performance degradation is long-lasting, although the detectors show signs of recovery 5 months later.

References

[1] A.-C. Knopf and A. Lomax, “In vivo proton range verification: a review,” Phys. Med. Biol., vol. 58, no. 15, p. R131, Jul. 2013. [Online]. Available: https://doi.org/10.1088/0031-9155/58/15/R131

[2] B. Zapien-Campos, Z. Ahmadi Ganjeh, G. Perotti-Bernardini, J. Free, S. Both, and P. Dendooven, “Instantaneous in vivo distal edge verification in intensity-modulated proton therapy by means of PET imaging,” Med Phys, vol. 52, no. 7, p. e17850, Jul. 2025. [Online]. Available: https://pmc.ncbi.nlm.nih.gov/articles/PMC12257898/

MIC-10-335

In-Beam All-Digital PET for Dose-Guided Particle Therapy: Vision, Roadmap, and Progress (#1518)

Ao Qiu[1], Qingguo Xie[1,2]

[1] Huazhong University of Science and Technology, Department of Biomedical Engineering, Wuhan, China; [2] University of Science and Technology of China, Department of Electronic Engineering and Information Science, Hefei, China

This work was supported by the National Natural Science Foundation of China under Grant 625B2079.

Abstract

Proton and heavy-ion therapy exploits the Bragg peak to concentrate dose within the tumor while sparing surrounding normal tissues; however, range uncertainties necessitate conservative safety margins and restrict clinical indications. To address this, we are developing an in-beam All-Digital positron emission tomography (PET) platform for dose-guided particle therapy. Two prototype systems have been designed, built, and tested at multiple proton and heavy-ion therapy centers: a 12-module pre-clinical partial-ring system for phantom and small-animal studies, and a 16-module research-clinical open-ring system for human-subject trials. Both employ lutetium-yttrium oxyorthosilicate scintillators read out via the multi-voltage threshold digitization architecture. In-beam PET imaging of proton-induced positron activity has been demonstrated in polymethyl methacrylate phantoms with approximately 1 mm range agreement, and in live rats where biological washout effects on image contrast were observed. A three-phase development roadmap is presented, progressing from online range monitoring to adaptive therapy and ultimately real-time feedforward therapy, aiming to narrow safety margins, broaden treatment indications, and provide the verification infrastructure for FLASH therapy.

References

[1] Parodi, K, Yamaya, T, Moskal, P 2023, 'Experience and new prospects of PET imaging for ion beam therapy monitoring', Zeitschrift für Medizinische Physik, vol. 33, no. 1, pp. 22–34, Munich: Elsevier

[2] Gao, M, Chen, H-H, Chen, F-H, Hong, J-H, Hsiao, I-T, Yen, T-C, Mao, J, Lu, JJ, Wang, W, D'Ascenzo, N, Xie, Q 2021, 'First Results From All-Digital PET Dual Heads for In-Beam Beam-On Proton Therapy Monitoring', IEEE Transactions on Radiation and Plasma Medical Sciences, vol. 5, no. 6, pp. 775–782, New York: IEEE

[3] Ma, Q, Mu, D, Zhang, R, Liu, Z, Wan, L, Liu, Y, Qiu, A, Yang, Z, Xie, Q 2025, 'Development and evaluation of an in-beam PET system for proton therapy monitoring', Physics in Medicine & Biology, vol. 70, no. 2, 025019, Bristol: IOP Publishing

[4] Fang, L, Zhang, B, Li, B, Zhang, X, Zhou, X, Yang, J, Li, A, Shi, X, Liu, Y, Kreissl, M et al. 2024, 'Development and evaluation of a new high-TOF-resolution all-digital brain PET system', Physics in Medicine & Biology, vol. 69, no. 2, 025019, Bristol: IOP Publishing

[5] Zhang, B, Li, B, Fang, L, Zhou, X, Li, A, Zhang, X, Liu, Y, Wang, Z, Kao, C-M, Liu, Y et al. 2025, 'Performance Evaluation of New PET/CT DigitMI 930', IEEE Transactions on Radiation and Plasma Medical Sciences, vol. 9, no. 5, pp. 578–585, New York: IEEE

[6] Hu, T, Hu, J, Zhang, X, Zheng, S, Zhou, T, Liu, Q, Hu, W, Qiu, A, Xia, Y, Li, B et al. 2026, 'Development and Performance Evaluation of an Open-Ring PET Prototype for Intraoperative Metabolic Monitoring', IEEE Transactions on Radiation and Plasma Medical Sciences, New York: IEEE

MIC-10-338

Feasibility Study of In-Beam Range Verification Using Pixelated CZT Detectors in Carbon Ion Therapy (#1646)

Dian Guo, Jianxiong Shao, Xiangdong Cai, Chunhui Zhang, Yongzhi Yin

Lanzhou University, LanZhou, China

Abstract

To overcome the limitations of existing beam range verification methods in terms of detection efficiency, system complexity, and real-time capability, this study proposes a carbon ion beam range verification method based on a pixelated cadmium zinc telluride (CZT) detector and machine learning. The pixelated CZT detector was used to measure the secondary particle response generated during carbon ion irradiation of a polymethyl methacrylate

(PMMA) target, and a machine learning regression model was then applied to predict the beam range. The experimental results demonstrate that the pixelated CZT detector can accurately measure secondary particle responses. In addition, the effects of different detection regions, defined by pixel ranges, were investigated at a monitor unit (MU) setting of 6 × 10⁶. Using data from a 16 × 16 pixel region, the proposed method achieved a mean absolute error (MAE) of 0.79 mm. These results indicate that the proposed approach provides a feasible technical strategy for online range verification in carbon ion beam therapy

References
[1] Wang S, Guo J H, Zhang Y, et al. High-resolution pixelated CdZnTe detector prototype system for solar hard X-ray imager. Nuclear Science and Techniques, 2019, 30(3): 42. https://doi.org/10.1007/s41365-019-0571-9
[2] Hui Zou, Trevor Hastie, Regularization and Variable Selection Via the Elastic Net, Journal of the Royal Statistical Society Series B: Statistical Methodology, Volume 67, Issue 2, April 2005, Pages 301–320, https://doi.org/10.1111/j.1467-9868.2005.00527.x

MIC-10-341

Experimental setup for radiobiological studies with laser-accelerated protons at high dose rates (#1921)

Lucia Velasco Peñarrubia[1], Lucía Martín Fernández[1], Jessica Juan-Morales[1], Diego de Luis Blanco[2], José Luis Henares González[2], Jon Imanol Apiñaniz Aginako[2], Michael Seimetz[1]

[1] Instituto de Instrumentación para Imagen Molecular (i3M), CSIC-Universitat Politècnica de València, Valencia, Spain; [2] Centro de Láseres Pulsados (CLPU, Salamanca, Spain

Grant PID2023-148992OB-C21 funded by MICIU/AEI/10.13039/501100011033 and cofunded by the European Union, ERDF

Abstract
Laser-driven sources of ionizing radiation provide unique possibilities for studying ground-breaking phenomena and for exploring novel applications of compact accelerators. An outstanding example is the controlled irradiation of biological samples with laser-accelerated, high-energy particles. After a pilot experiment at the Spanish Pulsed Laser Center (CLPU), the aim of the present study is an increase of the single-shot dose and the mean dose rate on monolayer cell cultures. Two possible scenarios at the same laboratory have been considered. On the one hand, the previous setup at the VEGA-3 laser line may be upgraded through a set of permanent quadrupole magnets to focalize the proton beam closely behind the laser target. On the other hand, a similar, more compact arrangement inside the VEGA-2 target vessel benefits from shorter flight paths and a 10-fold higher repetition rate. Particle tracking simulations with realistic beam control elements point towards a 5–15 times increase in proton fluence and single-shot dose.

References
[1] Daido, H., Nishiuchi, M., Pirozhkov, A.S. 2012, ‘Review of laser-driven ion sources and their applications’, *Reports on Progress in Physics*, 75, 056401.
[2] Chaudhary, P. et al. 2021, ‘Radiobiology Experiments With Ultra-high Dose Rate Laser-Driven Protons: Methodology and State-of-the-Art’, *Frontiers in Physics*, 9, 75.
[3] Reija Vecino, A. 2026, *Laser-driven radiation sources for in vitro radiobiological studies*, PhD thesis, Universidade de Santiago de Compostela.

[4] Reija, A., Esteban, D. et al. 2024, 'Design and Implementation of an Energy Selector for Laser-Accelerated Protons. Instruments', *Instruments*, 8, 36.
[5] Ehret, M. et al. 2024, 'Stability and debris-mitigation of a solid tape target delivery system for intense laser-matter interactions towards high-repetition-rate', *Plasma Physics and Controlled Fusion*, 66, 045003.
[6] Bin, J. et al. 2012, 'A laser-driven nanosecond proton source for radiobiological studie', *Applied Physics Letters*, 101, 243701.
[7] Pommarel, L. et al. 2017, 'Spectral and spatial shaping of a laser-produced ion beam for radiation-biology experiments', *Physical Review Accelerators and Beams*, 20, 032801.
[8] Salinas Morote, A.M. 2025, *Sistema de focalización para protones acelerados por láser*, Final degree project, Faculty of Physics, Universitat de València.

MIC-10-344

Design and Development of a BGO-based PET Scanner for Dose Verification after Proton Therapy (#1975)

Óscar Pietrzyk[1], **Marta Freire**[1], Marc Gil[1], Luis F. Vidal[1], Marcin Balcerzyk[2,3], Antonio J. Gonzalez[1]

[1] Instituto de Instrumentación para Imagen Molecular (I3M), Centro Mixto CSIC—Universitat Politècnica de València, 46022 Valencia, Spain, Valencia, Spain; [2] Bioaraba Health Research Institute, Vitoria, Spain; [3] IKERBASQUE, Basque Foundation of Science, Bilbao, Spain

This work was supported by the Agencia Valenciana de Innovacion under Grant No INNVA1/2024/72. M. Freire was supported by the CIAPOS Grant No. CIAPOS/2023/141 and M. Gil was supported by the ACIF Grant No. GVRTE/2024/5586404.

Abstract

Proton therapy is an advanced radiotherapy modality whose clinical advantage arises from the highly localized dose deposition produced at the Bragg peak. However, this feature makes the technique highly sensitive to uncertainties in patient positioning, anatomical changes, and beam delivery. Verifying the dose delivered to patients after treatment session is therefore essential to ensure treatment safety and reducing planning margins. During proton irradiation, nuclear interactions generate positron-emitting isotopes that can be detected with Positron Emission Tomography (PET). In this work, we focus on the detection of ^{18}F, whose long half-life enables offline PET acquisitions 60–150 min after treatment, when short-lived isotopes have decayed. Because the expected in-vivo ^{18}F activity is very low (0.1–1 Bq/mL), we propose a PET system optimized for low-count imaging, based on BGO scintillation crystals to avoid the intrinsic background of lutetium-based detectors typically used in commercial scanners.

The proposed PET prototype (*INSPIRE*) consists of 16 detector modules arranged in a single ring, each comprising a two-layer pixelated BGO block (19×19 and 20×20 arrays) coupled to a 12×12 SiPM array, thus enabling Depth of Interaction (DOI) information. The system, which has an inner diameter of 26 cm and an axial length of 5 cm, is intended for brain studies. In this work we present the design of the *INSPIRE* system and the experimental characterization of the detector modules, including pixel resolvability, layer separation, and energy performance, together with preliminary proton-irradiation simulations that illustrate the suitability of the ^{18}F signal for offline PET imaging.

MIC-10-347

A Software Framework for Real-Time Prompt Gamma Range Verification (#2107)

Letizia Santini[1,3], Korbinian Urban[1,3], Emma S. Bellotti[2], Beatrice Foglia[4], Andrea Forgione[1,3], Martina Piroddi[1,3], Christian Riboldi[1,3], Annamaria Contangelo[1], Giacomo Borghi[1,3], Marco Carminati[1,3], Stefano Agosteo[2,3], Davide Mazzucconi[2,3], Davide Bortot[2,3], Katia Parodi[4], Alessio Mereghetti[5], Carlo E. Fiorini[1,3]

[1] Politecnico di Milano, Department of Electronics, Information and Bioengineerin, Milano, Italy; [2] Politecnico di Milano, Department of Energy, Milano, Italy; [3] National Institute for Nuclear Physics, Section of Milan, Milano, Italy; [4] Ludwig-Maximilians-Universität Munich, Department for Medical Physics, Garching, Germany; [5] Centro Nazionale di Adroterapia Oncologica, Pavia, Italy

Abstract

Real-time monitoring in hadron therapy is essential to account for anatomical shifts and setup uncertainties that may compromise dose delivery. This work evaluates a software framework designed for online range verification via monitoring of the Prompt Gamma (PG) profile, which is know to be correlated to the Bragg peak position. The architecture employs a decoupled simulation pipeline: PG emission is modeled using MC codes, while the detector response is characterized through a dedicated Python-based tool, PGIPY. This simulated new profile, computed spot by spot, is then compared with measurement inside the software. To ensure spot-by-spot clinical correspondence, the software utilizes machine log files to synchronize simulated data with actual delivery sequences.

Experimental validation with an homogenoeus phantom was performed at the CNAO facility (Pavia, Italy). A high degree of correlation was observed between simulated and experimental profiles, confirming that the framework is free from significant systematic modeling errors. These results demonstrate that the proposed pipeline provides a robust, validated baseline for clinical integration, ensuring that any detected profile deviations during treatment are attributable to physical range shifts.

References

[1] M. Pinto, *Prompt-gamma imaging in particle therapy. Eur. Phys. J. Plus*, vol. 139, p. 10, 2024.

[2] J. Krimmer, D. Dauvergne, J. M. Létang, and É. Testa, *Prompt-gamma monitoring in hadrontherapy: A review. Nucl. Instrum. Meth. A*, vol. 878, 2018, pp. 58--73.

[3] K. Urban, *A New Software Tool for Modeling the Performance of Prompt Gamma Cameras for Range Verification in Hadron Therapy*. Presented at the IEEE Nuclear Science Symposium and Medical Imaging Conference (NSS/MIC), Yokohama, Japan, 2025. [Poster].

[4] K. Souris et al., *MCsquare – fast multipurpose Monte Carlo simulation framework. Med. Phys.*, 2016.

[5] B. Foglia et al., *Implementation and 3D extension of dose reconstruction strategies from prompt-gamma emissions in proton therapy. Physics in Medicine & Biology*, vol. 70, 235026, 2025.

MIC-10-350

Construction and positioning accuracy of a prototype Portable Organ Dosimetry Device (PODD) for RPT (#2213)

William C.J. Hunter, Robert S. Miyaoka

University of Washington, Radiology, Seattle, USA

This work was supported in part by NIH NCI R01CA287205.

Abstract

Purpose: To enable personalization dosage of ^{177}Lu-based Theranostic radiopharmaceutical therapy (RPT), we are developing a Portable Organ Dosimetry Device (PODD) for at-home use to monitor activity in regions of interest (ROI) such as tumors and organ at risk (OAR). To accurately estimate OAR activity, knowledge of the relative positions of probes and ROIs is required. This can be achieved either by consistency of initially measured locations, or by verifying locations for each measurement. Methods: We have constructed a prototype PODD, and we examine the variation of ROI-location estimates of an NEMA IQ phantom in the PODD reference frame by measuring PODD and ROI features from repeat x-ray CT scan with the phantom removed and replaced in the PODD between measurements. Results: The standard deviations of ROI translational location with the phantom in a supine orientation was 1.0mm axially, 0.2mm horizontally, and 0.1mm vertically. Standard deviations of rotational position were 0.7 degree in tilt and less than 0.1 degrees in roll about the PODD and CT scanner axis. Conclusion: Locating uncertainty of a rigid body phantom within our prototype PODD will not significantly affect the accuracy of time-integrated activity estimates using longitudinal measurements with the phantom removed and replaced in the PODD between measurements. We must repeat these measurements for a realistic deformable phantom or with real subjects.

MIC-10-353

^{224}Ra Experimental and simulation studies with the MACACO III+ Compton camera prototype (#2389)

Luis Barrientos[1], Karol Brzeziński[1], Deniel Rodríguez Almora[1], Siddharth Parashari[1], Matthew Strugari[2], Irene Torres-Espallardo[2], Gabriela Llosá[1]

[1] Instituto de Física Corpuscular (IFIC-CSIC/UVEG), Valencia, Spain; [2] La Fe Hospital (HUiP), Nuclear Medicine department, Valencia, Spain

This work has received funding from the Spanish MICIU / AEI (project MIDAS, PID2022-143246OB-I00) and from the European Union's EURATOM research and innovation program (AIDER project, G.A. 101061037). S.P. acknowledges the Severo Ochoa CEX2023-001292-S grant, funded by MCIN/AEI/10.13039/501100011033.

Abstract
Compton cameras are showing promise for targeted radionuclide therapy (TRT). The IRIS group of IFIC (Valencia, Spain) has developed a scintillator-based Compton camera prototype for medical imaging applications which is being assessed in TRT. The prototype MACACO III+ consists of two detector planes, with the second having an active area four times larger than the first. Previous tests performed on phantoms and small animals using ^{131}I demonstrated the suitability of the system for radiotracer imaging. The system is being employed to obtain initial experimental data with different radionuclides to validate the simulations carried out within the European project AIDER, which will develop a high performance Compton camera. In this work, experimental measurements with MACACO III+ were carried out at La Fe Hospital (Valencia, Spain) to image a vial filled with ^{224}Ra. GATE simulations were also performed to compare with experimental data. In addition, the prototype MACACO IV, composed of two planes with four detectors each, is under development. Simulation studies also include the configuration of the new prototype to assess influence of detector geometry on the overall system performance.

References
[1] Tashima, H and Yamaya, T., Phys. Technol., 2022, vol. 15(3). 187-205.
[2] LLosá, G and Rafecas, M., Eur. Phys. J. Plus, 2023, vol 138(3), 214.
[3] Fujieda, K et al., Nucl. Inst. and Meth. A, 2020, 958, 162802.
[4] Roser, J et al., Physica Medica., 2025, vol 132, 104928.
[5] Brzeziński, K et al., 2026, Article in preparation.
[6] Barrientos, L et al., Rad Phys and Chemi., 2023, vol. 208 110922.
[7] Agostinelli, S et al., Nucl. Inst. and Meth. A., 2003, vol. 506 (3):250-303.
[8] Muñoz, E et al., Phys. Med. Biol., 2018, vol. 63(13), 135004.

MIC-10-356

AIDER Compton Camera for Targeted Radionuclide Therapy (#2559)

Gabriela Llosá, On behalf of AIDER Collaboration

Instituto de Física Corpuscular (IFIC), CSIC-UV., Valencia, Spain

This work has received funding from the European Union's EURATOM research and innovation program (AIDER project, G.A. 101061037).

Abstract
Targeted radionulclide therapy (TRT) is a cancer treatment modality that employs radiopharmaceuticals to selectively deliver radiation to cancerous cells at specific target organs. Its use has increased drastically in the last years, and it has been extended to novel radiopharmaceuticals. The secondary photons emitted by the therapeutic radionuclides can be employed for imaging the compound distribution in the patient's body for treatment assessment and dosimetry. A precise quantification of the radiation dose delivered to lesions and organs at risk is crucial for improving patient treatment safety and reducing related side effects. Conventional imaging modalities

are not optimized for such secondary emission, in particular in the case of alpha-emitting radionuclides, which are gaining prominence due to their exceptional cytotoxicity. For targeted alpha therapy (TAT), image-based dosimetry is an unmet need as currently used gamma cameras are not effective in the case of these high energy and low activity emitters. The European project AIDER aims at developing a high-performance scintillator-based Compton camera to improve imaging in TRT and to enable image-based dosimetry in TAT. The project, coordinated by the IRIS group of IFIC, includes four academic partners, two hospitals, an SME and a patient association. Within the project, the system will be developed and tested with phantoms and patients. Initial work on system design optimization and image reconstruction, as well as detector and electronics development has been carried out.

References
[1] Ballal et al. 225Ac-PSMA-617-targeted alpha therapy for the treatment of metastatic castration-resistant prostate cancer: A systematic review and meta-analysis.. The prostate. Volume 81, Issue9 2021. Pages 580-591.
[2] Seo, Y. "Quantitative imaging of alpha-emitting therapeutic radiopharmaceuticals." Nuclear medicine and molecular imaging 53.3 (2019): 182-1s88.
[3] https://aider.ific.uv.es/aider/
[4] Sarrut D, … Krah N. GATE 10 Monte Carlo particle transport simulation: I. Development and new features. Phys Med Biol. 2026 Jan 14;71(1).
[5] L. Barrientos et al. Characterization and 131I tests with MACACO III+ Compton camera. Submitted to TRPMS.

MIC-10-359

Gamma Detection for Source Localisation in Targeted Alpha Therapy

(#2678)

Chiara De Sio, Lujin AbuSabah, Jinyan Duan, Yuyao Shi, Sean Williams, Jaap Velthuis

University of Bristol, School of Physics, Bristol, UK

Abstract

Targeted alpha therapy delivers highly localised dose, so treatment planning and delivery verification depend on whether the radionuclide source remains at the intended deposition site or is redistributed by diffusion or biological transport. This simulation study tests whether decay-chain gamma emissions can provide a detectable source-localisation signal in an AlphaGlue-like geometry. Photon transport was modelled for a thin loaded glue layer on a water phantom surrounded by six detector panels, with each photon entry into a panel counted as one hit. Seven source configurations were analysed: a retained-source baseline, broad redistribution of 10%, 50%, or 90% of the source in water, and localised displacement of 20%, 40%, or 60% of the source to a compact water region. Each configuration used ten repetitions of 10,000 primary decays and was normalised to a 3 µCi reference source. Total detector-hit yield changed only modestly, but baseline-subtracted spatial hit profiles showed strong source-dependent structure. The central glue-facing signal fell to 0.94, 0.72, and 0.47 of baseline for the broad-redistribution cases, and to 0.84, 0.67, and 0.50 for the localised-displacement cases. Profile-shape features recovered the broad diffusion fraction with an R2 value of 0.998, while a secondary-source metric identified all localised displaced-source cases. The reconstructed displaced-source position was centred at approximately 525–531 mm, compared with the simulated 500 mm source region. Time-window analysis showed that large redistributions reached three-standard-deviation thresholds within 30 minutes to 2 hours; the weakest broad redistribution required about 6 hours, and the 20% localised displacement produced detectable displaced-region

excess within about 1 hour. These results indicate that gamma-hit patterns provide source-location information beyond total count rate and could support activity verification and treatment-delivery monitoring.

MIC-10-362

Cellular-Scale Imaging of Theranostic Radiopharmaceutical Uptake with a Lensless Radiomicroscopy Sensor (#2746)

Nicola Belcari[1,2], Luca Pesce[3], Giancarlo Sportelli[1,2], Claudia Catarinicchia[4], Luca Menichetti[4], Daniele Panetta[4], Laura Colagiorgio[5], Aurora Leso[6], Davide Serafini[6], Alberto Arzenton[7], Laura Cansolino[8,9], Cristiana Alberghina[10,11], Francesco P. Cammarata[10,11], Chiara Bonanno[12,13], Massimo Ippolito[13], Fabrizio Scopelliti[13], Giorgio Grosso[14], Andrea Gandini[14], Antonietta Donzella[15,9], Emilio Mariotti[16,2], Giulia S. Valli[16], Alberto Andrighetto[6]

[1] University of Pisa, Department of Physics, Pisa, Italy; [2] INFN, Sezione di Pisa, Pisa, Italy; [3] University of Pisa, CISUP, Pisa, Italy; [4] CNR, IFC, Pisa, Italy; [5] Scuola Superiore Sant'Anna, Pisa, Italy; [6] INFN, Laboratori Nazionali di Legnaro, Legnaro, Italy; [7] University of Padova, Department of Physics and Astronomy, Padova, Italy; [8] University of Pavia, Department of Clinical Surgical Sciences, Pavia, Italy; [9] INFN, Sezione di Pavia, Pavia, Italy; [10] CNR, IBSBC, Cefalù, Italy; [11] INFN, Laboratori Nazionali del Sud, Catania, Italy; [12] University of Catania, Department of Chemical Sciences, Catania, Italy; [13] Cannizzaro Hospital, Catania, Italy; [14] LENA, Pavia, Italy; [15] University of Brescia, Department of Mechanical and Industrial Engineering, Brescia, Italy; [16] University of Siena, Department of Physical Sciences, Earth and Environment, Italy

This work is partially supported under the National Recovery and Resilience Plan (NRRP), Mission 4 Component 2 Investment 3.1 - DD MUR 3264/21 - funded by the European Union – NextGenerationEU. Project code IR00023 - Concession Decree No. 101 of 16/06/2022 adopted by MUR, CUP B53C22001810006, Project PNRR-SEE LIFE - Strengthening the Italian Infrastructure of Euro-Bioimaging.

Abstract

We present a low-cost lensless radiomicroscopy system for cellular-scale imaging of theranostic radiopharmaceutical uptake using a commercial CMOS image sensor. The device enables simultaneous brightfield and β-emission imaging with sub-10 μm spatial resolution, allowing direct correlation between morphology and radionuclide distribution. The system was validated using β^--emitting 111Ag and β^+-emitting 18F-FDG sources, demonstrating quantitative linearity and accurate radioactive decay measurements. Live-cell experiments on MDA-MB-231 breast cancer cells showed detectable intracellular uptake of 111Ag, while imaging of U87 glioblastoma spheroids revealed spatially localized 18F-FDG accumulation in a warm background environment. These results demonstrate the potential of lensless radiomicroscopy as a compact and affordable platform for quantitative in vitro evaluation of theranostic agents at single-cell and multicellular levels.

References
[1] Klein JS, Kim TJ, Pratx G. Development of a Lensless Radiomicroscope for Cellular-Resolution Radionuclide Imaging. J Nucl Med. 2023 Mar;64(3):479-484. doi: 10.2967/jnumed.122.264021.

MIC-10-365

Intercrystal Compton Scattering Detection in Pixelated LYSO Detectors via Quantum Localization (#2993)

Amirreza Hashemi, Xi Zhang, Hamid Sabet

Harvard Medical School/Massachusetts General Hospital, Radiology Department, Boston, USA

This work was supported in part by NIH grant R01EB034785.

Abstract

We introduce a novel quantum-inspired method for identifying intercrystal Compton scattering in pixelated scintillation detectors. The approach treats each SiPM readout as a spatial signal and converts it into a discrete eigenfunction representation using a Hamiltonian built from the measured intensity distribution. Event structure is then assessed through quantum localization, quantified by the participation ratio. Single-site events produce highly localized dominant modes, whereas Compton-scattered events produce multiple localized modes associated with distinct interaction sites. A dual criterion based on quantum localization and eigenvalue proximity is used to classify multi-site events without calibration-intensive response modeling or supervised training. The method was evaluated with Geant4 optical photon simulations and measurements from LYSO:Ce detector arrays with thicknesses from 2 to 25 mm. Experimental classification agreed closely with simulation, with differences below 1% for most thicknesses and below 5% in all cases. These results indicate that the proposed representation captures the topology of gamma-ray interactions directly from detector signals.

References

[1] M. S. Lee, H. S. Shim, and J. S. Lee, “Strategies for mitigating inter-crystal scattering effects in positron emission tomography: a comprehensive review,” *Biomedical Engineering Letters*, vol. 14, no. 6, pp. 1243–1258, Nov. 2024, doi: 10.1007/s13534-024-00427-7.

[2] S. Lee, K. Y. Kim, M. S. Lee, and J. S. Lee, “Recovery of inter-detector and inter-crystal scattering in brain PET based on LSO and GAGG crystals,” *Phys. Med. Biol.*, vol. 65, no. 19, p. 195005, Oct. 2020, doi: 10.1088/1361-6560/ab9f5c.

[3] M. N. Ullah and C. S. Levin, “Application of Artificial Intelligence in PET Instrumentation,” *PET Clinics*, vol. 17, no. 1, pp. 175–182, Jan. 2022, doi: 10.1016/j.cpet.2021.09.011.

[4] A. Hashemi, S. Dutta, B. Georgeot, D. Kouamé, and H. Sabet, “A novel perspective on denoising using quantum localization with application to medical imaging,” *AIP Advances*, vol. 15, no. 8, p. 085012, Aug. 2025, doi: 10.1063/5.0267924.

[5] A. Hashemi, S. Dutta, B. Georgeot, D. KouamÉ, and H. Sabet, “Quantum-Inspired Denoising via Adaptive Planck Constant and Image Patching,” in *2024 IEEE Nuclear Science Symposium (NSS), Medical Imaging Conference (MIC) and Room Temperature Semiconductor Detector Conference (RTSD)*, Oct. 2024, pp. 1–1. doi: 10.1109/NSS/MIC/RTSD57108.2024.10657709.

[6] A. Hashemi, H. Babaei, and S. Lee, “Effects of medium range order on propagon thermal conductivity in amorphous silicon,” *Journal of Applied Physics*, vol. 127, no. 4, p. 045109, Jan. 2020, doi: 10.1063/1.5124821.

MIC-10-368

A Learned Unfolded Deconvolution Framework for Partial Volume Correction in Total-Body PET Imaging (#3021)

Mohamed Saber Azimi[1,2], Vahid Felfelian[3], Maryam Cheraghi[4], Abass Alavi[5], Hossein Arabi[6], Habib Zaidi[6,2]

[1] Obuda University, Doctoral School of Applied Informatics and Applied Mathematics, Budapest, Hungary; [2] Obuda University, University Research and Innovation Center, Budapest, Hungary; [3] Shahid Beheshti University, Department of Medical Radiation Engineering, Tehran, Iran; [4] Shahid Beheshti University of Medical Sciences, Department of Nuclear Medicine, Tehran, Iran; [5] University of Pennsylvania, Department of Radiology, Philadelphia, USA; [6] Geneva University Hospital, Division of Nuclear Medicine & Molecular Imaging, Geneva, Switzerland

Abstract

Total-body PET imaging provides unprecedented sensitivity and extended axial coverage but remains affected by partial volume effects (PVE), particularly in small lesions and regions with spatially varying resolution. Conventional deconvolution approaches, such as Richardson–Lucy (RL), can improve spatial resolution but often suffer from noise amplification and inaccuracies in point spread function (PSF) modeling. In this work, we propose a learned unfolded deconvolution framework for robust PVE correction in total-body PET imaging. The method reformulates RL deconvolution as a fixed-depth network in which each iteration explicitly incorporates the system PSF while learnable parameters enable adaptive regularization and noise suppression. Standard-dose [^{18}F]FDG PET images were used as network inputs to isolate the PVE correction problem from low-count noise effects. The model was trained in a self-supervised manner using RL-generated surrogate references, eliminating the need for voxel-wise ground-truth images. Evaluation was performed on multicenter total-body PET datasets acquired from uEXPLORER and Biograph Vision Quadra systems. Quantitative assessment on an independent test set demonstrated high structural fidelity (PSNR = 47.38 ± 5.71, SSIM = 0.98 ± 0.01) and low reconstruction error (RMSE = 0.005 ± 0.003), while maintaining acceptable SUV bias (12.2% ± 23.1%). Qualitative analysis showed improved lesion delineation and enhanced uptake contrast without visible noise amplification. Bootstrap-based analysis further demonstrated stable performance with narrow confidence intervals across metrics. The proposed framework provides an interpretable and robust solution for PVE correction, improving image quality and quantitative consistency in total-body PET imaging.

References

[1] M. S. Azimi *et al.*, "Critical review of partial volume correction methods in PET and SPECT imaging: benefits, pitfalls, challenges, and future outlook," *European Journal of Nuclear Medicine and Molecular Imaging,* pp. 1–32, 2025.

[2] M.-S. Azimi *et al.*, "Deep learning-based partial volume correction in standard and low-dose positron emission tomography-computed tomography imaging," *Quantitative Imaging in Medicine and Surgery,* vol. 14, no. 3, p. 2146, 2024.

[3] M. Azimi *et al.*, "Attention-based deep neural network for partial volume correction in brain 18F-FDG PET imaging," *Physica Medica,* vol. 119, p. 103315, 2024.

[4] M. S. Azimi, F. MahdiMaleki, F. MahdiMaleki, M. Cheraghi, A. Alavi, and H. Zaidi, "Supervised vs. Unsupervised Radiomics Reproducibility Across Dose-Level Variations and Partial Volume Correction Methods in Total-Body PET Imaging," *Biomedical Signal Processing and Control,* In press 2026.

[5] H. Marquis, K. Erlandsson, and I. Buvat, "Addressing partial volume effects in clinical PET quantification: modern correction strategies and challenges," *PET clinics,* vol. 20, no. 4, pp. 407–422, 2025.

MIC-10-371

Direct Theranostic Dose Estimation using a Multi-Pinhole Model of the Sparse Portable Organ Dosimetry Device (#3220)

Gabriel Maliakal[1], Robert S. Miyaoka[2], William C.J. Hunter[2], Adam M. Alessio[1]

[1] Michigan State University, Institute for Quantitative Health, Biomedical Engineering, CMSE, and Radiology, East Lansing, USA; [2] University of Washington, Radiology, Seattle, USA

This work was supported by NIH Grant 1R01CA287205

Abstract

Many studies have proposed methods to estimate internal dosimetry, enabling patient-specific adjustment of radiopharmaceutical therapy. We are developing a practical, low-cost multi-pinhole collimated system (PODD) with on the order of 10 sensors at fixed locations around a subject. Estimation of internal dosimetry to organs at risk is extremely ill-posed with this sparse sensor placement. In this work, we hypothesize that use of objective functions with an accurate forward model and multiple regularization terms can directly estimate total accumulated activity using simulated PODD acquisitions of realistic distributions of Lu-177 DOTATATE. Methods: We developed a custom GPU-based forward projector enabling rapid multi-pinhole detection simulation. We propose an objective function for direct estimation of wash-in, wash-out, and total integrated activity (TIA) kinetic parameters from multi-time point, sparse sensor measurements. This objective function includes regularization based on a) matching sensor measurements to initial time-point SPECT acquisitions and b) promoting kinetic parameters similar to population kinetics. Evaluation was performed by simulating sensor acquisitions from public 4-time point SPECT/CT images (Dewaraja et al, 2021, Lu-177 DOTATATE Anonymized Patient Datasets). Conclusion: Direct estimation of clinically relevant TIA can be performed with on the order of 10 to 20 pinhole-collimated sensors acquiring data at four times post treatment.

MIC-10-374

FastPET for low-count reconstruction scenarios (#1498)

Vanessa Nadig[1], Deepak Bharkhada[2], Mael Millardet[3,2], Vladimir Panin[2], Josh Schaefferkoetter[2], Yifan Zheng[2], Mengxi Zhang[2], Naveen Murthy[2], Stephen Liu[2], Paul Schleyer[2]

[1] Siemens Healthcare Limited, London, UK; [2] Siemens Medical Solutions, Knoxville, USA; [3] University of Pennsylvania, Radiology Department, Philadelphia, USA

The authors would like to thank the Department of Nuclear Medicine at Bern University Hospital's Inselspital for providing patient data. They also extend their gratitude to King's College London for sharing image quality phantom data. This investigative work was supported by the National Institute of Biomedical Imaging and Bioengineering through grant number R01-EB031806. The content in this article is solely the responsibility of the authors and does not necessarily represent the official views of the National Institutes of Health.

Abstract

Highly sensitive long-axial-field-of-view (LAFOV) positron emission tomography (PET) scanners require fast and reliable reconstruction methods, where accurate quantification in short temporal frames is key to kinetic modeling applications. We extended FastPET - a direct neural network reconstruction method based on image loss - with an additional forwardprojection step and data loss penalty, modified the training database to specifically account for short temporal frames and evaluated its PET quantification accuracy in high- and lowcount regimes on the Biograph Vision Quadra. Compared to ordered subset expectation maximation (OSEM, 4i5s, all pass) reconstructions, FastPET based only on image loss resulted in smoothed images and an overshoot in the contrast recovery coefficient (CRC) by up to 20%. A combination of data loss and image loss counteracted this effect but still showed a degraded CRC for frame lengths ≤5s. Including low-count training data in the training stablized the image quality and slightly improved the CRC of small structures in short frames ≤5s.

References

[1] Overbeck et al. Near real-time reconstruction of dynamic [18F]FDG PET examinations for Total Body PET, Journal of Nuclear Medicine Jun 2025, 66 (supplement 1) 251340.

[2] Nadig et al. PET quantification accuracy using FastPET in ultra-short frames on the Biograph Vision Quadra PET/CT, EANM Innovation (2025): S1–S1013; 10(1): 63–73. doi: 10.1016/S3051-2913(25)00

[3] Whiteley et al., DirectPET: full-size neural network PET reconstruction from sinogram data, Journal of Medical Imaging, Vol. 7, Issue 3, 032503 (February 2020), doi: 10.1117/1.JMI.7.3.032503

[4] Whiteley et al., FastPET: Near Real-Time PET Reconstruction from Histo-Images Using a Neural Network, IEEE Transactions on Radiation and Plasma Medical Sciences, vol. 5, no. 1, pp. 65-77, Jan. 2021, doi: 10.1109/TRPMS.2020.3028364

[5] Millardet et al. Improved quantification in end-to-end deep learning Fast-PET reconstruction using multi-view histo-images of attenuation correction factors, IEEE Transactions on Radiation and Plasma Medical Sciences 2026 January; 10(1): 63–73. doi: 10.1109/TRPMS.2025.3569198

[6] Bharkada, Panin and Millardet, Methods and apparatus for deep learning based image reconstruction, US 2025/0148662 A1

MIC-10-377

Quantitative Reconstruction and Correction for Long-Axial FOV PET: Optimizing Component-Based Normalization and Scatter Estimation

(#1897)

Yue Chen, Runze Liao, Yucun Hou, Jianyong Jiang

Beijing Normal University, school of physics and astronomy, Beijing, China

This work was supported in part by the National Natural Science Foundation of China (No. 12475336), and the Fundamental Research Funds for the Central Universities (No. 310400209521).

Abstract

The extension of the axial field-of-view (AFOV) advances in positron emission tomography (PET), offering unprecedented sensitivity and enabling ultra-low-dose 4D total-body imaging. However, long-axial field-of-view (LAFOV) systems introduce significant challenges, including prohibitive computational loads and complex quantitative corrections necessitated by expanded axial acceptance angles. A primary obstacle is the extreme sparsity of acquired data relative to the vast lines-of-response (LOR) space. We present a robust quantitative correction strategy integrated into QuanTOF, a GPU-accelerated, list-mode reconstruction framework. Our primary contribution is the implementation of a modified component-based normalization (CBN) strategy tailored for axial-dependent variations, effectively mitigating noise amplification in sparse data environments. Furthermore, we introduce a simplified calibration protocol utilizing 0.5 m thin-ring and FOV-length line sources to derive geometric and plane efficiencies—an efficient alternative to conventional through-axial rotating rods. To ensure correction accuracy despite data sparsity, a moderate rebinning strategy was employed for scatter and random estimation. The framework was validated via GATE simulations of the 1.5 m uMI Panorama GS system. Reconstruction of a 1.5 m uniform cylinder phantom (8cm radius) demonstrated superior axial uniformity, with intensity fluctuations constrained to less than 2% within 70% of the FOV. Additionally, Derenzo phantom simulations confirmed the framework's high-resolution capabilities, successfully resolving 2.4 mm hot rods. These results show this framework successfully overcomes the inherent challenges of LAFOV data sparsity, securing the quantitative fidelity essential for total-body molecular imaging.

References
[1] Zhang, H, et al. 2024, ‘Performance Characteristics of a New Generation 148-cm Axial Field-of-View uMI Panorama GS PET/CT System with Extended NEMA NU 2-2018 and EARL Standards’, *Journal of Nuclear Medicine*, jnumed.124.267963, Reston: Society of Nuclear Medicine and Molecular Imaging
[2] Qi, J, Matej, S, Wang, G, and Zhang, X 2021, ‘3D/4D Reconstruction and Quantitative Total Body Imaging’, *PET Clinics*, 16(1), 41–54, Philadelphia: Elsevier
[3] Zhang, X, Badawi, RD, Cherry, SR, and Qi, J 2018, ‘Theoretical study of the benefit of long axial field-of-view PET on region of interest quantification’, *Physics in Medicine and Biology*, 63(13), 135010, Bristol: IOP Publishing
[4] Zhang, X, et al. 2020, ‘Total-Body Dynamic Reconstruction and Parametric Imaging on the uEXPLORER’, *Journal of Nuclear Medicine*, 61(2), 285–291, Reston: Society of Nuclear Medicine and Molecular Imaging
[5] Cherry, SR, Jones, T, Karp, JS, Qi, J, Moses, WW, and Badawi, RD 2018, ‘Total-Body PET: Maximizing Sensitivity to Create New Opportunities for Clinical Research and Patient Care’, *Journal of Nuclear Medicine*, 59(1), 3–12, Reston: Society of Nuclear Medicine and Molecular Imaging
[6] Yuan, Z, et al. 2025, ‘GPU-based list-mode TOF PET image reconstruction with complete correction techniques’, *Medical Physics*, 53(1), e70216, Alexandria: American Association of Physicists in Medicine

MIC-10-380

Optimized Partial Field-of-View Reconstruction by Limited TOF Axial Rebinning in Long-Axial PET (#2235)

Inki Hong, Ziad Burbar

Siemens Healthineers, R&D, Knoxville, USA

Abstract

This work addresses efficient partial axial field-of-view (aFoV) reconstruction for long-axial PET systems, where reconstructing the full long-axial dataset and subsequently cropping to a target aFoV is computationally expensive. This need may arise when CT coverage is intentionally limited (e.g., organ-focused protocols or pediatric imaging). However, simply limiting the PET aFoV reduces the effective sensitivity of a long-aFoV scanner to that of a shorter-aFoV system. We propose a limited axial rebinning strategy that retains a subset of oblique lines of response that would otherwise be discarded when truncating data to a partial aFoV, thereby leveraging the sensitivity of the long-aFoV system. The approach selects a starting rebin segment and a bounded set of additional oblique segments (up to a maximum rebin segment), and rebins eligible events into target segments while preserving time-of-flight (TOF) geometry. In an FDG human study on a long-aFoV system, the proposed limited rebinning substantially increases retained true counts for a Vision-equivalent aFoV versus truncation without rebinning, while maintaining comparable axial resolution and avoiding the cost of reconstructing the full long-aFoV image.

References
[1] LR. D. Badawi et al., “First Human Imaging Studies with the EXPLORER Total-Body PET Scanner,” J. Nucl. Med., 2019.
[2] S. Surti, A. R. Pantel, and J. S. Karp, “Total Body PET: Why, How, What for?,” IEEE Trans. Radiat. Plasma Med. Sci., 2020.
[3] M. Defrise et al.,“Continuous and Discrete Data Rebinning in Time-of-Flight PET,” IEEE Trans. Med. Imaging, 2008.
[4] M. Defrise et al., “Exact and approximate rebinning algorithms for 3-D PET data,” IEEE Trans. Med. Imaging, 1997.
[5] S. Cho et al.,“Exact and approximate Fourier rebinning of PET data from time-of-flight to non time-of-flight,” PMB, 2009.
[6] I. Hong, and Z. Burbar, “PET image reconstruction optimization for long aFoV scanner by using TOF axial rebinnig,” IEEE NSS/MIC, 2025.

MIC-10-383

Generalizable CT-Free Low-Dose PET Restoration: Few-Shot Adaptation Across Multi-Scanners (#2478)

Xiaoya Qiao[1], Hanzhong Wang[1], Bolin Yao[1], Jiwei Yu[2], Ziqi Zhuang[3], Qiu Huang[4]

[1] Shanghai Jiao Tong University, Department of Nuclear Medicine, Ruijin Hospital, Shanghai, China; [2] Shanghai Jiao Tong University, Department of Cardiology, Ruijin Hospital, Shanghai, China; [3] Wageningen University and Research, Wageningen, Netherlands; [4] Macao Polytechnic University, Faculty of Applied Sciences, Macao, Macau

The authors would like to thank all colleagues and collaborators who contributed to this project.

Abstract
PET/CT radiation exposure arises from both the injected PET radiotracer and the accompanying CT scan used for attenuation and scatter correction. Reducing PET dose while eliminating CT-based correction is therefore an attractive strategy for lower-radiation PET/CT imaging, but this setting substantially degrades image quality. In this study, we propose a deep learning framework for CT-free low-dose [18F]FDG PET restoration based on a Noise-Level-Estimation network and systematically evaluate its generalizability across different PET scanners. The model restores attenuation- and scatter-corrected PET images from reduced-dose non-corrected inputs using a mixed-dose training strategy. It was trained on a main cohort from Ruijin Hospital, acquired with [18F]FDG on a

uEXPLORER scanner, comprising 5,731 reconstructed PET volumes derived from 1,163 examinations. Scanner-domain validation was performed on 640 reconstructed PET volumes derived from 320 examinations acquired on three different scanners, including Discovery MI, Vision 450, and uMI 780. Direct pretrained inference, few-shot scanner-domain finetuning, and from-scratch training were compared. Direct application of the uEXPLORER-trained model showed performance degradation under scanner shifts, whereas few-shot finetuning consistently improved restoration fidelity. In the most challenging uMI 780 cohort, median PSNR increased from 35.24 dB to 47.58 dB after finetuning. These results demonstrate the feasibility of scanner-generalizable CT-free low-dose FDG PET restoration.

References
[1] Lammertsma, A, et al. 2017, 'Forward to the past: The case for quantitative PET imaging', *J. Nucl. Med.*, vol. 58, no. 7, pp. 1019–1024.
[2] Khosravi, B, et al. 2025, 'Temporal hindsight, clinical foresight: Longitudinal lymphoma analysis at PET/CT', *Radiol. Artif. Intell.*, vol. 7, no. 3, e250149.
[3] Wang, H, et al. 2025, 'Optimizing MR-based attenuation correction in hybrid PET/MR using deep learning: Validation with a flatbed insert and consistent patient positioning', *Eur. J. Nucl. Med. Mol. Imaging*, vol. 52, no. 7, pp. 2577–2588.
[4] Chen, G, et al. 2023, 'A total-body ultra-low dose PET reconstruction method via image space shuffle U-Net and body sampling', *IEEE Trans. Radiat. Plasma Med. Sci.*, vol. 8, no. 6, pp. 357–365.
[5] Wang, H, et al. 2025, 'Noise-Level-Estimation Network for CT-Less Low Dose Total-Body PET Imaging', *2025 IEEE Nuclear Science Symposium (NSS), Medical Imaging Conference (MIC) and Room Temperature Semiconductor Detector Conference (RTSD)*, Yokohama, Japan.

MIC-10-386

3D Photon Position Estimation Using Neural Networks in Monolithic-Based PET Systems (#2663)

Pau Piera-Sapiña, **Marta Freire**, Fernando Lopez-Berenguer, Andrea Gonzalez-Montoro, Antonio J. Gonzalez

Instituto de Instrumentación para Imagen Molecular (I3M), Centro Mixto CSIC—Universitat Politècnica de València, Valencia, Spain

This work was supported by the Generalitat Valenciana under Grant No. CIPROM/2021/003 and funding from the University of Virginia Focused Ultrasound Cancer Immunotherapy Center and the FUS Foundation. M. Freire was supported by the CIAPOS Program for Researchers in Postdoctoral Phase of the Generalitat Valenciana under Grant No. CIAPOS/2023/141.

Abstract
Neural Network (NN) models have emerged as a promising tool for determining 3D photon impact positions in Positron Emission Tomography (PET) detectors based on monolithic scintillators. Nevertheless, NNs typically require long acquisitions of reference data training, becoming a time-consuming process that requires extensive experimental data for each individual detector module. To reduce calibration time, we propose a new methodology based on NNs trained entirely using simulated data to predict the 3D impact position of gamma rays. The feasibility of the proposed approach was verified using a real preclinical PET system composed of two rings of 8 LYSO:Ce monolithic scintillators each.

The simulation of a single detector was implemented in GATE and reference data moving a pencil beam in 1 mm steps was simulated to train two Multilayer Perceptrons (MLPs), MLP_X and MLP_Y, to predict the *x*- and *y*- impact positions, respectively. To validate the introduced methodology at reconstructed image level, experimental data was acquired using a ^{22}Na point source at the center of the preclinical system and processed using both the presented framework and the system's standard calibration methodology.
Results have demonstrated that similar spatial resolution was obtained with both approaches, thus demonstrating that NNs trained exclusively with Monte Carlo simulations can generate coherent reconstructed images and thus eliminate the need for calibration measurements for each individual detector module.

References
[1] Gonzalez-Montoro A, et al. 2021, IEEE Trans. on Rad. and Plasma Med. Sci., 5, 282-305
[2] Iborra A, et. al. 2019, Phys. Med. Biol., 64, 195010
[3] Lopez-Berenguer F, et al. 2025, IEEE Trans. on Rad. and Plasma Med. Sci., 10, 789-798
[4] Gonzalez-Montoro A, et al. 2017, IEEE Trans. on Rad. and Plasma Med. Sci., 1, 229-237
[5] Freire M, et al. 2020, IEEE Trans. on Rad. and Plasma Med. Sci., 4, 350-360
[6] Jan S, et al. 2004, Phys. Med. Biol., 49, 4543-4543
[7] Freire M, et al. 2022, Phys. Med. Biol., 67, 245011

MIC-10-389

Depth Attention and Volume Attention Module for 3D Medical Image Segmentation (#1088)

Xiaoshuo Kan[1], Koichi Ogawa[2]

[1] Hosei University, Graduate School of Science and Engineering, Tokyo, Japan; [2] Hosei University, Faculty of Science and Engineering, Tokyo, Japan

Abstract
3D medical image segmentation of CT and MRI volumes is essential for clinical diagnosis and treatment planning. While deep learning methods such as 3D U-Net, Attention U-Net, and nnU-Net achieve strong performance, conventional 3D CNNs treat all slices equally along the axial direction, causing insufficient learning of lesion-containing slices. Existing attention mechanisms such as Attention U-Net focus on height×width (H×W) planar spatial attention without explicitly modeling slice-wise importance along the depth (D) axis. This paper proposes two attention modules to address these limitations. First, a Depth Attention Module (DAM) automatically learns the importance of each slice and integrates it into each decoder layer via residual connection. Second, a volume Attention Module (VAM) extends DAM to independently learn importance along H, W, and D axes, combining three independent axis-wise attention maps to achieve disease-adaptive spatial importance learning. DAM achieves Dice improvements of 7.61%, 4.71%, and 3.72% over 3D U-Net on brain hemorrhage CT (HemSeg-200), kidney CT, and ischemic stroke MRI, respectively, and 8.52% over nnU-Net on lung cancer CT (MSD Task06). On brain hemorrhage CT, DAM further improves over Attention U-Net by 4.54% and over nnU-Net by 1.03%. VAM achieves improvements of 7.76% over 3D U-Net on brain hemorrhage CT and 2.83% over nnU-Net on lung cancer CT. Experimental results confirm the effectiveness of the proposed modules across multiple diseases and imaging modalities.

References

[1] Ronneberger, O, Fischer, P, Brox, T 2015, 'U-Net: convolutional networks for biomedical image segmentation,' in *Proceedings of MICCAI*, pp. 234–241
[2] Çiçek, Ö, Abdulkadir, A, Lienkamp, SS, Brox, T, Ronneberger, O 2016, '3D U-Net: learning dense volumetric segmentation from sparse annotation,' in *Proceedings of MICCAI*, pp. 424–432
[3] Oktay, O, Schlemper, J, Folgoc, LL, Lee, M, Heinrich, M, Misawa, K 2018, 'Attention U-Net: learning where to look for the pancreas,' in *Proceedings of MIDL*
[4] Isensee, F, Jaeger, PF, Kohl, SAA, Petersen, J, Maier-Hein, KH 2021, 'nnU-Net: a self-configuring method for deep learning-based biomedical image segmentation,' *Nature Methods*, vol. 18, no. 2, pp. 203–211
[5] Hu, J, Shen, L, Sun, G 2018, 'Squeeze-and-excitation networks,' in *Proceedings of IEEE CVPR*, pp. 7132–7141
[6] Song, C et al. 2024, 'HemSeg-200: a voxel-annotated dataset for intracerebral hemorrhage segmentation in brain CT scans,' in *Proceedings of IEEE ISBI*, pp. 3376–3377
[7] Simpson, AL et al. 2019, 'A large annotated medical image dataset for the development and evaluation of segmentation algorithms,' arXiv:1902.09063
[8] Heller, N et al. 2021, 'The KiTS19 challenge: data, methods, and results,' *Medical Image Analysis*, vol. 67, art. no. 101821
[9] Liew, SL et al. 2022, 'ATLAS: a large stroke neuroimaging dataset,' *Scientific Data*, vol. 9, art. no. 320

MIC-10-392

Comparing the anatomical accuracy of a PET(O15) reconstructed algorithm (AGR) on Moyamoya Patients (#1252)

Azeezat Azeez[1], Andrew Zhang[1], Moss Zhao[2], Greg Zaharchuk[1], Fernando Boada[1]

[1] Stanford School of Medicine, Radiological Sciences Laboratory, Palo Alto, USA; [2] Stanford School of Medicine, Department of Neurosurgery, Palo Alto, USA

This work was supported in part by PHS Grant EB029306.

Abstract

PET(O15) is the gold standard for assessing cerebral perfusion in vivo. Assessment of perfusion deficits before surgical interventions in Moyamoya patients with PET(O15) is hampered by poor spatial resolution and low signal-to-noise ratio (SNR). We investigate the use of anatomically-guided reconstruction (AGR) for improving the assessment of baseline perfusion metrics in Moyamoya patients. To evaluate PET(O15) perfusion metrics in Moyamoya patients with and without the use of anatomically guided reconstructions. We assess perfusion metrics across different anatomical brain parcellations to evaluate the differences between the conventional and AGR-enhanced PET(O15) images. Regions that overlap with clinically relevant regions are significantly different in signal intensity when comparing the use of the reconstruction method. Many of which overlap with those reported in the Moyamoya literature. Implementation of the anatomy-guided PET reconstruction(AGR) algorithm can provide clinicians with a better understanding of the disease progression, especially if data integrity is limited, and of low resolution. Particularly in cases of radioisotopes with short decay half-life, such as O15, or when studying diseases of tissue perfusion and oxygen metabolism.

References
[1] Demartini Jr., Z., Teixeira, B. CA., Koppe, G. L., Gatto, L. A. M., Roman, A., & Munhoz, R. P. (2022). Moyamoya disease and syndrome: A review. Radiologia Brasileira, 55(1), 31–37. https://doi.org/10.1590/0100-3984.2021.0010 [doi]
[2] Karsonovich, T., & Lui, F. (2025). Moyamoya disease. StatPearls.
[3] Lee, S. U., Oh, C. W., Kwon, O.-K., Bang, J. S., Ban, S. P., Byoun, H. S., & Kim, T. (2018). Surgical treatment of adult moyamoya disease. Current Treatment Options in Neurology, 20(7). https://doi.org/10.1007/s11940-018-0511-8 [doi]

[4] Scott, R. M., Smith, J. L., Robertson, R. L., Madsen, J. R., Soriano, S. G., & Rockoff, M. A. (2004). Long-term outcome in children with moyamoya syndrome after cranial revascularization by pial synangiosis. Journal of Neurosurgery: Pediatrics, 100(2), 142–149. https://doi.org/10.3171/ped.2004.100.2.0142 [doi]
[6] Suzuki, J. (1969). Cerebrovascular "moyamoya" disease. Archives of Neurology, 20(3), 288. https://doi.org/10.1001/archneur.1969.00480090076012 [doi]
[5] Shang, S., Zhou, D., Ya, J., Li, S., Yang, Q., Ding, Y., Ji, X., & Meng, R. (2018). Progress in moyamoya disease. Neurosurgical Review, 43(2), 371–382. https://doi.org/10.1007/s10143-018-0994-5 [doi]
[7] Zhao, M. Y., Fan, A. P., Chen, D. Y.-T., Ishii, Y., Khalighi, M. M., Moseley, M., Steinberg, G. K., & Zaharchuk, G. (2022). Using arterial spin labeling to measure cerebrovascular reactivity in Moyamoya disease: Insights from simultaneous PET/MRI. Journal of Cerebral Blood Flow & Metabolism, 42(8), 1493–1506. https://doi.org/10.1177/0271678x221083471 [doi]
[8] Schramm, G., Rigie, D., Vahle, T., Rezaei, A., Van Laere, K., Shepherd, T., … Boada, F. (2021). Approximating anatomically-guided PET reconstruction in image space using a convolutional neural network. NeuroImage, 224, 117399. https://doi.org/10.1016/j.neuroimage.2020.117399 [doi]

MIC-10-395

MRI-Informed SPECT-only Spatial Normalization for Reliable Brain Perfusion Quantification (#1410)

Euijin You[1,2], Yu Jin Seol[1,2], Hyun Gee Ryoo[3], Seung Kwan Kang[4], Jae Sung Lee[1,2]

[1] Seoul National University, Interdisciplinary Program in Bioengineering, Seoul, South Korea; [2] Seoul National University, Integrated Major in Innovative Medical Science, Seoul, South Korea; [3] Seoul National University, Department of Nuclear Medicine, Seoul, South Korea; [4] Samsung Ventures, Seoul, South Korea; [5] Brightonix Imaging Inc., Seoul, South Korea

Abstract

Spatial normalization enables standardized volume-of-interest quantification in brain perfusion single-photon emission computed tomography, but accurate alignment is difficult because of low resolution, noise, partial volume effects, and uptake-dependent variation. We propose a MRI-informed, SPECT-only framework that distills anatomical deformation fields and feature guidance from a magnetic resonance imaging registration teacher. The student disentangles anatomical and uptake-related representations to suppress functional-uptake interference while requiring only single-photon emission computed tomography at inference. In 173 paired imaging datasets, the method improved standardized uptake value ratio consistency between subject and template spaces, especially for fine-grained volumes of interest, supporting MRI-free, single-pass template-based quantification.

References
[1] Li, R., Figueredo, G., Auer, D., Wagner, C. and Chen, X. 2024, 'MrRegNet: Multi-resolution Mask Guided Convolutional Neural Network for Medical Image Registration with Large Deformations', 2024 IEEE International Symposium on Biomedical Imaging (ISBI), pp. 2349–2353, Piscataway, NJ: IEEE.
[2] Woo, S., Park, J., Lee, J.-Y. and Kweon, I.S. 2018, 'CBAM: Convolutional Block Attention Module', Proceedings of the European Conference on Computer Vision (ECCV), pp. 3–19, Cham: Springer.
[3] Kang, S.K., Kim, D., Shin, S.A., Kim, Y.K., Choi, H. and Lee, J.S. 2023, 'Fast and Accurate Amyloid Brain PET Quantification Without MRI Using Deep Neural Networks', Journal of Nuclear Medicine, vol. 64, no. 4, pp. 659–666, Reston, VA: Society of Nuclear Medicine and Molecular Imaging.

MIC-10-398

When Do TAC and ROI Features Help? Residual Multimodal Learning for GFR Estimation in Dynamic ^{99m}Tc-DTPA Renography (#1697)

Yuanhao Zhu[1], Jinlin Li[2], Chunhao Li[1], Jiaqi Zhong[2], Wen Sun[2], Zhuoyuan Xu[1], Jingxian Chen[3], Yuecan Zeng[4], Jingzhang Sun[1], Huan Xiao[2]

[1] Hainan University, Department of Data Science and Big Data, Haikou, China; [2] The First Affiliated Hospital of Hainan Medical University, Department of Nuclear Medicine, Haikou, China; [3] Hainan General Hospital, Pediatric Intensive Care Unit, Haikou, China; [4] The Second Affiliated Hospital of Hainan Medical University, Department of Radiation Oncology, Cancer Treatment Center, Haikou, China

This work was supported in part by the National Natural Science Foundation of China (12505396) and the Science and Technology Talents Innovation Project of Hainan Province (KJRC2023D30).

Abstract

Dynamic ^{99m}Tc-DTPA renography provides both spatiotemporal image information and clinically interpretable time-activity curve (TAC) and region-of-interest (ROI) descriptors for renal functional assessment. However, how these heterogeneous information sources should be integrated for automated Gates-derived total glomerular filtration rate (GFR) estimation remains unclear. This study developed a residual multimodal learning framework in which a 3D CNN image branch first estimated Gates-derived total GFR from multi-frame renography sequences, and selected TAC/ROI descriptors were then used to predict a residual correction term rather than being directly concatenated with image features. A total of 471 complete paired examinations were retrospectively included, with 376 cases for training and 95 cases for held-out testing. Representative image-only, TAC-only, direct-fusion, ROI/TAC tabular, and residual-correction models were compared under the same test split. The dynamic image-only model outperformed perfusion TAC-only, function TAC-only, and pure ROI/TAC tabular models, indicating that the multi-frame renography sequence was the dominant information source. Direct fusion of image and TAC inputs did not improve image-only prediction. In contrast, the proposed residual-correction model achieved the best overall performance, with the lowest mean absolute error of 8.21 and root mean square error of 10.93. These findings suggest that TAC/ROI descriptors are more useful as clinically interpretable residual correction cues than as standalone predictors or directly fused inputs. The proposed framework provides a practical strategy for approximating total GFR from routine dynamic ^{99m}Tc-DTPA renography while clarifying the complementary role of TAC/ROI descriptors.

References

[1] B. Feng *et al.*, "The rotation method for correcting renal depth in the determination of glomerular filtration rate using Tc-99m diethylenetriamine pentaacetic acid (DTPA)-based renal dynamic imaging in patients with hydronephrosis," *Quantitative Imaging in Medicine Surgery*, vol. 15, no. 1, pp. 721-730, 2025.

[2] Y. Pi *et al.*, "Deep regression using 99mTc-DTPA dynamic renal imaging for automatic calculation of the glomerular filtration rate," *European Radiology*, vol. 33, no. 1, pp. 34-42, 2023.

MIC-10-401

Uncertainty-Guided Localized Diffusion Refinement for Lumbar Spine MRI Segmentation (#1924)

Quang Vinh Pham[1,2], Saerom Sung[1], Hyun Joon Choi[3], Sangwoon Jeong[3], Seoung Wan Nam[4], Hyunjung Kim[5], Chul Hee Min[1]

[1] Yonsei University, Department of Radiation Convergence Engineering, Wonju, South Korea; [2] Hanoi University of Science and Technology, Faculty of Engineering Physics, Hanoi, Vietnam; [3] Yonsei University Wonju College of Medicine, Department of Radiation Oncology, Wonju, South Korea; [4] Wonju Severance Christian Hospital, Wonju College of Medicine, Yonsei University, Department of Rheumatology, Wonju, South Korea; [5] Wonju Severance Christian Hospital, Wonju College of Medicine, Yonsei University, Department of Radiology, Wonju, South Korea

Abstract

Lumbar spine MRI segmentation is an important prerequisite for quantitative spine image analysis; however, it remains challenging due to complex anatomy, low contrast, and high inter-patient variability. Recent diffusion-based approaches have shown potential for medical image segmentation; nevertheless, preserving anatomically consistent boundaries remains challenging, particularly in low-contrast regions. We propose a conditional diffusion-based framework for lumbar spine MRI segmentation with uncertainty-guided localized refinement. The model integrates a UNet-based denoising backbone with multi-scale feature encoding to preserve anatomical structures during the diffusion process. Furthermore, an entropy-driven uncertainty mechanism is introduced to identify ambiguous regions, enabling localized refinement and selective diffusion re-sampling in low-confidence regions to support boundary delineation. The framework is evaluated using 5-fold cross-validation on multi-contrast (T1- and T2-weighted) MRI data, achieving Dice scores of 0.87-0.89 with low surface errors (ASSD ≈ 1-2 mm, HD95 < 10 mm). The current results demonstrate consistent segmentation performance across spinal canal, vertebral bodies, and intervertebral discs, indicating the feasibility of automated multi-structure lumbar MRI segmentation. These results suggest that the proposed framework can serve as a technical foundation for automated quantitative spine MRI analysis. In future work, this framework will be extended to vertebral body and corner-region analysis for edema detection, assessment of corner changes, and quantitative MRI evaluation of axial spondyloarthritis.

References

[1] A. Kazerouni *et al.*, *Med. Image Anal.*, vol. 88, p. 102846, Aug. 2023, doi: 10.1016/j.media.2023.102846.

[2] Z. Xing *et al.*, arXiv:2303.10326, 2023, doi: 10.48550/arXiv.2303.10326.

[3] M. Monzon *et al.*, *Proc. Mach. Learn. Res. (PMLR)*, vol. 156, pp. 1–18, 2025, accepted for MIDL 2025.

[4] J. W. Van Der Graaf *et al.*, *Sci. Data*, vol. 11, no. 1, p. 264, Mar. 2024, doi: 10.1038/s41597-024-03090-w.

MIC-10-404

PhysiCal-PET: Physics-based neural networks for the rapid position Calibration of PET Scanners (#2036)

Mojahed Abushawish[1], Pablo Galve[3,1], Iván Colmenarejo Allavena[1], Sara Gaitán Dominguez[1], Carlos Galindo-Morata[1], Victor Martínez Nouvilas[1], Jose Manuel Udias[1,2]

[1] Universidad Complutense de Madrid, Grupo de Física Nuclear, EMFTEL & IPARCOS, Madrid, Spain; [2] Health Research Institute of the Hospital Cínico San Carlos (IdISSC), Madrid, Spain; [3] Spanish National Research Council (CSIC), Institute for Physical and Information Technologies "Leonardo Torres Quevedo", ITEFI, Madrid, Spain

P. Galve acknowledges grant JDC2023-051754-I, funded by MCIU/AEI/10.13039/501100011033 and ESF+.

Abstract

Total-body positron emission tomography (PET) increases system sensitivity and enables whole-body dynamic imaging, but its extended axial field of view makes accurate depth-of-interaction (DOI) calibration essential for maintaining uniform spatial resolution and reducing parallax error. Conventional DOI calibration requires mechanically scanned collimated sources or detector-specific reference measurements, which become impractical as the number of detector modules increases. PhysiCal-PET introduces a physics-based neural-network framework for autonomous in-system DOI calibration of PET scanners. The method trains a network to map raw detector signals to DOI using coincidence data acquired with an uncollimated positron source at known positions. For each event, the loss function enforces annihilation geometry by requiring the predicted line of response to be consistent with the source position, thereby providing supervision without measured DOI labels. The framework was tested on realistic PET simulations and applied to data from a real preclinical PET scanner. Using this procedure, the DOI response of all 144 detector modules was calibrated in less than 2 hours of point-source measurement time. These results demonstrate that the annihilation physics can replace labor-intensive DOI calibration hardware and enable rapid, routine calibration of high-resolution PET systems. PhysiCal-PET therefore provides a scalable path toward autonomous calibration for total-body PET and other systems that rely on accurate DOI positioning. notionvc: 49ace5df-389b-489a-b611-1abe67c4c114

MIC-10-407

Nonsubsampled Contourlet Transform-based Generative Adversarial Networks for Anatomical Structure-Preserving Low Dose CT Denoising

(#2204)

Hyosung Cho, **Sanghyun Cho**

Yonsei University, Department of Radiation Convergence Engineering, Wonju, South Korea

This work was supported by the National Research Foundation of Korea(NRF) grant funded by the Korea government(MSIT)(RS-2025-16065119).

Abstract

This paper presents a Nonsubsampled Contourlet Transform-Based Generative Adversarial Network (NSCT-GAN) for low-dose computed tomography (LDCT) denoising. LDCT reduces radiation exposure but introduces quantum Poisson and electronic Gaussian noise, which blurs anatomical structures. Conventional deep learning methods using mean-squared error loss produce over-smoothed images, while existing image-domain generative adversarial networks (GANs) struggle with high-frequency CT noise. To address this, the proposed NSCT-GAN extracts multi-scale, multi-directional, and shift-invariant high-frequency features using the NSCT. The network trains a discriminator on these high-frequency images to distinguish noise from anatomical edges. The generator utilizes a U-Net architecture to maintain spatial consistency. The objective function combines a Wasserstein GAN with gradient penalty adversarial loss for high-frequency reconstruction, an L1 loss for accurate CT number recovery, and a multi-scale structural similarity (MS-SSIM) loss for global and local structural consistency. The method was evaluated using the 2016 NIH-AAPM-Mayo Clinic Low-Dose CT Grand Challenge dataset and compared against five deep learning-based denoising methods: WavResNet, SMGAN, CPCE, DU-GAN, and WDLP. Quantitative results demonstrate that NSCT-GAN achieves a peak signal-to-noise ratio (PSNR) of 27.1850 dB, a structural similarity index (SSIM) of 0.8215, and a feature similarity index (FSIM) of 0.9698, yielding the highest SSIM and FSIM values among the tested models. Qualitative evaluations show the method restores continuous vascular boundaries in the lungs and maintains heterogeneous parenchymal patterns in the liver without introducing over-smoothing or artifacts.

MIC-10-410

Preliminary Results of Generative Model-Based Positron Range Correction in PET Imaging (#2359)

Yucun Hou[1], Jiaru Ni[1], Yihao Chen[1], Fenglin Zhan[2,3], Jianyong Jiang[1]

[1] Beijing Normal University, School of Physics and Astronomy, Beijing, China; [2] The First Affiliated Hospital of USTC, Department of Nuclear Medicine, Hefei, China; [3] Jiangnan University, Wuxi School of Medicine, Wuxi, China

This work was supported in part by the National Natural Science Foundation of China (No. 12475336), and the Fundamental Research Funds for the Central Universities (No. 310400209521).

Abstract

Positron range is an inherent physical factor that degrades the spatial resolution of positron emission tomography (PET), particularly for radionuclides with high positron energies. This study investigated the feasibility of deep learning-based positron range correction for PET brain imaging. A total of 304 brain datasets acquired using a Siemens Biograph Vision PET/CT scanner at the First Affiliated Hospital of the University of Science and Technology of China were voxelized to generate brain phantoms. These phantoms were used as activity maps for GATE simulations with three emission settings: ^{18}F, ^{68}Ga, and back-to-back sources. The ^{18}F and ^{68}Ga simulations represented mild and severe positron range effects, respectively, whereas the back-to-back simulation served as the range-free reference. Two deep learning-based correction methods were evaluated, including a conditional denoising diffusion probabilistic model (C-DDPM) and a residual U-Net (Res-UNet). Visual results showed that C-DDPM better restored fine sulcal and gyral structures and achieved closer agreement with the back-to-back reference, especially for the more severe ^{68}Ga correction task. Although Res-UNet achieved superior PSNR, SSIM, and NRMSE values, its restored images exhibited noticeable oversmoothing and partial loss of subtle anatomical details. These findings suggest that diffusion-based generative restoration is a promising strategy for positron range correction, with the potential to reduce positron range induced blurring while preserving fine anatomical structures.

References

[1] Berg, E & Cherry, SR 2018, 'Innovations in Instrumentation for Positron Emission Tomography', *Seminars in Nuclear Medicine*, vol. 48, no. 4, pp. 311–331, Elsevier.

[2] Hou, Y, Zhan, F, Liu, J, Cheng, X, Li, C, Yuan, Z, et al. 2026, 'Cycle-constrained adversarial denoising convolutional network for PET image denoising: Multi-dimensional validation on large datasets with reader study and real low-dose data', *Medical Image Analysis*, vol. 107, 103826, Elsevier.

[3] Yuan, Z, Zhan, F, Lu, H, Hou, Y, Liao, R, Li, C, et al. 2026, 'GPU-based list-mode TOF PET image reconstruction with complete correction techniques', *Medical Physics*, vol. 53, no. 1, e70216, Wiley.

[4] Ho, J, Jain, A & Abbeel, P 2020, 'Denoising diffusion probabilistic models', *Advances in Neural Information Processing Systems*, vol. 33, pp. 6840–6851.

MIC-10-413

Wavelet-Conditioned Rectified Flow for Efficient Whole-Body Low-Dose PET Denoising (#2431)

Luxiang Xie, Weigang Duan, Jiali Yan, Hongyang Zhang, Shi Wang, Zhaoxia Wu, Hui Liu, Yaqiang Liu

Tsinghua University, Beijing, China

The authors gratefully acknowledge Xue Song, Kuangyu Shi, and Axel Rominger from the University of Bern, as well as Hanzhong Wang, Rui Guo, and Biao Li from Ruijin Hospital, Shanghai Jiao Tong University School of Medicine, for providing the PET data used in this study.

Abstract

Low-dose positron emission tomography (PET) reduces injected activity and acquisition time, but low-count statistics introduce strong noise, impaired lesion conspicuity, and unstable standardized uptake value (SUV) quantification in whole-body imaging. Recent 3D diffusion models improve PET denoising, and wavelet-conditioned diffusion further shows that the Haar low-frequency LLL subband can serve as a robust structural prior. However, diffusion sampling is computationally expensive for large 3D PET volumes. We propose Wavelet-Conditioned Rectified Flow (WCRF), a deterministic whole-body PET restoration framework that integrates wavelet-domain structural guidance with rectified-flow matching.To establish robust structural guidance, WCRF isolates the lowest-frequency (LLL) subband via a single-level 3D Haar decomposition. This frequency-derived information is then combined with the original noisy input to form a resilient conditioning signal. A lightweight ControlNet-style branch injects this condition into a time-conditioned rectified-flow network, which learns the velocity field from low-dose to full-dose PET along a straight transport path. During inference, WCRF restores full 3D volumes using sliding-window Euler integration with only a small number of function evaluations. Experiments against low-dose input, 3D U-Net, 3D GAN, and 3D DDPM baselines at the 1/20-dose setting show that WCRF achieves competitive overall restoration performance among the evaluated methods, while substantially reducing inference cost relative to DDPM.

References

[1] Wang, Y., Yu, B., Wang, L., Zu, C., Lalush, D. S., Lin, W., ... & Shen, D. (2018). 3D conditional generative adversarial networks for high-quality PET image estimation at low dose. NeuroImage, 174, 550-562.

[2] Yu, B., Ozdemir, S., Dong, Y., Shao, W., Pan, T., Shi, K., & Gong, K. (2025). Robust whole-body PET image denoising using 3D diffusion models: evaluation across various scanners, tracers, and dose levels. European Journal of Nuclear Medicine and Molecular Imaging (EJNMMI), 52(7), 2549-2562.

[3] Lyu, Q., Chen, T., Wang, Y., Guo, E., & Zhou, L. (2025). WID-PET: PET image reconstruction from low-dose data using a wavelet-informed diffusion model with fast inference. In International Conference on Medical Image Computing and Computer-Assisted Intervention (MICCAI) (pp. 684-693). Springer.

[4] Xue S, Guo R, Bohn KP, Matzke J, Viscione M, Alberts I, Meng H, Sun C, ZhangM, Zhang M, Sznitman R, EI Fakhri G, Rominger A, Li B and Shi K, A cross-scannerandcross-tracer deep learning method for the recovery of standard-dose imaging qualityfrom low-dose PET. European journal of nuclear medicine and molecular imaging, 2021. pp.1-14.

MIC-10-416

Adaptive Spatio-Temporal Denoising for Low-Dose Fluoroscopy via Motion-Gradient Weighting (#2582)

Nerea León[1,2], Xiaolin Ye[1], Jesús L. Longas[1], Juan Manuel Arco[1], Jose María Ortega[1], Mailyn Pérez-Liva[2], Joaquín López Herraiz[2], Alejandro Sisniega[1]

[1] Sedecal Molecular Imaging, Madrid, Spain; [2] Universidad Complutense de Madrid, Nuclear Physics Group and IPARCOS, Universidad Complutense de Madrid, Madrid, Spain

The authors would like to express their sincere gratitude to the Image Processing and AI Group at Sedecal Molecular Imaging for their invaluable technical support and expertise. We also thank the Nuclear Physics Group and IPARCOS at the Universidad Complutense de Madrid for their collaboration and the resources provided for this research.
We acknowledge support from the Comunidad de Madrid regional government through the LUNABRAIN project (TEC-2024/TEC-43) and the Industrial PhD program IND2023/BMD-28275.

Abstract

A spatio-temporal denoising training strategy for low-dose fluoroscopy is proposed, based on a spatially-adaptive temporal consistency metric. This approach acts on a small set of consecutive frames coupling a conventional denoising operator with an adaptive motion-gradient attention gate to selectively modulate the temporal consistency terms within the loss function, ensuring effective noise suppression and flickering reduction while maintaining high anatomical fidelity in dynamic regions.
The proposed method was used to train a denoising operator in which a three-frame temporal window is used as input. The model was trained across multiple dose reduction factors (qF), and demonstrated superior structural recovery and enhanced temporal stability in the processed image sequences, compared to single-frame models. Quantitative and qualitative evaluation of image quality, along with stability maps—defined as the Normalized Cross-Correlation (NCC) of temporal Coefficient of Variation (CV) maps—confirms high fidelity relative to high-dose reference acquisitions, effectively mitigating stochastic fluctuations without introducing motion artifacts.

References

[1] Dierckx, P. *et al.* 2007, "Spatio-temporal adaptive filter for low-dose fluoroscopy", *IEEE Nuclear Science Symposium Conference Record*, pp. 3450–3453.

[2] Wang, X. *et al.* 2019, "EDVR: Video restoration with enhanced deformable convolutional networks", *IEEE/CVF Conference on Computer Vision and Pattern Recognition Workshops (CVPRW)*.

[3] Chen, H. *et al.* 2017, "Low-dose CT with a residual encoder-decoder convolutional neural network", *IEEE Transactions on Medical Imaging*, vol. 36, no. 12, pp. 2524–2535.

[4] Lehtinen, J. *et al.* 2018, "Noise2Noise: Learning image restoration without clean data", *Proceedings of the International Conference on Machine Learning (ICML)*.

[5] Zhao, W., Rowlands, J. A. 1995, "X-ray imaging using amorphous selenium: Feasibility of a flat panel self-scanned detector for digital radiology", *Medical Physics*, vol. 22, no. 10, pp. 1595–1604.

[6] Cunningham, I. A. 2000, "Applied linear-systems theory", in *Handbook of Medical Imaging*, vol. 1, Sonka, M., Fitzpatrick, J. M. (eds.), pp. 79–160, Bellingham, WA: SPIE.

MIC-10-419

An Ensemble of Deep-Learning Classifiers for 3D Anatomical Change Reconstruction in Carbon-Ion Radiotherapy (CIRT) (#2644)

Patrice Schlegel[1,3], Rebekka Kirchgässner[1,2], Pamela Ochoa-Parra[1,2], Erik Bartelme[1,2], Ralf Mikut[4], Oliver Jäkel[1,2], Maria Martisikova[1,2]

[1] DKFZ, Division of Medical Physics in Radiation Oncology, E040, Heidelberg, Germany; [2] Heidelberg Institute for Radiation Oncology (HIRO), National Center for Research in Radiation Oncology (NCRO), Heidelberg, Germany; [3] University, Heidelberg, Medical Faculty, Heidelberg, Germany; [4] Karlsruhe Institute of Technology (KIT), Institute for Automation and Applied Informatics (IAI), Karlsruhe, Germany

Abstract

Carbon-ion radiotherapy (CIRT) combines high biological effectiveness with outstanding treatment precision. Since treatment plans are based on the most recent Computed Tomography (CT), anatomical changes during multi-week treatments may compromise dose delivery accuracy. To address the increasing uncertainty about the patient's anatomical state with time elapsed since the planning CT, our group developed an in vivo monitoring method using secondary charged particles emitted during therapy. This non-invasive approach requires no additional dose and reduces uncertainty about patient anatomy and thus, loss of treatment accuracy. It uses a custom detection system to detect nuclear fragments emmited from the patient and allows approximating their origin. To reconstruct these changes in 3D, we utilize our recently published method for detecting the depth (z) of changes along the beam axis and apply it to a sliding window (x,y) along the transverse plane. However, splitting reconstructed nuclear fragment origins into smaller subsets reduces the statistical stability of each subset distribution. In this study, we present an approach to robustly distinguish whether a windowed subset belongs to a region with or without an anatomical change based on correlation matrices generated by our depth detection method. These images contain location-wise correlations of joined frequency band variations between projections of nuclear fragment measurements from different treatment days. To classify regions of change and approximate change depth, we train an ensemble of deep learning-based image classifiers with different architectures *(i.e. ResNet, RegNet and ConvNeXt)* and combine their outputs into an ensemble decision. The approach was validated using dedicated irradiation measurements with coin-sized cavities inserted into PMMA head phantoms. Despite limited training data, we achieved robust improvements in change localization using an ensemble of different deep learning architectures.

References

[1] Schlegel, P., Kirchgässner, R., Ochoa-Parra, P., Kelleter, L., Gertz, M., Mikut, R., Jäkel, O. and Martišíková, M. 2025, 'A data analysis framework for in vivo monitoring in carbon-ion radiotherapy (CIRT): towards 3D reconstruction of interfractional anatomical changes', *Physics in Medicine & Biology*, 70, 245009, Bristol: IOP Publishing.

[2] Kirchgässner, R., Martišíková, M., Schlegel, P., Ochoa-Parra, P., Harrabi, S., Jäkel, O., Debus, J. and Kelleter, L. 2026, 'Out-of-beam artifact suppression in charged nuclear fragment-based carbon-ion radiotherapy monitoring', *Medical Physics*, 53, e70351, Hoboken: Wiley.

[3] Ghesquière-Diérickx, L., Félix-Bautista, R., Schlechter, A., Kelleter, L., Reimold, M., Echner, G., Soukup, P., Jäkel, O., Gehrke, T. and Martišíková, M. 2022, 'Detecting perturbations of a radiation field inside a head-sized phantom exposed to therapeutic carbon-ion beams through charged-fragment tracking', *Medical Physics*, 49, Hoboken: Wiley.

[4] Kelleter, L., Schmidt, S., Subramanian, M., Marek, L., Granja, C., Jakubek, J., Jäkel, O., Debus, J. and Martišíková, M. 2024, 'Characterisation of a customised 4-chip Timepix3 module for charged-particle tracking', *Radiation Measurements*, 173, Amsterdam: Elsevier.

MIC-10-422

Reduction of Breathing and Metallic Implant Artifacts in PET with Synthetic CT Attenuation (#2684)

Jaasiel Edwards[1,2], Zoe Wilson[1,2], Scott Wollenweber[3], Robert Johnsen[3], Hagit Ratner[3], Abolfazl Mehranian[3], Kevin M. Bradley[4], Daniel R. McGowan[1,2]

[1] University of Oxford, Oncology Department, Oxford, UK; [2] Oxford University Hospitals NHS Foundation Trust, Department of Medical Physics and Clinical Engineering, Oxford, UK; [3] GE HealthCare, Chicago, USA; [4] University Hospital of Wales, Wales Research and Diagnostic Positron Emission Tomography Imaging Centre, Cardiff, UK

Abstract

Despite its widespread use for compensating attenuation in positron emission tomography (PET), computed tomography (CT)-based attenuation correction has limitations which can create imaging artifacts associated with breathing motion and metallic implants. Using deep learning networks to create synthetic attenuation correction maps represents a data-driven, non-ionizing alternative with the potential to reduce the frequency and/or intensity of such errors. In this study, the authors aimed to demonstrate that using synthetic maps would reduce breathing motion and metallic implant artifacts. To achieve this, ten anonymized whole-body F^{18}-Fluorodeoxyglucose exams were assessed. Scans were divided into two Cohorts; Cohort 1 comprised exams with breathing motion artifacts, whilst Cohort 2 contained scans of patients with hip replacements. Each scan was corrected separately with CT-based attenuation correction and synthetic maps prior to identical reconstruction. Quantitative assessments of standardized uptake value (SUV) parameters were performed, and differences were tested for statistical significance. Additionally, each image's lesion detectability, diagnostic confidence and overall image quality were scored on a Likert scale by an experienced radiologist. After assessment, no statistically significant differences in SUV quantification were detected ($p > 0.05$). Images corrected with synthetic maps were preferred by the radiologist in Cohort 1, but no preference was expressed in Cohort 2. Moreover, a single Cohort 1 case was identified in which breathing motion artifacts impacted clinical diagnosis only for the image treated with CT-based attenuation correction. Thus, it was concluded that synthetic maps reduce breathing motion artifacts to an extent which may support clinical diagnoses, although their effects on metallic implant artifacts require further investigation.

MIC-10-425

Frozen Stable Diffusion VAE as a Slice-Wise Encoder for Scalable 3-D Medical Image Generation (#2828)

Youness Mellak, Antoine De Paepe, Alexandre Bousse, Dimitris Visvikis

Université de Bretagne Occidentale, LaTIM, INSERM, UMR 1101, Brest, France

Abstract

Full-volume 3-D medical image generation at clinical resolutions remains a significant challenge due to GPU memory constraints. Existing voxel-space generative methods are difficult to scale to large clinical volumes, as memory and compute costs grow rapidly with spatial resolution. Latent diffusion approaches offer a more scalable alternative [1], but they typically require training a dedicated medical autoencoder for each modality or dataset before generative modeling can begin, making the compression stage itself a major bottleneck [2], [3], [4]. A lighter alternative is to encode axial slices independently with a 2-D autoencoder and stack the resulting latent maps into a 3-D tensor [5]; however, this still requires training a modality-specific encoder from scratch, limiting generality across modalities and resolutions.

We propose a scalable latent flow framework that eliminates this bottleneck by using a frozen pretrained Stable Diffusion VAE as a ready-to-use slice-wise encoder for medical volumes, requiring no modality-specific retraining or adaptation. Each axial slice is resampled to a common resolution, intensity-normalized, and encoded independently by the frozen encoder, yielding a high in-plane compression factor compared to dedicated medical autoencoders. The resulting latent maps are stacked into a compact 3-D tensor, on which a full-volume 3-D U-Net flow model is trained directly. The objective predicts clean latents and supervises in velocity space [6], ensuring stable optimization and sharp generations in high-dimensional latent spaces, avoiding the blurriness and instability observed with standard diffusion objectives.

We validate our framework on CT, PET, and MRI volumes at clinical resolutions, demonstrating strong encoding fidelity and coherent full-volume generation across axial, coronal, and sagittal planes on a single consumer-grade GPU, without any modality-specific autoencoder training.

References

[1] Rombach, R., Blattmann, A., Lorenz, D., Esser, P. and Ommer, B., 2022. High-resolution image synthesis with latent diffusion models. In *Proceedings of the IEEE/CVF conference on computer vision and pattern recognition* (pp. 10684-10695).

[2] Guo, P., Zhao, C., Yang, D., Xu, Z., Nath, V., Tang, Y., Simon, B., Belue, M., Harmon, S., Turkbey, B. and Xu, D., 2025, February. Maisi: Medical ai for synthetic imaging. In *2025 IEEE/CVF Winter Conference on Applications of Computer Vision (WACV)* (pp. 4430-4441). IEEE.

[3] Khader, F., Müller-Franzes, G., Tayebi Arasteh, S., Han, T., Haarburger, C., Schulze-Hagen, M., Schad, P., Engelhardt, S., Baeßler, B., Foersch, S. and Stegmaier, J., 2023. Denoising diffusion probabilistic models for 3D medical image generation. *Scientific reports*, *13*(1), p.7303.

[4] Pinaya, W.H., Tudosiu, P.D., Dafflon, J., Da Costa, P.F., Fernandez, V., Nachev, P., Ourselin, S. and Cardoso, M.J., 2022, September. Brain imaging generation with latent diffusion models. In *MICCAI workshop on deep generative models* (pp. 117-126). Cham: Springer Nature Switzerland.

[5] Kebaili, A., Lapuyade-Lahorgue, J., Vera, P. and Ruan, S., 2024, May. 3d mri synthesis with slice-based latent diffusion models: Improving tumor segmentation tasks in data-scarce regimes. In *2024 IEEE International Symposium on Biomedical Imaging (ISBI)* (pp. 1-5). IEEE.

[6] Li, T. and He, K., 2025. Back to basics: Let denoising generative models denoise. *arXiv preprint arXiv:2511.13720*.

MIC-10-427

Deep learning-based 3D SPECT generation model for 225Ac-DOTATATE quantification using CT and 2D Planar images (#2434)

Jingyu Yang[1], Muath Almaslamani[1,2], Inki Lee[3], Ilhan Lim[3], Sang-Keun Woo[1,2]

[1] Korea Institute of Radiological and Medical Sciences, Division of Applied RI, Seoul, South Korea; [2] University of Science & Technology, Radiological & Medico-Oncological Sciences, Daejeon, South Korea; [3] Korea Institute of Radiological and Medical Sciences, Department of Nuclear Medicine, Seoul, South Korea

Abstract

Targeted alpha therapy using ^{225}Ac-DOTATATE has shown promise for patients with metastatic or inoperable neuroendocrine tumors. Image-based dosimetry is important for treatment optimization and toxicity assessment; however, quantitative ^{225}Ac SPECT imaging is challenging due to low injected activity and limited gamma-ray count statistics. This study aimed to investigate the feasibility of generating ^{225}Ac-DOTATATE SPECT images from planar and CT images using a deep learning-based image generation framework. Five patients were administrated administered with 205 μCi of ^{225}Ac-DOTATATE were included. Planar, SPECT and CT imaging was performed 24 h after administration using a dual-head Symbia T2 scanner with energy windows centered at 78, 218, and 440 keV. Fusion images were generated from planar and CT images using the conjugate view method described in MIRD Pamphlet No. 16. Planar images, fusion images, and CT images were used as multimodal inputs to a 3D U-Net encoder–decoder network to generate quantitative SPECT images. All images were resized to 128 × 128 × 128 voxels and normalized. The model was optimized using the Adam optimizer with a learning rate of 2×10^{-5}, batch size of 1, and 500 epochs, using L1 loss. The generated SPECT images showed uptake patterns comparable to acquired SPECT images. Quantitative organ-level analysis showed similar uptake distributions across major organs and tumor regions, with relative uptake error below 15% in most organs. These findings demonstrate the feasibility of planar-to-SPECT image generation using deep learning and suggest its potential to support ^{225}Ac-DOTATATE image-based dosimetry by providing three-dimensional radiopharmaceutical distribution from clinically practical planar and CT images.

MIC-10-428

No CT, No Problem: Synthetic PET Enables Attenuation Correction in Dedicated Brain Scanners (#2919)

Alejandro Merino-Balaguer[1], David Perez-Benito[1], Claire J. Brooks[1], Juan J. Vaquero[1,2], Juan E. Iglesias[3,4], David Izquierdo-Garcia[1]

[1] Universidad Carlos III de Madrid, Dpt. Bioengineering, Madrid, Spain; [2] Instituto de Investigación Sanitaria Gregorio Marañón, Madrid, Spain; [3] Massachusetts General Hospital, Harvard Medical School, Dpt. Radiology, Boston, USA; [4] Massachusetts Institute of Technology, Cambridge, USA

Abstract

Dedicated standalone brain positron emission tomography (PET) scanners have emerged in recent years as a promising technology for neuroimaging, offering high spatial resolution, increased sensitivity, reduced injected dose and shorter acquisition times. However, unlike hybrid PET/computed tomography (PET/CT) or PET/magnetic resonance imaging (PET/MRI) systems, these scanners do not provide an anatomical image from which attenuation information can be derived. We present a SynthSR-based framework to predict CT-derived attenuation maps from non-attenuation-corrected (NAC) PET images, aiming to enable attenuation correction in standalone brain PET. Building on SynthSR, a large and widely variable set of synthetic PET volumes is generated to sample a space larger than the potential clinically viable PET images, and thus increasing the robustness and clinical applicability of the model. The synthetic PET volumes are generated on-the-fly from anatomical labels using label-conditioned Gaussian-mixture intensity sampling, spatial/intensity augmentation and PET-specific priors estimated from real normalized PET data. A PET appearance model introduces count-based noise, correlated texture, smoothing, and controlled intensity variability. Finally, spatial transformations are used to increase sample diversity while preserving voxel-wise alignment. A three-dimensional U-Net was trained to predict normalized attenuation maps from synthetic PET, while validation and testing were performed on never-seen real PET/CT data. The model was optimized with 24,000 on-the-fly synthetic samples and evaluated on held-out real PET/CT data. The best validation checkpoint achieved MAE=0.03 (3%), PSNR=25.74 dB, and Pearson correlation r=0.859. On the independent test subject, the model achieved MAE=0.027 (2.7%), PSNR=26.35 dB, and r=0.854. These results support the feasibility of CT/MRI naive pseudo-CT generation for PET attenuation correction in novel standalone dedicated brain PET scanners.

References

[1] J. J. Vaquero and P. E. Kinahan, “Positron emission tomography: Current challenges and opportunities for technological advances in clinical and preclinical imaging systems,” Annu. Rev. Biomed. Eng., 2015

[2] Juan E. Iglesias et al., “SynthSR: A public AI tool to turn heterogeneous clinical brain scans into high-resolution T1-weighted images for 3D morphometry”, Sci. Adv.9,eadd3607, 2023

[3] D. Izquierdo-Garcia and C. Catana, “MR imaging-guided attenuation correction of PET data in PET/MR imaging,” PET Clinics, 2016

[4] B. Billot et al., “SynthSeg: Segmentation of brain MRI scans of any contrast and resolution without retraining,” Medical Image Analysis, 2023.

MIC-10-431

Alpha-CenterNet: A Heatmap-Based Detector for Alpha-Particle Localization in Scintillator-Camera Imagery (#3015)

Donghee Kang[1], Seohan Kim[2,3], Wonmo Sung[2,3]

[1] Agency for Defense Development, Chem-Bio Technology Directorate, Daejeon, South Korea; [2] The Catholic University of Korea, Department of Biomedical Engineering, College of Medicine, Seoul, South Korea; [3] The Catholic University of Korea, Department of Medical Sciences, Graduate School, Seoul, South Korea

Abstract

Targeted Alpha Therapy with actinium-225 induces double-strand DNA breaks through individual alpha decays, motivating quantitative imaging of single-event distributions for dose assessment. We address point detection in a cerium-doped gadolinium aluminum gallium garnet scintillator coupled to an electron-multiplying camera, in which each alpha produces a point-spread function of approximately 2-micrometer diameter at 10 to 150 events per 100-millisecond frame. We compare three method groups on Monte Carlo simulated images: 20 classical preprocessing-and-clustering pipelines, two deep learning detectors based on the U-Net and YOLOv8-nano architectures, and Alpha-CenterNet, a heatmap-based detector that adapts CenterNet with a feature pyramid network and a modified focal loss. The highest-F1 classical pipeline attains 0.641 with 447-nanometer mean localization error. U-Net reaches F1 = 0.978 with 302-nanometer error; YOLOv8-nano reaches 185-nanometer error with F1 = 0.938; the two metrics produce divergent rankings. Alpha-CenterNet (3.78 million parameters) achieves F1 = 0.965 and 244-nanometer error, reducing localization error by 19 percent relative to U-Net at 26 percent of its parameter count, and reaching the validation F1 plateau of 0.98 in 29 versus 86 epochs—a 2.97-fold convergence speedup within the same ablation. The modified focal loss decouples F1 from localization error: F1 changes by 0.0004 while the mean error decreases by 76 nanometers, and this effect persists across all tested densities. The method generalizes to clustered and edge source distributions at unseen densities, supporting point detection for Targeted Alpha Therapy monitoring.

References

[1] S. Yamamoto et al., "Real-time trajectory imaging of alpha particles emitted from actinium-225 and its daughter radionuclides," *Sci. Rep.*, vol. 15, no. 1, p. 2534, Jan. 2025, doi: 10.1038/s41598-025-87014-7.

[2] X. Zhou, D. Wang, and P. Krähenbühl, "Objects as points," *arXiv*:1904.07850, Apr. 2019.

[3] H. Law and J. Deng, "CornerNet: Detecting objects as paired keypoints," in *Proc. ECCV*, Munich, Germany, Sep. 2018, pp. 734–750.

MIC-10-434

AI-Assisted Circuitry Design for a Timing-Sensitive SiPM Front-End Readout (#3235)

Ziwen Lv[1], Zehao Hao[1], Xiaochun Lai[1], Pengwei Xie[2], Boren Wang[1]

[1] ShanghaiTech University, School of Biomedical Engineering, Shanghai, China; [2] Shanghai United Imaging Healthcare Advanced Technology Research Institute Co., Ltd., Shanghai, China

This work was supported by the Science and Tech-nology Commission of Shanghai Municipality under grant No. 24DIPA00700. We acknowledge the ShanghaiTech Material and Device Lab and HPC Platform of ShanghaiTech University.

Abstract

Artificial-intelligence-assisted PCB layout is an emerging capability that promises to reduce design iteration time and enable rapid exploration of placement and routing alternatives, which is particularly valuable for complex, multi-channel analog front-end boards where manual layout is labor-intensive and experience-dependent. In this work, we explore the application of an AI-assisted layout workflow to a timing-sensitive silicon photomultiplier (SiPM) front-end readout board for time-of-flight positron emission tomography (TOF-PET) detectors. A four-channel RF front-end readout board, extending a validated single-channel timing topology, underwent automated placement and routing via AI layout tools. To establish a performance baseline, a single-channel prototype of the same RF topology was fabricated and characterized using a coincidence measurement setup with LYSO scintillators, achieving a coincidence time resolution of 100.78 ps and confirming the near-100-ps timing capability of the front-end design. Preliminary evaluation of the AI-generated four-channel layout shows that the tool achieved high routing completion and produced a viable candidate layout. Based on these encouraging results, we plan to fabricate the AI-generated board and systematically compare its timing performance, energy response, and channel consistency against our manually designed baseline, providing a direct, measurement-level assessment of AI-assisted layout quality for timing-sensitive detector electronics.

References

[1] N. Zhang, A. Agnesina, N. Shbat, Y. Leader, Z. Zhang, and H. Ren, “Cypress: VLSI-inspired PCB placement with GPU acceleration,” in Proceedings of the 2025 International Symposium on Physical Design (ISPD), 2025, pp. 31–41, doi: 10.1145/3698364.3705346.

[2] L. Vassallo and J. Bajada, “Learning circuit placement techniques through reinforcement learning with adaptive rewards,” in Proc. Design, Automation & Test in Europe Conference & Exhibition (DATE), 2024, pp. 1–6.

[3] L. Chen, R. Chen, S. Hu, X. Yao, Z. Tang, S. Kai, S. Xu, M. Yuan, J. Hao, B. Yu, and J. Xu, “PCBAgent: An agent-based framework for high-density printed circuit board placement,” in Proceedings of the 30th Asia and South Pacific Design Automation Conference, 2025, pp. 781–787, doi: 10.1145/3658617.3697736.

[4] P. Lecoq, “Pushing the limits in time-of-flight PET imaging,” IEEE Transactions on Radiation and Plasma Medical Sciences, vol. 1, no. 6, pp. 473–485, Nov. 2017, doi: 10.1109/TRPMS.2017.2756674.

MIC-10-437

Simultaneous Dual Tracer PET Separation in reconstruction: Validation on LAFOV Data (#1161)

Zekai Li[1], Nikos Efthimiou[1], Sebastiaan L.M. Viol[2], Gert Luurtsema[1], Tom van Meerten[3], Kris Thielemans[4,5], Adrienne H. Brouwers[1], Adriaan A. Lammertsma[1], Charalampos Tsoumpas[1]

[1] University Medical Center Groningen, Department of Nuclear Medicine and Molecular Imaging, Groningen, Netherlands; [2] VU University Medical Center, Department of Radiology and Nuclear Medicine, Amsterdam UMC, Amsterdam, Netherlands; [3] University Medical Center Groningen, Department of Hematology, Groningen, Netherlands; [4] University College London, Institute of Nuclear Medicine, London, UK; [5] University College London, UCL Hawkes Institute, London, UK

Zekai Li was also supported by a Joint Scholarship from the China Scholarship Council and the University of Groningen (202210100011) and his placement at UCL by EPSRC CCP in Synergistic Reconstruction for Biomedical Imaging (EP/T026693/1).Charalampos Tsoumpas, Nikos Efthimiou and Zekail Li are supported by the NWO AES Vici Talent program (doi: 10.61686/REEAR02777).

Abstract

Simultaneous dual tracer PET provides complementary physiological information compared with single tracer imaging. For example, combining [^{89}Zr]labeled monoclonal antibodies (mAbs) with [^{18}F]fluorodeoxyglucose (FDG) enables the assessment of both targeted uptake and glucose metabolism, potentially improving patient selection [1]. Existing dual tracer separation methods exploiting differences in tracer kinetics are typically applied post-reconstruction in the image domain. However, these approaches may be sensitive to noise propagation. In this work, we evaluate a sinogram-domain iterative separation method that is incorporated directly into the reconstruction process, enabling direct generation of single tracer images.

References

[1] Li Z, de Boer JW, van Meerten T, *et al*. Separation of simultaneously acquired [^{89}Zr]atezolizumab and [^{18}F]FDG PET scans. Eur J Nucl Med Mol Imaging. 2026;53(2):705-707.

[2] Li Z, Mohr P, Brouwers AH, Lammertsma AA, Tsoumpas C. Reconstruction-Based Image Separation for Simultaneous Dual-Tracer PET Scanning. IEEE Nuclear Science Medical Imaging Conference (MIC). 2025. 1-1.

[3] Venet L, Pati S, Feldman MD, *et al*. Accurate and robust alignment of differently stained histologic images based on Greedy diffeomorphic registration. Appl Sci (Basel). 2021;11:1892.

[4] Thielemans K, Tsoumpas C, Mustafovic S, *et al*. STIR: software for tomographic image reconstruction release 2. Phys Med Biol. 2012;57(4):867-883.

MIC-10-440

High-Energy Proton Scattering Radiography of a Geant4 Hand Phantom under Constant-Energy Loss (#1435)

Reshma S. Ughade, Stylianos Chatzidakis

Purdue University, West Lafayette, USA

The present research is being conducted with the support of funding provided by the Purdue University School of Nuclear Engineering and the Purdue Research Foundation.

Abstract

Proton radiography and tomography often use residual energy or water equivalent path length (WEPL) to estimate relative stopping power (RSP). Since the maximum likelihood path (MLP) formalism of Schulte et al. (2008), proton trajectories in tissue have been modeled as curved paths constrained by entry and exit tracking. In full proton CT, this path estimation is coupled to energy dependent multiple Coulomb scattering and longitudinal energy loss, which becomes computationally and physically complex at low residual energies. Most MLP based reconstructions use the estimated path mainly to assign WEPL or RSP contributions to voxels. Here, we examine a thin object regime in which scattering itself provides imaging contrast. For high energy protons traversing a human hand, the integrated energy loss is small, allowing the scattering relevant βcp factor to be approximated as constant along the path. Under this constant energy approximation, we reconstruct a volumetric scattering density map using an M-value calculated from each proton scattering angle and kinetic energy, together with the μTRec Bayesian voxel attribution algorithm developed for muon scattering tomography. The method is demonstrated in Geant4 using an anthropomorphic hand phantom containing bones, muscles, tendons, and skin. A single orientation 200 MeV parallel proton beam with 10^7 protons is simulated and reconstructed on a 0.3 mm voxel grid. The resulting proton radiograph resolves carpals, metacarpals, and phalanges, and detects a submillimetre osteochondral gap at the thumb interphalangeal joint. These results suggest that constant energy, MLP inspired scattering radiography can provide a computationally lightweight alternative or complement to energy loss based proton imaging for thin anatomical sites.

MIC-10-443

Multiple Emission Tomography: A High-Sensitivity Single-Layer Simultaneous PET Compton-Camera (#1838)

Marco Pizzichemi[1,2], Giulia Terragni[2], Francesco Pennazio[3], Francesca Sgarbi[1], Laura Cassano[1], Lisa Arnone[1], Matteo N. Colombo[1], Elisa Fiorina[3], Fabio Cossio[3], Mohammad Fadavi Mazinani[3], Marco Paganoni[1], Etiennette Auffray[2], Luca Presotto[1]

[1] University of Milano-Bicocca, Milano, Italy; [2] CERN, Geneva, Switzerland; [3] INFN Torino, Torino, Italy

This work is supported by the European Union-Next Generation EU, Mission 4 Component 1 CUP H53D23007430001, and carried out in association with the CERN Crystal Clear Collaboration.

Abstract

The growing importance of theranostics and research with long-lived isotopes demands imaging systems far more sensitive than standard PET or SPECT. Many emerging isotopes lie outside current detector capabilities, resulting in low sensitivity, high background, and poor quantification, as seen with ^{90}Y verification and ^{124}I or ^{89}Sr imaging. The Multiple Emission Tomography (MET) project introduces a novel imaging device based on inorganic scintillators, capable of operating in dual modes: PET-style coincidence detection of 511 keV photon pairs and single-photon Compton-scattering detection in a single-layer configuration. The technical configuration of the MET prototype utilizes a DOI-capable light-sharing scheme. Each module consists of a 16x16 matrix of 1.53x1.53x20 mm^3 depolished LYSO crystals coupled to an 8x8 array of 3x3 mm^2 Hamamatsu Silicon Photomultipliers (SiPMs). The detector's readout electronics are based on the ALCOR ASIC, a low-power, mixed-signal device featuring single-photon sensitivity, a high bandwidth of up to 2 Mevents/s per channel, and a fine 25 ps time binning. Supported by a combination of analytic algorithms and a machine learning pipeline, the MET detector can successfully solve the temporal sequence of inter-crystal scatters, and determine the points of interaction and the energies deposited. To fully leverage these recovered events, a dedicated Compton image reconstruction algorithm has been developed, employing an event-by-event statistical model with ad-hoc projector functions. This technology is expected to significantly impact theranostics, collimator-less SPECT, and in-vivo range verification for CPT.

MIC-10-446

A Scalable NaI(Tl)-SiPM Photon-Counting Scintillator Detector for Gold and Gadolinium XRF Imaging (#2151)

Ana Luísa M. Silva[1], Bryan Casanelli[1], David Batista[1], Tiago Ferreira[1], Pedro M.M. Correia[1], Rodolfo G. Figueroa Saavedra[2], João Veloso[1]

[1] I3N -University of Aveiro, Physics Dpt., Aveiro, Portugal; [2] Center of Excellence in Physics and Engineering in Health (CFIS), University of La Frontera (UFRO), Temuco, Chile

This work was supported by Project TA24I10046 from the National Research and Development Agency of Chile (ANID) and
by Portuguese national funds through FCT – Fundação para a Ciência e a Tecnologia, I.P., under the project UID/50025/2025 (doi.org/10.54499/UID/50025/2025), UID/PRR/50025/2025 (doi.org/10.54499/UID/PRR/50025/2025), UID/PRR2/50025/2025 (doi.org/10.54499/UID/PRR2/50025/2025) and the Associate Laboratory I3N – LA/P/0037/2020 (doi.org/10.54499/LA/P/0037/2020)

Abstract

Gold and gadolinium-based nanoparticles have been investigated as theranostic agents whose characteristic X-ray fluorescence (XRF) emissions enable non-invasive, element-specific biodistribution imaging. This work presents the design, assembly, and characterization of a scalable NaI(Tl)-SiPM scintillation detector module developed as a building block for a 16-element detector array for the Confocal Orthovoltage X-Ray--Induced Radiation System (COXIRIS) Project. Each module comprises a 25.4x25.4x4 mm^3 monolithic NaI(Tl) crystal optically coupled to a custom SiPM array and read out by the TOFPET2 ASIC.

The architecture targets the K-shell fluorescence lines of gold ($K\alpha$ = 68 keV) and gadolinium ($K\alpha$ = 43 keV), while providing a large active area at low cost.

Four modules were characterized with a 2.0 μCi ^{241}Am source, whose 59.5 keV emission lies within the 40--80 keV target interval. The peak was clearly identified in all modules, with energy resolutions ranging from 47% to 65%. Per-pixel gain calibration produced an additional relative improvement of approximately 2% for each module. These results support the feasibility of the proposed assembly approach as a detector building block for XRF imaging applications.

References

[1] M. A. Kouri, K. Polychronidou, G. Loukas, A. Megapanou, I.-A.Vagena, A. M. Gerardos, E. Spyratou, and E. P. Eftsathopoulos, "Consolidation of gold and gadolinium nanoparticles: An extrastep towards improving cancer imaging and therapy," Journal of Nanotheranostics, vol. 4, no. 2, pp. 127–149, Apr. 2023. [Online]. Available: https://www.mdpi.com/2624-845X/4/2/7

[2] R. G. Figueroa, M. Valente, J. Guarda, J. Leiva, E. Quilaguilque, B. Casanelli, and F. Leyton, "OXIRIS project: Development of a new XRF device for the simultaneous detection and treatment of cancer," X-Ray Spectrometry, vol. 51, no. 3, pp. 251–261, May 2022. [Online]. Available: https://analyticalsciencejournals.onlinelibrary.wiley.com/doi/10.1002/xrs.3272

[3] PETsys Electronics, "TOFPET2 ASIC," https://www.petsyselectronics. com/, accessed: 2026-05-10. [Online]. Available: https://www.petsyselectronics.com/

MIC-10-449

A Preclinical PET System for Simultaneous Acquisition and Separation of Multiple Tracers (#2209)

Jackson W. Foster[1], Wen He[2], Muhammad N. Ullah[2], Yug B. Shah[2], Garry Chinn[2], Craig S. Levin[2,3]

[1] Stanford University, Electrical Engineering, Stanford, USA; [2] Stanford University, Radiology, Stanford, USA; [3] Stanford University, By courtesy Electrical Engineering, Bioengineering, Physics, Stanford, USA

This work is supported by NIH F31CA265205, the Falk Medical Research Trust (SPO 268891), Stanford Bio-X IIP and an SNMMI Mars Shot Award.

Abstract

Positron emission tomography (PET) is traditionally limited to scanning one tracer per session. Positron and prompt gamma emitters may be used to form triple coincidences that allow for signal separation based on energy. We present a proof-of-concept, preclinical PET system designed for detecting and distinguishing prompt gamma and annihilation photons in the same detector. We describe the data processing pipeline with advances for estimating randoms, scatter, and sensitivity of the prompt gamma photon. System performance is characterized with NEMA and Derenzo phantom studies. Next, we present multi-isotope studies using ^{52}Mn and ^{18}F in a custom image quality phantom. We compare two reconstruction methods and find alternating updates yield faster convergence and higher image quality. After correcting for injected activity and decay, the mean voxel intensity ratio between ^{18}F and ^{52}Mn across background ROIs is 0.95 ± 0.06, where 1 represents perfect quantitative agreement. The uncertainty reflects variability across ROIs and dose calibrator uncertainty (±2%), suggesting unmixing accuracy is within dose calibrator tolerance. Further, we scan the phantom after ^{18}F decay to determine the relative image quality between single (^{52}Mn only) and dual (^{52}Mn with ^{18}F) acquisition. We find the ^{52}Mn image has similar contrast recovery (0.65/0.62) and crosstalk ratio (0.24/0.24) between the single and dual acquisition. Due to low triples sensitivity, simultaneous acquisition of both radionuclides reduces the contrast to noise from 10.2 to 4.7. Despite limitations on axial field of view, data rate, and the high background from ^{52}Mn's 3 gamma cascade, we achieve high quantitative accuracy. Future studies will scale up the system, use more favorable tracers, add regularization to mitigate noise propagation and include preclinical animal scans.

References

[1] A. Andreyev, A. Sitek, and A. Celler, "EM reconstruction of dual isotope PET using staggered injections and prompt gamma positron emitters," *Medical Physics*, vol. 41, no. 2, p. 022501, Feb. 2014, doi: 10.1118/1.4861714.

[2] T. Fukuchi, T. Okauchi, M. Shigeta, S. Yamamoto, Y. Watanabe, and S. Enomoto, "Positron emission tomography with additional γ-ray detectors for multiple-tracer imaging," *Medical Physics*, vol. 44, no. 6, pp. 2257–2266, 2017, doi: 10.1002/mp.12149.

[3] E. Pfaehler, D. Niekämper, J. Scheins, N. J. Shah, and C. W. Lerche, "ML-EM based dual tracer PET image reconstruction with inclusion of prompt gamma attenuation," *Phys Med Biol*, vol. 70, no. 1, Dec. 2024, doi: 10.1088/1361-6560/ad9660.

[4] López-Montes A, Cabello J, Conti M, Badal A, Herraiz JL, "GPU-accelerated Monte Carlo-Based Scatter and Prompt-Gamma Corrections in PET," *IEEE Nuclear Science Symposium and Medical Imaging Conference* 2021, M-07-01, Nov. 2021

[5] J. Foster, G. Chinn, and C. Levin, "MLEM Method for Estimating Spatial Sensitivity Coefficients for Simultaneous Multi-Tracer Positron Emission Tomography (mPET) Reconstruction," in *2024 IEEE Nuclear Science Symposium and Molecular Imaging Conference*, Nov. 2024.

[6] A. Sitek, A. Andreyev, and A. Celler, "Reconstruction of dual isotope PET using expectation maximization (EM) algorithm," in *2011 IEEE Nuclear Science Symposium Conference Record*, Oct. 2011, pp. 4323–4326. doi: 10.1109/NSSMIC.2011.6153832.

[7] W. He, J. W. Foster, and C. S. Levin, "Alternating Update Method for Joint EM Estimation of Multiple Tracer Distributions in Multiplexed PET (mPET)," *IEEE Transactions on Radiation and Plasma Medical Sciences*, pp. 1–1, 2026, doi: 10.1109/TRPMS.2026.3688900.

MIC-10-452

On the Pseudo Dark-Field Signal in X-Ray Scattering Tensor Tomography (#2316)

Runtao Deng, Ruifeng Liu, Peixuan Song, Jincheng Lu, Li Zhang, Zhentian Wang

Tsinghua University, Department of Engineering Physics, Beijing, China

This work was supported in part by National Natural Science Foundation of China (No. 62227804), Beijing Municipal Natural Science Foundation (No. L232115) and National Key Research and Development Program of China (No. 2023YFC2605802).

Abstract

X-ray scattering tensor tomography retrieves directional dark-field projections from the focused, structured illumination produced by 2D diffractive optics, and is increasingly attractive as a route to anisotropic micro-structural imaging on laboratory sources. Quantitative tensor reconstruction requires the focused reference field to cancel out exactly in the Fourier-domain retrieval, a condition met only under monochromatic illumination. We show that beam hardening through an absorbing sample reshapes this focused reference field non-uniformly across its bright core and the surrounding plateau, so the retrieval assigns a non-zero scattering tensor to a purely absorbing object—a pseudo dark-field signal. We derive a closed-form expression for the pseudo dark-field signal, prove its exact isotropy arising from the circular symmetry of the focal spot, and identify the retrieved observables that are biased by beam hardening versus those that are not. The standard angular-consistency metric is blind to this bias, so a dedicated calibration is required. We describe a step-wedge calibration protocol that compresses the family of pseudo dark-field signals into a single thickness-dependent function suitable for per-pixel correction. Removing this artefact is a prerequisite for quantitative X-ray scattering tensor tomography on laboratory sources.

References

[1] M. Kagias, Z. Wang, P. Villanueva-Perez, K. Jefimovs, and M. Stampanoni, "2d-omnidirectional hard-x-ray scattering sensitivity in a single shot," *Physical Review Letters*, vol. 116, no. 9, p. 093902, 2016.

[2] M. Kagias, Z. Wang, M. E. Birkbak, E. Lauridsen, M. Abis, G. Lovric, K. Jefimovs, and M. Stampanoni, "Diffractive small angle x-ray scattering imaging for anisotropic structures," *Nature Communications*, vol. 10, p. 5130, 2019.

[3] F. Pfeiffer, M. Bech, O. Bunk, C. Bronnimann, C. Grünzweig, and C. David, "Hard-x-ray dark-field imaging using a grating interferometer," *Nature Materials*, vol. 7, no. 2, pp. 134–137, 2008.

[4] G. Giakoumakis, J. Primot, A. Jarnac, L. Guitard, and A. Stolidi, "Artifacts reduction in high-acutance phase images for x-ray grating interferometry," *Optics Express*, vol. 30, no. 23, pp. 41147–41156, 2022.

[5] G. Lautizi, V. Di Trapani, A. Studer, M.-C. Zdora, F. De Marco, J. Kim, F. Marone, M. Stampanoni, and P. Thibault, "Robust dark-field signal extraction for modulation-based x-ray tensor tomography," *Applied Physics Letters*, vol. 125, no. 26, p. 264103, 2024.

[6] M. Kagias, Z. Wang, G. Lovric, K. Jefimovs, and M. Stampanoni, "Simultaneous reciprocal and real space x-ray imaging of time-evolving systems," *Physical Review Applied*, vol. 15, no. 4, p. 044038, 2021.

MIC-10-455

A Proof-of-Concept Tri-Mode PET and SPECT Imager with a Shared Scintillator-as-Collimator Detector (#2390)

Xiangtao Zeng[1], Hang Yang[1], Ming Niu[1], Wenjie Huang[1], Xiaolong Jiang[1], Chen Huang[1], Yangyang Zhao[1], Jinpei Tian[1], Xiaoqin Zhang[1], Qingyang Wei[3], Jing Wu[5], Ying Liang[7], Zheng Gu[1]

[1] shenzhen bay laboratory, Shenzhen, China; [2] University of Science and Technology Beijing, School of Automation and Electrical Engineering, Beijing, China; [3] University of Science and Technology Beijing, School of Automation and Electrical Engineering, Beijing, China; [4] Beijing Normal University, School of Physics and Astronomy, Beijing, China; [5] Beijing Normal University, School of Physics and Astronomy, Beijing, China; [6] Cancer Hospital Chinese Academy of Medical Sciences, Shenzhen, China; [7] Cancer Hospital Chinese Academy of Medical Sciences, Shenzhen, China

This work is supported by the National Key R&D Program of China (No. 2023YFC2414800), the Major Program of Shenzhen Bay Laboratory (No. C1012530005), the National Natural Science Foundation of China (Nos. 12275182 and 62371314), Guangdong Basic and Applied Basic Research Foundation (Nos. 2024A1515012154), the Guangdong Provincial Project (Grant No. 2023TQ07A233) and the Shenzhen Bay Laboratory Proof-of Concept Grants (No. C1022430005).

Abstract

Simultaneous dual-radionuclide imaging offers complementary information for diagnosis, stratification, treatment planning, and therapy evaluation. However, the fundamental differences between PET and SPECT present significant challenges for integrated imaging. We propose a scintillator-as-collimator detector enabling both PET and SPECT. It consists of three scintillator layers separated by two light guides. Parallel holes in the upper portion function as a SPECT collimator, referred to as the scintillator-as-collimator volume (SCV). The lower portion serves as the SPECT detector (SD). In PET mode, the entire detector acts as a multi-resolution TOF-DOI PET detector. Thus, it serves as a self-collimated SPECT or TOF-DOI PET detector. A dual-panel prototype was developed with rotational acquisitions for PET, SPECT, and simultaneous imaging. SPECT events are selected using flood image mask, maximum SiPM channel energy (Pmax), and DOI-integrated charge (QDC). SPECT resolution reaches ~5 mm. PET performance is preserved, with best SD–SD CTR of 352 ps and two-layer DOI. The introduction of holes has minimal impact on PET detection, enabling high-quality PET images. In simultaneous imaging, a unified timing framework rejects 511 keV down-scatter, and residual artefacts were further mitigated using a 200–240 keV energy window for scatter correction. Phantom experiments validate tri-mode imaging. This detector eliminates external collimators, supports multi-tracer imaging, and offers a cost-effective single-detector-set PET&SPECT system.

References

[1] Huang, S. *et al.* (2026). Optimization of TOF and DOI Performance in a Multi-Resolution Detector for Brain-Dedicated PET. IEEE Transactions on Radiation and Plasma Medical Sciences, 10(3).

[2] Zeng X *et al.* (2025). Tri-Mode PET, SPECT, and PET&SPECT Imager Using a Novel Scintillator-as-Collimator Detector. *2025 IEEE NSS, MIC and RTSD*, Yokohama, Japan.

MIC-10-458

Zero-Shot PET Image Super-Resolution via Cross-Modal Mutual Information Guidance (#2526)

Yilin He, Yang Lv

Shanghai United Imaging Medical Technology Co., Ltd, Molecular Imaging Business Unit, Shanghai, China

This work was supported in part by Shanghai United Imaging Medical Technology Co., Ltd., through its internal research program. The authors gratefully acknowledge the Molecular Imaging team for their technical support and helpful discussions.

Abstract

Diffusion models have shown strong potential for improving PET image quality. However, existing methods based on unconditional pretrained diffusion priors often struggle to balance realism and fidelity, particularly in preserving high-resolution details. To address this issue, we propose MI-ResShift, a zero-shot mutual information-guided diffusion model with residual shifting for PET image super-resolution. MI-ResShift introduces a differentiable local-wise mutual information layer to guide the denoising process using structural information from CT or MRI, enabling robust cross-modal feature alignment in the statistical domain. By combining mutual information guidance with residual shifting, the proposed method enhances PET detail fidelity and robustness while reducing diffusion-based inference to only four steps. Experiments on PET/MR brain datasets demonstrate that MI-ResShift improves image quality over classical interpolation methods and provides an efficient solution for cross-modal PET super-resolution.

References

[1] Z. Wang et al., "Mutual Information Guided Diffusion for Zero-Shot Cross-Modality Medical Image Translation," in IEEE Transactions on Medical Imaging, vol. 43, no. 8, pp. 2825-2838, Aug. 2024, doi: 10.1109/TMI.2024.3382043.

[2] Z. Yue, J. Wang and C. C. Loy, "Efficient Diffusion Model for Image Restoration by Residual Shifting," in IEEE Transactions on Pattern Analysis and Machine Intelligence, vol. 47, no. 1, pp. 116-130, Jan. 2025, doi: 10.1109/TPAMI.2024.3461721.

MIC-10-461

Extracting total and Compton attenuation coefficients via ghost imaging-like photon counting (#2895)

Gregory R. Romanchek[1,2], Praveen G. Bharathi[2], Shiva Abbaszadeh[2]

[1] University of Illinois Urbana-Champaign, Department of Nuclear, Plasma, and Radiological Engineering, Urbana, USA; [2] University of California Santa Cruz, Department of Electrical and Computer Engineering, Santa Cruz, USA; [3] University of Illinois at Urbana-C hampaign, Department of Nuclear, Plasma, and Radiological Engineering, Urbana, USA

This work was supported by the National Institutes of Health under Grant R01-EB028091.

Abstract

Coincidence-based imaging with the back-to-back 511 keV photon pairs emitted during positron annihilation enables transmission imaging with reduced quantum noise. Conventional transmission imaging recovers only a single attenuation-related quantity per voxel or pixel. In this work, we extend coincidence-based imaging to simultaneously recover both the total and the Compton-scatter linear attenuation coefficients from a single acquisition, providing a second axis for material identification. Forward-scattered photons collected in coincidence within an analytically defined polar window, obtained by integrating the Klein-Nishina differential cross section over a 20-to-30-degree band, enable direct estimation of the Compton macroscopic cross section, while the idler channel provides the incident count for the total coefficient. We evaluate the approach using Monte Carlo simulations of opposing cadmium zinc telluride panels viewing a water phantom of thickness 2 to 10 millimeters. Idler-normalized transmission was recovered to within 0.1 percent across all thicknesses, while the extracted total and Compton coefficients exhibited 1 to 4 percent absolute error, with the Compton coefficient transitioning from over- to underestimation near 6 millimeters. These deviations arise from logarithmic amplification of small counting errors and from competing air-scatter contamination at thin phantoms and self-attenuation of scattered photons at thicker ones. The results establish that scatter data from coincidence-based annihilation imaging can recover a second material descriptor, motivating further development toward dose-efficient material identification.

References

[1] Romanchek, G, Yu, Z, Abbaszadeh, S 2026, 'Monte Carlo validation of signal-to-noise improvements in transmission imaging using correlated annihilation photon pairs', *Scientific Reports*, London: Nature Portfolio.

[2] Padgett, MJ, Boyd, RW 2017, 'An introduction to ghost imaging: quantum and classical', *Philosophical Transactions of the Royal Society A: Mathematical, Physical and Engineering Sciences*, vol. 375, no. 2099, 20160233, London: The Royal Society.

[3] Sarrut, D, Bała, M, Bardiès, M, Bert, J, Chauvin, M, Chatzipapas, K, Dupont, M, Etxebeste, A, Fanchon, LM, Jan, S, Kayal, G, Kirov, AS, Kowalski, P, Krzemień, W, Labour, J, Lenz, M, Loudos, G, Mehadji, B, Ménard, L, Morel, C, Papadimitroulas, P, Rafecas, M, Salvadori, J, Seiter, D, Stockhoff, M, Testa, E, Trigila, C, Pietrzyk, U, Vandenberghe, S, Verdier, MA, Visvikis, D, Ziemons, K, Zvolský, M, Roncali, E 2021, 'Advanced Monte Carlo simulations of emission tomography imaging systems with GATE', *Physics in Medicine & Biology*, vol. 66, no. 10, 10TR03, Bristol: IOP Publishing.

MIC-10-464

Enhancement of Charged-Particle Shielding via Lightweight Nanocomposites (#2978)

Gabrielle J. Grey[1], Niko Speck[2], Drew Vecchio[3], Kathleen A. Cotterill[4,5], Alan Taub[1], Mark Hammig[2]

[1] University of Michigan, Materials Science & Engineering Department, Ann Arbor, USA; [2] University of Michigan, Nuclear Engineering & Radiological Sciences, Ann Arbor, USA; [3] Amphionic, LLC., Plymouth, USA; [4] University of Michigan, Department of Math, Ann Arbor, USA; [5] University of Michigan, Department of Physics, Ann Arbor, USA

The authors would like to acknowledge the technical support of the University of Michigan's Michigan Center for Materials Characterization and Michigan Medicine Microscopy Core. G. J. Grey & N. P. Speck give special thanks to Dr. Tao Ma for guidance on TEM operation and Megan Bennett for support on ultramicrotome sample preparation.

Abstract

The development of lightweight radiation shielding materials is of high interest for a broad range of defense, space, and medical applications. In particular, mass-savings are desired in vehicles (ground, naval, and/or aerospace) and as wearable fabrics in high dosage environments such as those encountered in the medical setting. Here we investigate the potential of enhanced shielding via radiation attenuation of nanostructured materials which take advantage of interfacial and nanocrystalline loss processes increase the multiplicity of energy loss mechanisms within the shielding solid. In this work, colloidal metallic nanoparticles grown in an aqueous environment (such as palladium (Pd) and silver (Ag)) with sizes in the 5 - 50 nm range are imbedded in a polymeric matrix material (epoxy or aramid nanofiber (ANF)) to demonstrate photon and electron shielding while maintaining mechanical properties such as strength, durability, and form-factor flexibility. The mechanisms of energy loss at the interfaces of the nanomaterials and overall in the solid are quantified through transport modeling as well as the unorthodox usage of the Transmission Electron Microscope (TEM), in which a focused electron beam and state-of-the-art detector system are utilized to measure the effects of particle interactions within our material system to a near single particle resolution. Therefore, this work encompasses both an investigation of the potential enhancement of radiation attenuation by nanostructured materials while also introducing an innovative nanocomposite material system with manufacturing versatility enabling lightweight, flexible shielding.

References

[1] M. Wang et al., "Review of Passive Shielding Materials for High-Energy Charged Particles in Earth's Orbit," Materials (Basel), vol. 18, no. 11, p. 2558, May 2025, doi: 10.3390/ma18112558.W.-K. Chen, Linear Networks and Systems. Belmont, CA, USA: Wadsworth, 1993, pp. 123–135.

[2] N. Ipe, "Transmission of Shielding Materials for Particle Therapy Facilities," Nuclear Technology, no. 168(2), pp. 559–563, Apr. 2017, doi: https://doi.org/10.13182/NT09-A9243.

[3] R. L. Maughan, M. J. Hardy, M. J. Taylor, J. Reay, and R. Amos, "Radiation shielding and safety for particle therapy facilities," in Design and Shielding of Radiotherapy Treatment Facilities: IPEM Report 75, 2nd Edition, IOP Publishing, 2017. doi: 10.1088/978-0-7503-1440-4ch11.

[4] Q. Chang, S. Guo, and X. Zhang, "Radiation shielding polymer composites: Ray-interaction mechanism, structural design, manufacture and biomedical applications," Materials & Design, vol. 233, p. 112253, Sep. 2023, doi: 10.1016/j.matdes.2023.112253.

[5] D. A. Vecchio, M. D. Hammig, and N. A. Kotov, "High-Resolution Radiation Sensors from Flexible Network Nanocomposites of Nanoparticles and Aramid Nanofibers," ACS Nano, vol. 19, no. 12, pp. 11924–11935, Apr. 2025, doi: 10.1021/acsnano.4c15939.

[6] K. A. Cotterill et al., “Synthesis of Palladium Nanoparticles for Multifunctional Applications in Space and Hydrolysis Environments,” unpublished.
[7] J. Lyu et al., “Stretchable conductors by kirigami patterning of aramid-silver nanocomposites with zero conductance gradient,” Appl. Phys. Lett., vol. 111, no. 16, p. 161901, Oct. 2017, doi: 10.1063/1.5001094.

MIC-10-467

Detector Geometry Optimization of a Sensing Collimation Imager (SCI)

(#3067)

Ling Cai[1], Huitian Xia[2], Samarth Aggarwal[1], Fardeen Ahmed[2], Joseph A. O’Sullivan[1,3], Abhinav K. Jha[2,4], Yuan-Chuan Tai[3,4]

[1] Washington University in St. Louis, Imaging Science, St. Louis, USA; [2] Washington University in St. Louis, Department of Biomedical Engineering, St. Louis, USA; [3] Washington University in St. Louis, Department of Electrical and Systems Engineering, St. Louis, USA; [4] Washington University in St. Louis, Mallinckrodt Institute of Radiology, St. Louis, USA

This work was supported in part by the Mallinckrodt Institute of Radiology at Washington University at St. Louis through an internal fund allotment. We also acknowledge the support from NIH (R01-EB031962, R01-CA240711) and NSF CAREER Award (2239707).

Abstract

The Sensing Collimation Imager (SCI) is an ultrasensitive gamma detector that integrates multi-pinhole, coded aperture, and self-collimation imaging into a single compact device, achieving substantially higher sensitivity than conventional gamma cameras. Maximizing the spatial encoding capability of the SCI module requires optimizing the crystal arrangement over a high-dimensional combinatorial design space, which is too large for exhaustive search.

We propose an information-theoretic detector geometry optimization framework that uses the Fisher Information Matrix (FIM) spatial correlation map as a computationally efficient performance metric. The metric requires only computing the FWHM of the FIM column vector (O(n)), avoiding the O(n^3) cost of inverting the FIM for the Cramér–Rao bound, enabling broad geometry searches. A genetic algorithm (GA) guided by this metric searches over fixed-cardinality crystal arrangements to identify high-performing designs.

Applied to the SCI module, the GA converged within 50 generations and identified an optimized arrangement producing narrower FIM correlation peaks throughout the field of view than a heuristic design. GATE Monte Carlo simulations of a Derenzo phantom confirmed improved recovery of the 8 mm sphere group with clearer feature separation, validating the optimization framework.

References
[1] Cai et al., "An ultra-high sensitivity sensing collimation imager: design, modelling, and assessment," Proc. SPIE 13405, Medical Imaging 2025: Physics of Medical Imaging
[2] H H, Gifford H. Cone-beam tomography with discrete data sets[J]. Physics in Medicine & Biology, 1994, 39(3): 451.
[3] Qi and R. H. Huesman, "Wavelet crosstalk matrix and its application to assessment of shift-variant imaging systems," 2002 IEEE Nuclear Science Symposium Conference Record

MIC-10-470

Toward Whole-Body Whole Gamma Imaging: Monte Carlo Simulation of ^{89}Zr PET-Compton Hybrid Imaging (#3156)

Mizuki Miyahara[1,2], Hideaki Tashima[2], Mikio Suga[3], Sodai Takyu[2], Fumihiko Nishikido[2], Go Akamatsu[2], Taiga Yamaya[2]

[1] Chiba University, Graduate School of Science and Engineering, Chiba, Japan; [2] National Institutes for Quantum Science and Technology, Institute for Quantum Medical Science, Chiba, Japan; [3] Chiba University, Center for Frontier Medical Engineering, Chiba, Japan

Abstract

Whole gamma imaging (WGI) is a novel imaging technique that combines PET and Compton imaging by inserting a scatterer detector ring inside a PET detector ring. One of the suitable nuclides for WGI is ^{89}Zr. ^{89}Zr emits a 909 keV single gamma ray after undergoing positron emission or electron capture to form ^{89m}Y. Because these 909 keV gamma rays are emitted approximately four times more frequently than positrons, hybrid imaging of WGI combining both modalities is expected to improve image quality compared to conventional ^{89}Zr-PET which uses only annihilation gamma rays. In this study, we aimed at finalizing the design of a clinical whole-body WGI system. The hybrid imaging method was applied to Geant4-simulated data of a whole-body WGI system. We modeled a system employing HR-GAGG crystals as the scatterer and LGSO crystals as the absorber. Measurement of an ^{89}Zr-filled NEMA IEC body phantom placed at the center of the field of view was simulated. Images were reconstructed using the hybrid reconstruction method combining PET and Compton events and compared with PET images reconstructed by the list-mode OSEM algorithm using only PET events. We calculated the percent contrast ($Q_{H,j}$) and percent background variability (N_j) for each sphere size *j* (10-37 mm). The results showed that, for large spheres with diameters of 22 mm or more, hybrid imaging reduced N_j[if gte msEquation 12]><m:oMath><m:sSub><m:sSubPr><m:ctrlPr></m:ctrlPr></m:sSubPr><m:e><span lang=EN-US style='font-size:10.0pt;font-family:"Cambria Math",serif;mso-fareast-font-family: "ＭＳ 明朝";mso-fareast-theme-font:minor-fareast;mso-bidi-font-family:"Times New Roman"; mso-ansi-language:EN-US;mso-fareast-language:JA;mso-bidi-language:AR-SA'><m:r><m:rPr><m:scr m:val="roman"/><m:sty m:val="bi"/></m:rPr>N</m:r></m:e><m:sub><span lang=EN-US style='font-size:10.0pt;font-family:"Cambria Math",serif; mso-fareast-font-family:"ＭＳ 明朝";mso-fareast-theme-font:minor-fareast; mso-bidi-font-family:"Times New Roman";mso-ansi-language:EN-US;mso-fareast-language: JA;mso-bidi-language:AR-SA'><m:r><m:rPr><m:scr m:val="roman"/><m:sty m:val="bi"/></m:rPr>j</m:r></m:sub></m:sSub></m:oMath><![endif], but the maximum achievable $Q_{H,j}$ was lower than that of PET. In contrast, for small spheres with diameters of 17 mm or less, hybrid imaging demonstrated a specific advantage by suppressing noise amplification while accelerating contrast recovery in the early iterations. In conclusion, although the overall image quality improvement was limited in certain aspects, the

potential to enable novel applications such as multi-isotope imaging and positronium lifetime imaging using appropriate position emitters was suggested.

13 November, 2026

Time:
13 November, 2026
9:00 – 11:00

Room:
FEDERICO GARCÍA LORCA

MIC-11 | Young Investigator Session (oral)

Chairs:
Emilie Roncali (Davis)
Ciprian Catana (Charlestown)

MIC-11-01

Toward Clinical Deployment of Complex PET Designs via Fast In-System Calibration (#1486)

Julian Thull[1], **Julian Thull**[1], Yannick Kuhl[1], Yannick Kuhl[1], Bjoern Weissler[1,2], Bjoern Weissler[1,2], David Schug[1,2], David Schug[1,2], Volkmar Schulz[1,2], Volkmar Schulz[1,2]

[1] RWTH Aachen University, Chair of Imaging and Computer Vision, Aachen, Germany; [2] Hyperion Hybrid Imaging Systems GmbH, Aachen, Germany; [3] Fraunhofer Institute for Digital Medicine MEVIS, Bremen, Germany

This work was funded by BMFTR and the Ministry of Culture and Science of North Rhine-Westphalia through NHR4CES. We thank NVIDIA for four RTX 6000 Ada GPUs through its Grant Program.

Abstract

Accurate positron emission tomography (PET) depends on calibration of detector alignment, gamma interaction positioning, and coincidence timing, which jointly define line-of-response (LOR) and time-of-flight (TOF) information. Conventional workflows calibrate these quantities in separate stages using dedicated acquisitions, hardware, or phantoms. This is particularly burdensome for light-sharing detectors, where these quantities are coupled through the detector response but are typically treated as separate calibration tasks. We introduce a differentiable in-system calibration framework that enables rapid scanner-level calibration by replacing staged workflows with a single coincidence-level optimization. A shared neural network predicts local interaction positions and timing corrections from single-event readouts, while learnable detector poses map predictions into scanner coordinates. Singles are processed independently, and coincidence information enters only via physical LOR and TOF construction. This prevents source-label access at the network input while enforcing scanner-level consistency. The framework was trained on 28M coincidences from 450 randomized 22Na point-source positions acquired on a semi-monolithic preclinical PET system. In hot-rod reconstructions, the proposed calibration achieved image quality on par with a conventional blueprint and fan-beam workflow, as assessed by peak signal-to-noise ratio, structural similarity, coefficient of variation, recovery coefficients, and peak-to-valley ratios. Differentiable in-system calibration therefore compresses labor-intensive staged workflows into a unified physics-constrained optimization completed in hours, reducing effort and mechanical constraints without sacrificing reconstruction performance.

References

[1] Thull, J, Kuhl, Y, Mueller, F, Schug, D, Weissler, B & Schulz, V 2026, 'Beyond mechanics: Maximum-likelihood-driven PET detector alignment calibration', *Medical Physics*, 53(1), e70256, Wiley.

[2] Kuhl, Y, Mueller, F, Naunheim, S, Bovelett, M, Lambertus, J, Schug, D, Weissler, B, Gegenmantel, E, Gebhardt, P & Schulz, V 2024, 'A finely segmented semi-monolithic detector tailored for high-resolution PET', Medical Physics, 51(5), 3421–3436, Wiley.

[3] Kuhl, Y, Mueller, F, Thull, J, Naunheim, S, Schug, D & Schulz, V 2025, '3D in-system calibration method for PET detectors', Medical Physics, 52(1), 232–245, Wiley.

MIC-11-02

A Compact Preclinical PET Scanner Achieving NEMA-Standard Sub-0.5 mm Spatial Resolution via Analytic FBP Reconstruction (#1867)

Chenxi Li[1], Haoqi Wen[1], Yuhao Jiang[1,2], Yucun Hou[1], Kexin Wang[1], Jianyong Jiang[1]

[1] Beijing Normal University, Key Laboratory of Beam Technology of Ministry of Education, School of Physics and Astronomy, Beijing, China; [2] Beijing Normal University, Key Laboratory of Radiopharmaceuticals of the Ministry of Education, NMPA Key Laboratory for Research and Evaluation of Radiopharmaceuticals (National Medical Product Administration), College of Chemistry, Beijing, China

This work was supported in part by the NSFC (No. 12475336).

Abstract

PET is a cornerstone of preclinical imaging, where achieving ultra-high spatial resolution is paramount for the precise quantification of sub-regional metabolism. While commercial scanners typically yield 1.0–1.5 mm resolution, advanced research prototypes target sub-millimeter precision. This study introduces a compact preclinical PET scanner achieving NEMA-standard sub-0.5 mm spatial resolution via the analytic filtered back-projection (FBP) algorithm. To the best of our knowledge, this is the first reported system demonstrating such resolution through FBP. The dual-ring scanner features a 64 mm transaxial and 53.2 mm axial field of view, integrating 16 modules of 44 × 44 LYSO crystal arrays (0.497 × 0.497 × 5 mm^3 elements). These arrays are coupled to Hamamatsu Multi-Pixel Photon Counters (MPPCs, S14161-3050HS-08) and managed by a PETsys TOFPET2 ASIC system. System performance was characterized following NEMA NU 4-2008 protocols. The scanner demonstrated an overall energy resolution of 13.43% and an absolute sensitivity of 0.87% (350–650 keV). Peak true and noise equivalent count rates (NECR) were 7.61 kcps and 6.02 kcps, respectively, with a scatter fraction of 8.92%. FBP reconstruction of a point source demonstrated the system achieved average FWHM resolutions of 0.90 mm, 0.86 mm, and 0.69 mm in the radial, tangential, and axial directions, respectively, reaching a peak resolution of 0.48 mm. Imaging of a Micro-Derenzo phantom resolved 0.4 mm rods via iterative reconstruction. *In vivo* studies using ^{18}F-FDG and ^{18}F-Florbetazine delineated precise tracer distributions within sub-regional structures. While the 5-mm scintillator thickness involves a trade-off in sensitivity, the system establishes a benchmark for spatial fidelity in preclinical instrumentation. Future work will integrate thicker crystals with depth-of-interaction capabilities to enhance sensitivity without compromising spatial precision.

References

[1] S. Yamamoto *et al.*, "Development of an ultrahigh resolution Si-PM based PET system for small animals," Physics in Medicine and Biology, vol. 58, no. 21, pp. 7875-7888, October 2013, doi: 10.1088/0031-9155/58/21/7875.

[2] H. G. Kang, H. Tashima, H. Wakizaka, M. Higuchi, and T. Yamaya, "Sub-0.5 mm Resolution PET Scanner with 3-Layer DOI Detectors for Rodent Neuroimaging," IEEE Transactions on Medical Imaging, vol. 45, no. 4, pp. 1423-1431, April 2026, doi: 10.1109/TMI.2025.3627815.

[3] C. Li *et al.*, "Design and Initial Evaluation of a Prototype Preclinical PET Scanner with Submillimeter Spatial Resolution for Highprecision Imaging," in *2025 IEEE NSS/MIC/RTSD*, Yokohama, Japan, 2025, pp. 1-1, doi: 10.1109/NSS/MIC/RTSD57106.2025.11286554.

[4] Z. Yuan *et al.*, "GPU-based list-mode TOF PET image reconstruction with complete correction techniques," Medical Physics, vol. 53, no. 1, pp. e70216, 2026, doi: 10.1002/mp.70216.

MIC-11-03

Development of a ring-type Quantum Entanglement PET Imaging System and Application of a Novel Image Reconstruction Algorithm to In-Vivo Imaging (#1680)

Koki Nakamura[1], Macoto Fujimoto[2], Pietro Caradonna[1], Mizuki Uenomachi[3], Laura Stephenson[4], Dan Watts[4], Kenji Shimazoe[1,2]

[1] The University of Tokyo, Department of Nuclear Engineering and Management, Graduate School of Engineering, Tokyo, Japan; [2] The University of Tokyo, Department of Bioengineering, Graduate School of Engineering, Tokyo, Japan; [3] Institute of Science Tokyo, Institute of Integrated Research, Tokyo, Japan; [4] University of York, York, UK

Abstract

Current positron emission tomography (PET) imaging is fundamentally limited by physical background noise, such as scatter and random coincidences, which significantly degrade image quality and quantitative accuracy. Quantum-entangled PET (QEPET) is a promising solution that utilizes the inherent orthogonal polarization correlation of annihilation photon pairs to physically reject noise. However, its practical application to in-vivo imaging has been a major challenge due to the severe reduction in usable event statistics caused by strict event selection. In this study, we developed a triple-ring PET scanner consisting of 24 Ce:GAGG modules (8×8 arrays of 2.5×2.5×9.0 mm³ pixels at 3.2 mm pitch; 1536 pixels in total) arranged in three axial rings with an inner radius of 36.7 mm, read out by SiPMs via dynamic time-over-threshold circuits, achieving an energy resolution of 9.5% at 511 keV and a coincidence timing resolution of 16.8 ns. By selecting events within a scattering-angle range of 70°–121° and an azimuthal-angle difference of 80°–100°, we obtained a modulation contrast ratio of 1.91, which clearly exceeds the classical limit of 1.63, confirming the entanglement of annihilation photon pairs. Furthermore, to overcome the limited counting statistics of conventional QEPET, we developed a novel reconstruction algorithm that seamlessly integrates the high-statistics structural information of standard PET into the iterative MLEM process. In phantom experiments, this approach improved the SBR to ~1.25× that of raw QEPET while preserving an SNR ~1.27× that of standard PET, achieving the highest CNR among the compared methods. Finally, we performed in-vivo QEPET imaging of a tumor-bearing mouse. The developed method effectively suppressed the granular noise characteristic of conventional QEPET while demonstrating highly localized tracer accumulation, thereby verifying its superiority over both standard PET and conventional QEPET.

References
[1] Holmes, TJ, Snyder, DL, Ficke, DC 2007, 'The effect of accidental coincidences in time-of-flight positron emission tomography', IEEE Transactions on Medical Imaging, vol. 3, no. 2, pp. 68-79, New York: IEEE.
[2] Moskal, P 2024, 'Positron emission tomography could be aided by entanglement', Physics, vol. 17, p. 138, College Park: American Physical Society.
[3] Watts, DP et al. 2021, 'Photon quantum entanglement in the MeV regime and its application in PET imaging', Nature Communications, vol. 12, no. 1, p. 2646, London: Nature Publishing Group.
[4] Nakamura, K et al. 2025, 'Monte Carlo assessment of entanglement-based positron emission tomography', Acta Physica Polonica A, vol. 148, no. 6, p. S138, Warsaw: Polish Academy of Sciences.
[5] Cheng, J-C et al. 2017, 'Incorporating HYPR de-noising within iterative PET reconstruction (HYPR-OSEM)', Physics in Medicine & Biology, vol. 62, no. 16, pp. 6666-6687, Bristol: IOP Publishing.
[6] Mistretta, CA et al. 2006, 'Highly constrained backprojection for time-resolved MRI', Magnetic Resonance in Medicine, vol. 55, no. 1, pp. 30-40, Hoboken: Wiley.

MIC-11-04

SIMPLE-DIP: Positronium Lifetime Image Reconstruction Using Deep Image Prior (#2252)

Bangyan Huang, Jinyi Qi

University of California, Davis, Biomedical Engineering, Davis, USA

This work is supported by the National Institutes of Health, under Grant No. U01AG82845.

Abstract

Positronium lifetime tomography (PLT) is an emerging imaging modality for imaging positronium lifetime in vivo. Previously, we developed SIMPLE (Statistical IMage reconstruction of Positron Lifetime via time-wEighting), a reconstruction framework for estimating average positron lifetime images, and demonstrated high-resolution imaging on a phantom at clinical activity levels. However, the reconstruction problem remains highly ill-posed, particularly under low-count and high-random conditions. In this work, we propose SIMPLE-DIP, a deep image prior (DIP)-based reconstruction method that regularizes SIMPLE without requiring external training data. The proposed approach employs a single patient-specific U-Net that takes a prior anatomical image as input and jointly constrains both the activity and lifetime-weighted images during reconstruction. Computer simulations using a brain phantom show that SIMPLE-DIP effectively suppresses image noise while preserving lifetime contrast and improving lesion recovery, outperforming the compared SIMPLE formulations regularized by the quadratic penalty or independent DIPs. These results suggest that the proposed SIMPLE-DIP is a promising method for high-resolution positronium lifetime imaging.

References

[1] Moskal, P, Bilewicz, A, Das, M, et al., 2025, 'Positronium Imaging: History, Current Status, and Future Perspectives', *IEEE TRPMS*, Vol. 8, No. 9, 981-1001

[2] Huang, B, Dai, B, Lapi, SE, Liles, G, Karp, JS, Qi, J, 2025, 'High-Resolution Positronium Lifetime Tomography at Clinical Activity Levels on the PennPET Explorer', *Journal of Nuclear Medicine*, Vol. 66, No.9, Page 1464--1470

[3] Huang, B, Wang, Z, Zeng, X, Goldan, AH, Qi, J, 2025, 'Fast high-resolution lifetime image reconstruction for positron lifetime tomography', *Communications Physics*, Vol. 8, No. 1, Page 181

[4] Gong, K, Catana, C, Qi, J, Li, Q, 2019, 'PET Image Reconstruction Using Deep Image Prior', *IEEE TMI*, Vol. 38, No. 7, 1655-1665

[5] Moskal, M, Baran, J, Bass, S, et al., 2024, 'Positronium image of the human brain in vivo', *Science Advances*, Vol. 10, No. 37, Page eadp2840

MIC-11-05

AI-Based Predictive Dosimetry from PET for 177Lu-PSMA Radiopharmaceutical Therapy for Prostate Cancer (#2210)

Bowen Lei, Tzu-An Song, Fan Yang, Vibha Balaji, Joyita Dutta

University of Massachusetts Amherst, Biomedical Engineering, Amherst, USA

Abstract

Personalized 177Lu-PSMA-617 radiopharmaceutical therapy (RPT) for prostate cancer requires patient-specific dosimetry, but post-therapy SPECT imaging for dose computation is not universally performed. In contrast, pre-therapy PSMA PET is widely available and often mandatory for patient selection. PET-based predictive dosimetry therefore has the potential to enable personalized treatment planning before RPT administration. We developed a machine learning framework for organ-level predictive dosimetry from pre-therapy PET, where PET-derived organ features are used to predict kinetic parameters of post-therapy SPECT time-activity curves (TACs). Organ masks for the liver, spleen, and bilateral kidneys were used to extract PET features. Serial 177Lu-PSMA SPECT images at multiple post-injection time points provided reference organ activity values, from which mono-exponential fitting yielded organ TACs and time-integrated activities (TIAs). Absorbed dose was computed from TIAs using the MIRD formalism with organ-specific S values. Our deep learning model predicting kinetic parameters outperformed a comparable deep learning model predicting TIA directly, as well as three classical machine learning models predicting kinetic parameters. This workflow demonstrates the feasibility of forecasting organ absorbed dose from pre-therapy PET, supporting individualized therapeutic regimen planning.

MIC-11-06

Event-Resolved Parent-Progeny Discrimination Using CMOS Lensless Radiomicroscopy for ^{225}Ac Targeted Alpha Therapy (#2026)

Hyeyeun Chu[1,3], Jae Sung Lee[1,2]

[1] Seoul National University, Interdisciplinary Program in Bioengineering, College of Engineering, Seoul, South Korea; [2] Seoul National University, Department of Nuclear Medicine, Seoul, South Korea; [3] Seoul National Graduate School, Integrated Major in Innovative Medical Science, Seoul, South Korea

Abstract

Although targeted alpha therapy (TAT) using ^{225}Ac has demonstrated high therapeutic efficacy, clinical translation remains limited due to redistribution of daughter isotopes, leading to off-target dose. Therefore, discriminating localized emissions from redistributed emitting progeny is significant for small-scale dosimetry and radiopharmaceutical evaluation. Here, we propose a low-cost CMOS-based lensless radiomicroscopy system for direct / discrimination using cluster morphology. Event level features extracted from ^{210}Po and ^{90}Sr measurements

were used for classification applying both a physics-driven probability density function (PDF) approach and a data-driven multilayer perceptron (MLP). Both methods achieved > 98% accuracy with AUC > 0.99. Mixed-source experiments mimicking ^{225}Ac decay conditions demonstrated robust event-level discrimination. These results indicate that cluster morphology encodes sufficient physical information to monitor daughter isotope migration, enabling pathway toward quantifying parent and progeny distributions in radiopharmaceutical imaging.

References
[1] Robin, Peter, 2024, '*Digital autoradiography and small-scale dosimetry techniques for alpha-particle radiopharmaceutical therapy*', PhD dissertation, University of California, Berkeley: University of California

[2] Klein, Justin S., Tae Jin Kim, and Guillem Pratx. 2023, 'Development of a lensless radiomicroscope for cellular-resolution radionuclide imaging' *Journal of Nuclear Medicine* 64.3 (2023): 479-484.

MIC-11-07

Physics-Guided Implicit Neural Representation for 3D Ac-225 Compton Imaging (#1786)

Gyohyeok Song[1], Biswajit Das[2], Junhyeok Kim[3], Youngho Seo[2,4], Jisoo Kim[1], Gyuseong Cho[1], Javier Caravaca[5]

[1] Korea Advanced Institute of Science and Technology, Department of Nuclear and Quantum Engineering, Daejeon, South Korea; [2] University of California, San Francisco, Department of Radiology and Biomedical Imaging, San Francisco, USA; [3] Korea Atomic Energy Research Institute, Daejeon, South Korea; [4] University of California, Berkeley, Department of Nuclear Engineering, Berkeley, USA; [5] Lawrence Berkeley National Laboratory, Nuclear Science Division, Berkeley, USA

This work is supported by the National Institutes of Health (NIH) under grant R01EB032324 and the National Research Foundation of Korea(NRF) grant funded by the Korea government(MSIT)(RS-2024-00345521).

Abstract
Actinium-225 (Ac-225) is a promising alpha-emitting radionuclide for targeted alpha therapy, and Compton cameras have emerged as a potential imaging solution for this radionuclide. We developed a physics-guided implicit neural representation (PG-INR) framework for Ac-225 Compton image reconstruction that does not require any ground truth data. Unlike conventional deep learning approaches, the proposed method incorporates physical laws directly into the training process by embedding physics-based loss terms, including maximum-likelihood estimation and Klein-Nishina differential cross section. This enables unsupervised learning solely guided by the measurement results. Furthermore, by representing the reconstructed image as a continuous implicit neural function, the framework achieves resolution enhancement beyond the native voxel grid. The proposed method was evaluated against a conventional ordered subsets expectation maximization (OSEM) algorithm using measured Compton imaging data from a mouse phantom and a Monte Carlo-simulated resolution phantom (from 1.0 to 2.5 mm). For the mouse phantom experiments, PG-INR achieved up to 18-fold faster reconstruction compared to OSEM at comparable resolution. For the resolution phantom simulation, PG-INR successfully resolved 1.0 mm diameter rods with up to 4.8 dB peak signal-to-noise ratio improvement and 0.25 structural similarity index measure

enhancement over OSEM. These results suggest that the PG-INR performs significantly better than standard OSEM for Ac-225 Compton imaging.

References
[1] Thijssen, L., et al. 'Polymersomes as nano-carriers to retain harmful recoil nuclides in alpha radionuclide therapy: a feasibility study.' *Radiochimica Acta* 100.7 (2012): 473.
[2] De Kruijff, Robin M., Hubert T. Wolterbeek, and Antonia G. Denkova. 'A critical review of alpha radionuclide therapy—how to deal with recoiling daughters?.' *Pharmaceuticals* 8.2 (2015): 321-336.
[3] Fontana, Mattia, et al. 'Compton camera study for high efficiency SPECT and benchmark with Anger system.' *Physics in Medicine & Biology* 62.23 (2017): 8794-8812.
[4] Han, Li, et al. 'Statistical performance evaluation and comparison of a Compton medical imaging system and a collimated Anger camera for higher energy photon imaging.' *Physics in Medicine & Biology* 53.24 (2008): 7029-7045.
[5] Seo, Youngho. 'Quantitative imaging of alpha-emitting therapeutic radiopharmaceuticals.' *Nuclear medicine and molecular imaging* 53.3 (2019): 182-188.
[6] B. Das, et al. 'Compton Imaging of Ac-225 in Preclinical Phantoms With a 3D-positioning CZT Camera.' *IEEE Transactions on Radiation and Plasma Medical Sciences* 10.1 (2026): 112-125.
[7] J. Caravaca, et al. 'Compton and Proximity Imaging of Ac In Vivo With a CZT Gamma Camera: A Proof of Principle With Simulations.' *IEEE Transactions on Radiation and Plasma Medical Sciences* 6.8 (2022): 904-915.
[8] Skorokhodov, Ivan, et al. 'Adversarial generation of continuous images.' *Proceedings of the IEEE/CVF conference on computer vision and pattern recognition*. 2021.
[9] Xu, Xinyue, et al. 'Physics-guided Bayesian neural networks and their application in ODE problems.' *Verification and Validation* 87769. American Society of Mechanical Engineers, 2024.

MIC-11-08

Attenuation Map Estimation from NAC Brain PET Images Using a 3D Patch-Based U-Net: A Multi-Tracer Study on the NeuroEXPLORER

(#1934)

Max Keppens, Georg Schramm, Hélène Goesseye, Koen Van Laere

KU Leuven, Department of Imaging and Pathology, Leuven, Belgium

Abstract

Attenuation correction in PET/CT imaging typically uses a CT-derived attenuation map (μ-map), prone to misalignment artifacts, CT-induced artifacts, and additional radiation dose. CT-free alternatives are therefore clinically attractive, and deep learning methods are a promising solution. As clinical PET centres increasingly adopt diverse tracer protocols beyond FDG, a single attenuation correction model that generalizes across tracers without retraining would further reduce deployment complexity. In this work, we investigate the feasibility of supervised μ-map estimation from non-attenuation-corrected (NAC) brain PET images using a 3D patch-based U-Net, trained and evaluated on patient data from the NeuroEXPLORER, a brain- dedicated PET/CT scanner. A dataset of 353 scans across 12 different tracers was used to study the effect of tracer composition on model generalizability. To our knowledge, this is the first study to systematically assess how training tracer composition affects cross-tracer generalization in deep learning-based CT- free attenuation correction, using a large multi-tracer cohort. The tuned U-Net outperformed Attention U-Net, HighResNet, and Swin UNETR under matched conditions. FDG-only training showed poor generalization to non-FDG tracers, with Normalized Root Mean Squared Error (NRMSE) on average 5× higher in the brain for non-FDG tracers than multi-tracer models across different dataset sizes. Notably, a model trained without any FDG data produced FDG μ-maps as well as a FDG-only model, suggesting the network learns anatomy-based priors that generalize across tracer distributions. Tracer diversity during training did not degrade FDG performance and improved generalization. Weighted resampling to correct FDG/non-FDG imbalance

worsened performance when the non-FDG patient pool was small. These results indicate that training set diversity, rather than size or tracer-specific data, is an important driver of generalization.

References
[1] M. Jehl et al., “Beyond CT: Attenuation correction for stand-alone brain PET,” Zeitschrift f¨ur Medizinische Physik, 2026. DOI: https://doi.org/10.1016/j.zemedi.2026.02.001.
[2] J. Wasserthal et al., “TotalSegmentator: Robust segmentation of 104 anatomic structures in CT images,” Radiology: Artificial Intelligence, 2023. [Online]. Available: https://doi.org/10.1148/ryai.230024.
[3] W. Falcon and The PyTorch Lightning team, PyTorch Lightning, 2019. DOI: 10.5281/ zenodo .3828935. [Online]. Available: https: // github. com/Lightning- AI /lightning.
[4] M. J. C. et al., “Monai: An open-source framework for deep learning in healthcare,” arXiv:2211.02701, 2022.

Time:
13 November, 2026
9:00 – 11:00

Room:
MANUEL DE FALLA

MIC-12 | New Concepts and Emerging Applications

Chairs:
Magdalena Rafecas (Lübeck)

MIC-12-01

Direct clinical imaging of alpha therapy in a PET/CT scanner via cascade gamma-rays imaging (#1380)

Javier Caravaca[1,2], Youngho Seo[2], Jorge Cabello[3], Stefan Siegel[3], Robert R. Flavell[2], Thomas A. Hope[2]

[1] Lawrence Berkeley National Laboratory, Applied Nuclear Physics, Berkeley, USA; [2] University of California San Francisco, Radiology, San Francisco, USA; [3] Siemens Medical Solutions USA, Inc., Knoxville, USA

This work is supported by the Department of Energy and by the National Institutes of Health (NIH) under grant R01EB032324 and under clinical trial
LuTACT NCT07054346. This research used resources of the National Energy Research Scientific Computing Center (NERSC), a Department of Energy User Facility using NERSC awards BER ERCAP0034495, BER ERCAP0035599, and DDR-NESAP ERCAP0037956. \ac~was supplied by the U.S. Department of Energy Isotope Program, managed by the Office of Isotope R\&D and Production.

Abstract

Targeted alpha therapy is a very promising treatment modality for numerous types of cancer. Although PET presents an excellent resolution and signal-to-noise ratio, this modality is limited to radionuclides that emit positrons and cannot be used to image alpha radionuclides such as Ac-225 and Pb-212. Therefore, SPECT is the imaging modality of choice for these radionuclides, despite its poor signal-to-noise ratio and low quantitative accuracy due to the extremely limited sensitivity of this modality. We propose a new approach that enables imaging of alpha-emitting radionuclides in PET/CT scanners: time-of-flight cascade gamma-ray imaging. Our methodology exploits the coincidence detection of gamma-ray cascades emitted by ^{225}Ac or ^{212}Pb to perform tomography of non-positron emitters in PET/CT scanners. Our technique is evaluated with Ac-225 and Pb-212 phantoms at low concentrations of ~44kBq/mL and short scan sessions under 5-minutes in a commercial clinical PET/CT. We also present the first clinical image of a prostate cancer patient injected with 225Ac-PSMA-617 in a clinical PET/CT system. Lastly, we predict via simulations that next-generation long-axial field-of-view PET/CT scanners will achieve a sensitivity several orders of magnitude higher than SPECT with similar or better spatial resolution.

References

[1] A. Jang, A. T. Kendi, G. B. Johnson, T. R. Halfdanarson, and O. Sartor, “Targeted Alpha-Particle Therapy: A Review of Current Trials,” *Int. J. Mol. Sci.*, vol. 24, no. 14, p. 11626, Jul. 2023, doi: 10.3390/IJMS241411626.

[2] N. Benabdallah *et al.*, “Practical considerations for quantitative clinical SPECT/CT imaging of alpha particle emitting radioisotopes,” *Theranostics*, vol. 11, no. 20, pp. 9721–9737, 2021, doi: 10.7150/thno.63860.

[4] C.-C. Chiang, C.-C. Chuang, Y.-C. Ni, M.-L. Jan, K.-S. Chuang, and H.-H. Lin, “Time of flight dual photon emission computed tomography,” *Sci. Rep.*, vol. 10, no. 1, p. 19514, 2020, doi: 10.1038/s41598-020-76526-z.

[3] J. Caravaca, “Feasibility of ^225 \textAc Imaging with Time-Offlight Gamma-Ray Cascade Tomography,” in *2025 IEEE Nuclear Science Symposium (NSS), Medical Imaging Conference (MIC) and Room Temperature Semiconductor Detector Conference (RTSD)*, Nov. 2025, pp. 1–1. doi: 10.1109/NSS/MIC/RTSD57106.2025.11287360.

[5] J. Caravaca, B. Das, H. Chu, and R. Heller, “POSSUM: a Python Image Reconstruction Framework for Emerging and Combined Modalities,” *2025 IEEE Nucl. Sci. Symp. NSS Med. Imaging Conf. MIC Room Temp. Semicond. Detect. Conf. RTSD*, pp. 1–1, Nov. 2025, doi: 10.1109/NSS/MIC/RTSD57106.2025.11287697.

MIC-12-02

From MeV Gamma to PET Signal: Experimental Demonstration of Pair Production Tomography for Theranostic Imaging (#2289)

Biswajit Das[1,2], Robin Peter[3], Javier Caravaca[2,1], Youngho Seo[1,4]

[1] University of California, San Francisco, Department of Radiology and Biomedical Imaging, San Francisco, USA; [2] Lawrence Berkeley National Laboratory, Applied Nuclear Science Division, Berkeley, USA; [3] University of California, San Francisco, Department of Radiation Oncology, San Francisco, USA; [4] University of California, Berkeley, Department of Nuclear Engineering, Berkeley, USA

This work was supported by the National Cancer Institute (NCI) grant R01CA279203 and the National Institute of Biomedical Imaging and Bioengineering (NIBIB) grant R01EB032324.

Abstract

Imaging of theranostic radionuclides that emit high-energy (MeV range) γ rays remains extremely challenging with conventional imaging systems. SPECT performance degrades at MeV energies due to scatter and collimator penetration, while PET is inherently restricted to positron-emitting radionuclides. Pair production tomography (PPT) offers a new approach enabled by the high-energy γ interactions with matter to detectable coincidence signals. When a photon with energy ≥ $2m_ec^2$ (=1.022 MeV) undergoes pair production, the positron generated from this pair production leads to annihilation with the medium electron and emission of two 511 keV photons, enabling PET imaging. In this study, we experimentally demonstrate PPT using the ^{212}Pb decay chain, exploiting 2.617 MeV γ rays from ^{208}Tl. Monte Carlo simulations indicate that, despite long photon transport distances, the spatial distributions of pair production and annihilation events remain localized at the millimeter scale. Phantom experiments were performed on both clinical time-of-flight (TOF) PET and preclinical non-TOF PET systems without hardware modification using clinically and preclinically relevant ^{212}Pb activity levels. Reconstructed PPT images successfully recovered the spatial distribution of activity, with improved contrast observed when TOF information was available. Corresponding SPECT measurements under identical conditions showed reduced visibility for smaller structures. Our results demonstrate the feasibility of PPT for imaging high-energy γ-emitting radionuclides and suggest a route to extend PET beyond conventional principles requiring positron emissions directly from radionuclides.

MIC-12-03

Quantitative evaluation of pair-produced positrons using a clinical linear accelerator for pair-production tomography (#2445)

Ryosuke Ota[1,2], Qihui Lyu[3], Biswajit Das[4], Bruce Faddegon[3], Yongho Seo[4], Ke Sheng[3], Sun Il Kwon[1]

[1] University of California, Davis, Department of Biomedical Engineering, Davis, USA; [2] Hamamatsu Photonics K.K., Central Research Laboratory, Hamamatsu, Japan; [3] University of California, San Francisco, Department of Radiation Oncology, San Francisco, USA; [4] University of California, San Francisco, Department of Radiology and Biomedical Imaging, San Francisco, USA

This work was supported by NIH grants R01 EB030538 and R01EB031577.

Abstract

X-ray based radiotherapy is indispensable in modern cancer treatment yet has challenges because it is an open-loop treatment, with limited ability to verify during treatment whether the delivered dose matches the treatment plan. To address this problem, we investigated the use of positrons which are generated in a patient body during X-ray radiotherapy through pair production interactions between matter and MV X-rays, and proposed a novel imaging modality termed pair-production tomography (P2T). This is possible because the X-ray energy used for radiotherapy is a few MeV, and pair production can occur when the photon energy is higher than 1.022 MeV, producing an electron–positron pair. Their simulation results showed opportunities to utilize pair-produced positrons to not only monitor the treatment but also differentiate materials with similar density but different effective atomic numbers, which remains challenging in conventional computed tomography. However, to our best knowledge, there has been no experimental evidence of pair-produced positron detection using a clinical linear accelerator (LINAC). Therefore, in this study, we performed experimental detection of pair-produced positrons using a LINAC. Experiments were conducted using a LINAC and a pair of radiation detectors composed of photomultiplier tubes and LYSO scintillator crystals. We successfully observed positrons generated in various phantoms via pair production. Furthermore, we quantitatively investigated sensitivity of P2T by adjusting the effective atomic number of phantoms, showing consistent results with the previous simulation results. These results provide an important step toward experimental validation of P2T.

References

[1] Q. Lyu, *et al.*, "Tomographic detection of photon pairs produced from high-energy X-rays for the monitoring of radiotherapy dosing", *Nat. Biomed. Eng.*, 2022 vol. 7, pp 323

MIC-12-04

Terbium-149: a Laboratory for Three-Photon Events (#2764)

Lorenzo Mercolli[1,2], Pascal V. Grundler[3], Anzhelika N. Moiseeva[3], Lars Eggimann[2], Saverio Braccini[2], Ulli Köster[4], Nicholas P. van der Meulen[3,5], William M. Steinberger[6]

[1] Inselspital, Bern University Hospital, Department of Nuclear Medicine, Bern, Switzerland; [2] University of Bern, Albert Einstein Center for Fundamental Physics (AEC), Laboratory for High Energy Physics (LHEP), Bern, Switzerland; [3] PSI Center for Life Sciences, Center for Radiopharmaceutical Sciences, Villigen, Switzerland; [4] Institut Laue-Langevin, Grenoble, France; [5] PSI Center for Nuclear Engineering and Science, aboratory of Radiochemistry, Villigen, Switzerland; [6] Siemens Medical Solutions USA, Inc, Knoxville, USA

Abstract

Terbium-149 (^{149}Tb) is a promising radionuclide for targeted α therapy that also emits positrons and prompt photons γ across a wide energy range, which makes it a candidate for ortho-positronium (oPs) lifetime imaging (oPsLI). We present the first demonstration of oPsLI with a therapeutic radionuclide and with γ energies below 511 keV on a commercial long-axial field-of-view PET/CT system. Using a three-lifetime-component Bayesian fitting model, we determined the oPs lifetime for the following three γ energy windows: 310 to 420 keV, 590 to 710 keV and above 720 keV. The medium- and high-energy windows yielded oPs lifetime values consistent with each other and with literature values, while the low-energy window produced systematically lower values. Voxel-wise oPsLI with small voxel size was successfully demonstrated using a single γ energy window. These results establish ^{149}Tb as a versatile probe for exploring γ energy window effects in oPsLI, with future potential for in vivo microdosimetry and chelator stability studies.

MIC-12-05

The first in vivo quantum entanglement imaging of a human subject (#3065)

Pawel Moskal, Deepak Kumar, Sushil Sharma, Ewa Ł. Stępień

Jagiellonian University, Institute of Physics, KRAKOW, Poland

We acknowledge support by National Science Center in Poland (2021/42/A/ST2/00423,2021/43/B/ST2/02150, 2022/47/I/NZ7/03112), Polish Ministry MNiSW (IAL/SP/596235/2023 and SPUB/SP/627733/2025), and European Union through ERC Advanced Grant POSITRONIUM no. 101199807.

Abstract

We present the first in-vivo imaging of the degree of quantum entanglement in a human subject. The reported investigations were conducted at the Cracow University Hospital in Poland using a 50 cm long, multi-photon J-PET

scanner capable of registering and imaging the degree of quantum entanglement of photons originating from electron-positron annihilations in the patient's body.
A 48-year-old male patient, administered 145 MBq of [68Ga]Ga-DOTA-TATE, was scanned for 20 minutes starting 90 minutes post-injection, following the completion of his routine diagnosis. Data were collected in a triggerless mode, enabling the simultaneous registration of annihilation photons and Compton scattered photons. Event selection was based on the position, time, and energy deposition of the annihilation and scattered photons.
The angular distributions between the scattering planes of annihilation photons in the patient's liver and spleen were determined. These distributions were used to extract the degree of quantum entanglement for these organs. The obtained degree of quantum entanglement is larger than expected for separable photons and lower than expected for maximally entangled photons.
These results demonstrate, for the first time, the feasibility of measuring the degree of quantum entanglement in annihilation photons originating from patients during positron emission tomography. This finding motivates the further development of detectors for the construction of PET systems capable of simultaneously capturing annihilation and Compton-scattered photons, and supports future studies aimed at uncovering medically useful information gained by imaging the degree of quantum entanglement.

References
[1] M. L. H. Pryce and J. C. Ward, Nature 160 (1947) 435.
[2] I. Tkachev et al., Scientific Reports 15 (2025) 6064.
[3] P. Moskal et al., Science Advances 11 (2025) eads3046.

[4] P. Moskal, Bio-Algorithms and Med. Systems 22 (2026) 56.
[5] R. Bayerlein et al, Phys. Med. Biol. 71 (2026) 075026.

[6] K. Kacprzak et al., Bio-Algorithms and Med. Systems 22 (2026) 36

MIC-12-06

Constraining CP Invariance in Ortho-Positronium Decays at 7 T with NeuroSphere MR-Compatible PET Modules (#3078)

Magdelena S. Allen[1,2], Michele Scipioni[1], Caio Silva[2], Nikos Efthimiou[1], Maryam Hiradfar[1], Or Hen[2], Ciprian Catana[1]

[1] MGH and Harvard University, A. A. Martinos Center and Harvard Medical School, Cambridge, USA; [2] MIT, Physics, Cambridge, USA

This project is funded by the NIH BRAIN Initiative, 1U01EB029826-01.

Abstract
In addition to medical imaging applications, Positron Emission Tomography (PET) systems can be used to study fundamental physics. One pathway for positron-electron annihilation is the formation of ortho-positronium (oPs), an intermediate bound state that decays to photons after a short lifetime. The lifetime and decay kinematics of oPs can be used to probe material properties and test the Standard Model. Additional sources of charge conjugation-parity (CP) symmetry violation are required to explain the observed matter-antimatter imbalance in the Universe,

and CP violation can be constrained by measuring [if gte msEquation 12]><m:oMath><span style='font-size:12.0pt;line-height: 115%;font-family:"Cambria Math",serif;mso-fareast-font-family:Aptos; mso-fareast-theme-font:minor-latin;mso-bidi-font-family:"Times New Roman"; mso-ansi-language:EN-US;mso-fareast-language:EN-US;mso-bidi-language:AR-SA'><m:r>oPs</m:r><m:r>→3</m:r><m:r>γ</m:r></m:oMath><![endif][if gte vml 1]><v:shapetype id="_x0000_t75" coordsize="21600,21600" o:spt="75" o:preferrelative="t" path="m@4@5l@4@11@9@11@9@5xe" filled="f" stroked="f"> <v:stroke joinstyle="miter"/> <v:formulas> <v:f eqn="if lineDrawn pixelLineWidth 0"/> <v:f eqn="sum @0 1 0"/> <v:f eqn="sum 0 0 @1"/> <v:f eqn="prod @2 1 2"/> <v:f eqn="prod @3 21600 pixelWidth"/> <v:f eqn="prod @3 21600 pixelHeight"/> <v:f eqn="sum @0 0 1"/> <v:f eqn="prod @6 1 2"/> <v:f eqn="prod @7 21600 pixelWidth"/> <v:f eqn="sum @8 21600 0"/> <v:f eqn="prod @7 21600 pixelHeight"/> <v:f eqn="sum @10 21600 0"/> </v:formulas> <v:path o:extrusionok="f" gradientshapeok="t" o:connecttype="rect"/> <o:lock v:ext="edit" aspectratio="t"/></v:shapetype><v:shape id="_x0000_i1025" type="#_x0000_t75" style='width:50pt; height:16pt'> <v:imagedata src="file:////Users/msa54/Library/Group%20Containers/UBF8T346G9.Office/TemporaryItems/msohtmlclip/clip_image001.emz" o:title="" chromakey="white"/></v:shape><![endif] decays under the reversal of an applied magnetic field. A dedicated physics measurement platform was constructed from the architecture of the NeuroSphere brain PET insert for 7-T MRI, including a PET detector array, positronium target with lifetime trigger, and motorized gantry for control of the system orientation inside the 7-T environment. GATE simulations were used to inform the development of a custom data analysis pipeline for oPs event selection and multi-coincidence processing. Systematics were mitigated by combining runs with various target and detector positions (to average out artificial asymmetries caused by assembly or detector efficiency) and by applying a baseline correction from events in a kinematic region with vanishing analyzing power (to account for drift and more field- and material- related effects). [if gte msEquation 12]><m:oMath><span style='font-size:12.0pt;line-height: 115%;font-family:"Cambria Math",serif;mso-fareast-font-family:Aptos; mso-fareast-theme-font:minor-latin;mso-bidi-font-family:"Times New Roman"; mso-ansi-language:EN-US;mso-fareast-language:EN-US;mso-bidi-language:AR-SA'><m:r>oPs</m:r><m:r>→3</m:r><m:r>γ</m:r></m:oMath><![endif][if gte vml 1]><v:shape id="_x0000_i1025" type="#_x0000_t75" style='width:50pt;height:16pt'> <v:imagedata src="file:////Users/msa54/Library/Group%20Containers/UBF8T346G9.Office/TemporaryItems/msohtmlclip/clip_image003.emz" o:title="" chromakey="white"/></v:shape><![endif] decays in polyvinyltoluene (PVT) were measured at 7 T, finding a lifetime of 98.7 ± 1.0 ns and constraining CP violation to be zero at a level of 2×10^{-2}. This work demonstrates the unique opportunity provided by PET/MR instrumentation to perform high-field physics measurements, a pathway toward a leading measurement of CP violation in positronium, and proof-of-concept for measuring positronium decays with the full NeuroSphere system.

References
[2] Moskal, P., Bilewicz, A., Das, M., Huang, B., Khreptak, A., Parzych, S., Qi, J., Rominger, A., Seifert, R., Sharma, S., Shi, K., Steinberger, W. M., Walczak, R., & Stępień, E. (2025). Positronium Imaging: History, Current Status, and Future Perspectives. *IEEE Transactions on Radiation and Plasma Medical Sciences*, *9*(8), 981–1001. https://doi.org/10.1109/TRPMS.2025.3583554
[3] Moskal, P., Gajos, A., Mohammed, M., Chhokar, J., Chug, N., Curceanu, C., Czerwiński, E., Dadgar, M., Dulski, K., Gorgol, M., Goworek, J., Hiesmayr, B. C., Jasińska, B., Kacprzak, K., Kapłon, Ł., Karimi, H., Kisielewska, D., Klimaszewski, K., Korcyl, G., … Wiślicki, W. (2021). Testing CPT symmetry in ortho-positronium decays with positronium annihilation tomography. *Nature Communications*, *12*(1), 5658. https://doi.org/10.1038/s41467-021-25905-9
[1] Yamazaki, T., Namba, T., Asai, S., & Kobayashi, T. (2010). Search for C P Violation in Positronium Decay. *Physical Review Letters*, *104*(8), 083401. https://doi.org/10.1103/PhysRevLett.104.083401
[6] Rauscher, L. U., Allen, M. S., Judenhofer, M. S., Byars, L., Scipioni, M., Udias, J. M., Catana, C., Pichler, B. J., & Schmidt, F. P. (2025). Impact of DOI Capability on Detector Performance: A Comparative Study of DOI and Non-DOI Detectors for High-Resolution and Sensitivity Organ-Specific PET Inserts. *IEEE Transactions on Radiation and Plasma Medical Sciences*, 1–1. https://doi.org/10.1109/TRPMS.2025.3624609
[4] Scipioni, M., et al. (2025). Manufacturing and Assembly of the NeuroSphere PET Insert for the Human Dynamic NeuroChemical Connectome. *IEEE NSS MIC RTSD*.

[5] Allen, M. S., et al. (2024). Coincidence Timing Performance Optimization of the Detector for the Human Dynamic NeuroChemical Connectome Scanner. *IEEE NSS RTSD MIC*.

MIC-12-07

Novel Spatial Encoding Using Larmor Precession in Nuclear Medicine: A Study on Imaging Robustness (#1753)

Hiroto Suzuki[1], Boyu Feng[2], Motofumi Fushimi[3], Kenji Shimazoe[2], Hiroyuki Takahashi[2], Masaki Sekino[4]

[1] The University of Tokyo, Department of Electrical Engineering and Information Systems Graduate School of Engineering, Bunkyo, Japan; [2] The University of Tokyo, Department of Nuclear Engineering and Management, Department of Bioengineering, and Institute of Engineeing Innovation, Bunkyo, Japan; [3] Keio University, Department of Applied Physics and Physico-Informatics, Faculty of Science and Technology, Bunkyo, Japan; [4] The University of Tokyo, Department of Bioengineering, School of Engineering, Yokohama, Japan

This work was supported by JSPS KAKENHI Grant Number 22H04961.

Abstract

In nuclear medicine, positron emission tomography (PET) and single photon emission computed tomography (SPECT) exhibit high detection sensitivity by detecting γ-rays emitted from radiopharmaceuticals, but they are limited by poor spatial resolution. Conversely, Magnetic Resonance Imaging (MRI) achieves high spatial resolution by encoding positional information through Larmor precession induced by magnetic field gradients. To improve the spatial resolution in nuclear medicine, we propose a novel image reconstruction framework that integrates magnetic field–based spatial encoding, as utilized in MRI, with γ-ray detection as employed in PET and SPECT. By incorporating the effect of Larmor precession in perturbed angular correlation (PAC), we formulated a forward model that enables image reconstruction as an inverse problem. Numerical simulations demonstrated that our method can stabilize 7 by 7pixels imaging on a small-animal scale. Furthermore, condition number analysis revealed that the imaging process becomes increasingly stable as the neodymium magnets are scanned. However, since each magnetic field distribution requires several hours of measurement, future work will focus on designing more detailed field distributions to reduce measurement time while further enhancing spatial resolution.

References
[1] S. L. Pimlott and A. Sutherland, “Molecular tracers for the PET and SPECT imaging of disease,” vol. 40, no. 1. in Chem. Soc. Rev., no. 40, vol. 40. Royal Society of Chemistry (RSC), 2011.
[2] Y. Zheng, G. W. Miller, W. A. Tobias, and G. D. Cates, “A method for imaging and spectroscopy using γ-rays and magnetic resonance,” vol. 537, no. 7622. in Nature, no. 537, vol. 537. Springer Science and Business Media LLC, Sep. 01, 2016.
[3] G. Schatz and A. Weidinger, “Nuclear Condensed Matter Physics: Nuclear Methods and Applications,” 2nd ed. John Wiley & Sons, 1996. Nuclear Instruments and Methods in Physics Research Section A: Accelerators, Spectrometers, Detectors and Associated Equipment, Volume 1053, 2023, 168305, ISSN 0168-9002.
[4] R. M. Sterzex, “Influence of the Time-Dependent Quadrupole Interaction on the Directional Correlation of the Cd^{111} Gamma Rays.” 1956.

MIC-12-08

Real-Time Task-Based Adaptive SPECT Imaging via Optimized System Sampling Strategies Using a Robotic Clinical SPECT Platform (#2916)

Yifei Jin[1], Ling-Jian Meng[1,2]

[1] University of Illinois at Urbana and Champaign, Department of Nuclear, Plasma, and Radiological Engineering, Urbana, USA; [2] University of Illinois at Urbana and Champaign, Beckman Institute for Advanced Science and Technology, Urbana, USA

This work was supported by NIH under grant numbers R01HL145786 (NHLBI) and U01EB031798 and UH3EB034715 (National Institute of Biomedical Imaging and Bioengineering).

Abstract

Task-based adaptive SPECT imaging has long been limited by the computational complexity associated with optimizing acquisition strategies over high-dimensional system configuration spaces. In this work, we present a computational framework for adaptive SPECT imaging based on direct optimization of imaging time distribution (ITD) over discretized detector poses. We have demonstrated the effectiveness of this scheme on a simulated robotic SPECT platform. The framework finds the best imaging strategy by finding an optimized imaging noise property based on the modified uniform Cramér–Rao bound (MUCRB). We further improve the computation efficiency using a non-uniform object-space pixelation (NUOP), which makes it possible to compute the optimum imaging geometry in real time. A StarGuide-inspired multi-head robotic SPECT was simulated and evaluated using a Hoffman brain phantom and hot- and cold-rod resolution-phantoms. Compared with conventional whole-view and uniform ITDs under identical total acquisition time, the optimized ITDs achieved substantially improved region-of-interest (ROI) image quality in all three phantoms and ROIs. These results demonstrate that the proposed framework enables efficient task-specific optimization of acquisition strategies for highly reconfigurable SPECT systems.

References

[1] A. Zorz *et al.*, "Performance evaluation of the 3D-ring cadmium–zinc–telluride (CZT) StarGuide system according to the NEMA NU 1-2018 standard," *EJNMMI Phys.*, vol. 11, no. 1, p. 69, Jul. 2024, doi: 10.1186/s40658-024-00671-x.

[2] H. H. Barrett *et al.*, "Adaptive SPECT," *IEEE Trans. Med. Imaging*, vol. 27, no. 6, pp. 775–788, Jun. 2008, doi: 10.1109/TMI.2007.913241.

[3] E. Clarkson, M. A. Kupinski, H. H. Barrett, and L. Furenlid, "A task-based approach to adaptive and multimodality imaging," *Proc. IEEE*, vol. 96, no. 3, pp. 500–511, 2008, doi: 10.1109/JPROC.2007.913073.

[4] M. A. Kupinski, J. W. Hoppin, E. Clarkson, and H. H. Barrett, "Ideal-observer computation in medical imaging with use of Markov-chain Monte Carlo techniques," *JOSA A*, vol. 20, no. 3, pp. 430–438, Mar. 2003, doi: 10.1364/JOSAA.20.000430.

[5] L.-J. Meng and N. Li, "SPECT system optimization against a discrete parameter space," *Phys. Med. Biol.*, vol. 58, no. 9, p. 3037, 2013, doi: 10.1088/0031-9155/58/9/3037.

[6] A. Lin, L. C. Johnson, S. Shokouhi, T. E. Peterson, and M. A. Kupinski, "Using the Wiener estimator to determine optimal imaging parameters in a synthetic-collimator SPECT system used for small animal imaging," in *Medical Imaging 2015: Image Perception, Observer Performance, and Technology Assessment*, SPIE, Mar. 2015, pp. 124–131. doi: 10.1117/12.2082971.

Time:
13 November, 2026
11:30 – 12:45

Room:
FEDERICO GARCÍA LORCA

MIC-13 | New radiation detector technologies for medical imaging (2)

Chairs:
Paul R. Lecoq (Geneva)
Han Gyu Kang (Chiba)

MIC-13-01

Cramér–Rao–Efficient Timing with Photon Counting: Theory and Proof-of-Concept Demonstration for Cherenkov TOF-PET (#1437)

Nicolaus Kratochwil[1], Seungeun Lee[2], Joshua W. Cates[2], Gerard Ariño-Estrada[1,3]

[1] University of California, Davis, Department of Biomedical Engineering, Davis, USA; [2] Lawrence Berkeley National Laboratory, Nuclear Science Division, Berkeley, USA; [3] Barcelona Institute of Science and Technology, Institut de Fisica d'Altes Energies, Barcelona, Spain

NIH: R01EB034062, R01EB033402

Abstract

Fast timing with Cherenkov luminescence has attracted significant interest in the medical imaging community over the last decade. While detector time resolutions of 100–200ps FWHM have been reported, we recently demonstrated that current timing estimators fail to fully exploit the prompt nature of Cherenkov emission. In particular, simulations of a small BGO crystal coupled to a state-of-the-art silicon photomultiplier (SiPM) yield a detector time resolution (standard deviation) of σ_t = 158ps when using only the first detected photon, whereas the Cramér–Rao lower bound (CRLB) predicts a ≈ 4.5-fold improvement to σ_t = 35ps for the same configuration.

To approach this limit, we apply a maximum-likelihood estimation (MLE) framework incorporating the full photon arrival time distribution. Using all detected photons, we obtain a harmonic average detector time resolution of σ_t = 35 ± 2ps, demonstrating statistically efficient timing estimation consistent with the CRLB. The MLE framework also enables event classification, identifying variations in Cherenkov photon yield and time biases from light transport and photon production. Simulations suggest a 2-fold timing improvement compared to state-of-the-art classifiers such as the signal rise time.

To validate this approach experimentally, we apply the method to a semi-monolithic BGO photon-counting detector (42 × 2 × 20 mm^3) measured in coincidence with a reference detector and read out by 16 SiPMs. Events with different Cherenkov photon yield can be identified, improving time resolution from 199ps (all events) to 165ps and 140ps FWHM for tighter log-likelihood selections. We observe a stronger improvement over the first timestamp for Cherenkov-rich events and shallow interaction depths.

These results demonstrate that photon-counting-based MLE can fully exploit the information content of Cherenkov emission, enabling a pathway toward CRLB-limited timing performance for improved TOF-PET imaging.

References
[1] Arino-Estrada et al 2025, https://doi.org/10.1109/TRPMS.2025.3579673
[2] Loignoun-Houle et al 2023, https://doi.org/10.1109/trpms.2023.3279455
[3] Kratochwil et al 2026, https://doi.org/10.1109/TRPMS.2026.3665464
[4] Seifert et al 2012, https://doi.org/10.1088/0031-9155/57/7/1797
[6] Lee et al 2026, https://doi.org/10.1088/1361-6560/ae2db7
[7] Kratochwil et al 2020, https://doi.org/10.1088/1361-6560/ab87f9
[5] van Dam et al 2013, https://doi.org/10.1088/0031-9155/58/10/3243

MIC-13-02

Sparse-to-Dense SiPM Readout Upsampling for Position Estimation in PET Detectors (#1583)

Fiammetta Pagano, Paula Muñoz Izquierdo, Antonio J. Gonzalez, Francis Loignon-Houle

CSIC-Universitat Politècnica de València, Institute for Instrumentation in Molecular Imaging (I3M), Valencia, Spain

Abstract

Signal readout strategies of positron emission tomography detectors have an inherent compromise between resolution and complexity, where finer photosensor sampling improves interaction localization but increases the number of readout channels and associated hardware demands. Channel-reduction methods are therefore central to detector design, though they typically can incur some loss in performance. Recent advances in deep learning offer a pathway to mitigate this compromise by recovering information lost through reduced readout. In this work, we propose a neural network–based sparse-to-dense mapping that reconstructs high-resolution (8×8) silicon photomultiplier signals from low-resolution (4×4) inputs. Data was acquired using a semi-monolithic scintillator array with pinhole collimation across both the monolithic and depth-of-interaction directions. An initial upsampling network is trained to transform 4×4 signals into 8×8 representations, which are then used as input to a second network for interaction position estimation. Performance is evaluated by comparing positioning accuracy across four configurations: native 8×8 readout, reduced 4×4 readout, upsampled 4×4-to-8×8 signals, and a conventional row–column summation (8+8) scheme. Results demonstrate that the proposed upsampling approach effectively reconstructs higher-resolution signal structure, helping to improve the monolithic and DOI resolution compared to both 4×4 and 8+8 readouts. This approach could therefore remove the need for additional hardware coming with conventional multiplexing techniques, while recovering the benefits of denser photosensor sampling.

References

[1] Park, Haewook, Minseok Yi, and Jae Sung Lee. "Silicon photomultiplier signal readout and multiplexing techniques for positron emission tomography: a review." *Biomedical engineering letters* 12.3 (2022): 263-283.

[2] Pagano, Fiammetta, et al. "Performance evaluation of a multiplexing circuit combined with ASIC readout for cost-effective brain PET imaging." *Physics in Medicine & Biology* 70.20 (2025): 205001.

[3] Li, Yixin, et al. "Interleaved signal multiplexing readout in depth encoding prism-PET detectors." *Medical physics* 50.7 (2023): 4234-4243.

[4] Loignon-Houle, Francis, Fiammetta Pagano, and Antonio J. Gonzalez. "Multi-Input Interaction Positioning and Signal Demultiplexing With Deep Learning in Semi-Monolithic Detectors." *IEEE Transactions on Radiation and Plasma Medical Sciences* (2025).

MIC-13-03

Crosshair Light-Sharing Detectors with Diode-based Multiplexing for High-Resolution TOF-DOI PET (#2227)

Han Gyu Kang, Eiji Yoshida, Go Akamatsu, Taiga Yamaya

National Institutes for Quantum Science and Technology (QST), Advanced Nuclear Medicine Sciences, Chiba, Japan

This work was supported by Nakatani Foundation.

Abstract

Last year, we developed diode-based row-column multiplexing boards that can reduce the number of silicon photomultiplier (SiPM) channels by a factor of four without compromising the coincidence timing resolution (CTR). This technology is key to reducing the production costs of next-generation clinical whole-body time-of-flight positron emission tomography (TOF-PET) systems. However, we used one-to-one coupling detectors with a crystal pitch of 3.2 mm, which cannot provide depth-of-interaction (DOI) information. For brain PET applications, for example, DOI measurement capability with a finer crystal pitch is required. On the other hand, our group has developed crosshair light-sharing (CLS) detectors that can offer both TOF and DOI information with a crystal pitch half that of the SiPM pitch. In this work, therefore, we explored the performance of the CLS detectors with the multiplexing board in combination with a TOFPET2 ASIC module for high-resolution TOF-DOI brain PET imaging. The CLS detectors had a 14×14 array of fast-LGSO crystals (crystal pitch=1.6 mm, crystal thickness=15 mm) and an 8×8 SiPM array (Hamamatsu, S14161-3050HS). The multiplexed SiPM signals were digitized by the TOFPET2 ASIC module. We evaluated CTR at eight different detector positions of the multiplexing boards by shifting the CLS detector pairs and a ^{22}Na source. The diode multiplexing did not degrade the CTR and energy resolution compared to the case without multiplexing. The average CTR of 366±6 ps was obtained across the eight detector positions. In the future, we plan to further improve the CTR by using DOI information.

References

[1] H. Park et al., “Silicon photomultiplier signal readout and multiplexing techniques for positron emission tomography: a review”, *Biomed. Eng. Letters*, vol. 12, pp. 263-283, 2022.

[2] H.G. Kang et al., “Development of diode-based row-column multiplexing boards with the TOFPET2 ASIC for clinical TOF-PET systems”, *Phys. Med. Biol.*, vol. 70, no.22, pp. 225001, 2025.

[3] E. Yoshida et al., “Development of crosshair light sharing PET detector with TOF and DOI capabilities using fast LGSO scintillator”, *Phys. Med. Biol.*, vol. 66, no.22, pp. 225003, 2021.

[4] K. Narita et al., “Simulation and one-ring prototyping of 1 mm-rod-resolution hemispherical brain PET with TOF-DOI detectors”, *Phys. Med. Biol.*, vol. 70, no. 12, pp. 12NT01, 2025.

[6] F. Pagano al., “Performance evaluation of a multiplexing circuit combined with ASIC readout for cost-effective brain PET imaging”, *Phys. Med. Biol.*, vol. 70, no.22, pp. 205001, 2025.

[5] J. Jung et al., “A Diode-Based Symmetric Charge Division Circuit With Grounding Path to Reduce Signal Crosstalk and Improve Detector Performance”, *IEEE TRPMS*, vol. 6, no. 7, pp. 788-793, 2022.

[7] S.I. Kwon and Lee., “Signal encoding method for a time-of-flight PET detector using a silicon photomultiplier array”, Nucl. Instrum. Methods Phys. Res. A., vol. 761, pp. 39-45, 2014.

MIC-13-04

High-performance 4×4-channel microchannel plate photomultiplier tubes with bismuth germanate window faceplate (#2331)

Ryosuke Ota[1,2], Yuki Ichikawa[3], Tatsuo Sasaki[3], Koji Kuramoto[3], Kenshi Shimano[3], Takahiro Moriya[2], Simon R. Cherry[1], Sun Il Kwon[1]

[1] University of California, Davis, Department of Biomedical Engineering, Davis, USA; [2] Hamamatsu Photonics K.K., Central Research Laboratory, Hamamatsu, Japan; [3] Hamamatsu Photonics K.K., Electron Tube Division, Iwata, Japan

This work was supported by the National Institutes of Health under grant R01 EB033536.

Abstract

Positron emission tomography can benefit from time-of-flight information between a coincident pair of PET detectors to enhance image quality. Improved coincidence time resolution (CTR) can not only improve image quality but also obviate the need for image reconstruction when the spatial uncertainty derived from CTR becomes sufficiently small to directly localize positron annihilation events within the patient body, potentially making PET systems more compact and flexible. The first reconstruction-free positron emission imaging termed direct positron emission imaging (dPEI), was demonstrated using detectors with 32 ps CTR; however, limitations such as low detection efficiency, lack of energy information due to the use of a pure Cherenkov radiator, and a small active area resulting from the single-channel detector system remain. To address these limitations and make dPEI more practical, we developed the first prototypes of a multi-anode bismuth germanate-integrated microchannel plate photomultiplier tube (MA-BGO-IMP). The MA-BGO-IMP is position-sensitive and has a two-dimensional 4 × 4 anode array with a 5.75 mm readout pitch. At the detector level, the transit time spread and quantum efficiency were measured to be ~40 ps full width at half maximum (FWHM) without circuit optimization and 31.4% at 380 nm without Fresnel reflection correction, respectively. A coincidence experiment was conducted using a ^{22}Na point source paired with a barium fluoride-integrated microchannel plate photomultiplier tube. The preliminary energy resolution and CTR were 26% FWHM at 511 keV and 56.2 ps FWHM, respectively. These results were obtained using signals from only one anode. At the conference, we will present more detailed characterization of these newly developed MA-BGO-IMPs with 511 keV-based coincidence results, including energy resolution, CTR, and spatial resolution using a pair of MA-BGO-IMPs.

References

[1] S. I. Kwon, *et al.*, "Ultrafast timing enables reconstruction-free positron emission imaging", *Nat. Photon.*, 2021 vol. 15, pp 914

[2] R. Ota, *et al.*, "Coincidence time resolution of 30 ps FWHM using a pair of Cherenkov-radiator-integrated MCP-PMTs", *Phys. Med. Biol.*, 2019 vol. 64 07LT01

[3] R. Ota, *et al.*, "Scintillator-integrated microchannel plate photomultiplier tubes for ultrafast timing over keV-GeV energy scales", arXiv:2510.03488

[4] R. Ota, *et al.*, "Lead-free MCP to improve coincidence time resolution and reduce MCP direct interactions", *Phys. Med. Biol.* 2021 vol 66 064006

MIC-13-05

Achieving Sub-100 ps CTR and Sub-2 mm DOI Resolution in TOF-PET Modules (#2370)

Giulia Terragni[1], Ece Ucari[2], Matteo N. Colombo[3], Joshua W. Cates[4], Marco Pizzichemi[1,3], Etiennette Auffray[1]

[1] CERN, Meyrin, Switzerland; [2] Boston University, Boston, USA; [3] University of Milano-Bicocca, Milan, Italy; [4] Lawrence Berkeley National Laboratory, Berkeley, USA

This work is performed in the framework of the Crystal Clear Collaboration.

Abstract

Low-dose imaging and small-animal positron emission tomography (PET) require detectors with both high sensitivity and high spatial resolution. In this study, we investigate the performance of high-density scintillator matrices, such as BGO and LYSO:Ce, combined with multi-channel, low-noise, low-power, high-frequency (HF) readout electronics to enhance the Time-of-Flight (TOF) and Depth-of-Interaction (DOI) performance of pixelated detectors. High-frequency SiPM readout has demonstrated significant improvements in coincidence time resolution (CTR) by enabling the detection of ultrafast optical-photon production processes, such as Cherenkov emission in BGO and fast scintillation in LYSO:Ce. Two DOI-encoding detector designs are compared in this work: a double-sided readout and a single-sided readout employing a light guide to achieve DOI encoding through light sharing in laterally depolished crystal matrices. Experimental results demonstrate that they can achieve a timing resolution comparable to that of a standard pixelated matrix while also providing accurate DOI information. In particular, using 20 mm-long LYSO:Ce crystals, the light-sharing approach achieves a CTR of 133 ± 2 ps FWHM together with a DOI resolution of 2.2 ± 0.1 mm FWHM. Using a double-sided readout further improves the performance, reaching a CTR of 90 ± 2 ps FWHM and a DOI resolution of 1.9 ± 0.1 mm. Both DOI encoding methods provide similar DOI performance with LYSO:Ce matrices, while the advantage of collecting light from both ends of the scintillator becomes more evident with BGO crystals. In this case, the double-sided readout achieves a DOI resolution of 4.4 ± 0.1 mm, compared with 7.2 ± 0.2 mm obtained using the light-sharing approach. Future work will investigate the scalability of these detector concepts by extending the study from 16 to 64-channel prototypes and by comparing different readout electronics.

Time:
13 November, 2026
11:30 – 12:45

Room:
MANUEL DE FALLA

MIC-14 | Novel applications of AI in radiation-based medical imaging (2)

Chairs:
Joyita Dutta (Amherst)

MIC-14-01

Deep Learning Limited Angle Artefact Correction for dual panel PET in Shearlet Domain (#2587)

Jens Maebe, Maya Abi Akl, Boris Vervenne, Stefaan Vandenberghe

Ghent University, Gent, Belgium

Abstract

Dual-flat-panel positron emission tomography (PET) systems offer strong advantages such as improved sensitivity but suffer from reconstruction artefacts due to missing projection data. We propose a deep learning model to correct these artefacts in the shearlet domain. The shearlet transform provides a multiscale, multidirectional analysis of the image, decomposing it into its shearlet coefficients, each corresponding to a subset of projections. A U-Net is used to correct for artefacts in these coefficients, but by only modifying coefficients corresponding to missing projection data, we can obtain an overall more robust algorithm. The model is trained and evaluated on data from a dual-panel PET system simulated in GATE, using real patient PET scans as the ground truth activity maps. The resulting artefact-corrected images showed good visual agreement with reference images from a system with full angular sampling. The standardized uptake value (SUV) mean of a hotspot also showed improvement (being closer to the reference value), but further investigation is required with regards to the consistency of quantitative accuracy of the model. Future work will also include an extension to 3D, to better leverage projection data along the axial dimension.

References

[1] S. Vandenberghe et al., “Walk-through flat panel total-body PET: a patient-centered design for high throughput imaging at lower cost using DOI-capable high-resolution monolithic detectors,” Eur J Nucl Med Mol Imaging, vol. 50, no. 12, pp. 3558–3571, Oct. 2023, doi: 10.1007/s00259-023-06341-x.

[2] J. Gu and J. C. Ye, “Multi-Scale Wavelet Domain Residual Learning for Limited-Angle CT Reconstruction,” Mar. 04, 2017, arXiv: arXiv:1703.01382. doi: 10.48550/arXiv.1703.01382.

[3] S. Xue et al., “A cross-scanner and cross-tracer deep learning method for the recovery of standard-dose imaging quality from low-dose PET,” Eur J Nucl Med Mol Imaging, vol. 49, no. 6, pp. 1843–1856, May 2022, doi: 10.1007/s00259-021-05644-1.

[4] B. Goossens, J. Aelterman, H. Luong, A. Pizurica, and W. Philips, “Design of a tight frame of 2D shearlets based on a fast non-iterative analysis and synthesis algorithm,” in PROCEEDINGS OF SPIE, THE INTERNATIONAL SOCIETY FOR OPTICAL ENGINEERING, SPIE, 2011, pp. 81381Q–13. doi: 10.1117/12.893752.

MIC-14-02

Multi-Objective Bayesian Optimization of Self-Collimating SPECT System Design Using Quantitative Imaging Metrics (#3200)

Syed O. Shah[1], Harsh Tripathi[2], Tridev Methuku[2], Kirtirajsinh M. Parmer[3], Tessa Skirsky[2], Leslie Ying[4], Tianyu Ma[5], Rutao Yao[2]

[1] State University of New York at Buffalo, Engineering Science (Artificial Intelligence), Buffalo, USA; [2] State University of New York at Buffalo, Radiology, Buffalo, USA; [3] State University of New York at Buffalo, Computer Science and Engineering, Buffalo, USA; [4] State University of New York at Buffalo, Biomedical Engineering, Buffalo, USA; [5] Tsinghua University, Engineering Physics, Beijing, China

The work of Syed Omer Shah, Harsh Tripathi, Tridev Methuku, Tessa Skirsky, and Rutao Yao are supported by the National Institute of Biomedical Imaging and Bioengineering of the National Institutes of Health, USA, under Grant R21EB032993. Syed Omer Shah and Tessa Skirsky are also partially supported by the Career Design Center of State University of New York at Buffalo.
This work uses computational resources supported by the Center for Computational Research, State University of New York at Buffalo.

Abstract
Self-collimating (SC) SPECT employs a multi-layered, interspaced mosaic array detector structure to enable simultaneous gains in sensitivity and resolution. The complex configuration, however, demands a new set of imaging metrics and strategy to guide system design and optimization. In this work, we propose a Multi-Objective Bayesian Optimization (MOBO) framework based on four voxel-wise imaging metrics calculated from the projection probability density functions (PPDF) of the system: Angular Sampling Completeness Index (ASCI), average PPDF FWHM (full-width at half-maximum), Multiplex Index (MPXI), and sensitivity, to predict a design's performance and efficiently navigate the design space.
Through analytical simulations, we study a SC small animal SPECT that consists of a cylindrical tungsten high-resolution collimator ring surrounded by four concentric detector rings. In an initial test, we seek optimal design parameters for the aperture diameter, the number of apertures on the collimator ring, and crystal counts in two independent detector rings. The MOBO agent uses independent Gaussian process surrogates with log noisy expected hypervolume improvement to propose Pareto-improving configurations sequentially.
Results of MOBO search confirm that the four objectives genuinely conflict, which is desired, and provide recommended parameters balancing resolution, sensitivity, angular coverage, and multiplexing. Validation studies of the MOBO recommendations are underway.

References
[1] Ma, T et al. 2021, 'Self-collimating SPECT with multi-layer interspaced mosaic detectors', IEEE Trans. Med. Imaging, vol. 40, no. 8, pp. 2152-2169.
[2] Zhang, D et al., 2023, 'Characterization and Assessment of Projection Probability Density Function and Enhanced Sampling in Self-Collimation SPECT', IEEE Trans. Med. Imaging, vol. 42, no. 9, pp. 2787-2801
[3] Zhang, D et al., 2026, "A High-Performance Self-Collimation SPECT for Small Animal Imaging," IEEE Trans. Med. Imaging, vol. 45, no. 5, pp. 2403-2413.

MIC-14-03

Sensitivity-Aware Gated Deep Reconstruction for Cascade γ Coincidence Imaging (#2567)

Hao Jia[1], Hui Liu[2], Tan Gong[1], Yaqiang Liu[2], Zuoxiang He[3]

[1] Tsinghua University, School of Biomedical Engineering, Beijing, China; [2] Tsinghua University, Department of Engineering Physics, Beijing, China; [3] Tsinghua University Changgeng Hospital, Changgeng Hospital, Beijing, China

This work was supported in part by the National Key Research and Development Program of China (No. 2022YFC2402004, No. 2022YFC2403802), National Natural Science Foundation of China (No. 12205166) and High performance computing Center of Tsinghua University.

Abstract

Cascade γ coincidence imaging can provide stronger geometric constraints than conventional single-photon imaging by exploiting the coincident detection of two cascade photons, but its reconstruction is challenging due to the complex system response and spatially non-uniform sensitivity. This work proposes a physics-prior-driven deep reconstruction framework for small-animal cascade γ coincidence imaging. A direct back-projection(DBP) reconstruction image was used as a physics-informed initialization, and a cascade sensitivity map was incorporated into a gated 3D ResUNet as a system-level spatial prior. Patch-based training was further adopted for sparse point-source reconstruction to reduce foreground-background imbalance. Monte Carlo simulations showed that, for a single-point source, the proposed method reduced the mean FWHM from 1.50 mm to 0.87 mm, increased the PSNR from 43.85 dB to 54.48 dB, and reduced the peak localization error from 0.25 mm to nearly 0 mm compared with DBP reconstruction. For the hotrod phantom, the foreground MAE decreased from 0.886 to 0.142, indicating improved recovery of extended active structures. The sensitivity map comparison further showed that different incorporation strategies lead to different trade-offs between foreground recovery and background suppression. These results demonstrate that the proposed framework provides a feasible route toward fast, sensitivity-aware, and physically informed reconstruction for cascade γ coincidence imaging.

References

[1] X. Liu, H. Liu, L. Cheng, J. Wu, T. Bao, R. Yao, and Y. Liu, "A 3-dimensional stationary cascade gamma-ray coincidence imager," Phys. Med. Biol., vol. 66, no. 22, p. 225001, 2021.

MIC-14-04

Two-Stage Retrieval-Augmented 3D Detection of Bone Metastatic Lesions via SPECT/CT (#2324)

Yangshi Lin[3], DuoDuo Li[2], Na Dang[2], Fenghua Weng[1], Weiyan Chen[1], Gaoyu Chen[4], Ying Liang[2], Qiu Huang[1]

[1] Macao Polytechnic University, Applied Sciences, Macao, China; [2] Chinese Academy of Medical Sciences and Peking Union Medical College, National Cancer Center/National Clinical Research Center for Cancer/ Cancer Hospital & Shenzhen Hospital, Shenzhen, China; [3] Guangxi University of Foreign Languages, School of Digital Technology, Nanning, China; [4] Vplus Technology Ltd., Research and Development Department, Shanghai, China

This work was supported by the Macao Polytechnic University under Grant RP/FCA-10/2025.

Abstract

Bone metastases are common in advanced malignancies, and SPECT/CT provides complementary 3D radiotracer uptake and anatomy for screening and follow-up. Automatic whole-body lesion localization can reduce reading burden and improve consistency in patient-level assessment. However, it remains challenging because a detector needs to balance high-recall whole-body search, false-positive suppression, and fine-resolution local detail under memory and runtime constraints. To address this challenge, we propose a two-stage retrieval-augmented lesion detection framework: a 3D Swin Transformer-FPN-FCOS detector retrieves candidates from coarse-voxel-spacing whole-body SPECT/CT, and a candidate query retrieves fine-voxel-spacing local/context SPECT/CT evidence tokens for classification, box refinement, and rescoring. In validation, the base model achieves free-response receiver operating characteristic (FROC) scores of 0.511/0.471 for Mean-FROC/Low-FROC and reduces inference time from 14.9 to 3.6 s/patient; a final reranker raises Mean-FROC to 0.530 at 5.5 s/patient.

References

[1] Lin, Q., Li, T., Cao, C., Cao, Y., Man, Z., and Wang, H. 2021, 'Deep learning based automated diagnosis of bone metastases with SPECT thoracic bone images', Scientific Reports, vol. 11, article 4223.

[2] Zhang, Y., Li, J., Yang, Q., et al. 2025, 'A clinically applicable AI system for detection and diagnosis of bone metastases using CT scans', Nature Communications, vol. 16, article 4444.

[3] Chen, M., Chen, Z., Xi, Y., Qiao, X., Chen, X., and Huang, Q. 2023, 'Multimodal fusion network for detecting hyperplastic parathyroid glands in SPECT/CT images', IEEE Journal of Biomedical and Health Informatics, vol. 27, no. 3, pp. 1524-1534.

[4] Lewis, P., Perez, E., Piktus, A., et al. 2020, 'Retrieval-augmented generation for knowledge-intensive NLP tasks', Advances in Neural Information Processing Systems, vol. 33, pp. 9459-9474.

[5] Liu, Z., Lin, Y., Cao, Y., et al. 2021, 'Swin Transformer: Hierarchical vision transformer using shifted windows', Proceedings of the IEEE/CVF International Conference on Computer Vision, pp. 10012-10022.

[6] Lin, T.-Y., Dollar, P., Girshick, R., He, K., Hariharan, B., and Belongie, S. 2017, 'Feature pyramid networks for object detection', Proceedings of the IEEE Conference on Computer Vision and Pattern Recognition, pp. 2117-2125.

[7] Tian, Z., Shen, C., Chen, H., and He, T. 2019, 'FCOS: Fully convolutional one-stage object detection', Proceedings of the IEEE/CVF International Conference on Computer Vision, pp. 9627-9636.

[8] Lin, T.-Y., Goyal, P., Girshick, R., He, K., and Dollar, P. 2020, 'Focal loss for dense object detection', IEEE Transactions on Pattern Analysis and Machine Intelligence, vol. 42, no. 2, pp. 318-327.

[9] Chillakuru, Y. R., Kranen, K., Doppalapudi, V., et al. 2021, 'High precision localization of pulmonary nodules on chest CT utilizing axial slice number labels', BMC Medical Imaging, vol. 21, article 66.

MIC-14-05

Data Augmentation Strategy Analysis for Noninvasive Lung Cancer Subtype Classification (#2187)

Xinyu Hu[1], Xinyan Lin[1], Ruijie Yang[2], David Huang[1], Qinglong Yao[1], Ruiyang Yan[4], Kaiwen Li[3], Lisheng Geng[1]

[1] Beihang University, Beijing, China; [2] Department of Radiation Oncology, Cancer Center, Peking University Third Hospital, Beijing, China; [3] Department of Technology, CAS Ion Medical Technology Co., Ltd., Beijing, China; [4] Sun Yat-sen University, Guangzhou, China

The authors thank the MAASTRO Clinic and The Cancer Imaging Archive for making the NSCLC-Radiomics dataset publicly available. This work was partly supported by the Beijing Natural Science Foundation (Z230003), National Natural Science Foundation of China (No. 12475309) and Beijing Municipal Commission of Science and Technology Collaborative Innovation Project (Z221100003522028).

Abstract

Lung cancer remains a leading cause of cancer-related death, and distinguishing between the two major non-small cell lung cancer (NSCLC) subtypes, adenocarcinoma (ADC) and squamous cell carcinoma (SCC), is essential for treatment planning. To evaluate whether data augmentation strategies can improve subtype classification on computed tomography (CT) images with reduced annotation burden, we compared pseudo-color mapping, adaptive histogram equalization, pixel inversion, and rotation-based augmentation in combination with tumor-centric and lung-centric region extraction. Using the public NSCLC-Radiomics dataset, features were extracted with a pretrained ResNet-50 network and classified with support vector machine (SVM) and k-nearest neighbors (KNN) models, with all augmentation and feature selection performed within each cross-validation fold. Rotation consistently improved classification, with the best single model reaching 89.36% patient-level classification accuracy. Tumor-centric and lung-centric strategies showed complementary error patterns, and an ensemble of five complementary models achieved 100% patient-level classification accuracy on this cohort. The findings suggest that complementary augmentation pathways can diversify feature representations and improve classification stability in small-sample studies.

References

[1] H. Sung, J. Ferlay, R. L. Siegel, M. Laversanne, I. Soerjomataram, A. Jemal, and F. Bray, "Global cancer statistics 2020: GLOBOCAN estimates of incidence and mortality worldwide for 36 cancers in 185 countries," CA Cancer J. Clin., vol. 71, no. 3, pp. 209–249, May 2021, doi: 10.3322/caac.21660.

[2] H. J. W. L. Aerts, L. Wee, E. R. Velazquez, R. T. H. Leijenaar, C. Parmar, P. Grossmann, S. Carvalho, J. Bussink, R. Monshouwer, B. Haibe-Kains, D. Rietveld, F. Hoebers, M. M. Rietbergen, C. R. Leemans, A. Dekker, J. Quackenbush, R. J. Gillies, and P. Lambin, "Data from NSCLC-Radiomics," The Cancer Imaging Archive, 2015. [Online]. Available: https://doi.org/10.7937/K9/TCIA.2015.PF0M9REI.

[3] K. He, X. Zhang, S. Ren, and J. Sun, "Deep residual learning for image recognition," in Proc. IEEE Conf. Comput. Vis. Pattern Recognit. (CVPR), Las Vegas, NV, USA, 2016, pp. 770–778, doi: 10.1109/CVPR.2016.90.

[4] R. Tibshirani, "Regression shrinkage and selection via the lasso," J. Roy. Statist. Soc. B (Methodological), vol. 58, no. 1, pp. 267–288, 1996, doi: 10.1111/j.2517-6161.1996.tb02080.x.

[5] B. E. Boser, I. M. Guyon, and V. N. Vapnik, "A training algorithm for optimal margin classifiers," in Proc. 5th Annu. Workshop Comput. Learn. Theory, Pittsburgh, PA, USA, 1992, pp. 144–152, doi: 10.1145/130385.130401.

[6] T. Cover and P. Hart, "Nearest neighbor pattern classification," IEEE Trans. Inf. Theory, vol. IT-13, no. 1, pp. 21–27, Jan. 1967, doi: 10.1109/TIT.1967.1053964.

Time:
13 November, 2026
12:45 – 13:05

Room:
FEDERICO GARCÍA LORCA

M-LT-05 | Kinetic modeling, molecular connectivity analysis and radiomics, Theranostics, Imaging and dosimetry in therapy (particle, radiopharmaceutical, surgery), Total body imaging systems including applications

Chairs:
Paul R. Lecoq (Geneva)
Han Gyu Kang (Chiba)

M-LT-05-01

Pixelated Cherenkov Crystals for Prompt-Gamma Imaging in Proton Range Verification (#1181)

Leonor Rebolo[1,2], Salvador Moreno Gomez[6], Machiel Kolstein[6], Michael Backfish[5], Matthew Novotny[5], Rafiaullah Sahebzada[5], Sara St. James[4], Brahim Mehadji[2], Eric Prebys[5,3], Pedro M.M. Correia[1], Ana Luísa M. Silva[1], Gerard Ariño-Estrada[2,6]

[1] Universidade de Aveiro, Física, Aveiro, Portugal; [2] University of California Davis, Biomedical Engineering, Davis, USA; [3] University of California Davis, Physics, Davis, USA; [4] University of Utah, Huntsman Cancer Institute, Salt Lake City, USA; [5] Crocker Nuclear Laboratory, Davis, USA; [6] Institut de Fisica d'Altes Energies - Barcelona Institute of Science and Technology (IFAE-BIST), Bellaterra, Spain

This work was supported by NIH grant R01EB029533 (PI G.A.E.), by FCT projects UID/50025/2025, UID/PRR/50025/2025, UID/PRR2/50025/2025, and LA/P/0037/2020, and by FCT scholarship PRT/BD/154945/2023 (L.R.).

Abstract

Proton range verification (PRV) in proton therapy is an outstanding clinical need. Prompt-gammas (PG) emitted along the proton track constitute a strong signal to determine the Bragg Peak position. However, the high energy of PGs (1-7 MeV), the high particle flux and the presence of significant background radiation make prompt-gamma imaging (PGI) challenging.

We report on the development of pure Cherenkov pixelated detectors for PRV. The detector consisted of an 8×8 pixelated PbF2 crystal array coupled to an 8×8 S14161-3050HS-08 SiPM array from Hamamatsu, read out by a row-column signal processing board. Two analytical event reconstruction algorithms were evaluated: rise-to-the-power with k=2 (RTP2) and k=3 (RTP3).

The detector was exposed to both a sealed 228Th source and a 67.5 MeV proton beam at a current of 100 pA. Floodmaps were obtained using both RTP2 and RTP3 methods to resolve the 8×8 matrix of the crystal under laboratory source irradiation. Similar results were obtained under proton beam irradiation, showing the robustness of this detector concept.

In this contribution we demonstrate for the first time the ability of a pixelated pure Cherenkov detector to provide spatial resolution information in clinically relevant proton beam conditions. The prompt emission of Cherenkov light and exclusive sensitivity to highly energetic PGs offer a very high count rate capability, effective background rejection, and capacity to multiplex signals, enabling to use less channels and low power readout electronics. Future work will focus on quantitative floodmap quality metrics, detector modeling to optimize the detector geometry, and acquisition of additional data in the proton beam line at higher proton energies and beam currents.

References

[1] Jacquet, M. et al 2023, 'A high sensitivity Cherenkov detector for prompt gamma timing and time imaging', *Scientific Reports*, 13, 3609

[2] Ellin, J. et al 2024, 'Prompt gamma timing for proton range verification with TlBr and TlCl as pure Cherenkov emitters', *Physics in Medicine and Biology, 69, 11*

[3] Pinson, et al. 2026, 'Prompt Gamma Timing in Carbon Therapy: First Experimental Results with the TIARA Detector', arXiv:2602.18318

[4] Rebolo, L. et al. 2024, 'Cherenkov Light Emission in Pure Cherenkov Emitters for Prompt Gamma Imaging', *IEEE TRPMS*, 8, 1, pp. 15-20

M-LT-05-02

Coded-Mask PGI for Proton Range Verification With Pure Cherenkov Crystal Detectors (#1159)

Salvador M. Gómez[1], Machiel Kolstein[1], Carles Gomà[2], Sara Marcatili[3,4], Aleksandra Wrońska[5], Magdalena Rafecas[6], **Gerard Ariño-Estrada**[1,7]

[1] Institut de Física d'Altes Energies - Barcelona Institute of Science and Technology (IFAE-BIST), Medical Detector Instrumentation and Imaging Physics group, Cerdanyola del Vallès, Spain; [2] Institut d'Investigacions Biomèdiques August Pi i Sunyer (IDIBAPS), Translational genomics and targeted therapies in solid tumours, Barcelona, Spain; [3] Laboratoire de Physique Subatomique et de Cosmologie (LPSC), Physics at the service of energy and health - Medical Applications, Grenoble, France; [4] Centre National de la Recherche Scientifique (CNRS), Grenoble, France; [5] Marian Smoluchowski Institute of Physics, Jagiellonian University, Department of Hadron Physics (ZFH), Kraków, Poland; [6] Universität zu Lübeck, Biomedical Engineering - Medical Imaging, Lübeck, Germany; [7] University of California Davis, Department of Biomedical Engineering, Davis, USA

Abstract

Accurate proton range verification (PRV) in proton therapy (PT) is an unmet clinical need and is essential to exploit the full potential of PT to maximize treatment effectiveness and minimize toxicity. We present a Monte Carlo (GATE 10) study of a Cherenkov-based prompt gamma imaging system combining an array of PbF2 crystal detectors with a MURA coded-aperture collimator for real-time PRV. The detector response was studied through detected Cherenkov photon distributions generated by prompt-gammas with energies ranging from 0.5 MeV to 7.0 MeV in steps of 0.5 MeV. A threshold of 15 detected Cherenkov photons was applied to reject low-energy background, which effectively suppressed 511 keV annihilation gammas and sub-MeV contributions while retaining the prompt gammas of interest. Image reconstruction was performed using the Maximum Likelihood Expectation Maximization algorithm, with the system matrix computed with 4.4 MeV point-like sources. The imaging performance was validated on isotropic gamma point sources in both 1D and 2D coded-mask configurations across a field of view of ~130 mm. A direct comparison between discrimination based on energy deposition (E > 1 MeV) and discrimination based on the number of detected Cherenkov photons (nckv ≥ 15) showed comparable performance, with position residuals consistent with zero within statistical uncertainties in both cases. For the proton beam measurements, background rejection was performed exclusively via the Cherenkov photon count threshold. Under realistic proton beam conditions, the distal fall-off position was reconstructed with a systematic residual below 1.5 mm and a statistical precision of less than 2 mm for beam intensities above 10^8 protons, corresponding to approximately 10 ms of irradiation at a standard proton current of 2 nA (1.25 × 10^10 protons/s). This work presents the concept and shows the feasibility of using Cherenkov-based coded-aperture imaging for PRV by means of a simulation framework.

References
[1] Ariño-Estrada, G, et al., 2026, 'Current Status of Cherenkov-Based Gamma Detectors for TOF-PET and Proton Range Verification', *IEEE Transactions on Radiation and Plasma Medical Sciences*, Vol. 10, No. 1, pp. 1–15, New York: IEEE.

[2] André, A, et al., 2026, 'TIARA: A Fast Gamma-Ray Detector for Range Monitoring in Proton Therapy', *IEEE Transactions on Radiation and Plasma Medical Sciences*, Early Access, New York: IEEE.
[3] Hetzel, R, et al., 2023, 'Near-Field Coded-Mask Technique and Its Potential for Proton Therapy Monitoring', *Physics in Medicine and Biology*, Vol. 68, p. 245028, Bristol: IOP Publishing.
[4] Gottesman, S R, Fenimore, E E, 1989, 'New Family of Binary Arrays for Coded Aperture Imaging', *Applied Optics*, Vol. 28, No. 20, pp. 4344–4352, Washington, D.C.: Optical Society of America.
[5] Rebolo, L, et al., 2024, 'Cherenkov Light Emission in Pure Cherenkov Emitters for Prompt Gamma Imaging', *IEEE Transactions on Radiation and Plasma Medical Sciences*, Vol. 8, No. 1, pp. 15–20, New York: IEEE.

M-LT-05-03

Deep Learning-based CT-Free Deformable Registration for PET-CT Misalignment Correction (#1875)

Abolfazl Mehranian[1], Scott Wollenweber[2], Fotis Kotasidis[3], Zacharias Chalampalakis[4], Ariel Lulinsky[5], Hagit Ratner[5], Robert Johnsen[2], Gil Kovalski[5]

[1] GE HealthCare, Oxford, UK; [2] GE HealthCare, Waukesha, USA; [3] GE HealthCare, Zurich, UK; [4] GE HealthCare, Buc, France; [5] GE HealthCare, Haifa, Israel

This work has been sponsored by GE HeathCare.

Abstract

Respiratory phase mismatches between PET and CT commonly cause artifacts in PET/CT, especially at lung–liver and lung–spleen interfaces. Since CT captures a single respiratory phase while PET reflects an average over breathing, this misalignment leads to attenuation correction errors and inaccurate lesion quantification, particularly near the liver dome. We propose a deep learning framework that uses PET-based pseudo-CT to guide deformable CT-to-PET alignment. A retrospective dataset of 10 18F-FDG exams with respiratory phase mismatch (banana) artifacts, scanned on a Total-Body BGO-based PET/CT scanner, was used for evaluation. A previously trained 3D residual neural network was used to generate pseudo-CT images from non-attenuation corrected (NAC) PET images. The pseudo-CT images, inherently aligned with the PET data, were then used as a reference for deformable registration of the CT images. The original and registered CT images were used for attenuation correction and reconstruction of the PET data using a BSREM algorithm. Regions of interested were placed in dome of the liver to quantitatively measure the SUV changes in those regions affected by the artifacts. Compared to baseline PET/CT without correction, the proposed method effectively reduced or eliminated respiratory-induced PET/CT misalignment artifacts were significantly reduced or eliminated. Quantitatively, the method achieved improvements in liver SUVmean towards the expected values. By leveraging the native alignment between PET and the generated pseudo-CT, the method avoids direct multimodal registration and instead enables accurate deformable alignment of CT to PET space. This approach improves attenuation correction and quantitative accuracy, with potential to enhance diagnostic confidence in routine clinical PET/CT imaging

M-LT-05-04

Evaluation of TOF-DOI Crystal Topologies for the HD-MetaPET MRI Insert (#2140)

Thore Meyer[1], Giulia Terragni[2], David Schug[1,3], Yannick Kuhl[1], Bjoern Weissler[1,3], Eike Gegenmantel[3], Oliver Muelhens[3], Harald Radermacher[1], Marco Pizzichemi[2,4], Etiennette Auffray[2], Volkmar Schulz[1,3]

[1] RWTH Aachen University, Chair of Imaging and Computer Vision, Aachen, Germany; [2] CERN, Geneva, Switzerland; [3] Hyperion Hybrid Imaging Systems GmbH, Aachen, Germany; [4] University of Milano-Bicocca, Milan, Italy

This work is sponsored by the BMFTR, contract numbers 13GW0609A, 13GW0609B, 13GW0621A and 13GW0621B. Part of this work was performed in the framework of Crystal Clear Collaboration.

Abstract

The HD-MetaPET project is developing a high-resolution positron emission tomography insert for simultaneous magnetic resonance imaging. The insert will consist of 120 Hyperion Visor Max detector tiles with an area of 56.5 x 56.5 mm^2, arranged in two semi-circles and coupled to LYSO:Ce crystal scintillators. A crucial optimisation parameter for the upcoming system performance is the crystal topology. This study evaluates Time-of-Flight and Depth-of-Interaction positioning performance across several crystal topologies: continuous slabs, pseudoslabs, and pixelated arrays with a light guide coupled to the face opposite the photosensitive detector. The study utilizes the Hyperion Visor Max and a custom development board, both featuring the TOFPET2 ASIC. Experimental measurements are performed using a ^{22}Na point source. The preliminary results with crystals of different materials show that pixelated arrays with light guides outperform continuous slabs. Specifically, pixelated designs achieved a Coincidence Time Resolution of ≈235 ps, compared to >400 ps for the slabs. The results indicate that the pixelated designs utilizing the light guide also demonstrated superior accuracy in the evaluation of the Depth-of-Interaction. The pixelated light-guide topology shows promising performance, circumventing the traditional compromise between spatial depth accuracy and timing resolution. Consequently, this configuration emerges as a good candidate for integration into the upcoming HD-MetaPET scanner. While these preliminary results are promising, the comprehensive evaluations utilizing final-scale crystals of the same material and the final scanner electronics will be presented at the conference.

References

[1] Pizzichemi, Marco, 2019, 'On light sharing TOF-PET modules with depth of interaction and 157 ps FWHM coincidence time resolution', *Physics in Medicine & Biology*, Vol. 64, No. 15, 155008

[2] Terragni, Giulia, 2025, 'Exploring the performance of a DOI-capable TOF-PET module using different SiPMs, customized and commercial readout electronics', *Physics in Medicine & Biology*, Vol. 70, No. 2, 025015

[3] Mueller, Florian, 2022, 'A Semi-Monolithic Detector providing intrinsic DOI-encoding and sub-200 ps CRT TOF-Capabilities for Clinical PET Applications', *Medical Physics*, Vol. 49, No. 12, 7469–7488

[4] Cucurella, Neus, 2025, 'Single-Ended Readout PET Detector Based on Pixelated Crystals With TOF and DOI Capabilities', *IEEE Transactions on Radiation and Plasma Medical Sciences*, Vol. 9, No. 7, 866-871

M-LT-05-05

Noise-Robust Bayesian Parameter Estimation of Two-Tissue Compartment Kinetic Model for dynamic SPECT imaging (#1051)

Dandan Zhang[1], Hui Liu[2], Jingjing Qin[1], Yufan Gu[3], Wei Fang[3], Lei Wang[3], Jing Wu[1]

[1] Beijing Normal University, School of Physics and Astronomy, Beijing, China; [2] Tsinghua University, Department of Engineering Physics, Beijing, China; [3] Fuwai Hospital, Chinese Academy of Medical Sciences & Peking Union Medical College/National Center for Cardiovascular Diseases, Department of Nuclear Medicine, Beijing, China

This study was supported by National Natural Science Foundation of China (No. 12305379, No.12205166), Beijing Natural Science Foundation (Z220010), CIRP Open Fund of Radiation Protection Laboratories (TNMPP-2024-No.1)

Abstract

Tracer kinetic modeling using the two-tissue (2T) compartment model remains challenging in dynamic SPECT imaging, particularly under realistic noise conditions. In this study, we propose a noise-robust Bayesian parameter estimation method that incorporates physiological prior information for the 2T model in dynamic SPECT imaging. To validate the proposed method, we conducted both simulation study and dynamic ^{99m}Tc-4BOH clinical study. The proposed method was compared with the conventional nonlinear least-squares (NLS) method. In the simulation study, the proposed method yielded lower relative bias in the estimated kinetic parameters (K_1, k_2, k_3, and k_4) than the NLS method under both low and high noise conditions. In the clinical ^{99m}Tc-4BOH study, K_1 estimated using the proposed method demonstrated significantly stronger agreement and lower relative bias with respect to head-to-head ^{13}N-NH_3 PET myocardial blood flow (MBF), which was used as the reference standard, than the NLS method. In conclusion, the proposed method substantially improved the accuracy and precision of parameter estimation for the 2T model compared with the NLS method.

References

[1] Naganawa M, Li S, Nabulsi N, Henry S, Zheng MQ, Pracitto R, Cai Z, Gao H, Kapinos M, Labaree D, Matuskey D, Huang Y, Carson RE, 'First-in-Human Evaluation of ^{18}F-SynVesT-1, a Radioligand for PET Imaging of Synaptic Vesicle Glycoprotein 2A, J Nucl Med, 2021, 62(4): 561-567.

[2] Dandan Z, Yufan G, Hui L, Ding D, Jing Q, Wei F, Lei W, Jing W . Pharmacokinetic modelling of dynamic ^{99m}Tc-4BOH SPECT for myocardial perfusion imaging in patients with coronary artery disease. J Nucl Cardiol, 2025, 21: 102570.

M-LT-05-06

Conditional Flow-Matching-based Kinetic Refinement for Low-Count SRTM-based Parametric Imaging in Dynamic PET (#1873)

Yu Jin Seol[1,2], **Yu Jin Seol**[1,2], Seung Kwan Kang[3], Seung Kwan Kang[3], Eui Tae Kim[4], Eui Tae Kim[4], Jae Sung Lee[1,2], Jae Sung Lee[1,2]

[1] Seoul national university, Interdisciplinary Program in Bioengineering, Seoul, South Korea; [2] Seoul national university, Integrated Major in Innovative Medical Science, Seoul, South Korea; [3] Samsung Ventures, Seoul, South Korea; [4] Seoul National University Bundang Hospital, Department of Psychiatry, Seoul, South Korea

Abstract

We propose a kinetic-consistent conditional flow matching framework for dynamic *[11C* raclopride PET SRTM parametric imaging. Conventional indirect SRTM fitting is vulnerable to frame-wise count noise, causing unstable voxel-wise *R1* , *k2* , and *BPND* maps. Using 105 scans from 35 subjects, count-reduced datasets were generated at 50%, 25%, and 10% of the original counts. The model refines reduced-count indirect SRTM estimates toward full-count SRTM pseudo-reference maps using kinetic consistency, count/noise conditioning, and physiological constraints, reducing *BPND* deviation, high-percentile errors, and kinetic-parameter disagreement compared with indirect SRTM and denoising and regularization-based baselines

References

[1] Lammertsma, AA & Hume, SP 1996, 'Simplified reference tissue model for PET receptor studies', *NeuroImage*, vol. 4, no. 3 Pt 1, pp. 153–158, publisher/place of publication not specified.

[2] Zhou, Y, Endres, CJ, Brasic, JR, Huang, S-C & Wong, DF 2003, 'Linear regression with spatial constraint to generate parametric images of ligand-receptor dynamic PET studies with a simplified reference tissue model', *NeuroImage*, vol. 18, no. 4, pp. 975–989, publisher/place of publication not specified.

[3] Lipman, Y, Chen, RTQ, Ben-Hamu, H, Nickel, M & Le, M 2022, 'Flow matching for generative modeling', *arXiv preprint*, arXiv:2210.02747, publisher/place of publication not specified.

M-LT-05-07

Attenuation Images from Time-of-Flight PET for Metal Artifact Reduction: A Phantom Study (#1406)

Finn L. Peltzer[1,2], **Ann-Kristin Lüvelsmeyer**[1,3], Claus M. Bäcker[1,2], Jörg Wulff[1,2], Mohammadreza Teimoorisichani[4], Walter Jentzen[5], Beate Timmermann[1,6], Christian Bäumer[1,3]

[1] University Medicine of Essen, West German Proton Therapy Centre Essen, Essen, Germany; [2] University Medicine of Essen, West German Cancer Centre Essen, Essen, Germany; [3] TU Dortmund University, Physics, Dortmund, Germany; [4] Siemens Medical Solutions USA Inc., Knoxville, USA; [5] University Medicine of Essen, Clinic for Nuclear Medicine, Essen, Germany; [6] University Medicine of Essen, Department of Particle Therapy, Essen, Germany; [7] German Cancer Consortium, Heidelberg, Germany

This study was supported by the German Research Foundation (DFG) under grant number 525659135.

Abstract

Metal implants can degrade CT image quality and introduce artifacts that affect dose calculation in particle therapy. This study investigates attenuation images (μ-MLAA) reconstructed from time-of-flight PET data using maximum-likelihood reconstruction of attenuation and activity for metal artifact reduction. The linearity of a calibration curve relating CT number to relative electron density was first evaluated using a PMMA phantom with metal and tissue-equivalent inserts. Metal artifacts were then studied in a water phantom containing a Ti6Al4V total endoprosthesis (TEP) implant. μ-MLAA attenuation images reconstructed from PET list mode data and CT images reconstructed using iterative metal artifact reduction (iMAR) were evaluated using gamma index analysis (10%, 1 mm) relative to an artifact-free reference slice. The calibration curve remained linear in the presence of metal inserts ($R^2 > 0.999$). For the TEP phantom, μ-MLAA images achieved a higher gamma pass rate (96.3%) than iMAR CT (70.8%). Using the calibration curve, the relative electron density of the TEP shaft was estimated as $n_{e,rel} = 3.58 \pm 0.12$ corresponding to a 3.5% deviation from reported reference values. These results indicate the potential of μ-MLAA images for reducing metal artifacts and supporting implant characterization in radiotherapy imaging.

References

[1] Giantsoudi, D., De Man, B., Verburg, J., Trofimov, A., Jin, Y., Wang, G., Gjesteby, L., Paganetti, H. 2017, 'Metal artifacts in computed tomography for radiation therapy planning: dosimetric effects and impact of metal artifact reduction', *Physics in Medicine & Biology*, 62(8), R49–R80, Bristol: IOP Publishing

[2] Defrise, M., Rezaei, A., Nuyts, J. 2012, 'Time-of-Flight PET data determine the attenuation sinogram up to a constant', *Physics in Medicine & Biology*, 57(4), 885–899, Bristol: IOP Publishing.

[3] Wang, G. 2020, 'PET-enabled dual-energy CT: image reconstruction and a proof-of-concept computer simulation study', *Physics in Medicine & Biology*, 65(24), 245028, Bristol: IOP Publishing.

[4] Teimoorisichani, M., Panin, V., Rothfuss, H., Sari, H., Rominger, A., Conti, M. 2022, 'A CT-less approach to quantitative PET imaging using the LSO intrinsic radiation for long-axial FOV PET scanners', *Medical Physics*, 49(1), 309–323, Alexandria: AAPM.

[5] Bäumer, C., Bäcker, C. M., Conti, M., Fragoso Costa, P., Hermann, K., Kazek, S. L., Jentzen, W., Panin, V., Siegel, S., Teimoorisichani, M., Wulff, J., Timmermann, B. 2021, 'Can a ToF-PET photon attenuation reconstruction test stopping-power estimations in proton therapy? A phantom study', *Physics in Medicine & Biology*, 66(21), 215010, Bristol: IOP Publishing.

M-LT-05-08

An FPGA-based data acquisition system for remote wireless radiation monitoring (#1302)

Pavan S. Guntha[3], Ethan Ingalls[2], Thomas M. Whalen[2], Mia T. Kim[2], William C.J. Hunter[1], Geoff Jones[2], Scott A. Hauck[2], **Robert S. Miyaoka**[1]

[1] University of Washington, Radiology, Seattle, USA; [2] University of Washington, Electrical Engineering, Seattle, USA; [3] Microsoft, Azure, Redmond, USA; [4] University of Washington, Department of Radiology, Seattle, USA

This work was supported by NIH R01CA287205-01

Abstract

Purpose: We are developing a Personalized Remote Radiation Tracking Portable Organ Dosimetry Device (PRRT PODD) for at-home monitoring of patients receiving radiopharmaceutical therapy (RPT). We report on an FPGA-based data acquisition system capable of wireless communication in support of this goal.
Methods: Our acquisition system supports16-radiation detectors and outputs an energy histogram for each using a time-over-threshold (ToT) energy measurement. The electronics consists of a custom analog board that converts each detector's analog signal into a digital ToT signal; an FPGA board for signal processing; and a microcontroller board that serves as the system controller. The microcontroller communicates with the FPGA via UART to retrieve energy histogram data, manages system configuration parameters, and provides Bluetooth Low Energy connectivity to a mobile Android app. The electronics fits within the PODD's base assembly and can operate on cell phone battery power. Each detector has a small thermistor for individual probe temperature monitoring and to characterize MPPC gain versus temperature. An Android app was developed to control data acquisition and wireless transfer of data to a remote workstation. The detector and electronics acqusition system was tested using Tc-99m, Na-22 and Lu-177 radioactive sources at clinically relevant counting rates.
Results: Sixteen channel operation of our FPGA-based data acquisition system has been validated using a variety of radionuclides. The output properties of the probes have been characterized versus temperature to enable post acquisition normalization of signals.
Conclusion and future work: A compact, wireless 16-channel gamma spectroscopy system for remote monitoring of Lu-177 RTP was designed and tested. Future work includes implementing real-time temperature compensation based on continuous temperature readings, ensuring stable operation without post-processing.

M-LT-05-09

Energy-Shifting: an efficient approach for Monte Carlo Particle Therapy Dose Calculation (#3092)

Chi-Hieu Pham[1], Didier Benoit[1], Vincent Bourbonne[1,2], Ulrike Schick[1,2], Dimitris Visvikis[1], Julien Bert[1]

[1] University of Brest, LaTIM, INSERM-UMR1101, Brest, France; [2] Brest Hospital University, Radiotherapy Department, Brest, France

Abstract
While recent deep learning techniques for accelerating Monte Carlo (MC) radiotherapy dose calculation have shown promising results, most state-of-the-art methods rely on a denoising paradigm. This approach aims to predict a high-sampling (HS) reference dose map from a fast low-sampling (LS) input. However, information loss and stochastic noise in LS inputs often limit the accurate recovery of fine structural details and dose gradients, and may lead to hallucinations. To address these limitations, we propose a novel learning framework, Energy-Shifting, which reconstructs a time-intensive polyenergetic HS dose distribution from a GPU-accelerated monoenergetic dose map. Our results demonstrate that this method significantly outperforms conventional denoising approaches in accuracy.

M-LT-05-10

Treatment Monitoring System for Proton Therapy Based on Beam Range Measurement (#1067)

SeHyun Jang[1], Jaeho Cho[1], Goeun Lee[1], Taehyeon Eom[1], Junyoung Lee[1], Jong Hwi Jeong[2], Sung Hun Kim[2], Sungkoo Cho[3], Kwanghyun Jo[3], Chan Hyeong Kim[1]

[1] Hanyang University, Nuclear Engineering, Seoul, South Korea; [2] National Cancer Center, Proton Therapy Center, Goyang, South Korea; [3] Samsung Medical Center, Department of Radiation Oncology, Seoul, South Korea

Abstract

In proton therapy, range uncertainties can result in insufficient dose delivery to the tumor or unintended dose delivery to organs at risk (OARs). To address this, several range verification methods have been investigated, and prompt gamma imaging is considered a promising method due to the strong correlation between the dose profile and prompt gamma distribution at the distal dose fall-off location. Based on prompt gamma imaging, a treatment monitoring system was developed to measure the in vivo beam range and detect range shifts during the treatment. The developed system consists of a 72-slit parallel collimator, 144 CsI(Tl) scintillation detectors, a dedicated field-programmable gate array (FPGA)-based data acquisition (DAQ) system, and a dedicated program with a graphical user interface (GUI). The DAQ system calculates pulse height and timing of each signal from 144 detectors. The dedicated program reconstructs 1D prompt gamma distribution using pulse data and determines the beam range of each spot using a dedicated range estimation algorithm [1]. The system's performance was evaluated using a clinical proton beam prescribed to deliver 0.5 Gy to a spherical clinical target volume (CTV) with 50 mm diameter in a homogeneous PMMA phantom. To evaluate range shift detection performance, range shifts were induced at both the global range shift (1–10 mm) and local range shift (5 and 10 mm) conditions. At the same time, the computation time for range deviation analysis was evaluated. The system detected global range shifts with an accuracy of 1 mm and identified the presence and location of local range shifts exceeding 5 mm. Furthermore, the time required for range deviation analysis per layer was found much shorter than energy layer switching time. These results demonstrate the system can verify the in vivo beam range during treatment in clinical practice.

References

[1] Ku, Y, Jung, J, and Kim, CH 2022, 'New algorithm to estimate proton beam range for multi-slit prompt-gamma camera', *Nucl. Eng. Technol.*, vol. 54, no. 9, pp. 3422-3428, South Korea: Elsevier.

Time:
13 November, 2026
12:45 – 13:05

Room:
MANUEL DE FALLA

M-LT-06 | Signal and Data Processing, New Concepts and Emerging Applications

Chairs:
Joyita Dutta (Amherst)

M-LT-06-01

Development of a Dual-Modality Imaging Capsule for Laparoscopic Radio-Guided Surgery (#2174)

Krishan Patel[1], Lorenzo Confalonieri[1], Susie Huh[2], Matthew Wilson[3], Diana Caprotti[3], Naruhiko Ikoma[4], Elena M. Zannoni[1,5]

[1] The University of Texas at Austin, Walker Department of Mechanical Engineering, Austin, USA; [2] The University of Texas at Austin, Department of Biomedical Engineering, Austin, USA; [3] Rutherford Appleton Laboratory, Science and Technology Facilities Council, Didcot, UK; [4] MD Anderson Cancer Center, Department of Surgical Oncology, Houston, USA; [5] The University of Texas at Austin, Department of Diagnostic Medicine, Austin, USA

We thank the Cancer Prevention & Research Institute of Texas (grant # RP240462) and the 2024 Mitzi & William Blahd MD Pilot Research Grant, The Education and Research Foundation for their generous support.

Abstract

Minimally-invasive radio-guided surgery requires simultaneous functional nuclear guidance and anatomical visualization to enable precise intraoperative localization of radiolabeled targets [1]. We propose a dual-modality imaging drop-in capsule designed for deployment through a standard 15-mm laparoscopic trocar. It consists of a 2-mm thick semiconductor detector with a sub-millimeter pixel pitch [2,3], a custom lofthole collimator embedded within a 3D-printed tungsten capsule, and two miniaturized stereoscopic micro-cameras.

Preliminary results show: real-time 3D depth maps validated against an ultrasonic distance sensor; a seamless 360° panoramic view stitched from sequential frames using cylindrical warping and multi-band Laplacian blending [4,5]; spectral localization of multiple isotopes ^{57}Co and ^{241}Am within a scattering biological medium; and a preliminary 2D co-registration overlaying the functional dataset onto the anatomical scene. We will present the system design and components, and discuss the steps towards a fully integrated prototype for laparoscopic radio-guided surgery.

References

[1] I. Boekestijn et al., “The current status and future prospects for molecular imaging-guided precision surgery,” Cancer Imaging, vol. 22, Art. no. 48, 2022.

[2] R. Ballabriga, M. Campbell, and X. Llopart, “An introduction to the Medipix family ASICs,” Radiat. Meas., vol. 136, Art. no. 106271, 2020.

[3] L. Jones, P. Seller, M. Wilson, and A. Hardie, “HEXITEC ASIC—a pixellated readout chip for CZT detectors,” Nucl. Instrum. Methods Phys. Res. A, vol. 604, no. 1–2, pp. 34–37, 2009.

[4] M. Brown and D. G. Lowe, “Automatic panoramic image stitching using invariant features,” Int. J. Comput. Vis., vol. 74, no. 1, pp. 59–73, 2007.

[5] R. Szeliski, “Image alignment and stitching: A tutorial,” Found. Trends Comput. Graph. Vis., vol. 2, no. 1, pp. 1–104, 2006.

M-LT-06-02

Development of a High Sensitivity Cascade Gamma Photon Coincidence Imaging System (#2224)

Qingyang Wei[1], Yangyang Zhao[1,2], Kui Wang[1], Zijun Yan[1], Shuyu Xu[1], Xiangbao Zhou[1], Jiaxin Dang[1], Hao Jia[3], Hanshen Ye[4], Zhongbin Hang[5], Wenjie Huang[2], Zheng Gu[2], Hui Liu[6], Jing Wu[4], Yaqiang Liu[6], Zuoxiang He[5]

[1] University of Science and Technology Beijing, Beijing Engineering Research Center of Industrial Spectrum Imaging, School of Automation and Electrical Engineering, Beijing, China; [2] Shenzhen Bay Laboratory, Institute of Biomedical Engineering, Shenzhen, China; [3] Tsinghua University, School of Biomedical Engineering, Beijing, China; [4] Beijing Normal University, Center for Advanced Quantum Studies, School of Physics and Astronomy, Beijing, China; [5] Beijing Tsinghua Changgung Hospital, Department of Nuclear Medicine, Beijing, China; [6] Tsinghua University, Department of Engineering Physics, Beijing, China

This work was supported in part by the National Key Research and Development Program of China under Grant 2022YFC2402001, National Natural Science Foundation of China (Grant Number:12375337) and Beijing Natural Science Foundation (Grant Number: L232126).

Abstract

Lutetium-177 (^{177}Lu) is one of the most representative radionuclides in integrated nuclear medicine theranostics. To image ^{177}Lu, we have developed a full-ring, high-sensitivity cascade gamma photon coincidence imaging system. This work presents the system construction and preliminary performance evaluation.

The detector ring consists of 40 continuous $LaBr_3$ crystal modules arranged in 10 radial × 4 axial configuration (each 50 × 50 × 6 mm³). The inner diameter of the ring is 110 mm, with axial module spacing of 60 mm. Each crystal is coupled to four MPPC arrays and read out via PETsys FEM256 electronics, with three FEB/D boards and one DAQ for data acquisition. Both the ASICs and MPPCs are cooled by a water-cooling system, maintaining water at 8 °C and ASIC temperature below 20 °C.

The collimator assembly comprises 10 tungsten plates (26 × 128 × 8 mm³), each covering four axial detector modules. Plates are arranged alternately with pinholes and slits (1 mm), placed at a vertical distance of 36.5 mm from the ring center, creating an imaging field of Φ30 × 30 mm. The prototype hardware has been fully assembled and is capable of normal data acquisition.

Simulation results indicate a coincidence sensitivity of 2.97 × 10^{-5} at the central field of view, spatial resolution of ~1.7 mm, and hot cylindrical object resolution up to 1.2 mm. Preliminary experimental tests have validated the feasibility of the system. Ongoing optimization includes crystal position calibration, energy resolution improvement, and collimator geometry alignment. The full system performance evaluation is expected to be completed before the upcoming conference.

References

[1] Liu X, Liu H, Cheng L, et al. A 3-dimensional stationary cascade gamma-ray coincidence imager. Physics in Medicine & Biology. 2021 66(22):225001

[2] Xu S , Wei Q, Ding D, et al. *Cascade Gamma Photon Coincidence Imaging System: a Simulation Study*. IEEE NSS/MIC RTSD, 2023

[3] Zhao Y, Zhou X, Huang W, et al. Performance Evaluation of a TOFPET2 ASIC-Readout $LaBr_3$(Ce) Monolithic Detector for Cascade Gamma-Ray Coincidence Imaging System. IEEE NSS/MIC RTSD, 2025

[4] Jia H, et al. Multi-GPU-Based Ultra-Fast and High-Precision Reconstruction Algorithm for a Full-Ring Cascade γ Coincidence Imaging System,IEEE NSS/MIC RTSD, 2025

M-LT-06-03

Quantum entanglement of annihilation photons as a function of the annihilation mechanism (#2454)

Deepak Kumar[1,2], Sushil Sharma[1,2], Pawel Moskal[1,2]

[1] Jagiellonian University, Faculty of Physics, Astronomy and Applied Computer Science, Krakow, Poland; [2] Jagiellonian University, Center of Theranostics, Krakow, Poland

Supported by the National Science Centre of Poland (grants no. 2021/42/A/ST2/00423, 2021/43/B/ST2/02150, 2023/50/E/ST2/00574, 2024/53/N/ST2/04279) and ERC Advanced Grant No. 101199807. Computing resources were provided by PLGrid, Grant no. PLG/2024/017688 and PLG/2025/018762.

Abstract

In matter, a positron annihilates with an electron into two photons through several mechanisms, including direct annihilation and the formation of positronium, a metastable bound state that exists as either para-positronium or ortho-positronium. Each channel has a characteristic lifetime, allowing their contributions to be distinguished in time. The two photons are predicted to be entangled in their polarizations [1], and recent measurements indicate that the degree of entanglement depends on the annihilation channel [2]. In particular, the ortho-positronium decay is sensitive to the local concentration of molecular oxygen, and can serve as a probe of tissue hypoxia in PET imaging [3]. The Jagiellonian Positron Emission Tomograph is a scanner built from plastic scintillators, in which 511 keV photons interact predominantly through Compton scattering [4]. The Compton scattering plane of each photon is correlated with its polarization. We measure annihilations of positrons emitted by a sodium-22 source embedded in porous polymer. Sodium-22 emits a positron accompanied by a 1274 keV prompt photon, which provides a time reference for the positron lifetime. The polarization correlation distribution of the annihilation photon pairs is consistent with quantum entanglement, between the limits for maximally entangled and classically separable states [2]. Selecting events by positron lifetime reveals distinct polarization correlation distributions for different annihilation channels. A detailed comparison will be presented at the conference. These results motivate quantum-informed PET imaging, with tissue hypoxia as a clinical biomarker.

References

[1] Pryce, M.L.H., Ward, J. C. 1947,'Angular correlation effects with annihilation radiation', Nature, vol. 160, p. 435.

[2] Moskal, P. et al. 2025, 'Nonmaximal entanglement of photons from positron-electron annihilation demonstrated using a novel plastic PET scanner', Sci. Adv., vol. 11, no. 18, eads3046.

[3] Moskal, P. 2026, 'Quantum Entanglement Degree, Mean Positronium Lifetime, and the 3γ/2γ Annihilation-Rate Ratio as Novel PET Biomarkers for Hypoxia – Concept, Challenges, and Predictions', Bio-Algorithms and Med-Systems, vol. 22, no. 1, p. 56.

[4] Moskal, P. et al. 2024, 'Positronium image of the human brain in vivo', Science Advances, vol. 10, no. 37, p. eadp2840.

M-LT-06-04

First In-Vivo Positronium Ratio Imaging (PRI) using F-18 FDG: A Preliminary Study with Phantom and a Mouse Model (#2615)

Macoto Fujimoto[1], Koki Nakamura[2], Riku Sato[1], Peter Caradonna[2], Ayaka Ostuka[1], Seiichi Ohta[1], Mizuki Uenomachi[3], Laura Stephenson[4], Archie Montgomery[4], Daniel P. Watts[4], Kenji Shimazoe[1,2]

[1] The University of Tokyo, Department of Bioengineering, Bunkyo, Japan; [2] The University of Tokyo, Department of Nuclear Engineering and Management, Bunkyo, Japan; [3] Institute of Science Tokyo, Laboratory for Zero-Carbon Energy, Meguro, Japan; [4] University of York, School of Physics, Engineering and Technology, York, UK

Abstract

This research presents the development and first in-vivo demonstration of Positronium Ratio Imaging, a novel functional imaging technique that uses the three-photon to two-photon decay ratio of positronium. While conventional Positron Emission Tomography primarily maps radiopharmaceutical distribution, Positronium Ratio Imaging provides insights into the tissue microenvironment by exploiting the sensitivity of ortho-positronium to local oxygen levels and morphology. We characterized the system's geometric stability using a four-rod phantom with varying dimensions and evaluated the results against Monte Carlo simulations using the Geant4 toolkit. The phantom study identified a size-dependent uncertainty baseline of approximately twenty percent, primarily arising from detector sensitivity and geometric factors. Furthermore, we achieved the first in-vivo ratio imaging using a tumor-bearing mouse model administered with fluorine-18 fluorodeoxyglucose. Quantitative analysis revealed that the three-photon to two-photon ratio in brown adipose tissue was approximately two and a half times higher than in the heart and bladder. This significant contrast is consistent with theoretical trends derived from tissue-specific positronium lifetimes and far exceeds the established hardware-induced uncertainty. These findings validate the feasibility of using standard positron emitters for functional three-photon imaging without the need for specialized prompt-gamma emitters. Future work will focus on refining quantitative calculation methods, evaluating signal-to-noise ratios, and implementing hardware-specific calibrations to enhance absolute quantification. This technology lays a foundation for clinical applications such as the non-invasive visualization of tumor hypoxia and metabolic characterization of the tissue microenvironment, offering a breakthrough in functional molecular imaging.

References

[1] Moskal, P, et al. 2019, ‘Feasibility study of the positronium imaging with the J-PET tomograph’, Phys. Med. Biol., vol. 64, no. 5, 055017, Bristol: IOP Publishing.

[2] Mercolli, L, et al. 2024, ‘In Vivo Positronium Lifetime Measurements with Intravenous Tracer Administration and a Long Axial Field-of-View PET/CT’ (Preprint)

[3] Moskal, P, et al. 2024, ‘Positronium image of the human brain in vivo’, Sci. Adv., vol. 10, no. 2, eadj2840, Washington, D.C.: American Association for the Advancement of Science.

[4] Fujimoto, M, Shimazoe, K, et al. 2025, ‘Advancing PET through Direct Imaging of Three-Photon Decay using Pure Positron Emitters’, Communications Physics (Under Review), (Preprint)

M-LT-06-05

Quantitative 4D PET Imaging of Photosynthate Transport and Rhizosphere Carbon Partitioning in Intact Plant–Soil Systems (#3049)

Muhammad Nasir Ullah[1], Daniel Hastings[2], David Anders[1], Weixin Cheng[2], Shiva Abbaszadeh[3], Craig S. Levin[4,1]

[1] Stanford University, Department of Radiology and Molecular Imaging Program at Stanford ((MIPS)), stanford, USA; [2] University of California Santa Cruz, Department of Environmental Studies, Santa Cruz, USA; [3] University of California Santa Cruz, Electrical and Computer Engineering, Santa Cruz, USA; [4] Stanford University, Departments Physics, Electrical Engineering, and Bioengineering, Stanford, USA

This work was supported by the U.S. Department of Energy, Office of Science, Office of Biological & Environmental Research, under Award Numbers DE-SC0021975 and DE-SC0024712. The authors also acknowledge the Stanford Cyclotron Research Facility and UCSC Greenhouse Facilities for technical support and Ricky Padmore for assistance with the plant growth apparatus

Abstract

We present quantitative 4D PET imaging of photosynthate carbon transport and rhizosphere exudation in intact Phaseolus vulgaris plant–soil systems using the R-PET (Rhizo-PET) scanner with the ^{11}C radiotracer ($t_1/_2$ = 20.3 min). Across N = 6 plants, time–activity curves (TACs) extracted from 225 cross-pattern ROIs per dataset—spanning 3 roots × 3 axial depths × ±3 mm radial extent—reveal a reproducible source-to-sink carbon allocation hierarchy: upper root zones receive ≈50% of total plant carbon, while root 2 (primary taproot) dominates at 20.8 ± 6.3%. Time-to-peak (TTP) increases from 31.5±4.4 min (upper) to 48.0±13.1 min (lower root 2), corresponding to a phloem transport velocity of ≈2.4 mm min^{-1}. Rhizosphere carbon exudation follows an exponential decay AUC(r) = A e^{-kr} with k = 0.10–0.20 mm^{-1}, placing the active deposition zone within 4–14 mm of the root surface—the first spatially resolved 3D+t measurement of this process in intact soil.

References
[1] M. N. Ullah et al., “Quantitative Assessment of Imaging Performance of Rhizo-PET (R-PET): A PET Scanner Dedicated to Dynamic Plant Rhizosphere Imaging,” 2025 IEEE NSS MIC RTSD, pp. 1–2, 2025.
[2] M. N. Ullah et al., “Rhizo-PET: A Dedicated PET System for 4D Imaging of Carbon Dynamics in the Rhizosphere,” bioRxiv, 2026.
[3] M. Knoblauch et al., “Sieve elements in intact, unmanipulated phloem,” Plant Cell, vol. 28, pp. 2462–2474, 2016.
[4] S. Jahnke et al., “Combined 64Cu-PET/MR imaging of plants,” Plant J., vol. 59, pp. 634–644, 2009
[5] N. Kawachi et al., “Carbon-11 imaging of photosynthate transport in plants,” Plant Cell Physiol., vol. 52, pp. 333–342, 2011.
[6] T. Alexander et al., “Non-invasive imaging of 11C in plant stems,” New Phytol., vol. 196, pp. 366–375, 2012.e’, Journal, Edition, Page, Place of publication: publishers

M-LT-06-06

Comparative Evaluation of Respiratory Motion Correction Methods for Upright Walk-Through PET Using XCAT Simulations (#1444)

Rabia Aziz[1], Thibault D'Hulster[1], Jens Maebe[1], Christian Vanhove[1], Sun Tao[2], Stefaan Vandenberghe[1]

[1] University of Ghent, Institute of Biomedical Engineering, Ghent, Belgium; [2] Shenzhen Institute of Advanced Technology, Chinese Academy of Sciences, Shenzhen, China

Supported by the Research Foundation – Flanders (FWO) through a long-stay grant (File number: V402926N).

Abstract

Walk-through positron emission tomography (WT-PET) is an emerging upright imaging geometry based on two vertically opposing flat detector panels. Although this design may improve patient comfort and acquisition efficiency, respiratory motion remains a major source of image degradation. This study evaluates respiratory motion correction strategies for WT-PET using XCAT anthropomorphic simulations. A 30s acquisition was simulated in a WT-PET geometry and reconstructed using an in-house MLEM-based algorithm. Data-driven amplitude- and phase-based respiratory gating were followed by non-rigid motion correction using Advanced Normalization Tools (ANTs) and Fast Algorithms for Motion Correction (FALCON). Overlapping-frame reconstruction using 0.9375s windows shifted every 0.3125s was also evaluated to assess the effect of temporal smoothing. Performance was quantified against a motion-free reference using normalized root mean square error (NRMSE), diaphragm edge width, and line profile analysis. ANTs phase-based 4-gate correction achieved the best performance, reducing NRMSE from 64% to 6% and restoring the diaphragm edge width to the motion-free reference level (25.10 mm vs. 25.79 mm). FALCON phase-based 4-gate correction reduced NRMSE to 12% but showed limited recovery of diaphragm sharpness, with an edge width of 28.40 mm compared with 28.62 mm for no motion correction. Overlapping-frame ANTs correction reduced NRMSE to 15% and yielded an intermediate edge width of 27.13 mm, although line profiles indicated residual local displacement and smoothing. These findings show that data-driven respiratory gating combined with deformable registration can substantially improve image quality in upright WT-PET.

References

[1] S. Vandenberghe *et al.*, "Walk-through flat panel total-body PET: a patient-centered design for high throughput imaging at lower cost using DOI-capable high-resolution monolithic detectors," *EJNMMI*, 2023.

[2] R. Aziz *et al.*, "Quantitative analysis of patient motion in walk-through PET scanner and standard axial field of view PET scanner using infrared-based tracking," *EJNMMI Phys.*, 2024.

[3] M. D. Walker *et al.*, "Data-driven respiratory gating outperforms device-based gating for clinical 18F-FDG PET/CT," *Journal of Nuclear Medicine*, 2020.

[4] A. H. Dias *et al.*, "Validation and clinical impact of motion-free PET imaging using data-driven respiratory gating and elastic PET-CT registration," *EJNMMI*, 2024.

[5] N. J. Tustison *et al.*, "The ANTsX ecosystem for quantitative biological and medical imaging," *Sci. Rep.*, 2021.

[6] L. K. Shiyam Sundar *et al.*, "Fully Automated, Fast Motion Correction of Dynamic Whole-Body and Total-Body PET/CT Imaging Studies," *Journal of Nuclear Medicine*, 2023.

M-LT-06-07

Dementia Risk Estimation From a Positron Emission Tomography-Derived Latent Biomarker (#2058)

Cristóbal Vázquez García[1], Francisco J. Martínez Murcia[1], Javier Ramírez Pérez de Inestrosa[1], Fermín Segovia Román[1], Anabel Forte Deltell[2], Ignacio Álvarez Illán[1], Alejandro Hernández Segura[1], Carmen Jiménez-Mesa[3], Juan Manuel Górriz Sáez[1]

[1] University of Granada, Department of Signal Processing and Biomedical Applications, Granada, Spain; [2] University of Valencia, Department of Statistics and Operations Research, Valencia, Spain; [3] University of Málaga, Department of Communication Engineering, Málaga, Spain

This publication is part of the projects PID2022-137629OA-I00 and PID2022-137451OB-I00 funded by MICIU/AEI/10.13039/501100011033 and by ERDF/EU, and the C-ING-183-UGR23 project, cofunded by the Consejería de Universidad, Investigación e Innovación and by European Union, funded by Programa FEDER Andalucía 2021–2027. F.J.M.M. received support from grant RYC2021-030875-I, funded by MICIU/AEI/10.13039/501100011033 and European Union NextGener-ationEU/PRTR.
Data collection and sharing for the ADNI is funded by the National Institute on Aging (National Institutes of Health Grant U19AG024904).

Abstract
We investigated whether a positron emission tomography-derived latent biomarker can serve as a compact prognostic signal after longitudinal modeling. The study used 3,458 scans from 1,624 participants in the Alzheimer's Disease Neuroimaging Initiative. A Bayesian mixed-effects model was fitted to the biomarker trajectory and evaluated in two practical settings: forecasting future visits for previously observed subjects and estimating short-term dementia risk from predicted biomarker values. For subjects already observed during training, future visits were predicted with a mean root mean squared error of 0.298 and a mean absolute error of 0.250. For entirely new subjects, a change-from-baseline formulation reduced prediction error to a mean root mean squared error of 0.217 and a mean absolute error of 0.171 after an initial scan. A training-only logistic calibration applied to held-out predictions reached an area under the receiver operating characteristic curve of 0.826 for future dementia risk estimation. These results suggest that the latent biomarker can move beyond representation learning and support short-term longitudinal forecasting and clinically interpretable risk stratification.

M-LT-06-08

Data-Driven Selection of Representative Motion Models for Simulation in Dynamic Cardiac PET (#2952)

Nader Nemati[1], **Nader Nemati**[1], Oona Rainio[1], Oona Rainio[1], Santeri Palonen[1], Santeri Palonen[1], Eero Lehtonen[1,3], Eero Lehtonen[1,3], Teemu Maaniitty[1,2], Teemu Maaniitty[1,2], Jarmo Teuho[1], Jarmo Teuho[1], Jouni Tuisku[1], Jouni Tuisku[1], Muhammad Irfan[1], Muhammad Irfan[1], Nicole Miller[1], Nicole Miller[1], Lauri Nummenmaa[1], Lauri Nummenmaa[1], Juhani Knuuti[1], Juhani Knuuti[1], Riku Klén[1], Riku Klén[1]

[1] University of Turku and Turku University Hospital, Turku PET Centre, Turku, Finland; [2] Turku University Hospital, Department of Clinical Physiology, Nuclear Medicine and PET, Turku, Finland; [3] Turku University of Applied Science, ICT and Industrial Engineering, Data Engineering and AI technologies, Turku, Finland

This work was supported by the Research Council of Finland project #351482, the European Research Council (Advanced Grant #101141656), the Jane and Aatos Erkko Foundation, and the Sigrid Juselius Foundation. Jarmo Teuho reports funding from the Research Council of Finland Academy Research Fellowship grant #360120. Teemu Maaniitty reports funding from the Research Council of Finland grant #363775.

Abstract

Patient motion remains a common challenge in dynamic cardiac positron emission tomography (PET), as it degrades image quality and complicates reliable evaluation of motion correction methods. Realistic motion simulation requires motion models that capture the variability observed in clinical data, but this remains difficult when simulations rely on only a limited set of motion patterns. In this work, we propose a data driven framework for motion model selection and simulation in dynamic cardiac PET. We characterize motion trajectories using physically interpretable features and analyze them using clustering and trajectory similarity based on dynamic time warping to identify a compact set of representative motion models. These models are integrated with patient-specific motion scaling for frame-wise simulation of motion-corrupted PET data. The proposed framework produces stable normalized error levels across 1308 patient–model evaluations while using only a small number of representative motion models. The results suggest that the selected models effectively capture dominant motion behaviors observed in the dataset and enable realistic PET motion simulation.

M-LT-06-09

A Quality Control Framework for Deep Learning-based Attenuation Map Synthesis in PET (#2579)

Zhen Ji[1], Yue Li[2], Chenyao Jiang[2], Chen Sun[2], Xiong Wang[1], Yihuan Lu[2]

[1] ShanghaiTech University, School of Information Science and Technology, Shanghai, China; [2] Shanghai United Imaging Healthcare Co., LTD, Molecular Imaging Business Unit, Shanghai, China

Abstract

Deep learning-based attenuation correction (DL-AC) offers potential advantages over conventional CT-based attenuation correction (CT-AC) in PET imaging, including avoidance of additional radiation exposure and reduced susceptibility to PET–CT misalignment. However, in DL-AC application scenarios, when CT-derived attenuation maps (CT-μ) are unavailable as reference images, quality control (QC) of deep learning-derived attenuation maps (DL-μ) often relies on manual inspection. To address this limitation, we propose a patch-level 3D convolutional neural network (3D CNN) framework for automated anomaly detection and localization in DL-μ without requiring CT during inference. During training, CT-μ was used to assist patch-level annotation of DL-μ, and artifact-free CT-μ patches without observer-identified abnormalities were incorporated as normal samples to help the model learn normal attenuation patterns. During inference, only DL-μ was used, and sliding-window prediction was used to aggregate patch-level anomaly probabilities into a voxel-wise anomaly probability map. On the validation set (51 cases), the framework yielded patch-level performance with an AUC of 0.9984, an F1-score of 0.9802, a sensitivity of 97.06%, and a specificity of 98.86%. These results suggest that the proposed framework can provide spatial cues for DL-μ, potentially supporting efficient evaluation and reducing reliance on manual QC inspection.

References

[1] T. Di Noto *et al.*, "An anatomically-informed 3D CNN for brain aneurysm classification with weak labels," *arXiv preprint arXiv:2012.08645, 2020.*

[2] T.-Y. Lin, P. Goyal, R. Girshick, K. He, and P. Dollár, "Focal loss for dense object detection," in *Proc. IEEE Int. Conf. Comput. Vis. (ICCV)*, 2017, pp. 2999–3007.

M-LT-06-10

Characterizing Noise in Clinical Nuclear Medicine Modalities via Quantum-Inspired Framework (#2977)

Amirreza Hashemi, Shadi Abdar Esfahani, Pamela Silva, Anthony Sinagra, Pedram Heidari, Hamid Sabet

Harvard Medical School/Massachusetts General Hospital, Department of Radiology, Boston, USA

This work was supported in part by NIH grant R01EB034785.

Abstract
Quantum-inspired denoising is employed for clinical PET/CT, PET/MR, and SPECT imaging by treating images analogous to disordered materials and analyzing the eigenfunctions of an associated Hamiltonian. Quantum localization is quantified by the participation ratio, enabling filtering of non-localized, high-participation modes that dominate the mid-frequency range and are associated with diffusive noise. By suppressing these modes and reconstructing from the remaining localized modes, noise is reduced without training data or manual regularization. The framework is applied to 46 multi-vendor, multi-tracer patient datasets from Massachusetts General Brigham to characterize scanner-dependent noise structure and its impact on image appearance. Across the cohort, quantum-inspired filtering yields consistent decreases in blind image quality scores (PIQE and BRISQUE) together with increases in entropy and Laplacian variance, indicating lower perceived noise and enhanced structural detail in the denoised clinical images.

Time:
13 November, 2026
15:00 – 17:00

Room:
Poster Area

MIC-15 | MIC Poster Session 3

Chairs:
Georg Schramm
Charalampos Tsoumpas (Groningen)

MIC-15-003

Dual-ended Redout PET Detectors based on 0.25 mm pitch LYSO/GAGG arrays (#1104)

Jiahao Xie, Haibo Wang, Jinyi Qi, Ramsey D. Badawi, Simon R. Cherry, Junwei Du

University of California at Davis, Biomedical Engineering, Davis, USA

This work was supported by the NIH R01 EB031961.

Abstract

Spatial resolution and sensitivity are the two most critical characteristics of a positron emission tomography (PET) scanner, as they determine the accuracy and precision of reconstructed images. Achieving uniform ultra-high spatial resolution across the field of view (FOV) while maintaining **sufficient** sensitivity requires PET detectors **capable of resolving** ultra-fine, high-aspect-ratio crystals **and extracting** precise depth-of-interaction (DOI) information to mitigate parallax errors. In this study, we developed and evaluated two dual-ended readout detectors for small-animal brain PET applications. Each detector comprised a 36 × 36 array of lutetium yttrium oxyorthosilicate (LYSO) or gadolinium aluminum gallium garnet (GAGG) coupled to two linearly-graded silicon photomultipliers (LG-SiPMs). The crystal element size of the two crystal arrays was 0.20 × 0.20 × 9 mm³, while the pitch of the two crystal arrays was 0.25 mm. Despite the crystal element aspect ratio reaching 45:1, most crystal elements in both detectors were resolved, yielding average energy resolutions of 37.3 ± 5.6% and 31.7 ± 5.7%, respectively, for the LYSO and GAGG arrays, resepectively. The mean coincidence timing resolutions (CTRs) of the central 32 × 32 crystal elements, measured using a 200–1000 keV energy window to select events, were 1025 ± 40 ps (LYSO array) and 1205 ± 62 ps (GAGG array). Additionally, the average DOI resolutions across crystal elements were 1.48 ± 0.10 mm and 1.47 ± 0.10 mm, respectively, for the LYSO and GAGG arrays, respectively.

References

[1] R. S. Miyaoka and A. L. Lehnert, “Small animal PET: a review of what we have done and where we are going,” *Phys Med Biol*, vol. 65, no. 24, p. 10.1088/1361-6560/ab8f71, Dec. 2020, doi: 10.1088/1361-6560/ab8f71.

[2] J. Du and T. Jones, “Technical opportunities and challenges in developing total-body PET scanners for mice and rats,” *EJNMMI Phys*, vol. 10, no. 1, p. 2, Jan. 2023, doi: 10.1186/s40658-022-00523-6.

[3] E. Yoshida and T. Yamaya, “PET detectors with depth-of-interaction and time-of-flight capabilities,” *Radiol Phys Technol*, vol. 17, no. 3, pp. 596–609, Sep. 2024, doi: 10.1007/s12194-024-00821-x.

[4] F. Acerbi, S. Merzi, and A. Gola, “Large area tiles of position-sensitive silicon photomultipliers,” *Nuclear Instruments and Methods in Physics Research Section A: Accelerators, Spectrometers, Detectors and Associated Equipment*, vol. 1067, p. 169650, Oct. 2024, doi: 10.1016/j.nima.2024.169650.

[5] J. Xie *et al.*, “High spatial resolution PET detectors based on 10 mm × 10 mm linearly-graded SiPMs and 0.5 mm pitch LYSO arrays,” *Phys. Med. Biol.*, vol. 70, no. 2, p. 025016, Jan. 2025, doi: 10.1088/1361-6560/ada084.

MIC-15-006

Study of the response of comercial CMOS sensors to soft X-rays (#1477)

Lucía Velasco[2], Jessica Juan-Morales[2], Teresa Cebriano[1], Natividad Lara[1], José Luis Henares González[1], Juan Hernandez-Toro[1], Pablo Vicente[1], Diego De Luis[1], Eduardo Flores[1], Michael Seimetz[2], **Jon Imanol Apiñaniz Aginako**[1]

[1] Center of Pulsed Lasers (CLPU), Villamayor, Spain; [2] Instituto de Instrumentación para Imagen Molecular (I3M), CSIC-Universitat Politècnica de València, Valencia, Spain

This work has been supperted by PID2023-148992OB-C22 of the spanish Ministry of Science, Innovation and Universities and PR-084-2022 of the spanish Nuclear Security Council.

Abstract

High-repetition-rate (HRR) operation is a key limitation in laser-driven particle and photon sources, requiring diagnostics compatible with repetition rates of order 1 Hz or higher. We investigate standard industrial CMOS imaging sensors as soft X-ray detectors, analysing their single-photon response in the 5.5--12.6 keV range. The response is linear, and the sensors are calibrated in terms of generated electron--hole carriers versus incident photon energy. X-ray interactions in pixel sensors produce single-pixel (SPE) and multi-pixel events (MPE), which are analysed independently; removing MPEs significantly improves spectral resolution. This work is a first step toward the systematic study of commercial CMOS sensors under exposure to high-energy particles and photons, including response, radiation tolerance and dynamic range. Their compact size, low cost, and intrinsic compatibility with high-repetition-rate operation make them suitable for laser-plasma, nuclear and particle physics, and biomedical applications.

References

[1] H. Daido, M. Nishiuchi, and A. S. Pirozhkov, “Laser-driven ion sources,”Rep. Prog. Phys., vol. 75, no. 5, 056401, 2012.

[2] A. Macchi, M. Borghesi, and M. Passoni, “Ion acceleration in laser-plasma interaction,” Rev. Mod. Phys., vol. 85, pp. 751–793, 2013.

[3] J. Peñas, A. Alejo, A. Bembibre et al., “Production of carbon-11 for PET preclinical imaging using a high-repetition rate laser-driven proton source,” Sci. Rep., vol. 14, p. 11448, 2024.

[4] J. L. Henares, M. Ehret, J. Api˜naniz et al., “Online target normal sheath acceleration proton beam stabilization at 1 Hz in ultra-intense laser–matter interaction,” High Power Laser Sci. Eng., vol. 12, e94, 2024.

[5] C. Grupen, Particle Detectors. Berlin, Germany: Springer, 2008

[6] J. R. Janesick, T. Elliott, S. Collins, M. M. Blouke, and J. Freeman, “Scientific charge-coupled devices,” Opt. Eng., vol. 26, no. 8, 268692, 1987.

[7] D. E. Groom, “Temperature dependence of the mean number of e-h pairs per eV of X-ray energy deposit,” Lawrence Berkeley National Laboratory, Rep. LBNL-54952, 2004.

MIC-15-009

Asymmetric dual-ended readout using diode-based multiplexing circuits for TOF-DOI PET detectors (#1717)

Ruipeng Dai[1,2], Xiaolong Jiang[1,3], Xiangtao Zeng[1], Xiaoqin Zhang[1], Wenjie Huang[1], Yangyang Zhao[1], Jianlang Hua[1,3], Hang Yang[1,3], Ming Niu[1], Zheng Gu[1]

[1] Shenzhen Bay Laboratory, Institute of Biomedical Engineering, Shenzhen, China; [2] University of Science and Technology Beijing, School of Automation and Electrical Engineering, Beijing, China; [3] Harbin Institute of Technology, School of Electronics and Information Engineering, Harbin, China

This work is supported by the National Natural Science Foundation of China (Nos. 62371314 and 12275182), the National Key R&D Program of China (No. 2023YFC2414800), Guangdong Basic and Applied Basic Research Foundation (Nos. 2024A1515012154), the Guangdong Provincial Project (Grant No. 2023TQ07A233), the Major Program of Shenzhen Bay Laboratory (No. C1012530005) and the Shenzhen Bay Laboratory Proof-of Concept Grants (No. C1022430005).

Abstract

To address spatial resolution and sensitivity limitations in whole-body PET for small-organ imaging, such as heart, breast and prostate, this study developed an asymmetric dual-ended readout for TOF-DOI PET detectors.

The asymmetric readout design utilizes a 4×4 SiPM array (6×6 mm² pixels) with individual channel readout at the front end, for good timing performance . At the back end, an 8×8 SiPM array (3×3 mm² pixels) is read out using a diode-based row-column summing multiplexing circuit to facilitate event position decoding while reducing the number of readout channels. Specifically, the multiplexing scheme reduces the back end channels from 64 to 16, lowering the total channels per detector from 80 to 32. LYSO arrays with three crystal dimensions were evaluated: an 8×8 array (3.10×3.10×20 mm³ crystals), a 13×13 array (1.88×1.88×20 mm³ crystals), and a 16×16 array (1.50×1.50×20 mm³ crystals).

Detector performance was evaluated in an array-to-array coincidence setup, with two identical detector modules placed face-to-face. Flood images show all crystals in the three evaluated arrays can be clearly resolved under both non-multiplexed and multiplexed readout conditions. The average energy resolutions for the 8×8, 13×13, and 16×16 arrays are 12.49%, 11.71%, and 10.92%, respectively, which are comparable to those obtained with non-multiplexed readout . A preliminary evaluation of CTR for the 8×8 array yields 327 ps (non-multiplexed) and 365 ps (multiplexed), indicating limited timing degradation due to multiplexing.

The proposed asymmetric multiplexed readout design maintains acceptable spatial, energy, and timing resolution while substantially reducing electronic complexity . This configuration is suitable for developing cost-effective, high-performance organ-specific PET scanners . Future work will focus on optimizing the MPPC operating overvoltage and PETsys threshold settings, as well as implementing an interleaved multiplexing circuit to improve CTR performance.

References

[1] Niu M, Yang Y, Zhao Y, et al. Initial studies of high resolution PET detectors using a novel dual-ended readout for organ-dedicated imaging.2024 IEEE Nuclear Science Symposium (NSS), Medical Imaging Conference (MIC) and Room Temperature Semiconductor Detector Conference (RTSD). IEEE, 2024: 1-1.

[2] Huang S, Jiang X, Chen Z, et al. Optimization of TOF and DOI Performance in a Multi-Resolution Detector for Brain-dedicated PET. IEEE Transactions on Radiation and Plasma Medical Sciences, 2025.
[3] M Niu, X Jiang, S Huang, Z Chen, et al. A CNN-based demultiplexing method for an interleaved signal multiplexing readout with a TOF-DOI brain PET detector. IEEE Nuclear Science Symposium (NSS), Medical Imaging Conference (MIC) and Room Temperature Semiconductor Detector Conference (RTSD). IEEE, 2024.

MIC-15-012

Development of a TOF-DOI PET Detector Using Dual-ended Interleaved Multiplexing Readout (#1813)

Xiaolong Jiang[1,2], Ruipeng Dai[1], Xiaoqin Zhang[1], Hang Yang[1], Yangyang Zhao[1], Xiangtao Zeng[1], Wenjie Huang[1], Ming Niu[1], Zheng Gu[1]

[1] Shenzhen Bay Laboratory, Institute of Biomedical Engineering, Shenzhen, China; [2] Harbin Institute of Technology, School of Electronics and Information Engineering, Harbin, China

This work is supported by the National Key R&D Program of China (No. 2023YFC2414800), the National Natural Science Foundation of China (Nos. 62371314 and 12275182), Guangdong Basic and Applied Basic Research Foundation (Nos. 2024A1515012154), the Guangdong Provincial Project (Grant No. 2023TQ07A233), the Major Program of Shenzhen Bay Laboratory (No. C1012530005) and the Shenzhen Bay Laboratory Proof-of Concept Grants (No. C1022430005).

Abstract

Time-of-flight (TOF) and depth-of-interaction (DOI) information improve the spatial resolution and signal-to-noise ratio of PET imaging, but typically requires numerous readout channels, increasing system complexity and cost. In this work, we developed a TOF-DOI PET detector using a novel dual-ended interleaved multiplexing (DiMux) readout. The detector consists of an 8×8 LYSO crystal array with polished surfaces, where each crystal measures 3.1 × 3.1 × 20 mm^3 with a 3.2 mm crystal pixel pitch, and is optically isolated using $BaSO_4$ reflectors. Both ends are one-to-one coupled to 8×8 SiPM arrays and read out by two complementary interleaved multiplexing circuits, which use Schottky barrier diode-based charge division. In this approach, each crystal is encoded as a row signal on one end and a column signal on the opposite end, with multiplexed signals digitized by PETsys TOFPET2 ASICs. This dual-ended, complementary design enables accurate position decoding using a conventional center-of-gravity (CoG) method, eliminating the need for deep learning-based decoding.

Flood images with clearly resolved crystals are generated from the summed signals of both ends. The detector achieves a average DOI resolution of 2.97 mm and a coincidence time resolution (CTR) of 257 ps, which further improves to 234 ps after excluding inter-crystal scattering (ICS) events. Compared with a non-multiplexed dual-ended reference detector, the DiMux scheme reduces the number of readout channels by a factor of four while maintaining comparable TOF and DOI performance.

These results demonstrate that the DiMux readout provides a high performance, low complexity, and scalable solution for clinical PET imaging systems.

References
[1] Y. Li, *et al*, “Interleaved signal multiplexing readout in depth encoding prism-PET detectors,” Medical physics, vol. 50, no. 7, pp. 4234–4243, 2023.

[2] M. Niu *et al*, "Performance comparison of two signal multiplexing circuits using diodes with a tof-doi brain pet detector," in 2025 IEEE NSS MIC RTSD, 2025, pp. 1–1.
[3] S. Huang, *et al*, "Optimization of tof and doi performance in a multi-resolution detector for brain-dedicated pet," IEEE Transactions on Radiation and Plasma Medical Sciences, vol. 10, no. 3, pp. 380–390, 2026.
[4] H. Wang, J. Xie, and J. Du, "Development of whole-body tof-doi pet detector using dual-ended readout method," IEEE Transactions on Instrumentation and Measurement, vol. 74, pp. 1–9, 2025.

MIC-15-015

Design of a Single-Ended Readout DOI PET Detector with BGO and Deep Learning (#1952)

Sungwook Hong, Jin Ho Jung, Jiwoong Jung, Yong Choi

Sogang University, Department of Electronic Engineering, Intelligent Signal Processing System (ISPS) Laboratory, Seoul, South Korea

This research was supported by the Korea Medical Device Development Foundation Grant funded by the Ministry of Science and ICT, the Ministry of Trade, Industry and Resources, the Ministry of Health & Welfare, the Ministry of Food and Drug Safety (no. 2410019162, no. RS-2026-25540876) and by the National Research Foundation of Korea (NRF) grant funded by the Korea government (MSIT) (no. RS-2023-00280177, no. RS-2025-21682968) of the Republic of Korea.

Abstract
The purpose of this study was to design a single-ended readout PET detector with BGO providing DOI, to investigate the effects of lateral surface treatments and inter-crystal coupling conditions on detector performance, and to improve the performance using deep learning. A detector consisting of an 8 × 8 array of 3 mm × 3 mm × 20 mm BGO, each one-to-one coupled with a SiPM, was modeled using DETECT2000. Photon distributions were estimated for four detector configurations: polished + air (PA), polished + glue (PG), unpolished + air (UA), and unpolished + glue (UG). The x-, y-, and z-positions were analytically estimated using photon distribution information. To improve positioning accuracy, a deep learning model combining CNN and MLP was implemented. The CNN extracted features from photon distributions, and the MLP estimated the fine position using CNN-derived features concatenated with analytically calculated positions. The difference between the ground-truth and the estimated positions was evaluated using the mean absolute error (MAE). The accuracy of DOI estimation was assessed by evaluating the DOI identification accuracy in 20 mm long BGO divided into three equal segments. For x- and y-position estimations, the MAE values showed minimal variations (< 0.1 mm) across the four detector configurations, regardless of the estimation methods. For DOI estimation, the UA and UG achieved lower MAE (3.8 and 3.6 mm) and higher DOI identification accuracies (63% and 66%) than the other detector configurations. By applying deep learning, the MAE values for UA and UG were reduced to approximately 1 mm, and the DOI accuracies increased to 92% and 91%, respectively. These results indicate that three-level DOI identification can be achieved using photon distribution information obtained from a simple single-ended readout detector. In particular, the UA provided superior DOI estimation performance, and the incorporation of deep learning further enhanced DOI positioning accuracy.

References
[1] N. Cucarella, J. Barrio, D. Sanchez, J. M. Benlloch, and A. J. Gonzalez, “Single-ended readout PET detector based on pixelated crystals with TOF and DOI capabilities,” IEEE Trans. Radiat. Plasma Med. Sci., vol. 9, no. 7, pp. 866–871, 2025.
[2] M. Pizzichemi, G. Stringhini, T. Niknejad, Z. Liu, P. Lecoq, S. Tavernier, *et al.*, “A new method for depth of interaction determination in PET detectors,” Phys. Med. Biol., vol. 61, no. 12, pp. 4679–4698, 2016.
[3] N. Cucarella, L. Moliner, D. Sanchez, N. Pavon, C. Correcher, A. Ganzalez-Montoro, *et al.*, Detector block based on pseudo-slabs with DOI and TOF capabilities for a dedicated brain PET scanner. Presented at IEEE NSS/MIC/RTSD Conference [Online]. Available: https://ieeexplore.ieee.org/document/11287104. Accessed on: December 18, 2025.
[4] A. LaBella, P. Vaska, W. Zhao, and A. H. Goldan, “Convolutional neural network for crystal identification and gamma ray localization in PET,” IEEE Trans. Radiat. Plasma Med. Sci., vol. 4, no. 4, pp. 461–469, 2020.
[5] B. Dai, S. Krishnamoorthy, E. Morales, S. Surti, and J. S. Karp, “Depth-of-interaction encoding techniques for pixelated PET detectors enabled by machine learning methods and fast waveform digitization,” Phys. Med. Biol., vol. 70, no. 8, pp. 085009, 2025.

MIC-15-018

A pulse-train model for X-ray photon-counting scintillation detectors with pile-up (#2023)

Lukas Schröder, Dennis R. Schaart

Delft Univeristy of Technology, Radiation Science & Technology, Delft, Netherlands

Abstract

To investigate potential applications of indirect photon-counting detectors, we developed a model to simulate pulse trains with pile-up for a combination of scintillator and silicon photomultiplier (SiPM). We generated pulse trains for various input rates, and the output count rate (OCR) and the spectral degradation factor (SDF) were analyzed. This was performed for two scintillators and counting algorithms, various cut-off frequencies of the applied low-pass filter, event energy thresholds, and a mono- and a polychromatic source. The results were compared to experiments. For the OCR, the model and measurements produced very similar results for all investigated parameter combinations. While the SDF values of the simulations tended to show some differences compared to the measurements, the general trend was similar.

MIC-15-021

Monte Carlo Simulations of a Penumbra-Based Collimator-less SPECT Detector for Targeted Radionuclide Therapy Monitoring (#2115)

Iara Neves[1,2], Bryan Casanelli[2], Ana Luísa M. Silva[2], Pedro M.M. Correia[2]

[1] University of Porto, Faculty of Sciences, Porto, Portugal; [2] University of Aveiro, Institute for Nanostructures, Nanomodelling and Nanofabrication (i3N), Department of Physics (DFis), Aveiro, Portugal

This work was supported by the "la Caixa" Foundation ID CI25-10265 under the CaixaImpulse program, and by project HadronPET COMPETE2030-FEDER-00755500, funded by FEDER program and by national funds through the FCT, Portugal. It is also funded by national funds through FCT – Fundação para a Ciência e a Tecnologia, I.P., under the project UID/50025/2025 (doi.org/10.54499/UID/50025/2025), UID/PRR/50025/2025 (doi.org/10.54499/UID/PRR/50025/2025), UID/PRR2/50025/2025 (doi.org/10.54499/UID/PRR2/50025/2025) and the Associate Laboratory I3N – LA/P/0037/2020 (doi.org/10.54499/LA/P/0037/2020)

Abstract

This work investigates a collimator-less scintillator-based detector that uses penumbra maps to reconstruct the spatial origin of radioisotopes without photon losses from collimation, motivated by the need for in-vivo dosimetry monitoring during targeted radionuclide therapy (TRT) and the limitations for its broader clinical adoption. Monte Carlo simulations were performed in GATE to evaluate the method's viability, using a 218 keV mono-energetic point-like source to replicate the first gamma emission on Ac-225's decay scheme. Given its favorable photoelectric fraction for this energy, BGO was chosen as the detector's material on the simulations. Geometrical parameters such as crystal dimensions, inter-crystal spacing, and array layout were systematically varied. Results show that inter-crystal spacing significantly shapes the photon distribution pattern, the larger 0.4mm value produced a distinct visual artifact. Depth profiles vary with source position in a predictable manner and provide information regarding the radiation's penetration depth. The implemented dual-layer checkerboard geometry demonstrated complementary detection behavior between layers, improving spatial discrimination over single-layer designs. These findings support the feasibility of collimator-less gamma imaging and show that geometric optimization shapes the detector's spatial response.

References

[1] K. Ramonaheng, K. Banda, M. Qebetu, P. Goorhoo et al., "Clinical image-based dosimetry of actinium-225 in targeted alpha therapy,'' Cancers, vol. 18, no. 2, p. 321, Jan. 2026

[2] European Medicines Agency (EMA), "Xofigo (radium Ra223 dichloride): European Public Assessment Report'' EMA/H/C/002653. Accessed: May 11, 2025. Available: https://www.ema.europa.eu/en/medicines/human/EPAR/xofigo

[3] R. Eychenne, M. Chérel, F. Haddad, F. Guérard, and J.-F. Gestin, "Overview of the most promising radionuclides for targeted alpha therapy: The 'hopeful eight', Pharmaceutics vol. 13, no. 6, p. 906, Jun. 2021

[4] Y. Zhu, Z. Yu, Z. Lyu, Y. Liu, R. Yao, and T. Ma, "A collimator-less crisscrossed planar gamma scanner with a single-slim-scintillator detector'', J. Nucl. Med. vol. 64, no. suppl. 1, p. P788, 2023

[5] J. Caravaca et al., "A collimatorless detector for in vivo 225Ac tomography: A feasibility study,'' in Proc. IEEE Nucl. Sci. Symp. Med. Imaging Conf. (NSS/MIC), 2021

[6] D. Sarrut et al., "The OpenGATE ecosystem for Monte Carlo simulation in medical physics,'' Phys. Med. Biol., vol. 67, no. 18, p. 184001, Sep. 2022.

MIC-15-024

A covariance-based framework for quantifying circuit and intrinsic CTR limits in TOF-PET detectors (#2237)

Hyeongseok Shim[1,2], Guen Bae Ko[2]

[1] Korea Advanced Institute of Science and Technology, Department of Nuclear and Quantum Engineering, Daejeon, South Korea; [2] Korea Advanced Institute of Science and Technology, Mechanical Engineering Research Institute, Daejeon, South Korea

This work was supported by the National Research Foundation of Korea(NRF) grant funded by the Korea government(MSIT) (RS-2026-25490510). The authors gratefully acknowledge Broadcom Inc. for providing the NUV-DJ SiPM that enabled this characterization.

Abstract

CTR in PET detectors is a quadrature combination of scintillator photon statistics, intrinsic detector physics, and front-end circuit electronics, but conventional measurement reports only the combined FWHM, leaving the relative contributions indeterminate. This hinders rational optimization between circuit-side and detector-side improvements. We introduce a covariance-based framework that decomposes the CTR noise budget from a single coincidence measurement by simultaneously extracting timestamps from two independent readouts—the timing chain and the energy chain. The covariance $\mathrm{Cov}(\Delta T_T, \Delta T_E)$ isolates the common-mode intrinsic contribution, while variance differences identify chain-specific circuit noise in closed form, requiring no calibration beyond standard CTR acquisition. Applied to a 4 condition of LSO and GAGG:Ce (3×3×20 mm³) with Broadcom NUV-MT and NUV-DJ SiPMs, the framework extracts a circuit noise floor σ_{nT} = 11.2–18.5 ps per detector across all conditions, supporting its interpretation as a detector-independent electronics floor. Intrinsic contributions cluster sharply by crystal type (LSO 28–31 ps, GAGG 49–56 ps), exceeding the analytical CRLB by 1.42–1.62× due to DOI and transport effects. A walk asymmetry $\rho(\Delta T_E, dE)/\rho(\Delta T_T, dE)$ = 1.42–1.82× reflects front-end pulse-shape physics. The decomposition quantifies circuit-improvement leverage: LSO configurations retain 11–15% potential CTR reduction, while GAGG configurations operate within 2–6% of their photon-statistics bound. The framework provides a single-measurement diagnostic for prioritizing circuit-side versus detector-side investments in PET front-end development, and also provides the first quantitative noise-budget characterization of NUV-DJ SiPMs.

References
[1] Surti S, Karp JS. "Advances in time-of-flight PET." Phys. Med. Biol. 63, 055008 (2018).
[2] Hu K, et al. "Coincidence time resolution of radiation detector based on 6×6 mm² ToF SiPM detectors with different readout schemes." Front. Phys. 11, 1050234 (2023).
[3] Seifert S, et al. "A comprehensive model to predict the timing resolution of SiPM-based scintillation detectors." IEEE Trans. Nucl. Sci. 59(1), 190-204 (2012).
[4] Gundacker S, et al. "High-frequency SiPM readout advances measured coincidence time resolution limits in TOF-PET." Phys. Med. Biol. 64, 055012 (2019).

MIC-15-027

Identification and Mitigation of Inter-Crystal Scatter in Dual-Layer DOI Configurations Under Highly Multiplexed Readout (#2354)

Lukas U. Rauscher[1], Martin Judenhofer[2], Janina Hohnholz[1], Esther Haas[1], Elnaz Olyaei[1,4], Hong Phuc Vo[3], Magdalena Rafecas[3], Bernd Pichler[1], Fabian P. Schmidt[1,4]

[1] University Hospital Tuebingen, Department of Preclinical Imaging and Radiopharmacy, Tuebingen, Germany; [2] Siemens Medical Solutions, Inc, Knoxville, USA; [3] University of Luebeck, Institute of Medical Engineering, Luebeck, Germany; [4] University Hospital Tuebingen, Department of Nuclear Medicine and Clinical Molecular Imaging, Tuebingen, Germany

Funded by DFG 508064995

Abstract
Stacked scintillator configurations to obtain depth-of-interaction (DOI) information, combined with small crystal pitch, are commonly used to improve spatial resolution and maintain uniform performance across the field of view. Such configurations are prone to inter-crystal scatter (ICS), where energy deposition is shared across multiple crystals, leading to event mis-assignment and degradation of detector performance, including incorrect DOI estimation. Correction of these effects typically benefits from individual channel readout, which is often limited in highly multiplexed systems. In this work, we investigate ICS in a dual-layer LSO detector with 1.6 mm pitch, employing a 10×10/9×9 stacked crystal configuration coupled to a 4×4 SiPM array. The detector uses a highly multiplexed readout scheme with only three output channels (x, y, and total energy), imposing additional constraints on event discrimination. To analyze ICS effects, a hybrid simulation framework was developed, pairing Geant4-based modeling of gamma interactions with custom light transport and readout model. The simulations reproduce characteristic structures observed in experimental data, including patterns in floodmaps and energy-dependent light spread distributions. Based on these results, a light-pattern-based metric was introduced to identify ICS events using an energy-dependent threshold derived from single-interaction event distributions. This approach indicates that 32.9 ± 5.5% of events per crystal are affected by ICS and assigned to a non-optimal crystal, including mis-assignment between layers. Reassignment of these events to the most likely interaction crystal increased effective sensitivity by 4.1% and improved energy resolution from 10.6 ± 1.8% to 10.2 ± 1.8% FWHM. These results demonstrate that ICS as major effect in finely pixelated, DOI-capable detectors and that its identification and partial correction is feasible under highly multiplexed readout conditions.

References
[1] Rauscher, L. U. et al., 2025 IEEE NSS MIC RTSD, Yokohama

MIC-15-030

Characterization of a multiplexed SiPM readout with free-running ADC for BGO PET detectors (#2466)

Nicola Belcari[1,2], Matteo Morrocchi[1,2], Giancarlo Sportelli[1,2]

[1] University of Pisa, Department of Physics "E. Fermi", Pisa, Italy; [2] INFN - Istituto Nazionale di Fisica Nucleare, Sezione di Pisa, Pisa, Italy

Abstract
We present a modular FPGA-based data acquisition and real-time processing architecture for SiPM-based PET detectors, developed in the context of compact, low-cost PET imaging. The system combines a multiplexed readout of a SiPM array with free-running high-speed ADCs and on-chip FPGA processing to extract event energy, timestamp, and interaction position in real time. The approach emphasizes compactness, scalability, and low-latency operation, while reducing channel count and system complexity. First measurements demonstrate correct operation and clear crystal identification in flood maps, highlighting both the potential and current limitations of

SiPM multiplexing, such as the limited CTR. This work aims to enable cost-efficient, flexible, and scalable PET imaging systems.

References
[1] W. Hu et al., *Nucl. Instrum. Methods Phys. Res. Sect. Accel. Spectrometers Detect. Assoc. Equip.*, vol. 664, no. 1, pp. 370–375, 2012, doi.org/10.1016/j.nima.2011.05.053.
[2] R. Fontaine et al., *IEEE Trans. Nucl. Sci.*, vol. 56, no. 1, pp. 3–9, 2009, doi.org/10.1109/TNS.2008.2007485.
[3] E. Downie et al., *Phys. Med. Biol.*, vol. 58, no. 11, p. 3943, 2013, doi.org/10.1088/0031-9155/58/11/3943.

MIC-15-033

MIC-15-036

Evaluating a novel type of silicon photomultiplier for X-ray photon-counting CT applications (#2659)

Lukas Schröder, Marc Snoeyink, Dennis R. Schaart

Delft University of Technology, Radiation Science & Technology, Delft, Netherlands

We thank Broadcom Inc for providing the SiPM samples as well as preliminary PDE data. This work is partly funded by EU Horizon grant 101112053.

Abstract
Photon-counting computed tomography (PCCT) is a rapidly emerging (medical) imaging technology. PCCT commonly relies on finely pixelated room-temperature semiconductor detectors (RTSD). Scintillation detectors have long been considered too slow to handle the high X-ray fluence rates encountered in clinical PCCT. However, the fast signals provided by modern scintillators and silicon photomultipliers (SiPMs) allow us to reconsider this paradigm. SiPM-based scintillation detectors offer excellent image quality and are known to operate reliably in clinical time-of-flight positron emission tomography (TOF-PET) scanners. Recent research indicates that the combination of ultrafast SiPMs and scintillators could potentially provide a robust, scalable, and affordable X-ray photon-counting detector (PCD) technology. Here, we evaluate a novel type of silicon photomultiplier (SiPM) for this application. The SiPM is based on small (< 15 □m) single-photon avalanche diodes (SPADs), which have an innovative design that enables a fast recharge time (< 7 ns) as well as a high geometric efficiency (fill factor),

resulting in high photodetection efficiency (PDE) (~ 50%) over a broad wavelength range. These benefits can be exploited to mitigate the classical trade-off between dynamic range and PDE, which is of high interest for X-ray photon-counting applications. We perform experiments with different design variations of the new SiPM, coupled to small pixels of commercially available scintillators (e.g. LYSO:Ce, LaBr3:Ce). We report on the pulse shape, count-rate capability, and spectral performance achieved with different combinations of SPAD design and scintillator.

MIC-15-039

Ultra-High-Definition, 8 µm pitch, Low-Dose X-ray Detector for Microfocus Clinical Applications: From Dental to Medical Imaging (#2814)

Michele Sannino[1], **Renato A.D. Turchetta**[1], Daniel Uzbelger Feldman[2], Adrià Bofill-Petit[1], Erin Simons[3], Robert Raible[4]

[1] IMASENIC SL, Barcelona, Spain; [2] Real Time Imaging Technologies, LLC, Charlotte, USA; [3] Blur Product Development, Cary, USA; [4] University of Virginia Health Science Center, Charlottesville, USA

Abstract

We present the design and characterization of a 11.6 million pixel, 8 µm pitch, low noise (1.5 e rms), high dynamic range (93.5 dB), backside-illuminated (BSI) CMOS image sensor with microlenses (M) coupled to a scintillator for X-ray detection. Characterisation with a microfocus X-ray source shows high MTF, in excess of 30-line pairs per mm (lp/mm), while operating at an air kerma of 20.9 mGy per image.

MIC-15-042

Dual-Ended Readout PET Detector Based on Semi-Monolithic Laser-Engraved Scintillators (#2831)

Victor Sánchez-Tembleque[1], Lidia Jiménez Algarra[1], Luis Batres[1], David Perez-Benito[1], David Izquierdo-Garcia[1], Juan J. Vaquero[1]

[1] Universidad Carlos III, Biomedial science and engineering lab, Madrid, Spain; [2] 2 Instituto de Investigacion Sanitaria Gregorio Marañon, Madrid, Spain

This research has been supported by Universidad Carlos III de Madrid through the Young Doctors Research Activity Grant

Abstract

This work presents the development of a semi-monolithic laser-engraved PET detector with dual-ended readout for continuous Depth of Interaction (DOI) estimation. The detector is based on a monolithic LYSO scintillator structured using Subsurface Laser Engraving (SSLE) techniques, enabling controlled light sharing between neighboring pixels while pre-serving the simpler readout and calibration typically associated with pixelated detectors, together with the accurate interaction vertex determination characteristic of monolithic designs. The main objective of this work is to determine the optimal placement of a reduced number of photodetectors in order to maximize DOI performance while minimizing the system's complexity. The study is based on the direct experimental measurement of light sharing inside the scintillator crystal. For this purpose, two 61- channel SiPM matrices are coupled to both faces of a LYSO scintillator matrix featuring a honeycomb laser-engraved pattern of 181 crystals. Taking advantage of the fact that the existing electronics can process up to 64 channels, the light distribution measured on one side of the detector is combined with the signal collected by only three selected photodetectors on the opposite side to estimate the DOI and evaluate different configurations for these additional channels. Using fully instrumented matrices on both faces allows the evaluation of different three-SiPM configurations and provides a detailed understanding of scin-tillation light-sharing behavior. The proposed approach aims to identify compact dual-ended configurations capable of achieving continuous DOI estimation with reduced readout complexity for future high-resolution PET detectors.

References

[1] F. Cadoux, R. Cardella, G. Iacobucci, L. Iodice, D. Ferr`ere, S. Gonzalez-Sevilla, T. Kugathasan, F. Martinelli, L. Paolozzi, A. Picardi, J. Saidi, M. Vicente, and S. Zambito, "The 100pet project: A small-animal pet scanner for ultra-high resolution molecular imaging with monolithic silicon pixel detectors," Nuclear Instruments and Methods in Physics Research Section A, vol. 1048, 2023.
[2] A. Gonzalez-Montoro, A. J. Gonz´alez, S. Pourashraf, R. S. Miyaoka, P. Bruyndonckx, G. Chinn, L. A. Pierce, and C. S. Levin, "Evolution of pet detectors and event positioning algorithms using monolithic scintillation crystals," IEEE Transactions on Radiation and Plasma Medical Sciences, vol. 5, pp. 282–305, 2021.
[3] D. Perez-Benito, R. Chil, J. Udias, M. Desco, and J. Vaquero, "Sipmbased pet detector module for a 4 span scanner," Nuclear Instruments and Methods in Physics Research Section A, vol. 936, 2019, frontier Detectors for Frontier Physics: 14th Pisa Meeting on Advanced Detectors.
[4] M. Li and S. Abbaszadeh, "Depth-of-interaction study of a dual-readout detector based on tofpet2 application-specific integrated circuit," Physics in Medicine Biology, vol. 64, no. 17, sep 2019.
[5] G. Konstantinou, R. Chil, M. Desco, and J. J. Vaquero, "Subsurface laser engraving techniques for scintillator crystals: Methods, applications, and advantages," IEEE Transactions on Radiation and Plasma Medical Sciences, vol. 1, no. 5, 2017.

MIC-15-045

PETVision: An Ultra-High TOF Resolution PET System with 2.5D Modular Flat-Panel Detectors (#3008)

Yue Zhuo[1], Thibault Marin[1], David Gascón[2], Alberto Gola[3], Jose Maria Benlloch[4], David Sanchez Gonzalo[5], Rafael Ballabriga[6], Wolfgang Weber[7], Julio Barberá Ballester[5], Gianmario Bergamin[6], Juan Vicente Catret[2], Rok Dolenec[8,9], José María Fernández-Tenllado[2], Lluis Garrido[2], Kira Grogg[1], Ibrahim Hany[3,1], Priyanka Kachru[3], Samo Korpar[8,10], Peter Križan[8,9], Marijan Leban[8], Stanislaw Majewski[11], Joan Mauricio[2], David Mazzanti[2], Stefano Merzi[3], Laura Moliner Martinez[4], Tim Mulnix[1], Yassir Najmaoui[1], Stephan Nekolla[7], Matic Orehar[9], Giovanni Palu[3], Laura Parellada-Monreal[3], Giovanni Paternoster[3], Noriel Pavon Hernandez[4], Michele Penna[3], Sara Portero[2], Isabel Rauscher[7], Gašper Razdevšek[8], Miquel Ribalda[2], Andreu Sanuy[2], Andrej Seljak[8], Andrej Studen[8,9], Oscar de la Torre[2], Carina A. Trippl[3], Manuel Viqueira Rodriguez[6], Dejan Žontar[8], Rok Pestotnik[8], Georges El Fakhri[1]

[1] Yale University, Yale Biomedical Imaging Institute (YBII) at Yale School of Medicine, New Haven, USA; [2] University of Barcelona (IEEC-UB), Dept. Física Quàntica i Astrofísica, Institut de Ciències Del Cosmos (ICCUB), Barcelona, Spain; [3] Fondazione Bruno Kessler (FBK), Povo TN, Italy; [4] Instituto de Instrumentación Para Imagen Molecular (CSIC-UPV), Valencia, Spain; [5] Oncovision, Valencia, Spain; [6] CERN, Geneva, Switzerland; [7] Technical University of Munich (TUM-MED), Munich, Germany; [8] Jožef Stefan Institute, Ljubljana, Slovenia; [9] University of Ljubljana, Faculty of Mathematics and Physics, Ljubljana, Slovenia; [10] University of Maribor, Faculty of Chemistry and Chemical Engineering, Maribor, Slovenia; [11] University of California Davis, Davis, USA

This work was funded in parts by the National Institutes of Health under grant R01EB036642, the European Union's Horizon Europe research and innovation program through PetVision project under Grant 101099896; and in part by the Slovenian Research and Innovation Agency through Research core funding under Grant P1-0389 and Grant P1-0135.

Abstract

We report updates on the development and current progress of PETVision, a modular flat-panel positron emission tomography (PET) system designed to achieve ultra-high Time-of-Flight (TOF) resolution. Traditional cylindrical PET scanners often face limitations due to high crystal volume costs and geometries that restrict simultaneous medical intervention. By leveraging unprecedented Coincidence Time Resolution (CTR), the PETVision architecture enables limited-angle, flat-panel geometries that reduce material costs while maintaining high image resolution.

The Photo-Detection Module (PDM) of the PET system is utilizing a 2.5D integration configuration, where Silicon Photomultiplier (SiPM) arrays and readout ASICs are coupled to opposite sides of a passive interposer. The sensing layer employs state-of-the-art NUV-HD-MT technology, featuring custom "glass-less" Through Silicon Vias (TSVs) to achieve a Photon Detection Efficiency (PDE) of up to 65% and a Single Photon Time Resolution (SPTR) with Full Width at Half Maximum (FWHM) as low as 20 ps. Readout electronics development is proceeding in two stages: an initial 32-channel FastIC+ BGA chiplet demonstrating a CTR of (85±1) ps FWHM with 2×2×3 mm3 LYSO:Ce:0.2%Ca scintillator crystals. This is followed by the 64-channel Positron Emission Tomography Integrated

Circuit (PoETIC) ASIC, which targets an electronics jitter contribution below 12 ps r.m.s. to support the 10-picosecond challenge. This modular approach aims to provide a high-performance, cost-effective PET imaging system suitable for diverse clinical and research applications, including simultaneous PET/intervention procedures.

References
[1] E. K. Leung et al., Phys Med Biol, vol. 66, no. 20, 2021.
[2] H. Li et al., J Nuc Med, vol. 65, no. 8, 2024.
[3] L. Parellada-Monreal et al., in Proc IEEE NSS MIC RTSD, 2023.
[4] E. Petersen et al., J Nuc Med, vol. 62, no. supplement 1, 2021.
[5] S. Vandenberghe et al., in Japanese Soc Nuc Med. IEEE/JSNM, 2025.
[6] D. Mazzanti et al., IEEE Trans Rad Plasma Med Sci, 2026.
[7] E. Dhaenens et al., Frontiers in Physics, vol. 13, 2026.
[8] S. Merzi et al., J Instrum, vol. 18, no. 05, May 2023.
[9] L. Parellada-Monreal et al., Nucl Instrum Methods Phys Res A, vol. 1049, 2023.

MIC-15-048

Comparative Evaluation of NUV-MT and NUV-DJ SiPM Timing Performance for TOF-PET Detector Application (#3213)

Suhan Choi[1], Hyeong Seok Shim[1,2], Guen Bae Ko[1]

[1] Korea Advanced Institute of Science and Technology, Department of Nuclear and Quantum Engineering, Daejeon, South Korea; [2] Korea Advanced Institute of Science and Technology, Mechanical Engineering Research Institute, Daejeon, South Korea

This study was supported through the provision of NUV-DJ SiPMs by Broadcom.

Abstract

Recently developed Broadcom NUV-DJ SiPMs have improved photon detection efficiency (PDE) by placing the high-field region deeper than that of NUV-MT SiPMs. PDE is one of the major factors affecting coincidence timing resolution (CTR), and its performance varies depending on the scintillation light wavelength. Therefore, this study comparatively evaluated the CTR performance of LYSO:Ce, GAGG:Ce, and BGO scintillators, which have different peak emission wavelengths, coupled with NUV-MT and NUV-DJ SiPMs. The detectors consisted of 6 × 6 mm² NUV-MT and NUV-DJ SiPMs coupled with 3 × 3 × 20 mm³ LYSO:Ce and GAGG:Ce crystals and 3 × 3 × 3 mm³ BGO crystals using optical grease. Timing and energy signals were processed using a high-frequency (HF) readout board and acquired using an oscilloscope. CTR measurements were performed as a function of overvoltage for each detector. In addition, quartile-based rise-time analysis was conducted for the BGO detectors to investigate the effect of prompt Cherenkov photon detection on timing performance as indirect indicators. The detectors coupled with NUV-MT SiPMs achieved CTRs of 109.0 ps (LYSO:Ce), 182.8 ps (GAGG:Ce), and 210.8 ps (BGO) at an overvoltage of 12 V, whereas those coupled with NUV-DJ SiPMs achieved CTRs of 103.0 ps (LYSO:Ce), 172.4 ps (GAGG:Ce), and 187.2 ps (BGO), respectively. Compared with the NUV-MT SiPMs, the NUV-DJ SiPMs improved CTR by 5.2%, 4.5%, and 11.2% for LYSO:Ce, GAGG:Ce, and BGO, respectively. The quartile analysis further showed improved timing performance for fast rise-time events when using the NUV-DJ SiPMs. These results indicate that the improved PDE of the NUV-DJ SiPM enhances prompt photon detection and contributes to

improved CTR performance for BGO scintillators. Therefore, the proposed detector configuration may be beneficial for future TOF-PET and BGO-based timing detector applications.

References
[1] Gonzalez-Montoro, A, et al. 2021, 'Study of optical reflectors for a 100 ps coincidence time resolution TOF-PET detector design', Biomedical Physics & Engineering Express, vol. 7, no. 6, p. 065010, IOP Publishing
[2] Gola, A, et al. 2024, 'NUV-sensitive deep-junction (NUV-DJ) SiPMs, a new technology optimized for fast timing applications', PSMR 2024 – 10th Conference on PET, SPECT, and MR Multimodal Technologies, Total Body and Fast Timing in Medical Imaging

MIC-15-051

Decomposing Optical Photon Transport in PET Detectors: Geometric Priors and Generative Models of Residual Stochasticity (#1379)

Stephan Naunheim[1], Nicolaus Kratochwil[1], Elizabeth Melton[1], Brandon Pardi[2], Emilie Roncali[1]

[1] University of California, Davis, Department of Biomedical Engineering, Davis, USA; [2] University of California, Davis, Department of Computer Science, Davis, USA

This work is supported by NIBIB grant R01 EB034475.

Abstract

Monte Carlo simulations of optical photon transport are the gold standard for modeling PET detectors, but their step-by-step nature makes large-scale optical systems computationally prohibitive. Generative models are an attractive alternative, and we previously demonstrated conditional generative adversarial networks for single crystals and crystal arrays, in which physics knowledge enters the model through architectural extensions and a physics-informed loss. In this work, we propose a fundamentally different way of incorporating physics. Instead of acting on the loss, prior physical information is injected directly into the conditioning pathway of the generative model. A lightweight, geometry-agnostic light transport estimator (GALTE) propagates photons through the segmented crystal geometry under a simplified physical model and produces a compact descriptor of the expected sensor-level light response. This descriptor replaces the bare emission coordinates as conditioning input, leaving the generative model to capture only the residual stochastic structure that the analytical prior cannot resolve. We instantiate the framework with a conditional GAN whose architecture and trainable parameter count matches the published OptiGAN baseline, so that observed differences can be attributed to the conditioning rather than to model capacity. On a 3×3 BGO array, the GALTE-conditioned model preserves the distributional fidelity of the OptiGAN baseline across the full crystal array while reproducing physically interpretable structures of the joint position–momentum distribution more closely, particularly in regimes of high reflection multiplicity. Most notably, the GALTE-conditioned model reaches its best performance after roughly one third of the training epochs required by the OptiGAN baseline. Physics-informed conditioning thus opens a path toward generative models that combine physical priors with machine learning.

References
[1] C. Trigila, G. Mummaneni, B. Mehadji, B. Pardi, and E. Roncali, "Towards large nuclear imaging system optical simulations with optiGAN, a generative adversarial network," Phys. Med. Biol., vol. 70, no. 12, p. 125002, Jun. 2025, doi: 10.1088/1361-6560/adde0c.

[2] S. Naunheim, B. Pardi, G. Mummaneni, C. Trigila, and E. Roncali, “OptiGAN for Crystal Arrays: Physics-Informed Generative Modeling of Optical Photon Transport in PET Detector Arrays,” Jan. 26, 2026, arXiv: arXiv:2601.18780. doi: 10.48550/arXiv.2601.18780.
[3] D. Sarrut et al., “GATE 10 Monte Carlo particle transport simulation -Part I: development and new features,” Phys. Med. Biol., 2025, doi: 10.1088/1361-6560/ae237b.
[4] N. Krah et al., “GATE 10 Monte Carlo particle transport simulation -Part II: architecture and innovations,” Phys. Med. Biol., 2025, doi: 10.1088/1361-6560/ae237c.
[5] S. Naunheim et al., “Improving the Timing Resolution of Positron Emission Tomography Detectors Using Boosted Learning—A Residual Physics Approach,” IEEE Transactions on Neural Networks and Learning Systems, pp. 1–13, 2023, doi: 10.1109/TNNLS.2023.3323131.
[6] S. Naunheim et al., “Rethinking timing residuals: advancing PET detectors with explicit TOF corrections,” Front. Phys., vol. 13, Apr. 2025, doi: 10.3389/fphy.2025.1570925.

MIC-15-054

Scaling TOF-PET Timing Calibration via Structured Detector-Wise Learning (#1493)

Julian Thull[1], Yannick Kuhl[1], Thore Meyer[1], Marc Henning[1], Bjoern Weissler[1,2], David Schug[1,2], Volkmar Schulz[1,2]

[1] RWTH Aachen University, Institute of Imaging and Computer Vision, Aachen, Germany; [2] Hyperion Hybrid Imaging Systems GmbH, Aachen, Germany

This work was funded by BMFTR and the Ministry of Culture and Science of North Rhine-Westphalia through NHR4CES. We thank NVIDIA for four RTX 6000 Ada GPUs through its Grant Program.

Abstract

Time-of-flight positron emission tomography (PET) timing calibration is especially challenging for light-sharing detectors, where biases arise from interaction-dependent light transport, silicon photomultiplier response, and effects of readout electronics. Conventional skew and walk corrections are robust but leave high-dimensional event signatures underused. We introduce an in-system approach that learns detector-wise corrections from coincidence data without requiring pair-specific models. A shared network conditioned by detector embeddings estimates single-interaction offsets from singles observables, yielding a structured model with linearly scaling detector-specific parameters. We evaluate the method on two prototype PET systems: a 24-module semi-monolithic detector scanner and a 28-module multi-layer segmented-crystal detector scanner. For both, data were acquired at 450 randomized 22Na point-source positions and split by source position for fivefold cross-validation. We studied a residual multilayer perceptron, a geometry-aware transformer, and a lightweight edge multilayer perceptron. Across scanners and energy windows, learned models improved coincidence timing resolution over time-skew and time-walk correction. The residual multilayer perceptron achieved the best timing resolutions, reaching 431ps and 382ps for scanners 1 and 2. Transformer and edge variants performed similarly with smaller models and generalized to detector pairs excluded during training. Feature ablation identified light spread as the dominant auxiliary cue, with local position and energy adding further improvements. These results establish detector-wise learning as a practical route to scalable timing calibration for PET systems with complex light-sharing detector topologies.

References
[1] Naunheim, S, Lopes de Paiva, L, Nadig, V, Kuhl, Y, Gundacker, S, Mueller, F & Schulz, V 2025, 'Rethinking timing residuals: advancing PET detectors with explicit TOF corrections', Frontiers in Physics, 13, 1570925, Frontiers Media SA.
[2] Berg, E & Cherry, SR 2018, 'Using convolutional neural networks to estimate time-of-flight from PET detector waveforms', Physics in Medicine & Biology, 63(2), 02LT01, IOP Publishing.
[3] Loignon-Houle, F, Kratochwil, N, Toussaint, M, Lowis, C, Ariño-Estrada, G, Gonzalez, AJ, Auffray, E & Lecomte, R 2025, 'Improving timing resolution of BGO for TOF-PET: a comparative analysis with and without deep learning', EJNMMI Physics, 12(1), 2, Springer.
[4] Thull, J, Kuhl, Y, Mueller, F, Schug, D, Weissler, B & Schulz, V 2026, 'Beyond mechanics: Maximum-likelihood-driven PET detector alignment calibration', Medical Physics, 53(1), e70256, Wiley.
[5] Kuhl, Y, Mueller, F, Naunheim, S, Bovelett, M, Lambertus, J, Schug, D, Weissler, B, Gegenmantel, E, Gebhardt, P & Schulz, V 2024, 'A finely segmented semi-monolithic detector tailored for high-resolution PET', Medical Physics, 51(5), 3421–3436, Wiley.

MIC-15-057

GPU-Accelerated Monte Carlo Simulation for SPECT Imaging (#1616)

Feng Zhou[1], Zhongzhi Liu[1], Yusheng Li[2], Bo Gao[1], Songsong Tang[1], Chen Sun[1], Liuchun He[1]

[1] United Imaging Healthcare, Shang hai, China; [2] United Imaging Healthcare North America, Houston, USA

Abstract

Monte Carlo simulation (MCS) is essential for PET and SPECT system modeling and optimization. However, existing CPU-based toolkits such as GATE and Geant4 remain too slow for iterative system design. We present a GPU-accelerated SPECT simulation module within the United-Imaging Healthcare (UIH) Molecular-imaging Innovation Platform (uMIP), extending its validated PET capability to single-photon imaging with native support for both multi-pinhole and parallel-hole collimator geometries. The key innovation is a closed-form analytic ray-aperture intersection algorithm for multi-pinhole collimators, which eliminates iterative geometric traversal and enables massively parallel GPU execution. Its speed is approximately 2~3 orders of magnitude faster than a CPU-based simulation toolkits. Quantitative validation against Geant4 demonstrates excellent agreement for both multi-pinhole and parallel-hole configurations: point-source projection profiles across six field-of-view positions yield NRMSE <0.80% and Pearson correlation >90%, while transmitted-photon spatial distributions and energy spectra show consistent results at both 140 keV and 440 keV. The proposed framework provides a practical, high-fidelity simulation platform for rapid SPECT collimator design and imaging protocol optimization.

References
[1] S. Agostinelli et al., Geant4 - A Simulation Toolkit, Nucl. Instrum. Meth. A 506 (2003)
[2] S. Jan, et al., GATE: a simulation toolkit for PET and SPECT Phys Med Biol 49 4543-61
[3] He et al., GPU-accelerated Monte Carlo Simulation for PET imaging (part I): Validation of Imaging Physics Simulation, IEEE-NSS/MIC 2023
[4] Sun et al., GPU-accelerated Monte Carlo Simulation for PET imaging (part II): patient motion and dynamic imaging simulation, IEEE-NSS/MIC 2023
[5] Gao et al., Fast on-the-fly system matrix computation for broad-Energy multi-pinhole SPECT, IEEE-NSS/MIC 2026

MIC-15-060

Monte Carlo Validation of a Positron Emission Mammography Scanner Using GATE 9.4: Sensitivity Analysis with an Aluminum Sleeve Phantom (#1652)

Sara H. El-Sallabi[1,4], Othmane Bouhali[1,3], Hadi Fayad[2], Amer Ghujeh[2], Jim Ji[4]

[1] Texas A&M University at Qatar, Electrical & Computer Engineering, Doha, Qatar; [2] Hamad Medical Corportation, Occupational Health and Safety, Doha, Qatar; [3] Hamad Bin Khalifa University, Electrical Engineering, Doha, Qatar; [4] Texas A&M University, Electrical & Computer Engineering, College Station, USA

The authors thank the medical physics team at the National Center for Cancer Care and Research, Hamad Medical Corporation, for scanner access and experimental measurements. Computing resources were provided by the Texas A&M University at Qatar HPC cluster. This work was supported in part by Qatar Foundation and Texas A&M University at Qatar.

Abstract

Accurate Monte Carlo simulation of Positron Emission Mammography (PEM) scanners is essential for optimizing detector design, reconstruction algorithms, and dosimetry in dedicated breast imaging. This work presents a GATE 9.4 simulation of the Naviscan PEM scanner validated against clinical sensitivity measurements at Hamad Medical Corporation, Doha, Qatar. Scanner geometry was implemented from published specifications, with detector efficiency derived from LYSO crystal attenuation via the Beer-Lambert law (approximately 70% for 13 mm crystals, mu = 0.86 cm-1 at 511 keV). A cylindrical aluminum sleeve phantom in five configurations (zero to four 2.5 mm sleeves) was simulated using a 0.58 ns coincidence timing window and a 350-650 keV energy window, matching the hospital protocol. True coincidences were counted following clinical convention, including scattered events within the energy window. The base-case configuration achieved 96.8% agreement with hospital measurements. Mean agreement across all five configurations was 70.3%, with the correct exponential attenuation trend reproduced across increasing sleeve thicknesses. Systematic underestimation at higher attenuation is consistent with known GATE aluminum cross-section limitations and the absence of scatter recovery corrections. All parameters were derived from first principles without empirical tuning. Preliminary results demonstrate a rigorous, reproducible simulation framework for PEM, with complete validation to be presented at the conference.

References

[1] Moliner, L, Gonzalez, AJ, Soriano, A, Sanchez, F, Correcher, C, Orero, A, Carles, M, Vidal, LF, Barbera, J, Caballero, L, Seimetz, M, Lerche, CW, Bendriem, B, Pavon, N, Benlloch, JM 2012, 'Performance evaluation of the Flex Solo II dedicated PEM scanner', *Physics in Medicine and Biology*, vol. 57, no. 17, pp. 5669–5686

[2] Lamare, F, Turzo, A, Bizais, Y, Le Rest, CC, Visvikis, D 2006, 'Validation of a Monte Carlo simulation of the Philips Allegro/GEMINI PET systems using GATE', *Physics in Medicine and Biology*, vol. 51, no. 4, pp. 943–962

[3] Goertzen, AL, Bao, Q, Bergeron, M, Bhatt, DL, Colin, S, Gasecka, A, Beanlands, R 2012, 'NEMA NU 4-2008 comparison of preclinical PET imaging systems', *Journal of Nuclear Medicine*, vol. 53, no. 8, pp. 1300–1309

[4] Schmidtlein, CR, Kirov, AS, Nehmeh, SA, Erdi, YE, Humm, JL, Amols, HI, Bidaut, LM, Ganin, A, Stearns, CW, McDaniel, DL, Hamacher, KA 2006, 'Validation of GATE Monte Carlo simulations of the GE Advance/Discovery LS PET scanners', *Medical Physics*, vol. 33, no. 1, pp. 198–208

[5] Luo, W, Anashkin, E, Matthews, CG 2010, 'Monte Carlo simulation of a dedicated PEM scanner', *IEEE Transactions on Nuclear Science*, vol. 57, no. 5, pp. 2443–2449

MIC-15-063

Heuristic seeding for GA-based optimization of halbach magnets for PET-compatible low-field MRI (#1747)

Md Shahadat Hossain Akram[1], Fumihiko Nishikido[1], Mikio Suga[3], Takayuki Obata[2], Taiga Yamaya[1]

[1] National Institutes for Quantum Science and Technology (QST), Imaging Physics Group, Advance nuclear medicine science, Chiba, Japan; [2] National Institutes for Quantum Science and Technology (QST), Applied MRI Research, Chiba, Japan; [3] Chiba University, Center for Frontier Medical Engineering, Chiba, Japan

This work was supported by the JSPS Kakenhi grant number: 24K15805.

Abstract

This paper presents an optimization framework for Halbach magnet arrays targeting PET-compatible portable low-field MRI. Positioning an MRI system within existing PET rooms offers a practical alternative to PET-in-MRI inserts, as it simplifies compliance with radioisotope regulations. However, achieving high field uniformity in a 200-magnet Halbach array requires optimizing discrete rotation angles within an exponentially large search space. To address this, we developed a genetic algorithm (GA) utilizing adaptive mutation and dynamic elitism. To prevent premature convergence caused by rapid diversity loss in high-dimensional spaces, we investigated five population seeding strategies, including a novel Segmented Stochastic Progression (SSP) method using stratified complexity sampling. Performance was evaluated via fitness convergence and Hamming distance using progressive mutation step-size ranges (sigma = 6 to 1 and 10 to 1). Our results demonstrated that heuristic seeding maintained population diversity 1.3 to 2.6 times more effectively than random initialization. Specifically, the SSP method provided superior global search stability, yielding highly ordered magnetic flux streamlines across a 10 cm target region within a 20 cm diameter ring. Furthermore, mean time to solution (MTTS) remained consistent (0.94–1.00 relative to baseline), indicating the search quality was improved without increasing the computational overhead. This approach offers a robust, transferable methodology for complex electromagnetic design optimizations.

MIC-15-066

Experimentally Validated GATE Model of a Commercial PET System with Sub-200 ps TOF (#1879)

Michel Atieh[1,2], Emmanuel Durand[1,2], Olga Kochebina[2]

[1] Assistance publique – Hôpitaux de Paris (AP-HP), Department of Biophysics and Nuclear Medicine, Le Kremlin-Bicêtre, France; [2] Université Paris-Saclay, BioMaps Laboratory, Service Service Hospitalier Frédéric Joliot, CEA, Orsay, France

Abstract
This paper presents a GATE Monte Carlo model and its preliminary validation of the uMI Panorama 35™ PET system, which combines a 35 cm axial field-of-view with sub-200 ps time-of-flight performance. The model was validated for coincidence time resolution (CTR) and against NEMA NU 2-2018 measurements of sensitivity and noise equivalent count rate. The coincidence time resolution of 197 ps obtained with the model is comparable to 194 ps measured experimentally, and a system sensitivity of 21.0 versus 23.5 kcps/MBq. It also reproduced count-rate performance, with a peak noise equivalent count rate of 615 kcps at 43.7 kBq/mL, compared with 687 kcps at 43.2 kBq/mL experimentally. These results show the preliminary work on its validation and focuses mainly on the main counting performance characteristics of the scanner. Future work will extend validation to additional image tests, including spatial resolution and image quality.

References
[1] Sarrut, D. *et al.* 2022, 'The OpenGATE ecosystem for Monte Carlo simulation in medical physics', *Physics in Medicine & Biology*, vol. 67, no. 18, p. 184001.
[2] Peña-Acosta, M.M., Gallardo, S., Lorduy-Alós, M. & Verdú, G. 2024, 'Application of NEMA protocols to verify GATE models based on the digital Biograph Vision and the Biograph Vision Quadra scanners', *Zeitschrift für Medizinische Physik*.
[3] Pommranz, C.M. *et al.* 2025, 'A digital twin of the Biograph Vision Quadra long axial field of view PET/CT: Monte Carlo simulation and image reconstruction framework', *EJNMMI Physics*, vol. 12, no. 1, p. 31.
[4] Merlin, T. *et al.* 2018, 'CASToR: a generic data organization and processing code framework for multi-modal and multi-dimensional tomographic reconstruction', *Physics in Medicine & Biology*, vol. 63, no. 18, p. 185005.

MIC-15-069

Experimental and simulation-guided light-sharing characterization of hexagonal laser-engraved PET detectors. (#2003)

Clara N. Golhen Mateo[1], Mojahed Abushawish[1], Pablo Galve Lahoz[1,3], Victor Sanchez-Tembleque[2], David Perez-Benito[2], Luis Batres[2], Lidia Jiménez Algarra[2], Jose Udias[1], Juan Jose Vaquero[2]

[1] Universidad Complutense de Madrid, Departamento de Estructura de la Materia, Física Térmica y Electrónica, Madrid, Spain; [2] UC3M, Madrid, Spain; [3] Spanish National Research Council (CSIC), Institute for Physical and Information Technologies "Leonardo Torres Quevedo", ITEFI, Madrid, Spain

We acknowledge support from European Union as part of the European Innovation Council's Pathfinder Open Programme: RETIMAGER, 101099096; Spanish Government and Next Generation EU/PRTR: DI2M: Smart detectors for molecular imaging (2021/C005/00147498); P. Galve acknowledges grant JDC2023-051754-I, funded by MCIU/AEI/10.13039/501100011033 and ESF+.

Abstract
PET image quality depends on accurate identification of the gamma-ray interaction point. RETIMAGER proposes laser-engraved (LE) pixelated LYSO blocks, where inter-crystal transparency can be tuned through engraving density. This controlled light sharing can preserve crystal identification while providing XY position information. Previous GOSS optical simulations combined with artificial intelligence (AI) predicted the transparency range expected to optimize XY resolution for 1.25 mm pitch hexagonal crystals. Here, we extend this simulation-guided strategy to experimental data by analysing four LE matrices with different engraving densities and effective

transparencies. For each event, the seven largest SiPM signals were used to characterize the light-sharing pattern. A χ^2 classifier was developed from reference patterns associated with the two main configurations imposed by the hexagonal geometry: crystals above one SiPM and crystals close to a vertex shared by three SiPMs. GOSS simulations with different transparency values were processed with the same procedure and used to select a representative configuration and define the ROI criterion for extracting the χ^2 reference distributions. This criterion was transferred to the experimental matrix, separating the expected 1-SiPM-like and 3-SiPM-like populations. These results show that simulation-guided light-sharing analysis supports classification of the experimental response and future application of AI-based XY identification to LE matrices, aiming to determine the transparency that maximizes detector performance and enables intracrystal positioning.

References
[1] W. W. Moses, “Fundamental limits of spatial resolution in PET,” NIMA Accel. Spectrometers, Detect. Assoc. Equip., vol. 648, pp. S236–S240, Aug. 2011
[2] Perez-Benito, et al. (2019). SiPM-based PET detector module for a 4π span scanner. NIMA: Accelerators, Spectrometers, Detectors and Associated Equipment, 936, 18-2.
[3] C. N. Golhen-Mateo *et a l*(2025, November), "Vertex Reconstruction for the Laser-Engraved PET Detectors: A Study Through AI Methods," In 2025 IEEE NSS MIC RTS1
[4] Galve, P. ,et al. (2024, October). GOSS: GPU-based Optical Simulator of Scintillator Crystals. In 2024 IEEE NSS MIC RTS

MIC-15-072

Microstructure-Informed Single-Grid Dark-Field X-ray Imaging for Breast Microcalcification Typing (#2061)

Sunghoon Choi, Sora Park, Jun-Tae Kang, Jihwan Yeon, Jin-Woo Jeong

Electronics and Telecommunications Research Institute, Materials and Components Research Division, Daejeon, South Korea

This research was supported by the National Research Council of Science & Technology(NST) grant by the Korea government (MSIT) (No. CAP25021-000). This research was also supported by the National Research Foundation of Korea (NRF) funded by the Korea government (MSIT) (RS-2023-00302330).

Abstract
Dark-field X-ray imaging (DFXI) measures ultra-small-angle scattering from sub-resolution density fluctuations and provides contrast complementary to attenuation mammography. We present a wave-optics simulation of a compact single-grid spatial-harmonic imaging (SHI) DFXI system for breast microcalcification typing, focusing on type-II hydroxyapatite (HAp) and type-I calcium oxalate dihydrate (COD). Instead of a generic monodisperse-sphere model, the simulation uses a calibrated $\gamma(\xi)$-based microstructure interface: HAp is represented as a Gaussian-random-field medium, whereas COD is represented as a compact-crystal scatterer with weak surface-dominated dark-field response. For a 17.5 keV source, 20 μm focal spot, 47 μm grid period, and 2.0 m source-to-detector distance, the operating autocorrelation length is ξ_G=249 nm. Simulations with simplified Bakic-style Voronoi backgrounds over BI-RADS A--D show that large HAp clusters remain detectable under anatomy-limited conditions and that the dark-field-to-absorption ratio, $r=\Delta I_{df}/\Delta(1-T)$, separates HAp-like and COD-like clusters more robustly

than either channel alone. These results support compact tabletop SHI-DFXI for specimen-level microcalcification characterization and surgical-margin assessment.

References
[1] Z. Wang et al., *Nature Communications*, vol. 5, 3797, 2014, doi: 10.1038/ncomms4797.
[2] K. Scherer et al., *Nature Communications*, vol. 7, 10863, 2016, doi: 10.1038/ncomms10863.
[3] H. Lim et al., *Journal of Optics*, vol. 24, 035608, 2022, doi: 10.1088/2040-8986/ac3f93.
[4] M. Strobl, *Scientific Reports*, vol. 4, 7243, 2014, doi: 10.1038/srep07243.
[5] P. R. Bakic et al., *Medical Physics*, vol. 29, no. 9, pp. 2131-2139, 2002, doi: 10.1118/1.1501143.

MIC-15-075

SimTBPET: A faster framework for Total Body Monte Carlo PET simulations (#2141)

Arnau Farré-Melero[1,2], Charalampos Tsoumpas[3], Robert L. Harrison[4], Zekai Li[3], Nikos Efthimiou[3], Kris Thielemans[5], Fabian P. Schmidt[6,7], Christian M. Pommranz[7,8], Wenhong Lan[6], Raúl Tudela[9,10], Uxía Quintas[3], Claudia Dominguez-Borrero[2], Alba Garcia-Garrit[1], Jeremiah Poveda-Martínez[2], Jesús Silva-Rodríguez[11,12], Aida Niñerola-Baizán[1,9], Pablo Aguiar[2,12]

[1] Hospital Clínic de Barcelona - IDIBAPS, Department of Nuclear Medicine, Barcelona, Spain; [2] University of Santiago de Compostela, Center for Research in Molecular Medicine and Chronic Diseases (CiMUS), Santiago de Compostela, Spain; [3] University Medical Center Groningen, Department of Nuclear Medicine and Molecular Imaging, Groningen, Netherlands; [4] University of Washington Medical Center, Department of Radiology, Seattle, USA; [5] University College London, Institute of Nuclear Medicine, London, UK; [6] University Hospital Tuebingen, Department of Nuclear Medicine and Clinical Molecular Imaging, Tuebingen, Germany; [7] Eberhard Karls University Tuebingen, Werner Siemens Imaging Center, Department of Preclinical Imaging and Radiopharmacy, Tuebingen, Germany; [8] Eberhard Karls University Tuebingen, Institute for Astronomy and Astrophysics, Tuebingen, Germany; [9] Instituto de Salud Carlos III, Biomedical Research Networking Center of Bioengineering, Biomaterials and Nanomedicine (CIBER-BBN), Barcelona, Spain; [10] University of Barcelona, Faculty of Medicine and Health Sciences, Biophysics and Bioengineering Unit, Barcelona, Spain; [11] Instituto de Salud Carlos III, Reina Sofía Alzheimer Centre, CIEN Foundation, Madrid, Spain; [12] Instituto de Salud Carlos III, Biomedical Research Networking Center on Neurodegenerative Diseases (CIBERNED), Santiago de Compostela, Spain

Charalampos Tsoumpas, Nikos Efthimiou and Zekai Li are supported by the NWO AES Vici Talent program (doi: 10.61686/REEAR02777). Zekai Li was also supported by a Joint Scholarship from the China Scholarship Council and the University of Groningen (202210100011) and his placement at UCL by EPSRC CCP in Synergistic Reconstruction for Biomedical Imaging (EP/T026693/1). STIR is part-maintained by CCP SyneRBI, funded by the UKRI EPSRC grant EP/T026693/1 and by STFC through the UKRI Digital Research Infrastructure programme.

Abstract
Total Body Positron Emission Tomography (TBPET) scanners offer a substantial sensitivity increase compared to traditional scanners, leading to lower doses or acquisition times. In parallel, interest in modelling such tomographs through Monte Carlo simulations has raised. In this work, a faster framework to simulate TBPET scans is presented by modelling the Siemens Biograph Vision Quadra scanner. SimPET platform is used for simulation, which

combines the use of SimSET and STIR. To assess its performance, spatial resolution, sensitivity and image quality NEMA tests were run. Spatial resolution shows reasonable agreement, with an average deviation of 0.6 mm. Although our model overestimates the experimental sensitivity, as expected for a simple cylinder model, a calibration factor is proposed. Concerning image quality, recovery coefficients align with experimental data, while background variability is higher due to reduced maximum ring difference. To sum up, our approach represents a faster alternative (projected x40 speed-up), which could make feasible the large-scale databases simulation when fully adjusted and optimized.

References
[1] Y Sun, Z Cheng, J Qiu, W Lu, "Performance and application of the total-body PET/CT scanner: a literature review," *EJNMMI Res* 14(1):38, 2024.
[2] N Efthimiou, "New Challenges for PET Image Reconstruction for Total-Body Imaging," *PET Clin.*, 15(4): 453–61, 2020.
[3] CM Pommranz, EA Elmoujarkach, W Lan, J Cabello, PM Linder, H Vo, *et al.*, "A digital twin of the Biograph Vision Quadra long axial field of view PET/CT: Monte Carlo simulation and image reconstruction framework," *EJNMMI Phys*, 12(1):31, 2025.
[4] MM Peña-Acosta, S Gallardo, M Lorduy-Alós, G Verdú, "Application of NEMA protocols to verify GATE models based on the Digital Biograph Vision and the Biograph Vision Quadra scanners," *Z Med Phys*, 35(3): 318–30, 2025.
[5] J Paredes-Pacheco, F J López-González, J Silva-Rodríguez, N Efthimiou, A Niñerola Baizán, Á Ruibal, *et al.*, "SimPET—An open online platform for the Monte Carlo simulation of realistic brain PET data. Validation for ^{18}F-FDG scans," *Med Phys*, 48(5):2482–93, 2021.
[6] RL Harrison, SD Vannoy, D Haynor, SB Gillispie, M Kaplan, TK Lewellen, "Preliminary experience with the photon history generator module of a public-domain simulation system for emission tomography," *1993 IEEE NSS/MIC*, 1154–8.
[7] K Thielemans, C Tsoumpas, S Mustafovic, T Beisel, P Aguiar, N Dikaios, MW Jacobson, "STIR: software for tomographic image reconstruction release 2," *Phys Med Biol*, 57(4):867–83, 2012.
[8] Performance Measurements of Positron Emission Tomographs (PET), NEMA Standards Publication NU 2-2018, 2018.
[9] GA Prenosil, H Sari, M Fürstner, A Afshar-Oromieh, K Shi, A Rominger, M Hentschel. "Performance Characteristics of the Biograph Vision Quadra PET/CT System with a Long Axial Field of View Using the NEMA NU 2-2018 Standard," *J Nucl Med*, 63(3): 476–84, 2022.

MIC-15-078

Performance Comparison of Low-Multiplexing and High-Multiplexing Multi-Pinhole Collimators for a Large-Animal Cardiac SPECT System

(#2308)

Jiali Yan, Debin Zhang, Weigang Duan, Shi Wang, Zhaoxia Wu, Hui Liu, Yaqiang Liu

Tsinghua University, Beijing, China

This work was supported in part by the National Key Research and Development Program of China (No. 2022YFC2402002, No. 2022YFC2403802), and National Natural Science Foundation of China (No. 12205166)

Abstract

Large-animal preclinical studies are essential for translating cardiovascular imaging technologies toward clinical applications; however, dedicated SPECT systems optimized for large-animal cardiac imaging remain limited. In this study, we propose a full-ring large-animal cardiac SPECT system composed of six detector heads and investigate

the impact of multi-pinhole multiplexing on system performance. Two collimator configurations are compared: a low-multiplexing reference design with 6 pinholes per plate and a high-multiplexing system with 36 pinholes per plate. The 36-pinhole configuration is generated using a Halton sequence, serving as a specific high-multiplexing representative rather than an optimized arrangement. System performance is evaluated using sensitivity maps and multiple digital phantoms, including a Defrise disk phantom for axial sampling assessment, a Derenzo phantom for spatial resolution evaluation, and a hot-sphere phantom for contrast analysis. All studies employ analytic projection and the Maximum Likelihood Expectation Maximization reconstruction. Results demonstrate that the high-multiplexing system achieves a higher peak sensitivity (2.04×10^{-3} vs. 3.87×10^{-4}), improved hot-rod resolution (3.5 mm clearly resolved vs. 4.5 mm marginally resolved), and a smaller detectable hot-sphere diameter (4 mm vs. 5 mm). In conclusion, high-multiplexing multi-pinhole design may benefit spatial resolution and detectability in stationary SPECT systems, although projection-overlap-induced artifacts must be carefully managed.

References
[1] A. Rahman et al., "Large animal models of cardiac ischemia-reperfusion injury: Where are we now?," Zoological Research, vol. 44, pp. 1-13, 05/18 2023, doi: 10.24272/j.issn.2095-8137.2022.487.
[2] K. S. Kalluri et al., "Examination of aperture layout designs for an adaptive-stationary multi-pinhole brain-dedicated SPECT system," Medical Physics, vol. 52, no. 6, pp. 3734-3759, 2025/06/01 2025, doi: https://doi.org/10.1002/mp.17866.

MIC-15-081

Is 20 mm Still Optimal? Revisiting Scintillator Length in Modern TOF-PET Systems (#2332)

Mizuki Furuta[1,2], Han Gyu Kang[1], Hideaki Tashima[1], Go Akamatsu[1], Taiga Yamaya[1]

[1] National Institutes for Quantum Science and Technology (QST), Institutes for Quantum Medical Sciences, Chiba, Japan; [2] Chiba University, Faculty of Engineering, Chiba, Japan

This work was supported by Nakatani Foundation.

Abstract
Scintillator length of 20 mm has been considered a standard in positron emission tomography (PET); however, recent advances in time-of-flight (TOF) performance necessitate a re-evaluation of this assumption. While shorter scintillators improve coincidence timing resolution (CTR) at the expense of detection efficiency, enhanced TOF information may compensate for this loss in terms of image quality. In this work, we experimentally investigated the effects of crystal thickness on CTR and performed simulations of a clinical PET scanner to evaluate image quality. We used fast-LGSO crystals with a cross section of 4 × 4 mm2 and varying lengths, each coupled to a silicon photomultiplier (SiPM; Hamamatsu Photonics) that had an effective area of 4.0 × 4.0 mm². The timing and energy signals of the SiPM were extracted using a custom-made high frequency readout circuit and digitized with a CAMAC digitizer. The measured CTRs of 10 mm, 15 mm, and 20 mm fast-LGSO crystals were 121 ps, 129 ps and 134 ps, respectively. Based on the experimental results, we investigated the effects of crystal thickness on the image quality of a clinical PET scanner (ring diameter= 675 mm, axial coverage= 158 mm) by Geant4 simulation. Image quality was evaluated using an IQ phantom based on the NEMA NU 2 standard, and metrics including

contrast recovery and background variability. Among the three crystal thicknesses, the 20 mm thickness provided the highest contrast while keeping the background variability. At this stage, we have concluded that longer scintillators appear to provide better image quality. We are still investigating the performance of even longer lengths such as 25 mm and 30 mm, and their performance will be discussed at the conference.

References
[1] National Electrical Manufacturers Association (NEMA), NEMA NU 2-2024: Performance Measurements of Positron Emission Tomographs (PET), NEMA, 2024

MIC-15-084

Comparison Between GATE and SimSET Monte Carlo Simulations on GE Omni Legend PET scanner geometry (#2495)

SeyedAmir ZamanPour[1], Antonia Reeves[2,3], Simon Noe[1], Ahmadreza Rezaei[1], Johan Nuyts[1], Kris Thielemans[2,3], Georg Schramm[1]

[1] KU Leuven, Department of Imaging and Pathology, Leuven, Belgium; [2] University College London, Department of Medical Physics and Biomedical Engineering, London, UK; [3] University College London, Institute of Nuclear Medicine and the Hawkes Institute, London, UK

This work was supported by the i4Health Centre for Doctoral Training, UCL and GE Healthcare. Software used in this project is maintained by CCP SyneRBI (UKRI support: EPSRC grant EP/T026693/1 and STFC through the DRI programme).
This work was supported with the help of Kuan-Hao Su (Dylan), GEHC, and Robert Harrison.

Abstract
Monte Carlo (MC) methods are powerful tools for simulating physical processing such as estimating in positron emission tomography (PET) scattered and true coincidences in PET, with GATE considered the gold standard. However, the high computational costs can limit its clinical applicability. SimSET offers a substantially faster alternative while retaining the key photon-interaction physics required for accurate PET simulation. In this work, we present a systematic concordance study between SimSET and GATE for the GE Omni Legend PET scanner geometry. The two simulators are compared across four metrics: sensitivity sinograms for the true coincidences, 2D energy spectra, trues-only reconstructed images, and scatter fraction, using a uniform cylinder and a realistic [18F]PE2I brain phantom as test cases. Strong agreement was observed across all metrics, with scatter fractions differing by less than 0.03 percentage points (25.65% vs. 25.63%). SimSET was found to be approximately ~59x times faster than GATE for almost equivalent simulation conditions. These results demonstrate that SimSET reproduces GATE outputs with high fidelity on this state-of-the-art scanner geometry, establishing it as an efficient and accurate platform for MC-based scatter estimation in clinical PET imaging workflows.

MIC-15-087

Hybrid Least-Square and k-Nearest-Neighbour Event Positioning for a Compact Gamma Camera with Monolithic NaI(Tl) Scintillator (#2718)

Xiao Zhang[1], **Yujin Qi**[2], Andrea Fabbri[3], Valentino O. Cencelli[3], Huifeng Zou[4], Jian Zheng[1], Qiang Du[1], Zhongyi Wu[1], Benjamin M.W. Tsui[5]

[1] Suzhou Institute of Biomedical Engineering and Technology, Chinese Academy of Sciences, Department of Medical Imaging, Suzhou, China; [2] University of Wollongong, Centre for Medical Radiation Physics, Wollongong, Australia; [3] I.N.F.N, Roma, Italy; [4] Suzhou Hospital of Nanjing University, Medical School, Suzhou, China; [5] Johns Hopkins University, Department of Radiology, Baltimore, USA

Abstract

The purpose of this study is to develop an accurate event positioning algorithm for a compact scintillation camera to enhance its intrinsic resolution and useful field-of-view (FOV). The compact camera consists of a 50×50×7mm^3 continuous NaI(Tl) crystal directly coupled to a Hamamatsu H12700 position-sensitive photomultiplier tube (PSPMT) with an 8×8 multi-anode readout array. Two kinds of reference libraries of detector responses for event positioning were built by analytical model of scintillation light distribution in a monolithic crystal and GENT4-based GATE Monte Carlo (MC) simulation, respectively. Each entry of the discrete grids-based library contains a detector response distribution corresponding to a known interaction position in crystal volume. Then a hybrid event positioning framework combining least-square estimation (LSE) and k-nearest-neighbour (k-NN) was developed and experimentally validated using Tc-99m flood sources. Preliminary test results show that the proposed hybrid event positioning method with MC simulation-based reference library exhibits good positioning linearity and edge-event positioning accuracy to enhance detector's spatial resolution and useful FOV as compared to the conventional centroid positioning method. Experimental results also demonstrate that the hybrid algorithm provides robust and computationally efficient event positioning. In conclusion, the approach combing hybrid algorithm with MC simulation-based reference library offers a practical and accurate solution for next-generation monolithic gamma-camera systems requiring high throughput and high intrinsic resolution. Further experimental evaluations are continued under investigations.

References

[1] Gonzalez-Montoro A et al., "Evolution of PET detectors and event positioning algorithms using monolithic scintillation crystals," *IEEE Trans. Rad. Plas. Med. Sci.*, vol.5, no.3, pp.282–305, May 2021.

[2] A. Fabbri et al., "A new iterative algorithm for pixilated and continuous scintillating crystal," *Nucl. Instrum. Methods Phys. Res. A*, vol. 648, pp. S79-S84, Aug., 2011.

[3] Z Wu et al., "Design and development of a high-resolution handheld gamma camera for thyroid and sentinel nodes imaging," *IEEE Nucl. Sci. Symp. Conf. Rec.*, Nov. 2022.

[4] Sarrut D, et al. "The OpenGATE ecosystem for Monte Carlo simulation in medical physics," *Phys Med Biol.* 67(18), 184001, 2022.

MIC-15-090

Ultra-fast Positron Range Simulator for Patient-Specific PET Imaging

(#2851)

Robert J. Paneque-Yunta[1,2], Nerea Encina-Baranda[1,2], Joaquín López Herraiz[1,2], Khaled M Abushab[3,1], Jose M Udias[1,2], Paula Ibáñez[1,2]

[1] Complutense University of Madrid (UCM), Nuclear Physics Group and IPARCOS, Madrid, Spain; [2] Instituto de Investigación Sanitaria Hospital Clínico San Carlos (IdISSC), Nuclear Techniques and Instrumentation in Biomedicine, Madrid, Spain; [3] Al-Azhar University-Gaza, Medical Physics, Gaza, Palestine

We acknowledge support from the Comunidad de Madrid through the Industrial Doctorate Program (IND2023/BMD-28275), co-funded by the European Social Fund (ESF), and from 3PET (PDC2022-133057-I00), funded by the Spanish Ministry of Science, Innovation and Universities (MCIU) through AEI/10.13039/501100011033 and the European Union's NextGenerationEU/PRT program. RJPY also acknowledges support from the Complutense University Predoctoral Fellowship (CT22-25), funded by the Universidad Complutense de Madrid (UCM) and Banco Santander.

Abstract

Positron range (PR) degrades spatial resolution in positron emission tomography (PET), with its efect being radionuclide- and medium-dependent. Current accurate PR simulators are computationally intensive and cannot be used in clinical applications. This work presents the Hybrid Monte Carlo (HMC) PR simulator, a GPU-accelerated condensed-history code in CUDA Fortran for 3D annihilation imaging in heterogeneous voxelized geometries derived from CT images and μ-maps. Pre-computed interaction tables covering 24 reference-tissue materials and support for arbitrary β^+ emitters up to 3.55 MeV end-point energies (^{68}Ga, ^{82}Rb, etc.) allow both GPU and CPU implementations. Maximum speeds reach $4.77 \cdot 10^5$ (Intel Core i9-14900KF) and $3.32 \cdot 10^8$ (NVIDIA GeForece RTX 5080) histories/s, surpassing prior CPU-only PR simulators by up to 4 orders of magnitude. Close agreement with PenEasy 2024 is demonstrated: point-source simulations reach FWHM residuals are below 0.1 mm at 10^7 histories, and voxelwise R^2=0.982 and PSNR≈30.8 dB are achieved in a realistic myocardium phantom while decreasing the simulation time from 6 hours to 1 second (using HMC GPU). The resulting annihilation maps enable PET resolution modeling and patient-specific PR correction within clinically practical time frames.

References

[1] R. J. Paneque-Yunta *et al.*, "Analytical positron range model for PET with cross-code Monte Carlo benchmarking," *Phys Med Biol*, vol. 70, no. 16, p. 165013, Aug. 2025, doi: 10.1088/1361-6560/adf591.

[2] W. Schneider, T. Bortfeld, and W. Schlegel, "Correlation between CT numbers and tissue parameters needed for Monte Carlo simulations of clinical dose distributions," *Phys Med Biol*, vol. 45, no. 2, pp. 459–478, Feb. 2000, doi: 10.1088/0031-9155/45/2/314.

[3] P. Ibáñez *et al.*, "XIORT-MC: A real-time MC-based dose computation tool for low- energy X-rays intraoperative radiation therapy," *Med Phys*, vol. 48, no. 12, pp. 8089–8106, Dec. 2021, doi: 10.1002/mp.15291.

[4] J. L. Herraiz, A. Lopez-Montes, and A. Badal, "MCGPU-PET: An open-source real-time Monte Carlo PET simulator," *Comput Phys Commun*, vol. 296, p. 109008, Mar. 2024, doi: 10.1016/j.cpc.2023.109008.

[5] J. Sempau, A. Badal, and L. Brualla, "A PENELOPE-based system for the automated Monte Carlo simulation of clinacs and voxelized geometries—application to far-from-axis fields," *Med Phys*, vol. 38, no. 11, pp. 5887–5895, Nov. 2011, doi: 10.1118/1.3643029.

[6] J. Cal-González *et al.*, "Positron range estimations with PeneloPET," *Phys Med Biol*, vol. 58, no. 15, pp. 5127–5152, Aug. 2013, doi: 10.1088/0031-9155/58/15/5127.

[7] C. S. Levin and E. J. Hoffman, “Calculation of positron range and its effect on the fundamental limit of positron emission tomography system spatial resolution,” *Phys Med Biol*, vol. 44, no. 3, pp. 781–799, Mar. 1999, doi: 10.1088/0031-9155/44/3/019.

MIC-15-093

Analytic Determination of Minkhole Collimator Sensitivity With Penetration (#3082)

Yusheng Li

United Imaging Healthcare North America, MI, Houston, USA

Abstract

Multi-pinhole collimation in single-photon emission computed tomography (SPECT) trades aperture penetration against sensitivity and spatial resolution. Closed-form analytic sensitivities with penetration are known for the circular pinhole and the rectangular pinhole (recthole), but not for the recently introduced minkhole: a Minkowski-sum aperture lofting a circular waist into a rectangular exit. We close that gap with three knife-edge closed forms—an Anger three-term penetration expansion, an exact on-axis Stieltjes form in elementary moment integrals, and a Stieltjes-corrected hybrid—anchored to a two-dimensional level-set integral as the point-source-exact reference. The three-term expansion shares the universal penetration-order scaling of the circular-pinhole and recthole results; the minkhole’s first-order coefficient carries a disk-rectangle Steiner cross-term that vanishes at the recthole limit and is structurally absent from the cylindrical circular pinhole. The on-axis Stieltjes route recovers the Metzler–Moore recthole closed form term-by-term as the waist radius vanishes. Validation against a three-dimensional ray-tracing reference on a 12-panel benchmark grid gives worst relative errors of 1.01% (Anger), 0.69% (hybrid), and 0.39% (level-set exact). The hybrid enables sub-millisecond sensitivity evaluation for minkhole-based SPECT system-matrix construction.

References

[1] M. C. Goorden, M. C. M. Rentmeester, and F. J. Beekman, “Theoretical analysis of full-ring multi-pinhole brain SPECT,” Phys. Med. Biol., vol. 54, no. 21, pp. 6593–6610, Nov. 2009, doi: 10.1088/0031-9155/54/21/010.

[2] K. Van Audenhaege, R. Van Holen, S. Vandenberghe, C. Vanhove, S. D. Metzler, and S. C. Moore, “Review of SPECT collimator selection, optimization, and fabrication for clinical and preclinical imaging,” Med. Phys., vol. 42, no. 8, pp.4796–4813, Aug. 2015, doi: 10.1118/1.4927061.

[3] S. Pells, N. Zeraatkar, K. S. Kalluri, S. C. Moore, M. May, L. R. Furenlid, M. A. Kupinski, P. H. Kuo, and M. A. King, “Correction of multiplexing artefacts in multi-pinhole SPECT through temporal shuttering, de-multiplexing of projections, and alternating reconstruction,” Phys. Med. Biol., vol. 69, no. 12, p. 125004, Jun. 2024, doi: 10.1088/1361-6560/ad4f47.

[4] S. D. Metzler, J. E. Bowsher, M. F. Smith, and R. J. Jaszczak, “Analytic determination of pinhole collimator sensitivity with penetration,” IEEE Trans. Med. Imag., vol. 20, no. 8, pp. 730–741, Aug. 2002, doi: 10.1109/42.938241.

[5] S. D. Metzler and S. C. Moore, “Analytic determination of rectangular-pinhole sensitivity with penetration,” IEEE Trans. Med. Imag., vol. 39, no. 4, pp. 833–843, Apr. 2019, doi: 10.1109/TMI.2019.2936187.

[6] Y. Li and H. Li, “Minkhole collimators for SPECT: Minkowski-sum aperture geometry and closed-form ray tracing,” in Proc. IEEE Nucl. Sci. Symp. Med. Imag. Conf. (NSS/MIC), 2026, submitted.

[7] K. Deprez, L. R. Pato, S. Vandenberghe, and R. Van Holen, “Characterization of a SPECT pinhole collimator for optimal detector usage (the lofthole),” Phys. Med. Biol., vol. 58, no. 4, Jan. 2013, doi: 10.1088/0031-9155/58/4/859.

MIC-15-096

MIC-15-099

Performance evaluation of Compton-PET with MACACO-PET system

(#2666)

Siddharth Parashari[1], Karol Brzeziński[1], Luis Barrientos[1], Nataly Castellanos[1], Fernando Hueso-González[1], Ana Ros[1], Jorge Roser[2], Magdalena Rafecas[2], Gabriela Llosa[1]

[1] Instituto de Fisica Corpuscular (IFIC) CSIC-UV, Valencia, Spain; [2] University of Luebeck, Institute of Medical Engineering, Luebeck, Germany

This work has received funding from the Spanish MICIN/AEI (project MIDAS, PID2022-143246OB-I00). SP acknowledges the funding from Severo Ochoa Center of Excellence under the CEX2023-001292-S grant, funded by MCIN/AEI/10.13039/501100011033.

Abstract

Integration of Compton cameras (CC) with PET can be advantageous for multitracer imaging and to improve the resolution for simultaneous β^+-γ emitters. This technology is showing potential to become a viable option. The combination of PET and SPECT faces challenges due to collimation in SPECT and poor performance at high photon energies. CCs overcome this limitation and are more suitable for high-energy and multiple gamma emitting radiotracers. The IRIS group of IFIC (Valencia) has shown via simulations that combined CC and PET imaging of a Derenzo-like phantom with ^{89}Zr, ^{124}I, and both ^{18}F and ^{95}Tc is feasible, demonstrating the ability of Compton-PET to image multiple radionuclides. In continuation of this work, a performance evaluation of an experimental Compton-PET prototype is ongoing. An identical geometry is also studied through GATE simulations. The geometry consists of four identical detectors, of which two are combined as a CC and the other two are placed as PET detectors facing each other at either side of the geometrical center of the system. Image reconstruction is performed using a custom algorithm developed by the IRIS group. We present reconstructed images of a ^{22}Na source array obtained with the simulated Compton-PET system. Successful imaging results pave the way for subsequent laboratory testing of the Compton-PET system, enabling simultaneous β^+-γ and multitracer radionuclide imaging.

MIC-15-102

Dosimetry Assessment and Noise Scaling Laws in Proton Computed Tomography (#2724)

Carlo Civinini[1], Annamaria Falivene[2], Linhsia Noferini[2], Francesco Rossi[2], Monica Scaringella[1], Adriana Taddeucci[3], Francesco Tommasino[4,5], Enrico Verroi[5], Mara Bruzzi[6,1]

[1] INFN - Istituto Nazionale di Fisica Nucleare, Sezione di Firenze, Sesto Fiorentino (FI), Italy; [2] A.O.U. Careggi, U.O. Fisica Sanitaria, Firenze, Italy; [3] USL Toscana Centro, SOC Fisica Sanitaria Firenze ed Empoli, Firenze, Italy; [4] University of Trento, Department of Physics, Trento, Italy; [5] INFN - Istituto Nazionale di Fisica Nucleare, TIFPA, Povo (TN), Italy; [6] University of Florence, Department of Physics and Astronomy, Sesto Fiorentino (FI), Italy

This work was supported by INFN CSN5 with the PRAD research project.

Abstract

Proton Computed Tomography (pCT) is an emerging imaging modality designed to reduce uncertainties in proton therapy planning by directly mapping the Relative Stopping Power (RSP) of tissues. This study provides a comprehensive performance evaluation of the INFN pCT prototype, focusing on experimental dosimetric characterization and the determination of noise scaling laws. Utilizing a silicon tracker and a YAG:Ce calorimeter, measurements were conducted at the APSS Trento center with a 211.2 MeV proton beam. Dosimetry performed with TLD-100 thermoluminescent dosimeters revealed an absorbed dose of 1.4–1.5 mGy per10^8 trigger events, resulting in a total dose of 11.6 mGy for a high-quality 9-rotation scan. The investigation into image noise demonstrated that the system operates in a purely statistical regime, with the standard deviation of RSP following the inverse square root of the product of dose and voxel volume. No significant additive noise floor was detected. Analysis identified a 1 mm³ voxel volume as an optimal benchmark, constrained by Multiple Coulomb Scattering physical limits. At this resolution, measured noise levels ranged from 0.3% to 0.7%, significantly outperforming the 1% clinical requirement. These results validate the system's ability to provide high-accuracy RSP maps at low patient doses.

References
[1] C. Civinini et al 2020 Phys. Med. Biol. 65 225012
[2] M. Bruzzi et al 2026 Phys. Med. Biol. 71 01504
[3] M. Scaringella et al 2023 Phys. Med. Biol. 68 154001
[4] S. Rit et al. 2013 Med. Phys. 40 (3)
[5] A. C. Kak and Malcolm Slaney, Principles of Computerized Tomographic Imaging, Society of Industrial and Applied Mathematics, 2001
[6] E. Fogazzi et al 2023 Phys. Med. Biol. 68 124001
[7] Tommasino F et al 2017 NIM A 869 15–20
[8] Y.S. Horowitz et al 2008, Rad. Meas., 2-6, 203-207
[9] C. Civinini et al 2017 JINST 12 C01034

MIC-15-105

Feasibility of 511 keV photon detection in the presence of scattered x-rays for simultaneous PET and CT imaging (#2946)

Charles Hayward[1], Carolina Rabin[2], William C.J. Hunter[1], Robert S. Miyaoka[1], Ioannis Sechopoulos[3], **Paul E. Kinahan**[1]

[1] University of Washington, Department of Radiology, Seattle, USA; [2] Instituto de Física, Universidad de la República, Montevideo, Uruguay; [3] Department of Medical Imaging, Radboud University Medical Center, Nijmegen, Netherlands

Supported in part by NIH grant U01EB034222

Abstract

In PET/CT scanners the x-ray source is turned off during the PET acquisition for several reasons, including preventing saturation of the PET detectors due to pulse pile-up from lower-energy scattered x-rays. We conducted simulation and experimental studies to evaluate if there are operating conditions where simultaneous PET and CT imaging is feasible.

Simulation studies were used to estimate the flux and energy distribution of scattered x-rays for a dedicated breast PET/CT scanner using a tungsten x-ray tube operated at 65 kVp. The x-ray tube spectrum was used for tracking of x-rays scattered at roughly 90 deg into a PET detector. We also evaluated using metal filters in front of the PET detector to preferentially absorb the lower energy scattered x-rays. We then conducted experimental studies of 511 keV photon detection by a LYSO scintillator in the presence of scattered x-rays. The x rays were generated from a mammography scanner operated at 49 kVp. The scattering object was a water phantom in the mammography field of view. The PET detector was located at 90 deg to the x-ray beam direction. The outputs were evaluated in terms of timing and energy spectra.

The simulation studies indicated that for the CT and PET scanner geometry, the scattered x-ray flux was overall reduced by 90 %. The addition of 1 mm of Ag or Cu in front of the PET detector reduced the flux of scattered x-rays incident on the PET detector by 99.5% or 96.5%, while reducing the flux of 511 keV photons by only 9% or 16%. The experimental studies demonstrated the expected dominance of the scattered x-rays on the PET detector output. The use of 1 mm of Cu filtration restored the photopeak signal, except for the predicted 16% loss. Both simulations and experimental studies indicate that simultaneous PET and x-ray imaging may be possible under certain conditions of x-ray tube technique, scanner geometry, and pre-detector PET filtration.

MIC-15-108

Integrating X-ray Dark-Field and Fluorescence Modalities for Molecular Imaging in Personalized Medicine: Initial Specifications of Setup Design and Integration Parameters (#3110)

Kunal Kumar[1], Xiaolei Yan[1], Xiaolei Yan[1], Muna Abboush[1], Muna Abboush[1], Cecilia Riani[2], Cecilia Riani[3], Christoph Hoeschen[1], Christoph Hoeschen[1]

[1] Otto von Guericke University Magdeburg, Institute for medical technology, Chair of Medical Systems Technology, Magdeburg, Germany; [2] University of Pavia, Department of Physics "A. Volta", Pavia, Italy, Italy; [3] University of Pavia, Department of Physics "A. Volta", Pavia, Italy, Italy

IMMPRINT Project (G.A. 101061037).
The author would like to express sincere appreciation to the supervisor and colleagues of the team for their support.

Abstract

As innovative imaging tools, both X-ray dark-field and X-ray fluorescence imaging show significant potential for medical applications. However, each modality has technical trade-offs that can limit its effectiveness when used in isolation. While molecular imaging plays a crucial role in modern diagnostics by enabling early detection and personalized therapy, existing *in vivo* methods often suffer from low sensitivity, limited resolution, or high ionizing radiation exposure.To address these challenges, this proof-of-principle study proposes a hybrid approach leveraging the synergistic advantages of X-ray dark-field imaging (DFI) and X-ray fluorescence (XRF) imaging. DFI—characterized by high sensitivity to micro-level structural abnormalities at a low radiation dose—is utilized to identify targeted regions of interest (ROIs), thereby overcoming the inherent resolution and dose constraints of XRF. By confining XRF scans exclusively to DFI-guided ROIs, the distribution of molecular nanoprobes (nanoparticles) can be mapped with high precision. This approach ensures that the high radiation doses typical of body-wide nuclear imaging are restricted to localized areas, significantly enhancing patient safety. In this work, specifications for both modalities were investigated via simulations and experiments to establish optimal integration parameters. Subsequently, a CAD model was developed and implemented to assemble the final integrated setup.

References
[1] Wirtensohn, S., Schmid, C., Berthe, D., John, D., Heck, L., Taphorn, K., Flenner, S. and Herzen, J., 2024. "Self-supervised denoising of grating-based phase-contrast computed tomography." Scientific Reports, 14(1), p.32169.
[2] Glinz, J., 2024. Quantitative phase and dark-field contrast computed tomography for industrial applications on lightweight materials (Doctoral dissertation, Technische Universität Wien).
[3] Ando, M., Yamasaki, K., Toyofuku, F., Sugiyama, H., Ohbayashi, C., Li, G., Pan, L., Jiang, X., Pattanasiriwisawa, W., Shimao, D. and Hashimoto, E., 2005. Attempt at visualizing breast cancer with X-ray dark field imaging. Japanese journal of applied physics, 44(4L), p.L528.
[4] Stampanoni, M., Wang, Z., Thüring, T., David, C., Roessl, E., Trippel, M., Kubik-Huch, R.A., Singer, G., Hohl, M.K. and Hauser, N., 2011. The first analysis and clinical evaluation of native breast tissue using differential phase-contrast mammography. Investigative radiology, 46(12), pp.801-806.
[5] Willer, K., Fingerle, A.A., Noichl, W., De Marco, F., Frank, M., Urban, T., Schick, R., Gustschin, A., Gleich, B., Herzen, J. and Koehler, T., 2021. X-ray dark-field chest imaging for detection and quantification of emphysema in patients with chronic obstructive pulmonary disease: a diagnostic accuracy study. The Lancet Digital Health, 3(11), pp.e733-e744.

[6] Kumar, K., Fachet, M., Al-Maatoq, M., Chakraborty, A., Khismatrao, R.S., Oka, S.V., Staufer, T., Grüner, F., Michel, T., Walles, H. and Hoeschen, C., 2023. Characterization of a polychromatic microfocus X-ray fluorescence imaging setup with metallic contrast agents in a microphysiological tumor model. Frontiers in Physics, 11, p.1125143.
[7] Grüner, F., Blumendorf, F., Schmutzler, O., Staufer, T., Bradbury, M., Wiesner, U., Rosentreter, T., Loers, G., Lutz, D., Richter, B. and Fischer, M., 2018. Localising functionalised gold-nanoparticles in murine spinal cords by X-ray fluorescence imaging and background-reduction through spatial filtering for human-sized objects. Scientific reports, 8(1), p.16561.
[8] Staufer, T. and Grüner, F., 2023. Review of development and recent advances in biomedical X-ray fluorescence imaging. International Journal of Molecular Sciences, 24(13), p.10990.
[9] Ungerer, A., Staufer, T., Schmutzler, O., Körnig, C., Rothkamm, K. and Grüner, F., 2021. X-ray-fluorescence imaging for *in vivo* detection of gold-nanoparticle-labeled immune cells: a GEANT4 based feasibility study. Cancers, 13(22), p.5759.

MIC-15-111

A Dual-Head Positron Imaging System (#1322)

Matthias Streun[1], Antoina Chlubek[2], Robert Koller[2], Ralf Metzner[2], Daniel Pflugfelder[2], Benedikt Scherer[1], Nils Schramm[1], Peter Wüstner[1], Egon Zimmermann[1], Ghaleb Natour[1]

[1] Forschungszentrum Jülich GmbH, Institute of Technology and Engineering (ITE), Jülich, Germany; [2] Forschungszentrum Jülich GmbH, Institute of Bio- and Geosciences (IBG-2), Jülich, Germany

This work has been performed in the framework of the Crystal Clear Collaboration.

Abstract

In this paper we will introduce a system for two-dimensional imaging of positron emission. It has been developed for the investigation of plant roots grown in rhizotrones. A rhizotron is a narrow, transparent flower pot that forces the roots to grow in a virtually two-dimensional manner. For this reason, a 3D reconstruction, as done in a PET scanner, is not necessary, and for a 2D projection two opposing planar detector heads are sufficient. The heads cover an area of 134x134 mm^2 and each contains 4096 LYSO scintillation crystals of 1.85x1.85x10 mm^3 each. Digital Silicon Photomultipliers (Philips DPC) detect the scintillation events which are stored as list mode data on disk and are already used to instantly visualize an online image of the activity distribution. We will present first images and characterize the system based on evaluation measurements.

MIC-15-114

Development of the CT extension of the MERMAID PET prototype

(#1586)

Rebecca Kantorek[1,2], Steven Seeger[2], Magdalena Rafecas[1]

[1] University of Luebeck, Institute of Medical Engineering, Lübeck, Germany; [2] University of Luebeck, Isotope Laboratory of the Natural Science Section, Lübeck, Germany

This work is financially supported by the German Research Foundation (DFG) under Grant Agreement no. 496099829.

Abstract

Zebrafish play an important role in biomedical research as a key vertebrate model for disease studies and drug screening; however, PET imaging has not yet been translated to this animal model. To fill this gap, the PET prototype MERMAID has been specifically conceived for imaging adult zebrafish and other small aquatic animals. Initial studies have proven the feasibility of the concept, as well as the need for anatomical reference information. For the latter, we are developing a cone beam CT system to be integrated into MERMAID. Challenges are the low soft tissue contrast in zebrafish and its small thickness, the attenuation of the water-filled imaging chamber, and potentially high radiation doses for the target animal. Although synchrotron radiation and contrast agents have both proved successful in providing high resolution and contrast zebrafish CT images, neither is suitable for our case, nor phase-contrast CT imaging techniques. The current CT setup consists of a cesium iodide flat panel detector and a handheld x-ray tube with a tungsten filament. For image reconstruction simultaneous algebraic reconstruction technique (SART) adapted from the reconstruction toolkit (RTK) is used. This setup allows a resolution smaller than 0.4 mm. We have successfully imaged several characterization phantoms as well as adult zebrafish ex-vivo, allowing visualization of the skeleton and small soft tissue changes in both air and water. Further work will include image registration, soft-tissue contrast enhancement, and integration with the PET component.

References

[1] Choi, TY, et al., 2021, 'Zebrafish as an animal model for biomedical research', *Exp Mol Med*, **53**, 310–317, DOI: 10.1038/s12276-021-00571-5

[2] Tucker, C, et al. 2021, 'PET/CT Technology in Adult Zebrafish: A Pilot Study Toward Live Longitudinal Imaging', Frontiers in Medicine, 8, DOI: 10.3389/fmed.2021.725548

[3] Seeger, S, et al. 2022, 'Characterisation of the Upgraded MERMAID Prototype, a PET/CT Device for Small Aquatic Animals', *2022 IEEE Nuclear Science Symposium and Medical Imaging Conference (NSS/MIC)*, Milan, Italy, DOI: 10.1109/nss/mic44845.2022.10399085

[4] Seeger, S, et al. 2025, 'First in-Vivo Tests of Zebrafish with Mermaid, a PET Prototype for Small Aquatic Animals', 2025 IEEE Nuclear Science Symposium (NSS), Medical Imaging Conference (MIC) and Room Temperature Semiconductor Detector Conference (RTSD), Yokohama, Japan, DOI: 10.1109/NSS/MIC/RTSD57106.2025.11287003

[5] Rit, S, et al. 2014, 'The Reconstruction Toolkit (RTK), an open-source cone-beam CT reconstruction toolkit based on the Insight Toolkit (ITK)', *J. Phys.: Conf. Ser.* , **489**, 012079, DOI: 10.1088/1742-6596/489/1/012079

[6] Lohrabian, V, et al. 2019, 'Design and construction of a variable resolution cone-beam small animal mini-CT prototype for in vivo studies', *Radiat. Phys. Chem.*, 162, 199-207, DOI: 10.1016/j.radphyschem.2018.10.019

[7] Cherry, S, et al. 2012, 'chapter 15 - Image Quality in Nuclear Medicine', Physics in Nuclear Medicine, 4. Edition, W.B. Saunders, Philadelphia, DOI: 10.1016/B978-1-4160-5198-5.00015-0

MIC-15-117

Initial performance evaluation of a dual-panel, high-resolution TOF-DOI PET prototype (#1796)

Ming Niu[1], Hang Yang[1], Xiaolong Jiang[1], Xiangtao Zeng[1], Wenjie Huang[1], Ruipeng Dai[1,2], Xiaoqin Zhang[1], Jianlang Hua[1], Yangyang Zhao[1,2], Qingyang Wei[2], Ying Liang[3], Zheng Gu[1]

[1] Shenzhen Bay Laboratory, Institute of Biomedical Engineering, Shenzhen, China; [2] University of Science and Technology Beijing, School of Automation and Electrical Engineering, Beijing, China; [3] National Cancer Center, Cancer Hospital & Shenzhen Hospital, Department of Nuclear Medicine, Shenzhen, China

The National Key R&D Program of China (No. 2023YFC2414800), the Major Program of Shenzhen Bay Laboratory (No. C1012530005), the National Natural Science Foundation of China (Nos. 12275182 and 62371314), Guangdong Basic and Applied Basic Research Foundation (Nos. 2024A1515012154), the Guangdong Provincial Project (No. 2023TQ07A233) and the Shenzhen Bay Laboratory Proof-of Concept Grants (No. C1022430005).

Abstract

This study presents an initial evaluation of a dual-panel PET prototype with TOF-DOI capabilities for high-resolution local human organs imaging. The system consists of two flat panel detectors, offering an open geometry suitable for small anatomical regions. Each panel has a 212 × 212 mm² active area and consists of dual-layer, multi-resolution LYSO detectors. An interleaved multiplexing circuit was implemented to reduce the readout channels by a factor of four, with signals processed by TOFPET2 ASIC electronics.

At the detector level, clear flood images were obtained with well identified crystals. The average energy resolutions were 14.60% and 14.09% for the top and bottom layers. The bottom layer achieved an average DOI resolution of 3.37 mm. The best coincidence timing resolution was 280 ps for bottom–bottom events after excluding inter-crystal scatter events. With a panel distance of 30 cm, the spatial resolutions at the center of the FOV were 1.15, 1.53, and 3.63 mm FWHM in the three orthogonal directions. The peak sensitivity was 4.29% at the FOV center and 2.14% at a 5 cm axial offset.

For phantom imaging, 1.6-mm rods were clearly resolved at the FOV center and remained discernible at a 5 cm off-center when four DOI bins were used in reconstruction. These initial results indicate that the dual-panel TOF-DOI PET prototype is promising for high-resolution imaging of localized human anatomy and small lesions detection. Its open and flexible geometry may also support dose monitoring in proton therapy. Further work will focus on correction methods, a more comprehensive performance evaluation, and practical imaging demonstrations.

References

[1] Huang S, Jiang X, Chen Z, Zeng X, Huang W, Yang H, He W, Niu M, Wu J, Wei Q and Gu Z, "Optimization of TOF and DOI Performance in a Multi-Resolution Detector for Brain-dedicated PET", IEEE Transactions on Radiation and Plasma Medical Sciences. 2025.

MIC-15-120

Development of a Four-Layer DOI Detector Based Preclinical PET System (#1863)

Hang Yang[1,2], Xiaoqin Zhang[1], Xiaolong Jiang[1], Wenjie Huang[1], Yangyang Zhao[1], Xiangtao Zeng[1], Ming Niu[1], Ying Liang[3], Zheng Gu[1]

[1] Shenzhen Bay Laboratory, Institute of Biomedical Engineering, Shenzhen, China; [2] Harbin Institute of Technology, School of Astronautics, Harbin, China; [3] National Cancer Center/National Clinical Research Center for Cancer/Cancer Hospital & Shenzhen Hospital, Chinese Academy of Medical Sciences and Peking Union Medical College, Department of Nuclear Medicine, Shenzhen, China

This work is supported by the National Natural Science Foundation of China (Nos. 12275182 and 62371314), the National Key R&D Program of China (No. 2023YFC2414800), Guangdong Basic and Applied Basic Research Foundation (Nos. 2024A1515012154), the Guangdong Provincial Project (Grant No. 2023TQ07A233), the Major Program of Shenzhen Bay Laboratory (No. C1012530005) and the Shenzhen Bay Laboratory Proof-of Concept Grants (No. C1022430005).

Abstract

This work presents a Monte Carlo-based performance evaluation of a preclinical PET system based on a four-layer depth-of-interaction (DOI) detector. The detector with optimized layer thickness design comprises two LYSO arrays and two BGO arrays. The first and third layers adopt 60×30 LYSO arrays with pixel dimensions of 0.78×0.78×4 mm3 and 0.78×0.78×6 mm3, respectively, the second and fourth layers employ 40×20 BGO arrays with pixel dimensions of 1.21×1.21×4 mm3 and 1.21×1.21×10 mm3, respectively. System spatial resolution and sensitivity were characterized via Monte Carlo simulations following the NEMA NU 4 protocol. The single-ring system achieves the peak sensitivity of 16.6% and an average spatial resolution of 0.69 mm across the field of view (FOV). The complete dual-ring complete system could further improve the sensitivity to >25%. Compared with the two-layer detector system, the proposed four-layer DOI design exhibits significantly improved sensitivity while maintaining high and uniform spatial resolution. Experimental validation using the four-layer detector with total size of 51.6×25.8×25.5 mm3 demonstrated CNN classification accuracies of 84% for the LYSO layers and 76% for the BGO layers. Flood images using 45° oblique collimated incidence showed distinct event clustering patterns between upper- and lower-layers Future work will focus on developing the single-ring validation prototype and further improving the DOI layer discrimination accuracy.

References

[1] He W, Zhao Y, Zhao X, et al. 'A CNN-based four-layer DOI encoding detector using LYSO and BGO scintillators for small animal PET imaging', Physics in Medicine & Biology, 2023, 68(9): 095021.

[2] Yang H, Zeng X, Huang W, et al. 'Design Optimization of a CNN-Based Fourlayer DOI Detector for Preclinical PET Imaging', 2025 IEEE NSS MIC and RTSD, Yokohoma Japan.

[3] Yang H, He W, Zhao X, et al. 'Performance evaluation of S-PET, a compact, LYSO/BGO phoswich detector small animal PET prototype', Physics in Medicine & Biology, 2026, 71(5): 055013.

MIC-15-123

Experimental Evaluation of 3D Imaging Point Spread Function for the Ultra-High Performance Brain PET (UHB-PET) Scanner (#2170)

Nicolas A. Karakatsanis[1], Fiammetta Pagano[2], Francis Loignon-Houle[2], David Sanchez[3], Enrique Munoz[3], Ezzat Elmoujarkach[1], Juan Vicente Catret[3], Antonio J. Gonzalez[2], Sadek A. Nehmeh[1]

[1] Weill Cornell Medical College, Department of Radiology, New York, USA; [2] Instituto de Instrumentacion para Imagen Molecular (i3M), Valencia, Spain; [3] Oncovision SA, Valencia, Spain

This project is supported by the National Institutes of Health (NIH) under award number 1R01CA275942.

Abstract

We report preliminary experimental results on the 3D imaging point spread function response performance of the Ultra-High Performance Brain PET (UHB-PET) system employing semi-monolithic LYSO slabs, machine-learning–based event positioning, and list-mode 3D point spread function (PSF) reconstruction. Detector calibration was previously performed using a slit-collimated 22-Na point source translated across monolithic and depth dimensions. A previous multilayer perceptron (MLP) estimated monolithic and depth positions of interaction, while axial positioning was derived via a previous center-of-gravity algorithm.

List-mode coincidence events were registered encoding time, energy, time-of-flight, module pair and within-module 3D coordinates, discretized into virtual detector pixels (50 transaxial × 50 axial × 20 depth) and mapped to global cylindrical coordinates after depth-of-interaction correction. A list-mode MLEM algorithm with an optimized Gaussian PSF model kernel width was employed. The system 3D imaging PSF was evaluated from 3-min acquisitions by placing a 0.25 mm 22-Na point source across 25 axial positions spanning the full axial FOV along the transaxial FOV center.

3D PET images free of visual artifacts were obtained. A uniform 3D PSF with mean relative absolute deviation from FOV center of 5.83%, 5.87% and 7.32% for both FWHM and FWTM was observed in radial, tangential and axial PSF components, respectively, across all axial locations demonstrating an axially homogeneous 3D imaging PSF for UHB-PET.

Ongoing work includes implementation of classification-based MLP positioning with improved detector resolution, incorporation of experimentally derived spatially variant PSF kernels, and validation with an extended set of phantoms to further optimize 3D imaging PSF response and its uniformity in all directions across the entire FOV.

References

[1] Majewski, S., 2021, 'Perspectives of brain imaging with PET systems', *Bio-Algorithms and Med-Systems*, 17(4), pp. 269-29

[2] Pagano, F, *et al.*, 2024 'Performance evaluation of a multiplexing circuit combined with ASIC readout for cost-effective brain PET imaging', *Phys. Med. Biol.* 70 205001

[3] Karakatsanis, NA, et al, 2024, 'Monte Carlo Evaluation of the Ultra-High Physical Performance Brain PET (UHB-PET) scanner with semi-monolithic detectors' *IEEE NSS/MIC*

[4] Rahmim, A., Qi, J. and Sossi, V., 2013. 'Resolution modeling in PET imaging: theory, practice, benefits, and pitfalls',. *Medical physics*, *40* (Issue 6 Part 1), p.064301.

[5] Elmoujarkach, E, *et al.*, 2025, 'Sub-Millimeter 2D Intrinsic Resolution Recovery in Semi-Monolithic PET Detector using Neural Networks - a Monte Carlo Simulation', *IEEE NSS/MIC*

MIC-15-126

System integration of a Breast PET/MR Insert in a Whole-Body PET/MRI System: Data Driven Temperature Drift Correction and Synchronization

(#2428)

Janina Hohnholz[1], Lukas U. Rauscher[1], Martin Judenhofer[2], Elnaz Olyaei[1,3], Hong P. Vo[4], Magdalena Rafecas[4], Bernd Pichler[1,5], Fabian P. Schmidt[1,3]

[1] Werner Siemens Imaging Center, Department of Preclinical Imaging and Radiopharmacy, University of Tuebingen, Tuebingen, Germany; [2] Siemens Medical Solutions USA, Inc., Knoxville, USA; [3] University Hospital Tuebingen, Nuclear Medicine and Clinical Molecular Imaging, Tuebingen, Germany; [4] Insitute of Medical Engineering, University of Luebeck, Luebeck, Germany; [5] Cluster of Excellence iFIT (EXC2180), "Image Guided and Functionally Instructed Tumor Therapies", Tuebingen, Germany

Funding DFG 508064995

Abstract

Our PET/MR breast insert currently under development is designed to be compatible with a whole-body 3T PET/MRI system. The proposed insert comprises a ring geometry based on dual layer LSO detector blocks coupled via FFC cables to SiPM arrays. Such integration in the confined and RF-shielded PET/MR environment introduces challenges related to thermal stability, which are addressed using data-driven temperature monitoring and correction. In an isothermal setup, the photopeak remains stable (898.7 ± 0.5). Under a temperature gradient, a drift from 901.1 to 914.1 (~ 1.1 to 8.5 keV) within 30 min is observed, resulting in a shifted and broadened energy spectrum (photopeak 907.8, FWHM 76.9). After scaling energy values via the derived ratio of the peak shift to the reference, the photopeak is restored to 899.1 with reduced FWHM (75.7). In parallel, combined operation of insert and whole-body PET systems requires alignment of independent timestamp domains to enable mixed-coincidence reconstruction. Two detector blocks were operated with independent local clocks, a synchronized reference was established and desynchronized by introducing a delay. A data-driven algorithm estimates this offset via a sliding-window coincidence search (±100 ns), where the offset is determined by the maximum coincidence counts within the timing window. After correcting for the delay, time difference spectra within a narrow ±3 ns time window could be restored while preserving a 430 ps coincidence resolution time. These results demonstrate that data-driven correction and synchronization enable stable PET/MR operation and potentially enable mixed-coincidence imaging across independent systems. Future work will focus on scaling to multi-ring systems, enhancing in-situ temperature sensing during MR operation, and evaluating mixed-coincidence imaging between independent PET systems enabled by the proposed synchronization approach.

MIC-15-129

Performance Evaluation of the Motion-Adaptive Molecular and Behavioral Observation (MAMBO)-PET System (#2586)

Francisco E. Enriquez-Mier-y-Teran[1,2], Julien Bec[3], Martin Judenhofer[4], Stefan Siegel[4], Sun Il Kwon[3], Simon R. Cherry[3], Andre Z. Kyme[2,5], Steven R. Meikle[1,2]

[1] The University of Sydney, Faculty of Medicine and Health, Sydney, Australia; [2] The University of Sydney, Brain and Mind Centre, Sydney, Australia; [3] University of California Davis, Department of Biomedical Engineering, Davis, USA; [4] Siemens Healthineers, Knoxville, USA; [5] The University of Sydney, School of Biomedical Engineering, Sydney, Australia

The authors would like to acknowledge the mechanical workshop at the Faculty of Engineering, The University of Sydney, and the Advanced Manufacturing Hub at The University of Sydney for their machining of various aluminium components

Abstract

Conventional brain PET imaging of small rodents necessitates anesthesia to prevent motion artefacts. However, anesthesia may alter brain function and preclude the simultaneous assessment of brain function and animal behavior. The Motion-Adaptive Molecular and Behavioral Observation (MAMBO)-PET system aims to overcome these limitations by enabling brain imaging in awake, freely moving mice. The system consists of four detector panels. Two panels have been assembled, while the remaining two are in the final stages of assembly. Here, we report the initial performance of the two-panel MAMBO-PET system. The mean detector panel energy resolution ranged from 14.9% to 15.0%. The FWHM of the radial and tangential PSF profiles at the center of the FOV were 0.9 mm and 5.7 mm, respectively. Future work includes the NEMA characterization of the full 4-panel system.

References

[1] P. Vaska *et al.*, *IEEE Trans. Nucl. Sci.*, vol. 51, pp. 2718-22, 2004
[2] A. Z. Kyme *et al.*, *Neuroimage*, vol. 188, pp. 92-101, 2019
[3] A. Miranda *et al.*, *IEEE Trans. Med. Imaging*, vol. 36, pp. 1573-82, 2017
[4] A. Z. Kyme *et al.*, *Phys. Med. Biol.*, vol. 62, pp. 6207-6225, 2017
[5] F.E. Enriquez-Mier-y-Teran *et al.*, *2021 IEEE NSS/MIC*, pp. 1-3, 2021
[6] F.E. Enriquez-Mier-y-Teran *et al.*, *IEEE Trans. Radiat. Plasma Med. Sci.*, vol. 9, pp. 395-405, 2025
[7] R. Bugalho *et al.*, *JINST*, vol. 64, pp. P03029, March 2019
[8] D. Schug *et al.*, *IEEE Trans. Radiat. Plasma Med. Sci.*, vol. 3, pp. 444-53, 2019

MIC-15-132

First experimental and phantom results of the DC-SPECT scanner: a cardiac-dedicated SPECT with Laser-Processed CsI:Tl Detector Modules (#2799)

Xi Zhang, Arkadiusz Sitek, Mark P. Ottensmeyer, Fang Han, Hamid Sabet

Harvard Medical School, Massachusetts General Hospital, Boston, USA

This work was supported in part by NIH Grant No. R01HL145160 and R01EB034785.

Abstract

Our group is developing Dynamic Cardiac SPECT (DC-SPECT) featuring laser-processed CsI: Tl scintillators with converging pixels to avoid depth-of-interaction blurring. This work reports, for the first time, the initial imaging performance of the DC-SPECT scanner featuring laser-processed CsI: Tl detector modules with converging pixels. A 50×50×8.05 mm^3 CsI: Tl crystal was laserprocessed into a 25×25 converging-pixel array. The crystal was coupled to an 8×8 multi-pixel photon counter array , read out by a custom 64-channel analog front-end board and a 12-bit waveform digitizer. Three decoding algorithms were evaluated: MLE-Bicubic, MLE-Nearest, and a deep neural network (NN) decoder. A ^{57}Co point source and a ^{99m}Tc three-line source phantom were imaged using list-mode MLEM reconstruction. For the point source, FWHM values of 6.24, 6.58, and 5.67 mm were obtained for MLE-Bicubic, MLE-Nearest, and NN at 20 iterations, with NN yielding the sharpest response. At 50 iterations, FWHM values improved to 4.63, 4.98, and 5.02 mm, with MLE-Bicubic achieving the sharpest response. For the three-line source phantom, sources located near the center of the field of view yielded mean FWHM values as low as 3.55 mm (NN) and 4.04 mm (MLE-Bicubic). Sources near the field-of-view edge exhibited broader responses, consistent with the known degradation of detector sensitivity toward the detector periphery. The converging-pixel architecture effectively eliminates depth-of-interaction ambiguity without additional hardware, further supporting the practical viability of this detector design. Future work will focus on optimization of reconstruction parameters, and further phantom and cardiac imaging studies toward clinical deployment of the DC-SPECT system.

References

[1] L. Bläckberg et al., “Dynamic Cardiac SPECT for diagnostic and theranostics applications: latest results,” in 2020 IEEE NSS, MIC and RTSD, 2020, pp. 1–3.

[2] H. Sabet, L. Blackberg, D. Uzun-Ozsahin, and G. El Fakhri, “Novel laser-processed CsI:Tl detector for SPECT,” Med. Phys., vol. 43, no. 5, 2016, pp. 2630–2638.

[3] X. Zhang, A. Sitek, L. Blackberg, M. Kupinski, L. Furenlid, and H. Sabet, “Development and Performance Evaluation of a Laser Processed CsI:Tl Detector with Converging Pixels,” in 2025 IEEE NSS, MIC and RTSD, 2025, pp. 1–2.

MIC-15-135

Validation of an Image Based Method of Estimating Mechanical Offsets in a Rotating Flat-Panel PET Scanner with Phantom and Clinical Data

(#2997)

Anirudh Shahi[1], Brandon Baldassi[2], Borys Komarov[2], Ur Metser[3], Alla Reznik[1,4], Oleksandr Bubon[1,2]

[1] Lakehead University, Physics, Thunder Bay, Canada; [2] Radialis Inc., Thunder Bay, Canada; [3] Princess Margaret Cancer Center, Medical Imaging, Toronto, Canada; [4] Thunder Bay Regional Health Research Institute, Thunder Bay, Canada

The authors acknowledge financial support from OGS, INOVAIT, NSERC, and NRC.

Abstract

Accurate geometric calibration is essential for high-resolution 3D PET image reconstruction because detector element mispositioning can introduce spatial misalignment of lines-of-response (LORs) and image blur. This challenge is particularly important in rotating flat-panel PET scanners, where opposing detector panels rotate during acquisition to improve angular coverage and enable fully 3D reconstruction. In this work, we developed and evaluated an image-based calibration method for estimating linear offsets between detector centers and the axis of rotation in the Radialis PET Imager, an organ-targeted rotating flat-panel PET scanner. The calibration was performed using a ^{22}Na point source acquired with twelve step-and-shoot detector rotations from -90° to +75°. Four point source experiments were performed at different source locations. An iterative algorithm was implemented to estimate linear offsets by minimizing distances between reconstructed point sources from different detector angles and the target image acquired at 0°. The estimated offsets were fed into transformation matrices used for composite image reconstruction of list mode data from all detector angles. Performance was evaluated using spatial resolution measurements from composite images, Hoffman brain phantom scans, and a clinical ^{18}F-Florbetaben brain scan. Offset calibration improved the average spatial resolution (FWHM) from 3.3 mm to 2.9 mm, with axial FWHM improving from 5.2 mm to 3.0 mm. Hoffman phantom images reconstructed with offset calibration demonstrated improved contrast and visualization of internal structures. The calibration of ^{18}F-Florbetaben clinical brain images demonstrated improved visualization of anatomical features, including the septum pellucidum, as well as improved contrast and reduced apparent cortical tracer uptake relative to image reconstructed without offset calibration.

References

[1] J. Thull, T. Freye, Y. Kuhl and V. Schulz, "Beyond Mechanics: Maximum-Likelihooddriven Pet Detector Alignment," 2025 IEEE Nuclear Science Symposium (NSS), Medical Imaging Conference (MIC) and Room Temperature Semiconductor Detector Conference (RTSD), Yokohama, Japan, 2025, pp. 1-1, doi: 10.1109/NSS/MIC/RTSD57106.2025.11287313.

[2] L. Pierce, R. Miyaoka, T. Lewellen, A. Alessio, and P. Kinahan, “Detector position estimation for pet scanners,” Nuclear Instruments and Methods in Physics Research Section A: Accelerators, Spectrometers, Detectors and Associated Equipment, vol. 677, pp. 74–79, Jun. 2012. doi:10.1016/j.nima.2012.02.040

[3] Y. Chen, L. Cai, S. Komarov, J. A. O’Sullivan, and Y.-C. Tai, “A data-driven approach for spatial alignment of pet add-on detectors with sub-millimeter accuracy,” Physics in Medicine & Biology, vol. 70, no. 18, p. 185005, Sep. 2025. doi:10.1088/1361-6560/adf937

[4] M. Abella et al., “Misalignments calibration in small-animal pet scanners based on rotating planar detectors and parallel-beam geometry,” Physics in Medicine and Biology, vol. 57, no. 22, pp. 7493–7518, Oct. 2012. doi:10.1088/0031-9155/57/22/7493

[5] A. Shahi et al., "3D Brain Imaging Using a Rotating Flat-Panel PET Scanner with LYSO/SiPM-Based Detectors," 2025 IEEE Nuclear Science Symposium (NSS), Medical Imaging Conference (MIC) and Room Temperature Semiconductor Detector Conference (RTSD), Yokohama, Japan, 2025, pp. 1-2, doi: 10.1109/NSS/MIC/RTSD57106.2025.11286760.
[6] S. Siala, D. Homen, B. Smith, and C. Guimaraes, “Imaging of the septum pellucidum: Normal, variants and pathology,” The British Journal of Radiology, vol. 96, no. 1151, Nov. 2023. doi:10.1259/bjr.20221058

MIC-15-138

Detector Stability and Effects on Time and Energy Resolution in Novel Clinical Brain PET Scanners (#3125)

Luis Batres[1], Lidia Jiménez Algarra[1], Marcos Vidal[1], David Perez-Benito[1], Juan Jose Vaquero[1,2]

[1] Universidad Carlos III de Madrid, Departamento de Bioingeniería, Leganés, Spain; [2] Instituto de Investigación Sanitaria Gregorio Marañón, Madrid, Spain

We acknowledge support from European Union as part of the European Innovation Council's Pathfinder Open Programme: RETIMAGER, 101099096.

Abstract

Compact PET scanners based on highly integrated front-end ASICs require stable thermal conditions to preserve detector gain, timing response, energy resolution, and inter-module uniformity. This is especially relevant in low-footprint PET systems, where high channel density and closed mechanical integration limit conventional forced-air cooling.

This work presents a thermal stabilization strategy designed for a new family of clinical and preclinical PET scanners: BuckyPET, BrainPET and UltraPET. The solution combines adaptive SiPM bias compensation with active liquid cooling of the ASIC electronics using a cascade proportional--integral (PI) controller. The outer loop regulates an exponentially filtered high-percentile aggregate of ASIC temperature deviations from a learned baseline, while the inner loop controls the coolant temperature through the chiller command. Saturation, setpoint slew-rate limiting and anti-windup mechanisms are included to improve robustness under variable conditions.

The proposed strategy maintained the ASIC thermal deviation within the tolerance band for different ambient conditions and high data throughput acquisitions. Preliminary measurements show improvements of up to 15% in energy resolution and up to 8% in coincidence time resolution compared with worst-case thermal drift conditions. The architecture enables compact, silent, and patient-friendly scanner designs, while preserving reproducible PET performance.

MIC-15-141

Counting loss correction of photon counting detector: the need to consider the effective atomic number of the target object in clinical applications (#1049)

Natsumi Kimoto[1], Rina Nishigami[2], Takashi Asahara[3], Yuki Kanazawa[4], Akitoshi Katsumata[5], Shuichiro Yamamoto[6], Hiroaki Hayashi[7], This is a collaborative study between JOB CORPORATION and Junshin Gakuen University.

[1] Junshin Gakuen University, Department of Radiological Science, Faculty of Health Sciences, Fukuoka, Japan; [2] Kanazawa University, Graduate School of Medical Sciences, Kanazawa, Japan; [3] Okayama University, Department of Radiological Technology, Faculty of Health Sciences, Okayama, Japan; [4] Kumamoto University, Faculty of Life Science, Kumamoto, Japan; [5] Asahi University, Oral Radiology and Artificial Intelligence, Mizuho, Japan; [6] JOB CORPORATION, Yokohama, Japan; [7] Kanazawa University, College of Transdisciplinary Sciences for Innovation, Kanazawa, Japan

This research was supported by JSPS KAKENHI Grant Numbers 25K21600 and 24K03306.

Abstract

Correcting counting loss phenomena caused by pulse pile-up and dead time is essential for the medical application of an energy-resolving photon counting detector (ERPCD). At the IEEE 2025 MIC conference, we proposed a counting loss correction algorithm applicable to objects, but it was limited to an effective atomic number (Z_{eff}) of 7–13. In this study, we propose a novel counting loss correction algorithm that extends the target object to Z_{eff} = 3–20 to cover biological samples, and evaluate the quantitative performance of the Z_{eff} images related to the algorithm. The novelty is to estimate the effect of counting loss on objects with Z_{eff} = 3–20 using experimentally derived counting loss correction functions for polymethyl methacrylate (PMMA, Z_{eff} = 6.5) and aluminum (Al, Z_{eff} = 13). Using the correction function for each Z_{eff}, the measured counting rate can be converted to the expected counting rate under ideal conditions without counting loss. Since the Z_{eff} of the object is unknown at the beginning of the analysis, corrections for Z_{eff} = 3–20 are tentatively performed. The corrected counting rate is then applied to the material identification algorithm, which was proposed in a previous study, and Z_{eff} is derived. Finally, the Z_{eff} of an object is determined when the entire algorithm works properly. To demonstrate our method, reference samples with known Z_{eff} (PMMA, Al, bilayer structures of PMMA and Al, and Si powder) and tooth samples were measured using a prototype ERPCD system equipped with a cadmium zinc telluride (CZT) semiconductor detector. When applying the correction to the measurement of reference samples, the accuracy of the Z_{eff} image was +/-1 under general radiography conditions. For a dental sample, tooth structure and resin can be observed with proper Z_{eff}. This result demonstrates that counting loss correction is important for the clinical application of ERPCD.

References

[1] Hayashi H, Kimoto N, Asahara T, Asakawa T, Lee C, Katsumata A, 2021, 'Photon Counting Detectors for X-ray Imaging: Physics and Applications', *Springer*, 1, 1-119, Switzerland AG.

[2] Nishigami R, Kimoto N, Asahara T, Maeda T, Kobayashi D, Goto S, Haba T, Kanazawa Y, Yamamoto S, Hayashi H, 2026, 'Bone-enhanced high contrast X-ray images derived from attenuation estimation related to ultra-low energy X-rays – An application of an energy-resolving photon-counting detector (ERPCD)', *Radiation Physics and Chemistry*, 238, 113243.

[3] Asahara T, Okada S, Hayashi H, Maeda T, Nishigami R, Kobayashi D, Kurose C, Kimoto N, Goto S, Hisatomi M, Yanagi Y, Iguchi T, 2025, 'Helpfulness of effective atomic number image in forensic dental identification: Photon-counting computed tomography is suitable', *Computers in Biology and Medicine*, 184, 109333.
[4] Taguchi K, Iwanczyk JS, 2013, 'Vision 20/20: Single photon counting x-ray detectors in medical imaging', *Medical Physics*, 40, 100901.
[5] Kimoto N, Nishigami R, Kobayashi D, Maeda T, Asahara T, Goto S, Kanazawa Y, Katsumata A, Yamamoto S, Hayashi H, 2026, 'Counting-loss correction procedure of X-ray imaging detectors with consideration for the effective atomic number of biological objects', *Radiation Physics and Chemistry*, 239, 113237.
[6] Kimoto N, Hayashi H, Asakawa T, Lee C, Asahara T, Maeda T, Goto S, Kanazawa Y, Katsumata A, Yamamoto S, Okada M, 2021, 'Effective atomic number image determination with an energy-resolving photon-counting detector using polychromatic X-ray attenuation by correcting for the beam hardening effect and detector response', *Applied Radiation and Isotopes*, 170, 109617.

MIC-15-144

An algorithm to generate effective atomic number and mass density images from photon-counting CT: application for lung disease assessment (#1211)

Takashi Asahara[1], Rina Nishigami[2], Natsumi Kimoto[3], Mana Mitani[4,2], Noriaki Akagi[4], Mitsugi Honda[4], Toshihiro Iguchi[1], Takao Hiraki[5], Hiroaki Hayashi[6]

[1] Okayama University, Department of Radiological Technology, Faculty of Health Sciences, Okayama, Japan; [2] Kanazawa University, Graduate School of Medical Sciences, Kanazawa, Japan; [3] Junshin Gakuen University, Department of Radiological Science, Faculty of Health Sciences, Fukuoka, Japan; [4] Okayama University Hospital, Division of Radiological Technology, Medical Support Department, Okayama, Japan; [5] Okayama University, Department of Radiology, Faculty of Medicine, Dentistry and Pharmaceutical Sciences, Okayama, Japan; [6] Kanazawa University, College of Transdisciplinary Sciences for Innovation, Kanazawa, Japan

This study was supported by JSPS KAKENHI (25K21586 & 24K03306); JGC-S Foundation; Suzuki Memorial Foundation

Abstract

Photon-counting CT (PC-CT) enables acquisition of energy-resolved images. Analyzing these images provides potential for quantitative diagnosis based on material composition. This study aims to develop an algorithm that simultaneously generates effective atomic number (Z_{eff}) and effective mass density (ρ_{eff}) images from virtual monoenergetic images (VMIs) acquired by clinical PC-CT. To demonstrate the feasibility of our algorithm, phantom experiment and clinical lung datasets were analyzed as representative applications. In our algorithm, Z_{eff} and ρ_{eff} values are estimated voxel-wise from two VMIs. The CT values are converted to μ values, and their ratio is converted to the Z_{eff} value using a reference curve created from a known database of mass attenuation coefficient (μ/ρ). In addition, the tentative mass densities as a function of atomic number are estimated by fitting μ/ρ data of each atomic number to the measured μ values, and the ρ_{eff} is uniquely determined using the Z_{eff} information. The algorithm was validated using an in-house low-density phantom and clinical chest CT images from 10 patients. We analyzed Z_{eff} and ρ_{eff} values in diseased and normal lung tissue regions. From the phantom study, the measured ρ_{eff} values were consistent with the reference density of the samples. In clinical analysis, lung diseases exhibited characteristic changes in ρ_{eff}. A metastatic lung nodule showed a similar Z_{eff} value compared to normal lung tissue,

but its ρ_{eff} value was clearly higher. During pneumonia follow-up, ρ_{eff} values decreased by approximately 56% after one month of disease regression, while Z_{eff} values remained nealy unchanged. Our algorithm generates Z_{eff} and ρ_{eff} images from PC-CT data, allowing quantitative interpretation of conventional CT values. These results suggest that ρ_{eff} provides a useful quantitative indicator for lung lesion assessment.

References
[1] Nishii S, Asahara T, Morimitsu Y, Kajisaki S, Akagi N, Honda M, Hayashi H, Sugaya A, Munetomo K, Higaki F, Hiraki T, Iguchi T, 2026, 'Optimization of the reconstruction kernel for temporal bone imaging using photon-counting detector CT: a combined physical and visual evaluation', *Radiography*, 32(2), 103274.
[2] Hubbell JH and Seltzer SM, 1995. 'Tables of X-Ray Mass Attenuation Coefficients and Mass Energy-Absorption Coefficients 1 keV to 20 MeV for Elements Z = 1 to 92 and 48 Additional Substances of Dosimetric Interest'. http://physics.nist.gov/PhysRefData/XrayMassCoef/cover.html
[3] Asahara T, Mitani M, Kimoto N, Nishigami R, Takegami K, Morimitsu Y, Akagi N, Miyoshi T, Kanazawa Y, Iguchi T, Hayashi H, 2025, 'Applicability of Effective Atomic Number (Z_{eff}) Image Analysis of Coronary Plaques Measured With Photon-Counting Computed Tomography', *Investigative Radiology*, in press.
[4] Asahara T, Okada S, Hayashi H, Maeda T, Nishigami R, Kobayashi D, Kurose C, Kimoto N, Goto S, Hisatomi M, Yanagi Y, Iguchi T, 2025, 'Helpfulness of effective atomic number image in forensic dental identification: Photon-counting computed tomography is suitable', *Computers in Biology and Medicine*, 184, 109333.
[5] Kimoto N, Hayashi H, Asakawa T, Lee C, Asahara T, Maeda T, Goto S, Kanazawa Y, Katsumata A, Yamamoto S, Okada M, 2021, 'Effective atomic number image determination with an energy-resolving photon-counting detector using polychromatic X-ray attenuation by correcting for the beam hardening effect and detector response', *Applied Radiation and Isotopes*, 170, 109617.

MIC-15-147

Dual-Energy CT Metal Artifact Reduction Using VMI-Guided Iterative Reconstruction Refinement (#1325)

Sungmin Park, Younghwan Lim, Soohyun Lee, Hyosung Cho

Yonsei University, Department of Radiation Convergence Engineering, Yonsei University, Wonju, South Korea

Abstract

Metal artifacts in computed tomography (CT) degrade image quality and reduce quantitative reliability, particularly in the presence of metallic objects. Conventional metal artifact reduction (MAR) methods, such as sinogram interpolation and normalized correction, rely heavily on accurate metal segmentation and often fail to preserve fine anatomical structures. Although dual-energy CT (DECT) provides additional spectral information for material characterization, its potential has not been fully utilized in prior-guided iterative MAR frameworks. In this study, we propose a prior-guided iterative MAR method for DECT that incorporates virtual monoenergetic image (VMI) priors for improved artifact suppression and structural preservation. Metal regions are first identified in the image domain using residual-based metal segmentation from initial dual-energy reconstructed images, and the resulting metal mask is forward-projected to generate the metal trace in the projection domain. Dual-energy projection data are then corrected in the projection domain using prior-guided interpolation to reduce metal-induced inconsistencies. Material decomposition is then performed to generate VMIs, which provide structurally consistent priors for subsequent image-domain reconstruction refinement. The final images are obtained by iterative prior-guided reconstruction that enforces data consistency while incorporating VMI-based edge guidance and artifact-suppression regularization to suppress residual artifacts and preserve anatomical boundaries. Quantitative evaluations on simulated datasets demonstrate that the proposed method significantly reduces root mean square

error and improves structural similarity compared with normalized MAR. These results indicate that the proposed framework effectively suppresses metal artifacts while maintaining structural fidelity and quantitative accuracy.

MIC-15-150

Magnification Effect Evaluation for Novel Dual-Energy X-Ray Absorptiometry System (#1442)

Chanwoo Kwon, Youngbok Ahn, Sunghyun Min, Hyuntae Leem, Myungwoo Oh

Osteosys Co., Ltd., R&D Center, Seoul, South Korea

This research was financially supported by the Ministry of Trade, Industry and Resources (MOTIR) , Korea, under the “Global Industrial Technology Cooperation Center(GITCC) program” supervised by the Korea Institute for Advancement of Technology (KIAT).(Task No. P0030253)

Abstract

Accurate BMD measurement is essential for osteoporosis diagnosis and fracture risk assessment. Wide fan-beam DXA systems provide faster scan acquisition than pencil-beam systems; however, their geometric characteristics can introduce magnification errors when the distance between the X-ray source and the subject changes. These distortions affect bone mineral content (BMC), projected bone area, and ultimately BMD accuracy. The iNSiGHT C510 (OsteoSys Co., Korea) employs a 25° fan beam with a SID distance of 812 mm, substantially wider than the 4.5° narrow fan beam geometry of the PRIMUS, which operates at a 634 mm SID. To compensate for magnification-induced distortion, the iNSiGHT C510 incorporates the geometric correction within the LUCIDA software platform. The correction algorithm was evaluated using a custom lumbar spine phantom elevated from 0 to 200 mm above the tabletop in 10 mm increments, with 10 repeated measurements obtained at each height. Without correction, the iNSiGHT C510 showed BMD deviations ranging from approximately +40% to −40%. After applying the correction algorithm, residual BMD variability was reduced to within ±5%, comparable to the ±4–5% variation observed with the PRIMUS under identical conditions. Correlation analysis between corrected iNSiGHT C510 measurements and corresponding PRIMUS values demonstrated strong agreement, with a coefficient of determination (R^2) of 0.934 and a standard error below 2%. These results indicate that the proprietary correction algorithm effectively compensates for magnification errors inherent to the wide fan-beam geometry, enabling the iNSiGHT C510 to achieve clinically equivalent BMD accuracy suitable for routine bone density assessment.

References
[1] Scafoglieri, A et al. 2018, ‘Dual energy X-ray absorptiometry: gold standard for muscle mass?’, J Cachexia Sarcopenia Muscle, vol. 9, no. 4, pp. 786–787.
[2] Messina, C et al. 2020, ‘Body composition with dual energy X-ray absorptiometry from basics to new tools’, Quant Imaging Med Surg., vol. 10, no. 8.
[3] Libouban, H et al. 2002, ‘Comparison of pencil-, fan-, and cone-beam dual X-ray absorptiometers for evaluation of bone mineral content in excised rat bone’, J Clin Densitom., vol. 5, no. 4, pp. 355–361.
[4] Cole, JH et al. 2005, ‘Fan-beam densitometry of the growing skeleton: Are we measuring what we think we are?’, J Clin Densitom., vol. 8, no. 1, pp. 57–64.
[5] Griffiths, MR et al. 1997, ‘Correcting the magnification error of fan beam densitometers’, J Bone Miner Res., vol. 12, pp. 119–123.
[6] Tothill, P et al. 2001, ‘Comparisons between a pencil beam and two fan beam dual energy X-ray absorptiometers used for measuring total body bone and soft tissue’, Br J Radiol., vol. 74, pp. 166–176.

[7] Pocock, NA et al. 1997, 'Magnification error of femoral geometry using fan beam densitometers', Calcif Tissue Int., vol. 60, pp. 8–10.
[8] Blake, GM et al. 1996, 'Dual X-ray absorptiometry: a comparison between fan beam and pencil beam scans', Br J Radiol., vol. 66, pp. 902–906.
[9] Mazess, RB et al. 2000, 'Axial and total-body bone densitometry using a narrow-angle fan-beam', Osteoporos Int., vol. 11, pp. 158–166.

MIC-15-153

Transient radiative transport equation solution for ToF-CT ballistic X-ray photons (#2208)

Maëlle Fromont[1,2], Réjean Fontaine[1,2], Yves Bérubé-Lauzière[1,2]

[1] Université de Sherbrooke, Département de génie électrique et de génie, Sherbrooke, Canada; [2] Université de Sherbrooke, Institut interdisciplinaire d'innovation technologique - 3IT, Sherbrooke, Canada

Abstract

Computed tomography (CT) has made significant advances in reducing X-ray exposure while preserving image quality. A novel project to improve CT imaging involves subsituting anti-scatter grids with filtering out scattered photons using time-of-flight (ToF) measurements. A first approach resorting to ToF filtering was developed to eliminate the noise due to scattered photons, thereby improving the contrast-to-noise ratio. Additionally, ToF-CT has the potential to exploit both detected ballistic and scattered photons for reconstructing both 3D images of absorption and scattering using model-based image reconstruction.

In this approach, an X-ray radiation propagation model must be resorted to.

For this purpose, a transient radiative transport equation is presented herein. It is divided into ballistic and scattering propagation components. The present study focuses on the ballistic component, with the aim of evaluating various numerical methods to achieve better numerical temporal accuracy.

References
[1] Rossignol J, Turtos RM, Gundacker S, Gaudreault D, Auffray E, Lecoq P, Bérubé-Lauzière Y, Fontaine R., 2020 Apr 22;65(8):085013, 'Time-of-flight computed tomography - proof of principle.' Phys Med Biol. doi: 10.1088/1361-6560/ab78bf. PMID: 32084652.
[2] Bouza Dominguez J, Bérubé-Lauzière Y, 2012 'Diffuse optical tomographic imaging of biological media by time-dependent parabolic SP_N equations: a two-dimensional study', Journal of Biomedical Optics, vol. 17, no. 8, pp.086012-1-086012-14, Art no. 086012.
[3] Norris E T, 2017, 'Discrete ordinates CT organ dose simulator (DOCTORS)', Doctoral dissertation, Dept. Nucleat Eng. and Rad. Sc., Missouri S\&T
[4] Leveque R J, 2002, 'Finite-Volume Methods for Hyperbolic Problems', Cambridge University Press
[5] Courant R, Hilbert D, 1989, 'Methods of Mathematical Physics, Vol. 2', Wiley
[6] Reddy J N, Anand N K, Roy P, 2023, 'Finite Element and Finite Volume Methods for Heat Transfer and Fluid Dynamics', Cambridge Unisersity Press

MIC-15-156

Characterization of a Photon-Counting CT Modality for Preclinical PET/CT (#2155)

Regina G. Oliveira, Ana Luísa M. Silva, Pedro M.M. Correia, João F.C.A. Veloso

University of Aveiro, Physics, Aveiro, Portugal

This work was supported by project CENTRO2030-FEDER-02363500 (easyPET.CT), funded by FEDER program through CENTRO2030; and by national funds through FCT - Fundação para a Ciência e a Tecnologia, I.P. and the Ministry of Science, Technology and Higher Education under the project UID/50025/2025 (doi.org/10.54499/UID/50025/2025), UID/PRR/50025/2025 (doi.org/10.54499/UID/PRR/50025/2025), UID/PRR2/50025/2025 (doi.org/10.54499/UID/PRR2/50025/2025) and the Associate Laboratory I3N – LA/P/0037/2020 (doi.org/10.54499/LA/P/0037/2020); and grant to R. G. Oliveira (2022.09701.BD) through FCT, I.P, by project https://doi.org/10.54499/2022.09701.

Abstract

The easyPET/CT is a multimodal imaging system that integrates positron emission tomography and computed tomography (CT), using LYSO:Ce scintillator crystals coupled to silicon photomultipliers. CT acquisition is done in photon-counting (PC) mode, enabling energy discrimination and improving contrast-to-noise ratio. The radiation source used is a ^{241}Am radioactive source (2.89 MBq), which simplifies system integration. This work presents the first characterization of the integrated CT modality of the easyPET/CT of through simulation, evaluating CT number calibration, noise, and uniformity. A non-linear system response between pixel intensity and Hounsfield units was observed and successfully corrected using a second-order polynomial fit (R^2=0.99). Noise and uniformity assessment revealed peripheral non-uniformity attributed to reconstruction artifacts. Spatial resolution characterization is ongoing. These results establish a foundation for a compact, portable PCCT system with strong potential for multimodal preclinical imaging applications.

References

[1] Willemink, Martin J et al. “Photon-counting CT: Technical Principles and Clinical Prospects.” *Radiology* vol. 289,2 (2018): 293-312. doi:10.1148/radiol.2018172656

[2] Ribeiro, F. M., “Sensitivity and Spatial Resolution Optimization of a High-Resolution Preclinical PET With a Unique Acquisition Method”, IEEE Transactions on Radiation and Plasma Medical Sciences, vol. 9, no. 7, IEEE, pp. 959–969, 2025. doi:10.1109/TRPMS.2025.3546120.

MIC-15-159

Characterization of a LYSO:Ce/SiPM detector array for photon-counting CT (#2348)

Regina G. Oliveira, Afonso Xavier Pinto, Ana Luísa M. Silva, Pedro M.M. Correia, João Filipe C.D.A. Veloso

University of Aveiro, Physics, Aveiro, Portugal

This work was supported by project CENTRO2030-FEDER-02363500 (easyPET.CT), funded by FEDER program through CENTRO2030; and by national funds through FCT - Fundação para a Ciência e a Tecnologia, I.P. and the Ministry of Science, Technology and Higher Education under the project UID/50025/2025 (doi.org/10.54499/UID/50025/2025), UID/PRR/50025/2025 (doi.org/10.54499/UID/PRR/50025/2025), UID/PRR2/50025/2025 (doi.org/10.54499/UID/PRR2/50025/2025) and the Associate Laboratory I3N – LA/P/0037/2020 (doi.org/10.54499/LA/P/0037/2020); and grant to R. G. Oliveira (2022.09701.BD) through FCT, I.P, by project https://doi.org/10.54499/2022.09701.

Abstract

This work characterizes the LYSO:Ce/SiPM detector array of the easyPET/CT, a compact multimodal preclinical imaging platform. The characterization of the 16×2 array of LYSO:Ce crystals, coupled one-to-one to SiPMs was assessed per crystal in terms of energy resolution (ER), count rate, and sensitivity using a ^{241}Am radioactive source (59.5 keV). The mean ER was 33.8 ± 1.8% FWHM at 59.5 keV, competitive with current LYSO:Ce-based photon-counting detector systems reported in the literature. The mean count rate and sensitivity were 62.4 ± 5.3 photons/s and 0.7 ± 0.1 counts•photon^{-1}, respectively, both displaying a uniform spatial distribution across the array. The overall uniformity of the detector response validates the shared PET/CT hardware architecture as a viable approach for photon-counting CT, confirming that using the PET detector for CT operation preserves detector integrity. Future work will address pile-up characterization at higher count rates to further define the dynamic range of the system.

References

[1] van der Sar SJ, Leibold D, Schaart DR. Experimental investigation of the potential of LaBr 3 :Ce, LYSO:Ce, and YAP:Ce for scintillator-based x-ray photon-counting detectors . Phys Med Biol. 2026 Jan 28. doi:10.1088/1361-6560/ae1bf4

[2] van der Sar SJ, Brunner SE, Schaart DR. Silicon photomultiplier-based scintillation detectors for photon-counting CT: A feasibility study. Med Phys. 2021 Oct 1;48(10):6324–38. doi:10.1002/mp.14886 PubMed PMID: 34169535.

[3] Tiessen JE, Budden B, Burr K, Qiang Y. Exploring the Suitability of LYSO & LaBr3 Scintillator-SiPM Systems with Pulse Shaping for Photon-Counting Computed Tomography Applications. 2023.

MIC-15-162

Linearizing the Transformation from CT Hounsfield Units to Linear Attenuation Coefficient for PET Attenuation Map Generation using Virtual Non-Contrast Images (#2486)

Heba Alrakh[1,2], Lutz Tellmann[1], Omid Nikoubashman[3], Sebastian Faby[4], Debora Niekämper[1], Ali Abu arra[5], Martin Wiesmann[3], N. Jon Shah[1,2], Christoph W. Lerche[1]

[1] Forschungszentrum Jülich GmbH, INM-4, Jülich, Germany; [2] RWTH Aachen University, Department of Neurology, Aachen, Germany; [3] RWTH Aachen University, Department of Diagnostic and Interventional Neuroradiology, Aachen, Germany; [4] Siemens Healthineers AG, Department of Computed Tomography, Forchheim, Germany; [5] An-Najah National University, Department of Biophysics and Medical Imaging, Nablus, Palestine

This work is funded in part by the Palestinian-German Science Bridge (PGSB), the RETIMAGER project (Real Time Molecular Imager with Unsurpassed Resolution), and the Innovation Go Fund by Forschungszentrum Juelich.

Abstract

Attenuation correction (AC) is crucial for artefact-free PET/MR images. Currently, CT-derived PET attenuation maps (AMs) are based on transformation schemes from conventional CT scanners with data from polyenergetic X-ray spectra. It is known that converting from polyenergetic CT image data to monoenergetic 511 keV linear attenuation coefficients (LACs) introduces systematic errors in the LACs employed for AC in PET imaging. To address this issue, we investigated spectral CT to obtain more accurate AMs. Spectral CT offers advantages over conventional CT scanners by providing the possibility of material decomposition. It also allows to reconstruct virtual monochromatic images (VMI) from the inherently multiple polyenergetic data sets of CT. The spectral information can also be used to obtain virtual non-contrast (VNC). In our approach, we use angiographic spectral CT scans with an administration of iodinated contrast agents and computed VNC images from the obtained dataset. The linear transformation scheme from monochromatic CT images to LACs at 511 keV was obtained from VNC images for different tissue types using an electron density phantom and a photon counting (PC) CT scanner. The use of VNC images effectively simplifies the transformation from HUs to LACs requiring only a single linear function. It further minimizes residual deviations of the LACs for soft-tissues mimicking materials. Deriving the LACs from VNC images instead of standard CT images may lower the systematic errors of CT-based attenuation correction for PET scanners equipped with dual energy CT systems.

References

[1] J. P. J. Carney, D. W. Townsend, V. Rappoport, and B. Bendriem, 'Method for transforming CT images for attenuation correction in PET/CT imaging', *Med Phys*, vol. 33, no. 4, pp. 976–983, Apr. 2006.

[2] A. D. Sodickson, A. Keraliya, B. Czakowski, A. Primak, J. Wortman, and J. W. Uyeda, 'Dual energy CT in clinical routine: how it works and how it adds value', *Emerg Radiol*, vol. 28, no. 1, pp. 103–117, Feb. 2021.

[3] T. Xia, A. M. Alessio, and P. E. Kinahan, 'Dual energy CT for attenuation correction with PET/CT: DECT attenuation correction for PET/CT', *Med. Phys.*, vol. 41, no. 1, p. 012501, Dec. 2013.

[4] 'Multi-Energy CT Phantom (Gammex™ Technology) - Sun Nuclear'. Accessed: Available: https://www.sunnuclear.com/products/multi-energy-ct-phantom.

[5] 'Advanced Electron Density Phantom (Gammex™ Technology) - Sun Nuclear'. Available: https://www.sunnuclear.com/products/advanced-electron-density-phantom.

[6] K. Rajendran *et al.*, 'First Clinical Photon-counting Detector CT System: Technical Evaluation', *Radiology*, vol. 303, no. 1, pp. 130–138, Apr.

MIC-15-165

MIC-15-168

Image Improvement in X-ray Fluorescence Computed Tomography Using Deep Image Prior with X-ray Transmission Images (#2730)

Tomoki Ono[1], Sota Kusakari[1], Fumio Hashimoto[2], Ryuku Abe[1], Michihiro Kobayashi[1], Tenta Sasaya[3], Naoki Sunaguchi[4], Shin'ichiro Takeda[5], Hidekazu Kawashima[6], Tetsuya Yuasa[3], Tsutomu Zeniya[1]

[1] Hirosaki University, Graduate School of Science and Technology, Hirosaki, Japan; [2] University of Florida, J.Crayton Pruitt Family Department of Biomedical Engineering, Gainesville, USA; [3] Yamagata University, Graduate School of Science and Engineering, Yonezawa, Japan; [4] High Energy Accelerator Research Organization, Institute of Materials Structure Science, Tsukuba, Japan; [5] Fukushima Institute for Research, Education and Innovation, Namiemachi, Japan; [6] Kyoto Pharmaceutical University, Radioisotope Research Center, Kyoto, Japan

This study was supported by JSPS KAKENHI grants JP22K19501 (Corresponding author: Tsutomu Zeniya).

Abstract

X-ray fluorescence computed tomography (XFCT) enables nanoparticle imaging and biological function imaging without radioisotopes. We successfully improved image quality by applying Deep Image Prior (DIP), a self-supervised deep learning technique that does not require training datasets, to XFCT images. However, conventional DIP, which uses randomly generated input images, has problems such as reduced spatial resolution and deviation from the true image distribution. To address these problems, we propose CT-DIP, a modified DIP framework in which the network input is replaced with projection images acquired from simultaneous X-ray transmission computed tomography (XTCT). Monte Carlo simulations using Geant4 were performed to generate both XFCT and XTCT projection images of a mouse brain phantom, with iodine used as a contrast agent to mimic cerebral blood flow. Image reconstruction was carried out using the ordered subsets expectation maximization (OS-EM) algorithm after DIP denoising. Visual evaluation and quantitative evaluation using Peak Signal-to-Noise Ratio (PSNR) and Structural Similarity Index Measure (SSIM) demonstrated that CT-DIP outperformed conventional DIP, Gaussian filtering, and only OS-EM reconstruction. Furthermore, CT-DIP reduced training time from 75.3 minutes to 4.2 minutes, representing an approximately 18 times speedup. These results suggest that CT-DIP has strong

practical potential for XFCT imaging in low-count environments, and future work will focus on validation with real measurement data.

References
[1] T. Sasaya, N. Sunaguchi, K. Hyodo, T. Zeniya, and T. Yuasa, “Multi-pinhole fluorescent x-ray computed tomography for molecular imaging”, *Sci. Rep.*, vol. 7, 5742, 2017.
[2] S. Kusakari, K. Sato, Y. Tsushima, M. Matsuoka, T. Sasaya, N. Sunaguchi, K. Matsubara, H. Kawashima, K. Hyodo, T. Yuasa, and T. Zeniya, “Fundamental study on improving the quality of X-ray fluorescence computed tomography images by applying deep image prior to projection images as a pre-denoising method”, *Int. J. Comput. Assist. Radiol. Surg.*, vol. 20, pp. 665–676, 2025.
[3] F. Hashimoto, K. Ote, and Y. Onishi, "PET Image Reconstruction Incorporating Deep Image Prior and a Forward Projection Model," *IEEE Trans. Radiat. Plasma Med. Sci.*, vol. 6, no. 8, pp. 841–846, Nov. 2022.
[4] Q. Wang, S. L. Ding, Y. Li, J. Royall, D. Feng, P. Lesnar, et al., “The Allen Mouse Brain Common Coordinate Framework: A 3D Reference Atlas”, *Cell*, vol. 181, no. 4, pp. 936-953, 2020

MIC-15-171

Experimental Characterization and Materials-Driven Optimization of Fine-Pitch CZT Detectors for Photon-Counting CT (#2994)

Aziz Ikhlef, Salmon Arnab, Randy Luhta, Steve Utrup, Chris Vrettos

Analogic Corporation, Salem, USA

The authors acknowledge the support of Analogic Corporation and collaborating research partners.

Abstract
The performance of fine-pitch cadmium zinc telluride (CZT) photon-counting detectors is strongly governed by experimentally measurable charge transport and leakage current characteristics. We present the fabrication and experimental characterization of a pixelated CZT detector array with a nominal pixel pitch of 441 × 441 μm², targeting high-channel-count architectures for computed tomography (CT). CZT material properties were characterized using a custom-built time-of-flight (TOF) measurement system to extract electron mobility and lifetime under controlled electric field conditions. Dark current behavior was systematically measured as a function of bias voltage and pixel geometry to assess operational limits imposed by material quality. Experimentally derived transport and leakage parameters were used to perform a detector-level trade-off analysis linking CZT material properties, pixel pitch, and bias field. The results establish experimentally grounded constraints and design guidelines for scaling CZT detector arrays toward advanced photon-counting CT systems.

References
[1] Xiaochun Lai, Liang Cai, Kevin Zimmerman and Richard Thompson, Signal Generation in Semiconductor Detectors for Photon-Counting CT, Chapter 13 of Spectral, Photon Counting Computed Tomography, Technologies and Applications, 1st Edition, Edited by Katsuyuki Taguchi, Ira Blevis, Krzysztof Iniewski, CRC Press, 2020.
[2] J. Pipek et al. Charge Transport and Space-Charge Formation in $Cd_{1-x}Zn_xTe_{1-y}Se_y$ Radiation Detectors, Phys. Rev. Applied **15**, 054058 (2021)
[3] G. F. Knoll, Radiation Detection and Measurement, 4th ed., Wiley, 2010.
[4] A. Owens and A. Peacock, “Compound semiconductor radiation detectors,” Nucl. Instrum. Methods Phys. Res. A, vol. 531, pp. 18–37, 2004.

MIC-15-174

Longitudinal Cone-Beam CT and MRI Integration for High-Fidelity Synthetic CT Generation (#3003)

Vincent Jaouen[1,2], Vincent Bourbonne[2,3], Julien Bert[2,3], Ulrike Schick[2,3], Pierre-Henri Conze[1,2], Dimitris Visvikis[2]

[1] IMT Atlantique, Brest, France; [2] U1101 LaTIM, Inserm, Université de Bretagne Occidentale, Brest, France; [3] Brest University Hospital, Brest, France

Abstract

Cross-modality synthesis from cone-beam CT (CBCT) to CT is central to online adaptive radiotherapy and accurate dose recalculation. Although planning MRI provides valuable soft-tissue information, daily CBCT captures the patient's updated anatomy on the treatment couch. Its direct use remains limited by scatter artifacts and imperfect Hounsfield Unit (HU) calibration. This study investigates whether aggregating sequential on-treatment CBCTs improves deep learning-based synthetic CT (sCT) generation compared with single-fraction CBCT or static MRI priors alone.

We developed a conditional GAN with Residual-in-Residual Dense Blocks to generate high-fidelity sCTs. The model was evaluated on 190 patients with brain metastases, split into 152 training cases and 38 independent test cases. Each patient had a planning CT used as ground truth, a planning T1-weighted MRI, and up to three daily CBCT scans. Four input settings were compared: 1 CBCT, 1 CBCT+MRI, 3 CBCTs, and 3 CBCTs+MRI.

Adding temporal and multimodal information improved sCT accuracy. The single-CBCT baseline achieved 67.79 HU MAE and 29.12 dB PSNR, while the full 3 CBCTs+MRI configuration reached the best performance, with 59.81 HU MAE and 30.82 dB PSNR. Importantly, temporal accumulation alone using 3 CBCTs achieved 60.01 HU MAE, outperforming the static multimodal 1 CBCT+MRI setting at 65.98 HU. This suggests that longitudinal CBCT redundancy provides stronger density and attenuation constraints than a single CBCT complemented by a rigid planning MRI prior.

Sequential CBCT aggregation, especially when fused with MRI, improves HU calibration and reduces daily setup artifacts, supporting robust automated sCT generation for online adaptive radiotherapy.

References

[1] Johnstone, E, Wyatt, JJ, Henry, AM, Short, SC, Sebag-Montefiore, D, Murray, L, Kelly, CG, McCallum, HM & Speight, R 2018, 'Systematic review of synthetic computed tomography generation methodologies for use in magnetic resonance imaging-only radiation therapy', International Journal of Radiation Oncology, Biology, Physics, vol. 100, no. 1, pp. 199–217, Amsterdam: Elsevier.

[2] Edmund, JM & Nyholm, T 2017, 'A review of substitute CT generation for MRI-only radiation therapy', Radiation Oncology, vol. 12, article 28, London: BioMed Central.

[3] Bourbonne, V, Jaouen, V, Hognon, C, Boussion, N, Lucia, F, Pradier, O, Bert, J, Visvikis, D & Schick, U 2021, 'Dosimetric validation of a GAN-based pseudo-CT generation for MRI-only stereotactic brain radiotherapy', Cancers, vol. 13, no. 5, article 1082, Basel: MDPI.

[4] Dinkla, AM, Wolterink, JM, Maspero, M, Savenije, MHF, Verhoeff, JJC, Seravalli, E, Išgum, I, Seevinck, PR & van den Berg, CAT 2018, 'MR-only brain radiation therapy: Dosimetric evaluation of synthetic CTs generated by a dilated convolutional neural network', International Journal of Radiation Oncology, Biology, Physics, vol. 102, no. 4, pp. 801–812, Amsterdam: Elsevier.

[5] Kazemifar, S, McGuire, S, Timmerman, R, Wardak, Z, Nguyen, D, Park, Y, Jiang, S & Owrangi, M-A 2019, 'MRI-only brain radiotherapy: Assessing the dosimetric accuracy of synthetic CT images generated using a deep learning approach', Radiotherapy and Oncology, vol. 136, pp. 56–63, Amsterdam: Elsevier.

[7] Molina-Maza, JM, Viar-Hernandez, D, Rodriguez-Gonzalez, B, Sequeiro-Gonzalez, J, Vera-Sanchez, JA, Mazal, A, Malpica, N, Torrado-Carvajal, A, Perez-Moreno, JM & Rodriguez-Vila, B 2025, 'Enhancing CBCT-based CT synthesis using planning MRI in adaptive proton therapy for head cancer: A deep learning approach', Journal of Applied Clinical Medical Physics, vol. 26, no. 12, article e70367, Hoboken, NJ: Wiley Periodicals LLC.

[8] Wang, X, Yu, K, Wu, S, Gu, J, Liu, Y, Dong, C, Loy, CC, Qiao, Y & Tang, X 2018, 'ESRGAN: Enhanced super-resolution generative adversarial networks', ECCV Workshops, pp. 63–79, Cham: Springer.
[9] Thummerer, A, van der Bijl, E, Galapon, AJ, Kamp, F, Savenije, M, Muijs, C, Aluwini, S, Steenbakkers, RJHM, Beuel, S, Intven, MPW, Langendijk, JA, Both, S, Corradini, S, Rogowski, V, Terpstra, M, Wahl, N, Kurz, C, Landry, G & Maspero, M 2025, 'SynthRAD2025 Grand Challenge dataset: Generating synthetic CTs for radiotherapy from head to abdomen', Medical Physics, vol. 52, no. 7, article e17981, Hoboken, NJ: Wiley Periodicals LLC.
[10] Jaouen, V, Conze, P-H & Visvikis, D 2024, 'One-sided unsupervised medical image synthesis with normalized edge consistency', Proceedings of the IEEE International Symposium on Biomedical Imaging, pp. 1–5, Piscataway, NJ: IEEE.

MIC-15-177

Dynamic hepatocyte-specific liver imaging using a two-dimensional SiPM-based photon counting CT: Comparison between healthy and liver tumor mouse models (#3095)

Fitri Lucyana[1], Makoto Arimoto[1], Minori Oshima[1], Yu Futura[1], Shuma Midorikawa[1], Hiroki Kawashima[1], Satoshi Kobayashi[1], Kenichiro Okumura[1], Asuka Mizutani[1], Naoki Ohno[1], Jun Kataoka[2], Takahiro Ro[2], Ryotaro Minagawa[2], Kazuhiro Murakami[3], Shinsuke Terazawa[4], Yuta Maeno[4]

[1] Kanazawa University, Kanazawa, Japan; [2] Waseda University, Tokyo, Japan; [3] Ishikawa Prefectural University, Nonoichi, Japan; [4] Proterial Ltd., Osaka, Japan

We gratefully acknowledge financial support from JSPS KAKENHI Grant Numbers JP19H04483, JP19K22924, JST ERATO Grant Number JPMJER2102, JST SPRING Grant Number JPMJSP2135, the Naito Foundation, the Uehara Memorial Foundation, the Casio Science Promotion Foundation, and the JSPS Leading Initiative for Excellent Young Researchers program.

Abstract

Photon counting computed tomography (PC-CT) enables energy-resolved imaging and material-specific analysis through individual X-ray photon detection. In this study, dynamic hepatocyte-specific imaging was performed in healthy and liver tumor mouse using a developed two-dimensional (2D) PC-CT system consisting of a 16 × 64-channel YGAG scintillator array coupled with MPPC array, with a voxel size of 1×1×1 mm^3. Gd-EoB was intravenously administered, and time-resolved imaging was conducted before and after contrast injection. Reconstructed CT images in the 50–60 keV energy range and estimated Gd concentration maps were evaluated around the liver and bladder regions. Dynamic enhancement was observed after Gd administration in both healthy and liver tumor mice, with differences in temporal enhancement behavior and estimated Gd concentration tendency between the two models. Although the tumor region was not clearly distinguishable because of its small size and current image quality limitations, temporal changes in CT value and estimated Gd concentration were still observable. MRI comparison demonstrated a positive relationship between MRI signal intensity and PC-CT-derived Gd concentration, although quantitative tendencies differed because of differences in imaging mechanisms and contrast sensitivity between MRI and PC-CT. These results demonstrate the feasibility of scintillator-based PC-CT for dynamic hepatocyte-specific imaging in vivo.

References

[1] Reimer P, Vosshenrich R. Detection and characterization of liver lesions using gadoxetic acid as a tissue-specific contrast agent. Biologics. 2010;4:199-212. Published 2010 Aug 9. doi:10.2147/btt.s6479
[2] Cassol, Franca et al, ”Tracking Dynamics of Spontaneous Tumors in Mice Using Photon-Counting Computed Tomography,” iScience, vol. 21: 68-83, 2019 doi:10.1016/j.isci.2019.10.015
[3] M. Oshima et al, ”In vivo imaging demonstration using a two-dimensional SiPM-based photon-counting CT system: preliminary results”[Accepted for publication]
[4] M. Arimoto et al, ”Development of 64-channel LSI with ultrafast analog and digital signal processing dedicated for photon-counting computed tomography with multi-pixel photon counter”,Nucl. Instr. Meth. A,, 1047:167721, 2023

MIC-15-180

Improved Material Decomposition Method in DXA Using Scatter-Induced Arrival Time Difference (#3163)

Sena Kwon, Jiwoong Jung, Sang-hyun Chun, Jiwon Nam, Jin Ho Jung, Yong Choi

Sogang University, Department of Electronic Engineering, Intelligent Signal Processing System (ISPS) Laboratory, Seoul, South Korea

This research was supported by the Industrial Technology Innovation Program funded by the Ministry of Trade, Industry and Energy (no. P0030253), by the National Research Foundation of Korea (NRF) grant funded by the Korea government (MSIT) (no. RS-2023-00280177), and by the Basic Science Research Program through the National Research Foundation of Korea (NRF) funded by the Ministry of Education (no. RS-2026-25565373) of the Republic of Korea.

Abstract

Material decomposition is commonly based on the R-value, defined as the ratio of attenuated intensities measured at low-high X-ray energies. However, materials with similar compositions, such as fat and muscle, can exhibit overlapping R-values, limiting the accuracy of material decomposition. This study investigates the feasibility of improving material decomposition using scatter-induced arrival time difference. Scattered photons travel longer paths than primary photons, resulting in delayed arrival times. Photons with arrival time delay exceeding a threshold were distinguished as scattered photons. The scatter ratio (SR), defined as the ratio of scatter counts in low to high energy regions, was used for an additional identifier for material decomposition. DXA system was simulated using GATE with a detector consisting of 240 × 24 LYSO pixels with dimensions of 3 × 3 × 5 mm^3, an X-ray source operated at 83 kVp and 0.2 mA with a 0.025 mm Ce filter, and the source-to-detector distance set to 1000 mm. Fat, muscle, and bone phantoms were placed at the center between the source and detector. The arrival time delay threshold was set to 20 ps since the maximum time difference of direct photons within the 5 mm pixel depth is 16 ps under ideal timing resolution of 0 ps. Each material was represented in feature space using the R-value and SR. Material separability was evaluated using a separability index based on the difference between feature means and standard deviations. In the feature space, fat, muscle, and bone formed distinct clusters. SR derived from photon arrival time difference improved the separability index for all material pairs. For fat–muscle, the separability index increased from 13 to 17, achieving a 25% increase. For fat–bone and muscle–bone pairs, separability improved by 84% and 62%, compared with the R-value. These results demonstrate the feasibility of improving the material decomposition in DXA using scatter-induced arrival time difference.

References
[1] C. Messina, D. Albano, S. Gitto, L. Tofanelli, A. Bazzocchi, F. M. Ulivieri, et al., “Body composition with dual energy X-ray absorptiometry: from basics to new tools,” Quant Imaging Med Surg, vol. 10, no. 8, pp. 1687–1698, Aug. 2020.
[2] M. A. Laskey, “Dual-energy X-ray absorptiometry and body composition,” Nutrition, vol. 12, no. 1, pp. 45–51, Jan. 1996.
[3] J. Rossignol, G. Bélanger, D. Gaudreault, A. C. Therrien, Y. Bérubé-Lauziére, and R. Fontaine, “Time-of-flight scatter rejection in x-ray radiography,” Physics in Medicine and Biology, vol. 69, p. 055027, Mar. 2024.
[4] S. Jan, G. Santin, S. Staelens, K. Assié, D. Autret, S. Avner, et al., “GATE: a simulation toolkit for PET and SPECT,” Phys. Med. Biol., vol. 49, pp. 4543-4561, 2004.
[5] J. R. Rajagopal, F. Farhadi, J. Solomon, B. Saboury, P. Sahbaee, A. H. Negussie, et al. “Development of a separability index for task specific characterization of spectral computed tomography,” Physica Medica, vol. 122, 103382, 2024.

MIC-15-183

Limited-Angle and Few-View Image Reconstruction Using Point Spread Functions (#1111)

Gengsheng Zeng[1,2]

[1] Utah Valley University, Department of Computer Science, Orem, USA; [2] University of Utah, Radiology, Salt Lake City, USA

This work was supported in part by the National Institutes of Health under Grant R15EB024283.

Abstract

Limited-angle tomography and few-view tomography are extremely ill-conditioned problems. A usual way to reconstruct an image in limited-angle tomography or in few-view tomography is via an iterative algorithm that minimizes a two-term objective function. The objective function consists of a data fidelity term and a Bayesian term. A common Bayesian term is the total variation (TV) norm of the image. This paper proposes a different way to reconstruct the image in limited-angle tomography and few-view tomography by iteratively deconvolving the point spread function (PSF). Two PSFs are considered: the PSF of the filtered backprojection (FBP) and the PSF of pure backprojection. The method of using the PSF of pure backprojection gives better results.

References
[1] Tam, K. C., and Victor Perez-Mendez. "Tomographical imaging with limited-angle input." *Journal of the Optical Society of America* 71, no. 5 (1981): 582-592.
[2] LaRoque, Samuel J., Emil Y. Sidky, and Xiaochuan Pan. "Accurate image reconstruction from few-view and limited-angle data in diffraction tomography." *Journal of the Optical Society of America A* 25, no. 7 (2008): 1772-1782.
[3] Champley, Kyle M., Michael B. Zellner, Joseph W. Tringe, and Harry E. Martz Jr. "Methods for Few-View CT Image Reconstruction." *arXiv preprint arXiv:2410.07552* (2024).
[4] Frikel, Jürgen. "Sparse regularization in limited angle tomography." *Applied and Computational Harmonic Analysis* 34, no. 1 (2013): 117-141.
[5] Kazantsev, Ivan G., M. J. Samuel, and Robert M. Lewitt. "Limited angle tomography and ridge functions." In *2002 IEEE Nuclear Science Symposium Conference Record*, vol. 3, pp. 1706-1710. IEEE, 2002.

MIC-15-186

Accelerating CGCIS Iterative Reconstruction Based on Location Priors from the DBP Algorithm (#1203)

Kui Wang[1], Yangyang Zhao[1], Shuyu Xu[1], Zhongbin Hang[2], Hui Liu[3], Jing Wu[4], Yaqiang Liu[3], Zuoxiang He[2], Qingyang Wei[1]

[1] University of Science and Technology Beijing, Beijing Engineering Research Center of Industrial Spectrum Imaging and School of Automation and Electrical Engineering, Beijing, China; [2] Tsinghua University, Beijing Tsinghua Changgung Hospital, Beijing, China; [3] Tsinghua University, Department of Engineering Physics, Beijing, China; [4] Beijing Normal University, Center for Advanced Quantum Studies, School of Physics and Astronomy, Beijing, China

Abstract

To address the high computational complexity and low efficiency caused by traversing all field-of-view (FOV) voxels during image reconstruction in full-ring cascade gamma coincidence imaging systems (CGCIS), we propose a location priors algorithm to significantly accelerate image reconstruction. By restricting system matrix calculations, forward projection and back-projection operations to the ROI. This reduces the computational complexity from $O(N_x \times N_y \times N_z)$ to $O(m \times n \times l)$, thereby significantly improving reconstruction efficiency. Experimental results demonstrated that, compared to conventional iterative algorithm, the proposed location priors algorithm achieved an approximate 37.05-fold acceleration in reconstruction speed while preserving high imaging quality. Ultimately, this advancement provides robust technical support for real-time, dynamic imaging monitoring utilizing theranostic nuclides.

MIC-15-189

DeepDreaming SPECT: Gradient-Based Reconstruction via Differentiable Physics Simulation (#1364)

Francesc Massanes

Siemens Medical Solutions USA Inc, MI SPECT Research, Hoffman Estates, USA

Abstract

We present a gradient-based SPECT reconstruction framework that treats the physics-based forward model as a frozen differentiable operator and optimizes the 3D activity volume through backpropagation, an approach directly analo gous to Google's DeepDream algorithm. The forward model is implemented as a PyTorch module comprising gantry rotation via trilinear interpolation, photon attenuation correction, and depth-dependent detector blur via per-slice convolution with measured point response function (PRF) kernels. Reconstruction minimizes the Mighell modified chi-square, a Poisson-appropriate cost function, using adaptive gradient descent. We evaluate four first-

order optimizers (Adam, AdamW, RMSprop, SGD) on a hot/cold sphere phantom acquired on a Siemens Symbia Intevo with LEHR collimation and demonstrate that RMSprop achieves the fastest cost reduction. Preliminary reconstructions at 20 iterations recover the phantom geometry with visible hot sphere contrast, validating both the forward model accuracy and the gradient-based reconstruction pipeline.

References
[1] A. Mordvintsev, C. Olah, and M. Tyka, "Inceptionism: Going Deeper into Neural Networks," Google Research Blog, June 2015.
[2] A. Paszke et al., "PyTorch: An Imperative Style, High-Performance Deep Learning Library," Advances in Neural Information Processing Systems, vol. 32, 2019
[3] K. J. Mighell, "Parameter Estimation in Astronomy with Poisson distributed Data. I. The χ2 γ Statistic," The Astrophysical Journal, vol. 518, no. 1, pp. 380–393, 1999.
[4] A. H. Vija, "Characteristics of the xSPECT Reconstruction Method," White Paper, Siemens Healthineers, Sept. 2017.
[5] C.-Y. Liu, E.-J. Kuo, C.-H. A. Lin, S. Chen, J. G. Young, Y.-J. Chang, and M.-H. Hsieh, "Training Classical Neural Networks by Quantum Machine Learning," arXiv:2402.16465 [quant-ph], 2024

MIC-15-192

Plug-and-Play Learned Regularization in PET Reconstruction: Integration of DeepInverse and STIR through SIRF (#1578)

Kathiresan Chandrasekaran[1], George Webber[2], Alexander Denker[3,4], Matthias J. Ehrhardt[5]

[1] University of Bern, Department of Nuclear Medicine, Inselspital (Bern University Hospital), Bern, Switzerland; [2] King's College London, School of Biomedical Engineering and Imaging Sciences, London, UK; [3] Deutsches Elektronen-Synchrotron DESY, Helmholtz Imaging, Hamburg, Germany; [4] University College London, Department of Computer Science, London, UK; [5] University of Bath, Department of Mathematical Sciences, London, UK; [6] University of Bath, Department of Mathematical Sciences, London, UK

Abstract

This work presents a modular software integration framework that bridges physics-based PET reconstruction with modern deep learning regularization. While deep learning has shown significant promise in medical imaging, integrating learned priors into established reconstruction pipelines remains a challenge. We address this by developing a direct interface between the DeepInverse library and the Synergistic Image Reconstruction Framework (SIRF), which wraps the Software for Tomographic Image Reconstruction (STIR) engine. This integration enables the direct deployment of learned priors, such as the Deep Residual UNet (DRUNet) and Weakly Convex Ridge Regularizers (WCRR), within accurate physics-based forward models. To demonstrate the framework's flexibility, we integrate and evaluate three reconstruction strategies using learned regularization: PnP-PD3O (WCRR), PnP-SVRG (DRUNet), and PnP-HQS (DRUNet). Performance is validated using a simulated 2D thorax phantom, comparing the proposed framework against Ordered Subsets Maximum A Posteriori One Step Late (OSMAPOSL), corresponding to standard Ordered Subsets Expectation Maximization (OSEM) reconstruction when no prior is applied, and OSMAPOSL with Relative Difference Prior (RDP) baselines. Quantitative results demonstrate improved image fidelity using learned regularization. As a representative example, the PnP-SVRG approach achieved a Peak Signal-to-Noise Ratio (PSNR) of 45.90 dB, compared to 39.52 dB for baseline OSEM, showing improved reconstruction quality using this unified interface. The framework suppresses noise while

preserving structural details. By providing an open-source Python-based bridge, this work lowers the barrier for evaluating state-of-the-art inverse-problem techniques in realistic clinical PET imaging scenarios.

References
[1] K. Thielemans et al., "STIR: Software for tomographic image reconstruction release 2," Phys. Med. Biol., vol. 57, no. 4, pp. 867–883, 2012.
[2] J. Tachella et al., "DeepInverse: A Python package for solving imaging inverse problems with deep learning," J. Open Source Softw., vol. 10, no. 115, p. 8923, 2025.
[3] E. Ovtchinnikov et al., "SIRF: Synergistic image reconstruction framework," Comput. Phys. Commun., vol. 249, p. 107087, 2020.
[4] J. S. Jørgensen et al., "Core Imaging Library - Part I: a versatile Python framework for tomographic imaging," Phil. Trans. R. Soc. A, vol. 379, no. 2204, p. 20200192, 2021.
[5] E. Pasca et al., "Core Imaging Library (CIL)," Zenodo software archive, 2023.
[6] S. V. Venkatakrishnan, C. A. Bouman, and B. Wohlberg, "Plug-and-play priors for model based reconstruction," in 2013 IEEE Global Conference on Signal and Information Processing, 2013, pp. 945–948.
[7] S. Salzo and S. Villa, "Inexact and accelerated primal-dual three-operator splitting methods," Journal of Optimization Theory and Applications, vol. 188, no. 2, pp. 438–463, 2021.
[8] K. Zhang, Y. Li, W. Zuo, L. Zhang, L. Van Gool, and R. Timofte, "Plug-and-play image restoration with deep denoiser prior," IEEE Transactions on Pattern Analysis and Machine Intelligence, vol. 44, no. 10, pp. 6360–6376, 2022.
[9] G. Webber, K. Chandrasekaran, A. Denker, G. Van Hoey, and M. J. Ehrhardt, "PnP with DeepInverse," GitHub repository, 2026. [Online]. Available: https://github.com/GeorgeWebber/SIRF-Contribs-PnP-DI/blob/master/src/notebooks/PnP_LR_in_PET_Reconstruction.ipynb

MIC-15-195

Optimization of CT Reconstruction for Improved Image Quality in Lithium-Ion Battery Modules for Electric Wheelchairs (#1761)

Donghee Kim, Hyung Joo Choi, Chul Hee Min

Yonsei Unuversity, Department of Radiation Convergence Engineering, Wonju, South Korea

This research was supported by the Regional Innovation System & Education(RISE) program through the Gangwon RISE Center, funded by the Ministry of Education(MOE) and the Gangwon State(G.S.), Republic of Korea.(2026-RISE-10-006).

Abstract
Lithium-ion batteries (LIBs) are widely used in electric wheelchairs, and their safety is a critical concern due to the risk of thermal runaway caused by internal defects. In practical applications, batteries are operated as multi-cell modules, and periodic inspection is required as their condition degrades over time. X-ray computed tomography (CT) is widely used for non-destructive testing. However, CT inspection of compact multi-cell modules is challenging since overlapping attenuation from neighboring cells can lead to reconstruction artifacts and reduce defect contrast. In this study, CT reconstruction strategies for multi-cell LIB modules were evaluated using a Geant4-based simulation framework. Projection data were generated under the simulated conditions, and various combinations of projection processing and reconstruction methods were compared. Reconstructed image quality and defect detectability were quantitatively evaluated using the signal-to-noise ratio (SNR), contrast-to-noise ratio (CNR), and detectability index (d′). The results show that the combination of unfiltered projection data, OS-SART reconstruction, and Gaussian smoothing achieved the highest mean d′ across the nine cells. Compared with the

baseline reconstruction, SNR, CNR and d′ improved by 233%, 119% and 117%, suggesting improved defect-to-background separation. These results indicate that reconstruction strategy significantly affects defect detectability, and optimization of reconstruction methods is necessary. In future work, experimental validation will be conducted on a prototype radiography system.

References
[1] W. Chen, X. Han, Y. Pan, Y. Yuan, X. Kong, L. Liu, *et al.*, "Defects in lithium-ion batteries: From origins to safety risks," Green Energy and Intelligent Transportation, vol. 4, no. 3, Art. no. 100235, 2025.
[2] D. Tan, T. Chen, F. Meng, X. Tian, W. Li, C. Peng, *et al.*, "A fast iterative reconstruction method of sparse angle CT for cylindrical lithium battery," Sensors and Actuators A: Physical, vol. 398, Art. no. 117318, 2026.
[3] H.-J. Choi, D. Kim, and C. H. Min, "X-ray radiography instrument design for internal defect detection in lithium-ion battery modules for electric wheelchairs," Nuclear Engineering and Technology, vol. 58, no. 6, Art. no. 104194, 2026.

MIC-15-198

Frequency Guided Network for Quantitative PET Reconstruction with Improved Scatter Correction (#1823)

Yucun Hou[1], Yihao Chen[1], Haoqi Wen[1], Fenglin Zhan[2,3], Jianyong Jiang[1]

[1] Beijing Normal University, School of Physics and Astronomy, beijing, China; [2] The First Affiliated Hospital of USTC, Division of Life Sciences and Medicine, Hefei, China; [3] Jiangnan University, Wuxi School of Medicine, Wuxi, China

This work was supported in part by the National Natural Science Foundation of China (No. 12475336), and the Fundamental Research Funds for the Central Universities (No. 310400209521).

Abstract
PET reconstruction aims to recover the activity distribution from coincidence measurements, while accurate quantitative imaging relies on comprehensive modeling of the physical processes spanning positron annihilation, photon propagation, and detector response. Existing deep learning approaches commonly rely on end-to-end supervision using iterative reconstructions as reference labels, which limits quantitative accuracy and does not explicitly account for the physical degradation mechanisms governing PET measurements. In this work, we propose Wiener Wavelet Net (WieNet), a degradation aware reconstruction framework that models the geometric time of flight probabilistic (GTP) image as a blurred and bias contaminated observation of the underlying activity distribution. A two-stage learnable Wiener filtering strategy is introduced to address TOF induced spatial blurring through frequency domain deconvolution, while a wavelet attention fusion module performs multi energy guided scatter correction by selectively incorporating reliable low frequency information. A 3D denoiser suppresses residual stochastic noise, and an absolute activity calibration module restores the quantitative intensity scale using patient and acquisition parameters. Experiments on clinical and simulated datasets demonstrate that WieNet provides improved scatter compensation and quantitative accuracy compared with fully corrected OSEM and other baseline methods. These findings suggest that degradation aligned reconstruction integrating blur restoration,

scatter correction, and quantitative calibration offers a principled alternative to purely supervised deep learning PET reconstruction.

References
[1] Berg, E & Cherry, SR 2018, 'Innovations in Instrumentation for Positron Emission Tomography', *Seminars in Nuclear Medicine*, vol. 48, no. 4, pp. 311–331, Elsevier.
[2] Gonzalez, RC & Woods, RE 2008, *Digital Image Processing*, 3rd edn, Pearson Prentice Hall.
[3] Yang, B, Gong, K, Liu, H, Li, Q & Zhu, W 2024, 'Anatomically Guided PET Image Reconstruction Using Conditional Weakly-Supervised Multi-Task Learning Integrating Self-Attention', *IEEE Transactions on Medical Imaging*, vol. 43, no. 6, pp. 2098–2112, IEEE.
[4] Yuan, Z, Zhan, F, Lu, H, Hou, Y, Liao, R, Li, C, et al. 2026, 'GPU-based list-mode TOF PET image reconstruction with complete correction techniques', *Medical Physics*, vol. 53, no. 1, e70216, Wiley.
[5] Hou, Y, Zhan, F, Liu, J, Cheng, X, Li, C, Yuan, Z, et al. 2026, 'Cycle-constrained adversarial denoising convolutional network for PET image denoising: Multi-dimensional validation on large datasets with reader study and real low-dose data', *Medical Image Analysis*, vol. 107, 103826, Elsevier.

MIC-15-201

Image-guided depth-of-interaction recovery for parallax-mitigated PET image reconstruction (#2033)

Carlos Galindo-Morata[1], Pablo Galve[3,1], Iván Colmenarejo Allavena[1], Mojahed Abushawish[1], Jose Udias[1,2]

[1] Universidad Complutense de Madrid, Grupo de Física Nuclear, EMFTEL & IPARCOS, Madrid, Spain; [2] Health Research Institute of the Hospital Cínico San Carlos (IdISSC), Madrid, Spain, Madrid, Spain; [3] Spanish National Research Council (CSIC), Institute for Physical and Information Technologies "Leonardo Torres Quevedo", ITEFI, Madrid, Spain

We acknowledge support from European Union as part of the European Innovation Council's Pathfinder Open Programme: RETIMAGER, 101099096; Spanish Government and Next Generation EU/PRTR: DI2M: Smart detectors for molecular imaging (2021/C005/00147498); P. Galve acknowledges grant JDC2023-051754-I, funded by MCIU/AEI/10.13039/501100011033 and ESF+.

Abstract
Depth-of-interaction (DOI) information is essential to reduce parallax-related spatial blurring in PET systems using thick scintillation crystals, especially in compact preclinical scanners. We present an image-guided DOI estimation method for a preclinical PET scanner with dual-ended readout, aimed at DOI calibration from both signals. The method follows a superiterative reconstruction strategy. An initial image is reconstructed with a fixed DOI assignment and then used as a spatial prior. Then, from the list-mode file, for each event LOR indicated by a crystal-pair, several DOI candidates are compared for the said crystal pair, generating several possible DOI-LORs. Each candidate LOR is forward-projected onto the previous image, and the value of such projection is used as a compatibility metric. The DOI combination with the highest compatibility is selected to update the DOI-LOR for the given event. To assess consistency, the dual-ended energy ratio was represented as a function of the estimated DOI. The ratio-DOI distributions show a clear depth-dependent trend, indicating that the proposed method provides a DOI response correlated with detector light sharing.

References
[1] Arias-Valcayo F, et al. 2023 Reconstruction of multi-animal PET acquisitions with anisotropically variant PSF Biomed. Phys. Eng. Express 9 065018
[2] Wang H, et al. 2025 Dual-ended readout TOF-DOI PET detectors based on 3.2 mm and 1.6 mm pitch LYSO arrays EJNMMI Phys. 12 51Lastname, GN, Lastname, GN YYYY, 'Article', *Journal*, Edition, Page, Place of publication: publishers
[3] Kiyokawa M, et al. 2025 Monolithic U-shaped crystal design for TOF-DOI detectors: a flat top vs. a tapered top Biomed. Phys. Eng. Express 0–23
[4] Pizzichemi M, et al. 2016 A new method for depth of interaction determination in PET detectors Phys. Med. Biol. 61 4679–98

MIC-15-204

Patient-Adaptable Smoothing with Deep Learning Denoising for Cardiac-gated SPECT Studies (#2052)

Xirang Zhang[1,3], Yongyi Yang[1], Jovan G. Brankov[1], Michael A. King[2]

[1] Illinois Institute of Technology, Department of Electrical and Computer Engineering, Chicago, USA; [2] University of Massachusetts Medical School, Department of Radiology, Worcester, USA; [3] Hunan University of Technology and Business, School of Frontier Crossover Studies, Changsha, China

This work was supported by NIH Grants R01-HL154687 and EB036082.

Abstract

In cardiac-gated SPECT studies, the acquired data counts can exhibit significant inter-subject variability. Consequently, the reconstructed images are often processed with post-reconstruction filtering in which the smoothing level needs to be adjusted individually among subjects for optimal noise suppression. In this study, we investigate an operator-interpolation approach to achieve an adaptable level of smoothing with a deep learning (DL) denoising network for processing cardiac-gated images, enabling real-time, patient-specific adjustments without retraining the DL network. We assessed the performance of this approach on a set of 20 clinical gated acquisitions using a DL network pre-trained at two nominal smoothing levels on image data from 862 studies. The results indicate that the proposed approach could achieve nearly identical denoised output images compared to retraining the DL network for a specific target smoothing level, with an average relative mean-squared-error (rMSE) below 0.15% and the structural similarity index measure (SSIM) above 0.982.

References
[1] G. Lin, H. Hines, et al, "Automated quantification of myocardial ischemia and wall motion …," J Nucl Med Technol, vol. 34, 2006.
[2] M. Kortelainen, T. Koivumaki, *et al*, "Dependence of left ventricular functional parameters …," *J Nucl Cardiol*, vol. 22, 2015.
[3] P. Slomka, G. Germano, "Optimizing radiation dose and imaging time with conventional myocardial …," *J Nucl Cardiol*, vol. 24, 2017.
[4] M. D. Cerqueira, *et al.*, "Recommendations for reducing radiation exposure in myocardial...," *J. Nucl. Cardiol.*, vol. 17, 2010.
[5] C. Song, Y. Yang, *et al*, "4D non-local means post-filtering for cardiac gated SPECT," *Phys Med Biol.*, vol. 63, 2018.
[6] E. T. P. Slijpen and F. J. Beekman, "Comparison of post-filtering and filtering between …," *IEEE Trans Nuc Sci*, vol. 46, 1999.
[7] A. Ramon, Y. Yang, *et al*, "Improving diagnostic accuracy in low-dose SPECT …," *IEEE Trans Med Imag.*, vol. 39, 2020.

[8] J. Liu, *et al*, "Accounting for inter-subject variations in deep learning for reduced-…," *IEEE 28th Inter Conf Imag Proc*, 2021.
[9] B. Yu and K. Gong, "Adaptive whole-body PET image denoising using 3D diffusion …," *IEEE 22nd Inter Symp Biomed Imag*, 2025.

MIC-15-207

LAFOV scanner SAFOV imaging: Sensitivity Restoration by Local Tomography Approach (#2099)

Vladimir Panin[1], Deepak Bharkhada[1], Mael Millardet[2]

[1] Siemens Medical Solutions USA, Molecular Imaging, Knoxville, USA; [2] University of Pennsylvania, Department of Radiology, Philadelphia, USA

The authors would like to thank the Department of Nuclear Medicine at Bern University Hospital's Inselspital, the first site of the Siemens Vision Quadra, for providing patient data.

Abstract

The application of organ-specific imaging on axially long field-of-view (LAFOV) scanners is currently emerging, where an axially shorter CT acquisition defines the target region of imaging. Nevertheless, the PET system naturally acquires additional measurements, where high-polar-angle data contain contributions from both the CT-defined region and the region extending beyond it. Estimation of correction factors, including attenuation and scatter, requires knowledge of the object in the extended region using traditional approaches.

The modern scanner has TOF resolution of a few centimeters, and the TOF local tomography property can be exploited for this task. High-polar-angle PET data, truncated in the TOF domain, can be used, as they contribute to the targeted region. This paper investigates this approach with the goal of faster reconstruction of the target region of interest. Scatter correction is performed using quantitative knowledge of the object obtained from reconstruction of the subset of data for which correction factors are fully known (residual scatter approach). Attenuation can be obtained by a similar approach or by the ML-ACF method using full or TOF-truncated emission data. Alternatively, the attenuation map can be estimated from the full-extent emission data compressed into a single backprojection image using a fast DL method.

Preliminary investigations on the Siemens Vision Quadra show that the sensitivity of the targeted region can be restored with accurate quantification.

References

[1] Panin VY, Defrise M, Nuyts J, Rezaei A, and Casey ME, 2012. Reconstruction of uniform sensitivity emission image with partially known axial attenuation information in PET-CT scanners. *IEEE NSS MIC 2012*.
[2] Bal H, Panin VY, Schaefferkoetter J, Cabello J and Conti M, 2021. Fully 3D scatter estimation in axially long FOV PETCT scanners: residual estimation approach. *IEEE NSS MIC 2021*.
[3] Rezaei A, Defrise M, and Nuyts J, 2014. ML-reconstruction for TOF-PET with simultaneous estimation of the attenuation factors. *IEEE Transactions on Medical Imaging*, *33*(7), 1563-1572.
[4] Whiteley, W., Panin, V., Zhou, C., Cabello, J., Bharkhada, D. and Gregor, J., 2020. FastPET: near real-time reconstruction of PET histo-image data using a neural network. *IEEE Transactions on Radiation and Plasma Medical Sciences*, *5*(1), 65-77.
[5] Millardet, M., Bharkhada, D., Raj, J., Schaefferkoetter, J., Panin, V., Conti, M. and Matej, S., 2025. Improved quantification in end-to-end deep learning FastPET reconstruction using multi-view histo-images of attenuation correction factors. *IEEE transactions on Radiation and Plasma Medical Sciences*, 63-73.

[6] Panin V, Millardet M, Bharkhada D and Conti M, 2024. FastPET: Histo-projections approach. *IEEE NSS MIC 2024*.

MIC-15-210

Clinically Feasible Deep-Learning–Enabled Dual-Gating Reconstruction for Cardiac PET (#2156)

Kuan-Hao Su, Renato Keshet, Andrew Langholz, Bella Yuzefovich, Sofi Novofastovski, Eli Stern, Sivan Peleg-Cohen, Ariel Lulinsky, Yariv Grobshtein, Gil Kovalski

GE HealthCare, Chicago, USA

Abstract

Cardiac PET imaging is significantly affected by respiratory and cardiac motion, leading to image blurring and reduced quantification accuracy, particularly in motion-sensitive myocardial regions. Although dual-gating techniques can mitigate motion artifacts, their clinical adoption remains limited due to substantial noise amplification and degraded image quality. In this work, we propose a clinically feasible dual-gating reconstruction framework that integrates deep-learning–based denoising with motion-compensated reconstruction to address this fundamental limitation.

The proposed method was evaluated using both XCAT simulations with known ground truth and clinical datasets from 18 patients undergoing Flyrcado and Rubidium (Rb) cardiac PET imaging. A deep-learning denoising model is applied to enhance gated images and improve the robustness of motion estimation. Motion fields are estimated using a symmetric normalization approach and incorporated into a novel multi-pose reconstruction framework, where motion information is directly embedded into forward and backward projections for efficient motion-aware reconstruction.

Simulation results demonstrate accurate recovery of myocardial defects that are blurred or indistinguishable in standard reconstructions without motion correction. Clinical results show improved image sharpness, enhanced myocardial delineation, and preserved count statistics across both tracers, indicating consistent performance under realistic imaging conditions.

By effectively addressing the noise–motion trade-off while maintaining computational efficiency, the proposed framework enables practical clinical implementation of dual-gated cardiac PET imaging. This approach has the potential to improve diagnostic confidence and quantitative accuracy in routine cardiac PET applications.

References

[1] A. Mehranian, S. D. Wollenweber, M. D. Walker, et al., “Image enhancement of whole-body oncology [18F]-FDG PET scans using deep neural networks to reduce noise,” Eur. J. Nucl. Med. Mol. Imaging, vol. 49, pp. 539–549, 2022

[2] S. Ahn and J. A. Fessler, “Globally convergent image reconstruction for emission tomography using relaxed ordered subsets algorithms,” IEEE T. Med. Imag., vol. 22, no. 5, pp. 613–626, 2003

[3] B. B. Avants, C. L. Epstein, M. Grossman, and J. C. Gee, “Symmetric diffeomorphic image registration with cross-correlation: Evaluating automated labeling of elderly and neurodegenerative brain,” Med. Image Anal., vol. 12, no. 1, pp. 26–41, 2008

MIC-15-213

Regularized Tomographic Reconstruction for Fast Ultrasound-Modulated Optical Tomography (#2444)

Lucas Duclos[1], Anne Louchet-Chauvet[2], François Ramaz[2], Maïmouna Bocoum[2], Jean-Luc Gennisson[1], Claude Comtat[1]

[1] Université Paris Saclay, Inserm, CNRS, CEA, Laboratoire d'Imagerie Biomédicale Multimodale, Orsay, France; [2] ESPCI Paris, Université PSL, CNRS, Institut Langevin, Paris, France

Supported by France Life Imaging (ANR-11-INBS-0006 grant from the French “Investissements d’Avenir” program)

Abstract

Ultrasound-modulated optical tomography (UOT) is a hybrid biomedical imaging modality that uses a laser beam and ultrasound (US) to reveal optical properties deep within scattering living tissues. It exploits the acousto-optic effect and is based on the detection of photons whose frequency is shifted by the US frequency. Traditionally, focused US waves are used to directly sample the optical image pixel by pixel. To improve the signal-to-noise ratio of the optical image and reduce the acquisition time, US plane waves can be used, resulting in a tomographic problem. However, the finite numerical aperture of the US probe introduces a limited-angle problem, resulting in a loss of lateral resolution. To mitigate this issue, structuration of the plane waves (SW) has been successfully tested for long acquisition times. The objective of the study is to evaluate the performances of Least Squares with Total Variation (LS-TV) tomographic reconstruction in SW UOT for shorter acquisition times, using simulated data with realistic noise levels.

We show first that reducing the number of configurations of the US plane wave structuration from 1353 initially to 41 maintains reconstruction quality for a fixed total acquisition time. Then, we increase gradually the acquisition frame rate from 0.002 Hz initially to 3 Hz. Analysis with adapted regularization parameter reveals a trade-off between frame rate, noise in the reconstructed image, and contrast recovery coefficient (CRC) for an optical absorber mimicking a 1.35 mm radius tumor. Noise increases with frame rate while CRC remains stable below 0.19 Hz and drops significantly above 1.5 Hz.

This study shows for the simulated setup that LS-TV reconstruction enables SW UOT imaging up to a frame rate of 1.5 Hz. It also shows that noise is the primary limiting factor for high-speed UOT rather than sparsity in undersampled SW data.

References

[1] Bocoum, M., Louchet-Chauvet, A., Ramaz, F., Gennisson, J.-L. 2019, ‘Structured ultrasound-modulated optical tomography’, *Applied Optics*, 58(8), pp. 1933–1940, Washington, DC: Optica Publishing Group.

[2] Duclos, L., Louchet-Chauvet, A., Ramaz, F., Bocoum, M., Gennisson, J.-L., Comtat, C. 2026, ‘Iterative reconstruction algorithms for limited-angle UOT using structured planar waves’, *Proceedings of SPIE*, 12345, Strasbourg, France: SPIE.

[3] Chambolle, A., Pock, T. 2011, ‘A first-order primal-dual algorithm for convex problems with applications to imaging’, *Journal of Mathematical Imaging and Vision*, 40(1), pp. 120–154, New York, NY: Springer.

[4] Yagubbayli, F., Sinden, D., Simson, W. 2023, ‘*k-Wave-Python*’, GitHub, [Online]. Available: https://github.com/waltsims/k-wave-python.

MIC-15-216

Multiresolution Proximal Stochastic Denoising Regularization for Accelerated Sparse-View CT Reconstruction (#2515)

Antoine De Paepe[1,2], Dimitris Visvikis[1,2], Alexandre Bousse[1,2]

[1] *LaTIM, Inserm, UMR 1101, Brest, France;* [2] *Université de Bretagne Occidentale, Brest, France*

This work was supported by CPER 2021–2027 IMAGIIS (INNOV-XS) and by the Région Bretagne through the ARED doctoral research grant program.

Abstract

Sparse-view CT reconstruction can reduce radiation dose and acquisition time, but it leads to a severely ill-posed inverse problem. Recent denoiser-based methods such as SNORE provide effective image priors for this setting, yet remain computationally expensive at full resolution. In this work, we propose a multiresolution extension of Prox-SNORE for sparse-view CT. The method solves a sequence of reconstruction problems from coarse to fine resolution levels, using each intermediate solution to initialize the reconstruction at the next finer level. This strategy improves the conditioning of the optimization in the early stages and accelerates convergence at high resolution. Experiments on 30-view CT show that the proposed approach achieves a better time–quality trade-off than standard and annealed Prox-SNORE, while reaching comparable final reconstruction quality. These results suggest that multiresolution optimization is a simple and effective way to make stochastic denoiser-based reconstruction more practical for accelerated CT reconstruction.

References

[1] Renaud, M, Prost, J, Leclaire, A & Papadakis, N 2024, 'Plug-and-play image restoration with stochastic denoising regularization', *Forty-first International Conference on Machine Learning*.

[2] Renaud, M, Hermant, J & Papadakis, N 2025, 'Convergence analysis of a proximal stochastic denoising regularization algorithm', *International Conference on Scale Space and Variational Methods in Computer Vision*, pp. 17–29, Springer.

[3] Chung, H, Kim, J, McCann, MT, Klasky, ML & Ye, JC 2022, 'Diffusion posterior sampling for general noisy inverse problems', *arXiv preprint arXiv:2209.14687*.

[4] Laurent, N, Tachella, J, Riccietti, E & Pustelnik, N 2026, 'Multilevel Plug-and-Play Image Restoration', *IEEE Transactions on Computational Imaging*, vol. 12, pp. 445–456, IEEE.

[5] Jiang, X, Gang, GJ & Stayman, JW 2025, 'Ctorch: PyTorch-compatible GPU-accelerated auto-differentiable projector toolbox for computed tomography', *arXiv preprint arXiv:2503.16741*.

[6] De Paepe, A, Bousse, A, Phung-Ngoc, C, Mellak, Y & Visvikis, D 2025, 'Adaptive Diffusion Models for Sparse-View Motion-Corrected Head Cone-Beam CT', *IEEE Transactions on Radiation and Plasma Medical Sciences*, IEEE.

[7] Roth, HR, Lu, L, Seff, A, Cherry, K, Hoffman, J, Wang, S, Liu, J, Turkbey, E & Summers, RM 2014, 'A new 2.5 D representation for lymph node detection using random sets of deep convolutional neural network observations', *International Conference on Medical Image Computing and Computer-Assisted Intervention*, pp. 520–527, Springer.

MIC-15-219

MLEM Positron Range Corrector for PET/CT (#2681)

Joaquín López Herraiz[1,2], Robert J. Paneque-Yunta[1], Nerea Encina-Baranda[1], Jose M. Udias[1,2]

[1] Complutense University of Madrid, Grupo de Fisica Nuclear, EMFTEL & IPARCOS, Madrid, Spain; [2] Health Research Institute of the Hospital Clínico San Carlos (IdISSC), Madrid, Spain

We acknowledge support from the Comunidad de Madrid regional government through the LUNABRAIN project (TEC-2024/TEC-43) and the Industrial PhD program IND2023/BMD-28275. We also thank Dr. Jan Grimm for the 68Ga-mice acquisition.

Abstract

Positron range introduces a spatially variant, density-dependent blur in positron emission tomography (PET) images of high-energy emitters such as ^{68}Ga and ^{82}Rb, degrading quantification at tissue interfaces. We present a graphics-processing-unit (GPU) implementation of a heterogeneous maximum-likelihood expectation-maximization (MLEM) positron range correction with a joint expectation-maximization/total-variation (EM-TV) update, built on an exact density-weighted forward/adjoint pair derived from a recently published multi-branch range parametrization supporting eight isotopes. The forward operator combines near-field volume integration with far-field Fibonacci-sphere ray traversal of a CT-derived density volume; the adjoint is the matched transpose, and the iterative update conserves total counts exactly. The code corrects a clinical-scale 192x192x335 ^{68}Ga-PSMA volume in 2 minutes (1 iteration, 8 subsets, RTX 3090) and produces visibly sharper structures on a ^{68}Ga mouse acquisition with a preclinical scanner in 45 seconds. The code is publicly available at https://github.com/jlherraiz/PRC_OSEM.

References

[1] R. J. Paneque-Yunta et al., “Analytical positron range model for PET with cross-code Monte Carlo benchmarking,” Phys. Med. Biol., vol. 70, 165013, 2025.

[2] J. Cal-Gonzalez et al., “Tissue-dependent and spatially-variant positron range correction in 3D PET,” IEEE Trans. Med. Imag., vol. 34, no. 11, pp. 2394–2403, 2015.

[3] https://github.com/jlherraiz/PRC OSEM

[4] Deep-learning Evaluation for Enhanced Prognostics - DEEP-PSMA Grand Challenge, MICCAI 2025. https://deep-psma.grand-challenge.org/

MIC-15-222

Lutetium-176-Aided Joint Activity and Attenuation Reconstruction in TOF-PET Using Trust-Region Cubic Surrogate Optimization (#2772)

Xin Zhao, Zhijun Zhao, Zhao Wang, Zhaoheng Xie

Peking University, Beijing, China

This work was supported by National Natural Science Foundation of China (62394311) and National Biomedical Imaging Facility Grant.

Abstract
Joint Maximum Likelihood Activity and Attenuation (MLAA) provides a promising CT-less attenuation correction framework but suffers from global scaling ambiguity. Intrinsic Lu-176 background radiation provides patient-specific transmission information to reduce this issue, while introducing a highly nonlinear and ill-conditioned joint likelihood. We propose the Separable Cubic Surrogate with Trust Region (SCS-TR) algorithm, utilizing an analytical Lipschitz constant and a vectorized solver to ensure strictly monotonic convergence and avoid local optima. The reconstruction is initialized with Maximum Likelihood Transmission Reconstruction (MLTR) results. GATE simulations studies demonstrate that SCS-TR effectively recovers clear bone structures and smooth uniform regions without explicit regularization. The proposed method recovered clear bony structures and uniform soft-tissue regions without explicit regularization, and maintained structural fidelity under 20% count statistics.

References
[1] Omidvari N, Cheng L, Leung E K, et al. Lutetium background radiation in total-body PET–A simulation study on opportunities and challenges in PET attenuation correction[J]. Frontiers in Nuclear Medicine, 2022, 2: 963067.
[2] Cartis C, Gould N I M, Toint P L. Adaptive cubic regularisation methods for unconstrained optimization. Part I: motivation, convergence and numerical results[J]. Mathematical Programming, 2011, 127(2): 245-295.
[3] Li T, He L, Liu Z, et al. CT-Less Attenuation Correction for PET using Backward Inter-Crystal Scattered Events[C]//2024 IEEE Nuclear Science Symposium (NSS), Medical Imaging Conference (MIC) and Room Temperature Semiconductor Detector Conference (RTSD). IEEE, 2024: 1-1
[4] Nesterov Y, Polyak B T. Cubic regularization of Newton method and its global performance[J]. Mathematical programming, 2006, 108(1): 177-205.

MIC-15-225

Organ-based Motion Correction for PET Image Reconstruction using Artificial Intelligence to Segment Organs (#2922)

Eléonore V. Lieffrig[2,1], Vladimir Panin[1], Joshua Schaefferkoetter[1], Deepak Bharkhada[1]

[1] Siemens Medical Solutions USA, Inc., Molecular Imaging, Knoxville, USA; [2] Yale University, New Haven, USA

We are grateful to University hospital at Bern for providing the patient dataset used in this study.

Abstract
Respiratory, cardiac and patient motion during positron emission tomography imaging create artifacts in reconstructed images and can bias their interpretation. In this study, we propose a data-driven, organ-based method to correct motion. Our framework utilizes deep learning-based organ segmentation on no motion corrected images, followed by motion gating derived from centroid of tracer distribution computed within the segmented regions of interest on histo-images. Motion vector fields between the gated images are estimated using the Lucas-Kanade algorithm. Motion is subsequently corrected for in the corresponding gated sinograms and the motion-corrected image is reconstructed from the motion-free sinograms. We demonstrate the effectiveness of our method

by applying it to the liver, enabling accurate estimation and correction of respiratory motion. Qualitative and quantitative results show that our method significantly improves the quality of the reconstructed images compared to no motion correction, and that the organ-specific approach also outperforms motion correction based on motion estimation on the whole abdominal tracer uptake. The average mean and maximum lesion intensities increased by 23.4% and 26.9%, respectively. Combined with better contrast observed on the reconstructed image, these findings suggest that the organ-based approach can recover some true signal that would otherwise be lost due to motion. The proposed framework paves the way for more precise, organ-focused motion correction strategies, enabling the reconstruction of high-quality images tailored to specific anatomical regions.

References
[1] Kris Thielemans, Shailendra Rathore, Fredrik Engbrant and Pasha Razifar, Device-less gating for PET/CT using PCA, *IEEE NSS/MIC*, Valencia, Spain. 2011
[2] Silin Ren, Xiao Jin, Chung Chan, Yiqiang Jian, Tim Mulnix, Chi Liu and Richard E. Carson, Data-driven event-by-event respiratory motion correction using TOF PET list-mode centroid of distribution, *Phys. Med. Biol.*62 4741, 2017
[3] Luyao Shi, Yihuan Lu, Nicha Dvornek, Christopher A. Weyman, Edward J. Miller and Albert J. Sinusas, Automatic Inter-Frame Patient Motion Correction for Dynamic Cardiac PET Using Deep Learning, *IEEE Transactions on Medical Imaging*, vol. 40, no. 12, pp. 3293-3304, 2021
[4] Joshua Schaefferkoetter, Paul Schleyer and Maurizio Conti, A Deep Learning Approach for Semantic, Multi-Organ Segmentation of PET Images, *PSMR 2024*, Isola d'Elba, Italy
[5] Bruce Lucas and Takeo Kanade, An iterative image registration technique with an application to stereo vision. In *Proceedings of the International Joint Conference on Artificial Intelligence*, pp. 674– 679, 1981
[6] Vladimir Panin and Harshali Bal, TOF data non-rigid motion correction, *IEEE NSS/MIC*, San Diego, USA, 2015

MIC-15-228

Multi-information Joint Iterative Reconstruction Algorithm for Cascaded Gamma Photon Coincidence (#2956)

Shuyu Xu[1], Xinyao Liu[2], Kui Wang[1], Zijun Yan[1], Ge Liu[1], Qingyang Wei[1], Hui Liu[3], Jing Wu[4], Yaqiang Liu[3], Zuoxiang He[5]

[1] University of Science and Technology Beijing, School of Automation and Electrical Engineering, Beijing, China; [2] China Nuclear Power Engineering Co., Ltd, Beijing, China; [3] Tsinghua University, Department of Engineering Physics, Beijing, China; [4] Beijing Normal University, School of Physics and Astronomy, Beijing, China; [5] Beijing Tsinghua Changgung Hospital, Department of Nuclear Medicine, Beijing, China

This research was supported by the National Key R&D Program of China (Grant No. 2022YFC2402000), and the National Natural Science Foundation of China (Grant No. 12375337).

Abstract
In cascaded gamma photon coincidence imaging, coincidence events offer superior spatial localization accuracy. However, their low cascade branching ratio limits detection efficiency compared to single-photon events, resulting in elevated statistical noise and prolonged acquisition times.
Since simultaneously acquired single-photon events also encode the spatial distribution of the radionuclide, we propose a multi-information joint iterative reconstruction algorithm. This method fuses coincidence and single-photon events to construct a joint cost function.

Given the incomplete spatial sampling of single-photon events, linearly integrating these modalities via the MLEM algorithm causes high-count single-photon data to overwhelm the high-resolution coincidence features. This leads to image distortion and edge blurring.
To overcome this, we introduce a Maximum A Posteriori (MAP) estimation framework. Discarding the conventional image-domain spatial smoothing prior, the algorithm utilizes single-photon information simultaneously for direct image reconstruction and projection-domain regularization. Within this framework, a data weighting factor, α, governs the integration of single-photon data in the likelihood term, while a prior penalty factor, β, modulates the anti-distortion penalty.
For ultra-low dose or rapid scanning protocols, increasing α leverages the high detection efficiency of single photons to bolster effective statistical counts, suppress Poisson noise in count-starved coincidence events, and enhance sensitivity. Concurrently, synergizing with β to counteract image distortion yields substantial improvements in image quality and the contrast-to-noise ratio.

References
[1] Liu X, Liu H, Cheng L, et al. An mlem reconstruction method with mixed events based on a cascade gamma emission imager system[C]//2020 IEEE Nuclear Science Symposium and Medical Imaging Conference (NSS/MIC). IEEE, 2020: 1-3.

MIC-15-231

Detector-Block-Level Geometric Calibration for Full-Ring Multi-Aperture SPECT Using Analytical Ray-Tracing Simulation (#3028)

Qian Wang, Hongdi Li, Yusheng Li

United Imaging Healthcare North America, Houston, USA

Abstract
Full-ring multi-aperture single-photon emission computed tomography (SPECT) can provide excellent spatial resolution, but geometric misalignments of collimator apertures and detector blocks can substantially degrade image quality. We developed and evaluated a detector-block-level geometric calibration method for full-ring SPECT systems using analytical ray-tracing simulation. The simulated system used the geometry of Alpha-SPECT, consisting of 34 detector modules arranged on a ring with a 40.4-cm radius. Each module contained a 2 (transaxial) × 8 (axial) detector-block array, and each block comprised 40 × 40 CZT crystals with dimensions of 0.5 × 0.5 × 6 mm³. Each module was paired with an 18-mm-thick tungsten collimator containing sixteen 2-mm-diameter pinholes, each focused onto one detector block and separated from the detector surface by 3.1 cm. The proposed calibration estimated source-position offsets and local pinhole and detector-block misplacements by fitting three source-shift parameters and four pose-perturbation parameters for each pinhole–block pair. Simulated projection were generated by ray tracing from a 3 × 3 × 3 grid of 140-keV point sources with 2.5-cm spacing, after applying realistic random perturbations to source positions and system geometry. For each pinhole–block pair, nonlinear least-squares fitting minimized the discrepancy between measured and estimated block projections using independent multistart global optimization followed by two-stage local refinement. Across all detector blocks, the estimated geometric perturbations closely matched the known applied perturbations. Reconstruction of a small Jaszczak phantom using the calibrated geometry showed significantly improved image quality compared with

reconstruction using the perturbed geometry. These results demonstrate that detector-block-level calibration can accurately recover local geometric misplacements and support robust high-resolution full-ring multi-aperture SPECT imaging.

References
[1] Ozsahin, I, Chen, L, Könik, A, King, MA, Beekman, FJ & Mok, GSP 2020, 'The clinical utilities of multi-pinhole single photon emission computed tomography', *Quantitative Imaging in Medicine and Surgery*, 10(10), pp. 2006–2029, Hong Kong: AME Publishing Company.
[2] Huh, Y, Yang, J, Dim, OU, Cui, Y, Tao, W, Huang, Q, Gullberg, GT & Seo, Y 2021, 'Evaluation of a variable-aperture full-ring SPECT system using large-area pixelated CZT modules: A simulation study for brain SPECT applications', *Medical Physics*, 48(5), pp. 2301–2314, Hoboken: Wiley.
[3] Bequé, D, Nuyts, J, Bormans, G, Suetens, P & Dupont, P 2003, 'Characterization of pinhole SPECT acquisition geometry', *IEEE Transactions on Medical Imaging*, 22(5), pp. 599–612, Piscataway: IEEE.
[4] van der Have, F, Vastenhouw, B, Rentmeester, M & Beekman, FJ 2008, 'System calibration and statistical image reconstruction for ultra-high resolution stationary pinhole SPECT', *IEEE Transactions on Medical Imaging*, 27(7), pp. 960–971, Piscataway: IEEE.
[5] Zhang, J, Zannoni, EM, Du, Y, Frey, E & Meng, LJ 2019, 'Alpha-SPECT: Hyperspectral single photon imaging of targeted α-emission therapy', *Journal of Nuclear Medicine*, 60(Supplement 1), p. 311, Reston: Society of Nuclear Medicine and Molecular Imaging.

MIC-15-234

A flexible convex optimization framework for list-mode PET reconstruction with explicit regularization using Primal-Dual Hybrid Gradient (#3122)

Alejandro Lopez-Montes[1,2], Zhimei Ren[3], Joseph Steiner[4], Rina Foygel Barber[4], Axel Rominger[1], Chien-Min Kao[4], Kuangyu Shi[1,2], Emil Sidky[4]

[1] University of Bern, Department of Nuclear Medicine, Bern, Switzerland; [2] University of Bern, Department of Digital Medicine, Bern, Switzerland; [3] University of Pennsilvania, Department of Statistics and Data Science, The Wharton School, Philadelphia, USA; [4] University of Chicago, Department of Radiology, Chicago, USA; [5] Ludwig Maximillian University, Department of Nuclear Medicine, Munich, Germany; [6] Ludwig Maximillian University, Department of Nuclear Medicine, Munich, Germany; [7] University of Pretoria, Department of Nuclear Medicine, Pretoria, South Africa; [8] University of Pretoria, Department of Nuclear Medicine, Pretoria, South Africa; [9] Steve Biko Hospital, Nuclear Medicine Research Infrastructure, Pretoria, South Africa; [10] Steve Biko Hospital, Nuclear Medicine Research Infrastructure, Pretoria, South Africa

Abstract

Image reconstruction in Positron Emission Tomography (PET) is conventionally performed using Maximum Likelihood Expectation Maximization (MLEM) or Ordered Subsets Expectation Maximization (OSEM). While highly successful clinically, these approaches are limited in their ability to incorporate general regularization functions, particularly non-smooth penalties such as Total Variation (TV). In practice, most clinical reconstruction workflows combine OSEM with post-processing Gaussian filtering, which may lead to oversmoothing or residual noise in low-count acquisitions. In this work, we propose a Chambolle–Pock Primal-Dual Hybrid Gradient (CP-PDHG) framework for PET reconstruction compatible with both sinogram and list-mode representations. The proposed formulation introduces a stacked operator representation enabling simultaneous treatment of complete sinogram and list-mode likelihood terms while naturally incorporating convex regularization functions. We derive closed-form dual updates for the Poisson likelihood and implement Huber-regularized reconstruction as a differentiable

approximation to TV. The method was evaluated on simulated IQ phantom data with count levels ranging from 10^6 to 10^8 detected coincidences and on clinical long axial field-of-view (LAFOV) PET acquisitions acquired on a Siemens Biograph Vision Quadra system. In noiseless simulations, CP-PDHG achieved convergence rates comparable to MLEM, while in low-count scenarios it demonstrated substantially improved noise behavior. Regularized CP-PDHG consistently outperformed MLEM with Gaussian post-filtering in both simulated and clinical low-count reconstructions, showing improved lesion conspicuity and reduced noise propagation.

References
[1] Green PJ. Bayesian reconstructions from emission tomography data using a modified EM algorithm. IEEE Trans Med Imaging. 1990;9(1):84-93. doi: 10.1109/42.52985. PMID: 18222753.
[2] Antonin Chambolle, Thomas Pock. A first-order primal-dual algorithm for convex problems with applications to imaging. 2010. (hal-00490826)
[3] Zhang Z, Rose S, Ye J, Perkins AE, Chen B, Kao CM, Sidky EY, Tung CH, Pan X. Optimization-Based Image Reconstruction From Low-Count, List-Mode TOF-PET Data. IEEE Trans Biomed Eng. 2018 Apr;65(4):936-946. doi: 10.1109/TBME.2018.2802947. PMID: 29570054; PMCID: PMC5912805.
[4] Huber, P.J. (1964) Robust Estimation of a Location Parameter. The Annals of Mathematical Statistics, 35, 73-101.
https://doi.org/10.1214/aoms/1177703732
[5] Schramm G and Thielemans K (2024) PARALLELPROJ—an open-source framework for fast calculation of projections in tomography. Front. Nucl. Med. 3:1324562. doi: 10.3389/fnume.2023.1324562

MIC-15-237

Investigation of hybrid CT-free attenuation correction framework with TOF-MLAA and deep learning (#1209)

Yuya Onishi, Kibo Ote, Takashi Isobe

Hamamatsu Photonics K.K., Central Research Laboratory, Hamamatsu, Japan

This work was partially supported by the JSPS KAKENHI (grant number: JP24K10802).

Abstract
Positron emission tomography (PET) attenuation correction (AC) is essential for achieving quantitative accuracy and is conventionally performed using computed tomography (CT). However, CT-based AC introduces challenges such as image misregistration and additional radiation exposure. Although deep learning-based CT-free AC methods have shown promising performance, concerns remain regarding the reliability and physical consistency of purely data-driven attenuation estimates. In this study, we investigate a hybrid CT-free AC framework that combines deep learning-based attenuation estimation with maximum likelihood reconstruction of attenuation and activity using time-of-flight information (TOF-MLAA). As an initial step toward this integration, we focus on evaluating the TOF-MLAA performance for attenuation-map reconstruction using emission data alone. Monte Carlo simulation was conducted using a realistic digital brain phantom and a brain-dedicated PET scanner geometry. The results demonstrate that TOF-MLAA can reconstruct attenuation maps with anatomically plausible structures and physically meaningful spatial distributions, despite residual noise and quantitative inaccuracies. As a next step, tracer-agnostic deep learning-derived attenuation estimates will be incorporated into the TOF-MLAA framework.

This integration is expected to improve the stability and quantitative performance of attenuation reconstruction while enhancing the reliability and physical consistency of deep learning-generated attenuation maps.

References
[1] J. S. Lee. A Review of Deep-Learning-Based Approaches for Attenuation Correction in Positron Emission Tomography. *IEEE Trans. Radiat. Plasma. Med. Sci.*, 5, 160-84, 2020.
[2] R. Guo *et al*. Using domain knowledge for robust and generalizable deep learning-based CT-free PET attenuation and scatter correction. *Nat. Commun.*, 13, 5882, 2022.
[3] Y. Onishi *et al*. Cross-Tracer PET Attenuation Correction Using Diffusion Model With Slice-Positional Embedding. *2025 IEEE NSS/MIC/RTSD*, 2025.
[4] A. Rezaei *et al*. Joint activity and attenuation reconstruction of listmode TOF-PET data. *2015 IEEE NSS/MIC*, 2015.
[5] Y. Onishi *et al*. Performance evaluation of dedicated brain PET scanner with motion correction system *Ann. Nucl. Med.*, 2022.

MIC-15-240

Crystal-Wise Dead-Time Correction: Application to VRAIN (#1619)

Hideaki Tashima, Go Akamatsu, Yuma Iwao, Taiga Yamaya

National Institutes for Quantum Science and Technology, Institute for Quantum Medical Science, Chiba, Japan

Abstract
Dead-time correction is important for quantitative PET imaging; however, typical methods are approximate, as global dead-time correction is applied using system-level count-rate information. Even with more refined methods, such as block-wise correction, limitations remain. On the other hand, one-to-one coupled detectors, which provide independent signal readout for each crystal, may exhibit crystal-dependent variations in count rate and dead-time behavior. In this study, therefore, we developed a crystal-wise dead-time correction method for the brain-dedicated PET system VRAIN, in which each scintillator crystal is coupled to an individual SiPM. Singles count rates for each crystal were calculated from singles event data acquired during measurement of an ^{18}F-filled phantom over a wide range of radioactivity levels and the rates were used to estimate dead time. Dead-time factors representing sensitivity reduction due to count loss were modeled using both non-paralyzable and paralyzable models. The factors were estimated for arbitrary acquisition time frames and incorporated into the forward projection model of a list-mode OSEM reconstruction algorithm. To evaluate the proposed method, pool phantom measurements were performed and compared with a detector-wise correction method. The proposed method showed improved linearity with radioactivity compared with the detector-wise approach. Comparable performance was observed between the two dead-time models, while the non-paralyzable model showed slightly better linearity. These results demonstrate the feasibility of crystal-wise dead-time correction for improving quantitative accuracy in brain PET systems with one-to-one coupled detectors.

References
[1] S. Yamamoto, *et al.*, “Deadtime correction method using random coincidence for PET,” *JNM*, vol. 27, pp. 1925-8, 1986.
[2] A. S. M. Issa, *et al.*, “A detector block-pairwise dead time correction method for improved quantitation with a dedicated BrainPET scanner,” *Phys. Med. Biol.*, vol. 67, pp. 235004, Dec. 2022.
[3] M. Aykac, *et al.*, “Crystal-based deadtime correction for Siemens next generation SiPM based PET/CT scanner,” 2017 IEEE NSS/MIC, Atlanta, GA, USA, 2017.
[4] G. Akamatsu, *et al.*, “Evaluation of a Hamamatsu TOF-PET detector module with 3.2 mm pitch LFS scintillators and a 256-channel SiPM array,” *IEEE TRPMS*, vol. 5, pp. 645-50, Sep. 2021.

[5] G. Akamatsu, *et al.*, "Performance evaluation of VRAIN: a brain-dedicated PET with a hemispherical detector arrangement," *Phys. Med. Biol.*, vol. 67, pp. 225011, Nov. 2022.
[6] M. Takahashi, *et al.*, "Small nuclei identification with a hemispherical brain PET," *EJNMMI Physics*, vol. 9, pp. 69, Oct. 2022.

MIC-15-243

Beyond NEMA Standards: Spatial Resolution Assessment of a Dual-Rotation Preclinical PET System (#2011)

Fabiana M. Ribeiro[1], Leonor Moutinho[1], Ana C. Carvalho[1], Ana C. Santos[2], Pedro M.M. Correia[1], Ana Luísa M. Silva[1], João F.C.A. Veloso[1]

[1] University of Aveiro, Department of Physics, i3N, Aveiro, Portugal; [2] University of Coimbra, iCBR, CIMAGO, CIBB, CEMMPRE, Coimbra, Portugal

This work is financed by national funds through FCT, I.P. and the Ministry of Science, Technology and Higher Education under project UID/50025/2025, UID/PRR/50025/2025, UID/PRR2/50025/2025, and Associated Laboratory i3N – LA/P/0037/2020; and by FEDER program and national funds through FCT under project HadronPET COMPETE2030-FEDER-00755500.

Abstract

The easyPET.3D system is a preclinical positron emission tomography (PET) scanner featuring a non-conventional acquisition geometry based on the dual-rotation of two opposing detector modules, combining a fan rotation for angular sampling and an axial rotation for volumetric coverage. Its performance was previously evaluated following the NEMA NU 4-2008 standard, demonstrating consistent spatial resolution across the field-of-view. However, such assessment relies on filtered back projection, an analytical reconstruction method that may not accurately represent the performance of systems with unconventional geometries, where its application can be challenging, thereby limiting the direct applicability of the standard protocol. In this work, the easyPET.3D spatial resolution was further investigated using a micro-Derenzo phantom and iterative reconstruction (LM-MRP), enabling a more realistic and application-oriented evaluation. A quantitative metric based on the smallest resolvable rod diameter was introduced to formalize the commonly adopted smallest resolvable rod criterion and provide a simple and reproducible indicator under practical imaging conditions. The analysis was performed for the three predefined acquisition modes of the system (fast, medium, slow), previously established based on optimized operating parameters. These modes differ in axial rotation step angle and acquisition time, reflecting distinct sampling conditions while preserving the same hardware configuration. This work explores a more application-oriented approach for assessing spatial resolution in preclinical PET systems with non-conventional geometries.

References
[1] NEMA standards for the performance measurements of small animal positron emission tomographs, NEMA standards publication NU 4-2008, 2011.
[2] J. F. C. A. Veloso, *et al.*, *"Positron emission tomography system and method with tworotation shafts,"* patent granted: WO/2016/147130 A1/PCT/IB2016/051487, Sep. 22, 2016.
[3] F. M. Ribeiro, *et al.* (2025). doi: 10.1109/TRPMS.2025.3546120.
[4] F. M. Ribeiro, *et al.* (2025). doi: 10.1186/s40658-025-00757-0.
[5] P. M. C. C. Encarnação, *et al.* (2025). doi: 10.1088/1361-6560/ada718.

MIC-15-246

PET Spatial Resolution Repeatability and Reproducibility Following the NEMA NU 2 Standard (#2134)

Benjamin A. Spencer[1], Yifan Wu[2], Yun Dong[2], Lorenzo Nardo[1], Brahim Mehadji[1]

[1] UC Davis Health, Radiology, Sacramento, USA; [2] United Imaging Healthcare, Shanghai, China

Abstract

The NEMA NU 2 protocol provides the standard for positron emission tomography (PET) spatial resolution evaluation and benchmarking, yet its reproducibility and repeatability have not been rigorously evaluated for modern PET systems. In this study, we investigated the variability of NEMA spatial resolution measurements using the uEXPLORER total-body PET scanner under controlled experimental conditions. A total of 195 point source measurements were acquired to determine an estimate of NEMA spatial resolution uncertainty along with the effects of capillary size, activity concentration, and acquired counts. Spatial resolution was computed following the NEMA standard using in-house code and a vendor provided tool for filtered back projection reconstruction. Despite controlled experimental conditions, statistically significant differences were observed in 16 of 86 comparisons indicating limited reproducibility across experiments. From our measurements we determined that a single NEMA spatial resolution measurement exhibits an uncertainty of approximately 0.2 mm (≈5%), improving to 0.1 mm (≈3%) with repeated acquisitions. There was no observed impact to spatial resolution from capillary size (0.3–1.0 mm) or total counts acquired, while a potential dependence on activity concentration was identified but requires further validation. These findings highlight a discrepancy between reported precision in the literature and practical measurement variability. We recommend incorporating repeated measurements and reporting uncertainty to ensure meaningful benchmarking. Revisions to the NEMA protocol may be necessary to better reflect the performance of modern PET systems

References
[1] NU 2-2018. National Electrical Manufacturers Association; 2018.

MIC-15-249

Characterization and Correction of Dynamic Changes in Sensitivity Patterns for the Jülich BrainPET-7T (#2315)

Juergen J. Scheins[1], Lutz Tellmann[1], Debora Niekämper[1], Nadim J. Shah[1,2], Christoph W. Lerche[1]

[1] Forschungszentrum Jülich GmbH, Institute of Neuroscience and Medicine (INM-4), Jülich, Germany; [2] RWTH Aachen University, Department of Neurology, Aachen, Germany

The project "*Next generation BrainPET scanner for 7T MRI*" was supported by the Helmholtz Validation Fund No. 0051 and the Innovation Go funding of the Forschungszentrum Jülich GmbH for the project “BrainPET-7T”.

Abstract

In PET, the large dynamic range of activity in the scanner field-of-view (FOV) represents a significant challenge in accurately detecting and quantifying all incoming photons and coincidences. Block pileup and deadtime, well-known effects that increase non-linearly with the activity exposure, are unavoidable for all types of detector hardware. Thus, the observed global sensitivity at the block-level, as well as the detection efficiency at the crystal-pixel level, can be strongly impacted. The adequate characterization and correction of these sources of bias is imperative to obtain artifact-free quantitative images from the reconstruction process.In this work, we characterize such activity dependencies for our Jülich BrainPET-7T insert, which is designed as hybrid PET/MR system for advanced neuroscience applications. The new BrainPET-7T insert comprises 120 detector blocks with a three-staggered-layer design using a 12x12 matrix of digital silicon photomultipliers (dSiPM) from Philips DPC to detect light. A ^{11}C-decay experiment using a homogeneously filled cylinder was performed to quantify changes in terms of individual block deadtime and crystal efficiency maps as a function of the FOV activity. Assuming the low activity regime is (approx.) unbiased allows quantification of deviations with respect to higher activities by extrapolation of ground truth values. A block deadtime of 11-13% was found for a total FOV activity of 195 MBq. Furthermore, the crystal efficiency patterns showed a continuous evolution over the covered activity range, necessitating compensation in terms of dynamic adjustment of the scanner normalization to prevent streak artifacts in reconstructed images in the high activity regime.

References

[1] Lerche, C.W. et al., *First Performance Results of a UHF-MRI Compatible BrainPET Insert for Neuroscience*, IEEE NSS/MIC 2023

[2] Lerche, C.W. et al., *MR Compatibility Evaluation of a BrainPET Insert for UHF-MR Systems and Neuroscientific Applications*, IEEE NSS/MIC 2024

[3] Lerche, C.W. et al., *Fast maximum likelihood positioning for staggered layer scintillation PET detector*, Phys. Med. Biol., 2025, 70 175018

[4] Scheins, J.J. et al., *Fully-3D PET image reconstruction using scanner-independent, adaptive projection data and highly rotation-symmetric voxel assemblies*, Trans. Med. Imaging, 2011, Vol. 30, p.879-92

[5] Scheins, J. J. et al., *High-Throughput CPU/GPU Monte Carlo Scatter Simulation for the Jülich BrainPET-7T Insert,IEEE NSS/MIC 2025*

MIC-15-252

Evaluation of the Impact of Motion Correction on PET Quantification of Early Diagnosis of Alzheimer’s Disease (#2407)

Viet A. Dao[1,3], Ekaterina Mikhaylova[2], Daniel Lesnic[1], Charalampos Tsoumpas[3,1]

[1] University of Leeds, School of Mathematics, Leeds, UK; [2] Positrigo AG, Zurich, Switzerland; [3] University Medical Center Groningen, University of Groningen, Department of Nuclear Medicine and Molecular Imaging, Groningen, Netherlands

V. Dao is supported by an EPSRC CASE PhD scholarship in partnership with Positrigo and his placement at the University Medical Center Groningen by EPSRC CCP in Synergistic Reconstruction for Biomedical Imaging (EP/T026693/1). C. Tsoumpas is supported by the NWO AES Vici Talent program (doi: 10.61686/REEAR02777). Dr. M. Ahnen for overseeing the various clinical trials to obtain patient data. Leipzig hospital for conducting the clinical trials.

Abstract

In this work we apply the fully automated motion correction algorithm using open source Software for Tomographic Image Reconstruction (STIR) with automated motion detection for [^{18}F]-Flutemetamol ([^{18}F]-FMM) tracer for β-amyloid accumulation in the brain cortex region. The visual results show significant improvement in contrast in the Pons and Cerebellum region with decrease blurring at the edges around the cortex region of the brain. The quantitative results shows statistically significant agreement of centiloid, a metric for early diagnosis Alzheimers' disease, between the motion corrected [^{18}F]FMM tracer and the noisy longest frame without detectable motion using the single sided Wilcoxon test at 5% compared to no motion correction.

References
[1] E Keogh et al., ”An online algorithm for segmenting time series,” in Proc. IEEE Int. Conf. Data Mining, 289–96, 2001.
[2] BB Avants et al., ”A reproducible evaluation of ANTs similarity metric performance in brain image registration,” Neuroimage, 54(3):2033–44, 2011.
[3] K Thielemans et al., ”STIR: Software for Tomographic Image Reconstruction Release 2,” Phys. Med. Biol., 57(4):867–83, 2012.
[4] C Tsoumpas et al., ”The effect of regularization in motion compensated PET image reconstruction: a realistic numerical 4D simulation study”,Phys. Med. Biol., 58(6): 1759-73, 2013.
[5] V Dao et al. , ”Data driven motion detection, estimation and correction for brain PET scanners,” 2025 IEEE NSS MIC
[6] WE Klunk, et al., “The Centiloid Project: Standardizing quantitative amyloid plaque estimation by PET,” Alzheimer’s Dement., 11(1):1, 2015.

MIC-15-255

Investigation of PET-only Data-driven Motion Detection and Correction Methods (#2633)

Natia Beriashvili[1,3], Lutz Tellmann[1], Cláudia R. Brambilla[1], Keith G. Ciantar[1], Jürgen J. Scheins[1], Elisabeth Pfaehler[1], Mikheil Chikhradze[2], Nadim J. Shah[1,4], Christoph W. Lerche[1]

[1] Forschungszentrum Jülich, Institute of Neuroscience and Medicine 4, Jülich, Germany; [2] Georgian Technical University, Faculty of Engineering Physics, Tbilisi, Georgia; [3] RWTH Aachen University, Faculty of Medicine, Aachen, Germany; [4] RWTH Aachen University, Department of Neurology, Aachen, Germany

This work was supported by the Joint Research and Education Program for PhD Students funded by Forschungszentrum Jülich and the Shota Rustaveli
National Science Foundation of Georgia (Grant No. JFZ-II-22-035), awarded to Natia Beriashvili and by the RETIMAGER project, Horizon EIC 2022 Pathfinder Open, Grant ID:101099096.
Elisabeth Pfaehler is funded by the European Union, Marie-Curie Sklodowska Fellowship HORIZON-MSCA-2021-PF-01, grant 101068572.

Abstract
Spontaneous patient motion degrades image quality and compromises quantitative accuracy in brain PET imaging. In this work, we present and evaluate three data-driven approaches for rotational motion detection using list-mode PET data: a point-cloud-based principal component analysis (PCA) method operating on LOR midpoint coordinates, a PCA method applied to backprojected images, and a convolutional neural network (CNN)-based approach. Controlled measurements were performed using an anthropomorphic head phantom on a custom holder allowing isolated single-plane rotations, with ground truth determined via MRI at each position. The PCA-based methods achieved an angular precision of 1-3 degrees, with the backprojection-based implementation additionally reducing signal cross-talk between projection planes. A full comparison of all three methods will be presented at the conference.

References
[1] C. Catana, Semin. Nucl. Med., vol. 45, pp. 212–223, 2015.
[2] T. Zeng et al., Phys. Med. Biol, vol. 68, no. 24, p. 245019, 2023.
[3] Y. Lu et al., J. Nucl. Med., vol. 61, pp. 1397–1403, 2020.
[4] Y. Lu et al., Phys. Med. Biol., vol. 64, no. 6, p. 065002, 2019.
[5] E. M. Revilla et al., NeuroImage, vol. 252, p. 119031, 2022.
[6] L. Caldeira et al., IEEE Trans. Radiat. Plasma Med. Sci., vol. 3, no. 3, pp. 352–362, 2019.
[7] H. Iida et al., Ann. Nucl. Med., vol. 27, no. 1, pp. 25–36, 2013.
[8] P. J. Schleyer et al., Phys. Med. Biol., vol. 60, pp. 6441–6458, 2015.
[9] K. Thielemans et al., in Proc. IEEE NSS/MIC. IEEE, 2013.

MIC-15-258

Rigorous and accurate estimation of spatial resolution of MLEM reconstructions in PET (#2749)

Martin Rädler[1,2], Paweł Moskal[1,2], On behalf of the J-PET collaboration

[1] Jagiellonian University, Centre for Theranostics, Kraków, Poland; [2] Jagiellonian University, Faculty of Physics, Astronomy and Applied Computer Science, Kraków, Poland

National Science Centre of Poland (2021/42/A/ST2/ 00423, 2021/43/B/ST2/02150, 2022/47/I/NZ7/03112), SciMat and qLife under the Excellence Initiative at Jagiellonian University, and PLGrid (ACK Cyfronet AGH, PLG/2024/017688).

Abstract
Positron Emission Tomography (PET) detector systems are continuously being developed and optimized to enhance sensitivity and spatial resolution. Standards, such as those defined by the National Electrical

Manufacturers Association (NEMA), are essential for reliable performance assessment. However, little has changed between the first (NU 2-1994) and the latest (NU 2-2024) NEMA standard on spatial resolution assessment of PET scanners. Also, the small animal PET scanner standard (NU 4) has not been updated since 2008. Reconstructing point sources with outdated filtered back-projection remains mandatory. Although Maximum Likelihood Expectation Maximization (MLEM) algorithms are favored for achieving higher resolution and lower noise, their use for spatial resolution assessment is discouraged, since reconstructed point sources can become arbitrarily small with many iterations [1]. In this work, we propose a protocol for rigorous and accurate estimation of the spatial resolution of MLEM-reconstructed images. Our method relies on the Derenzo phantom [2], yet, any hot-rod phantom may be used. Spatial resolution is assessed in two steps. First, Modulation Transfer Function (MTF) values are extracted at spatial frequencies defined by the rod sizes. Then, a parametric MTF model is fitted to derive the resolution from the associated Point Spread Function (PSF). We show that this method converges, removing the dependence on the number of iterations. We further demonstrate that it yields spatial resolution values consistent with theoretical expectations. Therefore, we recommend updating the upcoming NEMA NU 2 and NU 4 standards to reflect established iterative reconstruction practices and enable a robust assessment of spatial resolution across PET systems.

References
[1] Gong, K. et al. 2016, 'On the assessment of spatial resolution of PET systems with iterative image reconstruction', *Physics in Medicine & Biology*, 61.5, N193–N202
[2] Cox, B. L. et al. 2016, 'Development of a novel linearly-filled Derenzo microPET phantom', *American journal of nuclear medicine and molecular imaging*, 6.3, 199

MIC-15-261

Randomand Scatter Correction for a Brain PET System Based on List-Mode Data (#2899)

Zexing Wu[1,2], Hang Yang[1], Hengyi Li[1], Chen Huang[1,2], Xiaolong Jiang[1], Wenjie Huang[1], Xiangtao Zeng[1], Ming Niu[1], Zheng Gu[1]

[1] Shenzhen Bay Laboratory, Institute of Biomedical Engineering, Shen zhen, China; [2] Southern University of Science and Technology, Shen zhen, China

This work is supported by the National Key R&D Program of China (No. 2023YFC2414800), the National Natural Science Foundation of China (Nos. 12275182 and 62371314), Guangdong Basic and Applied Basic Research Foundation (Nos. 2024A1515012154), the Guangdong Provincial Project (Grant No. 2023TQ07A233), the Major Program of Shenzhen Bay Laboratory (No. C1012530005) and the Shenzhen Bay Laboratory Proof-of Concept Grants (No. C1022430005).

Abstract
In this work, random and scatter corrections were developed for N-PET, a dedicated brain PET system, using the correction framework supported by CASToR. Each detector module contains dual-layer LYSO scintillator arrays with four DOI encoding bins. Random coincidences were estimated using the delayed window method, while scatter coincidences were estimated using a GATE Monte Carlo simulation model. Both random and scatter

estimates were incorporated as additive terms in the iterative reconstruction model. To improve the statistical stability of sparse LOR-level estimates, each 2×2 neighboring crystal array was grouped as one block. For each block-pair, the random and scatter counts from all corresponding crystal-level LORs were summed and evenly redistributed to the LORs within the same block-pair.
Random correction was evaluated experimentally with an image quality phantom containing three hot spheres with diameters of 13 mm, 22 mm, and 37 mm. The results showed that random correction reduced background noise outside the phantom, and normalization and attenuation correction further improved image uniformity and hot sphere visibility. Scatter correction was preliminarily evaluated using GATE simulation. The proposed method increased the CRC of the 13 mm hot sphere from 0.49 to 0.60, which was comparable to the scatter-free reconstruction result of 0.59. These results show that the proposed list-mode-based random and scatter correction method improves the reconstructed image quality of the N-PET system. Future work will validate the scatter correction with experimental data and further optimize the accuracy of both corrections.

MIC-15-264

Attenuation Correction Strategies for Bain Scans in State-of-the-art TOF PET/MRI (#2990)

Mohammadreza Teimoorisichani[1], Josh Schaefferkoetter[1], Jorge Cabello[1], Patrick Lehmann[2,3], Flemming L. Andersen[4,5], Thomas L. Andersen[4,5], Paul Schleyer[1]

[1] Siemens Medical Solutions USA Inc., Knoxville, USA; [2] Siemens Healthcare A/S, Ballerup, Denmark; [3] Siemens Healthineers AG, Research & Clinical Translation, Magnetic Resonance, Erlangen, Germany; [4] Copenhagen University Hospital Rigshospitalet, Department of Clinical Physiology and Nuclear Medicine, Copenhagen, Denmark; [5] University of Copenhagen, Department of Clinical Medicine, Copenhagen, Denmark

Abstract
Accurate patient attenuation maps (μ-maps) are essential for precise PET quantification. In this study, we compared four methods for generating brain μ-maps in TOF PET/MRI scans and evaluated their impact on reconstructed PET images. We analyzed MRI segmentation, MLAA-based attenuation correction, and two deep learning (DL) approaches: convolutional neural networks (CNN) and denoising diffusion probabilistic models (DM). Two clinical studies utilizing [^{18}F]-FDG and [^{18}F]FE-PE2I tracers on a Siemens BIOGRAPH One PET/MRI (Siemens Healthineers) were examined. The MR-based technique occasionally misclassified skull bone and paranasal sinuses as soft tissue. Both DL networks produced reasonable μ-maps for [^{18}F]-FDG but struggled with the [^{18}F]FE-PE2I data, which was absent from the training set. While MLAA-based μ-maps assisted in recovering missed bone and sinuses, they were more susceptible to noise. For [^{18}F]-FDG, μ-map variations did not cause major PET quantification differences, though MLAA showed a slight overcorrection. Conversely, for [^{18}F]FE-PE2I, CNN-based attenuation led to an activity underestimation of up to 10% in the striatum. This study highlights the importance of μ-map selection, and future work will utilize PET/CT for a systematic "ground truth" comparison.

References
[1] Catana, C., Attenuation correction for human PET/MRI studies. Phys Med Biol, 2020. 65(23): p. 23TR02
[2] Schaefferkoetter, J., P. Schleyer, and M. Conti, Medical Image Volume Generation Using 3D Conditional Diffusion Models, in 2025 IEEE Nuclear Science Symposium (NSS), Medical Imaging Conference (MIC) and Room Temperature Semiconductor Detector Conference (RTSD). 2025. p. 1-1.

[3] Nuyts, J., et al., Simultaneous maximum a posteriori reconstruction of attenuation and activity distributions from emission sinograms. IEEE Trans Med Imaging, 1999. 18(5): p. 393-403.
[4] Rezaei, A., et al., Simultaneous reconstruction of activity and attenuation in time-of-flight PET. IEEE Trans Med Imaging, 2012. 31(12): p. 2224-33.
[5] Henriksen, O.M., et al., First Clinical Experiences with the Ultra-Fast Time-of-Flight BIOGRAPH One Next-Generation Hybrid PET/MRI System. Diagnostics (Basel), 2026. 16(3).

MIC-15-267

Performance Evaluation of DSAC in LYSO and Plastic Scintillators: A Comparative Simulation Study for CT-less PET (#3027)

Satyam Tiwari, Sushil Sharma, Pawel Moskal

Jagiellonian University, Faculty of Physics, Astronomy and Applied Computer Science, Kraków, Poland

Work supported by National Science Centre, Poland: 2021/42/A/ST2/00423, 2021/43/B/ST2/02150, 2022/47/I/NZ7/03112, 2023/50/E/ST2/00574; Ministry of Science/Higher Education: IAL/SP/596235/2023; and Jagiellonian University (SciMat, qLife, Excellence Initiative).TgQPHd|[]

Abstract

Quantitative PET requires attenuation correction (AC) to compensate for the loss of annihilation photons due to absorption and scattering within the patient's body [1]. The current clinical gold standard is CT, but it increases radiation dose, hardware costs, and registration complexity [2]. These limitations motivate the exploration of CT-less AC approaches in PET imaging [3]. One such method is Detector Scattered Attenuation Correction (DSAC), which uses detector-scattered photons to estimate the attenuation map from the PET data itself [4]. In DSAC, detector-scattered (DS) coincidences are used. These coincidences define lines of response (LORs) in which a gamma ray undergoes Compton scattering in one detector module and then deposits its remaining energy in another detector module after passing through the patient. As these photons pass through the phantom, attenuation information is encoded through photoelectric absorption and scattering. In this comparative study, we use GATE simulations [5] with two different materials, plastic and LYSO, to estimate attenuation maps via DSAC. The results show that plastic scintillator based JPET Scanner [6,7] yield a significantly higher DS-coincidence fraction (47%) than LYSO (1.2%), representing a 6.3-fold increase in useful statistics despite the lower raw registration efficiency of plastic. Single Slice Rebinning (SSRB) reconstructions show lower absolute error, better uniformity, and reduced cupping for plastic, while the phantom remains visible for LYSO despite its lower DS statistics. Our study concludes that DSAC is feasible for PET imaging with both scintillator types, with plastic offering stronger DS statistics and improved preliminary quantitative metrics

References
[1] Zaidi, H, Hasegawa, B 2003, 'Determination of the attenuation map in emission tomography', *J. Nucl. Med.TgQPHd|[]*, 44, 291–315.
[2] Blodgett, TM, Mehta, AS, Laymon, CM, Carney, J, Townsend, DW 2011, 'PET/CT artifacts', *Clin. ImagingTgQPHd|[]*, 35, 49–63.TgQPHd|[]
[3] Berker, Y, Li, Y 2016, 'Attenuation correction in emission tomography using the emission data: A review', *Med. Phys.TgQPHd|[]*, 43, 807–832.
[4] Tiwari, S, Sharma, S, Moskal, P 2025, 'Feasibility study of using detector-scattered photons for attenuation correction in CT-less PET imaging', *Bio-Algorithms and Med-SystemsTgQPHd|[]*, 21, 13–20.TgQPHd|[]

[5] Jan, S, et al. 2004, 'GATE: a simulation toolkit for PET and SPECT', *Phys. Med. Biol.TgQPHd|[]*, 49, 4543–4561.
[6] Moskal, P, et al. 2014, 'Test of a single module of the J-PET scanner based on plastic scintillators', *Nucl. Instrum. Methods Phys. Res. ATgQPHd|[]*, 764, 317–321.
[7] Moskal, P, et al. 2024, 'Positronium image of the human brain in vivo', *Science AdvancesTgQPHd|[]*, 10, eadp2840.TgQPHd|[]

MIC-15-270

Random Estimation for a PET Scanner Dedicated to Plant Rhizosphere Imaging Using LORs Outside the Reconstruction Volume (#3071)

Muhammad Nasir Ullah[1], Garry Chinn[1], Grant H.-S. Park[1], David Anders[1], Shiva Abbaszadeh[2], Criag S. Levin[1,3]

[1] Stanford University, Department of Radiology and Molecular Imaging Program at Stanford ((MIPS)), stanford, USA; [2] University of California Santa Cruz, Department of Electrical and Computer Engineering, Santa Cruz, USA; [3] Stanford University, Departments Physics, Electrical Engineering, and Bioengineering, stanford, USA

This work is supported by U.S. DOE BER (DE-SC0021975, DE-SC0024712). We also acknowledge Stanford Sherlock HPC and the Stanford Cyclotron Facility.

Abstract

Accurate randoms correction in PET is typically achieved via delayed-window (DW) or singles-product (SP) methods, both requiring dedicated hardware unavailable on many research PET systems. We present Non-imaging Pairs Random Estimation (NPR), a calibration-free estimator that uses detector pairs whose lines of response (LORs) lie outside the reconstruction field of view (FOV) as a random-coincidence baseline. Per-pair randoms are estimated in three closed-form steps from prompt list mode data alone. Validated against GATE Monte Carlo ground truth on data acquired across 38 simulations spanning random fractions 9–99%, NPR achieves per-pair MAE = 0.45%, matching DW (0.50%) and SP (0.35%) for spatially distributed sources. Under a 5×-singles-asymmetry hot-sphere stress test, NPR retains 1.96% MAE (matching DW, which is also robust) while SP fails by +230%/-33%. A 20-pair FPGA configuration supporting NPR45 (neighbor pairs only, MAE = 0.50%) is demonstrated on R-PET with an ^{18}F capillary phantom.

References
[1] M. N. Ullah et al., "Imaging Performance of Rhizo-PET (R-PET),"2025 IEEE NSS MIC RTSD, pp. 1-2, 2025.
[2] M. N. Ullah et al., "Rhizo-PET: 4D Imaging of Carbon Dynamics,"bioRxiv, 2026.
[3] C. W. Williams et al., "Correction of random coincidences inPET," J. Nucl. Med., vol. 20, pp. 695-696, 1979.
[4] E. J. Hoffman et al., "Quantitation in PET," JCAT, vol. 5, pp.391-400, 1981.
[5] C. W. Stearns et al., "Random coincidence estimation," IEEE NSSCR, vol. 5, p. 3067, 2003.
[6] S. Jan et al., "GATE: a simulation toolkit," Phys. Med. Biol., vol.49, pp. 4543-4561, 2004.

MIC-15-273

An Exponential Total Variation Functional to Replace the Total Variation Norm (#1061)

Gengsheng L. Zeng[1], Ya Li[2]

[1] Utah Valley University, Computer Science, Orem, USA; [2] Utah Valley University, Mathematics, Orem, USA

This work was supported in part by the National Institutes of Health under Grant R15EB024283

Abstract

In iterative image restoration, the total variation (TV) norm is the most common regulator to control noise and enforce sharp edges in the images. This paper proposes an exponential version of the TV norm. This exponential version of the TV norm behaves similar to the L_p norm for $0 < p < 1$ and it promotes sharp image edges better than the TV norm. This exponential TV is easy to implement. We use computer simulations to compare the effectiveness of preserving sharp edges by the TV regulator and by the exponential version. The image restoration task is image denoising. The exponential regulator is demonstrated as more effective in obtaining piecewise-constant images than the popular TV regulator.

References

[1] [1] Rudin, Leonid I.; Osher, Stanley; Fatemi, Emad (1992), "Nonlinear total variation-based noise removal algorithms," *Physica D: Nonlinear Phenomena*, 60.1, 259-268, doi:10.1016/0167-2789(92)90242-F.

[2] Blomgren, Peter; Chan, Tony F. (1998), "Color TV: total variation methods for restoration of vector-valued images," *IEEE Transactions on Image Processing*, vol. 7, no. 3: 304-309, doi:10.1109/83.661180, PMID 18276250.

[3] Tony F. Chan and Jackie (Jianhong) Shen (2005), *Image Processing and Analysis - Variational, PDE, Wavelet, and Stochastic Methods*, SIAM, ISBN 0-89871-589-X.

[4] Wang, Zhou; Bovik, A.C.; Sheikh, H.R.; Simoncelli, E.P. (2004-04-01). "Image quality assessment: from error visibility to structural similarity," *IEEE Transactions on Image Processing*, vol. 13, no. 4, pp. 600–612.

MIC-15-276

Comparative Evaluation of Respiratory Motion Correction Methods for Upright Walk-Through PET Using XCAT Simulations (#1444)

Rabia Aziz[1], Thibault D'Hulster[1], Jens Maebe[1], Christian Vanhove[1], Sun Tao[2], Stefaan Vandenberghe[1]

[1] University of Ghent, Institute of Biomedical Engineering, Ghent, Belgium; [2] Shenzhen Institute of Advanced Technology, Chinese Academy of Sciences, Shenzhen, China

Supported by the Research Foundation – Flanders (FWO) through a long-stay grant (File number: V402926N).

Abstract

Walk-through positron emission tomography (WT-PET) is an emerging upright imaging geometry based on two vertically opposing flat detector panels. Although this design may improve patient comfort and acquisition efficiency, respiratory motion remains a major source of image degradation. This study evaluates respiratory motion correction strategies for WT-PET using XCAT anthropomorphic simulations. A 30s acquisition was simulated in a WT-PET geometry and reconstructed using an in-house MLEM-based algorithm. Data-driven amplitude- and phase-based respiratory gating were followed by non-rigid motion correction using Advanced Normalization Tools (ANTs) and Fast Algorithms for Motion Correction (FALCON). Overlapping-frame reconstruction using 0.9375s windows shifted every 0.3125s was also evaluated to assess the effect of temporal smoothing. Performance was quantified against a motion-free reference using normalized root mean square error (NRMSE), diaphragm edge width, and line profile analysis. ANTs phase-based 4-gate correction achieved the best performance, reducing NRMSE from 64% to 6% and restoring the diaphragm edge width to the motion-free reference level (25.10 mm vs. 25.79 mm). FALCON phase-based 4-gate correction reduced NRMSE to 12% but showed limited recovery of diaphragm sharpness, with an edge width of 28.40 mm compared with 28.62 mm for no motion correction. Overlapping-frame ANTs correction reduced NRMSE to 15% and yielded an intermediate edge width of 27.13 mm, although line profiles indicated residual local displacement and smoothing. These findings show that data-driven respiratory gating combined with deformable registration can substantially improve image quality in upright WT-PET.

References
[1] S. Vandenberghe *et al.*, “Walk-through flat panel total-body PET: a patient-centered design for high throughput imaging at lower cost using DOI-capable high-resolution monolithic detectors,” *EJNMMI*, 2023.
[2] R. Aziz *et al.*, “Quantitative analysis of patient motion in walk-through PET scanner and standard axial field of view PET scanner using infrared-based tracking,” *EJNMMI Phys.*, 2024.
[3] M. D. Walker *et al.*, “Data-driven respiratory gating outperforms device-based gating for clinical 18F-FDG PET/CT,” *Journal of Nuclear Medicine*, 2020.
[4] A. H. Dias *et al.*, “Validation and clinical impact of motion-free PET imaging using data-driven respiratory gating and elastic PET-CT registration,” *EJNMMI*, 2024.
[5] N. J. Tustison *et al.*, “The ANTsX ecosystem for quantitative biological and medical imaging,” *Sci. Rep.*, 2021.
[6] L. K. Shiyam Sundar *et al.*, “Fully Automated, Fast Motion Correction of Dynamic Whole-Body and Total-Body PET/CT Imaging Studies,” *Journal of Nuclear Medicine*, 2023.

MIC-15-279

Multi-parametric calibration and correction procedures for clinical and preclinical PET scanners: improving timing and energy resolution

(#1593)

Iván Colmenarejo Allavena[1], Mojahed Abushawish[1], Carlos Galindo-Morata[1], Pablo Galve[1,2], Jose Udias[1]

[1] Universidad Complutense de Madrid, Grupo de Física Nuclear and IPARCOS, Madrid, Spain; [2] Spanish National Research Council (CSIC), Institute for Physical and Information Technologies “Leonardo Torres Quevedo”, ITEFI, Madrid, Spain

This work was supported by the Spanish Ministry of Science, Innovation and Universities under the FPU Program (grant number FPU24/00918).

Abstract

Modern Positron Emission Tomography (PET) scanners are increasingly complex, incorporating a large number of modular detectors that require meticulous synchronization. Precise calibration of detector parameters, such as energy response, depth-of-interaction (DOI), and time-alignment, is essential to maintain image quality. This work presents a robust multi-parametric correction pipeline applied to two LYSO based, DOI capable PET scanners: a preclinical (12 cm transaxial FOV) device and a extended Field of View clinical geometry (23 cm transaxial FOV) scanner, targeting four primary sources of systematic degradation: crystal-by-crystal energy centroid offsets, individual crystal gain non-uniformities, time alignment, and DOI-dependent energy and time variations. Calibration data were acquired from reference point sources and specialized phantoms to ensure statistical reliability. The timing alignment pipeline, which iterates recursively over crystal- and detector-level centroids, improved the Coincidence Time Resolution (CTR) by 50% through the effective mitigation of electronic offsets and time-walk effects. Furthermore, DOI-dependent energy corrections linearized the crystal response, improving energy resolution from 25.0% to 12.6% FWHM. These results demonstrate that a modular multi-parametric calibration framework significantly optimizes timing and energy performance across heterogeneous PET architectures, providing a scalable solution for high-sensitivity molecular imaging.

References

[1] W. W. Moses, “Fundamental limits of spatial resolution in PET,” NIMA Accel. Spectrometers, Detect. Assoc. Equip., vol. 648, pp. S236–S240, Aug. 2011

[2] P. Lecoq, "Pushing the limits of PET scintillation detectors," *IEEE Trans. Radiat. Plasma Med. Sci.*, vol. 1, no. 6, pp. 473–485, Nov. 2017

[3] M. V. Nemallapudi *et al.*, "Single photon time resolution of state-of-the-art SiPMs," *J. Instrum.*, vol. 10, no. 10, p. P10016, Oct. 2015.

[4] A. Sanaat and H. Zaidi, "Depth of Interaction Estimation in a Preclinical PET Scanner Equipped with Monolithic Crystals Coupled to SiPMs Using a Deep Neural Network," *Appl. Sci.*, vol. 10, no. 14, p. 4753, Jul. 2020.

MIC-15-282

Dementia Risk Estimation From a Positron Emission Tomography-Derived Latent Biomarker (#2058)

Cristóbal Vázquez García[1], Francisco J. Martínez Murcia[1], Javier Ramírez Pérez de Inestrosa[1], Fermín Segovia Román[1], Anabel Forte Deltell[2], Ignacio Álvarez Illán[1], Alejandro Hernández Segura[1], Carmen Jiménez-Mesa[3], Juan Manuel Górriz Sáez[1]

[1] University of Granada, Department of Signal Processing and Biomedical Applications, Granada, Spain; [2] University of Valencia, Department of Statistics and Operations Research, Valencia, Spain; [3] University of Málaga, Department of Communication Engineering, Málaga, Spain

This publication is part of the projects PID2022-137629OA-I00 and PID2022-137451OB-I00 funded by MICIU/AEI/10.13039/501100011033 and by ERDF/EU, and the C-ING-183-UGR23 project, cofunded by the Consejería de Universidad, Investigación e Innovación and by European Union, funded by Programa FEDER Andalucía 2021–2027. F.J.M.M. received support from grant RYC2021-030875-I, funded by MICIU/AEI/10.13039/501100011033 and European Union NextGener-ationEU/PRTR.
Data collection and sharing for the ADNI is funded by the National Institute on Aging (National Institutes of Health Grant U19AG024904).

Abstract
We investigated whether a positron emission tomography-derived latent biomarker can serve as a compact prognostic signal after longitudinal modeling. The study used 3,458 scans from 1,624 participants in the Alzheimer's Disease Neuroimaging Initiative. A Bayesian mixed-effects model was fitted to the biomarker trajectory and evaluated in two practical settings: forecasting future visits for previously observed subjects and estimating short-term dementia risk from predicted biomarker values. For subjects already observed during training, future visits were predicted with a mean root mean squared error of 0.298 and a mean absolute error of 0.250. For entirely new subjects, a change-from-baseline formulation reduced prediction error to a mean root mean squared error of 0.217 and a mean absolute error of 0.171 after an initial scan. A training-only logistic calibration applied to held-out predictions reached an area under the receiver operating characteristic curve of 0.826 for future dementia risk estimation. These results suggest that the latent biomarker can move beyond representation learning and support short-term longitudinal forecasting and clinically interpretable risk stratification.

MIC-15-285

Affine rotation and scaling transformations directly over the sinogram domain images for data augmentation (#2059)

Alejandro Sanz-Sánchez[1], Francisco B. García-Aparisi[1], Joan Prats-Climent[1], Jorge R. Vergara Quezada[2], María J. Rodríguez-Álvarez[1]

[1] Universitat Politècnica de València, Instituto de Instrumentación para Imagen Molecular (I3M), Consejo Superior de Investigaciones Científicas, Valencia, Spain; [2] Universidad Tecnológica Metropolitana, Informática y Computación, Santiago, Chile

This work was supported by the UPV Subprograma-2 (PAID-01-22)-42694 grant. We thank the UPV for the access to the RIGEL Supercomputing cluster.
Project supported by the Fund for Scientific and Technological Equipment year 2024, code LE24-03, UTEM, Project supported by the Competition for Research Regular Projects, year 2023, code LPR23-17, Universidad Tecnológica Metropolitana and this research was supported by the Cluster Faraday UTEM (FONDEQUIP EQM180180).

Abstract

Data augmentation techniques applied in state-of-the-art image reconstruction with deep learning in the positron emission tomography (PET) modality are performed in the reconstructed image domain and subsequently forward-projected to the sinogram domain. In this work, we present a method for applying affine rotation and scaling transformations to sinogram images obtained from a series of simulations in GATE. The proposed algorithms were validated on 100 2D sinogram slices from Nema-like and Jaczack-like phantoms. The preliminary results from this study indicate that the proposed methods are visually indistinguishable from those obtained by applying the transformation in the image domain and then forward projecting to the sinogram domain. The quantitative evaluation was performed using the metrics Zero Mean Normalized Cross-Correlation (ZNCC), which yielded mean values over 0.95, and the Gradient Normalized Cross-Correlation (GNCC), which yielded mean values over 0.66, for both the rotation and scaling transformations. These preliminary results show that the implemented algorithms could be considered the first of their kind, designed to tackle data augmentation directly in the sinogram domain.

References
[1] Häggström, Ida, C. Ross Schmidtlein, Gabriele Campanella, Thomas J. Fuchs 2019, 'DeepPET: A deep encoder–decoder network for directly solving the PET image reconstruction inverse problem', Medical Image Analysis, Volume 54, Pages 253-262, Elsevier
[2] Yanchao Huang, Huobiao Zhu, Xiaoman Duan, Xiaotong Hong, Hao Sun, Wenbing Lv, Lijun Lu, Qianjin Feng 2021, 'GapFill-Recon Net: A Cascade Network for simultaneously PET Gap Filling and Image Reconstruction', Computer Methods and Programs in Biomedicine, Volume 208, 106271, Elsevier
[3] Sanz-Sanchez, Alejandro, Francisco B. García, Pablo Mesas-Lafarga, Joan Prats-Climent, and María José Rodríguez-Álvarez. 2024. "PIPET: A Pipeline to Generate PET Phantom Datasets for Reconstruction Based on Convolutional Neural Network Training" *Algorithms* 17, no. 11: 511. https://doi.org/10.3390/a17110511, MDPI
[4] National Electrical Manufacturers Association 2008, 'Performance Measurements of Small Animal Positron Emission Tomographs (NEMA NU 4-2008)', National Electrical Manufacturers Association, Rosslyn, VA: National Electrical Manufacturers Association
[5] Jaszczak, R. J., Greer, K. L., Floyd, C. E. Jr, Harris, C. C., Coleman, R. E. 1984, 'Improved SPECT quantification using compensation for scattered photons', Journal of Nuclear Medicine, Volume 25, Issue 8, Pages 893-900
[6] OpenGATE Collaboration 2022, 'The OpenGATE ecosystem for Monte Carlo simulation in medical physics', Physics in Medicine and Biology, Volume 67, Issue 18, 184001, Bristol: IOP Publishing
[7] Merlin, T., et al. 2018, 'CASToR: a generic data organization and processing code framework for multi-modal and multi-dimensional tomographic reconstruction', Physics in Medicine and Biology, Volume 63, Issue 18, 185005, Bristol: IOP Publishing
[8] Joseph, P. M. 1982, 'An Improved Algorithm for Reprojecting Rays through Pixel Images', IEEE Transactions on Medical Imaging, Volume 1, Issue 3, Pages 192-196, Piscataway, NJ: IEEE

MIC-15-288

Multi-Hit Event Recovery in Multiplexed PET (#2294)

Kurumi Narita[1,2], Jackson W. Foster[3,4], Taiga Yamaya[1], Craig S. Levin[3,5]

[1] National Institutes for Quantum Science and Technology (QST), Institute for Quantum Medical Sciences, Chiba, Japan; [2] Chiba University, Graduate School of Science and Engineering, Chiba, Japan; [3] Stanford University, Molecular Imaging Program, Stanford, USA; [4] Stanford University, Department of Electrical Engineering, Stanford, USA; [5] Stanford University, Department of Radiology by courtesy the Department of Bioengineering, Electrical Engineering, and Physics, Stanford, USA

This work was supported by JST SPRING, Grant Number JPMJSP2109, as well as in part by NIH-NCI grant 1F31CA265205-01A1.

Abstract
Multiplexed positron emission tomography (mPET) is an emerging method that enables two or more tracer distributions to be separated from data acquired in one PET scan. The technique requires high detection efficiency for triple coincidences resulting from a prompt-gamma and two annihilation photons emitted from a positron+prompt gamma emitter. In this study, we focus on multi-hit events occurring within the same coincidence timing window inside the same detector, which are typically discarded as multi-photon hits or inter-crystal scatter (ICS). We propose a recovery method for both annihilation and prompt-gamma events from these multi-hit events, thereby improving the detection sensitivity for triple coincidences. We first generated a new charge-to-digital converter (QDC)–based energy window derived from single-hit 511 keV events for each crystal. This crystal-specific window was then applied to each hit in multi-hit events, and then each hit was classified as either an ICS, annihilation photon, or prompt-gamma event. Evaluation with a ^{22}Na point source placed at the center of the scanner showed increases of 3.5% in annihilation photon singles, 10.8% in prompt-gamma singles, 1.1% in double coincidences, and 9.1% in triple coincidences. These results indicate that the proposed method recovers useful events and enhances triple-coincidence sensitivity for mPET.

References
[1] G. Soultanidis, J. L. Herraiz, Z. A. Fayad, J. Grimm, and A. J. P. Teunissen, "Multiplexed imaging of radionuclides," *Nat. Biomed. Eng*, vol. 9, no. 7, pp. 993–1006, Jun. 2025
[2] E. Lage *et al.*, "Recovery and normalization of triple coincidences in PET," *Medical Physics*, vol. 42, no. 3, pp. 1398–1410, 2015
[3] D. Niekämper, J. J. Scheins, E. Pfaehler, J. L. Herraiz, N. J. Shah, and C. Lerche, "Improved random coincidence estimation including triple coincidence detection in PET". Front. Nucl. Med. 6:1739575. 2026
[4] V. Nadig, D. Schug, B. Weissler, and V. Schulz, "Evaluation of the PETsys TOFPET2 ASIC in multi-channel coincidence experiments," *EJNMMI Phys*, vol. 8, no. 1, p. 30, Dec. 2021

MIC-15-291

Hyperion DAQ: A Versatile Data Acquisition and Processing Platform

(#2422)

David Schug[1,2], Oliver Muelhens[2], Eike Gegenmantel[2], Bjoern Weissler[1,2], Yannick Kuhl[1], Thore Meyer[1], Julian Thull[1], Harald Radermacher[1], Max Breuer[1], Volkmar Schulz[1,2]

[1] RWTH Aachen University, Chair of Imaging and Computer Vision, Aachen, Germany; [2] Hyperion Hybrid Imaging Systems GmbH, Aachen, Germany

German BMFTR, contract numbers 13GW0609A, 13GW0609B, 13GW0621A, 13GW0621B and 13GW0621C.

Abstract
We present the Hyperion DAQ (data acquisition platform), a versatile MRI-compatible infrastructure for PET detector data acquisition. It combines firmware on a sensor-tile FPGA and a mainboard FPGA with a software stack that splits between a Data Acquisition and Processing System (DAPS) host — receiving and processing the

ASIC data over a 10 Gig Ethernet downstream link — and a separate control computer that coordinates the platform components. The firmware handles ASIC configuration, capture and per-packet annotation; the higher-level calibration routines run in software. We have integrated the PETsys TOFPET2 ASIC as the first front-end digitization chip and built an end-to-end calibration suite on top of the platform: breakdown determination via bias sweeps, signal-level and threshold calibration via discriminator sweeps, a charge-to-digital converter (QDC) linearization sampled by on-tile test pulses and stored as a per-bin lookup table, and a time-to-digital converter (TDC) calibration driven by the natural random trigger stream from a 511 keV source. All four routines run in-system on the assembled scanner. We further report on the ASIC's test-pulse insensitivity window, showing that its position depends on the end phase of the test pulse rather than its start phase — a finding relevant to anyone calibrating the TDC with a test-pulse-based code-density method. On a Visor Max detector pair (8×8 6 mm Broadcom SiPMs read out by a single TOFPET2 ASIC, 64 LYSO crystals per tile), three ^{22}Na sources, 5 V over-voltage and 17°C cooling, we measure an energy resolution of 10.7 % FWHM at 511 keV and a coincidence time resolution of 248 ps FWHM. An end-to-end evaluation of the data-rate handling of the firmware and software acquisition chain will be presented at the conference. The platform is being prepared for the next generation of Hyperion-based PET/MRI scanners.

MIC-15-294

Quantifying the Effect of Partial Volume Correction on Lesion Dosimetry in ^{161}Tb-FAPI-2286 and ^{177}Lu-FAPI SPECT/CT imaging (#2883)

Mohamed Saber Azimi[1,2], Milad Peer-Firozjaei[3], Maryam Cheraghi[4], Ghasemali Divband[5], Swagat Dash[6], Vindhya Malasani[6], Kamal Yadav[6], Rakhee Vatsa[7], Parul Thakral[8], Priya Ashok[9], Naveen Sanchety[10], Vishnu Hari[11], Habibollah Dadgar[12], Majid Assadi[13], Hossein Arabi[14]

[1] Obuda University, Doctoral School of Applied Informatics and Applied Mathematics, Budapest, Hungary; [2] Obuda University, University Research and Innovation Center, Budapest, Hungary; [3] Babol University of Medical Science, Student Research Committee, Babol, Iran; [4] Shahid Beheshti University of Medical Sciences, PET-CT Unit, Department of Nuclear Medicine, Tehran, Iran; [5] Jam Hospital, Department of Nuclear Medicine, Tehran, Iran; [6] Sarvodaya Hospital, Dept. of Nuclear Medicine & Molecular Theranostics, Faridabad, India; [7] ABX-CRO Advanced Pharmaceutical Services, New Delhi, India; [8] Fortis Memorial Research Institute, Dept. of Nuclear Medicine, Gurugram, India; [9] GE HealthCare, Molecular Imaging Application Specialist, Bengaluru, India; [10] Sarvodaya Hospital, Dept. of Surgical Oncology, Faridabad, India; [11] Sarvodaya Hospital, Dept. of Medical Oncology & Bone Marrow Transplant, Faridabad, India; [12] Imam Reza International University, Cancer Research Center, RAZAVI Hospital, Mashhad, Iran; [13] Bushehr University of Medical Sciences, The Persian Gulf Nuclear Medicine Research Center, Bushehr, Iran; [14] Geneva University Hospital, Division of Nuclear Medicine & Molecular Imaging, Geneva, Switzerland

Abstract

Accurate lesion-level dosimetry is essential for evaluating therapeutic response in radiopharmaceutical therapy; however, its reliability in SPECT/CT imaging is limited by partial volume effects, which can significantly underestimate activity concentration in small or heterogeneous lesions. These limitations become particularly important when comparing radionuclides with different emission characteristics, such as the widely used ^{177}Lu and the emerging ^{161}Tb, which emits additional low-energy electrons that may enhance microscopic dose deposition. In

this study, we performed a lesion-level dosimetric analysis of ^{161}Tb-FAPI and ^{177}Lu-FAPI using a Monte Carlo simulation framework based on patient-specific SPECT/CT data. Two iterative partial volume correction methods, Richardson–Lucy and reblurred Van Cittert, were applied to assess their impact on absorbed dose estimation. Lesions were segmented on SPECT images, and voxel-wise dose maps were generated using GATE simulations, followed by lesion-level dose aggregation. Relative dose differences were calculated by comparing corrected and non-corrected images. Results show that partial volume correction significantly affects lesion dosimetry for ^{177}Lu-FAPI, with dose increases reaching approximately 30.6% in bone metastases and 23.2% in liver lesions, while changes in corresponding normal tissues remained minimal. In contrast, ^{161}Tb-FAPI exhibited more stable behavior, with lesion-level variations generally limited to below 10% and moderate reductions observed in lung lesions (≈ −15%). Both correction methods produced consistent trends, with slightly lower magnitude changes for the reblurred Van Cittert approach. Overall, these findings indicate that lesion-level dose estimation for ^{177}Lu is highly sensitive to image correction, whereas ^{161}Tb provides more robust dosimetric estimates.

References
[1] M. S. Azimi *et al.*, "Critical review of partial volume correction methods in PET and SPECT imaging: benefits, pitfalls, challenges, and future outlook," *European Journal of Nuclear Medicine and Molecular Imaging,* pp. 1-32, 2025.
[2] H. Dadgar *et al.*, "Targeted radioligand therapy: physics and biology, internal dosimetry and other practical aspects during 177Lu/225Ac treatment in neuroendocrine tumors and metastatic prostate cancer," *Theranostics,* vol. 15, no. 10, p. 4368, 2025.
[3] S. Lehenberger *et al.*, "The low-energy β– and electron emitter 161Tb as an alternative to 177Lu for targeted radionuclide therapy," *Nuclear medicine and biology,* vol. 38, no. 6, pp. 917-924, 2011.
[4] M. S. Azimi *et al.*, "Impact of partial volume correction on radiomics reproducibility in theranostic SPECT/CT imaging," *Medical Physics,* vol. 53, no. 4, p. e70427, 2026/04/03 2026, doi: 10.1002/mp.70427.

MIC-15-297

A Quality Control Framework for Deep Learning-based Attenuation Map Synthesis in PET (#2579)

Zhen Ji[1], Yue Li[2], Chenyao Jiang[2], Chen Sun[2], Xiong Wang[1], Yihuan Lu[2]

[1] ShanghaiTech University, School of Information Science and Technology, Shanghai, China; [2] Shanghai United Imaging Healthcare Co., LTD, Molecular Imaging Business Unit, Shanghai, China

Abstract
Deep learning-based attenuation correction (DL-AC) offers potential advantages over conventional CT-based attenuation correction (CT-AC) in PET imaging, including avoidance of additional radiation exposure and reduced susceptibility to PET–CT misalignment. However, in DL-AC application scenarios, when CT-derived attenuation maps (CT-μ) are unavailable as reference images, quality control (QC) of deep learning-derived attenuation maps (DL-μ) often relies on manual inspection. To address this limitation, we propose a patch-level 3D convolutional neural network (3D CNN) framework for automated anomaly detection and localization in DL-μ without requiring CT during inference. During training, CT-μ was used to assist patch-level annotation of DL-μ, and artifact-free CT-μ patches without observer-identified abnormalities were incorporated as normal samples to help the model learn normal attenuation patterns. During inference, only DL-μ was used, and sliding-window prediction was used to aggregate patch-level anomaly probabilities into a voxel-wise anomaly probability map. On the validation set (51 cases), the framework yielded patch-level performance with an AUC of 0.9984, an F1-score of 0.9802, a sensitivity

of 97.06%, and a specificity of 98.86%. These results suggest that the proposed framework can provide spatial cues for DL-μ, potentially supporting efficient evaluation and reducing reliance on manual QC inspection.

References
[1] T. Di Noto *et al.*, "An anatomically-informed 3D CNN for brain aneurysm classification with weak labels," *arXiv preprint arXiv:2012.08645, 2020.*
[2] T.-Y. Lin, P. Goyal, R. Girshick, K. He, and P. Dollár, "Focal loss for dense object detection," in *Proc. IEEE Int. Conf. Comput. Vis. (ICCV)*, 2017, pp. 2999–3007.

MIC-15-300

Generating synthetic PET/CT scans with latent diffusion models (#2763)

Kevin H. Leung[1], Esther Mena[2], Peter L. Choyke[2], Sangeeta Ray[1], Yong Du[1]

[1] Johns Hopkins University School of Medicine, Russell H. Morgan Department of Radiology and Radiological Science, Baltimore, USA; [2] National Cancer Institute, Center for Cancer Research, Bethesda, USA

Abstract
Artificial intelligence approaches require training on large amounts of data to achieve acceptable levels of performance as well as generalizability. However, there is a lack of available annotated datasets for nuclear medicine imaging modalities as they are a relatively low-volume clinical modality, especially when compared to other anatomical imaging modalities, such as CT and MRI. We aim to leverage a deep generative modeling approach based on latent diffusion models to generate synthetic PET/CT images to address this issue. ^{18}F-FDG PET/CT and ^{18}F-DCFPyL PET/CT scans of 668 patients with various types of cancer, including lung cancer, melanoma, lymphoma, and prostate cancer were used to train a latent diffusion model. The data were randomly partitioned into training and test sets using a 90%/10% split. A hierarchical, latent diffusion modeling approach was trained in multiple stages. A patch volume autoencoder was trained to learn a discrete latent representation of local image volume patches using a vector quantized-variational autoencoder. A diffusion model was then trained to generate image volumes sampled from random noise in the latent space. Image quality metrics, including peak signal to noise ratio (PSNR) and mean absolute error (MAE), were evaluated across the training and test sets. On the training set, the approach yielded PSNR values of 40.85 ± 5.50 dB and 36.77 ± 5.30 dB and MAE values of 0.015 ± 0.01 and 0.021 ± 0.011 between the generated and original PET and CT image volumes, respectively. On the test set, the approach yielded PSNR values of 40.00 ± 6.19 dB and 35.48 ± 5.75 dB and MAE values of 0.017 ± 0.012 and 0.030 ± 0.075 between the generated and original PET and CT scans, respectively. The approach achieved relatively high PSNR and low MAE values, respectively, indicating that the approach generated high fidelity PET and CT images. The present study demonstrated a proof of concept for generating realistic PET/CT volumetric scans.

MIC-15-303

Characterizing Noise in Clinical Nuclear Medicine Modalities via Quantum-Inspired Framework (#2977)

Amirreza Hashemi, Shadi Abdar Esfahani, Pamela Silva, Anthony Sinagra, Pedram Heidari, Hamid Sabet

Harvard Medical School/Massachusetts General Hospital, Department of Radiology, Boston, USA

This work was supported in part by NIH grant R01EB034785.

Abstract

Quantum-inspired denoising is employed for clinical PET/CT, PET/MR, and SPECT imaging by treating images analogous to disordered materials and analyzing the eigenfunctions of an associated Hamiltonian. Quantum localization is quantified by the participation ratio, enabling filtering of non-localized, high-participation modes that dominate the mid-frequency range and are associated with diffusive noise. By suppressing these modes and reconstructing from the remaining localized modes, noise is reduced without training data or manual regularization. The framework is applied to 46 multi-vendor, multi-tracer patient datasets from Massachusetts General Brigham to characterize scanner-dependent noise structure and its impact on image appearance. Across the cohort, quantum-inspired filtering yields consistent decreases in blind image quality scores (PIQE and BRISQUE) together with increases in entropy and Laplacian variance, indicating lower perceived noise and enhanced structural detail in the denoised clinical images.

MIC-15-306

Data-Driven Selection of Representative Motion Models for Simulation in Dynamic Cardiac PET (#2952)

Nader Nemati[1], **Nader Nemati**[1], Oona Rainio[1], Oona Rainio[1], Santeri Palonen[1], Santeri Palonen[1], Eero Lehtonen[1,3], Eero Lehtonen[1,3], Teemu Maaniitty[1,2], Teemu Maaniitty[1,2], Jarmo Teuho[1], Jarmo Teuho[1], Jouni Tuisku[1], Jouni Tuisku[1], Muhammad Irfan[1], Muhammad Irfan[1], Nicole Miller[1], Nicole Miller[1], Lauri Nummenmaa[1], Lauri Nummenmaa[1], Juhani Knuuti[1], Juhani Knuuti[1], Riku Klén[1], Riku Klén[1]

[1] University of Turku and Turku University Hospital, Turku PET Centre, Turku, Finland; [2] Turku University Hospital, Department of Clinical Physiology, Nuclear Medicine and PET, Turku, Finland; [3] Turku University of Applied Science, ICT and Industrial Engineering, Data Engineering and AI technologies, Turku, Finland

This work was supported by the Research Council of Finland project #351482, the European Research Council (Advanced Grant #101141656), the Jane and Aatos Erkko Foundation, and the Sigrid Juselius Foundation. Jarmo Teuho reports funding from the Research Council of Finland Academy Research Fellowship grant #360120. Teemu Maaniitty reports funding from the Research Council of Finland grant #363775.

Abstract
Patient motion remains a common challenge in dynamic cardiac positron emission tomography (PET), as it degrades image quality and complicates reliable evaluation of motion correction methods. Realistic motion simulation requires motion models that capture the variability observed in clinical data, but this remains difficult when simulations rely on only a limited set of motion patterns. In this work, we propose a data driven framework for motion model selection and simulation in dynamic cardiac PET. We characterize motion trajectories using physically interpretable features and analyze them using clustering and trajectory similarity based on dynamic time warping to identify a compact set of representative motion models. These models are integrated with patient-specific motion scaling for frame-wise simulation of motion-corrupted PET data. The proposed framework produces stable normalized error levels across 1308 patient–model evaluations while using only a small number of representative motion models. The results suggest that the selected models effectively capture dominant motion behaviors observed in the dataset and enable realistic PET motion simulation.

MIC-15-309

Initial Validation of a High-Precision External Head-Motion Tracking System for γβ⁺ Brain PET Imaging (#3196)

Clifford Lindsay[1], Kesava Kalluri[1], Sophia Pells[1], Matthew A. Kupinski[2], Phillip H. Kuo[3], Shiva Abbaszadeh[4], Michael A. King[1], Lars R. Furenlid[2]

[1] University of Massachusetts Chan Medical School, Department of Radiology, Worcester, USA; [2] University of Arizona, Wyant College of Optical Sciences and the Department of Radiology and Imaging Sciences, Tucson, USA; [3] Kuo Radiology, LLC, Phoenix, USA; [4] University of California Santa Cruz, Department of Electrical and Computer Engineering, Santa Cruz, USA

The research reported in this publication was supported by the National Institute of Biomedical Imaging And Bioengineering of the National Institutes of Health under Award Number UH3EB034686. The content is solely the responsibility of the authors and does not necessarily represent the official views of the National Institutes of Health.

Abstract
Patient head motion during positron emission tomography (PET) brain imaging degrades system spatial resolution and quantitative accuracy; even sub-millimeter displacements can blur fine structures in highresolution systems. We present the validation of an OptiTrack PrimeX 41 fourcamera near-infrared stereocamera system for use with a novel γβ⁺ brain-imaging prototype targeting ≤0.200mm spatial accuracy and ≤250ms temporal synchronization with list-mode data acquisition. System calibration achieved a mean residual of 0.075mm, below the manufacturer's 0.1

mm specification. Tracking accuracy was characterized over 360,000 Euclidean-distance measurements using a Capintec brain phantom displaced by Zaber precision stages (repeatability ≤0.050mm) as ground truth, yielding RMSE of 0.018–0.038mm and maximum outliers ≤0.135mm across three orthogonal directions that were at least 5× better than the 0.200mm target. Three temporal synchronization strategies were evaluated; a network-based UDP broadcast produced a correctable 17.2±2.4ms transmission delay, yielding a combined synchronization uncertainty of 57ms versus the 250ms requirement. Performance was maintained in a clinically realistic configuration with a mock 40-cm imaging bore and supine patient positioning.

References
[1] Arman Rahmim, Olivier Rousset, Habib Zaidi, Strategies for Motion Tracking and Correction in PET, PET Clinics, Volume 2, Issue 2, 2007, Pages 251-266, ISSN 1556-8598.
[2] Cherry SR, Jones T, Karp JS, Qi J, Moses WW, Badawi RD. Total-Body PET: Maximizing Sensitivity to Create New Opportunities for Clinical Research and Patient Care. J Nucl Med. 2018 Jan;59(1):3-12. doi: 10.2967/jnumed.116.184028. Epub 2017 Sep 21. PMID: 28935835; PMCID: PMC5750522.
[3] McNamara, J.E., et. al. A flexible multicamera visual-tracking system for detecting and correcting motion-induced artifacts in cardiac SPECT slices, Med. Phys, 2009, 36, (5), pp. 1913-1923. PMCID 2832034
[4] Pretorius PH, et al. Investigation of the physical effects of respiratory motion compensation in a large population of patients undergoing Tc-99m cardiac perfusion SPECT/CT stress imaging. J Nucl Cardiol 27: 80-95, 2020. PMCID 7714447
[5] Chemli Y, Tetrault M-A, Normandin M, Marin T, Bloch I, El Fakhri G, Ouyang J, Petibon Y, “Superresolution in brain PET Using a Real Time Motion Capture System,” J. Nucl. Med., 62 (S1) (2021), 34.
[6] Carson R, Berg E, Badawi R, Cherry S, Du J, Feng T, Fontaine K, Gravel P, Hillmer A, Honhar P, Hoye J, Hu L, Jones T, Leung E, Li T, Liu C, Liu H, Lu Y, Majewski S, Mulnix T, Schmall J, Selfridge A, Toyonaga T, Qi J, Li H, “Design of the NeuroEXPLORER, a next-generation ultra-high performance human brain PET imager,” J. Nucl. Med., 62 (S1) (2021), 1120.
[7] Zeng T, Lu Y, Jiang W, Zheng J, Zhang J, Gravel P, Wan Q, Fontaine K, Mulnix T, Jiang Y, Yang Z, Revilla EM, Naganawa M, Toyonaga T, Henry S, Zhang X, Cao T, Hu L, Carson RE. Markerless head motion tracking and event-by-event correction in brain PET. Phys Med Biol. 2023 Dec 12;68(24):245019. doi: 10.1088/1361-6560/ad0e37. PMID: 37983915; PMCID: PMC10713921.
[8] Shiva Abbaszadeh, Matthew Kupinski and Lars Furenlid, βγ imaging: simultaneous detection of single-gamma and position-annihilation with CZT-based PET scanner, Journal of Nuclear Medicine June 2023, 64 (supplement 1) P1282;
[9] OptiTrack, “PrimeX 41 Camera Specification Sheet,” OptiTrack Inc., 2023.

MIC-15-312

Noise-Robust Bayesian Parameter Estimation of Two-Tissue Compartment Kinetic Model for dynamic SPECT imaging (#1051)

Dandan Zhang[1], Hui Liu[2], Jingjing Qin[1], Yufan Gu[3], Wei Fang[3], Lei Wang[3], Jing Wu[1]

[1] Beijing Normal University, School of Physics and Astronomy, Beijing, China; [2] Tsinghua University, Department of Engineering Physics, Beijing, China; [3] Fuwai Hospital, Chinese Academy of Medical Sciences & Peking Union Medical College/National Center for Cardiovascular Diseases, Department of Nuclear Medicine, Beijing, China

This study was supported by National Natural Science Foundation of China (No. 12305379, No.12205166), Beijing Natural Science Foundation (Z220010), CIRP Open Fund of Radiation Protection Laboratories (TNMPP-2024-No.1)

Abstract

Tracer kinetic modeling using the two-tissue (2T) compartment model remains challenging in dynamic SPECT imaging, particularly under realistic noise conditions. In this study, we propose a noise-robust Bayesian parameter estimation method that incorporates physiological prior information for the 2T model in dynamic SPECT imaging. To validate the proposed method, we conducted both simulation study and dynamic ^{99m}Tc-4BOH clinical study. The proposed method was compared with the conventional nonlinear least-squares (NLS) method. In the simulation study, the proposed method yielded lower relative bias in the estimated kinetic parameters (K_1, k_2, k_3, and k_4) than the NLS method under both low and high noise conditions. In the clinical ^{99m}Tc-4BOH study, K_1 estimated using the proposed method demonstrated significantly stronger agreement and lower relative bias with respect to head-to-head ^{13}N-NH_3 PET myocardial blood flow (MBF), which was used as the reference standard, than the NLS method. In conclusion, the proposed method substantially improved the accuracy and precision of parameter estimation for the 2T model compared with the NLS method.

References
[1] Naganawa M, Li S, Nabulsi N, Henry S, Zheng MQ, Pracitto R, Cai Z, Gao H, Kapinos M, Labaree D, Matuskey D, Huang Y, Carson RE, 'First-in-Human Evaluation of ^{18}F-SynVesT-1, a Radioligand for PET Imaging of Synaptic Vesicle Glycoprotein 2A, J Nucl Med, 2021, 62(4): 561-567.
[2] Dandan Z, Yufan G, Hui L, Ding D, Jing Q, Wei F, Lei W, Jing W . Pharmacokinetic modelling of dynamic ^{99m}Tc-4BOH SPECT for myocardial perfusion imaging in patients with coronary artery disease. J Nucl Cardiol, 2025, 21: 102570.

MIC-15-315

Conditional Flow-Matching-based Kinetic Refinement for Low-Count SRTM-based Parametric Imaging in Dynamic PET (#1873)

Yu Jin Seol[1,2], Yu Jin Seol[1,2], Seung Kwan Kang[3], Seung Kwan Kang[3], Eui Tae Kim[4], Eui Tae Kim[4], Jae Sung Lee[1,2], Jae Sung Lee[1,2]

[1] Seoul national university, Interdisciplinary Program in Bioengineering, Seoul, South Korea; [2] Seoul national university, Integrated Major in Innovative Medical Science, Seoul, South Korea; [3] Samsung Ventures, Seoul, South Korea; [4] Seoul National University Bundang Hospital, Department of Psychiatry, Seoul, South Korea

Abstract

We propose a kinetic-consistent conditional flow matching framework for dynamic *[11C* raclopride PET SRTM parametric imaging. Conventional indirect SRTM fitting is vulnerable to frame-wise count noise, causing unstable voxel-wise *R1* , *k2* , and *BPND* maps. Using 105 scans from 35 subjects, count-reduced datasets were generated at 50%, 25%, and 10% of the original counts. The model refines reduced-count indirect SRTM estimates toward full-count SRTM pseudo-reference maps using kinetic consistency, count/noise conditioning, and physiological constraints, reducing *BPND* deviation, high-percentile errors, and kinetic-parameter disagreement compared with indirect SRTM and denoising and regularization-based baselines

References
[1] Lammertsma, AA & Hume, SP 1996, 'Simplified reference tissue model for PET receptor studies', *NeuroImage*, vol. 4, no. 3 Pt 1, pp. 153–158, publisher/place of publication not specified.
[2] Zhou, Y, Endres, CJ, Brasic, JR, Huang, S-C & Wong, DF 2003, 'Linear regression with spatial constraint to generate parametric images of ligand-receptor dynamic PET studies with a simplified reference tissue model', *NeuroImage*, vol. 18, no. 4, pp. 975–989, publisher/place of publication not specified.
[3] Lipman, Y, Chen, RTQ, Ben-Hamu, H, Nickel, M & Le, M 2022, 'Flow matching for generative modeling', *arXiv preprint*, arXiv:2210.02747, publisher/place of publication not specified.

MIC-15-318

Treatment Monitoring System for Proton Therapy Based on Beam Range Measurement (#1067)

SeHyun Jang[1], Jaeho Cho[1], Goeun Lee[1], Taehyeon Eom[1], Junyoung Lee[1], Jong Hwi Jeong[2], Sung Hun Kim[2], Sungkoo Cho[3], Kwanghyun Jo[3], Chan Hyeong Kim[1]

[1] Hanyang University, Nuclear Engineering, Seoul, South Korea; [2] National Cancer Center, Proton Therapy Center, Goyang, South Korea; [3] Samsung Medical Center, Department of Radiation Oncology, Seoul, South Korea

Abstract

In proton therapy, range uncertainties can result in insufficient dose delivery to the tumor or unintended dose delivery to organs at risk (OARs). To address this, several range verification methods have been investigated, and prompt gamma imaging is considered a promising method due to the strong correlation between the dose profile and prompt gamma distribution at the distal dose fall-off location. Based on prompt gamma imaging, a treatment monitoring system was developed to measure the in vivo beam range and detect range shifts during the treatment. The developed system consists of a 72-slit parallel collimator, 144 CsI(Tl) scintillation detectors, a dedicated field-programmable gate array (FPGA)-based data acquisition (DAQ) system, and a dedicated program with a graphical user interface (GUI). The DAQ system calculates pulse height and timing of each signal from 144 detectors. The dedicated program reconstructs 1D prompt gamma distribution using pulse data and determines the beam range of each spot using a dedicated range estimation algorithm [1]. The system's performance was evaluated using a clinical proton beam prescribed to deliver 0.5 Gy to a spherical clinical target volume (CTV) with 50 mm diameter in a homogeneous PMMA phantom. To evaluate range shift detection performance, range shifts were induced at both the global range shift (1–10 mm) and local range shift (5 and 10 mm) conditions. At the same time, the computation time for range deviation analysis was evaluated. The system detected global range shifts with an accuracy of 1 mm and identified the presence and location of local range shifts exceeding 5 mm. Furthermore, the time required for range deviation analysis per layer was found much shorter than energy layer switching time. These results demonstrate the system can verify the in vivo beam range during treatment in clinical practice.

References

[1] Ku, Y, Jung, J, and Kim, CH 2022, 'New algorithm to estimate proton beam range for multi-slit prompt-gamma camera', *Nucl. Eng. Technol.*, vol. 54, no. 9, pp. 3422-3428, South Korea: Elsevier.

MIC-15-321

Pixelated Cherenkov Crystals for Prompt-Gamma Imaging in Proton Range Verification (#1181)

Leonor Rebolo[1,2], Salvador Moreno Gomez[6], Machiel Kolstein[6], Michael Backfish[5], Matthew Novotny[5], Rafiaullah Sahebzada[5], Sara St. James[4], Brahim Mehadji[2], Eric Prebys[5,3], Pedro M.M. Correia[1], Ana Luísa M. Silva[1], Gerard Ariño-Estrada[2,6]

[1] Universidade de Aveiro, Física, Aveiro, Portugal; [2] University of California Davis, Biomedical Engineering, Davis, USA; [3] University of California Davis, Physics, Davis, USA; [4] University of Utah, Huntsman Cancer Institute, Salt Lake City, USA; [5] Crocker Nuclear Laboratory, Davis, USA; [6] Institut de Fisica d'Altes Energies - Barcelona Institute of Science and Technology (IFAE-BIST), Bellaterra, Spain

This work was supported by NIH grant R01EB029533 (PI G.A.E.), by FCT projects UID/50025/2025, UID/PRR/50025/2025, UID/PRR2/50025/2025, and LA/P/0037/2020, and by FCT scholarship PRT/BD/154945/2023 (L.R.).

Abstract

Proton range verification (PRV) in proton therapy is an outstanding clinical need. Prompt-gammas (PG) emitted along the proton track constitute a strong signal to determine the Bragg Peak position. However, the high energy of PGs (1-7 MeV), the high particle flux and the presence of significant background radiation make prompt-gamma imaging (PGI) challenging.

We report on the development of pure Cherenkov pixelated detectors for PRV. The detector consisted of an 8×8 pixelated PbF2 crystal array coupled to an 8×8 S14161-3050HS-08 SiPM array from Hamamatsu, read out by a row-column signal processing board. Two analytical event reconstruction algorithms were evaluated: rise-to-the-power with k=2 (RTP2) and k=3 (RTP3).

The detector was exposed to both a sealed 228Th source and a 67.5 MeV proton beam at a current of 100 pA. Floodmaps were obtained using both RTP2 and RTP3 methods to resolve the 8×8 matrix of the crystal under laboratory source irradiation. Similar results were obtained under proton beam irradiation, showing the robustness of this detector concept.

In this contribution we demonstrate for the first time the ability of a pixelated pure Cherenkov detector to provide spatial resolution information in clinically relevant proton beam conditions. The prompt emission of Cherenkov light and exclusive sensitivity to highly energetic PGs offer a very high count rate capability, effective background rejection, and capacity to multiplex signals, enabling to use less channels and low power readout electronics. Future work will focus on quantitative floodmap quality metrics, detector modeling to optimize the detector geometry, and acquisition of additional data in the proton beam line at higher proton energies and beam currents.

References

[1] Jacquet, M. et al 2023, 'A high sensitivity Cherenkov detector for prompt gamma timing and time imaging', *Scientific Reports*, 13, 3609

[2] Ellin, J. et al 2024, 'Prompt gamma timing for proton range verification with TlBr and TlCl as pure Cherenkov emitters', *Physics in Medicine and Biology, 69, 11*

[3] Pinson, et al. 2026, 'Prompt Gamma Timing in Carbon Therapy: First Experimental Results with the TIARA Detector', arXiv:2602.18318

[4] Rebolo, L. et al. 2024, 'Cherenkov Light Emission in Pure Cherenkov Emitters for Prompt Gamma Imaging', *IEEE TRPMS*, 8, 1, pp. 15-20

MIC-15-324

Coded-Mask PGI for Proton Range Verification With Pure Cherenkov Crystal Detectors (#1159)

Salvador M. Gómez[1], Machiel Kolstein[1], Carles Gomà[2], Sara Marcatili[3,4], Aleksandra Wrońska[5], Magdalena Rafecas[6], **Gerard Ariño-Estrada**[1,7]

[1] Institut de Física d'Altes Energies - Barcelona Institute of Science and Technology (IFAE-BIST), Medical Detector Instrumentation and Imaging Physics group, Cerdanyola del Vallès, Spain; [2] Institut d'Investigacions Biomèdiques August Pi i Sunyer (IDIBAPS), Translational genomics and targeted therapies in solid tumours, Barcelona, Spain; [3] Laboratoire de Physique Subatomique et de Cosmologie (LPSC), Physics at the service of energy and health - Medical Applications, Grenoble, France; [4] Centre National de la Recherche Scientifique (CNRS), Grenoble, France; [5] Marian Smoluchowski Institute of Physics, Jagiellonian University, Department of Hadron Physics (ZFH), Kraków, Poland; [6] Universität zu Lübeck, Biomedical Engineering - Medical Imaging, Lübeck, Germany; [7] University of California Davis, Department of Biomedical Engineering, Davis, USA

Abstract

Accurate proton range verification (PRV) in proton therapy (PT) is an unmet clinical need and is essential to exploit the full potential of PT to maximize treatment effectiveness and minimize toxicity. We present a Monte Carlo (GATE 10) study of a Cherenkov-based prompt gamma imaging system combining an array of PbF2 crystal detectors with a MURA coded-aperture collimator for real-time PRV. The detector response was studied through detected Cherenkov photon distributions generated by prompt-gammas with energies ranging from 0.5 MeV to 7.0 MeV in steps of 0.5 MeV. A threshold of 15 detected Cherenkov photons was applied to reject low-energy background, which effectively suppressed 511 keV annihilation gammas and sub-MeV contributions while retaining the prompt gammas of interest. Image reconstruction was performed using the Maximum Likelihood Expectation Maximization algorithm, with the system matrix computed with 4.4 MeV point-like sources. The imaging performance was validated on isotropic gamma point sources in both 1D and 2D coded-mask configurations across a field of view of ~130 mm. A direct comparison between discrimination based on energy deposition (E > 1 MeV) and discrimination based on the number of detected Cherenkov photons (nckv ≥ 15) showed comparable performance, with position residuals consistent with zero within statistical uncertainties in both cases. For the proton beam measurements, background rejection was performed exclusively via the Cherenkov photon count threshold. Under realistic proton beam conditions, the distal fall-off position was reconstructed with a systematic residual below 1.5 mm and a statistical precision of less than 2 mm for beam intensities above 10^8 protons, corresponding to approximately 10 ms of irradiation at a standard proton current of 2 nA (1.25 × 10^10 protons/s). This work presents the concept and shows the feasibility of using Cherenkov-based coded-aperture imaging for PRV by means of a simulation framework.

References

[1] Ariño-Estrada, G, et al., 2026, 'Current Status of Cherenkov-Based Gamma Detectors for TOF-PET and Proton Range Verification', *IEEE Transactions on Radiation and Plasma Medical Sciences*, Vol. 10, No. 1, pp. 1–15, New York: IEEE.

[2] André, A, et al., 2026, 'TIARA: A Fast Gamma-Ray Detector for Range Monitoring in Proton Therapy', *IEEE Transactions on Radiation and Plasma Medical Sciences*, Early Access, New York: IEEE.
[3] Hetzel, R, et al., 2023, 'Near-Field Coded-Mask Technique and Its Potential for Proton Therapy Monitoring', *Physics in Medicine and Biology*, Vol. 68, p. 245028, Bristol: IOP Publishing.
[4] Gottesman, S R, Fenimore, E E, 1989, 'New Family of Binary Arrays for Coded Aperture Imaging', *Applied Optics*, Vol. 28, No. 20, pp. 4344–4352, Washington, D.C.: Optical Society of America.
[5] Rebolo, L, et al., 2024, 'Cherenkov Light Emission in Pure Cherenkov Emitters for Prompt Gamma Imaging', *IEEE Transactions on Radiation and Plasma Medical Sciences*, Vol. 8, No. 1, pp. 15–20, New York: IEEE.

MIC-15-327

An FPGA-based data acquisition system for remote wireless radiation monitoring (#1302)

Pavan S. Guntha[3], Ethan Ingalls[2], Thomas M. Whalen[2], Mia T. Kim[2], William C.J. Hunter[1], Geoff Jones[2], Scott A. Hauck[2], **Robert S. Miyaoka**[1]

[1] University of Washington, Radiology, Seattle, USA; [2] University of Washington, Electrical Engineering, Seattle, USA; [3] Microsoft, Azure, Redmond, USA; [4] University of Washington, Department of Radiology, Seattle, USA

This work was supported by NIH R01CA287205-01

Abstract

Purpose: We are developing a Personalized Remote Radiation Tracking Portable Organ Dosimetry Device (PRRT PODD) for at-home monitoring of patients receiving radiopharmaceutical therapy (RPT). We report on an FPGA-based data acquisition system capable of wireless communication in support of this goal.

Methods: Our acquisition system supports16-radiation detectors and outputs an energy histogram for each using a time-over-threshold (ToT) energy measurement. The electronics consists of a custom analog board that converts each detector's analog signal into a digital ToT signal; an FPGA board for signal processing; and a microcontroller board that serves as the system controller. The microcontroller communicates with the FPGA via UART to retrieve energy histogram data, manages system configuration parameters, and provides Bluetooth Low Energy connectivity to a mobile Android app. The electronics fits within the PODD's base assembly and can operate on cell phone battery power. Each detector has a small thermistor for individual probe temperature monitoring and to characterize MPPC gain versus temperature. An Android app was developed to control data acquisition and wireless transfer of data to a remote workstation. The detector and electronics acqusition system was tested using Tc-99m, Na-22 and Lu-177 radioactive sources at clinically relevant counting rates.

Results: Sixteen channel operation of our FPGA-based data acquisition system has been validated using a variety of radionuclides. The output properties of the probes have been characterized versus temperature to enable post acquisition normalization of signals.

Conclusion and future work: A compact, wireless 16-channel gamma spectroscopy system for remote monitoring of Lu-177 RTP was designed and tested. Future work includes implementing real-time temperature compensation based on continuous temperature readings, ensuring stable operation without post-processing.

MIC-15-330

Attenuation Images from Time-of-Flight PET for Metal Artifact Reduction: A Phantom Study (#1406)

Finn L. Peltzer[1,2], **Ann-Kristin Lüvelsmeyer**[1,3], Claus M. Bäcker[1,2], Jörg Wulff[1,2], Mohammadreza Teimoorisichani[4], Walter Jentzen[5], Beate Timmermann[1,6], Christian Bäumer[1,3]

[1] University Medicine of Essen, West German Proton Therapy Centre Essen, Essen, Germany; [2] University Medicine of Essen, West German Cancer Centre Essen, Essen, Germany; [3] TU Dortmund University, Physics, Dortmund, Germany; [4] Siemens Medical Solutions USA Inc., Knoxville, USA; [5] University Medicine of Essen, Clinic for Nuclear Medicine, Essen, Germany; [6] University Medicine of Essen, Department of Particle Therapy, Essen, Germany; [7] German Cancer Consortium, Heidelberg, Germany

This study was supported by the German Research Foundation (DFG) under grant number 525659135.

Abstract

Metal implants can degrade CT image quality and introduce artifacts that affect dose calculation in particle therapy. This study investigates attenuation images (μ-MLAA) reconstructed from time-of-flight PET data using maximum-likelihood reconstruction of attenuation and activity for metal artifact reduction. The linearity of a calibration curve relating CT number to relative electron density was first evaluated using a PMMA phantom with metal and tissue-equivalent inserts. Metal artifacts were then studied in a water phantom containing a Ti6Al4V total endoprosthesis (TEP) implant. μ-MLAA attenuation images reconstructed from PET list mode data and CT images reconstructed using iterative metal artifact reduction (iMAR) were evaluated using gamma index analysis (10%, 1 mm) relative to an artifact-free reference slice. The calibration curve remained linear in the presence of metal inserts ($R^2 > 0.999$). For the TEP phantom, μ-MLAA images achieved a higher gamma pass rate (96.3%) than iMAR CT (70.8%). Using the calibration curve, the relative electron density of the TEP shaft was estimated as $n_{e,rel} = 3.58 \pm 0.12$ corresponding to a 3.5% deviation from reported reference values. These results indicate the potential of μ-MLAA images for reducing metal artifacts and supporting implant characterization in radiotherapy imaging.

References

[1] Giantsoudi, D., De Man, B., Verburg, J., Trofimov, A., Jin, Y., Wang, G., Gjesteby, L., Paganetti, H. 2017, 'Metal artifacts in computed tomography for radiation therapy planning: dosimetric effects and impact of metal artifact reduction', *Physics in Medicine & Biology*, 62(8), R49–R80, Bristol: IOP Publishing

[2] Defrise, M., Rezaei, A., Nuyts, J. 2012, 'Time-of-Flight PET data determine the attenuation sinogram up to a constant', *Physics in Medicine & Biology*, 57(4), 885–899, Bristol: IOP Publishing.

[3] Wang, G. 2020, 'PET-enabled dual-energy CT: image reconstruction and a proof-of-concept computer simulation study', *Physics in Medicine & Biology*, 65(24), 245028, Bristol: IOP Publishing.

[4] Teimoorisichani, M., Panin, V., Rothfuss, H., Sari, H., Rominger, A., Conti, M. 2022, 'A CT-less approach to quantitative PET imaging using the LSO intrinsic radiation for long-axial FOV PET scanners', *Medical Physics*, 49(1), 309–323, Alexandria: AAPM.

[5] Bäumer, C., Bäcker, C. M., Conti, M., Fragoso Costa, P., Hermann, K., Kazek, S. L., Jentzen, W., Panin, V., Siegel, S., Teimoorisichani, M., Wulff, J., Timmermann, B. 2021, 'Can a ToF-PET photon attenuation reconstruction test stopping-power estimations in proton therapy? A phantom study', *Physics in Medicine & Biology*, 66(21), 215010, Bristol: IOP Publishing.

MIC-15-333

Depth-Resolved Multi-Nuclide Decomposition of Carbon-Ion PET for Range Verification (#1499)

Ximeng Li[1], Ruolan Liu[1], Dengyun Mu[1], Ao Qiu[1], Wentao Hu[1], Jingmin Zhu[1], Tianjiao Hu[3], Lin Wan[5], Weiwei Li[4], Nitta Yuki[4], Jiping Liu[4], Ji Zhu[4], Qingguo Xie[1,2]

[1] Huazhong University of Science and Technology, Department of Biomedical Engineering, Wuhan, China; [2] Huazhong University of Science and Technology, Wuhan National Laboratory for Optoelectronics, Wuhan, China; [3] University of Science and Technology of China, Department of Electronic Engineering and Information Science, Hefei, China; [4] Chinese Academy of Sciences, Department of Radiation Oncology, Zhejiang Cancer Hospital, Hangzhou Institute of Medicine (HIM), Hangzhou, China; [5] Huazhong University of Science and Technology, School of Software Engineering, Wuhan, China

This work was supported by the National Natural Science Foundation of China (Grant No. 625B2079).

Abstract

PET-based range verification in ion-beam therapy requires decay correction for a depth-dependent mixture of positron emitters. We introduce a range-verification-oriented carbon-ion PET workflow that partitions beam-axis reconstructions into axial slices and fits post-beam-off time-activity curves with four fixed-half-life components (^{11}C, ^{15}O, ^{10}C, ^{13}N); the small ^{13}N term (~0.4%) was grouped with ^{11}C for comparison. The experiment contained 120 reconstructed 10-s frames, and corresponding GATE simulation modeled 221.48 MeV/u carbon ions with 2.0 x 10_7 primary particles and seven positron-emitting nuclides. Across 35 accepted PET slices (R^2 >= 0.9), fitted fractions were 82.6%, 12.1%, 4.9%, and 0.4%, showing clear ^{11}C dominance. After converting fitted amplitudes to observation-window counts, plateau PET fractions were 77.5%, 14.5%, and 8.0%, versus grouped simulation values of 63.2%, 27.1%, and 9.7% for ^{11}C+^{13}N, ^{15}O+^{14}O+^{17}F, and ^{10}C. Carbon-ion PET agreement is therefore nuclide dependent: ^{10}C showed the smallest residual bias after correction, whereas long-lived carbon/nitrogen activity remains high and oxygen-group activity remains low. This nuclide-aware comparison reveals isotope-group-specific discrepancies that total-activity range metrics cannot localize.

References

[1] K. Parodi, H. Paganetti, H. A. Shih, S. Michaud, J. S. Loeffler, T. F. DeLaney et al., “Patient study of in vivo verification of beam delivery and range, using positron emission tomography and computed tomography imaging after proton therapy,” Int J Radiat Oncol Biol Phys, vol. 68, no. 3, pp. 920–934, 2007.

[2] K. Parodi, T. Yamaya, and P. Moskal, “Experience and new prospects of PET imaging for ion beam therapy monitoring,” Z Med Phys, vol. 33, no. 1, pp. 22–34, 2023.

[3] K. Parodi, H. Paganetti, E. Cascio, J. B. Flanz, A. A. Bonab, N. M. Alpert et al., “PET/CT imaging for treatment verification after proton therapy: a study with plastic phantoms and metallic implants,” Med Phys, vol. 34, no. 2, pp. 419–435, 2007.

[4] K. Parodi, A. Ferrari, F. Sommerer, and H. Paganetti, “Clinical CT-based calculations of dose and positron emitter distributions in proton therapy using the FLUKA Monte Carlo code,” Phys Med Biol, vol. 52, no. 12, pp. 3369–3387, 2007.

[5] T. Hu, J. Hu, X. Zhang et al., “Development and performance evaluation of an open-ring PET prototype for intraoperative metabolic monitoring,” IEEE Trans Radiat Plasma Med Sci, 2026, early access; DOI to be confirmed at proof stage.

[6] L. Fang, B. Zhang, B. Li, X. Zhang, X. Zhou, J. Yang, A. Li, X. Shi, Y. Liu, M. C. Kreissl, N. D’Ascenzo, P. Xiao, and Q. Xie, “Develop- ment and evaluation of a new high-TOF-resolution all-digital brain PET system,” Phys Med Biol, vol. 69, no. 2, p. 025019, 2024.

[7] B. Zhang, B. Li, L. Fang, X. Zhou, A. Li, X. Zhang, Y. Liu, Z. Wang, C.-M. Kao, Y. Liu, X. Zhu, L. Wan, P. Xiao, X. Chen, H. Iida, J. Knuuti, and Q. Xie, "Performance evaluation of new PET/CT DigitMI 930," IEEE Trans Radiat Plasma Med Sci, vol. 9, no. 5, pp. 578–585, 2025.
[8] S. Jan, D. Benoit, E. B. Becheva, T. Carlier, F. Cassol, P. Descourt et al., "GATE V6: a major enhancement of the GATE simulation platform enabling modelling of CT and radiotherapy," Phys Med Biol, vol. 56, no. 4, pp. 881–901, 2011.
[9] K. McNamara, A. Schiavi, D. Borys, K. Brzezinski, J. Gajewski, R. Kopec´ et al., "GPU accelerated Monte Carlo scoring of positron emitting isotopes produced during proton therapy for PET verification," Phys Med Biol, vol. 67, no. 24, 2022.

MIC-15-336

FARO: Feasibility of Adaptative Surface-Guided Radiation Oncology

(#1580)

Nataly Castellanos[1], Jose V. Casaña[1], Rafael D. Espósito[2], Luisa Gavier[3], Gabriela Llosá[1], Carmen Salvador[3], Montserrat Carles[3], Ana Ros[1]

[1] IFIC - Insitute of Corpuscular Physics (CSIC-UV), 46980, Paterna, Spain; [2] La Fe University and Polytechnic Hospital, Nuclear Medicine, 46026, Valencia, Spain; [3] Health Research Institute La Fe, Biomedical Imaging Research Group, 46026, Valencia, Spain

This work has received financial support from the IIS La Fe through the VLCBIOMED FARO project and the SO project CEX2023-001292-S funded by MCIU/AEI, as well as support from INNAVA2/2023/8-Potenciación (UCIE-IFIC) and Triad Semiconductor, Inc.

Abstract

The IRIS group at IFIC-Valencia, as part of the FARO (Feasibility of Adaptive Surface-Guided Radiation Oncology) project, funded under the VLC-BIOMED 2024 call (AP2024VLC-01), has developed a prototype to ensure the reproducibility of patient positioning, movement management in oncology applications and correlate the patient position across different scans. The system, based on Lighthouse v2 technology, uses base stations that emit infrared light and detectors that record these pulses. Experimental measurements at La Fe University and Polytechnic Hospital have been carried out using a torso phantom coupled to a motor that emulates different respiratory patterns. The results show that our non-invasive prototype is capable of calculating static position and reproducing respiratory movement with millimeter accuracy.

References
[1] American Association of Physicists in Medicine (AAPM) 2017, 'Measurement and calculation of doses outside the treated volume from external-beam radiation therapy', AAPM Report TG-158, College Park, MD, USA: American Association of Physicists in Medicine.
[2]
Ji, Z, Qiu, B, Jiang, Y, Sun, H, Zhao, T, Chen, Y, Li, M & Wang, J 2025, 'Evaluation of cone-beam computed tomography (CBCT) correction magnitudes for patient positioning in radiotherapy', *Journal of Radiation Research and Applied Sciences*, vol. 18, no. 4, art. no. 102008, Elsevier.
[3]
Uribe, C, Iravani, A, Savir-Baruch, B, Jacene, H, Graves, SA, Dewaraja, YK, Heath, CL & Hope, TA 2025, 'SNMMI/ACNM procedure standard for posttreatment imaging of 177Lu-based radiopharmaceuticals', *Journal of Nuclear Medicine*, vol. 66, no. 10, pp. 1528–1537, Reston, VA: Society of Nuclear Medicine and Molecular Imaging.

[4]
Uribe, C, Dewaraja, YK, Heath, CL, Graves, SA, Savir-Baruch, B, Iravani, A, Jacene, H & Hope, TA 2022, 'Whole-body and SPECT/CT imaging for dosimetry of 177Lu-labeled radiopharmaceutical therapies', *Journal of Nuclear Medicine*, vol. 63, no. 8, pp. 1238–1245, Reston, VA: Society of Nuclear Medicine and Molecular Imaging.
[5]
Li, Z, Zhang, W & Liu, Q 2021, 'Light-based indoor positioning systems: A review', *IEEE Sensors Journal*, vol. 21, no. 5, pp. 5936–5949, New York, NY: IEEE.
[6]
Tiemann, J & Wietfeld, C 2018, 'Lighthouse positioning system: Dataset, accuracy, and precision for UAV research', *Proceedings of the International Conference on Indoor Positioning and Indoor Navigation (IPIN)*, pp. 1–8, Nantes, France: IEEE.

MIC-15-339

A Cherenkov-Based Prompt Gamma Imaging for Proton Range and Dose Prediction Using a Multilayer Perceptron (#1783)

Xiangtao Zeng[1], Chen Huang[1], Xiaolong Jiang[1], Hang Yang[1], Ming Niu[1], Junqin Lei[2,3], Enzhuo Quan[2,3], Zheng Gu[1]

[1] Shenzhen Bay Laboratory, Institute of Biomedical Engineering, Shenzhen, China; [2] National Cancer Center/National Clinical Research Center for Cancer, Shenzhen, China; [3] Chinese Academy of Medical Sciences and Peking Union Medical College, Cancer Hospital & Shenzhen Hospital, Shenzhen, China

This work is supported by the National Key R&D Program of China (No. 2023YFC2414800), the National Natural Science Foundation of China (Nos. 12275182 and 62371314), Guangdong Basic and Applied Basic Research Foundation (Nos. 2024A1515012154), the Guangdong Provincial Project (Grant No. 2023TQ07A233), the Major Program of Shenzhen Bay Laboratory (No. C1012530005) and the Shenzhen Bay Laboratory Proof-of Concept Grants (No. C1022430005).

Abstract

Accurate in vivo dose range verification is critical in proton therapy due to uncertainties in beam range. Prompt gamma imaging (PGI) is promising because PG emissions correlate with the Bragg peak. However, conventional detectors can suffer from signal pile-up under high-intensity proton beams. Cherenkov detectors are attractive for PGI due to their selective gamma sensitivity, ultrafast response, and high count-rate capability. In this work, a PGI system based on PbF_2, a pure Cherenkov-emitting material, was simulated, and a multilayer perceptron (MLP) model was employed to predict proton range and one-dimensional dose distributions. The detector comprises a 32 × 32 PbF_2 crystal array coupled to a silicon photomultiplier (SiPM) array, with a knife-edge slit collimator providing one-dimensional PG projections. Proton beams from 70 to 120 MeV in 10 MeV intervals were simulated in a PMMA phantom using Geant4, and 1000 PG profiles per energy were generated via Poisson resampling. The MLP was trained on 70–120 MeV beams (80% training, 20% validation), while intermediate energies from 75 to 115 MeV (in 10 MeV intervals) were reserved for testing. Predicted dose distributions agree well with ground truth, achieving sub-millimeter proton range accuracy and mean relative errors (MRE) of 0.6–2.4%. These results demonstrate the feasibility of combining Cherenkov-based PGI with machine learning for accurate dose and range prediction, supporting future real-time, beam-by-beam verification in proton therapy.

References
[1] L. Rebolo. et al. (2026). CHEMONO: A Cherenkov-Only Monolithic Detector for PGI in Proton Range Verification. IEEE Transactions on Radiation and Plasma Medical Sciences, 10(2)

MIC-15-342

Compact Handheld Compton Camera versus Planar Gamma Camera for Post-Iodine-131 Therapy Imaging: A GATE/Geant4 Monte Carlo Study (#1927)

Mina-Ermioni Tomazinaki[2], Aristotelis-Nikolaos Rapsomanikis[2], Efstathios Stiliaris[2,1]

[1] Institute of Accelerating Systems & Applications (IASA), Athens, Greece; [2] National and Kapodistrian University of Athens, Department of Physics, Athens, Greece

Abstract

Post-thyroidectomy whole-body imaging after Iodine-131 administration in differentiated thyroid cancer is performed to verify biodistribution, identify thyroid bed remnants, detect locoregional and distant metastases, and support patient-specific dosimetry. The clinical standard, planar scintigraphy with a high-energy parallel-hole collimator, suffers from photon collection efficiency below 1% and depth ambiguity that can mask small remnants. We present a GATE/Geant4 Monte Carlo comparison of a clinical planar gamma camera and a compact handheld silicon/cesium iodide Compton camera at the 364 keV photopeak of Iodine-131 This translates into shorter acquisition times in clinical practice. Preliminary results indicate a sensitivity advantage of 30% for the Compton camera over the gamma camera in planar mode. The handheld geometry enables point-of-care bedside imaging of high-activity post-therapy patients, with potential to transform post-radioiodine therapy monitoring and dosimetry in thyroid cancer.

References
[1] M. Luster et al., "Guidelines for radioiodine therapy of differentiated thyroid cancer", Eur. J. Nucl. Med. Mol. Imaging, vol. 35, no. 10, pp. 1941–1959, 2008.
[2] G. Autret et al., "Monte Carlo modeling of gamma cameras for I-131 imaging in targeted radiotherapy", Cancer Biother. Radiopharm., vol. 20, no. 1, pp. 77–84, 2005.
[3] T. Kim et al., "Development and applications of Compton camera-a review" Sensors, vol. 22, no. 19, art. no. 7374, 2022.
[4] M. Suzuki et al., "Tomographic imaging by a Si/CdTe Compton camera for In-111 and I-131 radionuclides", IEEE Trans. Radiat. Plasma Med. Sci., vol. 6, no. 6, pp. 689–696, 2022.
[5] M.-E. Tomazinaki, "Construction of a Compton-Camera Prototype based on Silicon Scatterer with Analytical Image Reconstruction for Medical Imaging", PhD Thesis, Department of Physics, National and Kapodistrian University of Athens, 2023.

MIC-15-345

Comparison of CNN-Based Reduced-Time-Point and Conventional Single-Time-Point Voxel Dosimetry for ^{177}Lu-DOTATATE SPECT/CT

(#2030)

Stathis Varzakis[1], Ana Denis-Bacelar[2], Sarah J. McQuaid[3], John Dickson[4], Mark Gaze[5], Dimitrios Priftakis[4], Kris Thielemans[1], This work is supported by the EPSRC-funded UCL Centre for Doctoral Training in Intelligent, Integrated Imaging in Healthcare (i4health) (EP/S021930/1), the National Physical Laboratory (NPL) and the UK National Measurement System of the UK Government's Department for Science, Innovation and Technology (DSIT). SIRF and STIR software maintenance is part-funded via CCP SyneRBI (funded by the EPSRC grant EP/T026693/1) and by STFC through the UKRI Digital Research Infrastructure programme.

[1] University College London, Insitute of Nuclear Medicine, London, UK; [2] National Physical Laboratory, Medical Physics, London, UK; [3] Barts Health NHS Trust, Department of Nuclear Medicine, London, UK; [4] University College London Hospitals, Department of Nuclear Medicine, London, UK; [5] University College London Hospitals, Department of Oncology, London, UK

Abstract

Patient-specific dosimetry in peptide receptor radionuclide therapy (PRRT) using ^{177}Lu-DOTATATE commonly requires multiple quantitative SPECT/CT acquisitions to estimate time-integrated activity and absorbed dose distributions. Although multi-time-point imaging improves kinetic characterization, it increases clinical workload and patient burden. Single-time-point (STP) dosimetry approaches have therefore been proposed as practical alternatives, although conventional analytic STP methods may have limited accuracy in heterogeneous activity distributions.

In this work, CNN-based voxel dosimetry frameworks for ^{177}Lu-DOTATATE SPECT/CT were compared against conventional Hänscheid-based STP dosimetry. Quantitative SPECT/CT datasets from 44 paediatric treatment cycles were retrospectively analysed. Reference voxel-level absorbed dose maps were generated using multi-time-point dosimetry and GATE Monte Carlo simulation. Conventional STP dosimetry was performed using the Hänscheid formalism and a GATE-derived dose voxel kernel (DVK). A 3D U-Net architecture was used to estimate voxel-level absorbed dose maps from co-registered activity and density distributions using either a single 96 h activity input or paired 4 h and 120 h activity inputs.

CNN-based dosimetry demonstrated reduced organ-level absorbed dose deviations across the liver, spleen, kidneys, and tumour volumes relative to conventional STP dosimetry. Mean voxel-wise NMAE and NRMSE values decreased from 45.0 % and 54.3 % for conventional Hänscheid-STP dosimetry to 20.6 % and 27.4 % for CNN-STP dosimetry using a single 96 h activity input. The CNN model using paired 4 h and 120 h activity inputs further reduced these values to 18.8 % and 25.1 %, respectively. Improved preservation of heterogeneous tumour absorbed dose distributions was additionally observed in dose-volume histogram analysis.

References

[1] M. G. Stabin, M. T. Madsen, and H. Zaidi, 'Personalized dosimetry is a must for appropriate molecular radiotherapy', *Medical Physics*, vol. 46, no. 11, pp. 4713–4716, 2019, doi: 10.1002/mp.13820.

[2] H. Hänscheid, C. Lapa, A. K. Buck, M. Lassmann, and R. A. Werner, 'Dose Mapping After Endoradiotherapy with 177Lu-DOTATATE/DOTATOC by a Single Measurement After 4 Days', *J. Nucl. Med.*, vol. 59, no. 1, pp. 75–81, Jan. 2018, doi: 10.2967/jnumed.117.193706.
[3] M. S. Lee, D. Hwang, J. H. Kim, and J. S. Lee, 'Deep-dose: a voxel dose estimation method using deep convolutional neural network for personalized internal dosimetry', *Scientific Reports 2019*, 9:1, vol. 9, no. 1, pp. 1–9, Jul. 2019, doi: 10.1038/s41598-019-46620-y.

MIC-15-348

Design and characterization of detector modules and readout electronics for a dual head PET system for proton therapy verification

(#2108)

Lluis Freixas, Jesús Marín, Javier Navarrete, Juan Carlos Oller, Oscar Vela, **Pedro Rato-Mendes**

CIEMAT, Technology Department, Madrid, Spain

This work was supported in part by Grant PID2022-127902OB-C22 funded by MCIN/AEI/10.13039/501100011033 and by "ERDF A way of making Europe".

Abstract

Positron emission tomography has been routinely used over the past 20 years for treatment delivery monitoring in charged particle radiotherapy. Based on previous work from our group on Monte Carlo simulations of real patient treatment plans, we report on the design and characterization of detector modules and readout electronics of a dedicated dual head PET system for treatment verification in proton therapy. The detector modules are made of LYSO:Ce matrices optically coupled to silicon photomultiplier matrices, with custom-designed compact readout electronics based on the 16-channel HRFlexToT ASIC, developed by our group in collaboration with the University of Barcelona. Each 64-channel detector module is read out by 4 ASICs, followed by an FPGA which records the time stamp of each event with respect to a global clock using a coarse and a fine counter, and digitizes the time-over-threshold output of each individual channel. Results from the characterization of the detector modules under irradiation of a 22Na source have shown that all channels are readout independently, with energy spectra for all channels yielding an average 16% energy resolution at the 511 keV photopeak. The time stamp of each event was calculated at FPGA level down to 87 ps binning, allowing time-of-flight PET image reconstruction. Moreover, individual readout of all channels allows the identification of intercrystal scatter events. We are currently developing a small prototype PET system based on these detector models and readout electronics to evaluate different treatment verification methods in proton therapy.

References
[1] W. Enghardt et al., "Charged hadron tumour therapy monitoring by means of PET," *Nucl. Instr. Meth. In Phys. Res. A*, vol. 525, pp. 284-288, June 2004. DOI. 10.1016/j.nima.2004.03.128.
[2] T. Nishio et al., "Dose-volume delivery guided proton therapy using beam on-line PET system," *Med. Phys.*, vol. 33, no. 11, pp. 4190-4197, Nov. 2006. DOI. 10.1118/1.2361079.
[3] X. Zhu and G. El Fakhri, "Proton therapy verification with PET imaging," *Theranostics*, vol. 3, no. 10, Sep. 2013. DOI. 10.7150/thno.5162.
[4] C. Toramatsu et al., "Biological washout modelling for in-beam PET: rabbit brain irradiation by 11C and 15O ion beams," *Phys. Med. Biol.*, vol. 65, no. 10, 105011, May 2020. DOI. 10.1088/1361-6560/ab8532
[5] P. Rato Mendes et al., "In-vivo treatment verification by TOF-PET for multiple proton fields: a Monte Carlo simulation study," *Radiat. Oncol.* vol. 161, Suppl. 1, S1286, Aug. 2021. DOI. 10.1016/S0167-8140(21)08012-9.

[6] P. Arce et al., "Monte Carlo simulation framework for the evaluation of PET detector designs in charged particle therapy applications," in *Proc. 2022 IEEE Nucl. Sci. Symp. Med. Imag. Conf.*, Milan, Italy, Nov. 2022. DOI. 10.1109/NSS/MIC44845.2022.10398937
[7] P. Rato Mendes et al., "A dedicated dual-head TOF-PET system for in-vivo quality control of beam delivery in proton therapy," in *Proc. to the 61st Annual Conference of the Particle Therapy Cooperative Group, Int. J. Part. Ther.*, vol. 10, no. 2, pp. 118-396, Nov. 2023. DOI. 10.14338/IJPT-23-PTCOG61-10.2.
[8] D. Sánchez et al., "HRFlexToT: A high dynamic range ASIC for time-of-flight positron emission tomography," *IEEE Trans. Radiat. Plasma Med. Sci.*, vol. 6, no. 1, pp. 51-67, Jan. 2022. DOI. 10.1109/TRPMS.2021.3066426.
[9] E. Yoshida et al., "Simultaneous time-skew and time-walk correction for TOF-PET detector," *Nucl. Instr. Meth. In Phys. Res. A*, vol. 1049, 168114, Apr. 2023. DOI. 10.1016/j.nima.2023.168114.

MIC-15-351

Characterization of Prompt Gamma-Ray Emission for Helium-Ion Beam Range Verification: A Monte Carlo Study (#2288)

Weigang Duan, Hongyang Zhang, Jiali Yan, Zhengyang Zhao, Shi Wang, Zhaoxia Wu, Hui Liu, Yaqiang Liu

Tsinghua University, Beijing, China

This work was supported in part by the National Key Research and Development Program of China (No. 2022YFC2402002, No. 2022YFC2403802), and National Natural Science Foundation of China (No. 12205166)

Abstract

Prompt gamma imaging is a promising technique for *in vivo* range verification in particle therapy. Compared with protons, Helium-ion (He^{2+}) beams may produce prompt gamma (PG) emissions different from proton beams, affecting energy-window (EW) selection and range-positioning performance. This study investigates the PG energy spectra, EW-dependent yields, and spatial distribution features of He^{2+} irradiation in a homogeneous PMMA phantom.

Monte Carlo simulations were performed using GATE for He^{2+} pencil beams from 70 to 230 MeV/u. Secondary gamma rays generated within the phantom were recorded using a *PhaseSpaceActor*, including their production positions, kinetic energies, direction vectors, and particle information. The PG spectra were analyzed and compared with proton-induced spectra. Several energy windows were selected according to characteristic spectral regions, and their PG yields, longitudinal distributions, and range-positioning performance were evaluated using *Falloff50%*, *Falloff80%*, and *Steepest Falloff* metrics.

The simulations showed He^{2+} irradiation produced substantially higher PG yields than proton irradiation over the investigated energy range, while the main spectral peaks appeared at similar energies. For He^{2+}, PG yield increased with incident energy in all selected windows. The broad 1.9–8 MeV window provided the highest yield and best statistical stability, whereas narrower characteristic windows showed stronger energy specificity but lower counting statistics. EW selection also affected the distal fall-off shape and the derived positioning value. Overall, the 1.9–8 MeV window combined with the Steepest Falloff metric provided the most robust PG range-positioning performance, supporting the development of helium-ion PGI range verification strategies.

References

[1] A. C. Kraan, "Range Verification Methods in Particle Therapy: Underlying Physics and Monte Carlo Modeling," *Frontiers in Oncology,* vol. 5, 2015-07-07, doi: 10.3389/fonc.2015.00150.
[2] M. Pinto, "Prompt-gamma imaging in particle therapy," *The European Physical Journal Plus 2024 139:10,* vol. 139, no. 10, 2024-10-09, doi: 10.1140/epjp/s13360-024-05664-4.
[3] A. Mairani *et al.*, "Roadmap: helium ion therapy," *Physics in Medicine & Biology,* vol. 67, no. 15, 2022-08-05, doi: 10.1088/1361-6560/ac65d3.
[4] H. Paganetti, "Range uncertainties in proton therapy and the role of Monte Carlo simulations," *Physics in Medicine & Biology,* vol. 57, no. 11, 2012-05-09, doi: 10.1088/0031-9155/57/11/R99.

MIC-15-354

GPU-Accelerated Voxel-Wise Mono/Bi-Exponential Fitting for Lu-177 SPECT Time-Integrated Activity Estimation (#2410)

Haotian Tan[1], Jingzhang Sun[2], Gefei Chen[2]

[1] Yunnan Vocational Institute of Energy Technology, Qujing, China; [2] Hainan University, Department of Data Science and Big Data, Haikou, China

This work was supported in part by the National Natural Science Foundation of China (12505396).

Abstract

Time-integrated activity (TIA) estimation is essential for patient-specific Lu-177 SPECT dosimetry, but voxel-wise time–activity curve fitting remains computationally demanding because nonlinear kinetic models must be solved independently across many voxels. This study developed a GPU-accelerated voxel-wise kinetic modeling framework for rapid Lu-177 SPECT TIA estimation. Four serial post-therapy SPECT/CT scans from anonymized Lu-177 DOTATATE datasets were analyzed. The framework used a hierarchical TAC model library, including one mono-exponential model and three bi-exponential variants, to characterize different uptake and clearance patterns. Model selection was performed using the Akaike information criterion, and voxels with insufficient fitting quality were processed using trapezoidal integration with tail extrapolation. GPU acceleration was implemented through batched voxel-wise optimization using CuPy-based array operations and compared with a CPU-based Levenberg–Marquardt implementation. Evaluation included fitting quality, model-selection distribution, agreement with dataset-provided reference TIA maps, organ/lesion-level relative error, and computation time. The GPU implementation preserved the CPU-derived model-selection distribution, with 60.7% mono-exponential, 31.2% bi-exponential, and 8.1% trapezoidal fallback voxels. The median regional voxel-wise fitting R^2 was 0.848. Relative differences from reference TIA maps were 4.2% for kidneys, 3.5% for spleen, 2.7% for liver, and 8.5% for tumor lesions. Computation time decreased from 552.1 s to 18.5 s per patient, corresponding to approximately 30-fold acceleration. These preliminary results support the technical feasibility of GPU-accelerated voxel-wise TAC fitting for practical Lu-177 SPECT dosimetry, although validation in larger multi-patient datasets remains necessary.

References
[1] K. Kim and S.-J. Kim, "Lu-177-based peptide receptor radionuclide therapy for advanced neuroendocrine tumors," *Nuclear Medicine Molecular Imaging,* vol. 52, no. 3, pp. 208-215, 2018.
[2] A. Nautiyal, S. Michopoulou, and M. Guy, "Dosimetry in Lu-177-DOTATATE peptide receptor radionuclide therapy: a systematic review," *Clinical Translational Imaging,* vol. 12, no. 2, pp. 157-175, 2024.
[3] Y. Dewaraja and B. Van, "Lu-177 DOTATATE anonymized patient datasets: multi-time point Lu-177 SPECT/CT scans," *Deep Blue Data website,* vol. 10, 2021.

[4] D. Y. Van BJ, "Lu-177 DOTATATE anonymized patient datasets: Lu-177 SPECT time integrated activity maps," *Deep Blue Data website*.
[5] A. Przybylski, B. Thiel, J. Keller-Findeisen, B. Stock, and M. Bates, "Gpufit: An open-source toolkit for GPU-accelerated curve fitting," *Scientific Reports*, vol. 7, no. 1, p. 15722, 2017.

MIC-15-357

A Three-Stage Scintillator-Compton Camera for BNCT: From Point-Source Resolution to Phantom Reconstruction (#2560)

Sergio López Martínez, Catarina Veiga, Robert Speller, Robert Moss

University College London, Department of Medical Physics and Biomedical Engineering, London, UK

This work is supported by the EPSRC-funded UCL Centre for Doctoral Training in Intelligent, Integrated Imaging in Healthcare (i4health) (EP/S021930/1).

Abstract
Boron Neutron Capture Therapy (BNCT) requires accurate in-vivo dose verification, yet current clinical methods rely on indirect blood-based boron concentration estimates that introduce substantial inter-patient variability. Imaging the 478 keV prompt gamma ray emitted during boron-10 neutron capture offers a direct route to real-time dose mapping. However, this requires a detector capable of efficient reconstruction at high gamma energies in the presence of significant background.

Building on our previously reported scintillator-based Compton camera concept [1], we present the full computational characterisation of a three-stage system comprising scintillator cylinders arranged in a three-dimensional spherical array. The non-planar geometry offers multi-directional cone orientations, improving global spatial resolution compared to conventional planar designs. Geant4 Monte Carlo simulations were used to model a realistic BNCT irradiation scenario [2], incorporating a modified Snyder head phantom with clinically representative boron concentrations (25 ppm brain / 65 ppm tumour) [3].

Reconstruction performance is evaluated across scenarios of increasing complexity: an idealised point source, a distributed gamma-ray source, a treatment-like gamma source, and a full phantom simulation. This progressive approach illustrates how reconstruction quality is affected by increasing complexity and the high neutron-induced background inherent to BNCT environments, providing insight into the current limitations of the design and potential strategies to address them. These results establish a validated simulation framework for a scintillator-based Compton camera tailored to BNCT prompt gamma imaging, providing the foundation for forthcoming experimental characterization and clinical translation.

References
[1] S. Lopez Martinez, R. Speller, and R. Moss, “A Scintillator-Based Compton Camera Concept for BNCT Treatment Optimisation,” in *2025 IEEE Nuclear Science Symposium (NSS), Medical Imaging Conference (MIC) and Room Temperature Semiconductor Detector Conference (RTSD)*, Nov. 2025, pp. 1–1. doi: 10.1109/NSS/MIC/RTSD57106.2025.11286503.

[2] N. Hu *et al.*, "Clinical evaluation of performance, stability, and longevity of an accelerator system designed for boron neutron capture therapy utilising a beryllium target," *Nuclear Instruments and Methods in Physics Research Section A: Accelerators, Spectrometers, Detectors and Associated Equipment*, vol. 1072, p. 170126, Mar. 2025, doi: 10.1016/j.nima.2024.170126.
[3] C. Gong, X. Tang, D. Shu, H. Yu, and C. Geng, "Optimization of the Compton camera for measuring prompt gamma rays in boron neutron capture therapy," *Applied Radiation and Isotopes*, vol. 124, pp. 62–67, Jun. 2017, doi: 10.1016/j.apradiso.2017.03.014.

MIC-15-360

Impact of PET Energy Window Selection on Y-90 Radioembolization Dosimetry (#2682)

Matthew Strugari[1], Sergio Romero García[2], Floris P. Jansen[3], Kuan-Hao Su[4], Matthew Spangler-Bickell[5], Pablo García-Polo[6], Daniel Pérez Enguix[7], Luis Martí-Bonmatí[1,7], Irene Torres Espallardo[1,2]

[1] Instituto de Investigación Sanitaria La Fe, Biomedical Imaging Research Group (GIBI230), Valencia, Spain; [2] Hospital Universitario y Politécnico La Fe, Department of Nuclear Medicine, Valencia, Spain; [3] GE HealthCare, Department of Engineering, Waukesha, USA; [4] GE HealthCare, Molecular Imaging and CT Engineering, Waukesha, USA; [5] GE HealthCare, PET/MR Engineering, Waukesha, USA; [6] GE HealthCare, Science and Technology Office, Madrid, Spain; [7] Hospital Universitario y Politécnico La Fe, Department of Radiology, Valencia, Spain

This work was supported by the ORION research project of the Spanish Society of Medical Physics.

Abstract

Selective internal radiation therapy using ^{90}Y microspheres provides targeted treatment of liver malignancies, with post-therapy PET enabling treatment verification and voxel-based dosimetry. Quantitative ^{90}Y PET imaging is challenged by a low signal-to-background ratio. The internal pair production branching ratio of ^{90}Y is low, yielding a weak 511 keV annihilation photon signal amid background contributions from bremsstrahlung following β^- decay and intrinsic radiation from ^{176}Lu in PET systems constructed with LYSO scintillation crystals. These background events increase random coincidences and degrade spatial localization and dosimetric accuracy. This study evaluated the effect of PET energy window selection on ^{90}Y radioembolization dosimetry using standard (425-650 keV) and narrow (480-542 keV) energy windows. Six patients underwent post-therapy PET/MR imaging. Images were reconstructed using TOF-OSEM, and absorbed dose distributions were calculated using local deposition modelling. Randoms fraction, apparent activity outside the perfused volume, dose-volume histograms, and dose-volume metrics were compared between protocols. The narrow-window protocol reduced the randoms fraction from 91 ± 3% to 60 ± 10% and apparent activity outside the perfused volume by 51 ± 16%, indicating reduced background contamination and improved confinement of the reconstructed activity distribution. Mean absorbed doses to the tumour and healthy liver were preserved, and healthy liver $V30$ decreased by 13 ± 8%. Tumour $D70$ changed by -15 ± 33%, and tumour dose redistribution effects varied substantially between patients without a consistent directional trend. These findings demonstrate that narrow-window PET acquisition improves activity localization in ^{90}Y radioembolization while preserving overall absorbed dose estimates and may influence patient-specific voxel-based dosimetry.

References
[1] Y. Seo, M. M. Khalighi, K. A. Wangerin, T. W. Deller, Y.-H. Wang, S. Jivan, M. P. Kohi, R. Aggarwal, R. R. Flavell, S. C. Behr, and M. J. Evans, "Quantitative and Qualitative Improvement of Low-Count [68Ga]Citrate and [90Y]Microspheres PET Image Reconstructions Using Block Sequential Regularized Expectation Maximization Algorithm," Molecular Imaging and Biology, vol. 22, no. 1, pp. 208–216, Feb. 2020. [Online]. Available: http://link.springer.com/10.1007/s11307-019-01347-0
[2] C. Chiesa, K. Sjogreen-Gleisner, S. Walrand, L. Strigari, G. Flux, J. Gear, C. Stokke, P. M. Gabina, P. Bernhardt, and M. Konijnenberg, "EANM dosimetry committee series on standard operational procedures: a unified methodology for 99mTc-MAA pre- and 90Y peri-therapy dosimetry in liver radioembolization with 90Y microspheres," EJNMMI Physics, vol. 8, no. 1, p. 77, Nov. 2021. [Online]. Available: https://ejnmmiphys.springeropen.com/articles/10.1186/s40658-021-00394-3

MIC-15-363

A Compton Camera Using GAGG Scintillators Coupled with SiPM Array Readout for Online Monitoring in Particle Therapy (#2860)

Yun Wang[1], Jiaxing Peng[1], Jianbo Chen[1], Yongzhi Yin[1], Jianxiong Shao[1], Chunhui Zhang[1]

[1] Lanzhou University, School of Nuclear Science and Technology, Lanzhou, China; [2] Lanzhou University, School of Nuclear Science and Technology, Lanzhou, China

Abstract

Particle therapy exploits the Bragg peak for precise dose deposition, yet the high-LET characteristic demands accurate real-time range verification and dose distribution monitoring. Compton cameras offer a promising collimator-free solution for the prompt gamma imaging induced during treatment. In this work, a Compton camera is constructed by using $Gd_3Al_2Ga_3O_{12}$:Ce (GAGG) scintillator coupled with silicon photomultiplier (SiPM) arrays. The scatter and absorber layers are both constructed from high-light-yield, high-energy-resolution GAGG with optimized geometry. An energy resolution of ~8% FWHM is obtained for 511 keV gamma rays, while the position resolution is 1.5 mm (scatter layer) and 2.0 mm (absorber layer) in both x and y directions. The scatter layer retains the capability for dual-ended readout, with an expected DOI resolution of ~2.5 mm. Image reconstruction is performed using GPU-accelerated LM-MLEM. Laboratory measurements with a ^{22}Na source demonstrate that an angular resolution of ~7° at 511 keV and ~6° at 1274 keV was achieved. Future work will focus on proton/carbon ion beam experiments and scaling the effective detector area to 100 mm × 100 mm.

References
[1] H. Paganetti, "Range uncertainties in proton therapy and the role of Monte Carlo simulations," Phys. Med. Biol., vol. 57, no. 11, pp. R99–R117, 2012.
[2] J. Krimmer et al., "Prompt-gamma monitoring in hadrontherapy: A review," Nucl. Instrum. Methods A, vol. 878, pp. 58–73, 2018.
[3] E. Draeger et al., "3D prompt gamma imaging for proton beam range verification," Phys. Med. Biol., vol. 63, no. 3, p. 035006, 2018.

MIC-15-366

In Silico Optimization of [^{177}Lu]Lu-PSMA-617 Therapy Regimens (#3011)

Marc Ryhiner[1,2], Ivata Fajnorova[2], Ines C. Azrour[2], Ava Fakharpour[2], Johannes Czernin[2], Axel Rominger[1], Catherine Meyer[2], Christine Mona[2], Kuangyu Shi[1]

[1] University of Bern, Department of Nuclear Medicine, Bern, Switzerland; [2] University of California, Los Angeles, Department of Nuclear Medicine, Los Angeles, USA

Abstract

This study presents a data-driven framework for optimizing dosimetry regimens in radiopharmaceutical therapy using *in vivo* data from [^{177}Lu]Lu-PSMA-617-treated murine models incorporating therapy resistance. Experimental data demonstrated improved long-term outcomes for cumulative (3 × 10 MBq) and de-escalation (20 MBq + 10 MBq) regimens compared with conventional single-dose (30 MBq) and escalation (10 MBq + 20 MBq) schedules. Building on these findings, additional treatment regimens were evaluated in silico to identify combinations of favorable therapeutic characteristics. Dose-rate kernels derived from dynamic SPECT/CT imaging were used to calibrate an integrated dose–response and tumor growth model. These kernels captured both the temporal evolution of dose rates following treatment and spatial intratumoral heterogeneity through region-specific dose quantiles. Therapy resistance across treatment cycles was incorporated using generalized dose-rate patterns derived from experimentally observed relationships between treatment response and previously administered activity ratios. The spatial distribution of dose-rate regions used for kernel generation was best described by an exponential decay model, yielding a lower Akaike Information Criterion (AIC: −139 ± 31) than alternative distributions. Simulations identified the 3–2–1 (15, 10, 5 MBq), 2–1–1 (15, 2 × 7.5 MBq), and 2–2–1 (2 × 12, 6 MBq) regimens as outperforming the experimentally tested schedules. These results demonstrate the potential of simulation-based optimization to support the design of biologically informed radiopharmaceutical therapy regimens and provide a framework for systematic *in silico* treatment planning.

MIC-15-369

Energy-Shifting: an efficient approach for Monte Carlo Particle Therapy Dose Calculation (#3092)

Chi-Hieu Pham[1], Didier Benoit[1], Vincent Bourbonne[1,2], Ulrike Schick[1,2], Dimitris Visvikis[1], Julien Bert[1]

[1] University of Brest, LaTIM, INSERM-UMR1101, Brest, France; [2] Brest Hospital University, Radiotherapy Department, Brest, France

Abstract

While recent deep learning techniques for accelerating Monte Carlo (MC) radiotherapy dose calculation have shown promising results, most state-of-the-art methods rely on a denoising paradigm. This approach aims to

predict a high-sampling (HS) reference dose map from a fast low-sampling (LS) input. However, information loss and stochastic noise in LS inputs often limit the accurate recovery of fine structural details and dose gradients, and may lead to hallucinations. To address these limitations, we propose a novel learning framework, Energy-Shifting, which reconstructs a time-intensive polyenergetic HS dose distribution from a GPU-accelerated monoenergetic dose map. Our results demonstrate that this method significantly outperforms conventional denoising approaches in accuracy.

MIC-15-372

Human Single Time Point Dosimetry Using Weight-Based Extrapolated Mouse Effective Half-Life (#3228)

Muath Almaslamani[1,2], Jingyu Yang[1], Ilhan Lim[2,3], Kwang il Kim[1,2], Sang Keun Woo[1,2]

[1] Division of Applied RI, Korea Institute of Radiological and Medical Sciences, Seoul, South Korea; [2] University of Science & Technology, Radiological & Medico-Oncological Sciences, Daejeon, South Korea; [3] Korea Institute of Radiological and Medical Sciences, Department of Nuclear Medicine, Seoul, South Korea

Abstract

Image-based dosimetry requires multiple-time-point (MTP) imaging to estimate the time-integrated activity (TIA), which can be challenging to implement in clinical practice. Moreover, Mouse-to-human extrapolation methods produces large errors. This study aimed to evaluate single-time-point (STP) dosimetry approach using extrapolated human effective half-life derived from preclinical activity scaling based on body weight and organ mass. Six patients underwent where administrated with ^{64}Cu-DOTA-rituximab and underwent MTP PET/CT imaging at 1, 24, and 48 h post-injection (p.i.), while four mice were imaged at 1, 24, 48, and 72 h p.i. Regions of interest were manually drawn for the kidney, liver, and spleen. Human MTP reference TIA was calculated using OLINDA with mono-exponential fitting. Mouse organ activity was converted to estimated human organ activity using body weight and organ mass scaling as: $(\%ID/organ)_{human}=(\%ID/g)_{mouse}\times(kg_{WB})_{mouse}\times(g_{Organ}/kg_{WB})_{human}$. Human TIA was then estimated from the extrapolated activity curve. In the proposed approach, the extrapolated human time–activity curve was used to derive the extrapolated human effective half-life. This effective half-life was then combined with the measured human organ activity from STP scan and TIA was calculated as following: $TIA=(A(T_{sc})/\ln(2))\times 2^{Tsc/Teff(extrapolated)}\times T_{eff(extrapolated)}$. [if gte msEquation 12]><m:oMath><span style='font-size: 10.0pt;line-height:107%;font-family:"Cambria Math",serif;mso-fareast-font-family: "Malgun Gothic";mso-fareast-theme-font:minor-fareast;mso-bidi-font-family: "Times New Roman";color:black;mso-themecolor:text1;mso-ansi-language:EN-US; mso-fareast-language:KO;mso-bidi-language:AR-SA'><m:r> </m:r></m:oMath><![endif][if gte vml 1]><v:shapetype id="_x0000_t75" coordsize="21600,21600" o:spt="75" o:preferrelative="t" path="m@4@5l@4@11@9@11@9@5xe" filled="f" stroked="f"> <v:stroke joinstyle="miter"/> <v:formulas> <v:f eqn="if lineDrawn pixelLineWidth 0"/> <v:f eqn="sum @0 1 0"/> <v:f eqn="sum 0 0 @1"/> <v:f eqn="prod @2 1 2"/> <v:f eqn="prod @3 21600 pixelWidth"/> <v:f eqn="prod @3 21600 pixelHeight"/> <v:f eqn="sum @0 0 1"/> <v:f eqn="prod @6 1 2"/> <v:f eqn="prod @7 21600 pixelWidth"/> <v:f eqn="sum @8 21600 0"/> <v:f eqn="prod @7 21600 pixelHeight"/> <v:f eqn="sum @10 21600 0"/> </v:formulas> <v:path o:extrusionok="f" gradientshapeok="t" o:connecttype="rect"/> <o:lock v:ext="edit"

aspectratio="t"/></v:shapetype><v:shape id="_x0000_i1025" type="#_x0000_t75" style='width:468pt; height:12.75pt'> <v:imagedata src="file:///C:/Users/muath/AppData/Local/Temp/msohtmlclip1/01/clip_image001.png" o:title="" chromakey="white"/></v:shape><![endif]. The proposed STP approach reduced the estimation error for kidney from 88.7% with the conventional extrapolation approach to 29.0%, 40.6%, and 66.7% at 1, 24, and 48 h p.i., respectively. The corresponding errors decreased from 406% to 26.8%, 35.1%, and 65.3% for the liver, and from 480% to 42.2%, 57.7%, and 76.2% for the spleen, respectively. These results demonstrate that incorporating measured human STP activity with extrapolated human effective half-life improves TIA estimation and provide a practical dosimetry approach when full MTP imaging is not feasible.

MIC-15-375

Deep Learning-based CT-Free Deformable Registration for PET-CT Misalignment Correction (#1875)

Abolfazl Mehranian[1], Scott Wollenweber[2], Fotis Kotasidis[3], Zacharias Chalampalakis[4], Ariel Lulinsky[5], Hagit Ratner[5], Robert Johnsen[2], Gil Kovalski[5]

[1] GE HealthCare, Oxford, UK; [2] GE HealthCare, Waukesha, USA; [3] GE HealthCare, Zurich, UK; [4] GE HealthCare, Buc, France; [5] GE HealthCare, Haifa, Israel

This work has been sponsored by GE HeathCare.

Abstract

Respiratory phase mismatches between PET and CT commonly cause artifacts in PET/CT, especially at lung–liver and lung–spleen interfaces. Since CT captures a single respiratory phase while PET reflects an average over breathing, this misalignment leads to attenuation correction errors and inaccurate lesion quantification, particularly near the liver dome. We propose a deep learning framework that uses PET-based pseudo-CT to guide deformable CT-to-PET alignment. A retrospective dataset of 10 18F-FDG exams with respiratory phase mismatch (banana) artifacts, scanned on a Total-Body BGO-based PET/CT scanner, was used for evaluation. A previously trained 3D residual neural network was used to generate pseudo-CT images from non-attenuation corrected (NAC) PET images. The pseudo-CT images, inherently aligned with the PET data, were then used as a reference for deformable registration of the CT images. The original and registered CT images were used for attenuation correction and reconstruction of the PET data using a BSREM algorithm. Regions of interested were placed in dome of the liver to quantitatively measure the SUV changes in those regions affected by the artifacts. Compared to baseline PET/CT without correction, the proposed method effectively reduced or eliminated respiratory-induced PET/CT misalignment artifacts were significantly reduced or eliminated. Quantitatively, the method achieved improvements in liver SUVmean towards the expected values. By leveraging the native alignment between PET and the generated pseudo-CT, the method avoids direct multimodal registration and instead enables accurate deformable alignment of CT to PET space. This approach improves attenuation correction and quantitative accuracy, with potential to enhance diagnostic confidence in routine clinical PET/CT imaging

MIC-15-378

Investigation of Image Quality Gains Using Variable Time Windows in Long-Axial PET Systems (#1914)

Yue Chen, Yucun Hou, Jianyong Jiang

Beijing Normal University, school of physics and astronomy, Beijing, China

This work was supported by the National Natural Science Foundation of China (No. 12475336)

Abstract

The extension of the axial field-of-view (AFOV) represents a transformative advancement in PET, offering superior sensitivity and enabling ultra-low-dose 4D imaging. However, the increased AFOV necessitates wider acceptance angles and correspondingly larger coincidence time windows, leading to a substantially higher proportion of random coincidence events compared to conventional scanners. While traditional random correction relies on noisy, sparse delayed coincidence sinograms, the singles-rate method has been approved as a superior alternative for long-axial FOV (LAFOV) systems. A critical yet underexplored challenge in LAFOV PET is the significant variation in the required time window across different ring differences. Although object-specific customized windows have shown promise in short-axial systems, their application to total-body PET remains largely unoptimized. In this study, we propose a novel reconstruction strategy utilizing a variable time window tailored to specific ring differences to minimize random fractions. Using GATE simulations of a 1.5-m total-body PET system (uMI Panorama GS), we designed and evaluated a variable time window set based on practical coincidence time resolution (CTR). This approach was benchmarked against a standard fixed window (6.0 ns) and a 3-step window (4.7, 6.2, and 8.3 ns). Systematic analysis of simulated coincidence data reveals that the variable window design significantly reduces the random fraction. Comparative reconstructions of a uniform cylinder, NEMA, and torso phantoms demonstrate that this reduction directly translates to lowered image noise levels and enhanced signal-to-noise ratios within a consistent reconstruction framework. These findings establish that ring-difference-specific time windows provide a robust technical pathway for maximizing the quantitative performance of next-generation LAFOV PET systems.

References

[1] Zhang, H, et al. 2024, 'Performance Characteristics of a New Generation 148-cm Axial Field-of-View uMI Panorama GS PET/CT System with Extended NEMA NU 2-2018 and EARL Standards', *Journal of Nuclear Medicine*, jnumed.124.267963, Reston: Society of Nuclear Medicine and Molecular Imaging

[2] Qi, J, Matej, S, Wang, G, and Zhang, X 2021, '3D/4D Reconstruction and Quantitative Total Body Imaging', *PET Clinics*, 16(1), 41–54, Philadelphia: Elsevier

[3] Zhang, X, Badawi, RD, Cherry, SR, and Qi, J 2018, 'Theoretical study of the benefit of long axial field-of-view PET on region of interest quantification', *Physics in Medicine and Biology*, 63(13), 135010, Bristol: IOP Publishing

[4] Zhang, X, et al. 2020, 'Total-Body Dynamic Reconstruction and Parametric Imaging on the uEXPLORER', *Journal of Nuclear Medicine*, 61(2), 285–291, Reston: Society of Nuclear Medicine and Molecular Imaging

[5] Cherry, SR, Jones, T, Karp, JS, Qi, J, Moses, WW, and Badawi, RD 2018, 'Total-Body PET: Maximizing Sensitivity to Create New Opportunities for Clinical Research and Patient Care', *Journal of Nuclear Medicine*, 59(1), 3–12, Reston: Society of Nuclear Medicine and Molecular Imaging

[6] Yuan, Z, et al. 2025, 'GPU-based list-mode TOF PET image reconstruction with complete correction techniques', *Medical Physics*, 53(1), e70216, Alexandria: American Association of Physicists in Medicine

MIC-15-381

Evaluation of TOF-DOI Crystal Topologies for the HD-MetaPET MRI Insert (#2140)

Thore Meyer[1], Giulia Terragni[2], David Schug[1,3], Yannick Kuhl[1], Bjoern Weissler[1,3], Eike Gegenmantel[3], Oliver Muelhens[3], Harald Radermacher[1], Marco Pizzichemi[2,4], Etiennette Auffray[2], Volkmar Schulz[1,3]

[1] RWTH Aachen University, Chair of Imaging and Computer Vision, Aachen, Germany; [2] CERN, Geneva, Switzerland; [3] Hyperion Hybrid Imaging Systems GmbH, Aachen, Germany; [4] University of Milano-Bicocca, Milan, Italy

This work is sponsored by the BMFTR, contract numbers 13GW0609A, 13GW0609B, 13GW0621A and 13GW0621B. Part of this work was performed in the framework of Crystal Clear Collaboration.

Abstract

The HD-MetaPET project is developing a high-resolution positron emission tomography insert for simultaneous magnetic resonance imaging. The insert will consist of 120 Hyperion Visor Max detector tiles with an area of 56.5 x 56.5 mm^2, arranged in two semi-circles and coupled to LYSO:Ce crystal scintillators. A crucial optimisation parameter for the upcoming system performance is the crystal topology. This study evaluates Time-of-Flight and Depth-of-Interaction positioning performance across several crystal topologies: continuous slabs, pseudoslabs, and pixelated arrays with a light guide coupled to the face opposite the photosensitive detector. The study utilizes the Hyperion Visor Max and a custom development board, both featuring the TOFPET2 ASIC. Experimental measurements are performed using a ^{22}Na point source. The preliminary results with crystals of different materials show that pixelated arrays with light guides outperform continuous slabs. Specifically, pixelated designs achieved a Coincidence Time Resolution of ≈235 ps, compared to >400 ps for the slabs. The results indicate that the pixelated designs utilizing the light guide also demonstrated superior accuracy in the evaluation of the Depth-of-Interaction. The pixelated light-guide topology shows promising performance, circumventing the traditional compromise between spatial depth accuracy and timing resolution. Consequently, this configuration emerges as a good candidate for integration into the upcoming HD-MetaPET scanner. While these preliminary results are promising, the comprehensive evaluations utilizing final-scale crystals of the same material and the final scanner electronics will be presented at the conference.

References

[1] Pizzichemi, Marco, 2019, 'On light sharing TOF-PET modules with depth of interaction and 157 ps FWHM coincidence time resolution', *Physics in Medicine & Biology*, Vol. 64, No. 15, 155008

[2] Terragni, Giulia, 2025, 'Exploring the performance of a DOI-capable TOF-PET module using different SiPMs, customized and commercial readout electronics', *Physics in Medicine & Biology*, Vol. 70, No. 2, 025015

[3] Mueller, Florian, 2022, 'A Semi-Monolithic Detector providing intrinsic DOI-encoding and sub-200 ps CRT TOF-Capabilities for Clinical PET Applications', *Medical Physics*, Vol. 49, No. 12, 7469–7488

[4] Cucurella, Neus, 2025, 'Single-Ended Readout PET Detector Based on Pixelated Crystals With TOF and DOI Capabilities', *IEEE Transactions on Radiation and Plasma Medical Sciences*, Vol. 9, No. 7, 866-871

MIC-15-384

Towards Clinically Compatible Dynamic PET: Enabling Kinetic Analysis with 20-Minute Acquisitions (#2711)

Irene Incicco[1], Daniele Dall'Olio[1], Irene Brusa[2], Riccardo Mei[2], Andrea Farolfi[2], Cristina Nanni[2], Benjamin A. Spencer[3], Guobao Wang[3], Lorenzo Nardo[3], Stefano Fanti[2,4], Gastone Castellani[1,5]

[1] University of Bologna, Department of Medical and Surgical Sciences, Bologna, Italy; [2] IRCCS Azienda Ospedaliero–Universitaria di Bologna, Nuclear Medicine, Bologna, Italy; [3] University of California-Davis, Department of Radiology, Davis, USA; [4] Alma Mater Studiorum University of Bologna, Nuclear Medicine, Bologna, Italy; [5] IRCCS Azienda Ospedaliero-Universitaria di Bologna S.Orsola, 40138, Bologna, Italy

Abstract

Dynamic PET imaging enables tracer kinetics characterization, offering complementary quantitative insights beyond static imaging. The advent of Long Axial Field-of-View (LAFOV) scanners, with high sensitivity, has renewed interest in kinetic modelling by enabling whole-body dynamic imaging in clinical settings. However, acquisitions can last up to 1 hour, limiting adoption due to reduced throughput. Clinically, reporting relies on late-phase images (1-hour post-injection), whereas kinetic modelling requires data from injection, creating a conflict between clinical requirements and feasibility. This work investigates whether dynamic protocols can be shortened to 20 minutes post-injection while preserving clinically relevant information by predicting late-phase time-activity curves (TACs) from early dynamic data. The cohort included 107 subjects imaged with ^{18}F-FDG, yielding 20,903 TACs extracted from multiple anatomical structures. Four approaches were compared: a three-exponential model, two-tissue compartment model (2TCM), a gated recurrent unit encoder-decoder, and a novel Neural Ordinary Differential Equation framework (NODE). At 60 minutes, all methods showed near-zero median residuals. Over 20–60 min, NODE outperformed competing approaches with the lowest root mean squared error (0.096) and χ^2 (0.43), and the highest concordance correlation coefficient (0.40), with reduced variability across TACs. Overall, prediction of late-phase PET information from 0–20 min data appears feasible. NODE provided the most accurate and stable results, although 2TCM remained competitive at 60 min, suggesting benefits from incorporating physiological priors. Future work will extend the analysis to voxel-wise reconstruction, with preliminary results showing promising outcomes, and will examine kinetic parameter consistency between observed early dynamics (0–20 min) and full predicted dynamic data (0–60 min).

MIC-15-387

SADCA-ResDiff: A Structure-Aware Dual Cross-Attention Residual Diffusion Network for MR-Free Partial Volume Correction in Amyloid Brain PET (#1005)

Runxiang Huang[1,2], Yibin Liu[1], Zhijie Fang[1], Zhanli Hu[2], Greta S.P. Mok[1,3]

[1] University of Macau, Biomedical Imaging Laboratory (BIG), Department of Electrical and Computer Engineering, Faculty of Science and Technology, Macao, China; [2] Chinese Academy of Sciences, Research Center for Medical AI, Shenzhen Institute of Advanced Technology, Shenzhen, China; [3] University of Macau, Centre for Cognitive and Brain Sciences, Institute of Collaborative Innovation, Macao, China

This work was supported by the Science and Technology Development Fund of Macau (0178/2024/AMJ) and University of Macau (CG2026-FST).

Abstract

Partial volume effects (PVE) degrade quantitative accuracy and blur boundaries in PET. MR-guided partial volume correction (PVC) can mitigate PVE, but it requires anatomical information from MR, which may be unavailable. This work aims to develop a 2-stage deep learning-based PET to MR synthesis framework, SADCA-ResDiff, to provide structural priors for MR-guided PVC in 18F-AV45 amyloid brain PET. A total of 135 pairs of 18F-AV45 PET and MR were selected from ADNI [1]. A coarse MR is first generated from PET using a dual cross-attention UNet, while a residual diffusion network with an edge-aware mechanism is applied to refine the coarse MR. Joint mutual information, diffusion, reconstruction, and structure-aware symmetric consistency losses derived from a pretrained MR segmentation model were used to optimize the 2-stage network. Synthesized MR was segmented into gray matter (GM), white matter (WM), and cerebrospinal fluid masks using FSL [2] and applied to the Iterative-Yang (IY) PVC [3]. SADCA-ResDiff was compared with DeepPVC [4], using standard IY as reference. Structural similarity index (SSIM) and peak signal-to-noise ratio (PSNR) was measured on the whole brain while regional error was evaluated using relative mean absolute error (RMAE) for GM and WM. Wilcoxon signed-rank test was used for statistical comparison.

SADCA-ResDiff achieved the highest SSIM and PSNR among all methods (0.97±0.02 and 32.62±3.43dB), significantly outperforming DeepPVC (0.93±0.02 and 27.95±3.67dB) and origin PET (0.90±0.02 and 26.73±3.89dB) (all $p<0.05$). It also yielded the lowest RMAE in GM and WM (0.12±0.05 and 0.08±0.05), compared with DeepPVC (0.14±0.04 and 0.15±0.03) and origin PET (0.16±0.04 and 0.15±0.03).

SADCA-ResDiff provides effective anatomical guidance for PVC in amyloid PET, offering a practical solution for MRI-free PET quantification.

References

[1] Weiner, et al. "2014 Update of the Alzheimer's Disease Neuroimaging Initiative: a review of papers published since its inception." Alzheimer's & dementia 11.6 (2015): e1-e120.

[2] Jenkinson M, Beckmann CF, Behrens TEJ, Woolrich MW, Smith SM. FSL. *NeuroImage*. 2012;62(2):782–790. doi:10.1016/j.neuroimage.2011.09.015.

[3] Erlandsson, Kjell, John Dickson, Simon Arridge, David Atkinson, Sebastien Ourselin, and Brian F. Hutton. "MR imaging-guided partial volume correction of PET data in PET/MR imaging." *PET clinics* 11, no. 2 (2016): 161-177.

[4] Matsubara, K., Ibaraki, M., Kinoshita, T. and Alzheimer's Disease Neuroimaging Initiative, 2022. DeepPVC: prediction of a partial volume-corrected map for brain positron emission tomography studies via a deep convolutional neural network. EJNMMI physics, 9(1), p.50.

MIC-15-390

A comparison of deep-learning-based attenuation correction methods in brain perfusion SPECT (#1100)

Raúl Osorio Durán[1,2], Gloria A. Adame Ocampo[1], Maria D.L. Martínez Gudiño[1], Mercedes Rodríguez Villafuerte[2], Arnulfo Martínez Dávalos[2]

[1] Instituto Nacional de Psiquiatría, Departamento de Imágenes Cerebrales, CDMX, Mexico; [2] Universidad Nacional Autónoma de México, Instituto de Física, CDMX, Mexico

The work of R. Osorio-Durán has been supported by a Ph.D. scholarship from SECIHTI and a travel grant from PAEP UNAM.

Abstract

A locally developed database of human brain studies from 113 subjects has been used to develop and train convolutional neural networks (CNNs) for attenuation correction in SPECT. All subjects underwent brain perfusion SPECT imaging studies with ^{99m}Tc-ECD, an X-ray CT scan, and MRI. Images were preprocessed for anonymization, removal of the table in CT, co-registration, and spatial and intensity normalization. Deep learning architectures encompassed U-Net, Residual U-Net, Attention U-Net and Residual Attention U-Net. Three methods were evaluated: (a) direct mapping of uncorrected SPECT to corrected SPECT, (b) multisequence MRI scans to synthetic CT (sCT) mapping, followed by iterative reconstruction with sCT attenuation correction, and (c) CNN reconstruction using sinograms to directly generate attenuation-corrected SPECT images. To evaluate the attenuation-corrected images, the mean square error (MSE), peak signal-to-noise ratio (PSNR) and structural similarity index (SSIM) were calculated. Attenuation corrections were successfully applied using three different approaches, addressing various clinical scenarios found in clinical medical equipment that does not have CT for attenuation correction, such as dedicated SPECT or SPECT/MRI.

References

[1] Catafau, A. M. “Brain SPECT in Clinical Practice. Part I: Perfusion”. J Nucl Med. 2001 Feb;42(2):259-71.
[2] Torkaman M. et. al. “Direct Image-Based Attenuation Correction using Conditional Generative Adversarial Network for SPECT Myocardial Perfusion Imaging”. Proc SPIE Int Soc Opt Eng. 2021.
[3] Murata, T. et. al. “Development of attenuation correction methods using deep learning in brain-perfusion single-photon emission computed tomography”. Med Phys. 2021 Aug;48(8):4177-4190.
[4] Ronneberger, O. et. al., “U-Net: Convolutional Networks for Biomedical Image Segmentation”. MICCAI, Springer, LNCS, Vol.9351: 234–241, 2015.
[5] Alom, Z. et. al. “Recurrent Residual Convolutional Neural Network based on U-Net (R2U-Net) for Medical Image Segmentation”. JoCAAA, 33(06), 46–54.
[6] Oktay, O. et. al. “Attention U-Net: Learning Where to Look for the Pancreas”. Preprint at https://doi.org/10.48550/arXiv.1804.03999 (2018).
[7] Kingma, D. P. Ba, J. “Adam: A Method for Stochastic Optimization”. In International Conference on Learning Representations (ICLR), 2015.
[8] Polson, L. A. et. al. “PyTomography: A Python Library for Medical Image Reconstruction”. SoftwareX, Volume 29, 2025, Page 102020.

MIC-15-393

Assisting Total-Body Multiplexed PET Separation Using Synthetic Paired Data (#1368)

Denis Prokopenko, Andrew J. Reader

King's College London, London, UK

This work was funded by the Australian Research Council (ARC) DP230102070.

Abstract

Multiplexed positron emission tomography (mPET) remains limited by the challenge of separating overlapping tracer signals, as tracers produce indistinguishable same-energy photon pairs.

Existing deep learning-based separation methods are constrained by the limited real data availability, particularly in the context of total-body imaging.

In this work, we propose a framework for training total-body dual-tracer mPET separation models using synthetic paired datasets generated from independent single-tracer acquisitions, and investigate the effect of synthetic data diversity on separation performance.

Two score-based generative models were trained to generate synthetic [18F]FDG and [18F]PSMA PET images conditioned on attenuation maps.

Complementary synthetic tracer images were combined with real PET acquisitions to construct paired dual-tracer datasets for training a Swin UNETR-based separation model.

Quantitative evaluation on dual-tracer combinations demonstrated the feasibility of the proposed framework and suggested that increased diversity of synthetic samples may improve separation robustness.

These results highlight the potential of generative augmentation as a scalable strategy for pretraining mPET separation models under limited paired-data availability.

References

[1] Pan, B, Marsden, PK, and Reader, AJ, 2023, “Dual-Tracer PET Image Separation by Deep Learning: A Simulation Study,” Applied Sciences, vol. 13, no. 7, p. 4089.

[2] Pan, B, Marsden, PK, Reader, AJ, 2024, “Kinetic model-informed deep learning for multiplexed PET image separation,” EJNMMI Physics, vol. 11, no. 1, p. 56.

[3] Pan, B, Marsden, PK, Reader, AJ, 2024, “Deep learned triple-tracer multiplexed PET myocardial image separation,” Frontiers in Nuclear Medicine, vol. 4, p. 1379647.

[4] Sanaat, A, Hu, Y, Boccalini, C, Salimi, Y, Mansouri, Z, Teixeira, EPA, Mathoux, G, Garibotto, V, Zaidi, H, 2025, “Tracer-Separator: A Deep Learning Model for Brain PET Dual-Tracer (18F-FDG and Amyloid) Separation,” Clinical Nuclear Medicine, vol. 50, no. 1, pp. 1–10.

[5] Song, Y, Sohl-Dickstein, J, Kingma, DP, Kumar, A, Ermon, S, Poole, B, 2021, “Score-Based Generative Modeling through Stochastic Differential Equations”.

[6] Ho, J, Salimans, T, 2022, “Classifier-Free Diffusion Guidance”.

[7] Song, J, Meng, C, Ermon, S, 2022, “Denoising Diffusion Implicit Models”.

[8] Hatamizadeh, A, Nath, V, Tang, Y, Yang, D, Roth, H, Xu, D, 2022, “Swin UNETR: Swin Transformers for Semantic Segmentation of Brain Tumors in MRI Images”

MIC-15-396

A Multi-Client Split Federated Diffusion Framework for Resource-Efficient Cardiac-Gated MP-SPECT Denoising (#1592)

Chunhao Li[1], Jiangshan Huang[2], Zhenmin Fu[2], Yankun Shi[2], Zhigang Sun[1], Zhuoyuan Xu[1], Yuecan Zeng[3], Huan Xiao[4], Hui Wang[2], Jingzhang Sun[1]

[1] Hainan University, Department of Data Science and Big Data, Haikou, China; [2] Hainan Hospital of Chinese PLA General Hospital, Department of Nuclear Medicine, Sanya, China; [3] The Second Affiliated Hospital of Hainan Medical University, Department of Radiation Oncology, Cancer Treatment Center, Haikou, China; [4] The First Affiliated Hospital of Hainan Medical University, Department of Nuclear Medicine, Haikou, China

This work was supported in part by the National Natural Science Foundation of China (12505396) and the Science and Technology Talents Innovation Project of Hainan Province (KJRC2023D30). Corresponding authors: Jingzhang Sun and Hui Wang.

Abstract

Diffusion models have shown strong potential for cardiac-gated myocardial perfusion single-photon emission computed tomography (CG MP-SPECT) denoising. However, centralized or fully federated diffusion training requires each client to process a complete high-capacity model, which may be impractical for resource-limited nuclear medicine departments. This study presents a multi-client split federated learning diffusion framework (SFLDiff) for resource-efficient CG MP-SPECT denoising. SFLDiff vertically partitions the diffusion network into lightweight client-side encoders and a server-side reconstruction module, enabling local clients to perform shallow feature extraction while computationally intensive generative restoration is executed on the server. This architecture reduced client-side GPU memory consumption from over 4300 MiB to approximately 257 MiB with a training time of 2950.39 s while maintaining competitive denoising performance. Experiments on 8-/16- cardiac gated datasets showed that SFLDiff achieved image restoration accuracy comparable to centralized and federated diffusion baselines and superior to standard split learning, particularly under high-noise gated conditions. These results suggest that multi-client split federated diffusion provides a practical quality–efficiency trade-off for deploying advanced generative denoising models in resource-constrained CG MP-SPECT environments.

References

[1] C. Li *et al.*, "SMGDiff: step mapping generalized diffusion model for efficient noise reduction in cardiac-gated myocardial perfusion SPECT images," *EJNMMI Phys*, vol. 13, no. 1, p. 7, Jan 17 2026.

[2] C. Thapa, P. C. M. Arachchige, S. Camtepe, and L. Sun, "Splitfed: When federated learning meets split learning," in *Proceedings of the AAAI conference on artificial intelligence*, 2022, vol. 36, no. 8, pp. 8485-8493.

MIC-15-399

Weakly Supervised Cyclic Disentanglement for Delayed PET Image Synthesis (#1702)

Zhigang Sun[1], Liqing Fu[2], Chunhao Li[1], Zhuoyuan Xu[1], Qian Wang[1], Yuecan Zeng[3], Huan Xiao[4], Liangqian Tong[2], Jingzhang Sun[1]

[1] Hainan University, Department of Data Science and Big Data, Haikou, China; [2] Haikou Affiliated Hospital of Xiangya Medical College, Department of Nuclear Medicine, Haikou, China; [3] The Second Affiliated Hospital of Hainan Medical University, Department of Radiation Oncology, Cancer Treatment Center, Haikou, China; [4] The First Affiliated Hospital of Hainan Medical University, Department of Nuclear Medicine, Haikou, China

This work was supported in part by the National Natural Science Foundation of China (12505396) and the Science and Technology Talents Innovation Project of Hainan Province (KJRC2023D30).

Abstract

Dual-time-point positron emission tomography (PET) provides complementary temporal uptake information for lesion characterization, but delayed imaging increases examination time and clinical workload. This study proposes UCD-Net, a weakly supervised cyclic disentanglement framework for synthesizing delayed-pass PET from first-pass PET. UCD-Net decompose first-pass PET images into a delayed-equivalent component, a signal-dependent residual component, and a signal-independent residual component, followed by cyclic re-decomposition to improve latent-component separation. Reconstruction, zero-mean, identity-consistency, and noise-statistical constraints are used to preserve image content and suppress residual interference. A three-dimensional projection-excitation module captures global spatial statistics along depth, height, and width to enhance anatomical consistency. Real delayed PET images are incorporated as weak distribution-level guidance through a rank-based consistency loss, allowing the model to better recover delayed uptake patterns without direct image-to-image supervision. This retrospective study included 90 PET scans from 70 patients, including 86 ^{18}F-FDG PET scans and 4 ^{68}Ga-PSMA PET scans, divided into training, validation, and test sets. The weakly supervised UCD-Net was compared with its unsupervised backbone and four baseline models, including EDCNN, CGAN, U-Net, and CVF-SID. Across three test scenarios, the weakly supervised UCD-Net achieved the best performance, with RMSE values of 0.0333, 0.0365, and 0.0236. Compared with unsupervised UCD-Net, weak delayed-image guidance reduced RMSE by 17.2%, 20.8%, and 30.0%. These results suggest that UCD-Net can synthesize delayed-equivalent PET images from first-pass PET and may reduce dependence on additional delayed imaging.

References

[1] R. L. Wahl, H. Jacene, Y. Kasamon, and M. A. Lodge, "From RECIST to PERCIST: Evolving Considerations for PET Response Criteria in Solid Tumors," (in English), *Journal of Nuclear Medicine,* vol. 50, pp. 122s-150s, May 1 2009, doi: 10.2967/jnumed.108.057307.

[2] R. Hong *et al.*, "st-DTPM: Spatial-Temporal Guided Diffusion Transformer Probabilistic Model for Delayed Scan PET Image Prediction," *IEEE Transactions on Radiation and Plasma Medical Sciences,* 2025.

MIC-15-402

Neural Radiance Field-Based Reconstruction of Object Changes in Stationary Computed Tomography with Linearly Distributed Sources

(#1936)

Haoyuan Qian[1], Yongshun Xiao[2]

[1] Tsinghua University, Department of Engineering Physics, Beijing, China; [2] Tsinghua University, Department of Engineering Physics, Beijing, China

This work was supported by Beijing Natural Science Foundation QY25007. I would like to thank Dr. Yongshun Xiao, Associate Professor at Department of Engineer Physics, Tsinghua University, for valuable guidance and support.

Abstract

This research aims to detect and reconstruct object changes using computed tomography (CT). We focus on stationary CT with linearly distributed sources (SLCT), which enables rapid projection data acquisition without mechanical rotation. However, due to the lack of sufficient angular coverage, SLCT inherently suffers from a severely limited-angle imaging problem, where direct reconstruction leads to strong anisotropic artifacts. To address this issue, we introduce the pre-change object as prior knowledge and propose two Neural Radiance Field (NeRF)-based change modeling strategies. The first method, Full-Object Nerf (FO-NeRF), continues optimization from a pre-trained NeRF representing the pre-change object, refining it into the post-change object. The second method, Change-Filed NeRF (CF-NeRF), explicitly models a change field and directly learns the residual component between the pre- and post-change objects. We validate the proposed methods on 2D simulated objects composed of simple geometric shapes. Experimental results demonstrate that, with prior constraints, both methods can successfully reconstruct object changes while effectively mitigating limited-angle artifacts. These results indicate that, by leveraging object priors within a NeRF-based representation, the highly ill-posed limited-angle reconstruction problem can be transformed into a more stable and tractable optimization problem, enabling reliable change detection and reconstruction under severely incomplete projection data.

References

[1] T. Zhang, Y. Xing, L. Zhang, X. Jin, H. Gao, and Z. Chen, “Stationary computed tomography with source and detector in linear symmetric geometry: Direct filtered backprojection reconstruction,” *Medical physics*, vol. 47, no. 5, pp. 2222–2236, 2020.

[2] B. Mildenhall, P. P. Srinivasan, M. Tancik, J. T. Barron, R. Ramamoorthi, and R. Ng, “Nerf: Representing scenes as neural radiance fields for view synthesis,” *Communications of the ACM*, vol. 65, no. 1, pp. 99–106, 2021.

[3] Z. Shen, C. Gong, W. Yu, and L. Zeng, “Guided image filtering reconstruction based on total variation and prior image for limited-angle ct,”*IEEE Access*, vol. 8, pp. 151 878–151 887, 2020.

MIC-15-405

Methods for Reconstruction Aware Completion of Partial PET Sinograms (#2029)

Ziad Burbar, Inki Hong

Siemens Molecular Imaging, Knoxville, USA

Abstract

A partial-detector-ring Positron Emission Tomography (PET) system may be an option to reduce cost and/or enable integration within another modality for multimodality imaging. In some use cases, the PET system may not be able to rotate continuously to collect all lines of response needed to form an image, yet a rapidly available image is still required for image quality control or organ-motion detection when the detectors are stationary. In this setting, missing angular coverage yields incomplete projection measurements and degraded reconstructions. This work describes a learning-based method to generate results equivalent to full-ring acquisition from partial-ring data This work proposes a reconstruction-aware sinogram completion network that predicts a full-ring-equivalent sinogram while enforcing consistency after tomographic reconstruction. This method combines supervision in projection space with an additional image-space objective computed after reconstructing the predicted sinogram using standard PET reconstruction operators, encouraging outputs that both match full-ring sinograms and yield accurate reconstructed images. By incorporating reconstruction consistency, the reconstruction-aware approach is intended to enable partial-ring systems to produce full-ring-equivalent sinograms that can be reconstructed with existing pipelines without modification, supporting more practical imaging workflows when mechanical rotation is constrained.

References

[1] P. Isola, J.-Y. Zhu, T. Zhou, and A. A. Efros, “Image-to-image translation with conditional adversarial networks,” in Proc. IEEE Conf. Comput. Vis. Pattern Recognit. (CVPR), 2017, pp. 1125–1134.

[2] J. Schlemper, J. Caballero, J. V. Hajnal, A. N. Price, and D. Rueckert, “A deep cascade of convolutional neural networks for dynamic MR image reconstruction,” IEEE Trans. Med. Imaging, vol. 37, no. 2, pp. 491–503, Feb. 2018.

[3] T. M. Quan, T. Nguyen-Duc, and W.-K. Jeong, “Compressed sensing MRI reconstruction using a generative adversarial network with a cyclic loss,” IEEE Trans. Med. Imaging, vol. 37, no. 6, pp. 1488–1497, Jun. 2018.

[4] H. Zhang, Y. Yang, M. Wang, Y. Zhang, Y. Liang, and J. Chen, “DuDoNet: Dual domain network for CT reconstruction,” in Proc. IEEE Nucl. Sci. Symp. Med. Imaging Conf. (NSS/MIC), 2018, pp. 1–4.

[5] E. Y. Sidky and X. Pan, “Image reconstruction in circular cone-beam computed tomography by constrained, total-variation minimization,” Phys. Med. Biol., 2008.

[6] K. Hammernik et al., “Learning a variational network for reconstruction of accelerated MRI data,” Magn. Reson. Med., 2018.

MIC-15-408

Symmetry-Enhanced YOLOv11 for Bone Metastatic Lesion Detection in Whole-Body Bone Scintigraphy (#2214)

Fenghua Weng[1], Hanmei Gong[1], Duoduo Li[2], Na Dang[2], Yangshi Lin[3], Gaoyu Chen[4], Yunlong Zan[4], Ying Liang[2], Qiu Huang[1]

[1] Macao Polytechnic University, Faculty of Applied Sciences, Macao, Macau; [2] National Cancer Center/National Clinical Research Center for Cancer/ Cancer Hospital & Shenzhen Hospital, Department of Nuclear Medicine, National Cancer Center/National Clinical Research Center for Cancer/ Cancer Hospital & Shenzhen Hospital, Chinese Academy of Medical Sciences and Peking Union Medical College, Shenzhen, China; [3] Guangxi University of Foreign Languages, School of Digital Technology, Nanning, China; [4] Vplus Technology Ltd., Research and Development Department, Shanghai, China

This work was supported by the Macao Polytechnic University under Grant RP/FCA-10/2025.

Abstract

Automated bone metastasis detection in whole-body bone scintigraphy (WBBS) is often hindered by subtle contrast, scale variation, and physiological interference. We propose an enhanced YOLOv11-based framework incorporating a symmetry-aware representation—utilizing ECC (Enhanced Correlation Coefficient)-registered mirrored images and difference maps—to model pathological asymmetry. To handle multi-scale lesions, we introduce a scale-sensitive architecture featuring a P2 detection branch and Efficient Multi-scale Attention (EMA). Furthermore, an extremity-specific refinement branch and an anatomical cross-view fusion strategy (integrating anterior/posterior projections) are employed to improve sensitivity in limbs and reduce single-view occlusion. Evaluated on 1,800 patient studies, our method achieved 0.959 recall, 0.820 precision and 0.785 mAP50, outperforming YOLOv8 and Faster R-CNN, particularly for small, low-contrast lesions. The exceptionally high recall demonstrates superior sensitivity to small and low-contrast lesions, highlighting the method's potential as a reliable screening tool to minimize missed diagnoses in clinical practice.

References

[1] Davila, D, Antoniou, A and Chaudhry, MA 2015, 'Evaluation of osseous metastasis in bone scintigraphy', *Seminars in Nuclear Medicine*, vol. 45, no. 1, pp. 3–15.

[2] Redmon, J, Divvala, S, Girshick, R and Farhadi, A 2016, 'You only look once: Unified, real-time object detection', *Proceedings of the IEEE Conference on Computer Vision and Pattern Recognition (CVPR)*, pp. 779–788.

[3] Evangelidis, GD and Psarakis, EZ 2008, 'Parametric image alignment using enhanced correlation coefficient maximization', *IEEE Transactions on Pattern Analysis and Machine Intelligence*, vol. 30, no. 10, pp. 1858–1865.

[4] Ouyang, D, He, S, Zhang, G, Luo, M, Guo, H, Zhan, J and Huang, Z 2023, 'Efficient multi-scale attention module with cross-spatial learning', *Proceedings of the IEEE International Conference on Acoustics, Speech and Signal Processing (ICASSP)*, pp. 1–5.

MIC-15-411

HyperAβ: Brain Region Hypergraph Neural Network with Dynamic Margin Loss for Amyloid PET/CT Classification (#2367)

Gan Zhan[1], **Xiaolin Sun**[2], Yulin Yang[5], Qing Zhang[2], Jie Yang[3], Xianchen Liu[4], Tong Ye[3], Zitao Zeng[3], Bingcheng Jiang[3], Lei Jiang[2], Jing Zou[3], Siwei Xie[3]

[1] Shenzhen Bay Laboratory, Institute of Biomedical Engineering, Shenzhen, China; [2] Guangdong Provincial People's Hospital, Department of Nuclear Medicine, Guangzhou, China; [3] Sun Yat-sen University, School of Biomedical Engineering, Shenzhen, China; [4] Florida State University, Tallahassee, USA; [5] Wenzhou University, Metaverse and Artificial Intelligence Institute, Wenzhou, China

This work was supported by grants from Shenzhen Medical Research Fund(A2403021), National Key Research and Development Program of China (2024YFF0727400) and the National Natural Science Foundation of China (82327809).

Abstract

Accurate Aβ PET/CT classification is critical for Alzheimer's diagnosis and anti-amyloid treatment eligibility, yet existing methods struggle to model higher-order inter-regionbrain relationships and handle class imbalance and per-class learning hardness. We propose HyperAβ, which constructs a 30 node brain-region hypergraph over SynthSeg-parcellated multimodal PET/CT features with 10 anatomically-defined hyperedges,and employs hypergraph convolution for higher-order multiregion interaction modeling. To address class imbalance and per-class learning hardness, we introduce GCA-D loss combining static per-class confidence calibration with EMA-based dynamic hardness tracking. Under 5-fold cross-validation, HyperAβ achieves ACC of 0.8784 and AUC of 0.9341, outperforming state of-the-art methods.

References

[1] S.Fan,M.R.Ponisio,P.Xiao, et al., "AmyloidPETNet:Classification of amyloid positivity in brain PET imaging using end-to-end deep learning,"Radiology,vol.311,no.3,2024.

[2] C.Kyobin, J. Jaehoon, L. Sangwon,et al., "Deep learning-basedCT brainparcellationfor amyloidPETanalysis,"Eur. J.Nucl.Med.Mol. Imaging,2025.

[3] C.Cortes,M.Mohri, and Y.Zhong, "Improved balanced classification with theoretically grounded loss functions,"inProc.NeurIPS,2025.

[4] Z.Deng,H.Wang,Z.Huang,etal.,"Brain foundation models with hypergraph dynamic adapter for brain disease analysis,"PatternRecognit., vol.172,2025.

[5] X.Chen,L.Chen,W.Yao, et al., "MR-guided graph learning of 18F-florbetapir PET,"NeuroImage,vol.321,2025.

MIC-15-414

A Wavelet-Enhanced Trajectory-Refined Flow Matching Model for MR-to-CT Synthesis in Nasopharyngeal Carcinoma (#2901)

Yueyu Huang[1], Zijian Zhang[2], Jiayu Da[5], Tao Jiang[4], Ming Yu[4], Lu Qiang[3], Tingting Chen[2], Yuchen He[3], Yifang Li[6]

[1] Shanghai University of Electric Power, College of Electronics and Information Engineering, Shanghai, China; [2] Xiangya Hospital, Department of Radiation Oncology, Changsha, China; [3] The First People's Hospital of Chenzhou, Chenzhou, China; [4] Fudan University, College of Biomedical Engineering, Shanghai, China; [5] ShanghaiTech University, School of Biomedical Engineering, Shanghai, China; [6] Shanghai University, School of Life Sciences, Shanghai, China

Abstract

Nasopharyngeal carcinoma (NPC) is common in southern China, Southeast Asia, and North Africa. Radiotherapy treatment planning (RTP) relies on magnetic resonance (MR) imaging and computed tomography (CT). MR provides superior soft-tissue contrast for target delineation, whereas CT provides electron density information for dose calculation. However, separate acquisition and subsequent registration of MR and CT not only increase time, cost, and radiation exposure, but also introduce registration and dosimetric errors. Diffusion model-based MR-to-CT synthesis offers an efficient, cost-effective, and radiation-free alternative for NPC radiotherapy. However, the nasopharyngeal region has highly complex anatomical structures. As a result, existing methods often fail to preserve anatomical details adequately and may suffer from mode averaging between adjacent slices, reducing slice-specificity and distributional separability. Accordingly, a wavelet-enhanced trajectory-refined flow matching model (WETR-FM) was proposed. A wavelet fusion convolution (WFConv) is introduced to strengthen the extraction of multi-frequency information in the feature space, particularly high-frequency structural details. A wavelet enhanced attention (WE-Attn) module is designed to enhance the network's ability to model critical multi-scale structural features through attention interactions among different frequency components. A trajectory refinement loss (TR loss) is incorporated to enlarge the differences among the denoising trajectories and terminal distributions of different slices. This helps alleviate distributional confusion between adjacent slices, while improving slice-specificity. Experimental results demonstrate that WETR-FM outperformed existing approaches (cycleGAN, sc-cycleGAN, pix2pix, DDPM, FM, SM) in terms of MSE and MAE by more than 35%, and improved by 4%-10% in PSNR. These findings demonstrated promising potential for application in NPC radiotherapy.

References

[1] Q. Liu *et al.*, "Global, regional, and national epidemiology of nasopharyngeal carcinoma in middle-aged and elderly patients from 1990 to 2021," *Ageing Res. Rev.*, vol. 104, p. 102613, 2025.

[2] M. Deng, H. Li, T. Li, Y. Du, and K. He, "Generative Modeling via Drifting," *arXiv preprint arXiv:2602.04770*, 2026.

[3] Y. Lipman, R. T. Chen, H. Ben-Hamu, M. Nickel, and M. Le, "Flow matching for generative modeling," *arXiv preprint arXiv:2210.02747*, 2022.

[4] E. M. Shalby, A. Y. Abdelaziz, E. S. Ahmed, and B. Abd-Elhamed Rashad, "A comprehensive guide to selecting suitable wavelet decomposition level and functions in discrete wavelet transform for fault detection in distribution networks," *Sci. Rep.*, vol. 15, no. 1, p. 1160, 2025.

MIC-15-417

Quantitative Unpaired Low-Dose PET Image Translation with a Poisson-Aware Identity Loss (#2489)

Sihyun Lee[1,2], Raehyun Lee[2], Euiheon Chung[3,1]

[1] Gwangju Institute of Science and Technology, AI Graduate School, Gwangju, South Korea; [2] RMTEC, Gwangju, South Korea; [3] Gwangju Institute of Science and Technology, Department of Biomedical Science and Engineering; AI Graduate School, Gwangju, South Korea

This work was supported in part by the Institute of Information and Communications Technology Planning and Evaluation (IITP) grant funded by the Korea government (MSIT) under Grant 2019-0-01842 (Artificial Intelligence Graduate School Program, GIST), and in part by the Ministry of Oceans and Fisheries (MOF) of the Republic of Korea and the Korea Institute of Marine Science and Technology Promotion (KIMST) under Grant RS-2023-00240908.

Abstract

Reducing positron emission tomography (PET) tracer dose lowers patient radiation exposure but degrades image quality and the quantitative accuracy of standardized uptake values (SUVs). Paired same-subject low/full-dose acquisitions
are impractical to obtain at scale, motivating unpaired image translation. Applying Contrastive Unpaired Translation (CUT)
to ultra-low-dose PET, we identify a quantitative failure mode in which the trained generator improves image appearance but
introduces high-uptake SUV underestimation that can exceed the bias of the unprocessed low-dose input itself. We interpret this
behavior as a mismatch between the fixed residual weighting of the intensity-space ℓ1 identity loss and PET's uptake-dependent
Poisson-derived noise. To address this, we propose PA-CUT (Poisson-Aware CUT), which replaces the ℓ1 identity loss with
one evaluated under the classical Anscombe transform, a Poisson-motivated variance-stabilizing reweighting of the identity term. A
multi-dose training scheme yields a single model across multiple dose reduction factors (DRFs). On the UDPET 2024 challenge
dataset, PA-CUT substantially reduces high-uptake SUV bias compared with CUT, with negligible changes in pixel-level and
perceptual quality.

References
[1] J. Schaefferkoetter et al., "Convolutional neural networks for improving image quality with noisy PET data," EJNMMI Res., vol. 10, art. 62, 2020.
[2] T. Park, A. A. Efros, R. Zhang, and J.-Y. Zhu, "Contrastive learning for unpaired image-to-image translation," in Proc. ECCV, 2020.
[3] F. J. Anscombe, "The transformation of Poisson, binomial and negative-binomial data," Biometrika, vol. 35, pp. 246–254, 1948.

[4] R. Zhang, P. Isola, A. A. Efros, E. Shechtman, and O. Wang, "The unreasonable effectiveness of deep features as a perceptual metric," in Proc. CVPR, 2018, pp. 586–595.
[5] S. Xue et al., "UDPET: Ultra-low dose PET imaging challenge dataset," in Proc. MICCAI, Lecture Notes in Computer Science, vol. 15972. Cham: Springer, 2026.

MIC-15-420

Deep Learning with Physics-Corrected Histo-Images for Robust Low-Dose Scatter Correction on uMI Panorama GS (#2657)

Xu Zhang, Yihang Zhu, Liuchun He, Qing Ye, Yun Dong, Hao Zeng, Hancong Xu

United Imaging Healthcare, Shanghai, China

Abstract

Quantitative accuracy in PET relies heavily on effective scatter correction (SC), especially for long axial field-of-view (LAFOV) systems such as the uMI Panorama GS where low-count scenarios are increasingly prevalent. Conventional SC requires an emission map generated through iterative OSEM reconstruction, which is inherently sensitive to noise and degrades at low doses. Our prior work demonstrated that a deep learning (DL) approach using physics-corrected histo-images achieves high quantitative accuracy for SC under standard-dose conditions [2].

In this work, we extend this framework to low-dose scenarios on the uMI Panorama GS PET/CT system. We collected 220 static ^{18}F-FDG cases and 21 dynamic cases. Low-dose conditions were simulated by randomly downsampling events at seven dose levels (0.1%–100%). A U-Net was trained to predict emission maps from physics-corrected histo-images, with full-dose reconstructions as targets.

At standard dose, both the proposed and conventional methods achieved relative differences below 2% compared with the ground truth. At the 0.1% dose level, the conventional method showed organ VOI deviations approaching 10%, while the proposed method remained below 2% across all dose levels. In dynamic studies, the proposed method preserved time-activity curve accuracy at 0.5% dose and produced reliable Patlak Ki images at 1% dose. Combined with regularized reconstruction, the proposed method enables ultra-low-dose PET data to yield clinically usable images with high quantitative accuracy, demonstrating its potential for low-dose PET applications.

References
[1] Whiteley W et al. FastPET: Near Real-Time PET Reconstruction from Histo-Images Using a Neural Network[J]. IEEE Transactions on Radiation and Plasma Medical Sciences.2021.
[2] X. Zhang et al. Deep Learning with Physics-corrected Histo-Images for Accurate Scatter Correction in Long Axial Field-of-view PET Systems. IEEE-NSS/MIC, 2025.

MIC-15-423

Quantum-Geometric Radiomics Classification of Pancreatic Lesions

(#2704)

Hyeonmin Yang[1], Chul Hee Min[1], Hyun Joon Choi[2], Sangwoon Jeong[2]

[1] Yonsei University, Department of Radiation Convergence Engineering, Wonju, South Korea; [2] Wonju Severance Christian Hospital, Department of Radiation Oncology, Wonju, South Korea

Abstract

This study proposes Quantum Barren-Plateau Correction via Information-theoretic Regularization (QBPCIR), a hybrid quantum-classical architecture for CT radiomics-based pancreatic lesion classification. A parameter-shift-rule diagonal quantum Fisher information matrix (QFIM) estimator quantifies per-class output curvature and adaptively amplifies minority-class gradient contributions to mitigate barren plateau-induced gradient suppression. Evaluated on 1206 training and 71 test portal-venous CT cases with 294 LASSO-selected PyRadiomics features, QBPCIR-VQC achieved AUC 0.916 and recall 0.859, outperforming a classical MLP (AUC 0.846) and a standard VQC (AUC 0.880), and approaching the recall of an expert radiologist reference (0.830). The BCE ablation confirmed that the inter-class Fisher trace asymmetry is a genuine quantum geometric effect, validating the information-theoretic rationale for the proposed correction

References

[1] H. Sung et al., "Global cancer statistics 2020," CA Cancer J. Clin., vol. 71, pp. 209–249, 2021.
[2] P. Lambin et al., "Radiomics," Eur. J. Cancer, vol. 48, pp. 441–446, 2012.
[3] M. Schuld et al., "Circuit-centric quantum classifiers," Phys. Rev. A, vol. 101, Art. no. 032308, 2020.
[4] M. Cerezo et al., "Cost function dependent barren plateaus," Nat. Commun., vol. 12, p. 1791, 2021.
[5] S. L. Braunstein and C. M. Caves, "Statistical distance and geometry of quantum states," Phys. Rev. Lett., vol. 72, pp. 3439–3443, 1994.
[6] J. Wasserthal et al., "TotalSegmentator," Radiol. Artif. Intell., vol. 5, Art. no. e230024, 2023.
[7] J. J. M. van Griethuysen et al., "Computational radiomics system," Cancer Res., vol. 77, pp. e104–e107, 2017.
[8] T. Akiba et al., "Optuna," in Proc. KDD, 2019, pp. 2623–2631.
[9] V. Bergholm et al., "PennyLane," arXiv:1811.04968, 2018.

MIC-15-426

Zero-Shot Vision-Language Refinement for PET-CT Multi-Organ Segmentation (#2885)

Cindy Duan[1], Georgios Krokos[1], Andrew J. Reader[1], David M.L. Lilburn[1,2]

[1] King's College London, School of Biomedical Engineering and Imaging Sciences, London, UK; [2] King's College London, PET Centre, London, UK

C. Duan is funded by the EPSRC, part of the EPSRC DTP, Grant Ref: [EP/W524475/1]

Abstract
Accurate organ segmentation in positron emission tomography (PET) is essential for quantitative analysis, treatment personalisation, and clinical decision-making. In current practice, organ masks are commonly derived from CT using tools such as TotalSegmentator (TS) and transferred to PET directly; however, PET–CT misalignment systematically degrades accuracy and biases downstream functional measurements. PET-native supervised approaches mitigate this misalignment but require costly expert annotation and lack generalisability to unseen organs or acquisition protocols. We propose a zero-shot vision-language refinement framework that adapts CT-derived anatomical priors to PET without any PET-specific training. TS masks are converted into multi-modal prompts for SAM3 — comprising organ bounding boxes, interior positive points, boundary negative points, and organ-specific radiological text descriptions — which are applied independently across axial, coronal, and sagittal views. A Prior-Anchored Refinement Gate (PARG) then constrains each SAM3 prediction by enforcing spatial overlap, area consistency, and eroded-core preservation with respect to the TS prior, suppressing anatomically implausible outputs. Evaluated on 12 held-out oncological PET-CT studies across liver, spleen, and bladder, our zero-shot refinement consistently outperforms TS, improving Dice from 0.744 to 0.835 for bladder, 0.936 to 0.941 for liver, and 0.870 to 0.879 for spleen. Our SAM3 features are further incorporated as auxiliary inputs to supervised training of nnUNet with very limited true labels. The resulting PET+TS+SAM3 configuration achieves Dice of 0.929 (bladder), 0.945 (liver), and 0.886 (spleen) with only eight annotated cases. These results demonstrate that our method effectively corrects PET–CT mismatch and offers a label-efficient, annotation-free pathway towards generalizable PET-CT multi-organ segmentation.

MIC-15-429

Beyond AUC: Decision-Level Discordance and XAI Interpretation of a CBAM-CNN and a Vision Transformer on PET Polar Maps (#2933)

Seyed Mohammadreza Hosseini[1], Anting Li[1], Amin Kazempour[2], Seyed Ehsan Roshan[2,1], Luis E. Juarez-Orozco[3,1], Monire Vatandoust[1], Juhani Knuuti[1], Antti Saraste[1], Teemu Maaniitty[1], Riku Klén[1], Jarmo Teuho[1]

[1] Turku PET Centre, Turku University Hospital and University of Turku, Turku, Finland; [2] Tabriz University, Tabriz, Iran; [3] University MedicalCenter Utrecht, Department of Cardiology, DivisionHeart & Lungs, Utrecht, Netherlands

Abstract
Convolutional neural networks and vision transformers are increasingly applied to medical image classification, yet their comparative decision-making behavior under equivalent aggregate performance remains poorly understood. We trained a convolutional neural network equipped with convolutional block attention modules and a vision transformer from scratch to predict major adverse cardiac events from nitrogen-13 ammonia positron emission tomography myocardial perfusion polar maps in a cohort of 1,079 patients. Across 100 independent training runs, both architectures achieved statistically indistinguishable area under the receiver operating characteristic curve (both 0.90; Wilcoxon signed-rank p = 0.897), yet discordance analysis revealed significantly different binary predictions on specific patients (McNemar p = 0.0013). Using architecture-appropriate explainability methods —

gradient-weighted class activation mapping (the improved variant) for the convolutional network and attention rollout for the vision transformer — we propose a mechanistic hypothesis that the transformer's global self-attention integrates large-territory perfusion defects that the convolutional network's local spatial attention fails to aggregate. These findings demonstrate that equivalence in area under the curve does not imply decision equivalence, and motivate consideration of decision-level discordance when comparing architectures for clinical deployment.

References
[1] Juarez-Orozco, LE, Martinez-Manzanera, O, van der Zant, A et al. 2020, 'Deep learning in quantitative PET myocardial perfusion imaging: A study on cardiovascular event prediction', *JACC Cardiovascular Imaging*, vol. 13, no. 1, pp. 180–182.
[2] Dosovitskiy, A, Beyer, L, Kolesnikov, A, Weissenborn, D, Zhai, X, Unterthiner, T, Dehghani, M, Minderer, M, Heigold, G, Gelly, S, Uszkoreit, J & Houlsby, N 2021, 'An image is worth 16×16 words: Transformers for image recognition at scale', *Proceedings of the International Conference on Learning Representations (ICLR)*.
[3] Woo, S, Park, J, Lee, J-Y & Kweon, IS 2018, 'CBAM: Convolutional block attention module', *Proceedings of the European Conference on Computer Vision (ECCV)*, pp. 3–19, Munich, Germany.
[4] Salih, A, Boscolo Galazzo, I, Gkontra, P et al. 2023, 'Explainable artificial intelligence and cardiac imaging: Toward more interpretable models', *Circulation: Cardiovascular Imaging*, vol. 16, no. 8, p. e014519.

MIC-15-432

Multitracer Conditional Diffusion Model for CT-Less Attenuation Correction in Preclinical PET Imaging (#3096)

Mathieu Vachon[1,5], Alexandre St-Georges[2], Christian Thibaudeau[3], Otman Sarrhini[4], Maxime Gaudreault[2], Roger Lecomte[2,3], Jean-Baptiste Michaud[1,5], University of Sherbrooke, Department of Electrical and Computer Engineering

[1] University of Sherbrooke, Department of Electrical and Computer Engineering, Sherbrooke, Canada; [2] University of Sherbrooke, Department of Medical Imaging and Radiation Sciences, Sherbrooke, Canada; [3] Imaging Research & Technology, Sherbrooke, Canada; [4] Sherbrooke Molecular Imaging Center, Sherbrooke, Canada; [5] Institut Interdisciplinaire d'Innovation Technologique, Sherbrooke, Canada

We thank our colleagues from the Molecular Imaging Center and Dr. Christophe Carpentier for sharing the preclinical data used in this study

Abstract
Accurately quantifying radiotracer uptake and metabolic activity in a subject using positron emission tomography (PET) requires correcting for photon attenuation. An attenuation map, typically produced using a second imaging modality, is required for attenuation correction but can increase radiation exposure, operational costs, and reconstruction complexity. To mitigate these drawbacks, methods for generating attenuation maps from the non-attenuation-corrected (NAC) PET image using deep neural networks were proposed. Preclinical PET images of small animals present additional challenges for artificial attenuation map generation because the attenuation is low and the subjects are not rigid bodies, making anatomical structures less consistent and more prone to artifacts. A conditional Denoising Diffusion Probabilistic Model (cDDPM) was implemented to generate attenuation maps from NAC PET images. The model was preliminarily trained on approximately 60 paired NAC PET and CT images acquired on the LabPET8 scanner. The dataset consisted of mouse whole-body and body-without-head scans

obtained with two radiotracers: ^{18}F-FDG, and ^{11}C-acetate. Preliminary slice-level evaluation showed that the generated pseudo-CT images were visually consistent with the reference CT images and preserved the main anatomical structures in the evaluated regions. The generated pseudo-CT images achieved a structural similarity index measure (SSIM) of 0.991, a mean squared error (MSE) of 4.47×10^{-5} and a mean absolute error (MAE) of 8.51. These preliminary results suggest the feasibility of cDDPM-based pseudo-CT generation for preclinical PET attenuation correction, although full-volume validation and PET reconstruction studies using the generated attenuation maps are still required. Full results for more tracers and scanners will be presented at the conference.

References
[1] St-Georges, A et al. 2025, 'CT-less attenuation correction using multiview ensemble conditional diffusion model on high-resolution uncorrected PET images', *arXiv preprint arXiv:2510.24805*, arXiv.
[2] Chen, X & Liu, C 2023, 'Deep-learning-based methods of attenuation correction for SPECT and PET', *Journal of Nuclear Cardiology*, vol. 30, no. 5, pp. 1859–1878, Springer, doi: 10.1007/s12350-022-03007-3.
[3] Tétrault, M-A et al. 2006, 'System integration of the LabPET small animal PET scanner', *2006 IEEE Nuclear Science Symposium Conference Record*, pp. 1880–1884, San Diego, CA, USA: IEEE, doi: 10.1109/NSSMIC.2006.354260.

MIC-15-435

Joint Self-Collimation Compton SPECT for Wide-Energy and High-SNR Imaging (#2)

Peize Li[1], Linxin Lei[1], Xingchun Zheng[1], Zhenlei Lyu[1], Rutao Yao[2], Tianyu Ma[1]

[1] Tsinghua University, Department of Engineering Physics, Beijing, China; [2] University at Buffalo SUNY, Department of Radiology, Jacobs School of Medicine & Biomedical Sciences, Buffalo, USA

Abstract

Mechanical collimators enforce a strict resolution-sensitivity trade-off, necessitate hardware exchanges for wide-energy imaging, and suffer from poor high-energy performance due to septal penetration. We propose Joint Self-Collimation Compton (JSCC) SPECT as a wide-energy solution using a multi-layer stochastic mosaic detector. JSCC integrates geometric constraints with Compton kinematics to screen pathways and suppress artifacts. Cylindrical-coordinate-based fast modeling accelerates volumetric reconstruction. Simulations using Hot-rod, Contrast, and Hoffman phantoms demonstrate that JSCC achieves a significantly superior signal-to-noise ratio compared to parallel-hole SPECT. At 511 keV, JSCC resolves 16-mm and 10-mm rods in 2-minute and 20-minute scans, outperforming the baseline (22-mm and 16-mm). At 140 keV, it resolves 9-mm rods in 30 seconds without hardware modification. These results demonstrate the potential of JSCC as a wide-energy, high-SNR SPECT imaging paradigm for next-generation molecular imaging and theranostic applications.

References
[1] T, Ma et al. 2021, 'Self-Collimating SPECT With Multi-Layer Interspaced Mosaic Detectors', IEEE Transactions on Medical Imaging, 40(8), 2152-2169
[2] Siemens Healthineers 2010, 'Symbia T Series SPECT/CT Specification Sheet', Siemens Medical Solutions, URL: https://marketing.webassets.siemens-healthineers.com/1800000001977049/5df0aa45b817/symbia-t-spec-sheet-2010_1800000001977049.pdf

MIC-15-438

A Robot-Assisted SPECT Platform for Adaptive Functional Imaging using Non-Conventional Trajectories (#1192)

Lorenzo Confalonieri[1,2], Luca Pezzotti[1], Farshid Alambeigi[1,2], Elena Maria Zannoni[1,2]

[1] The University of Texas at Austin, Walker Department of Mechanical Engineering, Austin, USA; [2] Texas Robotics, Austin, USA

We acknowledge the Rising Faculty Science and Technology Acquisition and Retention (STARs) Program, The University of Texas System, for the generous support and the NIH National Institute of Biomedical Imaging and Bioengineering (grant R21EB037274-01A1) as funding agency.

Abstract

The growing integration of robotics in medical imaging applications [1], the maturation of high-resolution room temperature semiconductor detectors, and the push towards safe, cost-effective and easy-to-use imaging platforms [2], motivates the development of a robotic SPECT system designed to overcome the inherent limitations of traditional platforms. The high flexibility of the robot enables acquisition trajectories not attainable with standard gantry-based systems, practically implementing the concept of adaptive SPECT [3].

We propose a system based on a collaborative 7-degrees-of-freedom robot, a CZT detector panel, a custom-designed multi-pinhole tungsten collimator, a LiDAR sensor for environment awareness, and a 3D structured light camera for object localization and occupancy.

Inverse kinematics and Bidirectional Rapidly exploring Random Trees are used for determining the robot configurations and collision-free movement. Energy calibration of the detector shows a FWHM of 4.94 keV at 122 keV, and an energy range up to 380 keV, suitable for imaging of most clinical and theranostics radiotracers. Integration of a LiDAR sensor and a 3D structured light camera shows high precision in object detection ($AP_{0.5}$>0.90) and point cloud stitching via Eye-in-Hand calibration.

Noisy Jaszczak phantom simulations show that robot-enabled spherical acquisition outperforms standard cylindrical scanning, yielding better metrics at the minimum NRMSE iteration: NRMSE improved by 18%, the peak-to-valley ratio for the 6.4 mm rods increased of 55.3%, and the average contrast-to-noise ratio and contrast recovery coefficient increased by 5.1% and 5.3%, respectively, with maximum gains over 13% for the smallest sphere.

References

[1] S. E. Salcudean, H. Moradi, D. G. Black and N. Navab, "Robot-Assisted Medical Imaging: A Review," in Proceedings of the IEEE, vol. 110, no. 7, pp. 951-967, July 2022, doi: 10.1109/JPROC.2022.3162840.

[2] H. Hricak et al., “Medical imaging and nuclear medicine: a Lancet Oncology Commission,” in The Lancet Oncology, vol. 22, no. 4, pp. e136–e172, Apr. 2021, doi: 10.1016/S1470-2045(20)30751-8.

[3] H. H. Barrett et al., "Adaptive SPECT," in IEEE Transactions on Medical Imaging, vol. 27, no. 6, pp. 775-788, June 2008, doi: 10.1109/TMI.2007.913241.

MIC-15-441

Estimating ejection fractions from standard of care F18-FDG PET/CT: a feasibility study (#1487)

Zoe Wilson[1,2], Floris P. Jansen[3], Kevin M. Bradley[4], Robert Johnsen[3], Kuan-Hao Su[3], Daniel R. McGowan[1,2]

[1] University of Oxford, Oncology Department, Oxford, UK; [2] Oxford University Hospitals NHS Foundation Trust, Department of Medical Physics and Clinical Engineering, Oxford, UK; [3] GE HealthCare, Chicago, USA; [4] University Hospital of Wales, Wales Research and Diagnostic Positron Emission Tomography Imaging Centre, Cardiff, UK

This work was supported by the COMPASS project (Grant Agreement No. 101253264).

Abstract

For patients undergoing cardiotoxic cancer therapies, baseline cardiac function is assessed using echocardiography to calculate left ventricle ejection fractions (LVEFs). At many sites, this requires additional patient visits and could delay treatment as use of these therapies increases. We investigate whether LVEF can be automatically derived from routine ^{18}F-fluorodeoxyglucose (FDG) PET/CT scans acquired on a high-sensitivity Omni Legend scanner. Our retrospective study of FDG PET lymphoma scans (n=437) was organised into three complementary cohorts addressing gating validity, preliminary clinical comparison, and real-world applicability. In 5 electrocardiogram(ECG)-gated PET/CT scans, algorithm-generated triggers showed strong agreement with ECG triggers, with standard deviation trigger shift < 0.03. Of patients with ground truth echocardiograms (n=5), algorithm-derived LVEFs showed good agreement with echocardiography (mean absolute error = 5.1%), within the clinically accepted range for echocardiographic reporting variability (10%). Across the full dataset, sufficient myocardial uptake for heart localization and edge detection was observed in 153/437 cases (35.0%), while 207/437 (47.4%) lacked sufficient uptake despite successful algorithm execution. This cohort data suggests the potential for automatic LVEF estimation for one third of patients. Future work will investigate pipeline improvements such as refining the basal plane localisation to enable a LVEF estimation for a greater proportion of patients. Overall, these preliminary results indicate the potential for FDG PET derived LVEF with good ECG gating agreement and acceptable early agreement against echocardiographic reference values. Ongoing analysis of ground truth EFs will further evaluate classification of abnormal LVEF (< 50%) and establish myocardial uptake thresholds to guide clinical applicability.

MIC-15-444

Experimental validation of inter-crystal scatter recovery using forward Compton kinematics and polarization correlations in PET imaging

(#2032)

Mihael Makek[1], Tomislav Bokulić[1], Ana Marija Kožuljević[2], Siddharth Parashari[3], Luka Pavelić[2]

[1] University of Zagreb Faculty of Science, Department of Physics, Zagreb, Croatia; [2] Institute for Medical Research and Occupational Health, Zagreb, Croatia; [3] Instituto de Fisica Corpuscular, Valencia, Spain

This work was supported by the Croatian Science Foundation under the project numbers IP-2022-10-3878 and PZS-2019-02-5829, and by the European Union – NextGenerationEU through the National Recovery and Resilience Plan 2021-2026 Institutional grants of University of Zagreb Faculty of Science (ProPubFO).

Abstract

Compton scatter of gamma-rays within detector elements, denoted as inter-crystal scatter events, has been considered a resource for sensitivity improvement in PET imaging. The obstacle for their exploitation has been the resolution and contrast degradation due to inclusion of these events, related to the lack of knowledge of the first interaction position. We studied inter-crystal scatter events experimentally using a modular system based on single-end readout modules, also able to perform Compton polarimetry. Two modules comprising 16 x 16 GAGG:Ce scintillator matrices read out by silicon photomultipliers were mounted on a rotating gantry with 430 mm diameter. Two types of events were selected: (i) with a single pixel firing in one module and a two-pixel hit with forward Compton kinematics in the opposite module, and (ii) two-pixel Compton events in both modules with a pronounced polarization correlation. We imaged Ge-68 rod sources, and a NEMA NU-4 phantom with a Ga-68 solution. They results show that the statistics increases by 18 % using (i) and by an extra 8 % when adding (ii), compared to pure single-pixel events. At the same time, the inclusion of the selected inter inter-crystal scatter events has a marginal effect on image resolution (central field-of-view), shifting it from 2.5 +/- 0.1 mm (FWHM) for the single pixel events, to 2.7 +/- 0.2 mm (FWHM) for the combined sample, while the signal-to-noise and contrast-to-noise values are moderately increased. This validates the use of the inter-crystal scatter events for improved sensitivity and image quality in PET.

References

[1] Lee, MS, Shim, HS, Lee, JS, 2024, 'Strategies for mitigating inter-crystal scattering effects in positron emission tomography: a comprehensive review', *Biomed. Eng. Lett.* 14, 1243–1258

[2] Makek, M et al., 2020, 'Single-layer Compton detectors for measurement of polarization correlations of annihilation quanta', *Nucl. Instrum. Methods Phys. Res. A*, vol. 958, pp. 162835

[3] Kožuljević, AM et al., 2024, 'Investigation of the spatial resolution of PET imaging system measuring polarization-correlated Compton events', *Nucl. Instrum. Methods Phys. Res. A*, vol. 1068, pp. 169795

[4] Kožuljević, AM et al., 2025, 'Towards polarization-enhanced PET: Study of random background in polarization-correlated Compton events', *Physica Medica*, vol. 145, pp. 105780

[5] Parashari, S et al., 2022, 'Optimisation of detector modules for measuring gamma-ray polarization in Positron Emission Tomography', *Nucl. Instrum. Methods Phys. Res. A*, vol. 1040, pp. 167186

[6] Makek, M et al., 2022, 'Development of the Quantum-PET Demonstrator', *Proc. IEEE Nucl. Sci. Symp. Med. Imag. Conf.*, pp. 1--3

[7] Wettenhovi, V et al., 2021, OMEGA - open-source emission tomography software', *Phys. Med. Biol.*, vol., pp. 065010

MIC-15-447

Development of a Dual-Modality Imaging Capsule for Laparoscopic Radio-Guided Surgery (#2174)

Krishan Patel[1], Lorenzo Confalonieri[1], Susie Huh[2], Matthew Wilson[3], Diana Caprotti[3], Naruhiko Ikoma[4], Elena M. Zannoni[1,5]

[1] The University of Texas at Austin, Walker Department of Mechanical Engineering, Austin, USA; [2] The University of Texas at Austin, Department of Biomedical Engineering, Austin, USA; [3] Rutherford Appleton Laboratory, Science and Technology Facilities Council, Didcot, UK; [4] MD Anderson Cancer Center, Department of Surgical Oncology, Houston, USA; [5] The University of Texas at Austin, Department of Diagnostic Medicine, Austin, USA

We thank the Cancer Prevention & Research Institute of Texas (grant # RP240462) and the 2024 Mitzi & William Blahd MD Pilot Research Grant, The Education and Research Foundation for their generous support.

Abstract

Minimally-invasive radio-guided surgery requires simultaneous functional nuclear guidance and anatomical visualization to enable precise intraoperative localization of radiolabeled targets [1]. We propose a dual-modality imaging drop-in capsule designed for deployment through a standard 15-mm laparoscopic trocar. It consists of a 2-mm thick semiconductor detector with a sub-millimeter pixel pitch [2,3], a custom lofthole collimator embedded within a 3D-printed tungsten capsule, and two miniaturized stereoscopic micro-cameras.

Preliminary results show: real-time 3D depth maps validated against an ultrasonic distance sensor; a seamless 360° panoramic view stitched from sequential frames using cylindrical warping and multi-band Laplacian blending [4,5]; spectral localization of multiple isotopes ^{57}Co and ^{241}Am within a scattering biological medium; and a preliminary 2D co-registration overlaying the functional dataset onto the anatomical scene. We will present the system design and components, and discuss the steps towards a fully integrated prototype for laparoscopic radio-guided surgery.

References

[1] I. Boekestijn et al., “The current status and future prospects for molecular imaging-guided precision surgery,” Cancer Imaging, vol. 22, Art. no. 48, 2022.

[2] R. Ballabriga, M. Campbell, and X. Llopart, “An introduction to the Medipix family ASICs,” Radiat. Meas., vol. 136, Art. no. 106271, 2020.

[3] L. Jones, P. Seller, M. Wilson, and A. Hardie, “HEXITEC ASIC—a pixellated readout chip for CZT detectors,” Nucl. Instrum. Methods Phys. Res. A, vol. 604, no. 1–2, pp. 34–37, 2009.

[4] M. Brown and D. G. Lowe, “Automatic panoramic image stitching using invariant features,” Int. J. Comput. Vis., vol. 74, no. 1, pp. 59–73, 2007.

[5] R. Szeliski, “Image alignment and stitching: A tutorial,” Found. Trends Comput. Graph. Vis., vol. 2, no. 1, pp. 1–104, 2006.

MIC-15-450

Development of a High Sensitivity Cascade Gamma Photon Coincidence Imaging System (#2224)

Qingyang Wei[1], Yangyang Zhao[1,2], Kui Wang[1], Zijun Yan[1], Shuyu Xu[1], Xiangbao Zhou[1], Jiaxin Dang[1], Hao Jia[3], Hanshen Ye[4], Zhongbin Hang[5], Wenjie Huang[2], Zheng Gu[2], Hui Liu[6], Jing Wu[4], Yaqiang Liu[6], Zuoxiang He[5]

[1] University of Science and Technology Beijing, Beijing Engineering Research Center of Industrial Spectrum Imaging, School of Automation and Electrical Engineering, Beijing, China; [2] Shenzhen Bay Laboratory, Institute of Biomedical Engineering, Shenzhen, China; [3] Tsinghua University, School of Biomedical Engineering, Beijing, China; [4] Beijing Normal University, Center for Advanced Quantum Studies, School of Physics and Astronomy, Beijing, China; [5] Beijing Tsinghua Changgung Hospital, Department of Nuclear Medicine, Beijing, China; [6] Tsinghua University, Department of Engineering Physics, Beijing, China

This work was supported in part by the National Key Research and Development Program of China under Grant 2022YFC2402001, National Natural Science Foundation of China (Grant Number:12375337) and Beijing Natural Science Foundation (Grant Number: L232126).

Abstract

Lutetium-177 (^{177}Lu) is one of the most representative radionuclides in integrated nuclear medicine theranostics. To image ^{177}Lu, we have developed a full-ring, high-sensitivity cascade gamma photon coincidence imaging system. This work presents the system construction and preliminary performance evaluation.

The detector ring consists of 40 continuous $LaBr_3$ crystal modules arranged in 10 radial × 4 axial configuration (each 50 × 50 × 6 mm³). The inner diameter of the ring is 110 mm, with axial module spacing of 60 mm. Each crystal is coupled to four MPPC arrays and read out via PETsys FEM256 electronics, with three FEB/D boards and one DAQ for data acquisition. Both the ASICs and MPPCs are cooled by a water-cooling system, maintaining water at 8 °C and ASIC temperature below 20 °C.

The collimator assembly comprises 10 tungsten plates (26 × 128 × 8 mm³), each covering four axial detector modules. Plates are arranged alternately with pinholes and slits (1 mm), placed at a vertical distance of 36.5 mm from the ring center, creating an imaging field of Φ30 × 30 mm. The prototype hardware has been fully assembled and is capable of normal data acquisition.

Simulation results indicate a coincidence sensitivity of 2.97 × 10^{-5} at the central field of view, spatial resolution of ~1.7 mm, and hot cylindrical object resolution up to 1.2 mm. Preliminary experimental tests have validated the feasibility of the system. Ongoing optimization includes crystal position calibration, energy resolution improvement, and collimator geometry alignment. The full system performance evaluation is expected to be completed before the upcoming conference.

References

[1] Liu X, Liu H, Cheng L, et al. A 3-dimensional stationary cascade gamma-ray coincidence imager. Physics in Medicine & Biology. 2021 66(22):225001

[2] Xu S , Wei Q, Ding D, et al. *Cascade Gamma Photon Coincidence Imaging System: a Simulation Study*. IEEE NSS/MIC RTSD, 2023

[3] Zhao Y, Zhou X, Huang W, et al. Performance Evaluation of a TOFPET2 ASIC-Readout $LaBr_3$(Ce) Monolithic Detector for Cascade Gamma-Ray Coincidence Imaging System. IEEE NSS/MIC RTSD, 2025

[4] Jia H, et al. Multi-GPU-Based Ultra-Fast and High-Precision Reconstruction Algorithm for a Full-Ring Cascade γ Coincidence Imaging System,IEEE NSS/MIC RTSD, 2025

MIC-15-453

Development of High-Time Resolution Ring-Type GFAG Pixel Detector System for pH Sensing via Time-Differential Perturbed Angular Correlation (#2325)

Mizuki Uenomachi[1], Boyu Feng[2], Macoto Fujimoto[2], Koki Nakamura[2], Kenji Shimazoe[2]

[1] Institute of Science Tokyo, Institute of Integrated Research, Tokyo, Japan; [2] The University of Tokyo, School of Engineering, Tokyo, Japan

This work was supported by JST, PRESTO (Grant Number JPMJPR23F1).

Abstract

Positron emission tomography and single photon computed emission tomography are widely used nuclear medicine modalities. These modalities provide information on physiological and metabolic functions by visualizing radiotracer distributions. However, they cannot obtain local information, such as intermolecular interactions, pH, and other microenvironmental factors. We have proposed and demonstrated a novel nuclear medicine imaging and quantum sensing method utilizing the characteristics of cascade radionuclides. For imaging, the coincidence detection of cascade gamma rays enables localization of the source position using directional detectors. For sensing, changes in angular correlation between cascade gamma rays provide local information, such as pH [1]. In our previous studies, angular distribution information was used as an indicator of angular correlation changes because the time resolution of measurement system of approximately 50 ns was insufficient for time-differential perturbed angular correlation analysis. In this study, we developed the improved time resolution of the measurement system using GFAG pixel scintillator detectors, originally designed 64-channel slew rate limited time-over-threshold integrated application specific intesgrated circuits, [2] and 62.5 ps sampling data acquisition systems [3]. The time-dependent perturbation factor exhibited pH-dependent decay behavior consistent with a previous study [4], with slower decay at low pH and faster decay at higher pH. In addition, ^{111}In-labeled OctreoScan showed different after-effect behavior from aqueous $^{111}InCl_3$ solutions, suggesting that time-differential analysis provides information beyond integrated angular distribution measurements. We will incorporate the time-differential perturbed angular correlation analysis into double-photon coincidence imaging and investigate its potential for nuclear medicine application.

References

[1] K. Shimazoe et al., ‘Imaging and sensing of pH and chemical state with nuclear-spin-correlated cascade gamma rays via radioactive tracer’, *Commun, Phys.*, **5**(1), 24, (2022)

[2] T. Orita et al., 'Time and Energy Resolving Time-over-Threshold ASIC for MPPC module in TOF-PET system (ToT-ASIC2)', *JINST*, **18**(09), P09033, (2023)

[3] S. Sato et al., 'Development of multichannel high time resolution data acquisition system for TOT-ASIC', *IEEE Trans. Nucl. Sci.*, **68**(8), 1801-1806, (2021).

[4] G. R. Demille, et al., 'PAC Studies of ‘^{111}In Binding to Transferrin, Tropolone and Acetylacetone in Aqueous Solutions', *Chem Phys Lett*, **44**(1), 164-16, (1976),

MIC-15-456

Quantum entanglement of annihilation photons as a function of the annihilation mechanism (#2454)

Deepak Kumar[1,2], Sushil Sharma[1,2], Pawel Moskal[1,2]

[1] Jagiellonian University, Faculty of Physics, Astronomy and Applied Computer Science, Krakow, Poland; [2] Jagiellonian University, Center of Theranostics, Krakow, Poland

Supported by the National Science Centre of Poland (grants no. 2021/42/A/ST2/00423, 2021/43/B/ST2/02150, 2023/50/E/ST2/00574, 2024/53/N/ST2/04279) and ERC Advanced Grant No. 101199807. Computing resources were provided by PLGrid, Grant no. PLG/2024/017688 and PLG/2025/018762.

Abstract

In matter, a positron annihilates with an electron into two photons through several mechanisms, including direct annihilation and the formation of positronium, a metastable bound state that exists as either para-positronium or ortho-positronium. Each channel has a characteristic lifetime, allowing their contributions to be distinguished in time. The two photons are predicted to be entangled in their polarizations [1], and recent measurements indicate that the degree of entanglement depends on the annihilation channel [2]. In particular, the ortho-positronium decay is sensitive to the local concentration of molecular oxygen, and can serve as a probe of tissue hypoxia in PET imaging [3]. The Jagiellonian Positron Emission Tomograph is a scanner built from plastic scintillators, in which 511 keV photons interact predominantly through Compton scattering [4]. The Compton scattering plane of each photon is correlated with its polarization. We measure annihilations of positrons emitted by a sodium-22 source embedded in porous polymer. Sodium-22 emits a positron accompanied by a 1274 keV prompt photon, which provides a time reference for the positron lifetime. The polarization correlation distribution of the annihilation photon pairs is consistent with quantum entanglement, between the limits for maximally entangled and classically separable states [2]. Selecting events by positron lifetime reveals distinct polarization correlation distributions for different annihilation channels. A detailed comparison will be presented at the conference. These results motivate quantum-informed PET imaging, with tissue hypoxia as a clinical biomarker.

References

[1] Pryce, M.L.H., Ward, J. C. 1947,'Angular correlation effects with annihilation radiation', Nature, vol. 160, p. 435.

[2] Moskal, P. et al. 2025, 'Nonmaximal entanglement of photons from positron-electron annihilation demonstrated using a novel plastic PET scanner', Sci. Adv., vol. 11, no. 18, eads3046.

[3] Moskal, P. 2026, 'Quantum Entanglement Degree, Mean Positronium Lifetime, and the 3γ/2γ Annihilation-Rate Ratio as Novel PET Biomarkers for Hypoxia – Concept, Challenges, and Predictions', Bio-Algorithms and Med-Systems, vol. 22, no. 1, p. 56.

[4] Moskal, P. et al. 2024, 'Positronium image of the human brain in vivo', Science Advances, vol. 10, no. 37, p. eadp2840.

MIC-15-459

First In-Vivo Positronium Ratio Imaging (PRI) using F-18 FDG: A Preliminary Study with Phantom and a Mouse Model (#2615)

Macoto Fujimoto[1], Koki Nakamura[2], Riku Sato[1], Peter Caradonna[2], Ayaka Ostuka[1], Seiichi Ohta[1], Mizuki Uenomachi[3], Laura Stephenson[4], Archie Montgomery[4], Daniel P. Watts[4], Kenji Shimazoe[1,2]

[1] The University of Tokyo, Department of Bioengineering, Bunkyo, Japan; [2] The University of Tokyo, Department of Nuclear Engineering and Management, Bunkyo, Japan; [3] Institute of Science Tokyo, Laboratory for Zero-Carbon Energy, Meguro, Japan; [4] University of York, School of Physics, Engineering and Technology, York, UK

Abstract

This research presents the development and first in-vivo demonstration of Positronium Ratio Imaging, a novel functional imaging technique that uses the three-photon to two-photon decay ratio of positronium. While conventional Positron Emission Tomography primarily maps radiopharmaceutical distribution, Positronium Ratio Imaging provides insights into the tissue microenvironment by exploiting the sensitivity of ortho-positronium to local oxygen levels and morphology. We characterized the system's geometric stability using a four-rod phantom with varying dimensions and evaluated the results against Monte Carlo simulations using the Geant4 toolkit. The phantom study identified a size-dependent uncertainty baseline of approximately twenty percent, primarily arising from detector sensitivity and geometric factors. Furthermore, we achieved the first in-vivo ratio imaging using a tumor-bearing mouse model administered with fluorine-18 fluorodeoxyglucose. Quantitative analysis revealed that the three-photon to two-photon ratio in brown adipose tissue was approximately two and a half times higher than in the heart and bladder. This significant contrast is consistent with theoretical trends derived from tissue-specific positronium lifetimes and far exceeds the established hardware-induced uncertainty. These findings validate the feasibility of using standard positron emitters for functional three-photon imaging without the need for specialized prompt-gamma emitters. Future work will focus on refining quantitative calculation methods, evaluating signal-to-noise ratios, and implementing hardware-specific calibrations to enhance absolute quantification. This technology lays a foundation for clinical applications such as the non-invasive visualization of tumor hypoxia and metabolic characterization of the tissue microenvironment, offering a breakthrough in functional molecular imaging.

References

[1] Moskal, P, et al. 2019, ‘Feasibility study of the positronium imaging with the J-PET tomograph’, Phys. Med. Biol., vol. 64, no. 5, 055017, Bristol: IOP Publishing.

[2] Mercolli, L, et al. 2024, ‘In Vivo Positronium Lifetime Measurements with Intravenous Tracer Administration and a Long Axial Field-of-View PET/CT’ (Preprint)

[3] Moskal, P, et al. 2024, ‘Positronium image of the human brain in vivo’, Sci. Adv., vol. 10, no. 2, eadj2840, Washington, D.C.: American Association for the Advancement of Science.

[4] Fujimoto, M, Shimazoe, K, et al. 2025, ‘Advancing PET through Direct Imaging of Three-Photon Decay using Pure Positron Emitters’, Communications Physics (Under Review), (Preprint)

MIC-15-462

Ortho-Positronium Lifetime Measurements from Pile-up Single Events

(#2939)

José A. Avellaneda[1], Sara Gaitán Dominguez[1], Victor Martínez Nouvilas[1], Eduardo Romero-Sanz[3], Marta Oteo Vives[3], Miguel Ángel Morcillo[3], Jose Udias[1], Luis M. Fraile[2,1], Joaquín López Herraiz[1]

[1] Universidad Complutense de Madrid, Grupo de física nuclear & EMFTEL & IPARCOS, Madrid, Spain; [2] CERN, ISOLDE, Geneva, Switzerland; [3] CIEMAT, Unidad de aplicaciones médicas de la radiación ionizante, Madrid, Spain

This work was supported by grants Prototwin Project (TED2021-130592B-I00) and Tecnologías Avanzadas para la Exploracíon del Universo y sus Componentes" (PR47/21 TAU-CM TAU-PRTR), funded by EU Resilient and NextGeneration funds. José A. Avellaneda received support in the form of FPI Predoctoral Grant (CT85/23) funded by the autonomous community of Madrid.

Abstract

Positronium annihilation lifetime spectroscopy (PALS) has recently attracted considerable interest as a potentially sensitive tool for tissue characterization. In standard PALS experimental setups, at least two detectors are needed to provide start and stop signals for positron emission and annihilation creation. However, due to the isotropic nature of prompt-gamma emission, in a very significant fraction of events, both prompt and annihilation photons are detected in the same detector, resulting in a pileup event. In this work, we propose using these pile-up events to simplify o-Ps lifetime estimation workflows,
enabling estimation with a single detector. Using a 22Na source sample, we successfully measured the o-Ps lifetime using both standard coincidence PALS and the proposed approach with excellent agreement (1.88±0.04 and 1.90±0.07 ns). Measurements of o-Ps lifetime in an isopropanol-based liquid using 44Sc, as well as in ex-vivo biological samples from mice (liver and plasma) after a PET acquisition using 52Mn, were also obtained. These results demonstrate the feasibility of single-detector o-Ps measurement and open new lines of research, by facilitating the characterization of samples from PET studies.

References
[1] Hourlier et al. Experimental uses of positronium and potential for biological applications. IEEE Trans. Radiat. Plasma Med. Sci., 2024.
[2] Sodai et al. Positronium lifetime measurement using a clinical pet system for tumor hypoxia identification. NIM Phys. Res. A, August 2024
[3] Avachat et al. Ortho-positronium lifetime for soft-tissue classification. Scientific Reports, 14(1), 2024.
[4] Dulski et al. The j-pet detector—a tool for precision studies of ortho-positronium decays. NIM Phys. Res. A, 1008:165452, August 2021.
[5] Avellaneda et al. Mltiming: Pairwise-constrained learning for improving timing resolution in tof-pet. IEEE Trans. Radiat. Plasma Med. Sci., 2026.

MIC-15-465

Quantitative 4D PET Imaging of Photosynthate Transport and Rhizosphere Carbon Partitioning in Intact Plant–Soil Systems (#3049)

Muhammad Nasir Ullah[1], Daniel Hastings[2], David Anders[1], Weixin Cheng[2], Shiva Abbaszadeh[3], Craig S. Levin[4,1]

[1] Stanford University, Department of Radiology and Molecular Imaging Program at Stanford ((MIPS)), stanford, USA; [2] University of California Santa Cruz, Department of Environmental Studies, Santa Cruz, USA; [3] University of California Santa Cruz, Electrical and Computer Engineering, Santa Cruz, USA; [4] Stanford University, Departments Physics, Electrical Engineering, and Bioengineering, Stanford, USA

This work was supported by the U.S. Department of Energy, Office of Science, Office of Biological & Environmental Research, under Award Numbers DE-SC0021975 and DE-SC0024712. The authors also acknowledge the Stanford Cyclotron Research Facility and UCSC Greenhouse Facilities for technical support and Ricky Padmore for assistance with the plant growth apparatus

Abstract

We present quantitative 4D PET imaging of photosynthate carbon transport and rhizosphere exudation in intact Phaseolus vulgaris plant–soil systems using the R-PET (Rhizo-PET) scanner with the ^{11}C radiotracer ($t_1/_2$ = 20.3 min). Across N = 6 plants, time–activity curves (TACs) extracted from 225 cross-pattern ROIs per dataset—spanning 3 roots × 3 axial depths × ±3 mm radial extent—reveal a reproducible source-to-sink carbon allocation hierarchy: upper root zones receive ≈50% of total plant carbon, while root 2 (primary taproot) dominates at 20.8 ± 6.3%. Time-to-peak (TTP) increases from 31.5±4.4 min (upper) to 48.0±13.1 min (lower root 2), corresponding to a phloem transport velocity of ≈2.4 mm min^{-1}. Rhizosphere carbon exudation follows an exponential decay AUC(r) = A e^{-kr} with k = 0.10–0.20 mm^{-1}, placing the active deposition zone within 4–14 mm of the root surface—the first spatially resolved 3D+t measurement of this process in intact soil.

References
[1] M. N. Ullah et al., “Quantitative Assessment of Imaging Performance of Rhizo-PET (R-PET): A PET Scanner Dedicated to Dynamic Plant Rhizosphere Imaging,” 2025 IEEE NSS MIC RTSD, pp. 1–2, 2025.
[2] M. N. Ullah et al., “Rhizo-PET: A Dedicated PET System for 4D Imaging of Carbon Dynamics in the Rhizosphere,” bioRxiv, 2026.
[3] M. Knoblauch et al., “Sieve elements in intact, unmanipulated phloem,” Plant Cell, vol. 28, pp. 2462–2474, 2016.
[4] S. Jahnke et al., “Combined 64Cu-PET/MR imaging of plants,” Plant J., vol. 59, pp. 634–644, 2009
[5] N. Kawachi et al., “Carbon-11 imaging of photosynthate transport in plants,” Plant Cell Physiol., vol. 52, pp. 333–342, 2011.
[6] T. Alexander et al., “Non-invasive imaging of 11C in plant stems,” New Phytol., vol. 196, pp. 366–375, 2012.e’, Journal, Edition, Page, Place of publication: publishers

MIC-15-468

Investigating an Optical Approach for Microliter-Scale Droplet Geometry Correction in Radioactivity Quantification (#3086)

Shawn Shin, Robert Carmichael, Weiting Deng, Juan Alexander Leal Doblado, David Prout, Robert Michael van Dam, Arion Chatziioannou

University of California, Los Angeles, Department of Molecular and Medical Pharmacology, Crump Institute for Molecular Imaging, Los Angeles, USA

Abstract

Positron-labeled tracers are powerful tools for studying diseases and developing new therapeutics, yet conventional radiochemistry platforms are complex, costly, and low-throughput, making PET tracer development slow and resource-intensive. To address this bottleneck, we are constructing a high-throughput radiochemistry system that will enable multiple radiosyntheses to be performed in parallel. A key challenge is accurately quantifying radioactivity in each microliter-scale droplet throughout the radiosynthesis process. While plastic scintillators and an overhead CMOS camera offer a compact detection approach, the scintillation signal is confounded by variations in droplet volume and geometry. Geometry correction is therefore critical for reliable activity quantification.

We investigated an optical approach to infer droplet geometry by leveraging its optical reflective and refractive properties. Droplets were illuminated with a ring light mounted around the camera lens, and we sought to infer their geometries from the resulting optical features. Experimental images were acquired from evaporating water droplets on a Teflon-coated silicon chip, and ray-tracing simulations were performed on droplet models reconstructed from side-profile images. Both revealed two distinct features from independent optical processes: a mirror reflection effect and a lensing magnification effect. These varied systematically with droplet volume, suggesting they encode geometry information and may provide complementary information for inference.

These preliminary findings support the feasibility of this optical method for geometry estimation and radioactivity quantification correction. The approach adds minimal complexity to the existing system and is well-suited for integration into a compact radiochemistry robot. Future work will focus on refining droplet shape models, extending the method to off-axis droplets, and evaluating image-analysis approaches for robust geometry inference.

References

[1] A. Rios, T. S. Holloway, P. H. Chao, C. De Caro, C. C. Okoro, and R. M. van Dam, “Microliter-scale reaction arrays for economical high-throughput experimentation in radiochemistry,” *Sci. Rep.*, vol. 12, no. 1, p. 10263, Jun. 2022, doi: 10.1038/s41598-022-14022-2.

[2] J. Jones, V. Do, Y. Lu, and R. M. van Dam, “Accelerating radiochemistry development: Automated robotic platform for performing up to 64 droplet radiochemical reactions in a morning,” *Chem. Eng. J.*, vol. 468, p. 143524, Jul. 2023, doi: 10.1016/j.cej.2023.143524.

Time:
13 November, 2026
17:30 – 19:00

Room:
FEDERICO GARCÍA LORCA

MIC-16 | Simulation and modeling of medical imaging systems (2)

Chairs:
Munetaka Nitta (Garching)
David Sarrut (Villeurbanne)

MIC-16-01

How well do we know non-collinearity in PET? A simulation and a new analysis of past and recent experiments (#2250)

Andrea Espinosa[1], Pablo Galve[2,1], Luis M. Fraile[1,3], Joaquín López Herraiz[1], **Jose M. Udias**[1]

[1] Universidad Complutense de Madrid, Grupo de Física Nuclear, EMFTEL & IPARCOS, Madrid, Spain; [2] Spanish National Research Council (CSIC), Institute for Physical and Information Technologies "Leonardo Torres Quevedo", ITEFI, Madrid, Spain; [3] CERN, ISOLDE, EP Department, Geneva, Switzerland

Supported by the European Innovation Council RETIMAGER (101099096), by the Spanish Government JDC2023-051754-I (P. Galve)

Abstract

Positron-electron **non-collinearity** of the 511 keV annihilation-photon has been derived from several experiments. In the one hand, of the (anti-)correlation between Doppler broadening induced by the transverse momentum component of the annihilating pair, and photon non-collinearity. Direct non-colinearity measurements with pin-hole or slits provide also noncolinearity information. In the past, discrepancies in the non-collinearity derived from both kinds of experiments have arised, and the non-collinearity value generally accepted has been solely derived from Doppler broadening experiments. To better understand non-collinearity, we review the correlation between the kinematics of the initial electron-positron pair and the emitted non-collinear photon. We then use a detailed 3D simulation of the kinematics annihilation of the e-e+ pair, including the motion of the initial pair of leptons, which in turns introduces the energy broadening of the 511 keV peak, and the non-collinearity of the final photons, linked to the underlying electron kinetic-energy distribution. To this end, initial electron kinetic energies are sampled from a semi-Gaussian distribution, while initial electron directions are sampled isotropically. We fit the initial kinetic energy distribution of the electron-positron pairs to reproduce, after the detailed 3D simulation, the observables in each kind of experiments, either Doppler broadening or actual non-collinearity in slit experiments. We find that the same initial electron kinetic energy distribution explains both Doppler broadening and accurate slit experiments in water at room temperature. Finally, we compare our extraction for non-collinearity distribution, and found it similar to the one presented by Tuoissant et al in 2024, confirming that non-collinearity is being underestimated in most MC simulations of PET scanners.

References

[1] Mogensen, O. E., & Eldrup, M. (1978). Vacancies in pure ice studied by positron annihilation techniques. Journal of Glaciology, 21(85), 85-99.

[2] Iwata, K., Greaves, R. G., & Surko, C. M. (1997). γ-ray spectra from positron annihilation on atoms and molecules. Physical Review A, 55(5), 3586.

[3] Toussaint, M., Loignon-Houle, F., Auger, É., Lapointe, G., Dussault, J. P., & Lecomte, R. (2024). On the implementation of acollinearity in PET Monte Carlo simulations. Physics in Medicine & Biology, 69(18), 18NT01.

[4] Shibuya, K., Yoshida, E., Nishikido, F., Suzuki, T., Tsuda, T., Inadama, N., ... & Murayama, H. (2007). Limit of spatial resolution in FDG-PET due to annihilation photon non-collinearity. In World Congress on Medical Physics and Biomedical Engineering 2006: August 27–September 1, 2006 COEX Seoul, Korea "Imaging the Future Medicine" (pp. 1667-1671). Springer Berlin Heidelberg.

Shibuya, K., Yoshida, E., Nishikido, F., Suzuki, T., Tsuda, T., Inadama, N., ... & Murayama, H. (2007). Annihilation photon acollinearity in PET: volunteer and phantom FDG studies. Physics in Medicine & Biology, 52(17), 5249.

MIC-16-02

PAL-G4: A Geant4-based code with PAL parametrisation (#2072)

Nataly Castellanos[1], Debora Niekämper[2], Wilson Ramírez[1], Lutz Tellmann[2], Juergen Scheins[2], Gabriela Llosá[1], Christoph W. Lerche[2], Ana Ros[1]

[1] Instituto de Fisica Corpuscular (CSIC-UV), Valencia, Spain; [2] Forschungszentrum Jülich, Institute of Neuroscience and Medicine 4, Jülich, Germany

This work was supported in part by and the SO project CEX2023-001292-S funded by MCIU/AEI and the JAE Intro2024 (JAEINT24_EX_1518) grant.

Abstract

Positron Annihilation Lifetime has previously been demonstrated to provide useful information in PET imaging. Due to the fact that the annihilation time depends on the tissue where the annihilation occurs, to disentangle the different times for heterogeneous tumors is extremely challenging. Geant4, the toolkit for the simulation of the passage of particles through matter developed at CERN, has been shown to be a good candidate for medical physics simulations. The main drawback is that Geant4 code does not include Positron Annihilation Lifetime information in the source code. The IRIS group at IFIC (Valencia) has developed PAL-G4, an unofficial version of Geant4 that introduces the possibility to add measured Positron Annihilation Lifetimes for different materials in order to be able to simulate realistic scenarios. In order to test the PAL-G4 code, the BrainPET-7T insert for magnetic resonance at the PET-physics group at the Forschungszentrum Jülich GmbH was simulated. Two cases were simulated, one in which the annihilation took place in a homogeneous medium, and another in a heterogeneous medium. The simulation results fit the expected behavior in terms of the detected annihilation times in both cases, thereby showing the suitability of using PAL-G4 for real case studies. Further measurements of annihilation times for various sources and tissues of interest in medical applications will be measured with the BrainPET-7T and used as input parameters for the PAL-G4 code. The simulations results will be compared with the measured data in all cases.

References

[1] Takyu S. et al., Applied Physics Express, 2022, vol. 15, no 10, p. 106001.
[2] Alkhorayef M. et al., Radiation Physics and Chemistry, 2021, vol. 188, p.109690.
[3] Avachat V. et al., Scientific reports, 2024, vol. 14, no 1, p. 21155.
[4] Tashima H. et al., 2023 IEEE NSS MIC RTSD, IEEE, 2023. p. 1-1.
[5] Moskal P. et al., Physics in Medicine & Biology, 2019, vol. 64, no 5, p.055017.
[6] Niekämper D. et al., 2024 IEEE NSS MIC RTSD, IEEE, 2024. p. 1-1.

MIC-16-03

Data-Driven System Response Modeling for SPECT via Maximum Likelihood Estimation (MLE) of Directional Penetration Maps from Experimental Sparse Scanning Data (#2923)

Yifei Jin[1], Shubham Mandot[1], Ling-Jian Meng[1,2]

[1] University of Illinois at Urbana and Champaign, Department of Nuclear, Plasma, and Radiological Engineering, Urbana, USA; [2] University of Illinois at Urbana and Champaign, Beckman Institute for Advance Science and Technology, Urbana, USA

This work was supported by the National Institutes of Health under grant numbers R01HL145786 (National Heart, Lung, and Blood Institute) and U01EB031798 (National Institute of Biomedical Imaging and Bioengineering).

Abstract

Accurate system response modeling is essential for quantitative SPECT, but system response functions (SRFs) generated from nominal collimator geometry can deviate from the response of the actual system due to aperture imperfections, mechanical misalignment, and septal penetration. This mismatch is especially significant for a non-conventional aperture. We propose a data-driven SRF modeling method that reconstructs a directional penetration map from sparse point-source scans. In the proposed aperture-domain representation, each source-detector measurement is indexed by its aperture crossing position and ray direction, allowing measurements from different source locations and detector pixels to be pooled into a shared position-direction map. The map represents the effective material path length, which is estimated by maximum likelihood under a Poisson model with latent detector-depth sublayers, and the resulting problem is solved using an expectation-maximization (EM) algorithm. SRFs for arbitrary source locations can then be generated through the ray-tracing method by combining geometric factors with the learned path length and the photon-energy-dependent attenuation coefficient. Preliminary Geant4 validation using a 16-aperture micro-ring CZT-based SPECT model with controlled collimator tilting demonstrates that scan-based SRFs recover aperture-level response features missed by nominal-design SRFs and agree more closely with the ground-truth tilted-collimator response at non-scanned source positions. Experimental validation on the clinical AlphaSPECT system and image-domain evaluation will be presented at the conference.

References

[1] T. Li, E. C. I. Ao, B. Lambert, B. Brans, S. Vandenberghe, and G. S. P. Mok, “Quantitative Imaging for Targeted Radionuclide Therapy Dosimetry - Technical Review,” *Theranostics*, vol. 7, no. 18, pp. 4551–4565, 2017, doi: 10.7150/thno.19782.

[2] S. Y. Chun, J. A. Fessler, and Y. K. Dewaraja, “Correction for Collimator-Detector Response in SPECT Using Point Spread Function Template,” *IEEE Trans. Med. Imaging*, vol. 32, no. 2, pp. 295–305, Feb. 2013, doi: 10.1109/TMI.2012.2225441.

[3] Z. El Bitar, R. H. Huesman, R. Buchko, V. Bekaert, D. Brasse, and G. T. Gullberg, “A detector response function design in pinhole SPECT including geometrical calibration,” *Phys. Med. Biol.*, vol. 58, no. 7, pp. 2395–2411, Apr. 2013, doi: 10.1088/0031-9155/58/7/2395.

[4] X. Song, W. P. Segars, Y. Du, B. M. Tsui, and E. C. Frey, “Fast modelling of the collimator-detector response in Monte Carlo simulation of SPECT imaging using the angular response function,” *Phys. Med. Biol.*, vol. 50, no. 8, pp. 1791–1804, 2005, doi: 10.1088/0031-9155/50/8/011.

[5] B. W. Miller, R. Van Holen, H. H. Barrett, and L. R. Furenlid, “A System Calibration and Fast Iterative Reconstruction Method for Next-Generation SPECT Imagers,” *IEEE Trans. Nucl. Sci.*, vol. 59, no. 5, pp. 1990–1996, Oct. 2012, doi: 10.1109/TNS.2012.2198243.

[6] X. Lai, E. M. Zannoni, J. George, and L.-J. Meng, "System modeling and evaluation of a prototype inverted-compound eye gamma camera for the second generation MR compatible SPECT," *Nucl. Instrum. Methods Phys. Res. Sect. Accel. Spectrometers Detect. Assoc. Equip.*, vol. 954, p. 162046, Feb. 2020, doi: 10.1016/j.nima.2019.04.001.
[7] E. M. Zannoni, C. Yang, and L.-J. Meng, "Design Study of an Ultrahigh Resolution Brain SPECT System Using a Synthetic Compound-Eye Camera Design With Micro-Slit and Micro-Ring Apertures," *IEEE Trans. Med. Imaging*, vol. 40, no. 12, pp. 3711–3727, 2021, doi: 10.1109/TMI.2021.3096920.

MIC-16-04

Wasserstein Pullback Metric for Intrinsic Difficulty of Scintillation Detector Inverse Problems (#2265)

Sangjin Bae[1,2], Jae Sung Lee[1,3]

[1] Seoul National University Graduate School, Interdisciplinary Program in Bioengineering, Seoul, South Korea; [2] Seoul National University Graduate School, Integrated Major in Innovative Medical Science, Seoul, South Korea; [3] Seoul National University Hospital, Department of Nuclear Medicine, Seoul, South Korea

Abstract

Scintillation detector inverse problems are limited by how sensitively photon distributions change with interaction or detector conditions. We propose a likelihood-free Wasserstein-geometric framework for quantifying this distributional sensitivity using a pretrained generative model for scintillation photon transport. By representing conditional photon distributions as pushforwards of a latent distribution, the Jacobian of the transport map induces a Wasserstein pullback metric on the condition space. We use the trace of this metric as a local sensitivity measure and its detector-level average as the expected distributional sensitivity (EDS). The proposed sensitivity captures DOI and crystal-dependent timing trends, correlates monotonically with interaction localization error across crystal dimensions (Spearman ρ=-0.88 for rough Teflon and -0.90 for polished ESR), and supports differentiable detector optimization. These results suggest that Wasserstein sensitivity can provide an estimator-independent measure of inverse-problem difficulty and a tool for detector characterization and optimization.

References
[1] Bae, S, Gong, K & Lee, JS 2025, 'Fast and Differentiable Optical Photon Transport for Scintillation Detectors Using Flow Matching', *2025 IEEE NSS-MIC-RTSD*, IEEE.
[2] Peyré, G & Cuturi, M 2019, 'Computational optimal transport: With applications to data science', *Now Foundations and Trends*.

MIC-16-05

Zero-Knowledge Calibration: PET Geometry Recovery from Unlocalized Point Sources (#2333)

Tim Freye[1], Julian Thull[1], Yannick Kuhl[1], Volkmar Schulz[1,2]

[1] RWTH Aachen University, Chair of Imaging & Computer Vision, Aachen, Germany; [2] Hyperion Hybrid Imaging Systems, Aachen, Germany

We thank NVIDIA for four RTX 6000 Ada GPUs through its Grant Program.

Abstract

Mechanical detector misalignments in positron emission tomography (PET) scanners, caused by manufacturing tolerances as well as mechanical and thermal stress, lead to inaccurate line of response (LOR) positioning and consequently degrade image quality and quantitative accuracy. Existing calibration methods typically rely on dedicated measurements with known tracer distributions, requiring either calibration phantoms or precisely positioned point sources. These procedures are time-consuming, operationally demanding, and difficult to integrate into PET-MRI systems due to magnetic field constraints. This work proposes an unsupervised detector alignment calibration method that estimates detector misalignments from point-source measurements with unknown source positions. The proposed approach estimates source locations using an iterative likelihood-based optimization and derives detector alignment parameters from the resulting LOR geometry, eliminating the need for externally calibrated source positioning. The method is evaluated on a simulated PET scanner and achieves translational and rotational alignment accuracies of 0.95mm and 0.41°, respectively, while the source positions are recovered with an accuracy of 0.61mm using only 3×10^5 LORs. By avoiding specialized calibration hardware and requiring only limited acquisition data, the proposed method enables rapid, flexible, and easily deployable PET calibration. Its low operational complexity and short acquisition time make it particularly promising for routine clinical recalibration and for hybrid imaging systems such as PET-MRI.

References

[1] Sabet, Hamid, Ishii, Keizou, Matsuyama, Shigeo, Kikuchi, Youhei, Nakazawa, K., Esmaili Torshabi, Ahmad, Yamazaki, Hiromichi 2009, 'A method to modify coordinates of detectors in positron emission tomography systems', *Nuclear Instruments and Methods in Physics Research Section A: Accelerators, Spectrometers, Detectors and Associated Equipment*, 600(3), 678-682, Elsevier

[2] Pierce, Larry, Miyaoka, Robert, Lewellen, Tom, Alessio, Adam, Kinahan, Paul 2009, 'Determining block detector positions for PET scanners', *2009 IEEE Nuclear Science Symposium Conference Record (NSS/MIC)*, 2976-2980, IEEE

[3] Thull, Julian, Kuhl, Yannick, Mueller, Florian, Schug, David, Weissler, Bjoern, Schulz, Volkmar 2026, 'Beyond mechanics: Maximum-likelihood-driven PET detector alignment calibration', *Medical Physics*, 53.1, e70256, Wiley

MIC-16-06

A Multi-Channel Positronium Decay Source Model in GATE (#2911)

Mateusz Bała[2], **Wojciech Krzemien**[1], Kamil Dulski[3], Wojciech Zdeb[2], Aurélien Coussat[4], For the IMPET project

[1] National Centre for Nuclear Research, Department of High Energy Physics, Otwock Swierk, Poland; [2] National Centre for Nuclear Research, Department of Complex Systems, Otwock Swierk, Poland; [3] Jagiellonian University, Faculty of Physics, Astronomy and Applied Computer Science, Krakow, Poland; [4] INSA-Lyon, Université Claude Bernard Lyon 1, CNRS, Inserm, CREATIS UMR 5220, Lyon, France

The work was supported by the Foundation for Polish Science through the FIRST TEAM FENG.02.02-IP.05-0152/23 programme co-financed by the European Union under the European Funds for Smart Economy 2021-2027 (FENG). by the “PHC POLONIUM” program (project number: 55194PB), funded by the French Ministry for Europe and Foreign Affairs, the French Ministry for Higher Education, Research, and Space, and the Polish NAWA (BPN/BFR/2025/1/00036/ and BPN/BAT/2025/1/00009), and co-supported by the Austrian Ministry for Women, Science and Research (project WTZ PL 11/2026).

Abstract

Positronium-based imaging [1-3] requires accurate Monte Carlo modelling of positronium decay in matter. Existing implementations in the Geant4 Application for Tomographic Emission simulation framework [4-5] are limited to at most two annihilation channels, which is insufficient to represent the multi-component lifetime structures observed in biological tissues and complex materials. We present a new modular positronium decay source model implemented in both GATE versions 9.4 and 10 [5], enabling the simultaneous definition of an arbitrary number of decay channels. Each channel is independently characterised by its mean lifetime, branching fraction, annihilation multiplicity into two or three photons, and optional prompt photon emission, as required for radionuclides such as scandium-44, gallium-68, and iodine-124. The model is validated through analytical and numerical benchmarks. Branching fractions are correctly reproduced within statistical uncertainties across all tested configurations. Practical applicability is demonstrated through simulations of a NEMA Image Quality phantom filled with tissue-mimicking positronium sources representing water, fat, muscle, and bone. The implementation is fully compatible with standard simulation workflows, providing the community with the first general-purpose, multi-channel positronium decay model integrated into a widely adopted medical physics simulation framework.

References

[1] Hourlier, A, Boisson, F & Brasse, D 2024, 'Experimental uses of positronium and potential for biological applications', *IEEE Transactions on Radiation and Plasma Medical Sciences*, vol. 8, no. 6, pp. 581–594.

[2] Moskal, P, Baran, J, Bass, S, Choiński, J, Chug, N, Curceanu, C, Czerwiński, E, Dadgar, M, Das, M, Dulski, K, Eliyan, KV, Fronczewska, K, Gajos, A, Kacprzak, K, Kajetanowicz, M, Kaplanoglu, T, Kapłon, Ł, Klimaszewski, K, Kobylecka, M, Korcyl, G, Kozik, T, Krzemień, W, Kubat, K, Kumar, D, Kunikowska, J, Mączewska, J, Migdał, W, Moskal, G, Mryka, W, Niedźwiecki, S, Parzych, S, del Rio, EP, Raczyński, L, Sharma, S, Shivani, S, Shopa, RY, Silarski, M, Skurzok, M, Tayefi, F, Ardebili, KT, Tanty, P, Wiślicki, W, Królicki, L & Stępień, Eł 2024, 'Positronium image of the human brain in vivo', *Science Advances*, vol. 10, no. 37, art. no. eadp2840.

[3] Mercolli, L, Steinberger, WM, Läppchen, T, Amon, M, Bregenzer, C, Conti, M, Cardoso, ÂRF, Mingels, C, Moskal, P, Rathod, N, Sari, H, Stępień, Eł, Weidner, S, Rominger, A, Shi, K & Seifert, R 2026, 'In vivo voxel-wise positronium lifetime imaging of thyroid cancer using clinically routine I-124 PET/CT', *EANM Innovation*, vol. 2, art. no. 100017.

[4] Sarrut, D, Bała, M, Bardiès, M, Bert, J, Chauvin, M, Chatzipapas, K, Dupont, M, Etxebeste, A, Fanchon, LM, Jan, S, Kayal, G, Kirov, AS, Kowalski, P, Krzemien, W, Labour, J, Lenz, M, Loudos, G, Mehadji, B, Ménard, L, Morel, C, Papadimitroulas, P, Rafecas, M, Salvadori, J, Seiter, D, Stockhoff, M, Testa, E, Trigila, C, Pietrzyk, U, Vandenberghe, S, Verdier, MA, Visvikis, D, Ziemons, K, Zvolský, M & Roncali, E 2021, 'Advanced Monte Carlo simulations of emission tomography imaging systems with GATE', *Physics in Medicine and Biology*, vol. 66, no. 10, art. no. 10TR03.

[5] Krah, N, Arbor, N, Baudier, T, Bert, J, Chatzipapas, K, Favaretto, M, Fuchs, H, Grevillot, L, Harb, H, Van Hoey, G, Jacquet, M, Jan, S, Jia, Y, Kagadis, GC, Kang, HG, Klever, P, Kochebina, O, Krzemien, W, Maigne, L, Mohr, P, Mummaneni, G, Paneta, V, Papadimitroulas, P, Pereda, A, Rannou, A, Resch, AF, Roncali, E, Toussaint, M, Trigila, C, Tsoumpas, C, Zhang, J, Ziemons, K & Sarrut, D 2026, 'GATE 10 Monte Carlo particle transport simulation: II. Architecture and innovations', *Physics in Medicine and Biology*, vol. 71, no. 1, art. no. 015043.

Time:
13 November, 2026
17:30 – 19:00

Room:
MANUEL DE FALLA

MIC-17 | Theranostics, Imaging and dosimetry in therapy (particle, radiopharmaceutical, surgery) (1)

Chairs:
Akram Hamato (Chiba)
Francesco Pennazio (Torino)

MIC-17-01

Detection of deep seated anatomical changes in patients undergoing ion beam radiotherapy (#2562)

Maria Martisikova[1,3], Rebekka Kirchgässner[4,1], Pamela Ochoa[1,3], Semi Harrabi[2,7], Patrice Schlegel[1,2], Erik Bartelme[1,5], Sevgi Yesilmen[1,6], Laurent Kelleter[1,3], Jan Jakubek[8], Marcus Winter[7], Juergen Debus[2,3], Oliver Jaekel[1,7]

[1] German Cancer Research Center, Division of Medical Physics in Radiation Oncology, Heidelberg, Germany; [2] University Hospital, Department of Radiation Oncology, Heidelberg, Germany; [3] Nationatl Center for Tumor Disseases (NCT), HIRO-Heidelberg Institute for Radiation Oncology, Heidelberg, Germany; [4] University of Heidelberg, Faculty of Physics, Heidelberg, Germany; [5] University of Heidelberg, Faculty of Informatics, Heidelberg, Germany; [6] University of Applied Sciences, Department of Science, Saarbruecken, Germany; [7] Heidelberg Ion Beam Therapy Center (HIT), Departmen of Medical Physics, Heidelberg, Germany; [8] ADVACAM s.r.o, Prague, Czech Republic

Abstract

Carbon-ion radiotherapy enables highly precise tumor treatment, particularly for locations near critical structures such as the brainstem or spinal cord. However, the focused dose distributions that make this modality effective also increase its sensitivity to variations in the beam path. Consequently, accurate monitoring and control of the dose distribution in the patient are essential. Despite this clinical need, radiation-free monitoring approaches are scarce. In order to investigate use of secondary ions for this purpose, we compare measured ion distributions across treatment fractions. For this approach, a contactless detection system for secondary-ion tracking was developed and clinically implemented at the Heidelberg Ion-Beam Therapy Facility (HIT), Germany. The system enables tracking of individual secondary-ions with high spatial and temporal resolution.

The performance of the developed monitoring approach is currently being assessed within the clinical study “InViMo.” To date, more than 100 patient measurements have been acquired. For the majority of patients, the measured data showed consistency across treatment fractions. However, pronounced inter-fractional variations were observed in several cases. These signals demonstrated clear spatial correlation with the anatomical ground truth derived from CT imaging, including challenging cases involving deep-seated tumors. In addition, the system enabled a worldwide first measurement of a patient treated with helium ions, a promising modality for several pediatric tumor indications. Considerable amount of secondary ion tracks was recorded.

Our results demonstrate that the proposed method can detect clinically relevant anatomical changes in treated patients with high sensitivity and accurate spatial localization.

MIC-17-02

Proton Range Verification in 3D Pencil Beam Scanning Lattice via a Dual-head Multi-slit 3D Prompt Gamma Imaging System (#2861)

Hongyang Zhang[2,3], Bo Zhao[1,2], Zishen Wang[4,5], Jie Wang[4], Peng Fan[6,7], Yancheng Yu[2,3], Weigang Duan[1,2], Lilei Gao[3], Shi Wang[1,2], Zhaoxia Wu[1,2], Tianyu Ma[1,2], Hui Liu[1,2], Yaqiang Liu[1,2]

[1] Ministry of Education, Key Laboratory of Particle & Radiation Imaging, Beijing, China; [2] Tsinghua University, Department of Engineering Physics, Beijing, China; [3] Chengdu NOVEL MEDICAL Equipment Co. Ltd., Beijing, China; [4] Hebei Yizhou Cancer Hospital, Zhuozhou, China; [5] China institute of Atomic Energy, Beijing, China; [6] China Academy of Space Technology and Science, Beijing Institute of Spacecraft Environment Engineering, Beijing, China; [7] Beijing Institute of Spacecraft Environment Engineering, Technology on Reliability and Environmental Engineering Laboratory, Beijing, China

The work is supported in part by the National Key Research and Development Program of China (No. 2022YFC2403802), National Natural Science Foundation of China (No. 12205166) and National Key Research and Development Program of China (No. 2016YFC0105405).

Abstract

Objective: Online range monitoring is critically important in proton therapy, as range uncertainties arising from patient positioning, anatomical variations, and range calculation algorithms remain a major limitation in precise dose delivery. Prompt gamma-ray imaging (PGI) offers a promising solution for real-time range verification due to the ultra-fast emission of prompt gamma rays. However, for the most advanced dose delivery technique—pencil beam scanning—proton beams are delivered in a three-dimensional (3D) lattice, necessitating 3D online monitoring systems capable of spot-by-spot range and dose verification within a single acquisition.

Approach: In this study, a dual-head 3D PGI system based on multi-slit collimated gamma-ray cameras was evaluated for proton beams delivered to 3D lattices. Experiments were conducted in a clinical proton therapy treatment room using a proton beam of typical therapeutic energy incident on a polymethyl methacrylate (PMMA) phantom. The precision and accuracy of both range verification and beam spot positioning were systematically assessed.

Main results: At a typical low proton count level of 1×10^8 protons per scanning spot, the system achieved accuracy and precision better than 1.5 mm for both range verification and beam spot positioning. At proton counts of 3×10^8 or higher, both metrics improved to sub-millimeter levels (<1 mm).

Significance: These findings demonstrate that the dual-head 3D PGI system is capable of high-precision, spot-by-spot range and beam spot verification even at low proton counts, highlighting its potential for effective online in vivo monitoring in 3D pencil beam scanning proton therapy.

References

[1] I. Perali, "A prompt gamma camera for real-time range control in proton therapy," Doctoral dissertation, Dipartimento di Elettronica e Informazione, Politecnico di Milano, Milan, Italy, 2015.

[2] W. Lu, D. Zhang, P. Fan, S. Wang, Z. Wu, T. Ma, and Y. Liu, "Simulation Study of a 3D Multi-slit Prompt Gamma Imaging System for Proton Therapy Monitoring," *IEEE Transactions on Radiation and Plasma Medical Sciences*, vol. 6, no. 3, pp. 355-365, 2021.

[3] H. Zhang, B. Zhao, P. Fan, S. Wang, W. Lu, Y. Yu, Z. Wu, T. Ma, H. Liu, and Y. Liu, "Proton Range Verification Realized via a Multislit Prompt Gamma Imaging System," *IEEE Transactions on Radiation and Plasma Medical Sciences*, vol. 9, 2025.

MIC-17-03

Design and Experimental Validation of the REALPATH Prompt Gamma Camera for Range Verification in Hadrontherapy (#2605)

Martina Piroddi[1,3], Korbinian Urban[1,3], Emma S. Bellotti[2,3], Andrea Forgione[1,3], Fabio Garzetti[1], Davide Mazzucconi[2,3], Christian Riboldi[1,3], Letizia Santini[1,3], Giacomo Borghi[1,3], Marco Carminati[1,3], Guido Baroni[1], Stefano Agosteo[2,3], Marco Pullia[4], Carlo E. Fiorini[1,3]

[1] Politecnico di Milano, Department of Electronics, Information and Bioengineering (DEIB), Milano, Italy; [2] Politecnico di Milano, Department of Energy (DENG), Milano, Italy; [3] National Institute for Nuclear Physics (INFN), Milano, Italy; [4] Centro Nazionale di Adroterapia Oncologica (CNAO), Pavia, Italy

This work was supported by the REALPATH project (Italian MUR), grant n. FISA-2022-00779

Abstract

Hadrontherapy is a kind of radiation therapy that delivers highly localized radiation doses to treat tumors spearing healthy tissues. In this context, Prompt Gamma Imaging (PGI) is a promising technique towards real-time monitoring of the particle beam range, thereby enhancing both treatment precision and patient safety. The REALPATH project aims to develop a compact range verification system based on passive collimation and a pixelated gamma camera. The detector utilizes LYSO scintillator crystals coupled to silicon photomultipliers (SiPMs), organized into 64- channel base units that scale up to a 512-channel instrument with a 20 × 10 cm² footprint. The primary objective of this project is to overcome the physical and operational barriers that currently prevent PGI systems from being used during standard treatment workflows. For this reason, the detector and electronics are engineered to maximize detection efficiency, minime acquisition dead time, while reducing the footprint of the system. A novel ”inverted” collimator design significantly reduces the overall instrument weight and allows the camera to be rigidly fixed beneath the patient couch. The experimental results obtained from measurement campaigns at CNAO facility in Pavia, Italy are also reported.

References
[1] Perali, Irene., et al. "Prompt gamma imaging of proton pencil beams at clinical dose rate." Physics in Medicine & Biology 59.19 (2014): 5849
[2] Pausch, Guntram, et al. "Detection systems for range monitoring in proton therapy: Needs and challenges." Nuclear Instruments and Methods in Physics Research Section A: Accelerators, Spectrometers, Detectors and Associated Equipment 954 (2020): 161227
[3] Riboldi, Christian et al. “Design of a 64-channel modular platform for high-speed readout of scintillator-based detectors for range monitoring in hadrontherapy.” *Journal of Instrumentation* 20 (2025).

MIC-17-04

First Tests of Hybrid n/gamma-ray Imaging for Proton Therapy Range Verification at a Clinical Proton Beam (#2027)

Sara T. Mueller[1,2], Sander Blorstad Thu[3], Thyrza Jagt[1,2], Ilker Meric[4], Anna Milde Bekkevoll[3], Guntram Pausch[5], Hunter Ratliff[4], Katja Roemer[6], Joseph Turko[6], Andreas Wolf[5], Toni Koegler[1,2], On behalf of the NOVO collaboration

[1] OncoRay – National Center for Radiation Research in Oncology, Dresden, Germany; [2] Helmholtz- Zentrum Dresden- Rossendorf, Institute of Radiooncology – OncoRay, Dresden, Germany; [3] University of Bergen, Bergen, Norway; [4] Western Norway University of Applied Sciences, Bergen, Norway; [5] Rapiscan Systems GmbH, Hofheim, Germany; [6] Helmholtz- Zentrum Dresden- Rossendorf, Institute of Radiation Physics, Dresden, Germany

This work is supported by the European Innovation Council, grant agreement No. 101130979

Abstract

Proton therapy provides highly conformal dose delivery and the integration of in-vivo range verification can further enhance treatment safety and efficacy by serving as a trigger for intervention and by decreasing safety margins [1]. The NOVO collaboration [2] investigates a novel hybrid detector concept that combines prompt gamma ray and fast neutron imaging in a compact organic-scintillator-based system to improve proton range verification. This dual-particle approach offers complementary particle information and thus improved localisation capabilities [3]. For the first time, the NOVO detector was operated at a clinical proton beam at the OncoRay proton therapy facility in Dresden, Germany [4]. The system's detection performance and imaging capability were investigated by irradiating different phantoms with numerous proton energies and beam currents and by varying the phantoms' position and compositions. The detector array demonstrated stable performance under clinically relevant mixed-field and high-rate conditions and achieved reliable neutron–photon discrimination. Furthermore, images could be reconstructed which provide the first experimental validation of the combined n/gamma approach in proton therapy and highlight its strong potential as a future real-time range verification technique.

References

[1] Berthold, Jonathan, et al. 2023 "Detectability of anatomical changes with prompt-gamma imaging: first systematic evaluation of clinical application during prostate-cancer proton therapy." *International Journal of Radiation Oncology* Biology* Physics* 117.3: 718-729.

[2] NOVO research project: Targeting Cancer with New Precision: https://www.novo-project.eu/

[3] Meric, Ilker, et al. 2023 "A hybrid multi-particle approach to range assessment-based treatment verification in particle therapy." *Scientific reports* 13.1: 6709.

[4] Horst, Felix, Bodenstein, Elisabeth, et al. 2025 "The research beamlines at the Dresden proton therapy facility: available infrastructure and experimental capabilities." *Frontiers in Oncology* 15: 1594973.

MIC-17-05

First Demonstration of Short-Interval Proton Range-Verification and FAZA PET on SIRMIO (#1636)

Chie Toramatsu[1], Caroline Steinbrecht[2], Francesco Evangelista[2], Giulio Lovatti[2], Maxin Chen[2], Munetaka Nitta[2], Jonathan Bortfeldt[2], Niels Bassler[3], Peter G. Thirolf[2], Brita S. Sorensen[3], Morten Busk[3], Taiga Yamaya[1], Katia Parodi[2]

[1] National Institutes for Quantum Science and Technology, Chiba, Japan; [2] Ludwig Maximilians-University, Munich, Germany; [3] Danish Centre for Particle Therapy, Aarhus, Denmark

This work was supported by EQAP, DFG GRK2274, CALA and JSPS KAKENHI 23KK0206. The authors gratefully acknowledge valuable contributions of Prof. Per Rugaard Poulsen and Dr. Fardous Reaz (DCPT).

Abstract

Biological washout, traditionally considered a source of error in range-verification PET in particle therapy, is now emerging as a potential new biomarker for tumor diagnosis. At QST, proof-of-concept studies using animal irradiation at HIMAC demonstrated a correlation between hypoxia PET maps and washout rate maps derived from range-verification PET. However, due to facility limitations, including radioisotope regulation constraints, hypoxia PET had to be performed on the day following irradiation. As a result, confounding factors such as tumor growth and delayed irradiation effects could not be fully excluded. In contrast, LMU has developed the Small Animal Proton Irradiator for Research in Molecular Image-Guided Radiation Oncology (SIRMIO) that includes an in-beam PET scanner, and conducted experiments at DCPT, which offers close integration with a nuclear medicine division. Leveraging this environment, we designed an experimental protocol to perform both proton range-verification PET (irradiation-PET) and hypoxia PET (FAZA-PET) on the same platform with a shortened interval using the SIRMIO system at DCPT. Considering that the activity level in range-verification PET is much lower than that in FAZA-PET, ^{18}F-FAZA administration was performed after the irradiation-PET. The time interval between the two PET scans was reduced to < 4 hours, which is sufficient for FAZA uptake while minimizing biological changes in the tumor. The first proof-of-concept experiment was conducted using mouse models bearing SCCVII tumors. Mouse was positioned in a custom-made holder, and co-registration was ensured by on-board μCBCT. A low washout rate in hypoxic areas was observed, which may be explained by poor blood perfusion. Correlation to in-beam PET data will be analyzed and reported.

References

[1] Toramatsu, Chie, Iwao Kanno, and Taiga Yamaya 2026 "Correction and utilization of the washout effect in range-verification PET for particle therapy." *Radiological Physics and Technology* , 1-11:Springer Nature

[2] Toramatsu, C., Mohammadi, A., Wakizaka, H., Sudo, H., Nitta, N., Seki, C., ... & Yamaya, T. 2022, 'Measurement of biological washout rates depending on tumor vascular status in 15O in-beam rat-PET', *Physics in Medicine & Biology, 67* (12), 125006: IOP Publishing

[3] Parodi, K., Yamaya, T., & Moskal, P. 2023, 'Experience and new prospects of PET imaging for ion beam therapy monitoring', *Zeitschrift für Medizinische Physik, 33* (1), 22-34: Elsevier

[4] Lovatti, G., et al., 2025 'Experimental assessment of novel PET detector components for online imaging of radioactive ion beams' *Physics in Medicine & Biology, 70*(19), 195008: IOP Publishing

[5] Chen, M., Bortfeldt, J., Berthe, D., Dedes, G., Pfeiffer, F., & Parodi, K, 2024 'PP27. 07 DEVELOPMENT AND INITIAL CHARACTERIZATION OF A PHOTON-COUNTING MICRO-CBCT SYSTEM FOR A SMALL ANIMAL PROTON IRRADIATION PLATFORM' *Physica Medica, 125*, 103944: Elsevier

[6] Parodi, K. et al., 2019 'Towards a novel small animal proton irradiation platform: the SIRMIO project' *Acta oncologica, 58*(10), 1470-1475:Taylor & Francis
[7] Bortfeldt J., et al., 2026 'Tailored Instrumentation for (Pre-)Clinical Proton Minibeam Radiotherapy: Collimator Mount, High-Resolution QA and Small-Animal Positioning' presented PMBT workshop

MIC-17-06

Beyond short-lived positron emitters: feasibility of ^{18}F detection for range verification in carbon ion therapy (#1521)

Akram Hamato[1], Chie Toramatsu[1], Hidekatsu Wakizaka[1], Hideaki Tashima[1], Yuma Iwao[1], Han Gyu Kang[1], Go Akamatsu[1], Katia Parodi[2], Taiga Yamaya[1]

[1] National Institutes for Quantum Science and Technology (QST), Advanced Nuclear Medicine Sciences, Chiba, Japan; [2] Ludwig Maximilian University, Department of Medical Physics, Munich, Germany

Abstract

In carbon ion therapy, positron emission tomography (PET) is one of the most investigated methods for range verification that relies on short half-life β^+ emitters such as ^{11}C and ^{15}O. Consequently, in-beam PET or off-beam PET performed immediately after irradiation have been considered mandatory, and little attention has been paid to the existence of longer-lived β^+ emitters than ^{11}C. With a recent increase in PET system sensitivity, delayed acquisitions targeting longer-lived β^+ emitters have become increasingly feasible. In this study, therefore, we focused on the feasibility of off-beam detection of an irradiation-induced ^{18}F component for range verification in carbon ion therapy. Monte Carlo simulations were first performed to estimate the yield of ^{18}F and the other most important β^+ emitters induced in a polymethyl methacrylate (PMMA) phantom irradiated by carbon ion beams. The yield of produced ^{18}F was one-eighth that of the ^{11}C, and the shifts of the dose peak and PET peak were 1.5 mm and 0.5 mm for in- and off-beam PET, respectively. To validate the simulation results, a PMMA phantom and a live tumor-bearing rat model were irradiated with a ^{12}C ion beam of 290 MeV/u at the carbon therapy facility of the Heavy Ion Medical Accelerator in Chiba (HIMAC) to evaluate ^{18}F production in both simplified and biologically relevant environments. One hour after irradiation, PET scans were carried out for 30 min for both the phantom and the rat. Time-activity curves (TACs) were extracted from the PET images, and they showed the presence and detectability of ^{18}F. A measured activity profile was obtained from the off-beam PET image of the phantom and compared with the measured dose. The dose peak and PET peak positions were matched, which is consistent with submillimeter (0.5 mm) shift of the peaks for off-beam PET predicted from the simulation. Our results demonstrate the feasibility of ^{18}F for range verification in carbon ion therapy using off-beam PET.

References
[1] W. Enghardt et al., Nucl. Instrum. Methods Phys., A 525, pp 284-8, 2004.
[2] A. Mohammadi et al., Phys Med Biol. 65, pp 125006, 2020.
[3] A. Mohammadi et al., Phys Med Biol. 67, pp 165001, 2022.
[4] S. Espana et al., Sci Rep. 12, pp 7075, 2022.
[5] H. G. Kang et al., Phys Med Biol. 70, pp 125014, 2025.

14 November, 2026

Time:
14 November, 2026
9:00 – 11:00

Room:
FEDERICO GARCÍA LORCA

MIC-18 | Advanced tomographic reconstruction techniques (2)

Chairs:
Jinyi Qi (Davis)

MIC-18-01

Steerable Kernel Based Emission Tomography Reconstruction (#2137)

Huanzhe Wei[1], Lefteris Livieratos[1,2], Andrew J. Reader[1]

[1] Kings College London, School of Biomedical Engineering and Imaging Sciences, London, UK; [2] Kings College London, Guy's and St Thomas' NHS Foundation Trust, London, UK

Abstract

Kernelized expectation maximization (KEM) has emerged as an effective and practical approach for improving image quality in emission tomographic reconstruction by incorporating high-quality prior information into the iterative reconstruction process. In conventional KEM, the kernel matrix is derived from a prior image and remains fixed throughout reconstruction. This may result in artifacts when the prior image and target emission data are not perfectly matched, especially in cross-modality or cross-scanner settings, such as MR-guided PET reconstruction and PET-guided SPECT reconstruction in theranostic imaging. In those settings, differences in scanner characteristics, acquisition time points, or tracer distributions may cause mismatch between the prior image and the target emission data. In this work, we propose a steerable kernel reconstruction framework that adapts the prior-derived kernel representation according to the measured data. The proposed method dynamically updates the kernel matrix during reconstruction to improve consistency with the measured data. We evaluate the proposed method on 2D brain phantom data for MR-guided PET reconstruction and on 2D thorax phantom data for PET-guided SPECT reconstruction in a theranostic setting. Experimental results demonstrate that the proposed steerable kernel method mitigates mismatch-induced artifacts and achieves improved reconstruction fidelity compared with conventional fixed-kernel approaches. These findings suggest that adaptive kernel steering offers a promising direction for robust prior-guided emission tomography reconstruction under realistic mismatch conditions.

References

[1] G. Wang and J. Qi, “PET image reconstruction using kernel method,”IEEE Trans. Med. Imag., vol. 34, no. 1, pp. 61–71, Jan. 2015.

[2] E. J. Hu, Y. Shen, P. Wallis et al., “LoRA: Low-rank adaptation of large language models,” 2021, arXiv:2106.09685.

[3] K. Thielemans, C. Tsoumpas, S. Mustafovic et al., “STIR: Software for tomographic image reconstruction release 2,” Phys. Med. Biol., vol. 57, no. 4, pp. 867–883, Feb. 2012.

[4] L. A. Polson, R. Fedrigo, C. Li et al., “PyTomography: A Python library for medical image reconstruction,” SoftwareX, vol. 29, p. 102020, Feb. 2025.

MIC-18-02

Cross-Tracer PET Image Reconstruction Using an ^{18}F-FDG-Trained Deep Kernel Model (#2782)

Siqi Li[1], Xiaoyun Long[2], Yang Lv[2], Guobing Liu[1], Jinyi Qi[1], Simon R. Cherry[1], Ramsey D. Badawi[1], Lorenzo Nardo[1], Benjamin A. Spencer[1], Guobao Wang[1]

[1] University of California, Davis, USA; [2] United Imaging Healthcare, Shanghai, China

Abstract

PET image quality is affected by limited-count statistics and the ill-posed nature of tomographic image reconstruction. Deep learning methods have shown promise for improving PET image quality. However, most existing models have primarily been developed and validated using ^{18}F-FDG datasets. The generalizability of ^{18}F-FDG- trained models to less common radiotracers, particularly non-^{18}F tracers with distinct biodistributions and physical properties, has not been well demonstrated. As the clinical and research use of diverse PET tracers continues to expand, there is a growing need for unified deep learning reconstruction methods capable of generalizing across tracers. We previously developed a pretrained deep kernel model using a large-scale ^{18}F-FDG total-body PET dataset and demonstrated its feasibility for tomographic image reconstruction in static PET imaging by using a single-frame MLEM image as the image prior. Unlike post-reconstruction denoising methods that learn tracer-specific activity distributions and directly output images, the deep kernel method learns to construct a kernel matrix that reflects spatial correlations, making it potentially transferable across tracers. In this work, we extend the deep kernel pretraining by incorporating additional ^{18}F-FDG data and then investigate whether the ^{18}F-FDG-trained model can be directly applied to other non-^{18}F tracers without any tracer-specific training or fine-tuning. The proposed method was evaluated on fourteen ^{68}Ga-DOTATATE scans acquired with the uEXPLORER total-body scanner and compared against a state-of-the-art deep-learning denoising model that is also trained on ^{18}F-FDG total-body datasets. Results demonstrate that the proposed method significantly reduces image noise and achieves improved lesion quantitative accuracy. This work demonstrates the feasibility of cross-tracer PET reconstruction using an ^{18}F-FDG-trained deep kernel model, supporting future evaluation in larger multi-tracer datasets.

References

[1] F. Hashimoto, Y. Onishi, Kibo Ote, H. Tashima, A. J. Reader, and Taiga Yamaya, "Deep learning-based PET image denoising and reconstruction: a review," *Radiological Physics and Technology*, Feb. 2024, doi: https://doi.org/10.1007/s12194-024-00780-3.

[2] S. Xue *et al.*, "A cross-scanner and cross-tracer deep learning method for the recovery of standard-dose imaging quality from low-dose PET," *European Journal of Nuclear Medicine and Molecular Imaging*, Dec. 2021, doi: https://doi.org/10.1007/s00259-021-05644-1.

[3] H. Liu, J. Wu, W. Lu, J. A. Onofrey, Y.-H. Liu, and C. Liu, "Noise reduction with cross-tracer and cross-protocol deep transfer learning for low-dose PET," *Physics in Medicine and Biology*, vol. 65, no. 18, pp. 185006–185006, Aug. 2020, doi: https://doi.org/10.1088/1361-6560/abae08.

[4] B. Yu *et al.*, "Robust whole-body PET image denoising using 3D diffusion models: evaluation across various scanners, tracers, and dose levels," *European Journal of Nuclear Medicine and Molecular Imaging*, Feb. 2025, doi: https://doi.org/10.1007/s00259-025-07122-4.

[5] G. Wang and J. Qi, "PET Image Reconstruction Using Kernel Method," *IEEE Transactions on Medical Imaging*, vol. 34, no. 1, pp. 61–71, Jan. 2015, doi: https://doi.org/10.1109/tmi.2014.2343916.

[6] S. Li and G. Wang, "Deep Kernel Representation for Image Reconstruction in PET," *IEEE Transactions on Medical Imaging*, vol. 41, no. 11, pp. 3029–3038, Nov. 2022, doi: https://doi.org/10.1109/tmi.2022.3176002.

[7] S. Li *et al.*, "Static PET Image Reconstruction Using A Pretrained Deep Kernel Method," *2025 IEEE Nuclear Science Symposium (NSS), Medical Imaging Conference (MIC) and Room Temperature Semiconductor Detector Conference (RTSD)*, pp. 1–1, Nov. 2025, doi: https://doi.org/10.1109/nss/mic/rtsd57106.2025.11287136.

MIC-18-03

List-mode PET Image Reconstruction with Neural Radiance Fields

(#1346)

Haoyu Lu[1,2], **Haoyu Lu**[1,2], Catherine E. Davey[1,2], Catherine E. Davey[1,2], Leigh A. Johnston[1,2], Leigh A. Johnston[1,2]

[1] University of Melbourne, Department of Biomedical Engineering, Parkville, Australia; [2] University of Melbourne, Melbourne Brain Centre Imaging Unit, Parkville, Australia; [3] University of Melbourne, Graeme Clark Institute, Parkville, Australia

This research was supported by a Melbourne Research Scholarship from the University of Melbourne, The University of Melbourne's Research Computing Services and the Petascale Campus Initiative. The authors acknowledge the facilities and scientific and technical assistance of the National Imaging Facility, a National Collaborative Research Infrastructure Strategy (NCRIS) capability, at the Melbourne Brain Centre Imaging Unit, University of Melbourne.

Abstract

Numerous AI-based solutions to PET image reconstruction, an ill-posed inverse problem, have been implemented to enhance image quality or convergence speed, yet most suffer from reliance on high-quality paired dataset and lack of robustness. As an emerging methodology, implicit neural representations (INRs) demonstrate tremendous potential in continuous modelling of spatial distribution. However, the existing INR-based PET reconstruction methods generally suffer from loss of information due to compression in sinograms they utilise as input, and do not include corrections for noise caused by the physical factors like attenuation and normalisation. In this work, we present a self-supervised PET reconstruction method based on neural radiance fields (NeRFs), a special type of INR with list-mode coincidences as input, where sensitivity is incorporated as both the weight for sampling points along each LOR and combined corrections for attenuation and normalisation. LORs with no recorded coincidences function as data-driven regularisation and are augmented as part of the input. Results using simulated and experimental data show that our proposed method can achieve excellent image quality and improved contrast, and outperform conventional iterative algorithms and other AI approaches, particularly in recovering fine details in small hot regions.

References

[1] B. Yang, P. He, S. Liu, and L. Zhou, "Neural Radiance Fields Enabled Continuous PET Image Modeling and High-Resolution Reconstruction," *Journal of Nuclear Medicine*, vol. 65, no. supplement 2, pp. 241396–241396, Jun. 2024.

[2] Y. Long *et al.*, "PD-INR: Prior-Driven Implicit Neural Representations for TOF-PET Reconstruction," in *Medical Image Computing and Computer Assisted Intervention – MICCAI 2025*, J. C. Gee, D. C. Alexander, J. Hong, J. E. Iglesias, C. H. Sudre, A. Venkataraman, P. Golland, J. H. Kim, and J. Park, Eds., Cham: Springer Nature Switzerland, 2026, pp. 459–469. doi: 10.1007/978-3-032-04947-6_44.

[3] B. Mildenhall, P. P. Srinivasan, M. Tancik, J. T. Barron, R. Ramamoorthi, and R. Ng, "NeRF: representing scenes as neural radiance fields for view synthesis," *Commun. ACM*, vol. 65, no. 1, pp. 99–106, Dec. 2021, doi: 10.1145/3503250.

[4] H. M. Hudson and R. S. Larkin, "Accelerated image reconstruction using ordered subsets of projection data," *IEEE Transactions on Medical Imaging*, vol. 13, no. 4, pp. 601–609, Dec. 1994, doi: 10.1109/42.363108.

[5] A. R. De Pierro and M. E. B. Yamagishi, "Fast EM-like methods for maximum 'a posteriori' estimates in emission tomography," *IEEE Transactions on Medical Imaging*, vol. 20, no. 4, pp. 280–288, Apr. 2001, doi: 10.1109/42.921477.
[6] K. Gong, C. Catana, J. Qi, and Q. Li, "PET Image Reconstruction Using Deep Image Prior," *IEEE Trans Med Imaging*, vol. 38, no. 7, pp. 1655–1665, Jul. 2019, doi: 10.1109/TMI.2018.2888491.

MIC-18-04

Dynamic image reconstruction for high-resolution SAVANT scanner using non-negative low-rank constraint (#3104)

Yassir Najmaoui[1,2], Yanis Djebra[1], Yanis Chemli[1], Maxime Gaudreault[2], Kathryn Fontaine[1], Maeva Dhaynaut[1], Jean-Dominique Gallezot[1], Marc-André Tétrault[2], Roger Lecomte[3], Marc Normandin[1], Georges El Fakhri[1], Chao Ma[1], Thibault Marin[1]

[1] Yale University, Yale Biomedical Imaging Institute, New Haven, USA; [2] Université de Sherbrooke, Institut interdisciplinaire d'innovation technologique, Sherbrooke, Canada; [3] Université de Sherbrooke, Centre hospitalier universitaire de Sherbrooke, Sherbrooke, Canada

This work was supported in part by the National Institutes of Health under the grants R01EB035093, U01EB027003.

Abstract

Dynamic Positron Emission Tomography (PET) imaging is an essential tool for research in neurodegenerative diseases through the modeling of tracer kinetics.

However, achieving ultra-high spatial resolution in PET systems tends to reduce their overall geometric sensitivity. This leads to a possible compromise between dynamic frame duration, spatial resolution, and noise.

This study presents the application of a non-negative low-rank-constrained reconstruction method tailored for the ultra-high-resolution SAVANT scanner.

Traditional algorithms reconstruct PET images frame-by-frame without taking into account the natural spatiotemporal correlations within the data. This redundancy is leveraged by this method to reconstruct all the dynamic frames simultaneously.

The method alternates between updating a matrix representing the spatial distribution for each temporal basis, and updating a matrix representing the translation from temporal bases to frame.

In order to accommodate for the large memory and computational requirements associated with the SAVANT, we extended the nonnegative low-rank model to support list-mode data and optimized its implementation through Graphical Processing Unit (GPU) acceleration.

In vivo evaluations using a dynamic [18F]DG scan demonstrate a visible improvement in image quality when using the proposed method compared to the conventional frame-by-frame MLEM algorithm. The low-rank constraint allows to preserve greater detail and shows sharper anatomical structures, which better showcases the high resolution of the SAVANT system.

References

[1] Lecomte, Roger et al. 'Scanner Approaching in Vivo Autoradiographic Neuro Tomography (SAVANT): Progress Towards µL Resolution for Imaging the Human Brain', SNMMI 2022.

[2] Djebra, Yanis et al. ''LR-PET: A Subspace-Based Dynamic PET Imaging via Explicit Non-Negative Low-Rank Factorization", IEEE NSS/MIC 2025.
[3] Parra L., Barrett H. "List-mode likelihood: EM algorithm and image quality estimation demonstrated on 2-D PET" IEEE Transactions on Medical Imaging 17, 228 (1998).
[4] Najmaoui, Yassir et al. "YRT-PET: An Open-Source GPU-Accelerated Image Reconstruction Engine for Positron Emission Tomography" IEEE Transactions on Radiation and Plasma Medical Sciences 10, 535 (2026).
[5] Paatero, P. and Tapper, U. "Positive matrix factorization: A non-negative factor model with optimal utilization of error estimates of data values" Environmetrics 5, 111 (1994).
[6] Siddon, R. L. "Fast calculation of the exact radiological path for a three-dimensional CT array" Medical Physics 12, (1985)

MIC-18-05

A Generalized Tuy-Type Completeness Analysis for X-Ray Scattering Tensor Tomography (#2612)

Ruifeng Liu[1,2], Runtao Deng[1,2], Peixuan Song[1], Li Zhang[1,2], Zhentian Wang[1,2]

[1] Tsinghua University, Department of Engineering Physics, Beijing, China; [2] Radiation Imaging of Ministry of Education, Key Laboratory of Particle, Beijing, China

This work was supported in part by National Natural Science Foundation of China (No. 62227804), Beijing Municipal Natural Science Foundation (No. L232115) and National Key Research and Development Program of China (No. 2023YFC2605802).

Abstract

X-ray scattering tensor tomography aims to recover orientation-dependent microstructural information beyond scalar attenuation or scalar dark-field CT. For quantitative reconstruction, however, an aquisition trajectory satisfying Tuy's condition should also provide enough independent angular sensitivity for the tensor model being reconstructed. We formulate this requirement as a generalized Tuy-type completeness condition for scattering tensor tomography, linking conventional geometric visibility with tensor sensitivity. This analysis shows that the former 15-component model is intrinsically incomplete: under each plane, only 12 independent tensor modes can be probed, so arbitrary 15-component fields require additional prior assumptions. In contrast, the reduced 6-component model satisfies the planar completeness requirement under sufficient angular coverage. Planar singular-value tests confirm both the 12-mode limit and the full rank of the reduced model, providing practical criteria for tensor-model selection and aquisition trajectory design and optimization.

References
[1] Kim, J, Kagias, M, Marone, F, Shi, Z & Stampanoni, M 2021, 'Fast acquisition protocol for X-ray scattering tensor tomography', *Scientific Reports*, vol. 11, article no. 23046.
[2] Sharma, Y, Schaff, F, Wieczorek, M, Pfeiffer, F & Lasser, T 2017, 'Design of acquisition schemes and setup geometry for anisotropic X-ray dark-field tomography (AXDT)', *Scientific Reports*, vol. 7, article no. 3195.
[3] Tuy, HK 1983, 'An inversion formula for cone-beam reconstruction', *SIAM Journal on Applied Mathematics*, vol. 43, no. 3, pp. 546–552.
[4] Quinto, ET 1993, 'Singularities of the X-ray transform and limited data tomography in R^2 and R^3', *SIAM Journal on Mathematical Analysis*, vol. 24, no. 5, pp. 1215–1225.
[5] Denisjuk, A 2006, 'Inversion of the X-ray transform for 3D symmetric tensor fields with sources on a curve', *Inverse Problems*, vol. 22, no. 2, pp. 399–411.

[6] Wieczorek, M, Schaff, F, Pfeiffer, F & Lasser, T 2016, 'Anisotropic X-ray dark-field tomography: A continuous model and its discretization', *Physical Review Letters*, vol. 117, no. 15, article no. 158101.
[7] Malecki, A et al. 2014, 'X-ray tensor tomography', *EPL (Europhysics Letters)*, vol. 105, no. 3, article no. 38002.
[8] Liu, R, Zhang, L, Zhu, P & Wang, Z 2025, 'Parameter constraints and ill-conditioning in tensor tomography reconstruction: a theoretical and numerical approach', *Optics Express*, vol. 33, no. 9, pp. 18810–18823.

MIC-18-06

Hamiltonian Monte Carlo Ensemble Features for DATSCAN SPECT Analysis in Parkinson's Disease (#1511)

Theodoros Leontiou[1,2], Shabnam Jaafari[2,7], Christodoulos Likartsis[3], Anna Frixou[4], Yiannis Parpottas[1,2], Efstathios Stiliaris[5,4], Costas N. Papanicolas[4,6]

[1] Frederick University, Department of Mechanical Engineering, School of Engineering, Nicosia, Cyprus; [2] Frederick Research Center, Nicosia, Cyprus; [3] Limassol General Hospital, Department of Nuclear Medicine, Limassol, Cyprus; [4] The Cyprus Institute, CaSToRC, Nicosia, Cyprus; [5] National and Kapodistrian University of Athens, Department of Physics, Athens, Greece; [6] The Cyprus Academy of Sciences, Letters and Arts, Nicosia, Cyprus; [7] European University Cyprus, Department of Histology and Embryology, School of Dentistry, Nicosia, Cyprus

Data used in the preparation of this article were obtained from the Parkinson's Progression Markers Initiative (PPMI) database (https://www.ppmi-info.org/data), RRID:SCR_006431. For up-to-date information on the study, visit https://www.ppmi-info.org.

This work was supported by the Cyprus Research and Innovation Foundation under the project PERSPECT (Project No. EXCELLENCE/0524/0410). PERSPECT project (https://perspect.frederick.ac.cy) is implemented in the frames of Cohesion Policy Programme "THALIA 2021-2027" and is co-funded by the European Union.

Abstract

Single-photon emission computed tomography (SPECT) reconstruction is an ill-posed inverse problem, and standard clinical methods typically provide a single reconstructed image without an explicit characterization of uncertainty. In this work, we adopt a stochastic reconstruction approach based on Hamiltonian Monte Carlo (HMC), which generates an ensemble of radiotracer distributions consistent with the measured projection data and the assumed forward model. Rather than relying solely on the reconstructed mean image, this formulation enables both uncertainty-aware evaluation of conventional measures and the construction of new descriptors derived from ensemble variability. We investigate whether such ensemble-derived features can provide additional diagnostic information for DATSCAN SPECT analysis, complementing standard metrics such as striatal binding ratios (SBR). We show that normalized fluctuation measures extracted from the HMC ensemble exhibit distinct behavior between control and Parkinson's disease cases. These findings suggest that the stochastic reconstruction framework may provide additional diagnostic information and enhance the diagnostic capabilities of SPECT.

MIC-18-07

Monte Carlo–based reconstruction in Ac-225 SPECT: impact on image quality, quantitative accuracy, and computational burden. (#1164)

Chenguang Li[1,2], Pedro Esquinas[1,3], James Fowler[1,2], Xinchi Hou[3], Arman Rahmim[1,2], Carlos Uribe[2,3]

[1] The University of British Columbia, Department of Physics & Astronomy, Vancouver, Canada; [2] BC Cancer Research Institute, Department of Basic & Translational Research, Vancouver, Canada; [3] BC Cancer, Department of Molecular Imaging & Therapy, Vancouver, Canada; [4] University of British Columbia, Department of Radiology, Vancouver, Canada

Abstract

Purpose: Quantitative ^{225}Ac SPECT is challenging because of low counts, complex emissions, scatter, and septal penetration[1]. This study developed and evaluated a Monte Carlo (MC)-based reconstruction framework for ^{225}Ac SPECT, focusing on image quality, quantitative accuracy, and computational cost.

Methods: SIMIND was used as an MC forward-projector for a vendor-specific SPECT system with a high-energy collimator, while an analytical back-projector was retained to improve efficiency[2]. Unlike conventional MLEM with TEW scatter correction, the MC model incorporated patient scatter, collimator penetration/scatter, detector backscatter, and system response. Performance was evaluated using both simulated and experimental phantom data. The simulated phantom contained 20, 40, and 72 mm spheres, and the experimental phantom contained a 60 mm sphere, both with a 10:1 sphere-to-background activity ratio. Reconstructions used a 218 keV photopeak with a 20% window and were assessed using the recovery coefficient(RC) and contrast recovery coefficient(CRC).

Results: In simulations, MC reconstruction improved contrast recovery and reduced scatter and septal-penetration artifacts. At 25 iterations, mean CRCs for the 72, 40, and 20 mm spheres were 90.1%, 61.3%, and 21.9%, compared with 45.4%, 29.1%, and 9.4% for conventional reconstruction. MC reconstruction directly estimated activity in MBq and achieved RCs of 90.2% and 94.5% for the 72 and 40 mm spheres. Experimental results showed consistent improvement, with MC reconstruction more than doubling CRC at 25 iterations (75.4% vs. 29.2%) and achieving an RC of 88.5% for the 60 mm sphere. Reducing photon histories from 600 to 30 million per projection preserved accuracy for the 72 mm sphere while reducing runtime from 53 to 3.1 min per iteration.

Conclusion: MC-based reconstruction substantially improves image quality and quantitative accuracy for ^{225}Ac SPECT and may support more reliable post-therapy imaging and dosimetry.

References

[1] Zacherl, MJ, Gildehaus, FJ, Mittlmeier, L, Boening, G, Gosewisch, A, Wenter, V, Unterrainer, M, Schmidt-Hegemann, N, Belka, C, Kretschmer, A, et al. 2021, 'First clinical results for PSMA-targeted α-therapy using 225Ac-PSMA-I&T in advanced-mCRPC patients', Journal of Nuclear Medicine, 62(5), 669–674, Society of Nuclear Medicine.

[2] Gustafsson, J, Brolin, G, Ljungberg, M 2018, 'Monte Carlo-based SPECT reconstruction within the SIMIND framework', Physics in Medicine & Biology, 63(24), 245012, IOP Publishing.

MIC-18-08

Sparse-View ^{177}Lu SPECT Reconstruction for Pre-Treatment Dosimetry using Gaussian Mixtures (#2004)

Hyun Ji Lee[1,2], Sangjin Bae[1,2], Jae Sung Lee[1,2]

[1] Seoul National University Graduate School, Interdisciplinary Program in Bioengineering, Seoul, South Korea; [2] Seoul National University Graduate School, Integrated Major in Innovative Medical Science, Seoul, South Korea; [3] Brightonix Imaging Inc., Seoul, South Korea

Abstract

Pre-treatment dosimetry for ^{177}Lu-DOTATATE therapy requires accurate reconstruction from low-dose sparse-view SPECT imaging, which remains challenging due to severe noise and limited projection information. We propose a Gaussian Mixture Model (GMM)-based reconstruction framework with projection-domain optimization for sparse-view ^{177}Lu SPECT imaging. Experimental results on multi-timepoint ^{177}Lu-DOTATATE SPECT datasets demonstrated competitive reconstruction and dosimetry performance with substantially faster optimization under sparse-view conditions.

References

[1] Kim, Keon Min, et al. "Pre-treatment Dosimetry using Synthetic Full-Dose SPECT generated from Low-Dose SPECT with Self-Supervised NERF." (2024): 241297-241297.

[2] Kerbl, Bernhard, et al. "3d gaussian splatting for real-time radiance field rendering." *ACM Trans. Graph.* 42.4 (2023): 139-1.

Time:
14 November, 2026
9:00 – 11:00

Room:
MANUEL DE FALLA

MIC-19 | Signal and data processing

Chairs:
Jae Sung Lee (Seoul)
Fumio Hashimoto (Gainesville)

MIC-19-01

Noise-Aware Brownian Bridge Diffusion Model for Denoising of Low-Dose PET Images (#2951)

Wolf De Mits[1], Elise Taragola[1], Boris Vervenne[1], Margaret E. Daube-Witherspoon[2], Christian Vanhove[1], Samuel Matej[2], Stefaan Vandenberghe[1], Joel S. Karp[2], Florence M. Muller[1,2]

[1] Ghent University, Faculty of Engineering and Architecture, Ghent, Belgium; [2] University of Pennsylvania, Department of Radiology, Philadelphia, USA

This work was supported by the Research Foundation Flanders (Vervenne: 1195125N, Muller: 11P0E24N) and the National Institutes of Health, R01 CA-113941 (Karp, PI). Data Courtesy (UPenn): J Dubroff, C Wiers, P Bravo.

Abstract

This study proposes a Noise-Aware Brownian Bridge Diffusion Model (NA-BBDM) for low-dose positron emission tomography (PET) denoising. The proposed NA-BBDM models a conditional diffusion path between paired low- and full-dose PET images and incorporates the estimated noise level from the input image into the network. The noise level is estimated from the variance of the residual between the low-dose image and a Gaussian-smoothed version. The diffusion path uses a parabolic variance schedule with zero variance at both endpoints (i.e., low- and full-dose images), parameterized by peak variance and number of diffusion steps. Both are treated as noise-dependent hyperparameters and optimized through grid search. Training data consisted of 25 ^{18}F-FDG datasets acquired on the PennPET Explorer and subsampled to emulate dose levels from 1/5 to 1/300 of total counts. Performance was compared with a U-Net and evaluated on independent ^{18}F-FDG and unseen ^{11}C-carfentanil (CFN) datasets. The NA-BBDM produced images with reduced noise speckles (still present with the U-Net) and better-preserved high-uptake regions at ultra-low-dose levels. Quantitatively, the NA-BBDM also achieved lower SUV variability and mean squared error for ^{11}C-CFN, especially below 1/60th dose. Our results suggest that the NA-BBDM provides a robust framework for ultra-low-dose and cross-tracer PET denoising.

References

[1] B. Yu, *et al.*, "Robust whole-body PET image denoising using 3D diffusion models," *Eur J Nucl Med Mol Imaging*, 2025.

[2] B. Li, *et al.*, "BBDM: Image-to-image translation with Brownian bridge diffusion models," in *Proc. IEEE on Comp Vision and Pattern Recogn*, 2023.

[3] B. Dai, *et al.*, "Performance evaluation of the PennPET Explorer with expanded axial coverage," *Phys Med Biol*, 2023.

[4] H. Xie, *et al.*, "Unified noise-aware network for low-count PET denoising," *IEEE Trans Radiat Plasma Med Sci*, 2024.

[5] F. Muller, *et al.*, "Impact of deep learning denoising on kinetic modelling for low-dose dynamic PET," *Eur J Nucl Med Mol Imaging*, 2025.

MIC-19-02

N2N-DiffPET: Self-supervised Diffusion for Low-dose PET Image Denoising (#2281)

Kailong Fan[2,1], Yichen Wu[1], Quanzheng Li[1], Huafeng Liu[2], Ning Guo[1]

[1] Massachusetts General Hospital and Harvard Medical School, Department of Radiology, Boston, USA; [2] Zhejiang University, Department of Optical Engineering, Hangzhou, China

Abstract

Low-dose positron emission tomography (PET) imaging can reduce radiation exposure and shorten acquisition time, but reduced photon counts introduce strong count-dependent noise and degrade quantitative reliability. Supervised deep learning methods usually require paired low-dose and normal-dose PET images, which are difficult to acquire in clinical practice. We propose N2N-DiffPET, a self-supervised diffusion framework for low-dose PET denoising without normal-dose supervision. Inspired by recent self-supervised diffusion MRI denoising, N2N-DiffPET adapts iterative diffusion refinement to PET using paired noisy PET observations generated from independent low-dose measurements by event splitting or Poisson resampling. To better model PET noise, N2N-DiffPET constructs a fusion trajectory between the paired noisy PET images and perturbs it using pair-derived PET noise rather than synthetic Gaussian noise. Co-registered MRI is incorporated as an anatomical condition to improve structural preservation. During inference, bidirectional deterministic denoising is performed, and the two directional outputs are averaged to reduce directional bias. Normal-dose PET images are not used for training and are only used for evaluation. Experiments on BrainWeb-based PET/MR simulation data show that N2N-DiffPET suppresses noise while preserving anatomical structures and regional uptake, outperforming conventional denoising methods and self-supervised baselines in visual quality and quantitative metrics.

References

[1] J. Lehtinen, J. Munkberg, J. Hasselgren, S. Laine, T. Karras, M. Aittala, and T. Aila, “Noise2Noise: Learning image restoration without clean data,” arXiv preprint arXiv:1803.04189, 2018.

[2] C. Wu, Q. Kong, Z. Jiang, and S. K. Zhou, “Self-supervised diffusion MRI denoising via iterative and stable refinement,” arXiv preprint arXiv:2501.13514, 2025.

[3] C. A. Cocosco, V. Kollokian, R. K.-S. Kwan, and A. C. Evans, “BrainWeb: Online interface to a 3D MRI simulated brain database,” Proceedings of the 3rd International Conference on Functional Mapping of the Human Brain, 1997.

MIC-19-03

Multi-Dose PET Image Denoising using Consistency Flow Matching

(#1864)

Joo Hyun Lee[1,2], Sangjin Bae[1,2], Jae Sung Lee[3,4]

[1] Seoul National University, Interdisciplinary Program in Bioengineering, Seoul, South Korea; [2] Seoul National University, Integrated Major in Innovative Medical Science, Seoul, South Korea; [3] Seoul National University, Department of Nuclear Medicine, Seoul, South Korea; [4] Brightonix Imaging Inc., Seoul, South Korea

This research was supported by the AI Computing Infrastructure Enhancement (GPU Rental Support) User Support Program funded by the Ministry of Science and ICT (MSIT), Republic of Korea. (No. RQT-25-090157)

Abstract

Low-dose PET reduces patient radiation burden by decreasing injected radiotracer dose or scan duration, but the resulting reduction in photon counts introduces statistical noise that degrades diagnostic image quality. Most deep learning denoising methods are trained at a single fixed dose reduction factor and do not generalize to unseen dose levels. We propose Consistency Flow Matching (CFM), a multi-dose denoising framework that augments flow matching with a cross-dose consistency regularization. During training, pairs of low-dose images at two different dose reduction factors are jointly processed, and a consistency loss enforces agreement between their predicted normal-dose outputs, promoting a dose-invariant flow field. Dose conditioning is achieved through Spatial Feature-wise Linear Modulation with a log-sinusoidal dose embedding. Experiments on the UltraLow-Dose PET Challenge dataset show that CFM improves perceptual image quality and out-of-distribution generalization over standard flow matching, confirming the benefit of cross-dose consistency regularization.

References

[1] Ronneberger, O, Fischer, P, Brox, T 2015, 'U-Net: Convolutional networks for biomedical image segmentation', *Proc. MICCAI*

[2] Lipman, Y et al. 2023, 'Flow matching for generative modeling', *Proc. ICLR*

[3] Song, Y, Dhariwal, P, Chen, M, Sutskever, I 2023, 'Consistency models', *Proc. ICML*

[4] Park, T, Liu, MY, Wang, TC, Zhu, JY 2019, 'Semantic image synthesis with spatially-adaptive normalization', *Proc. CVPR*

[5] Xue, S et al. 2025, 'UDPET: Ultra-low dose PET imaging challenge dataset', *Proc. MICCAI*, vol. 15972, Springer

MIC-19-04

High-Temporal-Resolution Data-Driven Respiratory Motion Estimation in Cardiac PET Imaging (#1890)

Hongrong Wei, Chen Sun, Zhiheng Feng, Yue Li, Duo Zhang, Qing Ye, Yihuan Lu

United Imaging Healthcare, Shanghai, China

Abstract

Cardiac PET is widely used for myocardial perfusion imaging and viability assessment, both of which require high image quality and quantitative accuracy. In free-breathing acquisitions, respiratory motion can induce cardiac displacement, particularly along the superior-inferior (SI, z-axis) direction, leading to image blurring, attenuation-emission mismatch, and quantitative bias. Reliable estimation of this translation is therefore essential for effective motion correction. In this work, we propose COD-S (Centroid of Distribution-Scaled), a data-driven method to estimate respiratory-induced SI cardiac translation in cardiac PET. COD-S integrates the high sensitivity and high temporal resolution of COD analysis with the physically scaled displacement provided by image registration. Specifically, the respiratory motion trajectory is decomposed into waveform and amplitude components, where the waveform is derived from COD and the amplitude are calibrated using registration-based estimates. This produces a high-temporal-resolution and physically interpretable cardiac translation trajectory without external respiratory hardware, providing a practical input for motion correction in cardiac PET.

References

[1] D. Zhang, Y. Li, C. Sun, H. Zeng, G. Yang, F. Kang, J. Wang, and Y.Lu, "A novel data-driven respiratory gating method in PET," in Proc. IEEE NSS/MIC/RTSD), Vancouver, BC, Canada, 2023, pp. 1.

[2] C. Sun, E. M. Revilla, J. Zhang, K. Fontaine, T. Toyonaga, J.-D. Gallezot, T. Mulnix, J. A. Onofrey, R. E. Carson, and Y. Lu, "An objective evaluation method for head motion estimation in PET–Motion corrected centroid-of-distribution," NeuroImage, vol. 264, pp. 119678, Dec. 2022.

[3] J. Zhang, C. Sun, E. M. Revilla, D. Zhang, S. P. Mok, C. Liu, K. Fontaine, R. Carson, and Y. Lu, "An objective evaluation method for respiratory motion correction in TOF PET," in Proc. IEEE NSS/MIC/RTSD), Boston, MA, USA, 2020, pp. 1.

MIC-19-05

Spatial-variant fast non-linear energy calibration for a high resolution SSLE pixelated PET detector (#3118)

Lidia Jiménez Algarra[1], Víctor Sánchez Tembleque[1], Luis Batres Mongil[1], David Perez-Benito[1], Juan J. Vaquero López[1,2]

[1] Departamento de Bioingeniería, Universidad Carlos III de Madrid, Madrid, Spain, Departamento de Bioingeniería, Leganés, Spain; [2] Instituto de Investigación Sanitaria Gregorio Marañón, Madrid, Spain, Madrid, Spain

Abstract

High-resolution PET detectors require position dependent energy calibration due to the spatial variability of their optical response. This work addresses that challenge for a novel hexagonal LYSO detector structured by subsurface laser engraving (SSLE) with a double honeycomb displaced crystal array, coupled to a custom 61-channel hexagonal SiPM. This design provides two depth-of-interaction (DOI) layers as well as a high-granularity for event's positioning. We first present a DOI separation method based on a dispersion metric computed from the per-channel light distribution, enabling crystal pixel specific calibration for each layer independently. After precise vertex identification, energy calibration is then performed per crystal pixel by fitting four reference points: the 202 and 307 keV intrinsic 176Lu peaks and the 511 and 1275 keV peaks from a 22Na source to a non-linear model accounting for SiPM saturation. These points are fitted to a non-linear response model that accounts for SiPM saturation and electronic nonlinearity. The proposed calibration produces stable photopeak positions across the detector and achieves an energy resolution of 15.2% at 511 keV, while preserving the DOI-resolved flood maps required for high-granularity event's positioning by PET imaging techniques.

MIC-19-06

Random Coincidence Correction for Inter-Crystal Scatter Events in PET

(#2588)

Hyeongseok Shim[1,2], Guen Bae Ko[2]

[1] Korea Advanced Institute of Science and Technology, Department of Nuclear and Quantum Engineering, Daejeon, South Korea; [2] Korea Advanced Institute of Science and Technology, Mechanical Engineering Research Institute, Daejeon, South Korea

This work was supported by the National Research Foundation of Korea(NRF) grant funded by the Korea government(MSIT) (RS-2026-25490510).

Abstract

Inter-crystal scatter (ICS) events in PET, in which a 511 keV photon deposits energy across multiple crystals, offer a route to higher effective sensitivity but are conventionally discarded by photopeak windowing. Prior work has focused on positioning the first-interaction crystal, yet positioning alone does not translate ICS recovery into a system-level sensitivity gain: accepting ICS events requires lowering the lower-level discriminator, which sharply increases the singles rate and raises three issues that have not been jointly addressed, how to group raw singles into candidate ICS events, how to reject uncorrelated groupings of independent-photon singles, and whether the resulting triple coincidences are compatible with the dual-coincidence random-correction framework. This study presents a unified pipeline that addresses all three. Candidate ICS events are formed from list-mode singles and screened for type-1 randoms (false ICS) by a joint timing–distance gate, suppressing the singles-level ICS-to-PE ratio from 15.5–18% to 7–7.5% with negligible activity dependence. Validated PE and ICS events are then paired into PE–PE and PE–ICS prompt coincidences, and the singles-prompt (SP) framework is extended to ICS events by symmetric deflation of the measured ICS rate, yielding a type-resolved SP estimator for type-2 random correction. Validated through GATE simulations of the Pharos PET scanner (Brightonix Imaging; Seoul, Korea), the type-resolved SP estimator achieves $\hat{R}/R_{true}$ = 0.97–1.01 for PE–ICS coincidences across six activity conditions

(200–667 μCi), outperforming the unified strategy and standard delayed-window and singles-rate methods. The complete pipeline delivers approximately 13% additional net true coincidences over a PE-only baseline, with essentially activity-invariant gain across the operating range examined.

References
[1] M. S. Comanor, P. R. G. Virador, and W. W. Moses, "Algorithms to identify detector Compton scatter in PET modules," IEEE Trans. Nucl. Sci., vol. 43, no. 4, pp. 2213–2218, Aug. 1996.
[2] G. Pratx and C. S. Levin, "Bayesian reconstruction of photon interaction sequences for high-resolution PET detectors," Phys. Med. Biol., vol. 54, no. 17, pp. 5073–5094, Sep. 2009.
[3] E. Lage, V. Parot, S. C. Moore, A. Sitek, J. M. Udías, S. R. Dave, M. Park, J. J. Vaquero, and J. L. Herraiz, "Recovery and normalization of triple coincidences in PET," *Med. Phys.*, vol. 42, no. 3, pp. 1398–1410, Mar. 2015.
[4] J. F. Oliver and M. Rafecas, "Modelling random coincidences in positron emission tomography by using singles and prompts: a comparison study," PLoS ONE, vol. 11, no. 9, e0162096, Sep. 2016.
[5] I. Torres-Espallardo, M. Rafecas, V. Spanoudaki, D. P. McElroy, and S. I. Ziegler, "Effect of inter-crystal scatter on estimation methods for random coincidences and subsequent correction," Phys. Med. Biol., vol. 53, no. 9, pp. 2391–2411, 2008.

MIC-19-07

A Software-Based Coincidence Sorters for Simultaneous PET Emission and Lu-176 Intrinsic Transmission Data Extraction (#1792)

Xin Zhao, **Xin Zhao**, Zhao Wang, Zhao Wang, Zhaoheng Xie, Zhaoheng Xie

Peking University, Beijing, China

This work was supported by National Natural Science Foundation of China (62394311) and National Biomedical Imaging Facility Grant.

Abstract
Conventional PET coincidence sorters focus on emission events, disregarding intrinsic Lu-176 background radiation in LYSO (Lutetium-Yttrium Oxyorthosilicate) crystals as unwanted noise. To enable simultaneous acquisition of emission and intrinsic transmission data, we developed a software-based multi-window coincidence processor capable of extracting mixed-energy coincidence events from list-mode singles data. The processor utilizes geometric constraints and a dynamic time-of-flight (TOF)-based limit to filter candidate pairs. To suppress severe 511 keV's backscatter contamination in the 202 keV transmission window, a dual-condition rejection strategy was integrated, reducing residual crosstalk to 15.9%. Quantitative validation against Monte Carlo simulation ground truth showed good agreement in count statistics, sinograms, and radial profiles. Tomographic reconstructions successfully recovered phantom structures, validating the fidelity of the simultaneously extracted emission and intrinsic transmission coincidences.

References
[1] Omidvari, N, Cheng, L, Leung, EK, et al. 2022, 'Lutetium background radiation in total-body PET–A simulation study on opportunities and challenges in PET attenuation correction', Frontiers in Nuclear Medicine, 2, 963067, Lausanne: Frontiers Media SA.
[2] Leung, EK, Judenhofer, MS, Cherry, SR, et al. 2018, 'Performance assessment of a software-based coincidence processor for the EXPLORER total-body PET scanner', Physics in Medicine & Biology, 63(18), 18NT01, Bristol: IOP Publishing.

[3] Li, T, He, L, Liu, Z, et al. 2024, 'CT-Less Attenuation Correction for PET using Backward Inter-Crystal Scattered Events', 2024 IEEE Nuclear Science Symposium (NSS), Medical Imaging Conference (MIC) and Room Temperature Semiconductor Detector Conference (RTSD), 1-1, New York: IEEE.

MIC-19-08

Characterisation of Positron Emission Particle Tracking (PEPT) Performance for In-vivo Blood Flow Estimation in Preclinical PET (#1869)

Laurence Vass, Tia Gibson, Rafa De Torres, Paul K. Marsden

King's College London, School of Biomedical Engineering and Imaging Sciences, London, UK

Abstract

Positron Emission Particle Tracking (PEPT) enables tracking of individual radiolabelled particles and is widely used in industrial applications (e.g. fluid dynamics), but remains underexplored for biomedical use. We recently demonstrated whole-body *in vivo* tracking of single nanoparticles in mice using a preclinical PET scanner, showing transit through the vasculature from the injection site. However, murine blood flow varies from a few to several hundred mm/s. Within this range, the conditions under which PEPT can reliably resolve motion remain poorly characterised. Trajectory estimation depends on a complex interplay between activity, particle velocity, acquisition settings (e.g. energy window, temporal sampling), and algorithm parameters, which have not been explored for murine blood flow estimation.

We address this by establishing a controlled framework to evaluate PEPT performance on a 3-ring PET/CT system (Mediso nanoScan 123S). A modified FLSUN 3D printer generated programmable trajectories of Ga-68 radiolabelled beads (0.4–350 kBq) at speeds of 6–170 mms^{-1}. Ground-truth motion was validated via high-frame-rate video and frame-by-frame analysis. Trajectories were reconstructed using the Birmingham method; estimated speeds and positions were compared to ground truth to quantify accuracy and localisation error.

Our results show that tracking a single particle at speeds up to 50 mms^{-1} with RMSE <2.5 mm requires activity >1.2 kBq. At ≥0.7 kBq, speeds had 18–34% error with large RMSE. At ≤0.5 kBq, trajectories were not reliably resolved. Localisation error increased with decreasing activity and increasing speed, exceeding 10 mm RMSE in low-activity, high-speed regimes. These findings suggest activities >1.2 kBq are required for reliable intravascular speed estimation.

References

[1] Windows-Yule, C. R. K., M. T. Herald, A. L. Nicuşan, et al. "Recent Advances in Positron Emission Particle Tracking: A Comparative Review." *Reports on Progress in Physics* 85, no. 1 (2022): 016101. https://doi.org/10.1088/1361-6633/ac3c4c.

[2] Pellico, Juan, Laurence Vass, Amaia Carrascal-Miniño, et al. "In Vivo Real-Time Positron Emission Particle Tracking (PEPT) and Single Particle PET." *Nature Nanotechnology* 19, no. 5 (2024): 668–76. https://doi.org/10.1038/s41565-023-01589-8.

[3] Nguyen, Hieu T. M., Neeladrisingha Das, Rohollah Nasiri, and Guillem Pratx. "In Vivo Positron Emission Particle Tracking (PEPT) of Single Cells Using an Expectation Maximization Algorithm." *IEEE Transactions on Medical Imaging* 45, no. 4 (2026): 1673–85. https://doi.org/10.1109/TMI.2025.3640076.

[4] Parker, D. J., C. J. Broadbent, P. Fowles, M. R. Hawkesworth, and P. McNeil. "Positron Emission Particle Tracking - a Technique for Studying Flow within Engineering Equipment." *Nuclear Instruments and Methods in Physics Research Section A: Accelerators, Spectrometers, Detectors and Associated Equipment* 326, no. 3 (1993): 592–607. https://doi.org/10.1016/0168-9002(93)90864-E.

Time:
14 November, 2026
11:30 – 12:45

Room:
FEDERICO GARCÍA LORCA

MIC-20 | Total body imaging systems including applications and kinetic modeling, molecular connectivity and radiomics

Chairs:
Stefaan Vandenberghe (Ghent)
Kevin Chung (Boston)

MIC-20-01

Evaluation of Sparse-Geometry Designs for Long-Axial Field-of-View Preclinical SPECT (#1427)

Elissa L. Avila[1], Lorenzo Confalonieri[1], Xiaochuan Pan[3], Chin-Tu Chen[3], Elena M. Zannoni[1,2]

[1] The University of Texas at Austin, Walker Department of Mechanical Engineering, Austin, USA; [2] The University of Texas at Austin, Department of Diagnostic Medicine, Austin, USA; [3] The University of Chicago, Department of Radiology, Chicago, USA

We thank the Rising Faculty Science and Technology Acquisition and Retention (STARs) Program, The University of Texas System, for the generous support.

Abstract

This study presents the design and preliminary performance evaluation of a long-axial field-of-view (LA-FOV) preclinical SPECT system for small-animal total-body imaging (TBI) [1]. The proposed full scanner consists of 240 CZT detectors distributed across 10 panels and coupled with a multi-pinhole collimator. The system offers a FOV of 74 mm in diameter, ideal for rat imaging, a high-sensitivity central region of 37 mm in diameter tailored for mice, and an axial coverage up to 20 cm.

System performance was characterized through simulations to compute the system response function, 3D sensitivity map, and reconstructed image quality, assessed using a digital long-axial Derenzo phantom under both noiseless and Poisson-noise conditions. A 50% checkerboard sparse configuration was compared against the full configuration [2-3]. While the sparse configuration yielded a proportional 50% reduction in sensitivity, the volumetric uniformity was preserved. Both configurations achieve similar spatial resolution. In noiseless conditions, both can resolve hot rods as small as 1.62 mm with average peak-to-valley ratios (PVR) of 4.35 (full) and 5.32 (sparse). Under noisy conditions, both configurations can fully resolve the 1.93-mm hot rods with average PVR of 7.22 (full) and 7.58 (sparse). Notably, this performance is consistent along the 20 cm axial extent of the phantom.

Future work will evaluate spiral sparse geometries at sparsity levels of 25%, 33%, 66%, and 75% to characterize the degradation of image quality, with quantitative analysis in terms of contrast-to-noise ratio and contrast recovery coefficient. This work supports a pathway toward cost-effective LA-FOV preclinical SPECT instrumentation suitable for TBI.

References

[1] J. Du and T. Jones, “Technical opportunities and challenges in developing total-body PET scanners for mice and rats,” *EJNMMI Physics*, vol. 10, no. 1, p. 2, Jan. 2023. [Online]. Available: https://doi.org/10.1186/s40658-022-00523-6

[2] Z. Zheng *et al.*, "Preliminary investigation of optimization-based image reconstruction for TOF PET with sparse configurations," in *Proc.SPIE*, 2019, vol. 11072, p. 110720L, doi: 10.1117/12.2534846. [Online]. Available: https://doi.org/10.1117/12.2534846

[3] N. A. Karakatsanis, M. H. Nehmeh, M. Conti, G. Bal, A. J. González, and S. A. Nehmeh, "Physical performance of adaptive axial FOV PET scanners with a sparse detector block rings or a checkerboard configuration," *Physics in Medicine & Biology*, vol. 67, no. 10, p. 105010, 2022/05/12 2022, doi: 10.1088/1361-6560/ac6aa1.

MIC-20-02

Feasibility study of ^{68}Ga/^{18}F multiplexed PET imaging on a total-body PET scanner (#2284)

Wen He[1], Craig S. Levin[1,2]

[1] Stanford University, Department of Radiology, Palo Alto, USA; [2] Stanford University, Departments of Electrical Engineering, Bioengineering, and Physics, Palo Alto, USA

This work was supported in part by a grant from the Neuroendocrine Tumor Research Foundation (NETRF).

Abstract

Multiplexed PET (*m*PET) enables simultaneous multi-tracer imaging by detecting prompt gamma in positron plus prompt gamma emitters for triple-photon coincidence tagging, thereby distinguishing them from pure positron emitters. ^{68}Ga is a commonly used PET isotope and emits a prompt gamma at 1077 keV in ~1% of its positron decays. In this study, we assessed the feasibility of ^{68}Ga/^{18}F *m*PET on the GE Omni 128 cm total-body PET/CT using Monte Carlo simulation.

The scanner model was validated against NU2-2018 sensitivity and NECR measurements. A NU2-2018 image-quality phantom was simulated with a 1:1 ^{68}Ga/^{18}F background (2.65 kBq/mL per isotope) and 4:1 hot-to-background ratio, with the two largest spheres assigned to ^{18}F and the four smaller spheres to ^{68}Ga to represent a challenging case for triple-coincidence detection. Isotope unmixing employed an “alternating-update joint EM (AU-EM) algorithm” that we developed with a prompt-gamma detection efficiency map simulated from a ^{68}Ga point-source array.

The simulation yielded 3.46 billion double and 57 million triple coincidences; triple events were dominated by randoms (55.6%), with ^{68}Ga true triples comprising 7.1%. Using true events only, AU-EM reconstructions successfully separated the ^{68}Ga and ^{18}F distributions and achieved percent contrast comparable to OSEM reconstructions from ground-truth events, although percent background variability was degraded. These results demonstrate the feasibility of ^{68}Ga/^{18}F *m*PET on a total-body PET scanner and motivate future work on random triple-coincidence estimation, variance reduction methods, and experimental validation.

References

[1] Y. Sanli *et al.*, “Neuroendocrine Tumor Diagnosis and Management: 68Ga-DOTATATE PET/CT,” *American Journal of Roentgenology*, vol. 211, no. 2, pp. 267–277, Aug. 2018, doi: 10.2214/AJR.18.19881.

[2] W. He, J. W. Foster, and C. S. Levin, “Alternating Update Method for Joint EM Estimation of Multiple Tracer Distributions in Multiplexed PET (mPET),” *IEEE Transactions on Radiation and Plasma Medical Sciences*, pp. 1–1, 2026, doi: 10.1109/TRPMS.2026.3688900.

[3] G. Schramm and K. Thielemans, “PARALLELPROJ—an open-source framework for fast calculation of projections in tomography,” vol. 3, Jan. 2024, doi: 10.3389/fnume.2023.1324562.

MIC-20-03

Positronium Lifetime Imaging on LAFOV PET: Impact of Estimation Methods and Count Statistics (#2317)

Lukas U. Rauscher[1], William Steinberger[2], Elisa Körner[3], Pia M.-L. Linder[3], Christian la Fougère[3,4], Fabian P. Schmidt[1,3]

[1] University Hospital Tuebingen, Department of Preclinical Imaging and Radiopharmacy, Tuebingen, Germany; [2] Siemens Medical Solutions, Inc., Knoxville, USA; [3] University Hospital Tuebingen, Department of Nuclear Medicine and Clinical Molecular Imaging, Tuebingen, Germany; [4] University of Tuebingen, Cluster of Excellence iFIT (EXC 2180) "Image Guided and Functionally Instructed Tumor Therapies", Tuebingen, Germany

Abstract

Positronium lifetime imaging (PLI) enables probing tissue microstructure via the lifetime of ortho-positronium (o-Ps). Robust voxel-wise lifetime estimation remains limited even for high-sensitivity long axial field-of-view (LAFOV) positron emission tomography (PET) systems due to a combination of low detection sensitivity for triple-coincidences and variability in o-Ps lifetime (o-PS-L) extraction methods. In this work, three established approaches for o-Ps-L estimation are presented: least-squares fitting (LS), Bayesian fitting (B), and exponential fitting of the late decay tail (LT). These methods were systematically evaluated using inorganic samples (Quartz, wet and dry Amberlite XAD-4) prepared with I-124. Data were acquired on a Siemens Healthineers Biograph Vision Quadra system in single event acquisition mode and analyzed using time difference distributions (TDDs). The o-PS-L for the Quartz sample was measured to be 1.572 | 1.573 | 1.574 ns (LS | B | LT), wet XAD-4 2.381 | 2.381 | 2.798 ns and dry XAD-4 2.719 | 2.719 | 2.915 ns. LS and B approaches showed consistent results across all samples, while the LT method exhibited systematic deviations under reduced o-Ps contribution. A subsampling analysis identified a minimum of 2500 events per TDD for stable o-PS-L estimation within 5% deviation from the full-statistics result. Based on this constraint, voxel-wise lifetime imaging was demonstrated in a metastatic thyroid cancer patient following injection of 37 MBq I-124 using a 15 min acquisition. To satisfy required statistics, a voxel size of 32 mm was selected, and lifetime estimates were restricted to regions with sufficient counts. These results identify count statistics as primary limiting factor for clinically viable PLI and define a practical threshold for stable voxel-wise lifetime imaging. Future work will focus on extending acquisition times to enable higher spatial resolution and improve robustness for clinical applications.

References

[1] K. Dulski et al., Acta Phys. Pol. A, vol. 132, no. 5, 2017

[2] W. M. Steinberger et al., EJNMMI Phys, vol. 11, no. 1, 2024

[3] M. Yamawaki et al., Jpn. J. Appl. Phys., vol. 59, no. 11, p. 2020

[4] L. Mercolli et al., *arXiv (Cornell University)*, 2025

MIC-20-04

Intercept Graphical Plot with Normalization for Total-Body PET Parametric Imaging with Reduced Input Function Data and Enhanced Inter-Subject Quantification (#2748)

Yiran Wang[1], Qing Ye[2], Siqi Li[3], Tiantian Li[1], Benjamin A. Spencer[3,4], Yasser Abdelhafez[3], Xishan Sun[1], Adam Chandler[1], Lingzhi Hu[1], Hongdi Li[1], Lorenzo Nardo[3], Moon S. Chen[5], Ramsey D. Badawi[3,4], Simon R. Cherry[4,6], Guobao Wang[3]

[1] United Imaging Healthcare, North America, Houston, USA; [2] United Imaging Healthcare, Shanghai, China; [3] University of California, Davis, Department of Radiology, Sacramento, USA; [4] University of California, Davis, Department of Biomedical Engineering, Davis, USA; [5] University of California, Davis, Department of Internal Medicine, Sacramento, USA; [6] King's College London, School of Biomedical Engineering and Imaging Sciences, London, UK

Abstract

The Patlak plot is a widely used kinetic modeling method for estimating the tracer net influx rate K_i in dynamic PET imaging. However, the requirement for a full time course input function limits its routine clinical use. The Relative Patlak (RP) plot mitigates this constraint effectively by reducing the required acquisition time. Nevertheless, the quantified RP slope K_i' introduces a time-dependent and subject-specific scaling factor relative to K_i, reducing the reliability for inter-subject analysis. In this study, we propose an Intercept Graphical (IG) plot with an associated normalization that requires the same imaging duration as the RP method. The quantified parameter K_{IG} has a time-independent and approximately subject-independent scaling factor for estimating K_i. We evaluated the proposed method using total-body dynamic PET images of 12 healthy and 10 cancer subjects. To evaluate inter-subject quantification performance, multi-organ and lesion K_i' and K_{IG} were generated using the RP and IG methods, respectively, and then rescaled using population-mean scaling factors to recover K_i. Using the Patlak K_i as the reference standard, the organ or lesion K_i estimated by the population-rescaled IG had an error that was 50–70% lower than that of the population-rescaled RP. Furthermore, group analysis indicates the K_i yielded by the population-rescaled IG exhibits statistical behavior more similar to that of the Patlak K_i and outperforms the population-rescaled RP K_i. Overall, the proposed IG approach with normalization retains the low imaging time requirement and improves inter-subject quantitative robustness. It may enable more accurate K_i quantification and improve the clinical feasibility of PET parametric imaging.

References

[1] C. S. Patlak, R. G. Blasberg, and J. D. Fenstermacher, "Graphical evaluation of blood-to-brain transfer constants from multiple-time uptake data," *J. Cereb. Blood Flow Metab.*, vol. 3, no. 1, pp. 1–7, Mar. 1983, doi: 10.1038/jcbfm.1983.1.

[2] Y. Zuo, J. Qi, and G. Wang, "Relative Patlak plot for dynamic PET parametric imaging without the need for early-time input function," *Phys. Med. Biol.*, vol. 63, no. 16, p. 165004, Aug. 2018, doi: 10.1088/1361-6560/aad444.

MIC-20-05

Generative Consistency Model for Bayesian Kinetic Model Selection in Dynamic Total-Body PET (#2512)

Yun Zhao[1], Qinlin Gu[1], Georgios I. Angelis[1], Katya Amadita[1], Andrew J. Reader[2], Yanan Fan[3], Steven R. Meikle[1]

[1] The University of Sydney, Camperdown, Australia; [2] King's College London, London, UK; [3] Commonwealth Scientific Industrial Research Organisation, Sydney, Australia

Abstract

The selection of compartmental models for dynamic PET analysis is compromised by three key scenarios—the unknown kinetics of novel tracers, mixed kinetics resulting from tissue heterogeneity and spillover, and the diverse multi-organ kinetics in total-body PET—where conventional model selection using nonlinear least squares and Akaike Information Criterion can fail. For this, we augmented our previous framework--kinetic parameter posterior estimation using generative consistency models--to perform Bayesian model selection. The objective is to simultaneously estimate both the model probability and the posterior distributions of the kinetic parameters across six commonly used kinetic models. The method involves training the consistency model on 6,000,000 simulated time-activity curves. Evaluation against a conventional method demonstrates significant improvements; across 6,000 simulated time-activity curves, the proposed method achieved an overall model selection accuracy of 86%, substantially outperforming the 34% accuracy of the conventional method. Furthermore, application to clinical total-body positron emission tomography data from a patient with metastatic cancer yielded physiologically plausible model selection maps that successfully differentiated complex underlying regional kinetics, such as healthy liver tissue versus tumour. Our results indicate that this proposed framework is useful in kinetic model selection in dynamic total-body PET and can have potential for evaluating new radiotracers in clinical practice.

Time:
14 November, 2026
11:30 – 12:45

Room:
MANUEL DE FALLA

MIC-21 | Theranostics, Imaging and dosimetry in therapy (particle, radiopharmaceutical, surgery) (2)

Chairs:
Youngho Seo (San Francisco)
Andrea Gonzalez Montoro (Valencia)

MIC-21-01

Experimental System Performance Characterization of Alpha-SPECT and Exploration of Angular Sampling Enhancement via Collimator Micro-Rotation (#3105)

Shubham Mandot[1], Yifei Jin[1], Elena M. Zannoni[2], Yong Du[3], George Sgouros[3], Eric Frey[3], Ling-Jian Meng[1,4]

[1] University of Illinois at Urbana-Champaign, Department of Nuclear, Plasma and Radiological Engineering, Champaign, USA; [2] University of Texas at Austin, Walker Department of Mechanical Engineering, Austin, USA; [3] Johns Hopkins University School of Medicine, Department of Radiology, Baltimore, USA; [4] University of Illinois at Urbana-Champaign, Beckman Institute for Advanced Science and Technology, Champaign, USA

We would like to thank National Institute of Health (NIH) for supporting this work under the grant U01EB031798.

Abstract

Targeted Alpha Therapy (TAT) requires dedicated imaging infrastructure capable of tracking alpha-emitting therapeutics and their daughters in vivo across a wide energy range. We present the experimental imaging performance of AlphaSPECT — a whole-body CZT-based clinical SPECT scanner comprising 32 detector panels integrating 512 micro-pinhole cameras in a dual field-of-view (FOV) configuration. Each panel integrates 16 CZT detectors (20×20×6 mm³, 500-µm pixel pitch) bump-bonded to HEXITEC ASICs. A CT-derived precision rotating gantry enables seamless switching between a large-FOV mode (5-mm pinholes, 40×40×20 cm³) and a high-resolution mode (2-mm pinholes, 20 cm spherical FOV), with sub-10-µm rotational accuracy. Energy calibration across all panels achieved 4–7 keV FWHM at 122 keV following charge-sharing correction. System response matrices were generated via voxel-driven ray-tracing, with geometry parameters estimated via nonlinear optimization against experimental point-source projections. Phantom reconstructions demonstrate uniform response across all detector panels and qualitative compartmental contrast in a 3D Hoffmann brain phantom (8 mCi Tc-99m, 30-minute acquisition), with resolution-limited blurring and partial-volume effects motivating investigation into angular sampling and reconstruction improvements. Ongoing studies include spatial resolution evaluation using a NEMA-compliant hot-rod phantom, collimator micro-rotation to enhance angular sampling, and joint dual-FOV reconstruction — to be presented at the conference.

MIC-21-02

First Validation of a BNCT-SPECT System Based on a Detector with Embedded AI in a Clinical-Like Facility (#2463)

Filippo Ghisio[1,2], Tommaso Ferri[1,2], Gianluca Mocerino[2,3], Luca Grisoni[2,3], Carlo E. Fiorini[1,2], Davide Mazzucconi[2,3], Marco Carminati[1,2], Stefano Agosteo[2,3], Kazuki Tsuchida[4], Yasuaki Ichikawa[4], Sachiko Yoshiashi[4], Giuseppe Iaselli[5,6], Nicoletta Protti[7,8], Giacomo Borghi[1,2]

[1] Politecnico di Milano, Dipartimento di Elettronica, Informazione e Bioingegneria, Milano, Italy; [2] Istituto Nazionale di Fisica Nucleare, Sezione di Milano, Milano, Italy; [3] Politecnico di Milano, Dipartimento di Energia, Milano, Italy; [4] Nagoya University, Graduate School of Engineering, Nagoya, Japan; [5] Politecnico di Bari, Dipartimento di Fisica, Bari, Italy; [6] Istituto Nazionale di Fisica Nucleare, Sezione di Bari, Bari, Italy; [7] Università di Pavia, Dipartimento di Fisica, Pavia, Italy; [8] Istituto Nazionale di Fisica Nucleare, Sezione di Pavia, Pavia, Italy

This work was supported in part by INFN Gruppo V, Italy (SPOC project) and in part by the PRIN PNRR 2022 Funding Program of Ministero Dell'Università e della Ricerca (MUR), Italy (BNCT-SPECT Project).

Abstract

Boron Neutron Capture Therapy (BNCT) requires precise, real-time monitoring of the distribution of boron neutron capture reactions to maximize its therapeutic selectivity.

This work presents a major hardware evolution of the BeNEdiCTE detector, a SPECT-based system designed to track the 478 keV prompt gamma rays emitted during neutron capture.
The detector is based on a co-doped LaBr3(Ce, Sr) monolithic crystal read out by Silicon Photomultipliers.
The custom readout electronics have been entirely redesigned, utilizing boron-free substrates to eliminate background interference at 478 keV.
Furthermore, the new module features embedded AI on a high-performance FPGA for real-time reconstruction of interaction coordinates (X, Y, and Depth-of-Interaction) of the gamma rays on the scintillator.
To meet the high-flux demands of clinical BNCT, the dead time of the system has been reduced from 5.4 µs to 2.1 µs, and an hardware-based energy discrimination circuit has been designed to process only the small percentage of useful gamma rays across the whole spectrum.

We report on the system's design and its upcoming validation at Nagoya University Accelerator-driven Neutron Source (Japan), marking the first SPECT measurement performed in a clinical-like facility.
Preliminary Monte Carlo simulations using a Derenzo-like phantom demonstrate the system's high spatial resolution and its ability to distinguish lesion-sized volumes with boron concentrations as low as a few hundred ppm.
These results set the stage for the upcoming SPECT validation, which aims to prove the system's readiness for the non-invasive, live monitoring of boron distribution during clinical patient treatment.

References
[1] W. Sauerwein et al., Neutron Capture Therapy: Principles and Applications. Springer Berlin Heidelberg, 2012.

[2] T. Ferri et al., "Design and Validation of a SPECT Prototype for Treatment Monitoring in BNCT and First Experimental Tomographic Results," IEEE Transactions on Radiation and Plasma Medical Sciences, pp. 1–1, 2025.
[3] A. Caracciolo et al., "A compact scintillator-based detector with collimator and shielding for dose monitoring in boron neutron capture therapy," Physics and Imaging in Radiation Oncology, vol. 29, 2024.

MIC-21-03

Imaging of TAT in Clinical Phantoms with a CZT Compton Camera

(#3012)

Biswajit Das[1,2], David Goodman[3], Michael Streicher[3], Jaewon Lee[2], Oscar H. Matousek[4,2], Ryan Heller[2], Victor Negut[2], Youngho Seo[1,4], Javier Caravaca[2,1]

[1] University of California, San Francisco, Department of Radiology and Biomedical Imaging, San Francisco, USA; [2] Lawrence Berkeley National Laboratory, Applied Nuclear Science Division, Berkeley, USA; [3] H3D Inc., Ann Arbor, USA; [4] University of California, Berkeley, Department of Nuclear Engineering, Berkeley, USA

This work was supported by the National Institutes of Health (NIH) under Grant R01EB032324. The authors thank Joshua Cates, Woon-Seng Choong, Seungeun Lee, Grant Gullberg, Gyohyeok Song, Uttam Shrestha, and Robin Peter for valuable discussions throughout this project. The ^{225}Ac was supplied by the U.S. Department of Energy Isotope Program, managed by the Office of Isotope Research and Development and Production.

Abstract

Targeted alpha therapy (TAT) has shown strong promise for cancer treatment because of its high linear energy transfer and localized cytotoxic effect. However, quantitative in-vivo imaging of TAT radiopharmaceuticals and its daughter remains challenging. The clinically administered activity is typically low, while the emitted gamma rays have low branching ratios, making conventional SPECT imaging sensitivity-limited and often requiring impractically long acquisition times. These limitations restrict accurate assessment of biodistribution, pharmacokinetics, and dosimetry, which are essential for optimizing TAT agents. This study investigates Compton imaging as a high-sensitivity alternative for visualizing TAT radiopharmaceuticals using a 5 cm × 5 cm single-layer 3D position-sensitive cadmium zinc telluride (CZT) camera. We performed a pilot imaging study with the alpha therapy radionuclide 225Ac in a clinical phantom filled with a low concentration of 6.2 kBq/mL surrounded by non-radioactive water. The phantom was scanned at 45° rotational steps with 15-minute acquisitions each, and Compton images were reconstructed to evaluate source localization below clinically relevant low-activity conditions. This is the first time such a low-activity concentration has been imaged in a clinical phantom. The results demonstrate clear visualization of the radioactive inserts, supporting the feasibility of CZT-based Compton imaging for TAT monitoring. Based on these measurements, a multi-head configuration with at least eight detector modules could enable in-vivo imaging of ^{225}Ac daughters of target organs within less than 30 minutes, and is being planned as the next step. Additional experiments with ^{212}Pb further suggest that the proposed approach can operate across a broad photon-energy range. Overall, this work provides experimental validation that compact 3D CZT Compton cameras may overcome key sensitivity barriers in alpha-emitter imaging and support future image-guided TAT.

MIC-21-04

Design of a PET&SPECT shared Detector with Low- and Medium-Energy Scintillator-as-Collimator for Lu-177 Imaging (#1720)

Xiangtao Zeng, Hang Yang, Wenjie Huang, Ming Niu, Zheng Gu

shenzhen bay laboratory, Shenzhen, China

This work is supported by the National Key R&D Program of China (No. 2023YFC2414800), the Major Program of Shenzhen Bay Laboratory (No. C1012530005), the National Natural Science Foundation of China (Nos. 12275182 and 62371314), Guangdong Basic and Applied Basic Research Foundation (Nos. 2024A1515012154), the Guangdong Provincial Project (Grant No. 2023TQ07A233) and the Shenzhen Bay Laboratory Proof-of Concept Grants (No. C1022430005).

Abstract

Lu-177, a promising theranostic radionuclide emitting β particles for therapy and γ photons for imaging, enables integrated diagnosis and therapy. Lu-177 imaging is increasingly important in treatments where imaging guides therapy. Previous work has demonstrated the use of scintillator as collimators to achieve simultaneous and separate imaging of F-18 and Tc-99m. In this work, we present a novel three-layer shared detector with variable collimator thickness, enabling simultaneous PET, SPECT, and Lu-177 imaging. The first two crystal layers are perforated, with the top layer functioning as a low-energy high-sensitivity (LEHS) collimator, the top and middle layers combined acting as a low-energy high-resolution (LEHR) collimator and medium-energy general-purpose (MEGP) collimator. This design allows flexible adaptation for Tc-99m and Lu-177 imaging without hardware changes.A 96 mm-diameter system was simulated to evaluate two collimation schemes. Simulation results indicate that for Tc-99m, the system can achieve both LEHS and LEHR imaging, with hot-rod phantom spatial resolution reaching 3.5 mm. For Lu-177 (208 keV), inserting high-density LYSO or BGO in the middle layer improved peak-to-valley ratio compared to GAGG, and BGO yielded 4 mm spatial resolution for hot-rod phantom imaging. This flexible collimator design enhances detector versatility and offers a promising solution for multi-radionuclide theranostic applications. Future work will focus on optimizing collimator thickness and evaluating the performance of a prototype system.

References

[1] Zeng. X et al. (2025). Tri-Mode PET, SPECT, and PET&SPECT Imager Using a Novel Scintillator-as-Collimator Detector. 2025 IEEE NSS, MIC and RTSD, Yokohama, Japan

MIC-21-05

Dosimetry Evaluation Studies in Non-Melanoma Skin Cancers Using a Novel Thin-Layer Scintillation Detector (#1851)

Giulia Tosetti[1], Jean-Marc Fontbonne[1], Dorothée Lebhertz[3], Ihssane Chaoufi[2], Cyril Moignier[3], Rémi Lafaye[1], This project has received financial support from the CNRS through the MITI interdisciplinary programs.

[1] Université de Caen Normandie, ENSICAEN, CNRS/IN2P3, LPC Caen UMR6534, CAEN, France; [2] Hassan II University, Laboratory of Mechanic and High Energy Physics, Department of Physics, Faculty of Sciences of Ain Chock, CASABLANCA, Morocco; [3] Centre François Baclesse, Service de radiophysique, CAEN, France

This project has received financial support from the CNRS through the MITI interdisciplinary programs.

Abstract

Conventional radiotherapy is a well-establish treatment for Non-Melanoma Skin Cancers (NMSCs). In this context, patient-specific quality assurance (PSQA) relies on accurate dose distribution measurements. However, current state-of-the-art technologies do not provide sufficient accuracy in assessing dose deposition within the superficial skin layers.

To compensate for the buildup effect in radiotherapy, a bolus material is commonly applied over the tumor to mimic tissue equivalence. Nevertheless, anatomical changes during treatment, such as tumor shrinkage, may introduce air gaps between the bolus and the skin, potentially leading to underdosage.

To address these limitations, a prototype detector, referred to as DQX, has been developed at Laboratoire de Physique Corpusculaire de Caen and experimentally evaluated at Centre François Baclesse . The device is based on a 100 µm thick plastic scintillator coupled to wavelength-shifting fibers and is designed to measure radiation dose in superficial tissue layers, targeting a relative measurement uncertainty below 1% for a 2 Gy photon beam at depths as shallow as 70 µm beneath the skin surface.

This contribution presents a comparison of the DQX prototype and a range of commonly used dosimetric devices employed in PSQA for conventional radiotherapy. These include tools such as ionization chambers and radiochromic films, each of which exhibits inherent limitations when applied to superficial dose measurements. The evaluation focuses on the response under possible clinical conditions such as air gaps variations. By benchmarking the DQX detector against these established technologies, this study also aims to assess its potential to improve dose verification in the buildup region.

References

[1] M. Butson, T. Cheung, P. Yu, and P. Metcalfe, “Effects on skin dose from unwanted air gaps under bolus in photon beam radiotherapy,” Radiation Measurements - RADIAT MEAS, vol. 32, pp. 201–204, 06 2000.

[2] C.-Y. Huang, B. Yang, W. W. Lam, K. K. Tang, T. C. Li, W. K. Law, K. Y. Cheung, and S. K. Yu, “Effects on skin dose from unwanted air gaps under bolus in an mr-guided linear accelerator (mr-linac) system,” Physics in Medicine and Biology, vol. 66, no. 6, p. 065021, mar 2021.

[3] C. Moignier, A. Batalla, L. Bonnor, P. Dutheil, D. Lebhertz, L. Lechippey, M. Lecornu, C. Loiseau, D. Stefan, and A. Vela, “Protontherapy for superficial tumors: validation of the tps dose calculation and comparison to high energy photon techniques,” in Proceedings of PTCOG 2023, 2023.

[4] Van Dyk, Jacob & Rosenwald, J.-C & Fraass, Benedick & Cramb, Jenna & Ionescu-Farca, F. & Sharpe, Michael. (2006). IAEA Technical Reports Series No. 430: Commissioning And Quality Assurance Of Computerized Planning Systems For Radiation Treatment Of Cancer. Medical Physics - MED PHYS. 33. 10.1118/1.2167371

[5] Miften M, Olch A, Mihailidis D, Moran J, Pawlicki T, Molineu A, Li H, Wijesooriya K, Shi J, Xia P, Papanikolaou N, Low DA. Tolerance limits and methodologies for IMRT measurement-based verification QA: Recommendations of AAPM Task Group No. 218. Med Phys. 2018 Apr;45(4):e53-e83.
[6] A.Niroomand-Rad, S.-T. Chiu-Tsao, M.P. Grams, D.F. Lewis, C.G. Soares, L.J. Van Battum et al., Report of aapm task group 235 radiochromic film dosimetry: An update to tg-55, Medical Physics 47 (2020) 5986.
[7] Syam Kumar SA, Sukumar P, Sriram P, Rajasekaran D, Aketi S, Vivekanandan N. A patient-specific quality assurance study on absolute dose verification using ionization chambers of different volumes in RapidArc treatments. Med Dosim. 2012 Winter;37(4):436-41.
[8] Ishmael Parsai E, Shvydka D, Pearson D, Gopalakrishnan M, Feldmeier JJ. Surface and build-up region dose analysis for clinical radiotherapy photon beams. Appl Radiat Isot. 2008 Oct;66(10):1438-42.

Time:
14 November, 2026
12:45 – 13:05

Room:
FEDERICO GARCÍA LORCA

MIC-22 | Closing

Chairs:
Vesna Sossi (Vancouver)
Roger Fulton (Sydney)

RTSD

9 November, 2026

Time:
9 November, 2026
15:00 – 17:00

Room:
ANDALUCÍA II & III

RTSD-01 | RTSD Opening

Chairs:
Michael Fiederle (Freiburg)
Gerard Arino-Estrada (Barcelona)

RTSD-01-01

Exploring 4x4x3 cm^3 3D-CdZnTe Semiconductor Gamma-Ray Detectors

(#1366)

Zhong He, Yuefeng Zhu

University of Michigan, Nuclear Engineering and Radiological Sciences, Ann Arbor, USA

This material is based upon work supported by the Defense Threat Reduction Agency (DTRA) under Contract No. HDTRA124C0002. Any opinions, findings and conclusions or recommendations expressed in this material are those of the author(s) and do not necessarily reflect the views of the Defense Threat Reduction Agency.

Abstract

Three-dimensional position-sensitive single-crystal CdZnTe detectors (3D-CZT), with energy resolution of ~0.3% FWHM for single-pixel events and ~0.5% FWHM for all events at 662 keV, had been demonstrated previously on detectors with dimensions up to 2x2x1.5 cm^3 (total 6 cm^3).Larger volumesingle-crystalCdZnTe semiconductor gamma-ray detectors are needed to achieve higher intrinsic detection efficiency at higher gamma-ray energies. 4x4x3 cm^3 (total 48 cm^3) 3D-CZT detectors manufactured by Redlen Technologies have been explored for the first time. Energy spectra of Cs-137 were obtained on all three 4x4x3 cm^3 CZT detectors. An energy resolution of 1.05% FWHM at 662 keV was obtained for single-pixel events on one 4x4x3 cm^3 CZT detector #12R2. The feasibility of achieving close to 1.0% FWHM energy resolution on CdZnTe gamma-ray detectors with single-crystal detection volume of 48 cm^3 has been demonstrated.

References

[1] https://h3dgamma.com/

[2] A.E. Bolotnikov et al. "*Performance of 8x8x32 and 10x10x32 mm^3 CdZnTe position-sensitive virtual Frisch-grid detectors for high-energy gamma ray cameras*", Nucl. Instr. and Meth. A 969 (2020) 164005.

[3] Y.F. Zhu, Z. He, “Evaluation of Pixelated 2×2×3 cm^3 CdZnTe Detectors”, 2025 IEEE Nucl. Sci. Sym. Conf. at Yokohama, Japan.

RTSD-01-02

Visualizing the Hidden Physics of CdTe Detectors: Direct Spatiotemporal Imaging of Charge Clouds (#1397)

Adriano Cola[1], Antonio Valletta[2], Isabella Farella[3], Vaclav Dědič[4], Lorenzo Dominici[5]

[1] CNR, IMM, Lecce, Italy; [2] CNR, IMM, Roma, Italy; [3] CNR, IMM, Lecce, Italy; [4] Charles University, Institute of Physics, Prague, Czech Republic; [5] CNR, Nanotec, Lecce, Italy

This research was partially funded by the PNRR MUR project PE0000023- NQSTI, financed by the European Union – Next Generation EU.

Abstract

Carrier Dynamics by Pockels Imaging (CDPI) is a novel all-optical, quantitative, and non-invasive method for direct spatiotemporal visualization of charge carrier clouds in CdTe radiation detectors. CDPI achieves micrometer-scale spatial resolution and nanosecond temporal resolution, with sensitivity to electric field differences down to ~2 V/cm – enabling tracking of carrier densities just above the intrinsic level. We directly observe electron cloud formation and evolution, including Gaussian shape preservation, diffusion-driven broadening, and field-dependent reshaping. Under high optical excitation, we resolve space-charge perturbed regimes with cloud expansion due to Coulomb repulsion (width up to 400 µm) and pronounced asymmetric tails due to detrapping processes, possibly correlated with a defective layer near the cathode surface. Crucially, CDPI correlates internal cloud dynamics with external circuit currents, linking microscopic physics to macroscopic detector performance. Although demonstrated in one dimension, CDPI is intrinsically two-dimensional and readily extendable to investigate charge sharing in segmented electrodes or pixel arrays. The technique also supports studies of ultra-high photogenerated charge densities relevant to synchrotron and free-electron laser applications and enables direct visualization of carrier injection from the contacts. CDPI offers a powerful new diagnostic tool for understanding and improving CdTe and other compound semiconductor radiation detectors.

RTSD-01-03

Compton Imaging Capability of 1-cm-Thick Pixelated TlBr Detectors

(#1525)

Keitaro Hitomi[1], Yoshiharu Kitayama[2], Mitsuhiro Nogami[1], Jiyon Lee[3], Kenichi Watanabe[4]

[1] Tohoku University, Department of Quantum Science and Energy Engineering, Graduate School of Engineering, Sendai, Japan; [2] Fukushima Institute for Research, Education and Innovation, Fukushima, Japan; [3] Korea Institute of Nuclear Safety, Division of Radiation Protection for NORM & Cosmic Radiation, Daejeon, South Korea; [4] Kyushu University, Department of Applied Quantum Physics and Nuclear Engineering, Graduate School of Engineering, Fukuoka, Japan

Abstract

Thallium bromide (TlBr) is a promising compound semiconductor for the fabrication of gamma-ray detectors because of its high atomic numbers (Tl: 81, Br: 35), high density (7.56 g/cm^3), and wide bandgap energy (2.68 eV). The Compton imaging capability of 1-cm-thick pixelated TlBr detectors was characterized in this study. Pixelated TlBr detectors were fabricated from a crystal grown by the traveling molten zone method using zone-purified material. The crystal size for the detector was 12 mm x 12 mm x 10 mm. The electrodes were formed on the two 12 mm x 12 mm surfaces by vacuum deposition of Tl, followed by Ni and Au. The anode consisted of nine pixel electrodes (2 mm x 2 mm each) surrounded by guard electrodes. The cathode on the opposite side was a planar electrode. For single-pixel events, the TlBr detector exhibited energy resolutions of approximately 2% full width at half maximum or better at 662 keV for all nine pixels with depth correction and event selection based on electron drift time. Compton images of a ^{137}Cs gamma-ray source were obtained using non-adjacent two-pixel events via

the list-mode maximum likelihood expectation maximization (LM-MLEM) algorithm. Clear images of the source were reconstructed at positions consistent with the actual source locations. These results demonstrate that the TlBr detector fabricated in this study possesses high energy resolution and Compton imaging capability.

RTSD-01-04

Effect of the Anode Irradiation by X-ray on the Polarization of a CdTe Imaging Sensor (#1944)

Petr Praus[1], Eduard Belas[1], Marián Betušiak[1], Roman Grill[1], Samuel Kacenga[1], Zuzana Melnikova[2], Jan Jakubek[2]

[1] Charles University, Faculty of Mathematics and Physics, Institute of Physics, Prague, Czech Republic; [2] ADVACAM s.r.o., Prague, Czech Republic

This project is co-financed from the state budget by the Technology Agency of the Czech Republic under the project TQ28000004 Semiconductors4All.

Abstract

This work presents a study of the influence of X-ray irradiation on the electric field profile in biased CdTe sensors with blocking contacts. The investigation focuses on the modification and potential stabilization of the internal electric field through controlled irradiation of the blocking anode under varying conditions. To emulate realistic detector operation, a silicon wafer was positioned in front of the anode to represent a readout chip, while the cathode was probed by laser-induced transient current technique to determine the electric field. A synchronized pulsed bias scheme enabled time-resolved monitoring of polarization dynamics. Transient current waveforms were recorded in a shielded setup with controlled X-ray exposure, and their temporal evolution was analyzed to assess changes in the electric field profile. The results show that, under dark conditions, the sensor exhibits pronounced space charge formation due to blocking anode. In contrast, appropriately tuned X-ray irradiation of the anode leads to a significant stabilization of the field within the sensor bulk. Under these conditions, the electric field remains nearly uniform over time. The observed behavior reflects the interplay between space-charge formation and X-ray–induced carrier generation, which can partially compensate accumulated charge, although the process remains sensitive to irradiation conditions and contact configuration. Furthermore, low-energy X-ray irradiation transmitted through a silicon layer produces effects comparable to optical excitation at the anode, indicating a similar mechanism of near-contact carrier generation. The presented results provide insight into the control of polarization effects and contribute to improving the operational stability of CdTe-based radiation detectors.

RTSD-01-05

Identification and control of interfacial limits enabling high-performance photon-counting perovskite radiation detectors (#2057)

Ganbaatar Tumen-Ulzii[1], **Samuel D. Stranks**[1,2]

[1] University of Cambridge, Department of Chemical Engineering and Biotechnology, Cambridge, UK; [2] University of Cambridge, Department of Physics, Cambridge, UK

G.T.-U. acknowledges funding from a Marie Skłodowska-Curie Postdoctoral Fellowship via UKRI Horizon Europe Guarantee, grant no. EP/Y016912/1. G.T.-U. acknowledges the Leverhulme Trust and Isaac Newton Trust (Leverhulme Early Career Fellowship). G.T.-U., and S.D.S. acknowledge the Engineering and Physical Sciences Research Council (EPSRC, EP/W004445/1) and the Medical Research Council (APP47651) for funding.

Abstract

Lead halide perovskite single crystals are promising for photon-counting radiation detection due to their high atomic number and favourable charge-transport properties. However, most perovskite detectors operate in hole-transport configurations, while currently existing readout electronics are optimised for electron collection. Bridging this mismatch requires a clear understanding of carrier-polarity-dependent transport and the underlying device physics governing perovskite detectors. We conducted polarity-resolved α-particle (^{241}Am, 5.48 MeV) measurements on $FAPbBr_3$ planar detectors (Au/$FAPbBr_3$/Bi). Polarity-resolved α-particle measurements reveal strongly asymmetric degradation, with irreversible degradation localised beneath the Bi contact, whereas the Au interface develops a defect-rich recombination region that can be mitigated by ultrathin Ti or Cr interlayers, enabling stable bipolar transport operation. Detectors remain stable after ~100 h of continuous biasing at 5,000 V cm^{-1} and ~3 months of shelf-life storage. The combination of high-quality crystals and interfacial protection layers enables the detectors to achieve 1.3% energy resolution for 662 keV (^{137}Cs γ-ray source) and 6.1% for 5.48 MeV α-particles in an electron-transport configuration. This work establishes interfacial degradation as the dominant performance-limiting factor in perovskite radiation detectors and identifies interfacial engineering as the key pathway toward stable and high-resolution electron-transport spectroscopy.

RTSD-01-06

High-Z Sensor Characterisation and Readout Development for X-ray Detectors at PSI (#2720)

Jonathan Mulvey, Dominic Greiffenberg, Bernd Schmitt, Michele Anastasi, On behalf of the detector group whose members include:J. Mulvey, M. Anastasi, A. Bergamaschi, M. Brueckner, M. Carulla, R. Dinapoli, S. Ebner, S. Emiliani,K. Ferjaoui, E. Fr¨ojdh, V. Gautam, D. Greiffenberg, S. Hasanaj, V. Hinger, V. Kedych, T. King, S. Li,C. Lopez-Cuenca, L. Lunin, A. Mazzoleni, D. Mezza, S. Moses, K. Moustakas, A. Mozzanica, M. Mueller,C. Ruder, B. Schmitt, S. Silletta, D. Thattil, X. Xie and J. Zhang

Paul Scherrer Institute, Center For Photon Science, Villigen, Switzerland

Abstract

The newly upgraded Swiss Light Source (SLS) 2.0, a fourth-generation synchrotron, has begun operation. Photons with energies up to 80 keV will be available at increased flux compared to the third-generation source it replaces. In particular, the brilliance is expected to increase by two orders of magnitude. In this energy range, silicon is no longer an efficient detection material. High-Z semiconductors are therefore required, with GaAs:Cr, CdTe, and CdZnTe being promising candidates. Single sensors (2 × 2) cm^2 made up of 256 × 256 pixels with a 75 µm pitch have been bump-bonded to the JUNGFRAU readout ASIC. Developed at PSI, JUNGFRAU is a charge-integrating readout chip with three gain levels and dynamic gain switching. In this talk, we will discuss the ongoing characterisation of high-Z sensors using JUNGFRAU, with a focus on charge transport properties of CdZnTe produced by Redlen Technologies. Furthermore, recent efforts to improve the linear dynamic range of JUNGFRAU in electron collection mode will be discussed. We will also look towards the future with a discussion of full JUNGFRAU modules using GaAs from Dectris or recently acquired (4 × 4) cm^2 CdZnTe sensors from Redlen. Additionally, the new MATTERHORN photon-counting ASIC has been designed for both silicon and high-Z sensors, with assemblies using GaAs undergoing characterisation.

References

[1] D. Greiffenberg et al., “Characterization of GaAs:Cr sensors using the charge-integrating JUNGFRAU readout chip,” Journal of Instrumentation, vol. 14, no. 05, pp. 05020, May, 2019, DOI 10.1088/1748-0221/14/05/P05020

[2] L. A. Franklin et al., “Characterization of high-flux cadmium zinc telluride detectors coupled to MM-PAD readout ASICs for high-flux X-ray applications,” IOP Publishing, vol. 21, no. 03, pp. 03014, March, 2026, DOI 10.1088/1748-0221/21/03/P03014

[3] D. Greiffenberg et al., “Signal stability of high-Z sensors at synchrotron light sources,” Journal of Instrumentation, vol. 20, no. 01, pp. 01031, January, 2025, DOI 10.1088/1748-0221/14/05/P05020

[4] J. Mulvey et al., (2025, July). CdZnTe (CZT) as a Material for Detecting Hard X-rays at Synchrotrons and FELs . presented at IWORID. Oral Presentation. Available: https://indi.to/5YCBb. Accessed on: May 11, 2026

[5] A. Mozzanica et al., “Prototype characterization of the JUNGFRAU pixel detector for SwissFEL,” Journal of Instrumentation, vol. 9, May, 2014, DOI 10.1088/1748-0221/9/05/C05010.

[6] A. Mozzanica et al., “The JUNGFRAU Detector for Applications at Synchrotron Light Sources and XFELs,” ynchrotron Radiation News, vol. 31, no. 06, pp. 16-20, 2018, DOI 10.1080/08940886.2018.1528429

[7] V. Kedych et al., (2025, July). Characterization of the JUNGFRAU 1.2 readout ASIC. presented at IWORID. Oral Presentation. Available: https://indi.to/KQWc4. Accessed on: May 11, 2026

[8] D. Mezza et al., ”The new Matterhorn detector for 4th generation synchrotrons,” 2023 IEEE Nuclear Science Symposium, Medical Imaging Conference and International Symposium on Room-Temperature Semiconductor Detectors (NSS MIC RTSD), Vancouver, BC, Canada, 2023, pp. 1-1, doi: 10.1109/NSSMICRTSD49126.2023.10338514.

RTSD-01-07

Response of a Timepix4 CdTe spectral imaging detector for radiographic applications (#2859)

Laura A. Cerbone[1,2], Jan Žemlička[4], Benedikt Bergmann[4], Petr Smolyanskiy[4], Petr Manek[4], Luigi Cimmino[2,3], Giovanni Mettivier[2,3], Stanislav Pospíšil[4], Paolo Russo[2,3]

[1] Scuola Superiore Meridionale, SPACE PhD program, Napoli, Italy; [2] University of Naples Federico II, Dept. of Physics, Napoli, Italy; [3] Istituto Nazionale di Fisica Nucleare, Sezione di Napoli, Napoli, Italy; [4] Institute of Experimental and Applied Physics, Prague, Czech Republic

L.A.C. acknowledges UNINA for supporting her research stay at IEAP through the STAR grant awarded for the DXA4A project (PI: L.A.C.).

Abstract

We characterized a Timepix4 application-specific integrated circuit bonded to a 1-mm-thick cadmium telluride sensor for photon-counting X-ray imaging in the diagnostic energy range. A per-pixel energy calibration was performed using X-ray fluorescence and gamma-ray sources, followed by a cluster-wise linear correction to compensate for spectral distortions associated with multi-pixel charge sharing and front irradiation. Flat-field, photon-counting, and spectral imaging tests were performed using a tungsten-anode microfocus X-ray tube operated at 80 kV. The detector achieved an energy resolution of 3.3 keV at 59.5 keV for the Am-241 source. Spectral images were reconstructed using 1 keV energy bins after offline clustering and fluorescence recovery correction. The detector demonstrated high-quality radiographic imaging capability after flat-field correction, despite spatial inhomogeneities typical of fine-pitch CdTe hybrid pixel detectors. A limiting spatial resolution of 8 lp/mm at 10% modulation transfer function was measured for the detector biased at -450 V, at a counting rate approaching 10^7 cps per chip. The results demonstrate the potential of the Timepix4 CdTe assembly for spectral imaging applications.

References

[1] X. Llopart, J. Alozy, R. Ballabriga, M. Campbell, R. Casanova, V. Gromov, et al., “Timepix4, a large area pixel detector readout chip which can be tiled on 4 sides providing sub-200 ps timestamp binning,” J. Instrum., vol. 17, no. 1, Jan. 2022, Art. no. C01044, doi: 10.1088/1748-0221/17/01/C01044.

[2] J. Jakubek, A. Cejnarova, T. Holy, S. Pospisil, J. Uher, and Z. Vykydal, “Pixel detectors for imaging with heavy charged particles,” Nucl. Instrum. Methods Phys. Res. A, vol. 591, no. 1, pp. 155–158, May 2008, doi: 10.1016/j.nima.2008.03.091.

RTSD-01-08

Exploring the X-ray imaging with single-crystalline integrated perovskite sensors (#1569)

Vitalii Bartosh[1,2], **Vitalii Bartosh**[1,2], Anastasiia Sakhatska[1,2], Anastasiia Sakhatska[1,2], Kostiantyn Sakhatskyi[1,2], Kostiantyn Sakhatskyi[1,2], Gebhard J. Matt[1,2], Gebhard J. Matt[1,2], Andrii Kanak[1,2], Andrii Kanak[1,2], Sergii Yakunin[1,2], Sergii Yakunin[1,2], Maksym Kovalenko[1,2], Maksym Kovalenko[1,2]

[1] ETH Zurich, Laboratory of Inorganic Chemistry, D-CHAB, Zürich, Switzerland; [2] EMPA, Laboratory for Thin Films and Photovoltaics, Dübendorf, Switzerland

The work was financially supported by the Swiss Innovation Agency (Innosuisse) under grant agreement 46894.1 IP-ENG and through the ETH+ Project SynMatLab: Laboratory for Multiscale Materials Synthesis. Authors also acknowledge Prof. Dr. Makhsud Saidaminov and his group from the University of Victoria, Canada, for providing $MAPbBr_3$ single crystals.

Abstract

Metal halide perovskites emerge as promising materials for direct X-ray detection due to their high absorption efficiency, favorable charge-transport properties, and compatibility with scalable fabrication methods[1, 2]. While thin polycrystalline perovskite films integrated with pixelated electronics have already demonstrated high-resolution imaging[3], extending these approaches toward thicker highly crystalline absorbers remains essential for practical low-dose applications. Here, we investigate several perovskite multi-pixel detector architectures coupled to charge-integrating readout electronics for low-dose X-ray imaging. The developed devices exhibit stable operation, uniform photoresponse, and spatial resolution approaching pixel pitch limit. Highly crystalline film $CsPbBr_3$ detectors demonstrate spatial resolution up to 20 lp mm^{-1}, keeping high X-ray absorption and efficient charge collection together with scalable fabrication potential, while bulk single-crystalline integrated absorbers provide further improvements in charge collection and uniform low-dose response. Thick 3-4 mm single crystal sensors achieve modulation transfer function values of 35% at the Nyquist frequency under X-ray doses as low as 4 μGy_{air} with a detective quantum efficiency of 48%. In addition, we demonstrate high-contrast radiographic imaging of packaged integrated circuit and computed tomography of small multi-material objects, highlighting the potential of perovskite detectors for next-generation high-resolution imaging systems.

References

[1] Yakunin, S., Dirin, D., Shynkarenko, Y., Morad, V., Cherniukh, I., Nazarenko, O. *et al.*, "Detection of gamma photons using solution-grown single crystals of hybrid lead halide perovskites," *Nature Photon,* vol. 10, pp. 585–589, 2016.

[2] He, Y., Petryk, M., Liu, Z., Chica, D. G., Hadar, I., Leak, C. *et al.*, "$CsPbBr_3$ perovskite detectors with 1.4% energy resolution for high-energy γ-rays," *Nature Photon,* vol. 15, pp. 36–42, 2021.

[3] Y. Kim, Kim, K.-H., Son, D.-Y., Jeong, D.-N., Seo J.-Y., Choi, Y. S. *et al.*, "Printable organometallic perovskite enables large-area, low-dose X-ray imaging," *Nature,* vol. 550, pp. 87–91, 2017

[4] Chen, H., Gu, M., Liu, X., Huang, S., Liu, B., Zhang, J., "Spatial resolution and light output of pixelated CsI(Tl) scintillation screen based on oxidized silicon micropore array template," *JINST,* vol. 13, no. P07002, 2018.

[5] Mei. K., Roshkovan, L., Halliburton, S.S., Sharma, S., Ross, S., Yu, Z. *et al.*, "Evaluation of a CZT-based photon-counting detector CT prototype for low-dose lung cancer screening using patient-specific lung phantoms," *medRxiv,* p. 2025.12.30.25343218, 2025.

[6] Haruta, Y., Ye, H., Huber, P., Sandor, N., Pavesic Junior, A. *et al.*, "Reproducible high-quality perovskite single crystals by flux-regulated crystallization with a feedback loop," *Nature Synthesis,* vol. 3, no. 10, pp. 1212–1220, 2024.

[7] R. Najjar, "Radiology's Ionising Radiation Paradox: Weighing the Indispensable Against the Detrimental in Medical Imaging," *Cureus,* vol. 15, no. 7, p. e41623, 2023.

Time:
9 November, 2026
17:30 – 19:00

Room:
ANDALUCÍA II & III

RTSD-02 | RTSD Aviation Inspection & Security Applications

Chairs:
Zhong He (Ann Arbor)
Jan S. Iwanczyk (Los Angeles)

RTSD-02-01

Next Generation Room Temperature Semiconductor Detectors, Sources, and Methods for Computed Tomography in Aviation Security

(#2984)

William C. Barber[1], **William C. Barber**[1]

[1] Rapiscan Systems, Detectors, Torrance, USA; [2] Rapiscan Systems, Detectors, Torrance, USA

Some work supported by the DHS S&T Directorate under Contract No. 70RSAT18CB0000002 and Contract No. 70RSAT21CB0000022. Any opinions, findings, conclusions or recommendations expressed in this material are those of the author(s) and do not necessarily reflect the views of the DHS.

Abstract

Advanced X-ray imaging is a principal pillar supporting aviation security and provides materially segmented images of bags, luggage, and cargo. The images are processed to provide a high probability of detection for contraband and/or threats, at an acceptably low false alarm rate to allow sufficient throughput. As the list of contraband and threats increases, the challenge to maintain a high detection probability at a low false alarm rate is advancing the state of art in detectors, sources, scanning methods, reconstruction, recognition, and decision, with the goal of clearing items for air transport. Room temperature semiconductor detectors are currently being used in commercially available diffraction scanners. These are based on pixellated Cadmium Zinc Telluride spectroscopic detectors, which are being developed further for better performance and lower cost. Cadmium Telluride and Cadmium Zinc Telluride photon counting detectors are currently being developed for potential use in multi-energy transmission scanners to improve detection and lower false alarms compared to the dual-energy dual-layer scintillator based scanners that are in wide use. Sensor performance requirements and cost constrains for widespread use of room temperature semiconductor detectors in both transmission and diffraction scanners are presented, with a focus on next generation computed tomography methods in multi-modal system of systems approaches to achieve the imaging workflows required for aviation security. Detector array and source geometries to achieve combined transmission and diffraction imaging in the different concepts of operation for the various scanning applications in aviation security are discussed.

RTSD-02-02

A new compact prototype for 3D gamma coded-aperture spectro-imaging (#1218)

Giulia Rosso, Guillaume Amoyal, David Fras, Quentin Gendre, Maugan Michel, Dominique Tromson

Université Paris-Saclay, CEA List F-91120, Palaiseau, France

Abstract

During nuclear dismantling, remote measurements, as radiation gamma imaging, are particularly advantageous since they reduce the risk for users, providing a visual map of radioactivity even in inaccessible environments. However, 2D gamma imaging does not directly provide the distance between source and detector, neither the 3D localization of the source. The goal of this work is to overcome these limits by developing a new compact and light 3D coded-aperture spectro-imager for applications in nuclear dismantling. This study presents the developments of the prototype, consisting of a coded-aperture gamma spectro-imager and an RGB-D (color and depth) camera, in carrying out 3D gamma imaging in experimental laboratory conditions. The device weight 325 g, with dimensions of 18 × 10 × 2.8 cm, and can distinguish among the most common radionuclides in the nuclear industry with energies ranging from the 59.5 keV gamma ray line of 241Am, up to the 60Co 1332 keV emission. The 3D hotspot localization and reconstruction are achieved with a triangulation from different viewpoints, which is made possible using a SLAM (Simultaneous Localization And Mapping) algorithm. We tested the prototype using point-like radioactive sources both in single and multiple sources configurations. In both cases, using a minimum of three static poses of few minutes' duration, the sources localizations are correctly achieved with errors in the order of 2 cm for measurements taken at almost one meter. New tests on volumetric and extended sources are currently on-going.

References

[1] T. Poikela *et al.*, "Timepix3: a 65K channel hybrid pixel readout chip with simultaneous ToA/ToT and sparse readout," *J. Instrum.*, vol. 9, no. 05, pp. C05013–C05013, May 2014, doi: 10.1088/1748-0221/9/05/c05013

[2] S. R. Gottesman and E. E. Fenimore, "New family of binary arrays for coded aperture imaging," *Appl. Opt.*, vol. 28, no. 20, p. 4344, Oct. 1989, doi: 10.1364/ao.28.004344

[3] G. Amoyal *et al.*, "Nanopix-v1: A compact miniaturized coded-aperture gamma imager," *Nucl. Instrum. Methods Phys. Res. Sect. Accel. Spectrometers Detect. Assoc. Equip.*, vol. 1068, p. 169718, Nov. 2024, doi: 10.1016/j.nima.2024.169718

[4] R. C. Smith and P. Cheeseman, "On the Representation and Estimation of Spatial Uncertainty," *Int. J. Robot. Res.*, vol. 5, no. 4, pp. 56–68, Dec. 1986, doi: 10.1177/027836498600500404

[5] A. Macario Barros, M. Michel, Y. Moline, G. Corre, and F. Carrel, "A Comprehensive Survey of Visual SLAM Algorithms," *Robotics*, vol. 11, no. 1, p. 24, Feb. 2022, doi: 10.3390/robotics11010024

RTSD-02-03

Characterization of a miniature prototype photon counting detector system and evaluation of its imaging performance for potential use in threat and explosive detection CT scanners; A new paradigm for security screening. (#1293)

Georgios Prekas, Brian Mercurio, Carl Bosch, Kurt Rogers, Eric Johnson

SureScan Corporation, Binghamton, USA

The authors would like to thank Dr. Zhong Zhong from Brookhaven National Laboratory for his invaluable help during setting up and testing at the beamline.

Abstract

Spectral photon counting technology (SPCCT) represents a critical leap for security screening, offering high-resolution imaging and accurate material identification to reduce false alarms and detect threats invisible to legacy systems. SureScan Corporation utilizes SPCCT and dual-energy CT (DECT) in airport explosive detection systems (EDS), focusing R&D on characterizing prototype components like the AMS-OSRAM AS5920M. This state-of-the-art, 4-side buttable system-in-package (BSIP) module features direct-conversion CdZnTe crystals with 341µm x 365µm pixels integrated with ultra-low noise ASICs. Each ASIC supports five configurable energy thresholds and operates with short dead times to sustain high photon flux without significant pile-up. Our performance evaluation includes per-bin count rates, spatial uniformity, and spectral fidelity under various beam conditions, alongside imaging metrics such as modulation transfer function (MTF) and detective quantum efficiency (DQE). Furthermore, we demonstrate the importance of spectrum unfolding to correct non-ideal detector responses. By utilizing energy response function models derived from synchrotron measurements at Brookhaven National Laboratory, we reconstructed true incident energy spectra, significantly improving the accuracy of material identification through proprietary empirical decomposition methodologies.

References
[1] home - SureScan Corporation
[2] ams AS5920M Photon Counting Module X-Ray Sensors | ams OSRAM
[3] BNL | NSLS-II | Beamline 27-ID (HEX) High Energy Engineering X-ray Scattering | Schedule

RTSD-02-04

Tileable Imager Architecture using HiSPECT Gamma Imaging Modules and Applications (#2049)

Guillaume Montémont, **Guillaume Montémont**, Nicolas Billon-Pierron, Nicolas Billon-Pierron, Mathis Moulin, Mathis Moulin, Hugo de las Heras Gala, Hugo de las Heras Gala, Sylvain Stanchina, Sylvain Stanchina

CEA-LETI, Grenoble, France

The authors would like to thank the French governmental program for CBRNE R&D program for its support and funding.

Abstract

For low-flux radiation imaging applications such as gamma-ray imaging, nuclear medicine, and X-ray diffraction, spectral and spatial resolution are performance drivers.However, detector efficiency is essential as it determines the quantity of information collected. The primary challenge is to achieve high-resolution performance at a reasonable cost. Then, it becomes possible to increase detection volume and the amount of information that the system can gather within a limited time.

Our HiSPECT CZT detector module addresses this challenge through several key principles: the anode is segmented into large pixels, which limits charge sharing, while high spatial resolution is achieved through sub-pixel positioning. The low electronics density reduces cost, power dissipation, and improves yield. Additionally, the absence of cathode readout simplifies integration, while the depth of interaction is retrieved through multiple anode readouts.

In this work, we present how modules are combined to build larger systems, detailing the readout electronics and showcasing various imaging application cases, including coded aperture, collimator, positron, and Compton imaging modes.

RTSD-02-05

Activity Quantification Using Experimentally Imaged Source Distributions (#2702)

Christopher G. Wahl, **Christopher G. Wahl**, Reid Sobota, Reid Sobota, David Goodman, David Goodman, Joseph Ghezzi, Joseph Ghezzi

H3D, Inc., Ann Arbor, USA

Abstract

Radioactive source activity quantification is critical in many applications. A limiting factor in estimating activity is often knowledge of the source distribution within a medium since the position of the activity can greatly impact the observed counts at the detector. Algorithms have been developed to use a Compton and coded aperture gamma-ray imaging detector to image the source distribution within the volume of interest using a set of stationary measurements or a free-moving measurement with a simultaneously localization and mapping (SLAM) system. The iterative 3D volumetric imaging algorithm will be described. The imaged source distribution can then be used to improve activity quantification over a uniform source assumption. This is demonstrated with measurements of various geometries.

10 November, 2026

Time:
10 November, 2026
9:00 – 11:00

Room:
ANDALUCÍA II & III

RTSD-03 | RTSD Pixel Detectors

Chairs:
Dominic Greiffenberg (Villigen)
Filippo Mele (Milano)

RTSD-03-01

Flat-Panel Intensity Normalization for Fully Spectroscopic CT-Based Material Identification with 1 mm CdTe Timepix3 Detectors (#2597)

Michael K. Schütz[1,2], Gerardo Roque Romero[1], Sebastian Useche Parra[1], Martin P. Pichotka[2], Michael Fiederle[1]

[1] University of Freiburg, Freiburg Materials Research Centre (FMF), Freiburg im Breisgau, Germany; [2] University of Freiburg, Medical Physics Division, Department of Radiology, Freiburg im Breisgau, Germany

We would like to thank Eurostars for funding this project under the project M3dicam, code 01QE2510B.

Abstract

Fully spectroscopic photon-counting CT enables material identification by recording the energy-dependent transmission spectrum of an object. Timepix3 (TPX3) detectors extend conventional threshold-based photon counting CT by recording position, time-of-arrival and energy information for individual events, allowing for post-acquisition energy binning and extraction of spectral features such as K-edges. However, fully spectroscopic photon counting CT with TPX3 detectors remains limited by detector area, photon statistics, scan time and raw data volume.

Previous work introduced a two-stage TPX3 acquisition scheme that combines frame-based and event-based readout. Here, we investigate whether the frame-based TPX3 intensity image can be replaced by a geometrically matched flat-panel intensity measurement. The CMOS/GdOS flat-panel detector provides full-field intensity projections, while a 12 x 1 TPX3 array with 1 mm CdTe sensors provides fully spectroscopic region-of-interest (ROI) information. The method combines the low-noise intensity information of the flat-panel detector with the material-specific spectroscopic information of TPX3. Projection geometry is matched by adapting cone-beam magnification, followed by empirical intensity mapping in the overlap region. The approach is benchmarked against the original TPX3-MPX-normalized acquisition reference. Initial results indicate that replacing the TPX3 intensity image with flat-panel projections preserves TPX3-derived material characteristics in the investigated ROI and enables material labels to be extrapolated to repeated structures in the full-field reconstruction.

References

[1] Schuetz, MK, Roque, G, Useche, JS, Procz, S, Jakubek, J, Pichotka, MP, Fiederle, M 2025, 'Optimized data acquisition for spectroscopic CT with Timepix3: combining photon-counting and data-driven readout modes with adaptive pixel masking', Journal of Instrumentation, 20(10), P10045.

[2] Schütz, MK, Fey, J, Procz, S, Useche, JS, Roque, G, Fiederle, M 2024, 'Element Identification by K-Edge Imaging Using Spectroscopic Photon Counting Detectors', IEEE Transactions on Nuclear Science, 71(1), 106-112.

[3] Yang, Q, Cong, W, Xi, Y, Wang, G 2016, 'Spectral X-Ray CT Image Reconstruction with a Combination of Energy-Integrating and Photon-Counting Detectors', PLOS ONE, 11(5), e0155374.

[4] Clark, DP, Badea, CT 2017, 'Hybrid spectral CT reconstruction', PLOS ONE, 12(7), e0180324.

[5] Holbrook, MD, Clark, DP, Badea, CT 2020, 'Dual source hybrid spectral micro-CT using an energy-integrating and a photon-counting detector', Physics in Medicine & Biology, 65(20), 205012.

[6] Treb, K, Hämisch, Y, Ullberg, C, Zhang, R, Li, K 2023, 'Photon counting-energy integrating hybrid flat panel detector systems for image-guided interventions: an experimental proof-of-concept', Physics in Medicine & Biology, 68(13), 135009.

[7] Teledyne DALSA 2019, 'Rad-icon 2329 Detector User Manual, GigE model', User Manual, Rev. 02, Milpitas: Teledyne DALSA.

RTSD-03-02

A Pixelated CCI TlBr Detector for Time-Resolved Multi-MeV Gamma Detection (#1612)

Leonor Rebolo[1,4], Salvador Moreno-Gómez[2], Hadong Kim[3], James Christian[3], Pedro M.M. Correia[4], Ana Luísa M. Silva[4], **Gerard Ariño-Estrada**[2,1]

[1] University of California Davis, Biomedical Engineering, Davis, USA; [2] Institut de Física d'Altes Energies - Barcelona Institute of Science and Technology, Medical Detector Instrumentation and Imaging Physics, Barcelona, Spain; [3] Radiation Monitoring Devices, Inc., Watertown, USA; [4] University of Aveiro, Aveiro, Portugal

This work was supported in part by grant R01EB029533 (PI Arino-Estrada) and by i3N - IDB/50025/2020, UIDP/50025/2020 and LA/P/0037/2020, financed by Portuguese national funds through the FCT/MEC. L.R. is supported by grant Prototera PRT/BD/154945/2023, financed by national funds through the FCT/MEC.

Abstract

Cherenkov Charge Induction (CCI) detectors consist of transparent semiconductor detectors that combine the conventional charge induction readout with the detection of Cherenkov light generated by gammas depositing energy above the Cherenkov threshold. CCI detectors show strong potential for applications requiring time-resolved multi-MeV gamma detection, such as proton range verification in proton therapy.

In this work we report on a pixelated CCI TlBr detector consisting of a 14×14×11 mm3 TlBr crystal with a 4×4 pixelated anode matrix of 2.3×2.3 mm2 pixels with 2.5 mm pitch. The lateral faces of the crystal were polished to maximize light extraction, and a 2×2 silicon photomultiplier (SiPM) array with 4×4 mm2 active area per channel was used for Cherenkov light detection. The detector was instrumented with a multi- channel acquisition system based on a CAEN R5560 open FPGA digitizer, enabling simultaneous acquisition of charge induction and Cherenkov light signals from all detector channels. The acquisition was triggered by the Cherenkov readout and a 22Na point source was used for detector characterization.

First results demonstrate the feasibility of simultaneous Cherenkov light and charge induction acquisition using a multi-channel readout, with the optical signal successfully providing the acquisition trigger and a timing reference to estimate the electron drift time. Future work will focus on optimization of the triggering and synchronization scheme, waveform processing methods, and detector operating conditions to improve event selection and detector characterization.

References

[1] Arino-Estrada, G. et al. 2019, 'First Cerenkov charge-induction (CCI) TlBr detector for TOF-PET and proton range verification', *Physics in Medicine & Biology*, 64, 17

[2] Arino-Estrada, G. et al. 2021, 'Energy and electron drift time measurements in a pixel CCI TlBr detector with 1.3 MeV prompt-gammas', *Physics in Medicine & Biology*, 66, 4

RTSD-03-03

Self-Consistent Simulation of Charge Sharing in CZT Pixel Detectors

(#2864)

Stefania Favilla[1], Manuele Bettelli[1], Leonardo Abbene[2], Matthew C. Veale[3], Andrea Zappettini[1]

[1] IMEM-CNR, Parma, Italy; [2] University of Palermo, aDipartimento di Fisica e Chimica (DiFC), Palermo, Italy; [3] STFC Rutherford Appleton Laboratory, Didcot, UK

PRIN 2022 “Toward Next-Generation X-ray Imagers: a High Resolution Spectroscopic System with Ultra-High Photon Flux Capabilities”, Cod. 2022ZEF2RE, CUP: B53D23004710006

Abstract

Cadmium Zinc Telluride (CZT) detectors are widely used for X-ray and γ-ray detection due to their high atomic number, wide band gap, and excellent room-temperature performance. Their response is governed by charge transport processes, including carrier mobility, trapping, diffusion, and electric-field nonuniformities, which are critical in pixelated geometries where charge sharing and weighting-field effects dominate signal formation. In this work, a 3D CZT detector model is developed in COMSOL Multiphysics, solving semiconductor transport equations self-consistently without Gaussian charge-cloud approximations. Signal induction is computed using the Ramo–Shockley theorem applied to the full carrier distribution. Validation against synchrotron measurements shows excellent agreement in normalized charge collection profiles (r = 0.98), confirming accurate reproduction of charge transport and sharing effects.

References

[1] L. Abbene et al, “Room-temperature X-ray response of cadmium–zinc–telluride pixel detectors grown by the vertical Bridgman technique”, J. Synchrotron Rad. (2020). 27, 319–328.

[2] COMSOL Multiphysics®, www.comsol.com. COMSOL AB, Stockholm, Sweden.

[3] E. Istatiadis et al, “A novel theoretical model framework for the 3D CdZnTe drift strip detector”, 2025 JINST 20 C02014

[4] M. Bettelli et al, "A first principle method to simulate the spectral response of CdZnTe-based X- and gamma-ray detectors”, Nucl. Instrum. Methods Phys. Res. A 960 (2020) 163663

RTSD-03-04

Waveform-Based Depth-of-Interaction Characterization in 5-mm Cross-Strip CdZnTe (#2149)

Max Teicheira[1], Lars R. Furenlid[2], Chiao Huang[2], Matthew A. Kupinski[2], Michael A. King[3], Shiva Abbaszadeh[1]

[1] University of California, Santa Cruz, Electrical and Computer Engineering, Santa Cruz, USA; [2] University of Arizona, Department of Radiology and Imaging Sciences, Tuscon, USA; [3] University of Massachusetts Chan Medical School, Radiology, Worcester, USA

All authors declare no conflicts of interest regarding competing financial interests or personal relationships that may influence the work reported in this paper. This work was supported by the National Institute of Biomedical Imaging and Bioengineering of the National Institutes of Health under Award Numbers R01EB028091 and UH3EB034686.

Abstract

Depth-of-interaction (DOI) estimation in CdZnTe detectors is conventionally based on the cathode-to-anode amplitude ratio (C/A), while timing-based methods have been explored as alternative indicators in pixelated geometries. However, DOI characterization in cross-strip CdZnTe detectors using digitized waveform signal parameters, including drift time, cathode amplitude, and anode rise time, and the degree to which these parameters provide independent depth information has not been systematically studied. In this work, we present a waveform-based DOI characterization of a 5 mm thick cross-strip CdZnTe detector (7 anode strips, 8 cathode strips, and 1 steering electrode). A collimated ^{137}Cs slit beam was scanned across 26 discrete depth positions 0.2 mm apart. Drift time and cathode amplitude exhibit a strong correlation (R^2 = 0.99), establishing that both contribute to the practical lower bound on the achievable single-event depth resolution. At each collimator slit position, the measured signal distributions reflect the distribution of interaction depths, due to finite beam width and intracrystal scatter. The C/A ratio computed from the two highest-amplitude cathode strips provides the best trade-off between DOI resolution and measurement consistency. Using a leave-one-step-out cross- validation framework, we obtain a DOI resolution of 1.35 mm RMSE with single-feature calibration and 1.12 mm RMSE using a 9-feature random forest regression model.

RTSD-03-05

Ultra-High Resolution CZT Gamma Camera Using Machine-Learning Based 3D Interaction Localisation (#2496)

Nathan Atkins, Matthew Exley, Ian Baistow, **Alexander Cherlin**

Kromek Ltd., Sedgefield, UK

Abstract

An ultra-high resolution CZT gamma camera platform is presented, integrating advanced detector readout, machine learning (ML) based signal processing and practical calibration procedures for sub-pixel 3D interaction localisation. The system employs Kromek's D-Matrix readout with 2 mm pixel pitch detectors and utilises an ML model trained on physics-based simulations and calibrated with experimental flood-field data. Recent developments focus on improving calibration flexibility, robustness to detector performance fluctuations and stability during prolonged operation through refined detector simulations, multi-model optimisation strategies and incorporation of measured data in the training process.

Performance evaluation demonstrates improved spatial uniformity and significant suppression of inter-pixel artefacts in uncorrected flood field images, with stable behaviour maintained over extended acquisition periods without recalibration. Previously reported intrinsic spatial resolution (~250 µm) and depth-of-interaction accuracy (~0.5–1 mm) are preserved, with improved consistency across the detector volume. Reduced reliance on flat-field correction limits amplification of Poisson noise in reconstructed images, enhancing effective image quality. The ML predicted energy incorporates corrections that effectively eliminate energy DOI dependence and charge sharing losses, resulting in a strongly reduced low-energy tail of the spectrum.These results demonstrate a robust and scalable CZT gamma camera platform, addressing key practical limitations of earlier implementations. The integrated detector, calibration and ML based data processing framework enable reliable high-resolution imaging under realistic operating conditions and supports straightforward scaling to larger field-of-view systems. A full-scale camera is currently under construction, highlighting the potential for integration into advanced nuclear imaging applications.

References

[1] Cherlin A, Atkins N, Baistow I "A feasibility prototype of a low-dose stationary tomographic Molecular Breast Imaging camera using 3D position sensitive CZT detectors", in 2022 IEEE NSS MIC, Milan, Italy.

[2] Cherlin A, Exley M, Atkins N "Redefining Gamma Ray Imaging with Highly Sub-Pixelised CZT Arrays", in 2025 IEEE RTSD, Yokohama, Japan.

[3] Cherlin A, Wirth A, Baistow I, Erlandsson K, Thielemans K, Hutton BF "Feasibility studies of a novel ultra-low dose stationary tomographic molecular breast imaging system utilising 3D position of interaction CZT detectors", 2023 iWoRiD, Oslo, Norway.

RTSD-03-06

Optimized femtosecond laser ablation processing of hybrid semiconductor detectors for enhanced spectroscopic and imaging performance (#2556)

Zuzana Melnikova[1], Eliska Soharova[1], Simon Syrovatka[2], Vojtech Kudrna[2], Jiri Syrovatka[2], Pavel Kozmin[2], Jan Jakubek[1]

[1] ADVACAM s.r.o., Prague 7, Czech Republic; [2] Hofmeister, s.r.o., Pilsen, Czech Republic

This work was supported by the Technological Agency of the Czech Republic within the grant FW10010210 "Sensor Chip and Technology for X-ray Imaging".

Abstract

Hybrid semiconductor detectors based on the TimePIX-family read-out chips enable direct detection of ionizing radiation with high spatial and spectroscopic resolution. This work investigates the application of femtosecond laser ablation for precise structural modification of detector components while minimizing thermal damage and preserving detector functionality. The study focused on three-dimensional shaping of the read-out chip in a MiniPIX TimePIX3 detector with a 1 mm thick cadmium telluride sensor and on edge cutting of silicon sensors. An optimized laser ablation process enables significant thinning of the read-out chip while maintaining full detector operation. The modified configuration allows backside illumination of the detector, resulting in reduced X-ray attenuation and improved detection efficiency for low-energy photons in the energy range from 5 to 25 keV. Experimental measurements also demonstrate improved spectroscopic performance and enhanced spatial resolution. In addition, femtosecond laser ablation was applied to precise cutting of silicon sensor edges, enabling efficient integration of individual modules into large-area monolithic detection systems. The presented results demonstrate that femtosecond laser ablation is a promising tool for advanced modification of hybrid semiconductor detectors and can significantly expand their applicability in future radiation detection systems.

RTSD-03-07

Energy, Spatial and Timing Performance of CZT Drift Strip Detectors (#2701)

Leonardo Abbene[1], Antonino Buttacavoli[1], Fabio Principato[1], Gaetano Gerardi[1], Manuele Bettelli[2], Andrea Zappettini[2], Natalia Auricchio[3], Stefano Del Sordo[4], Ezio Caroli[3]

[1] University of Palermo, Dipartimento di Fisica e Chimica E. Segrè, Palermo, Italy; [2] IMEM/CNR PARMA, Parma, Italy; [3] INAF/OAS of Bologna, Bologna, Italy; [4] INAF/IASF of Palermo, Palermo, Italy

Abstract
High resolution detection modules for multi-isotope SPECT imaging are strongly required in nuclear medicine. In this framework, we proposed and developed new cadmium–zinc–telluride (CZT) drift strip detectors for room temperature gamma-ray spectroscopic imaging. As widely demonstrated, CdZnTe (CZT) is one of the key materials for the development of room temperature X-ray and gamma ray detectors and several research groups are still involved in advances in both device and the crystal growth technologies. The CZT detectors, equipped with orthogonal anode/cathode collecting strips, drift strips and dedicated digital pulse processing allow a detection area of 6 x 20 mm^2, excellent room temperature energy resolution of 0.8% FWHM at 662 keV and sub-millimetre spatial resolution. The timing performance of the detectors will be also presented. These activities are within an Italian PRIN 2022 PNRR project (No. P2022SE49Y; CUP: B53D23024100001), funded by the Italian Ministry for University and Research (MUR).

RTSD-03-08

Circularity-Based Spectroscopic Correction for Small-Pixel CdTe/Timepix Detectors (#2745)

Anthony R. Whittemore[1], Krishan Patel[1], **Elena Maria Zannoni**[1,2]

[1] The University of Texas at Austin, Walker Department of Mechanical Engineering, Austin, USA; [2] The University of Texas at Austin, Department of Diagnostic Medicine, Dell Medical School, Austin, USA

We thank the Cancer Prevention & Research Institute of Texas (grant # RP240462) and the 2024 Mitzi & William Blahd MD Pilot Research Grant, The Education and Research Foundation for their generous support.

Abstract
High-resolution Cd(Zn)Te radiation detectors are essential for quantitative imaging in medical diagnostics, high-energy physics, and industrial non-destructive testing [1]. This study examines the impact of charge sharing (CS) [2] in a 2-mm CdTe/Timepix detector with 55 µm pixels [3], and proposes a spectroscopic correction method.

From Am-241 and Co-57 experimental data, we categorized interaction events by their multiplicity and a newly introduced shape descriptor called circularity. Analysis showed that non-circular events (C < 0.9) resulted in energy peaks shifting toward lower energies due to unrecorded below-threshold pixels. To address these high-multiplicity CS events, we developed a multi-stage spectroscopic correction method that corrects spectra based on circularity and multiplicity values. This approach improved the average FWHM for the Am-241 peak from 16.70% to 10.05% and for Co-57 from 9.64% to 6.73%.

Additionally, AllPix-Squared simulations [4] were used to model charge cloud dynamics and quantify losses occurring during both propagation and digitization. This work enabled a more robust energy calibration and unbiased spectroscopic performance for small-pixel semiconductor detectors.

References

[1] A. R. Whittemore and E. M. Zannoni, "Applications of Cd(Zn)Te Radiation Detectors in Non-Destructive Testing and Evaluation," *Sensors*, vol. 25, no. 6, doi: 10.3390/s25061776.
[2] M. C. Veale *et al.*, "Measurements of charge sharing in small pixel CdTe detectors," *Nuclear Instruments and Methods in Physics Research Section A: Accelerators, Spectrometers, Detectors and Associated Equipment*, vol. 767, pp. 218-226, 2014/12/11/ 2014, doi: https://doi.org/10.1016/j.nima.2014.08.036.
[3] R. Ballabriga, M. Campbell, and X. Llopart, "An introduction to the Medipix family ASICs," *Radiation Measurements*, vol. 136, p. 106271, 2020/08/01/ 2020, doi: https://doi.org/10.1016/j.radmeas.2020.106271.
[4] S. Spannagel *et al.*, "Allpix2: A modular simulation framework for silicon detectors," *Nuclear Instruments and Methods in Physics Research Section A: Accelerators, Spectrometers, Detectors and Associated Equipment*, vol. 901, pp. 164-172, 2018/09/01/ 2018, doi: https://doi.org/10.1016/j.nima.2018.06.020.

Time:
10 November, 2026
15:00 – 17:00

Room:
Poster Area

RTSD-04 | RTSD Poster Session

Chairs:
Michael Fiederle (Freiburg)
Gerard Arino-Estrada (Barcelona)

RTSD-04-350

Characterization of Bremsstrahlung Photon Contamination in Clinical Electron Beams via CdZnTe Detectors (#1036)

Chansun Park[1], Sangsu Kim[1], Hyojung Kim[2], Won-Young Jeong[2], Hochun Park[2], Jung-Yeol Yeom[3,4], Shinhaeng Cho[2]

[1] Korea University, Global Health Technology Research Center, Seongbuk-gu, South Korea; [2] Chonnam National University Medical School, Department of Radiation Oncology, Gwangju, South Korea; [3] Korea University, School of Biomedical Engineering, Seongbuk-gu, South Korea; [4] Korea University, Department of Bioengineering, Seongbuk-gu, South Korea

This work was supported by the National Research Foundation of Korea(NRF) grant funded by the Korea government(MSIT) (RS-2026-25474062, RS-2023-NR077190, RS-2023-00234651, RS-2025-00561749) and supported by the Chonnam National University Hwasun Hospital Institute for Biomedical Science (HCRI24-010).

Abstract

Accurate dosimetry of high-energy (≥ 15 MeV) clinical electron beams is challenged by bremsstrahlung-induced photon contamination (X-ray tail), which leads to unintended dose deposition in deep tissues. In this study, high-resistivity CdZnTe (CZT) detectors were investigated for sensitive characterization of this contamination. Two planar CZT detectors (5-mm and 8-mm thick) exhibited high bulk resistivity (~2.0 × 10^{10} Ω·cm) and competitive energy resolution (3.9–4.1% at 662 keV). Measurements were performed using clinical LINAC electron beams (6–18 MeV) at an SSD of 100 cm. To circumvent pulse pile-up under intense photon flux, the detector response was evaluated via time-integrated current in a mixed radiation field. The integrated charge increased markedly at 15 and 18 MeV, indicating enhanced bremsstrahlung production. The 8-mm detector showed higher sensitivity to penetrating photon components than the 5-mm detector, highlighting the importance of detector thickness. These results demonstrate that CZT detectors enable high-sensitivity characterization of photon contamination and are promising for real-time dosimetry and radiotherapy quality assurance.

References

[1] F. M. Khan and J. P. Gibbons, *Khan's The Physics of Radiation Therapy*. Philadelphia, PA, USA: Lippincott Williams & Wilkins, 2014.

[2] G. F. Knoll, *Radiation Detection and Measurement*, 4th ed. Hoboken, NJ, USA: John Wiley & Sons, 2010.

[3] A. Hossain et al., "Novel approach to surface processing for improving the efficiency of CdZnTe detectors," *J. Electron. Mater.*, vol. 43, no. 8, pp. 2771–2777, Aug. 2014.

[4] C. Park et al., "Preliminary study of CdZnTe for multipurpose radiation detection in broadband applications," *Radiat. Meas.*, vol. 186, Jan. 2025, Art. no. 107457.

RTSD-04-351

Engineering Low-Reverse-Current $CsPbBr_3$ Sensor Structures through Surface Passivation and Deposition of Different Contacts (#1094)

Volodymyr Gnatyuk[1], Xinxin Wang [2,3], Juha Kalliopuska[1], Dmytro Nalyvaiko[1], Noriyuki Masuda[1], Sami Vähänen[1], Shimao Wang[3], Gang Meng[3]

[1] Advafab Oy, Helsinki, Finland; [2] University of Science and Technology of China, Hefei, China; [3] Anhui Institute of Optics and Fine Mechanics, Hefei Insititutes of Physical Sciences, Chinese Academy of Sciences, Hefei, China

Abstract

$CsPbBr_3$ single crystals (CPB SCs) were grown by a modified inverse temperature crystallization method and processed to fabricate metal-insulator-semiconductor (MIS) sensor structures. A 5 nm Al_2O_3 layer was deposited by atomic layer deposition to passivate the crystal surface, suppress surface leakage, and provide environmental protection. Pt, Ti, Au, and Al contacts were subsequently deposited to form asymmetric barrier structures with different electrode combinations. X-ray diffraction measurements confirmed high crystalline quality of the as-grown CPB crystals. The rocking curve of the (004) plane exhibited a full width at half maximum of 0.19°. *I-V* measurements demonstrated pronounced rectification in all investigated MIS structures. The $Pt/Al_2O_3/CPB/Al_2O_3/Al$ sample exhibited the lowest reverse current (~ 25 nA at 1000 V) and the strongest blocking behavior. These results confirm that Al_2O_3 passivation combined with optimized asymmetric contacts is an effective approach for engineering low-leakage, polarization-resistant perovskite X/γ-ray sensors.

RTSD-04-352

Additive Engineering of $Cs_2AgBiBr_6$ Double Perovskite Single Crystals: Growth Optimization, Structural Characterization, and Radiation Detector Evaluation (#1418)

Nazire S. Sahsuvar[1], Michael Fiederle[1], Zeynep Cihan[1], Michael Daub[2]

[1] Albert-Ludwigs-Universität Freiburg, Freiburg Materials Research Center (FMF), Freiburg im Breisgau, Germany; [2] Albert-Ludwigs-Universität Freiburg, Institute of Inorganic and Analytical Chemistry, Freiburg im Breisgau, Germany

This work was supported by the BMBF under Grant No. 05K22VFA Perodet.

Abstract

This study presents a systematic investigation of additive engineering strategies for the solution-based growth of all-inorganic $Cs_2AgBiBr_6$ double perovskite single crystals and their evaluation as radiation detectors. Various

chemical additives including toluene, ethyl acetate, thiourea, sodium acetate (NaOAc), and potassium acetate (KOAc) were systematically introduced into the precursor solution to influence nucleation dynamics, crystal size, and structural quality. The combination of NaOAc and KOAc was identified as the most effective additive strategy, consistently producing large (up to 2.2 cm), well-faceted, phase-pure single crystals with high reproducibility. The optimized crystals were characterized using X-ray diffraction(XRD), high-resolution XRD(HR-XRD) with rocking curve analysis, scanning electron microscopy(SEM), energy-dispersive X-ray spectroscopy(EDX), laser-induced breakdown spectroscopy (LIBS), and Raman spectroscopy. HR-XRD rocking curves revealed exceptionally narrow full-width at half-maximum (FWHM) values as low as 0.0144°, confirming outstanding crystalline perfection. Electrical characterization, including current–voltage (I–V) profiling, space-charge-limited current (SCLC) analysis, signal-to-noise ratio (SNR) evaluation, was performed to assess the detector potential of the optimized crystals. While the crystals exhibited high bulk resistivity (~10^9–10^{10} Ω·cm), excellent phase purity, and radiation sensitivity, detector-level investigations revealed trap-limited charge transport and self-trapped exciton formation as intrinsic limitations. This work establishes dual-acetate additive engineering as a robust strategy for growing high-quality $Cs_2AgBiBr_6$ single crystals and provides critical insights into the gap between crystal quality and detector-scale performance.

References
[1] V. Murgulov, C. Schweinle, M. Daub, H. Hillebrecht, M. Fiederle et al., “Double perovskite $Cs_2AgBiBr_6$ *radiation sensor: synthesis and characterization of single crystals,” J. Mater. Sci.* 57:2758–2774, 2022.
[2] W. Yuan, G. Niu and Y. Xian et al., “In situ regulating the order-disorder phase transition in $Cs_2AgBiBr_6$ single crystal toward the application in an X-ray detector,” *Adv. Funct. Mater.* 29:1900234–1900242, 2019.
[3] N. S. Sahsuvar, M. Daub, C. Schweinle, M. Fiederle, and H. Hillebrecht, "All-inorganic $Cs_2AgBiBr_6$ *double perovskite single crystals for radiation detectors,"* KIT Scientific Publishing, Karlsruhe Institute of Technology, 2023.
[4] Z. Liu, X. Zhang, L. Liu, et al., “3D $Cs_2AgBiBr_6$/2D $Cs_3Bi_2Br_9$ heterostructures for hard X-ray detection with high sensitivity,” *Sci. China Mater.* vol. 67, 2024.

RTSD-04-353

Solution Growth and Material Characterization of $Cs_2AgBiBr_6$ Double Perovskite Crystals for X-Ray Detection: Crystal Quality, Electrical Transport Properties, and Structural Defects (#1556)

Zeynep Cihan, Michael Fiederle

Albert Ludwigs Üniversity of Freiburg / Freiburger Material Forschungszentrum (FMF), Fakultät für Umwelt und Natürliche Ressourcen Institut für Geo- und Umweltnaturwissenschaften Kristallographie, Freiburg, Germany

The authors gratefully acknowledge the support of the PERODET II project.

Abstract
This work builds upon our characterization of lead-free double perovskite $Cs_2AgBiBr_6$ single crystals for radiation detection applications, where high-quality, centimeter-scale crystals (up to ~2.2 cm) were synthesized via a low-cost standard solution-cooling growth method. Structural analysis confirmed a phase-pure cubic $Fm\bar{3}m$ structure with a dominant {111} orientation and narrow FWHM values, indicating high crystalline quality. Morphological and

compositional studies revealed smooth surfaces, uniform morphology, and near-stoichiometric composition, while electrical measurements showed low leakage current, ohmic behavior, and high resistivity (10^9–10^{10} Ω·cm)[4]. Despite these favorable properties, device performance remained limited due to defect-related charge transport.To address this, a constant-temperature, feed-controlled growth approach is introduced, where supersaturation is regulated via continuous precursor feeding under stable thermal conditions. This steady-state method suppresses uncontrolled nucleation and promotes the growth of larger, higher-quality crystals. The approach is expected to reduce defect densities and improve material performance, providing a pathway toward high-performance, environmentally friendly radiation detectors.

References
[1] N. S. Sahsuvar, M. Daub, C. Schweinle, M. Fiederle, and H. Hillebrecht, "All-inorganic $Cs_2AgBiBr_6$ double perovskite single crystals for radiation detectors," KIT Scientific Publishing, Karlsruhe Institute of Technology, 2023.
[2] Murgulov, V. (2021). Double perovskite radiation sensors: crystal growth and cha-racterisation of single crystals of $Cs_2AgBiBr_6$ and layered $(BA)_2CsAgBiBr_7$
[3] Y. Dang *et al.*, "Interface engineering strategies towards $Cs_2AgBiBr_6$ single-crystalline photodetectors with good Ohmic contact behaviours," *J. Mater. Chem. C*, vol. 8, no. 1, pp. 276–284, 2020.
[4] Z. Cihan, "Characterization of the Material Properties of Double Perovskite Crystals $Cs_2AgBiBr_6$ Dedicated for Application as X-Ray Detectors," M.S. thesis,University of Freiburg, Freiburg im Breisgau, Germany, Nov. 2025.

RTSD-04-354

A new approach for studying phase equilibria in the CdTe-MnTe system (#1669)

Oleh Kopach[1], Vasylyna Kopach[1], Petro Fochuk[1], Mykola Solodkyi[1], Mykola Kukurudziak[1], Aleksey Bolotnikov[2], Ralph B. James[3]

[1] Yuriy Fedkovych Chernivtsi National University, Chernivtsi, Ukraine; [2] Brookhaven National Laboratory, Upton, USA; [3] Savannah River National Laboratory, Aiken, USA

This work was partially supported by MESU(grant number 0125U000832, author M. K., M. S., V. K.). One of the authors (R.B.J.) received partial support from the NNSA Minority Serving Institution Partnerships Program.

Abstract
In this work we determined the peculiarities of high-temperature phase equilibria in the CdTe–MnTe system using a differential thermal analysis method in a thermocycling mode. Temperature dependences of the volume fractions of the liquid and solid phases in $Cd_{1-x}Mn_xTe$ (x=0÷0.5) alloys, as well as the minimum and maximum melting temperatures of the solid phase were obtained. These dependences allowed us to establish critical temperatures of equilibria between the solid phase and the melt and to construct the solidus and liquidus lines of the CdTe–MnTe phase diagram. It was shown that with an increase in the molar fraction of MnTe in alloys ranging from 0.1 to 0.5, the decreases in the temperatures for both the solidus and the liquidus did not exceed 20 °C. Plus, the temperature interval between them remains practically constant at 15-18°C. Also, we determined the temperature intervals of the pre-melting region and found that with an increase in the MnTe fraction, the region of pre-melting states of the

alloys expands. The results described in this work provide more reliable data on the equilibrium between phases, since the method reduces the influence of kinetic limitations of classical thermography.

References
[1] Cui, Y., Bolotnikov, A., et al. 'CdMnTe in X-ray and Gamma-ray Detection: Potential Applications', August 11, 2008; United States
[2] Yu, P., Chen, Y., et al. 'Study of Detector-Grade CdMnTe:In Crystals Obtained by a Multi-Step Post-Growth Annealing Method', *Crystals* 2018, 8, 387
[3] Zayets, V., 'Optical Isolation in $Cd_{1-x}Mn_xTe$ Magneto-Optical Waveguide Grown on GaAs Substrate', *J. of The Optical Society of America B-Optical Physics*, 2005
[4] Yu P., Shao T., et al. 'Preparation and characterization of pure phase CdMnTe nanopowders by a hydrothermal route', *RSC Adv*. 2022 Jun 29; 12(29):19006-19015
[5] Tribouet R. and Didier G., 'Growth and characterization of $Cd_{1-x}Mn_xTe$ and MnTe crystals; contribution to the CdTe-MnTe pseudo-binary phase diagram determination', *Journal of Crystal Growth* - 1981. - Vol. 52, P. - 614-618
[6] Huabei Qi, Youbao Ni, et al., 'Study of the Solid Solubility Limit and Growth of $Cd_{1-x}Mn_xTe$ Multicomponent Single Crystals for Miniaturized Magneto-Optical Isolators', *Inorganic Chemistry* 2025 64 (36), 18499-18508
[7] Kopach, O.; Kopach, V.,; et al. 'Melting and crystallization peculiarities of $Cd_{0.50}Mn_{0.50}Te$ solid solutions' *Proc. SPIE* 2023, *12696*, 126960J1-J7.
[8] Joost W. M. Frenken et al., 'Observation of Surface Melting', *Physical Review Letters*, 54(2), 134–137, 1985.

RTSD-04-355

First Clinical Evaluation of a Gallium Nitride Diode Array for Proton Pencil Beam Scanning (#1828)

Luisa Parschat[1,2], Nico F. Brosda[3], Jean-Yves Duboz[4,5], Eric Frayssinet[5], Stéphane Higueret[6], Maxime Hugues[4,5], Matilde Siviero[4,5], Christian Bäumer[1,2]

[1] TU Dortmund University, Department of Physics, Dortmund, Germany; [2] West German Proton Therapy Centre Essen, Essen, Germany; [3] Ruhr-University Bochum, Department of Physics, Bochum, Germany; [4] Université Côte d'Azur, Nice, France; [5] CNRS, CRHEA, Valbonne, France; [6] Université de Strasbourg, IPHC, CNRS, UMR7178, Strasbourg, France

This study was supported by the German Research Foundation (DFG) and the French National Research Agency (ANR) within the collaborative project “GaN diode array for proton monitoring and imaging”. Project number: DFG-505408069/ANR-22-CE92-0047

Abstract
To fully exploit the high-precision of proton therapy, advanced beam monitoring and quality assurance devices capable of reliable real-time dose verification are essential. This study presents the first performance evaluation of a Gallium Nitride (GaN) pin-diode array at a clinical proton therapy facility using Pencil Beam Scanning. The detector array is comprised of 11x11 diodes with a 500 µm pitch coupled to a low-noise multi-channel readout system, and the response of all 121 pixels was evaluated individually. The experimental characterization was carried out at a cyclotron-based proton therapy center using clinical proton energies of 100 MeV and 226.7 MeV. We investigated the detector response for different single proton spots ranging from 0.02 to 100 monitor units (MU), corresponding to 10^6 - 10^{10} protons. The results demonstrate excellent linearity between diode response and machine output. Regarding the time response characteristics, a bi-exponential decay model expresses the

observed signal fall-off after irradiation. The afterglow contribution was less than 5% of the integrated signal per measured spot. These initial results of a pixelated GaN pin-diode array under clinical pencil beam scanning conditions identify the proposed detector as a promising candidate for both real-time beam monitoring and high-precision quality assurance in clinical proton therapy environments.

RTSD-04-356

An Integrated Purification-Growth Strategy for High-Performance Perovskite $CsPbBr_3$ Crystals (#2068)

Junqiang Wang[1,3], Jie Ma[1,2], Shaohan Wang[1], Chengqian Zhong[1,2], Yong Zhu[1], Yugui Lu[1], Run Xu[2], **Junfeng Chen**[1,3]

[1] Shanghai Institute of Ceramics, Chinese Academy of Sciences, State Key Laboratory of Functional Crystals and Devices, Shanghai, China; [2] Shanghai University, School of Materials Science and Engineering, Shanghai, China; [3] University of Chinese Academy of Sciences, Center of Materials Science and Optoelectronics Engineering, Beijing, China

This work was funded by the National Natural Science Foundation of China (U2541244); and the opening fund of State Key Laboratory of Functional Crystals and Devices, Shanghai Institute of Ceramics, Chinese Academy of Sciences (SKLFCD202506SIC).

Abstract

All-inorganic perovskite $CsPbBr_3$ single crystals are promising candidates for room-temperature radiation detection; however, the conventional vertical Bridgman (VB) growth rates (<1 mm/h) severely constrain efficient growth and wide applications. In this study, we report a novel strategy for preparing high-performance single crystals via zone refining, which integrates the traditionally separate purification and crystal growth processes into a unified in-situ purification and growth process. This strategy accelerates the growth rate to 25 mm/h — approximately 25-fold faster than conventional vertical Bridgman (VB) growth methods — while preserving an X-ray rocking-curve FWHM of just 0.02°. The resulting crystals exhibit exceptional carrier transport properties, with a hole mobility-lifetime product ($\mu_h\tau_h$) of 1.2×10^{-3} cm^2 V^{-1} and a dark current of only 26 nA at 300 V for a 6-mm-diameter circular device. Asymmetric planar detectors fabricated from these crystals demonstrate outstanding room-temperature energy resolutions (ERs) of 7.3%, 5.8%, 5.0%, and 3.3% for ^{241}Am (59.5 keV), ^{57}Co (122 keV), ^{22}Na (511 keV), and ^{137}Cs (662 keV) γ-rays, respectively. This work breaks the crystal growth rate bottleneck and provides a practical pathway toward the scalable in-situ growth of high-performance perovskite $CsPbBr_3$ radiation detectors.

References
[1] C. C. Stoumpos et al., "Crystal growth of the perovskite semiconductor CsPbBr3: A new material for high-energy radiation detection," Cryst. Growth Des., vol. 13, no. 7, pp. 2722–2727, Jul. 2013.
[2] Y. He et al., "High spectral resolution of gamma-rays at room temperature by perovskite CsPbBr3 single crystals," Nat. Commun., vol. 9, no. 1, Art. no. 1609, Apr. 2018.
[3] D. Y. Chung et al., "Growth of high-purity CsPbBr3 crystals for enhanced gamma-ray detection," Cryst. Growth Des., vol. 24, no. 22, pp. 9590–9600, Nov. 2024.
[4] B. Xiao et al., "Ambipolar charge transport in perovskite $CsPbBr_3$ gamma-ray detectors with superior uniformity and spectral resolution by zone refining processing," Adv. Sci., vol. 12, no. 11, Art. no. 2408933, 2025.

[5] Y. Hua et al., "Suppressed ion migration for high-performance X-ray detectors based on atmosphere-controlled EFG-grown perovskite $CsPbBr_3$ single crystals," Nat. Photonics, vol. 18, pp. 1060–1068, Jul. 2024.
[6] Q. Sun et al., "High-performance industrial-grade $CsPbBr_3$ single crystal by solid-liquid interface engineering," Adv. Sci., vol. 11, no. 1, Art. no. 2305881, Jan. 2024.

RTSD-04-357

Spectral Performance of GaAs:Cr Photon-Counting Detectors with Various Thicknesses (#2228)

Boren Wang[1], Tao Zhong[1], He Li[2], Juha Kalliopuska[3], Dmytro Nalyvaiko[3], Volodymyr Gnatyuk[3], Xiaochun Lai[1]

[1] Shanghaitech University, School of Biomedical Engineering, ShanghaiTech University, Shanghai, Pudong, China; [2] Shanghai United Imaging Healthcare Advanced Technology Research Institute Co., Ltd., Pudong, China; [3] Advafab OY, Helsinki, Finland

Supported by the Science and Technology Commission of Shanghai Municipality (24DIPA00700) and the Ministry of Industry and Information Technology (TC230H0AB/111). We acknowledge the ShanghaiTech Material and Device Lab.

Abstract

Photon-counting detectors (PCDs) enable high spatial resolution, zero electronic noise, and multi-material decomposition. Chromium-compensated gallium arsenide (GaAs:Cr) is an outstanding candidate material for these applications. To address single-crystal inhomogeneities and ASIC-induced variations, we implemented a single-pixel energy calibration scheme based on K-edge absorption for high-resistivity GaAs:Cr detectors [1]. S-curve scans were performed for 0.6 mm, 1.0 mm, and 1.4 mm sensor thicknesses using 0.5 mm metallic filters (Ta, W, Pb). Calculating the differential intensity ratio between filtered and air spectra allowed accurate K-edge energy extraction, yielding highly linear fits ($R^2 > 0.99$) between energy (keV) and Digital-to-Analog Converter (DAC) thresholds. Crucially, incorporating electron mobility-lifetime ($\mu\tau_e$) products elucidates the physical mechanisms driving thickness-dependent gain variations and spectral shifts. Subsequent evaluations confirmed the calibration accuracy. This calibration and physical analysis validate the spectral imaging capabilities of thick GaAs:Cr detectors, advancing their clinical applications.

References
[1] Vespucci, S, Park, CS, Torrico, R, Das, M 2018, 'Robust energy calibration technique for photon counting spectral detectors', *IEEE Transactions on Medical Imaging*, vol. 38, no. 4, pp. 968–978.
[2] Danielsson, M, Persson, M, Sjölin, M 2021, 'Photon-counting x-ray detectors for ct', *Physics in Medicine & Biology*, vol. 66, no. 3, p. 03TR01.
[3] Becker, J et al. 2018, 'Characterization of chromium compensated gaas as an x-ray sensor material for charge-integrating pixel array detectors', *Journal of Instrumentation*, vol. 13, no. 01, p. P01007.
[4] Wang, B, Li, H, Zhong, T, Lai, X 2024, 'Temporal response of GaAs:Cr x-ray detector under intense irradiation', *2024 IEEE Nuclear Science Symposium, Medical Imaging Conference, and International Symposium on Room-Temperature Semiconductor Detectors (NSS MIC RTSD)*, IEEE, poster.

RTSD-04-358

Optical manipulation of space charge in rectifying CdZnTe/CdTe radiation detectors (#2589)

Samuel Kačenga, Marián Betušiak, Eduard Belas, Roman Grill, Petr Praus

Charles University, Faculty of Mathematics and Physics, Institute of Physics, Prague, Czech Republic

This project is co-financed from the state budget by the Technology Agency of the Czech Republic under the code TQ28000004 Semiconductors4All.

Abstract

This work investigates the polarization and depolarization processes in CdZnTe and CdTe radiation detectors with rectifying contacts. The electrical properties of the contacts were characterized by I–V measurements, while the evolution of space charge was studied using the Laser-induced Transient Current Technique (L-TCT) combined with Monte Carlo simulations of charge transport to determine electric field profiles. In both CdZnTe and CdTe detectors, the gradual formation of negative space charge within the detector volume after applying bias was observed due to the hole blocking anode. Depolarization methods based on optical irradiation were subsequently investigated. In the CdTe detector, continuous above-bandgap irradiation of the anode by a 565 nm diode resulted in a stable, nearly flat electric field profile, demonstrating effective suppression of polarization for at least 1000 s. Similar results were observed for above-bandgap anode irradiation of CdZnTe as well. In both CdZnTe and CdTe detectors, continuous side irradiation by a below-bandgap 904 nm diode decreased the space charge and improved stability as well. However, compared with the above-bandgap anode irradiation, polarization was only partially suppressed for the CdTe detector, and the internal electric field still evolved over time, albeit more slowly than in the dark. For the CdZnTe detector, the side irradiation completely stopped the polarization. The results confirm that controlled optical irradiation can significantly improve the stability of CdTe/CdZnTe detectors operated under bias.

References

[1] Szeles, C. 2004, ‘CdZnTe and CdTe materials for X-ray and gamma ray radiation detector applications’, Physica Status Solidi (b), 241(3), 783–790

[2] Schlesinger, T., Toney, J., Yoon, H., Lee, E., Brunett, B., Franks, L. and James, R. B. 2001, ‘Cadmium zinc telluride and its use as a nuclear radiation detector material’, Materials Science and Engineering R: Reports, 32(4–5), 103–189

[3] Gaubas, E., Ceponis, T., Deveikis, L., Kalensinskas, V., Kreiza, G., Malinauskas, T., Pavlov, J., Rumbauskas, V., Mychko, A. and Ivanov, V. 2020, ‘Study of the electrical characteristics of CdZnTe Schottky diodes’, Materials Science in Semiconductor Processing, 105, 104705

[4] Bell, R. O., Entine, G. and Serreze, H. B. 1974, ‘Time-dependent polarization of CdTe gamma-ray detectors’, Nuclear Instruments and Methods, 117(1), 267–271

[5] Tsuchiya, K., Takahashi, I., Kawaguchi, T., Yokoi, K., Morimoto, Y., Ishitsu, T., Suzuki, A., Ueno, Y. and Kobashi, K. 2010, ‘Basic performance and stability of a CdTe solid-state detector panel’, Annals of Nuclear Medicine, 24(4), 301–311

[6] Uxa, Š., Belas, E., Grill, R., Praus, P. and James, R. B. 2012, ‘Determination of electric-field profile in CdTe and CdZnTe detectors using transient-current technique’, IEEE Transactions on Nuclear Science, 59, 2402–2408

RTSD-04-359

High-Voltage Tolerant Ni/YSZ/4H-SiC MOS Detectors for Thick Active Layers (#2697)

Marcel Talacko[1], Bohumír Zaťko[1], Štefan Chromik[1], Marianna Španková[1], Eva Kováčová[1], Zdenko Zápražný[1], Igor Píš[1], Vadym Ukrainets[1], Ladislav Hrubčín[1], Andrea Šagátová[2]

[1] Slovak Academy of Sciences, Institute of Electrical Engineering, Bratislava, Slovakia; [2] Slovak University of Technology, Faculty of Electrical Engineering and Information Technology, Bratislava, Slovakia

This work was supported by the Slovak Research and Development Agency by grant No. APVV-22-0382 and PostdokGrant – the Grant Programme for postdoctoral fellows of the Slovak Academy of Sciences No. APD0163, and Funded by the EU Next Generation EU through the Recovery and Resilience Plan for Slovakia under the project No. 09I05-03-V02-00073.

Abstract

Conventional 4H-SiC Schottky barrier detectors (SBDs) with thick active layers (>50 μm) are often limited by high leakage currents and premature breakdown under high bias voltages. This work introduces an innovative approach using an ultrathin yttria-stabilized zirconia (YSZ) high- κ dielectric interlayer to form a metal-oxide-semiconductor (MOS) structure. While YSZ is a known ionic conductor at elevated temperatures, its ionic mobility is effectively frozen at room temperature, allowing it to function as a robust electrical insulator that suppresses carrier injection. Ni/YSZ/n-4H-SiC MOS structures, fabricated via pulsed laser deposition demonstrated stable operation up to 1 kV. The high-voltage stability enabled a depletion width of approximately 70 μm at 1000 V, establishing favorable conditions for efficient charge collection in thick epitaxial layers. Spectrometric evaluation with a triple-alpha source (^{238}Pu–^{239}Pu–^{244}Cm) confirmed enhanced performance, with stable energy resolution maintained across a broad bias range (100–1000 V) and optimal results observed between 200 V and 600 V. This architecture significantly improves high-voltage resilience while maintaining competitive spectroscopic qualities, paving the way for next-generation deep-depletion radiation detectors in nuclear and space applications.

RTSD-04-360

Polycrystalline Based Semiconductors (PBS) TlBr for High Energy X-ray Detection and Radiography (#2790)

Alireza Kargar, Matthias Muller, Arthur Kim, Mike S. Squillante, Jarek Glodo

RMD, Inc., Watertown, USA

This work has been supported in-part by the CWMD/DHS through University of Tennessee, Knoxville (UTK), under competitively awarded contracts: 22CWDARI00047-01-01. This support does not constitute an express or implied endorsement on the part of the Government.

Abstract

TlBr Polycrystalline Based Semiconductors (PBS) are investigated as promising ceramic materials for low-cost, high-energy x-ray detection. Ceramic samples were prepared through hot pressing followed by the fabrication of planar detectors for characterization and x-ray response measurements. Current-voltage (I-V) characteristics were evaluated for all devices, which exhibited high resistivity (≥10^9 Ω cm) and stable performance under applied bias. The samples demonstrated excellent sensitivity to 70 kVp x-rays, as well as outstanding response to 6 MeV and 9 MeV x-ray pulses from the Linatron M9A linear accelerator (linac) at the University of Tennessee, Knoxville (UTK). This work provides a general overview of the ceramic preparation process and detector characterization and summarizes low and high-energy x-ray responses measured at RMD and UTK.

RTSD-04-361

Lateral Expansion of the Active Region in Semi-Insulating GaAs Radiation Detectors with Different Schottky Contact Sizes (#3001)

Nikola Kurucova[1], Andrea Sagatova[1], Bohumir Zatko[2], Eva Kovacova[2]

[1] Slovak University of Technology, Faculty of Electrical Engineering and Information Technology, Institute of of Nuclear and Physical Engineering, Bratislava, Slovakia; [2] Slovak Academy of Sciences, Institute of Electrical Engineering, Bratislava, Slovakia

This work was partially supported by grants of the Slovak Research and Development Agency No. APVV-22-0382, No. DS-FR-24-0020 and by the EU NextGenerationEU through the Recovery and Resilience Plan for Slovakia under the project No. 09I05-03-V02-00073.

Abstract

This work investigates the influence of Schottky contact size on the charge collection efficiency (CCE) and lateral expansion of the active region in 350 μm thick semi-insulating GaAs detectors using alpha particle spectrometry. Measurements were performed for detectors with Schottky contact diameters ranging from 0.10 mm to 2.00 mm under reverse bias voltages up to 500 V. The results show that detectors with smaller contacts achieve higher CCE values and simultaneously higher counting rates, indicating spreading of the electric collection field beyond the geometrical contact area. The lateral extension of the active region was evaluated from the effective active diameter derived from alpha peak count analysis. The obtained results demonstrate an approximately linear increase of the lateral extension with increasing reverse bias voltage, reaching average values of about 80 μm at 200 V and 120 μm at 300 V. These findings are particularly relevant for pixelated detector systems with small pixel pitch, such as Timepix3-based detectors employing thick GaAs sensors.

RTSD-04-362

Depth-Resolved Measurement of Charge-Cloud Formation and Transport in a 2.0 mm CdTe-Timepix3 Detector (#3046)

Duarte S. Rodrigues[1,3], Alexandre M. Trindade[1,3], **Jorge M. Maia**[2,1], Rui M. Curado da Silva[1,3], Pedro G.H. Carmo[1,3], Jose F. Sousa[1], Mariana Letra[1]

[1] LIP–Laboratory of Instrumentation and Experimental Particle Physics, Coimbra, Portugal; [2] University of Beira Interior (UBI), Department of Physics, Covilhã, Portugal; [3] University of Coimbra, Department of Physics, Coimbra, Portugal

This work was supported by the European Space Agency, through the PRODEX Experiment Arrangement No 4000141332.

Abstract

Understanding charge cloud formation and transport in CdTe detectors is essential for precision spectroscopy, imaging, and Compton polarimetry in the sub-MeV gamma-ray band. We report a detailed experimental study of electron diffusion and electron-dispersion mechanisms in a 2.0 mm-thick CdTe-Timepix3 detector (256×256 pixels, 55 µm pitch), operated at a bias voltage of −300 V and temperature of ≈28 °C. Monochromatic 200 keV and 300 keV gamma-ray beams, collimated to 10 µm×10 µm, were provided by the ESRF ID15A beamline and directed along the detector's Y-axis. A depth-resolved scan was performed in 200 µm steps along the Z-axis, probing the evolution of the transverse charge cloud inside the CdTe volume. For each Z-position, thousands of photoelectric events were selected, and the 1D transverse distribution of the total collected charge was reconstructed along the X-axis. Gaussian fits to these distributions yielded depth-dependent width values. Fitting the squared width values with a function that models all contributions to the transverse charge distribution at the pixelated plane enabled the extraction of key charge-transport parameters: the initial radius of the primary photoelectron cloud and the electron transverse diffusion coefficient. Independent measurements of the electron drift velocity using throughgoing muon tracks were used to constrain this parameter. The measured evolution of sigma values is well described by a model that combines thermal diffusion, the finite initial radius of the primary photoelectron cloud, and Coulomb-driven charge-cloud expansion. This work provides the first depth-resolved experimental quantification of these combined effects in CdTe-Timepix3 detectors, improving charge-transport inputs for simulations of Compton imaging and polarimetry in the 0.1–1 MeV energy band.

References

[1] Sousa, JF, et al., Polarimetric Evaluation of CdTe-Timepix3 Detector Module for THOR-SR Compton Telescope, Astroparticle Physics 175 (2026) 103181

[2] Poikela, T, et al., Timepix3: a 65K channel hybrid pixel readout chip with simultaneous ToA/ToT and sparse readout, 2014 JINST 9 C05013.

[3] Trindade, AMF, et al., Development of a Device to Measure the Electron Transverse Diffusion in Gas Media, IEEE Trans. Nucl. Sci., vol. 70, no.3, pp. 254-261, 2023.

[4] Boggs, SE, Modeling charge cloud dynamics in cross-strip semiconductor detectors, Nuclear Inst. and Methods in Physics Research, A 1052 (2023) 168310.

[5] Benoit, M, Hamel, LA, Simulation of charge collection processes in semiconductor CdZnTe γ-ray detectors, Nuclear Inst. and Methods in Physics Research A 606 (2009) 508-516.

RTSD-04-363

When 0 V Is Not Really 0 V: Remnant Fields in $MAPbBr_3$ X-Ray Detectors (#1290)

Eric Gros-Daillon[1], Oriane Baussens[1], Ferdinand Lédée[2], Jean-Marie Verilhac[2]

[1] CEA, Leti, Grenoble, France; [2] CEA, Liten, Grenoble, France

This work received funding from the European Union's Horizon 2020 research and innovation program under the Photonics Public–Private Partnership (www.photonics21.org) with the project PEROXIS under Grant Agreement No. 871336.

Abstract

Methylammonium lead tribromide ($MAPbBr_3$) single crystals are intensively studied emerging materials for use in X-ray radiography and gamma-ray spectrometry [1] and their quality such as shape control, dislocation and point defect densities are improving but some of their properties remain elusive. In particular, transient X-ray-induced photocurrent can be measured in MAPbBr3 single crystals detectors after the bias is switched off. This response then slowly decays over time. In this study, we investigate the internal electrical field that builds up when a bias is applied2[4] by measuring the residual sensitivity of millimeter-thick Cr/$MAPbBr_3$/Cr-based detectors after switching off the bias from 10V to 0V. By fitting a numerical model, we compute the value of this internal field and infer the ionic charge density close to the electrodes. This model is also used to approximate the charge carrier mobility lifetime product.

References

[1] H. Wei et al., "Sensitive X-ray detectors made of methylammonium lead tribromide perovskite single crystals," Nat. Photonics 10(5), 333–339 (2016). DOI. 10.1038/nphoton.2016.41

[2] F. Lédée, J. Mayén-Guillen, S. Lombard, J. Zacarro, JM. Verilhac, E. Gros-Daillon; Evidence for a build-in remnant field in symmetrically contacted $MAPbBr_3$ x-ray detectors. *J. Appl. Phys.* 21 November 2023; 134 (19): 195703. DOI. 10.1063/5.0170580

RTSD-04-364

Vibration-suppressed solution growth of perovskite single crystals for high-resolution gamma-ray detection (#1577)

Bin Song[1], Yifu Chen[1], Shasha Xiao[1], Zimeng Li[2], Yongshuai Ge[1], Haodi Wu[1]

[1] Chinese Academy of Sciences, Research Center for Advanced Detection Materials and Medical Imaging Devices, Shenzhen Institute of Advanced Technology, Shenzhen, China; [2] Shenzhen Polytechnic University, School of Electronic and Communication Engineering, Shenzhen, China

This work was supported bythe National Natural Science Foundation of China (No. 62474185, 62501412), the Major State Basic Research Development Program of China (No. 2024YFF0507800).

Abstract

High-performance γ-ray spectroscopy with solution-grown metal halide perovskites has been persistently limited by uncontrolled defect formation during crystal growth. Here, we identify ambient mechanical vibration as a critical yet overlooked factor that destabilizes the concentration boundary layer and perturbs lattice ordering in hybrid perovskite single crystals. The resulting crystals exhibit an increased carrier mobility-lifetime product of 8.36×10^{-2} $cm^{-2}\,V^{-1}$, which contributes to a more efficient charge collection process. Detectors achieved an energy resolution of 9.5% at 59.5 keV and 5.2% at 122 keV. These results establish vibration control as a key principle for high-quality single-crystal growth and scalable perovskite radiation detectors.

References

[1] F. Liu, R. Wu, J Wei, W. Nie, H. Li, et al., “Recent progress in halide perovskite radiation detectors for gamma-ray spectroscopy,” ACS Energy Lett., vol. 7, no. 3, pp. 1066-1085, Feb. 2022. doi: 10.1021/acsenergylett.2c00031

[2] Z. Lei, L. Li, Y. Xu, D. Yang, Z. Ni, “Metal halide perovskite for room temperature gamma-ray spectrum detection,” Inf. Funct. Mater., vol. 2, no. 1, pp 40-61, Mar. 2025. doi: 10.1002/ifm2.29

[3] M. Li, S. Wang, A. Wood, J. D. Yeager, J. Huang, et al., “Defect repairing in lead bromide perovskite single crystals with biasing and bromine for X-ray photon-counting detectors,” Nat. Mater., vol. 24, pp 1993-2000, Aug. 2025. doi: 10.1038/s41563-025-02310-x

[4] J. Jiang, M. Xiong, K. Fan, C. Bao, D. Xin, et al., “Synergistic strain engineering of perovskite single crystals for highly stable and sensitive X-ray detectors with low-bias imaging and monitoring,” Nat. Photon., vol. 16, pp 575-581, Jul. 2022. doi: 10.1038/s41566-022-01024-9

RTSD-04-365

Investigation of the anisotropy of the electronic properties of $CsPbBr_3$ (#1667)

Valerii Skliarchuk[1], **Petro Fochuk**[1], Aleksey Bolotnikov[2], Ralph B. James[3]

[1] Chernivtsi National University, Chernivtsi, Ukraine; [2] Brookhaven National Laboratory, Upton, USA; [3] Savannah River National Laboratory, Aiken, USA

This work was partly supported by the Science@Technology Center of Ukraine under project 6437. This work was supported by a grant from the Simons Foundation (SFI-PD-Ukraine-00014579).

Abstract

The study of the electrical properties of perovskite $CsPbBr_3$ crystals, grown by the Bridgman method in our laboratory, showed that the stability of the dark current of the In/$CsPbBr_3$/In structure critically depends on the polarity of the applied voltage. The $CsPbBr_3$ crystal was cut perpendicular to the growth plane. Indium was deposited on both surfaces after treatment in an argon plasma. The contact area was 4x4 mm^2, and the thickness of the plates was 1-2 mm. The study was carried out at a temperature of T≈300 K and a voltage of 100 V. The surface of the sample, which was closer to the beginning of the ingot growth and crystallized first, will be designated as “cold”. When on the “cold” side was the “minus”, the current remained stable over time for 8 hours of

continuous operation, while with reverse polarity, a degradation of the blocking properties wais observed with an increase in the dark current by 2–3 orders of magnitude. A similar phenomenon (non-equivalence of opposite crystal surfaces) was observed in CdTe crystals, oriented in the (111) plane. Therefore, it can be assumed that when cutting a plate perpendicular to the growth axis, with there is a very high probability that one side will be enriched with a layer of Cs and Br atoms, and the opposite side, which is more chemically active, will be enriched with Pb and Br atoms. This may be the reason for the non-equivalence of their behavior in the electrical measurements.

RTSD-04-366

Controllable Fabrication of High-performance Perovskite Single Crystals in Solution toward Efficient X-ray Detection (#2024)

Yu Chen

Beijing Institute of Technology, HaiDian Beijing, China

The financial support from the National Natural Science Foundation of China (No.52373279) and the Beijing Natural Science Foundation (No.4232079).

Abstract

Perovskite single crystals demonstrate great potential in high energy radiation detection applications due to the unique semiconductor properties, while still suffers from uncontrollable growth progress and labile crystal quality. In this paper, we here develop a series of interdisciplinary growth methodologies for fabricating high-quality perovskite single crystals based on the solvent design and additive engineering, achieving high-performance and reliable robustness toward impressive X-ray detection performance.

References

[1] Liangji Li, Aijing Gao, Chen Sun, Xuhui Wu, Xiaoning Wang, Yubin Zhou, Jian Sun,* Haizheng Zhong, and Yu Chen*. *ACS Energy Lett.* **2026**, 11, 2993–3002

[2] Aijing Gao, Yu Chen,* Zining Li, Kai Gu, Shipei Sun, Haizheng Zhong, and Jian Sun*. *Adv. Funct. Mater.* **2024**, 2314237

[3] Zining Li, Shipei Sun, Haotian Jiang, Zhiyuan Ding, Chao Zhang, Zhili Cui, Yuling Wang, Yu Chen,* and Haizheng Zhong. *Adv. Funct. Mater.* **2024**, 2407629

[4] Shuyu Shi, Chao Zhang, Jiaming Su, Chen Sun, Songtao Su, Yanling Che, Yu Zhang, Zhili Cui, Gaoling Yang, Haizheng Zhong, and Yu Chen*. *Small***2025**, 2504160

[5] Haotian Jiang, Yu Chen,* Shipei Sun, Zining Li, Qingchen Wang, Tinglu Song, and Haizheng Zhong. *Cryst. Growth Des.* **2023**, 23, 7424–7431

RTSD-04-367

Improved Stability of Perovskite Single Crystal Semiconductor X-ray Detector via 2D Layer Formation (#2555)

Dakyoung Lee[1,2], Beomjun Park[3], Seungho Song[1,2], Jiwon Seo[5], Chansun Park[4], Jung-Yeol Yeom[1,6]

[1] Korea University, Department of Bioengineering, Seoul, South Korea; [2] Korea University, Interdisciplinary Program in Precision Public Health, Seoul, South Korea; [3] Seoul National University, Nuclear Research Institute for Future Technology and Policy (NIFTEP), Seoul, South Korea; [4] Korea University, Global Health Technology Research Center, Seoul, South Korea; [5] Korea Institute of Fusion Energy (KFE), Daejeon, South Korea; [6] Korea University, School of Bioengineering, Seoul, South Korea

This work was supported by the National Research Foundation of Korea (NRF), funded by the Ministry of Science and ICT (RS-2023-NR077190, RS-2022-00165164), and by the National Research Foundation of Korea and the Commercializations Promotion Agency for R&D Outcomes (RS-2023-00234651).

Abstract

Methylammonium lead tribromide ($MAPbBr_3$, MPB) single crystals are promising candidates for direct-conversion X-ray detection, but their practical use is hindered by ion migration that causes photocurrent drift and baseline instability under continuous X-ray exposure. In this work, a two-dimensional (2D) organic–inorganic hybrid layer is formed on MPB single crystals through a simple solution-dipping process using 4-fluorophenethylammonium iodide (4F-PEAI), and the impact on detector stability is systematically investigated. The 2D-layer formation, controlled through precursor concentration and dipping time, is confirmed by the emergence of a new low-angle XRD peak assigned to a $(4F\text{-}PEA)_2PbX_4$ 2D layered phase, and by a blue shift of the band-edge photoluminescence consistent with surface modification. Surface 2D-layer passivation reduces the dark-current hysteresis, suppresses the photocurrent drift under continuous X-ray exposure, and lowers the in-pulse relative standard deviation, while maintaining linear dose response across the measured dose-rate range. These results demonstrate that surface 2D-layer formation is a practical strategy for suppressing ion migration and improving the operational stability of perovskite single-crystal X-ray detectors.

References

[1] Wei, Haotong, and Jinsong Huang. "Halide lead perovskites for ionizing radiation detection." *Nature communications* 10.1 (2019): 1066.

[2] Pan, Weicheng, et al. "Cs2AgBiBr6 single-crystal X-ray detectors with a low detection limit." *Nature photonics* 11.11 (2017): 726-732.

[3] Ko, Juyoung, et al. "High-performance 110 kVp hard x-ray detector based on all-crystalline-surface passivated perovskite single crystals." *InfoMat* 6.8 (2024): e12560.

[4] Park, Ahreum, et al. "Exploration on high-energy and high-dose rate X-ray detection with Bridgman-grown CsPbBr3 single crystal." *Nuclear Engineering and Technology* (2025): 103799.

RTSD-04-368

Highly Radiation-Hard Flexible Perovskite Imaging Arrays for Real-Time Proton Beam Monitoring (#2700)

Yang Zhang, Guangda Niu

Huazhong University of Science and Technology, Wuhan National Laboratory for Optoelectronics and School of Optical and Electronic Information, WuHan, China

Abstract

Real-time proton beam monitoring is crucial for pencil beam scanning in proton therapy, but conventional solid-state detectors suffer from radiation-induced damage and structural rigidity, limiting their in-vivo applications. Building upon the lattice-anchoring dynamic repair mechanism in hybrid perovskites, we developed a highly stable, flexible perovskite thin-film transistor array for real-time proton beam profiling. The detector adopts a p-i-n architecture on a flexible substrate, protected by robust Parylene encapsulation to ensure long-term operational stability. Under 160 megaelectron-volt high-energy proton irradiation, the arrays demonstrated exceptional radiation hardness, maintaining robust operational stability even after accumulating a high fluence of $1.23*10^{10}$ p cm^{-2}. Spatial resolution remained uncompromised post-irradiation, with the spatial frequency at a modulation transfer function of 0.2 showing negligible degradation from about 3.03 line pairs per millimeter.. When deployed in a clinical setup, the TFT array achieved real-time proton beam imaging at a frame rate of 15 frames per second. At a 16-centimeter solid water depth, the measured beam full-width at half-maximum (FWHM) was 8.47 millimeters, perfectly matching the 8.27 millimeters theoretical value predicted by Monte Carlo simulations using FLUKA and Allpix, and it has achieved real-time tracking and prediction of the center of the proton beam. These results validate the immense potential of flexible perovskite TFT arrays for the real-time tracking of the Bragg peak and conformal dose monitoring, offering a transformative dosimetric tool for advanced precision radiotherapy and expanding the practical applications of room-temperature semiconductor detectors.

References

[1] K. Parodi and J. C. Polf, "In vivo range verification in particle therapy," Med. Phys., vol. 45, no. 11, pp. e1036–e1050, Nov. 2018, doi: 10.1002/mp.12960.

[2] H. Paganetti, "Range uncertainties in proton therapy and the role of Monte Carlo simulations," Phys. Med. Biol., vol. 57, no. 11, pp. R99–R117, May. 2012, doi: 10.1088/0031-9155/57/11/R99.

[3] J. Cayley, I. Filipev, J. A. Davis, V. de Rover, D. Cutajar, E. Li, B. M. Oborn, M. Petasecca, A. Rosenfeld, and M. L. F. Lerch, "Playing hard with Si: Challenges and opportunities for new materials in radiation therapy dosimetry," Adv. Mater., vol. 37, no. 36, Art. no. e2508478, Jul. 2025, doi: 10.1002/adma.202508478.

[4] H. Yin, H. Wu, Y. Zhang, F. Liu, Q. Bai et al., "Highly sensitive and stable perovskite detector for ultrahigh-energy radiations via dynamic repair regulation," Nat. Photon., vol. 20, no. 4, pp. 340–347, Feb. 2026, doi: 10.1038/s41566-026-01849-8.

[5] J. Ortigoza-Diaz et al., "Techniques and considerations in the microfabrication of Parylene C microelectromechanical systems," Micromachines, vol. 9, no. 9, Art. no. 422, Aug. 2018, doi: 10.3390/mi9090422.

[6] S. Agostinelli et al. (GEANT4 Collaboration), "Geant4—a simulation toolkit," Nucl. Instrum. Methods Phys. Res. A, vol. 506, no. 3, pp. 250–303, Jul. 2003, doi: 10.1016/S0168-9002(03)01368-8.

RTSD-04-369

FAPbBr3 Single Crystal Perovskite Radiation Detector with Embedded Electrode Array Architecture (#2833)

Seán Cardiff, Ganbaatar Tumen-Ulzii, Samuel D. Stranks

University of Cambridge, Chemical Engineering and Biotechnology, Cambridge, UK

This work was supported by the Engineer ing and Physical Sciences Research Council (EPSRC) grant EP/S022139/1- the Centre for Doctoral Training in Connected Electronic and Photonic Systems.

Abstract

Formamidinium lead bromide (FAPbBr3) single crystal perovskites have recently emerged as a key candidate for commercially viable radiation detectors for their high per formance and solution processability at low temperatures. An under-explored consequence of crystal growth from solution is the ability to crystallise around pre-placed structures, enabling detectors with an embedded electrode architecture. This work presents the growth of FAPbBr3 single crystals around a 2×2 array of gold wire electrodes, showing the first demonstration of this device architecture in a FAPbBr3 single crystal radiation detector as a proof of concept. By collecting charge carriers laterally, the charge carrier transit time and trap probability is reduced compared to the planar configuration. Initial charac terisation demonstrated a linear I–V response and sensitivity to X-rays. Future work will scale to a larger array with an increased area targeting γ-ray spectroscopic performance with fast signal pulse rise times.

References

[1] M. Li et al., “Defect repairing in lead bromide perovskite single crystals with biasing and bromine for X-ray photon-counting detectors,” Nature Mater., vol. 24, no. 12, pp. 1993–2000, 2025.

[2] M. I. Saidaminov et al., “Rapid low-temperature crystallization of phase pure formamidinium perovskite,” ACS Energy Lett., vol. 1, no. 4, pp. 840–845, Oct. 2016.

[3] S. Terzo et al., “Novel 3D pixel sensors for the upgrade of the ATLAS Inner Tracker,” Frontiers in Physics, vol. 9, p. 624668, 2021.

RTSD-04-370

RTSD-04-371

Evaluation of carrier transport properties of TlBr semiconductor detectors (#1686)

Kenichi Watanabe[1], Yusuke Sugai[1], Seishiro Tanaka[1], Yusuke Kawai[1], Mitsuhiro Nogami[2], Keitaro Hitomi[2]

[1] Kyushu University, Department of Applied Quantum Physics and Nuclear Engineering, Fukuoka, Japan; [2] Tohoku University, Department of Quantum Science and Energy Engineering, Sendai, Japan

This work was partially supported by JSPS KAKENHI Grant Numbers JP23K23276 and JP25H01210. This work was also supported by JAEA Nuclear Energy S&T and Human Resource Development Project Grant Number JPJA25P25134581.

Abstract

Thallium bromide (TlBr) is a highly promising material for next-generation gamma-ray detectors due to its wide band gap and high stopping power. To realize large-volume and high-performance detectors, it is essential to establish an efficient evaluation method for detector performance. This study aims to investigate the correlation between crystalline structural quality and carrier dynamics in TlBr single crystals. We developed a scanning time-of-flight (TOF) measurement system to evaluate the two-dimensional distribution of electron mobility and trapping characteristics. A 3-mm-thick TlBr wafer was characterized using both EBSD mapping and laser-induced TOF measurements. The results revealed a clear correlation between structural grain boundaries and localized degradations in electron mobility. Furthermore, spatial mapping of the residual charge ratio identified specific regions characterized by high trap densities. Subsequent evaluations of detectors fabricated from these regions showed significantly poor long-term stability. This study provides essential feedback for improving crystal growth processes and establishes a methodology for the quality assurance of compound semiconductor radiation detectors.

References

[1] K. Hitomi, T. Onodera, S.Y. Kim, T. Shoji, K. Ishii, Characterization of pixelated TlBr detectors with Tl electrodes, *Nucl. Instrum. Method Phys. Res. Sec. A*, **747**, 7-12 (2014).

[2] T. Nojima, M. Nogami, K. Hitomi, Enhancing the energy resolution of TlBr detectors through an adaptive shaping method, *Japanese Journal of Applied Physics*, **64**, 116001 (2025).

[3] K. Watanabe, Y. Sugai, S. Hasegawa, S. Tanaka, K. Hitomi, M. Nogami, T. Shinohara, Y. Su, J.D. Parker, W. Kockelmann, Comparison between carrier transport property and crystal quality of TlBr semiconductors, *Scientific reports.*, **14**, 25224 (2024).

[4] Y. Sugai, K. Watanabe, S. Hasegawa, K. Hitomi, M. Nogami, Development of Time-of-flight Measurement System for Carrier Transport Characterization of TlBr Semiconductor Detectors, *Sensors and Materials.*, **36**, 155-161 (2024).*l*, Edition, Page, Place of publication: publishers

RTSD-04-372

Fabrication of Flexible Nanostructured Polymer for Nanomaterial-based Detectors (#1099)

Ill-Hyuk Han[1], Jihwan Boo[1], Geehyun Kim[2,3]

[1] Seoul National University, Department of Energy System Engineering, Gwanak-gu, South Korea; [2] Seoul National University, Department of Nuclear Engineering, Gwanak-gu, South Korea; [3] Seoul National University, Institute of Engineering Research, Gwanak-gu, South Korea

This work was supported by the National Research Foundation of Korea (NRF) grant funded by the Korea government (Ministry of Science and ICT) (No. 2022M2D2A1A02063826).

Abstract

This study describes the fabrication of the aramid nanofiber (ANF) to produce flexible detectors based on nanomaterials, with short preparation and low surface leakage current. Flexible detectors offer the advantage of achieving improved detection efficiency and efficient use of space with curved surfaces. In previous studies, ANF was used as a porous nanostructured polymer for the fabrication of nanomaterial-based semiconductor detectors. However, it had the issues of a long preparation time and brittleness after drying. To address these issues, we used DMSO containing an aqueous KOH solution in the preparation of the ANF solution. with This reduced the preparation time from one week to two days. Furthermore, we compared the results of ANF coagulation in different soloutions—ethanol (EtOH), acetic acid (AcOH), and a mixed AcOH-EtOH (volume ratio was 7:3) solution—to alleviating the pore collapse of the nanostructure, with the conventional H_2O-based method. The synthesis solution containing PbS quantum dots (about dia. 5 nm) and Te nanorods (130 nm in length), as confirmed by TEM and XRD, was loaded into ANF samples using various coagulation solutions. We confirmed that uniform loading in dpeth occurred in the order of H_2O, EtOH, AcOH, and the AcOH-EtOH mixture. Furthermore, according to the I–V curves, the surface leakage current also tended to decrease in the same order of uniform loading, with a maximum 10,000-fold difference observed between the ANF samples prepared with H_2O (about 100 μA at 10 V) and the AcOH-EtOH mixed solution (about 2 nA at 10 V). Therefore, it was shown that ANF coagulated with the AcOH-EtOH mixed solution remained flexible even after drying, and the uniform embedding of nanomaterials according to depth reduced the surface leakage current.

References

[1] X. Ou, Z. Hong, Q. Wu, X. Che, L. Xie, Z. Zhang, Y. He, Q. Chen, H. Yang, 2024, 'Micro/Nano Engineering Advances Next-Generation Flexible X-ray Detectors', *ACS nano*, vol. 18, no. 40, pp. 27126-27137, USA: Amer. Chemical Soc.

[2] D. A. Vecchio, M. D. Hammig, N. A. Kotov, 2025, 'High-Resolution Radiation Sensors from Flexible Network Nanocomposites of Nanoparticles and Aramid Nanofibers', *ACS Nano*, vol. 19, no. 12, pp. 11927-11935, USA: Amer. Chemical Soc.

[3] V. D. Le, D. A. Vecchio, A. D. Uyulur, I. -H. Han, A. M. Ursu, G. Kim, M. D. Hammig, 2025, 'X-ray and γ-ray Sensing from Aqueous-Based Lead Sulfide Telluride Nanocomposites', *Small*, vol. 21, no. 49, pp. e04684-e04684, Germany: Wiley-V C H Verlag Gmbh

[4] Y. -J. Zhu, X. -L. Hu, W. -W. Wang, 2006, 'Poly(vinylpyrrolidone): a new reductant for preparation of tellurium nanorods, nanowires, and tubes from TeO2', *Nanotechnology*, vol. 17, no. 3, pp. 645-650, England: IOP Publishing Ltd.

[5] H. -J. Chen, Q. -Y. Bai, M. -C. Liu, G. Wu, Y. -Z. Wang, 2021, 'Ultrafast, Cost-Effective and Scaling-Up Recycling of Aramid Products into Aramid Nanofibers: Mechanism, Upcycling, Closed-Loop Recycling', *Green Chemistry*, 23, pp. 7646-7658, England: Royal Soc. Chemistry

[6] I. -H. Han, J. Boo, D. A. Vecchio, M. D. Hammig, G. Kim, 2025, 'Assessment of Charged Particle Response of PbS Quantum Dots in Nanostructured Polymer', *IEEE NSS-MIC-RTSD*, Yokohama, Japan, 2025, pp. 1-1
[7] J. Wu, J. Zhang, M. Sang, Z. Li, J. Zhou, Y. Wang, S. Xuan, KCF. Leung, X. Gong, 2023, 'Acid-assisted Toughening Aramid Aerogel Monoliths with Ultralow Thermal Conductivity and Superior Tensile Toughness', *Advanced Functional Materials*, vol. 34, issue 2, 2307072, Germany: Wiley-V C H Verlag Gmbh

RTSD-04-373

Enhanced Imaging Uniformity of Perovskite X-ray Detectors via Combined Uniform Particle Dispersion and Solution-assisted Hot Pressing Treatment (#1643)

Xulong Pang[1,2], Zimeng Li[3], Manling Sui[1], Yue Lu[1], Yongshuai Ge[2], Haodi Wu[2]

[1] Beijing University of Technology, State Key Laboratory of Materials Low-Carbon Recycling, Beijing, China; [2] Shenzhen Institute of Advanced Technology, Chinese Academy of Sciences, Research Center for Advanced Detection Materials and Medical Imaging Devices, Shenzhen, China; [3] Shenzhen Polytechnic University, School of Electronic and Communication Engineering, Shenzhen, China

This work was supported by the Major State Basic Research Development Program of China (No. 2024YFF0507800) and the National Natural Science Foundation of China (No. 62474185, 62501412).

Abstract

Perovskite materials are promising for low-cost direct X-ray detection, but their integration with thin-film transistor backplanes is limited by porosity, cracking, and poor imaging uniformity. Here, we report a combined strategy of uniform particle dispersion and solution-assisted hot pressing for fabricating uniform $MAPbI_3$ thick films on TFT substrates, where uniform particle dispersion stabilizes slurry dispersion and solution-assisted hot pressing promotes film densification, grain growth, and pore filling. The average particle size of the fabricated devices decreased from 32.07 μm to 15.14 μm, and the standard deviation reduced from 7.3 μm to 4.9 μm. At an electric field strength of 100 $V \cdot mm^{-1}$, the sensitivity reached 3514 $\mu C \cdot Gy_{air}^{-1}\ cm^{-2}$. A prototype $MAPbI_3$-based X-ray flat-panel detector further achieves a spatial resolution of 3.75 lp mm^{-1} at an modulation transfer function of 0.2, together with significantly improved imaging uniformity. This work provides a practical route toward scalable, thin-film transistor compatible perovskite X-ray flat-panel detectors.

References
[1] S. Deumel, A. van Breemen, G. Gelinck. et al. High-sensitivity high-resolution X-ray imaging with soft-sintered metal halide perovskites. Nat Electron., vol. 4, pp. 681–688, Sep. 2021. doi: org/10.1038/s41928-021-00644-3
[2] K. Sakhatskyi, B. Turedi, G. Matt, et al. Stable perovskite single-crystal X-ray imaging detectors with single-photon sensitivity. Nat. Photon. vol. 17, pp. 510–517, Jun. 2023. doi: org/10.1038/s41566-023-01207-y
[3] H.Wu, X.Chen, Z.Song, et al. Mechanochemical Synthesis of High-Entropy Perovskite toward Highly Sensitive and Stable X-ray Flat-Panel Detectors. Adv. Mater. vol. 35, no. 29, pp. 2301406, Jul. 2023. doi: org/10.1002/adma.202301406
[4] Y. Liu, C. Gao, D. Li, et al. Dynamic X-ray imaging with screen-printed perovskite CMOS array. Nat Commun. vol. 15, no. 1588. Feb. 2024. doi: org/10.1038/s41467-024-45871-2

RTSD-04-374

Investigation of Metal Oxides as Contact Materials for CdTe X-Ray, Gamma-Ray Detectors (#1816)

Madan Niraula, Masaya Tanimoto, Yamato Ohi, Rikuto Fukuda

Nagoya Institute of Technology, Graduate School of Engineering, Nagoya, Japan

This work was partly supported by JSPS Kakenhi grant (24K15592).

Abstract

CdTe is a well-established semiconductor for high-resolution X-ray, gamma-ray detector. However, its widespread application is limited by high dark current and long-term performance instability. The metal–semiconductor interface plays a critical role in governing these issues, as it strongly influenced by contact metal indiffusion and interfacial reactions. In this work, indium tin oxide (ITO) is investigated as a potential contact material for CdTe detectors to mitigate these limitations. ITO electrodes were deposited on one face of a high-resistivity p-like CdTe crystal by RF sputtering, while a gold electrode was formed on the opposite face by thermal evaporation. The fabricated device showed clear rectifying behavior, with reverse dark currents below 1 nA at 100 V bias for a 3 x 3 x 0.5 mm^3 device, representing a significant reduction compared to similar devices with Au contacts on both sides. Improved gamma-ray detection performance was also observed. Furthermore, the effects of CdTe substrate temperature during ITO deposition and post-deposition annealing on junction formation and detector performance, including dark current, energy resolution, and long-term stability, were systematically investigated.

RTSD-04-375

Transport Properties of CdTe Semiconductor after Laser Ablation (#2458)

Jakub Dřevo, Eduard Belas, Roman Grill, Pavel Moravec, Marián Betušiak

Charles University, Faculty of Mathematics and Physics, Institute of Physics, Prague, Czech Republic

This project is co-financed from the state budget by the Technology agency of the Czech Republic under the SIGMA Programme TACR TQ28000004 Semiconductors4All.The authors gratefully acknowledge Šimon Syrovátka and Vojtěch Kudrna (Hofmeister s.r.o.) for their assistance with laser ablation sample processing.

Abstract

This study investigates the characterization of conductive layers on CdTe semiconductor crystals fabricated via laser ablation. The layers were prepared at both ambient and elevated temperatures, with various ablation parameters evaluated to optimize their quality. Our analysis revealed the formation of conductive layers on the semiconductor surface, exhibiting high hole mobility. These layers were systematically characterized using a suite of electrical and optical techniques, including Hall effect measurements, photocurrent mapping, the Laser-induced Transient Current Technique (L-TCT), and stability tests focusing on time-dependent behavior.

References
[1] Zha, F. X., Zhou, S. M., Ma, H. L., Yin, F., Zhang, B., Li, T. X., Shao, J., Shen, X. C. 2008, 'Laser drilling induced electrical type inversion in vacancydoped -type HgCdTe', Appl. Phys. Lett., 93, 151113, Melville: AIP Publishing
[2] Hatanaka, Y., Niraula, M., Nakamura, A., Aoki, T. 2001, 'Excimer laser doping techniques for II–VI semiconductors', Applied Surface Science, 175–176, 462-467, Amsterdam: Elsevier
[3] Medvid', A., Korbutyak, D. V., Krylyuk, S. G., Kryuchenko, Yu. V., Kuznetsov, E. I., Kupchak, I. M., Fedorenko, L. L., Hlidek, P. 2004, 'Influence of powerful laser irradiation on impurity-defect structure of CdTe detector material', Nuclear Instruments and Methods in Physics Research A, 531, 157–160, Amsterdam: Elsevier
[4] Mychko, A., Medvid, A., Dauksta, E. 2015, 'Laser-induced increase of resistivity and improvement of optical properties of CdZnTe crystal', Journal of Crystal Growth, 415, 47-50, Amsterdam: Elsevier
[5] Gnatyuk, V., Maslyanchuk, O., Strebezhev, V., Fodchuk, I., Solovan, M., Sorokatyi, M., Boledzyuk, I., Kuzmin, A. 2023, 'Laser-Induced Modification of the Morphology and Defect Structure of Heterostructures Based on Detector-Grade CdTe Crystals', Journal of Nano- and Electronic Physics, 15, 01001, Sumy: Sumy State University
[6] Belas, E., Franc, J., Toth, A., Moravec, P., Grill, R., Sitter, H., Höschl, P. 1996, 'Type conversion of p-(HgCd)Te using H2/CH4 and Ar reactive ion etching', Semicond. Sci. Technol., 11, 1116–1120, Bristol: IOP Publishing
[7] Belas, E., Grill, R., Pipek, J., Praus, P., Bok, J., Musiienko, A., Moravec, P., Tolbanov, O., Tyazhev, A., Zarubin, A. 2020, 'Space charge formation in chromium compensated GaAs radiation detectors', J. Phys. D: Appl. Phys., 53, 475102, Bristol: IOP Publishing

RTSD-04-376

Contact Characterization of High-Flux Stable GaAs:Cr Detector (#3233)

Kaiwen Shi[1], Boren Wang[1], He Li[2], Tao Zhong[1], Zhijian Shen[2], Juha Kalliopuska[3], Dmytro Nalyvaiko[3], Volodymyr Gnatyuk[3], Xiaochun Lai[1]

[1] ShanghaiTech University, School of Biomedical Engineering, pudong, China; [2] Shanghai United Imaging Healthcare Advanced Tech-nology Research Institute Co., Ltd, pudong, China; [3] Advafab OY, Espoo, Finland

Supported by the Science and Technology Commission of Shanghai Municipality (24440730100, 24QB2703900). We ac-
knowledge the ShanghaiTech Material and Device Lab and HPC
Platform of ShanghaiTech University

Abstract

Chromium-compensated gallium arsenide (GaAs:Cr) is a highly promising material for spectral X-ray photon counting detectors (PCDs), offering high electron mobility (~4000 cm2/V · s), low K-shell fluorescence (9.2 keV and 10.5 keV), and ultra-high bulk resistivity (~109 Ω · cm). A critical factor governing the high-flux stability of such PCDs is the metal–semiconductor contact. While conventional detectors often rely on Schottky contacts—which trap space charge and cause polarization under sustained irradiation—the ultra-high resistivity of GaAs:Cr enables barrier-free Ohmic contacts. This approach relies entirely on bulk resistance to limit dark current, eliminating

interface charge accumulation and preserving a uniform electric field. In this work, we characterize the wide-bias (−1000 V to 1000 V) dark current–voltage (I–V) behavior of pixelated GaAs:Cr detectors. The devices exhibit highly linear, symmetric responses with distinct Ohmic and space-charge-limited current (SCLC) regimes, confirming high-quality Ohmic contact formation. Furthermore, the extracted bulk resistivity and demonstrated pixel-level uniformity validate the contact integrity required for stable high-flux photon counting applications.

References
[1] Hamann, E et al. 2013, 'Characterization of photon counting pixel detectors based on semi-insulating GaAs sensor material', J. Phys.: Conf. Ser., vol. 425, p. 062015, Bristol: IOP Publishing
[2] Sun, GC et al. 2007, 'Mobility-lifetime product in epitaxial GaAs X-ray detectors', Nucl. Instrum. Methods Phys. Res. A, vol. 573, no. 1–2, pp. 228–231, Amsterdam: Elsevier

RTSD-04-377

Validation of FAPbBr3 Perovskite Radiation Stability: Monte Carlo Simulation and Proton-Irradiation Experiment (#1624)

Zeqi Huang[1], Bin Song[1], Yifu Chen[1], Xulong Pang[1], Yong Sang[2], Jianan Wu[2], Haodi Wu[1], **Yongshuai Ge**[1]

[1] Shenzhen Institutes of Advanced Technology, Chinese Academy of Sciences, Shenzhen, China; [2] Cancer Hospital Chinese Academy of Medical Sciences, Shenzhen, Shenzhen, China

Abstract

A Geant4-based Monte Carlo framework was developed to predict the proton-irradiation stability of FAPbBr3 perovskite. Beyond calculating non-ionizing energy loss (NIEL), the framework records layer-resolved energy deposition across a 2 mm crystal divided into 50 slices. For 70, 100, 150, and 200 MeV protons, the NIEL values are 2.04, 2.01, 1.38, and 1.55*10^-3 MeV cm^2 g^-1, confirming non-ionizing displacement-damage channels. The deposited-energy fractions in the incident-side 0.20 mm are 11.83%, 10.69%, 19.57%, and 14.90%, respectively, following the same order as the measured electrical response: 150 MeV > 200 MeV > 70 MeV > 100 MeV. This agreement indicates that near-surface energy deposition can effectively predict mobility-lifetime product variation and supports the framework as a screening tool for perovskite radiation stability.

References
[1] He, Xuchang, Nannan Shen, Ruohan Ren, Sheng Lin, Bao Xiao, Ning Ding, Yuquan Wang, Wenjie Chen, and Yihui He. "Numerical Simulation Framework of Dynamic Charge Induction and Signal Generation in Pixelated Perovskite Semiconductor Detectors." IEEE Transactions on Nuclear Science 73, no. 1 (2025): 190-198.
[2] Zhao, Liang, Zhifang Shi, Ying Zhou, Xiaoming Wang, Yeming Xian, Yifan Dong, Obadiah Reid et al. "Surface-defect-passivation-enabled near-unity charge collection efficiency in bromide-based perovskite gamma-ray spectrum devices." Nature Photonics 18, no. 3 (2024): 250-257.
[3] Shim, Ha Eun, Jinhyung Park, Yeong Heum Yeon, Namho Lee, and Hui-Jeong Gwon. "Prediction of radiation-induced degradation for a FAPbBr3 perovskite solar cell." Journal of the Korean Physical Society 80, no. 3 (2022): 191-196.
[4] Kirmani, Ahmad R., Todd A. Byers, Zhenyi Ni, Kaitlyn VanSant, Darshpreet K. Saini, Rebecca Scheidt, Xiaopeng Zheng et al. "Unraveling radiation damage and healing mechanisms in halide perovskites using energy-tuned dual irradiation dosing." Nature Communications 15, no. 1 (2024): 696.

RTSD-04-378

CZT Strip Detectors Characteristics After the Euro Material Ageing Mission (#2468)

Manuele Bettelli[1], Natalia Auricchio[2], Ezio Caroli[2], Rui C. Silva[3], Claudio Ferrari[1], Elena Ferrari[1], Jorge M. Maia[4,6], Monia Vadrucci[5], Enrico Virgilli[2], **Andrea Zappettini**[1]

[1] CNR, IMEM, Parma, Italy; [2] INAF, OAS, Bologna, Italy; [3] University of Coimbra, Department of Physics, Coimbra, Portugal; [4] LIP, Coimbra, Portugal; [5] ASI, Rome, Italy; [6] University of Beira Interior, Physics Department, Covilha, Portugal

The authors acknowledge:
- Italian Space Agency, “Gamma-ray Laue Optics and Solid State detectors (GLOSS)”, ASI contract n. 2023-22-U.0, CUP: C33C23000620005
- European Space Agency (ESA) for the selection and integration of the scientific samples within the Euro Material Ageing (EMA) mission, as well as the French Space Agency (CNES) for the development of the EMA payload.

Abstract
The effect of the Low Earth Orbit (LEO) environment on future high energy instrument sensors is essential to optimize their performance, by minimizing orbital background noise. In the framework of the CNES-ESA European Material Ageing program (EMA), the ageing effects on critical components of a Laue lens telescope in the LEO space environment is investigated. Since more than a decade, the group has been developing CZT drift strip sensors to meet the stringent requirements of a Laue lens focal plane detector for high-energy photons. As part of the EMA proposal, two simplified samples of drift strip CZT detectors were exposed to outer space on the CNES Bartolomeo external platform of ISS for more than 12 months. The objective was to test the robustness and reliability of the surface passivation and metallization processes in the LEO space environment. The samples were taken down to earth on February 27. In this work, we report on the results of the simulations we carried out accounting for possible damages to the detector properties due to agents as oxygen and high energy ions. Also, preliminary measurements on the detectors come back from space will be shown.

RTSD-04-379

Development of a Compact CdTe-Based Gamma Spectroscopy System with Dual-Side Readout for High-Resolution Gamma Imaging (#1117)

Siyao Chang, Setsuo Sato, Yuki Mitsuya, Hiroyuki Takahashi

The University of Tokyo, School of Engineering, Tokyo, Japan

Abstract

We developed a compact CdTe-based gamma-ray spectroscopy system with a dual-side readout architecture for high-resolution gamma imaging. The system is designed for pixelated Schottky CdTe detector arrays. Cathode pixels at the same relative position across multiple detector chips are multiplexed, while the anode of each chip is read out independently. This configuration reduces the number of readout channels and system complexity while preserving energy information from the anode side and position information from the cathode side.

The system integrates custom JFET-input charge-sensitive preamplifiers and a waveform-sampling data acquisition system based on AFE5801 chips, enabling measurement of pulse height, risetime, and waveform information.

To evaluate the feasibility of the proposed method, spectral measurements were performed using a 2 × 1 CdTe detector array operated at +650 V with sealed ^{22}Na and ^{137}Cs sources. A 1 μs coincidence time window was applied to match the anode and cathode signals. Calibrated energy spectra were obtained from both sides. The anode signal showed slightly better energy resolution and was used as the primary signal for energy measurement, while the cathode signal can provide position information. After applying risetime selection, energy resolutions of 3.61% at 511 keV and 3.20% at 662 keV were achieved. These results demonstrate the feasibility of the proposed dual-side merged readout architecture.

A 5 × 5 CdTe detector array has also been assembled, and further verification experiments are in progress.

References

[1] R. Arlt and D. E. Rundquist, “Room temperature semiconductor detectors for safeguards measurements,” *Nucl Instrum Methods Phys Res A*, vol. 380, no. 1–2, pp. 455–461, Oct. 1996, doi: 10.1016/S0168-9002(96)00475-5.

[2] R. O. Bell, G. Entine, and H. B. Serreze, “Time-dependent polarization of CdTe gamma-ray detectors,” *Nuclear Instruments and Methods*, vol. 117, no. 1, pp. 267–271, May 1974, doi: 10.1016/0029-554X(74)90408-X.

RTSD-04-380

An Event Reconstruction ASIC for 3D CdZnTe Gamma-Ray Detectors

(#1375)

Farah Mohammed Rafee[1], Damon Anderson[2], Yuefeng Zhu[1], Zhong He[1]

[1] University of Michigan, Nuclear Engineering & Radiological Sciences, Ann Arbor, USA; [2] H3D, Inc., Ann Arbor, USA

Effort sponsored by the U.S. Government under Other Transaction number W15QKN-18-9-1004 between the CWMD Consortium and the Government. The US Government is authorized to reproduce and distribute reprints for Governmental purposes notwithstanding any copyright notation thereon. The views and conclusions contained herein are those of the authors and should not be interpreted as necessarily representing the official policies or endorsements, either expressed or implied, of the U.S. Government.

Abstract

Three-dimensional position-sensitive CdZnTe (3D-CZT) gamma-ray detector systems provide compact gamma-ray spectroscopy with 3D position sensing. Achieving high performance requires event-by-event energy and position reconstruction to compensate for charge loss, gain variation, and response nonlinearity. Such reconstruction calculations are typically performed on a powerful CPU. To reduce power consumption and minimize system

footprint, we propose implementing the reconstruction in an application-specific integrated circuit (ASIC). In this work, we focus on single-pixel event reconstruction, integrating depth and nonlinearity corrections along with a sub-pixel position calculation. This ASIC is implemented in TSMC 65 nm CMOS technology and is designed to interface with a DAQ-DSP back-end ASIC and four H3DD-UM front-end ASICs. Preliminary results demonstrate the feasibility of an event reconstruction ASIC with an area of 2.43 mm^2. This development represents a key step towards the development of more compact 3D-CZT systems.

References
[1] Z. He, W. Li, G.F. Knoll, D.K. Wehe, J. Berry, C.M. Stahle, "3-D position sensitive CdZnTe gamma-ray spectrometers," Nuclear Instruments and Methods in Physics Research Section A: Accelerators, Spectrometers, Detectors and Associated Equipment, vol. 422, no. 1–3, pp. 173-178, 1999.
[2] F. Zhang, "Events Reconstruction in 3-D Position Sensitive CdZnTe Gamma-Ray Spectrometers," Ph.D. Thesis, University of Michigan, 2005.
[3] D. Anderson, "Digital Signal Processing Techniques and ASIC Development for 3D CdZnTe Gamma-Ray Detectors," Ph.D. Thesis, University of Michigan, 2024.
[4] G. De Geronimo, Y. Zhu, J. E. Berry and Z. He, "Waveform-Sampling Front-End ASIC for 3-D Position-Sensitive Detectors," in IEEE Transactions on Nuclear Science, vol. 72, no. 3, pp. 925-935, March 2025.
[5] Y. Zhu, S. E. Anderson and Z. He, "Sub-Pixel Position Sensing for Pixelated, 3-D Position Sensitive, Wide Band-Gap, Semiconductor, Gamma-Ray Detectors," in IEEE Transactions on Nuclear Science, vol. 58, no. 3, pp. 1400-1409, June 2011.

RTSD-04-381

Spectroscopic Performance of SOI-CMOS Pixel Detector at Elevated Temperatures (#1803)

Haruno Takamoto[1], Ayaki Takeda[1], Koji Mori[1], Hiromasa Suzuki[1], Takeshi G. Tsuru[2]

[1] University of Miyazaki, Engineering, Miyazaki, Japan; [2] Kyoto University, Physics, Kyoto, Japan

Abstract

XRPIX is a silicon-on-insulator (SOI) CMOS pixel detector developed for next-generation X-ray astronomical observations. An X-ray camera, SUIM (Soipix for observing Upper atmosphere as Iss experiment Mission), is our first space mission employing XRPIX and is planned for launch to the International Space Station (ISS) in 2026. Thermal analysis of the SUIM instrument indicates that the camera housing may reach temperatures as high as +60°C in orbit, making it essential to verify XRPIX performance under elevated temperature conditions. The primary concern under such conditions is the degradation of spectroscopic performance due to increased dark current. Spectroscopic measurements using ^{241}Am were conducted over a temperature range from −30°C to +70°C, with a periodic reset of 100 µs applied to suppress dark current accumulation during integration. Only minimal degradation was observed, confirming that the periodic reset scheme effectively maintains good spectroscopic performance even at +70°C. The gain decreases at a rate of −0.132 µV e^{-1} $°C^{-1}$, which can be corrected through gain calibration. These results demonstrate that XRPIX maintains sufficient spectroscopic performance at least up to +70°C, indicating that its performance is also adequate for use in the SUIM instrument.

References
[1] K. K. Nobukawa, A. Takeda, S. Katsuda et al., “SUIM project: measuring the upper atmosphere from the ISS by observations of the CXB
transmitted through the Earth rim,” Proc. SPIE, 130932G, 2024.

[2] A. Takeda, Y. Arai, S. G. Ryu et al., “Design and evaluation of an SOI pixel sensor for trigger-driven X-ray readout,” IEEE Trans. Nucl. Sci.,
vol. 60, pp. 586–591, 2013.
[3] A. Takeda, K. Mori, Y. Nishioka et al., “Development of on-chip pattern processing in event-driven SOI pixel detector for X-ray astronomy with background rejection purpose,” J. Instrum., vol. 15, p. P12025, 2020.

RTSD-04-382

Development of Zero-Grid-Bias Operation in Coplanar Grid Type TlBr Detectors (#1807)

Seishiro Tanaka[1], Yusuke Kawai[1], Taisei Teshima[1], Kenichi Watanabe[1], Mitsuhiro Nogami[2], Keitaro Hitomi[2]

[1] Kyushu University, Department of Applied Quantum Physic and Nuclear Engineering, Fukuoka, Japan; [2] Tohoku University, Department of Quantum Science and Energy Engineering, Sendai, Japan

Abstract

TlBr is a promising compound semiconductor material for gamma-ray detectors[1] because of its wide bandgap, high-Z constituents, and high density, which enable room-temperature operation and high detection efficiency. However, because the hole mobility in TlBr is significantly lower than the electron mobility, single-polarity charge sensing techniques are required to achieve high energy resolution. In this study, a zero-grid-bias operation in a coplanar-grid electrode structure for TlBr gamma-ray detectors was investigated. Unlike conventional coplanar-grid detectors, the proposed structure operates without a bias voltage between adjacent grid electrodes, which may reduce leakage current.

A conventional comb-shaped electrode structure was evaluated experimentally and through simulations using a Cs-137 source. The simulation results reproduced the experimental pulse-height spectra well. In addition, pulse-height correction using the cathode-to-anode pulse-height ratio improved the energy resolutionTo further improve detector performance, the weighting-potential distribution inside the detector was analyzed, and a spiral-shaped electrode structure was proposed to suppress spatial nonuniformities in the weighting potential. Simulations indicated that the proposed spiral-shaped electrode structure suppressed spatial variations in the weighting potential between adjacent anodes, leading to improved energy resolution after correction. These results suggest that the proposed spiral-shaped zero-grid-bias coplanar-grid electrode structure is a promising approach for large active volume and high-resolution TlBr gamma-ray detectors.

References
[1] K. Hitomi, T. Onodera, S.Y. Kim, T. Shoji, K. Ishii, Characterization of pixelated TlBr detectors with Tl electrodes, *Nucl. Instrum. Method Phys. Res. Sec. A*, **747**, 7-12 (2014).
[2] T. Nojima, M. Nogami, K. Hitomi, Enhancing the energy resolution of TlBr detectors through an adaptive shaping method, Japanese Journal of Applied Physics, 64, 116001 (2025).

RTSD-04-383

A Monte-Carlo Simulation of Unipolar Charge-Sensing Amorphous Selenium X-ray Detector for Photon Counting Imaging (#2479)

Yagiz Mart[1,2], Arev Koc[3,2], Ahmet Camlica[5,4]

[1] Middle East Technical University, Electrical and Electronics Engineering, Ankara, Turkey; [2] Xera Medical Systems and Technology, R&D, Ankara, Turkey; [3] Chalmers University of Technology, Electrical Engineering, Goteborg, Sweden; [4] Hacettepe University, Institute of Informatics, Ankara, Turkey; [5] University of Waterloo, Electrical and Computer Engineering, Waterloo, Canada

The authors acknowledge financial support from the Natural Sciences and Engineering Research Council (NSERC) of Canada and XERA Medical Systems and Technology. The authors also thank Hyunsuk Jang of Vieworks, Inc., South Korea for valuable discussions.

Abstract

This study investigates the spectral performance of a unipolar charge-sensing amorphous selenium detector using Monte Carlo simulation and compares its response with that of a conventional amorphous selenium detector. The unipolar charge-sensing architecture mitigates the limitations associated with poor electron mobility and deep electron trapping in amorphous selenium by promoting hole-dominated signal formation. Both unipolar charge-sensing and conventional detector structures were simulated for a 20 μm pixel pitch under an average electric field of 8 V/μm. The simulated full-width at half maximum energy resolution was 8.02 keV for the unipolar charge-sensing detector, compared with 21.32 keV for the conventional detector. These results demonstrate that the unipolar charge-sensing architecture substantially improves the spectral performance of amorphous selenium detectors by suppressing depth-dependent signal variations and reducing sensitivity to electron trapping.

References

[1] Camlica, A., Lee, D., Jang, H., Arnab, S. M., Fang, Y., Kabir, M. Z., and Karim, K. S., 2020, "Performance of amorphous selenium-based unipolar charge sensing detector for photon counting X-ray imaging," Medical Imaging 2020: Physics of Medical Imaging, Vol. 11312, SPIE, p. 113120G.

[2] LasAgostinelli, S. et al., 2003, "Geant4—a simulation toolkit," Nuclear Instruments and Methods in Physics Research Section A: Accelerators, Spectrometers, Detectors and Associated Equipment, Vol. 506, No. 3, pp. 250–303.

[3] Allison, J. et al., 2006, "Geant4 developments and applications," IEEE Transactions on Nuclear Science, Vol. 53, No. 1, pp. 270–278.

[4] Ramo, S., 1939, "Currents induced by electron motion," Proceedings of the IRE, Vol. 27, No. 9, pp. 584–585.

[5] Shockley, W., 1938, "Currents to conductors induced by a moving point charge," Journal of Applied Physics, Vol. 9, No. 10, pp. 635–636.

[6] He, Z., 2001, "Review of the Shockley–Ramo theorem and its application in semiconductor gamma-ray detectors," Nuclear Instruments and Methods in Physics Research Section A: Accelerators, Spectrometers, Detectors and Associated Equipment, Vol. 463, No. 1, pp. 250–267.

[7] Stavro, J., Goldan, A. H., and Zhao, W., 2018, "Photon counting performance of amorphous selenium and its dependence on detector structure," Journal of Medical Imaging, Vol. 5, No. 4, p. 043502.

[8] Fang, Y., Badal, A., Allec, N., Karim, K. S., and Badano, A., 2011, "Spatiotemporal Monte Carlo transport methods in x-ray semiconductor detectors: Application to pulse-height spectroscopy in a-Se," Medical Physics, Vol. 39, No. 1, pp. 308–319.

[9] Kasap, S. O., Ed., 2022, 'Photoconductivity and Photoconductive Materials: Fundamentals, Techniques and Applications', Newark, NJ, USA: Wiley.

RTSD-04-384

Study of the spectroscopic performance of Timepix4 with highly ionizing particles (#2480)

Petr Smolyanskiy[1], Benedikt Bergmann[1], Petr Burian[1,2], Pavel Broulim[2], Radu E. Mihai[1,3]

[1] Czech Technical University in Prague, Institute of Experimental and Applied Physics, Prague, Czech Republic; [2] University of West Bohemia, Faculty of Electrical Engineering, Pilsen, Czech Republic; [3] Horia Hulubei National Institute for Physics and Nuclear Engineering, Department for Nuclear Physics, Magurele, Romania

We would like to thank the SPS team for providing Medipix collaboration with the beamtime. The authors, P.S., B.B. acknowledge funding from the Czech Science Foundation under Registration Number GM23-04869M.

Abstract

We report on the characterization of the Timepix4 hybrid pixel detector with a Si sensor under exposure to heavily ionizing particles. The device was configured sequentially in three gain modes: logarithmic (log), high, and low. Previously developed methodology of pixel's energy calibration beyond calibration with X- and γ-rays was adopted and applied to Timepix4 data. It uses the protons with energies in the range from 500 -- 2000 keV. Saturation of the pixel's energy response was observed at 1057, 1244, and 2030~keV in the low, high, and log gain modes, respectively. In a laboratory experiment, the detector was irradiated with α-particles from a ^{239}Pu^{241}Am^{244}Cm source, even higher energy α-particles were obtained from naturally occurring radon progeny decays recorded over several weeks of continuous operation. Both measurements yielded an energy resolution of about 2.5\%. The capability of Timepix4 for relativistic ion beam decomposition was investigated within fragment beams at the Super Proton Synchrotron (SPS) at CERN. A spectrum stripping technique based on iterative Landau curve fitting was applied to the measured energy-loss spectra, enabling ion charge identification up to Z = 10 at a track inclination of θ = 60 deg. with respect to the sensor normal.

RTSD-04-385

Investigation of Gain Instability of a 3-D CdZnTe Detector (#2768)

Matthew Granados, Yuefeng Zhu, Zhong He

University of Michigan, Ann Arbor, USA

Abstract

CdZnTe (CZT) detectors require stable calibration parameters for optimal spectroscopic performance. However, certain pixels exhibit random gain variation during or between measurements, complicating calibration and degrading detector performance. Digital ASICs allow for readout of event waveforms in a CZT detector exhibiting gain instability. Th-228 and Cs-137 measurements were utilized to characterize the gain instabilities, revealing a

decrease in the anode amplitudes proportional to the incident energy. Analysis of the neighbor pixel-anode waveforms reveal abnormally high tail amplitudes in the four side neighbors which exceed expectations based on the Shockley-Ramo theorem. The corner neighbors experience noticeable smaller increases in tail amplitudes. Sub-pixel position analysis demonstrates that the tail amplitude increase is not proportional to the neighbor signal amplitude. These findings suggest that the observed gain instability could be caused by issues with capacitance in the system rather than anomalous charge movement. Ongoing work aims to verify the cause of the shift and if the anode deficit can be entirely explained by the differences in the neighbor waveform signals.

References
[1] W. R. Kaye, "Energy and Position Reconstruction in Pixelated CdZnTe Detectors,'' Ph.D. dissertation, Dept. Nuclear Eng., Univ. of Michigan, Ann Arbor, MI, USA, 2012. p. 153.
[2] Y. Zhu, "Digital Signal Processing Methods for Pixelated 3-D Position Sensitive Room-Temperature Semiconductor Detectors,'' Ph.D. dissertation, Dept. Nuclear Eng., Univ. of Michigan, Ann Arbor, MI, USA, 2012. p. 85.

RTSD-04-386

Bias Scan Analysis of Si-Timepix Detector with Various Sensor Thickness (#2847)

Andrea Sagatova[1], Matej Balušík[1], Katarina Foss[1], Bohumir Zatko[2], Carlos Granja[1], Tomas Slavicek[3], Zdenek Kohout[3]

[1] Slovak University of Technology, Institute of Nuclear and Physical Engineering, Bratislava, Slovakia; [2] Slovak Academy of Sciences, Institute of Electrical Engineering, Bratislava, Slovakia; [3] Czech Technical University, Institute of Experimental and Applied Physics, Prague, Czech Republic

This work was supported by grants of the Slovak Research and Development Agency No. APVV-22-0382 and No. DS-FR-24-0020 and funded by the EU NextGenerationEU through the Recovery and Resilience Plan for Slovakia under the project No. 09I05-03-V02-00073.

Abstract
In the present work, we study the MiniPIX Timepix hybrid pixel detectors with silicon sensors of two different thicknesses and their response to high energy protons. Thermally stabilized detectors measured protons of five energies, 400, 700, 1000, 1400 and 1800 keV in vacuum. During the measurements, a bias scan was performed to investigate the efficiency of collection of charge carriers generated by the protons. With increasing reverse bias, the signal from the detector grew until it saturated. The 300 um thick detector required an electric field generated by a reverse bias of 30 to 40 volts for effective charge collection. A detector with a thicker 500 um sensor required approximately 70 V bias for complete charge collection when registering 400 keV protons and a gradually higher bias of up to 100 V in the case of 1800 keV protons. The much larger bias for a complete collection of the charge generated by protons in a thick detector is in correlation with the theory, where the semiconductor depleted region thickness increases proportionally to the square root of applied reverse bias.

RTSD-04-387

Multidimensional Parameter-Space Analysis of Fast Neutron-Induced Tracks in Timepix Detectors (#2992)

Matej Balušík[1], Carlos Granja[1], Andrea Sagatova[1], Katarina Foss[1], Tomas Slavicek[2], Bohumir Zatko[3]

[1] Faculty of Electrical Engineering and Information Technology, Slovak University of Technology, Institute of Nuclear and Physical Engineering, Bratislava, Slovakia; [2] Czech Technical University, Institute of Experimental and Applied Physics, Prague, Czech Republic; [3] Slovak Academy of Sciences, Institute of Electrical Engineering, Bratislava, Slovakia

Work at the STU was partially supported by funding grants APVV-22-0382 and DS-FR-24-0020 of the Slovak Research and Development Agency and funded by the EU NextGenerationEU program through the Recovery and Resilience Plan for Slovakia under the project No. 09I05-03-V02-00073.

Abstract

The Timepix family of pixel detectors provides high spatial resolution together with per-pixel spectroscopic response, allowing event-by-event analysis of radiation interactions through deposited energy and cluster morphology. In fast neutron fields, the detector response is indirect and is produced mainly by secondary particles generated in the sensor and surrounding materials. This work focuses on fast-neutron-induced tracks measured with a Timepix3 detector equipped with a 300 µm silicon sensor at the Van de Graaff laboratory of IEAP CTU in Prague, using neutrons produced trough D–T reaction, in the range of approximately 15–17.5 MeV. The data were processed using TraXEngine [1] and further evaluated through selected spectral and morphological cluster parameters. The selected parameters were analyzed in two- and three-dimensional parameter spaces, where high-density regions corresponding to characteristic event groups were identified. Based on these regions, five parameter-based classes were defined: high-energy ion-like events, low-energy ion-like events, a transition region toward electron-like events, photon-like events, and electron-like events. The developed parameter-space analysis shows that combinations of spectral and morphological parameters can be used to separate components of a fast-neutron-induced mixed radiation field and can support future automated particle-recognition methods.

References

[1] L. Marek, C. Granja, J. Jakůbek, J. Ingerle, D. Tureček, M. Vuolo, and C. Oancea, “Data Processing Engine (DPE): Data analysis tool for particle tracking and mixed radiation field characterization with pixel detectors Timepix,” J. Instrum., vol. 19, no. 4, Apr. 2024, Art. no. C04026, doi: 10.1088/1748-0221/19/04/C04026.J.

RTSD-04-388

A 512 × 256 a-IGZO Dual-Gate TFT 2T-APS Array for Low-Dose Direct-Conversion X-Ray Flat-Panel Detector (#2297)

Yihong Qi[1], Haorong Xie[2], Xulong Pang[1], Haodi Wu[1], Xinghui Liu[3], Yongshuai Ge[1], Kai Wang[2]

[1] Shenzhen Institute of Advanced Technology, Chinese Academy of Sciences, Research Center for Advanced Detection Materials and Medical Imaging Devices, Shenzhen, China; [2] Sun Yat-sen University, School of Electronics and Information Technology, Guangzhou, China; [3] Shenzhen Chipwey Innovation Technologies Co., Ltd, Shenzhen, China

This work was financially supported in part by the National Key Research and Development Program of China under Grant 2024YFF0507800.

Abstract

Direct-conversion X-ray flat-panel detectors are attractive for high-resolution and low-dose imaging compared to indirect conversion. However, conventional passive pixel sensors (PPS) without in-pixel gain are commonly used in direct-conversion detectors, causing low signal-to-noise ratio under low-dose exposure. In this work, a compact two-transistor active pixel sensor (2T-APS) with in-pixel current amplification based on amorphous indium-gallium-zinc-oxide (a-IGZO) dual-gate TFTs is proposed for low-dose direct-conversion X-ray imaging. The proposed pixel employs two subthreshold-biased dual-gate TFTs to realize logarithmic–exponential signal processing, enabling electrical tuning of the operating point and sensitivity.

A 512×256 2T-APS array was fabricated using an a-IGZO dual-gate TFT process with a pixel pitch of 75 μm×75 μm. Pixel-level characterization further demonstrated amplification of pA-level input currents, achieving a representative current gain over 10^3. The fabricated array was integrated with a perovskite layer to realize X-ray imaging. At the tube voltage of 50 kV, images acquired with tube currents from 0.5 mA to 2.0 mA clearly visualized the object outline. These results validate the feasibility of the proposed a-IGZO dual-gate 2T-APS pixel for low-dose, high-sensitivity direct-conversion X-ray flat-panel detectors.

References

[1] Y. Li, X. Wang, J. Liang, L. Zhang, and J. Zhang, “Recent Progress in Direct X-Ray Detectors Based on Metal Oxide Wide Bandgap Semiconductors: A Review,” IEEE Sensors Journal, vol. 24, no. 23, pp. 38569–38583, Dec. 2024.

[2] S. Deumel et al., “High-sensitivity high-resolution X-ray imaging with soft-sintered metal halide perovskites,” Nature Electronics, vol. 4, no. 9, pp. 681–688, Sept. 2021.

[3] Di Geng et al., “Thin-film transistors for large-area electronics,” Nature Electronics, vol. 6, no. 12, pp. 963–972, Dec. 2023.

[4] C. C. Scott et al., “High-energy micrometre-scale pixel direct conversion X-ray detector,” Journal of Synchrotron Radiation, vol. 28, no. 4, pp. 1081–1089, June 2021.

RTSD-04-389

Development of a Self-Triggering Pixelated TlBr Detector with Cherenkov Light Detection (#2504)

Tsubasa Komaki[1], Hikaru Sekiguchi[1], Mizuki Uenomachi[2], Keitaro Hitomi[3], Mitsuhiro Nogami[3], Ayaki Takeda[4], Hidenori Toyokawa[5], Kenji Shimazoe[1]

[1] The University of Tokyo, Bioengineering/Graduate School of Engineering, Tokyo, Japan; [2] Institute of Science Tokyo, Institute of Integrated Research, Tokyo, Japan; [3] Tohoku University, Department of Quantum Science and Energy Engineering/Graduate School of Engineering, Sendai, Japan; [4] University of Miyazaki, Faculty of Engineering, Miyazaki, Japan; [5] Konan University, Faculty of Science and Engineering, Kobe, Japan

Abstract

Simultaneous multi-nuclide imaging is a key challenge in nuclear medicine, promising benefits such as improved diagnostic accuracy, reduced examination frequency, and elimination of physiological variations between scans. However, conventional imaging systems such as positron emission tomography (PET) and single-photon emission computed tomography (SPECT) are based on fundamentally different principles, making their integration into a single system technically difficult. To address this, we have proposed and developed a Compton-PET camera that enables simultaneous visualization of PET and SPECT nuclides using PET and Compton imaging, respectively. In our previous implementation, the system employed GAGG scintillators as absorbers, but their limited energy resolution (11–15% FWHM above 100 keV) degraded the Compton imaging performance. Thallium bromide (TlBr) semiconductor detectors have been shown to offer both high energy resolution, such as 2% FWHM at 662 keV, and high time resolution, including 511 ps via Cherenkov photon detection, making TlBr a promising sensor material for improving Compton-PET performance. Based on these advantages, we developed a new multi-pixel TlBr semiconductor detector by bonding a TlBr crystal to a self-triggering, energy-resolving pixel application-specific integrated circuit (ASIC). We plan to present the results of I-V characteristic measurements and evaluate detector performance through energy spectrum measurements and time resolution analysis using radionuclide sources.

References

[1] Shimazoe, K. et al., Nucl. Instr. and Meth. A., 954, (2020), 161499.
[2] Uenomachi, M. et al., Sci. Rep., 11, (2021), 17933.
[3] Ogane, K. et al., Appl. Radiat. Isot., 176, (2021), 109864.
[4] Todd, R. W. et al., Nature, 251, (1974), 132–134.
[5] Hamdan, M. et al., JINST, 19, (2024), C11017K.
[6] Hitomi, K. et al., IEEE Trans. Nucl. Sci., 60, (2012), 1156–1161.
[7] Hitomi, K. et al., Jpn. J. Appl. Phys., 62, (2023), 081001.

RTSD-04-390

Readout Electronics of SPECTRE CZT detector (#2525)

Michela Greco[1,2], Vincenzo Monaco[1,2], Federico M. Melendi[4,3], Damanio Cabiati[1], On behalf of SPECTRE Collaboration

[1] INFN, -Torino, Torino, Italy; [2] University of Turin, Physics Dept., Torino, Italy; [3] University of Ferrara, Physics Dept., Ferrara, Italy; [4] INFN, -Ferrara, Ferrara, Italy

Abstract

The INFN SPECTRE (Single Photon Emission Computed Tomography Readout Electronics) project aims to design, assemble, and characterize a complete detection module based on CZT sensors for medical applications. As the demand for SPECT systems with higher spatial resolution, energy resolution, and sensitivity continues to grow, there is an increasing need to develop high-performance CZT detectors with small pixels and corresponding high-speed readout electronics [1,2].

For readout, SPECTRE uses electronics developed for a high-capacitance gas detector (CGEM@BESIII, IHEP, Beijing [3]): the TIGER (Torino Integrated GEM Electronics for Readout) ASIC for on-detector electronics and the off-detector FPGA-based GEMROC module for power and data processing [4]. TIGER is a mixed-signal chip with 64 channels on an area of 5 × 5 mm². Each channel has a complete readout chain with amplification, signal conditioning, and discrimination, as well as a data payload containing the time and charge information for each event. TIGER is versatile for the readout of radiation sensors up to 50 fC and for high rates up to 70 kHz. The TIGER/GEMROC readout circuit is compact, modular, scalable, and highly customizable. In typical CZT applications today, spectroscopic systems operate at rates of about 1 kcps/mm² because extracting energy information requires more processing time [5]. However, our system can acquire each sensor pixel at a rate of up to 70 kHz, or approximately 16 kcps/mm².

In this presentation, we will cover all phases of the project to date, including CZT sensor and electronics simulation with the Allpix Squared package [6], based on Geant4, current-voltage characterization of the CZT sensors, system design and construction, assembly of four modules onto an adapter board, and initial system characterization using X-rays.

References

[1] Ritt P., 2022-*Recent Developments in SPECT/CT*, doi:10.1053/j.semnuclmed.2022.01.004

[2] Israel O. et al., 2019- *Two decades of SPECT/CT – the coming of age of a technology: An updated review of literature evidence*, DOI:10.1007/s00259-019-04404-6

[3] Melendi FM on behalf of the CGEM-IT Working Group, 2026 *The CGEM-IT detector of the BESIII experiment* JINST 21 C01045

[4] Amoroso A *et al* 2021 The CGEM-IT readout chain *JINST* 16 P08065

[5] Nakanishi K. et al., 2024-A simple method to shorten the apparent dead time in the dosimetry of Lu-177 for targeted radionuclide therapy using a gamma camera, DOI: 10.1016/j.ejmp.2024.103298

[6] https://allpix-squared.docs.cern.ch/

RTSD-04-391

Spectral Response and Counting Characteristics of a Peak-finding ASIC for GaAs:Cr Detectors (#2540)

Junhao Bai[1], Guo Yu[1], Yaqing Zhao[1], Yawen Tong[1], He Li[2], Heyu Ren[2], Xiaochun Lai[1]

[1] ShanghaiTech University, School of Biomedical Engineering, Shanghai, China; [2] Shanghai United Imaging Healthcare Advanced Technology Research Institute Co., Ltd., Shanghai, China

This research is supported by the Science and Technology Commission of Shanghai Municipality under grant No. 24DIPA00700. The authors would like to thank ShanghaiTech Material and Device Lab and the HPC Platform of ShanghaiTech University.

Abstract

Photon-counting computed tomography requires readout ASICs with high count-rate capability and reliable spectral performance under clinical X-ray flux. In this work, a peak-finding ASIC for GaAs:Cr photon-counting detectors is presented. The prototype ASIC contains a 9 × 12 pixel array with a pixel pitch of 341 μm × 368 μm. Each pixel integrates a charge-sensitive preamplifier, shaper, peak-finding circuit, five energy bins, threshold DACs, and counters. The peak-finding circuit captures the amplitude of signal peaks, improving counting capability under high-flux conditions. Electrical measurements demonstrate reliable counting performance beyond 30 Mcps/pixel. After coupling with a GaAs:Cr sensor, X-ray measurements showed clear tungsten characteristic peaks, confirming the energy-discrimination capability of the detector module. These results demonstrate the potential of the proposed ASIC for high-flux GaAs:Cr-based PCCT detectors.

References

[1] M. Danielsson, M. Persson, and M. Sjölin, “Photon-counting x-ray detectors for CT,” Phys. Med. Biol., vol. 66, no. 3, p. 03TR01, Feb. 2021, doi: 10.1088/1361-6560/abc5a5.

[2] M. J. Willemink, M. Persson, A. Pourmorteza, N. J. Pelc, and D. Fleischmann, “Photon-counting CT: Technical Principles and Clinical Prospects,” Radiology, vol. 289, no. 2, pp. 293–312, Nov. 2018, doi: 10.1148/radiol.2018172656.

[3] T. Flohr, M. Petersilka, A. Henning, S. Ulzheimer, J. Ferda, and B. Schmidt, “Photon-counting CT review,” Phys Med., vol. 79, pp. 126–136, Nov. 2020, doi: 10.1016/j.ejmp.2020.10.030.

[4] M. C. Veale, P. Seller, M. Wilson, and L. J. K. Wilson, “Chromium compensated gallium arsenide detectors for X-ray and γ-ray spectroscopic imaging,” Nucl. Instr. and Methods A, vol. 752, pp. 6–14, Jun. 2014, doi: 10.1016/j.nima.2014.03.033.

RTSD-04-392

Thickness-dependent front-end noise in CdTe Timepix3 detectors

(#2649)

Juan S. Useche Parra[1], Gerardo Roque[1], Michael Schütz[1], Rafael Ballabriga[2], Simon Procz[1], Michael Fiederle[1]

[1] University of Freiburg, Freiburg Material Research Center, Freiburg, Germany; [2] CERN, EP, Geneva, Switzerland

Acknowledgement of funding through BMFTR in projects OSKAR: 02NUK070A and PERODET: 05K22VFA.

Abstract

Photon-counting detectors (PCDs) with high-Z sensors are widely used for spectroscopic X-ray imaging in medical, security, and industrial applications. Hybrid PCDs can be coupled to different semiconductor sensors (Si, CdTe, GaAs), tailoring the assembly to the application. CdTe is the sensor of choice for energies above 50 keV, given its higher absorption efficiency compared to Si. The Timepix3 is a pixelated hybrid PCD that records each individual photon interaction in the sensor, providing the time-over-threshold (energy) and time-of-arrival of each event at fluxes up to 40 MhitsHits/cm^2/s. The spectral resolution of CdTe-Timepix3 assemblies degrades with sensor thickness, and the relative weight of front-end electronic noise and sub-threshold charge-sharing losses has not yet been quantified at 55 µm pitch. An empirical equivalent-noise-charge (ENC) model exists for Si-Timepix3 but, to our knowledge, has not been reported for CdTe at this pitch. This work addresses this gap by measuring the front-end ENC of three CdTe-Timepix3 assemblies (1 mm, 3 mm, and 5 mm sensor thickness) from internal test-pulse scans, fitting an empirical ENC model with the detector capacitance estimated from per-pixel geometry, and decomposing the photopeak FWHM at the ^{241}Am (59.5 keV) line into Fano, front-end, and sub-threshold contributions. A Si-Timepix3 of the same ASIC family is included as a cross-check for the front-end term. The result is a quantitative basis for predicting CdTe-Timepix3 spectral performance as a function of sensor thickness on this ASIC.

References

[1] Siemens Healthineers, 2021, `NAEOTOM Alpha with Quantum Technology', Siemens Healthineers Webpage.
[2] De Gaspari, M. et al, 2014, `Design of the analog front-end for the Timepix3 and Smallpix hybrid pixel detectors in 130 nm CMOS technology', J. Instrum., vol. 9, no. 01, p. C01037.
[3] Llopart Cudie, X 2007, `Design and characterization of 64K pixels chips working in single photon processing mode', Ph.D. dissertation, Sundsvall, Sweden: Mid Sweden University.
[4] Poikela, T et al. 2014, `Timepix3: a 65K channel hybrid pixel readout chip with simultaneous ToA/ToT and sparse readout', J. Instrum., vol. 9, p. C05013.
[5] Koenig, T et al. 2013, `Charge summing in spectroscopic x-ray detectors with high-Z sensors', IEEE Trans. Nucl. Sci., vol. 60, no. 6, pp. 4713--4718.
[6] Radeka, V., 1988. `Low-noise techniques'. Annu. Rev. Nucl. Part. Sci, 38, pp.217-277.
[7] Ballabriga, R et al. 2024, `A simulator for Timepix-like pixel front-ends', J. Instrum., vol. 19, no. 3, p. C03022.

RTSD-04-393

SiC Timepix3 detector response to fast neutrons: effect of varying sensor bias (#1226)

Katarina Foss[1], Carlos Granja[1], Matej Balušík[1], Tomáš Slavíček[3], Bohumír Zaťko[2], Andrea Šagátová[1]

[1] Faculty of Electrical Engineering and Information Technology, Slovak University of Technology in Bratislava, Bratislava, Slovakia; [2] Institute of Electrical Engineering, Slovak Academy of Sciences, Bratislava, Slovakia; [3] Institute of Experimental and Applied Physics, Czech Technical University in Prague, Prague, Czech Republic

This work was partially supported by grants of the Slovak Research and Development Agency Nos. APVV 22 0382 and DS-FR-24-002. Funded by the EU NextGenerationEU through the Recovery and Resilience Plan for Slovakia under the project No. 09I05-03-V02-00073

Abstract

In semiconductor radiation detectors such as silicon (Si) and silicon carbide (SiC) the sensor bias determines the radiation sensitive volume. Varying the sensor applied bias can thus significantly change and even distort the detector response, sensitivity and spectral-tracking properties. These effects can be studied and described when the sensor is bump-bonded to the Timepix3 detector which provides particle counting response, high-granularity imaging detection and spectral-tracking ability to single particles. These properties make possible to analyze and resolve particle-type events which is useful for mixed-field decomposition. In this work we examine and experimentally investigate the response of the SiC Timepix3 detector to well-defined fast neutrons to quantify and analyze the changes induced by varying the sensor applied bias voltage. The main effects are further decreasing the detection efficiency, which is overall low (≤ 1%), and only partly reducing the spectral-tracking resolving power to particle-type discrimination.

References

[1] R. Ballabriga, et. al., “ASIC developments for radiation imaging applications: The medipix and timepix family”, Nucl. Instrum. Meth. A, vol. 878, pp. 10-23, 2018.

[2] C. Granja, et al., “Resolving power of pixel detector Timepix for wide-range electron, proton and ion detection”, Nuclear Instr. Methods A, vol. 908, 2018, Art no. 60-71.

[3] M. De Napoli, SiC detectors: A review on the use of silicon carbide as radiation detection material, Front. Phys, vol. 12, 2022, Art no. 10:898833.

[4] F. H. Ruddy, et al., "Silicon Carbide Neutron Detectors for Harsh Nuclear Environments: A Review of the State of the Art," *IEEE Trans. Nuclear Sci.*, vol. 69, 2022, pp. 792-803.

[5] B. Zatko, et al., Detection of fast neutrons using 4H-SiC radiation detectors, EPJ Web of Conf., vol. 288, 2023, Art no. 03004.

[6] B. Zatko, et al. "From a single silicon carbide detector to pixelated structure for radiation imaging camera." *J. of Instrument.*, vol. 17, 2022, Art. no. C12005.

[7] C. Granja, et al., "Detection resolving power of SiC Timepix3 detector to electrons, neutrons, ions and protons." *J. of Instrument.*, vol. 19, 2024, Art no. C11007.

[8] C. Granja, et al, "Detection resolving power of SiC Timepix3 detector to electrons, neutrons, ions and protons", J. of Instrum. vol. 19, 2024, Art no. C11007.

RTSD-04-394

A neural network determining the gamma interaction position in pixelated CZT detectors (#2330)

Adeiza S. Anumah[1], Peter Dendooven[1], Andreas Hauptmann[2], Matti Kalliokoski[1], Mihaela Bezak[1]

[1] University of Helsinki, Helsinki Institute of Physics, Helsinki, Finland; [2] University of Oulu, Research Unit of Mathematical Sciences of University of Oulu, Finland, Oulu, Finland

This work was supported by the Research Council of Finland (Flagship of Advanced Mathematics for Sensing Imaging and Modelling grant 359182 Helsinki and 359186 Oulu)
Finnish Ministry of Education and Culture's Pilot for Doctoral Programmes (Pilot project Mathematics of Sensing, Imaging and Modelling)

Abstract

This study presents an experimental and computational framework for gamma-ray imaging using a position-sensitive Cadmium Zinc Telluride (CZT) detector combined with deep learning–based reconstruction techniques. A GDS-100 CZT detector with an 11 × 11 pixelated anode matrix was irradiated using a tightly collimated 662 keV Cs-137 gamma-ray beam scanned across the detector surface with 1 mm step size. Detector waveforms were used to train a compact ResNet-based convolutional neural network capable of reconstructing higher-resolution spatial information by mapping 11 × 11 detector inputs to 22 × 22 outputs. Kernel density estimation (KDE) analysis of reconstructed events shows that the predicted interaction positions remain strongly localized around the true coordinates, demonstrating accurate spatial learning. Average spatial spreads of σx = 1.375 mm and σy = 1.398 mm, together with positional deviations below 1 mm, indicate stable and nearly symmetric localization performance. Although edge and corner regions exhibit slightly broader distributions due to detector-related physical effects, the reconstructed interaction densities remain well confined around the true positions. Overall, the results demonstrate that deep learning–based CZT signal analysis can significantly improve spatial reconstruction performance in semiconductor gamma-ray imaging systems.

RTSD-04-395

Robust and reliable radionuclide identification under realistic measurement conditions (#2743)

Nicola Sarzi Amadè[1], Gang Li[2], Martin Thompson[2], Jude Alexander[2], MIke Echlin[2], Liqian Li[2], Nicola Zambelli[1], Valentina Vicini[3], Manuele Bettelli[3], Ghaouti Bentoumi[2], Andrea Zappettini[3]

[1] due2lab, Reggio Emilia, Italy; [2] Canadian Nuclear Laboratories, Chalk River Ontario, Canada; [3] IMEM-CNR, Parma, Italy

Abstract

Reliable radioisotope identification with handheld instruments remains challenging due to limited detector resolution, shielding, low counting statistics, and variable background conditions. We present a convolutional neural network algorithm for automated multi-isotope identification from gamma-ray spectra acquired with low-resolution detectors. The algorithm is trained using an optimized synthetic spectral library of 48 radionuclides and evaluated using measured data acquired under controlled shielding, signal-to-noise ratio, and count-rate conditions. Results show near-perfect identification accuracy for moderate to high signal-to-noise ratio regimes and for low to high statistics. At low signal-to-noise ratio the algorithm is still able to recognize some radionuclides with decent accuracy. These results demonstrate that the method provides a practical and scalable solution for real-time isotope identification in nuclear security and radiation detection systems.

RTSD-04-396

In-situ high-resolution gamma spectroscopy for characterization of radiological environmental sites. (#2318)

Bertrand Rossé, Ludivine Fevre, Maxime Allerme, Pascal Chotard

CEA, DAM, DIF, F-91297 Arpajon, France

Abstract

In the context of in-situ radiological characterization of sites (natural or artificial radioactivity) and for the dismantling of nuclear installations, high-resolution gamma-ray spectrometry is a powerful tool to both identify and quantify gamma-emitters. This technique makes it possible to better define the state of radiologically polluted soils without having to collect samples. To perform mapping of large areas (a few hundred square meters) and to detect radiological hotspots, we first use a 2''x2'' NaI(Tl) scintillator probe (Mirion® SG2R) at 20 cm from the ground in pedestrian mode, called C.R.E.M.P (Caractérisation Radiologique En Mode Piéton, radiological characterization in pedestrian mode). Then, for each particular points, high-resolution gamma spectrometry is performed with an HPGe Ortec® DETECTIVE-X. To obtain a reliable transfer function, the absolute efficiency of the detectors must be known. We therefore used our radiological characterization platform located at CEA/DAM Ile de France. Thanks

to these measurements, a geometric model of the HPGe detector was developed and optimized using the MCNP Monte Carlo simulation code taking into account real position and shape of the germanium crystal including mechanical supports and dead layers. To validate the model, experiments on radiologically marked standard soils were performed. Extrapolated data from MCNP simulations make it possible to obtain the transfer functions for each detected radionuclide. The whole method, measurements and simulations will be described.

RTSD-04-397

Gamma Spectroscopy Analysis and Benchmarking of Nuclear Fuel for Next Generation Reactor Designs (#3247)

Daryl T. Giglio, Tommy V. Holschuh, Scott J. Thompson, Jay D. Hix, David L. Chichester, Jeff Sanders

Idaho National Laboratory, Idaho Falls, USA

Abstract

This paper contains the findings associated with the collection of gamma spectroscopy of a variety of fuel types being utilized in the deployment of the next generation of nuclear reactors. Gamma spectroscopy of TRISO fuel types at HALEU levels of enrichment were collected and analyzed prior to installment in their respective reactor designs. Preliminary measurements of these fuels establish a strong baseline that serve as important experimental data points for simulation validation and monitoring fuel characteristics that are underexplored in next generation reactor designs such as burnup rates, and fuel stability (physical, chemical, performance).

In addition, the established baseline also serves as an important benchmark for quality assurance and nuclear nonproliferation by providing reference spectrum for archiving purposes in a nuclear fuel landscape that is rapidly expanding. This ensures enrichment reporting is accurate in the event of fuel mixing/reprocessing prior to reactor loading.

RTSD-04-398

Comparison of the simulated response of the in-house DT hybrid pixel detector with synchrotron beam tests (#2098)

Mélissa Leroy[1,2], Mathieu Dupont[1], Elena Gaborieau-Borissenko[2], Christian Morel[1], Yannick Boursier[1]

[1] Aix Marseille Univ., CNRS/IN2P3, CPPM, Marseille, France; [2] Detection Technology Oyj., R&D, Moirans, France

We acknowledge the European Synchrotron Radiation Facility (ESRF) for the provision of synchrotron radiation facilities under proposal ID MI-1525 and on beamline ID11. We thank Loic Jegou and the beamline staff for assistance and support during the beamtime.
The authors also thank G. Gey, T. Pierson, M. Plainemaison, O. Loukkola and M. Matikkala for their support during data acquisition and experimental preparation.

Abstract
Simulation of Photon Counting Detectors (PCD) is essential to optimize detector design and to assess detector response for photon counting CT. In this work, synchrotron measurements performed with the new PCD tiles, developed by Detection Technology (DT) are compared to simulated data. The detector prototype is a pixelated array of CdTe and CZT pixel with 350 µm pixel pitch. Each pixel has 6 energy thresholds. Measurements were carried out at the European Synchrotron Radiation Facility (ESRF) using pencil beam scan to study charge-sharing and fluorescence escape. The experiment was reproduced in a simulation framework that encompasses physics interaction within the sensor, charge generation, drift, and diffusion and Coulomb repulsion. The comparison focuses on counts of distribution across pixel positions and single pixel spectral response. Results show a good agreement for central pixel irradiation, but discrepancies are observed near pixel boundaries. The assessment of the modeling for interpixel irradiation is currently under study.

References
[1] M. Leroy et al., 2025, “A comprehensive simulation framework for cadmium telluride hybrid pixels,” IEEE NSS/MIC/RTSD’2025, (Yokohama)
[2] M. Leroy et al., (2026),“Modelling of charge sharing and fluorescence escape in the XPAD3.2-S/CdTe hybrid pixel detector,” to be subm. to
Nucl. Instr. and Meth. A, IEEE Trans. Radiat. Plasma Med. Sci.
[3] Y. Boursier et al. (2026), “2D-CdZnTe detector prototype characterization for simulation validation,” Experimental report, Proposal MI-1525,
Beamline ID11, ESRF, DOI: 10.15151/ESRF-ES-2266935027

RTSD-04-399

Characterization and Compensation of Radiation-Induced Leakage Current in CdTe/CZT Detectors Under High-flux X-ray Irradiation (#2377)

Xinchi Ran, Zhi Deng, Haibo Luo, Hanzhe Dong

Tsinghua University, Beijing, China

This work is supported by the Beijing Natural Science Foundation under Grant L242002 and the State Key Program of National Natural Science of China under Grant 62031020.

Abstract
Radiatio-induced leakage current has been found in ohmic CdTe/CZT detectors under high-flux X-ray irradiation scenario such as photon-counting X-ray CT and new generation light sources. Slowly evolving radiation-induced leakage current that compromises signal stability. In this work, we experimentally characterize the dynamic behavior of this leakage current using step-irradiation and rapid-chopping measurements on a custom 32×32 pixel

CdTe detector module. The results reveal a two-timescale response consisting of a fast photocurrent component and a slow, history-dependent leakage component that increases approximately exponentially during irradiation and decays over minutes after beam-off. This behavior is attributed to trap occupancy dynamics that modulate carrier injection at the contacts. A first-order exponential model is proposed to describe the temporal evolution, and a recursive deconvolution framework is explored for signal correction. However, observed nonlinearities and flux/history dependence indicate that a linear time-invariant (LTI) assumption is insufficient, suggesting the need for a more general nonlinear model. These findings provide insight into the instability mechanisms of Ohmic CdTe detectors and offer experimental support for the development of improved dynamic correction strategies for high-flux X-ray imaging applications.

RTSD-04-400

Compton Polarimetric Potential of a Low Power CdTe Timepix3 Frame Mode Detector (#2920)

Gregoire Veyrac[1], **Rui M. Curado Da Silva**[1,2], Jorge M. Maia[3,1], João Campos[4], Pedro G.H. Carmo[1,2], Gabriel Falcão[5], Cristiana Francisco[1,6], Mariana Letra[1,2], Fernando Pinheiro[6], Duarte Rodrigues[1,2], José Sousa[1,2], Alexandre Trindade[1,2], Carlos Granja[7], Matouš Kasal[7], Martin Konečný[7], Jan Jakůbek[7], Lukáš Marek[7]

[1] LIP - Laboratório de Instrumentação e Física Experimental de Partículas, Coimbra, Portugal; [2] University of Coimbra, Department of Physics, Coimbra, Portugal; [3] University of Beira Interior, Physics Department, Covilhã, Portugal; [4] University of Coimbra, Department of Informatics Engineering, Coimbra, Portugal; [5] University of Coimbra, Department of Electrical and Computer Engineering, Coimbra, Portugal; [6] University of Coimbra, Geophysical and Astronomical Observatory, Coimbra, Portugal; [7] ADVACAM s.r.o., Prague, Czech Republic

This work is supported by the ESA-PRODEX Experiment Arrangement (PEA No. 4000141332).“THOR-SR: TGF and High-energy astrophysics Observatory for gamma-Rays on board the Space Rider”.
Cristiana Francisco work is supported by UI/BD/154752/2023 fellowship.

Abstract

CdTe Timepix3 based instruments are an excellent option to perform fine Compton gamma-ray polarimetry. Its high pixelization level (55×55 μm^2) allows to maximize instruments modulation factor and to deliver the higher polar angular resolution in the soft gamma-ray domain. This level of performance is especially important for future gamma-ray astrophysics’ telescopes, since high-energy polarimetry is still a domain with a vast research potential. Timepix3 can be operated in two modes: frame mode and data-driven mode. In data-driven mode each interaction full detection data is available: pixel position (x and y), energy and time. In the frame mode only position (x and y) and energy are available for a given time interval, during which all interactions are integrated in a single frame. However, in this mode less intensive front-end electronics’ processing capacity is required leading to substantial lower power consumption. This is an advantage that can be decisive for applications where high sensitive polarimetry must be performed in low electric power platforms, such as cubesat platforms. An experimental set of measurements with a CdTe Timepix3 operating in frame mode was performed at ESRF under a ~99% polarized

200 keV beam. A Q polarization modulation factor of 0.71 ± 0.014 was obtained, proving that under certain conditions and constraints, frame-mode polarimetry is not only a valid method but also a performant one.

References
[1] D. Turecek et al., “Single layer Compton camera based on Timepix3 technology”, JINST, 15 (2020), Article C01014, 10.1088/1748-0221/15/01/C01014
[2] P. Laurent et al. “PHEMTO: The Polarimetric High Energy Modular Telescope Observatory”, Exp Astron 51, 1143–1173 (2021). https://doi.org/10.1007/s10686-021-09723-x
[3] R. Caputo et al., “All-sky Medium Energy Gamma-ray Observatory eXplorer mission concept”, J Astro Tele Instr Systems, Vol. 8, 4, 2022. https://doi.org/10.1117/1.JATIS.8.4.044003
[4] Vincent Tatischeff et al., “Gamma-Ray Polarimetry”, Astrophys.Space Sci.Libr. 460 (2019) 109-146, DOI: 10.1007/978-3-030-19715-5_5
[5] R. M. Curado Da Silva et al., "THOR-SR: TGF and High-energy astrophysics Observatory for gamma-Rays on board the Space Rider," 2024 IEEE Nuclear Science Symposium (NSS), Medical Imaging Conference (MIC) and Room Temperature Semiconductor Detector Conference (RTSD), Tampa, FL, USA, 2024, pp. 1-2, doi: 10.1109/NSS/MIC/RTSD57108.2024.10655687.
[6] J.F. Sousa et al., “Polarimetric evaluation of CdTe-Timepix3 detector module for THOR-SR Compton telescope”, Astroparticle Physics,Vol. 175, 2026, 103181, https://doi.org/10.1016/j.astropartphys.2025.103181.

RTSD-04-401

Imaging Performance Comparison of a GaAs Photon-Counting Detector and an Energy-Integrating Detector under Various Photon-Flux Conditions (#3232)

Luyuan Yang[1], He Li[3], Dmytro Nalyvaiko[4], Volodymyr Gnatyuk[4], Juha Kalliopuska[4], Xu Ji[2], Xiaochun Lai[1], **Boren Wang**[1]

[1] ShanghaiTech University, School of Biomedical Engineering, Shanghai, China; [2] Southeast University, School of Computer Science and Engineering, Nanjing, China; [3] Shanghai United Imaging Healthcare Advanced Technology Research Institute Co.,Ltd., Shanghai, China; [4] Advafab OY, Espoo, Finland

This work was supported by the Science and Tech-nology Commission of Shanghai Municipality under grant No. 24DIPA00700. We acknowledge the ShanghaiTech Material and Device Lab and HPC Platform of ShanghaiTech University.

Abstract

This work compares the imaging performance of a GaAs photon-counting detector (PCD) and an energy-integrating detector (EID) under various photon-flux conditions. The detectors were characterized using the modulation transfer function (MTF), noise power spectrum (NPS), and detective quantum efficiency (DQE), and were evaluated under similar effective spatial-resolution conditions. An NPS-based noise prediction model was then used to estimate the image standard deviation as a function of photon count. The results show that the GaAs PCD and the resolution-matched EID exhibit comparable frequency-domain performance and image quality under the reference photon-flux condition. At low photon flux, however, the PCD shows a markedly lower predicted noise level. Finally, phantom imaging experiments further confirm that the PCD provides lower background fluctuations and clearer structural visibility under low-flux conditions. These results demonstrate the noise advantage of GaAs photon-counting detectors for low-flux X-ray imaging.

References
[1] Willemink, Martin J., et al. "Photon-counting CT: technical principles and clinical prospects." Radiology 289.2 (2018): 293-312.
[2] Acciavatti, Raymond J., and Andrew DA Maidment. "A comparative analysis of OTF, NPS, and DQE in energy integrating and photon counting digital x-ray detectors." Medical Physics 37.12 (2010): 6480-6495.
[3] Sandrik, John M., and Robert F. Wagner. "Radiographic screen–film noise power spectrum: variation with microdensitometer slit length." Applied optics 20.16 (1981): 2795-2798.

11 November, 2026

Time:
11 November, 2026
9:00 – 11:00

Room:
ANDALUCÍA II & III

RTSD-05 | RTSD Perovskite Detectors

Chairs:
Andrea Zappettini (Parma)
Paul Sellin (Guildford)

RTSD-05-01

Performance Improvements on Perovskite Gamma-Ray Detectors Using Depth-Dependent Shaping Optimizations (#1338)

Max Robbins[1], Mustafa Unal[2], Quoc Vuong Phan[2], Khasim S. Bayikadi[2], Duck C. Young[2], Mercouri G. Kanatzidis[2,3], Zhong He[1]

[1] University of Michigan, NERS, Ann arbor, USA; [2] Argonne National Labs, Materials Science Division, Lemont, USA; [3] Northwestern University, Department of Chemistry, Evanston, USA

The work was supported by the Interaction of Ionizing Radiation with Matter - University Research Alliance, DOD DTRA award HDTRA 12020002, and by the Office of Defense Nuclear Nonproliferation Research and Development within the U.S. Department of Energy's National Nuclear Security Administration through a subcontract from Argonne National Laboratory (DOE Contract No. DE-AC02-06CH11357.)

Abstract

$CsPbBr_3$ is a perovskite room-temperature semiconductor crystal, with properties for high-resolution gamma-ray detection. This material has been fabricated in large volumes, with detectors up to 12 mm thick demonstrated to remain stable for up to 4 months under continuous bias, achieving energy resolutions of 1.1%-1.6% FWHM at 662 keV. This research employs depth-of-interaction analysis on a 12 mm-thick pixelated detector to investigate how optimizing digital pulse shaping parameters as a function of interaction depth and pixel electrode can improve energy resolution. Rather than applying a uniform set of shaping parameters across all events, each waveform is processed independently, allowing shaping to be tuned to the charge-transport characteristics specific to each depth bin and pixel pair. Two optimization methods are compared: a Linear 1D approach, in which rise time and flat-top time are constrained to be equal, and a Grid 2D approach, in which both parameters are varied independently across a wider search space. Our results show that both depth-dependent methods consistently outperform uniform shaping across all drift times. The 2D grid method achieves lower energy resolution than the 1D method but at a significantly higher computational cost (up to an order of magnitude slower). Using 1D optimization, per-pixel energy-resolution improvements of 4.1% to 15.4% were observed, with a best achieved resolution of 0.65% FWHM at 662 keV for near-pixel-side events, representing an improvement over previously reported thinner detectors while maintaining comparable stability.

References

[1] M. Petryk, "Algorithms and electronics for processing data from pixelated semiconductor gamma-ray detectors," Ph.D. dissertation, University of Michigan, 2023.

RTSD-05-02

On Technological Aspects In The Development Of Perovskite Gamma Radiation Detectors (#1472)

Normunds Grundmanis[1], Vladimir Gostilo[1], Aleksandr Lupilov[1], Alan Owens[2]

[1] Baltic Scientific Instruments, Riga, Latvia; [2] Czech Technical University, Institute of Experimental and Applied Physics, Prague, Czech Republic

Abstract

This paper outlines the technological steps and methods used to manufacture perovskite semiconductor radiation detectors and compares them with those used in the manufacture of other semiconductor materials, such as HPGe, Si, CZT, CdTe, and TlBr. We analyse the problems and limitations arising when implementing these technologies at this early stage of perovskite detector development. We examine and critique the technologies involved in crystal growth and processing; for example, mechanical (cutting, grinding, polishing...), chemical (etching, washing...), contact deposition and patterning (masking, photolithography) as well as the welding of contacts and micro assembly of detector crystals.

Applying the processes described above to $CsPbBr_3$ crystals of dimensions of 5´5´3 mm^3, we have manufactured a number of radiation detectors with different contact architectures - a planar contact structure, a planar structure with a guard ring and a ring-electrode type structure. The detectors provided FWHM energy resolutions of less than 1% at 662 and 1332 keV (0.79% and 0.86%, respectively) with a peak to Compton ratio of 11, The FWHM energy resolutions at 59.5 keV, 122 keV and 5.9 kV were 2.7 keV (4.5%), 3.9 keV (3.2 %) and ≤2.6 keV, respectively.

RTSD-05-03

Metal-Halide Perovskites for Fast Hard-Radiation Detection (#1576)

Anastasiia Sakhatska[1,2], Kostiantyn Sakhatskyi[1,2], Gebhard J. Matt[1,2], Andrii Kanak[1,2], Alexander Szola[1], Yevhenii Padnuik[1,2], Yuliia Kominko[1,2], Aditya Bhardwaj[1,2], Sergii Yakunin[1,2], Maksym Kovalenko[1,2]

[1] ETH Zurich, Laboratory of Inorganic Chemistry, Department of Chemistry and Applied Biosciences, Zürich, Switzerland; [2] EMPA, Laboratory for Thin Films and Photovoltaics, Zürich, Switzerland

The work at ETH Zürich was financially supported by ETH Zürich through the ETH+ Project SynMatLab: Laboratory for Multiscale Materials Synthesis, by the Ukrainian-Swiss Joint Research Programme grant #IZURZ2_224877, and also by the Swiss Innovation Agency (Innosuisse) under grant agreement 46894.1 IP-ENG.

Abstract

Metal-halide perovskites are promising low-cost semiconductors for photon-counting X-ray imaging. However, their temporal response is often hindered by ion migration induced field screening, which can lead to an underestimation of charge carrier mobility. Here, charge transport is studied in $CsPbBr_3$single-crystal detectors using time-of-flight technique and ^{241}Am (60 keV) gamma-counting spectroscopy under direct-current (DC) and alternating-current (AC) bias. In DC operation, polarization effects restrict the extracted hole mobility to ~36 $cm^2V^{-1}s^{-1}$. Applying AC bias suppresses ionic accumulation and reveals substantially higher hole mobility, reaching up to ~560 $cm^2V^{-1}s^{-1}$. Gamma counting under AC operation preserves energy resolution (~10–11%) while accelerating charge collection: the mean response time decreases from ~460 ns (DC) to ~110 ns (AC). These results show that alternating biasing mitigates ion migration induced field distortion and enables perovskite detectors to approach the response speeds required for fast photon counting.

References
[1] He, Y, Petryk, M, Liu, Z, Chica, DG, Hadar, I, Leak, C, Ke, W, Spanopoulos, I, Lin, W, Chung, DY, Wessels, BW, He, Z, Kanatzidis, MG 2021, 'CsPbBr3 perovskite detectors with 1.4% energy resolution for high-energy γ-rays', *Nature Photonics*, 15(1), 36–42, London: Springer Nature.
[2] Wang, YQ, Ren, RH, Shen, NN, Xiao, B, He, XC, Sun, QH, He, YH 2024, 'Determining the Carrier Mobility-Lifetime Product in the Perovskite CsPbBr3 Semiconductor with a Pulsed Laser', *Journal of Instrumental Analysis*, 43(10), 1645–1650, Guangzhou: Journal of Instrumental Analysis Editorial Office.
[3] Sakhatskyi, K, John, RA, Guerrero, A, Tsarev, S, Sabisch, S, Das, T, Matt, GJ, Yakunin, S, Cherniukh, I, Kotyrba, M, Berezovska, Y, Bodnarchuk, MI, Chakraborty, S, Bisquert, J, Kovalenko, MV 2022, 'Assessing the Drawbacks and Benefits of Ion Migration in Lead Halide Perovskites', *ACS Energy Letters*, 7(10), 3401–3414, Washington, DC: American Chemical Society.
[4] Eames, C, Frost, JM, Barnes, PRF, O'Regan, BC, Walsh, A, Islam, MS 2015, 'Ionic transport in hybrid lead iodide perovskite solar cells', *Nature Communications*, 6(1), 7497, London: Springer Nature.
[5] Calado, P, Telford, AM, Bryant, D, Li, X, Nelson, J, O'Regan, BC, Barnes, PRF 2016, 'Evidence for ion migration in hybrid perovskite solar cells with minimal hysteresis', *Nature Communications*, 7(1), 13831, London: Springer Nature.

RTSD-05-04

Growth of $MAPbBr_3$ Single Crystals for X-Ray, Gamma Ray Detection by Slow Solvent Evaporation at Room-Temperature (#1827)

Madan Niraula, **Madan Niraula**, Ryuto Ohshima, Ryuto Ohshima, Seita Kamon, Seita Kamon

Nagoya Institute of Technology, Graduate School of Engineering, Nagoya, Japan

This work was partly supported by JSPS Kakenhi grant (24K15592).

Abstract

Solution-grown lead halide perovskites are promising materials for next-generation radiation detectors. Inverse temperature crystallization (ITC) growth is widely used to obtain large crystals within a relatively short time. However, the rapid increase in supersaturation during heating promotes spontaneous nucleation, leading to compositional inhomogeneity and elevated defect density. To address this limitation, we investigated the growth of $MAPbBr_3$ single crystals using a slow solvent evaporation-induced crystallization method performed at a controlled, constant temperature near room temperature. X-ray diffraction confirmed the formation of high-quality single crystals with improved crystallinity compared to our standard ITC-grown crystals. Detectors fabricated in an Au/$MAPbBr_3$/Cr planar configuration exhibited reduced dark current and enhanced X-ray sensitivity relative to

devices based on ITC-grown crystals. These results demonstrate that this growth strategy provides a viable pathway to improved crystal quality and device performance.

RTSD-05-05

Millimeter-Thick Perovskite Single-Crystal X-ray Detectors with Unity Charge Extraction in Photovoltaic Mode (#1868)

Bekir Turedi[1,2], Kostiantyn Sakhatskyi[1,2], Vitalii Bartosh[1,2], Gebhard J. Matt[1,2], Anastasiia Sakhatska[1,2], Quang Lung[1,2], Sergii Yakunin[1,2], Maksym Kovalenko[1,2]

[1] ETH Zurich, Department of Chemistry and Applied Biosciences, Zurich, Switzerland; [2] Empa - Swiss Federal Laboratories for Materials Science and Technology, Laboratory for Thin Films and Photovoltaics, Dubendorf, Switzerland

The work at ETH Zurich was financially supported by the Swiss Innovation Agency (Innosuisse) under grant agreement 46894.1 IP-ENG, by ETH Zurich through the ETH+ Project SynMatLab: Laboratory for Multiscale Materials Synthesis, and by the UkrainianSwiss Joint Research Programme grant #IZURZ2_224877. We acknowledge ams-OSRAM for providing the AS5920M detector.

Abstract

Low-dose diagnostic X-ray imaging requires detector materials that combine high stopping power, low electronic noise, fine spatial resolution, and stable operation under clinically relevant X-ray energies. Cadmium telluride currently provides this performance in direct-conversion imagers, but its cost and crystal-growth constraints limit scalability. We report direct conversion detectors working in photovoltaic mode based on solution-grown mixed-cation methylammonium-formamidinium lead triiodide single crystals. The crystals were grown with controlled thicknesses up to 1 mm on charge-selective contacts and patterned indium tin oxide arrays. Optical and X-ray detection characterization shows millimeter-scale charge extraction without an externally applied field, with electron mobility-lifetime products up to 0.17 $cm^2 V^{-1}$ and diffusion lengths of 3.5 mm. The devices achieve single-photon sensitivity and detective quantum efficiency above 90% at 60 keV, while the same growth route enables conformal integration into 40 µm-pitch linear arrays with spatial resolution up to 19-line pairs per millimeter. The detectors also maintain a stable response over up to two years of intermittent operation and storage. These results indicate that solution-grown perovskite single crystals can approach cadmium telluride-level low-dose imaging performance while retaining a scalable low-temperature materials platform for medical and industrial X-ray imaging.

References
[1] Del Sordo, S et al. 2009, ‘Progress in the development of CdTe and CdZnTe semiconductor radiation detectors for astrophysical and medical applications’, Sensors, vol. 9, pp. 3491–3526, Basel: MDPI.
[2] He, Y, Hadar, I & Kanatzidis, MG 2022, ‘Detecting ionizing radiation using halide perovskite semiconductors processed through solution and alternative methods’, Nature Photonics, vol. 16, pp. 14–26, London: Springer Nature.
[3] Sakhatskyi, K et al. 2023, ‘Stable perovskite single-crystal X-ray imaging detectors with single-photon sensitivity’, Nature Photonics, vol. 17, pp. 510–517, London: Springer Nature.
[4] Kabir, MZ & Kasap, S 2002, ‘Sensitivity of X-ray photoconductors: charge trapping and absorption-limited universal sensitivity curves’, Journal of Vacuum Science & Technology A, vol. 20, pp. 1082–1086, Melville: AIP Publishing.
[5] Sakhatskyi, K et al. 2025, ‘Characterizing emerging detector materials for low-dose X-ray imaging’, Advanced Materials, article e12795, Weinheim: Wiley-VCH.

RTSD-05-06

Multipixel 2D Perovskite Thin-Film Array for High-Resolution Proton Beam Profiling (#2090)

Ilaria Fratelli[1,2], Laura Basiricò[1,2], Giulia Napolitano[1], Andrea Ciavatti[1,2], Enrico Verroi[4], Ioannis Kymissis[3], Beatrice Fraboni[1,2]

[1] University of Bologna, Department of Physics and Astronomy, Bologna, Italy; [2] INFN, Bologna, Bologna, Italy; [3] Columbia University, Department of Electrical Engineering, New York City, USA; [4] Trento Institute for Fundamental Physics and Applications, Trento, Italy

I.F. has received funding from Horizon Europe under the Marie Skłodowska-Curie grant agreement No 101105245

Abstract

We present a scalable and calibrated proton dosimetry platform based on flexible 2D perovskite (PEA_2PbBr_4) thin films, enabling high-resolution beam profiling in clinically relevant conditions. The devices consist of solution-processed thin films deposited on 75 μm Kapton substrates and operated as two-terminal coplanar detectors. Their response has been characterized under therapeutic proton beams (70–200 MeV), showing stable operation, good radiation tolerance up to 20 Gy, and a linear dependence of the collected charge on the total dose. The current response exhibits a reproducible sublinear dependence on dose rate, enabling the definition of calibration protocols. The scalability of the technology is demonstrated through multipixel linear arrays composed of up to 28 devices arranged side-by-side, showing good uniformity with pixel-to-pixel variations below 25% in sheet resistance and 15% in calibration parameters. After calibration, the system enables accurate reconstruction of transverse proton beam profiles in agreement with nominal beam shapes. A key feature of these detectors is their angular-independent response (<2% variation up to 90°), which enables operation in an edge-on configuration and a transition from pixel-pitch-limited to thickness-limited spatial resolution. This concept is extended to a stacked pixel-on-pixel multipixel architecture for high-resolution beam profiling (77 μm). Finally, the devices have been validated in an anthropomorphic phantom under clinical 200 MeV proton irradiation, demonstrating the capability to discriminate beam position shifts and reconstruct dose profiles consistently with radiochromic film and commercial dosimetry measurements. These results highlight the potential of flexible 2D perovskite detectors as a versatile platform for scalable, high-resolution, and real-time proton beam dosimetry.

References

[1] I. Filipev *et al.*, *Radiat. Meas.*, vol. 177, Sep. 2024, doi: 10.1016/j.radmeas.2024.107272.
[2] A. B. Rosenfeld, *et al.*, 2020, *IOP Publishing Ltd.* doi: 10.1088/1361-6560/aba163.
[3] I. Fratelli *et al.*, *Advanced Science*, no. 2401124, 2024, doi: 10.1002/advs.202401124.
[4] I. Fratelli *et al.*, "Angular-Independent Flexible Perovskite Dosimeters for High-Resolution Proton Beam Mapping", submitted

RTSD-05-07

Phase-Pure Orthorhombic $CsPbBr_3$ Perovskite Materials for Low-Lag, Ultrahigh-Resolution Direct X-ray Detectors (#3093)

Amlan Datta, Brandon Dunham, Shariar Motakef

CapeSym, Inc., Research and Developement, Natick, USA

This research was supported by the U.S. National Institutes of Health under award R44EB038123.

Abstract

Room-temperature direct-conversion X-ray imagers require sensor materials that combine high stopping power, efficient charge transport, spatially confined charge collection, and stable temporal response. We report an all-inorganic perovskite detector platform in which phase purity of cesium lead bromide ($CsPbBr_3$, CPB) is used as the central materials control parameter. Low-impurity, spectroscopic-grade CPB crystals were produced by purification and optimized Bridgman growth, milled to nanopowder, and blade-coated into dense sensor films on active-pixel readout arrays at temperatures compatible with backplane electronics. X-ray diffraction of both precursor crystals and sensor films showed the stable orthorhombic Pnma phase with characteristic reflections, indicating preservation of phase through crystal-to-powder-to-film conversion. In contrast, unoptimized starting material contained a $CsPb_2Br_5$ tetragonal secondary phase, generated nonuniform slurries and aggregate-rich films, and produced degraded X-ray images due to interpixel charge sharing. The optimized CPB sensors demonstrated linear response to 30 keV X-rays, sensitivity of 55,400 μC Gy_{air}^{-1} cm^{-2} at 0.5 V/μm, a limit of detection of 417 pGy_{air} s^{-1}, and a hole mobility-lifetime product of 8.0×10^{-4} cm^2/V. Phase-pure CPB also produced low residual lag, reducing detector lag from 8.9% to 1.1%, while enabling 6.9 lp/mm at 20% modulation transfer function on a 100 μm-pitch amorphous-silicon array and 20 lp/mm on a fine-pitch CMOS readout. These results identify phase-pure orthorhombic CPB as a scalable room-temperature semiconductor for low-lag, high-sensitivity, high-resolution X-ray imagers.

Time:
11 November, 2026
11:30 – 13:00

Room:
ANDALUCÍA II & III

RTSD-06 | RTSD Perovskite Detectors II

Chairs:
Juan S. Useche Parra (Freiburg)
Ge Yang (Raleigh)

RTSD-06-01

Influence of the Active Layer Thickness on the Performance of Metal-Halide-Perovskite Thin Films for X-ray Detectors (#1972)

Marco Girolami[1], Fabio Matteocci[2], Mina Bagheri Khorasgani[2], Zeynab Skafi[2], Antonello Ranieri[4], Sara Pettinato[3], Stefano Salvatori[3], Thomas M. Brown[2], Aldo Di Carlo[2], Daniele M. Trucchi[1]

[1] CNR - Consiglio Nazionale delle Ricerche, DiaTHEMA Lab, ISM - Istituto di Struttura della Materia, Montelibretti, Italy; [2] University of Rome Tor Vergata, C.H.O.S.E. (Centre for Hybrid and Organic Solar Energy), Department of Electronic Engineering, Roma, Italy; [3] Università degli Studi Niccolò Cusano, Faculty of Engineering, Roma, Italy; [4] CNR - Consiglio Nazionale delle Ricerche, IC - Istituto di Cristallografia, Montelibretti, Italy

Abstract

The performance under X-rays (with energies up to 40 keV) of self-powered detectors with a submicrometric metal-halide-perovskite ($FAPbBr_3$) active layer was systematically investigated as a function of the $FAPbBr_3$ film thickness, ranging from 180 to 840 nm. Results show that an intermediate thickness of 710 nm represents the best trade-off among sensitivity (up to 571.07 μC Gy^{-1} cm^{-2}), limit of detection (down to 39.55 nGy s^{-1}), linearity with the dose-rate, and stability over time (signal fluctuations <1% within 1 h of continuous irradiation).Very significantly, it is here shown that, in the case of submicrometric $FAPbBr_3$ film-based X-ray detectors, a better performance is not necessarily connected to a larger thickness; the benefits of a better X-ray absorption are indeed nullified by a drastic decrease of the photoconductive gain, due to increased interface charge accumulation and enhanced recombination.

RTSD-06-02

Optimization of $FAPbBr_3$ Single Crystals for Photon Counting Radiation Detection (#2520)

Jayana Jayarathne[1], Amy J. Dickinson[1], Jenson Green[1], Muzzamer Zahid[1], Carol Crean[2], Sithumini Perera[1], Paul Sellin[1]

[1] University of Surrey, School of Mathematics and Physics, Guildford, UK; [2] University of Surrey, School of Chemistry and Chemical Engineering, Guildford, UK

Abstract

The organic hybrid perovskite $FAPbBr_3$ shows great potential as a radiation detector, particularly due to its synthesis using cost-effective room-temperature solution-based growth processes. In this paper we report on recent improvements in the quality of solution-grown $FAPbBr_3$ single crystals using a sulfonic zwitterionic ligand 3-(Decyldimethylammonio)-propane-sulfonate inner salt (DPSI). By optimizing the growth process we have produced X-ray and gamma ray detectors that show excellent charge transport properties, with a high hole mobility of 190

cm^2/Vs and a high hole mobility-lifetime (μτ) product of 2.7 x 10^{-3} cm^2/V, combined with a low dark current of 2.9 nA cm^{-2} operating at a field strength of 1000 V/cm. These $FAPbBr_3$ detectors show well-resolved low energy gamma peaks from 241Am, with an energy resolution of 25.6% FWHM at 59.5 keV.

RTSD-06-03

Transient Currents in 4H–SiC Radiation Sensors with Graphene Electrodes (#2924)

Eduard Belas[1], Marián Betušiak[1], Roman Grill[1], Petr Praus[1], Jan Kunc[1], Ritwik Nag[2], Krishna C. Mandal[2]

[1] Charles University, Faculty of Mathematics and Physics, Institute of Physics, Prague 2, Czech Republic; [2] University of South Carolina, Department of Electrical Engineering, Columbia, USA

This project is co-financed from the state budget by the Technology agency of the Czech Republic under the TACR 13 SIGMA DC5 Programme TQ28000004.

Abstract

We investigate charge transport in both 4H–SiC semiinsulating bulk graphene/semiinSiC/Ni sensor and epitaxial graphene/epiSiC/subsSiC/Ni Schottky barrier diode structure. Using the laser-induced Transient Current Technique (L–TCT), combined with alpha spectroscopy and I–V characterization, we investigate charge transport across either the bulk or epilayer and adjacent substrate. Our results reveal rapid space charge formation at all structures, even under pulsed bias, attributed to electron depletion. It is shown that in contrast to metallic electrodes showing fast damped oscillations, the graphene electrodes lead to significantly slower non-oscillating exponential-like current waveforms. Observed phenomena were successfully described by theoretical model based on surface plasmons in both sensors. These findings highlight the importance of the transient current technique for the investigation of SiC sensors.

RTSD-06-04

Perovskite $CsPbBr_3$ Cherenkov charge induction gamma-ray detector with sub-ns timing resolution (#2971)

Lei Pan[1], Quoc Vuong Phan[3], Mustafa Unal[3], Seungeun Lee[1], Duck Young Chung[3], Joshua W. Cates[1], Om Aggarwal[2], Marcos Turqueti[2], Gerard Ariño-Estrada[4], Mercouri G. Kanatzidis[3], Javier Caravaca[1]

[1] Lawrence Berkeley National Laboratory, Nuclear Science Division, Berkeley, USA; [2] Lawrence Berkeley National Laboratory, Engineering Division, Berkeley, USA; [3] Argonne National Laboratory, Materials Science Division, Lemont, USA; [4] University of California Davis, Department of Biomedical Engineering, Davis, USA

This research was supported by the DOE Laboratory Directed Research and Development Program through Lawrence Berkeley National Laboratory.

Abstract

Perovskite $CsPbBr_3$ is promising as next-generation room temperature semiconductor gamma-ray detector. While remarkable energy resolution has been achieved (e.g., 1% at 662 keV) for $CsPbBr_3$, its timing resolution is expected to be limited by the charge transport process as semiconductor (as a reference, timing resolution is several ns or worse for semiconductor CdZnTe or TlBr). Here, we report sub-nanosecond time resolution utilizing the prompt Cherenkov emission from the $CsPbBr_3$ as fast timing signal while maintaining its good energy resolution. We demonstrate successful simultaneous readout of semiconductor charge induction signal and SiPM Cherenkov light signal. By associating the Cherenkov light signal with the charge signal, good energy resolution of ~3% at 511 keV and sub-ns coincidence timing resolution of ~ 583 ps with ^{22}Na gamma-ray source were achieved simultaneously. We expect further improvement of time and energy resolution with a high-frequency SiPM read-out PCB and a dedicated charge-readout PCB with integrated high-performance pre-amplifiers. Built upon the high energy resolution and the ability to provide spatial information of gamma-ray interaction, the sub-ns fast timing capability would markedly broaden the applications of $CsPbBr_3$ gamma-ray detectors that are projected to have low cost compare to CdZnTe.

References

[1] G. Ariño-Estrada *et al.*, "First Cerenkov charge-induction (CCI) TlBr detector for TOF-PET and proton range verification," *Physics in Medicine & Biology,* vol. 64, no. 17, p. 175001, 2019.

[2] G. Ariño-Estrada *et al.*, "Towards time-of-flight PET with a semiconductor detector," *Physics in Medicine & Biology,* vol. 63, no. 4, p. 04LT01, 2018.

[3] G. Ariño-Estrada *et al.*, "Study of Čerenkov light emission in the semiconductors TlBr and TlCl for TOF-PET," *IEEE transactions on radiation and plasma medical sciences,* vol. 5, no. 5, pp. 630-637, 2020.

[4] K. Hitomi, C. Kim, M. Nogami, K. Shimazoe, and H. Takahashi, "Characterization of coincidence time resolutions of TlBr x Cl1− x crystals as Cherenkov radiators," *Japanese Journal of Applied Physics,* vol. 62, no. 8, p. 081001, 2023.

[5] G. Terragni *et al.*, "Time resolution studies of thallium based Cherenkov semiconductors," *Frontiers in Physics,* vol. 10, p. 93, 2022.

[6] K. Hitomi *et al.*, "Timing performance of TlBr detectors," *IEEE Transactions on Nuclear Science,* vol. 60, no. 4, pp. 2883-2887, 2013.

[7] N. Shen *et al.*, "Single photon γ-ray imaging with high energy and spatial resolution perovskite semiconductor for nuclear medicine," *Nature Communications,* vol. 16, no. 1, p. 8113, 2025.

[8] Y. He, I. Hadar, and M. G. Kanatzidis, "Detecting ionizing radiation using halide perovskite semiconductors processed through solution and alternative methods," *Nature Photonics,* vol. 16, no. 1, pp. 14-26, 2022.

[9] L. Pan *et al.*, "Geant4 Simulation of Cherenkov Photons in Perovskite CsPbBr3 Gamma-Ray Detectors," *IEEE Transactions on Radiation and Plasma Medical Sciences,* 2025.

RTSD-06-05

Unraveling Atmosphere-Dependent Trap-Mediated X-Ray Detection in Organic Field-Effect Transistors (#2896)

Giulia Napolitano[1], Ilaria Fratelli[1,2], Carme Martínez-Domingo[3], Manikanta Makala[4], Lamiaa Fijahi[5], Ioannis Kymissis[2], Oana Jurchescu[4], Beatrice Fraboni[1,6], Marta Mas-Torrent[5], Laura Basiricò[1,6]

[1] University of Bologna, Department of Physics and Astronomy, Bologna, Italy; [2] Columbia University, Department of Electrical Engineering, New York, USA; [3] Institute of Microelectronics of Barcelona, IMB-CNM-CSIC, Bellaterra, Spain; [4] Wake Forest University, Deparment of Physics and Center for Functional Materials, Winston-Salem, USA; [5] Institut de Ciència de Materials de Barcelona, ICMAB-CSIC, Bellaterra, Spain; [6] INFN-BO, Bologna, Italy

L.B. acknowledges INNOVARE project funded by Fondazione Compagnia di S. Paolo-CARIPLO-CDP grant “vEIColo – accompagnamento per la
valorizzazione della ricerca” Grant No. 2025.1624; I.F. has received funding from Horizon Europe under the Marie Skłodowska-Curie grant agreement No 101105245, “Hybrid detectors for medical radiation therapies – IDEATE”.

Abstract

Organic field-effect transistors are promising candidates for ionizing radiation dosimetry due to their low-cost fabrication, large-area processability, and tissue-equivalent composition. However, their response is strongly affected by environmental species, such as oxygen and moisture, which can induce charge traps and compromise detector stability. Here, we investigate the role of Parylene-C encapsulation in TMTES:PS-based OFET X-ray detectors. The encapsulation layer preserves the pristine electrical performance while significantly improving shelf stability. Under X-ray irradiation, uncoated devices exhibit air-dependent transient dynamics, with recovery in air and integrative behavior in vacuum. In contrast, Parylene-C-coated devices show stable and cumulative response independently of the surrounding environment, indicating that encapsulation suppresses air-induced trap formation. Trap density of states analysis supports this interpretation, revealing additional shallow trap states only in uncoated devices irradiated in air. Encapsulated OFETs further display a dose-dependent threshold-voltage shift, with a maximum sensitivity of 0.109 ± 0.002 V Gy^{-1} and long-lived retention of the absorbed dose information. These results demonstrate that Parylene-C encapsulation is not only an effective strategy to improve environmental stability, but also a key tool to control the radiation response of organic transistor-based dosimeters.

References

[1] Basiricò, L., Ciavatti, A., & Fraboni, B. (2021). 'Solution-Grown Organic and Perovskite X-Ray Detectors: A New Paradigm for the Direct Detection of Ionizing Radiation.' *Advanced Materials Technologies*, 6.1: 2000475

[2] Fratelli, I., Basiricò, L., Ciavatti, A., Lamport, Z. A., Anthony, J. E., Kymissis, I., & Fraboni, B. (2023). Trap States Ruling Photoconductive Gain in Tissue-Equivalent, Printed Organic X-Ray Detectors. *Advanced Materials Technologies*, 8.3: 2200769.

[3] Haneef, H. F., Zeidell, A. M., & Jurchescu, O. D. (2020). Charge carrier traps in organic semiconductors: a review on the underlying physics and impact on electronic devices. *Journal of Materials Chemistry C*, 8.3: 759-787.

[4] Giglio, M. E., Colantoni, E., Fratelli, I., Martinez-Domingo, C., Martinez-Zaragoza, P., Napolitano, G., ... & Mas-Torrent, M. (2025). Vertical Phase Separation in Blended Organic Semiconducting Films and Impact on Their Electrical and Direct X-Ray Detection Properties. *Advanced Electronic Materials*, 11.17: 2400887.

[5] McKeen, L. W. (2017). *Film properties of plastics and elastomers*. William Andrew.

[6] Jong, W. L., Wong, J. H. D., Ung, N. M., Ng, K. H., Ho, G. F., Cutajar, D. L., & Rosenfeld, A. B. (2014). Characterization of MOSkin detector for in vivo skin dose measurement during megavoltage radiotherapy. *Journal of applied clinical medical physics*, 15.5: 120-132.
[7] Bordoni, C., Ciavatti, A., Cortinhal, M., Pereira, M., Cramer, T., Barquinha, P., & Fraboni, B. (2024). Dielectric multilayers impact on radiation-induced charge accumulation in highly sensitive oxide field effect transistors. *APL Materials*, 12.3.

RTSD-06-06

Li- and B-Doped $CsPbBr_3$ Composites for Fast Radiation Scintillation Detection (#2944)

Mohamed Boukhicha, Spencer A. Reisbick, Cultrera Luca, Tsang Thomas

Brookhaven National Laboratory, Instrumentation, Upton, USA

Abstract

Efficient and scalable scintillators are critical for applications in medical imaging, nuclear security, and environmental monitoring. Here, we investigate lithium-6 and boron-10 doped $CsPbBr_3$ perovskite-polymer composites for dual-mode neutron and X-ray detection. A scalable ball-milling process was used to incorporate neutron-sensitive isotopes into $CsPbBr_3$ nanocrystals embedded in PMMA and PDMS matrices. The resulting composites combine the neutron capture capabilities of lithium-6 and boron-10 with the favorable optical properties of $CsPbBr_3$, including high light yield, emission near 520 nm, and sub-nanosecond decay times. HR-TEM analysis confirmed a homogeneous distribution of ~10 nm nanocrystals throughout the polymer matrix. Synchrotron-based measurements further demonstrated strong radioluminescence and fast scintillation response under X-ray excitation. Preliminary studies also indicate promising neutron and alpha-particle scintillation performance, highlighting the potential of these flexible and scalable composites for next-generation radiation detection technologies.

Time:
11 November, 2026
15:00 – 17:00

Room:
ANDALUCÍA II & III

RTSD-07 | RTSD Pixel Detectors II

Chairs:
Krishna C. Mandal (Columbia)
Chris G. Wahl (Ann Arbor)

RTSD-07-01

Physics-Informed 3D Gaussian Splatting for Multi-View Compton Camera Imaging (#1292)

Rui Ma, Liang Li

Tsinghua University, Department of Engineering Physics, Beijing, China

This work was supported by National Key R&D Program of China (No. 2023YFA1608401).

Abstract

High-resolution 3D Compton imaging is essential for quantitative environmental monitoring. Traditional Maximum Likelihood Expectation Maximization (MLEM) suffers from voxel discretization penalties. Without ground-truth references, MLEM's required early stopping creates a dilemma between severe depth-elongation and late-stage noise deterioration. Meanwhile, modern deep learning models suppress noise but lack zero-shot generalization. To bridge this gap, we present a zero-shot, physics-informed 3D Gaussian Splatting (3DGS) framework. Although likelihood computation utilizes differentiable voxelization, the fundamentally continuous nature of 3DGS introduces implicit spatial regularization, bypassing rigid voxel constraints. It rigorously decouples the morphological probability density from overall source activity via an analytical optimal scaling mechanism. In simulations, 3DGS eliminates background artifacts, yielding up to 5.7 dB Peak Signal-to-Noise Ratio (PSNR) improvement over MLEM in 4-view phantom reconstructions. Validated experimentally on an H3D M400 detector within a 0.125 m³ workspace, 3DGS overcomes MLEM's depth-elongation and noise deterioration without arbitrary early stopping. It achieves an angular resolution of ~9° and excels in practical multi-isotope identification while strictly preserving relative activity linearity. This training-free paradigm offers a robust, quantitative tool for radiation monitoring.

References

[1] Wu, C, Zhang, S, Li, L 2022, 'An accurate probabilistic model with detector resolution and Doppler broadening correction in list-mode MLEM reconstruction for Compton camera', Physics in Medicine & Biology, vol. 67, no. 12, 125017, Bristol, UK: IOP Publishing.

[2] Yao, Z, et al. 2022, 'Technical note: Rapid and high-resolution deep learning-based radiopharmaceutical imaging with 3D-CZT Compton camera and sparse projection data', Medical Physics, vol. 49, no. 11, 7336-7346, Hoboken, NJ, USA: Wiley.

[3] Kerbl, B, Kopanas, G, Leimkuehler, T, Drettakis, G 2023, '3D Gaussian splatting for real-time radiance field rendering', ACM Transactions on Graphics, vol. 42, no. 4, 139, New York, NY, USA: Association for Computing Machinery.

[4] Zha, R, et al. 2024, 'R^2-Gaussian: rectifying radiative Gaussian splatting for tomographic reconstruction', Proceedings of the 38th International Conference on Neural Information Processing Systems (NeurIPS), 1427, Red Hook, NY, USA: Curran Associates Inc.

[5] H3D, Inc. 2024, 'M400 Custom Integrable Detector Module', [Online], Available: https://h3dgamma.com/M400Specs.pdf, Ann Arbor, MI, USA: H3D, Inc.

RTSD-07-02

Benchmark of the H3DD_UMv5 Waveform Sampling ASIC for Pixelated Room-Temperature Semiconductor Detectors (#1336)

Yuefeng Zhu, Gianluigi D. Geronimo, Zhong He

University of Michigan, Nuclear Engineering and Radiological Sciences, Ann Arbor, USA

This material is based upon work supported by the Defense Threat Reduction Agency under Contract # HDTRA1-24-C-0002. Any opinions, findings and conclusions or recommendations expressed in this material are those of the author(s) and do not necessarily reflect the views of the Defense Threat Reduction Agency.

Abstract

H3DD_UM ASIC has been developed at the University of Michigan since 2017. This paper summarizes the performance of the most recent version H3DD_UMv5 ASIC. The electronic noise was measured to be 1.2 keV FWHM at 700-keV dynamic range with a 20×20×15 mm^3 CdZnTe detector attached but not biased. Such low noise enables an excellent energy resolution of 0.37% FWHM at 662 keV for single-pixel events. For all events, the measured energy resolution is 0.52 % FWHM. The low-energy threshold can be as low as 2.0 keV using the 200 keV dynamic range. The nonlinearity of the AISC is around 0.6% and it can be calibrated using the internal test pulse.

RTSD-07-03

Optimizing Array Configurations of Position-Sensitive Virtual Frisch-grid Detectors for Coded Aperture Telescopes (#3134)

Aleksey Bolotnikov[1], Piotr G. Maj[1], Erik Muller[2], Utpal Roy[3], Ralph B. James[3]

[1] Brookhaven National Laboratory, Upton, USA; [2] Stony Brook University, Stony Brook, USA; [3] Savannah River National Laboratory, Aiken, USA

Abstract

We report recent progress in the development of CdZnTe (CZT) and CdZnTeSe (CZTS) position-sensitive virtual Frisch-grid (VFG) gamma-ray detectors and detector arrays. The high 3D position sensitivity enabled by the VFG design allows correction of response non-uniformities caused by crystal defects. A key challenge in current large-volume CZT/CZTS detectors is the lateral displacement of charge carriers, which may exceed 1-2 mm over a >1 cm drift distance, strongly affecting the imaging capabilities of gamma cameras. These displacements are closely tied to crystal defects, such as dislocations and sub-grain boundaries, which are always present even in the highest-quality crystals. To address this issue, we propose using detectors with smaller-than-typical cross-sectional

areas (4×4 or 5×5 mm²), which match the size of the basic element in a coded-aperture imaging system. Improving position and energy resolution through the application of neural network algorithms is critical for the development of high-performance and reliable detector systems. We demonstrate that the neural network approach yields better results and requires significantly less calibration data because it handles the continuous distribution of events within the detector, whereas the conventional correction-matrix approach relies on discretized values resulting from detector segmentation. We present the results of testing these devices and discuss their advantages and shortcomings.

References
[1] Bolotnikov, AE, Camarda, GS, De Geronimo, G, Fried, F, James,RJ, 'A 4×4 array module of position-sensitive virtual Frisch-grid CdZnTe detectors for gamma-ray imaging spectrometers', Nuclear Instruments and Methods in Physics Research, A954, 2020, 161036.

RTSD-07-04

Measurement of the energy response function of a photon counting prototype detector using the HEX-27 beamline at the Brookhaven National Laboratory; A method to derive an empirical model of the detector non-ideal behavior and to improve material discrimination by spectrum deconvolution. (#2142)

Georgios Prekas[1], Brian Mercurio[1], Carl Bosch[1], Kurt Rogers[1], Zhong Zhong[2], Eric Johnson[1]

[1] SureScan Corporation, Binghamton, USA; [2] BrookHaven National Laboratory, Upton, USA

Abstract

Spectrum unfolding, or deconvolution, is a critical preprocessing step in X-ray image formation, particularly for spectral photon-counting detectors (PCDs). While an ideal detector records the full energy of an incident photon at a single pixel, realistic semiconductor detectors are governed by complex physical phenomena. Charge sharing, K-fluorescence escape, and pulse pile-up are the dominant factors that distort the recorded energy of the recorded signal. Thes first two effects are significantly exacerbated as pixel sizes decrease, leading to spectral degradation that compromises material discrimination and CNR, challenging the multi-energy imaging system.

This study presents a comprehensive characterization of the energy response function (ERF) for a PCD module developed by AMS-OSRAM, utilizing a CdZnTe (CZT) crystal with a native pixel pitch of 341 µm × 365 µm coupled to three ultra-low noise ASICs. The work was conducted at the HEX-27 (High Energy X-ray Scattering) beamline at Brookhaven National Laboratory. The detector was exposed to monochromatic X-ray beams from 30 keV to 140 keV at a flux of 9 Mcps/mm². The complete spectral response was mapped at high resolution, by sweeping the detector's five energy thresholds. The measurements enabled the derivation of an empirical model describing the ERF of the AS5920M/CZT module, accurately capturing inherent spectral features and tailing effects. To verify this empirical model, the derived response was convoluted with ideal spectra generated via SpekCalc. The resulting reconstructed distorted spectra matched well the measured detector output.

Finally, we propose a correction methodology applied to individual energy bins. By compensating for spectral

distortions, enhanced contrast-to-noise ratio (CNR) can be achieved, thereby significantly improving the accuracy of material separation.

References
[1] ams AS5920M Photon Counting Module X-Ray Sensors | ams OSRAM
[2] BNL | NSLS-II | Beamline 27-ID (HEX) High Energy Engineering X-ray Scattering | Schedule
[3] Schlomka, J. P., Roessl, E., Dorscheid, R., Dill, S., Martens, G., Istel, T., Bäumer, C., Herrmann, C., Grass, R., Proksa, R., & Martens, G. (2008). Experimental feasibility of multi-energy photon-counting K-edge imaging in pre-clinical computed tomography. *Physics in Medicine & Biology*, *53*(15), 4031–4047. https://doi.org/10.1088/0031-9155/53/15/002
[4] P. Zambon et.al, A fitting model of the pixel response to monochromatic X-rays in photon counting detectors, Nuclear Inst. and Methods in Physics Research, A 905 (2018) 188–192. https://doi.org/10.1016/j.nima.2018.07.069 .

RTSD-07-05

3D Integration and Interconnects for the Readout of Hybrid Pixel Detectors (#2576)

Francisco Piernas Diaz[1,2], Jerome A. Alozy[2], Mateus V. Barreto Pinto[3], Tea Bodova[2], Antonio Fernandez Prieto[1], Kostas Kloukinas[2], Mark I. Kovacs[2], Xavier Llopart Cudie[2], Carmelo Scarcella[2], Ken Wyllie[2], On behalf of the Medipix Collaboration and the EP R&D Work Package 5.

[1] Instituto Galego de Física de Altas Enerxías (IGFAE), Santiago de Compostela, Spain; [2] European Organization for Nuclear Research (CERN), Experimental Physics Department, Geneva, Switzerland; [3] University of Geneva, Geneva, Switzerland

This work was supported by the CERN EP R&D Work Package 5 and the Medipix Collaboration.

Abstract

Future hybrid pixel detectors for particle tracking and imaging require dense, low-inductance interconnections that can distribute clean power, sustain multi-gigabit data transmission, and minimize non-sensitive area. Conventional wire-bonding constrains input and output access to the die periphery, and results in long internal power routing as well as dead area which prevents close tiling of chips. This contribution presents a three-dimensional integration approach for the readout of hybrid pixel detectors based on Through-Silicon Vias (TSVs) fabricated after complementary metal-oxide-semiconductor processing. Timepix4 readout chips are used as a test vehicle. Vias are etched from the back side of thinned chips, insulated from the substrate, metallized, and connected to a back-side redistribution layer that routes power and signals to an array of bonding pads on which solder balls can be deposited. The resulting interconnects replace wire bonds and allow the chip to be soldered directly to a carrier printed circuit board. Several processed Timepix4 batches have been evaluated. A custom-designed test system allows measurement of interconnect quality for signal transmission and power delivery. TSV-processed chips have also been co-integrated together with silicon-photonics into module demonstrators. The tests demonstrate successful operation of Timepix4 after TSV processing, including 5 Gbit/s data transmission and stable power delivery through the back-side interconnect stack. The presentation will discuss the processing flow, test system

design choices, assembly and test results, and the suitability of solder ball-grid arrays and anisotropic conductive paste for permanent chip-to-board attachment.

References
[1] X. Llopart et al., "Timepix4, a large area pixel detector readout chip which can be tiled on 4 sides providing sub-200 ps timestamp binning", 2022 JINST 17 C01044 https://iopscience.iop.org/article/10.1088/1748-0221/17/01/C01044
[2] F. Laerme et al., "Bosch deep silicon etching: improving uniformity and etch rate for advanced MEMS applications", Technical Digest. IEEE Inter national MEMS 99 Conference. Twelfth IEEE International Conference on Micro Electro Mechanical Systems (Cat. No.99CH36291), Orlando, FL, USA, 1999, pp. 211-216, doi: 10.1109/MEMSYS.1999.746812. https://ieeexplore.ieee.org/document/746812
[3] J. Troska et al., "The VTRx+, an optical link module for data transmission at HL-LHC", 2018 PoS TWEPP-17 048 https://pos.sissa.it/313/048
[4] C. Scarcella et al., “Silicon Photonics Circuits for the optical readout of CERN detectors”, 2025 JINST 20 C02043 https://iopscience.iop.org/article/10.1088/1748-0221/20/02/C02043

RTSD-07-06

Carrier Dynamics and Polarization in GaAs:Cr Detectors Under High X-ray Flux (#2747)

Tao Zhong[1], Boren Wang[1], Yalong Yang[1], He Li[2], Juha Kalliopuska[3], Dmytro Nalyvaiko[3], Volodymyr Gnatyuk[3], Xiaochun Lai[1]

[1] ShanghaiTech University, School of Biomedical Engineering, Shanghai, China; [2] Shanghai United Imaging Healthcare Advanced Technology Research Institute Co.,Ltd., Shanghai, China; [3] Advafab OY, Helsinki, Finland

Supported by the Science and Technology Commission of Shanghai Municipality (24DIPA00700, 24440730100, 24QB2703900) and the Ministry of Industry and Information Technology (TC230H0AB/111). We acknowledge the ShanghaiTech Material and Device Lab.

Abstract

Gallium arsenide (GaAs) has broad application prospects as a material for photon counting detectors (PCDs). In this study, we investigate carrier dynamics and polarization in Cr-compensated GaAs (GaAs:Cr) via infrared transient current analysis and clinical X-ray temporal response experiments. The transient current results indicate that while massive carrier generation under high-intensity illumination can induce localized polarization, the deep energy levels introduced by Cr doping effectively preserve dynamic charge neutrality. By capturing and recombining excess carriers, this Cr-compensation successfully mitigates polarization effects, significantly improving detector signal stability up to an ultra-high clinical flux of 2.7 Gcps/mm^2.

References
[1] Hamann, E., et al. "Characterization of photon counting pixel detectors based on semi-insulating GaAs sensor material." *Journal of Physics: Conference Series*. Vol. 425. No. 6. 2013.
[2] Sun, G. C., et al. "Mobility-lifetime product in epitaxial GaAs X-ray detectors." *Nuclear Instruments and Methods in Physics Research Section A: Accelerators, Spectrometers, Detectors and Associated Equipment* 573.1-2 (2007): 228-231.
[3] Kolesnikova, Irina A., et al. "Optical pump–terahertz probe study of HR GaAs: Cr and SI GaAs: EL2 structures with long charge carrier lifetimes." *Photonics*. Vol. 8. No. 12. MDPI, 2021.
[4] Zambon, P. "Simulation of polarization dynamics in semi-insulating, Cr-compensated GaAs pixelated sensors under high x-ray fluxes." *AIP Advances* 11.7 (2021).

RTSD-07-07

Evaluation of Cr-Compensated GaAs Sensors with Different Thicknesses by Photon-Counting ReadoutElectronics (#2806)

Juha Kalliopuska[1], Dmytro Nalyvaiko[1], Volodymyr Gnatyuk[1], Noriyuki Masuda[1], Sami Vähänen[1], Eliska Soharova[2], Jan Jakubek[2], Pavel Spisek[2], Boren Wang[3], He Li[3], Tao Zhong[3], Xiaochun Lai[3]

[1] ADVAFAB, Helsinki, Finland; [2] ADVACAM, Prague, Czech Republic; [3] School of Biomedical Engineering, ShanghaiTech University, Shanghai, China

This research has received co-funding from the Business Finland under grant agreement 5700/31/2024 and from the Science and Technology Commission of Shanghai Municipality under grants 24QB2703900 and 24440730100.

Abstract

Advances in the fabrication of detector-grade GaAs semiconductors through chromium compensation have enabled the development of imaging sensors with high detection efficiency, energy resolution, high-flux tolerance, and enhanced radiation hardness, providing improved performance in the mid-energy X-ray range compared to conventional Si and Cd(Zn)Te sensors. Detection efficiency in semiconductor sensors strongly depends on sensor thickness, as the active detection volume scales directly with it. High absorption efficiency up to 80 keV is required in medical computed tomography (CT) and security imaging, which can be achieved using 2 mm thick GaAs sensors.

GaAs sensors with thicknesses from 0.3 mm to 2 mm manufactured by Advafab were developed, characterized, and evaluated with different photon-counting readout electronics. High-resistivity GaAs wafers were processed using Cr compensation, followed by lithography, metallization, dicing, and flip-chip bonding to various readout ASICs. The sensors were evaluated under X-ray irradiation to investigate detection efficiency, count-rate uniformity, charge transport, stability, and imaging performance. The 2 mm thick sensors demonstrated excellent image uniformity and operation at extreme X-ray fluxes up to 1100 Mcnt/s/mm2 with stability better than 2% over 30 s. Sidewall etching of diced GaAs improved sensor performance by reducing leakage current and enhancing electric field uniformity. The results highlight GaAs:Cr as an effective material for photon-counting X-ray imaging in medical, synchrotron, and industrial applications.

References

[1] B. D. Milbrath, A. J. Peurrung, M. Bliss, and W. J. Weber, “Radiation detector materials: An overview,” J. Mater. Res., vol. 23, no. 10, pp. 2561–2581, Oct. 2008, 10.1557/JMR.2008.0319.

[2] C. Michail, P. Liaparinos, N. Kalyvas, I. Kandarakis, G. Fountos, and I. Valais, “Radiation detectors and sensors in medical imaging,” Sensors, vol. 24, no 19, pp. 1–65, Sep. 2024, Art. no. 6251, 10.3390/s24196251.

[3] M. Fiederle, S. Procz, E. Hamann, A. Fauler, and C. Fröjdh, “Overview of GaAs and CdTe pixel detectors using Medipix electronics,” Cryst. Res. Technol., vol. 55, no. 9, pp. 1–6, Aug. 2020, Art. no. 2000021, 10.1002/crat.202000021.

[4] J. Becker, M. W. Tate, K. S. Shanks, H. T. Philipp, J. T. Weiss, P. Purohit, et al., “Characterization of chromium compensated GaAs as an X-ray sensor material for charge-integrating pixel array detectors,“ J. Instrum., vol. 13, no. 1, pp. 1–28, Jan. 2018, Art. no. P01007, 10.1088/1748-0221/13/01/P01007.

[5] J. Kalliopuska, D. Nalyvaiko, E. Hogenbirk, E. Maddox, J. Jakubek, J. Alozy, et al., “Chromium compensated gallium arsenide sensor evaluation using photon counting readout electronics,” in Book of Abstracts of The 26th International Workshop on Radiation Imaging Detectors (iWoRiD 2025), 2025, pp. 86–87, Bratislava, Slovakia.

[6] J. Kalliopuska, D. Nalyvaiko, V. Gnatyuk, S. Vähänen, J. Jakubek, J. Lange, et al., “Evaluation of different thicknesses of chromium compensated gallium arsenide sensors using photon counting readout electronics,” in Proc. 2025 IEEE NSS/MIC/RTSD, 2025, RTSD-10-02 (#1859), Yokohama, Japan. 10.1109/NSS/MIC/RTSD57106.2025.11287298.
[7] T. Poikela, J. Plosila, T. Westerlund, M. Campbell, M. De Gaspari, X. Llopart, et al., Timepix3: a 65K channel hybrid pixel readout chip with simultaneous ToA/ToT and sparse readout, J. Instrum., vol. 9, no 5, pp. 1–8, May 2014, Art. no. C05013, 10.1088/1748-0221/9/05/C05013.

Time:
11 November, 2026
17:30 – 19:00

Room:
ANDALUCÍA II & III

RTSD-08 | RTSD Medipix/Timepix Detectors

Chairs:
Amlan Datta (Natick)
Christer Frojdh

RTSD-08-01

The Timepix ASIC Family: Past, Present, and Future (#3005)

Rafael Ballabriga, Xavier Llopart Cudie, Michael Campbell, On behalf of the Medipix2, Medipix3 and Medipix4 Collaborations

CERN, Meyrin, Switzerland

Abstract

This summary reviews the evolution of the Timepix family of hybrid pixel detector readout ASICs, from Timepix in 2006 through to the recently released Timepix4 and the forthcoming Picopix demonstrator. The early versions had a regular matrix of 256x256 pixels. Each generation introduced an architectural innovation: per-pixel programmable Time-of-Arrival (ToA) or Time-over-Threshold (ToT) mode selection (Timepix, 250 nm MOS, 2006, Medipix2 Collaboration); data-driven triggerless readout with simultaneous time and energy measurement (ToA/ToT) and a 1.56 ns on-pixel TDC (Timepix3,130 nm CMOS, 2013, Medipix3 Collaboration); simultaneous ToA/ToT with logarithmic gain mode, improved energy resolution, and dead-time-free continuous read/write (Timepix2,130 nm CMOS, 2018, Medipix2 Collaboration); and 195 ps ToA binning over a four-side buttable 448x512 matrix using through-silicon via (TSV) technology (Timepix4, 65 nm CMOS, 2019, Medipix4 Collaboration). The forthcoming Picopix (28 nm CMOS, submission foreseen in 2026) targets ~35 ps ToA binning with on-pixel clustering, on-chip time calibration, and packet sorting. Key quantitative parameters—timing resolution, hit rate, active area, power consumption, and readout bandwidth—are compared across all five generations. Representative applications and the knowledge-transfer impact of the Medipix Collaborations model are discussed.

RTSD-08-02

Timepix4 based photon-counting detector for full-spectral X-ray micro computed tomography (#1355)

Paolo Cardarelli[1], Nicolò Vladi Biesuz[1], Francesco Brun[2,3], Viola Cavallini[1,5], Pasquale Delogu[6,7], Alessandro Feruglio[6,7], Massimiliano Fiorini[1,5], Renata Longo[2,4], Vittoria Mazzini[1,5], Piernicola Oliva[7,6], Valeria Rosso[7,6], Simone Velardita[1], Luca Brombal[2,3]

[1] INFN, Ferrara Division, Ferrara, Italy; [2] INFN, Trieste Division, Trieste, Italy; [3] Università di Trieste, Dipartimento di Ingegneria e Architettura, Trieste, Italy; [4] Università di Trieste, Dipartimento di Fisica, Trieste, Italy; [5] Università di Ferrara, Dipartimento di Fisica e Scienze della Terra, Ferrara, Italy; [6] Università di Pisa, Dipartimento di Fisica, Pisa, Italy; [7] INFN, Pisa Division, Pisa, Italy

This work was supported by the INFN-CSN5 experiment TIMEPIX4.

Abstract

Timepix4 is the latest generation of the readout ASIC developed by the Medipix4 Collaboration for hybrid pixel detector technology, featuring a 448 x 512 matrix with a 55 µm pitch. Operating in data-driven mode, it provides simultaneous Time of Arrival (ToA) and Time over Threshold (ToT) information for each hit. This allows for multi-pixel signal clustering to mitigate charge sharing and fluorescence escape, while calibrated ToT values provide per-pixel energy measurement. Such capabilities enable high-resolution X-ray spectral imaging, providing accurate energy deposition information for each detected event and greater post-processing flexibility compared to traditional threshold-based photon-counting systems. In this work, we present the first full-spectral micro-CT images acquired with a Timepix4-based detector operating in data-driven mode. The detector is equipped with a 1 mm-thick CdTe sensor, making it suitable for X-ray energies commonly used in biomedical applications. Tomographic scans were performed at the INFN PEPI laboratory using a microfocus X-ray tube (80 kV, 20 µA). The study evaluated a custom plastic phantom containing three distinct contrast agents: silver, iodine, and gadolinium. Projections were acquired over 360° with a reconstructed voxel size of 33 µm. The resulting 3D attenuation spectra were processed using a basis material decomposition algorithm, producing independent 3D density maps for each contrast agent. The results confirm the feasibility of full-spectral micro-CT imaging using the Timepix4 ASIC, demonstrating its ability to capture 3D attenuation spectra at high spatial resolution. While data rate management remains a challenge, the ability to resolve full attenuation spectra in 3D enables precise multi-material identification in a single scan. This capability offers significant potential for advanced applications in biomedical research and materials science.

References
[1] X. Llopart, J. Alozy, R. Ballabriga, M. Campbell, R. Casanova, V. Gromov, E. Heijne, T. Poikela, E. Santin, V. Sriskaran et al., “Timepix4, a large area pixel detector readout chip which can be tiled on 4 sides providing sub-200 ps timestamp binning,” Journal of Instrumentation, vol. 17, no. 01, p. C01044, 2022.
[2] V. Cavallini, N. V. Biesuz, R. Bolzonella, E. Calore, M. Fiorini, A. Gianoli, X. L. Cudie, and S. F. Schifano, “DataPix4: A C++ framework for Timepix4 onfiguration and read-out,” Comput. Phys. Commun., p. 109658, 2025
[3] L. Brombal, F. Arfelli, R. H. Menk, L. Rigon, and F. Brun, “PEPI lab: a flexible compact multi-modal setup for x-ray phase-contrast and spectral imaging,” Scientific Reports, vol. 13, no. 1, p. 4206, 2023.
[4] P. Delogu, N. V. Biesuz, R. Bolzonella, L. Brombal, V. Cavallini, F. Brun, P. Cardarelli, A. Feruglio, M. Fiorini, R. Longo, and V. Rosso, “Validation of Timepix4 Energy Calibration Procedures with Synchrotron X-ray Beams,” Nuclear Instruments and Methods in Physics Research A, vol. 1068, p. 169716, 2024.

RTSD-08-03

Machine learning pipeline for spectral material identification with a CdTe-Timepix3 detector (#1932)

Juan S. Useche Parra, Michael Schütz, Gerardo Roque, Simon Procz, Michael Fiederle

University of Freiburg, Freiburg Material Research Center, Freiburg, Germany

The authors acknowledge funding of DFG under the nanoCT-project (PR1897/1-1) and of BMFTR under PERODET (05K22VFA).

Abstract

X-ray imaging systems are widely used in industries such as homeland security, non-destructive testing, archaeological research, and medicine, where accurate material identification is often essential. Examples include explosives screening in airport luggage, product quality testing on a production line, and content characterization in historical manuscripts. Photon-counting detectors provide high spatial and energy resolution, along with full spectroscopic information on a per-event basis, and are therefore well suited for machine learning (ML) approaches to material identification. One example of such a detector is the Timepix3, which records single events at fluxes up to 40 Mhits/cm^2/s. Previous work, presented at this conference, demonstrated the feasibility of training an ML classifier (Gradient-Boosted Trees) on measured X-ray spectra acquired with a 12x1 Timepix3 (bump-bonded to 1 mm CdTe) detector and reported initial identification results on a multi-material phantom. This contribution extends that work, addressing two limitations of its results: the restricted size of the experimental material database and the lack of quantitative model diagnostics. The database is supplemented with simulated spectra (generated with the Allpix Squared framework) for materials that are difficult to obtain as pure reference samples, and the consistency between simulated and measured data is assessed. The extended database is then used to retrain the classifier, and standard ML diagnostics are reported to characterize model behavior. The performance of this approach will be compared to classical techniques such as base-material decomposition.

References
[1] Clouet, A. 2022, 'Digital X-ray Imaging Report' *YOLE Intelligence*
[2] Dudak, J et al. 2022, 'Multi bin energy-sensitive micro-CT using large area photon-counting detectors Timepix', J. Instrum., vol. 17, p. C01028
[3] Llopart Cudié, X 2007, 'Design and characterization of 64K pixels chips working in single photon processing mode', Ph.D. dissertation, Sundsvall, Sweden: Mid Sweden University.
[4] Poikela, T et al. 2014, 'Timepix3: a 65K channel hybrid pixel readout chip with simultaneous ToA/ToT and sparse readout', J. Instrum., vol. 9, p. C05013.
[5] Koenig, T et al. 2013, 'Charge summing in spectroscopic x-ray detectors with high-Z sensors', IEEE Trans. Nucl. Sci., vol. 60, no. 6, pp. 4713–4718.
[6] Žemlička, J et al. 2009, 'Energy- and position-sensitive pixel detector Timepix for X-ray fluorescence imaging', Nucl. Instrum. Methods Phys. Res. A, vol. 607, no. 1, pp. 202–204.
[7] Schütz, MK et al. 2024, 'Element identification by K-edge imaging using spectroscopic photon counting detectors', IEEE Trans. Nucl. Sci., vol. 71, no. 1, pp. 106–112.
[8] Spannagel, S et al. 2018, 'Allpix2: A modular simulation framework for silicon detectors', Nucl. Instrum. Methods Phys. Res. A, vol. 901, pp. 164–172.
[9] Ballabriga, R et al. 2024, 'A simulator for Timepix-like pixel front-ends', J. Instrum., vol. 19, no. 3, p. C03022.

RTSD-08-04

Full Scale Microstructural Imaging Based on Energy dispersive X-ray Diffraction using Timepix3/4 with CdTe Sensor (#2737)

Jan Jakubek[1], Roman Nebel[1], Jiri Volny[1], Daniel Vavrik[2]

[1] ADVACAM s.r.o., Prague, Czech Republic; [2] Institute of Theoretical and Applied Mechanics, Czech Academy of Sciences, Prague, Czech Republic

Abstract

This contribution extends the technique of the fast energy dispersive X-ray diffraction (XRD) in transmission mode for inspection of macroscopic objects, as described in our previous work [1], published recently by Nature Scientific Reports. This technique utilizes the event-based registration of diffracted X-ray photons with simultaneous timing

and energy information as provided by Timepix3/4 detectors. It enables rapid diffraction measurements with a polychromatic X-ray source, eliminating the need for mechanical angular scanning while preserving spatially resolved structural information.
Current XRD systems utilize relatively low-energy monochromatic X-ray beam (5-20 keV) which can only penetrate shallow layer close to the sample surface. Therefore, thick or dense parts cannot be analyzed through their entire volume using standard approaches. An alternative is the use of synchrotron sources, however, these are generally impractical for industrial applications.
A hard polychromatic X-ray source (X-ray tube) in combination with spectrally sensitive imaging detector such as Timepix3 or Timepix4 equipped with high-Z sensor (CdTe or CZT) overcomes above listed limits. This work focuses on optimizing detector performance by suppressing unwanted effects such as internal X-ray fluorescence and charge-sharing. Both of these effects degrade energy resolution, which directly impacts the quality of recorded XRD data. It will be demonstrated that an optimized detector, together with an event-sorting algorithm, can provide high-quality XRD data within a fraction of a second. Such speed enables 2D scanning across the entire volume of the inspected sample.
[1] Vavrik, D., Georgiev, V., Jakubek, J. *et al.* Transmission energy dispersive X-ray diffraction as a tool for the laboratory study of fast processes in metals. *Sci Rep***15**, 31752 (2025). https://doi.org/10.1038/s41598-025-16314-9

RTSD-08-05

Energy-resolved Grating-based Phase-contrast Imaging with Timepix4

(#2862)

Markus Schneider[1], Gisela Anton[1], Benedikt Bergmann[2], Petr Burian[2], Tomáš Čelko[2], Petr Mánek[2], Stanislav Pospíšil[2], Constantin Rauch[1], Martin Rongen[1], Petr Smolyanskiy[2], Stefan Funk[1]

[1] Friedrich-Alexander-Universität Erlangen-Nürnberg, Erlangen Centre for Astroparticle Physics, Erlangen, Germany; [2] Czech Technical University in Prague, Institute for Experimental and Applied Physics, Prague, Czech Republic

This work was supported by the Bavarian-Czech Academic Agency from funds of the Bavarian State Ministry of Science and the Arts, and by the Ministry of Education, Youth and Sports of the Czech Republic under Grant BTHA-JC-2024-80.

Abstract
Grating-based phase-contrast imaging (gbPCI) is a powerful tool for non-destructive testing and material analysis. In conventional X-ray imaging, only the attenuation of the X-rays is measured, resulting in low contrast between structures with similar absorption characteristics. With gbPCI, it is possible to not only get information about the absorption, but also the phase-shift of X-rays when propagating through material. For non-destructive testing and material analysis, the dark-field image provides complementary information, since it is sensitive to structures below the resolution limit of the system, which is primarily given by the pixel sizes of the detector. The pixel pitch is typically 50 µm or higher. With the dark-field image, it is possible to see porous or fibrous structures and estimate their sizes. A photon-counting and energy-resolving Timepix4 detector is used in this work. By setting energy cuts,

the sensitivity range can be maximized, allowing a more detailed structural analysis. Additionally, the quality of the imaging system can be improved by cutting unwanted energies. First test measurements with Timepix4 have shown the feasibility of phase-contrast imaging with this detector, by acquiring energy-resolved dark-field images of lycopodium spores and a piece of wood.

12 November, 2026

Time:
12 November, 2026
9:00 – 11:00

Room:
ANDALUCÍA II & III

RTSD-09 | RTSD CZT Detectors

Chairs:
Aleksey E. Bolotnikov (Upton)

RTSD-09-01

4π Visualization of Extended, Low-Level GammaEmission Sources Using a Rotating 3-D PositionSensitive CdZnTe Imager (#1204)

Amii O. Lamm, Peter G. Hotvedt, Zhong He

University of Michigan, Nuclear Engineering and Radiological Sciences, Ann Arbor, USA

The authors acknowledge H3D, Inc. for the loan of the M400 CdZnTe detector and Jim Berry for constructing the stepper-motor rotary table.

Abstract

Direct image reconstruction methods for Compton imaging such as Simple Back Projection (SBP) are widely used for their simplicity and robustness. Difficulties arise when imaging low-activity, non-point sources that span a significant portion of the detector's field of view (FOV). The detector's directional photopeak efficiency will heavily skew the collected data, and may result in a biased image that does not accurately visualize the extent and intensity of the whole object. This work proposes a SBP imaging algorithm with rotational corrections that smooth out the directional efficiency of the CdZnTe detector and generate a 4π FOV Compton image that accurately visualizes the distribution of an extended radioactive source. Experimental results demonstrate the ability to differentiate between naturally occurring radioactive material (NORM) such as Ra-226 and Th-232 found in the concrete masonry unit (CMU) walls and the lack of NORMs from the windows. This was achieved by placing the detector 6" away from a CMU wall and a floor-to-wall window of roughly the same size and rotating it continuously as it collected data. The resulting Compton image clearly showed regions of high and low intensity corresponding to the locations of the CMU wall and window, successfully mitigating the effects of directional efficiency. Further work will investigate source-to-detector distance dependence and field applications, with the goal of applying similar methods to environmental monitoring and surveying scenarios to visualize areas of elevated radiation levels and contamination.

RTSD-09-02

High-Energy Gamma Transmission Imaging with a 3D-CZT Detector Using Ring Localization (#1362)

Peter G. Hotvedt, Yuefeng Zhu, Matthew Granados, Zhong He

University of Michigan, Nuclear Engineering and Radiological Sciences, Ann Arbor, USA

This material is based upon work supported by the Defense Threat Reduction Agency (DTRA) under Contract No. HDTRA124C0002. Any opinions, findings and conclusions, or recommendations expressed in this material are those of the author(s) and do not necessarily reflect the views of DTRA.

Abstract

Transmission imaging requires a backing photon-sensing detector to accurately measure the interaction site and energy of each incident photon in future systems for material identification. 3D-CdZnTe detectors currently approximate the centroid of each electron cloud as the gamma interaction site with subpixel position sensing, but at high photon energies this measure may be biased by several millimeters from the true gamma interaction position, creating a noisy image. The ring localization technique constructs a ring of potential locations of the interaction site. The ring has its center at the measured centroid and has a radius equal to the average displacement between the interaction site and the centroid. Overlapping multiple rings on a per-event basis recovers this positional error. To demonstrate this recovery, a Th-228 source was placed behind a tungsten collimator with a 0.5-mm gap, which was aligned across a row of pixel electrodes to create centroid and ring images. Images were made using suspected Compton scattering events with a total event energy > 2 MeV. Two specific pixels were investigated in both images: one in the exposed region and one in the shielded region. The ring localization image shows an improved signal-to-noise ratio in both the exposed and shielded pixels compared to the centroid image. The pixels in the ring image also demonstrate a statistically significant difference between the average signal in the exposed and shielded regions. Subdividing the pixels reveals a count gradient on the investigated pixel, with the higher average signal in line with the collimator region. Future work will add more event types to get a better measure of the image resolution.

References

[1] Y. Zhu and Z. He, “Subpixel sensing for charge-sharing events in pixelated CdZnTe detectors,” vol. 69, no. 6, pp. 1385–1388.

[2] P. G. Hotvedt, Y. Zhu, and Z. He, “Improving the position resolution of high energy photon measurements in 3d-CZT using rings,” in 2025 IEEE Nuclear Science Symposium (NSS), Medical Imaging Conference (MIC) and Room Temperature Semiconductor Detector Conference (RTSD), pp. 1–1. ISSN: 2577-0829.

[3] G. De Geronimo, Y. Zhu, J. E. Berry, and Z. He, “Waveform-sampling front-end ASIC for 3-d position-sensitive detectors,” vol. 72, no. 3, pp. 925–935.

RTSD-09-03

A 128-Channel Mixed-Signal Readout ASIC for 3D Position-Sensitive CZT Detectors with Integrated ADC and TDC (#2014)

Zirui Yang[1], Hao Chang[1], Yan Huang[2], Xutao Zheng[1], Jiahuan Zhu[1], Yang Tian[1], Yulan Li[1], Feng Liu[2], Hua Feng[3], Wei Shen[2], Ming Zeng[1]

[1] Tsinghua University, Department of Engineering Physics, Beijing, China; [2] MicroParity Tech Inc., Hangzhou, China; [3] Chinese Academy of Sciences, Institute of High Energy Physics, Beijing, China

This work is supported by the Tsinghua University Initiative Scientific Research Program, the National Natural Science Foundation of China under grants Nos. 12025301 and 12103027, and the Tsinghua-Kunshan Student Innovation and Entrepreneurship Talent Cultivation Agreement.
The authors thank the technical staff at MicroParity for their support during the ASIC fabrication process.

Abstract

Three-dimensional position-sensitive Cadmium-Zinc-Telluride (3D-CZT) detectors are promising in astrophysics. However, the specific space environment and scientific observation requirements impose numerous challenges on the readout electronics, including achieving low noise, high timing precision, and high count rates, while balancing high integration with low power consumption. Thus, we propose MPT3128, a 128-channel mixed-signal application-specific integrated circuit (ASIC) for 3D-CZT detectors. Each channel integrates a low-noise charge-sensitive amplifier (CSA), fast and slow shapers, a 12-bit ADC (shared between two channels), and a time-to-digital converter (TDC) with a resolution of 312.5 ps. Specifically, for cathode timing, it features an adjustable fast-shaper peaking time and a triple-threshold timing scheme. Experimental results demonstrate that the analog front-end achieves low timing jitter (~2 ns even at 4.5 fC charge input), low electronic noise (202 e^- rms), and high energy resolution (5.7 keV FWHM at 511 keV), while featuring fully digital output and control interfaces, facilitating system integration. Furthermore, with all channels active, the triggering rate reaches 55 kHz per channel. The unit has a relatively low power consumption (6.34 mW/channel), making it a promising solution for advanced radiation applications.

References

[1] Kierans, C. et al, “Compton Telescopes for Gamma-Ray Astrophysics”, *Handbook of X-ray and Gamma-ray Astrophysics*, Springer Nature Singapore, pp. 1–72, 2022. doi:10.1007/978-981-16-4544-0_46-1.

[2] Lucchetta, G. et al, “Introducing the MeVCube concept: a CubeSat for MeV observations”, *Journal of Cosmology and Astroparticle Physics*, vol. 2022, IOP Publishing, 2022. doi:10.1088/1475-7516/2022/08/013.

[3] Zhu, J. et al, “MeV astrophysical spectroscopic surveyor (MASS): a compton telescope mission concept”, *Experimental Astronomy*, vol. 57, no. 1, Springer, pp. 2, 2024. doi:10.1007/s10686-024-09920-4.

[4] Shy, D. et al, “Development of the cadmium zinc TElluride Radiation Imager”, *Journal of Astronomical Telescopes, Instruments, and Systems*, vol. 10, no. 4, SPIE, pp. 044009–044009, 2024. doi:10.1117/1.JATIS.10.4.044009.

[5] Lehner, C. E. et al, “4π Compton Imaging Using a 3-D Position-Sensitive CdZnTe Detector Via Weighted List-Mode Maximum Likelihood”, *IEEE Transactions on Nuclear Science*, vol. 51, no. 4, IEEE, pp. 1618–1624, 2004. doi:10.1109/TNS.2004.832573.

[6] Valluvan, A. B. et al, “In-orbit Spectral Calibration Prospects for the COSI Space Telescope”, *IEEE Transactions on Nuclear Science*, IEEE, pp. 1–1, 2026. doi:10.1109/TNS.2026.3659066.

[7] Abbaszadeh, S. et al, “Characterization of a sub-assembly of 3D position sensitive cadmium zinc telluride detectors and electronics from a sub-millimeter resolution PET system”, *Physics in Medicine & Biology*, vol. 61, no. 18, IOP Publishing, pp. 6733, 2016. doi:10.1088/0031-9155/61/18/6733.

RTSD-09-04

X-ray direct detectors from solution-processed CdZnTe quantum dots

(#2395)

Marco Ruggieri[1], Muhammad Waqas[4,1], Mattia Scagliotti[2], Matteo Rapisarda[2], Antonio Valletta[2], Paolo Branchini[1], Luca Tortora[3], Andrea Fabbri[1]

[1] INFN, Roma Tre Section, Rome, Italy; [2] CNR, IMM, Rome, Italy; [3] Roma Tre University, Dep. of Sciences, Rome, Italy; [4] Padova University, Padova, Italy

Abstract

The growing role of solution-processable materials in novel, sensible radiation detectors has established materials like organic semiconductors and perovskites as promising alternatives to traditional ones. Solution-processable materials posses the unique characteristic to be semiconductors that can be processed in liquid form, and thus are extremely useful to develop thin, large-area and inexpensive devices. Quantum Dots have only recently started to draw attention as candidates for innovative, tunable detectors. These nanoparticles possess wide tunability possibilities, facile synthesis, ambient stability and are constituted often of High-Z elements such as Pb, Cd, Se etc. QDs' optoelectronic properties are strongly dependent on their size, which is tunable during synthesis. Within a size range for every QD material, it is then possible to select the best ones for each application. Recent results suggest that QD-based detectors have high X-ray sensitivity even with low-power operation, are radiation hard and retain their stability under ambient condition. However, a still unexplored and exciting question is if the best materials for direct radiation detection could still perform efficiently in QD form. A positive answer would mean a new, unprecedented way to fabricate such detectors, exploiting the advantages of solution-processable materials such as low-cost, large-area deposition, casting on flexible substrates etc. With this question in mind, and inspired by the excellent detection characteristics of CdZnTe detectors, in this work we synthesized CZT QD and employed them in drop-cast photodetectors. We assessed their X-ray detection capabilities in the 5-50 keV range with low-power biasing, observing a ready, repeatable response to the radiation. This result, albeit still early, seems to suggest a positive answer to our question, paving the way for the use of already established materials (CZT) in QD form for the development of new, advanced direct detectors.

References

[1] M. Helal Miah, M. Uddin Khandaker, M. A. Islam, M. Nur-E-Alam, H. Osman, e M. Habib Ullah, «Perovskite materials in X-ray detection and imaging: recent progress, challenges, and future prospects», *RSC Adv.*, vol. 14, fasc. 10, pp. 6656–6698, 2024, doi: 10.1039/D4RA00433G.

[2] A. L. Efros e L. E. Brus, «Nanocrystal Quantum Dots: From Discovery to Modern Development», *ACS Nano*, vol. 15, fasc. 4, pp. 6192–6210, apr. 2021, doi: 10.1021/acsnano.1c01399.

[3] C.-M. Zhang, R. Quaglia, A. Shulga, V. Goossens, P. B. Cruz, e P.-F. Rüedi, «A Quantum-Dot-Coated Image Sensor With a Wide-Spectral Sensitivity From X-rays to SWIR Photons», *IEEE Sens. Lett.*, vol. 8, fasc. 8, pp. 1–4, ago. 2024, doi: 10.1109/LSENS.2024.3428608.

[4] M. Ruggieri *et al.*, «Low-Voltage and Highly Sensitive PbS Quantum Dot Thin-Film X-ray Monitors», *ACS Appl. Electron. Mater.*, vol. 5, fasc. 10, pp. 5642–5650, ott. 2023, doi: 10.1021/acsaelm.3c00986.

[5] G. N. Ankah *et al.*, «PbS quantum dot based hybrid-organic photodetectors for X-ray sensing», *Org. Electron.*, vol. 33, pp. 201–206, giu. 2016, doi: 10.1016/j.orgel.2016.03.023.

[6] B. J. Davis e M. D. Hammig, «PbSe Quantum Dots for X-ray and γ-Ray Sensors», *ACS Appl. Nano Mater.*, vol. 4, fasc. 7, pp. 6936–6946, lug. 2021, doi: 10.1021/acsanm.1c00942.

[7] M. Ruggieri *et al.*, «Electrohydrodynamic Jet-Printed X-ray Sensor Based on Iodide-Exchanged Lead(II) Sulfide Quantum Dots», *ACS Appl. Electron. Mater.*, vol. 7, fasc. 12, pp. 5549–5558, giu. 2025, doi: 10.1021/acsaelm.5c00527.

[8] M. D. Alam, S. S. Nasim, e S. Hasan, «Recent progress in CdZnTe based room temperature detectors for nuclear radiation monitoring», *Prog. Nucl. Energy*, vol. 140, p. 103918, ott. 2021, doi: 10.1016/j.pnucene.2021.103918.

[9] J. Cheng, D. Li, T. Cheng, B. Ren, G. Wang, e J. Li, «Aqueous synthesis of high-fluorescence CdZnTe alloyed quantum dots», *J. Alloys Compd.*, vol. 589, pp. 539–544, mar. 2014, doi: 10.1016/j.jallcom.2013.11.207.

RTSD-09-05

High-Flux Performance of a Photon-Counting Detector for Spectral CT Based on the ColorCT ASIC (#1491)

Andrea Brambilla, Arnaud Peizerat, Kim Abdoul-Carime, Adrien Poizat, Jonathan Jonsson, Daniel Tran, Loick Verger

Univ. Grenoble Alpes, CEA-Leti, DOPT, Grenoble, France

CEA-Leti is a member of the Carnot institute network. This work was supported by the French ANR via Carnot institute funding.

Abstract

ColorCT is a novel readout ASIC for energy-resolved photon-counting detectors (ER-PCDs) dedicated to spectral X-ray computed tomography (CT). It is designed to sustain very high photon fluxes while preserving spectral performance under strict power consumption constraints. The ColorCT test chip features an 11 × 11 pixel matrix (330 µm pitch) and 8 energy bins. A fast analog front-end delivers short pulses (13 ns peaking time, 24 ns FWHM), enabling high count rate capability. A Digital Reset circuit mitigates pile-up and prevents detector paralysis, ensuring a monotonic increasing behavior of the count rate with the X-ray flux with a saturation value of 30 Mcps. A digital charge sharing correction (CSC) improves the spectral accuracy. The ASIC was coupled to a CdTe crystal to perform X-ray characterizations. Experimental results demonstrate improved count rate and spectral response obtained with the Digital Reset and the CSC, with a power consumption of 3 mW/mm² at 3 10^7 cps/px (3 10^8 cps/mm²).

RTSD-09-06

A CZT Readout ASIC for Double-Layer Compton Imaging Applications (#2191)

Will B. Wright[1], Tarun Prakash[1], Carl Grace[1], Marcos Turqueti[1], Javier Caravaca[2,3]

[1] Lawrence Berkeley National Laboratory, Engineering Division, Berkeley, USA; [2] Lawrence Berkeley National Laboratory, Nuclear Science Division, Berkeley, USA; [3] University of California San Francisco, Department of Radiology & Biomedical Imaging, San Francisco, USA

This work is supported by the National Institutes of Health (NIH) and the Department of Energy (DOE).

Abstract

CZT Compton cameras have demonstrated great promise for nuclear medicine. We are designing a dual layer CZT Compton camera to enhance angular resolution with respect to current single-layer cameras. An application specific integrated circuit (ASIC) that provide excellent 3D position, energy resolution and high data throughout is required for this. A multi-channel ASIC is presented in this work to overcome these challenges. It is composed of 16 anode readout channels, plus a cathode channel, that each contain a charge sensitive amplifier (CSA), pulse shaper, programmable gain amplifier (PGA), peak detector, and configurable peak detector reset dissipating 12 mW per channel to support low-noise and high dynamic range. The channels are designed for a target energy of 218keV & 440keV used in ^{225} Ac Compton imaging, with a worst-case 0.81% non-linearity over the dynamic range of 30 keV to 2.2 MeV. Each channel can handle up to 2 nA of leakage current without performance degradation and yields 1.33% FWHM at 662 keV with a single-pixel capacitance of 29.1 pF for each (1.225 mm)x(1.225 mm) pixel. The rise time of each CSA is 150 ns while the shaper peaking time is 320 ns to enable fast readout with a configurable gain of 7, 13, 45, 81, and 132 mV/fC from the PGA. This work demonstrates a compact, scalable readout platform for CZT-based Compton imagers and other room-temperature semiconductor detector systems requiring high energy resolution.

References

[1] J. Caravaca, Y. Huh, G. T. Gullberg and Y. Seo, "Compton and Proximity Imaging of Ac In Vivo With a CZT Gamma Camera: A Proof of Principle With Simulations", in IEEE Transactions on Radiation and Plasma Medical Sciences, vol. 6, no. 8, pp. 904-915, Nov. 2022

[2] G. Song, B. Das, Y. Seo, G. Cho and J. Caravaca, “Performance Evaluation of Single- and Double-Layer CZT Compton Cameras for 225Ac Imaging,” in IEEE Transactions on Nuclear Science, vol. 73, no. 4, pp. 1481-1494, April 2026

[3] G. De Geronimo, P. O'Connor and J. Grosholz, "A generation of CMOS readout ASICs for CZT detectors," *IEEE Nuclear Science Symposium*, 1999

[4] Emerson Vernon, Gianluigi De Geronimo, et al., "Front-end ASIC for spectroscopic readout of virtual Frisch-grid CZT bar sensors," Nuclear Instruments and Methods in Physics Research Section A: Accelerators, Spectrometers, Detectors and Associated Equipment, Volume 940, 2019, Pages 1-11, ISSN 0168-9002

RTSD-09-07

Performance evaluation of CZTS grown with higher purity CdSe starting material (#2698)

Utpal N. Roy, Joshua Kleppinger, Ralph B. James

Savannah River National Laboratory, ELM, Aiken, USA

The authors acknowledge support from the U.S. Department of Energy, Office of Defense Nuclear Nonproliferation Research and Development (DNN R&D).

Abstract

CdZnTe (CZT) has been the most commercially successful semiconductor material for room-temperature X-ray and gamma-ray radiation detector applications. It is considered as the gold standard for detector applications that

require spectral and often spatial information in a compact instrument. However, CZT still contains a high density of performance-limiting defects such as high concentrations of sub-grain boundary networks, Te inclusions and compositional inhomogeneity in as-grown ingots. Adding a small amount of selenium (Se) in the CZT matrix was found to successfully mitigate the performance-limiting defects and provide for better compositional homogeneity. Thus, the new quaternary $Cd_xZn_{1-x}Te_ySe_{1-y}$ (CZTS) is emerging as a next-generation compound semiconductor, potentially surpassing the material quality of CZT. However, the purity of CZTS material is not on par with commercial CZT, principally due to the lack of availability of commercial high-purity CdSe. The presence of the impurities in CZTS caused by the lower-purity CdSe starting material was found to impose a detrimental effect on the charge transport properties of CZTS, resulting in adverse effects on the charge collection and detector performance. Here, we report for the first time on the growth and characterization of $Cd_{0.9}Zn_{0.1}Te_{0.98}Se_{0.02}$ grown by vertical Bridgman and by the traveling heater method (THM) using higher-purity CdSe starting material.

RTSD-09-08

Merit-Function-Guided Porosity Control in Directional Solidification of CZT (#2985)

Aimen E. Gheribi[1], Khedija Younsi[1], Nikolay Chorbadzhiev[1], Elhadi Hammoutene[1], Frederic Belanger[1]

[1] 5Nplus, R&D, Montreal, Canada; [2] 5Nplus, R&D, Montreal, Canada

Abstract

Directional solidification (DSM) enables rapid growth of cadmium zinc telluride (CZT) ingots with superior scalability and geometric flexibility compared to the travelling heater method (THM). However, the strongly non-equilibrium conditions inherent to DSM promote gas bubble nucleation, growth, transport, and coalescence, leading to porosity that degrades detector performance. Bubble-induced defects distort internal electric fields, enhance charge trapping, reduce the carrier mobility–lifetime product ($\mu\tau$), and increase leakage current and electronic noise through impurity segregation and secondary phase formation. In contrast, THM operates closer to thermodynamic equilibrium and therefore minimizes such defects, albeit at reduced growth rate and scalability.

DSM-grown CZT typically exhibits axial heterogeneity, with increasing bubble density and size toward the last-to-solidify region. This results from coupled interactions between volatile-species thermodynamics, buoyancy-driven transport, capillarity, coalescence, and solidification kinetics. Bubble coalescence and accumulation in the upper melt region significantly amplify porosity near the end of solidification, producing larger pores that are more easily entrapped and more detrimental to detector uniformity.

To describe these mechanisms, a physics-based dimensionless framework is introduced using transport, thermodynamic, and interfacial scaling parameters, including an escape number comparing bubble migration and interface growth velocities, as well as Bond and Capillary numbers governing deformation and stability. Within an atomistic-informed thermophysical model at 5N Plus, temperature- and composition-dependent properties are used to evaluate these parameters and define a predictive merit function for DSM optimization. This framework identifies

conditions that promote bubble escape, suppress coalescence and entrapment, and reduce porosity while preserving the advantages of rapid CZT crystal growth.

Time:
12 November, 2026
11:30 – 13:00

Room:
ANDALUCÍA II & III

RTSD-10 | RTSD Awards and Closing

Chairs:
Michael Fiederle (Freiburg)
Gerard Arino-Estrada (Barcelona)

RTSD-10-01

Energy-Resolved Effective Focal-Spot Characterization of a CdTe-Timepix3 Nanofocus XCT System Using Orthogonal Slanted-Edge Measurements (#1354)

Gerardo A. Roque, Michael K. Schütz, Juan S. Useche, Simon Procz, Michael Fiederle

Albert-Ludwigs-Universität Freiburg, FMF, Freiburg, Germany

Abstract

Spatial resolution in high-magnification X-ray imaging is limited by the detector's pixel aperture and the X-ray source focal spot size. The latter caps the achievable geometric magnification, and depends on photon energy, observation direction, and sample X-ray attenuation. This work presents an energy-resolved characterization of the effective focal spot size of the Freiburg Materials Research Center nanofocus X-ray imaging system, that combines the Hamamatsu L10711-03 Tungsten-anode nanofocus X-ray tube with a 12 × 1 Timepix3 spectroscopic photon-counting detector (PCD) array equipped with 1 mm thick Cadmium Telluride (CdTe) sensors. A single high-absorbing Steel slanted edge is used to implement the double-distance edge-response method, applied in horizontal and vertical orientations to measure the focal spot size in both principal directions. For energy bins from 15 keV to 50 keV, an in-contact edge image captures detector-generated blur, while a magnified edge image embeds both detector blur and source penumbra. After energy calibration, flat-field correction, and event declustering, edge-spread functions are oversampled, differentiated to obtain line-spread functions (LSF), and Fourier-transformed to obtain energy-resolved Optical Transfer Functions, OTF(E). The per-bin ratio of the mixed and contact OTF removes the detector contribution to image blur and yields a source-plane OTF and LSF, from which the effective focal spot size is extracted. Preliminary analysis suggests measurable variation in the recovered source-plane profiles across energy windows and between horizontal and vertical orientations, indicating that the effective focal spot cannot be treated as energy-independent. The study relies on a practical method for source characterization in spectroscopic photon-counting X-ray systems, to achieve a thorough resolution characterization of the nanofocus imaging system.

References

[1] A. A. Harms, et al 1977, 'A New Formulation of Total Unsharpness in Radiography', *Phys. Med. Biol.*, 22(1), pp. 70-80

[2] G. Roque, et al 2025, 'Spectrally-Resolved Modulation Transfer Function and Effective Focal-Spot Characterization of a CdTe-Timepix3 Nanofocus XCT System', *Proceedings of IEEE NSS/MIC/RTSD*

[3] M. Nishiki, et al 2020, 'Measurement of the x-ray effective focal spot size with edge response analysis using digital detectors', *J. Med. Imag.*, 7(2), pp. 023502

[4] M. Schütz, et al 2025, 'Voxel-wise Element Identification in Spectroscopic PCCT with Cadmium-Telluride Timepix3 Detectors', *Proceedings of IEEE NSS/MIC/RTSD*

[5] G. Roque, et al 2024, 'A CdTe Timepix3-based Sub-micron XCT System for Non-Destructive Testing', *Proceedings of IEEE NSS/MIC/RTSD*

[6] T. Poikela, et al 2014, 'Timepix3: a 65K channel hybrid pixel readout chip with simultaneous ToA/ToT and sparse readout', *J.Inst.*, 9(5), pp. C05013

[7] M. Schütz, et al 2025, 'Optimized data acquisition for spectroscopic CT with Timepix3: combining photon-counting and data-driven readout modes with adaptive pixel masking', *J. Inst.*, 20, pp. P10045

[8] M. Schütz, et al 2020, 'Element discrimination via spectroscopic X-ray imaging with a CdTe Medipix3RX detector', *J. Inst.*, 15, pp. P01006

[9] G. Roque, et al 2022, 'Sub-pixel energy-weighting techniques for metallic contaminant highlighting in a pharmaceutical hard capsule using a Timepix3 CdZnTe hybrid pixel detector', *J. Inst.* 17, pp. P10030

RTSD-10-02

Digital Signal Processing of Large-Volume, Pixelated $CsPbBr_3$ for Gamma-ray Spectroscopy (#1601)

Michael Streicher[1], Matthew Petryk[1], Josh Palmer[2], Indra Pandey[2], Sara Abraham[1], Ryan Parsons[1]

[1] H3D, Inc., Ann Arbor, USA; [2] Actinia, Inc., Evanston, USA

This material is based upon work supported by the Defense Threat Reduction Agency under Contract No. HDTRA225CE001. Any opinions, findings and conclusions or recommendations expressed in this material are those of the author(s) and do not necessarily reflect the views of the Defense Threat Reduction Agency.

Abstract

Over the course of the past decade, $CsPbBr_3$ has emerged as perhaps the most promising alterative room temperature semiconductor material for gamma-ray spectroscopy. $CsPbBr_3$ has been shown to be grown quickly, and relatively inexpensively, while being surprisingly defect tolerant. Fifteen 1-cm-thick $CsPbBr_3$ samples, attached to printed circuit boards with a low-temperature melting alloy, were evaluated over the course of this project. A custom evaluation system containing COTS preamplifiers and oscilloscopes was used to correct these samples for depth-of-interaction effects. While yields were initially fairly poor, the best sample achieved better than 1.5% FWHM energy resolution at 662 keV for the entire 0.25 cm^3 volume. Eight of the nine pixels in the device achieved energy resolution better and 1.5% FWHM at 662 keV. The device exhibited predicable conditioning effects. The device has been operating for several months, albeit not at continuous bias. The failing samples tended to have attachment issues; either the attachment failed and the $CsPbBr_3$ disconnected from the carrier board or all pixels exhibited poor performance and instability which could also be due to issues with the device attachment to the substrate. At the time of the conference, the authors expect to have preliminary results of a $CsPbBr_3$ gamma-ray spectrometer with volume greater than 1 cm^3 read out with pulse-waveform sampling preamplifiers integrated into an Application Specific Integrated Circuit (ASIC).

References

[1] Y. He et. al., "High spectral resolution of gamma-rays at room temperature by perovskite $CsPbBr_3$ single crystals", Nature Comm. Apr 23 2018.

[2] D. Liu et. al. "High-performance $CsPbBr_3$ perovskite single crystals for gamma-ray detection." Adv. Photon Nexus. May 2026.

RTSD-10-03

A spectroscopic CdZnTe/CMOS hybrid linear array detection system based on wedge-bondable HDI interposer (#2346)

Filippo Mele[1,2], Jacopo Quercia[1], Yinhe Zhu[1], Leonardo Abbene[3], Manuele Bettelli[4], Toby Brookes[5], Antonino Buttacavoli[3], Navid Ghorbanian[5], Fabio Principato[3], Matthew C. Veale[5], Andrea Zappettini[4], Giuseppe Bertuccio[1,2]

[1] Politecnico di Milano, Department of Electronics, Infomration and Bioengineering, Milano, Italy; [2] Istituto Nazionale di Fisica Nucleare (INFN), Sezione di Milano, Milano, Italy; [3] University of Palermo, Department of Physics and Chemistry (DiFC), Palermo, Italy; [4] Istituto Materiali per l'Elettronica e il Magnetismo (IMEM), Parma, Italy; [5] UKRI STFC Rutherford Appleton Laboratory, Didcot, UK

This work was supported by the Italian Ministry for University and Research (MUR), under PRIN2022 PNRR (P2022SE49Y, 2022ZEF2RE) projects, and the UKRI STFC Centre for Instrumentation SMART Managed Programme 24 - 26.

Abstract

In this work, we present a CdZnTe/CMOS spectroscopic linear-array detection system enabled by a wedge-bondable High Density Interconnect (HDI) interposer that allows bump-bonding on the detector side and wedge-bonding toward the readout electronics, significantly simplifying the interconnection constraints between the two elements [1],[2],[3]. The interposer layout is optimized to suppress inter-channel parasitics, yielding measured pixel-to-pixel and pixel-to-guard capacitances of 10.2 fF and 25.7 fF, respectively. Two custom 8-pixel CdZnTe detectors (500 µm pitch, 25 µm gap with 1 mm and 2 mm thickness respectively) were integrated with an 8-channel ultra-low-noise SIRIO charge-sensitive amplifier [4],[5] and characterized at room temperature. After integration, spectroscopic characterization was performed with 55Fe, 241Am, and 57Co radioactive calibration sources, demonstrating the capability of the system to cover a wide energy range (5–150 keV). Using a 50 ns peaking time on an external digital pulse processor, an average FWHM of 744 eV (Detector 1) and 850 eV (Detector 2) was measured on the pulser line, recording an optimum energy resolution of 1.4% at 122 keV, and paving the way for additional studies on larger detector arrays in high-flux spectroscopy applications.

References

[1] Schneider, A. et al., 2015, "Interconnect and bonding techniques for pixelated x-ray and gamma-ray detectors," *JINST*, vol. 10, no. 02, pp. C02 010–C02 010.

[2] Veale, M.C. et al., 2018, "Hexitec: A high-energy x-ray spectroscopic imaging detector for synchrotron applications," *Synchrotron Radiation News*, vol. 31, no. 6, pp. 28–32.

[3] Veale, M.C. et al., 2022, "Characterisation of the hexitec4s x-ray spectroscopic imaging detector incorporating through-silicon via (tsv) technology," *NIMA*, vol. 1025, p. 166083.

[4] Mele, F. et al., 2023, "Advances in high-energy-resolution cdznte linear array pixel detectors with fast and low noise readout electronics," *MDPI Sensors*, vol. 23, no. 4, p. 2167.

[5] Mele, F. et al., 2021, "Sirio: A high-speed cmos charge-sensitive amplifier for high-energy-resolution x-γ ray spectroscopy with semiconductor detectors," *IEEE TNS*, vol. 68, no. 3, pp. 379–383.

RTSD-10-04

Stabilizing the Detector Response of $CsPbBr_3$ Gamma-Ray Detectors

(#2010)

Matthew Petryk[1], Michael Streicher[1], Ryan Parsons[1], Sara Abraham[1], Josh Palmer[2], Indra Pandey[2]

[1] H3D, Inc., Ann Arbor, USA; [2] Actinia Detectors, Inc., Evanston, USA

This material is based upon work supported by the Defense Threat Reduction Agency under Contract No. HDTRA225CE001. Any opinions, findings and conclusions or recommendations expressed in this material are those of the author(s) and do not necessarily reflect the views of the Defense Threat Reduction Agency.

Abstract

With greater photopeak efficiency and lower temperature growth processes, $CsPbBr_3$ is a promising alternative to CdZnTe (CZT) for room temperature semiconductor-based gamma-ray detectors. H3D, Inc. has characterized the stability of both single-pixel and pixelated 10mm thick $CsPbBr_3$ gamma-ray detectors. The best pixelated devices show a pattern of conditioning, whereby the device response stabilizes after 60 hours of bias. The best resolution obtained is 1% at 662 keV on a by-pixel basis, and 1.5% overall. The most stable detectors show clear photopeaks from ^{137}Cs during over 1200 hours of continuous operation. Though the stability is improved by contact engineering, surface polishing, and encapsulation, there is still significant drift in the peak over time. This drift causes the resolution to deteriorate over time and invalidates earlier calibrations. H3D has developed an algorithm to stabilize the response of these $CsPbBr_3$ detectors further by utilizing the known relationships between photopeaks and escape peaks. The algorithm operates on a per-measurement basis, requiring no knowledge of what isotope is being measured nor the past history of the device. This enables it to be applied in the field to arbitrary measurements, without requiring a convenient check source for pre-measurement calibration.

This material is based upon work supported by the Defense Threat Reduction Agency under Contract No. HDTRA225CE001. Any opinions, findings and conclusions or recommendations expressed in this material are those of the author(s) and do not necessarily reflect the views of the Defense Threat Reduction Agency.

References

[1] He, Y. et. al. 2018, 'High spectral resolution of gamma-rays at room temperature by perovskite $CsPbBr_3$ single crystals', Nature Comm. 9, 1609

[2] Kang J. et. al. 2017, 'High Defect Tolerance in Lead Halide Perovskite $CsPbBr_3$', J Phys Cehm Lett. 8(2):489-493

[3] Pan, L. et. al. 2025, 'Ion Migration Enhances the Performance of Perovskite $CsPbBr_3$ y-Ray Detectors', Adv. Mater. Technol. 10, 2401548

RTSD-10-05

Neutron Irradiation Effects in β-Ga_2O_3 Radiation Detector Materials Investigated by Raman and Positron Annihilation Spectroscopy (#2161)

Shams Noor, Ming Liu, Austin Wells, Ge Yang

NCSU, Nuclear Engineering, Raleigh, USA

This work was supported by the U.S. Department of Energy (DOE) Office of Nuclear Energy under its Nuclear Energy University Program (NEUP) (Award No: DE-NE0009192) and under DOE Idaho Operations Office Contract DE-AC07- 051D14517 as part of a Nuclear Science User Facilities experiment (Award No: 21-24020). The authors also thank Colby Fleming for her assistance in irradiation experiments.

Abstract

Gallium oxide (Ga_2O_3) is an emerging material for next-generation nuclear sensors due to its ultra-wide bandgap, high thermal stability, and large critical breakdown field. However, its radiation tolerance and defect evolution mechanisms in reactor environments remain insufficiently understood, limiting predictive assessment of long-term device reliability and performance. In this work, we systematically investigate the effects of neutron irradiation with simultaneous thermal annealing on β-Ga_2O_3 using positron annihilation lifetime spectroscopy (PALS), Raman spectroscopy, and polarized optical microscopy to probe irradiation-induced changes across atomic, defect, and microstructural length scales, providing complementary insight into defect formation, evolution, and recovery mechanisms under neutron exposure.

Monoclinic β-Ga_2O_3 samples were irradiated in the North Carolina State University PULSTAR reactor at room temperature (RT) and 700 °C. Microstructural characterization and PALS confirmed vacancy-type defects in the RT irradiated samples, while their absence at high temperature suggests thermally activated point defect suppression through increased atomic mobility. Raman spectroscopy revealed irradiation-induced microtilting in both cases, whereas the absence of Raman modes associated with gallium-clusters and oxygen-vacancy indicates overall defect concentrations remained low though detectable by the highly sensitive PALS technique. Together, these results show β-Ga_2O_3 is a promising material for nuclear sensing while unveiling key insights into its behavior under irradiation.

References

[1] Higashiwaki, M, et al. 2016, 'Recent progress in Ga_2O_3 power devices', Semiconductor Science and Technology, vol. 31, no. 3, Art. no. 034001, Bristol: IOP Publishing, doi: 10.1088/0268-1242/31/3/034001.

[2] Angeloni, LA, Shan, I-J, Leach, JH & Schroeder, WA 2024, 'Iron dopant energy levels in β-Ga_2O_3', Applied Physics Letters, vol. 124, no. 25, Art. no. 252104, Melville, NY: AIP Publishing, doi: 10.1063/5.0213263.

[3] Kranert, C, Sturm, C, Schmidt-Grund, R & Grundmann, M 2016, 'Raman tensor elements of β-Ga_2O_3', Scientific Reports, vol. 6, Art. no. 35964, London: Nature Publishing Group, doi: 10.1038/srep35964.

[4] Singh, AK, Krishnamoorthy, S, Xia, Z, Rajan, S & Ramanathan, S 2023, 'Optical characterization of β-Ga_2O_3 using spectroscopic ellipsometry and Raman spectroscopy', Applied Optics, vol. 62, no. 15, pp. 3848–3855, Washington, DC: Optica Publishing Group, doi: 10.1364/AO.485308.

[5] Huso, J, Dutton, B, Remple, C, McCluskey, MD, McCloy, JS, Bhattacharyya, A, Krishnamoorthy, S, Rebollo, S, Speck, JS, Varley, JB & Voss, LF 2025, 'Evidence for Ga clusters in β-Ga_2O_3 from Raman spectroscopy and density functional theory', Applied Physics Letters, Melville, NY: AIP Publishing, doi: 10.1063/5.0292434.

Awards and closing remarks

Michael Fiederle

Uni Freiburg, Freiburg, Germany

Special Events

11 November, 2026

Time:
11 November, 2026
11:30 – 13:00

Room:
Seminar Room 3/4

TS-02 | Technical Sessions 2

TS-02-01

ROIC/ASICs for Radiation Detection and Imaging (#3349)

Dirk Meier

Integrated Detector Electronics AS - IDEAS, Oslo, Norway

Abstract
IDEAS has a long heritage in designing detector readout integrated circuits (ROICs) and electronic systems for scientific applications. You can use our VATA and IDE-type chips for reading out your high-channel-count detectors, e.g., strips or pixels on silicon, CZT, or scintillators with PMTs or SiPMs. For space applications, and with flight heritage, our radiation-hardened ASICs enable compact, low-power detectors. Building on this foundation, IDEAS is contributing to next-generation instruments and missions: Space radiation monitors deliver real-time dosimetry and particle spectra (NORM, and Galileo RMU). CZT-based systems (SRE4001, GDS-100) deliver high-resolution gamma spectroscopy and x-ray imaging in a modular form. Our new designs of ADC- and infrared controller ASICs (NIRCA) help minimizing infrared imaging systems and cameras. In my presentation I will focus on the ASICs and ROICs that we can supply and our new developments.

TS-02-02

Toward Information-Efficient Photon Detection: CMOS SiPMs and Multi-Threshold Readout ASICs (#3352)

Hui Lao, Guanning Su

RAYQUANT Technology Co., Ltd., Ezhou, China

Abstract
Detecting photons is only the beginning. How can we preserve and make better use of the information they carry? At Rayquant, we develop both CMOS silicon photomultipliers (SiPMs) and multi-voltage-threshold (MVT) readout ASICs, linking photon detection with timing readout. This presentation highlights our latest SiPM devices, measured photon detection and timing performance, and timing results from our MVT ASIC and SiPM–MVT experiments. We will also share applications of our SiPMs in PET imaging and radiation detection.
Beyond existing products, we will explore how detector-specific requirements can shape new SiPM and readout ASIC development, turning real detection challenges into working silicon.

TS-02-03

From Semiconductor Sensors to Hybrid Pixel Detectors: Advafab's Fabrication and Integration Capabilities (#3301)

Ben Panesar, **Juha Kalliopuska**, Sami Vahanen

ADVAFAB, Helsinki, Finland

Abstract
Advanced radiation imaging requires sensor materials, electrode structures and interconnection processes tailored to the application and readout electronics. This presentation introduces Advafab's sensor fabrication and hybrid integration capabilities, with a focus on silicon and compound semiconductor sensors, including GaAs and Cd(Zn)Te, for scientific, medical and industrial imaging.
We present the manufacturing route from sensor design and electrode processing to under-bump metallisation, wafer-level solder bumping, precision dicing and flip-chip bonding to readout ASICs. Particular attention is given to material-dependent processing requirements, compatibility between sensor contacts and interconnects, and electrical characterisation supporting detector quality.
The presentation also outlines Advafab's development of compound semiconductor foundry capabilities and opportunities for customer-specific sensor fabrication and process development. Attendees will gain a practical overview of how Advafab supports detector development from initial prototypes towards repeatable production, connecting sensor manufacturing with the requirements of complete hybrid pixel detector assemblies.

TS-02-04

Real-Time Pile-Up Recovery and High-Resolution Signal Processing for SDDs using PurSamurAI (#3305)

Yoshihiro Endou[1], Masaki Takamaru[2], Kazuki Otomo[2]

[1] TechnoAP Co.,Ltd., Research and Development Department, Hitachinaka-City, Japan; [2] TechnoAP Co.,Ltd., Sales Department, Hitachinaka-City, Japan

N/A

Abstract
In spectroscopy using Silicon Drift Detectors (SDDs), signal pile-up in high count rate environments remains a primary challenge, significantly degrading energy resolution and throughput. This presentation introduces "PurSamurAI" (Pile-up Recovery via Smart Algorithm for Multi-pulse Unmixing and Reconstruction AI), a novel algorithm designed to overcome this limitation. By implementing a pre-trained inference model specialized for

waveform unmixing, PurSamurAI separates and recovers overlapping pulses in real time—events that are conventionally discarded. This approach minimizes spectral degradation even at extremely high input count rates, successfully achieving both high throughput and high energy resolution simultaneously. Furthermore, the architecture provides the flexibility for users to optimize the inference model tailored to their specific measurement applications. We will discuss the technical details of the PurSamurAI signal processing architecture and evaluate its real-time performance capabilities.

TS-02-05

Sci-Compiler: Towards Cross-Platform FPGA Development and Automated CI/CD Workflows for Scientific Data Acquisition (#3405)

Andrea Abba[1], Stefano Carsi[1], Davide Bianchi[1], Francesco Caponio[1], Alberto Cusimano[1], Valentina Arosio[1], Monica Lazari[1], Alessando Giannini[1], Simone Cuzzolin[1], Yuri Venturini[2], Gianluca Beccuzi[2], Matteo Bianchini[2], Luca Colombini[2], Carlo Tintori[2], Annalisa Mati[2]

[1] Nuclear Instruments SRL, Lambrugo, Italy; [2] CAEN S.P.A., Viareggio, Italy

Abstract

Sci-Compiler is a graphical FPGA development environment for custom digital signal processing and data acquisition in nuclear physics, radiation detection, and scientific instrumentation. This contribution presents a major evolution of the platform, including the highly anticipated introduction of Linux support and automated firmware compilation through CI/CD pipelines.

The new alpha release for Linux represents a significant milestone, addressing a long-standing requirement from the scientific community and enabling Sci-Compiler to operate natively in Linux-based research environments. Together with newly introduced pipeline licenses, it opens the way to automated FPGA compilation, integration with Git-based workflows, reproducible firmware builds, and continuous validation of scientific instrumentation firmware.

The signal processing library has been substantially expanded with advanced FFT/IFFT architectures, real-time frequency-domain filtering, programmable FIR and CIC filters, digital modulation, waveform averaging, statistical analysis, and configurable signal generators. Extensive support for time-multiplexed processing enables efficient implementation of multichannel algorithms for high-sampling-rate digitizers.

Detector-oriented developments include improved trapezoidal processing for high-count-rate spectroscopy, pile-up rejection, rise-time discrimination, and flexible event packet generation. Extended simulation capabilities allow acquisition chains to be tested and waveforms, spectra, and event streams to be exported without physical hardware.

A redesigned graphical editor further improves productivity through intelligent signal connections, searchable processing blocks, hierarchical design tools, and integrated documentation.

These advances mark a transition towards an accessible, cross-platform and automated FPGA development ecosystem for modern scientific experiments.

TS-02-06

Broadcom's Silicon Photomultiplier: Technology, Performance, Status and Roadmap (#3399)

Stefan Brunner, on behalf of the Broadcom SiPM team

Broadcom Inc, Regensburg, Germany

Abstract
This presentation provides an overview of Broadcom's silicon photomultiplier (SiPM) and photodetection technologies, including NIR- and NUV-SiPMs. Special focus is placed on initial results for the new HDR-NUV-MT SiPM, as well as the newly developed BroadR and NUV-DJ SiPM technologies.
HDR-NUV-MT We present the recently released HDR-NUV-MT SiPM, a 3×3 mm² device designed for applications requiring high dynamic range. This is achieved using an 18 µm SPAD pitch, combined with a fast recharge time constant of about 17 ns. Additionally, this is the first SiPM in the NUV family featuring four subsegmented quadrants that can be read out individually.
BroadR The newly developed BroadR technology utilizes a novel SPAD architecture enabling an unprecedented flat spectral response. A high photon detection efficiency (PDE) of 50% is maintained from 400 nm to 750 nm, bridging the spectral ranges traditionally covered by separate NUV- and NIR-SiPM technologies. Along with the high and flat PDE, the BroadR technology offers superior dynamic range. Indeed, the this PDE level is achieved with a SPAD pitch of 14 µm and a recharge time constant that can be designed to be well below 10ns.
NUV-DJ The NUV-DJ technology significantly increases PDE at wavelengths above 420 nm compared to NUV-MT, while maintaining excellent NUV sensitivity from 250 nm to 420 nm. At 500 nm, PDE improves from 52% to 62% with the same 40 µm SPAD pitch. The correlated noise of NUV-DJ is also lower compared to NUV-MT at the same PDE. This high PDE and low noise enable best-in-class coincidence time resolution (CTR) for LYSO-based TOF-PET, expand applications to green-emitting scintillators like GAGG, and enable BGO-based Cherenkov TOF-PET. Initial characterization results for NUV-DJ will be presented.

Broadcom's NUV SiPMs find application in TOF-PET, Cherenkov-PET, radiation spectroscopy, photon-counting X-ray detection & PCCT, flow cytometry, and time-gated fluorescence.

Time:
11 November, 2026
13:15 – 14:30

Room:
ALBÉNIZ & MACHUCA

SimSET | SimSET User Meeting (onsite only)

Chairs:
Paul E. Kinahan (Seattle)
Robert S. Miyaoka (Seattle)

Summary

The Simulation System for Emission Tomography (SimSET) toolkit has been in the nuclear medicine physics research landscape for over 30 years. First released in 1993, SimSET has become a primary resource for many nuclear medicine imaging research groups around the world.

The University of Washington Imaging Research Laboratory and collaborators are continuing to develop SimSET, adding new functionality and utilities. The direction of development is driven in part by the SimSET users.

We encourage SimSET users, or those just interested, to participate in the meeting to learn about proposed developments, provide feedback and new directions, and to meet other users.

For further information, email simset@u.washington.edu

Time:
11 November, 2026
15:00 – 17:00

Room:
Seminar Room 3/4

TS-03 | Technical Sessions 3

TS-03-01

Recent Advances in Photosensors and Radiation Detectors for Nuclear Science and High Energy Physics (#3391)

Mauro Bombonati

Hamamatsu Photonics Italia Srl, Arese, Italy

The work presented here reflects the contributions of numerous colleagues across Hamamatsu Photonics. The author gratefully acknowledges the efforts of the photosensor, detector, device development and application engineering teams in Japan, whose expertise and continuous innovation make these developments possible.

Abstract
Hamamatsu Photonics continues to develop a broad portfolio of photosensors and radiation detector technologies addressing the evolving requirements of nuclear science, high energy physics, medical imaging, and related applications. This presentation will provide an overview of recent developments across several detector platforms, including silicon photomultipliers (SiPMs), advanced silicon electron multiplication devices, vacuum photodetectors, and emerging radiation detection technologies. Particular attention will be given to ongoing efforts aimed at improving photon detection efficiency, noise performance, timing characteristics, operation in demanding environments and detector integration. The presentation is intended as an overview of current development activities, providing attendees with insights into emerging detector solutions and their potential impact on future nuclear science and high energy physics experiments.

TS-03-02

Introduction to Representative Achievements of Jinan Laboratory of Applied Nuclear Sciences in the Field of Nuclear Technology Applications (#3425)

Kunliang Liu[1,2], Xiaolei Yang[1,3], Guangbin Wei[1,3], Jie Cao[1,3], Xianhui Xie[1,3], Ray Image Testing Technology；The Palace Museum；Shandong Nuclear Power Co., Ltd

[1] Jinan Laboratory of Applied Nuclear Sciences, Department of Research management, Jinan, China; [2] Institute of High Energy Physics, Chinese Academy of Sciences, Nuclear Technology Application Center, Beijing, China; [3] CAEA Center of Excellence on Nuclear Technology Applications for Nuclear Detection and Imaging, Jinan Base, Beijing, China

This work is supported by Jinan Haiyou Talents Introduction Program.

Abstract

Jinan Laboratory of Applied Nuclear Sciences is a research platform established by the Institute of High Energy Physics, Chinese Academy of Sciences. Our team focuses on nuclear technology applications in three key areas: non-destructive testing, radiation monitoring, and molecular imaging. We have developed and industrialized a broad portfolio of nuclear instruments. This presentation introduces our recent achievements and flagship products.

Non-destructive testing — We invented the world's first curved-surface XRF spectrometer used for cultural heritage conservation, producing high-resolution 3D elemental maps of irregular bronze and jade relics. It has analyzed precious artifacts for the Palace Museum and other museums.

Radiation monitoring — Our portfolio includes personal dosimeters, portable gamma cameras, radionuclide identifiers, neutron detectors, and nuclear electronics modules. Over 3,000 units are in service at universities, nuclear power plants, and hospitals. Our digital monitoring system supports wide-area imaging and semi-quantitative analysis to safeguard plant operations.

Molecular imaging — Our panoramic small-animal PET-CT offers a 213 mm axial FOV, capturing whole-body dynamic rat imaging in a single bed position at sub-millimeter resolution for radiopharmaceutical R&D. XTOMO-CUBE, the world's smallest micro-CT, is compact, portable, and domestically built, delivering micron-resolution 3D reconstruction for archaeology, materials research, and teaching.

Core components — We have also independently developed 150 kV X-ray source components with decetn in-lab performance, and we are carrying out equipment integration to further validate and optimize this technology.

Visit us at Booth 53 for specifications, application cases, and live demos. We look forward to discussing collaboration with you.

12 November, 2026

Time:
12 November, 2026
13:00 – 15:00

Room:
Z1

WIE & YP | WIE & YP

Chairs:
Audrey Corbeil Therrien (Sherbrooke)
Andrea Gonzalez Montoro (Valencia)

Join us at the IEEE 2026 WIE+YP Event in Granada for an interactive and engaging experience focused on career development, leadership, networking, and collaboration within the NPSS community.

We have prepared a dynamic program with inspiring discussions, interactive activities, and opportunities to connect with colleagues and friends from different career stages and technical backgrounds. Whether you are a student, postdoc, young professional, or senior researcher, we hope this event will provide a welcoming space to exchange experiences, build new connections, and strengthen our community.

The event will include a complimentary lunch, a few YP goodies, great networking opportunities with friends and colleagues, and a lineup of very engaging activities.

We are really looking forward to seeing you in Granada!

Time:
12 November, 2026
19:00 – 21:30

Room:
ANDALUCÍA II & III

STIR | STIR Users' & Developers' Meeting (onsite only)

Summary

STIR is Open Source software for use in tomographic imaging. Its aim is to provide a Multi-Platform Object-Oriented framework for all data manipulations in tomographic imaging. The emphasis is on image reconstruction in emission tomography (PET and SPECT). During the annual meeting experienced users and developers will present their recent work with STIR with technical emphasis on software and algorithmic development and demos. Additional time will be allowed for discussion between the speakers and the audience. If interested in presenting contact the chairs before the 1st of September.

For up-to-date information please always check STIR website: https://nssmic.ieee.org/2026/hannah-wakeling/

Contact

Daniel Deidda, National Physical Laboratory (daniel.deidda@npl.co.uk)
Nikos Efthymiou, Harvard Medical School (neftymiou@mgh.harvard.edu)
Charalampos Tsoumpas, University of Groningen (c.tsoumpas@umcg.nl)
Kris Thielemans, University College London (k.thielemans@ucl.ac.uk)
Ludovica Brusaferri, London South Bank University (ludovica.brusaferri@lsbu.ac.uk)

STIR-10

Welcome and Introduction (#3452)

Charalampos Tsoumpas

University of Groningen, Groningen, Netherlands

STIR-01

A STIR-based reconstruction pipeline for the Philips Vereos PET/CT scanner (#3453)

Claudia C. Dominguez Borrero[1], Nikos Efthimiou[2], Pablo Aguiar[1], Charalampos Tsoumpas[3]

[1] Universidade de Santiago de Compostela, Santiago de Compostela, Spain; [2] Harvard Medical School, Boston, USA; [3] University of Groningen, Groningen, Netherlands

STIR-02

Scatter Correction for Long Axial Field-of-View PET Scanners in STIR Library (#3454)

Aparna Jayaraj[1], MIchael Needham[1], Paul Clegg[1], Benjamin Wynne[1], Charalampos Tsoumpas[2]

[1] University of Edinburgh, London, UK; [2] University of Groningen, Groningen, Netherlands

STIR-03

Adding time-of-flight scatter estimation to STIR (#3455)

Manil Z. Sabeur[1], Seyed Amir Zaman Pour[1], Kris Thielemans[2]

[1] KU Leuven, Leuven, Netherlands; [2] University College London, Institute for Nuclear Medicine, London, UK

STIR-04

Fully Automated Motion Detection, Estimation and Correction For Rigid Motion (#3456)

Viet A. Dao[1], Evgenia Mikhaylova[1], Daniel Lesnic[1], Charalampos Tsoumpas[2]

[1] University of Leeds, Leeds, UK; [2] University of Groningen, Groningen, Netherlands

STIR-05

Simultaneous Dual Tracer PET Separation in reconstruction: Validation on LAFOV Data (#3457)

Zekai Li, Nikos Efthimiou, Sebastiaan L. Meyer Viol, Gert Luurtsema, Tom van Meerten, Kris Thielemans, Adrienne Brouwers, Adriaan A. Lammertsma, Charalampos Tsoumpas

University Medical Center Groningen, Groningen, Netherlands

STIR-06

Simulation-Based Evaluation of SPECT Image Reconstruction in STIR (#3458)

Stathis Varzakis, Kris Thielemans

University College London, London, UK

STIR-11

Exploring Starguide GX SPECT-CT system in STIR (#3459)

Valentina Ferri, Elise Emond

GE HealthCare, Barcelona, Spain

STIR-07

Introduction to the STIR new SPECT GPU projector (#3460)

Daniel Deidda[1], David Roddy[2], Chris Buck[2], Wei Huanzhe[3], Jeremiah Chan[3]

[1] National Physical Laboratory, London, UK; [2] TBA, TBA, United Arab Emirates; [3] Kings College London, London, UK

STIR-13

Optimization of GPU memory management in STIR (#3461)

Valerio Cosmi[1], Casper O. Da Costa-Luis[2], Nikos Efthimiou[1], Charalampos Tsoumpas[1], Kris Thielemans[3]

[1] University of Groningen, Groningen, Netherlands; [2] Sci. & Tech. Facilities Council, London, UK; [3] University College London, London, UK

STIR-14

Dead-time correction for STIR and PETSIRD (#3462)

Alan Osys[1], Pawel Markiewicz[2]

[1] London South Bank University, London, UK; [2] University College London, London, UK

STIR-12

PETRIC2: overview and results (#3463)

Casper O. Costa-Luis[1], Manil Sabeur[2], Kris Thielemans[2]

[1] *London South Bank University, London, UK;* [2] *University College London, London, UK*

STIR-08

Democratizing AI attenuation correction research with STIR: results and experiences from the BIC-MAC MICCAI challenge (#3464)

Christian Hinge[1], Valeria Bahel[1], Flemming Littrup Andersen[2], Claes N. Ladefoged[3]

[1] *TBA, TBA, UK;* [2] *Rigshospitalet, Copenhagen, Denmark;* [3] *DTU, Copenhagen, Denmark*

STIR-09

Future of STIR and related projects (#3465)

Kris Thielemans

Univesity College London, London, UK

Index

Author Index

A

Aarabi, Seyed Sahab
MIC-10-317 1171
Abadi, Ehsan
MIC-05-310 968
Abba, Andrea
N-LT-02-13 ..... **317**
N-LT-03-13 548
NSS-01-081 ..... **354**
NSS-01-145 380
NSS-01-305 ..... 46, ***443***
NSS-03-04 464
NSS-13-078 595
NSS-13-306 689
NSS-20-04 ..... 83, ***744***
TS-02-05 ..... 183, ***1588***
Abbaneo, Duccio
NSS-12-04 532
Abbasi, Maysam
MIC-10-317 1171
Abbaszadeh, Shiva
MIC-05-208 937
MIC-05-436 1008
MIC-10-461 1217
MIC-15-270 1356
MIC-15-309 1367
MIC-15-465 1417
M-LT-06-05 1268
NSS-13-310 691
RTSD-03-04 1488
WS-02-15 ..... 19, ***235***
WS-04-01 ..... **245**
WS-04-16 259
Abbene, Leonardo
RTSD-03-03 1487
RTSD-03-07 ..... **1490**
RTSD-10-03 1579
Abboush, Muna
MIC-15-108 1306
Abdar Esfahani, Shadi
MIC-15-303 1366
M-LT-06-10 1272
Abdelhafez, Yasser
MIC-20-04 1456
Abdelli, Mohamed
NSS-09-01 508
Abdollahi, Mirsaeed
MIC-10-317 1171
Abdoul-Carime, Kim
RTSD-09-05 1572
Abe, Mitsuru
NSS-02-02 456
Abe, Ryogo
MIC-05-091 ..... **900**
MIC-05-454 1014
Abe, Ryuku
MIC-15-168 1325
Abe, Tomohisa
NSS-01-023 ..... 31, ***330***
Abgrall, Nicolas
NSS-22-01 759
Abi Akl, Maya
MIC-14-01 1248
Abid, Chayma
MIC-05-337 977
Abraham, Sara
RTSD-10-02 1578
RTSD-10-04 1580
Abrate, Matteo
NSS-17-05 726
Abu arra, Ali
MIC-15-162 1324
AbuSabah, Lujin
MIC-10-359 1183
Abushab, Khaled M
MIC-15-090 1301
Abushawish, Mojahed
MIC-10-023 1084
MIC-10-404 ..... 138, ***1197***
MIC-15-069 1294
MIC-15-201 1335
MIC-15-279 1358
M-LT-03-06 ..... 120, ***1042***
Acerbi, Fabio
JS-02-03 271
JS-02-04 272
NSS-01-293 438
NSS-21-02 751
NSS-21-08 757
Achard, Cyrille
NSS-01-101 362
Acikgoz, Sena
NSS-13-076 594
Acosta, Luis
NSS-25-04 780
Adame Ocampo, Gloria A.
MIC-15-390 1393
Adhikari, Govinda
NSS-07-03 494
NSS-16-07 719
Adinehpour, Zohreh
MIC-05-313 969
Adler, Stephen
WS-04-15 ..... 23, ***258***
Adsley, Philip
N-LT-01-05 296
NSS-01-019 328
NSS-01-129 372
Afshari, Shaghayegh
MIC-05-415 ..... 114, ***1002***
Afshar-Oromieh, Ali
MIC-01-01 823
Aggarwal, Om
NSS-01-319 449
NSS-14-01 699
RTSD-06-04 1549
Aggarwal, Samarth
MIC-05-364 ..... 112, ***986***
MIC-10-467 1219
Aghakhanolia, Narges
MIC-08-03 ..... 122, ***1060***
Agnese, Franck
N-LT-03-10 545
NSS-13-134 619
Agosteo, Stefano
MIC-05-082 897
MIC-10-347 1180
MIC-17-03 1430
MIC-21-02 1460
Aguiar, Pablo
MIC-05-073 894
MIC-05-388 ..... 113, *994*
MIC-15-075 1296
STIR-01 1597
Ahmad, Salleh
NSS-03-06 466
Ahmed, Fardeen
MIC-10-107 1108
MIC-10-467 1219
Ahmed, Zeeshan
NSS-13-104 607
Ahn, Jae Joon
NSS-01-201 400

Author Index

NSS-13-166 632
Ahn, Sangtae
MIC-10-203 1136
Ahn, Youngbok
MIC-10-149 1120
MIC-10-158 1122
MIC-15-150 1320
Aimè, Chiara
NSS-24-01 ..... 86, ***772***
Akagi, Noriaki
MIC-05-145 917
MIC-15-144 1318
Akamatsu, Go
MIC-05-091 ..... 102, *900*
MIC-05-094 901
MIC-05-124 910
MIC-05-454 ..... 115, ***1014***
MIC-09-01 1067
MIC-10-470 1220
MIC-13-03 1244
MIC-15-081 1298
MIC-15-240 1347
MIC-17-06 1433
Akatsuka, Takumi
MIC-05-055 ..... 101, ***889***
MIC-10-056 ..... 126, ***1094***
Akedo, Jun
NSS-13-230 659
Akgun, Bora
NSS-01-137 376
Akimitsu, Nobuyoshi
MIC-07-02 1034
Akram, Md Shahadat Hossain
MIC-05-076 ..... **895**
MIC-15-063 ..... **1293**
Al Khouri, Khalil
NSS-01-239 ..... 42, ***415***
Alabedi, Mahmoud
MIC-05-319 971
Alamaniotis, Miltiadis
NSS-26-01 784
Alambeigi, Farshid
MIC-15-438 1408
Alavi, Abass
MIC-10-368 1186
Alawabdeh, Sara
NSS-01-295 ..... 45, ***439***
Alberghina, Cristiana
MIC-10-362 1184
Albert, Mitchell
MIC-05-106 905
Albert, Patrick
NSS-16-07 719
Alcaide, Ariel A.
NSS-05-06 ..... 50, ***481***
NSS-13-274 ..... 75, ***677***
Alderman, Oliver L.G.
N-LT-02-10 315
NSS-01-267 426
Alessio, Adam M.
MIC-10-371 ..... 137, *1187*
WS-04-04 248
Alexa, Petr
NSS-01-273 429
Alexander, Jude
RTSD-04-395 1532
Alexandre Baptista Bonifacio, Daniel
NSS-13-010 567
Alexandrov, Alexander
NSS-01-073 350
NSS-13-062 588
Alexeev, Maxim
NSS-14-02 700
Alhashim, Maryam
MIC-05-319 971
Alice, Chiara
NSS-14-02 700
Alipio, Andrea G.
N-LT-04-07 ..... 59, ***556***
NSS-13-208 ..... 71, ***650***
Alizadehsani, Roohallah
MIC-10-317 1171
Allen, Magdelena S.
MIC-12-06 ..... 142, ***1237***
Allen, Trevor
NSS-02-01 455
Allerme, Maxime
RTSD-04-396 1532
Allevi, Alessia
NSS-03-04 464
Allwork, Chris
N-LT-01-04 295
NSS-01-033 334
NSS-13-040 579
Almaslamani, Muath
MIC-10-427 1205
MIC-15-372 ..... **1387**
Alnajjar, Dawood
NSS-10-04 519
Alonso-Monsalve, Saul
NSS-12-01 529
Alonso-Sañudo, Odette
N-LT-01-07 298
NSS-01-039 336
Alozy, Jerome A.
MIC-05-019 878
MIC-09-08 1074
NSS-01-139 377
NSS-03-05 465
RTSD-07-05 1556
Alrakh, Heba
MIC-10-260 1153
MIC-15-162 ..... 152, ***1324***
Altamura, Anna Rita
NSS-12-03 531
NSS-28-07 807
Altana, Carmen
NSS-25-04 780
Altet, Josep
N-LT-03-02 539
NSS-13-098 604
NSS-20-06 746
Altingün, Ali
NSS-05-05 480
NSS-13-268 674
Altmann, Yoann
N-LT-04-08 556
NSS-13-200 646
Altube, Jose
MIC-10-293 1163
Alvado, Ludovic
NSS-20-06 746
Alvarado Orozco, Santiago
MIC-05-241 ..... 108, ***947***
M-LT-02-06 ..... 96, ***851***
Álvarez Illán, Ignacio
MIC-10-281 1160
MIC-10-296 1164
MIC-10-308 1168
MIC-15-282 1359
M-LT-06-07 1270
Alvarez, Arthur
N-LT-01-05 296
NSS-01-019 328
NSS-01-129 372
Álvarez, Vicente
NSS-01-099 361
Alva-Sánchez, Héctor
MIC-05-049 ..... 101, *887*
MIC-05-112 906
Alviggi, Mariagrazia
N-LT-04-11 559
NSS-13-290 683
Alwuhaib, Enas
MIC-05-319 971
Amadita, Katya
MIC-20-05 1457
Amadori, Mattia
MIC-10-038 1089

Author Index

M-LT-04-04 1051
NSS-23-05 769
Amaya, Kenji
MIC-03-07 861
Amini, Mehdi
MIC-10-206 1137
Ammour, Luis
N-LT-03-10 545
NSS-13-134 619
Amorim, Beatriz
NSS-13-278 678
Amoyal, Guillaume
RTSD-02-02 1479
Amratisha, Koth
NSS-01-281 432
NSS-16-04 716
An, Ke
NSS-18-04 731
An, Shaohui
MIC-05-046 886
MIC-10-284 1161
Anand, Vivek
NSS-01-045 339
NSS-01-157 ..... **385**
NSS-07-02 493
NSS-13-022 ..... **572**
Anastasi, Michele
NSS-01-093 358
RTSD-01-06 1473
Anders, David
MIC-15-270 1356
MIC-15-465 1417
M-LT-06-05 1268
Andersen, Flemming L.
MIC-15-264 1354
Andersen, Flemming Littrup
STIR-08 1600
Andersen, Thomas L.
MIC-10-212 ..... 131, *1139*
MIC-15-264 1354
Anderson, Damon
RTSD-04-380 1518
Andoh, Sampson
NSS-28-06 806
André, Adélie
MIC-05-337 977
Andreazza, Attilio
NSS-13-284 681
Andrighetto, Alberto
MIC-10-362 1184
Angelis, Georgios I.
MIC-20-05 1457
Angelucci, Bruno
NSS-15-02 708
Anokhin, Igor E.
NSS-01-189 ..... 40, ***396***
Anraku, Yasutaka
MIC-07-02 1034
Anreus-Valero, Álvaro
MIC-05-379 ..... **991**
Anton, Gisela
RTSD-08-05 1564
Antonelli, Matias
NSS-12-02 530
Antonioli, Pietro
NSS-20-05 745
NSS-21-02 751
Antonsanti, Pierre-Louis
NSS-11-02 523
NSS-13-206 ..... 71, ***649***
Anuchit, Kanatip
NSS-01-281 432
Anumah, Adeiza S.
RTSD-04-394 ..... 176, ***1531***
Anwar, Muhammad Adeel
N-LT-03-01 ..... 57, ***538***
NSS-13-094 ..... 65, ***602***
Aoki, Masaharu
N-LT-03-11 546
NSS-13-150 625
Aoki, Masahiko
MIC-05-199 934
Aoyama, Kei
NSS-13-066 590
Apiñaniz Aginako, Jon Imanol
MIC-10-341 1178
MIC-15-006 ..... **1276**
Apresyan, Artur
NSS-20-07 ..... **747**
Arabi, Hossein
MIC-05-319 971
MIC-05-367 987
MIC-10-206 1137
MIC-10-368 1186
MIC-15-294 1363
Aragones, Xavier
N-LT-03-02 539
NSS-13-098 604
Aragonés, Xavier
NSS-20-06 746
Arai, Ryusei
NSS-13-320 694
Araujo, Gabriela R.
N-LT-02-12 316
NSS-01-085 356
Arbor, Nicolas
NSS-04-03 470
Arcidiacono, Roberta
NSS-28-07 807
NSS-28-08 808
Arco, Juan E.
MIC-10-281 1160
MIC-10-290 1162
Arco, Juan Manuel
MIC-10-416 1201
M-LT-03-07 1043
Arfelli, Fulvia
NSS-12-02 530
Argiento, Benedetta
N-LT-04-11 559
NSS-13-290 683
Ariesanti, Elsa
NSS-27-06 ..... 89, ***796***
Arimoto, Makoto
MIC-05-151 919
MIC-05-157 921
MIC-15-177 1328
M-LT-02-04 849
M-LT-02-05 850
Ariño-Estrada, Gerard
MIC-05-004 873
MIC-09-04 1070
MIC-10-071 1098
MIC-10-185 1130
MIC-13-01 1242
MIC-15-321 1371
MIC-15-324 ..... **1372**
M-LT-05-01 1254
M-LT-05-02 ..... **1255**
RTSD-03-02 ..... **1486**
RTSD-06-04 1549
Arnab, Salmon
MIC-15-171 1326
Arnone, Lisa
MIC-10-443 1211
NSS-26-04 ..... **786**
Arosio, Valentina
N-LT-02-13 317
NSS-01-081 354
NSS-01-305 443
NSS-20-04 744
TS-02-05 1588
Arridge, Simon
MIC-05-268 955
M-LT-02-09 853
Arutinov, David
MIC-10-008 1079
Arvanitidis, Georgios
JS-03-05 282

Author Index

Arveuf, Nicolas
NSS-20-06 746
Arzenton, Alberto
MIC-10-362 1184
Asahara, Takashi
MIC-05-145 917
MIC-10-143 1118
MIC-15-141 1317
MIC-15-144 ..... 152, ***1318***
Aschauer, Stefan
NSS-08-01 500
Ashok, Priya
MIC-05-367 987
MIC-15-294 1363
Asou, Kazuki
NSS-13-020 571
Aspinall, Michael D.
NSS-18-05 732
NSS-22-02 759
Assadi, Majid
MIC-05-367 987
MIC-15-294 1363
Asuncion-Astronomo, Alvie
N-LT-04-07 556
NSS-13-208 650
Atieh, Michel
MIC-15-066 ..... 149, ***1293***
Atkins, Nathan
MIC-09-05 1071
RTSD-03-05 1489
ATLAS Collaboration, ATLAS Collaboration
NSS-20-01 ..... 83, ***742***
Au, Samuel
NSS-06-05 488
Auffray, Etiennette
MIC-05-028 880
MIC-10-443 1211
MIC-13-05 1246
MIC-15-381 1390
M-LT-05-04 1257
N-LT-04-11 559
NSS-07-08 498
NSS-13-290 683
NSS-26-04 786
Auricchio, Natalia
RTSD-03-07 1490
RTSD-04-378 1517
Austin, Mark
NSS-13-120 613
Avellaneda, José A.
MIC-15-462 ..... 163, ***1416***
Avila, Elissa L.
MIC-20-01 ..... 167, ***1453***
Ayers, Timothy
NSS-25-06 782
Ayyildiz, Meyra
NSS-01-137 376
Azeez, Azeezat
MIC-10-257 ..... 133, ***1152***
MIC-10-392 ..... 138, ***1193***
Azevedo, Carlos D.R.
NSS-01-143 379
Azimi, Mohamed Saber
MIC-05-319 ..... 111, ***971***
MIC-05-367 ..... 112, ***987***
MIC-10-368 ..... 137, ***1186***
MIC-15-294 ..... 157, ***1363***
N-LT-04-09 ..... 60, ***557***
NSS-13-194 ..... 71, ***644***
NSS-13-210 ..... 71, ***651***
NSS-15-06 ..... 79, ***712***
Aziz, Rabia
MIC-15-276 ..... 156, ***1357***
M-LT-06-06 ..... 146, ***1269***
Azrour, Ines C.
MIC-15-366 1386

B

Babiano-Suárez, Victor
MIC-10-098 1105
M-LT-04-02 1049
NSS-02-04 ..... 48, ***458***
Babiano-Suárez, Víctor
MIC-05-361 985
Back, Keum M.
MIC-10-080 1100
Bäcker, Claus M.
MIC-10-320 1172
MIC-15-330 1374
M-LT-05-07 1259
Backfish, Michael
MIC-15-321 1371
M-LT-05-01 1254
Badawi, Ramsey D.
MIC-10-245 1149
MIC-10-248 1150
MIC-15-003 1275
MIC-18-02 1437
MIC-20-04 1456
Badel, Jean Nöel
MIC-06-02 1028
Badran, Hussam
NSS-13-006 ..... 61, *566*
Bae, Hanwook
NSS-01-141 378
Bae, Jooyoung
NSS-23-02 766
Bae, Sangjin
MIC-16-04 ..... 164, ***1423***
MIC-18-08 1443
MIC-19-03 1447
Baek, Cheol-Ha
NSS-01-269 427
Baek, Hee Kyun
NSS-01-169 ..... 39, ***389***
NSS-13-222 656
Bagheri Khorasgani, Mina
RTSD-06-01 1547
Bahel, Valeria
STIR-08 1600
Bähr, Alexander
NSS-04-04 471
Bai, Junhao
RTSD-04-391 ..... **1528**
Bai, Yizhou
MIC-03-05 859
Baillif, Christophe
MIC-10-197 1134
M-LT-03-02 1038
NSS-13-212 652
Baistow, Ian
MIC-09-05 1071
RTSD-03-05 1489
Bajpai, Utkarsh
NSS-13-022 572
Bakalis, Christos
NSS-01-147 381
NSS-10-04 ..... 55, *519*
NSS-20-08 747
Baker, Peter J
NSS-13-078 595
Bała, Mateusz
MIC-16-06 1425
Balaji, Vibha
MIC-11-05 1228
Balasmeh, Yazeed
MIC-05-406 ..... 114, ***1000***
Balcerzyk, Marcin
MIC-05-355 983
MIC-10-344 1179
Balcon, Nicolas
NSS-13-322 695
Baldassi, Brandon
MIC-05-106 905
MIC-15-135 1315
Baldesi, Lucia
NSS-12-06 534

Author Index

Baldini, Luca
NSS-14-08 705
Balibrea-Correa, Javier
MIC-05-361 985
MIC-10-098 ..... 127, ***1105***
M-LT-04-02 ..... 120, ***1049***
NSS-02-04 458
Ballabriga, Rafael
JS-02-04 272
MIC-05-019 878
MIC-09-08 1074
MIC-15-045 1287
NSS-01-139 377
NSS-03-05 465
NSS-23-04 768
RTSD-04-392 1529
RTSD-08-01 ..... 180, ***1561***
WS-02-03 228
WS-02-06 ..... 17, ***230***
Ballard, Richard
NSS-13-284 681
Ballester, Francisco
NSS-01-099 361
Balušík, Matej
RTSD-04-386 1523
RTSD-04-387 ..... 175, ***1524***
RTSD-04-393 1530
Bandstra, Mark
NSS-01-159 386
NSS-22-01 759
Bannwart Perina, Andrea
NSS-13-304 688
Bansal, Bhavika
NSS-07-02 ..... 52, ***493***
NSS-13-022 572
NSS-13-038 ..... ***578***
Bao, Ziyu
NSS-13-060 ..... 63, ***587***
Barajas, Enrique
N-LT-03-02 539
NSS-13-098 604
NSS-20-06 746
Barbagiovanni, Matteo
N-LT-01-10 ..... 28, ***301***
NSS-01-061 ..... 33, ***345***
Barber, William C.
RTSD-02-01 ..... 170, ***1478***
Barberá Ballester, Julio
MIC-15-045 1287
Barbieri, Marco
NSS-12-01 529
Barbon, Alice
NSS-25-04 780
Barcella, Pietro
N-LT-03-13 548
NSS-01-305 443
NSS-08-05 ..... 53, ***503***
NSS-08-06 504
NSS-13-306 689
Bardelli, Giulio
NSS-28-08 808
Barion, Luca
NSS-20-05 745
Barkhof, Frederik
MIC-05-265 954
Baroni, Guido
MIC-17-03 1430
Barraud, Loris
MIC-10-197 1134
M-LT-03-02 1038
Barreto Pinto, Mateus V.
RTSD-07-05 1556
Barrientos, Luis
MIC-05-088 899
MIC-05-358 984
MIC-05-460 1016
MIC-10-293 1163
MIC-10-326 1174
MIC-10-353 ..... 136, ***1181***
MIC-15-099 1303
Barrio, John
MIC-05-460 1016
Barsuk, Sergey
NSS-12-04 532
Bartelme, Erik
MIC-10-419 1202
MIC-17-01 1428
M-LT-03-08 1044
Bartoldus, Rainer
NSS-23-02 766
Bartosh, Vitalii
RTSD-01-08 ..... 170, ***1475***
RTSD-05-05 1543
Bartsch, Robert
N-LT-01-05 296
NSS-01-019 328
NSS-01-129 372
Bascuñana, Pablo
MIC-10-140 1117
Basiricò, Laura
NSS-12-06 534
RTSD-05-06 1544
RTSD-06-05 1550
Bassler, Niels
MIC-05-130 912
MIC-17-05 1432
Batarchuk, Viktoriia
MIC-05-106 905
Batista, David
MIC-10-446 1212
Batres Mongil, Luis
MIC-19-05 1448
Batres, Luis
MIC-02-05 833
MIC-10-023 1084
MIC-15-042 1285
MIC-15-069 1294
MIC-15-138 ..... 151, ***1316***
Baudier, Thomas
MIC-06-02 1028
Baudin, David
NSS-01-079 353
Baudot, Jérome
N-LT-03-10 545
NSS-13-134 619
Bäumer, Christian
MIC-10-098 1105
MIC-10-320 ..... 135, *1172*
MIC-15-330 1374
M-LT-04-02 1049
M-LT-05-07 1259
RTSD-04-355 1498
Baumgartner, Wayne H.
NSS-10-01 516
Baussens, Oriane
RTSD-04-363 1505
Bautista, Meriam Gay
NSS-13-106 607
Bayikadi, Khasim S.
RTSD-05-01 1540
Beaudoin, Jean-François
MIC-02-03 831
MIC-10-092 1104
M-LT-04-07 1054
Beaumont, Tiffany
WS-04-03 247
Beaupere, Nicolas
NSS-16-08 720
Beauregard, Jean Mathieu
MIC-05-319 971
Bec, Julien
MIC-15-129 1313
Beccherle, Roberto
NSS-14-08 705
Beccuzi, Gianluca
TS-02-05 1588
Bechetoille, Edouard
NSS-20-06 746
Becuzzi, Gianluca

Author Index

NSS-20-04 744
Beekman, Freek
WS-04-10 254
Behera, Prafulla
NSS-17-03 724
Behling, Spencer
N-LT-04-06 ..... 59, ***555***
NSS-13-192 ..... 70, ***643***
Bekaert, Virgile
NSS-13-122 613
Belanger, Frederic
RTSD-09-08 1574
Belanger, Gabriel
MIC-03-08 ..... 98, ***861***
Belas, Eduard
RTSD-01-04 1471
RTSD-04-358 1501
RTSD-04-375 1514
RTSD-06-03 ..... 178, ***1548***
Belcari, Nicola
MIC-10-362 ..... 136, ***1184***
MIC-15-030 ..... 148, ***1283***
N-LT-03-08 544
NSS-13-136 619
Belkacem, Rafik
NSS-01-079 ..... **353**
Bellazzini, Ronaldo
NSS-14-08 705
Bellotti, Emma S.
MIC-10-347 1180
MIC-17-03 1430
NSS-09-04 511
Belzunce, Martín A.
MIC-05-388 994
Benaglia, Andrea
N-LT-04-11 559
NSS-13-290 683
Beneš, Milan
NSS-01-287 435
Beney, Jean-Luc
NSS-16-08 720
Benhabiles, Halim
NSS-16-08 720
Benkechkache, Mohamed El Amine
NSS-01-151 ..... 38, ***382***
Benlloch, Jose Maria
JS-02-04 272
MIC-05-355 983
MIC-09-08 1074
MIC-15-045 1287
WS-02-03 228
Benoit, Didier
MIC-15-369 1386
M-LT-05-09 1261
Bensedik, Youcef
NSS-02-01 455
Bentoumi, Ghaouti
RTSD-04-395 1532
Berardi, Vincenzo
NSS-12-01 529
Bergamaschi, Anna
NSS-01-093 358
NSS-08-04 502
Bergamin, Gianmario
MIC-09-08 1074
MIC-15-045 1287
NSS-23-04 768
Bergauer, Thomas
NSS-12-03 531
Bergmann, Benedikt
JS-03-04 281
MIC-05-292 963
NSS-01-135 375
NSS-01-287 435
RTSD-01-07 1474
RTSD-04-384 1522
RTSD-08-05 1564
Bergont, Mathieu
NSS-13-322 695
Beriashvili, Natia
MIC-15-255 ..... 156, ***1351***
Berlea, D. Vlad
NSS-17-03 724
Bernardini, Leonardo
NSS-14-03 ..... 78, ***700***
Bernhardt, Alexander
MIC-10-281 1160
Bernier, Alexandre
MIC-10-092 ..... 127, ***1104***
M-LT-04-07 ..... 121, ***1054***
Bernier, Nikita
N-LT-01-07 298
NSS-01-039 336
NSS-01-131 373
Berr, Stuart
MIC-05-121 909
M-LT-02-10 854
Bert, Julien
MIC-15-174 1327
MIC-15-369 ..... 160, *1386*
M-LT-05-09 ..... 145, *1261*
Bertaina, Mario E.
NSS-17-05 726
Bertolin, Eleonora
NSS-21-02 751
Bertuccio, Giuseppe
NSS-13-112 610
RTSD-10-03 1579
Bérubé-Lauzière, Yves
MIC-03-08 861
MIC-15-153 1321
Berzin, Elizabeth
NSS-20-08 747
Besnard-Vauterin, Clément
NSS-02-01 455
Betelgueriev, Djokhar
NSS-04-03 470
Bettelli, Manuele
RTSD-03-03 1487
RTSD-03-07 1490
RTSD-04-378 1517
RTSD-04-395 1532
RTSD-10-03 1579
Betušiak, Marián
RTSD-01-04 1471
RTSD-04-358 1501
RTSD-04-375 1514
RTSD-06-03 1548
Beyer, Kurt
NSS-11-03 524
Bez Baruah, Suomi
NSS-01-293 ..... 45, ***438***
Bezak, Mihaela
RTSD-04-394 1531
Bezshyyko, Oleg
NSS-12-04 532
Bharathi, Praveen G.
MIC-10-461 1217
Bhardwaj, Aditya
RTSD-05-03 1541
Bharkhada, Deepak
MIC-10-374 1187
MIC-15-207 1337
MIC-15-225 ..... 154, *1342*
Bhat, Sheethal
MIC-05-418 1003
Bi, Dongdong
MIC-10-284 1161
Bianchi, Davide
TS-02-05 1588
Bianchini, Matteo
NSS-20-04 744
TS-02-05 1588
Biasini, Maurizio
N-LT-04-11 559
NSS-13-290 683
Biasiol, Giorgio
NSS-12-02 530
Bichard, Henry

Author Index

NSS-13-284 681
Biesuz, Nicolò Vladi
NSS-01-139 ..... 37, ***377***
RTSD-08-02 1561
Biggs, James
NSS-01-171 ..... 39, ***390***
NSS-11-06 ..... 56, ***527***
Bilki, Burak
NSS-13-076 ..... 64, ***594***
Billon-Pierron, Nicolas
RTSD-02-04 1481
Bilyeu, Brooke
NSS-22-05 761
Bisht, Ashish
N-LT-01-11 302
NSS-01-063 346
NSS-28-07 807
Bisi, Samuele
JS-02-05 ..... 25, ***273***
N-LT-01-08 299
NSS-01-015 326
NSS-21-04 753
WS-02-02 ..... 17, ***228***
Bisignani, Valeria
N-LT-04-11 559
NSS-13-290 683
Bisogni, Maria Giuseppina
NSS-12-06 534
NSS-28-04 804
Bjorklid, Anders
N-LT-01-10 301
NSS-01-061 345
Blanchard, Guillaume
NSS-20-06 746
Blas, Sheraz
NSS-01-195 ..... 40, ***398***
Blick, Cara
NSS-13-312 692
Blideanu, Valentin
NSS-01-239 415
Blomgren, August
MIC-05-133 ..... 104, ***913***
Blorstad Thu, Sander
MIC-17-04 1431
Boada, Fernando
MIC-10-257 1152
MIC-10-392 1193
Bobba, Kondapa N.
MIC-05-334 976
Bobin, Jérôme
NSS-01-197 399
Boccalini, Cecilia
MIC-05-403 999
Boccanfuso, Daniele
N-LT-04-11 559
NSS-13-290 683
Boch, Jerome
NSS-13-256 669
Bocoum, Maïmouna
MIC-15-213 1339
Bodova, Tea
RTSD-07-05 1556
Boening, Guido
MIC-01-01 823
Bofill-Petit, Adrià
MIC-15-039 1285
Boggs, Steven E.
NSS-01-053 341
NSS-04-06 473
Boiano, Ciro
NSS-01-009 324
NSS-13-074 ..... 64, *593*
Boisson, Frederic
NSS-13-122 613
Bokulić, Tomislav
MIC-15-444 1410
Bollack, Ariane
MIC-05-265 954
Bolotnikov, Aleksey
RTSD-04-354 ..... 172, *1497*
RTSD-04-365 ..... 173, *1506*
RTSD-07-03 ..... 179, ***1554***
Bolzonella, Riccardo
NSS-01-139 377
Bombonati, Mauro
TS-03-01 ..... 183, ***1592***
Bonanno, Chiara
MIC-10-362 1184
Bonanno, Gabriele
NSS-12-02 530
NSS-13-304 688
Bonick, Sam
NSS-13-308 690
Bonini, Chiara
NSS-13-298 686
Bonito, Gregory
NSS-13-310 691
Bonnard, Jonathan
NSS-01-101 362
Bonney, Lara M.
MIC-10-311 ..... 135, ***1169***
Bony, Mathis
NSS-01-239 415
Boo, Jihwan
N-LT-01-12 ..... 28, ***302***
NSS-01-065 ..... 34, ***347***
RTSD-04-372 1512
Booker, Paul
NSS-13-278 678
Boonen, Marcel M.
NSS-01-113 ..... 36, ***366***
Boreel, Daan
MIC-10-251 1151
Borge, Luigi
NSS-17-04 725
Borges, Filipa I.G.M.
NSS-24-06 775
Borghi, Giacomo
MIC-05-082 897
MIC-10-038 1089
MIC-10-347 1180
MIC-17-03 1430
MIC-21-02 1460
M-LT-04-04 1051
N-LT-03-03 540
N-LT-03-13 548
NSS-01-133 374
NSS-03-02 462
NSS-03-03 463
NSS-08-05 503
NSS-08-06 504
NSS-09-04 511
NSS-13-102 606
NSS-13-260 671
NSS-13-306 689
NSS-14-03 700
NSS-14-06 703
NSS-23-05 769
Borgwardt, Tyler C.
N-LT-01-03 294
NSS-05-06 481
NSS-13-329 453
Borri, Marcello
NSS-01-301 441
NSS-13-088 ..... **599**
NSS-13-278 678
Borriello, Lucrezia
N-LT-04-11 559
NSS-13-290 683
Bortfeldt, Jonathan
MIC-05-130 912
MIC-17-05 1432
Bortoletto, Daniela
NSS-17-03 724
Bortolussi, Silva
MIC-05-361 985
Bortone, Alberto
N-LT-01-10 301
NSS-01-061 345

Author Index

Bortot, Davide
MIC-10-347 1180
NSS-09-04 511
Boscardin, Maurizio
N-LT-01-11 302
NSS-01-063 346
NSS-28-04 804
NSS-28-07 807
NSS-28-08 808
Bosch, Carl
RTSD-02-03 1480
RTSD-07-04 1555
Bossis, Théo
NSS-16-08 720
WS-04-03 ..... **247**
Boston, Andrew
NSS-06-03 487
Boswinkel, Milou
MIC-10-251 1151
Botella Asunción, Pablo
MIC-05-355 983
Bottaro, Marcio
NSS-13-010 567
Bottau, Vincent
NSS-09-01 508
Bottinelli, Sergio
NSS-10-05 520
Bouchard, Jonathan
MIC-02-03 831
Bouchez-Delotte, Sacha
MIC-05-301 ..... 110, ***966***
Bouhali, Othmane
MIC-15-060 1292
Boukhicha, Mohamed
RTSD-06-06 ..... 179, ***1551***
Bourbonne, Vincent
MIC-15-174 1327
MIC-15-369 1386
M-LT-05-09 1261
Boursier, Yannick
MIC-05-337 977
RTSD-04-398 1533
Bousse, Alexandre
MIC-01-02 824
MIC-08-08 1065
MIC-10-425 1204
MIC-15-216 1340
Bouvard, Sandrine
N-LT-03-10 545
NSS-13-134 619
Bouvet, Françoise
WS-04-03 247
Bowron, Daniel T.
N-LT-02-10 315
NSS-01-267 426
Boyarintsev, Andrey
NSS-12-04 532
Boyarintseva, Ianina
NSS-12-04 532
Braaksma, Jan
MIC-05-097 902
MIC-10-260 1153
Braccini, Saverio
MIC-12-04 1236
Braddock, Isabel
JS-01-01 ..... 23, ***264***
Bradley, Kevin M.
MIC-04-07 870
MIC-10-311 1169
MIC-10-422 1203
MIC-15-441 1409
Brajnik, Gabriele
NSS-12-02 530
Brambilla, Andrea
RTSD-09-05 ..... 181, ***1572***
Brambilla, Cláudia R.
MIC-10-242 1148
MIC-15-255 1351
Brambilla, Sergio
NSS-01-009 324
NSS-13-074 593
Branchini, Paolo
RTSD-09-04 1571
Brankov, Jovan G.
MIC-10-227 ..... 132, ***1144***
MIC-15-204 1336
Bravin, Alberto
NSS-15-05 711
Bravo, Javier
N-LT-02-02 308
NSS-01-275 430
Bravo, Paco
MIC-05-262 953
Breidenbach, Marc
N-LT-04-06 555
NSS-13-192 643
Breitenmoser, David
NSS-05-01 477
NSS-09-03 510
NSS-11-04 ..... 56, ***525***
NSS-13-014 569
NSS-13-196 ..... 71, ***645***
NSS-22-03 760
Breton, Dominique
NSS-01-079 353
NSS-12-04 532
NSS-13-084 597
NSS-20-06 746
Breton, Vincent
NSS-01-101 362
Breuer, Max
MIC-05-103 904
MIC-15-291 1362
Brez, Alessandro
NSS-14-08 705
Brini, Matteo
NSS-01-173 391
Briz, José A.
N-LT-01-07 298
NSS-01-027 332
NSS-01-039 336
NSS-01-131 373
Broadbent, Emily
NSS-04-06 473
Brombal, Luca
RTSD-08-02 1561
Brookes, Toby
RTSD-10-03 1579
Brooks, Claire J.
MIC-05-283 ..... 109, ***960***
MIC-10-428 1206
Brosda, Nico F.
RTSD-04-355 1498
Broulim, Pavel
RTSD-04-384 1522
Broulím, Pavel
NSS-01-287 435
Brouwers, Adrienne
STIR-05 1598
Brouwers, Adrienne H.
MIC-05-445 1011
MIC-10-437 1209
Brown, Thomas M.
RTSD-06-01 1547
Brown, William
JS-01-01 264
Brubaker, Erik
NSS-03-01 462
Brücken, Erik
NSS-13-006 ..... **566**
Brueckner, Martin
NSS-01-093 358
Brun, Francesco
RTSD-08-02 1561
Brunamonti, Alessio
MIC-10-293 1163
NSS-03-02 ..... 48, ***462***
Brune, Carl
NSS-05-06 481

Author Index

Brunner, Stefan
TS-02-06 ..... 183, ***1589***
Brunskog, Rickard
N-LT-01-10 301
NSS-01-061 345
Brunt, Benjamin
MIC-05-133 913
Brusa, Irene
MIC-15-384 1391
Brusasco, Benedetta
MIC-10-098 1105
M-LT-04-02 1049
Bruschi, Paolo
NSS-14-08 705
Bruschini, Claudio
JS-02-05 273
N-LT-01-08 299
NSS-01-015 326
NSS-12-01 529
NSS-19-06 739
NSS-21-04 753
NSS-21-05 754
NSS-21-06 755
SC-02-07 12
Bruzzi, Mara
MIC-15-102 ..... 150, *1304*
NSS-12-03 531
NSS-12-06 ..... 57, ***534***
Brzezinski, Karol
MIC-10-293 1163
Brzeziński, Karol
MIC-05-088 899
MIC-05-358 ..... 112, ***984***
MIC-05-460 1016
MIC-10-032 ..... 125, ***1087***
MIC-10-326 1174
MIC-10-353 1181
MIC-15-099 1303
Bubon, Oleksandr
MIC-05-106 ..... 103, *905*
MIC-10-302 ..... 134, *1166*
MIC-15-135 1315
Buchanan, Emma
NSS-01-283 433
Buck, Chris
STIR-07 1599
Buckland, Matthew
NSS-01-301 441
NSS-13-088 ..... 65, *599*
NSS-13-278 ..... 75, ***678***
Buda, Filippo
NSS-06-08 491
Buffet, Jean-Claude
NSS-24-04 774
Bugby, Sarah
NSS-15-05 711
Bui, My Hoang Hoa
MIC-06-02 1028
Burbar, Ziad
MIC-10-380 1189
MIC-15-405 ..... 161, ***1398***
Burdyko, Alexander
NSS-21-07 756
Burian, Petr
MIC-05-292 963
NSS-01-135 375
NSS-01-287 435
RTSD-04-384 1522
RTSD-08-05 1564
Buridon, Victor
NSS-27-03 794
Burom, Sunruthai
NSS-01-281 432
Busato, Emmanuel
NSS-01-101 362
Busk, Morten
MIC-17-05 1432
Bussi, Matteo
NSS-17-05 726
Bustillo, John Paul
NSS-06-05 488
Buttacavoli, Antonino
RTSD-03-07 1490
RTSD-10-03 1579
Buttar, Craig
NSS-17-03 724
Buttler, Werner
NSS-14-07 704
Buvat, Irene
MP-01-03 ..... 92, ***817***
Buvat, Irène
WS-03-04 ..... **240**
Buzug, Thorsten M.
MIC-05-391 995
Byun, Soo Hyun
NSS-24-05 774

C

Caballero Rodríguez, Miriam
N-LT-01-07 ..... 28, ***298***
NSS-01-027 332
NSS-01-039 ..... 32, ***336***
NSS-01-131 373
NSS-13-086 ..... 65, ***598***
Cabello, Jorge
MIC-05-424 1005
MIC-10-212 1139
MIC-12-01 1233
MIC-15-264 1354
WS-04-17 260
Cabiati, Damanio
RTSD-04-390 ..... 176, *1527*
Cabrera-Martín, María Nieves
MIC-10-140 1117
Cai, Huawei
MIC-05-451 1013
WS-04-08 252
Cai, Jiale
NSS-13-126 615
Cai, Ling
MIC-05-364 986
MIC-10-467 ..... 140, ***1219***
Cai, Xiangdong
MIC-10-065 1097
MIC-10-338 1177
NSS-13-034 577
Cai, Zhuochen
NSS-01-031 ..... 32, ***333***
NSS-27-04 ..... 89, ***795***
Calderón Ochoa, Eduardo
MIC-08-07 1064
Caliskan, Furkan
NSS-01-137 376
Caliskan, Hasan O.
NSS-01-137 376
Camera, Franco
NSS-13-074 593
NSS-13-260 671
Cameron, Matthew
NSS-06-05 488
Camlica, Ahmet
RTSD-04-383 1521
Cammarata, Francesco P.
MIC-10-362 1184
Campajola, Marcello
N-LT-04-11 ..... 60, ***559***
NSS-13-290 ..... 76, ***683***
NSS-21-07 ..... 84, ***756***
Campbell, Colleen
NSS-13-046 ..... 63, ***581***
Campbell, Michael
NSS-01-139 377
RTSD-08-01 1561
Campdell, MIchael
MIC-05-019 878
Campos, João
RTSD-04-400 1535
Canfield, Brian

Author Index

NSS-13-308 690
Cansolino, Laura
MIC-10-362 1184
Cantrel, Eric
NSS-13-206 649
Cao, Guohua
MIC-10-188 1131
Cao, Jie
TS-03-02 1592
Cao, Lei R.
NSS-01-323 450
Cao, Raymond
NSS-12-08 ..... 57, ***536***
Cao, Xin
NSS-01-121 369
Capocasa, Francesca
NSS-01-307 443
NSS-08-03 ..... 53, ***502***
Caponio, Francesco
N-LT-02-13 317
NSS-01-081 354
NSS-01-305 443
NSS-13-078 595
NSS-20-04 744
TS-02-05 1588
Caprotti, Diana
MIC-15-447 1411
M-LT-06-01 1264
Caradonna, Peter
MIC-15-459 1415
M-LT-06-04 1267
Caradonna, Pietro
MIC-11-03 1226
Carasco, Cédric
N-LT-02-07 312
NSS-01-231 412
NSS-09-01 508
Caravaca, Javier
MIC-05-139 915
MIC-05-235 945
MIC-10-185 1130
MIC-11-07 1229
MIC-12-01 ..... 142, ***1233***
MIC-12-02 1234
MIC-21-03 1461
RTSD-06-04 1549
RTSD-09-06 1572
WS-04-01 ..... **245**
WS-04-13 256
Cardarelli, Paolo
RTSD-08-02 ..... 180, ***1561***
Cardella, Giuseppe
NSS-25-04 780
Cardenas, Joseph
NSS-01-117 367
Cardiff, Seán
JS-01-01 264
RTSD-04-369 ..... 174, ***1510***
Caricato, Anna Paola
NSS-27-08 798
Carini, Gabriella
NSS-08-03 502
Carles, Montserrat
MIC-15-336 1376
Carlier, Thomas
MIC-04-04 867
MIC-10-305 1167
Carlotti, Edoardo
NSS-01-305 443
Carmichael, Robert
MIC-15-468 1418
N-LT-02-09 ..... 29, ***314***
NSS-01-249 ..... 43, ***420***
Carminati, Marco
MIC-05-082 897
MIC-10-038 1089
MIC-10-347 1180
MIC-17-03 1430
MIC-21-02 1460
M-LT-04-04 1051
N-LT-03-03 540
N-LT-03-13 548
NSS-01-305 443
NSS-03-02 462
NSS-03-03 463
NSS-08-05 503
NSS-08-06 504
NSS-09-04 511
NSS-13-102 606
NSS-13-260 671
NSS-13-306 689
NSS-14-03 700
NSS-14-06 703
NSS-19-03 ..... 82, ***736***
NSS-23-05 769
Carmo, Pedro G.H.
RTSD-04-362 1504
RTSD-04-400 1535
Carnesecchi, Francesca
NSS-21-02 751
Caroli, Ezio
RTSD-03-07 1490
RTSD-04-378 1517
Carrato, Sergio
NSS-12-02 530
NSS-13-130 617
Carrel, Frédérick
NSS-01-197 399
Carsi, Stefano
N-LT-02-13 ..... 30, *317*
NSS-01-081 ..... 34, *354*
NSS-01-145 380
NSS-01-305 443
NSS-03-04 ..... 49, ***464***
NSS-20-04 744
TS-02-05 1588
Carson, Richard E.
MIC-04-08 871
MIC-05-244 948
M-LT-02-08 852
Carson, Richard: **239**
Carter, Lukas
WS-04-17 260
Cartiglia, Nicolò
NSS-28-07 807
NSS-28-08 808
Carturan, Sara M.
NSS-27-08 798
Carulla, Maria
NSS-01-093 358
Carvalho, Ana C.
MIC-15-243 1348
Casaña, Jose V.
MIC-15-336 1376
Casanelli, Bryan
MIC-05-043 ..... 101, ***885***
MIC-05-370 ..... 113, *988*
MIC-10-446 ..... 140, *1212*
MIC-15-021 1280
Caselles, Olivier
WS-04-03 247
Casini, Giovanni
NSS-12-06 534
Caso, Fabiola
JS-02-04 272
NSS-21-02 751
Cassano, Laura
MIC-10-443 1211
Cassese, Antonio
NSS-28-08 808
Castellani, Gastone
MIC-15-384 1391
Castellanos, Nataly
MIC-15-099 1303
MIC-15-336 ..... 158, ***1376***
MIC-16-02 ..... **1421**
Castillo, Killian
NSS-01-197 ..... **399**
Castoldi, Andrea

Author Index

N-LT-03-12 547
NSS-01-291 437
NSS-06-08 ..... 52, ***491***
NSS-08-01 500
NSS-08-07 505
NSS-13-300 687
NSS-25-04 780
Catana, Ciprian
MIC-12-06 1237
MP-02-12 ..... 117, ***1024***
Catarinicchia, Claudia
MIC-10-362 1184
Cateret, Juan
MIC-09-02 1068
Cates, Joshua W.
JS-02-08 ..... 25, ***276***
MIC-05-037 ..... 100, ***883***
MIC-13-01 1242
MIC-13-05 1246
N-LT-03-04 541
NSS-01-116 611
RTSD-06-04 1549
WS-04-01 ..... **245**
WS-04-13 256
Catret, Juan Vicente
MIC-10-020 1083
MIC-10-140 1117
MIC-15-045 1287
MIC-15-123 1311
Cautero, Giuseppe
NSS-12-02 530
NSS-13-130 617
Cautero, Marco
NSS-12-02 530
NSS-13-130 617
Cavalieri, Andrea
NSS-12-06 534
Cavallini, Louis
NSS-01-241 416
Cavallini, Viola
RTSD-08-02 1561
Cavazzini, Leo
N-LT-01-11 ..... 28, ***302***
NSS-01-063 ..... 33, ***346***
Cave, Frank
NSS-18-05 732
Cayley, James
NSS-04-01 ..... **468**
Cazalas, Edward
NSS-13-312 ..... 77, ***692***
NSS-13-318 ..... 77, *694*
Cazzoli, Sara
NP-01-02 ..... 26, ***287***
Cebriano, Teresa
MIC-15-006 1276
Ceccanti, Marco
NSS-14-08 705
Cecchi, Claudia
N-LT-04-11 559
NSS-13-290 683
Cech, Daniel
NSS-01-295 439
Čelko, Tomáš
NSS-01-135 375
RTSD-08-05 1564
Cencelli, Valentino O.
MIC-15-087 1300
Centis Vignali, Matteo
N-LT-01-11 302
NSS-01-063 346
NSS-08-05 503
NSS-28-04 804
NSS-28-07 807
NSS-28-08 808
Cerasole, Davide
NSS-20-03 743
Cerbone, Laura A.
MIC-05-292 963
RTSD-01-07 ..... 169, ***1474***
Cerello, Piergiorgio
NSS-05-07 482
NSS-12-07 535
Cerna, Manuel
MIC-05-370 988
Čeřovský, Jaroslav
NSS-06-06 489
Cha, Bo Kyung
N-LT-01-01 292
NSS-01-021 329
Cha, Hyemi
NSS-13-242 664
Chae, Jung-Seok
NSS-13-238 662
Chaffin, Jeffrey M.
NSS-01-299 440
Chaiwongkhot, Kullapha
NSS-01-281 ..... 45, ***432***
NSS-16-04 716
Chakrabarti, Sukanya
NSS-10-01 516
Chalampalakis, Zacharias
MIC-10-203 1136
MIC-15-375 1388
M-LT-05-03 1256
Chalil, Achment
NSS-09-01 508
Chan, Jeremiah
STIR-07 1599
Chanal, Hervé
NSS-01-101 ..... 35, ***362***
NSS-12-04 ..... 57, ***532***
Chandler, Adam
MIC-20-04 1456
Chandrasekaran, Kathiresan
MIC-15-192 ..... 153, ***1332***
Chang, Chun-Yen
N-LT-02-03 309
NSS-01-253 421
Chang, Hao
RTSD-09-03 1569
Chang, Haoran
MIC-01-05 ..... 94, ***827***
Chang, Haoxiang
NSS-09-05 ..... **512**
Chang, Siyao
RTSD-04-379 ..... 175, ***1517***
Chang, Ya-Chen
N-LT-02-03 309
NSS-01-253 421
Chaoufi, Ihssane
MIC-21-05 1463
Charbon, Edoardo
JS-02-05 273
N-LT-01-08 299
NSS-01-015 326
NSS-12-01 529
NSS-19-06 739
NSS-21-04 753
NSS-21-05 754
NSS-21-06 755
Charlebois, Serge
SC-02-05 12
Charlebois, Serge A.
NSS-05-08 483
NSS-21-03 ..... 84, *752*
WS-02-04 ..... 17, ***229***
Chartier, Gabriel
NSS-01-241 ..... 43, ***416***
Chatzidakis, Stylianos
MIC-10-440 1210
Chatziioannou, Arion
MIC-10-077 1100
MIC-15-468 1418
N-LT-02-09 314
NSS-01-249 420
Chatzipapas, Konstantinos
MIC-10-251 1151
Chaudhary, Shivam
MIC-05-418 ..... 114, ***1003***

Author Index

Chaudhuri, Sandeep K.
JS-03-01 279
Chauhan, Shivani L.
N-LT-01-04 295
NSS-01-033 334
Cheiney, Pierrick
NSS-13-322 695
Chembakan, Theertha
NSS-17-03 724
Chemli, Yanis
MIC-02-03 831
MIC-10-236 1146
MIC-18-04 1439
Chen, Boping
NSS-01-121 369
Chen, Changyu
MIC-10-182 1129
Chen, Chenxi
NSS-01-111 ..... 36, ***366***
Chen, Chin-Tu
MIC-10-047 1091
MIC-20-01 1453
NSS-01-025 331
NSS-13-050 583
Chen, Faguo
MIC-05-226 943
M-LT-01-02 836
NSS-13-270 675
Chen, Gaoyu
MIC-14-04 1251
MIC-15-408 1399
Chen, Gefei
MIC-15-354 1382
Chen, Jianbo
MIC-15-363 1385
Chen, Jingbin
NSS-01-105 364
Chen, Jingxian
MIC-10-239 1147
MIC-10-398 1195
Chen, Junfeng
NSS-01-025 ..... 32, *331*
NSS-07-05 495
RTSD-04-356 ..... 172, ***1499***
Chen, Junyu
MIC-10-314 1170
Chen, Kai
MIC-05-160 922
Chen, Kexin
WS-04-08 252
Chen, Maxin
MIC-17-05 1432
Chen, Mengxin
MIC-05-325 973
Chen, Moon S.
MIC-20-04 1456
Chen, Pengfei
MIC-10-161 ..... **1123**
Chen, Qingxiang
MIC-10-164 ..... 129, ***1124***
Chen, Ruohua
MIC-05-385 993
MIC-08-05 1062
Chen, Sidong
NSS-25-06 782
Chen, Simeng
NSS-01-111 366
Chen, Tingting
MIC-15-414 1401
Chen, Wei
NSS-01-303 442
Chen, Weiyan
MIC-14-04 1251
Chen, Xu
MIC-05-046 886
Chen, Yang
MIC-05-160 922
Chen, Yifu
RTSD-04-364 1505
RTSD-04-377 1516
Chen, Yihao
MIC-02-02 830
MIC-05-184 ..... 106, ***929***
MIC-05-253 ..... 108, ***950***
MIC-08-01 1058
MIC-10-119 ..... 128, ***1111***
MIC-10-131 1115
MIC-10-410 1199
MIC-15-198 1334
Chen, Yu
RTSD-04-366 ..... 173, ***1507***
Chen, Yue
MIC-02-02 830
MIC-05-184 929
MIC-05-253 950
MIC-05-352 982
MIC-10-119 1111
MIC-10-131 1115
MIC-10-377 ..... **1188**
MIC-15-378 ..... **1389**
Chen, Zhiqiang
MIC-10-182 1129
Chen, Zhongjian
NSS-01-127 371
Cheng, Jianping
NSS-01-041 337
NSS-15-04 710
Cheng, Li
MIC-08-04 1061
Cheng, Weixin
MIC-15-465 1417
M-LT-06-05 1268
NSS-13-310 691
Cheng, Wendi
WS-04-08 252
Cheng, Zhaoping
MIC-05-385 993
Cheraghi, Maryam
MIC-05-319 971
MIC-05-367 987
MIC-10-368 1186
MIC-15-294 1363
N-LT-04-09 557
NSS-13-194 644
NSS-13-210 651
NSS-15-06 712
Cherlin, Alexander
MIC-09-05 ..... 123, ***1071***
MIC-10-068 1097
RTSD-03-05 ..... 171, ***1489***
WS-04-10 ..... 22, ***254***
Cherry, Simon R.
MIC-05-007 874
MIC-10-041 1090
MIC-10-104 1107
MIC-13-04 1245
MIC-15-003 1275
MIC-15-129 1313
MIC-18-02 1437
MIC-20-04 1456
M-LT-03-04 1040
NSS-16-01 714
WS-04-02 246
Cheung, Chi C.
JS-03-06 283
Chevillon, Nicolas
NSS-13-122 613
Chi, Wangzhao
MIC-05-451 1013
WS-04-08 252
Chiang, Gloria C.-Y.
MIC-10-137 1116
Chiariello, Matteo
NSS-13-118 ..... **612**
Chiba, Komei
N-LT-02-15 318
NSS-01-325 451
Chichester, David L.
NSS-09-03 510

Author Index

NSS-13-196 645
RTSD-04-397 1533
Chiesa, Federico
NSS-14-06 703
Chikhradze, Mikheil
MIC-15-255 1351
Chindaratchakul, Sarawit
NSS-01-281 432
Chinn, Garry
MIC-05-274 957
MIC-07-04 1035
MIC-10-449 1213
MIC-15-270 1356
Chlubek, Antoina
MIC-15-111 1307
Chmeissani, Mokhtar
MIC-05-004 873
Chmeissani, Mokthar
MIC-10-185 1130
Cho, Gyuseong
MIC-05-334 976
MIC-11-07 1229
NSS-01-155 384
NSS-01-209 403
NSS-13-096 603
Cho, Hyosung
MIC-05-289 962
MIC-10-407 1198
MIC-15-147 1319
Cho, Jaeho
MIC-15-318 1370
M-LT-05-10 1262
NSS-02-05 459
Cho, Jaeyoung
NSS-01-327 452
Cho, Min Jeong
MIC-04-01 ..... 98, ***864***
Cho, Sanghyun
MIC-05-289 ..... 109, *962*
MIC-10-407 ..... 138, ***1198***
Cho, Seungryong
MIC-05-277 958
Cho, Shinhaeng
RTSD-04-350 1494
Cho, Sung Oh
N-LT-01-01 292
NSS-01-021 329
Cho, Sungkoo
MIC-15-318 1370
M-LT-05-10 1262
Chock, Christopher
MIC-05-022 879
NSS-01-117 367
NSS-10-03 518
NSS-14-05 702
Choi, Chang Heon
MIC-10-062 1096
Choi, Gyeongjin
NSS-13-252 ..... 74, ***668***
Choi, Hyun Joon
MIC-07-01 1033
MIC-10-401 1196
MIC-15-423 1404
Choi, Hyung Joo
MIC-15-195 1333
NSS-13-222 ..... 72, ***656***
Choi, Ilwoong
NSS-13-172 635
Choi, Jihoon
NSS-13-008 566
Choi, Seong Hun
NSS-01-169 389
Choi, Seung A
NSS-01-201 ..... **400**
Choi, Suhan
MIC-10-029 1086
MIC-15-048 ..... 148, ***1288***
Choi, Sunghoon
MIC-15-072 ..... 149, ***1295***
Choi, Yong
MIC-10-179 1128
MIC-15-015 1279
MIC-15-180 1329
NSS-01-047 340
NSS-23-03 767
Choi, Young Seung
N-LT-01-01 292
NSS-01-021 329
Choi, Youngchol
MIC-05-169 925
NSS-01-211 ..... 41, *404*
Choong, Woon-Seng
JS-02-08 276
MIC-05-037 883
N-LT-03-04 541
NSS-01-116 611
Chorbadzhiev, Nikolay
RTSD-09-08 1574
Chotard, Pascal
RTSD-04-396 1532
Chou, Cheng-Ying
MIC-05-415 1002
Choudhary, Deepa
MIC-10-245 ..... 132, ***1149***
Choy, Jennifer
NSS-12-08 536
Choyke, Peter L.
MIC-15-300 1365
Christensen, Emil S.
MIC-10-212 ..... **1139**
Christian, James
NSS-01-151 382
RTSD-03-02 1486
Christy, Eric
NSS-13-310 691
Chromik, Štefan
RTSD-04-359 1502
Chu, Hyeyeun
MIC-11-06 ..... 141, ***1228***
Chu, Shaoping
JS-02-06 274
Chug, Neha
MIC-05-457 ..... 116, ***1015***
Chun, Sang-hyun
MIC-15-180 1329
NSS-01-047 340
Chun, Sang-Hyun
MIC-10-179 ..... 130, ***1128***
Chung, Duck Young
RTSD-06-04 1549
Chung, Euiheon
MIC-15-417 1402
Chung, Hyun-Thai
MIC-10-323 1173
Chung, Kevin
WS-03-06 ..... **240**
Chung, Kevin Jaeyoung
MP-02-13 ..... 117, ***1024***
Chung, Kyoung-Jae
NSS-13-252 668
Chung, Yong Hyun
NSS-01-169 389
NSS-01-175 391
NSS-01-201 400
NSS-01-255 422
NSS-13-166 632
NSS-13-246 666
Chung, Yoon Soo
NSS-01-175 391
NSS-01-255 ..... **422**
NSS-13-166 632
Cianci, Cameron
NSS-01-179 393
Ciantar, Keith G.
MIC-10-008 1079
MIC-15-255 1351
Ciarlantini, Sabrina
NSS-13-298 686
Ciavarella-Ciavarella, Adele

Author Index

NSS-08-06 ..... 53, ***504***
NSS-14-03 700
NSS-14-06 703
Ciavatti, Andrea
RTSD-05-06 1544
Cicero, Valentina
NSS-13-324 ..... 77, ***696***
Cieri, Davide
NSS-01-113 366
Cihan, Zeynep
RTSD-04-352 1495
RTSD-04-353 ..... 172, ***1496***
Cimmino, Luigi
RTSD-01-07 1474
Cinausero, Marco
NSS-27-08 798
Cirotto, Francesco
N-LT-04-11 559
NSS-13-290 683
Civinini, Carlo
MIC-15-102 ..... **1304**
NSS-12-06 534
Cizel, Jean-Baptiste
NSS-03-06 466
Clagett, Vaun
NSS-01-299 440
Clark, Peter
MIC-10-077 1100
Clarke, Shaun D.
NSS-05-01 477
NSS-09-03 510
NSS-11-03 524
NSS-11-04 525
NSS-13-014 569
NSS-13-196 645
NSS-13-224 657
NSS-16-05 717
NSS-22-03 ..... 85, ***760***
NSS-27-07 797
Clegg, Paul
STIR-02 1597
Clemmensen, Andreas
MIC-10-212 1139
Closier, Joel
NSS-06-01 485
Codesido, Jessica
MIC-05-073 894
Cola, Adriano
RTSD-01-02 ..... 169, ***1469***
Colagiorgio, Laura
MIC-10-362 1184
Colarieti Tosti, Massimiliano
MIC-08-06 1063
Colja, Matija
NSS-12-02 530
NSS-13-130 617
Collado Soto, Pablo
N-LT-04-13 ..... 60, *561*
NSS-13-288 ..... 76, *682*
Collazuol, Gianmaria
NSS-21-07 756
Collij, Lyduine E.
MIC-05-265 954
Collins-Price, Patrick M.
NSS-22-02 ..... 85, ***759***
Colmenarejo Allavena, Iván
MIC-10-404 1197
MIC-15-201 1335
MIC-15-279 ..... 156, ***1358***
M-LT-03-06 1042
Colombini, Luca
TS-02-05 1588
Colombo, Matteo N.
MIC-05-217 ..... 107, ***940***
MIC-10-443 1211
MIC-13-05 1246
NSS-26-04 786
Colzani, Luca
NSS-13-304 688
Comtat, Claude
MIC-15-213 1339
Confalonieri, Lorenzo
MIC-15-438 ..... 162, ***1408***
MIC-15-447 1411
MIC-20-01 1453
M-LT-06-01 1264
Congedo, Liliana
NSS-20-03 ..... 83, ***743***
Connolly, Patrick
N-LT-04-03 552
NSS-13-180 638
Constanza, Corentin
MIC-05-214 ..... 107, ***938***
M-LT-01-06 ..... 95, ***839***
Contalbrigo, Marco
NSS-20-05 745
Contangelo, Annamaria
MIC-10-347 1180
Conti, Maurizio
MIC-05-424 1005
WS-04-17 260
Conventi, Francesco
N-LT-04-11 559
NSS-13-290 683
Conze, Pierre-Henri
MIC-15-174 1327
Coode, Piers
NSS-13-078 595
Cooper, Reynold
NSS-01-159 386
NSS-22-01 759
Corbeil Therrien, Audrey
MIC-03-08 861
Corde, Stephanie
NSS-06-05 488
Correia, Pedro M.M.
MIC-05-043 885
MIC-05-058 890
MIC-05-166 ..... 105, ***923***
MIC-05-349 981
MIC-05-448 1012
MIC-09-04 1070
MIC-10-446 1212
MIC-15-021 1280
MIC-15-156 1322
MIC-15-159 1323
MIC-15-243 1348
MIC-15-321 1371
M-LT-05-01 1254
NSS-01-143 ..... 37, *379*
RTSD-03-02 1486
WS-04-01 ..... **245**
Cortés, Guillem
NSS-02-04 458
Corti, Gloria
NSS-01-289 436
NSS-06-01 485
NSS-13-080 595
Cosmi, Valerio
MIC-05-280 959
STIR-13 ..... **1599**
Cossio, Fabio
MIC-10-443 1211
NSS-20-05 745
Cossío, Unai
MIC-05-358 984
Costa, Andrea
NSS-12-02 530
NSS-13-130 617
NSS-13-304 688
Costa, Marco
NSS-28-07 807
Costa-Luis, Casper O.
STIR-12 ..... **1600**
Cotroneo, Timothy
MIC-05-115 ..... 103, ***907***
M-LT-02-01 ..... 96, ***846***
Cotterill, Kathleen A.
MIC-10-464 1218

Author Index

N-LT-01-13 303
NSS-01-311 445
Cottrell, Stephen P.
NSS-13-078 595
Courbon, Frédéric
WS-04-03 247
Coussat, Aurélien
MIC-05-223 942
MIC-10-221 ..... 131, ***1142***
MIC-16-06 1425
M-LT-01-07 840
Cowen, Douglas F.
NSS-16-06 718
Crane, Tom
N-LT-01-04 295
NSS-01-033 334
NSS-13-244 665
Crean, Carol
JS-03-02 280
NSS-07-04 495
RTSD-06-02 1547
Crespi, Pierre
NSS-16-08 720
Croci, Tommaso
NSS-28-07 807
NSS-28-08 808
Croft, Stephen
NSS-01-057 343
NSS-13-228 658
NSS-18-05 732
Croizet, Hervé
NSS-01-101 362
Croteau, Étienne
MIC-02-03 831
Csige, Lóránt
NSS-27-05 796
Cucarella, Neus
MIC-05-118 ..... 103, ***908***
MIC-05-379 991
MIC-09-06 1072
M-LT-02-02 ..... 96, ***847***
Cuccaro, Sylvain
NSS-24-04 774
Cuccui, Chiara
MIC-05-448 1012
Cuciuc, Mihai
JS-01-06 267
Cui, Yingying
NSS-01-127 371
Cuozzo, Marie
NSS-11-02 523
NSS-13-206 649
Curado da Silva, Rui M.
RTSD-04-362 1504
Curado Da Silva, Rui M.
RTSD-04-400 ..... **1535**
Curcio, Davide
NSS-12-02 530
Curras Rivera, Esteban
NSS-21-08 757
Curtis, Travis
NSS-08-08 505
Cusimano, Alberto
NSS-01-305 443
NSS-20-04 744
TS-02-05 1588
Cutajar, Dean
NSS-04-01 ..... 49, *468*
NSS-04-02 ..... 49, *469*
NSS-06-05 ..... 51, *488*
Cuzzolin, Simone
TS-02-05 1588
Czernin, Johannes
MIC-15-366 1386

D

d'Enterria, David
NSS-12-04 532
Da Costa-Luis, Casper O.
STIR-13 1599
Da Rocha Rolo, Manuel D.
N-LT-01-10 301
NSS-01-061 345
NSS-17-04 725
NSS-21-07 756
Da, Jiayu
MIC-15-414 1401
D'Adda, Ilenia
N-LT-03-03 540
NSS-13-102 606
Dadgar, Habibollah
MIC-05-367 987
MIC-15-294 1363
D'Agata, Giuseppe
NSS-25-04 780
Dai, Bing
MIC-04-03 ..... 98, ***866***
Dai, Ji
MIC-05-127 911
Dai, Ruipeng
MIC-15-009 ..... 147, ***1277***
MIC-15-012 1278
MIC-15-117 1309
Dai, RuiPeng
MIC-05-013 876
Dai, Tiantian
MIC-05-109 906
NSS-13-184 640
NSS-13-220 655
WS-04-05 249
WS-04-06 250
Dal Zilio, Simone
NSS-12-02 530
Dall'Olio, Daniele
WS-03-13 ..... **242**
Dalla Betta, Gian-Franco
NSS-27-08 798
Dall'Olio, Daniele
MIC-15-384 1391
Dalmasson, Jacopo
JS-02-04 272
d'Almeida, Filip
NSS-09-01 ..... 54, ***508***
Danagoulian, Areg
NSS-13-250 ..... 74, ***667***
NSS-13-316 693
NSS-18-03 730
Danek, Adrian
MIC-10-281 1160
Dang, Hong-Phuong
MIC-01-02 824
Dang, Jiaxin
MIC-09-03 1069
MIC-15-450 1412
M-LT-06-02 1265
Dang, Na
MIC-14-04 1251
MIC-15-408 1399
Dang, Yongle
NSS-13-214 652
Daniel, Geoffrey
NSS-06-07 490
NSS-11-02 523
NSS-13-084 597
Daniel, Kirk
NSS-13-078 595
Daniel, Nixon
NSS-13-078 595
Danielsson, Mats
N-LT-01-10 301
NSS-01-061 345
Danilevski, Cyril
N-LT-03-12 547
NSS-08-07 505
NSS-13-300 687
NSS-13-304 688
Danzeca, Salvatore
NSS-01-245 418

Author Index

NSS-13-256 669
Dao, Valerio
NSS-17-03 724
Dao, Viet A.
MIC-10-194 1133
MIC-15-252 ..... 155, ***1350***
STIR-04 ..... **1598**
Darambara, Dimitra
MIC-03-02 857
Das, Biswajit
MIC-05-139 915
MIC-11-07 1229
MIC-12-02 ..... 142, ***1234***
MIC-12-03 1235
MIC-21-03 ..... 168, ***1461***
Dash, Ganapati
NSS-17-03 724
Dash, Swagat
MIC-05-367 987
MIC-15-294 1363
Dassanayake, Movindu
MIC-05-220 ..... 107, ***941***
M-LT-01-09 ..... 95, ***842***
Dastgerdi, Shaghayegh
MIC-05-313 969
Data, Emanuele M.
NSS-05-07 482
Datta, Amlan
MIC-10-044 ..... 125, ***1090***
M-LT-03-05 ..... 120, ***1041***
RTSD-05-07 ..... **1545**
Daub, Michael
RTSD-04-352 1495
Daube-Witherspoon, Margaret E.
MIC-04-03 866
MIC-05-262 953
MIC-19-01 1445
D'Avanzo, Antonio
N-LT-04-11 559
NSS-13-290 683
Davarpanah, Shideh
N-LT-02-11 ..... 30, ***315***
NSS-01-077 ..... 34, ***352***
Davey, Catherine E.
MIC-18-03 1438
Davies, Gareth
NSS-01-223 409
Davis, Joseph M.
NSS-01-279 431
Davolio, Fabio
NSS-01-263 ..... 44, ***425***
NSS-15-02 ..... 79, ***708***
Day, Jack
N-LT-02-10 315
NSS-01-267 426
De Astis, Stefano
NSS-12-07 535
NSS-28-04 804
De Benetti, Elliott
MIC-10-302 1166
De Bie, Nicolas
MIC-08-06 ..... 122, ***1063***
De Filippo, Enrico
NSS-25-04 780
De Geronimo, Gianluigi
NSS-10-01 ..... 55, ***516***
NSS-13-128 616
SC-01-01 11
SC-01-03 11
SC-01-05 11
De Guzman, John Patrick Ryan S.
MIC-10-170 ..... 130, ***1126***
De Izarra, Grégoire
NSS-06-02 486
De Jong, Hugo W.
WS-04-11 255
De La Rosa, Nathaly
NSS-24-04 774
de la Torre, Oscar
MIC-09-06 1072
MIC-09-08 1074
MIC-15-045 1287
de las Heras Gala, Hugo
MIC-10-233 1146
RTSD-02-04 1481
de Lorenzo, Gabriel G.
N-LT-01-07 298
NSS-01-039 336
de Luca, Saverio
NSS-25-04 780
de Luis Blanco, Diego
MIC-10-341 1178
De Luis, Diego
MIC-15-006 1276
De Matteis, Giovanni
NSS-13-324 696
De Matteis, Marcello
NSS-13-118 612
De Mits, Wolf
MIC-19-01 ..... 166, ***1445***
De Nardo, Guglielmo
N-LT-04-11 559
NSS-13-290 683
NSS-21-07 756
De Paepe, Antoine
MIC-01-02 824
MIC-08-08 ..... 122, *1065*
MIC-10-425 ..... 139, *1204*
MIC-15-216 ..... 154, ***1340***
De Pretto, Francesco
NSS-25-04 780
De Robertis, Giuseppe
NSS-20-03 743
de Rover, Vincent T.
NSS-06-05 ..... **488**
De Sio, Chiara
MIC-10-359 ..... **1183**
De Torres, Rafa
MIC-19-08 1451
Debernardis, Francesco
NSS-24-02 ..... 86, ***772***
Debus, Juergen
MIC-17-01 1428
Dědič, Vaclav
RTSD-01-02 1469
Defay, Xavier
NSS-10-04 519
DeFranchis, Matteo
NSS-12-04 532
Degenkolb, Skyler
NSS-01-315 447
Deguchi, Soma
NSS-02-02 456
Deidda, Daniel
MIC-10-194 1133
STIR-07 ..... ***1599***
STIR-09 185
Del Bene, Cristiana
NSS-01-263 425
NSS-15-02 708
Del Sordo, Stefano
RTSD-03-07 1490
Delafosse, Clément
NSS-13-048 582
Delagnes, Eric
NSS-13-084 597
Delenne, Julie
N-LT-04-11 559
NSS-07-08 498
NSS-13-290 683
Delker, Astrid
MIC-01-01 823
Della Casa, Giulio
NSS-20-05 745
Delogu, Pasquale
NSS-14-08 705
RTSD-08-02 1561
Demenev, Evgeny
NSS-01-067 348

Author Index

Demir, Ugur
NSS-01-137 376
Dendooven, Peter
MIC-10-332 1176
RTSD-04-394 1531
Deng, Mingxue
NSS-07-05 ..... 52, *495*
Deng, Runtao
MIC-10-452 ..... **1214**
MIC-18-05 1440
Deng, Tianyi
MIC-10-065 ..... 126, ***1097***
Deng, Weiting
MIC-15-468 1418
Deng, Zhi
NSS-18-02 729
RTSD-04-399 1534
Denis-Bacelar, Ana
MIC-15-345 1379
Denisov, Oleg
NSS-14-02 700
Deniz, Bayram
NSS-01-089 ..... 35, ***357***
NSS-01-137 ..... 37, *376*
Denker, Alexander
MIC-15-192 1332
Deptuch, Grzegorz W.
NSS-13-146 623
Derrien, Cyrille
NSS-03-06 466
Deut, Umberto
NSS-28-04 804
Dewji, Shaheen
N-LT-04-03 552
NSS-13-180 638
Dhamgaye, Vishal
JS-01-01 264
Dhaynaut, Maeva
MIC-18-04 1439
D'Hulster, Thibault
MIC-05-373 ..... 113, ***989***
MIC-15-276 1357
M-LT-06-06 1269
Di Capua, Francesco
NSS-21-07 756
Di Carlo, Aldo
RTSD-06-01 1547
Di Fraia, Carlo
N-LT-04-11 559
NSS-13-290 683
Di Fulvio, Angela
N-LT-01-06 297
N-LT-04-08 556
NSS-01-017 327
NSS-09-03 510
NSS-09-05 512
NSS-13-196 645
NSS-13-200 646
Di Martino, Fabio
NSS-12-06 534
Di Salvo, Andrea
NSS-17-05 ..... 81, ***726***
Di Venere, Leonardo
NSS-20-03 743
Dias, André
N-LT-01-14 305
NSS-01-313 446
Dickinson, Amy J.
JS-03-02 280
NSS-07-04 ..... 52, ***495***
RTSD-06-02 1547
Dickson, John
MIC-15-345 1379
Diehl, Inge
NSS-13-100 605
Diel, Felix
N-LT-04-06 555
NSS-13-192 643
Dieminger, Till C.
NSS-12-01 529
NSS-21-05 754
Dierlamm, Alexander
NSS-12-03 531
Dietze, Martijn M.A.
WS-04-11 255
Diglio, Sara
NSS-16-08 720
Dijk, Nienke
MIC-05-265 954
Dilsizian, Matthew
NSS-13-176 ..... 70, ***637***
Din, Huay
MIC-04-06 ..... **869**
Dinapoli, Roberto
NSS-01-093 358
NSS-08-04 502
D'Incà, Tommaso
N-LT-03-03 ..... 57, *540*
NSS-13-102 ..... 66, *606*
Ding, Dongzhou
JS-02-02 ..... 24, ***270***
Ding, Wenwan
NSS-15-04 710
Ding, Xiangxiang
WS-04-07 251
Divband, Ghasemali
MIC-05-313 969
MIC-05-319 971
MIC-05-367 987
MIC-15-294 1363
NSS-13-194 644
NSS-15-06 712
Djebra, Yanis
MIC-10-236 ..... **1146**
MIC-18-04 1439
Doblado, Juan Alexander Leal
MIC-15-468 1418
Doering, Dionisio
NSS-01-087 356
NSS-10-04 519
Dolenec, Rok
JS-02-04 272
MIC-05-019 878
MIC-09-08 1074
MIC-15-045 1287
NSS-19-06 739
NSS-21-06 ..... 84, ***755***
WS-02-03 ..... 17, ***228***
WS-02-10 ..... **232**
Dolmeta, Alessandra
NSS-17-04 725
Domenech, Alexandre Germain Philippe
NSS-21-06 755
Domingo-Pardo, César
MIC-05-361 985
MIC-10-098 1105
M-LT-04-02 1049
NSS-02-04 458
Dominguez Borrero, Claudia C.
STIR-01 ..... **1597**
Dominguez-Borrero, Claudia
MIC-05-073 ..... 102, ***894***
MIC-05-388 994
MIC-15-075 1296
Dominici, Lorenzo
RTSD-01-02 1469
Domnanich, Katharina
NSS-13-310 691
Dong, Hanzhe
RTSD-04-399 1534
Dong, Jiahui
MIC-10-239 1147
Dong, Minghao
NSS-13-266 673
Dong, Roushi
NSS-13-284 681
Dong, Sheng
NSS-01-121 369

Author Index

Dong, Yun
MIC-05-064 891
MIC-05-211 938
MIC-05-382 992
MIC-15-246 1349
MIC-15-420 1403
Dong, Zhengkun
WS-04-07 ..... 22, ***251***
Donghui, Hou
NSS-01-281 432
Doniger, Will
NSS-13-308 690
D'Onofrio, Adelina
N-LT-04-11 559
NSS-13-290 683
Donzella, Antonietta
MIC-10-362 1184
Doornenbal, Pieter
NSS-25-06 782
Doostparast, Armin
MIC-10-317 1171
Dopke, Jens
NSS-13-284 681
Doroud, Katayoun
MIC-10-206 1137
D'Ottavi, Fabio
NSS-13-118 ..... 66, *612*
Dragone, Angelo
MIC-03-06 860
NSS-10-04 519
NSS-23-02 766
Drakopoulos, Michael Drakopoulos
NSS-01-303 442
Dřevo, Jakub
RTSD-04-375 ..... 174, ***1514***
Driussi, Francesco
NSS-12-02 530
Drouet, Lance M.
NSS-13-158 ..... 69, ***628***
Du, Junwei
MIC-05-007 ..... 99, *874*
MIC-10-041 1090
MIC-10-104 1107
MIC-15-003 ..... 147, *1275*
M-LT-03-04 1040
WS-04-02 246
Du, Qiang
MIC-15-087 1300
Du, Tianxue
MIC-05-346 980
Du, Yanzhen
MIC-05-352 ..... 112, ***982***
Du, Yong
MIC-04-05 ..... 99, *868*
MIC-05-271 ..... 109, *956*
MIC-10-314 ..... 135, *1170*
MIC-15-300 1365
MIC-21-01 1459
Duan, Cindy
MIC-15-426 ..... 162, ***1404***
Duan, Jinyan
MIC-10-359 1183
Duan, Weigang
MIC-10-413 1200
MIC-15-078 1297
MIC-15-351 ..... 159, ***1381***
MIC-17-02 1429
Duan, Yanhua
MIC-05-385 993
Dubovik, Alexender M.
NSS-12-04 532
Duboz, Jean-Yves
RTSD-04-355 1498
DuBridge, Seth
NSS-22-05 761
Duch, Marta
N-LT-01-14 305
NSS-01-313 446
Duclos, Lucas
MIC-15-213 ..... 154, ***1339***
Duffy, Jon
NSS-15-05 711
Dufour, Arnaud
NSS-13-054 ..... 63, ***584***
Dulohan, Christine L.
N-LT-04-07 556
NSS-13-208 650
Dulski, Kamil
MIC-16-06 1425
Dumazert, Jonathan
NSS-01-241 416
Dunham, Brandon
MIC-10-044 1090
M-LT-03-05 1041
RTSD-05-07 1545
Dupont, Mathieu
MIC-05-337 977
N-LT-03-10 ..... 58, ***545***
NSS-06-07 490
NSS-13-084 597
NSS-13-134 ..... 67, ***619***
RTSD-04-398 1533
Dupraz, Kevin
NSS-15-05 711
Durand, Emmanuel
MIC-15-066 1293
Durand, Thibaud
NSS-13-206 649
Durandetto, Sofia
NSS-17-05 726
Durando, Matteo
NSS-28-08 808
Durando, Stefano
NSS-17-04 725
Dutta, Joyita
MIC-08-02 1059
MIC-11-05 1228

E

Eaton, Megan A.
MIC-05-421 ..... 114, ***1004***
Ebner, Simon
NSS-01-093 358
Echlin, MIke
RTSD-04-395 1532
Ecoffet, Robert
NSS-13-054 584
Edelstein, Michal
MIC-05-247 ..... 108, *949*
M-LT-02-07 ..... 97, *851*
Edwards, Jaasiel
MIC-10-422 ..... **1203**
Efe, Baris Can
NSS-21-06 755
Efthimiou, Nikos
MIC-05-280 ..... 109, ***959***
MIC-10-194 ..... 130, ***1133***
MIC-10-437 1209
MIC-12-06 1237
MIC-15-075 1296
STIR-01 1597
STIR-05 1598
STIR-13 1599
Eggimann, Lars
MIC-12-04 1236
Egwolf, Bernhard
N-LT-04-07 556
NSS-13-208 650
Ehrhardt, Matthias J.
MIC-15-192 1332
Eisch, Jonathan
NSS-13-120 613
Eksim, Ali
NSS-01-089 357
El Akel, Sara
NSS-13-212 652
El Bitar, Ziad
NSS-11-02 523

Author Index

El Fakhri, Georges
JS-02-04 272
MIC-02-03 831
MIC-05-019 878
MIC-09-08 1074
MIC-10-236 1146
MIC-15-045 1287
MIC-18-04 1439
WS-02-03 228
El katera, Samir
N-LT-03-10 545
NSS-13-134 619
Eleon, Cyrille
NSS-09-01 508
Elesgaray, Oihan
MIC-10-032 1087
Elgewaily, Dina O.E.
JS-02-04 272
NSS-21-02 751
Elihar, Andreas
N-LT-01-10 301
NSS-01-061 345
Elkayee Dehno, Avishan
MIC-05-445 ..... 115, ***1011***
Elkin-Basudo, Gali
MIC-05-247 949
M-LT-02-07 851
Ellin, Justin
NSS-22-05 761
Elmoujarkach, Ezzat
MIC-09-02 1068
MIC-10-020 ..... **1083**
MIC-15-123 1311
El-Sallabi, Sara H.
MIC-15-060 ..... 149, ***1292***
Emiliani, Simone
NSS-01-093 358
Emond, Elise
MIC-10-203 ..... 131, ***1136***
STIR-11 1599
WS-03-09 ..... **241**
Enari, Yuji
NSS-17-03 724
Encina-Baranda, Nerea
MIC-05-424 ..... 114, ***1005***
MIC-15-090 1301
MIC-15-219 1341
WS-04-17 ..... **260**
Endo, Shunsuke
NSS-27-01 792
Endou, Yoshihiro
TS-02-04 ..... **1587**
Engels, Elette
NSS-04-01 468
NSS-06-05 488
Enomoto, Kazuyuki
N-LT-02-04 310
NSS-01-219 408
Enriquez-Mier-y-Teran, Francisco E.
MIC-05-307 ..... 110, ***967***
MIC-15-129 ..... 151, ***1313***
Eo, Jung-Hyeon
NSS-01-269 427
Eom, Doyoon
NSS-13-082 596
Eom, Taehyeon
MIC-15-318 1370
M-LT-05-10 1262
NSS-02-05 459
Ercolani, Daniele
NSS-12-02 530
Erlandsson, Kjell
MIC-05-265 954
MIC-09-05 1071
MIC-10-068 ..... **1097**
Erojo, Mary
MIC-06-02 1028
Erwin, William
NSS-01-299 440
Esmaeilzadeh, Sajedeh
NSS-26-05 ..... 88, ***787***
Espagnet, Romain
MIC-02-03 831
NSS-21-03 752
Espinosa, Andrea
MIC-16-01 1420
Espinya Rojas, Albert
MIC-09-08 1074
NSS-23-04 768
Esposito, Ciro
NSS-13-118 612
Espósito, Rafael D.
MIC-15-336 1376
Esquibel, Adam
NSS-13-236 662
Esquinas, Pedro
MIC-08-03 1060
MIC-18-07 1442
Esser, Johannes N.
MIC-10-320 ..... **1172**
Esteve, Raúl
NSS-01-099 361
Etxebeste, Ane
MIC-05-088 899
MIC-05-214 938
MIC-06-02 ..... **1028**
M-LT-01-06 839
Evangelisat, Francesco
MIC-05-130 912
Evangelist, Francesco
MIC-10-083 1101
M-LT-04-09 1055
Evangelista, Francesco
MIC-10-059 1095
MIC-17-05 1432
M-LT-04-08 1054
Exley, Matthew
MIC-09-05 1071
RTSD-03-05 1489

F

Fabbri, Andrea
MIC-15-087 1300
RTSD-09-04 1571
Fabris, Lorenzo
MP-01-16 ..... 93, ***821***
NSS-05-06 481
NSS-05-08 483
NSS-21-03 752
Faby, Sebastian
MIC-10-260 1153
MIC-15-162 1324
Facchinelli, Tiziano
NSS-01-067 348
Fadavi Mazinani, Mohammad
MIC-10-443 1211
NSS-12-07 535
Faddegon, Bruce
MIC-12-03 1235
Fadini, Giulia
NSS-21-02 751
Fahey, Frederic
MIC-10-275 1158
Fajnorova, Ivata
MIC-15-366 1386
Fakharpour, Ava
MIC-15-366 1386
Falcão, Gabriel
RTSD-04-400 1535
Falchieri, Davide
NSS-01-109 365
NSS-13-298 686
NSS-20-05 ..... 83, ***745***
NSS-21-07 756
Falivene, Annamaria
MIC-15-102 1304
Falkenberg, Gerald
NSS-08-05 503

Author Index

Fan, Kailong
MIC-19-02 ..... **1446**
Fan, Peng
MIC-17-02 1429
Fan, Qing
NSS-13-270 675
Fan, Yanan
MIC-20-05 1457
Fan, Yu-Ming
MIC-05-394 996
Fanals-i-Batllori, Llorenç
NSS-10-04 519
NSS-23-02 766
Fanchini, Erica
NSS-15-02 708
Fanciulli, Giuseppe
MIC-05-337 977
Fang, Ming
N-LT-04-08 556
NSS-09-03 ..... 54, ***510***
NSS-09-05 512
NSS-13-196 645
NSS-13-200 646
Fang, Shilong
NSS-01-075 ..... **351**
Fang, Wei
MIC-15-312 1368
M-LT-05-05 1258
Fang, Zhijie
MIC-15-387 1392
Fanti, Stefano
MIC-15-384 1391
Farella, Isabella
RTSD-01-02 1469
Farkaš, Martin
NSS-01-287 435
Farolfi, Andrea
MIC-15-384 1391
Farré-Melero, Arnau
MIC-15-075 ..... 149, ***1296***
Fasselt, Lucian
NSS-17-03 724
Fatemi, Setareh
MIC-05-361 985
Faure, Jean-Louis
NSS-07-08 498
Favilla, Leonardo
N-LT-04-11 559
NSS-13-290 683
Favilla, Stefania
RTSD-03-03 ..... **1487**
Fayad, Hadi
MIC-15-060 1292
Febbraro, Michael
NSS-05-06 481
Felfelian, Vahid
MIC-10-368 1186
Felipe-Maestre, María
MIC-05-283 960
Feng, Boyu
MIC-07-02 ..... 119, ***1034***
MIC-12-07 1239
MIC-15-453 1413
Feng, Hua
NSS-01-127 371
RTSD-09-03 1569
Feng, Shaojie
MIC-05-100 903
Feng, Yuemeng
MIC-10-191 1132
MIC-10-326 ..... 135, ***1174***
Feng, Yuzhong
NSS-13-026 573
NSS-13-240 663
Feng, Zhiheng
MIC-19-04 1448
Ferjaoui, Khalil
NSS-01-093 358
Fernandez Garcia, Marcos
N-LT-01-11 302
NSS-01-063 346
Fernandez Moreira, Miguel D.
NSS-12-07 535
Fernandez Prieto, Antonio
RTSD-07-05 1556
Fernández Prieto, Antonio
MIC-05-328 974
Fernández-Tejero, Javier
N-LT-01-14 ..... 28, ***305***
NSS-01-313 ..... 46, ***446***
Fernández-Tenllado, José María
MIC-05-019 878
MIC-09-08 1074
MIC-15-045 1287
NSS-03-05 465
NSS-23-04 768
Ferrari, Claudio
RTSD-04-378 1517
Ferrari, Elena
RTSD-04-378 1517
Ferrari, Sara
NSS-01-067 348
Ferreira Brito Filho, Carlos H.
NSS-06-01 485
Ferreira, Kelley M.
MIC-04-07 ..... 99, ***870***
Ferreira, Tiago
MIC-10-446 1212
Ferrero, Marco
NSS-12-03 531
NSS-28-04 804
NSS-28-07 ..... 90, ***807***
NSS-28-08 ..... 90, ***808***
Ferrero, Veronica
MIC-05-391 995
MIC-10-191 1132
NSS-05-07 482
NSS-12-07 535
Ferretti, Andrew E.
MIC-10-053 ..... 125, ***1093***
Ferri, Tommaso
MIC-05-082 ..... 102, ***897***
MIC-21-02 ..... 168, *1460*
Ferri, Valentina
STIR-08 185
STIR-11 ..... ***1599***
Feruglio, Alessandro
RTSD-08-02 1561
Fevre, Ludivine
RTSD-04-396 1532
Ficorella, Andrea
JS-02-04 272
NSS-21-02 751
Ficorella, Francesco
N-LT-01-11 302
NSS-01-063 346
NSS-08-05 503
Fiederle, Michael
RTSD-03-01 1485
RTSD-04-352 1495
RTSD-04-353 1496
RTSD-04-392 1529
RTSD-08-03 1562
RTSD-10-01 1577
Fiederle, Michael: **1582**
Fienga, Francesco
NSS-21-07 756
Fietzek, Urban
MIC-10-281 1160
Figge, Martin
WS-02-16 235
Figueroa Saavedra, Rodolfo G.
MIC-05-370 ..... **988**
MIC-10-446 1212
Fijahi, Lamiaa
RTSD-06-05 1550
Filliatre, Philippe
NSS-06-02 486
Finne, Theodore T.

Author Index

NSS-01-279 431
Fiore, Salvatore
NSS-01-245 ..... 43, ***418***
NSS-13-256 669
Fiorillo, Giuliana
NSS-21-07 756
Fiorina, Elisa
MIC-10-443 1211
NSS-05-07 482
NSS-12-07 535
Fiorini, Carlo E.
MIC-05-082 897
MIC-10-038 1089
MIC-10-293 1163
MIC-10-347 1180
MIC-17-03 1430
MIC-21-02 1460
M-LT-04-04 1051
N-LT-03-03 540
N-LT-03-13 548
NSS-01-133 374
NSS-01-305 443
NSS-03-02 462
NSS-03-03 463
NSS-08-01 500
NSS-08-05 503
NSS-08-06 504
NSS-09-04 511
NSS-13-102 606
NSS-13-260 671
NSS-13-306 689
NSS-14-03 700
NSS-14-06 703
NSS-23-05 769
Fiorini, Massimiliano
NSS-01-139 377
RTSD-08-02 1561
Fissum, Kevin
NSS-24-04 774
Fitzhugh, Richard
NSS-01-055 342
Fiumicelli, Gabriele
NSS-12-02 530
NSS-13-130 617
NSS-13-304 ..... 76, ***688***
Flatt, Jason
NSS-25-06 782
Flavell, Robert R.
MIC-05-334 976
MIC-12-01 1233
Fleck, Ivor
MIC-05-406 1000
Fleta, Celeste
JS-02-09 276
N-LT-02-02 308
NSS-01-275 430
NSS-12-05 ..... 57, *532*
Fleury, Julien
NSS-03-06 466
Flores, Eduardo
MIC-15-006 1276
Floris, Tommaso M.
NSS-10-05 520
NSS-21-07 756
WS-02-09 ..... 18, ***231***
Flors Marti, Joan
MIC-05-355 ..... 112, ***983***
Floyd, Nicholas
N-LT-01-05 296
NSS-01-019 328
NSS-01-129 372
NSS-13-236 662
Fochuk, Petro
RTSD-04-354 1497
RTSD-04-365 ..... **1506**
Fogg, Thomas
MIC-10-332 ..... 135, ***1176***
Foglia, Beatrice
MIC-10-347 1180
Folley, Damilola
NSS-13-228 658
Follo, Umberto
N-LT-01-10 301
NSS-01-061 345
Fondacci, Alessandro
NSS-28-07 807
NSS-28-08 808
Fondement, Valentin
NSS-05-04 ..... 50, ***479***
Fontaine, Kathryn
MIC-05-244 948
MIC-10-236 1146
MIC-18-04 1439
M-LT-02-08 852
Fontaine, Réjean
JS-02-07 275
MIC-02-03 831
MIC-03-08 861
MIC-15-153 1321
NSS-21-03 752
Fontbonne, Jean-Marc
MIC-21-05 1463
For the IMPET project
MIC-16-06 1425
Forcieri, Leonardo
NSS-12-06 534
Ford, Michael
NSS-13-274 677
Forgione, Andrea
MIC-10-347 1180
MIC-17-03 1430
NSS-03-03 ..... **463**
NSS-09-04 511
Formenti, Samuele
NSS-14-03 700
Forsythe, Eyan
NSS-01-117 367
NSS-10-03 518
NSS-14-05 702
Forte Deltell, Anabel
MIC-15-282 1359
M-LT-06-07 1270
Forza, Camilla
NSS-21-02 751
Foss, Katarina
RTSD-04-386 1523
RTSD-04-387 1524
RTSD-04-393 ..... 176, ***1530***
Fosset, Steven
NSS-13-322 695
Foster, Jackson W.
MIC-10-449 ..... 140, ***1213***
MIC-15-288 1361
Fowler, James
MIC-08-03 1060
MIC-18-07 1442
Fox, Harald
NSS-13-284 681
Fox, Oliver
JS-01-01 264
Foygel Barber, Rina
MIC-15-234 1345
Fraboni, Beatrice
NSS-12-06 534
RTSD-05-06 1544
RTSD-06-05 1550
Fraile, Luis M.
MIC-15-462 1416
MIC-16-01 1420
N-LT-01-07 298
NSS-01-027 332
NSS-01-039 336
NSS-01-131 373
NSS-13-086 598
Fraioli, Francesco
MIC-10-068 1097
Francesconi, Marco
N-LT-04-11 559
NSS-13-290 683

Author Index

Francisco, Cristiana
RTSD-04-400 1535
François, Brieuc
NSS-12-04 532
Fras, David
RTSD-02-02 1479
Fratelli, Ilaria
RTSD-05-06 ..... 178, ***1544***
RTSD-06-05 1550
Frayssinet, Eric
RTSD-04-355 1498
Freeman, Patrick
NSS-22-05 761
Freire, Marta
MIC-05-118 908
MIC-05-379 991
MIC-10-344 ..... 136, ***1179***
MIC-10-386 ..... 137, ***1191***
M-LT-02-02 847
M-LT-03-10 ..... 120, ***1046***
Freitas Pacifico, Andre
NSS-06-01 485
Freixas, Lluis
MIC-15-348 1380
Frey, Eric
MIC-21-01 1459
Freye, Tim
MIC-16-05 ..... 164, ***1424***
Friday, David
NSS-01-283 433
Fritchie, Jacob W.
N-LT-01-06 ..... **297**
NSS-01-017 ..... **327**
Fritz, Shayden
N-LT-01-05 296
NSS-01-019 328
NSS-01-129 372
Fritzsche, Nick
NSS-19-02 ..... 82, ***735***
Frixou, Anna
MIC-05-463 ..... 116, ***1017***
MIC-18-06 1441
Froehlich, Thomas
JS-01-03 265
Froejdh, Erik
NSS-01-093 358
Frojdh, Erik
NSS-08-04 502
Fromont, Maëlle
MIC-15-153 ..... 152, ***1321***
Frontini, Luca
NSS-01-109 365
NSS-14-08 705
Fu, Liqing
MIC-15-399 1396
Fu, Weibin
MIC-10-275 ..... **1158**
Fu, Yi
NSS-23-01 ..... 85, ***765***
Fu, Zhenmin
MIC-15-396 1395
Fuchs, Christian
NSS-13-122 613
Fujii, Yuki
NSS-13-144 622
Fujimoto, Macoto
MIC-11-03 1226
MIC-15-453 1413
MIC-15-459 ..... 163, ***1415***
M-LT-06-04 ..... 146, ***1267***
Fujita, Yowichi
NSS-01-071 349
Fujiwara, Chihaya
NSS-01-029 333
NSS-22-06 762
NSS-27-05 ..... 89, ***796***
Fujiwara, Takeshi
N-LT-02-14 ..... 30, ***318***
NSS-01-321 ..... 47, ***450***
NSS-13-030 575
Fukao, Yoshinori
NSS-01-071 349
Fuke, Hideyuki
NSS-13-064 589
Fukuda, Rikuto
RTSD-04-374 1514
Fulton, Roger
MP-01-01 ..... 92, ***817***
MP-02-01 ..... 116, ***1021***
Funaki, Hironori
NSS-01-153 383
NSS-13-152 626
Funk, Stefan
RTSD-08-05 1564
Furenlid, Lars R.
MIC-05-208 937
MIC-05-436 1008
MIC-15-309 1367
RTSD-03-04 1488
WS-04-16 259
Furuse, Hiroaki
NSS-01-011 325
Furuta, Mizuki
MIC-05-094 ..... 102, ***901***
MIC-15-081 ..... 149, ***1298***
Furuta, Yu
MIC-05-151 ..... 105, ***919***
MIC-05-157 921
M-LT-02-04 849
M-LT-02-05 ..... 96, ***850***
Fushimi, Motofumi
MIC-12-07 1239
Futura, Yu
MIC-15-177 1328

G

Gaborieau-Borissenko, Elena
RTSD-04-398 1533
Gagliardi, Francesco
NSS-14-08 705
Gaioni, Luigi
NSS-01-109 ..... 36, ***365***
NSS-14-08 705
Gaitán Dominguez, Sara
MIC-10-404 1197
MIC-15-462 1416
M-LT-03-06 1042
N-LT-01-07 298
NSS-01-027 ..... 32, ***332***
NSS-01-039 336
NSS-01-131 373
NSS-13-086 598
Galarneau, Tommy
MIC-02-03 831
Galindo-Morata, Carlos
MIC-10-023 1084
MIC-10-404 1197
MIC-15-201 ..... 154, ***1335***
MIC-15-279 1358
M-LT-03-06 1042
Galletto, Simone
NSS-28-07 807
Gallezot, Jean-Dominique
MIC-10-236 1146
MIC-18-04 1439
Gallin Martel, Marie-Laure
MIC-05-337 977
Galve Lahoz, Pablo
MIC-15-069 1294
Galve, Pablo
MIC-10-023 1084
MIC-10-404 1197
MIC-15-201 1335
MIC-15-279 1358
MIC-16-01 1420
M-LT-03-06 1042
Gamage, Kelum A.A.
NSS-07-07 497

Author Index

NSS-13-198 645
Gameiro, Bernardo
MIC-05-361 985
Gandini, Andrea
MIC-10-362 1184
Gang, Grace J.
MIC-04-06 869
MIC-05-178 ..... 105, *928*
Gao, Bo
MIC-05-064 ..... 101, ***891***
MIC-15-057 1291
Gao, Lilei
MIC-08-04 1061
MIC-17-02 1429
Gao, Ting
NSS-25-06 782
Gao, Yanyan
NSS-13-284 681
Garbolino, Sara
N-LT-01-10 301
NSS-01-061 345
NSS-17-05 726
García Fernández, Daniel
MIC-05-328 974
Garcia Garcia, Lucia Victoria
NSS-04-03 ..... 49, ***470***
García Rivas, Iris
MIC-05-328 ..... **974**
García-Aparisi, Francisco B.
MIC-15-285 1360
García-Barrena, Jara
NSS-01-099 ..... 35, ***361***
Garcia-Garrit, Alba
MIC-15-075 1296
García-Otero, Xurxo
MIC-05-073 894
García-Polo, Pablo
MIC-15-360 1384
Garcia-Sciveres, Maurice
NSS-13-106 607
García-Varela, Lara
MIC-05-073 894
Gardikiotis, Alexandros
NSS-05-05 480
NSS-13-268 674
Gargano, Fabio
NSS-20-03 743
Gariazzo, Gabriella
N-LT-01-06 297
NSS-01-017 327
Garibotto, Valentina
MIC-05-403 999
Garnier, Alicia
MIC-05-337 977
Garosi, Paola
NSS-01-263 425
NSS-15-02 708
Garrido, Lluis
MIC-15-045 1287
Garvey, Declan D.
MIC-10-089 ..... 127, ***1103***
M-LT-04-05 ..... 121, ***1052***
Garzetti, Fabio
MIC-17-03 1430
NSS-03-03 463
NSS-09-04 511
NSS-12-02 530
NSS-13-130 ..... **617**
NSS-13-304 688
Gascón, David
JS-02-04 272
MIC-05-019 878
MIC-09-06 1072
MIC-09-08 ..... 123, ***1074***
MIC-15-045 1287
NSS-03-05 465
NSS-23-04 768
WS-02-03 228
Gaudino, Giovanni
N-LT-04-11 559
NSS-13-290 683
Gaudreault, Maxime
MIC-02-03 831
MIC-10-092 1104
MIC-15-432 1406
MIC-18-04 1439
M-LT-04-07 1054
Gautam, Viveka
NSS-01-093 358
NSS-08-04 ..... 53, ***502***
Gavier, Luisa
MIC-15-336 1376
Gaze, Mark
MIC-15-345 1379
Ge, Yongshuai
MIC-05-148 ..... **918**
RTSD-04-364 1505
RTSD-04-373 1513
RTSD-04-377 ..... **1516**
RTSD-04-388 1525
Gegenmantel, Eike
MIC-05-028 880
MIC-05-103 904
MIC-15-291 1362
MIC-15-381 1390
M-LT-05-04 1257
Gelmi, Luca
NSS-13-118 612
Geminiani, Sandro
NSS-20-05 745
Gendre, Quentin
RTSD-02-02 1479
Geng, Lisheng
MIC-14-05 1252
Gennisson, Jean-Luc
MIC-15-213 1339
Gensolen, Fabrice
N-LT-03-10 545
NSS-13-134 619
Georgeous, Joel
NSS-14-06 ..... 78, ***703***
Georgii, Robert
NSS-01-315 447
Geppert, Christopher
MIC-05-355 983
Geraci, Angelo
NSS-03-03 463
NSS-12-02 530
NSS-13-130 617
NSS-13-304 688
Geraci, Elena
NSS-25-04 780
Gerard, Rovira L.
NSS-27-01 792
Gerardi, Gaetano
RTSD-03-07 1490
Gerardin, Simone
NSS-01-109 365
Gerber, Julian
NSS-01-053 ..... 33, ***341***
NSS-04-06 473
Gerenton, Valentin
NSS-06-02 ..... 51, ***486***
Gernhäuser, Roman
NSS-01-315 447
Geronimo, Gianluigi D.
RTSD-07-02 1554
Geslot, Benoit
N-LT-02-07 312
NSS-01-231 412
Gheribi, Aimen E.
RTSD-09-08 ..... 181, ***1574***
Ghezzi, Joseph
RTSD-02-05 1481
Ghisetti, Maurizio
N-LT-03-12 ..... 58, ***547***
NSS-08-07 505
NSS-13-300 ..... 76, ***687***
Ghisio, Filippo

Author Index

MIC-05-082 897
MIC-10-293 1163
MIC-21-02 ..... **1460**
NSS-03-02 462
Ghislotti, Luca
NSS-14-04 ..... 78, ***701***
Ghodsi-Rad, Mohammad A.
MIC-05-319 971
NSS-13-194 644
NSS-15-06 712
Ghorbanian, Navid
RTSD-10-03 1579
Ghosh, Joydip
NSS-07-04 495
Ghosh, Uttal
NSS-13-100 605
Ghujeh, Amer
MIC-15-060 1292
Giacomini, Gabriele
NSS-08-03 502
Giangrande, Luca
NSS-25-02 ..... 87, ***778***
Giannini, Alessando
TS-02-05 1588
Gianoli, Chiara
MIC-05-130 912
Giaz, Agnese
NSS-01-009 324
NSS-13-074 593
Gibson, Tia
MIC-19-08 1451
Giglio, Daryl T.
RTSD-04-397 ..... 176, ***1533***
Gignac, Matthew
NSS-01-147 381
Gil, Marc
MIC-05-118 908
MIC-05-379 991
MIC-10-344 1179
M-LT-02-02 847
Gil-Bosch, Laura
MIC-05-118 908
M-LT-02-02 847
Giliberti, Mario
NSS-20-03 743
Gingu, Cristinel V.
NSS-20-07 747
Ginsz, Michael
NSS-13-262 672
Giordanengo, Simona
NSS-05-07 482
NSS-12-07 ..... **535**
NSS-28-04 804
Giordano, Ferdinando
NSS-01-173 391
Giordano, Raffaele
JS-01-06 ..... 24, ***267***
Giovagnoli, Debora
NSS-16-08 720
Girard, Sylvain
NSS-13-322 695
Giri, Naresh
NSS-28-06 806
Girolami, Marco
RTSD-06-01 ..... 178, ***1547***
Gispert López, Juan Domingo
MIC-05-265 954
Giubilato, Piero
NSS-13-298 ..... 76, ***686***
Giuffrida, Luigi
NSS-17-04 725
Glaser De Senna, Pedro
NSS-06-01 485
Glodo, Jarek
MIC-10-041 ..... 125, ***1090***
M-LT-03-04 ..... 119, ***1040***
NSS-07-03 494
NSS-07-06 ..... 52, ***496***
NSS-13-046 581
NSS-16-01 714
NSS-16-07 719
RTSD-04-360 ..... 173, *1502*
Glover, James J.
NSS-13-088 599
Gnanvo, Kondo
NSS-13-310 691
Gnatyuk, Volodymyr
NSS-13-056 585
RTSD-04-351 ..... 172, ***1495***
RTSD-04-357 1500
RTSD-04-376 1515
RTSD-04-401 1536
RTSD-07-06 1557
RTSD-07-07 1558
Godfrey, Liam
NSS-13-088 599
NSS-13-278 678
Goesseye, Hélène
MIC-11-08 1230
Goh, YoungMoon
MIC-10-080 ..... 126, ***1100***
Goicoecheaca, Victor
NSS-22-05 761
Gola, Alberto
JS-02-03 271
JS-02-04 272
JS-02-05 273
MIC-05-019 878
MIC-09-08 1074
MIC-15-045 1287
N-LT-01-08 299
NSS-01-015 326
NSS-01-293 438
NSS-21-02 751
NSS-21-04 ..... 84, ***753***
NSS-21-08 757
WS-02-03 228
WS-02-07 ..... 17, ***230***
Goldan, Amir H.
MIC-10-137 1116
Golhen Mateo, Clara N.
MIC-10-023 1084
MIC-15-069 ..... 149, ***1294***
Golina-Bezshyyko, Larysa
NSS-12-04 532
Gomà, Carles
MIC-15-324 1372
M-LT-05-02 1255
Gomes, Andrea
NSS-11-01 ..... 55, ***523***
Gomes, Tomás
MIC-05-448 1012
Gómez, Salvador M.
MIC-15-324 ..... 158, *1372*
M-LT-05-02 ..... 144, *1255*
Gomez, Sergio
MIC-09-06 1072
NSS-03-05 465
Gómez, Sergio
MIC-05-019 878
N-LT-03-02 539
N-LT-04-14 561
NSS-13-098 604
NSS-13-292 684
NSS-20-06 746
Gómez-Cadenas, Juan José
MIC-05-034 882
NSS-01-099 361
Gómez-González, Juan Pablo
MIC-05-388 994
Gómez-Lado, Noemí
MIC-05-073 894
Gómez-Muñoz, María
MIC-05-073 894
Gong, Datao
NSS-20-07 ..... 83, *747*
Gong, Hanmei
MIC-15-408 1399
Gong, Jingzhe

Author Index

MIC-05-046 886
Gong, Kuang
MIC-01-04 826
MIC-10-269 1156
Gong, Shenghuan
MIC-02-02 830
Gong, Tan
MIC-05-190 ..... **931**
MIC-14-03 1250
Gong, Weile
NSS-17-06 727
Gong, Wenxuan
NSS-01-121 369
Gonski, Julia
NSS-23-06 770
Gonzalez, Antonio J.
MIC-05-118 908
MIC-05-121 909
MIC-05-238 946
MIC-05-379 ..... 113, *991*
MIC-09-02 1068
MIC-09-06 1072
MIC-10-020 1083
MIC-10-344 1179
MIC-10-386 1191
MIC-13-02 1243
MIC-15-123 1311
M-LT-02-02 847
M-LT-02-10 854
M-LT-03-10 1046
WS-04-13 256
Gonzalez-Montoro, Andrea
MIC-05-058 890
MIC-05-118 908
MIC-05-121 ..... 103, *909*
MIC-05-379 991
MIC-05-448 1012
MIC-09-06 1072
MIC-10-386 1191
M-LT-02-02 847
M-LT-02-10 ..... 97, *854*
M-LT-03-10 1046
WS-04-01 ..... **245**
WS-04-13 256
González-Ramírez, Mario A.
MIC-05-049 ..... **887**
Gonzalez-Tarrio, Pablo
N-LT-01-07 298
NSS-01-039 336
Goodman, David
MIC-21-03 1461
RTSD-02-05 1481
Goodwin, Matthew
NSS-06-03 487
Goorden, Marlies C.
MIC-10-251 1151
Gorni, Dominik S.
NSS-13-146 623
Górriz Sáez, Juan Manuel
MIC-15-282 1359
M-LT-06-07 1270
Gorriz, Juan M.
MIC-10-317 1171
Górriz, Juan M.
MIC-10-296 1164
MIC-10-308 1168
Gorriz, Juan Manuel
MIC-10-281 1160
MIC-10-290 1162
Gostilo, Vladimir
RTSD-05-02 1541
Gourishetty, Anil K.
NSS-01-043 ..... 32, *338*
NSS-01-045 ..... 33, *339*
NSS-01-157 ..... 38, *385*
NSS-07-02 493
NSS-13-022 ..... 61, *572*
NSS-13-038 ..... 62, *578*
NSS-13-204 648
Goyes-Acosta, Karol F.
MIC-05-112 906
Graafsma, Heinz
NSS-10-02 516
Grabmaier, Anton
WS-02-16 235
Grace, Carl
MIC-05-037 883
NSS-13-106 607
RTSD-09-06 1572
Gracequist, Kevin
NSS-26-05 787
Graham, Colton
NSS-13-014 569
Grams, Michael
NSS-06-05 488
Granados, Matthew
RTSD-04-385 ..... 175, ***1522***
RTSD-09-02 1568
Granger, Charles-Etienne
NSS-26-05 787
Granja, Carlos
NSS-01-273 ..... 44, ***429***
RTSD-04-386 1523
RTSD-04-387 1524
RTSD-04-393 1530
RTSD-04-400 1535
Grazioso, Ron
NSS-01-295 439
Greco, Michela
RTSD-04-390 ..... **1527**
Green, Brendan
NSS-01-057 343
NSS-13-228 ..... 72, ***658***
Green, Jenson
RTSD-06-02 1547
Greiffenberg, Dominic
NSS-01-093 358
RTSD-01-06 1473
Greuter, Marcel J.W.
MIC-05-097 902
MIC-10-260 1153
Grey, Gabrielle J.
MIC-10-464 ..... 140, ***1218***
N-LT-01-13 303
NSS-01-311 445
Grievson, Alex
NSS-18-05 732
Grill, Roman
RTSD-01-04 1471
RTSD-04-358 1501
RTSD-04-375 1514
RTSD-06-03 1548
Grimm, Jan
WS-04-17 260
Grisoni, Luca
MIC-21-02 1460
Groba de Antas, Soraya
MIC-05-073 894
Grobshtein, Yariv
MIC-05-247 949
MIC-15-210 1338
M-LT-02-07 851
Grogg, Kira
MIC-15-045 1287
Groschupf, Dennis
MIC-01-01 823
Gros-Daillon, Eric
NSS-27-03 794
RTSD-04-363 ..... **1505**
Grossmann, Martin
MIC-05-058 890
MIC-05-349 981
MIC-05-448 1012
Grosso, Giorgio
MIC-10-362 1184
Groves, Douglas M.
JS-03-06 283
Gruel, Adrien
NSS-02-01 455

Author Index

Gruev, Viktor
NSS-09-05 ..... 54, *512*
Grundler, Pascal V.
MIC-12-04 1236
Grundmanis, Normunds
RTSD-05-02 ..... 177, ***1541***
Grüner, Christoph
NSS-01-315 447
Gu, Qinlin
MIC-20-05 1457
Gu, Yufan
MIC-15-312 1368
M-LT-05-05 1258
Gu, Zheng
MIC-05-013 876
MIC-05-067 892
MIC-05-127 911
MIC-05-250 949
MIC-05-253 950
MIC-05-343 979
MIC-09-03 1069
MIC-09-07 1073
MIC-10-224 1143
MIC-10-455 1215
MIC-15-009 1277
MIC-15-012 1278
MIC-15-117 1309
MIC-15-120 1310
MIC-15-261 1353
MIC-15-339 1377
MIC-15-450 1412
MIC-21-04 1462
M-LT-06-02 1265
Guan, Zilong
MIC-05-385 993
Guardiola, Consuelo
JS-02-09 ..... 25, ***276***
MIC-10-017 1082
M-LT-03-03 1039
N-LT-02-02 308
NSS-01-275 430
NSS-12-05 ..... **532**
Guatelli, Susanna
NSS-04-02 469
NSS-06-05 488
Guazzoni, Chiara
N-LT-03-12 547
NSS-01-291 ..... 45, ***437***
NSS-06-08 491
NSS-08-07 505
NSS-13-300 687
NSS-25-04 ..... 87, ***780***
Guberman, Daniel
MIC-05-019 878
MIC-09-06 1072
MIC-09-08 1074
Guedan, Fernando
MIC-05-430 ..... 115, ***1006***
Guerard, Bruno
NSS-24-04 774
Guérard, Bruno
N-LT-02-01 307
NSS-01-271 428
Gullberg, Grant T.
MIC-05-439 ..... **1009**
Gundacker, Stefan
JS-02-05 273
N-LT-01-08 299
NSS-01-015 326
NSS-21-04 753
SC-02-03 11
Gunji, Shuichi
N-LT-02-15 318
NSS-01-325 451
Guntha, Pavan S.
MIC-15-327 1373
M-LT-05-08 1260
WS-04-04 248
Guo, Cheng
NSS-01-095 359
Guo, Dian
MIC-10-338 ..... 136, ***1177***
Guo, Fangyi
NSS-12-04 532
Guo, Haoran
NSS-17-06 727
Guo, Liang
MIC-04-08 871
Guo, Ning
MIC-19-02 1446
Guo, Peiyuan
MIC-03-03 858
NSS-18-02 729
Gupta, Aseem
MIC-03-06 860
NSS-01-087 ..... 35, *356*
NSS-10-04 519
NSS-23-02 766
NSS-23-06 ..... 86, ***770***
Gupta, Tanmay
NSS-13-064 589
Gür, Fatih N.
MIC-05-193 932
Gushchina, Liudmila
MIC-10-011 1080

H

Ha, Hyun-Soo
NSS-01-269 427
Ha, Won Yong
NSS-21-06 755
Haas, Esther
MIC-15-027 1282
Haberl, Sebastian
NSS-17-03 724
Habib, Alexandre
NSS-10-04 519
Haddar, Amar
NSS-03-06 466
Hadžić, Šejla
NSS-04-04 ..... 49, ***471***
Haefeli, Guido
NSS-13-080 595
NSS-21-08 757
Haefner, Andrew
NSS-22-05 761
Haese, Harald
NSS-01-315 447
Hagemann, Felix
NSS-01-053 341
Hagura, Naoto
NSS-13-248 667
Haight, Sophia E.
NSS-04-06 ..... 49, ***473***
Hait-Fraenkel, Ester
MIC-05-247 949
M-LT-02-07 851
Hajianfar, Ghasem
MIC-05-403 999
MIC-10-206 1137
Hakulinen, Mikko
MIC-06-02 1028
Halfon, Orith
NSS-13-260 ..... 74, ***671***
Haller, Gunther
NSS-13-104 607
Hamada, Eitaro
NSS-01-071 349
NSS-01-141 378
Hamaguchi, Kenji
NSS-02-02 456
Hamato, Akram
MIC-05-346 980
MIC-17-06 ..... 165, ***1433***
NSS-16-01 ..... 79, ***714***
Hambley, David
NSS-13-228 658
Hamdan, Moh

Author Index

MIC-07-02 1034
Hammad Ali, Omar
NSS-28-07 807
NSS-28-08 808
Hammad Alì, Omar
N-LT-01-11 302
NSS-01-063 346
Hammer, Mike
MIC-03-06 860
NSS-08-02 501
NSS-10-04 519
Hammers, Alexander
MIC-01-03 825
MIC-05-265 954
Hammi, Abdelkhalek
MIC-10-320 1172
Hammig, Mark
MIC-10-464 1218
N-LT-01-13 303
NSS-01-311 445
Hammoutene, Elhadi
RTSD-09-08 1574
Han, Dae Yup
MIC-05-289 962
Han, Dejun
NSS-21-01 750
Han, Fang
MIC-15-132 1314
Han, Haonan
MIC-10-188 1131
Han, Ill-hyuk
NSS-13-238 662
Han, Ill-Hyuk
NSS-13-252 668
RTSD-04-372 ..... 174, ***1512***
Han, Jifeng
NSS-02-03 457
Han, Ki-Taek
MIC-05-322 972
Han, LiHui
NSS-01-069 ..... 34, ***348***
NSS-13-068 591
Han, Siyuan
MIC-10-125 1113
Han, Xiaorou
MIC-05-040 884
Han, Zhenjie
JS-02-06 274
Haneishi, Hideaki
MIC-05-187 930
MIC-10-014 1081
M-LT-01-10 843
Hang, Zhongbin
MIC-15-186 1331
MIC-15-450 1412
M-LT-06-02 1265
WS-04-05 249
WS-04-06 250
Hankins, Travis
N-LT-01-05 296
NSS-01-019 328
NSS-01-129 372
Hanna, Andrea
MIC-10-293 1163
Hansen, Karsten
NSS-08-01 500
NSS-13-100 605
NSS-13-304 688
Hantrakul, Wutthiphat
NSS-01-281 432
Hany, Ibrahim
JS-02-04 272
MIC-15-045 1287
Hao, Yao
MIC-05-364 986
Hao, Zehao
MIC-10-434 1208
Hao, Zifan
MIC-05-046 886
Harano, Hideki
NSS-27-02 793
Hari, Vishnu
MIC-05-367 987
MIC-15-294 1363
Harrabi, Semi
MIC-17-01 1428
Harrington, Thomas
NSS-01-223 409
Harrison, Robert L.
MIC-15-075 1296
Hart, Shanyn
NSS-01-243 ..... **417**
NSS-13-216 653
Hartman, Johan
N-LT-01-10 301
NSS-01-061 345
Harvey, Bryan
N-LT-01-05 296
NSS-01-019 328
NSS-01-129 372
Hasanaj, Shqipe
NSS-01-093 358
Hashemi, Amirreza
MIC-05-316 ..... 110, ***970***
MIC-05-469 ..... **1018**
MIC-10-365 ..... 137, ***1185***
MIC-15-303 ..... 157, ***1366***
M-LT-04-03 ..... 121, ***1050***
M-LT-06-10 ..... 146, ***1272***
Hashimoto, Fumio
MIC-01-04 ..... 94, ***826***
MIC-05-196 933
MIC-05-205 936
MIC-09-01 1067
MIC-15-168 1325
Hashimoto, Takeyuki
MIC-05-196 933
MIC-05-205 936
Hassan, Andrew B.
MIC-10-311 1169
Hastings, Daniel
MIC-15-465 1417
M-LT-06-05 1268
Hata, Nao
NSS-13-320 ..... 77, ***694***
Hauberg, Søren
JS-03-05 282
N-LT-04-01 551
NSS-13-162 630
Hauck, Scott A.
MIC-15-327 1373
M-LT-05-08 1260
WS-04-04 248
Hauptmann, Andreas
RTSD-04-394 1531
Hausladen, Paul
NSS-05-08 483
NSS-21-03 752
Havla, Joachim
MIC-10-281 1160
Hawrami, Rastgo
NSS-13-044 ..... 63, ***580***
NSS-27-06 796
Hayashi, Hiroaki
MIC-05-145 917
MIC-10-143 ..... 129, ***1118***
MIC-15-141 1317
MIC-15-144 1318
Hayashi, Masateru
NSS-13-058 586
Hayashi, Tasuku
NSS-13-320 694
Hayek, Antoine
NSS-11-02 ..... 56, ***523***
Hayward, Charles
MIC-15-105 1305
Hayward, Jason P.
NSS-05-03 479
NSS-13-226 658

Author Index

He, Li
NSS-01-069 348
NSS-13-068 591
NSS-13-110 ..... 66, ***609***
He, Liuchun
MIC-04-02 865
MIC-05-064 891
MIC-05-211 938
MIC-05-382 ..... 113, *992*
MIC-15-057 1291
MIC-15-420 1403
He, Wen
MIC-10-449 1213
MIC-20-02 ..... 167, ***1454***
He, Yilin
MIC-10-458 ..... 140, ***1216***
M-LT-03-09 ..... 120, ***1045***
He, Yuchen
MIC-15-414 1401
He, Zhong
JS-03-06 283
RTSD-01-01 ..... 169, ***1469***
RTSD-04-380 1518
RTSD-04-385 1522
RTSD-05-01 1540
RTSD-07-02 1554
RTSD-09-01 1568
RTSD-09-02 1568
He, Zuoxiang
MIC-05-190 931
MIC-05-226 943
MIC-14-03 1250
MIC-15-186 1331
MIC-15-228 1343
MIC-15-450 1412
M-LT-01-02 836
M-LT-06-02 1265
WS-04-05 249
WS-04-06 250
Heather, Tom
N-LT-01-04 295
NSS-01-033 334
Heidari, Pedram
MIC-15-303 1366
M-LT-06-10 1272
Heim, Timon
NSS-13-106 607
Heino, Jouni
NSS-13-006 566
Heinrich, Sophie
NSS-12-05 532
Helej, Markus
NSS-11-01 523
Heller, Matthieu
NSS-25-02 778
Heller, Ryan
JS-02-08 276
MIC-21-03 1461
Hellwege, Laura
MIC-05-391 ..... **995**
Helsby, William
NSS-01-301 441
NSS-13-278 678
Hemperek, Tomasz
NSS-10-05 520
Hen, Or
MIC-12-06 1237
Henao, Ángela
NSS-12-05 532
Henares González, José Luis
MIC-10-341 1178
MIC-15-006 1276
Henderson, Robert K.
WS-02-11 ..... 18, ***233***
Henderson, Shawn W.
NSS-13-104 607
NSS-13-106 607
Hennig, Wolfgang
NSS-01-295 439
Henning, Marc
MIC-15-054 1290
Henriksen, Otto M.
MIC-10-212 1139
Henry, William
NSS-13-106 607
Hensel, Martin
NSS-04-04 471
Heo, Jae seung
NSS-01-169 389
Heo, Kang
N-LT-01-01 292
NSS-01-021 329
Herbst, Ryan
NSS-10-04 519
NSS-20-08 747
NSS-23-02 766
Heriot, William
NSS-05-01 ..... 50, ***477***
Hermann, Raphael
NSS-27-06 796
Hernández Segura, Alejandro
MIC-15-282 1359
M-LT-06-07 1270
Hernández, Alejandro
MIC-10-296 1164
MIC-10-308 ..... 134, ***1168***
Hernandez, Hugo
MIC-03-06 860
NSS-10-04 519
NSS-23-02 766
Hernandez, Ryan
MIC-09-04 1070
Hernandez-Toro, Juan
MIC-15-006 1276
Herraiz, Joaquín López
MIC-05-424 1005
MIC-10-416 1201
MIC-15-090 1301
MIC-15-219 ..... 154, ***1341***
MIC-15-462 1416
MIC-16-01 1420
M-LT-03-07 1043
WS-04-17 ..... 23, ***260***
Herrero, Vicente
NSS-01-099 361
Hervo, Amaury
NSS-16-08 720
Herweg, Katrin
JS-02-05 273
N-LT-01-08 ..... 28, ***299***
NSS-01-015 ..... 31, ***326***
NSS-21-04 753
Herzen, Julia
N-LT-01-10 301
NSS-01-061 345
Herzog, Hans
MIC-10-242 1148
Heshmat, Amirreza
MIC-05-172 926
M-LT-01-05 838
Hesp, David
NSS-25-06 782
Hide, Bob
NSS-25-06 782
Higuchi, Mikio
NSS-13-230 659
Higueret, Stéphane
NSS-04-03 470
RTSD-04-355 1498
Hildén, Timo
NSS-13-006 566
Hill, Andrew
NSS-01-301 441
NSS-13-088 599
NSS-13-278 678
Hillemanns, Hartmut
NSS-19-04 ..... ***737***
Hinge, Christian
STIR-08 ..... ***1600***

Author Index

STIR-13 185
Hinger, Viktoria
NSS-01-093 358
Hiradfar, Maryam
MIC-12-06 1237
Hiraki, Takao
MIC-05-145 917
MIC-15-144 1318
Hirato, Misaki
NSS-01-257 ..... 43, ***423***
NSS-13-230 659
Hitchens, Jack R.
N-LT-01-04 ..... **295**
NSS-01-033 ..... **334**
Hitomi, Keitaro
N-LT-02-04 310
NSS-01-219 408
RTSD-01-03 ..... 169, ***1470***
RTSD-04-371 1511
RTSD-04-382 1520
RTSD-04-389 1526
Hix, Jay D.
RTSD-04-397 1533
Ho, James D.
MIC-05-274 ..... 109, ***957***
Hoang, Trang
MIC-05-058 ..... 101, ***890***
Hoarau, Christophe
MIC-05-337 977
Hocquet, Sébastien
NSS-02-01 455
Hodge, Wesley
NSS-10-01 516
Hoe, Kahiwa
NSS-01-117 367
NSS-14-05 702
Hoegberg, Erick
NSS-01-151 382
Hoeschen, Christoph
MIC-05-142 915
MIC-10-032 1087
MIC-15-108 1306
Hoffman, Ashton
NSS-01-323 450
Hohnholz, Janina
MIC-05-052 888
MIC-05-070 893
MIC-10-122 ..... 128, ***1112***
MIC-15-027 1282
MIC-15-126 ..... 151, ***1312***
Hölinger, Gunter
MIC-10-281 1160
Holman, Beverley
MIC-05-265 954
Holschuh, Tommy V.
RTSD-04-397 1533
Honda, Mitsugi
MIC-15-144 1318
Hong, Huicong
NSS-01-151 382
Hong, Inki
MIC-10-380 ..... 137, ***1189***
MIC-15-405 1398
Hong, Jintae
NSS-13-258 670
Hong, Qiliang
MIC-03-04 858
Hong, Sungwook
MIC-15-015 ..... 147, ***1279***
Hong, Wooseong
N-LT-04-04 553
NSS-13-164 631
Hong, Yoonsang
NSS-01-207 402
Hop, Joost F.
MIC-05-097 902
Hope, Thomas A.
MIC-12-01 1233
Hori, Jun-ichi
NSS-01-229 411
Hori, Kensuke
MIC-05-196 ..... 106, ***933***
MIC-05-205 936
Horikawa, Justine
NSS-01-117 367
Horodynski, Jean-Michel
NSS-04-03 470
Horsfield, Colin
NSS-01-223 409
Hosseini, Seyed Mohammadreza
MIC-05-433 1007
MIC-15-429 ..... **1405**
Hosseinzadeh, Elinaz
MIC-05-313 969
Hostalet, Enrique
JS-01-03 265
Hotvedt, Peter G.
RTSD-09-01 1568
RTSD-09-02 ..... 181, ***1568***
WS-04-12 ..... 23, *256*
Hou, Xinchi
MIC-18-07 1442
Hou, Yingrui
NSS-12-04 532
Hou, Yucun
MIC-02-02 830
MIC-05-184 929
MIC-08-01 ..... 122, ***1058***
MIC-10-119 1111
MIC-10-377 1188
MIC-10-410 ..... 138, ***1199***
MIC-11-02 1225
MIC-15-198 ..... 153, ***1334***
MIC-15-378 1389
N-LT-04-10 558
NSS-13-280 679
Hrubčín, Ladislav
RTSD-04-359 1502
Hruska, Carrie
MIC-09-05 1071
Hsieh, Scott
JS-01-02 ..... 24, ***264***
Hu, Ankang
NSS-26-06 788
Hu, Hai
MIC-05-226 943
M-LT-01-02 836
WS-04-06 250
Hu, Kaiming
MIC-05-286 ..... **961**
MIC-07-03 1034
Hu, Lingzhi
MIC-20-04 1456
Hu, Tianjiao
MIC-05-331 975
MIC-10-329 1175
MIC-15-333 1375
Hu, Wentao
MIC-05-325 ..... **973**
MIC-05-331 975
MIC-15-333 1375
Hu, Xinyu
MIC-14-05 ..... 144, ***1252***
Hu, Xueye
NSS-01-111 366
NSS-13-108 608
Hu, Yifan
MIC-04-08 ..... 99, ***871***
MIC-05-244 948
MIC-05-451 1013
M-LT-02-08 852
WS-04-08 252
Hu, Yiyi
MIC-05-403 ..... 114, ***999***
Hu, Yuchen
NSS-01-111 366
Hu, Zhanli
MIC-05-385 993
MIC-07-05 1036

Author Index

MIC-15-387 1392
Hua, Jianlang
MIC-05-013 ..... 100, ***876***
MIC-05-127 911
MIC-15-009 1277
MIC-15-117 1309
Hua, Michael Y.
NSS-01-295 439
NSS-22-03 760
Huang, Bangyan
MIC-11-04 ..... 141, ***1227***
Huang, Chen
MIC-05-127 911
MIC-05-343 979
MIC-09-07 1073
MIC-10-224 1143
MIC-10-455 1215
MIC-15-261 1353
MIC-15-339 1377
Huang, Chiao
RTSD-03-04 1488
Huang, Chia-Wei
NSS-06-06 ..... 51, ***489***
Huang, David
MIC-14-05 1252
Huang, Huandong
N-LT-03-07 543
NSS-13-140 621
Huang, Hui
MIC-05-010 875
MIC-07-05 1036
Huang, Jiangshan
MIC-15-396 1395
Huang, Jiarui
MIC-10-188 ..... 130, ***1131***
Huang, Mingyue
NSS-21-01 750
Huang, Ping-Chen
NSS-10-04 519
NSS-23-02 766
Huang, Qiu
MIC-10-383 1190
MIC-14-04 1251
MIC-15-408 1399
Huang, Runxiang
MIC-15-387 ..... 160, ***1392***
Huang, Wenbo
MIC-05-190 931
MIC-05-400 998
Huang, Wenjie
MIC-05-127 911
MIC-09-03 1069
MIC-09-07 1073
MIC-10-455 1215
MIC-15-009 1277
MIC-15-012 1278
MIC-15-117 1309
MIC-15-120 1310
MIC-15-261 1353
MIC-15-450 1412
MIC-21-04 1462
M-LT-06-02 1265
Huang, Xianchao
MIC-05-040 ..... 100, *884*
Huang, Yan
RTSD-09-03 1569
Huang, Yannan
NSS-01-041 337
NSS-15-04 710
Huang, Yixing
MIC-10-209 1138
Huang, Yueyu
MIC-15-414 ..... 161, ***1401***
Huang, Ze
MIC-05-130 912
Huang, Zeqi
MIC-05-148 918
RTSD-04-377 ..... 174, *1516*
Huang, Zhenxing
MIC-08-05 ..... **1062**
Huang, Ziqian
MIC-01-04 826
Huanzhe, Wei
STIR-07 1599
Huerst, Markus
NSS-01-093 358
Hueso-González, Fernando
MIC-05-328 ..... 111, *974*
MIC-10-035 1088
MIC-10-089 1103
MIC-15-099 1303
M-LT-04-05 1052
Hugg, James
MIC-05-001 873
Hughes, Terri-Louise
N-LT-02-10 315
NSS-01-267 426
Hugues, Maxime
RTSD-04-355 1498
Huh, Susie
MIC-15-447 1411
M-LT-06-01 1264
Huh, Yoonsuk
MIC-05-334 976
MIC-10-062 ..... **1096**
Hull, Giulia
NSS-12-04 532
Huneau, Clément
MIC-05-301 966
Hung, Guang-Uei
MIC-05-394 996
Hunter, William C.J.
MIC-10-350 ..... 136, ***1181***
MIC-10-371 1187
MIC-15-105 1305
MIC-15-327 1373
M-LT-05-08 1260
WS-04-04 248
Hunyadi, Mátyás
NSS-27-05 796
Hur, Seop
NSS-13-174 636
Hurani, Zaina J.
MIC-05-088 ..... 102, ***899***
Huser, Thomas
MIC-10-101 1106
M-LT-04-01 1048
Hutcheson, Anthony L.
JS-03-06 283
NSS-01-279 431
NSS-25-01 ..... 87, ***778***
Hutchinson, Elizabeth
NSS-13-284 681
Hutinet, Henri
NSS-01-195 398
Hutton, Brian F.
MIC-09-05 1071
MIC-10-068 1097
Hwang, Junseong
N-LT-02-08 313
NSS-01-165 388
NSS-01-247 419
Hyeon, Suyeon
MIC-10-029 ..... 125, ***1086***
Hyesun, Yang
MIC-05-289 962
Hyun, Subong
MIC-05-277 ..... 109, ***958***

I

Iaselli, Giuseppe
MIC-21-02 1460
Ibáñez, Paula
JS-02-09 276
MIC-15-090 1301
Ibrahim, Nahid
MIC-05-319 971
Ichiba, Yuta

Author Index

NSS-15-01 707
Ichikawa, Yasuaki
MIC-21-02 1460
Ichikawa, Yuki
MIC-13-04 1245
Ide, Ryutaro
MIC-10-278 ..... 133, ***1159***
Idier, Jérôme
MIC-05-301 966
NSS-16-08 720
Igarashi, Youichi
NSS-01-071 349
NSS-01-141 378
NSS-13-144 622
Iglesias, Juan E.
MIC-10-428 1206
Iguchi, Toshihiro
MIC-05-145 917
MIC-15-144 1318
Iida, Hidehiro
MIC-10-242 1148
Iiyama, Haruki
NSS-02-02 456
Ikawa, Hiroaki
MIC-05-346 980
Ikhlef, Aziz
MIC-15-171 ..... 152, ***1326***
Ikoma, Naruhiko
MIC-15-447 1411
M-LT-06-01 1264
Ilie, Gabriela
NSS-13-072 ..... 64, ***592***
NSS-13-326 ..... 77, ***697***
Illana, Andrés
N-LT-01-07 298
NSS-01-039 336
NSS-01-131 373
Ilosalo, Mikko
NSS-28-06 806
Iltis, Alain
MIC-10-293 1163
NSS-03-02 462
Im, Jaeyoung
N-LT-01-01 292
NSS-01-021 329
Imai, Yoichi
MIC-05-454 1014
Imam, Safdar
NSS-01-151 382
Imas, Lucas J.
MIC-09-08 1074
Inada, Tomohiro
NSS-17-03 724
Inagaki, Shunsuke
MIC-05-322 972
Inaniwa, Taku
MIC-05-346 980
Incicco, Irene
MIC-15-384 ..... 160, ***1391***
Ingalls, Ethan
MIC-15-327 1373
M-LT-05-08 1260
WS-04-04 248
Inoue, Tomonao
NSS-01-049 341
Insa, Christophe
NSS-01-101 362
Inyong, Kwon
NSS-01-083 355
NSS-01-259 423
Iorio, Orso Alberto Maria
N-LT-04-11 559
NSS-13-290 683
Ippolito, Massimo
MIC-10-362 1184
Irfan, Muhammad
MIC-15-306 1366
M-LT-06-08 1271
Irvine, Christian A.
N-LT-01-03 ..... 27, ***294***
NSS-13-329 ..... 47, ***453***
Ishibashi, Mariko
MIC-05-454 1014
Ishihara, Itsutoshi
NSS-13-020 571
Ishihara, Shintaro
NSS-13-090 ..... 65, ***600***
Ishii, Junya
NSS-13-066 590
NSS-27-02 793
Ishikawa, Taiyo
MIC-10-014 ..... 124, ***1081***
Ishizawa, Satoshi
MIC-10-011 1080
NSS-16-03 715
Işık, Fuat Kerem
NSS-17-03 ..... 81, ***724***
Iskra, Peter
NSS-14-07 704
Isobe, Takashi
MIC-15-237 1346
Issever, Cigdem
NSS-17-03 724
Ito, Shigeki
MIC-05-454 1014
MIC-06-03 1029
Iwao, Yuma
MIC-05-124 910
MIC-05-346 980
MIC-05-454 1014
MIC-15-240 1347
MIC-17-06 1433
Iyomoto, Naoko
NSS-13-320 694
Izquierdo-Garcia, David
MIC-10-428 1206
MIC-15-042 1285
NSS-13-178 638
Izumitani, Keisuke
MIC-05-187 ..... 106, ***930***
M-LT-01-10 ..... 96, ***843***
Izzo, Vincenzo
N-LT-04-11 559
NSS-13-290 683

J

Jaafari, Shabnam
MIC-18-06 1441
Jaakkola, Maria K.
MIC-05-409 1001
Jäck, Alexander
MIC-10-281 1160
Jack, Day
NSS-13-078 595
Jackson, Mark
NSS-06-03 487
Jacquet, Marie
NSS-15-05 711
Jaekel, Oliver
MIC-17-01 1428
Jafari, Hamid
NSS-13-052 583
Jafarizadeh, Ali
MIC-10-317 1171
Jagt, Thyrza
MIC-17-04 1431
Jäkel, Oliver
MIC-10-419 1202
M-LT-03-08 1044
Jakubek, Jan
MIC-17-01 1428
RTSD-01-04 1471
RTSD-03-06 1490
RTSD-07-07 1558
RTSD-08-04 ..... 180, ***1563***
Jakůbek, Jan
RTSD-04-400 1535
Jamadar, Sharna

Author Index

WS-03-07 ..... **241**
James, Ben
MIC-10-164 1124
James, Ralph B.
RTSD-04-354 1497
RTSD-04-365 1506
RTSD-07-03 1554
RTSD-09-07 1573
Jamlongkul, Paparin
NSS-01-281 432
Jang, Mee
NSS-13-242 664
Jang, Sehyun
NSS-02-05 459
Jang, SeHyun
MIC-15-318 ..... 158, ***1370***
M-LT-05-10 ..... 145, ***1262***
Jang, Seoyun
NSS-01-155 ..... 38, ***384***
NSS-01-209 403
Janot, Patrick
NSS-12-04 532
Jansen, Andreas
N-LT-03-11 546
NSS-13-150 625
Jansen, Floris P.
MIC-15-360 1384
MIC-15-441 1409
Jaouen, Vincent
MIC-15-174 ..... 153, ***1327***
NSS-16-08 720
Järvenpää, Magdalena
NSS-28-06 806
Jaworski, Jason
JS-03-06 283
Jayaraj, Aparna
STIR-02 ..... **1597**
Jayarathne, Jayana
JS-01-01 264
JS-03-02 280
RTSD-06-02 ..... **1547**
Jayatissa, Heshani
N-LT-01-05 296
NSS-01-019 328
NSS-01-129 372
NSS-13-236 662
Jazvac, Gabriela
NSS-01-037 ..... 32, ***335***
NSS-06-04 487
Jdid, Lamyae
JS-02-07 ..... 25, ***275***
Jegal, Jin
MIC-10-062 ..... 126, *1096*
Jelinek, Jindrich
JS-03-04 ..... 26, ***281***
Jentzen, Walter
MIC-15-330 1374
M-LT-05-07 1259
Jeon, Byoungil
JS-01-05 ..... 24, ***267***
Jeon, Duhee
MIC-05-289 962
Jeong, Dongwoo
NSS-01-327 ..... 47, ***452***
Jeong, Jihun
NSS-01-059 ..... 33, ***344***
Jeong, Jin-Woo
MIC-15-072 1295
Jeong, Jong Hwi
MIC-15-318 1370
M-LT-05-10 1262
Jeong, Sangwoon
MIC-07-01 1033
MIC-10-401 1196
MIC-15-423 1404
Jeong, Seong Jae
NSS-01-169 389
Jeong, Won-Young
RTSD-04-350 1494
Jha, Abhinav K.
MIC-10-107 1108
MIC-10-467 1219
Ji, Huimin
NSS-28-05 ..... 90, ***805***
Ji, Jim
MIC-15-060 1292
Ji, Wanook
NSS-01-213 405
Ji, Xu
RTSD-04-401 1536
Ji, Young-Yong
NSS-01-213 ..... 41, ***405***
Ji, Zhen
MIC-15-297 ..... **1364**
M-LT-06-09 ..... **1272**
Jia, Hao
MIC-05-190 ..... 106, *931*
MIC-14-03 ..... 144, ***1250***
MIC-15-450 1412
M-LT-06-02 1265
WS-04-06 250
Jia, Tong
MIC-10-161 1123
MIC-10-200 ..... 131, ***1135***
MIC-10-218 ..... 131, *1141*
Jiang, Bingcheng
MIC-15-411 1400
Jiang, Chenyao
MIC-15-297 1364
M-LT-06-09 1272
Jiang, Jianyong
MIC-02-02 830
MIC-05-184 929
MIC-05-253 950
MIC-08-01 1058
MIC-10-119 1111
MIC-10-131 ..... 128, *1115*
MIC-10-377 ..... 137, *1188*
MIC-10-410 1199
MIC-11-02 1225
MIC-15-198 1334
MIC-15-378 ..... 160, *1389*
N-LT-04-10 558
NSS-13-280 679
Jiang, Junan
MIC-10-314 ..... **1170**
Jiang, Lei
MIC-15-411 1400
Jiang, Nianming
NSS-01-225 410
Jiang, Shan
MIC-10-059 ..... 126, ***1095***
MIC-10-083 ..... 127, ***1101***
M-LT-04-08 ..... 121, ***1054***
M-LT-04-09 ..... 121, ***1055***
Jiang, Tao
MIC-15-414 1401
Jiang, Weichun
NSS-01-127 371
Jiang, Xiao
MIC-05-175 927
M-LT-01-04 837
Jiang, Xiaolong
MIC-05-127 911
MIC-05-343 ..... 111, ***979***
MIC-09-07 1073
MIC-10-455 1215
MIC-15-009 1277
MIC-15-012 ..... 147, ***1278***
MIC-15-117 1309
MIC-15-120 1310
MIC-15-261 1353
MIC-15-339 1377
Jiang, Xiaopan
NSS-13-126 615
Jiang, Yuhao
MIC-11-02 1225
Jiang, Zirui
MIC-10-314 1170

Author Index

Jimenez Algarra, Lidia
MIC-02-05 833
Jiménez Algarra, Lidia
MIC-10-023 1084
MIC-15-042 1285
MIC-15-069 1294
MIC-15-138 1316
MIC-19-05 ..... 167, ***1448***
NSS-13-178 ..... 70, ***638***
Jiménez-Mesa, Carmen
MIC-10-281 1160
MIC-10-290 ..... 134, ***1162***
MIC-10-296 1164
MIC-10-308 1168
MIC-15-282 1359
M-LT-06-07 1270
Jimenez-Serrano, Santiago
MIC-05-379 991
Jiménez-Serrano, Santiago
MIC-05-238 946
Jin, Xiao
WS-04-07 251
Jin, Yifei
JS-01-04 266
MIC-10-104 ..... 127, ***1107***
MIC-12-08 ..... 143, ***1240***
MIC-16-03 ..... 164, ***1422***
MIC-21-01 1459
WS-04-02 ..... **246**
Jo, Kwanghyun
MIC-15-318 1370
M-LT-05-10 1262
Jo, Seongmin
NSS-13-024 572
John, Dominik
N-LT-01-10 301
NSS-01-061 345
Johnsen, Robert
MIC-10-422 1203
MIC-15-375 1388
MIC-15-441 1409
M-LT-05-03 1256
Johnson, Eric
RTSD-02-03 1480
RTSD-07-04 1555
Johnson, Jyothisraj
MIC-05-037 883
Johnson, Mark
NSS-13-216 653
Johnson, Owen A.
NSS-01-055 ..... 33, ***342***
NSS-13-308 ..... 77, ***690***
Johnson, Wiley N.
JS-03-06 283
NSS-01-279 431
NSS-25-01 778
Johnson-Rambert, Mary V.
JS-03-06 283
NSS-01-279 431
NSS-25-01 778
Johnston, Leigh A.
MIC-18-03 1438
Joly, Baptiste
NSS-20-06 746
Joly, Candie
MIC-05-283 960
Jones, Geoff
MIC-15-327 1373
M-LT-05-08 1260
WS-04-04 248
Jones, Pete
NSS-01-243 417
NSS-13-216 ..... 72, ***653***
Jones, Tim
NSS-13-284 681
Jonsson, Jonathan
RTSD-09-05 1572
Joo, Hosung
NSS-01-211 ..... **404**
Joseph, Maxim B.
NSS-13-244 665
Joshi, Ketaki
NSS-13-226 ..... 72, ***658***
Joshi, Pankaj
NSS-25-06 782
Joshi, Sarina
JS-01-01 264
Jovanovic, Igor
NSS-01-317 448
NSS-05-04 479
NSS-13-224 657
NSS-16-06 718
Joyce, Malcolm J.
NSS-01-057 343
NSS-13-228 658
NSS-18-05 ..... 82, *732*
NSS-22-02 759
Juan-Morales, Jessica
MIC-10-341 1178
MIC-15-006 1276
Juarez-Orozco, Luis E.
MIC-15-429 1405
Judenhofer, Martin
MIC-10-122 1112
MIC-15-027 1282
MIC-15-126 1312
MIC-15-129 1313
Jung, Jin Ho
MIC-10-179 1128
MIC-15-015 1279
MIC-15-180 1329
NSS-01-047 340
NSS-23-03 767
Jung, Jiwoong
MIC-10-179 1128
MIC-15-015 1279
MIC-15-180 1329
NSS-01-047 340
NSS-23-03 767
Jung, Kyung-Hwan
NSS-01-269 427
Jurchescu, Oana
RTSD-06-05 1550
Jurisa, Noah
MIC-10-101 1106
M-LT-04-01 1048

K

Kabongo, Luis
MIC-10-167 1125
Kabra, Saurabh
NSS-18-04 731
Kaburagi, Masaaki
NSS-27-02 793
Kacenga, Samuel
RTSD-01-04 1471
Kačenga, Samuel
RTSD-04-358 ..... 172, ***1501***
Kachel, Maciej
N-LT-03-10 545
NSS-13-134 619
Kachru, Priyanka
JS-02-04 272
MIC-15-045 1287
NSS-21-02 751
NSS-21-04 753
Kada, Wataru
NSS-13-090 600
Kajiyama, Kengo
NSS-02-06 460
Kakimoto, Koichi
NSS-07-01 493
Kalavakuru, Pradeep
NSS-08-01 500
NSS-13-100 ..... 66, ***605***
Kalliokoski, Matti
RTSD-04-394 1531
Kalliopuska, Juha

Author Index

NSS-28-06 ..... 90, ***806***
RTSD-04-351 1495
RTSD-04-357 1500
RTSD-04-376 1515
RTSD-04-401 1536
RTSD-07-06 1557
RTSD-07-07 ..... 180, ***1558***
TS-02-03 ..... **1587**
Kalluri, Kesava
MIC-15-309 1367
Kamada, Kei
JS-02-03 271
MIC-05-025 879
MIC-05-454 1014
MIC-10-011 1080
NSS-07-01 ..... 52, ***493***
NSS-16-03 715
NSS-27-02 ..... 89, ***793***
Kamiya, Naoki
NSS-28-03 803
Kamon, Seita
RTSD-05-04 1542
Kamp, Sebastian
MIC-10-281 1160
Kan, Xiaoshuo
MIC-10-389 ..... 137, ***1192***
Kanak, Andrii
RTSD-01-08 1475
RTSD-05-03 1541
Kanan, Riad
JS-01-03 265
Kanatzidis, Mercouri G.
NSS-01-151 382
RTSD-05-01 1540
RTSD-06-04 1549
Kanazawa, Yuki
MIC-15-141 1317
Kandlakunta, Praneeth
NSS-01-323 ..... **450**
Kaneko, Junichi H.
NSS-13-230 659
Kaneshige, Nate
NSS-01-295 439
Kaneyasu, Kodai
NSS-12-01 529
NSS-21-05 ..... 84, ***754***
WS-02-08 ..... 18, ***231***
Kang, Donghee
MIC-10-431 ..... 139, ***1207***
Kang, Gujin
NSS-13-258 670
Kang, Han Gyu
MIC-05-079 ..... 102, ***896***
MIC-05-130 912
MIC-05-340 978
MIC-05-346 980
MIC-05-454 1014
MIC-06-05 ..... 118, ***1030***
MIC-13-03 ..... 143, ***1244***
MIC-15-081 1298
MIC-17-06 1433
Kang, Jeongsoo
NSS-13-238 662
Kang, Jin-Goo
NSS-13-238 ..... 73, ***662***
Kang, Jun-Tae
MIC-15-072 1295
Kang, Juwan
NSS-01-175 391
NSS-01-255 ..... 43, *422*
NSS-13-166 ..... 69, ***632***
NSS-13-246 666
Kang, Seung Kwan
MIC-04-01 864
MIC-10-395 1194
MIC-15-315 1369
M-LT-03-01 1038
M-LT-05-06 1259
Kang, Zhe
NSS-01-031 333
NSS-27-04 795
Kanno, Marina
NSS-01-023 330
NSS-01-309 444
Kantorek, Rebecca
MIC-10-074 1099
MIC-15-114 ..... 150, ***1308***
M-LT-04-10 1056
Kao, Chien-Min
MIC-10-047 ..... 125, *1091*
MIC-10-110 ..... 127, *1109*
MIC-15-234 1345
NSS-01-025 331
NSS-13-050 ..... 63, *583*
Kappler, Steffen
MIC-05-172 926
M-LT-01-05 838
Kaprelian, Theo
NSS-06-07 490
NSS-13-084 597
Karaca, Utku
NSS-21-06 755
Karakatsanis, Nicolas A.
MIC-09-02 1068
MIC-10-020 ..... 124, *1083*
MIC-15-123 ..... 151, ***1311***
Karcz, Jason
NSS-13-158 628
Kargar, Alireza
NSS-01-151 382
RTSD-04-360 ..... **1502**
Karkour, Nabil
NSS-13-124 ..... 67, ***614***
Karp, Joel S.
MIC-04-03 866
MIC-05-262 953
MIC-19-01 1445
Kasal, Matouš
RTSD-04-400 1535
Kasprzak, Jona
MIC-05-391 995
MIC-10-191 1132
MIC-10-326 1174
Kasue, Takuya
MIC-05-145 917
MIC-10-143 1118
Katabuchi, Tatsuya
NSS-01-229 411
NSS-27-01 792
Kataoka, Jun
MIC-05-151 919
MIC-05-157 921
MIC-15-177 1328
M-LT-02-04 849
M-LT-02-05 850
Kato, Hidetoshi
MIC-05-187 930
M-LT-01-10 843
NSS-13-030 575
Kato, Masahiro
NSS-27-02 793
Kato, Takumi
NSS-01-011 325
NSS-01-035 335
NSS-13-012 568
NSS-13-028 574
Katsioulas, Ioannis
NSS-05-05 ..... 50, ***480***
NSS-13-268 674
Katsumata, Akitoshi
MIC-15-141 1317
Katz, Sander
NSS-16-06 ..... 80, ***718***
Katzdobler, Sabrina
MIC-10-281 1160
Kavrigin, Pavel
MIC-05-337 977
Kawachi, Naoki
MIC-05-340 978

Author Index

N-LT-02-04 310
NSS-01-219 408
Kawaguchi, Noriaki
NSS-01-011 325
NSS-01-035 ..... 32, ***335***
NSS-13-012 568
NSS-13-028 ..... 62, ***574***
Kawai, Yusuke
RTSD-04-371 1511
RTSD-04-382 1520
Kawamoto, Amane
NSS-13-320 694
Kawamura, Hiroshi
N-LT-02-14 318
NSS-01-321 450
Kawano, Shukei
NSS-13-002 564
Kawarabayashi, Jun
NSS-13-248 ..... 74, ***667***
Kawasaki, Kohei
N-LT-02-14 318
NSS-01-321 450
Kawashima, Hidekazu
MIC-15-168 1325
Kawashima, Hiroki
MIC-05-151 919
MIC-05-157 921
MIC-15-177 1328
M-LT-02-04 849
M-LT-02-05 850
Kawashima, Rikuto
NSS-13-232 660
Kaye, Willy
JS-03-06 283
Kazempour, Amin
MIC-15-429 1405
Ke, Pengyu
MIC-05-046 886
Kebbiri, Mariam
NSS-05-05 480
Kedych, Vadym
NSS-01-093 358
Kee, Youngwook
MIC-10-272 1157
Kelleter, Laurent
MIC-17-01 1428
Kempf, Sebastian
NSS-01-315 447
Kemppainen, Jukka
MIC-05-409 1001
Kennedy, Andrew
NSS-13-228 658
Kenny, Chris
NSS-10-04 519
Keppens, Max
MIC-11-08 ..... 142, ***1230***
Kerboub, Nourdine
NSS-13-322 ..... 77, ***695***
Kerckhaert, Camiel E.
WS-04-11 255
Kerr, Phil
NSS-05-03 479
Keshet, Renato
MIC-15-210 1338
Khalid, Usman
MIC-10-242 ..... 132, ***1148***
Khalighi, Mehdi
MIC-10-257 1152
Khaplanov, Anton
NSS-18-04 ..... 82, ***731***
Kharwadkar, Neha S.
NSS-20-07 747
Khonsri, Pakorn
NSS-01-281 432
Kiatkongkaew, Krittanai
NSS-01-229 411
Kiefer, Lena S.
MIC-08-07 1064
Kierans, Carolyn
NSS-01-053 341
Kim, Arthur
MIC-10-041 1090
M-LT-03-04 1040
NSS-13-046 581
NSS-16-07 719
RTSD-04-360 1502
Kim, Bongjin
NSS-23-02 766
Kim, Byoung Soo
NSS-01-251 420
Kim, Byoung-Jik
NSS-26-02 ..... 88, ***784***
Kim, Chan Hyeong
MIC-15-318 1370
M-LT-05-10 1262
NSS-02-05 459
Kim, Chanho
N-LT-02-08 313
N-LT-04-05 ..... **554**
NSS-01-165 388
NSS-01-247 419
NSS-13-160 ..... **629**
NSS-13-174 636
Kim, Daeseung
NSS-01-155 384
NSS-01-209 403
Kim, Dong Seok
N-LT-03-01 538
NSS-13-094 602
Kim, Dong Sik
MIC-05-163 ..... 105, *923*
NSS-13-016 ..... 61, ***569***
Kim, Donghee
MIC-15-195 ..... 153, ***1333***
Kim, Donghyun
MIC-05-277 958
Kim, Duckhyun
NSS-13-096 ..... 65, ***603***
Kim, Eui Tae
MIC-15-315 1369
M-LT-05-06 1259
Kim, Geehyun
N-LT-01-12 302
N-LT-04-04 553
NSS-01-065 347
NSS-13-164 631
NSS-13-238 662
RTSD-04-372 1512
Kim, Geon
N-LT-02-08 313
N-LT-04-05 554
NSS-01-165 ..... 39, ***388***
NSS-01-247 419
NSS-13-160 629
Kim, Geon-bo
NSS-01-317 448
Kim, Grace H.
MIC-04-06 869
Kim, Hadong
RTSD-03-02 1486
Kim, Haksoo
MIC-10-323 1173
Kim, Heejong
MIC-10-047 1091
NSS-01-025 ..... **331**
NSS-13-050 ..... **583**
Kim, Ho Kyung
NSS-01-177 392
NSS-01-207 402
Kim, Hong Joo
NSS-01-327 452
Kim, Hyojung
RTSD-04-350 1494
Kim, Hyund-Dong
NSS-01-269 427
Kim, Hyunjoon
MIC-03-06 860
NSS-01-087 356
NSS-10-04 ..... **519**

Author Index

NSS-23-02 ..... 86, ***766***
Kim, Hyunjung
MIC-10-401 1196
Kim, Jae-Hyeon
NSS-01-269 427
Kim, Jaehyo
N-LT-04-04 553
NSS-13-164 631
Kim, Jeongho
NSS-13-008 ..... 61, ***566***
Kim, Jeonghyeon
NSS-01-177 392
Kim, Jin
NSS-13-258 670
Kim, Jinhwan
NSS-13-218 654
Kim, Jinjoo
NSS-13-258 670
Kim, Jisoo
MIC-11-07 1229
NSS-01-155 384
NSS-01-209 403
Kim, Jongbum
NSS-13-258 670
Kim, Jong-Guk
NSS-01-251 ..... 43, ***420***
Kim, Jong-Yul
NSS-01-269 427
Kim, Jung-in
MIC-10-062 1096
Kim, Junhyeok
MIC-11-07 1229
NSS-13-218 ..... 72, ***654***
Kim, Kiyoung
NSS-01-163 387
Kim, Kum Bae
MIC-10-062 1096
Kim, Kwang il
MIC-15-372 1387
Kim, Kyoung Jin
MIC-05-454 1014
NSS-27-02 793
Kim, Kyungmin
NSS-01-213 405
Kim, Mia T.
MIC-15-327 1373
M-LT-05-08 1260
WS-04-04 248
Kim, Minho
MIC-10-146 1119
Kim, Minjong
NSS-13-154 ..... 68, ***627***
Kim, Myoung Jung
NSS-01-213 405
Kim, Sang Yong
NSS-01-169 389
Kim, Sangsu
RTSD-04-350 1494
Kim, Seil
NSS-01-059 344
Kim, Seohan
MIC-10-095 1104
MIC-10-431 1207
Kim, Seul Ah
NSS-01-201 400
Kim, Soo Mee
NSS-13-242 664
Kim, Sung Hun
MIC-15-318 1370
M-LT-05-10 1262
Kim, Sung-Woo
MIC-10-080 1100
Kim, Sunjin
NSS-13-258 670
Kim, Suyoung
MIC-10-041 1090
M-LT-03-04 1040
NSS-16-07 719
Kim, Tae Hoon
MIC-10-323 1173
Kim, Wonku
NSS-13-258 670
Kim, Woojin
NSS-13-246 666
Kim, Yeaeun
NSS-01-209 403
Kim, Yeongjun
N-LT-04-05 ..... 59, *554*
NSS-13-160 ..... 69, *629*
Kim, Yeon-Wook
NSS-01-163 ..... 39, ***387***
Kim, Yong Kyun
MIC-10-323 1173
Kim, Yongho
NSS-22-01 759
Kimoto, Natsumi
MIC-05-145 917
MIC-10-143 1118
MIC-15-141 ..... 151, ***1317***
MIC-15-144 1318
Kimura, Atsushi
NSS-27-01 792
Kimura, Hiromi
N-LT-02-14 318
NSS-01-321 450
NSS-13-028 574
NSS-13-030 ..... 62, ***575***
Kimura, Yura
MIC-05-199 ..... 106, ***934***
Kinahan, Paul E.
MIC-15-105 ..... 150, ***1305***
Kind, Charlie
NSS-01-187 395
King, Andrew P.
MIC-01-03 825
King, Michael A.
MIC-05-208 937
MIC-05-436 1008
MIC-10-227 1144
MIC-10-275 ..... 133, *1158*
MIC-15-204 1336
MIC-15-309 ..... 157, *1367*
RTSD-03-04 1488
WS-04-16 259
King, Pietro
MIC-03-06 860
NSS-10-04 519
King, Thomas
NSS-01-093 358
Kirchgässner, Rebekka
MIC-10-419 1202
MIC-17-01 1428
M-LT-03-08 1044
Kirschner, Nicholas
JS-03-06 ..... 26, ***283***
Kiselev, Oleg
NSS-13-278 678
Kishishita, Tetsuichi
NSS-01-071 349
Kitagawa, Yuichi
NSS-13-230 659
Kitahara, Masanori
NSS-07-01 493
Kitaura, Mamoru
N-LT-02-15 318
NSS-01-325 451
Kitayama, Yoshiharu
N-LT-02-04 ..... 29, ***310***
NSS-01-219 ..... 41, ***408***
RTSD-01-03 1470
Kitsuki, Wakako
NSS-01-217 407
Kjaer, Andreas
MIC-10-212 1139
Klatte, Lukas
MIC-10-281 1160
Klaus, Franz L.
N-LT-01-10 301
NSS-01-061 345

Author Index

Klein, Kyle
MIC-10-077 ..... 126, ***1100***
Klein, Martin
NSS-13-268 674
Klekots, Denys
NSS-12-04 532
Klén, Riku
MIC-05-409 1001
MIC-05-433 1007
MIC-15-306 1366
MIC-15-429 1405
M-LT-06-08 1271
Kleppinger, Joshua
RTSD-09-07 1573
Kloukinas, Kostas
RTSD-07-05 1556
Klujev, Alexander
NSS-10-02 516
Knecht, Kalie
NSS-13-158 628
Knol, Remco J.
MIC-05-433 1007
Knuuti, Juhani
MIC-05-433 1007
MIC-15-306 1366
MIC-15-429 1405
M-LT-06-08 1271
Ko, Guen Bae
MIC-05-016 877
MIC-05-085 898
MIC-10-026 1085
MIC-10-029 1086
MIC-10-095 ..... 127, *1104*
MIC-15-024 1281
MIC-15-048 1288
MIC-19-06 1449
Ko, Kilyoung
NSS-13-258 ..... 74, ***670***
Kobayashi, Daiki
MIC-05-145 917
MIC-10-143 1118
Kobayashi, Michihiro
MIC-15-168 1325
Kobayashi, Satoshi
MIC-05-151 919
MIC-05-157 921
MIC-15-177 1328
M-LT-02-04 849
M-LT-02-05 850
Kobayashi, Tatsuya
NSS-28-03 803
Kobayashi, Yosuke
JS-02-03 271
Koc, Arev
RTSD-04-383 ..... 175, *1521*
Kochebina, Olga
MIC-15-066 1293
Kochurikhin, Vladimir
NSS-07-01 493
Koda, Yuya
NSS-18-06 733
Koegler, Toni
MIC-17-04 1431
Koffmane, Christian
NSS-04-04 471
Kögler, Toni
MIC-05-328 974
Kohout, Zdenek
RTSD-04-386 1523
Kojima, Kazutoshi
NSS-01-071 349
Kojima, Yuya
NSS-26-08 ..... 89, ***789***
Koller, Robert
MIC-15-111 1307
Kolnikaj, Arjana
NSS-07-07 ..... 52, ***497***
Kolnsberg, Stephan
WS-02-16 235
Kolodziej, Magdalena
MIC-10-074 ..... 126, ***1099***
M-LT-04-10 ..... 121, ***1056***
Kolstein, Machiel
MIC-10-185 1130
MIC-15-321 1371
MIC-15-324 1372
M-LT-05-01 1254
M-LT-05-02 1255
Kolthammer, Jeff
MIC-01-05 827
MIC-10-269 1156
MIC-10-299 1165
Komaki, Tsubasa
RTSD-04-389 ..... 176, ***1526***
Komarov, Borys
MIC-15-135 1315
Komeda, Masao
NSS-01-221 408
NSS-13-234 661
Kominko, Yuliia
RTSD-05-03 1541
Kondasani, Basanth
NSS-04-04 471
Kondo, Shinichiro
NSS-01-029 ..... 32, ***333***
Kondrashov, Vladislav
NSS-13-182 ..... 70, ***639***
Konečný, Martin
RTSD-04-400 1535
Kononov, Anton
NSS-13-070 592
Konstantinou, Georgios
MIC-06-04 ..... 118, ***1030***
MIC-10-197 ..... 130, ***1134***
M-LT-03-02 ..... 119, ***1038***
NSS-13-212 ..... 72, ***652***
Kontaxakis, George
MIC-05-430 1006
Konvalov, Val
NSS-13-308 690
Koo, Seo Ryong
N-LT-03-01 538
NSS-13-094 602
Kopach, Oleh
RTSD-04-354 ..... **1497**
Kopach, Vasylyna
RTSD-04-354 1497
Körner, Elisa
MIC-20-03 1455
WS-04-17 260
Korpar, Samo
MIC-15-045 1287
NSS-21-06 755
Kortner, Oliver
NSS-01-113 366
NSS-24-03 773
Kortner, Sandra
NSS-01-113 366
NSS-24-03 773
Koshimizu, Masanori
NSS-13-018 ..... 61, ***570***
NSS-13-020 ..... 61, ***571***
Kossakowski, Michał
JS-03-05 282
N-LT-04-01 ..... 59, ***551***
NSS-13-162 ..... 69, ***630***
Köster, Ulli
MIC-12-04 1236
Kosugi, Ryoji
NSS-01-071 349
Kotasidis, Fotis
MIC-10-203 1136
MIC-15-375 1388
M-LT-05-03 1256
Kotenko, Andrii
NSS-12-04 532
Kotera, Katsushige
NSS-25-03 779
Koto, Masashi

Author Index

MIC-05-346 980
Koukopoulou, Aikaterini
MIC-10-215 1140
Kovacova, Eva
RTSD-04-361 1503
Kováčová, Eva
JS-03-03 280
RTSD-04-359 1502
Kovacs, Mark I.
RTSD-07-05 1556
Kovalenko, Maksym
RTSD-01-08 1475
RTSD-05-03 1541
RTSD-05-05 1543
Kovalski, Gil
MIC-15-210 1338
MIC-15-375 1388
M-LT-05-03 1256
Kowitt, Nolan I.
NSS-13-316 ..... 77, ***693***
NSS-18-03 730
Kozai, Masayoshi
NSS-13-064 589
Kozioł, Anna
NSS-13-168 ..... 69, ***633***
Kozmin, Pavel
RTSD-03-06 1490
Kožuljević, Ana Marija
MIC-15-444 1410
NSS-01-037 335
NSS-06-04 ..... 51, ***487***
Kracmar, Vojtech
NSS-12-03 531
Kral, Jan
NSS-07-08 498
Krämer, Jörg
MIC-05-355 983
Kratochwil, Nicolaus
MIC-05-004 873
MIC-09-04 1070
MIC-10-071 ..... 126, ***1098***
MIC-13-01 ..... 143, ***1242***
MIC-15-051 1289
NSS-16-01 714
Kraus, Veronika
N-LT-01-11 302
NSS-01-063 346
Krauze, Bohdan
MIC-05-106 ..... **905**
Krieger, Amanda
NSS-13-088 599
Krings, Thomas
NSS-01-307 443
NSS-13-070 592
Križan, Peter
MIC-15-045 1287
NSS-21-06 755
Kroha, Hubert
NSS-24-03 773
Krokos, Georgios
MIC-15-426 1404
Kroll, Jiri
NSS-12-03 531
Krueger, Hans
NSS-10-02 516
Krzemien, Wojciech
MIC-05-223 ..... 107, ***942***
MIC-16-06 ..... 164, ***1425***
M-LT-01-07 ..... 95, ***840***
Kuang, Zhonghua
MIC-07-05 1036
Kuchta, John R.
WS-04-12 ..... **256**
Kuczewski, Anthony J.
NSS-01-303 442
NSS-01-307 443
NSS-08-03 502
Kudo, Soshi
NSS-13-232 660
Kudo, Tetsuo
MIC-05-025 879
NSS-16-03 715
Kudrna, Vojtech
RTSD-03-06 1490
Kuhl, Yannick
MIC-05-028 880
MIC-11-01 1224
MIC-15-054 1290
MIC-15-291 1362
MIC-15-381 1390
MIC-16-05 1424
M-LT-05-04 1257
Kukurudziak, Mykola
RTSD-04-354 1497
Kulhánek, Tomáš
NSS-01-287 435
Kulkarni, Kirti
MIC-10-173 1127
Kumar, Deepak
MIC-12-05 1236
MIC-15-456 ..... 163, ***1414***
M-LT-06-03 ..... 146, ***1266***
Kumar, Kunal
MIC-10-032 1087
MIC-15-108 ..... **1306**
Kumar, Tanuj
NSS-01-045 ..... **339**
Kunc, Jan
RTSD-06-03 1548
Kunitomo, Risa
NSS-01-229 411
NSS-27-01 792
Kuo, Phillip H.
MIC-15-309 1367
Kupinski, Matthew A.
MIC-05-208 ..... 106, ***937***
MIC-05-436 1008
MIC-15-309 1367
RTSD-03-04 1488
WS-04-16 ..... 23, ***259***
Kuramoto, Koji
MIC-13-04 1245
Kurosawa, Shunsuke
NSS-01-029 333
NSS-02-02 456
NSS-05-02 478
NSS-11-05 526
NSS-22-06 ..... 85, ***762***
NSS-27-05 796
Kurucova, Nikola
RTSD-04-361 ..... 173, ***1503***
Kusakari, Sota
MIC-15-168 1325
Kushida, Junko
NSS-02-02 456
Kuvvetli, Irfan
JS-03-05 282
N-LT-04-01 551
NSS-13-162 630
Kuwabara, Soken
N-LT-02-15 ..... 30, ***318***
NSS-01-325 ..... 47, ***451***
Kwak, Sung-Woo
NSS-13-222 656
NSS-13-246 ..... 73, ***666***
Kwatra, Neha
MIC-10-275 1158
Kwon, Beomkyu
N-LT-04-04 ..... 59, ***553***
NSS-13-164 ..... 69, ***631***
NSS-13-252 668
Kwon, Chanwoo
MIC-10-149 1120
MIC-10-158 1122
MIC-15-150 ..... 152, ***1320***
Kwon, Inyong
N-LT-03-01 538
NSS-01-059 344
NSS-01-167 388

Author Index

NSS-13-094 602
NSS-13-096 603
Kwon, Jinhyung
NSS-13-154 627
Kwon, Sena
MIC-10-179 1128
MIC-15-180 ..... 153, ***1329***
NSS-01-047 340
Kwon, Sun Il
MIC-12-03 1235
MIC-13-04 1245
MIC-15-129 1313
NSS-01-103 363
NSS-03-05 465
NSS-16-01 714
Kyme, Andre Z.
MIC-05-307 967
MIC-15-129 1313
Kymissis, Ioannis
RTSD-05-06 1544
RTSD-06-05 1550

L

la Fougère, Christian
MIC-08-07 1064
MIC-20-03 1455
Labalme, Marc
NSS-01-241 416
Labiche, Marc
NSS-13-278 678
NSS-25-06 782
Lacasta, Carlos
MIC-10-032 1087
Ladarescu, Ion
MIC-05-361 985
MIC-10-098 1105
M-LT-04-02 1049
NSS-02-04 458
Ladefoged, Claes N.
STIR-08 1600
LAfay, Xavier
NSS-13-124 614
Lafaye, Rémi
MIC-21-05 1463
Laforest, Richard
MIC-05-364 986
Lafoux, Pauline
NSS-13-122 ..... 67, ***613***
Lai, Adriano
NSS-10-06 ..... **521**
Lai, Xiaochun
MIC-10-434 1208
RTSD-04-357 1500
RTSD-04-376 1515
RTSD-04-391 ..... 176, *1528*
RTSD-04-401 1536
RTSD-07-06 1557
RTSD-07-07 1558
Lai, Yanlin
NSS-01-123 370
Lai, Yuhang
MIC-05-325 973
Lakronwat, Jidapa
NSS-01-281 432
Lamblin, Jacob
NSS-09-01 508
Lamm, Amii O.
RTSD-09-01 ..... 180, ***1568***
Lammertsma, Adriaan A.
MIC-05-097 902
MIC-05-445 1011
MIC-10-437 1209
STIR-05 1598
Lamperti, Marco
NSS-03-04 464
Lampoudis, Christos
NSS-05-05 480
NSS-13-268 674
Lan, Hao
NSS-15-03 709
Lan, Wenhong
MIC-15-075 1296
Lang, Youdong
MIC-10-110 ..... **1109**
Lange, Sabine
NSS-10-02 516
Langholz, Andrew
MIC-15-210 1338
Lanièce, Phillipe
N-LT-03-10 545
NSS-13-134 619
Lanteri, Leonardo
NSS-28-07 807
Lanza, Jack
NSS-12-08 536
Lao, Hui
NSS-01-105 ..... 36, ***364***
TS-02-02 ..... 182, ***1586***
Lao, Jonathan
NSS-01-101 362
Lara, Natividad
MIC-15-006 1276
Latronico, Luca
NSS-14-08 705
Laurence, Jérome
N-LT-03-10 545
NSS-13-134 619
Laurent, Baptiste
MIC-05-232 944
Laurent, Benoit
NSS-01-241 416
Lavallée, Éric
MIC-02-03 831
Law, Ian
MIC-10-212 1139
Lazari, Monica
NSS-01-305 443
TS-02-05 1588
Lazzaroni, Paolo
NSS-08-02 ..... 53, ***501***
NSS-10-05 520
NSS-14-04 701
Le Grand, Roger
MIC-05-283 960
Le Guyader, Loïc
N-LT-03-12 547
NSS-08-07 505
NSS-13-300 687
Le Loirec, Cindy
NSS-01-195 398
Le Ray, Patrick
NSS-16-08 720
Le, The-Duc
NSS-04-03 470
Leal Doblado, Juan Alex
MIC-10-077 1100
Leatherland, Alex
NSS-01-223 409
Leban, Marijan
MIC-15-045 1287
LeBeau, Alexander H.
MIC-09-04 1070
Lebhertz, Dorothée
MIC-21-05 1463
Lebreton, Malo
N-LT-02-07 ..... 29, ***312***
NSS-01-231 ..... 42, ***412***
Lecomte, Roger
MIC-02-03 ..... 94, ***831***
MIC-10-092 1104
MIC-15-432 1406
MIC-18-04 1439
M-LT-04-07 1054
NSS-21-03 752
Lecoq, Paul
MIC-06-04 1030
Lédée, Ferdinand
RTSD-04-363 1505

Author Index

Lee, Dakyoung
N-LT-01-02 293
NSS-01-013 325
RTSD-04-367 ..... 173, ***1508***
Lee, Eunae
MIC-05-163 ..... **923**
Lee, Goeun
MIC-15-318 1370
M-LT-05-10 1262
NSS-02-05 ..... 48, ***459***
Lee, Hakjae
NSS-13-024 572
NSS-13-172 635
Lee, Hojin
NSS-01-097 360
Lee, Hyun Ji
MIC-18-08 ..... 166, ***1443***
Lee, Inki
MIC-10-427 1205
Lee, Jae Sung
MIC-04-01 864
MIC-05-016 877
MIC-10-026 1085
MIC-10-395 1194
MIC-11-06 1228
MIC-15-315 1369
MIC-16-04 1423
MIC-18-08 1443
MIC-19-03 1447
M-LT-03-01 1038
M-LT-05-06 1259
Lee, Jaewon
MIC-05-139 915
MIC-05-235 ..... 107, ***945***
MIC-21-03 1461
Lee, JeongHee
MIC-05-169 ..... 105, ***925***
NSS-01-211 404
Lee, Jeonghoon
NSS-01-155 384
NSS-01-209 403
Lee, Jin Won
NSS-01-169 389
Lee, Jisoo
MIC-10-095 ..... **1104**
Lee, Jiyon
RTSD-01-03 1470
Lee, Joo Hyun
MIC-19-03 ..... 166, ***1447***
Lee, Juhyun
NSS-13-238 662
Lee, Junho
NSS-01-177 392
NSS-01-207 ..... 41, ***402***
Lee, Junyoung
MIC-15-318 1370
M-LT-05-10 1262
NSS-02-05 459
Lee, Kisung
NSS-13-024 572
NSS-13-172 635
Lee, Ki-Yoon
NSS-01-269 ..... 44, ***427***
Lee, Kyo Chul
NSS-01-251 420
Lee, Min Sun
MIC-10-029 1086
NSS-13-242 ..... 73, ***664***
Lee, MyeongJae
NSS-13-144 622
Lee, Myung-Jae
NSS-13-082 596
Lee, Raehyun
MIC-15-417 1402
Lee, Sangho
MIC-05-334 ..... 111, ***976***
NSS-01-209 403
Lee, Sangmin
NSS-13-154 627
Lee, Seoyoung
MIC-05-277 958
Lee, Seung J.
NSS-13-310 691
Lee, Seungbae
NSS-01-059 344
Lee, Seungeun
JS-02-08 276
MIC-13-01 1242
RTSD-06-04 1549
Lee, Seungjoon
MIC-05-001 ..... **873**
Lee, Sihyun
MIC-15-417 ..... 161, ***1402***
Lee, Soo Min
MIC-05-322 ..... **972**
Lee, Soohyun
JS-01-02 264
MIC-15-147 1319
Lee, Sungho
NSS-01-233 413
NSS-13-190 ..... 70, ***642***
Lee, Taewoong
NSS-13-024 572
Lee, Uijin
NSS-01-155 384
NSS-01-209 ..... 41, ***403***
Lee, Ui-Seob
MIC-10-080 1100
Lee, Yeon Woo
NSS-01-201 ..... 40, *400*
Leem, Hyuntae
MIC-10-149 ..... 129, ***1120***
MIC-10-158 1122
MIC-15-150 1320
Lefevre, Frédéric
NSS-16-08 720
Lefrançois, Jacques
NSS-12-04 532
Lega, Alessandro
NSS-01-067 348
Leganés-Nieto, José Luis
NSS-02-04 458
Lehmann, Patrick
MIC-10-212 1139
MIC-15-264 1354
Lehtonen, Eero
MIC-05-433 1007
MIC-15-306 1366
M-LT-06-08 1271
Lei, Bowen
MIC-11-05 ..... 141, ***1228***
Lei, Junqin
MIC-05-343 979
MIC-15-339 1377
Lei, Linxin
MIC-15-435 1407
NSS-01-203 ..... 41, ***401***
Leite, Flávia Daniela
NSS-13-004 ..... **565**
Leland, John
N-LT-01-06 ..... 28, *297*
N-LT-04-08 ..... 60, ***556***
NSS-01-017 ..... 31, *327*
NSS-03-01 462
NSS-13-200 ..... 71, ***646***
Lemaire, Gaétan
MIC-03-08 861
NSS-21-03 752
Lemaire, Olivier
NSS-16-08 720
Lemaitre, Julien
MIC-05-283 960
Lenardo, Brian
NSS-13-106 607
Lennartz, Manfred
MIC-10-242 1148
Leo, Emmanuel
NSS-13-198 ..... 71, ***645***
León, Nerea

Author Index

MIC-10-416 ..... 138, ***1201***
M-LT-03-07 ..... 120, ***1043***
Leonida, Evgenia
NSS-13-256 ..... 74, ***669***
Leontiou, Theodoros
MIC-18-06 ..... 166, ***1441***
Lepine, Antoine
NSS-24-04 774
Lerch, Michael
NSS-04-01 468
NSS-04-02 469
NSS-06-05 488
Lerche, Christoph W.
MIC-05-028 880
MIC-05-103 904
MIC-10-008 1079
MIC-10-242 1148
MIC-10-260 1153
MIC-15-162 1324
MIC-15-249 1349
MIC-15-255 1351
MIC-16-02 1421
Lerendegui-Marco, Jorge
MIC-05-361 985
MIC-10-098 1105
M-LT-04-02 1049
NSS-02-04 458
Leroy, Mélissa
RTSD-04-398 ..... 176, ***1533***
Lesmes, Catalina
NSS-01-287 ..... 45, ***435***
Lesnic, Daniel
MIC-15-252 1350
STIR-04 1598
Leso, Aurora
MIC-10-362 1184
Lessard, Gabriel
NSS-05-08 483
NSS-21-03 ..... **752**
Létang, Jean Michel
MIC-10-221 1142
MIC-10-233 1146
NSS-01-195 398
Leterrier, Laurent
NSS-20-06 746
Letra, Mariana
RTSD-04-362 1504
RTSD-04-400 1535
Leung, Kevin H.
MIC-15-300 ..... 157, ***1365***
Levin, Craig S.
MIC-05-274 957
MIC-07-04 1035
MIC-10-449 1213
MIC-15-288 1361
MIC-15-465 1417
MIC-20-02 1454
M-LT-06-05 1268
Levin, Criag S.
MIC-15-270 1356
Levin, Johannes
MIC-10-281 1160
MIC-10-308 1168
Lewis, Emma
MIC-05-421 1004
Li, Anting
MIC-05-409 ..... 114, ***1001***
MIC-15-429 ..... 162, *1405*
Li, Canming
NSS-01-121 369
Li, Chen
NSS-17-02 ..... 81, ***723***
Li, Chenguang
MIC-18-07 ..... 166, ***1442***
Li, Chengyi
JS-02-02 270
Li, Chenxi
MIC-02-02 830
MIC-05-184 929
MIC-10-119 1111
MIC-11-02 ..... 141, ***1225***
N-LT-04-10 558
NSS-13-280 679
Li, Chunhao
MIC-05-400 998
MIC-10-239 1147
MIC-10-398 1195
MIC-15-396 ..... **1395**
MIC-15-399 1396
Li, Deyuan
NSS-01-265 ..... 44, ***426***
Li, Duoduo
MIC-15-408 1399
Li, DuoDuo
MIC-14-04 1251
Li, Elizabeth J.
MIC-05-262 953
Li, Fei
NSS-01-121 369
Li, Gang
RTSD-04-395 1532
Li, Gengchen
NSS-27-01 ..... 89, ***792***
Li, Haifang
MIC-10-272 1157
Li, Haiyi
MIC-10-272 ..... **1157**
Li, Haonan
MIC-05-010 875
MIC-07-05 ..... 119, ***1036***
Li, He
RTSD-04-357 1500
RTSD-04-376 1515
RTSD-04-391 1528
RTSD-04-401 1536
RTSD-07-06 1557
RTSD-07-07 1558
Li, Hengyi
MIC-05-067 892
MIC-05-127 911
MIC-05-250 ..... 108, ***949***
MIC-15-261 1353
Li, Hong
NSS-01-127 371
NSS-28-01 ..... 90, ***801***
Li, Hongdi
MIC-04-02 865
MIC-06-01 1027
MIC-15-231 1344
MIC-20-04 1456
NSS-13-176 637
Li, Hua
MIC-05-226 943
M-LT-01-02 836
NSS-13-270 675
Li, Hui
NSS-01-265 426
NSS-13-270 ..... 75, ***675***
Li, Ji
NSS-01-303 442
Li, Jie
WS-04-07 251
Li, Jinghuai
NSS-01-215 406
Li, Jinlin
MIC-10-239 1147
MIC-10-398 1195
Li, Junjun
NSS-26-03 ..... 88, ***785***
Li, Junli
NSS-26-06 788
Li, Kaiwen
MIC-14-05 1252
Li, Liang
MIC-05-442 ..... 115, *1010*
MIC-10-152 1121
RTSD-07-01 1553
Li, Lianghua
MIC-05-385 993

Author Index

MIC-08-05 1062
Li, Liqian
RTSD-04-395 1532
Li, Long
NSS-17-03 724
Li, Longhao
NSS-13-282 680
Li, Lu
NSS-01-105 364
Li, Minghang
NSS-01-127 371
Li, Nan
WS-04-07 251
Li, Peize
MIC-15-435 ..... 162, ***1407***
Li, Qicai
NSS-17-06 727
Li, Quanzheng
MIC-19-02 ..... 166, *1446*
Li, Shuqi
NSS-01-093 358
Li, Sichun
MIC-08-05 1062
Li, Siqi
MIC-18-02 ..... 165, ***1437***
MIC-20-04 1456
Li, Tiantian
MIC-05-211 938
MIC-20-04 1456
Li, Wei
NSS-13-060 587
Li, Weiwei
MIC-05-331 975
MIC-10-329 1175
MIC-15-333 1375
Li, Wenbin
MIC-05-286 961
MIC-05-376 990
MIC-07-03 1034
MIC-10-113 1110
MIC-10-116 1111
Li, Xiaohui
N-LT-03-05 542
NSS-13-092 601
NSS-13-126 615
NSS-28-05 805
Li, Xiaoxuan
NSS-13-126 615
Li, Ximeng
MIC-15-333 ..... **1375**
Li, Xin
NSS-13-026 573
NSS-13-240 ..... 73, *663*
Li, Xinbin
NSS-18-02 729
Li, Xiuxia
NSS-01-069 348
Li, XiuXia
NSS-13-068 591
Li, Xuan
NSS-17-03 724
Li, Ya
MIC-15-273 1357
Li, Yazhi
MIC-05-100 903
Li, Yifang
MIC-15-414 1401
Li, Yiming
NSS-13-284 681
Li, Yuanjing
NSS-01-069 348
NSS-13-068 591
NSS-13-110 609
Li, Yue
MIC-15-297 1364
MIC-19-04 1448
M-LT-06-09 1272
Li, Yulan
NSS-01-069 348
NSS-13-068 591
NSS-13-110 609
RTSD-09-03 1569
Li, Yusheng
MIC-04-02 ..... 98, ***865***
MIC-06-01 ..... 118, ***1027***
MIC-15-057 1291
MIC-15-093 ..... 150, ***1302***
MIC-15-231 1344
NSS-13-176 637
Li, Zekai
MIC-05-280 959
MIC-05-445 1011
MIC-10-194 1133
MIC-10-437 ..... 139, ***1209***
MIC-15-075 1296
STIR-05 ..... **1598**
Li, Zhenjie
NSS-13-060 587
Li, Zhihao
MIC-10-209 ..... 131, ***1138***
Li, Zhihua
NSS-28-05 805
Li, Zimeng
RTSD-04-364 1505
RTSD-04-373 1513
Liang, Da
MIC-02-01 829
MIC-05-286 961
MIC-05-376 ..... **990**
MIC-07-03 1034
MIC-10-113 ..... **1110**
MIC-10-116 1111
MIC-10-125 1113
Liang, Dong
MIC-05-385 993
Liang, Felix
N-LT-01-05 ..... 27, ***296***
NSS-01-019 ..... 31, ***328***
NSS-01-129 ..... 37, ***372***
NSS-13-236 ..... 73, ***662***
Liang, Futian
NSS-01-095 359
Liang, Kun
NSS-21-01 750
Liang, Ying
MIC-05-127 911
MIC-09-07 1073
MIC-10-455 1215
MIC-14-04 1251
MIC-15-117 1309
MIC-15-120 1310
MIC-15-408 1399
Liang, Zhengrong J.
MIC-10-272 1157
Liao, Hanri
MIC-05-040 884
Liao, Haolong
NSS-01-127 371
NSS-13-126 ..... **615**
Liao, Runze
MIC-02-02 830
MIC-10-131 ..... **1115**
MIC-10-377 1188
Liao, Suyu
MIC-05-178 ..... **928**
Liberali, Valentino
NSS-14-08 705
Licciulli, Francesco
NSS-20-03 743
NSS-21-07 756
Lieffrig, Eléonore V.
MIC-05-259 ..... 108, ***952***
MIC-15-225 ..... **1342**
Liguori, Antonio
NSS-20-03 743
Likartsis, Christodoulos
MIC-18-06 1441
Lilburn, David M.L.
MIC-15-426 1404

Author Index

Lim, Anthony
NSS-13-078 595
Lim, Chang Hwy
MIC-05-169 925
NSS-01-211 404
Lim, Dohyun
MIC-05-277 958
Lim, Gei Y.
NSS-25-03 779
Lim, Ilhan
MIC-10-427 1205
MIC-15-372 1387
NSS-01-251 420
Lim, Jungman
NSS-01-059 344
Lim, Soobin
JS-01-05 267
Lim, Younghwan
MIC-15-147 1319
Lin, Cheng T.
MIC-05-172 926
M-LT-01-05 838
Lin, Chia-Yu
MIC-05-394 996
Lin, Ming-Wei
N-LT-02-03 309
NSS-01-253 421
Lin, Tzu-Hsiang
N-LT-02-03 309
NSS-01-253 421
NSS-01-323 ..... 47, *450*
Lin, Xinyan
MIC-14-05 1252
Lin, Yangshi
MIC-14-04 ..... 144, ***1251***
MIC-15-408 1399
Lin, Ying
MIC-05-286 961
MIC-05-376 990
MIC-07-03 1034
MIC-10-113 1110
Lin, Yuejie
MIC-05-286 961
MIC-05-376 990
MIC-07-03 1034
MIC-10-113 1110
MIC-10-116 ..... **1111**
Linder, Pia M.-L.
MIC-20-03 1455
Lindman, Alec
N-LT-02-12 ..... 30, ***316***
NSS-01-085 ..... 35, ***356***
NSS-14-01 699
NSS-28-02 802
Lindsay, Clifford
MIC-15-309 ..... **1367**
Ling, Cai
MIC-10-107 1108
Linhart, Vladimír
NSS-06-06 489
Liotino, Rocco
NSS-20-03 743
Lipp, John
NSS-13-278 678
Litaize, Olivier
NSS-09-01 508
Liu, Baodong
MIC-10-200 1135
Liu, Bicheng
JS-02-02 270
NSS-13-214 652
Liu, Dong
NSS-01-121 ..... 36, ***369***
Liu, Feng
RTSD-09-03 1569
Liu, Gang
MIC-03-06 860
NSS-01-087 ..... **356**
NSS-10-04 519
NSS-23-02 766
Liu, Ge
MIC-15-228 1343
Liu, Guobing
MIC-18-02 1437
Liu, Guorong
NSS-01-215 ..... 41, ***406***
Liu, Han
MIC-02-01 829
MIC-05-286 961
MIC-05-376 990
MIC-07-03 ..... 119, ***1034***
MIC-10-113 1110
MIC-10-116 1111
MIC-10-125 1113
Liu, Hongbin
NSS-01-123 370
NSS-17-06 ..... **727**
Liu, Hong-Da
N-LT-02-03 ..... 29, ***309***
NSS-01-253 ..... 43, ***421***
Liu, Hongwei
NSS-01-127 371
Liu, Huafeng
MIC-19-02 1446
Liu, Huan
NSS-13-148 ..... 68, ***624***
Liu, Hui
MIC-05-190 931
MIC-05-226 943
MIC-05-352 982
MIC-08-04 1061
MIC-10-224 1143
MIC-10-413 1200
MIC-14-03 1250
MIC-15-078 1297
MIC-15-186 1331
MIC-15-228 1343
MIC-15-312 1368
MIC-15-351 1381
MIC-15-450 1412
MIC-17-02 1429
M-LT-01-02 836
M-LT-05-05 1258
M-LT-06-02 1265
WS-04-05 249
WS-04-06 250
Liu, Jianjun
MIC-05-385 993
MIC-08-05 1062
Liu, Jiaqi
NSS-16-02 ..... 80, ***715***
Liu, Jinbo
NSS-01-031 333
NSS-27-04 795
Liu, Jiping
MIC-05-331 975
MIC-10-329 1175
MIC-15-333 1375
Liu, Kunliang
TS-03-02 ..... 183, ***1592***
Liu, Lei
NSS-13-214 652
Liu, Liye
NSS-13-270 675
Liu, Manwen
NSS-28-05 805
Liu, Ming
RTSD-10-05 1581
Liu, Qi
MIC-05-325 973
MIC-10-008 ..... 124, ***1079***
Liu, Qiao
MIC-05-193 ..... 106, ***932***
Liu, Qibin
NSS-23-06 770
Liu, Qiong
MIC-10-299 ..... **1165**
Liu, Ruifeng
MIC-10-452 ..... 140, *1214*

Author Index

MIC-18-05 ..... 166, ***1440***
Liu, Ruolan
MIC-05-331 975
MIC-10-329 ..... **1175**
MIC-15-333 1375
Liu, Shuangquan
N-LT-03-05 542
NSS-13-092 601
Liu, Stephen
MIC-10-374 1187
Liu, Wei
MIC-05-376 990
MIC-10-113 1110
WS-04-07 251
Liu, Xianchen
MIC-05-100 903
MIC-15-411 1400
Liu, Xiaohua
NSS-01-127 371
Liu, Xiaoqing
NSS-13-032 ..... 62, ***576***
Liu, Xin
NSS-01-225 410
Liu, Xinghui
RTSD-04-388 1525
Liu, Xinyao
MIC-15-228 1343
Liu, Yantao
NSS-13-026 ..... 62, ***573***
NSS-13-240 ..... **663**
Liu, Yaoguang
NSS-13-060 587
Liu, Yaqiang
MIC-05-190 931
MIC-05-226 943
MIC-05-352 982
MIC-08-04 1061
MIC-10-413 1200
MIC-14-03 1250
MIC-15-078 1297
MIC-15-186 1331
MIC-15-228 1343
MIC-15-351 1381
MIC-15-450 1412
MIC-17-02 1429
M-LT-01-02 836
M-LT-06-02 1265
NSS-01-225 410
WS-04-05 249
WS-04-06 250
Liu, Yi
MIC-10-164 1124
NSS-13-126 615
Liu, Yibin
MIC-15-387 1392
Liu, Yi-Chien
MIC-05-394 996
Liu, Yilin
MIC-05-382 992
Liu, Yongjian
MIC-05-364 986
Liu, Yu Xiang
NSS-13-264 ..... 74, ***673***
Liu, Yuanyuan
NSS-01-041 337
NSS-15-04 710
Liu, Yujie
NSS-01-225 410
Liu, Zhenan
NSS-01-121 369
Liu, Zheng
MIC-05-010 ..... 99, ***875***
MIC-07-05 1036
Liu, Zhongzhi
MIC-05-211 ..... 107, ***938***
MIC-15-057 1291
Liu, Zimo
MIC-05-175 927
M-LT-01-04 837
Liu, Ziwei
MIC-08-02 1059
Livieratos, Lefteris
MIC-05-202 935
MIC-18-01 1436
M-LT-01-01 835
Llido, Olivier
NSS-27-03 794
Llop, Jordi
MIC-05-358 984
Llopart Cudie, Xavier
NSS-01-139 377
RTSD-07-05 1556
RTSD-08-01 1561
Llosa, Gabriela
MIC-05-460 1016
MIC-10-035 1088
MIC-15-099 1303
Llosá, Gabriela
MIC-05-088 899
MIC-05-358 984
MIC-10-032 1087
MIC-10-089 1103
MIC-10-293 1163
MIC-10-326 1174
MIC-10-353 1181
MIC-10-356 ..... 136, ***1182***
MIC-15-336 1376
MIC-16-02 1421
M-LT-04-05 1052
NSS-03-02 462
Lockhart, Madeline L.
NSS-05-03 ..... 50, ***479***
Lohmann, Philipp
MIC-10-242 1148
Loignon-Houle, Francis
MIC-05-118 908
MIC-09-02 1068
MIC-09-06 ..... 123, ***1072***
MIC-10-020 1083
MIC-13-02 ..... 143, *1243*
MIC-15-123 1311
M-LT-02-02 847
WS-04-13 256
Loizzo, Pierpaolo
NSS-20-03 743
Lomidze, David
N-LT-03-12 547
NSS-08-07 505
NSS-13-300 687
NSS-13-304 688
Long, Xiaoyun
MIC-18-02 1437
Longas, Jesús L.
MIC-10-416 1201
M-LT-03-07 1043
Longo, Renata
RTSD-08-02 1561
Loparco, Francesco
NSS-20-03 743
López Martínez, Sergio
MIC-15-357 ..... 159, ***1383***
Lopez Paz, Ivan
MIC-10-017 ..... 124, ***1082***
M-LT-03-03 ..... 119, ***1039***
López, Alberto
N-LT-03-02 539
NSS-13-098 604
NSS-20-06 ..... **746**
Lopez, Iván
N-LT-02-02 308
NSS-01-275 430
López, Iván
JS-02-09 276
NSS-12-05 532
López, Rafael
MIC-10-296 1164
Lopez-Berenguer, Fernando
MIC-05-121 ..... **909**
MIC-10-386 1191

Author Index

M-LT-02-10 ..... **854**
M-LT-03-10 1046
Lopez-Cuenca, Carlos
NSS-01-093 358
López-González, Francisco J.
MIC-05-388 994
Lopez-Montes, Alejandro
MIC-01-01 ..... 93, ***823***
MIC-05-424 1005
MIC-08-03 1060
MIC-15-234 ..... 155, ***1345***
WS-04-17 260
Lord, James S
NSS-13-078 ..... **595**
Lorenzon, Altea
MIC-05-175 ..... 105, ***927***
M-LT-01-04 ..... 95, ***837***
Lorusso, Leonarda
NSS-20-03 743
Los, Sergey
NSS-20-07 747
Lotina, Luka
NSS-01-037 335
NSS-06-04 487
Louchet-Chauvet, Anne
MIC-15-213 1339
Loughney, Kerri L.
NSS-13-040 ..... **579**
Lovatti, Giulio
MIC-05-130 912
MIC-10-059 1095
MIC-10-083 1101
MIC-17-05 1432
M-LT-04-08 1054
M-LT-04-09 1055
Lowell, Alex
NSS-13-128 616
Loyd, Matthew
N-LT-02-06 ..... 29, ***311***
NSS-01-227 410
NSS-01-235 ..... 42, ***414***
NSS-27-06 796
Lu, Haoyu
MIC-18-03 ..... 165, ***1438***
Lu, Jincheng
MIC-03-03 858
MIC-03-05 859
MIC-10-452 1214
Lu, Ming
WS-04-07 251
Lu, Qiuyu
NSS-04-02 469
Lu, Wengao
NSS-01-127 371
Lu, Yihuan
MIC-15-297 ..... 157, *1364*
MIC-19-04 1448
M-LT-06-09 ..... 146, *1272*
Lu, Yue
RTSD-04-373 1513
Lu, Yugui
RTSD-04-356 1499
Lu, Zhenrui
MIC-10-284 1161
Luca, Cultrera
RTSD-06-06 1551
Lucchini, Marco Toliman
N-LT-04-11 559
NSS-13-290 683
Luck, Marcus
MIC-05-022 ..... **879**
Lucyana, Fitiri
MIC-05-151 919
M-LT-02-05 850
Lucyana, Fitri
MIC-05-157 921
MIC-15-177 ..... 153, ***1328***
M-LT-02-04 849
Luhta, Randy
MIC-15-171 1326
Lukosi, Eric
NSS-01-055 342
NSS-01-151 382
NSS-13-308 690
Lulinsky, Ariel
MIC-15-210 1338
MIC-15-375 1388
M-LT-05-03 1256
Lung, Quang
RTSD-05-05 1543
Lunin, Leonid
NSS-01-093 358
Luo, Gongning
MIC-05-286 961
Luo, Haibo
RTSD-04-399 1534
Luo, Jingqin
MIC-05-310 968
Luo, Jun
NSS-28-05 805
Luo, Qingfei
MIC-10-272 1157
Luo, Tian
NSS-01-127 371
Luo, Xuhan
MIC-04-05 868
MIC-05-271 956
Lupilov, Aleksandr
RTSD-05-02 1541
Lusardi, Nicola
NSS-12-02 ..... 56, ***530***
NSS-13-130 ..... 67, *617*
NSS-13-304 688
Luurtsema, Gert
MIC-10-437 1209
STIR-05 1598
Lüvelsmeyer, Ann-Kristin
MIC-15-330 ..... 158, ***1374***
M-LT-05-07 ..... 145, ***1259***
Lv, Chao
NSS-13-108 608
Lv, Xinyu
JS-02-06 274
MIC-05-046 886
Lv, Yang
MIC-05-193 932
MIC-10-188 1131
MIC-10-458 1216
MIC-18-02 1437
M-LT-03-09 1045
Lv, Ziwen
MIC-10-434 ..... **1208**
Lyashenko, Alexey
MIC-10-047 1091
NSS-13-084 597
Lynde, Clément
NSS-11-02 523
Lyu, Qihui
MIC-05-439 1009
MIC-12-03 1235
Lyu, Zhenlei
MIC-02-04 832
MIC-05-451 1013
MIC-15-435 1407
NSS-01-203 401
WS-04-08 252

M

Ma, Chao
MIC-10-236 1146
MIC-18-04 1439
Ma, Jie
NSS-07-05 495
RTSD-04-356 1499
Ma, Qianyue
MIC-03-05 ..... 98, ***859***
Ma, Qiuhui
MIC-05-325 973

Author Index

Ma, Rui
RTSD-07-01 ..... 179, ***1553***
Ma, Tianyu
MIC-02-04 832
MIC-05-451 1013
MIC-10-230 1145
MIC-14-02 1249
MIC-15-435 1407
MIC-17-02 1429
NSS-01-203 401
WS-04-08 252
Ma, Wangquan
MIC-02-01 829
MIC-05-376 990
MIC-10-113 1110
Ma, Yuanjue
MIC-10-152 ..... 129, ***1121***
Maa-Hacquoil, Henry
MIC-10-302 ..... **1166**
Maalmi, Jihane
NSS-12-04 532
NSS-13-084 597
NSS-20-06 746
Maaniitty, Teemu
MIC-15-306 1366
MIC-15-429 1405
M-LT-06-08 1271
Macchiarulo, Luca
MIC-05-022 ..... 100, *879*
NSS-01-117 ..... 36, ***367***
NSS-10-03 ..... 55, ***518***
NSS-14-05 ..... 78, ***702***
Machida, Masahiko
NSS-15-01 707
Madhan, Kavish
NSS-13-204 648
Mae, Shunichiro
N-LT-02-14 318
NSS-01-321 450
Maebe, Jens
MIC-05-373 989
MIC-14-01 ..... 143, ***1248***
MIC-15-276 1357
M-LT-06-06 1269
Maeda, Makoto
NSS-01-221 408
NSS-13-234 ..... 73, ***661***
Maeno, Yuta
MIC-05-151 919
MIC-05-157 921
MIC-15-177 1328
M-LT-02-04 849
M-LT-02-05 850
Maffessanti, Stefano
N-LT-03-12 547
NSS-08-01 ..... 53, ***500***
NSS-08-07 505
NSS-13-100 605
NSS-13-300 687
NSS-13-304 688
Magalhães, Ana C.
MIC-05-349 ..... **981**
Magaud, Gilles
NSS-01-101 362
Magazzu, Guido
NSS-14-08 705
Maggio, Camilla
NSS-20-04 744
Magistris, Matteo
NSS-11-01 523
Magne, Magali
NSS-01-101 362
NSS-12-04 532
Mahé, Charly
NSS-11-02 523
Mahgoub, Omer
NSS-13-216 653
Maia, Jorge M.
RTSD-04-362 ..... **1504**
RTSD-04-378 1517
RTSD-04-400 1535
Maiatska, Olga
NSS-13-260 671
Maier, Andreas
MIC-05-418 1003
Maiolino, Cettina
NSS-25-04 780
Maiorino, Marino
MIC-05-004 873
Maj, Piotr G.
NSS-13-146 ..... 68, ***623***
RTSD-07-03 1554
Majewski, Stanislaw
JS-02-04 272
MIC-05-019 878
MIC-09-08 1074
MIC-15-045 1287
Majumder, Shweta
MIC-05-262 953
Makala, Manikanta
RTSD-06-05 1550
Makek, Mihael
MIC-15-444 ..... 162, ***1410***
NSS-06-04 487
Malaguti, Roberto
NSS-20-05 745
Malanchini, Mirco
NSS-13-118 612
Malasani, Vindhya
MIC-05-367 987
MIC-15-294 1363
Malec, Štěpán
NSS-06-06 489
Maliakal, Gabriel
MIC-10-371 ..... **1187**
WS-04-04 248
Malliolio, Lisa
NSS-13-078 595
Maloney, Maxwell C.
NSS-27-01 792
Mamalakis, Michail
MIC-10-290 1162
Manabe, Seiya
NSS-13-066 590
NSS-27-02 793
Manber, Richard
MIC-05-265 954
Mandal, Krishna C.
JS-03-01 ..... 25, ***279***
RTSD-06-03 1548
Mandot, Shubham
JS-01-04 266
MIC-05-136 ..... 104, ***914***
MIC-16-03 1422
MIC-21-01 ..... 168, ***1459***
M-LT-02-03 ..... 96, ***848***
NSS-09-05 512
Manek, Petr
RTSD-01-07 1474
Mánek, Petr
MIC-05-292 ..... 110, ***963***
NSS-01-135 ..... 37, ***375***
NSS-01-287 435
RTSD-08-05 1564
Manen, Samuel
NSS-20-06 746
Manera Escalero, Rafel
NSS-23-04 768
Manera, Rafel
MIC-05-019 878
N-LT-03-02 539
NSS-13-098 604
Maneval, Daniel
MIC-05-337 977
Manfreda, Alberto
NSS-14-08 705
Manfredi, Enrico
NSS-17-04 725
Manfredi, Juan J.

Author Index

NSS-01-299 ..... 46, ***440***
NSS-05-06 481
NSS-13-274 677
Manghisoni, Massimo
NSS-08-02 501
NSS-10-05 520
NSS-14-04 701
NSS-14-08 705
Mangiagalli, Giacomo
NSS-01-263 425
Mann, Sarah E.
N-LT-02-10 ..... 29, ***315***
NSS-01-267 ..... 44, ***426***
NSS-09-06 513
Mannel, Eric J.
N-LT-04-12 ..... 60, ***560***
NSS-13-294 ..... 76, ***685***
Mano, Charles-Philippe
NSS-01-197 399
Manoni, Elisa
N-LT-04-11 559
NSS-13-290 683
Mansouri, Zahra
MIC-05-319 971
Manuthasna, Shariff
NSS-01-281 432
Marcatili, Sara
MIC-05-337 ..... 111, ***977***
MIC-15-324 1372
M-LT-05-02 1255
Marcellino, Lorenzo
NSS-14-02 700
Marchais, Thomas
NSS-02-01 455
Marchal, Julien
N-LT-02-01 307
NSS-01-271 428
NSS-24-04 774
Marek, Lukáš
RTSD-04-400 1535
Maresca, Luca
NSS-21-07 756
Margato, Luis M.
N-LT-02-01 ..... 29, ***307***
NSS-01-271 ..... 44, ***428***
Marín, Daniel David
N-LT-03-02 ..... 57, ***539***
NSS-13-098 ..... 65, ***604***
NSS-20-06 746
Marín, Jesús
MIC-15-348 1380
Marin, Thibault
MIC-02-03 831
MIC-04-08 871
MIC-10-236 ..... 132, *1146*
MIC-15-045 1287
MIC-18-04 1439
Mariotti, Emilio
MIC-10-362 1184
Markiewicz, Pawel
STIR-14 1599
Markiewicz, Pawel J.
MIC-05-265 ..... 109, ***954***
Markovic, Bojan
MIC-03-06 860
NSS-01-087 356
NSS-10-04 519
NSS-23-02 766
Marles, Jussi
NSS-28-06 806
Marleu, Peter
NSS-05-01 477
Marques, Afonso P.
NSS-24-06 ..... 87, ***775***
Marras, Alessandro
NSS-10-02 516
Marsden, Paul K.
MIC-05-220 941
MIC-19-08 1451
M-LT-01-09 842
Marshall, William
NSS-25-06 782
Marsri, Tanawish
NSS-01-281 432
Mart, Yagiz
RTSD-04-383 ..... **1521**
Marth, Lena
MIC-10-281 1160
Martí-Bonmatí, Luis
MIC-15-360 1384
Martín Fernández, Lucía
MIC-10-341 1178
Martina, Luigi
NSS-13-324 696
Martina, Maurizio
NSS-17-04 725
Martínez Dávalos, Arnulfo
MIC-15-390 1393
Martínez Gudiño, Maria D.L.
MIC-15-390 1393
Martínez Murcia, Francisco J.
MIC-10-281 ..... 134, ***1160***
MIC-10-290 1162
MIC-10-296 1164
MIC-10-308 1168
MIC-15-282 1359
M-LT-06-07 1270
Martínez Nouvilas, Victor
MIC-10-404 1197
MIC-15-462 1416
M-LT-03-06 1042
N-LT-01-07 298
NSS-01-039 336
Martínez Nouvilas, Víctor
NSS-01-027 332
NSS-01-131 ..... 37, ***373***
NSS-13-086 598
Martinez, Paul N.
WS-04-09 253
Martínez-Dávalos, Arnulfo
MIC-05-049 887
MIC-05-112 906
Martínez-Domingo, Carme
RTSD-06-05 1550
Martín-Noguerol, Teodoro
MIC-10-296 1164
Martisikova, Maria
MIC-10-419 ..... 139, *1202*
MIC-17-01 ..... 164, ***1428***
M-LT-03-08 ..... 120, *1044*
Mas Milian, Felix
NSS-05-07 482
NSS-12-07 ..... 57, *535*
Mas, Roser
N-LT-01-14 305
NSS-01-313 446
Masbou, Julien
NSS-16-08 720
Masek, Vladimir
NSS-07-08 498
Masera, Guido
NSS-17-04 725
Mashinini, Sello
NSS-01-243 ..... 43, *417*
Mason, Andrea
NSS-01-291 437
NSS-08-07 ..... 53, ***505***
NSS-25-04 780
Mason, James
JS-03-06 283
Massaccesi, Ludovico
NSS-28-07 807
Massaharu Murata, Helio
NSS-13-010 567
Massanes, Francesc
MIC-05-229 ..... 107, ***944***
MIC-15-189 ..... 153, ***1331***
Massey, Thomas
NSS-05-06 481

Author Index

Mas-Torrent, Marta
RTSD-06-05 1550
Mastroianni, Stefano
NSS-01-149 ..... 38, ***382***
Masuda, Akihiko
NSS-13-066 590
NSS-27-02 793
Masuda, Noriyuki
RTSD-04-351 1495
RTSD-07-07 1558
Masuda, Takamitsu
MIC-05-346 980
Matej, Samuel
MIC-19-01 1445
Mateo, Diego
N-LT-03-02 539
NSS-13-098 604
NSS-20-06 746
Mathez, Hervé
NSS-20-06 746
Mathur, Kartikey
NSS-13-228 658
Mati, Annalisa
NSS-20-04 744
TS-02-05 1588
Matousek, Oscar H.
MIC-05-139 ..... 104, ***915***
MIC-21-03 1461
Matsubayashi, Nishiki
NSS-05-02 ..... 50, ***478***
NSS-11-05 526
NSS-27-05 796
Matsumoto, Tetsuro
NSS-13-066 590
NSS-27-02 793
Matsumura, Toru
NSS-25-03 ..... 87, ***779***
Matsunaga, Daisuke
NSS-01-133 374
Matsunaga, Kai
NSS-02-02 456
Matsunaga, Yusuke
NSS-28-03 803
Matsuyama, Shigeo
NSS-13-090 600
Matt, Gebhard J.
RTSD-01-08 1475
RTSD-05-03 1541
RTSD-05-05 1543
Matta, James
NSS-05-06 481
Mattayom, Nattasit
NSS-16-04 716
Matteocci, Fabio
RTSD-06-01 1547
Matthews, David
NSS-05-06 481
Mattiazzo, Serena
NSS-13-298 686
Mattingly, John
N-LT-01-03 294
NSS-13-329 453
Maurer, Linus
NSS-14-07 704
Mauri, Giacomo
N-LT-02-10 315
NSS-01-267 426
NSS-09-06 ..... 54, ***513***
Mauricio Ferré, Joan
NSS-23-04 768
Mauricio, Joan
MIC-05-019 878
MIC-09-08 1074
MIC-15-045 1287
N-LT-03-02 539
NSS-03-05 465
NSS-13-098 604
NSS-20-06 746
Mayet, Céline
MIC-05-283 960
Mazorra, José
NSS-20-06 746
Mazza, Giovanni
NSS-14-02 ..... 78, ***700***
Mazza, Simone
NSS-10-03 518
NSS-14-05 702
Mazzanti, David
JS-02-04 272
MIC-05-019 ..... 100, ***878***
MIC-09-06 1072
MIC-09-08 1074
MIC-15-045 1287
Mazzini, Vittoria
RTSD-08-02 1561
Mazziotta, Mario Nicola
NSS-20-03 743
NSS-21-07 756
Mazzoleni, Alice
NSS-01-093 358
Mazzucconi, Davide
MIC-10-347 1180
MIC-17-03 1430
MIC-21-02 1460
NSS-09-04 511
Mazzuzzoni, Davide
MIC-05-082 897
Mc Lean, Chris
MIC-03-01 856
McAleer, Daniel
JS-01-01 264
McColl, Taylor J.
MIC-05-313 969
McGowan, Daniel R.
MIC-04-07 870
MIC-10-311 1169
MIC-10-422 1203
MIC-15-441 1409
McHugh, Annamaria R.
NSS-11-03 ..... 56, ***524***
McNitt-Gray, Michael F.
MIC-04-06 869
McQuaid, Sarah J.
MIC-15-345 1379
Mead, Lewis
NSS-01-187 ..... 40, ***395***
Medaer, Sacha E.R.
NSS-01-289 ..... 45, ***436***
NSS-06-01 ..... 51, ***485***
NSS-13-080 ..... 64, ***595***
Medina, Elisabetta
MIC-05-004 873
MIC-10-185 ..... 130, ***1130***
Meer, David
MIC-05-349 981
Mehadji, Brahim
MIC-09-04 1070
MIC-10-185 1130
MIC-10-245 1149
MIC-10-248 ..... **1150**
MIC-15-246 1349
MIC-15-321 1371
M-LT-05-01 1254
Mehranian, Abolfazl
MIC-10-203 1136
MIC-10-422 1203
MIC-15-375 ..... 160, ***1388***
M-LT-05-03 ..... 144, ***1256***
Mehta, Siddharth
MIC-10-230 ..... **1145**
Mei, Filippo
NSS-13-324 696
Mei, Riccardo
MIC-15-384 1391
Mei, Zhusong
NSS-13-214 ..... 72, ***652***
Meier, Dirk
TS-02-01 ..... 182, ***1586***
Meier, Nick

Author Index

NSS-24-03 773
Meigo, Shin-ichiro
NSS-01-141 378
Meikle, Steven
WS-03-01 ..... **239**
Meikle, Steven R.
MIC-05-307 967
MIC-15-129 1313
MIC-20-05 1457
MP-01-04 ..... 92, ***818***
MP-01-06 ..... 92, ***818***
MP-01-08 ..... 92, ***819***
MP-01-10 ..... 92, ***819***
MP-01-12 ..... 93, ***820***
MP-01-14 ..... 93, ***820***
MP-01-15 ..... 93, ***820***
MP-02-03 ..... 116, ***1021***
Meirose, Bernhard
NSS-24-04 774
Mekki, Julien
NSS-13-054 584
NSS-13-322 695
Mele, Filippo
NSS-10-04 519
NSS-13-112 610
RTSD-10-03 ..... 182, ***1579***
Melendi, Federico M.
RTSD-04-390 1527
Mellak, Youness
MIC-08-08 ..... **1065**
MIC-10-425 ..... **1204**
Melnikova, Zuzana
RTSD-01-04 1471
RTSD-03-06 ..... 171, ***1490***
Melovská, Karolína
NSS-06-06 489
Melton, Elizabeth
MIC-15-051 1289
Memis, Ceren
MIC-10-242 1148
Men, Longchao
MIC-03-03 ..... 97, ***858***
MIC-03-05 859
NSS-18-02 729
Mena, Esther
MIC-15-300 1365
Menard, Laurent
WS-04-03 ..... 21, *247*
Meng, Fanhui
N-LT-03-05 542
NSS-13-092 601
Meng, Gang
RTSD-04-351 1495
Meng, Ling-Jian
JS-01-04 266
MIC-04-05 868
MIC-05-136 914
MIC-05-271 956
MIC-10-104 1107
MIC-12-08 1240
MIC-16-03 1422
MIC-21-01 1459
M-LT-02-03 848
NSS-09-05 512
WS-04-02 ..... 21, ***246***
Meng, Lingxin
NSS-13-284 681
Meng, Ruiqing
MIC-05-286 961
Meng, Xiangxi
WS-04-07 251
Menge, Peter
MIC-05-031 881
Menichetti, Luca
MIC-10-362 1184
Menk, Ralf H.
NSS-12-02 530
Menzio, Luca
NSS-28-08 808
Merasli, Alexandre
MIC-05-304 966
Mercado, Angel
N-LT-04-03 ..... **552**
NSS-13-180 ..... **638**
Mercolli, Lorenzo
MIC-12-04 ..... 142, ***1236***
Mercurio, Brian
RTSD-02-03 1480
RTSD-07-04 1555
Mereghetti, Alessio
MIC-10-347 1180
NSS-05-07 482
Meric, Ilker
MIC-17-04 1431
Merino-Balaguer, Alejandro
MIC-10-428 ..... 139, ***1206***
Merlin, Thibaut
MIC-05-232 ..... 107, ***944***
Mertens, Susanne
NSS-14-06 703
Merzi, Stefano
MIC-15-045 1287
Metcalfe, Alex
NSS-01-057 343
Methuku, Tridev
MIC-10-230 1145
MIC-14-02 1249
Metser, Ur
MIC-15-135 1315
Mettivier, Giovanni
RTSD-01-07 1474
Metzler, Scott D.
MIC-05-136 914
M-LT-02-03 848
Metzner, Ralf
MIC-15-111 1307
Meurer, Tobias
MIC-10-242 1148
Meyer Viol, Sebastiaan L.
STIR-05 1598
Meyer, Catherine
MIC-15-366 1386
Meyer, Steyn
NSS-13-216 653
Meyer, Thore
MIC-05-028 ..... 100, ***880***
MIC-05-103 904
MIC-15-054 1290
MIC-15-291 1362
MIC-15-381 ..... 160, ***1390***
M-LT-05-04 ..... 144, ***1257***
Mezza, Davide
NSS-01-093 ..... 35, ***358***
NSS-08-04 502
Miceli, Antonino
MIC-03-06 860
NSS-08-02 501
Michaud, Jean-Baptiste
MIC-02-03 831
MIC-10-092 1104
MIC-15-432 1406
M-LT-04-07 1054
Michel, Maugan
RTSD-02-02 1479
Michel, Tobias
NSS-14-07 ..... 78, ***704***
Michelet, Claire
N-LT-02-07 312
NSS-01-231 412
Michishio, Koji
NSS-13-030 575
Middents, Wilko
NSS-13-070 592
Midorikawa, Shuma
MIC-05-151 919
MIC-05-157 ..... 105, ***921***
MIC-15-177 1328
M-LT-02-04 ..... 96, ***849***
M-LT-02-05 850

Author Index

Mießner, Danilo
NSS-04-04 471
Mieszkalski, Romain
NSS-02-01 455
Mignone, Marco
NSS-14-02 700
NSS-17-04 725
NSS-17-05 726
Mihai, Radu E.
MIC-05-292 963
NSS-01-135 375
RTSD-04-384 1522
Mihara, Satoshi
NSS-01-071 349
Mikhaylova, Ekaterina
MIC-15-252 1350
Mikhaylova, Evgenia
STIR-04 1598
Mikusu, Satoshi
NSS-01-049 341
Mikut, Ralf
MIC-10-419 1202
M-LT-03-08 1044
Mikuz, Marko
MIC-10-032 1087
Milde Bekkevoll, Anna
MIC-17-04 1431
Millardet, Mael
MIC-10-374 1187
MIC-15-207 1337
Miller, Brian W.
WS-04-14 ..... 23, ***257***
Miller, Nicole
MIC-15-306 1366
M-LT-06-08 1271
Mills, Robert
NSS-13-228 658
Miloudi, Abdelwahab
NSS-02-01 455
Min, Chul Hee
MIC-05-322 ..... 111, *972*
MIC-07-01 1033
MIC-10-401 1196
MIC-15-195 1333
MIC-15-423 1404
NSS-01-003 321
NSS-01-201 400
NSS-13-222 656
Min, Sunghyun
MIC-10-149 1120
MIC-10-158 1122
MIC-15-150 1320
Minagawa, Ryotaro
MIC-05-151 919
MIC-15-177 1328
M-LT-02-05 850
MInagawa, Ryotaro
MIC-05-157 921
M-LT-02-04 849
Minagawa, Tomoya
MIC-05-205 ..... 106, ***936***
Minot, Michael
MIC-10-047 1091
NSS-13-084 597
Minuti, Massimo
NSS-14-08 ..... 78, ***705***
Mirra, Marco
N-LT-04-11 559
NSS-13-290 683
Mitani, Mana
MIC-05-145 917
MIC-15-144 1318
Mitchell, Lee J.
NSS-01-279 431
Mitsou, Eleni
MIC-10-215 1140
Mitsuda, Kazuhisa
NSS-13-320 694
Mitsuya, Yuki
RTSD-04-379 1517
Mitthumsiri, Warit
NSS-01-281 432
Miuchi, Kentaro
NSS-02-02 456
Miyahara, Ayumu
NSS-01-153 ..... 38, ***383***
NSS-13-152 626
Miyahara, Mizuki
MIC-10-470 ..... 141, ***1220***
Miyai, Haruki
NSS-01-141 378
NSS-13-144 622
Miyajima, Keita
NSS-01-011 325
NSS-01-035 335
Miyako, Katsuki
N-LT-02-14 318
NSS-01-321 450
Miyamura, Makoto
N-LT-03-09 545
NSS-13-142 622
Miyao, Sotaro
MIC-07-02 1034
Miyaoka, Robert S.
MIC-10-350 1181
MIC-10-371 1187
MIC-15-105 1305
MIC-15-327 ..... 158, ***1373***
M-LT-05-08 ..... 145, ***1260***
WS-04-04 ..... 21, ***248***
Miyataki, Masaki
N-LT-03-11 546
NSS-13-144 622
NSS-13-150 625
Mizrachi, Yaniv
MIC-05-247 949
M-LT-02-07 851
Mizumura, Yoshitaka
NSS-02-02 456
Mizuno, Hayato L.
MIC-07-02 1034
Mizuno, Hideyuki
MIC-05-340 978
MIC-05-346 980
Mizutani, Asuka
MIC-05-157 921
MIC-15-177 1328
M-LT-02-04 849
Mo, Xiaodong
NSS-13-034 ..... 62, ***577***
Mocerino, Gianluca
MIC-05-082 897
MIC-21-02 1460
Mochizuki, Brent
NSS-13-128 616
Moffatt, Jacob
NSS-16-06 718
Mogler, Carolin
N-LT-01-10 301
NSS-01-061 345
Mohammed Rafee, Farah
RTSD-04-380 ..... 175, ***1518***
Moignier, Cyril
MIC-21-05 1463
Moiseeva, Anzhelika N.
MIC-12-04 1236
Mok, Greta S.P.
MIC-05-385 993
MIC-15-387 1392
Molina Gonzalez, Emmanuel Josue
NSS-01-297 ..... 46, *440*
Moliner Martinez, Laura
MIC-15-045 1287
Moll, Michael
N-LT-01-11 302
NSS-01-063 346
Mona, Christine
MIC-15-366 1386
Monaco, Vincenzo

Author Index

RTSD-04-390 1527
Moncada-Gutiérrez, Fernando G.
MIC-05-112 906
Mondal, Parmita
JS-01-02 264
Moneta, Stefano
N-LT-04-11 559
NSS-13-290 683
Moniz, Marta
NSS-01-143 ..... **379**
Montagna, Elisabetta
NSS-21-02 751
Montalvan Olivares, Diango M.
NSS-05-07 482
NSS-12-07 535
NSS-28-04 ..... 90, ***804***
Montanari, Alessandro
NSS-13-324 696
NSS-21-02 751
Montaruli, Teresa
NSS-25-02 778
Monteil, Stéphane
NSS-12-04 532
Montémont, Guillaume
MIC-10-233 1146
RTSD-02-04 ..... 170, ***1481***
Montero, Isabel
MIC-05-310 968
Montgomery, Archie
MIC-15-459 1415
M-LT-06-04 1267
Moore, Jared W.
WS-04-14 257
Moore, Joshua
NSS-01-057 343
Moore, Stephen C.
MIC-04-03 866
Mora, Francisco J.
NSS-01-099 361
Moralles, Mauricio
NSS-13-010 567
Moravec, Pavel
RTSD-04-375 1514
Morcillo, Miguel Ángel
MIC-15-462 1416
Morel, Christian
MIC-05-337 977
N-LT-03-10 545
NSS-06-07 490
NSS-13-084 597
NSS-13-134 619
RTSD-04-398 1533
Morellato, Beatrice
NSS-03-02 462
Morenas, Maxime
NSS-03-06 466
Moreno Gomez, Salvador
MIC-15-321 1371
M-LT-05-01 1254
Moreno, Brahim A.
NSS-05-05 480
Moreno-Gómez, Salvador
RTSD-03-02 1486
Moretto, Sandra
NSS-27-08 798
Mori, Koji
RTSD-04-381 1519
Mori, Masaki
NSS-02-02 456
Morichi, Massimo
NSS-01-263 425
NSS-15-02 708
Morishita, Yuki
NSS-01-023 330
NSS-01-153 383
NSS-01-309 ..... 46, ***444***
NSS-02-06 ..... 48, ***460***
NSS-11-05 526
NSS-13-152 626
NSS-13-230 ..... 73, ***659***
Moriya, Takahiro
MIC-13-04 1245
Moriyama, Rintaro
NSS-13-320 694
Morley, Sam
NSS-01-223 409
Mormino, Elizabeth
MIC-10-257 1152
Morozov, Andrey
N-LT-02-01 307
NSS-01-271 428
Morozzi, Arianna
NSS-12-03 ..... 56, *531*
NSS-28-07 807
NSS-28-08 808
Morrall, Paul
NSS-13-278 678
Morris, Luke G.
NSS-13-244 ..... 73, ***665***
Morrocchi, Matteo
MIC-15-030 1283
N-LT-03-08 544
NSS-13-136 619
Morsani, Fabio
NSS-14-08 705
Morteau, Eric
NSS-16-08 720
Moscatelli, Francesco
NSS-12-03 ..... **531**
NSS-28-07 807
NSS-28-08 808
Moses, Scharon
NSS-01-093 358
Moskal, Pawel
MIC-12-05 ..... 142, ***1236***
MIC-15-267 1355
MIC-15-456 1414
M-LT-06-03 1266
Moskal, Paweł
MIC-05-457 1015
MIC-10-128 1114
MIC-15-258 1352
Moss, Robert
MIC-15-357 1383
Mostafanezhad, Isar
MIC-05-022 879
NSS-01-117 367
NSS-10-03 518
NSS-14-05 702
Mostafapour, Samaneh
MIC-05-097 ..... 103, ***902***
MIC-10-260 1153
Mostardi, Franco
NSS-28-04 804
Motakef, Shariar
MIC-10-044 1090
M-LT-03-05 1041
RTSD-05-07 ..... 178, *1545*
Motoyoshi, Makoto
JS-02-05 273
Moulin, Mathis
MIC-10-233 ..... 132, ***1146***
RTSD-02-04 1481
Mourani, Cristo
NSS-01-099 361
Moussaoui, Saïd
MIC-10-263 1154
Moussaoui, Younes
MIC-10-263 1154
Moustafa, Ahmed
NSS-01-227 ..... 42, ***410***
Moustakas, Konstantinos
NSS-08-04 502
Moustakas, Kostantinos
NSS-01-093 358
Moutinho, Leonor
MIC-15-243 1348
Mowen, Derian M.
NSS-26-01 ..... 88, ***784***

Author Index

Mozzanica, Aldo
NSS-01-093 358
Mu, Dengyun
MIC-05-325 973
MIC-05-331 975
MIC-10-329 1175
MIC-15-333 1375
Mu, Junxu
MIC-10-284 ..... 134, ***1161***
Muangha, Pradiphat
NSS-01-281 432
Muelhens, Oliver
MIC-05-028 880
MIC-05-103 904
MIC-15-291 1362
MIC-15-381 1390
M-LT-05-04 1257
Mueller, Martin
NSS-01-093 358
Mueller, Sara T.
MIC-17-04 ..... 165, ***1431***
Muenstermann, Daniel
NSS-13-284 681
Mukhopadhyay, Sharmistha
N-LT-04-03 ..... 59, *552*
NSS-13-180 ..... 70, *638*
Muller, David A.
MIC-10-137 1116
Muller, Erik
RTSD-07-03 1554
Muller, Florence M.
MIC-04-03 866
MIC-05-262 ..... 108, ***953***
MIC-05-298 965
MIC-19-01 1445
Muller, Matthias
MIC-10-041 1090
M-LT-03-04 1040
NSS-13-046 581
NSS-16-07 719
RTSD-04-360 1502
Mulnix, Tim
MIC-04-08 871
MIC-15-045 1287
Mulvey, Jonathan
NSS-01-093 358
RTSD-01-06 ..... 169, ***1473***
Munakata, Yusuke
NSS-02-02 456
Muñoz Izquierdo, Paula
MIC-13-02 1243
Munoz, Enrique
MIC-15-123 1311
Muñoz, Enrique
MIC-10-140 ..... 129, ***1117***
Muntean, Andrada
JS-02-05 273
Murakami, Kazuhiro
MIC-05-151 919
MIC-05-157 921
MIC-15-177 1328
M-LT-02-04 849
M-LT-02-05 850
Murakami, Rikito
MIC-10-011 1080
NSS-07-01 493
NSS-16-03 715
Muraz, Jean-François
MIC-05-337 977
Murrieta-Rodríguez, Tirso
MIC-05-112 906
Murthy, Naveen
MIC-10-374 1187

N

Nadig, Vanessa
MIC-10-374 ..... 137, ***1187***
Naesseth, Christian A.
JS-03-05 282
Nag, Ritwik
RTSD-06-03 1548
Nagai, Kanta
NSS-13-066 ..... 64, ***590***
NSS-13-232 660
Nagai, Ryo
NSS-13-002 ..... 60, ***564***
Nagao, Yuto
MIC-05-340 978
Nagarkar, Vivek
NSS-07-03 494
Nagicheva, Galina
NSS-01-073 350
NSS-13-062 ..... 64, ***588***
Nagy, Gergeley
NSS-18-04 731
Nahuel, Franco
MIC-05-019 878
Najmaoui, Yassir
MIC-02-03 831
MIC-10-236 1146
MIC-15-045 1287
MIC-18-04 ..... 165, ***1439***
Nakai, Hiromi
N-LT-02-04 310
NSS-01-219 408
Nakamori, Takeshi
NSS-02-02 456
Nakamura, Eiken
N-LT-02-15 318
NSS-01-325 451
Nakamura, Koki
MIC-11-03 ..... 141, ***1226***
MIC-15-453 1413
MIC-15-459 1415
M-LT-06-04 1267
Nakamura, Takashi
NSS-13-066 590
Nakanishi, Kohei
MIC-10-011 1080
Nakanishi, Takayuki
NSS-01-011 325
Nakano, Yuuki
NSS-13-002 564
Nakasone, Takamasa
NSS-01-023 330
Nakata, Yuhei
MIC-05-025 879
NSS-16-03 ..... 80, ***715***
Nakatsugawa, Yohei
N-LT-03-11 546
NSS-13-150 625
Nakauchi, Daisuke
NSS-01-011 325
NSS-01-035 335
NSS-13-012 568
NSS-13-028 574
NSS-13-030 575
Nakaye, Yasukazu
NSS-01-049 ..... 33, ***341***
Nakazawa, Yu
NSS-01-141 378
NSS-13-144 622
Nalyvaiko, Dmytro
RTSD-04-351 1495
RTSD-04-357 1500
RTSD-04-376 1515
RTSD-04-401 1536
RTSD-07-06 1557
RTSD-07-07 1558
Nam, Jiwon
MIC-10-179 1128
MIC-15-180 1329
NSS-01-047 ..... 33, ***340***
Nam, Seoung Wan
MIC-10-401 1196
Nania, Rosario
NSS-21-02 751
Nanink, Thibaut

Author Index

MIC-05-283 960
Nanjo, Hajime
NSS-25-03 779
Nanni, Cristina
MIC-15-384 1391
Napolitano, Giulia
RTSD-05-06 1544
RTSD-06-05 ..... 178, ***1550***
Nardo, Lorenzo
MIC-10-248 1150
MIC-15-246 1349
MIC-15-384 1391
MIC-18-02 1437
MIC-20-04 1456
Narita, Kurumi
MIC-05-124 ..... 104, ***910***
MIC-15-288 ..... 157, ***1361***
Nascimento, Camila
WS-04-03 247
Nassi, Leonardo
N-LT-03-03 ..... **540**
NSS-13-102 ..... **606**
National Research and Development Agency of Chile (ANID) and the Frontera Uninversity
MIC-05-370 988
Natour, Ghaleb
MIC-15-111 1307
Naunheim, Stephan
MIC-15-051 ..... 148, ***1289***
Navarrete, Javier
MIC-15-348 1380
Navarro-Cozcolluela, Laura
MIC-05-034 ..... 100, ***882***
Nebel, Roman
RTSD-08-04 1563
Needham, MIchael
STIR-02 1597
Neely, Erin
NSS-13-014 569
NSS-16-05 ..... 80, ***717***
Negut, Victor
MIC-21-03 1461
NSS-22-04 761
Nehmeh, Sadek A.
MIC-09-02 1068
MIC-10-020 1083
MIC-15-123 1311
Nekolla, Stephan
MIC-15-045 1287
Nelson, Brian
N-LT-03-06 542
NSS-13-132 618
Nelson, Timothy K.
NSS-01-147 381
NSS-20-08 747
Nemallapudi, Mythra V.
MIC-10-047 1091
NSS-13-050 583
Nemati, Nader
MIC-15-306 ..... 157, ***1366***
M-LT-06-08 ..... 146, ***1271***
Neulinger, Thomas
NSS-01-315 ..... 46, ***447***
NSS-24-04 774
Neves, Iara
MIC-05-043 885
MIC-15-021 ..... 147, ***1280***
Newman, Harvey
NSS-16-07 719
Neyt, Sara
MIC-05-298 965
Nguyen, Trong-Nghia
WS-04-17 260
Ni, Jiaru
MIC-10-410 1199
Ni, Yu-Ching
MIC-05-394 ..... 113, *996*
Nicassio, Nicola
NSS-20-03 743
Nicholls, Tim
JS-01-01 264
Nickkholgh, Babak
MIC-05-313 969
Nie, Shuming
NSS-09-05 512
Niekämper, Debora
MIC-10-260 ..... 133, ***1153***
MIC-15-162 1324
MIC-15-249 1349
MIC-16-02 1421
Niel, Elisabeth M.
NSS-13-080 595
Niess, Valentin
NSS-01-101 362
Nikiforou, Nikiforos
N-LT-04-13 ..... **561**
NSS-01-297 ..... **440**
NSS-13-288 ..... **682**
Nikoubashman, Omid
MIC-15-162 1324
Ninci, Daniele
NSS-20-04 744
Niñerola-Baizán, Aida
MIC-15-075 1296
Ninković, Jelena
MIC-10-032 1087
NSS-04-04 471
Niraula, Madan
RTSD-04-374 ..... 174, ***1514***
RTSD-05-04 ..... 177, ***1542***
Nishigami, Rina
MIC-05-145 ..... 104, ***917***
MIC-10-143 1118
MIC-15-141 1317
MIC-15-144 1318
Nishiguchi, Hajime
NSS-01-071 349
Nishikawa, Akihiro
NSS-13-028 574
Nishikido, Fumihiko
MIC-05-025 ..... 100, ***879***
MIC-05-076 ..... 102, *895*
MIC-05-454 1014
MIC-10-470 1220
MIC-15-063 ..... 149, *1293*
Nitta, Munetaka
MIC-05-130 ..... 104, ***912***
MIC-10-035 1088
MIC-10-059 1095
MIC-10-083 1101
MIC-17-05 1432
M-LT-04-08 1054
M-LT-04-09 1055
Nitta, Yuki
MIC-05-331 975
MIC-10-329 1175
Niu, Guangda
RTSD-04-368 1509
Niu, Ming
MIC-05-013 876
MIC-05-067 892
MIC-05-127 ..... 104, ***911***
MIC-05-250 949
MIC-05-253 950
MIC-05-343 979
MIC-09-07 1073
MIC-10-455 1215
MIC-15-009 1277
MIC-15-012 1278
MIC-15-117 ..... 151, ***1309***
MIC-15-120 1310
MIC-15-261 1353
MIC-15-339 1377
MIC-21-04 1462
Noe, Simon
MIC-05-268 955
MIC-15-084 1299
M-LT-02-09 853

Author Index

Noë, Simon
MIC-05-256 ..... 108, ***951***
MIC-10-086 ..... 127, ***1102***
Noferini, Daria
NSS-24-04 774
Noferini, Linhsia
MIC-15-102 1304
Nogami, Mitsuhiro
N-LT-02-04 310
NSS-01-219 408
RTSD-01-03 1470
RTSD-04-371 1511
RTSD-04-382 1520
RTSD-04-389 1526
Nomachi, Masaharu
N-LT-03-14 ..... 59, ***548***
NSS-13-138 ..... 67, ***620***
Nomura, Tadashi
NSS-25-03 779
Noor, Shams
RTSD-10-05 ..... 182, ***1581***
Noordzij, Walter
MIC-05-445 1011
Normandin, Marc
MIC-10-236 1146
MIC-18-04 1439
Novel, David
NSS-01-067 ..... **348**
Novofastovski, Sofi
MIC-15-210 1338
Novotny, Matthew
MIC-15-321 1371
M-LT-05-01 1254
Novotny, Radek
NSS-12-03 531
Nowack, Aaron
NSS-03-01 ..... 48, ***462***
Nummenmaa, Lauri
MIC-15-306 1366
M-LT-06-08 1271
Nurdan, Kıvanc
NSS-01-137 376
Nuyts, Johan
MIC-05-256 951
MIC-10-086 1102
MIC-10-254 1152
MIC-15-084 1299

O

O'Sullivan, Joseph A.
MIC-10-107 1108
MIC-10-467 1219
Oancea, Cristina
NSS-01-273 429
Obara, Hideki
MIC-05-199 934
Obata, Fujino
MIC-05-454 1014
Obata, Takayuki
MIC-05-076 895
MIC-15-063 1293
Obermaisser, Roman
MIC-05-406 1000
Obertino, Maria Margherita
NSS-28-07 807
Ocal, Selin
MIC-05-172 926
M-LT-01-05 838
Ochoa, Pamela
MIC-17-01 1428
Ochoa-Parra, Pamela
MIC-10-419 1202
M-LT-03-08 1044
O'Connor, David
N-LT-01-09 ..... 28, *300*
NSS-01-001 ..... 30, *321*
O'Connor, Michael
MIC-09-05 1071
Oddland, Odd Harald
NSS-04-02 469
O'Donnell, David
NSS-25-06 782
Ogallar Ruiz, Francisco
NSS-11-01 523
Ogawa, Koichi
MIC-05-055 889
MIC-10-056 1094
MIC-10-278 1159
MIC-10-389 1192
Ogren, Kristofer
NSS-13-224 657
Oh, Dae yang
N-LT-02-08 ..... 29, ***313***
N-LT-04-05 554
NSS-01-165 388
NSS-01-247 ..... 43, ***419***
NSS-13-160 629
Oh, Jin-Seok
NSS-01-083 ..... 34, ***355***
NSS-01-259 ..... 44, ***423***
Oh, Kyung-Min
NSS-01-269 427
Oh, Myungwoo
MIC-10-149 1120
MIC-10-158 ..... 129, ***1122***
MIC-15-150 1320
Oh, Seokwon
NSS-01-177 ..... 39, ***392***
NSS-01-207 402
Ohashi, Ryotaro
MIC-06-03 ..... 118, ***1029***
Ohi, Yamato
RTSD-04-374 1514
Ohno, Naoki
MIC-05-151 919
MIC-05-157 921
MIC-15-177 1328
M-LT-02-04 849
M-LT-02-05 850
Ohshima, Ryuto
RTSD-05-04 1542
Ohta, Seiichi
MIC-15-459 1415
M-LT-06-04 1267
Oishi, Kou
NSS-01-141 378
NSS-13-144 622
Ojeda, Fernando
N-LT-03-06 ..... 58, ***542***
NSS-13-132 ..... 67, ***618***
Oka, Masaya
NSS-01-049 341
Oka, Tomohiko
NSS-02-02 456
Okabe, Kenya
NSS-01-071 ..... 34, ***349***
Okamoto, Kanaho
NSS-02-02 456
Okamoto, Takayuki
MIC-05-187 930
M-LT-01-10 843
Okazaki, Kai
NSS-01-011 325
NSS-01-035 335
Okazaki, Yuta
NSS-17-03 724
Okfen, Julia
NSS-24-03 ..... 86, ***773***
Okubo, Yuji
NSS-01-133 ..... 37, ***374***
Okumura, Kenichiro
MIC-05-151 919
MIC-05-157 921
MIC-15-177 1328
M-LT-02-04 849
M-LT-02-05 850
Okumura, Sana
NSS-02-02 456

Author Index

Oliva, Piernicola
RTSD-08-02 1561
Oliveira, Regina G.
MIC-15-156 ..... **1322**
MIC-15-159 ..... **1323**
Oller, Juan Carlos
MIC-15-348 1380
Olmos Risen, Antonio
WS-04-13 256
Olmos-Risen, Antonio
MIC-09-06 1072
Olyaei, Elnaz
MIC-05-052 888
MIC-05-070 ..... 102, ***893***
MIC-08-07 ..... 122, ***1064***
MIC-10-122 1112
MIC-15-027 1282
MIC-15-126 1312
Omidvari, Negar
MIC-10-245 1149
WS-03-01 ..... **239**
Omidvari, Negar:..... **240**, **241**
On behalf of Linear Collider Time Projection Chamber International Collaboration
NSS-01-005 322
On behalf of 1MICRON Collaboration
N-LT-01-10 301
NSS-01-061 345
On behalf of AIDER Collaboration
MIC-10-356 1182
On behalf of ASPIDES-Collaboration
WS-02-09 231
On behalf of CMS Collaboration
NSS-24-01 772
On behalf of EduPET Collaboration
MIC-05-058 890
MIC-05-448 1012
On behalf of GRID Collaboration
NSS-13-282 680
on behalf of IGNITE-Collaboration
NSS-10-06 521
On behalf of IMPET project
MIC-05-223 942
M-LT-01-07 840
On behalf of J-PET collaboration
MIC-05-457 1015
On behalf of KATRIN Collaboration
NSS-19-03 736
On behalf of NEXT collaboration
NSS-01-099 361
On Behalf of NOVO Collaboration
NSS-01-137 376
On behalf of NUSES Collaboration
N-LT-02-11 315
NSS-01-077 352
On behalf of PetVision project
NSS-23-04 768
On behalf of SPECTRE Collaboration
RTSD-04-390 1527
On behalf of the ALICE Collaboration
NSS-19-04 737
On behalf of the ASPIDES collaboration
WS-02-12 233
On behalf of the ATLAS Collaboration
N-LT-04-13 561
NSS-01-297 440
NSS-13-288 682
NSS-19-02 735
NSS-20-01 742
on behalf of the Broadcom SiPM team
TS-02-06 1589
On behalf of the CMS Collaboration
NSS-19-01 735
On behalf of the CRYSP group
MIC-05-034 882
On behalf of the detector group whose members include
J. Mulvey, M. Anastasi, A. Bergamaschi, M. Brueckner, M. Carulla, R. Dinapoli, S. Ebner, S. Emiliani, K. Ferjaoui, E. Fr¨ojdh, V. Gautam, D. Greiffenberg, S. Hasanaj, V. Hinger, V. Kedych, T. King, S. Li, C. Lopez-Cuenca, L. Lunin, A. Mazzoleni, D. Mezza, S. Moses, K. Moustakas, A. Mozzanica, M. Mueller, C. Ruder, B. Schmitt, S. Silletta, D. Thattil, X. Xie and J. Zhang 1473
On behalf of the detector group whose members include M. Anastasi, M. Bruckner, S. Ebner, S. Emiliani, K. Ferjaoui, D. Greiffenberg, S. Hasanaj, V. Hinger, V. Kedych, T. King, S. Li, C. Lopez-Cuenca, L. Lunin, A. Mazzoleni, S. Moses, A. Mozzanica, J. Mulvey, M. Muller, C. Ruder, B. Schmitt, S. Silletta, D. Thattil, X. Xie and J. Zhan 502
on behalf of the fARCOS collaboration
NSS-01-291 437
On behalf of the GAPS collaboration
NSS-25-05 781
On behalf of the HYPATIA Collaboration
NSS-25-06 782
On behalf of the IBIS and IBIS_NEXT Collaborations
NSS-21-02 751
On behalf of the INSIGHT collaboration
NSS-01-125 370
On behalf of the JEM-EUSO Collaboration
NSS-17-05 726
On behalf of the joint research group of Kanazawa University, Waseda University, Ishikawa Prefectural University, and Proterial Ltd.
MIC-05-151 919
M-LT-02-05 850
On behalf of the J-PET collaboration
MIC-10-128 1114
MIC-15-258 1352
on behalf of the LHCb ECAL Upgrade II R&D Group
NSS-19-05 738
On behalf of the LHCb ECAL Upgrade II R&D Group
NSS-20-06 746
on behalf of the LHCb ECAL Upgrade II RD Group
N-LT-04-14 561
NSS-13-292 684
On behalf of the LHCb VELO group
NSS-01-283 433
On Behalf of the LiquidO Consortium
NSS-16-06 718
On behalf of the Medipix Collaboration and the EP R&D Work Package 5.
RTSD-07-05 1556
On behalf of the Medipix2, Medipix3 and Medipix4 Collaborations
RTSD-08-01 1561
On behalf of the NOVO collaboration
MIC-17-04 1431
on behalf of the XENON Collaboration
NSS-01-149 382
Oñate Melecio, Karla G.
NSS-01-279 ..... 45, ***431***
Oncel, Dilek
MIC-05-172 926
M-LT-01-05 838
Onder, Sebastian A.
NSS-12-03 531
Onishi, Yuya
MIC-09-01 ..... 123, ***1067***
MIC-10-005 1078
MIC-15-237 ..... 155, ***1346***
Ono, Tomoki

Author Index

MIC-15-168 ..... **1325**
Onofrey, John
MIC-05-259 952
Orehar, Matic
MIC-15-045 1287
Orero, Carlos
N-LT-01-14 305
NSS-01-313 446
Orozco, Luis J.
MIC-05-433 1007
Orsini, Leonardo
NSS-14-08 705
Ortega, Jose María
MIC-10-416 1201
M-LT-03-07 1043
Ortiz, Andres
MIC-10-290 1162
Ortuño, Juan Enrique
MIC-05-430 1006
Oshima, Minori
MIC-05-151 919
MIC-05-157 921
MIC-15-177 1328
M-LT-02-04 849
M-LT-02-05 850
Oshima, Yuya
NSS-01-217 407
Oshiro, Justin
NSS-22-05 761
Osorio Durán, Raúl
MIC-15-390 ..... 160, ***1393***
Ostling, William
NSS-13-064 589
Ostuka, Ayaka
MIC-15-459 1415
M-LT-06-04 1267
O'Sullivan, Joseph
MIC-05-364 986
Osys, Alan
STIR-11 185
STIR-14 ..... ***1599***
Ota, Ryosuke
MIC-09-01 1067
MIC-10-005 ..... 124, *1078*
MIC-10-014 1081
MIC-12-03 ..... 142, ***1235***
MIC-13-04 ..... 143, ***1245***
NSS-03-05 465
NSS-16-01 714
Otaegui, Jaume R.
MIC-05-364 986
Ote, Kibo
MIC-09-01 1067
MIC-15-237 1346
Oteo Vives, Marta
MIC-15-462 1416
Otomo, Kazuki
TS-02-04 ..... 183, *1587*
Ott, Jennifer
NSS-10-03 518
NSS-14-05 702
Ottensmeyer, Mark P.
MIC-15-132 1314
Otto, Benedikt
NSS-01-125 ..... 37, ***370***
Ou, Shiyu
MIC-05-325 973
Ouyang, Zhonghua
WS-04-12 256
Ovcharenko, Yevheniy
N-LT-03-12 547
NSS-13-300 687
Overbeek, Daniel
MIC-10-260 1153
Over-Winter, Tobias
NSS-13-070 ..... 64, ***592***
Owens, Alan
RTSD-05-02 1541
Ozaki, Sho
MIC-05-199 934

P

P. Reinert, Christian
MIC-08-07 1064
Pacher, Luca
NSS-10-06 ..... 55, *521*
Pacini, Matteo
NSS-13-206 649
Padnuik, Yevhenii
RTSD-05-03 1541
Pagano, Emanuele V.
NSS-25-04 780
Pagano, Fiammetta
MIC-05-118 908
MIC-09-02 ..... 123, ***1068***
MIC-09-06 1072
MIC-10-020 1083
MIC-13-02 ..... **1243**
MIC-15-123 1311
M-LT-02-02 847
WS-04-13 ..... 23, ***256***
Paganoni, Marco
MIC-05-217 940
MIC-10-443 1211
NSS-26-04 786
Pagliarino, Valerio
NSS-17-04 ..... 81, ***725***
Pal, Debojyoti
MIC-05-310 ..... 110, ***968***
Palini, Luca
NSS-13-118 612
NSS-14-08 705
Pallás, Max
MIC-10-098 1105
M-LT-04-02 1049
Palleis, Carla
MIC-10-281 1160
Palm, Marcus
MIC-05-133 913
Palmer, Josh
RTSD-10-02 1578
RTSD-10-04 1580
Palonen, Santeri
MIC-15-306 1366
M-LT-06-08 1271
Palu, Giovanni
MIC-15-045 1287
Pan, Lei
RTSD-06-04 ..... 178, ***1549***
Pan, Li
MIC-03-04 ..... **858**
Pan, Xiaochuan
MIC-10-053 1093
MIC-10-173 ..... 130, *1127*
MIC-20-01 1453
MP-02-09 ..... 117, ***1023***
Pancheri, Lucio
N-LT-01-10 301
NSS-01-061 345
NSS-21-07 756
Pandey, Indra
RTSD-10-02 1578
RTSD-10-04 1580
Pandocchi, Maurizio
MIC-10-038 ..... 125, ***1089***
M-LT-04-04 ..... 121, ***1051***
Paneque-Yunta, Robert J.
MIC-05-424 1005
MIC-15-090 ..... 150, ***1301***
MIC-15-219 1341
Panesar, Ben
TS-02-03 ..... 182, ***1587***
Panetta, Daniele
MIC-10-362 1184
Pang, Xulong
RTSD-04-373 ..... 174, ***1513***
RTSD-04-377 1516
RTSD-04-388 1525

Author Index

Pangaud, Patrick
N-LT-03-10 545
NSS-13-134 619
Pani, Silvia
MIC-05-421 1004
Panin, Vladimir
MIC-10-374 1187
MIC-15-207 ..... 154, ***1337***
MIC-15-225 1342
NSS-04-02 469
Pantano, Devis
NSS-13-298 686
Pantouvakis, Caterina
NSS-13-298 686
Panyalert, Thanayuth
NSS-01-281 432
Panza, Matilda
NSS-20-05 745
Panzarini, Giuliana
NSS-20-03 743
Paolucci, Pierluigi
N-LT-04-11 559
NSS-13-290 683
Papadakis, Nicolas
MIC-10-167 1125
Papadopoulou, Aikaterini
NSS-13-106 607
Papaevangelou, Thomas
NSS-05-05 480
Papanicolas, Costas N.
MIC-05-463 1017
MIC-18-06 1441
Pappas, Kaliroë
NSS-13-064 589
Paradis, Hugues
NSS-01-197 399
Parajuli, Bal
NSS-13-274 677
Parashari, Siddharth
MIC-05-460 ..... 116, ***1016***
MIC-10-032 1087
MIC-10-035 ..... 125, ***1088***
MIC-10-293 1163
MIC-10-326 1174
MIC-10-353 1181
MIC-15-099 ..... 150, ***1303***
MIC-15-444 1410
NSS-06-04 487
Pardi, Brandon
MIC-15-051 1289
Pare, David
MIC-05-115 907
M-LT-02-01 846
Parellada-Monreal, Laura
JS-02-04 272
JS-02-05 273
MIC-15-045 1287
N-LT-01-08 299
NSS-01-015 326
NSS-21-02 751
NSS-21-04 753
Park, Beomjun
N-LT-01-02 293
N-LT-01-12 302
NSS-01-013 325
NSS-01-065 347
RTSD-04-367 1508
Park, Byeonghyeon
NSS-13-154 627
Park, Byungdo
NSS-13-008 566
Park, Chansun
N-LT-01-02 293
NSS-01-013 325
RTSD-04-350 ..... 171, ***1494***
RTSD-04-367 1508
Park, Chanwho
NSS-23-02 766
Park, Grant H.-S.
MIC-05-274 957
MIC-07-04 ..... 119, ***1035***
MIC-15-270 1356
Park, Hochun
RTSD-04-350 1494
Park, HyeoungWoo
NSS-01-327 452
Park, Jin-Hyung
NSS-01-269 427
Park, Jiwon
MIC-05-289 ..... **962**
Park, Jiyoung
NSS-13-242 664
Park, Jonghoon
NSS-13-154 627
Park, Jonghyun
NSS-13-172 ..... 69, ***635***
Park, Jongwon
MIC-05-169 925
NSS-01-211 404
Park, Min Yong
NSS-01-169 389
Park, Sean
NSS-06-05 488
Park, Seungwoo
MIC-10-146 ..... 129, *1119*
Park, Sora
MIC-15-072 1295
Park, Sung Min
NSS-01-169 389
Park, Sungmin
MIC-15-147 ..... 152, ***1319***
Park, Wonu
MIC-05-274 957
Park, Youngjoo
NSS-13-024 ..... 62, ***572***
NSS-13-172 635
Parker, Andrew
NSS-18-05 ..... **732**
Parker, Cody
NSS-05-06 481
Parma, Michael J.
MIC-05-262 953
Parmer, Kirtirajsinh M.
MIC-14-02 1249
Parnell, Julia
N-LT-01-10 301
NSS-01-061 345
Parodi, Katia
MIC-05-130 912
MIC-05-346 980
MIC-10-035 1088
MIC-10-059 1095
MIC-10-083 1101
MIC-10-347 1180
MIC-17-05 1432
MIC-17-06 1433
M-LT-04-08 1054
M-LT-04-09 1055
Parpottas, Yiannis
MIC-18-06 1441
Parrilla, Hannah
NSS-01-159 ..... 38, ***386***
NSS-22-01 ..... 85, ***759***
Parschat, Luisa
RTSD-04-355 ..... 172, ***1498***
Parsons, Ryan
JS-03-06 283
RTSD-10-02 1578
RTSD-10-04 1580
Paschalis, Stefanos
NSS-13-278 678
NSS-25-06 782
Passeri, Daniele
NSS-12-03 531
NSS-28-07 807
NSS-28-08 808
Pastrone, Nadia
NSS-28-07 807
Patel, Krishan

Author Index

MIC-15-447 ..... 163, ***1411***
M-LT-06-01 ..... 145, ***1264***
RTSD-03-08 1491
Paterno, Andrea
MIC-05-019 878
Paterno, Gianfranco
NSS-15-05 711
Paternoster, Giovanni
JS-02-04 272
MIC-15-045 1287
N-LT-01-11 302
NSS-01-063 346
NSS-21-02 751
NSS-21-04 753
NSS-28-07 807
NSS-28-08 808
Patricelli, Colin
NSS-13-308 690
Patryl, Luc
NSS-01-197 ..... 40, *399*
Patt, Bradley
MIC-05-001 873
Pausch, Guntram
MIC-17-04 1431
NSS-13-260 671
Pavelić, Luka
MIC-15-444 1410
NSS-01-037 335
NSS-06-04 487
Pavlovsky, Ryan
NSS-22-05 ..... 85, ***761***
Pavon Hernandez, Noriel
MIC-15-045 1287
Paylan, David
WS-04-12 256
Pedretti, Beatrice
N-LT-03-13 ..... 58, ***548***
NSS-01-305 443
NSS-08-05 503
NSS-13-306 ..... 76, ***689***
Peer-Firozjaei, Milad
MIC-05-367 987
MIC-15-294 1363
Peizerat, Arnaud
RTSD-09-05 1572
Peleg-Cohen, Sivan
MIC-15-210 1338
Pellegri, Luna
NSS-01-243 417
NSS-13-216 653
Pells, Sophia
MIC-15-309 1367
Peltzer, Finn L.
MIC-15-330 1374
M-LT-05-07 1259
Pena, Cristian
NSS-20-07 747
Pena-Perez, Aldo
MIC-03-06 ..... 98, *860*
NSS-01-087 356
NSS-10-04 519
NSS-13-106 607
NSS-23-02 766
Peng, Jiangpeng
MIC-10-284 1161
Peng, Jiaxing
MIC-15-363 1385
Peng, Qiyu
MIC-02-01 829
MIC-05-286 ..... 109, *961*
MIC-05-376 ..... 113, *990*
MIC-07-03 1034
MIC-10-113 ..... 128, *1110*
MIC-10-116 ..... 128, *1111*
MIC-10-125 1113
Peng, Sheng
MIC-03-05 859
Peng, Wenyi
NSS-01-095 359
Penna, Michele
JS-02-04 ..... 25, ***272***
JS-02-05 273
MIC-09-08 1074
MIC-15-045 1287
N-LT-01-08 299
NSS-01-015 326
NSS-21-04 753
Penna, MIchele
MIC-05-019 878
Pennazio, Francesco
MIC-05-217 940
MIC-05-391 995
MIC-10-191 1132
MIC-10-443 1211
NSS-05-07 482
NSS-12-07 535
NSS-26-04 786
Pennicard, David
NSS-10-02 516
Pentenero, Jerome
NSS-24-04 774
Pepin, Catherine M.
NSS-05-08 483
NSS-21-03 752
Peralta, Agnette
MIC-10-170 1126
Perea, Rose S.
NSS-01-279 431
Perera, Sithumini
RTSD-06-02 1547
Pérez Curbelo, Javier
MIC-10-293 1163
Pérez Enguix, Daniel
MIC-15-360 1384
Perez, Emmanuel
NSS-12-04 532
Perez, Kerstin
NSS-13-064 589
Pérez, Martín
N-LT-02-02 308
NSS-01-275 430
Perez-Benito, David
MIC-02-05 ..... 94, ***833***
MIC-05-283 960
MIC-10-023 1084
MIC-10-428 1206
MIC-15-042 1285
MIC-15-069 1294
MIC-15-138 1316
MIC-19-05 1448
Pérez-Benito, David
NSS-13-178 638
Pérez-Liva, Mailyn
MIC-10-416 1201
M-LT-03-07 1043
Pérez-Martínez, Valeria
MIC-05-112 ..... 103, ***906***
Peric, Ivan
NSS-13-284 681
Perkins, Stephanie
MIC-05-364 986
Perna, Simone
N-LT-04-11 559
NSS-13-290 683
Pernegger, Heinz
NSS-17-03 724
Pérot, Bertrand
N-LT-02-07 312
NSS-01-231 412
NSS-02-01 ..... 47, ***455***
NSS-09-01 508
Perrez, Florent
NSS-03-06 466
Persson, Henrik
NSS-01-179 ..... **393**
Persson, Mats
N-LT-01-10 301
NSS-01-061 345
Pesce, Luca

Author Index

MIC-10-362 1184
Pesce-Rollins, Melissa
NSS-14-08 705
Pessanha, Sofia
NSS-13-004 565
Pestotnik, Rok
JS-02-04 272
MIC-05-019 878
MIC-09-08 1074
MIC-15-045 1287
NSS-21-06 755
WS-02-03 228
Petasecca, Marco
NSS-04-02 469
NSS-06-05 488
Peter, Robin
MIC-12-02 1234
Peterson, John
NSS-01-295 439
Petisiwaveth, Phasit
NSS-07-04 495
Petit, Odile
NSS-01-195 398
Petitjean, Arlo
N-LT-01-09 300
NSS-01-001 321
Petri, Marina
NSS-13-278 678
NSS-25-06 782
Petryk, Matthew
RTSD-10-02 1578
RTSD-10-04 ..... 182, ***1580***
Pettinato, Sara
RTSD-06-01 1547
Pezzotti, Luca
MIC-15-438 1408
Pfaehler, Elisabeth
MIC-15-255 1351
Pfeiffer, Dorothea
NSS-24-04 774
Pflugfelder, Daniel
MIC-15-111 1307
Pham, Chi-Hieu
MIC-15-369 ..... **1386**
M-LT-05-09 ..... **1261**
Pham, Khang
N-LT-01-05 296
NSS-01-019 328
NSS-01-129 372
Pham, Quang Vinh
MIC-10-401 ..... 138, ***1196***
Pham, Trinh T.D.
NSS-01-163 387
Phan, Quoc Vuong
RTSD-05-01 1540
RTSD-06-04 1549
Phillips, Claire
NSS-06-05 488
Phillips, John Paul
MIC-10-053 1093
MIC-10-173 ..... **1127**
Phlips, Bernard F.
JS-03-06 283
NSS-01-279 431
NSS-25-01 778
Phung-Ngoc, Clémentine
MIC-01-02 ..... 93, ***824***
Phunpueok, Akapong
NSS-16-04 716
Pia, Valerio
NSS-13-324 696
Picard, David
NSS-01-101 362
NSS-12-04 532
Picatoste, Eduardo
N-LT-03-02 539
N-LT-04-14 ..... 60, ***561***
NSS-13-098 604
NSS-13-292 ..... 76, ***684***
NSS-19-05 ..... 82, ***738***
NSS-20-06 ..... 83, *746*
Picchi, Andrea
NSS-20-04 744
Pichler, Bernd
MIC-05-070 893
MIC-10-122 1112
MIC-15-027 1282
MIC-15-126 1312
Pichot, Patrice
NSS-16-08 720
Pichotka, Martin P.
MIC-05-292 963
RTSD-03-01 1485
Pickford Scienti, Oliver L.P.
MIC-03-02 ..... 97, ***857***
Piekar, Johann
NSS-13-272 ..... 75, ***676***
Piera-Sapiña, Pau
MIC-10-386 1191
M-LT-03-10 1046
Piernas Diaz, Francisco
RTSD-07-05 ..... 179, ***1556***
Pierre-Louis, Alix
NSS-13-054 584
Pietrzyk, Óscar
MIC-10-344 1179
Pike, Sean N.
NSS-01-053 341
NSS-04-06 473
Pilger, Christian
MIC-10-101 1106
M-LT-04-01 1048
Pillera, Roberta
NSS-20-03 743
Pilotto, Alessandro
NSS-12-02 530
Pinaroli, Giovanni
NSS-01-307 443
NSS-08-03 502
Pinchera, Michele
NSS-14-08 705
Pinheiro, Fernando
RTSD-04-400 1535
Pinot, Laurent
WS-04-03 247
Pinson, Maxime
MIC-05-337 977
Pinto, Afonso Xavier
MIC-05-004 873
MIC-09-04 ..... 123, ***1070***
MIC-15-159 1323
Pinto, Marco
MIC-05-346 980
Piotto, Massimo
NSS-14-08 705
Piroddi, Martina
MIC-10-347 1180
MIC-17-03 ..... 165, ***1430***
NSS-03-03 ..... 48, *463*
NSS-09-04 511
Pirrone, Sara
NSS-25-04 780
Píš, Igor
RTSD-04-359 1502
Piscopo, Valeria
NSS-17-04 725
Pittayang, Yaowarat
NSS-01-281 432
Pizzichemi, Marco
MIC-05-028 880
MIC-05-217 940
MIC-10-443 ..... 140, ***1211***
MIC-13-05 1246
MIC-15-381 1390
M-LT-05-04 1257
NSS-26-04 786
Plazas, María C.
WS-04-09 253
Plumanut, Ratchanonth

Author Index

NSS-01-281 432
Poizat, Adrien
RTSD-09-05 1572
Politi, Guseppe
NSS-25-04 780
Polo, Matteo
NSS-27-08 ..... 90, ***798***
Polovykh, Mikhail
NSS-04-04 471
Pomeroy, Marc J.
MIC-10-272 1157
Pommranz, Christian M.
MIC-15-075 1296
Pontius, Niko
NSS-08-08 505
Pooley, Daniel E.
NSS-13-078 ..... 64, *595*
Poon, Alan
NSS-14-01 699
NSS-28-02 802
Popecki, Mark
MIC-10-047 1091
NSS-13-084 597
Popoola, Olaoluwa R.
NSS-07-07 497
NSS-13-198 645
Popov, Kristiyan M.
MIC-10-035 1088
Porro, Matteo
N-LT-03-12 547
NSS-08-01 500
NSS-08-06 504
NSS-08-07 505
NSS-13-300 687
NSS-13-302 ..... 76, ***687***
NSS-13-304 688
Portero Castillo, Sara
NSS-23-04 768
Portero, Sara
MIC-05-019 878
MIC-09-08 1074
MIC-15-045 1287
Pospisil, Stanislav
NSS-01-273 429
Pospíšil, Stanislav
MIC-05-292 963
NSS-01-287 435
RTSD-01-07 1474
RTSD-08-05 1564
Posteraro, Edoardo
N-LT-01-10 301
NSS-01-061 345
Postuma, Ian
MIC-05-361 985
Potenza, Alberto
NSS-01-173 391
Poudyal, Nabin
NSS-10-01 516
Poulsen, Per
MIC-05-130 912
Poveda-Martínez, Jeremiah
MIC-05-388 ..... **994**
MIC-15-075 1296
Pozzi, Mattia
NSS-01-291 437
NSS-25-04 780
Pozzi, Sara A.
MP-01-02 ..... 92, ***817***
MP-02-01 ..... 116, ***1021***
NSS-05-01 477
NSS-09-03 510
NSS-11-03 524
NSS-11-04 525
NSS-13-014 569
NSS-13-196 645
NSS-13-224 657
NSS-16-05 717
NSS-22-03 760
NSS-27-07 797
Pozzoli, Alex
NSS-03-04 464
Prakash, Tarun
N-LT-03-04 ..... **541**
NSS-01-116 ..... **611**
RTSD-09-06 1572
Prats-Climent, Joan
MIC-15-285 1360
Pratt, Edwin C.
WS-04-17 260
Pratte, Jean-François
NSS-05-08 483
NSS-21-03 752
Pratx, Guillem
MIC-05-439 1009
Praus, Petr
RTSD-01-04 ..... 169, ***1471***
RTSD-04-358 1501
RTSD-06-03 1548
Prchlik, Jakub
N-LT-01-09 ..... **300**
NSS-01-001 ..... **321**
Prebys, Eric
MIC-15-321 1371
M-LT-05-01 1254
Preghenella, Roberto
NSS-20-05 745
NSS-21-02 ..... 84, ***751***
NSS-21-07 756
Prekas, Georgios
RTSD-02-03 ..... 170, ***1480***
RTSD-07-04 ..... 179, ***1555***
Presotto, Luca
MIC-05-217 940
MIC-10-443 1211
NSS-26-04 ..... 88, *786*
Priestley, Henry
NSS-15-05 ..... 79, ***711***
Priftakis, Dimitrios
MIC-15-345 1379
Principato, Fabio
RTSD-03-07 1490
RTSD-10-03 1579
Prins, Nicholas
NSS-13-158 628
Privitera, Marco
NSS-13-118 612
Priyadarshi, Ayush
NSS-13-204 ..... 71, ***648***
Procz, Simon
RTSD-04-392 1529
RTSD-08-03 1562
RTSD-10-01 1577
Profeti, Alessandro
NSS-14-08 705
Prokopenko, Denis
MIC-15-393 ..... 161, ***1394***
Proserpio, Edoardo
N-LT-02-13 317
NSS-01-081 354
NSS-01-305 443
Prosperi, Paolo
NSS-14-08 705
Protti, Nicoletta
MIC-21-02 1460
Prout, David
MIC-10-077 1100
MIC-15-468 1418
Psarras, Dimitrios
MIC-05-337 977
Puigdengoles, Carles
MIC-05-004 873
Pullia, Marco
MIC-05-337 977
MIC-17-03 1430
NSS-05-07 482
NSS-12-07 535
Puprasit, Kunlanan
NSS-01-281 432
NSS-16-04 ..... 80, ***716***

Author Index

Purschke, Martin L.
NSS-20-02 ..... 83, ***742***

Q

Qi, Chi
MIC-05-352 982
Qi, Haotian
NSS-13-282 680
Qi, Huirong
NSS-01-005 ..... 30, ***322***
Qi, Jinyi
MIC-01-05 827
MIC-05-007 874
MIC-10-137 1116
MIC-11-04 1227
MIC-15-003 1275
MIC-18-02 1437
Qi, Pengyuan
MIC-05-325 973
Qi, Wenyuan
MIC-01-05 827
MIC-10-269 1156
MIC-10-299 ..... 134, *1165*
Qi, Xinren
NSS-01-119 ..... 36, ***368***
Qi, Yihong
RTSD-04-388 ..... 175, ***1525***
Qi, Yujin
MIC-15-087 ..... **1300**
Qian, Haoyuan
MIC-15-402 ..... 161, ***1397***
Qian, Shuo
NSS-18-04 731
Qiang, Lu
MIC-15-414 1401
Qiao, Hongyang
MIC-05-160 922
Qiao, Xiaoya
MIC-10-383 ..... 137, ***1190***
Qiao, Zhihong
NSS-01-225 410
Qin, Jingjing
MIC-05-226 943
MIC-15-312 1368
M-LT-01-02 836
M-LT-05-05 1258
Qiu, Ao
MIC-05-325 973
MIC-05-331 975
MIC-10-329 1175
MIC-10-335 ..... 135, ***1176***
MIC-15-333 1375
Qiu, Peng
JS-02-02 270
Qiu, Rui
NSS-26-06 788
Qiu, Yuhang
NSS-13-184 ..... 70, ***640***
NSS-13-220 ..... 72, ***655***
Qu, Wenkang
MIC-05-286 961
MIC-07-03 1034
Quan, Enzhuo
MIC-05-343 979
MIC-15-339 1377
Quaranta, Alberto
NSS-27-08 798
Quattrocchi, Lucia
NSS-25-04 780
Quercia, Jacopo
RTSD-10-03 1579
Quintas, Uxía
MIC-15-075 1296
Quiter, Brian J.
NSS-22-04 ..... 85, *761*

R

Ra, Jiwon
NSS-01-175 ..... 39, ***391***
NSS-01-255 422
NSS-13-166 632
Rabant, Valentin
NSS-01-101 362
Rabin, Carolina
MIC-15-105 1305
Raczyński, Lech
MIC-05-223 942
M-LT-01-07 840
Radaideh, Majdi I.
NSS-11-03 524
Radermacher, Harald
MIC-05-028 880
MIC-05-103 904
MIC-15-291 1362
MIC-15-381 1390
M-LT-05-04 1257
Rädler, Martin
MIC-10-128 ..... 128, ***1114***
MIC-15-258 ..... 156, ***1352***
Rado, Janos
NSS-01-073 350
NSS-13-062 588
Rafecas, Magda
MIC-05-070 893
Rafecas, Magdalena
MIC-05-052 888
MIC-05-391 995
MIC-10-050 1092
MIC-10-074 1099
MIC-10-122 1112
MIC-10-191 1132
MIC-10-326 1174
MIC-15-027 1282
MIC-15-099 1303
MIC-15-114 1308
MIC-15-126 1312
MIC-15-324 1372
M-LT-04-06 1053
M-LT-04-10 1056
M-LT-05-02 1255
Raffanti, Richard
NSS-08-08 505
Rafiei Sardouei, Alireza
MIC-08-03 1060
Rahali, Hamza Ezzaoui
NSS-26-05 787
Rahman, Maahir
NSS-13-216 653
Rahmim, Arman
MIC-05-313 969
MIC-05-319 971
MIC-08-03 1060
MIC-18-07 1442
Raible, Robert
MIC-15-039 1285
Rainio, Oona
MIC-05-409 1001
MIC-15-306 1366
M-LT-06-08 1271
Ralet, Damian
NSS-13-262 ..... 74, ***672***
Ram, Eegan
MIC-05-274 957
Ramakers, Ruud M.
MIC-10-251 1151
Ramaz, François
MIC-15-213 1339
Ramazanov, Dmytro
NSS-01-189 396
Ramírez Pérez de Inestrosa, Javier
MIC-15-282 1359
M-LT-06-07 1270
Ramirez, Javier
MIC-10-281 1160
MIC-10-290 1162
Ramírez, Javier
MIC-10-296 1164

Author Index

MIC-10-308 1168
Ramírez, Wilson
MIC-16-02 1421
Ramonaheng, Kamo
MIC-01-01 823
Ramos-Docampo, Emma
MIC-05-073 894
Ramsi, Yohann
NSS-16-08 ..... 80, ***720***
Ran, Xinchi
NSS-18-02 729
RTSD-04-399 ..... 177, ***1534***
Ranatunge, Lochana
NSS-13-088 599
Rand, Stephen
NSS-13-046 581
Ranga, Virendra
NSS-13-204 648
Ranieri, Antonello
RTSD-06-01 1547
Ranjbar, Sahar
NSS-05-07 482
NSS-12-07 535
Rao, Xingzhe
MIC-05-325 973
Rapisarda, Matteo
RTSD-09-04 1571
Rapp, Benjamin
NSS-01-239 415
Rapsomanikis, Aristotelis-Nikolaos
MIC-05-061 ..... 101, ***891***
MIC-15-342 1378
Raspino, Davide
NSS-01-145 ..... 38, ***380***
NSS-24-04 774
Ratliff, Hunter
MIC-17-04 1431
Ratner, Hagit
MIC-10-422 1203
MIC-15-375 1388
M-LT-05-03 1256
Rato-Mendes, Pedro
MIC-15-348 ..... 159, ***1380***
Ratti, Lodovico
NSS-01-109 365
NSS-08-02 501
NSS-10-05 ..... 55, ***520***
NSS-14-04 701
NSS-14-08 705
NSS-21-07 756
SC-01-07 11
WS-02-12 ..... 18, ***233***
Rauch, Constantin
RTSD-08-05 1564
Rauscher, Isabel
MIC-15-045 1287
Rauscher, Lukas
MIC-05-052 888
Rauscher, Lukas U.
MIC-05-070 893
MIC-10-122 1112
MIC-15-027 ..... 147, ***1282***
MIC-15-126 1312
MIC-20-03 ..... 167, ***1455***
Ravel, Bruce
NSS-01-307 443
Ravotti, Federico
NSS-01-245 418
Ray Image Testing Technology ; The Palace Museum ; Shandong Nuclear Power Co., Ltd
TS-03-02 1592
Ray, Paul S.
NSS-10-01 516
Ray, Sangeeta
MIC-15-300 1365
Razdevšek, Gašper
MIC-15-045 1287
Re, Valerio
NSS-01-109 365
NSS-08-02 501
NSS-10-05 520
NSS-14-04 701
Reader, Andrew
WS-03-03 ..... **239**
Reader, Andrew J.
MIC-01-03 825
MIC-05-202 935
MIC-05-220 941
MIC-05-388 994
MIC-15-393 1394
MIC-15-426 1404
MIC-18-01 1436
MIC-20-05 1457
M-LT-01-01 835
M-LT-01-09 842
Rebolo, Leonor
MIC-09-04 1070
MIC-15-321 ..... 158, ***1371***
M-LT-05-01 ..... 144, ***1254***
RTSD-03-02 ..... 171, *1486*
Reckleben, Christian
NSS-08-01 500
NSS-13-100 605
Reese, Benjamin
NSS-01-147 ..... 38, ***381***
Reese, Benjamin A.
NSS-13-104 ..... 66, ***607***
NSS-20-08 ..... 83, ***747***
Reeves, Antonia
MIC-05-268 ..... 109, ***955***
MIC-10-086 1102
MIC-15-084 1299
M-LT-02-09 ..... 97, ***853***
Regnery, Brendan
NSS-12-03 531
Reis, João M.
MIC-05-166 923
Reisbick, Spencer A.
RTSD-06-06 1551
Reiser, Ingrid
MIC-10-173 1127
Reiss, Justin
NSS-16-07 719
Ren, Heyu
RTSD-04-391 1528
Ren, Jing
NSS-02-03 457
Ren, Ning
MIC-07-05 1036
Ren, Qiushi
MIC-05-376 990
MIC-10-113 1110
WS-04-07 251
Ren, Zhimei
MIC-15-234 1345
Renard, Christophe
NSS-16-08 720
Renn, Philipp
MIC-10-101 ..... 127, ***1106***
M-LT-04-01 ..... 120, ***1048***
Resch, Sandra
MIC-01-01 823
Retiere, Fabrice
NSS-18-01 ..... 81, *729*
SC-02-01 11
WS-02-05 ..... 17, ***229***
WS-02-14 ..... 18, ***234***
Rey, Jean-Michel
NSS-13-262 672
Reynaud, Federico
NSS-17-05 726
Rezaei, Ahmadreza
MIC-05-256 951
MIC-10-086 1102
MIC-10-254 1152
MIC-15-084 1299
Reznik, Alla
MIC-05-106 905

Author Index

MIC-10-302 1166
MIC-15-135 1315
NSS-01-073 350
NSS-13-062 588
Rhodes, Nigel J.
N-LT-02-10 315
NSS-01-267 426
NSS-09-06 513
Ria, Andrea
NSS-14-08 705
Riani, Cecilia
MIC-15-108 1306
Riazanova, Irina
NSS-04-04 471
Ribalda Galvez, Miquel
NSS-23-04 768
Ribalda, Miquel
MIC-05-019 878
MIC-09-08 1074
MIC-15-045 1287
Ribeiro, Fabiana M.
MIC-15-243 ..... **1348**
Riboldi, Christian
MIC-10-347 1180
MIC-17-03 1430
NSS-03-03 463
NSS-09-04 511
NSS-13-260 671
Riboldi, Stefano
NSS-01-009 ..... 31, ***324***
NSS-13-074 ..... **593**
Ricci, Riccardo
NSS-21-02 751
Rice, Simon
NSS-01-223 409
Riceputi, Elisa
NSS-08-01 500
NSS-14-04 701
Richter, Matthias
NSS-04-02 469
Richter, Rainer H.
NSS-04-04 471
Richter, Robert
NSS-24-03 773
Riedler, Petra
NSS-17-03 724
Riera-Llobet, Carla
JS-02-09 276
Rignanese, Luigi
NSS-21-02 751
NSS-21-07 756
Rignanese, Luigi P.
NSS-20-05 745
Rignanese, Michele
NSS-13-298 686
Rigotti Caiano, Solano
NSS-13-010 ..... 61, ***567***
Rios, Alfonso
MIC-05-379 991
Ripoche, Xavier
MIC-10-167 1125
Risitano, Fabio
NSS-25-04 780
Rit, Simon
MIC-10-167 1125
MIC-10-221 1142
Ritschl, Ludwig
MIC-05-172 926
M-LT-01-05 838
Ritt, Stefan
MIC-05-448 1012
MP-01-01 ..... 92, ***817***
NP-01-01 ..... 26, ***287***
Rius, Gemma
MIC-10-017 1082
M-LT-03-03 1039
Rivas Ortiz, Iram B.
NSS-05-07 ..... 50, ***482***
NSS-12-07 535
Rivero-Buceta, Eva
MIC-05-355 983
Rivetti, Angelo
NSS-17-04 725
NSS-17-05 726
Rizzo, Francesca
NSS-25-04 780
Ro, Takahiro
MIC-05-151 919
MIC-15-177 1328
M-LT-02-05 850
Robbins, Max
RTSD-05-01 ..... 177, ***1540***
Robert, Tom
NSS-13-122 613
Roberts, Jarred
NSS-04-06 473
NSS-10-01 516
Roberts, Jarred M.
NSS-01-053 341
NSS-13-128 616
Robinson, Andrew P.
MIC-04-07 870
Roche, Grant
N-LT-01-06 297
NSS-01-017 327
Roddy, David
STIR-07 1599
Rodrigues, Duarte
RTSD-04-400 ..... 177, *1535*
Rodrigues, Duarte S.
NSS-24-06 775
RTSD-04-362 ..... 173, *1504*
Rodriguez Almora, Deniel
MIC-10-293 ..... 134, ***1163***
Rodríguez Almora, Deniel
MIC-10-353 1181
Rodríguez Villafuerte, Mercedes
MIC-15-390 1393
Rodríguez, Jorge
MIC-05-358 984
Rodríguez-Álvarez, María J.
MIC-15-285 1360
Rodriguez-Rubio, Marina
MIC-10-281 1160
Rodríguez-Silva, Jesús
MIC-05-073 894
Rodríguez-Villafuerte, Mercedes
MIC-05-049 887
MIC-05-112 906
Roemer, Katja
MIC-17-04 1431
Rofors, Emil
NSS-22-04 ..... **761**
Rogers, Field R.
NSS-01-053 341
NSS-13-128 616
Rogers, Kurt
RTSD-02-03 1480
RTSD-07-04 1555
Röhrich, Dieter
NSS-04-02 469
Rojas, Solangel
NSS-07-08 498
Rolo, Manuel
NSS-13-298 686
Romancheck, Gregory
MIC-05-436 1008
Romanchek, Gregory R.
MIC-10-461 ..... 140, ***1217***
Römer, Katja
MIC-05-328 974
Romero García, Sergio
MIC-15-360 1384
Romero-Sanz, Eduardo
MIC-15-462 1416
Rominger, Axel
MIC-01-01 823
MIC-05-133 913
MIC-15-234 1345

Author Index

MIC-15-366 1386
WS-04-17 260
Roncali, Emilie
MIC-10-071 1098
MIC-15-051 1289
Ronchetti, Federico
NSS-13-080 595
Ronchi, Michele
MIC-10-038 1089
M-LT-04-04 1051
NSS-23-05 ..... 86, ***769***
Ronconi, Enrico
NSS-03-03 463
NSS-12-02 530
NSS-13-130 617
NSS-13-304 688
Rong, Jianming
MIC-08-05 ..... 122, *1062*
Rongen, Martin
RTSD-08-05 1564
Roque Romero, Gerardo
RTSD-03-01 1485
Roque, Gerardo
RTSD-04-392 1529
RTSD-08-03 1562
Roque, Gerardo A.
RTSD-10-01 ..... 181, ***1577***
Ros, Ana
MIC-15-099 1303
MIC-15-336 1376
MIC-16-02 ..... 164, *1421*
Rose, Luke
NSS-13-278 678
Rosenfeld, Anatoly
NSS-04-01 468
NSS-04-02 469
NSS-06-05 488
Rosenhahn, Axel
NSS-08-05 503
Roser, Jorge
MIC-05-052 888
MIC-10-050 ..... 125, ***1092***
MIC-10-074 1099
MIC-10-191 1132
MIC-10-326 1174
MIC-15-099 1303
M-LT-04-06 ..... 121, ***1053***
M-LT-04-10 1056
Roshan, Seyed Ehsan
MIC-15-429 1405
Rossé, Bertrand
RTSD-04-396 ..... 176, ***1532***
Rossi, Biaggio
N-LT-04-11 559
NSS-13-290 683
Rossi, Elvira
N-LT-04-11 559
NSS-13-290 683
Rossi, Francesco
MIC-15-102 1304
Rossi, Ian M.
WS-04-09 ..... 22, ***253***
Rossignol, Julien
MIC-03-08 861
NSS-01-103 ..... 35, ***363***
NSS-03-05 ..... 49, ***465***
Rossignol, Tommy
NSS-05-08 483
NSS-21-03 752
Rosso, Giulia
RTSD-02-02 ..... 170, ***1479***
Rosso, Valeria
RTSD-08-02 1561
Rossomme, Severine
MIC-10-098 1105
M-LT-04-02 1049
Rota, Lorenzo
MIC-03-06 ..... **860**
NSS-01-087 356
NSS-10-04 519
NSS-13-106 607
NSS-23-02 766
NSS-23-06 770
Roughley, Kiarn
NSS-06-05 488
Round, Thomas
NSS-01-057 ..... 33, ***343***
Roupas, Efstratios
MIC-10-215 ..... 131, ***1140***
Rovati, Edoardo
NSS-21-02 751
Roy, Nicolas
NSS-05-08 483
NSS-21-03 752
Roy, Utpal
RTSD-07-03 1554
Roy, Utpal N.
RTSD-09-07 ..... 181, ***1573***
Ruckman, Larry
NSS-01-087 356
NSS-23-06 770
Ruddy, Frank H.
JS-03-01 279
Ruder, Christian
NSS-01-093 358
Ruffolo, David
NSS-01-281 432
Ruggieri, Marco
RTSD-09-04 ..... 181, ***1571***
Rumaiz, Abdul
NSS-08-03 502
NSS-13-146 623
Rumaiz, Abdul K.
NSS-01-303 442
NSS-01-307 ..... 46, ***443***
Ruskowski, Jennifer
WS-02-16 ..... 19, ***235***
Russo, Paolo
MIC-05-292 963
RTSD-01-07 1474
Russotto, Paolo
NSS-25-04 780
Rutstrom, Daniel
NSS-05-06 481
Růžička, Ondrej
NSS-01-287 435
Ruzzarin, Maria
JS-02-04 272
NSS-21-04 753
Ruzzarin, Maria S.
NSS-01-293 438
Ryhiner, Marc
MIC-15-366 ..... 160, ***1386***
Rynders, Michael
NSS-01-299 440
Ryoo, Hyun Gee
MIC-10-395 1194
M-LT-03-01 1038
Ryu, Jinho
NSS-13-246 666

S

Sabatini, Fabrizio
NSS-13-284 681
Saberi Manesh, Abdollah
MIC-10-206 ..... 131, ***1137***
Sabet, Hamid
MIC-05-022 879
MIC-05-316 970
MIC-05-469 ..... 116, *1018*
MIC-10-365 1185
MIC-15-132 1314
MIC-15-303 1366
M-LT-04-03 1050
M-LT-06-10 1272
NSS-13-044 580
NSS-17-01 722
Sabeur, Manil

Author Index

MIC-10-263 ..... 133, ***1154***
STIR-12 1600
Sabeur, Manil Z.
STIR-03 ..... **1597**
Sabirzyanova, Kamilla
NSS-06-06 489
Sabiu, Bianca
NSS-21-02 751
Sabuncu, Mert
MIC-10-020 1083
Sacchi, Roberto
NSS-05-07 482
NSS-12-07 535
NSS-28-04 804
Sadowy, Jérôme
NSS-13-054 584
Saenz-Arevalo, William
NSS-24-04 ..... 87, ***774***
Sagara, Hiroshi
NSS-01-229 411
Sagardia, Joan
MIC-05-370 988
Sagatova, Andrea
NSS-01-273 429
RTSD-04-361 1503
RTSD-04-386 ..... 175, ***1523***
RTSD-04-387 1524
Šagátová, Andrea
JS-03-03 280
RTSD-04-359 1502
RTSD-04-393 1530
Sagawa, Naoki
NSS-13-036 ..... 62, ***577***
NSS-13-230 659
Saheb, Khasim
NSS-01-151 382
Sahebzada, Rafiaullah
MIC-15-321 1371
M-LT-05-01 1254
Sahsuvar, Nazire S.
RTSD-04-352 ..... 172, ***1495***
Saito, Yutaro
NSS-01-217 ..... 41, ***407***
Sakai, Toshiaki
MIC-05-079 896
Sakama, Makoto
MIC-05-340 978
Sakamoto, Kyohei
JS-02-03 271
Sakamoto, Toshitsugu
N-LT-03-09 545
NSS-13-142 622
Sakhatska, Anastasiia
RTSD-01-08 1475
RTSD-05-03 ..... 177, ***1541***
RTSD-05-05 1543
Sakhatskyi, Kostiantyn
RTSD-01-08 1475
RTSD-05-03 1541
RTSD-05-05 ..... 178, *1543*
Sakuma, Yasutaka
NSS-01-049 341
Sakumura, Takuto
NSS-01-049 341
Salas-González, Diego
MIC-10-308 1168
Salathe, Marco
NSS-22-01 759
Saleh, Lemise
MIC-05-115 907
M-LT-02-01 846
Salimi, Yazdan
MIC-05-319 971
MIC-10-206 1137
Salvador, Carmen
MIC-15-336 1376
Salvatori, Stefano
RTSD-06-01 1547
Samimi, Rezvan
MIC-05-313 969
Samouilidis, Evangelos
NSS-05-05 480
NSS-13-268 ..... 75, ***674***
Samson, Arnaud
MIC-02-03 831
San Martín Valenzuela, Claudio
MIC-05-004 ..... 99, ***873***
Sanaat, Amirhossein
MIC-05-403 999
Sanchety, Naveen
MIC-05-367 987
MIC-15-294 1363
Sanchez Gonzalo, David
MIC-15-045 1287
Sánchez Tembleque, Víctor
MIC-19-05 1448
Sanchez, David
MIC-05-118 908
MIC-05-379 991
MIC-09-02 1068
MIC-09-08 1074
MIC-10-020 1083
MIC-15-123 1311
M-LT-02-02 847
Sánchez, David
MIC-10-140 1117
Sanchez, David G.
WS-02-03 228
Sanchez, Kevin
NSS-18-03 ..... 81, ***730***
Sanchez-Tembleque, Victor
MIC-15-069 1294
Sánchez-Tembleque, Victor
MIC-10-023 1084
MIC-15-042 ..... 148, ***1285***
Sánchez-Tembleque, Víctor
NSS-13-086 598
Sandberg, Hampus
NSS-01-087 356
Sanders, Jeff
RTSD-04-397 1533
Sandmann, Tim
NSS-01-315 447
Sang, Yong
RTSD-04-377 1516
Sankaran, Rajesh
NSS-22-01 759
Sannino, Michele
MIC-15-039 ..... 148, *1285*
Santini, Letizia
MIC-10-347 ..... **1180**
MIC-17-03 1430
NSS-09-04 511
Santoro, Romualdo
NSS-13-298 686
NSS-21-07 756
Santos, Ana C.
MIC-15-243 1348
Santos, Filomena P.
NSS-24-06 775
Sanuy, Andreau
JS-02-04 272
Sanuy, Andreu
MIC-05-019 878
MIC-09-08 1074
MIC-15-045 1287
Sanzen, Arisa
MIC-10-005 ..... **1078**
Sanz-Sánchez, Alejandro
MIC-15-285 ..... 157, ***1360***
Sapkas, Michail
NSS-01-173 ..... **391**
Sapozhnikov, Leonid
NSS-13-104 607
Saraste, Antti
MIC-15-429 1405
Sari, Adrien
NSS-13-272 676
Sari, Hasan

Author Index

WS-04-17 260
Sarrhini, Otman
MIC-02-03 831
MIC-15-432 1406
Sarrut, David
MIC-05-088 899
MIC-05-214 938
MIC-06-02 ..... 118, *1028*
M-LT-01-06 839
Sartor, Nicolas
NSS-24-04 774
Sarzi Amadè, Nicola
RTSD-04-395 ..... **1532**
Sasaki, Miyuki
NSS-01-153 383
NSS-05-02 478
NSS-11-05 ..... 56, ***526***
NSS-13-152 626
Sasaki, Tatsuo
MIC-13-04 1245
Sasano, Makoto
NSS-13-058 ..... 63, ***586***
Sasaya, Tenta
MIC-15-168 1325
Sathekge, Mike
MIC-01-01 823
Sato, Akira
NSS-13-002 564
Sato, Joe
NSS-26-07 ..... 88, ***789***
Sato, Masahiro
MIC-10-002 1077
Sato, Riku
MIC-15-459 1415
M-LT-06-04 1267
Sato, Setsuo
RTSD-04-379 1517
Sato, Taiyo
NSS-02-02 ..... 48, ***456***
Sato, Yuki
NSS-15-01 707
Satoh, Daiki
NSS-18-06 ..... **733**
Saut, Olivier
MIC-01-02 824
Savazzi, Simone
MIC-05-337 977
Savino, Umberto
NSS-13-286 ..... 75, ***682***
Sawada, Rikuto
MIC-03-07 ..... 98, ***861***
Sawano, Tatsuya
NSS-02-02 456
Sawhney, Kawal
JS-01-01 264
Sbuelz, Luca
NSS-12-02 530
Scagliotti, Mattia
RTSD-09-04 1571
Scamardella, Julia
N-LT-04-11 559
NSS-13-290 683
Scarcella, Carmelo
RTSD-07-05 1556
Scaringella, Monica
MIC-15-102 1304
Schaart, Dennis
JS-01-02 264
Schaart, Dennis R.
MIC-05-031 881
MIC-15-018 1280
MIC-15-036 1284
WS-04-11 ..... 22, ***255***
Schaefer, Jamin
MIC-05-172 926
M-LT-01-05 838
Schaefferkoetter, Josh
MIC-10-374 1187
MIC-15-264 1354
Schaefferkoetter, Joshua
MIC-05-397 ..... 114, ***997***
MIC-08-07 1064
MIC-15-225 1342
Schäfer, Noah R.
MIC-05-292 963
Schäfers, Jakob
MIC-10-101 1106
M-LT-04-01 1048
Schäfers, Klaus
MIC-10-101 1106
M-LT-04-01 1048
Scheins, Juergen
MIC-16-02 1421
Scheins, Juergen J.
MIC-15-249 ..... 155, ***1349***
Scheins, Jürgen
MIC-10-242 1148
MIC-10-260 1153
Scheins, Jürgen J.
MIC-15-255 1351
Scherer, Benedikt
MIC-15-111 1307
Schick, Ulrike
MIC-15-174 1327
MIC-15-369 1386
M-LT-05-09 1261
Schilling, Alexander
NSS-04-02 469
Schlegel, Patrice
MIC-10-419 ..... **1202**
MIC-17-01 1428
M-LT-03-08 ..... **1044**
Schleyer, Paul
MIC-05-397 997
MIC-10-374 1187
MIC-15-264 1354
WS-03-10 ..... **242**
Schlueter, Lisa
N-LT-02-12 316
NSS-01-085 356
Schmidt, Christian J.
NSS-13-268 674
Schmidt, Fabian
MIC-10-122 1112
WS-04-17 260
Schmidt, Fabian P.
MIC-05-052 888
MIC-05-070 893
MIC-08-07 1064
MIC-15-027 1282
MIC-15-075 1296
MIC-15-126 1312
MIC-20-03 1455
Schmidt, Malte
MIC-10-191 1132
Schmitt, Bernd
NSS-01-093 358
RTSD-01-06 1473
Schnabel, Julia A.
MIC-05-220 941
M-LT-01-09 842
Schneider, Ethan
NSS-13-014 ..... 61, ***569***
NSS-16-05 717
Schneider, Markus
RTSD-08-05 ..... 180, ***1564***
Schnorrenberg, Elizabeth
N-LT-01-05 296
NSS-01-019 328
NSS-01-129 372
Schönecker, Sonja
MIC-10-281 1160
Schooneveld, Erik
NSS-01-145 380
Schooneveld, Erik M.
N-LT-02-10 315
NSS-01-267 426
NSS-09-06 513
Schopper, Florian

Author Index

NSS-04-04 471
Schramm, Georg
MIC-05-241 947
MIC-05-256 951
MIC-10-086 1102
MIC-10-254 1152
MIC-11-08 1230
MIC-15-084 1299
M-LT-02-06 851
Schramm, Nils
MIC-15-111 1307
Schröder, Lukas
MIC-05-031 881
MIC-15-018 ..... 147, ***1280***
MIC-15-036 ..... 148, ***1284***
WS-04-11 255
Schug, David
JS-02-05 273
MIC-05-028 880
MIC-05-103 904
MIC-11-01 1224
MIC-15-054 1290
MIC-15-291 ..... 157, ***1362***
MIC-15-381 1390
M-LT-05-04 1257
N-LT-01-08 299
NSS-01-015 326
NSS-21-04 753
Schulz, Volkmar
JS-02-05 273
MIC-05-028 880
MIC-05-103 904
MIC-11-01 1224
MIC-15-054 1290
MIC-15-291 1362
MIC-15-381 1390
MIC-16-05 1424
M-LT-05-04 1257
N-LT-01-08 299
NSS-01-015 326
NSS-21-04 753
Schune, Marie-Hélène
NSS-12-04 532
Schüßler-Langeheinee, Christian
NSS-08-08 505
Schütz, Michael
RTSD-04-392 1529
RTSD-08-03 1562
Schütz, Michael K.
RTSD-03-01 ..... 171, ***1485***
RTSD-10-01 1577
Schwartzman, Ariel G.
NSS-23-02 766
Scialdone, Antonio
NSS-13-256 669
Scipioni, Michele
MIC-12-06 1237
Scopelliti, Fabrizio
MIC-10-362 1184
Scott, Tom
NSS-01-187 395
Scoullar, Paul
MIC-03-01 ..... 97, ***856***
Searfus, Oskar
NSS-13-224 657
Sechopoulos, Ioannis
MIC-15-105 1305
Seddon, Dave
NSS-13-278 678
NSS-25-06 782
Sedgwick, Iain
NSS-13-088 599
Seeger, Steven
MIC-10-074 1099
MIC-15-114 1308
M-LT-04-10 1056
Segovia Román, Fermín
MIC-15-282 1359
M-LT-06-07 1270
Segovia, Fermin
MIC-10-281 1160
MIC-10-290 1162
MIC-10-296 ..... 134, ***1164***
Segovia, Fermín
MIC-10-308 1168
Seifert, Robert
MIC-01-01 823
Seimetz, Michael
MIC-05-355 983
MIC-10-341 1178
MIC-15-006 1276
Sekhniaidze, Givi
N-LT-04-11 559
NSS-13-290 683
Sekiguchi, Hikaru
RTSD-04-389 1526
Sekino, Masaki
MIC-12-07 1239
Seljak, Andrej
MIC-15-045 1287
NSS-21-06 755
Sellin, Paul
JS-01-01 264
JS-03-02 280
NSS-07-04 495
RTSD-06-02 ..... 178, *1547*
Sellin, Paul J.
NSS-13-040 579
Selvaggi, Michele
NSS-12-04 532
Semkiv, Nazard
NSS-12-04 532
Semnani, Farbod
MIC-10-317 ..... 135, ***1171***
Seo, Jiwon
N-LT-01-02 293
NSS-01-013 325
RTSD-04-367 1508
Seo, Jungmin
NSS-13-242 664
Seo, Yongho
MIC-12-03 1235
Seo, Youngho
MIC-05-058 890
MIC-05-334 976
MIC-05-439 ..... 115, *1009*
MIC-05-448 1012
MIC-10-062 1096
MIC-11-07 1229
MIC-12-01 1233
MIC-12-02 1234
MIC-21-03 1461
MP-02-05 ..... 117, ***1022***
MP-02-08 ..... 117, ***1023***
MP-02-11 ..... 117, ***1024***
WS-04-01 ..... 21, ***245***
Seol, Yu Jin
MIC-10-395 1194
MIC-15-315 ..... 158, ***1369***
M-LT-03-01 1038
M-LT-05-06 ..... 145, ***1259***
Seop, Hur
NSS-01-083 355
NSS-01-259 423
Seo-Ryong, Koo
NSS-01-083 355
NSS-01-259 423
Serafini, Davide
MIC-10-362 1184
Sergo, Rudi
NSS-12-02 530
NSS-13-130 617
Serrano, Joan
N-LT-03-02 539
NSS-13-098 604
NSS-20-06 746
Seung, Minuk
NSS-13-174 ..... 69, ***636***
Sevenois, Matthijs

Author Index

MIC-05-241 947
M-LT-02-06 851
Severin, Gregory
NSS-13-310 691
Seyssaud, Jérémy
NSS-13-206 649
Sgalaberna, Davide
NSS-12-01 ..... 56, ***529***
NSS-21-05 754
WS-02-08 ..... **231**
WS-02-13 ..... 18, ***234***
Sgarbi, Francesca
MIC-10-443 1211
Sgouros, George
MIC-21-01 1459
Sgrò, Carmelo
NSS-14-08 705
Sguazzoni, Giacomo
NSS-28-08 808
Sha, Fei
NSS-13-282 680
NSS-17-02 723
Shabani Sichani, Soroush
MIC-10-137 ..... 128, ***1116***
Shah, Kuneh
NSS-01-157 385
Shah, N. Jon
MIC-10-008 1079
MIC-10-260 1153
MIC-15-162 1324
Shah, Nadim J.
MIC-10-242 1148
MIC-15-249 1349
MIC-15-255 1351
Shah, Syed O.
MIC-14-02 ..... 144, ***1249***
Shah, Yug B.
MIC-10-449 1213
Shahi, Anirudh
MIC-15-135 ..... 151, ***1315***
Shahkarami, Sean
NSS-22-01 759
Shao, Jianxiong
MIC-10-338 1177
MIC-15-363 1385
Shao, Zefeng
NSS-27-01 792
Sharma, Anjali
NSS-13-022 572
Sharma, Deepika
NSS-01-043 ..... **338**
Sharma, Kartikeya
NSS-18-01 ..... **729**
Sharma, Sushil
MIC-12-05 1236
MIC-15-267 1355
MIC-15-456 1414
M-LT-06-03 1266
Sharpe, Joshua
NSS-25-06 782
Sharpe, Zoe H.
NSS-13-040 ..... 62, *579*
Sharyy, Viatcheslav
NSS-06-07 490
NSS-13-084 ..... 65, ***597***
Shearman, Robert
NSS-25-06 782
Shelden, David
N-LT-01-05 296
NSS-01-019 328
NSS-01-129 372
Shen, Wei
RTSD-09-03 1569
Shen, Zhijian
RTSD-04-376 1515
Sheng, Ke
MIC-12-03 1235
Sheng, Shuqi
NSS-21-08 757
Shenton-Taylor, Caroline
N-LT-04-02 551
NSS-01-171 390
NSS-11-06 527
NSS-13-156 628
NSS-13-170 634
Shenyi, Zhang
NSS-01-281 432
Shepelytskyi, Yurii
MIC-05-106 905
Shi, Dawei
MIC-05-286 961
MIC-05-376 990
MIC-07-03 1034
MIC-10-113 1110
MIC-10-116 1111
Shi, Gengxin
MIC-05-172 ..... **926**
M-LT-01-05 ..... **838**
Shi, Henry
MIC-03-06 860
NSS-10-04 519
Shi, Kaiwen
RTSD-04-376 ..... **1515**
Shi, Kuangyu
MIC-01-01 823
MIC-05-133 913
MIC-08-03 1060
MIC-15-234 1345
MIC-15-366 1386
WS-04-17 260
Shi, Yankun
MIC-15-396 1395
Shi, Yuan
NSS-01-127 371
Shi, Yuyao
MIC-10-359 1183
Shibuya, Tatsunori
MIC-05-187 930
M-LT-01-10 843
Shih, Albert
NSS-04-06 473
Shim, Chaeyun
NSS-23-02 766
Shim, Hyeong Seok
MIC-15-048 1288
Shim, Hyeongseok
MIC-05-085 ..... 102, ***898***
MIC-15-024 ..... 147, ***1281***
MIC-19-06 ..... 167, ***1449***
Shimano, Kenshi
MIC-13-04 1245
Shimazoe, Kenji
JS-02-03 ..... 24, ***271***
MIC-07-02 1034
MIC-11-03 1226
MIC-12-07 1239
MIC-15-453 1413
MIC-15-459 1415
M-LT-06-04 1267
NSS-13-066 590
NSS-13-232 660
NSS-27-02 793
RTSD-04-389 1526
Shimizu, Yuki
NSS-13-064 589
Shin, Byungha
N-LT-01-01 ..... 27, ***292***
NSS-01-021 ..... 31, ***329***
Shin, Dongseong
NSS-01-167 ..... 39, ***388***
Shin, Jung Ki
NSS-01-169 389
Shin, Jung-ki
NSS-13-222 656
Shin, Jung-Ki
NSS-01-003 321
Shin, Jungwook
MIC-05-334 976
Shin, JunYoung

Author Index

NSS-01-269 427
Shin, Kibeak
NSS-13-258 670
Shin, Shawn
MIC-15-468 ..... 163, ***1418***
Shinoto, Makoto
MIC-05-346 980
Shiokawa, Asahi
NSS-13-232 660
Shiomi, Koji
NSS-25-03 779
Shiozaki, Ryozo
NSS-28-03 803
Shoen, Luke
NSS-12-08 536
Shoghi, Kooresh I.
MIC-05-310 968
Shojaei, Fatemeh
NSS-21-07 756
Shoji, Masayoshi
NSS-01-071 349
Shoji, Yasuhiro
JS-02-03 271
NSS-07-01 493
Shoji, Yasushi
N-LT-02-14 318
NSS-01-321 450
Shoop, Greyson
MIC-05-436 ..... 115, ***1008***
Shoorian, Sarah
NSS-13-052 ..... 63, ***583***
Shtepura, Olena
NSS-28-06 806
Shu, Shangzhen
JS-01-04 266
Shuai, Lei
NSS-13-126 615
Shy, Daniel
JS-03-06 283
Siddons, David P.
NSS-01-303 ..... 46, ***442***
NSS-01-307 443
NSS-08-03 502
NSS-13-146 623
Sidiropoulou, Ourania
NSS-05-05 480
NSS-24-04 774
Sidky, Emil
MIC-10-053 1093
MIC-10-173 1127
MIC-15-234 1345
Siegel, Stefan
MIC-12-01 1233
MIC-15-129 1313
Silletta, Saverio
NSS-01-093 358
Silva García, Juan José
NSS-23-04 768
Silva, Ana Luísa M.
MIC-05-043 885
MIC-05-058 890
MIC-05-166 923
MIC-05-349 ..... 112, *981*
MIC-05-370 988
MIC-05-448 ..... 115, ***1012***
MIC-09-04 1070
MIC-10-446 ..... **1212**
MIC-15-021 1280
MIC-15-156 1322
MIC-15-159 1323
MIC-15-243 1348
MIC-15-321 1371
M-LT-05-01 1254
NSS-01-143 379
NSS-13-004 ..... 61, *565*
RTSD-03-02 1486
Silva, Caio
MIC-12-06 1237
Silva, Juan J.
MIC-05-019 878
MIC-09-08 1074
Silva, Pamela
MIC-15-303 1366
M-LT-06-10 1272
Silva, Rui C.
RTSD-04-378 1517
Silva-Rodríguez, Jesús
MIC-05-388 994
MIC-15-075 1296
Silvestri, Stefano
NSS-14-08 705
Simic, Vesna
NSS-13-272 676
Simons, Andrew
NSS-01-223 409
Simons, Erin
MIC-15-039 1285
Sinagra, Anthony
MIC-15-303 1366
M-LT-06-10 1272
Singh, Prabhleen
NSS-19-06 ..... 82, ***739***
NSS-21-06 755
WS-02-10 ..... 18, ***232***
Sirri, Gabriele
NSS-21-02 751
Sisniega, Alejandro
MIC-10-416 1201
M-LT-03-07 1043
Sitek, Arkadiusz
MIC-15-132 1314
Siviero, Federico
NSS-28-07 807
NSS-28-08 808
Siviero, Matilde
RTSD-04-355 1498
Sjolin, Martin
N-LT-01-10 301
NSS-01-061 345
Skafi, Zeynab
RTSD-06-01 1547
Skee, Chelsey
NSS-04-01 468
Skirsky, Tessa
MIC-10-230 1145
MIC-14-02 1249
Skliarchuk, Valerii
RTSD-04-365 1506
Slavicek, Tomas
NSS-01-273 429
RTSD-04-386 1523
RTSD-04-387 1524
Slavíček, Tomáš
JS-03-03 280
RTSD-04-393 1530
Sleator, Clio
NSS-13-128 ..... 67, ***616***
Smolyanskiy, Petr
NSS-01-135 375
NSS-01-287 435
RTSD-01-07 1474
RTSD-04-384 ..... 175, ***1522***
RTSD-08-05 1564
Snoeyink, Marc
MIC-05-031 ..... 100, ***881***
MIC-15-036 1284
WS-04-11 255
Snoeys, Walter
NSS-17-03 724
Snow, Jesse
NSS-13-318 ..... **694**
So, Chanyoung
NSS-04-04 471
Sobel, Peter
NSS-13-158 628
Sobota, Reid
RTSD-02-05 1481
Soerensen, Jan
NSS-21-05 754

Author Index

Soharova, Eliska
RTSD-03-06 1490
RTSD-07-07 1558
Soharová, Eliška
NSS-06-06 489
Sohma, Mitsugu
NSS-13-230 659
Sohn, Jongdae
NSS-01-097 ..... 35, ***360***
Sokolowski, Andrzej
MIC-10-257 1152
Sola, Valentina
NSS-12-03 531
NSS-28-07 807
NSS-28-08 808
Solans Sanchez, Carlos A.
NSS-17-03 724
Soleti, Stefano Roberto
MIC-05-034 882
Solf, Torsten
JS-01-03 ..... 24, ***265***
Solodkyi, Mykola
RTSD-04-354 1497
Solovov, Vladimir
N-LT-02-01 307
NSS-01-271 428
Son, Doo-Hee
NSS-13-082 ..... 65, ***596***
Son, Min Hyeong
NSS-23-03 ..... 86, ***767***
Sonawane, Manda
NSS-01-043 338
Song, Bin
RTSD-04-364 ..... **1505**
RTSD-04-377 1516
Song, Gyohyeok
MIC-11-07 ..... 141, ***1229***
NSS-01-155 384
NSS-01-209 403
Song, Peixuan
MIC-10-182 ..... 130, ***1129***
MIC-10-452 1214
MIC-18-05 1440
Song, Seungho
N-LT-01-02 ..... 27, ***293***
NSS-01-013 ..... 31, ***325***
RTSD-04-367 1508
Song, Si Y.
MIC-10-080 1100
Song, Tzu-An
MIC-08-02 1059
MIC-11-05 1228
Song, Zhiyong
MIC-05-046 ..... **886**
Sonobe, Hironori
NSS-28-03 ..... 90, ***803***
Sonoda, Shinya
NSS-18-06 ..... 82, *733*
Sorensen, Brita S.
MIC-17-05 1432
Sosa, Charles
MIC-10-041 1090
M-LT-03-04 1040
NSS-01-151 382
NSS-16-05 717
Sossi, Vesna
MP-01-01 ..... 92, ***817***
MP-02-01 ..... 116, ***1021***
Soundara Pandian, Lakshmi
NSS-07-03 ..... 52, ***494***
NSS-07-06 496
NSS-16-07 ..... 80, ***719***
Sousa, José
RTSD-04-400 1535
Sousa, Jose F.
RTSD-04-362 1504
Sousa, José F.
NSS-24-06 775
Spandre, Gloria
NSS-14-08 705
Spangler-Bickell, Matthew
MIC-05-256 951
MIC-15-360 1384
Španková, Marianna
RTSD-04-359 1502
Spannagel, Simon
NSS-10-02 516
Sparger, John
NSS-13-158 628
Speck, Niko
MIC-10-464 1218
Speck, Niko P.
N-LT-01-13 ..... 28, ***303***
NSS-01-311 ..... 46, ***445***
Speller, Robert
MIC-15-357 1383
Spencer, Benjamin A.
MIC-10-245 1149
MIC-10-248 ..... 132, *1150*
MIC-15-246 ..... 155, ***1349***
MIC-15-384 1391
MIC-18-02 1437
MIC-20-04 1456
Spiga, Jenny
NSS-15-05 711
Spillmann, Uwe
NSS-13-070 592
Spisek, Pavel
RTSD-07-07 1558
Sportelli, Giancarlo
MIC-10-362 1184
MIC-15-030 1283
N-LT-03-08 ..... 58, ***544***
NSS-13-136 ..... 67, ***619***
Squillante, Mike S.
RTSD-04-360 1502
St. James, Sara
MIC-15-321 1371
M-LT-05-01 1254
Stabile, Alberto
NSS-01-109 365
NSS-13-118 612
NSS-14-08 705
Staempflin, Martin
NSS-16-08 720
Staine, Courtnee
NSS-13-308 690
Stamati, Maria Elisso
NSS-11-01 523
Stanchina, Sylvain
RTSD-02-04 1481
Stayman, J Webster
MIC-05-175 927
M-LT-01-04 837
Stayman, Joseph W.
MIC-04-06 ..... 99, *869*
Stebel, Luigi
NSS-12-02 530
NSS-13-130 617
Steele, John
NSS-03-01 462
Stein, Juergen
NSS-13-260 671
Steinberger, William
MIC-20-03 1455
Steinberger, William M.
MIC-12-04 1236
Steinbrecht, Caroline
MIC-17-05 1432
Steiner, Joseph
MIC-15-234 1345
Steinhebel, Amanda
NSS-05-08 ..... 51, ***483***
Steinhebel, Amanda L.
NSS-21-03 752
Stennes, Oscar
NSS-27-07 797
Stephenson, Laura
MIC-11-03 1226

Author Index

MIC-15-459 1415
M-LT-06-04 1267
Stępień, Ewa Ł.
MIC-12-05 1236
Stern, Eli
MIC-15-210 1338
St-Georges, Alexandre
MIC-15-432 1406
Stieh, Amy
NSS-01-073 350
NSS-13-062 588
Stiliaris, Efstathios
MIC-05-061 891
MIC-05-463 1017
MIC-10-215 1140
MIC-15-342 1378
MIC-18-06 1441
Stille, Maik
MIC-05-391 995
Stodart, Nieldane
NSS-13-216 653
Stöhlker, Thomas
NSS-13-070 592
Stokes, Thomas C.
NSS-06-03 ..... 51, ***487***
Stott, Aaron
NSS-01-223 409
Stranks, Samuel
JS-01-01 264
Stranks, Samuel D.
RTSD-01-05 ..... **1472**
RTSD-04-369 1510
Streicher, Michael
JS-03-06 283
MIC-21-03 1461
RTSD-10-02 ..... 182, ***1578***
RTSD-10-04 1580
Streun, Matthias
MIC-15-111 ..... 150, ***1307***
Strüder, Lothar
NSS-08-01 500
Strugari, Matthew
MIC-10-353 1181
MIC-15-360 ..... 159, ***1384***
Studen, Andrej
MIC-10-032 1087
MIC-15-045 1287
Stute, Simon
MIC-04-04 867
MIC-05-301 966
MIC-05-304 966
MIC-10-263 1154
MIC-10-305 1167
NSS-16-08 720
Stutzmann, Jean-Sébastien
NSS-16-08 720
Su, Guanning
NSS-01-105 364
NSS-15-03 ..... 79, *709*
TS-02-02 1586
Su, Kuan-Hao
MIC-10-203 1136
MIC-15-210 ..... 154, ***1338***
MIC-15-360 1384
MIC-15-441 1409
Su, Ni
NSS-15-04 710
Su, Pengwen
NSS-26-06 788
Suckling, John
MIC-10-290 1162
Suezumi, Hisato
MIC-10-011 ..... 124, ***1080***
Suga, Mikio
MIC-10-470 1220
MIC-15-063 1293
Sugai, Yusuke
RTSD-04-371 1511
Sugiyama, Akira
MIC-07-02 1034
Sui, Manling
RTSD-04-373 1513
Sukharnikov, Konstantin
NSS-13-304 688
Sul, Yong Hwan
MIC-10-026 ..... 124, ***1085***
Sun, Baohua
NSS-13-282 680
Sun, Chen
MIC-15-057 1291
MIC-15-297 1364
MIC-19-04 ..... 166, *1448*
M-LT-06-09 1272
Sun, Huahai
MIC-05-442 ..... **1010**
Sun, Jingzhang
MIC-05-400 998
MIC-10-239 1147
MIC-10-398 1195
MIC-15-354 1382
MIC-15-396 1395
MIC-15-399 1396
Sun, Lubing
MIC-05-385 993
Sun, Siyuan
N-LT-03-11 ..... 58, ***546***
NSS-13-150 ..... 68, ***625***
Sun, Wen
MIC-10-239 1147
MIC-10-398 1195
Sun, Xiaolin
MIC-15-411 ..... **1400**
Sun, Xishan
MIC-20-04 1456
Sun, Yi
WS-04-07 251
Sun, Yuchang
NSS-13-186 ..... 70, ***641***
Sun, Zhengyi
NSS-13-056 585
Sun, Zhigang
MIC-05-400 ..... 114, *998*
MIC-10-239 1147
MIC-15-396 ..... 161, *1395*
MIC-15-399 ..... 161, ***1396***
Sunaguchi, Naoki
MIC-15-168 1325
Sundramoorthy, Subramanian
NSS-01-025 331
NSS-13-050 583
Sung, Kyeong Hyeon
NSS-01-003 ..... 30, ***321***
Sung, Saerom
MIC-07-01 ..... 118, ***1033***
MIC-10-401 1196
Sung, Wonmo
MIC-10-095 1104
MIC-10-431 1207
Sung, Yongjin
MIC-05-439 1009
Surti, Suleman
MIC-05-262 953
MP-02-06 ..... 117, ***1022***
Sutowski, Konrad
NSS-01-301 441
NSS-13-278 678
Suzuki, Erika
NSS-22-05 761
Suzuki, Hiromasa
RTSD-04-381 1519
Suzuki, Hiroto
MIC-12-07 ..... 142, ***1239***
Suzuki, Kazuhiro
NSS-01-153 383
NSS-13-152 ..... 68, ***626***
Suzuki, Ryoichi
NSS-13-030 575
Suzuki, Shun
NSS-02-02 456

Author Index

Suzuki, Takahito
NSS-13-066 590
Svihra, Peter
NSS-12-03 531
Sweany, Melinda
NSS-03-01 462
Swinson, Bryan
NSS-18-05 732
Swoboda, Anna
NSS-17-03 724
Syal, Chinar
NSS-20-07 747
Sykora, G. Jeff
N-LT-02-10 315
NSS-01-267 426
Sykora, Jeff
NSS-01-145 380
Sykora, Jeff G.
NSS-09-06 513
Sýkora, Rudolf
JS-03-03 280
Sylvia, Christophe
NSS-20-06 746
Syrovatka, Jiri
RTSD-03-06 1490
Syrovatka, Simon
RTSD-03-06 1490
Szezurek, Dimitri
MIC-10-236 1146
Szola, Alexander
RTSD-05-03 1541
Szornel, Joanna
NSS-04-06 473
Szornel, Joanna M.
NSS-04-05 ..... 49, ***472***
Szyszko, Teresa
MIC-05-265 954

T

Taddeucci, Adriana
MIC-15-102 1304
Taggart, Matt P.
N-LT-01-04 ..... 27, *295*
NSS-01-033 ..... 32, *334*
NSS-13-244 665
Taguchi, Katsuyuki
MIC-03-07 861
MIC-05-154 ..... 105, ***920***
M-LT-01-03 ..... 95, ***837***
Taguchi, Ken
MP-02-10 ..... 117, ***1023***
Taheri, Nasrin
MIC-05-304 ..... 110, ***966***
MIC-10-305 ..... 134, ***1167***
Tai, Yuanchuan
MIC-02-02 830
MIC-10-131 1115
Tai, Yuan-Chuan
MIC-05-364 986
MIC-10-107 1108
MIC-10-119 1111
MIC-10-467 1219
Tajiri, Minoru
MIC-05-346 980
Takabayashi, Yusuke
NSS-13-248 667
Takada, Atsushi
NSS-02-02 456
NSS-18-06 733
Takahashi, Akira
N-LT-02-15 318
NSS-01-325 451
Takahashi, Hiroyuki
MIC-05-295 964
MIC-12-07 1239
RTSD-04-379 1517
Takahashi, Miwako
MIC-05-124 910
MIC-05-454 1014
MIC-06-03 1029
Takahashi, Yoshiyuki
NSS-01-229 411
Takahiro, Ro
MIC-05-157 921
M-LT-02-04 849
Takamaru, Masaki
TS-02-04 1587
Takamoto, Haruno
RTSD-04-381 ..... 175, ***1519***
Takata, Takushi
NSS-27-05 796
Takeda, Ayaki
NSS-13-232 ..... 73, ***660***
RTSD-04-381 1519
RTSD-04-389 1526
Takeda, Shin'ichiro
MIC-15-168 1325
Takyu, Sodai
MIC-10-470 1220
Talacko, Marcel
RTSD-04-359 ..... 172, ***1502***
Talent, Philippe
NSS-01-261 ..... 44, ***424***
Tamm, Moa Y.
N-LT-01-10 301
NSS-01-061 345
Tan, Haotian
MIC-15-354 ..... 159, ***1382***
Tan, Wanbin
MIC-10-137 1116
Tan, Yaw-Ren E.
NSS-04-01 468
Tan, Yuhang
MIC-05-148 918
Tanabe, Kosuke
NSS-01-229 ..... 42, ***411***
Tanaka, Hiroki
NSS-27-05 796
Tanaka, Seishiro
RTSD-04-371 1511
RTSD-04-382 ..... 175, ***1520***
Tanaka, Yasunori
NSS-01-071 349
Tang, Hui
MIC-05-160 922
Tang, Peng
NSS-01-007 ..... 31, ***323***
Tang, Songsong
MIC-05-211 938
MIC-15-057 1291
Taniguchi, Nanae
N-LT-03-09 545
NSS-13-142 622
Tanimori, Toru
NSS-02-02 456
NSS-18-06 733
Tanimoto, Masaya
RTSD-04-374 1514
Tanner, Sebastian
NSS-01-223 409
Tao, Jingyong
MIC-05-286 961
Tao, Jinyong
MIC-02-01 829
MIC-05-376 990
MIC-07-03 1034
MIC-10-113 1110
MIC-10-116 1111
MIC-10-125 1113
Tao, Sun
MIC-15-276 1357
M-LT-06-06 1269
Tao, Xuetong
MIC-05-385 993
Taragola, Elise
MIC-05-298 ..... 110, ***965***
MIC-19-01 1445
Tarifeño-Saldivia, Ariel

Author Index

MIC-10-098 1105
M-LT-04-02 1049
NSS-02-04 458
Tarpau, Cecilia
N-LT-04-08 556
NSS-13-200 646
Tashima, Hideaki
MIC-05-079 896
MIC-05-091 900
MIC-05-094 901
MIC-05-124 910
MIC-05-346 ..... 112, ***980***
MIC-05-454 1014
MIC-06-05 1030
MIC-09-01 1067
MIC-10-470 1220
MIC-15-081 1298
MIC-15-240 ..... 155, ***1347***
MIC-17-06 1433
Tashiro, Mutsumi
MIC-05-322 972
Tatachak, Idris
MIC-10-167 ..... 129, ***1125***
Tateishi, Dai
NSS-15-01 ..... 79, ***707***
Tatsumi, Toshifumi
MIC-07-02 1034
Taub, Alan
MIC-10-464 1218
Taub, Alan I.
N-LT-01-13 303
NSS-01-311 445
Taylor, Glen
NSS-13-216 653
Taylor, Gregor G.
NSS-21-06 755
Tba, Tba
MP-01-05 ..... 92, ***818***
MP-01-07 ..... 92, ***818***
MP-01-09 ..... 92, ***819***
MP-01-11 ..... 93, ***819***
MP-01-13 ..... 93, ***820***
MP-02-04 ..... 117, ***1021***
Tehei, Moeava
NSS-06-05 488
Teicheira, Max
RTSD-03-04 ..... 171, ***1488***
Teimoorisichani, Mohammadreza
MIC-10-266 ..... 133, ***1155***
MIC-15-264 ..... 156, ***1354***
MIC-15-330 1374
M-LT-05-07 1259
Tellmann, Lutz
MIC-10-242 1148
MIC-10-260 1153
MIC-15-162 1324
MIC-15-249 1349
MIC-15-255 1351
MIC-16-02 1421
Templeman, Dave
NSS-13-078 595
Teodorescu, Liliana
NSS-13-088 599
Terada, Kazushi
NSS-01-229 411
Teranishi, Nobukazu
NSS-13-058 586
Terasaka, Yuta
NSS-15-01 707
Terazawa, Shinsuke
MIC-05-151 919
MIC-05-157 921
MIC-15-177 1328
M-LT-02-04 849
M-LT-02-05 850
Tercero, Dennis
NSS-08-08 505
Terlizzi, Livia
NSS-19-04 ..... 82, *737*
Terragni, Giulia
MIC-05-028 880
MIC-05-217 940
MIC-10-443 1211
MIC-13-05 ..... 143, ***1246***
MIC-15-381 1390
M-LT-05-04 1257
NSS-26-04 786
Terray, Luca
NSS-01-101 362
Teshima, Taisei
RTSD-04-382 1520
Tetley, Luke
NSS-25-06 ..... 88, ***782***
Tétrault, Marc-André
MIC-02-03 831
MIC-03-08 861
MIC-18-04 1439
Teuho, Jarmo
MIC-05-433 1007
MIC-15-306 1366
MIC-15-429 1405
M-LT-06-08 1271
Thacker, Daniel
NSS-01-301 ..... 46, ***441***
Thakral, Parul
MIC-05-367 987
MIC-15-294 1363
Thattil, Dhanya
NSS-01-093 358
Theis, Christian
NSS-11-01 523
Therrien, Audrey C.
JS-02-07 275
NSS-26-05 787
Thers, Dominique
NSS-16-08 720
Thibaudeau, Christian
MIC-02-03 831
MIC-15-432 1406
Thielemans, Kris
MIC-05-268 955
MIC-05-280 959
MIC-09-05 1071
MIC-10-068 ..... 126, *1097*
MIC-10-086 1102
MIC-10-194 1133
MIC-10-263 1154
MIC-10-437 1209
MIC-15-075 1296
MIC-15-084 1299
MIC-15-345 1379
M-LT-02-09 853
STIR-03 ..... *1597*
STIR-04 184
STIR-05 1598
STIR-06 ..... *1598*
STIR-07 185
STIR-09 ..... ***1600***
STIR-10 185
STIR-12 ..... 185, *1600*
STIR-13 ..... *1599*
STIR-14 185
Thirolf, Peter
MIC-05-130 912
MIC-10-059 1095
MIC-10-083 1101
M-LT-04-08 1054
M-LT-04-09 1055
Thirolf, Peter G.
MIC-10-035 1088
MIC-17-05 1432
This is a collaborative study between JOB CORPORATION and Junshin Gakuen University.
MIC-15-141 1317
This is a collaborative study between Kanazawa University and Okayama University.
MIC-05-145 917

Author Index

This project has received financial support from the CNRS through the MITI interdisciplinary programs. MIC-21-05 1463
This work is supported by the EPSRC-funded UCL Centre for Doctoral Training in Intelligent, Integrated Imaging in Healthcare (i4health) (EP/S021930/1), the National Physical Laboratory (NPL) and the UK National Measurement System of the UK Government's Department for Science, Innovation and Technology (DSIT). SIRF and STIR software maintenance is part-funded via CCP SyneRBI (funded by the EPSRC grant EP/T026693/1) and by STFC through the UKRI Digital Research Infrastructure programme. 1379
This work was supported in part by the Consortium for Monitoring, Technology, and Verification under Department of Energy National Nuclear Security Administration, award number DE-NA0003920. NSS-05-01 477
Thomas, Allan
MIC-05-310 968
Thomas, Tsang
RTSD-06-06 1551
Thompson, Alena
JS-03-06 283
Thompson, Alena M.
NSS-25-01 778
Thompson, Martin
RTSD-04-395 1532
Thompson, Scott
NSS-09-03 510
NSS-13-196 645
Thompson, Scott J.
RTSD-04-397 1533
Thomson, Francis
NSS-25-06 782
Thorek, Daniel
MIC-05-364 986
Thorimbert, Fanny
NSS-27-03 ..... 89, ***794***
Thull, Julian
MIC-05-103 904
MIC-11-01 ..... 141, ***1224***
MIC-15-054 ..... 148, ***1290***
MIC-15-291 1362
MIC-16-05 1424
Tian, Jie
NSS-18-02 729
Tian, Jinpei
MIC-10-455 1215
Tian, Yang
NSS-01-069 348
NSS-13-068 591
NSS-13-110 609
RTSD-09-03 1569
Timmermann, Beate
MIC-10-320 1172
MIC-15-330 1374
M-LT-05-07 1259
Tinoco Mendes, Andre David
NSS-12-04 532
Tintori, Carlo
NSS-01-173 ..... 39, *391*
NSS-01-305 443
NSS-20-04 744
TS-02-05 1588
Tisseur, David
NSS-27-03 794
Titov, Maksym
NSS-01-005 322
Tiwari, Satyam
MIC-15-267 ..... 156, ***1355***
Toh, Yosuke
NSS-01-221 ..... 41, ***408***
NSS-13-234 661
Toledo, Jose F.
NSS-01-099 361
Tomaszewski, Lukasz
N-LT-04-02 ..... 59, ***551***
NSS-13-156 ..... 68, ***628***
NSS-13-170 ..... 69, ***634***
Tomazinaki, Mina-Ermioni
MIC-05-061 891
MIC-15-342 ..... 159, ***1378***
Tomida, Taketoshi
NSS-07-01 493
Tominey, William
NSS-01-223 409
Tommasino, Francesco
MIC-15-102 1304
Tomoda, Takahiro
MIC-05-151 919
M-LT-02-05 850
Tompkins, Lauren
NSS-20-08 747
Tomsick, John
NSS-04-06 473
Tomsick, John A.
NSS-01-053 341
NSS-13-128 616
Tong, Liangqian
MIC-15-399 1396
Tong, Teng
N-LT-03-05 542
NSS-13-092 601
Tong, Yawen
RTSD-04-391 1528
Tong, Ye
MIC-05-100 903
Tong, Yuhan
NSS-12-08 536
Toramatsu, Chie
MIC-05-346 980
MIC-17-05 ..... 165, ***1432***
MIC-17-06 1433
Torii, Tatsuo
NSS-05-02 478
NSS-11-05 526
Tornago, Marta
NSS-12-03 531
NSS-28-07 807
Torres Espallardo, Irene
MIC-15-360 1384
Torres-Espallardo, Irene
MIC-05-379 991
MIC-10-353 1181
Torres-Sánchez, Pablo
MIC-05-361 ..... 112, ***985***
MIC-10-098 1105
M-LT-04-02 1049
NSS-02-04 458
Torromeo, Giovanni
NSS-20-05 745
Torteeka, Peerapong
NSS-01-281 432
Tortora, Luca
RTSD-09-04 1571
Tosato, Pietro
NSS-01-067 ..... 34, *348*
Toschi, Nicola
MIC-05-337 977
Tosetti, Giulia
MIC-21-05 ..... 168, ***1463***
Tosi, Nicolò
NSS-13-324 696
NSS-21-02 751
Tosun, Mehmet
NSS-13-076 594
Toubon, Hervé
NSS-02-01 455
Toumi, Mehdi

Author Index

MIC-10-227 1144
Touron, Anthony
NSS-01-195 398
Toussaint, Maxime
MIC-02-03 831
MIC-04-04 ..... 98, ***867***
MIC-05-304 966
Toyama, Sho
NSS-13-090 600
Toyokawa, Hidenori
RTSD-04-389 1526
Toyonaga, Takuya
MIC-05-244 948
MIC-05-259 952
MIC-10-236 1146
M-LT-02-08 852
Tran, Daniel
RTSD-09-05 1572
Tran, Dung T.
MIC-10-146 ..... **1119**
Tran, Gia Van
NSS-21-06 755
Tran, Linh
NSS-04-02 ..... **469**
Trang, Hoang T.K.
MIC-05-448 1012
Traversi, Gianluca
NSS-01-109 365
NSS-14-08 705
Treesakul, Natthapong
NSS-01-281 432
Treis, Johannes
MIC-10-032 1087
NSS-04-04 471
Tremmel, Josef
NSS-01-315 447
Tremsin, Anton
NSS-08-08 ..... 54, ***505***
Treves, S. Ted
MIC-10-275 1158
Trimarchi, Marina
NSS-25-04 780
Trindade, Alexandre
RTSD-04-400 1535
Trindade, Alexandre M.
RTSD-04-362 1504
Trindade, Alexandre M.F.
NSS-24-06 775
Triossi, Andrea
NSS-01-173 391
Tripathi, Harsh
MIC-10-230 1145
MIC-14-02 1249
Trippl, Carina
JS-02-04 272
MIC-09-08 1074
NSS-21-02 751
Trippl, Carina A.
MIC-15-045 1287
Trippl, Carina Antonia
NSS-21-08 ..... 84, ***757***
Tromson, Dominique
NSS-27-03 794
RTSD-02-02 1479
Trossarello, Emanuele
NSS-17-05 726
Trucchi, Daniele M.
RTSD-06-01 1547
Trunk, Ulrich
NSS-10-02 ..... 55, ***516***
Tse, Che S.
NSS-13-088 599
Tseng, Fan-Pin
MIC-05-394 996
Tsitsimpelis, Ioannis
NSS-22-02 759
Tsoumpas, Charalampos
MIC-05-097 902
MIC-05-280 959
MIC-05-445 1011
MIC-10-194 1133
MIC-10-260 1153
MIC-10-437 1209
MIC-15-075 1296
MIC-15-252 1350
STIR-01 ..... 184, *1597*
STIR-02 ..... 184, *1597*
STIR-03 184
STIR-04 ..... *1598*
STIR-05 ..... 184, *1598*
STIR-06 185
STIR-10 ..... ***1597***
STIR-13 1599
Tsuchida, Kazuki
MIC-21-02 1460
Tsuda, Michiko
MIC-05-340 ..... 111, ***978***
Tsui, Benjamin M.W.
MIC-15-087 1300
Tsukahara, Haruhisa
NSS-13-018 570
Tsuru, Takeshi G.
RTSD-04-381 1519
Tudela, Raúl
MIC-15-075 1296
Tudisco, Salvo
NSS-25-04 780
Tuisku, Jouni
MIC-15-306 1366
M-LT-06-08 1271
Tumen-Ulzii, Ganbaatar
JS-01-01 264
RTSD-01-05 ..... 169, *1472*
RTSD-04-369 1510
Tupitsyna, Irina
NSS-12-04 532
Turbiner, Victor
NSS-23-02 766
Turcato, Monica
NSS-08-07 505
NSS-13-302 687
NSS-13-304 688
Turchetta, Renato A.D.
MIC-15-039 ..... **1285**
Turedi, Bekir
RTSD-05-05 ..... **1543**
Türk Çakır, İlkay
NSS-17-03 724
Turko, Joseph
MIC-17-04 1431
Turqueti, Marcos
N-LT-02-12 316
N-LT-03-04 ..... 58, *541*
NSS-01-085 356
NSS-01-116 ..... 66, *611*
NSS-01-319 ..... 47, ***449***
NSS-14-01 ..... 78, ***699***
NSS-28-02 ..... 90, ***802***
RTSD-06-04 1549
RTSD-09-06 1572
Tyagi, Mohit
NSS-01-043 338
Tyler, Schuyler
NSS-27-07 ..... 89, ***797***
Tytgat, Michael
NSS-19-01 ..... 82, ***735***

U

Ucari, Ece
MIC-13-05 1246
Uchida, Yoshi
N-LT-03-11 546
NSS-13-150 625
Uchida, Yukimune
NSS-13-090 600
Udee, Nantawat
NSS-16-04 716
Udias, Jose

Author Index

MIC-10-023 ..... 124, ***1084***
MIC-15-069 1294
MIC-15-201 1335
MIC-15-279 1358
MIC-15-462 1416
N-LT-01-07 298
NSS-01-027 332
NSS-01-039 336
NSS-13-086 598
Udias, Jose M
MIC-15-090 1301
Udias, Jose M.
MIC-15-219 1341
MIC-16-01 ..... 164, ***1420***
WS-04-17 260
Udias, Jose Manuel
MIC-10-404 1197
M-LT-03-06 1042
Udías, José Manuel
NSS-01-131 373
Ueda, Shunya
NSS-01-141 ..... 37, ***378***
NSS-13-002 564
NSS-13-144 622
Uehara, Greg
NSS-01-117 367
Uehara, Gregory
NSS-10-03 518
NSS-14-05 702
Ueno, Kazuki
N-LT-03-09 ..... 58, ***545***
N-LT-03-11 546
NSS-01-141 378
NSS-13-002 564
NSS-13-142 ..... 68, ***622***
NSS-13-144 622
NSS-13-150 625
Ueno, Takehiro
NSS-13-320 694
Uenomachi, Mizuki
MIC-07-02 1034
MIC-11-03 1226
MIC-15-453 ..... 163, ***1413***
MIC-15-459 1415
M-LT-06-04 1267
NSS-13-232 660
RTSD-04-389 1526
Ughade, Reshma S.
MIC-10-440 ..... 139, ***1210***
Uguccioni, Carlo
NSS-01-263 425
NSS-15-02 708
Ukai, Mifuyu
NSS-25-03 779
Ukrainets, Vadym
RTSD-04-359 1502
Ulin-Briseño, Edwing Y.
MIC-05-238 ..... 108, ***946***
Ullah, Muhammad N.
MIC-05-274 957
MIC-07-04 1035
MIC-10-449 1213
Ullah, Muhammad Nasir
MIC-15-270 ..... 156, ***1356***
MIC-15-465 ..... 163, ***1417***
M-LT-06-05 ..... 146, ***1268***
Ullán, Miguel
N-LT-01-14 305
NSS-01-313 446
Unal, Mustafa
RTSD-05-01 1540
RTSD-06-04 1549
University of Sherbrooke, Department of Electrical and Computer Engineering
MIC-15-432 1406
Unsworth, Carl
NSS-25-06 782
Urano, Yusuke
NSS-22-06 762
NSS-27-05 796
Urban, Korbinian
MIC-10-347 ..... 136, *1180*
MIC-17-03 1430
NSS-03-03 463
NSS-09-04 ..... 54, ***511***
NSS-13-260 671
Urban, Ondrej
NSS-01-287 435
Uribe, Carlos
MIC-05-313 969
MIC-18-07 1442
Useche Parra, Juan S.
RTSD-04-392 ..... 176, ***1529***
RTSD-08-03 ..... 180, ***1562***
Useche Parra, Sebastian
RTSD-03-01 1485
Useche, Juan S.
RTSD-10-01 1577
Usenko, Sergey
NSS-08-07 505
Ustuner, Fuat
NSS-13-284 681
Utrup, Steve
MIC-15-171 1326
Uzbelger Feldman, Daniel
MIC-15-039 1285

V

Vacchi, Carla
NSS-10-05 520
NSS-21-07 756
Vachon, Frederic
NSS-05-08 483
Vachon, Frédéric
NSS-21-03 752
Vachon, Mathieu
MIC-15-432 ..... 162, ***1406***
Vadalà, Valeria
NSS-13-118 612
Vadrucci, Monia
RTSD-04-378 1517
Vahanen, Sami
TS-02-03 1587
Vähänen, Sami
NSS-28-06 806
RTSD-04-351 1495
RTSD-07-07 1558
Vaigneur, Keith
NSS-05-01 477
Valente, Mauro A.
MIC-05-370 988
Valladares-Sánchez, Sebastián
MIC-05-361 985
Vallari, Giulia
MIC-05-346 980
Vallerand, Philippe
NSS-20-06 746
Vallerga, John
NSS-08-08 505
Valletta, Antonio
RTSD-01-02 1469
RTSD-09-04 1571
Vállez García, David
MIC-05-265 954
Vallgren, Christina
MIC-05-133 913
Valli, Giulia S.
MIC-10-362 1184
Vallot, Delphine
WS-04-03 247
Valluvan, Aravind
NSS-04-06 473
Valverde Mahou, Alejandro
JS-03-05 ..... 26, ***282***
N-LT-04-01 551
NSS-13-162 630
van Dam, Mike

Author Index

MIC-10-077 1100
van Dam, Robert Michael
MIC-15-468 1418
Van de Velde, Wout
MIC-05-298 965
van der Meulen, Nicholas P.
MIC-12-04 1236
Van Laere, Koen
MIC-11-08 1230
van Loef, Edgar
NSS-07-03 494
NSS-07-06 496
van Meerten, Tom
MIC-10-437 1209
STIR-05 1598
van Niekerk, Ferdinand
NSS-13-216 653
van Rijnbach, Milou
NSS-17-03 724
van Sluis, Joyce
MIC-05-097 902
MIC-05-445 1011
van Tubbergh, Christo
NSS-01-243 417
NSS-13-216 653
Vanat, Tomas
NSS-10-02 516
Vandaele, Richard
NSS-20-06 746
Vandenberghe, Stefaan
MIC-05-298 965
MIC-05-373 989
MIC-14-01 1248
MIC-15-276 1357
MIC-19-01 1445
M-LT-06-06 1269
Vanhove, Christian
MIC-05-298 965
MIC-15-276 1357
MIC-19-01 1445
M-LT-06-06 1269
Vanker, Ahmed
NSS-13-216 653
Vaquero López, Juan J.
MIC-19-05 1448
NSS-13-178 638
Vaquero, Juan J.
MIC-02-05 833
MIC-10-428 1206
MIC-15-042 1285
Vaquero, Juan Jose
MIC-15-069 1294
MIC-15-138 1316
Vaquero, Juan José
MIC-05-283 960
MIC-10-023 1084
Varga, Marian
JS-03-03 280
Varzakis, Stathis
MIC-15-345 ..... 159, ***1379***
STIR-06 ..... **1598**
Vaska, Paul
MIC-05-115 907
M-LT-02-01 846
Vass, Laurence
MIC-05-220 941
MIC-19-08 ..... 167, ***1451***
M-LT-01-09 842
Vatandoust, Monire
MIC-05-433 ..... 115, ***1007***
MIC-15-429 1405
Vatsa, Rakhee
MIC-05-367 987
MIC-15-294 1363
Vavrik, Daniel
RTSD-08-04 1563
Vázquez García, Cristóbal
MIC-15-282 ..... 157, ***1359***
M-LT-06-07 ..... 146, ***1270***
Vázquez Regueiro, Pablo
MIC-05-328 974
Vazquez-Garcia, Cristobal
MIC-10-290 1162
Vazquez-Garcia, Cristóbal
MIC-10-281 1160
Vázquez-García, Cristóbal
MIC-10-296 1164
MIC-10-308 1168
Veale, Matthew
JS-01-01 264
Veale, Matthew C.
RTSD-03-03 1487
RTSD-10-03 1579
Vecchio, Drew
MIC-10-464 1218
Vecchio, Drew A.
N-LT-01-13 303
NSS-01-311 445
Vehmanen, Ahti
MIC-05-409 1001
Veiga, Catarina
MIC-15-357 1383
Vela, Oscar
MIC-15-348 1380
Velardita, Simone
RTSD-08-02 1561
Velasco Peñarrubia, Lucia
MIC-10-341 ..... 136, ***1178***
Velasco, Lucía
MIC-15-006 ..... 147, *1276*
Veloso, João
MIC-05-349 981
MIC-05-448 1012
MIC-09-04 1070
MIC-10-446 1212
NSS-13-004 565
Veloso, João F.
MIC-05-058 890
Veloso, João F.C.A.
MIC-15-156 ..... 152, *1322*
MIC-15-243 ..... 155, *1348*
NSS-01-143 379
Veloso, João Filipe C.D.A.
MIC-15-159 ..... 152, *1323*
Velthuis, Jaap
MIC-10-359 1183
NSS-01-283 433
Velthuis, Jaap J.
NSS-13-284 ..... **681**
Venara, Julien
NSS-11-02 523
NSS-13-206 649
Venturini, Yuri
NSS-01-305 443
NSS-20-04 744
TS-02-05 1588
Verdier, Marc Antoine
N-LT-03-10 545
NSS-13-134 619
Verdier, Marc-Antoine
WS-04-03 247
Vergara Quezada, Jorge R.
MIC-15-285 1360
Verger, Loick
RTSD-09-05 1572
Verilhac, Jean-Marie
NSS-27-03 794
RTSD-04-363 ..... 173, *1505*
Verroi, Enrico
MIC-15-102 1304
NSS-12-06 534
RTSD-05-06 1544
Vervenne, Boris
MIC-14-01 1248
MIC-19-01 1445
Vetter, Kai
MIC-05-139 915
NSS-22-05 761
Veyrac, Gregoire

Author Index

RTSD-04-400 1535
Vicente, Pablo
MIC-15-006 1276
Vicini, Valentina
RTSD-04-395 1532
Vickers, Sarah
NSS-13-064 589
Vidal, Luis F.
MIC-05-379 991
MIC-10-344 1179
Vidal, Marcos
MIC-02-05 833
MIC-15-138 1316
Viel, Simon
NSS-26-05 787
Vignati, Anna
NSS-05-07 482
NSS-12-07 535
NSS-28-04 804
Vija, Alexander H.
MIC-05-229 944
Vija, Lavinia
WS-04-03 247
Vijay, Anusree
NSS-17-03 724
Viliani, Lorenzo
NSS-28-08 808
Villar, Natalia S.
MIC-05-370 988
Villarreal, Oscar A.M.
JS-02-04 272
NSS-21-02 751
NSS-21-08 757
Vinattieri, Anna
NSS-12-06 534
Vincke, Helmut
NSS-11-01 523
Vinoy, Jeanne
NSS-13-272 676
Viol, Sebastiaan L.M.
MIC-10-437 1209
Viqueira Rodriguez, Manuel
MIC-09-08 1074
MIC-15-045 1287
NSS-23-04 ..... 86, ***768***
Virgilli, Enrico
RTSD-04-378 1517
Viscione, Marco
MIC-05-133 913
Viscogliosi, Nicolas
MIC-02-03 831
Visvikis, Dimitris
MIC-01-02 824
MIC-05-232 944
MIC-08-08 1065
MIC-10-425 1204
MIC-15-174 1327
MIC-15-216 1340
MIC-15-369 1386
M-LT-05-09 1261
MP-02-07 ..... 117, ***1022***
MP-02-14 ..... 117, ***1025***
Vo, Hong P.
MIC-05-070 893
MIC-10-050 1092
MIC-10-074 1099
MIC-10-122 1112
MIC-15-126 1312
M-LT-04-06 1053
M-LT-04-10 1056
Vo, Hong Phuc
MIC-05-052 ..... 101, ***888***
MIC-15-027 1282
Vo, Nghia
NSS-01-303 442
Vogt, Sebastian
MIC-05-172 926
M-LT-01-05 838
Vohradsky, James
NSS-04-02 469
Volny, Jiri
RTSD-08-04 1563
Volpi, Tommaso
MIC-05-244 948
M-LT-02-08 852
WS-03-05 ..... **240**
vom Stein, Peter
WS-02-16 235
Vos, Marcel
N-LT-01-14 305
NSS-01-313 446
Vostokov, Mikhail
NSS-01-073 ..... 34, ***350***
NSS-13-062 588
Vrettos, Chris
MIC-15-171 1326
Vykydal, Zdenek
NSS-01-273 429

W

Wagemann, Olivia
MIC-10-281 1160
Wagenknecht, Gudrun
MIC-10-008 1079
Wahl, Christopher G.
RTSD-02-05 ..... 170, ***1481***
Wakeling, Hannah
NP-02-01 ..... **290**
Wakizaka, Hidekatsu
MIC-05-025 879
MIC-05-454 1014
MIC-17-06 1433
Wan, Lin
MIC-05-325 973
MIC-05-331 975
MIC-10-329 1175
MIC-15-333 1375
Waner, Arden
NSS-13-120 613
Wang , Xinxin
RTSD-04-351 1495
Wang, Beien
MIC-05-064 891
Wang, Boren
MIC-10-434 ..... 139, *1208*
RTSD-04-357 ..... 172, ***1500***
RTSD-04-376 ..... 174, *1515*
RTSD-04-401 ..... 177, ***1536***
RTSD-07-06 ..... 179, *1557*
RTSD-07-07 1558
Wang, Cai L.
NSS-09-02 ..... 54, ***509***
Wang, Chengmin
MIC-10-161 1123
MIC-10-200 1135
Wang, Dehao
NSS-01-191 ..... 40, ***397***
Wang, Guobao
MIC-15-384 1391
MIC-18-02 1437
MIC-20-04 1456
WS-03-02 ..... **239**
Wang, Haibo
MIC-05-007 874
MIC-15-003 1275
Wang, Haiyan
MIC-05-385 ..... 113, ***993***
Wang, Hanzhong
MIC-10-383 1190
Wang, Haoshuai
NSS-24-05 ..... 87, ***774***
Wang, Haoxin
NSS-01-121 369
Wang, Hui
MIC-15-396 1395
Wang, Jie
MIC-17-02 1429
Wang, Jing

Author Index

NSS-01-105 364
Wang, Jinghong
NSS-01-111 366
Wang, Jinhong
NSS-13-108 608
Wang, Jun
NSS-07-03 494
Wang, Junqiang
RTSD-04-356 1499
Wang, Kai
RTSD-04-388 1525
Wang, Ke
NSS-01-127 ..... 37, *371*
NSS-02-03 457
NSS-13-126 615
Wang, Kexin
MIC-02-02 ..... 94, ***830***
MIC-05-184 929
MIC-10-119 1111
MIC-10-131 1115
MIC-11-02 1225
N-LT-04-10 558
NSS-13-280 679
Wang, Kui
MIC-05-109 ..... 103, ***906***
MIC-09-03 1069
MIC-15-186 ..... 153, ***1331***
MIC-15-228 1343
MIC-15-450 1412
M-LT-06-02 1265
WS-04-05 ..... **249**
Wang, Lei
MIC-15-312 1368
M-LT-05-05 1258
Wang, Li
NSS-01-041 337
NSS-15-04 710
Wang, Liqiang
NSS-13-186 641
Wang, Meiyun
MIC-05-385 993
Wang, Mingmin
NSS-13-270 675
Wang, Mingxin
NSS-23-01 765
Wang, Minjie
MIC-05-100 ..... 103, *903*
Wang, Na
NSS-01-127 ..... **371**
Wang, Qian
MIC-04-02 865
MIC-05-400 ..... **998**
MIC-15-231 ..... 155, ***1344***
MIC-15-399 1396
Wang, Qidong
NSS-13-282 ..... 75, ***680***
Wang, Rui
MIC-05-046 ..... 101, *886*
Wang, Shan-Ying
MIC-05-394 996
Wang, Shaohan
NSS-07-05 495
RTSD-04-356 1499
Wang, Shen
NSS-01-285 434
Wang, Shi
MIC-05-352 982
MIC-08-04 1061
MIC-10-413 1200
MIC-15-078 1297
MIC-15-351 1381
MIC-17-02 1429
Wang, Shimao
RTSD-04-351 1495
Wang, Tao
NSS-01-031 333
NSS-13-056 585
NSS-27-04 795
Wang, Wanchang
NSS-13-108 608
Wang, Weidun
MIC-10-125 1113
Wang, Xiaoming
NSS-13-026 573
Wang, Xinzhe
NSS-01-095 359
Wang, Xiong
MIC-15-297 1364
M-LT-06-09 1272
Wang, Yanfang
MIC-10-200 1135
Wang, Yifan
MIC-10-218 ..... **1141**
Wang, Yimin
NSS-16-07 719
Wang, Yingjie
MIC-10-047 ..... **1091**
NSS-01-025 331
NSS-13-050 583
Wang, Yiran
MIC-20-04 ..... 167, ***1456***
Wang, Yonggang
N-LT-03-07 543
NSS-01-119 368
NSS-13-140 621
Wang, Yun
MIC-15-363 ..... 159, ***1385***
Wang, Yusa
NSS-13-060 587
Wang, ZeKun
NSS-01-285 ..... 45, ***434***
Wang, Zereng
NSS-01-105 364
Wang, Zhao
MIC-10-209 1138
MIC-15-222 1341
MIC-19-07 1450
M-LT-01-08 841
Wang, Zhe
MIC-10-161 ..... 129, *1123*
MIC-10-200 1135
Wang, Zhentian
MIC-03-03 858
MIC-03-05 859
MIC-10-452 1214
MIC-18-05 1440
NSS-18-02 729
Wang, Zhexin
NSS-18-02 ..... 81, ***729***
Wang, Zipai
MIC-10-137 1116
Wang, Ziqi
MIC-05-160 922
Wang, Zishen
MIC-17-02 1429
Wannasorn, Jetawee
NSS-01-281 432
Waqas, Muhammad
RTSD-09-04 1571
Warnier, Alexis
MIC-10-098 1105
M-LT-04-02 1049
Wastie, Roy
NSS-13-088 599
Watabe, Hiroshi
MIC-05-340 978
Watanabe, Hiroaki
NSS-25-03 779
Watanabe, Kenichi
NSS-01-217 407
NSS-13-018 570
NSS-13-030 575
RTSD-01-03 1470
RTSD-04-371 ..... 174, ***1511***
RTSD-04-382 1520
Watts, Dan
MIC-11-03 1226
Watts, Daniel P.
MIC-15-459 1415

Author Index

M-LT-06-04 1267
Weaver, Matt
NSS-20-08 747
Webber, George
MIC-01-03 ..... 93, ***825***
MIC-05-202 935
MIC-05-388 994
MIC-15-192 1332
M-LT-01-01 835
Weber, Günter
NSS-13-070 592
Weber, Wolfgang
MIC-15-045 1287
WS-02-03 228
Wegner, Mathias
NSS-01-315 447
Wehe, David
NSS-13-046 581
Wei, Aoyang
NSS-13-026 573
NSS-13-240 663
Wei, Cunfeng
MIC-10-161 1123
MIC-10-200 1135
MIC-10-218 1141
N-LT-03-05 542
NSS-13-092 601
NSS-13-126 615
Wei, Guangbin
TS-03-02 1592
Wei, Hongrong
MIC-19-04 ..... **1448**
Wei, Huanzhe
MIC-05-202 ..... 106, ***935***
MIC-18-01 ..... 165, ***1436***
M-LT-01-01 ..... 95, ***835***
Wei, Ke
NSS-01-127 371
Wei, Long
MIC-05-040 884
MIC-10-200 1135
N-LT-03-05 542
NSS-13-092 601
NSS-13-126 ..... 67, *615*
NSS-13-240 663
Wei, Qingyang
MIC-05-109 906
MIC-05-127 911
MIC-09-03 1069
MIC-09-07 1073
MIC-10-224 1143
MIC-10-455 1215
MIC-15-117 1309
MIC-15-186 1331
MIC-15-228 1343
MIC-15-450 ..... 163, ***1412***
M-LT-06-02 ..... 145, ***1265***
NSS-01-225 410
NSS-13-184 640
NSS-13-202 647
NSS-13-220 655
WS-04-05 ..... 22, ***249***
WS-04-06 250
Wei, Wei
NSS-01-127 371
Wei, Xingzhan
NSS-01-075 ..... 34, *351*
Weicherding, Teo
N-LT-03-10 545
NSS-13-134 619
Weidinger, Endy
MIC-10-281 1160
Weinberg, Jacob
NSS-01-299 440
Weingarten, Jens
MIC-10-320 1172
Weisenberger, Andrew
MIC-05-001 ..... 99, *873*
NSS-13-310 ..... 77, ***691***
Weissler, Bjoern
MIC-05-028 880
MIC-05-103 ..... 103, ***904***
MIC-11-01 1224
MIC-15-054 1290
MIC-15-291 1362
MIC-15-381 1390
M-LT-05-04 1257
Weldon Jr., Robert A.
N-LT-01-03 294
NSS-13-329 453
Wells, Austin
RTSD-10-05 1581
Wen, Haoqi
MIC-02-02 830
MIC-11-02 1225
MIC-15-198 1334
N-LT-04-10 ..... 60, ***558***
NSS-13-280 ..... 75, ***679***
Wen, Xianfei
NSS-13-226 658
Wendel, Garrett
NSS-16-06 718
Weng, Fenghua
MIC-14-04 1251
MIC-15-408 ..... 161, ***1399***
Werner, Julius
MIC-05-391 ..... 113, *995*
MIC-10-191 ..... 130, ***1132***
MIC-10-326 1174
West, Malachi
N-LT-04-03 552
NSS-13-180 638
Whalen, Thomas M.
MIC-15-327 1373
M-LT-05-08 1260
WS-04-04 248
Wheadon, Richard
NSS-17-05 726
Wheadon, Richard J.
NSS-14-02 700
White, Robert
NSS-12-03 531
NSS-28-07 807
Whittemore, Anthony R.
RTSD-03-08 1491
Wiehe, Moritz
N-LT-01-11 302
NSS-01-063 346
Wiesmann, Martin
MIC-10-242 1148
MIC-15-162 1324
Wiest, Florian
NSS-14-07 704
Wijnen, Niek
WS-04-11 255
Wilhelm, Andrew
NSS-16-06 718
Willers, Michael
NSS-14-06 703
Williams, Mark
MIC-05-121 909
M-LT-02-10 854
Williams, Sean
MIC-10-359 ..... 136, *1183*
NSS-13-284 ..... 75, *681*
Williams, Sean J.
NSS-01-283 ..... 45, ***433***
Willis, Michael
NSS-13-158 628
Wilson, Adrian
NSS-15-05 711
Wilson, Benjamin
JS-01-02 264
Wilson, Caryanne R.
NSS-13-224 ..... 72, ***657***
Wilson, Fergus
NSS-13-284 681
Wilson, Lucy A.
NSS-01-223 ..... 42, ***409***

Author Index

Wilson, Matt
MIC-05-421 1004
Wilson, Matthew
MIC-15-447 1411
M-LT-06-01 1264
Wilson, Zoe
MIC-10-422 ..... 139, *1203*
MIC-15-441 ..... 162, ***1409***
Wilson-Hodge, Colleen A.
NSS-10-01 516
Wink, Alle Meije
MIC-05-265 954
Winter, Axel
MP-02-02 ..... 116, ***1021***
Winter, Marcus
MIC-17-01 1428
Wirtensohn, Sami
N-LT-01-10 301
NSS-01-061 345
Wng, Na
NSS-13-126 615
Wolf, Andreas
MIC-17-04 1431
Wolf, Joshua M.
NSS-01-279 431
Wollenweber, Scott
MIC-10-422 1203
MIC-15-375 1388
M-LT-05-03 1256
Wolz, Robin
MIC-05-265 954
Woo, Sang Keun
MIC-15-372 1387
Woo, Sang-Keun
MIC-10-427 1205
Wood, Ryan
NSS-01-317 ..... 47, ***448***
Woodborne, Stephan
NSS-13-216 653
Woolf, Richard S.
NSS-01-279 431
Woolhead, Verity
NSS-01-223 409
Worm, Steven
NSS-17-03 724
Wright, David
NSS-01-223 409
Wright, Will B.
RTSD-09-06 ..... 181, ***1572***
Wrobel, Frederic
NSS-13-256 669
Wrońska, Aleksandra
MIC-15-324 1372
M-LT-05-02 1255
Wu, Chen
N-LT-03-11 546
NSS-13-150 625
Wu, Chengpeng
NSS-18-02 729
Wu, Haodi
MIC-05-148 918
RTSD-04-364 ..... 173, *1505*
RTSD-04-373 1513
RTSD-04-377 1516
RTSD-04-388 1525
Wu, Jianan
RTSD-04-377 1516
Wu, Jing
MIC-05-127 911
MIC-05-226 943
MIC-05-250 949
MIC-10-224 1143
MIC-10-455 1215
MIC-15-186 1331
MIC-15-228 1343
MIC-15-312 1368
MIC-15-450 1412
M-LT-01-02 836
M-LT-05-05 1258
M-LT-06-02 1265
WS-04-05 249
WS-04-06 250
Wu, Jing: **239**
Wu, Jinyuan
NSS-01-277 ..... 44, ***431***
NSS-13-120 ..... 66, ***613***
Wu, Liangyu
NSS-23-06 770
Wu, Shuoxing
NSS-20-07 747
Wu, Tong
NSS-07-05 495
Wu, Weihao
NSS-23-01 765
Wu, Yaping
MIC-05-385 993
Wu, Yen-Wen
MIC-05-394 996
Wu, Yichen
MIC-19-02 1446
Wu, Yifan
MIC-05-382 992
MIC-15-246 1349
Wu, Yiming
NSS-13-108 608
Wu, Yini
NSS-15-04 710
Wu, Yuzhe
NSS-07-05 ..... **495**
Wu, Zexin
MIC-05-067 892
MIC-10-224 1143
Wu, Zexing
MIC-05-127 911
MIC-15-261 ..... 156, ***1353***
Wu, Zhan
MIC-05-160 922
Wu, Zhaoxia
MIC-05-352 982
MIC-08-04 1061
MIC-10-413 1200
MIC-15-078 1297
MIC-15-351 1381
MIC-17-02 1429
Wu, Zhen
NSS-26-06 788
Wu, Zhongyi
MIC-15-087 ..... 150, *1300*
Wulf, Eric A.
NSS-10-01 516
NSS-13-128 616
Wulff, Joerg
MIC-10-098 1105
M-LT-04-02 1049
Wulff, Jörg
MIC-10-320 1172
MIC-15-330 1374
M-LT-05-07 1259
Wunderer, Cornelia B.
NSS-10-02 516
Wüstner, Peter
MIC-15-111 1307
Wyllie, Ken
RTSD-07-05 1556
Wyngaard, Donovan
NSS-13-216 653
Wynne, Benjamin
STIR-02 1597
Wyrsch, Nicolas
MIC-10-197 1134
M-LT-03-02 1038
NSS-13-212 652

X

Xi, Daoming
MIC-03-04 858
Xia, Huitian
MIC-10-467 1219

Author Index

Xiao, Huan
MIC-05-400 998
MIC-10-239 1147
MIC-10-398 1195
MIC-15-396 1395
MIC-15-399 1396
Xiao, Mengjiao
NSS-13-064 589
Xiao, Peng
MIC-03-04 858
MIC-10-329 1175
Xiao, Shasha
RTSD-04-364 1505
Xiao, Yongshun
MIC-15-402 1397
NSS-13-266 ..... 74, *673*
NSS-26-03 785
Xie, Haorong
RTSD-04-388 1525
Xie, Huidong
MIC-02-04 832
Xie, Huifang
MIC-10-188 1131
Xie, Jiahao
MIC-05-007 ..... **874**
MIC-10-041 1090
MIC-15-003 ..... **1275**
M-LT-03-04 1040
Xie, Luxiang
MIC-10-413 ..... 138, ***1200***
Xie, Pengwei
MIC-10-434 1208
Xie, Qingguo
MIC-03-04 858
MIC-05-325 ..... 111, *973*
MIC-05-331 ..... 111, *975*
MIC-10-110 1109
MIC-10-329 ..... 135, *1175*
MIC-10-335 1176
MIC-15-333 ..... 158, *1375*
NSS-01-105 364
NSS-13-148 624
NSS-15-03 709
Xie, Shili
MIC-10-161 1123
Xie, Shipeng
MIC-05-160 922
Xie, Si
NSS-20-07 747
Xie, Siwei
MIC-05-100 903
MIC-15-411 1400
Xie, Xiangyu
NSS-01-093 358
Xie, Xianhui
TS-03-02 1592
Xie, Zhaoheng
MIC-05-376 990
MIC-10-113 1110
MIC-10-209 1138
MIC-15-222 1341
MIC-19-07 1450
M-LT-01-08 841
WS-04-07 251
Xin, Shuiting
JS-02-06 ..... 25, ***274***
Xing, Tianyu
N-LT-03-11 546
NSS-13-150 625
Xing, Yuxiang
MIC-05-181 928
MIC-10-182 1129
Xiu, Qinglei
NSS-01-123 370
Xu, Bowen
NSS-15-03 ..... **709**
Xu, Hancong
MIC-05-382 ..... **992**
MIC-15-420 1403
Xu, Haoxuan
NSS-01-105 364
Xu, Jiachang
WS-04-08 252
Xu, Jiawei
NSS-01-025 331
Xu, Jingyan
MIC-05-154 920
M-LT-01-03 837
Xu, Junnv
MIC-05-400 998
Xu, Qiong
MIC-10-218 1141
Xu, Run
RTSD-04-356 1499
Xu, Shuyu
MIC-15-186 1331
MIC-15-228 ..... 155, ***1343***
MIC-15-450 1412
M-LT-06-02 1265
Xu, Xinchi
N-LT-03-07 543
NSS-13-140 621
Xu, Yanwei
NSS-13-214 652
Xu, Ying
MIC-05-376 990
MIC-10-113 1110
Xu, Zhuoyuan
MIC-10-239 ..... 132, ***1147***
MIC-10-398 1195
MIC-15-396 1395
MIC-15-399 1396
Xue, Zhongjun
JS-02-02 270

Y

Yabe, Takuya
MIC-05-340 978
Yadav, Kamal
MIC-05-367 987
MIC-15-294 1363
Yakunin, Sergii
RTSD-01-08 1475
RTSD-05-03 1541
RTSD-05-05 1543
Yamada, Chihiro
N-LT-03-11 546
NSS-01-141 378
NSS-13-144 ..... 68, ***622***
NSS-13-150 625
Yamada, Miho
NSS-13-232 660
Yamada, Naoto
N-LT-02-04 310
NSS-01-219 408
Yamada, Susumu
NSS-15-01 707
Yamada, Tsutomu
NSS-01-023 330
NSS-02-06 460
Yamada, Yoshiki
NSS-01-071 349
Yamaguchi, Mitsutaka
MIC-05-340 978
Yamaguchi, Yoshiki
NSS-01-071 349
Yamaishi, Naoya
NSS-13-230 659
Yamaji, Akihiro
NSS-01-029 333
NSS-22-06 762
NSS-27-05 796
Yamamoto, Shuichiro
MIC-15-141 1317
Yamamoto, Takeshi O.
NSS-25-03 779
Yamasaki, Noriko
NSS-13-320 694

Author Index

Yamaya, Taiga
MIC-05-025 879
MIC-05-076 895
MIC-05-079 896
MIC-05-091 900
MIC-05-094 901
MIC-05-124 910
MIC-05-130 912
MIC-05-340 978
MIC-05-346 980
MIC-05-454 1014
MIC-06-03 1029
MIC-06-05 1030
MIC-09-01 1067
MIC-10-014 1081
MIC-10-470 1220
MIC-13-03 1244
MIC-15-063 1293
MIC-15-081 1298
MIC-15-240 1347
MIC-15-288 1361
MIC-17-05 1432
MIC-17-06 1433
NSS-16-01 714
Yamazaki, Makoto
MIC-10-002 ..... 124, ***1077***
Yan, Chenyu
MIC-05-226 ..... 107, ***943***
M-LT-01-02 ..... 95, ***836***
Yan, Jiali
MIC-10-413 1200
MIC-15-078 ..... 149, ***1297***
MIC-15-351 1381
Yan, Ruiyang
MIC-14-05 1252
Yan, Xiaolei
MIC-05-142 ..... 104, ***915***
MIC-15-108 ..... 150, 1306
Yan, Xuewen
NSS-01-265 426
Yan, Yongqiang
NSS-21-01 ..... 84, ***750***
Yan, Zijun
MIC-09-03 1069
MIC-15-228 1343
MIC-15-450 1412
M-LT-06-02 1265
NSS-13-202 ..... 71, ***647***
Yanagida, Takauyuki
NSS-01-035 335
NSS-13-028 574
Yanagida, Takayuki
NSS-01-011 ..... 31, ***325***
NSS-13-012 ..... 61, ***568***
NSS-13-030 575
Yang, Chengzhi
MIC-05-226 943
MIC-10-224 ..... 131, ***1143***
M-LT-01-02 836
Yang, Chunyan
MIC-08-05 1062
Yang, Dongam
NSS-01-233 ..... 42, ***413***
Yang, Fan
MIC-08-02 1059
MIC-11-05 1228
Yang, Ge
RTSD-10-05 1581
Yang, Hang
MIC-05-013 876
MIC-05-067 ..... 101, ***892***
MIC-05-127 911
MIC-05-250 949
MIC-05-343 979
MIC-09-07 1073
MIC-10-455 1215
MIC-15-009 1277
MIC-15-012 1278
MIC-15-117 1309
MIC-15-120 ..... 151, ***1310***
MIC-15-261 1353
MIC-15-339 1377
MIC-21-04 1462
Yang, Hui-Chieh
MIC-05-394 ..... **996**
Yang, Hye Jeong
MIC-10-323 ..... 135, ***1173***
Yang, Hyeonmin
MIC-15-423 ..... 162, ***1404***
Yang, Hyun Jong
NSS-01-211 404
Yang, Jaewon
MIC-10-062 1096
Yang, Jie
MIC-05-100 903
MIC-15-411 1400
Yang, Jingyu
MIC-10-427 ..... 139, ***1205***
MIC-15-372 ..... 160, *1387*
Yang, Luyuan
RTSD-04-401 1536
Yang, Mingxin
NSS-01-069 348
Yang, MingXin
NSS-13-068 591
Yang, Ru
NSS-21-01 750
Yang, Ruijie
MIC-14-05 1252
Yang, Sen
MIC-07-05 1036
Yang, Shihan
MIC-05-040 ..... **884**
Yang, Xiaolei
TS-03-02 1592
Yang, Yalong
RTSD-07-06 1557
Yang, Yao
N-LT-03-05 ..... 58, ***542***
NSS-13-092 ..... 65, ***601***
NSS-13-126 615
Yang, Yigang
N-LT-02-05 310
NSS-01-191 397
NSS-01-205 401
NSS-01-237 414
NSS-13-264 673
Yang, Yongfeng
MIC-05-010 875
MIC-07-05 1036
Yang, Yongyi
MIC-10-227 1144
MIC-10-275 1158
MIC-15-204 1336
Yang, Yuhao
N-LT-03-07 ..... 58, ***543***
NSS-13-140 ..... 68, ***621***
Yang, Yulin
MIC-15-411 1400
Yang, Zhi
WS-04-07 251
Yang, Zhiyong
MIC-05-325 973
Yang, Zirui
RTSD-09-03 ..... 181, ***1569***
Yao, Bolin
MIC-10-383 1190
Yao, Qinglong
MIC-14-05 1252
Yao, Qiulei
MIC-10-188 1131
Yao, Rutao
MIC-05-451 1013
MIC-10-230 ..... 132, *1145*
MIC-14-02 1249
MIC-15-435 1407
Yaqub, Maqsood
MIC-05-265 954
Ye, Hanshen

Author Index

MIC-05-226 943
MIC-10-224 1143
MIC-15-450 1412
M-LT-01-02 836
M-LT-06-02 1265
WS-04-06 ..... 22, ***250***
Ye, Hua
NSS-04-04 471
Ye, Qing
MIC-15-420 1403
MIC-19-04 1448
MIC-20-04 1456
WS-03-11 ..... ***242***
Ye, Qiqi
MIC-02-04 ..... 94, ***832***
Ye, Tong
MIC-15-411 1400
Ye, Xiaolin
MIC-10-416 1201
M-LT-03-07 1043
Yee, Kelsey
NSS-13-064 ..... 64, ***589***
NSS-25-05 ..... 87, ***781***
Yeh, Minfang
NSS-16-06 718
Yennello, Sherry
N-LT-01-05 296
NSS-01-019 328
NSS-01-129 372
Yeom, Jungyeol
NSS-13-024 572
Yeom, Jung-Yeol
N-LT-01-02 293
N-LT-02-08 313
NSS-01-013 325
NSS-01-165 388
NSS-01-247 419
RTSD-04-350 1494
RTSD-04-367 1508
Yeom, Yeon soo
MIC-10-062 1096
Yeon, Jihwan
MIC-15-072 1295
Yeresko, Mykhailo
NSS-12-04 532
Yerli, Burcu
NSS-01-137 ..... ***376***
Yeroshenko, Vsevolod
NSS-03-06 ..... 49, ***466***
Yesilmen, Sevgi
MIC-17-01 1428
Yi, Minseok
MIC-05-016 ..... 100, ***877***
MIC-10-026 1085
Yildirim, Halil Kerim
NSS-21-06 755
Yin, Weigang
NSS-01-123 ..... 36, ***370***
Yin, Yongzhi
MIC-10-065 1097
MIC-10-338 1177
MIC-15-363 1385
NSS-13-034 577
Yin, Ziang
NSS-01-031 333
NSS-27-04 795
Yin, Ziqi
NSS-01-041 ..... ***337***
NSS-15-04 710
Ying, Leslie
MIC-10-230 1145
MIC-14-02 1249
Yokie, Eric
N-LT-01-09 300
NSS-01-001 321
Yokota, Yuui
MIC-10-011 1080
NSS-16-03 715
Yoneda, Hiroki
NSS-02-02 456
Yoo, Seungjun
NSS-01-177 392
NSS-01-207 402
Yoon, Changyeon
NSS-01-185 ..... 40, ***394***
NSS-13-188 ..... 70, ***642***
Yoon, Hyosang
NSS-01-097 360
Yoshiashi, Sachiko
MIC-21-02 1460
Yoshida, Eiji
MIC-05-124 910
MIC-05-340 978
MIC-05-454 1014
MIC-13-03 1244
Yoshikawa, Akira
MIC-05-025 879
MIC-05-454 1014
MIC-10-011 1080
NSS-07-01 493
NSS-16-03 715
NSS-27-02 793
Yoshimochi, Hiroshi
N-LT-02-14 318
NSS-01-321 450
Yoshino, Masao
JS-02-03 271
MIC-10-011 1080
NSS-07-01 493
NSS-16-03 715
NSS-27-02 793
You, Euijin
MIC-10-395 ..... 138, ***1194***
M-LT-03-01 ..... 119, ***1038***
You, Sei Hwan
MIC-07-01 1033
You, Yi-Hsiang
N-LT-02-03 309
NSS-01-253 421
You, Zhen-Fan
N-LT-02-03 309
NSS-01-253 421
Youmans, Amanda
NSS-05-03 479
Young, Christina
MIC-10-257 1152
Young, Duck C.
RTSD-05-01 1540
Young, Perry
NSS-01-295 439
Young, Rhys
NSS-01-323 450
Younsi, Khedija
RTSD-09-08 1574
Yousefirizi, Fereshteh
MIC-05-313 ..... 110, ***969***
Yu, Boxiao
MIC-10-269 ..... 133, ***1156***
Yu, Guo
RTSD-04-391 1528
Yu, Jiangyuan
WS-04-07 251
Yu, Jiwei
MIC-10-383 1190
Yu, Junhao
NSS-01-105 364
NSS-13-148 624
Yu, Minfeng
N-LT-02-05 ..... 29, ***310***
NSS-01-237 ..... 42, ***414***
Yu, Ming
MIC-15-414 1401
Yu, Siyuan
NSS-01-069 348
NSS-13-068 ..... 64, ***591***
Yu, Wenjie
NSS-13-266 ..... ***673***
Yu, Xin
MIC-02-01 ..... 94, ***829***

Author Index

MIC-05-286 961
MIC-05-376 990
MIC-07-03 1034
MIC-10-113 1110
MIC-10-116 1111
MIC-10-125 1113
Yu, Yancheng
MIC-17-02 1429
NSS-01-225 ..... 42, ***410***
Yu, Zerui
MIC-10-284 1161
Yuan, Bo
NSS-01-265 426
Yuan, Hang
MIC-05-040 884
Yuan, Ling
WS-04-07 251
Yuan, Ye
N-LT-03-11 546
NSS-13-150 625
Yuan, Yijie
MIC-04-06 869
Yuan, Yimie
NSS-17-06 ..... 81, *727*
Yuan, Ziquan
MIC-02-02 830
MIC-05-184 929
MIC-10-119 1111
MIC-10-131 1115
Yuasa, Tetsuya
MIC-15-168 1325
Yuki, Nitta
MIC-15-333 1375
Yuluo, Yikuang
MIC-10-209 1138
Yuzefovich, Bella
MIC-15-210 1338
Yvon, Dominique
NSS-06-07 490
NSS-13-084 597
Yvon, Dominique F.
NSS-01-079 ..... 34, *353*

Z

Zabloudil, Vojtech
NSS-07-08 ..... 53, ***498***
Zagami, Cristina
NSS-25-04 780
Zaharchuk, Greg
MIC-10-392 1193
Zahid, Muzzamer
JS-03-02 ..... 25, ***280***
RTSD-06-02 1547
Zahnreich, Sebastian
MIC-05-355 983
Zaidi, Habib
MIC-05-319 971
MIC-05-403 999
MIC-10-206 1137
MIC-10-368 1186
N-LT-04-09 557
NSS-13-194 644
NSS-13-210 651
NSS-15-06 712
Zaitseva, Natalia
NSS-05-06 481
Zaman Pour, Seyed Amir
MIC-10-086 1102
STIR-03 1597
ZamanPour, SeyedAmir
MIC-05-268 955
MIC-10-254 ..... 133, ***1152***
MIC-10-263 1154
MIC-15-084 ..... 149, ***1299***
M-LT-02-09 853
Zambelli, Nicola
RTSD-04-395 1532
Zambolo, Riccardo
NSS-01-291 437
NSS-25-04 780
Zamorano, Felipe
N-LT-02-02 ..... 29, ***308***
NSS-01-275 ..... 44, ***430***
Zan, Yunlong
MIC-15-408 1399
Zanetti, Marco
NSS-01-173 391
Zannoni, Elena
JS-01-04 266
Zannoni, Elena M.
MIC-15-447 1411
MIC-20-01 1453
MIC-21-01 1459
M-LT-06-01 1264
Zannoni, Elena Maria
MIC-15-438 1408
RTSD-03-08 ..... 171, ***1491***
Zant, Friso V.D.
MIC-05-433 1007
Zanzottera, Riccardo
NSS-13-284 681
Zappettini, Andrea
RTSD-03-03 ..... 171, *1487*
RTSD-03-07 ..... 171, *1490*
RTSD-04-378 ..... 174, ***1517***
RTSD-04-395 ..... 176, *1532*
RTSD-10-03 1579
Zápražný, Zdenko
RTSD-04-359 1502
Zarkos, Panagiotis
NSS-13-106 ..... 66, ***607***
Zatko, Bohumir
RTSD-04-361 1503
RTSD-04-386 1523
RTSD-04-387 1524
Zaťko, Bohumír
JS-03-03 ..... 25, ***280***
RTSD-04-359 1502
RTSD-04-393 1530
Zbijewski, Wojciech
MIC-05-172 ..... 105, *926*
MIC-05-175 927
M-LT-01-04 837
M-LT-01-05 ..... 95, *838*
Zdeb, Wojciech
MIC-16-06 1425
Zeghni, Isaac
NSS-13-048 ..... 63, ***582***
Zeltser, Danielle
MIC-05-247 ..... **949**
M-LT-02-07 ..... **851**
Žemlička, Jan
MIC-05-292 963
RTSD-01-07 1474
Zeng, Gengsheng
MIC-15-183 ..... 153, ***1330***
Zeng, Gengsheng L.
MIC-15-273 ..... 156, ***1357***
Zeng, Hao
MIC-15-420 1403
Zeng, Jiayang
MIC-05-376 990
MIC-10-113 1110
Zeng, Larry
MIC-10-272 ..... 133, *1157*
Zeng, Ming
NSS-13-282 680
NSS-17-02 723
RTSD-09-03 1569
Zeng, Shenghui
NSS-13-284 681
Zeng, Tianchen
NSS-13-186 641
Zeng, Tianyi
MIC-05-244 948
M-LT-02-08 852
Zeng, Xiangtao
MIC-05-067 892

Author Index

MIC-05-127 911
MIC-05-250 949
MIC-05-253 950
MIC-05-343 979
MIC-09-07 1073
MIC-10-455 ..... 140, ***1215***
MIC-15-009 1277
MIC-15-012 1278
MIC-15-117 1309
MIC-15-120 1310
MIC-15-261 1353
MIC-15-339 ..... 158, ***1377***
MIC-21-04 ..... 168, ***1462***
Zeng, Yuecan
MIC-05-400 998
MIC-10-239 1147
MIC-10-398 1195
MIC-15-396 1395
MIC-15-399 1396
Zeng, Zhi
MIC-05-181 928
Zeng, Zitao
MIC-15-411 1400
Zenger, Todd
NSS-20-07 747
Zeniya, Tsutomu
MIC-15-168 ..... 152, *1325*
Zhan, Fenglin
MIC-08-01 1058
MIC-10-410 1199
MIC-15-198 1334
Zhan, Gan
MIC-05-100 ..... **903**
MIC-15-411 ..... 161, *1400*
Zhang, Andrew
MIC-10-392 1193
Zhang, Chen
NSS-18-04 731
Zhang, Chengshuo
NSS-17-06 727
Zhang, Chunhui
MIC-10-065 1097
MIC-10-338 1177
MIC-15-363 1385
NSS-13-034 577
Zhang, Dandan
MIC-15-312 ..... 158, ***1368***
M-LT-05-05 ..... 145, ***1258***
Zhang, Debin
MIC-02-04 832
MIC-15-078 1297
NSS-01-203 401
Zhang, Duo
MIC-19-04 1448
Zhang, Feng
JS-03-06 283
Zhang, Haoyu
MIC-05-181 ..... 106, ***928***
Zhang, Hongqiang
MIC-10-065 1097
Zhang, Hongyang
MIC-10-413 1200
MIC-15-351 1381
MIC-17-02 ..... 164, ***1429***
Zhang, Hui
NSS-26-06 788
Zhang, Jiaguo
NSS-01-093 358
Zhang, Jianjie
NSS-01-041 337
NSS-15-04 710
Zhang, Jiazhen
MIC-05-244 ..... 108, ***948***
MIC-05-259 952
M-LT-02-08 ..... 97, ***852***
Zhang, Jing
NSS-01-025 331
Zhang, Kainan
NSS-26-06 ..... 88, ***788***
Zhang, Li
MIC-03-03 858
MIC-03-05 859
MIC-10-452 1214
MIC-18-05 1440
NSS-18-02 729
Zhang, Linjun
MIC-05-010 875
Zhang, Liyuan
NSS-16-07 719
Zhang, Mengxi
MIC-10-374 1187
Zhang, Na
MIC-05-385 993
Zhang, Pengpeng
NSS-01-265 426
Zhang, Qing
MIC-15-411 1400
Zhang, Qinghua
MIC-10-065 1097
Zhang, Weijian
JS-01-04 ..... 24, ***266***
Zhang, Xi
MIC-10-365 1185
MIC-15-132 ..... 151, ***1314***
M-LT-04-03 1050
NSS-17-01 ..... 80, ***722***
Zhang, Xiang
JS-02-06 274
N-LT-03-07 543
NSS-13-140 621
Zhang, Xianggang
NSS-01-031 333
NSS-27-04 795
Zhang, Xiao
MIC-15-087 1300
Zhang, Xiaoqin
MIC-05-013 876
MIC-05-127 911
MIC-10-455 1215
MIC-15-009 1277
MIC-15-012 1278
MIC-15-117 1309
MIC-15-120 1310
Zhang, Xiaoqing
MIC-09-07 1073
Zhang, Xiaoyin
MIC-07-03 1034
MIC-10-116 1111
Zhang, Xiaoying
MIC-05-286 961
Zhang, Xirang
MIC-15-204 ..... 154, ***1336***
Zhang, Xu
MIC-15-420 ..... 162, ***1403***
NSS-21-01 750
Zhang, Xuezhu
MIC-05-247 949
M-LT-02-07 851
Zhang, Yacong
NSS-01-127 371
Zhang, Yang
RTSD-04-368 ..... 173, ***1509***
Zhang, Yao
N-LT-03-11 546
NSS-13-150 625
Zhang, Yaofen
NSS-15-04 710
Zhang, Yaofeng
NSS-01-041 ..... 32, *337*
Zhang, Yibin
MIC-02-01 829
MIC-05-286 961
MIC-05-376 990
MIC-07-03 1034
MIC-10-113 1110
MIC-10-116 1111
MIC-10-125 1113
Zhang, Yirong
MIC-10-251 ..... 132, ***1151***

Author Index

Zhang, Yufang
MIC-05-451 1013
WS-04-08 252
Zhang, Yunzhuo
NSS-01-095 ..... 35, ***359***
Zhang, Yuxi
MIC-05-451 ..... 115, ***1013***
NSS-01-203 401
WS-04-08 ..... 22, ***252***
Zhang, Zexin
NSS-13-026 573
Zhang, Zhe
NSS-01-285 434
Zhang, Zheng
MIC-10-173 1127
Zhang, Zhiming
MIC-05-040 884
N-LT-03-05 542
NSS-13-092 601
NSS-13-126 615
NSS-13-240 663
Zhang, Zhong
NSS-01-205 ..... 41, ***401***
Zhang, Zijian
MIC-15-414 1401
Zhao, Bo
MIC-17-02 1429
Zhao, Bozhen
JS-02-02 270
Zhao, Chaoyang
NSS-02-03 ..... 48, ***457***
Zhao, Huiping
MIC-02-01 829
MIC-05-286 961
MIC-05-376 990
MIC-07-03 1034
MIC-10-113 1110
MIC-10-116 1111
MIC-10-125 1113
Zhao, Jingzhou
NSS-01-121 369
Zhao, Lei
MIC-10-125 1113
Zhao, Liyan
MIC-10-125 1113
Zhao, Moss
MIC-10-392 1193
Zhao, Qianyuan
NSS-01-121 369
Zhao, Qinghua
NSS-01-031 333
NSS-13-056 ..... 63, ***585***
NSS-27-04 795
Zhao, Ri
MIC-05-226 943
M-LT-01-02 836
Zhao, Shuwei
MIC-05-295 ..... 110, ***964***
Zhao, Shuwen
JS-02-02 270
Zhao, Wenbo
MIC-04-05 ..... **868**
MIC-05-271 ..... **956**
Zhao, Xiandong
MIC-05-364 986
Zhao, Xiaowen
MIC-05-385 993
Zhao, Xin
MIC-05-127 911
MIC-10-209 1138
MIC-15-222 ..... 154, ***1341***
MIC-19-07 ..... 167, ***1450***
M-LT-01-08 ..... 95, ***841***
NSS-01-041 337
NSS-15-04 710
Zhao, Yangyang
MIC-05-067 892
MIC-05-127 911
MIC-05-343 979
MIC-09-03 ..... 123, ***1069***
MIC-09-07 ..... 123, ***1073***
MIC-10-455 1215
MIC-15-009 1277
MIC-15-012 1278
MIC-15-117 1309
MIC-15-120 1310
MIC-15-186 1331
MIC-15-450 1412
M-LT-06-02 1265
NSS-13-202 647
Zhao, Yaqing
RTSD-04-391 1528
Zhao, Yubin
NSS-01-123 370
Zhao, Yun
MIC-20-05 ..... 168, ***1457***
Zhao, Yun: **240**, **241**
Zhao, Zeqing
MIC-05-451 1013
WS-04-08 252
Zhao, Zhengyang
MIC-15-351 1381
Zhao, Zhijun
MIC-10-116 1111
MIC-15-222 1341
M-LT-01-08 841
Zheng, Hairong
MIC-05-385 993
Zheng, Haowen
MIC-08-04 ..... 122, ***1061***
Zheng, Jian
MIC-15-087 1300
Zheng, Peng
NSS-13-108 ..... 66, ***608***
Zheng, Rui
MIC-03-04 ..... 97, *858*
Zheng, Xingchun
MIC-15-435 1407
Zheng, Xutao
NSS-13-282 680
NSS-17-02 723
RTSD-09-03 1569
Zheng, Yifan
MIC-05-424 1005
MIC-10-374 1187
Zhong, Chengqian
RTSD-04-356 1499
Zhong, Jiaqi
MIC-10-239 1147
MIC-10-398 1195
Zhong, Tao
RTSD-04-357 1500
RTSD-04-376 1515
RTSD-07-06 ..... **1557**
RTSD-07-07 1558
Zhong, Zhong
NSS-01-303 442
RTSD-07-04 1555
Zhou, Feng
MIC-05-064 891
MIC-15-057 ..... 148, ***1291***
Zhou, Hao
NSS-01-215 406
Zhou, Junjie
MIC-05-160 ..... 105, ***922***
Zhou, Wei
NSS-13-026 573
NSS-13-240 663
Zhou, Xiangbao
MIC-15-450 1412
M-LT-06-02 1265
Zhou, Xiaohong J.
MIC-10-272 1157
Zhou, Xiaopeng
NSS-13-282 680
Zhou, Xunsheng
NSS-09-02 509
Zhou, Yujie
NSS-17-06 727

Author Index

Zhou, Zhi
NSS-15-04 ..... 79, ***710***
Zhou, Ziyuan
MIC-08-02 ..... 122, ***1059***
Zhu, Ji
MIC-05-331 975
MIC-10-329 1175
MIC-15-333 1375
Zhu, Jiahuan
RTSD-09-03 1569
Zhu, Jingmin
MIC-05-325 973
MIC-05-331 ..... **975**
MIC-10-329 1175
MIC-15-333 1375
Zhu, Jiongtao
MIC-05-148 ..... 104, *918*
Zhu, Kejun
NSS-01-121 369
Zhu, Ruiying
MIC-10-107 ..... 127, ***1108***
Zhu, Shangzhen
NSS-09-05 512
Zhu, Wenjing
MIC-02-01 829
MIC-05-376 990
MIC-10-113 1110
MIC-10-116 1111
Zhu, Yihang
MIC-15-420 1403
Zhu, Yinhe
NSS-13-112 ..... 66, ***610***
RTSD-10-03 1579
Zhu, Yong
RTSD-04-356 1499
Zhu, Yuanhao
MIC-10-398 ..... 138, ***1195***
Zhu, Yuefeng
JS-03-06 283
RTSD-01-01 1469
RTSD-04-380 1518
RTSD-04-385 1522
RTSD-07-02 ..... 179, ***1554***
RTSD-09-02 1568
Zhu, Zhiqiang
MIC-05-010 875
Zhu, Ziyue
NSS-27-01 792
Zhuang, Ziqi
MIC-10-383 1190
Zhuo, Yue
MIC-15-045 ..... 148, ***1287***
Zich, Jan
NSS-01-287 435
Zickefoose, Jim
NSS-01-179 ..... 39, *393*
Ziempekis, Konstantinous
MIC-05-133 913
Zimmer, Luc
N-LT-03-10 545
NSS-13-134 619
Zimmerman, Thomas
NSS-20-07 747
Zimmermann, Egon
MIC-15-111 1307
Zimmermann, Jörg
NSS-24-03 773
Zingaretti, Alessandra
NSS-13-298 686
Zobundzija, Zoe
NSS-13-084 597
Zobundzija, Zoé
NSS-06-07 ..... 51, ***490***
Zoglauer, Andreas
NSS-01-053 341
NSS-04-06 473
Zong, Chunguang
NSS-13-214 652
Žontar, Dejan
MIC-15-045 1287
Zorrilla, Álvaro
MIC-10-296 1164
Zorzi, Nicola
JS-02-04 272
NSS-21-04 753
Zou, Haoyu
MIC-05-376 990
MIC-10-113 1110
MIC-10-116 1111
MIC-10-125 ..... 128, ***1113***
Zou, Huifeng
MIC-15-087 1300
Zou, Jing
MIC-05-100 903
MIC-15-411 1400
Žugec, Petar
NSS-06-04 487